

OFFICE OF  
NAVAL RESEARCH  
Arlington, Virginia 22217-5000

ONR 33395-12

Tenth  
International  
DETONATION  
Symposium

Boston, Massachusetts  
July 12 - 16, 1993

19960307 085



DISTRIBUTION STATEMENT A

Approved for public release;  
Distribution Unlimited

Approved for public release; distribution is unlimited.

# **PROCEEDINGS**

## **Tenth International Detonation Symposium**

**Sponsored by:**

**Office of Naval Research  
Naval Sea Systems Command  
Naval Surface Warfare Center,  
Dahlgren Division  
Army Research Laboratory/  
Weapons Technology Directorate  
Army Armament Research, Development  
and Engineering Center  
Wright Laboratory/Armament Directorate**

**July 12 - 16, 1993**

---

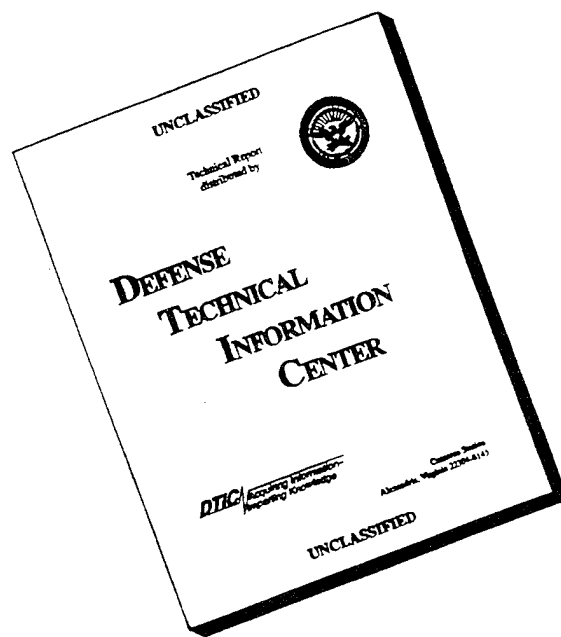
**Boston Park Plaza Hotel,  
Boston, Massachusetts**

---

Approved for public release; distribution is unlimited.



# DISCLAIMER NOTICE



**THIS DOCUMENT IS BEST QUALITY AVAILABLE. THE COPY FURNISHED TO DTIC CONTAINED A SIGNIFICANT NUMBER OF PAGES WHICH DO NOT REPRODUCE LEGIBLY.**

## FOREWORD

The Tenth International Detonation Symposium was held at the Boston Park Plaza Hotel in Boston, Massachusetts, July 12-16, 1993. These Proceedings include all manuscripts provided to us by authors for unlimited public release.

The character of the Symposium changed in several ways since the Ninth Symposium, held in 1989, in terms of title, attendance, and sponsorship. The name of the Symposium has been simplified to make clear that it is always open to papers from the international scientific community. The number of registrants in Boston was only 330 (115 fewer than attended the Ninth). Participants from outside the United States, representing 18 countries, numbered 104 (down 18 from the Ninth). For the first time since the Fifth Symposium, the number of sponsors also declined. This change reflected the realignment and closure of facilities within the United States Department of Defense. Moreover, the United States Department of Energy (DOE) laboratories, i.e., the Los Alamos, Livermore, and Sandia National Laboratories, were unable to sponsor this Symposium. As a consequence of the DOE withdrawal, we lost the organizational services of many long time contributors to The Detonation Symposium. In particular, we lost the invaluable services of Mrs. Alita Roach.

Among the Defense closures are the explosives research facilities located at the White Oak laboratory of the Naval Surface Warfare Center (NSWC), Dahlgren Division. Effective April, 1994, the White Oak capability was administratively transferred to the NSWC Indian Head Division. The physical movement to Indian Head from White Oak is scheduled for completion during 1997. This closure contributed to the delay in printing of these Proceedings. Of particular disappointment to us is the departure from White Oak of Ms. Wanda J. Morat, editor of the Ninth Symposium Proceedings. She has left us for a new job at the United States Department of Justice.

The banquet was held on the Thursday of the conference, and was attended by the conference attendees, many with their families. We were pleased that Dr. William E. Deal of the Los Alamos National Laboratory was able to serve as the Master of Ceremonies. As he remarked during the banquet, this symposium was the first not to have present an attendee of the first symposium (1951). Dr. Deal was the only person in Boston who had also attended the second symposium (1955). The guest speaker was The Reverend Robert W. Gollidge, the vicar of Old North Church in Boston, who both entertained and educated us with his talk: *Boston - Its Past as a Prelude to its Future*.

On behalf of everyone that contributed to making the physical arrangements in Boston, we wish to thank the authors of the papers for their essential contributions. In our roles as cochairmen, we wish to thank the sponsors and members of the Organizing Committee, both for contributing to the success of the Symposium and for their dedication in coordinating the review and selection of papers for presentation at the Symposium:

### THE ORGANIZING COMMITTEE

Naval Surface Warfare Center,  
Dahlgren Division -

James M. Short, Cochairman  
Douglas G. Tasker, Cochairman  
Richard R. Bernecker  
Wanda J. Morat

Office of Naval Research -  
Richard S. Miller

Army Research Laboratory/  
Weapons Technology Directorate -  
Robert Frey

Army Armament Research, Development  
and Engineering Center -  
Pai Lu

Wright Laboratory/Armament Directorate,  
Eglin AFB -  
Joseph C. Foster  
Martin Zimmer

## **SPONSORS**

Office of Naval Research  
Naval Sea Systems Command  
Naval Surface Warfare Center,  
Dahlgren Division  
Army Research Laboratory/  
Weapons Technology Directorate  
Army Armament Research, Development  
and Engineering Center  
Wright Laboratory/Armament Directorate

## **SUMMARY REVIEW**

Papers were selected based on a review of summaries by members of the organizing committee under the leadership of Robert Frey. We were assisted by colleagues from three DOE laboratories.

Lawrence Livermore National Laboratory -  
Edward L. Lee  
William C. Tao

Los Alamos National Laboratory -  
Allan B. Anderson  
William E. Deal  
Alita M. Roach

Sandia National Laboratories -  
Dennis E. Mitchell  
Phillip L. Stanton

## **REGISTRATION**

Army Armament Research, Development  
and Engineering Center -  
Anita Fehsal  
Rita Weshefsky

Army Research Laboratory/Weapons  
Technology Directorate -  
Evelyn McDougal

We mourn the passing of Mrs. Leona Hicks. Mrs. Hicks, a long time employee of the Lawrence Livermore National Laboratory, began her association with The Detonation Symposium at the Sixth Symposium in San Diego. She was the first mentor for one of us (James Short) at the onset of his association with The Detonation Symposium. Her enthusiasm for The Detonation Symposium will be sadly missed.

Naval Surface Warfare Center,  
Dahlgren Division -  
Barbara Jackson  
Ruth Maticic  
Janet Sutton

## **PREPARATION OF PROCEEDINGS**

Naval Surface Warfare Center,  
Dahlgren Division -  
Wanda J. Morat  
James M. Short  
Douglas G. Tasker

Management Resources Incorporated

## **BOSTON ARRANGEMENTS**

Naval Surface Warfare Center,  
Dahlgren Division -  
Wanda J. Morat  
James M. Short  
Douglas G. Tasker

## **AUDIOVISUAL SERVICES**

Projection Video Services, Inc.

Naval Surface Warfare Center,  
Dahlgren Division -  
Ernie Inman, retired

## **BOSTON CONTRACT ARRANGEMENTS**

Sacks and Co  
Executours  
Boston Park Plaza Hotel and Towers

**James M. Short, Cochairman**  
**Douglas G. Tasker, Cochairman**  
White Oak, Silver Spring, Maryland  
July 11, 1995

## CONTENTS

Page

### WAVE PROPAGATION

#### General Session

Cochairmen: James Kennedy and Brian Lambourn

#### Energy Transfer in Solid Explosives

C.M. Tarver, L.E. Fried, A.J. Ruggerio, and D.F. Calef . . . . . 3

#### Mach Reflection of Spherical Detonation Waves

L.M. Hull . . . . . 11

#### Understanding Curved Detonation Waves

B.G. Bukiet, K.S. Lackner, and R. Menikoff . . . . . 19

#### Streamline Dynamics Method for Highly Curved Detonation Waves

R.H. Guirguis . . . . . 27

#### Propagation Phenomena on the Detonation Wave Front

J.M. Chevalier, and N. Carion . . . . . 37

#### Computing the Transient Self-Sustained Detonation After a New Model

L. Brun, J.-M. Kneib, and P. Lascaux . . . . . 43

#### The Shape Analysis of a Steady Detonation Front in Right Circular Cylinders of High Density Explosive. Some Theoretical and Numerical Aspects

F. Chaissé, and J.N. Oeconomos . . . . . 50

#### Numerical Simulations of Detonation in High Explosive Charges of Finite Diameter

V.E. Fortov, A.L. Ni, A.V. Shutov, and A.V. Utkin . . . . . 58

#### Experimental Study of Detonation in PBXW-123, A Large Failure-Diameter, Non-Ideal Explosive

W.H. Wilson, J.W. Forbes, P.K. Gustavson, and G.T. Sutherland . . . . . 63

#### Some Characteristics of Bow Wave Initiation and Desensitization

M. Chick, T.J. Bussell, and R.B. Frey . . . . . 69

#### Reflected-Shock Initiation of Explosives

E.N. Ferm, and L.M. Hull . . . . . 78



## CONTENTS (Cont.)

Page

### POSTER PAPERS-2

**Cochairmen: Philip Stanton and Henry Moulard**

<b>Reaction of Aluminium and Ammonium Nitrate in Non-Ideal Heterogeneous Explosives</b> G.A. Leiper, and J. Cooper . . . . .	267
<b>An Extensive Experimental Study of Pressed NTO</b> P. Gimenez, P. Chabin, J. Mala, and C. Spyckerelle . . . . .	276
<b>Influence of Intragranular Cavities of RDX Particle Batches on the Sensitivity of Cast Wax Bonded Explosives</b> L. Borne . . . . .	286
<b>Sensitivity Study of Nitroparaffin-Based Blends</b> C.J. Anderson, M.E. Pinco, and S.B. Murray . . . . .	294

### POSTER PAPERS-3

**Cochairmen: Joseph Foster, Jr. and Brian Hammant**

<b>A Testing Method to Evaluate Explosiveness</b> C. Bélanger . . . . .	305
<b>The Application of Ballistic Impact and Radiant Ignition Techniques for Characterization of Violent Reaction in Cased Propellant</b> S.A. Finnegan, A.I. Atwood, J.K. Pringle, N.G. Zwierzchowski, P.O. Curran, and J. Wiknich . . . . .	320
<b>Thin-Film Methods for Examining the Decomposition Chemistry of Explosives</b> K.L. Erickson, W.M. Trott, and A.M. Renlund . . . . .	340
<b>Recovery Technique for Shocked Explosive Samples</b> T.P. Liddiard, J.W. Forbes, J.W. Watt, R.N. Baker, J. Sharma, and B.C. Beard . . . . .	347
<b>Portable, Solid State, Fiber Optic Coupled Doppler Interferometer System for Detonation and Shock Diagnostics</b> K.J. Fleming, and O.B. Crump . . . . .	351
<b>Synthesis, Characterization, and Sensitivity of Novel Nitramino Substituted Cyclotriphosphazenes</b> C.D. Bedford, M. Chaykovsky, M.-K. Rho, P.R. Dave, F. Forohar, T. Axenrod, and R. Gilardi . . . . .	358

## CONTENTS (Cont.)

Page

### EQUATIONS OF STATE

#### General Session

Cochairmen: Edward Lee and Graeme Leiper

<b>Equation of State for Detonation Products</b>	
William C. Davis . . . . .	369
<b>Development of the Williamsburg Equation of State to Model Non-Ideal Detonation</b>	
W. Byers Brown, and M. Braithwaite . . . . .	377
<b>A Review of Developments in the W-B-L Detonation Model</b>	
D.C. Swift, and B.D. Lambourn . . . . .	386
<b>An Application of Variable Metric Nonlinear Optimization to the Parameterization of an Extended Thermodynamic Equation of State</b>	
E.L. Baker . . . . .	394
<b>Direct Monte Carlo Simulation of the Chemical Equilibrium Composition of Detonation Products</b>	
M.S. Shaw . . . . .	401
<b>Calibrating the BKW-EOS with a Large Product Species Data Base and Measured C-J Properties</b>	
M.L. Hobbs, and M.R. Baer . . . . .	409
<b>Unlike-Pair Interactions at High Pressure and High Temperature</b>	
F.H. Ree, and M. van Thiel . . . . .	419
<b>The Significance of Interaction Potentials of Water with Other Molecules in the EOS of High Explosive Products</b>	
M. van Thiel, F.H. Ree, and L.C. Haselman, Jr. . . . .	425
<b>Analysis of Hugoniot and Detonation Properties of Explosives with JCZ3 Equation of State</b>	
L.I. Stiel, V.M. Gold, and E.L. Baker . . . . .	433
<b>A Theoretical Study for Gas-Gas Separation in High Temperature and High Pressure Fluid</b>	
M. Koshi, H. Matsui, T. Saito, and K. Takayama . . . . .	441
<b>Multipole Effects on the Equation of State for Reaction Products of Explosives</b>	
H.D. Jones, and F.J. Zerilli . . . . .	449

## CONTENTS (Cont.)

Page

### SDT, DDT, AND XDT

#### General Session

Cochairmen: Craig Tarver and James M. Short

<b>Initiation of Preshocked High Explosives PBX-9404, PBX-9502, and PBX-9501, Monitored with In-Material Magnetic Gauging</b> R.N. Mulford, S.A. Sheffield, and R.R. Alcon . . . . .	459
<b>Velocimetry Studies on the Prompt Initiation of PBX 9502</b> J. Wackerle, H.L. Stacy, and W.L. Seitz . . . . .	468
<b>Prompt and Delayed Detonation From Two-Dimensional Shock Loadings</b> R.R. Bernecker, A.R. Clairmont, Jr., and L.C. Hudson III . . . . .	476
<b>Temperature Effects on Failure Thickness and the Deflagration-to-Detonation Transition in PBX 9502 and TATB</b> B.W. Asay, and J.M. McAfee . . . . .	485
<b>Influence of Fresh Damage on the Shock Reactivity and Sensitivity of Several Energetic Materials</b> H.W. Sandusky, and R.R. Bernecker . . . . .	490
<b>Shock Initiation Studies of Cast, Damaged, and Granulated PBXs</b> R.R. Bernecker, and A.R. Clairmont, Jr. . . . .	499
<b>Effect of a Preshock on the Initiation of HMX, TATB and HMX/TATB Compositions</b> J.P. Plotard, R. Belmas, M. Nicollet, and M. Leroy . . . . .	507
<b>Numerical Modeling of an Aquarium Test for a Nonideal Explosive</b> J. Lee, J.H. Kuk, K.Y. Choi, and F.W. Sandstrom . . . . .	515

## CONTENTS (Cont.)

Page

### PHYSICAL CHEMISTRY

#### Specialist Session

Cochairmen: Richard Bardo and Conrad Bélanger

#### Optical Techniques for Strength Studies of Polymer Bonded Explosives

H.T. Goldrein, J.M. Huntley, S.J.P. Palmer, M.B. Whitworth, and J.E. Field . . . . . 525

#### Shock Response of Pure and Sensitized (0.1 wt% Ethylenediamine) Nitromethane: Time-Resolved Raman Measurements

G.I. Pangilinan, and Y.M. Gupta . . . . . 536

#### Radiation of Condensed Explosives and Its Interpretation (Temperature Measurements)

M.F. Gogulya, and M.A. Brazhnikov . . . . . 542

#### Temperature Measurements of Energetic Materials Containing Aluminum Using Infrared Detectors

D.L. Woody, and J.J. Davis . . . . . 549

#### Laser Ignition of Explosives: A LIF Study of the RDX Ignition Zone

H. Östmark, K. Ekvall, M. Carlson, H. Bergman, and A. Pettersson . . . . . 555

#### Detonation Reaction Steps Frozen by Free Expansion and Analyzed by Mass Spectrometry

N.R. Greiner, H.A. Fry, N.C. Blais, and R.P. Engelke . . . . . 563

#### The Thermal Decomposition of Pure and Amine-Sensitized Nitrocompounds

C.P. Constantinou, and M.M. Chaudhri . . . . . 570

#### Pressure Dependence of the Reaction Propagation Rate of PETN at High Pressure

M.F. Foltz . . . . . 579

#### The Calculation of Electrostatic Interactions and Their Role in Determining the Energies and Geometries of Explosive Molecular Crystals

J.P. Ritchie, E.M. Kober, and A.S. Copenhaver . . . . . 586

#### Thermodynamics of Detonation Products

S. McCahan, and J.E. Shepherd . . . . . 596

#### Products of Al Containing Explosives Detonated in Argon and Underwater

F. Volk, and F. Schedlbauer . . . . . 601

#### Thermal Stability Studies on Nitroarenes

J. Oxley, J. Smith, H. Ye, J. Wang, H. Feng, R.L. McKenney, and P.R. Baldac . . . . . 608



## CONTENTS (Cont.)

Page

### UNDERWATER EXPLOSIVES

#### Specialist Session

**Cochairmen: Ruth Doherty and Masatake Yoshida**

#### **Detonation Chemistry of Underwater Explosives**

J.S. Deiter, and G.B. Wilmot . . . . . 619

#### **Understanding Composite Explosive Energetics: IV. Reactive Flow Modeling of Aluminum Reaction Kinetics in PETN and TNT Using Normalized Product Equation of State**

W.C. Tao, C.M. Tarver, J.W. Kury, C.G. Lee, and D.L. Ornellas . . . . . 628

#### **An Aluminum Reaction Time Limit in Underwater Detonation of an Encased Aluminized Explosive**

J.W. Enig . . . . . 637

#### **A Reaction Model for Aluminized PBX Applied to Underwater Explosion Calculations**

G. Baudin, and D. Bergues . . . . . 646

#### **Nonideal Detonation in a Composite CHNO Explosive Containing Aluminum**

M. Cowperthwaite . . . . . 656

#### **Modelling Shock Initiation and Detonation in the Non-Ideal Explosive PBXW-115**

D.L. Kennedy, and D.A. Jones . . . . . 665

#### **Time-Dependent Equations of State for Aluminized Underwater Explosives**

R.H. Guirguis, and P.J. Miller . . . . . 675

### DDT AND SDT

#### Specialist Session

**Cochairmen: Harold Sandusky and Michel Samirant**

#### **The Influence of Parameter Variations on the Deflagration to Detonation Transition**

R. Verbeek, A.C. van der Steen, and E. de Jong . . . . . 685

#### **A New Look at the Run Distance Correlation and its Relationship to Other Non-Steady-State Phenomena**

P.W. Cooper . . . . . 690

## CONTENTS (Cont.)

	<u>Page</u>
<b>Multiple Shock Initiation of LX-17</b>	
C.M. Tarver, T.M. Cook, P.A. Urtiew, and W.C. Tao . . . . .	696
<b>Novelties of Detonation Phenomenon Study</b>	
A.N. Dremin . . . . .	704
<b>Visualization and Modelling of Delayed Detonation in the Card Gap Test</b>	
B. Salvetat, and J.F. Guery . . . . .	709
<b>Deflagration-to-Detonation in Granular HMX: Ignition, Kinetics, and Shock Formation</b>	
J.M. McAfee, B.W. Asay, and J.B. Bdzil . . . . .	716
<b>A Physical Model of Shock to Detonation Transition in Heterogeneous Explosives</b>	
R. Belmas, J.P. Plotard, and C. Bianchi . . . . .	724
<b>The Analysis of Modified Gap Test Data for Several Insensitive Explosives</b>	
E.R. Lemar, T.P. Liddiard, J.W. Forbes, G.T. Sutherland, and W.H. Wilson . . . . .	731

## EMULSION EXPLOSIVES

### Specialist Session

Cochairmen: Allen Tulis and Albert van der Steen

<b>Detonation Behaviour of a 'Water-in-Oil' Type Emulsion Explosive Containing Glass Microballoons of Selected Sizes</b>	
M.M. Chaudhri, L.-Å. Almgren, and A. Persson . . . . .	741
<b>Effect of Glass Microballoons on Shock Wave Sensitivity and Detonation Critical Diameter of Condensed Explosives</b>	
B.A. Khasainov, B.S. Ermolaev, and H.N. Presles . . . . .	749
<b>Shock Initiation of Nitromethane-PMMA Mixtures with Glass Microballoons</b>	
J.C. Gois, J. Campos, and R. Mendes . . . . .	758
<b>Isothermal and Shock Compression of High Density Ammonium Nitrate and Ammonium Perchlorate</b>	
F.W. Sandstrom, P.-A. Persson, and B. Olinger . . . . .	766

## CONTENTS (Cont.)

Page

### HOT SPOTS

#### Specialist Session

Cochairmen: William Deal, Jr. and Anatolij Dremin

<b>A Numerical Study of Drop-Weight Impact Testing of Solid Rocket Propellants</b> K.P. Duffy, and A.M. Mellor . . . . .	777
<b>A Frictional Work Predictive Method for the Initiation of Solid High Explosives from Low-Pressure Impacts</b> S.K. Chidester, L.G. Green, and C.G. Lee . . . . .	786
<b>An Investigation of Compression and Shear Wave Propagation in Explosives</b> M. Cowperthwaite, and Y.M. Gupta . . . . .	793
<b>Comparison of Damage-Created Voids With Other Void Types in Energetic Materials</b> J.B. Ramsay, H.P. Richter, and R.R. Bernecker . . . . .	802
<b>The Influence of Microstructure on the Sensitivity of Explosive Compositions</b> H. Cherin . . . . .	808
<b>Influence of Crystal Defects on Sensitivity of Explosives</b> F. Baillou, J.M. Dartyge, C. Spyckerelle, and J. Mala . . . . .	816
<b>The Initiation of Explosive Crystals by Shock or Impact</b> C.S. Coffey . . . . .	824
<b>Shock Solicitation of PETN Single Crystals Presenting Defects. Visualisation of Hot Spots Initiation</b> D. Spitzer, and M. Samirant . . . . .	831
<b>Detonation Parameters of Condensed High Explosive Charges with Long Ceramic Elements</b> I.A. Balagansky, S.V. Razorenov, and A.V. Utkin . . . . .	841

### RESPONSE TO STIMULUS

#### Specialist Session

Cochairmen: John Kury and Manfred Held

<b>Interpretation of Time-to-Explosion Tests</b> J.E. Shepherd, and T.B. Brill . . . . .	849
---	-----

## CONTENTS (Cont.)

	<u>Page</u>
<b>On the Theory of Ignition of a Reactive Solid by a Non-Constant Energy Flux</b> G.A. Leiper, and G.F. Roach . . . . .	856
<b>A Study of the Sensitivity and Decomposition of Keto-RDX</b> H. Bergman, H. Östmark, K. Ekvall, and A. Langlet . . . . .	862
<b>Chemical Sensitisation in C-Nitro Explosives</b> M.D. Cook, and P.J. Haskins . . . . .	870
<b>The Influence of Particle Size and Mechanical Properties on the Sensitivity of High Explosive Charges (PBX)</b> F. Schedlbauer, and A. Kretschmer . . . . .	876

## NEW FORMULATIONS

### Specialist Session

Cochairmen: Gary Parsons and Joël Mala

<b>Conception, Synthesis and Characterization of a New Insensitive High Explosive: DANTNP</b> P. Charrue, Ch. Wartenberg, and F. Laval . . . . .	885
<b>Development and Characterization of a Cold-Cast Composite/Molecular Explosive</b> J.D. Renick, and K. Bell . . . . .	891
<b>Effect of Inert Binder Mechanical Properties on Kinetic Parameters in HMX-Based Cast PBX</b> S. Lecume, P. Gimenez, J. Mala, and J.F. Guery . . . . .	898

## SAFETY RELATED TOPICS

### Specialist Session

Cochairmen: Joseph Lannon and Henric Östmark

<b>Simulated Fragment Attack on Cased Munitions</b> Pauline J. Roberts, and J.E. Field . . . . .	909
<b>Detonation and Reaction of Class 1.1 Explosives and Propellants Due to Water Jet Impact</b> S.G. Giltner, O.C. Sitton, and P.N. Worsey . . . . .	918



## CONTENTS (Cont.)

	<u>Page</u>
<b>Simulating Sympathetic Detonation Effects</b>	
J.G. Glenn, and M. Gunger . . . . .	928
<b>Electrostatic Discharge (ESD) Hazards of Energetic Materials</b>	
J. Covino, F.E. Hudson III, D.R. Dreitzler, B. Hammant, and R.J. Lee . . . . .	936

## HOT SPOT MODELS

### General Session

Cochairmen: Jerry Wackerle and Per-Anders Persson

<b>A Study of the Role of Homogeneous Process in Heterogeneous High Explosives</b>	
P.K. Tang . . . . .	947
<b>An Energy Transport Model for the Shock Initiation of Composite Explosives and Propellants</b>	
A.J. Lindfors, and O.E.R. Heimdahl . . . . .	955
<b>Modeling Shock Initiation in Composition B</b>	
M.J. Murphy, E.L. Lee, A.M. Weston, and A.E. Williams . . . . .	963
<b>Computational Analysis of Slip in PETN</b>	
J.P. Ritchie . . . . .	971
<b>The Viscoplastic Hot Spots in Pore Collapse</b>	
P.C. Chou, D. Liang, and Z. Ritman . . . . .	979
<b>The Simulation of Shock Initiation of Less Sensitive Explosives Using the Hydrocode AUTODYN</b>	
R. Verbeek, and A.C. van der Steen . . . . .	987
<b>An Assessment of the Performance of the Original and Modified Versions of the Forest Fire Explosive Initiation Model</b>	
J. Starkenberg . . . . .	992
<b>The Calculation of the Constants for the Forest Fire Model</b>	
D. Liang, W.J. Flis, and P.C. Chou . . . . .	1003

## CONTENTS (Cont.)

	<u>Page</u>
<b>Indexes of the Proceedings for the Ninth Symposium (International) on Detonation, 1989</b>	
S.L. Crane, W.E. Deal, J.B. Ramsay, A.M. Roach, and B.E. Takala . . . . .	1013
<b>Tenth International Detonation Symposium Registrants . . . . .</b>	<b>1041</b>
<b>Author Index . . . . .</b>	<b>1051</b>



## ENERGY TRANSFER IN SOLID EXPLOSIVES

C. M. Tarver, L. E. Fried, A. J. Ruggiero and D. F. Calef  
Lawrence Livermore National Laboratory  
Livermore, CA 94550

The nonequilibrium Zeldovich-von Neumann-Doring theory of detonation in solid explosives is extended to include recent nanosecond and picosecond experimental and theoretical results on each of the four main regions of the reaction zone. The first region is the three-dimensional, Mach stem dominated leading shock front which excites the phonon modes of the explosive molecules in less than a picosecond. The second region is the multiphonon up-pumping process in which the excited phonons anharmonically couple to the low frequency (doorway) vibrational modes which in turn equilibrate with the higher frequency modes by internal vibrational redistribution. This process may require on the order of tens of picoseconds. The third region is the chemical reconstitution region in which the vibrationally equilibrated transition state decomposes in a series of chain reaction steps into highly vibrationally excited diatomic and triatomic molecules in approximately one nanosecond. The fourth region is dominated by vibrational deexcitation and solid species formation as chemical and thermal equilibrium is approached. This is the region measured by current nanosecond resolution techniques and can last from nanoseconds to microseconds depending on the oxygen balance of the solid explosive.

### INTRODUCTION

The nonequilibrium Zeldovich-von Neumann-Doring model of detonation waves in gaseous and condensed explosives<sup>1-3</sup> identified the four main regions shown in Figure 1 that exist within the reaction zones of detonation waves. The first region is a very narrow three-dimensional, leading shock wave front structure in which the phonon modes are excited and equilibrate in less than a picosecond to a phonon quasitemperature. This is the translational temperature overshoot region discussed by Dremine et al.<sup>4</sup> The second region is the flow of this excess phonon energy into the vibrational modes of the explosive molecule through the lowest frequency modes to the highest frequency modes. Dlott and Fayer<sup>5</sup> and Tokmakoff et al.<sup>6</sup> termed this process "multiphonon up-pumping" and labeled the lowest frequency vibrational modes "doorway modes" through which the energy flows. They estimated that this process occurs in approximately 100 picoseconds. The third region is the chemical reconstitution zone in which the vibrationally equilibrated transition state is attained

before endothermic bond breaking and subsequent exothermic chain reactions can occur. Tarver<sup>3</sup> postulated that, in the highly compressed transition state attained in condensed explosives, the initial bond breaking reaction rate may be influenced by the neighboring vibrational modes with which the decomposition mode has equilibrated. This is the underlying principle of the "starvation kinetics" transition state theory of Eyring.<sup>7</sup> The calculated reaction rates for these types of transition states are on the order of a nanosecond. The high temperatures, close proximity and high vibrational excitation of the reaction product intermediates make most collisions effective in causing further exothermic reaction. This implies that the stable gaseous reaction product molecules are formed in times on the order of a nanosecond. The fourth region consists of the relatively slow deexcitation of the highly vibrationally excited stable reaction product molecules (mainly CO<sub>2</sub>, H<sub>2</sub>O, and N<sub>2</sub>) and, in underoxidized explosives, the even slower diffusion controlled coagulation of solid carbon into large chains of graphite, diamond or amorphous carbon as chemical and thermal

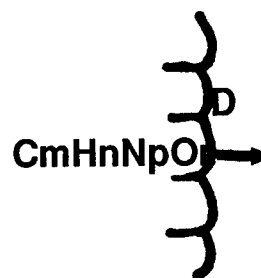


CO<sub>2</sub>\*  
H<sub>2</sub>O\*  
N<sub>2</sub>\*  
C(s)

CO<sub>2</sub>\*\*  
H<sub>2</sub>O\*\*  
N<sub>2</sub>\*\*  
C, C<sub>2</sub>, C<sub>3</sub>

NO<sub>2</sub>\*\*\*  
C<sub>x</sub>H<sub>y</sub>O<sub>z</sub>\*\*\*  
C<sub>a</sub>H<sub>b</sub>N<sub>c</sub>\*\*\*  
C<sub>d</sub>N<sub>e</sub>O<sub>f</sub>\*\*\*

CmHnNpOr\*



## CJ DEEXCITATION REACTION UP-PUMPING SHOCK

FIGURE 1. THE NONEQUILIBRIUM ZND MODEL OF DETONATION WAVES IN CONDENSED EXPLOSIVES

equilibrium at the Chapman-Jouguet (CJ) state is approached.<sup>8</sup> This fourth region may last several hundred nanoseconds in carbon rich monomolecular explosives, such as triaminotrinitrobenzene (TATB).<sup>9</sup> This region is currently being thoroughly studied using several embedded gauge<sup>10</sup> and laser interferometric<sup>11,12</sup> techniques, which have nanosecond resolution. Recent advances in picosecond and femtosecond laser spectroscopy<sup>13</sup> and molecular dynamic modeling<sup>14</sup> are now being applied to detonating solid explosives and are yielding new information on the states attained prior to chemical reaction. In this paper each of the four regions is discussed in terms of these recent experimental and theoretical developments.

### THE LEADING SHOCK FRONT

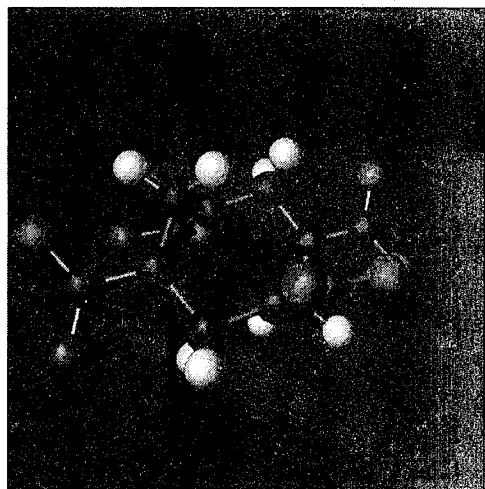
The three-dimensional cellular structure of self-sustaining detonation waves has been well documented for gaseous and liquid explosives.<sup>15</sup> Similar structures have been inferred for solid explosives from experiments that record the interaction of the detonation wave with inert surroundings.<sup>3,15</sup> In heterogeneous solid explosives, the structure must be less regular than those in gases and liquids due to the interactions of the shock front with voids, cracks, and grain boundaries. Direct experimental proof of the cellular structure still eludes experimentalists, because of the extremely high pressure, short time duration, and spatial nonuniformity. Additional indirect evidence of the existence of the three-dimensional structure has been obtained in recent Fabry-Perot and VISAR experiments on detonating<sup>9</sup> and supracompressed<sup>12</sup> (overdriven) solid explosives. These experiments use transparent impedance matching salt crystals plated with 1000 Angstroms of gold as a reflecting surface. Solid explosives with long reaction zones, such as TNT and TATB, and ones with extremely short reaction zones,

such as PETN, do not disrupt the gold surface. Thus excellent particle velocity histories of the interface between the explosive and the salt crystal are obtained which clearly show the reaction zone and the expansion (Taylor) wave. However, high energy solid explosives with intermediate length reaction zones, such as HMX, routinely disrupt the gold surface, and several microns of mylar must be placed on the explosive surface to obtain good records. High pressures and particle velocities in the direction of propagation do not cause disruption of the gold surface in supracompression experiments at pressures exceeding one megabar.<sup>12</sup> Particle motion in the transverse direction is the mostly likely cause of the gold surface disruption, and a cellular structure of the correct size and magnitude is the most likely cause of transverse motion. From these experiments and optical data, Green<sup>16</sup> has estimated the

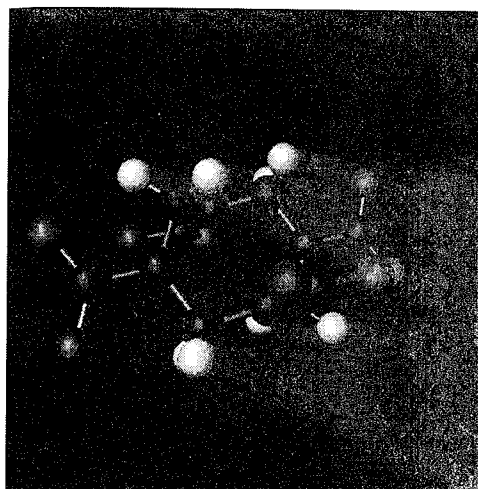
spacing between transverse waves in HMX-based explosives to be less than 2 nanoseconds. Theoretically it is known that all detonation fronts are unstable with respect to perturbations caused by exothermic chemical reactions which overtake, amplify and sustain the shock process.<sup>3</sup> Therefore, although direct experimental verification of the cellular structure of solid explosive detonation waves on the subnanosecond or picosecond time scale has not yet been obtained, a growing body of indirect experimental and theoretical evidence supports its existence.

### MULTIPHONON UP-PUMPING

Immediately behind the various shocks making up the leading shock front structure, only the phonon modes are excited. The phonons rapidly equilibrate in approximately one picosecond to a phonon quasitemperature of tens of thousands of degrees.<sup>4-6</sup> However, these extreme translational energies are completely ineffective in causing chemical reaction,



Crystal structure (expt).



3-21g ab initio geometry

FIGURE 2. THE AB INITIO GEOMETRY OF HMX COMPARED TO THE EXPERIMENTAL CRYSTAL STRUCTURE

because chemical decomposition requires that the high frequency vibrational modes of the molecules be excited. Therefore a region of "multiphonon up-pumping"<sup>5,6</sup> must exist in which the phonons anharmonically couple with the lowest frequency vibrational ("doorway"<sup>5,6</sup>) modes. These modes in turn rapidly equilibrate with higher frequency vibrational modes through intramolecular vibrational energy redistribution processes.

The multiphonon up-pumping process in crystals of explosive molecules is currently being studied by a combination of molecular dynamics simulation<sup>14</sup> and femtosecond laser spectroscopy<sup>13</sup>. Molecular dynamics simulations of multiphonon up-pumping were undertaken in HMX crystals. The potentials were derived from Hartree-Fock ab initio electronic structure calculations with the GAMESS<sup>17</sup> program. The molecular geometry was first optimized using the 3-21g basis set.<sup>18</sup> The resulting optimized gas phase geometry is shown in Figure 2 to correspond closely with the crystal geometry. This comparison is an important consistency check on the applicability of gas phase electronic structure calculations to condensed phase problems.

At the optimized geometry, the Hessian or force constant matrix was found at the 3-21g level. The frequencies of the six translational and rotational modes of HMX were set to zero. The HMX intramolecular potential (HMX1) was taken to be of the DREIDING<sup>19</sup> form with the addition of bond stretch-

bond stretch, bond stretch-bend, and bend-bend cross terms. Coulomb interactions were calculated between atoms separated by more than 4 Angstroms using Mulliken charges. The parameters of the intramolecular potential were then adjusted to minimize the root mean square difference between the second derivatives of the intramolecular potential and the ab initio Hessian. The intermolecular forces were taken to be the sum of Lennard-Jones and Coulomb interactions. A more detailed description of the HMX1 potential and its parameters will be published elsewhere.

The potential was tested by simulating the inelastic neutron scattering spectrum of HMX, which has been measured experimentally.<sup>20</sup> The spectrum calculation involved finding the self Van Hove correlation function of a sample of 32 HMX molecules and applying quantum correction factors.<sup>21</sup> Figure 3 shows the calculated and experimental spectra. The good agreement implies that the HMX1 potential is capable of reproducing the dynamic behavior of HMX at frequencies below 500  $\text{cm}^{-1}$ . No inelastic neutron scattering data exists above 500  $\text{cm}^{-1}$ , but efforts are underway to test the higher frequency behaviour of HMX1 by simulating infrared absorption spectra.

The HMX1 potential was then used in nonequilibrium molecular dynamics<sup>22</sup> studies of phonon-vibron upconversion. Periodic samples of 32 or 128 HMX molecules were used; the results for 32 molecules are reported here. Before beginning the upconversion process, the sample was equilibrated at

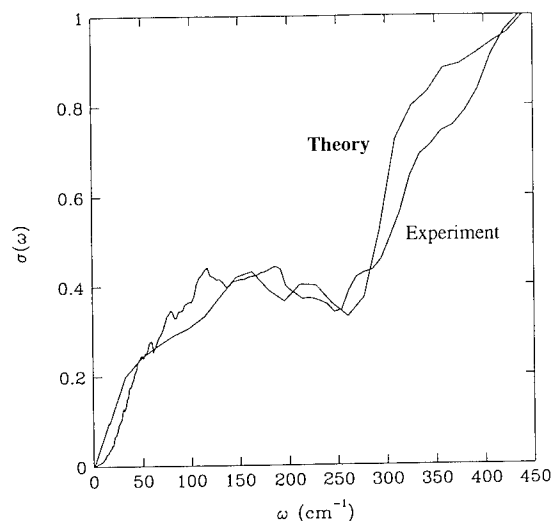


FIGURE 3. SIMULATED INELASTIC NEUTRON SCATTERING COMPARED TO EXPERIMENT

room temperature (300K) for several ps. A timestep of 0.5 fs was used in the simulation. Equilibration was accomplished by scaling velocities every 10 fs to maintain a kinetic energy equal to  $3NkT/2$ , where  $N$  is the number of atoms in the simulation,  $T$  is the temperature, and  $k$  is Boltzmann's constant. Since HMX has a large number of low frequency modes (12 normal modes under  $200\text{ cm}^{-1}$ ),<sup>23</sup> its lattice modes are amalgamated with low frequency molecular vibrations. This complicates the distinction between intramolecular and lattice vibrations. Phonons and vibrons were distinguished as follows: to each molecule a rotating frame was attached, as described in Ref. 24. In this frame, the molecular kinetic energy is divided into three parts: the translational temperature  $T_{\text{trans}}$ , the rotational temperature  $T_{\text{rot}}$ , and the vibrational temperature  $T_{\text{vib}}$ . In the molecular dynamics simulation, the phonon temperature is equal to  $T_{\text{trans}} + T_{\text{rot}}$ , while the vibron temperature is equal to  $T_{\text{vib}}$ .

The phonon velocities of the equilibrated HMX sample were chosen from a Maxwell-Boltzmann distribution of 16,000K, while the vibron velocities were left at 300K. The transfer of energy from the excited thermal phonons to vibrons is shown in Fig. 4, which displays  $T_{\text{trans}}$ ,  $T_{\text{rot}}$ , and  $T_{\text{vib}}$  as functions of time. A fast relaxation occurs in about 50 fs, followed by a slower component of about 2 ps. Even slower components of the relaxation could also be present, but are not resolved in this simulation. The fast relaxation is probably due to phonon energy rapidly entering low frequency molecular vibrations through collisions

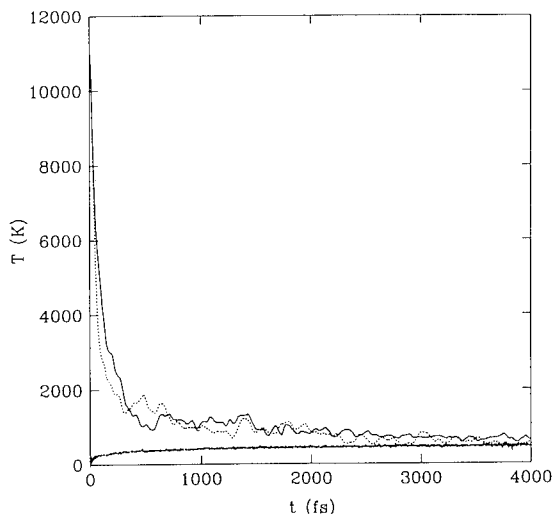


FIGURE 4. MULTIPHONON UP-PUMPING IN HMX [ $T_{\text{trans}}$  (solid),  $T_{\text{rot}}$  (dotted), and  $T_{\text{vib}}$  (thick hashed)]

between neighboring molecules, while the slower timescale corresponds to multiphonon upconversion.

This simulation exhibits faster phonon-vibron relaxation rates than the 30 - 100 ps rates recently predicted by Tokmakoff et al.<sup>6</sup> for naphthalene, which has fewer low frequency modes than HMX, and measured by Dlott et al.<sup>25</sup> in liquid nitromethane, which has only 15 vibrational modes compared to 78 for HMX. The maximum time required for vibrational equilibration behind a strong shock is approximately 10 ns, measured for diatomic liquids, such as  $\text{N}_2$  and  $\text{CO}$ , by Schmidt et al.<sup>26</sup> The relatively large number of low frequency (doorway) modes in HMX accounts for the rapid up-pumping. Experimental verification of this hypothesis by direct measurement of these energy transfer rates in HMX is currently being pursued. Measurements based on incoherent femtosecond Raman pump-probe spectroscopy will be employed. This experiment is unique in that it directly measures vibrational population transfer rates without being affected by dephasing. This allows direct comparison with the simulation results.

#### CHEMICAL RECONSTITUTION

Upon completion of the vibrational equilibration process, the explosive molecules can be described by transition state theory. The effects of shock pressures and temperatures on the activation energy, entropy, and volume of this transition state are unknown at present,<sup>3,7</sup> but are likely to be small with respect to the

40 - 60 kcal/m energy barriers to exothermic reaction measured for thermal decomposition of solid explosives.<sup>27</sup> Reaction rate constants for several condensed phase explosives at average von Neumann spike conditions have been calculated<sup>3</sup> using Eyring's "starvation kinetics" formalism and Gruneisen equations of state which incorporate heat capacity as a function of temperature,  $C_v(T)$ , data to calculate shock temperatures.<sup>28</sup> The basic assumption in "starvation kinetics" is that the high frequency vibrational mode in the compressed, equilibrated transition state which reacts endothermically to start the multistep decomposition process is statistically excited to a sufficient vibrational level to dissociate by the "pool" of vibrational energy contained in its nearest neighbor vibrational modes. This mode must also rapidly equilibrate with these neighboring modes any excess vibrational energy it instantaneously receives from any process, such as the relaxation of an electronically excited state to the ground electronic level with the accompanying high vibrational excitation.<sup>29</sup> The main effect of this transition state formalism is to decrease the dependence of the initial reaction rate on shock temperature.<sup>3</sup> Eyring<sup>7</sup> proposed this idea to explain the existence of finite reaction rates in detonation, but the requirement that the multiphonon up-pumping process be completed before chemical reaction can begin limits reaction rates at all shock pressures.

The existence of such a transition state in a solid explosive detonation wave has not yet been observed experimentally. Current experimental techniques measure pressures or particle velocities averaged over several nanoseconds in time and several microns in space. Since the cellular structure is believed to be smaller than those dimensions, some of the explosive molecules are heated to higher shock temperatures than others and are releasing chemical energy while others are still being up-pumped to the transition state. In VISAR and Fabry-Perot experiments, the initial resolvable particle velocities are always decreasing indicating exothermic reaction. No plateaus in pressure or particle velocity have been observed, even in TATB.<sup>9,11,12</sup> Thus direct observation of the transition state will require subnanosecond resolution.

When chemical reaction occurs, the large explosive molecule (20-30 atoms) reconstitutes into 7-10 diatomic and triatomic molecules plus solid carbon if the explosive is underoxidized. This multistep chain reaction process is quite rapid, because most collisions are reactive. The intermediate reactive fragments are formed in highly vibrationally excited states and thus react orders of magnitude faster than equilibrated fragments. Therefore large quantities of vibrationally

excited product gas are created on a nanosecond time scale. Again this process is too fast to observe with current hydrodynamic measurement techniques. However, electrical conductivity probes with nanosecond time response have long been used to detect the presence of solid carbon in the detonation reaction zone.<sup>30-32</sup> Since at least partial decomposition must have occurred before carbon can be formed, electrical conductivity measurements yield an upper limit for the time duration of the transition state. Hayes<sup>30</sup> and Antipenko et al.<sup>31</sup> have both measured some electrical conductivity within one nanosecond of the passage of the detonation front. The magnitude of the electrical conductivity continues to increase as more solid carbon is formed and then decreases as the diffusion controlled coagulation of carbon into large chains reduces the amount of carbon available to conduct electricity.

### VIBRATIONAL DEEXCITATION

The remaining portion of the detonation reaction zone is the vibrational deexcitation of the reaction products as chemical and thermal equilibrium is approached. This equilibration process can be quite fast. In Fabry-Perot studies of detonating PETN, which contains sufficient oxygen to react with all of its hydrogen and carbon yielding little or no solid carbon, no chemical reaction zone has been measured.<sup>9,33</sup> All of the PETN experiments can be accurately calculated using a CJ model and the Jones-Wilkins-Lee (JWL) equation of state derived by Green<sup>34</sup> from supracompression data. Therefore all four reaction zone processes must occur within a few nanoseconds, the Fabry-Perot time resolution, for PETN. Similar results have been obtained for hexanitrohexazaisowurtzitane (HNIW) on a limited number of experiments.

Underoxidized solid explosives which produce solid carbon exhibit measurable vibrational deexcitation regimes in both self-sustaining and supracompression experiments. HMX's main energy release due to deexcitation occurs in approximately 20 ns, while the slower carbon coagulation process requires another 100 ns.<sup>9,12,35</sup> TNT's main energy release takes approximately 60 ns followed by another 150 ns for carbon formation.<sup>9,12,36</sup> TATB's main energy release occurs in approximately 80 ns and the carbon formation tail lasts another 200-300 ns.<sup>9,12,37</sup> Reaction zone lengths of solid explosive formulations containing aluminum, ammonium perchlorate, etc. are orders of magnitude longer.<sup>38</sup> The rate of vibrational deexcitation<sup>3</sup> or "cooling"<sup>5,6</sup> is controlled by the initial degree of vibrational excitation in the products, the overall energy available in the wave, and the amount of

solid carbon present in the mixture. Collisions between diatomic and triatomic molecules are extremely efficient in causing internal vibrational energy redistribution. However, collisions between vibrationally excited diatomics or triatomics with atomic species, such as carbon, are very inefficient in converting vibrational energy into translational energy. Therefore the presence of significant quantities of solid carbon increases the time required for thermal equilibration. The diffusion controlled formation of long chain carbon species is a complex kinetic and phase problem currently being studied by several experimental and theoretical techniques.<sup>39,40</sup>

The question of whether complete chemical and thermal equilibration is attained at a true CJ state is still open. Certainly total equilibrium is closely approached after long run distances in large diameter charges. Laser interferometric measurements on self-sustaining detonation waves at several different run distances and on supracompressed waves appear to be converging to the same CJ pressure. Hydrodynamic reactive flow models<sup>41,42</sup> of ZND-type detonation waves with a fast reaction followed by a slow one to the CJ state accurately calculate metal acceleration, spall, rock dynamics, underwater shocks, and other explosive applications. Reactive flow modeling also helps explain older experimental data and interpretations in which CJ pressures varied greatly.<sup>43</sup> Some techniques measured only the energy delivered by the fast reaction and yielded higher CJ pressures, while others measured the effect of the complete reaction zone and implied lower CJ pressures. Continued experimentation and modeling with ever improving resolution will shed more light on the elusive CJ state in detonating condensed explosives.

## CONCLUSIONS

Recent experimental and theoretical progress in measurement and analysis of detonation of solid explosives has provided confirmation of the four regions described by the nonequilibrium ZND model and has reduced the uncertainty in the duration of each region. The three dimensional leading shock front excites phonons in a picosecond. Multiphonon up-pumping to vibrational equilibrium requires less than 100 picoseconds. The transition state and chemical reconstitution region lasts a nanosecond. The deexcitation of the highly vibrationally excited products can take tens to hundreds of nanoseconds depending on the amount of solid carbon present. The diffusion controlled formation of the final solid carbon structure can last for hundreds of nanoseconds.

Work performed under the auspices of the United States Department of Energy by the Lawrence Livermore National Laboratory under Contract No. W-7405-ENG-48.

## REFERENCES

1. Tarver, C. M., *Combustion and Flame* 46, 111 (1982).
2. Tarver, C. M., *Combustion and Flame* 46, 135 (1982).
3. Tarver, C. M., *Combustion and Flame* 46, 157 (1982).
4. Dremine, A. N.; Klimenko, V. Yu.; Davidova, O. N.; and Zoludeva, T. A., Ninth Symposium (International) on Detonation, Office of Naval Research OCNR113291-7, Portland, Oregon, 1989, p.724.
5. Dlott, D. D. and Fayer, M. D., *J. Chem. Phys.* 92, 3798 (1990).
6. Tokmakoff, A.; Fayer, M. D.; and Dlott, D. D., *J. Phys. Chem.* 97, 1901 (1993).
7. Eyring, H., *Science* 199, 740 (1978).
8. Tarver, C. M., "On the Difference between Self-Sustaining Converging Detonation Waves and Piston-Supported Overdriven Detonation Waves," Lawrence Livermore National Laboratory Report UCRL-90714, March 1984.
9. Tarver, C. M.; Breithaupt, R. D.; and Kury, J. W., International Symposium on Pyrotechnics and Explosives, Beijing, China, October 1987, p. 692.
10. Hayes, B. and Tarver, C. M., Seventh Symposium (International) on Detonation, Naval Surface Warfare Center NSWC MP82-334, White Oak, MD, 1981, p. 1029.
11. Sheffield, S. A.; Bloomquist, D. D.; and Tarver, C. M., *J. Chem. Phys.* 80, 3831 (1984).
12. Green, L. G.; Tarver, C. M.; and Erskine, D. J., Ninth Symposium (International) on Detonation, Office of Naval Research OCNR113291-7, Portland, OR, 1989, p. 670.

13. Nelson, K. A. and Ippen, E. P., *Adv. Chem. Phys.* 75, 1 (1989).
14. Allen, M. P. and Tildesley, D. J., "Computer Simulation of Liquids", Clarendon Press (Oxford), 1987.
15. Fickett, W. and Davis, W. C., *Detonation*, University of California Press, Berkeley, CA, 1979.
16. Green, L. G., LLNL, private communication, 1993.
17. Schmidt, M. W.; Baldrige, K. K.; Boatz, J. A.; Jensen, J. H.; Koseki, S.; Gordon, M. S.; Nguyen, K. A.; Windus, T. L.; and Elbert, S. T., *QCPE Bull.*, 10, 52 (1990).
18. Szabo, A. and Ostlund, N. S., "Modern Quantum Chemistry: Introduction to Advanced Electronic Structure Theory", Macmillan Publishing Co. Inc., New York, 1988.
19. Mayo, S. L.; Olafson, B. D.; Goddard III, W. A.; *J. Phys. Chem.* 94, 8897 (1990).
20. Boutin, H. P.; Prask, H. J.; Trevino, S., *Picatinny Arsenal Repts.*, 1967.
21. Ullo, J. J. and Yip, S., *J. Chem. Phys.*, 85, 4056(1986).
22. Allen, M. P. and Tildesley, D. J., "Computer Simulation of Liquids", Clarendon Press, Oxford, 1987, Chapter 8.
23. Fried, L. E. and Ruggiero, A. J., *Mat. Res. Soc. Symp. Proc.* 296, 35 (1993).
24. Jellinek, J. and Li, D. H., *Phys. Rev. Lett.* 62, 241 (1989).
25. Chen, S.; Lee, I.-Y. S.; Tolbert, W. A.; Wen, X.; and Dlott, D. D., *J. Phys. Chem.*, in press.
26. Schmidt, S. C.; Moore, D. S.; Shaw, M. S.; and Johnson, J. D., *J. Chem. Phys.* 98, 9379 (1993).
27. McGuire, R. R. and Tarver, C. M., *Seventh Symposium (International) on Detonation*, Naval Surface Weapons Center NSWC MP82-334, White Oak, MD, 1981, p. 56.
28. Cowperthwaite, M. and Shaw, R., *J. Chem. Phys.* 53, 555 (1970).
29. Srinivasan, J. and Vincenti, W. G., *Phys. Fluids* 18, 670 (1975).
30. Hayes, B., *Fourth Symposium (International) on Detonation*, Office of Naval Research ACR-126, Washington, D.C., 1965, p. 595.
31. Antipenko, A. G.; Dremine, A. N.; and Yakushev, Y., *Combustion, Explosion and Shock Waves* 14, 101 (1978).
32. Tasker, D. G.; Lee, R. J.; and Gustavson, P. K., *Naval Surface Warfare Center Report NSWCDD/TR-92/218*, March 1993.
33. Tarver, C. M.; Breithaupt, R. D.; and Kury, J. W., "Detonation Waves in PETN," manuscript in preparation.
34. Green, L. G., *Shock Waves in Condensed Matter -1987*, Schmidt, S. C. and Holmes, N. C., eds., North Holland, Amsterdam, 1988, p. 507.
35. Breithaupt, R. D.; Tarver, C. M.; and Kury, J. W., "Detonation Waves in HMX-Based Explosives," manuscript in preparation.
36. Kury, J. W.; Breithaupt, R. D.; and Tarver, C. M., "Detonation Waves in TNT," manuscript in preparation.
37. Tarver, C. M.; Kury, J. W.; and Breithaupt, R. D., "Detonation Waves in TATB-Based Explosives," manuscript in preparation.
38. Tao, W. C.; Tarver, C. M.; Kury, J. W.; Lee, C. G.; and Ornella, D. L., "Understanding Composite Explosive Energetics IV. Reactive Flow Modeling of Aluminum Reaction Kinetics in PETN and TNT," paper presented at this Symposium.
39. Johnson, J. D., *Ninth Symposium (International) on Detonation*, Office of Naval Research OCNR113291-7, Portland, OR, 1989, p. 417.
40. Volk, F. and Schedlbauer, F., *ibid.*, p. 962.
41. Murphy, M. J.; Simpson, R. L.; Breithaupt, R. D.; and Tarver, C. M., *ibid.*, p. 525.
42. Tang, P. K., *ibid.*, p. 657.
43. Davis, W. C. and Venable, D., *Fifth Symposium (International) on Detonation*, Office of Naval Research ACR-184, Pasadena, CA, 1970, p. 13.

## DISCUSSION

DR. FRED VOLK

Fraunhofer Institut für Chemische Technologie,  
Pfinztal, Germany

What about AP reaction?

## REPLY BY CRAIG TARVER:

Aluminum would begin to react with  $\text{CO}_2$  and/or  $\text{H}_2\text{O}$  produced by the organic explosive as soon as these products form. Because the aluminum particles generally have a layer of  $\text{Al}_2\text{O}_3$  that must melt and be penetrated by the hot gases, the diffusion-controlled aluminum oxidation reaction lasts much longer than the fourth region of vibrational deexcitation discussed here. We have measured aluminum reaction rates in the detonation products of PETN and TNT. Please see the paper by W. C. Tao, *et al.*, in these Proceedings.

## DISCUSSION

MICHEL M. S. SAMIRANT

French German Research Institute, Saint-Louis, Cedex,  
France

You consider that the change in reflectivity of a gold film impacted by a detonation wave is due to the front roughness. Have you an idea of the size of the detonation cells?

## REPLY BY CRAIG TARVER:

Because of these and other optical experiments, LeRoy Green of Lawrence Livermore National Laboratory has estimated the cell size in a detonating HMX explosive to be approximately 2 nanoseconds or 18  $\mu\text{m}$ . The cells in TATB-based explosives appear to

be 5 to 10 times larger. We are planning new experiments to address this issue directly.

## DISCUSSION

JOSEPH C. FOSTER, JR.

Wright Laboratory, Eglin Air Force Base, Florida

The four-stage model of the solid-phase detonation process is longer than previously pictured by many researchers and appears to be inconsistent with the hydrodynamic interpretation of particle velocity measurements which identify a large shift in particle velocity in the 10-20 ns time period after shock wave arrival. Could you comment on your interpretation of these data in light of your four-stage model and reference any supporting data for the sonic locus being 100-200 ns behind the shock for HMX- or RDX-based materials?

## REPLY BY CRAIG TARVER:

The four-stage model is consistent with gauge and laser interferometry experiments. The first three stages cannot be observed experimentally as yet, because they take only on the order of a nanosecond. The fourth stage (vibrational deexcitation of the reaction products as thermal and chemical equilibrium is approached) is being observed experimentally as the rapid decrease in particle velocity (an exothermic process) which generally lasts tens of nanoseconds. In both detonation and supercompression (overdriven detonation) experiments, we have observed this rapid particle velocity decrease followed by a slower particle velocity decrease which lasts hundreds of nanoseconds. Several research groups around the world have attributed this slower exothermic process to the diffusion-controlled coagulation of solid carbon into particles of diamond, graphite, or amorphous carbon depending on the pressure and temperature conditions.

## MACH REFLECTION OF SPHERICAL DETONATION WAVES

L. M. Hull  
Los Alamos National Laboratory  
Los Alamos, NM 87544

When two detonation waves collide, the shape of the wave front at their intersection can be used to categorize the flow as regular or irregular reflection. In the case of regular reflection, the intersection of the waves forms a cusp. In the case of irregular reflection, the cusp is replaced by a leading shock locus that bridges the incident waves. Many workers have studied irregular or Mach reflection of detonation waves,<sup>1-4</sup> but most of their experimental work has focused on the interaction of plane detonation waves. Reflection of spherical detonation waves has received less attention. This study also differs from previous work in that the focus is to measure the relationship between the detonation velocity and the local wave curvature for irregular reflection of spherical detonation waves. Two explosives with different detonation properties, PBX 9501 and PBX 9502, are compared.

### INTRODUCTION

Recent work in this country and in the UK indicates that divergent detonation wave propagation can be described in terms of a relationship between the local wave curvature and the local normal detonation velocity (see Refs. 5-7). In the U.S.A., the theory is called Detonation Shock Dynamics (DSD). The application of DSD to convergent waves has a less solid theoretical foundation because the flow behind the convergent wave is subsonic and can thus be influenced by disturbances propagated forward to the wave front. Whitham's<sup>8</sup> method for treating shock diffraction in gas dynamics suffers from the same difficulty; nevertheless, it has been successful. The results presented here, along with those of Bdzil and Davis,<sup>9</sup> show that the detonation velocity is related to the local wave curvature in a continuous manner from convergent to divergent configurations. Thus it may be possible to apply wave-tracking methods, based on DSD, to arbitrary convergent and divergent geometries, with success similar to that enjoyed by Whitham's method.

When two divergent spherical detonation waves collide, regular reflection is first observed and, subsequently, irregular reflection develops. The Mach stem is the bridge that develops between the spheres, (Herein, any irregular reflection is called a Mach reflection.) The saddle surface generated by the collision (Figure 1) is a surface of revolution that is truncated because of the finite dimensions of the explosive. Therefore, the intersection of the surface with a plane results in a record of the temporal evolution of the surface. To describe the entire surface generated when two divergent spherical waves collide, all the usual parameters that describe

wave reflection must be measured or estimated, as well as the parameters that describe the expanding spherical waves. Experimental wave-arrival-time data are modeled with analytic functions to describe the wave shape and propagation for both the convergent and divergent waves. We also use metal plate acceleration experiments and assumed equations of state to provide independent measurements of the pressure in the Mach reflection region.

A surface has two principal radii of curvature. We have chosen the mean curvature as the descriptive parameter. The sign of the mean curvature  $\kappa$  is chosen so that a divergent wave has positive curvature. The mean curvature of the saddle point (Mach stem) is negative and approaches zero as the spheres expand and the Mach stem grows. The data analysis technique assumes that the  $D(\kappa)$  relationship is linear, primarily because this is the simplest form. The convergent wave results are only slightly dependent on this assumption. The linear relationship can be written as

$$D = D_j (1 - v\kappa), \quad (1)$$

where  $D$  is the local detonation velocity,  $D_j$  is the CJ detonation velocity,  $v$  is a coefficient dependent on the explosive, and  $\kappa$  is the mean curvature of the detonation wave. For a spherical wave,  $D = dr/dt$ , so substitution of Equation (1) and integration with respect to time gives

$$D_j(t - t_0) = r - r_0 + v \ln \frac{r - v}{r_0 - v}. \quad (2)$$

Equation 1 applies to both convergent and divergent flow, but Equation 2 applies only to the spherically expanding waves.



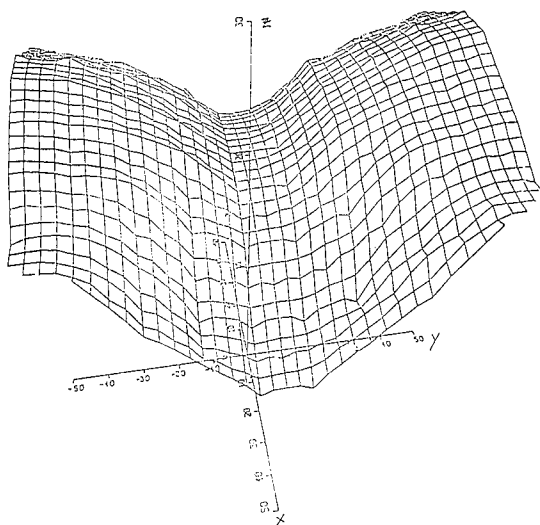


**FIGURE 1. MACH REFLECTION OF SPHERICAL DETONATION WAVES. DETONATIONS WERE INITIATED AT  $(0, \pm 50, 0)$  AND WAVE FRONT ARRIVAL RECORDED BY A SMEAR CAMERA. THE RECORDS WERE ANALYZED AND INTERPOLATED TO OBTAIN AN APPROXIMATION OF THE SHAPE OF THE COMPLETE SURFACE.**

## EXPERIMENTAL

The divergent-wave detonation-velocity-curvature relationship for PBX 9501 was determined with the experiment shown schematically in Figure 2. Two detonator-booster systems were placed so as to initiate the explosive under two thicknesses of the test explosive. The arrival time of the detonation wave at the observation surface over the center of each detonator was recorded through a single slit with the smear camera (Figure 3). Camera data corresponding to each wave were modeled as a sphere located at some arbitrary origin; the sphere expanded at a constant velocity only for the duration of the breakout at the free surface. Position-time data from the region directly over the detonators were fit to the model equation to determine the radius of each wave. When the measured radii and time differences are used to solve Equation (2) with  $D_j = 8.802 \text{ mm}/\mu\text{s}$ ,  $v = 0.639 \text{ mm}$ . Then Equation (1) gives the corresponding values of  $D$  so that we have two  $D(\kappa)$  points.

To determine the variation of the detonation velocity with the local mean surface curvature for convergent detonations, the Mach reflections of two propagating spherical detonation waves are measured. The mean curvature of the saddle surface, and thus the Mach stem, is the mean of the two principal curvatures. These principal curvatures are the inverse of the radius of curvature of the intersection of the saddle with the  $x$ - $z$  plane ( $r_m$ ), and the inverse of the radius of curvature of the intersection of the saddle with the  $y$ - $z$  plane at  $y = 0$  ( $r_s$ ) (Figure 4). The radius of curvature  $r_s$  is much smaller than the radius

of curvature  $r_m$ , so  $r_s$  dominates the estimated mean Mach stem curvature from the data. On the other hand, the velocity of the Mach stem is the rate of increase of  $r_m$ . Therefore, accurate measurement of both  $r_m$  and  $r_s$  is necessary to determine the  $D(\kappa)$  relationship for the convergent region.

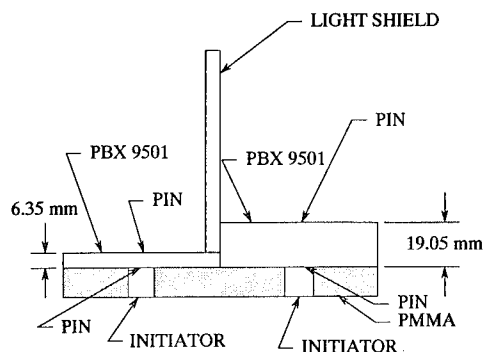


**FIGURE 2. DIVERGENT WAVE CHARACTERIZATION EXPERIMENT**

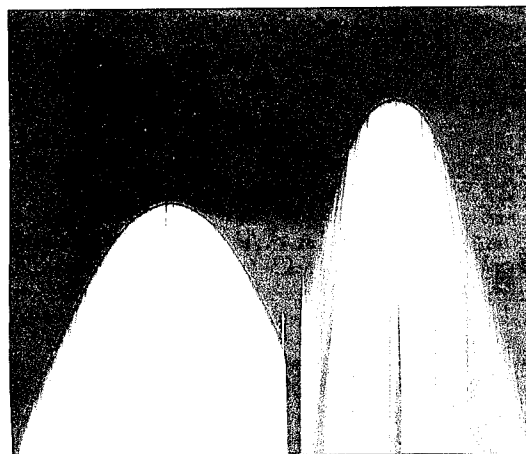


**FIGURE 3. SMEAR CAMERA RECORD OF THE BREAKOUT OF THE TWO DIVERGING SPHERICAL WAVES GENERATED BY THE TEST ASSEMBLY SHOWN IN FIGURE 2. CLEAR PAINT WAS USED TO PROVIDE A SHARP TRACE. TIME INCREASES UPWARD.**

Test pieces used for the convergent wave studies are right-circular cylinders with one end cut at an angle, with respect to the charge axis (see Figure 5). Two detonators are placed on the  $y$ -axis at  $y = \pm y_0$  and are initiated simultaneously. The arrival of the detonation wave at the angled observation surface is recorded through 11 slits with a smear camera. Slits are arranged parallel to the  $y$ -axis with the center slit at  $x = 0$ . A typical camera record is shown in Figure 6. The curved Mach stem can be clearly seen at the intersection of the two spheres.

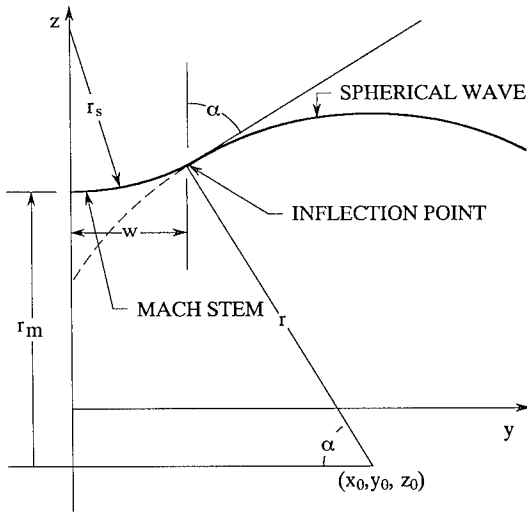


FIGURE 4. THE GEOMETRY OF THE MACH REFLECTION OF SPHERICAL WAVES

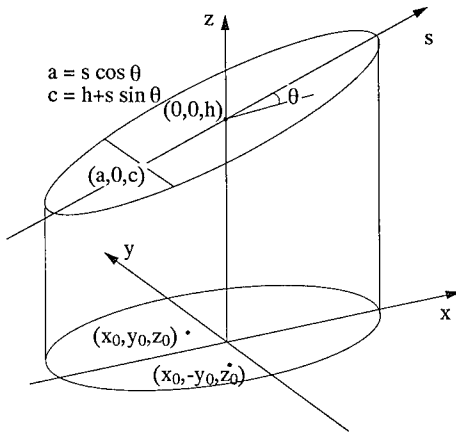


FIGURE 5. SHOT GEOMETRY FOR MACH STEM EXPERIMENTS

The arrival time data, well away from the Mach stem, are fit to the equation of a sphere centered at  $(x_0, y_0, z_0)$  and expanding as given by Equations 1 and 2. At each slit, the values of  $x = a$  and  $z = c$  are known from the geometry. Therefore, the model function for the expanding wave becomes

$$(a - x_0)^2 + (y - y_0)^2 + (c - z_0)^2 = r^2, \quad (3)$$

the data set is  $t = t(y)$ , and the parameters determined by the fit are  $x_0, y_0, z_0$ , and  $t_0$ . The  $r_0$  value in Equation (1) is taken to be  $|z_0|$ . The use of Equations (1) and (2), rather than a sphere expanding at the CJ velocity, result in a small correction because the radius of the sphere is large, compared with  $v$ . A fixed value of  $v = 0.6$  mm was used for PBX 9501 and a value of  $v = 2.0$  mm was used for PBX 9502. An example of the result of this

curve fit is given in Figure 7. The value of  $r_m$  for each slit is given by

$$(r_m)^2 = (a - x_0)^2 + (c - z_0)^2. \quad (4)$$

The corresponding arrival time of the Mach stem at  $y = 0$  is known from the data; differentiation of this  $(r_m, t)$  data gives the normal velocity of the Mach stem,  $D = dr_m/dt$ .

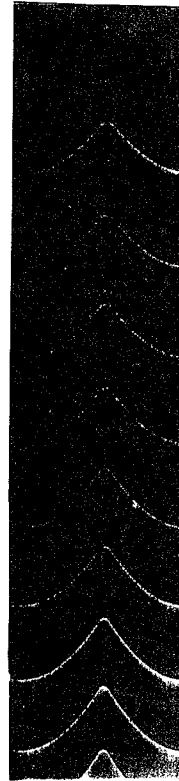


FIGURE 6. A MULTISLIT SMEAR CAMERA RECORD OF SPHERICAL DETONATION WAVE INTERACTION IN PBX 9501. TIME INCREASES UPWARD.

The arrival time data in the saddle region defines the shape of the Mach stem and allows the estimation of the Mach stem radius of curvature  $r_s$ . Mach stem data are fit to the equation of a circle lying in the  $y-\vec{n}$  plane ( $\vec{n}$  is the normal direction of the Mach stem). The center of the circle is moving in the  $\vec{n}$  direction at the velocity for that particular slit, and the radius of the circle is  $r_s$ . Therefore, the model equation we use to determine  $r_s$  is

$$(y - y_0)^2 + D^2(t - t_0)^2 = (r_s)^2,$$

where data to be fit are  $t = t(y)$  and the parameters are  $y_0, t_0$ , and  $r_s$  (note that this is a different origin than in the previous discussion). The result of this curve-fitting procedure for the center slit is shown in Figure 8; judgment

was used to select the number of data points to be included in the curve fit. The  $r_s$  data for PBX 9501 are in the approximate interval  $4 < r_s < 27$  mm and for PBX 9502 in the approximate interval  $9 < r_s < 34$  mm. Thus we are approaching the region where the radius of curvature of the wave front is comparable to the reaction zone thickness (the distance from the leading shock to the sonic locus), a region of questionable applicability of DSD. The theoretical basis of DSD and the applicability of Equation (1) are dependent on the condition that the inverse of the wave curvature is much greater than the reaction zone thickness.

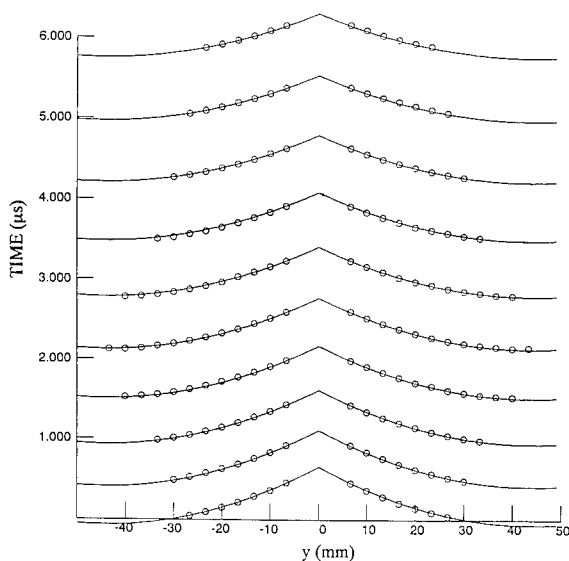


**FIGURE 7. DATA AND CURVE FIT USED TO FIND THE ORIGIN OF THE SPHERICALLY EXPANDING PART OF THE DETONATION WAVE FOR THE RECORD SHOWN IN FIGURE 6**

The mean curvature,  $\kappa = 1/2 (1/r_m - 1/r_s)$ , can now be calculated and the  $D(\kappa)$  relationship plotted (see Figure 9). Results for PBX 9501 indicate that, to within a good approximation over the measured range, the  $D(\kappa)$  relationship is continuous and linear for both  $\kappa > 0$  and  $\kappa < 0$ . The  $D(\kappa)$  relationship for PBX 9502 is linear in the convergent region evaluated here. Slope  $v$  for PBX 9502 is large, in comparison with that of PBX 9501. The PBX-9502  $D(\kappa)$  relationship for  $\kappa > 0$  is nonlinear.<sup>9</sup> The data from Bdzil and Davis's study<sup>9</sup> and this study patch together: the  $D(\kappa)$  relationship appears to be continuous in both slope and magnitude across  $\kappa = 0$ . These relations can now be used with a detonation-front tracking routine (see Reference 10) to predict wave profiles for both convergent and divergent waves.

Properly defined, the Mach stem width is the transverse distance from the plane of symmetry to the position of the intersection of the incident detonation and the disturbance reflected into the product. The position of the reflected disturbance is not readily available from arrival time data. Therefore, we choose to assume that the transverse position of the inflected point of the leading

wave front defines the stem width. Figure 10 shows the Mach stem width data as a function of position  $r_m$ . The estimated Mach stem width  $w$  completes the information necessary to calculate the interaction angle  $\alpha$  from  $r \cos \alpha = y_0 - w$  (see Figure 4). By this calculation, we show that the measurements are for interaction angles that vary from about  $70^\circ$  to  $75^\circ$  for both PBX 9501 and PBX 9502. Although we have made measurements over a limited range of interaction angle, the Mach stem dimensions detected are initially only slightly larger than the reaction zone thickness and they are observed until nearly plane wave conditions are achieved. Over the measured range, the growth rate of the Mach stem is approximately constant. From the linear fit shown in Figure 10, the growth angle for PBX 9501 is  $\chi = 2.4^\circ$  and for PBX 9502,  $\chi = 7.4^\circ$ . Extrapolating the linear relationship to  $w = 0$  allows the estimation of the critical angle (the value  $\alpha_c$ , at which an irregular reflection first appears). For PBX 9501  $\alpha_c = 56^\circ$ , and for PBX 9502  $\alpha_c = 63^\circ$ . This extrapolation is expected to overestimate the critical angle because of the neglected variation of the growth rate of the stem.

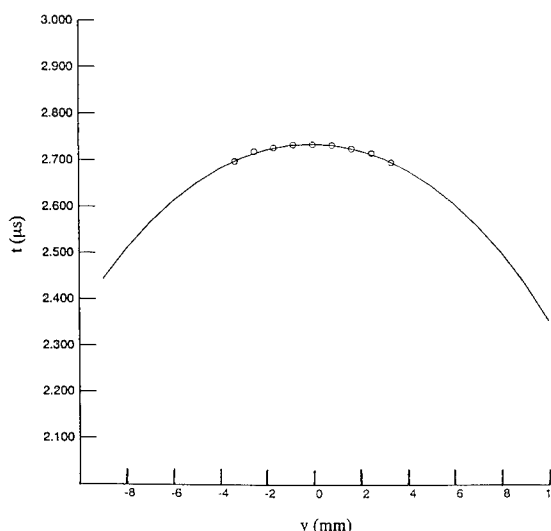


**FIGURE 8. DATA AND CURVE FIT TO THE CENTER SLIT MACH STEM REGION OF THE RECORD SHOWN IN FIGURE 6. THE RADIUS VALUE OBTAINED IS 16.4 mm.**

In the reflectance-change flash gap (RCFG) test, a 2-mm-thick aluminum plate is placed on top of a right-circular cylinder of explosive, along with a piece of Lucite® in which a gap is machined and polished.\* The plate surface is illuminated with an argon lamp, and the slit of a smear camera is aligned parallel with the line defined by the detonators and the gap. When a shock wave arrives at the metal-air interface, the diffuse reflectivity of

\* Lucite is a registered trademark for acrylic resins, E. I. du Pont de Nemours & Co.

the surface is reduced. This is recorded by the smear camera as reduced exposure on the film. The metal plate arrives at the Lucite surface and causes the trapped air to flash, and the subsequent shock induced in Lucite causes the Lucite to become opaque. This is recorded on the smear camera as a thin line of bright light. From the known gap depth and time difference, we calculate the average free-surface velocity of the aluminum plate.

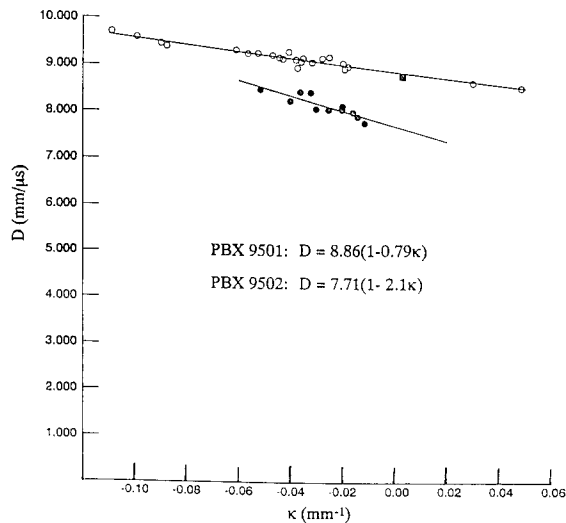


FIGURE 9. THE DETONATION VELOCITY-CURVATURE RELATIONSHIP FOR PBX 9501 (THE OPEN CIRCLES) AND PBX 9502 (THE SOLID CIRCLES). THE BLACK SQUARE IS A PBX-9404 POINT TAKEN FROM REFERENCE 14.

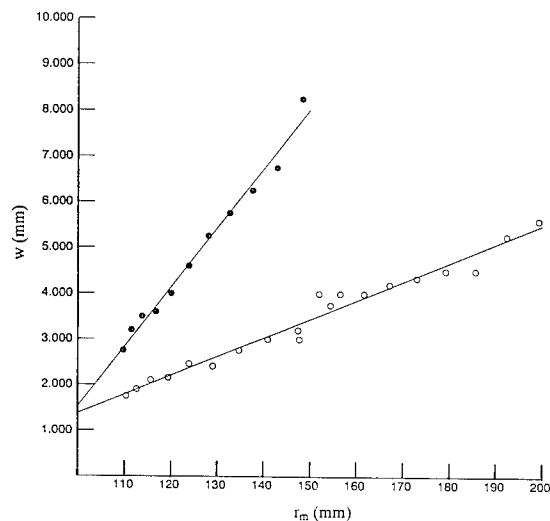


FIGURE 10. THE MACH STEM WIDTH AS A FUNCTION OF DISTANCE. THE SLOPE OF THE LINE GIVES THE GROWTH ANGLE OF THE STEM.

Figure 11 reproduces records obtained in reflectance-change flash gap experiments. The absence of a cusp in the reflectance-change trace in Figure 11a indicates irregular or Mach reflection. The presence of a cusp in Figure 11b indicates regular reflection. Dips toward earlier time at the center line of the flash trace imply that greater velocity is induced in the plate by higher pressure in the interaction region. We assumed that the particle velocity of the aluminum is one-half the measured free-surface velocity and that the free-surface velocity vector bisects the original surface normal and the shock front normal. To find the detonation wave pressure, the pressure and particle velocity of the explosive products and aluminum are shock matched (assuming the products follow the JWL equation of state). A curve-fitting procedure similar to the multistreak technique outlined above is used to find the interaction angle  $\alpha$ .

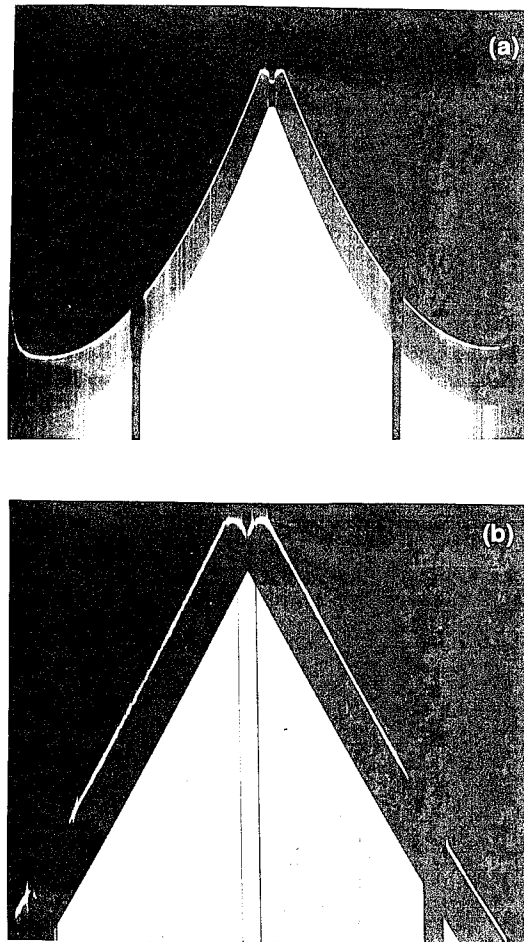


FIGURE 11. RECORD OBTAINED FROM REFLECTANCE-CHANGE FLASH-GAP EXPERIMENTS IN PBX 9501. (A) IRREGULAR OR MACH REFLECTION. (B) REGULAR REFLECTION. TIME INCREASES UPWARD.

## ANALYSIS

The data are best discussed in the context of an analysis. The most basic analysis is to approximate the flow as the intersection of two plane waves that are tangents to the spheres. Flow is separated into regions by the detonation and shock waves, the flow in each region is assumed to be one-dimensional, and all waves are assumed to follow the appropriate jump conditions. This is the classical shock polar theory of gas dynamics, a tool found useful over the decades and still in use today.<sup>11-13</sup> The quasi-steady assumption now encompasses the effects of interaction angle variation with time.

Figure 12 represents the geometry of the classical Mach reflection analysis. The plane of symmetry of the colliding spherical waves is represented as a perfectly rigid wall. Figure 12 shows the Mach stem as a straight line. However, other assumptions can be made about the shape of the Mach stem and the resulting trajectory of the triple point. The triple point follows a path that makes an angle  $\chi$  with the wall. In a stem that grows, the velocity of the point P is given by

$$\vec{V}_P = -D_j \csc(\alpha - \chi) \cos \chi \vec{i} + D_j \csc(\alpha - \chi) \sin \chi \vec{j}. \quad (6)$$

In general,  $\chi$  is variable and the path can have curvature. Additionally, for interacting spheres,  $\alpha$  is variable.

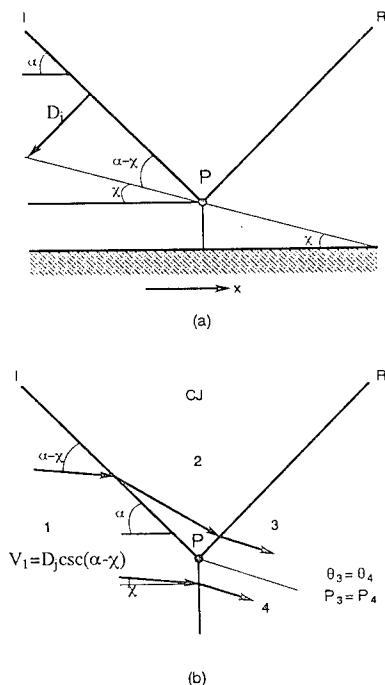


FIGURE 12. MACH REFLECTION OF A PLANE WAVE FROM A RIGID WALL. (A) LABORATORY COORDINATES. (B) COORDINATES ATTACHED TO P.

The system of equations is closed by requiring the flow velocity in regions 3 and 4 to be parallel and the pressures in regions 3 and 4 to be equal. Regions 3 and 4 are separated by a contact discontinuity (slip stream); the velocities differ, but the pressures are equal.

Our experimental observation is that the Mach stems are curved, they grow, and they are normal to the plane of symmetry. Thus the flow is at least two-dimensional in the region behind the stem and the "triple point" may degenerate into a region of interaction between the incident detonation and the reflected disturbance. In general, the rate of growth of the Mach stem will not be constant. On the other hand, our data (Figure 10) show that the growth rate is fairly constant over the interval observed. Because the observed stems are curved, we also expect that the straight-stem assumption will overpredict the growth rate. Therefore, we compare our pressure data to the results of the shock polar analysis using both the straight-stem assumption and the constant growth rate (measured) assumption. From Figure 12, if the growth rate and interaction angle are both specified, the pressure behind the stem is easily calculated from the jump conditions.

The explosive is assumed to follow the JWL equation of state. Figure 13 shows the pressure produced by the wave interaction for both regular and Mach reflection as a function of interaction angle. For low values of  $\alpha$ , regular reflection occurs. As the critical angle  $\alpha_c$  is approached, the pressure increases. When Mach reflection first appears, the pressure jumps discontinuously to very high values. As  $\alpha$  becomes larger in the Mach reflection regime, the pressure decreases and eventually approaches the CJ value. Mach stems near the critical angle would be the size of the reaction zone or smaller. Thus the classical theory, which assumes a jump from the initial state to the fully detonated state, may not apply.

For regular reflection ( $\chi = 0$ ,  $\theta_3 = 0$ ), the pressure calculated from the theory and the data from the RCFG experiments agree reasonably well. For Mach reflection, pressure calculated from the theory using the straight-stem assumption is significantly greater than the data from the RCFG experiments. Use of the measured value of  $\chi$ , which forces the measured Mach stem velocity, brings the calculation into agreement with the pressure measured in the RCFG experiments. The values of  $\chi$  calculated from the straight-stem assumption are considerably larger than the measured values. This results in overprediction of the phase velocity along the plane of symmetry, and so also overpredicts the pressure behind the stem.

## CONCLUSION

The data show that, over the measured interval, the detonation velocity is a continuous function of curvature for convergent flow, in spite of the presence of subsonic flow behind the Mach stem. The  $D(\kappa)$  relationships provided by this study combined with that of Reference 9 allow the calculation of convergent and divergent detonation wave propagation in PBX 9501 and PBX 9502

using DSD wave trackers. Comparisons of such calculations with experiments are required to determine the extent of applicability of DSD to convergent detonation waves.

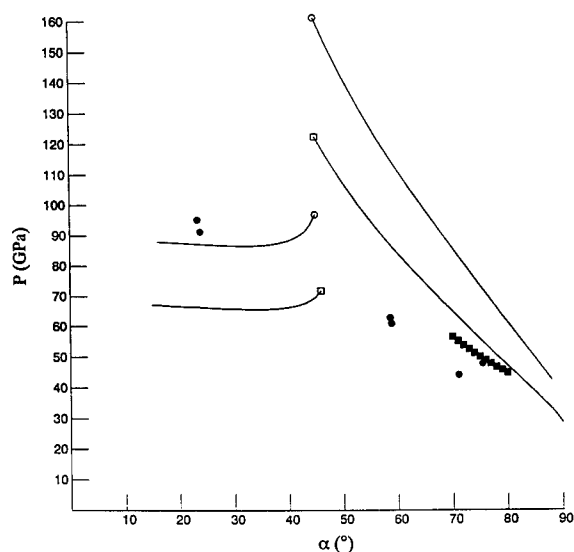


FIGURE 13. PRESSURE BEHIND THE REFLECTED WAVE AS A FUNCTION OF INTERACTION ANGLE. THE OPEN CIRCLES INDICATE PBX 9501 AND THE OPEN SQUARES INDICATE PBX 9502. THE BLACK SQUARES INDICATE THE PRESSURE CALCULATED WITH THE MEASURED GROWTH ANGLE AND THE BLACK DOTS INDICATE THE PRESSURE MEASURED WITH THE RCFG TECHNIQUE, BOTH FOR PBX 9501.

The classical shock polar theory fails to accurately replicate the parameters of the flow when the straight Mach stem assumption was used, but use of the measured stem growth rate brings the theory into agreement with the experiment. Therefore, the analytic treatment requires proper handling of the curved-stem growth rate dynamics. Equation (1) used with Whitham's method suggests a nonlinear diffusive Mach stem growth process.<sup>7</sup> For application to spherical wave interactions, the process must be convoluted with the time-dependent boundary condition introduced by the spherically expanding wave. This modeling approach seems valid and is a current topic of our research.

Both the classical shock polar theory and the use of DSD wave trackers are expected to be applicable when the features such as the Mach stem width and the inverse of the surface curvature are relatively large, compared with the reaction zone thickness. The study of the flow

where the features of interest are smaller than the reaction zone thickness remains unprobed by this study. Recent computer simulations<sup>15</sup> by Stewart suggest that reflection configurations familiar from gas dynamics may occur entirely within the reaction zone or span across the reaction zone.

## REFERENCES

1. Gardner, S. D., and Wackerle, J., "Interactions of Detonation Waves in Condensed Explosives," *Proceedings of the Fourth Symposium (International) on Detonation*, October 1965, pp. 154-155.
2. Lambourn, B. D., and Wright, P. W., "Mach Interaction of Two Plane Detonation Waves," *Proceedings of the Fourth Symposium (International) on Detonation*, October 1965, pp. 142-152.
3. J. P. Argous, C. Peyre, and J. Thouvenin, "Observation and Study of the Conditions for Formation of Mach Detonation Waves," *Proceedings of the Fourth Symposium (International) on Detonation*, October 1965, pp. 135-141.
4. Mader, C. L., "Detonation Wave Interactions," *Proceedings of the Seventh Symposium (International) on Detonation*, June 1981, pp. 669-677.
5. Stewart, D. S., and Bdzil, J. B., "The Shock Dynamics of Stable Multidimensional Detonation," in *Combustion and Flame*, **72**, 311-323 (1988).
6. Bdzil, J. B., Fickett, W., and Stewart, D. S., "Detonation Shock Dynamics: A New Approach to Modeling Multi-dimensional Detonation Waves," *Proceedings of the Ninth Symposium (International) on Detonation*, August 1989, pp. 730-742.
7. Lambourn, B. D. and Swift, D. C. "Application of Whitham's Shock Dynamics Theory to the Propagation of Divergent Detonation Waves," *Proceedings of the Ninth Symposium (International) on Detonation*, August 1989, pp. 784-797.
8. Whitham, G. B., *Linear and Nonlinear Waves*, John Wiley & Sons, New York, 1974.
9. Bdzil, J. B. "DSD Calibration for PBX 9502", *Proceedings of the Tenth Symposium (International) on Detonation*, July 1993.
10. Fickett, W. and Bdzil, J., "DSD Technology - A Detonation Reactive Huygens Code" Los Alamos National Laboratory report LA-12235-MS, (1992).
11. Courant, R. and Friedrichs, K. O., *Supersonic Flow and Shock Waves*, Interscience, New York, 1948.
12. Hornug, H., "Regular and Mach Reflection of Shock Waves," *Ann. Rev. Fluid Mech.* Vol. 18, No. 33, (1986) pp. 58.

13. Ben-Dor, G. and Takayama, K., "The Phenomena of Shock Wave Reflection — A Review of Unsolved Problems and Future Research Needs," *Shock Waves* Vol. 2, 1992, pp. 211-223.
14. Campbell, A. W. and Engelke, Ray, "The Diameter Effect in High-Density Heterogeneous Explosives," *Proceedings of the Sixth Symposium (International) on Detonation*, August 1976, pp. 642-652.
15. Stewart, D. S. "CMHOG Calculations of a Reactive Wave Interaction" personal communication, 1993.

## DISCUSSION

B. D. LAMBOURN  
AWE, Aldermaston, England

In view of the fact that for an overdriven wave, the wave is subsonic with respect to the flow behind, is the D- $\kappa$  relation for convergent wave unique?

### REPLY BY L. M. HULL

At this point in time, we have only indirect evidence that the D- $\kappa$  relationship is unique. First, the relationship derived for PBX9502 by John Bdzil was measured in rate stick geometry. Rate stick geometry has a sonic locus whereas a Mach stem flow does not, but the curves derived in the two studies match in both slope and magnitude.

Secondly, the colliding spherical wave experiments on PBX9501 used to derive the D- $\kappa$  relationship were done with two different lengths of cylinders, yet the experiments define a single straight line that again fits data points in the positive curvature region that were

found via a completely different technique. These facts suggest that the D- $\kappa$  relationship is unique, but this could be coincidence of the geometry selected. Another observation is that for inert flow, Whitham's theory does an adequate job of predicting Mach stem development, yet suffers from the same theoretical difficulty. In the case of detonation, the premise is that when disturbances reach the Mach stem through the following flow, the shape adjusts to any induced velocity variations. We plan to test this premise experimentally.

## DISCUSSION

BRUCE BUKIET  
New Jersey Institute of Technology,  
Newark, New Jersey

Your method of calculating curvature assumes that the shape of fronts when two expanding spherical detonations intersect is smooth. Is there really a cusp

there

or is it smooth?



### REPLY BY L. M. HULL

Figure 11(b) shows a regular reflection recorded in an aluminum cover plate. Similar sharpness is recorded in self-light experiments for regular reflection of both PBX9501 and PBX9502. These data were not included because of space limitations. Thus, to within the resolution of the experimental technique applied, a cusp occurs with regular reflection and a smooth surface with Mach reflection.

## UNDERSTANDING CURVED DETONATION WAVES

Bruce G. Bukiet  
Department of Mathematics  
Center for Applied Mathematics and Statistics  
New Jersey Institute of Technology  
Newark, NJ 07102

and

Klaus S. Lackner and Ralph Menikoff  
Los Alamos National Laboratory  
Los Alamos, NM 87545

The reaction zone of a detonation wave is very small compared to the hydrodynamic length scale for a typical application. Consequently, it is impractical for numerical calculations to resolve the reaction zone. Yet accounting for the width of the reaction zone is critical because it affects the wave speed of a curved detonation. The curvature effect results from the interaction between the rate of energy release and geometric source terms within the reaction zone. When the reaction zone width is determined by the computational cell size rather than the physical scale, the numerics introduces an artificial curvature effect which frequently dominates the physical effect and leads to mesh dependence of simulations. Modified Hugoniot jump conditions are derived which characterize the curvature effect. They express the conservation laws and are not sensitive to the detailed reaction dynamics but instead depend only on the reaction zone width, and averages of pressure and of mass, momentum and energy densities.

### INTRODUCTION

The reaction zone of a detonation wave is very small compared to the hydrodynamic length scale for a typical application. Consequently, it is impractical for numerical calculations to resolve the reaction zone. In contrast to a shock wave, small changes in the dynamics of the reaction zone affect the detonation shock Hugoniot while the large energy release has a significant effect on the subsequent flow. Here, we focus on understanding the detonation jump conditions as a necessary step to incorporating the correct detonation dynamics into hydrodynamic calculations in which one cannot afford to resolve the reaction zone.

Detonation waves may be modeled using the reactive Euler equations. In planar geometry with one irreversible exothermic reaction, this leads for a large class of reaction rates to the Zel'dovich-von Neumann-Doering (ZND) model<sup>1</sup> in which a detonation wave consists of a zero-width shock wave

followed by an extended reaction zone. The ZND model predicts that the state behind a steady detonation wave is determined by the strong branch of the detonation shock Hugoniot equations independent of the reaction rate or the reaction zone width. Moreover, there is a unique Chapman-Jouguet (CJ) wave with the minimum detonation velocity and a sonic state behind the detonation front. The CJ wave corresponds to an underdriven detonation. In addition, the reactive flow equations determine the reaction zone dynamics and with sufficient resolution, any non-steady planar flows with detonation waves can be accurately computed.

More complicated detonation dynamics than predicted by the ZND model arise when other length scales are present. For example, when the shock width is comparable to the reaction zone length, the state behind the detonation front can lie on the weak branch of the detonation shock Hugoniot. The shock width may have a physical origin or may be a numerical artifact due to artificial viscosity<sup>2</sup> or other dis-



sipative mechanisms introduced by shock capturing algorithms.

In more than one spatial dimension, detonation waves are subject to an instability involving transverse waves within the reaction zone. This phenomenon has been observed experimentally (see e.g., Ref. 1, chpt. 7), a linear analysis of the reactive Euler equations shows this instability<sup>3-5</sup>, and it also has been studied in numerical calculations with a well resolved reaction zone.<sup>6, 7</sup> Both the experiments and the simulations show that the amplitude of the instability saturates. On a scale large compared to both the width of the reaction zone and the wavelength of the instability, the detonation front is well defined. Moreover, heterogeneous explosives have an additional length scale set by the grain size. In effect, a reaction rate used in a numerical model can only account for the instabilities and the inhomogeneities in an average sense and thus is phenomenological. By neglecting the instability, the simplified model of the detonation wave dynamics allows one to identify the relevant parameters describing the propagation of the detonation waves. However, the effective rate law cannot be simply related to the kinetics of the underlying chemical reaction and must be deduced from wave propagation data. Quantities which are sensitive to the details of the phenomenological model, such as the failure diameter, are not captured by the simplified flow equations.

For many applications, burn models are used to avoid the computational expense of resolving the small spatial and temporal scales within the reaction zone. Similar to a shock capturing algorithm, a burn model gives a detonation wave an artificial width which for a good model is a few cells. With crude resolution, even well designed and physically motivated rate equations will at best deteriorate to such capturing algorithms. Furthermore, in multi-dimensional simulations great care must be taken to avoid having the effective reaction rate introduce an artificial transverse instability on the scale of the mesh. Typically, this smoothing is achieved with sufficient numerical dissipation.

Programmed burn is a particularly simple model in which a detonation wave is propagated in multiple spatial dimensions using a Huygens wave construction with the planar CJ detonation velocity. Rather than explicitly tracking the wave, behind the wave front the equation of state is switched from the reactant to the reaction products. The concurrent energy release increases the pressure and drives the wave. One numerical difficulty with this model is that the reaction front and the hydrodynamic front may separate because they are not calculated self-consistently. Such a model clearly is not adequate for overdriven detonation waves and as we will discuss does not correctly describe multi-dimensional effects.

A rate stick experiment provides a good example of an important multi-dimensional effect on propagating detonation waves that is not accounted for in the ZND model or programmed burn. In a rate stick, the steady state consists of a curved detonation wave propagating at a velocity lower than the minimum planar CJ detonation velocity. The change in the detonation velocity is caused by the interaction within the reaction zone between the geometric source term due to the curvature of the detonation front and the source term for energy release from the chemical reaction. An analysis of a curved detonation wave shows that the detonation velocity of an underdriven diverging wave is a function of the mean front curvature.<sup>8, 9</sup> To first order the effect is proportional to the product of the reaction zone width and the front curvature. The fact that a detonation wave fails to propagate when this ratio is still small emphasizes the importance of the curvature effect. In addition to the curvature effect, the failure radius also depends on 2-D instabilities and inhomogeneities in the explosive.

For numerical calculations, burn models are important for both initiation and propagation of detonation waves. Here we focus entirely on wave propagation. In this case, the burn model plays a role similar to artificial viscosity for non-reactive shock waves. It gives the detonation wave an artificial thickness determined by the cell size rather than the physical length scale of the reaction zone. Because of the artificial reaction zone width, one expects curvature effects in numerical simulations. However, the artificial curvature effect may have the wrong functional form and thus may be quantitatively inaccurate. Since the numerical width of the detonation front is proportional to the cell size, the artificial curvature effect is one cause of mesh size and mesh orientation dependence of numerical computations.

An example of this common numerical effect is seen in the calculation of a rate stick experiment in Ref. 10 using a burn model similar to Forest Fire.<sup>11</sup> The steady state detonation velocity as a function of tube radius approaches the experimental value as finer meshes are used; Ref. 10, Fig. 7. As expected from theory, the detonation velocity increases as the reaction zone width decreases with a smaller cell size. A very fine mesh, in this case 0.075 mm, is needed to obtain good agreement with the experiments. Furthermore, sufficient resolution was not available to verify convergence with mesh resolution. At the expense of very high resolution, the model will resolve the reaction zone and then the computation should converge to the curvature effect which corresponds to the reaction rate used in the simulation.

An improved version of programmed burn which accounts for the curvature effect of an underdriven diverging detonation wave is known as detonation shock dynamics (DSD).<sup>12-14</sup> It can be thought of as using a Huygens like construction in which the

local wave speed is a function of front curvature. In addition, the state behind the detonation wave is a function of curvature and for a given rate law would be determined by integrating the quasi-steady ODEs for the detonation wave profile. The principal simplification of the DSD algorithm is that it decouples the propagation of the wave front from the flow behind it.

The decoupling is a property only of an underdriven detonation wave and is a consequence of a sonic point within the reaction zone. As a result of the sonic point (which does not occur for a shock wave or an overdriven detonation wave) the flow behind an underdriven detonation wave is supersonic relative to the front and consequently acoustic waves cannot overtake such a wave from behind and affect its motion. Thus, the DSD algorithm is limited to computing underdriven diverging detonation waves. In addition, care must be taken in the DSD algorithm to set the state behind the front in a consistent manner such that the hydrodynamic front and reactive front of the detonation wave propagate in lock-step. This may entail small violations of the conservation equations. The DSD algorithm is not appropriate for either overdriven or converging detonation waves since their dynamics is affected by both front curvature and the flow behind the front.

The front tracking algorithm<sup>15</sup> is a method which is capable of accounting for the dynamics of both an underdriven and a strong detonation wave without resolving the reaction zone. The analytic behavior of a propagating detonation wave is characterized by the curvature dependent detonation wave curve.<sup>16</sup> For a given rate law, the wave curve can be obtained by integrating the quasi-steady ODEs for the detonation wave profile. In contrast to the planar case, for a curved detonation front the wave curve depends on the reaction zone dynamics. Consequently, there are corrections to the Hugoniot jump relations proportional to the front curvature. The curvature corrections on the Hugoniot jump conditions imply that the flux in and out of a sharp front would not be equal. A resolved reaction zone can accommodate this flux difference either by accumulating the conserved quantities within its volume or by equalizing the integrated fluxes by a corresponding difference in the front and back surface area. Because the curvature changes slowly, the effect on overall conservation is small and less important than getting the front dynamics correct.

In this paper we determine the modified jump relations under the assumption that the reaction zone is quasi-steady. The correction terms are proportional to the product of the front curvature and terms involving a few volume averaged quantities within the reaction zone. Using these quantities as empirical parameters, the curvature dependence of

the wave curve may be determined by solving algebraic equations rather than solving ODEs for the wave profile. Using the relevant integral quantities captures the dominant physical effects while avoiding the uncertainties inherent in a detailed reaction rate model.

## PLANAR DETONATIONS

Planar detonation waves may be modeled using the reactive Euler equations which represent the conservation of mass, momentum and energy. A fourth equation describes the progress of the chemical reaction taking place in the reaction zone. In conservation form the equations are

$$\rho_t + (\rho u)_x = 0, \quad (1)$$

$$(\rho u)_t + (\rho u^2 + P)_x = 0, \quad (2)$$

$$(\rho \mathcal{E})_t + (\rho u [\mathcal{E} + PV])_x = 0, \quad (3)$$

$$(\rho \lambda)_t + (\rho u \lambda)_x = \rho \mathcal{R}, \quad (4)$$

where  $\rho$ ,  $u$ ,  $E$  and  $P(V, E, \lambda)$  are the fluid density, particle velocity, specific internal energy (thermal + chemical) and pressure,  $V = 1/\rho$  is the specific volume,  $\mathcal{E} = \frac{1}{2}u^2 + E$  is the specific total energy,  $\lambda$  is the mass fraction of the reaction products and  $\mathcal{R}(V, E, \lambda)$  is the specific reaction rate.

The state behind a steady-state planar detonation wave is determined by the Hugoniot jump relations

$$J[\rho(u - D)] = 0, \quad (5)$$

$$J[\rho(u - D)^2 + P] = 0, \quad (6)$$

$$J[\rho(u - D) (\frac{1}{2}(u - D)^2 + E + PV)] = 0, \quad (7)$$

where  $J[f] = f_0 - f_1$  is the jump across the detonation wave from the ahead state ( $\lambda = 0$ ) to the behind state ( $\lambda = 1$ ), denoted by the subscripts '0' and '1' respectively. It follows that the detonation velocity  $D$  is given by

$$(\rho_0 D)^2 = (P_1 - P_0)/(V_0 - V_1) \quad (8)$$

when  $u_0 = 0$ .

For a given ahead state, these algebraic equations have a one parameter family of solutions. The CJ state corresponds to the minimum detonation velocity. The solutions with  $P > P_{CJ}$  are called strong detonations and those with  $P < P_{CJ}$  weak detonations. In the ZND model, the strong branch corresponds to overdriven detonation waves and the weak branch represents unphysical solutions.

The wave curve formed by the union of strong detonations plus the composite waves consisting of a CJ detonation followed by a rarefaction or Taylor wave can be used to define the dynamics to propagate a detonation wave with the front tracking method.<sup>17</sup> This method is a self-consistent extension of programmed burn that is applicable to both underdriven and overdriven detonation waves. However, it corresponds to the limit of an infinite reaction rate or zero-width reaction zone. In this limit the curvature effect is absent.

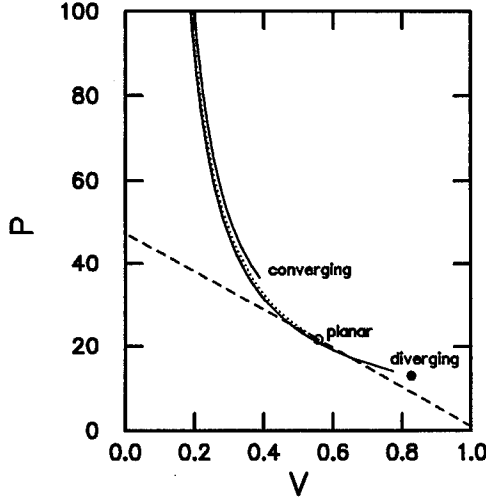


FIGURE 1. The locus in the  $P$ - $V$  plane of detonation wave final states. Converging and diverging geometry are represented by the solid lines for  $\kappa=0.02$ . The dotted line is the planar case. The Rayleigh line through the planar CJ state is shown as a dashed line. The planar CJ state is shown with an open circle and the underdriven diverging wave with a solid circle. The initial state is  $P=1$  and  $V=1$ .

### CURVED DETONATION WAVE CURVE

In contrast to a planar detonation wave, a non-zero reaction zone width has an important effect on the dynamics of a curved detonation wave. In order to model the reaction zone we introduce the natural coordinate frame formed by the detonation front and the stream lines. Within a local stream tube, the reactive Euler equations reduce to the reactive duct equations

$$(\rho A)_t + (\rho A u)_x = 0, \quad (9)$$

$$(\rho A u)_t + (\rho A [u^2 + PV])_x = P A_x, \quad (10)$$

$$(\rho A \mathcal{E})_t + (\rho A u [\mathcal{E} + PV])_x = 0, \quad (11)$$

$$(\rho A \lambda)_t + (\rho A u \lambda)_x = \rho A \mathcal{R}. \quad (12)$$

The cross sectional area of the stream tube is  $A$ , the coordinate in the stream direction is  $x$  and the stream velocity is  $u$ . We note that the duct equations depend only on the geometric quantity  $\kappa = (dA/dx)/A$ . In the limit that the diameter of the stream tube shrinks to zero,  $\kappa$  is a measure of the divergence of the stream lines and is frame dependent. In the frame in which the flow ahead of the detonation wave is at rest,  $\kappa$  is the mean front curvature.

When the spatial and temporal scales of the reaction zone are smaller than those of the hydrodynamic flow in the reaction products, a detonation wave can be approximated as quasi-steady with the reaction zone equilibrating adiabatically to changes in the flow behind the wave. The quasi-steady

approximation reduces the system of PDEs Eqs. (9–12) to a system of ODEs which represent the generalization of the planar equations for the reaction zone profile that includes the curvature effect to leading order in the product of the reaction zone width and the curvature of the front.

For a given  $\kappa$ , these ODEs can be used to determine the quasi-steady detonation waves. To illustrate the curvature effect, Fig. 1 shows the locus of final states in the  $P$ - $V$  plane of quasi-steady detonation waves for the simple example calculated in Ref. 16. The planar case corresponds to the standard detonation shock Hugoniot which is determined entirely from the equation of state by the usual jump conditions Eqs. (5–7). The converging and diverging cases are for  $\kappa = 0.02$ . As a consequence of the non-zero reaction zone width, neither a converging nor diverging detonation wave satisfy the standard jump conditions. Moreover, there is a qualitative difference between the detonation locus for the converging and diverging case. The diverging detonation locus has an isolated point which corresponds to an underdriven detonation wave. This is a consequence of the structure of the ODEs because only the diverging case has a critical point within the physical region,  $0 < \lambda < 1$ . Converging geometry forces a detonation into the overdriven regime.

The underdriven diverging detonation wave is determined by solving an eigenvalue like problem for the separatrix, the trajectory through the critical point, by using a shooting algorithm.<sup>18</sup> This leads to a sonic point within the reaction zone. As a consequence, an underdriven detonation wave decouples from the flow behind. This is the basis for detonation shock dynamics.<sup>8</sup> It uses the relation between the detonation velocity and the front curvature,  $D(\kappa)$ , to propagate an underdriven detonation wave. For the same example as in Fig. 1, the minimum detonation velocity as a function of curvature is shown in Fig. 2. Increasing curvature decreases the detonation velocity in diverging geometry while increasing it in converging geometry. Though the minimum detonation velocity joins up continuously between the diverging and converging case, using detonation shock dynamics in converging geometry would cause numerical problems since acoustic waves from behind the detonation would cause the reactive front and the hydrodynamic front to separate in a similar manner to that which occurs with programmed burn.

From the results in Figs. 1 and 2 which have been derived from the reactive Euler equations, it is clear that the Hugoniot jump conditions, Eqs. (5–7), are not satisfied for a curved detonation wave with non-zero width. In particular, the state behind the underdriven detonation wave lies above the Rayleigh line in the  $P$ - $V$  diagram of Fig. 1. Based on this, Eq. (8) would imply that the detonation velocity is higher than the planar CJ velocity. Nevertheless, Fig. 2 shows that it is lower.

The dynamics of the detonation front is affected by the interaction of the geometric source term

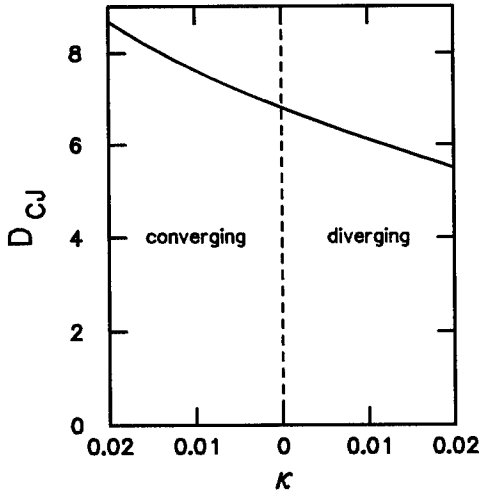


FIGURE 2. The underdriven detonation wave speed versus curvature. Both the converging and diverging cases are shown.

with the rate of chemical energy release. This can be seen by comparing in the  $P$ - $V$  plane the locus of the sonic points of underdriven diverging waves of varying curvature with the locus of planar CJ states corresponding to a partially burned Hugoniot parametrized by  $\lambda$ . From Fig. 3 it is clear that the family of partially burned planar CJ states is a poor approximation for the sonic states in an underdriven diverging detonation wave even though they too can be characterized by their value of  $\lambda$ . Unlike the planar detonation Hugoniot which is determined from the equation of state alone, the curved detonation Hugoniot depends on some aspects of the reaction dynamics and can not be derived solely from the equation of state. This shows that the introduction of a new length scale, even if small compared to the mesh size, can significantly modify the large scale flow.

In a tracking algorithm the question arises whether the end state of an underdriven detonation should be the sonic point or the fully burned state. Figure 3 shows that the loci of sonic points and end states for the underdriven diverging detonation almost overlap. However, the end states are displaced to lower pressures as can be seen from the difference in the end points of the two lines. The end points correspond to the same front curvature.

### MODIFIED JUMP CONDITIONS

The curved detonation shock Hugoniot must be insensitive to the uncertainties in the reaction rate if it is to be useful for propagating detonation waves. Here we use the conservation laws to derive jump conditions that account for the width of the detonation wave and use only integral quantities within the reaction zone. By determining these integral quantities empirically from wave propagation experiments

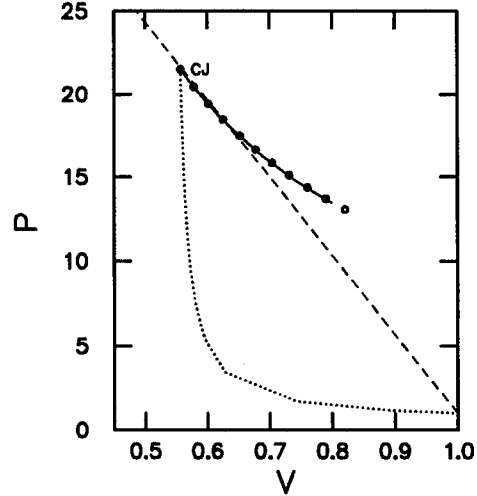


FIGURE 3. Comparison of the loci of underdriven diverging detonation waves and partially burnt planar detonation waves. Diverging waves are parametrized by front curvature and planar waves by burn fraction. Dotted line is locus of partially burnt sonic points. Dashed line is Rayleigh line through planar CJ state. Solid line is locus of sonic points of diverging detonations. The circles define the locus of states at the end of the reaction zone.

we expect to capture the important wave properties in a manner that is insensitive to the detailed reaction dynamics.

Suppose the detonation wave speed is slowly varying in time and that the reaction zone is quasi-steady. This motivates the assumption that to leading order  $\partial_t D$  can be neglected, and the state variables depend on  $x - Dt$ . Under these assumptions, integrating Eqs. (9-11) through the reaction zone from  $x_1$  (the end of the reaction) to  $x_0$  (the unburned state) leads to the equations for mass, momentum and energy fluxes through the reaction zone<sup>16</sup>

$$J[A\rho(u-D)] + \kappa w \langle \rho \rangle D A_0 = 0, \quad (13)$$

$$J[A\rho u(u-D) + AP] + \kappa w (\langle \rho u \rangle D - \langle P \rangle) A_0 = 0, \quad (14)$$

$$J[A\rho(u-D)\mathcal{E} + AuP] + \kappa w \langle \rho \mathcal{E} \rangle D A_0 = 0, \quad (15)$$

where  $w = x_0 - x_1$  is the reaction zone length, and the average quantities within the reaction zone are defined by

$$\begin{aligned} \langle \rho \rangle w A_0 &= \int_{x_1}^{x_0} A dx \rho, \\ \langle \rho u \rangle w A_0 &= \int_{x_1}^{x_0} A dx \rho u, \\ \langle \rho \mathcal{E} \rangle w A_0 &= \int_{x_1}^{x_0} A dx \rho \mathcal{E}, \\ \langle P \rangle w A_0 &= \int_{x_1}^{x_0} A dx P. \end{aligned}$$

In deriving these equations we have used the approximation

$$(dA/dx)/A = \kappa \approx \text{constant}.$$

Previously, we had approximated these integrals by the average of the end points<sup>16</sup> which is equivalent to the trapezoidal rule. For example, the mass in the reaction zone is given by

$$\int_{x_1}^{x_0} dx \rho A = \frac{1}{2}(\rho_0 A_0 + \rho_1 A_1) w [1 + O(w^2)].$$

However, the coefficient of the error is proportional to  $d^2\rho/dx^2$ . Since the end points  $\rho(x_0)$  and  $\rho(x_1)$  are almost constant, the shape of the profile causes  $d^2\rho/dx^2$  to increase as  $w$  gets small. Thus, the approximation does not give the leading order correction to the jump conditions.

Suppose the average densities are known. Then we can express the fluxes through the reaction zone by the following modified jump equations

$$J[\rho(u - D)] = -\kappa w [\rho_1(u_1 - D) + \langle \rho \rangle D], \quad (16)$$

$$J[\rho u(u - D) + P] = -\kappa w [\rho_1 u_1(u_1 - D) + P_1 + \langle \rho u \rangle D - \langle P \rangle], \quad (17)$$

$$J[\rho \mathcal{E}(u - D) + uP] = -\kappa w [\rho_1 \mathcal{E}_1(u_1 - D) + u_1 P_1 + \langle \rho \mathcal{E} \rangle D], \quad (18)$$

where we have used the approximation

$$A_0 - A_1 \approx w dA/dx = \kappa w A_0.$$

The right hand side of the flux equations is proportional to the dimensionless quantity  $\kappa w$  which is positive for a diverging wave and negative for a converging wave. For  $\kappa w = 0$ , they reduce to the planar jump conditions, Eqs. (5-7). The modified jump equations use the same approximation and are valid to the same order as the quasi-steady ODEs for the reaction zone profile discussed in the previous section. Equations (16-18) represent the leading order correction to the Hugoniot jump relations that accounts for the interaction between the geometric source terms from the front curvature and the rate at which chemical energy is released. For a fixed front curvature  $\kappa$ , as the reaction rate increases the reaction zone length decreases. Consequently, the correction terms to the jump relations decrease and hence the curvature effect diminishes. In a numerical simulation with a capturing algorithm, decreasing the cell size has the same effect.

The correction terms have a physical interpretation. The first term on the right hand side of Eqs. (16-18) corrects the outgoing integrated flux for the change in cross sectional area of the stream tube through the reaction zone. The term proportional to  $\langle P \rangle$  in Eq. (17) represents a transverse momentum transfer within the reaction zone. The terms proportional to the product of the detonation velocity

and the average densities represent the increase in the total of the conserved quantities within the reaction zone as the radius of curvature of the front and hence the volume of the reaction zone increases. Though the sum of these corrections is frame independent, their relative magnitudes are not. For a rate stick, it is natural to use the frame in which the reaction zone is stationary. In this case, the wave speed vanishes and the conserved quantities within the reaction zone are time independent. For an expanding detonation wave the natural frame is the lab frame in which the origin is at rest. In this frame the increase of the reaction zone volume is a significant term. We note that only in the lab frame, which we have tacitly been assuming in deriving Eqs. (16-18), is  $(dA/dx)/A$  equal to the front curvature. In general  $A(x)$  depends on the frame and as a consequence the average quantities are frame dependent. The frame invariance will be analyzed in detail elsewhere.

The modified jump relations depend on five parameters; the reaction zone width and the volume averages over the reaction zone of the pressure and of the mass, momentum and energy densities. Once these parameters have been determined experimentally as a function of wave strength, the curvature effect can be determined by solving algebraic equations. Rather than requiring a detailed understanding of the reaction zone dynamics this procedure makes use of a small number of integral quantities. It therefore provides the framework for a simple phenomenological description of wave propagation of curved detonations.

We have checked the plausibility of this idea with the simple model explosive used in the previous section as follows:

1. The reaction zone length and the average densities are calculated for a planar detonation;
2. For a given  $\kappa$  the quasi-steady ODEs are solved to determine the end state of the detonation shock Hugoniot;
3. The modified jump conditions are tested using the end states from (2) and the integral quantities from (1) with the corresponding detonation velocity.

The results of this test are shown in Fig. 4 and 5 for the diverging and converging cases respectively. As a dimensionless measure of the error we use the  $[(\text{left hand side}) - (\text{right hand side})]/\text{Eqs. (16-18)}$  divided by the flux into the detonation front. From the figures we see that the error is  $\mathcal{O}((\kappa w)^2)$  until it is dominated by numerical roundoff errors. Because the quasi-steady approximation is only valid to first order in  $\kappa w$ , it is consistent with the accuracy of the approximation to use the volume averages obtained from the planar wave for small values of  $\kappa$ . In effect this shows that the curved detonation wave can be determined as a perturbation of the planar detonation wave with the same detonation speed.

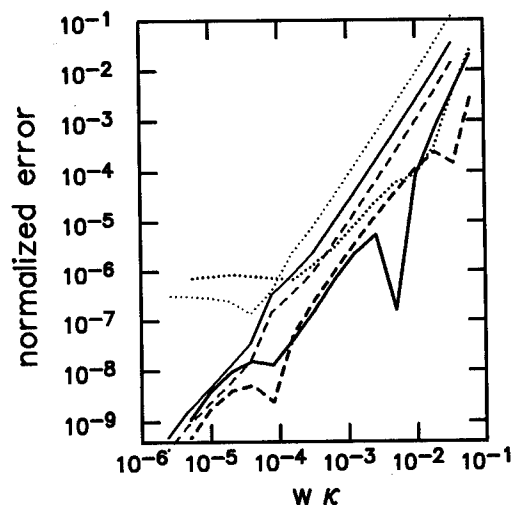


FIGURE 4. Error of modified jump conditions for diverging waves. Solid, dashed and dotted lines are mass, momentum and energy flux respectively. Thick and thin lines correspond to detonation velocities of approximately  $D_{CJ}$  and  $2D_{CJ}$  respectively.

#### SUMMARY

In order for a simulation of the reactive flow equations to predict the behavior of an explosive, a numerical algorithm must accurately propagate detonation waves. As with a non-reactive material the dominant wave behavior of an explosive is determined by its equation of state. However, in contrast to a shock wave, the width of a detonation wave cannot be neglected. This gives rise to a significant correction to the propagation of a detonation wave known as the curvature effect. The numerical width of a detonation wave in capturing algorithms gives rise to an artificial curvature effect which results in a mesh dependence of numerical simulations.

Analysis of the dynamics of the reaction zone has led to an understanding that the curvature effect is due to the interaction between geometric source terms from the curvature of the detonation front and the rate at which energy is released by the chemical reaction.<sup>8,9</sup> Underdriven detonation waves decouple from the flow behind, and the wave front can be correctly propagated with detonation shock dynamics.<sup>12-14</sup> However, the state behind the front must be carefully chosen such that the reactive front and the hydrodynamic front are propagated consistently.

We are studying a unified approach that can be used with a front tracking algorithm to propagate both underdriven and overdriven detonation waves. The sub-grid structure (reaction zone dynamics) needed to propagate a detonation wave can be

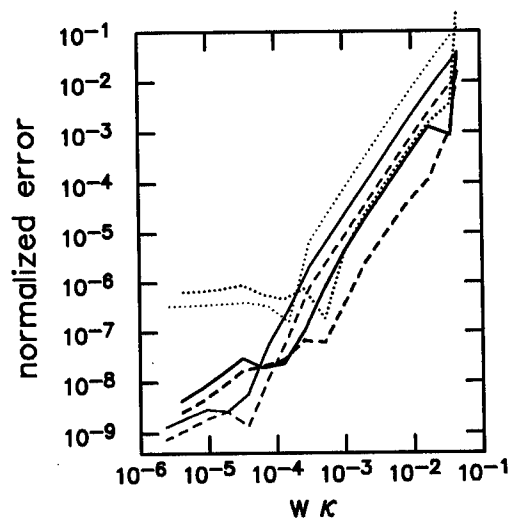


FIGURE 5. Error of modified jump conditions for converging waves. Solid, dashed and dotted lines are mass, momentum and energy flux respectively. Thick and thin lines correspond to detonation velocities of approximately  $D_{CJ}$  and  $2D_{CJ}$  respectively.

characterized analytically by the curvature dependent detonation shock Hugoniot. Given an equation of state and a reaction rate law, the curved detonation shock Hugoniot can be determined by integrating the ODEs for the quasi-steady reaction zone profile.

Numerical calculations use effective rate laws which average over complicated and frequently incompletely understood chemistry, and over length scales associated with material heterogeneities and transverse wave instabilities. At present, it is not possible to derive an averaged reaction rate from microscopic chemical data. It is therefore necessary to use macroscopic data, such as a Pop Plot or the front curvature and detonation velocity in a rate stick experiment, in order to empirically determine the effective rate law. Because of the difficulty of determining the functional form of a rate law, it is preferable to use the integral quantities we identified and which completely determine the curvature effect on wave propagation.

Constraints on the curvature effect from the conservation laws can be expressed as modified Hugoniot jump relations. The reaction zone dynamics enters the jump relations only through the reaction zone width and average values of pressure and of the mass, momentum and energy densities. At least for a simple rate law and equation of state, we have shown that the curved detonation shock Hugoniot can be obtained from the modified jump conditions as a perturbation of a planar detonation.

## ACKNOWLEDGEMENT

This work was supported by the U. S. Department of Energy. Support for BGB was provided under the New Jersey State Budget for Research Program through the NJIT Office of Sponsored Programs.

## REFERENCES

1. W. Fickett and W. C. Davis, *Detonation* (Univ. of California Press, Berkeley, 1979).
2. P. Colella, A. Majda and V. Roytburd, *Theoretical and Numerical Structure for Reacting Shock Waves*, SIAM J. Sci. Stat. Comp. **7**, pp. 1059–1080 (1986).
3. J. J. Erpenbeck, *Detonation Stability for Disturbances of Small Transverse Wavelength*, Phys. Fluids **9**, pp. 1293–1306 (1966).
4. J. J. Erpenbeck, *Nonlinear Theory of Unstable Two-Dimensional Detonation*, Phys. Fluids **13**, pp. 2007–2026 (1970).
5. G. E. Abouseif and T.-Y. Toong, *Theory of Unstable Two-Dimensional Detonations: Genesis of the Transverse Waves*, Combust. and Flame **63**, pp. 191–207 (1986).
6. S. U. Schöffel and F. Ebert, *Numerical Analyses Concerning the Spatial Dynamics of an Initially Plane Gaseous ZND Detonation*, in *International Colloquium on Dynamics of Explosions and Reactive Systems*, edited by A. L. Kuhl (AIAA, Washington, 1988) pp. 3–31.
7. E. S. Oran, K. Kailasanath and R. H. Guirguis, *Numerical Simulations of the Development and Structure of Detonations*, in *International Colloquium on Dynamics of Explosions and Reactive Systems*, edited by A. L. Kuhl (AIAA, Washington, 1988) pp. 155–169.
8. S. Stewart and J. B. Bdzil, *The Shock Dynamics of Stable Multidimensional Detonation*, Combust. and Flame **72**, pp. 311–323 (1988).
9. J. Jones, *The Spherical Detonation*, Adv. Appl. Math. **12**, pp. 147–186 (1991).
10. P. Donguy and N. Legrand, *Numerical Simulations of Non-Ideal Detonations of a Heterogeneous Explosive with the Two Dimensional Eulerian Code C.E.E.*, in *Proceedings of the Seventh International Symposium on Detonation* (Naval Surface Weapons Center, White Oak, MD, 1981) pp. 695–702.
11. C. Mader, *Numerical Modeling of Detonations* (Univ. of California Press, Berkeley, 1979).
12. J. Bdzil and D. S. Stewart, *Modeling Two-Dimensional Detonations with Detonation Shock Dynamics*, Phys. Fluids A **1**, pp. 1261–1267 (1989).
13. J. Bdzil, W. Fickett and D. S. Stewart, *Detonation Shock Dynamics: A New Approach to Modeling Multi-Dimensional Detonation Waves*, in *Proceedings of the Ninth International Symposium on Detonation*, edited by W. J. Morat (OCNR 113291-7, Office of Naval Research, U. S. Gov. Printing Office, Washington, D. C., 1989) pp. 730–742.
14. B. D. Lambourn and D. C. Swift, *Application of Whitham's Shock Dynamics Theory to the Propagation of Divergent Detonation Waves*, in *Proceedings of the Ninth International Symposium on Detonation*, edited by W. J. Morat (OCNR 113291-7, Office of Naval Research, U. S. Gov. Printing Office, Washington, D. C., 1989) pp. 784–797.
15. I.-L. Chern, J. Glimm, O. McBryan, B. Plohr and S. Yaniv, *Front Tracking for Gas Dynamics*, J. Comp. Phys. **62**, pp. 83–110 (1986).
16. B. G. Bukiet and R. Menikoff, *Detonation Waves and the Front Tracking Method*, Phys. Fluids A **4**, pp. 2070–2081 (1992).
17. B. Bukiet, *Application of Front Tracking to Two Dimensional Curved Detonation Fronts*, SIAM J. Sci. Stat. Comp. **9**, pp. 80–99 (1988).
18. B. Bukiet and J. Jones, *The Competition Between Curvature and Chemistry in a Spherically Expanding Detonation*, Appl. Phys. Letters **52**, pp. 1921–1923 (1988).

## STREAMLINE DYNAMICS METHOD FOR HIGHLY CURVED DETONATION WAVES

Raafat H. Guirguis  
Detonation Physics Branch  
Naval Surface Warfare Center  
Dahlgren Division, White Oak Detachment  
Silver Spring, MD 20903-5640

A semi-analytical method for solving steady detonations, called Detonation Streamline Dynamics, is introduced. It is used in this work to establish that the detonation curvature and velocity deficit are nothing but consequences of the self-adjustment steady flows go through in order to reach and transition through sonic conditions, commonly known as flow choking, resulting in a unique front curvature, that is an eigen value in the subdomain of steady solutions, and a unique flow structure, that is the corresponding eigen function. The method is almost as accurate as analytic solutions, but yields a much simpler formulation. It can be used to solve highly curved detonations, can deal with complex equations of state and rates of reaction, and can solve the whole domain of the detonation problem, from the axis to the edge of the explosive charge, and even the confinement, simultaneously.

### INTRODUCTION

Attempts to formulate a mathematically rigorous theory that explains the curvature of the detonation front in finite-size charges date back to the 1940's.<sup>1,2</sup> The milestones are the studies of Wood and Kirkwood<sup>3</sup> in the 1950's, Cowperthwaite<sup>4</sup> and Bdzil<sup>5</sup> in the 1970's, and Bdzil and Stewart<sup>6-8</sup> in the 1980's. Except for the recent work of Bdzil and Stewart on Detonation Shock Dynamics,<sup>8</sup> these analytical methods concentrate on the flow near the axis, and often use series expansion to solve the two-dimensional (2-D) axisymmetric flow equations in the special case resulting from slightly curved detonation fronts. They cannot be used to study highly curved detonations. These occur, for example, in heavily aluminized explosives,<sup>9</sup> now favored in underwater applications because of their higher bubble energy, or when the critical diameter is approached, such as detonations in long thin explosive cords often used in the neutralization of mined fields. The flow near the edge of the explosive charge is usually treated separately. The mathematical complexity of these methods prohibits all but the simplest of equations of state, usually a constant- $\gamma$  law, and the simplest of rates of reaction. In highly non-ideal explosives, a substantial amount of energy is released far behind the detonation front, requiring elaborate expressions for the rate of reaction, and the combustion of metals in the explosive results in products that have to be described by even more complicated equations of state than the products of ideal explosives.<sup>10,11</sup>

In principle, numerical methods are not subject to the same limitations. Usually, the unsteady flow equations are solved, starting at initiation. However, concepts like the critical diameter, which are inherently defined in terms of the capability of the explosive to sustain a steady detonation wave, can only be investigated approximately. This is because the detonation flow structure asymptotically reaches steady state, but numerical simulations have to be arbitrarily stopped early due to computer storage and CPU time limitations. As the detonation wave propagates downstream, more grid points are continuously engulfed in the domain of solution. If we use a fixed uniform grid, the storage and CPU time requirements will be enormous, because the reaction zone has to be finely resolved. If we use adaptive gridding, allowing the finely resolved region to move with the detonation front, the grid stretch will eventually cause a loss of accuracy. An important drawback to solving the unsteady flow equations is that the fine grid needed to resolve the reaction zone, also helps capture instabilities and other unsteady details of the flow structure,<sup>12</sup> for example, the transverse waves, even if the simple steady solution, that only includes the main features, is desired.

In this paper, we introduce a new method called Detonation Stream-Line Dynamics (DSL<sub>D</sub>), that does not suffer from any of the limitations described above, and is almost as accurate as analytical methods. It is limited to steady detonations, but can solve the whole domain, from the axis to the edge of the charge, without separating the two regions, and can as easily solve the flow in the confining medium. DSL<sub>D</sub> can accurately solve highly curved detonation waves. Any complex set of equation(s) of state and rate(s) of reaction can be used. It can even be used for stratified explosives, in which the composition changes from the inner core to the outer

This work was performed under the auspices of ONR 6.2 Explosives and Undersea Warheads Block Program and the Explosives and Warheads Division in NSWCWDET.



layers. DSLD also produces a complete picture - the structure of the flow, as well as the detonation front.

However, the strongest motivation for the work was the need to relate the detonation curvature and velocity deficit to a simple physical concept, from which all the properties of detonation waves propagating in finite size charges can be easily predicted. In DSLD, mathematical complexity is avoided without sacrificing generality. This is an important advantage, because the simpler the formulation, and the smaller the number of functions involved, the easier it is to devise an algorithm to solve it, and track down then remedy any potential sources of inaccuracy, for example, by using the double-precision option in the code implementing it. As will be explained below, when solving the problem of detonation curvature, we are solving for the very small differences between the actual 2-D and idealized one-dimensional (1-D) flow. In general, solving for small differences can cause a loss of accuracy. Had it not been for the other limitations described above, the technique of series expansion would have been ideal, because it solves for these differences directly, after the leading terms are canceled.

## DETONATION CURVATURE=FLOW CHOKING

The starting point is to establish that the detonation curvature and resulting velocity deficit are nothing but consequences of the phenomenon called flow choking, common in supersonic nozzles. When a steady flow cannot accommodate the mass flow rate compatible with the upstream boundary conditions, and at the same time reach sonic conditions, or transition from subsonic to supersonic, downstream, it self-adjusts by restricting the mass flow rate. The adjustment process, which is unsteady but transient, is achieved through sound waves that propagate upstream and change the boundary conditions there. After the adjustment, a new steady flow that is compatible with all the boundary conditions is achieved. As will be proved below, there is a unique detonation front profile that can produce a flow which smoothly transitions through sonic conditions, and a corresponding unique flow structure. Any other detonation front curvature does not produce a proper steady flow. *Within the subdomain of steady solutions*, the detonation curvature is an eigen value, and the resulting flow structure, the corresponding eigen function.

In a frame of reference moving with the front, a steady detonation transforms into a *steady compressible laminar flow with coupled changes in area and stagnation temperature*. For this type of flow,<sup>13</sup>

$$\frac{d \ln M^2}{d \xi} = \frac{1 + \frac{\gamma-1}{2} M^2}{1 - M^2} \left\{ -2 \frac{d \ln A}{d \xi} + (1 + \gamma M^2) \frac{d \ln T_o}{d \xi} \right\}. \quad (1)$$

In Eq. 1,  $d/d\xi$  describes the variation along a streamline, specifically, along an infinitesimal streamtube of area  $A$  surrounding the streamline,  $M$  is the Mach number,  $T$  is the temperature, and the subscript  $o$  denotes stagnation conditions, i.e., conditions reached if the flow at that

location is isentropically expanded to velocity  $u=0$ . In Eq. 1, a constant- $\gamma$  equation of state is assumed in order to explain the theory in terms of simple equations. But the theory itself is general and valid for any equation of state.

In a detonation wave,  $T_o$  increases due to chemical reaction, while the area is controlled by the curvature of the streamlines, which, in turn, are affected by the front profile. Because of the factor  $1-M^2$  in the denominator, the flow is controlled by the properties at the sonic plane, where  $M=1$ . For example, let  $dA=0$ , such as in 1-D detonations. From Eq. 1, if  $M<1$ ,  $dT_o>0$  yields  $dM^2>0$ , i.e., exothermic chemical reaction increases the Mach number. Once  $M=1$  is reached, the factor  $1-M^2$  changes sign, making any further heat release impossible. This is because there is no solution at  $M=1$  to the incipient change in  $M$ . If  $M$  tends to increase to  $M>1$ ,  $1-M^2<0$  yields  $dM^2<0$ , i.e.,  $M$  has to decrease. And vice-versa, if the flow tries to go back to subsonic speeds. Thus, heat cannot be released after the Chapman-Jouguet (CJ) plane of a 1-D detonation.

If the size of the charge is finite, the divergence of the flow due to lateral expansion yields  $dA>0$ . Equation 1 implies that the energy released in a 1-D detonation, which is just able to heat the flow to  $M=1$  when  $dA=0$ , won't be enough to do the same when  $dA>0$ , *if the flow starts at the same Mach number  $M(0)$  after the detonation shock front*. The detonation responds by lowering its velocity  $D$  and by curving. Each of these changes independently increases  $M(0)$  a little closer to  $M=1$ . A reduction in the mass flow rate across the detonation front follows, i.e., the flow is choked. Equation 1 also implies that in 2-D detonations, energy release does not stop at the CJ plane and continues after it, because the divergence term  $d \ln A/d\xi$  balances the effects of the heat release term  $d \ln T_o/d\xi$ , making the RHS of the equation zero and negative, respectively. In 2-D detonations, the CJ plane is defined as the surface at which  $M=1$ . It does not coincide any more with the surface at which energy release ends, now located further downstream. The pathological nature of 2-D detonations is also easily predicted by Eq. 1. If either  $dA$  or  $dT_o$  vanishes, we can eliminate  $\xi$ , which allows us to (separate the remaining two variables and) integrate Eq. 1, whereby the Mach number becomes a unique function of the local stagnation temperature or area, respectively. Such is the case in 1-D detonations, where all flow properties in the reaction zone are unique functions of the reaction progress variable  $\lambda$ . But if both  $dA \neq 0$  and  $dT_o \neq 0$ , the Mach number will depend on the paths  $A(\xi)$  and  $T_o(\xi)$ .

If we construct a grid  $(\xi, \eta)$  of orthogonal curvilinear coordinates, such that  $\xi$  is always aligned with the streamlines, as illustrated in Fig. 1,

$$\frac{d \ln A}{d \xi} = \frac{\partial \phi}{\partial \eta} + \frac{\sin \phi}{r}, \quad (2)$$

where  $\phi$  denotes the inclination of the streamlines to the axis of propagation. In 2-D planar geometry, for example, the case of a detonation propagating in a slab of explosive, the term  $\sin \phi/r$  in Eq. 2, describing the change

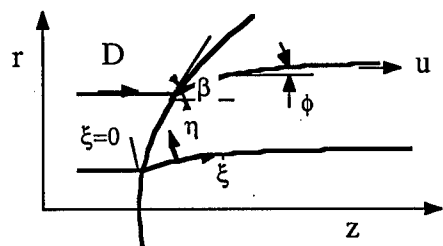


FIGURE 1. NOMENCLATURE

in area in axisymmetric  $(r,z)$  geometry due to a change in radius  $r$ , vanishes. But all other equations remain the same. As a result of the normal gradient in pressure  $p$ , the streamlines curve, such as to satisfy the momentum conservation relation,

$$\frac{d\phi}{d\xi} = -\frac{1}{\rho u^2} \frac{\partial p}{\partial \eta} = -\frac{\partial \ln p / \partial \eta}{\gamma M^2}. \quad (3)$$

The second equality in Eq. 3 is only valid for a constant- $\gamma$  equation of state. Lastly, the change in  $T_o$  can be expressed in terms of the reaction rate  $d\lambda/dt$  by

$$\frac{d \ln T_o}{d\xi} = \frac{d \ln h_o}{d\xi} = \frac{Q}{h_o u} \frac{d\lambda}{dt}, \quad (4)$$

since for a steady flow,  $d/dt = u d/d\xi$ .  $Q$  is the heat of reaction per unit mass,  $h_o$  the stagnation enthalpy ( $h_o = C_p T_o$ ), and  $u$  the flow velocity along the streamline, which is the same as the velocity vector in steady flows. In Eqs. 1 to 4,  $d/d\xi$  is used instead of  $\partial/\partial\xi$ , in order to emphasize that the integration along the streamline is carried out as if we are solving an ODE.

### EXAMPLE

Equations 1 to 4 are solved for an axisymmetric detonation wave propagating at  $D=8$  km/s in a stick of explosive 8 mm in diameter and density  $\rho^o=2$  g/cc. The superscript  $o$  will be used from now on to denote the undisturbed conditions ahead of the shock front. We assume that the products obey a constant- $\gamma$  equation of state, with  $\gamma=3$ , and that the ambient pressure is negligible compared to the pressures generated by the detonation wave. When used with a constant- $\gamma$  equation of state, assuming  $p^o=0$  is equivalent to assuming that the detonation is propagating at an infinite Mach number. In a frame of reference moving with the detonation wave,  $M^o=\infty$  yields the following flow properties immediately after the shock front leading the detonation wave, defined from now on as the location where  $\xi=0$ .

$$M^2(0) = \frac{\gamma-1}{2\gamma} \left\{ 1 + \left( \frac{\gamma+1}{\gamma-1} \right)^2 \frac{1}{\tan^2 \beta} \right\},$$

$$\frac{\rho(0)}{\rho^o} = \frac{\gamma+1}{\gamma-1},$$

$$\frac{p(0)}{\rho^o D^2} = \frac{2}{\gamma+1} \sin^2 \beta,$$

and

$$\frac{u(0)}{D} = \frac{\gamma-1}{\gamma+1} \sin \beta \left\{ 1 + \left( \frac{\gamma+1}{\gamma-1} \right)^2 \frac{1}{\tan^2 \beta} \right\}^{\frac{1}{2}},$$

where  $\beta = \tan^{-1}(dr/dz)$  is the angle between the tangent to the front and the  $z$ -axis, as illustrated in Fig. 1. The inclination of the streamlines at the front  $\phi(0)$  is given by

$$\phi(0) = \tan^{-1} \left\{ \frac{2 \tan \beta}{(\gamma-1) \tan^2 \beta + (\gamma+1)} \right\}.$$

The rate of reaction is assumed to follow a simple first order law  $d\lambda/dt = k(1-\lambda)p$ . The amount of energy released per unit mass  $Q$  has to be defined in relation to the minimum value  $Q_{min}$  needed to choke the 1-D flow, or, alternatively, to reach CJ conditions at  $\lambda=1$  in a 1-D detonation. Both methods are equivalent.  $Q_{min} = h_o^* - h_o(0)$  can be evaluated by integrating Eq. 1 with  $dA=0$  between  $M(0) = \sqrt{[(\gamma-1)/2\gamma]}$  and  $M^*=1$ . The superscript  $*$  will be used from now to indicate sonic conditions. We get,  $T_o^*/T_o(0) = h_o^*/h_o(0) = \gamma^2/(\gamma^2-1)$ . But  $h_o(0) = h_o^o$ , because the stagnation enthalpy does not change upon crossing a shock. Furthermore, when  $p^o=0$ ,  $h_o^o = \text{kinetic energy} = D^2/2$ . Substituting, we calculate  $Q_{min} = 0.04$  Mbar.cc/gm for  $\gamma=3$  and  $D=0.8$  cm/ $\mu$ s. Alternatively,  $Q_{min}$  can be determined from  $D^2 = 2(\gamma^2-1)Q$ , resulting from the simple 1-D detonation theory. At the CJ point,  $p = \rho^o D^2/(\gamma+1)$  and  $u = \gamma D/(\gamma+1)$ . The value of  $k$  in  $d\lambda/dt$  is adjusted such as to yield in 1-D, a reaction zone thickness ( $\lambda=0$  to  $\lambda=0.99$ ) of 0.01 cm, if  $d\lambda/dt$  is integrated assuming  $p$  is constant at a value equal to the arithmetic average of the pressure after the shock and the pressure at the CJ point. The same is assumed for the velocity  $u$ .

The domain of solution is illustrated in Fig. 2. It is the region between the shock front and the  $\eta$ -line passing through the intersection of the shock front with the edge of the charge. Although DSLD can be used to calculate the structure of the flow further downstream, the limited domain is selected in this example in order to illustrate the principal features of the theory, *without introducing the effects of the confinement yet*.

As the solution proceeds downstream, the  $(\xi-\eta)$  curvilinear grid is simultaneously generated using the calculated flow parameters.  $(r,z)$  are evaluated from  $\phi(\xi)$

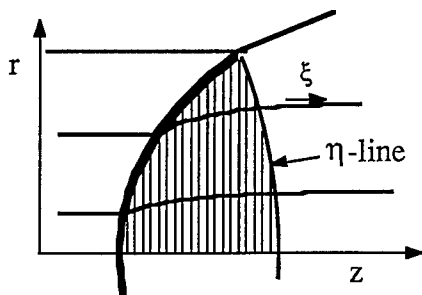


**FIGURE 2. DOMAIN OF SOLUTION**

using  $r = r(0) + \int \sin \phi \, d\xi$  and  $z = z(0) + \int \cos \phi \, d\xi$ . In the simulations presented below, and except when stated otherwise, a very coarse grid with only 20  $\xi$ -lines (streamlines) equally spaced in the radial direction (at the front) is used. The differential  $\partial/\partial \eta$  in Eqs. 2 and 3 is approximated by a 2<sup>nd</sup> order finite difference. In addition to Eq. 1, two more ODE's,  $d\lambda/d\xi = (d\lambda/dt)/u$  and  $d \ln(\rho u)/d\xi = -d \ln A/d\xi$ , are solved using 4<sup>th</sup> order Runge-Kutta, yielding  $M^2(\xi)$ ,  $\lambda(\xi)$ , and  $\rho u(\xi)$ , respectively. The velocity, density, and pressure are calculated from these using  $h_o(\xi) = D^2/2 + \lambda Q$ ,  $h_o(\xi)/h(\xi) = 1 + (\gamma - 1)M^2(\xi)/2$ ,  $u(\xi)/u(0) = M(\xi)/M(0) \times \sqrt{[h(\xi)/h(0)]}$ ,  $\rho(\xi) = \rho u(\xi)/u(\xi)$ , and  $p(\xi)/p(0) = \rho(\xi)h(\xi) / \rho(0)h(0)$ .

Because in the subsonic region behind the shock, disturbances downstream can affect the front, it may appear contradictory that in the algorithm described above, the solution downstream cannot affect the already calculated values upstream. But the method is in fact correct, because for a given shock profile and detonation velocity, the flow downstream is completely determined, provided it is steady. The only way disturbances downstream can affect the flow upstream is by changing the shape of the shock front, and that is done through unsteady processes. It may also be confusing that we can obtain the flow structure without considering the confinement. Here, we are deriving the front profile for a given detonation velocity. We cannot derive both without considering the confinement. But if both are determined, so is the flow downstream in the limited domain in Fig. 2, without introducing the effects of the boundary.

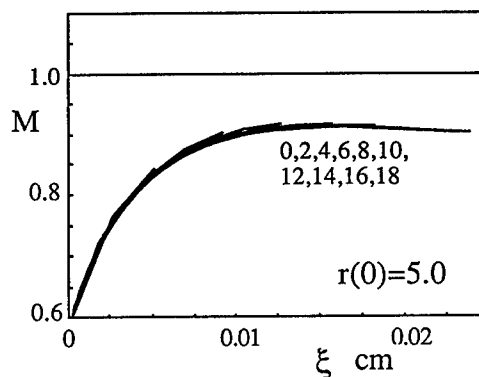
Figures 3a to 3e illustrate the solution for  $Q=0.04$  Mbar.cc/gm, assuming a spherical shock front of radius  $r_o=5.0$  cm. Since  $Q$  was selected equal to the minimum value  $Q_{min}$  needed to choke the flow in 1-D geometry, any finite curvature of the front will prevent the flow from reaching  $M=1$ , as implied by Eq. 1. Figure 3a indeed shows that the Mach number of the flow decays after only reaching  $M=0.9$ . In all figures, the 20 streamlines are labeled 0 to 20, starting from the axis, which is also a streamline. Streamline number  $n$  starts at the front at  $r = 0.02n$  cm

Figure 3b shows the resulting streamlines. For clarity, the scale of the  $z$ -axis is expanded. The streamlines appear to be straight lines parallel to the axis. But they are actually curved lines inclined to the axis, as is

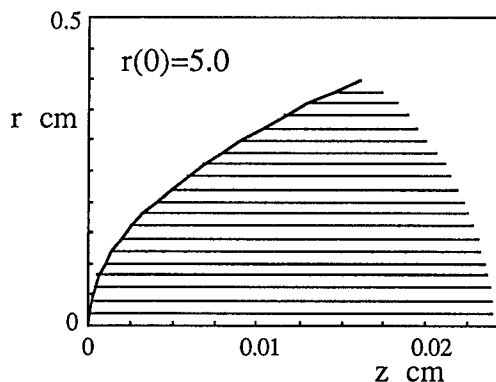
obvious from Fig. 3c, showing the change in the angle  $\phi$  (radians). The maximum value of  $\phi=4.58^\circ$ , the inclination of the 20<sup>th</sup> streamline at the front. Although  $\phi$  is generally very small ( $\leq 4.58^\circ$ ), both the angle  $\phi$  and the curvature  $d\phi/d\xi$  of the streamlines cannot be neglected. In fact, it is the change in  $\phi$  that controls the behavior of the flow and determines whether the curvature of the front is compatible with the assumed equation of state and rate of reaction.

Figure 3d exhibits an interesting similarity feature of streamlines resulting from a constant curvature detonation front. Normalized by the angle  $\phi(0)$  after the shock front, all streamlines satisfy the same function. Since  $\phi(0)$  is completely determined once the detonation front profile is known, the similarity can be useful in deriving analytical solutions for this class of detonations.

The convergence of the algorithm used in getting the solution is displayed in Fig. 3e, where  $\phi(\xi)$  resulting from two separate calculations, one twice as resolved as the other, is plotted. The more resolved calculation uses



**FIGURE 3A. MACH NUMBER ALONG STREAMLINES FOR  $Q=0.04$  MBAR.CC/GM,  $D=8$  KM/S, AND RADIUS OF CURVATURE=5.0 CM**



**FIGURE 3B. STREAMLINES FOR  $Q=0.04$  MBAR.CC/GM,  $D=8$  KM/S, AND RADIUS OF CURVATURE=5.0 CM**

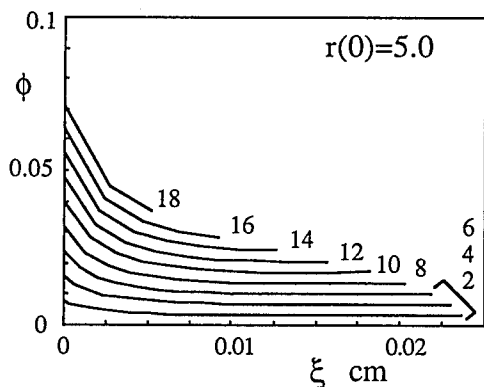


**FIGURE 3C. INCLINATION OF STREAMLINES FOR  $Q=0.04$  Mbar.cc/gm,  $D=8$  km/s, AND RADIUS OF CURVATURE=5.0 CM**

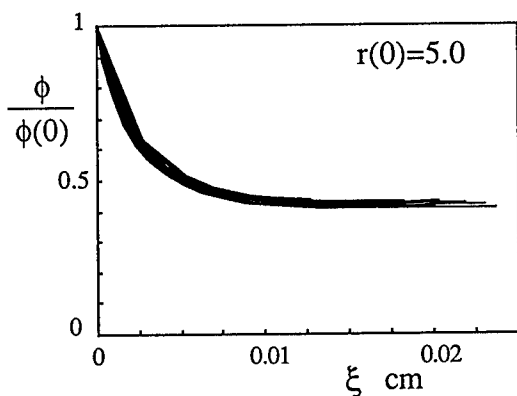


**FIGURE 3D. SIMILARITY OF STREAMLINES RESULTING FROM CONSTANT CURVATURE DETONATION FRONTS**

40 streamlines instead of 20 to cover the same radius  $r=0.4$  cm.  $M(\xi)$  profiles for both grids completely coincide. The plot showing the comparison of  $M(\xi)$  is not presented here, because it is a replica of Fig. 3a. The accuracy exhibited in Fig. 3e is both remarkable and misleading. It is remarkable, because the solution for very small angles  $\phi$  was obtained using the raw functions. In the computer code, no attempt was made to redefine these functions, such as to preserve their accuracy for small values of  $\phi$ . Also, Eqs. 1 to 4, effectively solving for small differences of large but nearly equal quantities, were not reformulated.

The technique of series expansion has an advantage in this regard, because it solves directly for the differences, after the leading terms are canceled. Yet, series expansion has serious drawbacks. In principle, it is only valid for small departures from the 1-D configuration.

And it gets too complicated when a real equation of state and/or a complicated rate of reaction are used. Here, using a simple formulation, a coarse grid, and a computer with a word structure 32-bit wide, we still get an accurate solution. And although a simple problem was selected to prove the theory, the method described in this paper is general, and has none of the limitations of series expansion. However, the accuracy of the solution is also misleading, because the flow does not choke in this problem, i.e., does not reach  $M=1$ . As explained later,  $M=1$  is a saddle-point singularity. Integrating into  $M=1$  is an ill-conditioned procedure, and convergence has to be defined accordingly.

If we slightly increase  $Q$  beyond  $Q_{\min}$  to  $Q=0.041$  Mbar.cc/gm, while using the same values  $D=8$  km/s and  $r_0=5.0$  cm, all streamlines will reach  $M=1$ , as shown in Fig. 4a. For comparison,  $Q=0.041$  Mbar.cc/gm and  $\gamma=3$  can sustain a 1-D detonation propagating at  $D = \sqrt{2(\gamma^2-1)Q} = 0.8099$  cm/ $\mu$ s. If  $D$  is smaller than this 1-D velocity, we can *always* find a detonation front which curvature satisfies the flow choking conditions. In Fig. 4a, each streamline remains at  $M=1$  for a short  $\delta\xi$  after reaching it. As explained earlier, a steady solution does not exist, if the RHS of Eq. 1 remains positive after reaching  $M=1$ . The only way the flow can proceed to  $M>1$  is if the RHS becomes negative. In the algorithm, the flow is allowed to remain at  $M=1$ , until the energy release slows down enough for the divergence  $d\ln A/d\xi$  to overcome its effects. Although such a flow cannot physically occur, this trick allows us to examine the tentative solution beyond  $\xi^*$ . Physically, sound waves propagate upstream and reduce the radius of curvature of the shock front, such that the transition from  $M<1$  to  $M>1$  occurs smoothly. But this is an unsteady effect that cannot be modeled here, because it is outside the scope of the formulation.

Figure 4b shows the flow near the axis of symmetry, when the radius of curvature of the shock is reduced to  $r_0=4.19$  cm. Streamlines 0 to 6 now transition smoothly through  $M=1$ . However, streamlines 8 to 18 still choke too early, as illustrated in Fig. 4c. If we

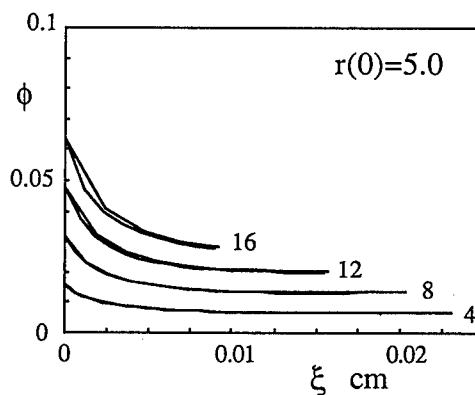


**FIGURE 3E. INCLINATION OF STREAMLINES FROM TWO DIFFERENT CALCULATIONS, ONE TWICE AS REFINED AS THE OTHER**

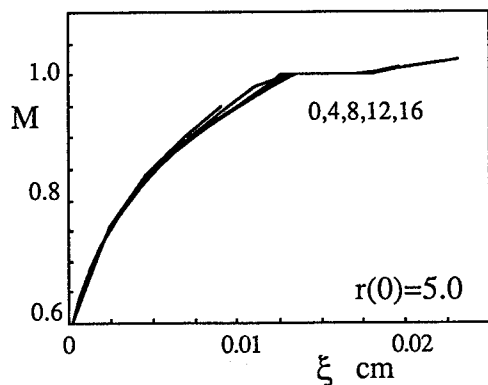


**FIGURE 4A. MACH NUMBER ALONG STREAMLINES FOR  $Q=0.041$  MBAR.CC/GM,  $D=8$  KM/S, AND RADIUS OF CURVATURE=5.0 CM**

further reduce  $r_0$  to 4.18 cm, streamline 0 comes near, but does not reach  $M=1$ . But there is no physical basis for the assumption often made that there exist a single curvature for the whole front which can make all the streamlines smoothly transition through  $M=1$ . A shock front profile  $z=k_2r^2 + k_4r^4 + k_6r^6 + \dots$  can have different curvatures, at different radii, while maintaining the same value for the radius of curvature  $r_0$  at  $r=0$  (in order not to disturb the already obtained compatible solution near the axis of symmetry), if we select  $k_2=1/2r_0$ . This profile produces a paraboloid instead of a spherical shock front. Figure 4d shows all the streamlines going smoothly through  $M=1$  when  $k_4=0$  and  $k_6=0.6$ . It is important to notice, however, that this conclusion is not universal, since it depends on the equation of state and rate of reaction used in the calculations. It is not too far from the behavior of actual detonations though. Detonations in solid explosives have most of the time fronts remarkably

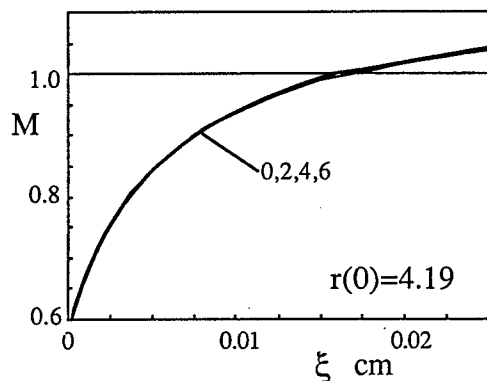


**FIGURE 4B. MACH NUMBER ALONG STREAMLINES 0 TO 6 FOR  $Q=0.041$  MBAR.CC/GM,  $D=8$  KM/S, AND RADIUS OF CURVATURE=4.19 CM**

close to a spherical surface. For  $k_4=0$  and  $k_6=0.6$ , the departure from a spherical front is minimal.

### ACCURACY AND CONVERGENCE OF ALGORITHM

In Figs. 4e, 4f, again we compare the results of two separate calculations, one with 20 and the other with 40  $\xi$ -lines. In Fig. 4e,  $M(\xi)$  profiles for different streamlines are separated along  $\xi$  for clarity. In Fig. 4f, we compare  $\phi(\xi)$  for the two cases. Except for streamlines 0 to 3 near the axis, both calculations converge to the same answer. It is also worth noticing that Fig. 4f, representing the case when the flow did choke, looks similar to Fig. 3c, when all streamlines did not reach  $M=1$ . Obviously, the differences between the two flows are small. But these small differences is what determines whether the front curvature is compatible with the assumed equation of state and rate of reaction.

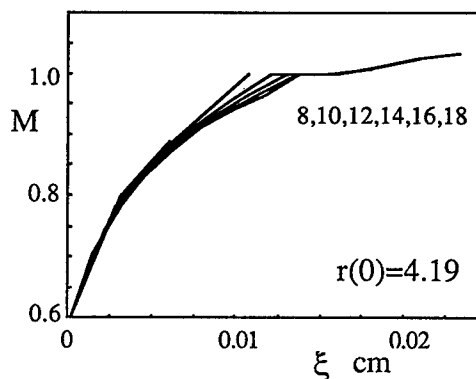


**FIGURE 4C. MACH NUMBER ALONG STREAMLINES 8 TO 18 FOR  $Q=0.041$  MBAR.CC/GM,  $D=8$  KM/S, AND RADIUS OF CURVATURE=4.19 CM**

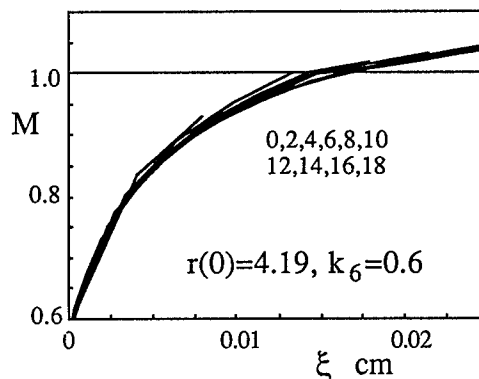


**FIGURE 4D. MACH NUMBER ALONG STREAMLINES FOR  $Q=0.041$  MBAR.CC/GM,  $D=8$  KM/S, AND RADIUS OF CURVATURE=4.19 CM + CORRECTION  $\delta z=0.6 R^6$**

The convergence of the algorithm was further tested by investigating the effects of the accuracy of integration on the solution. In calculating the solutions presented in Figs. 3 and 4, we used a 4<sup>th</sup> order explicit Runge-Kutta to integrate all  $d/d\xi$  differentials, except  $d\phi/d\xi$ , which was integrated using a 1<sup>st</sup> order explicit Euler method. When the case presented in Figs. 4b, 4c was recalculated using the 4<sup>th</sup> order Runge-Kutta to integrate  $d\phi/d\xi$  also, the value of  $r_0$  at which the streamlines 0 to 6 transition smoothly through  $M=1$ , changed from  $r_0=4.19$  to  $r_0=4.07$  cm.

To explain the sensitivity of the solution near  $M=1$ , we follow the analysis often invoked in studying the effects of moisture condensation in supersonic nozzles.<sup>13</sup> Eq. 1 is rewritten as  $dM^2/d\xi = \kappa(\xi)/(1-M^2)$ , which we can easily integrate for select functions  $\kappa(\xi)$ . In the actual detonation problem, the value of the RHS of Eq. 1 is affected by the shape of the shock front through its dependence on the behavior of the surrounding streamlines, since  $d\ln A/d\xi$  couples the RHS of Eq. 1 to the differentials  $\partial/\partial\eta$  in Eqs. 2 and 3. However, for the sake of

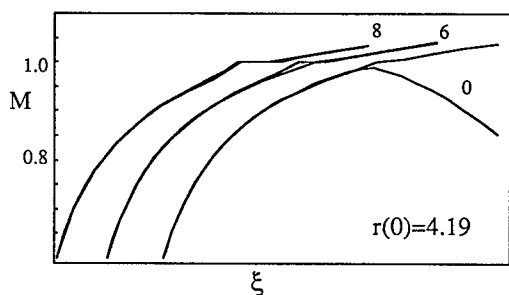


FIGURE 4E. MACH NUMBER ALONG STREAMLINES FROM TWO DIFFERENT CALCULATIONS, ONE TWICE AS REFINED AS THE OTHER

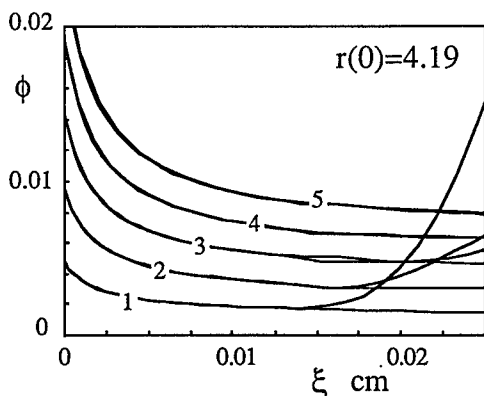


FIGURE 4F. INCLINATION OF THE STREAMLINES FROM TWO DIFFERENT CALCULATIONS, ONE TWICE AS REFINED AS THE OTHER

simplicity, let us assume that the RHS of Eq. 1 can be written as  $\kappa(\xi)/(1-M^2)$ . Here, we are only interested in the subset of functions  $\kappa(\xi)$  that change sign from  $\kappa>0$  to  $\kappa<0$  at some  $\xi^*>0$ .

Figure 5 explains what happens when we try to integrate towards  $M=1$ , starting from  $M<1$  at  $\xi=0$ . The dotted lines are impossible within the limited scope of the detonation problem, but are included here for the sake of completeness. If  $M(0)$  is below some critical value, the Mach number increases, but only reaches a maximum  $M<1$  at  $\xi^*$ , where  $dM^2/d\xi=0$ , then starts decreasing. The case presented in Figs. 3a to 3e corresponds to this class of integral curves. The integral curves starting above that critical value, reach  $M=1$  within  $\kappa>0$ , where  $dM^2/d\xi=\infty$ , and cannot transition to  $M>1$  (because there is no solution to the incipient change in  $M$ ), as explained above. All the streamlines in Fig. 4a, 4c that choke early, and remain fixed at  $M=1$  for some  $\delta\xi$ , belong to that class.

Only one integral curve reaches  $M=1$  at  $\kappa=0$ , where  $dM^2/d\xi$  is finite, then proceeds either to  $M>1$ , or reverts back to  $M<1$ . Similarly, in the detonation problem, there is a critical front profile which yields the only steady flow that can transition through  $M=1$ , and no others. Within the subdomain of steady solutions, the detonation curvature is an eigen value, and the resulting flow structure, the corresponding eigen function.

The point  $(\xi=\xi^*, M=1)$  is a saddle point singularity. Integrating towards that point is ill-conditioned, because any error resulting from the numerical integration can throw the solution off, either right, where it does not reach  $M=1$ , or left, where it reaches it earlier than it should. That does not mean that getting the solution is impossible. But it means that a proper method for the integration of the ODEs into the singularity should be used. For example, we can build in a small bias into the ODE solver, such as to prevent the solution from following noise. Alternatively, one can try to locate the saddle-point singularity in some phase-plane, and integrate out of it. If  $\kappa$  is a known function, locating the singularity is relatively easy. But in the detonation curvature problem, where all properties are interrelated, locating the singularity in the general case, without limiting

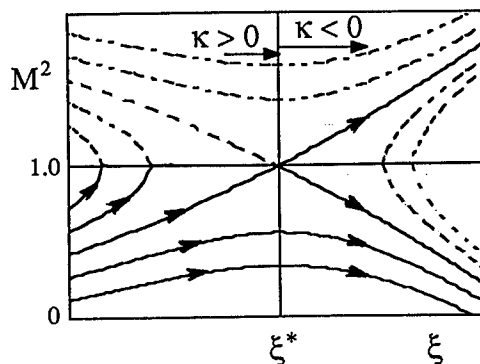


FIGURE 5.  $M=1$  IS A SADDLE POINT SINGULARITY

the scope of the method, for example, by choosing the technique of series expansion, may prove difficult.

Finding ways to reach the critical point accurately is beyond the scope of this work, which main objective is to introduce DSLD, and explain flow choking as applied to detonations. However, it is important to notice that:

1. The effect of the detonation curvature on the behavior of the flow follows a consistent trend, as long as the same integration scheme and the same spatial resolution are used.

2. Because the shock front is locally normal at the axis of symmetry, there isn't much variation from one streamline to the next. Near  $r=0$ , the differences are small enough to cause a loss of accuracy. But as  $r$  increases, and the shock becomes more oblique, these differences get larger, resulting in more accurate solutions. In Figs. 4e, 4f, streamlines 0 to 3 are the least accurate. Starting at streamline number 4,  $\phi(\xi)$  curves resulting from two calculations, with two different resolutions, are indistinguishable.

3. We can expect more accurate solutions when solving highly curved detonation waves, because the change from one streamline to an adjacent one increases with curvature (decreases with  $r_0$ ).

## CONCLUSIONS

Within the subdomain of steady solutions, the detonation curvature is an eigen value, and the flow structure, the corresponding eigen function. Without considering the effects of the confinement, we can derive the front profile for a given detonation velocity, but not both. The detonation curvature and velocity deficit in finite size charges are consequences of the flow choking, needed in order to reach the sonic surface, and transition smoothly to supersonic speeds.

In the Detonation Streamlines Dynamics method, we solve a set of ODEs describing the quickly changing flow properties along the streamlines. High-order integration schemes are already developed for ODEs. These high-order schemes can be coupled with small steps  $\delta\xi$ , without heavily taxing any computer's resources. The slow variation in flow properties from one streamline to the next allows us to use relatively low-order finite difference expressions for  $\partial/\partial\xi$ .

The formulation is simpler when we align the grid with the streamlines. That is always the case, even when we use more complex equations of state. In fact, most of the equations described above remain the same. Along the streamlines, the already existing methods for integrating the mass, momentum, and energy equations in quasi-one-dimensional geometry can be used.<sup>14</sup>

## REFERENCES

1. Jones, H., "A theory of the Dependence of the Rate of Detonation of Solid Explosives on the Diameter of the

Charge," *Proc. R. Soc. London, Ser. A*, Vol. 189, 1947, pp. 415-427.

2. Hill, R. and Pack, D. C., "An Investigation, by the Method of Characteristics, of the Lateral Expansion of the Gases Behind a Detonating Slab of Explosives," *Proc. R. Soc. London, Ser. A*, Vol. 191, 1947, pp. 524-541.

3. Wood, W. W. and Kirkwood, J. G., "Diameter Effect in Condensed Explosives. The Relation Between Velocity and Radius of Curvature of the Detonation Wave," *J. Chem. Phys.*, Vol. 22, 1954, pp. 1920-1924.

4. Cowperthwaite, M., "Two-Dimensional Steady-State Detonation Waves," *Thirteenth Symposium (International) on Combustion*, The Combustion Institute, Pittsburgh, 1971, pp. 1111-1117.

5. Bdzil, J. B., "Perturbation Methods Applied to Problems in Detonation Physics," *Sixth Symposium (International) on Detonation*, Office of Naval Research, Washington, D.C., ACR-221, 1976, pp. 352-369.

6. Bdzil, J. B., "Steady-State Two-Dimensional Detonation," *J. Fluid Mech.*, Vol. 108, 1981, pp. 195-226.

7. Bdzil, J. B. and Stewart, D. S., "Time-Dependent Two-Dimensional Detonation: The Interaction of Edge Rarefactions with Finite-Length Reaction Zones," *J. Fluid Mech.*, Vol. 171, 1986, pp. 1-26.

8. Bdzil, J. B. and Stewart, D. S., "Modeling Two-Dimensional Detonations with Detonation Shock Dynamics," *Phys. Fluids A*, Vol. 1, No. 7, 1989, pp. 1261-1267.

9. Forbes, J. W., Lemar, E. R. and Baker, R. N., "Detonation Wave Propagation in PBXW-115," *Ninth Symposium (International) on Detonation*, Naval Surface Warfare Center, Silver Spring, MD, OCNR 113291-7, Vol. 1, 1989, pp. 806-815.

10. Guirguis, R. H., "Modeling the Late Reactions in Aluminized Underwater Explosives," *Proceedings of the 1992 JANNAF PSHS Meeting*, Chemical Propulsion Information Agency, Columbia, MD, 1992.

11. Guirguis, R. H. and Miller, P., "Time-Dependent Equations of State for Aluminized Underwater Explosives," paper number 22, *this Symposium*, 1993.

12. Guirguis, R. H., Oran, E. S. and Kailasanath, K., "Numerical Simulations of the Cellular Structure of Detonations in Liquid Nitromethane - Regularity of the Cell Structure," *Comb. Flame*, Vol. 65, 1986, pp. 339-365.

13. Shapiro, A. H., *The Dynamics and Thermo-dynamics of Compressible Fluid Flow*, Vol. 1, The Ronald Press Company, New York, 1953, pp. 219-262.

14. Fickett, W. and Davis, W. C., *Detonation*, University of California Press, Berkeley, 1979, pp. 199-219.

## DISCUSSION

M. COWPERTHWAIT  
SRI INTERNATIONAL  
333 Ravenswood Avenue  
Menlo Park, California 94025

I would like to make a comment about the shape of the streamlines in a stationary, steady-state, cylindrically symmetric detonation wave. The curvature of these streamlines is governed by the following equation

$$\frac{d^2 r}{dz^2} = \frac{1}{u^2} \left( \frac{dw}{dt} - \frac{w}{u} \frac{du}{dt} \right) \quad (1)$$

where the axial particle velocity  $u = dz/dt$  and the radial particle velocity  $w = dr/dt$ . Equation 1 is obtained by differentiating the relation  $dr/dz = w/u$  with respect to  $z$ . Because  $du/dt > 0$  in the frame attached to the shock,  $d^2 r/dz^2 < 0$  when  $dw/dt < 0$  and  $\partial p/\partial r > 0$ ,  $d^2 r/dz^2 = 0$  when  $dw/du = w/u$ , and  $d^2 r/dz^2 > 0$  when  $dw/dt > (w/u) \times du/dt$ . In the neighborhood of the shock,  $d^2 r/dz^2 < 0$  when the pressure decreases faster along a streamline than along the shock. Further behind the shock wave, the flow is influenced largely by the lateral boundary,  $dw/dt > 0$ ,  $d^2 r/dz^2 > 0$ , and the streamlines bend away from the axis.

### REPLY BY R. GUIRGUIS:

Using series expansion, Bdzil formally investigated the curvature of the streamlines after crossing the leading shock front (reference 6 in paper). Also refer to the reply after Dremine's comment.

## DISCUSSION

A. N. DREMINE  
Institute of Chemical Physics  
Russian Academy of Sciences  
Moscow Region  
Chernogolovka 142432, Russia

Are you going to perform your calculations for smaller diameters of the explosive charge? In our investigation of the problem, we observed that the curvature of the streamlines just behind the detonation wave front changed from positive to negative at some proper diameter (perhaps, failure diameter).

### REPLY BY R. GUIRGUIS:

The streamline curvature is  $d\phi/d\xi$ . From Eq. 3 in the paper,  $d\phi/d\xi \sim -\partial p/\partial \eta \approx -(p_2 - p_1)/(\eta_2 - \eta_1)$  for streamline # 1 in Fig. 1' below, for example. Since the pressure behind an oblique shock decreases the more the shock is inclined to the incoming flow,  $p_2 < p_1$ . But, energy release also causes a drop in pressure, unless the flow diverges significantly (see reference 13 in paper). Thus,  $p_1' < p_1$ . The inequalities,  $p_2 < p_1$  and  $p_1' < p_1$  being parallel, the deflection of streamline #1 depends on which of these two competing effects, the inclination of

the shock or the energy release, decreases the pressure faster.

In all the cases presented in the paper, the reaction zone thickness is so small in comparison to the radius of curvature of the shock,  $p_2 > p_1'$ , whence  $d\phi/d\xi < 0$  always. But if the detonation becomes highly curved to the extent where  $p_2 < p_1'$ , then  $d\phi/d\xi > 0$ , i.e., the streamlines will bend further away from the axis after crossing the shock. As explained in the introduction of the paper, highly curved detonations were observed in some recent non-ideal underwater explosives, and they also occur when the critical diameter is approached. Both cases are similar as far as the detonation curvature is concerned, because in both cases, a significant fraction of the energy is released after the CJ plane.

The example presented in the paper yields a slightly curved detonation. It was selected for its simplicity, and in order to allow the reader to compare the results with those of other analytical methods. However, unlike other methods, DSLD can be also used to study highly curved detonations, because there are no assumptions inherent in the method, other than the flow has to be steady. In the Detonation Shock Dynamics method (see reference 8 in paper), for example, the streamline direction is approximated by the normal to the shock front, which is true in slightly curved detonations. But as obvious from Fig. 1', the more the shock front is curved, the larger is the angle between the normal  $n$  and the streamline. In future publications, cases of highly curved detonations, in which the streamlines bend further away from the axis after crossing the shock, will be presented.

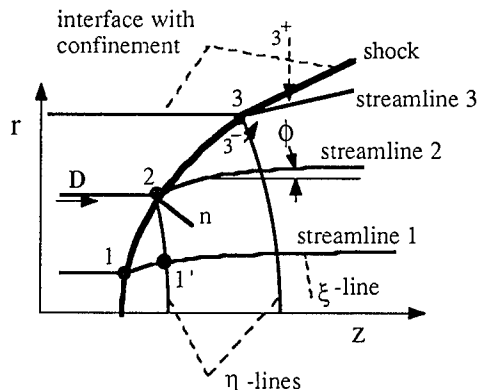


FIGURE 1'. FLOW CONFIGURATION FOR A SLIGHTLY CURVED DETONATION IN A HEAVILY CONFINED EXPLOSIVE

## DISCUSSION

J. E. KENNEDY  
Los Alamos National Laboratory  
Los Alamos, New Mexico 87545, USA

Do you intend to include the effects of confinement in the future?



## REPLY BY R. GUIRGUIS:

The effect of confinement is an important issue that will be addressed separately in a future publication. As explained in the paper, the limited domain in Fig. 2 was selected in order to illustrate the principal features of the DSLD method, without the complications the effect of confinement introduces. This limited domain allows us to derive the detonation curvature for a given detonation velocity, but not both. A further simplification is also implicit in the case study presented in the paper. The flow is subsonic at the edge of the domain of solution, point 3 in Fig. 1', i.e.,  $M_3(0) < 1$ . As in the paper,  $\xi=0$  is used here to designate the state immediately after the detonation shock front. The superscript (-) denotes conditions on the explosive side of streamline #3, while (+) denotes conditions on the confinement side. The resulting flow can be either considered representative of only the central part (near the axis) of the steady flow resulting from detonation of a larger diameter unconfined charge, or the whole flow in a heavily confined charge.

When the charge is heavily confined by an inert medium, a shock that is attached to the edge point 3, and that travels with the detonation wave, is formed in the confinement. This is the configuration illustrated in Fig. 1'. Across the detonation shock front, the pressure jumps to  $p_{3-}(0)$ . Since the pressure is continuous across streamline #3,  $p_{3+}(0) = p_{3-}(0)$ .  $p_{3+}(0)$  can be much higher than the ambient pressure  $p^0$ , because a shock in a heavy confinement can provide the needed discontinuous jump from the ambient pressure to  $p_{3+}(0)$ .

When the charge is unconfined,  $p_{3+}(0) \approx 0$ . In this case, a Prandtl-Meyer rarefaction wave, centered at point 3, is needed to drop the pressure instantaneously from  $p_{3-}(0)$  to zero at  $3^+$ , as illustrated in Fig. 2' below. But such a wave is impossible unless  $M_3(0) \geq 1$ . Here, the superscripts (-) and (+) are used to denote the states before and after the centered rarefaction wave, respectively. The flow also makes an abrupt turn at point 3, from  $u_{3-}(0)$  to  $u_{3+}(0)$ . Except at point 3, where it is centered, this rarefaction wave is not a simple wave, because upstream, the flow is rotational, and energy is released in the flow within the wave.

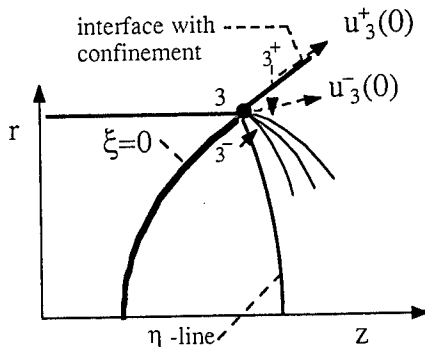


FIGURE 2'. FLOW CONFIGURATION FOR AN UNCONFINED EXPLOSIVE

If the shock front profile is continuous, and the Mach number at the edge  $M_e(0) > 1$ , there must be a point s on the front, where  $M_s(0) = 1$ , as illustrated in Fig. 3' below. After crossing the shock between s and e, the flow is still supersonic. Unless this flow is highly divergent, the energy released by the chemical reaction will decrease its Mach number towards  $M=1$  again. In this case, the sonic locus has two separate segments meeting at s. The outer segment will either intersect the rarefaction wave from the edge, which is impossible, bend away from it, or become tangent to its leading characteristic. In all three of these conjectures, the shock segment between point o, on the axis, and point s, is isolated from any information about the existence of the edge (also, see reference 6 in paper), which is unphysical. Thus, the only remaining option is  $M_3(0) = 1$ .

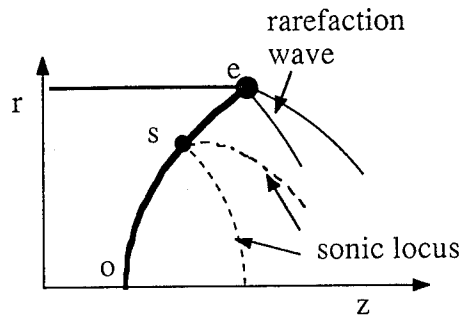


FIGURE 3'.  $M_e(0) > 1$  IS IMPOSSIBLE

Since in DSLD we solve along the streamlines, the edge of the unconfined charge introduces two separate problems. Even if  $M_3(0) > 1$ , streamline #3 discontinuously turns from  $u_{3-}(0)$  to  $u_{3+}(0)$ . In addition,  $M=1$  is a singularity, as obvious from for Eq. 1 in the paper. Figure 4' below shows that solving along the streamlines can still be accurately performed in the case a sonic flow turning over a convex corner to  $M=2$ . In Fig. 4', the  $\xi$  and  $\eta$ -lines predicted by the streamline dynamics method are compared to those obtained from the analytical solution of this simple wave.

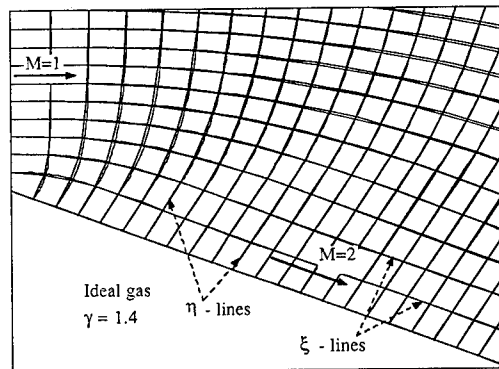


FIGURE 4'. COMPARISON BETWEEN ANALYTICAL AND STREAMLINE DYNAMICS SOLUTION OF A PRANDTL-MEYER FLOW

## PROPAGATION PHENOMENA ON THE DETONATION WAVE FRONT

J. M. Chevalier, N. Carion

Commissariat à l'Energie Atomique, CEV-M - BP  
n°7 - 77181 COUNTRY - France

A new theoretical approach to the unsteady detonation in condensed explosives was developed. The first experimental results presented in this paper confirm that the evolution of the front can be described by the propagation of front-waves, as predicted by the model. It seems, also, that the speed of these waves is a decreasing function of detonation velocity and does not depend on the confinement of the explosive.

### INTRODUCTION

A new model describing the detonation front propagation in condensed explosives (named Jr model) has been recently proposed by L. Brun.<sup>1-2</sup> First macroscopic model of the unsteady detonation, the Chapman-Jouguet model<sup>3</sup> assumes an instantaneous and complete decomposition across a downstream sonic discontinuity. But the condition of a detonation propagation at constant velocity doesn't agree with the curved steady revolution detonation (SRD) fronts observed on condensed explosives. The Zeldovitch-Von Neuman-Döring model ZND<sup>4-5</sup> assumes that the decomposition goes on behind a non reactive and hence subsonic discontinuity. The ZND model agrees for interpretations of the SRD<sup>6</sup>, but can't be extended to unsteady cases like spherically diverging detonation.

In the Jr model, the front acceleration is related to its curvature by two functions of the local detonation velocity: the characteristic curvature, which has been already studied (Aveillé, Bdzil)<sup>7-11</sup>, and a new function, the characteristic speed, which describes the front-wave propagation.

Original experiments were performed in order to check the model, in TATB and HMX based compositions, to confirm the front-waves propagation.

### THE RELAXED JOUGUET MODEL (Jr)

Three assumptions govern the model. The detonation front is assumed to be taken as an infinitely thin and downstream sonic discontinuity. But this model does not suppose, as Jouguet's did, a total decomposition within the front, and thus accordingly releases Jouguet's condition  $D=D_c$ <sup>1</sup>. The acceleration of a self-sustained detonation wave front is given by the relation:

$$\delta D / \delta t = 2 C^2(D) [K(D) - \mathcal{C}]$$

where  $\mathcal{C}$  is the curvature of the front,  $C(D)$  the transverse front-waves velocity and  $K(D)$  the celerity-curvature relationship. The associated boundary condition is:  $B(\theta_b, D_b) = 0$ , where  $\theta_b$  is the front inclination on the unperturbed interface and  $D_b$  the front velocity at the boundary.

The characteristic angle connects the transverse front-wave speed with the detonation velocity by the relation :

$$\operatorname{tg} \varphi = C(D)/D.$$

### ASSOCIATED EXPERIMENTS

The Jr model can easily be used to describe what would happen in a cylindrical geometry :

if a steady detonation propagates in an explosive cylinder, a sudden reduction of the diameter generates a circular perturbation which propagates inwards.

As shown figure 1, the model tells that, if the perturbation starts at time  $t_0$ , at  $t_0 + dt$  a length  $Cdt$  of the front will be modified. The  $TT'$  surface is not yet affected, and is determined by a translation of the  $NN'$  surface.

These phenomena must be experimentally observed in order to check the model.

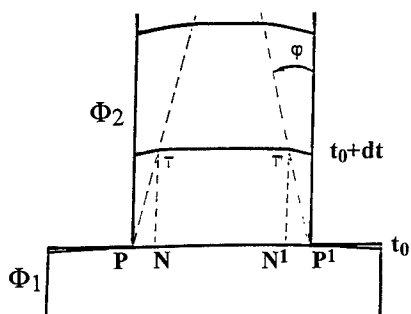


FIGURE 1. DISPLAY PRINCIPLE OF FRONT WAVES

#### EXPERIMENTAL SET-UP

The experimental set-up used to observe the detonation front and to measure the front-wave speed is presented figure 2.

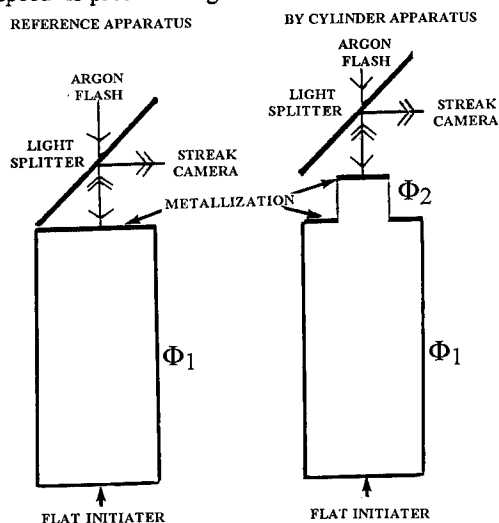


FIGURE 2. DISPLAY EXPERIMENTAL SET-UP OF FRONT WAVES

A plane wave generator initiates a detonation wave in an unconfined explosive cylinder (diameter  $\phi_1$ ). Its length  $H_1$  is chosen in order to achieve a steady detonation. The cylinder free surface is metallized for the optical recording of the front motion.

An argon flash-light is reflected by the surface and focused on a streak camera. When the detonation wave interacts with the surface, the damage of the metal spray is recorded on the film.

In another experiment a cylinder of diameter  $\phi_2$  ( $\phi_2 < \phi_1$ ) and length  $H_2$  is added to the previous one, and the detonation front is observed by using the same technics. Comparison of the shapes of the waves which emerge from both cylinders yields the velocity of the front-waves.

#### EXPERIMENTAL RESULTS

##### TATB Based Composition $T_2$ (97% TATB)

In order to study the variation of the transverse front-waves speed  $C$  versus the detonation velocity  $D$ , several cylinder diameters  $\phi_1$  have been tested. For  $T_2$  composition, as for other TATB compositions, the detonation velocity is strongly dependent on the cylinder diameter (Aveillé). <sup>10-11</sup>

Figure 3 presents the optical records obtained in one configuration. In the first experiment, the dimensions were  $\phi_1 = 30$  mm,  $H_1 = 120$  mm. In the second experiment, a cylinder  $\phi_2 = 15$  mm,  $H_2 = 15$  mm is added.

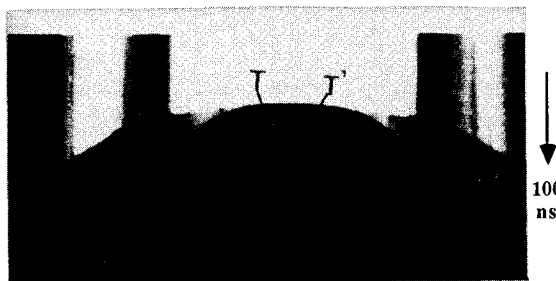


FIGURE 3. EXTENDING SUPERPOSITION OF  $T_2$   
 $\phi_1 = 30$  mm AND  $\phi_2 = 15$  mm WAVES OUT

No noise perturbs the records. The superposition of the two measurements gives an accurate determination of the transverse front-waves speed. The central part of the front, delimited by the two points  $T$  and  $T'$ , is not yet affected by the perturbations propagated by the transverse front-waves, as predicted by the Jr model.

As defined figure 1,  $D$  and  $C$  are given by the relation :  $D = NT/dt$ ,  $C = PN/dt$ .  $C$  is the average value of the transverse front-waves velocity.  $D$  is in good agreement with previous measurements. <sup>10-11</sup>

The values of  $C(D)$ , reported in table 1, show that  $C$  is a decreasing function of  $D$ .

TABLE 1. MEASURED VALUES ON T<sub>2</sub> COMPOSITION

$\Phi_1/\Phi_2$ mm	H <sub>2</sub> mm	D m/s	C(D) m/s	$\varphi$ (°)	$\Delta D$ m/s	$\Delta C$ m/s	$\Delta \varphi$ (°)
30/15	15	7538	2810	20.4	35	250	2
		7519	2810	20.5	35	250	2
75/50	40	7627	1880	13.8	20	140	1
100/50	40	7603	2170	15.9	20	140	1

To complete the determination of function C(D), a series of experiments has been performed with cylinder diameters  $\phi_1$  decreasing from 75 to 10 mm. In these conditions the detonation velocity decreases from 7630 to 7290 m/s.<sup>10-11</sup> The C(D) measured values are reported on table 2. The variations of transverse front-wave speed C versus the detonation velocity are recorded on figure 4. These results confirm that C is decreasing function of D. The last value seems to express that the front-wave speed increases strongly near the critical diameter ( $\phi_c=8.5$  mm for T<sub>2</sub> composition). Nevertheless, this value needs to be confirm.

TABLE 2. TRANSVERSE FRONT-WAVE SPEED VERSUS DETONATION VELOCITY

$\Phi_1/\Phi_2$ mm	H <sub>1</sub> mm	H <sub>2</sub> mm	D m/s	C(D) m/s	$\varphi$ (°)	$\Delta D$ m/s	$\Delta C$ m/s	$\Delta \varphi$ (°)
75/50	510	40	7626	1990	14.6	8	100	0.8
60/40	370	30	7612	1990	14.7	10	130	1
40/20	240	14	7560	2320	17.1	20	140	1
30/15	160	10	7558	2490	18.2	30	200	1.5
20/14	100	9	7502	2670	19.6	30	220	2
15/10	75	4	7438	3350	24.2	70	400	3
		6	7413	3210	23.4	45	270	2
10/6	50	2	7326	5860	38.7	135	840	6

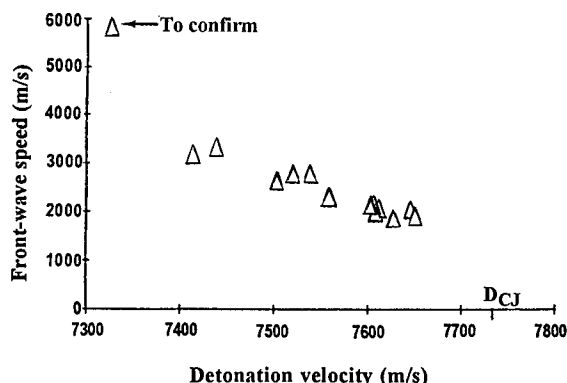


FIGURE 4. VARIATION OF TRANSVERSE FRONT-WAVE SPEED C VERSUS DETONATION VELOCITY

In a second study a series of experiments has been performed to observe the variation of transverse front-wave speed C with the time.

In this case, configurations with  $\phi_1=50$  mm,  $\phi_2=30$  mm and H<sub>2</sub>=10 to 50 mm by 10 mm step has been tested. For this configuration the detonation velocity on the axis wouldn't vary.

The experimental results are reported on table 3. The measured values of C confirm that to one detonation velocity value D is associated one transverse front-waves speed C, taking the experimental accuracy into account.

TABLE 3. MEASURED VALUES OF TRANSVERSE FRONT-WAVE SPEED VERSUS TIME ON T<sub>2</sub> COMPOSITION

$\Phi_1/\Phi_2$ mm	H <sub>1</sub> mm	H <sub>2</sub> mm	D m/s	C(D) m/s	$\varphi$ (°)	$\Delta D$ m/s	$\Delta C$ m/s	$\Delta \varphi$ (°)
50/30	300	10	7612	2090	15.4	30	390	3
		20	7607	2020	14.9	15	195	1.5
		30	7607	1990	14.7	10	130	1
		40	7606	2170	15.9	8	65	0.5
		50	7609	2025	14.9	6	40	0.5

#### HMX Based Compositions X<sub>1</sub> and X<sub>2</sub> (96 and 94.2% HMX)

These two HMX based compositions differ essentially by their binders. The C(D) measured values are reported in table 4.

TABLE 4. MEASURED VALUES ON X<sub>1</sub> AND X<sub>2</sub> COMPOSITIONS

Compo sition	$\Phi_1/\Phi_2$ mm	H <sub>2</sub> mm	D m/s	C(D) m/s	$\varphi$ (°)	$\Delta D$ m/s	$\Delta C$ m/s	$\Delta \varphi$ (°)
X <sub>1</sub>	25/10	20	8755	1450	9.4	40	100	1
X <sub>1</sub>	50/30	30	8744	1530	9.9	25	100	1
X <sub>2</sub>	100/50	40	8767	1420	9.2	20	100	1
X <sub>2</sub>	100/50	80	8760	1320	8.5	10	100	1

In both compositions, the values are nearly the same, as expected, and lower than those found for the TATB composition.

For these HMX based compositions experiments, the decrease of the detonation velocity is not significant enough to check whether the function  $C(D)$  is decreasing or not.

### Influence of the Confinement

The Jr model predicts that  $C$  is a function of the detonation velocity and will not depend on the boundary conditions. Some experiments were performed with a case (aluminum or steel) around the second explosive cylinder. The results are given in table 5.

TABLE 5. INFLUENCE OF CONFINEMENT

Comp. / Wall	$\Phi_1/\Phi_2$ mm	H <sub>2</sub> mm	D m/s	C(D) m/s	$\varphi$ (°)	$\Delta D$ m/s	$\Delta C$ m/s	$\Delta \varphi$ (°)
X <sub>2</sub> / Air			8767	1420	9.2	20	100	1
X <sub>2</sub> / 2024	100/50	40	8787	1370	8.9	20	100	1
T <sub>2</sub> / Air			7603	2170	15.9	20	140	1
T <sub>2</sub> / Steel	100/50	40	7646	2060	15.1	20	140	1
T <sub>2</sub> / 2024			7651	1940	14.2	20	140	1

The measured values of  $C$ , with and without confinement, are very close to each other.

Of course, the shapes of the detonation fronts are very different : the transverse front-waves move with the same speed, but they do not carry the same information.

### UNSTEADY REGIME

In the experiment depicted in figure 5 the detonation was initiated in a cylinder of T<sub>2</sub> composition by a plane detonation making an angle of 74° with the axis. It appears that the detonation in the T<sub>2</sub> cylinder evolves toward the stationary shape which would be observed when initiation is perpendicular to the axis.

Indeed several configurations have been performed with T<sub>2</sub> cylinders which dimensions are respectively  $\phi=50$  mm and  $H=100, 200, 400$  and 600 mm. For the first one, the optical record presented (figure 6) shows an asymmetrical detonation front with regard to the axis. For the third, the detonation front (figure 7) was nearly steady, presenting a weak asymmetry.

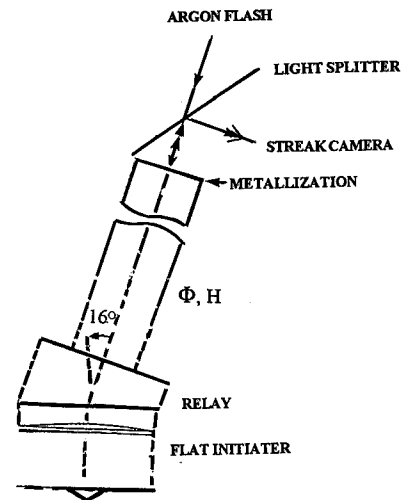


FIGURE 5. EXPERIMENTS IN UNSTEADY DETONATION FIELD

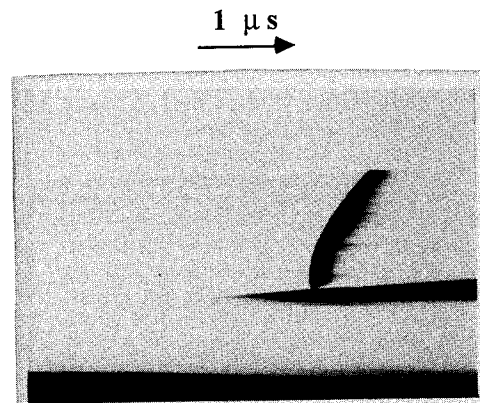


FIGURE 6. OPTICAL RECORD OF DETONATION IN T<sub>2</sub> CYLINDER (  $\Phi=50$  mm AND  $H=100$  mm) INITIATED BY A PLANE DETONATION MAKING AN ANGLE OF 74° WITH THE AXIS

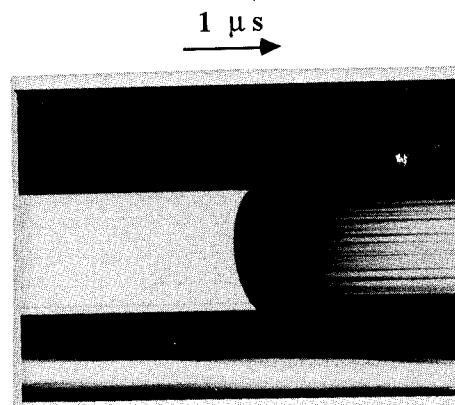


FIGURE 7. OPTICAL RECORD OF DETONATION IN T<sub>2</sub> CYLINDER (  $\Phi=50$  mm AND  $H=400$  mm) INITIATED BY A PLANE DETONATION MAKING AN ANGLE OF 74° WITH THE AXIS

For this configuration, the perturbation due to the diameter reduction which propagates inwards, arrives at center of the cylinder and reverberates two times before the detonation emergence. For the last one, the recorded detonation front is steady and presents the same characteristics as a detonation front with initiation perpendicular to the axis.

#### ASSOCIATED BOUNDARY CONDITION

For this study, two methods were used to measure the front inclination.

The first (classical method) is based on the front detonation record at the end of an explosive cylinder. For the second (zero method), this cylinder is terminated in cone ("pencil") with an inclination  $\theta_b$  corresponding to the presumed value. This method allows a more accurate measure of the motion at this presumed value. The experimental set-up of this method and the optical record obtained for  $T_2$  cylinder with 15 mm diameter are presented respectively figures 8 and 9. Measures were obtained after digitization and linear approximation on 0.7 mm of boundary front wave. The measured values for  $T_2$  composition are shown on table 6. The boundary detonation velocity is given by the relation  $D_b = D \cdot \cos\theta_b$ , where the  $D$  values were measured by Aveillé et al. <sup>10-11</sup> The classical method, though less accurate, gave interesting results.

These results show that  $\theta_b$  is (like  $C$ ) a decreasing function of  $D$ .

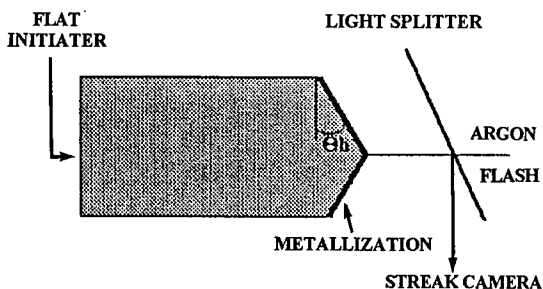


FIGURE 8. EXPERIMENTAL SET-UP OF THE ZERO METHOD FOR BOUNDARY CONDITION DETERMINATION

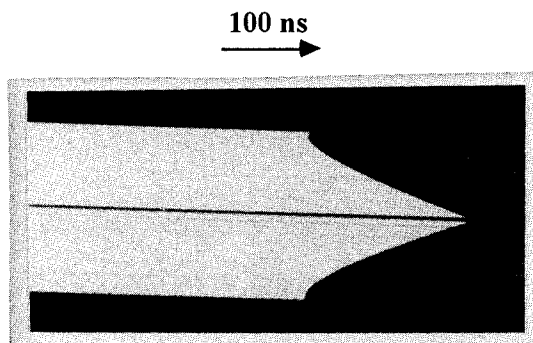


FIGURE 9. OPTICAL RECORD FOR  $T_2$  "PENCIL"  
( $\Phi = 15$  mm AND  $H = 180$  mm)

TABLE 6. MEASURED VALUES OF THE BOUNDARY CONDITION ON  $T_2$  COMPOSITION

$\Phi$ mm	(Zero method)		(Classical method)	
	$D_b$ m/s	$\theta_b$ (°)	$D_b$ m/s	$\theta_b$ (°)
50			7145	20.1
40			7095	20.2
30	7095	19.8	7110	19.8
20	7020	20.7	7065	19.6
15	6885	22.7	6925	21.1
10			6450	28.3
9			6340	29.6

$$\Delta\theta_b \sim 1^\circ$$

#### CONCLUSION

The experimental results presented in this paper are in general agreement with the front wave propagation phenomena as described by the Jr model. They were obtained for TATB or HMX based compositions, which exhibit very different front curvatures and these preliminary results seem to confirm the basic assumption of a transverse front-wave speed that only depends upon the detonation velocity.

The results on TATB based composition show that  $C$  is a decreasing function of  $D$ . Experiments performed on HMX based compositions can't lead to same conclusions. Results on TATB ( $C(D)$  function associated with the boundary condition values) would certainly allow us to treat more physically the detonation in calculations.

## REFERENCES

1. L. Brun "Une théorie de la détonation dans les explosif condensés fondée sur l'hypothèse de Jouguet" CEA Report (Unpublished 1989)
2. L. Brun "Un nouveau modèle macroscopique de la détonation non soutenue dans les explosifs condensés" Symposium International Hautes Pressions Dynamiques, la Grande Motte p.103-107, CEA eds (1989)
3. E. Jouguet "Mécanique des explosifs" Doin et fils eds (1917)
4. R. Courant and K.O. Friedrichs "Supersonic flow and shock waves" I.P. (1948)
5. W. Fickett and D.C. Davis "Detonation" University of California Press (1979)
6. J.B. Bdzil "Steady - state two - dimensional detonation" J. Fluid. Mech., 108, 195-226 (1981)
7. J.B. Bdzil and D.S. Stewart "Modeling two dimensional detonations with detonation shock dynamics" Phys. of Fluids, 1,7, P. 1261-67 (1989)
8. C. Bianchi, N. Carion and J. Aveille CEA Report (Unpublished 1987)
9. C. Perennes, C. Bianchi, N. Carion and F. Chaisse CEA Report (Unpublished 1988)
10. J. Aveille, J. Baconin, N. Carion and J. Zoe "Experimental study of spherically diverging detonation waves" The Eighth Symposium International on Detonation, 523-527, Albuquerque (1985)
11. F. Chaisse, J. M. Servas, J. Aveille, J. Baconin, N. Carion and P. Bongrain "A theoretical analysis of the shape of a steady axisymmetrical reactive shock front in cylindrical charges of high explosive. A curvature-diameter relationship" The Eighth Symposium International on Detonation, 539-547, Albuquerque (1985)

## ACKNOWLEDGEMENTS

We wish to thank J.C. Protat and J.C Redasse for their enthusiasm and diligence in executing our experiments with great care.

## DISCUSSION

A. N. DREMIN  
Institute of Chemical Physics, Chernogolovka, Russia

The velocity of the surface waves you discuss has an unusually low value. Could you comment on the wave's nature and, in particular, how the waves relate to the explosive state beside the detonation wave front?

## REPLY BY J. M. CHEVALIER:

C is the velocity with which infinitesimal perturbations of the detonation wave front propagate along the front. Because by construction the Jr model views the front as infinitely thin in the same way as Riemann-Hugoniot relating does, it does not refer to the structure of the front. The resulting expression for C, by nature exclusively thermodynamic, depends only on the values of the adiabatic index  $\gamma = v(p + \delta e / \delta v) / (p \delta e / \delta p)$  along the sonic locus via a formula given in Brun's original paper and to be found for instance in the paper of Brun et al. in the symposium.

## COMPUTING THE TRANSIENT SELF-SUSTAINED DETONATION AFTER A NEW MODEL

L. Brun - Commissariat à l'Energie Atomique - B.P. 7 - 77181 COURTRY (France)  
J-M. Kneib - CISI-Ingénierie - Centre d'Etudes Nucléaires de Saclay\*  
P. Lascaux - Centre d'Etudes de Limeil-Valenton

When a self-sustained smoothly propagating detonation wave encounters an abrupt change in, say, the boundary conditions, it undergoes a transient evolution in order to adapt to the new situation. Correctly modelling the transient regime is of importance if one is to successfully predict the subsequent position of the front. A theory has recently been put forward by one of us<sup>1a,b</sup> along Jouguet's line of thought, which combines in a single equation the effects of curvature, explosive decomposition and propagation of signals along the front. This fundamental equation turns out to reduce to Chisnel-Whitham's A-M relation in the absence of the reactivity source-term, and the associated mathematical problem to be of hyperbolic type. In order to assess the new approach, an experimental program is currently being developed with special emphasis on the geometrically simple 'trapezium test' which, while showing off specific features of the transient regime, lends itself to a variety of measurements and a comparatively safe numerical solution of the model equations. After reviewing general aspects of the model, we concentrate on preliminary computational results obtained within the context of the trapezium test.

### THE MODEL

The simplest theory, as expounded in Jouguet's treatise<sup>2</sup>, views the self-sustained detonation as a transition zone in a reactive medium with a single progress variable and negligible transport phenomena, that obeys the three conditions of being (i) vanishingly thin; (ii) downstream sonic; (iii) totally reactive. It implies a constant velocity<sup>2</sup>  $D_{cj}$  and infinitely steep gradients downstream of any curved front<sup>3</sup>. While shortcomings of the theory for gases<sup>4</sup> are mainly attributable to the inadequacy of assumption (i), thus entailing reconsideration of (ii) and (iii) as well, experimental evidence for condensed explosives of a narrow ( $\leq 1$  mm) detonation zone, and fairly steep gradients<sup>5,6</sup> suggests that merely removing condition (iii) should allow by itself an improvement to Jouguet's theory<sup>7</sup>. Indeed, without further ingredient, the mathematical treatment<sup>1a</sup> of the customary hydrodynamic equations<sup>4</sup> leads to the front propagation law:

$$(1) \quad \frac{\delta D}{\delta t} = 2 C^2(D) [K(D) - \phi],$$

where  $D$  is the local detonation velocity,  $\delta D/\delta t$  the acceleration normal to and  $\phi$  the mean curvature of the front.

Functions  $K$  and  $C$  turn out to be connected<sup>1a</sup> to the sequence of values of the decomposition-rate  $r$ , the adiabatic index  $\gamma$  and the coefficient of thermicity  $\sigma$  along the sonic locus<sup>4</sup> through formulas:  $2K = (\gamma + 1) \sigma r/D$ ,  $C^2/D^2 = (3(\gamma + 1)/\gamma - 2 \ln \gamma / \ln D)^{-1}$ . These last will not be needed in the present study, since both  $K$  and  $C$  are supposed to be inferred from experiment thanks to the more or less direct consequences of Eq. (1) that follow.

- At a point of zero acceleration the *characteristic curvature*  $K$  is seen to equal the front mean curvature. At such a point, the detonation velocity and the curvature are thus in a one-to-one relationship, a property first pointed out by Wood and Kirkwood for the particular case of the apex of a stationary axisymmetric detonation.

- Function  $C$  has the dimensions of a velocity.

\*under contract CEL-V



Indeed, after converting Eq. (1) into a second order PDE in  $F$ , with  $z = F(x, y, t)$  the equation of the front surface  $\Sigma_t$ , function  $C$  comes out to be the *characteristic speed* associated with "front waves". Such a prediction is currently being investigated<sup>8</sup>.

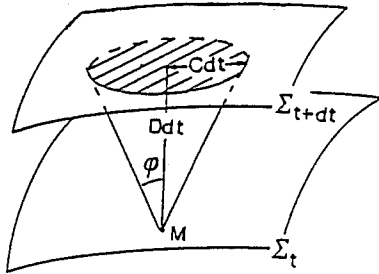


FIGURE 1. A PERTURBATION LOCATED AT POINT M AT TIME  $t$  EXTENDS OVER THE HATCHED DISK AT TIME  $t + dt$

The circular intersection of  $\Sigma_{t+dt}$  and the cone having its axis normal to  $\Sigma_t$  at the vertex M and its half-angle equal to the *characteristic angle*  $\varphi(D) = \tan^{-1}(C/D)$  thus delimits the domain of influence of M at time  $t + dt$ .

When  $K$  is equal to zero, Eq. (1) readily integrates to such a  $D$ - $A$  relation between  $D$  and the local surfacic dilatation  $A$  of the front as is at the root of Whitham's geometrical shock dynamics<sup>9</sup>.

#### APPLICATION TO PLANE AND SPHERICAL DETONATIONS

We identify the zero of  $K$  with  $D_{cj}$  and suppose that  $\lim_{D \rightarrow D_{cj}} K(D)/(D_{cj} - D) = a$ , whereas  $C_{cj} \neq 0$ .

Then  $D_{cj} - D$  decreases exponentially to zero according to an inverse characteristic time  $\tau^{-1} = 2a D_{cj}^{-2} \tan^2 \varphi_{cj}$ . Example : for the 94,2 % HMX-based composition X2, we adopt  $D_{cj} = 8760 \text{ m.s}^{-1}$ ,  $a = 0,89 \text{ s.m}^{-2}$ ,  $\varphi_{cj} = 9^\circ$ , and get  $\tau \sim 3.10^{-7} \text{ s}$ .

In the spherically diverging case, it may be shown<sup>1a,b</sup> that the value of  $D$  at radius  $R$  is necessarily *less* than the velocity of the cylindrical stationary detonation with the same radius of curvature  $R$  on the axis. This is in broad agreement with the experimental results of Aveillé et al.<sup>10</sup>.

#### THE TRAPEZIUM TEST - PRINCIPLE, PHENOMENOLOGY AND GOVERNING EQUATIONS

Let an unconfined explosive slab with thickness  $d$  extend to infinity in directions  $y \pm$  and  $z_+$ . Let too, at time zero, an ideally plane CJ-detonation

front parallel to the  $y$ -axis be inclined at an angle  $i$  to the  $x$ -axis (figure 2). As the detonation runs

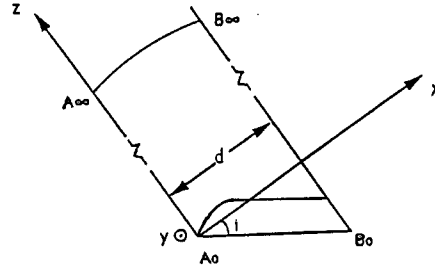


FIGURE 2. CONFIGURATION OF THE TRAPEZIUM TEST (SUPERSONIC CASE)

down the  $z_+$  direction, the front keeps the shape of a cylinder the cross section of which eventually modifies from the initial segment  $A_0B_0$  to the asymptotically stable profile  $A_\infty B_\infty$  (we suppose that  $d$  exceeds the failure thickness).

According to the model, the transition to the steady regime begins as follows. A rarefaction wave headed by a second-order discontinuity propagating with speed  $C_{cj}$  starts from the left, bringing the angle  $\theta$  of the normal to the front with the  $z$ -axis, a function of  $x$  and  $t$  initially equal to  $-i$ , to a positive value  $\theta_1(t) = \theta(0, t)$  on the left interface (the inclination  $i$  is supposed to be small enough to allow to disregard a possible dead-zone effect on the overall motion).

At the same time, a similar phenomenon may occur or not from the opposite direction according to whether the motion of the trace of the right interface along the front is subsonic (with respect to the local characteristic speed  $C_{cj}$ ), that is  $i < \varphi_{cj}$ , or supersonic, that is  $i > \varphi_{cj}$ . In the supersonic case (figure 2), the front does not "feel" the presence of the right interface until the release wave from the left has increased the angle  $\theta_r(t) = \theta(d, t)$  to such a value that the motion of the trace becomes subsonic.

The corresponding mathematical formulation consists of general equations and boundary conditions. We first have the system of geometrical relationships :

$$(2) \quad \frac{\partial F}{\partial x} = -\tan \theta$$

$$(3) \quad \frac{\partial F}{\partial t} = \frac{D}{\cos \theta}$$

between  $F$ ,  $D$  and  $\theta$ . Both  $D$  and  $\theta$  satisfy the first-order system made up of the front propagation law

(4), with the notation  $s = -2C^2K$  for the source term, and the compatibility equation (5) that results from equating the cross-derivatives of  $F$  deduced from the preceding system :

$$(4) \quad \frac{\partial D}{\partial t} + D \sin \theta \frac{\partial D}{\partial x} + C^2(D) \cos \theta \frac{\partial \theta}{\partial x} - s(D) = 0$$

$$(5) \quad \frac{\partial \theta}{\partial t} + D \sin \theta \frac{\partial \theta}{\partial x} + \cos \theta \frac{\partial D}{\partial x} = 0.$$

This is a quasilinear hyperbolic system, with eigenvalues

$$(6) \quad \lambda^\pm = D \sin \theta \pm C(D) \cos \theta,$$

which may be rewritten in the equivalent form

$$(7) \quad \frac{d^+ D}{dt} + C(D) \frac{d^+ \theta}{dt} - s(D) = 0$$

$$(8) \quad \frac{d^- D}{dt} - C(D) \frac{d^- \theta}{dt} - s(D) = 0,$$

where we have set

$$\frac{d^\pm}{dt} = \frac{\partial}{\partial t} + \lambda^\pm \frac{\partial}{\partial x}.$$

The boundary conditions follow in part from the previous phenomenological description : in the supersonic case, none is to be applied. They will be specified further without appeal to physical arguments, while demanding that they be simple and likely to render the solution to the problem unique. Let the index  $b$  refer to any of the boundaries and  $\theta_b = \theta_l$  or  $-\theta_r$ . In the subsonic case,  $\theta_b$  is accordingly assumed<sup>1a</sup> to be a function  $\Theta$  of the single variable  $D_b$  subject to the condition  $\Theta(D) \leq \varphi(D)$ . For lack of published data concerning both  $\Theta$ ,  $\varphi$  for the same composition, we shall adopt the limiting dependance

$$(9) \quad \theta_b = \varphi(D_b).$$

This dependence holds from the beginning on the left, causing one of the eigenvalues to cancel :

$$(10) \quad \lambda^-(D_l, \theta_l) = 0.$$

As soon as it holds on the right as well (see above), the other eigenvalue cancels :  $\lambda^+(D_r, \theta_r) = 0$ .

One remark is in order. The slab is actually of finite extent so right from the start rarefaction waves propagate from both sides that border it in the  $y$ -direction, destroying the cylindrical

conformation of the front in their wake : our bidimensional picture only applies to a steadily diminishing portion of the front until the waves meet.

## NUMERICAL SCHEME

The mesh points  $(x_j, t^{n+1})$  of the finite differences scheme used are defined by :

$$\begin{aligned} x_j &= (j-1) \Delta x \quad j = 1, \dots, N \\ \Delta x &= d/(N-1) \\ t^{n+1} &= t^n + \Delta t_n, \end{aligned}$$

where  $N$  is the number of space intervals taken to be equal,  $\Delta t_n$  the time step deduced from the C.F.L. condition

$$(11) \quad \Delta t_n = \Delta x / \max_j \{ |\lambda_j^{n+1}|, |\lambda_j^n| \},$$

and  $f_j^n$  the approximation to a function  $f(x, t)$  at point  $x_j, t^n$ .

The overall procedure is as follows. Starting from the general equations appropriately discretized will allow to determine  $F_j^{n+1}, D_j^{n+1}$  for  $j = 1, \dots, N$  from the already known  $F_j^n, \theta_j^n, D_j^n$ . The same holds true for  $\theta_j^{n+1}$ , for  $j = 2, \dots, N-1$ . The boundary conditions will finally come into play to determine the boundary values  $\theta_b^{n+1}$  ( $b = 1$  or  $N$ ).

The geometrical relationships (2) and (3) are accordingly first discretized as

$$(12) \quad F_j^{n+1} = F_j^n + \Delta t_n D_j^n / \cos \theta_j^n \quad j = 1, \dots, N$$

$$(13) \quad \theta_j^{n+1} = -\tan^{-1} \frac{F_{j+1}^{n+1} - F_{j-1}^{n+1}}{x_{j+1} - x_{j-1}} \quad j \neq 1, N.$$

As is at once clear from the inspection of Eqs. (4-8), any equation that may serve the purpose of approximating  $D$  involves directional derivatives of the form

$$(14) \quad E = \frac{\partial f}{\partial t} + v(\theta, D) \frac{\partial f}{\partial x}$$

(with  $v$  being equal to  $D \sin \theta$ ,  $\lambda^+$  or  $\lambda^-$ ), which must be discretized. There results from a first-order Taylor expansion that the expression  $\{f(t^{n+1}, x_j) - f(t^n, \xi)/\Delta t_n\}$ , where  $\xi = x_j - v(\theta_j^n, D_j^n) \Delta t_n$ , is adequate to start with. The abscissa  $\xi$  belongs to some interval  $(x_k, x_{k+1})$  which only depends on  $j$  and  $v$ . Linearly interpolating between  $f_k^n$  and  $f_{k+1}^n$  then yields a certain approximation  $f_{(i)}^n$  to  $f(t^n, \xi)$

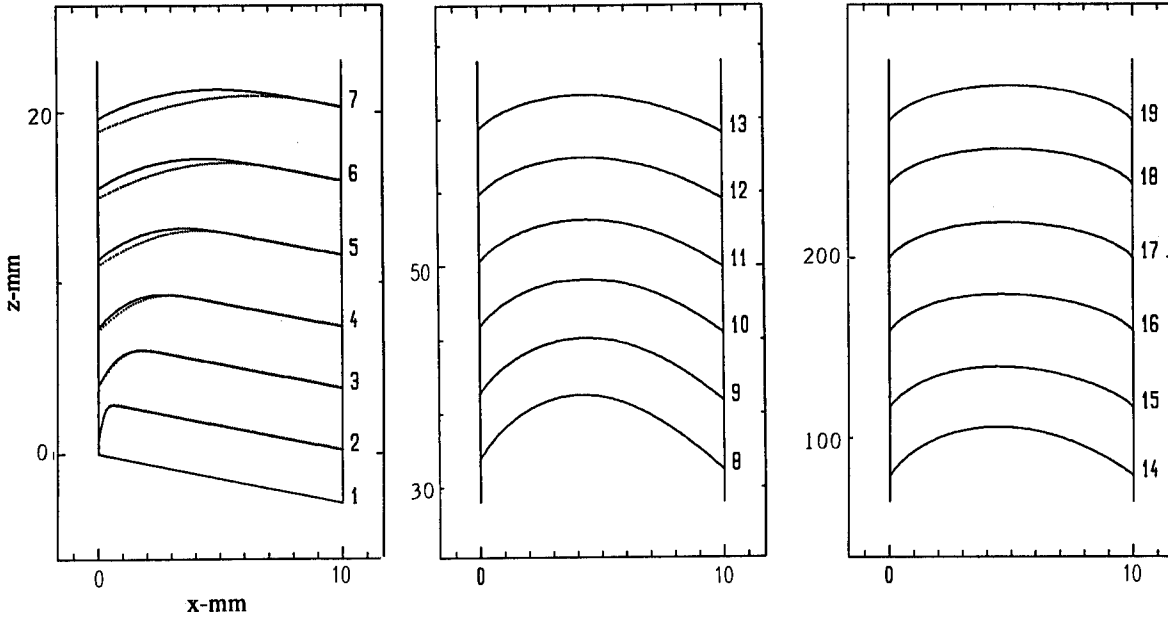


FIGURE 3. PROFILES OF THE FRONT THROUGH TIME.

which will be adopted to discretize E according to the formula

$$(15) \quad E_j^n = \frac{1}{\Delta t_n} (f_j^{n+1} - f_{(vj)}^n).$$

For the ensuing algorithm to work,  $v$  should never cancel. The cancelation of  $v$  is undesirable indeed because it may entail either approximations that converge towards nonphysical solutions<sup>11</sup> or instability through oscillations. None of the aforementioned equations may be uniformly used, since  $\theta$  cancels in the interior,  $\lambda^+$  at the right and  $\lambda^-$  at the left end of the  $x$ -interval. It may be seen however that Eq.(4) will be suitable at the boundary, whereas rewriting this same equation in the form of a combination of Eqs. (7) and (8), that is

$$(16) \quad \frac{1}{2} \left( \frac{d^+ D}{dt} + \frac{d^- D}{dt} \right) + \frac{C}{2} \left( \frac{d^+ \theta}{dt} - \frac{d^- \theta}{dt} \right) - s = 0,$$

will do in the interior. Denote  $f_{(vj)}^n$  by  $f_j^{on}$ ,  $f_j^{+n}$  or  $f_j^{-n}$  whenever  $v$  is equal to  $D \sin \theta$ ,  $\lambda^+$  or  $\lambda^-$ . Discretizing Eq.(16) given Eq.(15), we end up with the formulas :

$$(17) \quad D_j^{n+1} = \frac{1}{2} (D_j^{+n} + D_j^{-n}) + \frac{1}{2} C (D_j^n) (\theta_j^{+n} - \theta_j^{-n}) + \Delta t_n s (D_j^n), \quad j = 2, \dots, N-1$$

$$(18) \quad D_b^{n+1} = D_b^{on} - \Delta t_n \left\{ C^2 (D_b^n) \left( \cos \theta \frac{\partial \theta}{\partial x} \right)_b^n - s (D_b^n) \right\}$$

Finally, let  $a = |\tan^{-1}(\partial F / \partial x)_b^{n+1}|$  and  $\varphi_b = \tan^{-1} (C(D)/D)_b^{n+1}$ . We adopt

$$(19) \quad \theta_b^{n+1} = a \text{ if } a < \varphi_b, \text{ otherwise } \theta_b^{n+1} = \varphi_b.$$

The complete algorithm is made up of formulas (12), (13), (17), (18) and (19). It has been successfully tested in two ways : firstly while comparing the asymptotic profile of the front at large times with the one derived from the integration of the second-order ODE which governs the stationary motion<sup>1a,b</sup> ; secondly in the case of  $K \equiv 0$  and  $i > \varphi_{cj}$ , for which an explicit solution<sup>9</sup> is available up to the time when the motion ceases to be a simple wave.

### SOME COMPUTATIONAL RESULTS

Computations have been performed on the assumption of a linear dependence of the characteristic curvature on the detonation velocity and a constant characteristic angle, specifically :

$K \text{ (m}^{-1}\text{)} = 0,89 \text{ (8760 - } D \text{ (ms}^{-1}\text{))}$  and  $\varphi(D) = 90^\circ$ . These data apply to the 94,2 % HMX-based composition X2 at "sufficiently" high values of the detonation velocity.

Figure 3 represents results of the calculations in the case of  $d = 10 \text{ mm}$ ,  $i = 16^\circ$ , which is relevant to experiments under way. The y-axis of the figure is parallel to the vertical page side. From the bottom left to top right, profiles of the front are to be seen at successive times  $t_n$ , specified as follows:

n	1	2	3	4	5	6	7	8	9	10
$t_n(\mu\text{s})$	0	.08	.47	.87	1.3	1.8	2.3	2.8	3.8	4.8
n	11	12	13	14	15	16	17	18	19	
$t_n(\mu\text{s})$	5.8	6.9	7.9	9.1	13	18	23	28	32	

Numbers of the left of a column mark off the approximate distance travelled by the front. To exaggerate the curvature, dilatations along the y-direction by a factor varying with the column have been effected (the left end of a profile and the vertical distance between ends are preserved in the first column, both ends are in the other two).

The propagation of the initial rarefaction wave from the left is apparent. The linear part of the profile vanishes at time  $2.67 \mu\text{s}$  close to  $t_g$ , a result confirmed by elementary geometry. Not until time  $6,34 \mu\text{s}$ , between  $t_{11}$  and  $t_{12}$ , when the motion of

the right end of the profile becomes subsonic, does the presence of the right interface make itself felt. From then on, the ordinate of the right end progressively catches up with the left one, and at time  $t_9$ , the profile may be considered to be stabilized.

The dotted curves figure, up to time  $t_7$ , the solution to the same problem for the characteristic curvature  $K$ , and consequently the reactivity, artificially set equal to zero while maintaining the boundary conditions. At early times, profiles of both kinds are indistinguishable so the source term  $s$  is negligible in the true problem. This can be confirmed by reasoning. With time, an increasing portion of the artificial profile lags behind the actual one, as expected.

Figure 4 is a plot of the velocity  $V$  of the left end or trace of the profile against time. For the artificial problem, the corresponding quantity would keep constant over a certain time interval and be given by the analytic expression:

$$(20) \quad V_{art}(t) = D_{cj}/\cos \varphi \exp \{(\varphi + i) \operatorname{tg} \varphi\}.$$

Confirming the negligible role of the source term in the beginning, the starting value  $V(0)$  is seen to agree closely with  $V_{art}$ , which on its part equals the low value of  $8277 \text{ ms}^{-1}$  (cross on the V-axis). The corresponding value  $V(0) \cos \varphi$  of the initial detonation velocity at the boundary is lower still and at variance with it being assume from the outset not too different from  $D_{cj}$ . Besides, it may well be less than the failure detonation velocity of the explosive. Unlike  $V_{art}$ , the velocity  $V$  first strongly increases under the influence of the reactivity, then quickly proceeds to converge from about  $5 \mu\text{s}$  onwards to the asymptotic value  $8755 \text{ ms}^{-1}$ , which coincides with the steady velocity of the profile.

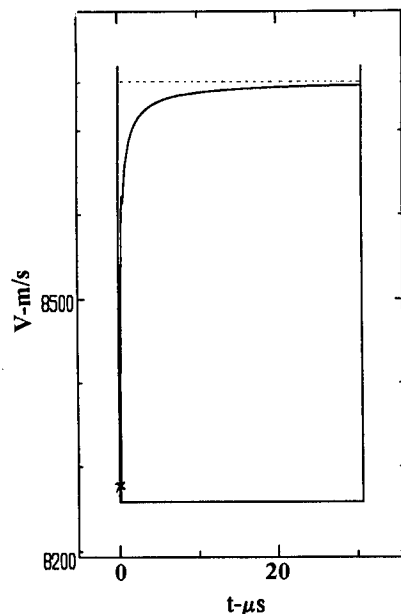


FIGURE 4. VELOCITY OF THE LEFT TRACE OF THE PROFILE VS TIME

## CONCLUSION

The model we have been discussing is intended to deal with transient detonation regimes. It proves able to provide quantitative predictions within the context of the trapezium test. These are still to be compared with experimental results. A comparison with another model<sup>12,13</sup> based on the assumption of a detonation velocity-curvature relationship will also help to display the physical content of the present model and assess its limitations. A first improvement should consist in making it capable of accounting for dead-zone effects when necessary.

## REFERENCES

1. Brun, L., a. "Une théorie de la détonation dans les explosifs condensés fondée sur l'hypothèse de Jouguet", *CEA-DAM report*, 1989.  
b. "Un nouveau modèle macroscopique de la détonation non soutenue dans les explosifs condensés", *3ème Symposium International HDP*, la Grande Motte, 1989, p.103.
2. Jouguet, E., *Mécanique des Explosifs*. Doin et Fils Eds, 1917.
3. Brun, L., "Sur l'autonomie des ondes de choc à état aval sonique. Cas de la détonation", *J. de Méc. Th. et Appl.*, 1982, p. 623.
4. Fickett, W.; and Davis, D.C., *Detonation*, University of California Press, 1979.
5. Craig, B.G., "Measurements of the detonation front structure in condensed-phase explosives", *Tenth Symposium (Intl) on Combustion*, The Combustion Institute, 1965, p. 863.
6. Seitz, W.L.; Stacy, H.L.; Engelke, R.; Tang, P.K.; and Wackerle, J., "Detonation reaction-zone structure of PBX 9502", *Ninth Symposium (Intl) on Detonation*, Portland, 1989, p. 657.
7. Brun, L., "How to propagate the explosive wave?", *Chocs* (scientific and technical review of the DAM), No 5, 1992, p. 53.
8. Chevalier, J.-M.; Carion, N.; Protat, J.C.; and Redasse, J.C., "Propagation phenomena on the detonation wave front", paper presented at this present symposium.
9. Whitham, G.B., *Linear and Nonlinear Waves*, John Wiley & Sons, 1974.
10. Aveillé, J.; Baconin, J.; Carion, N.; and Zoé, J., "Experimental study of spherically diverging detonation waves", *Eighth Symposium (Intl) on Detonation*, Albuquerque, N.W., 1985.
11. Roe, P.L., "Sonic flux formulas", *Siam J. Sc. Stat. Comp.*, Vol. 13, No 2, 1992.
12. Bdzil, J.B.; and Stewart, D.S., "Modeling two-dimensional detonations with detonation shock dynamics", *Phys. Fluids A*, Vol. 1, No 7, 1989, p. 1261.

13. Lambourn, B.D.; and Swift, D.C., "Application of Whitham's shock dynamics theory to the propagation of divergent detonation waves" *Ninth Symposium (Intl) on Detonation*, Portland, 1989, p. 784.

## DISCUSSION

R. SARRACINO

AECI Explosives, Modderfontein, South Africa

The relaxation of the C-J assumptions which lead to the JR model is similar to the relaxation which led to the original Zel'dovich-von Neumann-Döring model, the difference being that ZND is restricted to one dimension, whereas JR allows for two-dimensional detonation. Does the JR model reduce to standard ZND detonation at infinite diameter?

## REPLY BY LOUIS BRUN:

The ZND model deals with the planar stationary detonation wavefront viewed as a reactive wave of finite extent headed by an ordinary shock wave. The JR model is more generally concerned with the curved, nonstationary front, without regard to its internal structure because the front is being viewed as infinitely thin. Accordingly, the two models are quite dissimilar. With increasing rate-stick diameter, the stationary wavefront profile of the JR detonation evolves in a way that depends on both the asymptotic behavior of  $K$ ,  $C$  for  $D \rightarrow D_{cj}$  and the boundary condition. Assuming for instance the powerlaw  $K \propto (1-D/D_{cj})^n$ ,  $C/C_{cj} > 0$  and the boundary condition retained in the present paper, it is found that for  $n \geq 1$  the height of the profile increases without limit, while it is bounded for  $n < 1$ . Besides, the limiting shape of the profile is never flat because the angle between the tangents at the ends always exceeds  $2 \tan^{-1}(C_{cj}/D_{cj})$ .

(See also related question by R. Sarracino in paper by F. Chaisé and J. N. Oeconomos entitled, "The Shape Analysis of a Steady Detonation Front in Right Circular Cylinders of High Density Explosive - Some Theoretical and Numerical Aspects.")

## DISCUSSION

A. DREMIN

Institute of Chemical Physics, Chernogolovka, Russia

I wonder if your analysis can be used to describe the unstable detonation front shape?

#### REPLY BY LUIS BRUN

This is an open question to me.

#### DISCUSSION

B. D. LAMBOURN  
AWE Aldermaston, Reading, England

The JR model has an evolutionary equation for detonation velocity requiring knowledge of the variation of detonation velocity along the initial wavefront and leading to a hyperbolic set of equations for wavefront propagation. The DSD model assumes detonation velocity instantaneously responds to wavefront curvature and leads to a parabolic set of equations for wavefront propagation. The two models both lead to curved wave fronts but are sufficiently different in kind that an experiment needs to be devised which will clearly distinguish between them.

#### REPLY BY LUIS BRUN

I agree, although devising the suggested experiment may turn out to be difficult considering the present achievable precision.

The two models were compared within the context of the trapezium test for the particular set of data (explosive properties and boundary conditions) retained in the present paper. There resulted no sizable differences between the velocities of the left trace of the profile against time, except in the very first times,  $t \lesssim 0.1 \mu\text{s}$  say, when the DSD model, along

with a numerical scheme not precisely aimed at handling such short times, predicts much lower values. These conclusions still require confirmation and extension to other situations.

#### DISCUSSION

DAMIAN SWIFT  
AWE Aldermaston, Reading, England

Is the resolution of the radiographs sufficient to distinguish between a wavefront with a kinked profile (indicating a hyperbolic system), or a sharply curved profile (indicating a parabolic system)?

#### REPLY BY LOUIS BRUN:

The optical records of the transient profiles dealt with by Chevalier in a companion communication at this symposium show a regular inflexion, sharper in the case of HMX-based rather than TATB-based compositions, but no evidence of a kink. One cannot, however, in my opinion infer any definite conclusion from this as to the type of the underlying set of equations. The reason is that the type in question makes sense for short times only, while the records rather concern the delayed behavior of the system and, as known, the long and short time characteristics of a perturbation may be highly unrelated.

Comparing transient profiles through time should, however, provided the resolution is sufficient, allow distinguishing between a "parabolic" and a "hyperbolic" long-time behavior.

# THE SHAPE ANALYSIS OF A STEADY DETONATION FRONT IN RIGHT CIRCULAR CYLINDERS OF HIGH DENSITY EXPLOSIVE. SOME THEORETICAL AND NUMERICAL ASPECTS

F. Chaissé, J.N. Oeconomos

CEA-Centre d'Etudes de Vaujours-Moronvilliers  
BP n°7 - 77181 Courtry - France

Concerning the axial steady detonation waves observed in right-circular cylinders of a high-density explosive ( $T_2$  : TATB formulation), we present an accurate front shape analysis of the waves.

In this paper, with regard to the front locus, we selected the experimental data obtained for two diameters of the sticks (100 and 50 mm). They are analysed using the "AIDE" plan and then are well represented by the relationship :  $z = \alpha_1 \ln [J_0(\alpha_2 r)]$ .

We make use of different theoretical models in the interpreting of the data.

## INTRODUCTION

The shape analysis of a steady self-sustained detonation front in right-circular cylinders of high density explosive is a challenging problem starting mainly in 1954 with the work of W.W. Wood and J.G Kirkwood.<sup>1</sup> These authors propounded, using the Z.N.D. approximation, a solution concerning the axial flow in the reaction zone leading to a linear velocity deficit versus the axial curvature of the front in a circular approximation.

Allowing the setting up of a relationship between detonation velocity and curvature of the front in a steady flow, the Z.N.D. model obtained its "letters patent of nobility" in the scientific community. It was real progress compared to the classical C.J. model which, for a given explosive, provides only a single value of the detonation velocity independent of the front curvature, for the self-sustained detonation. Later in 1981 J.B. Bdzil<sup>2</sup> developed the Wood and Kirkwood approximation to the radial flow and got analytic representations for diameter effects and the shock profile.

It appears now that the Z.N.D. model is not the only one in the analysis of velocity deficit for such experiments. In 1989 L. Brun<sup>3</sup> renewed with the Jouguet approximation for the analysis of a self-sustained detonation wave (sonic shock) and forsook the condition of chemical equilibrium. This is the Jouguet relaxed model (J.R.) leading to a dynamical equation governing the front motion.

In this paper, we first inspect the three main models used in the analysis of the steady detonation front in right-circular cylinders of high-density explosive. Secondly we present our experimental data analysis on a TATB composition ( $T_2$ ) (we focus on such an explosive because the curvature effects on the front are marked in this case). Then we compare the data to theories and argue about the results.

## Index of notation :

-  $z, r$  : axial and radial coordinates of a point  $m$  of the detonation front.

-  $z(r)$  : equation of the front meridian

-  $W$  : detonation speed on the charge axis

-  $\theta$  : angle between the normal to the front at a point  $m$  and the charge axis :

$$\operatorname{tg} \theta = \frac{dz}{dr} = z'.$$

$\theta_b$  : angle at the boundary of the charge

-  $D$  : normal celerity of the wave :

$$D = W \cdot \cos \theta$$

-  $D_{CJ}$  : C.J. celerity of detonation

$$- \ell = \frac{W}{D_{CJ}}$$

-  $\mathcal{C}$  : exact mean curvature of the shock surface

$$- \mathcal{C} = \frac{1}{2} \left[ z'' (1+z'^2)^{-3/2} + \frac{z'}{r} (1+z'^2)^{-1/2} \right]$$

-  $\mathcal{C}_a$  : approximate mean shock curvature

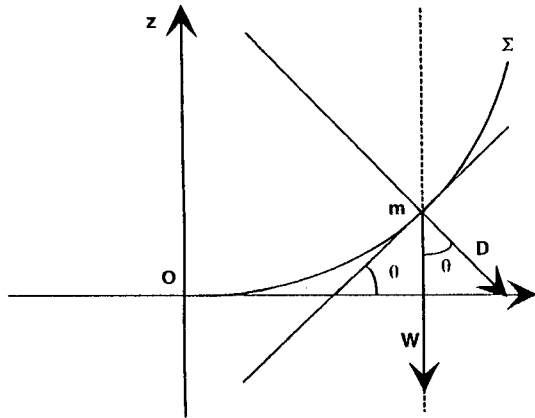
$$\mathcal{C}_a = \frac{1}{2} \left[ z'' + \frac{z'}{r} \right]$$

-  $\mathcal{C} = K(D)$  : curvature - velocity relationship

-  $\emptyset$  : diameter of the charge

-  $L$  : a scale of length

-  $\mathcal{C}_0$  : curvature of the front on the axis



### DETONATION FRONT SHAPE : THEORETICAL ASPECT

We summarize here the main results with regard to the problem studied here.

#### THE BDZIL MODEL 2

Extending the analysis of Wood and Kirkwood to the radial part of the reactive flow, J.B. Bdzil found that a solution of the flow problem may be constructed between the shock and the sonic point if the following relation is verified :

$$\ell^4 - \ell^2 + \ell^{1-n} \cdot \overline{\mathcal{C}}_a - z' \cdot 2 = 0 \quad (1)$$

In Equation (1)  $\overline{\mathcal{C}}_a$  is the approximate scaled mean shock curvature :

$$\overline{\mathcal{C}}_a = 2 L \mathcal{C}_a = L \left( z'' + \frac{z'}{r} \right). \quad (2)$$

Noting that  $z(0) = z'(0) = 0$  by integration of Equation (1) we get the shock locus solution :

$$z = -L \cdot \ell^{1-n} \cdot \text{Ln} \left[ J_0 \left( \frac{\ell^n (1-\ell^2)^{1/2}}{L} \cdot r \right) \right] \quad (3),$$

where  $J_0$  is the Bessel function of zero order and "n" a parameter introduced in the steady-state reaction rate.

At this point of the analysis the formal solution of the shock front problem is clear.

On the other hand, Bdzil's analysis gives, for the the central streamline limit, the following curvature-velocity relationship :

$$\mathcal{C}_0 = \frac{1}{2L} \ell^{1+n} (1-\ell^2) \quad (4).$$

### THE CURVATURE-VELOCITY RELATIONSHIP

In a 1-D flow, using the Z.N.D. approximation we can study the self-sustained detonation wave. The curvature effect is a necessary condition for the flow to exist between the shock front and the critical point (sonic point). If we apply locally the  $\mathcal{C} = K(D)$  relation to any point of the steady detonation front we can obtain with proper conditions at the boundary of the charge, the diameter effect and shock profile.<sup>4,5</sup> Here our approach is similar to the one followed by B.D. Lambourn<sup>4</sup> and based on the integration of the  $\mathcal{C} = K(D)$  relation for a given  $K(D)$  function. This relation is written as :

$$z'' = (1+z'^2) \left( \frac{2K(W \cos \theta)}{\cos \theta} - \frac{z'}{r} \right) \quad (5)$$

with  $z(0) = z'(0) = 0$ .

Recalling Bdzil's result we look for a standard solution as :

$$z = -\alpha \text{Ln} [f(x)] \text{ with } x = \beta r. \quad (6)$$

The combination of Equation (5) and (6) gives :



$$f'' + \frac{1}{x} f' + \frac{2K}{\alpha \beta^2 \cos \theta} f + \left[ \frac{2\alpha K}{\cos \theta} - 1 \right] \frac{f^2}{f} + \frac{\alpha^2 \beta^2}{x} \frac{f^3}{f^3} = 0. \quad (7)$$

Using a Taylor's series of  $\frac{K(W \cos \theta)}{\cos \theta}$  in the vicinity of  $\theta = 0$ , Equation (7) becomes :

$$f'' + \frac{1}{x} f' + \frac{2K(W)}{\alpha \beta^2} f + (3\alpha K(W) - 1 - \alpha W K'(W)) \frac{f^2}{f} + \frac{\alpha^2 \beta^2}{f^2} + 0 \left( \frac{f^4}{f^3} \right) = 0 \quad (8)$$

A solution  $f = J_0(x) + o(x^6)$  may be found for  $f(x)$  if the two following conditions are satisfied :

$$(9) \begin{cases} \alpha \beta^2 = 2K(W) \\ 4K^2(W) = \beta^2 [1 + \alpha W K'(W)] \end{cases}$$

Then it is possible, if  $K'(W) < 0$ , to obtain the needed real and positive parameters  $\alpha$  and  $\beta$  :

$$(10) \begin{cases} \alpha = \left[ 2K(W) \left( 1 - \frac{1}{2} \frac{d \ln K}{d \ln W} \right) \right]^{-1} \\ \beta = 2K(W) \left( 1 - \frac{1}{2} \frac{d \ln K}{d \ln W} \right)^{1/2} \end{cases}$$

By this way, for a general  $K(W)$  function with  $K'(W) < 0$ , it is always possible to get an over-osculating representation of the  $f(r)$  profile (solution of  $\mathcal{E} = K(D)$ ) as :

$z = -\alpha \ln [J_0(\beta r)]$ , with  $\alpha$  and  $\beta$  defined by Equations (10). This result is an extension of the one obtained by Lambourn <sup>4</sup> using a linear relationship for  $K(D)$ .

#### THE JOUGUET RELAXED MODEL (J.R.)

The Chapman-Jouguet scheme of a self-sustained detonation wave allows a sonic line on the downstream side of the totally reactive shock front, which is nonreactive. L. Brun <sup>3</sup> reconsidered Jouguet's hypothesis (sonic shock), and gave up the chemical equilibrium condition. This new model leads to a dynamical equation governing the front motion :

$$\frac{\delta D}{\delta t} = 2\eta(D).D^2 [K(D) - \mathcal{E}] \quad (11)$$

In this relation,  $\frac{\delta}{\delta t}$  is the time derivative in the normal direction to the front shock. Two main functions  $K(C)$  and  $\eta(D)$  appear in this analysis. The first one is associated with the curvature-velocity relationship when the normal wave acceleration is rendered null. The second one is a consequence of the model, it represents the square of the acoustical perturbation celerity moving on the front :

$$C^2 = \eta(D).D^2.$$

The two functions  $K(D)$  and  $\eta(D)$  are necessarily positive.

This model is used to describe the steady front shape detonation wave propagating along the axis of a right circular cylinder ; we get a first order differential equation governing the  $\theta(r)$  function :

$$\left[ 1 - \frac{\text{tg}^2 \theta}{\eta(W \cos \theta)} \right] \frac{d\theta}{dr} + \frac{\text{tg} \theta}{r} - \frac{2K(W \cos \theta)}{\cos \theta} = 0 \quad (12).$$

Now we focus on this equation :

The shock profile is obtained in a parametric form  $r=r(\theta)$  ;  $z=z(\theta)$ , by solving the two simultaneous equations :

$$(13) \begin{cases} \frac{dr}{d\theta} = \left( 1 - \frac{\text{tg}^2 \theta}{\eta} \right) \left[ 2 \frac{K}{\cos \theta} - \frac{\text{tg} \theta}{r} \right]^{-1} \\ \frac{dz}{d\theta} = \text{tg} \theta \cdot \frac{dr}{d\theta} \end{cases}$$

With the conditions :  $r(0) = 0$  ;  $z(0) = 0$ . From Equation (13), L. Brun gives an a priori condition for the radius of the explosive cylinder,

$$\text{tg}^2 \theta_b \leq \eta [W \cos(\theta_b)] \quad (14)$$

to get a single-valued solution of the profile, and he admits that, for an unconfined charge, the inequality (14) may become an equality :

$$\theta_b = \text{tg}^{-1} [\eta^{1/2} (W \cos \theta_b)] \quad (15).$$

Now we analyse the Equation (12) which becomes :

$$z'' \left[ 1 - \frac{z'^2}{\eta} \right] = \left( 1 + z'^2 \right) \left[ \frac{2K}{\cos\theta} - \frac{z'}{r} \right] \quad (16).$$

We may notice the similarity of formulation (5) and (16). Resorting to Brun's formulation (11), the accelerating effect on the front, out of the charge axis, is taken into account.

As in the former models, we introduce a new function  $f$  and new variable  $x$  by :

$$z = -\alpha \ln [f(x)] \text{ with } x = \beta r.$$

Using a Taylor's series of  $\frac{K(W \cos\theta)}{\cos\theta}$  and  $\eta(W \cos\theta)$  at  $x=0$ , we get a solution :

$$f = J_0(x) + o(x^6) \text{ if :}$$

$$(17) \begin{cases} \alpha \beta^2 = 2K(W) \\ 4K^2(W) \left( 1 + \frac{1}{2\eta(W)} \right) = \beta^2 [1 + \alpha W K'(W)]. \end{cases}$$

Knowing the  $K(W)$  and  $\eta(W)$  functions, in Brun's analysis, a fourth-order representation of the  $f(r)$  profile may still be found :

$$z = -\alpha \ln [J_0(\beta r)],$$

with the  $\alpha$  and  $\beta$  parameters calculated by :

$$(18) \begin{cases} \alpha = \left[ 2K(W) \left( 1 + \frac{1}{2\eta(W)} - \frac{1}{2} \frac{d \ln K}{d \ln W} \right) \right]^{-1} \\ \quad (K'(W) < 0) \\ \beta = 2K(W) \left[ 1 + \frac{1}{2\eta(W)} - \frac{1}{2} \frac{d \ln K}{d \ln W} \right]^{1/2} \end{cases}$$

As a conclusion of these three theoretical investigations about the shock locus in axial steady-state detonation, we may confirm that the  $\ln [J_0(\beta r)]$  representation for  $z(r)$  is the major function. The same functional form is justified for the Z.N.D. and J.R. models. Now we have to compare these theoretical data to the experimental ones.

## CONSEQUENCE ON DATA ANALYSIS : THE "AIDE" PLAN

In order to compare the different models mentioned above, we need accurate experimental data analysis. To that end, we developed the "AIDE" plan (Image Analysis in Experimental Detonics).

Firstly, we use all tools of modern image processing and particularly contour segmentation to obtain a data set of about 500 points from the original experimental pictures (streak camera photograph).<sup>7</sup>

Secondly, interpretation of experimental data set is performed using least-squares fitting of  $\ln(J_0)$  function. The resolution of such a non-linear problem requires to carry out new methods based on an iterative algorithm (simplex algorithm).<sup>6</sup>

The image is processed by the AIDE system and we get, knowing the axial velocity of detonation front, the desired shock profile :  $z(r)$ .

On the following Figures 1 and 2 we present the final results obtained on a  $T_2$  composition (TATB) for two charges diameters :

$$\begin{aligned} \varnothing &= 100 \text{ mm, } W = (7633 \pm 30) \text{ m/s ;} \\ \varnothing &= 50 \text{ mm, } W = (7620 \pm 30) \text{ m/s.} \end{aligned}$$

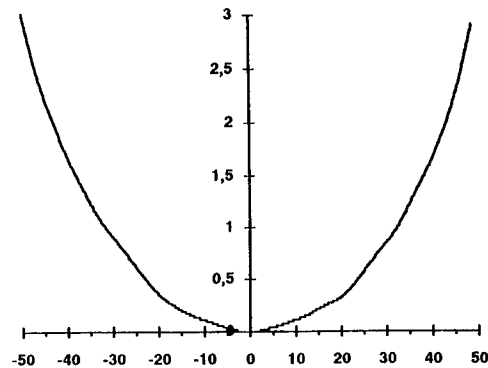


FIGURE 1 : THE AIDE PLAN : SHOCK PROFILE  $z(r)$  FOR  $\Phi = 100$  mm

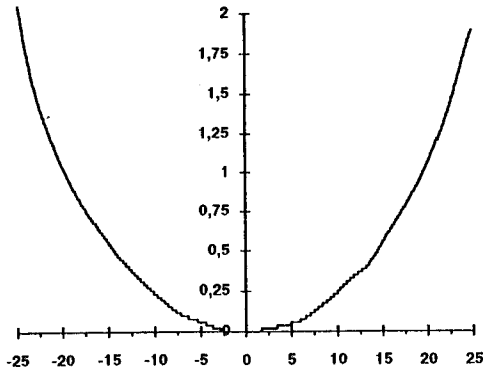


FIGURE 2 : THE AIDE PLAN : SHOCK PROFILE  $z(r)$  FOR  $\Phi = 50$  mm

#### THE MODELS COMPARISON WITH EXPERIMENTS

To make relevant our comparison of the three previous models with the experimental data, we use Bdzil's formulation (4) for  $K(D)$  and for the J.R model of Brun, we retain a linear relationship for  $\eta(D)$ . These two functions are adjusted to experimental data : Aveillé et al. <sup>8</sup> for  $K(W)$ , and Chevalier, Carion for  $\eta(D)$  (paper submitted to this symposium).

The results are the following for  $T_2$  composition (TATB) :

$$K(W) = \frac{1}{2L} \ell^{1+n} (1 - \ell^2) \quad (19)$$

$$\text{with } \begin{cases} L = 9,518 \cdot 10^{-3} (\text{m}) \\ n = -47,716 \\ D_{CJ} = 7733 (\text{ms}^{-1}) \end{cases}$$

(Figure 3).

$$\eta(D) = \eta_0 \left( 1 - \frac{D}{D_{CJ}} \right) \quad (20)$$

with  $\eta_0 = 4,798$

(Figure 4).

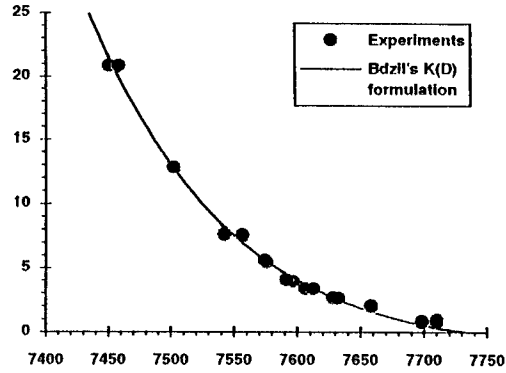


FIGURE 3 : CURVATURE VERSUS AXIAL CELERITY  $D$  OF THE WAVE FOR  $T_2$  COMPOSITION

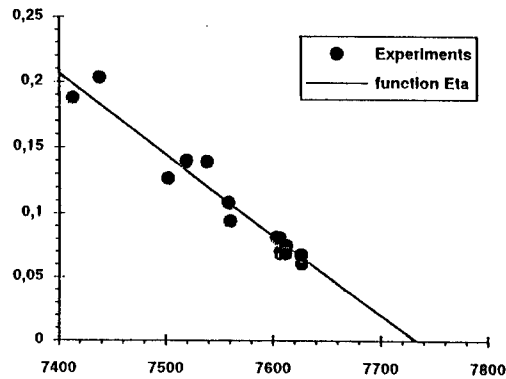


FIGURE 4 : BRUN'S FUNCTION  $\eta(D)$  FOR  $T_2$  COMPOSITION

First, using the AIDE Plan we analyse the data presented on Figures 1, 2 using the following representation for  $z(r)$  :

$$z = -\alpha \ln \left[ J_0 \left( 2\beta \frac{r}{\phi} \right) \right] \quad (21).$$

The results are :

TABLE 1 :

	$\varnothing = 100 \text{ mm}$	$\varnothing = 50 \text{ mm}$
$\alpha \text{ (m)}$	$2,51427.10^{-3}$	$1,36706.10^{-3}$
$\beta$	1,86465	1,96554
$\mathcal{E}_0 = \frac{2\alpha\beta^2}{\phi^2} (\text{m}^{-1})$	1,748	4,225
$W(\text{m.s}^{-1})$	7653	7596
$\ell = \frac{W}{D_{CJ}}$	0,9897	0,98235
$z(\varnothing/2) \text{ (mm)}$	3,007	1,929
$\theta_b \text{ (degree)}$	10,226	14,312
$\frac{d\text{Ln}K}{d\text{Ln}W} \text{ (19)}$	- 142,242	- 101,87
$\eta(W) \text{ (20)}$	0,04945	0,08469

In this table, we note :

$$z(\varnothing/2) = -\alpha \text{Ln} [J_0(\beta)] \text{ and}$$

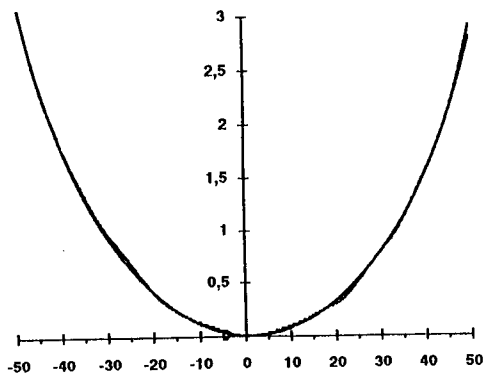
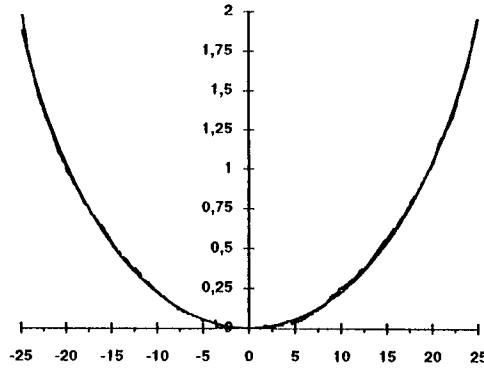
$$\theta_b = \text{tg}^{-1} \left[ \frac{2\alpha\beta J_1(\beta)}{\phi J_0(\beta)} \right].$$

The least-squares fitting of the experimental data by formulation (21) provides a high correlation factor (near 1) :

$$\begin{aligned} \rho &= 1-5,2.10^{-4} \quad (\phi = 100 \text{ mm}) \\ \rho &= 1-4,1.10^{-3} \quad (\phi = 50 \text{ mm}) \end{aligned}$$

This result indicates that the formulation (21) is an advantageous one for a such analysis.

On Figures 5, 6 the experimental data and the analytic representation (Equation (21)) are presented.

FIGURE 5 : EXPERIMENTAL SHOCK PROFILE  $z(r)$  FOR  $\Phi = 100 \text{ mm}$  AND ITS  $\text{Ln}(J_0)$  APPROXIMATIONFIGURE 6 : EXPERIMENTAL SHOCK PROFILE  $z(r)$  FOR  $\Phi = 50 \text{ mm}$  AND ITS  $\text{Ln}(J_0)$  APPROXIMATION

Secondly, we compare our experimental data with the three competing models for this kind of analysis :

- ① . the explicit relation of Bdzil (Equation (3) )
- ② . the integration of velocity-curvature relationship (Equation (5) )
- ③ . the integration of the Brun's formulation (Equation (16) )

For this purpose we first get the values of  $\alpha$  and  $\beta$  defined by Equation (21) which are associated to Bdzil's formulation (3) and to the over-osculating approximation deduced from Brun's model [equation (18)] and the velocity-curvature model [equation (10)] :

TABLE 2 :

	$\varnothing = 100 \text{ mm}$	$\varnothing = 50 \text{ mm}$
① $\begin{cases} \alpha = L\ell^{1-n} [\text{m}] \\ \beta = \frac{\ell^n (1-\ell^2)^{1/2}}{L} \frac{\phi}{2} \end{cases}$	$5,7449.10^{-3}$ 1,2333	$3,9972.10^{-3}$ 1,1493
② $\begin{cases} \alpha(10) [\text{m}] \\ \beta(10) \end{cases}$	$3,966.10^{-3}$ 1,4845	$2,2787.10^{-3}$ 1,5224
③ $\begin{cases} \alpha(18) [\text{m}] \\ \beta(18) \end{cases}$	$3,4784.10^{-3}$ 1,5851	$2,0461.10^{-3}$ 1,6066

From the three models, we note that the values of  $\alpha$  and  $\beta$  are of the same order than those of table 1. On figures 7 and 8 are presented the final results obtained by the three models ① ② ③.

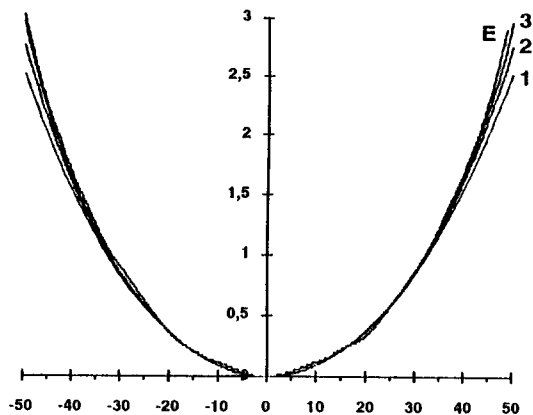


FIGURE 7 : THE 3 MODELS AND EXPERIMENT : SHOCK PROFILES  $z(r)$  FOR  $\Phi = 100$  mm

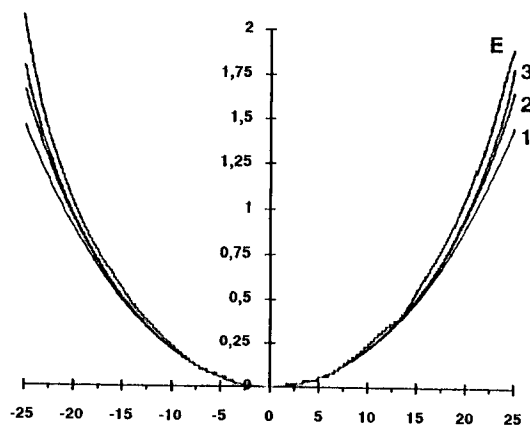


FIGURE 8 : THE 3 MODELS AND EXPERIMENT : SHOCK PROFILES  $z(r)$  FOR  $\Phi = 50$  mm

For  $r \in \{-\phi/4, +\phi/4\}$  the three models can't be distinguished. Only in the vicinity of the charge diameter do we observe the difference. As a result it appears that the Brun's model gives a better fit to the front locus.

Now we focus on the Brun's model to get the theoretical relation governing the axial celerity of the front versus inverse diameter deduced from the integration of Equation (13) at different values of  $W$  associated with the "sonic" condition described by Equation (15). For that, we use the Equations (19)

and (20) for  $K (W \cos \theta)$  and  $\eta (W \cos \theta)$  and by integration we get the result presented on figure 9 for the  $T_2$  composition.

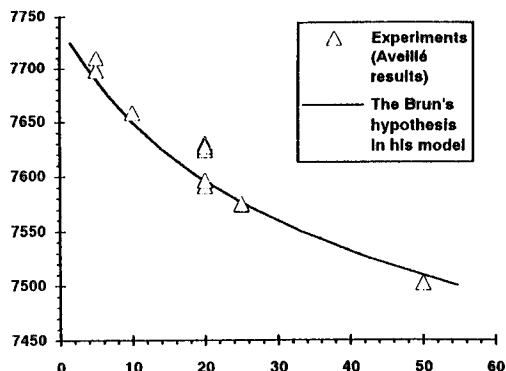


FIGURE 9 :  $W(1/\phi)$  FOR  $T_2$  COMPOSITION

It may be noticed that, for a given  $W$ , the theoretical inverse diameter must be lower than the experimental one (equation (14)). We can see the good agreement between the experimental results and the one obtained by Brun's model knowing the main functions  $K(D)$  and  $\eta(D)$ .

## CONCLUSION

By a theoretical analysis of the differential equations governing the front shape, and using different detonation models, it was possible to show that the steady detonation front shape, in right circular cylinders of high density explosive, is well represented by a functional relationship :

$z = \alpha_1 \cdot \ln(J_0(\alpha_2 \cdot r))$ . This result was well confirmed by the experimental data fitting, using the "AIDE" plan. Finally, using numerical integration, we performed on a TATB composition, an accurate comparison between the three main models and the experimental results.

## REFERENCES

1. W.W. Wood and J.G. Kirkwood  
"Diameter effect in condensed explosives. The relation between velocity and radius of curvature of the detonation wave"  
Journal of Chemical Physics 22, 1920, (1954)

2. J.B. Bdzil  
"Steady-state two-dimensional detonation"  
Journal of Fluid Mechanics Vol. 108, pp.195-226  
(1981)
  
3. L. Brun  
"Un nouveau modèle macroscopique de la  
détonation non soutenue dans les explosifs  
condensés"  
3ème Symposium International sur le  
comportement des milieux denses sous hautes  
pressions dynamiques (CEA), pp. 103-107  
La Grande Motte - France (juin 1989)
  
4. B.D. Lambourn and D.C. Swift  
"Application of Whitham's shock dynamics theory  
to the propagation of divergent detonation waves.  
9th Symposium (international) on detonation,  
Office of Naval Research, Arlington - Virginia -  
Vol. 1, pp. 308-313, (1965)
  
5. B.G. Bukiet and R. Menikoff  
"Detonation waves and the front tracking method  
Phys. Fluids - vol. 4, n°9 - pp. 2070-2081 (1992)
  
6. J.A. Nelder and R. Mead  
"A simplex method for function minimisation"  
The Computer Journal, vol. 7, pp. 308-313,  
(1965)

7. J.N. Oeonomos  
"Sidebar 5 of Chaissé's paper in CHOCS issue #  
5 p. 49 (1992)  
Publication of CEA-DAM - France
  
8. F. Chaissé, J.M. Servas, J.Aveillé et al .  
"A theoretical analysis of the shape of a steady  
axisymetrical reactive shock front in cylindrical  
charges of high explosive, a curvature-diameter  
relationship"  
8th Symposium (International) on Detonation, Naval  
Surface Weapons Center, White Oak, Silver Spring,  
Maryland (USA) (1985).

---

## DISCUSSION

R. SARRACINO  
AECI Explosives, Modderfontein, South Africa

It seems to me that the velocity-curve relationship mentioned in this paper is a special case of the JR model (ref. Brun *et al.*, "Computing the Transient Self-Sustained Detonation After a New Model").

## REPLY BY FRANCIS CHAISSÉ:

Letting the front wave speed  $C$  in the r.h.m of Eq. (1) of the JR model in the Brun paper grow to infinity, while keeping the acceleration of the front in the l.h.m. finite, results indeed in the velocity-curvature relationship referred to by example in that paper.

# NUMERICAL SIMULATIONS OF DETONATION IN HIGH EXPLOSIVE CHARGES OF FINITE DIAMETER

V.E. Fortov, A.L. Ni, A.V. Shutov, A.V. Utkin  
Institute of Chemical Physics  
142432, Chernogolovka, Russia

Results of numerical simulations of detonation in high explosive charges of finite diameter are presented. Dependence of self-sustained detonation velocity from charge diameter and the failure diameter for TNT are obtained. Numerical results are in a good agreement with available experimental data.

## INTRODUCTION

The failure diameter problem is the problem of minimum explosive charge diameter for which a self-sustained detonation can exist. The problem has been investigated by many researchers qualitatively,<sup>1,2</sup> theoretically,<sup>3-5</sup> and numerically.<sup>6,7</sup> In the work<sup>2</sup> an estimation of diameter  $d = \lambda$  ( $\lambda$  is the width of chemical reaction zone) was given. This simple estimation corresponds to the case when rarefaction wave from the side surface of explosive charge reaches the axis of symmetry at a point being at  $\lambda$  distance from the initial shock wave front. Rarefaction waves reach the reaction zone with decreasing of charge diameter. It results in decreasing temperature and pressure in reacting substance and in decelerating reaction and finally in failure of detonation.

The numerical analysis of detonation for charges of finite diameter has been performed.<sup>6,7</sup> Failure diameter obtained is in a reasonable agreement with experiments. The results of the numerical simulation given below do not contain any new quantitative data in addition to the cited works. The goal of this work is to demonstrate possibilities for the numerical algorithm, its flexibility and adaptability to the geometry and physics of flow under consideration.

## CONSISTUTIVE RELATIONS

Assume that the following equation of state connecting specific internal energy  $e$  with pressure  $p$ , density  $\rho$ , and depth of reaction  $\alpha$  is valid:

$$e = e_x + (p - p_c)/p\Gamma$$

where  $e_x$  is the energy of cold compression  $p_x = -\partial e_x / \partial v$  the cold component of pressure,  $\Gamma$ —Gruneisen coefficient. In the initial and completely reacted explosive  $\alpha = 0, 1$  correspondingly. The depth of reaction is governed by the following kinetic equation

$$\begin{aligned} d\alpha/dt &= k\alpha^\gamma(1-\alpha)^{1-\gamma} p E_f = \Phi, \\ k &= 1.2 \cdot 10^{-9} (c \cdot J \cdot Pa)^{-1}, \quad \gamma = 0.3 \end{aligned}$$

Here and below  $d/dt$  designates the lagrangian derivative. Equation of state and kinetics correspond to TNT.<sup>6,8</sup> As distinct from<sup>8</sup> the expression for Gruneisen coefficient was obtained by matching its values for nonreacted substance and products by conversion parameter  $\alpha$  but not by density. Parameter  $E_f$  in the kinetic equation needs to be discussed separately. It remains constant in time for every liquid particle behind the shock front being equal to  $p_f (V_0 - V_f)/2$ , where  $p_f$  and  $V_f$  are the pressure and specific volume at the moment of the crossing of the shock by the particle. The following equation is valid for  $E_f$ :

$$dE_f/dt = 0$$

Equations of state and the kinetic equation given above close the governing media equations. Their divergent form is

$$\begin{aligned} \partial \rho / \partial t + \nabla \rho u + \rho v(v-1)/r &= 0 \\ \partial \rho u / \partial t + \nabla (\rho u : u + p) + \rho v u / r &= 0 \\ \partial \rho E / \partial t + \nabla u (p + rE) + (p + \rho E) v / r &= \rho Q d\alpha / dt \end{aligned}$$

They differ from the usual hydrodynamics equations only by the equation of energy where the term responsible for the energy release in a chemical reaction with heat effect  $Q$  appears.

Multiplying the governing equations for  $E_f$  and  $\alpha$  by  $\rho$ , and combining the obtained relations with a conservation of mass equation we come to the following divergent equations

$$\begin{aligned} \partial \rho \alpha / \partial t + V \rho u \alpha + \alpha \rho v (v-1) / r &= \rho \Phi \\ \partial \rho E_f / \partial t + V (\rho u E_f) + E_f \rho v (v-1) / r &= 0 \end{aligned} \quad (1)$$

Shock conditions can easily be obtained from the divergent equations in the usual way. The first three equations give Rankin-Hugoniot relationships. The two last equations lead to

$$[\alpha] = 0, [E_f] = 0$$

## NUMERICAL ALGORITHM

Let us outline the problems met in numerical simulations of detonation.

Along with detonation propagation along the charge the size of the region involved in the motion increases. To elucidate whether the detonation becomes steady or not it is necessary to calculate the evolution of the detonation process at distance for at least several (perhaps ten) diameters.

In spite of the fact that the memory problem is not nowadays crucial for computers, the problem of the linear increase with time of the volume of computations is real. The other problem is connected with determination of front position. This point is significant because the downstream flow behind the shock is determined by the chemical reaction kinetics and, in particular, by the value  $E_f$ . A shock is reproduced by most of numerical schemes as a continuous region. Therefore the shock position and its parameters can be determined with some degree of arbitrariness.

A brief description of the numerical algorithm being free from some of these disadvantages is given below. The algorithm is based on Godunov method in moving grids.<sup>9</sup> The flow region under consideration can be subdivided into several subregions. Boundaries of subregions can be both real flow singularities (characteristics, boundary between substance and vacuum, the contact boundary between two substances, the axis (plane) of symmetry, the shock (wave) and therefore to move in accordance with their physical nature or can be inserted for some computational reasons and to move by the demands of the problem.

Algorithms for movement of contacts and shock waves and also formula for filling of total boundary by the positions of its nodes are given.<sup>9</sup> They were used as a whole or with some modifications in the complex of programs.

Let flow parameters and grids be known at time  $t_0$ . Flow parameters for a next discrete moment of time  $t_0 + \Delta t$  are calculated by performing three sequential steps

- 1) Determination of new boundaries.
- 2) Construction of grids in regions inside these boundaries.
- 3) Calculations of flow parameters for the new time step.

Now we describe schematically a sequence of operations by realization of each stage.

1) The boundary of each subregion is represented as an array of node coordinates. Any boundary between adjacent subregions represents a unification of nodes belonging to boundaries of adjacent subregions. The node coordinates are also stored in special arrays establishing the sequence of nodes. Nodes corresponding to the beginning and to the end of different segments of boundaries are also marked. It means that each boundary segment is represented as a sequence of points belonging to the boundaries of different subregions and that of special end-points of boundaries. The total number of nodes representing the boundary exceeds, generally speaking, the number of cells being in contact from the side of adjacent sub fields.

The Riemann problem with flow parameters from adjacent cells being in contact along every link is solved. If a Riemann solver gives a negative pressure a rebound along the link is assumed to have happened. This fact is taken into account by inserting some new special boundary points in the array. In more complex physical models the coupling force can be prescribed to the contact surface and the rebound can be inserted when the tensile strengths exceeds it.

This procedure on contacts and shocks permits us to calculate the velocities of their nodes, displacements of the nodes and new positions of boundaries. Note that all parameters necessary to compute the fluxes of mass, momentum and energy through boundaries are calculated at this stage.

2) Now, when the new boundaries have been found and nodes on them arranged, grids are constructed inside the computed fields. For this purpose the algorithm<sup>9</sup> is used.



This algorithm is based on mapping of a unit square at a parametric plane  $(\xi, \eta)$  to a subregion under consideration in the physical plane  $(x, y)$  of flow.

The algorithm described above has been applied to the simulation of detonation. Boundaries of the computed field (Fig. 1) are the shock S, free surface between the detonation products and vacuum F, an axis (in case of plane geometry—a plane) of symmetry A and a moving boundary B—a segment of the straight line normal to the axis of symmetry situated between boundaries A and F. The velocity of motion of B at a fixed time is determined from the following reasons. The velocity is regarded as being directed along the axis and to be equal to  $\max(u+a, D)$ , where  $D$  is the shock velocity at the axis of symmetry,  $u+a$  is the velocity of characteristic surface moving along the axis and calculated with parameters of a computed cell adjacent to B. The maximum is taken for all the cells adjacent to B. It is clear from the choice of the motion law for B that parameters from internal cells adjacent to B enter to expression of fluxes of mass, momentum and energy through B. This strategy of simulations is not applicable for all possible situations. It cannot be used for example if in a flow region outside of the region under consideration a shock arises, overtaking the detonation wave. Such cases are excluded from consideration. Nevertheless the way of generalizing algorithm to this situation is evident. An analogy between under flow under consideration and the problem of a supersonic underexpanded jet<sup>10</sup> should be pointed out. The flow in such a case is well studied and has a so called "barrel structure." However, the question for a steady solution is open, because of the "gradient catastrophe" leading to appearance of shock followed by subsonic region and ultimately to transformation of the flow.

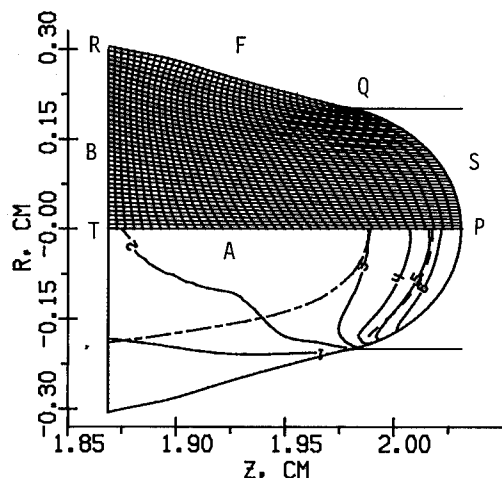


FIGURE 1.

An algorithm<sup>9</sup> for fitting the shock surface was used. The boundary conditions in this case are obvious. The fluxes are computed from the shock relationships.

There is a problem (it should be said) particularly about the boundary condition for  $E_r$  at the shock front. The value  $E_r$  behind front calculated formally from the divergent form (1) is equal to zero and it is obviously wrong. In accordance with definition of  $E_r$  a singular situation exists at the front. The flow of  $E_r$  through the shock is equal to  $jE_r$ , where  $j$  is the mass flux through the front and  $E_r$  is calculated with the parameters of flow behind the shock front.

A computational grid in curvilinear region PQRT is constructed in a following way. The sides PQ, RT and QR, RT are divided into M and N segments correspondingly with a uniform distribution by length along each side of a curvilinear quadrangle. Then a map of PQRT to a square in parametric space with uniform division of corresponding sides is constructed.

If it is necessary, the numerical algorithm allows the transition to refined grids. The transition is organized in a following way. A grid of dimension  $M \times N$  is used initially.

After achievement of steady detonation the transition to the grid  $2N \times 2M$  takes place and this process can be repeated if it is necessarily.

## RESULTS OF SIMULATIONS

The dependence of detonation velocity on time for charges of TNT with diameters 6, 4, 3 and 2.4 mm are shown on Fig. 2 (curves 1, 2, 3, 4, correspondingly). Pressure  $p=200$  kbar, density  $\rho=\rho_0$  -normal

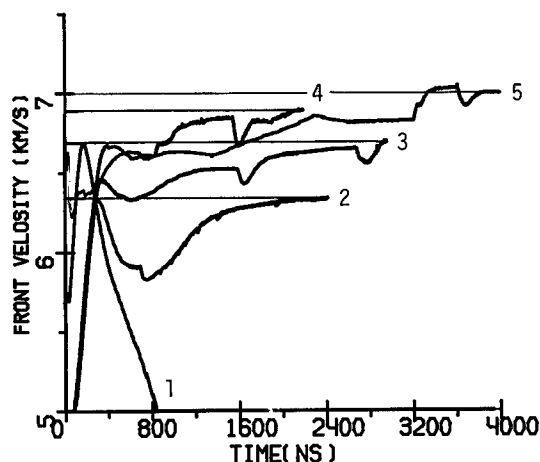


FIGURE 2.

density,  $u=0$  were used as initial data for the calculations. The velocity increases on the figure correspond to the transition to a refined grid.

Fig. 3 demonstrates the dependence of detonation velocity on charge diameter. Experiments are marked by the dashed line. Numerical data are in a good agreement with the experiments.

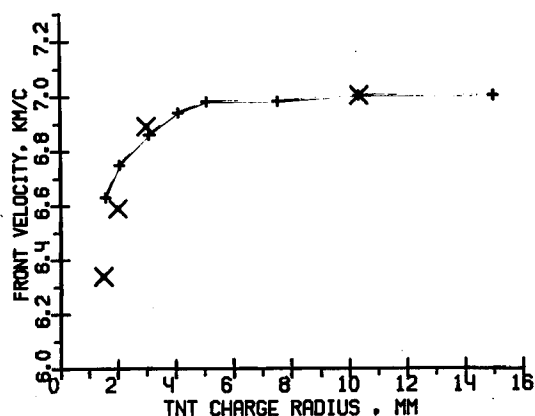


FIGURE 3.

In case 4, as seen in Fig. 2, detonation decays. Calculations for this diameter were performed with different initial pressures. In all cases the steady detonation was not obtained. This fact allows us to draw a conclusion that the failure diameter of TNT lies within the interval 2, 4 and 3 mm, which also agrees with experiment.

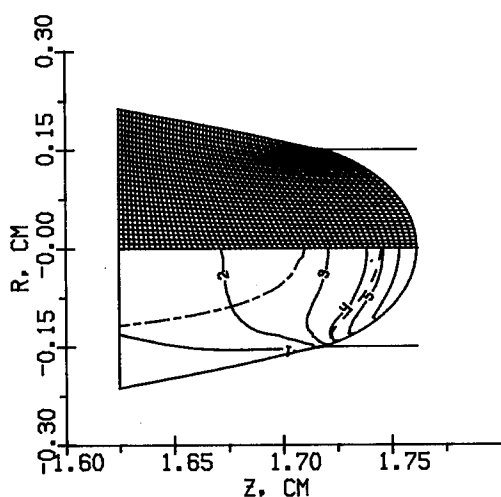


FIGURE 4a.

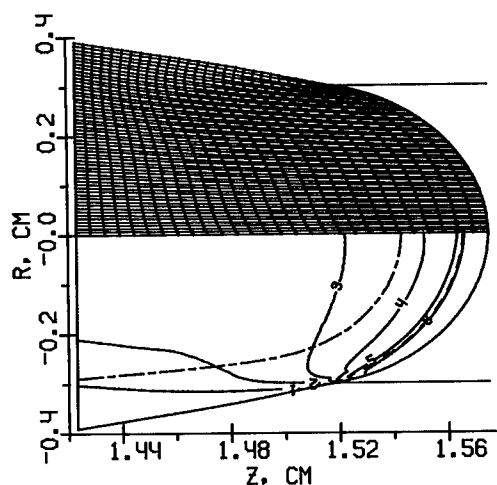


FIGURE 4b.

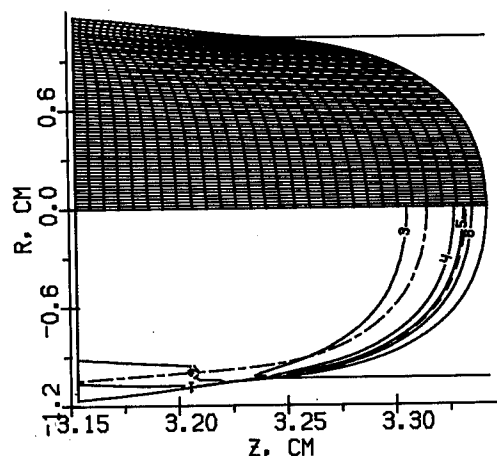


FIGURE 4c.

P = PRESSURE, KB

FIGURE 4. (a, b, c)

a - D = 3mm  
b - D = 6mm  
c - d = 20mm

1-P = 25.714  
2-P = 51.429  
3-P = 77.143  
4-P = 102.857  
5-P = 128.571  
6-P = 154.286

Fig. 4 a-c demonstrate computing grids and equal pressure level lines for different charge diameters after reaching steady detonation. Size of zone of energy release increases with decreasing of charge diameter. The dashed line in Fig. 4 corresponds to the reaction depth  $\alpha = 0.01$ . The dotted line corresponds to the flow Mach number  $M=1$  in the moving coordinate system connected with the shock wave.

## REFERENCES

1. Khariton, Yu.B.; and Rosing, V.O., *Dan SSSR*, Vol. 26, No. 5, 1940, p. 360.
2. Khariton, Yu.B., *The Problems of Explosion Theory*, Academic Press (in Russian), Moscow, Leningrad, 1947, Vol. 1., p. 7.
3. Mikhailjuk, K.M.; and Trofimov, V.S., "On Possible Stationary Detonation Spreading Limits," *Fizika Gorenia i Vzriva*, Novosibirsk, Vol. 11, No. 4, 1977, p. 606.
4. Kobilkin, I.F.; Soloviev, V.S.; and Boiko, M.M., "Stationar Detonation Critical Diameter Nature of Condensed Explosives," *Reports of Moscow Bauman Highest Technical School*, No. 387, Moscow, p. 13.
5. Chaisse, F.; Servas, J.M.; Aveitle, J.; Baconin, J.; Carion, N.; and Bongrain, P., "A Theoretical Analysis of the Shape of a Steady Axisymmetrical Reactive Shock Front in Cylindrical Charges of High Explosive. A Curvature Diameter Relationship," *8th Symposium (Int) on Detonation, Preprints, Albuquerque*, Vol. 1, 1985, p. 539.
6. Utkin, A.V.; Fortova, T.N.; Kanel, G.I.; and Shkadinskij, K.G., "Calculation of Nonideal Detonation in TNT on the Base of Macrokinetics Empirical Equation," *Chemical Physics, Russia*, Vol. 7, No. 9, 1988, p. 1257.
7. Maider, Ch., *Numerical Simulation of Detonation*, Mir, Moscow, 1985.
8. Fortov, V.E.; and Dremin, A.N., "The Semi-empirical Equation of State of TNT," *DAN SSSR*, Vol. 222, No. 1, 1975, p. 162.
9. Godunov, S.K.; Zabrodin, A.V., Ivanov, M.Ya.; et.al., *Numerical Solver of Multidimensional Gas Dynamics Problems*, Nauka, Moscow, 1976.
10. Ovsyannikov, L.V., *Lectures on Gas Dynamics*, Nauka, Moscow, 1981.

## EXPERIMENTAL STUDY OF DETONATION IN PBXW-123, A LARGE FAILURE-DIAMETER, NON-IDEAL EXPLOSIVE

W. H. Wilson, J. W. Forbes,  
P. K. Gustavson and G. T. Sutherland  
Naval Surface Warfare Center  
Dahlgren Division White Oak Detachment  
Silver Spring, MD 20903-5000

The stability of detonation wave propagation in PBXW-123, an aluminized, non-ideal explosive based upon ammonium perchlorate (AP) and trimethylol-ethane trinitrate (TMETN), has been studied experimentally. Streak camera and shock output pressure records showed that detonation was gradually failing in lengths of unconfined samples of 75 mm, 100 mm, and 126 mm diameters. After a run length of 548 mm in the 126 mm diameter charges, both PVDF and manganin gauge measurements showed a peak output pressure of only 30 kbar. Confinement of the charges was found to have a significant effect upon detonation wave stability. Detonation velocity was found to be steady, in 76 mm diameter samples confined in brass tubes of 6.4 mm wall thickness, along the full 152 mm test length. For the confined charges, detonation velocity was measured using embedded carbon resistor time-of-arrival gauges.

### INTRODUCTION

A major concern for those using explosives in any application is the avoidance of unwanted detonation, primarily out of a concern for safety, but also because such incidents are very costly and result in loss of operational resources. Consequently, considerable research effort has been directed over the years to the development of less sensitive explosive formulations. An obvious trade-off which often must be made in these developments has been loss of performance in exchange for increased insensitivity. A more subtle detriment which can occur as sensitivity is reduced is an increase in critical diameter or loss of detonation stability, even in cases where performance may be kept high. As greater input shock is required to initiate a main charge explosive, larger initiator-booster systems are required. As the critical diameter of an explosive grows, not only does the required booster size grow, but also the minimum practical size of the explosive main charge.

In non-ideal explosives, the issue of detonation stability can be particularly difficult to resolve, because

very vigorous sub-detonation reactions may continue for long run lengths, propagating at high velocity which only gradually decreases. Thus, results of uninstrumented small scale tests of such non-ideal explosives can be misleading, because vigorous sub-detonation reactions can easily be confused for detonation.

The purpose of the work reported here was to study definitively the character of detonation in PBXW-123, an insensitive, non-ideal underwater explosive which was developed for improved insensitivity. Experiments were conducted which were intended to determine detonation velocity, critical diameter, and detonation pressure. Such data are needed so that questions of adequate booster size and minimum charge size can be addressed.

### SAMPLE MATERIAL DESCRIPTION

PBXW-123 is a non-ideal explosive that relies largely on a combination of aluminum (Al) and ammonium perchlorate (AP) to give it a high heat of detonation. It is similar in some respects to PBXN-103.

The main constituents of each of these explosives are AP, Al, and trimethylethane trinitrate (TMETN) (with the remainder made up of inert binder, plasticizer, emulsifier, etc.). TMETN is included in both materials in continuous phase, providing an easily detonable energetic constituent. The aluminum content in each explosive provides a heat-producing fuel, but also leads to increased non-ideal detonation behavior. PBXW-123, however, uses a rubbery polycaprolacton binder system, in an effort to improve insensitivity properties, whereas PBXN-103 has an energetic polymer binder. By comparison to PBXN-103, it indeed has been found that PBXW-123 has greatly reduced sensitivity. In the NSWC Modified Gap Test (MGT) PBXW-123 has a sustained ignition threshold of 69 kbar (estimated shock in the explosive), compared to a 50 kbar sustained ignition threshold for PBXN-103.<sup>1</sup> In the NOL Large Scale Gap Test (LSGT), the 50% point (gap thickness for which there is a 50% probability of detonation) for PBXW-123 was 0.52 inches, corresponding to approximately 80 kbar in the polymethylmethacrylate (PMMA) gap.<sup>2</sup> By comparison, PBXN-103 has a shock sensitivity 50% point corresponding to approximately 59 kbar in the PMMA gap for the LSGT.<sup>3</sup>

Both PBXW-123 and PBXN-103 are produced in a cold cast cure process. The typical density of PBXN-103<sup>4</sup> is 1.89 g/cc; the average density of the PBXW-123 samples studied in these experiments was 1.92 g/cc.

## EXPERIMENTAL DESCRIPTION

### Unconfined Sample Experiments

The stability of reaction propagation in unconfined cylinders of PBXW-123 was studied in a series of experiments in which the sample was overdriven at one end using a Pentolite plane wave booster (PWB) to initiate a detonation. The reaction propagating at the far end was then monitored either by measuring the propagation velocity using streak photography, or by measuring the strength of the output shock wave. Four experiments were run using unconfined samples of three sizes. Figure 1 compares the sample sizes used, and also illustrates the sizes of the plane wave boosters used, relative to the sample diameters. In the experiments using the 75 mm or the 100 mm diameter samples, the plane wave booster diameter was 108 mm. A 159 mm diameter PWB was used in the experiment using a 126 mm diameter sample. In each experiment, the Pentolite output end of the PWB was in direct contact with the input end of the PBXW-123 sample. The shock front at the PWB output end is planar over at

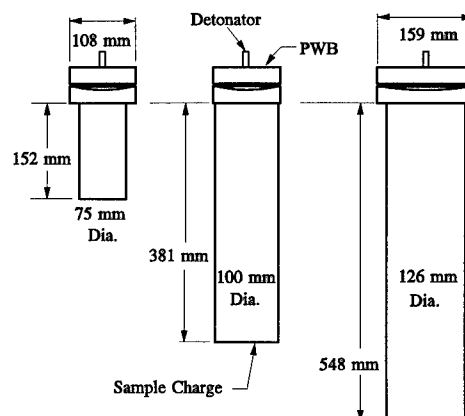
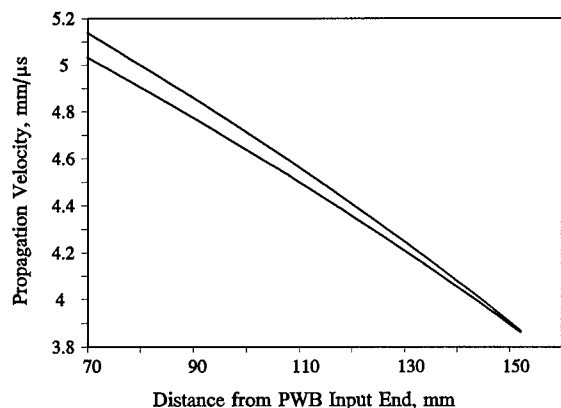


FIGURE 1. SIZE COMPARISONS FOR PWB AND UNCONFINED SAMPLES TESTED

least 80% of the PWB diameter. In each case, the shock input to the PBXW-123 sample was much greater than the 69 kbar estimated to be needed to initiate a detonation at the input end of the sample, thus insuring that an overdriven detonation was initiated at the input end of each sample tested.

Two streak camera experiments were run using the 75 mm diameter sample size. As illustrated in Figure 1, the sample length-to-diameter (L/D) ratio for these tests was approximately 2. The position of the reaction front, at points where it intersected the outer edge of the charge as it propagated, was monitored along the final 80 mm of the charge. The camera records of the reaction-front position vs. time showed that the propagation velocity was gradually slowing in each test, and was below the expected level for a detonation velocity. At the point of first observation in the experiments, approximately 70 mm from the PWB input end, the reactions were each propagating at only slightly more than 5 mm/ $\mu$ s. PBXN-103, the explosive to which PBXW-123 is being compared, has a failure diameter of approximately 28 mm and a detonation velocity of 6.2 mm/ $\mu$ s.<sup>5</sup> Figure 2 shows plots of the velocity of propagation as a function of distance from the PWB input for each of these two tests; these plots were derived from second order functions approximating the records of reaction position vs. time using a least squares routine. From these curves it is obvious that reaction is not stable for an unconfined PBXW-123 charge diameter of 75 mm. However, the reactions observed in these two experiments were failing relatively gradually, in contrast to a more abrupt cessation of reaction more typically found for ideal explosives. In each test the propagation velocity steadily decreased with run distance, decaying to approximately



**FIGURE 2. REACTION PROPAGATION VELOCITY VS. DISTANCE FROM PWB, 75 MM SAMPLES**

3.9 mm/μs before the ends of the samples were reached. Although the overdriven detonation had failed in these samples, the reaction wave propagating the full run length was still quite strong.

A third streak camera experiment was run using a 100 mm PBXW-123 sample size; for this test the sample L/D ratio was increased to approximately 3.8. The position of the reaction front was monitored along the final 140 mm of the sample's 381 mm length. As in the 75 mm diameter tests, the reaction was gradually failing by the time it had reached the observed portion of the sample. Figure 3 shows the approximate velocity of reaction propagation, as a function of distance from the PWB input end of the sample, derived from

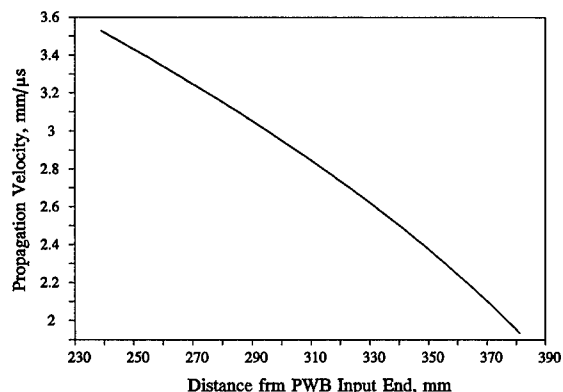


**FIGURE 3. REACTION PROPAGATION VELOCITY VS. DISTANCE FROM PWB, 100 MM CHARGE.**

a least squares second order fit to the position vs. time streak camera record. At the point where the reaction was first monitored, after running approximately 238 mm from the PWB input end, it had a propagation velocity of approximately 3.6 mm/μs. Over the next 142 mm of travel the velocity of the reaction front decayed to approximately 2 mm/μs. Again, it is observed that the reaction in the 100 mm diameter sample was failing only relatively slowly, as was the case in the two tests at 75 mm diameter. Based on the second order fits for the streak camera records, the rate at which the propagation velocity was decelerating was less than 0.1 mm/μs<sup>2</sup> in each of these three tests.

One test using an unconfined 126 mm diameter sample was conducted to measure the output shock pressure at the end of a 548 mm charge. Note that for this test the L/D ratio was again increased, to approximately 4.3. For this test, the diameter of the PWB was increased also, to 159 mm. Thus, as in the previous tests, the PBXW-123 was overdriven at the PWB input end, assuring that detonation was initiated near that end. The shock pressure in the reaction wave reaching the output end of the charge was measured using PVDF and manganin pressure gauges.<sup>6</sup> The gauges were mounted on a Teflon cylinder attached to the end of the charge, as shown in Figure 4. Two Metravib PVDF

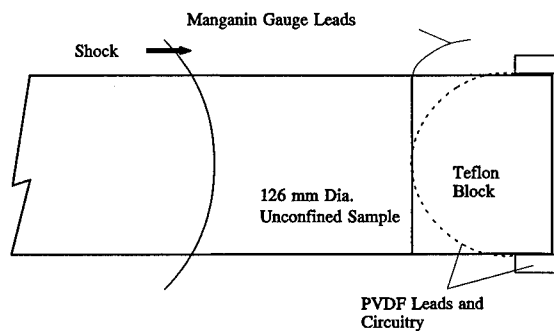


**FIGURE 4. EXPERIMENTAL ARRANGEMENT FOR OUTPUT PRESSURE MEASUREMENT FROM 126 MM CHARGE**

transducer elements were used, each 25 μm thick, with a 5 mm by 5 mm active area. A single Dynasen gauge package, consisting of one manganin gauge sandwiched between thin sheets of Teflon, was epoxied in front of the PVDF packages. The gauges were laterally offset so that each was approximately 8 mm off center, and they did not shadow each other.

The PVDF transducers were used in two modes of operation; one was operated in the so-called "charge

mode", while the other was used in the "current mode". In the current mode, the voltage at a small resistor across the gauge leads is recorded; the signal is proportional to stress rate  $d\sigma/dt$ . In the charge mode, the transducer output is integrated by a capacitor across its leads; the record of the capacitor voltage is then proportional to the stress history at the gauge element.

The stress records derived from the three gauges are shown in Figure 5. There is good general agreement among the three records for the general structure

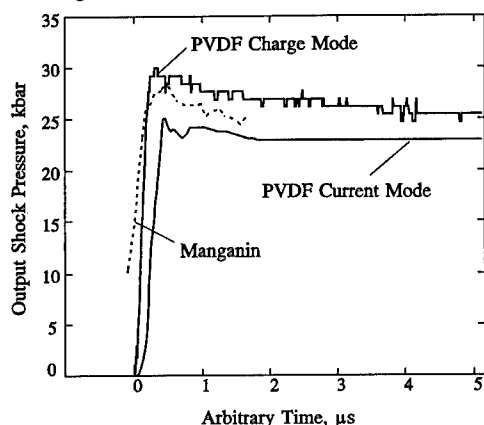


FIGURE 5. OUTPUT PRESSURE AT END OF 126 MM DIAMETER SAMPLE

and magnitude of the output pressure history. Note, however, that the shock front did not reach the three gauges simultaneously; the two PVDF gauge records have been shifted in time so that their structures can more easily be compared. In actuality the charge mode PVDF gauge responded approximately 200 ns before the current mode gauge. This was most likely due to an offset of the reaction wave from the charge centerline, as well as slight differences in the offset distance of each gauge from the charge centerline; it is an indication that there was large curvature in the propagating wavefront. (See Appendix A for a brief discussion of reaction wave curvature in PBXW-123.) The peak stress in the PVDF gauge used in the charge mode was approximately 30 kbar. The current mode PVDF gauge record shown has been numerically integrated, and shows a peak stress of about 25 kbar. The manganin gauge record reached a peak of approximately 28 kbar; however, its apparent rise time was longer than that of either PVDF gauge. The manganin gauge was closer to the end of the charge, so it responded before the two PVDF gauges; wave curvature effects could also have contributed to a difference in its response compared to that of the PVDF gauges. Based upon the peak stress at the charge output end, as measured in these three gauge records it is obvious that detonation failed for the unconfined 126 mm charge of PBXW-123, just as

it did for the smaller diameter, shorter charges. However, the magnitude of the output shock pressure was significant, and implies again that the reaction which was propagating was only gradually failing.

### Confined Sample Experiments

Three experiments were conducted using confined sample charges of PBXW-123. The sample charge and PWB configuration, illustrated in Figure 6, was very similar to that of the unconfined 75 mm diameter tests. Confinement was provided by brass cylinders which had an inner diameter of 76 mm and wall thickness of

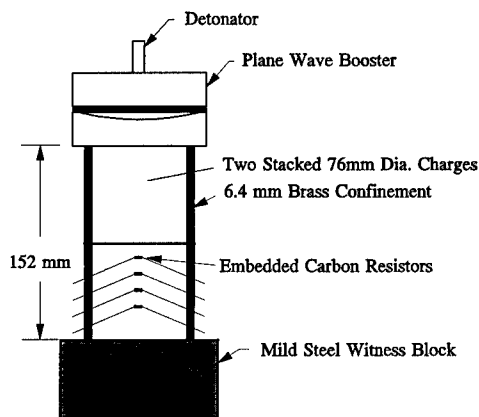


FIGURE 6. PBXW-123 CONFINED SAMPLE TEST CONFIGURATION

6.4 mm. The explosive charges were cast and cured in 76 mm lengths in the brass cylinders. In each of the three confined sample tests, the sample length of 152 mm was made up by stacking two such charges; the interfaces between the charges were coated with a thin layer of vacuum grease to fill in any voids and maintain good contact. The first of these three experiments was uninstrumented, using only the mild steel witness cylinder at the output end, as shown in Figure 6, to gauge reaction strength at that point. In each of the three confined sample tests, the back end of the 64 mm thick steel cylinder was spalled off, and the remaining steel was shattered into numerous fragments, indicating that detonation in the sample had propagated the full charge length.

In the final two confined sample experiments, carbon composition resistors embedded within the PBXW-123 were used to estimate the propagation velocity of the reaction along the charge centerlines. These gauges function essentially as time of arrival gauges when exposed to detonation pressures. However, for subdetonation reaction pressures up to approximately 100 kbar their resistance change with pressure has been

calibrated,<sup>7</sup> so the gauge output can be used to estimate shock pressure in such cases. The gauge leads were angled back from the resistor bodies, relative to the expected direction of shock propagation, as illustrated in Figure 6. In the first of these experiments, four gauge resistors were used within the lower half of the test length only. In the second test, eight gauge resistors, four in each half of the test charge, were used. In both of these instrumented tests, the magnitude of all of the resistor gauges' signals exceeded the 100 kbar maximum calibrated response, an indication that reaction in the sample material was not significantly declining as it propagated along the charge. Plots of the position of the reaction front vs. time, based upon the signal arrival times at the gauge resistors, also indicate that the reaction propagation velocity in each test was steady along the full length of the test charges. The slope of a linear least squares fit of the position-time data for the first of the instrumented confined charge tests, in which the gauge resistors were in the last half of the charge length, gives a propagation velocity of approximately 5.4 mm/ $\mu$ s. Note that this is significantly greater than the highest velocity which was observed in the unconfined tests. Higher-order least squares functions did not fit the same position-time data well, also indicating that the propagation velocity was steady.

Similar results were obtained in the second of the instrumented confined charge tests. The position-time plot of the signal arrival at the eight embedded resistor gauges, shown relative to distance from the PWB input end of the sample charge, is shown in Figure 7. As in the previous test, it was found that a linear fit worked best for these data, indicating negligible slowing of the reaction propagation within this charge length. The

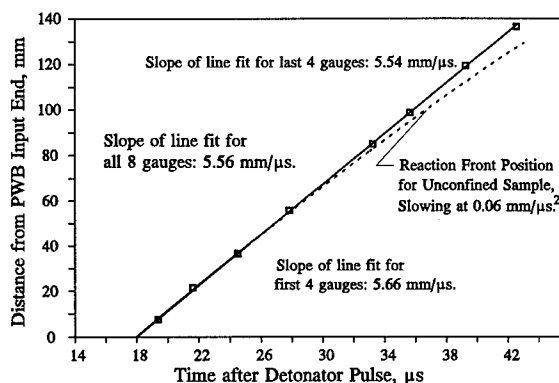


**FIGURE 7. SIGNAL ARRIVAL TIMES AT EIGHT EMBEDDED RESISTOR GAUGES, CONFINED SAMPLE TEST**

slope of the least squares line fit using all eight gauge

times was approximately 5.6 mm/ $\mu$ s. The apparent propagation velocity based on the first four gauges only was slightly higher, but this is to be expected, since the detonation was at first overdriven. The average propagation velocity for the two instrumented confined charge tests was 5.5 mm/ $\mu$ s.

Based upon the fragmentation of the witness cylinders in the three confined sample tests, the shock pressure in excess of 100 kbar at all internal gauge locations, and the apparently steady reaction propagation velocity, it may be concluded that detonation continued along the full 152 mm lengths of the confined 76 mm diameter samples of PBXW-123. Within the experimental error of our time-of-arrival measurements, detonation was stable for these confined samples. For purposes of comparison, the position of the slowly failing reaction front in a 75 mm diameter unconfined sample, observed in the first streak camera test, is shown in Figure 7 as a function of time. From this comparison, it appears that the detonation in the unconfined samples began to fail after propagating approximately 28 mm from the PWB input. If similar behavior had occurred in the confined samples it would have been detected from the available arrival time data.

## CONCLUSIONS

PBXW-123 has an unconfined failure diameter greater than 126 mm. Brass confined 76 mm diameter charges propagate stable detonation waves with a velocity of approximately 5.5 mm/ $\mu$ s.

PBXW-123 in unconfined charges up to 126 mm in diameter does not propagate steady detonation waves; however, it does propagate strong reaction waves for long distances. These reaction waves fail very slowly by comparison to failure in more ideal explosives, typically at less than 0.1 mm/ $\mu$ s<sup>2</sup>. The shock pressure propagated by these failing reaction waves also remains quite high for long distances.

## ACKNOWLEDGEMENTS

The authors wish to thank K. D. Ashwell, R. N. Baker, and J. H. O'Connor, who contributed valuable skills and suggestions in conducting the present experiments. E. R. Lemar and P. M. Ladd are gratefully acknowledged for their assistance in the data reduction. This work was sponsored by the Office of Naval Research, Code 4525, as part of the Explosives and Undersea Warheads Technology Block Program PE602314N.



## APPENDIX A

Wave curvature was also investigated in another part of the study of PBXW-123 detonation behavior. Reaction wave breakout at the far end of a cylindrical charge, identical to the 100 mm sample shown in Figure 1, was observed by streak photography. The arrival time along a diameter was measured from the film record. As described above, for this unconfined diameter in PBXW-123 the wave propagating the length of the sample was not a detonation wave, but rather was a slowly decaying subdetonation reaction wave. Figure A1 shows wave arrival times measured along the central 50% of the charge diameter, as well as a second order least squares fit to the data. As can be seen, there is large curvature in the wave, and the wave is approximately 3 mm off-center. As mentioned in the body of the paper, both of these types of behavior could contribute to differences in gauge arrival times such as that seen in the 126 mm diameter test.

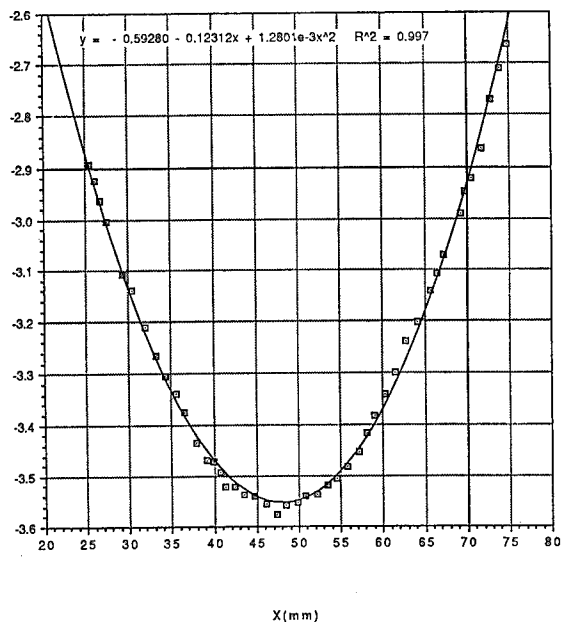


FIGURE A1. BREAKOUT TIME ALONG DIAMETER AT END OF CHARGE

## REFERENCES

1. Lemar, E. R.; Liddiard, T. P.; Forbes, J. W.; Sutherland, G. T.; and Wilson, W. H., *The Analysis of Modified Gap Test Data for Several Selected Insensitive Explosives*, NAVSWC TR 89-290, Sep 1993, NAVSWC, Dahlgren, VA.
2. Hutcheson, R. S. Jr., unpublished test data from *Large Scale Gap Test Firing Sheet*, NAVSWC White Oak Detachment, Silver Spring, MD, 25 Jun 1990.
3. Hall, T. N. and Holden, J. R., *Navy Explosives Handbook - Explosions Effects and Properties - Part III. Properties of Explosives and Explosive Compositions*, NSWC MP 88-116, Oct 1988, NAVSWC, Dahlgren, VA, p 8-16.
4. Hall, T. N. and Holden, J. R., *Navy Explosives Handbook - Explosions Effects and Properties - Part III. Properties of Explosives and Explosive Compositions*, NSWC MP 88-116, Oct 1988, NAVSWC, Dahlgren, VA, p 4-12.
5. Hall, T. N. and Holden, J. R., *Navy Explosives Handbook - Explosions Effects and Properties - Part III. Properties of Explosives and Explosive Compositions*, NSWC MP 88-116, Oct 1988, NAVSWC, Dahlgren, VA, p 1-6 and p 7-8.
6. Gustavson, P. K.; Tasker, D. G. and Forbes, J. W., *PVDF Pressure Transducers for Shock Wave and Explosive Research* (U), NAVSWC TR 91-506, 1993, Dahlgren, VA.
7. Watson, R. W., "Gauge for Determining Shock Pressures," *The Review of Scientific Instruments*, Vol. 38, No. 7, July 1967, pp 978-980.

## DISCUSSION

K. GRAHAM

Atlantic Research Corporation, Gainesville, Virginia

Does PBXW-123 steadily detonate unconfined underwater? At what diameter?

## REPLY BY RUTH DOHERTY:

Yes, in ~6-inch-diameter, confined only with PVC pipe.

## SOME CHARACTERISTICS OF BOW WAVE INITIATION AND DESENSITIZATION

M. Chick and T.J. Bussell  
DSTO, Materials Research Laboratory  
Ascot Vale, Victoria 3032, Australia

and  
R.B. Frey  
Army Research Laboratory  
Aberdeen Proving Ground, Maryland 21005, USA

We report on the use of bow waves as a new approach to the study of shock initiation processes. The material of the cover adjacent to explosive is shown to have a significant effect on the run to detonation distance for a given jet velocity and this is related to the characteristics of the wave ahead of the jet. Variation in RDX particle size in Composition B has a marked influence on jet impact sensitivity but not on bow wave shock sensitivity. Within limits side confinement reduces the critical jet velocity for detonation by supporting bow waves that would otherwise fail; some controlling parameters are discussed.

### INTRODUCTION

Shock initiation studies have been mostly undertaken with wave shapes that approximate to either rectangular or triangular profiles. However, recent investigations<sup>1,3</sup> into the interaction of shaped charge jets with explosives have demonstrated that a major initiation mechanism is by the bow wave shock from the jet penetration of the explosive. The discovery opens up the opportunity of being able to study initiation processes by the third type of shock wave profile; that is where the pressure significantly increases after the initial shock, rather than either remaining constant (rectangular) or decreasing (triangular). This type of shock wave profile arises since jet penetration in the explosive is almost always supersonic and the initial shock is following by increasing pressure to the stagnation point at the jet/explosive interface. The ramp pressure profile is significant since it is a few microseconds wide with a peak pressure several times greater than the preceding shock and its confining effect on the reaction may play a significant role in explosive initiation. A further aspect of this approach is that the bow wave shape from the jet penetration of a cover is dependent on the

shock properties of the host material and can vary from a ramp, simple shock or combination of the two. However, these waves also ramp up to the high pressure at the stagnation point at the jet/cover material interface. The analysis in reference two and the elegant experiments of Ferm and Ramsay<sup>4</sup> with Plexiglas (PMMA) as an explosive surrogate shows that the wave transmitted to an adjacent explosive layer initially retains the basic structure of the bow wave from the jet penetration of the cover. The transmitted precursor waves may be expected to have the potential to desensitise or shock initiate the explosive.

These proposals suggest that an examination of the interaction of bow waves with explosives offer a new avenue for the study of shock initiation processes.

In this paper we report on three different aspects of bow wave initiation. These are; (a) the relative ability of bow waves from the jet penetration of perspex and steel to initiate adjacent explosive (b) the effect of RDX type on the relative jet impact and bow wave shock sensitivity of Composition B, and (c) the effect of the interaction of bow waves with side confinement on the initiation process.

## EXPERIMENTAL

The 38 mm diameter and 66 mm LAW shaped charges were fired from 2 charge diameters standoff coaxial with the receptor. The characteristics of the jet from the 66 mm LAW round were taken from our measurements and those reported by McAfee.<sup>5</sup> The characteristics of the 38 mm diameter shaped charge have been previously reported.<sup>6,7</sup>

The critical detonation threshold for a given receptor was determined from a series of firings (8 to 10 shots) where the jet was fired through a predetermined, but variable thickness of steel. The results were analysed statistically and expressed as the thickness of steel that produced a 50% probability of detonation.<sup>8</sup> The steel thickness was converted to the critical jet velocity for the detonation threshold using the standard incompressible Bernoulli penetration equations and reported data.<sup>5,7</sup> For jet penetration bow wave initiation tests the steel was in intimate contact with the explosive while for jet impact sensitivity tests the steel was stood off from the receptor to avoid precursor wave effects.<sup>1-4</sup>

Run to detonation measurements were made using the jet from the 38 mm diameter shaped charge. In most experiments the time of the event progressing through the receptor charge was recorded with electric probes; however a few measurements on unconfined receptors were carried out using multiple flash radiography to allow direct observation of the event. In these tests the jet velocity was varied by varying the thickness of a steel or PMMA cover. Unless it is explicitly stated the cover used for a particular test was steel. This was because our results show that the bow wave transmitted to adjacent explosive from jet penetration of steel only causes initiation through small cover thicknesses (i.e. < 12 mm) which is equivalent to a jet velocity of about 7.4 km/s. The distance time history for the jet penetration of PMMA was taken from our compressibility study previously reported<sup>6</sup> which is based on the treatment by Flis and Chou.<sup>9</sup> Run to detonation distances were determined from the approach of Ramsay and Popolato.<sup>10</sup> If it is assumed that the jet penetration bow wave shock velocity ( $U_s$ ) approximates the jet penetration velocity,  $U_{pen}$ , then the run to detonation,  $d$ , can be represented by;

$$d = \ell - V_D t / (1 - V_D / U_{pen})$$

where  $\ell$  the length of the explosive charge,  
 $t$  the time for the event through the charge, and

$V_D$  the velocity of detonation for the explosive, in these tests Composition B, where  $V_D = 7.77$  km/s.

We estimate that the accuracy of the run distances are to within a few millimetres.

The two sets of Composition B receptors were based on a different type of RDX. Class A RDX had an average particle diameter (APD) of 200 microns and its preparation included a final recrystallisation process. Class B RDX had an APD of 75 microns and its preparation included boiling and milling without the final recrystallisation process. Scanning electron microscopy showed both materials to be similar in shape and contain a similar, but small number of inclusions. The Composition B made from the Class A RDX had a density of 1.67 g cm<sup>-3</sup> and a composition of RDX/TNT/WAX, 58/41/1. The Composition B made from the Class B RDX had a density of 1.65 g cm<sup>-3</sup> and a composition of RDX/TNT/WAX, 55/44/1. We conclude that the major difference between the two types of Composition B is the particle size of the RDX. Unless otherwise stated Composition B made from the Class B RDX was used as the receptor material.

## CASE GENERATED WAVE EFFECTS ON INITIATION

The run to detonation in Composition B from the jet penetration of steel, PMMA and 30 mm thick steel/variable PMMA thickness combinations are plotted in Figure 1. Data analysis has converted the cover thicknesses to the jet velocity at the cover/Composition B interface; this allows a comparison of the run values from the 3 types of cover for the same initial jet velocity.

After an initial, almost zero run distance from thin covers (up to 12 mm) the curve for steel jumps to about a 20 mm run and then steadily increases to 40-50 mm at the approaching detonation threshold (corresponding to a jet velocity of 5.2 km/s). The run distance for plexiglas remains less than 8 mm for most of the curve and then rapidly increases to 30 mm at the approaching failure condition which our results give as 4.95 km/s. We interpret these results in terms of the competing initiation waves produced by the jet penetration of the cover material and the jet penetration of Composition B.

The short runs for PMMA are associated with the fact that a bow wave shock forms in front of the jet in PMMA (the penetration rate is supersonic). This shock can cause prompt initiation of the explosive.

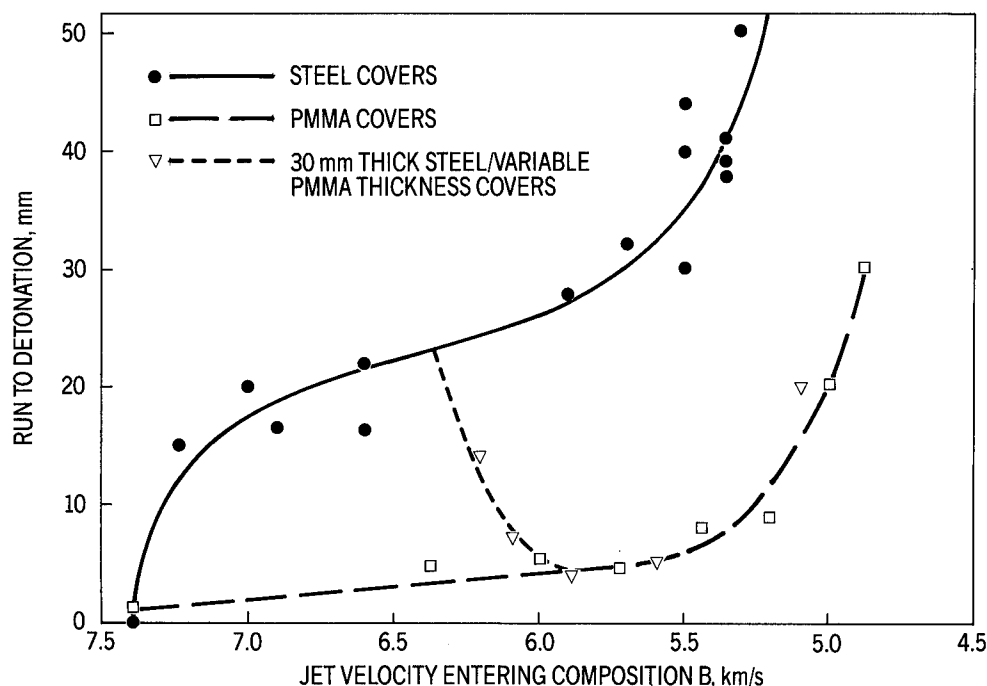


FIGURE 1. RUN TO DETONATION VS INITIAL JET VELOCITY FOR COMPOSITION B WITH COVERS OF STEEL, PMMA AND 30 mm THICK STEEL/PMMA COMBINATIONS

Thus, for  $V_j = 5.4$  km/s and using Hugoniot matching, an initiating pressure in the Composition B of 4.7 GPa is obtained. This is high compared to the critical shock pressure from the large Scale Gap Test (LSGT) of 2.0 GPa (see Table 1), and it is not surprising that the run distance is short. With a PMMA cover, the bow shock in the cover, after transmission into the Composition B, is always somewhat stronger than the bow shock that forms in the Composition B (for the same jet velocity). Therefore, one might suppose that the transmitted shock from the PMMA cover would always be responsible for the initiation. The following observations indicate that this is not true; 1) the run distance increases rapidly as jet velocity is reduced below 5.4 km/s, 2) the critical jet velocity, where initiation just fails, is similar for steel, aluminium, and PMMA covers.<sup>3</sup> Thus, it appears that for jet velocities above 5.4 km/s, the transmitted bow shock is the causative agent, but for lower jet velocities, the bow shock that forms in the explosive is responsible.

What is somewhat puzzling is that the transition between the two mechanisms appears to occur at a jet velocity of about 5.4 km/s and a transmitted shock pressure of about 4.7 GPa. We base this inference on the fact that the run distance begins to increase rapidly as jet velocity is reduced from this point. We would

have guessed, based on the comparison to the LSGT, that the transmitted shock would still be an effective initiator under these conditions. A complication in the comparison is that the bow shock from PMMA will be divergent and hence produce a smaller volume of shock ignited explosive than the confined donor in the LSGT. Hence, it may require compensation by a stronger shock to reach the critical condition. However, the bow shock from the jet penetration of Composition B is also divergent, and yet the critical initiation pressure is estimated to be 2.5 GPa.<sup>1,3,10</sup> While we do not completely understand this difference, it is clear that at the critical condition, the bow shock requires the support of the jet over long run distances to enable the lower pressure, divergent shock to attain detonation.

The situation with the steel cover is quite different because the jet penetration in the steel is subsonic, and for sufficiently thick covers the leading edge of the bow wave will be a ramp, rather than a shock. Following from Reference 2, further study has been undertaken of the shock structure produced in steel from jet impact and penetrator using the CTH hydrocode<sup>12</sup>. The previous results referred to a quasi-steady state bow wave structure with an elastic wave ramping to a plastic bow shock followed by a ramp to

the stagnation pressure at the jet tip. The CTH hydrocode calculations indicated that at 10 mm into steel the transient wave from jet impact is still important. At this point, the calculations indicate that there is a weak elastic precursor which leads a plastic shock by about 0.8 mm. When the precursor enters the Composition B, it will be weak and propagate at just above the sound velocity, or about 2.8 km/s. The leading plastic shock will have an amplitude of about 20 GPa in the steel and produce a shock of about 5.8 GPa in the Composition B. This wave will overtake the elastic precursor in about 0.5  $\mu$ s. Hence, shock initiation should take place promptly as observed in Figure 1 at the start of the steel cover curve; thus for thin covers, even out to 10 mm, it is the transient impact shock that causes initiation. For a 14 mm steel cover, the code calculations show that the leading shock in the transient wave has turned into a ramp in front of the second, plastic shock. This wave structure may not be an efficient initiator and thus may desensitize the explosive to the following plastic shock. Initiation can only occur when this structure has "shocked up" in the explosive (presumably, it evolves in some continuous fashion into the bow shock which precedes the penetrating jet in Composition B under quasi-steady state conditions). Initiation can only occur when a bow shock has formed in the explosive; thus, there is a dramatic increase in the run to detonation as shown in Figure 1. Thereafter the run increases steadily as the jet velocity decreases until the rapid rise at the approaching detonation threshold.

The discussion above and the run distances in Figure 1 suggest that for the same jet velocity, PMMA is a more efficient initiating cover system than steel. This effect was confirmed with a combination cover system comprising 30 mm thick steel/and various thicknesses of PMMA with the latter in contact with the explosive.

The data plotted in Figure 1 represents PMMA thicknesses of 5, 10, 20, 40 and 80 mm. It shows that the run to detonation vs jet velocity relationship falls sharply from the steel cover curve to follow that produced by the PMMA covers. Thus the run to detonation distance of 23 mm from a 30 mm thick steel cover ( $V_j = 6.3$  km/s) drops to 4 mm for a 30 mm thick steel/20 mm thick PMMA cover ( $V_j = 5.9$  km/s).

The comparison of the relative magnitude of the critical shocks from the steel and PMMA covers appears to support the proposition that ramp waves are desensitising. Thus the CTH calculations show that at 14 mm into steel the transient wave has a ramp followed by a shock that produces an estimated 6.3

GPa peak in Composition B. In comparison, PMMA does not produce a ramp and the critical shock in the explosive is 4.7 GPa.

## EFFECT OF PARTICLE SIZE ON JET SENSITIVITY

### Review of Particle Size effects on Shock Initiation

Particle size has a significant effect on the shock to detonation process in solid explosives. The effect is complicated because particle size may have one effect on the ignition of hot spots by a shock and a different effect on the buildup of reaction after ignition has occurred. We will briefly review some of the published work here. References 13 and 14 discuss tests that were performed on pressed TNT. Samples with a particle size of about 250 micron and 70 micron were pressed to a density of 1.55 g cm<sup>-3</sup>. Flyer plate impact experiments were conducted, and the downstream surface of the samples were monitored for evidence of reaction (a free surface velocity in excess of what would be expected for an inert sample). When density was held constant, the large particle size material ignited at a lower pressure. However, full detonation was obtained at a lower pressure in the small particle size sample. The authors suggested that hot spots could form more easily in the large particle size material, but that the buildup to detonation proceeded more rapidly in the fine particle size material (which has a larger internal surface area).

Because of these competing effects, particle size can affect the threshold conditions for the initiation of detonation in different ways for different levels of shock pressure. Honodel, et. al,<sup>15</sup> conducted experiments on pressed charges prepared from different types of TATB with different particle sizes. In gap tests, where the shock pressure is relatively low and the duration is relatively long, the finest particle size material (mean particle size about 9  $\mu$ m) was significantly less sensitive than the larger particle size materials. However, when tests were done with thin (0.05 mm), high velocity flying foils, the fine particle material was more sensitive. Setchell and Taylor,<sup>16</sup> came to the same conclusion with pressed hexanitrostilbene. They impacted their samples with thin flyer plates and observed the downstream surface with VISAR. When the duration of the shock pulse was 0.19 microseconds, they found that the larger particle size material was more sensitive than the fine particle material (it initiated at a lower shock pressure); but for very short pulse durations (0.04 microseconds), the situation reversed.

The studies mentioned above involved pressed explosive without a binder. Moulard et al<sup>17,18</sup> demonstrated that very similar conclusions apply to plastic bonded explosives. They studied RDX/polyurethane mixtures using three different particle sizes of RDX. In flyer plate impact experiments where the pulse duration was in the range of 0.5 to 2.5 microseconds, the fine particle material (circa 8 microns in diameter) was markedly less sensitive. However, the fine material had a small failure diameter (evidence that it reacts faster at detonation pressures), and wedge tests showed that the fine material was the most sensitive at high pressures (12.0 GPa). The conclusion was that the initiation process was controlled by the growth aspect of the process for high pressures and short durations and by the ignition aspect for low pressures and long durations. Small particles inhibit ignition but promote growth. The general picture is that small particle materials are less sensitive at lower pressures and larger particle materials are less sensitive at higher pressures. However, the definition of "low" and "high" probably depends on the range of particle sizes which is being considered. Belanger<sup>19</sup> obtained data on a polybutadiene/dioctyladipate/RDX explosive. He used two particle size distributions, one peaking at about 200 microns and the other at about 700 microns. He conducted flyer plate impact experiments where the duration was in the range from 0.5 to 2.0 microseconds and where the pressure was 3.0 to 9.0 GPa. For this range of pressures and durations, the experiments discussed above would indicate that the fine particle material should be less sensitive, but in Belanger's case, the coarse particle material was less sensitive.

However, in Belanger's case, even the fine material was probably coarse enough that it could easily be ignited throughout the experimental pressure range; thus the buildup was controlled by growth.

## Results and Discussion

The results from the effect of RDX particle size as incorporated into Composition B on jet sensitivity are given in Table 1. We note that the two particle sizes of RDX are both relatively coarse compared to most material covered by the literature summary above.

Jet impact on explosives produces high pressure, short duration shocks and there is no rising ramp behind the front. The data in Table 1 shows that the smaller particle material is more sensitive to impact initiation (i.e. lower  $V_j$ ) and is therefore in agreement with the literature summary above for high pressure shocks. In the moderate shocks from the gap tests the smaller particles were also more sensitive (see Table 1). These particles (mean average particle diameter 75 microns) are relatively large and in this context the gap test results show a similar trend to those reported by Belanger<sup>19</sup> where reaction growth is considered the controlling influence.

Table 1 shows that the critical jet velocities for the bow wave initiation of the two types of Composition B for the jets from both the 38 mm and 66 mm LAW shaped charges are similar. As discussed earlier, bow wave shock profiles are quite different to those produced by jet impact. Flash radiography has shown

TABLE 1. RDX PARTICLE SIZE EFFECT ON JET SENSITIVITY  
(RDX INCORPORATED INTO COMPOSITION B)

EXPLOSIVE DETAILS		JET SENSITIVITY, $\text{mm}^3/\mu\text{s}^2$				GAP TEST SENSITIVITY	
Mean RDX Particle Size (Microns)	Composition B Type	Bow Wave Shock Initiation		Impact Shock Initiation		Small Scale $M_{50\%}$ , mm	Large Scale GPa
		38 mm $\varnothing$ Charge Jet	66 mm $\varnothing$ LAW Jet	38 mm $\varnothing$ Charge Jet	66 mm $\varnothing$ LAW Jet		
75	RDX/TNT/WAX 55/45/1 $\rho = 1.65 \text{ g/cm}^3$	41 ( $V_j = 5.2 \text{ km/s}$ $d = 1.5 \text{ mm}$ )	$\sim 48$ ( $V_j \approx 5.5$ $d \approx 1.6 \text{ mm}$ )	14 ( $V_j = 3.2 \text{ km/s}$ $d = 1.4 \text{ mm}$ )	$\sim 10$ ( $V_j \approx 2.6 \text{ km/s}$ $d \approx 1.5 \text{ mm}$ )	16	2.0
200	RDX/TNT/WAX 58/41/1 $\rho = 1.67 \text{ g/cm}^3$	41 ( $V_j = 5.2 \text{ km/s}$ $d = 1.5 \text{ mm}$ )	$\sim 50$ ( $V_j \approx 5.6$ $d \approx 1.6 \text{ mm}$ )	38 ( $V_j = 5.0 \text{ km/s}$ $d = 1.5 \text{ mm}$ )	$\sim 15$ ( $V_j \approx 3.2 \text{ km/s}$ $d \approx 1.5 \text{ mm}$ )	< 0	2.5

that bow shocks are a few microseconds wide<sup>1</sup> and the shock front pressure of the critical wave for the initiation of Composition B is moderate at 2.5 GPa.<sup>1,11</sup> The reason for a lack of a significant particle size effect in these materials for the moderate shock pressure is not clear. It may be influenced by the type of shock profile. Thus the shock front ignites hot spots and the ensuing growth of reaction will be enhanced by the local pressure produced by the confining effect of the ramp component of the wave. Thus the growth of reaction may be insensitive to the variation in the surface area of the two types of RDX for the bow wave profiles.

### SIDE CONFINEMENT EFFECTS

The effect of various thicknesses of steel and aluminium side confinement on the critical jet velocity for the initiation of Composition B are shown in Figure 2. Jets were generated from the 38 mm shaped charge and the critical jet velocities are at the surface of the Composition B. All explosive receptors were 38 mm diameter. This diameter was selected since previous work<sup>20</sup> showed that steel side confinement in this geometry will affect the critical jet initiation velocity whereas the unconfined charge is sufficiently large to be independent of self confinement effects.

The critical jet velocities in Figure 2 are for initiation from the jet penetration bow wave shock in the explosive where the results in Figure 3 indicate that the run to detonation is in excess of several tens of millimetres. Our unpublished data shows that the jet diameter,  $d$ , remains relatively constant at 1.4 to 1.5 mm for the initiation conditions of these tests. Thus the variation in the critical jet velocity,  $V_j$ , for bow wave initiation can be used to signify the change in the initiation criteria value of  $V_j^2 d$  (or more strictly,  $Up^2 d$ , since the penetrating jet is producing the critical bow wave shock). The data for steel cases in Figure 2 show that the critical velocity for bow wave shock initiation starts to decrease at a thickness of 2 mm and continues to a minimum value at a thickness of 10 mm. Thereafter the jet velocity remains constant with increasing case thickness, even for massive confinement (30 mm); thus there is no case inertia effect. Aluminium cases up to 19 mm thickness did not reduce the critical jet velocity below the unconfined value and hence exhibited no confinement effect.

The steel case results suggest that the component of the bow shock reflected from the explosive/steel interface supports the bow shock at least at the region of the critical condition. In this situation side

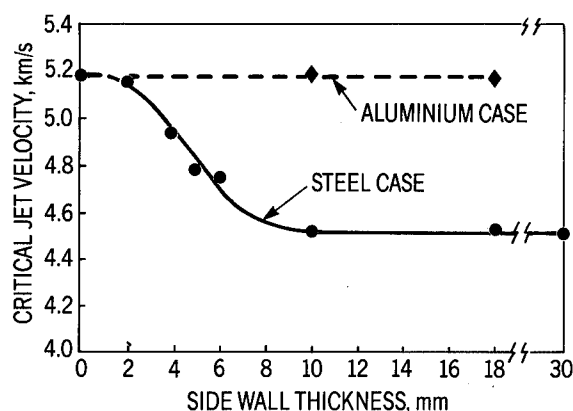


FIGURE 2. EFFECT OF SIDE CONFINEMENT MATERIAL AND THICKNESS ON BOW WAVE INITIATION OF COMPOSITION B

refractions are important since the penetrating jet continues to provide rear support for the shock. Therefore we assume that the component of the shock transmitted to the steel produces free surface movement which sends a rarefaction back into the case and through to the explosive. The rarefaction then limits the supporting effect of the reflected bow wave on the initiation process in the region of the critical condition. As the case wall thickness increases the rarefaction is delayed and the reinforcing effect of the reflected bow wave continues to be enhanced producing more effective initiation and thus the critical jet velocity decreases. The limiting case thickness may be linked to the characteristics of the bow wave and hence to the jet diameter and its relation to the diameter of the charge. Thus the charge diameter/jet diameter ratio (i.e.  $38/1.5 \approx 25$ ) and its relationship to the limiting case thickness (10 mm) may be useful in predicting steel confinement effects for other systems. The aluminium case results show that the reflected shock for this material is insignificant with respect to the bow shock's initiation capability and suggests that there is a minimum shock impedance mismatch requirement for a confinement effect.

Figure 3 shows the effect of variation of jet velocity entering Composition B on the run to detonation of confined charges of various diameters. All cases were 19 mm thick and well above the value to maximise the confinement effect. Apart from the zero value, the run to detonation distances are for the bow wave shock for the jet penetration of the explosive. Figure 3 shows two distinct features. Firstly, the run to detonation distances are independent of charge diameter for jet velocities up to about the critical value for unconfined charges (i.e. at  $V_j \approx 5.2$  km/s). These results demonstrate that this part of the initiation curve is

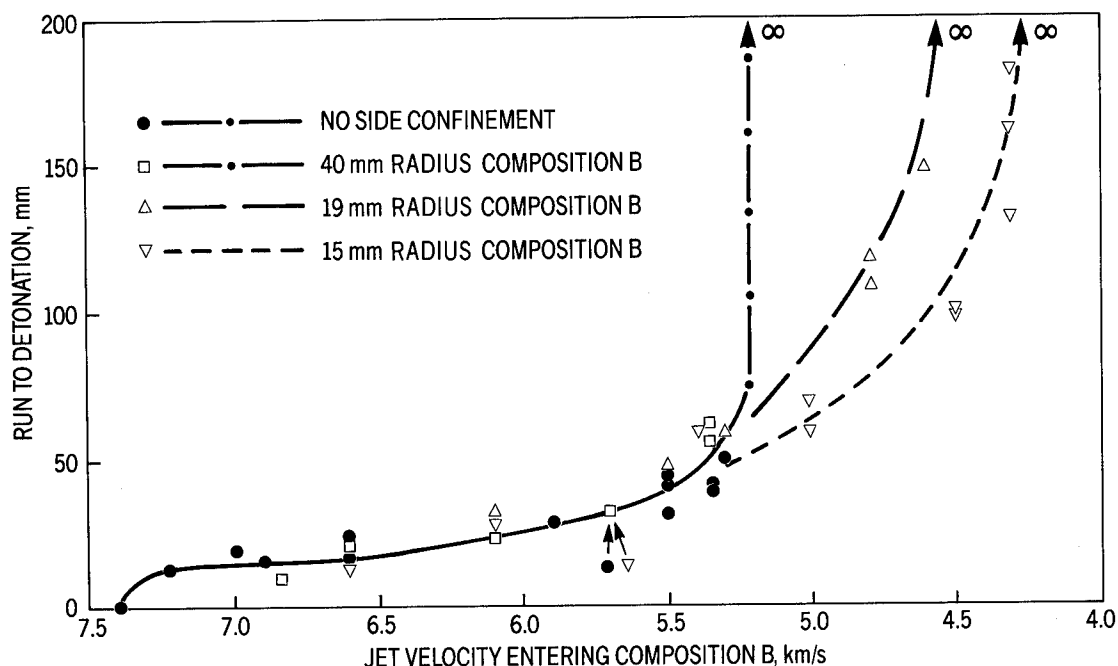


FIGURE 3. THE RUN TO DETONATION IN COMPOSITION B CHARGES OF VARIOUS DIAMETERS WITH 19 mm THICK STEEL SIDE CONFINEMENT

independent of confinement and is simply related to the jet penetration velocity and hence its bow wave shock without reinforcement from side reflections. Secondly, the curves fan out from about the unconfined critical value to asymptot at a critical velocity which decreases with decreasing charge diameter. Some of these run distances are very long (150 mm). The results demonstrate that the waves reflected from the wall are only able to influence the bow wave during the latter part of its run up to detonation and then only those waves that were otherwise going to fail. Note that the confined 40 mm radius charge exhibits no confinement effect with a curve and critical value similar to that for unconfined Composition B.

## CONCLUSION

Some features of bow wave initiation have been studied. Thus it has been shown that the run to detonation distance in Composition B for a given jet velocity is dependent on the material of the adjacent cover. The different behaviour produced by steel and PMMA covers has been discussed in terms of the wave

structure ahead of the jet. The general conclusions are supported by a model experiment using a steel/PMMA combination cover system. This produces a run to detonation vs jet velocity relationship that initially exhibits a dramatic increase in the run distance which then slows; this is followed by a sharp drop prior to increasing rapidly as the jet velocity approaches the detonation threshold value.

The effect of RDX particle size (as incorporated into Composition B) on jet impact shock initiation is marked and is in accordance with the literature, whereas our results suggest that bow wave shock initiation may be insensitive to the effect. The results support the importance of wave shape in determining the effect of particle size on shock initiation.

A qualitative description has been produced for the role of side confinement on the jet penetration bow wave initiation of Composition B. The study shows that the ratio of the jet/charge diameter is a controlling parameter, that there is a limiting thickness effect and that there is a minimum to the shock impedance mismatch at the explosive/case interface.



## ACKNOWLEDGEMENTS

We wish to record our thanks to Darren McQueen and Lyn McVay of MRL for assistance with the experiments.

## REFERENCES

1. Chick, M.; and Hatt, D.J.; Seventh Symposium (International) on Detonation, Naval Surface Weapons Centre, NSWC MP 82-334, 1981, p 352.
2. Chick M.; Bussell, T.J.; Frey, R.B.; and Bines, A.; Ninth Symposium (International) on Detonation, Office of the Chief of Naval Research, OCNR 113291-7, 1989, p 1404.
3. Chick, M.; Macintyre, I.B.; and Frey, R.B.; Eighth Symposium (International) on Detonation, Naval Surface Weapons Centre, NSWC MP 86-194, 1985, p 318.
4. Ferm, E; and Ramsay, J.B.; Propellants Explosives and Pyrotechnics, Vol. 16, 1991, pp 123-130.
5. McAfee, J.M.; LA-UR-87-3169, 1987, Los Alamos Scientific Laboratory.
6. Chick, M.C.; Frey, R.B.; and Bines, A.; International Journal Impact Engineering, Vol. 9, No. 4, 1990, pp 433-439.
7. Chick, M.C.; Bussell, T.J.; and Frey, R.B.; Journal of Energetic Materials, Vol. 5, 1987, pp. 327-342.
8. Chick, M.; Wolfson, M.C.; and Learmonth, L.A.; 18th International Annual Conference of ICT, Karlsruhe, FRG, 1987, p 56.
9. Flis, W.J.; and Chou, P.C.; Seventh International Symposium on Ballistics, The Hague, Netherlands, 1983, p 617.
10. Ramsay, J.B.; and Popolato, A.; Fourth Symposium (International) on Detonation, Office of Naval Research, ACR-126, 1965, p 233.
11. Chick, M.C.; Bussell, T.J.; and Frey R.B.; 19th International Annual Conference of ICT, Karlsruhe, FRG, 1988, p 24.
12. Kimsey, K.; and Frey, R.B.; ARL, Aberdeen Proving Ground, Md, January 1992.
13. Howe, P.; Frey, R.B.; Taylor, B.; and Boyle, V.; Sixth Symposium (International) on Detonation, Office of Naval Research, ACR-221, 1976, p 11.
14. Taylor, B.; and Ervin, L.; Sixth Symposium (International) on Detonation, Office of Naval Research, ACR-221, 1976, p 3.
15. Honodel, C.A.; Humphrey, J.R.; Weingart, R.C.; Lee, R.S.; and Kraner, P.; Seventh Symposium (International) on Detonation, Naval Surface Weapons Center, NSWC MP 82-334, 1981, p 425.
16. Setchell, R.; and Taylor, P.; Ninth International Colloquium on the Dynamics of Explosions and Reactive Systems, Poitiers, France, 1983.
17. Moulard, H.; Kury, J.; and Delclos, A.; Eighth Symposium (International) on Detonation, Naval Surface Weapons Center, NSWC MP 86-194, 1985, p 902.
18. Moulard, H.; Ninth Symposium (International) on Detonation, Office of the Chief of Naval Research, OCNR 113291-7, 1989, p 18.
19. Belanger, C.; Pelletier, P.; and Drolet, J.; Eighth Symposium (International) on Detonation, Naval Surface Weapons Center, NSWC MP 86-194, 1985, p 361.
20. Chick, M.C.; Bussell, T.J.; and McVay, L.; Eleventh International Symposium on Ballistics, Brussels, Belgium, 1989.

---

## DISCUSSION

### BLAINE ASAY

Lawrence Livermore National Laboratory, Livermore, California

The large particle RDX showed a very small difference in  $V^2d$  between impact and bow shock insults. Could you explain that behavior?

#### REPLY BY M. CHICK:

The small difference between the impact and bow wave shock sensitivities ( $V^2d$ ) for the large RDX material is observed for the tests using the jet from the 38-mm LAW charge, i.e., only for the relatively smaller diameter jet. Flash radiography shows that for the smaller diameter jet, the large diameter RDX material exhibits poor detonation corner turning during impact initiation, whereas the finer RDX material exhibits prompt detonation corner turning. Thus, we propose that the smaller diameter jet requires a higher velocity when impacting the larger diameter RDX material in order to produce a sufficient amount of initial reaction that can expand to the minimum detonation diameter and, thus, accomplish the shock to detonation transition. As a consequence the  $V^2d$  value for impact initiation increases and approaches that for bow wave initiation. Hence we suggest that the effect is related to the ratio of the jet diameter and minimum detonation diameter. Further work examining the effect, including measurement of the minimum detonation diameter of the two materials, is underway.

#### DISCUSSION

M. M. CHAUDHRI

University of Cambridge, Cambridge, England

Would you please explain why you expect (found) the smaller particles much more sensitive than the larger particles, especially when we know that the explosive crystals are very weak and very fragile, and that probably all of them are likely to disintegrate extensively at the shock front, thus multiplying the initial particle size differences.

#### REPLY BY M. CHICK:

There is a bulk of literature demonstrating that particle size can have a significant effect on the shock to detonation process in solid explosives. Literature

quoted in the paper, and our results, suggest that the interrelationship between shock shape and particle size is important in determining the relative importance of hot spot formation and the growth phase in the initiation process.

#### DISCUSSION

HAROLD J. GRYTING

Gryting Energetics Science Company, San Antonio, Texas

Were the 76- and 200-micrometer explosives of approximately those sizes, or did they have wide or normal distributions?

#### REPLY BY M. CHICK:

The material with an average particle size (APD) of 200  $\mu\text{m}$  exhibited an approximately normal distribution with limits between 50 and 500  $\mu\text{m}$ . The smaller size material did not exhibit a normal distribution, the curve being skewed toward the lower end.

#### DISCUSSION

M. HELD

DASA, Schrobenhausen, Germany

Your experimental results I can confirm: that with Al, Plexiglas, plastics (different types), lead (Pb), the buildup distances are much shorter compared with steel. My explanation is that steel has much greater bulging behavior before jet exit, which is desensitizing the HE charge, compared with the other cover materials.

#### REPLY BY M. CHICK:

These results are compatible with the data and discussion in our paper, with the bulging behavior of the steel being related to the effect of the ramp wave.

## REFLECTED-SHOCK INITIATION OF EXPLOSIVES

E. N. Ferm and L. M. Hull

Explosives Technology and Applications Division  
Los Alamos National Laboratory  
Los Alamos, New Mexico 87545

In a study of initiations caused by reflected shock from a high-impedance boundary attempts to establish sufficient conditions for initiation are described. Shock polar analysis is used to discover the ranges of various flow regimes, general shock structures and pressure estimates of states behind the reflected wave. Using this knowledge, wave structure growth rates from hydrocode simulations are estimated and standard-shock initiation criteria are used; experiments are designed in which the initiation from a reflected-shock wave structure appears likely. Two experiments are described in which a reflected-shock wave from a uranium surface initiated PBX 9502. The experimental evidence is in good agreement with the assumptions and results of the analysis.

### INTRODUCTION

Shock initiation of explosives has been studied extensively and has resulted in useful models that describe the run to detonation, given the initial shock pressure. The experiments leading to these models were designed to eliminate boundary effects. The work presented here studies the influence of high-impedance boundaries on shock initiation of explosives. When boundaries are included in the problem, more analysis is required to determine the effect of wave reflections from the boundaries. Our approach to this problem was to examine the shock structure of the nonreactive reflected-wave problem using shock polar analysis and hydrocode simulations. We then looked for the shock structures that appear likely to initiate the explosive, considering the known explosive properties.

To obtain the shock structure, we studied the simple geometrical configuration of the reflection of a nonreactive, plane shock traveling in the explosive impacting a flat high-impedance metal plate like uranium. In this case, classical shock polar theory applies. This simple analysis determines the pressure behind the reflected wave as a function of the interaction angle and incident shock pressure. If the wave reflection is regular, the incident wave and the reflected wave are attached to the wall. If it is irregular, a more complicated shock structure must exist between the incident and reflected shock and the wall in order to satisfy boundary conditions. Shock polar analysis is only a local analysis, and it has limitations because the flow configurations are assumed in order to do the analysis.

Our hydrocode calculations of the wave reflection problem were made to validate the shock polar analysis and to obtain growth rate information of the irregular reflection.

To find a case in which a reflected shock is likely to initiate an explosive, we expected the following conditions must be met: (1) the incident shock must not desensitize the explosive,<sup>1</sup> (2) the amplified pressure must be sustained over the distances approximately equal to the single-shock run-to-detonation distance corresponding to the amplified pressure,<sup>2</sup> and (3) the pressure must be sustained over a width of explosive approximately the same as the failure radius of the explosive.<sup>3</sup> These conditions are the same used on any shock to estimate whether initiation might occur; the only difference is that we are applying them to a local shock structure that occurs from a boundary interaction.

All the experimental work reported here studies the initiation of PBX 9502 by reflected waves from uranium boundaries. For PBX 9502, we found that irregular reflection was most likely to result in initiation. The primary reason is that the irregular reflection results in an amplified pressure wave running into explosive that was not preshocked. This wave structure, often referred to as a Mach stem or Mach reflection, is not the classical triple-point solution, but rather a curved-stem structure. We will discuss the analysis that suggests shock initiation with an irregular reflection or Mach reflection is possible, two experiments in which such initiation was detected for PBX 9502, and possible situations that may degrade or enhance the effect.

# CHARACTERIZATION OF REFLECTIVE WAVE BEHAVIOR

## Local Analysis

The geometrical configuration we studied is a plane shock incident on a flat uranium plate. We applied the classical shock polar theory, shown in Fig. 1, to shock reflection in explosive, with appropriate equations of state (see Table I).

The shock polar in the pressure-flow angle plane is a convenient means of examining the possible solutions. Figure 2 indicates how the shock polar is generated: the phase velocity  $V_0$  is fixed and the angle between this velocity vector and the shock is varied. Jump conditions are used to calculate the normal component of the velocity behind the shock, and because the tangential component is unaltered, the flow angle can also be found. Flow angle and the pressure, the two variables of interest, are plotted in Fig. 3. The polar labeled **I**

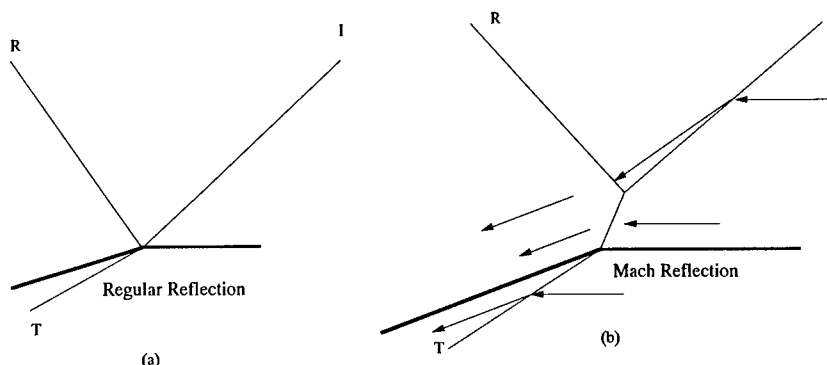


FIGURE 1. REGULAR AND MACH REFLECTION FLOW DIAGRAM

TABLE 1. MIE-GRÜNEISEN EQUATION-OF-STATE PARAMETERS

Material	Density (g/cm <sup>3</sup> )	Shock Hugoniot (mm/μs)	Grüneisen Gamma
PBX 9502	1.894	$u_s = 2.36 + 2.23u_p$	1.2
Uranium	18.93	$u_s = 2.51 + 1.51u_p$	2.2

When a shock wave obliquely encounters a high-impedance interface, two basic kinds of shock reflection occur. Regular reflection is the case in which the incident wave and the reflected wave intersect at the interface (Fig. 1a). Irregular reflection includes all other possibilities, of which there are many. The most famous irregular reflection is "classical" Mach reflection in which the interaction results in a triple-shock structure and a contact discontinuity separating the double-shocked material from the single-shock material that has flowed through the stem structure (see Fig. 1b). For brevity, any wave reflection structure that features a stem, where a single-shock processes material from zero pressure to the amplified pressure behind the reflection, will be called a Mach reflection.

In the local shock polar analysis, the flow in the regions delineated by the shocks is assumed to be one-dimensional. Shock jump conditions (conservation of mass, momentum, and energy subject to the equation of state) are satisfied across each shock. The incident shock turns the flow toward the wall and the reflected wave turns the flow back away from the wall. At the walls, the boundary conditions are such that the flow behind the shock structure must be parallel to the flow in the wall and pressure is continuous across the boundary. An irregular reflection appears when a regular reflection cannot meet this compatibility conditions.

indicates the states achievable behind the incident shock. The polar labeled **R** indicates the states achievable behind the reflected shock starting from the state behind the incident shock. The polar labeled **T** indicates the states achievable behind the shock transmitted in the uranium. In regular reflection (see Fig. 3a), the flow behind the shock structure satisfies the boundary conditions at the intersection of the **T** and **R** polars, where the flow across the wall is parallel and no pressure gradient exists across the wall.

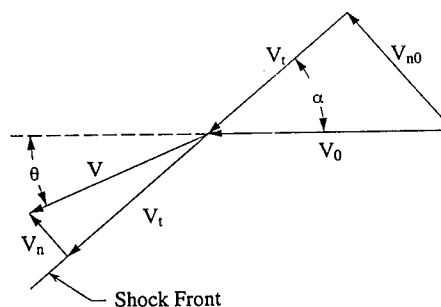
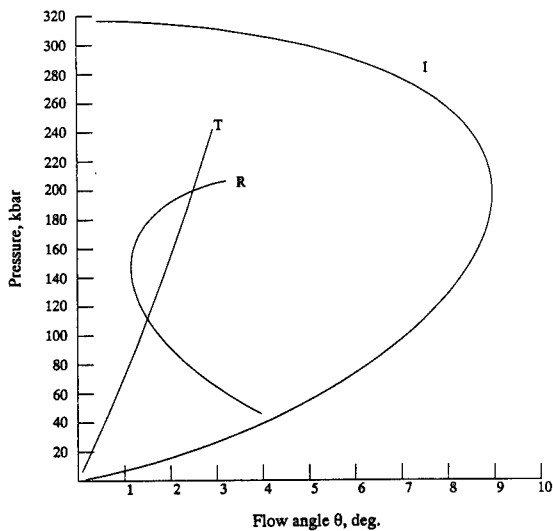
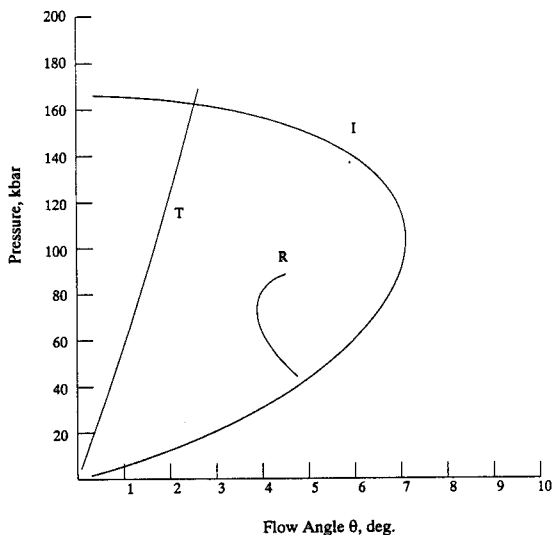


FIGURE 2. VELOCITY DECOMPOSITION OF 1-D FLOW ACROSS SHOCK



**FIGURE 3a. SHOCK POLAR FOR REGULAR REFLECTION IN PBX 9502**



**FIGURE 3b. SHOCK POLAR FOR IRREGULAR REFLECTION IN PBX 9502**

In Mach reflection (see Fig. 3b), the *T* and *R* polars do not intersect. A classical Mach reflection (triple point solution) would be possible if the *I* and *R* polars had intersected more than once. In this case (Fig. 3b), the triple point solution is not allowed and a more complicated Mach stem arrangement must exist to turn the shocked flow away from the plate. One admissible solution is a Mach stem which smoothly curves as the plate is approached. The states on the curved Mach stem will lie on a family of shock polars having a small variation in phase velocity due to the growth of the stem. The incident shock polar, *I*, has been used to estimate these states. Based on the data described later in this paper, this approximation is accurate to within about 8%

in phase velocity. Because of this continuous variation, the precise definition of the size of the Mach stem or its growth rate is lost. However, the shape of the *I* polar indicates that some region of the flow will have reached amplified pressure levels through a single shock (the top of the shock polar is relatively flat).

Solutions to the reflection problem can also be plotted in the pressure-interaction angle plane. In this case, the wall pressure behind the reflected wave is given as a function of the interaction angle for fixed-incident shock pressure. That was done for a 42-kbar incident shock in Fig. 4.

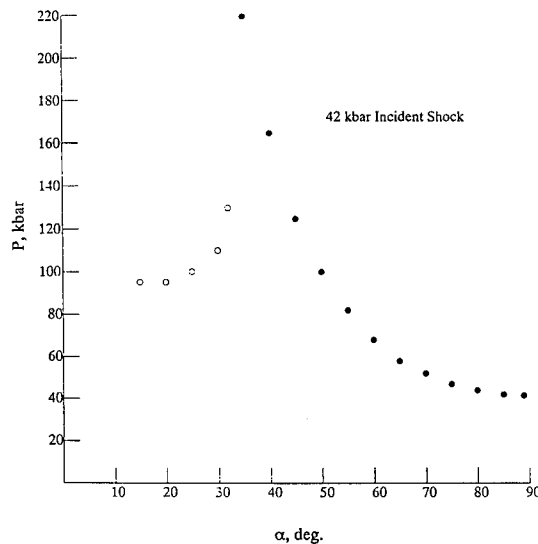


**FIGURE 4. THE WALL PRESSURE - INTERACTION ANGLE PLOT FOR A 42-KBAR SHOCK. THE OPEN POINTS INDICATE REGULAR REFLECTION, WHEREAS THE SOLID POINTS INDICATE IRREGULAR SHOCK REFLECTION.**

In either regular or mach reflection, the pressure is elevated to a level that will initiate unshocked PBX 9502. In regular reflection, the elevated pressure propagates into material that has been preshocked and desensitized by the incident wave to some extent. In Mach reflection, however, the stem, with sufficiently elevated pressure behind it, propagates into unshocked explosive and represents a likely initiation mechanism. The shock polar analysis is convenient for giving critical angles and estimates of pressures; however, the analysis does not lead to any growth rate information, nor does it examine the stability of the flow configuration. To answer these questions, we examined this flow with the MESA hydrodynamics code.

#### HYDROCODE ANALYSIS

With MESA, we calculated several reflected-wave solution pressures and interaction angles, using a 0.5-mm

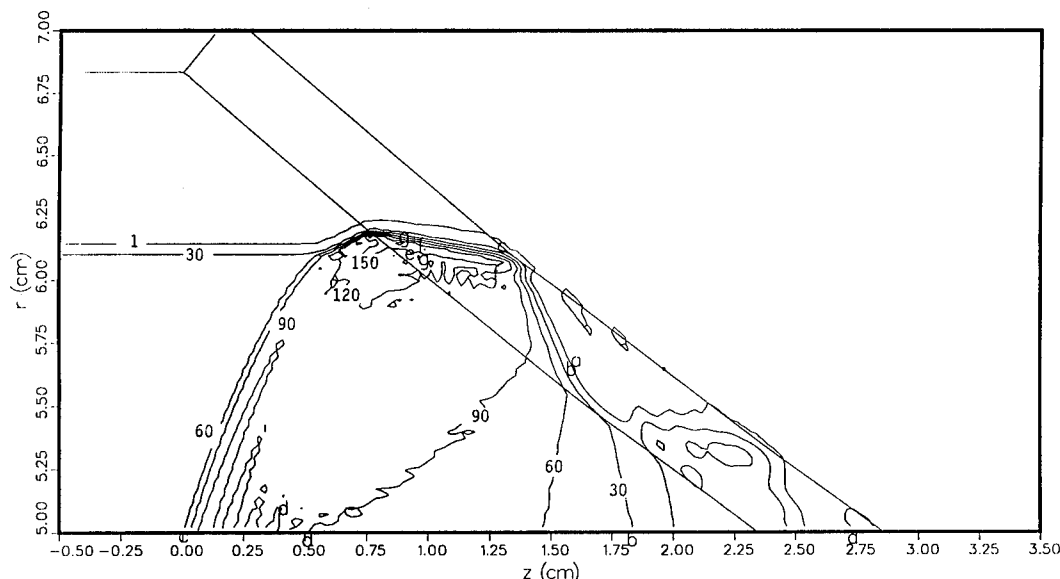


**FIGURE 5. MESA CALCULATION OF A 42-KBAR SHOCK INCIDENT ON A 3-MM URANIUM PLATE. PRESSURE CONTOURS ARE LABELED IN KILOBARS.**

mesh. Shown in Figure 5 is the calculation of a 42-kbar incident shock obliquely impacting a 3-mm-thick uranium plate at  $40^\circ$  incident angle  $22 \mu s$  after the initial impact of the plate. Here a significant shock stem leads the incident shock. The 120-kbar region backs a substantial portion of the stem and the 150-kbar contour extends into the reflected-wave region. Even if the shock wave looks rather straight in this region, there is curvature in the shock wave and a more obvious continuous rise in shock pressure as the wall is approached.

Although these calculations are rather straight forward to complete and analyze, a subtle detail exists at the beginning of the calculation in how to resolve the initial point singularity on a finite mesh. In these calculations we took no special precautions, and if one looks carefully at the stem width in time, it appears to grow more rapidly at early times, then slows its growth significantly, and finally reaches an intermediate value. This appears to be the result of not being able to resolve the singularity at the beginning of the calculation. Hence, at early times in the calculation, the calculation appears to overestimate the stem width and underestimate the pressure. This problem appears to resolve itself in time. However, some caution should be used in the examination of early results from the simulations.

In summary, the hydrocode simulations are in qualitative agreement with the shock polar analysis, although the pressure values from the hydrocode tend to be somewhat lower than the estimates from shock polar theory. The growth angle of the stem region found in these calculations ranges from  $1^\circ$  to  $5^\circ$ , depending on the incident shock pressure and angle. The small growth angles can be used to rationalize the use of the quasi-steady approximation in the previous section. This range

of angles is typical for growth rates of Mach stems seen in gas dynamics<sup>5</sup> and detonation experiments.<sup>6</sup>

## INITIATION ANALYSIS

The preceding analysis has shown that in either regular or irregular reflection, the pressure amplification is sufficiently large to dramatically reduce the distance to detonation of unshocked explosive.<sup>2</sup> In considering the possibility of initiating by a regular reflection, many cases can be ruled out because the flow behind the second shock is highly supersonic, and any energy release in the double-shocked material has no possibility of influencing either the reflected or the incident shock. As the incidence angle approaches the critical angle, this argument cannot be used because the flow behind the reflected shock becomes subsonic. In these cases, consider the thickness of material that can travel through the incident shock and reach the second shock before it has been desensitized by the incident shock. This width can be estimated by assuming the time that the material is in the incident-shock region must be less than the time it takes for the explosive to be desensitized. We used the time estimate from Campbell and Travis's paper<sup>1</sup> for PBX 9404, because no desensitization data are available for PBX 9502. For a 50-kbar shock at  $25^\circ$  incidence angle, the width of material in the second shock region conforming to this criterion is 0.5 mm, which is much smaller than the self-confined failure thickness, and even smaller than the run-to-detonation distance for the pressure in the double-shocked explosive region. This material may react, but it has low probability of developing into a detonation because it is significantly smaller than the failure radius.<sup>3</sup> A more positive statement is precluded because the self-confined failure radius of the

precompressed explosive has never been studied. This initiation scenario may be much more important in more sensitive explosives like PBX 9501. These have much smaller failure thicknesses than do insensitive explosives, and much lower incident shock pressures result in much larger critical angles. In all, we were led to examine the Mach reflection regime, where preshock was not an issue.

In Mach reflection, with sufficiently elevated pressure behind it, the stem propagates into unshocked explosive and presents a likely initiation case because the explosive has not been desensitized. Another aspect of Mach reflection enhances the likelihood of a situation in which initiation can occur: the flow behind a large portion of the curved shock wave section is subsonic. This implies that energy release from the shocked explosive has a chance of reinforcing the shock wave and of building to a detonation wave.

The remaining requirement is that the Mach stem must be sufficiently large. Classical shock polar analysis provides no stem growth information in this curved-stem case. However, the hydrocode calculations indicated a growth angle of  $1^\circ$  to  $5^\circ$ . This would imply that initiation would occur after a run of 44 to 229 mm along the surface of the uranium plate, depending on the shock pressure and angle. Using this analysis, we designed the experiments to detect the transition from shock to detonation when a 40-kbar plane shock in PBX 9502 is reflected from a flat uranium plate with an incidence angle of  $40^\circ$  and  $50^\circ$ .

## EXPERIMENTAL RESULTS

The PBX-9502 test pieces were six-sided prisms (see Fig. 6). Top and bottom surfaces defined two horizontal planes 96.4 mm apart. Two sides defined planes that were perpendicular to the top and bottom planes. One of the other two surfaces (A in Fig. 6) was angled at  $30^\circ$  to the bottom plane and was defined as the observation surface. The other surface (B in Fig. 6) was angled at  $40^\circ$  or  $50^\circ$  with respect to the bottom plane and was covered with a 3-mm-thick uranium plate providing the reflective boundary. A plane shock wave was driven into the bottom of the prism with the plane wave attenuator system shown in Fig. 7.

The phase velocity of the wave along the uranium surface, the width of the Mach stem, and the incident wave velocity, pressure, and position must be observed to obtain a complete experimental record of the experiment. The shock arrival time along the uranium surface (B) was monitored with a series of time-of-arrival pins that we placed at known distances along the uranium plate. Each pin reported the time at which the shock transmitted (at some angle) through the uranium plate arrived at the free surface. We estimated the phase velocity of the wave at the explosive-metal interface from these data by assuming the flow to be steady. We obtained the width, shape, and velocity of the Mach stem, as well as the incident wave velocity by using a multiple-slit smear camera technique. The intersection of surfaces A and B and at least 25 mm of surface A were observed with a series of argon flash gaps. Each camera slit was aligned

so that a record of the flash gave the wave arrival time of the Mach stem and incident shock at 11 different run distances into the explosive.

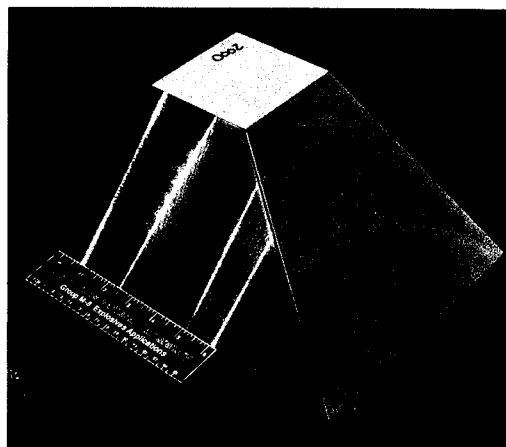


FIGURE 6. PBX-9502 TEST PIECE WITH URANIUM PLATES ATTACHED

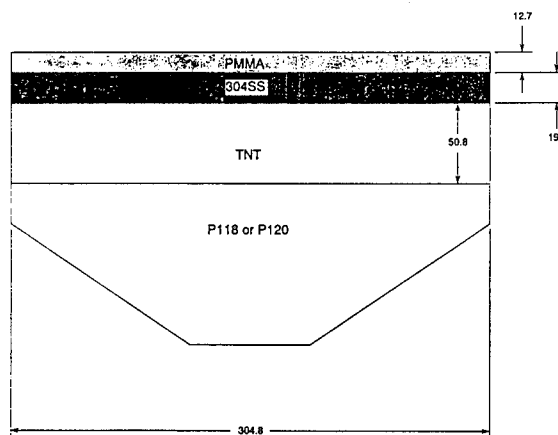


FIGURE 7. THE PLANE SHOCK DRIVER SYSTEM USED TO DRIVE A 42-kbar SHOCK INTO THE TEST PIECE OF PBX 9502. DIMENSIONS ARE IN MILLIMETERS.

Shown in Fig. 8 are the shock arrival times on the uranium surface for the  $40^\circ$  experiment. Straight-line fits show that the incident phase velocity associated with the propagation of the inert Mach reflection is about  $6.02 \text{ mm}/\mu\text{s}$ . About 75 mm from the corner, a transition to  $7.43 \text{ mm}/\mu\text{s}$  occurs. Similar results for the  $50^\circ$  interaction angle, also shown in Fig. 8, indicate that the wave accelerates from  $4.92 \text{ mm}/\mu\text{s}$  to  $7.68 \text{ mm}/\mu\text{s}$  after transiting the surface for 70 mm.

In Fig. 9 is the digitized camera record from the  $40^\circ$  shot, and the smear camera record of the  $50^\circ$  experiment is shown in Fig. 10. Each slit was oriented so that a record of the wave arrival time was obtained for a constant distance from the bottom surface of the prism. Each slit recorded the arrival of the incident wave as a

horizontal line in the region away from the uranium interface. These were used to obtain the velocity of the incident shock and thus to estimate the incident pressure. The Mach stem developed at the uranium-PBX-9502 interface was recorded as the early-arrival part of each trace. When the location of the break in the horizontal trace was measured, the width of the Mach stem or detonation front could be estimated as a function of run distance along the uranium plate. Assuming that the Mach stem is normal to the wall, a conservative estimate for the Mach stem width can be obtained. The assumption that the Mach stem is normal to the wall may be relaxed if one is willing to accept a calculated value for this angle. Mach stem width data are plotted as a function of position along the uranium plate in Fig. 11. A sudden change in wave width is associated with the transition to detonation. This is in good agreement with the previously described pin data. The last slit recorded a detonation wave 7 mm wide in the 40° case and 17 mm wide in the 50° case.

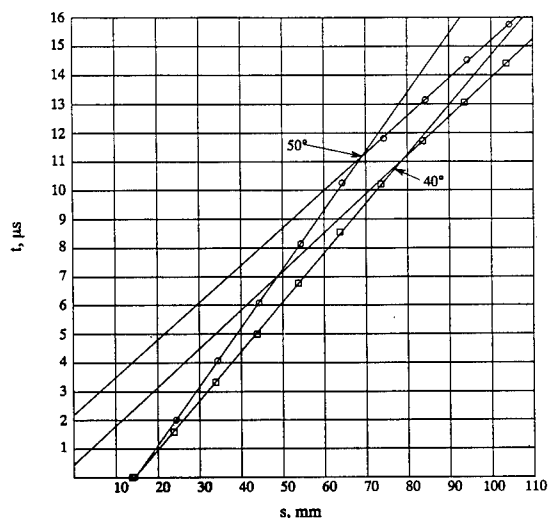


FIGURE 8. PIN DATA FOR SHOT Nos. C-6496 AND C-6543

The two smear camera records clearly show the development of curved Mach stems with growth angles of 1.7° and 3.6°. The transition occurred when the stem reached a width between 2 and 4 mm in the 40° case and between 4 and 6 mm in the 50° case. After the transition, a detonation wave is clearly observed with a growth angle of more than 5° in the 40° incident angle case and more than 15° in the 50° case. We expect that this angle is strongly influenced by corner-turning and preshock-desensitization processes. These runs to detonation, measured from the driver system, are 1/5 of what one would expect from extrapolating existing run-to-detonation data to the incident shock pressure.

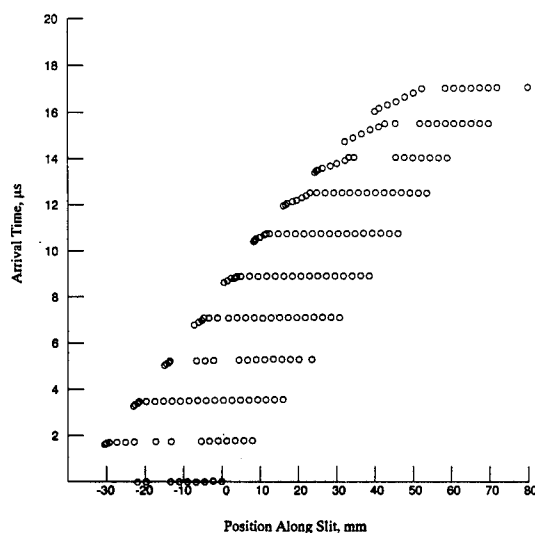


FIGURE 9. DIGITIZED SMEAR CAMERA RECORD FOR SHOT No. C-6496. INCIDENT SHOCK WAS 42-kbar AT 40° INCIDENCE.

## DISCUSSION

These experiments demonstrate that, in PBX 9502, a Mach reflection can transit into a detonation for two different incident angles. Diameter effect data<sup>3</sup> indicate that a 7-mm-radius rate stick of PBX 9502 would detonate at 7.49 mm/μs and a 17-mm-radius rate stick detonates at 7.62 mm/μs. The final pin velocities agree well with these values. Minimum width of the detonation observed is about 4 mm, and this is close to the failure radius of 4.5 mm for PBX 9502.<sup>3</sup> Pressure behind the Mach stem was estimated at 160 kbar for 40° and 100 kbar at 50°, based on the shock polar theory. Run-to-detonation distance for a planar, well-supported shock at these pressures is about 4 mm and 13 mm, respectively.<sup>2</sup> Our experiments sustained the shock pressures much longer than this. However, the flow behind the stem shock is substantially more complicated than that found in a wedge experiment. Therefore, the conditions we detected are in agreement with our expectations derived from other aspects of explosive behavior. Because the shock initiation estimates of where initiation occurs appear to hold, one would expect a multiple-shock Forest Fire model to be able to model these problems adequately. Calculations<sup>6</sup> done by Ed Kober show that this is indeed true and give extra evidence that the initiations in these cases are due to the shock-reflection structure.

Further work continues on this topic in the areas of other explosive materials, divergence effects of the incident shock wave, and the effect of convergent and divergent wall interfaces. We are using PBX 9501 to assess the implications of this initiation mechanism on much more sensitive explosives. Classical analysis indicates that for PBX 9501, the angles at which Mach stems become important are about 20° greater than those of PBX 9502, primarily because the pressure at which initiation from a plane shock occurs are significantly



smaller. Although the range of possible angles is smaller, the initiation appears likely because the failure diameter is much smaller and the run to detonation is significantly shorter than for that of PBX 9502. Also, for PBX 9501, some cases of initiation by regular reflection may be possible.



**FIGURE 10. SMEAR CAMERA RECORD FOR SHOT No. C-6543. INCIDENT SHOCK WAS 42-kbar AT 50° INCIDENCE. FOR EACH SLIT, TIME IS INCREASING IN THE VERTICAL DIRECTION. THE OVEREXPOSURE ON THE STEM IN THE LAST FOUR SLITS IS DUE TO THE BRIGHT FLASH RESULTING FROM THE DETONATION, AS COMPARED WITH THE EXPOSURE OF THE INCIDENT SHOCK.**

In summary, we have experimentally observed the transition of a Mach reflection into a detonation in PBX 9502. This initiation mechanism can radically reduce the run to detonation in explosive charges with high-impedance boundaries. Classical analysis can bound the incident shock pressures and angles of Mach reflection initiation. The resulting shock configurations and knowledge of explosive behavior can be used to help decide whether initiation is likely. However, growth angle and stem size information is not found by means of the classical analysis. Computer simulations are useful

for obtaining growth angle estimates and Forest Fire models can be used to examine the initiation process. Even so, there are still mesh resolution problems to address, and equation of state (especially sensitive materials) information for the explosive at low pressures will need to be refined before simulations are reliable. Therefore, further experiments and analysis will be necessary to completely describe the initiation criterion for shock reflection from high-impedance boundaries.

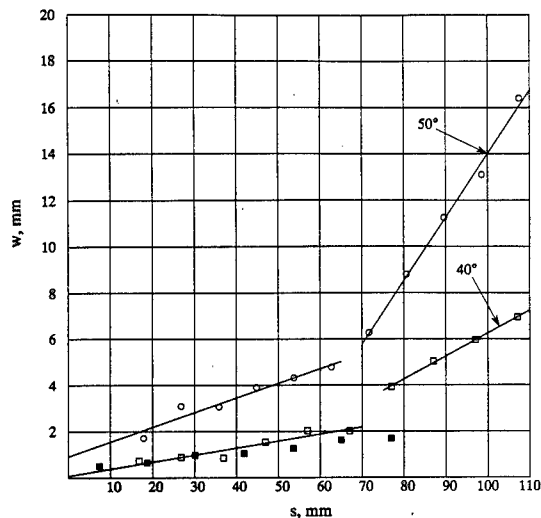


**FIGURE 11. STEM WIDTH MEASUREMENTS FOR SHOT Nos. C-6496 AND C-6543. THE SOLID SQUARES ARE STEM WIDTHS MEASURED FROM THE MESA CALCULATION OF THE REFLECTION OF A 42-kbar SHOCK INCIDENT AT 40° ON A URANIUM SURFACE.**

#### ACKNOWLEDGEMENTS

We express our appreciation to Victor Sandoval, Willie Spencer, Rudy Archuleta, Bob Critchfield, Andreas Krause, and Walter Quintana, who are responsible for, or assisted in, firing these experiments. We thank Ed Kober for discussing with us his Forest Fire simulations of initiation by shock-wave reflection. We acknowledge that LeRoy Green had the insight to suggest the possibility of initiation of a Mach stem. We thank John Ramsay for many helpful discussions and support. We also thank Larry Hantel and John Ramsay for their persistent support in obtaining funding.

This work was performed under the auspices of the U.S. Department of Energy, Contract No. W-7405-ENG-36 with the Los Alamos National Laboratory, Los Alamos, New Mexico.

#### REFERENCES

1. Campbell, A. W. and Travis, J. R., "The Shock Desensitization of PBX-9404 and Composition B-3," *Proc. of the 8th Symp. (Int.) on Detonation*, Albuquerque, New Mexico, July 15-19, 1985, NSWC MP 86-194 (1986), pp. 1057-1068.

2. Dick, J. J.; Forest, C. A.; Ramsay, J. B.; and Seitz, W. L., "The Hugoniot and Shock Sensitivity of a Plastic-Bonded TATB Explosive PBX 9502," *J. Appl. Phys.*, Vol. 63, May 1988, pp. 4881-4888.
3. Cambell, A. W. and Engelke, R., "The Diameter Effect in High-Density Heterogeneous Explosives," *Proc. of the 6th Symp. (Int.) on Detonation*, Coronado, California, August 24-27, 1976, ACR-221 (1977), pp. 642-652.
4. Courant, R. and Friedrichs, K. O., *Supersonic Flow and Shock Waves*, Interscience Publishers, Inc., New York, 1948, pp. 318-349.
5. Bleakney, W. and Taub, A. H., "Interaction of Shock Waves," *Rev. Mod. Phys.*, Vol. 21, No. 4, 1949, pp. 584-605.
6. Hull, L., "Mach Reflection of Spherical Detonation Waves," paper presented at this symposium.
7. Kober, E., Technical Staff Member of Group T-14, Los Alamos National Laboratory, Los Alamos, New Mexico, conversations with E. Ferm and L. Hull concerning his Forest Fire calculations of initiation owing to shock reflection, March-April 1992.

## **SESSIONS ON**

## **IMPACT**

**Cochairmen:**    **John Starkenberg**  
                         **U.S. Army Research Laboratory/**  
                         **Weapons Technology Directorate**

**Peter Haskins**  
**Defence Research Agency**

# THE DEPENDENCE OF THE RESPONSE OF HEAVILY-CONFINED EXPLOSIVES ON THE DEGREE OF PROJECTILE PENETRATION

H.R. James and M.A. Grixti

Atomic Weapons Establishment, Foulness Island, Essex SS3 9XE, UK  
and

M.D. Cook, P.J. Haskins and K. Stuart Smith  
Defence Research Agency, RARDE, Fort Halstead,  
Sevenoaks, Kent, TN14 7BP, UK

Experimental evidence is presented which shows a complex, but consistent, pattern of sub-detonative responses for a frangible, highly-confined explosive impacted by a given projectile. A violent reaction is generated by impacts which are below the ballistic limit for thick barriers, but which produce significant case distortion. The level of this reaction at first decreases with increasing projectile penetration, and then increases again before full detonation is achieved. Both ionisation probe data and comparisons with data from a plastic explosive of similar shock sensitivity - but having no violent sub-detonative response - indicate that detonation is caused by a shock-induced mechanism, even for relatively thick barriers. Previously developed predictive criteria for shock initiation give both qualitative and, over a more limited range, quantitative agreement with this detonation threshold.

## INTRODUCTION

Two explosives of similar shock sensitivity, but with very different mechanical properties, were used to explore the response of heavily confined charges to projectile impact. From the results obtained, it will be shown that the ignition threshold lies just below the ballistic limit of the barrier in the region where the barrier thickness is of the same order as the projectile length. It will also be shown that ignition takes place for barriers much thicker than the projectile length, and for which no perforation was recorded. The variation in response in the region between the ignition and detonation thresholds will be discussed, and evidence will be examined that the detonation threshold is entirely determined by a shock mechanism over a wide range of barrier thicknesses for the explosives tested.

## EXPERIMENTAL DETAILS

The two explosives used were Bridgwater Type A (RDX/TNT/Beeswax 59.5/39.5/1.0, density  $1.66 \pm 0.02 \text{ Mg/m}^3$ ), a cast, fairly brittle explosive

known to fracture easily, and PE4 (RDX/grease 88/12, density  $1.60 \pm 0.01 \text{ Mg/m}^3$ ), a pressed plastic explosive.

The explosive was heavily confined in a steel cylindrical container. The container used for the sub-detonative response work had a wall thickness of 23.25mm and an end-plate thickness of 25mm. The assembly was firmly bolted together to ensure that a rise in pressure could not prematurely blow off an end-cap before a final level of response was achieved. The charge was 141mm long by 93.5mm diameter. A rather smaller charge was used to establish the detonation threshold. This charge was 114mm long by 57mm diameter, and both case and end-plate were 9mm thick.

Impacts were normal to a steel coverplate, the thickness of which could be varied, protecting one of the flat ends of the explosive cylinder. The projectile was a right circular steel cylinder, 13.15mm in diameter and either 25.4mm or 12.75mm long, the shorter projectile being used for the sub-detonative work. Impact velocity was measured by foil screen while explosive response

was deduced from case fragmentation, timing probes, blast gauges and film records.

The density of the projectile was  $7.81 \text{ Mg/m}^3$  while that of the barrier was  $7.78 \text{ Mg/m}^3$ . The respective Brinell hardnesses were  $280 \pm 20 \text{ BHN}$  and  $115 \pm 15 \text{ BHN}$ .

Deformation of the coverplate was determined by firing projectiles at containers in which explosive had been replaced by an inert substitute, designed to model the density but not the fracture properties of the explosive. Three conditions were noted. An uncracked bulge in the barrier. A cracked bulge, in which the crack was on the charge side of the barrier and did not extend through the coverplate. Penetration, in which the projectile passed through the barrier preceded by a plug of plate material. In no instance did the projectile completely penetrate the simulant with the coverplate present. The range of impact velocities used against explosive fillings was designed to cover the velocities used against the inerts. The response was then matched to the degree of barrier deformation.

The division of sub-detonative responses into different degrees has always been open to interpretation and argument. The important factor, of which any division must take account, is the possibility of the presence of a measurable air blast which is distinct from the burning reactions on the one hand, but is below a detonation on the other. This response is unacceptable in that it produces case fragments and a blast pressure that would constitute a severe hazard to personnel or other munitions in the vicinity. However, as will be shown, it can be caused by projectile velocities that are considerably below those needed to ensure detonation. In this paper the responses have been divided into no reaction; burn (reaction but no measurable air blast, with case either intact or in very large parts and unreacted explosive present); explosion (air blast and large case fragments) and detonation (blast and small case fragments).

## EXPERIMENTAL RESULTS

### Sub-Detonative Response

The degree of sub-detonative response was found to depend heavily on the properties of the explosive. Confined PE4 could only be made to give a mild burn, while Bridgwater, under the

same circumstances, would give an explosion. This tends to confirm the hypothesis that brittle materials, that can fracture to form large surfaces available to support burning, will give a higher degree of response if other factors are constant.

Figure 1 shows the response of Bridgwater Type A to impact. Data on the damage to the inert-filled vehicle have been over-laid on the explosive reaction obtained from the same range of impacts.

With no coverplate (but otherwise confined) the explosive shows either a burn (usually mild) or detonation. The 5mm thick barrier shows no response below the point of maximum bulge in the plate. Above this point (although the data are somewhat sparse) only burns are observed, with one explosion at larger penetrations. Discussion on the detonations is left until later. The 8mm and 10mm barriers show a similar pattern to each other. There is no reaction until (approximately) the point of maximum plate bulge is reached. In this region, and for small penetrations, an explosion occurs. At larger penetrations the response falls to a burn, with only the occasional explosion. The response rises to an all-explosion regime as the penetration/impact velocity increases further. The 20mm barrier has explosions occurring well below the point at which the plate cracks. At this point, somewhat surprisingly since there is no perforation, the response drops to a burn, only to rise again at higher impact velocities (projectile velocities up to  $2120 \text{ m/s}$  - the maximum tested against an inert - failed to penetrate this thickness of plate).

An order-of-magnitude estimate was made of the reaction time relative to impact. This method consisted of looking at case movement and only provides some idea of the relative order of times rather than an absolute measure of charge reaction. Timings from this method, given in Table 1, showed that there was a significant delay in moving the case by an explosion compared to a detonation. They also showed that this delay decreased for explosions as the impact velocity increased from the region around the ballistic limit to that close to the detonation threshold.

The onset of severe reaction occurs below the ballistic limit (although not far removed from it for the 8 and 10mm plates) for barriers having the same order of thickness as the projectile length. For very thick barriers, there is no question of perforation

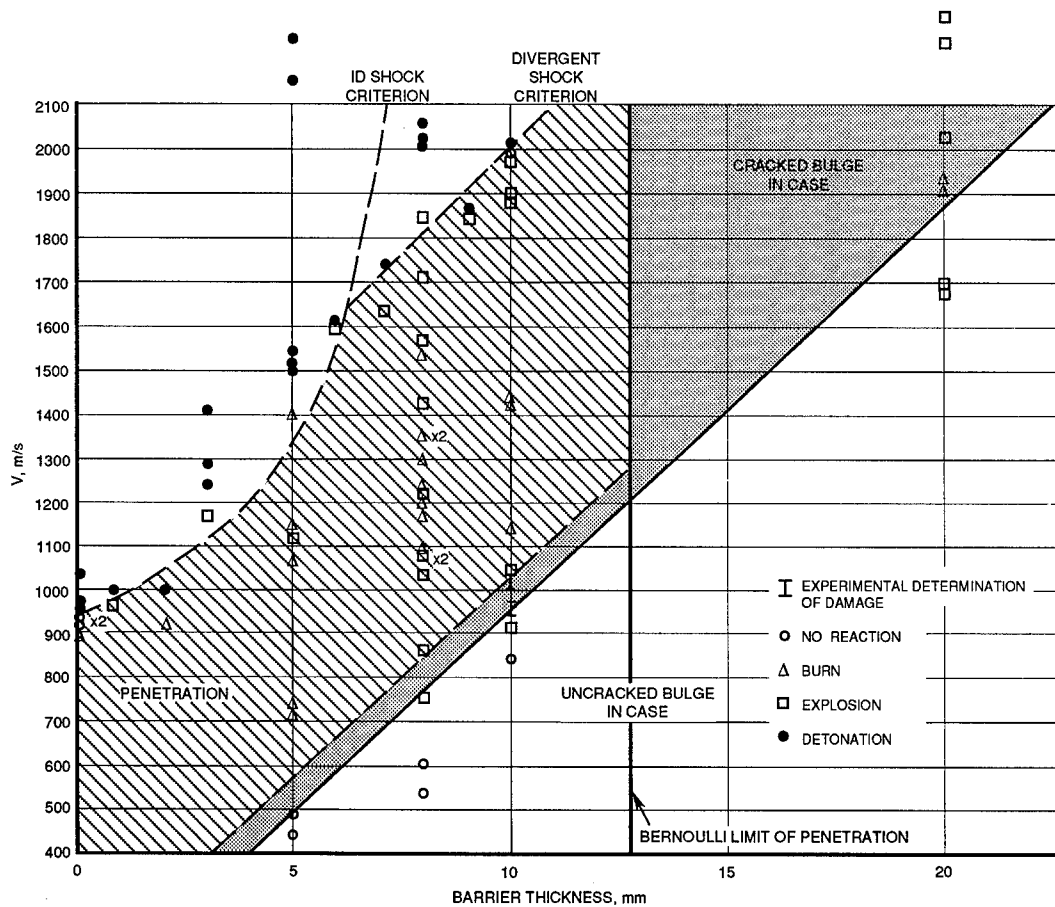


FIGURE 1. STEEL ROD IMPACTING BARE AND COVERED, CONFINED BRIDGWATER TYPE A

TABLE 1. DELAYS IN RESPONSE FOR EXPLOSIONS

Plate thickness							
5mm		8mm		10mm		20mm	
v(m/s)	t(ms)	v(m/s)	t(ms)	v(m/s)	t(ms)	v(m/s)	t(ms)
1120	1.1	753	3.5	910	1.5	1680	0.9
		833	0.8	1040	2.0	2050	0.6
		1085	1.8	1880	0.2	2060	0.6
		1220	0.5	1890	0.5	2230	0.5
		1441	0.5			2280	0.5
		1567	0.5				
		1712	0.2				
		1859	0.2				

N.B. Detonations, measured by this method, are of the order of 0.1 ms or less, corresponding to the highest resolution of the system.

occurring in the region in which explosions are observed. It appears that case distortion is the main cause of reaction in this region for the 8, 10 and 20mm plates, with the lack of venting ensuring a vigorous response. It is hypothesized that this response level is maintained until the projectile has sufficient velocity to clear the perforation in a timescale which is short compared to the growth in reaction. The relatively long delays for explosions to occur in this region support the idea that any venting will play a significant role in the final response level. This is reflected by the drop in severity of response for impacts which are well above the ballistic limit.

The rise in response at the higher impact velocities appears to result from a complex balance of increased reaction caused by a greater compression of a larger volume of damaged material (or possibly a compression of an increasingly damaged material), which offsets the increase in vent area. The smaller delays presumably restrict the importance of venting in this regime.

#### Detonation Threshold

The detonation thresholds for bare charges of PE4 and Bridgwater are similar for this projectile. For a bare configuration there is no question of mechanisms other than shock causing this response, and so the two explosives are seen to have a similar shock sensitivity. Both explosives continue to follow almost the same threshold over the range of barrier thicknesses in which detonation was observed (up to 10mm - see Table 2). This is despite the fact that PE4 went from mild burn to detonation across this threshold, while Bridgwater generally went from explosion to detonation. This indicates that sub-detonative responses are very different and are probably based on the mechanical differences between the explosives. However, there appears to be a common mechanism which triggers detonation, the most likely being shock sensitivity.

This is supported by a separate study using aluminium barriers. In this work ionisation probes in both PE4 and Bridgwater show detonation occurs within about 5 $\mu$ s of impact, regardless of barrier thickness. Hydrocode simulations show no sign of significant barrier distortion in this timescale, but there is a high level of shock generated in the explosive at these impact velocities

for even the thickest barriers. Hence there is little doubt that detonation is triggered by a shock mechanism in both explosives for this barrier material. A similar pattern of threshold behaviour (described more fully below) is found in the steel-covered explosives, leading to the conclusion that the same mechanism is at work.

#### THEORETICAL INVESTIGATION OF THE DETONATION THRESHOLD

The shape of the detonation threshold for impacts into steel-covered Bridgwater closely follows the pattern described for impacts into aluminium-covered PE4.<sup>1,2</sup> For flat-nosed rods impacting thin barriers, a significant portion of non-diverging shock is passed to the explosive and provides the controlling mechanism in triggering detonation. Predictive techniques have been described<sup>3</sup> for this regime based on a critical energy concept,<sup>4,5</sup> and figure 1 shows such a prediction using a critical energy of 1.90 MJ/m<sup>2</sup>. As can be seen, this criterion follows the experimental data up to barrier thicknesses of about 6-7mm. Above this point the nature of the threshold curve changes, and it is postulated that the divergent portion of the shock supplies the controlling mechanism.

#### DISCUSSION AND CONCLUSIONS

The present study shows that for a frangible explosive, an ignition, leading to an explosion, is possible for impacts which are below the ballistic limit for relatively thick cases. From the experimental data it is postulated that the distortion of the case, coupled with a lack of venting, triggers a slow growth in reaction. Indeed the level of response to impacts ranging from just below to some way above the ballistic limit, appears to be significantly affected by the degree of venting. Impacts which are above the ballistic limit, and which presumably clear the case perforation in a timescale which is short compared to the growth in reaction, lead to lower levels of response.

The increase in reaction growth rate for higher velocity impacts reduces the dependence of the response on the amount of venting. The increasing amount of compression associated with the penetrator and its effect on increasingly damaged material, become the significant factors in this regime.

TABLE 2. CRITICAL VELOCITY (m/s) FOR DETONATION THRESHOLDS IN CONFINED EXPLOSIVES WITH STEEL BARRIERS

Barrier Thickness (mm)	Bridgwater	PE4
0	854-929	982-1034
1	972-1003	965-974
2	926-1000	
3	1188-1240	1147-1214
5	1406-1497	1395-1435
6	1600	
7	1648-1746	1605-1653
8	1859-2008	1894-1982
9	1842-1864	> 1985
10	1990	

In those barrier thicknesses for which detonations were observed there is strong evidence to indicate that the detonation threshold is determined by a shock mechanism. However, no detonations were obtained for barrier thicknesses greater than 10mm due to constraints on launch velocities imposed by the use of a powder gun. Consequently the conclusion reached by Howe, Watson and Frey <sup>6</sup>, that shear can be the dominant factor for highly confined charges, could not be tested above this point.

#### REFERENCES

1. Cook, M.D., Haskins, P.J., and James, H.R., "An investigation of Projectile and Barrier Geometry Effects on Impact Initiation of a Secondary Explosive," in *Shock Compression of Condensed Matter 1991*, Ed. Schmidt, S.C., Dick, R.D., Forbes, J.W., and Tasker, D.G., Elsevier Science Publishers B.V. 1992, p 675.
2. James, H.R., Haskins, P.J., and Cook, M.D., "Effect of Case Thickness and Projectile Geometry on the Shock Initiation Threshold for a Given Explosive", in *AGARD Conference Proceedings 511 on Insensitive Munitions*, Bonn, Germany, 21 - 23 Oct 1991, p 18.
3. Cook, M.D., Haskins, P.J., and James, H.R., "Projectile Impact Initiation of Explosive Charges", in *Ninth Symposium (International) on Detonation*, Portland, Oregon, 28 Aug - 1 Sep 1989, p 1441.
4. Walker, F.E., and Wasley, R.J., "Critical Energy for Shock Initiation of Explosives", *Explosivestoffe*, Vol. 17, No. 1, 1969, p 9.
5. James, H.R., "Critical Energy Criterion for the Shock Initiation of Explosives by Projectile Impact", *Propellants, Explosives, Pyrotechnics*, Vol. 13, 1988, p 35.
6. Howe, P.M., Watson, J.L., and Frey, R.B., "The Response of Confined Explosive Charges to Fragment Attack", in *Seventh Symposium (International) on Detonation*, Annapolis, Maryland, 16-19 June, 1981, p 1048.

British Crown Copyright 1993/MOD.  
Published with the permission of the Controller  
of Her Britannic Majesty's Stationery Office.



# HIGH STRAIN-RATE IMPACT IGNITION OF ROCKET PROPELLANTS

S.Y. Ho

Explosives Ordnance Division, Salisbury  
Materials Research Laboratory

P.O. Box 1750, Salisbury, SOUTH AUSTRALIA 5108.

The high strain-rate ( $10^3$ - $10^4$  s<sup>-1</sup>) fracture properties and impact ignition sensitivity of several in-service and research composition rocket propellants were assessed using a modified Hopkinson Bar, and the deformation/fracture and ignition events during projectile impact photographed. The predominant impact ignition mechanisms under various conditions of strain-rates, specimen geometry and material properties were identified, and the stress-strain states related to deformation/fracture and ignition processes. The effect of pre-damage on the impact ignition sensitivity was investigated. Pre-damage in the propellants was induced by constant stress tests and the damage characterized by a failure criteria derived from a Cumulative Damage model.

## INTRODUCTION

Bullet/fragment impact phenomena generally occur in the plastic wave regime, and involves large-scale deformation, heating and mechanical failure of the solid. In this elastic-plastic or viscoelastic impact regime, the geometry of the specimen as well as the material properties both play an important role in determining the impact response. The key factors that govern the impact sensitivity of rocket and gun propellants and plastic bonded explosives include temperature, high strain-rate mechanical properties and thermal properties<sup>1-5</sup>. In addition, damage in energetic materials (eg. induced by the thermal and pressure stresses built up in the propellant grain of a solid rocket motor during its service life, or resulting from multiple impact) must be considered, as this can increase the impact sensitivity as a result of the larger surface area available for burning.

Currently accepted mechanisms by which hot spots are formed include (1) plastic flow and adiabatic shearing resulting in localization of the heat generated in shear bands<sup>6-10</sup>, (2) friction between the impacted surfaces of explosives and/or additives<sup>11</sup>, (3) fracture of explosives crystals and adiabatic heating at tips of fast propagating cracks<sup>12</sup>, (4) viscous heating by viscoplastic work<sup>13,14</sup>, (5) stress concentration in cracks, cavities or voids<sup>7,15,16</sup>, and (6) adiabatic compression of gas

pockets and gas phase heating following cavity collapse<sup>11</sup>.

Although there have been many studies on the impact ignition mechanisms of thin layers of explosives and model materials, such as lead azide, silver azide, RDX, HMX, PETN, etc., studies on the impact ignition mechanisms of rocket and gun propellants have been limited. The predominant mechanisms by which hot spots are formed may be different for charge samples of rocket and gun propellants as they are very heterogeneous. The binder in heterogeneous energetic materials has been shown to play an important role in controlling the impact sensitivity - they have a strong influence on the sensitization or desensitization mechanisms of RDX/Ethylene Vinyl Acetate (EVA) booster compositions<sup>5</sup>. Furthermore, the effect of sample size has not been previously considered. This is important in terms of scaling up to full weapons systems tests.

Earlier studies<sup>2-4,15</sup> of the impact ignition sensitivity of rocket and gun propellants has shown that the heating/energy dissipation mechanisms are determined to a large extent by the high strain-rate deformation/fracture behaviour. In addition, transitions from ductile to brittle failure modes can occur with a change in specimen geometry and/or temperature<sup>2,17</sup>.

In this paper, the high strain-rate mechanical behaviour and impact ignition sensitivity of a series of AP-, PETN-, RDX-, HMX/RDX- based composite propellants and a NC/NG cast double based propellant were assessed using a modified Hopkinson Bar. The deformation/fracture, ignition, and burning events during projectile impact were photographed using a microflash photography technique<sup>7,15</sup>. One of the aims of this study is to identify the predominant impact ignition mechanisms of typical in-service and research composition rocket propellants under various conditions of strain-rate, specimen geometry and material properties. The effect of pre-damage on the impact sensitivity and ignition mechanisms is investigated.

## EXPERIMENTAL

### Materials

The propellant types and their compositions are listed in Table 1. The composite propellants and cast double base propellant were made by standard processing techniques as described previously<sup>7</sup>. The processed propellants were machined into cylindrical pellets with various geometry for the modified Hopkinson Bar test. Specimen diameter-to-thickness ratios were 8:6, 8:8, 8:15, 10:8 and 15:8 mm.

### Measurements

The modified Hopkinson Bar test and experimental arrangement for photographing the impact event have been described in detail in previous papers<sup>1-5,7,15</sup>.

In order to study the effect of pre-damage on the impact sensitivity, the propellants were deformed by subjecting them to constant stress tests prior to testing on the modified Hopkinson Bar. Constant stress experiments were conducted using a Rheometrics Dynamic Mechanical Thermal Analyser, Model RSA2. Measurements were made in a compression mode using a parallel plate geometry or in a shear mode using a shear sandwich fixture (specially designed for cylindrical samples). The constant stress experiments were made at ambient temperature at stress levels in the range 0.1 to 0.5 MPa. From the incremental loading time and constant stress level, the state of damage in the propellant specimens can be characterized by a damage parameter derived from a Cumulative Damage model<sup>18,19</sup> (where failure occurs over a critical stress level over a finite time).

## RESULTS AND DISCUSSION

### High Strain-Rate Mechanical Behaviour - Effect of Specimen Geometry and Prestress Damage

Typical stress-strain curves (strain-rate ca.  $10^3 \text{ s}^{-1}$ ) for the various propellants are shown in Fig.1. All the rubbery composite propellants undergo extensive plastic deformation before ductile failure, whereas the stress-strain curve of the PEG,PCP/RDX,HMX propellant is characteristic of elastomeric polymers undergoing quasi-rubber-like deformation. Shear failure was also evident in the HTPB/AP propellant when the surface of the impacted pellets were examined visually and by scanning electron microscopy (SEM). This propellant

TABLE 1. PROPELLANT COMPOSITIONS

Propellant Type	Binder Prepolymer	Curative	Oxidiser (wt. %)
<i>Composite</i>			
HTPB/AP	Hydroxyterminated polybutadiene	Dimeryl diisocyanate (DDI)	Ammonium perchlorate (80%)
HTPB/PETN	Hydroxyterminated polybutadiene	Isophorone diisocyanate (IPDI)	Pentaerythritol tetranitrate (80%)
HTPB/RDX	Hydroxyterminated polybutadiene	DDI	Cyclotrimethylene trinitramine (80%)
PEG,PCP/RDX,HMX	Polyethylene glycol and polycaprolactone		Cyclotrimethylene trinitramine (47%) and Cyclotetramethylene tetranitramine (20%)
<i>Double Base</i>			
CDB	Nitrocellulose-nitroglycerine (42:46 wt. %)		

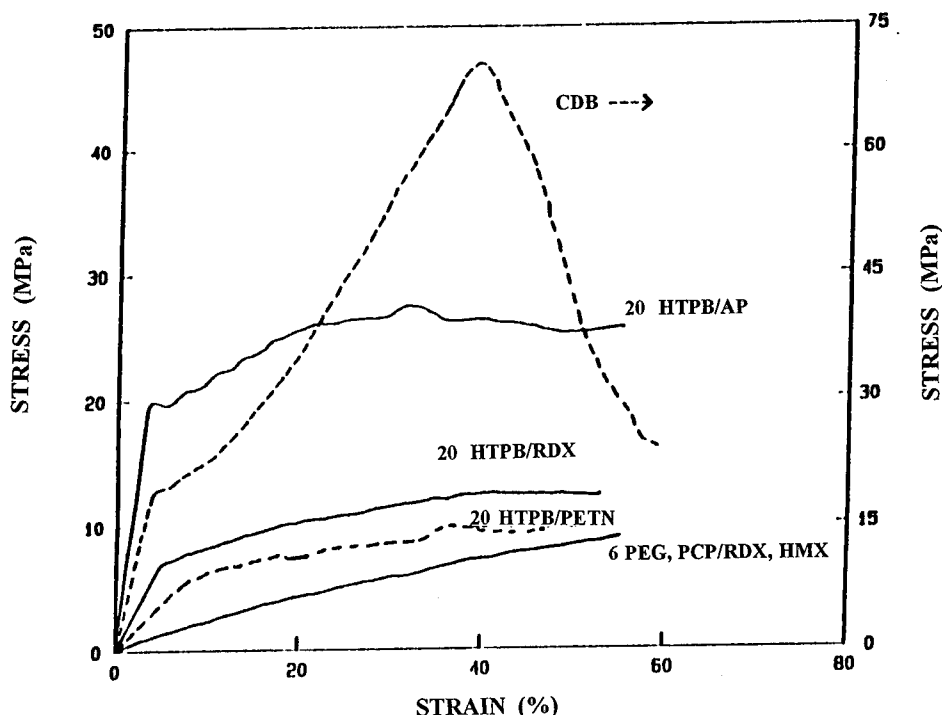


FIGURE 1. STRESS-STRAIN BEHAVIOUR OF VARIOUS PROPELLANTS, WITH SPECIMEN DIAMETER-TO-LENGTH RATIO OF 10:8, FROM MODIFIED HOPKINSON BAR TEST

has a higher fracture resistance and a greater ability to undergo plastic deformation than the HTPB/RDX and HTPB/PETN propellants.

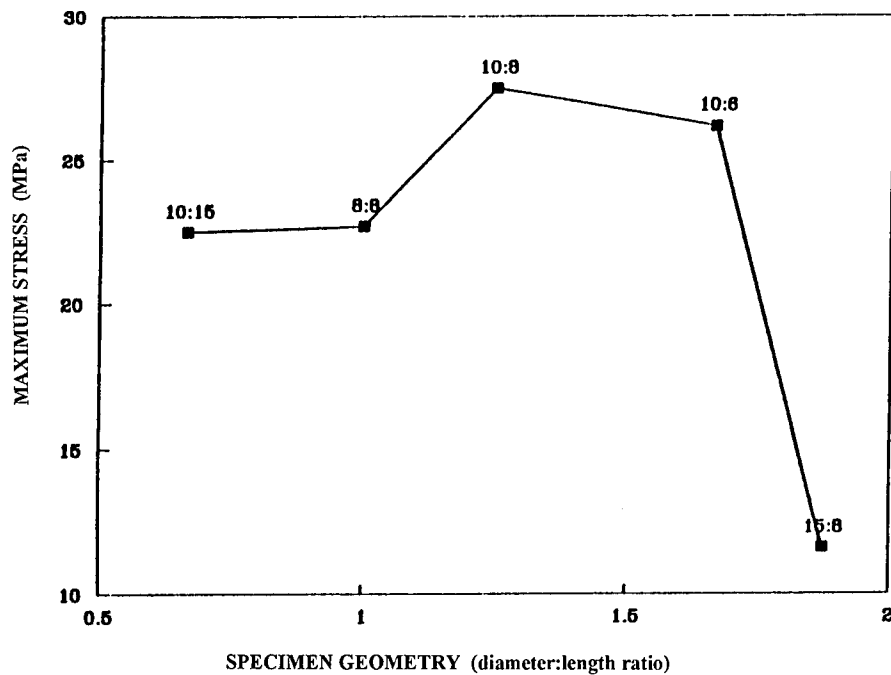
The CDB propellant undergoes brittle failure and shows comparatively less plastic deformation. This propellant has the highest maximum stress, modulus and fracture toughness but has a low strain to failure.

The PEG,PCP/RDX,HMX propellant is mechanically weak (low maximum stress and modulus) and exhibits the low load capability and large strain viscoelastic behaviour characteristic of elastomers. Localized melting (as evidenced by the smooth surface inside the cavity formed in the centre of the pellet) occurred during impact<sup>7</sup>, as a result of the high temperatures produced in the regions of maximum shear stress during compression.

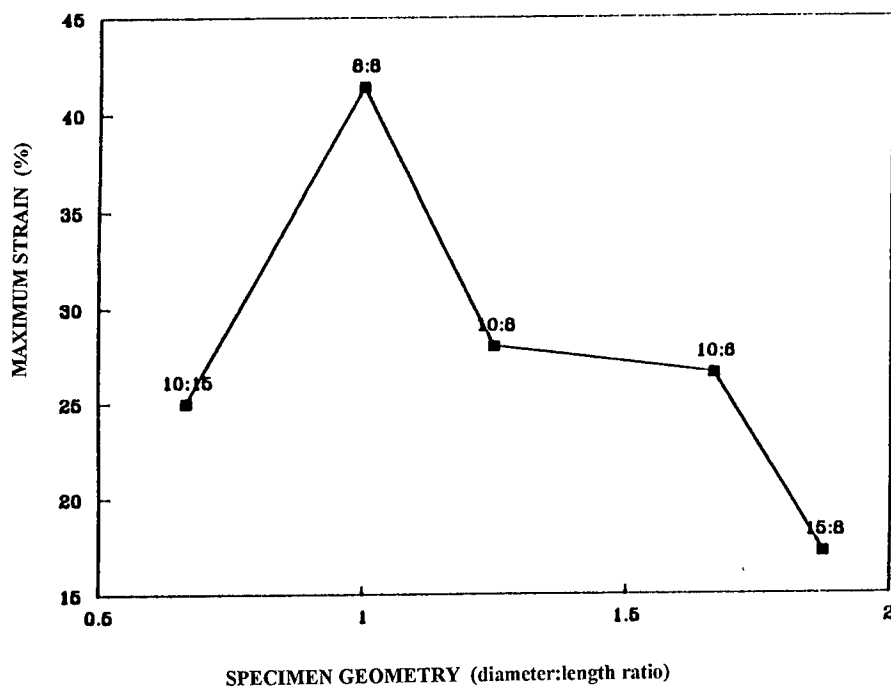
A change in specimen geometry can result in a ductile-to-brittle transition<sup>7</sup>. This arises from (1) the loading condition changes from plane stress to plane strain as the specimen thickness is increased<sup>20</sup>, or (2) an increase in the strain-rate as the specimen size is decreased. In addition, a change in failure mode may occur when the specimen diameter exceeds the projectile diameter.

For the HTPB/AP propellant, changes in specimen geometry, at ambient temperature, did not induce a ductile-to-brittle transition. The relative extent of ductile and shear failure changed with specimen geometry; shear failure became more significant when the specimen diameter to length ratio increased. When the specimen diameter exceeded that of the projectile, shear failure predominated. The propellant appeared less ductile when the thickness was increased, due to the stress state changing to plane strain conditions. Decreasing the specimen size resulted in higher strain-rates, and higher compressive stresses were measured for the specimens with shorter lengths (Fig.2a and b).

It is well known that in rubbery composite propellants rehealing (ie. damage is reduced with time) can occur when the propellant is left in an unstrained condition over a period of time. Thus the critical factor that determines the sensitization effect of predamage is the amount of damage at the time of impact initiation and not the amount of deformation the specimen had been subjected. Stress relaxation experiments on some of the deformed samples were conducted in the shear and compression modes using the RSA2 Dynamic Mechanical Thermal Analyser, to determine the amount of recovery and the effect of



(a)



(b)

FIGURE 2. (a) MAXIMUM STRESS OF HTPB/AP PROPELLANT PLOTTED AS FUNCTION OF SPECIMEN GEOMETRY (diameter:length ratio). (b) MAXIMUM STRAIN OF HTPB/AP PROPELLANT PLOTTED AS FUNCTION OF SPECIMEN GEOMETRY.

recovery time on the induced mechanical damage. The hysteresis energy losses in composite propellants, in the form of non-recoverable damage, can be attributed to plastic deformation, dewetting (oxidiser-binder debonding), microvoiding and subsequent craze formation and microcracking<sup>21</sup>.

A damage measure (failure criterion),  $D$ , based on the work by Martin<sup>22</sup>, following Miner's linear Cumulative Damage hypothesis<sup>19</sup>, was used here to quantify the amount of predamage in the propellants. In this model,  $D=0$  for an undamaged material, while for a completely damaged material,  $D=1$ . Our preliminary results indicate that the high strain-rate mechanical properties (modulus and maximum stress), measured in the Hopkinson Bar test, decreased when sufficient pre-damage was induced in the propellant. More details on characterization of predamage, and its effect on the impact sensitivity and impact ignition mechanism will be published in a later paper<sup>18</sup>.

### Impact Ignition Sensitivity

The ease of ignition of the propellants ranked according to their ignition threshold velocity (in increasing order) are as follows:

HTPB/RDX < PEG,PCP/RDX,HMX < HTPB/PETN < CDB < HTPB/AP.

The HTPB/RDX, PEG,PCP/RDX,HMX and HTPB/PETN propellants are hard to ignite compared to the HTPB/AP and CDB propellants. This may be partly attributed to the relatively high heats of fusion of RDX, PETN and HMX compared to AP, which helps restrain temperature rises<sup>23</sup>. The low impact sensitivity of propellants with RDX as an oxidiser may also be due to the ability of RDX to form a stable liquid at its melting temperature<sup>24</sup>. There is some evidence from photographs taken during impact that ignition in the RDX propellant occurs on the surface, ie. in the gaseous phase<sup>7</sup>.

Preliminary Hopkinson Bar tests on the predamaged HTPB/AP propellant samples indicate that the ignition threshold velocity is decreased (ie. sensitization occurred) when sufficient damage was induced in the samples prior to testing. More details on this work will be reported in a later paper<sup>18</sup>.

### Impact Ignition Mechanisms AP-Based Propellant

Photographs taken during impact of the HTPB/AP propellant provide clear evidence for the role of plastic deformation and adiabatic shear in the

ignition process (Fig.3). Although a change in specimen geometry affects the relative extent of ductile and shear failure, the overall impact ignition mechanism is not altered<sup>7</sup> - the first signs of ignition are at the specimen-projectile interface and around cracks, after plastic deformation and flow had occurred. The negative slope of the stress-strain curve (Fig. 3e and f), before ignition was first observed, may be due to adiabatic strain softening which could lead to localization of plastic flow and the formation of shear bands. Shear bands in crystalline oxidiser particles have been observed by Winter and Field<sup>6</sup> and Coffey et. al<sup>9,10</sup>, and are believed to be sites for hot spots. Cracks and voids (formed by dewetting of the crystalline oxidiser particles from the polymer binder matrix), where stress concentration can occur, also act as sites for hot spot formation, as indicated in Fig. 3f.

### PETN- and RDX-Based Propellants

The impact ignition mechanisms of the PETN and RDX-based rubbery composite propellants are somewhat similar. The sequence of events leading to fracture and ignition of the PETN propellant are shown in Fig. 4. Cracking and extensive plastic deformation/flow occurs (Fig. 4a-e) followed by localized melting and jetting (Fig. 4f), as a result of the melted propellant being forced out of the centre of the pellet. The propellant was in a partial "melt" (rubbery-viscous) state when the first signs of ignition were visible as brown bands along cracks and at the specimen-projectile interface. A swollen and fluid-like propellant, indicating a viscous state, and further burning are observed in Fig. 4g. These photographs give clear evidence that the mechanism of ignition of the PETN propellant is by viscous heating due to viscoplastic work, after the heat produced by plastic deformation/flow has partially melted the propellant in the region of maximum shear stress, ie. at the specimen-projectile interface.

### Elastomeric RDX,HMX-Based Propellant

The deformation, ignition and burning behaviour of this propellant are shown in Fig. 5. This propellant exhibits typical elastomeric deformation characteristics, undergoing large strain viscoelastic/plastic deformation with little or no cracking (Fig. 5a-d). There is some evidence of ignition starting at the specimen-projectile interface in Fig. 5e, after localized melting had occurred (see Fig. 5d, note that the propellant had become lighter in colour and the volume had increased slightly).

Two very distinct phases, a solid layer and a

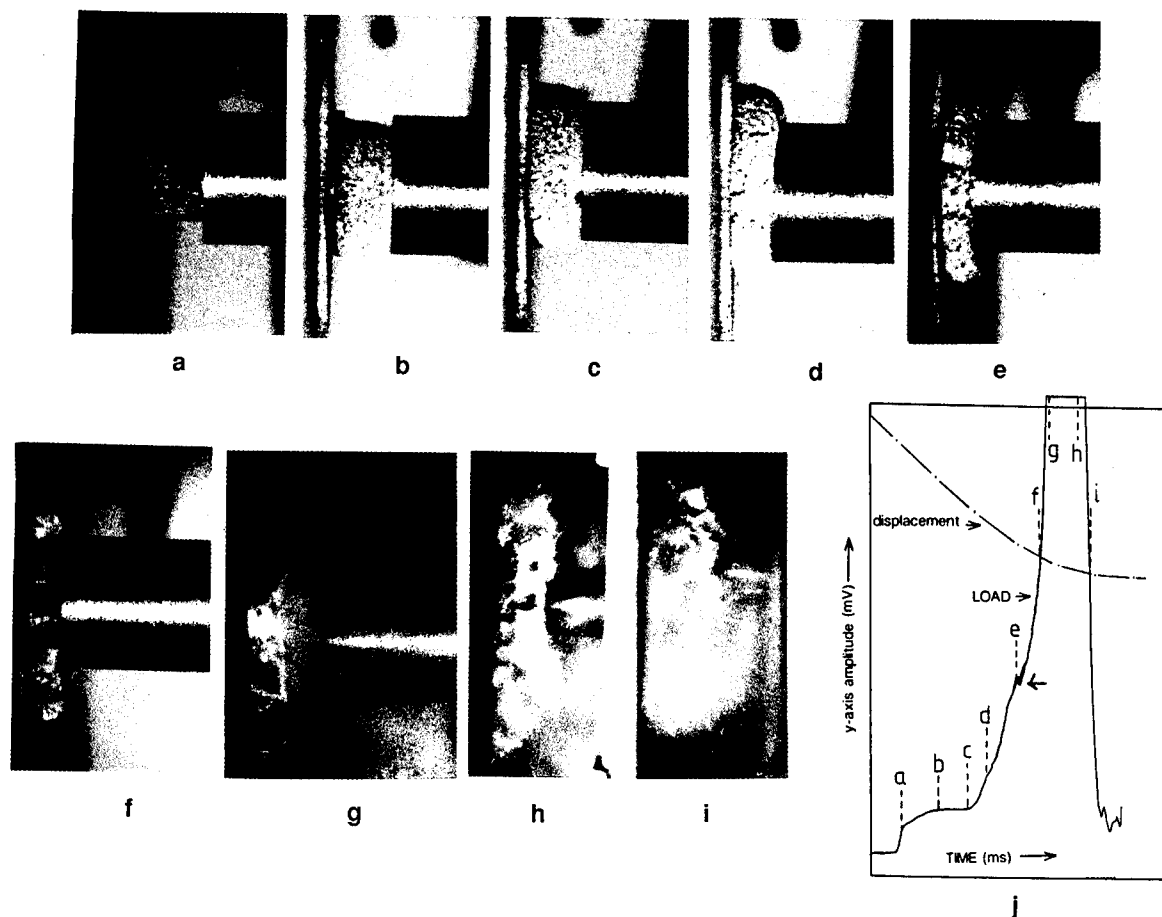
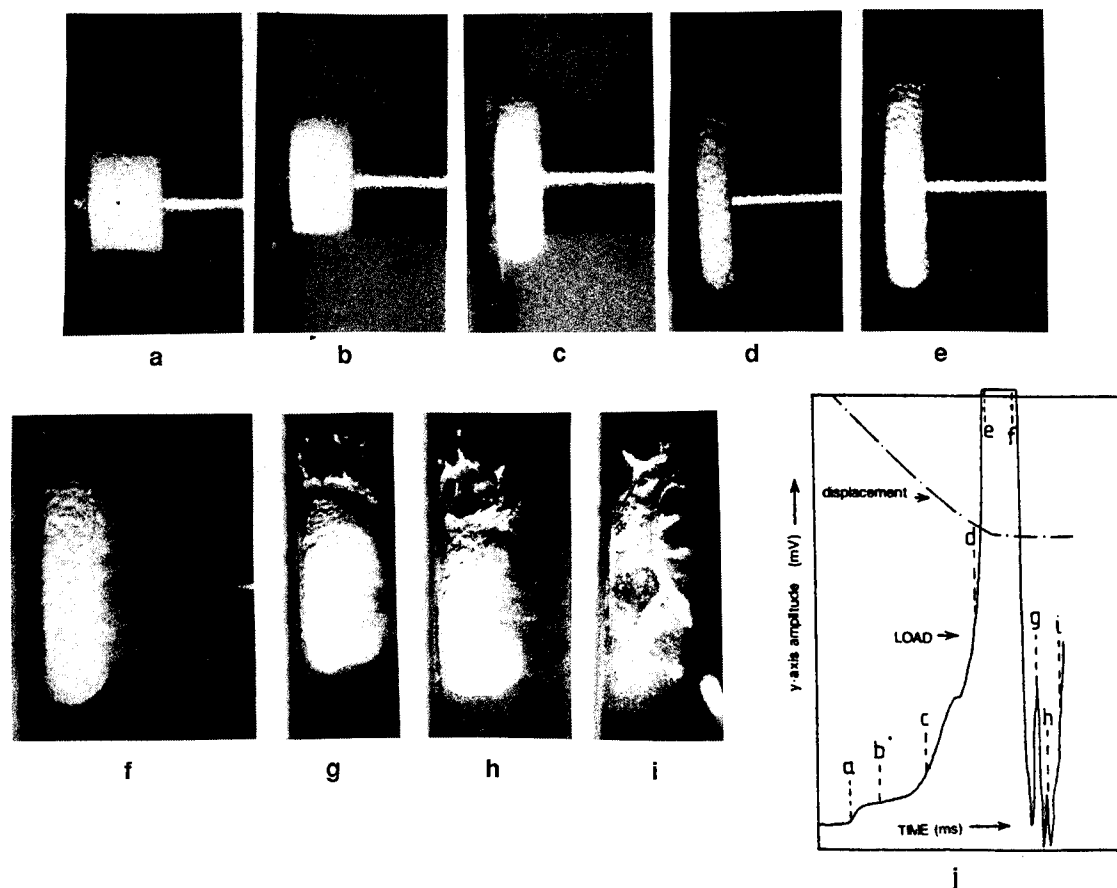


FIGURE 3. (a) TO (i) PHOTOGRAPHS SHOWING THE SEQUENCE OF EVENTS LEADING TO FRACTURE AND IGNITION FOR HTPB/AP PROPELLANT. ORIGINAL IN COLOUR. (j) CORRESPONDING LOAD-TIME AND DISPLACEMENT-TIME CURVES FOR HTPB/AP PROPELLANT. VERTICAL LINES ON LOAD TIME CURVE INDICATE WHEN PHOTOGRAPHS WERE TAKEN. N.B. ARROW INDICATES WHERE CORRESPONDING STRESS-STRAIN CURVE SHOWS A NEGATIVE SLOPE.

white translucent rubbery-viscous ("melt") layer, and jetting are evident in Fig. 5f. An ignition site is observed in the rubbery viscous layer, suggesting that ignition is by deformation work of the viscous layer. Ignition appears to occur near the junction of the solid and molten layers, where the shear stress is expected to be maximum because of the high velocity gradient. The next few photographs (Fig. 5f-i) show the molten region nucleating as a thin layer and then increasing in thickness. Ignition is confined in the molten layer, providing clear evidence that plastic deformation in the solid phase does not generate enough heat to ignite this propellant. A deflagration is observed in the last photograph, when the propellant is completely molten.

#### Cast Double-Base (NC/NG) Propellant

This propellant exhibits brittle fracture behaviour under impact loading at high strain-rate. It undergoes relatively less plastic flow before fracture (Fig. 6a-d) compared with the rubbery composite propellants. Ignition occurs after brittle fracture and is first visible around the grains of the propellant where cracking had occurred (Fig. 6e,f). Calculations from the photographs and displacement vs. time plots indicate that the projectile was not yet in contact with the output bar when ignition was first visible, ie. the initiation is not due to a grinding/pinching mechanism (where heating by friction or localization of strain occur). These observations suggest that ignition by



**FIGURE 4. (a) TO (i) PHOTOGRAPHS SHOWING SEQUENCE OF EVENTS LEADING TO FRACTURE AND IGNITION FOR HTPB/PETN PROPELLANT. ORIGINAL IN COLOUR. (j) CORRESPONDING LOAD-TIME AND DISPLACEMENT TIME CURVES FOR HTPB/PETN PROPELLANT. VERTICAL LINES ON LOAD-TIME CURVE INDICATE WHEN PHOTOGRAPHS WERE TAKEN.**

brittle fracture, as a result of the heat released during fast crack propagation, is a possible heating mechanism.

The calculated temperature rise generated by fast crack growth, assuming adiabatic conditions and that crack instability arises during high strain-rate impact is ca.  $750^{\circ}\text{C}$ <sup>7</sup>. Since the ignition temperature of this propellant is  $204^{\circ}\text{C}$  the temperature rise generated by fast crack growth is sufficient for ignition to occur, supporting the suggested heating mechanism.

## CONCLUSIONS

The experimental results from this study clearly show that the impact sensitivity and ignition mechanism of rocket propellants are controlled to a

large extent by (1) high strain-rate mechanical properties which influence the failure mode (eg. ductile vs. brittle), and (2) thermal properties (eg. when the melt point of the propellant is lower than its ignition temperature, ignition is likely to occur by viscous heating).

For the AP-based composite propellant, photographs taken during impact provide clear evidence of the role of plastic deformation and adiabatic shear in the ignition process. A change in specimen geometry affected the relative extent of ductile and shear failure, but the overall impact ignition mechanism was not altered.

The impact ignition mechanisms of the PETN and RDX-based propellants are somewhat similar.

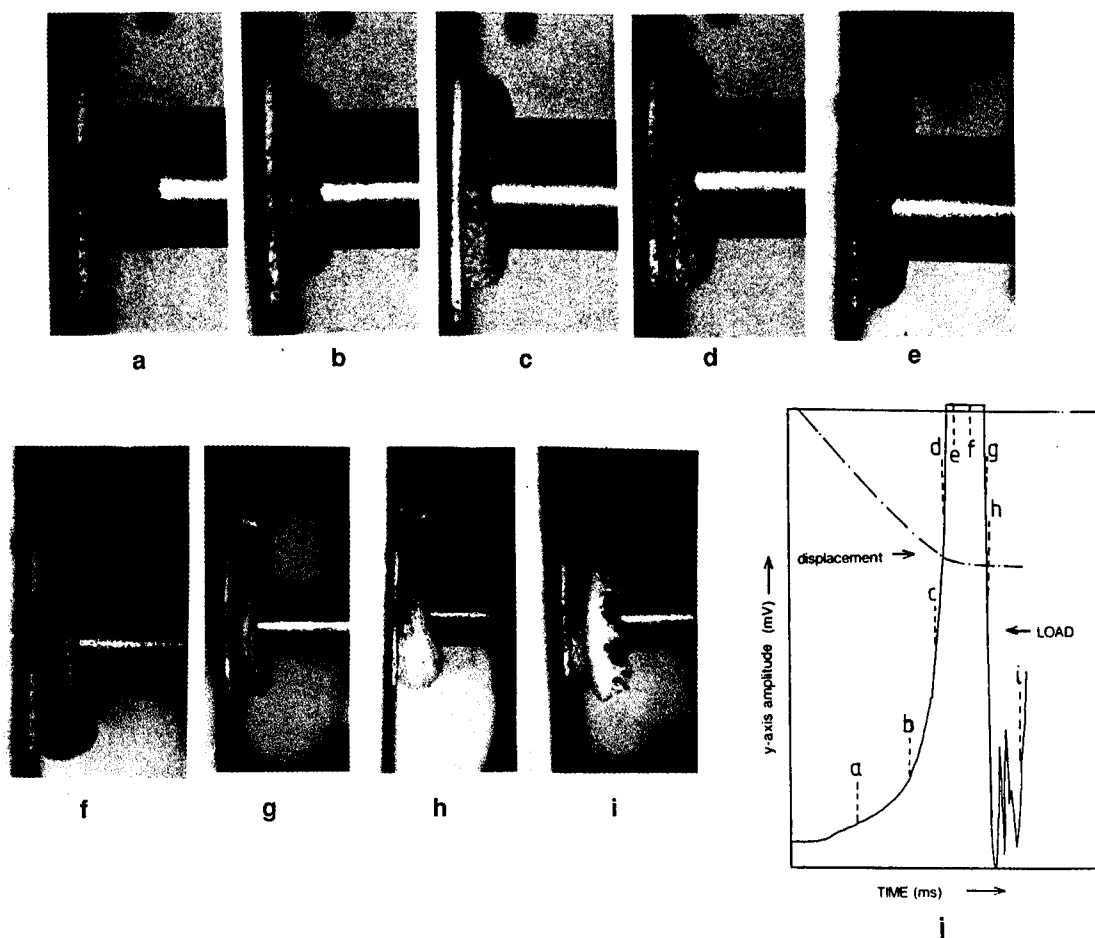


FIGURE 5. (a) TO (i) PHOTOGRAPHS SHOWING SEQUENCE OF EVENTS LEADING TO FRACTURE AND IGNITION FOR PEG,PCP/RDX,HMX PROPELLANT. ORIGINAL IN COLOUR. (j) CORRESPONDING LOAD-TIME AND DISPLACEMENT-TIME CURVES FOR PEG,PCP/RDX,HMX PROPELLANT. VERTICAL LINES ON LOAD-TIME CURVE INDICATE WHEN PHOTOGRAPHS WERE TAKEN.

Ignition occurred by viscous heating from viscoplastic work, after the heat produced by plastic deformation/flow had partially melted the propellant in the region of maximum shear stress.

Definitive evidence for localized melting and ignition by viscous heating from viscous flow was obtained for the elastomeric PEG,PCP/RDX,HMX propellant. Two very distinct phases, a solid layer and a rubbery-viscous ("melt") layer, were formed during high strain-rate impact. Ignition occurred in the rubbery-viscous phase.

For the CDB propellant, ignition was first visible around the grains of the propellant where brittle

cracking had occurred. This indicates that the heat released during fast crack propagation is a possible ignition mechanism.

The sensitizing effect of predamage was investigated. Preliminary results showed that the level of test response to projectile impact was increased when sufficient predamage was induced in the propellant.

#### REFERENCES

1. Ho, S.Y.; and Fong, C.F., Polymer, Vol. 28, 1987, p739.



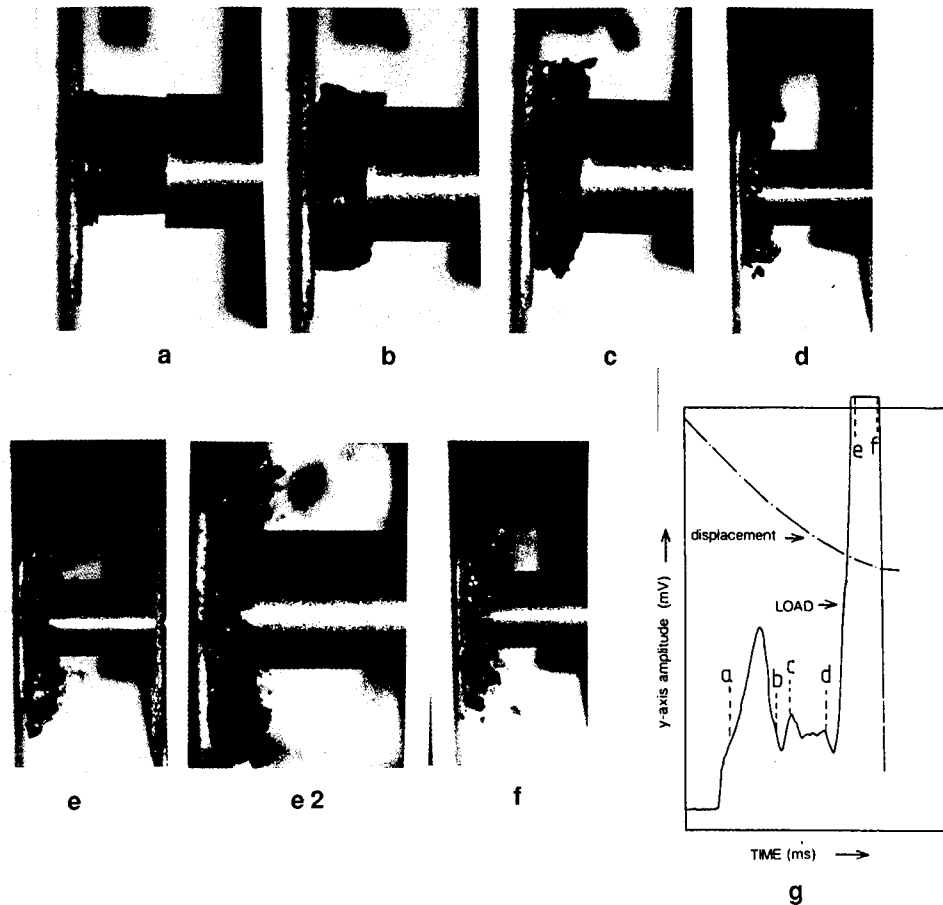


FIGURE 6. (a) TO (f) PHOTOGRAPHS SHOWING SEQUENCE OF EVENTS LEADING TO FRACTURE AND IGNITION FOR CDB PROPELLANT. ORIGINAL IN COLOUR. (g) CORRESPONDING LOAD-TIME AND DISPLACEMENT-TIME CURVES FOR CDB PROPELLANT. VERTICAL LINES ON LOAD-TIME CURVE INDICATE WHEN PHOTOGRAPHS WERE TAKEN.

2. Ho, S.Y.; and Fong, C.F., J. Mater. Sci., Vol. 22, 1987, p3023.

3. Ho, S.Y.; and Fong, C.F., Combust. Flame, Vol. 75, 1989, p139.

4. Ho, S.Y.; Fong, C.F.; and Hamshere, B.L., Combust. Flame, Vol. 77, 1989, p395.

5. Dagley, I.J.; Ho, S.Y.; Montelli, L.; and Louey, C.N., Combust. Flame, Vol. 89, 1992, p271.

6. Winter, R.E.; Field, J.E., Proc. R. Soc. Lond. A, Vol. 343, 1975, p399.

7. Ho, S.Y., Combust. Flame, Vol. 91, 1992, p131.

8. Afanas'ev, G.T.; and Bobolev, V.K., "Initiation of Solid Explosives by Impact", translated from Russian by Israel Program for Scientific Translations, Jerusalem, 1971.

9. Coffey, C.S.; Frankel, M.J.; Liddiard, T.P.; and Jacobs, S.J., Proceedings of the Seventh Symposium (International) on Detonation, 1981, p334.

10. Coffey, C.S., Proceedings of the Ninth Symposium (International) on Detonation, 1989, p58.

11. Bowden, F.P.; and Yoffe, A.D., "Initiation and Growth of Explosions in Liquids and Solids", Cambridge University Press, 1952.
12. Fuller, K.N.G.; Fox, P.G.; and Field, J.E., Proc. R. Soc. Lond. A, Vol. 341, 1975, p537.
13. Swallowe, G.M.; Field, J.E.; and Hutchingson, C.D., "Shock Waves Condensation", Proceedings of the American Physical Society Top. Conference (Gupta, Y.M., Ed.), Plenum, New York, 1985, p891.
14. Frey, R.B., Proceedings of the Eighth Symposium (International) on Detonation, 1985, p68.
15. Ho, S.Y.; Hammond, R.T.; Schebella, K.T.; and Wilson, A.G., WSRL Report WSRL-TN-40/89, Weapons Systems Research Laboratory, South Australia, 1989.
16. Howe, P.M.; Frey, R.B.; Taylor, B.C.; and Boyle, V.M., Proceedings of the Sixth Symposium (International) on Detonation, 1970, p11.
17. Weimann, R.M.; Ho, S.Y.; and Winch, P.C., WSRL Report WSRL-TR-43/89, Weapons Systems Research Laboratory, South Australia, 1989.
18. Ho, S.Y., J. Mater. Sci., in preparation.
19. Miner, M.A., J. Applied Mechanics, Vol. A160, 1945, p159.
20. Williams, J.G., "Fracture Mechanics Of Polymers", Halstead, New York, 1984.
21. Ho, S.Y.; and Tod, D.A., "Fracture and Hysteresis Characteristics of Rubbery Composite Propellants", Proceedings of the 21st ICT Conference, Karlsruhe, FRG, July 1991.
22. Martin, D.L., Jr., Chemical Propulsion Information Agency Publication 331, The Johns Hopkins Univ., Applied Physics Lab., Laurel, MD, Dec. 1980, p85-105.
23. Swallowe, G.M.; Field, J.E.; and Horn, L.A., J. Mater. Sci., Vol. 21, 1986, p4089.
24. Karpowicz, R.J.; and Brill, T.E., Combust. Flame, Vol. 56, 1984, p317.

---

## DISCUSSION

ARTHUR METZNER

NSWC, Indian Head, Maryland

In the samples which showed melting in the center of the sample: is there shear there?

### REPLY BY SOOK-YING HO:

Because the first signs of melting are at the sample-projectile interface, where the shear stress is expected to be a maximum, melting is due to the high temperatures produced in the regions of maximum shear stress during compression.

## DISCUSSION

PEI CHI CHOU

Drexel University, Philadelphia, Pennsylvania

What is the strain-rate regime of your tests? How is the strain rate measured?

### REPLY BY SOOK-YING HO:

The strain-rate regime of the Modified Hopkinson Bar is  $10^3 - 10^4 \text{ s}^{-1}$ . The strain rate was calculated from the change in true strain of the sample with time. Displacement of the projectile (after impact), and therefore of the sample at a given time, was measured using a coaxial capacitor, as described in detail in earlier work (Refs. 1-4).

## JET INITIATION THRESHOLDS OF NITROMETHANE

Blaine W Asay, Deanne J. Pauley, and Eric N. Ferm  
Los Alamos National Laboratory  
Los Alamos, NM 87544

The initiation criterion for nitromethane and diethylenetriamine-sensitized solutions has been established over a confined range of jet diameters, velocities, and failure diameters. The data were normalized with the failure diameter that was chemically modified, and they support the hypothesis that the failure diameter should be made part of the critical initiation function. The difference between physically- and chemically sensitized NM in promptness of initiation, as measured by corner turning distance, was not statistically significant. The diameter of the Viper jet has been characterized over a wide range of velocities.

### INTRODUCTION

Munitions safety concerns underlie a significant effort to develop and understand the initiation characteristics, response thresholds, and performance of modern energetic materials. Inherent differences between the insensitive high explosives (IHEs) and propellants and the common military explosives are more complex than merely improved resistance to single-shock initiation. Even low-level insults may cause transition to detonation in granular propellant or damaged explosive. Non-prompt processes leading to detonation are poorly understood, and thresholds have not yet been established.

In a study of vulnerability, the questions include the level of stimulus required for initiation to detonation or violent reaction, the effect of explosive failure diameter on initiation (in relation to jet/fragment properties), the qualitative and quantitative differences between homogeneous and heterogeneous materials, and the effects of confinement materials, thickness, and geometry.

Liquid propellants are homogeneous explosives, whereas solid propellants are heterogeneous. Both types of propellants can have large failure diameters ( $>125$  mm). No published work systematically covers jet initiation of materials with failure diameters greater than five jet diameters (except for a preliminary study of PBX 9502 by McAfee<sup>1</sup>), although nonsteady initiation of nitromethane (NM) by shaped-charge jets has been reported.<sup>2</sup>

Until recently, the only predictor for jet initiation of explosives was the  $v^2d$  criterion first postulated by Held.<sup>3</sup> Chick and coworkers, in a series of papers (summarized by Chick et al.<sup>4</sup>), have shown that  $v^2d = k$  describes only one initiation mechanism; that caused by

the contact shock produced from the initial jet-HE or jet-thin-cover-plate interaction. They have also demonstrated that initiation can occur as a result of the jet bow shock. They postulate that when the ratio of jet diameter to the failure diameter exceeds  $1/5$ , the contact shock is responsible for initiation, whereas when the ratio is less than  $1/5$ , initiation occurs by means of the bow shock. However, substantially different values of  $k$  apply, depending on what type of mechanism initiates the HE, and whether the jet penetration rate in the explosive is supersonic or subsonic.

Chick et al.<sup>4</sup> have also determined that the commonly used predictive criteria apply only to jets with a limited range of diameters. For smaller jets, with diameters much less than  $1/5$  the failure diameter of the explosive, the predictive relationships appear to have a form other than  $v^2d$ . Because liquid or solid gun propellant and IHE can have failure diameters several times larger than most common HE, the interaction of most jets with these materials will be in this largely unstudied region.

Chick's work is based on the results from several explosives with a variety of material properties; so the exact value of the ratio of the jet diameter to the failure diameter for the transition between initiation mechanisms is uncertain. The nature of this transition from large-jet to small-jet initiation may be precipitous or smooth. Our study was designed to provide further information about the interaction by using an HE that could be easily modified to meet our needs.

We chose NM as the test explosive because it is a clear, liquid high explosive and it has several other advantages. Its failure diameter is easily increased by dilution with acetone, or reduced by sensitization with diethylenetriamine (DETA).<sup>5</sup> Therefore, the ratio of jet diameter to failure diameter can be continuously varied

while using only a single type of jet. This technique greatly reduces the amount of work necessary because only one jet must be characterized. Also, NM can be made heterogeneous by the addition of particles and a thickener.<sup>6</sup>

Using NM as either a homogeneous or heterogeneous material connects the work done previously in high-density explosives, in particulate-solid-gun propellants, and in liquid propellants. An added advantage is that since NM is a liquid, gauge placement is facilitated, and because it is transparent, optical diagnostics are possible that would be either impossible or prohibitively expensive in solid materials. With the above techniques, NM serves as a surrogate for both heterogeneous and homogeneous propellants and explosives.

This paper describes research designed to elucidate the initiation behavior as the mechanism changes from contact- to bow shock initiation. The differences in physical and chemical sensitization have also been investigated by measuring corner-turning distances. Jet interaction with NM was characterized with framing-camera and streak photography. Quantitative characterization of the jet by flash radiography (see McAfee<sup>7</sup>) was used to determine the jet's velocity and diameter.

## EXPERIMENTAL RESULTS AND DISCUSSION

### Materials

Commercial-grade NM has various impurities; however, they are typically in low concentrations. The composition of the NM used in this program was measured when received, and the impurities constituted less than 1.4% by volume. The failure diameter was also determined to be  $16.4 \pm 1.1$  mm but is subject to change, depending on storage conditions. It has been observed to decrease with time, but the mechanism for this change is unknown. Thus, extreme caution should be exercised in the storage and handling of NM.

Technical-grade diethylenetriamine (DETA, Lot D13632, H768-07, 500 ml, purchased from J. T. Baker, Inc.) was used for chemical sensitization. DETA is also subject to chemical degradation.

Boron carbide (B<sub>4</sub>C) and fumed silica were chosen as the substitutes for the glass beads and guar gum previously used by Engelke<sup>8</sup> to obtain heterogeneous mixtures with NM. Boron carbide particles with an average particle size of 1.3  $\mu$ m were used for the physical sensitization. The Cab-o-Sil fumed silica (TS720) was produced by the Cabot Corporation.

### Failure Diameter Determination

Plate dent tests were used to determine failure diameters for neat NM, mixtures of NM with DETA, and NM gelled with TS720 to which B<sub>4</sub>C particles have been added. Lengths of the standard-wall pyrex tubing exceeded 13 times the internal diameter of the tube. Steel

witness plates were used to record the dents from detonation. Failure diameters were calculated as the average of the inner diameters of the two adjacent tubes for which the detonation propagated and failed. Ranges for the failure diameters are given as one-half the difference between the inner diameters.

NM. The critical diameter of an explosive is known to be affected by changes in confinement, density, particle size, and initial temperature. For NM, the effect of temperature change is significant. NM critical diameter data<sup>9</sup> were fit as a function of temperature. A derivative of this equation with respect to temperature was used to define the average failure diameter change over the experimental temperature range (see Ref. 10):

$$\frac{d(d_f)}{d(T)} = -35.5e^{-T/60.913} \quad (1)$$

where T is the temperature in kelvin, and the failure diameter  $d_f$  is in units of millimeters. For our plate dent tests the temperatures ranged from 19° to 28°C. Across this range, the average change in failure diameter is approximately -0.27 mm/°C. The failure diameters were temperature-corrected with this value from our experimentally measured diameters to 22°C.

NM/DETA. Nitromethane with selected concentrations of DETA were tested to confirm the reproducibility of the data first published by Engelke.<sup>5</sup> However, the initial results indicated that the DETA we were using had a greater effect on the failure diameter than expected. Therefore, we completed more tests to reproduce the entire curve and check the precision of some of the new points. Our temperature-corrected values are compared with Engelke's temperature-corrected results in Figure 1.

NM/B<sub>4</sub>C/TS720. In each of these tests, the concentration of TS720 was held constant at 3.0 wt%. These results are given in Figure 2. When the failure diameter data for the NM/DETA mixtures and the NM/B<sub>4</sub>C/TS720 mixtures are compared, DETA is much more effective at modifying the failure diameter of the NM, in terms of the concentration of additive required. Also, the boron carbide mixtures are more effective in reducing the failure diameter than are glass beads,<sup>8</sup> when equal concentrations of additive are used. These differences demonstrate the effect of the impedance of inclusions on HE sensitivity.

### Experimental Configuration

A Viper shaped charge was chosen as the impactor for these studies because of its reproducibility and availability. The copper cone diameter is 63 mm.

The experimental configuration was designed using a simple one-dimensional (1-D) penetration algorithm using virtual-origin information from hydrocode simulations. The virtual-origin information used initially is given in Table 1. By linear extrapolation, separate particles arising from particulated jets imaged by radiography show that particulation of the Viper occurs between 100

and 120  $\mu$ s. However, at 100  $\mu$ s, shadowgraphs show a continuous jet.

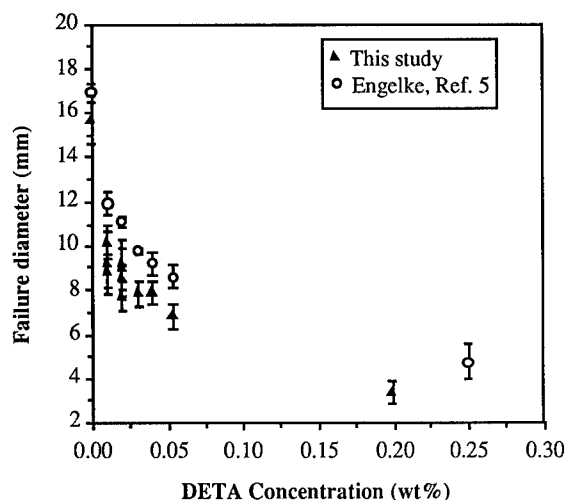


FIGURE 1. FAILURE DIAMETER OF NM AS A FUNCTION OF CONCENTRATION OF DETA (WT%). DATA FROM ENGELKE<sup>5</sup> HAVE BEEN GIVEN FOR COMPARISON. BOTH SETS OF DATA ARE SHOWN WITH RANGES AND HAVE BEEN CORRECTED TO 22°C

A typical experimental configuration is shown in Figure 3. Several different stand-offs (distance from the jet face to the first attenuator plate) were examined, ranging from 50 mm to 150 mm. Several competing objectives must be considered in choosing this distance. A larger stand-off will provide more control over the residual velocity of the jet, less scatter for repeat shots at

the same attenuation, and more accurate predictions of the residual velocity. On the other hand, shorter stand-offs will cause the jet to exit the target sooner, so the jet is not as close to particulation. Also, shorter stand-offs between the face of the jet and the first attenuator plate allow for more distance between the attenuator plates and the target, which simplifies the radiography. In weighing these considerations we determined that the 50 mm stand-off was optimal for the present work.

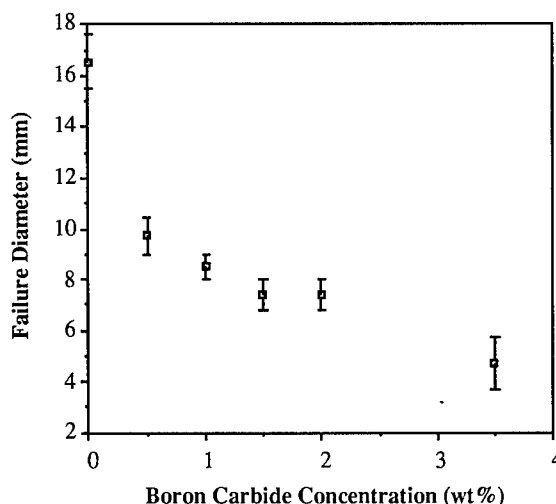


FIGURE 2. FAILURE DIAMETER OF NM AS A FUNCTION OF CONCENTRATION OF B<sub>4</sub>C (WT%) AND TS720 (3.0 WT%). THESE VALUES HAVE NOT BEEN TEMPERATURE CORRECTED. AMBIENT TEMPERATURES FOR ALL SHOTS WERE WITHIN 2°C OF THE NOMINAL TEMPERATURE 26°C

TABLE 1. VIRTUAL ORIGIN REPRESENTATION OF VIPER

Tip Velocity (mm/ $\mu$ s)	Tail Velocity (mm/ $\mu$ s)	Calculated (x <sub>vo</sub> ) <sup>a</sup> (mm)	Calculated t <sub>vo</sub> ( $\mu$ s)	Experimental (x <sub>vo</sub> ) <sup>a</sup> (mm)	Experimental t <sub>vo</sub> ( $\mu$ s)
9.17	9.17	0.0	21.81		
9.17	7.17	-85.4	14.35		
7.17	5.17	-39.2	20.80		
5.17	3.17	-21.3	24.25		
3.17	1.17	-3.1	30.00		
9.17	7.64			-105.9	11.59
7.64	2.45			-29.2	21.63

<sup>a</sup>Constant velocity segment tip at 0 mm and tail at -17 mm.

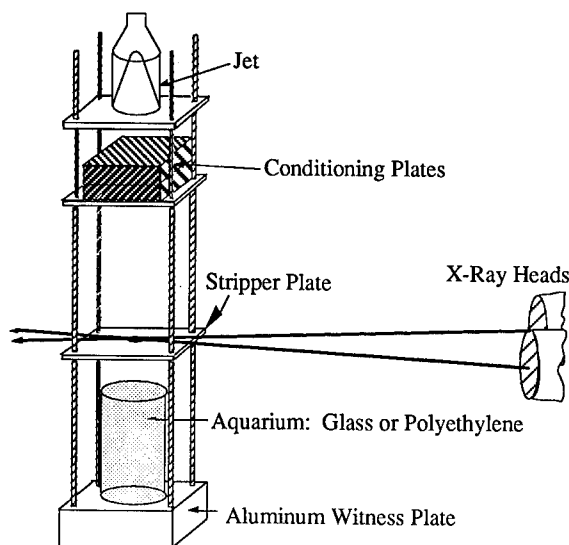


FIGURE 3. SCHEMATIC OF A TYPICAL SHOT SET UP USED FOR  $v_{nd}$  AND CTD MEASUREMENTS

For the initial screening experiments we used 1-in.-thick cold-rolled steel plates exclusively. However, while determining the critical conditions, we used a combination of 1-in. and 0.25-in. plates, with the last plate in the stack being 0.25-in. thick. This reduced the scatter in residual velocities. The free surface of the NM was placed either 10 in. or 13 in. from the top of the first attenuator plate. The 10-in. spacing ensures that the residual jet is unparticulated, whereas the 13-in. spacing was used with thicker attenuation systems that required more room to obtain reliable radiographs of the penetrator. Although the 13-in. spacing can result in impact times greater than 110  $\mu$ s, no particulation has been observed in the residual penetrators during these tests, even when 8.25 in. of attenuation was used. A stripper plate, 0.25-in. steel with a 0.5-in. hole in the center, was placed 3 in. above the NM level to minimize the amount of spall from the attenuator plates that impacts the NM surface.

### Shaped-Charge Characterization

The jet diameter and velocity are critical parameters in the initiation of explosives. The jet's residual velocity can easily be measured by several techniques; however, x-ray shadowgraphs have been the most reliable. The jet diameters are much more difficult to obtain reliably, primarily because they are relatively small, and they change as a function of both time and position. Typically, the tip is mushroom-shaped, and its diameter is several times larger than the shank diameter. The shank diameter was used in the correlations that we present.

**Jet Velocity.** For each test, radiographs of the residual penetrator were obtained at two different times. Two 150-keV or two 450-keV flash x-ray units served as

sources, and the magnification factor for the experiments was nominally 120%. Jet velocities are determined directly from the radiographs by measuring the distance traveled between the two x-ray flashes. The velocities are easily measured to within 1% because of the distances involved and the accuracy of our time measurements ( $\pm 5$  ns). The data shown in Figure 4 demonstrate the reproducibility of this system.

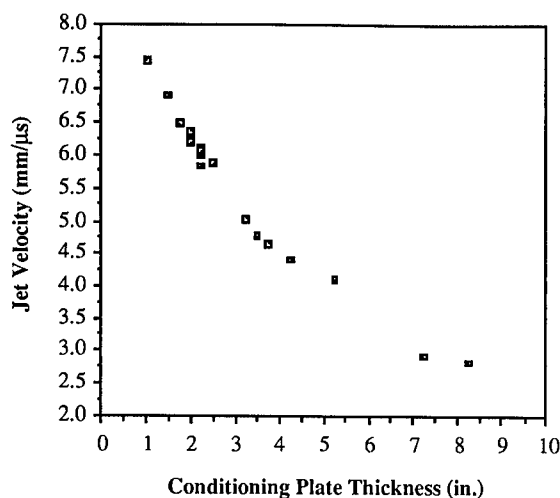


FIGURE 4. VIPER JET VELOCITY AS A FUNCTION OF ATTENUATOR THICKNESS

**Jet Diameter.** We have approached the difficult job of accurately determining the jet diameter using two different methods. A radiographic method was used to acquire the data presented here. More recently, we have developed an optical technique. However, those data are currently incomplete and will be reported later.

Unaided measurements of the diameters from radiographs are estimated to be accurate to  $\pm 0.5$  mm when the nominal diameter is  $\sim 2$  mm. Optical magnification of the image is not a practical method of improving accuracy because the grain size of the film and the blurred edge definition from the finite x-ray source size results in poor contrast in magnified images. To improve this accuracy, we scanned the radiographs with a densitometer.

A Leeds and Northrup microdensitometer was used to scan the radiographs across the axis of the jet. Measurements were made at the tip, and then 5 mm, 15 mm, and 25 mm from the tip, as measured on the film. The method we used to obtain diameters from these data is a modified version of that described by McAfee.<sup>7</sup> He found that an "effective spot size" of the x-ray source could be determined using a stepped calibration rod that covered the range of typical jet diameters using the relation

$$d_j = \frac{I - (m-1)s}{m} \quad (2)$$

where  $d_j$  = jet/calibration rod diameter,  
 $I$  = image width at the base line,  
 $m$  = magnification factor, and  
 $s$  = spot size of the x-ray source.

Our data obtained from the calibration rods did not yield a constant spot size, especially in the 450-keV calibration, but had a gentle trend to larger spot sizes for smaller rod diameters. We fit a linear relation of the image width to the diameters of the calibration rod for each x-ray setup used. This method improved the accuracy of the diameter measurement to within  $\pm 8\%$  with the occasional outliers reaching 10% at the extreme edge of the calibration range of  $\sim 1$ –3 mm.

We defined the shank diameter as the average of the three values behind the tip. This diameter is not measured at the NM surface, but rather at the time of the selected radiograph. To estimate the diameter when the jet impacts the NM surface, we assume that the stretching-jet segment is conserving volume and has the same stretch rate as the unattenuated jet estimate given in Table 1. The formula for estimating the stretched diameter is

$$d_j(t_i) = d_j(t_x) \sqrt{\frac{t_x - t_{vo}}{t_i - t_{vo}}} \quad (3)$$

where  $d_j(t)$  = jet diameter at time  $t$ ,  
 $t_i$  = time of impact of the NM surface,  
 $t_x$  = x-ray time,  
 $t_{vo}$  = experimental virtual-origin time corresponding to the velocity of the attenuated jet given in Table 1.

The accuracy of this extrapolation is a function of the constant-volume approximation (i.e., it ignores thermal expansion from plastic work and any void in the rod). It also assumes that the attenuated jet is stretching at the same rate as the unattenuated jet, and that the jet is not particulating.

Figure 5 shows a tip profile determined from radiographs after the jet passed through 2 in. of attenuation. Two cases are plotted, one in which the jet was attenuated by two 1-in. plates, and one in which the jet was attenuated by one 1-in. plate and four 0.25-in. plates. The scan was made every millimeter on the film from the tip back to 25 mm. The diameter quickly drops from the tip diameter to the shank diameter, especially in the second case. These data indicate that the average shank diameter is not greatly affected by the attenuation system, but less scatter is apparent when the series of 0.25-in.-thick attenuator plates was used.

#### Establishment of $v^nd$ Criterion

Chick and Bussell<sup>11</sup> proposed that the empirical ratio of  $d_f/d_j$  may be used to estimate the transition in the mode of initiation for several different bare solid

explosives: pressed TNT, Composition B, PBX 9502, Octol, H-6, and Cast TNT. They proposed that when  $d_f/d_j < 5$ , jet initiation on bare solid explosive would occur by contact shock, and when  $d_f/d_j > 5$ , the bow shock would cause initiation. To compare the data, the jet diameters were scaled with the explosive's failure diameter ( $d_f/d_j$ ). For our studies, this ratio was always less than 1/5 for neat NM and always greater than 1/5 for the NM/DETA mixtures. Following Chick and Bussell's predictions, this would indicate bow shock initiation for neat NM and contact shock initiation for the NM/DETA mixtures.

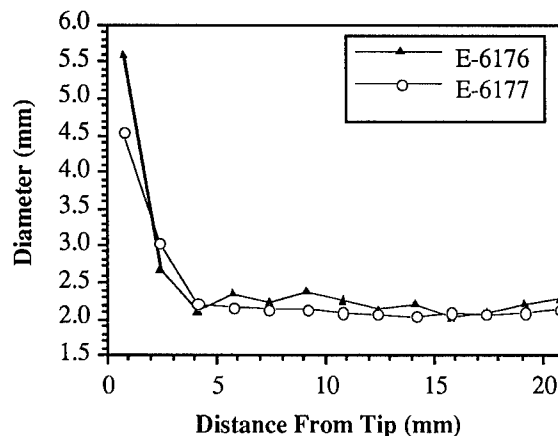


FIGURE 5. JET DIAMETER AS A FUNCTION OF THE DISTANCE FROM THE VIPER JET TIP FOR TWO DIFFERENT EXPERIMENTS. THE JET IN SHOT NO. E-6176 WAS ATTENUATED WITH TWO 1.0-IN. CONDITIONING PLATES. SHOT NO. E-6177 USED ONE 1.0-IN. AND FOUR 0.25-IN. CONDITIONING PLATES. SHOT DIAMETERS WERE DETERMINED FROM SCANNING DENSITOMETER MEASUREMENTS OF THE CORRESPONDING RADIOGRAPHS

Because of our choice of explosive, we have the unique opportunity to change the failure diameter of the explosive without grossly changing the explosive composition. By very modest addition of chemical sensitizers or by the addition of particulates to NM, the failure diameter can be decreased by a factor of 4. If we assume that the explosive's characteristic length (that is, its reaction zone length) is proportional to  $d_f$ , then the critical conditions for jet initiation should be dependent on  $d_f/d_j$ . This is a generalization of the work of Chick et al.,<sup>4,11</sup> in which they stated that the mechanism of jet initiation depends on the jet size relative to the failure diameter of the explosive.

Go/no-go criteria were established for neat NM and NM/DETA. Results are shown in Figure 6, plotted as jet velocity versus the ratio of the jet diameter to the failure diameter of the explosive. The vertical line indicates where the ratio  $d_f/d_j$  is equal to 1/5. Neat NM data lie to the left of this line, and the NM/DETA data lie to the right.

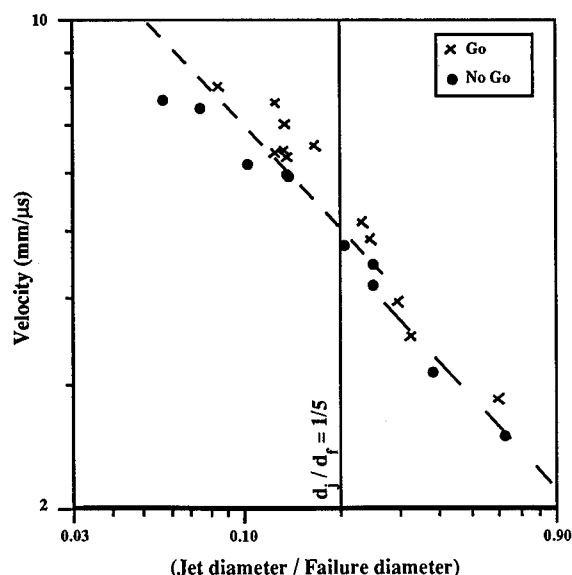


FIGURE 6. JET VELOCITY AS A FUNCTION OF THE RATIO  $d_j/d_f$ . THE VERTICAL LINE INDICATES WHERE  $d_j/d_f = 1/5$ . NEAT NM AND NM/DETA DATA LIE TO THE LEFT AND RIGHT OF THIS LINE RESPECTIVELY. THE DASHED LINE AT THE UPPER LEFT IS CALCULATED FROM  $v^2 d_j/d_f = 5.1$ . THE DASHED LINE AT THE LOWER RIGHT IS CALCULATED FROM  $v^2 d_j/d_f = 4.2$ . ALL  $d_f$  VALUES USED FOR THESE DATA WERE CORRECTED TO THE CORRESPONDING SOLUTION TEMPERATURE MEASURED AT THE TIME OF THE EXPERIMENT.

Choosing to fit the experimental data with a  $v^2 d_j/d_f$  form produces two different values for the constant  $k$ . These two fits are depicted in Figure 6 as the dashed, diagonal lines. The line at the upper left produced a value of 5.1 and the line at the lower right produced a value of 4.2. However, because the midpoints between go and no go data were not used to fit the lines, this type of fit implies that several of the go or no go points had a higher probability of occurring than others. In actuality, equal probabilities should be assigned to the corresponding go/no go pairs, and the midpoints between the data should be fit with  $v^n d_j/d_f = k$  to determine values for  $n$  and  $k$ . When this is done, the fit produced the values of  $n = 2.3$  and  $k = 8.2$  for the data at the upper left, and  $n = 2.6$  and  $k = 8.2$  for the data at the lower right. These results indicate that the exponent might actually have a value other than 2. Further examination of the data using either fit clearly indicates that the transition between modes of initiation is not smooth, and probably occurs in the  $d_j/d_f$  range  $\sim 1/4$ – $1/5$ .

An examination of the  $v^2 d_j = k_1$  criterion for other published experiments combinations shows a range from 4–100  $\text{mm}^3/\mu\text{s}^2$  (see Table 2). If one rewrites the criterion as  $v^2 d_j/d_f = k_2$ , the critical value of  $k_2$  falls in

the range of 2–17  $\text{mm}^2/\mu\text{s}^2$ . The  $d_f$  scaling law shows an encouraging compression of the range of the critical parameters, considering the variety of impacts represented in Table 2 (both continuous and particulated jets as well as thin flyer plates). This scaling of  $d_j$  with  $d_f$  accounts only for explosive properties that scale with the failure diameter. Thus, we should expect some variation of  $k_2$ , with respect to explosive, impactor dimension, equation of state, and initiation properties of the explosive (e.g. the Pop plot). As other researchers have noted<sup>4,11</sup> the relation may be different than  $v^2 d_j/d_f = k_2$ . Indeed, it may change depending on whether the impactor is a continuous or particulated jet or a thin flyer, compared with a long projectile. The form might also change as the ratio  $d_j/d_f$  changes.

### Comparison of Physical and Chemical Sensitization

The corner-turning distances (CTD) is an effective measure of the promptness of initiation of detonation. It has been shown that CTD can indicate the effect of initiator diameter and acceptor temperature on TATB.<sup>14</sup>

We measured corner-turning distances to determine how chemical modification (heterogeneous) compares with modification by addition of particles (homogeneous) in affecting the promptness of initiation by jet attack. From the prior  $v^n d = k$  measurements, we established that the go/no-go boundary for neat NM with our shot design and Viper jet occurred with 2.00–2.25 in. of attenuation. Therefore, all CTD tests were executed with 2.25 in. of attenuation. Data were obtained with an argon flash gap and a Cordin model 330A streak camera.

The results of the CTD shots are given in Figure 7 plotted against their  $v^2 d_j/d_f$  values. The concentration effects showed that as additive concentration was increased, the failure diameter decreased, and the CTD decreased proportionally. The method of sensitization did not affect the CTD response. These results indicate that, within the accuracy of the data, failure diameter, and not the initiation mechanism, is the single most important variable in determining the promptness of initiation by shaped charge jet. The actual mechanism, whether by means of hot spots or thermal explosion, was not observed to influence the results.

Although this result is rather surprising, it may indicate that in the shock initiation regime, the largest contribution to CTD is the distance required for the shock conditions to evolve to a point where the initiation criteria are met. The addition of DETA to NM modestly influences the sound speed and density. Sheffield, et al.,<sup>15</sup> have measured the sound speed and density of NM/DETA solutions as well as NM/guar/silica mixtures. Their results reveal that, for these mixtures, the density and sound speed vary by about 1.5%. Density measurements have not been made on NM/B<sub>4</sub>C/TS720 mixtures; however, the volumetric calculations of NM with B<sub>4</sub>C show that density will probably change only by 0.7%/wt% B<sub>4</sub>C. These changes are small in comparison with the changes in material properties that occur by



using different explosives. Because the material properties of the explosive were not greatly modified by heterogenization, the CTD required was similar for the two compositions.

## CONCLUSIONS

The diameter of the jet is the largest single source of error in determining the initiation thresholds of explosives. This variable is typically measured with a scale, and consistency between tests is usually assumed. Few if any of the published data are determined with more sophisticated methods. We have taken great care to accurately establish the errors associated with our measurements and to improve them as much as possible. Using the microdensitometer has reduced the maximum error of the radiographic measurements to ~10%, which is substantially less than previously achieved. We have also begun to use optical methods that promise to reduce the error even further. Optical methods have the added advantage of providing a dynamic determination of the jet profile, which will lead to improved understanding of jet parameters in general.

The initiation threshold of NM had not previously been determined. The  $v^2d_j$  criterion has now been bounded over a significant range of jet velocities and failure diameters. More work needs to be done to fully

understand the nature and position of the transition from bow- to contact shock initiation. This will have far-reaching implications for understanding the initiation of explosives in general.

NM that is sensitized physically or chemically, and that has the same failure diameter, demonstrated the same CTD when penetrated with a shaped-charge jet, within the errors of the data. Although differences may exist, additional study is needed before firm conclusions can be drawn.

## ACKNOWLEDGMENTS

We express our appreciation to the firing crews responsible for conducting these experiments. We also thank Aaron Honey for film processing, Robert Critchfield for expert optical assistance, Gordon Robinson for machining of fixtures, and Gerald Langner for the many jet diameter measurements. Their contributions to this work were exceptional.

This study was supported by the Department of Energy and the Department of Defense/Office of Munitions, under the Joint DoD/DOE Munitions Technology Development Program. Their support is gratefully acknowledged.

TABLE 2. COMPARISON OF  $v^2d_j/d_f$  VALUES FOR DIFFERENT EXPLOSIVES

Explosive	$v^2d_j$ (mm <sup>3</sup> /μs <sup>2</sup> )	$d_f$ (mm)	$v^2d_j/d_f$ (mm <sup>2</sup> /μs <sup>2</sup> )
Neat NM <sup>a</sup>	83.9 ± 5.7	16.4 ± 1.1	5.1
NM/DETA <sup>a</sup> 99.99/0.01 wt%	54.1 ± 5.0	9.9 ± 1.0	5.5
NM/DETA <sup>a</sup> 99.947/0.053 wt%	29.6 ± 3.5	7.0 ± 0.6	4.2
NM/DETA <sup>a</sup> 99.75/0.25 wt%	15.8 ± 0.5	3.5 ± 0.6	4.5
Comp. B <sup>b</sup>	15	4.28	3.5
Pressed TNT <sup>b</sup>	13	2.6	5.0
PBX 9404 <sup>c</sup>	4	1.18	3.4
H-6 <sup>c</sup>	16.5	~6.4	2.6
TATB <sup>c</sup>	108	6.35	17
PBX 9502 <sup>c,e</sup>	128	9.00	14.2
PBX 9502 <sup>d,e</sup>	46.1	9.00	5.12

<sup>a</sup>This study.

<sup>b</sup>References 11 and 12.

<sup>c</sup>Reference 13.

<sup>d</sup>Reference 1.

<sup>e</sup>Several differences existed between the determination of these two values: the most important was that one study<sup>13</sup> used particulated jets, whereas the other<sup>1</sup> used the jet before it had particulated.

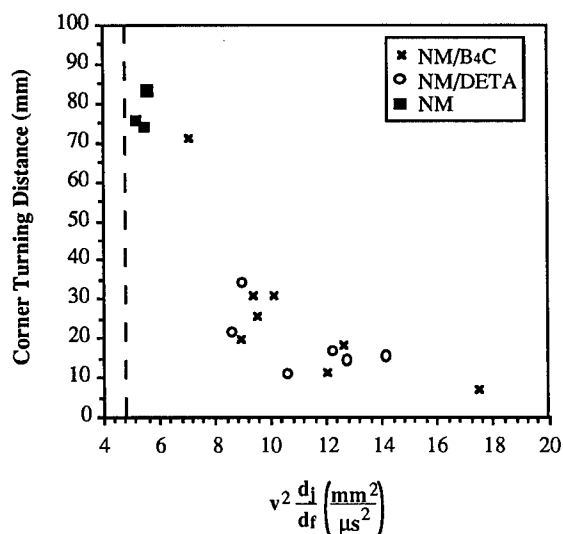


FIGURE 7. CTD AS A FUNCTION OF  $v^2 d_i / d_f$ . ALL VALUES OF  $d_f$  WERE CORRECTED TO THE CORRESPONDING SOLUTION TEMPERATURE MEASURED AT THE TIME OF THE EXPERIMENT. THE EXPERIMENTS WERE FIRED USING 2.25 IN. OF COLD-ROLLED, MILD STEEL ATTENUATION. VIPER JETS ATTENUATED BY 2.25 IN. WILL NOT DETONATE NEAT NM AT ROOM TEMPERATURE. THIS LIMIT IS INDICATED ON THE FIGURE WITH A VERTICAL DASHED LINE. THE THREE POINTS SHOWN FOR NEAT NM WERE OBTAINED WITH A JET ATTENUATED BY 2.0 IN. OF CONDITIONING PLATES

## REFERENCES

- McAfee, J. M., "Initiation of PBX 9502 by Copper Jets as Measured by Corner Turning," *DEA-AF-F.G-7304 Physics of Explosives*, Schrobhausen, FRG (July 1987).
- Asay, B. W.; McAfee, J. M.; and Ferm, E. N., "Nonsteady Detonation Driven by a Hypervelocity Jet in a Homogeneous Explosive," *Phys. Fluids*, **4** (7), 1558 (1992).
- Held, M., "Initiating Explosives, A Multiple Problem of the Physics of Explosives," *Explosivstoffe*, **5**, 121 (1968).
- Chick, M.; Bussell, T. J.; Frey, R. B.; and Bines, A., "Jet Initiation Mechanisms and Sensitivities of Covered Explosives," *Ninth Symp. (Int.) on Detonation*, pp. 1404-1415 (1989).
- Engelke, R., "Effect of a Chemical Inhomogeneity on Steady-State Detonation Velocity," *Phys. Fluids* **23**(5), 875 (1980).
- Engelke, R. and Bdzil, J. B., "A Study of the Steady-State Reaction-Zone Structure of a Homogeneous and a Heterogeneous Explosive," *Phys. Fluids*, **26**, (5), 1210 (1983).
- McAfee, J. M., "Accurate Diameter Measurement of Explosively Formed Metal Jets and Effective X-ray Source Size," *Proc. 1989 Flash Radiography Topical Symposium*, Welches, Oregon, 249 (1989).
- Engelke, R., "Effect of the Number Density of Heterogeneities on the Critical Diameter of Condensed Explosives," *Phys. Fluids*, **26**(9), 2420 (1983).
- Dobratz, B. N., *LLNL Explosives Handbook: Properties of Chemical Explosives and Explosive Simulants*, 8-31 (1982).
- Belyaev, A. F. and Kurbangalina, R. Kh., "Effect of Initial Temperature on Critical Diameter of Nitroglycerin and Trinitrotoluene," *Russ. J. Phys. Chem.*, **34**(3), pp. 285-289, March 1960.
- Chick, M. C. and Bussell, T. J., "The Effect of Minimum Detonation Diameter on The Mechanism of Jet Initiation of Bare Explosives," *J. Appl. Phys.*, **63**(9), 4761 (1988).
- Chick, M. C.; Macintyre, I. B.; and Frey, R. B., "The Jet Initiation of Solid Explosives," *Eighth Symp. (Int.) on Detonation*, pp. 318-327 (1985).
- Held, M., "Initiation Phenomena with Shaped Charge Jets," *Ninth Symp. (Int.) on Detonation*, pp. 1416-1426 (1989).
- Cox, M. and Campbell, A. W., "Corner-Turning in TATB," *Seventh Symp. (Int.) on Detonation*, pp. 624-633 (1981).
- Sheffield, S. A.; Engelke, R.; and Alcon, R. R., "In-Situ Gauging Experiments in Homogeneous Initiation Experiments", Group M-9 Quarterly Report, M-9-QR-89-2, pp. 43-45, August 4, 1989.

## DISCUSSION

M. HELD

DASA, 86523 Schrobhausen, Germany

(1) What were the dimensions of your acceptor charge?

(2) How did you measure the reaction level (detonation, partial detonation, deflagration, etc.)?

**REPLY BY BLAINE ASAY:**

(1) Two different containers were used. One was a glass box that was 4 x 4 x 6 inches, and the other was a polyethylene cylinder 3.5 inches in diameter and 6 inches deep.

(2) To determine the v<sup>2</sup>d criterion, only a "go" or "no-go" result was desired. This was determined by examining the witness plate after the experiment. Other diagnostics described in the paper were used to determine corner-turning distance and other aspects of the reaction.

**DISCUSSION**

**HAROLD GRYPING**

Gryping Energetics Science Co., San Antonio, Texas

How are the shaped charge jets kept uniform? Are the percentages of theoretical kept at the same value for the different explosive charges?

**REPLY BY BLAINE ASAY:**

We used the Viper shaped charge in the as-received condition. The charges were center-initiated with a machined adapter to assure reproducibility.

**DISCUSSION**

**ALAIN L. KERDRAON**

GIAT INDUSTRIES, BOURGES, FRANCE

What is your feeling if we were to use aluminum as a shaped charge liner instead of copper?

**REPLY BY BLAINE ASAY:**

Penetration velocity and shock strength are functions of the density and impedance of the jet. Thus we would expect different behavior of the explosive given two jets with the same initial velocity but having different compositions. There may also be an additional difference resulting from the enhanced reaction occurring from turbulent mixing of the aluminum with the explosive.

## FRAGMENT IMPACT INITIATION OF CAST PBXs IN RELATION WITH SHOCK SENSITIVITY TESTS

M. QUIDOT - S. HAMAIDE - J. GROUX  
P. GIMENEZ - J. ISLER

*S.N.P.E.*

Centre de Recherches du Bouchet - BP 2  
91710 VERT-LE-PETIT  
FRANCE

In this study, we have analyzed experimental results of fragment impact initiation on RDX, HMX and NTO based cast PBXs with inert and energetic binders and some other energetic materials. Two fragment impact results are considered : the heavy fragment (250 g steel sphere) performed at DCN Lorient (GERBAM) and light fragments (14 g steel cubes). The critical velocities for shock to detonation transition at these fragment impact tests are correlated with classical laboratory shock sensitivity tests, i.e. gap-test, flyer plate impact test and wedge-test. The results indicate an overall good correlation for cast PBXs but we found that the sensitivity order may be reversed for light fragment impact with respect to heavy fragment impact and laboratory tests. Numerical simulations with reactive flow modeling are in agreement with experimental results.

### INTRODUCTION

Hazard assessment methods for high explosives subjected to fragment impact are of great interest in developing insensitive munitions. The impact of fragments or projectiles on a warhead may induce its accidental detonation by different ways.

Heavy fragments impacting with high velocity will generate a shock pressure sufficient to induce a prompt shock to detonation transition (SDT). Less hazardous fragments or medium caliber projectiles, leading to a shock pressure weak enough to avoid an SDT reaction, will penetrate both the case and the high explosive loading and highly damage it just before ignition. The burning of the damaged high explosive may lead to a

deflagration to detonation transition (DDT).

Before coming to the main topic of this paper, it is useful to explain how cast PBXs behave when the impact will not directly induce an SDT reaction. As presented in previous publications<sup>1,2</sup>, the DDT process involves both damage during the loading (cracks, fragmentation) in relation with the HE dynamic mechanical properties, and burning with a very high gas production rate.

Many works performed to study the response of cast PBXs to bullet impact have shown that due to their good mechanical properties and moderate burning rate, the risk of DDT is very low for such energetic materials. Since the same event sequence occurs for

fragment impact, the risk of DDT is also very low. Then, the main responses of cast PBXs charges to fragment impact are detonation by an SDT process (and partial detonation close to the SDT threshold) and no-detonation which is identified by a weak overpressure blast, recovered case in large fragments or even complete and sometimes recovered fragments of HE.

In this paper we analyse experimental results of a heavy fragment impact test for RDX, HMX and NTO based cast PBXs as well as cast TNT and Hexol (Comp B) and two energetic propellants, in comparison to results of shock sensitivity (gap-test and flyer-plate impact test). The experimental light fragments impact results for two cast PBXs (ORA86 and B3108) show that the sensitivity order is reversed with respect to heavy fragment impact test. The last section presents, for these two explosives, fragment impact modeling with a LEE-TARVER<sup>3</sup> model based on wedge-test and pressure measurements which explain this behavior.

## CORRELATION IN LABORATORY SHOCK SENSITIVITY TESTS

Several laboratory tests are currently used to evaluate the shock sensitivity of energetic materials. It is interesting to determine what is similar in these different tests, and how the differences can be interpreted. Some such work has already been done<sup>4,5</sup> but disregarding the pressure range. On another hand, analysis of particle size effect<sup>6,7</sup> has shown that sensitivity is the sum of two terms related to ignition sensitivity and reaction rate which have their own dependance on shock pressure.

Then, the shock sensitivity tests used at SNPE (gap-test, flyer plate impact test and wedge-test) are analyzed here only in the low pressure regime, the term low being relative to the shock sensitivity of the energetic material considered.

## Shock Sensitivity Tests

The French LSGT uses an RDX/Wax-95/5 donor (40 mm diameter) and a test sample (diameter 40 mm, length 200 mm) confined by a 4 mm thick steel tube. The result is the critical barrier thickness (0.19 mm cellulose acetate cards) for a no detonation propagation between the donor and the explosive sample. This test has been calibrated by both pressure measurements for different barrier thickness and hydrocode simulations using a JWL EOS for the donor. The Hugoniot of the PBXs have been determined by both wedge-test results and light gas gun impact experiments at lower shock pressure. The pressure threshold is then calculated from the critical barrier thickness by a 1-D impedance matching method.

The flyer plate impact test (FPI) is used to determine the critical energy for shock initiation of explosives. The shock wave is generated by an explosively driven flyer plate impacting a 63 mm diameter, 60 mm long sample. The experimental result is identified by the transit time measurement and the fragmentation of a rear steel support plate. The critical energy as a function of shock time duration is obtained by varying the plate velocity and thickness. Since the number of shots is restricted and the response is of the go-no go type, the critical energy determination is not very accurate. In this study, we have used the critical energy corresponding to about a 2  $\mu$ s time duration.

The experimental arrangement for the wedge-test used at SNPE has been described previously<sup>8</sup>. The wedge-test gives space time diagrams and run distance to detonation as a function of the impact shock pressure. In order to compare wedge-test results to the other tests, we used here the pressure corresponding to a 25 mm run distance to detonation.

## Results

The energetic materials studied are listed in Table 1. For comparison, two melt-cast HE, TNT and Hexol (Comp B) and two energetic propellants XLDB1 and XLDB2 are also reported. Figure 1 shows the correlation between the three sensitivity tests. For each composition, the pressure in the FPI,  $P_T$ , and the pressure in the wedge-test,  $P_X$ , are normalized by the pressure threshold in gap-test,  $P_g$ ; the experimental values  $P_X$  and  $P_T$  for TNT and Hexol are from references 9 and 10. Figure 1 shows that all energetic material are close, except TNT on account of the great sensitivity to pulse

duration of this HE.

As we recall above, the sensitivity of energetic material depends on two terms. In this way, the wedge-test is not exactly a sensitivity test because the run to detonation depends as much on bulk reaction rate as on the ignition rate. Figure 1 shows this interpretation since we find a logical order for the ratio  $P_X/P_T$  for TNT, TNT/RDX, RDX/IB, HMX/IB and HMX/EB compositions, the B2214 composition being particular due to its high insensitivity and large critical diameter<sup>11</sup>. Nevertheless other explosive data and more accurate critical energy would be useful to support this analysis.

TABLE 1. DETONATION VELOCITY AND SHOCK HUGONIOT DATA

NAME	COMPOSITION	DENSITY g/cm <sup>3</sup>	DETONATION VELOCITY (m/s)	HUGONIOT		
				c (m/s)	s	REFERENCE
ORA86A	HMX/IB	1.71	8380	2356	2.18	This work
B2203	RDX/IB	1.51	7630	2035	2.26	This work
B2214	HMX/NT0/IB	1.63	7420	2300	2.10	Estimate
B2220	RDX/IB	1.55	7870	2427	1.78	This work
B3108	HMX/AL/EB	1.82	7760	2437	1.86	This work
TNT	TNT	1.60	6820	2570	1.88	(9)
HEXOL	RDX/TNT/60/40	1.72	7910	2710	1.86	(9)
XLDB1	HMX/PA/AL/EB	1.85	7920	2241	2.13	This work
XLDB2	HMX/PA/AL/EB	1.77	8400*	2300	2.10	Estimate

\* : BKW calculation

IB : Inert binder

EB : Energetic binder

c, s : Parameters for the classical shock velocity / particle velocity relation  $U = c + s u$

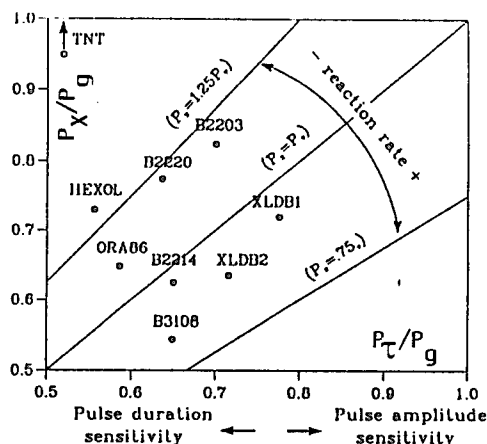


**FIGURE 1. CORRELATION IN SHOCK SENSITIVITY TESTS :  $P_g$  LSGT PRESSURE,  $P_T$  FPI PRESSURE ( $\tau \approx 2 \mu s$ ),  $P_X$  WT PRESSURE (25 mm run to detonation)**

### HEAVY FRAGMENT IMPACT TEST

This test (referred to as Spherical Projectile Impact, SPI) performed at DCN/Lorient (GERBAM), has been described

previously<sup>12</sup>. The experimental results are given in Table 2 ; the two velocities given are for a non detonation and detonation. Numerical simulations for the calculation of the shock pressure transmitted to the energetic material were performed with DYNA2D<sup>13</sup>. The method has been described in reference 2 (the slight differences in the values reported here take into account new additional experimental data for Hugoniot of energetic materials and LSGT calibration). The calculated pressure threshold in the SPI test is compared in Table 2 with the LSGT and FPI threshold.

For all materials, except for TNT, the critical pressure for SDT at the heavy fragment impact test is between LSGT and FPI pressure threshold. This result can be explained by the different shapes of the shock waves in these tests. The shock wave is divergent but quasi-sustained (2 to 3  $\mu s$ ) in the SPI test whereas it is divergent and unsustained in the LSGT test and not divergent and sustained in the FPI test. As seen above, the result for TNT corroborates its great sensitivity to shock duration.

**TABLE 2. PRESSURE THRESHOLD IN GAP-TEST (LSGT), FLYER PLATE IMPACT TEST (FPI) AND HEAVY FRAGMENT IMPACT TEST (SPI)**

NAME	LSGT		FPI		SPI		SPI/LSGT $P_s/P_g$	SPI/FPI $P_s/P_T$
	cards	$P_g$ (GPa)	$E_c$ (J/cm <sup>2</sup> )	$P_T$ (GPa)	Velocity (m/s)	$P_s$ (GPa)		
ORA86A	150	6.0	400	3.5	1772-1781	4.1	0.7	1.2
B2203	215	3.1	200	2.1	1363-1433	2.2-2.4	0.7	1.1
B2214A	25	17.0	3200	12.0	> 2373	> 6.3	> 0.4	> 0.5
B2220	150	5.5	450	3.5	1761-1771	3.7	0.7	1.1
B3108	140	6.6	550	4.3	1967-2056	5.1-5.5	0.8	1.2
TNT	135	6.6	420 *	3.4	1300-1350	2.4-2.6	0.4	0.7
HEXOL	150	3.7	150 *	2.1	$\approx$ 1150	2.0	0.5	1.0
XLDB1	150	6.1	650	4.7	2100-2180	5.8-6.2	1.0	1.3
XLDB2	155	5.7	525	4.1	1812-1905	4.3-4.7	0.8	1.1

\* : From reference (10)

## LIGHT FRAGMENT IMPACT

An explosive launcher has been designed to launch 14 g steel cubic fragments at a velocity of 1750 m/s. Four fragments impact a target which is a cylinder, diameter 125 mm, length 90 mm, with a 20 mm thick steel case and a steel cover plate of variable thickness. The minimum plate to ensure a non-detonation is determined for the explosive studied.

The experimental results are given in Table 3 for three cast PBXs. The main result is that the sensitivity order for ORA86A and B3108 is reversed with respect to the heavy fragment impact test and laboratory sensitivity tests. The difference between heavy and light fragment impact is the pressure for initiation ( $\approx 50$  kbar to more than 100 kbar) in relation to the time duration of the shock wave sensitivity tests, this result accounts for the difference of sensitivity of explosives in the low and high pressure regimes.

The bulk reaction rate (and perhaps the energy released) is greater for the composition with energetic binder but the ignition term ("hot spot" reaction) is lower. Reactive flow modeling has been performed to investigate this behavior.

TABLE 3. EXPERIMENTAL COVER THICKNESS THRESHOLD (mm) IN LIGHT FRAGMENTS IMPACT TEST (IMPACT VELOCITY 1750 m/s)

EXPLOSIVE	COVER THICKNESS
ORA 86A	6.5 - 7.0
B 2214	< 4.0
B 3108	8.0 - 9.0

## REACTIVE FLOW MODELING

We use a LEE-TARVER<sup>3</sup> model implemented in DYNA2D<sup>13</sup>. The unreacted explosive and the reaction products are both described by a JWL EOS of the form

$$P = A e^{-R_1 V} + B e^{-R_2 V} + \frac{\omega C_v T}{V} \quad (1)$$

where  $P$ ,  $V$  and  $T$  are pressure, relative volume and temperature. The coefficients  $A$ ,  $B$ ,  $R_1$ ,  $R_2$ ,  $\omega$  are based on the cylinder test for the reaction products and on the Hugoniot for the unreacted explosive (Table 1). A pressure and temperature equilibrium between the two phases is assumed and the reaction rate law is of the form :

$$\frac{\partial F}{\partial t} = \frac{I(F_m - F)(\rho/\rho_0 - 1)^m + G(1 - F)^{x_1} F^{x_2} p^n}{\quad} \quad (2)$$

where  $F$  is the mass fraction reacted.

The ORA 86A model has been described previously<sup>8</sup> and used in various problems<sup>2,8,14</sup>. The B3108<sup>15</sup> model is based on wedge-test space-time diagrams and pressure measurements in light gas gun experiments. Comparison of experimental and numerical results are shown for space time diagrams for 6.1 GPa and 10.6 GPa impact shock pressures (Figure 2) and pressure at 0, 3 and 6 mm distance for a 4.3 GPa impact shock pressure (Figure 3). Lastly, the B2214 model is based on an heuristic method<sup>16</sup> owing to its very high insensitivity.



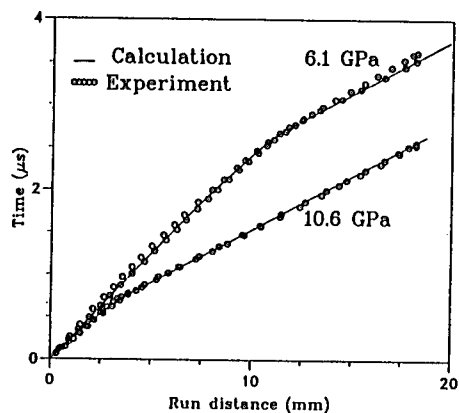


**FIGURE 2. COMPARISON OF CALCULATION AND EXPERIMENT (right and left slant face) FOR B3108 IN DOUBLE WEDGE-TEST FOR 6.1 GPa AND 10.6 GPa IMPACT SHOCK PRESSURE**

The reactive models have been used to investigate the shock sensitivity of ORA 86A and B3108 in laboratory tests. The "pop-plots" of these two compositions are very similar but the critical energies are different. As example, Figure 4 shows the calculated SDT threshold in FPI test for B3108. The gap-test have also been calculated for ORA 86A and B3108 and the results are given in Table 4. Figure 5 shows the numerical simulation of the gap-test with 130 and 140 cards for B3108.

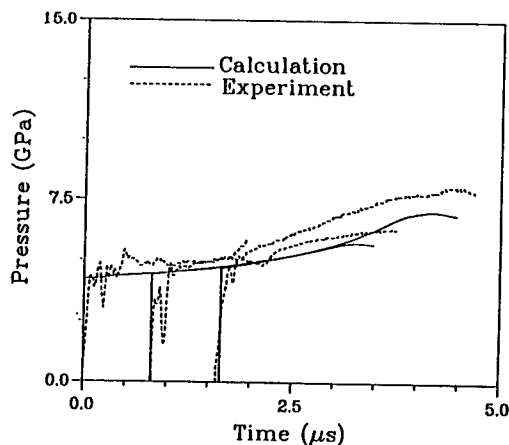


**FIGURE 3. PRESSURE IN B3108 AT 0, 3 AND 6 mm DISTANCE FOR A 4.3 GPa IMPACT SHOCK PRESSURE**

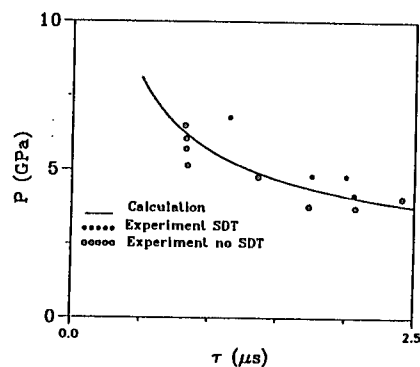
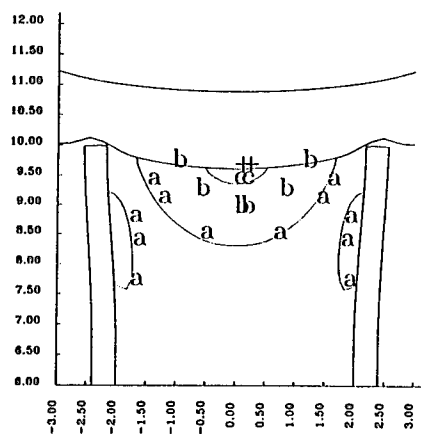
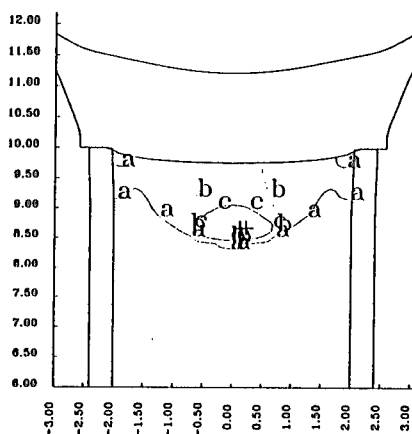


**FIGURE 4. FLYER PLATE IMPACT TEST - PRESSURE VS TIME DURATION**



a = 0.05 - b = 0.1 - c = 0.15 - max = 0.17 at t = 35 μs)

A) 140 cards No Detonation



a = 0.0 - b = 0.25 - c = 0.5 - max = 1.0 at t = 29 μs)

B) 130 cards Detonation

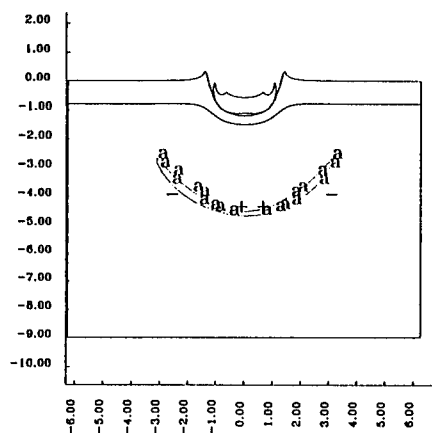
**FIGURE 5. B3108 GAP-TEST CALCULATIONS. CONTOURS OF MASS FRACTION REACTED**

The capability of 2D and 3D reactive flow modeling to predict the velocity threshold for SDT in the heavy fragment impact test has been demonstrated previously<sup>2,14</sup>. The comparison of experimental and numerical results are given Table 4. Since the multiple fragments impact is not experimentally well known, an accurate numerical simulation of the light fragments impact test is impossible. Nevertheless, numerical simulations have been performed to check the

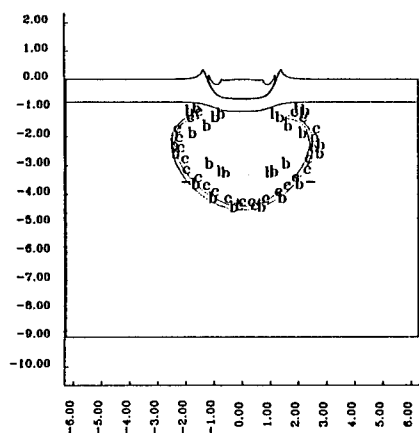
capability of the reactive model to reproduce qualitatively the reverse sensitivity order of B3108 and ORA 86A. The numerical modeling uses a one cylinder fragment impact. The Figure 6 shows the no detonation and detonation (with a classical retonation phenomena) of ORA 86A for a 8 mm plate cover thickness. Numerical and experimental results are summarized Table 4.

TABLE 4. COMPARISON OF EXPERIMENTAL AND NUMERICAL RESULTS IN GAP-TEST, HEAVY FRAGMENT IMPACT TEST AND LIGHT FRAGMENTS IMPACT TEST

TEST		EXPLOSIVE		
		ORA 86A	B2214	B3108
Gap-test (cards)	Experiment	150	25	140
	Calculation	150		140
Heavy fragment (velocity m/s)	Experiment	1770	> 2273	1956
	Calculation	1700	3200	1875
Light fragment (cover plate thickness mm)	Experiment	6.5 - 7.0	< 4.0	8.0 - 9.0
	Calculation	7.5	ND for 0.0	8.4



V = 1800 m/s (t = 12.5  $\mu$ s)



V = 1850 m/s (t = 7.5  $\mu$ s)

FIGURE 6. ORA 86A LIGHT FRAGMENT IMPACT. CONTOURS OF PRESSURE  
(a = 0.5 GPa - b = 5 GPa - c = 20 GPa)

Different models have been developed for the initiation of explosives by fragment impact<sup>17,18,19,20</sup>. For the steel fragment considered here, we find that the reactive flow calculations agree with a Rindner formula which is of the form :

$$V^2 = V_0^2(d) \frac{e^{\alpha t/d}}{1 + \beta t/d} \quad (3)$$

where  $V$  is the threshold velocity,  $V_0(d)$  the threshold velocity for bare explosive,  $t$  the covering plate thickness,  $d$  the diameter of the cylindrical fragment and  $\alpha, \beta$  two constants,  $\alpha = 2.66$ ,  $\beta = 1.64$  from the original Rindner formula. The Figure 7 shows that the results obtained for ORA 86A and B3108 are close to this formula.

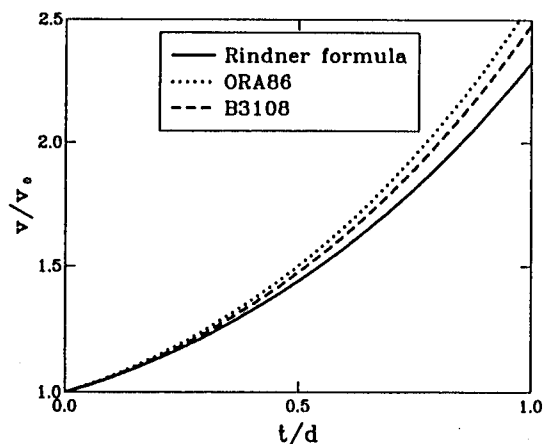


FIGURE 7. NORMALIZED VELOCITY THRESHOLD VS NORMALIZED COVER PLATE THICKNESS (Eq. 3)

## CONCLUSIONS

The experimental results presented in this paper show the relation between shock sensitivity tests (gap-test, flyer plate impact test and wedge-test) and an analysis in terms of ignition and bulk reaction rate. The different weight of these two terms in low and high pressure regimes is an

explanation for the experimental reversed shock sensitivity order in heavy and light fragments impact observed for two compositions.

Reactive flow modeling with reaction rate based on trajectories in wedge-test and pressure measurements in light gas gun experiments is in accordance with experimental results and supports this analysis. Nevertheless, further experimental and numerical work should be done to better characterize explosives in the high pressure regime and in multiple fragment impact.

## REFERENCES

1. Isler J., "Contribution du mode de combustion des explosifs aux processus de TDD", *19th International Annual Conference of ICT*, 1988.
2. Isler J. ; Quidot M., "Evaluation du risque de transition des chargements en explosifs", *22nd International Conference of ICT*, 1991.
3. Lee E.L. ; Tarver C.M., *Phys. Fluids*, vol. 23, 1980, p. 2362.
4. Weston A.M. ; Kincaid J.F. ; James E. ; Lee E.L. ; Green L.G. ; Walton J., "Correlation of the results of shock initiation tests" in *proceedings of the Seventh International Symposium on Detonation*, Annapolis, 1981, p. 887
5. Lundstrom E., "A new approach to shock sensitivity testing of energetic materials", JANNAF, CPIA, Pub. 509, 1989,
6. Price D, "Effect of particle size on the shock sensitivity of pure porous HE", NSW-TR-86-336, 1986.
7. Moulard H. ; Kury J. ; Delclos A., "The effect of RDX particle size on the shock sensitivity of cast PBX formulation", in *proceedings of the Eight Symposium International on Detonation*, 1985, pp 903-913.

8. Quidot M. ; Groux J., "Reactive modeling in shock initiation of heterogeneous explosives", in *proceedings of the Ninth Symposium International on Detonation*, Portland, 1989, pp 1217 à 1223.
9. Gibbs ; Popolato, LASL Explosive property data
10. Walker F.E. ; Wasley R.J., *Propellants, Explosives Pyrotechnics*, vol. 1, pp 73-80, 1976.
11. Becuwe A. ; Delclos A., "Use of oxynitrotriazole to prepare an insensitive high explosive", in *proceedings of the Ninth Symposium International on Detonation*, Portland, 1989, pp 1008-1013
12. Artaud A. ; Saliou O., "Safety specifications and criteria concerning munitions intended for the French Navy", *AGARD Conference on Insensitive Munitions*, Bonn 1991.
13. Hallquist J.O., User's manual for DYNA2D, LLNL 18 756, 1984.
14. Nouguez B. ; Quidot M. ; Gimenez P. ; Derrien J.C., "Phénomène de détonation par influence : approche numérique et expérimentale", *AGARD Conference on Insensitive Munitions*, BONN 1991.
15. Quidot M., "Modélisation des régimes transitoires de détonation", SNPE Report CR 8/92/CRB/S/TRE, 1992
16. Quidot M., "Modelisation de l'amorçage par choc des explosifs. Application à l'Octorane 86A et à la composition B 2214", SNPE Report 18/89/CRB/S/TRE, 1990.
17. Rindner R.M., "Response of explosive to fragment impact", *Annals of New York Academy of Sciences*, vol 152, AR 1, p 250, 1962.
18. Green L., "Shock initiation of explosives by the impact of small diameter cylindrical projectiles", in *proceedings of the Eight Symposium International on Detonation*, Albuquerque, pp 1091-1101, 1985.
19. Roslund L.A. ; Liddiard F.P., "Fragment impact sensitivity of explosives, NSWG, TR 89-184.
20. Cook M.P. ; Haskins P.J. ; James H.R., "Projectile impact initiation of explosive charges", in *proceedings of the Ninth Symposium International on Detonation*, Portland, 1989, pp 1441-1450

---

#### DISCUSSION

HAROLD J GRYTING

Gryting Energetics Science Company,  
San Antonio, Texas

It is realized that utmost care is taken by your agency in preparing your product. The question is: when the cast PBX is examined for possible initiation, how are the composition, density, and shrinkage kept constant for each specimen of the cast PBX being investigated:

#### REPLY BY JEAN ISLER AND ALAIN BECUWE:

By nature, cast PBXs are homogeneous materials with uniform composition and density. In addition, the specimens for a kind of characterization are coming from a single batch. Usually quality of the samples is checked by X-ray.

# A SHOCK-TO-DETONATION TRANSITION MODEL FOR HIGH-ENERGY ROCKET PROPELLANT APPLIED TO PREDICT JET INITIATION THRESHOLD\*

D. BERGUES; G. BAUDIN; H. TRUMEL  
DGA / Centre d'Etudes de Gramat (CEG)  
46500 Gramat - France

(\*) Work supported by the French Ministry of Defense (DGA / DME / STPE)

In this article, experiments and analytical methods used for standard explosives have been adapted to characterize the decomposition process and shock-to-detonation transition (SDT) of an HMX-rich rocket propellant. The chemical kinetic model thus validated is used to predict the  $V^2d$  critical detonation threshold of this propellant when attacked by a shaped charge jet. This approach is validated by a comparison between experimental results and calculations.

## INTRODUCTION

The use of high-energy rocket propellants containing increasing amounts of HMX has given rise to extensive studies into how these products operate under detonation<sup>1</sup> and their vulnerability to different types of attack, such as those due to shaped charge jets or kinetic projectiles. The phenomena leading to the detonation of this rocket propellant can only be modelled if their decomposition kinetics are thoroughly understood.

## EXPERIMENTAL STUDY OF SDT

The rocket propellant studied was not a conventional product. In addition to the usual constituents found in propellants, such as ammonium perchlorate (AP) and aluminum, it also contained a high percentage of HMX and a nitroglycerin (NG)-based active binder.

The plane shock generator used for the SDT study was the "Arès" launcher. This is a 98 mm-borehole single-stage launcher tube, with a length of 11 m. Depending on the required velocity, it can be used either in a gun propellant version (800 → 2300 m/s), or in a compressed helium or air version (100 → 1200 m/s). In the standard configuration, the impact of the projectile on the target occurred in an evacuated

chamber. The target was composed of two disks of test material of varying thickness, between which a manganin gage was inserted. This instrumentation was completed by self-shorting pins, used to trigger the instruments, measure the velocity of the projectile and check the tilt at the impact (typically less than 1.5 mrad).

First of all, this lagrangian pressure measurement technique, generally used with explosives<sup>2</sup>, was applied to the propellant. This direct transfer was a failure because the signals obtained were inconsistent. Firing conditions were as follows: Duralumin projectile, 1200 m/s impact velocity and 5 mm gage insertion depth.

A typical signal is shown in Figure 1, revealing the following phenomena:

- (i) the initial shock level  $P_{sh}$  recorded (approx. 8 GPa) was different from that actually applied (approx. 6 GPa);
- (ii) the presence of an "electromagnetic precursor" which appeared at the moment when the shock penetrated the sample.

Experiments conducted at the Centre d'Etudes de Gramat more than 10 years ago<sup>3,4</sup> showed that with some macromolecular materials subjected to shock, an electromagnetic interference occurred on the pressure signals recorded using manganin gages. Probably due

to shock polarization, this interference occurs when the shock wave penetrates the material and distorts the incident pressure level reading on the gage. The solution used by these authors<sup>3,4</sup> for the elimination of this precursor signal was then applied to our case. This involves protecting the gage with a metal sheet, connected to ground and glued on the side of the gage receiving the incident shock.

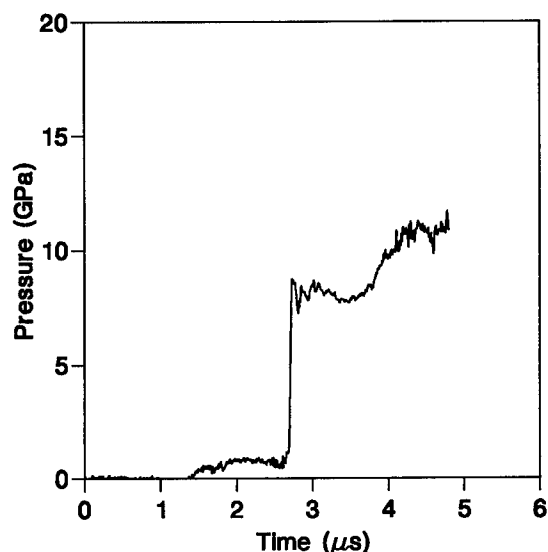


FIGURE 1. INCORRECT EXPERIMENTAL PRESSURE SIGNAL IN THE PROPELLANT -  $P_{Sh}=6$  GPa;  $h=5$  mm

In spite of this precaution, the signal obtained was unsatisfactory. By listing the differences liable to explain this phenomena, it was found that one of the major differences between this type of rocket propellant and conventional ones is that in the case studied, one of the main constituents of the binder was nitroglycerin. Given its exceptional migrational characteristics<sup>5,6</sup>, this constituent could be concentrated at the interfaces, notably in the polyurethane glue used for assembly. This phenomenon was no doubt enhanced by the fact that the experimental set-up was placed in primary vacuum in the target holder of the launcher for several hours.

In order to assess the effects of vacuum conditions, small samples of propellant were therefore subjected to thermogravimetric analysis at a temperature of 30°C in a vacuum of 1 mbar. After periods of 15 h and 48 h, 41 % and 82 % of nitrated oil was extracted from the propellant binder (see Figure 2). These results showed that the propellant must be stored at ambient pressure during SDT firings.

For all the other experiments, a consumable Duralumin target holder was used. This made it possible (Figure 3) to evacuate the launcher tube while keeping the experimental set-up in the open air. The symmetrical impact created between the projectile and the transmitter sheet, made of the same material, induced a shock in the propellant which was identical to that created by direct impact.

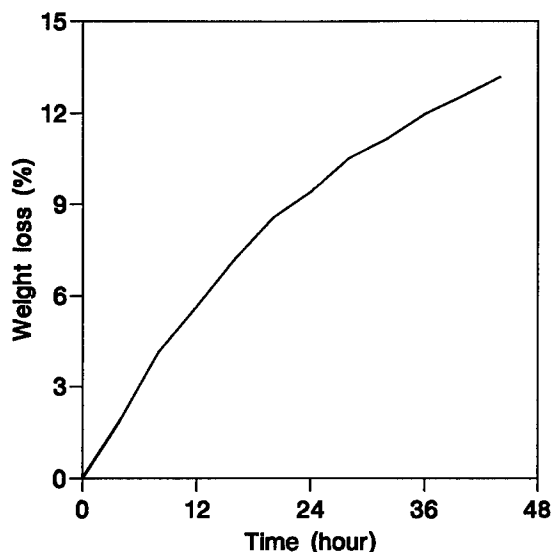


FIGURE 2. PROPELLANT WEIGHT LOSS IN A VACUUM OF 1 hPa AT 30°C

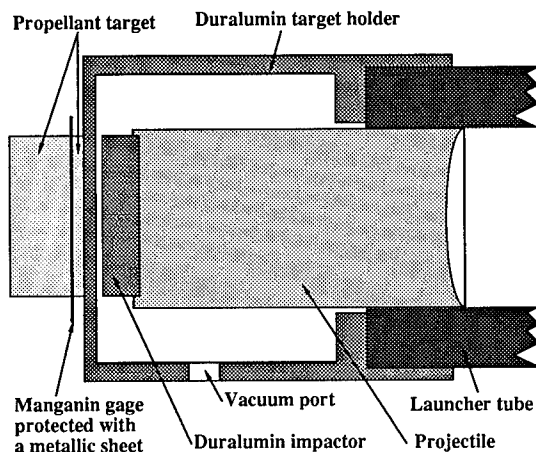


FIGURE 3. TARGET HOLDER DEVICE

The use of a consumable target holder in conjunction with a metal protective sheet on the gage yielded correct experimental signals. The presence of the metal protective sheet (20  $\mu$ m) may, however, reduce the accuracy (usually 5%) of the readings recorded by manganin gage.

Three  $P_{Sh}$  pressure levels were tested. These were approximately 5, 6 and 8 GPa. The corresponding projectile velocities were 1000, 1200 and 1500 m/s. The penetration depths tested were: 10 mm at 5 GPa, 5 mm at 8 GPa and 2, 5, 10 mm at 6 GPa. Pressure signals are given in Figures 4, 5 and 6.

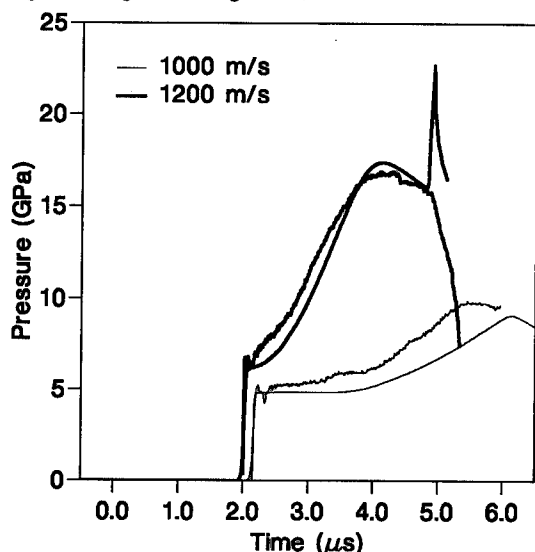


FIGURE 4. PRESSURE SIGNALS IN PROPELLANT (EXPERIMENT AND CALCULATION) -  $P_{Sh}=5$  AND 6 GPa;  $h=10$  mm

### PROPELLANT REACTIVITY MODELLING

All the experimental results obtained at the CEG, added to values obtained by the SNPE / CRB, were used to construct the propellant reactivity kinetic model. This is a hot-spots initiation model which also takes into account the effects resulting from the slow reactions of aluminum.

The decomposition of the rocket propellant is assumed to occur in 4 phases:

- (1) initiation of reactions in the form of hot-spots in the most reactive constituent (NG),
- (2) decomposition of HMX, AP and the remainder of the binder,
- (3) heating of aluminum particles\* through the absorption of some of the thermal energy released by decomposition products,
- (4) oxidation of aluminum heated above ignition temperature, releasing a large quantity of energy.

This article focusses on the first two phases, as these are the only ones which need to be considered in modelling the shock-to-detonation transition of the propellant.

Since the effects of aluminum burning are only important in studying the end effects of detonation, readers interested in this aspect are invited to refer to the article of Baudin and Bergues <sup>7</sup> in this symposium, which focusses on the choice and study of the reactive characteristics of aluminum with oxidizing gaseous products and heat transfer aspects.

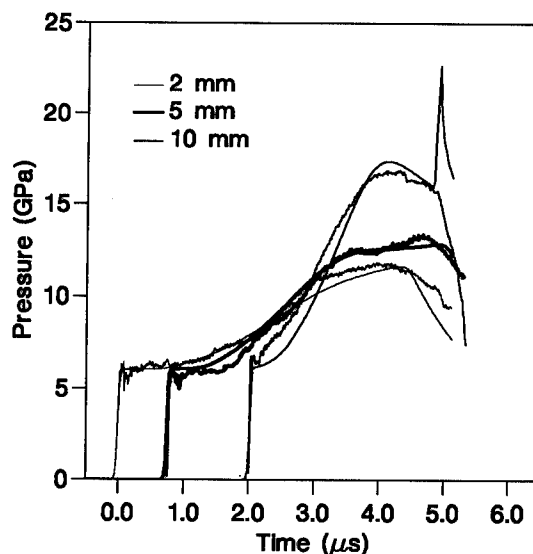


FIGURE 5. PRESSURE SIGNALS IN PROPELLANT (EXPERIMENT AND CALCULATION) -  $P_{Sh}=6$  GPa;  $h=2, 5$  et 10 mm

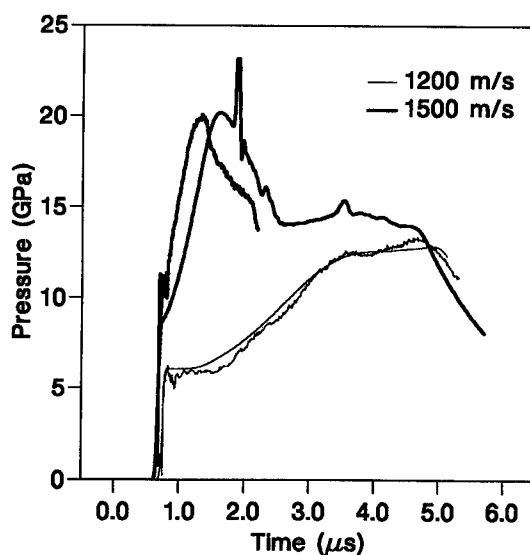


FIGURE 6. PRESSURE SIGNALS IN PROPELLANT (EXPERIMENT AND CALCULATION) -  $P_{Sh}=6$  et 8 GPa;  $h=5$  mm

The weight fractions of the nitroglycerin (NG) and aluminum (Al) contained in the propellant are termed

$\mu$  and  $\psi$ . The remainder, with a weight fraction of  $1-\mu-\psi$ , will be termed Re.

The comparison of adiabatic explosion times <sup>8</sup> of different explosive constituents (see Figure 7) shows that nitroglycerin is a far more reactive product than HMX. In the phase (1) of the reaction model selected, the reactions around the hot-spots therefore develop primarily in the nitroglycerin. Then, they propagate to the remainder of the propellant Re when a sufficient fraction of nitroglycerin has decomposed.

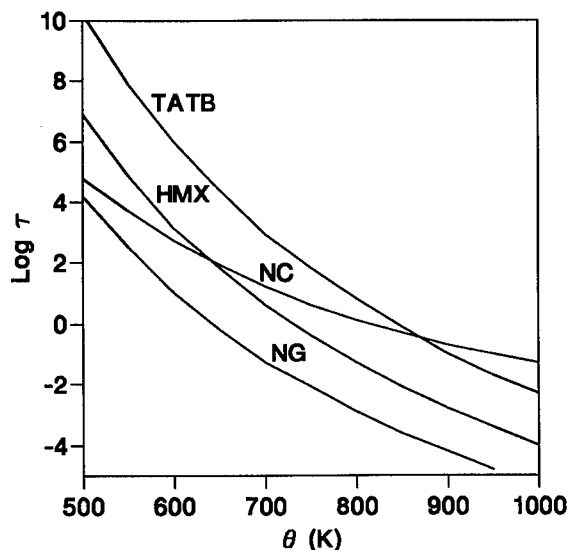
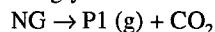


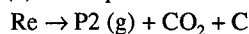
FIGURE 7. ADIABATIC EXPLOSION TIME ACCORDING TO HOT-SPOTS TEMPERATURE FOR DIFFERENT EXPLOSIVES

The phases considered are:

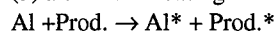
(1) decomposition of the weight fraction  $\mu$  of nitroglycerin



(2) decomposition of the propellant fraction  $1-\mu-\psi$

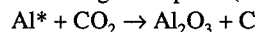


(3) aluminum heating



where  $\text{Prod.} = [\text{P1(g)} + \text{P2(g)} + \text{CO}_2 + \text{C}]$ ,  $\text{Al}^*$  is the heated aluminum and  $\text{Prod}^*$  are the cooled products

(4) oxidation of aluminum when its temperature reaches ignition point (alumina melting temperature)



P1 and P2 represent the reaction products of NG and Re, without the carbon dioxide and the solid carbon.

Having balanced the weight of the chemical reactions (1), (2) and (4), the method generally used in chemical kinetics makes it possible to express reaction speeds in

terms of the variation in weight concentrations <sup>7</sup>.

These are given for phases (1) and (2) by:

$$\begin{aligned} \frac{d[\text{NG}]}{dt} &= -\frac{[\text{NG}]^{A1}}{\tau_{\text{NG}}} \\ \frac{d[\text{P1}]}{dt} &= -0.418 \frac{d[\text{NG}]}{\tau_{\text{NG}}} \\ \frac{d[\text{Re}]}{dt} &= -\frac{[\text{Re}]^{A2}}{\tau_{\text{Re}}} \\ \frac{d[\text{P2}]}{dt} &= -m_3 \frac{d[\text{Re}]}{dt} \end{aligned}$$

where  $m_3$  is the weight of all the reaction products from 1 kg of Re with the exception of  $\text{CO}_2$  and C.

For phases (3) and (4), refer to <sup>7</sup>.

If the reacted weight fractions of aluminum, nitroglycerin and the rest of the propellant are termed  $\alpha$ ,  $f$  and  $g$ , the total weight fraction  $r$  of the reacted propellant is expressed as follows:

$$r = (1-\psi)\lambda + \psi\alpha$$

where

$$\lambda = \left( \frac{\mu}{1-\psi} \right) f + \left( 1 - \frac{\mu}{1-\psi} \right) g$$

The concentrations  $[\text{NG}]$  and  $[\text{Re}]$  are thus written:

$$[\text{NG}] = \mu(1-f)$$

$$[\text{Re}] = (1-\mu-\psi)(1-g)$$

For the concentration rates, we find:

$$\begin{aligned} \dot{f} = \frac{df}{dt} &= \frac{(1-f)^{A1}}{\tau_{\text{NG}}} \mu^{A1-1} \\ \dot{g} = \frac{dg}{dt} &= \frac{(1-g)^{A2}}{\tau_{\text{Re}}} (1-\mu-\psi)^{A2-1} \end{aligned}$$

The expressions used for the characteristic times  $\tau_{\text{NG}}$  and  $\tau_{\text{Re}}$  are those used by Johnson, Tang and Forest<sup>9</sup> in their hot-spots initiation model (JTF) applied to HMX-based explosives.

In the case of nitroglycerin,  $\tau_{\text{NG}}$  is the adiabatic explosion time calculated as follows:

$$\tau_{\text{NG}} = \frac{\theta^2}{\theta_{\text{Act}} \beta Z} e^{\frac{\theta_{\text{Act}}}{\theta}}$$

where  $\theta$ ,  $Z$ ,  $\theta_{\text{Act}}$  and  $\beta$  are the hot-spots temperature, the pre-exponent factor, the activation temperature and the adiabatic temperature elevation.

For the remainder Re of the propellant,  $\tau_{\text{Re}}$  is given by the Forest-Fire model, corrected for low pressures by a term  $G_0 P$ :

$$\tau_{\text{Re}} = \left( G_0 \frac{P}{P_0} + A \left( \frac{P}{P_0} \right)^n + B \left( \frac{P}{P_0} \right)^7 \right)^{-1} \frac{f-f_0}{1-f_0}$$

where  $P_0$  is a reference pressure and where  $f_0$  is a threshold value beyond which the decomposition



reaction of the remainder of the propellant Re can start.

As the values of the orders of reaction A1 and A2 are parameters which are difficult to assess under experimental conditions, they are assumed to be equal to 1 as in the JTF model<sup>9</sup>.

The mean hot-spots temperature reached under a shock of intensity  $P_{Sh}$ , is calculated by the empirical equation<sup>9</sup>:

$$\theta_{Sh} = \theta_0 \left( 1 - m \frac{\theta_0}{\theta_{Act}} \ln \left( \frac{P_{Sh}}{P_0} \right) \right)^{-1}$$

Following the shock, the change in hot-spots temperature is described by an adiabatic compression process:

$$\dot{\theta} = \frac{d\theta}{dt} = \theta \Gamma k \dot{P}$$

where  $\Gamma$  and  $k$  are the Gruneisen coefficients and the isentropic compressibility of the unreacted propellant.

The thermodynamic state of the global reactive system is described by a potential which is a function of advance parameters  $\lambda$  and  $\alpha$ . The potential selected is the Helmholtz free energy potential,  $F(V, T, \lambda, \alpha)$ <sup>7</sup> which can be expressed as follows:

$$F(V, T, \lambda, \alpha) = (1 - \lambda) F_S(V, T) + \lambda F_G(V, T) + \alpha \psi Q_{A1}$$

where  $V$  is the specific volume,  $T$  is the temperature of the mixture and  $Q_{A1}$  is the amount of energy released when the aluminum is oxidized by the carbon dioxide (20.1 MJ/kg of aluminum).  $F_S$  and  $F_G$  are respectively the free energy of the unreacted propellant and that of the mixture composed of aluminum in the solid or liquid state and decomposition products.

The third term of the expression  $F(V, T, \lambda, \alpha)$  is only involved when the decomposition of the binder, the HMX and the ammonium perchlorate is completed ( $\lambda=1$ ) and when the temperature of the aluminum particles has exceeded ignition temperature. The pressure  $P$  and the internal energy  $E$  can be deduced from the free energy using thermodynamic equations expressing the basic principle of thermodynamics:

$$P = - \left( \frac{\partial F}{\partial V} \right)_{T, \lambda, \alpha}$$

$$E = F - T \left( \frac{\partial F}{\partial T} \right)_{V, \lambda, \alpha}$$

The internal energy and pressure expressions used for inert propellant are of the Mie-Gruneisen type<sup>7</sup>. The mixture composed of inert aluminum and decomposition products is described by a JWL-type equation of state<sup>7</sup>. The parameters of this equation are

adjusted to reproduce the isentropic expansion of the decomposition products from the Chapman-Jouguet point and calculated using the BKW thermochemical code when aluminum is assumed to be inert.

This model is then implemented in the one-dimensional (1-D) MONODIM and two-dimensional (2-D) EPIC2 lagrangian calculation codes. As aluminum oxidation occurs downstream from the reaction zone, only the first two terms of the model (initiation) were implemented in a 2-D eulerian HULL code.

## IDENTIFICATION OF THE MODEL - NUMERICAL RESULTS

Lagrangian analysis was applied to the experimental signals recorded at 6 GPa. The software used is a version of that developed by Lynn Seaman<sup>10</sup> adapted to reactive flows<sup>2</sup>. The signals are time-adjusted using the Hugoniot established by the SNPE/CRB.

The equations of state used to represent the thermodynamic development of the reactive system make it possible to calculate the parameter  $\lambda(t)$  for each lagrangian abscissa.

Using the weight induction times recorded under experimental conditions at 6 GPa, the parameters  $\theta_0$ ,  $f_0$  and  $\mu$  can be interrelated. A set of different possible combinations of the parameters  $\theta_0$  et  $f_0$  can be determined by taking the value of  $\mu$  to be equal to the weight fraction of nitroglycerin contained in the propellant and by assuming that the induction times are reproduced by the first term of the kinetic model, provided that  $f$  remains less than  $f_0$ .

The results of numerical simulations performed using the 1-D code are compared with experimental results in Figures 4, 5 and 6. This comparison is excellent given the simplicity of the model and the fact that the composition of the propellant is not ideal. Since the Forest-Fire term is included in the global kinetic model, the initiation depths are automatically reproduced. One can notice that the numerical detonation wave corresponds exactly to the gage breaking. As the aluminum oxidation time constant is clearly greater than  $\tau_{NG}$  and  $\tau_{Re}$ , simulations of the vulnerability of the propellant to shaped charge jets can be reasonably performed by cancelling the aluminum oxidation term.

2-D numerical impact simulations were carried out at 6 GPa using the HULL and EPIC2 codes and gave

identical results to those obtained using the 1-D MONODIM code.

## SHAPED CHARGE JET IMPACT BEHAVIOR

The above-mentioned model is capable, when implemented in the HULL code, of simulating the response of the propellant under shaped charge jet impact conditions. The present section deals with some experimental results and the corresponding simulations.

### Impact on covered propellant

The experimental set-up is depicted in Figure 8.

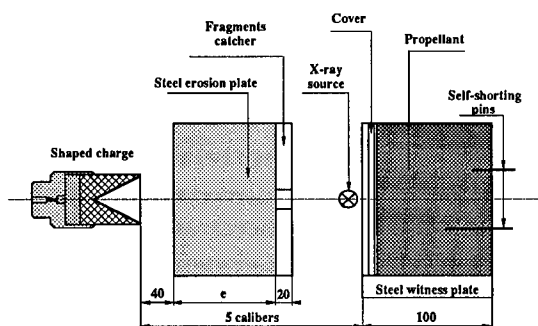


FIGURE 8. EXPERIMENTAL SET-UP

A steel barrier is placed between the shaped charge and the propellant. Its thickness controls the residual velocity of the jet. The rocket propellant sample is covered with a few millimeters of low impedance materials representative of rocket motor casing. Observations are made by means of streak and frame cameras, self-shortening pins and a witness plate placed under the sample.

The stimulus level is evaluated by the Held's criterion<sup>11</sup>  $[V^2d]_{\text{crit}}$  where  $V$  and  $d$  are respectively the velocity and the diameter of the impinging jet. The measurement of  $d$  is performed by flash X-ray just before impact. It should be noted that this diameter may be adjusted by varying the barrier-propellant distance.

Provided that the jet has been previously well characterized, the jet diameter may be calculated with a reasonable degree of accuracy. Under such conditions and using various caliber charges, the  $[V^2d]_{\text{crit}}$  detonation threshold has proven to lie between 60 and 100  $\text{mm}^3/\mu\text{s}^2$ . These values agree with other experiments<sup>11</sup> for the same protected propellant:

$$78 \text{ mm}^3/\mu\text{s}^2 < [V^2d]_{\text{crit}} < 98 \text{ mm}^3/\mu\text{s}^2.$$

### Impact on bare propellant

The  $[V^2d]_{\text{crit}}$  detonation threshold greatly depends on the kind of stimulus delivered to the propellant. For the bare material, it has been shown that the threshold is lower than 21  $\text{mm}^3/\mu\text{s}^2$ . It is probably due to the stress conditions. In the case of bare propellant, the impact generates a strong 1-D shock wave. If the propellant is covered with low impedance materials, the 1-D shock is absorbed by the cover, and in most cases a supersonic penetration regime takes place. The crater is then preceded by an axisymmetric shock wave, the level of which can be calculated by means of the Bernoulli theorem. In any case, the stimulus is much lower than for the bare propellant.

### Impact by a broken-up jet

If standoff is notably increased, the jet breaks up before impacting the propellant sample. Some experiments have been conducted, leading to  $[V^2d]_{\text{crit}}$  values between 25 and 31  $\text{mm}^3/\mu\text{s}^2$ . This means that the propellant is much more sensitive to a fragmented jet than to a continuous one.

Consider two successive fragments. The first one penetrates the cover and the propellant. Provided that the threshold of covered material is not reached, detonation does not occur. After total erosion of the first fragment, impact of the second one occurs, producing a brief but strong shock, comparable to what happens on bare propellant.

With such a scenario, it could be thought that the threshold under broken-up jet impact conditions might vary between covered and bare propellants when standoff progressively increases.

### Numerical simulations

Some experimentally tested configurations concerning covered propellant have been simulated with the HULL 2-D code for  $V^2d$  values below and above the threshold. For a 62 mm diameter charge, the jet diameter is 2.6 mm which seems to be a realistic value; jet velocities lie between 5200 and 6200 m/s ( $70 < V^2d < 100 \text{ mm}^3/\mu\text{s}^2$ ). The cover materials are replaced by 7 mm of PMMA modeled using a Mie-Gruneisen equation of state. The mesh uses 0.2 mm constant dimension cells.

Simulations have produced a  $[V^2d]_{\text{crit}}$  numerical threshold of 80  $\text{mm}^3/\mu\text{s}^2$  which is consistent with the experimental value. This value is displayed on figure 9

together with experimental results from this study and Cueff<sup>12</sup>.

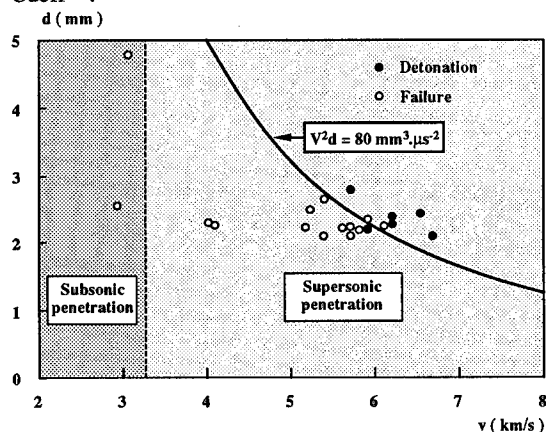


FIGURE 9. ROCKET PROPELLANT EXPERIMENTAL AND NUMERICAL THRESHOLD IMPACT VELOCITY AS A FUNCTION OF SHAPED CHARGE JET DIAMETER

## CONCLUSIONS

A numerical model has been built and identified from experimental results obtained under plane shock conditions on a high-energy rocket propellant, doped with HMX. It takes into account reactions occurring in nitroglycerin, aluminum and the remainder of the propellant.

Used to predict the  $V^2d$  critical detonation threshold of protected propellant when attacked by a shaped charge jet, the validated model yields values which are close to those obtained under experimental conditions.

In view of the good agreement between calculations and experimental results, the model developed would appear to be able to predict the response of this propellant when subjected to other types of attack, such as a broken-up jet, to validate different types of protective material and thereby reduce the vulnerability of the propellant and even predict the effects of its reaction on the environment (e.g., velocity of rocket motor casing fragments or blast effects).

## REFERENCES

1. Tarver C.M., Green L.G. (1989), "Using small scale tests to estimate the failure diameter of a propellant", *9th Symp. (Int.) on Det.*, pp 701-710, August 1989
2. Baudin G., Cau J.F., Saint Martin C., Gimenez P.(1988) , "Etude des régimes transitoires de détonation dans un explosif comprimé à l'octogène", Journées de Détonique 1988, Centre d'Etudes de Gramat, NC-14
3. Germain-Lacour M., de Gliniasty M. (1980), "Insertion d'une jauge piézorésistive au manganin dans des matériaux macromoléculaires - Etude du signal sous choc", Note technique T80-43, Centre d'Etudes de Gramat
4. Germain-Lacour M., de Gliniasty M. (1981), "Electromagnetic precursor in shock loaded polymers", *8th AIRAPT and 19TH EHPRG conference*, August 17-22 1981, Uppsala, Sweden
5. Agrawal J.P., Bouzon J., Vergnaud J.M. (1989), "Modelling of nitroglycerine and water migration behaviour through unsaturated chloropolyesters", *Polymer*, 1989, Vol. 30, pp. 1488-1492
6. Shu-Yun H., Tong-Xue P., Yang-Hui K., Zi-Ru L.(1991), "The nitroglycerin content distribution in the coating of the solid propellant and the service life prediction of the charge", *Propellants, Explosives, Pyrotechnics*, 1991, 16, pp. 31-35
7. Baudin G., Bergues D. (1993), "A reaction model for aluminized PBX applied to underwater explosion calculations", *10th Symp. on Det.*, July 1993
8. Bowden F.P., Yoffe Y.D.(1952), "Initiation and growth of explosion in liquids and solids", Cambridge University Press , Cambridge Science Classics
9. Johnson J.N., Tang P.K., Forest C.A. (1985), "Shock wave initiation of heterogeneous solids", *J. Appl. Phys.*, 57(9), May 1 1985
10. Seaman L.(1984), "Lagrangian analysis for stress and particle velocity gages", SRI Technical Report, August 1984
11. Held M. (1968), "Initiation of explosives, a multiple problem of the physics of detonation", *Explosivstoffe*, 1968, 5, pp. 98-113
12. Cueff C. (1991), "Etude expérimentale de la vulnérabilité d'un propergol énergétique", *2ème journées scientifiques Paul Vieille*, 16-18 octobre 1991, Brest, France

## DISCUSSION

R. SARRACINO

AECI Explosives, Modderfontein, South Africa

I would expect the CJ zone and the aluminum reaction zone to overlap. Your model assumes aluminum reaction to begin beyond the sonic surface. Did you make this as a simplifying assumption - to make the model more tractable - or do you have other reasons for making this assumption?

## REPLY BY DIDIER BERGUES:

In our model, heating of aluminum (Phase 3) is computed from the shock entering the propellant to the end of the event. If aluminum particles reach a temperature greater than their alumina crust melting

temperature<sup>7</sup>, aluminum oxidation can start even before the end of the Phase 2 (CJ plane in the case of steady-state detonation). But with our composition and with our particle size, ignition of aluminum does not occur before the CJ plane, whether in steady-state detonation or, of course, in an SDT process. It is due to the fact that detonation or SDT characteristic time (0.5-5 $\mu$ s) is always smaller than that of aluminum reaction (20-50  $\mu$ s).

The choice of the aluminum reaction scheme is justified by the following experimental proof<sup>7</sup>: if, in a similar rocket propellant composition, we replace aluminum with a non-reacting material such as lithium fluoride, which is "the" quasi-perfect mock material of aluminum, while remaining inert in detonation products, detonation velocity is unchanged, indicating that there is no energy release due to aluminum within the CJ zone.

## TEMPERATURE-DEPENDENT SHOCK INITIATION OF TATB-BASED HIGH EXPLOSIVES

J. C. Dallman and J. Wackerle  
Los Alamos National Laboratory  
Los Alamos, New Mexico 97544

The effects of temperature on the shock sensitivity of two TATB formulations PBX 9502 and LX-17 are studied over the temperature range -54°C to 252°C. The shock Hugoniot curves over this same temperature range are developed. Thermal expansion properties and porosities are used to help determine the mechanisms of thermal sensitization. Impact sensitivities over the range from ambient to 300°C are reported. Analyses of these results imply that thermal sensitization is the result of purely chemical kinetics enhancement and intracrystalline hot-spot growth. Additional results on the ambient shock sensitivity of PBX 9502 and LX-17 following thermal cycling to 252°C and back to ambient is presented.

### INTRODUCTION

TATB (1,3,5-triamino 2,4,6-trinitro-benzene) is a high explosive (HE) that is extremely stable under thermal insult, showing an exotherm only at temperatures above 310°C. It does not burn to detonation in confined or unconfined geometries; however, it has about 30% less energy than HMX (octahydro-1,3,5,7-tetranitro-1,3,5,7-tetrazocine). Two formulations of TATB have been investigated: PBX 9502\* and LX-17-01\*\* (hereafter LX-17). The chemical synthesis procedure differs for the TATB used in the two formulations. The TATB used in PBX 9502 is produced in a waterless amination process and results in a particle size distribution with 60% by weight being less than 45 microns. The TATB used in LX-17 is produced in a wet amination procedure and results in a particle size distribution with 75% by weight of the particles being less than 45 microns. These two procedures result in slightly different chloride and other impurity content of the resulting TATB product. To meet the higher density specification for LX-17 (1.91 g/cm<sup>3</sup>), it must be pressed at a slightly higher pressure. These differences are significant and produce differences in the thermal response and the shock sensitivity.

With a sufficiently strong shock, the shock-induced decomposition in heterogeneous explosives will accelerate and develop into a detonation. The evolution of this process is called the shock-to-detonation transition (SDT). The length of time or the distance a shock wave runs into an HE before it changes to a detonation wave is one measure of the shock sensitivity of an HE. The shock sensitivity of a wide variety of explosives have been tested in this way.<sup>1</sup> Plane-shock initiation measurements (wedge tests) can be used by themselves for quantitative comparison of the shock sensitivity among different explosives formulations or for the same formulation at different temperatures or densities. A number of models of initiation and detonation behavior depend upon or can use this type of data<sup>2,3</sup> for calibration. Use of these models in hydrocodes allows the examination of a wide variety of shock impulses and potential accident scenarios.

This study reports the effect of temperature on the shock initiation of the insensitive HEs PBX 9502 and LX-17. The measurements reported were carried out at ambient (12°C to 22°C) 75°C and 252°C. These results, coupled with the work of previous investigators at -55°C and at ambient, detail the planer-shock sensitivity of these TATB-based formulations over the temperature range -55°C to 252°C. In addition, materials that have been cycled to 252°C and returned to ambient will be studied.

\*95% TATB/5% Kel-F 800.

\*\*92.5% TATB/7.5% Kel-F 800.

The impact sensitivity of TATB will be reported showing first an increase and then a decrease in its impact sensitivity with increasing temperature. Some thermo-mechanical properties of PBX 9502 and LX-17 will be described

## BACKGROUND

Prior to this study, a number of investigators have shown that TATB alone or in formulation with Kel-F 800 has a temperature-dependent initiation sensitivity. In 1975, Schwartz<sup>4</sup> showed that a lower velocity flyer plate could be used to initiate TATB when its temperature was raised to 260°C from 25°C. In 1980, Seitz and Wackerle<sup>5</sup> reported a comparison of PBX 9502 wedge measurements at -55°C and ambient temperature. Their measurements show a 50% increase in the distance to detonation from ambient to -55°C. Also in 1980, Scheloske, Green, and Weingart<sup>6</sup> showed that raising the temperature of TATB to 250°C reduced the kinetic energy required of a thin flyer plate to initiate a heated sample by 33% for pressed TATB at 1.80 g/cm<sup>3</sup> and by 50% for RX03BB (an early experimental version of LX-17). They also observed about 4 times the total reaction in the Susan test with 260°C TATB over ambient material for identical conditions. In 1984, Campbell<sup>7</sup> reported that the failure diameter of PBX 9502 went from 5.85 ± 0.15 mm at 75°C to about 10.5 mm at -55°C. In addition, the detonation velocity decreased with decreasing temperature for small charge diameters.

Scanning electron micrographs (SEM) of dry aminated TATB crystals clearly show a complicated intracrystal hole structure. The hole structure for wet aminated TATB crystals shows a different pattern than for the dry aminated; however, both materials clearly have a hole structure. It is speculated that these holes result from the washout of ammonium chloride, during a part of the production process. Whether these holes play an important role in the initiation of TATB remains an unanswered question.

This work extends the temperature range of the planer-shock-initiation studies of Seitz and Wackerle<sup>5</sup> and the work of a number of investigators whose measurements on ambient temperature PBX 9502 are summarized in Dick et al.<sup>8</sup> The first measurements involved planer-shock-initiation studies on wedges of PBX 9502 and LX-17 at ambient temperature. These provided a basis of comparison with previous investigators both for similarity of the HE batch response and experimental technique. Following these ambient tests, the experiments at 75°C and subsequently at 252°C were pursued.

## THERMAL PROPERTIES

### Materials Properties

Cady<sup>9</sup> used 1-cm cubes of PBX 9502 and LX-17 to examine the gross decomposition of the constituent TATB in thermal heating tests. In these tests Cady measured both the weight loss of the cubes and the change of dimension of the cubes as a function of temperature. These HE cubes were subjected to 2°C/min temperature up and down ramps with the maximum temperature being maintained for 20 minutes, repeated up to four times. In Fig. 1 the cumulative weight loss of the cubes is shown. The weight loss at 201°C appears to be the loss of interstitial water since no substantial loss was measured with an additional cycle. However, at 250°C there appears to be an increased initial weight loss followed by additional small losses with each cycle. Still these weight losses were quite small. At 260°C the weight loss is increased and there is a clear change in the slope of the curve through the subsequent cycles.

Figure 2 shows the effect of temperature on the density of PBX 9502 and LX-17 over the range from -60°C to 260°C. Initially LX-17 has a higher density than PBX 9502, but by about 125°C there is very little difference in the density of the two materials. From about 25°C to about 125°C LX-17 grows more rapidly than PBX 9502; thereafter the volumetric growth with temperature is identical. Note in Fig. 2 that, at about 70°C, the slope of the density-temperature curve changes. The change in slope is probably due to the relief of "frozen-in" stress that occurs as the materials are pressed at about 70°C.

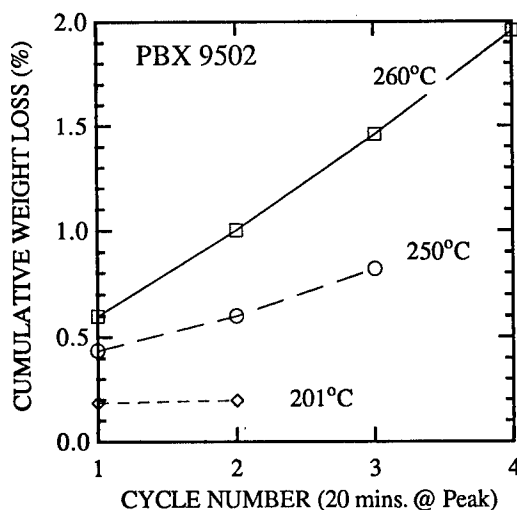


FIGURE 1. CUMULATIVE WEIGHT LOSS AFTER HEATING TO PEAK TEMPERATURES WITH 20 MIN AT PEAK AND A 2°C/MIN RAMP

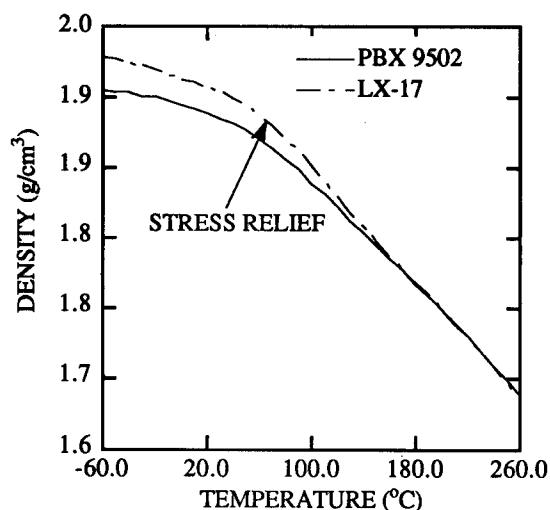


FIGURE 2. DENSITY OF PBX 9502 AND LX-17 OVER THE TEMPERATURE RANGE -60 TO 260°C

The coefficients of thermal expansion have been measured from -54°C to 100°C for TATB crystals<sup>10</sup> and to 75°C for Kel-F 800. Using linear and nonlinear extrapolations of these measurements, Cady<sup>9</sup> has calculated the porosity of PBX 9502 and LX-17 over the temperature range -60°C to 260°C. Figure 3 shows the porosity of PBX 9502 and LX-17 with increasing temperature. It appears that the porosities of these materials decrease with temperature. Thus, any enhanced sensitivity with increasing temperature does not appear to be due to increased porosity of the explosive.

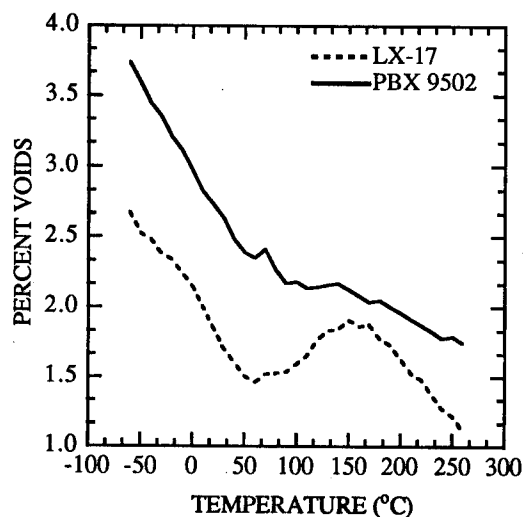


FIGURE 3. PERCENT VOIDS IN PBX 9502 AND LX-17 OVER THE TEMPERATURE RANGE -60°C TO 260°C

## Impact Sensitivity Results

Buntain<sup>11</sup> performed impact tests on dry aminated TATB powder at both ambient and elevated temperatures. Table I shows the results of his study. TATB powder was placed on an anvil and a 2.5 kg weight was dropped from 320 cm above the sample. A go/no go determination is made by a sound energy threshold. TATB at ambient temperature gives no reaction. However, Buntain found that at 250°C, 11 out of 50 drops registered as "goes." Note that at 300°C the number of "goes" drops dramatically for TATB held at temperature for 20 to 40 seconds before impact. When the TATB was held at 300°C for 120 seconds, even fewer "goes" were registered. At 300°C some reaction is taking place in the TATB; however, the products of reaction do not appear to catalyze further reaction, nor do the products appear to be more sensitive than the original TATB. A conclusion that can be drawn from these data is that thermal decomposition creates reaction products that make TATB less sensitive.

The thermal weight loss measurements, the impact sensitivity data, and the available one-dimensional time-to-explosion data<sup>12</sup> caused us to use 252°C as the target temperature for the shock sensitivity tests. We felt that temperatures above this would cause the measurement to have a dependence on the length of time the test samples were held at temperature. The 252°C temperature target provides a small cushion for thermal overshoot during the heating process.

## SHOCK-SENSITIVITY EXPERIMENTS

### Hardware

The experiments performed were a modified design of the Los Alamos wedge test. The wedges of test explosive were machined to a pyramidal shape providing two active sides of information per wedge. Figure 4 shows a schematic of the wedge experiment design. A

TABLE 1. SUMMARY OF IMPACT RESULTS

Material	No. of Tests	T <sub>0</sub> (°C)	No. of Goes
TATB	35	Rm	None
TATB	50	250 ± 10°C (25 to 45 s)	11
TATB	25	300 ± 10°C (120 s)	2
TATB	25	300 ± 10°C (20 to 40 s)	5
PBX 9502	25	250 ± 10°C (45 s)	None

plane-wave lens with additional booster explosive was used to create a high-pressure shock wave in a layer of inert material. With the proper choice of explosive and inert materials, the pressure of the shock wave entering the test sample can be tailored. A complicating factor for the 252°C test was the requirement that the inert attenuator plates remain dimensionally stable, effectively restricting the inert materials to stress-relieved metals.

The pyramidal wedge and the final attenuator plate forms the top of a hot-air furnace used to heat the sample. The expendable furnace doubled as an alignment fixture for the streak photography. To ensure even heating of the test piece, an electric-stove resistance heater, which is mounted on a copper plate for even heat distribution, is used to heat the outside of the attenuator plate that forms the furnace top wall, and to which, the wedge of test explosive is attached. Thermocouples were located on the top surface of the wedge and between the wedge and the final attenuator plate directly beneath the apex of the wedge. Additional thermocouples monitored the temperature of the air in the furnace, the hot air inlet, and the copper plate directly below the resistance heater. The rate of temperature rise on the wedge surfaces was about 2°C/min.

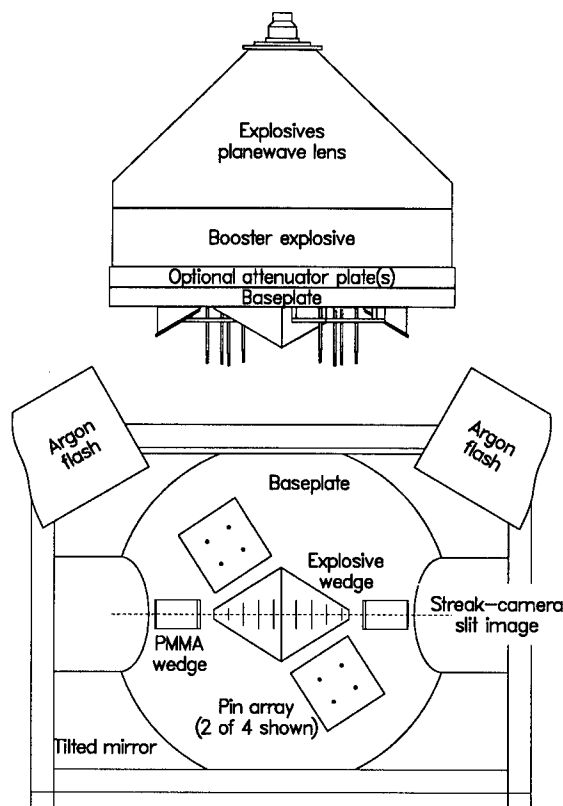


FIGURE 4. WEDGE-EXPERIMENT DESIGN

No radiography was performed on the test pieces, but visual observation of the wedges indicated highly uniform and voidless surfaces. In addition, the photographic films record stable velocities indicating the interiors of the wedges were free of imperfections of a size that would produce a macroscopic effect in the measured shock or detonation velocities. The density at 23°C of each wedge was floatation measured; the densities had a high degree of uniformity with all values falling in the range of  $1.888 \pm 0.002 \text{ g/cm}^3$  for PBX 9502 and  $1.913 \pm 0.004 \text{ g/cm}^3$  for LX-17.

A 20-min thermal "soak" time was used based on temperature measurements in the wedge geometry with thermocouples placed at the top, bottom, and center of the interior of a wedge of PBX 9502. These measurements indicated that, once the surfaces reached 252°C, the interior of the wedge reached 252°C within 10 minutes. These results provided us the confidence to use 20 minutes as the minimum time for thermal equilibrium in the test pieces.

#### Data Analysis

High-explosive driving systems were used to transmit plane shock waves through standard (materials of known shock properties) attenuator plates into the test explosive. Streak-camera observations of the evolution of the shock front along the inclined wedge surface and free-surface velocity measurements on the base plate provide the data necessary to determine the shock state in the test explosive, the shock buildup history, and the time and distance to detonation. The height of the toe, that region where the wedge is thinnest, at the location of the photographic slit was measured and is accounted for in the data analyses. A complete description of these analyses can be found in Reference 1. Thermal expansion was measured by Cady<sup>9</sup> on identical material in the laboratory, and those measurements were confirmed by optical measurements on the HE pieces under test conditions. These dimensional changes have been accounted for in the analyses.

Measurement of the initial shock state in the sample wedge requires the measurement of the free-surface velocity of the final attenuator plate and the shock velocity in the sample wedge. The free-surface velocity of the final attenuator plate is measured by a series of four blocks of velocity pins placed about the wedge as shown in Fig. 4. In each pin block four velocity pins measure the time of arrival of the plate's free surface. The four blocks were used to detect possible wave tilt and uneven pressure input and to provide redundancy and increased measurement accuracy.

The shock velocity in the test sample is measured photographically using a streak camera. Two separate



argon shock tubes provide light to the surface of the wedge. The reflection of this light from the top surfaces of the pyramidal wedge is recorded by a streak camera. Arrival of the input shock turns the surface sufficiently to reduce film exposure, producing a strong demarcation of light and dark regions on the streak-camera film and yielding a space-time record of wave arrival. The resulting films are digitized and the space-time data, as well as distances and times to detonation, are extracted. Shock velocities as a function of run distance and run time are obtained by performing a least-squares fit of the space-time points and differentiating to obtain the local slope. The initial shock velocities are obtained by extrapolating the shock velocity-distance curves back to

zero distance or by measuring the initial slope of the space-time record on the streak-camera film.

## RESULTS

### Shock to Detonation

The detailed results of the shock sensitivity experiments are shown in Table II. These results are presented in Fig. 5 as run distance-to-detonation transition as a function of shock pressure input to the test piece. This figure contains the results of Seitz and Wackerle,<sup>5</sup> Dick et al.,<sup>8</sup> as well as those of the current study. A clear progression from least sensitive at -54°C to most sensitive at 252°C is observed. In fact, at 75°C

TABLE 2. SUMMARY OF WEDGE EXPERIMENT DATA ON PBX 9502 AND LX-17

Shot Number		$\rho_0$ (g/cm <sup>3</sup> )	$T_0$ (°C)	$u$ (mm/ $\mu$ s)	$U$ (mm/ $\mu$ s)	$P$ (Gpa)	$h_d$ (mm)	$t_d$ ( $\mu$ s)	Remarks
<b>PBX 9520 Data</b>									
2088	A	1.886	17	1.02	4.62	8.89	19.6	4.01	
	B			1.01	4.80	9.12	19.6	3.83	
2100	A	1.890	10	1.23	5.10	11.86	10.6	1.83	
	B			1.24	5.08	11.9	10.0	1.77	
2089	A	1.889	17	1.34	5.37	13.6	7.0	1.25	
	B			1.35	5.31	13.6	7.0	1.21	
4189	A	1.785	13	1.09	4.75	9.3	7.3	1.42	Temperature cycled;
2134	A	1.785	16	1.34	5.70	13.6	3.2	0.68	note 0.08 porosity
									on these two shots
2105	A	1.857	75	0.79	4.05	5.91	$\geq 32.2$	$\geq 7.9$	Run distance more
	B			0.80	3.93	6.13	$\geq 31.4$	$\geq 7.5$	than wedge thickness
2074	A	1.857	75	0.84	4.47	7.03	21.4	4.85	
	B			0.85	4.30	6.81	22.1	4.91	
2084	A	1.857	75	0.91	4.28	7.23	19.4	4.35	
	B			0.91	4.25	7.19	19.8	4.38	
2083	A	1.857	75	1.04	4.80	9.26	10.0	2.14	
	B			1.06	4.55	8.93	10.0	2.04	
2080	A	1.857	75	1.25	5.00	11.6	6.4	1.22	
	B			1.26	4.88	11.4	5.9	1.18	
2135	A	1.857	75	1.26	4.95	11.7	6.7	1.27	
	B			1.25	4.92	11.6	6.8	1.34	
2068	A	1.857	75	1.38	5.28	13.5	4.2	0.80	
	B			1.38	5.20	13.4	4.1	0.77	
2078	A	1.857	75	1.39	5.24	13.5	4.0	0.72	
	B			1.37	5.40	13.8	3.5	0.66	
2132	A	1.70	252	0.28	2.22	1.05	$\gg 35$	$\gg 10$	Low-pressure
	B			0.27	2.47	1.15	$\gg 35$	$\gg 10$	Hugoniot data only
2118	A	1.70	252	0.50	2.87	2.46	22.2	7.28	
	B			0.50	2.86	2.45	23.2	7.45	
2114	A	1.70	253	0.52	2.87	2.53	19.2	6.62	Pins lost; u and p
	B			0.54	2.95	2.71	19.6	6.67	from U (u) Hugoniot
2119	A	1.70	250	0.63	3.15	3.38	11.1	3.19	
	B			0.63	3.14	3.37	10.9	3.16	
2122	A	1.70	252	0.81	3.92	5.41	4.5	1.07	
	B			0.81	3.95	5.44	4.7	1.11	
2124	A	1.70	253	0.91	4.12	6.36	3.4	0.77	
	B			0.91	4.13	6.37	3.6	0.82	
2111	A	1.70	252	1.31	4.62	10.3	0.90	0.17	Short run; U from
	B			1.31	4.62	10.3	0.98	0.19	U (u) Hugoniot
2155	A	1.912	12	1.03	4.47	8.84	est. 38	est. 7.5	Slightly overran;
	B			1.03	4.51	8.88	est. 38	est. 7.5	Hugoniot data good

*Continued on next page*

TABLE 2. SUMMARY OF WEDGE EXPERIMENT DATA ON PBX 9502 AND LX-17 (continued)

Shot Number		$\rho_0$ (g/cm <sup>3</sup> )	$T_0$ (°C)	$u$ (mm/ $\mu$ s)	$U$ (mm/ $\mu$ s)	$P$ (Gpa)	$h_d$ (mm)	$t_d$ ( $\mu$ s)	Remarks
<b>LX-17 Data</b>									
2159	A	1.914	14	1.12	4.62	9.89	31.5	6.41	
	B			1.11	4.69	9.97	32.1	6.60	
2163	A	1.911	21	1.20	5.02	11.6	15.9	3.06	
	B			1.21	4.96	11.5	15.7	3.02	
2178	A	1.917	19	1.23	4.92	11.6	21.6	4.15	Pantex pressed;
	B			1.23	5.01	11.8	20.7	4.03	note lower porosity
2154	A	1.913	7	1.36	5.53	14.5	8.5	1.47	
	B			1.36	5.48	14.4	8.0	1.43	
2156	A	1.912	14	1.46	5.85	16.4	4.35	0.72	
	B			1.44	6.04	16.6	4.52	0.76	
2165	A	1.807	21	1.17	5.12	11.0	4.38	0.85	Thermal cycled;
	B			1.18	5.35	11.3	4.26	0.80	note 0.07 porosity
2153	A	1.71	251	0.48	2.56	2.10	>>28	>>13	Overran data range;
	B			0.47	2.62	2.11	>>28	>>13	Hugoniot data only
2162	A	1.71	251	0.52	2.88	2.60	18.8	6.71	Faint record
	B			0.53	2.89	2.61	20.3	6.8	
2137	A	1.71	252	0.61	3.58	3.76	11.8	3.33	Pantex pressed
	B			0.62	3.50	3.69	11.9	3.40	
2161	A	1.71	250	0.85	3.85	5.54	5.1	1.26	
	B			0.85	3.84	5.54	5.2	1.27	
2138	A	1.71	252	0.91	4.49	6.96	3.7	0.82	Pantex pressed
	B			0.91	4.53	7.02	3.5	0.78	

the distance-to-detonation has shortened by a factor of 2 for the same pressure, and at 252°C the distance-to-detonation has shortened by over a factor of 10. A line representing a fit to ambient data on PBX 9501\* is

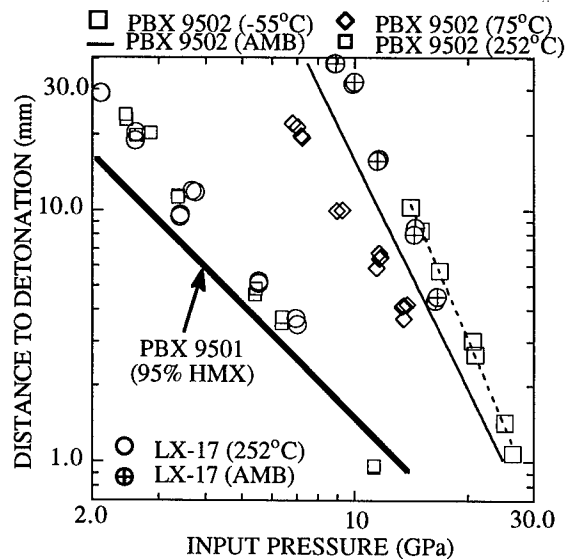


FIGURE 5. SHOCK SENSITIVITY (POP PLOT) OF PBX 9502 AND LX-17 OVER THE TEMPERATURE RANGE -54°C TO 252°C

\*95% HMX/2.5% Estane/2.5% BNDPA-F.

shown for comparison. It is important to notice that the 252°C data fall above this line especially in the region of low-pressure shock inputs. Most real or envisioned shock-to-detonation accident scenarios with HE occur at these much lower pressures. In the region of 2.5 GPa the distance-to-detonation of the TATB formulations at 252°C is about 50% greater than that of ambient PBX 9501.

Figure 6 shows the shock Hugoniot data in the shock velocity-particle velocity plane for all the tests. The following are linear fits to the PBX 9502 shock velocity,  $U_s$ , and particle velocity,  $u_p$ , data of Fig. 6:

$$U_s = 3.31 + 1.65 u_p \quad -55^\circ\text{C}$$

$$U_s = 2.60 + 1.91 u_p \quad 75^\circ\text{C} \pm 2^\circ\text{C}$$

$$U_s = 1.33 + 3.08 u_p \quad 252^\circ\text{C} \pm 2^\circ\text{C}$$

For the LX-17 data the linear fits are

$$U_s = 1.05 + 3.65 u_p \quad \text{Ambient}$$

$$U_s = 0.85 + 3.46 u_p \quad 252^\circ\text{C} \pm 2^\circ\text{C}$$

Note that Hugoniot data from wedge tests have, by nature, a limited range of input particle velocities, which makes the increase in slope with increasing temperature of the linear fits to the data interesting, but suspect. Dick et al.<sup>8</sup> showed that a fit to a wide range of Hugoniot data for ambient PBX 9502 required a three-part fit to adequately represent the data. The linear fits given are valid only for the limited range of available data.

### Thermally Cycled Material

Wedges of PBX 9502 and LX-17 were taken to 252°C and returned to ambient temperature. Subsequently, the shock sensitivity of these materials was tested. Figure 7 shows the results of the wedge tests on the cycled materials. Because TATB formulations exhibit permanent growth during heating (ratchet growth), the density of the cycled HE was considerably lower than that of uncycled HE. The densities were 1.785 g/cm<sup>3</sup> and 1.81 g/cm<sup>3</sup> for PBX 9502 and LX-17, respectively. Also shown in Fig. 7 are lines fit to the data for PBX 9502 at other temperatures. The cycled HEs are considerably more sensitive than uncycled materials; however, note the line representing shock-initiation data of Seitz<sup>13</sup> on neat TATB at 1.80 g/cm<sup>3</sup>. The relative sensitivity of the cycled materials compared to that of the 1.80 g/cm<sup>3</sup> TATB indicates that the dominant effect on sensitivity for the cycled TATB/Kel-F formulations is that of porosity (density decrease). The relative sensitivity of the cycled materials indicates that no significant catalytic daughter species from thermal decomposition are present. This agrees with Buntain's impact results showing a decrease in sensitivity with thermal decomposition.

Also shown in Fig. 6 is a line indicating the distance-to-detonation of PBX 9502 at 165°C. This line is the result of a nonlinear interpolation developed by Engleke.<sup>14</sup> Note, the measured density of PBX 9502 at 165°C is 1.785 g/cm<sup>3</sup>. PBX 9502 at 165°C is about 3 times more sensitive than the cycled HEs with the same density.

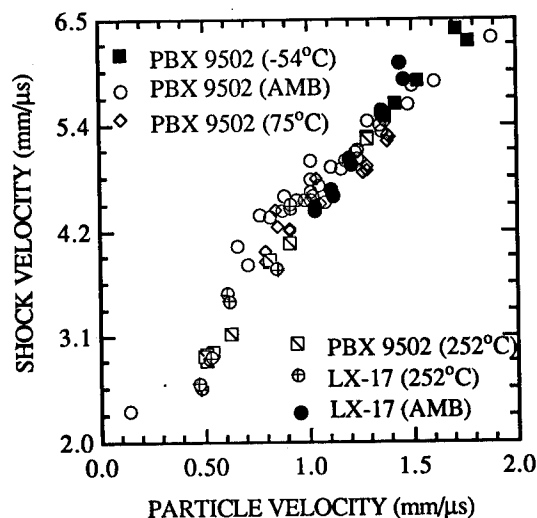


FIGURE 6. SHOCK VELOCITY-PARTICLE VELOCITY HUGONIOT CURVES FOR PBX 9502 AND LX-17 FROM -54°C TO 252°C

### DISCUSSION

#### Other High Explosives at High Temperatures

Three other explosive formulations have been examined by Ramsay et al.<sup>15</sup> at temperatures up to 150°C. They report that the shock sensitivities of PBX 9501\* and X-0299\*\* show no temperature dependence up to 100°C. However, at 150°C they observe about a 30% decrease in the run-to-detonation. TNT was also tested at 25°C and 73°C, but little or no temperature effect was observed. Notice that the shock sensitivity for low input pressures of PBX 9502 even at 252°C is still less than the conventional HE PBX 9501 at ambient temperature. The shock-sensitivity response to temperature of PBX 9502 is stronger than that of these other HEs and appears to be present even at low temperatures.

#### Sources of Increased Shock Sensitivity in TATB

The increase in sensitivity of TATB formulations with increasing temperature does not appear to result from more sensitive short- or long-lived thermal decomposition products. This is supported by the temperature dependent impact sensitivity of Buntain<sup>11</sup> showing a decrease in sensitivity when the temperature was changed from 250°C to 300°C. Additionally, no enhanced shock sensitivity above that expected from the reduced density of the thermally cycled (ambient-252°C-ambient) TATB formulations was observed.

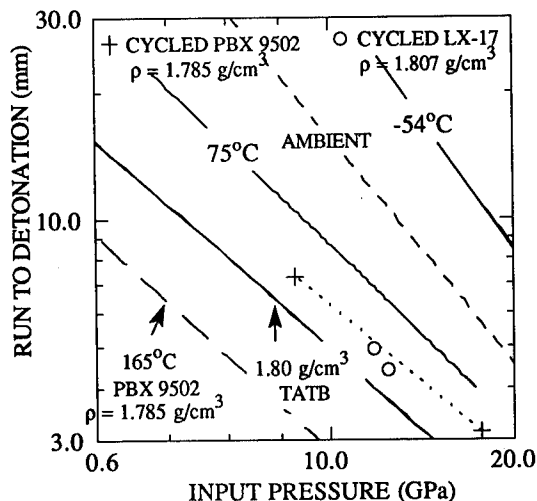


FIGURE 7. COMPARISON OF THE AMBIENT SENSITIVITY OF TEMPERATURE-CYCLED PBX 9502 AND LX-17

\*95% HMX/2.5% Estane/2.5% BDNPA/BDNPF.

\*\*95% 1,3-diamino-2,4,6-trinitrobenzene/5% viton A.

The increase in sensitivity with temperature is not the result of increased porosity of the higher temperature TATB formulation. This is strongly supported by the density measurements and calculated porosities. In fact, porosity appears to decrease with increasing temperature.

The observed buildup histories (shock velocity at the front as functions of time and distance after shock entry) in 252°C PBX 9502 and LX-17 also show initiation properties more resembling a low-porosity explosive than one with a relatively large void fraction. In particular, our data for these heated explosives—especially at longer run distances—have little increase in shock velocity for most of the run to detonation, with an abrupt increase just before the transition to detonation. These observations are quite similar to those in ambient-temperature, high-density, plastic-bonded HMX tested over a comparable range of shock strength. By contrast, buildup histories in 1.8-g/cm<sup>3</sup>, pressed TATB, are more gradual in both wedge and embedded-gauging experiments.<sup>16</sup>

Two prime candidates for the increased sensitivity of TATB with increasing temperature are the enhanced chemical reaction rates behind the lead shock wave or an increase in the number and intensity of active initiation hot spots. The temperature effect may be caused by TATB having a very strong dependence of reaction rates on temperature. But a reaction rate response this strong at low temperatures is not typical of other explosives such as HMX, DATB, and TNT.

The strong effect of temperature on shock sensitivity could also be related to an enhancement of the active hot spots. Note that TATB has a considerable intra-crystalline void structure. If these voids are related to initiation hot spots, then as the temperature of the TATB crystals increase the average size of the voids will increase. If some of the hot spots are too small to cause significant reaction behind a given strength shock at ambient temperature, then at elevated temperatures they could become effective and contribute to the initiation of the explosive.

It is likely that both of these phenomena contribute to the nonlinear and non-Arrhenius-like increase in the shock sensitivity of TATB with temperature. In any case, TATB is a very unique energetic material. It has good thermal stability coupled with excellent shock and impact insensitivity. It has not been shown to experience deflagration-to-detonation transitions even in heavy confinement at 250°C. And finally, in strictest safety terms, if TNT, RDX, or HMX were subjected to similar thermal insults, they would have a high probability of explosion or even of transitioning to a detonation. TATB is a unique HE with unparalleled safety properties.

## REFERENCES

1. Gibbs, T. and Popolato, A., *LASL Explosives Data*, University of California Press, Los Alamos Series in Basic and Applied Sciences, 1980.
2. Mader, C. L., *Numerical Modeling of Detonations*, University of California Press, Los Alamos Series in Basic and Applied Sciences, 1979.
3. Johnson, J. N.; Tang, P. K.; and Forest, C. A., "Shock Wave Initiation of Heterogeneous Reactive Solids," *Journal of Applied Physics* 57 (9), 1985.
4. Schwartz, A. C., "Flyer Plate Performance and the Initiation of Insensitive Explosives by Flyer Plate Impact," SAND75-0461 (1975).
5. Seitz, W. L. and Wackerle, J., "Prompt Initiation Studies of PBX 9502 and PBX 9503," The Fifth Annual Joint Firing System Conference (LFSC/XUSC) (Oct. 1980).
6. Scheloske, R.; Green, L.; and Weingart, R., "Sensitivity of Triaminotrinitrobenzene (TATB) at Elevated Temperatures," UCID-18336 (1980).
7. Campbell, A. W., "Diameter Effect and Failure Diameter of a TATB-Based Explosive," *Propellants, Explosives, and Pyrotechnics* 9, 183-187 (1984).
8. Dick, J. J.; Forest, C. A.; Ramsay, J. B.; and Seitz, W. L., "The Hugoniot and Shock Sensitivity of a Plastic-Bonded TATB Explosive PBX 9502," *Journal of Applied Physics* 63 (10), 4881-4888 (1988).
9. Cady, H. H., Los Alamos National Laboratory, M-1, informal written report to J. C. Dallman, M-1, concerning high-temperature materials property measurements on PBX 9502 and LX-17, May 1993.
10. Kolb, J. R.; Rizzo, H. F., "Growth of 1,3,5-Triamino-2,4,6-Trinitrobenzene (TATB), I. Anisotropic Thermal Expansion," *Propellants and Explosives* 4, 10-16, (1979).
11. Buntain G. A., Los Alamos National Laboratory, M-1, informal written report to J. C. Dallman, M-1, concerning the impact sensitivity of TATB powders at ambient, 250°C and 300°C, June 1990.
12. Dobratz, B. M. and Crawford, P. C., "LLNL Explosives Handbook, Properties of Chemical Explosives and Explosive Simulants," LLNL report UCRL 52997, Change 2, Jan. 31, 1985.
13. Seitz, W. L., "Short-Duration Shock Initiation of Triaminotrinitrobenzene (TATB)," *Shock Waves in Condensed Matter, 1983*, Asay, J. R.; Graham, R. A.; and Straub, G. K., eds., Elsevier Science.
14. Engleke, R., Los Alamos National Laboratory, M-7, informal quarterly report titled "Analysis of the Temperature Dependence of PBX 9502 Pop Plots," April 1991.
15. Ramsay, J. B.; Craig, B. G.; and Dick, J. J., "High-Temperature Shock Initiation of Explosive," Los Alamos National Laboratory report LA-7158 (1978).

16. Anderson, A. B.; Ginsberg, M. J.; Seitz, W. L.;  
and Wackerle, J., "Shock Initiation of Porous  
TATB," Seventh Symposium (international) on  
Detonation, 1981, p. 385
- 

#### **DISCUSSION**

R. H. GUIRGUIS

NSWC White Oak, Silver Spring, Maryland

Can you elaborate on why the voids are reduced  
when you heat the explosive? Do the TATB crystals  
expand into the voids?

**NO REPLY FROM THE AUTHOR**

## SHOCK SENSITIVITY OF IHE AT ELEVATED TEMPERATURES

P. A. Urtiew, T. M. Cook, J. L. Maienschein and C. M. Tarver  
Lawrence Livermore National Laboratory  
Livermore, California 94550

Insensitive high explosives (IHE's) based on triamino-trinitrobenzene (TATB) have been demonstrated to be very insensitive to shock, thermal, friction and other stimuli. Hazard scenarios can involve more than one stimulus, such as heating followed by fragment impact (shock). The shock sensitivity of the IHE's LX-17 and PBX-9502 preheated to a temperature (250°C) just below thermal runaway is quantitatively studied using embedded manganin pressure gauges. The thermal expansion of TATB to 250°C is measured to determine the state of the explosive prior to shock initiation. LX-17 and PBX-9502 are found to be significantly more sensitive at 250°C than at lower temperatures, but still less sensitive than ambient temperature HMX-based explosives. An ignition and growth reactive flow computer model of the shock initiation of hot IHE is developed to allow predictions of the response of hot IHE to impact scenarios which can not be tested directly.

### INTRODUCTION

With safety issues playing a dominant role in the present-day energetic materials technology, concern is growing about the safety of explosives exposed to extreme environmental conditions. In particular, this concern is expressed regarding so-called insensitive high explosives (IHEs), which normally are very insensitive to shock and other threatening initiation stimuli. However, when such an IHE is exposed to heat, it may become more sensitive to impact or to any other initiation mechanism.

Previous experiments<sup>1,2</sup> with the TATB-based explosive LX-17,\* have shown that it indeed does become more sensitive to shock but may still be regarded as an IHE when compared to other HMX-based conventional HEs. Recently, experiments at Los

Alamos<sup>3</sup> showed that IHE (PBX-9502\*\*) and LX-17 not only become more sensitive to impact at 250°C but become nearly as sensitive as the conventional PBX 9404\*\*\* when plotted on the run distance to detonation vs impact pressure plot usually called the "Pop-plot".<sup>4</sup>

Because of the important impact these observations may have on the accepted view of IHE and overall safety of various explosives systems, new experiments were undertaken to compare the results obtained by other techniques. This attempt to obtain more detailed information on the behavior of IHE under severe thermal environmental conditions formed the basis for this investigation. The main objectives here are to determine the impact thresholds for LX-17 and PBX-9502 heated to 250°C, to determine rates below the thresholds for detonation and to develop a reactive flow computer model for predictions of shock initiation of hot IHE's in untestable scenarios.

\* TATB/Kel-F 800 (92.5/7.5)

\*\* TATB/Kel-F800 (95/5)

\*\*\* HMX/NC/CEF (94/3/3)

## THERMAL EXPANSION OF LX-17

To characterize the behavior of heated IHE under dynamic loading, it is very important to know its physical state at high temperature before it is shocked. Measurements were made of the static thermal expansion of LX-17 up to 290°C, since the literature data do not extend beyond 100°C.<sup>5-7</sup> Pellets of LX-17, with length/diameter of 8.5 mm/4.4 mm or 2.9 mm/8.7 mm, were uniaxially pressed; these dimensions were chosen to give a wide range of the length/diameter (L/D) ratio. Most pellets were pressed at 20°C, and had densities of  $\approx 1.89$  g/cc (97.4% TMD). Thermal expansion was measured in the axial (i.e. along the axis of the cylinder) and radial (i.e., from center to edge of cross-section of cylinder) directions for both L/D ratios; from this, the coefficient of thermal expansion (CTE) and density were calculated. Thermal expansion measurements were made with a DuPont 941 Thermal Mechanical Analyzer (TMA) which was controlled by a DuPont 990 Thermal Analyzer, with an accuracy of  $\pm 3\%$  of the actual reading. Expansion measurements were made at a heating rate of 5°C/minute. More detail on sample preparation and further experimental results are given by Maienschein.<sup>8</sup>

Axial and radial growth data for cold-pressed LX-17 pellets are shown, as percent of initial length, in Figure 1. The axial expansion is, on average, 55% greater than the radial expansion. The thermal expansion of crystalline TATB perpendicular to the aromatic ring is  $\approx 30$  times larger than thermal expansion in the plane of the aromatic ring,<sup>5</sup> so the enhanced axial expansion of LX-17 indicates partial orientation of the TATB crystals, with the aromatic ring being forced perpendicular to the axis along which compaction pressure is applied.

Samples with both L/D ratios are included in Figure 1. If thermal expansion were driven by gas bubbles evolving in the LX-17, the axial and radial expansions would be different for different L/D ratios.<sup>8</sup> However, the results were indistinguishable for the two L/D ratios, so all data were combined in one plot.

The CTEs in the axial and radial directions are given by the derivatives of the data in Figure 1. Using the second-order polynomials shown in Figure 1, the CTEs are (in units of  $10^{-6}$  m/m/°C):

$$\text{CTE}_{\text{axial}} = 117 + 0.420 T \quad (1)$$

and

$$\text{CTE}_{\text{radial}} = 92.4 + 0.161 T \quad (2)$$

where T is temperature in °C. The volumetric CTE is

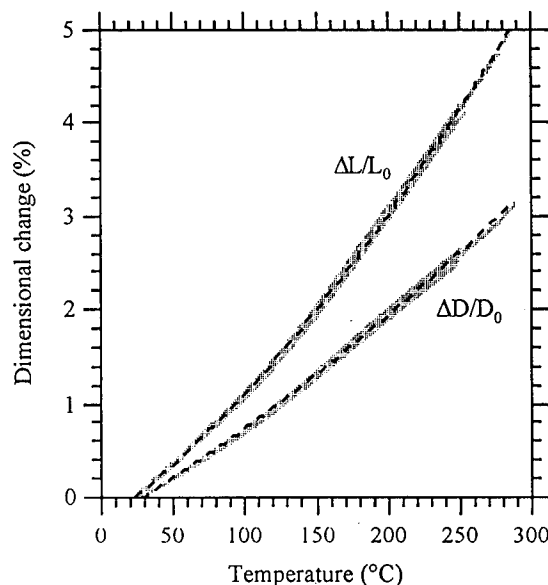


**FIGURE 1. DIMENSIONAL CHANGE IN LX-17 PELLETS WHEN HEATED TO 250-290°C.  $\Delta L/L_0$ =AXIAL GROWTH,  $\Delta D/D_0$ =RADIAL GROWTH. DATA FROM SEVERAL RUNS ARE SHOWN AS SHADED AREAS, AND 2-ND ORDER POLYNOMIAL FITS ARE SHOWN AS DASHED LINES.**

given by:

$$\text{CTE}_{\text{volumetric}} \approx 2 * \text{CTE}_{\text{radial}} + \text{CTE}_{\text{axial}}. \quad (3)$$

The resultant CTE values are shown in Figure 2, along with literature data (at lower temperatures). One may note that use of a different function to fit the expansion data will give a different dependence of CTE on temperature; however, in the absence of a physical model the simplest function that fits well (i.e. 2nd-order polynomial) is suitable. The volumetric CTE reported by Kolb<sup>5</sup> is reasonably consistent with the present data, but the other literature data<sup>6,7</sup> are lower than these results.

It was observed that, for pellets pressed at 100°C, additional expansion above that shown in Figure 1 occurred as the sample passed from 70 to 140°C. The higher density of hot-pressed pellets is apparently achieved by freezing extra strain into the solid, and this strain is released during thermal cycling. Calculation of CTEs for hot-pressed LX-17 is discussed by Maienschein.<sup>8</sup>

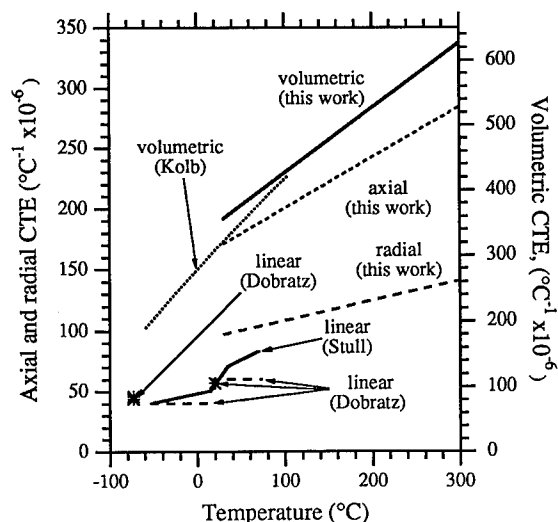


**FIGURE 2. MEASURED AND REPORTED VALUES FOR COEFFICIENTS OF THERMAL EXPANSION FOR LX-17**

#### DYNAMIC TESTS

In contrast to other experiments, which provide data only on shock and detonation velocity, the present approach is to do the experiments in the 4-in. smooth-bore gas gun, which will provide much more detailed information on pressure variation within the heated sample. The 4-in. gun thermal experiment is illustrated in Figure 3. Here, the target is much more complex than usual because it must contain not only the thin foil manganin gauges to measure dynamic changes of pressure but also two nichrome heaters to heat up the sample and eight thermocouples to monitor the temperature. All the placements within the target have to be thin and properly bonded to provide a unit without voids and with the least amount of dynamic impedance mismatch. All components such as adhesives, Teflon armor, solder joints, and signal cables had to be checked separately for strength and compatibility to withstand a full thermal load of 250°C. The gauges themselves had to be checked as well under the heated environment to make sure that they operate properly and respond to pressure as they do under ambient conditions.

A typical gas gun experiment with IHE is illustrated in Figure 4. Here a target assembly is shown in (a) before and after heating. With the aluminum back plates fixed at the target holder, IHE is allowed to

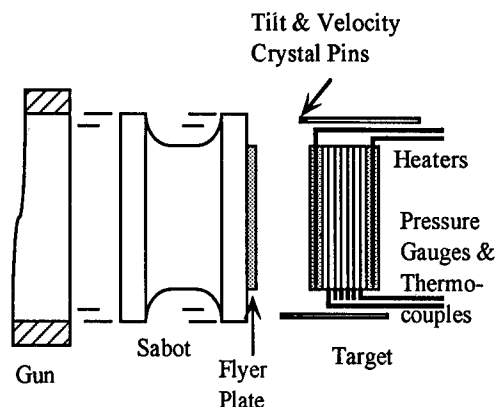


**FIGURE 3. EXPERIMENTAL SET-UP FOR THE 4" GAS GUN THERMAL EXPERIMENT**

thermally expand towards the impact surface. Locations of the gauge stations are also shown in (a). The waves generated by the impact of the projectile with the target is shown on the time distance plot in (b). Here the shock waves are represented as solid lines, particle motion as broken lines and rarefaction waves as chain dotted lines. The zero time on this plot is taken as the time the projectile strikes the crystal pins which were originally set flush with the impact surface to measure the flyer velocity as well as the tilt of the impactor. Since the tilt pins are not heated and hence do not thermally expand, their impact time occurs later than the impact with the target assembly. This accounts for the negative time of the first pressure trace and allows additional estimate of the extent of thermal expansion. Plotted to the same time scale in (c) are the pressure profiles recorded by all six gauge stations. These show the initial impact pressure pulse followed by a gradual buildup and eventual transition to detonation. The last gauge station was placed at the IHE-aluminum interface and hence the excursion in pressure is due to reflection from an impedance mismatch between aluminum and IHE.

In this case the aluminum flyer velocity was 0.9 mm/ $\mu$ s, but the pressure pulse into the LX-17 sample is only 42 kbar. At ambient temperatures, this pressure would have no effect on the material and would not have caused any reaction resulting in pressure buildup. Here, the transition to detonation took place just prior to the fifth gauge, which, after taking into account axial thermal expansion of 4%, translates into a turnover distance of 12 mm. Because of the thermal expansion



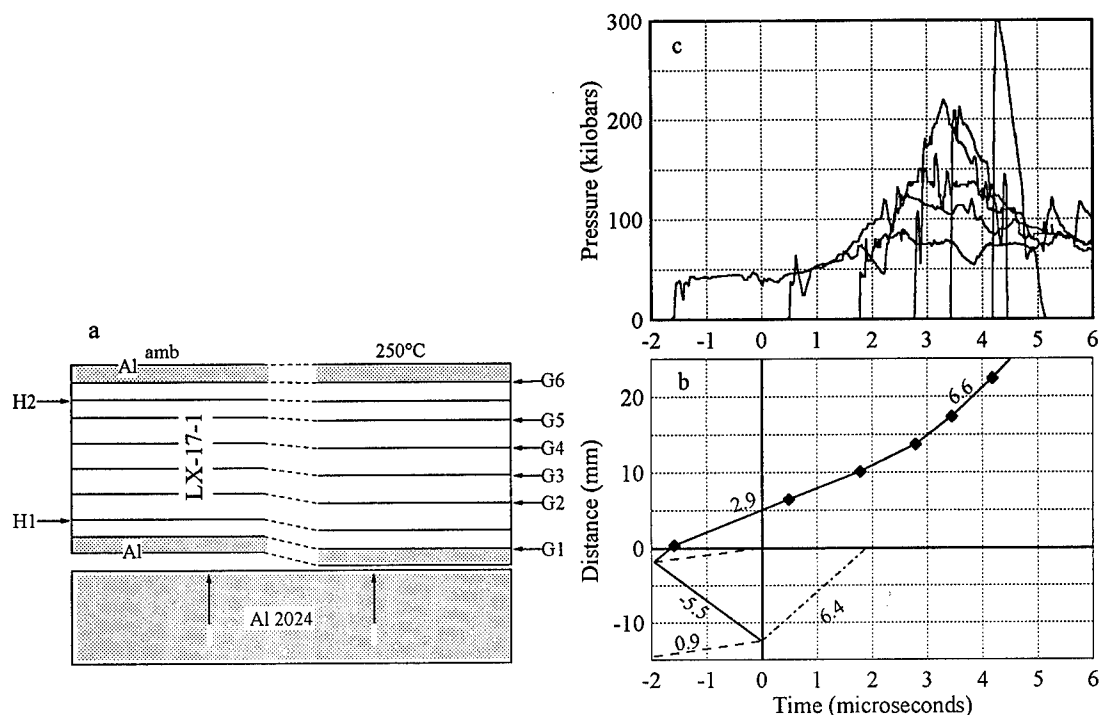


**FIGURE 4. GAS GUN EXPERIMENT WITH LX-17 TARGET HEATED TO 250°C.**

- (A) TARGET ASSEMBLY BEFORE AND AFTER HEATING WITH THE ALUMINUM FLYER JUST BEFORE IMPACT.
- (B) DISTANCE-TIME PLOT SHOWING WAVES GENERATED BY THE IMPACT (NUMBERS ABOVE LINES INDICATE VELOCITY IN mm/μs).
- (C) PRESSURE PROFILES AS RECORDED BY MANGANIN PRESSURE GAUGES.

of the material and its newly acquired lower density, the detonation parameters of heated LX-17 are also lower than those known to exist under ambient conditions. In our case, detonation pressure of LX-17 at 250°C was about 200 kbar and the detonation velocity was about 6.5 mm/μs. These agree well with the values estimated by empirical means described elsewhere<sup>9</sup>, as well as numerical calculations described below.

## MODELING

The ignition and growth reactive flow model of shock initiation and detonation of LX-17 has successfully calculated a great deal of one and two dimensional experimental data on LX-17 at ambient temperature,<sup>10, 11</sup> -54°C,<sup>2</sup> and + 88°C.<sup>2</sup> The thermal expansion measurements on LX-17 imply that at 250°C LX-17 and PBX-9502 are approximately 10% porous with a density of approximately 1.7 g/cm<sup>3</sup>. Therefore, the unreacted Hugoniot for 250°C IHE must reflect the mechanical properties, such as sound speed, of the hot, porous explosive.

The Jones-Wilkins-Lee (JWL) equation of state

which is used for both the unreacted material and the products is written as:

$$P = Ae^{-R_1V} + Be^{-R_2V} + WC_vT/V \quad (4)$$

where  $P$ ,  $V$ ,  $C_v$  and  $T$  are pressure, specific volume, specific heat at constant volume and temperature respectively and  $A$ ,  $B$ ,  $R_1$ ,  $R_2$ , and  $W$  are constants. The numerical values of all these constants are listed in Table 1.

The unreacted JWL equation of state, that is used in the ignition and growth model, is temperature based so an initial temperature of 523 K is used. To determine the shock velocity and compressibility of hot IHE, embedded manganin pressure gauge records are analyzed from the experiments which were exposed to the lowest shock pressure loadings of 2.5 and 3 GPa. These showed little or no growth of reaction at the shock front at several gauge positions. The shock arrival times at various gauge positions yield accurate shock velocities, and the measured pressures yield shock compressibility data. The unreacted Hugoniot parameters for hot IHE in Table 1 are fitted to these

**TABLE 1. JWL EQUATION OF STATE PARAMETERS FOR MODELING HOT IHE**

Parameters	Unreacted	Products
$\rho_0$ g/cc	1.7	-
A Mbars	244.8	6.5467
B Mbars	-0.0454	0.0712
$R_1$	11.3	4.45
W	0.894	0.35
$C_v$ Mbars/°K	2.487	$1 \times 10^{-5}$
T °K	523	-
$E_0$ Mbars cc/ccg	-	0.062
S Mbars	0.017	-
Y Mbars	0.002	-

experimental records. The product JWL equation of state in Table 1 is based on thermochemical code and empirical estimations of the differences in detonation properties between 250°C, 1.7 g/cm<sup>3</sup> TATB and 25°C, 1.9 g/cm<sup>3</sup> TATB.

The reaction rate equation of the ignition and growth reactive flow model is of the form:

$$\frac{\partial F}{\partial t} = I(1-F)^b(\rho/\rho_0-1-a)^x + G_1(1-F)^c F^d P^y + G_2(1-F)^e F^g P^z \quad (5)$$

where F is the fraction reacted,  $\rho$  is density, P is pressure and I, a, b, x,  $G_1$ , c, d, y,  $G_2$ , e, g and z are constants. The values of these constants are listed in Table 2. For 250°C, 1.7 g/cm<sup>3</sup> IHE, the first term in

**TABLE 2. IGNITION AND GROWTH PARAMETERS FOR MODELING HOT IHE**

CONSTANTS			
I	=	$1 \times 10^4$	a = 0.22
$G_1$	=	75	b = 0.667
$G_2$	=	400.0	c = 0.667
x	=	7.0	d = 0.111
y	=	2	e = 0.333
z	=	3.0	g = 1.0
LIMITS			
F(I)max	=	0.4	
F( $G_1$ )max	=	0.5	
F( $G_2$ ) min	=	0.5	

Equation (5) representing ignition of "hot spots" created by the shock compression is more important than in ambient temperature, 1.9 g/cm<sup>3</sup> (approximately 2% porous) LX-17 and PBX-9502, because the increased porosity of the heated IHE results in a greater number of heated regions during shock compression. The magnitude of this effect is measured by embedded gauges recording the increases in shock front strengths at greater depths in the shocked explosives. The second term in Equation (5) models the growth of reaction from isolated hot spots into the shocked, heated explosive. This growth rate is much faster than the corresponding rate for ambient IHE, because the hot spots spread more rapidly in the preheated explosive and heated regions.<sup>11</sup> The third term in Equation (5) represents the completion of reaction as detonation is approached. This reaction rate is quite rapid even for ambient TATB and thus is, most likely, not very sensitive to initial temperature.

## DISCUSSION OF RESULTS

In the following figures ignition and growth calculations are compared with experimental results. Numerical calculations match all experiments reasonably well with the set of constants which are listed in Table 2.

Figure 5 shows a record that resulted from an impact of an aluminum flyer at 0.81 mm/ $\mu$ s generating a pressure of 30 kb in the LX-17 target. The first gauge which was at an interface between IHE and aluminum buffer saw very little reaction. However, the next two gauges, located 5 and 10 mm deeper into the sample,

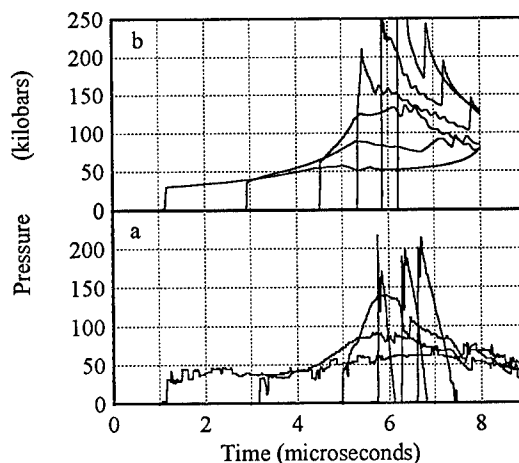


**FIGURE 5. PRESSURE PROFILES IN LX-17 HEATED TO 250°C AND IMPACTED BY AN ALUMINUM FLYER PLATE AT 0.81 mm/ $\mu$ s (A) EXPERIMENT; (B) COMPUTATION**

respectively, showed a drastic increase of reaction with the eventual transition to detonation taking place at or near the fourth gauge originally located 12 mm into the IHE. The last three gauges show a fully developed detonation wave.

Records from another experiment with a stronger impact are shown in Figure 6. The impact velocity of the aluminum flyer onto the aluminum buffer was 0.98 mm/ $\mu$ s, with a pressure pulse into the heated LX-17 of 39 kbar as shown by the first pressure jump at 0.35  $\mu$ s. The second gauge, located 5 mm into

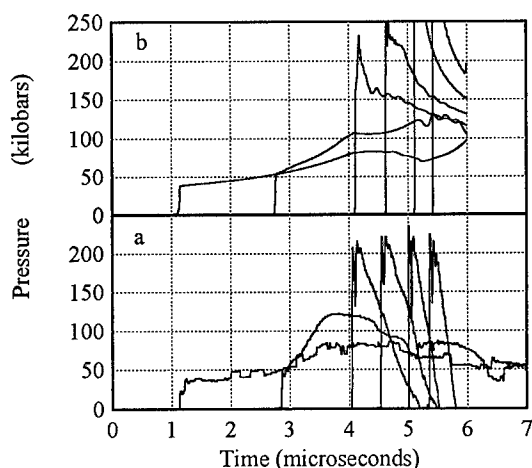


**FIGURE 6. PRESSURE PROFILES IN LX-17 HEATED TO 250°C AND IMPACTED BY AN ALUMINUM FLYER AT 0.98 mm/ $\mu$ s. (A) EXPERIMENT; (B) COMPUTATION**

the target, recorded an initial pulse of 50 kbar, followed by a very active chemical reaction that caused the pressure to rise immediately after the shock front. The next gauge that was only 5 mm deeper shows a signal that represents a fully developed detonation wave. Thus, transition to detonation, assuming again the axial thermal expansion of 4%, must have occurred approximately 7.5 mm into the heated sample.

A similar build-up regime is illustrated in Figure 7. Here the explosive is PBX-9502 which is the Los Alamos version of IHE. It contains 2.5% more TATB. The flyer velocity was 0.8 mm/ $\mu$ s and the pressure measured by the first gauge at the buffer-target interface was only 30 kbar. As one can again see at that pressure the first trace remained flat for over 6  $\mu$ s showing no evidence of any reaction taking place at that interface. The following three gauges registered typical pressure profiles of a regime representing a strong

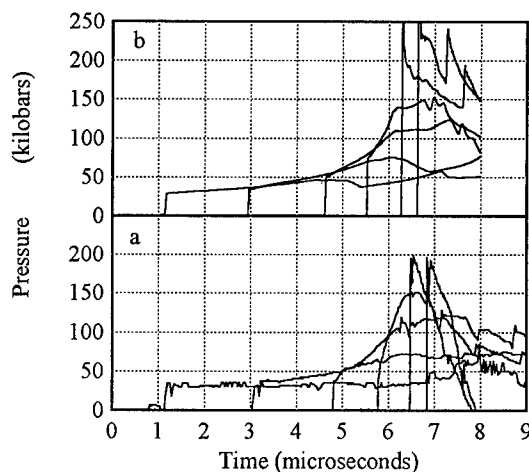


**FIGURE 7. PRESSURE PROFILES IN PBX-9502 HEATED TO 250°C AND IMPACTED BY AN ALUMINUM FLYER AT 0.8 mm/ $\mu$ s. (A) EXPERIMENT; (B) COMPUTATION**

build-up to detonation and finally the last two gauges located originally 16 and 18 mm into the target showed a fully developed detonation wave. Again, taking into account the proper thermal expansion the run distance to detonation for this system was estimated as 14.5 mm.

Another example with PBX-9502 at a slightly higher impact loading is shown in Figure 8. In this case in addition to a single element manganin gauge in its

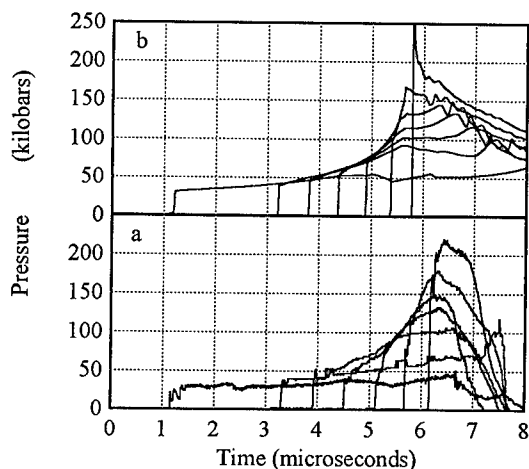


**FIGURE 8. PRESSURE PROFILES IN PBX-9502 HEATED TO 250°C AND IMPACTED BY AN ALUMINUM FLYER AT 0.88 mm/ $\mu$ s. (A) EXPERIMENT; (B) COMPUTATION**

usual place between the aluminum buffer and the IHE a multi element manganin gauge was placed at the inclined surface of the wedge sample. The target was impacted with an aluminum flyer traveling at a velocity of 0.88 mm/ $\mu$ s. The loading pressure, as measured by the first gauge, was taken as 31 kb. While the first gauge showed no evidence of reaction, throughout the test, the elements of the multimanganin gauge saw consistently rising reaction rates. The transition to

detonation probably occurred just behind the last gauge element which again after taking into account thermal expansion of 4% was estimated to be about 15 mm into the heated sample.

Experimental results of all these and other experiments in this series are listed in Table 3. This table also shows calculated values of shock velocity and pressure which one would expect from known

**TABLE 3. COMPARISON OF EXPERIMENTAL DATA ( $T_0=25^\circ\text{C}$ ) WITH CALCULATED VALUES ( $T_0=25^\circ\text{C}$ )**

	Flyer Vel (mm/ $\mu$ s)	Calculation (amb)		Experiment 250°		
		Us (mm/ $\mu$ s)	P (kbar)	Us (mm/ $\mu$ s)	P (kbar)	run dist. (mm)
IHE						
LX-17-1	0.74	3.52	34.4	2.68	25	>20
LX-17-1	0.81	3.64	39.0	2.7	30	12
LX-17-1	0.814	3.63	38.8	2.79	30	14
LX-17-1	0.898	3.77	44.5	3.0	42	11.7
LX-17-1	0.98	3.88	49.0	3.15	39	7.5
LX-17-1	1.295	4.32	70.3	3.5	65	3.3
PBX 9502	0.8	3.62	38.4	2.9	30	14.5
PBX 9502	0.88	3.73	42.76	2.97	31	15
PBX 9502	0.885	3.74	43.0	3.0	40	12

equations of state at ambient temperature. Also listed in the table are estimated values of the distances at which the transition to detonation took place. The results do support previous findings<sup>3</sup> that heated IHE does increase in shock sensitivity rather dramatically but still remains less sensitive than HMX based explosives at ambient temperatures. This is best illustrated in Figure 9 on the well known "Pop plot", which shows the run distance to detonation plotted against the impact shock pressure. On this plot the sensitivity is measured by the slope of the curve and its proximity to some already known explosives. The results here are compared with ambient LX-17 and PBX-9404, and they agree well with those obtained at Los Alamos<sup>3</sup>.

In all heated experiments the detonation wave pulses are very short, lasting less than 1  $\mu$ s and do not represent the expected detonation wave profile with the usual Taylor wave expansion. This is probably due to

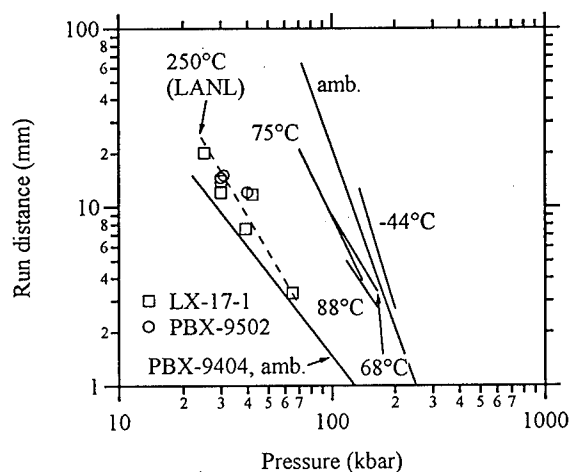


**FIGURE 9. DISTANCE TO DETONATION vs IMPACT SHOCK PRESSURE ILLUSTRATING THE SENSITIVITY OF HEATED IHE**

weakening of Teflon armor and consequential failure of small gauge elements under extremely large strains. Under normal conditions thickening of armor prolongs the active life of a gauge element but, at the same time, it reduces the accuracy of the measurement. In the heated environment thickness of the armor may not offer any significant protection because it would also be affected by the heat and weakened by it.

The pressure range covered by the four inch gun experiments is approximately 4 GPa, from 2.5 GPa, where some reaction occurs behind the shock front but transition to detonation does not occur within the 22.5 mm thick hot IHE charge, to approximately 6.5 GPa where the run distance to detonation is 3 mm. The ignition term rapidly reacts up to 10% of the explosive at shock pressures much lower than observed for ambient temperature LX-17, where shock pressures of approximately 6.5 GPa are required to start the initiation process.<sup>10</sup> The subsequent growth of reaction coefficient  $G_1$ , for hot IHE in Table 2 is approximately three times that used for ambient LX-17 initiation modeling. This demonstrates the effect of the much higher surrounding temperatures on the growth of the hot spots in these hot IHE experiments.

## CONCLUSION

The dynamic experiments provided a significant improvement in our understanding of the problem. However, because of extreme environmental conditions to which the target material is exposed, there is still a lot to be learned about the processes taking place during the event.

The results show that both TATB-based IHE's, LX-17-1 and PBX-9502, at elevated temperatures become significantly more sensitive to shock than they are at ambient temperatures. In fact their shock sensitivity approaches that of an ambient temperature HMX-based explosive such as PBX-9404.

The ignition and growth reactive flow model for hot IHE has been shown to agree reasonably well with embedded gauge records and run distance to detonation data over the pressure regime (2.5-6.5 GPa) studied. Therefore, the model can be reliably used to calculate the effects of more complex hazard scenarios that can not be studied experimentally if these scenarios deal with roughly the same pressure regimes. Model predictions for scenarios involving very different pressure regimes should be used with caution.

## ACKNOWLEDGMENTS

The authors wish to express their gratitude to E.

L. Lee, L. G. Green and W. C. Tao for their continued interest in this work, to L. Meegan and F. Garcia for their valuable assistance in performing the experiment and to C. Ynzunza for her help with typing of the manuscript. Work performed under the auspices of the U.S. Department of Energy by the Lawrence Livermore National Laboratory under contract No. W-7405-ENG-48.

## REFERENCES

1. Scheloske, R., Green, L., and Weingart, R., Sensitivity of Triaminotrinitrobenzene (TATB) at Elevated Temperatures, UCID-18336, 1980, Lawrence Livermore National Laboratory, Livermore, CA.
2. Urtiew, P. A., Erickson, L. M., Aldis, D. E., and Tarver, C. M., "Shock Initiation of LX-17 as a Function of Its Initial Temperature," Ninth Symposium (International) on Detonation, office of the Chief of Naval Research, OCNR-113291-7, Arlington, VA, 1990, pp. 112-122.
3. Dallman, J. C. and Wackerle, J., "Temperature-Dependent Shock Initiation of TATB-Based High Explosives," This Symposium.
4. Ramsey, J. B. and Popolato, A., "Analysis of Shock Wave and Initiation Data for Solid Explosives," Fourth Symposium (International) on Detonation, ACR-126, Office of Naval Research, 1965, pp. 233-238.
5. Kolb, J. R., and Rizzo, H. F., "Growth of 1, 3, 5-triamino-2,4,6-trinitrobenzene (TATB). I-Anisotropic Thermal Expansion," Propellants and Explosives, Vol. 4, 1979, p.10.
6. Stull, T. W. and Ashcraft, R. W., "Coefficient of thermal expansion of LX-17-1," MHSMP-89-13, Mason & Hanger - Silas Mason Co., Pantex Plant, April 1989.
7. Dobratz, B. and Crawford, P. C., "LLNL Explosives Handbook," UCRL-52997 Change 2, Lawrence Livermore National Laboratory, January 31, 1985.
8. Maienschein, J. L. and Garcia, F., "Thermal expansion of TATB-based explosives from 300 to 520 K," manuscript in preparation.
9. Urtiew, P. A. and Hayes, B., "Empirical Estimate of Detonation Parameters in Condensed Explosives," J. Energetic Materials, 2, No. 4, Nov.

1991, pp. 299-318.

Pyrotechnics, 15, 1990, p. 132.

10. Bahl, K., Bloom, G., Erickson, L., Lee, R., Tarver, C., Von Holle, W. and Weingart, R., "Initiation studies on LX-17 Explosives," Eighth Symposium (International) on Detonation, NSWC MP 86-194, Naval Surface Weapons Center, White Oak, Silver Spring, MD, 1986, pp. 1045-1056.
11. Tarver, C. M., "Modeling Shock Initiation and Detonation Divergence Tests on TATB-Based Explosive," Propellants, Explosives, and
12. Dobralz, B. M., Finger, M., Green, L. G., Humphrey, J. R., McGuire, R. R. and Rizzo, H. F., "Selected Sensitivity Tests of Triaminotrinitrobenzene (TATB) Formulation and their Evaluations," Lawrence Livermore National Laboratory, Livermore, CA, UCID-18026 1979.
13. Gibbs, T. R. and Popolato, A., "LASL Explosive Property Data," University of California Press, Berkeley, CA 1980, p. 363.

## AN INVESTIGATION OF XDT EVENTS IN THE PROJECTILE IMPACT OF SECONDARY EXPLOSIVES

P. J. Haskins, M. D. Cook and P. J. Cheese

Defence Research Agency  
Fort Halstead, Sevenoaks, Kent TN14 7BP, UK.

In this paper we describe the experimental arrangements and results of some recent projectile impact experiments on RDX/TNT (59.5: 39.5 + 1% beeswax) and HMX/RDX/TNT (70.25: 4.0: 24.75 + 1% beeswax). The main objective of these experiments was to study the occurrence of significantly delayed detonations; such processes being referred to as XDT events. We find such events occur under a range of projectile impact conditions, and at velocities well below those required for prompt shock initiation. These results are interpreted in terms of a two-stage process, involving charge break-up followed by initiation of the more sensitive damaged material.

### INTRODUCTION

It is well known that impact of certain energetic materials can lead to delayed detonations, these being commonly referred to as XDT events. XDT events are of considerable importance in assessing accident type situations as the threshold energies required are often considerably less than those necessary for direct shock initiation. There have been a number of previous studies<sup>1</sup> that have examined XDT in a range of possible accident configurations. However, to our knowledge none of these has examined the arrangement studied here, which represents an energetic store covered by a barrier and impacted by a small (cf. the target) projectile.

In recent years, a number of studies<sup>2,3</sup> have addressed both the measurement and modelling of prompt shock initiation thresholds. The results of such studies have given us a good qualitative understanding of such events with a moderate predictive capability. In general, prompt-shock initiation can be divided into two broad categories, namely that due to a 1-D shock and that resulting from a divergent shock. The former process being considerably more efficient than the

later. 1-D shock initiation only operates for impacts by flat-ended (180°) projectiles through thin (cf. projectile diameter) barriers. For barriers beyond a certain critical thickness the release waves in the barrier will erode the 1-D shock before it reaches the energetic material, for these cases and for pointed (or curved) projectiles a divergent shock mechanism operates. The threshold velocities for detonation with flat-ended projectiles show a marked increase at this critical barrier thickness. We have only observed XDT events with flat-ended projectiles when the barrier thickness was sufficient to eliminate the highly efficient 1-D shock mechanism. However, for conical tipped projectiles (where a 1-D shock never operates) XDT events have been observed for a range of barrier thicknesses.

### EXPERIMENTAL

Two explosives were used in this study, the majority of the experiments being carried out on RDX/TNT (59.5: 39.5 +1% beeswax) with a few additional experiments on an HMX/RDX/TNT (70.25: 4.0: 24.75 + 1% beeswax) composition. The RDX/TNT test charges were open cast to a density of

1.66 g/cc, and the HMX/RDX/TNT vacuum cast to a density of 1.81 g/cc. The majority of the experiments were carried out on unconfined cylinders of RDX/TNT covered, on the front face only, by various thicknesses of barrier plate. All impacts were carried out on the flat front face of the cylindrical test charges. The test charges were 100 mm long in four different diameters (50, 57, 70 and 100 mm). Some experiments were also carried out on the 57 mm diameter charges encased in 9 mm thick steel bodies. For the HMX/RDX/TNT composition only 57 mm diameter uncased charges were used. Most of the experiments employed aluminum barrier plates although some experiments were also carried out with PMMA and steel as barrier materials.

Flat-ended projectiles in two diameters (13.15 and 8 mm), and 13.15 mm diameter conical-tipped (165°, 150°, 120°, 90° and 30°) projectiles were employed in the study. These projectiles were housed in a nylon sabot and fired from a rifled 30 mm RARDEN gun. This arrangement allowed velocities in the range 800-2000 m/s to be studied with very few projectile stability problems. All firings were filmed with a Fastax camera, fitted with a quarter height block, framing at ca. 30,000 fps. The film record was used to determine projectile velocities and to check on projectile stability. In the firings where XDT events occurred the film record was also used to give an approximate delay time between impact and detonation. In some of the experiments ionization probes were mounted at a number of points on the surface of the charge to give more accurate estimates of the delay time and the position at which transition to detonation occurred.

## RESULTS

This study has entailed approximately 300 separate firings of which over 60 have yielded XDT type events. The experiments showed that the occurrence, or otherwise, of XDT events depended strongly on the degree of lateral confinement. No XDT events were observed with steel-cased and 100 mm diameter charges for any barrier thickness (including bare) or projectile type. The only detonations achieved with these targets were the result of prompt shock induced reaction. However, 50 mm, 57 mm and 70 mm charges all gave XDT events under a wide range of conditions, at velocities below those required for prompt shock initiation. The XDT events obtained with these charges are described below.

Considering the RDX/TNT results first. Figure 1 shows the region (shaded) in which XDT events were observed for 13.15 mm flat-ended projectiles relative to

the prompt shock threshold curve. The results of the firings for all projectile types are summarized in table 1. In this table we give the velocity window in which XDT events were observed for various barrier and projectile type combinations. The minimum velocities quoted in the table represent the lowest for XDT events regardless of charge diameter. The upper velocities quoted are the prompt shock threshold values, some of which lie above the maximum (2000 m/s) achievable with the gun system employed. It should be noted that not all impacts within this velocity window yielded an XDT event. A number of factors appear to influence the probability of obtaining an XDT, and whilst they are not fully understood, a number of trends are apparent. For the three charge diameters for which we have observed XDT events there appears to be no significant difference in threshold velocities. However, the probability of obtaining XDT events does appear to decrease as the charge diameter increases. Another factor that appears to influence the probability is the presence, or otherwise, of a barrier plate. It was found to be easier to obtain XDT events when the charge was covered by a moderately thick barrier. The reason why all impacts within the velocity window do not yield an XDT event is not totally clear, however slightly off-centre strikes may well be a contributory factor. A further factor, particularly for flat-ended projectiles, could be slight deviations in the impact angle. It is also possible that the inherently statistical nature of charge break-up plays an important role (the significance of charge break-up is discussed in the next section). For many of the configurations studied (particularly those employing 50 mm diameter charges) most XDT events were found to occur at the lower end of the velocity window.

Despite the reservations expressed above, concerning XDT velocity windows, some clear trends are discernible. Firstly, as can be seen from table 1, for impacts with flat-ended projectiles there is an increase in threshold velocity with increasing barrier thickness. Secondly, the results obtained with 7 mm aluminum barriers show a general trend of increasing threshold velocity with decreasing projectile cone angle. However, the effect of cone angle is less marked than for prompt shock thresholds.<sup>3</sup> Thirdly, as might be expected there is an increase in the threshold velocity for XDT events with decrease in projectile diameter.

For all the experiments the delay time between projectile impact and onset of detonation was estimated from the high speed cine records. In general XDT events were found to exhibit delays in the region of 50 - 200  $\mu$ s. For delay times at low end of this range the projectile was inside the charge at the time of transition



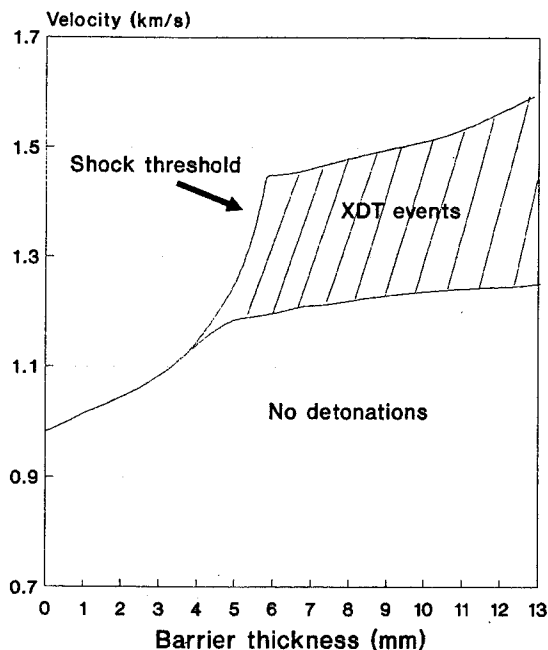


FIGURE 1. PROMPT SHOCK THRESHOLD CURVE FOR RDX/TNT

TABLE 1. XDT VELOCITY WINDOWS FOR RDX/TNT CHARGES

Barrier	Projectile Cone Angle (degrees)	Projectile Diameter (mm)	XDT Window (m/s)
5 mm Al	180	13.15	1032-1152
7 mm Al	180	13.15	1153-1455
9 mm Al	180	13.15	1228-1710
12 mm Al	180	13.15	1230->2000
7 mm Al	165	13.15	1282-1644
7 mm Al	150	13.15	1269->2000
7 mm Al	120	13.15	1366->2000
7 mm Al	90	13.15	1419->2000
7 mm Al	30	13.15	1542->2000
Bare	120	13.15	1398-1816
7 mm Al	180	8	1742->2000

to detonation, however for some of the longer delay times the projectile could be seen emerging from the rear surface of the charge when detonation occurred. For these long delay times the film records appear to show onset of detonation at or near the rear surface of the charge (i.e., close to the projectile). Whilst a precise correlation could not be established (the error in estimating delay times from the cine records was ca.  $\pm 30\mu\text{s}$ ) there were trends towards longer delays

with thicker barriers and with decrease in projectile cone angle. Examples of two high speed cine records are shown in figures 2 and 3. Both figures are of the same experimental arrangement, namely a 57 mm diameter RDX/TNT charge covered by a 7 mm aluminum barrier and impacted by a 13.15 mm flat-ended projectile. The only difference between these experiments was the projectile velocity which was 1650 m/s for figure 2 and 1445 m/s for figure 3. It can clearly be seen that the event depicted in figure 2 is 'prompt' (i.e., less than  $30\mu\text{s}$ ) whereas that shown in figure 3 is delayed by some three frames (ca.  $100\mu\text{s}$ ). In a few specific experiments ionization probes were attached to the charge surface to give more accurate measurements of the delay time and point of initiation. The results of the probe timings were consistent with the estimates from the cine records, although probes were not employed on any firings in which the projectile emerged from the charge prior to detonation. By way of example, 3 typical results from probe timings are shown in table 2. Whilst the delay between impact and break-out of detonation could be assessed fairly accurately from the probe readings it was not possible to precisely identify the point of initiation. However, it is clear that XDT events are initiated well inside the charge and not at the front face as in prompt shock initiation.

TABLE 2. PROBE TIMINGS FOR 57 MM DIAMETER RDX/TNT CHARGES AND FLAT-ENDED PROJECTILES

Barrier	Velocity (m/s)	Delay time ( $\mu\text{s}$ )*
5 mm Al	1129	50
7 mm Al	1178	66
9 mm Al	1228	70

\*Delay times quoted are from projectile impact to break-out of detonation on the charge surface.

A small number of experiments were carried out on 57 mm diameter uncased HMX/RDX/TNT charges covered by PMMA or steel barrier plates. These experiments showed that XDT events were not unique to the RDX/TNT - aluminum barrier plate combination. The most significant results obtained from these experiments were those pertaining to flat-ended projectiles impacting through thick PMMA or steel barriers. In these experiments XDT events were observed for PMMA thicknesses ranging from 7 to 25 mm. Even for the thickest of these barriers an XDT event was observed at the relatively low velocity of 1682 m/s. For this barrier thickness the prompt shock threshold is well above the 2000 m/s achievable with

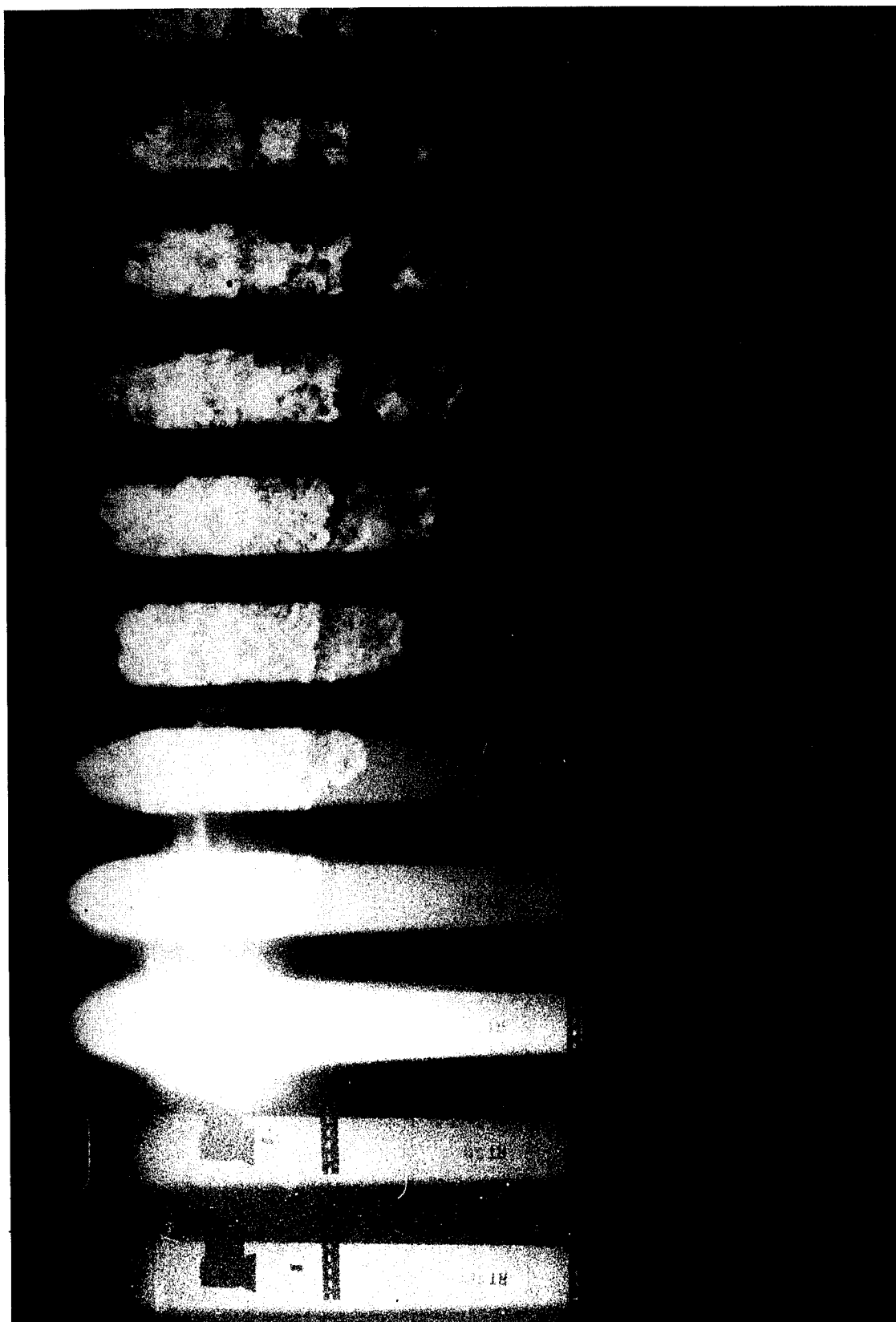


FIGURE 2. HIGH SPEED CINE SEQUENCE ILLUSTRATING A PROMPT SHOCK INDUCED DETONATION

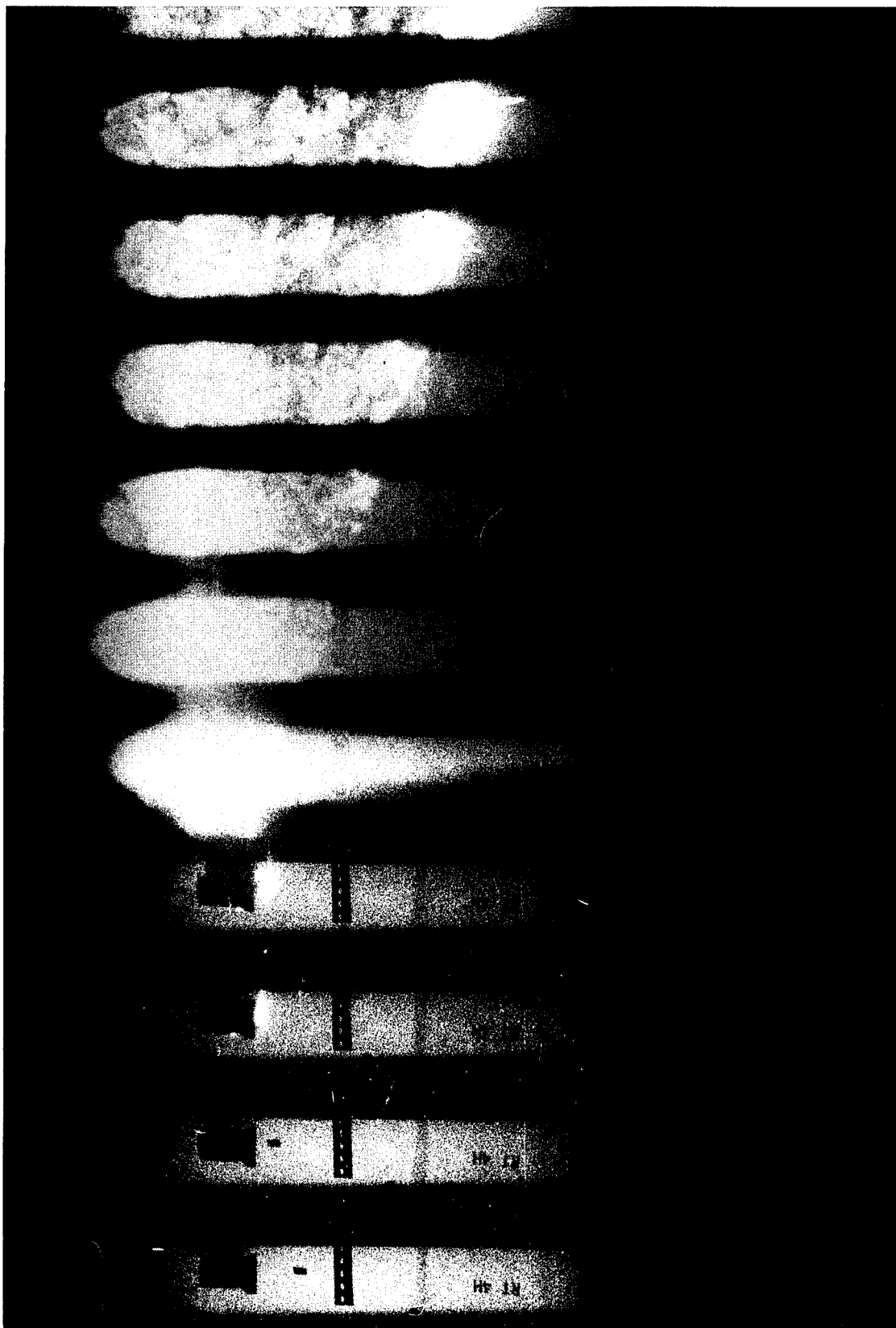


FIGURE 3. HIGH SPEED CINE SEQUENCE ILLUSTRATING AN XDT EVENT

our gun system. For PMMA barriers of 10 mm and greater long delays were observed, and the projectiles were at or near the rear surface of the charge when detonation occurred. The experiments with a 7 mm barrier showed significantly shorter delays. Only a few experiments were carried out with steel barriers, but an XDT event was obtained at 1487 m/s with a 10 mm barrier, and after a delay of ca. 200  $\mu$ s.

## DISCUSSION

The results in this paper and reference 1 have shown that delayed detonations can be obtained under a wide variety of conditions and at stimulus levels well below those required for prompt shock initiation. An understanding of events of this type is therefore crucial if we are to develop a fully predictive hazard response capability.

It is well known that the mechanical properties of an energetic material play a large part in determining its hazard properties. In brittle materials, such as those studied here, damage is not only easily sustained but usually results in significant sensitization. In looking to explain XDT events one is therefore drawn to proposing a mechanism in which damaged material plays a significant role. In this context Green et al<sup>1</sup> proposed charge break-up followed by initiation through recompaction of the now more sensitive material. In the paragraph below we propose a similar mechanism to explain our results.

When a projectile impacts the centre of a covered or bare cylindrical charge, a shock wave travels ahead of the projectile and diverges, ultimately reaching the sides of the charge whereupon it is reflected towards the axis as a tensile wave. We propose that in the time scale of our experiments that the most important source of damaged material arises from this reflected tensile wave. The strength of this tensile wave, and therefore the amount of damage that ensues, is dependent on the diameter of the charge. The time that the tensile wave reflects back on axis is also diameter dependent. For large diameter charges damage caused by this mechanism will therefore occur at later times and be less severe. For steel cased charges there is clearly no tensile wave of this type, the shock merely being reflected. 2D hydrocode calculations support our hypothesis that this reflected tensile wave is the major source of damage. An illustration of such a calculation is shown in Figure 4. This figure shows a DYNA2D negative pressure contour plot at 19  $\mu$ s after impact of a 13.15 mm diameter flat-ended projectile. The projectile velocity was 1400 m/s and the explosive was covered with a 7 mm aluminum barred plate. In this example the strong rarefaction caused by the reflected

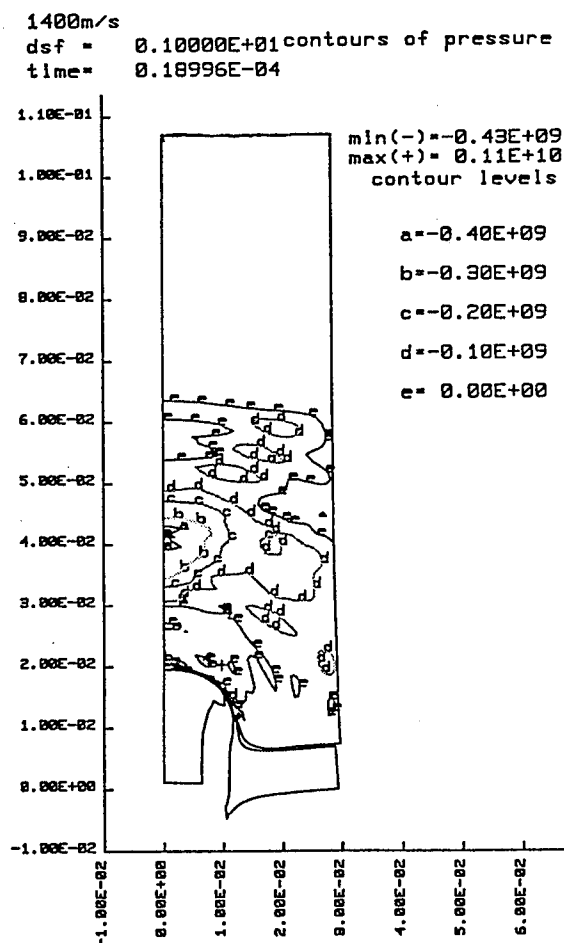


FIGURE 4. DYNA2D NEGATIVE PRESSURE CONTOUR PLOT

tensile wave can clearly be seen on the charge axis about 2 cm ahead of the projectile.

In those circumstances where damage occurs in an appropriate time-scale (i.e., by the mechanism suggested above) the onset, or otherwise, of detonation is dependent upon an additional stimulus sufficient to initiate the more sensitive damaged material. This stimulus could take the form of the recompaction wave generated by the projectile (as proposed by Green et al<sup>1</sup>), as it penetrates the charge. It is highly plausible that recompaction will result in badly damaged material undergoing SDT at substantially reduced pressures. Whilst this appears to be the most likely source of an appropriate initiation stimulus, others cannot be ruled out. Clearly high temperatures, and therefore ignition sites, could also be generated by a number of processes such as adiabatic shear and friction. Such ignitions in

sufficiently powdered material may then transit to detonation via a rapid DDT type process.

The two stage mechanism proposed above is consistent with the main results that we have presented in this paper, in particular explaining the lack of XDT events with cased and large (100 mm) diameter charges. With steel cased charges the results being simply explained by the absence of a reflected tensile wave and therefore an appropriate level of damage. For the 100 mm diameter charges the reflected tensile wave will be weaker and will arrive later than for the smaller targets. Either of these factors could be responsible for there being an inadequate level of damage at the appropriate time (namely the projectile arrival time for a recompression process). The fact that XDT events are more easily obtainable with thick barriers could possibly be interpreted in terms of the extra time available for damage before projectile arrival.

The results that we have presented here are particularly relevant to projectile or fragment impact on bare or lightly cased energetic materials. It is clear that for such systems, the material properties of the explosives will play a large part in determining the hazard response, and that for brittle materials the prompt shock threshold does not provide a safe go-no go level.

This study further highlights the importance of understanding the behaviour of dynamically (as well as statically) damaged energetic material. While the work reported here, and elsewhere, has given us a qualitative understanding of the processes involved, much work has still to be done if a predictive capability is to be achieved.

## REFERENCES

1. Green, L.; James, E. and Lee, E.; "Energetic Response of Propellants to High Velocity Impact," *Eighth Symposium (International) on Detonation*, Albuquerque, New Mexico, p. 284, 1985, and reference therein.
2. Cook, M. D.; Haskins, P. J. and James, H. R.; "Projectile Impact Initiation of Explosive Charges," *Ninth Symposium (International) on Detonation*, Portland, Oregon, p. 1441, 1989.
3. Cook, M. D.; Haskins, P. J. and James, H. R.; "An Investigation of Projectile and Barrier Geometry Effects on Impact Initiation of a Secondary Explosive," *American Physical Society Topical Conference on Shock Compression of Condensed Matter*, Williamsburg, Virginia, p. 675, 1991.

---

## DISCUSSION

BLAINE ASAY

Los Alamos National Laboratory, Los Alamos,  
New Mexico

What is your estimate of the bow wave pressure that arises from penetration of the bullet?

### REPLY BY MALCOLM COOK:

Although we have not estimated the bow wave pressure, we are confident that it is significantly less than that required for shock initiation leading to SDT.

## DISCUSSION

PEI CHI CHOU

Drexel University, Philadelphia, Pennsylvania

Do you think shear strain plastic deformation and viscosity could be the mechanism in causing ignition and burn in your experiments? In your code simulation, is the shear-generated heat included in the calculation?

### REPLY BY MALCOLM COOK:

Could cause ignition, although in many cases the initial shock is strong enough to cause deflagration, but not detonation. No, shear generated heat was not included in our calculations.

**SESSIONS ON**  
**NEW METHODS**

**Cochairmen:**    **LeRoy Green**  
                         **Lawrence Livermore National Laboratory**

**Hugh James**  
                         **Atomic Weapons Establishment (Foulness)**

# THE USE OF QUANTUM CHEMISTRY TO ESTIMATE THE PERFORMANCE AND PROPERTIES OF EXPLOSIVES

James P. Ritchie  
Los Alamos National Laboratory  
Los Alamos, NM 87544

Quantum chemistry techniques were applied to investigate two problems involving explosives. In the first instance, cyclotriphosphazenes were examined. Using calculated heats of formation, geometries, and vibrational frequencies when needed, the detonation performance of these compounds was qualitatively assessed. It was found that the burning of phosphorous contributes importantly to  $Q$ , which is not as large as in aluminized explosives. In addition, calculated values of  $P_{CJ}$  and  $V_{19}$  are in the range of common organic explosives like RDX and TNT. In the second example, *ab initio* molecular orbital techniques were used to obtain a charge distribution for benzotrifuroxan (BTF). This was then used in crystal structure modeling. A hypothetical polymorph of BTF was found to have a density greater than that of the observed polymorph. This is in violation of the close-packing principle. An analysis of intermolecular interactions showed that strong, highly-directed, and atom-specific electrostatic interactions are responsible.

## INTRODUCTION

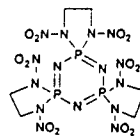
In the course of estimating the performance and properties of explosives, two problems arose that were particularly unusual. The interesting aspect of both these problems was that quantum chemistry techniques were used to calculate quantities normally obtained from experiment. These quantities were then used as input to other computations to estimate observable properties of explosives. In one instance, calculated heats of formation and vibrational frequencies were used to examine the explosive potential of some novel phosphorous-containing compounds. In the other case, beginning with a space-group specification, the structure and energy of a hypothetical polymorph of BTF was modeled using the molecular geometry and charge distribution from *ab initio* molecular orbital calculations.

## CYCLOTRIPHOSPHAZENES

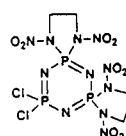
Compounds I - III have been synthesized as possible energetic materials.<sup>1</sup>

The use of phosphorous in an explosive is novel.

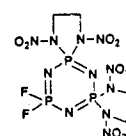
It is interesting to compare and contrast the use of phosphorous in an explosive with that of alu-



TEDNCP  
I

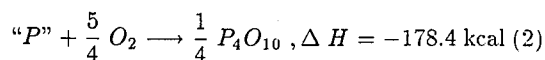
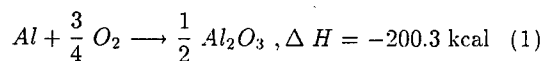


Dichloro  
II

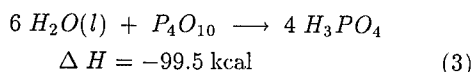


Difluoro  
III

minum. As shown below, oxidation of both these third-row elements is strongly exothermic, with phosphorous being less so by about 10%.<sup>2</sup>



On the other hand, alumina is a refractory solid, whereas  $P_4O_{10}$  melts in the range 580-585°C. An additional complicating factor is that  $P_4O_{10}$  reacts with water according to Equation 3 to produce phosphoric acid. It melts at 43°C.



These simple considerations suggest that the burning of phosphorous in I – III will contribute significantly to the heat of detonation (Q). In addition, because phosphorous is incorporated intramolecularly, its burning should be fast, thereby avoiding the complications encountered in aluminum explosives, which require fast reaction of hot gases with the metal particles to deliver their full energy. Finally, the phosphorous content by weight is: I, 16.0%; II, 18.5%; III, 19.8%. This loading is similar to that found in some common aluminized explosives; eg., Alex 20, 44/32.3/19.8/4 RDX/TNT/Al/Wax and H-6, 45/30/20/5 RDX/TNT/Al/Wax.<sup>3</sup>

To provide some information about the potential explosive performance of these compounds, some semi-empirical quantum-chemistry calculations were performed. PM3 has been parametrized to treat phosphorous, in addition to the other elements in I – III.<sup>4</sup> It was, thus, used to obtain heats of formation of these compounds. The results of these calculations are shown in Table I. Heats of formation of I – III<sup>4</sup> are for gas-phase molecules, while condensed phase quantities are desired. These were obtained by subtracting 25 kcal/mol from the gas phase numbers, as an approximation to the heat of sublimation.

Unlike aluminum, the thermodynamic state of phosphorous in I – III is not known *a priori*. It

**TABLE I. HEATS OF FORMATION FOR I-III FROM PM3 CALCULATIONS. ALSO SHOWN ARE THERMODYNAMIC FUNCTIONS FOR PHOSPHOROUS CONTAINING DETONATION PRODUCTS**

PM3 Heats of formation (kcal/mol)			
I	II	III	
5.4	-61.5	-163.9	
Calculated (unscaled) Vibrational Frequencies in cm <sup>-1</sup> (degeneracy)			
P <sub>4</sub> O <sub>10</sub>	H <sub>3</sub> PO <sub>4</sub>	HPO <sub>3</sub>	
183.9 (2), 194.2 (3), 200.0 (3),	137.6, 169.3, 177.3	292.7, 327.8, 346.9	
218.3 (2), 298.7 (3), 322.7 (3),	221.3, 260.9, 312.1	391.9, 766.0, 934.4	
455.1 (3), 478.9, 604.8, 656.6 (3)	342.4, 357.4, 728.9	960.5, 1172.9, 3952.6	
673.7 (3), 679.5 (2), 912.4 (3)	788.3, 799.5, 946.6		
1050.0 (3), 1097.6	984.5, 1012.3, 1088.0		
	3950.5, 3952.0, 3961.8		
Thermodynamic Functions (in cal/mol and cal/mol-deg)			
S(T) = A + BT + CT <sup>2</sup> + DT <sup>3</sup> + ET <sup>4</sup>			
H <sub>T</sub> <sup>o</sup> - H <sub>0</sub> <sup>o</sup> = BT <sup>2</sup> /2 + 2CT <sup>3</sup> /3 + 3DT <sup>4</sup> /4 + 4ET <sup>5</sup> /5 + IC			
$\Delta H_{f0}^o(g) = \Delta H_{f300}^o(c) + \Delta H_{sublimation} - (H_{300}^o - H_0^o)_{compound} + \sum (H_{300}^o - H_0^o)_{elements}$			
A	71.565850	64.890956	58.107995
B	0.160496	7.506319E - 2	4.756117E - 02
C	-5.163160E - 05	-2.316231E - 5	-1.495102E - 05
D	8.563724E - 09	3.796199E - 09	2.463246E - 09
E	-5.375657E - 13	-2.374797E - 13	-1.543124E - 13
IC	6.000000E + 03	4.000000E + 03	3.000000E + 03
$\Delta H_{f0}^o(g)$	-696.2E + 03	-283.0E + 03	-206.1E + 03
$\Delta H_{f300}^o(c)$	-720.0E + 03*	-306.2E + 03*	-228.1E + 03*
$\Delta H_{sublimation}$	17.6E + 03*	20.0E + 03**	20.0E + 03**
$(H_{300}^o - H_0^o)_{compound}$	9.4E + 03	5.3E + 03	3.5E + 03
$\sum (H_{300}^o - H_0^o)_{elements}$	15.62E + 03***	8.48E + 03***	5.43E + 03***

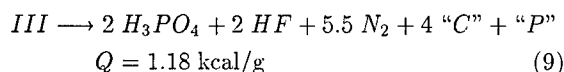
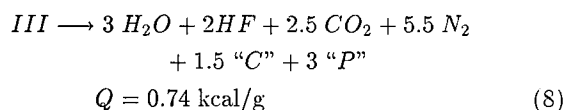
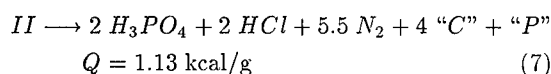
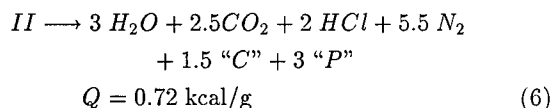
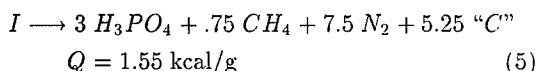
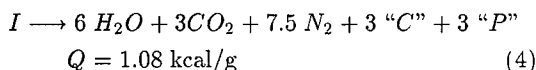
\* F.D. Rossini, D.D. Wagman, W.H. Evans, S. Levine, I. Jaffe *Circular of the National Bureau of Standards* 500, 1952.

\*\* Estimated.

\*\*\* Reference 2.



may, therefore, provide either more or less energy than the pure element, shown in Equation 2. Using the heat of formation of I - III, as described above, heats of detonation were computed. The value of this quantity was obtained in two different ways. In one set of calculations, phosphorous was treated as the element in its standard state, while in the other it was allowed to burn to produce phosphoric acid, as shown:



Thus, it is predicted that the burning of phosphorous contributes importantly to  $Q$ . In addition, the value of this quantity for I is greater than that of HMX (1.48 kcal/g, but BTF is higher yet at 1.69 kcal/g), but not so large as that for typical aluminized explosives (HBX-1: 1.84 kcal/g; HBX-3: 2.11 kcal/g; MINOL-2: 1.86 kcal/g).  $Q$  for II and III is similar, but lower than that for I, due to incomplete burning of phosphorous. Nonetheless, these values are near that found for TATB (1.08 kcal/g). Thus, the heats of detonation for I - III are in the range of common organic explosives.

The errors in  $Q$  arise from uncertainties in the PM3 estimate of the heats of formation of I - III. The root-mean-square error in this quantity for P containing compounds is 14.3 kcal/mol.<sup>4</sup> Although this error is relatively large, it is less than 5% of  $Q$ .

Although  $Q$  is an important factor to consider in assessing explosive performance, additional information is desirable. BKW<sup>5</sup> was selected to estimate the CJ state and expansion isentrope for I - III. It requires a description of the temperature dependence of the enthalpy and entropy, in addition to

a value of the co-volume for each of the detonation products. These quantities have not been previously obtained for phosphorous-containing detonation products. The thermodynamic functions can be obtained from the molecular vibrational frequencies and geometry, which were obtained from PM3 calculations. A previous study showed that O-H frequencies calculated in this way are, on average, 6.4% too high, while heavy-atom stretches are 3.4% too high.<sup>6</sup> The frequencies found for  $P_4O_{10}$ ,  $H_3PO_4$ , and  $HPO_3$ , shown in Table I, were thus scaled uniformly by a factor of .95 to account for this systematic error. Scaled values of the vibrational frequencies and molecular geometries were then used in the manner described by Mader<sup>5</sup> to obtain temperature fits for the enthalpy and entropy, in addition to geometric co-volumes. Finally, crystal densities are required for I-III. This quantity has been determined from x-ray analysis for I and II,<sup>1</sup> but was unavailable for III. It was estimated by fitting the density of I using Stine's C,H,N, and O increments<sup>7</sup> to obtain a corresponding value for the ring P. This value ( $18.9\text{\AA}^3$ ) was then used to estimate the density of III.

Using the quantities discussed above to describe the phosphorous-containing compounds, BKW calculations were performed. The resulting CJ parameters are shown in Table II.

**TABLE II. CALCULATED BKW RESULTS FOR I - III**

	Density (g/cc)	$E_0$ (kcal /mol)	$P_{cj}$ (kbar)	$D_{cj}$ (mm / $\mu$ s)	$T_{cj}$ (K)	$V_{cj}$ (cc/g)	$\gamma_{cj}$
I	1.887	44.34	330	8.555	2533	0.403	3.19
II	1.898	-52.60	316	7.912	1941	0.387	2.76
III	1.960	-155.00	315	8.458	1685	0.395	3.44

The CJ parameters along with the estimates of  $Q$  indicate that I-III may be explosives. These quantities and the expansion isentropes indicate that I is likely to perform best of the three. Furthermore, as will be argued next, it is probable that the quantities shown in Table II are upper limits for the performance of these explosives. This is because values of the CJ parameters shown in Table II are quite sensitive to the co-volumes and because, for usual detonation products, the geometric co-volume is frequently found to be similar to or less than that required to fit explosive and Hugoniot data, where it exists. Thus, a geometric co-

volume for phosphorous-containing detonation products is probably the largest plausible value for this quantity. To investigate the sensitivity of the CJ parameters to the co-volumes, BKW calculations were performed for I, using the nominal set of co-volumes and ones reduced both individually and uniformly by 20% and 50%. The results of this parameter study are shown in Table III. The nominal geometric co-volumes are shown in the first column. In addition, a one-dimensional hydrocode simulation of a 1 inch cylinder test was performed to estimate  $V_{19}$ . This provides information about the expansion isentrope. For comparison, a similar calculation yields: HMX, .198; RDX, .193; Comp-B, .176; TNT, .156 cm/ $\mu$ s. These calculated values are often about 10% too large, but provide qualitative information about the likely performance of the cyclotriphosphazenes. The results of this parameter study are shown in Table III. The nominal geometric co-volumes are shown in the first column.

It was found that the chemical composition is extremely sensitive to the co-volumes employed, even moreso than the CJ quantities. The balance between the detonation products spans a wide range with the variations examined. The computed CJ parameters, with one exception, are reduced relatively uniformly with reductions in the co-volumes. For  $\text{HPO}_3$ , it was found that a 20% reduction from nominal of the covolume gave CJ quantities and a  $V_{19}$  similar to those obtained using nominal values. Further reduction of the co-volume resulted in a corresponding reduction of the performance parameters. Somewhat remarkably,  $V_{19}$  proved much less sensitive to variations in values of the co-volumes than  $P_{CJ}$ . However, the trend is the same, with reductions in the co-volumes causing a reduction in  $V_{19}$ . Thus, it appears that the use of geometric co-volumes provides an upper limit for estimating the performance of these explosives. The values of these

quantities covers a very wide range, but are in the range of common organic explosives.

As noted above, co-volumes for phosphorous-containing compounds are subject to large uncertainties. Although we followed the recommended procedure for deriving their values, further adjustment of them may be required. A practical approach to this would be to scale all the co-volumes uniformly to fit a small amount of experimental data. These values could then be used to estimate the performance of other phosphorous containing compounds, or the compounds examined here at different densities or in admixture with other compounds.

**Conclusion:** A qualitative assessment has been made of the likely performance of I - III using quantum chemical techniques and BKW. The results show that the burning of phosphorous contributes importantly to Q. Additional calculations predict that the compounds I - III will likely perform in the range of common organic HE's. Further adjustment of the covolumes of phosphorous containing compounds may prove necessary, and this may be done with a uniform scaling factor being applied to all the pertinent co-volumes. Finally, the approach described here serves as an example for evaluating other novel explosives and the thermodynamic functions of detonation products.

## POLYMORPHS OF BENZOTRIFUROXAN

Holden, Du, and Ammon recently developed a procedure to predict possible crystal structures of C,H,N,O, and F containing organic compounds.<sup>8</sup> In addition to identifying an observed structure of a molecular crystal, this procedure may also yield alternative possible polymorphs. For many explosives, especially those that are conformationally flexible, polymorphism is well-known.<sup>9</sup> Under standard

**TABLE III. VARIATION OF CJ PARAMETERS AND  $V_{19}$  FOR I WITH CHANGES IN COVOLUMES FOR PHOSPHOROUS CONTAINING DETONATION PRODUCTS. ALL OTHER QUANTITIES WERE HELD CONSTANT.**

CV $\text{H}_3\text{PO}_4$ =	1790	1432	1432	1790	1790	895	1790	1790
CV $\text{HPO}_3$ =	1600	1280	1600	1280	1600	800	1600	800
CV $\text{P}_4\text{O}_{10}$ =	4600	3680	4600	4600	3680	2300	2300	4600
$P_{CJ}$ (kbar)	330	271	270	335	299	204	237	258
$D_{CJ}$ (km/s)	8.56	7.60	7.60	8.59	7.85	6.38	6.96	7.32
$T_{CJ}$ (K)	2533	3013	3015	2488	2768	3569	3202	2834
$\gamma_{CJ}$	3.19	3.03	3.04	3.16	2.89	2.77	2.87	2.92
mols $\text{H}_3\text{PO}_4$	2.97	2.99	3.00	2.52	0.11	2.89	0.00	0.00
mols $\text{HPO}_3$	0.00	0.01	0.00	0.48	0.00	0.11	0.00	3.00
mols $\text{P}_4\text{O}_{10}$	0.01	0.00	0.00	0.00	0.72	0.00	0.75	0.00
$V_{19}$ (cm/ $\mu$ s)	0.184	0.178	0.178	0.184	0.185	0.168	0.179	0.173

conditions, the common polymorph is typically the densest. This observation resulted in the principle of close-packing, which was advanced many years ago by Kitaigorodsky as a guide to the prediction of crystal structures.<sup>10</sup> Exceptions to this principle are therefore of interest because identification of the responsible factors could lead to new strategies in the design and development of novel explosives. Moreover, the occurrence of polymorphism and the transitions between polymorphs in explosives is of interest in its own right.

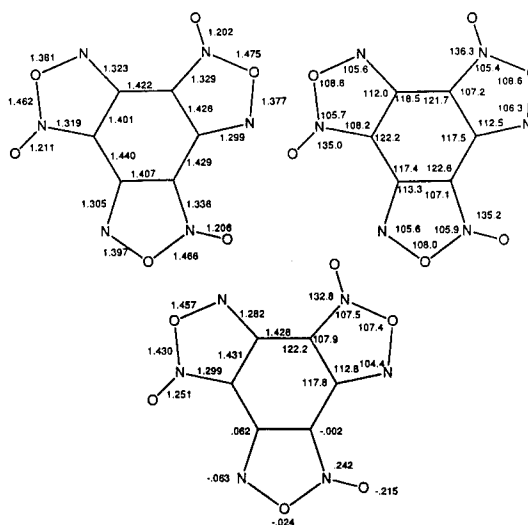


**FIGURE 1. OBSERVED (ABOVE) AND THEORETICAL STRUCTURES (BELOW) FOR BTF. BOND LENGTHS (Å) ON LEFT, BOND ANGLES (°) ON RIGHT. ATOM CHARGES FROM ACME's ARE SHOWN NEAR THE DOWNWARD POINTING FUROXAN RING.**

TABLE IV. ENERGY-OPTIMIZED CELL PARAMETERS FROM PCK/ME IN SPACE GROUP Pna2<sub>1</sub> WITH Z=4.

a=6.7438, b=19.3552, c=6.6793 Å, α = β = γ = 90°				
atom		cell		
ia	label	x	y	z
1	C	0.41524	0.10026	0.00163
2	C	0.38153	0.16685	-0.31744
3	C	0.68141	0.09361	-0.25838
4	C	0.30814	0.14635	-0.12622
5	C	0.60120	0.07466	-0.06784
6	C	0.56884	0.13970	-0.38013
7	N	0.32491	0.08813	0.16689
8	N	0.30355	0.20732	-0.44748
9	N	0.84972	0.06527	-0.29359
10	N	0.14482	0.16328	-0.03545
11	N	0.72578	0.03283	0.01774
12	N	0.60758	0.16461	-0.55648
13	O	0.14285	0.12842	0.15335
14	O	0.44585	0.20846	-0.61164
15	O	0.88947	0.02384	-0.11590
16	O	0.00298	0.20156	-0.0829
17	O	0.72486	0.00222	0.18265
18	O	0.75033	0.15694	-0.67394

of the P $\bar{1}$  structure. Thus, the crystal structure calculations predict the existence of a hypothetical polymorph of BTF that is less stable, but more dense, than that observed.

An understanding of the factors responsible for this behavior may be obtained by closer inspection of Table VI. It is found that the Pna2<sub>1</sub> structure is preferentially stabilized by electrostatic interactions. In fact, the sum of the dispersion and overlap repulsion terms favors the hypothetical polymorph. Thus, we find that electrostatic interactions occurring in the Pna2<sub>1</sub> structure are especially strong. Further insight into this behavior is afforded by inspection of Figure 2. There, contour plots showing the electrostatic potential in two different planes are displayed. The panel illustrating the potential in the molecular plane shows that negative potentials occur in a continuous ring around the edges of the BTF molecule. Also, the most negative potentials

TABLE V. ENERGY-OPTIMIZED CELL PARAMETERS FROM PCK/ME IN SPACE GROUP P $\bar{1}$ , WITH Z=2.

a=10.8753, b=9.0353, c=9.0368 Å, α=119.99, β=33.80, γ=114.54				
atom		cell		
ia	label	x	y	z
1	C	-0.25000	-0.30949	-0.06359
2	C	-0.25000	-0.18608	0.25337
3	C	-0.25000	-0.50310	0.05983
4	C	-0.25000	-0.16628	0.10640
5	C	-0.25000	-0.47628	-0.08337
6	C	-0.25000	-0.35612	0.22658
7	N	-0.25000	-0.26542	-0.17825
8	N	-0.25000	-0.07142	0.41207
9	N	-0.25000	-0.66183	0.01579
10	N	-0.25000	-0.02816	0.09566
11	N	-0.25000	-0.62512	-0.22146
12	N	-0.25000	-0.34539	0.37541
13	O	-0.25000	-0.07924	-0.08184
14	O	-0.25000	-0.16787	0.50182
15	O	-0.25000	-0.75157	-0.17037
16	O	-0.25000	0.12726	0.20563
17	O	-0.25000	-0.67053	-0.37685
18	O	-0.25000	-0.45540	0.42083

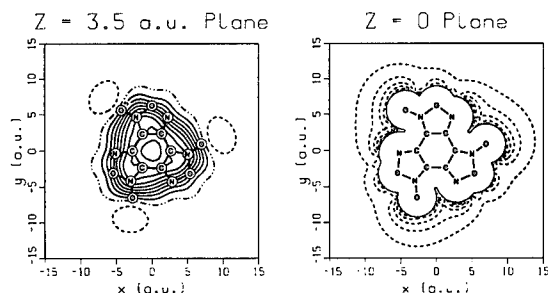


FIGURE 2. COMPUTED ELECTROSTATIC POTENTIAL OF BTF IN THE MOLECULAR PLANE (RIGHT) AND 3.5 A.U. ABOVE (LEFT). VALUES GREATER THAN ZERO ARE SHOWN WITH SOLID LINE, LESS THAN ZERO WITH DASHED LINE, AND THE ZERO CONTOUR WITH A CHAIN-DOT-DOT LINE. THE CONTOUR SPACING IS 5 KCAL/MOL/E. THE OUTERMOST CONTOUR IN THE RIGHT-HAND PANEL IS -5 KCAL/MOL/E.

TABLE VI. ENERGY COMPONENTS (KCAL/MOL/MOLECULE) FOR TWO BTF POLYMORPHS. DISPERSION ( $E_{dis}$ ), REPULSION ( $E_{rep}$ ), COULOMB ( $E_{coul}$ ) ENERGIES, AND THEIR SUMS, ARE SHOWN.

Space Group	$E_{coul}$	$E_{dis}$	$E_{rep}$	$E_{dis} + E_{rep}$	$E_{tot}$
Pna2 <sub>1</sub>	-9.565	-36.417	16.698	-19.719	-29.284
P $\bar{1}$	-6.187	-37.793	15.983	-21.811	-27.998

are found near the divalent N and exo-cyclic oxygen. Less negative potentials are found near the ring oxygen. In contrast, the plane approximately 1.85 Å above the molecule shows strong positive potentials over the carbon ring. Relatively weak negative potentials are found centered some distance from the N-O bonds. Clearly then, effective coulomb interactions in the crystal will be found when regions of positive and negative potential are brought into close proximity. This can be accomplished by pairing the negative nitrogen and oxygen atoms with positive centers or regions.

An illustration of a small fragment of the structure of the hypothetical polymorph is shown in Figure 3. In this structure, molecules of BTF are arranged in sheets; this packing motif is reminiscent of that found in TATB. The sheets are stacked ABAB ..., with a separation of about 3.0 Å. Inspection of Figure 3 shows that the carbon-containing rings of one sheet are aligned under a region encircled by the oxygens of three N-O bonds in the sheet above. As illustrated in Figure 2, this pairs regions of positive and negative potentials. This arrangement is relatively efficient, leading to its high density, but results in unfavorable electrostatic interactions within the sheets. This effectively destabilizes this polymorph relative to that observed.

In order to understand the electrostatic stabilization of the observed polymorph, the PCK/ME

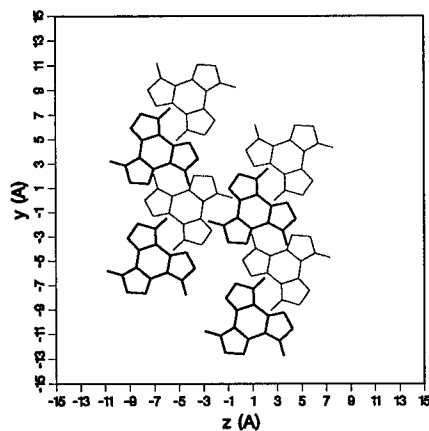


**FIGURE 3. PROJECTIONS OF MOLECULES IN TWO SHEETS OF THE HYPOTHETICAL POLYMORPH. MOLECULES IN THE UPPER SHEET ARE DRAWN WITH HEAVY LINES. THOSE BELOW WITH LIGHT LINES.**

calculation was analyzed. Two very strong intermolecular coulomb interactions were found. These occurred between a divalent nitrogen atom in one molecule and a trivalent nitrogen atom in another. The relative orientation of the respective molecules was edge-to-face. In addition, very strong electrostatic interactions between an oxygen atom of one molecule and a trivalent nitrogen of another was found. The relative orientation of these molecules was face-to-face with an offset. Inspection of Figure 4<sup>17</sup> shows the arrangement clearly. The atom charges shown in Figure 2 show that these atom pairs are comprised of positive and negative atoms. The actual value of the charges is only suggestive, because multipoles up to quadrupoles all contribute to the interaction. This is especially true for the divalent nitrogens, which requires a large dipole to describe the effects of the lone-pair of electrons. The coulomb interactions between these two atom-pairs are larger than the most favorable coulomb interactions in the hypothetical polymorph by more than a factor of two. The interactions are highly directed in that their energy is dependent upon the relative molecular orientations and separations, rather than just upon the separations alone. Although the distances involved in these interactions are not remarkably short (2.902 and 3.168 Å) they pair the strongly positively charged trivalent nitrogen with atoms of the opposite polarity. Thus, the electrostatic stabilization of the observed polymorph is found to result from edge-to-plane and plane-to-plane interactions between BTF molecules. This mixture of arrangements, while energetically favorable, packs less efficiently than the hypothetical polymorph.

## CONCLUSION

Coulomb interactions play a critical role in stabilizing the observed polymorph of BTF. A hypothetical polymorph, found by Ammon using MOLPAK, was also computationally characterized. Comparison of the two polymorphs showed that the energetic stabilization achieved in the observed polymorph was accompanied by a decrease in the computed crystal density. This violates the principle of closest-packing, although the density difference is only 2%, and illustrates the importance of electrostatics in determining crystal structures. These calculations also suggest that the hypothetical polymorph may be experimentally observable at high pressure.

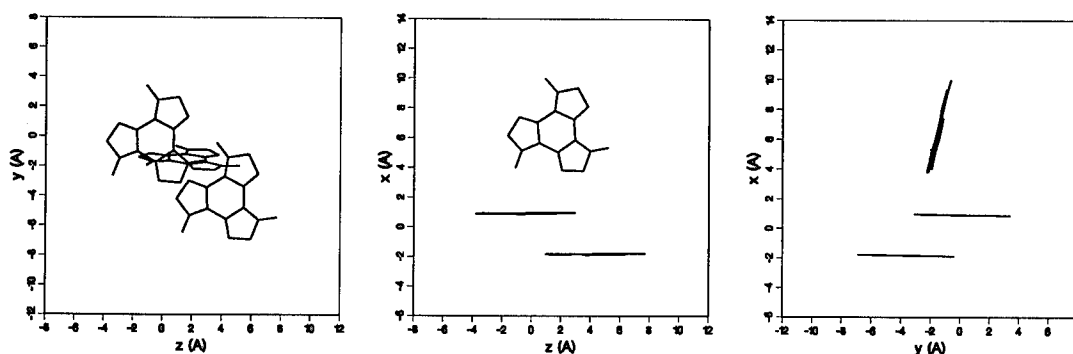


**FIGURE 4. ORTHOGRAPHIC PROJECTION OF A THREE-MOLECULE FRAGMENT SHOWING THE FACE-TO-EDGE MOTIF THAT GIVES RISE TO THE STRONGEST ATOM-ATOM COULOMB INTERACTIONS. THE FRAGMENT IS FROM THE CALCULATED STRUCTURE OF THE OBSERVED POLYMORPH AND IS NEARLY INDISTINGUISHABLE FROM THAT OF THE ACTUAL FRAGMENT IN THIS PROJECTION**

## REFERENCES

1. a) Forohar, F.; Dave, P. R.; Axenrod, T.; and Bedford, C. D., *Eleventh Annual Working Group Institute on Synthesis of High Energy Density Materials*, 8-11 Jun 1992. b) See Also: Dave, P.; Forohar, F.; Axenrod, T.; Bedford, C. D.; Chaykovsky, M.; Rho, M. K.; Gilardi, R.; Anderson, J. F.; George, C., This Symposium.
2. Thermodynamic data from: CRC Handbook of Chemistry and Physics, 63rd Ed. Weast, R. C., Ed. CRC Press: Florida, 1982.
3. LLNL Explosives Handbook: Handbook of Chemical Explosives and Explosive Simulants, Dobratz, B. M. Ed., UCRL-52997, 1981.
4. Stewart, J. J. P., *J. Comput. Chem.*, Vol. 10, 1989, p. 221.
5. Mader, C. L., *Numerical Modeling of Detonations*, University of California Press, Berkeley, CA, 1979, Appendix E.
6. Coolidge, M. B.; Marlin, J. E.; Stewart, J. J. P., *J. Comput. Chem.*, Vol. 12, 1991, p. 948.
7. Stine, J. R., *Prediction of Crystal Densities of Organic Explosives by Group Activity (U)*, LA-8920, 1981, LANL, Los Alamos, NM.
8. Holden, J. R.; Du, Z.; Ammon, H. L., *J. Comput. Chem.*, Vol. 14, 1993, p. 422.
9. Witness Table 4-3 of Reference 3.
10. Kitaigorodsky, A. I., *Molecular Crystals and Molecules*, Academic: New York, 1973, pp. 1-33.
11. Ammon, H. L., personal communication. The author thanks Professor Ammon for communicating these results.
12. Ritchie, J. P.; Kober, E. M.; Copenhaver, A. S., This Symposium.
13. a) Williams, D. E. and Cox, S. R., *Acta Cryst. B*, Vol. 40, 1984, p. 404.; b) Cox, S. R.; Hser, L. Y. and Williams, D. E., *Acta Cryst.*, Vol. A37, 1981, p. 293.
14. Ritchie, J. P., *J. Am. Chem. Soc.*, Vol. 107, 1985, p. 1829.
15. Hehre, W. J.; Radom, L.; Schleyer, P. R. and Pople, J. A., *Ab Initio Molecular Orbital Theory*, Wiley, New York, 1986.
16. Cady, H. H.; Larson, A. C.; Cromer, D. T., *Acta Cryst.*, Vol. 20, 1966, p. 336.
17. The molecules of the triplet shown in Figure 4 may be constructed from the cell and molecular coordinates in Table IV as follows: molecule 1: apply identity; molecule 2: apply symmetry operator  $.5+x, .5-y, z$ ; molecule 3: translate by  $-\vec{c}$ . Space limitations prevent presentation of the ACME's, but they may be obtained via mail or e-mail to [jpr@lanl.gov](mailto:jpr@lanl.gov).

## DISCUSSION

W. BYERS BROWN

University of Manchester, Manchester, England

I am impressed by the sophisticated quantum chemistry computations presented in this paper, but unimpressed by the use of the crude, empirical, old-fashioned BKW equation of state. My question is: How do you justify putting the new wine of quantum chemistry into the old BKW bottle? A new bottle would be one of the ideal detonation codes using equations of state based on statistical mechanics and intermolecular potentials such as F. H. Ree's CHEQ code.

### REPLY BY JAMES RITCHIE:

Equations of state for explosives based upon statistical mechanics, such as those referred to in the question, depend upon the availability of intermolecular potentials that are very accurate at high pressures and temperatures. When available, these have been obtained via fits to experimental data and corresponding states arguments. It has proven difficult, however, to obtain them from ab initio quantum chemistry. This is because the calculation of accurate two-body potentials requires large basis sets and extensive accounting for electron correlation. In addition, many-body effects may well be important in determining molecular interactions that occur at the conditions found near the CJ state. Thus, generation of the required intermolecular potentials would require a large investment of time and be of uncertain accuracy. On the other hand, vibrational frequencies and heats of formation for novel species can be efficiently calculated using quantum chemistry and utilized directly in BKW in the manner described. Consequently, the use of BKW was justified by the desire to predict the performance of novel explosive compositions in at least a qualitative manner.

## DISCUSSION

RUTH DOHERTY

NSWC White Oak, Silver Spring, Maryland

The performance estimates one obtains from such programs as BKW can be quite sensitive to the product species that are included in the library. Phosphorus is not a common component of explosives, so the number of phosphorus-containing species in a standard library is likely to be very limited. Did you include species such

as PN or suboxides of phosphorus in the library for your BKW calculations?

### REPLY BY JAMES RITCHIE:

The table below shows observed heats of formation of the species referred to in the question, in addition to some related ones. The  $H_f$  for  $P_3N_5$  was obtained by combustion in oxygen and yielded  $P_4O_{10}$  as a product. Thus, these species are thermodynamically unstable with respect to the products that were used in the calculations. The relative concentrations of such species is frequently found to depend sensitively upon their co-volumes. The data in Table III show that a calculated  $V_{19}$  is much less sensitive to chemical composition than is the calculated CJ state. This is because  $V_{19}$  samples over a wide range of the expansion isentrope. It is consequently frequently related to  $Q$ , rather than any detailed chemistry. Interestingly, for compound I, although the calculated  $Q$  for compound is larger than that for RDX and HMX and although its crystal density is quite high, the calculated  $V_{19}$  is substantially lower. This is attributed to the formation of large product species with many internal degrees of freedom, such as the ones considered, and is not anticipated to be sensitive to concentrations of thermodynamically unstable species.

Species	$\Delta H^\circ_{f,298}$ (kcal/mol)	Reference
$P_2$	42.7	1
P	4.3	1
$PO_2$	-71.0	1
PO	-1.5	1
PN	25.0	1
PH	60.6	1
CHP	40.0	1
CP	111.7	1
$P_3N_5$ (c)	-76.5	2

<sup>1</sup> JANAF Thermochemical Tables 2nd Ed.; D.R. Stull, H. Prophet, Eds. NSRDS-NBS 37, 1971.

<sup>2</sup> M.W. Chase, Jr.; C.A. Davies; J.R. Downey, Jr.; K.J. Frurip; R.A. McDonald; and A.N. Syverud, J. Phys. Chem. Ref. Data **14**, 1564(1985), Supplement 1.

## SHOCK INITIATION STUDIES OF LOW DENSITY HMX USING ELECTROMAGNETIC PARTICLE VELOCITY AND PVDF STRESS GAUGES

Stephen A. Sheffield, Richard L. Gustavsen, and Robert R. Alcon  
Los Alamos National Laboratory  
Los Alamos, New Mexico 87545

Robert A. Graham and Mark U. Anderson  
Sandia National Laboratories  
Albuquerque, NM 87185

Magnetic particle velocity and PVDF stress rate gauges have been used to measure the shock response of low density HMX ( $1.24 \text{ g/cm}^3$ ). In experiments done at LANL, magnetic particle velocity gauges were located on both sides of the explosive. In nearly identical experiments done at SNL, PVDF stress rate gauges were located at the same positions so both particle velocity and stress histories were obtained for a particular experimental condition. Unreacted Hugoniot data were obtained and an EOS was developed by combining methods used by Hayes, Sheffield and Mitchell (for describing the Hugoniot of HNS at various densities) with Hermann's  $P$ - $\alpha$  model. Using this technique, it is only necessary to know some thermodynamic constants or the Hugoniot of the initially solid material and the porous material sound speed to obtain accurate unreacted Hugoniots for the porous explosive. Loading and reaction paths were established in the stress-particle velocity plane for some experimental conditions. This information was used to determine a global reaction rate of  $\approx 0.13 \mu\text{s}^{-1}$  for porous HMX shocked to 0.9 GPa. At low input stresses the transmitted wave profiles had long rise times (up to 1  $\mu\text{s}$ ) due to the compaction processes.

### INTRODUCTION

Porous octotetramethylene tetranitramine (HMX) at a density of  $1.24 \text{ g/cm}^3$  has been shown to reproducibly undergo a deflagration-to-detonation transition (DDT) from small energy inputs when suitably confined.<sup>1</sup> This gives rise to safety concerns which is the principal reason for studying it under low shock input conditions.

Studies of low-density explosives (less than 80% of theoretical maximum density -- TMD) have been conducted on several explosive materials over the past 30 years. Seay and Seely<sup>2</sup> studied shock initiated low density PETN and showed that, at a density of  $1.0 \text{ g/cm}^3$  (65% TMD), this material could be initiated with shock inputs as low as 0.25 GPa. Evans et al.,<sup>3</sup> made measurements on ammonium perchlorate at a density of  $1.0 \text{ g/cm}^3$  (51% TMD) and found that shock inputs as

low as 1.7 GPa would initiate it. Dremin et al.,<sup>4</sup> used magnetic gauges to study the initiation of bulk density TNT and tetryl charges. They found inputs of 1.1 GPa produced runs to detonation between 16 and 54 mm, depending on the TNT particle size. Lindstrom<sup>5</sup> did a rather large study on tetryl at densities of 1.3, 1.4, 1.5, 1.6, and  $1.7 \text{ g/cm}^3$ . At a density of  $1.30 \text{ g/cm}^3$  (75% TMD) an input of 0.47 GPa gave a run distance to detonation of 10 mm.

Two studies with direct application to this work have been done on low density HMX. Dick performed several explosively driven cutback tests in which he measured the average transit time through HMX compacts of different thicknesses (at a density of  $1.24 \text{ g/cm}^3$ ) for inputs of 0.8 and 2.1 GPa.<sup>6</sup> By plotting transit time vs. compact thickness, he was able obtain some Hugoniot and initiation information. He determined the distance to detonation was 3.0 mm for



an input of 2.1 GPa and 5.2 mm for an input of 0.8 GPa. Elban and Chiarito subjected two different HMX powders to slow compaction conditions up to 0.2 GPa.<sup>7</sup> They found that the breakage of HMX crystals starts at stresses below 1 MPa and that widespread crystal fracture takes place between 62 and 75% of TMD. At a stress of 0.2 GPa, 96% of TMD was obtained. The data from these studies are not sufficient to construct a reliable equation of state (EOS) so we embarked upon a study to make time-resolved measurements as an extension of Dick's work with manganin gauges.<sup>8</sup>

Nearly all the previous experimenters have used explosive driver/attenuator systems to obtain the desired input shocks so the exact input shock amplitudes and shapes were not well known. In addition, many of them used diagnostics (such as measurement of shock breakout with a streak camera) which did not give detailed shock parameter histories. The samples were in the form of wedge or pellet shaped compacts, carefully pressed and shaped before assembly to the attenuator plate of the driver system. Only Dremine et al.,<sup>4</sup> made in-situ measurements of particle velocity histories in bulk density TNT; this allowed them to measure details of the reactive-wave growth process.

In our experiments magnetic particle velocity measurements were made at Los Alamos National Lab. (LANL) and polyvinylidene difluoride (PVDF) stress rate measurements<sup>9,10</sup> were done at Sandia National Labs. (SNL) in experiments that were nearly identical. Time resolved measurements of these two properties allows tracking of any process occurring (e.g. compaction or reaction) in the stress vs. particle velocity plane. In this paper we develop an EOS for low density HMX, discuss the experimental methods, the data obtained, and their interpretation.

## EQUATION OF STATE

Equation of state information is difficult to obtain on porous explosives for several reasons. At low input stresses, compaction behavior dominates and transmitted waves become disperse. At higher inputs, because the materials are very sensitive to the shock initiation of detonation, reaction occurs and shock velocity information is not reliable, i.e., transit time measurements cannot be used. Even at pressures of only a few kbars, the explosive may start to react and accelerate the wave. In wedge tests, wave acceleration is often apparent well before the onset of detonation. Because of the dynamic compaction processes and early onset of reaction, measurements of pressure or particle

velocity in transmitted waves provide unreliable EOS information as well. The best information has been obtained in flying plate experiments using flyers made of well characterized materials whose velocities were accurately measured and when pressure or particle velocity was measured at the flyer/explosive interface. Data from these types of experiments is uncommon, as most researchers have been more interested in the initiation properties, and have used wedge experiments.

Equations of state have been developed for porous explosive materials in the past. Lindstrom<sup>5</sup> developed an EOS for tetryl. Erkman and Edwards<sup>11</sup> constructed an EOS form in which different parameter values could be used to describe the behavior of RDX, tetryl, PETN, and ammonium nitrate. Sheffield, Mitchell, and Hayes<sup>12</sup> used an EOS based on the Helmholtz potential and a Murnaghan isotherm to model HNS (hexanitrostilbene) shock behavior. We use the Helmholtz form as the basis for the EOS development in this paper.

Because of the difficulties in making reliable EOS measurements on porous explosives it is often useful to construct a Hugoniot using thermodynamic constants obtained from static and hydrostatic measurements, the bulk sound speed of the porous explosive, and then to properly account for the porosity. If hydrostatic data is unavailable, the thermodynamic constants can be obtained by fitting to Hugoniot measurements of near 100% TMD explosives or single crystal explosives. These materials are generally much less sensitive to shock initiation.

## Porous Explosive EOS

The formalism for the equation of state which is used in this paper was developed by Hayes, and was first used to describe the porous explosive, HNS by Sheffield, Mitchell and Hayes.<sup>12</sup> It was later amended by Setchell and Taylor<sup>13</sup> to be used in Hermann's  $P$ - $\alpha$  model.<sup>14</sup> Thus, the ideas are not new, but neither have they seen widespread application.

The method is based on constructing a complete thermodynamic potential function for the fully dense explosive, namely the Helmholtz Free Energy. The specific form which Hayes chose for the Helmholtz Free Energy is<sup>12</sup>

$$F(T, V) = C_v \left[ (T - T_0) \left( 1 + \frac{\gamma}{V} (V_0 - V) \right) + T \ln \left( \frac{T_0}{T} \right) \right] + \frac{K_{T_0} V_0}{N(N-1)} \left[ \left( \frac{V_0}{V} \right)^{N-1} - (N-1) \left( 1 - \frac{V}{V_0} \right) - 1 \right] \quad (1)$$

where  $C_V$  is the specific heat at constant volume,  $\gamma$  is Gruneisen's parameter,  $V_0$  is the specific volume of the fully dense explosive at zero pressure,  $K_T$  is the bulk modulus at constant temperature, and  $N$  is a constant. This construction assumes  $C_V$  and  $\gamma/V$  are constants, while the bulk modulus is

$$K_T = K_{T_0} \left( \frac{V_0}{V} \right)^N \quad (2)$$

These constants are readily obtained from static thermodynamic measurements and hydrostatic pressure-volume measurements.

In order to describe the compaction of the porous explosive in the framework of Hermann's  $P$ - $\alpha$  model,<sup>14</sup> Eq. (1) must be recast in the form  $P(E, V)$  or  $E(P, V)$ . Setchell and Taylor<sup>13</sup> have shown that

$$\begin{aligned} E(P, V) = & \frac{P}{\gamma/V} - \frac{\gamma}{V} C_V T_0 (V_0 - V) \\ & - \frac{K_{T_0}}{N\gamma/V} \left[ \left( \frac{V_0}{V} \right)^N - 1 \right] \\ & + \frac{K_{T_0} V_0}{N(N-1)} \left[ \left( \frac{V}{V_0} \right)^{1-N} \right. \\ & \left. - (N-1) \left( 1 - \frac{V}{V_0} \right) - 1 \right] \end{aligned} \quad (3)$$

Eq. (3) describes the behavior of the fully dense explosive. While Eq. (1) is a complete thermodynamic EOS, Eq. (3) is not.

Hermann's theory,<sup>14</sup> as modified by Carroll and Holt<sup>15</sup> states that in a porous material, Eq. (3) describes the solid portion. The distention of the porous material is

$$\alpha = V/V_s, \quad (4)$$

where  $V$  is the specific volume of the porous explosive at a given pressure and energy, and  $V_s$  is the specific volume of the solid explosive at the same pressure and energy. If in the porous material the average pressure is  $P$  and the average specific volume  $V$ , then the pressure in the solid portion is  $P\alpha$  and the specific volume of the solid portion is  $V/\alpha$ . Equation (3) can thus be used to describe the energy at average pressure  $P$  and volume  $V$  in the porous explosive if modified to describe only the solid portion:

$$E = E(P\alpha, V/\alpha). \quad (5)$$

Eqs. (3), (4), and (5) are now augmented by defining  $\alpha$  as a function of the shock pressure  $P$ . A simple form for  $\alpha(P)$ , such as the following one suggested by Herman,<sup>14</sup> is often sufficient.

$$\begin{aligned} \alpha &= 1 + (\alpha_0 - 1)(1 - P/P_s)^2 & (P \leq P_s) \\ \alpha &= 1 & (P \geq P_s) \end{aligned} \quad (6)$$

In Eq. (6),  $\alpha_0$  is the original distention,  $\alpha_0 = V_{00}/V_0$ , and  $V_{00}$  is the initial specific volume of the porous explosive.  $P_s$  is the pressure at which the material crushes to solid density. Herman has also shown how  $P_s$  can be determined from measurements of the sound speed in the porous material.<sup>14</sup> Different values of  $P_s$  must be used for different initial porosities; generally it is smaller for larger porosities.

Given  $P$  and  $\alpha(P)$ , Eq. (5) is then iteratively solved for  $V$  such that the energy is the same as that given by the Hugoniot jump condition  $E = P/2(V_{00} - V)$ . Given the quality of much of the experimental EOS data, further sophistication in an EOS is unwarranted. Constants used in the EOS analysis will be discussed later when the HMX Hugoniot data are presented.

## EXPERIMENTAL DETAILS

Experiments at both labs utilized gas gun driven projectiles to obtain sustained-shock input conditions. Projectile velocities were nearly the same at both labs for a given experimental setup so that in separate, similar experiments, both stress and particle-velocity histories were measured.

HMX powder was confined in sample cells which had a polychlorotrifluoroethylene (Kel-F) front face (on which the projectile impacted) and a poly 4-methyl-1-pentene (TPX) cylindrical plug back. (TPX is a low impedance plastic and a reasonable impedance match to the pressed HMX.) Gauges were epoxied on the HMX side of both pieces. The front face was screwed to a Kel-F confining cylinder with an outside diameter of 68.6 mm and an inside diameter of 40.6 mm. The pressed HMX (between the Kel-F and TPX) was  $\approx 4$  mm thick and had a density of 1.24 g/cm<sup>3</sup>. Figure 1 is a cross-section of the cylindrical experimental setup showing the various parts.

The HMX powder used in all the experiments was coarse HMX from Holston (Lot HOL 920-32) with a bulk density of  $\approx 1.16$  g/cm<sup>3</sup> (see Ref. 6). The material was screened to eliminate agglomerates and a few of the largest particles.

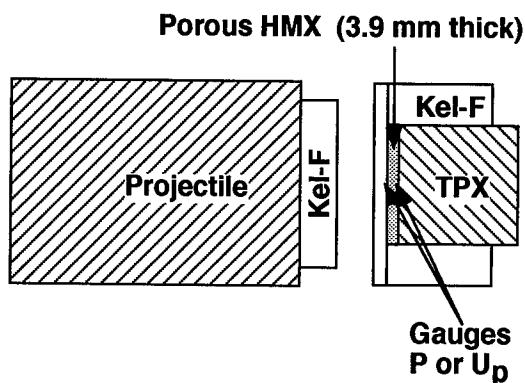


FIGURE 1. CROSS SECTION OF EXPERIMENTAL SETUP.

In the LANL experiments the magnetic particle-velocity gauges were  $5\text{ }\mu\text{m}$  thick aluminum "stirrup" gauges bonded to  $13\text{ }\mu\text{m}$  thick FEP Teflon sheet. Active region of the gauge was  $10\text{ mm}$  by  $0.5\text{ mm}$ . In the SNL experiments PVDF stress-rate gauges were composed of  $25\text{ }\mu\text{m}$  thick PVDF with plated electrodes on each side and a  $13\text{ }\mu\text{m}$  thick FEP Teflon film on the HMX side. The active area of this gauge is  $3\text{ mm}$  by  $3\text{ mm}$ . The side next to the HMX was coated with aluminum to eliminate any pyroelectric effects in the PVDF. Although gauge conditions were not exactly identical, they were as close as possible to being the same.

## RESULTS

Experiments were performed at projectile velocities ranging from  $0.15$  to  $0.7\text{ km/s}$  with corresponding stress inputs to the HMX samples between  $0.1$  and  $0.9\text{ GPa}$ . At the lower input stresses, the compaction process dominated and the transmitted waves as measured by the back gauges had long rise times; over  $1\text{ }\mu\text{s}$  for the lowest input experiments. At the higher projectile velocities, evidence of reaction was apparent at both the front and back gauges. Figure 2 shows the particle velocity history plots obtained in the lowest input experiment (Shot 931). The projectile velocity was  $0.158\text{ km/s}$  and the stress about  $0.1\text{ GPa}$ . The transmitted gauge record has a risetime of over  $3\text{ }\mu\text{s}$  with the front looking almost like an elastic precursor. This wave shape undoubtedly has to do with the dynamics of crushing and compaction of the HMX. The HMX was not compacted to  $100\%$  TMD in this experiment.

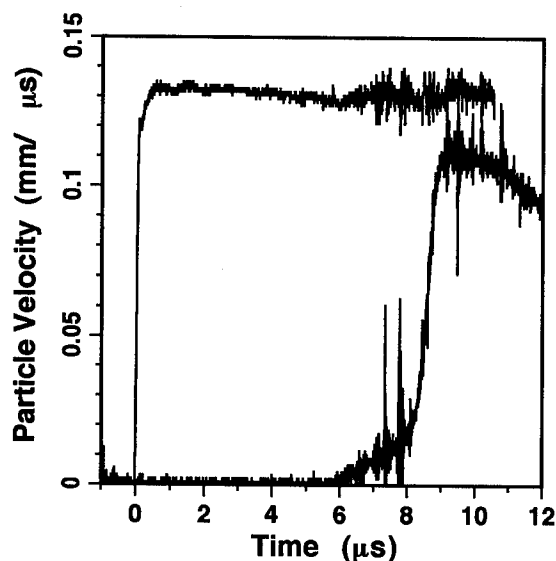


FIGURE 2. PARTICLE VELOCITY WAVEFORMS FOR SHOT 931.

The Hugoniot data obtained from this and other experiments are presented in Table 1. Some of the experiment are paired (one shot at LANL and one at SNL) at the conditions where we were trying to make identical experiments. This turned out to be harder than expected because of a number of difficulties with the biggest one being making the two different guns produce the same projectile velocity on demand. At the lower projectile velocities, this was more difficult than expected. In any case we succeeded in getting some of the shot pairs very close in projectile velocity. The pairs are shown in Table 1. For these pairs the Hugoniot point was obtained by taking the particle velocity from the LANL experiment and the stress from the SNL experiment. Hugoniot points were taken at a time when the gauge and HMX were in equilibrium.

Figure 3 shows particle velocity and stress waveforms obtained in two experiments (Shot 912 and Shot 2477) in which the projectile velocity was  $\approx 0.29\text{ km/s}$ . In the front PVDF gauge measurement, there is a considerable overshoot in stress because of the Kel-F front plate (this overshoot was observed in all the front PVDF gauge measurements). The stress measurement in the HMX begins after this overshoot - about  $40\text{ ns}$  into the record. Rounding at the top of both the front gauge waveforms results from the viscoelastic wave shaping that occurs in the shock as it moves through the Kel-F cell front. The back gauge waveforms show a very disperse wave with a risetime of  $\approx 700\text{ ns}$ . This is due to the compaction process in the HMX that develops as the wave progresses through the sample. We do not know if the profile is steady but assume that

TABLE 1. EXPERIMENTAL PARAMETERS AND HUGONIOT POINTS

Shot No.	Lab	Projectile Vel. km/s	Measured $u_p$ km/s	Measured $P$ GPa	Calculated $U_s$ km/s	Calculated $\rho$ g/cm <sup>3</sup>
931	LANL	0.158	0.132			
2489	SNL	0.189		0.087	0.532	1.651
912	LANL	0.288	0.23			
2477	SNL	0.285		0.20	0.701	1.844
942	LANL	0.406	0.29			
2488	SNL	0.412		0.35	0.973	1.767
929	LANL	0.509	0.37			
2487	SNL	0.496		0.48	1.046	1.919
928	LANL	0.599	0.43			
2486	SNL	0.591		0.65	1.219	1.916
913	LANL	0.696	0.50			
2478	SNL	0.669		0.90	1.45	1.890

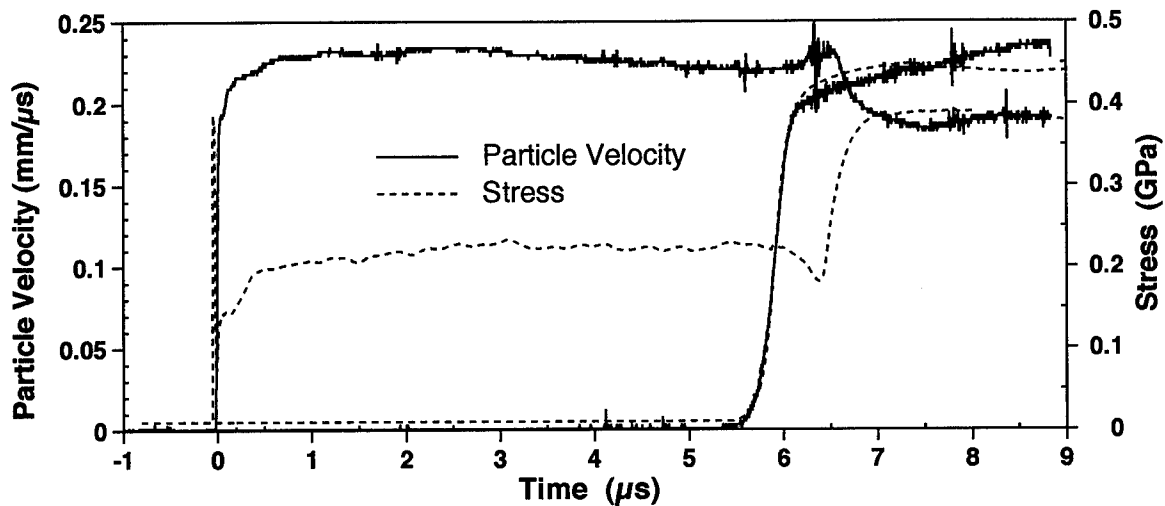


FIGURE 3. PARTICLE VELOCITY (LANL SHOT 912) AND STRESS WAVEFORMS (SNL SHOT 2477).

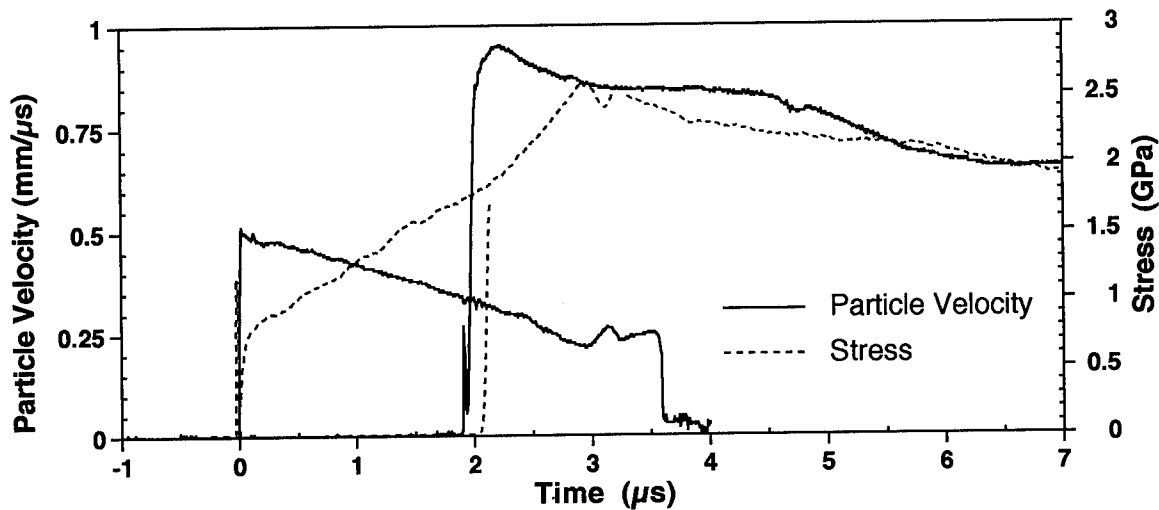


FIGURE 4. PARTICLE VELOCITY (LANL SHOT 913) AND STRESS WAVEFORMS (SNL SHOT 2478).

it is not. There was apparently little reaction at this experimental condition.

Figure 4 gives the particle velocity and stress waveforms obtained in two experiments (Shot 913 and Shot 2478) in which the projectile velocity was  $\approx 0.68$  km/s. In these experiments there is evidence of reaction in both the front and back gauge measurements. Reaction in the front gauge is manifested by a decrease in particle velocity (the reacting HMX is slowing down the cell front) and a corresponding increase in stress. The wave grows as it traverses the HMX sample because of reaction in the shock front so rather than the 0.5 km/s expected when a nonreactive wave interacts with the TPX back, a particle velocity of 0.95 km/s is measured. (The back PVDF gauge measurement was lost.) The risetime in the back particle velocity gauge was also considerably faster than in the lower input experiments (without reaction). However, it is still about 50 ns, longer than expected for a sharp shock. There is apparently competition between the reaction (trying to sharpen up the wave) and the compaction (trying to smear it out).

In this experiment the LANL projectile velocity was 4% higher than the SNL experiment. This is manifested in the data because the arrival time was later for the PVDF measurement. This gives an indication of the accuracy of the Hugoniot data from these experiments; it is on the order of 5% in the worst case and somewhat better in the best case.

## DISCUSSION

The Hugoniot data from the experiments in Table 1 were used to determine the adequacy of the EOS development described above. Table 2 lists the thermodynamic constants for the explosives HMX, HNS, and PETN. The latter two explosives have been included for comparison purposes. More information about the EOS and its application to HMX, HNS, PETN and other explosives can be found in Ref. 16. Brief comments about where the HMX constants were obtained, and how well the data were fit follow.

TABLE 2. THERMODYNAMIC CONSTANTS

Explosive	$\rho_0$ g/cm <sup>3</sup>	$K_{T_0}$ Mbar	$N$	$\gamma/V$ g/cm <sup>3</sup>	$C_V$ cm <sup>2</sup> /μs <sup>2</sup> /K
HMX	1.90	0.129	10.3	2.09	1.05(10 <sup>-5</sup> )
HNS	1.74	0.146	3.5	2.82	0.89(10 <sup>-5</sup> )
PETN	1.77	0.110	7.1	2.04	1.00(10 <sup>-5</sup> )

$K_{T_0}$  and  $N$  for HMX were obtained from fits to the hydrostatic pressure - volume data of Olinger, Roof and Cady.<sup>17</sup>  $\gamma$  and  $C_V$  are as reported in Ref. 17, as well. When these constants are used in the EOS given above, the curves shown in Figures 5 and 6 are produced. The initial density is noted beside each symbol. Smooth curves were calculated using the initial density noted beside the curve symbol. These constants, reproduce the 1.891 g/cm<sup>3</sup> HMX Hugoniot<sup>18</sup>

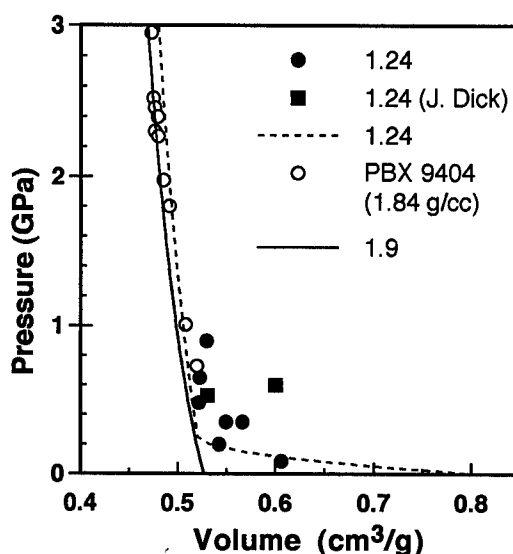


FIGURE 5. HUGONIOTS FOR HMX IN THE P-V PLANE.

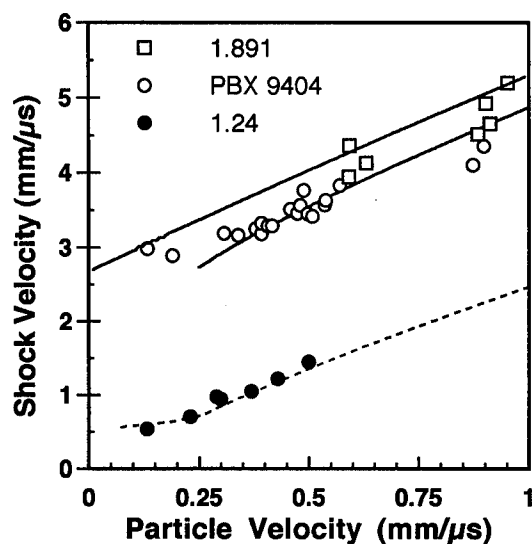


FIGURE 6. HUGONIOTS FOR HMX IN THE  $U_s-u_p$  PLANE.

and the PBX 9404 Hugoniot quite well up to pressures of about 10 GPa. Above 10 GPa, neither the PBX 9404, the 1.891 HMX, nor the single crystal HMX Hugoniots<sup>19</sup> are reproduced very well, possibly because of a phase transition in the HMX at a pressure near 10 GPa.<sup>20</sup> These constants, with  $P_r$  set equal to 0.25 GPa, nicely reproduce our Hugoniot measurements on 1.24 g/cc HMX as is shown in the figures. As is typical there is more scatter in the  $P$ - $V$  than the  $U_s$ - $u_p$  plane.

The risetimes of the transmitted waves are interesting in terms of indicating the competition between the dynamic compaction process (spreading out the wave) and the reaction process (steepening up the wave). Figure 7 shows the risetimes of the transmitted waves as a function of the input stress. At about 0.5 GPa the risetimes get to be below 100 ns, the minimum risetime for these experiments.

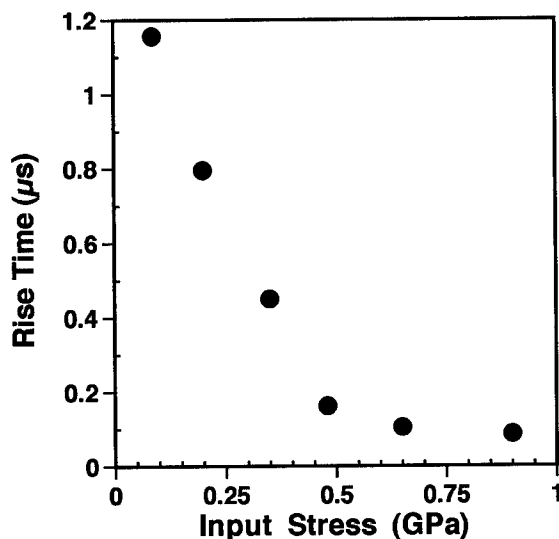


FIGURE 7. PLOT OF RISETIME FOR TRANSMITTED GAUGE WAVEFORMS VS. INPUT STRESS.

Using the particle velocity and stress data from the experiments, these two properties can be plotted against each other at the appropriate times in the stress vs. particle velocity plane. This plot can be superimposed on a Hugoniot cross plot to give some understanding of the processes occurring in the experiment. This has been done for the data shown in Fig. 3, where there was no reaction, and is reported in Ref. 21. The case with reaction is discussed next.

The data shown in Fig. 4 are definitely in the regime where reaction is taking place. Using the front

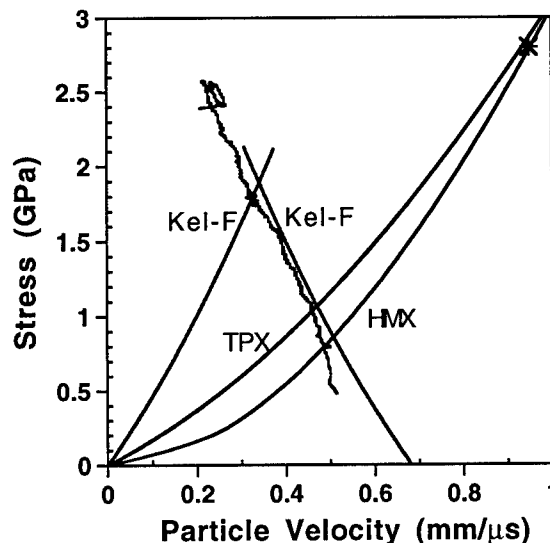


FIGURE 8. STRESS VS. PARTICLE VELOCITY PLOT OBTAINED USING THE DATA OF FIG. 4.

gauge data and plotting the stress vs. particle velocity results in the wiggly curve shown in Fig. 8. (The appropriate Hugoniots for Kel-F, low density HMX, and TPX are shown for reference purposes.) It starts somewhat low in stress, due to the viscoelastic effects in the Kel-F, but then moves along the backward facing Kel-F Hugoniot clear off the figure. In other words, the state at the front gauge as the reaction occurs moves up along the Kel-F Hugoniot because this is what it is in contact with. In this experiment the maximum stress at the front gauge was about 2.8 GPa at the end of the record. Ritchie<sup>22</sup> has calculated the BKW reaction product equation of state for 1.24 g/cm<sup>3</sup> HMX. Figure 8 has been expanded in Fig. 9 so that the BKW product isentrope and the porous HMX Hugoniot are shown. Using the product curve as the approximate end state for the reaction if it went to completion, it appears that the HMX has reacted to about the 40% point. This has taken place in about 3 μs, leading to an estimated global reaction rate of  $\approx 0.13 \mu s^{-1}$ . Of course there are many assumptions in this rough analysis but it gives an indication of the order of the reaction rate that is occurring in the shocked porous HMX.

The back magnetic gauge had a maximum particle velocity of 0.95 km/s, which corresponds to a stress of 2.8 GPa on the unreacted HMX Hugoniot and a shock velocity of 2.4 km/s. An asterisk has been put on this point on the unreacted Hugoniot of Fig. 8. The average shock velocity through the sample was 1.96 km/s, considerably above the 1.36 km/s expected if there were no reaction. Considerable reaction is occurring in the shock front (as is normally the case for

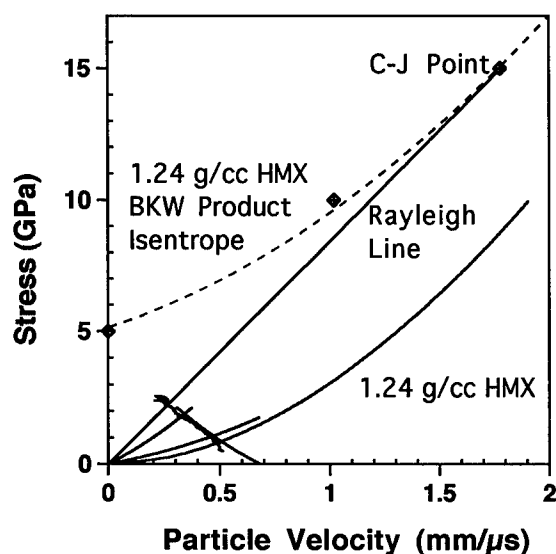


FIGURE 9. EXPANDED VIEW OF FIG. 8 SHOWING THE BKW PRODUCT ISENTROPE.

heterogeneous explosives) to strengthen the shock to this level. If the porous HMX were detonating, the detonation velocity would be 6.7 km/s so it is obvious that there is still a rather long buildup process to occur before detonation is achieved.

This set of experiments demonstrates the usefulness of making both stress and particle velocity measurements in near identical experiments. It is clear that to really understand the compaction and reaction processes in detail, computer modeling with accurate material, compaction, micromechanical, and reaction models will be required.

#### ACKNOWLEDGEMENTS

We would like to thank Ronald Rabie for useful discussions concerning the  $P$ - $\alpha$  model, and Jerry Dick and Jerry Wackerle for discussions concerning general properties of porous explosives.

#### REFERENCES

1. J. M. McAfee, B. W. Asay, A. W. Campbell, and J. B. Ramsay, Ninth Symposium (Intl.) on Detonation, Office of the Chief of Naval Research Report OCNR-113291-7, Arlington, VA (1989) p. 265.
2. G. E. Seay and L. B. Seely, Jr., *J. Appl. Phys.* **32**, 1092 (1961).
3. M. W. Evans, B. O. Reese, L. B. Seely, and E. L. Lee, Fourth Symposium (Intl.) on Detonation, Office of Naval Research Report ACR-126, Washington, D.C. (1965), p. 359.
4. A. N. Dremin, S. A. Koldunov, and K. K. Shvedov, *Comb. Expl. and Shock Waves* **7** (1), 87 (1971).
5. I. E. Lindstrom, *J. Appl. Phys.* **41**, 337 (1970).
6. J. J. Dick, *Combustion and Flame* **54**, 121 (1983).
7. W. L. Elban and M. A. Chiarito, *Powder Tech.*, **46**, 181 (1986).
8. J. J. Dick, *Combustion and Flame* **69**, 257 (1987).
9. F. Bauer, in *Shock Waves in Condensed Matter*, Y. M. Gupta, ed. (Plenum Press, New York, 1986), p. 483.
10. R. A. Graham, L. M. Lee, and F. Bauer, in *Shock Waves in Condensed Matter 1987*, S. C. Schmidt and N. C. Holmes, eds. (North-Holland, Amsterdam 1988), p. 619.
11. J. O. Erkman and D. J. Edwards, Sixth Symposium (intl.) on Detonation, Office of Naval Research Report ACR-221, Arlington, VA (1976), p. 766.
12. S. A. Sheffield, D. E. Mitchell, and D. B. Hayes, Sixth Symposium (Intl.) on Detonation, Office of Naval Research Report ACR-221, Arlington, VA (1976), p. 748.
13. R. E. Setchell and P. A. Taylor, *J. Energetic Mat.* **6**, 157 (1988).
14. W. Hermann, *J. Appl. Phys.* **40**, 2490 (1969).
15. M. M. Carroll and A. C. Holt, *J. Appl. Phys.* **45**, 3864 (1974).
16. R. L. Gustavsen and S. A. Sheffield, presented at the joint AIRAPT/APS Conference, June 28 - July 2, 1993, Colorado Springs, CO.
17. B. Olinger, B. Roof, and H. Cady in "Symposium H.D.P. (Commissariat a l'Energie Atomique)", 1978. pg. 3.
18. LASL Shock Hugoniot Data, S.P. Marsh Ed. U. of California Press, Berkeley, (1980) pg. 596.
19. Ref. 18, pg. 595.
20. J. J. Dick, *J. Energetic Mat.* **1**, 275 (1983).
21. S. A. Sheffield, R. L. Gustavsen, R. R. Alcon, R. A. Graham, and M. U. Anderson, presented at the joint AIRAPT/APS Conference, June 28 - July 2, 1993, Colorado Springs, CO.
22. J. P. Ritchie, Los Alamos National Lab., Group T-14, private communication.

## **DISCUSSION**

**PER-ANDERS PERSSON**

Research Center for Energetic Materials, Socorro, New Mexico

Were you able to recover unreacted HMX in any of the low-pressure experiments?

**REPLY BY STEPHEN SHEFFIELD:**

We have not seen anything that resembles HMX powder in the debris from any of the shots, including the lowest input experiments. Wood and steel plates are used to stop the shot debris in the catch system and it

would be hard to identify HMX powder after it had undergone this harsh treatment. There has been no attempt to "soft catch" the debris and look for unreacted HMX. We cannot be sure that some unreacted HMX was not among the pieces of plastic, wood, aluminum, etc., in the debris; we can only say that we have never identified any. In the lowest-pressure experiments (in which the input to the HMX was only 0.2 GPa) there was no evidence of reaction in the experimental records during the recording time. However, it is felt that some low-level reaction may occur at even these low pressures and over the several milliseconds it takes for the projectile/target assembly to move into the catch take and be slowed down, there is ample time for the HMX to react.



## RIPPLE FREE LINE INITIATION

A. M. Collyer, A. M. Johnson and D. C. Swift

Atomic Weapons Establishment, Aldermaston  
Reading, RG7 4PR, UNITED KINGDOM

Line initiation of explosives is typically achieved by many points of initiation, but the wave front is usually perturbed. A geometric form for a ripple free line initiator has been mathematically derived and experimentally tested. The experiments have demonstrated that consideration has to be given to the centre of initiation, uniformity, and corner turning ability of the explosive in order to achieve a perfect ripple free detonation wave. Although a final version has yet to be tested, the concept has been proven.

### INTRODUCTION

Many experiments studying detonation and shock wave phenomena require line initiation. This is currently achieved at AWE Aldermaston with a number of explosive trains, of equal length, originating from a single point. The resulting line of multiple initiation points is subsequently smoothed using two explosive layers separated by a perspex (PMMA) strip. The emerging detonation wave is typically rippled with time variations up to  $\pm 50\text{ns}$ . However, current applications require better planarity and a target of  $\pm 10\text{ns}$  has been set.

### GEOMETRIC LINE INITIATOR

If an infinite number of explosive paths of equal length can be created then ripple free line initiation is theoretically possible. This continuum of paths can be obtained if a sheet of explosive can be formed around a geometric shape such that the shortest path from the detonator to each point on the required initiation line is the same.

Consider a half-cone of sheet explosive initiated at the apex. All points on a circle, at a given distance from the apex, are initiated simultaneously. Now consider a plane sheet of explosive intersecting the cone at a variety of angles. When the plane contains the cone axis the detonator acts as a point initiator and produces a diverging wave along the sheet (figure 1).

If the plane is perpendicular to the axis, the intersection is a semicircle and a converging wave is produced on one side (figure 2). Hence there ought to be an intersection angle which gives at least an approximation to a line at the end of the plane sheet.

In fact, an exact line initiator is produced if the plane is parallel to the opposite generator of the cone (appendix I). To maximise the length of the initiation line it should intersect the cone axis (figure 3).

### PROTOTYPE DESIGN

A prototype design for a 70mm wide line initiator was manufactured by securing 1.5mm thick PETN based Detasheet explosive around a perspex former. The cone had a half-angle of  $\theta = 30^\circ$ , but was truncated to provide a flat area on which a detonator could more easily be mounted.

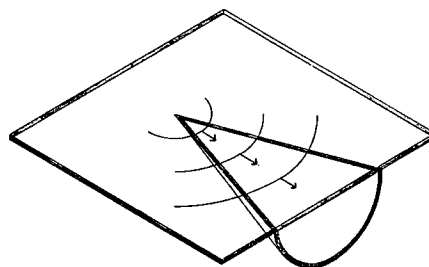


FIGURE 1.

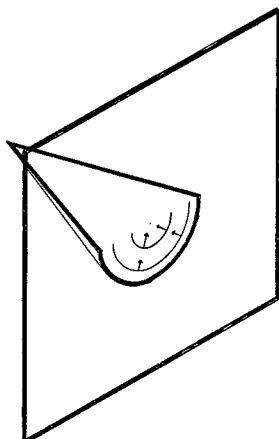


FIGURE 2.

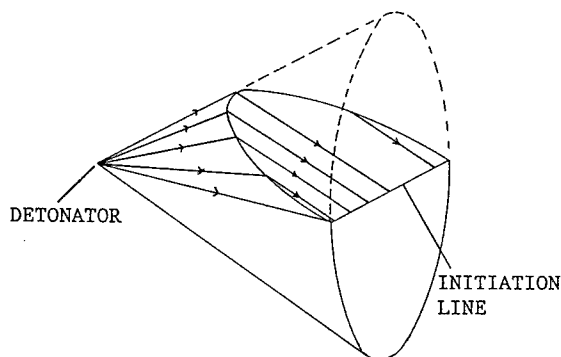


FIGURE 3. EXACT LINE INITIATOR

#### EXPERIMENTAL TECHNIQUE

A simple streak camera technique was adopted to measure the planarity of the detonation wave emerging along the initiation line. The aluminised surface of a glass mirror is placed in contact with the explosive. Two strips of the reflective coating are removed to act as fiducial markers, and allow the camera slit to be focused along the initiation line through the glass, taking account of refraction. Light from an argon flash bomb is reflected in this mirror and recorded by a Cordin 134 camera via an auxiliary mirror (figure 4).

The detonation wave shape is revealed as the light is extinguished on destruction of the reflective surface. In all experiments the camera was run with a nominal writing speed of  $30\text{mm}/\mu\text{s}$ .

#### PROTOTYPE RESULTS

Figure 5 shows the streak record obtained. This shows the detonation wave to be far from the required planarity of  $\pm 10\text{ns}$ . The apparent systematic tilt is

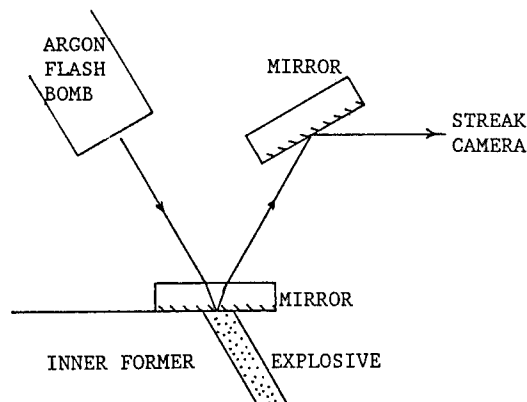


FIGURE 4. EXPERIMENTAL TECHNIQUE

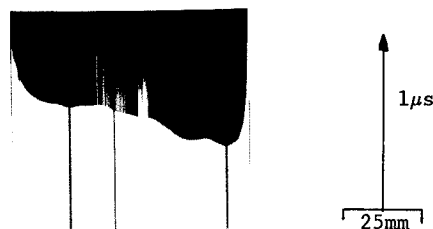


FIGURE 5. PROTOTYPE WAVE SHAPE

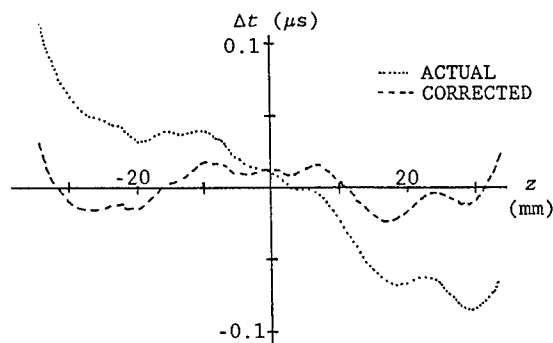


FIGURE 6. DIGITISED WAVE SHAPE

caused by an offset initiation point and is discussed later.

After separating the tilt from the digitised data points, a symmetrically curved wave with time deviations within  $\pm 40\text{ns}$  is revealed (figure 6). The time of arrival generally decreases from edge to centre, but this trend is broken with a time lag starting about  $\pm 18\text{mm}$  from the centre. This is attributed to a corner turning effect.

#### CORNER TURNING EFFECT

The angle  $\delta$  through which the detonation wave must turn in travelling from the conical surface onto the

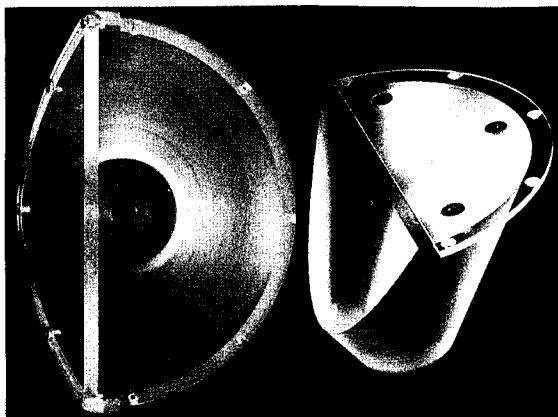


FIGURE 7. PERSPEX FORMERS FOR PLASTIC EXPLOSIVE CONICAL LINE INITIATOR

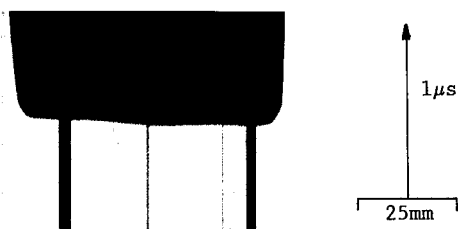


FIGURE 8. PLASTIC EXPLOSIVE RESULT

plane sheet varies from apex to edge. It has a maximum value of twice the cone half-angle  $\theta$  on the axis of symmetry (appendix II).

The time lag in the centre of the prototype result extends to about 18mm ( $\psi \approx 54^\circ$ ) either side of the axis, and is believed to be caused by a corner turning effect. For  $\psi < 54^\circ$  the corner turning angle exceeds  $53^\circ$ , hence the effect should be removed if  $\delta \leq 53^\circ$ .

In the practical design, the cone was truncated and the detonation wave must turn through an angle of  $90 - \delta$  from the base onto the sides of the cone. Any delays in the detonation wave turning such a corner do not interfere with the operation of the line initiator since the device is axisymmetric at this stage.

#### REVISED DESIGN

Cutting and assembling the sheet explosive into this geometry was difficult. Uneven edges created the possibility of small gaps between explosive sections. Stretching of the explosive, while attaching it to the perspex former was also a problem and may have resulted in undesirable local changes in the detonation properties. The straightness and orientation of the final initiation line are affected by these problems and consequently limit the achievable planarity and reproducibility of such a device.

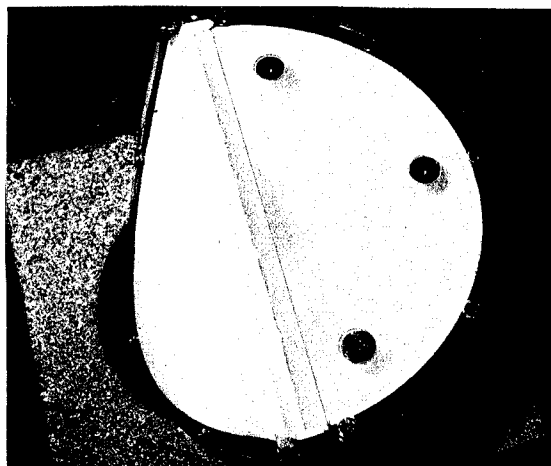


FIGURE 9. ASSEMBLED PLASTIC EXPLOSIVE INITIATOR

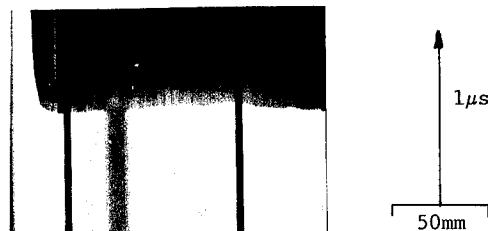


FIGURE 10. 152mm ENGINEERED RESULT

To overcome these difficulties the design was revised to use a PETN based plastic explosive pressed between two perspex formers (figure 7). A nominal thickness of 2mm was chosen for the explosive layer, and the cone half angle was reduced to  $28^\circ$ .

The detonation wave emerging from a 62mm wide prototype plastic explosive initiator has a smaller systematic tilt and is uniformly curved (figure 8), however the time spread is within 30ns. A fully engineered 152mm wide version (figure 9) also produced a curved wave, but this time late at the centre compared with the edges (figure 10). The wave was not tilted and the time spread was within 40ns across the whole width.

Perturbations on the wave fronts are assumed to arise from inhomogeneities in the packing of the explosive. A further trial with an improved filling technique reduced the perturbations, but the planarity was considerably poorer (figure 11).

None of the observed waves have shown the planarity expected from theory, however the tilt and curvature can be explained by a shift in position of the initiation point away from the axis.

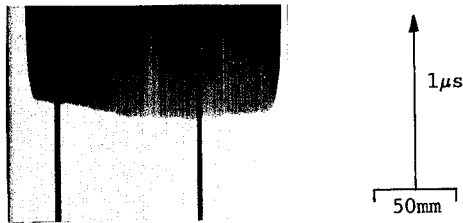


FIGURE 11. IMPROVED EXPLOSIVE FILL

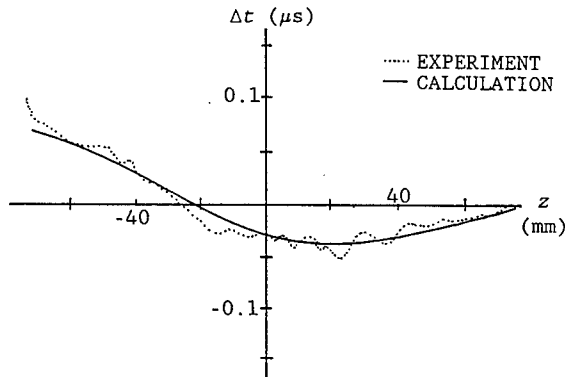


FIGURE 12. COMPUTED EFFECT OF INITIATION POINT OFFSET

#### EFFECT OF INITIATION POINT SHIFT

For the device to work correctly the initiation point must be coincident with the cone axis. The device is assembled by wrapping a layer of the plastic explosive around the inner perspex former, and then pressing this into the outer former which locates the detonator on axis. The inner piece defines the required geometric form, but its precise location relative to the outer is difficult. It is therefore possible for the initiation point to be offset by a small translation or slight tilt of the inner with respect to the outer former.

The effect of an offset initiation point, on the detonation wave shape, can be calculated (appendix III). Figure 12 shows good agreement between experimental and computed time deviations for the result shown in figure 11. In this case the offset position is found to be 0.5mm from the cone axis, and is consistent with possible variations in the experimental assembly. Similar offsets and shape agreements are obtained with other results.

Several results have had detonation waves with better planarity than existing line initiators at AWE. Removing the effect of an offset initiation point reveals wave shapes which are almost within the  $\pm 10$ ns objective. Hence improving the engineering to minimise the possibility of offsets should enable the objective to be met consistently.

#### CONCLUSIONS

A geometric form for a theoretically ripple free line initiator has been mathematically defined and the concept experimentally proven.

The planarity is capable of being better than current line initiators, but has so far been limited by practical problems such as the uniformity and corner turning ability of the explosive, and the precise location of the initiation point.

The practical difficulties are understood and further engineering work is planned to improve the design to achieve the required planarity.

#### APPENDIX I

The equation of a cone of half-angle  $\theta$  about the x-axis, with apex at the origin (figure 13) is:

$$\alpha^2 x^2 - y^2 - z^2 = 0 \quad (1)$$

where  $\alpha = \tan\theta$ , whilst the equation of a plane parallel to the z-axis, intersecting the y-axis at  $h$  and at an angle  $\epsilon$  to the x-axis (figure 13) is:

$$\beta x + y - h = 0 \quad (2)$$

where  $\beta = \tan\epsilon$ . Eliminating  $y$  gives the equation of the intersection:

$$(\alpha^2 - \beta^2)x^2 + 2h\beta x - z^2 - h^2 = 0 \quad (3)$$

which of course describes a conic section.

It is more useful to consider a coordinate  $\xi$ , the distance along the sloping plane (figure 14), rather than  $x$ , where:

$$d\xi^2 = dx^2 + dy^2 = dx^2(1 + \beta^2) \quad (4)$$

since  $dy = -\beta dx$ . The origin of  $\xi$  is defined to be where the plane meets the y-axis, so  $\xi = \gamma x$  with

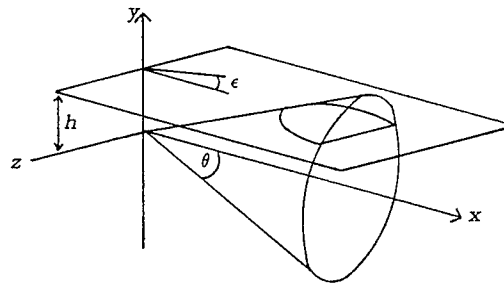


FIGURE 13. INTERSECTING CONE & PLANE - VARIABLE DEFINITIONS

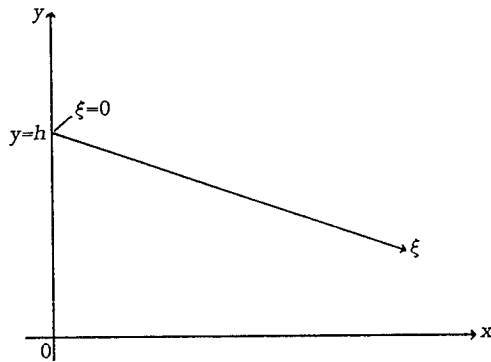


FIGURE 14. RELATION BETWEEN  $\xi$ ,  $x$  &  $y$

$\gamma = (1 + \beta)^{1/2}$ . The intersection (3) in terms of  $\xi$  is:

$$(\alpha^2 - \beta^2) \frac{\xi^2}{\gamma^2} + 2h\beta \frac{\xi}{\gamma} - (z^2 + h^2) = 0 \quad (5)$$

The desired result is that all points in a line  $\xi = \xi_0$  in the plane should be initiated simultaneously. In this case, "rays" in the direction of propagation of the detonation wave would spread from the apex of the cone, but bend to become parallel as they move onto the plane (figure 3). The distance along a ray from the apex to the line  $\xi = \xi_0$  must be independent of  $z$ . This distance is composed of a section of length  $l_1$  on the cone surface, and another of length  $l_2$  on the plane.

$l_1(z)$  is just the straight line distance between the origin and a point  $(x, y, z)$  on the intersection line, so:

$$\begin{aligned} l_1(z) &= [x^2(z) + y^2(z) + z^2]^{1/2} \\ &= \left[ \frac{\xi^2(z)}{\gamma^2} + \left[ h - \beta \frac{\xi(z)}{\gamma} \right]^2 + z^2 \right]^{1/2} \\ &= \left[ \frac{\xi^2(z)}{\gamma^2} (1 + \beta^2) - 2h\beta \frac{\xi(z)}{\gamma} + z^2 + h^2 \right]^{1/2} \end{aligned} \quad (6)$$

whilst  $l_2(z)$  is the distance in the  $\xi$  direction between the intersection and  $\xi_0$ , and is equal to  $\xi_0 - \xi(z)$ , where:

$$\xi(z) = \begin{cases} \frac{-b \pm \sqrt{b^2 - 4ac}}{2a} & : a \neq 0 \\ -\frac{c}{b} & : a = 0 \end{cases} \quad (7)$$

and  $a = (\alpha^2 - \beta^2)/\gamma^2$ ,  $b = 2h\beta/\gamma$  and  $c = -(z^2 + h^2)$ .

In general the total distance  $l_1(z) + l_2(z)$  is a complicated function of  $z$ , but simplifies to  $l_1 + l_2 = \xi_0$  in the case  $a = 0$  for which:

$$\xi(z) = \gamma \frac{z^2 + h^2}{2h\beta} = \frac{z^2 + h^2}{2h\sin\theta} \quad (8)$$

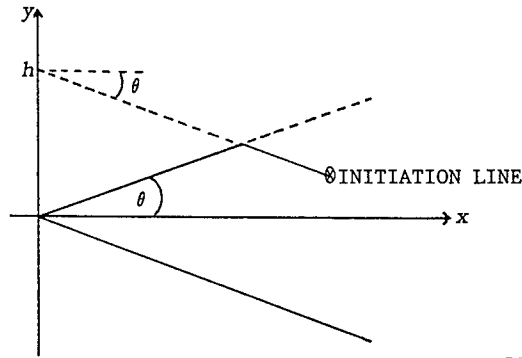


FIGURE 15. CONDITION FOR LINE INITIATION

This condition occurs when  $\theta = \epsilon$ , hence an exact line initiator is produced if the plane is parallel to the opposite generator of the cone (figure 15).

## APPENDIX II

The variation of the corner turning angle  $\delta$  can be calculated by taking direction vectors for rays on the cone and plane.

A direction vector  $\mathbf{r}_c$  lying in the cone consists of two parts. An axial vector:  $\mathbf{r}_a = (1, 0, 0)$  and a radial vector in the  $y$ - $z$  plane:  $\mathbf{r}_r = (0, \cos\psi, \sin\psi)$ , where  $\psi$  is the rotation angle about the  $x$ -axis with the  $y$ -axis and  $\psi = 0^\circ$  in the plane of symmetry. These vectors must satisfy:

$$\begin{aligned} \mathbf{r}_c &= a_a \mathbf{r}_a + a_r \mathbf{r}_r \\ |\mathbf{r}_c| &= 1 \\ \mathbf{r}_c \cdot \mathbf{r}_a &= \cos\theta \end{aligned} \quad (9)$$

where  $a_a$  and  $a_r$  are coefficients to be determined. The direction vector which satisfies these equations is:

$$\mathbf{r}_c = (\cos\theta, \sin\theta \cos\psi, \sin\theta \sin\psi) \quad (10)$$

For a ray in the plane, the direction vector is:

$$\mathbf{r}_p = (\cos\theta, -\sin\theta, 0) \quad (11)$$

As these are both unit vectors the angle  $\delta$  between them is defined by:

$$\cos\delta = \mathbf{r}_c \cdot \mathbf{r}_p = \cos^2\theta - \sin^2\theta \cos\psi \quad (12)$$

and stationary values of  $\cos\delta$  are given by:

$$\frac{\partial(\cos\delta)}{\partial\psi} = \frac{1}{2} \sin\psi (1 - \cos 2\theta) = 0 \quad (13)$$

Rays from the detonator only reach the initiation line when  $-90^\circ < \psi < 90^\circ$ , so the relevant stationary value is a minimum in  $\cos\delta$  when  $\psi = 0^\circ$ . Hence  $\delta$  has a maximum value of  $2\theta$  on the axis of symmetry.

### APPENDIX III

Any offset of the initiation point **I** results in a time deviation caused by a change in the distance from **I** to any point **P** on the edge of the base (figure 16). If **I** is at  $(e\cos\phi, e\sin\phi)$  and **P** at  $(r\cos\psi, r\sin\psi)$ , in the plane of the base, then their separation is defined by:

$$d^2 = (e\cos\phi - r\cos\psi)^2 + (e\sin\phi - r\sin\psi)^2 \quad (14)$$

$$= e^2 + r^2 - 2re\cos(\psi - \phi)$$

Assuming that the initiation point displacement  $e$  is very much less than the base radius  $r$ , equation 14 can be approximated as a perfect square which gives:

$$d \approx r - e\cos(\psi - \phi) \quad (15)$$

Hence the time deviations are given by:

$$\Delta t \approx -\frac{e}{D}\cos(\psi - \phi) \quad (16)$$

where  $D$  is the detonation velocity of the explosive.

The experimental wave shapes are measured as a function of  $z$ , hence equation 16 is more useful if cast into a form with  $\Delta t$  as a function of  $z$  rather than  $\psi$ .

$l_1$  is defined by a line in the direction of  $r_c$  (equation 10) which passes through the origin and satisfies the equation of the plane (equation 2):

$$l_1(\psi) = \frac{h}{\sin\theta(1 + \cos\psi)} \quad (17)$$

However  $l_1(z) = \xi(z)$  since  $l_1(z) + l_2(z) = \xi_0$  and  $l_2(z) = \xi_0 - \xi(z)$ , hence:

$$l_1 = \frac{z^2 + h^2}{2h\sin\theta} = \frac{h}{\sin\theta(1 + \cos\psi)} \quad (18)$$

which can be rearranged to give  $\psi$  in terms of  $z$ :

$$\cos\psi = \frac{h^2 - z^2}{h^2 + z^2} \quad (19)$$

Since the initiation line crosses the cone axis,  $h$  is equal to half its length  $W$ , i.e.  $h = \omega = W/2$ , hence:

$$\cos\psi = \frac{\omega^2 - z^2}{\omega^2 + z^2} \quad (20)$$

where  $-\omega \leq z \leq \omega$ .

The actual offset ( $e$  &  $\phi$ ) is not known and must be deduced from the experimental data. At the ends of the initiation line  $z = \pm\omega$  hence  $\cos\psi = 0$  and  $\psi = \pm 90^\circ$ , therefore from equation 16:

$$\Delta t \approx -\frac{e}{D}\cos(\pm 90 - \phi) \quad (21)$$

$$\approx \mp \frac{e}{D}\sin\phi$$

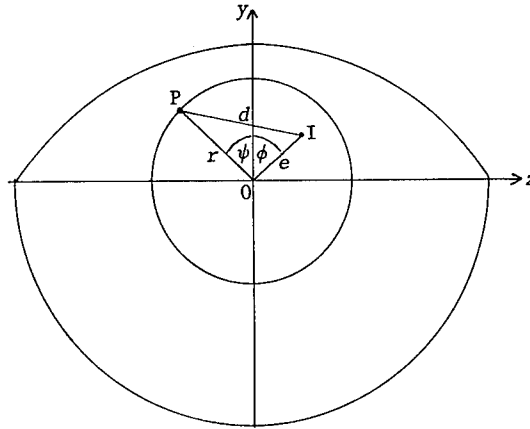


FIGURE 16. INITIATION POINT OFFSET

At the centre  $\psi = 0$ , hence:

$$\Delta t \approx -\frac{e}{D}\cos\phi \quad (22)$$

The rotation angle of the offset  $\phi$  can be estimated using these two equations and corresponding times from the experimental wave shape:

$$\frac{e}{D}\sin\phi / \frac{e}{D}\cos\phi = \tan\phi \quad (23)$$

The distance from the cone axis  $e$  follows once  $\phi$  has been evaluated.

© British Crown Copyright 1993/MOD

Published with the permission of the Controller of Her Britannic Majesty's Stationery Office

### DISCUSSION

DAVID DAVISON  
Shock Transients, Inc., Hopkins, Minnesota

How is the explosive extruded into the gap?

### REPLY BY ALAN COLLYER:

The inside of the outer former is lined with a layer of the plastic explosive slightly thicker than required. The inner former is then pressed into place and excess explosive extruded out as the device is removed.

# CONDENSED-PHASE THERMAL DECOMPOSITION OF TATB INVESTIGATED BY ATOMIC FORCE MICROSCOPY (AFM) AND SIMULTANEOUS THERMOGRAVIMETRIC MODULATED BEAM MASS SPECTROMETRY (STMBMS)

T.A. Land, W.J. Siekhaus, M.F. Foltz

Chemistry and Materials Science Dept.,  
Lawrence Livermore National Laboratory,  
Livermore, California 94550

R. Behrens, Jr.

Combustion Research Facility,  
Sandia National Laboratory,  
Livermore, California 94551

A combination of techniques has been used to investigate the condensed-phase thermal decomposition of TATB. STMBMS has been used to identify the thermal decomposition products and their temporal correlations. These experiments have shown that the condensed-phase decomposition proceeds through several autocatalytic pathways. Both low and high molecular weight decomposition products have been identified. Mono-, di- and tri-furazans products have been identified and, their temporal behaviors are consistent with a stepwise loss of water. AFM has been used to correlate the decomposition chemistry with morphological changes occurring as a function of heating. Patches of small 25-140 nm round holes were observed throughout the lattice of TATB crystals that were heated briefly to 300 °C. It is likely that these holes show where decomposition reactions have started. Evidence of decomposition products have been seen in TATB that has been held at 250 °C for one hour.

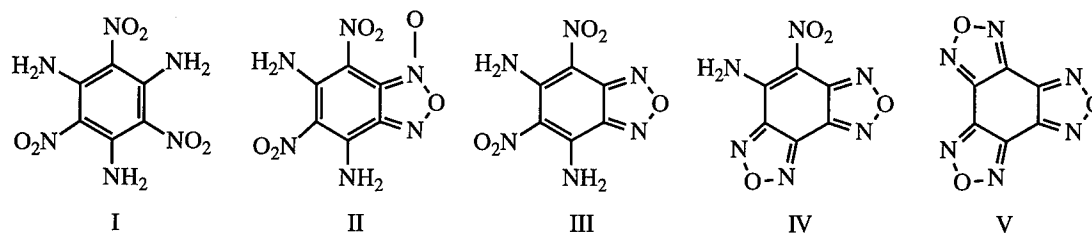
## INTRODUCTION

An important aspect of the safety and surety of weapons is being able to predict the response of the energetic material to abnormal thermal environments. To do this, one needs to understand the slow thermal processes that occur and, how these processes affect the thermal response and the impact and shock sensitivity of the material. In order to develop predictive models for thermal hazards of energetic materials both the physical and the chemical nature of the thermal reactions must be understood.

The compound 1,3,5-triamino-2,4,6-trinitrobenzene (TATB-I) is an energetic material of considerable interest due to its high thermal stability and relative insensitivity to shock and impact. There have been numerous studies addressing the unique properties of TATB.<sup>1-7</sup> A comprehensive literature review of TATB is presented in reference.<sup>1</sup> Even with all the studies focused on TATB there are still many important parameters that are not yet understood. For example, after being heated at 250 °C for a period of time, TATB exhibits an increased sensitivity to shock.<sup>2</sup> However,

the physical and chemical changes in the material due to heating at this temperature, as well as the causes for the observed change in sensitivity, are not understood. Other important parameters not yet understood are the identities and rates of formation of the thermal decomposition products. Differential scanning calorimetry (DSC) was used by Rogers et.al. to investigate qualitative aspects of the thermal decomposition of TATB.<sup>3,4</sup> The observed peak shape was consistent with a complex set of autocatalytic reactions. In addition, using deuterium-labeled TATB, they observed a deuterium kinetic isotope effect (DKIE) that is consistent with breaking of the N-H bond and formation of H<sub>2</sub>O in the slow step of the reaction. At this time, the decomposition products have yet to be fully characterized and the reaction mechanisms are still uncertain.

Sharma et.al. used various surface science techniques to investigate the effects of sub-initiation shock and impact on TATB.<sup>5,6,7</sup> Scanning electron microscopy (SEM) was used to investigate the physical effects of the stimuli on the surface of TATB. Small "ragged" 0.1 to 5 micron size holes surrounded by a fine



deposit of debris were observed. X-ray photoelectron spectroscopy (XPS) was then used to analyze the debris surrounding the holes. A marked decrease in the nitro-group N 1s peak indicated that loss of the NO<sub>2</sub> group was the main result from shock and impact. Other more subtle changes were also observed. Shifts of the N 1s peaks, resulting in shoulders on the main peaks, were consistent with the formation of furoxan (II) and furazan (III) derivatives.<sup>5,7</sup> Chemical ionization mass spectrometry was used to detect the presence of mono-furazan III in the residue of impacted TATB. The existence of debris around these holes, which may be the remnants of hot spots, may act as sensitization centers in the material. The increased sensitivity may be due to morphological defects, such as small micron-size holes, or due to the properties of the decomposed material.

The focus of our research is to gain an understanding of the important physical and chemical parameters that affect the thermal stability of TATB. A combination of techniques has been used to investigate the various aspects of the thermal decomposition of TATB. One area of research is directed at understanding the physical changes that occur in the material as a function of heating, impact and shock. In experiments done so far, atomic force microscopy (AFM) has been used to observe the morphological changes that occur when TATB has been thermally cycled. The high resolution capabilities of the AFM allows us to investigate the formation and growth of reaction centers or hot spots where reactions may have initiated and subsequently died out. It is important to correlate these observed physical changes with chemical changes in the material. The other area of our research focuses on understanding the chemical kinetics of the condensed-phase decomposition reactions. Simultaneous thermogravimetric modulated beam mass spectrometry (STMBMS) and time-of-flight (TOF) velocity-spectra measurements are used to elucidate details of the solid-state decomposition reactions of TATB. The results from these measurements are used to identify the reaction products and to determine their gas formation rates. From this information the reaction pathways are elucidated. Since the decomposition of TATB occurs in the solid phase, both the physical and the chemical nature of the thermal reactions need to be understood and incorporated in any model that is developed to predict its response in abnormal thermal environments.

The results presented in this paper cover our initial analysis of the thermal decomposition of TATB and are used to show the qualitative behavior. Quantification of our results requires further experiments

and will be presented at a later time.

## EXPERIMENTAL

### Materials

Wet aminated TATB, with particles sizes of 50-60 microns, from LLNL lot C084 has been used in the mass spectrometry experiments unless otherwise stated. It was also used as the raw material for recrystallization. Crystals used in these experiments were grown by recrystallization from nitrobenzene that was taken to the boiling point and cooled slowly over several days.

### Atomic Force Microscope

A Digital Instruments Nanoscope III AFM has been used to investigate changes in crystal morphology as a function of heating. The AFM is an ideal tool to characterize surface structure and defects. It offers the unique advantage of being able to directly obtain real space images of virtually any sample without modification or the need to expose the sample to damaging radiation. The AFM is capable of producing high resolution, nanometer scale, three dimensional images while operating in air or fluids. In our experiments, the AFM is used to investigate changes in morphology changes of the surface and also in the bulk of TATB crystals as a function of heating. Information about the bulk is obtained by cleaving crystals and examining the exposed surfaces. Thermal cycling is performed in the controlled environment of a DSC. The sample is placed in a sealed pan and heating is done in a background of nitrogen. After heating, the sample pan is immediately removed and cooled to room temperature. Interior (bulk) features of the cooled crystals are observed by removing surface layers. This can be accomplished by using a pin to cleave the crystal. The crystal is then mounted on the AFM stage. All AFM images are obtained in air at room temperature taking care to minimize the force used during imaging in order to prevent the AFM tip from removing material during scanning.

### Simultaneous Thermogravimetric Modulated Beam Mass Spectrometer

STMBMS has been used to investigate the condensed-phase decomposition chemistry of TATB. The STMBMS apparatus and the basic data analysis procedures have been described previously.<sup>8,9</sup> Briefly,



this instrument allows the concentration and rate of formation of each gas-phase species in a reaction cell to be measured as a function of time by correlating the ion signals measured with the mass spectrometer with the force measured by the microbalance at any instant. In the experiments, a small sample (~10 to 30 mg) is placed in an alumina reaction cell that is then mounted on a thermocouple probe that is seated on a microbalance. The reaction cell is enclosed in a high vacuum environment ( $<10^{-6}$  torr) and is radiatively heated. The gas phase molecules that are formed exit the reaction cell through a small diameter (0.00025 to 0.096 cm) orifice in the cap of the reaction cell. The molecules then traverse two beam-defining orifices before entering the electron-bombardment ionizer of the mass spectrometer where the ions are created by collisions of the electrons with the different molecules in the gas flow. A low ionization energy (20 eV) is used to minimize the amount of fragmentation that occurs in the mass spectrometer. The different  $m/z$ -value ions are then scanned with a quadrupole mass filter and counted with an ion counter. The background pressure is below  $10^{-9}$  torr in the detector chamber. The gas flow from the reaction cell is modulated with a chopping wheel and only the modulated signal is recorded. The containment time of a gas in the reaction cell is a function of the area of the orifice, the free volume within the reaction cell, and the characteristics of the flow of gas through the orifice. Relative rates of reactant loss due to evaporation and reactant decomposition are controlled by adjusting the size of the reaction cell orifice. Using a larger orifice (0.096 cm) results in a greater net evaporation rate of the material while using a smaller diameter orifice (0.00025 to 0.0025 cm) decreases the net evaporation rate, thus increasing containment and the length of time for decomposition to occur.

### Identification of Decomposition Products

The decomposition products are identified by: 1) using unlabeled and deuterium-labeled TATB to determine the formulas of the  $m/z$  values measured with the mass spectrometer, 2) performing an autocorrelation analysis on all of the ion signals measured during one thermal decomposition experiment and separating the different  $m/z$  values into temporally correlated groups that represent the major ion signals in the mass spectra of each product, and 3) measuring TOF velocity-spectra of ion signals at  $m/z$  values representing each decomposition product to determine the molecular weight of the product giving rise to the ion signal. Explicit details of this procedure have been described previously for the case of HMX decomposition.<sup>9</sup>

## RESULTS AND DISCUSSION

### AFM Results

In our experiments, the AFM is used to investigate morphological changes on the surface and, also in the bulk, of TATB crystals as a function of heating. Information about the bulk was obtained by cleaving crystals that have been heated and examining the

exposed surfaces. AFM was first used to characterize the surface, and the cleaved surface, of unheated TATB crystals. The 9 nm x 9 nm image in Figure 1 shows the arrangement of TATB molecules as seen by the AFM. One must use caution when interpreting molecular scale AFM images as it is likely that the AFM senses the overall periodicity of the lattice rather than actually resolving the individual molecules. Never-the-less, one can indeed see the hexagonal arrangement of the TATB molecules that exhibit the expected lattice spacing of  $a \approx b \approx 0.9$  nm.<sup>10</sup> In larger-scale images up to 125 microns, many flat terraces (a few nanometers to microns wide) are observed. A larger scale  $3.8 \mu \times 3.8 \mu$  image of the unheated crystal surface is shown in Figure 2. In this image one sees many step edges and terraces. In these images the lowest step height between terraces is 0.68 nm, as is expected for the  $c$ -axis of the TATB crystal<sup>10</sup> and, step heights at the terrace edges are always multiples of 0.68 nm. The unheated crystal surface appears to be relatively defect free as seen in Figure 2.

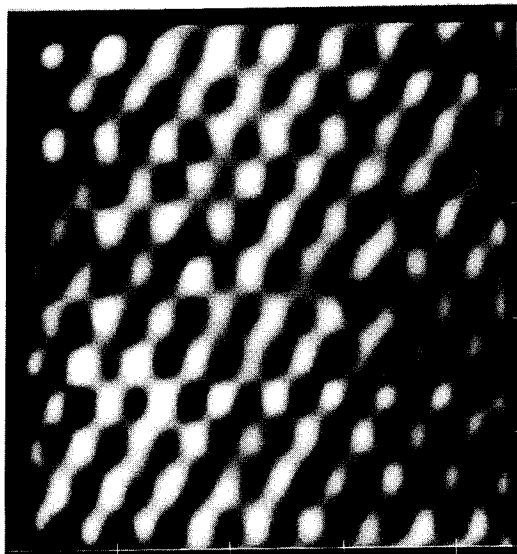


FIGURE 1. A 9 nm X 9 nm AFM IMAGE OF THE TATB CRYSTAL SURFACE. THE IMAGE SHOWS THE HEXAGONAL ARRANGEMENT OF THE TATB MOLECULES WITH A LATTICE SPACING OF 0.9 nm.

AFM was then used to observe changes in the morphology as a function of thermal cycling. After the TATB crystal is heated in the DSC at  $5^\circ\text{C}/\text{min}$  to  $300^\circ\text{C}$  and quickly recooled to room temperature, many defects from re-condensed material are seen to cover the surface. To observe details of any morphological changes it is necessary to remove the surface layers. The  $5 \mu \times 5 \mu$  image in Figure 3 was obtained after cleaving a TATB crystal that was heated to  $300^\circ\text{C}$ . In this image several patches of sub-micron size holes are observed. This is the first time that such holes have been observed in the bulk of thermally cycled TATB. In contrast to holes previously observed to be concentrated on the surface of shock and impacted TATB,<sup>5</sup> these



FIGURE 2. A  $3.8\ \mu\text{m} \times 3.8\ \mu\text{m}$  IMAGE OF THE UNHEATED TATB CRYSTAL SURFACE. THE STEP HEIGHT IS  $0.68\ \text{nm}$  CORRESPONDING TO THE C LATTICE PARAMETER OF TATB.



FIGURE 3. A  $5\ \mu\text{m} \times 5\ \mu\text{m}$  IMAGE ON A CLEAVED SURFACE OF A TATB CRYSTAL THAT HAS BEEN HEATED TO  $300\ ^\circ\text{C}$ . PATCHES OF HOLES ARE OBSERVED IN SEVERAL AREAS OF THE IMAGE.

thermally produced holes have been observed throughout the crystal. Shown in Figure 4 is a higher resolution  $1.1\ \mu\text{m} \times 1.1\ \mu\text{m}$  image of typical holes that were observed. The larger holes are  $100\text{--}140\ \text{nm}$  in diameter and the smaller holes range from  $25$  to  $50\ \text{nm}$  in diameter. Line scans through both the larger and smaller holes show that they have depths on the order of  $10\ \text{nm}$ . One often observes one larger hole surrounded by many smaller holes. It is also noted that the holes have fairly

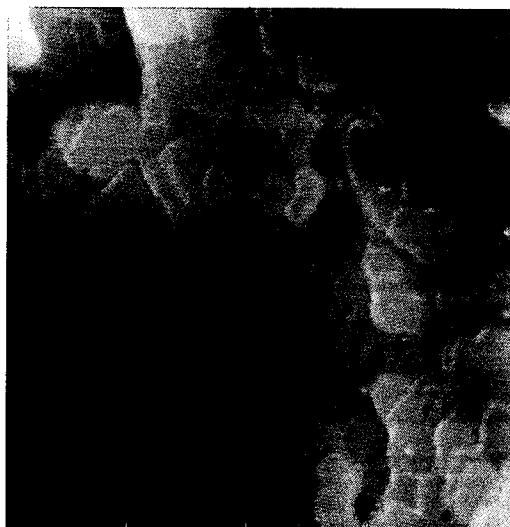


FIGURE 4. A  $1.1\ \mu\text{m} \times 1.1\ \mu\text{m}$  IMAGE SHOWING TYPICAL HOLES THAT ARE CREATED BY HEATING A TATB CRYSTAL TO  $300\ ^\circ\text{C}$ . THIS IMAGE WAS OBTAINED ON A CLEAVED SURFACE OF A THERMALLY CYCLED TATB CRYSTAL. THE LARGER HOLES ARE  $\sim 125\ \text{nm}$  IN DIAMETER AND THE SMALLER HOLES RANGE FROM  $25$  TO  $50\ \text{nm}$ .

regular shapes. All of the holes are rounded as opposed to being irregular and, many even have a defined hexagonal shape which is consistent with the hexagonal symmetry of the TATB lattice. The fact that the holes we observed in thermally cycled TATB, shown in Figure 4, are similar to the micron size holes observed on the surface of shocked and impacted TATB suggest that there may be a relationship between the slow thermal processes and higher order shock and impact events. If a relationship exists, it would mean that one may be able to obtain useful information, in the more easily investigated slow thermal regime, that is applicable to higher order shock and impact events that are much more difficult to study. The physical and chemical aspects of this relationship are currently being investigated.

It is possible that these holes are remnants of hot spots where reactions have started and died out. The high resolution capability of the AFM is being used to look for the beginnings of these reaction centers and how they may change with time and temperature. TATB crystals were heated in the DSC at  $5\ ^\circ\text{C}/\text{min}$  to  $200\ ^\circ\text{C}$  and quickly recooled to room temperature. In AFM images, the crystal surface appears relatively defect free as did the unheated crystal; however, one observes several small  $\sim 15\text{--}40\ \text{nm}$  size holes which may be the beginnings of the decomposition reactions. Experiments are currently in progress to look at morphological changes occurring as a function of time in the temperature range of  $200$  to  $300\ ^\circ\text{C}$  and, also any effects that may be due to different crystallization methods.

## STMBMS Results

It is important to correlate the observed changes in morphology with the reaction chemistry. STMBMS and TOF velocity-spectra measurements can be used to elucidate details of the solid-state decomposition reactions of TATB. In this paper we present the results on the mass spectra of TATB at low electron energies, the identification of thermal decomposition products above 300 °C, and the temporal behavior of the various decomposition product signals. These initial results show the qualitative behavior of the thermal decomposition of TATB. Quantification of our results requires further analysis and will appear in a future publication.

Using a larger (0.096 cm) orifice the evaporation of TATB at 250 °C was characterized and the major ion signals observed in the mass spectra of TATB at 20 eV are shown in Table I. The ion formulas shown in Table I were obtained by correlating  $m/z$  values from unlabeled-TATB with those from deuterium-labeled TATB. The molecular ion  $C_6N_6O_6H_6^+$  ( $m/z=258$ ) is by far the largest peak observed in the mass spectrum. The other major species observed in the mass spectrum is  $C_6N_5O_5H_6^+$  ( $m/z=228$ ) and it accounts for 28 % of the daughter ions. Other major peaks in the mass spectrum are approximately a factor of 16 lower than that of  $m/z=258$ .

TABLE I. MAJOR PEAKS IN THE MASS SPECTRA OF TATB AT AN ELECTRON ENERGY OF 20 EV.

Ion Signal	Fraction	TATB-d6	Formula
119	2%	122	$C_6N_2OH_3$
120	1%	121 or 124	?
147	1%	150	$C_6N_4OH_3$
165	2%	170	$C_6N_4O_2H_5$
182	2%	188	$C_6N_4O_3H_6$
224	3%	228	$C_6N_6O_4H_4$
228	15%	234	$C_6N_5O_5H_6$
229	1%		?
241	1%	246	$C_6N_6O_5H_5$
258	47%	264	$C_6N_6O_6H_6$

THE ION SIGNALS GREATER THAN 1% OF THE TOTAL ION SIGNAL ARE SHOWN FOR THE EVAPORATION OF TATB. ION FORMULAS ARE BASED ON CORRELATION'S OF ION SIGNALS AT DIFFERENT  $m/z$  VALUES FOR UNLABELED-TATB AND DEUTERIUM-LABELED TATB. THE SAMPLE WAS HELD AT 250 °C.

A smaller (0.0025-0.00025 cm) orifice is used to contain the material and investigate the decomposition of TATB. The ion signals of the products formed from the isothermal decomposition of TATB, when it is contained in a reaction cell with a 0.0025 cm diameter orifice at 340 °C, are shown in Table II. The thermal decomposition products associated with the ion signals were obtained by correlating  $m/z$  values of unlabeled-TATB with those from deuterium-labeled

TATB and these formulas appear at the  $m/z$  values listed in Table II. The major decomposition products formed are the lower molecular weight species:  $H_2O$ ,  $HCN$ ,  $CO$ ,  $NO$ ,  $HNCO$ ,  $CO_2$  and  $C_2N_2$ . Another smaller low molecular weight product is  $NH_3$ . Significant higher molecular weight decomposition products include three furazan derivatives, mono- ( $C_6N_6O_5H_4^+$ ,  $m/z=240$ , III), di- ( $C_6N_6O_4H_2^+$ ,  $m/z=222$ , IV), and tri-furazan ( $C_6N_6O_3^+$ ,  $m/z=204$ , V), that are formed by the loss of one, two and three water molecules from the parent TATB molecule. This is the first time that the tri-furazan product has been observed in the decomposition of TATB. It should also be noted that the loss of water can be intra- or intermolecular due to the hydrogen bonding and proximity of the TATB molecules in the lattice. In the case of furazan formation the ring remains intact but the aromaticity is lost. Ion signals associated with higher molecular weight decomposition products are observed at  $m/z$  values of 68, 120, 164, 176 and 177. Whether these are ion fragmentation products formed from the furazan products or additional thermal decomposition products will be determined by further TOF velocity spectra measurements and analysis of these species.

TABLE II. TATB THERMAL DECOMPOSITION PRODUCTS FORMULAS.

Ion Signal	Fraction <sup>c</sup>	TATB-d6	Formula <sup>a</sup>
17	2%	20	$NH_3$
18	14%	20	$H_2O$
27	8%	28	$HCN$
28	5%	28	$CO$
30	20%	30	$NO$
43	8%	44	$HNCO$
44	16%	44	$CO_2$
52	7%	52	$C_2N_2$
68 <sup>b</sup>	1%	68	$C_2N_2O$
120 <sup>b</sup>	2%	120	$C_4N_4O$
164 <sup>b</sup>	2%		?
176 <sup>b</sup>	1%		?
177 <sup>b</sup>	2%		?
204	1%	204	$C_6N_6O_3$
222	4%	224	$C_6N_6O_4H_2$
240	4%	244	$C_6N_6O_5H_4$

<sup>a</sup> Formulas of the thermal decomposition products formed during the decomposition of TATB. Identity of the formulas are determined from correlation's between the  $m/z$  values from unlabeled-TATB and deuterium-labeled TATB and TOF velocity-spectra measurements. Question marks indicate uncertainty in the identity of the product formula at this time.

<sup>b</sup> Some of these ion signals may be ion fragments from heavier thermal decomposition products.

<sup>c</sup> Approximate fraction of product ion signals for qualitative estimates of the amount of each product formed during the thermal decomposition of TATB. This has not been corrected for ion sensitivity factors and actual quantitative results may differ by up to 50% for ion signals at  $m/z$  values up to 52 and greater amounts at higher  $m/z$  values.

STMBMS/TOF experiments aid in determining the identity of the products and, also provide insight to the reaction mechanisms. The ion signal peaks resulting from evaporation rise early and remain constant throughout the isothermal experiment whereas, the peaks due to decomposition have a much different behavior. Figures 5 and 6 show the temporal behaviors of the ion signals associated with the major products formed during the isothermal decomposition of TATB. The signals in the left portion of the plot were obtained during the thermal ramp of the sample and those in the right shaded portion of the plot were obtained at the isothermal temperature. In these experiments decomposition begins at about 275 °C and rapidly increases as the sample reaches the isothermal temperature of 340 °C. For a simple first order reaction, one would expect the signals arising from decomposition products to rise as the reaction begins and to fall as the amount of sample in the reaction cell is depleted. However, this is not the behavior observed in the decomposition of TATB. As shown in Figures 5 and 6, the decomposition product signals all have an induction period followed by an accelerating rate of product formation as the sample is being depleted. This temporal behavior exemplifies the classic shape associated with solid-phase/autocatalytic decomposition. Further analysis of the temporal behavior of the ion signals in Figure 5 shows that the initial evolution of the three distinct furazan products is sequential. The peak associated with the mono-furazan product shows the earliest increase in signal and continues to rise until the sample is depleted. The peaks associated with the di- and tri-furazan products have a longer induction period and a later rise in signal that continues to increase. This suggests that the mono-, di-, and tri-furazan products are formed by a sequential step-wise loss of water.

An important step in determining the decomposition reaction pathways is correlating products with like temporal behaviors. Figure 6 shows that the temporal behaviors of H<sub>2</sub>O, CO<sub>2</sub>, CO and HCN exhibit an early rise time and are correlated with the mono-furazan product. Whereas, cyanogen (C<sub>2</sub>N<sub>2</sub>), NO, HNCO and NH<sub>3</sub> exhibit a later rise time and are correlated with the di- and tri-furazan products. The varied temporal behaviors of the ion signals associated with the decomposition of TATB suggest a multiple pathway decomposition mechanism. A detailed understanding of the reaction mechanisms requires further experiments that are presently being pursued.

### Correlation of Morphology with Chemistry

STMBMS can be used to investigate the chemistry associated with morphology changes observed by AFM that were discussed earlier in this paper. One would like to know what is the nature of these holes observed in thermally cycled TATB, i.e., are they gas-filled bubbles with the products trapped inside or, are they hollow voids lined with a non-volatile residue? If indeed these holes are reaction centers, one would expect to find evidence of the reaction products left behind. STMBMS mass spectrometry can be used to correlate the physical aspects of decomposition with the reaction chemistry. Crystals that have been thermally

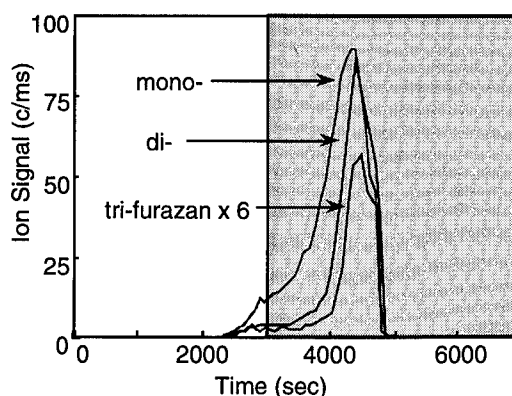


FIGURE 5. ION SIGNAL ASSOCIATED WITH THE FURAZAN THERMAL DECOMPOSITION PRODUCTS OF TATB. THE SIGNALS IN THE LEFT PORTION OF THE PLOT WERE OBTAINED DURING THE THERMAL RAMP (8 °C/MIN) OF THE SAMPLE AND THE SIGNALS IN THE RIGHT SHADED AREA WERE OBTAINED AT THE ISOTHERMAL TEMPERATURE OF 340 °C. THIS FIGURE SHOWS THAT THE INITIAL EVOLUTION OF THE THREE DISTINCT FURAZAN PRODUCTS IS SEQUENTIAL.

cycled can be evaporated in the mass spectrometer and the products present due to thermal cycling can be distinguished. Likewise, the spectrometer can also be used to investigate the real time decomposition of TATB at lower temperatures. If the holes observed by AFM are hollow voids lined only with a non-volatile residue one would only expect to see the higher molecular weight products. In this case, the ion signals of the products are expected to be correlated with the TATB molecular ion and exhibit temporal behaviors consistent with evaporation. This is in contrast to experiments where actual decomposition is occurring during the experiment and product signals exhibit autocatalytic characteristics that are not correlated to the molecular ion signal as was seen in Figure 6. On the other hand, if the holes are gas-filled bubbles and, the gases have not escaped between experiments, one would expect to see both high and low molecular weight products. In this case the product signals may not be correlated with the molecular ion since variations in the product signals may occur as the bubbles are ruptured and products are released. Preliminary results from evaporation of TATB and TATB crystals, that were previously heated for one hour at 250 °C, show evidence of some decomposition. In the early part of the evaporation experiment ( $t < 15$  min), the decomposition products observed were temporally correlated with the molecular ion  $m/z = 258$  and, did not show evidence of condensed phase autocatalytic decomposition. This behavior indicates that these decomposition products were present before the evaporation began (note that decomposition products are not observed in evaporation of untreated TATB). As evaporation continues and the sample is held for longer times at 250 °C, we see evidence of real-time decomposition occurring. A slow increase in the decomposition product signal indicates that TATB

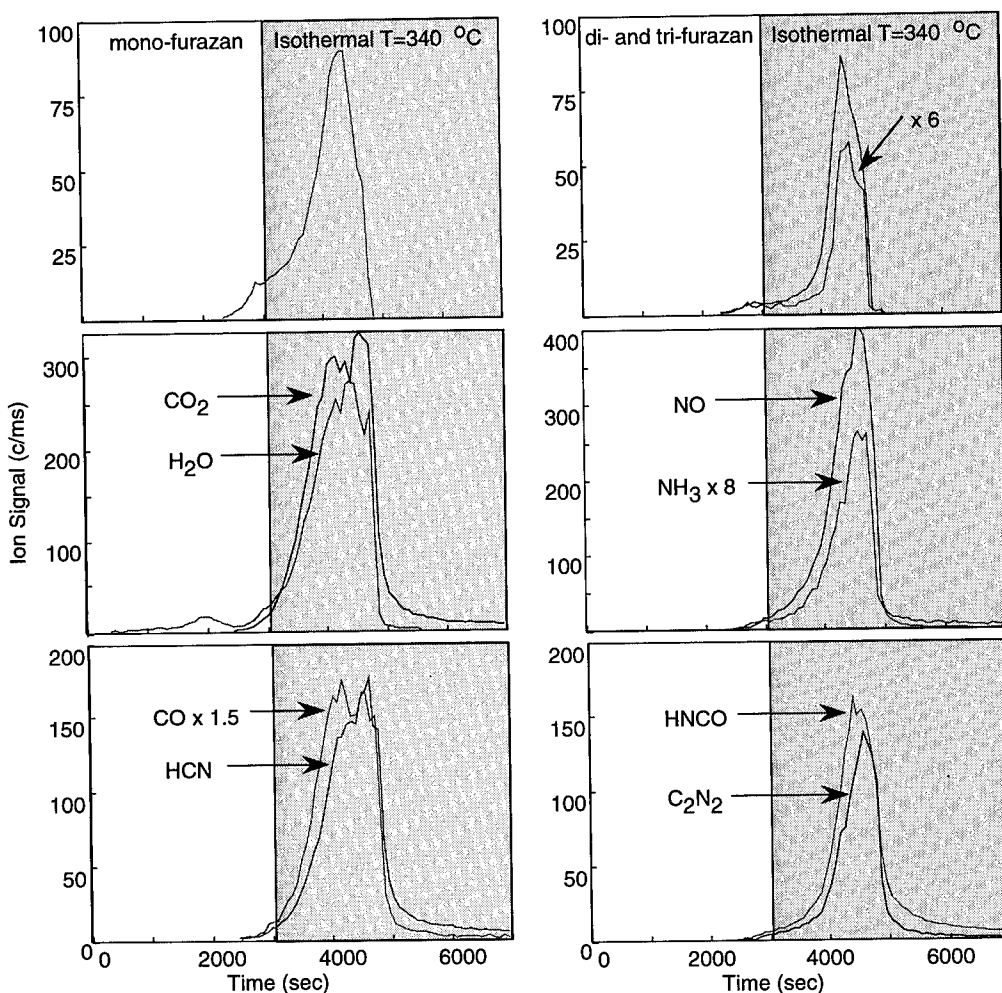


FIGURE 6. ION SIGNAL ASSOCIATED WITH THE THERMAL DECOMPOSITION PRODUCTS OF TATB. THE SIGNALS IN THE LEFT PORTION OF THE PLOT WERE OBTAINED DURING THE THERMAL RAMP (8 °C/MIN) OF THE SAMPLE AND THE SIGNALS IN THE RIGHT SHADED AREA WERE OBTAINED AT THE ISOTHERMAL TEMPERATURE OF 340 °C.

continues to slowly decompose during the ~2 hour experiment at 250 °C. The products detected in the STMBMS experiments may be correlated with the holes observed in the AFM images presented earlier in this paper. It is also possible that these holes may bear some relation to the holes observed by Sharma et. al.<sup>5</sup> on shocked and impacted TATB and, that they may be responsible for increased sensitivity of the material. More experiments are necessary to investigate the details of these correlation's.

## CONCLUSIONS

A combination of techniques has been used to investigate the condensed-phase thermal decomposition of TATB. AFM has been used to study morphological changes induced by thermal cycling. Patches of small 25-140 nm round holes were observed throughout the

lattice of TATB crystals that were heated briefly to 300 °C. This is the first time that such holes have been observed in thermally cycled TATB. It is likely that these holes show where decomposition reactions have started. This would imply that decomposition does not occur uniformly but rather that it is catalyzed by certain "sites". We are currently using STMBMS to look for evidence of reaction products remaining in the holes. Correlation's of the holes created by thermal processes with those created by sub-initiation shock and impact are also being investigated.

STMBMS has been used to investigate the reaction products formed by the thermal decomposition of TATB. These experiments have shown that thermal decomposition of TATB occurs in the condensed phase and, proceeds through several pathways that exhibit autocatalytic behavior. Both low and high molecular weight products have been identified. The major

decomposition products formed are  $\text{H}_2\text{O}$ ,  $\text{HCN}$ ,  $\text{CO}$ ,  $\text{NO}$ ,  $\text{HNCO}$ ,  $\text{CO}_2$  and  $\text{C}_2\text{N}_2$ . Another smaller low molecular weight product is  $\text{NH}_3$ . Significant higher molecular weight decomposition products include three furazan derivatives, mono- ( $\text{C}_6\text{N}_6\text{O}_5\text{H}_4^+$ ,  $m/z=240$  III), di- ( $\text{C}_6\text{N}_6\text{O}_4\text{H}_2^+$ ,  $m/z=222$ , IV), and tri-furazan ( $\text{C}_6\text{N}_6\text{O}_3^+$ ,  $m/z=204$ , V). This is the first time that the tri-furazan product has been observed in the decomposition of TATB. The furazan products are formed by the elimination of one, two and three water molecules from the parent TATB molecule. From these experiments, it has been determined that the initial formation of the three furazan products is sequential, with tri-furazan having the longest induction period as shown in Figure 5. The first step towards determining the decomposition reaction mechanisms is correlating products with like temporal behaviors. Presently, many of the lower molecular weight products have been correlated with the different furazans. Further experiments are required to identify other decomposition products, to elucidate details of the reaction mechanisms and to quantify the gas formation rates of the products.

#### ACKNOWLEDGEMENTS

The Authors thank D.M. Puckett for assistance in running experiments, F. Garcia for assistance in heating the crystals in the DSC and, P. Pagoria for synthesizing the deuterium-labeled TATB growing the TATB crystals.

Work performed under the auspices of the U.S. Department of Energy by the Lawrence Livermore National Laboratory under contract No. W-7405-ENG-48.

#### REFERENCES

1. S. F. Rice and R. L. Simpson; UCRL-LR-103683 (1990).
2. P. A. Urtiew, T. M. Cook, J. L. Maienschein, C. M. Tarver; Tenth Intl. Det. Symp. (1993).
3. R. N. Rogers, J. L. Janney and M. H. Ebinger; *Thermochimica Acta*, 59 (1982) 287.
4. R. N. Rogers, J. L. Janney; *Int. Jahrestag.-Fraunhofer-Inst. Treib-Explosivst.*, (1980) 411.
5. J. Sharma, J. W. Forbes, C. S. Coffey, and T. P. Liddiar; *J. Phys. Chem.* 91, (1987) 5139.
6. J. Sharma and B. C. Beard; *Phil. Trans. R. Soc. Lond. A*, 339 (1992) 285.
7. *Shock Waves In Condensed Matter-1983*; Ed. J. R. Asay, R. A. Graham, G. K. Straub Elsevier Science Publishes B. V., Holland, 1984, Ch. XII.
8. R. Behrens, Jr.; *Rev. Sci. Instrum.* 58(3) (1987) 451.
9. R. Behrens, Jr.; *Int. J. Chem. Kinetics*, 22 (1990) 135.
10. H. Cady and A. C. Larson; *Acta Cryst.* 18 (1965) 485.

#### DISCUSSION

JACQUES BOILEAU  
DRET, Paris, France

Did you observe the effect of traces of chlorine or chloric acid products (e.g., ammonium chloride) on the decomposition mechanism of TATB?

#### REPLY BY TERRY LAND:

TATB used in these experiments was prepared by the wet aminated process which typically is cleaner and has less ammonium chloride residue than material prepared by the dry aminated process. The TATB that was used in these experiments had ~0.06% chlorine impurity. Decomposition experiments were performed using TATB and recrystallized TATB. In experiments using recrystallized TATB the amount of chlorine is even lower. We have not increased the amount of chlorine products to investigate possible effects on the decomposition mechanisms.

#### DISCUSSION

DR. FRED VOLK  
Fraunhofer Institut für Chemische Technologie,  
Pfinztal, Germany

In your reaction products I missed the formulation of  $\text{N}_2\text{O}$ . Did you look for this decomposition product?

#### REPLY BY TERRY LAND:

We find a decomposition product ion signal with a  $m/z=44$ . This ion could be from  $\text{CO}_2$  or  $\text{N}_2\text{O}$ . We are currently using  $^{15}\text{N}$  labeled TATB to confirm the identity of the product.

#### DISCUSSION

DENIS SPITZER  
French German Research Institute, Saint-Louis, France

How do you evaluate the potential role of the residual crystallization solvent in the spatial nucleation and defect creation during the heating process? Is there any evidence that the solvent participates in the creation of the defects?

**REPLY BY TERRY LAND:**

STMBMS has been used to determine that the solvents used for recrystallization, nitrobenzene and DMSO, are not incorporated into the crystalline lattice. We observe nitrobenzene or DMSO evaporating very early in the experiment but all presence of the solvent is gone or below the detection limit by the time TATB

decomposition begins. This behavior suggests that the solvent is left as a residue on the outer surface of the crystals and is not incorporated into the lattice. The stimulus for decomposition at the sites observed by AFM is not known. It is possible that decomposition upon heating is initiated at defect sites or perhaps at sites where impurities (below the detection limit of ~0.001 wt%) are included in the lattice.

## FRACTURE SURFACE TOPOGRAPHY OF TNT, COMPOSITE B AND OCTOL

M. Yvonne D. Lanzerotti and J. Pinto

U. S. Army ARDEC  
Picatinny Arsenal, NJ 07806-5000

A. Wolfe

New York City Technical College  
Brooklyn, NY 11201-0000

David J. Thomson  
AT&T Bell Laboratories  
Murray Hill, NJ 07974

This paper describes new experimental and analysis techniques that allow us to characterize quantitatively and to compare the fracture surfaces of different energetic materials, and to deduce the specific fracture mechanisms. These techniques are widely applicable to other composite systems. In the materials discussed herein, topographical profiles spaced 1.0 mm apart across the fracture surfaces of TNT, Composition B, and Octol have been obtained with a diamond stylus profilometer. Spatial power spectra (wavelengths of 1.0  $\mu\text{m}$  to 1.0 cm) have been calculated using a prolate spheroidal data window in the horizontal space domain prior to using a fast Fourier transform algorithm. The spatial power density of the fracture surface profiles is found in general to decrease with increasing spatial frequency over the region of interest,  $\approx 1 \text{ mm}^{-1}$  to  $\approx 1 \text{ cm}^{-1}$ . Quasi-periodic peaks corresponding to the TNT grain size are observed in the TNT spatial power spectra; these peaks indicate the nonuniform grain size distribution in the TNT fracture surface. Quasi-periodic peaks corresponding to RDX and HMX particle sizes are observed in the Composition B and Octol spatial power spectra, respectively. These peaks indicate the inhomogeneous RDX and HMX grain size distribution in the Composition B and Octol fracture surfaces, respectively. The peaks in the TNT power spectra also indicate that much of the fracture in this material is occurring at grain boundaries: intergranular failure. Peaks in the Composition B and Octol spectra indicate that intergranular fracture often occurs between the TNT and RDX or HMX grains, respectively. Fractal analysis of the TNT, Composition B, and Octol power spectral slopes and amplitudes indicate the regions of deterministic intergranular failure and the regions of the nondeterministic trans-granular failure through TNT, RDX, or HMX grains. This non-deterministic (fractal) failure is chaotic and may indicate the origin of failure in the sample.

### INTRODUCTION

We have introduced several new fields of research to study the mechanical behavior of energetic materials during high acceleration by using an ultracentrifuge<sup>1</sup>, and to characterize the mechanical failure surfaces of energetic materials by power spectral statistical techniques<sup>2</sup>.

We have underway a program for studying in detail the fracture behavior of TNT, Composition B (59% cyclotrimethylenetrinitramine (RDX), 40% TNT, and 1% wax), and two types of Octol (70% cyclotetramethylenetetranitramine (HMX) and 30% TNT;  $\approx 83\%$  HMX and  $\approx 17\%$  TNT) using an ultracentrifuge<sup>2</sup>.

This program includes especially the study of the characteristics of the fracture surfaces of the materials. In this paper, the results and conclusions obtained from statistical studies of the fracture surface topography along several parallel scans across the fracture surfaces of TNT, Composition B, and Octol are described.

### TECHNIQUE

The fracture surfaces of the energetic materials under study are obtained by accelerating prepared samples in a Beckman preparative model L8-80 ultracentrifuge. The TNT, Composition B, and 70/30 Octol samples are melt cast in polycarbonate tubes<sup>2</sup>. The sedimentation cast 83/17 Octol sample is machined into the shape of a frustum of a cone. The large diameter is



11-mm, the small diameter is 9-mm. The angle between the base and the side is 80°. The sample is fitted into a 5-mm long, 11-mm outer diameter aluminum cylinder. The sample under study can be rotated up to 60,000 rpm (500,000 g). When the tensile or shear strength of the object material is exceeded, a fracture surface is obtained. A diamond stylus profilometer has been used to measure the topography of the surface after removal of the sample. Profiles have been obtained at several locations spaced approximately 1.0 mm apart across the surface. Spatial wavelengths along each trace of 1.0  $\mu\text{m}$  to approximately 1.0 cm have been statistically characterized. Spatial power spectra have been calculated from the data of the individual traces using a prolate spheroidal data window<sup>3,4</sup> applied in the horizontal space domain prior to using a fast Fourier transform algorithm<sup>5</sup>. The spatial frequency bands for which power spectral amplitudes are reported are designated A and C in Table 1.

## RESULTS

**TNT.** The sample of melt-cast TNT reported here was found to fracture at an acceleration of 50,000 g at 25°C. The spatial power spectra of the fracture surface profiles across traces g and i (see inset) are shown in Figure 1. The distribution of peaks in the spatial power spectra show the nonuniform TNT grain size. The TNT grain size varies discontinuously from  $\approx 0.1$  mm to  $\approx 1.0$  mm. Figure 1 also shows how the nonuniform TNT grain size varies with location across the surface. As has been shown previously<sup>2</sup>, the spatial power spectra for TNT falls off with increasing spatial frequency. The solid and starred lines superimposed on the spectra traces are linear fits to the sections of the spectra corresponding to the line lengths.

The variation of the spectral slope across the surface is of considerable interest. In the frequency interval  $10^0 \text{ mm}^{-1}$  to  $10^1 \text{ mm}^{-1}$  the spectral slope of trace g is -3.5. We have found values similar to this for the spectral slopes in our previous studies of TNT<sup>2</sup>. The spectral slope of trace i is -2.1 in this frequency interval. The absolute value of the spectral slopes for profiles g through k of Figure 1 are plotted in Figure 2 as a function of the sample trace. Typical errors in the slopes are shown. Similar results are obtained for sample traces a through f.

For spectral slopes  $\leq -3$ , the fractal dimension of the respective wavelength interval equals one<sup>6,7</sup>. Such a slope suggests that the failure process is deterministic. As we have noted before, this interpretation is consistent with the occurrence in the spectrum of quasi-harmonic peaks. That is, the occurrence of the peaks, which correspond to TNT grain sizes, as well as the magnitude of the spectral slopes, indicate that, in general, the fracture is occurring at grain boundaries: intergranular failure.

For spectral slopes,  $s$ , that lie in the range  $-3 < s \leq -2$ , the fractal dimension is given<sup>6,9</sup> by

$$s = -(5-2D), \quad (1)$$

where  $D$  is the fractal dimension. The fractal dimensions for profiles i and d are 1.5 and 1.8, respectively. This indicates that the failure is non-deterministic chaos. That is, transgranular failure occurs through the TNT grain. The region of non-deterministic chaos suggests that the origin of the failure is in the center of the sample.

Also of considerable interest is the nature of the spectral variations across the fracture surface. This has been investigated by determining the frequencies and amplitudes of the spectral peaks in each of the spectra computed from profile data taken for the sample traces a through k. The most prominent spectral peak is listed in Table 1 and is designated C. Spectral value A corresponds to a low frequency spectral value selected outside a distinct peak.

The power amplitudes for each of the spectral values of Table 1 are plotted in Figure 3 as a function of the sample trace. There is a distinct tendency for the high peak power levels to occur for those traces taken closer to the sample edges (i.e., the spectra from profiles g and k) for the spatial frequency value, C, corresponding to spectral peaks. The lowest spectral frequency has a peak amplitude in the center of the sample (profile trace i). Similar results are obtained for traces a through f. The high peak power levels occur for edge traces for the spatial frequency values, 2.1-2.6  $\text{mm}^{-1}$ , corresponding to spectral peaks. The lowest spectral frequency, A, also has a peak amplitude in the center of the sample (profile trace d).

Table 1. Spatial frequency bands for which TNT power amplitudes are plotted in Figure 3

A	1.0 $\text{mm}^{-1}$
C	1.4-1.8 $\text{mm}^{-1}$

**Composition B.** The sample of melt-cast Composition B reported here was found to fracture at an acceleration of 41,000 g at 25°C. The logarithmic normal crystal size distribution of RDX as specified by military specification Class 1<sup>10</sup> is shown in Figure 4. Figure 5 shows the spatial power spectra of the fracture surface profiles across traces i and j (see inset). The distribution of peaks in the spatial power spectra shows the inhomogeneous grain size of the RDX in the Composition B. The RDX grain size varies discontinuously from  $\approx 0.1$  mm to  $\approx 1.0$  mm in contrast to Class 1 RDX particle sizes in Figure 4. Figure 5 also shows how the inhomogeneous RDX particle size varies with location across the surface.

In the frequency interval  $10^0 \text{ mm}^{-1}$  to  $10^1 \text{ mm}^{-1}$  the spectral slope of trace i is -4.0. We have found values similar to this for the spectral slopes in our previous studies of Composition B<sup>2</sup>. The spectral slope of trace j is -2.1 in this frequency interval. The absolute value of the spectral slopes for profiles i through m are plotted in Figure 6 as a function of the sample trace. Similar results are obtained for sample traces a through h.

As noted above, for spectral slopes  $\leq -3$ , the fractal dimension = 1<sup>6,7</sup>. As we have noted before, this

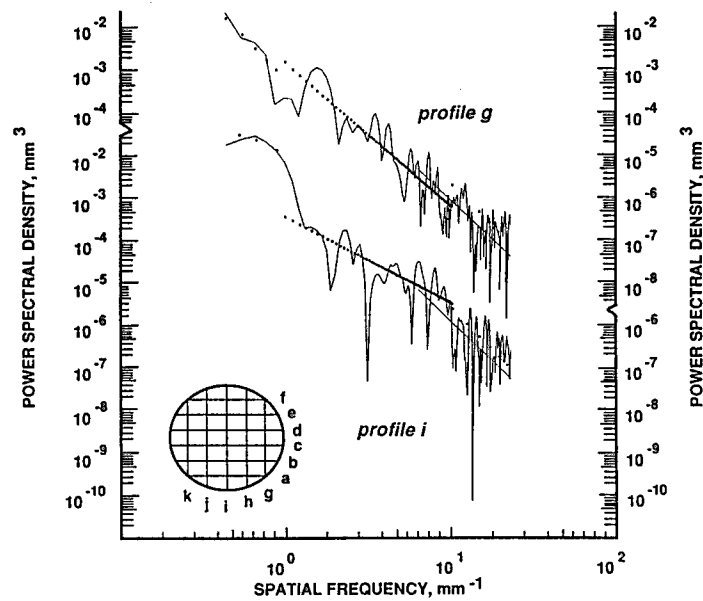


Figure 1. Spatial power spectra of the fracture surface profiles for sample traces g and i of TNT. The locations of the profile traces across the sample surface are shown in the inset. Diamond stylus horizontal spacing is 0.004 mm.

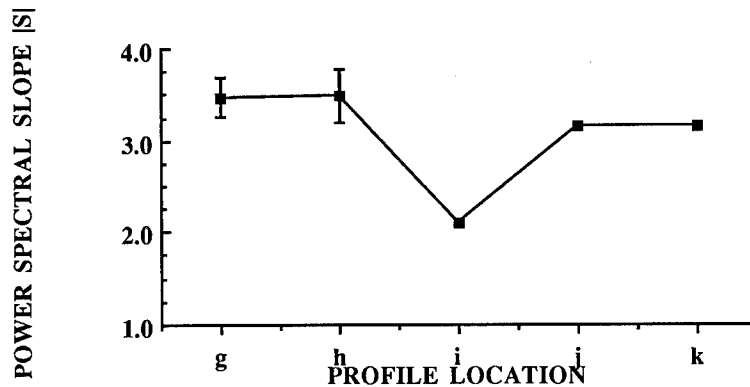


Figure 2. Spectral slopes versus profile location g through k of TNT for spatial frequency interval  $10^0 \text{ mm}^{-1}$  to  $10^1 \text{ mm}^{-1}$ .

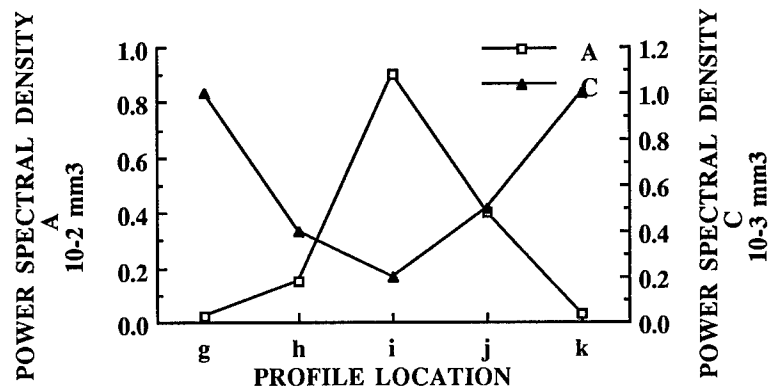


Figure 3. Power amplitudes for the spatial frequencies A and C in Table 1 plotted as a function of profile location g through k of TNT in Figure 1.

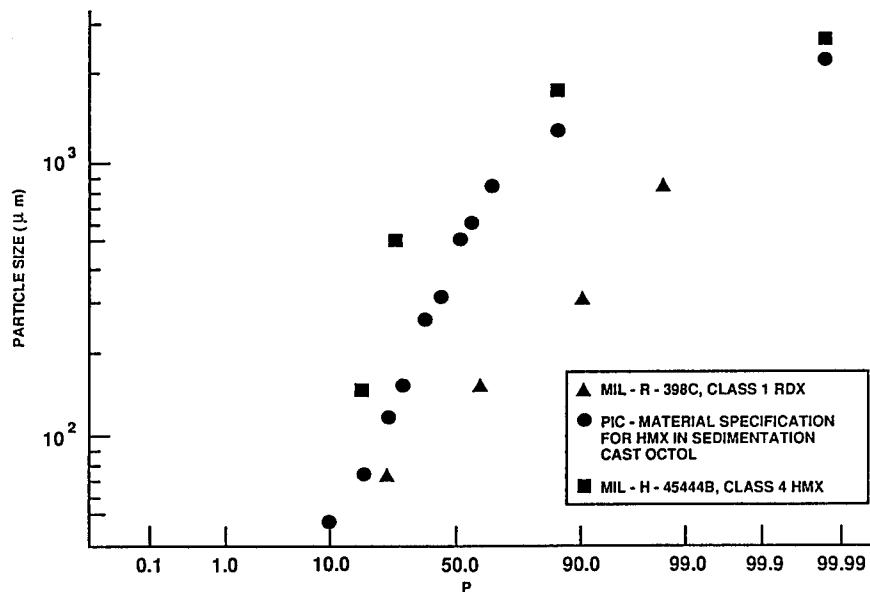


Figure 4. RDX and HMX Particle Size Distributions.  $P$  is the cumulative percentage of measurements less than or equal to the particle size.

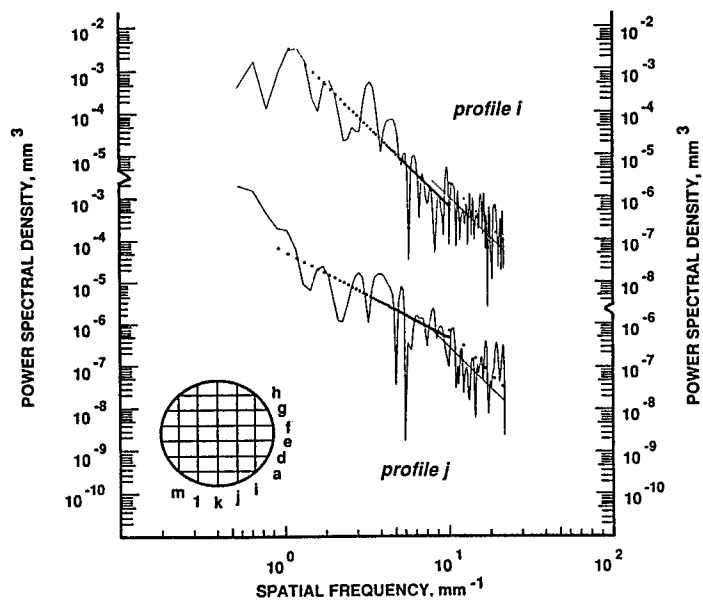


Figure 5. Spatial power spectra of the fracture surface profiles for sample traces i and j of Composition B. The locations of the profile traces across the sample surface are shown in the inset. Diamond stylus horizontal spacing is 0.003 mm.

interpretation of a deterministic failure process is consistent with the occurrence in the spectrum of quasi-harmonic peaks. That is, the occurrence of the peaks, that correspond to RDX crystal sizes, as well as the magnitude of the spectral slopes, indicate that, in general, the fracture is occurring between TNT and RDX grains: intergranular failure.

Equation (1) indicates that the fractal dimension for profiles j and e are 1.4 and 1.3, respectively. This indicates that the failure is chaotic and transgranular failure occurs through the grain. The chaotic region suggests that the origin of the failure, as for TNT, is in the center of the sample.

**Octol.** The sample of melt-cast 70/30 Octol reported here was found to fracture at an acceleration of 41,000 g at 25°C. The logarithmic normal crystal size distribution of HMX as specified by military specification Class 4<sup>11</sup> is shown in Figure 4. The spatial power spectra of the fracture surface profiles across traces g and h (see inset) of 70/30 Octol are shown in Figure 7. The distribution of peaks in the spatial power spectra shows the inhomogeneous grain size of the HMX in 70/30 Octol. The HMX grain sizes vary discontinuously from  $\approx 0.1$  mm to  $\approx 1.0$  mm in contrast to Class 4 HMX particle size in Figure 4. Figure 7 also shows how the inhomogeneous HMX grain size distribution changes with location across the surface.

In the frequency interval  $10^0$  mm<sup>-1</sup> to  $10^1$  mm<sup>-1</sup> the spectral slope of trace g is -3.9. The spectral slope of trace h is -2.7 in this frequency interval. The absolute value of the spectral slopes for profiles c through h are plotted in Figure 8 as a function of the sample trace. The spectral slopes for profiles i through m and c through g are  $\leq -3$ . The fractal dimension equals one for these profiles. Peaks, that correspond to HMX grain sizes, as well as the fractal dimensions of one indicate that, in general, intergranular failure is occurring at grain boundaries.

Equation (1) indicates that the fractal dimension for profile h is 1.1. This chaotic failure indicates that transgranular failure occurs through the grain. The chaotic region may indicate that the origin of the failure is at the edge of the sample.

The sample of sedimentation-cast 83/17 Octol reported here was found to fracture at an acceleration of 60,000 g at 25°C. The logarithmic normal crystal size distribution of HMX as specified by PIC Material Specification for Sedimentation Cast Octol<sup>12</sup> is shown in Figure 4. The spatial power spectra of the fracture surface profiles across traces a and f (see inset) of 83/17 Octol are shown in Figure 9. The distribution of peaks in the spatial power spectra shows the inhomogeneous grain size of the HMX in 83/17 Octol. The HMX grain size varies discontinuously from  $\approx 0.1$  mm to  $\approx 1.0$  mm in contrast to the HMX particle size distribution used in sedimentation cast Octol as shown in Figure 4. Figure 9 also shows how the inhomogeneous HMX grain size distribution changes with location across the surface.

In the frequency interval  $10^0$  mm<sup>-1</sup> to  $10^1$  mm<sup>-1</sup> the spectral slope of trace f is -4.1. The spectral slope of trace a is -2.4 in this frequency interval. The absolute value of the spectral slopes for profiles a through f of 83/17 Octol is plotted in Figure 10 as a function of the sample trace. The spectral slopes of sample traces g through l and c through f are  $\leq -3$ . The fractal dimension equals one for these sample traces. Peaks that correspond to HMX grain sizes, as well as fractal dimensions of one, indicate that, in general, intergranular failure is occurring at grain boundaries.

The fractal dimension for profiles a and b are 1.3 and 1.2, respectively. This chaotic failure indicates that failure occurs through the grain: transgranular failure. The chaotic region suggests that the origin of the failure is at the edge of the sample.

## DISCUSSION

The results of Figures 1-3 as well as our previous work<sup>2</sup> show clearly that the fracture process under high acceleration of our TNT sample tends to occur at grain boundaries. The results of Figure 2 show that the grain-boundary determination of the fracture is strongest at the edges of the sample. That is, the spectral peaks have their largest values for the profiles near the edges of the samples. A fractal dimension of 1 for these profiles is consistent with this interpretation.

Further, the largest power level at the lowest frequency occurs for two central traces. This lowest spatial frequency is of the order of the sample size. At the center of the sample, therefore, the fracture occurs in the bulk: transgranular failure. Such a failure mode is non-deterministic, i. e. chaotic. Fractal dimensions found for two traces through the center are consistent with this interpretation.

The results of Figures 5-6 as well as our previous work<sup>2</sup> show clearly that the fracture process under high acceleration of our Composition B sample tends to occur between the TNT and RDX grains. The results of Figure 6 show that the grain-boundary determination of the fracture is strongest at the edges of the sample. A fractal dimension of 1 for these profiles is consistent with this interpretation. Figure 6 shows that transgranular failure occurs in the center of the Composition B sample. Fractal dimensions found for two traces through the center are consistent with this interpretation.

The results of Figures 7-8 show clearly that the fracture process under high acceleration of our 70/30 Octol sample tends to occur between the TNT and HMX grains. The results of Figure 8 show that the grain-boundary determination of the fracture is strongest at the center and at three of the four edges of the sample. A fractal dimension of 1 for these profiles is consistent with this interpretation. Figure 8 shows that transgranular failure occurs at one edge of the 70/30 Octol sample. The fractal dimension found for the other edge trace is consistent with this interpretation.

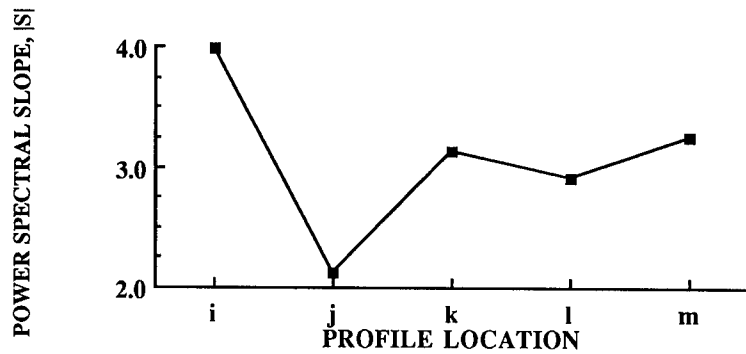


Figure 6. Spectral slopes versus profile location i through m of Composition B for spatial frequency interval  $10^0 \text{ mm}^{-1}$  to  $10^1 \text{ mm}^{-1}$ .

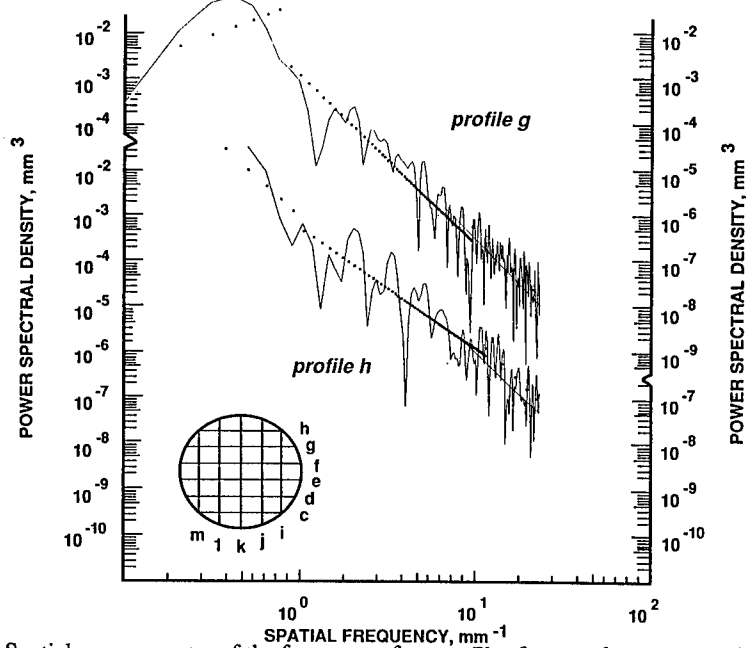


Figure 7. Spatial power spectra of the fracture surface profiles for sample traces g and h of 70/30 Octol. The locations of the profile traces across the sample surface are shown in the inset. Diamond stylus horizontal spacing is 0.004 mm.

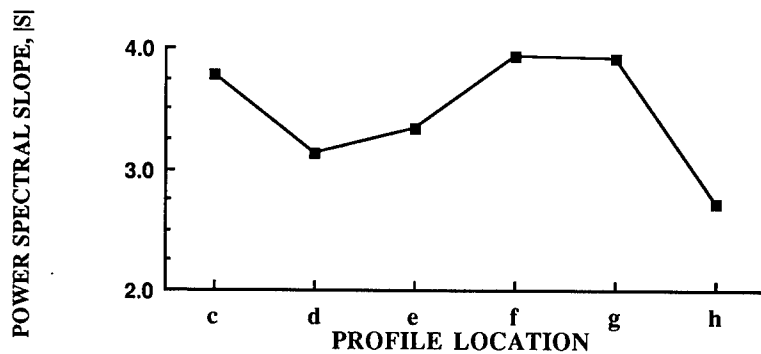


Figure 8. Spectral slopes versus profile location c through h of 70/30 Octol for spatial frequency profile  $10^0 \text{ mm}^{-1}$  to  $10^1 \text{ mm}^{-1}$ .

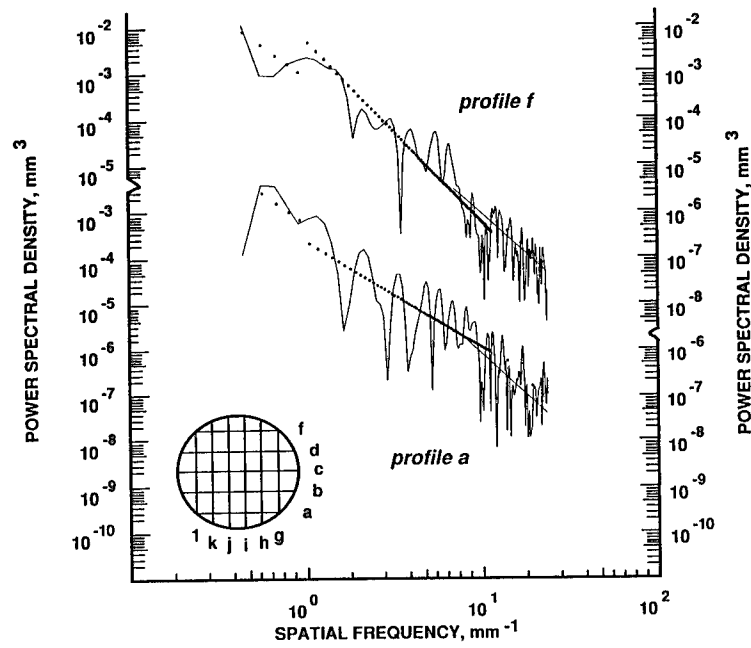


Figure 9. Spatial power spectra of the fracture surface profiles for sample traces a and f of 83/17 Octol. The locations of the profile traces across the sample surface are shown in the inset. Diamond stylus horizontal spacing is 0.004 mm.

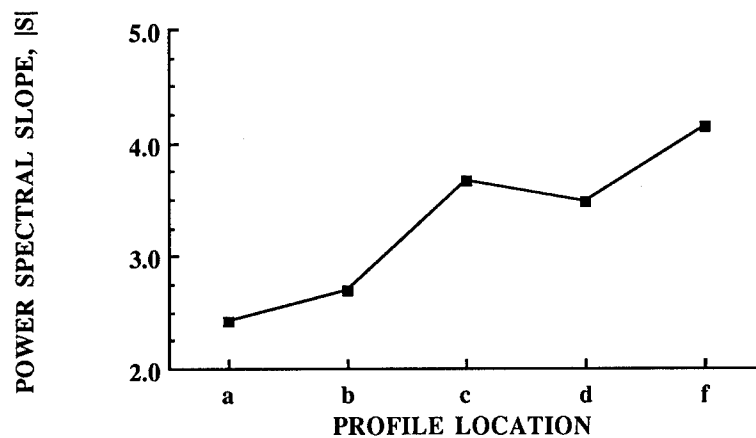


Figure 10. Spectral slopes versus profile location a through f of 83/17 Octol for spatial frequency interval  $10^0 \text{ mm}^{-1}$  to  $10^1 \text{ mm}^{-1}$ .

The results of Figures 9-10 show clearly that the fracture process under high acceleration of our 83/17 Octol sample tends to occur between the TNT and HMX grains. The results of Figure 9 show that the grain-boundary determination of the fracture is strongest at the center and at three of the four edges of the 83/17 Octol sample. A fractal dimension of 1 for these profiles is consistent with this interpretation. Figure 10 shows that transgranular failure occurs at the other edge of the sample. The fractal dimensions found for two traces at the same edge are consistent with this interpretation.

## CONCLUSIONS

Understanding of the fracture and rupture of energetic materials subjected to high acceleration is a key to better practical designs in several fields, including ordnance, the extraction industry, and space propulsion. In such applications the materials can often be subjected to high, fluctuating, and/or sustained accelerations. We have introduced fractal concepts and techniques to characterize the fracture surface topography of energetic materials obtained at high acceleration. These concepts have provided new statistical ways to characterize grain sizes of explosives. Of particular importance, these experimental and analysis techniques now allow quantitative comparisons to be made between different energetic materials so that improvements and changes in cast and composition of energetic materials can be verified. These concepts have also provided unique insights into the fundamental physics of the fracture process of explosives. For example, we have demonstrated that in general intergranular fracture occurs at grain boundaries or between grains in a mixture. We have also observed chaotic transgranular fracture through the grain that may indicate the origin of the failure in the sample. We have shown that the chaotic failure through the sample center appears to be similar for Composition B and TNT. We have also shown that the chaotic failure through the sample edge appears to be similar for 70/30 Octol and 83/17 Octol. The origin of the chaotic failure varies systematically with the percentage of TNT in the composition.

This work, both in the laboratory and in the field verification, is a major breakthrough in improving the understanding of the behavior of energetic materials during the gun launch process. This work also confirms that the value of relatively inexpensive laboratory experiments conducted in an ultracentrifuge, combined with sophisticated analysis and statistical techniques, can provide important new discoveries that are relevant and important to the gun launch process. We believe the experimental and analysis techniques used here have wide applicability in future studies of energetic materials.

## ACKNOWLEDGEMENT

We would like to thank J. Rowe, R. Dunne, and C. G. MacLennan, AT&T Bell Laboratories, Murray Hill, NJ, for helpful discussions regarding the data analysis.

## REFERENCES

1. M. Y. D. Lanzerotti and J. Sharma, *App. Phys. Lett.* **39** (1981) 455.
2. M. Y. D. Lanzerotti, J. Pinto and A. Wolfe, "Broad Bandwidth Study of the Topography of the Fracture Surfaces of Explosives", in The Ninth Symposium (International) on Detonation, Volume 1, pp. 355-361, 28 August - 1 September 1989, Portland OR.
3. D. J. Thomson, Spectral Analysis of Short Series, Ph. D. Dissertation, Department of Electrical Engineering, Polytechnic Institute of Brooklyn, Brooklyn NY, 1971.
4. D. J. Thomson, *Proc. IEEE*, **70**, 1055 (1982).
5. D. J. Thomson, M. F. Robbins, C. F. MacLennan, and L. J. Lanzerotti, *Physics of the Earth and Planetary Interiors*, **12**, 217 (1976).
6. S. R. Brown and C. H. Scholz, *J. Geophys. Res.* **90**, 12,575 (1985).
7. S. E. Hough, *Geophys. Res. Lett.* **16**, 673 (1989).
8. B. B. Mandelbrot, The Fractal Geometry of Nature (Freeman, NY, 1983).
9. B. B. Mandelbrot, *Physica Scripta*, **32**, 257 (1985).
10. RDX, MIL-R-398C, 22 August 1962.
11. HMX, MIL-H-4544B (PA), 27 February 1974.
12. PIC Material Specification for Sedimentation Cast Octol, 1986.

## DISCUSSION

R. R. BERNECKER

NSWC White Oak, Silver Spring, Maryland

It is well known that the cooling rate influences the size of crystallites formed during the casting process and also that the center will cool less rapidly than the outer regions. Hence, do you have any information indicating that your results (deterministic fracture at edges vs. chaotic fracture in the center for TNT, etc.) are not related to the manner in which the samples were cooled or their cooling rates?

## REPLY BY M. Y. D. LANZEROTTI:

No. When TNT is melt-cast in polycarbonate (thermal conductivity 0.193 W/m-K) sleeves the crystallites range in size from approximately 100 to 500  $\mu\text{m}$  and are randomly arranged (Reference 2 in paper).

When TNT is melt-cast in 4340 steel (thermal conductivity 51.9 W/m-K) sleeves, we have observed that the crystallites are approximately 5 mm long and point to the center of the circular cast.

In addition, due to the mismatch between the thermal expansion coefficient of polycarbonate ( $70.0 \times 10^{-6}$  in/in °C) and TNT ( $67.1 \times 10^{-6}$  in/in °C), the TNT sample is likely to be compressed by the polycarbonate. When TNT is melt-cast in 4340 steel ( $11.3 \times 10^{-6}$  in/in °C), the TNT is not compressed.

Chaotic failure is more likely to occur if there are defects or strain in the crystal.

#### DISCUSSION

M. DEFOURNEAUX  
NIMIC, NATO, 111 Brussels, Belgium

The fractal theory may lead to infinite surface areas. However, for the understanding of such phenomena as flame-spreading or DDT, you need to define finite surface areas. Can you correlate such surface areas with your fracture profiles?

#### REPLY BY M. Y. D. LANZEROTTI

No.

#### DISCUSSION

J. BOILEAU  
DRET, Paris, France

Do you observe an effect of tensio-active additives added in Comp B or Octol, e.g., some kinds of waxes, having a surface effect between TNT and the nitramine crystals (Comp B contains 1% wax)?

#### REPLY BY M. Y. D. LANZEROTTI

No. We will follow the role of wax in subsequent work.

#### DISCUSSION

J. F. GUERY  
Center de Recherches du Bouchet, BP 02, 91710 Vert-le-Petit, France

Do you think that the fracture surface topography depends on strain rate, stress state and the mode of failure?

#### REPLY BY M. Y. D. LANZEROTTI

There is some evidence for this. The strain rate in these experiments is approximately  $10^{-4}$  s<sup>-1</sup>. At these strain rates we have observed that the fracture tends to go around the RDX crystals in Comp B. However, at a strain rate of  $4 \times 10^{-3}$  s<sup>-1</sup> in the laboratory and at a higher strain rate in a gun firing, Smith and Thorpe, *Journal of Materials Science*, **8**,759(1973), report that the fracture tends to go through the RDX crystals in Comp B. Similar effects have been observed in high strength concrete by Bentur and Mindess, *Cement and Concrete Research*, **16**,59(1986).

#### DISCUSSION

H. GRYTING  
Gryting Energetics Science Company, San Antonio, Texas

Several of your pictures show a reddish color. Have you identified that material causing the color? Several years back we had a very dark Comp B that we were characterizing. I put a solution of it through an Al<sub>2</sub>O<sub>3</sub> column chromatographically separating a dark red ring. I ran IR curves on this after elution and purification. It turned out to be an addition complex of the ketone that was used in the processing of the explosive and TNT. These complexes are known as "Messenheimer Complexes."

#### REPLY BY M. Y. D. LANZEROTTI

No.



# CALCULATION OF REACTIVE FLOW USING SMOOTHED PARTICLE HYDRODYNAMICS

L.D. Libersky    A.G. Petschek    Per-Anders Persson

Energetic Materials Research Testing Center (EMRTC) and  
Department of Physics  
New Mexico Institute of Mining and Technology  
Socorro, NM 87801

Reactive flow is incorporated within the framework of Smoothed Particle Hydrodynamics and a mixture rule is formulated which allows for treatment of large grained explosives and propellants. The method is tested using length scales fine enough to resolve the reaction zone. The simulation seems to reproduce ideal detonation theory quite well for planar steady-state detonation in Composition-B.

## INTRODUCTION

Smoothed Particle Hydrodynamics (SPH) is a relatively new computational technique that seems well suited to simulation of reactive flow. The method uses Lagrangian fluid elements (particles) that are not tied to any underlying spatial grid. The gridless nature of the technique makes it possible to compute highly distorted flow in a pure Lagrangian frame. The method has other nice features such as the relative ease of adding new physics and of extending calculations to three dimensions. Application of SPH to the calculation of reactive flow has the potential, therefore, for improved accuracy and extended applicability. The main purpose of this paper is to describe the inclusion of reactive flow within the SPH framework. In so doing, we introduce new ways of treating the temperature in which (a) thermal equilibrium is not a mixture rule and (b) the temperature reference curve is determined analytically. A simulation of planar steady-state detonation in Composition-B is shown to reproduce ideal detonation theory quite well.

## THEORY

The SPH representation of the fluid conservation equations are given below<sup>1</sup>.

$$\frac{d\rho_i}{dt} = \rho_i \sum_j \frac{m_j}{\rho_j} (U_i^\beta - U_j^\beta) \frac{\partial W_{ij}}{\partial x_i^\beta} \quad (1)$$

$$\frac{dU_i^\alpha}{dt} = - \sum_j m_j \left( \frac{P_i}{\rho_i^2} + \frac{P_j}{\rho_j^2} + \Pi_{ij} \right) \frac{\partial W_{ij}}{\partial x_i^\alpha} \quad (2)$$

$$\frac{dE_i}{dt} = \sum_j m_j (U_i^\alpha - U_j^\alpha) \left( \frac{P_i}{\rho_i^2} + \frac{1}{2} \Pi_{ij} \right) \frac{\partial W_{ij}}{\partial x_i^\alpha} \quad (3)$$

Variables are coordinates ( $x$ ), time ( $t$ ), mass ( $m$ ) density ( $\rho$ ), velocity ( $U$ ), specific internal energy ( $E$ ), pressure ( $P$ ) and artificial viscosity ( $\Pi$ ). The subscripts refer to a given particle ( $i$ ) and its neighbors ( $j$ ). Superscripts  $\alpha$  and  $\beta$  are coordinate labels for the equations written in tensor notation. Interactions between particles are weighted by the interpolation kernel  $W$  called the smoothing function. Typically,  $W$  is a B-spline whose width is measured by the parameter  $h$ , the smoothing length. Notice that only gradients of  $W$  appear in these equations. Because of this, no underlying spatial grid is required. The formulation can be extended to include reactive flow by adding a constitutive relation and a rate equation for the unburned fraction ( $\lambda$ ) of reacting material. From this point on we drop the particle index in order to use subscript notation for other purposes.

$$P = P(\rho, E, \lambda) \quad (4)$$

$$\frac{d\lambda}{dt} = f(P, \rho, \lambda) \quad (5)$$

Reacting material is partitioned into unburned solid (s) and reacted gas (g) phases according to conservation laws for mass and energy.

$$V = \lambda V_s + (1 - \lambda) V_g \quad (6)$$

$$E = \lambda E_s + (1 - \lambda) E_g \quad (7)$$

Here,  $V=1/\rho$  is the specific volume. In order to close the system of equations (1-5) two additional constraints are required. For high density military explosives, it has often been assumed that the chemical reaction occurs homogeneously, therefore one chooses pressure and temperature equilibrium between the solid and gas phases of the burning material. However, for composite reacting materials having grain sizes typical of many explosives and propellants, the assumption of temperature equilibrium is not valid. A more realistic assumption for large grained materials would be that negligible heat transfer occurs between the two phases, i.e., the unreacted solid behaves isentropically. We therefore close the system of equations (1-6) by imposing the constraints of pressure equilibrium and an adiabatic solid.

$$P_s = P_g \quad (8)$$

$$\frac{\partial E_s}{\partial V_s} = -P_s \quad (9)$$

In order to use (9) we must know which isentrope the reacting material is on. For ideal steady state detonations this is the isentrope passing through the von-Neumann point. For transitions to detonation a family of adiabats defined by the solid Hugoniot are encountered by the reacting material. A prognostic equation for the entropy is added for this purpose.

$$\frac{dS}{dt} = \frac{dQ}{T} \quad (10)$$

The heat added ( $dQ$ ) is the artificial viscous work (II terms in equation 3). Equation (10) also introduces the temperature  $T$  which we compute by linear extrapolation from the principal adiabat.

$$T = T_s + (E - E_s) / C_v \quad (11)$$

Using the First Law

$$dE = TdS - PdV, \quad (12)$$

the following relations can be derived

$$\left( \frac{\partial T}{\partial V} \right)_s = \left( \frac{\partial P}{\partial S} \right)_V \quad \left( \frac{\partial E}{\partial S} \right)_V = T \quad (13)$$

Assuming a Gruneisen equation of state

$$P(V, E) = P_H(V) + \frac{\gamma}{V} [E - E_H(V)], \quad (14)$$

the pressure derivative in (13) can be written as

$$\left( \frac{\partial P}{\partial S} \right)_V = \left( \frac{\partial T}{\partial V} \right)_s = \left( \frac{\partial P}{\partial E} \right)_V \left( \frac{\partial E}{\partial S} \right)_V = \frac{\gamma}{V} T \quad (15)$$

An equation for the solid adiabat temperature is, therefore,

$$\left( \frac{\partial T}{\partial V} \right)_s = \frac{\gamma}{V} T \quad (16)$$

which, for  $\gamma/V = \text{const.}$  integrates to

$$T_s e^{(\gamma/V_o)V} = T_o e^{\gamma_o} \quad (17)$$

We obtain the adiabat energy  $E_s$  by integration.

$$E_s(V) = - \int_{V_o}^V P dV = \int_{V_o}^V \left[ P_H + \frac{\gamma}{V} (E - E_H) \right] dV \quad (18)$$

where the Hugoniot pressure and energy are given by

$$P_H = \frac{C^2 (V_o - V)}{[V_o - S(V_o - V)]^2} \quad (19)$$

$$E_H = \frac{1}{2} P_H (V_o - V) \quad (20)$$

Here,  $C$  and  $S$  are coefficients in the linear shock speed - particle speed relationship  $U_s = C + S U_p$  and  $V_o$  is the normal volume. Choosing  $\gamma/V = a$  to be constant, and letting  $F = E \exp[aV]$  we have

$$F = - \int_{V_o}^V e^{aV} \left[ P_H - \frac{\gamma}{V} E_H \right] dV \quad (21)$$

which integrates to

$$F(V) = \frac{1}{2S^3} \left\{ -C^2 (3S - aV_o) e^{aV_o} + \left[ 1 + \frac{(2 - aV_o/S)}{(SV/V_o - S + 1)} \right] \right\} + \frac{C^2 (2S^2 - 4aSV_o + a^2V_o^2)}{2S^4} \{ Ei[a(V_o - V)] + aV_o/3 - Ei(aV_o/S) \} \quad (22)$$

where  $Ei$  is the exponential integral. The adiabat energy is therefore,

$$E_s(V) = F(V)e^{-\frac{\gamma_s V}{V_0}} \quad (23)$$

Equations (11), (17) and (23) are used to calculate the temperature of the solid required in (10). Methods<sup>2</sup> using fits to the Hugoniot temperature for the reference curve have caused us difficulties, apparently because we require temperatures outside the region of validity of the fit. The analytic nature of our method eliminates such problems.

## EQUATIONS OF STATE

For the unreacted solid material the Gruneisen equation of state (14,19) is used. A HOM representation<sup>2</sup> of the BKW equation of state is used for the gaseous detonation products.

$$P = P_A + \frac{1}{\beta}(E - E_A)/V \quad (24)$$

$$\ln(P_A) = A + B(\ln V) + C(\ln V)^2 + D(\ln V)^3 + E(\ln V)^4 \quad (25)$$

$$\ln(E_A) = K + L(\ln P) + M(\ln P)^2 + N(\ln P)^3 + O(\ln P)^4 \quad (26)$$

$$-1/\beta = R + S(\ln V) + T(\ln V)^2 + U(\ln V)^3 \quad (27)$$

Here, the subscript "A" represents the adiabat passing through the CJ point. The coefficients are computed using the "BKW" code<sup>3</sup>.

For a partially reacted particle ( $0 < \lambda < 1$ ) we apply the mixture rules (8,9) in the following way. First we identify which adiabat the particle is on by comparing the particle entropy with the entropy on the solid Hugoniot. The family of adiabats is characterized by the solid Hugoniot curve for the unreacted material. Second, upper limits on the volume ( $V/\lambda$ ) and energy ( $E/\lambda$ ) of the solid are provided by (6,7) to ensure positive  $V_g$  and  $E_g$ . Next, we identify the lower limit for the solid volume as  $V(E/\lambda)$  on the adiabat. Having an acceptable volume range for the partially reacted solid, we pick the arithmetic mean as the starting guess for  $V_s$  and compute  $V_g$  using (8). The starting solid energy is  $E_s(V_s)$  with (9) providing  $E_g$ . A Newton-Raphson iteration is then used toward pressure equilibrium between the solid and gas phases, constraining the solid to move along its adiabat.

## CALCULATION

A one-dimensional simulation was performed in order to examine planar steady-state detonation in Composition-B explosive using the new formalism within the framework of Smoothed Particle Hydrodynamics. For this calculation we took the

smoothing length ( $h$ ) to be 1  $\mu\text{m}$ . Burning was initiated by impacting the explosive with equivalent inert material. The shock pressure input to the sample was kept just below  $P_{CJ}$  (290 Kb) so as to minimize the run distance to detonation. A Forest-Fire rate<sup>4</sup> was used to describe the decomposition.

$$\frac{d\lambda}{dt} = \lambda \sum_{i=1}^{14} C_i P^{i-1} \quad (28)$$

The coefficients in (27) were obtained using the ATFIRE code<sup>5</sup> and are listed in Table 1. Fits for the Comp-B isentrope (25,26,27) are given in Table 2. Solid parameters used were:  $V_0 = 0.583 \text{ cc/g}$ ,  $C = 0.21 \text{ cm}/\mu\text{s}$ ,  $S = 1.5$  and  $\gamma = 2.0$ .

$i$	$C_i$	$i$	$C_i$
1	-1.035458043E+01	8	8.206591093E+09
2	4.734274495E+02	9	-4.298662700E+10
3	-1.675370422E+04	10	1.618379369E+11
4	4.475674643E+05	11	-4.260581743E+11
5	-8.493147154E+06	12	-7.728984899E+11
6	1.155593435E+08	13	7.437676727E+11
7	-1.140256515E+09	14	3.616777570E+11

TABLE 1. FOREST-FIRE RATE COEF'S FOR COMP-B

A-E	K-O	Q-U
-3.525848E+00	-1.560876E+00	7.502780E+00
-2.334291E+00	5.331214E-01	-4.412090E-01
5.972673E-01	8.063108E-02	1.512926E-01
3.045104E-03	3.338168E-03	6.778832E-02
-1.752264E-01	-6.843999E-04	-2.424033E-02

TABLE 2. HOM FIT TO BKW EOS FOR COMP-B

Figures 1,2 and 3 show different aspects of the SPH computed steady-state detonation in Composition-B explosive. Only fully or partially reacted particles are plotted for clarity. Inert "flyer plate" particles and particles not yet shocked are omitted. Figure 1 shows the pressure profile. The peak pressure at the shock front is 450 Kb which is the von-Neumann spike. The reaction is 100% complete 400  $\mu\text{m}$  behind the spike at 290 Kb, the Chapman-Jouguet (CJ) state. The reaction is 75% complete 80  $\mu\text{m}$  behind the shock front. These numbers compare well with experimentally measured values for Composition-B.

In Figure 2 the pressure is plotted on the ordinate and the reaction extent on the abscissa. The von-Neumann spike is seen near  $\lambda=1$  and the CJ point is seen near  $\lambda=0$ . Notice the large number of particles (~100) comprising the reaction zone. Notice also that adequate resolution of the shock front is achieved in the sense that no substantial reaction takes place until the von-Neumann spike is reached. In Figure 3 the pressure is

again plotted on the ordinate but now the specific volume is used for the abscissa. This representation clearly shows the Rayleigh line extending from the von-Neumann spike to the CJ point. That compression to the von-Neumann point is not abrupt, and that the path to this point is curved, are both due to the artificial viscosity spreading out the shock. In addition to the results presented here we have also modeled cases using lower flyer-plate speeds (reduced shock input) and observe build-up to steady-state detonation consistent with wedge test results. We expect to present this data orally at the conference.

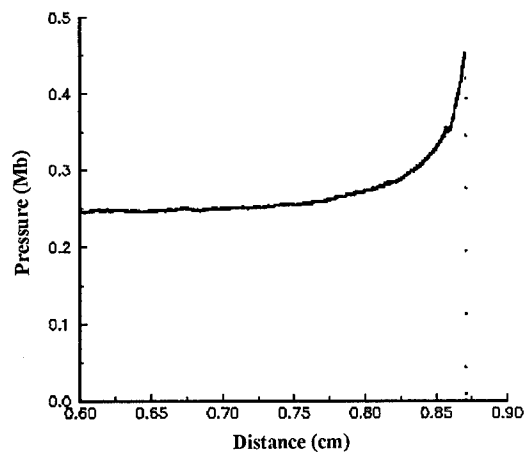


FIGURE 1. SPH COMPUTED PRESSURE PROFILE FOR STEADY-STATE PLANAR DETONATION IN COMPOSITION-B EXPLOSIVE

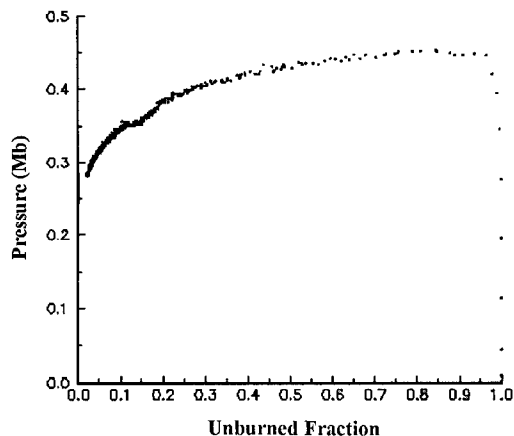


FIGURE 2.  $P$  vs  $\lambda$  SHOWS APPROXIMATELY 100 PARTICLES COMPRISING THE REACTION ZONE

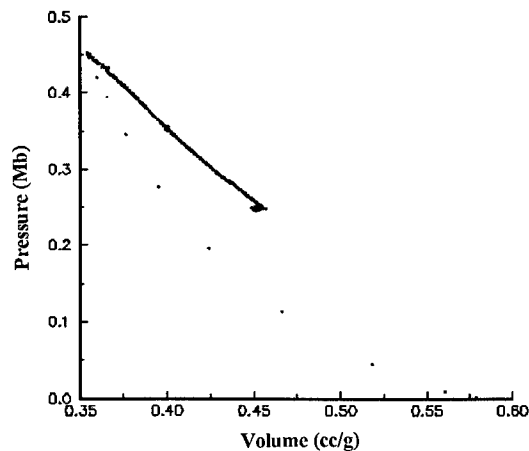


FIGURE 3.  $P$  vs  $V$  SHOWS THE VON-NEUMANN SPIKE, RAYLEIGH LINE AND CJ POINT

## CONCLUSIONS

We have derived a new formalism for treating reactive flow and have incorporated it within the framework of Smoothed Particle Hydrodynamics. The mixture rules extend the applicability of reactive flow calculations to large-grained materials and the SPH computing technique allows for easy extension to three-dimensions and improved accuracy. We have tested the approach by calculating planar steady-state detonation in Composition-B. Results show ideal detonation theory to be reproduced quite well.

## REFERENCES

1. Libersky, L.D.; Petschek, A.G.; Carney, T.C.; Hipp, J.R.; Allahdadi, F.A.; *J. Comput. Phys.*, accepted for publication, Feb., 1993.
2. Mader, C.L., Numerical Modeling of Detonations, Univ. of Calif. Press, Los Angeles, CA, 1979, p.327.
3. ATBKW Computer Program, Los Alamos Code No. LP-181 Los Alamos National Lab., NM, 1986.
4. Mader, C.L.; Forest, C.A., *Two-Dimensional Homogeneous and Heterogeneous Detonation Wave Propagation*, LA-6259, Los Alamos National Lab., N.M., 1976.
5. ATFIRE Computer Program, Mader Consultant Co., Honolulu, HI, 1986.

## DISCUSSION

DR. R. SARRACINO

AECI Explosives, Modderfontein, South Africa

Larry, this seems to me to be a very exciting development. I have a question about the assumed expansion curve - in the summary and your talk, you referred to it in different places as an "isentropes" and an "adiabat" (beyond the CJ point the two curves are virtually equivalent, but between the von Neumann spike and the CJ point, chemical reaction would result in an appreciable entropy rise along the adiabat). Which curve did you use?

## REPLY BY L.D. LIBERSKY

I take "isentropes" and "adiabat" as synonymous. Our model restricts the solid part of the partially reacted material to move along the solid adiabat (isentropes).

## DISCUSSION

C. P. CONSTANTINOU

Dept of Physics, Washington State University,  
Pullman, Washington

I would like to address two issues: (a) the Forest-Fire reaction rate-law that was applied here, has no temperature dependence. Physically, this can have no physical validity, for either ideal or non-ideal explosives. I was wondering what influence a more realistic rate-law would have on your calculations. (b) Is there an extent of reaction at the von Neumann point, and what is your calculated reaction zone length behind the front?

## REPLY BY L.D. LIBERSKY

We plan to implement a variety of rate laws in our code and observe the effects. SPH provides a nice framework for such explorations.

Figure 2 shows a reaction extent of around 3% at the von-Neumann point. Figure 1 shows 95% reaction at 0.4 mm behind the shock front.

## SESSIONS ON POSTER PAPERS-1

**Cochairmen:** **Pier Tang**  
**Los Alamos National Laboratory**

**Ries Verbeek**  
**Prins Maurits Laboratory TNO**

## NUMERICAL SIMULATION OF THE BEHAVIOR OF EXPLOSIVES SUBJECT TO A THERMAL HAZARD

C. Castille, F. Soulès

Commissariat à l'Energie Atomique  
BP 7 - 77181 COURTRY - FRANCE

CAT, a F.E.M. code computing thermal initiation and burning of explosives, has been developed in order to study the behavior of explosive devices subject to a fire or, more generally, to a thermal attack. This code includes two independent routines, based on small tests performed in our laboratories : in the first modeling, a multi-staged kinetics of decomposition of the explosive, defined in order to reproduce ODTX data, determines the time and place of thermal initiation. In the second one, the burning propagation is calculated by a front method. The front velocity, the temperature reached on the front, the rate of released energy are deduced from experimental data. For instance, we present the behavior of a spherical TATB device subject to a kerosene fire. This example shows that CAT code is a useful tool to evaluate the pyrotechnic risks.

### INTRODUCTION

The constant search for increased pyrotechnic security is an important concern in CEA. Its application field is large : munitions storage, explosive buildings handling in a workshop, in a military base... Despite all the safety measures and the respect for proceedings and for the security instructions, risks of accidents still exist and must be elaborated in the perspective of security improvement. In this context, CEA develops new unsensitive compounds, based on TATB, and also experimental and theoretical studies.<sup>1</sup> In this program, the physical phenomena are : thermal initiation and combustion, shock-detonation transition, combustion - deflagration - detonation transition, X-detonation transition. The main difficulty is to conceive experiments allowing a good approximation of physics, and therefore modeling.

So, we have chosen the following procedure :

1) Experiments to understand physical phenomena.

2) Building physical models accounting for these phenomena.

3) Introduction of these models in a calculation code.

4) Authentification of the calculations implement thus created by the adapted calculation-experiment comparisons.

So, an anticipation implement of the behavior of an explosive substance in front of a thermal attack is available.

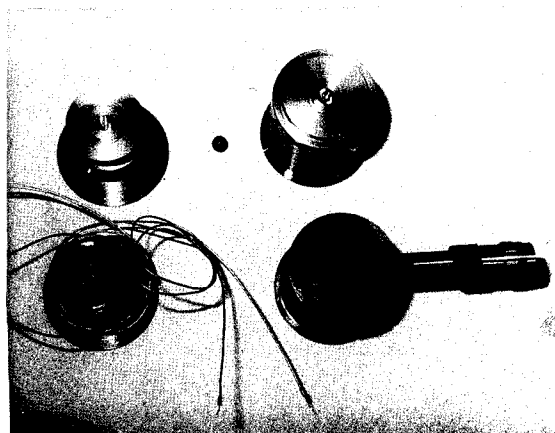
The works on the first two phenomena are very advanced and the means for analysis and for simulation are from now on operational. We are going to show, in the following report, the works relating to the reaction of thermally attacked explosive structures. When heated, the TATB/HMX compounds can become the basis of a slow decomposition of a combustion type. We must take into account two phenomena, which are required for the analysis of this reactional process : the thermal initiation and the spreading of combustion in the reactive field.

## EXPERIMENTAL STUDIES

### Thermal initiation

#### ODTX

The ODTX (One Dimensional Time to eXplosion) test has been developed at the Lawrence Livermore National Laboratory.<sup>2</sup> We have transposed and modified it to spread the field of its possibilities. This test consists in a spherical sample of explosive between two steel anvils regulated at a given temperature by means of heating collars (see Photograph 1 and Figure 1).



PHOTOGRAPH 1. ODTX ANVILS

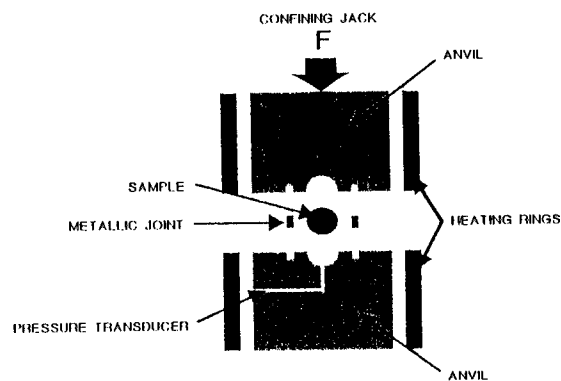


FIGURE 1. ODTX - SCHEME OF PRINCIPLE

In this experiment we measure the instant when we get a reaction detected by the division of the matrixes under the effect of the decomposition gas pressure. The evolution of the pressure is also

recorded with a directly connected pressure transducer, through calibrated dead volume, to the cavity filled by the sample.

We can then draw point by point the curve Time of explosion ( $t$ ) versus Test temperature ( $T$ ). This curve leads to linear relation between  $\log(t)$  and  $1/T$ . An example relative to a TATB composition, T2, is presented Figure 2.

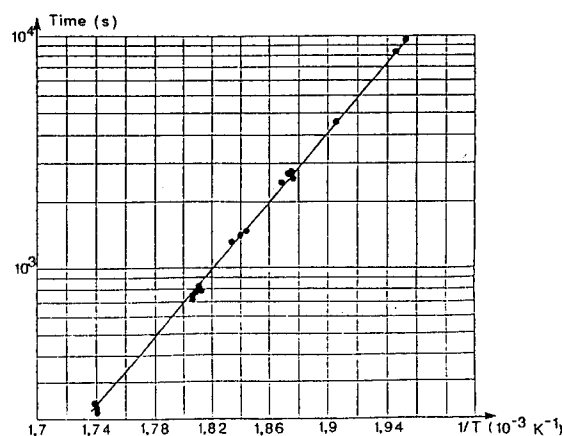


FIGURE 2. ODTX-EXPLOSION TIMES OF T2 COMPOSITION

The evolutions of measured pressure, for the same composition, at 250°C with various dead volumes are drawn Figure 3.

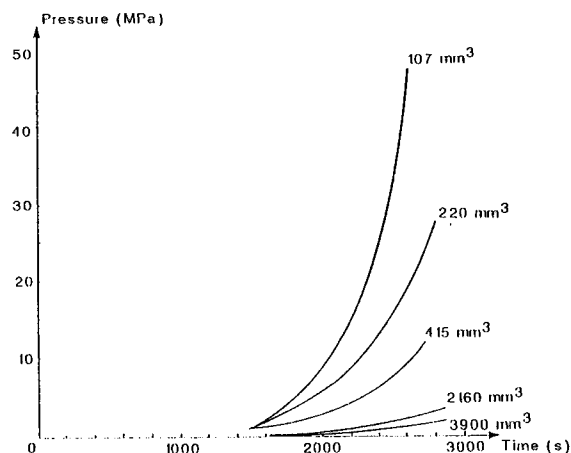


FIGURE 3. ODTX-PRESSURE EVOLUTIONS-T2 COMPOSITION

The main application of these measurements, beyond the comparison of the sensitivity of explosive



compositions, lays in the determination of the parameters of the kinetics used to describe the phenomenon of thermal initiation.

### TEMPERATURE GRADIENTS

The ODTX equipment was modified to perform experiments at temperatures functions of time. We make thus some rises in temperature at constant speeds ( $\leq 2^\circ\text{C/s}$ ). Particular heating systems and anvils of low thermal inertia are used for the highest speeds.

The interest of these tests is to allow the validation, by comparing calculations-experiments, of the kinetics finalized by means of the classical ODTX test (constant call).

### Combustion Test

The experimental set-up is presented Figure 4.

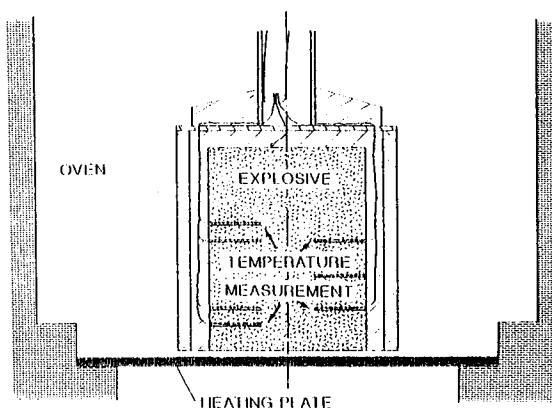
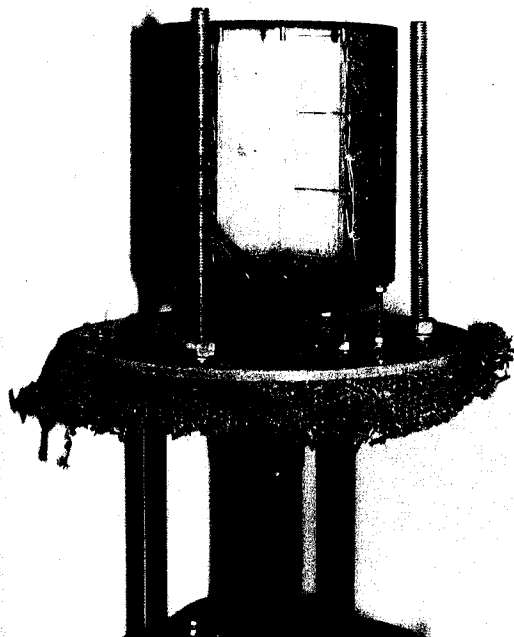


**FIGURE 4. COMBUSTION-EXPERIMENTAL SET-UP**

A cylindrical explosive sample (Photograph 2) is brought a few millimeters above a hot plate the temperature of which is kept constant in a furnace.

After an induction period depending on the heating plate temperature, thermal initiation happens from the basis of the sample and the combustion spreads to the top of the device.

The temperature is measured at various depths in the explosive by means of thermocouples. An example of obtained temperatures records with the T2 composition is presented Figure 5.



**PHOTOGRAPH 2. COMBUSTION SET-UP**

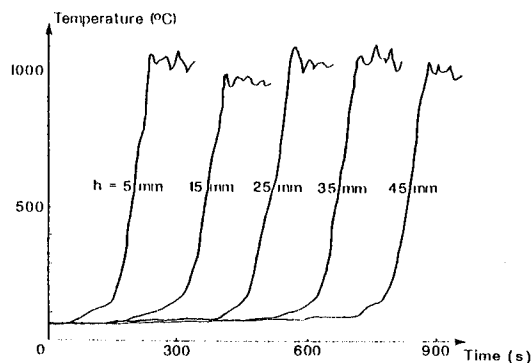


**FIGURE 5. COMBUSTION-TEMPERATURE PROFILES**

This figure shows the temperature variation when passing over the combustion front. We can thus determine numerous useful data for building a model :

- maximum combustion temperature of the explosive (about  $1100^\circ\text{C}$  for T2),
- propagation speed of the decomposition front (about  $3,5 \text{ mm/min}$  for T2),
- thickness of the reaction area.

The samples can be preheated at a given temperature before testing. This variant of the combustion test allows us to measure the influence of the initial temperature on the reaction phenomenon.

## MODELING AND NUMERICAL SIMULATION

### Calculation Code

We have developed a code with finite elements method : CAT (Calcul d'Amorçage Thermique) for the simulation of the explosive structures behavior under thermal attacks.

This code is based on the numerical treatment of the classical equation of thermal transfers with a term  $Q$  : exothermic decomposition heat of the explosive.

The main specificities of this code consist in :

- its bidimensional character (plane or axisymetrical geometry),
- a non-linear calculation algorithm (variation of the thermal conductivity and of the specific heat according to the calculated temperature),
- taking into account radiative and/or convective exchanges inside cavities or with the environment.

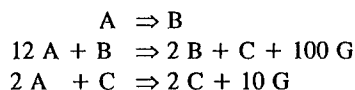
### Thermal Initiation

$Q$  depends on the chosen kinetics to describe the explosive decomposition. Some studies carried out at the LLNL have shown that a right restitution of the experimental phenomena needed the use of multi-staged kinetics.<sup>3</sup> The models proposed by Mc Guire and Al.<sup>3</sup> include some disadvantages as the necessity to be associated to arbitrary criteria to reconstitute instants of reaction. To cope with these difficulties, we have developed models allowing restitution of thermal effects (heat emission) and mechanical effects (rise of the pressure).

These models have been built taking into account the following constraints :

- elementary nature of the reactional scheme allowing processing without prohibitive calculations time,
- need of a first endothermic or weakly exothermic stage to reconstitute the long times of reaction obtained for weak test temperatures,
- need of autocatalytic stages to take into account dynamic phenomena experimentally observed.

The selected kinetics for T2 composition is presented below :



Coefficients have been determined by ensuring the restitution of the ODTX tests results (see Figures 6 and 7).

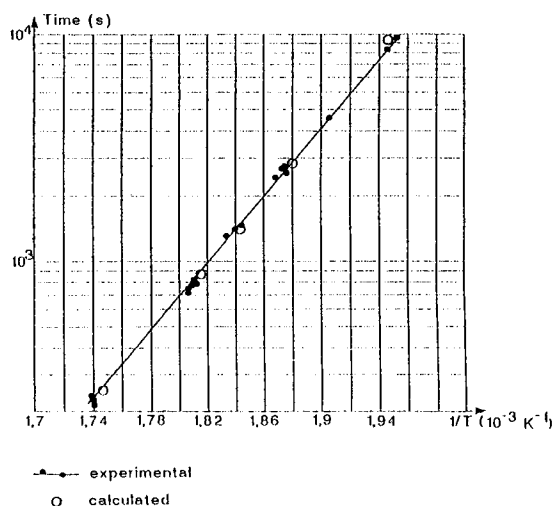


FIGURE 6. ODTX-REACTION TIMES-COMPARISON CALCULATIONS/EXPERIMENTS

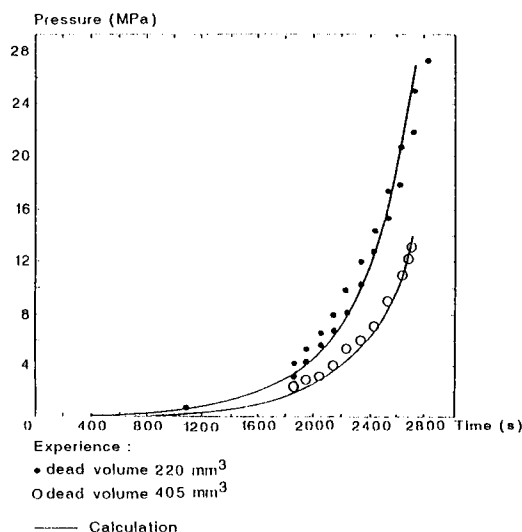


FIGURE 7. ODTX-PRESSURE EVOLUTIONS-COMPARISON CALCULATIONS/EXPERIMENTS

Some comparisons calculations/experiments, in the case of the temperature gradients, validate the previously determined kinetics (see the following chart).

**TABLE 1. ODTX RESULTS**

Temperature rise speed (°C/s)	Measured time of reaction (s)	Calculated time of reaction (s)
0,1	2880	2904
0,05	5446	5580
0,025	10400	10680

### Combustion

The CAT code has been adapted to simulate combustion spreading and associated thermal effects according to a front method. This combustion spreads from thermal initiation points determined by calculations. In the model, fire front moves to the experimentally measured value. When the front reaches a meshing element, it starts burning and emits a heat flux  $q$  during a time  $t$  which depends upon this element temperature before the combustion starts. This simple model allows us to use a relatively rough meshing which limits calculations durations.

Figure 8 presents comparisons between experimental and calculated profiles of temperature obtained with the previously presented model. The observed gap between measures and numerical simulation, at 15 mm depth, is due to an experimental problem (unintentional cooling of the set-up).

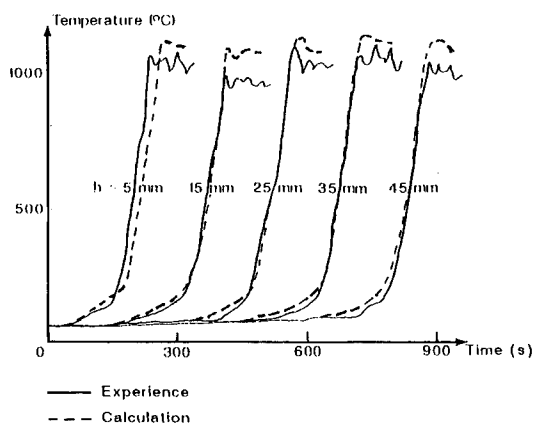


**FIGURE 8. COMBUSTION-TEMPERATURE PROFILES-COMPARISON CALCULATIONS/ EXPERIMENTS**

Another calculation/experiment comparison was made in the case of a kerosene fire test on a full-size structure, and allowed the authentication of the CAT code.

### AN EXAMPLE OF NUMERICAL SUMULATION OF A FIRE ON A PYROTECHNIC BUILDING

We consider a sphere the constitutive materials of which are presented Figure 9.

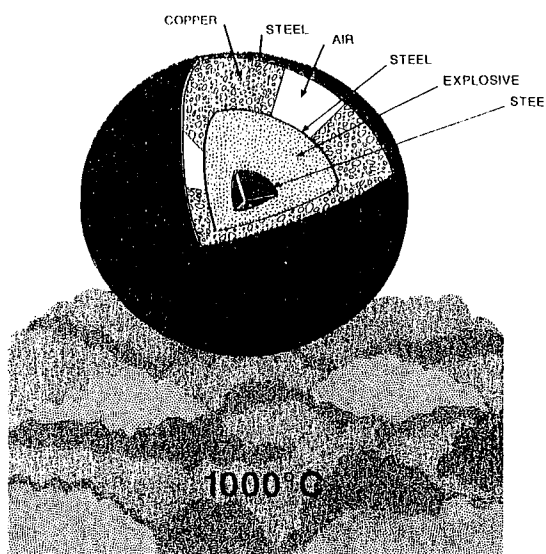


**FIGURE 9. FIRE ON A PYROTECHNIC BUILDING-SIMULATED STRUCTURE**

This pyrotechnic building is put through a kerosene fire, the conditions at the imposed limits on the external shell correspond to those experimentally obtained during the full-size test. We will find Figure 10 the temperature profile applied to the equatorial plane. After 33 minutes, the kerosene fire stops and we can observe the environment temperature decrease. The presence of an air cavity imposes us to take into account convective and radiative exchanges.

The explosive decomposition kinetics is the TATB "ODTX" type's. After 2,5 minutes, the explosive located at the equatorial plane initiates. The thermal initiation happens more lately under the cavity due to the weak air conduction coefficient. The combustion front begins to radially spread except in the under cavity area.

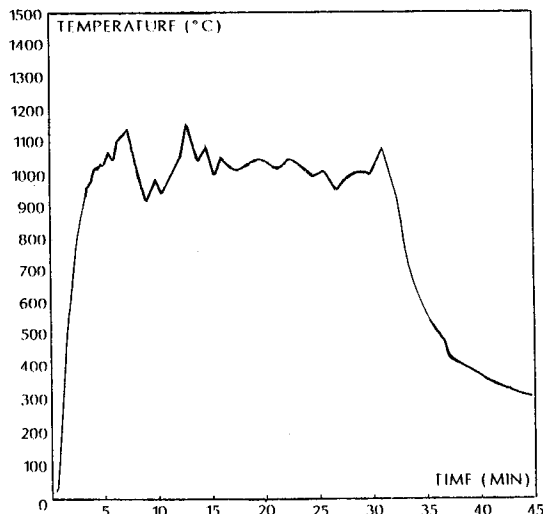


**FIGURE 10. SIMULATION OF A KEROSENE FIRE-THERMIC CALL ON THE SHELL OF THE BUILDING**

After 5 minutes, all the explosive was initiated and the combustion front goes on concentrically spreading to the inner material. The explosive burns at a temperature of 1100°C. When it stops burning, its thermal characteristics change and become those of a burnt gas. The copper and the steel shell are in a thermal balance at a temperature of about 1050°C through the imposed external temperature. The explosive which hasn't burnt and the inner material are at that time still cold.

After 11 minutes, half of the explosive has burned. We note two combustion fronts meeting in front of the cavity.

The explosive combustion stops after 18,4 minutes. We can observe Figure 11 the temperature evolution according to time in explosive near inner material. We distinguish its combustion peak at about 1050°C and a step which corresponds to the heat conduction coming from the kerosene fire in the burnt gas.

After 33 minutes, the temperature decrease becomes very clear. The inner material temperature (see Figure 12), facing the explosive presented Figure 11, reaches its maximum when the kerosene fire stops, that is 1000°C.

This value corresponds to that of the external call at the same time. When the explosive stopped

burning, the temperature is 500°C. This can be explained by the fact that the explosive protects the inner material because of its relatively weak conductivity.

Therefore, we have shown that CAT is a predictive code, which allows us to determine temperature at any time and everywhere in a structure including explosive and subject to any thermal attack.

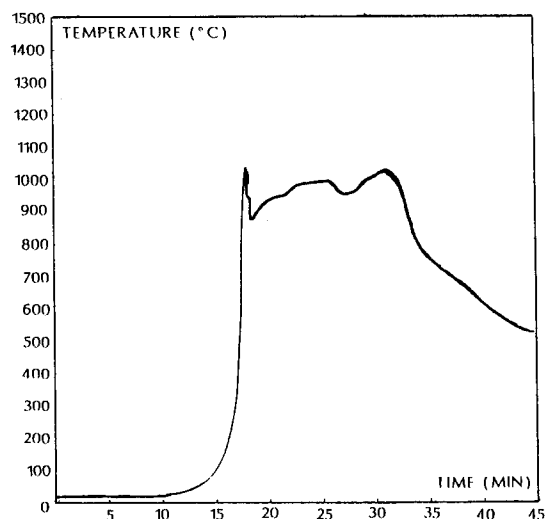


**FIGURE 11. NUMERICAL SIMULATION-TEMPERATURE VERSUS TIME IN THE EXPLOSIVE**

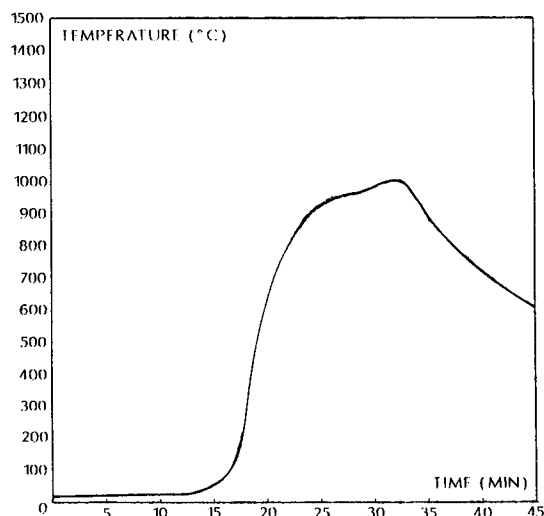


**FIGURE 12. NUMERICAL SIMULATION-TEMPERATURE VERSUS TIME IN THE INNER MATERIAL**

## CONCLUSION

We have developed models we included in a calculation code, CAT, and which allow to analyse and to simulate thermal initiation and combustion phenomena of explosives.

The aim of these works is to study the security of structures including unsensitive explosives and subject to thermal hazards.

## BIBLIOGRAPHY

1. Castille, C., Bainville, D., Reynier, P. and Belmas, R., "Etude expérimentale et simulation numérique de l'amorçage thermique et de la combustion des compositions explosives", in *Proceedings of the 4ème Congrès international de Pyrotechnie du GTPS*, La Grande Motte - FRANCE, 1989.
2. Catalano, E., Mc Guire, R., Lee, E.L., Wrenn, E. and Ornellas, D., in *Proceedings of the 6th Symposium (International) on Detonation*, Coronado - USA, 1976.
3. Mc Guire, R. and Tarver, C.M., in *Proceedings of the 7th Symposium (International) on Detonation*, Annapolis - USA, 1981.

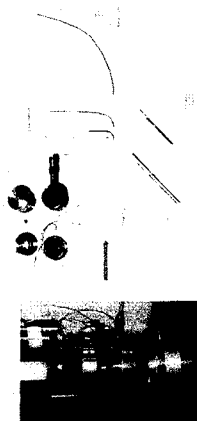
C. CASTILLE - F. SOULES

THE UNIVERSITY OF CHICAGO PRESS

[illegible]

# EXPERIMENTAL APPROACH OF THE PHENOMENA

**ΟΔΗΓΙΕΣ**



### COMBUSTION TEST



## MODELING

### KINETICS:

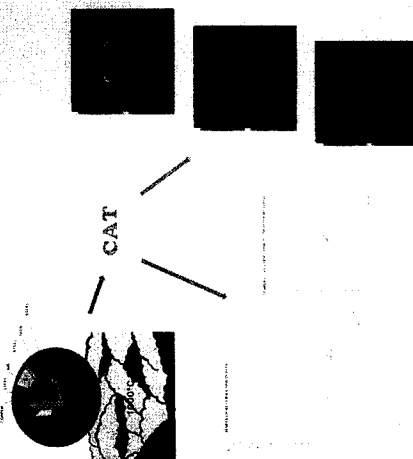
A - B  
12 A : B - 2 B  
2 A + C - 2 C



#### FRONT METHOD:

When the front reaches a meshing element, it starts burning and emits a heat flux  $q$  during a time  $t$  which depends upon this element temperature before the combustion starts.

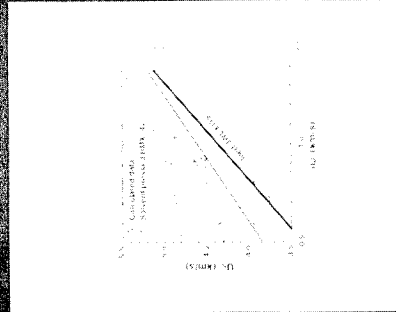
### EXAMPLE OF NUMERICAL SIMULATION



# Non-Reactive HMX Shock Hugoniot Data

*Explosives reactive-flow modeling requires knowledge of both the inert and product equations of state as boundaries for the global kinetic expression.*

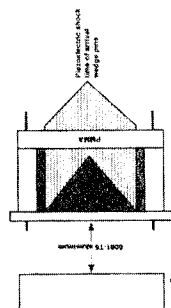
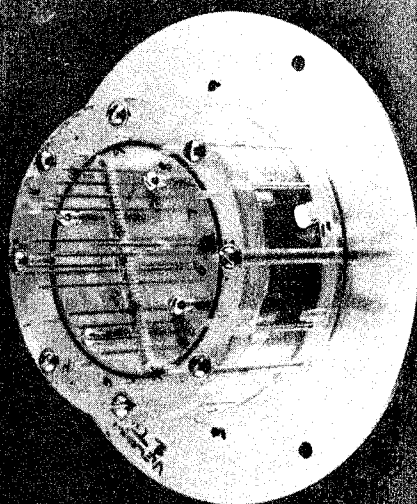
*High explosives Hugoniot based on shock-front measurements are likely to be in error (too stiff) as a consequence that the front is supported by reaction.*



Reactive-flow modeling indicates the effect of reaction on shock velocity. The consequences of 3, 6, and 10-ns reaction times are shown. Curves for reaction times of 10 ns to 100 ns give nearly the same initial shock velocities.

Most of the adjacent plotted data indicate that about 3% to 7% of the HMX reacted in less than about 100 ns. At 6.0 GPa about 4% reacted in the HMX-water system.

# Shock Velocity Measurements



Modified wedge tests have been used to measure the shock velocity as a function of pressure.

To determine the Hugoniot with HMX, a very insensitive mixture was manufactured by using fluid-energy-milled 5- $\mu$ m HMX in water.

Making the assumption that the mixture is macroscopically homogeneous and isotropic, these data and literature values for the equation of state of water are used to deduce the Hugoniot of pure HMX.

$$P = P_0 + U_0 \rho_0 (U_0 - U_p)$$

$$P_{HUG} = P_{HUG} + U_{HUG} \rho_{HUG} (U_{HUG} - U_p)$$

$$P_{HUG} = P_{HUG} + U_{HUG} \rho_{HUG} (U_{HUG} - U_p)$$

$$U_{HUG} = \frac{P_{HUG} - P_{HUG}}{\rho_{HUG} (U_{HUG} - U_p)}$$

$$U_{HUG} = \frac{P_{HUG} - P_{HUG}}{\rho_{HUG} (U_{HUG} - U_p)}$$

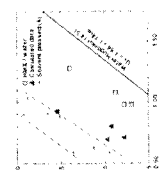
Experimental results for 48 vol% of 5  $\mu$ m HMX in water.

Experiment	$U_p$ (km/s)	$U_0$ (km/s)	$P$ (GPa)	$\rho$ (g/cm <sup>3</sup> )	Technique
1	1.42	0.706	0.044	1.00	1.00
2	1.42	0.706	0.044	1.00	1.00
3	1.42	0.706	0.044	1.00	1.00
4	1.42	0.706	0.044	1.00	1.00

Calculated HMX shock Hugoniot data.

Experiment	$U_p$ (km/s)	$U_0$ (km/s)	$P$ (GPa)	$\rho$ (g/cm <sup>3</sup> )	Technique
1	1.42	0.706	0.044	1.00	1.00
2	1.42	0.706	0.044	1.00	1.00
3	1.42	0.706	0.044	1.00	1.00
4	1.42	0.706	0.044	1.00	1.00

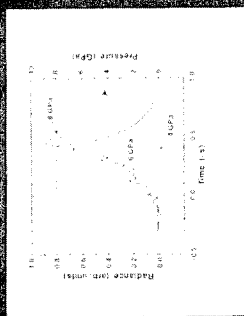
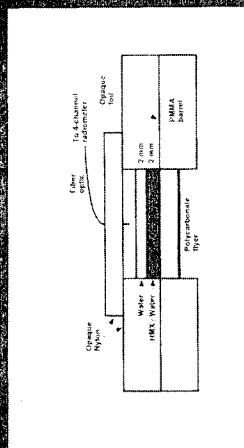
These data are summarized at left in the  $U_0$ - $U_p$  plane. The measured data are shown along with the water Hugoniot. The calculated Hugoniot for the HMX-water mixture is shown as a dashed line. The reported measured results for high-density, pure solvent-pressed HMX are shown as  $\square$ . These solvent-pressed HMX have theoretical maximum density and very insensitive Hugoniot as the solvent-pressed HMX is very near can only be used for a given particle velocity for these solvent-pressed data at pressures less than 6.0 GPa. This is attributed to a reaction-supported shock front. At higher pressures, the reaction is supported by reaction.





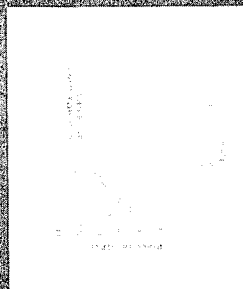
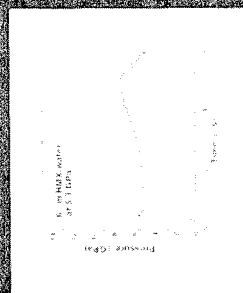
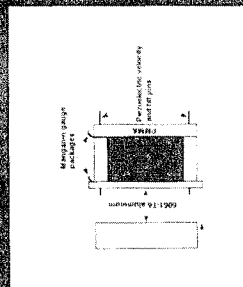
# Radiometric Measurements

To consider further the possibility of reaction, radiometric shock initiations were done using an electric gun. At 8.0 GPa the radiometric observation is that significant reaction is occurring.



# Pressure Measurements

*In situ* manganin pressure time histories were obtained from the results. At 5.5 GPa there was no discernible pressure build-up for 1.5  $\mu$ s. An equivalent shot done at 8.0 GPa showed rapid pressure build-up immediately after the time of impact.



## **Summary:**

*Hugoniot determined via shock-front measurements on energetic materials are likely to be supported by reaction at moderate pressures. Such Hugoniot are insufficient to define the unreactive shock compression behavior in reactive-flow modeling.*

*With HMX, shock strengths below 6.0 GPa produced no significant reaction near the shock front. Radiometric and in situ pressure measurements support this conclusion. Reactions of 3%-7% within 10 ns to 100 ns behind the shock front are sufficient to affect the front dramatically.*

## **Paper 52**

*Randall L. Simpson,  
Frank H. Helm and  
John W. Kury*

*Energetic Materials Center*

*Lawrence Livermore  
National Laboratory*



# HOT SPOT INITIATION OF PLASTIC-BONDED EXPLOSIVES DURING THE RAPID FLOW PHASE OF THE DROP WEIGHT IMPACT TEST

A.P. Metzner and C.S. Coffey  
Naval Surface Warfare Center  
Indian Head Division  
Indian Head, MD  
and  
Dahlgren Division, White Oak Detachment  
Silver Spring, MD

Hot spots generated in plastic-bonded explosive samples during the drop weight impact test were studied with heat-sensitive films. The hot spots occurred between pairs of radial cracks in the perimeter of the explosive. The effects on the rapid flow phase of RDX size and binder adhesiveness, modulus, and Poisson's ratio are discussed.

## INTRODUCTION

The behavior of plastic-bonded explosives (PBXs) during the drop weight impact test is characterized by three phases.<sup>1</sup> First, there is an initial pressure buildup phase. Secondly, there is a rapid flow phase produced by the failure of the sample. This phase is characterized by a decrease in the rate of pressure rise and rapid radial flow of the sample. Finally, there is a pinch phase during which the sample pressure increases greatly and the radial deformation slows to a stop. Photographic evidence suggests that failure of the sample, which triggers the rapid flow phase, is dominated by hoop stresses and strains near the perimeter of the sample. Ignition occurs midway between pairs of radial cracks.

Since samples do not ignite until the rapid flow phase begins,<sup>1</sup> understanding the nature of the rapid flow phase produces insights on how to delay or prevent initiation of an explosive. Calculations are presented that show how the binder modulus and adhesiveness and the filler particle size affect the start of the rapid flow phase.

## BACKGROUND

The rapid flow phase is started by a rupture of the impact test sample. During the pressure buildup phase, the sample has slowly expanded as its internal pressure

increases.<sup>1</sup> This creates large shear and hoop stresses and strains near the perimeter of the sample. Hoop stresses and strains are perpendicular to the radius of the sample and act in the  $\theta$  direction in the  $r$  and  $\theta$  coordinates (Figure 1). If the drop height is high enough, the internal sample pressure and the shear and hoop stresses and strains eventually become large enough to rupture the sample. The sample should fail near the perimeter because only compressive stresses are present near the center of the sample.

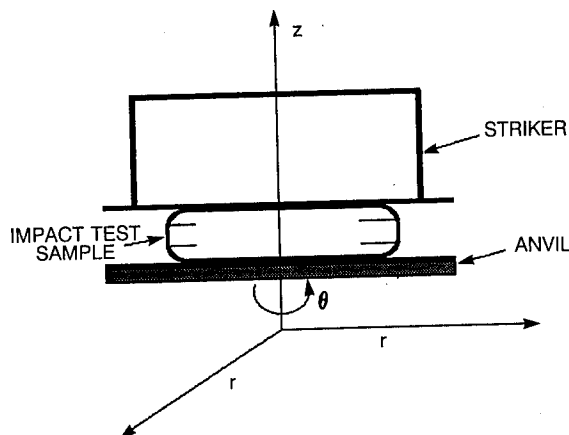


FIGURE 1. IMPACT TEST SAMPLE

After the sample ruptures, hoop stresses near the rupture should approach zero, so only shear stresses are

available to oppose the pressure from the center of the sample. The sudden reduction in hoop stress should lead to increased radial flow velocities next to the rupture. It also should lead to a reduction in sample pressure or a reduction in the rate of increase of sample pressure. The rupture in the sample perimeter should continue to grow towards the center of the sample as the sample expands outwards and so should be visible as a crack in impacted samples.

The results of impact tests with novel ring-shaped samples, which highlight the cracks, and heat-sensitive film, which highlights the hot spots in the sample,<sup>2</sup> were photographed.

## EXPERIMENTAL

Drop weight impact tests were run at the Naval Surface Warfare Center, Indian Head Division in 1991. The PBXs chosen for the tests consisted of a solid filler, RDX, with a polyurethane binder. The filler content was in the range of castable PBXs, 80% to 90% by weight.

The polyurethane binder contained long, flexible polymer chains made of polypropylene glycol (PPG) molecules linked together by a mixture of isocyanate molecules. Varying the type and amount of isocyanate molecules produced tensile strengths varying from 0.115 to 0.470 MPa when measured at a strain rate of  $0.7407 \text{ min}^{-1}$ . The binder also contained a plasticizer, isodecyl pelargonate.

The explosive samples were sandwiched between a sheet of sandpaper and a sheet of heat-sensitive film. The sandpaper used for most of the experiments was 180 Garnet Norton A511. However, 80 Garnet and 40 Garnet 3M sandpapers were sometimes used. The 40 Garnet sandpaper was generally too coarse to use for impact testing. The top layer of the "sandwich" was a sheet of 3M No. 382 Transparency Film for infrared copiers. This film darkens when heated and indicates the presence of "hot spots" next to the film.<sup>2</sup>

The explosive samples were ring shaped instead of disk shaped (Figure 2). This allowed both inward and outward deformation. A 5-kg drop weight was used for all tests. The drop heights ranged from 200 to 900 mm.

## RESULTS

Impacted samples are shown in Figures 2 through 5. The drop height, sandpaper type, and mechanical properties of the explosive are listed for each sample. The samples expanded both internally and

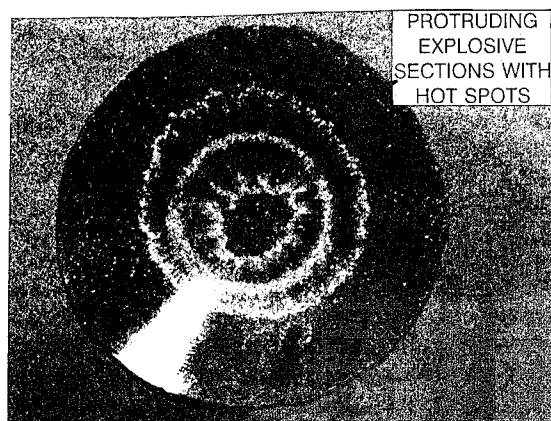


**FIGURE 2. SAMPLE X-19**  
[700-mm drop; 80 Garnet sandpaper; 0.126-MPa stress; 76.11% strain]

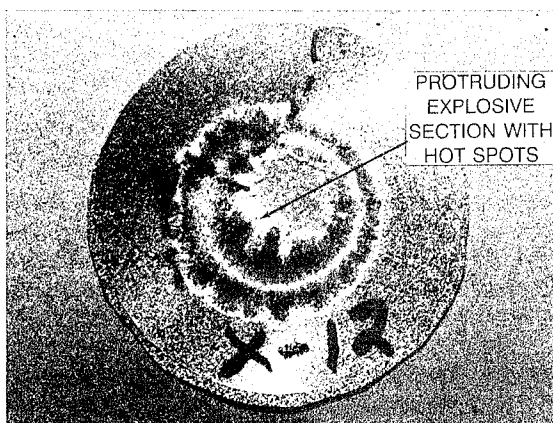


**FIGURE 3. SAMPLE X-12**  
[700-mm drop; 180 Garnet sandpaper; 0.470-MPa stress; 15.96% strain]

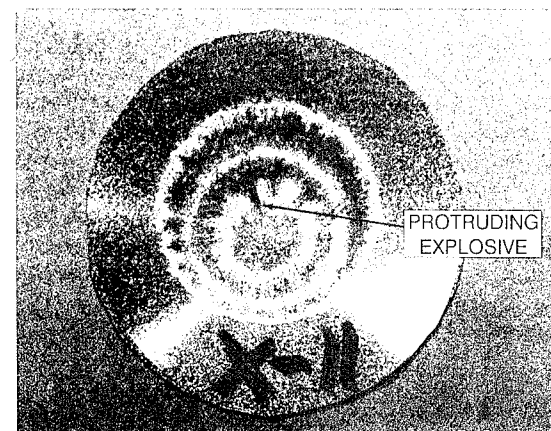


**FIGURE 4. SAMPLE X-11**  
[600-mm drop; 80 Garnet sandpaper; 0.470-MPa stress; 15.96% strain]

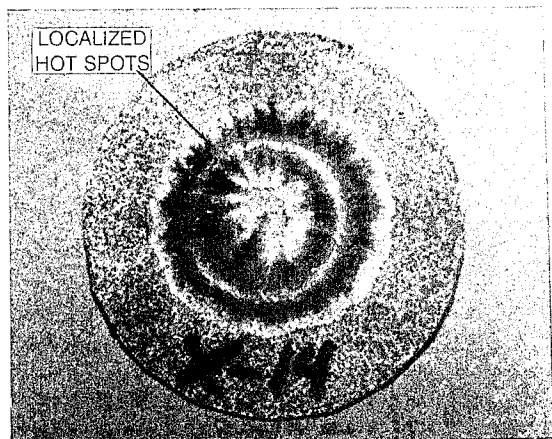


**FIGURE 5. SAMPLE X-14**  
[800-mm drop; 180 Garnet sandpaper; 0.126-MPa stress; 76.11% strain]

externally. The centerlines of the samples, where no shear stress occurs, did not heat the films even though the highest pressures should have occurred there.

The deformation of the samples in both the inward and outward direction was not uniform. Instead the samples formed finger-like projections of varying widths. These projections appeared to be formed by the explosive between two radial cracks in the sample perimeter. The radial cracks removed hoop stress, allowing the pressure in the center of the sample to drive the explosive away from the centerline. The resulting high shear strain rate flow fractured the RDX crystals, causing them to heat<sup>2</sup> and possibly ignite. The heating was strongest in the center of the finger-like projections. It appeared to be quenched effectively by the binder.

Adiabatic compression of the air in the center of the samples did not cause any noticeable darkening of the film. Also, heated air did not seem trapped in the explosive itself since the centerlines of the impacted rings were quite cool.

## ANALYSIS

The radial cracks contribute to the rapid flow of the sample by removing the hoop stresses opposing deformation. Therefore, it should be possible to minimize the rapid flow and ignition of the sample by minimizing the radial cracks.

The rupture of PBXs and composite propellants is preceded by the unbonding of the filler from the rubbery matrix.<sup>3</sup> Therefore, the unbonding of the filler

along the radial cracks must be a precursor to the rapid flow phase. The stress required to unbond a filler particle from an elastic matrix was derived by Nicholson in 1979.<sup>4</sup> Specifically,

$$p^2 = \frac{(B)(Y)(4)(1+\nu)}{9(r)(1-\nu)^2} \quad (1)$$

where:

$p$  is the uniform tensile stress applied to the binder surrounding the particle, which causes it to unbond;

$B$  is the energy absorbed in unbonding a unit area of particle surface;

$Y$  is the elastic modulus of the binder;

$\nu$  is the Poisson's ratio of the binder;

$r$  is the radius of the unbonding particle.

The Nicholson formula shows that the radial cracks can be minimized by increasing the adhesiveness, modulus, and Poisson's ratio of the binder. Cracks can also be minimized by reducing the particle size of the filler. Reducing the particle size of the filler of a PBX increases its dynamic strength and reduces its LABSET explosiveness.<sup>1,5</sup> However, part of this decrease in explosiveness may have been due to the fact that smaller particles are inherently less sensitive<sup>6</sup> and not due to interaction with the polymeric binder.

Equation (1) can be simplified when all explosive samples contain identical RDX particle sizes and percentages. In that case:

$$Y_{\text{explosive}} = (Y_{\text{binder}})(\text{filler factor}) \quad (2)$$

Since the filler factor is a constant, the Nicholson relation simplifies to:

$$p^2 \propto \frac{(B)(Y_{\text{explosive}})(1+\nu)}{(r)(1-\nu)^2} \quad (3)$$

Equation (3) shows that increasing the modulus of the explosive (while keeping the filler particle size and percentage constant) should increase the rupture stress. However, Figure 6 shows that this was not true for all the samples produced for this study. The samples labeled as "brittle" do not meet this criterion. There is a limit at which increasing modulus no longer increases tensile stress.

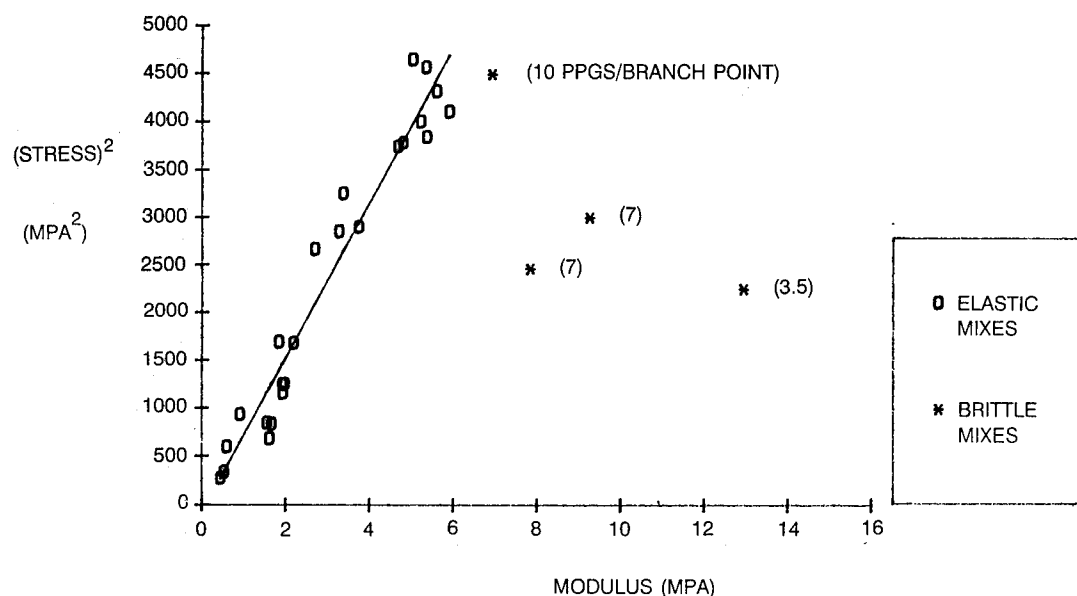


FIGURE 6. NICHOLSON DETACHMENT RELATION

The transition from elastic to brittle behavior occurs when the possible molecular weight of the polymer chains of the binder becomes infinite.<sup>7</sup> This represents a binder consisting of a single, giant polymer chain whose size is limited only by the amount of PPG and isocyanate reactants added to the mix. The extent of reaction,  $X$ , necessary to produce such a polymer chain can be calculated by the Carothers equation,<sup>8</sup>

$$X = 2/f \quad (4)$$

where  $f$  represents the functionality of the system.

Functionality is defined as the number of reactive sites per molecule. For example, PPG has two reactive sites per molecule, so its functionality is two. The formulations with seven PPG molecules per branch point had fourteen reactive sites ( $7 \times 2$ ) plus one reactive site from the branch point. This resulted in fifteen reactive sites per seven PPG molecules.

$$f = 15/7 = 2.14 \quad (5)$$

$$X = 2/2.14 = 0.93 \quad (6)$$

The formulations with seven PPGs per branch point would become brittle when 93% of the reactive sites on the PPG molecules are reacted. Since enough isocyanate curative was added to react 95% of the PPG reactive groups,<sup>7</sup> the formulations were brittle and the Nicholson relation did not apply.

## SUMMARY

The rapid flow phase of the drop weight impact test has important effects on the generation of hot spots in the sample. The authors suggest that the beginning of the phase is dominated by hoop stresses and strains near the perimeter of the sample. Photographic evidence is presented to support this theory. The authors also suggest that the rapid flow and ignition of a PBX sample could be minimized by decreasing the particle size of the filler and increasing the adhesiveness and Poisson's ratio of the binder. Increasing the modulus of the binder should also help as long as the binder does not become brittle as predicted by Carothers equation.

## REFERENCES

- (1) J.E. Fields, S.J.P. Palmer, P.H. Pope, R. Sundarajan, and G.M. Swallowe, "Mechanical Properties Of PBX's And Their Behavior During Drop-Weight Impact," *Proceedings of the Eighth Symposium (International) On Detonation*, July 15-19, 1985, Albuquerque, NM, pp. 635-644.
- (2) C.S. Coffey and S.J. Jacobs, "Detection Of Local Heating In Impact Or Shock Experiments With Thermally Sensitive Films," *J. Appl. Phys.* 52(11), November 1981.

- (3) A.E. Oberth and R.S. Bruenner, "Tear Phenomena Around Solid Inclusions In Castable Elastomers," *Trans. Soc. Rheol.*, 9(2), 1965, pp. 165-185.
- (4) D.W. Nicholson, "On The Detachment Of A Rigid Inclusion From An Elastic Matrix," *J. Adhesion*, 10, 1979, pp. 255-260.
- (5) K.A. Fleming, R. Bird, M.W.G. Burt, and C.E. Whatmore, "The Influence Of Formulation Variables On The Growth Of Reaction In Plastic Bonded Explosives," *Proceedings of the Eighth Symposium (International) On Detonation*, July 15-19, 1985, Albuquerque, NM, pp. 1035-1044.
- (6) R.W. Armstrong, C.S. Coffey, V.F. DeVost, and W.L. Elban, "Crystal Size Dependence For Impact Initiation Of Cyclotrimethylenetrinitramine Explosive," *J. Appl. Physics*, 68(3), Aug. 1990, pp. 979-984.
- (7) A.P. Metzner, *Mechanical Properties And Binder Structure Of PBX(AF)-108 Explosive*, IHMR 92-279, Indian Head, MD: Indian Head Division, Naval Surface Warfare Center; to be published.
- (8) W.H. Carothers, "Polymers And Polyfunctionality," *Trans. Faraday Soc.*, 32, 39, 1936.

## INAPPROPRIATE USE OF INCLINED ELECTROMAGNETIC VELOCITY GAUGES IN EXPLOSIVES\*

J. F. Cau  
Centre d'Etudes de Gramat  
46500 Gramat - FRANCE

This paper presents a set of experimental results obtained in the explosive under several plane, one dimensional configurations (single shock, double shock, ramp wave) for Los Alamos National Laboratory type electromagnetic particle velocity gauges. The problems encountered in the use of these gauges are highlighted (overshoot and a level lower than the level estimated with the Hugoniot). A numerical simulation makes it possible to partly explain overshoot and experiments performed using inert material show the negative influence of the inclined configuration of the experimental set-up which affects the one dimensional character of flow and leads to velocity measurements that are approximately 10% lower than the expected velocity measurements. Future research, focussed on finding the best position for the location of these gauges, should result in a positive solution concerning the quantitative use of these gauges which possess qualities that would make them an excellent tool in the study of the transient detonation flows of explosives.

### INTRODUCTION

Two of the major parameters that have been addressed when investigating the transient detonation conditions of solid high explosives are pressure and particle velocity. Although the time resolved experimental technics used to measure pressure have been widely described and used, those used to measure particle velocity, which have also been described to a large extent, have, until the last few years, been used to a lesser degree.

The technological progress achieved over the last few years has produced a renewed interest in the development of embedded electromagnetic velocity gauges used to record particle velocities.

Based on the gauges developed by the Los Alamos National Laboratory (LANL)<sup>1</sup> and used by the Lawrence Livermore National Laboratory<sup>2</sup>, the CENTRE D'ETUDES DE GRAMAT has produced similar gauges in order to use them in the study of the transient detonation flows of explosives alongside pressure gauges.

A description of the experiments conducted will be given first, followed by the presentation of the results obtained in various configurations with the two types of gauge.

The problems encountered with electromagnetic velocity gauges are set out and answers are provided.

\*Work performed under the auspices of French Ministry of Defense, Délégation Générale pour l'Armement.



## DESCRIPTION OF THE EXPERIMENTS

### Launcher, Target Chamber and Target

The experiments described in this document are plane, one dimensional impacts performed using the "ARES" powder launcher belonging to the Centre d'Etudes de Gramat. The single stage launcher has an inner diameter of 98 mm and is 11 m long. With a powder weight varying from 1 to 6 kg and a projectile weight of 10 to 1.5 kg, a velocity of 800 to 2300 m/s can be obtained. Velocity reproducibility is 1% and parallelism on impact is approximately 1.5 mrad. Impact takes place in an evacuated target chamber which covers the end of the gun. The target including a support, the instrumented explosive block and the short-circuit pins for measuring velocity and tilt, is secured by three rods used for adjusting tilt.

### The Gauges Used

- Pressure gauges. These are manganin gauges 3, manufactured at the Centre d'Etudes de Gramat which have an impedance of 13 m $\Omega$ .

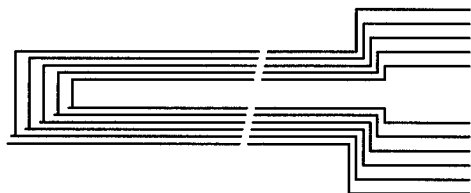


FIGURE 1. ELECTROMAGNETIC VELOCITY GAUGE

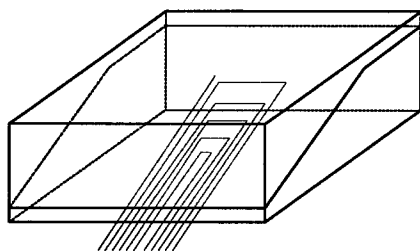


FIGURE 2. INSTRUMENTED TARGET WITH EMV GAUGE

The electric integrity of these gauges is provided by gluing two teflon sheets (250-150  $\mu$ m) around the gauge. The gauge is inserted at the required depth by gluing it between appropriate explosive blocks. The accuracy of

the results obtained with such gauges is  $\pm 5\%$ . Only one gauge is used per shot.

- Electromagnetic velocity gauges.<sup>4</sup> Using the concept developed at the LANL, gauges (fig. 1) with five active elements and associated measuring tabs were made by photoengraving onto a presensitized 50  $\mu$ m copper coated polyester film. The gauge is inclined in the explosive so that each active element is at a different depth (fig. 2). The instrumented explosive block is placed between two permanent magnets which provide a magnetic field of 200 to 300.10<sup>-4</sup> T according to the position of the active element in question. The angle of inclination of the gauge is 23° with respect to the perpendicular plane of the shot axis.

### Explosives Tested

Depending on the experiments performed, the results of which are given hereafter, three explosives were used:

- an HMX-based pressed explosive with energetic binder called X1 ;
- an HMX-based pressed explosive with inert binder called X2;
- a TATB-based pressed explosive with inert binder called T.

### Experimental Results

Three types of experiment were carried out :

- single shock: this was carried out on explosive X1 (fig. 3) with a PMMA flyer (5 mm) at 1050 m/s and on explosive T (fig. 4) with an alumina flyer (Al<sub>2</sub>O<sub>3</sub> - 15 mm) at 1300 m/s ;
- double shock: this was carried out on explosive X2 (fig. 5) with a teflon-polyethylene flyer (3 - 30 mm) at 1050 m/s and on explosive T (fig. 6) with a PMMA - Al<sub>2</sub>O<sub>3</sub> flyer (3-15 mm) at 1800 m/s;
- ramp wave: this was implemented at 1050 m/s by symmetrical impact of glass ceramics . The explosive X1 (fig. 7) was glued to the impacted ceramic (15 mm).

The signals were recorded either on a Tektronix 7612D, HP 5411D or Tektronix DSA 602 transient analyzer.

### Comments

The signals presented are "raw" signals which have not been smoothed. The velocity levels resulting from the Hugoniot curves of the explosives and the pressure levels obtained in other experiments have been indicated. There appears to be two main problems:

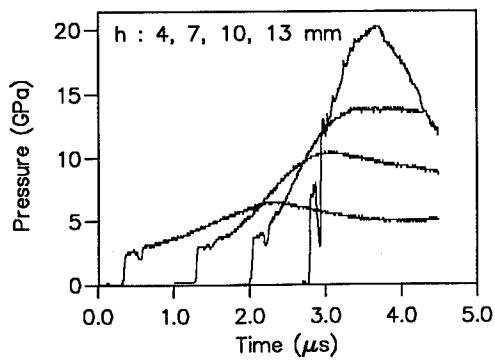


FIGURE 3. SINGLE SHOCK ON X1 EXPLOSIVE: PMMA FLYER (5 MM) AT 1050 M/S

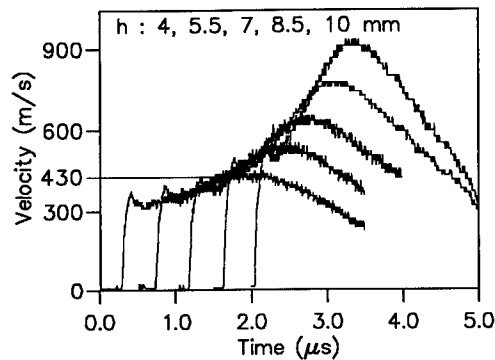


FIGURE 4. SINGLE SHOCK ON T EXPLOSIVE:  $\text{Al}_2\text{O}_3$  FLYER (15 MM) AT 1300 M/S

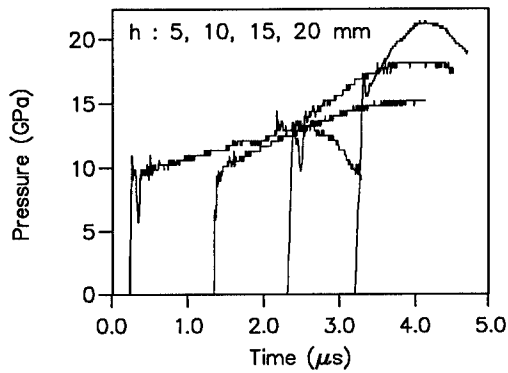


FIGURE 5. DOUBLE SHOCK ON X2 EXPLOSIVE: POLYETHYLENE-TEFLON (3-30 MM) AT 1050 M/S

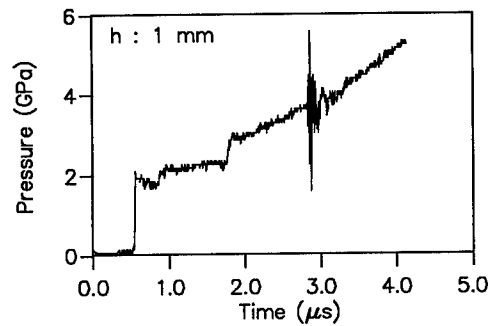
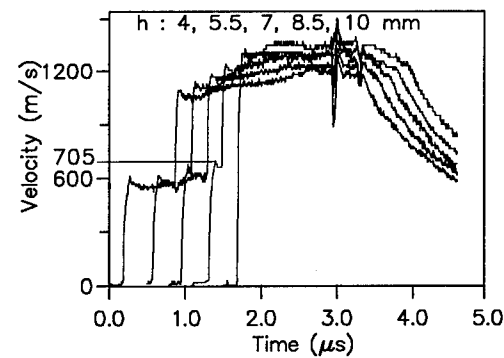
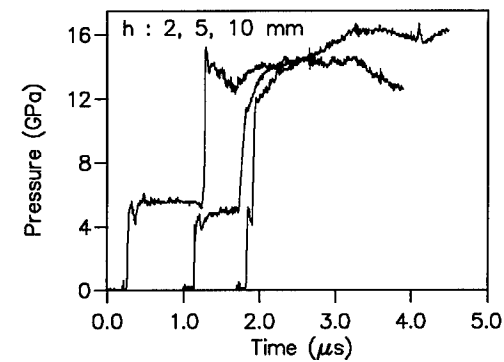
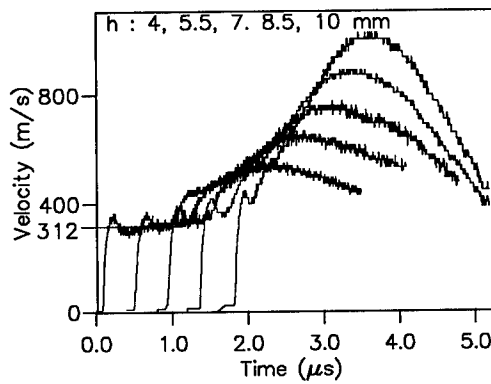
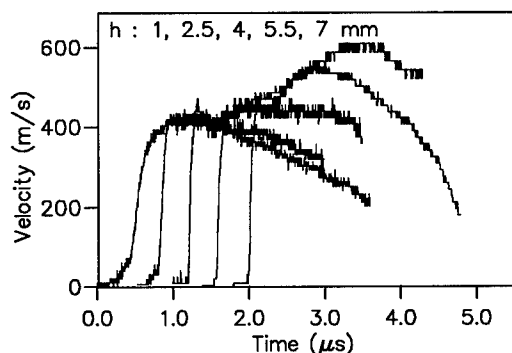
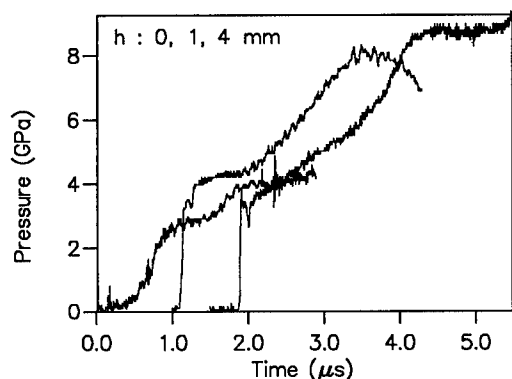


FIGURE 6. DOUBLE SHOCK ON T EXPLOSIVE: PMMA- $\text{Al}_2\text{O}_3$  FLYER (3-15 MM) AT 1800 M/S





**FIGURE 7. RAMP-WAVE ON X1 EXPLOSIVE: GLASS CERAMIC FLYER (15 MM) AT 1050 M/S**

- an initial overshoot before return to steady-state flow conditions ;
- a steady-state flow condition after the overshoot is lower than the level expected by the Hugoniot curves.

Apart from these two major problems, these gauges appear to monitor the different types of flow very well and seem to be very sensitive. The two problems mentioned above led to a finer analysis of these gauges

## ANALYSIS OF THE EXPERIMENTAL RESULTS

### Difference in Level in Steady-State Flow

Firstly, it was necessary to overcome the reactivity of the explosive. To do this, teflon, a non reactive material, with a Hugoniot close to those of the explosives studied and, what is more, electrically neutral. under shock conditions, was selected.

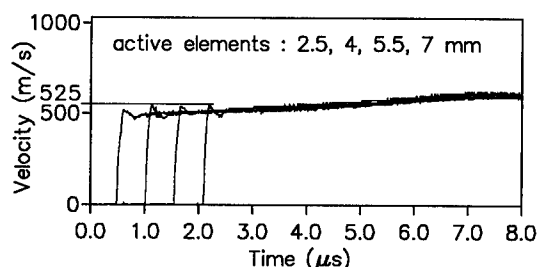


**FIGURE 8. SYMMETRICAL IMPACT ON TEFLON AT 1050 M/S: INCLINED GAUGE**

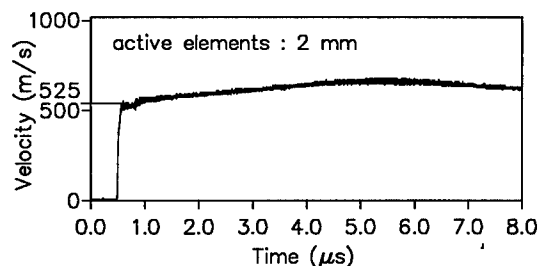


**FIGURE 9. SYMMETRICAL IMPACT ON TEFLON AT 1050 M/S: FLAT LYING GAUGE**

Symmetrical impact at 1050 m/s was implemented and the signals illustrated in figure 8 and obtained at various depths, show that the expected level of 525 m/s was not reached. The level after the overshoot is between 8% and 12% less than 525 m/s (on average 10%; i.e. 472 m/s) depending on the active element.

Moreover, the signals show an overshoot. The velocity level on the first hundred nanoseconds was analyzed. The analysis of the general increase in velocity over four or five microseconds is not the subject of this work. It therefore seemed of interest to install a flat lying gauge (perpendicular to flow) with all the active elements at the same depth (2 mm).

Symmetrical impact was performed at 1050 m/s under these conditions and the signals (fig. 9) demonstrate two points:

- they confirm the good reproducibility of the gauges and the quality of the data reduction and measurement methods used;

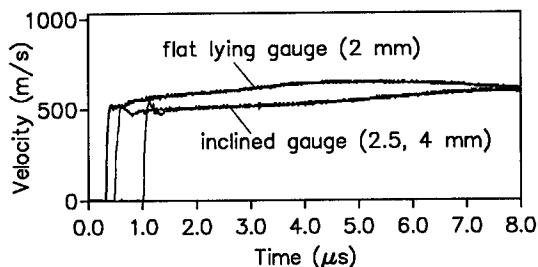


**FIGURE 10. SYMMETRICAL IMPACT ON TEFLON AT 1050 M/S: FLAT LYING AND INCLINED GAUGES**

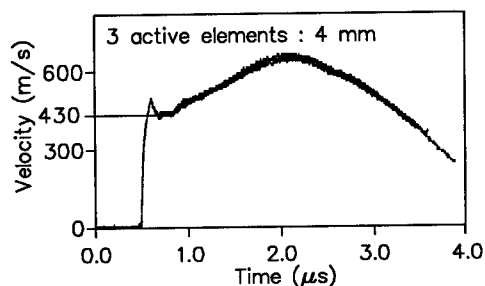


**FIGURE 11. SINGLE SHOCK ON X1 EXPLOSIVE: PMMA FLYER (5 MM) AT 1050 M/S; FLAT LYING GAUGE**

- the signals exhibit the expected level of 525 m/s, at least for the first hundreds of nanoseconds.

To make it easier to compare the flat lying and the inclined gauges, the first two signals of the inclined gauge (2.5 - 4 mm) were grouped with one of the signals of the flat lying gauge (2 mm) (fig. 10). There is a clear difference in level and the angle of the gauge seems to decrease the expected level.

The excellent behavior of the gauges when used flat was confirmed in explosive X1 with a PMMA flyer (5 mm) at 1050 m/s, with the gauge and its five active elements at a depth of 4 mm. The signals obtained (fig. 11) show that the expected level of 430 m/s is reached after the overshoot (only 3 active elements worked).

The excellent reproducibility can also be noted on the three active elements for which results were obtained.

One of the results of the flat lying gauge (4 mm) was grouped with the 4 mm result of the inclined gauge (fig. 12). This comparison with the explosive confirms

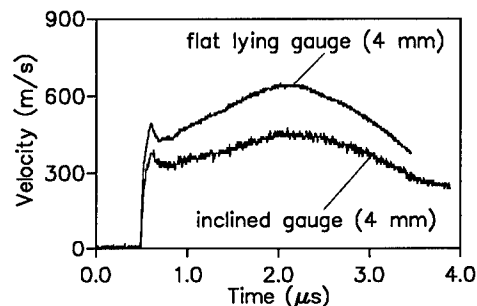


**FIGURE 12. SINGLE SHOCK ON X1 EXPLOSIVE: PMMA FLYER (5 MM) AT 1050 M/S; FLAT LYING AND INCLINED GAUGES**

the negative role of inclining the gauge on the velocity level obtained.

The previous experiments have only a demonstrative character with respect to the problem encountered and require additional theoretical or practical study to resolve this problem.

It should simply be noted that the complexity of the gauge arrangement, which is notably due to the diversity of materials present, to the lack of knowledge on the mechanical behavior of constitutive materials and to the small thicknesses concerned, do not make it easy to understand the behavior of the set-up and the response of the gauge.

### Overshoot

The level obtained with the flat lying gauges is correct and the overshoot on the velocity recording obtained, especially with the explosive, still remains to be solved. This overshoot is assumed to be due to the expansion of the active element into the polyester support and the glue which secures them to the explosive.

A numerical simulation with a one dimensional Lagrangian code in which the Johnson - Tang - Forest 5 kinetic is implemented, was carried out. The case illustrating the configuration was meshed at 100 meshes/mm and is shown in figure 13. The polyester support of the gauge (25 μm) and the glue thicknesses (100 + 20 μm) were simulated by PMMA (145 μm). The velocity recording obtained at the teflon-PMMA interface was compared to the velocity obtained with a flat lying gauge (4 mm) (fig. 14). Apart from the difference in level which appears both on the overshoot and in the steady-state flow conditions and which is probably due to inaccurate identification of the Hugoniot of the explosive, this comparison seems to confirm the

validity of the afore-mentioned assumption on the origin of the overshoot.

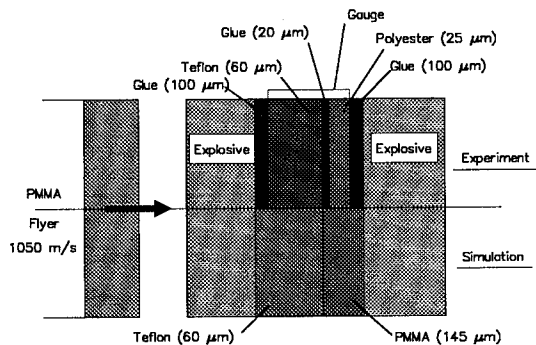


**FIGURE 13. LAYOUT OF SIMULATION**

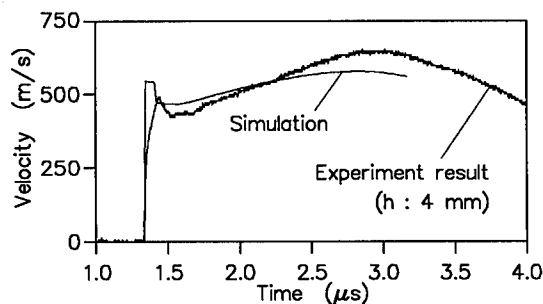


**FIGURE 14. COMPARISON BETWEEN EXPERIMENT AND NUMERICAL SIMULATION**

The origin of the overshoot can be found in the fact that the active element in this configuration is a flat element and not a wire. Y.M. Gupta<sup>6</sup> considers this difference as the likely cause of the overshoot.

### Improvement in the Design of the Gauges

Following the previous work, it seemed necessary to optimize the gauges to make their mechanical characteristics as close as possible to those of the materials in which they are inserted.

The manufacture of teflon-aluminum-teflon gauges was therefore undertaken, teflon being chosen for its features mentioned earlier, and aluminum for its Hugoniot which is lower than copper, thus allowing a faster response time.

After overcoming several difficulties, the manufacture of these gauges is now fully mastered. They have a total thickness of 170  $\mu\text{m}$ , with the active element being 30  $\mu\text{m}$  thick for a width of 250  $\mu\text{m}$ .

# DEMONSTRATING A FLOW COMPONENT THAT IS NOT ONE DIMENSIONAL WHEN AN INCLINED GAUGE IS USED

The analysis of the previous results led us to assume that the inclination of the gauge could disturb the one dimensional conditions of the initial flow.

Two configurations which were symmetrical to one another in relation to the vertical plane passing through the shot axis were set up (fig. 15) and magnets providing the magnetic field were placed on an axis shifted  $45^\circ$  in respect of the shot axis (and not  $90^\circ$  as was the case during the experiments previously discussed).

These configurations make it possible to measure the component of the particle velocity lying on a plane perpendicular to the magnet axis, with this axis also being shifted by  $45^\circ$  with respect to the vertical plane passing through the shot axis (cf. fig. 15). If flow is one dimensional, the values measured on the two projections that are perpendicular to each other should be the same.

The first experiment was conducted with the axis of the magnets shifted by  $-45^\circ$  in relation to the shot axis (in the conventional sense of positive upwards on a top view of the configuration, cf. fig. 15) and the measurement was therefore the projection of the particle velocity on the plane shifted by  $+45^\circ$  with respect to the axis. As was the case previously, this is teflon-teflon symmetrical impact at 1050 m/s with the gauge described above being positioned at an angle in the impacted block as shown in figure 15, with the angle of the gauge always being  $23^\circ$  in relation to the impact plane.

The signals shown on fig. 16 illustrate a steady flow velocity after the overshoot of about 370 m/s during the first hundreds of nanoseconds, with a general decrease in velocity over several microseconds probably being due to the configuration for which the value of the magnetic

field is lower than previously ( $150 \cdot 10^{-4}$  T instead of  $200 - 300 \cdot 10^{-4}$  T in the usual configuration) and to the permanent magnet arrangement which does not make it possible to provide a constant value of the field over a considerable range of movement.

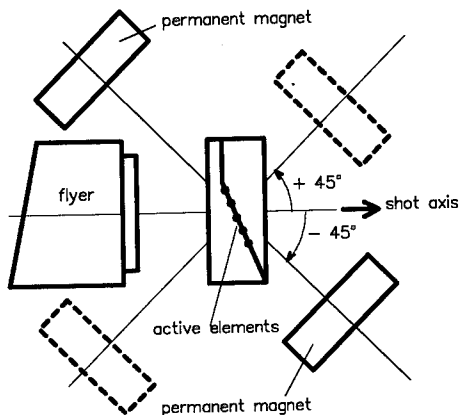


FIGURE 15. LAYOUT OF 45° EXPERIMENTS

As the non uniformity of the magnetic field was not a major preoccupation, no further experiments were carried out to extend its uniform range.

The second experiment concerned the symmetrical configuration with the axis of the magnets shifted by  $+45^\circ$ . This was also a symmetrical impact on teflon, with the gauge and the geometry of the block remaining unchanged.

The signals depicted in fig. 17 show a steady flow velocity of approximately 310 m/s. This case also looked at the velocity on the first hundreds of nanoseconds, and the increase in velocity over several microseconds had the same origins as described above. The measurement errors cannot be held responsible for such a difference (60 m/s, i.e. 18%) insofar as five measurements were performed simultaneously for each shot using different active elements of different lengths and varying magnetic field values for each active element. The reproducibility of the five signals is good enough to be confident in the measurements.

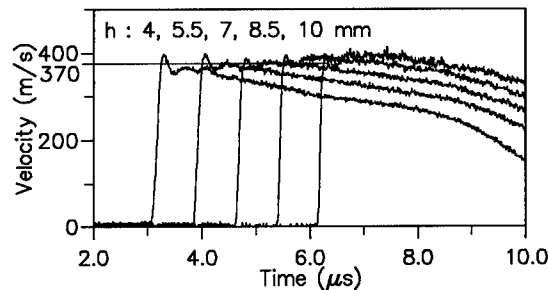


FIGURE 16. EXPERIMENTAL RESULTS OF THE  $+45^\circ$  PROJECTION OF VELOCITY

Moreover, a confirmation of the values obtained during these two experiments can be provided.

It should be remembered that during the experiments on teflon-teflon symmetrical impacts similar to these ones, the results with the flat lying gauge were naturally 525 m/s, whereas with the inclined gauge the values obtained for electromagnetic velocity were approximately 10% lower, i.e. 472 m/s.

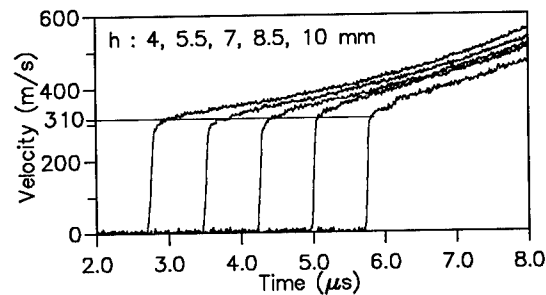


FIGURE 17. EXPERIMENTAL RESULTS OF THE  $-45^\circ$  PROJECTION OF VELOCITY

The diagram in fig. 18 where the particle velocity vector  $V$  appears, the components of which on the two perpendicular axes  $x$  and  $y$  were measured respectively as 370 m/s and 310 m/s, has an absolute value  $V$  of 483 m/s. This makes it possible to calculate the  $\alpha$  angle of the vector  $V$  with respect to the shot axis which was  $5^\circ 02'$  with values of 370 m/s and 310 m/s, which gives a projection  $v$  on the shot axis ( $v = V \cos \alpha$ ) equal to 481 m/s which is very close (2 %) to the 472 m/s measured during the first experiments and is in fact the measurement of the projection of vector  $V$  on the shot axis.

## Conclusions on the use of inclined gauges

It is therefore reasonable to think that an inclined electromagnetic particle velocity gauge leads to a degradation of the one dimensional character of flow which does not make it possible to measure the exact values of the particle velocity of the undisturbed flow field.

These observations are based on the results of experiments and lead to the conclusion that there is no possibility of using these gauges for accurate particle velocity measurements.

However, all the work done has made it possible to show the extremely sensitive nature of these gauges and the excellent reproducibility of the results obtained with them. These qualities, as well as the fact that a single shot can be used to obtain several measurements at different depths without any time resetting nor uncertainty concerning reproducibility, mean that research concentrating on finding an improved geometrical arrangement for the gauge should be envisaged (for example staircase configuration).

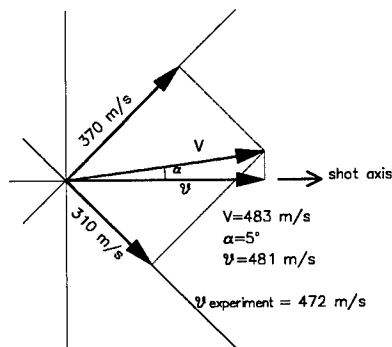


**FIGURE 18. SCHEME OF VELOCITY VECTOR WITH THE DIFFERENT PROJECTIONS**

## CONCLUSION

Two major problems were encountered in the use of electromagnetic velocity gauges: an overshoot in the velocity recording and a steady flow level that was lower than the one expected.

The studies conducted show that the overshoot is partly due to the impedance mismatch between the target material and the constitutive materials of the gauge package, but this remains to be confirmed.

As concerns the difference in flow level, it is reasonable to think that the inclined configuration disturbs the normal one dimensional flow and does not make it possible to measure the exact values of the flow field particle velocity (-10% discrepancy on average). This observation has an adverse effect on the use of these gauges in the above configuration. However, the intrinsic qualities of these gauges imply that research should be continued with a view to technically mastering their installation to be able to eventually benefit from their quantitative use.

## REFERENCES

1. Vorthman, J. ; Andrews, G. ; Wackerle, J. ; "Reactions rate from electromagnetic gauge data", Eighth Symposium (International) on Detonation, Naval Surface Weapons Center, NSWC MP 86-194, 1985, p. 99.
2. Urtiew, P., A. ; Erickson, L., M. ; "Multiple gauges for in situ measurements of pressure and particle velocity in condensed materials", Twelfth International Colloquium on the Dynamics of Explosions and Reactive Systems, University of Michigan, Ann Arbor, MI, 1989.
3. Courteix, R. ; Bedoch, J.P. ; "Utilisation des jauges manganin basse impédance en milieu réactif", CEG T 87-18, 1987, Centre d'Etudes de Gramat, Gramat, France.
4. Cau, J.F. ; Joubert, M. ; "Mise en oeuvre de jauges de vitesse matérielle dans l'explosif", CEG T 90-65, 1990, Centre d'Etudes de Gramat, Gramat, France.
5. Baudin, G. ; Cau, J.F. ; Saint-Matin, C. ; Gimenez, P. ; "Etudes des régimes transitoires de détonation dans un explosif comprimé à l'octogène", Journées Détonique, 1988, Gramat, France.
6. Gupta, Y.M. ; Keough, D.D. ; Walter, D.F. ; "Experimental facility to produce and measure compression and shear waves in impacted solids", Review of Scientist Instrum, Vol 51, February 1980, Poulter Laboratory, SRI International, Menlo Park, California 94025.



## **INAPPROPRIATE USE OF INCLINED ELECTROMAGNETIC VELOCITY GAUGES IN EXPLOSIVES**

J.F. CAU

Centre d'Etudes de Gramat  
46500 Gramat – FRANCE

This poster presents a set of experimental results obtained in high explosives under various types of plate–impact experiments (single shock, double shock, ramp wave) for pressure and multiple electromagnetic particle velocity gauges (LANL<sup>1</sup> type EMV gauge).

Two problems encountered in the use of the EMV gauges are highlighted :

- overshoot on particle velocity signals.
- a steady state velocity level lower than the expected one by the Hugoniot.

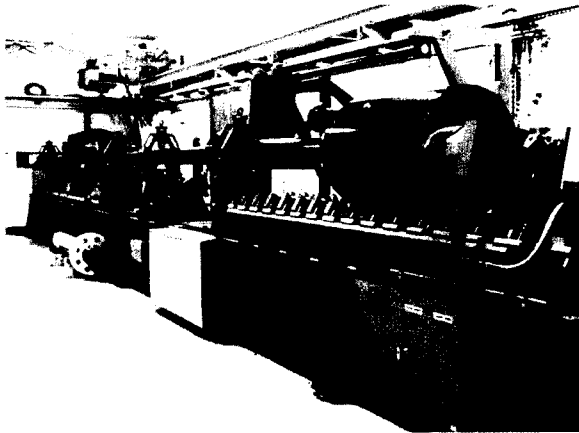
A numerical simulation makes it possible to partly explain the overshoot. Experiments performed using inert material show the negative influence of the inclined configuration of the experimental set–up which affects the one dimensional character of flow and leads to velocity measurements that are approximately 10% lower than the expected velocity measurements.



## EXPERIMENTAL FACILITIES

### "ARES" Powder Gun

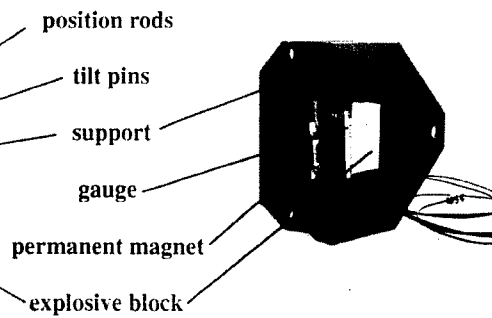
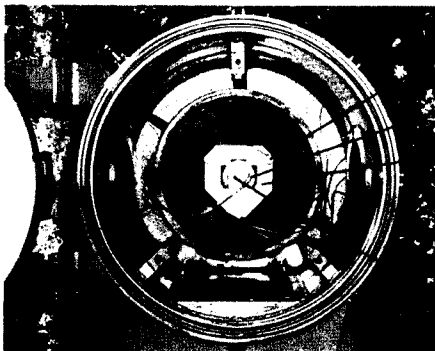
Characteristics and performances :



- Inner diameter : 98 mm
- Tube length : 11 m
- Projectile weight : 1.5 – 10 kg
- Powder mass : 1 – 6 kg
- Velocity reproducibility : 1%
- Tilt : < 1.5 mrad

### VACUUM TARGET CHAMBER

### TARGET



## GAUGES

Electromagnetic Velocity gauges  
(Los Alamos National Laboratory type) <sup>1,2,4</sup>



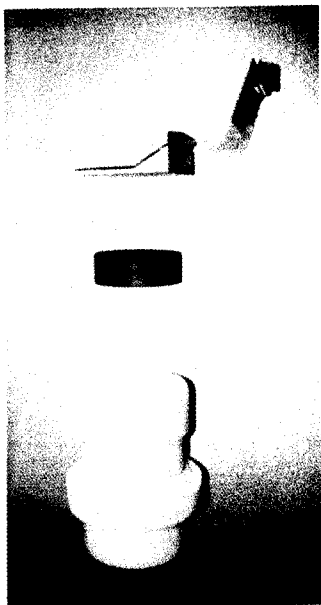
- Presensitized copper coated polyester film
- Photoengraving
- Gluing of a teflon sheet (50  $\mu\text{m}$ )

Piezo resistive pressure gauges <sup>3</sup>

- Manganin gauges
- 13 m $\Omega$
- Two teflon sheet embedded  
(250 – 150  $\mu\text{m}$ )

# EXPERIMENTS

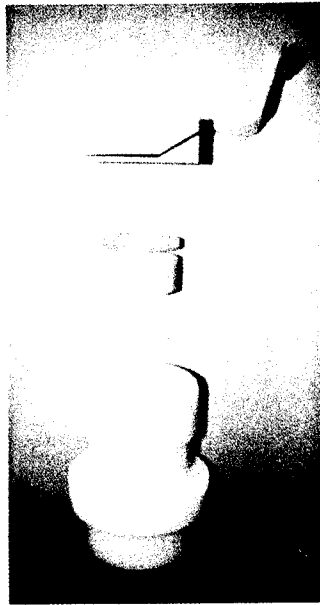
Single shock :



TESTED EXPLOSIVES :

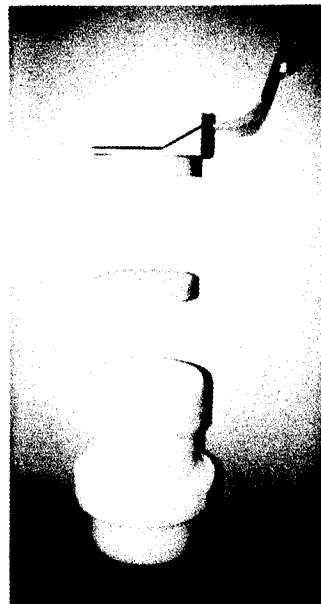
HMX-based pressed explosive  
with energetic binder (called X1).

Double shock :



HMX-based pressed explosive  
with inert binder (called X2).

Ramp wave :

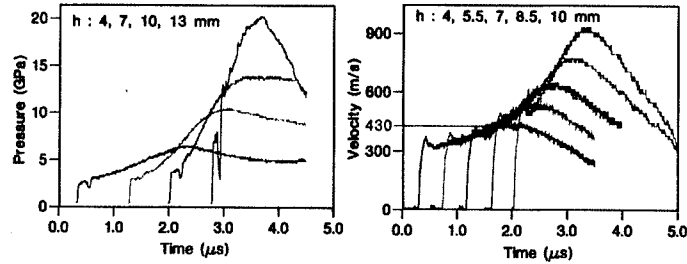


TATB-based pressed explosive  
with inert binder (called T).

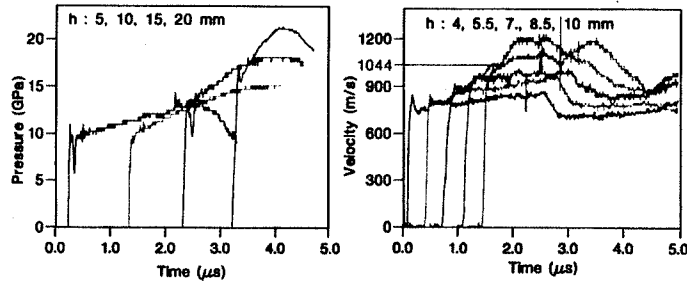
## RESULTS

— : Velocity level obtained from the Hugoniot and confirmed by the pressure gauges measurements

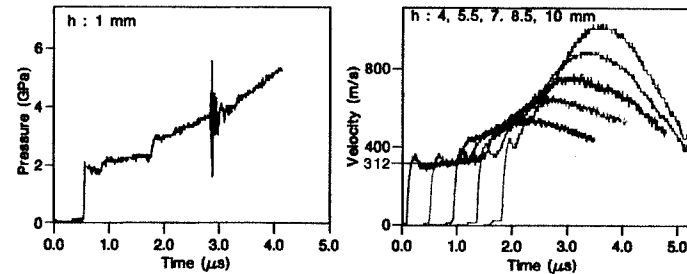
Single shock  
X1 explosive  
PMMA flyer (5 mm)  
1050 m/s



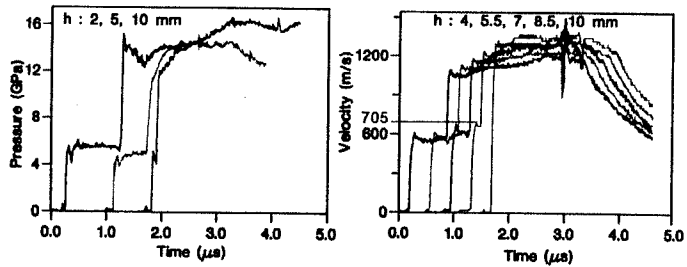
Single shock  
T explosive  
 $\text{Al}_2\text{O}_3$  flyer (15 mm)  
1300 m/s



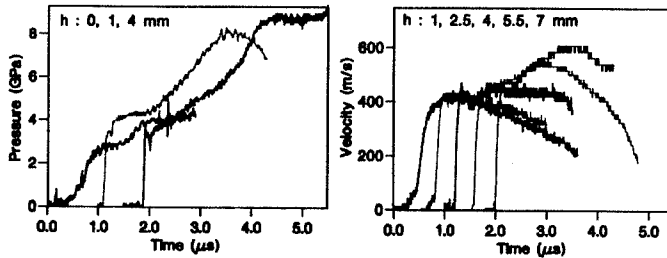
Double shock  
X2 explosive  
polyethylene-terflon  
flyer (3-30 mm)  
1050 m/s



Double shock  
T explosive  
PMMA- $\text{Al}_2\text{O}_3$  flyer  
(3-15 mm)  
1800 m/s



Ramp-wave  
X1 explosive  
glass ceramic flyer  
(15 mm)  
1050 m/s



## **EMV GAUGES**

### **QUALITIES :**

- Good monitoring of the different types of flows.
- Sensitive gauges.

### **PROBLEMS :**

- Initial overshoot.
- Steady state flow following the overshoot lower than the level expected by the Hugoniot.

## ANALYSIS OF THE TWO PROBLEMS AND QUESTIONING THE INCLINATION OF THE GAUGE

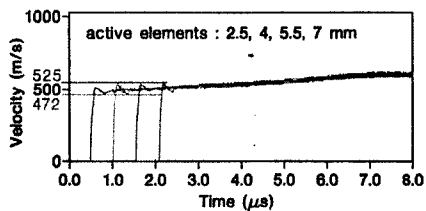
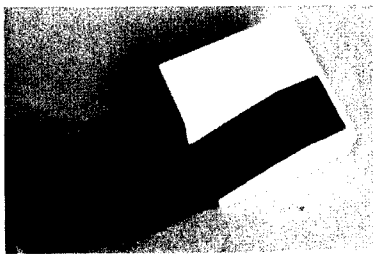
### DIFFERENCE IN LEVEL IN STEADY STATE FLOW

– Overcoming the reactivity of explosive using PTFE (teflon) :

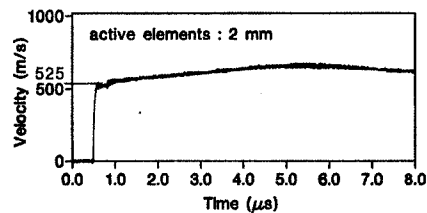
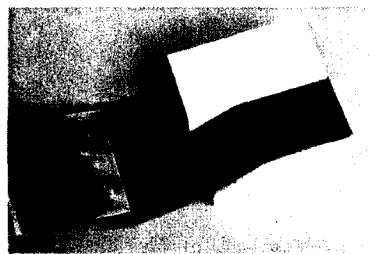
- . non reactive material.
- . Hugoniot close to those of explosives.
- . Electrically neutral under shock conditions.

– Experiments : symmetrical impact on teflon at 1050 m/s

inclined gauges



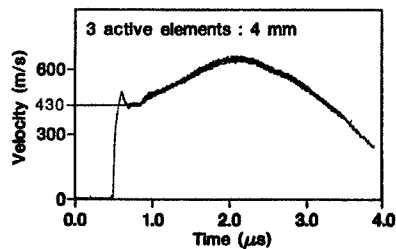
flat lying gauges



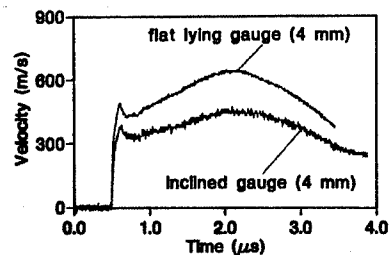
– Difference of about 10% (525m/s–472m/s) between the levels of the two experiments (inclined and flat lying gauges)

**Confirmation in explosive of the good behaviour of the gauges when they are used flat**

Experiment : single shock on X1 explosive  
PMMA flyer (5 mm) at 1050 m/s  
flat lying gauge at 4 mm



Comparison with an inclined  
gauge experiment

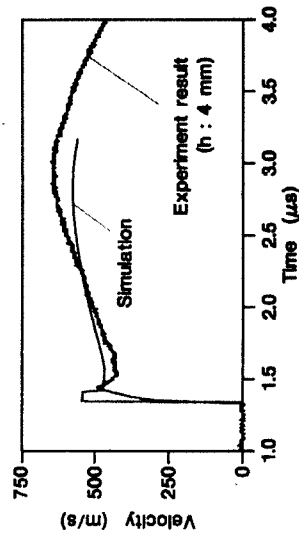
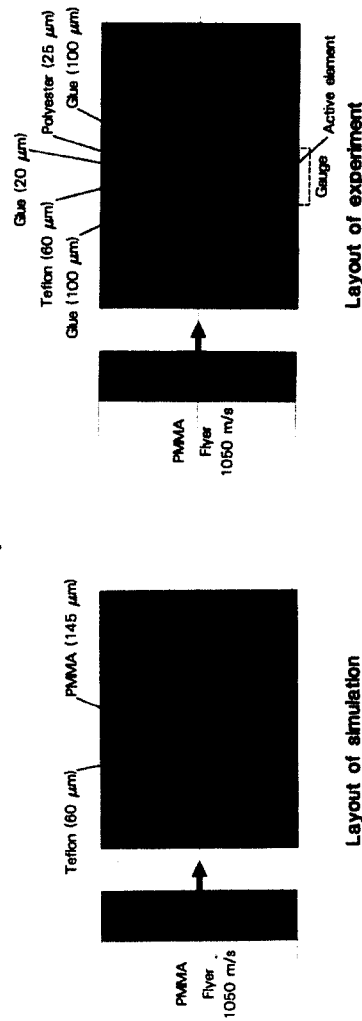


## OVERSHOOT :

- We assume that the overshoot is due to the expansion of the active element into the polyester support and the glue which secures them to the explosive.
- Simulation of the experiment was performed with a one dimensional lagrangian code in which the Johnson-Tang-Forest kinetic<sup>5</sup> is implemented.

The case was meshed at 100 meshes/mm.

The polyester support of the gauge (25  $\mu\text{m}$ ) and the glue thicknesses (100 + 20  $\mu\text{m}$ ) were simulated by PMMA (145  $\mu\text{m}$ ).



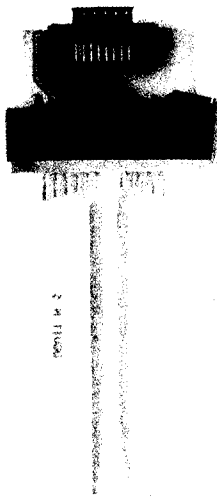
Another cause could be that it is a flat 30  $\mu\text{m}$  thick active element. Y.M Gupta<sup>6</sup> assumes that using a foil and not a wire element eliminates the overshoot.

## IMPROVEMENT IN THE DESIGN OF THE EMV GAUGES

– Gauges teflon–aluminum–teflon were realized to ensure a better behaviour and a better response.

Total thickness : 170  $\mu\text{m}$

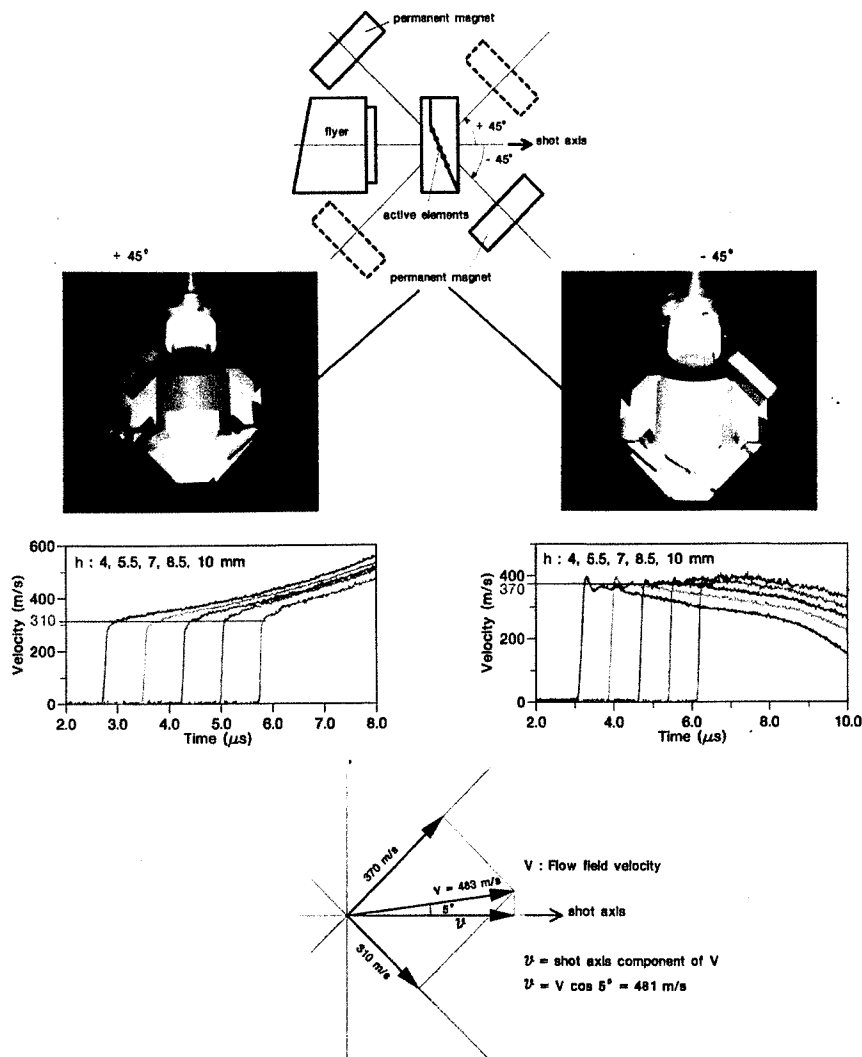
Active element thickness : 30  $\mu\text{m}$



## DEMONSTRATION THAT A FLOW COMPONENT IS NOT ONE DIMENSIONAL WHEN AN INCLINED GAUGE IS USED

If flow is one dimensional, the components of the velocity on two symmetrical planes in relation to the vertical plane passing through the shot axis would be equal.

To verify this previous hypothesis, the axis of permanent magnets are rotated of  $\pm 45^\circ$  in order to define two symmetrical planes of particle velocity measurements. These are symmetrical impact experiments on teflon performed at 1050 m/s.



The increase or decrease of the signals is due to the experimental arrangement which does not permit to establish a constant magnetic field over a range of several millimeters.

These results confirm the degradation of the one dimensional character of flow.

This result is supported by the previous experiment where the measured particle velocity is about 472 m/s very close (2%) to the result obtained (481 m/s) by the two component measurement experiments.



## CONCLUSIONS

A set of experimental results obtained in explosives have permitted :

- to show the qualities of the LANL type EMV gauges :  
good monitoring and sensitiveness.
- to highlight two problems :  
overshoot and steady state flow lower than expected by the Hugoniot

. Experiments with teflon allowed to attribute the cause of lower steady state flow to the inclination of the gauge. Numerical simulation let to think that the expansion of active element causes the overshoot.

. Updated teflon-Al-teflon were developped and velocity symmetrical component measurements were performed. The velocity results which are not equal prove that the flow become non one dimensional through the inclined gauge.

Actually these results, which are confirmed by the previous measurements, question the quantitative use of these gauges but it would be interesting to master their installation to be able to eventually benefit from their intrinsic qualities.

## REFERENCES

1. Vorthman, J. ; Andrews G. ; Wackerle, J. : "Reactions rate from electromagnetic gauge data". Eighth Symposium (International) on Detonation, Naval Surface Weapons Center, NSWC MP 86-194, 1985, p 99.
2. Urtiew, P.A. ; Erickson, L. M. : "Multiple gauges for in situ measurements of pressure and particle velocity in condensed materials", Twelfth International Colloquium on the Dynamics of Explosions and Reactive Systems, University of Michigan, Ann Arbor, MI, 1989.
3. Courteix, R. ; Bedoch, J.P. : "Utilisation des jauges manganin basse impedance en milieu reactif", CEG T87-18, 1987, Centre d'Etudes de Gramat, Gramat, France.
4. Cau, J.F. ; Joubert, M. : "Mise en oeuvre de jauges de vitesse materielle dans l'explosif", CEG T90-65, 1990, Centre d'Etudes de Gramat, Gramat, France.
5. Baudin, G. ; Cau, J.F. ; Saint-Martin, C. ; Gimenez, P. : "Etudes des regimes transitoires de detonation dans un explosif comprime a l'octogene", Journees Detonique, 1988, Gramat, France.
6. Gupta, Y.M. ; Keough, D.D. ; Walter, D.F. : "Experimental facility to produce and measure compression and shear waves in impacted solids", Review of Scientist Instrum, Vol 51, February 1980, Poulter Laboratory, SRI International, Menlo Park, California 94025.

Special thanks to M. Joubert, Y. Lagarde and J.C. Goutelle for their help.

## EXPERIMENTAL INVESTIGATION INTO THE DEFLAGRATION TO DETONATION TRANSITION IN SECONDARY EXPLOSIVES

P. E. Luebcke, P. M. Dickson, and J. E. Field  
Cavendish Laboratory, University of Cambridge,  
Madingley Road, Cambridge, CB3 0HE, United Kingdom.

Deflagration-to-detonation transition has been studied in prepared columns of granular secondary explosive. The secondary explosive 2-(5-cyanotetrazolato) pentammine cobalt (III) perchlorate or 'CP' was chosen for the study due to its known propensity to undergo DDT within a few millimetres of ignition. Confinement within polycarbonate allowed direct high-speed streak photography of the event. Deflagration and detonation velocities and the run-to-detonation lengths were measured with variation of charge pressed density. Ignition of the CP column was attained thermally through a barrier with a gasless pyrotechnic. Deflagration and detonation velocities were seen to depend strongly upon pressed density. There appeared to be a maximum density conducive to DDT but no minimum with this explosive.

### INTRODUCTION

The mechanism by which a deflagration makes the transition to a detonation is yet to be fully understood. The salient features observed in the DDT of a granular secondary explosive are an accelerating combustion wave which moves through the unreacted charge, followed by the onset of detonation at some point downstream from the combustion wave. A detonation wave can sometimes be seen to run upstream from the point of initiation. The process by which a shock wave becomes a detonation wave is fairly well understood; it is the mechanism by which sufficiently strong shock waves are formed which still requires an explanation.

The phenomenon of DDT has been investigated for many decades since Dixon<sup>1</sup> and Bone et al.<sup>2</sup> examined the transition to detonation in explosive gas mixtures. Pioneering work by Kistiakowsky<sup>3</sup> resulted in the hypothesis that upon ignition of an explosive, convective burning would govern the combustion process until initiation of detonation. Griffiths and Grocock<sup>4</sup> suggested that detonation was brought about via a sequence of stages; conductive burning, convective burning, and then compressive burning leading to shock formation of increasing strength until the critical shock initiation pressure had been attained. Gipson and Macek<sup>5</sup> postulated the production of compression waves of increasing strength which emanate from the burning zone. These

waves converge at a point, forming a shock which causes an increase in temperature, leading to chemical reaction and the initiation of detonation.

In studies of granular HMX, Campbell<sup>6</sup> tested the importance of convective burning in the run-up to detonation. His results from experiments in which gas-impermeable disks were inserted into the column of explosive to prevent the penetration of hot gaseous products ahead of the combustion wave, showed that convective combustion was only important during the initial stages of deflagration. As the pressure in the porous bed rises, intrusion of hot gases into the bed becomes increasingly impeded due to compaction. Eventually the bed compacts to such an extent that an impermeable 'plug' is formed. The plug is propelled downstream by the gaseous reaction products forming a compaction wave at the leading edge of the plug, which increases in strength as stress waves of a higher pressure originating from the accelerating combustion wave overtake it.

This experimental work was continued by McAfee et al.<sup>7</sup> and led to the formulation of a more detailed description of the DDT process which also seems consistent with previous observations. In this model, the pressure rise at the initial deflagration front sends a compaction wave into the unreacted material which initiates reaction by friction and shear between explosive grains. The combustion products do not readily permeate the compacted material and so a well-defined deflagration

wave follows the compaction wave, accelerating as the pressure rises with the extent of the reaction and so propagating increasingly strong stress waves which coalesce further along the column and further compact the bed to nearly 100% of the theoretical maximum density (TMD). The downstream boundary of this fully compacted region is a shock wave supported by the upstream boundary which behaves as a piston, and this shock wave accelerates slowly until the deflagration wave overtakes the upstream boundary, accelerating the piston and causing more rapid acceleration of the shock wave until it exceeds the critical shock initiation pressure of the compacted explosive.

This model is consistent with the observed data and differs from most previous models in that convective combustion plays little part in the process, other than affecting the rate of reaction and hence pressure rise in the initial stages.

## CP

The granulated explosive chosen for this study was 2-(5-cyanotetrazolato) pentammine cobalt (III) perchlorate or 'CP'. This explosive has been shown<sup>8</sup> to be highly reactive with growth to detonation occurring after only a few millimetres from the point of ignition, which is due to CP being able to undergo DDT at low pressures. This makes CP ideally suited to small-scale laboratory investigation. CP is a yellow free-flowing crystalline material with crystal density  $1.97 \text{ g cm}^{-3}$ . Baer et al.<sup>8</sup> reported the average particle diameter to be of the order of  $140 \text{ }\mu\text{m}$ , but that under the action of pressing the particles would easily fragment, resulting in an average particle size of  $10\text{--}15 \text{ }\mu\text{m}$ . The chemical structure of CP is more closely related to that of many inorganic primary explosives, such as mercuric-5-nitrotetrazole, than to most secondary explosives which are generally organic CHNO compounds.

Much work has been carried out on the possibility of replacing primary explosives in detonators by CP.<sup>9-14</sup> Leslie et al.<sup>9</sup> found that CP will undergo DDT following low-voltage hot-wire ignition, and that in terms of safety could replace materials such as lead azide. The recognition of CP as a potential replacement for primary explosives has led to the investigation of the burning characteristics of related cobalt coordination compounds. Lieberman and Fleming<sup>15</sup> compared the performances of fifteen complexes, mainly amine ligand coordinated with perchlorate anions, by loading them into a standard detonator and measuring the projection velocity of the end plate. The velocities were measured using the Velocity Interferometer System for Any Reflector (VISAR), this data being supplemented with

data from x-radiographs of the fired charge holders. The results obtained indicated that although a good oxygen balance in the complex was important to achieve the velocity jumps associated with detonation, it was the presence of a trigger group such as an azido or tetrazolato ligand which was the greatest determining factor affecting the detonability of the complexes.

Unfortunately, due to the toxicity of CP, its production has been discontinued.

## EXPERIMENTAL

High-speed photography was used to record the reaction of thermally initiated columns of CP. The confinement normally used for DDT studies is metallic, which does not permit direct photographic study, although some workers<sup>16,17</sup> have employed fibre-optic probes to follow the reaction zone in beds of energetic material. The confinement material chosen here was polycarbonate, which, although having a lower yield strength than metals, is strong enough to permit DDT to occur in CP and has the advantage of allowing direct visual observation of the reaction.

Figure 1 shows the construction of the test-pieces. A fibre-optic probe was positioned at the ignition end of the CP column so that light emitted from the initial stages of deflagration would be transmitted to the triggering system to trigger the camera. The acceptance angle of the fibre-optic could be reduced to prevent premature triggering by lengthening the fibre sleeving at the end of the fibre. The external surface of the test-piece was polished to improve the optical finish, allowing better definition in the photographic record.

The explosive column was prepared by pressing the CP incrementally. The height of each increment was less than the diameter of the channel in order to ensure a consistent pressed density. Stepped density columns were also prepared in order to investigate the effect on run-to-detonation lengths when the deflagration moves from a higher density pressing to a lower density. It was thought that the production of a shock wave at the density discontinuity might result in the reduction of the run-to-detonation length of the lower density section.

Ignition of the CP column was attained thermally with a virtually gasless pyrotechnic mixture of boron and potassium dichromate in a finely divided state. This avoided any pre-pressurisation of the explosive column which would complicate the interpretation of the initial CP deflagration. Emission of light from the pyrotechnic, which might otherwise

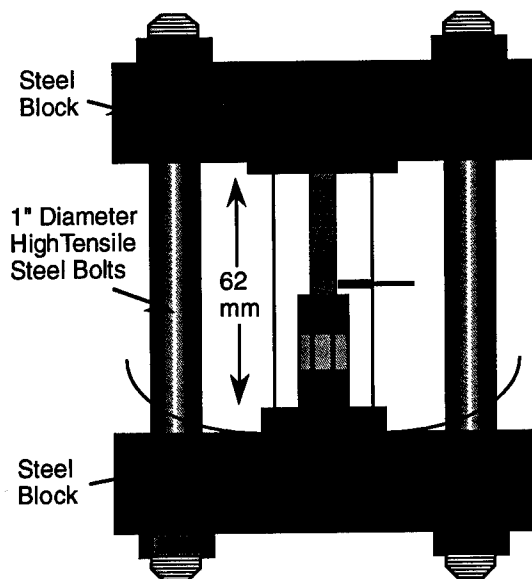


FIGURE 2. CLAMP FOR TEST-PIECE PROVIDING LONGITUDINAL CONFINEMENT

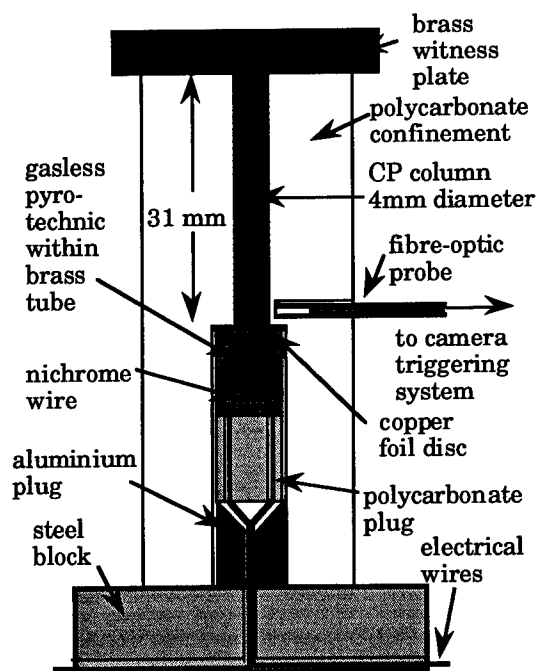


FIGURE 1. TEST-PIECE ARRANGEMENT

prematurely trigger the camera, was prevented by pressing the pyrotechnic into a brass sleeve and separating it from the CP by a 0.025 mm thick copper disk. At the end of the CP column, a brass witness plate was positioned to give an indication of the occurrence of detonation. Figure 2 shows the clamping system used to provide longitudinal confinement. The test-piece was held between the two heavy steel blocks by firmly tightening the connecting bolts, thus preventing rear-venting. The test-piece was then placed inside a vented firing-box fitted with polycarbonate windows to allow photography and to protect the camera and surroundings from fragments.

The charge was fired by passing a current through the bridge-wire in the pyrotechnic. The fibre-optic was coupled through a fast light detector to a delay generator. When the output voltage from the light detector exceeded a preset threshold value, the camera was triggered after a delay depending upon the initial burning characteristics of the explosive column. The Imacon 790 streak speed was calibrated after each firing by feeding a modulating signal of known frequency to the camera's y-deflection plates and photographing an illuminated card at the streak speed used.

## RESULTS

The CP was examined by scanning electron microscopy to determine the particle size distribution. The particles, which ranged in size from 20 to 200  $\mu\text{m}$ , appeared to consist of loosely-bonded clusters of smaller octahedral crystals in the range 5 – 20  $\mu\text{m}$ . Examination of pressed samples showed that these clusters usually disintegrate during the pressing process.

The high-speed streak photographs of the progress of the reaction front through CP were scanned and digitised to facilitate accurate measurement of deflagration and detonation velocities and run-to-detonation lengths. The results of these measurements are shown in figures 3 to 5. The digitised records of position of reaction front with time were also differentiated to give velocity-time profiles.

Figure 3 shows the variation in maximum deflagration velocity reached as a function of %TMD, this velocity either being the deflagration velocity just before DDT, or in the case of those samples which did not undergo DDT, the deflagration velocity at the end of the column. The general trend is that the deflagration velocity at DDT increases with pressed density.

Figure 4 shows the resulting detonation velocities as a function of %TMD; these are in broad agreement with values found by earlier workers.<sup>8</sup> The detonation velocities above about 75 %TMD were obtained by allowing DDT in a lower density column and then letting the detonation run into a higher density pressing.

Figure 5 is a plot of run-to-detonation length

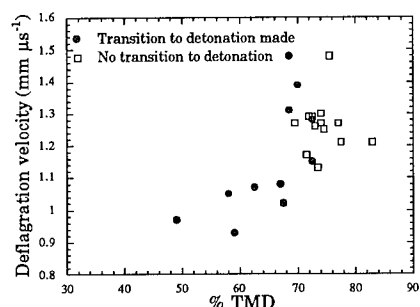


FIGURE 3. DEFLAGRATION VELOCITY VERSUS %TMD

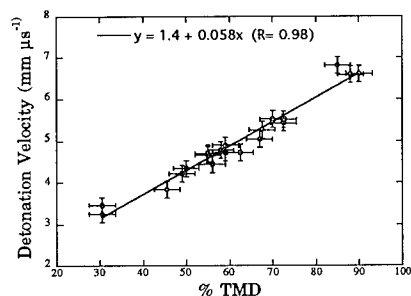


FIGURE 4. DETONATION VELOCITY VERSUS %TMD

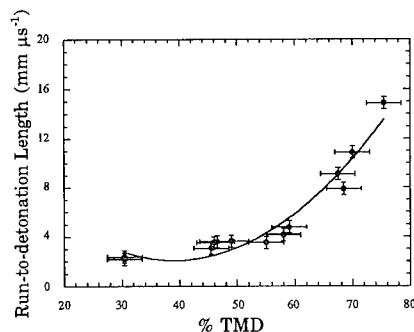


FIGURE 5. RUN-TO-DETONATION LENGTH VERSUS %TMD

against %TMD, which indicates that this rises with pressed density up to the point at which it exceeds the length of the columns used in these tests. It differs from the commonly observed "U-shaped" plots of many other secondary explosives in that there is no evidence of the run-to-detonation length also increasing at lower densities.

Run-to-detonation lengths for the stepped density columns were not significantly different to those for uniform pressings, indicating that shock wave formation at density discontinuities have little effect on the DDT process in this situation.

Figures 6 to 9 show streak photographs together with their corresponding velocity-time and distance-time profiles. Figure 6 shows DDT in a column pressed to 67 %TMD which exhibits a run-to-detonation length of 12 mm and an accelerating deflagration which increases to  $1.5 \text{ mm } \mu\text{s}^{-1}$  immediately prior to DDT. The velocity and distance profile with time for this streak record can be seen in figure 7.

Figure 8 shows DDT in a column pressed to 58%TMD; there is a 6 mm run-to-detonation length and an apparently constant deflagration velocity of  $1.1 \text{ mm } \mu\text{s}^{-1}$  (labelled A) which increases to  $1.5 \text{ mm } \mu\text{s}^{-1}$  immediately prior to DDT (labelled B). At DDT, the change in velocity appears to be discontinuous, with an initial detonation velocity of  $6.0$  to  $6.5 \text{ mm } \mu\text{s}^{-1}$  (labelled C) which is maintained for 2 to 3 mm, before decreasing to a stable value of  $5.5$  to  $6.0 \text{ mm } \mu\text{s}^{-1}$  (labelled D). A low velocity shock wave is visible moving upstream from the point of DDT at a velocity of about  $1.7 \text{ mm } \mu\text{s}^{-1}$ . This velocity does not appear to depend on either the velocity of the preceding deflagration or the subsequent detonation. Figure 9 shows the corresponding velocity and distance profiles at this density.

At higher densities, columns of CP frequently exhibited long induction times from ignition of the end of the column to propagation of a deflagration wave. This type of burning can be seen in figure 10 (labelled E). Figure 11 shows an initial deflagration velocity of the order of  $0.6$ – $0.8 \text{ mm } \mu\text{s}^{-1}$  (labelled F), followed after a few millimetres by an increase to  $1.0$ – $1.2 \text{ mm } \mu\text{s}^{-1}$ . As in many of the streak photographs of reaction in high density CP columns, two light-emitting waves can be seen here (labelled G), the second wave initially travelling  $0.3 \text{ mm } \mu\text{s}^{-1}$  slower than the first.

Some streak records, particularly of samples pressed to higher densities, show an increase in light output just before DDT. Figure 12 is typical of this type of behaviour (labelled H). The two waves are typically  $2.5$  to  $3.0 \text{ mm}$

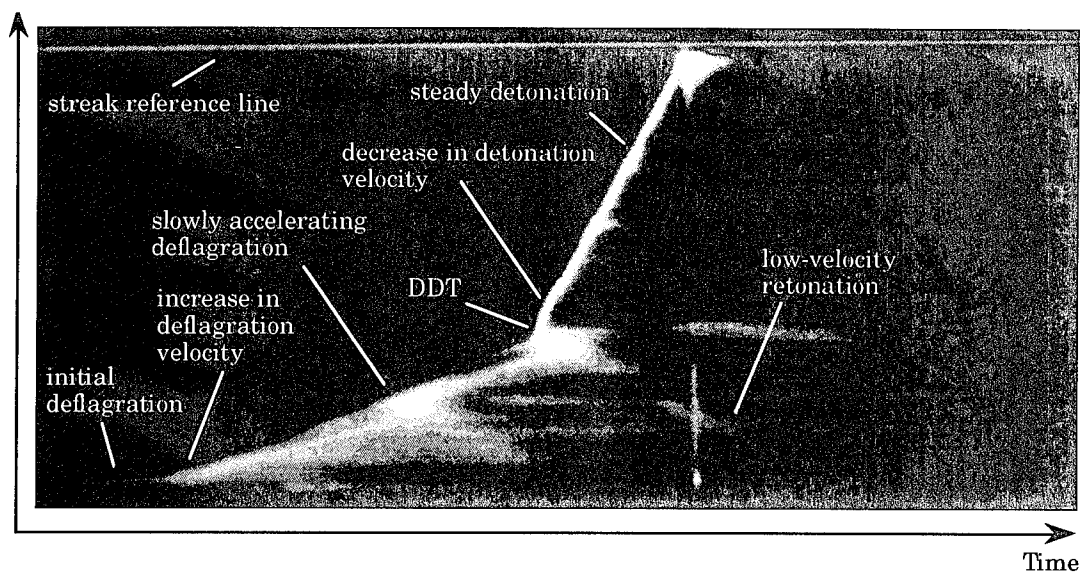


FIGURE 6. STREAK RECORD OF DDT IN 67 %TMD CP

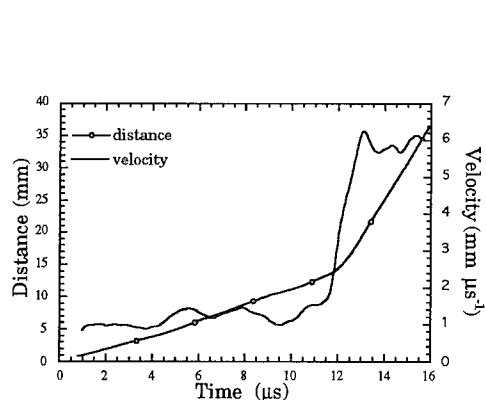


FIGURE 7. BURN FRONT VELOCITY AND DISTANCE VERSUS TIME IN 67 %TMD CP

apart at the start of this light emission which then continues for 2 to 3  $\mu\text{s}$  until the transition. In columns where no DDT occurs, the reaction wave accelerates down the column without emission light.

Occasionally a near vertical line appeared on the photograph at the time when the detonation reached the witness plate, see for example figure 6. This could be due to adiabatic compression of the small air-space at the end of the column causing light emission which is scattered by the decomposition products throughout the column.

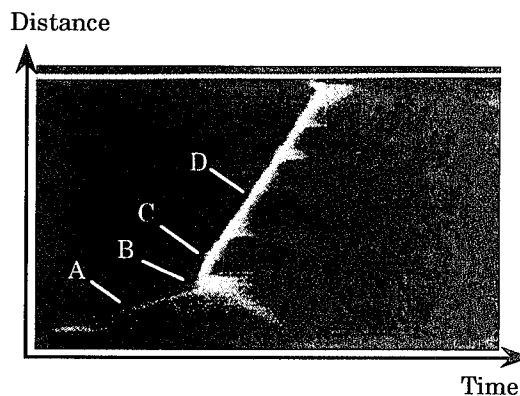


FIGURE 8. STREAK RECORD OF DDT IN 58 %TMD CP

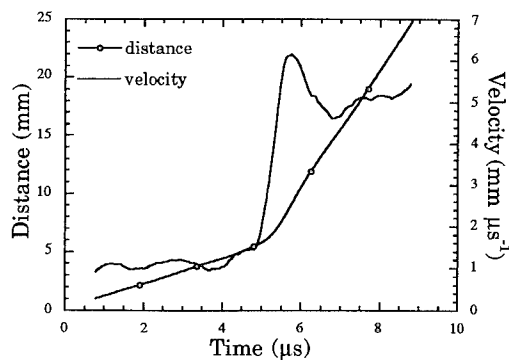


FIGURE 9. BURN VELOCITY AND DISTANCE VERSUS TIME IN 58 %TMD CP

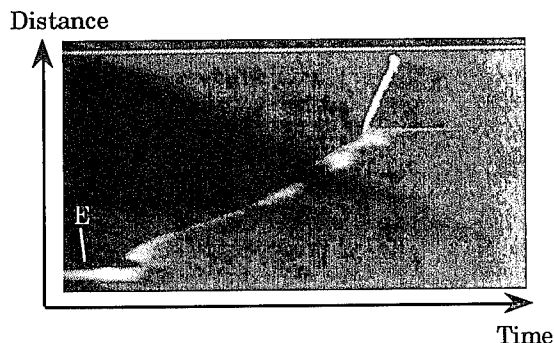


FIGURE 10. STREAK RECORD OF DDT IN 70 %TMD CP

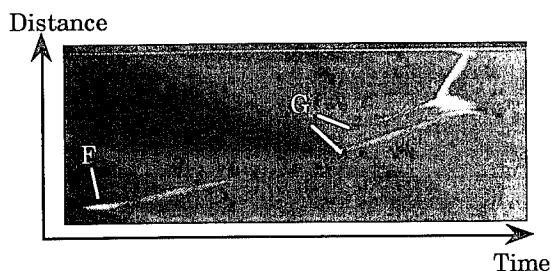


FIGURE 11. STREAK RECORD OF DDT IN 72 %TMD CP

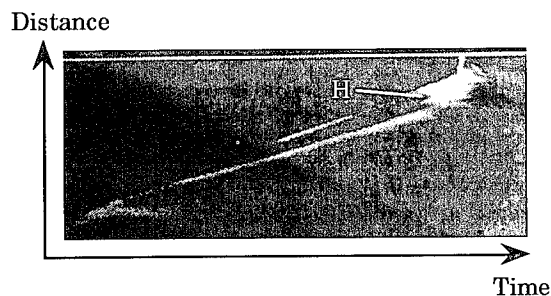


FIGURE 12. STREAK RECORD SHOWING LIGHT EMISSION PRIOR TO DDT IN 74 %TMD

## DISCUSSION

CP will undergo DDT in the confinement dimensions employed only up to ~75 %TMD. At densities greater than this, it is possible that DDT may occur in longer columns. However, this relatively slow attainment of the critical shock initiation pressure could allow the polycarbonate confinement to fail, making DDT unobtainable in columns over a certain length.

Three burning stages, distinguishable by their velocities, can be seen in the streak photographs. The slow initial burning stage is seen, especially at high densities, where long induction times in columns of CP are exhibited,

but is seemingly absent in columns pressed to less than about 55 %TMD. This could be due to increased importance of a conductive burning stage at higher densities, where slow, layer by layer burning precedes the faster convective stage caused by intrusion of hot gaseous reaction products. The light emitted frequently triggered the camera prematurely as the duration of this initial burn was greater than the recording time of the streak camera.

An increase in burning velocity to 0.6-0.8 mm  $\mu\text{s}^{-1}$ , which continues for only a few microseconds, could be attributed to a convective burning stage. The deflagration wave then increases in velocity to 1.0-1.2 mm  $\mu\text{s}^{-1}$  which could be due to compressive burning. In low density pressings, the run-to-detonation length is relatively short and the deflagration velocity appears to be constant. In higher density columns the deflagration accelerates to the point of DDT, or to the end of the charge in columns not undergoing DDT. There is a pronounced double-wave structure in the streak records of this higher velocity mode of burning. The first wave is followed by a 2-3 mm long region of comparatively lower radiance. The second wave follows with a similar radiance to the first, with light emission continuing for up to 10  $\mu\text{s}$ . The first of the two waves could be a leading compaction front as suggested by Baer et al.<sup>8</sup>, which causes adiabatic compression of air-spaces yielding light emission, or alternatively could be a leading combustion wave which results in only partial decomposition of the CP. This theory was put forward by Ermolaev,<sup>18</sup> who postulated that the first combustion wave which travels through the larger pores of an explosive was followed by a secondary combustion wave which moves through the remaining smaller pores. The emission of light between the two waves immediately prior to DDT is consistent with the model of McAfee et al.<sup>7</sup>, where the coalescence of stress waves between the leading compaction wave and the combustion wave gives rise to shock wave formation. The initial detonation velocity observed in the streak photographs is typically 0.5 to 1.0 mm  $\mu\text{s}^{-1}$  faster than the subsequent velocity. This is also consistent with the model proposed by McAfee et al.<sup>7</sup> in which the detonation wave starts in a pre-compacted region of the explosive and then slows down when it overtakes the compression wave.

The absence of long run-to-detonation lengths at relatively low densities, which contrasts with the results found by Baer et al.<sup>8</sup> could be due to the difference in the ignition method. They utilised a hot-wire igniter whereas the use of a pyrotechnic igniter through a barrier in our study, although virtually gasless, could produce a degree of compaction in the low density pressings.

## CONCLUSIONS

The granular explosive CP exhibited DDT in prepared columns confined within polycarbonate. The run-to-detonation lengths were seen to increase appreciably with pressed density. Above 75 % TMD, no transitions occurred with the standard column dimensions for the test-pieces used. There appears to be no minimum run-to-detonation length for CP, with loose powder columns undergoing DDT after only a few millimetres. In this respect, CP is unlike many other secondary explosives, where run-to-detonation lengths increase at low, as well as high, densities. The streak photographs clearly show the presence of two light-emitting waves. The first may be a leading compressive wave, or a combustion wave which results in only partial decomposition. This double wave structure is most clearly observed in the relatively higher density columns.

## ACKNOWLEDGEMENTS

We thank Sandia National Laboratories for the provision of the CP and to AWE for acquiring the CP for use at the Cavendish. P.E.L. wishes to thank the Science and Engineering Research Council for providing financial support in the form of a Postgraduate Study Award. ICI are thanked for supporting the early stage of this research.

## REFERENCES

- Dixon, H. B. , *Phil. Trans. Roy. Soc. (London)*, 200, (1903), 315 .
- Bone, W. A. , Fraser, R. P. , and Wheeler, W. H. , *Phil. Trans. Roy. Soc. (London)*, A235, (1936), 29.
- Kistiakowsky, G. B. , "Initiation of Detonation of Explosives," *Third Symp. on Combustion, Flame and Explosion Phenomena*, University of Wisconsin, Madison, Wisconsin, 1948, pp.560-565.
- Griffiths, N. and Groocock, J. M. , "The Burning to Detonation of Solid Explosives," *J. Chem. Soc.*, 11, (1960), 4154-4162.
- Gipson, R. W. and Macek, A. , "Flame Fronts and Compression Waves During Transition from Deflagration to Detonation in Solids," *Eighth Symposium (International) on Combustion*, Baltimore, Maryland, (1962) , pp. 847-854.
- Campbell, A. W. , "Deflagration to Detonation Transition in Granular HMX," Los Alamos National Laboratory Document, (1980), LA-UR 80-2016.
- McAfee, J. M. , Asay, B. W. and Campbell, A. W. , "Deflagration to Detonation in Granular HMX," *Ninth Symp. (International) on Detonation*, Portland, Oregon, Vol. 1, (1989), 265.
- Baer, M. R. , Gross, R. J. , Nunziato, J. W. and Igel, E. A. , "An Experimental and Theoretical Study of Deflagration to Detonation Transition (DDT) in the Granular Explosive, CP," *Combust. Flame*, 65(1), (1986), 15-30.
- Leslie, W. B. Dietzel, R. W. and Searcy, J. Q. , "A New Explosive for Low Voltage Detonator Applications," *Sixth Symp. (International) on Detonation*, Coronado, Ca. , (1976), 455-459.
- Ewick, D. W. , "Header Effects on the Hot-Wire Ignition Characteristics of a CP DDT Detonator," *Proc. Int. Pyrotech. Semin.* , 8th, (1982), 206-213.
- Lieberman, M. L. , "CP DDT Detonators (II): Output Characterisation," *Proc. Symp. Explos. Pyrotech.* , 12th, (1984), 3/105-3/112.
- Lieberman, M. L. , Begeal, D. R. , Durand, N. A. and Fleming, W. , "CP DDT Detonators (III): Powder Column Effects," *Proc. Int. Pyrotech. Semin.* , 9th, (1984), 371-392.
- Lieberman, M. L. , Hughes, R. L. and Heames, L. E. , "CP DDT Detonators (V): Output Performance and Analysis of Multiple-Out Devices," *Proc. Int. Pyrotech. Semin.* 11, (1986), 767-788.
- Kopczewski, M. R. and Weinmaster, R. R. , "Percussion Primer / DDT Detonator," *Proc. Int. Pyrotech. Semin.* , 11, (1986), 751-766.
- Lieberman, M. L. and Fleming, W. , "DDT Performance of Energetic Cobalt Coordination Compounds," *Proc. Int. Pyrotech. Semin.* , 11, (1986), 721-735.
- Demissy, M. and Michot, C. , *Proc. Int. Pyrotech. Semin.* , 13th, (1988), pp. 163-171.
- Dickson, P. M. , Field, J. E. and Luebcke, P. E. , "Experimental Investigation into Deflagration to Detonation Transition in Secondary Explosives," Cavendish Report, Cavendish Laboratory, Cambridge, December 1991.
- Ermolaev, B. S. , Sulimov, A. A. , Okunev, V. A. and Khrapovskii, V. E. , *Fiz. Goreniya Vzryva*, 24, No. 1, (1988), pp. 65-68.



# **Experimental Investigation into the Deflagration-to-Detonation Transition in Secondary explosives.**

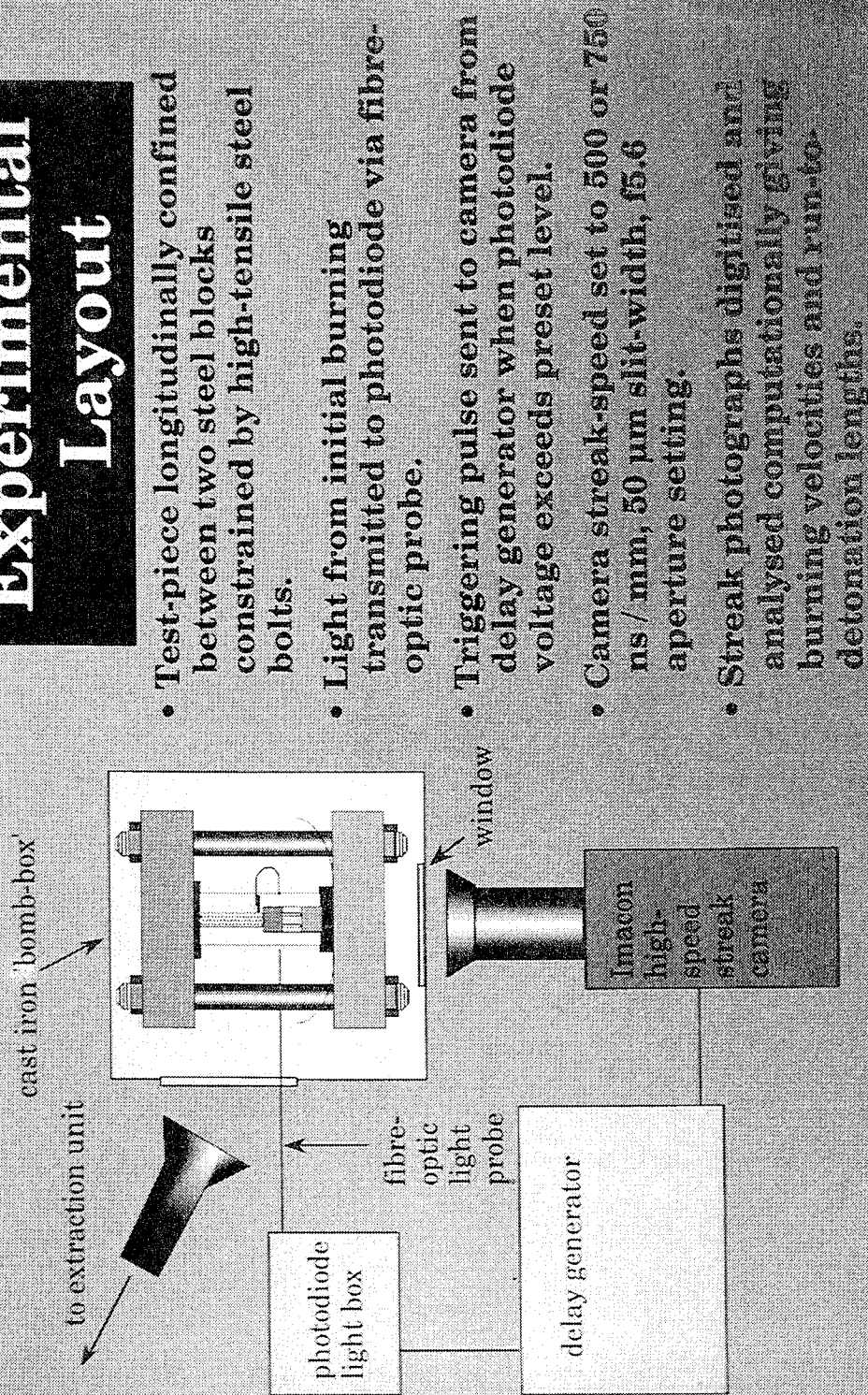
**Cavendish Laboratory,  
Madingley Road,  
Cambridge, CB3 0HE,  
United Kingdom.**

**P.E.Luebcke, P.M.Dickson and J.E.Field**

# Abstract

Deflagration-to-detonation transition has been studied in prepared columns of granular secondary explosive. The secondary explosive 2-(5-cyanotetrazolato) pentammine cobalt (III) perchlorate or 'CP' was chosen for the study due to its known propensity to undergo DDT within a few millimetres of ignition. Confinement within polycarbonate allowed direct high-speed streak photography of the event. Deflagration and detonation velocities and the run-to-detonation lengths were measured with variation of charge pressed density. Ignition of the CP column was attained thermally through a barrier with a gasless pyrotechnic. Deflagration and detonation velocities were seen to depend strongly upon pressed density. There appeared to be a maximum density conducive to DDT but no minimum with this explosive.

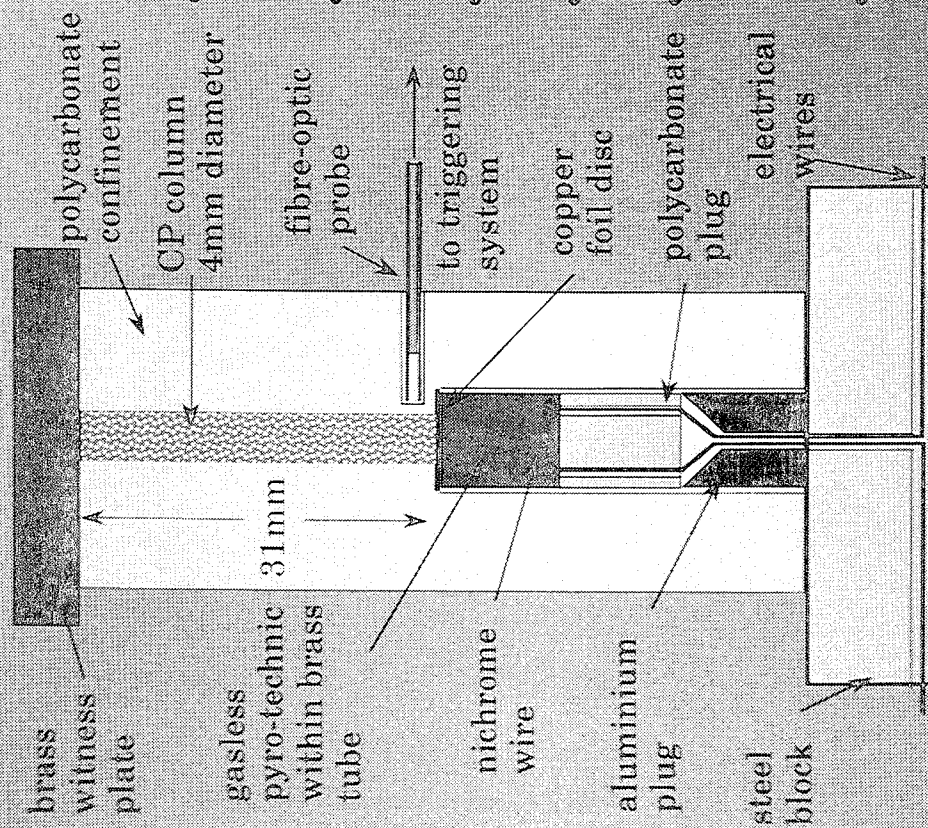
# Experimental Layout



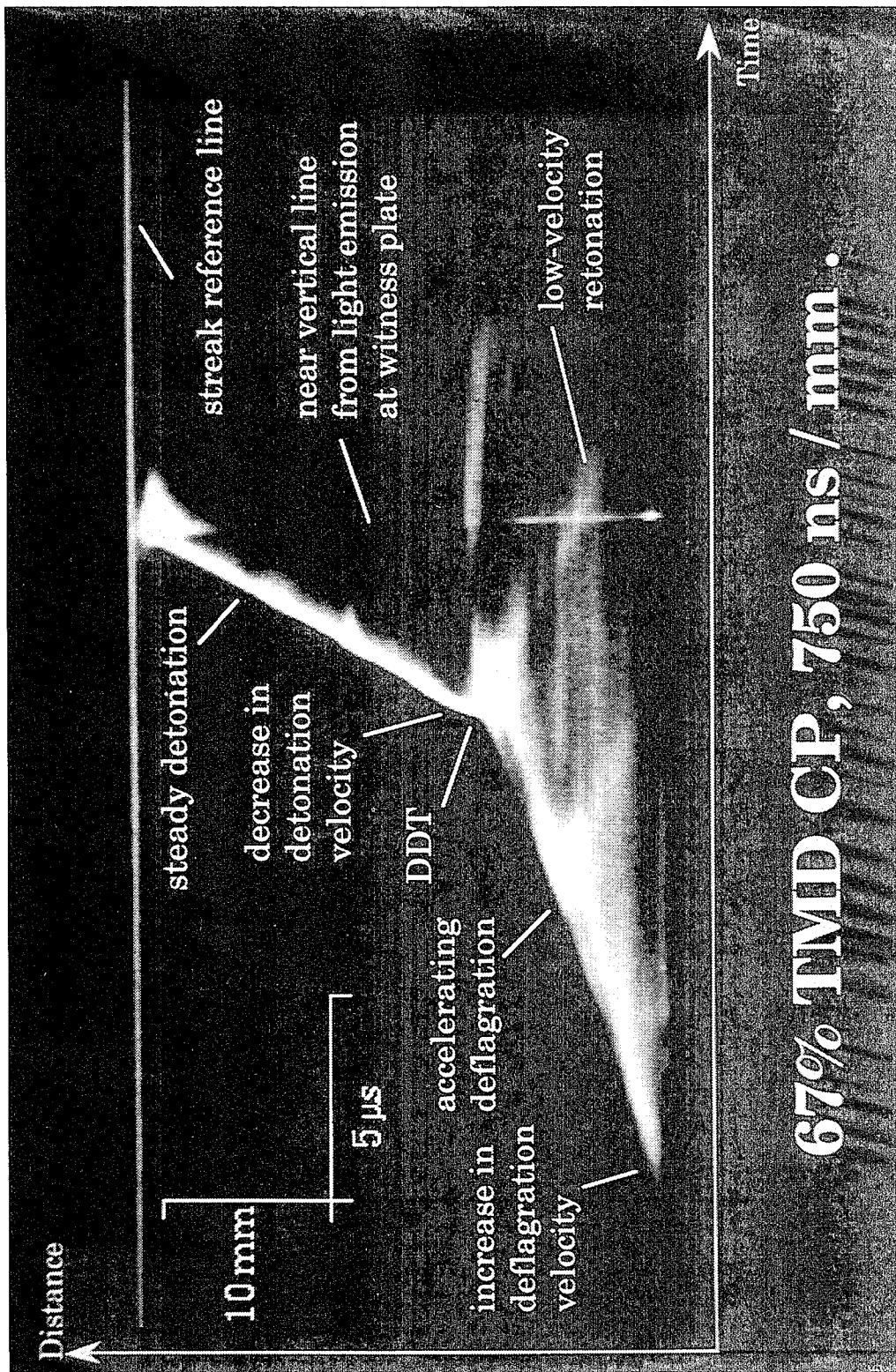
- Test-piece longitudinally confined between two steel blocks constrained by high-tensile steel bolts.
- Light from initial burning transmitted to photodiode via fibre-optic probe.
- Triggering pulse sent to camera from delay generator when photodiode voltage exceeds preset level.
- Camera streak speed set to 500 or 750 ns / mm, 50  $\mu$ m slit-width, f5.6 aperture setting.
- Streak photographs digitised and analysed computationally giving burning velocities and run-to-detonation lengths.

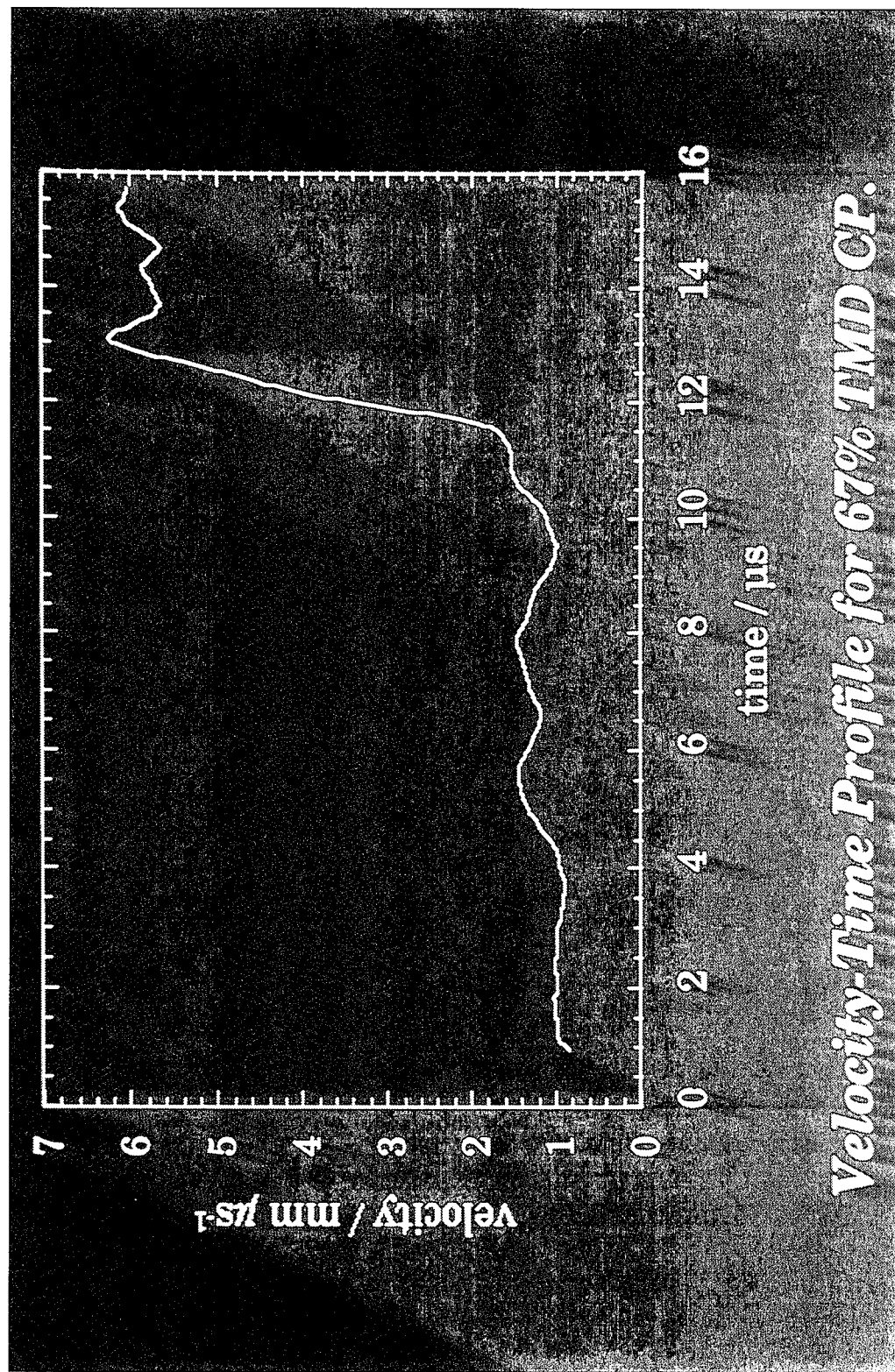


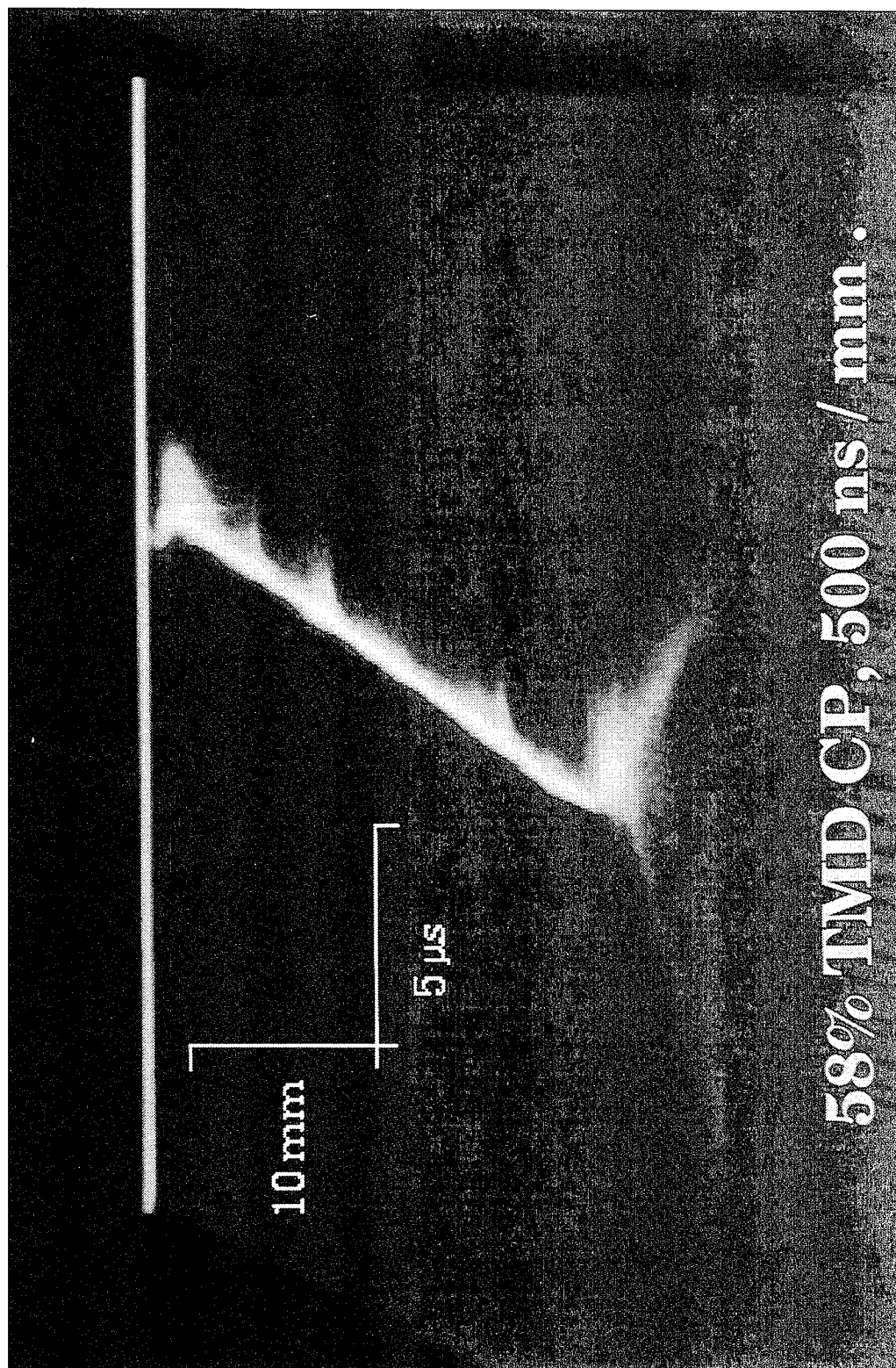
# Test-piece System



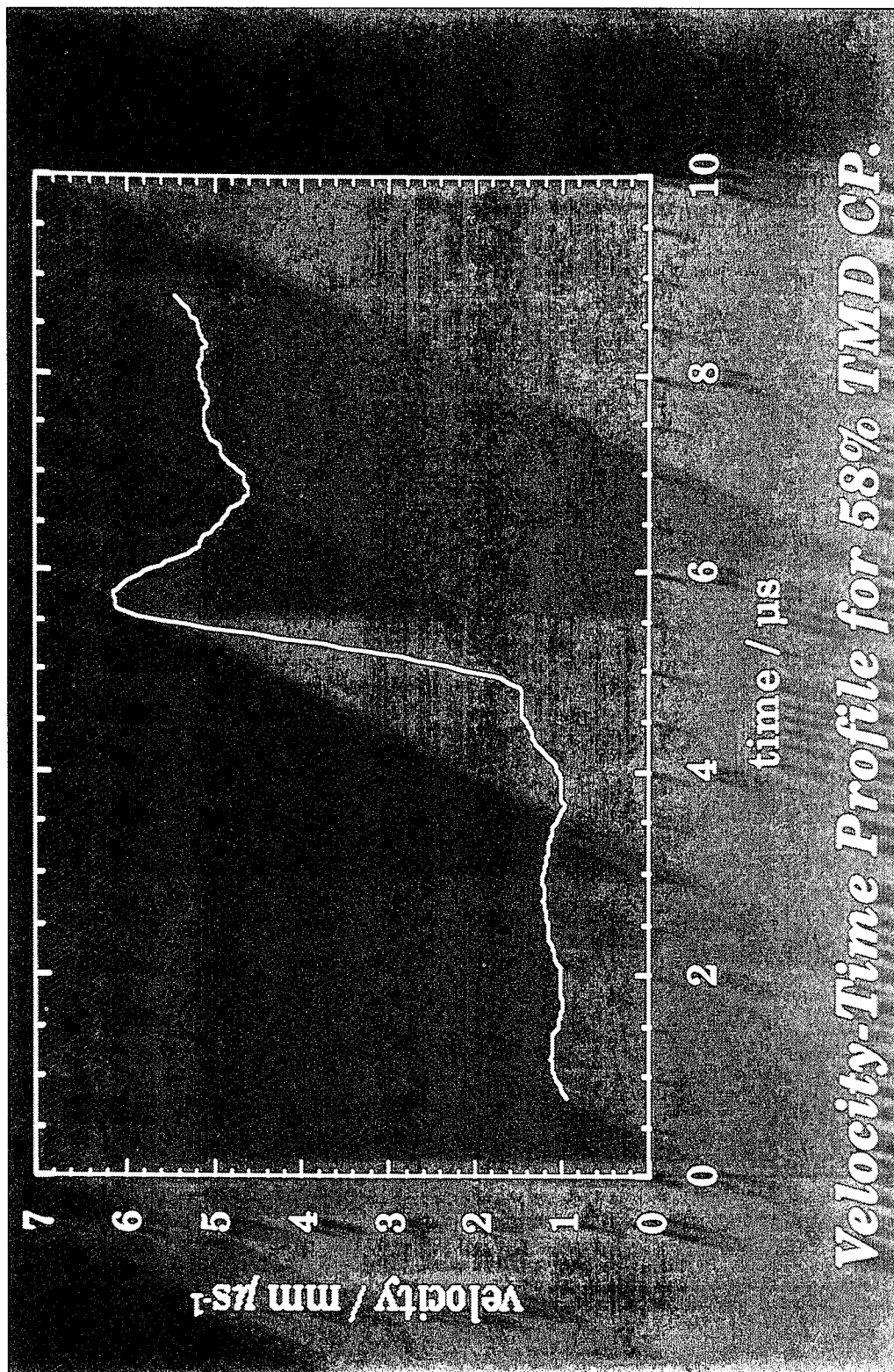
- CP confined within 25mm diameter polycarbonate confinement.
- 4mm Diameter explosive column prepared by incrementally pressing to a known density.
- explosive ignited by potassium dichromate / boron pyrotechnic.
- Fibre-optic probe positioned at the start of the CP column.
- Rear confinement maintained by incorporating a 'self-sealing' polycarbonate and aluminium coned plug system.
- Brass witness plate gives an additional indication as to the occurrence of DDT.



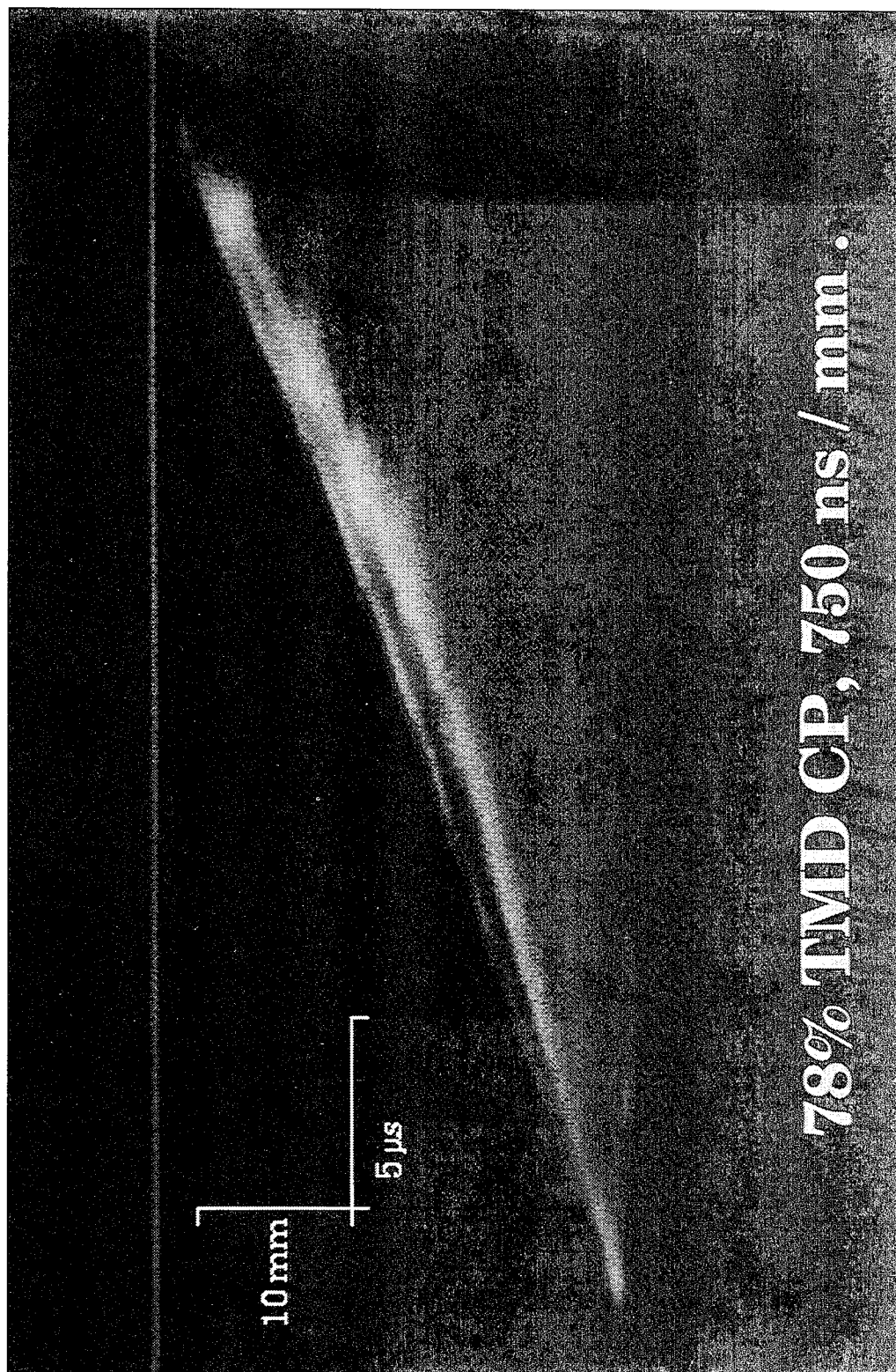


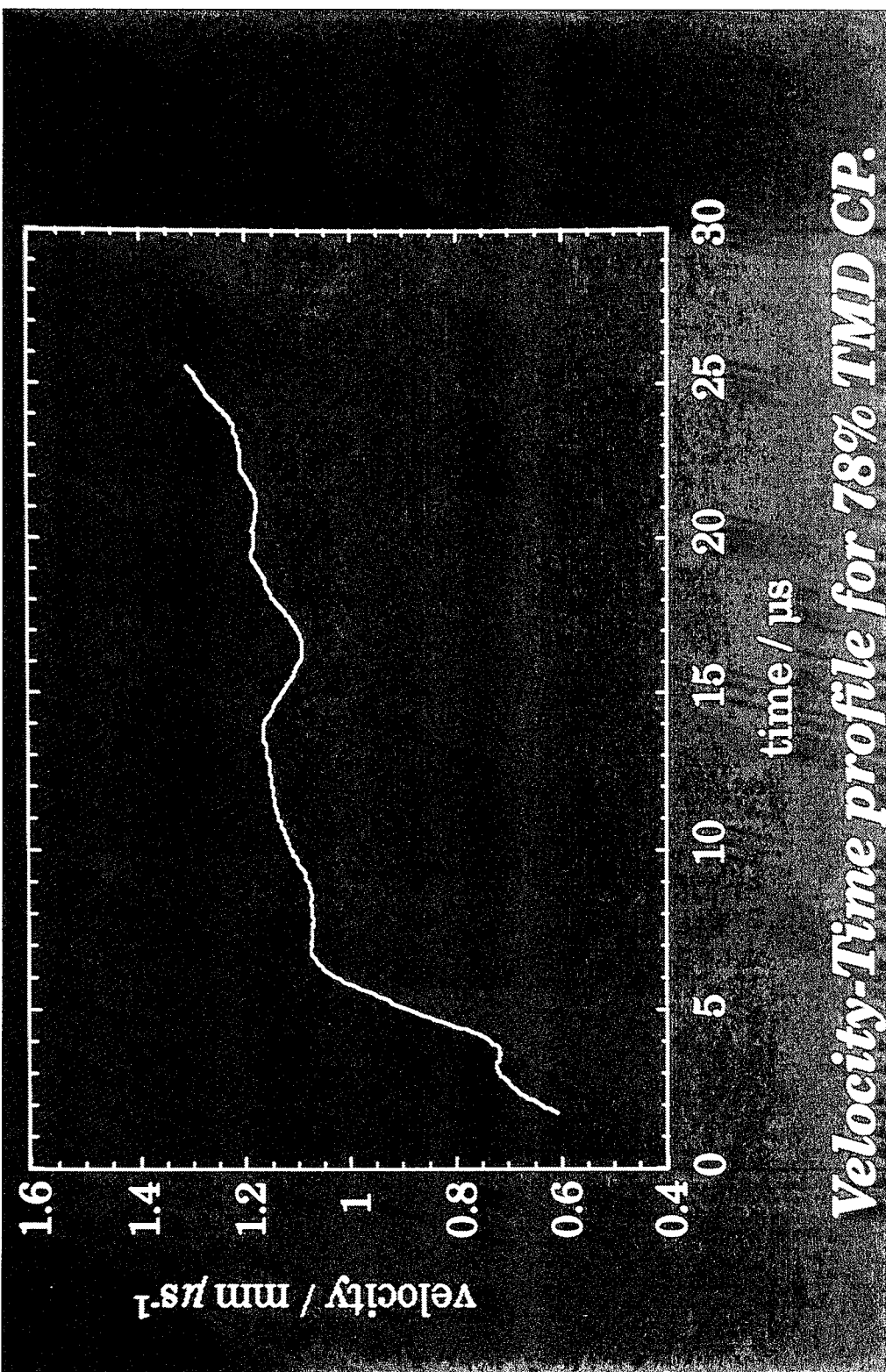


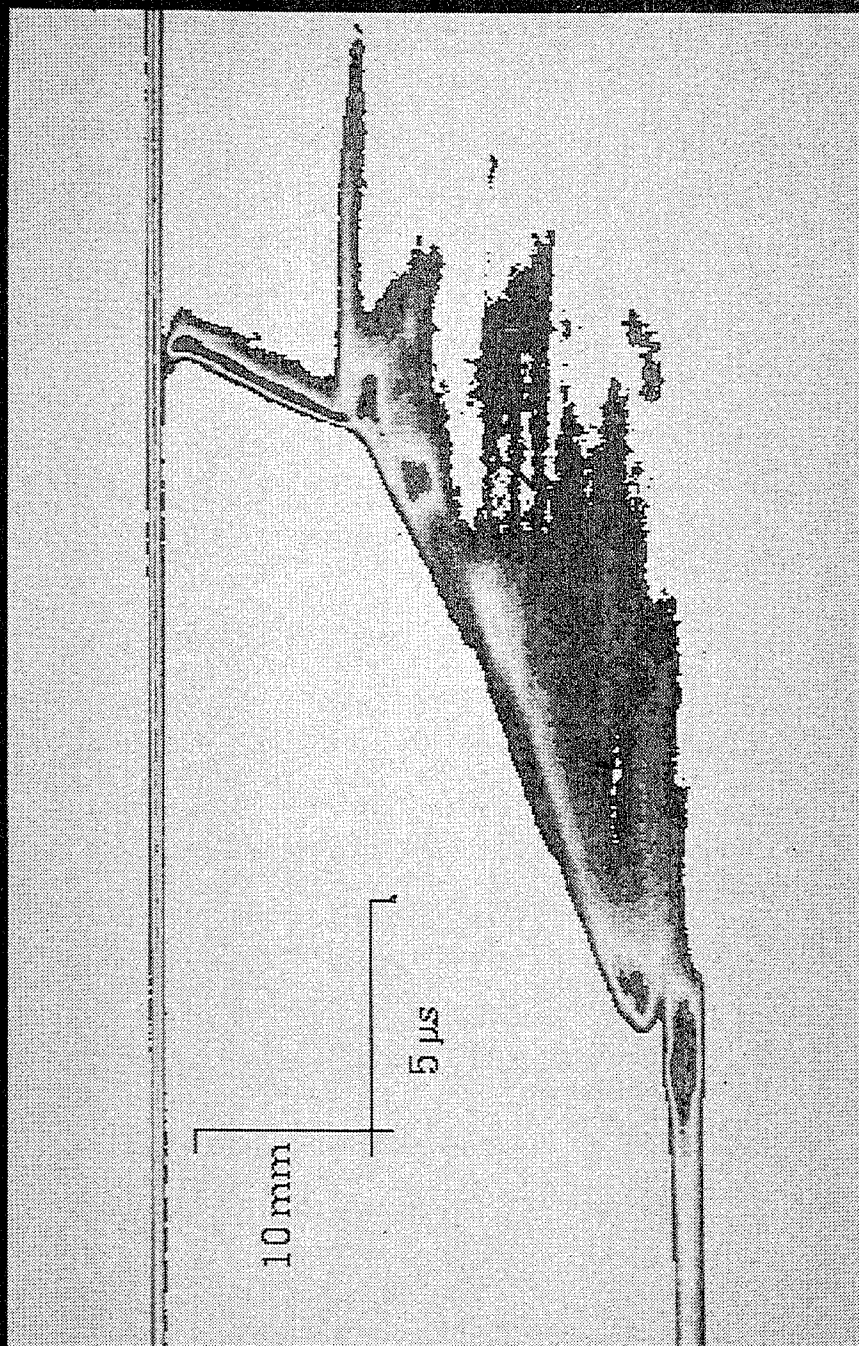




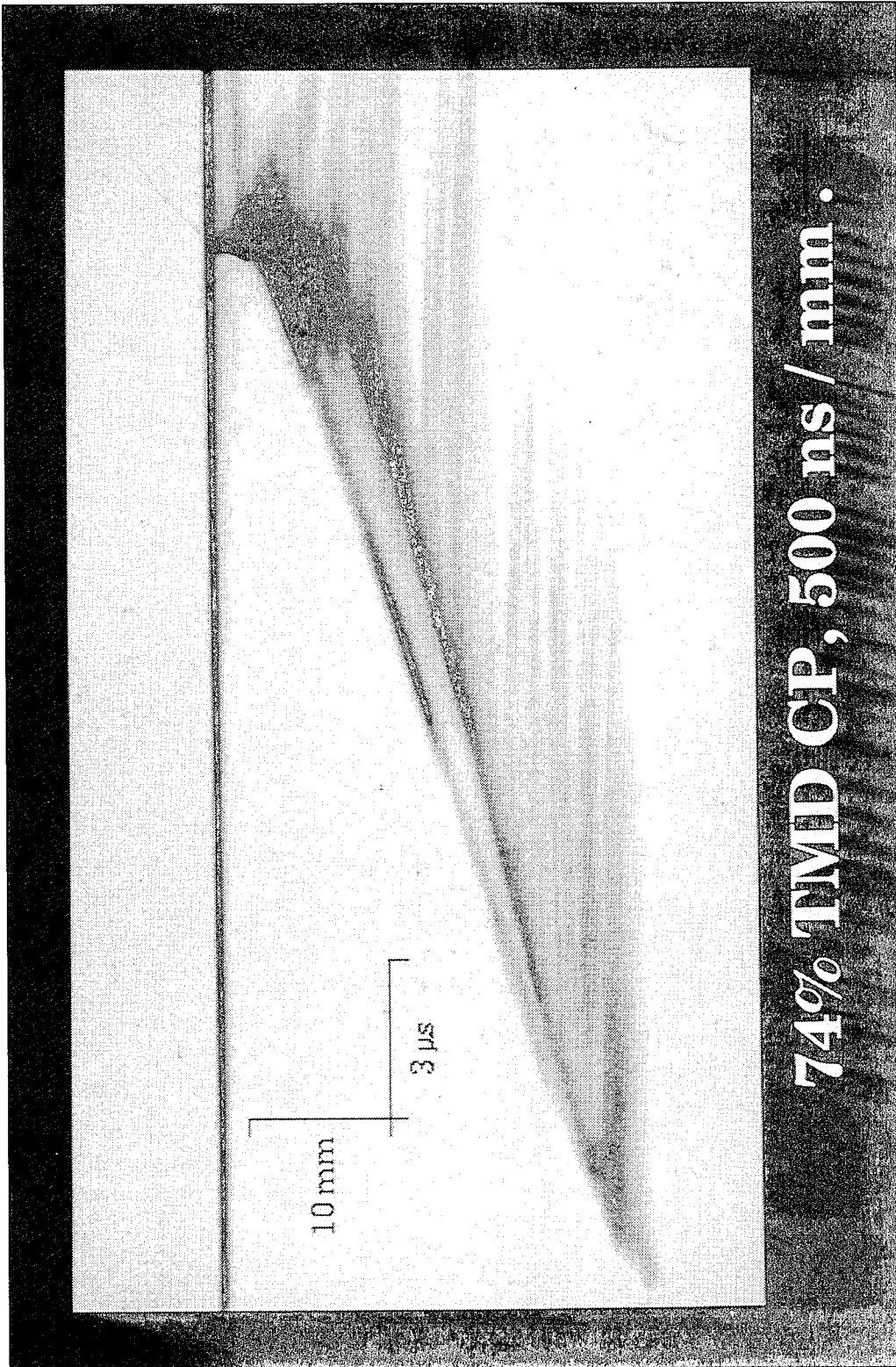


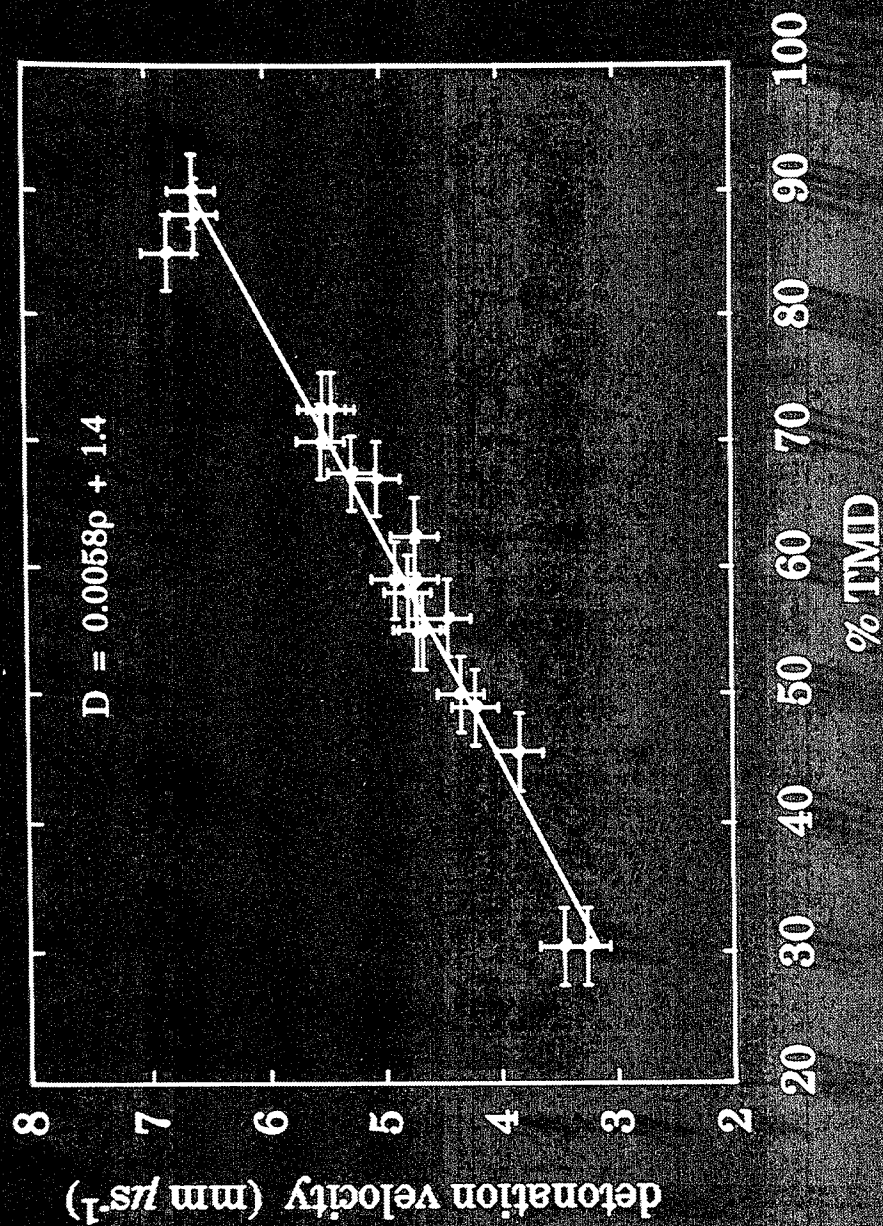






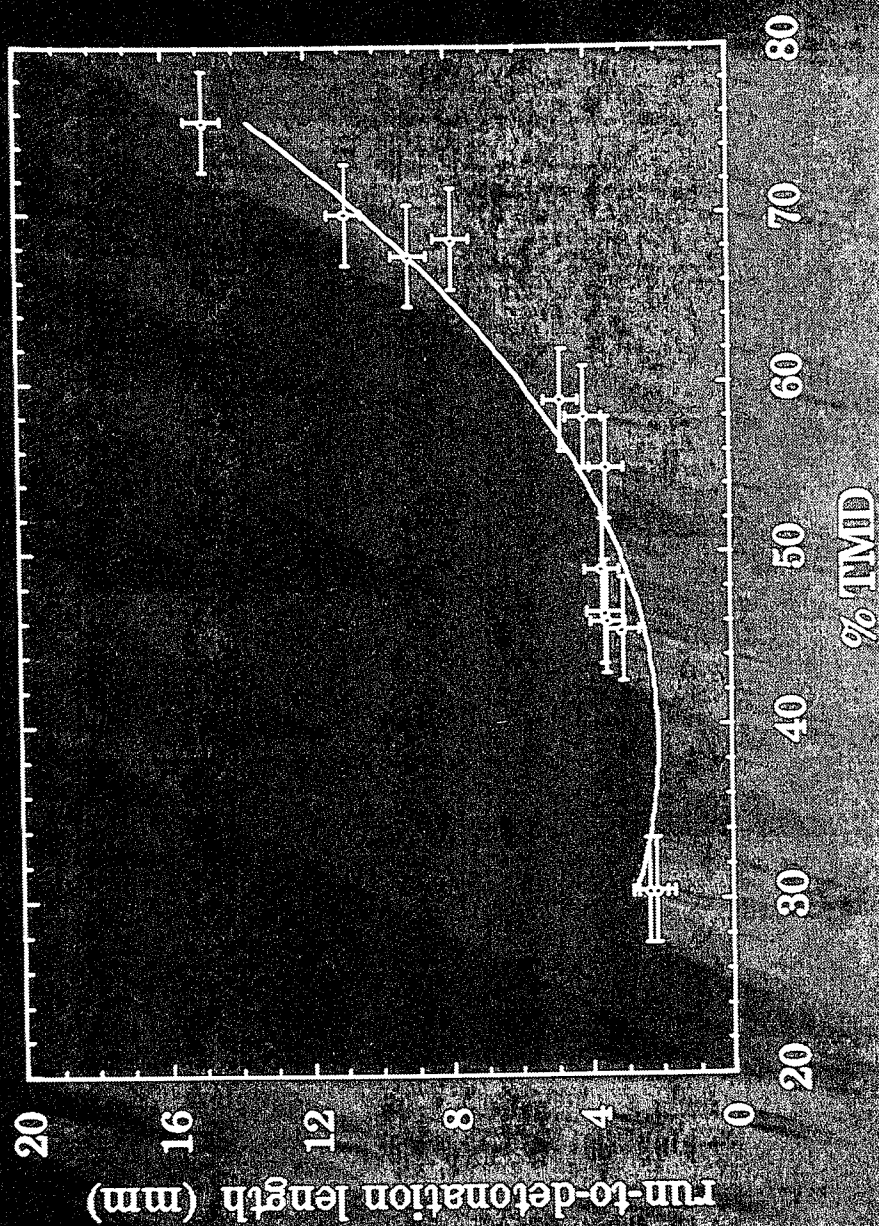
**70% TMD CP, 750 ns / mm .**





*Detonation velocity versus density in CP.*





*Run-to detonation length versus density in CP.*

- Detonation velocities varied linearly with density for CP.
- Initial lower velocity modes of burning during deflagration appear to be more prevalent at higher densities and are seemingly absent in relatively low density pressings.
- Detonation velocities are seen to slow to a steady value after the first 3-4 mm following DDT.
- Deflagrations in higher density pressings accelerate to the point of DDT.
- Increased light emission prior to DDT can be seen in many of the streak photographs of higher density CP columns.

## Conclusions

- The experimental arrangement allowed direct high-speed photography of DDT occurring in CP up to a maximum density.
- There appeared to be no minimum run-to-detonation length for CP with this experimental set-up. This could be due to the ignition method.
- Run-to-detonation lengths for stepped density columns were not found to vary significantly from those of single density columns. It was anticipated that run-to-detonation lengths would be reduced due to shock formation at a high-to-low density discontinuity.
- During deflagration, the presence of two distinct light-emitting waves, especially at high densities, can be seen in the streak photographs.



**SESSIONS ON**  
**POSTER PAPERS-2**

**Cochairmen:**    **Philip Stanton**  
                         **Sandia National Laboratories**

**Henry Moulard**  
                         **French German Research Institute (ISL)**

## REACTION OF ALUMINIUM AND AMMONIUM NITRATE IN NON-IDEAL HETEROGENEOUS EXPLOSIVES

G.A. Leiper and J. Cooper  
ICI Explosives  
Stevenston, KA20 3LN,  
United Kingdom

The behavior of particulate ammonium nitrate and aluminium in a commercial composite explosive was studied experimentally. The detonation performance of a model formulation, based on a paint grade aluminium sensitised slurry containing large mass fractions of atomised aluminium and crystalline ammonium nitrate (AN), was measured by monitoring the variation of detonation velocity and shock front radius of curvature with charge diameter. The mean particle size of the aluminium and ammonium nitrate was varied over a large range. Changes in detonation performance with varying solid particle sizes were interpreted using a slightly divergent flow detonation model to estimate the heat release rates within the explosive, and the reaction times of the AN and aluminium. Linear surface regression rates for AN crystals were found to be in good agreement with other results in the literature. The ignition delay time of aluminium was found to be dependent on the flame temperature of the explosive, the particle size of the aluminium, and the oxygen content of the reaction products. A turbulent heating model was used to demonstrate that ignition times close to those measured experimentally were achievable in the system.

### INTRODUCTION

Many explosives exhibit a significant variation in steady detonation performance with varying charge diameter, confinement, and ingredient morphology. This variation may be seen experimentally as a pronounced detonation velocity decrement at failure, or as an extended zone of chemical reaction within the explosive, causing deformation to surrounding material to differ from that expected. Explosives displaying such behaviour are generally classed as non-ideal.

Formulations which display non-ideal detonation performance have common characteristics. The chemical and physical structure is heterogeneous on a distance scale comparable to the reaction zone in the explosive. Also the reaction rates of the various components in the explosive may have widely differing values. Typical examples are inter-molecular fuel-oxidiser systems such as air-sensitised civil mining explosives, or nitramine sensitised composite explosives which include metallic fuels and crystalline oxidisers.

One of the most common of metallic fuels is aluminium. As a recently discovered metal, its use in explosives was recorded as early as 1906. The usefulness of aluminium in explosives is the subject of debate since much of the released energy is trapped as sensible heat in solid products, and the energising effect mitigated by a reduction in performance due to production of less working fluid i.e. gaseous species.<sup>1</sup> The behaviour of aluminium in detonations is not well understood, though in combustion studies it has been shown to be governed by thermal transport into the bulk of the sample, giving rise to a characteristic ignition delay before the onset of combustion.<sup>2</sup>

Inorganic oxidisers, such as ammonium nitrate (AN) have a long history of use in explosives as a means of balancing compositions to maximise performance and minimise smoke and noxious fume. Much experimental work has been carried out on the effect of oxidiser particle size and concentration on explosives performance, but little has been done to quantify and understand the measurements made.

In this work a series of closely controlled experiments was performed, wherein various previously determined size distributions of AN and aluminium were added to a slurry explosive sensitised by paint grade (pg) aluminium filled air bubbles. The detonation performance was assessed by measuring the variation of detonation velocity and shock front curvature with charge diameter for unconfined cartridges, between the critical and fifteen times the critical diameter. From the measured performance data, the reaction mechanism and reactivity of each component was ascertained by computational analysis using a non-ideal detonation model.

## EXPERIMENTAL

### Ingredient Preparation and Examination

Particulate AN and aluminium were both prepared by sieving on a motorised vibrator for approximately 1 hour, until the mass of material in each sieve fraction became constant. The sieve fractions were sealed into bottles, which in the case of AN were stored in a warm dry store at a constant temperature of approximately 25°C. The sieve fractions used in this study are detailed in tables 1 and 2.

TABLE 1.  
AN SIEVE FRACTIONS

Designator $\mu\text{m}$	Fraction $\mu\text{m}$
SMAN	10
125	+100-150
364	+300-425
1200	+1000-1400

TABLE 2.  
ALUMINIUM SIEVE FRACTIONS

Designator $\mu\text{m}$	Fraction $\mu\text{m}$
64	+53-75
128	+106-150
256	+212-300
600	+400-800
1100	+1000-1200

In the case of aluminium, all sieve cuts were taken from a single lot of "60 to dust" atomised material. A single examination of each sieve cut was made, measuring chemical purity, surface topography by scanning electron microscopy, and surface area by BET gas absorption.

In the case of AN, several sources of raw material were used. For coarse particle fractions, "ICI Ardeer Run Of Plant" was used, for intermediate fractions "ICI Ardeer Fine Dense"; for fine fractions ball milled "ICI Ardeer Fine Dense" was used. Various samples of each of these were examined as per aluminium over the duration of the project.

The finest grade of AN was prepared by suspension milling in a saturated AN aqueous solution with 0.5% by mass sodium carboxy-methyl-cellulose stabiliser. This "SMAN" grade was examined only by optical microscopy.

### Explosive Formulation and Manufacture

A model explosive was developed from a paint grade aluminium sensitised water gel system. The explosive contained a continuous aqueous phase of guar-thickened saturated AN solution, into which was mixed particulate aluminium and AN crystals. The resulting slurry was aerated by chemical gassing, after which paint grade hydrophobic aluminium flake was introduced into the bubbles by agitation. The guar was subsequently cross-linked using zinc chromate.

Three distinct formulations were used, with varying fractions of continuous aqueous phase, table 3. The formulations were designed such that both the matrix and fillers were oxygen balanced by themselves, giving an overall oxygen balanced system. It should be noted that the flame temperature achieved in the liquid phase of each formulation was somewhat different, due to the varying levels of guar used to control the slurry viscosity. Voidage was controlled by chemical gassing conditions and was held constant at a nominal 30%. In general the standard deviation on density for a batch of 18 charges (3 at each of 6 diameters) was better than 0.02 g/cc.

TABLE 3.  
EXPLOSIVE FORMULATIONS

	F1	F2	F3
AN(1)	22.7	29.25	39.0
AN(s)	39.5	41.0	25.4
Al(pg)	4.0	4.0	4.0
Aluminium	11.0	9.0	9.0
Guar	0.5	1.0	1.5
H <sub>2</sub> O	12.3	15.75	21.1

The explosive was mixed in 3 kg batches and cartridge into right-cylindrical manilla paper shells. The gel viscosity was sufficiently high to prevent segregation of the ingredients before the guar cross-

link was complete. All charges were tested within 3 hours of manufacture to minimise dissolution and re-crystallisation of the AN crystals.

During mixing and storage the temperature of all ingredients and the resulting explosive was controlled to  $25^{\circ}\text{C} \pm 1^{\circ}$ .

### Explosive Testing

Each of the slurry formulations was tested with various sieve cuts of AN and aluminium, and with the AN and aluminium replaced with glass beads of similar dimension.

Detonation velocity was measured by a two point time of flight technique using shock collapsible probes manufactured from 1.3 mm o.d. aluminium tubing and 26 s.w.g. detonator wire. The probes were isolated from each other and from earth by fast response opto-isolators which switched a digital timer of resolution 100 ns. The probes were separated by a fixed distance of 200 mm, the first probe being 6 charge diameters from the initiator, an 8\* detonator. For larger charge diameters, greater than 40 mm, measurements were performed at a remote field test site where VOD determination was by the D'Autriche<sup>3</sup> method. The effect of the presence of collapse tube probes on the detonation velocity in 10 mm diameter cartridges was assessed using streak photography and was found to be negligible.

Typical results for various slurries are presented in figure 1. The results are from single batches of explosive, with each point being an average of three experimental results. The average error for any one datum was  $\pm 100$  m/s.

The radius of curvature of the shock front within the explosive was measured by streak photography using an image converter camera. The charges were of a minimum 6 charge diameters in length and initiated by a large diameter pentolite primer. A carbon black loaded thin PVC film of good shock impedance match to the explosive was placed over the end of the charge to obscure light from the detonation products. During the streak experiments, small holes in this film, on the periphery of the charge, served to delimit the charge boundaries. Several streaks were taken of uncovered charges to confirm that the PVC film had no effect on the results.

Streak photographs were also taken using fibre optic straps, manufactured by mounting plastic fibre into printed circuit board. The technique proved especially useful at large charge diameters, where

simultaneous foam noise suppression could be used.

The streak photographs were digitised manually. An arc was fitted to the data using a least squares fitting routine. Allowance was made for tilt in the detonation wave. Data was only used from the central region of the shock front to avoid possible edge effects. The relationship of shock front radius of curvature to charge diameter is shown in figure 2, in a normalised fashion as described by Kirby and Leiper.<sup>4</sup> Within the resolution of the experiment the particle size of the energising ingredients did not affect shock front curvature.

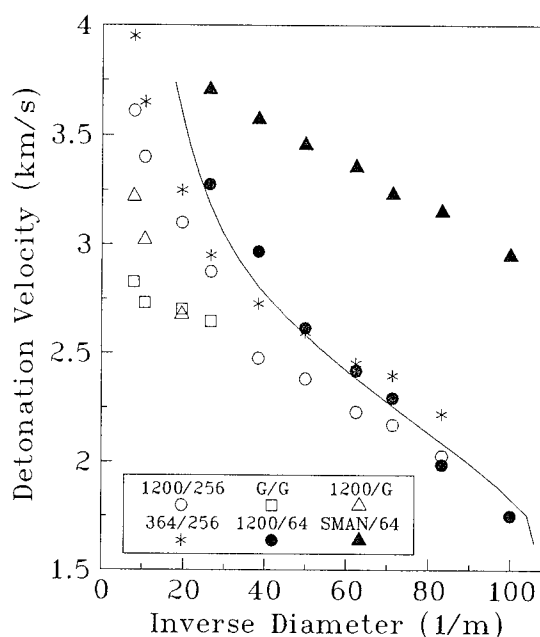


FIGURE 1.  
THE CHARGE DIAMETER EFFECTS

Legend refers to AN and Aluminium sizes respectively, as defined by the designator in tables 1 and 2. The identifier "G" signifies glass beads at 1200  $\mu\text{m}$  and 256  $\mu\text{m}$  replacing AN or Aluminium.

### GENERAL DISCUSSION AND DATA ANALYSIS

Several aspects of the data were unusual. The detonation velocity at failure was very low, less than 40% of the ideal value of 5.55 km/s as calculated by the DTNATE code.<sup>5</sup> However the critical diameter was small  $\approx 10$  mm. Stable propagation occurred at low velocity in small diameters, even for the case of very large particles of AN and aluminium. The failure diameter and velocity were only weak functions of the particle size of the AN and aluminium. All the diame-

ter effect curves were strongly upward concave from the failure point to the ideal value.

The diameter effect curves, viewed in reciprocal diameter space, were well approximated by a linear region extending from the failure point to an intermediate diameter, after which the curve sloped abruptly toward the ideal value. The gradient of the lower linear region was a strong function of the particle size of the aluminium, as was the diameter at which the inflection occurred. Changes to the AN particle size displaced the whole curve to high or lower detonation velocity, without significant alteration to the gradient or inflection point.

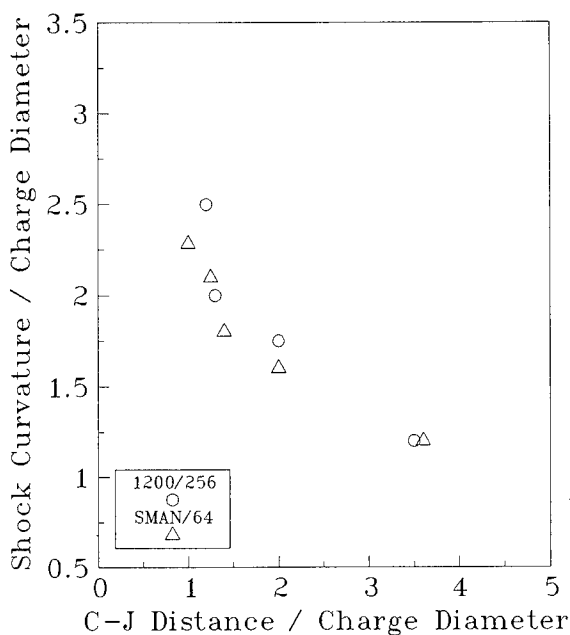


FIGURE 2.  
VARIATION OF SHOCK FRONT CURVATURE

Legend as explained in figure 1.

These results were consistent with the traditional view of the reaction mechanism of AN and aluminium in deflagrating reactions. Reaction of aluminium is controlled by an ignition event, therefore reaction of aluminium only affects the diameter effect curve when the ignition delay time is shorter than the C-J time in the diameter of interest. Reaction of AN is by surface grain burning, and increased reaction due to higher surface areas is apparent in all charge diameters.

When glass beads were used to replace sieve fractions of AN above 1200  $\mu\text{m}$  and aluminium above 256  $\mu\text{m}$ , no change was measured in the diameter

effect curve in the region below 38 mm diameter. In this region, AN and aluminium of those particle sizes could therefore be assumed to be effectively inert.

The data was analysed using a slightly divergent one dimensional detonation model.<sup>4</sup> The model was used to derive the variation of Chapman-Jouguet (C-J) pressure, of extent of chemical energy release at the C-J plane, of C-J distance, and of C-J time, with charge diameter. A typical fit of the theory to the diameter effect curve for 1200  $\mu\text{m}$ /64  $\mu\text{m}$  AN/aluminium is shown in figure 1. In obtaining the fit, the shock front curvature data was used as explained in Kirby and Leiper,<sup>4</sup> and the fit created by manipulation of the kinetic rate constants of the model.<sup>6</sup>

The variation of C-J extent of reaction with C-J time displayed a sigmoid relationship for all systems, figure 3. Close to the failure point (shortest C-J times), the detonation was supported by reaction of only the paint grade aluminium and AN solution in the collapsed voids. As the charge diameter increased, the C-J extent of reaction increased until the detonation was supported by reaction of the collapsed voids and all of the aqueous phase. As charge diameter further increased, the C-J extent of reaction remained approximately constant until the "break" in the charge diameter effect curve was reached. Thereafter the C-J extent of reaction increased with increasing diameter to complete reaction.

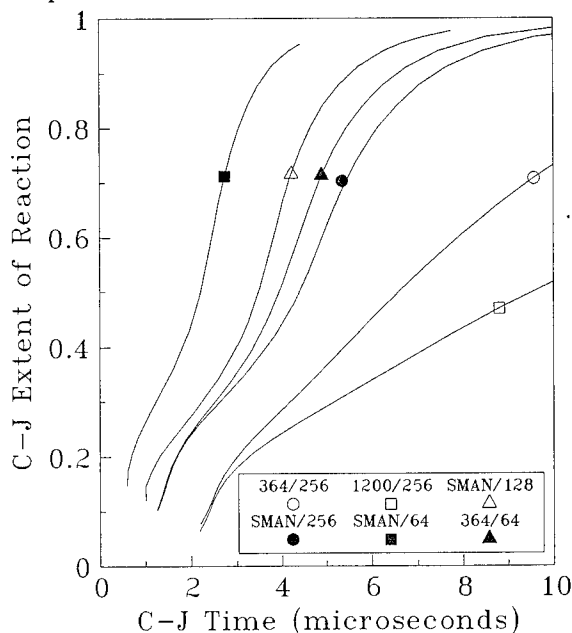


FIGURE 3.  
VARIATION OF C-J REACTION

Legend as explained in figure 1

The effect of the AN and aluminium particle size was visible. A scatter plot of the degree of reaction of each composition in 50 mm diameter charges is shown as a function of AN and aluminium particle size in figure 4. Smaller particles of AN and aluminium increased the overall C-J degree of reaction. There was evidence that for compositions containing the finest AN or aluminium, the particle size effect was enhanced: the reaction rate of AN was increased due to the increase in reaction zone temperature upon reaction of aluminium;<sup>7</sup> and the aluminium ignition delay time was decreased with increased concentration of oxidising moieties in the reaction zone due to increased AN decomposition.<sup>2</sup>

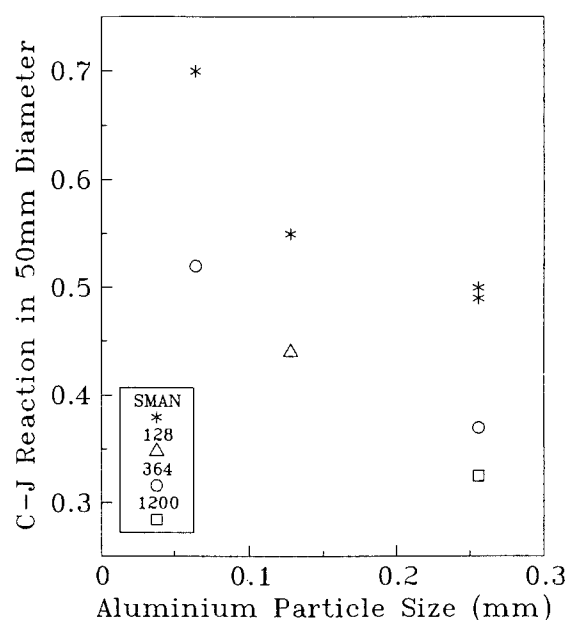


FIGURE 4.  
VARIATION OF REACTION  
IN 50 mm DIAMETER

Legend as explained in figure 1.

Quantitative analysis of the data required a knowledge of the total AN surface area available for reaction. This was not a simple function of the particle size. Particles were agglomerated in the case of the prilled material, and highly fractured in the case of the milled materials. Gas adsorption measurements were therefore used to determine the effective surface area of each AN sieve fraction, table 4.

TABLE 4.  
EXPERIMENTAL SPECIFIC SURFACE AREAS

$\phi$ AN $\mu$ m	SSA (m <sup>2</sup> /g)
128	0.12
364	0.07
1200	0.06

#### REACTION OF AMMONIUM NITRATE

The C-J extent of reaction and reaction time for formulations with differing AN particle sizes were compared at constant aluminium particle size. Based on the increased extent of reaction with increased AN surface area, estimates were made of the amount of crystalline AN consumed within the reaction zone.

These estimates were obtained by using an ideal detonation model, based on the Cook  $\alpha(v)$ <sup>8</sup> equation of state and a Van Zeggeren and Storey<sup>9</sup> chemical equilibrium solver to contour the variation in heat of reaction of the formulations with degree of reaction of AN and aluminium respectively. In the calculations, unreacted material was treated as being in mechanical, but not thermal equilibrium with the detonation products.

The calculations were used to convert the increase in reaction estimated from the experimental data to a corresponding volume of AN consumed. Using the surface area data, the rate of linear surface regression (burn rate) was calculated. The burn rate was found to range between 0.72 and 2.25 m/s, table 5. The rate was enhanced by use of finer grades of aluminium, and in formulations containing lower fractions of liquid phase, that is in compositions where the temperature of the reaction products surrounding the combusting AN would be hotter. There was excellent agreement between data extracted from formulations containing 10  $\mu$ m and 364  $\mu$ m AN particles. The data was also in good agreement with the work of previous authors.<sup>10</sup>

TABLE 5.  
AN COMBUSTION VELOCITIES

$\phi$ AN $\mu$ m	Liquid %	$\phi$ AL $\mu$ m	Vb mm/s
20	60	64	2.25
	60	128	1.56
	60	256	0.72
364	60	64	2.20
	60	128	1.43
	45	256	1.42

## REACTION OF ALUMINIUM

Based on the slightly divergent flow analyses, ignition delay times were estimated for the various particle sizes of aluminium used in the three slurry formulations. The ignition delay time was taken to be the C-J time of the charge diameter at which the inflection was seen in the diameter effect curve. This inflection was found to be associated with an inflection in the variation of C-J extent of reaction with C-J time. It is suggested that the acceleration of the rate after the inflection point was caused by an increase in temperature upon ignition of the aluminium.

As a thermodynamic check, the extent of reaction in the diameter at which ignition was seen, was compared to that obtained from the thermodynamic calculations detailed above. In all cases, ignition was at a degree of reaction obtainable by reaction only of the liquid phase and the crystalline AN.

The ignition time was found to be a strong function of aluminium particle size, AN particle size, and mass fraction of the liquid phase in the explosive, figure 5. The relationship between ignition time,  $\tau$ , and particle diameter,  $\phi$ , was well described by the equation:

$$\tau = a\phi^b \quad (1)$$

Typical values of  $a, b$  were calculated for four compositions, table 6.

TABLE 6.  
FITS TO IGNITION DATA

$\phi$ AN	Formulation	a	b	
1200	F2	-0.70	0.50	+/- 0.02
20	F3	-0.62	0.47	0.03
364	F3	-0.44	0.47	0.03
1200	F3	-0.53	0.52	0.03

Equation 1 has previously been used to describe results from studies of aluminium ignition in low pressure laminar flames.<sup>2</sup> However, the values of the exponents above are substantially below that found previously,  $1 < b < 2$ . It is suggested that the discrepancy may result from the highly turbulent nature of the detonation reaction zone, enhancing thermal and mass transfer to the surface of the igniting particle. Alternatively, it is noted that the temperature history seen by the particle is a function of detonation velocity: larger particles ignite in larger charge diameters and hence at higher detonation velocities. Due to the high voidage in the system, the shock temperature in the liquid phase of the explosive is a strong function of detona-

tion velocity. This is a second possible mechanism which would lead to artificially low exponents in table 6.

The variation of ignition delay with AN particle size, and with mass fraction of liquid can be claimed in terms of changes to the local environment of the igniting particle. Previous studies have shown that the ignition delay time is reduced by increased concentrations of gaseous oxidising species, and higher external temperatures.<sup>2,11</sup>

The flame temperatures of the liquid phases of the three formulations in table 1 were estimated by calculating the overall temperature rise due to shock compression of the porous explosive, followed by adiabatic reaction of the liquid phase. The shock temperature rise was evaluated by integrating along the porous hugoniot calculated after the method of Afanasenkov,<sup>12</sup> using the method of Cowperthwaite and Shaw.<sup>13</sup> The hugoniot excess energy associated with collapse of the pores was redistributed through the liquid phase, assuming a well-stirred system.

For an initial shock pressure of 2 GPa, flame temperatures of 2307 K and 2103 K for the F2 and F3 variants were calculated. At 4 GPa these values rose to 2687 K and 2403 K, respectively. In the detonation experiments, the hotter F2 variant consistently gave smaller ignition delay times.

The decrease in ignition delay time with decreasing AN particle size is believed to be caused by the large increase in the concentration of oxidising species, associated with increased reaction of the finer AN particles.

The coefficients in table 6 were used to estimate the ignition delay of paint-grade aluminium flake (100 nm), which had previously been measured by both optical and electromagnetic particle velocity gauge techniques.<sup>14</sup> Ignition delay times extrapolated from the fits, ranged from 160 ns to 220 ns, in good agreement with the measured value of 200 ns +/- 20 ns.

In order to further understand the results, a model of a spherical particle heated by a finite volume of a well-stirred fluid,<sup>15</sup> was used to examine the thermal history of the aluminium particles. The internal temperature fields of 64  $\mu$ m, 128  $\mu$ m and 256  $\mu$ m particles were calculated at times corresponding to the experimentally determined ignition delay, figure 6. At the ignition point, the surface region is well above the softening point of aluminium oxide,  $\approx 1750$  K,<sup>16</sup> the thermal gradient close to the surface is low, and the melting front has progressed a significant distance into

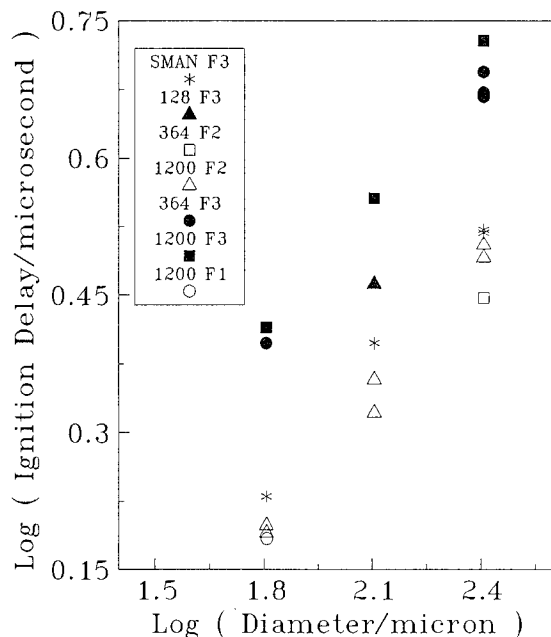


FIGURE 5  
ALUMINIUM IGNITION DELAY TIMES

Legend refers to aluminium particle size and explosive formulation as designated in tables 2 and 3.

the particles. At a pressure of 2 GPa the melting point is 1060 K.<sup>17</sup>

Given the 14% density decrease upon melting, there exists an internal pressure available to split the oxide skin, giving rise to a local surface exotherm and a possible ignition event.

In a separate calculation, after the work of Roberts,<sup>18</sup> the self-heating rate of particles was shown to be small, with a best case of  $5 \times 10^6$  K/s, and therefore negligible in the above model.

## CONCLUSION

The reaction behaviour of particulate AN and aluminium under detonation conditions has been investigated.

AN and aluminium of various particle sizes were incorporated into a slurry explosive, which was then characterised in terms of the variation of detonation velocity and shock front radius of curvature with charge diameter.

The resulting data was used in a slightly divergent flow detonation model to extract the heat release rate

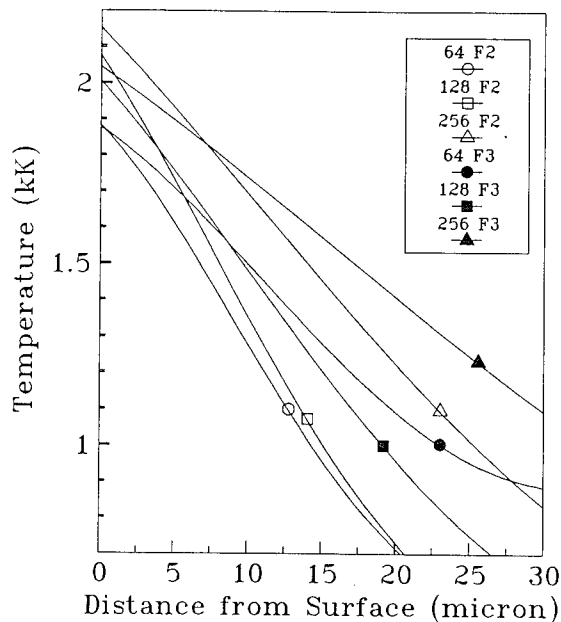


FIGURE 6.  
THERMAL PROFILES IN PARTICLES  
AT IGNITION

Legend shows particle size and formulations

of the explosive as a function of AN and aluminium particle size. From this the reaction rates of AN and aluminium were computed.

Ammonium nitrate was found to react by inward grain burning. The estimated burning velocity was shown to agree with other data in the literature. Aluminium was found to undergo an ignition event which was affected by local reaction zone temperature and chemical composition, and particle size.

A simple model of the heating of an aluminium particle in a well-stirred fluid was used to investigate the ignition event. Ignition occurred after significant heat transfer to the particle had taken place, sufficient to cause extensive melting. It is suggested that the volume change due to melting might be sufficient to cause cracking of the oxide sheath on the particle, and hence cause ignition.

## ACKNOWLEDGEMENTS

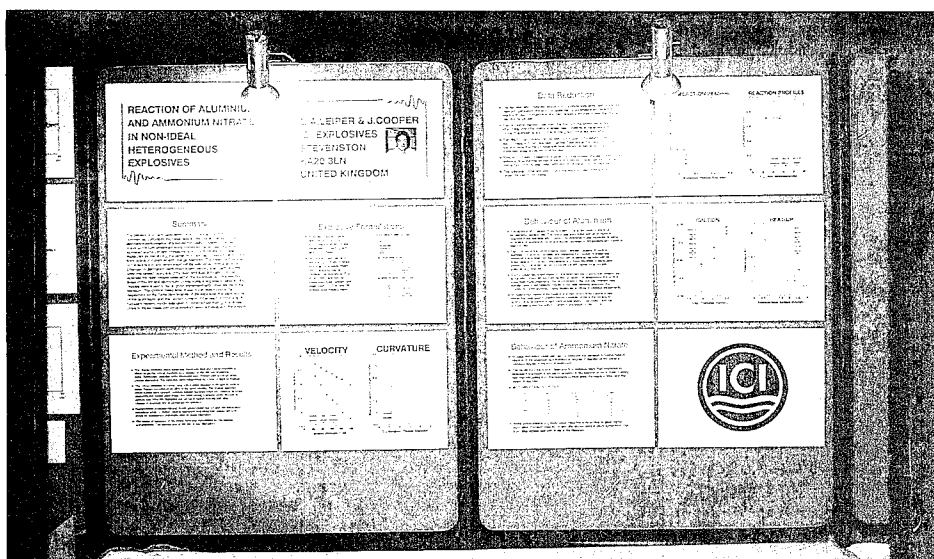
The authors acknowledge with thanks the permission of ICI Explosives to publish this work, and the many formative discussions held with Dr. C.M. Lownds. M.D. Harding was responsible for much of the explosive preparation and experimental testing.



The surface area determination on the powders was carried out by Dr. P. Snowden, ICI, Billingham.

#### REFERENCES

1. Cook, M.A. et al, "Aluminised Explosives," J. Physical Chemistry, 61, 180-196, 1957.
2. Macek, A., "Fundamentals of Combustion of Single Particle Aluminium and Beryllium," in Proceedings of the Eleventh Symposium (International) on Combustion, The Combustion Institute, Pittsburgh, 1967.
3. Meyer, R., "Explosives," Verlag Chemie, Basel, 1981, 2nd edition, p78.
4. Kirby, I.J.; Leiper, G.A., "A Small Divergent Detonation Theory for Intermolecular Explosives," Proceedings of the Eighth Symposium (International) on Detonation, Albuquerque, New Mexico, 1985, 176-185.
5. Brownlie, N., "Computer Program 'DTNATE' Detonation Properties of Explosives," ICI Canada Report, E-759-2, June 1968.
6. Leiper, G.A., "Numerical Modelling of Detonation Performance," Phil. Trans. R. Soc. Lond. A, 339, 419-429, 1992.
7. Cook, M.A.; Mayfield, E.B.; Partridge, W.S., "Reaction Rates of Ammonium Nitrate in Detonation," J. Physical Chemistry, 59, 675-680, 1954.
8. Cook, M.A., "The Science of High Explosives," Reingold, New York, 1958.
9. Van Zeggeren, F.; Storey, S.H.; "The Computation of Chemical Equilibria," Cambridge University Press, London, 1970.
10. Leiper, G.A., "The Behaviour of Non-Ideal Explosives in the Ballistic Mortar," J. Energetic Materials, 7(4-5), 381-403, 1989.
11. Merzhanov, A.G., "Thermal Theory of Metal Particle Ignition," AIAA J., 13(2), 209-14, 1975.
12. Afanasenkov, A.N.; Bogolomov, V.M.; Vostobionikov, I.M., "Generalised Shock Hugoniot of Condensed Substances," Zhur. Prok. Mekh. Tekh., 10, 137-147, 1969.
13. Cowperthwaite, M.; Shaw, R., " $C_v(T)$  Equation of State for Liquids, Calculation of the Shock Temperature of Carbon Tetrachloride, Nitromethane, and Water in the 100-kbar Region," J. Chemical Physics, 33(2), 555-560, 1970.
14. Leiper, G.A.; Kirby, I.J; and Hackett A., "Determination of Reaction Rates in Intermolecular Explosives Using the Electromagnetic Particle Velocity Gauge Technique," Proceedings of the Eight Symposium (International) on Detonation, Albuquerque, New Mexico, 1985, 186-195.
15. Paterson, S., "The Heating or Cooling of a Solid Sphere in a Well-Stirred Fluid," Proc. Phys. Soc, 59, 50-58, 1947.
16. Jaffe, R.I.; Maykuth, D.J., "Refractory Materials Part II-High-Temperature Behavior," Aero/Space Engineering, 19, 39-44, 1960.
17. Lees, J.; Williamson, B.H.J., "Combined Very High Pressure/High Temperature Calibration of the Tetrahedral Anvil Apparatus, Fusion Curves of Zinc, Aluminium, Germanium and Silicon to 60 kilobars," Nature, 208, 278-9, 1965.
18. Roberts, T.A.; Burton, R.L.; Krier, H., "Ignition and Combustion of Aluminium/Magnesium Alloy particles in  $O_2$  at High Pressures," Combustion and Flame, 92, 125-143, 1993.



## AN EXTENSIVE EXPERIMENTAL STUDY OF PRESSED NTO

P. GIMENEZ - P. CHABIN - J. MALA - C. SPYCKERELLE

*S.N.P.E.*

Centre de Recherches du Bouchet - BP 2  
91710 VERT-LE-PETIT  
FRANCE

NTO is used as an insensitive explosive component but its intrinsic detonation properties are not well known. We present experimental results regarding about 50 shots of pressed NTO cylinders for various densities and diameters and for two widely different grain sizes. The behaviour of NTO appears to be close to those of other insensitive molecules. The infinite diameter velocity for the maximum theoretical density is larger than 8460 m/s and the failure diameter for fine NTO is less than 14 mm.

### INTRODUCTION

NTO is becoming increasingly used in insensitive explosive compositions. SNPE has already published some results related to the vulnerability behaviour of NTO based compositions.<sup>1</sup>

We have also studied many compositions of the cast PBX type, consisting of different mixtures of NTO, HMX and inert or energetic binders, in order to optimize the trade off between vulnerability and performances.

To understand the detonics behaviour of these compositions, the behaviour of each component must be known. Until now, there exists very few data on pure NTO. This is the reason why we have undertaken this large experimental program in order to gather informations on the behaviour of pure NTO.

In the next chapters we describe the NTO used in this study, the experimental set-up, the

results and their analysis.

### PREPARATION AND MAIN PROPERTIES OF NTO USED IN THE STUDY

The NTO used in this study is produced at an industrial level in the SNPE plant of SORGUES in southeastern FRANCE.

NTO is obtained by nitration of TO. The NTO is then recrystallized in hot water to remove nitric acid and get coarse particles.

By sieving, this NTO conducts to classes I and II with, respectively, 450  $\mu\text{m}$  and 320  $\mu\text{m}$  for mean grain size. The grain size distribution and the shape of the grains for NTO class I are given in figures 1 and 2.

The classes III and IV are obtained by grinding and sieving the recrystallized NTO. The grain size distribution and the shape of the grains for NTO class IV are given in figures 3 and 4.

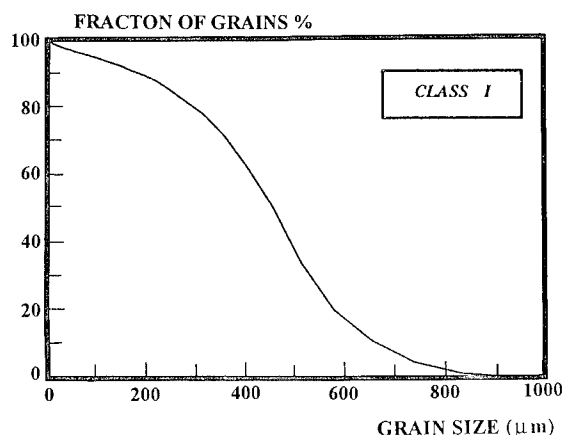


**FIGURE 1. GRAIN SIZE DISTRIBUTION FOR NTO CLASS I**

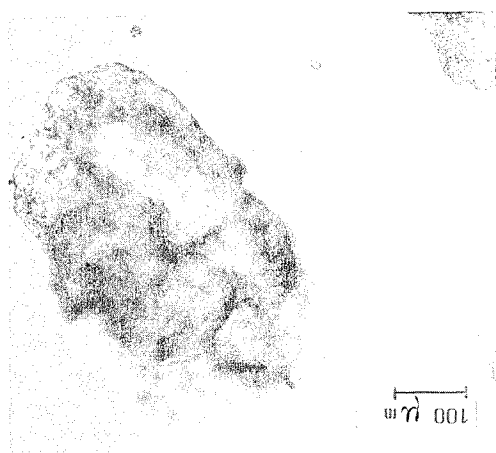


**FIGURE 2. MORPHOLOGY AND STRUCTURE OF NTO CLASS I.**

The mean grain size is 68  $\mu\text{m}$  for class III and 17  $\mu\text{m}$  for class IV.

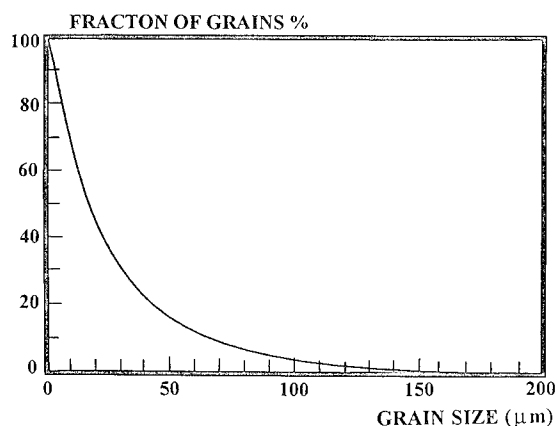


**FIGURE 3. GRAIN SIZE DISTRIBUTION FOR NTO CLASS IV**

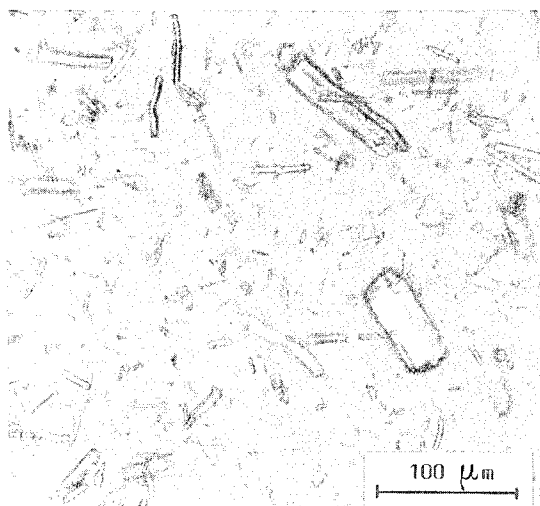


**FIGURE 4. MORPHOLOGY AND STRUCTURE OF NTO CLASS IV.**

Only the classes I and IV, that is the largest and the smallest grain size, are involved in this study.

#### EXPERIMENTAL SET-UP

In the experiments, the NTO was pressed at the required density in the form of cylindrical pellets with a diameter to length ratio of one.

For each diameter and each tested density, a cylinder was made from a minimum of eight pellets.

For the low densities, the cylinders were lightly confined in a paper tube allowing their handling.

The NTO cylinders were initiated by a pressed RDX/wax booster of the same diameter and with a length of twice the diameter.

The detonation velocity was obtained from three independent means :

- ▣ four small conducting wires located between the pellets ;
- ▣ ten short circuit pins on both sides of the cylinder.

The signals were recorded by a 32 channels THOMSON recording chronometer with a 1 ns accuracy.

A picture of a ready to shot set-up is given in figure 5.

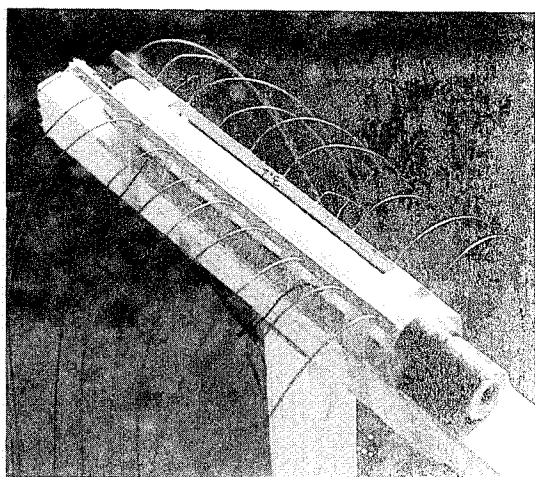


FIGURE 5. PICTURE OF A READY TO SHOT NTO CYLINDER.

The results were linearly fitted with a least squares method. From the accuracy on the location of the pins, we believe that the velocity is obtained at  $\pm 25$  m/s.

In some cases, the trajectory was separated in two regions independently fitted. This was made necessary for the non propagating cases as the first part of the trajectory is a detonation and the second is due to an attenuating shock wave.

The density was obtained simply by dividing the mass by the volume of each pellet. The precision on this parameter is about  $\pm 0.01$  g/cm<sup>3</sup>.

#### EXPERIMENTAL RESULTS

During this study, we tried to explore the widest possible range of loading densities. Practically, this conducted to test densities from 0.6 to 1.85 g/cm<sup>3</sup>, that is ratio  $\Delta$  of the tested density to the theoretical maximum density (1.93 g/cm<sup>3</sup>) ranging from 0.3 to 0.96.

Regarding the diameter, we performed tests from 14 to 40 mm.

Only one shot was made for a given configuration (diameter and density) except in few cases to check a particular result.

More than 50 shots were performed, the results are given in the tables 1 and 2. The figures 6 and 7 illustrate these tables in the plane (detonation velocity versus  $\Delta$ ).

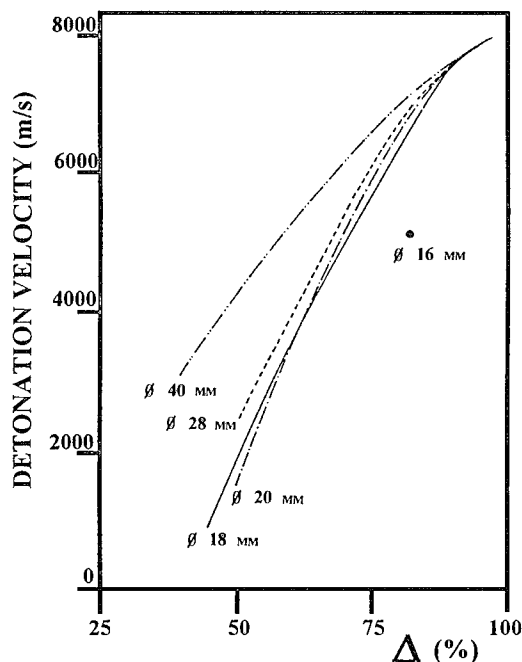


FIGURE 6. EXPERIMENTAL RESULTS FOR NTO CLASS I IN THE D VERSUS  $\Delta$  PLANE.

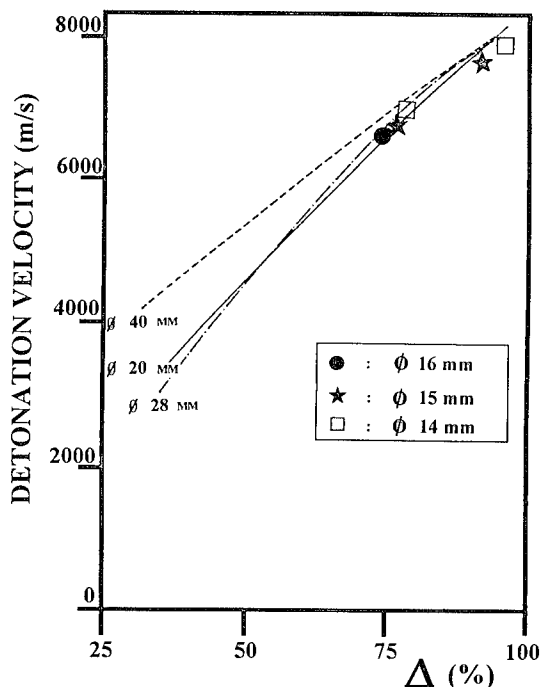


FIGURE 7. EXPERIMENTAL RESULTS FOR NTO CLASS IV IN THE D VERSUS  $\Delta$  PLANE.

**Table 1. Experimental results for NTO class I.**

DIAMETER (mm)	DENSITY (g/cm <sup>3</sup> )	DETONATION VELOCITY (m/s)
14	1.85	No Go
15	1.85	No Go
16	1.85	No Go
18	1.85	7970
20	1.85	8020 (2 No Go + one low velocity at 4125 m/s)
28	1.85	8115
40	1.85	8090
14	1.74	No Go
18	1.74	7690
20	1.75	7645
28	1.75	7740
40	1.75	7725
14	1.58	No Go
15	1.62	No Go
16	1.62	4870
18	1.58	6550
40	1.65	7385
20	1.49	6220
28	1.49	6460
18	0.9	1000
20	1	1610
28	1	2565
40	0.88	3150

**Table 2. Experimental results for NTO class IV.**

DIAMETER (mm)	DENSITY (g/cm <sup>3</sup> )	DETONATION VELOCITY (m/s)
14	1.83	7930
16	1.85	Detonation without measurement
18	1.84	7973
20	1.85	8040
28	1.85	8187
20	1.80	7940
28	1.80	7970
40	1.78	7940
15	1.75	7780
20	1.75	7780
28	1.75	7690
40	1.75	7850
20	1.70	7680
40	1.66	7570
20	1.60	7220
28	1.59	7330
14	1.50	6835
15	1.46	6744
16	1.44	6657
18	1.50	6878
20	1.50	6990
28	1.47	6850
20	0.67	3380
28	0.64	2895
40	0.58	4110

## ANALYSIS

### Infinite Diameter Velocities

For each tested density, the detonation velocities were linearly fitted with respect to the inverse of the diameter  $\phi$ :<sup>2</sup>

$$D = D_{\infty} (1 - a/\phi) \quad (1)$$

where  $D_{\infty}$  is the infinite diameter velocity.

The results of this fitting are reported in table 3.

This infinite diameter velocity is reported in figure 8 as a function of  $\Delta$  for  $\Delta > 0.75$ . On this figure we have also reported the experimental values obtained at LASL by L.B. CHAPMAN<sup>3</sup> for a 41 mm diameter but with a confinement.

The figure 8 shows a good agreement between the two classes of NTO and also between SNPE and LASL results. It also shows that the infinite diameter velocity is linearly increasing with  $\Delta$  at least in this range of densities.

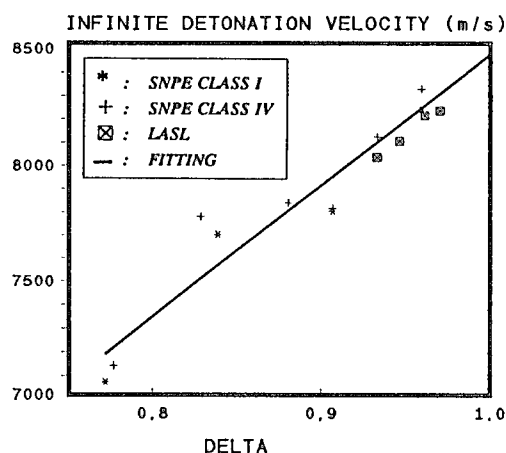


**FIGURE 8.** EXPERIMENTAL RESULTS AND FITTING FOR BOTH CLASSES IN THE PLANE ( $D_{\infty}$ ,  $\Delta$ )

A linear fitting of the SNPE data for this range of densities is given by :

$$D_{\infty} = D_{\infty,1} [1 - b(1-\Delta)] \quad (2)$$

with  $D_{\infty,1} = 8462$  m/s and  $b = 0.667$

As it can be seen in table 3, for  $\Delta > 0.75$ , the calculated velocities agree within less than 2 % for most of the experimental data. The 3.6 % obtained with class IV at  $\Delta = 0.829$  can be related to the lack of experimental data for the corresponding density ( $1.6$  g/cm<sup>3</sup>).

For each class, we also obtained an experimental value for the velocity at the lowest available density. These two measured velocities are located on both sides of the linear fitting and about at the same distance (8 or 9 % as indicated in table 3). This is due to the poor quality of the experimental data in the low densities range as :

- reproducibility of the density is not obtained ;
- low shock levels lead to scattering in the functioning of the short-circuit pins ;
- the slope of the  $D(\phi)$  curve is large and this decreases the precision of the infinite diameter velocity.

### Thermodynamical Calculations

A first way to calculate the CJ parameters of NTO is to use the KAMLET's method:<sup>4</sup>

$$D_{\infty} = A (1 + B \rho) \Phi^{0.5} \quad (3)$$

$$P_{cj} = \rho^2 K \Phi \quad (4)$$

$$\Phi = N (MQ)^{0.5} \quad (5)$$

$N$ ,  $M$  and  $Q$  being respectively, the number of moles of gas produced per weight unit of the explosive, the average molecular weight of the gases and the chemical energy released in the detonation.

These parameters can be calculated from :

- the formula of NTO :  $C_2H_2O_3N_4$  ;
- the enthalpy of formation of NTO : -14 kcal/mole;<sup>5</sup>
- hypothesis regarding the chemical equilibrium in the products.

Table 3.  $D_{\infty}$  and  $a$  from the fitting (1).

$\Delta$	density (g/cm <sup>3</sup> )	Experimental infinite diameter velocity (m/s)	Parameter $a$ of (1) (mm)	Calculated infinite diameter velocity (m/s)	difference (%)	Class
0.518	1	5269	13.6	5741	-8	I
0.772	1.49	7059	2.19	7175	-1.6	I
0.839	1.62	7687	2.28	7553	1.8	I
0.907	1.75	7788	0.28	7937	-1.9	I
0.959	1.85	8223	0.51	8231	-0.1	I
0.311	0.60	4995	9	4573	9	IV
0.777	1.50	7128	0.49	7203	-1	IV
0.829	1.60	7765	1.4	7497	3.6	IV
0.881	1.70	7824	0.37	7790	0.4	IV
0.907	1.75	7801	0.075	7937	1.7	IV
0.933	1.80	8108	0.43	8084	0.3	IV
0.959	1.85	8313	0.56	8231	1	IV

For NTO, this calculation gives :

$$D_{\infty} = D_{\infty,1} [1 - b (1-\Delta)] \quad (6)$$

with  $D_{\infty,1} = 8268$  m/s and  $b = 0.715$

In the reference,<sup>6</sup> F. BUGAUT provides ETARC calculation results showing a linear variation of  $D_{\infty}$  with  $\Delta$  in the range  $\Delta > 0.8$ .

In the reference,<sup>3</sup> L. B. CHAPMAN gives some results obtained at LASL with the BKW code.

As it can be seen from (3), KAMLET's method assumes a linear variation of  $D_{\infty}$  with respect to the density  $\rho$  that is, to  $\Delta$ . The results can then be expressed in the form (2).

The results of these calculations are reported in figure 9. In this figure we also indicate the experimental linear fitting given by (2).

At SNPE, we performed calculations, with the TIGER code and a JCZ3 equation of state, for  $\Delta$  ranging from 0.5 to 1.

In the high loading density region ( $\Delta > 0.87$ ), the agreement between experimental and calculated data is better with the TIGER calculations.

For  $\Delta < 0.87$ , the Tiger calculations are very close to the KAMLET's results and both are parallel to the experimental data but 200 m/s below.



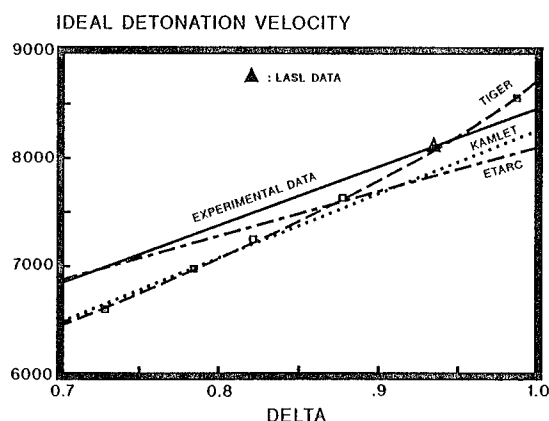


FIGURE 9. THERMODYNAMICAL CALCULATIONS FOR NTO. COMPARISON WITH THE EXPERIMENTAL FITTING OF FIGURE 8.

We do not know if these results can be interpreted in the light of the differences in the assumptions in the BKW, TIGER and ETARC codes.

In this range of lower density, the ETARC calculation provides a better comparison with the experimental data.

#### Failure Diameter

All the samples in class IV have conducted to a detonation. This result shows that, for very fine NTO, the failure diameter is less than 14 mm whatever the loading density.

The results regarding the coarse NTO (class I) are illustrated in the plane (diameter  $\phi$ ,  $\Delta$ ) of the figure 10. In this plane, a full circle indicates a detonation and a square (with a star in it) indicates a non-detonation.

The figure 10 indicates that the failure diameter for NTO increases with the density at least in the high density region. It seems also that the slope of the limiting curve is sharply steepening as we reach  $1.85 \text{ g/cm}^3$ . This is confirmed by the two non-detonation results obtained at 20 mm for a density of  $1.85 \text{ g/cm}^3$  (table 1) and by the failure diameter of 25 mm claimed by L.B. CHAPMAN<sup>3</sup> for large grain NTO at  $1.868 \text{ g/cm}^3$ .

#### Failure diameter Class I

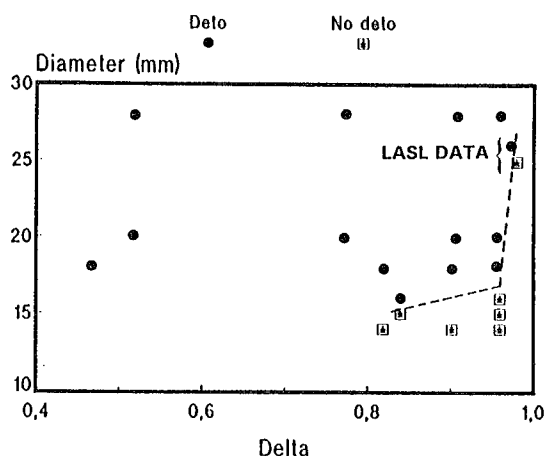


FIGURE 10. LIMITING CURVE OF DETONATION IN THE DIAMETER  $\phi$  VERSUS  $\Delta$  PLANE

The different results obtained at  $1.85 \text{ g/cm}^3$  for 20 mm diameter could be attributed to the modification of the grain size during the pressing process. Nevertheless, a reduction of the grain size would promote the detonation as it can be seen from the results for class IV. Such an effect seems therefore unable to explain the increase of failure diameter with density.

#### DISCUSSION

In a general way, for all the cartridge diameters, experimental detonation velocity increases with loading density and gets closer to the theoretical values.

For a given density and a given sample diameter, the detonation velocity is always higher for fine NTO than for coarse one. These features show a group I behaviour according to the classification by D. PRICE.<sup>7</sup>

Nevertheless, when density approaches its theoretical maximum value, velocity versus density curves seem to deviate from the ideal curve.

In some cases (see table 1 for a 20 mm diameter and a  $1.85 \text{ g/cm}^3$  density), getting a

detonation becomes very difficult and sometimes impossible. Moreover, the results obtained for the class I with small sample diameters show that failure diameter increases with loading density (for  $\Delta > 0.8$ ). These last observations would rather be an evidence for a group II behaviour.<sup>7</sup>

The same conclusion could be inferred from the detonation temperatures computed by SNPE which exhibit much lower values (about - 1000 K) with respect to classical materials such as HMX, RDX or PETN.

Finally, NTO has a behaviour which is too complicated to enable it to enter easily the simple classification proposed by D. Price. But it is important to notice that NTO seems to show the same type of detonation behaviour as other less sensitive molecules such as "high bulk density" nitroguanidine, DINGU (dinitroglycoluril) and TATB.<sup>8-9-10</sup>

It is also important to recall that the maximum detonation velocity for NTO is fairly large (8460 m/s) and that NTO has a rather small failure diameter (less than 14 mm for fine NTO) for an insensitive explosive.

This work has been performed under the auspices of French MOD (STPE).

## REFERENCES

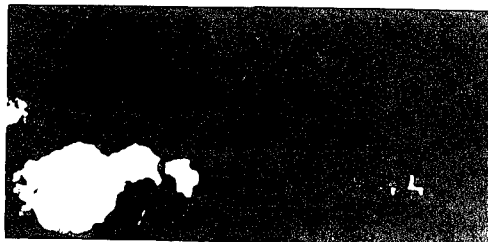
1. Becuwe, A. and Delclos, A., "Use of Oxynitrotriazole to Prepare an Insensitive High Explosive," *Proceedings of the Ninth Symposium International on Detonation*, Portland, Oregon, pp. 1008-1013.
2. Eyring, H.; Powell, R. E.; Duffey, G. H. and Parlin, R. B., "The Stability of Detonation," *Chemical Review*, Vol. 45, pp. 69-181, 1949.
3. Chapman, L. B., "NTO Development at Los Alamos," *Proceedings of the Ninth Symposium International on Detonation*, Portland, Oregon, 1989, pp. 1001-1007.
4. Kamlet, M. J. and Jacobs, S. J., "Chemistry of Detonation. A Simple Method for Calculating Detonation Properties of C-H-O-N Explosives," *J. Chem. Phys.*, Vol. 48, 1982, p. 23.
5. Lee, K. Y. and Coburn, M. D., "3-Nitro-1,2,4-Triazol-5-One, A Less Sensitive Explosive," LA 10302, MS UC 45, 1986.
6. Bugaut, F.; Bernard, S. and Chirat, R., "Theoretical Prediction of High Explosives Efficiency: Application to NTO," *Proceedings of the Ninth Symposium International on Detonation*, Portland, Oregon, 1989, pp. 489-497.
7. Price, D., "Contrasting Patterns in the Behavior of High Explosives," *Proceedings of the 11th Symposium on Combustion*, 1967, pp. 693-701.
8. Price, D. and Clairmont, A. R., Jr., "Explosive Behavior of Nitroguanidine," *Proceedings of the 12th Symposium on Combustion*, 1969, pp. 761-770.
9. de Longueville, Y.; Derrien, J. C.; Gaudin, C. and Ousset, R., "Caractérisation Détonique du Dinitroglycoluril," *Proceedings of the Symposium on Behaviour of Dense Media Under High Dynamic Pressure*, Paris, 1978, pp. 321-332.
10. Deneuille, P.; Gaudin, C.; Mala, J. and de Longueville, Y., "Comparison of TATB and DINGU Explosive Properties," *Proceedings of the 7th Symposium on Detonation*, Annapolis, MD, 1981, pp. 540-547.

# AN EXTENSIVE EXPERIMENTAL STUDY OF PRESSED NTO

P. GIMENEZ - P. CHABIN - J. MALA - C. SPYCKERELLE

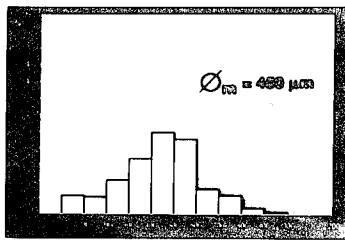
## REASON FOR THIS WORK

NTO is becoming increasingly used in insensitive explosive compositions, but until now, there exist few detonation data on pure NTO



STACK OF WARHEADS FILLED WITH A NTO-BASED CAST PBX RESISTING SYMPATHETIC DETONATION

## NTO USED IN THE STUDY

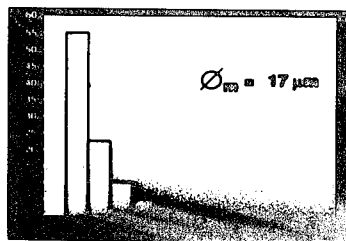


GRAIN SIZE DISTRIBUTION

NTO CLASS I.  
(made by SNPE)

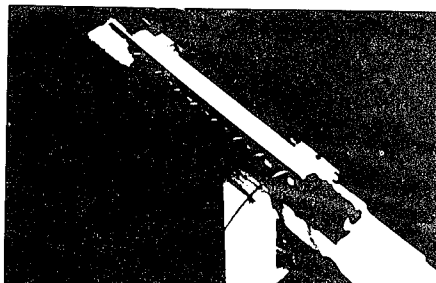
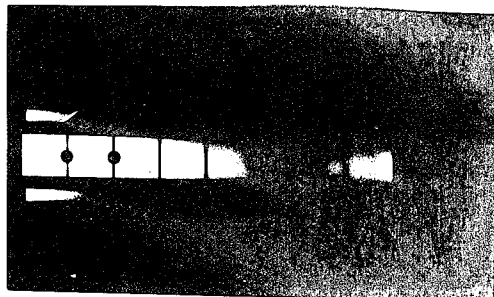


MORPHOLOGY



NTO CLASS IV.  
(made by SNPE)

## EXPERIMENTAL SET-UP FOR MEASURING DETONATION VELOCITY

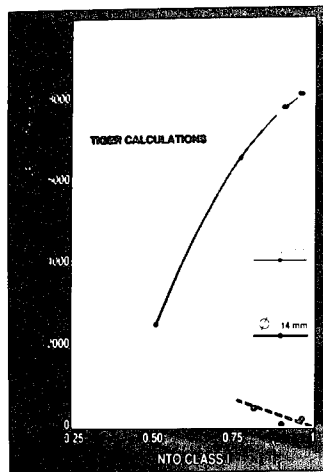


READY - FOR - SHOT NTO CYLINDER

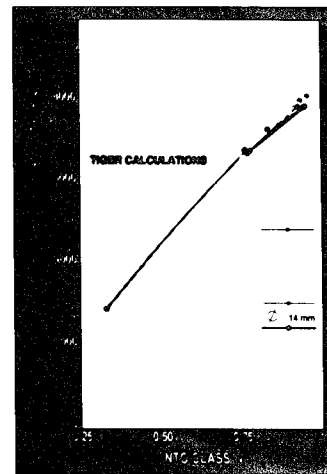
# SNPE

Défense Espace

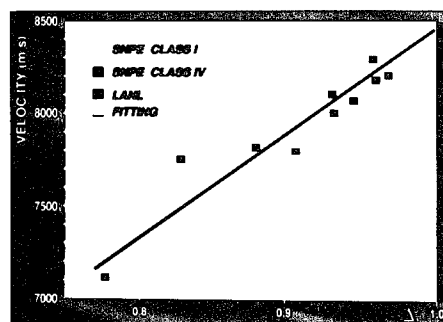
## EXPERIMENTAL RESULTS



$$\Delta = \frac{\text{loading density}}{\text{crystal density}}$$



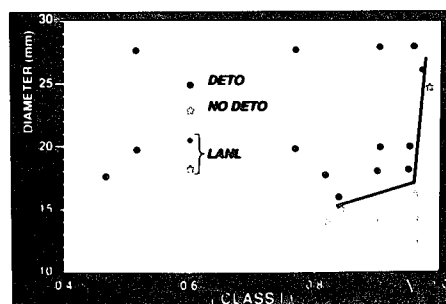
## IDEAL DETONATION VELOCITY (m / s)



$$D_{\infty} \text{ (m / s)} = 8462 [1 - 0.667 (1 - \Delta)]$$

## FAILURE DIAMETER $\phi_c$

FOR NTO CLASS IV,  $\phi_c < 14 \text{ mm}$



# SNPE

# Défense Espace

# INFLUENCE OF INTRAGRANULAR CAVITIES OF RDX PARTICLE BATCHES ON THE SENSITIVITY OF CAST WAX BONDED EXPLOSIVES

L. Borne

Franco-German Research Institute (ISL)  
P.O.Box 301 - 68301 Saint-Louis, FRANCE

Optical microscopy in a liquid of matching refractive index of RDX batches exhibits various intragranular cavities. Based on apparent particle density variations, flotation is used to produce RDX batches with calibrated internal defects. The influence of these cavities on the shock-detonation transition is checked on monomodal cast wax bonded RDX formulations. Shock wave transit time across targets of calibrated thickness are recorded using chronometric PVDF gauges. These incident shock waves are generated by the impact of projectiles launched by a 45 mm powder gun. Experimental results point out the variation of the shock detonation transition mechanisms with the incident shock pressure level. Near the initiation threshold, at 4 or 5 GPa, internal cavities ranging from 50 to 100  $\mu\text{m}$  are shown to be the potential hot spots of the usual shock initiation model. The role of other parameters is shown. Particle shapes and surface defects are valuable candidates.

## INTRODUCTION

Many efforts are made to reduce the sensitivity of explosives and propellants. In this way, shock-to-detonation transition (SDT) of cast-plastic bonded explosives is studied. Some formulation parameters have already been pointed out: the influence of the binder,<sup>1,2,3</sup> the influence of the explosive particle size,<sup>4,5</sup> and the influence of the explosive particle shape.<sup>6</sup> Our goal is to check the influence of internal volume defects of RDX particles.

Crystals defects are well known in crystallography. They are pointed out by optical microscopy of samples immersed in a liquid of matching refractive index.<sup>7</sup> Surprisingly, few available works deal with the influence of these internal cavities with the detonative behaviour of explosive formulations. Mishra and Vande Kieft have shown the link between the recrystallization process and these defects.<sup>1</sup> They obtain void free, needle-like RDX crystals by recrystallizing from a solvent such as a mixed alkyl phosphine oxides, consisting of long aliphatic chains. Dealing with qualitative observations of various nitramine samples, these micropores are good candidates to produce hot spots. Our work provides the experimental checking and

quantitative measurements of these internal cavities.

## DESCRIPTION OF EXPERIMENTS

### Explosive Formulations

It is well known that porosity has a strong effect on the shock sensitivity.<sup>8,9,10</sup> All these papers deal with porosity located outside of the explosive particles. Our purpose is to deal with compositions varying only in the internal defect population of RDX particles. In order to test homogeneous compositions with well coated particles, we choose to cast a mixture of 70% RDX and 30% wax (montanwachs BJ HOECHST). This inert binder has a melting point of 75 °C, a low viscosity and a convenient wetting capacity. Components are mixed under vacuum. Then formulation is casted by gravity and a controlled cooling is done. This gives us homogeneous cylinders with a good loading density. Targets for sensitivity tests are extracted from these raw cylinders and their density is controlled. The density variations recorded are below 0.5%. The average density is close (99,5%) to the theoretical maximum density (TMD=1.443 g/cm<sup>3</sup>). As usual, wax density is obtained by the flotation technique (0.986

g/cm<sup>3</sup>). The average RDX particle density is provided by the following study performed on crystal cavities (1.799 g/cm<sup>3</sup>).

### Explosive Particle Batches

Four similar formulations have been processed, using four different batches: 1,2,1- and 1+.

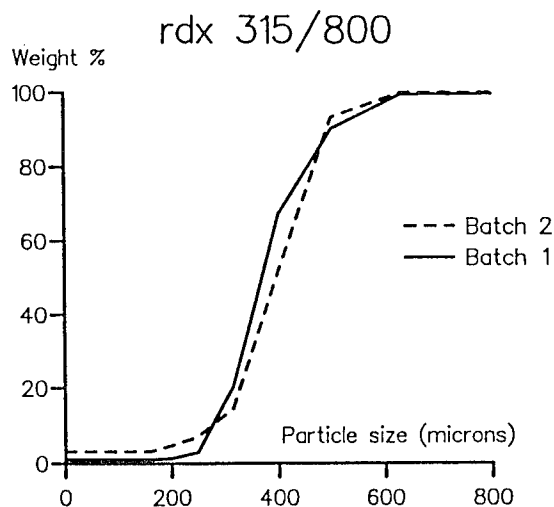


FIGURE 1. RDX PARTICLE SIZE

Batch 1 and 2 are commercial grade RDX. They have been selected for their same particle size distribution and their different internal defect population. Figure 1 shows particles between 315 and 800  $\mu\text{m}$ , centered on two sieves: 400 and 500  $\mu\text{m}$ .

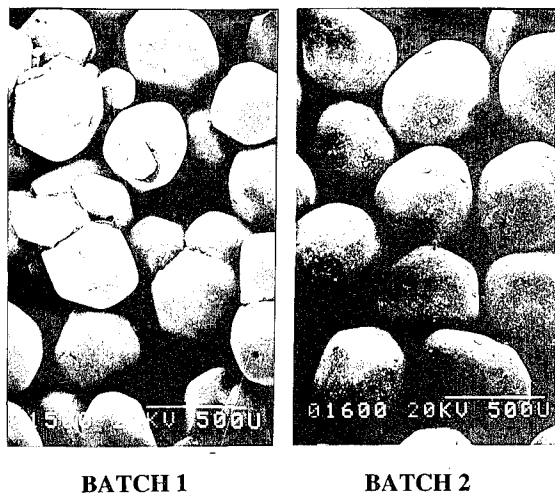


FIGURE 2. RDX PARTICLES

Scanning electron microscopy gives a qualitative insight of shape and surface defects of particles. In figure 2, batch 1 exhibits aggregates of particles.

Batch 2 points out isolated particles with more spherical shapes. Micrographs show a more important surface defect population for batch 2 than for batch 1. This is supported by mercury intrusion porosimetry measurements. This technique is based on the law which describes the penetration of a liquid into a small orifice. The minimum cylindrical pore diameter  $d$ , through which a non-wetting liquid will flow at a pressure  $P$ , is given by  $d=k/P$ , where  $k$  is a function of the surface tension of the liquid and the contact angle between the liquid and the solid. The experiment consists in the evacuation of the sample tube, which contains the RDX particle specimen, to a pressure of  $10^{-2}$  Torr and back filling with mercury for increasing pressure. The records of cumulative mercury intrusion for decreasing pore diameters (or increasing pressures) are given in figure 3 for three experiments on each batch. For pores, whose size is between 1 and 10  $\mu\text{m}$ , batch 2 shows a mercury intrusion of about 0.003 cm<sup>3</sup>/g, which is significant, in view of the experimental resolution of 0.0007 cm<sup>3</sup>/g. The similar batch 1 porosity is close to zero. For this diameter range, pores are particle surface defects.

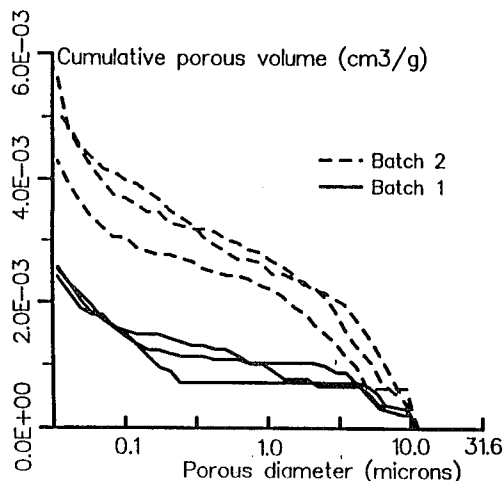


FIGURE 3. MERCURY POROSIMETRY

Optical microscopy in a liquid of matching refractive index allows in depth particle analysis.<sup>7</sup> Reducing refractive index discontinuities at particle boundaries emphasizes index gradients inside the particles. This points out crystal defects, such as internal cavities.<sup>1</sup> We have used a mixture of CS<sub>2</sub> and n-Hexane to fit the refractive index ( $n_{20} = 1.599$ ). Figures 4 show these volume defect populations for batch 1 and 2. Qualitatively, batch 2 has more defects than batch 1.

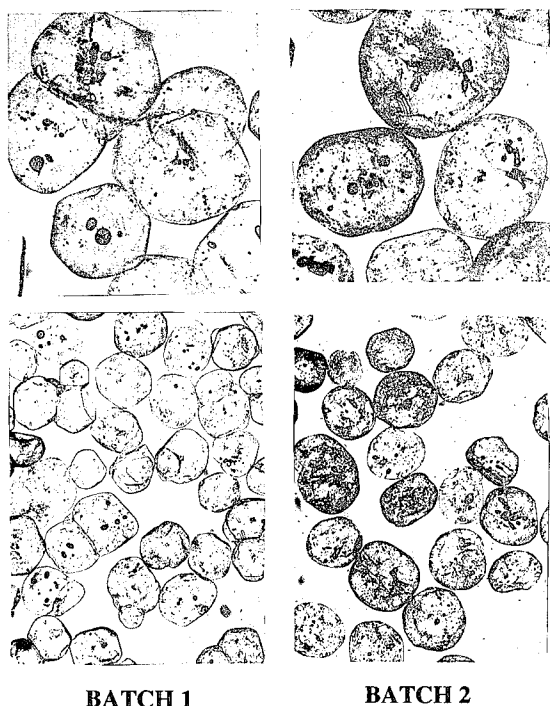


FIGURE 4. OPTICAL MICROSCOPY IN A LIQUID OF MATCHING REFRACTIVE INDEX

In conclusion, batch 2 has more defects than batch 1, but this concerns both volume defects and surface defects. We need, at least, another batch to check the influence of RDX internal volume defects on the shock-detonation transition. Moreover, the variations of another hidden parameter, linked with the RDX particle recrystallization process, is still possible for batch 1 and 2. Unfortunately, it was not possible to find the desired batch among the various commercial grade RDX. Hence, we have chosen to produce small quantities of two new batches 1- and 1+, starting from the unique batch 1.

Recrystallizing RDX from the right solvent can give cavity free nitramines.<sup>1</sup> But this affects the crystal shape. Needle-like particles are obtained. Various volume defects generate different apparent density from one particle to another. The following rough theoretical estimation of these apparent densities give an order of magnitude of these variations. On the basis of an academic cubic grain of 500  $\mu\text{m}$ , two cubic free cavities of 20  $\mu\text{m}$  generate a relative apparent density variation of 0.01%. In the same way, one cubic cavity of 100  $\mu\text{m}$ , another of 50  $\mu\text{m}$ , and three of 20  $\mu\text{m}$  give a relative variation of 0.91%. Figure 5 shows how this prediction is representative for batch 1. Taking into account the presence of solvent in the cavities would reduce the previous order of magnitude.

This leads us to set up a well-instrumented experiment to sort lower and higher apparent density particles (with more or less cavities). The separation is performed by flotation in a mixture of Methylene Iodide ( $\text{CH}_2\text{I}_2$ ) and Toluene, in order to achieve a mixture density of about 1.799  $\text{g}/\text{cm}^3$ .<sup>11</sup> RDX has a low solubility in this mixture, and the wetting capacities are good. Preliminary tests performed with a mixture of water and a heavy salt failed because of the lower wetting capacities of water. A PAAR densimeter, using the vibrating tube principle, allows us to control the mixture density with accuracy (0.001  $\text{g}/\text{cm}^3$ ). This obviously requires a fine control of the temperature (0.1  $^\circ\text{C}$ ). In this way, particles are sorted, then washed with Ethanol and dried.

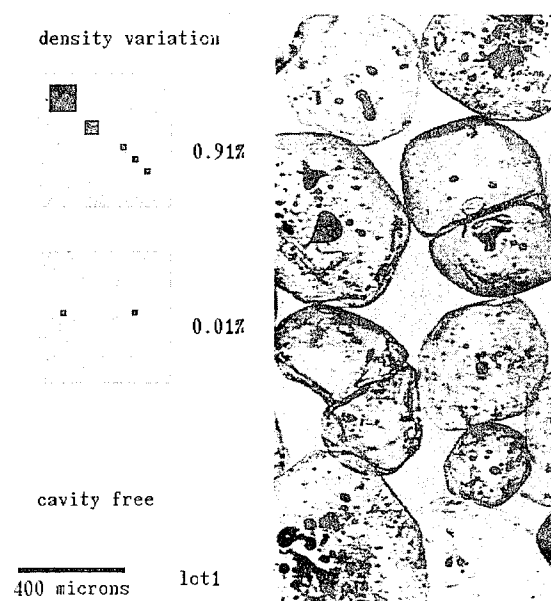
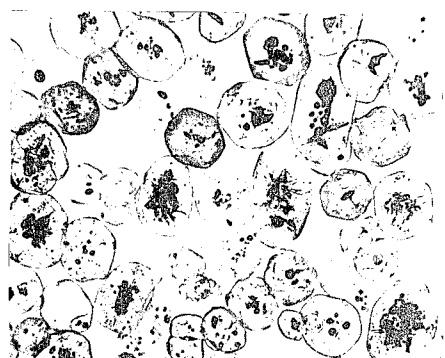


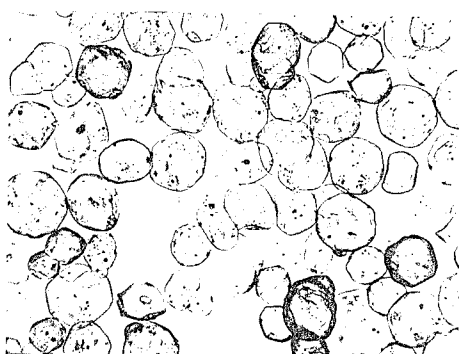
FIGURE 5. PARTICLE APPARENT DENSITY VARIATIONS

Starting from batch 1, a first mixture, fitted to a density of 1.798  $\text{g}/\text{cm}^3$  and a temperature of 20  $^\circ\text{C}$ , gives the batch 1+ in the upper part. The average apparent density of 1+ particles is then below 1.798  $\text{g}/\text{cm}^3$ . Figure 6 shows the volume defect population of batch 1+. It shows an increase of the cavity population. Cavity sizes involved are ranging from 50 to 100  $\mu\text{m}$ . These are the biggest cavities of batch 1.

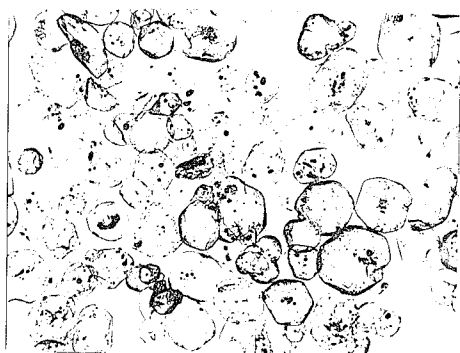
A last flotation, fitted to a density of 1.799  $\text{g}/\text{cm}^3$  and a temperature of 20  $^\circ\text{C}$ , gives the batch 1- in the lower part, starting from the rest of the previous experiment (batch 1 minus batch 1+). The average apparent density of 1- particles is higher than 1.799  $\text{g}/\text{cm}^3$ . A micrograph of batch 1- (figure 6) only shows small cavities. Their average size is about 10  $\mu\text{m}$ .



**BATCH 1+**



**BATCH 1-**



**RESIDUUM BATCH (BATCH 1 MINUS BATCH 1+ MINUS BATCH 1-).**

**FIGURE 6: ISL LABORATORY RDX BATCHES**

Finally, the residuum batch from batch 1 after sorting batches 1- and 1+ shows the separation power of our experiment. Its defect population is intermediate (figures 6). Developments are in progress to use this laboratory RDX production method as a quantification tool for internal cavities in explosive particle batches.

## Experimental Set-Up

SDT characterization of formulations is done by recording the transit time of a sustained plane incident shock wave in calibrated thickness samples. Each measure gives one point of the usual space-time diagram provided by the usual wedge test.<sup>4</sup> A good time resolution is achieved by using two chronometric PVDF gauges. The first gives the time of entrance of the shock wave in the sample. The second, on the rear, records the time the shock wave leaves the sample. Their rise time are less than 10 ns and their total thickness (with insulation) are limited to 0.05 mm. This experimental set-up provides accurate measurements and needs a limited amount of explosive formulations. A 45 mm powder gun launches the projectile. To get a high quality incident plane shock wave, the target and projectile designs have been controlled and optimized using both numerical simulations (NIKE2D and DYNA2D), and experimental checking. The sample thickness is limited to 20 mm and the impact tilt is below  $10^{-3}$  rad.

## EXPERIMENTAL RESULTS

### Checking of the Experimental Set-up

For each test, the level of chemical reaction is evaluated by comparing the recorded transit time with its theoretical evaluation in the same unreacted formulation. A mixture theory is used to predict the shock behaviour of the unreacted formulation from shock characteristics of wax and unreacted RDX.<sup>12</sup> The RDX Hugoniot data come from the literature.<sup>13</sup> They are usually available in the form  $U_s = a + b \cdot u_p$ , where  $a$  and  $b$  are empirical constants,  $U_s$  is the shock velocity, and  $u_p$  is the particle velocity. The wax Hugoniot data have been measured using the previous experimental set-up. All these data are given in table I. These Hugoniot predictions have been checked experimentally. 20 mm thick formulation samples, based on batch 1 and 2, have been tested below the initiation threshold (3.6 GPa).

**TABLE I: HUGONIOT DATA**

	a	b
Wax	2.937	1.21
RDX	2.87	1.61
Wax + RDX (30%) (70%)	2.715	1.446



Figure 7 shows the experimental transit time records in the usual form of a space-time diagram. The agreement with the theoretical prediction is quite good.

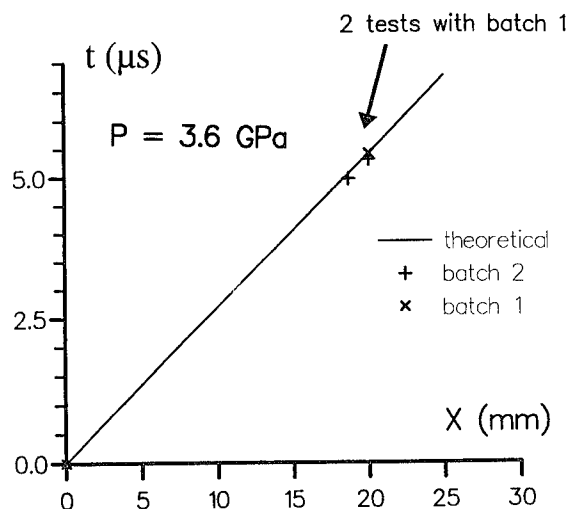


FIGURE 7. SPACE-TIME DIAGRAM TO CHECK HUGONIOT DATA

For each experimental measurement, at least two tests have been performed. Reproducibility is below 30 ns for the measure of the shock transit time. This is in agreement with the experimental set-up, taking into account the two PVDF gauge performances, their setting on the target, and the thickness calibration of the RDX/wax based target.

#### New Physical Results

Figure 8 shows experimental points of the space-time diagram obtained with the batch 1 and 2 based formulations, and for four shock pressure levels:

- At 4.7 and 5.7 GPa the batch 2 based formulation has the shortest transit times. More surface and volume defects for RDX particles give shorter transit times.

- This trend is less marked at 6.7 GPa than at 4.7 GPa. Defect influence reduces with increasing pressure.

- At 8.2 GPa, the highest shock pressure studied, results are reversed. The amount of defects of batch 2 does not lead to the shorter transit time at this high pressure level.

Recorded differences have the same order of magnitude (250 ns at 4.7 GPa) for two similar formulations, using two RDX particle size distributions (100/200 and 315/800  $\mu\text{m}$ ) used to check RDX particle size effects.<sup>4</sup>

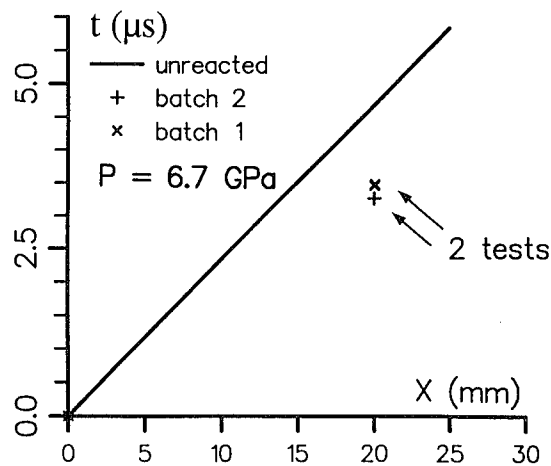
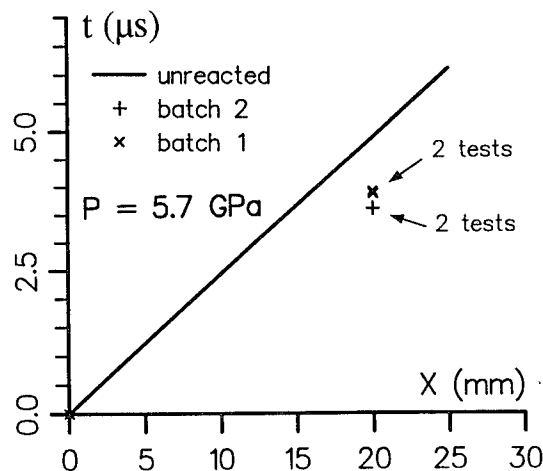
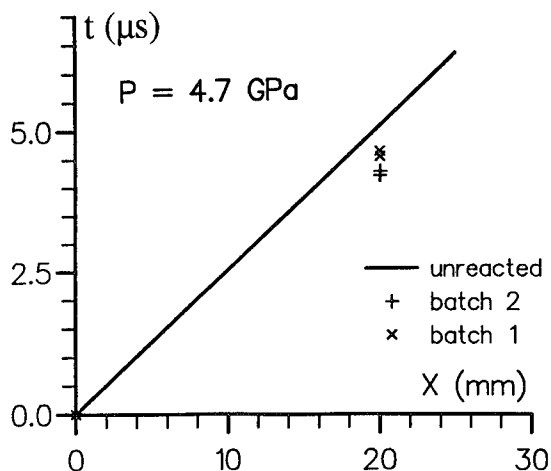


FIGURE 8. SPACE-TIME DIAGRAM FOR BATCH 1 AND 2 BASED FORMULATIONS

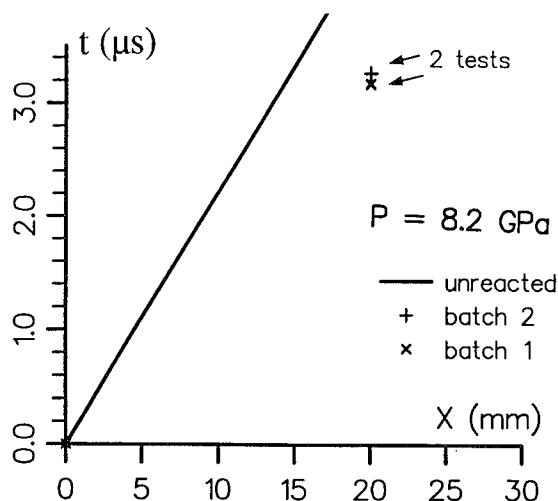


FIGURE 8. SPACE-TIME DIAGRAM FOR BATCH 1 AND 2 BASED FORMULATIONS

In the same way, figures 9 give the experimental results obtained with batch 1- and 1+ based formulations, whose only difference is the internal defect population of RDX particles. Cavity sizes in batch 1- are below 10  $\mu\text{m}$ . Batch 1+ exhibits bigger cavities, between 50 and 100  $\mu\text{m}$ . Variations recorded between these two formulations are smaller than the previous ones, but have the same order of magnitude. The time scale used for space-time diagram of figures 9 has been dilated to underline the time resolution of our experiments. The same trends are pointed out:

-At the lowest shock pressure (4.7 GPa), the shortest transit times are recorded for the batch 1+ based formulations with the biggest cavities.

-Transit time variations between batch 1- and 1+ based formulations decrease with increasing pressure. It is close to zero at 6.7 GPa.

This shows the influence of the biggest internal cavities (50 - 100  $\mu\text{m}$ ) at the lowest shock pressure (4.7 GPa).

## INTERPRETATION AND DISCUSSION

In the framework of the usual two step shock-detonation transition model (ignition and build up), batches 1+ and 1- show that RDX internal cavities are true potential hot spots of the ignition step. At about 5 GPa, effective hot spots have sizes between 50 and 100  $\mu\text{m}$ . But variations recorded between batches 1- and 1+ are smaller than those recorded with batches 1 and 2.

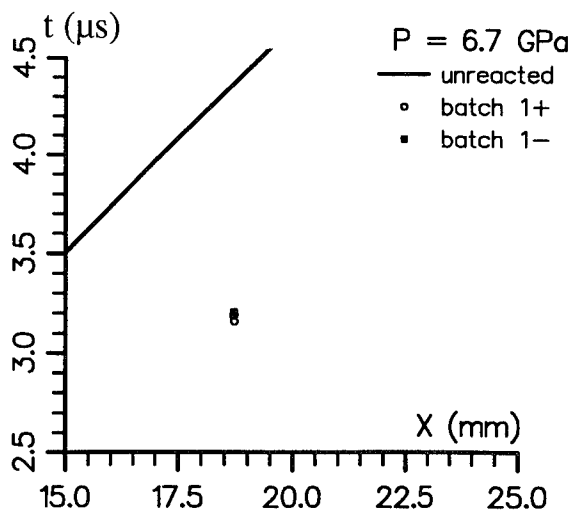
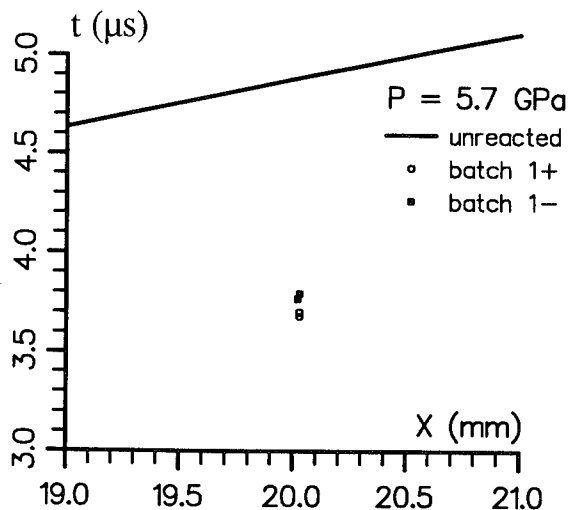
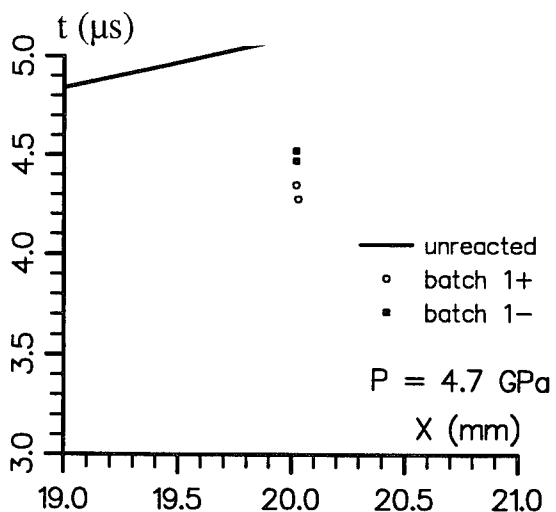


FIGURE 9. SPACE-TIME DIAGRAM FOR BATCH 1+ AND 1- BASED FORMULATIONS

This shows the influence of others parameters . Surface defects of batch 2 particles could be valuable candidates. This requires further experiments. Parameters linked with the partially known elaboration process of batches 1 and 2, could also have an influence.

Our results confirm that the shock-detonation transition behaviour depends on the incident shock pressure level.<sup>4</sup> They also give a more precise physical understanding. This shock pressure effect can be explained by the variations of the relative weight of the two steps: ignition of hot spots and build-up to detonation by growth of reactions.

At low shock pressures, shock-detonation transition is controlled by the first step: the ignition of hot spots. These are internal cavities in RDX particles, whose sizes are between 50 and 100  $\mu\text{m}$ . According to previous works, the heating mechanism can involve hydrodynamic compression or viscoplastic work, depending on the material viscosity.<sup>14,15</sup>

At higher shock pressures, shock-detonation transition is governed by the last step: the build-up to detonation. At low shock pressures, the population of hot spots (the biggest cavities) is limited. Increasing the shock pressure reduces the size threshold needed for a cavity to become an efficient hot spot. As observed qualitatively with batches 2 and 1-, this leads to an increase in the number of hot spots, which involve smaller cavities. The build-up of a reaction front is then easier and faster. This is supported by the following analysis of our experimental results.

Up to now, a lot of these PVDF chronometric tests have been performed on our four compositions , on three similar polyurethane based formulations used by Moulard,<sup>4</sup> and on inert materials. Various sample thicknesses have been used: 5,10,15 or 20 mm. The experimental time resolution recorded for all transit time measurements is below 30 ns, in agreement with the experimental set-up.

Nevertheless, for 20 mm thick samples, at the lowest shock pressure (4.7 GPa), tests on our four formulations are only reproducible within 80 ns. This is not a loss of accuracy, but the physical recording of the build-up to detonation from localized sites. The comparison of these recorded transit times with their theoretical evaluation in the same unreacted formulation shows that at a distance of 20 mm shock-detonation transition just starts. As a consequence of the limited amount of ignited sites and their spacing, the build-up to detonation starts from isolated sites and is slower. Increasing the incident shock pressure increases the amount of hot spots. This reduces the heterogeneity of

the starting step of the build-up to detonation, and transit time records are more reproducible. This suggests that the spacing of cavities in RDX particles and in compositions are important parameters. This analysis is also supported by a work on the shock sensitivity of nitromethane with a well defined hot spot distribution.<sup>16</sup> The role of the spacing of the hot spots is experimentally checked.

## CONCLUSIONS

Internal cavities of RDX particles observed by optical microscopy with matching refractive index are shown to be true hot spots. The sorting of RDX particles according to their apparent density give encouraging results for a quantitative characterization of defects in particle batches, and for their effects on the shock-detonation transition of cast formulations. Efforts are in progress to improve these first results.

## REFERENCES

1. Mishra, I.B. and Vande Kieft, L.J., "Novel Approach To Insensitive Explosives", in *Proceedings of the 19th International Annual Conference of ICT 1988*, Fraunhofer-Institut für Chemische Technologie, Karlsruhe, Federal Republic of Germany, June 25-July 1, 1988, 25-1
2. Van Ham, N.H.A.; Van der Steen, A.C. and Meulebrugge, J.J., "Less Sensitive Explosives", in *Agard conference proceedings 511 Insensitive Munitions*, Bonn Germany, 21st-23rd October 1991, 9-1
3. Mala, J. and Groux, J., "Participation des Liants Inertes a la Detonation," in *Proceedings of 4eme Journees Detonique*, Bourges - France, 19 March- 21 March 1991,
4. Moulard, H., "Particular Aspect of the Explosive Particle Size Effect on Shock Sensitivity of Cast PBX Formulations", in *Proceedings of the Ninth Symposium (International) on Detonation*, Portland, Oregon, August 28 - September 1, 1989, pp. 18-24.
5. Simpson, R.L.; Helm, F.H.; Crawford, P.C. and Kury, J.W., "Particle Size Effects in the Initiation of Explosives Containing Reactive and Non-Reactive Continuous Phases", in

- Proceedings of the Ninth Symposium (International) on Detonation*, Portland, Oregon, August 28 - September 1, 1989, pp25-38
6. Van der Steen, A.C.; Verbeek, H.J. and Meulenbrugge, J.J., "Influence of RDX Crystal Shape on the Shock Sensitivity of PBXs," in *Proceedings of the Ninth Symposium (International) on Detonation*, Portland, Oregon, August 28 - September 1, 1989, pp. 83-88.
  7. Johnson, J.R., "Report on Crystallographic Studies of RDX, HMX and Related Compounds," OSRD No. 694 Serial No. 289, Cornell University, June 30, 1942, Office of Scientific Research and Development.
  8. Campell, W.C.; Davis, W.C.; Ramsay, J.B. and Travis, J.R., "Shock Initiation of Solid Explosives," *The Physics of Fluids*, Vol. 4, No. 4, April 1961, p. 511.
  9. Lindstrom, I.E., "Planar Shock Initiation of Porous Tetryl," *Journal of Applied Physics*, Vol. 41, No. 1, January 1970, p. 337.
  10. Stirpe, D.; Johnson, J.O. and Wackerle, J., "Shock Initiation of XTX-8003 and Pressed PETN," *Journal of Applied Physics*, Vol. 41, No. 9, August 1970, p. 3884.
  11. Craig, R.E.R., "Determination of the Density of Crystalline Solids in the Undergraduate Laboratory," *Journal of Chemical Education*, Vol. 66, No. 7, July 1989, p. 599.
  12. Torvik, P.J., "A Simple Theory for Shock Propagation in Homogeneous Mixtures," AFIT TR 70-3, May 1970, Air Force Institute of Technology.
  13. Dobratz, B.M., and Crawford, P.C., "LLNL Explosives Handbook," UCRL-52997, 1985.
  14. Khasainov, B.A.; Borisov, A.A.; Ermolaev, B.S. and Korotkov, A.I., "Two-Phase Visco-Plastic Model of Shock Initiation of Detonation in High Density Pressed Explosives," in *Proceedings of the Seventh Symposium (International) on Detonation*, Naval Surface Weapons Center, NSWC MP 82-334, Annapolis, 1981, p. 435.
  15. Frey, R.B., "Cavity Collapse in Energetic Materials," *Eighth Symposium (International) on Detonation*, Naval Surface Weapon Center, NSWC MP 86-194, Albuquerque, 1985, p. 68.
  16. Fauquignon, C. and Moulard, H., "Shock Sensitivity of Nitromethane with well defined Hot Spots Distribution," *Acta Astronautica*, Vol. 5, 1978, pp 1035-1040.

## SENSITIVITY STUDY OF NITROPARAFFIN-BASED BLENDS

C.J. Anderson and M.E. Pinco  
Mining Resource Engineering Limited  
Kingston, Ontario  
CANADA, K7L 4V4

and  
S.B. Murray  
Defence Research Establishment Suffield  
Ralston, Alberta  
CANADA, T0J 2N0

Nitromethane is a very versatile compound and its use as an explosive is well known. There are two main disadvantages to its use as a bulk explosive: i) although classed as a flammable liquid, its relative sensitivity limits its transport to thin-walled, 200 kg containers; and ii) it freezes at  $-28.5^{\circ}\text{C}$ , which is well above a Canadian operational limit of  $-40^{\circ}\text{C}$ . This study investigates potential compounds which could be used to desensitize nitromethane to allow bulk transport and to reduce the blended product freezing point to a minimum of  $-40^{\circ}\text{C}$ . Methods of resensitizing the blend to levels approaching neat nitromethane were also investigated. The work conducted to date and presented here has identified blends of a minimum 50 percent by weight nitroethane in nitromethane as the best candidates to meet the requirements set at the start of this study.

### INTRODUCTION

Liquid explosives offer several advantages in their use, including ease of handling and the ability of the liquid to take the shape of any containment device. Perhaps the most rudimentary liquid explosive (and certainly the most studied) is nitromethane (NM). This material is considered a flammable liquid, however it is sensitive enough to shock stimulation that certain restrictions apply for its handling and storage.

Nitromethane is used in a wide range of industrial applications including: as a stabilizer for chlorinated hydrocarbons; as a component for special fuels in internal combustion engines; as a solvent for many chemical reactions such as polymerizations; and as a raw material in the synthesis of many useful chemicals. NM was first prepared in 1872 by Kolbe, and for many years was considered to be a very stable compound.<sup>1</sup> It was not until

1938 that McKittrick reported that NM could be detonated under conditions of strong confinement.<sup>2</sup>

During World War II, the U.S. Army Chemical Corps and the California Institute of Technology, while investigating the potential of NM as a monopropellant rocket fuel, discovered two conditions under which NM could be detonated.<sup>3-5</sup> These conditions were: (a) the addition of a few percent of certain compounds, particularly amines, sensitized NM so that it could be detonated by a #8 blasting cap; and (b) severe and very rapid compression under adiabatic conditions can result in detonation of the NM. It was also found during these studies that liquid NM, under confinement, could explode when heated to its critical temperature ( $315^{\circ}\text{C}$ ).

These conditions for explosive decomposition are so extreme that nitromethane is generally regarded as a safe material for industrial purposes, provided that certain

of its hazardous properties are understood by persons using this material so that they can take the relatively few simple precautions required to avoid unsafe conditions. These precautions have been detailed in technical specification sheets and are available from various NM manufacturers/suppliers. Furthermore, Hershkowitz and Dobratz have published a compendium of NM data which is an excellent reference source for investigations of NM regarding the various detonation properties (including shock sensitivity, detonation pressure and velocity, stability and the desensitization of NM using various liquid diluents).<sup>6</sup>

Based on considerations of safe handling and storage, temperature stability, toxicity, availability, and cost, it is clear that NM can be a preferred candidate for selection in many applications requiring the use of a liquid explosive. There are, however, some negative factors associated with the selection of NM as an explosive. As a flammable liquid, NM can only be transported and stored in 200 kg drums. Large scale applications such as ditching require considerably more than one drum of NM; thus it would be ideal to desensitize the NM such that tank-car capacities could be transported as a flammable liquid. However, the desensitized solution should be detonable using the appropriate sized booster charge. It may also be possible to sensitize the mixture (amine addition) just prior to the liquid's use in the explosive configuration.

A second disadvantage to the use of NM, particularly in northern climates, is the liquid's freezing point of approximately  $-29^{\circ}\text{C}$ . A freezing point of  $-40^{\circ}\text{C}$  would be more advantageous. The desensitized NM should therefore also have its freezing point depressed to this latter temperature.

This paper summarizes the results of an investigation into the freezing point depression and desensitization of NM to shock initiation. Shock sensitivity has been evaluated as a function of the minimum charge diameter necessary to sustain detonation, and minimum booster charge necessary to initiate detonation.

## EXPERIMENTAL

The mixtures were tested in ABS or PVC plastic pipe of the appropriate diameter with a cap fitted to one end of the pipe. Standard charge diameters used to determine an approximate critical diameter for each blend were limited to 2.5, 5, 7.5, 10, 15, and 20 cm. Charge

lengths were 70 to 75 cm; this was considered sufficient to confirm detonation had occurred. In the larger diameters, however, full run up to detonation may not have been achieved within the lengths tested.

Each blend was initiated from the capped end of the tube using varying weights of composition C-4, which were in turn initiated with an electric blasting cap. Primers larger than 1 kg were not considered. To confirm detonation or failure, a continuous velocity of detonation (VOD) probe was fixed to the tube. The test setup is illustrated in Figure 1. Cooling of the mixtures was performed in a metal container submerged in a slurry of alcohol and dry ice. The mixtures were cooled to approximately  $2^{\circ}$  below the required temperature to allow for warming during liquid transfer and test preparation. Similarly, mixtures were heated in a steam-jacketed vessel to approximately  $5^{\circ}$  above the target temperature. All final temperatures were monitored and recorded.

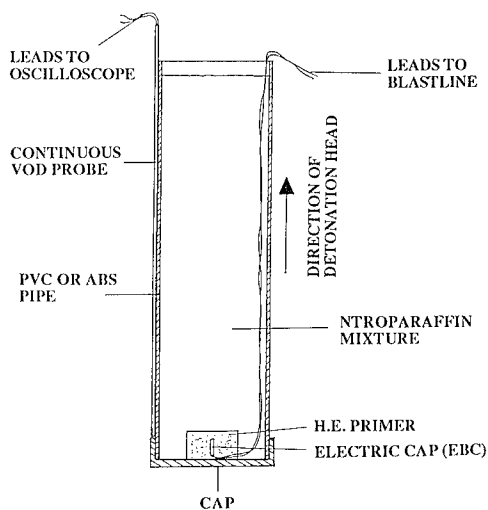


FIGURE 1. TEST SETUP TO DETERMINE THE CRITICAL DIAMETER AND MINIMUM INITIATION ENERGY FOR VARIOUS NITROMETHANE BLEND CONFIGURATIONS

## RESULTS AND DISCUSSION

This section summarizes the results of an investigation into various compounds to act as a desensitizing agent/freezing point depressant for NM. Minimum diameter and minimum initiation energy

(minimum booster size) trials were conducted for selected NM/diluent blends (unsensitized and sensitized) spanning the composition range from 0% to 100% NM, and a temperature range of 40 °C to -40 °C. The analysis of these results indicated strong relationships between the nitromethane content of the blend, the blend temperature, sensitization, and the initiation energy. Each of these factors will be discussed separately and their inter-relationships with the other factors considered. Finally, it should be noted that the detonation velocities, determined for all blends as an indication of detonation/failure, were of the order of 5200-6200 m/s.

### Desensitization and Freezing Point Suppression

Based on the bulk transport considerations, the most obvious place to begin is with the list of co-solvents which have already been approved by regulatory bodies as acceptable diluents for the bulk transport of NM. These co-solvents and the required degrees of dilution are listed in Table 1. This table also includes other candidates which the investigators believe have a good chance of being approved. Several of the candidates can be dismissed immediately. The freezing points of cyclohexanone, 1,4-dioxane, and methyl chloroform are too high for the blend to maintain a liquid state at -40 °C. 1,2-butylene oxide is too costly, methylene chloride is toxic and volatile (it boils at 40 °C), and 2-nitropropane (2-NP) is a suspected carcinogen. The remaining candidates include methanol, acetone, nitroethane (NE), and 1-nitropropane (1-NP).

TABLE 1. POTENTIAL CANDIDATES FOR DESENSITIZATION/FREEZING POINT DEPRESSION OF NITROMETHANE

CHEMICAL	WEIGHT %	MELTING POINT (°C)
*1,2-Butylene Oxide	40%	-95 (estimated)
*Cyclohexanone	25%	-16
*1,4-Dioxane	35%	12
*Methanol	45%	-94
*Methyl Chloroform	50%	-30
*1-Nitropropane	48%	-104
*2-Nitropropane	47%	-91
Acetone		-95
Ethylene Glycol Mononitrate		N/A
Methylene Chloride		-95
Nitroethane		-90

\* Approved DOT diluent for NM

The diluent used in the nitromethane blend is an important consideration in its sensitivity. Data in the literature and from the present investigation show that a freezing point of a blend of NM with the candidate diluents can be lowered to -40 °C with the addition of approximately 25-30% diluent. Figure 2 outlines the reduction in freezing point of NM as a function of NE content. Initial experiments showed that blends containing acetone or methanol in amounts of 20-30% were desensitized to the point where even a 1 kg booster charge could not initiate room temperature mixtures. These diluents were eliminated from the study. Figure 3 shows curves of temperature versus initiation energy for 50/50 blends of NM with NE and 1-NP using 4% and 10% sensitizer. As can be clearly seen, NE blends are more sensitive than blends using 1-NP at all but the highest temperatures. As will be further illustrated, the selected diluent plays a significant role in the detonation sensitivity of a blend.

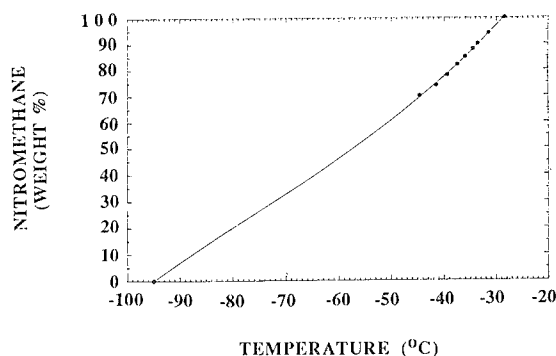
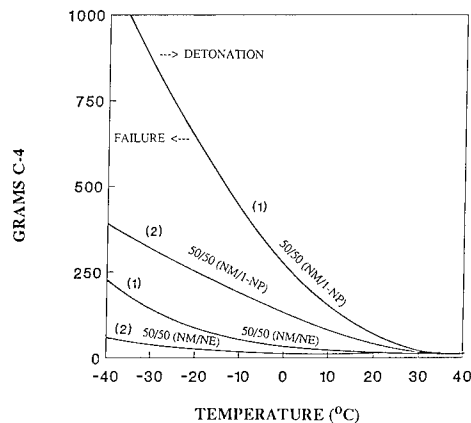


FIGURE 2. FREEZING POINT DEPRESSION CURVE FOR VARIOUS MIXTURES OF NITROMETHANE AND NITROETHANE

While the temperature requirement can be met with the addition of approximately 30% by weight diluent, analysis of the blends approved for transport have shown that approximately 50% by weight diluent is required. Such blends will not detonate at temperatures of up to 40°C using boosters with up to 1000 g of C-4 without sensitization. Thus, the most recent work in this area has been concentrated on blends with a minimum of 50% by weight diluent.

### Sensitization

The addition of a sensitizing agent such as certain amines to a blend of nitroparaffins significantly increases its sensitivity to shock initiation and decreases its critical diameter. Although ethylene diamine, diethylene triamine, and triethylene tetramine are more effective



(1) SENSITIZED WITH 4% TRIETHYLAMINE  
(2) SENSITIZED WITH 10% TRIETHYLAMINE

FIGURE 3. PLOT SHOWING ESTIMATES OF THE MINIMUM INITIATION ENERGY (G C-4) AS A FUNCTION OF BLEND TEMPERATURE FOR BLENDS OF 50/50 NM/NE AND 50/50 NM/1-NP SENSITIZED WITH 4 PERCENT AND 10 PERCENT TRIETHYLAMINE

sensitizing agents for NM, these agents were not used in this investigation because of the requirement that the sensitizing agent be effective at temperatures as low as  $-40^{\circ}\text{C}$ .<sup>7</sup> These amines all have freezing points higher than this benchmark temperature. Triethylamine, although not as effective a sensitizing agent, has a freezing point of approximately  $-115^{\circ}\text{C}$ . In addition, its boiling point of  $89^{\circ}\text{C}$  means that the toxic fumes associated with this liquid will not represent a severe handling hazard.

BLENDS which are not capable of initiation by the largest boosters considered when unsensitized, can be made to detonate with a considerably smaller booster when sensitized. It is even possible at selected NM content and temperature combinations to obtain a sensitivity similar to neat NM. For example, at ambient temperature an unsensitized blend of 50/50 NM/NE will not detonate at a diameter of 20 cm with 1 kg of C-4. When this blend is sensitized with the addition of 4 percent by weight triethylamine, it can be detonated with as little as 12.5 g of C-4 in plastic tube diameters of 5 cm. This represents almost a 100 fold increase in its shock initiation sensitivity and a 4 fold decrease in its critical diameter. Figure 4 demonstrates the effectiveness of increasing the amount of sensitizer in NM/NE blends. This figure shows curves representing combinations of minimum NM content and blend temperature which can be detonated with 250 g C-4 using various weights of sensitizer. The influence of a sensitizer on blend sensitivity is discussed further in the following sections.

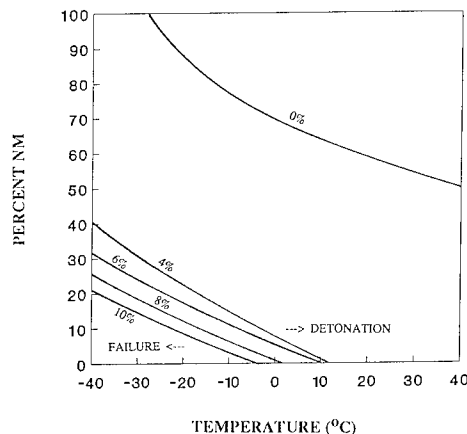


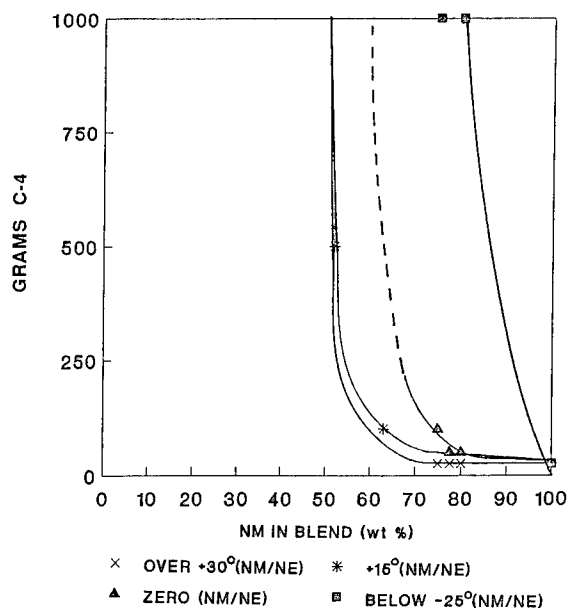
FIGURE 4. PLOT SHOWING MINIMUM BLEND NITROMETHANE CONTENT AND BLEND TEMPERATURE REQUIRED TO DETONATE NM/NE BLENDS SENSITIZED WITH VARIOUS PERCENTAGES OF TRIETHYLAMINE, AND USING A 250 g C-4 BOOSTER

#### Nitromethane Content

The addition of less sensitive nitroparaffins such as NE or 1-NP has been used in an effort to reduce the shock initiation risks associated with handling neat NM and to lower the freezing point to below  $-40^{\circ}\text{C}$ . For a given temperature and sensitizer combination, the NM content within the blend can be decreased until a point is reached after which detonation will not occur at the largest booster sizes considered (1 kg). Figures 5, 6, and 7 illustrate curves estimating the minimum initiation energy required for detonation as a function of nitromethane content at various temperatures and sensitizer additions. As can be seen from these curves, as the amount of sensitizer is increased from 0% to 4% to 10% by weight, the amount of nitromethane required in the blend at a specific temperature can be decreased while still maintaining the detonability of the blend using practical booster sizes. This becomes more clear in Figure 8 on which the  $0^{\circ}\text{C}$  NM/NE curves from Figures 5, 6, and 7 have been plotted. Figure 8 also clearly illustrates the effectiveness of triethylamine as a sensitizer in reducing the initiation energy required for detonation of all nitroparaffin blends and blend temperatures.

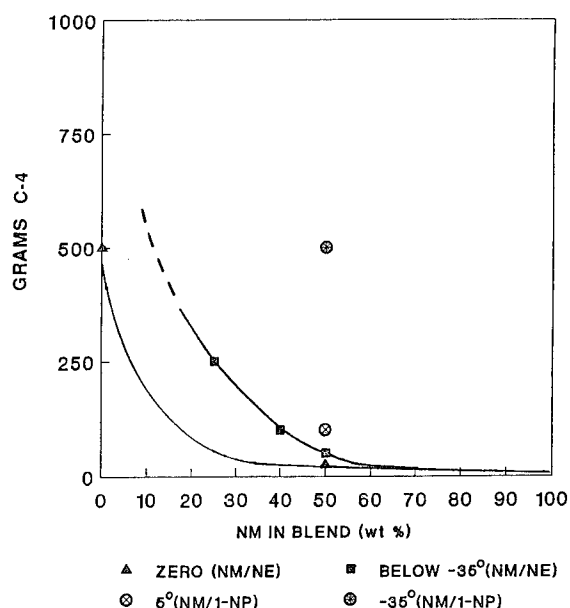
Figures 6 and 7 include points representing a sensitized 50/50 blend of NM and 1-NP. As can be seen, these points fall above the corresponding initiation energy curves for NM/NE blends at similar temperatures. This indicates that the addition of 1-NP reduces the shock





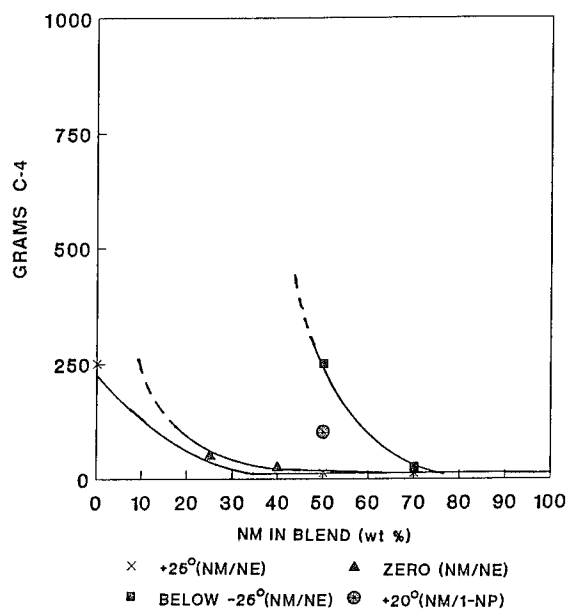
DETONATIONS ONLY PLOTTED

FIGURE 5. PLOT SHOWING INITIATION ENERGY (g C-4) AS A FUNCTION OF NITROMETHANE IN BLEND FOR UNSENSITIZED BLENDS AT VARIOUS TEMPERATURES



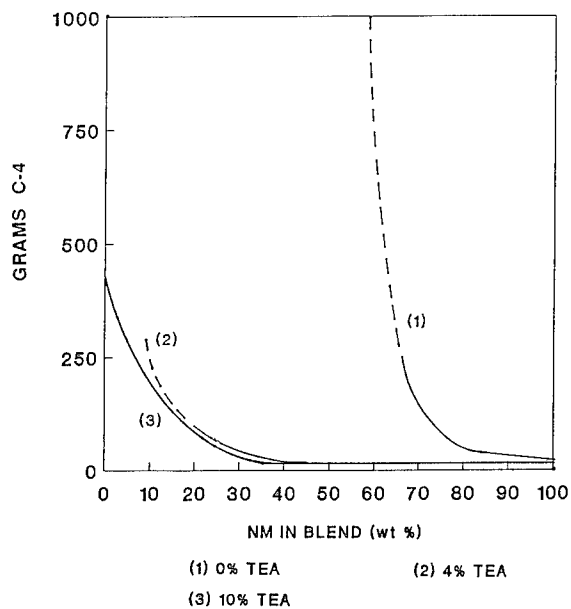
DETONATIONS ONLY PLOTTED

FIGURE 7. PLOT SHOWING INITIATION ENERGY (g C-4) AS A FUNCTION OF PERCENT NITROMETHANE IN BLEND FOR BLENDS SENSITIZED WITH 10 PERCENT TRIETHYLAMINE AT VARIOUS TEMPERATURES



DETONATIONS ONLY PLOTTED

FIGURE 6. PLOT SHOWING INITIATION ENERGY (g C-4) AS A FUNCTION OF PERCENT NITROMETHANE IN BLEND FOR BLENDS SENSITIZED WITH 4 PERCENT TRIETHYLAMINE AT VARIOUS TEMPERATURES



TEA = TRIETHYLAMINE

FIGURE 8. PLOT SHOWING INITIATION ENERGY (g C-4) AS A FUNCTION OF PERCENT NITROMETHANE IN BLEND FOR BLENDS SENSITIZED WITH 0, 4 AND 10 PERCENT TRIETHYLAMINE AT 0°C

sensitivity of NM to a greater extent than the addition of NE.

### Blend Temperature

It has been shown that as the temperature of the nitroparaffin blends decreases, their sensitivity to initiation also decreases. This decrease in sensitivity with temperature can reach a point below which detonation will not occur even with the largest boosters considered (1 kg C-4). Figures 9 and 10 show curves of temperature versus the initiation energy required for detonation in NM/NE blends with a maximum 50% by weight NM using 4% and 10% sensitizer. These figures show the significant desensitization effects of low temperatures, particularly below approximately 0°C. These temperature desensitization effects can be countered with the addition of increasing amounts of sensitizer, or an increase in the NM content, as the temperature of the blend decreases.

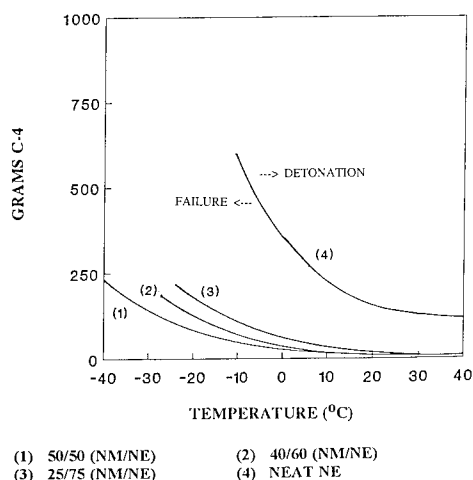


FIGURE 9. PLOT SHOWING ESTIMATES OF THE MINIMUM INITIATION ENERGY (g C-4) AS A FUNCTION OF BLEND TEMPERATURE FOR VARIOUS BLENDS OF NM AND NE SENSITIZED WITH 4 PERCENT TRIETHYLAMINE

### Initiation Energy

The energy (g C-4) used to initiate the nitroparaffin blend is directly related to the detonation sensitivity of the blend. The less energy required for detonation the more sensitive the blend is to shock initiation. As previously observed, the initiation energy is a function of the nitromethane content, blend temperature and the amount of sensitizer used. The

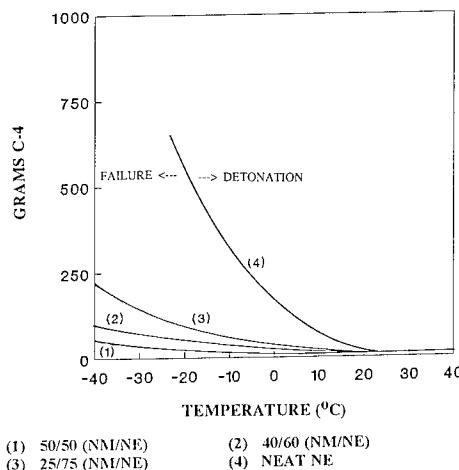


FIGURE 11. PLOT SHOWING MINIMUM BLEND NITROMETHANE CONTENT AND BLEND TEMPERATURE REQUIRED TO DETONATE NM/NE BLENDS SENSITIZED WITH 4 PERCENT TRIETHYLAMINE WITH VARIOUS SIZES OF BOOSTER (g C-4)

curves presented in Figures 11 and 12 represent the minimum blend nitromethane content (in NE) and temperature combinations which can be detonated with a given weight of booster using 4% and 10% by weight sensitizer respectively. These curves can be used to estimate the minimum blend NM content and blend temperature combinations which will assure detonation using a given booster size. A comparison of Figures 11 and 12 shows the effectiveness of increasing the amount of sensitizer on reducing the size of the booster required for detonation for all combinations of blend NM content and temperature.

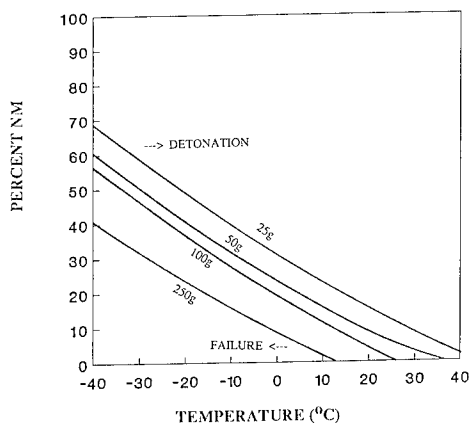


FIGURE 10. PLOT SHOWING ESTIMATES OF THE MINIMUM INITIATION ENERGY (g C-4) AS A FUNCTION OF BLEND TEMPERATURE FOR VARIOUS BLENDS OF NM AND NE SENSITIZED WITH 10 PERCENT TRIETHYLAMINE

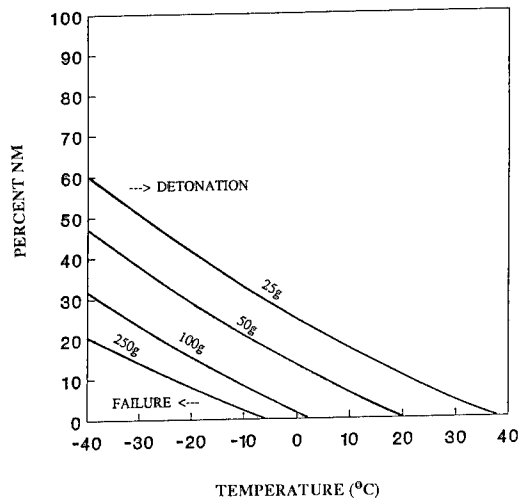
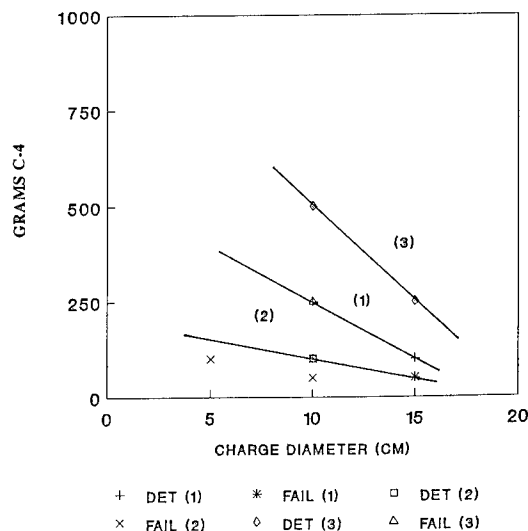


FIGURE 12. PLOT SHOWING MINIMUM BLEND NITROMETHANE CONTENT AND BLEND TEMPERATURE REQUIRED TO DETONATE NM/NE BLENDS SENSITIZED WITH 10 PERCENT TRIETHYLAMINE WITH VARIOUS SIZES OF BOOSTER (g C-4)



- (1) UNSENSITIZED 63/37 (NM/NE)  
 (2) SENSITIZED 50/50 (NM/1-NP)  
 (3) SENSITIZED NEAT NE

FIGURE 13. DETONATION/FAILURE PLOT OF CHARGE DIAMETER AS A FUNCTION OF INITIATION ENERGY (g C-4) FOR VARIOUS BLENDS AT AMBIENT TEMPERATURES

### Charge Diameter

All explosives have a diameter below which a detonation can not be sustained. This critical diameter can be altered by using various additives such as sensitizers or diluents. For the nitroparaffin systems considered in this study, it has been observed that the NM content of the blend, blend temperature, and sensitization all significantly affect sensitivity to shock initiation. This study has not focussed specifically on determination of critical diameters, however the results are useful in determining the general effect of charge diameter on detonation of nitroparaffin blends.

It has been shown that the critical charge diameter increases with decreasing nitromethane content and decreasing temperature. It has also been shown that the addition of a sensitizer reduces the critical diameter of the blends. In addition to these general observations, it is apparent that the amount of energy required to detonate the mixtures can be influenced by the charge diameter, particularly if the selected diameter is close to the critical diameter. Figure 13 illustrates a Detonation/Failure plot of the initiation energy as a function of charge diameter for selected blends at ambient temperature. The curves demonstrate that more energy is required for detonation

at smaller charge diameter which indicates they may be close to the critical diameter.

### CONCLUSIONS

This study was initiated to investigate compounds which could be added to nitromethane to desensitize it to levels which made it safe to handle in bulk quantities, and lower its freezing point to the level where the NM would remain liquid throughout a wide operating temperature range (40 °C to -40 °C). Nitroethane has been shown to be the most effective desensitizing agent/freezing point depressant for nitromethane. It is apparent that both the amount of added NE and the temperature have significant effects on the sensitivity of NM to detonation, however these effects can be generally offset with the addition of increasing amounts of sensitizer. Of the blends investigated, it has been shown that a 50/50 NM/NE blend meets the requirements outlined at the start of this investigation. This is demonstrated by the fact the blend cannot be detonated with up to one kilogram of C-4, but can be resensitized with the addition of reasonable amounts of sensitizer (10% by weight) to levels approaching neat NM, even at the lowest temperature tested.

## ACKNOWLEDGEMENTS

This work was performed under contract with the Canadian Department of National Defence for Defence Research Establishment Suffield.

## REFERENCES

1. Kolbe, H., *Prakt. Chemie* 5, 1872, p.427.
2. McKittrick, D., Irvine, R., Bergensteinsson, I., *Ind. Eng. Chem., Anal. Ed.* 10, 1938, p.630.
3. Bellinger, F., Friedman, H., Bauer, W., Eastes, J., Bull, W., Gross, J., *Ind. Eng. Chem.* 40, 1948, pp. 1320-1324.
4. Griffin, D., *J. Am. Chem. Soc.* 71, 1949, p.1423.
5. Kaplan, N., Johnson, S., Peebles, L., "Thermal and Shock Sensitivity of Nitromethane", Progress Report No. 1-35, Jet Propulsion Laboratory, California Institute of Technology, 1945.
6. Hershkowitz, J., Dobratz, B., "Compendium of Nitromethane Data Relevant to the Tactical Explosive System (TEXS) Program", U.S. Army Armament Research Development and Engineering Center, Picatinny Arsenal, NJ, 1989, Publication Number ARFSK-SP-89001.
7. Egly, R., "Recent Developments in Nitromethane-Based Liquid Explosives", in *Proceedings of the Symposium on Military Applications of Commercial Explosives*, The Technical Cooperation Program, Defence Research Establishment Valcartier, Quebec, Canada, 1972, p.190.

**SESSIONS ON  
POSTER PAPERS-3**

**Cochairmen: Joseph Foster, Jr.**  
**Wright Laboratory/Armament Directorate**

**Brian Hammant**  
**Defense Research Agency**

## A TESTING METHOD TO EVALUATE EXPLOSIVENESS

C. Bélanger

Défense Research Establishment Valcartier  
Québec, Canada G0A 1R0

A method which was developed to characterize explosives as main charges with respect to hazard assessment of munitions, is described. This laboratory scale method evaluates their propensity to propagate a reaction initiated by any stimuli other than the initiation system. This propensity is usually referred to as the explosiveness. The instrumented method described proved to be effective and reliable in evaluating the explosiveness of a great variety of explosives. In decreasing order of explosiveness LX-14 with the greatest explosiveness was followed by Octol 75/25, Composition B, Composition A-3, tetryl, TNT, PBXW-115, CX-84A, CX-85 and PBX-9502.

### INTRODUCTION

The development of new munitions called insensitive munitions requires the evaluation of their vulnerability to unplanned stimuli such as slow cook-off, fuel fire, bullet/fragment impact, shaped charge jet attack, electrostatic discharge and sympathetic detonation. Thus, insensitive munitions must be designed to avoid reaction or to react mildly when exposed to unplanned stimuli; this includes the use of explosives with low vulnerability characteristics. The vulnerability characteristics of energetic materials are mainly based on their propensity to propagate a reaction that may be initiated by any stimuli other than the initiation system in configurations such as those found in munitions. This propensity to propagate a reaction through different reaction thus leading to different intensities of reaction is usually referred to as explosiveness.

An experimental method to evaluate the explosiveness of high explosives has been developed at the Defence Research Establishment Valcartier. The method is used to characterize main explosive charges with respect to hazard assessment of munitions. This instrumented method, reported in References 1 and 2, is based on the DREV Setback Simulator, an apparatus designed to study the behavior of explosives under specific

gun launch or setback conditions. This apparatus, when used under specific testing conditions, has demonstrated its effectiveness in evaluating the explosiveness of explosives. Based on a large series of tests, not all of which are presented in this document, the explosiveness remained the same for each explosive regardless of the severity of the testing conditions used.

### EXPERIMENTAL METHOD

#### Apparatus

The experimental method is very similar to that described for the DREV setback simulator<sup>3 4</sup>. This apparatus, shown schematically in Figure 1, is based on a piston with a controlled mass which is accelerated in a reproducible manner by a square-wave force. The piston compresses a 0.9 mm thick air gap. When the gap collapses, a reproducible stress is applied on the heavily confined explosive specimen for  $4.3 \pm 0.2$  ms. The square-wave force is obtained by crushing a honeycomb piece with a 75-kg hammer. The aluminum honeycomb piece gives a constant crushing force for a major portion of its initial deformation distance. This force of  $108 \pm 7$  kN accelerates the piston of 420 g at  $25\,000\text{ g}_n$  prior to applying stresses of  $213 \pm 14$  MPa on the specimen. These stresses are applied very rapidly i.e. at the

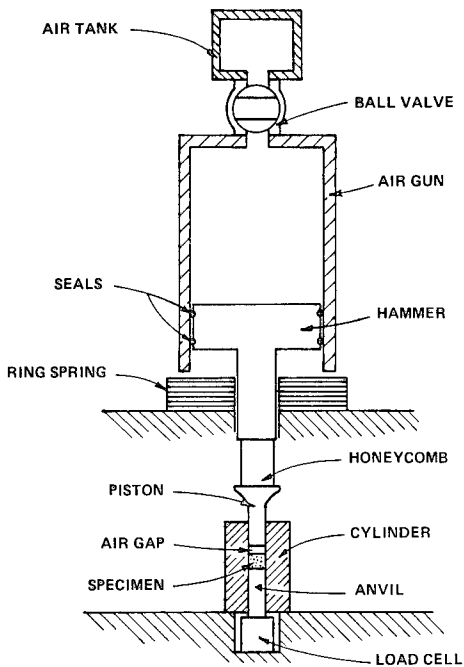


FIGURE 1. SCHEMATIC OF THE DREV SETBACK SIMULATOR

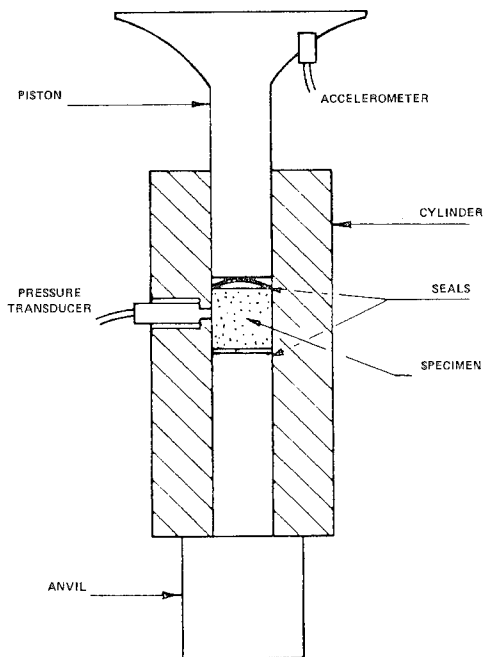


FIGURE 2. SPECIMEN MOUNTING HARDWARE

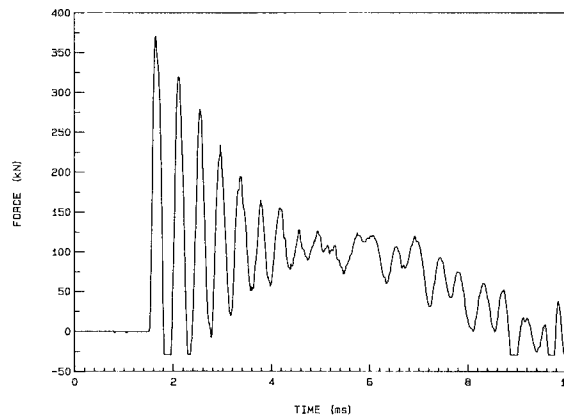


FIGURE 3. TYPICAL FORCE RECORDING

rate of 2.1 GPa/ms. The 75-kg hammer, accelerated by an air gun, reaches a velocity of  $25.0 \pm 0.5$  m/s, measured just before crushing the honeycomb piece. At the end of the test, a large ring spring stops the hammer over a very short distance and also damps any significant rebounds of the hammer.

The cylindrical explosive specimen, weighing approximately 21 g, is highly confined in a rigid steel cylinder between the piston and an anvil as shown in Figure 2. Seals are used at each end of the specimen to avoid any extrusion of explosive between the piston and the cylinder wall which could occur despite the very tight tolerances which allow a maximum free play of 0.04 mm. Furthermore, the top seal (piston side) prevents any air leakage in addition to providing an air gap of  $0.9 \pm 0.05$  mm above the sample, as given in the design specification.

This apparatus is instrumented to monitor the test conditions. The speed of the hammer, in addition to the force applied on the specimen by the honeycomb, are measured for every test. The hammer velocity is measured by laser, whereas a load cell, Lebow Model 3156, measures the force. This load cell has a capacity of 1000 kN. A typical recording, reproduced here in Figure 3, shows an initial impulse in addition to the constant force applied. This impulse is generated mainly by the momentum of the piston which theoretically reaches a velocity of 21.0 m/s at an acceleration of 25 000  $g_n$  over a distance of 0.9 mm. On this recording, the constant force of 115 kN for a duration of 4.4 ms is calculated directly

by computer. Furthermore, the load cell recordings indicate reliably and precisely any explosive reactions via a rapidly rising reaction peak and quantify the time delay before this response occurs. The experimental signals are monitored by digital recorders and they are stored and processed by a microcomputer.

A theoretical simulation reproducing the experimental conditions has shown that a temperature of 1052°C can be reached when the volume of air is compressed under the conditions described. The surface temperature of the specimen can reach temperatures from 325 to 365°C depending on the thermal conductivity of the explosives being tested. This theoretical simulation, initiated last year, has not yet been completed and the data mentioned previously are only preliminary. The simulation is conducted using an approach similar to that used by H.J. Pasman<sup>5</sup>.

The explosiveness of an explosive is assessed by analyzing load cell recordings and examining the components upon dismantling the specimen mounting pieces, including any residual portion of the specimen. The load cell recordings give measurements of the reaction peaks, if any, and the delays before they occurred. The reaction peaks are evaluated by measuring the portion of the peak which is higher than the initial impulse. The reaction delays reported are the time intervals between the starting point of the application of stress and the beginning of the reaction peak. The explosiveness is evaluated from a series of three tests.

The explosiveness results are classed into four categories. An explosion (E) is reported when the explosive specimen is completely consumed, the components of the mounting hardware for the specimen are badly damaged or broken into pieces and a strong reaction peak greater than 300 kN is recorded with delays generally shorter than 0.2 ms. A heavy partial reaction (PP) is assessed whenever more than 50% but not all of the specimen is consumed. In general, the hardware components for the specimen mounting are bulged, sometimes broken into a few parts, and significant reaction signals with peaks from 50 to 200 kN and delays from 0.2 to 0.4 ms are recorded. A light partial reaction (p) is identified when 5% or more but less than 50% of the original specimen is consumed and a reaction can be seen on the force recordings but no reaction peak is present. The components of the specimen mounting hardware are barely damaged. The reaction delays with light partial reactions

are generally longer than 0.8 ms. Finally, a mild partial burning (b) is reported when less than 5% of the specimen is burned. An indication of reaction is barely seen on the force recordings and the components of specimen's mounting hardware are undamaged except for some erosion on the piston. The delays recorded for these light partial burnings are usually longer than 1.0 ms.

### Explosive Specimens

The explosive specimens were produced from larger cylinder molds or pressing dies and machined precisely to the final dimensions required. These cylindrical specimens were machined to a diameter of  $25.38 \pm 0.013$  mm and a length of  $25.40 \pm 0.13$  mm.

The specimens tested were conventional cast and pressed explosives as well as plastic bonded explosives (PBXs) produced by a cast-cure process or by coating and pressing techniques. The conventional explosives tested included TNT with a density of  $1.56 \pm 0.01$  Mg/m<sup>3</sup>, Composition B (RDX/TNT/wax - 59.5/39.5/1.0) with a density of  $1.680 \pm 0.005$  Mg/m<sup>3</sup> and Octol (HMX/TNT-75/25) with a density of  $1.832 \pm 0.004$  Mg/m<sup>3</sup>. These TNT-based explosive specimens were all cast. The pressed explosives assessed were Composition A-3 (RDX/wax - 91/9) and tetryl pressed to densities of  $1.590 \pm 0.005$  Mg/m<sup>3</sup> and  $1.660 \pm 0.005$  Mg/m<sup>3</sup> respectively. The cast-cured plastic bonded explosives tested were PBXW-115, a US formulation made of RDX/AP/Al/binder - 20/43/25/12, and CX-84A and CX-85, two PBXs developed at DREV. PBXW-115 had a density of  $1.786 \pm 0.002$  Mg/m<sup>3</sup>. CX-84A is made of 84% RDX and 16% HTPB binder with a density of  $1.550 \pm 0.002$  Mg/m<sup>3</sup>. CX-85 contains 84.25% HMX and 15.75% HTPB binder with a density of  $1.620 \pm 0.002$  Mg/m<sup>3</sup>. The explosiveness of PBX-9502 and LX-14, two US explosives produced by pressing techniques were also evaluated. PBX-9502 is made of 95% TATB and 5% Kel-F as binder and was pressed to a density of  $1.645 \pm 0.001$  Mg/m<sup>3</sup>. LX-14 contains 95.5% HMX and 4.5% binder. It was pressed to a density of  $1.820 \pm 0.002$  Mg/m<sup>3</sup>.

### RESULTS AND DISCUSSION

Series of tests were carried out to evaluate the explosiveness of the explosives mentioned. All of the explosives tested reacted to varying degrees, each giving similar results for each of the three trials as indicated in Table I. LX-14 showed the highest explosiveness with the most violent reactions called explosions (E). No trace of explosive residue was found. The compo-



TABLE 1. EXPLOSIVENESS TEST RESULTS

EXPLOSIVES	REACTIONS			Type	Specimens Consumed
	Frequency	Peak (kN)	Delays (ms)		(%)
LX-14	3/3	375-600	≤ 0.1	E	100
Octol 75/25	3/3	375-450	≤ 0.1	E	100
COMP. B	3/3	500-700	≤ 0.1	E	100
COMP. A-3	3/3	250-400	0.13-0.20	E	100
TETRYL	3/3	250-350	0.15-0.20	PP	85-90
TNT	3/3	50-200	0.30-0.45	PP	70-85
PBXW-115	3/3	0	0.9-2.2	p	5-8
CX-84A	3/3	0	2.0-4.0	b	≤ 5
CX-85	3/3	0	3.3-3.5	b	≤ 4
PBX-9502	3/3	0	0.9-1.1	b	≤ 1.5

E: Explosion, PP: Heavy Partial Reaction, p: Light Partial Reaction, b: Mild Partial Burning

nents of the specimen mounting hardware were shattered into pieces as shown in Figure 4. Reaction peaks from 375 to 600 kN were measured with delays shorter than 0.1 ms from load cell recordings, as shown in Figure 5. Delays shorter than 0.1 ms are too short to measure since they are superimposed on the initial pulse which has a rise time slightly less than 0.1 ms. Octol 75/25 and Composition B produced very similar explosions (E) with reaction delays shorter than 0.1 ms but with a slightly lower explosiveness, particularly for Composition B. The components of the specimen mounting hardware after a reaction of Octol 75/25, as illustrated in Figure 6, were significantly more damaged than those for Composition B (Figure 7) but less than those for LX-14. However, based on the reaction peaks measured on the force recordings, one could conclude that Composition B, with reaction peaks from 500 to 700 kN, produced the most violent reactions. Reaction peaks were from 375 to 450 kN for Octol 75/25 and from 375 to 600 kN for LX-14. Force recordings for reactions of Octol 75/25 and Composition B are shown in Figures 8 and 9 respectively. An explanation for the lower reaction peaks recorded for LX-14 and Octol 75/25 is that these HMX-based explosives shattered the

cylinders that housed the specimens earlier than did Composition B. Therefore, these shatterings occurred in a time frame too short to allow a more complete recording of the pressure build-up as in the case of Composition B.

Composition A-3 also produced violent explosions (E) without any explosive residue. However the reactions were significantly less violent than those obtained for Composition B. Figure 10 shows a typical recording of a reaction of Composition A-3. Reaction peaks were measured between 250 and 400 kN with delays from 0.13 to 0.20 ms. As shown in Figure 11, the cylindrical portion of the piston was shattered into pieces but the cylinder remained in one piece.

All other explosives tested produced only partial reactions or burnings. Tetryl resulted in the strongest heavy partial reactions where 85 to 90% of the specimens were consumed. The reaction peaks, one of which is shown in Figure 12, were measured between 250 and 350 kN with delays from 0.15 to 0.20 ms. The components of the specimen mounting hardware were damaged and bulged but none were broken into pieces (Figure 13). TNT produced reactions very similar to

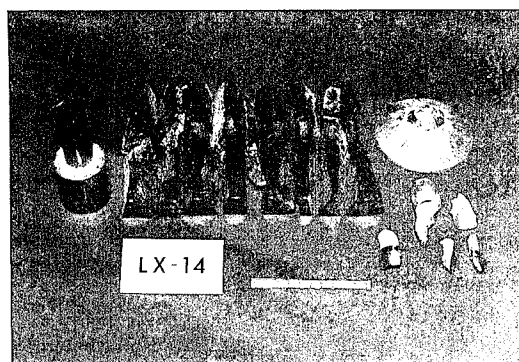


FIGURE 4. SPECIMEN MOUNTING HARDWARE AFTER A REACTION OF LX-14

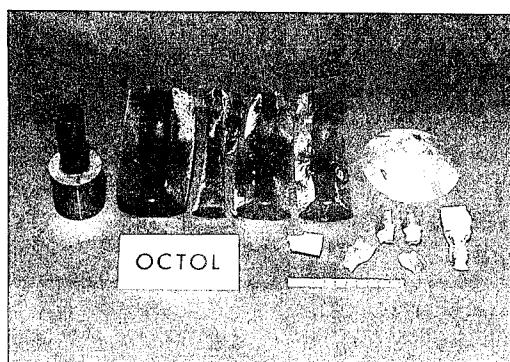


FIGURE 7. SPECIMEN MOUNTING HARDWARE AFTER A REACTION OF COMPOSITION B

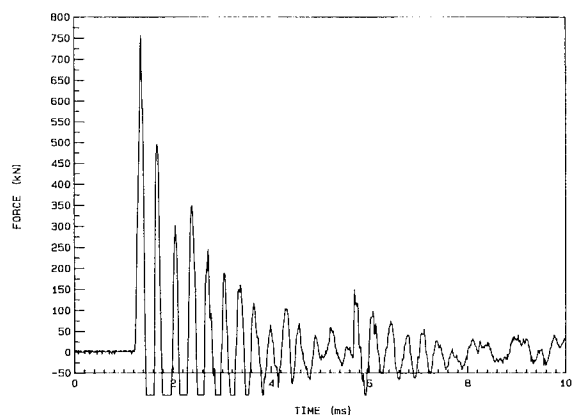


FIGURE 5. FORCE RECORDING OF A REACTION OF LX-14

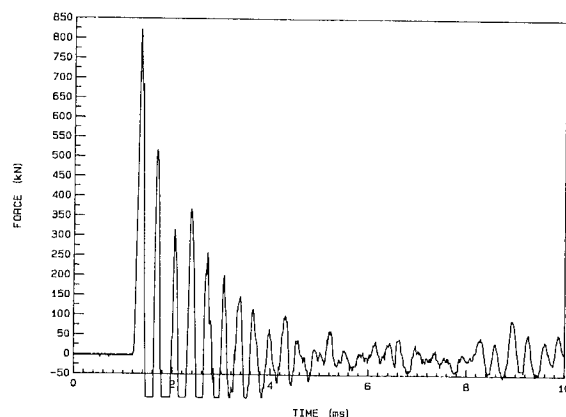


FIGURE 8. FORCE RECORDING OF A REACTION OF OCTOL 75/25

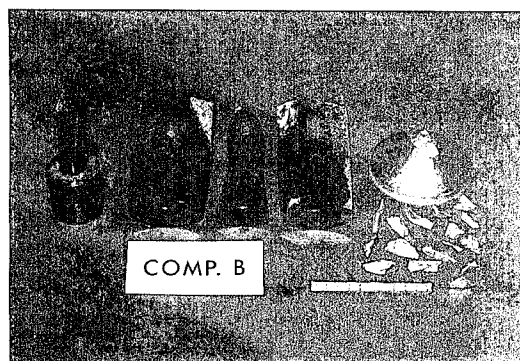


FIGURE 6. SPECIMEN MOUNTING HARDWARE AFTER A REACTION OF OCTOL 75/25

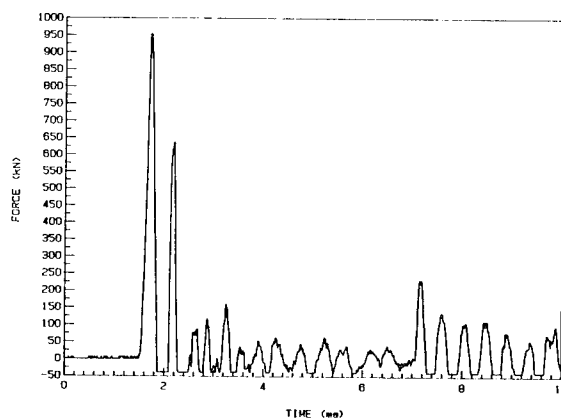


FIGURE 9. FORCE RECORDING OF A REACTION OF COMPOSITION B

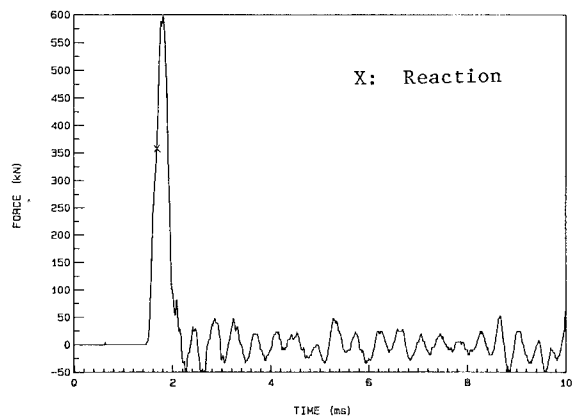


FIGURE 10. FORCE RECORDING OF A REACTION OF COMPOSITION A-3

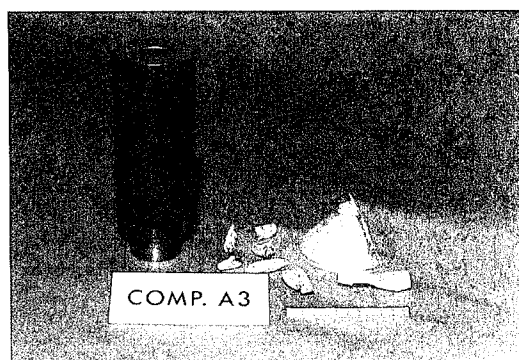


FIGURE 11. SPECIMEN MOUNTING HARDWARE AFTER A REACTION OF COMPOSITION A-3

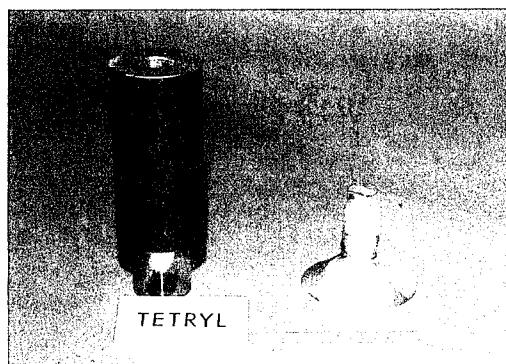


FIGURE 13. SPECIMEN MOUNTING HARDWARE AFTER A REACTION OF TETRYL

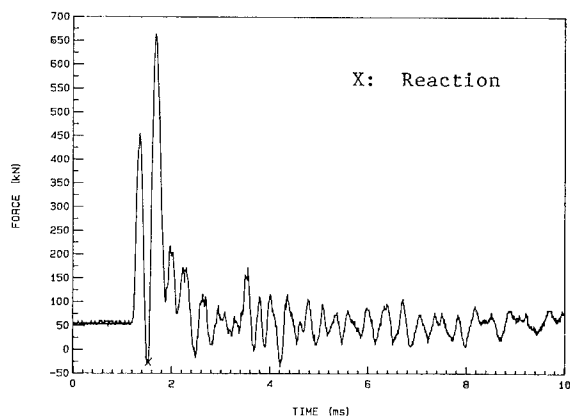


FIGURE 14. FORCE RECORDING OF A REACTION OF TNT

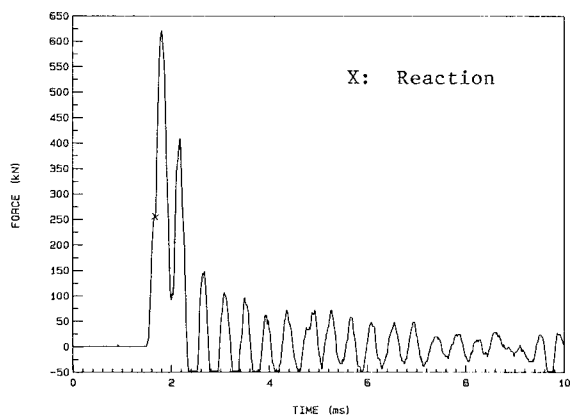


FIGURE 12. FORCE RECORDING OF A REACTION OF TETRYL

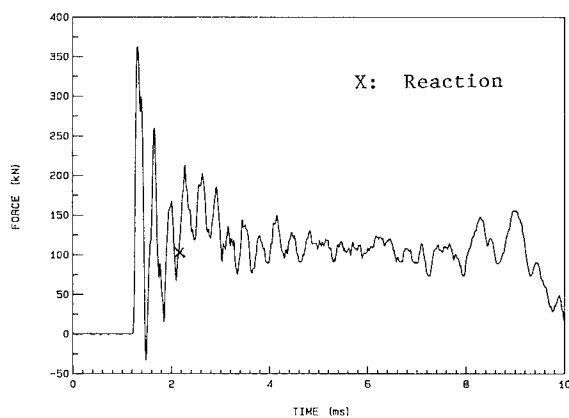


FIGURE 15. FORCE RECORDING OF A REACTION OF PBXW-115

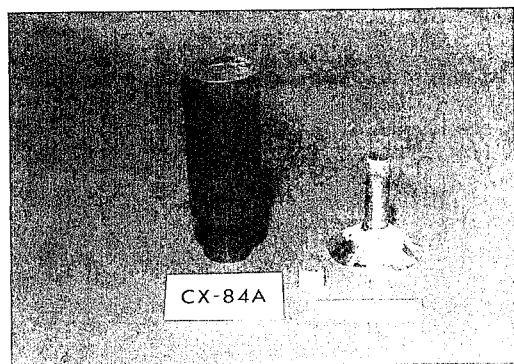


FIGURE 16. SPECIMEN MOUNTING HARDWARE AFTER A REACTION OF CX-84A

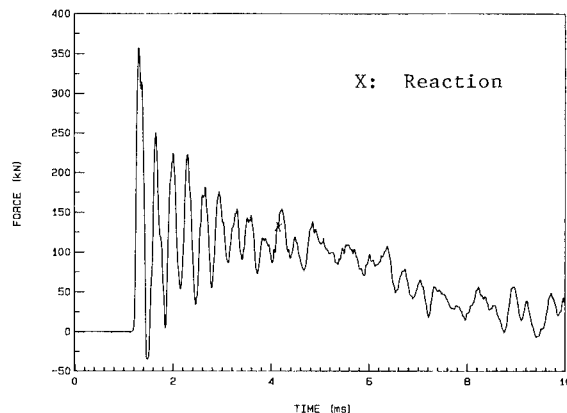


FIGURE 19. FORCE RECORDING OF A REACTION OF CX-85

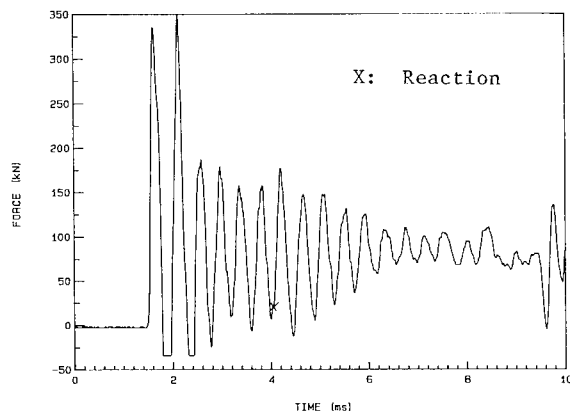


FIGURE 17. FORCE RECORDING OF A REACTION OF CX-84A

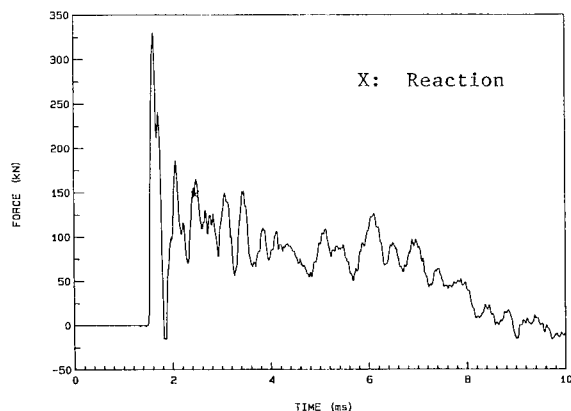


FIGURE 18. FORCE RECORDING OF A REACTION OF PBX-9502

those for tetryl. The specimens were consumed from 70 to 85% with reaction peaks between 50 to 200 kN with delays from 0.30 to 0.45 ms. A typical recording of a reaction of TNT is shown in Figure 14. PBXW-115 produced only light partial reactions (p). The portion of the specimen consumed was from 5 to 8% with reaction delays from 0.9 to 2.2 ms. The reactions were so feeble that no reaction peak was recorded as indicated in Figure 15. The specimen mounting hardware in each case was undamaged except for some erosion on the piston, which was very similar to that shown in Figure 16 for CX-84A.

CX-84A, CX-85 and PBX-9502 produced only light partial burnings (b). A reaction of CX-84A consumed less than 5% of the specimen. The specimens showed some indication of burning on the surface adjacent to the air gap. These reactions were so feeble that no reaction peak was recorded, as shown in Figure 17. Furthermore, it is difficult to determine precisely on the recording when the reaction occurred. Delays from 2.0 to 4.0 ms were obtained. Very similar light partial burnings were obtained for CX-85 and PBX-9502 but lower percentages of the specimens were consumed. Almost no erosion was observed on the piston particularly for PBX-9502. Less than 1.5% of PBX-9502 was consumed and for CX-85 it was less than 4%. The reaction delays were from 0.9 to 1.1 ms and from 3.3 to 3.5 ms respectively. Furthermore, these two explosives demonstrated that they are less likely to propagate a reaction than CX-84A. At the end of the test when the stimulus was no longer applied, the reaction died for PBX-9502 and CX-85 as indicated in Figures 17 and 18 respectively, whereas for CX-84A the record-

ings indicated that the reaction continued after the stresses ceased to be applied and seemed to continue until the moment the piston was ejected from the cylinder. The specimen mounting hardware after a reaction of CX-85 and PBX-9502 was similar to those shown in Figure 16 for CX-84A, except the erosion on the piston was reduced according to the percentage of specimen consumed for each explosive.

These explosiveness results, obtained under heavy confinement, are valuable data as an initial evaluation of the vulnerability of explosives to unplanned stimuli when loaded in a munition.

## CONCLUSIONS

The method described gives a consistent and reliable measure of explosiveness for a variety of explosives from TNT-based to insensitive PBXs, including pressed explosives.

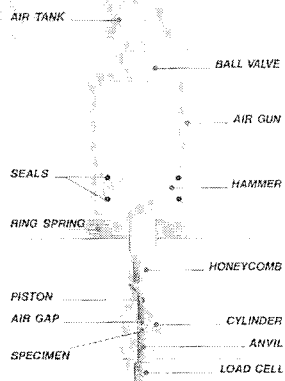
LX-14 gave the highest explosiveness or the highest propensity to react. It resulted in the greatest violence among the explosives tested. In decreasing order of explosiveness, LX-14 was followed by Octol 75/25, Composition B, Composition A-3, tetryl, TNT,

PBXW-115, CX-84A, CX-85 and PBX-9502 with the lowest explosiveness.

## REFERENCES

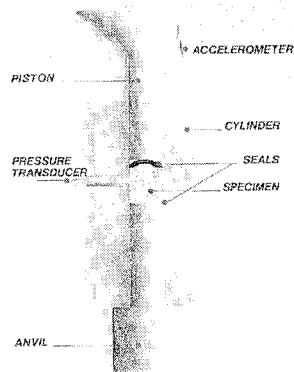
1. Bélanger, C., "DREV Setback Simulator as an Explosiveness Test", DREV M-3117/92, November 1992.
2. Bélanger, C., "Méthode d'évaluation de l'explosivité des explosifs", 22nd International Conference of ICT Karlsruhe, pp. 10-1 to 10-15, July 1991.
3. Bélanger, C. and Walker, G.R., "DREV Setback Simulator: Design and Performance", DREV R-4274/82, November 1982.
4. Bélanger, C., "Study of Explosive Shell Fillings with Defects in Simulated Gun Launch Conditions", Ninth Symposium (International) on Detonation, pp. 1480-1488, Portland Oregon, August-September 1989.
5. Pasman, H.J., "Shell Premature by Compression Ignition and their Laboratory Simulation", DREV R-707/75, April 1975.

## ••A P P A R A T U S

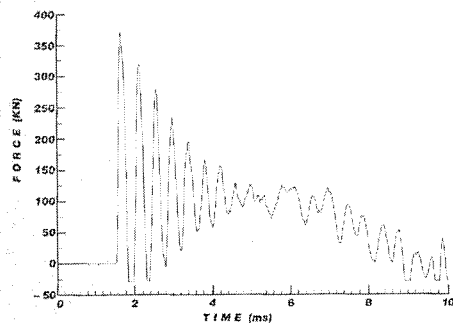


*DREV setback simulator*

## ••SPECIMEN MOUNTING



## ••TYPICAL FORCE RECORDING



*inert specimen*

## ••TEST CONDITIONS

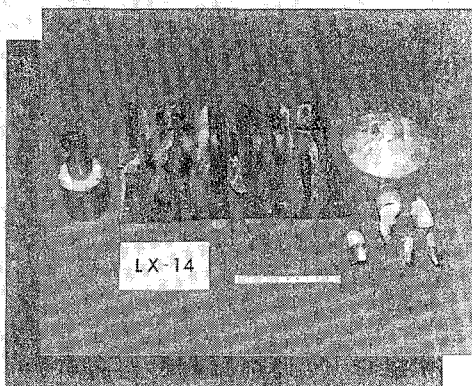
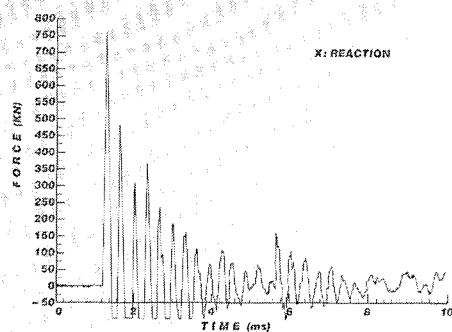
### ◊SPECIMEN

◊SIZE                      ◊WEIGHT  
 dia.: 25.38mm      2lg  
 l: 25.4mm

◊AIR GAP  
 0.9mm

◊PRESSURIZATION RATE: 2.1 GPa/ms  
 ◊PRESSURE: 2.3 MPa  
 ◊DURATION: 4.3 ms

## LX - 14

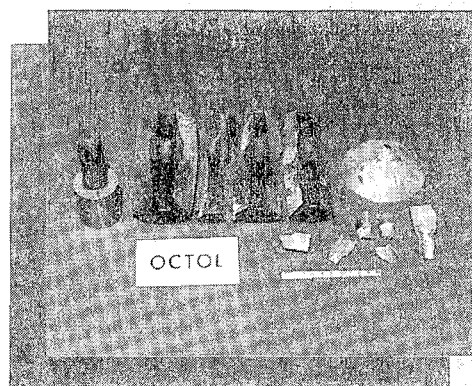
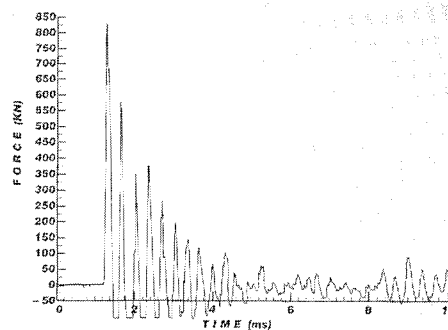


## RESULTS

◊REACTION			◊SPECIMEN
peak (kN)	delay (ms)	type	consumed (%)
375-600	≈0.1	E	100

E : Explosion

## OCTOL 75/25

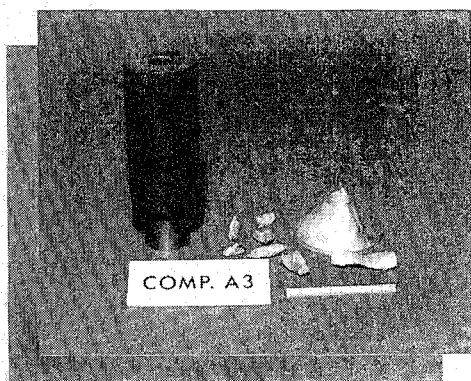
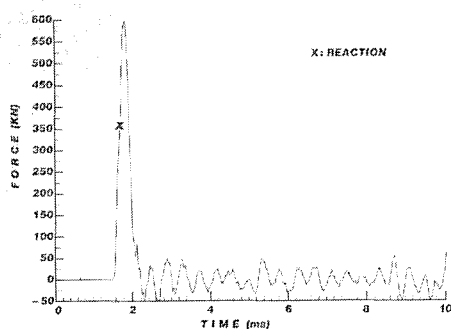


## RESULTS

◊REACTION			◊SPECIMEN
peak (kN)	delay (ms)	type	consumed (%)
375-450	≈0.1	E	100

E : Explosion

## COMP. A-3

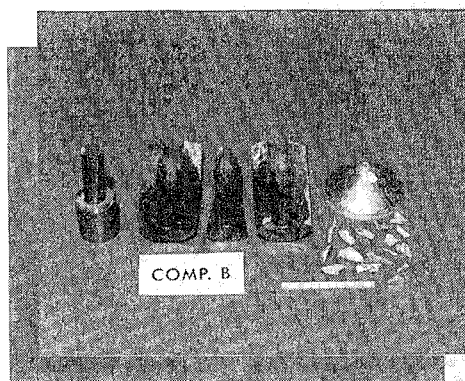
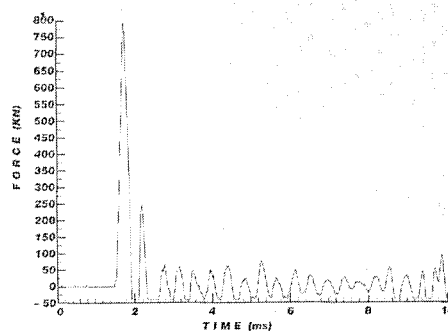


## RESULTS

◇REACTION			◇SPECIMEN
peak (kN)	delay (ms)	type	consumed (%)
250-400	0.13-0.20	E	100

E: Explosion

## COMP. B



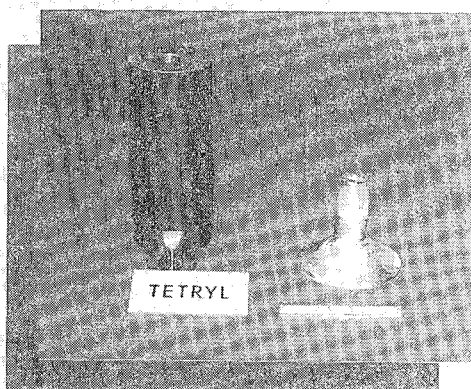
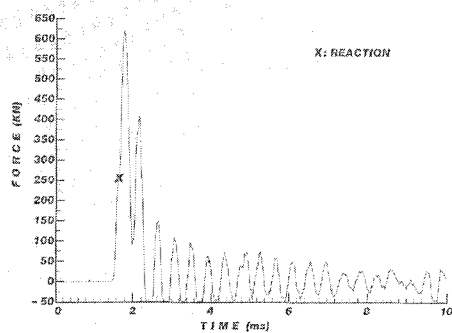
## RESULTS

◇REACTION			◇SPECIMEN
peak (kN)	delay (ms)	type	consumed (%)
500-700	<0.1	E	100

E: Explosion



## TETRYL

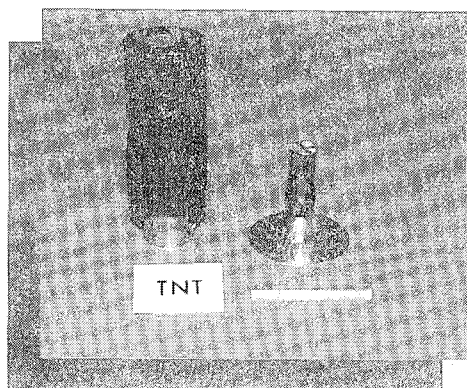
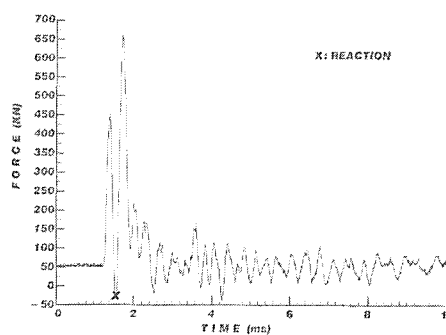


## RESULTS

◇REACTION			◇SPECIMEN
peak (kN)	delay (ms)	type	consumed (%)
250-350	0.15-0.20	PP	85-90

PP: Heavy Partial Reaction

## TNT

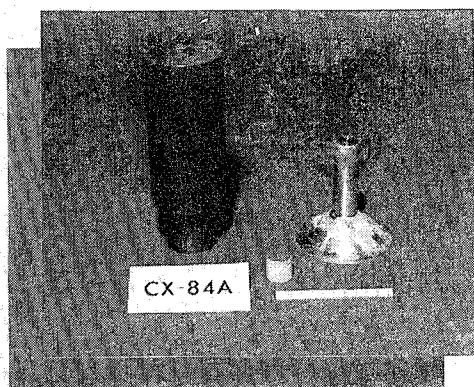
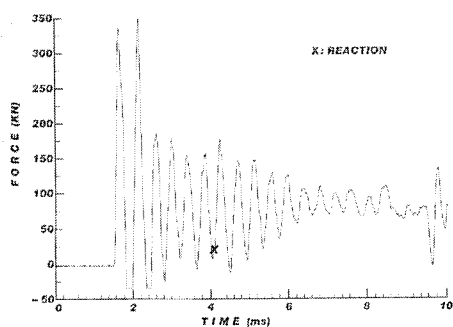


## RESULTS

◇REACTION			◇SPECIMEN
peak (kN)	delay (ms)	type	consumed (%)
50-200	0.30-0.45	PP	70-85

PP: Heavy Partial Reaction

## CX-84A

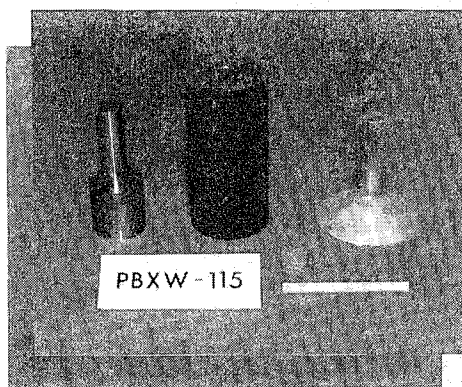
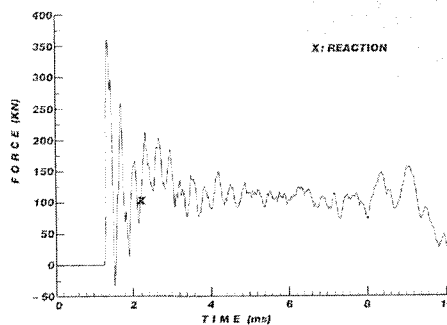


## RESULTS

REACTION			SPECIMEN
peak (kN)	delay (ms)	type	consumed (%)
O	2.0-4.0	b	≤5

b: Mild Partial Burning

## PBXW-115

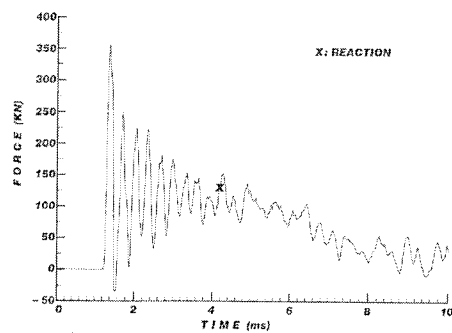


## RESULTS

REACTION			SPECIMEN
peak (kN)	delay (ms)	type	consumed (%)
O	0.9-2.2	p	5-8

p: Light Partial Reaction

## CX-85

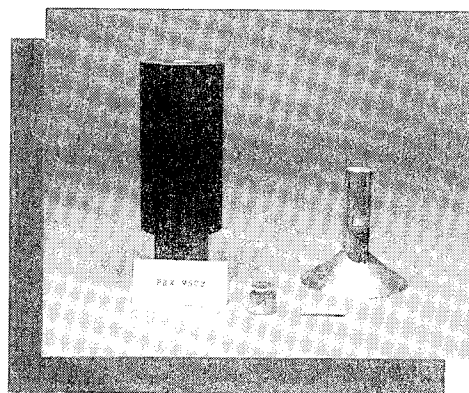
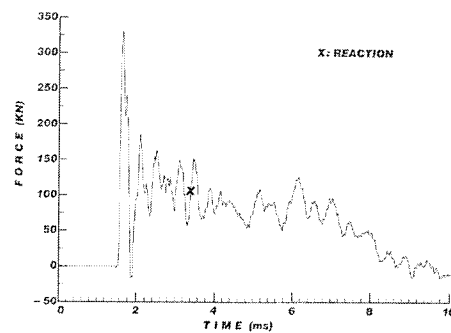


## RESULTS

◊REACTION			◊SPECIMEN
peak (kN)	delay (ms)	type	consumed (%)
0	3.3-3.5	b	≈4

b: Mild Partial Burning

## PBX - 9502



## RESULTS


◊REACTION			◊SPECIMEN
peak (kN)	delay (ms)	type	consumed (%)
0	0.9-1.1	b	≈1.5

b: Mild Partial Burning

# ***CONCLUSIONS***

---

- ***CONSISTENT AND RELIABLE MEASURE OF EXPLOSIVENESS FOR A VARIETY OF EXPLOSIVES***
- ***EXPLOSIVENESS IN DECREASING ORDER***

<b>HIGH</b>		<b>LX-14</b>
		<b>OCTOL 75/25</b>
		<b>COMPOSITION B</b>
		<b>COMPOSITION A-3</b>
		<b>TETRYL</b>
		<b>TNT</b>
		<b>PBXW~115</b>
		<b>CX~84 A</b>
		<b>CX~85</b>
<b>LOW</b>		<b>PBX~9502</b>

## THE APPLICATION OF BALLISTIC IMPACT AND RADIANT IGNITION TECHNIQUES FOR CHARACTERIZATION OF VIOLENT REACTION IN CASED PROPELLANT

S. A. Finnegan, A. I. Atwood, J. K. Pringle,  
N. G. Zwierzchowski, and P. O. Curran

Research Department  
Naval Air Warfare Center Weapons Division  
China Lake, California 93555-6001

and  
J. Wiknich  
Comarco, Inc.  
Ridgecrest, California 93555

A planar model of a solid rocket motor with a central bore has been developed that allows visual observation of impact-induced violent reaction processes. A comparison of explosive burn reactions in planar model and full-scale motor tests shows a number of similarities. In particular, displays of burning, fragmented propellant ejecta are qualitatively the same. In planar motor tests, these displays result from two reactions: a brief, intense one within the bore, and a longer duration, less intense one within the web. These tests also show an apparent inverse relation between the two reactions in some instances. This paper describes the results of a study to define the relationship between the two. Results indicate that web ignition occurs primarily by thermal transfer from in-bore processes at relatively low pressures. They also indicate that the lower web reaction levels sometimes associated with intense in-bore reactions are most likely caused by incomplete ignition or depressurization-induced extinction.

### INTRODUCTION

Bullet or fragment impact against a solid rocket motor can cause a reaction ranging from mild burning to detonation. Prompt detonation may occur immediately on contact through the mechanism of shock-to-detonation transition (SDT). Delayed reaction (either burning or detonation) may occur at later times. Delayed reactions are believed to be associated with damage and fragmentation of propellant during penetration; however, the underlying mechanisms are not well understood.<sup>1</sup>

The study of delayed reaction phenomena is complicated by the fact that these processes occur within the motor case. To aid in characterization, a planar model of a solid rocket motor with a central bore has been developed that allows impact and reaction events within the interior to be studied visually.

Previous papers have described the use of the planar model for the study of impact-induced reactions.<sup>2-4</sup> These studies show that a "bubble" of propellant debris forms in the air gap between two propellant layers as a result of projectile perforation of one of the layers. Ignition of bubble debris occurs upon impact with the second propellant layer followed by a reaction ranging from mild burning to detonation, depending on the degree of integrity and velocity of the debris bubble, propellant thermochemistry, and degree of confinement.

A comparison of planar model and full-scale motor test behavior shows many similarities. In particular, the subscale test appears to duplicate reasonably well those

reactions that involve the violent expulsion of burning propellant debris (Figure 1). These kinds of explosive burn reactions are of particular importance because of the increased hazard caused by burning ejecta.



FIGURE 1. HIGH-SPEED PHOTOGRAPH OF BULLET-IMPACT-INDUCED EXPLOSIVE BURN REACTION IN LARGE-SCALE MOTOR

In planar model tests, these reactions appear to be largely the result of two different processes, a brief (microsecond range), intense reaction within the central air gap (i.e., bore) and a much longer (millisecond or greater), less-intense reaction within the main propellant layers (i.e., web). The first, as the principal source of internal pressurization, is responsible for the breakup and expulsion of case and propellant material while the second is responsible for burning ejecta.

Recent experiments indicate that the relation between these two reactions is not always direct. For some propellants, intense in-bore reactions are not followed by reaction of web material, while less-intense in-bore reactions are followed by extensive web reaction. Any of several phenomena would account for this behavior. For example, the more rapid loss of confinement that occurs in regions of intense reaction (attributed primarily to faster debonding/fracturing of the Plexiglas sidewalls) could result in depressurization rates sufficient to extinguish combustion.<sup>5</sup> Similarly, the decrease in in-bore reaction intensity that accompanies depressurization could also result in incomplete ignition. The lack of reaction could also be the result of fluid-like movements of post-impact bubble debris that occur in regions of high intensity.<sup>3</sup> Rapid movement of debris along web surfaces could act to suppress reaction.

This paper summarizes some of the more significant results from a study to examine the relation between in-bore and web reaction processes observed in planar model tests.<sup>6</sup> Although the relation would appear to be fairly complex because of the number of possible web ignition mechanisms (thermomechanical as well as thermal), some effects can be estimated from previous studies. For example, tests of hydroxy-terminated polybutadiene/ammonium perchlorate (HTPB/AP) propellants showed that penetration processes alone were not sufficient to produce sustained ignition of the web.<sup>2</sup> In these tests, perforating impacts of single, covered propellant layers did not result in sustained ignition, while similar impacts against planar models containing a center bore resulted in ignition of both layers. This particular result also demonstrated that the effects of hot metal fragments from case perforation were not very large, either. These same tests also showed that, ignoring indirect ignition from reaction of bubble debris, debris bubble impact processes were not capable of producing sustained ignition of the bore surface. At air gaps where the bubble was fragmented and where fluid-like behavior could not inhibit ignition, there was no evidence of ignition from impact of individual propellant particles. A more recent test, involving impact of a unbroken debris bubble on a propellant layer with a central hole to allow the projectile to pass through unimpeded, also showed no evidence of ignition (also indicating that the principal ignition mechanism for bubble debris is projectile impact ejecta).<sup>7</sup> In summary, evidence from previous planar model tests indicates that, for impacts resulting in complete perforation of the target, thermomechanical processes do not appear to be the principal web ignition mechanisms. Although they may be important sensitizing mechanisms (e.g., by introducing damage and increasing local temperatures) and possibly ignition sources (of localized preignition or sustained combustion reactions, principally in penetration cavities), widespread ignition of the kind seen in planar model tests appears to require a large, diffuse thermal source like that produced by in-bore reaction processes.

On the basis of studies indicating that thermal processes (e.g., radiant, convective, and conductive heat sources) associated with in-bore reactions may be the most important factor in web ignition, it was decided to use radiant energy to examine web ignition behavior in the current study. While radiant ignition is probably not

the primary thermal mechanism in this instance (convective ignition is more likely because of the high-velocity, high-temperature reaction gases present in the bore), this method provides the best means for comparing the thermal ignition behavior of different materials because of the precise control over input conditions that it allows.<sup>8</sup> There is also some experimental evidence that radiant ignition may be important in flame spreading processes involving rough surfaces.<sup>9</sup> In addition to radiant ignition measurements, burn rate measurements were also made to examine the relation between burn rate and ignition behavior.<sup>10</sup>

## PROPELLANT SAMPLES

Four of the six materials studied<sup>6</sup> are compared in this paper. All are aluminized hydroxy-terminated polybutadiene/ammonium perchlorate (Al/HTPB/AP) formulations. One formulation (propellant A) exhibits very explosive behavior and violent expulsion of large amounts of burning propellant ejecta in both planar model tests and bullet impact tests of full-scale motors. Another (propellant B) shows no expulsion of burning ejecta in either test.<sup>11</sup> The third and fourth formulations (propellants C and D) are intermediate in behavior in planar model tests; expulsion of burning ejecta occurs under some conditions but not under other.

## EXPERIMENT

### Ballistic Impact

A sketch of the planar motor model used in the ballistic impact experiments is shown in Figure 2. The model consists of a steel plate, a layer of propellant, an air gap, a second layer of propellant, and a second steel plate. The air gap simulates a central bore in a rocket motor. A spherical projectile impacts the target perpendicular to the plates and layers. The addition of transparent Plexiglas sidewalls provides a measure of lateral confinement for enhancing in-bore combustion processes.

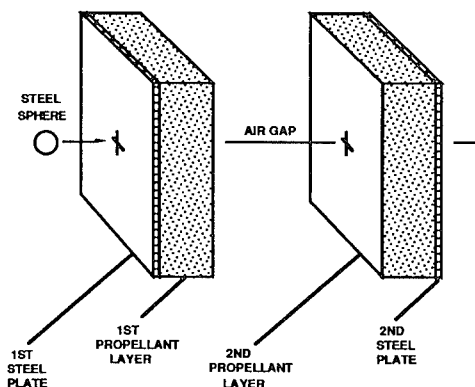


FIGURE 2. PLANAR ROCKET MOTOR MODEL

For the present tests, propellant layers were 127 mm wide by 38 mm thick while plates were 152 mm wide by 1.6 mm thick. Hardness values for the first and second plates were 370 BHN and 95 BHN, respectively.

Plexiglas sidewalls were 6.3 mm thick. Fast-setting urethane adhesive (Hardman, Inc., Belleville, NJ) was used to bond the various components together.

Four air gaps, 12.7, 38.1, 76.2, and 114.3 mm, were examined. Air gaps were chosen to sample reaction behavior at more-or-less regular intervals across the zone containing the most severe in-bore reactions.

Projectiles, consisting of 19-mm-diameter mild steel spheres, were fired at constant velocity ( $1190 \pm 60$  m/s) using a smooth-bore powder gun. In-flight velocities were measured using a 16,000 frame/s Photec high-speed camera. Backlighting was provided by an array of flash lamps and a diffusing screen. Impact processes and in-bore reactions were observed using a 32,000 frame/s Fastax high-speed camera and a separate, similar backlighting system. Longer-term reaction processes were examined using real-time video.

### Radiant Ignition

When a material is exposed to a thermal stimulus, a series of events (illustrated graphically in the log flux versus log time plot of Figure 3) occur which may lead to complete combustion.<sup>12</sup> Following the vertical dotted line in Figure 3, and starting at the time of initial exposure, these events include: (1) a period of inert heating, during which the surface temperature is raised and a thermal profile established, (2) a period of pre-ignition reactions, starting when gasification begins and gaseous products start to react, and ending when gasification and reaction rates are both sufficient for sustaining combustion when the external heat source is removed, and (3) a period of sustained combustion. The boundary separating regions of inert heating and pre-ignition reactions is called the first light/first gasification line, while the boundary separating regions of pre-ignition reactions and sustained combustion is called the go/no-go line. Propellant formulation, external energy level, and test pressure all contribute to the time relationship between the establishment of the thermal profile and self-sustained combustion.

Radiant ignition data were obtained using a CO<sub>2</sub> laser ignition system.<sup>12</sup> Samples of undamaged propellant were tested at 1.01 bars (absolute) nitrogen pressure, and 209, 419, and 837 J/cm<sup>2</sup>s radiant flux levels. Seventeen tests were required to establish each go/no-go point.

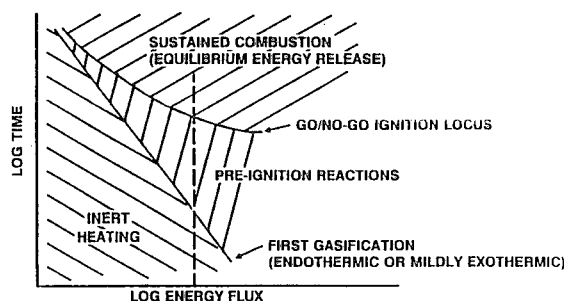


FIGURE 3. GENERAL DEPICTION OF IGNITION PROCESS

### Burn Rate

The rate that the propellant is converted from solid to reactive species (i.e., the rate of regression of the solid) is commonly referred to as the burn rate of the propellant.<sup>12</sup> Burn rates are dependent on several variables including the composition of the propellant and particle sizes of the ingredients, the surrounding pressure, and initial temperature of the propellant.

Burn rate data were obtained using a photographic window bomb system.<sup>13</sup> Samples of undamaged propellant were burned at 1.01, 1.72, 3.45, 6.90, 34.48, 68.95, and 103.42 bars (absolute) nitrogen pressure. Three tests were required to establish each data point.

## RESULTS

### Ballistic Impact

Results for the planar model impact tests are summarized in Table 1. Tabulated data include initial projectile velocity, maximum debris bubble velocity, average outward expulsion velocity of the two end plates after reaction (used as a measure of in-bore reaction levels),<sup>3-4</sup> and estimated reaction level of the web (parent layer) material. A sequence of high-speed photographs, showing the highly-luminous in-bore reactions commonly observed in these propellants at air gaps where the debris bubble was unbroken at impact, is also displayed in Figure 4. For these propellants, bubble breakup occurred at expansion distances between 38.1 and 76.2 mm.

As discussed earlier, the in-bore reaction is largely responsible for breakup and expulsion of case and propellant material. Previous studies have shown a direct relation between in-bore reaction levels and average case (end plate) expulsion velocities.<sup>3-4</sup> However, a preliminary comparison of velocity values for the C and D formulations showed poor agreement with other data. These disparities were finally attributed to mechanical response differences resulting from propellant density dissimilarities. A significant mechanical response, in terms of case expulsion velocities, had been previously measured in targets containing inert simulant. To eliminate mechanical response differences, expulsion velocities were corrected by subtracting out the mechanical component (Figure 5). The direct relation between mechanical response and propellant density shown in Figure 5 is attributed largely to the increased energy dissipation that results from higher penetration resistance in denser media.<sup>6</sup> The data in Figure 5 represents only a very rough estimate of the mechanical response. To make this estimate, both mechanical property variations and possible mechanical damage contributions to reaction behavior were ignored. The assumption was also made, based on test data, that the mechanical response was independent of air gap and impact velocity variations.

TABLE 1. BALLISTIC IMPACT RESULTS

Propellant	Air Gap, mm	Initial Vel., m/s	Bubble Vel., m/s	Average Plate Vel., m/s	Web (Parent Layer) Reaction Description
A	12.7	1188	<i>a</i>	75	Both layers nearly all consumed; some scattering of burning fragments about test site.
A	38.1	1202	650	98	Both layers burnt; some scattering of burning fragments about test site; unburnt material recovered.
A	76.2	1179	770	77	Both layers nearly all consumed; burning fragments scattered about test site.
A	114.3	1206	823	42	Both layers nearly all consumed; burning fragments widely scattered about test site (out to 60-90 meters).
B	12.7	1244	<i>a</i>	83	Minor reaction.
B	38.1	1230	746	92	Minor reaction.
B	76.2	1236	748	77	Minor reaction.
B	114.3	1208	849	19	Minor reaction.
C	12.7	1213	<i>a</i>	68	Minor reaction.
C	38.1	1170	<i>a</i>	74	Minor reaction.
C	76.2	1187	<i>a</i>	34	Minor reaction; some scattering of unburnt propellant fragments about test site.
C	114.3	1179	<i>a</i>	28	Second layer burnt completely; unburnt propellant fragments scattered about test site.
D	12.7	1209	<i>a</i>	67	Both layers burnt; burning occurred next to test site (propellant material not scattered).
D	38.1	1203	661	84	Minor reaction; unburnt propellant fragments scattered out to 30-45 meters.
D	76.2	1205	792	58	Both layers burnt; small unburnt propellant fragments scattered out to 30-45 meters.
D	114.3	1216	833	43	Both layers burnt; small unburnt propellant fragments found 30-60 meters from test site.

*a* Velocity could not be measured.

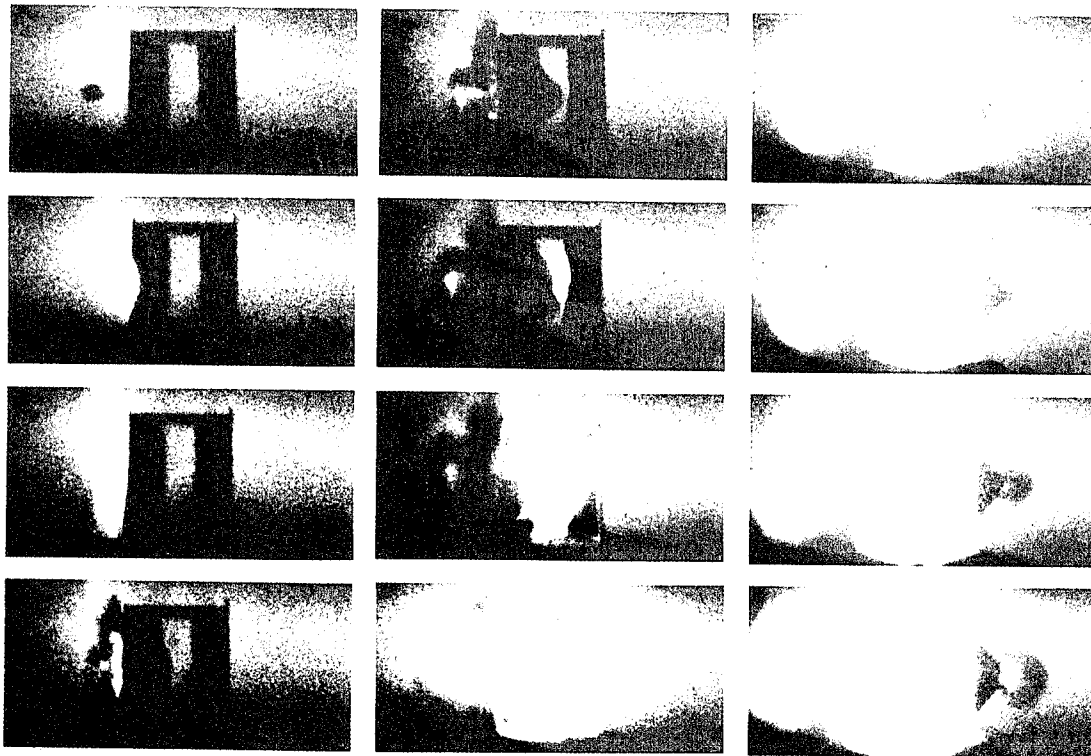


FIGURE 4. PHOTOGRAPHIC SEQUENCE OF PLANAR MODEL IMPACT AT 1230 M/S (PROPELLANT B, 38.1 MM AIR GAP)



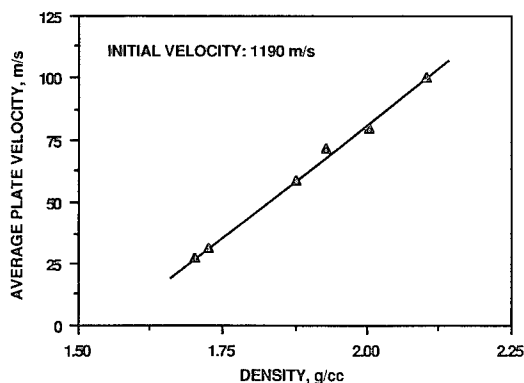


FIGURE 5. MECHANICAL COMPONENT OF AVERAGE PLATE VELOCITY VERSUS PROPELLANT DENSITY

Plots of corrected plate velocity values versus air gap, for the four propellants listed in Table 1, are shown in Figure 6. For all propellants, maximum reaction occurred at the 38.1 mm air gap, where the debris bubble was unbroken at impact. These results are consistent with previous studies.<sup>3-4</sup> At this air gap, a ranking of propellants in order of decreasing in-bore reaction level, based on the data in Figure 6, is:  $A > B > D > C$ . From an inspection of Figure 6, it is apparent that these rankings are highly dependent on air gap.

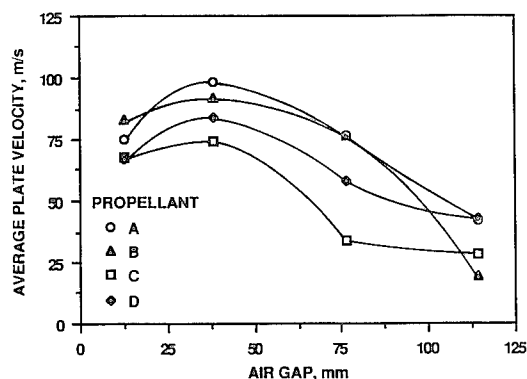


FIGURE 6. CORRECTED AVERAGE PLATE VELOCITY VERSUS AIR GAP

Using the information from Table 1 regarding web (parent layer) reaction behavior, a ranking of propellants on the basis of average web reaction levels (over the four air gaps) was also made. In order of decreasing level, the rankings are:  $A > D > C > B$ .

A comparison of in-bore and web rankings at all four air gaps indicates that, except perhaps at the largest air gap, there is no consistent relation between in-bore and web reaction levels for these propellants. For these propellants, the relation between the two reactions appears to be highly specific.

While web reaction levels appear to be largely independent of in-bore reaction levels for propellants A and

B, an interdependency between the two was observed for propellant D, as seen in Figure 7. For this propellant, the relation appears to be an inverse one. Propellant C also tends to show this behavior to a limited extent.

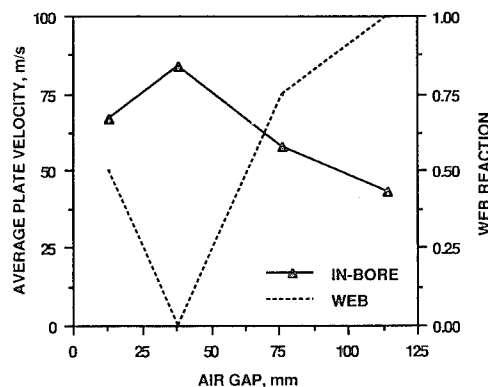


FIGURE 7. ILLUSTRATIVE COMPARISON OF IN-BORE AND WEB REACTION LEVELS VERSUS AIR GAP FOR PROPELLANT D (WEB REACTION NOT TO SCALE)

#### Radiant Ignition

Test results for the radiant ignition studies are illustrated in Figure 8. An inspection of Figure 8 shows that a ranking system based on the time delay between flux application and sustained ignition (go/no-go line) varies with flux level. At the lowest level the rankings, in order of decreasing ignitability, are:  $A > C > B > D$ . At the highest level, they become:  $A > D > C > B$ . Trend differences largely account for these changes. For example, propellant B exhibits a rising trend with increasing flux, while propellants A and D exhibit declining trends.

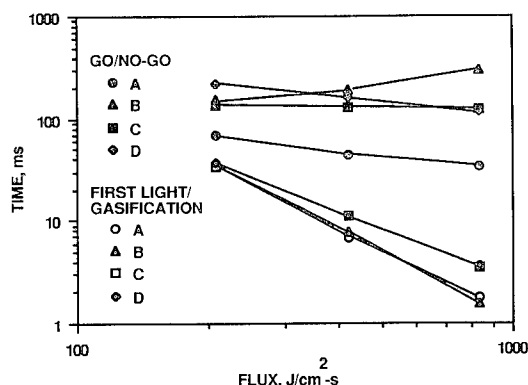


FIGURE 8. A COMPARISON OF FIRST LIGHT/FIRST GASIFICATION AND GO/NO-GO TRENDS AT 1.01 BARS PRESSURE

The rising trend, exhibited by propellant B, results when gasification rates and pressures become sufficiently high to cause pyrolysis products to be blown away from the surface prior to complete ignition. This process, the result of increasing gas velocities, results in larger flame standoff distances which reduces thermal feedback to the surface. At some higher flux level or longer time, the

effect will be large enough to prevent sustained ignition. When this occurs, the effect is described as overdriven ignition.<sup>12, 14</sup> The same phenomenon is also responsible for combustion extinguishment when pressures are suddenly reduced.<sup>15</sup>

It is interesting to note that propellants which exhibit little or no web reaction in planar model tests also tend to show flat-to-upward trending go/no-go lines over this flux range at lower pressures. On this basis, a heuristic argument could be made that go/no-go trends may be of more importance than delay times as an ignition criterion in this situation. Using this assumption, an approximate ranking in order of decreasing ignitability, would be: A > D > C > B. (Propellant A is still assumed to be more ignitable than the others because of the significantly lower delay times over this flux range.)

A more rigorous argument for using go/no-go trends for estimating relative ignitabilities can be made on the basis that, for most propellants, the average slope of the go/no-go boundary decreases as the surrounding pressure is reduced.<sup>8</sup> As the pressure approaches the minimum for sustaining ignition, the slope tends to become positive at the higher flux levels, as seen for propellant B in Figure 8. The trend differences seen in Figure 8 can be viewed as a reflection of differences between the test pressure and a minimum for sustaining ignition. On this basis, the propellant that appears to be furthest from a minimum (propellant A) would be the most ignitable and the propellant that appears to be closest (propellant B), the least ignitable.

## Burn Rate

A comparison of burn rates for the four propellants, at pressures between 1.01 and 6.90 bars, is shown in Figure 9. An inspection of Figure 9 shows that propellants rank consistently in the pressure regime between 1.72 and 6.90 bars. Below that range, data are too limited for comparison (only propellant A ignited reliably at 1.01 bars), while at 34.48 bars and above, rankings are different at each pressure.<sup>6</sup> Within this range, a ranking in terms of decreasing burn rate is: A > D > C > B.

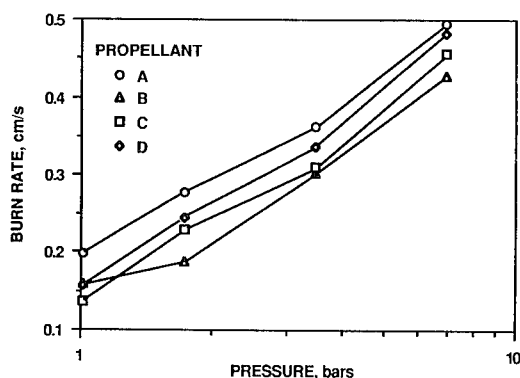


FIGURE 9. BURN RATE COMPARISON AT PRESSURES BETWEEN 1.01 AND 6.90 BARS

## Test Comparison

A comparative listing of the principal sensitivity rankings derived from the ballistic impact, radiant ignition, and burn rate studies is shown in Table 2.

TABLE 2. COMPARISON OF PROPELLANT SENSITIVITY RANKINGS

Reaction/ Ignitability/ Burn Rate Rank	In-Bore <sup>a</sup>	Web	Radiant Ignition <sup>b</sup>	Burn Rate <sup>c</sup>
Highest	A	A	A	A
	B	D	D	D
	D	C	C	C
Lowest	C	B	B	B

<sup>a</sup> 38.1 mm air gap

<sup>b</sup> Based on go/no-go trend differences.

<sup>c</sup> 1.72-6.90 bars pressure

An inspection of the various rankings in Table 2 shows an apparently strong correlation between web reaction levels and both low pressure ignitability and burn rate data. This result supports the idea of a direct relation between burn rate and ignitability, as concluded by previous investigators.<sup>10</sup> It also supports the idea that web ignition occurs at relatively low pressures.

## Analysis of Planar Model Reactions

A number of mechanisms have been proposed to account for the apparent inverse relation between in-bore and web reaction processes seen in Figure 7. These include: (1) a mechanical mechanism associated with debris bubble impact flow processes, and (2) several thermal mechanisms associated with high flux levels or in-bore depressurization rates.

At air gaps where the debris bubble is unbroken at impact, post-impact bubble debris tends to flow, fluid-like, along bore surfaces.<sup>3</sup> It was conjectured that material flow along web surfaces might inhibit ignition. This behavior should occur at the two smaller air gaps (12.7 and 38.1 mm) in the present situation.

However, a comparison of web reaction levels at these air gaps (Table 1) showed no pattern that could be attributed to mechanical flow processes. The influence of material flow was expected to manifest itself by a more uniform suppression of web reactions in all propellants. This was clearly not the case as shown by the large differences in web reaction levels at these air gaps. As a result, it was concluded that mechanical flow processes were not the principal cause of the phenomenon seen in Figure 7.

Maximum in-bore reaction also occurs in the air gap regime where the bubble is unbroken at impact. For the present tests, the most severe in-bore reactions occurred at the 38.1 mm air gap (Figure 6). Planar model tests show a direct relation between reaction severity and degree of breakup of the Plexiglas sidewalls. Assuming the increased breakup represents a more rapid loss of confinement, the result should be a higher rate of depressurization and decline in in-bore reaction levels at this air gap.

Any of three thermal mechanisms, resulting from high in-bore depressurization and thermal flux rates, could account for the drop in web reaction levels seen at the 38.1 mm air gap. A sufficiently high rate of depressurization will extinguish an ongoing reaction although reignition can occur for propellants with very low (sub-atmospheric) low-pressure deflagration limits.<sup>5</sup> At the same time, a sufficient decrease in thermal flux caused by a rapid decline in in-bore reaction levels with depressurization, will result in only partial ignition. Finally, sufficiently high flux levels or times could result in extinction through overdriven ignition.<sup>12, 14</sup>

Of the three mechanisms, the two based on depressurization (extinction or incomplete ignition) appear to be more probable. As both result from the same process, separation would normally be difficult without additional evidence. Thermomechanical ignition, because of the brief ignition delay times associated with localized heating, would tend to favor the first, while thermal ignition, because of the much longer delay times, might tend to favor the second.

In the case of the third mechanism (i.e., overdriven ignition), it is unlikely that this mechanism is a principal factor because of the probable preeminence of hot gas flow processes in this situation. Although ignition studies of unfilled polymers show that flow velocities above a certain level can result in increasing ignition delay times similar to the trends observed at high radiant flux levels for some propellants,<sup>16</sup> comparable data for filled materials (e.g., propellants) is lacking.

## CONCLUSIONS

A comparison of in-bore and web reactions for four aluminized hydroxy-terminated polybutadiene/ammonium perchlorate propellants, impacted in a planar motor model test, showed the relation between the two reactions to be highly specific. For one propellant, an inverse relation between in-bore and web reaction levels was noted. It was concluded that the reduced web reaction level found in a region of high in-bore reaction levels was most likely the result of incomplete ignition or depressurization-induced extinction.

A comparison of average web reaction levels with low-pressure burn rates and radiant ignition go/no-go times/trends, for the four propellants, showed a direct correspondence between the three parameters. This correspondence, along with data from previous studies, indicated that web ignition occurred primarily as a result of thermal transfer from the in-bore reaction process at relatively low (1.01-6.90 bars) pressures.

## ACKNOWLEDGEMENTS

Support for this work was provided by the Navy Insensitive Munitions Advanced Development Program. This support, along with that provided by the Warhead Test Branch of the Range Department, which conducted the planar model impact tests, is gratefully acknowledged.

## REFERENCES

1. Mellor, A. M.; Boggs, T. L.; Covino, J.; Dickinson, C. W.; Dreitzler, D.; Thorn, L. B.; Frey, R. B.; Gibson, P. W.; Roe, W. E.; Kirshenbaum, M.; and Mann, D. M., "Hazard Initiation in Solid Rocket and Gun Propellants and Explosives," *Prog. Energy Combust. Sci.*, Vol. 14, 1988, p. 213-244.
2. Finnegan, S. A.; Pringle, J. K.; Schulz, J. C.; and Alexander, M. D., "A Study of Impact-Induced Ignition/Combustion in Propellants Using a Planar Rocket Motor Model," *Proceedings of the 1990 JANNAF Propulsion Systems Hazards Subcommittee Meeting*, CPIA Pub. 538, Vol. 1, April 1990, pp.13-24.
3. Finnegan, S. A.; Schulz, J. C.; Pringle, J. K.; and Lindfors, A. J., "The Relationship Between Ballistic Impact Damage and Violent Reaction in Cased Propellant," *Proceedings of the 1991 JANNAF Propulsion Systems Hazards Subcommittee Meeting*, CPIA Pub. 562, Vol. 1, March 1991, pp. 399-408.
4. Finnegan, S. A.; Pringle, J. K.; Heimdahl, O. E. R.; and Schulz, J. C., "Impact-Induced Delayed Reactions in Rocket Motors: Further Studies With a Planar Model," *Proceedings of the 1992 JANNAF Propulsion Systems Hazards Subcommittee Meeting*, CPIA Pub. 582, Vol. 1, April 1992, pp. 267-283.
5. Reed, R. and Brady, V. L., "The Chemistry of Extinguishable Propellants," *Proceedings of the 18th International Pyrotechnics Seminar*, IIT Research Institute, 1992, pp. 715-725.
6. Finnegan, S. A.; Atwood, A. I.; Pringle, J. K.; Zwierzchowski, N. G.; Curran, P. O.; and Wiknich, J., "A Study of Impact-Induced Violent Reactions in Cased Propellant Using Planar Impact Model and Radiant Ignition/Burn Rate Measurements," *1993 JANNAF Propulsion Systems Hazards Subcommittee Meeting*, Fort Lewis, WA, 11-13 May 1993.
7. Unpublished Data.
8. Hermance, C. E., "Solid Propellant Ignition Theories and Experiments," in *Fundamentals of Solid-Propellant Combustion*, Vol. 90, *Progress in Astronautics and Aeronautics*, American Institute of Aeronautics and Astronautics, 1984, pp. 239-304.
9. McAlevy, R. M.; Magee, R. S.; Wrubel, J. A.; and Horowitz, F. A., "Flame Spreading Over the Surface of Igniting Solid Rocket Propellants and Propellant Ingredients," *AIAA Journal*, Vol. 5, No. 2, 1967, pp. 265-271.

10. Derr, R. L. and Fleming, R. W., "A Correlation of Solid Propellant Arc-Image Ignition Data," *Proceedings of the 10th JANNAF Combustion Meeting*, CPIA 243, Vol. 3, Dec. 1973, pp. 157-168.
11. Reed, R.; Brady, V. L.; and Hitner, J. M., "HTPB Propellants With Reduced Sensitivity," *Proceedings of the Insensitive Munitions Technology Symposium*, Williamsburg VA, 15-18 June 1992, American Defense Preparedness Association, Alexandria, VA, 1992, pp. 265-272.
12. Atwood, A. I.; Price, C. F.; Curran, P. O.; and Zwierchowski, N. G., "Burning Rate, Radiant Ignition, and Global Kinetics of a Nitrocellulose Propellant," *Proceedings of the 25th JANNAF Combustion Meeting*, CPIA Pub. 498, Vol. 1, Oct. 1988, pp. 69-81.
13. Boggs, T. L.; Crump, J. E.; Kraeutle, K. J.; and Zurn, D. E., "Cinematography and Scanning Electron Microscopy as Used to Study Solid Propellant Combustion," *Experimental Diagnostics in Combustion of Solids*, Vol. 63, *Progress in Astronautics and Aeronautics*, American Institute of Aeronautics and Astronautics, 1978, pp. 20-47.
14. Ohlemiller, T. J.; Caveny, L. H.; DeLuca, L.; and Summerfield, M., "Dynamic Effects on Ignitability Limits of Solid Propellants Subjected to Radiative Heating," *Proceedings of the 14th Symposium (International) on Combustion*, The Combustion Institute, 1973, pp. 1297-1307.
15. Kuo, K. K.; Gore, J. P.; and Summerfield, M., "Transient Burning of Solid Propellants," in *Fundamentals of Solid-Propellant Combustion*, Vol. 90, *Progress in Astronautics and Aeronautics*, American Institute of Aeronautics and Astronautics, 1984, pp. 599-659.
16. T. Niioka, T.; Takahashi, M.; and Izumikawa, M., "Gas-Phase Ignition of a Solid Fuel in a Hot Stagnation-Point flow," *Proceedings of the 18th Symposium (International) on Combustion*, The Combustion Institute, 1981, pp. 741-747.

## ***The Application of Ballistic Impact and Radiant Ignition Techniques for Characterization of Violent Reaction in Cased Propellant***

S. A. FINNEGAN, A. I. ATWOOD, J. K. PRINGLE,  
N. G. ZWIERZCHOWSKI, AND P. O. CURRAN  
RESEARCH DEPARTMENT  
NAVAL AIR WARFARE CENTER WEAPONS DIVISION  
CHINA LAKE, CALIFORNIA

J. WIKNICH  
COMARCO, INC  
RIDGECREST, CALIFORNIA

A planar model of a solid rocket motor with a central bore has been developed that allows visual observation of impact-induced violent reaction processes. A comparison of explosive burn reactions in planar model and full-scale motor tests shows a number of similarities. In particular, displays of burning, fragmented propellant ejecta are qualitatively the same.

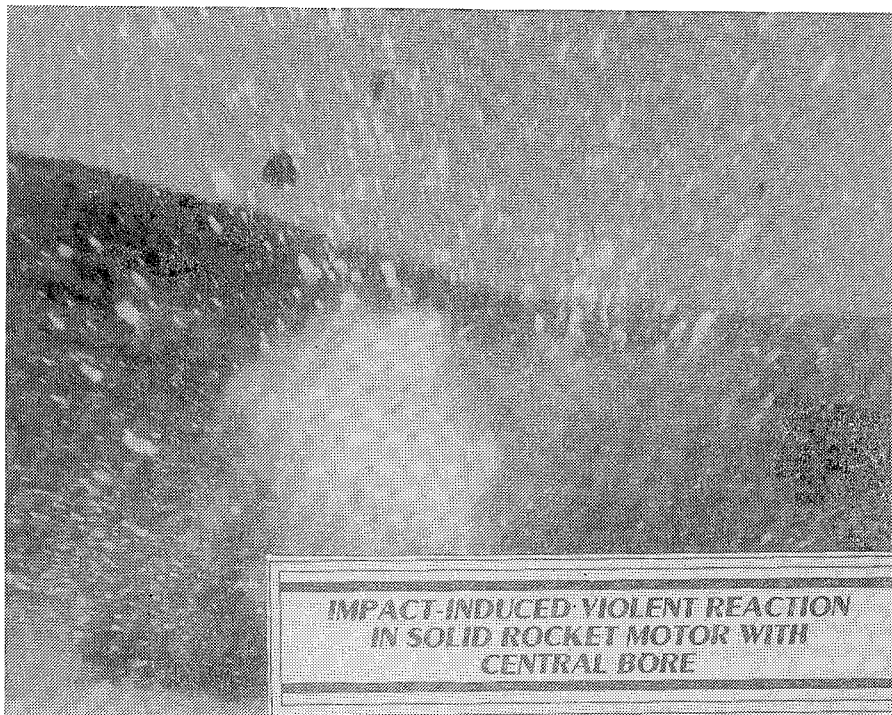
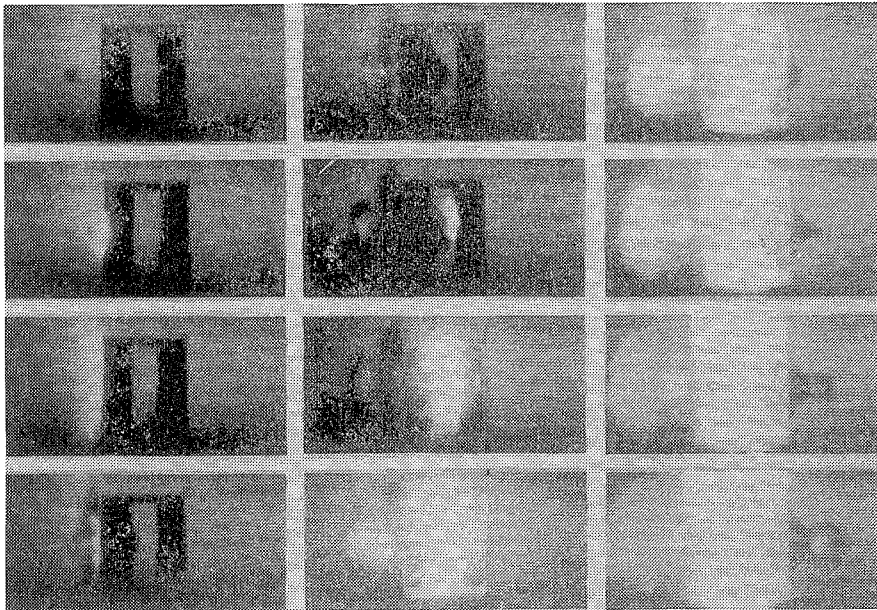
In planar motor tests, these displays result from two reactions:

- a brief, intense one within the bore, and
- a longer duration, less intense one within the web.

The first, as the principal source of internal pressurization, is responsible for the breakup and expulsion of case and propellant material while the second is responsible for the burning debris. These tests also show an apparent inverse relation between the two reactions in some instances.

*This paper describes the results of an experimental study, involving planar model impact tests along with radiant ignition and burn rate measurements, to examine the relation between these two reactions.*

**HIGH SPEED PHOTOGRAPHIC SEQUENCE  
OF PLANAR MOTOR MODEL IMPACT  
AND BURN REACTION PROCESSES**



**IMPACT-INDUCED VIOLENT REACTION  
IN SOLID ROCKET MOTOR WITH  
CENTRAL BORE**

## TEST PROPELLANTS

All of the test propellants are aluminized hydroxy-terminated polybutadiene/ammonium perchlorate (AI/HTPB/AP) formulations.

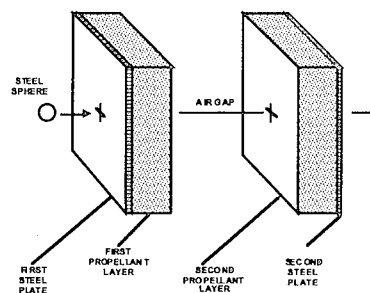
Propellant A exhibits very explosive behavior and violent expulsion of large amounts of burning propellant debris in both planar model tests and bullet impact tests of larger-scale motors.

Propellant B shows no expulsion of burning debris in either test.

Propellants C and D are intermediate in behavior in planar model tests; expulsion of burning debris occurs under some conditions but not under other.

## BALLISTIC IMPACT STUDY

### PLANAR TEST MODEL



The planar motor model, used in the ballistic impact experiments, consists of a steel plate, a layer of propellant, an air gap, a second layer of propellant, and a second steel plate. The air gap simulates a central bore in a rocket motor. A spherical projectile impacts the target perpendicular to the plates and layers. The addition of transparent Plexiglas sidewalls provides a measure of lateral confinement for enhancing in-bore combustion processes.

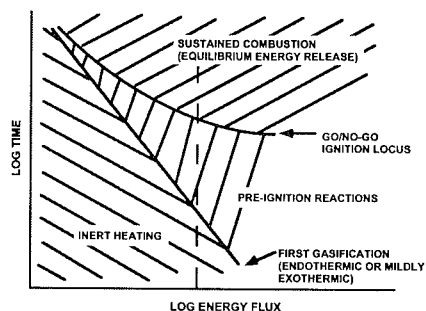
For the present tests, propellant layers were 127 mm wide by 38 mm thick while plates were 152 mm wide by 1.6 mm thick. Hardness values for the first and second plate were 370 and 95 BHN, respectively. Plexiglas sidewalls were 6.3 mm thick.

Four air gaps, 12.7, 38.1, 76.2, and 114.3 mm, were examined. Air gaps were chosen to sample reaction behavior at more-or-less regular intervals across the zone containing the most severe in-bore reactions.

Projectiles, consisting of 19-mm-diameter mild steel spheres, were fired at constant velocity ( $1190 \pm 60$  m/s) using a smooth-bore powder gun.

## RADIANT IGNITION STUDY

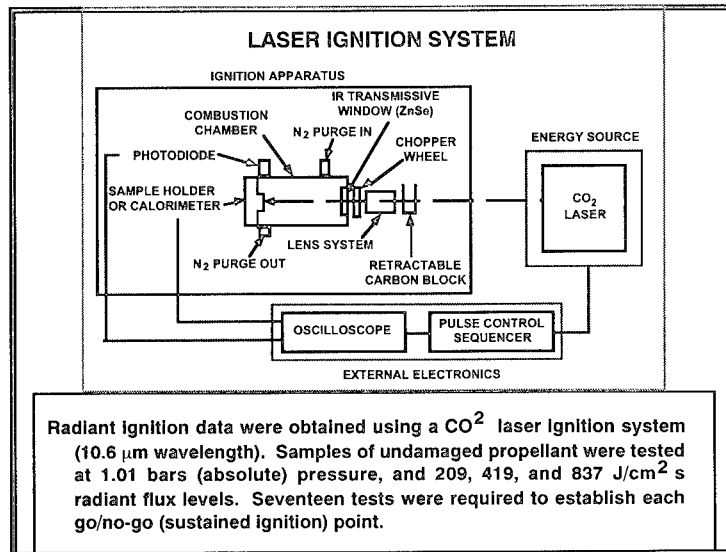
### THERMAL IGNITION PROCESS





When a material is exposed to a thermal stimulus, a series of events occur which may lead to complete combustion. These events include:

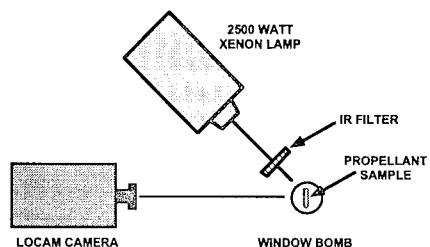
- (1) a period of inert heating, during which the surface temperature is raised and a thermal profile established,
- (2) a period of preignition reactions, starting when gasification begins and gaseous products begin to react, and ending when gasification and reaction rates are both sufficient for sustaining combustion when the external heat source is removed, and
- (3) a period of sustained combustion. The boundary separating regions of inert heating and preignition reactions is called the *first light/first gasification line*, while the boundary separating regions of preignition reactions and sustained combustion is called the *go-no/go line*.



## **BURN RATE STUDY**

The rate that the propellant is converted from solid to reactive species (i.e., the rate of regression of the solid) is commonly referred to as the burn rate of the propellant. Burn rates are dependent on several variables including the composition of the propellant and particle sizes of the ingredients, the surrounding pressure, and the initial temperature. The burn rate is considered to be a direct measure of Ignitability.

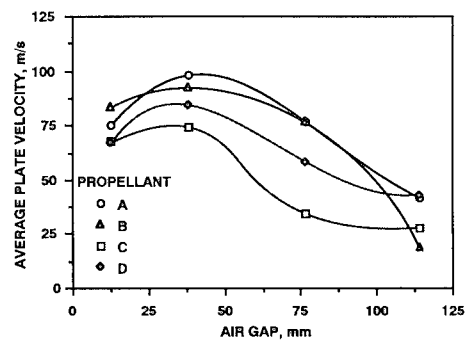
### **PHOTOGRAPHIC WINDOW BOMB SYSTEM**



Burn rate data were obtained using a photographic window bomb system. A heated wire (Nichrome or tungsten) was used as an ignition source. Samples of undamaged propellant were burned at 1.01, 1.72, 3.45, 6.90, 34.48, 68.95, and 103.42 bars (absolute) nitrogen pressure. Three tests were required to establish each data point.

## BALLISTIC IMPACT RESULTS

### IN-BORE REACTION COMPARISON



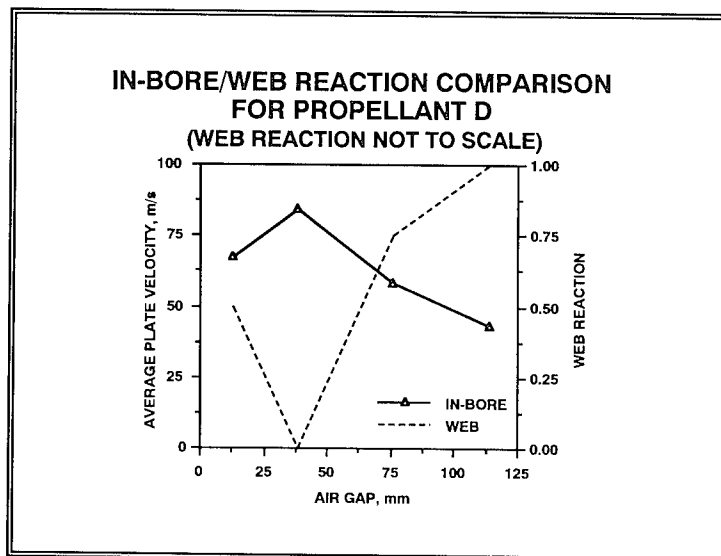
The average outward expulsion velocity of the two cover plates, corrected to remove the mechanical response, was used as the primary measure of in-bore reaction. Plate velocities were measured from high-speed photographs. These were obtained using a 32,000 frame/s Fastax camera coupled to a backlighting system consisting of an array of flash lamps and a diffusing screen. A Vanguard motion analyzer was used to analyze the photographs.

For all four propellants, maximum in-bore reaction occurs at the 38.1 mm air gap. At this air gap, a ranking of propellants in order of decreasing reaction level is: A > B > D > C. For these propellants, rankings appear to be highly dependent on air gap.

WEB REACTION COMPARISON	
PROPELLANT	WEB (PARENT LAYER) REACTION DESCRIPTION
A	BOTH LAYERS BURNT ALMOST COMPLETELY (12.7, 38.1, 76.2, AND 114.3 mm AIR GAPS)
B	MINOR REACTION (12.7, 38.1, 76.2, AND 114.3 mm AIR GAPS)
C	MINOR REACTION (12.7, 38.1, AND 76.2 mm AIR GAPS). SECOND LAYER BURNT (114.3 mm AIR GAP).
D	BOTH LAYERS BURNT (12.7, 76.2, and 114.3 mm AIR GAPS). MINOR REACTION (38.1 mm AIR GAP).

An estimate of the amount of original material burnt was used as the primary measure of web (parent layer) reaction. Recovered debris and real-time video were used for this purpose. The second, by providing visual displays of debris pyrotechnics, was particularly useful for establishing relative burning levels.

A ranking of propellants in order of decreasing average web reaction level is: A > D > C > B.

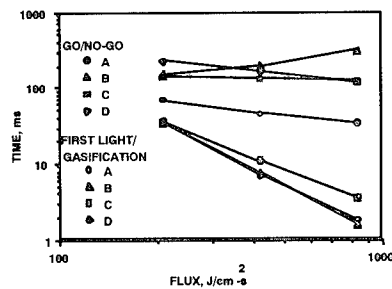


While web reaction levels appear to be largely independent of in-bore reaction levels for propellants A and B, an interdependency between the two is observed for propellant D. For this propellant, the relation appears to be an inverse one.

Two thermal mechanisms have been proposed to explain the reduction in web reaction levels observed at the 38.1 mm air gap. These mechanisms are associated with increased depressurization rates. Planar model tests show a direct relation between reaction severity and target breakup rate. A sufficiently high rate of depressurization will extinguish an ongoing reaction. At the same time, a sufficient decrease in thermal flux caused by a rapid decline in in-bore reaction levels with depressurization, will result in only partial ignition.

## RADIANT IGNITION RESULTS

### RADIANT IGNITION DATA COMPARISON



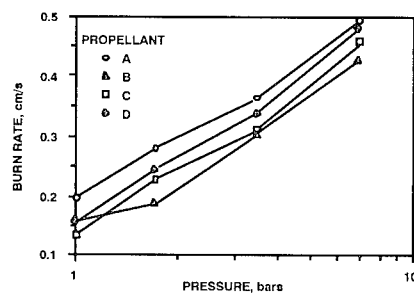
The delay time between application of a thermal stimulus and sustained combustion is generally considered to be an inverse measure of ignitability. Using this criterion, a ranking of the four propellants in order of decreasing ignitability varies considerably with flux level.

Because of these variations, an alternate ranking method was devised. This method is based on the observation that, for most propellants, the average slope of the go/no-go boundary decreases as the surrounding pressure is reduced. As the pressure approaches the minimum for sustaining ignition, the slope tends to become positive at the higher flux levels. Trend differences for different propellants can be viewed as a reflection of differences between the test pressure and a minimum for sustaining ignition.

On this basis, the propellant that appears to be furthest from a minimum (propellant A) would be the most ignitable and the propellant that appears to be closest (propellant B, the least ignitable). Using this criterion, a ranking of the four propellants in order of decreasing ignitability is:  $A > D > C > B$ .

## BURN RATE RESULTS

BURN RATE DATA COMPARISON



A ranking of the four propellants tested, on the basis of relative burn rates, was observed to be invariant only in the pressure regime between 1.72 and 6.90 bars. Within this regime, a ranking on the basis of decreasing burn rate is: A > D > C > B.

### COMPARATIVE ANALYSIS

#### BALLISTIC IMPACT, RADIANT IGNITION, AND BURN RATE RESULTS COMPARISON

REACTION/ IGNITABILITY/ BURN RATE	IN- BORE <sup>a</sup>	WEB	RADIANT IGNITION <sup>b</sup>	BURN RATE <sup>c</sup>
HIGHEST	A	A	A	A
	B	D	D	D
	D	C	C	C
LOWEST	C	B	B	B

<sup>a</sup> AT 38.1 mm AIR GAP

<sup>b</sup> BASED ON GO/NO-GO TREND DIFFERENCES

<sup>c</sup> BETWEEN 1.72-6.90 bars PRESSURE

A comparison of in-bore and web reaction levels for the four propellants indicates that there is no consistent relation between the two reactions; i.e., the relation is highly specific. On the other hand, a comparison of web reaction levels with low pressure ignitability and burn rate data shows a direct relationship. This result supports the idea of a direct correspondence between burn rate and ignitability. It also supports the idea that web ignition susceptibility is largely controlled by low pressure reaction processes.

## **CONCLUSIONS**

**FOR HTPB / AP / AL PROPELLANTS STUDIED,  
RELATION BETWEEN IN-BORE AND WEB  
REACTIONS APPEARS TO BE HIGHLY SPECIFIC**

**A COMPARISON OF WEB REACTION DATA WITH  
RADIANT IGNITION AND BURN RATE  
MEASUREMENTS INDICATES THAT WEB  
IGNITION SUSCEPTIBILITY IS LARGELY  
DETERMINED BY LOW PRESSURE REACTION  
BEHAVIOR**

**REDUCED WEB REACTION LEVELS THAT OCCUR IN  
REGIONS OF INTENSE IN-BORE REACTION MOST  
LIKELY RESULT FROM INCOMPLETE IGNITION OR  
DEPRESSURIZATION- INDUCED EXTINCTION**



## THIN-FILM METHODS FOR EXAMINING THE DECOMPOSITION CHEMISTRY OF EXPLOSIVES

K. L. Erickson, W. M. Trott, and A. M. Renlund  
Sandia National Laboratories  
Albuquerque, New Mexico 87185

Experimental techniques using thin-film samples and infrared spectroscopy have been developed to examine thermally-induced condensed-phase decomposition chemistry of explosives. Experiments with nitrocellulose (NC) and 1,3,5-triamino-2,4,6-trinitrobenzene (TATB) were done to examine the effect of confining the decomposition products so that intimate contact was maintained with the remaining explosive during isothermal decomposition at temperatures below those of the respective DTA exotherms. The NC experiments showed that substantial NC decomposition occurred at 150 C and confinement of the decomposition products influenced the decomposition reactions. Some of the mechanisms and reaction rates with confined samples compared favorably with published mechanisms and rates from unconfined samples, while other mechanisms and reaction rates differed. The TATB experiments showed that significant TATB degradation occurred at temperatures as low as 210 C, and substantial degradation occurred within 24 hours at 250 C which is about 80 C below the temperature of the DTA exotherm for TATB.

### INTRODUCTION

The response of energetic materials to thermal, shock, or combined thermal and shock stimuli can depend substantially on the thermally and mechanically induced decomposition chemistry of the materials. Development of reliable models for design, performance, and hazard analyses requires knowledge of the controlling chemical reaction mechanisms. These can be particularly important in determining the nature of an explosive's response (for example, burning versus explosion or detonation) in a cook-off situation or in predicting the shock sensitivity and detonation of thermally degraded explosives. Furthermore, a knowledge of decomposition mechanisms can guide development of new, less sensitive materials. The rate-determining decomposition mechanisms can occur in either the gas or condensed phase or can involve gas-surface reactions. Reactions occurring in the condensed phase have been particularly difficult to study previously because of the inability to probe chemistry directly in the condensed phase under isothermal conditions and with the spatial and temporal resolution needed at high temperatures and reaction rates. Thin-film samples provide an opportunity to overcome these difficulties. Using such samples, con-

densed-phase materials at constant, elevated temperatures can be examined spectroscopically with micro-second temporal resolution.

We are developing experimental techniques that use thin-film samples and multiple diagnostics to examine thermally induced condensed-phase decomposition chemistry. These experiments complement larger scale gas-gun tests that are investigating the shock sensitivity and detonation of thermally degraded explosives. The thermal decomposition experiments involve sample heating rates, reaction temperatures, and reaction times that can be varied from about  $10^8$  to less than 1 C/s, from ambient to about 600 C, and from  $10^{-4}$  to  $10^5$  s, respectively. Conventional infrared spectroscopy and time-resolved infrared spectral photography (TRISP), which provides 10-ns "snapshots" of selected regions of the infrared spectrum, are used for direct detection of condensed-phase decomposition products. Time-of-flight mass spectrometry (TOFMS) is used to monitor evolved gas species. Results from initial thermal decomposition experiments were reported previously.<sup>1</sup>

This paper discusses results from subsequent work with nitrocellulose (NC) and 1,3,5-triamino-2,4,6-trinitrobenzene (TATB) that focused on examining the effects of confining the samples so that intimate contact is maintained between the decomposition products and the remaining condensed-phase explosive during slow

\* This work performed at Sandia National Laboratories supported by the U.S. Department of Energy under contract DE-ACO4-76DP00789

decomposition at elevated temperatures below those of the respective DTA exotherms. The effects of maintaining intimate contact are particularly important because such confinement may significantly affect thermophysical phenomena and decomposition reaction rates.

The accumulation of decomposition products in the condensed phase can affect several physical phenomena that influence energetic material response in an abnormal thermal environment. The nature of these effects will depend on the degree of miscibility between the decomposition products and the remaining explosive. In the case of low miscibility, the separation of decomposition products into separate phases, possibly accompanied by fracturing of solid phases, can result in an extremely heterogeneous, reacting system. In the case of high miscibility, the dissolution of decomposition products in the explosive can result in: (1) volume changes leading to void or bubble formation and (2) lowering of the temperatures at which phase transitions occur, either solid-liquid or solid-solid, which can be accompanied by additional volume as well as enthalpy changes. Such physical changes can increase the sensitivity of explosives to impact as well as increase the severity of the thermal response of the material.

The accumulation of decomposition products also can have a substantial effect on the overall rate of reaction during decomposition. The overall rate can be influenced by the reaction of a particular decomposition product with another and by reaction of decomposition products with the remaining explosive, in which case, autocatalytic mechanisms are particularly important. Furthermore, a phase transition induced by dissolution of decomposition products can result in increased reaction rates.

Results from the experiments with NC showed that for some mechanisms, the reaction rates for confined NC samples compared favorably with published reaction rates for unconfined samples. However, the results also demonstrated that for other mechanisms, the reaction rates were significantly affected by confinement of the decomposition products.

Results from the experiments with TATB showed that significant degradation occurred slowly at temperatures as low as 210 C, and substantial degradation occurred within 24 hours at 250 C. However, reported DTA results<sup>2</sup> indicate negligible change in TATB at such temperatures, which are at least 80 C below the temperature of the DTA exotherm for TATB.

In the following discussion, the thin-film experimental techniques that have been developed are briefly summarized. Then, the results from experiments with NC and TATB samples are presented and discussed.

## EXPERIMENT

The objective of the experimental work was to examine the decomposition chemistry of explosives such as NC and TATB when intimate contact was maintained between decomposition products and the remaining explosive. The experiments required a sample configuration which provided maximum confinement of the decomposition products, involved minimum free volume around the explosive, and allowed the condensed-phase chemistry to be probed directly using infrared spectroscopy. This was accomplished using the configuration shown schematically in Figure 1. Samples of a single energetic material, NC or TATB, were used to study decomposition of initially pure explosives. The NC used was 11.8 weight percent N.

To prepare samples of NC and TATB, a thin-film, about 2 to 5 microns thick, of the explosive was deposited on an inert infrared-transmitting substrate, such as a barium fluoride or sodium chloride optical window. A second window was pressed against the surface of the explosive, and the perimeter around the film and windows sealed. In the NC experiments, the sealed sample was placed in a secondary stainless steel container that was sealed and then placed in an oven maintained at the desired reaction temperature. Typical aging temperatures were about 130 to 170 C, and typical aging times about 2 to 48 hours. Afterwards, the secondary container was removed from the oven and cooled in air. Cooling required about one hour. The sample was then removed from the secondary container and placed in an infrared spectrophotometer for postmortem analysis. In the TATB experiments, the sealed sample was placed in a heated IR-transmitting cell, which was essentially a small oven. The cell was placed in the sample compartment of the spectrophotometer and permitted continuous monitoring of a single sample. An inner gold wire seal also was added to reduce the free volume around the deposited TATB film.

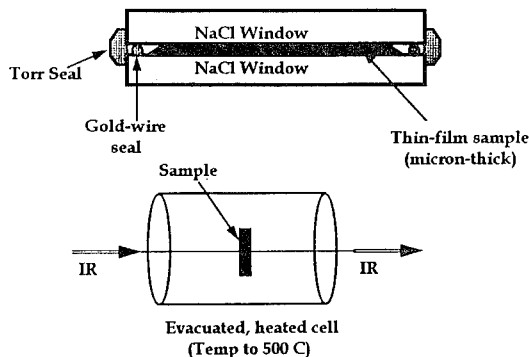


FIGURE 1. SAMPLE CONFIGURATION USED IN THERMAL AGING EXPERIMENTS

While considerable effort was made to confine decomposition products in intimate contact with the remaining explosive, some loss of gaseous products may have occurred. Postmortem visual examination of the samples indicated that most of the sample material had remained between the optical windows, and no seal failures could be detected with an optical microscope. However, undetected failure may have occurred, and some gaseous products could have escaped by permeation through the Torr Seal (Figure 1) at elevated temperatures.

The preparation of thin-film explosive samples has been discussed previously.<sup>3</sup> Briefly, the procedures for preparing samples are based on either physical vapor deposition or deposition from solution. Physical vapor deposition provides reasonably precise control of film properties. The technique can be used with any material, such as RDX, HMX, HNS, and TATB that exerts sufficient vapor pressures at temperatures low enough to preclude decomposition of the material. However, polymeric materials such as NC do not exert sufficient vapor pressure. For these materials, the simplest alternative is deposition from solution, which may not permit as precise control of film properties. Using physical vapor deposition, good quality samples of RDX, HMX, HNS, and TATB have been deposited on a variety of substrate materials that include tungsten, aluminum, nickel, gold, pyrex, barium fluoride, and sodium chloride. Film thicknesses have been varied between about 0.04 to 10 microns. Good quality films of NC, about 0.5 to 5 microns thick, have been prepared by evaporation of acetone solutions containing 0.1 to 1 weight percent NC.

The characterization of sample films prepared using the above procedures also has been discussed previously.<sup>3</sup> In general, films that are uniform and well-crystallized should be chemically representative of bulk materials. To determine uniformity and crystallinity, several thin-film samples were examined by optical and scanning electron microscopy, x-ray diffraction, and transmission electron microscopy. Optical and scanning electron microscopes were used to examine film morphology and uniformity. The films exhibited some microscopic surface roughness, but overall, they appeared relatively uniform, flat, and nearly fully dense. X-ray diffraction was used to examine the crystal structure of samples having thicknesses of about 2 microns or greater. The diffraction patterns obtained from the thin-film samples agreed with published data and exhibited very narrow peaks, which indicated that the films were well-crystallized. The films were polycrystalline, but the grains appeared to be highly oriented. To determine the uniformity and crystal structure of submicron-thick films, procedures were developed to examine samples with a transmission electron microscope. The electron diffraction patterns from 0.5-micron-thick RDX films showed that the crystal structure of the films was that of

bulk RDX. The 0.5-micron films were also polycrystalline and highly oriented, with the [001] zone of most of the grains being perpendicular to the substrate plane, which is consistent with the x-ray diffraction results from thicker films. In addition to examining film uniformity and crystallinity, infrared spectra were obtained from RDX, HMX, and TATB films, 2 to 5 microns thick. These spectra were in good agreement with the corresponding published spectra.

## RESULTS

The decomposition of unconfined NC films was studied previously by Phillips et al.<sup>4</sup> and Jutier et al.,<sup>5</sup> who used infrared spectroscopy to examine decomposition mechanisms and kinetics. The principal infrared absorption frequencies for NC are shown in Table 1.

TABLE 1. INFRARED ABSORPTION FREQUENCIES FOR NC

Frequency (cm <sup>-1</sup> )	Relative Intensity	Assignment
3515	weak	OH stretching
3512	weak	OH stretching
2973	medium	CH <sub>2</sub> asymmetric stretching
2927	medium	CH stretching
2883	medium	CH <sub>2</sub> symmetric stretching
1653	very strong	NO <sub>2</sub> asymmetric stretching
1424	weak	CH <sub>2</sub> bending
1375	medium	CH bending
1282	very strong	NO <sub>2</sub> symmetric stretching
1160	medium	asymmetric ring stretching
1118	medium	asymmetric ring stretching
1070	very strong	C-O stretching in Cl-O-C4
1025	weak	C-O stretching
1004	medium	C-O stretching
0910	weak	C-O stretching
0840	very strong	O-NO <sub>2</sub> stretching
0749	medium	O-NO <sub>2</sub> deformation
0692	medium	O-NO <sub>2</sub> deformation

Phillips et al. examined isothermal decomposition into vacuum. Decomposition temperatures were varied between 140 and 200 C. The NC films were typically 3 microns thick. The principal decomposition mechanisms observed by Phillips et al. were scission of the O-N bond in the nitrate groups, the corresponding carbonyl (C=O) formation by scission of an adjacent C-C bond, and the

scission of the C-O-C bonds involving both ring and linking oxygen atoms. Scission of the O-N bond, carbonyl formation, and scission of the C-O-C bond all appeared to be first-order processes, for which Arrhenius expressions, activation energies and frequency factors, were evaluated. The rate of scission of the C-O-C bond was approximately equal to the rate of scission of the O-N bond, and the rate of carbonyl formation appeared to be approximately equal to or greater than the rate of O-N bond scission. The spectra reported by Phillips et al. also indicated scission of the C-H bonds. Furthermore, a broad, but weak absorption in the O-H/N-H stretching region appeared to develop slowly.

Jutier et al. conducted nonisothermal experiments using a heating rate of 0.5 C/s. FTIR spectra were acquired between 140 and 200 C. Their results were similar to those of Phillips et al., except that Jutier et al. claimed that the C-O-C bond involving the linking oxygen atom remained intact during their experiments.

In general, some of the reaction mechanisms, particularly O-N bond scission, implied by the infrared spectra obtained during decomposition of confined samples would be expected to be similar to those observed by Phillips et al. and Jutier et al. during decomposition of unconfined samples. However, other mechanisms could be dissimilar. The infrared spectra obtained during decomposition of the confined samples do indicate similarities as well as differences. Figure 2 shows the spectra from 5-micron-thick, confined NC films aged at 130 and 150 C for 16 hours. The initial spectrum prior to heating is also shown for comparison. At 130 C, some decomposition is evident. With respect to the baseline, a small decrease in absorption, relative to the initial spectrum, occurred at the NO<sub>2</sub> stretching frequencies, indicating scission of the O-N bond. Some absorption at the C=O stretching frequency was present, indicating carbonyl formation. A small loss in absorption due to C-O-C

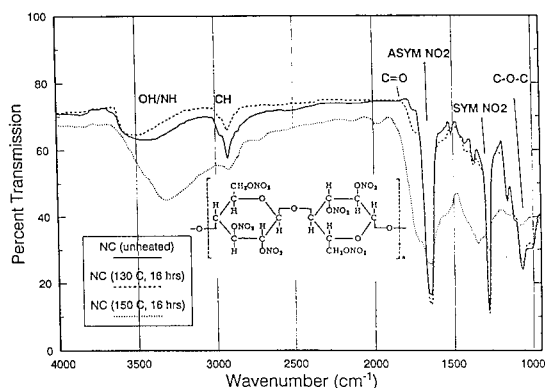


**FIGURE 2. INFRARED SPECTRA FROM 5- $\mu$ m-THICK NC SAMPLES AGED FOR 16 HOURS AT 130 AND 150 C**

stretching also occurred, indicating scission of the C-O-C bond, and a loss in absorption at the C-H stretching frequencies was evident, indicating some hydrogen abstraction. Increased absorption also appeared to occur at 1580, 1350, and 1200 cm<sup>-1</sup>. At 150 C, the changes in the absorptions, relative to the initial spectrum, at the O-N, C=O, C-O-C, and C-H stretching frequencies are much more pronounced and indicate that scission of the O-N bond, carbonyl formation, scission of the C-O-C bond, and hydrogen abstraction are substantial. The absorption in the O-H/N-H stretching region has broadened, shifted, and substantially increased, and the absorptions at about 1580, 1350, and 1200 cm<sup>-1</sup> also have increased substantially. Most of these effects are also evident even after relatively short aging times, as shown in Figure 3, which compares the spectra from samples aged for 2 and 16 hours, respectively, at 150 C.

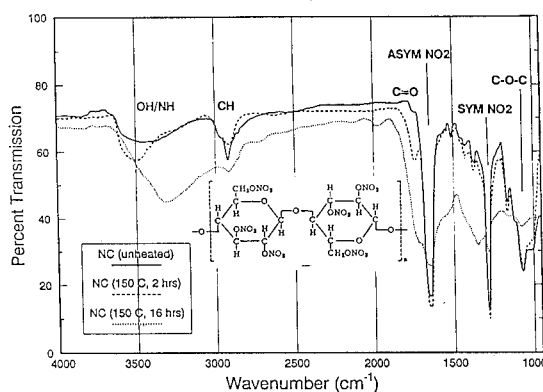


**FIGURE 3. INFRARED SPECTRA FROM 5- $\mu$ m-THICK NC SAMPLES AGED FOR 2 AND 16 HOURS AT 150 C**

The decrease in the absorptions at the O-N, C-O-C, and C-H stretching frequencies and the growth of the absorption at the C=O stretching frequency are evident in the spectra from both confined and unconfined samples. The significant absorptions at the O-H/N-H stretching frequencies and the apparent absorptions at about 1580, 1350, and 1200 cm<sup>-1</sup> are unique to the confined samples, and may be associated with degraded NC or may be due to accumulation of decomposition products.

Beer's law was assumed to examine the reaction rates associated with the spectral changes shown in Figure 3. The results are summarized in Table 2 which shows the various changes in absorbance  $A$  at time  $t$  relative to the absorbance  $A_0$  prior to aging. In the case of carbonyl formation (C=O), the ratio  $A/A^*$  is shown, where  $A^*$  is the value of  $A$  at 16 hours. Values of the ratio  $[-\ln(A/A_0)]/t$  also are shown as a function of time. The values for the NO<sub>2</sub> stretching frequencies, which indicate scission of the O-N bond, and the values for C-O-C stretching, which indicate scission of the C-O-C

bonds, are approximately constant with time, indicating that bond scission occurs by a first-order mechanism. However, the decrease in reaction rate implied by the changes in absorption at the C-H stretching frequencies and the changes in reaction rate implied by the increase in the N-H/O-H stretching frequencies do not indicate first order mechanisms. In the case of C-H stretching, the ratio  $A/A_0$  initially decreases much faster than the ratio for O-N and C-O-C bond scission, but between 2 and 16 hours decreases much slower. In the case of O-H/N-H stretching, the broadening and shifting of the absorption probably results from multiple mechanisms involving decomposition of the NC and interaction between the decomposition products. Furthermore, the values of  $A/A^*$  for C=O stretching indicate that carbonyl formation is not first-order with respect to O-N bond scission

The results from decomposition experiments with confined samples and the results from experiments with unconfined samples are similar with respect to O-N and C-O-C bond scission. With both confined and unconfined samples, the bond scissions apparently occur by first-order processes. However, the relative rates at

TABLE 2. ANALYSIS OF SPECTRA FROM NC SAMPLES AGED AT 150 C

Absorp.	<i>t</i> (hr)	<i>A/A<sub>0</sub></i>	<i>A/A*</i>	$\ln\left(\frac{A}{A_0}\right)$ $\frac{t}{(\text{hr}^{-1})}$	<i>k</i> (hr <sup>-1</sup> )	
					This work	ref. 4
NO <sub>2</sub> asym	0	1.0	---	---		
	2	0.77	---	0.13	0.12	0.10
	16	0.19	---	0.10		
NO <sub>2</sub> sym	0	1.0	---	---		
	2	0.84	---	0.09	0.10	0.10
	16	0.21	---	0.10		
C=O	0	---	0	---		
	2	---	0.35	---	---	0.10
	16	---	1.0	---		
C-O-C	0	1.0	---	---		
	2	0.77	---	0.13	0.14	0.11
	16	0.09	---	0.15		
C-H	0	1.0	---	---		
	2	0.58	---	0.27	---	---
	16	0.32	---	0.07		
O-H/N-H	0	1.0	---	---		
	2	1.48	---	-0.20	---	---
	16	2.78	---	-0.06		

which scission occurs differ between confined and unconfined samples. Phillips et al. reported that with their unconfined samples, the rate of C-O-C bond scission was approximately equal to the rate of O-N bond scission. However, with the confined samples described above, the rate of C-O-C bond scission appeared to be slightly faster (approximately 30%) than the rate of O-N bond scission.

The results also differ with respect to carbonyl formation. Phillips et al. reported that carbonyl formation was a first-order process having rates approximately equal to, or greater than the rate of O-N bond scission. However, with confined samples, carbonyl formation does not appear to be first-order, and the rate of formation between 2 and 16 hours appears slower than the rate of O-N bond scission at 150 C. The results further differ with respect to the strong absorption which develops at the O-H/N-H stretching frequencies. Apparently, the formation of products containing OH or NH groups was much more significant with confined samples.

The decomposition of thin films of TATB has not been studied by previous investigators. The results described below are from experiments using only confined samples, because the relatively high vapor pressure of TATB at decomposition temperatures militates against experiments with unconfined samples. The experiments with confined samples show that substantial changes in the infrared spectra occurred during aging experiments done at temperatures well below that of the DTA exotherm for TATB. Figures 4a and 4b show spectra taken at 0.5, 4, and 43 hours during the aging of a TATB sample at 210 C. The room temperature spectrum is also shown for comparison. The 0.5-hour spectrum is significantly different from the room-temperature spectrum. In addition to well-known physical effects (such as the significant temperature-induced broadening of peaks due to N-H symmetric and asymmetric stretching modes near 3220 cm<sup>-1</sup> and 3320 cm<sup>-1</sup>, respectively), changes in the spectrum indicate that some decomposition or degradation of the TATB occurred relatively fast. The spectra continue to change with time, as indicated by the 4- and 43-hour spectra, and significant degradation of the TATB appeared to have occurred after 43 hours.

The spectrum taken after 24 hours during aging of a TATB sample at 250 C is shown in Figure 5. Again, the room temperature spectrum is shown for comparison. In this case, the TATB appears to have been substantially degraded after aging for 24 hours at 250 C. However, reported DTA results<sup>2</sup> indicate that negligible change in TATB should occur at such temperatures, which are at least 80 C below the temperature of the corresponding DTA exotherm. Quantitative analysis of the TATB spectra, similar to that given for the NC spectra, has been hampered by the conflicting assignments reported for the bond frequencies in TATB.<sup>6-9</sup>

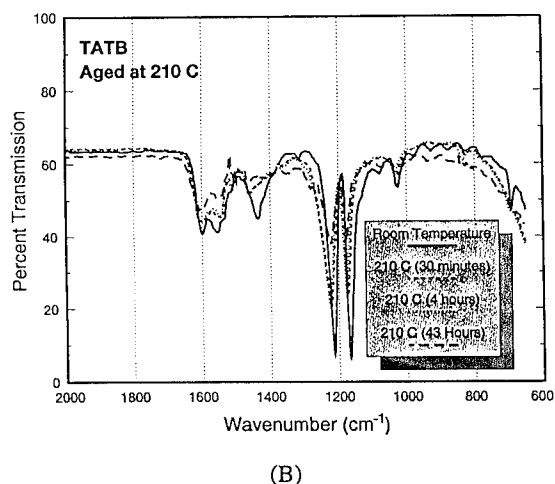
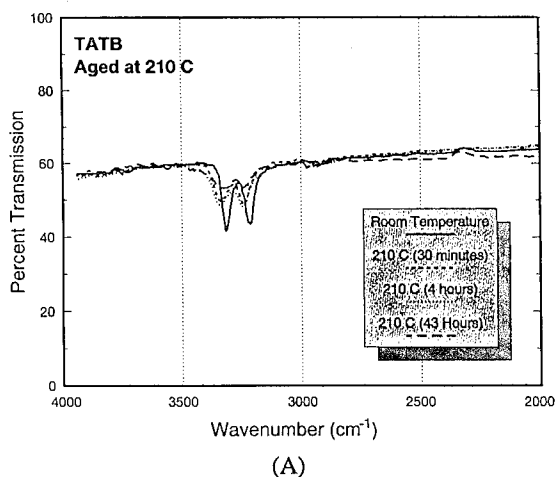


**FIGURE 4. INFRARED SPECTRA FROM 2- $\mu$ m-THICK TATB SAMPLE AGED AT 210 C: (A) 4000-2000  $\text{cm}^{-1}$  (B) 2000-600  $\text{cm}^{-1}$**

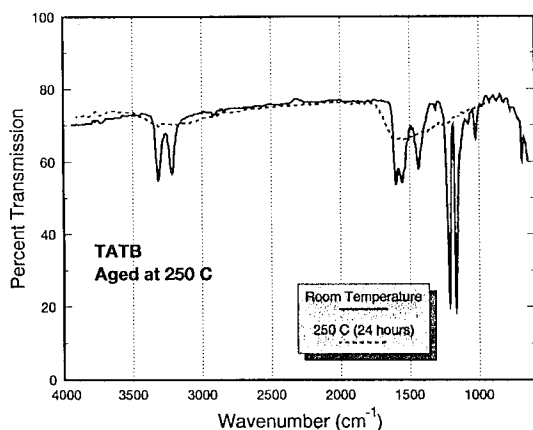


**FIGURE 5. INFRARED SPECTRA FROM 2- $\mu$ m-THICK TATB SAMPLE AGED AT 250 C**

## SUMMARY AND CONCLUSIONS

The results from the isothermal aging experiments show that IR spectroscopy can be used in conjunction with thin-film samples to probe the condensed-phase chemistry of confined explosives. The experiments with NC demonstrated that confinement of decomposition products in intimate contact with the remaining explosive can influence decomposition reactions. Some of the reaction rates determined from the experiments with confined samples compared favorably with published reaction rates from unconfined samples. However, some reaction rates differed between confined and unconfined samples. These differences should currently be considered tentative, since uncertainty exists in evaluating overlapping absorbances at some frequencies, and deviations from Beer's law can occur.

The experiments with TATB showed that degradation of TATB can occur slowly at temperatures as low as 210 C, and substantial degradation can occur within 24 hours at 250 C, which is about 80 C below the temperature of the DTA exotherm for TATB. These results further indicate that confinement can affect decomposition mechanisms and kinetics. Subsequent experiments have indicated that degradation may be extremely sensitive to the degree of confinement of the explosive. These effects are being further investigated.

A disadvantage of the postmortem analyses used in the NC experiments was that the sample had to be cooled before infrared analysis. In the TATB work, this disadvantage was overcome by placing the sample assembly in a heated cell which fits in the sample chamber of the infrared spectrophotometer. Further improvements to the experiments will include: (1) improved metal seals, which will allow experiments at higher temperatures, and (2) the use of FTIR, which will allow frequent, real-time data acquisition while samples are at their aging temperatures, and will facilitate acquiring data at several aging temperatures and times. With these improvements, the isothermal aging experiments should provide substantial insight into the decomposition mechanisms of a variety of explosives.

## ACKNOWLEDGMENTS

The authors gratefully acknowledge the technical assistance provided by F. D. Chavez.

## REFERENCES

1. Erickson, K. L., Trott, W. M., and Renlund A. M., "Use of Thin-Film Samples to study Thermal Decomposition Chemistry of Explosives," in *Proceedings of the Eighteenth International Pyrotechnics Seminar*, Breckenridge, Colorado, 12 - 17 July 1992, pp. 241-254.
2. Dobratz, B. M., *Properties of Chemical Explosives*

- and Explosive Simulants, UCRL-51319 Rev. 1, July 31, 1974, Lawrence Livermore Laboratory, Livermore, CA.
3. Erickson, K. L., Skocypec, R. D., Trott, W. M., and Renlund, A. M., "Development of Thin-Film Samples for Examining Condensed-Phase Chemical Mechanisms Affecting Combustion of Energetic Materials," in *Proceedings of the 15th International Pyrotechnics Seminar*, Boulder, Colorado, July 1990, pp. 239-260.
  4. Phillips, R. W., Orlick, C. A., and Steinberger R., "The Kinetics of the Thermal Decomposition of Nitrocellulose," *Journal of Physical Chemistry*, Vol. 59, 1955, p.1034.
  5. Jutier, J.-J., Harrison, Y., Premont, S., and Prud'homme, R. E., "A Nonisothermal Fourier Transform Infrared Degradation Study of Nitrocelluloses Derived from Wood and Cotton," *Journal of Applied Polymer Science*, Vol. 33, 1987, p. 1359.
  6. Vergoten, G., Fleury, G., Blain, M. and Odier, S., "Structure Moléculaire des Dérivés Nitres Aromatiques 5 - Spectres de Vibration et Analyse par Coordonnées Normales du 1,3,5-Triamino-2,4,6-trinitrobenzene," *Journal of Raman Spectroscopy*, Vol. 16, No. 3, 1985, p. 143.
  7. Deopura, B. L. and Gupta V. D., "Vibration Spectra of 1,3,5-Triamino-2,4,6-trinitrobenzene," *Journal of Chemical Physics*, Vol.54, No. 9, 1971, p. 4013.
  8. Towns, T. G., "Vibrational Spectrum of 1,3,5-triamino-2,4,6-trinitrobenzene," *Spectrochimica Acta*, Vol. 39A, No. 9, 1983, p. 801.
  9. Catalano E. and Rolon, C. E., "On the Solid State Products of the Thermal Decomposition of Confined and Unconfined Triaminotrinitrobenzene," *Thermo-chimica Acta*, Vol. 61, 1983, p. 53.

## RECOVERY TECHNIQUE FOR SHOCKED EXPLOSIVE SAMPLES\*

T. P. Liddiard, J. W. Forbes, J. W. Watt,  
R. N. Baker, J. Sharma, and B. C. Beard  
Naval Surface Warfare Center  
Dahlgren Division; White Oak Detachment  
10901 New Hampshire Ave.  
Silver Spring, MD 20903-5640

A reliable technique for recovering shocked explosive samples has been developed. Small explosive samples are mounted in Teflon holders. Samples are typically 5 mm diameter by 1 mm thick weighing 30 mg. The samples are placed underwater at prescribed distances from a one pound pentolite sphere. Samples have been recovered for peak shock stresses up to 26 kbar. New chemical reactions have been discovered in TATB and HMX samples that were shocked to stresses below that required to initiate detonation.

### INTRODUCTION

Pre-ignition reactions in explosives subjected to shock compression is of fundamental importance to the study of explosive behavior. Recovery of samples subjected to strong shocks has been a problem. The sample must be contained and remain relatively uncontaminated. In addition, some means of determining the shock history in the sample should be available. The present recovery technique is the result of a number of experiments in which various degrees of success occurred. Several modifications of the recovery system finally led to a reliable recovery technique.

### EXPERIMENTAL TECHNIQUE

In our technique, the recovery of small explosive samples subjected to high levels of shock compression is accomplished by using the donor charge and aquarium of the Underwater Sensitivity test<sup>1</sup>(UST) and explosive sample holders. Typically, 30 mg samples, 5 mm diameter by 1 mm thick, are mounted

in Teflon holders. The sample holders are mounted in thin-walled tubes of steel and placed around a spherical pentolite charge with the flat surface towards the donor. A number of samples are placed around the sphere in the tank on individual rigs to allow more samples to be tested per experiment. The explosive samples are set at different distances from the donor to obtain various peak pressures. The underwater shock system was carefully calibrated previously.<sup>2</sup> The sample holders are recovered following the detonation of the pentolite sphere. The explosive samples are removed from the holders for chemical and physical(microscopic) analysis. Recovery of samples shocked to peak stresses of up to 25 kbar with pulse widths of a few microseconds has been accomplished.

In most recovery techniques, the impedances of the surrounding material are quite different from the explosive samples and the outer boundaries of the surrounding material are close to the sample's location. Both these conditions lead to relief waves significantly affecting the strain histories of recovered samples. The recovery system presented in this paper results in simple strain histories for samples. The simple strain histories result from (1) the Teflon, water and explosive samples having similar shock impedances which greatly reduces the magnitude of the reflected waves in the sample and (2) relief waves from the boundaries of the water tank being quite weak when they reach the test samples. The stress conditions of the

\*This work was performed for the Office of Naval Research, Code 4525.



underwater sensitivity test subject explosive samples to relatively long, low-pressure shocks of spherical geometry. The shock duration (decay time to one-half peak pressure) is 20-40  $\mu$ s in the water. The donor system is an 82 mm diameter sphere of cast pentolite (50%TNT/50%PETN), weighing 470-480 g. A pressed pellet of pentolite is used to insure that the initiation of the sphere occurs at the center. The spherical donor is suspended by a nylon cord harness in the center of a supporting rig made of aluminum. The detonator axis is located in a position normal to the plane of the acceptors. This orientation reduces irregularities in the shock front, since the initiation of the donor is observed to be more symmetrical around the detonator axis. The complete donor/acceptor system mounted in the rig is submerged in a cubic tank of water, 60 cm on an edge. The aluminum frame fits just inside the cubic box. The general arrangement of capsule holders around the sphere is shown in Figure 1. The peak pressure in water is obtained from a published calibration of the UST system.<sup>2</sup> Peak stresses induced in the samples are obtained by the impedance matching technique.

The Teflon sample holder is in two parts as given in Figure 2, a cap and a threaded rod (plug) with a cavity in the end for the sample. A 1.6 mm bleed hole is located at the end of the cavity in the cap to permit air to escape when the threaded rod with the sample in the cavity is inserted into the cap. In early versions of the sample holder the rod was threaded its entire length, which made it difficult to be sure of complete assembly since the Teflon rod would sometimes warp and cause it to bind. The design was changed to use only 19 mm of thread (17 mm for the plug). To seal the sample holder after assembly, the

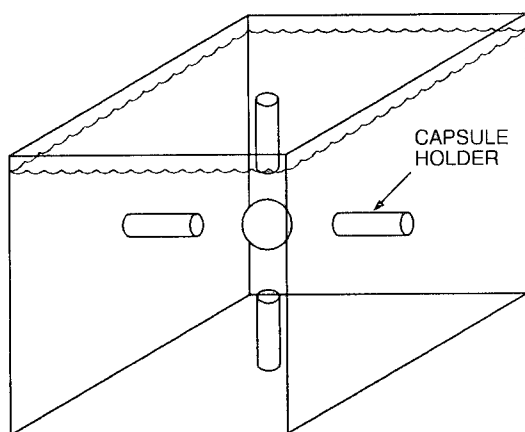
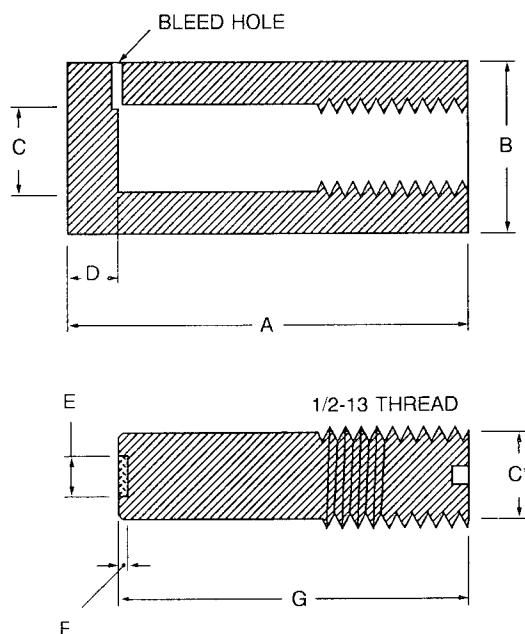


**FIGURE 1. CAPSULE PLACEMENT AROUND PENTOLITE SPHERE**

first sample holder models used chemical etching and special epoxy which made it extremely difficult to unscrew the assembly and recover the sample. The final design used the 19 mm long thread without cement. A Teflon paste was used to seal the threads. After assembly, the bleed hole is plugged with duxseal. The steel support tube is bored out to a diameter which just allows the sample holder to slide into the tube. This boring is just deep enough to allow the sample holder to be pushed in flush with the edge of the steel tube. The sample holder is pushed into that cavity and held in place by the close fit. The steel support tube has several 2.4 mm holes drilled in the side along its length to permit water to fill the tube completely. A Plexiglas collar attached to the aluminum frame supports the steel tube. The collar can be made so that the tube can be positioned at any desired angle. In earlier experiments, the impact of the tube against the aluminum frame caused excessive damage to the Teflon holder, so holes were cut in the aluminum frame to allow the steel tube to slip through the Plexiglas collar when the shock impacted the tube.



**DIMENSIONS IN mm**

A	50.8	E	5.2 (dia)
B	21.3 (dia)	F	0.89
C	10.71 (dia)	G	44.5
D	6.4		

\* SNUG FIT

**FIGURE 2. TEFLON SAMPLE CAPSULE: CAP (TOP) AND THREADED PLUG**

This led to a successful recovery of all samples in a subsequent experiment.

## SUMMARY OF RESULTS

The recovery technique described above has facilitated the study of explosives after being subjected to sub-ignition shock. Table 1 gives the summary of the experiments done to date. The stress at a depth of 6.4 mm in the Teflon cap of the recovery capsule was found using standard impedance calculations using the known equations of state of water<sup>3</sup> and Teflon.<sup>4</sup> The stress in water at 6.4 mm beyond the location of the capsule end was taken from the calibration of stress in water from a pentolite sphere.<sup>2</sup> This was done to approximately account for the attenuation of the pressure as a function of distance from the pentolite sphere. Note that the later recovery experiments were successful in recovery samples at higher pressures than

earlier experiments. These recoveries were successful because the steel tubes (capsule holders) were allowed to move when the shocks hit them. In the earlier experiments, the steel tubes were rigidly fixed on the aluminum frame. A number of papers<sup>5,6,7,8</sup> have reported the chemical and physical changes found in shocked samples recovered after shocking to threshold pressures. In shock recovered TATB, sub-micron ragged holes were found, accompanied with a fine deposit of furoxan and furazan derivatives of TATB. Since the furoxans are more sensitive than TATB, this alteration of the molecule provides a chemical basis of "hot spot" formation and sensitization of the explosive. The furazans are produced by the formation of a water molecule and identified as the first of the exothermic steps in the decomposition reaction of the molecule. In RDX and HMX, the products from shocking are mostly volatile. Analysis of the recovered nitramine material observed a loss of nitro functional groups. In HMX,

TABLE 1. RESULTS OF RECOVERY EXPERIMENTS\*

Expt. No.	Sample	Dist. capsule is from sphere (mm)	Pressure in Teflon (Kbar)	Results
83-77A	TATB	135	4.9	Sample reacted, no recovery
83-79	TATB	125	5.5	Sample recovered
83-81	TATB(A)	76	10.3	Sample recovered
	TATB(B)	64	13.1	" "
	TATB(C)	57	14.9	" "
	TATB(D)	51	17.3	" "
88-665	HMX(A)	159	4.2	Sample recovered, 3 pieces found
	HMX(B)	182	3.5	" " "
	HMX(C)	129	5.1	" " , 2 pieces found
	HMX(D)	130	5.1	Sample recovered intact
	NTO(E)	67	12.4	" " "
	NTO(F)	49	18.1	" " "
92-R1	TNT(I)	100	7.4	Sample recovered
	TNT(II)	120	5.7	" "
	TATB(III)	50	17.7	" "
	TATB(IV)	40	22.8	" "
	CaF(V)	150	4.5	No sample inside capsule
	RDX-XTAL(VI)	50	17.7	End blown off capsule, small parts of Xtal found
	RDX-XTAL(VII)	40	22.8	End blown off capsule, no recovery
	CL20/OIL(VIII)	100	7.4	Capsule recovered, soot around air hole, residue found
	CL20/OIL(IX)	150	4.5	Capsule recovered, soot around air hole, residue found

\*TATB, TNT, NTO, AND HMX SAMPLES WERE PRESSED TO 95-97% THEORETICAL MAXIMUM DENSITY.

subjected to under water shock of 4.1 kbar, a 16% loss of nitro groups was observed.

## CONCLUSIONS

A technique has been developed to recover shocked explosives for stresses as high as 26 kbar. The optical and chemical examination of recovered explosive samples has led to the discovery of new chemical reactions occurring in these explosives.

Future improvements of this recovery technique will be based on the results of two-dimensional hydrocode modeling of the experiment. Plastic capsule holders will be used to reduce the impedance between the explosive holders and the capsule holders.

## REFERENCES

1. Liddiard T. P., Forbes J. W., and Price D., "Physical Evidence of Different Chemical Reactions in Explosives as a Function of Stress," Ninth Symposium (International) on Detonation, Portland, OR, 28 Aug - 1 Sep 1989, pp. 1235-1242.
2. Liddiard T. P., Forbes J. W., "A Summary Report of the Modified Gap Test and The Underwater Sensitivity Test" NSWC TR 86-350, 12 March 1987.
3. Rice, M. H., and Walsh, J. M., "Equation of State of Water to 250 Kilobars," J. Chem Phys., vol. 26, No. 4, 1957, pp.824-830.
4. Champion, A. R., "Shock Compression of Teflon from 2.5 to 25 kbar-Evidence for a Shock-Induced Transition," J. Appl. Phys., vol. 42 No. 13, 1971, pp. 5546-5550.
5. Sharma J., Beard B. C., Forbes J., Coffey C. S., "Physical and Chemical Nature of Hot Spots in TATB and HMX," Ninth Symposium (International) on Detonation, Portland, OR, 28 Aug -1 Sep 1989, pp. 897-905.
6. Sharma J., Forbes J. W., Coffey C. S., Liddiard T. P., "The Physical and Chemical Nature of Sensitization Centers Left from Hot Spots Caused in Triaminotrinitrobenzene by Shock or Impact," J. Phys. Chem., 10, 1987, pp. 5139-5144.
7. Sharma J., Hoffsommer J. C., Glover D. J., Coffey C. S., Forbes J. W., Liddiard T. P., Elban W. L., and Santiago F., "Sub-Ignition Reactions at Molecular Levels in Explosives Subjected to Impact and Underwater Shock," Eighth Symposium (International) on Detonation, Albuquerque, NM, 15-19 July 1985, pp. 725-733.
8. Sharma J., Beard B. C., Energetic Materials, (Edited by J. E. Field and P. Gray), The Royal Society, London, (1992), PP. 285-292.

## PORTABLE, SOLID STATE, FIBER OPTIC COUPLED DOPPLER INTERFEROMETER SYSTEM FOR DETONATION AND SHOCK DIAGNOSTICS

K. J. Fleming, O.B. Crump  
Sandia National Laboratories  
Albuquerque, New Mexico, 87123

VISAR (Velocity Interferometer System for Any Reflector) is a specialized Doppler interferometer system that is gaining world-wide acceptance as the standard for shock phenomena analysis. The VISAR's large power and cooling requirements, and the sensitive and complex nature of the interferometer cavity has restricted the **traditional** system to the laboratory. This paper describes the new portable VISAR, its peripheral sensors, and the role it played in optically measuring ground shock of an underground nuclear detonation (UGT). The Solid State VISAR uses a prototype diode pumped Nd:YAG laser and solid state detectors that provide a suitcase-size system with low power requirements. A special window and sensor was developed for fiber optic coupling (1 kilometer long) to the VISAR. The system has proven itself as a reliable, easy-to-use instrument that is capable of field test use and rapid data reduction employing only a personal computer (PC).

### INTRODUCTION

Detailed analysis and accurate models of shock phenomena and high speed motion require an instrument that is capable of measuring the high acceleration of surfaces accurately and non-intrusively. Dent blocks and stress gauges can only infer the **final** velocity of detonations while critical information pertaining to the acceleration is unknown. A versatile instrument that optically measures acceleration, displacement and velocity is VISAR. The VISAR (Velocity Interferometer System for Any Reflector) uses coherent, single frequency laser light to illuminate a target that has some reflectivity. The reflected light is collected and routed through a modified, unequal leg, Michelson interferometer. As the target moves, the resulting Doppler information is detected and electronically analyzed, then the data are converted to velocity and displacement time histories using software operating on a personal computer (PC). The sensitivity, accuracy, and high bandwidth of VISAR are

attributed to the optical method of measurement and its 400 MHz bandwidth is primarily limited only by the electronics in the system.

Although the VISAR technique is excellent to measure shock phenomena, there are some limitations with the conventional VISAR, such as; inherent sensitivity to adverse environments found outside the laboratory, hazardous unenclosed laser beam, high current, voltage and cooling requirements, and inability to measure devices not in the "line of sight" of the laser beam, e.g. through smoke, tunnels, or inside chambers. In an attempt to improve on the versatility of VISAR, a solid state system with fiber optic coupling and rugged components has been developed and rigorously tested in harsh environments. The fiber optic coupled sensor used to send and collect the light at the target is unique from previous techniques and, in recent tests, has performed flawlessly even after four months encapsulation in curing concrete. The solid state VISAR described in this paper was used to measure

ground shock generated by a nuclear detonation at the Nevada Test Site (NTS).

## BACKGROUND

The VISAR was invented by Barker and Hollenbach<sup>1</sup> primarily for measuring free surface velocities of materials in gas gun experiments. An improved version of VISAR, developed by Hemsing<sup>2</sup>, electronically inverts and adds the 180° out-of-phase optical signals that were previously wasted, which effectively cancels target self-light effects and doubles the signal intensity. During fast shock jumps, the system may miss Doppler information which can cause discrepancies in measured velocity. For this reason, Kennedy and Crump<sup>3</sup> developed the double-delay-leg system. This VISAR takes the return light, splits the optical signal and routes it through two interferometer cavities with different sensitivities. The data can then be more accurately reduced by comparing the results of the two systems. The conventional VISAR has many sensitive components mounted on an optical table but the Fixed-Cavity VISAR (developed by Stanton, Crump and Sweatt<sup>4</sup>,) simplifies the interferometer cavity by cementing the movable components together. The result is a rugged, small, easy-to-use system that requires a minimal amount of adjustment.

A low cost, portable VISAR using a diode laser and a fiber optic coupled sensor has been developed by Fleming and Crump<sup>5</sup> with successful velocity measurements taken on electrical slappers. The diode's invisible laser light makes alignment to the target difficult and the aberrated, high divergence beam profile of the laser is difficult to propagate through space for any extended length. Both problems are solved by the development of an imaging fiber optic coupled sensor<sup>6</sup> that has intra-optic video capabilities. The sensor allows for remote target measurements and verification of the correct area of target illumination.

## THEORY OF OPERATION

In a typical experiment, a laser beam is focused to a small spot onto a target of interest. The reflected light is collected and routed to the interferometer cavity (*figure 1*). A dichroic mirror is inserted into the light collecting assembly to transmit the laser light and reflects the other wavelengths (This technique is valuable for viewing the target, allowing for precise alignment of the laser beam.).

The return light, containing equally distributed *S* and *P* polarization components, is collimated and sent through the interferometer cavity (*figure 2*). A 50/50

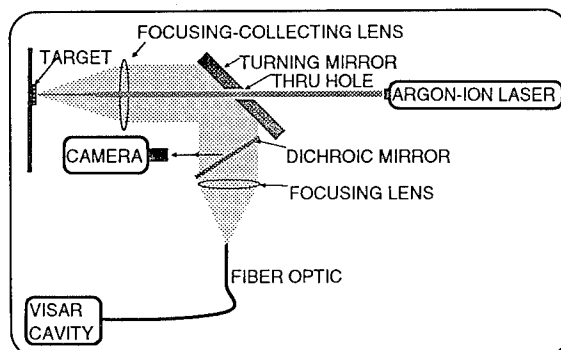


FIGURE 1. CONVENTIONAL METHOD FOR COLLECTING DOPPLER INFORMATION FROM TARGET

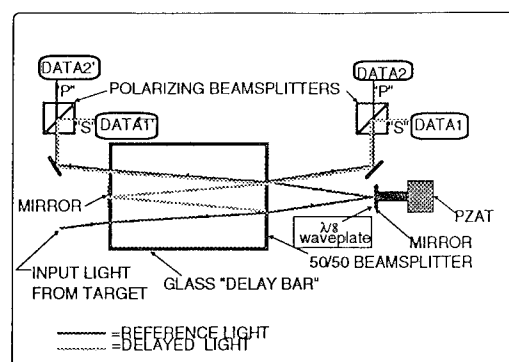


FIGURE 2. FIXED CAVITY VISAR SCHEMATIC SHOWING BEAM PATHS AND PIEZO ANGULAR TRANSLATOR (PZAT). "DATA" FIGURES ARE PHOTODETECTORS

beamsplitter separates the light so that one beam travels through the glass "delay bar" and the other travels through air and an 1/8 wave retarder before recombining and producing an interference (fringe) pattern.

In order to obtain quality fringe patterns, the image distances in both legs of the interferometer must be equal to within a few thousandths of an inch. If both legs of the interferometer are air, the measured distance would be equal. However, the refractive properties of glass make the image distance in the glass *delay* leg farther away than the image distance in the *air reference* leg. This relationship is defined by:

$$x = h(1 - 1/n) \quad (1)$$

where *h* is the delay leg length and *n* is the index of refraction. The distance the light has to travel in the delay leg is farther than the reference leg and the

velocity of light is slower in glass than in air. Using the relationship from equation (1), the delay time  $\tau$  is given by:

$$\tau = (2hc)/(n-1/n) \quad (2)$$

where  $c$  is the speed of light in a vacuum. Using these relationships, the fringe count  $F(t)$  relates to target velocity  $u(t-\tau/2)$  as<sup>7</sup>:

$$u(t-\tau/2) = \frac{\lambda F(t)}{2\tau(1+\Delta v/v)} \cdot \frac{1}{1+\delta} \quad (3)$$

in which  $\lambda$  is the wavelength of the laser light,  $\Delta v/v$  is an index of refraction correction factor if a window is used, and  $\delta$  is a correction factor with wavelength for dispersion in the delay bar. Varying the amount of delay in the interferometer cavity will give the user a greater or lesser amount of fringes to analyze. Equation (3) may be manipulated to obtain the *velocity-per-fringe* (VPF) constant for the interferometer. The VPF equation is:

$$\text{VPF} = \frac{\lambda}{2\tau(1+\Delta v/v)} \cdot \frac{1}{1+\delta} \quad (4)$$

With these relationships, VISAR interferometer cavities with different sensitivities can be designed for optimal performance with regard to anticipated velocity versus Doppler resolution parameters. In any experiment, it is helpful to know that everything is operating correctly. Active feedback from the measuring instrument is a good method of assuring proper operation. The piezoelectric angular translator (PZAT) performs one such function by electrically moving a mirror in the cavity, effectively changing the reference leg dimension. When the dimension changes by  $\lambda/2$ , a  $180^\circ$  phase change occurs which effectively simulates the fringe record for a velocity change equivalent to one-half the VPF value. The return interference signal is monitored and the experimenter is now able to verify that the system is functioning correctly. In *figure 2*, one component of light passes twice through the  $1/8$ -th wave retarder, which makes it  $90^\circ$  out of phase with the other component. The polarizing beam splitting cubes then separate the  $S$  from the  $P$  light and each beam is sent to a photo detector coupled to a digitizer.

Recording two  $90^\circ$  out of phase signals is advantageous because the interference pattern produced is a sinusoidal plot. Phase resolution of the signal is poor when the intensity of the sine wave is at a maxima or minima. Thus, recording two sinusoidal traces  $90^\circ$  out of phase insures that at any point in time one of the signals will be in a region of good resolution

resulting in greater accuracy in the final data.

Also, target acceleration or deceleration can be discriminated. During target acceleration, one signal pattern will lead the other by  $90^\circ$  and a deceleration will cause the opposite to occur.

## SOLID STATE VISAR DEVELOPMENT

The original intent for the development of the Solid State VISAR was for a portable "in house" tool that could be shared by several experimenters and used in the laboratory or in the field. At the same time, the Defense Nuclear Agency (DNA) was interested in optical based instrumentation for use at the Nevada Test Site (NTS). One particular experiment required an "up close" measurement of ground shock generated by the detonation. Since the nuclear event yields radiation and electro-magnetic fields, optical sensors are preferred because of their relative insensitivity to EMP and radiation. Also, the sensors require no electricity which adds a greater margin of safety to personnel. The following are some of the requirements for the system to function:

- Doppler measurement over kilometer-length fiber optics
- Rugged system, operating on 120 VAC
- Must run several days with no adjustments
- Sensors must withstand mechanical and chemical abuse
- Window and sensors must survive concrete encapsulation and measure ground shock at a distance of 7 meters from the detonation
- Data acquisition bandwidth limited to 20 MHz

## EXPERIMENT DESCRIPTION

Measurement of ground shock produced by the detonation is important because it contains valuable information used for analyzing and modeling of the test. This ground shock measurement method uses a window, with fiber optic coupled sensors connected to the VISAR cavity. The window is oriented towards the device so that the induced motion is normal to the face of the glass cylinder. Laser light is injected into the fiber optic, to the sensor which focus the light onto the reflective coating deposited on the front of the window in contact with the grout material. The reflected light is collected and injected into the return fiber optic which is connected to the VISAR cavity, then the entire area is filled with concrete. When the device detonates, a shock wave is transmitted through the concrete and into the window where the shock wave imparts a particle velocity in the window. The Doppler shift,

which corresponds to the particle velocity, is transmitted through the fiber optic to the VISAR cavity. The fringe data are converted to electronic signals and stored on digitizing oscilloscopes (digitizers).

The mechanism for triggering the digitizers is a time of arrival (TOA) gauge. The TOA gauge is simply a loop of fiber optic protruding in front of the window with a laser connected to one end and a photodetector attached to the other. When the shock wave breaks the fiber optic, laser light no longer reaches the detector and the output voltage drops, triggering the digitizers to record the VISAR data.

The characteristics of the window and the material transmitting the shock wave into the window **must** be known for accurate particle velocity measurements. The simplest way to use a window is to choose a material that has already been characterized. Unfortunately, the unusual laser wavelength and the large window thickness required for adequate recording time (40  $\mu$ s) did not allow previously characterized materials to be used. The material chosen for the window used in this experiment is Schott BK-7 glass, which has good broadband optical transmittance and is available in the thickness required (8" thick x 14" dia.). Several specimens of BK-7 as well as cored samples of the concrete were analyzed for their shock properties by impacting them into other known window materials, then into themselves using a gas gun as the target accelerator. The results from the analysis, commonly called a Shock Hugoniot, determine whether the

material is suitable for the shock pressure predicted for the event. The data also correlate the impedance mismatch at the grout/glass interface. The anticipated shock pressure for the NTS test, at 7 meters from the device, is  $\approx 70$  kBar in the grout. **Figure 3** is a display of the type of plots for the shock pressure tests obtained using BK-7 as the impacted material. Although at pressures above 90 kBar, the non-linear "shock-up" makes particle velocity correlations more difficult.

The VISAR designed for the underground test contains a diode pumped Nd:YAG laser operating at 1319 nm wavelength, with a CW output of 160 mW, and a 5 kHz, single frequency linewidth. This laser is a good choice for this system because it is stable, has low sensitivity to optical feedback, and the wavelength exhibits very low attenuation and high bandwidth in silica fiber optics. This high performance is due, in part, to the self cancellation of different wavelength-dependent dispersion effects that occur in the fiber. The photodetectors in the system are comprised of indium-gallium-arsenide (InGaAs) photodiodes coupled to low noise/high gain operational amplifier circuitry. The peak sensitivity for these detectors is at 1320 nm wavelength, which not only affords greater sensitivity, but also increases the signal to noise ratio. The linear response range for the detector/amplifiers is DC to 125 MHz with a linear response better than 3% and an output voltage of 40 mV/uW of light at 1320 nm wavelength (The flat linear response is critical for accurate data collection).

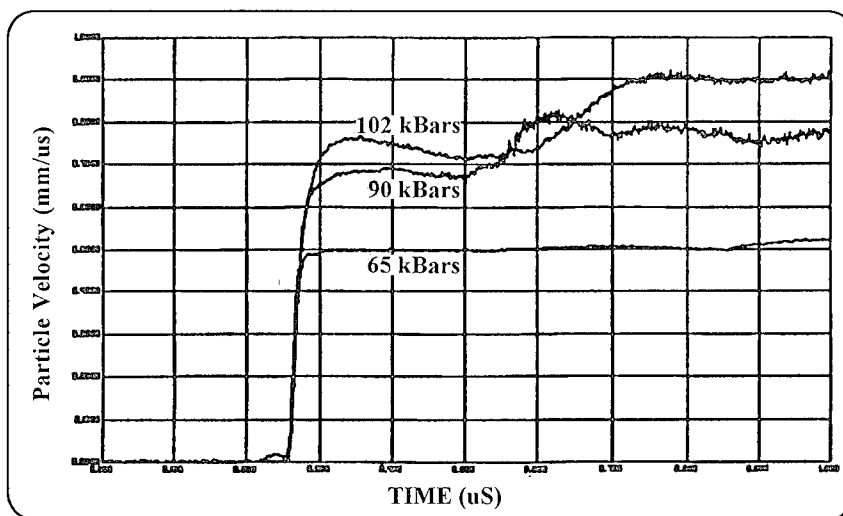
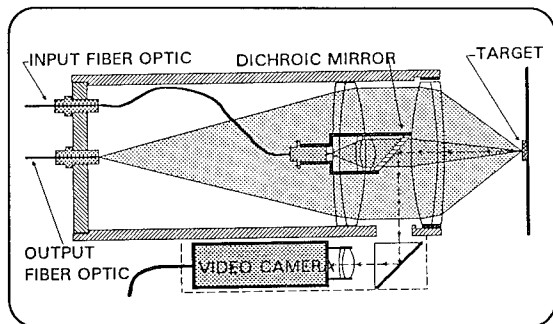


FIGURE 3. BK-7 SHOCK PROFILE CHARACTERIZATION FOR 65, 90, 102 kBar IMPACT PRESSURE

One of the most critical parts of the system design is the fiber optic coupled sensors. *Figure 4* illustrates the sensor used for collecting the Doppler information.



**FIGURE 4. DRAWING OF IMAGING OPTICAL FEEDBACK SENSOR FOR VISAR**

Laser radiation is injected into a 50 micron graded index, multimode fiber optic connected to sensors which image the fiber optic onto the rear surface of the window. The return light reflected from the window's front surface is collected and injected into a 100 um step index, multimode fiber optic connected to the VISAR cavity. A redundant sensor is linked to the VISAR cavity in the event of damage to primary sensor (*figure 5*). Correctly designing the optical train is paramount to attaining good signal strength that won't degrade under harsh environmental conditions. After the sensors are encapsulated in 100 foot thick concrete, re-aligning is impossible.

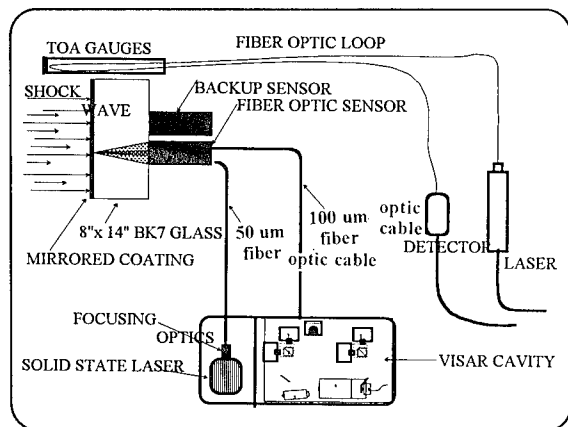


**FIGURE 5. DIAGRAMMATIC LAYOUT OF THE WINDOW, SENSORS, TIME OF ARRIVAL (TOA) GAUGES, VISAR CAVITY, AND LASER**

There was some concern about stress induced polarization after observing wildly fluctuating  $S$  and  $P$  ratios when the fiber optic was bent. These fluctuations in polarization change the sine-cosine relationship critical to accurate data analysis. In most cases, this polarization problem occurs when highly polarized laser beams are injected in short lengths of fibers. The root cause is the modes are not fully mixed and stressing the fiber optic redistributes these modes causing a change in the polarization. Since there was no room for error on the real test, three solutions were incorporated to remedy the problem: a mode scrambler to pinch the fiber optic into a serpentine shape was installed, a long fiber optic was used to mix the modes, and a rotatable linear polarizer was installed at the entry into the interferometer cavity. The modifications worked well.

The sensors perform three functions; collimating and focusing the laser radiation onto the front surface of the window, collecting the return light, and injecting the light into the return fiber optic. The sensor configuration was similar to *figure 4* except that the camera is omitted, because there was no need to see the front window surface.

Although the primary function of the TOA gauge is to trigger the digitizers, utilizing the TOA array provided additional shock data. Several gauges were placed around the window with the tips of the TOA's staggered to intercept the shock wave front at different points in time (*figure 6*). As the shock front breaks the TOA's, the digitizers record the time-of-break that is then correlated to the shock's arrival time and velocity.

## EXPERIMENTAL RESULTS

The VISAR and TOA gauges performed with strong, clean signals recorded on all instrumentation channels. The Doppler information, in unreduced form, is shown in *figure 7*. The signal strength is at 1 V peak to peak which is well above the noise floor that has, in the past, caused difficulty in accurate data reduction. The  $90^\circ$  phase relationship between the two traces indicates the stress induced polarization problem was cured.

*Figure 8* shows the reduced data. There is an impedance mismatch between the BK-7 and the grout but the shock Hugoniot for these materials is known and was used in calculating the final particle velocity. The peak recorded particle velocity was on the order of  $0.6 \text{ mm}/\mu\text{s}$ , which corresponds to a pressure at the interface of 85 kBar. The results indicate that the yield of



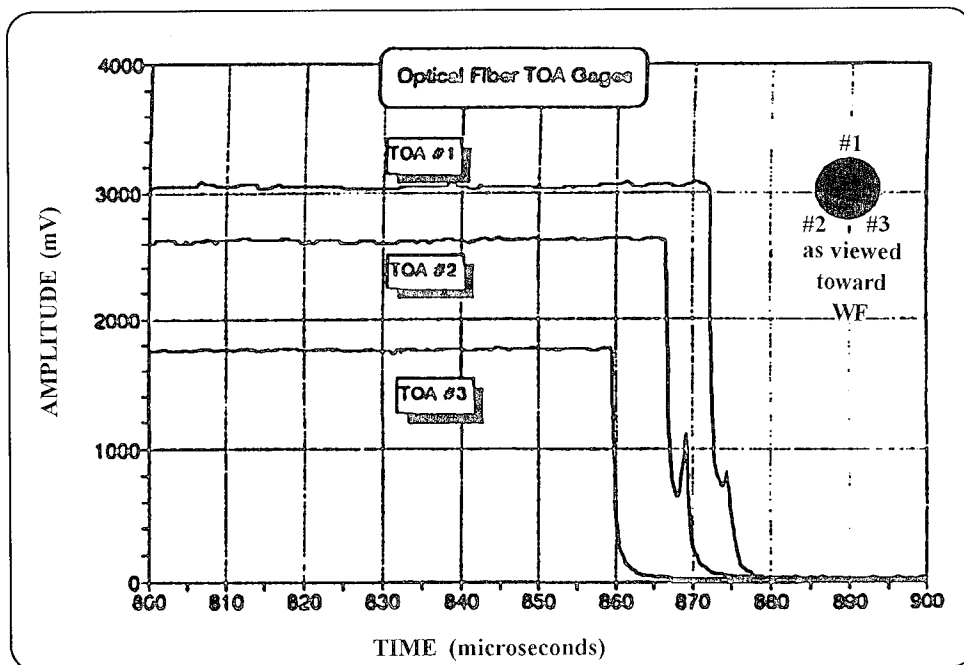


FIGURE 6. DATA FROM THREE TOA GAUGE FIBER BREAK SENSORS

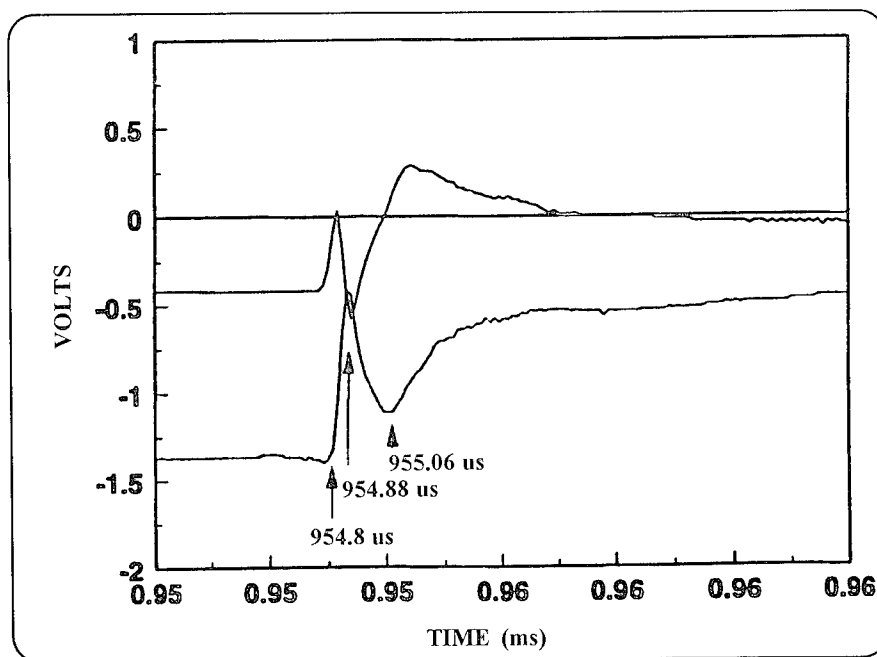


FIGURE 7. UNREDUCED DIGITIZED DATA FROM VISAR ILLUSTRATING THE 90° OUT-OF-PHASE RELATIONSHIP

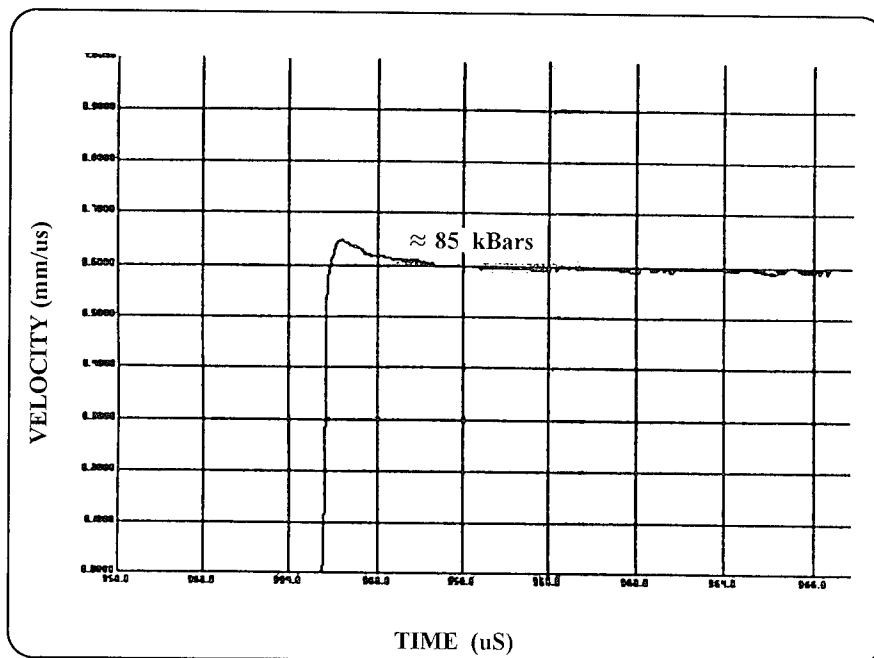


FIGURE 8. PARTICLE VELOCITY FOR THE BK-7 WINDOW AT THE GROUT/WINDOW INTERFACE. MAXIMUM PRESSURE = 85 kBar.

the device was greater than expected (60 kBar). The choice of BK-7 was fortunate because if fused silica was available and used the data would have been lost because it is known to become opaque at pressures above  $\approx 82$  kBar. The BK-7 is apparently able to withstand slightly greater shock pressures before going opaque and at 1/3 the cost, it is significantly less expensive.

#### ACKNOWLEDGEMENTS

This work was performed at Sandia National Laboratories, Albuquerque, NM for the United States Department of Energy under Contract DE-AC04-76DP00789. This project was truly a team effort and the authors gratefully thank the following people for their participation: *Leonard Duda*- financial and technical design support, *John Matthews* and *Richard Wickstrom*- software support, *Larry Weirick*, *Mike Navarro*, *Heidi Anderson*- BK-7 characterization and gas gun support, *Bill Brigham*, *Theresa Broyles*, *Dan Sanchez*- electronic design and fabrication, *Dan Dow*- mechanical fabrication, *Terry Steinfert*, *Robert Vasquez*- mechanical design and installation, and *William Tarbell*- shock analysis. A special thanks to *Lloyd Bonzon* for supporting the concept in its infancy.

#### REFERENCES

1. L. M. Barker and R. E. Hollenbach, "Laser Interferometer for Measuring High Velocities of Any Reflecting Surface," *Journal of Applied Physics* 43:11 (Nov 1972).
2. W. F. Hemsing, "Velocity Sensing Interferometer (VISAR) Modification," *Review of Scientific Instruments* 50:1 (Jan 1979).
3. J. E. Kennedy, Org 7130, Sandia National Laboratories, private communication.
4. K. J. Fleming, O. B. Crump, "Portable, Solid State VISAR," *SAND92-1361* (to be published).
5. O. B. Crump Jr., P. L. Stanton, W. C. Sweatt, "The Fixed Cavity VISAR," *SAND92-0162* (March 1992).
6. K. J. Fleming, "Fiber Optic Coupled Probe for Versatile Interferometry," *Department of Energy Patent Disclosure* SD-5034, S-74, 181
7. L. M. Barker and K. W. Schuler, *Journal of Applied Physics*. 45,3692 (1974).

## SYNTHESIS, CHARACTERIZATION, AND SENSITIVITY OF NOVEL NITRAMINO SUBSTITUTED CYCLOTRIPHOSPHAZENES

Clifford D. Bedford\*, Michael Chaykovsky, Man-Khyun Rho\*\*

Naval Surface Warfare Center

10901 New Hampshire Avenue, Silver Spring, MD 20903-5000

Paritosh R. Dave and Farhad Forohar

GEO-CENTERS, INC. at ARDEC

762 Route 15 South, Lake Hopatcong, NJ 07849

Theodore Axenrod

City College of the City Univ. of New York

New York, NY 10031

Richard Gilardi

Laboratory for the Structure of Matter

Naval Research Laboratory, Washington, DC 20375

\* To whom correspondence should be addressed

\*\* Visiting scientist at Naval Surface Warfare Center from the Agency for Defense Development, Republic of Korea

A new initiative directed toward understanding the chemistry, synthesis, and properties of non or low carbon-based energetic compositions was undertaken. Initial synthesis work has focused on reactions of hexachlorocyclotriphosphazene **1**, with ethylenediamino and azido functional groups. The reaction of **1** with ethylenediamine, N,N'-dinitroethylenediamine, N,N'-bis(trimethylsilyl)ethylenediamine yielded novel di and trispiro(ethylenediamino)cyclotriphosphazenes. Subsequent nitration with either nitronium fluoroborate or nitric acid (100%)/acetic anhydride gave various mono, di, and tri-spiro(N,N'-dinitroethylenediamino)cyclotriphosphazenes.

### INTRODUCTION

Considerable current interest has centered on the reactions of hexachlorocyclotriphosphazene, **1**, with difunctional reagents.<sup>1</sup> Of particular note are the biogenic diamines which offer potential application in the design of more selective antitumorals.<sup>2</sup> Difunctional reagents have been shown to react with **1** to give three different types of products: a) bino derivatives by the displacement of two chlorine atoms from phosphorus atoms in different rings leading to cycloliner polymers, b) ansa compounds derived from the displacement of two chlorine atoms from different phosphorus atoms in the same ring and c) spiro derivatives formed by the displacement of chlorine atoms from the same phosphorus atom.

A large number of substituted phosphazenes with bino and/or ansa and/or spiro configuration have been reported.<sup>1,2</sup>

The reaction of **1** with 1,2-diaminoethane and 1,3-diaminopropane leads exclusively to spiro fused derivatives.<sup>3</sup> It is interesting to note that while treatment of **1** with an excess of 1,3-diaminopropane leads to the tris-spiro derivative,<sup>4</sup> only the mono-spiro product can be obtained in pure form from 1,2-diaminoethane. The bis-spiro compound was detected by <sup>31</sup>P NMR, while the tris-spiro adduct still remains unknown.<sup>3c</sup> The failure to isolate the bis-spiro and tris-spiro adducts has been attributed to the presence of reactive PNHR units on the mono-spirocyclotriphosphazene coupled with the reduced stability of five-membered spiro rings compared to six-membered

congeners.<sup>1,5</sup> This hypothesis was reinforced by the observation that the reaction of **1** with an excess of N,N'-dimethylethylenediamine leads to the expected tris-spiro product containing only PNRR units.<sup>6</sup> We present here the results of our investigation of the reaction of **1** with N,N'-bis(trimethyl-silyl)ethylenediamine<sup>7</sup>, N,N'-dinitroethylenediamine, and 1,2-diaminoethane. The resulting products were converted to the novel 1,1,3,3,5,5-tris-spiro(N,N'-dinitroethylene-diamino)cyclotriphosphazene compound which is of significant interest to energetic materials research.

## EXPERIMENTAL RESULTS

**CAUTION!** All polynitramine compounds are considered toxic and potentially explosive and should be handled with appropriate precautions. In all nitrations with nitronium tetrafluoro-borate, upon removal of acetonitrile, ice cold water must be added immediately to the residue to quench any excess NO<sub>2</sub>BF<sub>4</sub>.

Melting points are uncorrected. NMR spectra were recorded on a Bruker NR 300 spectrometer. Chemical shifts are reported in ppm downfield from internal tetramethylsilane except for <sup>31</sup>P NMR spectra, which are referenced to phosphoric acid. THF was dried by distilling from benzophenoneketyl. Hexachlorocyclotriphosphazene was obtained from Aldrich Chemical Co. and nitronium tetrafluoroborate from Ozark-Mahoning, Inc. All spirocyclotriphosphazenes incorporating both NH and P-Cl linkages were found to be moisture sensitive and unstable in solution. These materials were used immediately without further purification in subsequent reaction steps. Elemental analyses were performed by Galbraith Laboratories, Inc., Knoxville, TN.

**3,3,5,5-Bis-spiro(N,N'-dinitro-ethylenediamino)-1,1-dichlorocyclotriphosphazene, 3.** (CAUTION: compound **3** exhibits explosive behavior on heating). A solution of hexachlorocyclotriphosphazene, **1** (20.0 g, 57.3 mmol) in dry THF (180 mL) was added dropwise to a refluxing solution of N,N'-bis(trimethylsilyl)-ethylenediamine (60.0 g, 294 mmol) in THF (500 mL) under an inert atmosphere over 4 h. The mixture was then stirred at reflux overnight. The resulting mixture was cooled to room temperature

and concentrated under reduced pressure. Upon removal from the rotary evaporator, ice cold water (300 mL) was added immediately and the resulting cloudy solution extracted with methylene chloride (3 x 200 mL). The organic extracts were combined and dried over MgSO<sub>4</sub>. The solution was then filtered and concentrated in vacuo to yield a viscous material.

The material obtained above was stirred in dry acetonitrile (500 mL) for 10 minutes. The suspension was then cooled in an ice bath (5-10 °C) and nitronium tetrafluoroborate (31.3 g, 236 mmol) was added over a 10 minute period. The solution was stirred for another 2 h at 5-10 °C, and then concentrated under reduced pressure. To the residue ice cold water (800 mL) was immediately added and the mixture stirred for 30 minutes whereupon the product separated as a white solid and was collected by filtration. Recrystallization from aqueous acetone yielded **3** as a colorless solid (21.2 g, 73% from **1**), mp 242-244 °C.

Alternatively, NO<sub>2</sub>BF<sub>4</sub> (1.5 g, 11.3 mmol) was added to an ice cooled solution of **6** (1.6 g, 3.8 mmol) in acetonitrile under dry atmosphere and the resulting solution was stirred at 0 °C for 1 h. The cooling bath was removed and stirring was continued overnight. The reaction mixture was then concentrated under reduced pressure and to the residue was immediately added ice cold water and methylene chloride. The organic phase was separated, washed successively with saturated NaHCO<sub>3</sub> solution, and brine, then dried (Na<sub>2</sub>SO<sub>4</sub>), filtered and concentrated. The residue was chromatographed on silica gel to give **3** (1.0 g, 2.0 mmol, 52%). IR (KBr), 1570 (N-NO<sub>2</sub>), 1275 (N-NO<sub>2</sub>), 1195 cm<sup>-1</sup>; <sup>1</sup>H NMR (acetone-d<sub>6</sub>) δ 4.25-4.50 (m); <sup>13</sup>C NMR (acetone-d<sub>6</sub>) δ 43.0 (br.); <sup>31</sup>P NMR (acetone-d<sub>6</sub>) δ 0.0 (d), 38.0 (t, J<sub>P-P</sub> = 68.8 Hz). Anal. Calcd for C<sub>4</sub>H<sub>8</sub><sup>35</sup>C<sub>12</sub>N<sub>11</sub>O<sub>8</sub>P<sub>3</sub>: (M + H)<sup>+</sup>, 500.9147. Found: (M + H)<sup>+</sup>, 500.9142.

**1,1-Spiro(N,N'-dinitroethylene-diamino)-3,3,5,5-tetrachlorocyclotriphosphazene, 5.** To a cooled solution (5-7 °C) of 1,1-spiro(ethylenediamino)-3,3,5,5-tetrachlorocyclotriphosphazene, **4** (1.6 g, 5 mmol) in acetonitrile (50 mL) was added nitronium tetrafluoroborate (1.5 g, 11.3 mmol) in one portion. The resulting suspension was stirred at 5-7 °C for 1 h and then stirred overnight at room temperature. The

reaction mixture was then concentrated under reduced pressure. The residue was taken up in methylene chloride (50 mL) and washed successively with water (50 mL), saturated NaHCO<sub>3</sub> solution (50 mL) and brine (50 mL). The organic phase was dried over MgSO<sub>4</sub>, filtered and the filtrate was concentrated in vacuo to give a pale yellow solid. Recrystallization from acetone/hexanes afforded pure **5** as a colorless microcrystalline solid (1.1 g, 2.6 mmol, 52%), mp 225-227 °C.

Alternatively, 100% nitric acid (3.0 g, 47.6 mmol) was added dropwise with stirring to acetic anhydride (7.39 g, 72.4 mmol) cooled to -5 °C (salt-ice). The solution was then warmed to 20 °C over 1 h, cooled again to -5 °C, and to this was added **4** (1.0 g, 3.0 mmol) all at once. After stirring at -5 °C for 1.5 h, the mixture was poured onto a mixture of ice and water (50 mL), and the precipitated white solid was filtered, washed with cold water and dried to give **5** (1.13 g, 89%); mp 223-226 °C. Recrystallization from benzene/hexane gave colorless prisms; mp 225-227 °C. IR (KBr) 1575 (N-NO<sub>2</sub>), 1275 (N-NO<sub>2</sub>), 1210 cm<sup>-1</sup> (PNP); <sup>1</sup>H NMR (CDCl<sub>3</sub>) δ 4.10 (d, J<sub>P-H</sub> = 6.6 Hz); <sup>13</sup>C NMR (CDCl<sub>3</sub>) δ 41.0 (d, J<sub>C-P</sub> = 10.13 Hz); <sup>31</sup>P NMR (CDCl<sub>3</sub>) δ -7.2 (t), 28.6 (d, J<sub>P-P</sub> = 59.1 Hz). HRMS EI (M = H)<sup>+</sup> Calcd. 422.8291; Found 422.8301. Anal. Calcd. for C<sub>2</sub>H<sub>4</sub>Cl<sub>4</sub>N<sub>7</sub>O<sub>4</sub>P<sub>3</sub>: C, 5.65; H, 0.95; Cl, 33.38; N, 23.08; P, 21.87. Found: C, 6.14; H, 0.95; Cl, 33.68; N, 22.47; P, 21.99.

**1,1-Spiro(ethylenediamino)-3,3-spiro-(N,N'-dinitroethylenediamino)-5,5-dichlorocyclotriphosphazene, 6.** Ethylene-diamine (1.0 g, 12.5 mmol) was slowly added to a stirred solution of **5** (0.05 g, 0.11 mmol) in methylene chloride (15 mL) at 25 °C. The mixture was stirred at 25 °C for 1 h. A suspension was obtained and was extracted with water (60 mL). The organic layer was kept over CaCl<sub>2</sub> for 1 h, filtered, and concentrated by rotary evaporator to yield **6** (0.04 g, 81%). IR (KBr) 3400 (NH), 2890 (NH), 1550 (N-NO<sub>2</sub>), 1270 (N-NO<sub>2</sub>), 1230 (PNP) cm<sup>-1</sup>; <sup>1</sup>H NMR (acetone-d<sub>6</sub>) δ 2.81 (d), 3.45 (m), 4.10 (d); <sup>13</sup>C NMR (CDCl<sub>3</sub>) δ 41.3 (d, J<sub>C-P</sub> = 9.0 Hz), 42.1 (d).

**1,1-Spiro(ethylenediamino)-3,3,5,5-bis-spiro(N,N'-dinitroethylenediamino)cyclotriphosphazene, 7.** To a refluxing solution of ethylenediamine (54 g, 900 mmol) in methylene

chloride (150 mL) under inert atmosphere was added dropwise a solution of **3** (12 g, 24 mmol) in methylene chloride (150 mL) over 2 h. Additional methylene chloride (100 mL) was then added and the resulting suspension was heated at reflux for a further 24 h. The solvent was removed by rotary evaporation and the resulting residue was suspended in water. Product **7** was collected by filtration (9.0 g, 20 mmol, 84%), mp 145-149 °C: IR (KBr) 3450 (NH), 2880 (NH), 1550 (N-NO<sub>2</sub>), 1275 (N-NO<sub>2</sub>), 1230 cm<sup>-1</sup> (PNP); <sup>1</sup>H NMR (DMSO-d<sub>6</sub>) δ 3.15 (d, 4H, J<sub>H-P</sub> = 12.6 Hz), 4.1 (d of m, 8H), 4.4 (d, 2H, J<sub>H-P</sub> = 14.6 Hz); <sup>31</sup>P (DMSO-d<sub>6</sub>); δ 5.4 (d, J<sub>P-P</sub> = 56.6 Hz), 35.0 (t, J<sub>P-P</sub> = 56.6 Hz). HRMS m/e Calcd. for (C<sub>6</sub>H<sub>15</sub>N<sub>13</sub>O<sub>8</sub>P<sub>3</sub>)<sup>+</sup> 490.0379. Found 490.0383

**1,1,3,3,5,5-tris-spiro(N,N'-dinitroethylenediamino)cyclotriphosphazene, 8.**

**CAUTION: Compound 8 exhibits explosive behavior on heating or when subjected to shock.**

**Method A.** A suspension of **7** (28.7 g, 58.6 mmol) in CH<sub>3</sub>CN (700 mL) was stirred at ice bath temperature and NO<sub>2</sub>BF<sub>4</sub> (16.4 g, 123.5 mmol) was added to it over ten minutes. The resulting clear colorless solution was stirred at 0-5 °C for 2 h. The solvent was then removed under vacuum and the resulting yellow solid was immediately added to 500 mL of ice cold water. Continued stirring gave **8** as a faint-yellow solid (21.3 g, 36.9 mmol, 63%). This solid was washed with methanol (15 mL) and recrystallized from 5% aqueous acetone to give pure **8**, m.p. 203-205 °C (dec).

Alternatively, compound **8** was prepared by treating **7** with acetylnitrate. To 12 mL of 100% nitric acid cooled to -5 °C was added dropwise with stirring 78 mL of acetic anhydride. The mixture was warmed to room temperature and stirred for an additional 1 h. It was then cooled to -5 °C whence compound **7** (12.7 g, 25.9 mmol) was added at once. The resulting suspension was stirred at -5 °C for 1 h and then at room temperature for 3 h more. The curde product was poured over ice (300 g), and the precipitated white product, **8**, (14.0 g, 24.1 mmol, 93%) was collected by filtration.

**Method B.** A stirred suspension of **9** (399 mg, 1.0 mmol) in CH<sub>3</sub>CN (30 mL) was cooled to 0 °C and then NO<sub>2</sub>BF<sub>4</sub> (671 mg of 84%, 5.0

mmol) was added all at once. The resulting solution was stirred at 0 °C for 4 h and then evaporated under vacuum to give a pale yellow oil. Addition of water (25mL) precipitated a white solid which was filtered, washed with methanol, and dried to yield **8** (380 mg, 66%): mp 203-205 °C (dec).

Compound **8** was also prepared by treating **9** with acetylnitrate. Nitric acid (3.0 g, 47.6 mmol of 100%) was added dropwise with stirring to acetic anhydride (7.39 g, 72.4 mmol) cooled to -5 °C (salt-ice). The solution was then warmed to 20 °C over 1 h, cooled again to -5 °C and to this was added **9** (1.197 g, 3.0 mmol) all at once. After stirring at -5 °C for 2 h the solution was poured onto a mixture of ice and water (150mL) and the precipitated white solid filtered, washed with water (50mL), then with methanol (25mL) and dried to give **8** (1.595 g, 90%): mp 203-205 °C (dec). Recrystallization from acetone/methanol gave colorless prisms: mp 205 °C (violent dec). IR (KBr) 1580 (N-NO<sub>2</sub>), 1285 (N-NO<sub>2</sub>), 1200 cm<sup>-1</sup> (PNP); <sup>1</sup>H NMR (acetone-d<sub>6</sub>) δ 4.3 (m); <sup>13</sup>C NMR (acetone-d<sub>6</sub>) δ 42.5 (d, J<sub>C-P</sub> = 9.8 Hz); <sup>31</sup>P NMR (acetone-d<sub>6</sub>) δ 5.7 (s). HRMS CI (NH<sub>3</sub>) m/e Calcd. 597.0346. Found: 597.0352. Anal. Calcd for C<sub>6</sub>H<sub>12</sub>N<sub>15</sub>O<sub>12</sub>P<sub>3</sub>: C, 12.44; H, 2.09; N, 36.28; P, 16.04. Found: C, 12.42; H, 2.02; N, 35.87; P, 16.09.

**1,1-spiro(N,N'-dinitroethylene-diamino)-3,3,5,5-bis-spiro(ethylenediamino)cyclotriphosphazene, 9.** A solution of ethylenediamine (3.60 g, 60 mmol) in CH<sub>2</sub>Cl<sub>2</sub> (100 mL) was added dropwise over 1 h to a stirred, refluxing solution of **5** (4.25 g, 10 mmol) in CH<sub>2</sub>Cl<sub>2</sub> (50 mL). Refluxing was continued for an additional 24 h, during which time a white solid precipitated. The mixture was cooled and the solid filtered, suspended in water (130 mL), and the pH brought to 9 by the addition of NH<sub>4</sub>OH. After stirring for 30 minutes the solid was filtered, washed with water (50 mL), then acetone (20 mL), and dried to give **9** (3.67 g, 92%): mp 278-280 °C (dec). The analytical sample, recrystallized from DMF, had mp 290 °C (dec). IR (KBr) 1540 (N-NO<sub>2</sub>), 1280 and 1250 cm<sup>-1</sup> (N-NO<sub>2</sub> and/or PNP); <sup>1</sup>H NMR (DMSO-d<sub>6</sub>) δ 3.97(d, CH<sub>2</sub>), 3.77 (m, NH), 3.00 (m, CH<sub>2</sub>). Anal. Calcd for C<sub>6</sub>H<sub>6</sub>N<sub>11</sub>O<sub>4</sub>P<sub>3</sub>: C, 18.05; H, 4.04; N, 38.60; P, 23.28. Found: C, 18.42; H, 4.31; N, 38.11; P, 23.03.

**1,1,3,3-Bis-spiro(N,N'-dinitroethylene-**

**diamino)-5,5-diazidocyclotriphosphazene, 10.** A stirred solution of **3** (3.20 g, 6.37 mmol) in DMSO (50 mL) was cooled in a cold water bath during the addition of lithium azide (9.3 g, 0.19 mmol), in portions, over 5 minutes. The mixture was stirred at room temperature for 48 h, then poured into cold water (200 mL), and the precipitate filtered and dried to yield **10** (2.35 g, 72%) as a white solid. Recrystallization from acetone/H<sub>2</sub>O gave colorless needles: mp 238 °C (violent dec). IR (KBr) 2182 (N<sub>3</sub>), 1560 (N-NO<sub>2</sub>), 1285 (N-NO<sub>2</sub>), 1196 cm<sup>-1</sup> (PNP); <sup>1</sup>H NMR (DMSO-d<sub>6</sub>) δ 4.08 (m, CH<sub>2</sub>), 4.26 (m, CH<sub>2</sub>). Anal. Calcd for C<sub>4</sub>H<sub>8</sub>N<sub>17</sub>O<sub>8</sub>P<sub>3</sub>: C, 9.32; H, 1.57; N, 46.23; P, 18.04. Found: C, 9.67; H, 1.55; N, 46.22; P, 18.13.

**1,1-Spiro(N,N'-dinitroethylenediamino)-3,3,5,5-tetraazidocyclotriphosphazene, 12.**

Tetrazide **11** was prepared from **4** and lithium azide in acetone. The crude oil (3.0 mmol) was dissolved in dry CH<sub>3</sub>CN (25 mL) and cooled in an ice-bath. With stirring, NO<sub>2</sub>BF<sub>4</sub> (1.21 g of 84%, 9.0 mmol) was then added at once. After stirring at 0 °C for 1 h the solution was poured onto a mixture of ice and water (60 mL) and extracted with CH<sub>2</sub>Cl<sub>2</sub>. The extracts were washed twice with water, dried (Na<sub>2</sub>SO<sub>4</sub>) and then evaporated under vacuum to leave a solid residue which was triturated with cold ether and filtered to give **12** (545 mg, 40%): mp 144-145 °C (colorless prisms from benzene/hexane). IR (KBr) 2180 (N<sub>3</sub>), 1565 (N-NO<sub>2</sub>), 1300 (N-NO<sub>2</sub>), 1270 and 1200 cm<sup>-1</sup> (PNP). <sup>1</sup>H NMR (acetone-d<sub>6</sub>) δ 4.40 (m, CH<sub>2</sub>). Anal. Calcd for C<sub>2</sub>H<sub>4</sub>N<sub>19</sub>O<sub>4</sub>P<sub>3</sub>: C, 5.32; H, 0.89; N, 59.00; P, 20.60. Found: C, 5.61; H, 0.93; N, 59.32; P, 20.45.

**1-(2-Ethylammonium)amino-1-oxido-3,3,5,5-tetraazidocyclotriphosphazene hemihydrate, 13.** A mixture of **4** (5.02 g, 0.015 mmol) and powdered lithium azide (7.34 g, 0.15 mmol) in dry acetone (150 mL) was stirred at room temperature for 18 h, then filtered. The filtrate was evaporated under vacuum to leave a mixture of oil and solid. The oil was dissolved in CH<sub>2</sub>Cl<sub>2</sub> (50 mL), washed with H<sub>2</sub>O (2 X 25 mL), dried (Na<sub>2</sub>SO<sub>4</sub>) and then evaporated under vacuum to leave crude **11** (6.0 g) as a colorless oil. IR (NaCl film) 2200 cm<sup>-1</sup>(N<sub>3</sub>); <sup>1</sup>H NMR(CDCl<sub>3</sub>) δ 3.53 (d, CH<sub>2</sub>), 2.77 (unsym.d, NH). This material was then dissolved in a mixture of CH<sub>3</sub>CN (40 mL) and H<sub>2</sub>O (10 mL) and allowed to stand at ambient temperature for 3

days, during which time a white solid precipitated. Filtration of the solid and drying gave **13** (5.01g, 86%): mp 139-140 °C (dec). Recrystallization from hot CH<sub>3</sub>CN/H<sub>2</sub>O gave colorless needles: mp 140-141 °C (dec). Single crystal X-ray crystallographic analysis confirmed structure **13**. Anal. Calcd for C<sub>2</sub>H<sub>8</sub>N<sub>17</sub>OP<sub>3</sub> 0.5H<sub>2</sub>O: C, 6.19; H, 2.34; N, 61.35; P, 23.94. Found: C, 6.22; H, 2.49; N, 61.51; P, 24.22.

## RESULTS AND DISCUSSION

Hexachlorocyclotriphosphazene, **1**, was treated with an excess of N,N'-bis(trimethylsilyl)ethylenediamine in refluxing tetrahydrofuran (THF) to give, after aqueous work-up, a product mixture containing principally 3,3,5,5-bis-spiro(N,N'-bistrimethylsilylethylenediamino)-1,1-dichlorocyclotriphosphazene, **2**. Compound **2** was found to be extremely reactive and was consumed in a subsequent reaction step without further purification, Figure 1. Nitration of

which was nitrated with nitronium tetrafluoroborate to give **3**, Figure 2.

The proton decoupled <sup>13</sup>C NMR (CDCl<sub>3</sub>) of compound **5** showed one signal at δ 41.4 (d, J<sub>C-P</sub> = 10.13 Hz), and <sup>31</sup>P NMR exhibited a doublet at δ -7.2 and a triplet at δ 28.6 (J<sub>P-P</sub> = 59.1 Hz). The proton decoupled <sup>13</sup>C NMR spectrum in acetone-d<sub>6</sub> of compound **3** showed a broad signal at δ 42.1, and the <sup>31</sup>P NMR showed a doublet at δ 0.0 and a triplet at δ 38.0 (J<sub>P-P</sub> = 68.8 Hz). The structure of compound **3** was further confirmed by X-ray crystallography.

Addition of ethylenediamine to **3** was found to be slow. However, upon extended reflux (24 h) a 84% yield of 1,1-spiro(ethylenediamino)-3,3,5,5-bis-spiro(N,N'-dinitroethylenediamino)-cyclotriphosphazene, **7**, was realized. As depicted in Figure 3, nitration of **7** with nitronium tetrafluoroborate proceeds smoothly to yield 1,1,3,3,5,5-tris-spiro(N,N'-dinitroethylenediamino)cyclotriphosphazene, **8**. Compound **8** was also obtained from 1,1-spiro(N,N'-

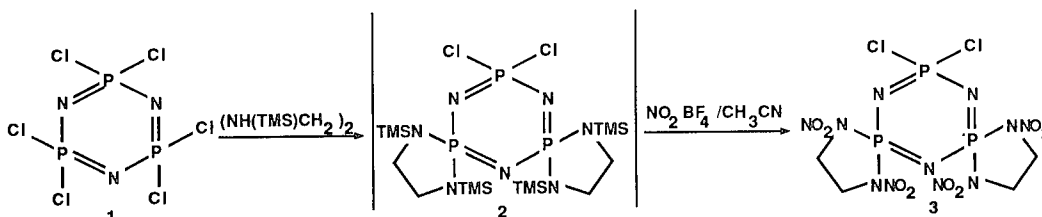


FIGURE 1. SYNTHESIS OF BIS-SPIRO(N,N'-DINITROETHYLENEAMINO)-DICHLOROCYCLOTRIPHOSPHAZENE, (**3**)

this product with nitronium tetrafluoroborate in acetonitrile afforded 3,3,5,5-bis-spiro(N,N'-dinitroethylenediamino)-1,1-dichlorocyclotriphosphazene, **3** (70% from **1**). No tris-spiro product was detected in the product mixture.

Alternatively, compound **3** was prepared by treating hexachlorocyclotriphosphazene with ethylenediamine by the method of Krishnamurthy et al.<sup>3</sup> to obtain 1,1-spiro(ethylenediamino)-3,3,5,5-tetrachlorocyclotriphosphazene, **4**. Nitration of **4** was carried out using either nitronium tetrafluoroborate in acetonitrile or with an acetic anhydride/100% nitric acid mixture to give 1,1-spiro(N,N'-dinitroethylenediamino)-3,3,5,5-tetrachlorocyclotriphosphazene, **5**. Brief treatment of **5** with an excess of ethylenediamine in methylene chloride gave 1,1-spiro(ethylenediamino)-3,3-spiro(N,N'-dinitroethylenediamino)-5,5-dichlorocyclo-triphosphazene, **6**,

dinitroethylenediamino)-3,3,5,5-tetrachlorocyclotriphosphazene, **5**. Treatment of compound **5**, with excess ethylenediamine under reflux afforded 1,1-spiro(N,N'-dinitroethylenediamino)-3,3,5,5-bis-spiro(ethylenediamino)cyclotriphosphazene, **9**, in high yield after aqueous workup. Compound **8** was prepared in high yield by treating compound **9** with an acetic anhydride/100% nitric acid mixture, Figure 4. The structure of the compound **8** was deduced on the basis of <sup>13</sup>C and <sup>31</sup>P NMR. Both exhibited a single signal attesting to the high symmetry of the molecule. The structure of **8** was further confirmed by X-ray crystallography.

Nucleophilic azide displacement of the residual chloro groups on compounds **3** and **5** also was examined. Compound **3** was converted to the 1,1,3,3-bis-spiro(N,N'-dinitroethylenediamino)-5,5-diazidocyclotriphosphazene, **10**, by treatment with lithium azide in DMSO, Figure 5. The

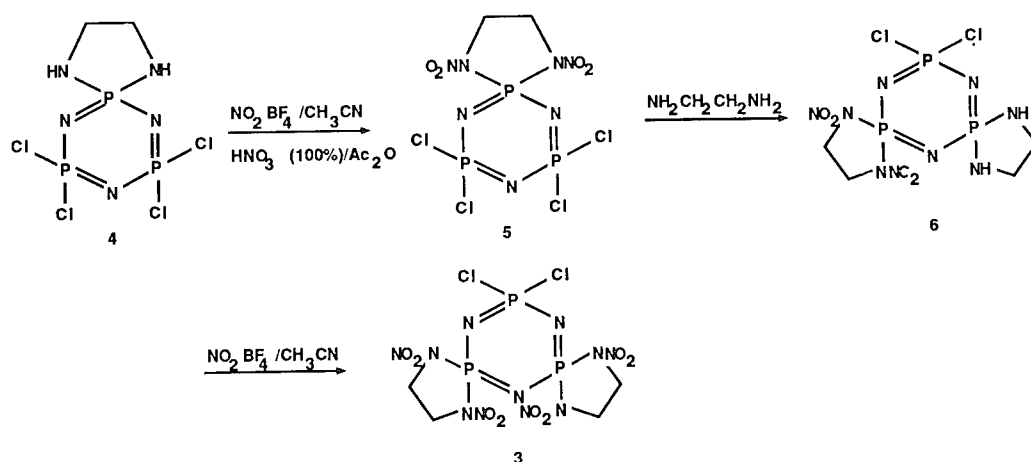


FIGURE 2. ALTERNATIVE SYNTHESIS OF BIS-SPIRO(N,N'-DINITROETHYLENEDIAMINO)-DICHLOROCYCLOTRIPHOSPHAZENE, (3)

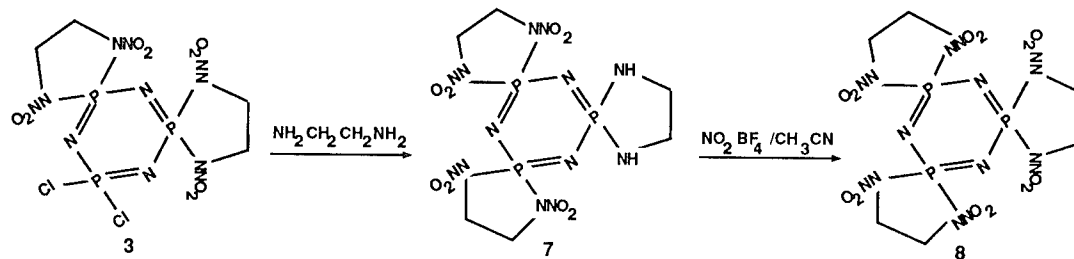


FIGURE 3. SYNTHESIS OF TRIS-SPIRO(N,N'-DINITROETHYLENEDIAMINO)-CYCLOTRIPHOSPHAZENE, (8)

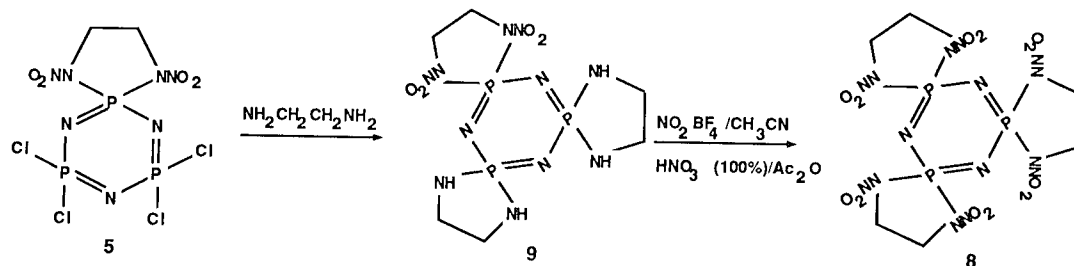


FIGURE 4. ALTERNATE SYNTHESIS OF TRIS-SPIRO(N,N'-DINITROETHYLENEAMINO)-CYCLOTRIPHOSPHAZENE, (8)

corresponding 1,1-spiro(N,N'-dinitroethylenediamino)-3,3,5,5-tetrachlorocyclotriphosphazene, **5**, did not yield the expected tetraazido compound **12** under similar conditions. Compound **12** was prepared by first converting **4** to the corresponding tetraazido compound **11** followed by nitration of **11** with nitronium tetrafluoro-borate, Figure 5. No nitramino displacement was observed in any of the above reactions. This is attributed to the increased steric crowding introduced by the N,N'-dinitro-ethylenediamino moiety.

A second product was isolated during our studies of the azide displacement reaction. If compound **11** was not converted immediately to

the corresponding nitramine, or if compound **11** was treated with aqueous acetonitrile, a new material was isolated. This material proved to be the 1-oxido compound **13** which resulted from ring opening of the N,N'-ethylenediamino moiety by water. The structure of **13** was unambiguously confirmed by single crystal X-ray.

Compounds **3** and **8** represent the first examples of potentially useful energetic materials made from a cyclotriphosphazene nucleus. They have extremely high melting points, 242-244 °C and 203-205 °C, respectively, show no thermal instability in their DSC traces, and demonstrate impact and friction sensitivities similar to existing



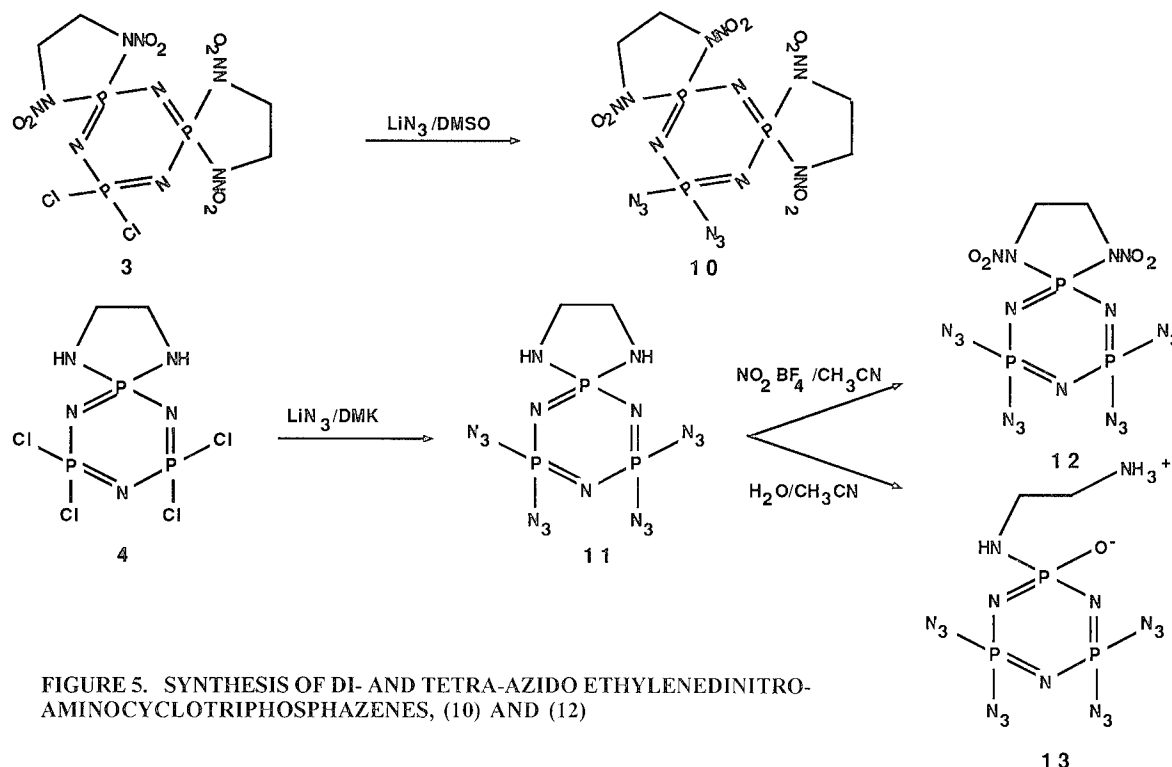


FIGURE 5. SYNTHESIS OF DI- AND TETRA-AZIDO ETHYLENEDINITRO-AMINOCYCLOTRIPHOSPHAZENES, (10) AND (12)

cyclic energetic nitramino materials 1,3,5-trinitro-2,4,6-hexahydrotriazine (RDX). The azido substituted cyclotriphosphazenes proved to be extremely impact sensitive<sup>8</sup>. **Extreme caution must be taken when working with these shock sensitive materials.**

The X-ray crystal structure of compounds 3 and 8 were done at NRL giving densities of 1.898 and 1.887 g/cc, respectively. The density of the the parent cyclotriphosphazene is 1.980 g/cc while that of  $\text{N,N}'$ -ethylenedinitramine is 1.171 g/cc. The incorporation of both moieties clearly enhances the overall density of the resulting energetic material.

## CONCLUSIONS

Novel bis-spiroethylenedinitramino and tris-spiroethylenedinitramino derivatives of cyclotriphosphazenes have been synthesized in good yields and their structures confirmed by X-ray crystallography. The materials were found to have moderate impact sensitivity, high melting points, and excellent densities. These new energetic polynitraminocyclo-triphosphazenes are the first examples of this novel class of energetic

compounds and promise to be the vanguard of many new energetic materials for explosive and propellant applications.

## ACKNOWLEDGEMENTS

Drs. G. Doyle, A. Bazhir-Hashemi and D. Stec, III, are thanked for their many useful suggestions. This work was performed under the auspices of the Naval Surface Warfare Center SBIR contract N60921-91-C-0009.

## REFERENCES

1. Chandrasekhar, V.; Muralidhara, M.G.R.; Selvaraj, I.I. *Heterocycles*, 1990, 31, 2231.
2. Labarre, J-F. *Topics in Current Chemistry*, 1985, 129, 173.
3. a) Krishnamurthy, S.S.; Ramachandran, K.; Vasudeva Murthy, A.R.; Shaw, R.A.; Woods, M. *Inorg. Nucl. Chem. Lett.*, 1977, 13, 407; b) *ibid.* *J. Chem. Soc. Dalton Trans.*, 1980, 840; c) Willson, M.; Lafaille, L.; Commenges, G.

Labarre, J-F. Phosphorus and Sulfur, 1985, 25, 273.

4. El Murr, N.; Lahana, R.; Labarre, J-F.; DeClercq, J-P. J. Mol. Struct., 1984, 117, 73.

5. a) Shaw, R.A. Phosphorus, Sulfur & Silicon, 1989, 45, 103; b) Chandrasekhar, V.; Krishnamurthy, S.S.; Manohar, H.; Vasudeva Murthy, A.R.; Shaw, R.A.; Woods, M. J. Chem. Soc. Dalton Trans., 1984, 621.

6. a) Chivers, T.; Hedgeland, R. Can. J. Chem., 1972, 50 1017; b), B.D.; Kuipers, G.; Bijlaart, J.H.; Van De Grampel, J.C. Z. Naturforsch, 1982, 376, 1425.

7. West, R.; Ishikawz, M.; Murai, S. J. Am. Chem. Soc., 1968, 90, 727.

8. Chang, M.S.; Matuszko, A.J. J. Am. Chem. Soc., 1960, 82, 5756.

**SESSIONS ON**  
**EQUATIONS OF STATE**

**Cochairmen:**    **Edward Lee**  
                      **Lawrence Livermore National Laboratory**

**Graeme Leiper**  
                      **ICI Explosives**

## EQUATION OF STATE FOR DETONATION PRODUCTS

William C. Davis  
Los Alamos National Laboratory  
Los Alamos, New Mexico 87545

An equation of state for detonation products, with the usual form  $p = p(v, E)$ , is proposed. It allows independent calibration of the adiabatic gamma and the Grüneisen gamma, and gives them forms in agreement with recent theoretical studies. The equation of state is given by

$$p = \frac{E}{v} \left[ k - 1 + F(v) \left\{ 1 + b \left( 1 - \frac{E}{E^S(v)} \right) \right\} \right]$$

where  $F(v)$  drops from a finite value at small  $v$  to zero at large  $v$ ,  $b$  is a constant, and  $E^S(v)$  is the specific internal energy on the principal isentrope. Its relationship to the polytropic gas equation of state  $p = (E/v)(\gamma - 1)$  is easily seen, and it reduces to this form at large volume.

## INTRODUCTION

Studies<sup>1,2</sup> of the equation of state of detonation products using statistical mechanics have provided new insights into the behavior of the products, and studies<sup>3,4</sup> of the interaction of the equations of hydrodynamics with the equation of state have provided new constraints for the equation of state. Experiments<sup>5</sup> have shown that data for calibration of an equation of state can be obtained. Many empirical fitting forms have been proposed earlier, but they do not represent these new developments. Here we suggest an empirical fitting form that gives the important features their proper form.

A basic premise of this work has been to accept the fact that designers will modify any equation of state to compensate for the errors in their computer codes and in their representation of the device being modeled. An equation of state form that has the right physical properties, particularly the sound speed or adiabatic gamma, will give reasonable results even when severely adjusted. The forms considered here have the property that the physical properties are correctly represented. They are easy to adjust, and detailed instructions for adjusting them are included. The underlying physical constraints are discussed, to help users see where modification may lead to nonphysical results. Computer codes for hydrodynamic problems need an equation of state of the form  $p = p(E, v)$ . The equations suggested here have that form.

The simplest equation of state that has been used successfully for detonation products is the polytropic gas form

$$p = (E/v)(k - 1), \quad (1)$$

where  $p$  is the pressure,  $E$  is the specific internal energy,  $v$  is the specific volume, and  $k = -(v/p)(\partial p / \partial v)_S$  is the adiabatic exponent. At low density  $k$  is 1.2 or 1.3 for ordinary detonation product gases and is equal to the ratio of the specific heats. At high density the same form is often used, with  $k \cong 3$ , and it works fairly well at densities near the CJ density for many explosives. When the energy of the explosive products is transferred to the inert components in the pressure region where  $k$  falls from its high value to its low value, the polytropic equation of state fails.

The polytropic equation of state can be modified to

$$p = (E/v)[k - 1 + F(v)] \quad (2)$$

where  $F(v)$  has the value 0 at large specific volume, so the equation of state assumes its proper form at low density, and increases monotonically as the specific volume decreases, approaching a constant value at small volume. This simple modification gives the proper behavior on the principal isentrope, the isentrope through the CJ point, but is not sufficiently flexible off that isentrope to fit data such as the velocities of

overdriven detonations. M. S. Shaw, in a private communication, provided an analysis that showed how to make the equation of state more general.

A specialization of Shaw's result, with the required flexibility, is

$$p = \frac{E}{v} \left[ k - 1 + F(v) \left\{ 1 + b \left( 1 - \frac{E}{E^S(v)} \right) \right\} \right] \quad (3)$$

where  $b$  is a constant and  $E^S(v)$  is the specific internal energy on the principal isentrope. The parenthesis multiplied by  $b$  is zero on the principal isentrope, and the form is that of Eq. (2). The bracket multiplied by  $b$  decreases the value of  $F(v)$  on isentropes above the principal isentrope, describing products that behave more like an ideal gas at a higher temperature, and increases the value for lower isentropes. The simple form for this term is consistent with the assumption that the region of interest for an equation of state for detonation products is always near the principal isentrope.

## DEVELOPMENT

Now let us proceed to develop the expression for the important physical quantities. The Grüneisen gamma

$$\Gamma = - \frac{v}{T} \left( \frac{\partial T}{\partial v} \right)_S = \frac{v}{T} \left( \frac{\partial p}{\partial S} \right)_v = v \left( \frac{\partial p}{\partial E} \right)_v, \quad (4)$$

describes the variation of temperature along an isentrope, or the separation of isentropes with different internal energy at a constant volume. The adiabatic gamma

$$\gamma = - \frac{v}{p} \left( \frac{\partial p}{\partial v} \right)_S = \frac{v}{p} \frac{p + \left( \frac{\partial E}{\partial v} \right)_p}{\left( \frac{\partial E}{\partial p} \right)_v} = \frac{c^2}{pv} \quad (5)$$

is the non-dimensional sound speed, and describes the transport of energy by compression and rarefaction waves. These two quantities are the only<sup>3,4</sup> features of the equation of state that enter directly into the differential equations of hydrodynamics. It is important that their behavior is properly represented.

The equation of state is

$$p = \frac{E}{v} \left[ k - 1 + F(v) \left\{ 1 + b \left( 1 - \frac{E}{E^S(v)} \right) \right\} \right] \quad (6)$$

On the principal isentrope, where  $E = E^S$ , we have

$$p^S = (E^S/v)(k - 1 + F) \quad (7)$$

and by straightforward differentiation, using the fact that

on an isentrope  $dE/dv = -p$ , we find that

$$\gamma^S = k + F - \frac{vF'}{k - 1 + F} \quad (8)$$

where  $F' = dF/dv$ . Notice that  $F'$  is negative, so the last term in the expression for  $\gamma^S$  may make  $\gamma^S$  have a maximum. Now from the definition of  $\gamma$  we see that

$$\int \frac{dp^S}{p^S} = - \int \gamma^S \frac{dv}{v} = - \int \frac{k dv}{v} - \int \frac{F dv}{v} + \int \frac{dF}{k - 1 + F}. \quad (9)$$

From the integration we obtain  $p^S(v)$ , and by substitution into Eq. (7) we find  $E^S(v)$  as

$$E^S(v) = p^S v / (k - 1 + F). \quad (10)$$

Introducing  $F(v)$  in Eq. (6) avoids the second integration that arises when a form for  $\gamma(v)$  is assumed in Eq. (8). If we integrate Eq. (9) from a chosen volume  $v_c$  to an arbitrary volume  $v$ , and substitute the result into Eq. (10), we find

$$\frac{E^S(v)}{E^S(v_c)} = \left( \frac{v_c}{v} \right)^{k-1} \exp \left( - \int_{v_c}^v \frac{F(v) dv}{v} \right) \quad (11)$$

The polytropic gas has the exponential term equal to one, that is,  $F(v) = 0$ , and the energy on the isentrope varies as an inverse power of the volume. With  $F(v) \neq 0$ , the specific internal energy on the isentrope increases more rapidly as the volume is reduced.

The same differentiation of the general equation of state gives the expression for  $\gamma(E, v)$  everywhere as

$$\gamma(E, v) = \gamma^S + bF \left( 1 - \frac{E}{E^S} \right) \left[ 1 + \frac{1 - \frac{vF'}{F}}{E/pv} - \frac{E}{E^S} \frac{1 - \frac{p^S E}{pE^S}}{1 - \frac{E}{E^S}} \right] \quad (12)$$

where  $p = p(E, v)$  and  $p^S = p^S(E^S, v)$ .

Similarly we find

$$\Gamma(E, v) = k - 1 + F \left[ 1 + b \left( 1 - \frac{2E}{E^S} \right) \right] \quad (13)$$

and

$$\Gamma^S(E^S, v) = k - 1 + F(1 - b). \quad (14)$$

Notice here that choice of the constant  $b$  makes it possible to choose the value of  $\Gamma$  at small specific

volume independent of the value of  $\gamma$ .

For shock stability and monotonicity of the Hugoniot curve in the  $p$ - $u$  plane, we must have

$$\gamma \geq \Gamma - 1. \quad (15)$$

On the isentrope, this can be seen to be true from Eqs. (8) and (14), since  $F'(v) < 0$ , as long as  $b > 0$ .

The fundamental derivative of gas dynamics,<sup>3,4</sup> which measures the convexity of isentropes and must be positive everywhere for ordinary detonation products, is given by

$$\mathcal{G} = \frac{1}{2}[\gamma + 1 - (v/\gamma)(\partial\gamma/\partial v)_S]. \quad (16)$$

$\mathcal{G}$  can be easily found by differentiating  $\gamma$ .

The material velocity on an isentrope is found by integrating the Riemann equation

$$du/dp = \pm (v/\gamma p)^{1/2} \quad (17)$$

This equation cannot be integrated in closed form for useful choices of  $F(v)$ . It must be integrated numerically.

The temperature and specific heats are not represented accurately by a simple equation of state of the kind proposed here. The evaluation of their values may be useful because a zero or a pole in  $T$  or  $C_v$  would indicate a serious flaw in the equation of state. The temperature on an isentrope is found<sup>6</sup> by integrating the differential equation

$$(v/T)(\partial T/\partial v)_S = -\Gamma \quad (18)$$

The specific heat at constant volume is found in a similar way from the differential equation<sup>3</sup>

$$(v/g)(\partial g/\partial v)_S = \Gamma + 1 - \gamma - (\Gamma p/g)(\partial \Gamma/\partial p)_v, \quad (19)$$

where  $g = pv/C_v T$ . The ratio of specific heats<sup>3</sup>  $C_p/C_v = \gamma/(\gamma - \Gamma^2/g)$  can be found once  $g$  is known.

#### EXAMPLE: A SIMPLE CHOICE FOR $F(v)$

A simple form for  $F(v)$  that has appropriate properties is

$$F(v) = 2a(v/v_c)^{-n}/[(v/v_c)^n + (v/v_c)^{-n}], \quad (20)$$

where  $a$ ,  $n$ , and  $v_c$  are constants to be determined in the calibration of the equation of state. For large  $v$ ,  $F = 0$ ; for small  $v$ ,  $F = 2a$ ; and  $F(v_c) = a$ .  $F(v)$  is a smeared out step function; the constant  $a$  determines the height of the step,  $v_c$  the volume where the rise is half the total rise, and the exponent  $n$  the steepness of the rise. For use in

the expressions developed above we need the derivative of  $F(v)$ . It is easy to show that

$$vF' = -\frac{4an}{\left[\left(\frac{v}{v_c}\right)^n + \left(\frac{v}{v_c}\right)^{-n}\right]^2} \quad (21)$$

This value can be substituted into Eqs. (8) and (12) for  $\gamma$ .

To integrate  $\gamma$  to find an expression for the principal isentrope we need the value of the integral

$$\int \frac{F dv}{v} = \ln \left[ \frac{\left(\frac{v}{v_c}\right)^n}{\left(\frac{v}{v_c}\right)^n + \left(\frac{v}{v_c}\right)^{-n}} \right]^{a/n} \quad (22)$$

Using the expressions developed above, we can now write the expression for the principal isentrope as

$$\frac{p^s}{p_c} = \frac{\left[ \frac{1}{2}\left(\frac{v}{v_c}\right)^n + \frac{1}{2}\left(\frac{v}{v_c}\right)^{-n} \right]^{a/n}}{\left(\frac{v}{v_c}\right)^{k+a}} \times \frac{k-1+F}{k-1+a} \quad (23)$$

In this expression,  $p_c$  is a constant to be determined in the calibration. The value for  $p^s$  is to be substituted into the equation of state to determine  $E^s$ .

Although the thermal properties of the equation of state play no part in hydrodynamics calculations, it is instructive to take a brief look at some of them. The temperature is obtained by integrating Eq. (18) to get

$$\frac{T^s}{T_c} = \frac{\left[ \frac{1}{2}\left(\frac{v}{v_c}\right)^n + \frac{1}{2}\left(\frac{v}{v_c}\right)^{-n} \right]^{(a/n)(1-b)}}{\left(\frac{v}{v_c}\right)^{k-1+a(1-b)}} \quad (24)$$

Notice that as  $v$  becomes very large, the right hand side reduces to  $(v/v_c)^{-(k-1)}$ , the expected value at low density. Notice also, however, that if  $b = 1$ , it has this value for all values of the density. The value of  $b$ , which does not affect the pressure along the isentrope, has a strong effect on the temperature.

It is also possible to use the expressions for  $p^s$  and  $T^s$  to see how  $p v / RT$  varies along the isentrope. We find

$$\frac{p^s v}{p_c v_c} = \frac{\left[ \frac{1}{2} \left( \frac{v}{v_c} \right)^n + \frac{1}{2} \left( \frac{v}{v_c} \right)^{-n} \right]^{ab/n}}{\left( \frac{v}{v_c} \right)^{ab}} \times \frac{k-1+F}{k-1+a} \quad (25)$$

The values of this function are

$$\frac{p^s v}{p_c v_c} = \frac{T^s}{T_c} = \begin{cases} (k-1) / [2^{ab/n} (k-1+a)] & v \rightarrow \infty \\ 1 & v = v_c \\ (k-1+2a) / [2^{ab/n} (k-1+a)] (v/v_c)^{-2ab} & v \rightarrow 0 \end{cases} \quad (26)$$

Notice that if  $b = 0$  the function reaches a finite value as  $v$  becomes small, and becomes large for other values of  $b$ . It always reaches a constant value for large  $v$ , as expected, where  $p v / RT = 1$ .

## CALIBRATION ON THE PRINCIPAL ISENTROPE

The constraints on an equation of state are (1) the principal isentrope must pass through the CJ point; (2) the principal isentrope must be tangent to the Rayleigh line at the CJ point; (3) the work done at a chosen truncation volume must be simply correlated with the Gurney energy; (4) the work done at complete expansion must be equal to the total chemical energy; (5) the adiabatic gamma at large expansion must be that of the product gases when they behave as ideal gases. These five constraints allow the calibration of five constants in the equation of state.

Constraints (1) and (2) lead to the equations

$$v_j / v_0 = \gamma_j / (\gamma_j + 1) \quad (27)$$

$$p_j = \rho_0 D^2 / (\gamma_j + 1) \quad (28)$$

where the subscript  $j$  indicates value at the CJ point, so  $v_j$ ,  $p_j$ , and  $\gamma_j$  are values of these quantities at the CJ point,  $\rho_0$  is the initial density of the explosive and  $v_0$  is its reciprocal, the initial specific volume, and  $D$  is the detonation velocity. The density  $\rho_0$  is known from measurement, or may be estimated using one of several rules. If  $p_j$  has been measured,  $\gamma_j$  may be calculated from the equation above. More often  $p_j$  is not known.

In this case,  $\gamma_j$  may be estimated from the empirical relationship

$$\gamma_j = 1.6 + 0.8 \rho_0 \quad (29)$$

or another similar relationship. The usefulness of an equation of state for most engineering calculations is not much affected by small errors in the CJ values. The tangency requirement, however, must be satisfied.

The Gurney energy is a measure of the energy available from the explosive to drive metal. In most applications, little energy is imparted to the metal after the pressure has fallen to 0.1 GPa, so the desired calibration quantity is the available energy between the CJ point and the volume at which the pressure on the isentrope is 0.1 GPa. The iteration to obtain this volume exactly is tedious, and it has been found satisfactory to assume the cutoff volume to be  $7v_0$  instead of calculating an exact value. Figure 1 shows the Fickett-Jacobs diagram<sup>8</sup> with the area that will correspond to the Gurney energy shaded. The Gurney energy is obtained from a cylinder test or a dent plate test. The cylinder at 19-mm expansion has a volume expansion of about 7; the energy is given as  $E_{19}$ . Standard practice is to measure the apparent wall velocity  $u_{19}$  in mm/ $\mu$ s, and

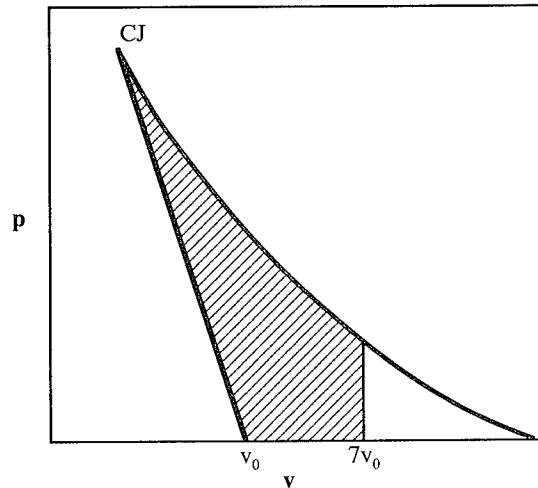


FIG. 1. THE FICKETT-JACOBS DIAGRAM OF THE QUASISTATIC CYCLE FOR DETONATIONS. THE TOTAL AREA OF THE DIAGRAM IS APPROXIMATELY EQUAL TO THE TOTAL ENERGY OF THE EXPLOSIVE. THE SHADED AREA IS THE ENERGY RELATED TO THE GURNEY ENERGY. IT REPRESENTS THE USEFUL WORK DONE BY THE EXPLOSIVE DRIVING AN AVERAGE METAL SYSTEM.

express the energy as  $E_{I9} = \frac{1}{2}u_{I9}^2$ , with units of  $(\text{mm}/\mu\text{s})^2$  or  $\text{kJ/g}$ . The Gurney energy, with units  $\text{kJ}/\text{cm}^3$ , is

$$e_g = E_{I9}(M/V)[1 + \frac{1}{2}\rho_0/(M/V)] \quad (30)$$

where  $M$  is the mass per unit length of the copper tube, usually  $19.501 \text{ g/cm}$ ,  $V$  is the volume of the tube per unit length, usually  $5.067 \text{ cm}^3/\text{cm}$ , and  $\rho_0$  is the initial density of the explosive. Lower case  $e$  is used because the upper case  $E$  is used for specific energy, or energy per unit mass;  $e$  means energy per unit volume, and has dimensions of pressure. It is obtained by multiplying  $E$  by the initial density, that is,  $e_g = \rho_0 E_g$ . The Gurney energy may also be obtained from the standard dent plate test, where, in units of  $\text{kJ}/\text{cm}^3$ ,

$$e_g = (\text{dent}/\text{refdent})(1 + \rho_0/\rho_{\text{ref}})(1 + 4\rho_{\text{ref}}/\rho_0) \quad (31)$$

with dent equal to the measured dent in inches, refdent a constant equal to 0.510, and  $\rho_{\text{ref}}$  a constant equal to  $1.250 \text{ g}/\text{cm}^3$ .

The shaded area of the Fickett-Jacobs diagram is

$$[E(p_j, v_j) - \frac{1}{2}p_j(v_0 - v_j)] - E(p_7, 7v_0) \quad (32)$$

where  $p_7$  is the pressure on the isentrope at volume  $7v_0$ . A useful calibration rule is to make

$$1.115E_g = [E(p_j, v_j) - \frac{1}{2}p_j(v_0 - v_j)] - E(p_7, 7v_0) \quad (33)$$

where the empirical factor 1.115 has been determined<sup>9</sup> from experiment. This equation assures that constraint (3) is approximately satisfied.

The chemical energy of the explosive is obtained by assuming the composition of the products at expansion to one atmosphere, and calculating the energy released as the explosive molecule transforms to those products. For ordinary CHNO explosives the products are usually assumed to be  $\text{N}_2$ ,  $\text{H}_2\text{O}$ ,  $\text{CO}_2$ , and  $\text{C}$ . The  $\text{H}_2\text{O}$  is assumed to be vapor at  $100^\circ\text{C}$ . The total area of the Fickett-Jacobs diagram is set equal to the chemical energy as,

$$E_0 = E(p_j, v_j) - \frac{1}{2}p_j(v_0 - v_j) \quad (34)$$

where  $E_0$  is the chemical energy, satisfying the fourth constraint. This notation is correct, and  $E_0$  is the energy at the initial state before detonation. The usual convention is followed here, with the energy of the products set to zero at expansion down the principal isentrope to one atmosphere. For calibration, to get energy per unit volume, we write  $e_0 = \rho_0 E_0$ .

The explosive product gases are  $\text{N}_2$ ,  $\text{H}_2\text{O}$ ,  $\text{CO}_2$ ,  $\text{CO}$ , and some solid carbon. We assume that a reasonable

value for the adiabatic gamma is obtained with  $k = 1.3$ . With this assumption, there are five constraints to determine the five parameters,  $a$ ,  $k$ ,  $v_c$ ,  $p_c$ , and  $n$  of the assumed form of the equation of state.

To summarize, the four equations to solve simultaneously are

$$\gamma_j = k + F_j + \frac{4an}{(k-1+F_j)G_j^2} \quad (35)$$

$$p_j = p_c \times \frac{k-1+F_j}{k-1+a} \times \frac{(\frac{1}{2}G_j)^{a/n}}{(v_j/v_c)^{k+a}} \quad (36)$$

$$\rho_0 E_0 = \frac{p_j(v_j/v_0)}{k-1+F_j} - \frac{1}{2}p_j(1 - v_j/v_0) \quad (37)$$

$$\rho_0 E_0 - 1.115e_g = \frac{p_7(v_7/v_0)}{k-1+F_7} \quad (38)$$

where

$$F = \frac{2a(v/v_c)^{-n}}{(v/v_c)^n + (v/v_c)^{-n}} \quad (39)$$

$$G = (v/v_c)^n + (v/v_c)^{-n} \quad (40)$$

$$v_7 = 7v_0 \quad (41)$$

$$p_7 = p_c \times \frac{k-1+F_7}{k-1+a} \times \frac{(\frac{1}{2}G_7)^{a/n}}{(v_7/v_c)^{k+a}} \quad (42)$$

and the subscripts  $j$  and  $7$  on  $F$  and  $G$  indicate the volume to be used in the expression.

Some values chosen for calibration input, some derived quantities, and the values for the calibrated parameters are given in Table I. The values chosen for input are believed to be in reasonable agreement with available experimental results, but this paper is not the place for a review of the experiments. The value for  $k$ , although listed with the calibrated parameters, was fixed at 1.3 as stated above.

## CALIBRATION OFF THE PRINCIPAL ISENTROPE

To calibrate the equation of state off the principal isentrope, which really means determining a value for the constant  $b$ , there must be data available that sample the behavior of the explosive off the principal isentrope. For some explosives, detonation velocities for overdriven detonations have been measured.<sup>7</sup> These measurements sample the high pressure branch of the detonation Hugoniot curve.



TABLE I. CALIBRATION INPUT, DERIVED QUANTITIES, AND CALIBRATED PARAMETERS

Calibration Input					
Explosive	D (m/s)	p <sub>j</sub> (GPa)	ρ <sub>0</sub> (kg/m <sup>3</sup> )	E <sub>19</sub> (MJ/kg)	e <sub>0</sub> (GJ/m <sup>3</sup> )
PBX-9404	8790	35.7	1844	1.620	10.78
LX-17	7630	26.0	1904	1.070	8.13

Derived Values					
Explosive	v <sub>0</sub> (m <sup>3</sup> /kg)	v <sub>j</sub> (m <sup>3</sup> /kg)	v <sub>7</sub> (m <sup>3</sup> /kg)	γ <sub>j</sub>	e <sub>g</sub> (GJ/m <sup>3</sup> )
PBX-9404	5.423 × 10 <sup>-4</sup>	4.064 × 10 <sup>-4</sup>	37.96 × 10 <sup>-4</sup>	2.991	7.728
LX-17	5.252 × 10 <sup>-4</sup>	4.020 × 10 <sup>-4</sup>	36.76 × 10 <sup>-4</sup>	3.263	5.137

Calibrated Parameters						
Explosive	k	a	n	v <sub>c</sub> (m <sup>3</sup> /kg)	p <sub>c</sub> (GPa)	b
PBX-9404	1.3	0.8067	1.4470	8.727 × 10 <sup>-4</sup>	3.376	0.62
LX-17	1.3	0.8767	1.8644	6.325 × 10 <sup>-4</sup>	5.511	0.65

The detonation Hugoniot curve is given by

$$E - E_0 = \frac{1}{2} p (v_0 - v). \quad (43)$$

The equation of state is

$$p = \frac{E}{v} \left[ k - 1 + F(v) \left\{ 1 + b \left( 1 - \frac{E}{E^s(v)} \right) \right\} \right] \quad (44)$$

These two equations must be solved simultaneously to obtain p(v) and E(v) on the detonation Hugoniot curve. A simple approach is to eliminate p from the equation of state by using the Hugoniot relation, which then gives a quadratic equation for E. The solution is

$$E = \frac{\epsilon}{2} \left[ \left\{ (\alpha - \beta)^2 + 4\alpha \frac{E_0}{\epsilon} \right\}^{1/2} - (\alpha - \beta) \right] \quad (45)$$

where  $\alpha = 2v/(v_0 - v)$ ,  $\beta = k - 1 + F(1+b)$ , and  $\epsilon = E^s/Fb$ . The result for E is substituted into the equation of state to get p. The detonation velocity D is obtained from the Raleigh line equation

$$D = \sqrt{\frac{pv_0^2}{v_0 - v}} \quad (46)$$

The particle velocity u is obtained from the jump condition

$$u = \sqrt{p(v_0 - v)}. \quad (47)$$

Fits to the data of reference 7, shown in Figs. 2 and 3, were obtained by eye rather than with the use of a least squares code. The values for b are given in Table I. The lowest point on the curves in Figs. 2 and 3, where there

is a horizontal tangent, is fixed by the choice of a value for the detonation velocity. The tangent point is fixed in the horizontal direction by the choice for the CJ pressure, which in turn fixes the CJ particle velocity. Changing the constant b moves the right end of the curve in the high velocity region. For these reasons, the curves do not fit the data as well as they might if there were freedom to make them fit only these data.

With the assumption that the detonation is really exactly a CJ detonation, it can be shown<sup>10</sup> by differentiating the Hugoniot curve and the Rayleigh line with respect to initial state values, that

$$\frac{\rho_0}{D} \frac{dD}{d\rho_0} = \frac{\gamma - 1 - \Gamma}{2 - \Gamma/\gamma}, \quad (48)$$

with  $\gamma$  and  $\Gamma$  evaluated at the CJ state. For PBX-9404, measured values of detonation velocity at different densities give a value of about 0.69 for this function. The calibration of this equation of states gives, at the CJ state,  $\gamma = 2.991$  and  $\Gamma = 0.853$ . Substituting these values into the equation above gives 0.664 for the function. The disagreement is in keeping with the results discussed in ref. 10 and 11, where it was shown that the derivatives at the CJ state obtained from the simple theory did not agree with experiment. The fit to the velocities for overdriven detonations does not depend on derivatives nor on the CJ assumption, and the value of found from them is to be preferred over one found from the variation of velocity with density.

## DISCUSSION

Plots of  $\gamma$  and  $\Gamma$  for PBX-9404 and LX-17 are shown in Figs. 4 and 5. The fit for  $\Gamma$  is monotone, while the fit for  $\gamma$  has a maximum. The value for n is higher for LX-

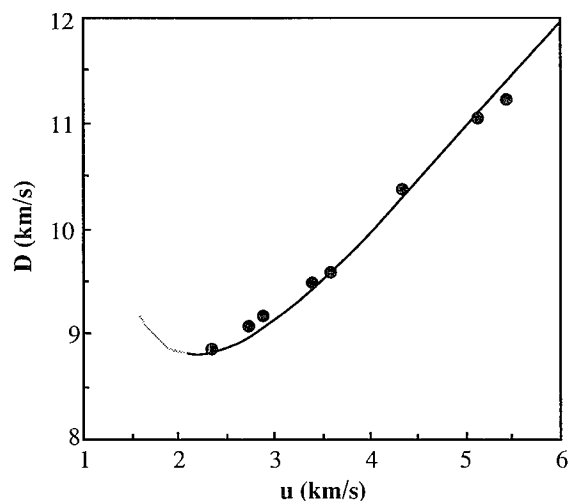


FIG. 2. DIAGRAM IN  $D$ - $u$  SPACE SHOWING THE DATA FOR OVERDRIVEN DETONATION IN PBX-9404, AND THE FIT TO THE DATA FOR CALIBRATION OF THE EQUATION OF STATE, WITH  $b = 0.62$ .

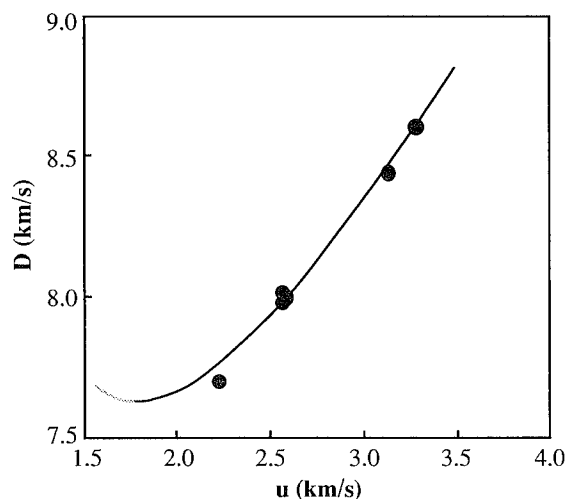


FIG. 3. DIAGRAM IN  $D$ - $u$  SPACE SHOWING THE DATA FOR OVERDRIVEN DETONATION IN LX-17, AND THE FIT TO THE DATA FOR CALIBRATION OF THE EQUATION OF STATE, WITH  $b = 0.65$ .

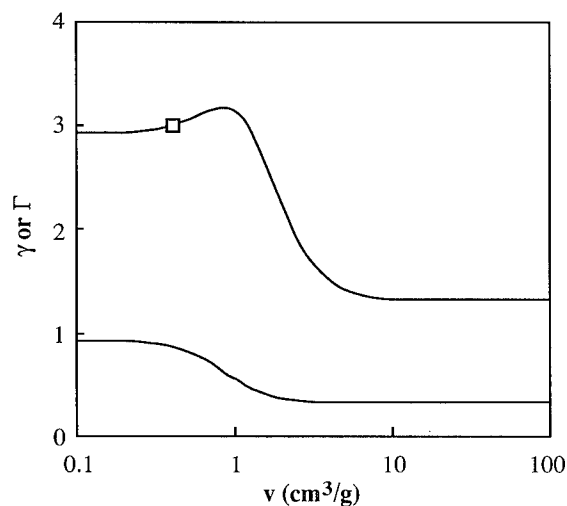


FIG. 4. PLOT OF  $\gamma$  AND  $\Gamma$  vs  $\log v$  FOR PBX-9404. THE UNITS OF VOLUME ARE  $\text{cm}^3/\text{g}$ . THE CJ POINT IS MARKED ON THE CURVE FOR  $\gamma$ .

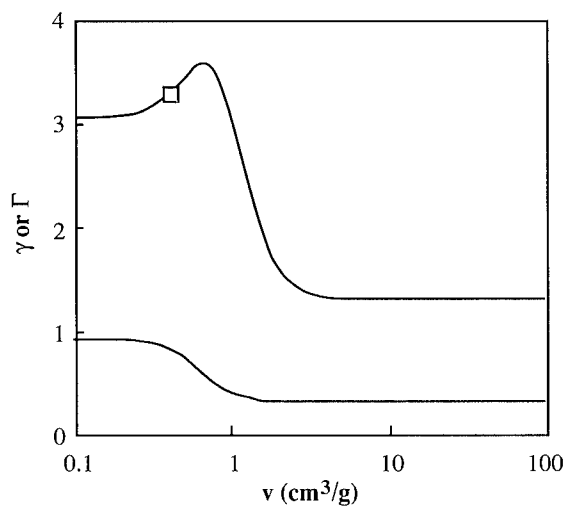


FIG. 5. PLOT OF  $\gamma$  AND  $\Gamma$  vs  $\log v$  FOR LX-17. THE UNITS OF VOLUME ARE  $\text{cm}^3/\text{g}$ . THE CJ POINT IS MARKED ON THE CURVE FOR  $\gamma$ .

17 than for PBX-9404, and as a result the maximum is more pronounced for LX-17.

The form of the function  $F(v)$ , and the linear function (with parameter  $b$ ) for states off the principal isentrope, were chosen to have the right number of constants to determine using the calibration procedure described for the usual data available. If more measurements are available, then more complicated

functions can be used. In particular if the equation of state were to be used as a fitting form for  $\gamma$  and  $\Gamma$  computed from a statistical mechanical treatment of intermolecular forces, the functions could be made more complicated for a better fit.

In engineering use, it is often necessary to change the equation of state a little to reproduce experiments. Usually adjustment of the constant used to multiply the

Gurney energy in Eqs. (33) and (38) and then recalibrating will be sufficient.

## ACKNOWLEDGEMENTS

Drs. J. B. Bdzil, W. Fickett, M. S. Shaw, and R. Menikoff have all contributed important concepts to this work.

## REFERENCES

1. M. S. Shaw and J. D. Johnson, "The Theory of Dense Molecular Fluid Equations of State with Application to Detonation Products," *Eighth Symposium (International) on Detonation*, pp. 531-539, 1985; M. S. Shaw, "A New Simulation Method for the Efficient Calculation of Benchmarks for Detonation Products Equations of State," *Ninth Symposium (International) on Detonation*, pp. 452-460, 1989.
2. F. H. Ree, "A Statistical Mechanical Theory of Chemically Reacting Multiphase Mixtures: Application to the Detonation Properties of PETN," *J. Chem. Phys.* **81**, pp. 1251-1263, 1984.
3. W. C. Davis, "Equation of State for Detonation Products," *Eighth Symposium (International) on Detonation*, pp. 785-795, 1985.
4. R. Menikoff and B. J. Plohr, "The Riemann Problem for Fluid Flow of Real Materials," *Rev. Mod. Phys.* **61**, pp. 75-130, 1989.
5. W. A. Bailey, R. A. Belcher, D. K. Chilvers, and G. Eden, "Explosive Equation of State by the AWRE Method," *Seventh Symposium (International) on Detonation*, Albuquerque, NM, 15 July 1985, pp. 678-685.
6. W. Fickett and W. C. Davis, *Detonation*, University of California Press, Berkeley, 1979, pp. 121-124.
7. L. Green, E. Lee, A. Mitchell, and C. Tarver, "The Supra-Compression of LX-07, LX-17, PBX-9404, and RX-26-AF and the Equations of State of the Detonation Products" *Eighth Symposium (International) on Detonation*, pp. 587-595, 1985.
8. Reference 6, pp. 35-38.
9. The empirical factor that relates the Gurney energy and the truncated Fickett-Jacobs energy is the crucial parameter of the calibration. The value used

in Eq. (33) was obtained by computing the ratios for calibrated equations of state that have been found sufficiently accurate to be useful, for example, the JWL constants given in Table 8-7 of B. M. Dobratz and P. C. Crawford, *LLNL Explosives Handbook*, UCRL-52997 Change 2, 1985. Users may find it advisable to make small adjustments to the factor for particular applications.

10. Reference 6, pp. 69-74.

11. W. C. Davis, B. G. Craig, and J. B. Ramsay, "Failure of the Chapman-Jouguet Theory for Liquid and Solid Explosives", *Phys. Fluids* **8**, pp. 2169-2182, 1965.

---

## DISCUSSION

R. GUIRGUIS  
NSWC, Silver Spring, Maryland

The gamma appears always to have a peak to the right of the CJ point. Is that a coincidence, or a result of getting the parameters of the equation of state (eos) from fitting experiments where the principal isentrope plays the major role, thus giving a bias to the location of the peak? The eos should not know where the CJ point is. If we compress the same gases with a piston, we should get the same peak. If there is no bias, we should get some peaks to the right and some to the left of the CJ point.

## REPLY BY WILLIAM DAVIS:

The peak in adiabatic gamma ( $\gamma$ ) is found in equations of state based on statistical mechanics as well as those more directly calibrated to detonation data, and seems to be a real physical effect. The maximum shifts to smaller specific volume at higher entropy, and to larger at lower entropy. Its location is in the region of specific volume where the gas changes from one where the molecules are far enough apart that they rarely collide, to one where the molecules are so close together that they interact and exert force on each other. On isentropes near the principal isentrope for explosives, the change occurs near where the specific volume is  $1 \text{ cm}^3/\text{g}$ . The location of the CJ point for high-density military explosives on the left of the maximum is a coincidence, and it is found there because their CJ specific volume is usually less than  $\frac{1}{2} \text{ cm}^3/\text{g}$ . Low-density explosives and commercial blasting explosives have their CJ points to the right of the maximum.

## DEVELOPMENT OF THE WILLIAMSBURG EQUATION OF STATE TO MODEL NON-IDEAL DETONATION

W. Byers Brown  
Mass Action Research Consultancy  
Devonshire House  
14 Corbar Road, Buxton, Derbyshire SK17 6RQ, UK  
and  
M. Braithwaite  
ICI Explosives Group Technical Centre  
Ardeer Site  
Stevenston, Ayrshire KA20 3LN, Scotland UK

A simple analytical equation of state for the internal energy  $E$  as a function of volume  $V$  and entropy  $S$  is proposed which is valid from the low densities of perfect gases up to the high densities and temperatures of detonation product fluids. The volume dependence can describe correctly the adiabatic and Grüneisen gamma coefficients along an adiabat, and the dependence on entropy is a generalization of a scaling law which is exact for a model fluid whose monatomic molecules repel each other with an inverse  $n$ -power potential. The EOS is intended to be fitted to the accurate results of an ideal detonation code involving explicit chemistry, for subsequent use in modelling non-ideal detonation. It is tested by fitting to calculated adiabats and shocks for PETN and ANFO, and compared with the JWLE equation.

### INTRODUCTION

There are now in existence quite a few sophisticated ideal detonation codes incorporating an equation of state (EOS) for detonation products based on statistical mechanics and intermolecular forces.<sup>1-3</sup> They are being increasingly used by engineers and by researchers pursuing experimental and theoretical studies in condensed phase detonation. However, to fit experimental detonation results from cylinder tests for the expansion adiabat, comparatively simple equations relating the pressure  $P$  and the internal energy  $E$  to the volume  $V$ , in which the complex chemistry of the detonation products is implicit, are almost mandatory for

hydrocode speed with all but the fastest computers. The assumption behind such simple implicit equations is that all the chemical reactions are at equilibrium. A similar but more general EOS describing also the earlier non-equilibrium stages in which not all the explosive has yet reacted, and which contains one or more extent-of-reaction parameters  $\lambda$ , is required to model non-ideal detonation.

By contrast with sophisticated and fundamental EOS used in modern detonation codes, the implicit equations most commonly used to describe detonation products are either empirical (eg. JWL equation) or simplistic (eg. polytropic EOS), and are usually inconsistent with known experimental facts (eg. assume constant Grüneisen gamma, or constant heat

capacity). They are typically (and deliberately) only *mechanical* EOS giving  $E(P,V)$  or  $P(E,V)$ . Such equations are incomplete in two senses. First of all the variables  $P,V$  or  $E,V$  are not independent since at high density, even at absolute zero,  $P$  and  $E$  have minimum non-zero values  $P_\infty(V)$  or  $E_\infty(V)$ , due to intermolecular repulsion, which have to be specified; the JWL equation is anomalous in this respect. Secondly, they do not involve any thermal quantities such as temperature  $T$  or entropy  $S$  which are necessary in *complete* equations of state. They are adequate for treating the fluid dynamics of detonation products in chemical equilibrium in a post-CJ expansion, but are not suitable as the fluid part of a reactive EOS, whose thermal interaction with the condensed explosive remaining at any stage must be taken into account, and the temperature of which must be involved in any realistic rate laws.

W. C Davis<sup>4</sup> has written a stimulating article describing all the features a useful implicit non-reactive EOS for detonation products should possess for fitting to experimental results. Our objective is somewhat different, in that we seek an EOS for detonation fluid primarily to fit thermodynamic properties calculated from a sophisticated ideal detonation code for use in hydrocodes to model non-ideal aspects of detonation, and only secondarily to fit cylinder and other experimental tests directly. Our desiderata for an implicit EOS are:

- (a) a basis in statistical mechanics and intermolecular forces;
- (b) a simple analytical form which reduces to perfect gas behaviour at low pressures;
- (c) a complete EOS capable of describing the thermal as well as the mechanical properties;
- (d) independent variables volume  $V$  and entropy  $S$ , for ease of describing adiabats and shocks;
- (e)  $S$  easily eliminated when only mechanical properties are required;
- (f) all parameters determined from a principal adiabat.

A new EOS satisfying most of these criteria and suitable for describing fluids up to CJ pressures and temperatures has been proposed by us recently,<sup>5</sup> based on some earlier work on an adiabatic EOS presented at the Williamsburg APS meeting in 1991.<sup>6,7</sup> We have therefore dubbed the new equation the *Williamsburg EOS*.

The object of this paper is to review the development of the new EOS, to apply it for the first time to the detonation product fluid of explosives (PETN and ANFO), and to compare it with the Jones-Wilkins-Lee (JWL) equation.

## STATISTICAL MECHANICAL BASIS

The chief characteristic of high pressure behaviour is that it is dominated by repulsive intermolecular forces. The simplest realistic repulsive potential is that involving the inverse- $n$  power of the intermolecular distance. The dimensionless excess properties of a fluid of  $N$  such molecules possess the simplifying feature that they are a function only of the combined volume-temperature variable  $x=VT^{3/n}$ , and are known accurately from a combination of statistical mechanics and computer simulation.<sup>8</sup> We wish to introduce the entropy  $S$  as a variable rather than the temperature  $T$ , and pose the question: Is it possible that a combined volume-entropy variable exists for the inverse- $n$  power potential fluid? The first thing to investigate is the ideal contribution to the entropy, which is given by

$$S_{id} = S_{id}^0 + C_V^{id} \log(T/T_0) + Nk_B \log(V/V_0) \quad (1)$$

where  $T_0, V_0$  is a reference state with ideal entropy  $S_{id}^0$ , and it has been assumed that the ideal heat capacity  $C_V^{id}$  is constant, independent of temperature. It follows that the ideal adiabatic gamma coefficient, given by

$$\gamma = C_P^{id}/C_V^{id} = 1 + Nk_B/C_V^{id}, \quad (2)$$

is also constant; such a feature could be called *ideal polytropic*. The excess entropy is a function only of  $x$ , and we can therefore write the total entropy

$$S = S_{id} + S_{ex} \quad (3)$$

in the form

$$S = Nk_B \log(VT^{\frac{1}{\gamma-1}}) + S_{ex}(VT^{\frac{3}{n}}) + const. \quad (4)$$

If we now define a dimensionless entropy factor  $\sigma$  by

$$\sigma = \exp\left(\frac{S - S_0}{Nk_B}\right), \quad (5)$$

where  $S_0$  is the reference entropy, then

$$\sigma = VT^{\frac{1}{\gamma-1}} \phi(VT^{\frac{3}{n}}), \quad (6)$$

where  $\phi$  is some function. It follows by elementary manipulation of indices that  $x = VT^{3/n}$  is some function of the combined volume-entropy variable  $y = V\sigma^\alpha$ , where the index  $\alpha$  is given by

$$\alpha = \frac{\gamma - 1}{\frac{n}{3} + 1 - \gamma} \quad (8)$$

A simple scaling argument then reveals that the internal energy  $E$  can be written as a function of volume  $V$  and entropy  $S$  in the form

$$E(V, S) = \left(\frac{\sigma}{V}\right)^{\gamma-1} \psi(V\sigma^\alpha), \quad (9)$$

where  $\psi$  is some function, and the zero of energy is the perfect gas state at the absolute zero of temperature.

The form (9) is already in marked contrast to that of the JWL equation: it combines the perfect gas factor and the term describing intermolecular repulsion *multiplicatively*, while the purely empirical JWL equation,<sup>9</sup> which may be expressed as

$$E_{JWL}(V, S) = K\left(\frac{\sigma}{V}\right)^{\gamma-1} + W(V) \quad (10)$$

(where  $W$  is the exponential terms) combines them *additively*. This leads to a striking difference in the relationship between the important adiabatic and Gruneisen gamma coefficients

$$\Gamma_S = \left(\frac{\partial \log P}{\partial \log V}\right)_S, \quad \Gamma_G = \left(\frac{\partial \log T}{\partial \log V}\right)_S. \quad (11)$$

The JWL equation implies that  $\Gamma_G$  is a constant, independent of volume (therefore strictly equal to the ideal value  $\gamma-1$ ) and unrelated to  $\Gamma_S$ , while equation (9) leads to the linear relationship,<sup>10</sup> valid for all states

$$\Gamma_S = \gamma_\infty - \left(\frac{\gamma_\infty - \gamma}{\gamma - 1}\right) \frac{\Gamma_G}{Z}, \quad (12)$$

where  $Z = PV/Nk_B T$  and  $\gamma_\infty = n/3 + 1$ . It can then be shown that the gamma coefficients have the following upper and lower bounds for this model system (and also for the Lennard-Jones  $n:6$  potential):

$$\left. \begin{aligned} \frac{n}{3} + 1 &\geq \Gamma_S \geq \gamma, \\ \frac{n}{3} - 1 &\geq \Gamma_G \geq \gamma - 1; \end{aligned} \right\} \quad (13)$$

the first of these inequalities is quoted without reference by Davis.<sup>4</sup> In addition, the third independent second derivative of  $E(V, S)$ , namely the total heat capacity at constant volume  $C_V$ , can be shown<sup>10</sup> to have the bounds

$$\frac{1}{\alpha} \geq \frac{C_V}{Nk_B} \geq \frac{1}{\gamma - 1} \quad (14)$$

where  $\alpha$  is given by equation (8).

We now seek a specific form for the internal energy  $E(V, S)$  of the model system.

## EQUATION OF STATE OF MODEL SYSTEM

The function  $E(V,S)$  is not a familiar one in the statistical mechanics of systems of interacting molecules (it corresponds to the micro-canonical ensemble of Gibbs), and a suitable form for the excess factor  $\psi$  does not suggest itself. We therefore return to the description of the excess properties of the inverse- $n$  power potential fluid, and in particular to the compressibility factor  $Z = PV/Nk_B T$ , which is a function only of  $x = VT^{3/n}$ . The exact analytical solution of the Percus-Yevick theory for hard spheres leads to a rational form for  $Z(V)$ , that is the ratio of two polynomials, which was preserved by Carnahan and Starling in their very successful semi-empirical equation for describing the properties of the hard-sphere fluid. A natural form for  $Z(x)$  is therefore the ratio of two polynomials in  $x = VT^{3/n}$ . It follows that since for our model system  $Z$  is only a function of  $y = V\sigma^\alpha$ , we should try

$$Z = D(y)/C(y) \quad (15)$$

where  $C$  and  $D$  are polynomials of low degree.

To develop the implications and consequences of this ansatz we need to derive an expression for  $Z$  from  $E(V,S)$ . The pressure  $P$  and temperature  $T$  are first derivatives given by

$$P = -\left(\frac{\partial E}{\partial V}\right)_S \text{ and } T = \left(\frac{\partial E}{\partial S}\right)_V, \quad (16)$$

and hence from (9)

$$\frac{PV}{E} = -\left(\frac{\partial \log E}{\partial \log V}\right)_S = \gamma - 1 - \chi(y), \quad (17)$$

$$\frac{Nk_B T}{E} = \left(\frac{\partial \log E}{\partial \log \sigma}\right)_V = \gamma - 1 + \alpha \chi(y). \quad (18)$$

where  $\chi(y)$  is a logarithmic derivative of logy. The compressibility factor  $Z = PV/Nk_B T$  is therefore the ratio of equation (17) to

equation (18). It is a natural extension of the ansatz (15) to represent (17) and (18) themselves by the ratio of polynomials in  $y$ . We define two dimensionless functions  $g$  and  $f$  by

$$g = 1 + PV/E, \quad f = Nk_B T/E \quad (19)$$

and set

$$\left. \begin{aligned} g &= A(y)/B(y) \\ f &= C(y)/B(y) \end{aligned} \right\} \quad (20)$$

where  $A, B$  are low degree polynomials like  $C$  and  $D = A + B$  in (15). Examination of the limiting behaviour of  $g$  and  $f$  shows that both are finite for  $y=0$  to  $\infty$ , and  $f(\infty)=0$ , so that  $A$  and  $B$  are of the same degree, say  $m$ , and  $C$  is of degree  $m-1$ .

In order to deduce the corresponding form for  $E$  it is necessary to integrate equation (17) or (18), and this requires us to put  $g$  or  $f$  in partial fractions thus

$$g = \gamma + \sum_{j=1}^m \frac{\gamma_j}{1 + \beta_j y} \quad (21)$$

where  $\beta_j$  and  $\gamma_j$  are constants replacing the coefficients of the polynomials  $A$  and  $B$ . By substituting (21) into (19), and (19) into (17), and integrating with respect to  $V$  at constant  $\sigma$ , we get

$$E(V,S) = \frac{E_0}{v^{\gamma_\infty-1}} \prod_{j=1}^m \left( \frac{1 + \beta_j v^\alpha \sigma^\alpha}{1 + \beta_j} \right)^{\gamma_j} \quad (22)$$

where we have introduced again a reference state  $S_0, V_0$  with internal energy  $E_0$ , and defined a reduced volume  $v = V/V_0$ . The parameters  $\gamma_j$  must satisfy the relation

$$\gamma_\infty = \gamma + \sum_{j=1}^m \gamma_j, \quad (23)$$

so that (22) behaves correctly in the perfect gas limit; for the same reason  $\alpha$  must be given by (8).

Equation (22) appears to be a very satisfactory EOS for describing the adiabats of the model system for low values of  $m$ ; even the  $m=1$  approximation can be fitted quite satisfactorily to accurate computer simulations.<sup>8</sup> However, it is not flexible enough as it stands to describe an ideal polytropic Lennard-Jones potential fluid, nor one with the more realistic Buckingham exponential potential. It is therefore necessary to generalize the equation in some way to make it more flexible.

## WILLIAMSBURG EQUATION OF STATE

The obvious generalization of (22) is to allow each denominator term to have a different value of  $\alpha$ , say  $\alpha_j$ . Thus the Williamsburg EOS of order  $m$  is defined by the equation

$$E(V,S) = \frac{E_0}{v^{\gamma_\infty-1}} \prod_{j=1}^m \left( \frac{1+\beta_j v \sigma^{\alpha_j}}{1+\beta_j} \right)^{\gamma_j} \quad (24)$$

where  $\gamma_\infty$  is defined by (23), and the  $\alpha_j$  must satisfy the condition

$$\sum_{j=1}^m \alpha_j \gamma_j = \gamma - 1 \quad (25)$$

so that (24) behaves correctly in the perfect gas limit. The EOS is defined to have energy  $E_0$  at the reference state  $S_0, V_0$ , and in addition has  $3m$  parameters  $\alpha_j, \beta_j, \gamma_j$ . The logarithmic first derivatives already introduced are now given by

$$\left. \begin{aligned} g &= \gamma + \sum_{j=1}^m \frac{\gamma_j}{1 + \beta_j v \sigma^{\alpha_j}} \\ f &= \gamma - 1 - \sum_{j=1}^m \frac{\alpha_j \gamma_j}{1 + \beta_j v \sigma^{\alpha_j}} \end{aligned} \right\} \quad (26)$$

All the Greek parameters can be obtained from thermodynamic data for  $g = 1 + PV/E$  and  $f = Nk_B T/E$  as functions of  $v$  along the isentrope (principal adiabat)  $S = S_0$ , or  $\sigma = 1$ , which goes through the reference state. The simplest technique is to write  $g_0(v)$  and  $f_0(v)$  as rational functions  $A/B$  and  $C/B$  where  $A(v)$ ,  $B(v)$  and  $C(v)$  are polynomials of degree  $m$ , and to solve the linear equations  $A - gB = 0$  and  $C - fB = 0$  by least squares. The  $\beta$  parameters can then be found from the roots of  $B=0$ , the  $\gamma$  from the partial fraction residues and remainders of  $A/B$ , and the  $\alpha$  from those of  $C/B$ ; the mathematics of rational functions involved is familiar from signal processing, and has been described briefly.<sup>6,7</sup> Since the roots of  $B=0$  may be complex, the parameters can occur in complex pairs, and often do. This presents no difficulties as the physical quantities are always real. If more accurate parameters are required for any order  $m$ , a pseudo-linear iterative technique is available to improve the fit.

The adiabatic and Grüneisen gammas, defined by (11), are given by

$$\Gamma_S = g - \left( \frac{\partial \log(g-1)}{\partial \log v} \right)_\sigma, \quad (27)$$

$$\Gamma_G = g - 1 - \left( \frac{\partial \log f}{\partial \log v} \right)_\sigma, \quad (28)$$

and are therefore easily calculated from equations (26), in particular along the principal adiabat.

## APPLICATION TO DETONATION PRODUCT FLUID

The results of fitting the Williamsburg (WB) EOS to accurate statistical mechanical computations for the Lennard-Jones 12:6 and exponential-13.5:6 potentials have been reported recently,<sup>5</sup> and will not be repeated here. By fitting  $g$  and  $f$  to a principal adiabat as described above, very good fits to the pressure and other properties can be obtained



over a range  $\log \sigma \approx \pm 2$  with  $m=2$ . Very good fits to Rankine-Hugoniot (shock) curves can also be obtained up to entropies corresponding to  $\sigma = 10^5$ , but these require the  $m=4$  approximation.

The object of this section is to report some preliminary applications of the WB EOS to fit adiabats and shocks for explosive detonation products calculated by the IDeX ideal detonation code.<sup>11</sup> Two of the basic assumptions involved in the construction of the WB equation are violated by detonation product fluid, viz.

1. The ideal gamma coefficient  $\gamma$  given by (2) is not constant, because (a) some internal vibrations of some of the polyatomic products become excited thermally in the fitting range, and (b) the equilibrium composition changes in the fitting range causing extra changes in the ideal heat capacity.
2. For a given mass of explosive, the number of product (gas) molecules  $N$  (or moles  $n$ ) changes along the adiabats and shocks due also to equilibrium composition shifts. We are dealing with a *Gibbsian* EOS, in which the elements are in total equilibrium, and only the elemental composition is constant.<sup>3</sup>

There is no problem in fitting any given adiabat satisfactorily with the WB equation, but the agreement for neighbouring isentropes can be less good. Although the change in  $\gamma$  itself is usually less than 5%, the underlying changes in  $CV$  may be much larger. As far as the second point is concerned, the changes in  $n$  vary a good deal in sign and magnitude, but can be as large as 5%. The effects are therefore not trivial, and there are a number of ways of attempting to overcome them. The simplest is to use average values of  $\gamma$  and of  $n$  over the range it is desired to fit. Another is to fit strictly *molar* quantities, and to allow for the fact that although the *specific* entropy is constant along an expansion adiabat, the *molar* entropy is changing slightly. A third is to use an extended form of the WB equation in which the  $\alpha$ 's are allowed to depend slightly on

volume; this allows a description of the effect of changes in  $\gamma$ . In the present paper we stick to the use of simple averages.

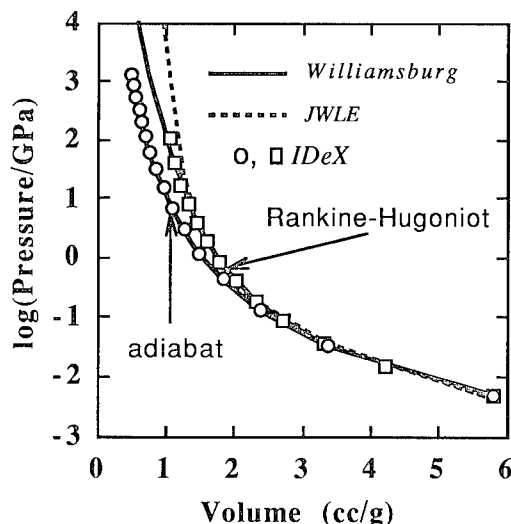


FIGURE 1. COMPARISON OF IDeX, WB AND JWLE ADIABAT AND SHOCK HUGONIOT FOR PETN (INITIAL DENSITY 1.5 G/CC)

In Figure 1 is shown WB fits (solid lines) to the expansion adiabat from the CJ point to 1 kbar and a shock Hugoniot for PETN at an initial density of 1.5 g/cc,

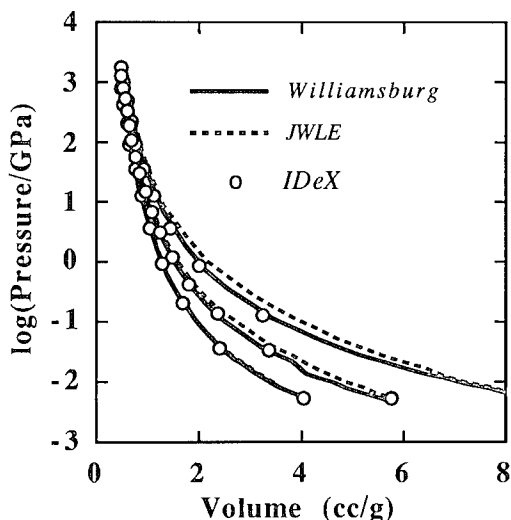
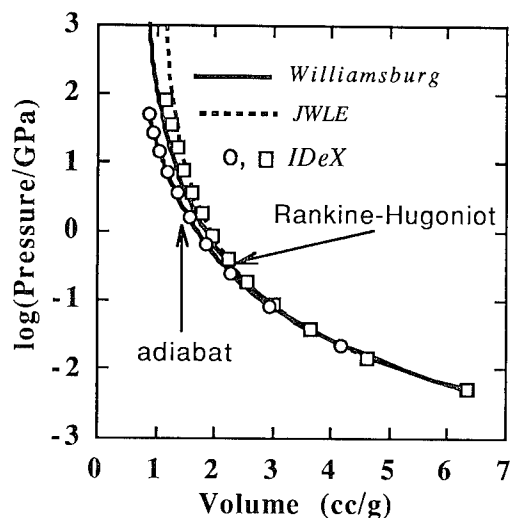


FIGURE 2. COMPARISON OF IDeX, WB AND JWLE ADIABATS FOR PETN (INITIAL DENSITY 1.5 G/CC)

compared with IDeX calculations (circles and squares). Also shown is the extended JWL equation<sup>4,12</sup> (dashed line), which uses parameters from unconstrained least squares fits to the adiabat, and the accurate IDeX values for the Grüneisen gamma coefficient along the adiabat. The adiabat is fitted with  $m=2$ , but the shock, going up to large  $\sigma$  values, requires  $m=4$ . Figure 2 shows the same principal adiabat with WB (solid lines) and JWL (dashed lines) fits to IDeX adiabats (circles) on either side. The JWL equation fitted to one adiabat cannot strictly be used to calculate another adiabat, as the inclusion of the ideal entropy dependence, as in equation (10), is quite inadequate. However, by modifying the ideal term so that it passes through the initial  $PV$ -state of a neighbouring adiabat, a comparison with an accurate adiabat is possible, and is labelled JWLE in the Figure. The WB adiabats ( $m=2$ ) have also been modified slightly so that they too pass through the initial  $PV$ -states.



**FIGURE 3. COMPARISON OF IDeX, WB AND JWLE ADIABAT AND SHOCK HUGONIOT FOR ANFO (INITIAL DENSITY 0.84 G/CC)**

Figures 3 and 4 show the same comparisons for an ANFO composition at 0.84 g/cc. In Figure 3 the fits of the WB and JWLE equations to the shock Hugoniot are comparable, but the WB is much simpler in that all the parameters are obtained by fitting

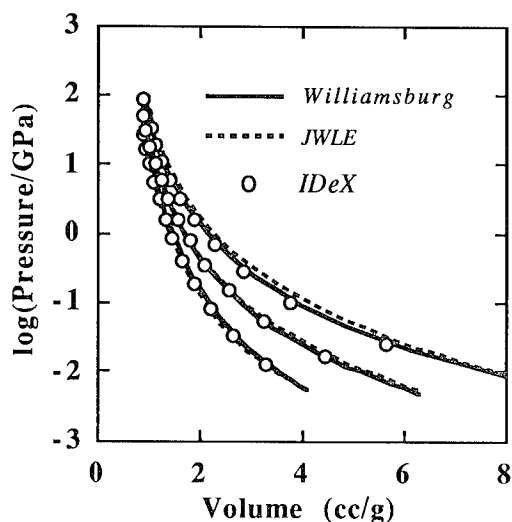


**FIGURE 4. COMPARISON OF IDeX, WB AND JWLE ADIABATS FOR ANFO (INITIAL DENSITY 0.84 G/CC)**

the principal adiabat, and an extra fit to the Grüneisen gamma (needed in the JWLE<sup>12</sup>) is not required. In Figure 4 both the JWL (labelled JWLE) and WB adiabats are constrained to pass through the IDeX initial states ( $P=1$  kbar), but again, this is necessary for the JWL but optional for the WB.

## CONCLUSIONS

The Williamsburg EOS is a comparatively simple semi-empirical equation for  $E(V,S)$  for describing adiabats, shocks and other states from low to detonation pressures. It is based on a generalization of a scaling law for the inverse-power potential, and a rational form for  $Z$ , both derived from statistical mechanics. It has been shown to give excellent fits to single adiabats for the detonation products of two explosives, from which very good fits to shocks can be calculated without further parameterization. The fits to neighbouring adiabats using a simple averaging technique for the variation of the ideal gamma  $\gamma$  and the number of moles  $n$ , while better than JWL, are not of comparable accuracy, and a more elaborate fitting method needs to be explored.

An important feature of the WB EOS from the point of view of modelling non-ideal detonation, is that it is a *complete* EOS, from which the temperature can easily be obtained in order to describe the thermal interaction of unreacted explosive and detonation products, and to appear in Arrhenius-type reaction rates. On the other hand, for high performance explosives in which non-ideality is ignored, the entropy can be easily eliminated between  $P$  and  $E$  to yield the mechanical EOS  $P(V,E)$ , not restricted to the principal adiabat, for use in hydrocodes.

## REFERENCES

1. Chirat, R.; and Pittion-Rossillon, G., "Detonation Properties of Condensed Explosives Calculated with an Equation of State based on Intermolecular Potentials", *Proceedings of the 7th Symposium (International) on Detonation*, 1981, p. 703.
2. Ree, F. H., "A Statistical Mechanical Theory of Chemically Reacting Multiphase Mixtures: Application to the Detonation Properties of PETN", *J.Chem.Phys.*, Vol. 81, 1984, p. 1251.
3. Byers Brown, W.; and Braithwaite, M., "Sensitivities of Adiabatic and Grüneisen Gammas to Errors in Molecular Properties of Detonation Products", *Proceedings of the 9th Symposium (International) on Detonation*, 1989, p. 271.
4. Davis, W. C., "Equation of State for Detonation Products", *Eighth Symposium (International) on Detonation*, 1985, p. 785.
5. Byers Brown, W.; and Braithwaite, M., "Williamsburg Equation of State for Detonation Product Fluid", *Shock Compression of Condensed Matter 1993*, Colorado Springs, June 1993 (to be published).
6. Byers Brown, W.; and Braithwaite, M., "Analytical Representation of the Adiabatic Equation for Detonation Products based on Statistical Mechanics and Intermolecular Forces", *Shock Compression of Condensed Matter 1991*, Elsevier, 1992, p. 325.
7. Byers Brown, W., "Analytical Representation of the Adiabatic Equation for Detonation Products based on Statistical Mechanics and Intermolecular Forces", *Phil.Trans.Roy.Soc.*, Vol. A 339, 1992, p. 345.
8. Hoover, W. G.; Ross, M.; Johnson, K. W.; Henderson, D.; Barker, J. A.; and Brown, B. C. J., *J.Chem.Phys.*, 52, 1970, p. 4931.
9. Lee, E. L.; Hornig, H. C.; and Kury, J. W., "Adiabatic Expansion of High Explosive Detonation Products", *Lawrence Radiation Laboratory Report No. UCRL-50422*, 1968.
10. Byers Brown, W., (to be published).
11. Freeman, T. L.; Gladwell, I.; Braithwaite, M.; Byers Brown, W.; Lynch, P.M.; and Parker, I.B., "Modular Software for Modelling the Ideal Detonation of Explosives", *Math. Eng. Industry*, Vol. 3, 1990, p. 97.
12. Baker, E. L., "An Explosives Products Equation of State appropriate for Material Acceleration and Overdriven Detonation: Theoretical Background and Formulation", *Picatinny Arsenal Technical Report ARAED-TR-91013*, 1991.

## DISCUSSION

R. GUIRGUIS  
NSWC, Silver Spring, Maryland

The gamma appears always to have a peak to the right of the CJ points. Is that a

coincidence, or a result of getting the parameters of the equation of state (eos) from fitting experiments where the principal isentrope plays the major role, thus giving a bias to the location of CJ relative to the peak? the eos should not know where the CJ point is. If we compress the same gases in a piston, we should get the same peak. If there is no bias, we should get some peaks to the right and some to the left of the CJ point. NOTE: the question is not whether there is a peak or not, but: why does the peak appear to fall always to the right of the CJ point?

#### REPLY BY MARTIN BRAITHWAITE:

Theoretically, that is on the basis of accurate statistical mechanics, the isentrope of the adiabatic gamma coefficient  $\Gamma_S = -(\delta \log P / \delta \log V)_S$  as a function of volume  $V$  has a single maximum at a sufficiently small value of  $V$  provided the repulsion between the molecules depends exponentially on the intermolecular distance, as with the Buckingham

exponential  $-a:6$  potential: no maximum occurs for inverse power potential, as with the Lennard Jones  $N:6$  potential. Thus, a maximum is predicted to occur for pure nitrogen, whose behavior can be modeled well by the Buckingham potential. The position and magnitude of the maximum depends on the entropy; or in other words, on the initial state in an adiabatic compression or expansion. Similarly, a mixture of actual detonation product gases is predicted to have a maximum in  $\Gamma_S$  along an isentrope at sufficiently high density, whether or not the mixture is in chemical equilibrium or frozen in composition. The  $\Gamma_S$  maximum for the detonation products of PETN, initially at its crystal density of  $1.77 \text{ g/cm}^3$ , occurs at a slightly larger specific volume than that of CJ point. However, for an initial density of  $1 \text{ g/cm}^3$ , the maximum occurs at a smaller specific volume along the principal adiabat than the CJ volume. Thus, some  $\Gamma_S$  peaks occur to the left and some to the right of the CJ point, as the questioner surmises.

## A REVIEW OF DEVELOPMENTS IN THE W-B-L DETONATION MODEL

D C Swift and B D Lambourn  
Atomic Weapons Establishment, Aldermaston  
Reading, RG7 4PR, UNITED KINGDOM

The W-B-L model incorporates an application of Shock Dynamics to diverging detonation waves, allowing the calculation of multidimensional and boundary effects on the propagation of detonation wavefronts without having to resolve the reaction zone explicitly. Its asymptotic solutions in rods and slabs have been investigated further, and the theory extended to 3D, including a prototype computer program. The 2D program has been used successfully to simulate recent experiments.

The second part of the model depicts the way in which the boundary effects and wavefront curvature affect the ability of explosive charges to drive metal plates. An energy release model is presented for explosive behind the detonation wave, based on a quasisteady solution of the equations for 1D spherically diverging flow.

### INTRODUCTION

Because of the large reaction zone sizes in insensitive high explosives, an improved detonation model is required for metal-moving hydrocode calculations. Most codes use either a constant-speed Huygens construction to calculate programmed burn times, or a full reaction zone model. The problem with the constant-speed model is that it implicitly assumes a reaction zone of zero thickness, and hence predicts no effects from the wave curvature and inert boundaries on the thermodynamic states and the progress of energy release within the reaction zone. These effects are accounted for in calculations with a fully-resolved reaction zone, but the meshing has to be extremely fine, and such calculations are far too time-consuming to be used in iterating towards designs with large masses of explosive. The W-B-L model is a way of approximating the effects of curvature and the boundary on the detonation process whilst preserving the advantages of programmed burn for design calculations.

The model has two parts:

- a. Detonation shock dynamics, which determines the evolution of a diverging wavefront, assuming that its speed is a function of the local

wavefront curvature, and that inert boundaries exert a 'dragging' effect which diffuses across the wavefront, increasing its curvature.

- b. A model of energy release which is dependent on the local wavefront curvature, and hence modifies the equation of state (EOS) of the detonation products locally.

Previous work<sup>1,2</sup> has shown that this model is a computationally efficient approach to take account of some of the multidimensional effects governing the propagation of detonation waves without resolving the reaction zone. This paper reviews the current status of the model and shows how it has been extended to deal with the effect of wavefront curvature on the EOS of the detonation products.

### BASIC W-B-L ASSUMPTIONS

The modelling of the propagation of a detonation wave ('detonation shock dynamics') is a variant of Whitham's theory of Shock Dynamics,<sup>3</sup> using the following assumptions:

- A1 The speed  $D$  of the detonation wave depends on the local curvature  $K$  of the wavefront.
- A2 The maximum angle the wavefront can make with the boundary of the explosive depends on

the effective impedance of the material adjacent to the boundary.

These assumptions can be expressed as partial differential equations and boundary conditions, whose solution describes the motion of a detonation wave through explosive material of arbitrary shape and composition. The equations are non-linear, and are solved numerically. They are of parabolic character for diverging waves, which influences the choice of numerical scheme. Convergent waves lead to hyperbolic equations, solved by Whitham's method.<sup>4</sup> The work done recently has concentrated on diverging systems, so the results are not generally applicable to the Mach stems produced when diverging waves collide, or to the inside of a wave converging toroidally.

In a diverging detonation wave, some of the energy is used to compensate for the divergence. In addition, if the full Chapman-Jouguet (C-J) plane wave energy is released behind a shock wave moving at other than the C-J speed, the pressure profile in the 'reaction zone' is incorrect. Controlling the energy release of the detonating explosive in the W-B-L model therefore requires a further assumption:

A3 The EOS of the detonation products depends on the curvature or wave speed when the wave passed.

(A consequence of these assumptions is that a C-J state exists only for a plane wave in a charge of infinite diameter.) Assuming the effects of lateral flow are negligible in the reaction zone, then applying these assumptions to the reactive flow equations leads to a correspondence between the  $D(K)$  relation and the chemical reaction rate.

## DETONATION SHOCK DYNAMICS

### 2D Theory

The derivation of the equations of motion of a detonation wave<sup>2</sup> proceeded by considering the expansion of a section of the surface of the wave. Simple geometrical constructions give a pair of partial differential equations for the curvatures of the wave and a 'ray' normal to it. These can be combined to give a single equation

$$\frac{\partial \theta}{\partial t} = -\frac{dD}{dK_T} \frac{1}{h} \frac{\partial}{\partial \sigma} \left[ \frac{1}{h} \frac{\partial \theta}{\partial \sigma} \right] \quad (1)$$

where  $\theta$  is the angle between a ray and some reference direction,  $t$  is the time,  $\sigma$  is a Lagrangian co-ordinate increasing with distance around the trace of the wave,  $h$  is a local expansion factor (in effect converting  $\sigma$  into distance), and  $K_T$  is the curvature of the trace of the wave in the 2D plane. Eq. 1 is of diffusive character provided that the rate of change of  $D$  with  $K$  is negative.

It has been found sufficient in most cases to use a linear  $D(K)$  relation:

$$D = D_{CJ}(1 - aK) \quad (2)$$

where  $D_{CJ}$  and  $a$  are explosive-dependent parameters determined by experiment.

### 3D Theory

The theory above is readily extended to 3D by considering instead the expansion of a patch on the surface of the wave bounded by a 'ray tube' (Fig. 1). The curvature of the wave is given by the solid angle equivalent of similar triangles, and the curvature of the ray from a 2D treatment in the plane containing the maximum change in  $D$  across the wave, i.e. the

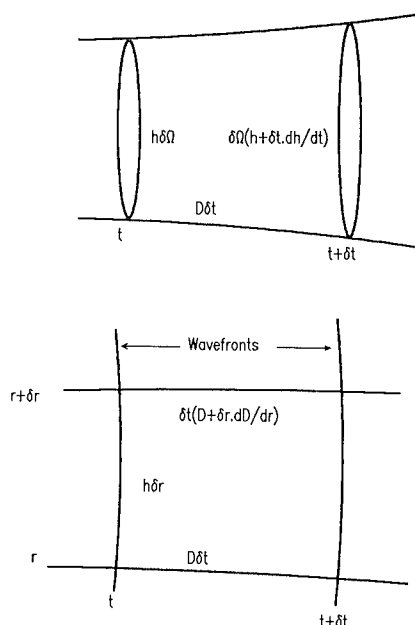


FIGURE 1. W-B-L WAVE DIAGRAMS IN 3D

plane containing  $\nabla D$ . The equations of motion in this case are

$$\frac{\partial \vec{n}}{\partial t} = -\nabla D, \quad \frac{\partial h}{\partial t} = hDK \quad (3)$$

where  $\vec{n}$  is the normal to a point on the wave.

These equations have been implemented in a program to calculate the motion of a detonation wave in a rod or slab of explosive.

### Curvature

An appropriate measure of curvature can be derived by considering the expansion of a region on the surface of a detonation wave. Reasoning heuristically, a detonation wave should move more slowly when the energy from material to the rear of the reaction zone is spread over a greater area by the time it reaches the leading shock.

Considering the rate of change of area  $A_P$  of a section of a wavefront surface about a point  $P$  with distance  $\xi$  as the wave propagates along the normals to the surface, the result

$$\frac{1}{A_P} \frac{\partial A_P}{\partial \xi} = \frac{1}{\pi} \oint_0^{2\pi} K_\phi d\phi \quad (4)$$

is obtained, where  $K_\phi$  is the curvature of the trace of the surface in the plane containing the normal at  $P$  and an azimuthal line in the  $\phi$ -direction.

This expansion-based measure can be related to the curvature used in a  $D(K)$  relation by comparison with the result for a sphere of initial radius  $r$ . It is easy to show that in this case

$$\frac{1}{A_P} \frac{\partial A_P}{\partial \xi} = \frac{2}{r}, \quad (5)$$

since  $A_P \propto (r + \xi)^2$ . Now,  $K = 1/r$  for a sphere, so for a general surface,

$$K = \frac{1}{2\pi} \oint_0^{2\pi} K_\phi d\phi. \quad (6)$$

(Considering the expansion of hoops in an axisymmetric surface, the result

$$K = \frac{1}{2} \left( K_T + \frac{\sin \theta}{r} \right) \quad (7)$$

can be proved, where  $\theta$  is the angle between the normal to the surface and the axis of symmetry. Similarly, the curvature of a surface with plane symmetry is  $K_T/2$ .)

### D(K) Relations for Four Explosives

The asymptotic waveshapes  $z(r)$  in long rods and slabs of explosive were deduced in a way similar to the work of J Bdzil.<sup>5</sup> These were used in calculating parameters for the model, by comparing with the shapes of detonation waves in long rods and slabs of explosive, measured with a streak camera. In this way, parameters have so far been calculated for 4 explosives (Table 1). Note that  $D_{CJ}$  is greater than the speeds observed in cylinder tests, because the cylinder test waves become curved.

### Relaxation to a 2D Steady Shape

A simple approximate solution to the diffusion equation (Eq. 1) predicts an exponential relaxation towards an asymptotic solution (a circular arc) as the effects of the boundary conditions diffuse along the wavefront. The most significant distance constant in the diffusion is

$$\sigma = \frac{2d^2}{(\alpha + 1)a\pi^2} \quad (8)$$

where  $d$  is the slab thickness or rod diameter and  $\alpha$  is a symmetry indicator: 0 for plane and 1 for axisymmetric geometry. The distance required for the exponential part to decay to  $e^{-\nu}$  is  $z \simeq \nu\sigma$ . Therefore  $\nu = z/\sigma$  is a reasonable stability index for any rod or slab experiment. Ideally,  $\nu$  should be at least 3 to give confidence that a stable waveshape has developed.

Table 1. D(K) PARAMETERS FOR 4 EXPLOSIVES

Explosive	Composition	Geometry	$D_{CJ}$ (mm/ $\mu$ s)	$a$ (mm)
Baratol	30/70 TNT/Barium Nitrate	25 mm slab	5.12	4.10
EDC29	95/5 HMX/Polyurethane	10 mm rod	8.77	0.30
EDC32	85/15 HMX/Viton	25 mm rod	8.50	0.28
EDC35	95/5 TATB/Kel-F	25 mm slab	7.81	1.56

When a 'point' initiator is used, the boundary conditions will not be applied until the angle of incidence has decreased to the minimum angle  $\theta_c$ . Thus there is an initial 'free run' radius from the detonator:

$$r_f = \frac{d}{2 \sin \theta_c} \quad (9)$$

This means that for equal initial perturbations from a steady shape, a plane-initiated wave should reach the steady shape before a point-initiated wave.

### Performance for 2D Wave Motion

As an example of the wave propagation model, wave motion comparisons have been made against the block experiments of Aveillé et al<sup>6</sup> using  $D_{CJ}$  and  $a$  measurements from their logosphere experiments<sup>7</sup> on the TATB-based explosive T2. The experiments were as shown in Fig. 2. The waveshapes at the end of the block were measured with a streak camera, and the time differences plotted relative to the latest arrival time (Fig. 3).

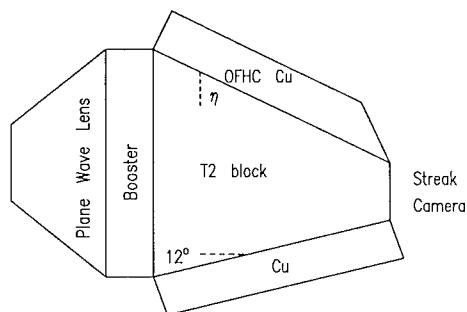


FIGURE 2. BLOCK EXPERIMENTS

These experiments were simulated assuming a plane wave input to the T2 block.  $a$  and  $D_{CJ}$  were obtained from the logosphere experiments (2.48 mm and 7.68 mm/μs respectively). The boundary angle  $\theta_c$  was varied until a reasonable fit was obtained, when  $\theta_c = 0.22$  radians (Fig. 4). For fitting purposes, the waveshapes were normalised to the earliest arrival time (in the centre of each profile) because the latest time was measured at only a single point, which was also the most difficult to calculate accurately. Reasonable agreement is obtained with the observed waveshapes, although the experimental traces show a lag at the edges which the model would not predict.

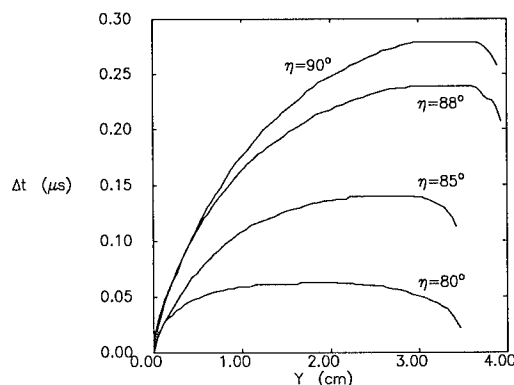


FIGURE 3. EXPERIMENTAL ARRIVAL TIMES

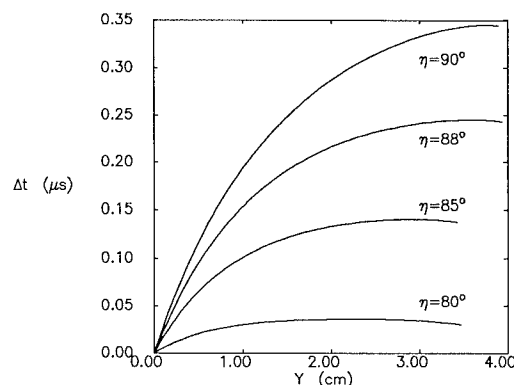


FIGURE 4. W-B-L ARRIVAL TIMES

### CONTROLLING ENERGY RELEASE

#### Overview

In an expanding wave where the sonic surface is a finite distance behind the leading shock, some of the energy released is used to balance the effect of divergence. Hence the wavespeed increases as the curvature decreases. Reaction at varying states alters the amount of energy available for driving material adjacent to the explosive, which can be regarded as a dependence of the products EOS on the wavefront curvature.

The release of chemical energy behind the detonation wave is modelled by considering a quasi-steady solution of the reactive flow equations for a spherically diverging wave. This is based on previous unpublished work by A F Devonshire, which is



related to that of Eyring et al.<sup>8</sup> A simple form is used for the EOS of partially-reacted explosive.<sup>9</sup>

To avoid ambiguity, we define the 'detonation zone' as being the region between the leading shock and the sonic surface, and the 'reaction zone' as the region where the reaction rate is significant. The reaction zone of a curved detonation wave generally extends past the sonic surface. In a 1D detonation, the flow in the detonation zone is independent of the degree of confinement, whereas the flow behind is influenced by the boundary conditions, which can therefore affect the progress of the reaction.

Assuming that lateral flow can be neglected in the detonation zone, then flow is confined to the direction perpendicular to the wavefront. Given a rate law and an EOS for explosive and products in all stages of reaction, the conservation equations in spherical geometry can be used to determine a value of  $D$  which satisfies the condition of quasisteady flow for any given wavefront curvature. Conversely, an experimental  $D(K)$  relation and EOS can be used to determine a parameter in the rate law, enabling the chemical energy in the explosive to be released over a more realistic period in the improved model of programmed burn.

The Rankine-Hugoniot equations are solved to find the state immediately behind the leading shock of the detonation wave. This state defines the initial values for integrating the conservation equations and reaction parameter through the reaction zone. The process can be repeated with different rate laws, until a solution is obtained which produces a physically consistent sonic point.

A wide variety of reaction rates has been investigated. These range from simple forms, the rate being a function only of the distance behind or time from the leading shock, to types such as DAGMAR and Forest Fire.<sup>10</sup>

### Conservation Equations Through the Detonation Zone

The conservation equations can be regarded in slightly different ways, depending on whether the chemical energy release is considered as an external source dumping energy in a material or as an equation of state transformation giving a higher pressure in the detonation products for a given internal energy. Both approaches give the same result where

comparable, and the derivation below uses the latter approach.

In a frame stationary with respect to the detonation zone, the steady-state conservation equations take the form

$$\begin{aligned}\frac{dw}{dy} &= \frac{\sigma(\rho^2 \partial e / \partial \rho - p) - \rho w \partial e / \partial \lambda \cdot d\lambda / dy}{\rho^2 (c^2 - w^2) \partial e / \partial p} \\ \frac{dp}{dy} &= -\rho w \frac{dw}{dy} \\ \frac{d\rho}{dy} &= -\frac{\rho}{w} \left[ \frac{dw}{dy} + \sigma \right]\end{aligned}\quad (10)$$

where  $y$  is the space coordinate relative to the leading shock,  $w$  the relative particle velocity ( $D - u$  where  $u$  is the particle velocity in the laboratory frame),  $e$  the specific internal energy, and the symmetry switch  $\alpha$  is now 2 for spherical symmetry.  $\sigma = \alpha(D - w)/(r - y)$  is a curvature term, and  $r = 1/K$ .

### Behaviour at the Sonic Point

The denominator of  $dw/dy$  is identically zero at the sonic point. For the solution to remain physical this implies that the numerator of  $dw/dy$  must also tend to zero in the approach to the sonic point. Therefore, as Devonshire pointed out, the effects of curvature are exactly balanced by the energy release rate at the sonic point, so not all the explosive energy is available in the detonation zone.

Algorithms have been developed to determine  $D$  given an EOS, reaction rate and value of  $K$ , and to determine a reaction rate parameter given an EOS and value of  $D$  at some  $K$ . In both processes, values of the unknown parameter are found which bracket the correct value and lead to invalid Mach numbers on integration: either no sonic point, or an imbalance of the energy release rate and the curvature at the sonic point. The correct value is then found by bisection.

### Use In a Hydrocode

The advantage of the W-B-L model is its ability to calculate detonation without resolving the detonation zone in a hydrocode. The hydrocode uses programmed burn information to deduce the pressure in a mesh.

The traditional approach for a C-J wave has been to estimate the fraction of the mesh crossed by the detonation wave at any given time and return a geometrical average of the unreacted ( $p = 0$ ) and fully reacted states.

Approaches extending this concept to detonation with a known reaction rate are under active investigation. One possibility is to produce tables of pressure against position in the detonation zone, for a range of curvatures, and use this to deduce the average pressure in a mesh. A simpler approach is to perform a geometrical average of an unreacted (but compressed) state and a partially reacted state. As a first guess, the partially reacted state used has  $\lambda = \lambda_{\text{sonic}}$ , the fraction reacted at the sonic point, but this value may be altered empirically for particularly coarse meshes. Once the detonation wave has passed completely through a mesh, the reaction rate (or a simplified form of it) can be used explicitly for the final, slower portion of the reaction.

### A Full EOS

As stated, the energy release model requires an EOS covering unreacted explosive, products and intermediate states. Suitable versions have been developed for EOS of the perfect gas and Jones-Wilkins-Lee (JWL) forms. In the current hydrocode conventions, the initial internal energy  $e_0$  is equivalent to the specific detonation energy of the unshocked explosive, because a pressure multiplier is used to control detonation and so the unreacted EOS is not used.

For a simple unreacted EOS, we require that  $p = 0$  when  $e = e_0$  and  $\lambda = 0$ . This leads to a modified JWL EOS for a partially reacted explosive in which for simplicity the transition from solid to reaction products is assumed to take place at constant volume:

$$p = \omega \rho e + A \left[ 1 - \frac{\omega \rho}{R_1 \rho_0} \right] e^{-R_1 \rho_0 / \rho} + B \left[ 1 - \frac{\omega \rho}{R_2 \rho_0} \right] e^{-R_2 \rho_0 / \rho} - (1 - \lambda) \omega \rho (e_0 + e^*) \quad (11)$$

where  $e^*$  is the region between the principal adiabat and the  $p = 0$  line (Fig. 5),

$$e^* = \frac{1}{\omega \rho_0} \left[ A \left( 1 - \frac{\omega}{R_1} \right) e^{-R_1} + B \left( 1 - \frac{\omega}{R_2} \right) e^{-R_2} \right]. \quad (12)$$

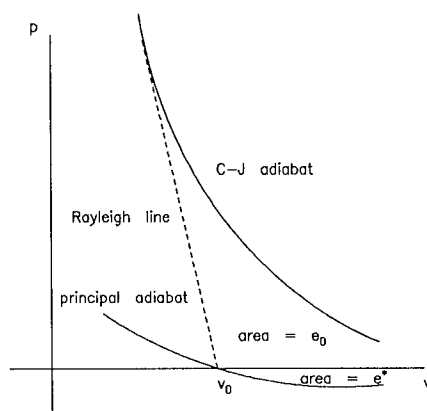


FIGURE 5. EOS FOR CONSTANT-VOLUME REACTION

### Application to EDC35

EDC35 is a TATB-based IHE of density  $\rho_0 = 1.904 \text{ g cm}^{-3}$ , whose products behind a C-J detonation are modelled by a JWL EOS with the following parameters:

$$\begin{aligned} e_0 &= 0.04 \text{ Mb cm}^3 \text{ g}^{-1} \\ p_{\text{CJ}} &= 0.319 \text{ Mb} \\ R_1 &= 3.8218 \\ R_2 &= 1.0 \\ \omega &= 0.3 \\ v_{\text{CJ}} &= 0.38089 \text{ cm}^3 \text{ g}^{-1} \\ A &= 4.7103 \text{ Mb} \\ B &= 2.3178 \times 10^{-2} \text{ Mb} \end{aligned}$$

The form of reaction rate with the most interesting properties encountered so far is a type of Forest Fire law:<sup>10</sup>

$$\dot{\lambda} = \dot{\lambda}_0 (1 - \lambda) \left( \frac{p}{p_{\text{ref}}} \right)^r \left[ 1 + f \left( \frac{p}{p_{\text{ref}}} \right)^s \right] \quad (13)$$

Approximate parameter values (not tuned to TATB) were taken from Johnson, Tang and Forest.<sup>10</sup>

$$\begin{aligned} r &= 2.85 \\ s &= 4.15 \\ f &= 4.2 \times 10^{-4} \\ p_{\text{ref}} &= 0.035 \text{ Mb} \end{aligned}$$

Values of  $\dot{\lambda}_0$  were found to match the  $D(K)$  relation of Table 1. To fasten on a single reaction rate, the

value of  $\lambda_0$  was chosen corresponding to the approximate curvature of the wavefront in the experiment used to derive the  $D(K)$  relation. This curvature was  $K = 0.1 \text{ cm}^{-1}$  (i.e.  $D = 0.769 \text{ cm } \mu\text{s}^{-1}$ ), giving  $\lambda_0 = 5.906 \times 10^{-3} \text{ } \mu\text{s}^{-1}$ .

The  $D(K)$  relation derived from this rate law demonstrates apparent detonation failure (Fig. 6). (Most of the other rate laws gave convex-down  $D(K)$  relations for the parameters chosen, which did not predict detonation failure.) Failure occurs at too small a curvature for this to be an accurate representation of the behaviour of EDC35, but it seems likely that altering the other parameters in the reaction rate will produce a more realistic  $D(K)$  relation. (The waveshape experiment did not produce curvatures sufficiently near failure to normalise the rate law to give a realistic failure curvature.) Figs 7 and 8 show the variation of the detonation zone length and  $\lambda_{\text{sonic}}$  with curvature.

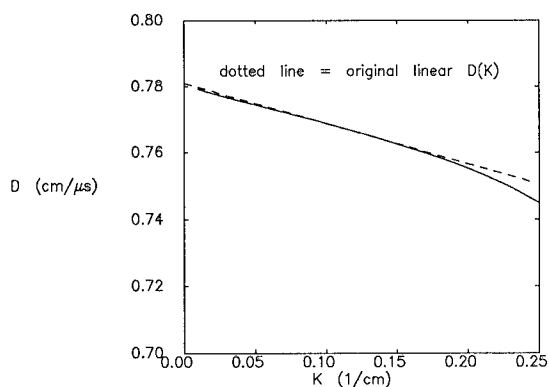


FIGURE 6.  $D(K)$  FROM A FOREST FIRE RATE

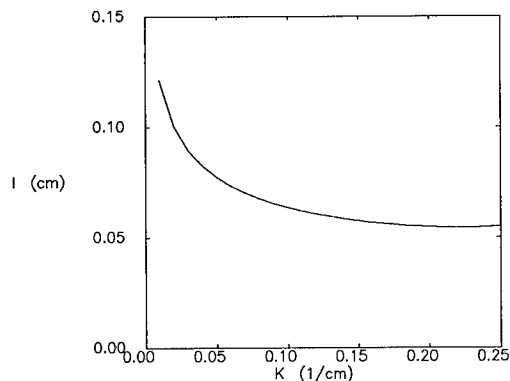


FIGURE 7. DETONATION ZONE LENGTH

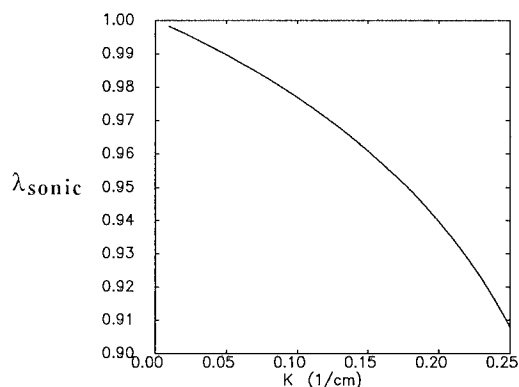


FIGURE 8. VARIATION OF  $\lambda_{\text{sonic}}$

## CONCLUSIONS

The W-B-L wave propagation theory has been extended for detonation waves in 3D. The 2D theory has been modified to predict how close a detonation wave will be to a steady shape at the end of a long rod or slab of explosive. This has applications in designing experiments to determine parameters for the wave propagation theory.

Further experimental evidence has confirmed the predictive capabilities of the model, by successful calculation of the waveshapes observed by Aveillé et al at the ends of TATB charges.

An energy release model has been developed for the explosive behind the detonation wave. Reaction rate laws can be calculated given an EOS for the explosive and reaction products, and a  $D(K)$  relation in the explosive. This theory allows more consistent use of the model in hydrocodes.

## FUTURE WORK

Further experiments are due to be performed to calculate a more accurate  $D(K)$  relation for the TATB-based explosive EDC35. These will include rods predicted to give much more stable waveshapes, and also designs such as the logosphere enabling more direct measurements to be made. Comparisons will be made between slabs and cylinders of the same explosive.

Efforts will be made to find a unique reaction rate law for EDC35. Hydrocode calculations will be

made to determine the effects of the energy release model for metal moving in cylinder test and other geometries.

## ACKNOWLEDGEMENTS

The authors wish to acknowledge the contributions of J Aveillé in providing data on experiments performed at the CEA, and the reviewers for their helpful suggestions.

## REFERENCES

1. Bdzil, J. B.; Fickett, W.; and Stewart, D. S., "Detonation Shock Dynamics: A New Approach to Modeling Multi-Dimensional Detonation Waves", in *Proceedings of the 9th Symposium (International) on Detonation*, 1989, pp 730-742.
2. Lambourn, B. D.; and Swift, D. C., "Application of Whitham's Shock Dynamics Theory to the Propagation of Divergent Detonation Waves", in *Proceedings of the 9th Symposium (International) on Detonation*, 1989, pp 784-797.
3. Whitham, G. B., *Linear and Non Linear Waves*, Wiley - Interscience, 1974, pp 263-311.
4. Lambourn, B. D.; and Wright, P. W., "Mach interactions", in *Proceedings of the 4th Symposium (International) on Detonation*, 1965, pp 142-152.
5. Bdzil, J. B., "Steady-state two-dimensional detonation", *Journal of Fluid Mechanics*, Vol. 108, 1981, pp 195-226.
6. Aveillé, J.; Carion, N.; Vacellier, J; and Servas, J. M.; "Experimental and Numerical Study of Oblique Interactions of Detonation Waves with Explosive/Solid Material Interfaces", in *Proceedings of the 9th Symposium (International) on Detonation*, 1989, pp 842-852.
7. Aveillé, J.; Baconin, J.; and Zoé, J., "Experimental study of spherically diverging detonation waves", in *Proceedings of the 8th Symposium (International) on Detonation*, 1985, pp 151-156.
8. Eyring, H.; Powell, R. E.; Duffey, G. H.; and Parlin, R. B., *Chemical Review*, Vol. 45, No. 69, 1949.
9. Fickett, W.; and Davis, W. C., *Detonation*, University of California, 1979.
10. Johnson, J. N.; Tang, P. K.; and Forest, C. A., "Shock-wave initiation of heterogeneous reactive solids", *Journal of Applied Physics*, Vol. 57, No. 9, 1985.

© British Crown Copyright 1993 /MOD

Published with the permission of the Controller of Her Britannic Majesty's Stationary Office

---

## DISCUSSION

DR. R. SARRACINO  
AECI Explosives, Modderfontain, South Africa

I have a question about your curvature. There's no unambiguous way to get a suitable curvature for this application in three dimensions (i.e., the Gaussian curvature of a cylinder is zero, whereas clearly VOD would depend on radius, in the case of cylindrical detonation). What did you use for curvature?

## REPLY BY DAMIAN SWIFT:

We use the mean curvature. If you assume that curvature-slowness is caused by the fact that energy released some way back in the reaction zone is spread over a different area by the time it reaches the leading shock, the mean curvature is the appropriate quantity, because it measures this change of area.

# AN APPLICATION OF VARIABLE METRIC NONLINEAR OPTIMIZATION TO THE PARAMETERIZATION OF AN EXTENDED THERMODYNAMIC EQUATION OF STATE

E.L. Baker  
U.S. Army, ARDEC  
Picatinny Arsenal, NJ 07806-5000

Variable metric nonlinear optimization was applied to the parameterization of an extended detonation products thermodynamic equation of state applicable to problems involving overdriven detonation and material acceleration. The equation of state was formulated to adequately describe the high pressure regime produced by overdriven detonation, and yet retain the moderate pressure expansion behavior required for standard material acceleration modeling. In addition, the form was chosen to maintain computational speed and robustness, while reproducing the predicted behavior with a minimum of constants. Nonlinear optimization was used to parameterize the equation of state to both cylinder test results and thermochemical calculations. Empirically based parameters were developed for TATB, LX-17, PETN, TNT, Octol, LX-14 and PAX2A that closely reproduce both cylinder test results, as well as BKWR predicted overdriven detonation behavior. The Gruneisen parameter was parameterized to the BKWR predicted behavior over the same specific volume range. Methodology, equation of state parameter sets, and modeling comparison to available experimental results are presented. The equation of state has been implemented and used extensively in the high rate continuum modeling programs DYNA2D, DYNA3D and CALE.

## INTRODUCTION

Many modern high explosive applications require continuum modeling (finite element, finite difference, and SPH) of explosives products behavior over a broad range of specific volume. Overdriven detonation requires a high pressure description of the products behavior above the Chapman-Jouguet state. Large detonation wave shaping and multiple point initiation are typical overdriven detonation applications. Material acceleration by contacting high explosives requires a moderate pressure description from the Chapman-Jouguet state to about seven volume expansions. Shaped charge jet formation and explosively formed penetrator acceleration are typical high explosive contact material acceleration applications. Near field blast applications require a low pressure description above seven volume expansions. Current thermodynamic equations of state used in continuum modeling programs are either parameterized to give agreement with thermochemical calculations<sup>16</sup> or empirical data.<sup>15,21</sup> Thermochemical calculations have proven to be very useful for the prediction of explosive products properties,

particularly near and above the Chapman-Jouguet state.<sup>4,17</sup> Unfortunately, they often do not reproduce explosives experimental detonation state or products expansion behavior accurately enough for typical continuum modeling applications. Although considerable work has been done on overdriven detonation equation of state prediction and parameterization<sup>6,10,11,13,14</sup>, currently used thermodynamic equations of state for warheads design (JWL, Wilkins) are normally parameterized to give agreement only with copper cylinder explosive expansion experiments and are not commonly parameterized for high pressures above the Chapman-Jouguet state or lower pressure behavior above seven volume expansions. Experimentation<sup>9</sup> and comparison with thermochemical calculations<sup>2-3</sup> have demonstrated that a poor description of the high pressure region often exists.

## EQUATION OF STATE

In order to achieve a suitable thermodynamic equation of state for both overdriven and high

explosive contact material acceleration, an appropriate equation of state form was derived.<sup>2</sup> The equation of state form was chosen so as to adequately describe the high pressure regime produced by overdriven detonation, and yet retain the moderate pressure expansion behavior required for standard material acceleration modeling. To this end, the derived form is based on the Jones-Wilkins-Lee (JWL) equation of state due to its computational speed and robustness, as well as an asymptotic approach to an ideal gas at high expansions. Additional exponential terms and a variable Gruneisen parameter have been added to more appropriately describe the physical behavior of the detonation products including the high pressure region above the Chapman-Jouguet state. The resulting equation of state form, named Jones-Wilkins-Lee-Baker (JWLb), is

$$P = \sum_i A_i \left(1 - \frac{\lambda}{R_i V}\right) e^{-R_i V} + \frac{\lambda E}{V} + C \left(1 - \frac{\lambda}{\omega}\right) V^{-(\omega+1)} \quad (1)$$

where,

$$\lambda = \sum_i (A_{\lambda i} V + B_{\lambda i}) e^{-R_{\lambda i} V} + \omega \quad (2)$$

Some important characteristics of the equation of state are that the Gruneisen Parameter,  $\lambda$  is represented as an analytic function of specific volume,  $V$ .  $\lambda + 1$  approaches a constant adiabatic gamma,  $\left. \frac{V}{P} \frac{\partial P}{\partial V} \right|_s = \omega + 1$  for large  $V$ , so that ideal gas behavior is asymptotically approached. The principle isentrope description,

$$P_s = \sum_i A_i e^{-R_i V} + C V^{-(\omega+1)} \quad (3)$$

is essentially identical to JWL, with the exception of an increased number of exponential terms. The Gruneisen parameter functional form is based on the predicted Gruneisen parameter behavior along the principle isentrope and reactive Hugoniot from revised Becker-Kistiakowsky-Wilson (BKWR) and Jacobs-Cowperthwaite-Zwisler (JCZ3) equilibrium calculations.<sup>2-3</sup> The form was chosen to maintain computational speed and robustness, while reproducing the predicted behavior with a minimum of constants. The JWLb form has the disadvantage that an increased number of highly nonlinear equation of state parameters are required. This is a common modeling problem in which desired functional forms

are often highly nonlinear with a large enough number of parameters to make parameterization relatively difficult. In addition, equality and inequality relationships are often imposed on the parameterization. Detonation products equations of state are normally parameterized with an equality constraint to produce a chosen Chapman-Jouguet (CJ) state. As a result, mathematical modeling descriptions are often chosen for their ease of parameterization, rather than their applicability and computational robustness. JWL is often parameterized by hand, due to the small number of equation of state constants. This type of parameterization can be very time consuming and nearly impossible with a large number of parameters.

## NONLINEAR OPTIMIZATION

Within the last two decades, there has been a dramatic increase in the efficiency and reliability of optimization methods for almost all discrete parameter problem categories.<sup>8</sup> Improvements of discrete nonlinear parametric optimization methods have been primarily based on the rigorous application of optimization theory,<sup>20</sup> as well as an increased utilization of numerically stable linear algebraic methods.<sup>7</sup> In particular, variable metric sequential quadratic programming has proven to be a particularly successful method for discrete parametric optimization of nonlinear systems.<sup>19</sup> This method successively minimizes a quadratic subproblem with linearized constraints. The quadratic cost function matrix (variable metric matrix) is updated for each quadratic subproblem. Currently, the most widely accepted variable metric matrix update is the Broyden, Fletcher, Goldfarb and Shanno (BFGS) update.<sup>7</sup> In order to overcome the problem of equation of state parameterization in a generalized fashion, variable metric nonlinear optimization has been incorporated into an equation of state parameterization program.<sup>1</sup> The parameterization program uses a BFGS variable metric matrix update along with a merit function based on the work of Powell<sup>18</sup> in order to efficiently address equality and inequality constraints. The nonlinear optimization has been used to parameterize the equation of state to both cylinder test results and thermochemical calculations.

## EMPIRICAL BASED PARAMETERS

Empirically based parameters were developed for TATB, LX-17, PETN, TNT, Octol, LX-14 and

PAX2A, that closely reproduce both cylinder test results (within 1% of experimental wall velocities) as well as BKWR predicted overdriven detonation behavior. The principle isentrope was parameterized using a least squares cost function combining predicted cylinder expansion velocities in the 2-7 volume expansion regime, and BKWR predicted pressure above the CJ state to 1 Mbar. The Gruneisen parameter was parameterized to the BKWR predicted behavior over the entire specific volume range. The CJ state ( $DCJ$ ,  $PCJ$ ) and  $E_0$  were used as equality constraints. The cylinder expansion velocities were predicted using an analytic cylinder test model<sup>1</sup> and verified using the DYNA2D Lagrangian finite element modeling program. Figure 1 presents a DYNA2D cylinder expansion computational mesh and material boundaries at 6  $\mu$ s intervals.

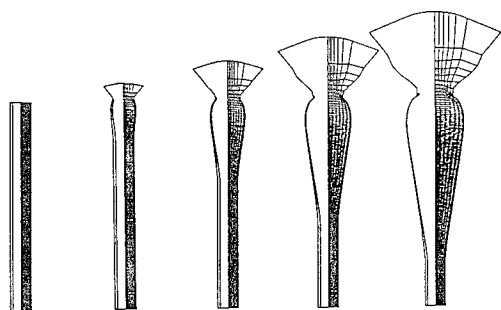


**FIGURE 1. DYNA2D CYLINDER EXPANSION COMPUTATIONAL MESH AND MATERIAL BOUNDARIES AT 6  $\mu$ S INTERVALS**

Table 1 presents the resulting JWLb parameter sets. Although the equation of state form has been implemented using five exponential terms, it has been found that three exponential terms are normally adequate to describe the principle isentrope over both the high pressure region above the Chapman-Jouguet state and the moderate pressure expansion region. It was found that the JWL form (two exponential terms) could not closely reproduce both the cylinder test behavior as well as the BKWR overdriven behavior for PAX2A and Octol 70/30. Parameterization using the two term form was not investigated for the other explosives. Figure 2 presents a comparison of Octol JWLb, BKWR, and commonly used JWL<sup>5</sup> predicted principle isentropes and reactive Hugoniot above the Chapman-Jouguet state. Although the Gruneisen parameter behavior was more accurately tailored using an increased number of exponential terms, a single exponential parameterization is presented as

little quantitative empirical data exists for Gruneisen parameter values and significant differences of Gruneisen parameter values exist between calculations using different thermochemical equations of state.<sup>1</sup> Figure 3 presents a comparison of the cylinder expansion radius time histories finite element results to experimental data. Table 2 presents a comparison of cylinder test velocities at 2, 4, and 7 inside area expansions for the empirical based JWLb finite element calculations to experimental results.

**TABLE 1. EMPIRICALLY BASED JWLb PARAMETER SETS**

	TATB	LX-17	PETN
$\rho_0$ (g/cc)	1.800	1.908	1.765
$E_0$ (Mbar)	.06400	.05628	.10530
$DCJ$ (cm/ $\mu$ s)	.7478	.7629	.8277
$PCJ$ (Mbar)	.2629	.2809	.3105
A1 (Mbar)	550.01	749.64	549.98
A2 (Mbar)	4.2564	3.9475	5.3127
A3 (Mbar)	.011369	.016852	.11850
R1	16.571	14.936	14.739
R2	3.8813	3.6460	4.1972
R3	.51558	.55551	1.1182
C (Mbar)	.0069666	0.0000	.010025
$\omega$	.37565	.35171	.25479
$A\lambda_1$	.97083	0.0000	1.3430
$B\lambda_1$	.021173	.51503	-.25479
$R\lambda_1$	1.0319	.13784	1.0001

	TNT	Octol 70/30	LX-14	PAX2A
$\rho_0$	1.631	1.803	1.821	1.770
$E_0$	.06739	.09370	.09708	.090798
$DCJ$	.6941	.8410	.8774	.85173
$PCJ$	.1998	.3252	.3529	.32416
A1	549.96	549.97	210.84	909.14
A2	4.3679	6.3704	3.1503	10.195
A3	.030198	.038937	.009061	.76191
R1	18.647	16.299	11.500	16.266
R2	4.3230	4.1487	3.15212	5.6415
R3	.70314	.54876	.28229	2.1540
C	.005310	.0046251	.0060900	.011325
$\omega$	.20807	.27859	.38547	.36989
$A\lambda_1$	1.4346	1.5539	1.4577	1.5621
$B\lambda_1$	-.20807	-.27859	-.38547	-.27665
$R\lambda_1$	1.0025	1.0920	1.1639	1.0841

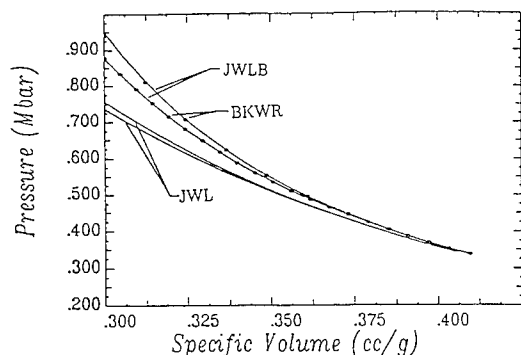


FIGURE 2. COMPARISON OF OCTOL JWLB, BKWR, AND COMMONLY USED JWL PREDICTED PRINCIPLE ISENTROPES AND REACTIVE HUGONITS ABOVE THE CHAPMAN-JOUQUET STATE

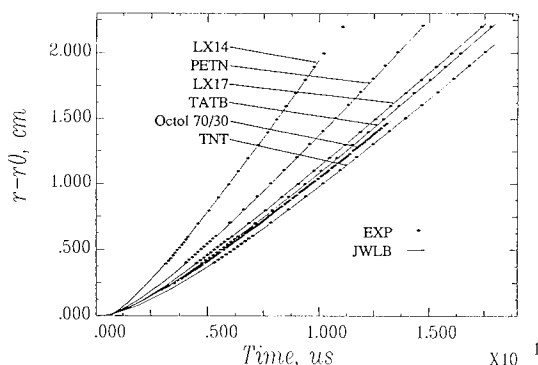


FIGURE 3. CYLINDER EXPANSION RADIUS TIME HISTORIES COMPARISON OF THE EMPIRICAL BASED JWLB CALCULATED FINITE ELEMENT RESULTS TO EXPERIMENTAL DATA

#### THERMOCHEMICAL BASED PARAMETERS

The nonlinear optimization was also used to parameterize the equation of state form for LX-17, PETN, and Octol 70/30 directly to TIGER thermochemical calculations (BKWR and JCZ3) in order to compare the different predicted products behavior. Table 3 presents the resulting JWLB parameter sets. Figures 4-6 present comparisons of the cylinder expansion radius time histories of the calculated results to experimental data. Table 4 presents a comparison of cylinder test velocities at 2, 4, and 7 inside area expansions for the empirical, BKWR and JCZ3 based JWLB finite element calculations to experimental results.

TABLE 2. COMPARISON OF CYLINDER TEST VELOCITIES AT 2, 4, AND 7 INSIDE AREA EXPANSIONS FOR THE EMPIRICALLY BASED JWLB FINITE ELEMENT CALCULATIONS TO EXPERIMENTAL RESULTS

TATB 1" LLNL Cylinder Test, Full Wall		
Area Ratio $A_{in}/A_{0in}$	Exp. Vel. cm/ $\mu$ s	JWLB Vel. cm/ $\mu$ s
2.0005	.1216	.1227
4.1605	.1392	.1391
6.8288	.1448	.1449

LX-17 1" LLNL Cylinder Test, Full Wall		
Area Ratio $A_{in}/A_{0in}$	Exp. Vel. cm/ $\mu$ s	JWLB Vel. cm/ $\mu$ s
2.0005	.1296	.1284
4.1605	.1412	.1417
6.8288	.1467	.1455

PETN 1" LLNL Cylinder Test, Full Wall		
Area Ratio $A_{in}/A_{0in}$	Exp. Vel. cm/ $\mu$ s	JWLB Vel. cm/ $\mu$ s
2.0005	.1512	.1508
4.1605	.1703	.1712
6.8288	.1782	.1774

TNT 1" LLNL Cylinder Test, Full Wall		
Area Ratio $A_{in}/A_{0in}$	Exp. Vel. cm/ $\mu$ s	JWLB Vel. cm/ $\mu$ s
2.0005	.1147	.1136
4.1605	.1325	.1338
6.8288	.1399	.1395

Octol 70/30 3/4" ARDEC Cylinder Test		
Area Ratio $A_{in}/A_{0in}$	Exp. Vel. cm/ $\mu$ s	JWLB Vel. cm/ $\mu$ s
2	.1062	.1073
4	.1284	.1284
7	.1371	.1374

LX-14 1" LLNL Cylinder Test, Half Wall		
Area Ratio $A_{in}/A_{0in}$	Exp. Vel. cm/ $\mu$ s	JWLB Vel. cm/ $\mu$ s
1.9280	.2034	.2016
3.9414	.2295	.2286
6.5295	.2387	.2398



TABLE 3. THERMOCHEMICAL BASED JWLb PARAMETER SETS

BKWR			
	LX-17	PETN	Octol
$\rho_0$ (g/cc)	1.908	1.765	1.803
$E_0$ (Mbar)	.05628	.1053	.09370
$D_{CJ}$ (cm/ $\mu$ s)	.7957	.8336	.8411
$P_{CJ}$ (Mbar)	.2809	.3105	.3252
$A_1$ (Mbar)	2338.1	549.73	2875.8
$A_2$ (Mbar)	9.0271	44.796	9.4178
$A_3$ (Mbar)	.10899	.99314	.27198
$R_1$	17.855	42.956	18.634
$R_2$	4.7661	8.2640	5.0834
$R_3$	1.1386	2.1161	1.2746
$C$ (Mbar)	0.0000	.008670	.002689
$\omega$	.35171	.25479	.27859
$A_{\lambda 1}$	0.0000	1.3430	1.5539
$B_{\lambda 1}$	.51503	-.25479	-.27859
$R_{\lambda 1}$	.13784	1.0001	1.0920
JCZ3			
	LX-17	PETN	Octol
$\rho_0$ (g/cc)	1.908	1.765	1.803
$E_0$ (Mbar)	.05911	.1075	.09616
$D_{CJ}$ (cm/ $\mu$ s)	.7778	.8156	.8258
$P_{CJ}$ (Mbar)	.2398	.2789	.2864
$A_1$ (Mbar)	3480.9	549.65	5193.9
$A_2$ (Mbar)	9.9262	60.521	20.678
$A_3$ (Mbar)	.0044231	.98035	.39089
$R_1$	17.565	44.366	19.807
$R_2$	4.7486	8.5767	6.3451
$R_3$	.18067	2.2736	1.5402
$C$ (Mbar)	.0016839	.012964	.004413
$\omega$	.12321	.25616	.17443
$A_{\lambda 1}$	.54670	1.8003	2.2765
$B_{\lambda 1}$	.61518	-.25616	-.17443
$R_{\lambda 1}$	.66185	1.2644	1.1892

TABLE 4. COMPARISON OF CYLINDER TEST VELOCITIES AT 2, 4, AND 7 INSIDE AREA EXPANSIONS FOR THE EMPIRICAL, BKWR, JCZ3, AND PANDA BASED JWLb FINITE ELEMENT CALCULATIONS TO EXPERIMENTAL RESULTS

LX-17 1" LLNL Cylinder Test, Full Wall			
Area Ratio $A_{in}/A_{0in}$	Exp. Vel. cm/ $\mu$ s	BKWR Vel. cm/ $\mu$ s	JCZ Vel. cm/ $\mu$ s
2.0005	.1296	.1300	.1025
4.1605	.1412	.1436	.1173
6.8288	.1467	.1454	.1247

PETN 1" LLNL Cylinder Test, Full Wall			
Area Ratio $A_{in}/A_{0in}$	Exp. Vel. cm/ $\mu$ s	BKWR Vel. cm/ $\mu$ s	JCZ Vel. cm/ $\mu$ s
2.0005	.1512	.1617	.1495
4.1605	.1703	.1755	.1659
6.8288	.1782	.1805	.1726

Octol 70/30 3/4" ARDEC Cylinder Test			
Area Ratio $A_{in}/A_{0in}$	Exp. Vel. cm/ $\mu$ s	BKWR Vel. cm/ $\mu$ s	JCZ Vel. cm/ $\mu$ s
2	.1062	.1192	.1141
4	.1284	.1372	.1286
7	.1371	.1408	.1328

FIGURE 4. LX-17 CYLINDER EXPANSION RADIUS TIME HISTORIES COMPARISON OF THE THERMOCHEMICAL BASED JWLb FINITE ELEMENT CALCULATED RESULTS TO EXPERIMENTAL DATA

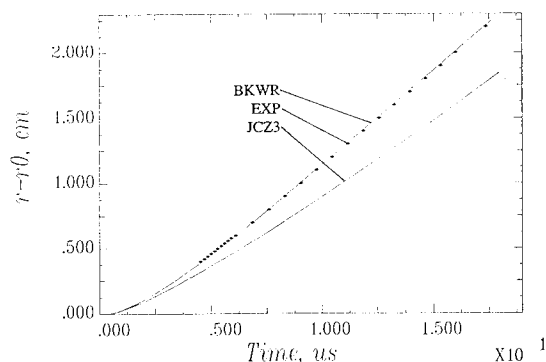
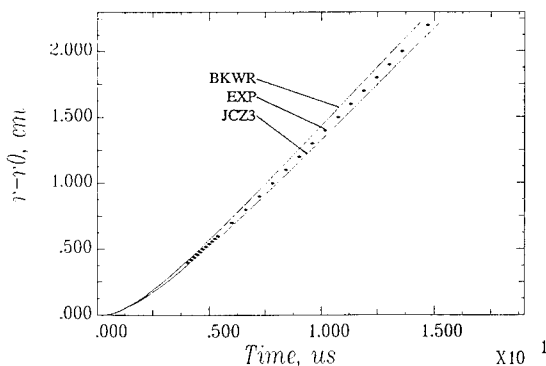
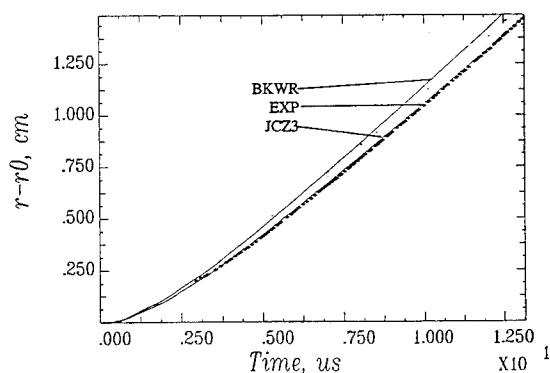


FIGURE 5. PETN CYLINDER EXPANSION RADIUS TIME HISTORIES COMPARISON OF THE THERMOCHEMICAL BASED JWLb FINITE ELEMENT CALCULATED RESULTS TO EXPERIMENTAL DATA





**FIGURE 6. OCTOL 70/30 CYLINDER EXPANSION RADIUS TIME HISTORIES COMPARISON OF THE THERMOCHEMICAL BASED JWLb FINITE ELEMENT CALCULATED RESULTS TO EXPERIMENTAL DATA**

The thermochemical calculations generally did quite well at predicting detonation velocities, with the exception of the LX-17 BKWR predicted overdriven detonation velocity. Although the BKWR LX-17 predicted detonation velocity is 4.3% higher than the experimental value, the BKWR based LX-17 predicted cylinder test velocities are in excellent agreement with the experimental results. The BKWR based calculations over predict the late time PETN and Octol 70/30 cylinder test velocities by 1.3% and 2.7% respectively. The JCZ based cylinder test calculations are in generally less agreement with the experimental results, under predicting late time cylinder velocities by 15.0%, 3.1%, and 3.1% for LX-17, PETN, and Octol 70/30 respectively. Finally, it is interesting to note that JCZ based Octol 70/30 cylinder test radius time history is in relatively good agreement to the experimental results due to the over prediction of cylinder test velocities at early volume expansions, and under prediction of cylinder test velocities at later volume expansions.

## CONCLUSIONS

The application of a BFGS variable metric sequential quadratic programming algorithm to detonation products thermodynamic equation of state parameterization has contributed significantly to the conventional explosives technology base. An extended thermodynamic equation of state (JWLb) has resulted with improved agreement to empirical cylinder test results and overdriven detonation thermochemical equation of state calculations. JWLb

has been implemented and used extensively in the high rate continuum modeling programs DYNA2D, DYNA3D and CALE. The generalized JWLb equation of state parameterization has allowed an investigation of the BKWR and JCZ3 thermochemical equilibrium equations of state using finite element modeling and existing cylinder test data. These results, as well as previous investigation by Kury and Souers<sup>12</sup>, indicate that some formal optimization of thermochemical equation of state parameters may lead to improved quantitative predictive capabilities. Future high explosives detonation products thermodynamic equation of state work will concentrate on quantitative agreement with empirical overdriven detonation data and high expansion (blast) behavior, while maintaining empirical agreement in the moderate pressure regime.

## REFERENCES

1. Baker, E.L., *Modeling and Optimization of Shaped Charge Liner Collapse and Jet Formation*, ARAED-TR-92019, Jan 1993, Picatinny Arsenal, NJ.
2. Baker, E.L., *An Explosives Products Thermodynamic Equation of State Appropriate for Material Acceleration and Overdriven Detonation: Theoretical Background and Formulation*, ARAED-TR-91013, July 1991, Picatinny Arsenal, NJ.
3. Baker, E.L. and J. Orosz, *Advanced Warhead Concepts: An Advanced Thermodynamic Equation of State for Overdriven Detonation*, ARAED-TR-91003, May 1991, Picatinny Arsenal, NJ.
4. Cowperthwaite, M. and W.H. Zwisler, *TIGER Computer Program Documentation*, SRI Publication No. Z106, 1973, Stanford Research Institute, Menlo Park, CA.
5. Dobratz, B.M., *LLNL Explosives Handbook: Properties of Chemical Explosives and Explosive Simulants*, UCRL-52997, 1981, University of California.
6. Fickett, W., *Detonation Properties of Condensed Explosives Calculated with an Equation of State Based on Intermolecular Potentials*, Los Alamos Scientific Laboratory Report, LA-2712, 1962.
7. Gill, P.E. et al., "Model Building and Practical

- Aspects of Nonlinear Programming.", *Computational Programming*, NATO ASI Series, Vol. F15, Springer-Verlag, Berlin, 1985.
8. Gill, P.E., W. Murray, and M.H. Wright, *Practical Optimization*, Academic Press, London., 1981.
  9. Green, L.G., C.M. Tarver, and D.J. Erskine, *Reaction Zone Structure in Supracompressed Detonating Explosives*, UCRL-101862, 1989, University of California.
  10. Green, L.G., E.L. Lee, D. Breithaupt and J. Walton, *Shock Waves in Condensed Matter--1987*, S.C. Schmidt and N.C. Holmes, Eds. Elsevier Science Publishers B. V., 1988, p. 507.
  11. Hornig, H.C., E.L. Lee, M. Finger and J. Kurrle, "Equation of State of Detonation Products," in *Proceedings, 5th Symposium (International) on Detonation*, ACR-184 Office of Naval Research, Pasadena, CA., 18-21 Aug. 1970.
  12. Kury, J.W. and C. Souers, *How Accurate is TIGER?*, private communication, LLNL, 1992.
  13. Lee, E.L., M. Van Thiel, L.G. Green and A. Mitchell, *Shock Waves in Condensed Matter--1983*, J.R. Asay, R.A. Graham and G.K. Straub, Eds., Elsevier Science Publishers B. V., 1984, p. 617.
  14. Lee, E.L. and H.C. Hornig, "Equation of State of Detonation Product Gases," in *Proceedings, 12th Symposium (International) on Combustion*, 1969, p. 493.
  15. Lee, E.L., H.C. Hornig, and J.W. Kury, *Adiabatic Expansion of High Explosive Detonation Products*, UCRL-50422, 1968, University of California.
  16. Mader, C.L., *Numerical Modeling of Detonations*, University of California Press, 1979.
  17. Mader, C.L., *FORTTRAN BKW - A Code for Computing the Detonation Properties of Explosives*, LA-3704, 1967, University of California.
  18. Powell, M.J.D., "A Fast Algorithm for Nonlinearly Constrained Optimization Calculations," in *Proceedings, Biennial Conference*, Dundee 1977, Lecture Notes in Mathematics 630, Springer-Verlag, 1978.
  19. Schittkowski, K., *More Test Examples for Nonlinear Programming Codes*, Lecture Notes in Economics and Mathematical Systems 188, Springer-Verlag, 1987.
  20. Vincent, T.L. and W.J. Grantham, *Optimality in Parametric Systems*, John Wiley & Sons, New York, 1981.
  21. Wilkins, M.L., *The Equation of State of PBX 9404 and LX04-01*, UCRL-7797, 1964, University of California.

## DIRECT MONTE CARLO SIMULATION OF THE CHEMICAL EQUILIBRIUM COMPOSITION OF DETONATION PRODUCTS

M. S. Shaw  
Group T-14, Mail Stop B214  
Los Alamos National Laboratory  
Los Alamos, New Mexico 87545

A new Monte Carlo simulation method has been developed by the author which gives the equilibrium chemical composition of a molecular fluid directly. The usual NPT ensemble (isothermal-isobaric) is implemented with  $N$  being the number of atoms instead of molecules. Changes in chemical composition are treated as correlated spatial moves of atoms. Given the interaction potentials between molecular products, "exact" (with statistical error  $\approx 1\%$ ) EOS points including the equilibrium chemical composition can be determined from the simulations. This method is applied to detonation products at conditions in the region near the Chapman-Jouguet state. For the example of NO, it is shown that the CJ detonation velocity can be determined to a statistical uncertainty of a few meters per second. A rather small change in cross potentials is shown to shift the chemical equilibrium and the CJ conditions significantly.

### INTRODUCTION

The equation of state (EOS) of high explosives detonation products is a crucial part of any calculation of the behavior of reacting explosives and its effect on adjacent inert materials. In principle, one could calculate an *ab initio* EOS by first using quantum mechanics methods for the potentials between molecular products and second using statistical mechanics for the resulting EOS given these potentials. The first step is limited by the accuracy of available quantum mechanics methods and the required computer time. Where available, these potentials are qualitatively accurate rather than quantitative. Given an accurate method for the second step of statistical mechanics, however, the potentials can be refined from the evaluation of experimental data.

This second step is typically evaluated using thermodynamic perturbation theories. For a single molecular species interacting through a spherical potential, there are several quantitative methods in use. The precision for these methods is not well characterized for multiple species mixtures such as occur in detonation products. In particular, equilibrium

chemical composition and possible fluid-fluid phase segregations can have substantial influence on the total EOS of these mixtures. In addition to approximate perturbation theories, there are simulation methods such as Monte Carlo and molecular dynamics which are essentially exact except for small (less than 1%) statistical error. These methods are well established for  $P$ ,  $V$ ,  $T$ , and  $E$ . However, quantities such as free energies, entropy, and chemical potentials are much more difficult to calculate. By standard simulation methods, the chemical equilibrium composition of a multi-component mixture would be nearly intractable.

The Metropolis Monte Carlo method<sup>1</sup> has been the basis for a wide variety of simulation methods for statistical mechanics. Some of the properties requiring the most effort to evaluate accurately are those related to free energies, e. g. chemical potentials, phase equilibrium, and chemical equilibrium. Recently, Panagiatopoulos<sup>2,3</sup> has introduced the Gibbs-ensemble Monte Carlo which allows for the evaluation of gas-liquid phase equilibria directly without the intermediate calculation of chemical potentials. Coker and Watts<sup>4</sup> and Kofke and Glandt<sup>5</sup> have used

modifications of Grand Canonical ensemble Monte Carlo to determine the chemical equilibrium composition of molecular fluid mixture. Sindzingre *et al.*<sup>6,7</sup> have shown that chemical potential differences can be evaluated more easily and accurately than individual chemical potentials through their 'difference method'. This generalization of a method by Shing<sup>8,9</sup> involves an interchange of one particle type for another rather than the addition or removal of a particle.

The author has recently developed a Monte Carlo simulation method<sup>10,11</sup> which allows for chemical equilibration as a natural part of a single simulation. (This method is designated  $N_{atoms}PT$  ensemble Monte Carlo since the number of atoms is held constant). Starting from an atomic rather than a molecular viewpoint, the equilibrium chemical composition of a molecular fluid mixture is evaluated without explicit calculation of chemical potentials. The partition function for this collection of atoms is rewritten as a sum over all molecular partition functions consistent with this set of atoms. That is, each set of atoms can be grouped into a variety of sets of molecules. Each set of molecules has its own molecular partition function which contributes to the total atomic partition function. That part of the atomic partition function which does not match up atoms into molecular groups is completely negligible for the region of interest.

For this particular study we will concentrate on a common approximation to the molecular partition function which treats each molecule as a single particle with internal degrees of freedom such as vibration and rotation. Instead of restricting this simulation to a given set of molecules, we allow for changes of in the set of molecules corresponding to an exchange of atoms. In the  $N_{atoms}PT$  ensemble Monte Carlo simulation, the chemical reaction steps are for an interchange of atoms between molecules. This step is treated like any other Monte Carlo step except that the acceptance probability is more complicated to evaluate. Note that this correlated move is like a "teleporter" from one likely configuration to another likely configuration. For most chemical reactions, the barrier between these two configurations is so high that a direct route involving a series of small changes in configuration would pass through very unlikely states. Hence, the correlated move allows for efficient sampling of a configuration space that has islands of locally high probability separated by regions of low probability. A further complication

is that of reactions involving a change in the number of molecules. The bookkeeping is simplified by fixing the total number of particles in the simulation, but allowing for a variable number of them to be noninteracting.

In this paper, the new method is applied to test cases of relevance to detonation products. One example is that of  $N_2 + O_2 \rightleftharpoons 2NO$  at 30GPa and 3000K. Variations in the cross-potentials (i.e. between unlike species) are shown to cause significant shifts in the equilibrium composition. For a 50/50 mix of N and O, a few percent shift in the distance scale of cross potentials leads to an equilibrium mole fraction of NO varying from 8-40%. On the other hand, the Lorentz-Berthelot rules for choosing cross potentials gives chemical equilibrium that is almost exactly reproduced by the ideal mixing approximation.

Another example is the accurate determination of the CJ state. This involves the simulation of  $N_2 + O_2 \rightleftharpoons 2NO$  for a variety of P and T near the CJ point. The Hugoniot is constructed by interpolation of appropriate EOS points. The Hugoniot is plotted in  $u_s$  vs.  $u_p$  space to search for the minimum shock velocity. The uncertainty of the detonation velocity from this method is shown to be a few meters per second. The effect of the cross potentials on the detonation velocity is shown to be significant.

## METHOD

The classical partition function for the atomic-canonical ensemble, with all atoms identical, is just

$$Q(N, V, T) = \frac{\Lambda^{-3N}}{N!} Z(N, V, T), \quad (1)$$

where N is the number of atoms,  $\Lambda$  is the de Broglie thermal wavelength and  $Z(N, V, T)$  is the configuration integral given by

$$Z(N, V, T) = \int \exp[-\beta U(\mathbf{r}_1, \dots, \mathbf{r}_N)] d\mathbf{r}_1 \dots d\mathbf{r}_N. \quad (2)$$

With A different types of atoms,  $N_i$  atoms of type i, and a total of  $N = \sum N_i$  atoms of all types, the partition function becomes

$$Q(N_1, N_2, \dots, N_A, V, T) = \frac{\Lambda_1^{-3N_1} \dots \Lambda_A^{-3N_A}}{N_1! \dots N_A!} Z(N_1, \dots, N_A, V, T). \quad (3)$$

Likewise, the partition function for a molecular mixture, within the approximation of separable molecular internal degrees of freedom, can be written as

$$Q(M_1, \dots, M_B, V, T) = \frac{Z(M_1, \dots, M_B, V, T)}{M_1! \dots M_B! \Lambda_1^{3M_1} \dots \Lambda_B^{3M_B}} q_1^{M_1} \dots q_B^{M_B} \quad (4)$$

The  $q_i$ 's are those parts of the partition function, such as vibration and rotation, which correspond to an isolated molecule. Eq. (4) is the restriction (e.g. the rigid rotor-harmonic oscillator approximation) of Eq. (3) to those atomic coordinates which correspond to the chosen molecular mixture composition. Now we can relax this restriction slightly to include any set of atomic coordinates which corresponds to any set of  $M_i$ 's which preserves the atomic compositions. Those atomic coordinates associated with each set of  $M_i$ 's can be separately approximated by Eq. (4) and the integral over all coordinates allowed by the relaxed restriction becomes a sum of the form

$$Q(N_1, \dots, N_A, V, T) = \sum' Q(M_1, \dots, M_B, V, T), \quad (5)$$

where  $\sum'$  indicates only those sets of  $M_i$ 's which preserve the set of  $N_i$ 's. Note that each set of  $M_i$ 's samples a different nonoverlapping region of atomic coordinate space due to the different sets of atomic correlations which define the molecules. The atomic-isothermal-isobaric ensemble partition function is

$$\Delta(N_1, \dots, N_A, P, T) = \int_0^\infty \exp(-\beta PV) Q(N_1, \dots, N_A, V, T) dV. \quad (6)$$

A Monte Carlo simulation can be made in these ensembles if a type of move between nonoverlapping regions can be found which is reasonably likely. This can be accomplished by interchanging atoms between molecules. In general, the number of molecules could change. Let  $M$  denote the total number of molecules, i.e.  $M = \sum_{i=1}^B M_i$ . A change of variables to a reduced distance  $s$  given by

$$\mathbf{s}_i = V^{-\frac{1}{3}} \mathbf{r}_i, \quad (7)$$

which has the normalization

$$\int d\mathbf{s}_i = 1. \quad (8)$$

Each molecular  $Q$  can be rewritten as

$$Q(M_1, \dots, M_B, V, T) = V^M \frac{q_1^{M_1} \dots q_B^{M_B}}{M_1! \dots M_B! \Lambda_1^{3M_1} \dots \Lambda_B^{3M_B}} \times \int \exp[-\beta U(\mathbf{s}_1, \dots, \mathbf{s}_M)] d\mathbf{s}_1 \dots d\mathbf{s}_M. \quad (9)$$

Since  $\int d\mathbf{s}_i = 1$ , integrations over  $\mathbf{s}_i$  were added such that  $M' \geq M$  for all molecular compositions of interest. Then Eq. (6) becomes

$$\Delta(N_1, \dots, N_A, P, T) = \int_0^\infty \int \sum' e^W dV d\mathbf{s}_1 \dots d\mathbf{s}_M \dots d\mathbf{s}_{M'}, \quad (10)$$

where

$$W(\mathbf{s}_1, \dots, \mathbf{s}_M, M_1, \dots, M_B) = -\beta[U(\mathbf{s}_1, \dots, \mathbf{s}_M) + PV] + M \ln V + \sum_{i=1}^B [M_i(\ln q_i - 3 \ln \Lambda_i) - \ln(M_i!)]. \quad (11)$$

Note that the first two terms on the righthand side are just those of an NPT ensemble with fixed molecular composition.

A Markov chain giving a limiting distribution proportional to  $e^W$  is then obtained<sup>1</sup> by accepting a move from state  $r$  to states  $s$  with the probability  $P_{r \rightarrow s}$  given by

$$P_{r \rightarrow s} = \text{Min}[1, \exp(W_s - W_r)]. \quad (12)$$

This assumes the usual condition  $p_{r \rightarrow s} = p_{s \rightarrow r}$  where the  $p$ 's indicate the unweighted probability of a move. It is sometimes convenient to relax this condition so that a low probability move is tried less often with a higher chance of being accepted when it is tried. We still want the net flow from  $r \rightarrow s$  to be the same as  $s \rightarrow r$  at the required distribution. The condition

$$\exp(W_r) p_{r \rightarrow s} P_{r \rightarrow s} = \exp(W_s) p_{s \rightarrow r} P_{s \rightarrow r}, \quad (13)$$

leads to the choice

$$P_{r \rightarrow s} = \text{Min}[1, \exp(W_s - W_r) p_{s \rightarrow r} / p_{r \rightarrow s}]. \quad (14)$$

We now have to evaluate the unweighted probabilities of moves for a specific scheme of choosing chemical reactions. The bookkeeping is somewhat easier to follow if we do not keep track of labels for a particular molecule. That is, only the set of positions,  $\mathbf{s}_i$ , and

corresponding molecule type,  $t_i$ , at each position are used to characterize a state. This indistinguishability of molecules of any given type cancels the  $\ln M_i!$  terms from Eq. (8) which were originally included to take into account indistinguishability in the usual labeled representation. For  $m$  types of molecules allowed in the simulation, let each positive integer through  $m$  denote one molecule type. Also, let  $t=0$  be a null particle which keeps track of the extra integration variables introduced in Eq. (9). A given chemical reaction can be written in the form

$$\sum_{t=0}^m \nu_t F_t \rightleftharpoons \sum_{t=0}^m \xi_t F_t, \quad (15)$$

where  $F_t$  is the formula for molecule  $t$ . For example, the reaction  $2CO + O_2 \rightleftharpoons 2CO_2$  would be characterized by  $F_0 = \text{null}$ ,  $F_1 = CO$ ,  $F_2 = O_2$ ,  $F_3 = CO_2$ ,  $\nu_0 = 0$ ,  $\nu_1 = 2$ ,  $\nu_2 = 1$ ,  $\nu_3 = 0$ ,  $\xi_0 = 1$ ,  $\xi_1 = 0$ ,  $\xi_2 = 0$ ,  $\xi_3 = 2$ . Likewise,  $N_2 + O_2 \rightleftharpoons 2NO$  would be characterized by  $F_0 = \text{null}$ ,  $F_1 = N_2$ ,  $F_2 = O_2$ ,  $F_3 = NO$ ,  $\nu_0 = 0$ ,  $\nu_1 = 1$ ,  $\nu_2 = 1$ ,  $\nu_3 = 0$ ,  $\xi_0 = 0$ ,  $\xi_1 = 0$ ,  $\xi_2 = 0$ ,  $\xi_3 = 2$ .

For a given simulation, one or more chemical reactions can be included at fixed or random intervals in the same way that occasional volume changes are included in a standard NPT ensemble simulation. For convenience, we pick a reaction at random after a fixed number of Monte Carlo steps. For a given state  $r$ , the number of ways to choose a forward reaction is given by

$$N_f(r) = \prod_{t=0}^m \binom{M_t}{\nu_t}. \quad (16)$$

Similarly, the backward reaction has a number of choices given by

$$N_b(r) = \prod_{t=0}^m \binom{M_t}{\xi_t}. \quad (17)$$

For a given chemical reaction step, we choose the forward path with probability  $\frac{N_f}{N_f + N_b}$  and the backward reaction with probability  $\frac{N_b}{N_f + N_b}$ . Then the reactants are chosen randomly from the available molecules of the proper type. This is equivalent to choosing  $\nu = \sum \nu_i$  particles at random and proceeding with the trial reaction if the set of molecules is that of either side of Eq. (15). Otherwise, the process is repeated with another set of  $\nu$  particles chosen at random until an acceptable set of particles is found.

Let  $s$  denote a specific final state for the forward reaction and  $t$ , a specific final state for the reverse

reaction. The final state molecule types are assigned randomly over the chosen  $\nu$  particles for the reaction. The number of distinct final states for this process is  $\nu! / \prod \xi_t!$  for the forward reaction and  $\nu! / \prod \nu_t!$  for the reverse reaction where we have used  $\nu = \xi$ . So the unweighted probability of choosing a move from state  $r$  to state  $s$  is given by

$$p_{r \rightarrow s} = \frac{\prod_{t=0}^m \xi_t!}{\nu! (N_f(r) + N_b(r))}. \quad (18)$$

Similarly,

$$p_{s \rightarrow r} = \frac{\prod_{t=0}^m \nu_t!}{\nu! (N_f(s) + N_b(s))}, \quad (19)$$

and consequently

$$\frac{p_{s \rightarrow r}}{p_{r \rightarrow s}} = \frac{\prod_{t=0}^m \nu_t! ((N_f(r) + N_b(r)))}{\prod_{t=0}^m \xi_t! (N_f(s) + N_b(s))} \quad (20)$$

and likewise for the reverse reaction

$$\frac{p_{t \rightarrow r}}{p_{r \rightarrow t}} = \frac{\prod_{t=0}^m \xi_t! ((N_f(r) + N_b(r)))}{\prod_{t=0}^m \nu_t! (N_f(t) + N_b(t))}. \quad (21)$$

The acceptance probabilities for a chemical reaction move are obtained from a combination of Eq.(11), Eq.(14), Eq.(20), and Eq.(21). These can be compared with a specific case given in reference 10. For spatial moves not involving a chemical reaction, the usual canonical ensemble probabilities are used. In the isothermal-isobaric ensemble, moves in volume are also allowed in the standard fashion.

## RESULTS

Monte Carlo simulations have been performed in the atomic-isothermal-isobaric ensemble using the method described above. A series of simulations have been made with nitrogen/oxygen mixtures at high  $P$  and  $T$ . Allowed molecular species are  $N_2$ ,  $O_2$ , and  $NO$ . The contribution to  $W$  from  $q_i$ 's and  $\Lambda_i$ 's is given using molecular constants and expressions found in McQuarrie<sup>12</sup> and supplemented with electronic level constants<sup>13,14</sup>. The molecular constants used for this evaluation are given in Table 1.  $M$  is the molecular weight,  $\Theta_r$  is the characteristic rotational temperature,  $\sigma$  is the symmetry number,  $\Theta_v$  is the vibrational temperature,  $D_0$  is the energy difference between the lowest vibrational level and the dissociated molecule,  $\epsilon_i$  is the  $i$ th electronic energy level, and  $\omega_i$  is the degeneracy of the  $i$ th level. Only those

TABLE 1. MOLECULAR CONSTANTS

symbol	$N_2$	$O_2$	$NO$
M	28.0134	31.988	30.0007
$\Theta_r(K)$	2.88	2.07	2.45
$\sigma$	2	2	1
$\Theta_v(K)$	3374	2256	2719
$D_0$ (kcal/mol)	225.1	118.0	150.0
$\omega_1$	1	3	2
$\epsilon_1(cm^{-1})$	0	0	0
$\omega_2$	3	2	2
$\epsilon_2(cm^{-1})$	49754.78	7882.39	119.82
$\omega_3$		1	8
$\epsilon_3(cm^{-1})$		13120.91	38440.
$\omega_4$		1	
$\epsilon_4(cm^{-1})$		32664.1	

TABLE 2. EXPONENTIAL-SIX POTENTIAL PARAMETERS FOR THE BASE CASE

#	Species	$\epsilon$ (K)	$r^*$ (Å)	$\alpha$
1	$N_2 - N_2$	75.	4.251	13.474
2	$N_2 - O_2$	75.	4.1805	13.2955
3	$N_2 - NO$	93.715	4.123	12.777
4	$O_2 - O_2$	75.	4.110	13.117
5	$O_2 - NO$	93.715	4.0525	12.5985
6	$NO - NO$	117.1	3.995	12.08

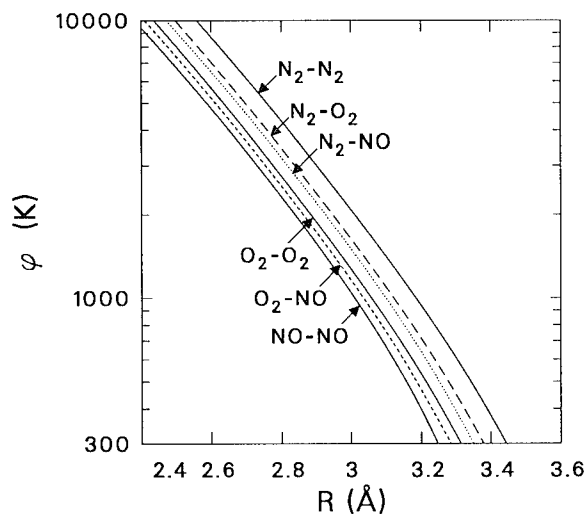


FIGURE 1. POTENTIALS VERSUS RADIUS FOR THE BASE CASE

electronic levels which contribute at  $T < 5000K$  are included. Note that conversion factors for the units include kcal/mole=503.22K and  $^{\circ}K=0.695026cm^{-1}$ .

TABLE 3. LABELS FOR SETS OF CROSS POTENTIALS

Label	$N_2 - O_2$	$N_2 - NO$	$O_2 - NO$
base	2	3	5
A	1	3	5
B	2	6	6
C	2	6	5
D	*	3	5
E	4	3	5
F	2	1	4

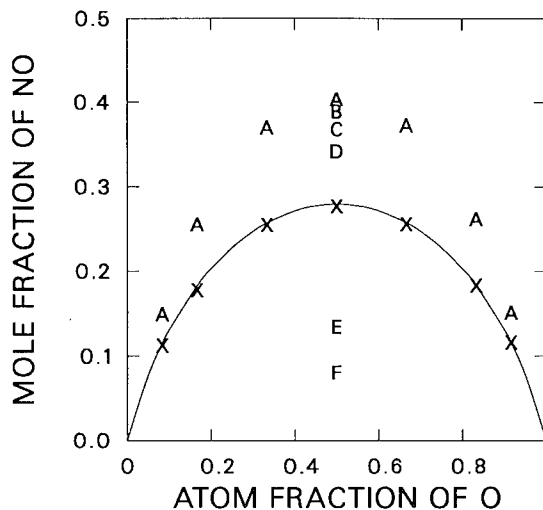


FIGURE 2. EQUILIBRIUM MOLE FRACTION OF NO VS. THE ATOMIC FRACTION OF O AT 3000K AND 30GPA. BASE SET OF POTENTIALS X, SETS A-F AS LABELED, AND PERTURBATION THEORY

Initial conditions are a random set of positions for 120 molecules. Only  $N_2$  and  $O_2$  molecules are allowed in the initial configuration. The potentials are of the exponential-six form,  $\phi = \epsilon(6\exp(\alpha(1 - r/r^*)) - \alpha(r/r^*)^{-6})/(\alpha - 6)$ , with parameters given in Table 2. The repulsive part of these potentials are shown in Figure 1. The interactions between like molecules are chosen to fit shock wave data<sup>15</sup>. The cross potentials for the baseline case are given by the Lorentz-Berthelot rules and the arithmetic mean for  $\alpha$ 's. Variations in the cross potentials are labeled in Table 3. Runs of  $10^6$  steps were made with the first  $2 \times 10^5$  steps ignored for the purpose of evaluating averages of quantities. Atomic exchanges were attempted every 37 steps and volume changes every 120 steps.



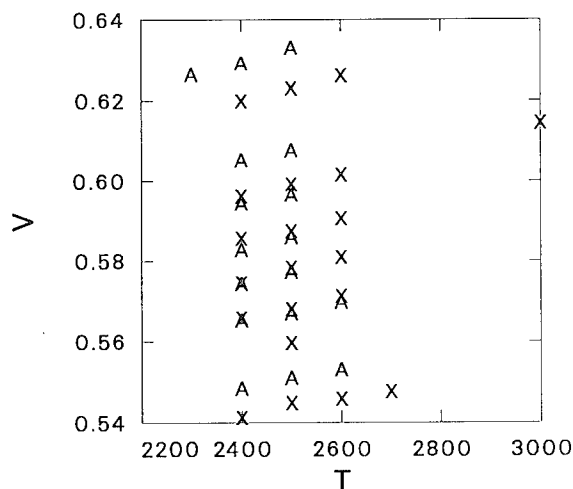


FIGURE 3. VOLUME VS. TEMPERATURE AT VARIOUS VALUES OF P

Figure 2 shows results from a previous paper<sup>11</sup> for  $P=30\text{ GPa}$  and  $T=3000\text{ K}$  to illustrate the substantial effect of cross potentials on the equilibrium composition. Comparison is made with perturbation theory<sup>15</sup> using ideal mixing. The relatively small differences in potentials leads to an accurate representation with ideal mixing for the baseline set of potentials. Other choices for cross potentials lead to significantly different equilibrium compositions. Note that since the potentials between like molecules are not changed, the ideal mixing composition is also unchanged.

In this study we have expanded the set of calculated states to include the region near the CJ conditions for the detonation of liquid NO. This is the first time a CJ state has been calculated by an (essentially) exact method such as a Monte Carlo simulation. The simulation results for the base set of potentials is given in Table 4. The same set of P and T points for the A set of potentials is given in Table 5. Units used in the tables are P(Mbar), T(K), V( $\text{cm}^3/\text{g}$ ), E(Mbar- $\text{cm}^3/\text{g}$ ), and u(m/s). Statistical uncertainties from the Monte Carlo simulations are  $E \pm .00007$ ,  $V \pm .00040$ ,  $u_s \pm 7$ ,  $u_p \pm 2$ , and  $x_{NO} \pm .002$  where  $x_{NO}$  is the mole fraction of NO in the products. Note that in these tables the difference between the specific internal energy of a state and the corresponding energy on a Hugoniot ( $E_H = E_0 + \frac{1}{2}P(V_0 - V)$ ) is given. The initial conditions are taken as  $\rho_0 = 1.294\text{ g/cm}^3$  and  $E_0 = 19.03\text{ kcal/mol}$  relative to  $N_2$  and  $O_2$  at  $T=0$  and  $P=0$ . The simulation data

TABLE 4. MONTE CARLO RESULTS FOR THE BASE SET OF POTENTIALS

P	T	E	V	$E-E_H$	$x_{NO}$
.080	2400	.031918	.61986	-.00074	.056
.080	2500	.033104	.62307	.00058	.059
.080	2600	.034778	.62628	.00238	.079
.090	2400	.033237	.59617	-.00125	.063
.090	2500	.034471	.59918	.00012	.067
.090	2600	.035851	.60159	.00161	.078
.090	3000	.041297	.61444	.00763	.115
.095	2400	.033759	.58553	-.00168	.060
.095	2500	.035219	.58734	-.00013	.072
.095	2600	.036588	.59055	.00139	.083
.100	2400	.034418	.57449	-.00204	.063
.100	2500	.035701	.57830	-.00056	.070
.100	2600	.037034	.58091	.00090	.079
.105	2400	.034761	.56586	-.00264	.058
.105	2500	.036359	.56807	-.00093	.075
.105	2600	.037709	.57128	.00059	.086
.110	2500	.037045	.55964	-.00122	.080
.120	2400	.036815	.54117	-.00362	.070
.120	2500	.038112	.54478	-.00211	.079
.120	2600	.039596	.54579	-.00057	.095
.120	2700	.041065	.54759	.00101	.105

TABLE 5. MONTE CARLO RESULTS FOR THE A SET OF POTENTIALS

P	T	E	V	$E-E_H$	$x_{NO}$
.080	2300	.031517	.62648	-.00088	.072
.080	2400	.032775	.62929	.00049	.078
.080	2500	.034277	.63310	.00215	.093
.090	2400	.034110	.60520	.00003	.085
.090	2500	.035482	.60761	.00151	.095
.095	2400	.034770	.59436	-.00025	.090
.095	2500	.036189	.59657	.00128	.100
.100	2400	.035626	.58272	-.00042	.098
.100	2500	.036777	.58593	.00089	.101
.105	2400	.036117	.57429	-.00085	.097
.105	2500	.037536	.57730	.00073	.108
.110	2400	.036862	.56526	-.00109	.102
.110	2500	.038068	.56706	.00021	.109
.110	2600	.039716	.56987	.00202	.127
.120	2400	.038268	.54839	-.00174	.115
.120	2500	.039615	.55100	-.00023	.125
.120	2600	.041025	.55301	.00130	.135

is plotted in Figure 3 in the form V versus T. With the help of the tables, groupings of data at a give value of P are readily identified. Note that the base case and the A case are significantly shifted relative to one another. Some of the apparent similar values between sets are actually from different values of P.

TABLE 6. INTERPOLATED HUGONIOT FOR THE BASE SET OF POTENTIALS

P	T	E	V	$u_s$	$u_p$
.080	2456	.03259	.62167	5623	1100
.090	2488	.03438	.59854	5554	1252
.095	2509	.03531	.58827	5545	1324
.100	2539	.03566	.57894	5550	1392
.105	2561	.03719	.57003	5561	1459
.110	2581	.03815	.56174	5579	1524
.120	2636	.04012	.54643	5627	1648

TABLE 7. INTERPOLATED HUGONIOT FOR THE A SET OF POTENTIALS

P	T	E	V	$u_s$	$u_p$
.080	2370	.03233	.62815	5747	1076
.090	2398	.03408	.60515	5662	1228
.095	2416	.03500	.59472	5644	1301
.100	2432	.03599	.58374	5620	1375
.105	2454	.03688	.57590	5643	1438
.110	2470	.03787	.56688	5648	1505
.120	2516	.03982	.55140	5690	1630

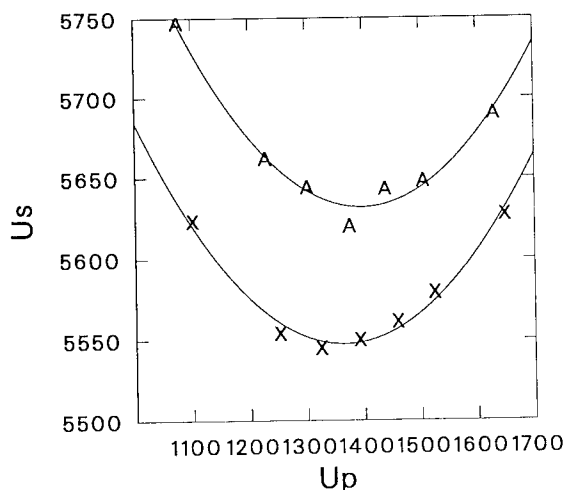


FIGURE 4. SHOCK VELOCITY VS. PARTICLE VELOCITY

## DISCUSSION

The interpolations to give the Hugoniot are shown in Table 6 and Table 7. These results include the conversion of  $P, V$  to  $u_s, u_p$  from the standard for-

mulae  $u_s = V_0 \sqrt{\frac{P-P_0}{V_0-V}}$  and  $u_p = \sqrt{(P-P_0)(V_0-V)}$  and conversion to units of meters per second. The  $u_s$  vs.  $u_p$  data are shown in Figure 4 along with least square fits of a quadratic to the data. Note that the small change in cross potentials leads to almost 100m/s difference in detonation velocities. This change is due to a combination of changes in the EOS per se and changes in the equilibrium composition for the products.

We have demonstrated a new method for the calculation of the CJ state of an explosive using a set of Monte Carlo simulations giving directly the equilibrium chemical composition. A general derivation has been given which allows for multiple species, multiple chemical reactions, and reactions involving a change in the total number of moles. The precision of the detonation velocity is a few meters per second for reasonable length simulations. Future application will be made of the method to more standard explosives. The extension of the method to the inclusion of solid products such as carbon is straightforward. Likewise, the method is easily extended to include fluid-fluid phase segregation (e.g. oil and water) utilizing the Gibbs ensemble method<sup>2</sup> as has already been demonstrated<sup>16</sup>. The net result of this combination of methods will be to allow essentially exact calculation of detonation products EOS and CJ conditions for any given set of intermolecular potentials with a given free energy representation of solid products.

## ACKNOWLEDGEMENTS

This work is supported by the U. S. Department of Energy.

## REFERENCES

1. N. Metropolis, A. W. Rosenbluth, M. N. Rosenbluth, A. H. Teller, and E. Teller, "Equation of State Calculations by Fast Computing Machines," J. Chem. Phys. **21** (1953) 1087.
2. A. Z. Panagiotopoulos, "Direct Determination of Phase Coexistence Properties of Fluids by Monte Carlo Simulation in a New Ensemble," Mol. Phys. **61** (1987) 813.
3. A. Z. Pangiatopoulos, N. Quirke, M. Stapleton, and D. J. Tildesley, "Phase Equilibria by Simulation in the Gibbs Ensemble," Mol. Phys. **63** (1988) 527.

4. D. F. Coker and R. O. Watts, "Chemical Equilibria in Mixtures of Bromine and Chlorine," *Mol. Phys.* **44** (1981) 1303.
5. D. A. Kofke and E. D. Glandt, "Monte Carlo Simulation of Multicomponent Equilibria in a Semigrand Canonical Ensemble," *Mol. Phys.* **64** (1988) 1105.
6. P. Sindzingre, G. Ciccotti, C. Massobrio, and D. Frenkel, "Partial Enthalpies and Related Quantities in Mixtures from Computer Simulation," *Chem. Phys. Lett.* **136** (1987) 35.
7. P. Sindzingre, C. Massobrio, G. Ciccotti, and D. Frenkel, "Calculation of Partial Enthalpies of an Argon-Krypton Mixture by NPT Molecular Dynamics," *Chem. Phys.* **129** (1989) 213.
8. K. S. Shing, "Infinite-dilution Activity Coefficients of Quadrupolar Lennard-Jones Mixtures from Computer Simulation," *J. Chem. Phys.* **85** (1986) 4633.
9. K. S. Shing, "Infinite-dilution Activity Coefficients from Computer Simulation," *Chem. Phys. Lett.* **119** (1985) 149.
10. M. S. Shaw, "Monte Carlo Simulation of Equilibrium Chemical Composition of Molecular Fluid Mixtures in the  $N_{atoms}PT$  Ensemble," *J. Chem. Phys.* **94** (1991) 7550.
11. M. S. Shaw, "Direct Monte Carlo Simulation of Chemical Equilibrium Composition of Molecular Fluid Mixtures under Shock Conditions," in *Shock Compression of Condensed Matter 1991*, eds. S. C. Schmidt et al. (Elsevier, Amsterdam, 1992), pp.131-134.
12. Donald A. McQuarie, *Statistical Mechanics* (Harper & Row, New York, 1976), Chap. 6.
13. M. W. Chase, Jr., C. A. Davies, J. R. Downey, Jr., D. J. Frurip, R. A. McDonald, and A. N. Syverud, *JANAF Thermochemical Tables*, 3rd Edition, *J. Phys. Chem. Ref. Data*, **14** (1985) Suppl. 1.
14. K. P. Huber and G. Herzberg, *Molecular Spectra and Molecular Structure IV. Constants of Diatomic Molecules* (Van Nostrand Reinhold, New York, 1979).
15. G. L. Schott, M. S. Shaw, and J. D. Johnson, "Shocked States from Initially Liquid Oxygen-Nitrogen Systems," *J. Chem. Phys.* **82**, 4264 (1985).
16. J. K. Johnson, A. Z. Panagiatopoulos, and K. E. Gubbins, "Reactive Canonical Monte Carlo: A New Simulation Technique for Chemical Reactions," to be published.

## CALIBRATING THE BKW-EOS WITH A LARGE PRODUCT SPECIES DATA BASE AND MEASURED C-J PROPERTIES

M. L. Hobbs and M. R. Baer\*  
Sandia National Laboratories  
Albuquerque, New Mexico 87185

*The Becker-Kistiakowsky-Wilson equation of state (BKW-EOS) has been calibrated over a wide initial density range near C-J states using 188 measured detonation properties from 62 explosives. Values for the empirical BKW constants  $\alpha$ ,  $\beta$ ,  $\kappa$ , and  $\theta$  were 0.5, 0.298, 10.5, and 6620, respectively. Co-volumes were assumed to be invariant. Model evaluation included comparison to 239 measurements from 94 explosives composed of combinations of Al, B, Ba, C, Ca, Cl, F, H, N, O, P, Pb, and Si. Adequate agreement between predictions and measurements were obtained with a few exceptions for nonideal explosives. However, detonation properties for the nonideal explosives were predicted adequately by assuming partial equilibrium.*

### INTRODUCTION

Determination of product species, equations of state (EOS), and thermochemical properties of high explosives, propellants, and pyrotechnics remains a major unsolved problem. A large product species data base is needed to develop and optimize equations of state and related constants, especially for materials with complex compositions. For example, 122 species found in the JANNAF tables<sup>1</sup> are composed of C, H, N, O, Cl, and Al. In this work, the BKW-EOS parameters were optimized using a large product species data base and measured C-J detonation properties.

An equation of state extensively used to calculate detonation properties is the Becker-Kistiakowsky-Wilson equation of state (BKW-EOS). Mader<sup>2</sup> gives the historical background and molecular covolumes for the BKW-EOS. A form of the EOS used in the present study is attributed to Cowan and Fickett:<sup>3</sup>

$$\frac{PV}{RT} = 1 + X e^{\beta X} \quad \text{with} \quad X = \frac{\kappa \sum n_i k_i}{V(T + \theta)^\alpha} \quad (1)$$

where  $P$ ,  $V$ ,  $R$ ,  $T$ , and  $n_i$  represent pressure, molar gas volume, gas constant, absolute temperature, and mole fraction of the  $i^{\text{th}}$  gaseous component, respectively. The summation extends over all components of the gaseous mixture. The covolume factors,  $k_i$ , representing excluded volume, are discussed subsequently.

\* This work performed at Sandia National Laboratories supported by the U.S. Department of Energy under contract DE-ACO4-76DP00789

The values  $\alpha$ ,  $\beta$ ,  $\kappa$ , and  $\theta$  are empirical constants. The quantity  $\theta$  was added to the equation to prevent  $P$  from approaching infinity as  $T$  approaches zero.<sup>2</sup> Typically, the parameters  $\alpha$ ,  $\beta$ ,  $\kappa$ ,  $\theta$ , and  $k_i$  are adjusted to fit measured detonation properties. For example, Finger et al.<sup>4</sup> attempted to determine these parameters using measured detonation properties and calorimetry data. The resulting data fit is the basis for the BKWR-EOS. Upon revisiting this data with additional measurements of detonation temperature, we have observed that variations due to parameters  $\beta$ ,  $\kappa$ , and  $\theta$  were most sensitive.

Recently, thermochemical data fits for approximately 900 gaseous and 600 condensed species found in the JANNAF tables have been completed for use with the TIGER thermoequilibrium code.<sup>5</sup> Furthermore, the TIGER code has been modified to allow systems containing up to 400 gaseous and 100 condensed constituents composed of up to 50 elements. Gaseous covolumes have been estimated following a procedure outlined by Mader<sup>2</sup> using estimates of van der Waals radii for 48 elements and three-dimensional molecular mechanics.

A thermal-elastic equation of state<sup>6</sup> was used for solid reaction products. However, thermal expansion and compressibility data were not available for all 600 condensed species. In the present study, most condensed phase species were assumed to be incompressible, although temperature and pressure dependent compressibility can be easily added when such information becomes available. Condensed Al, AlN, Al<sub>2</sub>O<sub>3</sub>, Al<sub>4</sub>C<sub>3</sub>, C and H<sub>2</sub>O were included as compressible species.

## PARAMETER OPTIMIZATION

Experimental Chapman-Jouguet (C-J) detonation velocity, pressure, and temperature were required to calibrate  $\beta$ ,  $\kappa$ , and  $\theta$ . These detonation characteristics depend on composition, density, and size of the initial explosive charge. Detonation velocities are measured at various charge diameters and extrapolated to an "infinite diameter" for comparison with steady-state calculations. Detonation velocities can typically be measured to within a few percent.<sup>2</sup>

In contrast to detonation velocity, the detonation pressure and temperature are not well resolved measurements. For example, detonation pressures determined by various indirect methods span a range of 10-20% (e.g. see Davis and Venable<sup>7</sup>). Nonequilibrium effects in reaction zones may contribute to this uncertainty. For example, measured pressures may be higher than equilibrium calculations if the measurement is taken behind the von Neumann spike and in front of the C-J plane.

Detonation temperatures are measured by the brightness of the detonation front interacting with a detector with absolute accuracies estimated to be  $\pm 100$  K for liquid explosives and  $\pm 200$  K for solid explosives.<sup>8</sup> Void free systems such as liquid explosives or single crystal systems are believed to be more accurate. Measurements in porous systems include the effects of shocked air or perhaps low-density explosive material jetting into the voids rather than the brightness of the pure detonation products.

Measurements in low density materials contain uncertainty due to nonhomogeneities caused by uneven packing or settling.<sup>9</sup> To add to this uncertainty, critical charge diameters are also affected adversely by low density materials. To account for uncertainty in low density C-J measurements, the following density weighted cost function was used to optimize the BKW parameters:

$$\text{cost} = \sum_i \frac{\rho_i}{\rho_i^{\text{max}}} \left[ \left( \frac{D_i^c - D_i^m}{D_i^m} \right)^2 + \left( \frac{P_i^c - P_i^m}{P_i^m} \right)^2 + \left( \frac{T_i^c - T_i^m}{T_i^m} \right)^2 \right] \quad (2)$$

where  $\rho$ ,  $D$ ,  $P$ , and  $T$  represents initial density, detonation velocity, pressure, and temperature, respectively. The superscripts  $c$ ,  $m$ , and  $\text{max}$  represent calculated and measured detonation properties, and maximum, respectively.

The cost function, which represents a density weighted squared residual, was minimized by using Nelder and Mead's<sup>10</sup> downhill simplex method for multidimensional minimization. The cost function described by Eq. (2) was based on 62 explosives, 111 initial densities, and 188 measurements. The 188 measurements included 107 velocities, 67 pressures and 14 temperatures. In the computations, temperature was affected greatly by changing  $\alpha$  and  $\theta$ , although in the final optimization,  $\alpha$  was not changed from Cowen and

Fickett's<sup>3</sup> original value of 0.5. Detonation velocity and pressure were affected by changing  $\beta$  and  $\kappa$ . Values for the optimized BKW constants  $\alpha$ ,  $\beta$ ,  $\kappa$ , and  $\theta$  were 0.5, 0.298, 10.5, and 6620, respectively. Use of these parameters with the BKW covolumes determined previously<sup>5</sup> constitutes the BKWS-EOS.\*

The experimental detonation properties used to optimize the BKW parameters are given in Table 1.<sup>†</sup> The compositions of explosives 1-44, 45-48, 49-54, 55-62 are CHNO, CNO, CHNOF, and CHNOCIF, respectively. All possible product species found in the JANNAF tables were considered for each calculation. For example, 138 product species were considered for explosives containing C, Cl, F, H, N, and O.

## PREDICTING DETONATION PROPERTIES

Predicted and experimental detonation properties using the BKWR and BKWS parameters are given in Fig. 1 and Table 1 for explosives 1-54. The mean absolute error in  $D$ ,  $P$  and  $T$ , for these explosives,  $|(\text{measured} - \text{predicted})| / (\text{measured}) \times 100$ , is shown in Table 2.

The BKWR predictions of detonation velocity are slightly better than the BKWS predictions. However, the BKWS predictions of detonation pressure and temperature are better than the BKWR predictions. The BKWR-EOS was calibrated with explosives with initial densities greater than 1 g/cc, and consequently performs well at higher densities. The BKWS-EOS was calibrated over the entire density range and tends to perform better than the BKWR-EOS over the intermediate and low density ranges as shown for RDX in Fig. 2. Similar conclusions can be deduced from Fig. 1 and Tables 1 and 2, noting that higher velocities and pressures usually correspond to higher initial densities.

Table 2. Error in Predicted Detonation Properties<sup>a</sup>

Parameters	D	P	T	Total <sup>b</sup>
BKWR	3.2	9.6	14.3	6.3
BKWS	3.5	7.2	3.4	4.8
BKWR	2.0	7.5	14.3	4.9
BKWS	2.6	5.8	3.4	3.7

a. Unshaded error calculated with measurements 1-54 in Table 1. Shaded error calculated with measurements obtained with initial densities  $\geq 1.0$ .

b. Weighted by number of measurements. There are 103, 64, and 14 D, P, and T measurements for the unshaded densities and 93, 54, and 14 D, P, and T measurements for the shaded densities.

\* BKWR ( $\alpha=0.5$ ,  $\beta=0.176$ ,  $\theta=1850$ ,  $\kappa=11.8$ ) and BKWS ( $\alpha=0.5$ ,  $\beta=0.298$ ,  $\theta=6620$ ,  $\kappa=10.5$ ) are used to distinguish between Finger et al.<sup>4</sup> re-parameterized BKW-EOS and the optimized BKW parameters discussed herein.

† Tables 1 and 3-5, which contain experimental data for 91 explosives at 141 densities, are located at the end of this work due to the large number of entries.

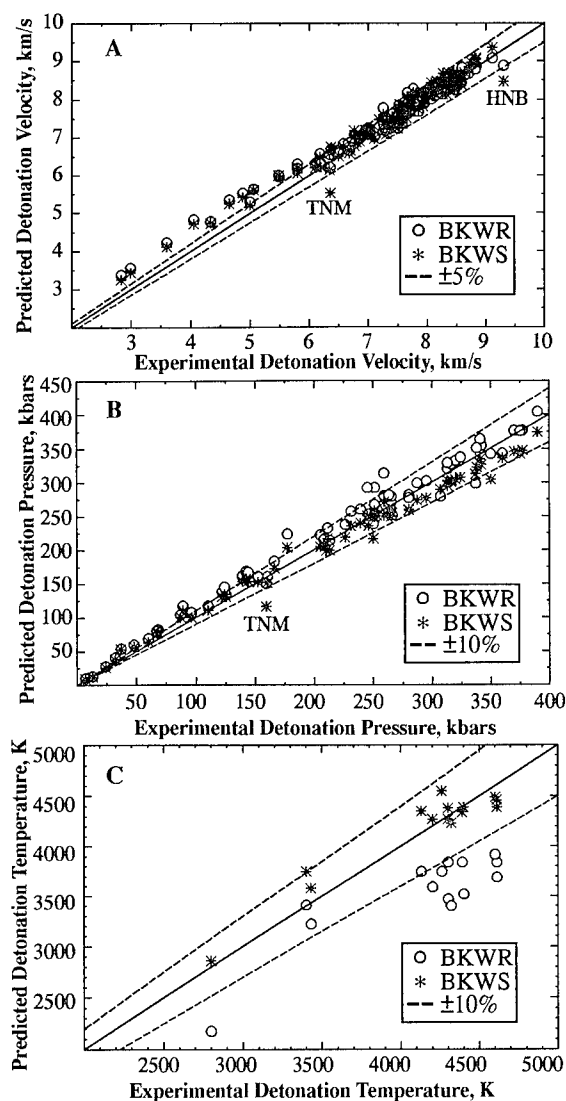


Figure 1. Comparison between predicted and experimental A) velocities, B) pressures, and C) temperatures.

Both BKWR and BKWS predict adequate detonation velocity. The predicted detonation velocity for TNM and HNB using BKWS are low when compared to experimental data as shown in Fig. 1. These explosives are composed of only CNO and might be classified as a distinct family of explosives (e.g. see Ref. 11). Detonation properties for the CNO family of explosives can be predicted better by changing  $\beta$  and  $\kappa$  to 0.0692 and 21.4, and retaining  $\alpha$  and  $\theta$ , at 0.5 and 6620, respectively.

#### NONIDEAL EXPLOSIVES

Nonideal explosives have significantly different detonation properties than predicted by equilibrium, one-dimensional, steady-state calculations. Physical separation of the fuel and oxidizer in such explosives result in extended chemical reaction zones and diffusion may

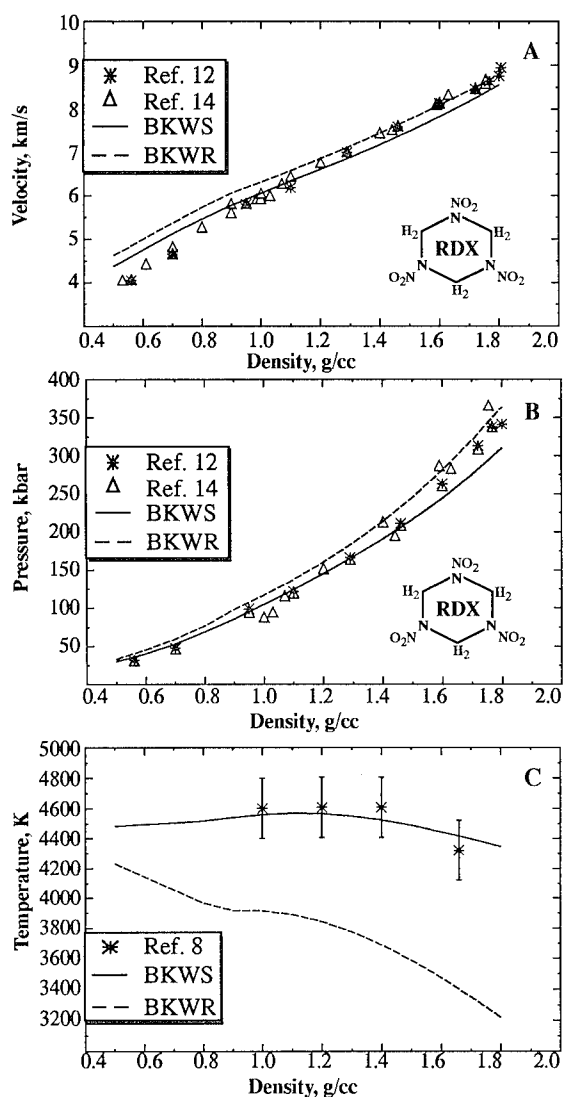


Figure 2. Comparison between predicted and experimental detonation properties of RDX.

play a major role in experimentally determined detonation properties. Furthermore, the amount of reacted material may be a function of the reaction zone length. Aluminized composite explosives or explosive nitrate salts can be classified as nonideal explosives.

As a simple approximation, partial equilibrium can be used, rather than a complex reacting mechanism, to predict detonation properties for nonideal explosives. Partial equilibrium is invoked by specifying the amount of the initial Al and/or AN that is assumed to react. For example, inert Al atoms were included in the product species data base that could only form solid, liquid or gaseous Al, thus preventing reactions with oxygen or other reactive species.

The behavior of reacting Al on detonation velocity is shown in Fig. 3 for Al composites of HMX. Prevention of Al from forming such products as  $\text{Al}_2\text{O}_3$  causes an increase in the number of gaseous molecules and an accompanying decrease in the amount of condensed C. The higher gas yield results in higher detonation pressure and velocity. When complete equilibrium is assumed, more condensed  $\text{Al}_2\text{O}_3$  is produced, forcing oxygen to react with Al rather than carbon; thus producing a hot, fuel-rich gas phase and more solid carbon. The higher temperature is a result of the large negative heat of formation of  $\text{Al}_2\text{O}_3$ .

Uncertainty in the detonation velocities for composites that contain less than 30% Al is too large to make definite conclusions about the percent of reacted Al because of the insensitivity of the detonation velocity to the percent of reacted Al. However, the experimental detonation velocities for the composites with greater than 30% Al suggest that only 40% of the Al has reacted prior to the C-J plane. The 40% reacted Al corresponds to the crossover temperature, roughly 4,000 K, shown in Fig. 3. The crossover temperature is the mixture average temperature possibly representing the high pressure boiling point of  $\text{Al}_2\text{O}_3$ . These results suggest that the  $\text{Al}_2\text{O}_3$  passivates the Al by a sudden change in reactivity at the interface as the reactive mixture expands to the C-J point. Similar conclusions can be made for Al composites of RDX, TNT, and TNETB as shown in Fig. 4.

Predicted and experimental detonation properties of nonideal explosives examined in this study are given in Table 3 and 4. The predictions are from the BKWS-EOS using full and partial equilibrium. The partial equilibrium predictions were obtained by assuming only 50% of the Al or AN interacts with the combustion products.

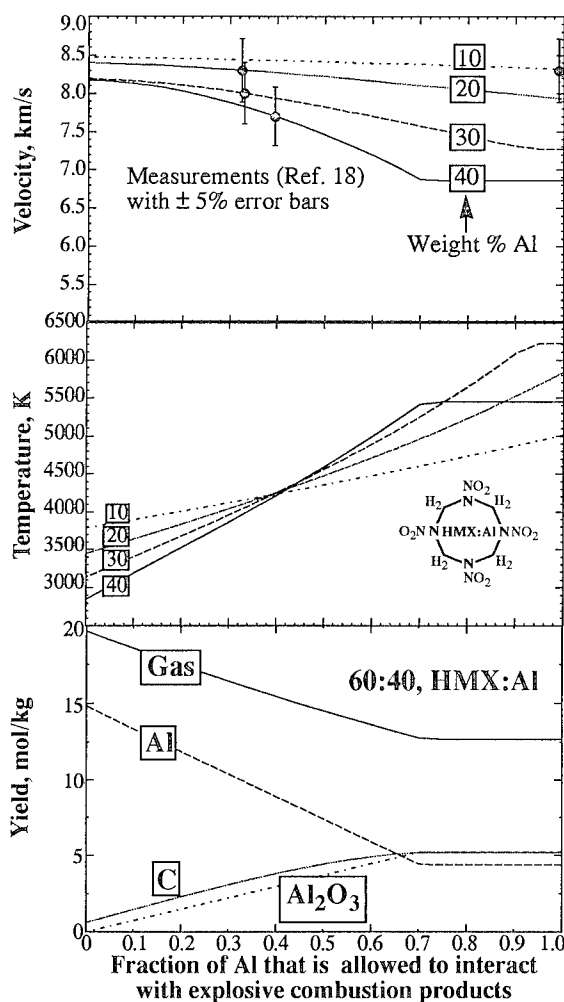


Figure 3. Effect of nonreacting Al on detonation properties of HMX/Al mixtures.

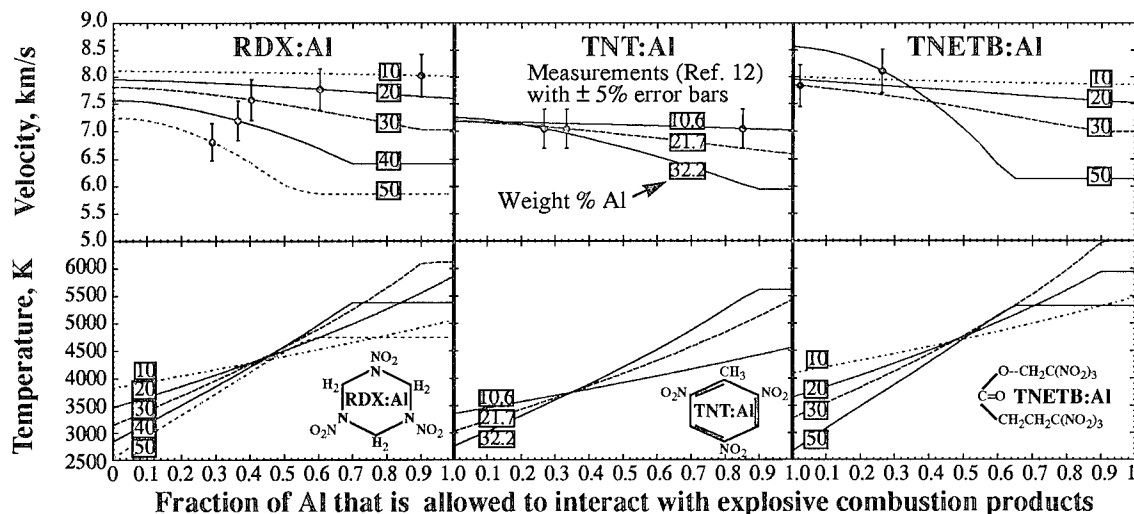


Figure 4. Effect of nonreacting Al on detonation properties of aluminized composites of RDX, TNT, and TNETB.

## EXPLOSIVES CONTAINING B, Pb, AND Si

Predicted and experimental detonation properties for explosives that contain B, Pb, and Si are given in Table 5. Detonation properties for boracitol, lead azide, and LX-02 are predicted adequately using BKWS. LX-02 has trace amounts of Si and is essentially unaffected by the Si content. However, predictions of detonation properties with BKWS for lead styphnate and explosives containing large amounts of Si are inadequate. Detonation properties of lead styphnate can be predicted by changing  $\beta$  from 0.298 to 0.04. Similarly, detonation properties of explosives with large amounts of Si can be calculated by changing  $\beta$  from 0.298 to 0.249.

## SUMMARY AND CONCLUSIONS

The BKW parameters have been optimized using 188 measurements from 62 explosives at 111 initial densities. The 188 measurements included 107 velocities, 67 pressures and 14 temperatures. Values for the BKWS constants  $\alpha$ ,  $\beta$ ,  $\kappa$ , and  $\theta$  were 0.5, 0.298, 10.5, and 6620, respectively. BKWS predictions were compared to BKWR predictions and measurements.

The BKWR detonation velocities were slightly better than the BKWS velocities, however the BKWS-EOS predicted better detonation pressures and temperatures. BKWR was calibrated with explosives having initial densities greater than unity, and consequently performs well at higher densities. BKWS was calibrated over the entire density range and tends to perform better than the BKWR over the intermediate and low density ranges.

Detonation properties for explosives containing Al and/or nitrate salts were predicted adequately by using partial equilibrium. However, detonation performance for several families of explosive could not be predicted accurately with BKWS. These included explosives which contained large amounts of silicon, TNM and lead styphnate. The performance of explosives containing large amounts of silicon can be predicted adequately by changing  $\beta$  from 0.298 to 0.249. Performance of TNM and lead styphnate can also be predicted by adjusting  $\beta$  and/or  $\kappa$ .

As discussed in this paper, measurements of detonation characteristics can be used to optimize equations of states and related constants. However, there are still uncertainties associated with measuring detonation properties, modeling the detonation process, and choosing appropriate cost functions. Therefore, the predictions may not be quantitatively accurate in every detail. Still the predictions do replicate experimental data and the BKW-EOS can be used to deduce relative performance.

## REFERENCES

- Chase, M. W. Jr., Davies, C. A., Downey, J. R., Jr., Frurip, D. J., McDonald R. A., and Syverud, A. N., "JANAF Thermochemical Tables Third Edition," *J. Phy. and Chem. Ref. Data*, Vol. 14, 1985.
- Mader, C. L., *Numerical Modeling of Detonations*, Univ. of California Press, Los Angeles, CA 1979.
- Cowan, R. D. and Fickett, W., "Calculation of the Detonation Products of Solid Explosives with the Kistiakowsky-Wilson Equation of State," *J. Chem Physics*, Vol. 24, 1956, p. 932.
- Finger, M., Lee, E., Helm, F. H., Hayes, B., Hornig, H., McGuire, R., Kahara, M., and Guidry, M., "The Effect of Elemental Composition on the Detonation Behavior of Explosives," *Sixth Symposium (International) on Detonation*, ACR-221, 1976, p. 710.
- Hobbs, M. L. and Baer, M. R., "Nonideal Thermoequilibrium Calculations Using a Large Product Species Data Base," SAND92-0482, also in *Shock Waves*, Vol. 2, No. 3, 1992, p. 177.
- Cowperthwaite, M. and Zwisler, W. H., *TIGER Computer Program Documentation*, Stanford Research Institute, Menlo Park, California, 1973.
- Davis, W. C. and Venable, D., "Pressure Measurements for Composition B-3," *Fifth Symposium (International) on Detonation*, ACR-184, 1970, p. 13.
- Kato, Y., Mori, N., Sakai, H., Sakurai, T., and Hikita, T., "Detonation Temperature of Some Liquid and Solid Explosives," *Ninth Symposium (International) on Detonation*, OCNR 113291-7, 1989, p. 939.
- Fedoroff B. T. and Sheffield, O. E., *Encyclopedia of Explosives and Related Items*, PATR 2700, Vol. 4, Picatinny Arsenal, Dover, New Jersey, 1969, p. 645.
- Nelder, J. A. and Mead, R., "A Simplex Method for Function Minimization," *Computer Journal*, Vol. 7, 1965, p. 308.
- Tanaka, K., "Detonation Properties of High Explosives Calculated by Revised Kihara-Hikita Equation of State," *Eighth Symposium (International) on Detonation*, NSWC MP 86-194, 1985, p. 548.
- Hall, T. N. and Holden, J. R., *Navy Explosives Handbook*, NSWC MP 88-116, 1988.
- Dobratz, B. M., *LLNL Explosives Handbook*, DE85-015961, 1981.
- Steinberg, D. J., "Comparison of Experimental data on Detonation Velocity and C-J Pressure vs HE Density with Predictions From Ree's Model EOS," *Eighth Symposium (International) on Detonation*, NSWC MP 86-194, 1985, p. 513.
- Kato, Y., Mori, N., Sakai, H., Tanaka, K., Sakurai, T., and Hikita, T., "Detonation Temperature of Nitromethane and some solid High Explosives," *Eight Symposium (International) on Detonation*, NSWC MP 86-194, 1985, P. 558.
- Burton, J. T. A., Hawkins, S. J., and Hooper, G., "Detonation Temperature of Some Liquid Explosives," *Seventh Symposium (International) on Detonation*, NSWC-MP 82-334, 1981, p. 759.
- Hornig, H. C., Lee, E. L., and Finger, M., "Equation of State of Detonation Products," *Fifth Symposium (International) on Det.*, ACR-184, 1970, p. 503.
- Price, D. and Clairmont, A. R. Jr., "Deflagration to Detonation Transition Behavior of Aluminized HMX," *Propellants and Explosives*, Vol. 4, 1979, p.132.



Table 1. Experimental and Calculated Detonation Properties<sup>a</sup>

EXPLOSIVE <sup>b</sup>	EXP	BKWR <sup>c</sup>	BKWS <sup>d</sup>
1. ABH, +116.0 C <sub>24</sub> H <sub>6</sub> N <sub>14</sub> O <sub>24</sub> ρ <sup>o</sup> = 1.64	7.20 <sup>12</sup> --- ---	7.28 (+1.1) 230 3960	7.14 (-0.8) 211 4710
2. COMP A-3, +2.84 C <sub>1.87</sub> H <sub>3.74</sub> N <sub>2.46</sub> O <sub>2.46</sub> ρ <sup>o</sup> = 1.64	8.47 <sup>13</sup> --- ---	8.26 (-2.5) 287 3090	8.25 (-2.6) 266 3670
3. COMP B, +1.00 C <sub>2.03</sub> H <sub>2.64</sub> N <sub>2.18</sub> O <sub>2.67</sub> ρ <sup>o</sup> = 1.72	7.92 <sup>13</sup> 295 <sup>13</sup> ---	8.12 (+2.5) 302 (+2.4) 3230	8.20 (+3.5) 276 (-6.4) 3950
4. COMP B-3 60/40 RDX/TNT ρ <sup>o</sup> = 1.72	7.89 <sup>13</sup> 287 <sup>13</sup> ---	8.08 (+2.4) 299 (+4.2) 3260	8.16 (+3.4) 273 (-4.9) 4000
5. COMP C-3, -6.45 C <sub>1.90</sub> H <sub>2.83</sub> N <sub>2.34</sub> O <sub>2.60</sub> ρ <sup>o</sup> = 1.60	7.63 <sup>13</sup> --- ---	7.77 (+1.8) 253 3150	7.74 (+1.4) 230 3790
6. COMP C-4, +3.33 C <sub>1.82</sub> H <sub>3.54</sub> N <sub>2.46</sub> O <sub>2.51</sub> ρ <sup>o</sup> = 1.66	8.37 <sup>13</sup> --- ---	8.30 (-0.8) 296 3120	8.32 (-0.6) 273 3760
7. CYCLOTOL-78/22 78/22 RDX/TNT ρ <sup>o</sup> = 1.76	8.31 <sup>12</sup> 317 <sup>12</sup> ---	8.40 (+1.1) 329 (+3.8) 3240	8.53 (+2.6) 302 (-4.7) 4070
8. CYCLOTOL-77/23 77/23 RDX/TNT ρ <sup>o</sup> = 1.74	8.25 <sup>12</sup> 313 <sup>12</sup> ---	8.33 (+1.0) 320 (+2.2) 3260	8.44 (+2.3) 294 (-6.1) 4070
9. CYCLOTOL-75/25 75/25 RDX/TNT ρ <sup>o</sup> = 1.76	8.30 <sup>13</sup> 316 <sup>13</sup> ---	8.37 (+0.8) 327 (+3.5) 3240	8.49 (+2.3) 300 (-5.1) 4050
CYCLOTOL-75/25 75/25 RDX/TNT ρ <sup>o</sup> = 1.62	7.95 <sup>12</sup> 265 <sup>12</sup> ---	7.91 (-0.5) 271 (+2.3) 3400	7.95 (0.0) 249 (-6.0) 4130
10. CYCLOTOL-70/30 70/30 RDX/TNT ρ <sup>o</sup> = 1.73	8.06 <sup>13</sup> --- ---	8.22 (+2.0) 311 3270	8.31 (+3.1) 285 4040
11. CYCLOTOL-65/35 65/35 RDX/TNT ρ <sup>o</sup> = 1.72	8.04 <sup>13</sup> 292 <sup>13</sup> ---	8.13 (+1.1) 303 (+3.8) 3270	8.22 (+2.2) 277 (-5.1) 4030
12. CYCLOTOL-60/40 60/40 RDX/TNT ρ <sup>o</sup> = 1.74	8.09 <sup>12</sup> --- ---	8.15 (+0.7) 307 3240	8.24 (+1.9) 281 3990
CYCLOTOL-60/40 60/40 RDX/TNT ρ <sup>o</sup> = 1.72	7.90 <sup>13</sup> --- ---	8.08 (+2.3) 299 3260	8.16 (+3.3) 273 4000
13. CYCLOTOL-50/50 50/50 RDX/TNT ρ <sup>o</sup> = 1.63	7.66 <sup>12</sup> 231 <sup>12</sup> ---	7.69 (+0.4) 257 (+11.3) 3340	7.71 (0.7) 235 (+1.7) 4000
14. DATB, -23.6 C <sub>6</sub> H <sub>5</sub> N <sub>5</sub> O <sub>6</sub> ρ <sup>o</sup> = 1.80	7.60 <sup>12</sup> 251 <sup>12</sup> ---	7.92 (+4.2) 292 (+16.3) 2860	7.86 (+3.4) 258 (+2.8) 3550
DATB, -23.6 C <sub>6</sub> H <sub>5</sub> N <sub>5</sub> O <sub>6</sub> ρ <sup>o</sup> = 1.78	7.60 <sup>12</sup> 251 <sup>12</sup> ---	7.85 (+3.3) 280 (+11.6) 2870	7.79 (+2.5) 250 (-0.4) 3550

Table 1. Experimental and Calculated Detonation Properties<sup>a</sup>

EXPLOSIVE <sup>b</sup>	EXP	BKWR <sup>c</sup>	BKWS <sup>d</sup>
15. DEGN, -99.4 C <sub>4</sub> H <sub>8</sub> N <sub>2</sub> O <sub>7</sub> ρ <sup>o</sup> = 1.38	6.76 <sup>13</sup> --- ---	7.08 (+4.7) 189 3240	7.19 (+6.4) 183 3690
16. DIPM, -6.8 C <sub>12</sub> H <sub>6</sub> N <sub>8</sub> O <sub>12</sub> ρ <sup>o</sup> = 1.76	7.40 <sup>13</sup> --- ---	7.62 (+3.0) 266 3310	7.56 (+2.2) 239 4040
17. EXP D, -94.0 C <sub>6</sub> H <sub>6</sub> N <sub>4</sub> O <sub>7</sub> ρ <sup>o</sup> = 1.55	6.85 <sup>13</sup> --- ---	7.02 (+2.5) 195 2840	6.91 (+0.9) 176 3360
EXP D, -94.0 C <sub>6</sub> H <sub>6</sub> N <sub>4</sub> O <sub>7</sub> ρ <sup>o</sup> = 1.48	6.70 <sup>12</sup> --- ---	6.78 (+1.2) 175 2890	6.66 (-0.6) 158 3380
18. HMX, +17.9 C <sub>4</sub> H <sub>8</sub> N <sub>8</sub> O <sub>8</sub> ρ <sup>o</sup> = 1.89	9.11 <sup>13</sup> 390 <sup>13</sup> ---	9.08 (-0.3) 405 (+3.8) 3090	9.35 (+2.6) 374 (-4.1) 4070
HMX, +17.9 C <sub>4</sub> H <sub>8</sub> N <sub>8</sub> O <sub>8</sub> ρ <sup>o</sup> = 1.60	7.91 <sup>14</sup> 280 <sup>4</sup> 4300 <sup>15</sup>	8.10 (+2.4) 281 (+0.4) 3470 (-19.3)	8.14 (+2.9) 259 (-7.5) 4270 (-0.7)
HMX, +17.9 C <sub>4</sub> H <sub>8</sub> N <sub>8</sub> O <sub>8</sub> ρ <sup>o</sup> = 1.40	7.30 <sup>14</sup> 210 <sup>4</sup> ---	7.45 (+2.1) 213 (+1.4) 3680	7.41 (+1.5) 199 (-5.2) 4380
HMX, +17.9 C <sub>4</sub> H <sub>8</sub> N <sub>8</sub> O <sub>8</sub> ρ <sup>o</sup> = 1.20	6.58 <sup>14</sup> 160 <sup>4</sup> ---	6.85 (+4.1) 160 (0.0) 3830	6.78 (+3.0) 151 (-5.6) 4450
HMX, +17.9 C <sub>4</sub> H <sub>8</sub> N <sub>8</sub> O <sub>8</sub> ρ <sup>o</sup> = 1.00	5.80 <sup>14</sup> 110 <sup>4</sup> ---	6.31 (+8.8) 117 (+6.4) 3900	6.20 (+6.9) 110 (0.0) 4480
HMX, +17.9 C <sub>4</sub> H <sub>8</sub> N <sub>8</sub> O <sub>8</sub> ρ <sup>o</sup> = 0.75	4.88 <sup>14</sup> 60 <sup>4</sup> ---	5.54 (+13.5) 69 (+15.0) 4000	5.42 (+11.1) 64 (+6.7) 4440
19. HNAB, +67.9 C <sub>12</sub> H <sub>4</sub> N <sub>8</sub> O <sub>12</sub> ρ <sup>o</sup> = 1.60	7.31 <sup>13</sup> 205 <sup>13</sup> ---	7.22 (-1.2) 222 (+8.3) 3900	7.09 (-3.0) 204 (-0.5) 4620
20. HNS, +18.7 C <sub>14</sub> H <sub>6</sub> N <sub>6</sub> O <sub>12</sub> ρ <sup>o</sup> = 1.60	6.80 <sup>13</sup> --- ---	6.96 (+2.4) 206 3580	6.88 (+1.2) 187 4150
HNS, +18.7 C <sub>14</sub> H <sub>6</sub> N <sub>6</sub> O <sub>12</sub> ρ <sup>o</sup> = 1.70	7.00 <sup>13</sup> --- ---	7.26 (+3.7) 236 3500	7.22 (+3.1) 214 4120
21. LX-01, -27.5 C <sub>1.52</sub> H <sub>3.73</sub> N <sub>1.69</sub> O <sub>3.39</sub> ρ <sup>o</sup> = 1.24	6.84 <sup>13</sup> --- ---	6.97 (+1.9) 172 3670	7.05 (+3.1) 165 4230
22. LX-14, +1.50 C <sub>1.52</sub> H <sub>2.92</sub> N <sub>2.59</sub> O <sub>2.66</sub> ρ <sup>o</sup> = 1.84	8.83 <sup>13</sup> 370 <sup>13</sup> ---	8.86 (+0.3) 377 (+1.9) 3030	9.04 (+2.4) 345 (-6.8) 3910
23. MEN-II, -74.3 C <sub>2.06</sub> H <sub>7.06</sub> N <sub>1.33</sub> O <sub>3.10</sub> ρ <sup>o</sup> = 1.02	5.49 <sup>13</sup> --- ---	5.97 (+8.7) 95 2520	6.00 (+9.3) 94 2720
24. NG, -90.8 C <sub>3</sub> H <sub>5</sub> N <sub>3</sub> O <sub>9</sub> ρ <sup>o</sup> = 1.60	7.70 <sup>13</sup> 253 <sup>13</sup> 4260 <sup>16</sup>	7.94 (+3.1) 260 (+2.8) 3750 (-12.0)	8.01 (+4.0) 250 (-1.2) 4550 (6.8)

Table 1. Experimental and Calculated Detonation Properties<sup>a</sup>

EXPLOSIVE <sup>b</sup>	EXP	BKWR <sup>c</sup>	BKWS <sup>d</sup>
25.NM, -27.0 $C_7H_5N_7O_2$ $\rho^0 = 1.13$	6.35 <sup>13</sup> 125 <sup>13</sup> 3430 <sup>16</sup>	6.56 (+3.3) 134 (+7.2) 3220 (-6.1)	6.59 (+3.8) 130 (+4.0) 3580 (+4.4)
26.NONA, +27.4 $C_{18}H_5N_9O_{18}$ $\rho^0 = 1.70$	7.40 <sup>12</sup> --- ---	7.35 (-0.7) 241 3780	7.26 (-1.9) 221 4510
27.NQ, -23.6 $C_7H_4N_4O_2$ $\rho^0 = 1.78$	8.59 <sup>12</sup> --- ---	8.83 (+2.8) 317 2090	8.53 (-0.7) 272 2740
NQ, -23.6 $C_7H_4N_4O_2$ $\rho^0 = 1.72$	--- 245 <sup>12</sup> ---	8.58 292 (+19.2) 2130	8.26 250 (+2.0) 2760
NQ, -23.6 $C_7H_4N_4O_2$ $\rho^0 = 1.62$	7.93 <sup>13</sup> --- ---	8.17 (+3.0) 252 2210	7.82 (-1.4) 217 2790
NQ, -23.6 $C_7H_4N_4O_2$ $\rho^0 = 1.55$	7.65 <sup>13</sup> --- ---	7.89 (+3.1) 227 2260	7.52 (-1.7) 198 2830
28.OCTOL-78/22 77.6/22.4 HMX/TNT $\rho^0 = 1.82$	--- 342 <sup>12</sup> ---	8.59 355 (+3.8) 3160	8.76 326 (-4.7) 4020
29.OCTOL-76/23 76.3/23.7 HMX/TNT $\rho^0 = 1.81$	8.45 <sup>12</sup> 338 <sup>12</sup> ---	8.54 (+1.1) 350 (+3.6) 3170	8.70 (+3.0) 321 (-5.0) 4020
30.OCTOL-75/25 75/25 HMX/TNT $\rho^0 = 1.81$	8.48 <sup>13</sup> --- ---	8.53 (+0.6) 349 3170	8.69 (+2.5) 320 4010
31.OCTOL-60/40 60/40 HMX/TNT $\rho^0 = 1.80$	8.16 <sup>12</sup> 320 <sup>12</sup> ---	8.34 (+2.2) 332 (+3.8) 3160	8.47 (+3.8) 304 (-5.0) 3950
32.PBX-9007, +7.13 $C_{1.97}H_{3.22}N_{2.43}O_{2.44}$ $\rho^0 = 1.64$	8.09 <sup>13</sup> --- ---	8.09 (0.0) 279 3190	8.08 (-0.1) 256 3810
33.PBX-9011, -4.05 $C_{1.73}H_{3.18}N_{2.45}O_{2.61}$ $\rho^0 = 1.77$	8.50 <sup>13</sup> 324 <sup>13</sup> ---	8.56 (+0.7) 337 (+4.0) 2980	8.65 (+1.8) 307 (-5.2) 3720
34.PBX-9205, +5.81 $C_{1.83}H_{3.14}N_{2.49}O_{2.51}$ $\rho^0 = 1.67$	8.17 <sup>13</sup> --- ---	8.22 (+0.6) 295 3190	8.25 (+1.0) 271 3870
35.PBX-9501, +2.30 $C_{1.47}H_{2.86}N_{2.60}O_{2.69}$ $\rho^0 = 1.84$	8.83 <sup>13</sup> --- ---	8.87 (+0.5) 379 3070	9.07 (+2.2) 348 3970
36.PENTOLITE 50/50 PETN/TNT $\rho^0 = 1.71$	7.75 <sup>12</sup> --- ---	7.72 (-0.4) 277 3290	7.91 (+2.1) 258 3990
PENTOLITE 50/50 PETN/TNT $\rho^0 = 1.70$	7.53 <sup>13</sup> --- ---	7.69 (+2.1) 274 3300	7.87 (+4.5) 255 4000
PENTOLITE 50/50 PETN/TNT $\rho^0 = 1.68$	7.65 <sup>12</sup> 251 <sup>12</sup> ---	7.63 (-0.3) 267 (+6.4) 3320	7.80 (+2.0) 248 (-1.2) 4010

Table 1. Experimental and Calculated Detonation Properties<sup>a</sup>

EXPLOSIVE <sup>b</sup>	EXP	BKWR <sup>c</sup>	BKWS <sup>d</sup>
PENTOLITE 50/50 PETN/TNT $\rho^0 = 1.64$	7.53 <sup>12</sup> --- ---	7.51 (-0.3) 253 3360	7.65 (+1.6) 235 4030
37.PETN, -129.0 $C_5H_8N_4O_{12}$ $\rho^0 = 1.76$	8.27 <sup>17</sup> 337 <sup>17</sup> ---	8.23 (-0.5) 298 (-11.6) 3330	8.67 (+4.8) 312 (-7.4) 4280
PETN, -129.0 $C_5H_8N_4O_{12}$ $\rho^0 = 1.70$	8.07 <sup>17</sup> 307 <sup>17</sup> ---	8.02 (-0.6) 279 (-9.1) 3400	8.43 (+4.5) 289 (-5.9) 4320
PETN, -129.0 $C_5H_8N_4O_{12}$ $\rho^0 = 1.60$	7.75 <sup>17</sup> 266 <sup>17</sup> 4400 <sup>15</sup>	7.70 (-0.6) 251 (-5.6) 3520 (-20.0)	8.03 (+3.6) 254 (-4.5) 4390 (-0.2)
PETN, -129.0 $C_5H_8N_4O_{12}$ $\rho^0 = 1.45$	7.18 <sup>17</sup> 208 <sup>17</sup> ---	7.27 (+1.3) 215 (+3.4) 3710	7.48 (+4.2) 208 (0.0) 4490
PETN, -129.0 $C_5H_8N_4O_{12}$ $\rho^0 = 1.23$	6.37 <sup>17</sup> 139 <sup>17</sup> ---	6.71 (+5.3) 161 (+15.8) 3940	6.76 (+6.1) 153 (+10.1) 4600
PETN, -129.0 $C_5H_8N_4O_{12}$ $\rho^0 = 0.99$	5.48 <sup>17</sup> 87 <sup>17</sup> ---	6.01 (+9.7) 104 (+19.5) 4150	5.99 (+9.3) 100 (+14.9) 4640
PETN, -129.0 $C_5H_8N_4O_{12}$ $\rho^0 = 0.88$	5.06 <sup>17</sup> 68 <sup>17</sup> ---	5.65 (+11.7) 82 (+20.6) 4240	5.61 (+10.9) 78 (+14.7) 4640
PETN, -129.0 $C_5H_8N_4O_{12}$ $\rho^0 = 0.48$	3.60 <sup>17</sup> 24 <sup>17</sup> ---	4.24 (+17.8) 28 (+16.7) 4460	4.12 (+14.4) 26 (+8.3) 4560
PETN, -129.0 $C_5H_8N_4O_{12}$ $\rho^0 = 0.30$	2.99 <sup>17</sup> 13 <sup>17</sup> ---	3.57 (+19.4) 13 (0.0) 4470	3.44 (+15.1) 12 (-7.7) 4450
PETN, -129.0 $C_5H_8N_4O_{12}$ $\rho^0 = 0.25$	2.83 <sup>17</sup> 8 <sup>17</sup> ---	3.38 (+19.4) 10 (+25.0) 4460	3.25 (+14.8) 9 (+12.5) 4400
38.PICRATOL 52/48 EXP D/TNT $\rho^0 = 1.63$	6.97 <sup>12</sup> --- ---	7.23 (+3.7) 221 2990	7.19 (+3.2) 200 3520
39.PICRIC ACID, -51.3 $C_6H_3N_3O_7$ $\rho^0 = 1.76$	7.57 <sup>12</sup> --- ---	7.51 (-0.8) 259 3280	7.52 (-0.7) 237 4010
PICRIC ACID, -51.3 $C_6H_3N_3O_7$ $\rho^0 = 1.71$	7.26 <sup>13</sup> --- ---	7.36 (+1.4) 243 3330	7.35 (+1.2) 222 4030
PICRIC ACID, -51.3 $C_6H_3N_3O_7$ $\rho^0 = 1.60$	7.10 <sup>13</sup> --- ---	7.03 (-1.0) 210 3420	6.97 (-1.8) 192 4080
40.RDX, +14.7 $C_3H_6N_6O_6$ $\rho^0 = 1.80$	8.75 <sup>12</sup> 341 <sup>12</sup> ---	8.77 (+0.2) 364 (+6.7) 3220	8.96 (+2.4) 334 (-2.1) 4140
RDX, +14.7 $C_3H_6N_6O_6$ $\rho^0 = 1.77$	8.70 <sup>13</sup> 338 <sup>13</sup> ---	8.67 (-0.3) 351 (+3.8) 3260	8.84 (+1.6) 322 (-4.7) 4160

Table 1. Experimental and Calculated Detonation Properties<sup>a</sup>

EXPLOSIVE <sup>b</sup>	EXP	BKWR <sup>c</sup>	BKWS <sup>d</sup>
<b>RDX, +14.7</b> <chem>C3H6N6O6</chem> $\rho^0 = 1.72$	8.46 <sup>12</sup> 313 <sup>12</sup> ---	8.50 (+0.5) 329 (+5.2) 3330	8.63 (+2.0) 302 (-3.5) 4200
<b>RDX, +14.7</b> <chem>C3H6N6O6</chem> $\rho^0 = 1.66$	8.24 <sup>14</sup> --- 4320 <sup>8</sup>	8.30 (+0.7) 304 3400 (-21.3)	8.38 (+1.7) 279 4230 (-2.1)
<b>RDX, +14.7</b> <chem>C3H6N6O6</chem> $\rho^0 = 1.60$	8.13 <sup>12</sup> 263 <sup>12</sup> ---	8.10 (-0.4) 281 (+6.8) 3480	8.15 (+0.2) 260 (-1.1) 4280
<b>RDX, +14.7</b> <chem>C3H6N6O6</chem> $\rho^0 = 1.46$	7.60 <sup>12</sup> 211 <sup>12</sup> ---	7.64 (+0.5) 232 (+10.0) 3630	7.63 (+0.4) 216 (+2.4) 4360
<b>RDX, +14.7</b> <chem>C3H6N6O6</chem> $\rho^0 = 1.4$	7.46 <sup>14</sup> 213 <sup>14</sup> 4610 <sup>8</sup>	7.45 (-0.1) 214 (+0.5) 3690 (-20.0)	7.42 (-0.5) 199 (-6.6) 4390 (-4.8)
<b>RDX, +14.7</b> <chem>C3H6N6O6</chem> $\rho^0 = 1.29$	7.00 <sup>12</sup> 166 <sup>12</sup> ---	7.12 (+1.7) 183 (+10.2) 3780	7.06 (+0.9) 172 (+3.6) 4430
<b>RDX, +14.7</b> <chem>C3H6N6O6</chem> $\rho^0 = 1.20$	6.77 <sup>14</sup> 152 <sup>14</sup> 4610 <sup>8</sup>	6.86 (+1.3) 160 (+5.3) 3840 (+16.7)	6.79 (+0.3) 152 (0.0) 4460 (-3.3)
<b>RDX, +14.7</b> <chem>C3H6N6O6</chem> $\rho^0 = 1.10$	6.18 <sup>12</sup> 122 <sup>12</sup> ---	6.58 (+6.5) 138 (+13.1) 3890	6.49 (+5.0) 130 (+6.6) 4480
<b>RDX, +14.7</b> <chem>C3H6N6O6</chem> $\rho^0 = 1.00$	6.10 <sup>14</sup> 89 <sup>14</sup> 4600 <sup>8</sup>	6.32 (+3.6) 117 (+31.5) 3920 (-14.8)	6.21 (+1.8) 110 (+23.6) 4490 (-2.4)
<b>RDX, +14.7</b> <chem>C3H6N6O6</chem> $\rho^0 = 0.95$	5.80 <sup>12</sup> 96 <sup>12</sup> ---	6.19 (+6.7) 107 (+11.5) 3920	6.06 (+4.5) 100 (+4.2) 4490
<b>RDX, +14.7</b> <chem>C3H6N6O6</chem> $\rho^0 = 0.70$	4.65 <sup>12</sup> 48 <sup>12</sup> ---	5.36 (+15.3) 60 (+25.0) 4060	5.25 (+12.9) 57 (+18.8) 4450
<b>RDX, +14.7</b> <chem>C3H6N6O6</chem> $\rho^0 = 0.56$	4.05 <sup>12</sup> 32 <sup>12</sup> ---	4.84 (+19.5) 41 (+28.1) 4180	4.72 (+16.5) 38 (+18.8) 4450
<b>41. TACOT, +111.0</b> <chem>C12H4N8O8</chem> $\rho^0 = 1.85$	7.25 <sup>12</sup> --- ---	7.79 (+7.4) 288 3330	7.62 (+5.1) 253 4040
<b>42. TATB, -36.9</b> <chem>C6H6N6O6</chem> $\rho^0 = 1.88$	7.76 <sup>15</sup> --- ---	8.28 (+6.7) 328 2550	8.19 (+5.5) 285 3250
<b>TATB, -36.9</b> <chem>C6H6N6O6</chem> $\rho^0 = 1.85$	7.66 <sup>12</sup> 259 <sup>12</sup> ---	8.18 (+6.8) 314 (+21.2) 2580	8.07 (+5.4) 271 (+4.6) 3260
<b>43. TETRYL, +4.67</b> <chem>C7H5N5O8</chem> $\rho^0 = 1.73$	7.72 <sup>12</sup> --- ---	7.75 (+0.4) 277 3460	7.81 (+1.2) 255 4210
<b>TETRYL, +4.67</b> <chem>C7H5N5O8</chem> $\rho^0 = 1.71$	7.85 <sup>15</sup> --- ---	7.69 (-2.0) 270 3480	7.74 (-1.4) 248 4220

Table 1. Experimental and Calculated Detonation Properties<sup>a</sup>

EXPLOSIVE <sup>b</sup>	EXP	BKWR <sup>c</sup>	BKWS <sup>d</sup>
<b>TETRYL, +4.67</b> <chem>C7H5N5O8</chem> $\rho^0 = 1.68$	7.50 <sup>12</sup> 239 <sup>12</sup> ---	7.60 (+1.3) 260 (+8.8) 3520	7.63 (+1.7) 239 (0.0) 4240
<b>TETRYL, +4.67</b> <chem>C7H5N5O8</chem> $\rho^0 = 1.61$	7.58 <sup>12</sup> 226 <sup>12</sup> 4200 <sup>8</sup>	7.39 (-2.5) 237 (+4.9) 3590 (-14.5)	7.38 (-2.6) 218 (-3.5) 4270 (1.7)
<b>TETRYL, +4.67</b> <chem>C7H5N5O8</chem> $\rho^0 = 1.40$	--- --- 4130 <sup>8</sup>	6.78 178 3750 (-9.2)	6.70 165 4350 (5.3)
<b>TETRYL, +4.67</b> <chem>C7H5N5O8</chem> $\rho^0 = 1.36$	6.68 <sup>12</sup> 142 <sup>12</sup> ---	6.67 (-0.1) 168 (+18.3) 3780	6.59 (-1.3) 157 (+10.6) 4360
<b>TETRYL, +4.67</b> <chem>C7H5N5O8</chem> $\rho^0 = 1.20$	6.34 <sup>12</sup> --- 4300 <sup>8</sup>	6.24 (-1.6) 133 3840 (-10.7)	6.15 (-3.0) 127 4380 (+1.9)
<b>TETRYL, +4.67</b> <chem>C7H5N5O8</chem> $\rho^0 = 1.00$	--- --- 4390 <sup>8</sup>	5.75 97 3840 (-12.5)	5.68 95 4340 (-1.1)
<b>44. TNT, -15.0</b> <chem>C7H5N3O6</chem> $\rho^0 = 1.64$	6.93 <sup>13</sup> 210 <sup>13</sup> ---	7.20 (+3.9) 223 (+6.2) 3210	7.19 (+3.8) 203 (-3.3) 3720
<b>TNT, -15.0</b> <chem>C7H5N3O6</chem> $\rho^0 = 1.45$	6.50 <sup>12</sup> 144 <sup>12</sup> ---	6.60 (+1.5) 167 (+16.0) 3330	6.51 (+0.2) 153 (+6.3) 3780
<b>TNT, -15.0</b> <chem>C7H5N3O6</chem> $\rho^0 = 1.36$	6.20 <sup>12</sup> 124 <sup>12</sup> ---	6.32 (+1.9) 145 (+16.9) 3380	6.22 (+0.3) 134 (+8.1) 3790
<b>TNT, -15.0</b> <chem>C7H5N3O6</chem> $\rho^0 = 1.00$	5.00 <sup>12</sup> 67 <sup>12</sup> 3400 <sup>8</sup>	5.30 (+6.0) 80 (+19.4) 3410 (+0.3)	5.21 (+4.2) 77 (+14.9) 3750 (+10.3)
<b>TNT, -15.0</b> <chem>C7H5N3O6</chem> $\rho^0 = 0.80$	4.34 <sup>12</sup> 37 <sup>12</sup> ---	4.79 (+10.4) 54 (+45.9) 3330	4.74 (+9.2) 53 (+43.2) 3610
<b>45. BTF, +144.0</b> <chem>C6N6O6</chem> $\rho^0 = 1.86$	8.49 <sup>13</sup> 360 <sup>13</sup> ---	8.43 (-0.7) 343 (-4.7) 4590	8.40 (-1.1) 336 (-6.7) 5570
<b>BTF, +144.0</b> <chem>C6N6O6</chem> $\rho^0 = 1.76$	8.26 <sup>2</sup> --- ---	8.14 (-1.5) 307 4700	8.14 (-1.5) 302 5600
<b>46. HNB, +10.0<sup>12</sup></b> <chem>C6N6O12</chem> $\rho^0 = 1.97$	9.30 <sup>2</sup> --- ---	8.89 (-4.4) 382 4360	8.47 (-8.9) 329 5470
<b>47. TNM, +13.0</b> <chem>C4N4O8</chem> $\rho^0 = 1.64$	6.36 <sup>2</sup> 159 <sup>2</sup> 2800 <sup>2</sup>	6.22 (-2.2) 150 (-5.7) 2180 (-22.1)	5.54 (+12.9) 116 (-27.0) 2860 (+2.1)
<b>48. TNTAB, +270.0</b> <chem>C6N12O6</chem> $\rho^0 = 1.74$	8.58 <sup>2</sup> --- ---	8.44 (-1.6) 321 4600	8.39 (-2.2) 312 5640
<b>49. FEFO, +178.0</b> <chem>C5H6N4O10F2</chem> $\rho^0 = 1.59$	7.50 <sup>12</sup> 250 <sup>12</sup> ---	7.20 (-4.0) 234 (-6.5) 3520	7.19 (-4.1) 211 (-15.6) 4390

Table 1. Experimental and Calculated Detonation Properties<sup>a</sup>

EXPLOSIVE <sup>b</sup>	EXP	BKWR <sup>c</sup>	BKWS <sup>d</sup>
50.LX-04 85/15 HMX/VIT <sup>e</sup> $\rho^0 = 1.86$	8.46 <sup>13</sup> 350 <sup>13</sup> ---	8.41 (-0.6) 342 (-2.3) 2940	8.39 (-0.8) 304 (-13.1) 3840
51.LX-07 90/10 HMX/VIT $\rho^0 = 1.87$	8.64 <sup>13</sup> --- ---	8.64 (0.0) 364 2990	8.70 (+0.7) 327 3920
52.LX-09, +2.00 C <sub>1.43</sub> H <sub>2.74</sub> N <sub>2.59</sub> O <sub>2.72</sub> F <sub>0.2</sub> $\rho^0 = 1.84$	8.81 <sup>13</sup> 377 <sup>13</sup> ---	8.84 (+0.3) 377 (0.0) 3120	9.05 (+2.7) 347 (-8.0) 4050
53.LX-10 95/5 HMX/VIT $\rho^0 = 1.86$	8.82 <sup>13</sup> 375 <sup>13</sup> ---	8.79 (-0.3) 376 (+0.3) 3070	8.93 (+1.2) 342 (-8.8) 4010
54.LX-11 80/20 HMX/VIT $\rho^0 = 1.87$	8.32 <sup>13</sup> --- ---	8.24 (-1.0) 328 2860	8.15 (-2.0) 288 3750
55.AP, -70.6 Cl <sub>1</sub> H <sub>4</sub> N <sub>1</sub> O <sub>4</sub> $\rho^0 = 1.00$	3.70 <sup>12</sup> --- ---	--- --- ---	4.02 (+8.6) 40 2010
56.LX-15 95/5 HNS/KEL <sup>f</sup> $\rho^0 = 1.58$	6.84 <sup>13</sup> --- ---	--- --- ---	6.73 (-1.6) 181 4210
57.LX-17 92.5/7.5 TATB/KEL $\rho^0 = 1.91$	7.63 <sup>13</sup> --- ---	--- --- ---	8.08 (+5.9) 289 3361
58.PBX-9010 90/10 RDX/KEL $\rho^0 = 1.78$	8.37 <sup>13</sup> 328 <sup>13</sup> ---	--- --- ---	8.46 (+1.1) 307 (-6.4) 4250
59.PBX-9404, +0.81 C <sub>1.4</sub> H <sub>2.75</sub> N <sub>2.57</sub> O <sub>2.69</sub> Cl <sub>0.03</sub> F <sub>0.01</sub> , $\rho^0 = 1.84$	8.80 <sup>13</sup> 375 <sup>13</sup> ---	--- --- ---	8.98 (+2.0) 341 (-9.1) 3910
60.PBX-9407, +0.81 C <sub>1.41</sub> H <sub>2.66</sub> N <sub>2.54</sub> O <sub>2.69</sub> Cl <sub>0.07</sub> F <sub>0.09</sub> , $\rho^0 = 1.60$	7.91 <sup>13</sup> 287 <sup>13</sup> ---	--- --- ---	7.92 (+0.1) 248 (-13.6) 4170
61.PBX-9502 95/5 TATB/KEL $\rho^0 = 1.90$	7.71 <sup>13</sup> --- ---	--- --- ---	8.12 (+5.3) 287 3320
62.PBX-9503 80/15/5 TATB/HMX/KEL $\rho^0 = 1.90$	7.72 <sup>13</sup> --- ---	--- --- ---	8.28 (+7.3) 300 3450

a. The entries under EXP, BKWR, and BKWS are detonation velocity (D) in km/s, detonation pressure (P) in kbars, and detonation temperature (T) in K, respectively. The numbers in parenthesis are percent error.

b. Common acronyms are followed by the heat of formation in kcal/mol. When no heat of formation is given, the heat of formation of the individual components can be found elsewhere in the paper. Acronym details are given in references 12 and 13. The density units are g/cc.

c. BKWR parameters  $\beta$ ,  $\theta$ , and  $\kappa$  are 0.176, 1850, and 11.8.

d. BKWS parameters  $\beta$ ,  $\theta$ , and  $\kappa$  are 0.298, 6620, and 10.5.

e. VIT (Viton A), C<sub>5</sub>H<sub>3.5</sub>F<sub>6.5</sub>,  $h_f = -332.7$  kcal/mol

f. KEL, C<sub>8</sub>H<sub>2</sub>Cl<sub>3</sub>F<sub>11</sub>,  $h_f = -161.0$  kcal/mol

Table 3. Detonation Properties of Explosives Containing Al<sup>a</sup>

EXPLOSIVE	EXP	FULL	PARTIAL <sup>b</sup>
63.H-6, -0.81, 20% Al C <sub>1.89</sub> H <sub>2.59</sub> N <sub>1.61</sub> O <sub>2.01</sub> Al <sub>0.74</sub> Ca <sub>0.005</sub> Cl <sub>0.009</sub> $\rho^0 = 1.75$	7.90 <sup>13</sup> --- ---	7.22 (-8.6) 215 5250	7.49 (-5.2) 216 4050
64.HBX-1, -2.54, 17% Al C <sub>2.06</sub> H <sub>2.62</sub> N <sub>1.57</sub> O <sub>2.07</sub> Al <sub>0.63</sub> Ca <sub>0.005</sub> Cl <sub>0.009</sub> $\rho^0 = 1.71$	7.31 <sup>13</sup> 220 <sup>13</sup> ---	7.18 (-1.8) 211 (-4.1) 4990	7.38 (+0.96) 209 (-5.0) 3980
65.HBX-3, -2.53, 35% Al C <sub>1.66</sub> H <sub>2.18</sub> N <sub>1.21</sub> O <sub>1.60</sub> Al <sub>1.29</sub> Ca <sub>0.005</sub> Cl <sub>0.009</sub> $\rho^0 = 1.84$	7.12 <sup>13</sup> --- ---	6.27 (-11.9) 152 5270	6.91 (-2.9) 173 4150
66.HMX/Al (90/10) 90/10% HMX/Al $\rho^0 = 1.76$	8.3 <sup>18</sup> --- ---	8.32 (+0.2) 291 5020	8.41 (1.3) 285 4360
67.HMX/Al (80/20) 80/20% HMX/Al $\rho^0 = 1.82$	8.3 <sup>18</sup> --- ---	7.93 (-4.5) 271 5840	8.22 (-1.0) 268 4480
68.HMX/Al (70/30) 70/30% HMX/Al $\rho^0 = 1.86$	8.0 <sup>18</sup> --- ---	7.27 (-9.1) 224 6210	7.82 (-2.3) 235 4560
69.HMX/Al (60/40) 60/40% HMX/Al $\rho^0 = 1.94$	7.7 <sup>18</sup> --- ---	6.86 (-10.9) 180 5450	7.46 (-3.1) 204 4590
70.MINOL-2 40/40/10% AN/TNT/AL $\rho^0 = 1.68$	5.82 <sup>13</sup> --- ---	7.23 (+24.2) 211 4930	6.30 (+8.2) 144 3030
71.RDX/Al (90/10) 90/10% RDX/Al $\rho^0 = 1.68$	8.03 <sup>12</sup> 246 <sup>12</sup> ---	8.02 (-0.12) 264 (+7.3) 5070	8.08 (+0.6) 257 (+4.5) 4400
72.RDX/Al (80/20) 80/20% RDX/Al $\rho^0 = 1.73$	7.77 <sup>12</sup> 227 <sup>12</sup> ---	7.60 (-2.2) 244 (+7.5) 5880	7.81 (+0.5) 237 (+4.4) 4500
73.RDX/Al (70/30) 70/30% RDX/Al $\rho^0 = 1.79$	7.58 <sup>12</sup> 210 <sup>12</sup> ---	7.03 (-7.3) 205 (-2.4) 6120	7.49 (-1.2) 212 (+0.95) 4570
74.RDX/Al (60/40) 60/40% RDX/Al $\rho^0 = 1.84$	7.20 <sup>12</sup> 211 <sup>12</sup> ---	6.42 (-10.8) 156 (-26.1) 5380	6.93 (-3.8) 174 (-17.5) 4580
75.RDX/Al (50/50) 50/50% RDX/Al $\rho^0 = 1.89$	6.81 <sup>12</sup> 190 <sup>12</sup> ---	5.78 (-15.1) 120 (-36.8) 5130	6.02 (-11.6) 119 (-37.4) 4490
76.TNETB <sup>c</sup> /Al (90/10) 90/10% TNETB/Al $\rho^0 = 1.75$	8.12 <sup>12</sup> 262 <sup>12</sup> ---	7.85 (-3.3) 269 (+2.7) 4804	7.91 (-2.6) 258 (-1.5) 4710
77.TNETB/Al (80/20) 80/20% TNETB/Al $\rho^0 = 1.82$	7.99 <sup>12</sup> 248 <sup>12</sup> ---	7.53 (-5.8) 256 (+3.2) 6310	7.73 (-3.3) 244 (-1.6) 4750
78.TNETB/Al (70/30) 70/30% TNETB/Al $\rho^0 = 1.88$	7.84 <sup>12</sup> 227 <sup>12</sup> ---	6.99 (-10.8) 219 (-3.5) 6510	7.43 (-5.2) 219 (-3.5) 4770

Table 3. Detonation Properties of Explosives Containing Al<sup>a</sup>

EXPLOSIVE	EXP	FULL	PARTIAL <sup>b</sup>
79.TNT/Al (89.4/10.6)	7.05 <sup>12</sup>	7.02 (-0.4)	7.12 (+1.0)
89.4/10.6% TNT/Al	---	203	200
$\rho^0 = 1.72$	---	4570	3910
80.TNT/Al (78.3/21.7)	7.05 <sup>12</sup>	6.59 (-6.5)	6.94 (-1.6)
78.3/21.7% TNT/Al	189 <sup>12</sup>	183 (-3.2)	187 (-1.1)
$\rho^0 = 1.80$	---	5450	4080
81.TNT/Al (67.8/32.2)	7.05 <sup>12</sup>	5.94 (-15.7)	6.71 (-4.8)
67.8/32.2% TNT/Al	---	144	168
$\rho^0 = 1.89$	---	5620	4200

a. See Table 1 footnotes.

b. Only 50% of the Al or AN is assumed to interact with the combustion products.

c. TNETB, C<sub>6</sub>H<sub>6</sub>N<sub>6</sub>O<sub>14</sub>, h<sub>f</sub> = -119.0 kcal/molTable 4. Detonation Properties of Explosives Containing NO<sub>3</sub><sup>-a</sup>

EXPLOSIVE	EXP	FULL	PARTIAL <sup>b</sup>
82.AN, -87.4	1.50 <sup>12</sup>	3.57 (+138)	2.23 (+48.7)
H <sub>4</sub> N <sub>2</sub> O <sub>3</sub>	---	23.6	8.9
$\rho^0 = 0.7$	---	1720	837
83.AMATEX-20	7.55 <sup>2</sup>	8.05 (+6.6)	7.53 (-0.3)
21/41/38% AN/RDX/TNT	---	255	221
$\rho^0 = 1.66$	---	3710	3330
84.AMATEX-40	7.01 <sup>2</sup>	7.97 (+13.7)	6.84 (-2.4)
42/20/38% AN/RDX/TNT	---	236	172
$\rho^0 = 1.61$	---	3430	2650
85.AMATOL-80/20	5.20 <sup>13</sup>	8.46 (+62.7)	5.65 (+8.7)
80/20% AN/TNT	---	248	102
$\rho^0 = 1.60$	---	3070	1440
86.AMATOL-60/40	5.76 <sup>2</sup>	8.05 (+39.8)	6.24 (+8.3)
60/40% AN/TNT	---	234	136
$\rho^0 = 1.60$	---	3200	2040
87.BARATOL	4.93 <sup>12</sup>	6.56 (+33.1)	4.95 (+1.6)
24/76% TNT/BN <sup>c</sup>	140 <sup>12</sup>	195 (+39.3)	109 (-22.1)
$\rho^0 = 2.61$	---	2880	1900
BARATOL	4.87 <sup>13</sup>	6.34 (+30.2)	4.78 (-1.8)
24/76% TNT/BN	---	182	101
$\rho^0 = 2.55$	---	2890	1900
(66). MINOL-2	5.82 <sup>13</sup>	7.23 (+24.2)	6.30 (+8.2)
40/40/10%	---	211	144
AN/TNT/AL	---	4930	3030
$\rho^0 = 1.68$			

a. See Table 1 footnotes.

b. Only 50% of the Al or AN is assumed to interact with the combustion products.

c. BN, Ba<sub>1</sub>N<sub>2</sub>O<sub>6</sub>, h<sub>f</sub> = -237.0 kcal/molTable 5. Detonation Properties of Explosives with B, Pb, and Si<sup>a</sup>

EXPLOSIVE	EXP	BKWS	BKWS <sup>b</sup>
88.BORACITOL	4.86 <sup>13</sup>	4.84 (-0.4)	---
40/60% TNT/Boric	---	60	---
Acid, <sup>c</sup> $\rho^0 = 1.55$	---	1440	---
89.LEAD AZIDE, +112	5.18 <sup>12</sup>	4.98 (-3.9)	---
N <sub>6</sub> Pb <sub>1</sub>	---	183	---
$\rho^0 = 4.00$	---	4080	---
LEAD AZIDE, +112.0	---	4.50	---
N <sub>6</sub> Pb <sub>1</sub>	158 <sup>12</sup>	147 (-7.0)	---
$\rho^0 = 3.70$	---	4130	---
90.LEAD STYPHNATE, +92.3	5.20 <sup>12</sup>	7.09 (+36.3)	5.19 (-0.2)
C <sub>6</sub> H <sub>3</sub> N <sub>3</sub> O <sub>9</sub> Pb <sub>1</sub>	---	326	231
$\rho^0 = 2.90$	---	5300	5640
91.LX-02, -49.1	7.37 <sup>13</sup>	7.13 (-3.3)	6.63 (-10.0)
C <sub>2.77</sub> H <sub>4.86</sub> N <sub>0.93</sub> O <sub>2.99</sub>	---	177	162
Si <sub>0.03</sub> , $\rho^0 = 1.44$	---	3090	3120
92.LX-08, -44.0	6.56 <sup>13</sup>	7.30 (+11.3)	6.92 (+5.5)
C <sub>1.93</sub> H <sub>4.39</sub> N <sub>0.81</sub> O <sub>2.95</sub>	---	178	168
Si <sub>0.50</sub> , $\rho^0 = 1.42$	---	4210	4230
93.XTX-8003, -39.0	7.30 <sup>13</sup>	7.84 (+7.4)	7.36 (+0.8)
C <sub>1.80</sub> H <sub>3.64</sub> N <sub>1.01</sub> O <sub>3.31</sub>	---	225	209
Si <sub>0.27</sub> , $\rho^0 = 1.53$	---	4280	4330
94.XTX-8004, -1.42	7.22 <sup>13</sup>	8.09 (+12.0)	7.59 (+5.1)
C <sub>1.62</sub> H <sub>3.78</sub> N <sub>2.16</sub> O <sub>2.43</sub>	---	235	218
Si <sub>0.27</sub> , $\rho^0 = 1.55$	---	4210	4250
XTX-8004, -1.42	7.45 <sup>12</sup>	7.86 (+5.5)	7.39 (-0.8)
C <sub>1.62</sub> H <sub>3.78</sub> N <sub>2.16</sub> O <sub>2.43</sub>	---	218	203
Si <sub>0.27</sub> , $\rho^0 = 1.50$	---	4230	4270

a. See Table 1 footnotes.

b. For Lead Styphnate, BKW parameter  $\beta$  changed from 0.298 to 0.04. For explosives with Si, BKW parameter  $\beta$  changed from 0.298 to 0.249.c. Boric Acid, H<sub>3</sub>B<sub>1</sub>O<sub>3</sub>, h<sub>f</sub> = -262.0 kcal/mol

## UNLIKE-PAIR INTERACTIONS AT HIGH PRESSURE AND HIGH TEMPERATURE

F. H. Ree and M. van Thiel  
Lawrence Livermore National Laboratory  
University of California  
Livermore, CA 94550

Although there are more unlike-pairs than like-pairs in detonation products, information on unlike-pair interactions is scarce at present. We describe how unlike pair-interactions involving dissociation products of CO and CO<sub>2</sub> can be derived by means of an accurate statistical mechanical theory of mixtures and recent shock wave data of CO and CO<sub>2</sub>. We then extend this complex study further by interpreting shock data of liquid NO and N<sub>2</sub> + O<sub>2</sub> mixture. It was done by constraining the resulting potentials to agree with all available Hugoniot data of chemical species occurring in detonation products in a self-consistent manner.

### INTRODUCTION

The primary constituents of condensed explosives are C, O, H, and N atoms. A study of complex explosives with full atomic compositions requires information on like- and unlike-pair interactions among dissociation products. There are more unlike-pairs than like-pairs in detonation products. Nevertheless, information on unlike-pair interactions is mostly unavailable at present. An approximation known as the Lorentz-Berthelot rule is currently being used to circumvent difficulties associated with the lack of information. On the other hand, shock wave data of N<sub>2</sub>, O<sub>2</sub>, NO, N<sub>2</sub>+O<sub>2</sub> mixtures, liquid air, CO, and CO<sub>2</sub> have recently become available. The data indicate that these molecular species will dissociate behind strong shock waves and that the use of the Lorentz-Berthelot rule cannot satisfactorily describe the shock wave data.

Earlier analyses of shock wave data were limited to individual detonation products. Such an approach is not useful if dissociation occurs. A correct approach in this case is to include shock data of all relevant detonation products and carry out the analyses simultaneously in a self-consistent manner without changing interaction parameters to match each case individually. We have given a brief description<sup>1</sup> on how to do such a self-consistent study in the case of NO and CO. The present work is its elaboration and extension to

other detonation products. In a separate paper<sup>2</sup> of this Proceedings, we report similar work to extract unlike-pair interactions from high explosive data (RX23-AB, HNB, PETN).

The present work considers much more detailed equations of state of graphite and diamond than our previous analyses. In addition, we have included a previously neglected phase of carbon,<sup>3</sup> i.e., liquid carbon, which is predicted when CO and CO<sub>2</sub> molecules are strongly shocked. Inclusion of liquid carbon explains a previous theoretical discrepancy in matching experimental Hugoniot data of liquid CO and CO<sub>2</sub>.

### THEORY OF PURE SYSTEMS

We need to understand pure systems before understanding mixtures. The essential equilibrium thermodynamics of pure systems is due to van der Waals who more than one hundred years ago considered a harsh repulsive portion, rather than the long-range portion, of an intermolecular potential to control thermodynamics and structural properties of condensed phases. Five ingredients are needed to formulate his idea into a mathematically rigorous framework. They are:

- (a) an optimum way to break an intermolecular potential  $V(r)$  into a hard-sphere-like interaction  $V_0(r)$  and a perturbation term  $W(r)$ ,

$$V(r) = V_0(r) + W(r), \quad (1)$$

(b) a specific expression for  $V_0(r)$  and  $W(r)$ ,

(c) an expression for the Helmholtz free energy  $A$ ,

$$A = A_0 + A_1, \quad (2)$$

in terms of the Helmholtz free energy  $A_0$  for the reference system and another ( $A_1$ ) for the perturbation potential,

(d) an expression for the hard-sphere (HS) diameter to represent the reference potential,

(e) convenient expressions for the HS equation of state (EOS) and radial distribution function  $g^{HS}(r)$ .

Specific expressions needed for items (a) - (e) are available for classical fluids.<sup>4,5</sup> One approach is to use our perturbation theory (PT)<sup>4</sup> which extends earlier theories to high pressure. The second approach is to employ a variational theory (VAR) developed by Ross.<sup>5</sup> Both give about equally reliable results. As an example, Fig. 1 compares  $PV/NkT$  ( $P$  = pressure,  $V$  = volume,  $T$  = temperature;  $\rho = N/V$ ) data based on the PT and Monte Carlo (MC) simulation data for an exponential-6 (exp-6) potential, where parameters,  $\alpha$ ,  $\epsilon$ , and  $r^*$  are specific to each chemical species and can be obtained from experimental data. It is noteworthy that PT is about equally reliable as MC (within MC's statistical errors). Yet, its computation time takes several orders of magnitude less than those required for MC.

$$V(r) = \epsilon/(\alpha - 6) \{ 6 \exp[\alpha(1 - r/r^*)] - \alpha (r^*/r)^6 \}$$

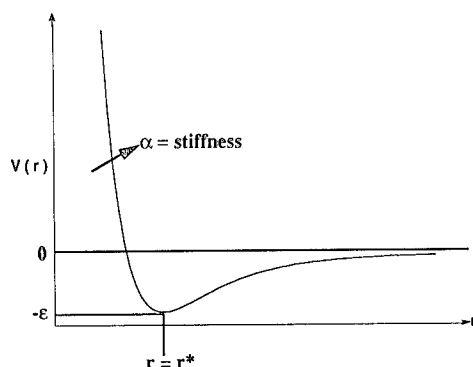


FIGURE 1. EXP-6 POTENTIAL (WITH  $\alpha=13$ ) AND ITS EOS.

## THEORY OF MIXTURES

Compared to like-pair potentials described above, the exp-6 parameters for unlike-pairs are experimentally less well known. But they can be expressed as

$$\begin{aligned} r_{ij}^* &= k_{ij}(r_{ii}^* + r_{jj}^*)/2, \\ \epsilon_{ij} &= l_{ij}\sqrt{\epsilon_{ii}\epsilon_{jj}}, \\ \alpha_{ij} &= m_{ij}\sqrt{\alpha_{ii}\alpha_{jj}}, \end{aligned} \quad (3)$$

in terms of like-pair parameters ( $r_{ii}^*, \epsilon_{ii}, \alpha_{ii}$ ) and small multiplicative constants ( $k_{ij}, l_{ij}, m_{ij}$ ) which can be fixed if appropriate theoretical or experimental data are available. Otherwise, we set  $k_{ij} = l_{ij} = m_{ij} = 1$  which is commonly referred to as the Lorentz-Berthelot rule.

We assume that mixtures of chemical species interacting with exp-6 potentials [Fig. 1 and Eq. (3)] are represented by a *hypothetical one-component* system interacting with a composition ( $x_i$ )-dependent exp-6 parameters,<sup>6</sup> as shown in Fig. 2 below.

The fact that one-component calculations are much simpler than mixture calculations provides a reasonable justification for using this so-called improved van der Waals one-fluid model. In fact, comparisons with two-component MC for He-H<sub>2</sub> mixtures in Fig. 2 shows that the effective one-component model (using VAR) produces excellent results at high pressure and temperature.

PV/NkT			
	Density $\rho(r^*)3/\sqrt{2}$	Exact	Perturbation Theory
fluid	0.9	3.27	3.27
	1.0	3.81	3.80
	1.5	8.08	8.04
	2.05	16.58	16.65
solid	2.308	20.28	20.19
	2.7	30.66	30.84

Pressure (GPa)			
$T$ (K)	$V$ (cm <sup>3</sup> /mol)	2-component Monte Carlo	Effective 1-component theory
50	20	0.047±0.01	0.05
100	14	0.338±0.008	0.35
300	10	1.856±0.02	1.91
4000	8	12.43±0.02	12.6
7000	4.5	54±1	55.3

$$(r^*)^3 = \sum_{i,j \geq 1} x_i x_j (r_{ij}^*)^3$$

$$\epsilon = \sum_{i,j \geq 1} x_i x_j \epsilon_{ij} (r_{ij}^*)^3 / (r^*)^3$$

$$\alpha = \sum_{i,j \geq 1} x_i x_j \epsilon_{ij} \alpha_{ij} (r_{ij}^*)^3 / (r^*)^3 \epsilon$$

( $x_i$  = concentration of species  $i$ )

FIGURE 2. EFFECTIVE ONE-COMPONENT EXP-6 PARAMETERS AND COMPARISONS OF THE RESULTING PRESSURE (GPa) OF AN EQUIMOLAR MIXTURE OF H<sub>2</sub> AND He WITH THE EXACT MONTE CARLO RESULTS.

#### SHOCK CHEMISTRY AND SELF-CONSISTENCY CRITERION

We will focus our analyses on shock data of liquid samples of CO,<sup>7</sup> CO<sub>2</sub>,<sup>8</sup> NO, and N<sub>2</sub>+O<sub>2</sub> mixtures.<sup>9</sup> A strong shock forces these molecules to dissociate into a mixture of chemical species with C, O, N atoms. Obviously, CO and CO<sub>2</sub> will produce the same dissociation products, as are true for liquid NO and N<sub>2</sub>+O<sub>2</sub> mixtures. Intermolecular potentials for dissociated species should be applicable to all shock data. Hence, the correct way to find intermolecular potentials is to consider all shock data together. This condition imposes a strong self-consistency criterion on intermolecular potentials.

We assume these dissociation products and their parent molecules (CO, CO<sub>2</sub>, NO, or N<sub>2</sub>+O<sub>2</sub>) to establish a chemical equilibrium. Their chemical concentrations  $\{n_i\}$  will change with  $T$  and  $P$  and have to be determined by minimizing the Gibbs free energy  $G(P, T, \{n_i\})$ ,

$$G(P, T, \{n_i\}) = \sum_i n_i \mu_i, \quad (4)$$

with respect to  $\{n_i\}$ . The connection between the statistical mechanical theories discussed above (including interaction potentials  $V_{ij}(r)$ ) and  $G(P, T, \{n_i\})$  occurs strictly through the chemical potentials  $\mu_i$ . The minimization is done by the chemical equilibrium code CHEQ<sup>10</sup> which evaluates  $\mu_i$  using the variational theory and the effective one-component mixture model.

#### LIKE- AND UNLIKE-PAIR POTENTIALS

A large number of intermolecular potentials are needed for such analyses. We will first discuss how unlike pair-interactions involving dissociation products of CO and CO<sub>2</sub> can be derived by means of the aforementioned statistical mechanical theory of mixtures and recent shock wave data of CO and CO<sub>2</sub>. We need to know interactions of dissociation products involving single elements (O-O, CO<sub>2</sub>-O, O<sub>2</sub>-O<sub>2</sub>), molecule-molecule interactions (CO-CO, CO<sub>2</sub>-CO<sub>2</sub>, CO<sub>2</sub>-O<sub>2</sub>, O<sub>2</sub>-CO), and molecule-atom and atom-atom interactions (CO-O, CO<sub>2</sub>-O). In addition, there will be carbon residues in graphitic, diamond, or liquid phase. The present work considers much more detailed equations of state of graphite and diamond than those used in the previous work. We have also included a previously neglected phase of carbon, i.e., liquid carbon.<sup>2</sup>

Our calculations employ exp-6 potentials with parameters,  $\epsilon$ ,  $r^*$ , and  $\alpha$ , which are varied until they satisfactorily describe all shock wave data. Like-pair interaction parameters can be determined at low pressure where the dissociation is unimportant, while unlike-pair interactions are determined by adjusting them until they can describe shock wave data at high pressure. Among the nine interactions described earlier, however, there are only three like-pair interactions (O<sub>2</sub>-O<sub>2</sub>, CO-CO, CO<sub>2</sub>-CO<sub>2</sub>) which can be determined from shock data of liquid O<sub>2</sub>, CO, and CO<sub>2</sub> at low pressures where dissociation is insignificant. The rest have to be determined by adjusting  $(k_{ij}, l_{ij}, m_{ij})$  parameters in Eq. (3) until they can satisfactorily describe shock wave data at high pressure. The exp-6 parameters for O<sub>2</sub>-O<sub>2</sub>, O<sub>2</sub>-O, O-O were



derived from the Hugoniot data of liquid O<sub>2</sub>.<sup>11</sup> We test the self-consistency of the resulting potentials obtained by using all relevant Hugoniot data. If the self-consistency test fails, we further fine-tune the exp-6 parameters until the desired self-consistency is achieved by such an iteration.

Figure 3 shows the Hugoniot of liquid CO and CO<sub>2</sub> obtained by adjusting the interactions parameters in such a manner. They are compared with the experimental data.<sup>7,8</sup> As shock pressures increase, CO<sub>2</sub> will partially dissociate into CO and O species,  $CO_2 \rightarrow CO + O$ . At pressures above 40 GPa, our calculation predicts that a significant proportion of carbon atoms will condense into the liquid phase,  $CO_2 \rightarrow CO + O \rightarrow \frac{1}{2}(\text{liquid C} + CO + O)$ .

The appearance of the liquid carbon gives rise to a shoulder-like structure seen in the experimental data near 40 GPa.

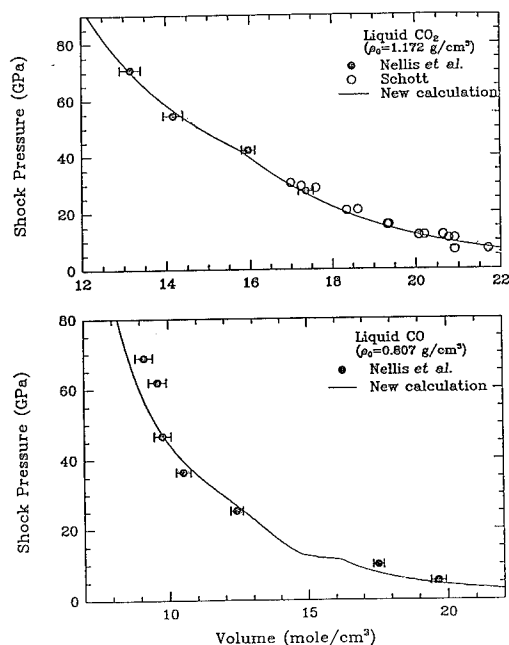


**FIGURE 3. THEORETICAL AND EXPERIMENTAL HUGONIOTS OF LIQUID CO<sub>2</sub> AND CO**

The same set of interaction parameters also gives a satisfactory Hugoniot for liquid CO.<sup>7</sup> Such an additional test provides a strong self-consistency criterion for unlike-pair potentials. In the case of liquid CO, the shoulder-like structure in the Hugoniot occurs near 13 GPa and is due to the graphite-diamond transition. At pressures below

13 GPa, the experimental data follows close to a nonreactive Hugoniot of CO, while the theoretical calculation predicts liquid CO to dissociate. This difference accounts for the deviations in Fig. 3 at  $P < 13$  GPa. From this observation, we conclude that the experimental shock data represent a metastable CO. Otherwise, one would expect the experimental data to agree with the theoretical calculation. Interaction parameters used in the present studies are:  $\{r^*(\text{\AA}), \epsilon/k(K), \alpha\} = (4.12, 108.3, 13)$  and  $(4.20, 245.6, 13.5)$  for CO-CO and CO<sub>2</sub>-CO<sub>2</sub>, respectively.

We next analyze the shock data of liquid N<sub>2</sub>+O<sub>2</sub> and NO.<sup>9</sup> Analyses of shock data of N<sub>2</sub>+O<sub>2</sub> and NO, done at low pressures, mostly require molecular species (not atomic species). In contrast, high temperatures attained in liquid air<sup>8</sup> will produce atomic O and N and will require accurate knowledge of effective interactions of O and N atoms with other molecular species. Nevertheless, we have allowed atomic O and N in our calculations. Even ignoring minor decomposition products such as O<sub>3</sub>, N<sub>2</sub>O, and NO<sub>2</sub>, there are a large number of dissociation products (N<sub>2</sub>, O<sub>2</sub>, NO, O, and N), hence, a large number of pair interactions to consider. Our study considers five like-pair interactions (N<sub>2</sub>-N<sub>2</sub>, N-N, O<sub>2</sub>-O<sub>2</sub>, O-O, and NO-NO) and ten unlike-pair interactions (N<sub>2</sub>-N, O<sub>2</sub>-O, N<sub>2</sub>-O<sub>2</sub>, N<sub>2</sub>-NO, O<sub>2</sub>-NO, NO-N, NO-O, N<sub>2</sub>-O, O<sub>2</sub>-N, and N-O). We use the same interaction parameters for O<sub>2</sub>-O<sub>2</sub>, O<sub>2</sub>-O, O-O as used in the analyses of the CO and CO<sub>2</sub> shock data. The exp-6 parameters for N<sub>2</sub>-N<sub>2</sub>, N<sub>2</sub>-N, N-N were derived from the Hugoniot data of liquid N<sub>2</sub>.<sup>12-15</sup> The Hugoniot data<sup>9</sup> of liquid NO are taken at low pressures where we can ignore a negligible amount of monatomic species (N or O). Thus, we can use the NO data to infer the exp-6 parameters for NO-NO, N<sub>2</sub>-O<sub>2</sub>, N<sub>2</sub>-NO, O<sub>2</sub>-NO. We test the self-consistency of the resulting potentials obtained by using the Hugoniot data of doubly shocked NO, liquid N<sub>2</sub>+O<sub>2</sub>,<sup>9</sup> and liquid air.<sup>8</sup>

Figure 4 shows the theoretical Hugoniot of NO at the end of such an iterative procedure. Agreement with the experimental Hugoniot data<sup>9</sup> is satisfactory. The self-consistency condition mentioned above implies that the same parameter set should also give a reasonable agreement for liquid N<sub>2</sub>, O<sub>2</sub>, and air. Interactions parameters for NO-NO are:  $\{r^*(\text{\AA}), \epsilon/k(K), \alpha\} = (3.97, 112.9, 12.2)$ . A more detailed analysis of the exp-6 parameters for all like- and unlike-pairs and the analyses of Hugoniots of other detonation products containing C, H, N, O atoms are beyond the scope of the limited space of this paper. Some preliminary

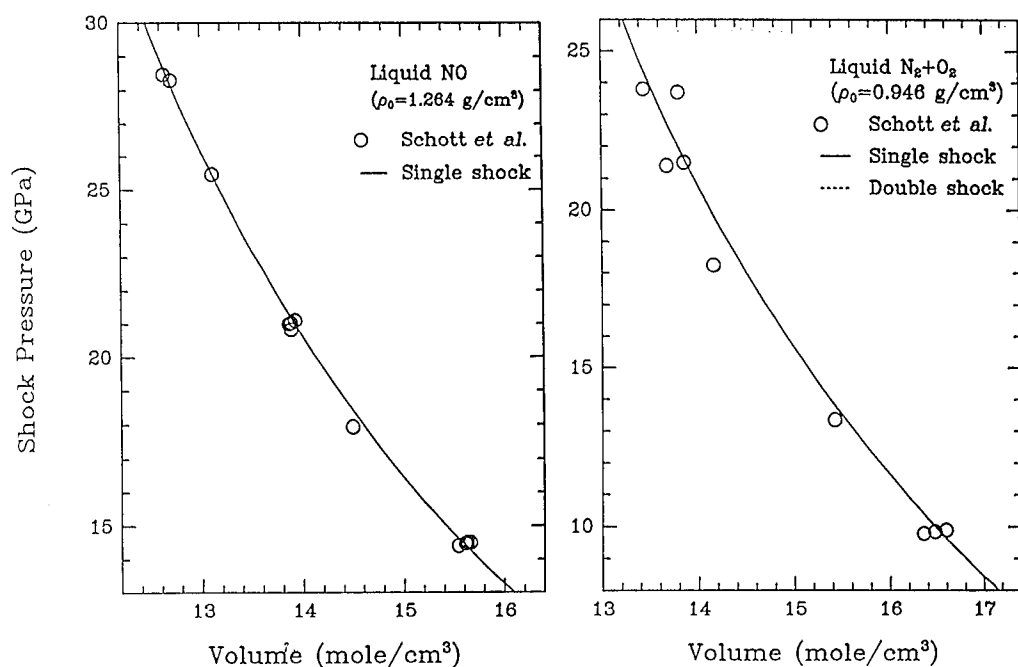


FIGURE 4. THEORETICAL AND EXPERIMENTAL HUGONIOTS OF LIQUID N<sub>2</sub>+O<sub>2</sub> AND NO

results are given in the following paper.<sup>3</sup> Final results will be given in a separate paper.<sup>16</sup>

## CONCLUDING REMARKS

We have described how to extract information on like- and unlike-pair interactions among various chemical species by examining shock wave data of these systems. The resulting potentials we obtained describe all available Hugoniot data in a self-consistent manner. This is particularly useful for unlike-pair interactions, because such an information is scarce at present. The present investigations also showed an important role that the liquid carbon plays in interpreting the shock wave data of liquid CO and CO<sub>2</sub>.

Unlike-pair interactions are also important in the description of supercritical fluid-fluid phase separations. Since the free energy difference between two fluid phases must vanish at the phase transition point, it is sensitive to unlike-pair interactions. One accurate way of determining the unlike-pair interaction in condensed phases is to try to match experimental phase-boundary data by adjusting unlike-pair potential parameters in a theoretical model as used here. Recent advent of the heated diamond-anvil cell technology makes

such experiments possible at high pressure and temperature.<sup>17,18</sup>

Finally, it is worthwhile to state that shocks can produce different chemical reactions in different samples. Reactions will depend on inherent properties such as the strength of chemical bonds, stoichiometry, and intermolecular forces. In addition, the variation of the strength of shock waves also provides an additional external variable to change the nature of chemical reactions. In accordance with Le Chatelier principle, shock pressures and temperatures work against each other, as we have seen that the former favoring recombination reactions and the latter dissociation reactions.

## ACKNOWLEDGMENTS

This work was performed under the auspices of the U. S. Department of Energy by the LLNL under contract number W-7405-ENG-48.

## REFERENCES

1. Ree, F. H. and van Thiel, M., "Effective Like- and Unlike-Pair Interactions at High Pressure and High Temperature," in *Shock Compression of Condensed Matter*, 1991, New York: North Holland, 1992, pp. 225-228.

2. (a) van Thiel, M. and Ree, F. H., "Thermodynamic Properties and Phase Diagram of the Graphite-Diamond-Liquid Carbon System," *High Pressure Research*, Vol. 7, No. 10, 1992, p. 607; (b) van Thiel, M. and Ree, F. H., "A High Pressure Liquid-Liquid Phase Change in Carbon," *Phys. Rev. B*, to appear.
3. van Thiel, M., Ree, F. H.; and Haselman Jr., L. C., "The Significance of Interaction Potentials of Water with Other Molecules in the EOS of High Explosive Products," paper presented at this Symposium.
4. Kang, H. S.; Lee, C. S.; Ree, T.; and Ree, F. H., "A Perturbation Theory of Classical Equilibrium Fluids," *J. Chem. Phys.*, Vol. 82, No. 1, 1985, p. 414.
5. Ross, M., "A High-Density Fluid-Perturbation Theory Based on an Inverse 12th-Power Hard-Sphere Reference System," *J. Chem. Phys.*, Vol. 71, No. 4, 1979, p. 1567.
6. Ree, F. H., "Simple Mixing Rule for Mixtures with Exp-6 Interactions," *J. Chem. Phys.*, Vol. 78, No. 1, 1983, p. 409.
7. Nellis, W. J.; Ree, F. H.; van Thiel, M.; and Mitchell, A. C., "Shock Compression of Liquid Carbon Monoxide and Methane to 90 GPa (900 kbar)," *J. Chem. Phys.*, Vol. 75, No. 6, 1981, pp. 3055-3063.
8. Nellis, W. J.; Mitchell, A. C.; Ree, F. H.; Ross, M.; Holmes, N. C.; Trainor, R. J.; and Erskine, D. J., "Equation of State of Shock-Compressed Liquids: Carbon Dioxide and Air," *J. Chem. Phys.*, Vol. 95, No. 7, 1991, p. 5268; G. L. Schott, *High Pressure Research*, Vol. 6, No. 3, 1991, p. 187.
9. Schott, G. L., Shaw, M. S.; and Johnson, J. D., "Shocked States from Initially Liquid Oxygen-Nitrogen Systems," *J. Chem. Phys.*, Vol. 82, No. 9, 1985, pp. 4264.
10. Ree, F. H., "A Statistical Mechanical Theory of Chemically Reacting Multiphase Mixtures: Application to the Detonation Properties of PETN," *J. Chem. Phys.*, Vol. 81, No. 3, 1984, p. 1251.
11. Hamilton, D. C.; Nellis, W. J.; Mitchell, A. C.; and van Thiel, M., "Electrical Conductivity and Equation of State of Shock-Compressed Liquid Oxygen," *J. Chem. Phys.*, Vol. 88, No. 8, 1988, p. 5042.
12. Ross, M., "The Dissociation of Dense Liquid Nitrogen," *J. Chem. Phys.*, Vol. 86, No. 12, 1987, p. 7110.
13. Hamilton, D. C. and Ree, F. H., "Chemical Equilibrium Calculations on the Molecular-to-Nonmolecular Transition of Shock-Compressed Liquid Nitrogen," *J. Chem. Phys.*, Vol. 90, No. 9, 1989, p. 4972.
14. Nellis, W. J.; Holmes, N. C.; Mitchell, A. C.; and van Thiel, M., "Phase Transition in Fluid Nitrogen at High Densities and Temperatures," *Phys. Rev. Lett.*, Vol. 53, No. 17, 1984, p. 1661.
15. Wackerle, J.; Seitz, Q. W. L.; and Jamieson, J. C., "Shock-Wave Equation of State for High-Density Oxygen," in *Behavior of Dense Media Under High Dynamic Pressure*, Gordon and Breach, New York, 1968, pp. 85-93.
16. Ree, F. H. and van Thiel, M., manuscript in preparation.
17. Costantino, M. and Rice, S. F., "Supercritical Phase Separation in H<sub>2</sub>O-N<sub>2</sub> Mixture," *J. Phys. Chem.*, Vol. 95, 1991, p. 9034.
18. van Hinseberg, M. G. E.; Verbrugge, R.; Schouten, J. A., presented at the *Eleventh Symposium on Thermophysical Properties*, Boulder, CO, June 23-27, 1991.

## THE SIGNIFICANCE OF INTERACTION POTENTIALS OF WATER WITH OTHER MOLECULES IN THE EOS OF HIGH EXPLOSIVE PRODUCTS

M. van Thiel, F. H. Ree, and L. C. Haselman, Jr.  
Lawrence Livermore National Laboratory  
Livermore, CA 94550

We have made a systematic set of improvements in the interaction potentials pertinent to nitrogen-water-carbondioxide mixtures, based on previous improvements of the high pressure interactions of molecular products of O, N, and C. This work continues our effort to remove canceling errors in the intermolecular potentials used to compute detonation properties. The present work tests the effect of the presence of hydrogen in post-detonation mixtures. To minimize canceling errors, we evaluate the interactions of N<sub>2</sub>, H<sub>2</sub>O, and CO<sub>2</sub> in HNB, RX-23-AB and PETN. This work indicates that the H<sub>2</sub>O-CO<sub>2</sub> interaction is quite non-ideal. The resulting set of potential constants is compared to the empirical EOS for experimental systems that use HMX formulations.

### INTRODUCTION

The chemical equilibrium and thermodynamic properties of detonated explosive mixtures at high temperature (T) and pressure (P) depend critically on all interactions between the major products. Improvements in the homomolecular interaction of nitrogen, carbon-dioxide, and condensed carbon have had significant effects on detonation properties of LX-14 (an HMX formulation). Extensive work on O, N, and C products<sup>1</sup> also showed the importance of including high temperature unstable species in determining the potential-constant of the major products of detonation. That work also showed the need to improve the unlike pair interaction constants in our statistical mechanical chemical equilibrium theory (CHEQ). Thirdly, a recent comparison of experimental and theoretical detonation velocities<sup>2</sup> (D) indicated that the original set of interaction potentials used contains canceling errors that limit the overall effectiveness of the code as a predictor of high P and T properties of reactive mixtures.

This study proceeds from explosives with simple product mixtures, RX-23-AB, HNB, and PETN, to HMX-like mixtures. The present set of potential constants is compared to the experimental EOS used for a number of experimental systems that use LX-14.

### THEORY

The equations of state (EOS) of high pressure molecular mixtures are determined by our chemical equilibrium code CHEQ. This code uses a statistical mechanical model for the EOS of the hot gaseous molecular mixture and EOS models based on Grüneisen forms for condensed systems.<sup>3</sup> The intermolecular potentials used for the gas phase components are of the exponential repulsive and inverse sixth power attractive (exp-6) form

$$\phi_{ij} = \frac{\epsilon_{ij}}{\alpha_{ij} - 6} \{ 6 \exp[\alpha_{ij}(1 - r/r_{ij}^*)] - \alpha_{ij}(r_{ij}^*/r)^6 \} \quad (1)$$

which has been the preferred form for high pressure work for some time.<sup>4</sup> The most general form of  $\epsilon$  is

$$\epsilon_{ii} = \epsilon_{ii}^* (1 + \lambda_{ii}/T), \quad (2)$$

where  $\lambda_{ii} \neq 0$  for polar molecules.

Interactions between unlike pairs (i.e. N<sub>2</sub>-CO<sub>2</sub>) are obtained using the combination rules:

$$\epsilon_{ij} = k_{ij} \sqrt{\epsilon_{ii} \epsilon_{jj}}; \quad r_{ij}^* = \frac{1}{2} \ell_{ij} (r_{ii} + r_{jj}); \quad \alpha_{ij} = m_{ij} \sqrt{\alpha_{ii} \alpha_{jj}}, \quad (3)$$

with the exp-6 potential constants used for the homomolecular interactions. The refinement of the

unlike pair interaction parameters  $k_{ij}$ ,  $\ell_{ij}$ , and  $m_{ij}$ , originally set equal to 1, is a primary result of our recent work.

## BACKGROUND

### Need for refinement

The original potentials were obtained with the corresponding states principle and with some preliminary Hugoniot data for  $O_2$ ,  $N_2$ ,  $CO_2$ ,  $CO$ ,  $H_2O$ ,  $NH_3$ , and  $CH_4$ . Graphite and diamond were modeled by Murnaghan forms.<sup>5</sup> Early work, on PBX-9404,<sup>6</sup> allowed for a refinement of  $\ell_{ij}$  in the  $CO_2$ - $H_2O$  and  $H_2O$ - $N_2$  interactions. More recent shock wave data, that extend the range and accuracy of the experimental database, are now available for  $O_2$ ,  $N_2$ , air,  $CO$ ,  $CO_2$ , and  $NO$ .<sup>1</sup> These data improved the accuracy of the intermolecular potentials and required the inclusion of additional reaction products in the theoretical description of the reactive mixtures. A discussion of those results is beyond the scope of this work and will be discussed elsewhere in these proceedings. We have used the results of the analysis of the new data in this study.

### Carbon

In addition, refinements of the carbon EOS allowed us to compute the regions of stability of the three known phases: graphite, diamond, and liquid carbon.<sup>7</sup> The model uses Grüneisen forms for solid graphite and diamond, including electronic effects for graphite and liquid. This carbon model fits all available data for graphite and diamond. The liquid state is defined by a liquid scaling model that is based on the heat capacity of known liquids. The properties of the liquid are scaled on the melting line, which is defined by an improved Lindemann law<sup>8</sup> for anisotropic systems, needed to explain graphite melting data. Since liquid carbon, graphite, and diamond are present in high-temperature and -pressure mixtures, we can offer a more accurate description of the effect of carbon in such mixtures.

### Preliminary refinements

To clarify the effect the above corrections have on the behavior of explosives, a systematic study was done to show how each one of the component changes affects the detonation velocity ( $D$ ) of LX14. This study, shown in Fig. 1, allowed us to isolate the significant effects of the refinements. The original mixture allowed for a second nitrogen-rich

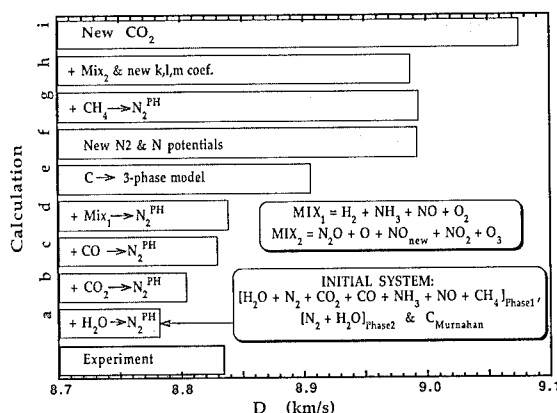


FIGURE 1. EFFECT OF CHANGES IN THE COMPONENT INTERACTION POTENTIALS ON THE DETONATION VELOCITY OF LX-14: SEE TEXT FOR DETAILS

gas phase which originally contained only  $H_2O$  and  $N_2$ . Subsequent refinements to the CHEQ code<sup>9</sup> facilitated the introduction of additional species, already present in phase 1 to the second phase. The effect of these additions, shown by b, c, and d, improved the agreement with experiment. Replacing the Murnaghan form of diamond with a more realistic and accurate 3-phase carbon EOS further increased  $D$ , as did the more accurate  $N_2$  EOS.<sup>10</sup> Minor components like  $CH_4$  and those designated as  $Mix_2$  ( $= N_2O, O, NO_{new}, NO_2, O_3$ ), and their interaction parameters had a minor effect, but the improvements made in  $CO_2$  are significant. The  $mix_2$  components are required to produce agreement with the more recent Hugoniot data.<sup>1</sup>

These changes all increase the detonation velocity, indicating that additional interactions need refinement. In particular, the absence of the effects of hydrogen products in the data studied up to this point need to be considered. This work extends the study to the  $N_2$ - $CO_2$ - $H_2O$  interactions.

### $N_2$ - $H_2O$ - $CO_2$ INTERACTIONS

There are essentially three materials that can be used as sources for the triad of interactions;  $N_2$ - $H_2O$ ,  $N_2$ - $CO_2$  and  $CO_2$ - $H_2O$ . These are: a mixture of Hydrazine-nitrate, hydrazine, and water, which produces an essentially binary mixture of  $H_2O$  and  $N_2$ ; Hexanitrobenzine, which produces primarily  $N_2$  and  $CO_2$ , and PETN, whose mayor products are  $CO_2$  and  $H_2O$  with a lesser amount of  $N_2$  near the Chapman Jouguet (CJ) point. Since good data are now also available for these three components. A careful scrutiny of these data now follows.

## Water, Nitrogen & RX-23-AB

Since these results were recently covered in a separate report,<sup>11</sup> this work will only be summarized here. We have refined the potentials of water and nitrogen with special attention to the data in the explosive CJ pressure range and below. Figure 2 shows two possible fits for water. The data of Rice<sup>12</sup> match up reasonably well to more recent data.<sup>13</sup> Hugoniot **a** fits the high pressure points quite adequately but is slightly lower than experiment at  $P \leq 10$  GPa and higher than data near 40 GPa. Close scrutiny of the experimental Hugoniot in the  $U_s$ - $U_p$  plane suggests a two-line fit with the lines meeting in this 40 GPa region. The data is, however not accurate enough to clearly indicate a second order transition, and a single potential appears to be adequate. Potential **b** is closer to the 40 GPa cluster and covers the low pressure points better.

Another reason for increasing the pressure for  $P \leq 10$  GPa is the empirical EOS obtained from hydrodynamic simulations of the acceleration of copper cylinders filled with HMX mixtures or PETN.<sup>14</sup> These indicate somewhat higher pressures in that range than theoretically predicted, qualitatively consistent with the deviation from experiment obtained with potential **a**.

Reflected shock data are equally well fitted by either potential, with perhaps a slight improvement for some points near  $P \approx 150$  GPa. The uncertainty is too large here to make a judgment about the potential in that pressure range.

Similar observations were made on the  $N_2$  Hugoniot and adjustments to the potentials were

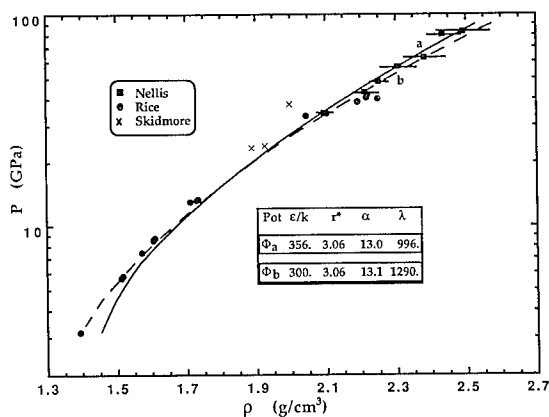


**FIGURE 2. WATER HUGONIOTS: EXPERIMENT VS. THEORY**

made, as indicated in Table 1.  $N_{2,a}$  are the original constants that predates the new high pressure data. Those data require coefficients  $N_{2,b}$  or  $N_{2,c}$ . The curvature of the Hugoniot had to be changed by reducing the value of the exponential parameter  $\alpha$  in  $N_{2,c}$  to improve the agreement with Zubarev's low pressure data.<sup>14</sup> Unlike water, nitrogen exhibits significant dissociation behind strong shocks with  $P > P_{CJ}$ . The two N atom potentials are included since  $N_b$  should be used with  $N_{2,a}$  and  $N_{2,c}$  potentials, while  $N_a$  yields best results with  $N_{2,b}$  for these overdriven shocks.

**TABLE 1. EXPONENTIAL-6 COEFFICIENTS**

Material	$\epsilon_{ij}/k$ K	$r_{ij}^*$ Å	$\alpha_{ij}$	$\lambda_{ij}$ K
H <sub>2</sub> O <sub>a</sub>	356	3.06	13.0	996
H <sub>2</sub> O <sub>b</sub>	300	3.06	13.1	1290
N <sub>2,a</sub>	101.9	4.09	13.2	0.0
N <sub>2,b</sub>	101.9	4.15	13.2	0.0
N <sub>2,c</sub>	293.0	3.91	11.5	0.0
N <sub>a</sub>	600	2.39	10.0	0.0
N <sub>b</sub>	600	2.47	10.0	0.0
CO <sub>2,a</sub>	245.6	4.28	13.0	0.0
CO <sub>2,b</sub>	245.6	4.20	13.5	0.0
CO <sub>2,c</sub>	245.6	4.17	13.5	0.0
CO <sub>2</sub>	245.6	4.17	13.0	0.0
CO	108.3	4.12	13.0	0.0
O <sub>2</sub>	125.0	3.86	13.2	0.0
O	700.0	2.40	11.0	0.0
O <sub>3</sub>	211.0	4.82	13.0	0.0

The detonation velocity of the water - hydrazine-nitrate - hydrazine mixture, RX-23-AB, was not sensitive to the difference between the two water potentials in Table 1, but was affected by the changes in the  $N_2$  potential. The  $N_{2,c}$  constants are consistent with the data if  $\ell_{ij} = 1.04$  in Eq. (3). The uncertainty range of the RX-23-AB detonation velocity does not distinguish between  $N_{2,b}$  and  $N_{2,c}$  constants, consequently, only the above considerations for selection apply.

## Nitrogen, carbondioxide, & HNB

Hexanitrobenzene is a light sensitive explosive that produces CO<sub>2</sub> and N<sub>2</sub> on detonation. We use the parameters for  $N_{2,c}$  for this study and those that follow. Figure 3 shows CO<sub>2</sub> hugoniot computed with several potentials and the recent data of Schott<sup>16</sup> and Nellis.<sup>17</sup> The potentials used for the non reactive curve<sup>5</sup> were obtained with argon-based corresponding states theory and

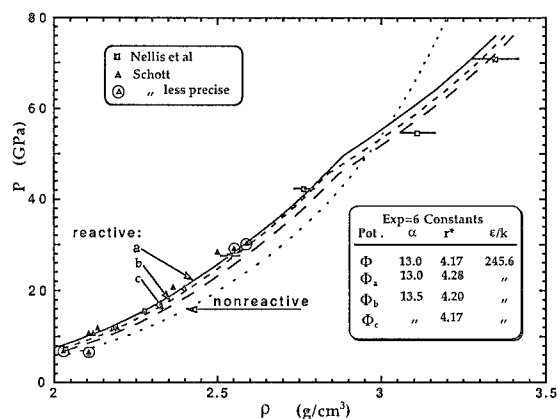


FIGURE 3. THEORETICAL AND EXPERIMENTAL CO<sub>2</sub> HUGONIOTS

agreed reasonably well with the original solid CO<sub>2</sub> data.<sup>18</sup> The other potential constants in Table 1 give increasingly better fits to the low pressure data, but appear to be too stiff in the region of dissociation. Previous work with somewhat smaller  $r^*_{ii}$  for CO than used here yielded somewhat more dissociation and a better fit to the high pressure data. We will use parameters of CO<sub>2,a</sub> in further work, since they also offer the best fit at pressures as low as 0.1 GPa. Below that pressure the curves converge as the ideal gas state is approached.

The components of hexanitrobenzene products are more numerous at high pressures than below CJ. At the Chapman Jouguet state, CO plays a small (7%) role in the CO<sub>2</sub>-N<sub>2</sub> mixture. Some atomic oxygen (3%) and NO (3%) are also present. At higher pressures a number of other species including liquid carbon play a (cumulative, 43% at 100 GPa) role in the EOS.

A single experimental cylinder test has been done using hexanitrobenzene, which has recently been reanalyzed.<sup>14,19</sup> A JWL EOS,

$$P = A(1 - \frac{\omega}{R_1 V})e^{-R_1 V} + B(1 - \frac{\omega}{R_2 V})e^{-R_2 V} + \frac{\omega E}{V}, \quad (4)$$

traditionally derived from these data, has coefficients:  $A = 1131.79$  GPa,  $B = 16.53$  GPa,  $\omega = 0.47$ ,  $R_1 = 4.713$ ,  $R_2 = 1.209$ , and  $E_0 = 12$  GPa. The JWL EOS from that test has been used to compute the Hugoniot ( $E = E_0 + [P + P_0][1 - V]/2$ ) with  $V = \rho_0/\rho$  near the CJ point in Fig. 4. The most significant result in Fig 4 is the improved agreement of the new CO<sub>2</sub> and N<sub>2</sub> parameters with

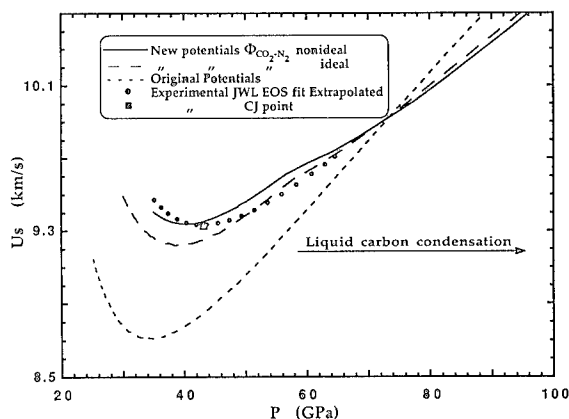


FIGURE 4. SHOCK SPEEDS FROM THEORETICAL CALCULATIONS AND JWL EXPERIMENTAL FIT FOR HNB

this experiment, even assuming ideal interaction. Use of  $(k/\ell/m)_{N_2-CO_2} = 1/1.0315/1$  allows an exact match of the experimental HNB detonation velocity (9.34 km/s), using the above mentioned potentials. No overdriven Hugoniot exists to test the high pressure calculation. Analysis of the preliminary cylinder-expansion test yielded a JWL isentrope

$$P_s = Ae^{R_1 V} + Be^{R_2 V} + CV^{-(\omega+1)} \quad (5)$$

(with the above constants and  $C = 1.976$  GPa) that may be compared to our calculations. The deviations vary from 0 near CJ to .85 GPa (at 25 GPa). Somewhat better agreement (-0.23 to 0.45 GPa) is obtained with the more recent analysis of the data<sup>19</sup> (which yielded  $A = 1047.883$  GPa,  $B = 7.9824$  GPa,  $C = 1.39612$  GPa,  $\omega = 0.28$ ,  $R_1 = 4.472$ ,  $R_2 = 0.85$ ,  $\rho_0 = 1.965$  g/cm<sup>3</sup>, and  $E_0 = 13.2$  GPa).

#### Carbondioxide-water interaction in PETN

Water and carbondioxide are known to form a number of metastable structures that may also exist at high pressure. One may therefore expect that strong non-ideal interactions between these two exist at high pressure. Shock and detonation data of PETN (C<sub>5</sub>H<sub>8</sub>N<sub>4</sub>O<sub>12</sub>) offer the best experimental data, to date, that allow us to quantitatively study this interaction at high pressure. Figure 5 shows the major high-pressure high-temperature decomposition products of this molecule.

The mixture, consisting primarily of CO<sub>2</sub>, H<sub>2</sub>O and N<sub>2</sub>, becomes heterogeneous just above the detonation pressure where a nitrogen-rich phase

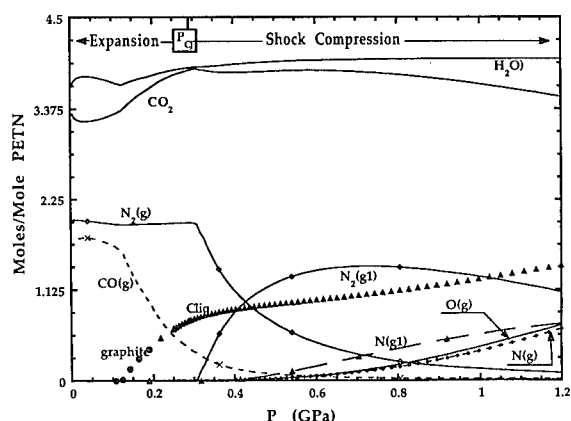


**FIGURE 5. COMPOSITION OF PETN PRODUCT MIXTURE BEHIND OVERDRIVEN SHOCK AND ON EXPANSION FROM THE DETONATION STATE**

(with major components labeled  $N_2(g1)$  and  $N(g1)$ ) separates out behind the overdriven shock front as the nitrogen content of the water-rich phase,  $N_2(g)$ , decreases. The other significant component is CO, which is roughly 3% of the total amount of gas just behind the detonation front, and rapidly increases as the pressure drops and the amount of condensed (liquid or graphitic) carbon decreases. At the detonation pressure the major components are therefore  $N_2$  and  $CO_2$ , with  $N_2$  coming in at 20% of the gaseous mixture. The  $\Phi(N_2-CO_2)$  and  $\Phi(N_2-H_2O)$  were determined above, so that the  $CO_2-H_2O$  interaction may be refined with these data.

Figure 6 shows the states reached by expansion from the CJ state as pressure differences from the experimental JWL isentrope of Green et al.,<sup>20</sup> with  $A = 1032.16$  GPa,  $B = 90.57014$ ,  $C = 3.72735$  GPa, and  $\omega = 0.56$ ,  $E_0 = 0.108$  GPa, and  $\rho_0 = 1.763$  g/cm<sup>3</sup>. The original EOS set assumed ideal unlike specie interaction while the final fit includes the constants for the two major species ( $[k/l/m]_{CO_2-H_2O} = 1.0/0.974/0.9$ ). Two improved potential sets that include the parameters of the recent high pressure analysis discussed in these proceedings show the effect of including the  $CO_2-H_2O$  interaction constants. The absence of these constants in Fig. 1 is the major cause for the deviation observed there due to the improved  $CO_2-CO_2$  potential. The difference between the latest fit and the improved EOS is the change in the water and  $N_2$  potentials discussed above.

The overdriven Hugoniot data in Fig. 7 also show the effect of the improvements made as a

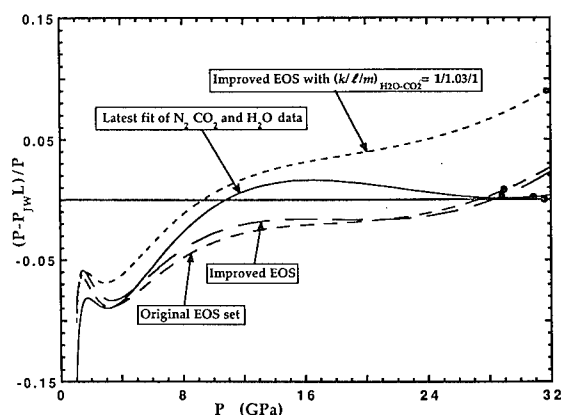


**FIGURE 6. ISENTROPIC EXPANSION STATES RELATIVE TO THE EXPERIMENTAL JWL ISENTROPE OF PETN**

consequence of including the high-temperature species. The old potential set produces a much higher curvature than the newer equations of state. The effect of including the  $CO_2-H_2O$  interaction again is clear from the curves representing the new EOS with and without the unlike interaction constants. The data appear to show a slightly higher compression between 50 and 90 GPa that is not observed by the present EOS. This could be spurious or a consequence of the complexity of the  $CO_2-CO_2$  and  $CO_2-H_2O$  interactions. The low pressure adjustments to the potentials of the components has not noticeably affected the EOS in this range.

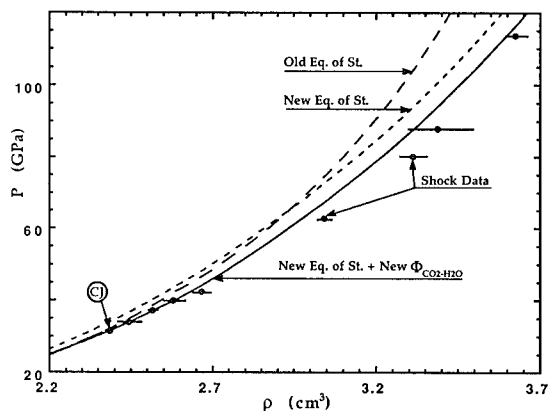


**FIGURE 7. EXPERIMENTAL AND THEORETICAL PETN HUGONIOTS**



## HMX MIXTURES

Some results of the application of the EOS set determined above will now be considered. The composition diagram in Fig. 8. is considerably more complex than that of PETN. Nitrogen and carbon are comparable to the water content while  $\text{CO}_2$  plays the secondary role. At the CJ point carbon is in the diamond form, which does not liquefy until the shock pressure reaches 80 GPa. The nitrogen content (both N and  $\text{N}_2$ ) is primarily in the  $\text{N}_2$ -rich phase, with only 10% or less N atoms in the water-rich phase. The non-ideal effect of carbon, is the main unknown here.

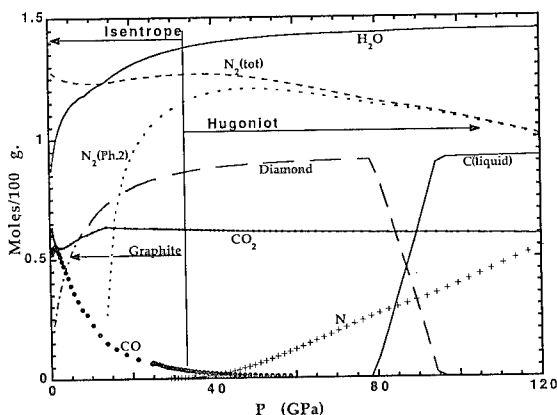


**FIGURE 8. THE MAJOR REACTION PRODUCTS OF LX-14 ALONG THE PRINCIPAL ISENTROPE AND THE OVERDRIVEN HUGONIOT**

The shock velocity is plotted as a function of pressure in Fig. 9. The original calculations have a stronger pressure dependence than experiment, as reported earlier.<sup>6</sup> The present set of potential constants greatly improved the high pressure slope. The minimum in the curve (the detonation velocity) is somewhat higher than experiment. Additional work on high carbon explosives is needed to determine whether this is due to our representation of the carbon EOS or to uncertainties in the potentials governing the six interactions between the major products excluding carbon, i.e.  $\text{N}_2$ ,  $\text{CO}_2$ , and  $\text{H}_2\text{O}$ .

The release isentrope is obtained from hydrodynamic simulations of experiments on various metal-explosive configurations: flat plates, cylindrical tubes, and other 2-D structures. The traditional EOS form has been the JWL form of Eq. (4) or (5). Figure 10 is a plot of the deviations of two empirical JWL isentropes from our theory.

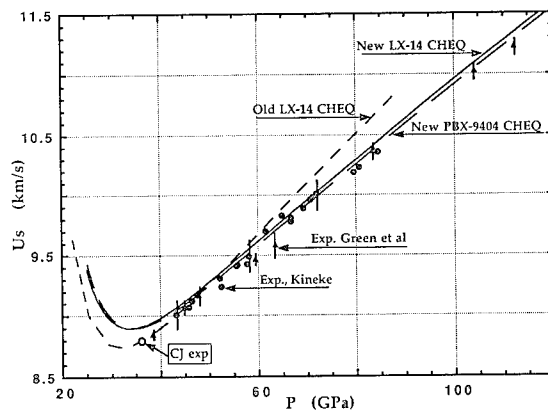


**FIGURE 9. SHOCK SPEED VERSUS PRESSURE FOR LX-14 AND PBX-9404: OLD AND NEW THEORY VS. EXPERIMENT**

Two-dimensional configurations (cylinders or other curved plates) tend to yield more consistent results and are perhaps less sensitive to transient effects caused by slow reactions (with relaxation times  $\tau \approx 10$  to 50 ns) near the detonation front. We therefore emphasize here two fits that offer the best agreement with two-dimensional systems.

Two features stand out in this plot. First, the sharp fluctuation below 12 GPa is due to the diamond to graphite transition observed in the theory, which is not representable in the JWL form. Secondly, the relatively large deviation from 0 at the CJ point. This is due to the disagreement in  $P_{CJ}$  between the theoretical equilibrium CJ point and experimental shock pressure, which is generally affected by the reactive wave-front profile. Furthermore, the use of an EOS with a detonation

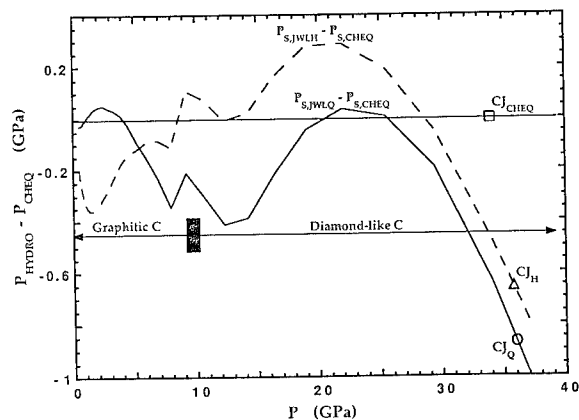


**FIGURE 10. PRESSURE DIFFERENCE BETWEEN TWO LX-14 JWL FORMS FROM HYDRO SIMULATIONS OF EXPERIMENTAL SYSTEMS, AND CHEQ**

velocity that is not consistent with experiment leads to significant deviations between hydro-simulation and experiment. It is therefore important for the theory to match the experimental detonation velocity. Since carbon is a significant component, the effect of different carbon cluster structures on the EOS need to be evaluated to determine the cause for the deviation in Fig. 9.

## SUMMARY

The improved accuracy of intermolecular potentials for  $N_2$ ,  $O_2$ ,  $NO$ ,  $N_2O$ ,  $NO_2$ ,  $CO$ ,  $CO_2$ , and their dissociation products required the investigation of systems containing water to explain the deviation between computed and experimental detonation velocities. The  $N_2$ - $N_2$ ,  $CO_2$ - $CO_2$ , and  $H_2O$ - $H_2O$  interactions were carefully reevaluated with added emphasis on the region below  $P = 40$  GPa, important to detonation waves. The unlike interactions between these molecules were obtained from the three explosives: HNB, RX-23-AB and PETN. The resulting set of potentials gave a good match to the overdriven Hugoniot of PBX-9404 and empirical release isentropes of LX-14. The detonation velocity, however, is  $\approx 0.8\%$  larger than experiment. Hydrodynamic simulations require a better match between experiment and theory. The effect of non-equilibrium carbon clusters needs to be evaluated.

## ACKNOWLEDGMENTS

We wish to acknowledge very helpful discussions with Cliff Coon, Clark Souers, John Kury, Don Ornellas, and Randy Simpson on various aspects of the explosive properties. The work Al Nichols has done to improve CHEQ and keep the new versions working has been very helpful in improving the efficiency of this effort. This work was performed under the auspices of the U. S. DOE by the Lawrence Livermore National Laboratory under contract W-7405-ENG-48.

## REFERENCES

1. Ree, F. H. and van Thiel, M., "Effective like-and unlike-pair interactions at high pressure and high temperature," *Shock Compression of Condensed Matter*, 1991, North Holland, New York, 1992, pp. 225-228.
2. Simpson, R. L., Kury, J. W., Nichols III, A. L., Breithaupt, R. D., and Crawford, P. C., "Performance Evaluation of Insensitive Explosives," LLNL, P. O. Box 808, Livermore, California, unpublished preprint 1991.
3. Ree, F. H., "A statistical mechanical theory of chemically reacting multiphase mixtures: application to the detonation properties of PETN," *J. Chem. Phys.* Vol. **81**, No. 3, 1984, p. 1251.
4. van Thiel, M. and Alder, B. J., "Shock Compression of Argon," *J. Chem. Phys.* Vol. **44**, No. 3, (1966), pp. 1056-65.
5. Ree, F. H., "Post detonation behavior of condensed high explosives by modern methods of statistical mechanics," in *Proc. of the Seventh Symposium International on Detonation*, Naval Surface Weapons Center, White Oak, MD 20910, 1982 pp. 646-659.
6. Ree, F. H. and van Thiel, M., "Detonation behavior of LX-14 and PBX-9404: theoretical aspect," *Proc. Eighth Symposium International on Detonation*, Naval Surface Weapons Center MP 86-194, White Oak, Silver Spring, Maryland, 1985, pp. 501-512.
7. van Thiel, M. and Ree, F. H., "Theoretical description of the Graphite, Diamond and Liquid Phases of Carbon," *Int. J. of Thermophys.* Vol. **10**, No. 3, (1989), p. 227 and references quoted therein.
8. van Thiel, M., "Lindeman melting law for anisotropic crystals: graphite  $\rightarrow$  liquid carbon," *Shock Compression of Condensed Matter - 1991*, editors S. C. Schmidt, R. D. Dick, J. W. Forbes and D. G. Tasker, North Holland, New York, 1992, p. 165f.
9. Nichols III, A. L., and Ree, F. H., "CHEQ 2.0 User's Manual," LLNL Report #UCRL-MA-106754, Dec. 1990, Lawrence Livermore National Laboratory, P. O. Box 808, Livermore, CA 94550.
10. Hamilton, D. C., and Ree, F. H., "Chemical equilibrium calculations in the molecular-to-non-molecular transition of shock compressed liquid nitrogen," *J. Chem. Phys.* Vol. **90**, No. 9, 1989, pp. 4972-81.
11. van Thiel, M. and Ree, F. H., "Unlike Pair Interactions in  $N_2$ - $H_2O$  Mixtures," *High Pressure Science and Technology-1993*, to be published.
12. Rice, M. H., and Walsh, J. M., "Equation of State of Water to 250 Kilobars" *J. Chem. Phys.* Vol. **26**, No. 4, 1957, pp. 824-30.
13. Mitchell, A. C., and Nellis, W. J., "Equation of state and electrical conductivity of water and ammonia shocked to the 100 GPa pressure range," *J. Chem. Phys.* Vol. **76**, No 12, 1982, p. 6273.
14. Souers, P. C., and Kury, J. W., *Propellants Explosives and Pyrotechnics*, to be published.

15. Zubarev, V. N. and Telegen, G. S., *Soviet Phys. Doklady* Vol. 7, No. 1, 1962, p. 34-6.
16. Schott, G. L., , "Shock compressed carbon dioxide: liquid measurements and comparisons with selected models," *High Press. Res.* Vol. 6, No. 3, 1990, p. 187.
17. Nellis, W. J., Mitchell, A. C., Ree, F. H., Holmes, N. C., Trainor, R. J., and Erskine, D. J., "Equation of State of Shock-Compressed Liquids: Carbon Dioxide and Air, *J. Chem. Phys.* Vol. 95, No. 7. 1991, pp. 5268-72.
18. van Thiel, M., Ed., *Compendium of Shock Wave Data*, NTIS, NBS, Springfield, Virginia, 1977, Vol. 2, p. 342.
19. McGuire, R., private communication, LLNL, P. O. Box 808, Livermore, Cal., concerning the HNB EOS, 1981
20. Green, L. G., Lee, E. L., Breithaupt, D., and Walton, J., "The equation of state of PETN detonation products," in *Shock Waves in Condensed Matter 1987*, Editors, S. C. Schmidt and N. C. Holmes, North Holland, New-York, 1988, pp. 507-13.

# ANALYSIS OF HUGONIOTS AND DETONATION PROPERTIES OF EXPLOSIVES WITH JCZ3 EQUATION OF STATE\*

L. I. Stiel  
Polytechnic University  
Brooklyn, New York 11201

V. M. Gold and E. L. Baker  
U.S. ARMY ARDEC  
Picatinny, New Jersey 07800

A study has been conducted on the accuracy of the Exp-6 potential parameters currently utilized for the JCZ3 equation of state. Hugoniot curves for the major reaction products calculated with JCZ3 have been compared with the available experimental data to identify potential sources of improvement. Similar studies were conducted for the C-J pressures and detonation velocities of explosives, and for PBX-9404 at overdriven conditions. Generally good agreement with the experimental values resulted for the present JCZ3 parameters, with some improvement indicated for an optimized set. Computer procedures were also developed to investigate the possibility of gas-gas equilibria at elevated temperatures and pressures. Calculations with JCZ3 did not predict phase separation for nitrogen-water mixtures at temperatures above 1000 K.

## INTRODUCTION

The JCZ3 equation of state is widely used in the Tiger chemical equilibrium program for the calculation of thermodynamic properties of explosive mixtures. This equation of state, developed by Jacobs, Cowperthwaite, and Zwisler<sup>1,2</sup> is of the form

$$P = P_0(V) + G(V, T) \frac{RT}{V} \quad (1)$$

The first term in Equation (1) represents the limiting lattice pressure, and the second term includes the contributions of intermolecular forces.

\* Work supported by the Armament Research, Development and Engineering Center under the auspices of the U.S. Army Research Office Scientific Services Program administered by Battelle (Contract No. DAALO3-86-D-0001).

The values of  $P_0$  and  $G$  are calculated by the use of parameters for the Exp-6 potential function,

$$\phi = \epsilon \left[ \frac{6}{m-6} e^{m \left( 1 - \frac{r}{r^*} \right)} - \frac{m}{m-6} \left( \frac{r}{r^*} \right)^6 \right] \quad (2)$$

In the JCZ3 procedure, the exponent  $m$  is 13.5 for all reaction products, and the parameters  $\epsilon$  and  $r^*$  for the mixture are calculated from the combining rules:

$$\epsilon = \sum_i \sum_j x_i x_j \epsilon_{ij} \quad (3)$$

$$(r^*)^3 = \sum_i \sum_j x_i x_j (r_{ij}^*)^3 \quad (4)$$

where,

$$\epsilon_{ij} = \sqrt{\epsilon_i \epsilon_j} \quad (5)$$

$$r_{ij}^* = \frac{r_i^* + r_j^*}{2} \quad (6)$$

The older BKW equation of state is also used with the Tiger program. Finger et al<sup>3</sup> reparameterized the constants and component covolumes for the BKW equation of state by the use of data for detonation velocities and C-J pressures for explosives with a wide range of reaction products. Good agreement with the experimental C-J properties were obtained with the revised set of parameters (known as BKWR) for the explosives considered. These investigators found that the detonation velocities and pressures calculated with JCZ3 were in general slightly lower than those for BKWR, but in reasonable agreement with the experimental values. Improved results for C-J temperatures and isentropic expansion curves were obtained with the JCZ3 relationships.

The Exp-6 parameters  $\epsilon/k$  and  $r^*$  used with the JCZ3 equation of state for the major reaction products are essentially those established previously by Fickett<sup>4</sup> for the Lennard-Jones and Devonshire equation of state, with values of the exponent  $m$  in the range 14-15. These parameters have not been reanalyzed with more recent Hugoniot data for the reaction products, and with C-J pressures, velocities, and other data for explosives. In this study, Hugoniot curves resulting from available experimental data for water, carbon dioxide, nitrogen, and oxygen have been compared with values calculated with the JCZ3 equation of state, in an attempt to identify sources of improvement for the parameters, and their effects on the properties of explosive mixtures.

## ANALYSIS OF HUGONIOTS OF PRODUCTS

For water, experimental Hugoniot pressures were related to  $VS = (V_0/V-1)$  through relationships of the form

$$P = P_0 + A(VS) + B(VS)^2 + C(VS)^3 \quad (7)$$

where  $P_0$  is the initial pressure and  $V_0$  is the initial specific volume of the fluid.

In Figure 1, Hugoniot pressures for water as a function of  $VS$  calculated with JCZ3 and the parameters of Fickett<sup>4</sup> ( $r^* = 3.35$  and  $\epsilon/k = 138$ ) are seen to be in good agreement with the experimental values of Walsh and Rice<sup>5</sup> and of Mitchell and Nellis<sup>6</sup> for pressures to 850 kbar. The calculated curve represents values from the least squares relationship, Equation (7). The small deviations below 200 kbar are primarily due to the neglect of dipole-dipole interactions in the intermolecular potential function<sup>7</sup>, since the temperatures are below 1000 K for this region. The Hugoniot pressures calculated with the BKWR equation of state are essentially identical to those for the JCZ3 method, while the calculated temperatures are considerably lower, particularly at the highest pressures, as shown in Figure 2. It also can be seen from this figure that experimental Hugoniot temperatures<sup>8</sup> for water are intermediate to those calculated by these two procedures.

Comparisons between experimental Hugoniot pressures for nitrogen<sup>9,10,11</sup> and values calculated with JCZ3 are shown in Figure 3. The parameters obtained by Fickett<sup>4</sup> for this substance are  $\epsilon/k = 120$  and  $r^* = 4.05$  (with  $m = 15$ ). It can be seen that increased deviations result by this procedure at pressures above 300 kbars. Nitrogen is considered to dissociate at pressures above 400 kbars<sup>12</sup>, and this behavior can not be modeled with the present version of Tiger. However, values calculated for undissociated nitrogen with the BKWR relationships are considerably lower than the corresponding values with JCZ3 for this substance in the range 300 - 400 kbars, as shown in Figure 3.

For carbon dioxide, Nellis et al<sup>13</sup> and Schott<sup>14</sup> have recently reported experimental Hugoniot pressures for an initial state of the liquid at 218 K. It can be seen from Figure 4 that the Hugoniot pressures calculated with JCZ3 and the parameters determined by Fickett<sup>4</sup> ( $\epsilon/k = 200$ ,  $r^* = 4.2$ ) are somewhat lower than the corresponding experimental values from these sources. Similar deviations result with the BKWR procedure. Large deviations with JCZ3 also result for the earlier Hugoniot data of Zubarev and Telegin<sup>11</sup> for an initial state of solid carbon dioxide at 196 K. However, pressure-volume values which were corrected from the shock and particle measurements presented in this reference as suggested by Ross and Ree<sup>15</sup> are more consistent with those calculated with the JCZ3 relationships.

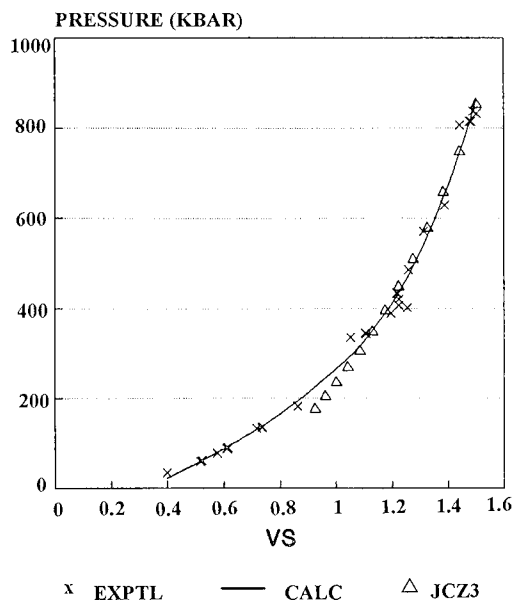


FIGURE 1. EXPERIMENTAL AND CALCULATED HUGONIOTS FOR WATER

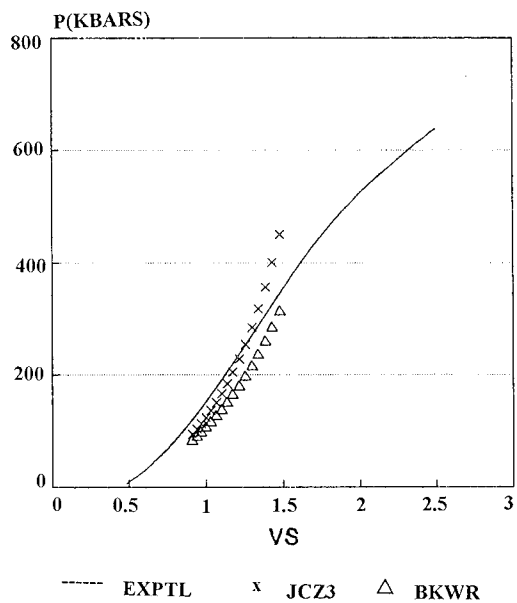


FIGURE 3. EXPERIMENTAL AND CALCULATED HUGONIOTS FOR NITROGEN

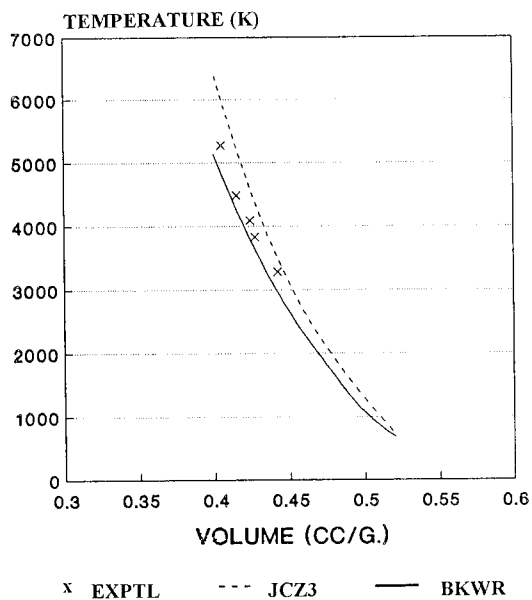


FIGURE 2. EXPERIMENTAL AND CALCULATED HUGONIOT TEMPERATURES FOR WATER

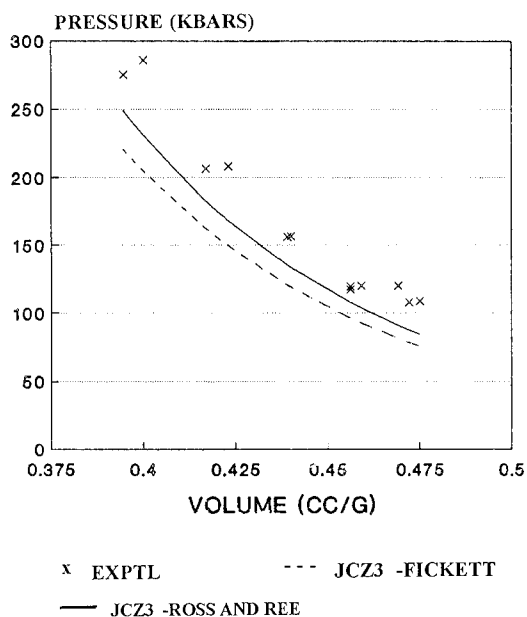


FIGURE 4. EXPERIMENTAL AND CALCULATED HUGONIOT CURVES FOR CARBON DIOXIDE.

In Figure 5, Hugoniot pressures for oxygen calculated with JCZ3 are seen to be in good agreement with the experimental values<sup>10,16</sup> for pressures to 600 kbars. It can also be seen that the values for this substance calculated with BKWR are somewhat lower for the complete pressure range.

Ross and Ree<sup>15</sup> have shown that parameters of the Exp-6 potential suitable for the calculation of Hugoniot curves for simple molecules such as argon and nitrogen should follow corresponding states relationships. Parameters  $r^*$  and  $\epsilon/k$  with  $m=13$  were determined for argon from liquid shock wave data by the use of relationships based on hard-sphere variational theory. From parameters determined for argon, the following dimensionless relationships were developed:

$$\frac{r^*}{V_c} = 0.759 \quad (8)$$

$$\frac{\epsilon/k}{T_c} = 0.808 \quad (9)$$

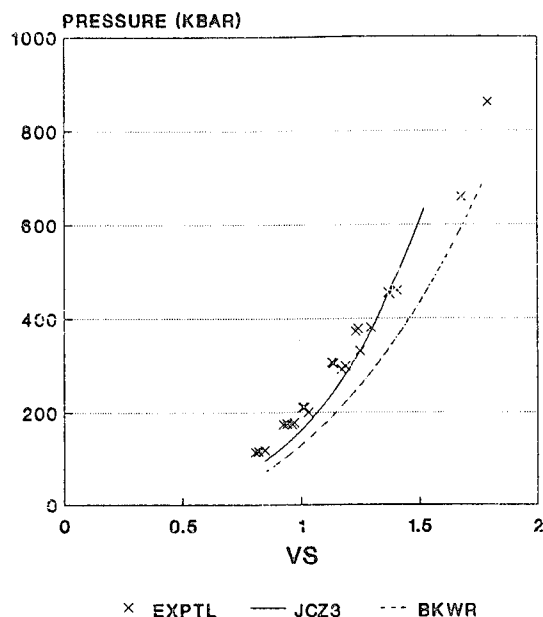


FIGURE 5. EXPERIMENTAL AND CALCULATED HUGONIOTS FOR OXYGEN

Parameters calculated from Equations (8) and (9) for simple molecules are similar to the Exp-6 parameters of Fickett<sup>4</sup> utilized with JCZ3, as shown in Table 1. Calculations with JCZ3 with parameters from Equations (8) and (9) and  $m=13.5$  result in small changes in the Hugoniot curves for nitrogen, carbon dioxide, and oxygen. For carbon dioxide, the Hugoniot pressures calculated with these parameters are in closer agreement with the experimental liquid shock values, as shown in Figure 4. The calculated pressures were found to increase with increasing values of  $m$  at constant  $r^*$  and  $\epsilon/k$ , and were slightly higher with  $m=13.5$  than for  $m=13$ .

#### DETONATION PROPERTIES FOR EXPLOSIVES

In order to investigate further the accuracy of JCZ3 with the present Exp-6 parameters, C-J pressures and detonation velocities were calculated for several explosive mixtures. Initial comparisons were made for nitric oxide, which dissociates almost entirely to nitrogen and oxygen at detonation conditions. In Table 2, calculated C-J pressures and velocities for nitric oxide are compared with the experimental values of Ramsay and Chiles<sup>17</sup>. It can be seen that the values calculated with BKWR and JCZ3 with the original parameters are in reasonable agreement with the experimental values. Slightly higher pressures and detonation velocities, which are in closer agreement with the experimental values, resulted for JCZ3 with  $m=13.5$  and parameters  $r^*$  and  $\epsilon/k$  for nitrogen, oxygen, and nitric oxide calculated with the generalized relationships, Equations (8) and (9).

In Table 3 calculated detonation properties for PETN with an initial density of 1.77 g/cc. are compared with the experimental values of Hornig et al<sup>18</sup>). It can be seen that the detonation velocities and C-J pressures calculated with JCZ3 with the original molecular parameters are slightly lower than the experimental values and those calculated with BKWR. It can also be seen that improved results are obtained for JCZ3 with  $m=13.5$  and parameters for nonpolar components calculated from Equations (8) and (9).

Calculated pressures and shock velocities at C-J and overdriven conditions for PBX-9404 with an initial density of 1.84 g/cc were also compared with the experimental values of Kineke and West<sup>19</sup> and

of Lee et al<sup>20</sup>. For the overdriven explosive, the Hugoniot pressures were calculated from the relationship<sup>12</sup>

$$D = V_o [P / (V - V_o)]^{1/2} \quad (10)$$

It can be seen from Figure 6 that the shock velocities calculated with JCZ3 are in good agreement with the experimental values, particularly at moderately overdriven pressures. It can also be seen that the shock velocities calculated with BKWR are lower at overdriven conditions. Calculations with JCZ3 with parameters from Equations (8) and (9) and  $m = 13.5$  resulted in slightly higher C-J and overdriven shock velocities than with the original procedure.

Ree<sup>12</sup> obtained large deviations in these detonation properties for PBX-9404 with his theoretical equation of state, and postulated that gas-gas phase separation may occur at these elevated temperatures and pressures. The present results indicate that reasonable agreement with the experimental overdriven properties of PBX-9404 can be obtained with JCZ3 or BKWR without the necessity for the inclusion of an additional gas phase in the Tiger calculations.

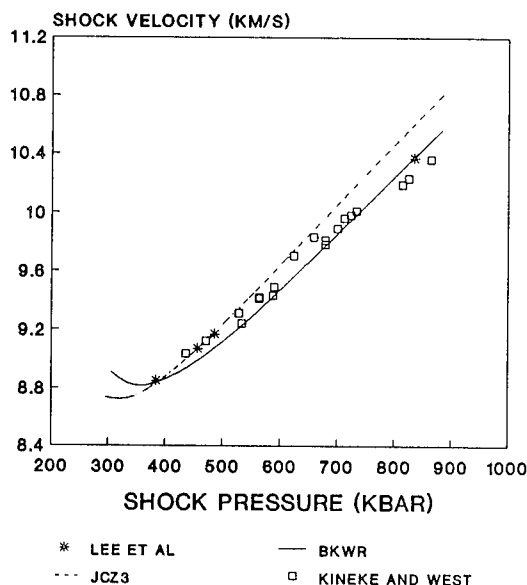


FIGURE 6. EXPERIMENTAL AND CALCULATED SHOCK VELOCITIES FOR PBX-9404

TABLE 1. COMPARISON OF EXP-6 PARAMETERS

	FICKETT <sup>4</sup>		ROSS AND REE <sup>15</sup>	
	$r^*$	$\epsilon/\kappa$	$r^*$	$\epsilon/\kappa$
Ar	3.87	123.	3.85	122.0
N <sub>2</sub>	4.05	120.	4.09	101.9
O <sub>2</sub>	3.73	132.	3.84	125.0
CO	4.05	120.	4.09	108.3
CO <sub>2</sub>	4.20	200.	4.17	245.6
CH <sub>4</sub>	4.29	154.	4.22	154.1
NO	3.97	105.	3.97	112.9

TABLE 2. DETONATION PROPERTIES FOR NITRIC OXIDE

	PRESSURE (KBAR)	DETONATION VELOCITY (KM/S)	(K)
EXPTL <sup>17</sup>	100	5.62	-
BKWR	100.5	5.53	2484
JCZ3(1)	97.6	5.625	2846
JCZ3(2)	96.6	5.54	2769
JCZ3(3)	101	5.74	2777

TABLE 3. DETONATION PROPERTIES OF PETN

	PRESSURE (KBAR)	DETONATION VELOCITY (KM/S)	T(K)
EXPTL <sup>18</sup>	317.	8.30	4200
BKWR	310.	8.34	3335
JCZ3(1)	279.	8.16	4256
JCZ3(2)	271.	7.99	4252
JCZ3(3)	284.	8.30	4235

- (1) Parameters of Fickett<sup>4</sup>,  $m=13.5$   
 (2) Equations (8) and (9),  $m=13.0$   
 (3) Equations (8) and (9),  $m=13.5$



In order to investigate further the possibility of gas-gas equilibrium behavior for explosive products, computer programs were developed to calculate fugacities with JCZ3 for nitrogen and water mixtures at detonation conditions. For conditions at which a second gas phase is formed, the equilibrium compositions are calculated by the equality of the fugacities of each component in each gas phase. In Figure 7, calculated fugacities of nitrogen and water at 2000 K and 300 kbars are plotted against mole fraction of nitrogen in the mixture. These conditions were chosen to be typical of temperatures and pressures at the C-J point of explosives. If phase separation occurs, the slope of the fugacity of each component would change sign from positive to negative in several regions of the composition range. It can be seen from Figure 7 that at these conditions the signs of the slopes of the fugacities are constant for the entire mole fraction range. For an actual explosive, the presence of carbon dioxide and additional polar components would tend to diminish the possibility of phase separation.

For nitrogen-water, gas-gas equilibria should be favored at lower temperatures and higher pressures, and with an interaction constant  $k_{12}$  less

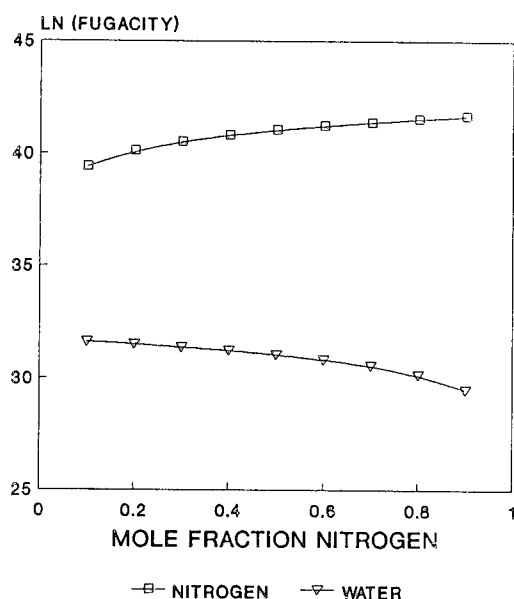


FIGURE 7. CALCULATED FUGACITIES FOR NITROGEN-WATER AT 2000 K AND 300 KBAR

than 1.0 in Equation (5). This behavior was also not observed with JCZ3 at 1000 K and 400 kbars and  $k_{12} = 0.8$ . Gas-gas equilibrium did result with JCZ3 for this system at 700 K and 100 kbars with  $k_{12} = 1.0$ . Limited gas phase miscibility has been found experimentally for this system at 658 K and pressures above 2200 atm<sup>21</sup>.

## DISCUSSION

The results of this study indicate that the JCZ3 equation of state with the parameters determined by Fickett<sup>4</sup> for the Exp-6 potential enables the calculation of Hugoniot curves of the major explosive products with reasonable accuracy, with some improvement indicated to be possible for nitrogen and carbon dioxide. This procedure was also found to result in good agreement with experimental shock velocities and pressures for several explosives at C-J and overdriven conditions. Calculations with JCZ3 and the present parameters did not predict the formation of an additional gas phase at normal detonation conditions.

Exp-6 parameters determined by Ross and Ree<sup>20</sup> by generalized procedures were found to lead to similar results with JCZ3 for the Hugoniot curves of the components, with some improvement resulting for carbon dioxide. For the explosives investigated, the use of these parameters and  $m=13.5$  resulted in slightly higher C-J shock velocities and pressures, which were in better agreement with the experimental values, than for the original JCZ3 procedure.

Based on the results of these analyses, a comprehensive study with experimental Hugoniot and C-J data is being conducted to determine optimum Exp-6 parameters for the JCZ3 equation of state. Improved potential parameters are particularly required for secondary polar detonation products, such as ammonia for which the present parameters are the same as for water. More advanced mixing rules for the mixture parameters of the JCZ3 equation of state are also being investigated.

## REFERENCES

1. Jacobs, S.J., "On the Equation of State for Detonation Products at High Density", *Proc. of the 12th Symposium (International) on Combustion*, 1969, pp. 501-510.

2. Cowperthwaite, M.; and Zwisler, W.H., "The JCZ Equations of State for Detonation Products and Their Incorporation Into the TIGER Code", in *Proc. of the Sixth Symposium (International) on Detonation*, Coronado, CA, Aug 24-27, 1976, pp.162-172.
3. Finger, M.; Lee, E.; Helm, F.H.; Hayes, B.; Hornig, H.; McGuire, R.; Kahara, M.; and Guidry, M., "The Effect of Elemental Composition on the Detonation Behavior of Explosives", in *Proc. of the Sixth Symposium (International) on Detonation*, Coronado, CA, Aug 24-27, 1976, pp.710-722.
4. Fickett, W., *Intermolecular Potential Functions for Some Simple Molecules from Available Experimental Data*, Los Alamos Scientific Laboratory Report LA-2665, 1962.
5. Walsh, J.M.; and Rice, M.H., "Dynamic Compression of Liquids from Measurements on Strong Shock Waves", *J. Chem. Phys.*, 26, 957, p.815.
6. Mitchell, A.C.; and Nellis, W.J., "Equation of State and Electrical Conductivity of Water and Ammonia Shocked to the 100 GPa (1MBar) Pressure Range", *J. Chem. Phys.*, 76, 1982, p.6273.
7. Chirat, R.; and Pittion-Rossillon, G., "Detonation Properties of Condensed Explosives Calculated with an Equation of State Based on Intermolecular Potentials", in *Proc. of the Seventh Symposium (International) on Detonation*, Annapolis, Md., June 16-19, 1981, pp.703-715.
8. Lyzenga, G.A.; Ahrens, T.J.; Nellis, W.J.; and Mitchell, A.C., "The Temperature of Shocked Compressed Water", *J. Chem. Phys.*, 73, 1980, p.6282.
9. Marsh, S.P., *LANL Shock Hugoniot Data*, University of California, Berkeley, 1980.
10. Nellis, W.J.; and Mitchell, A.C., "Shock Compression of Liquid Argon, Nitrogen, and Oxygen to 90 GPa (900 kbar)" *J. Chem. Phys.*, 73, 1980, p.6137.
11. Zubarev, V.N.; and Telegin, G.S., "The Impact Compressibility of Liquid Nitrogen and Solid Carbon Dioxide", *Sov. Phys. Dokl.*, 7, 1962, p.34.
12. Ree, F.H., "Supercritical Fluid Phase Separations: Implications for Detonation Properties of Condensed Explosives", *J. Chem. Phys.*, 84, 1986, p.5845.
13. Nellis, W.J.; Mitchell, A.C.; Ree, F.H.; Ross, M.; Holmes, N.C.; Trainor, R.J.; and Erskine, D.J., "Equation of State of Shock-Compressed Liquids: Carbon Dioxide and Air", *J. Chem. Phys.*, 95, 1991, p.5268.
14. Schott, G.L., "Shock-Compressed Carbon Dioxide: Liquid Measurements and Comparisons with Selected Models", *High Pressure Research*, 6, 1991, p.187.
15. Ross, M.; and Ree, F.H., "Repulsive Forces of Simple Molecules and Mixtures at High Density and Temperature", *J. Chem. Phys.*, 73, 1980, p.6146.
16. Wackerle, J.; Seitz, W.L.; and Jamieson, C.C., in *Behavior of Dense Media Under High Dynamic Pressure*, Gordon and Breach, 1968, p.85.
17. Chiles, W.C.; and Ramsay, J.B., "Detonation Characteristics of Liquid Nitric Oxide", in *Proc. of the Sixth Symposium (International) on Detonation*, Coronado, CA, Aug.24-27, 1976, pp.723-728.
18. Hornig, H.C.; Lee, E.L.; Finger, M.; and Kurrle, J.E., "Equation of State of Detonation Products", in *Proc. of the Fifth Symposium (International) on Detonation*, Pasadena CA, Aug.18-21, 1970, pp.503-512.
19. Kineke, Jr., J.H.; and West, Jr., C.E., "Shocked States of Four Overdriven Explosives", in *Proc. of the Fifth Symposium (International) on Detonation*, Pasadena, CA, Aug.18-21, 1970, pp.533-546.
20. Lee, E.L.; Van Thiel, M.; Green, L.G.; and Mitchell, A., in *Shock Waves in Condensed Matter-1983*, Elsevier Science Publishers, 1984, p617.

21. Prokhorov, V.M.; and D.S. Tsiklis, D.S., "Gas-Gas Equilibrium in the Nitrogen-Water System", *Russ. J. Phys. Chem.*, 44, 1970, p.1173.

change as you improve your parameters. In particular, your CO<sub>2</sub> fit seemed to be low in P. Does that mean that your detonation velocity will increase?

#### REPLY BY L. I. STIEL

The calculations presented in this paper are with the original JCZ3 parameters and with parameters resulting from corresponding states relationships. Optimized parameters for the major reaction products will result in better agreement for their Hugoniot curves and should also result in improvement for mixture properties, including C-J velocities. The accuracy of these results is also dependent on the optimization of the JCZ3 parameters for all the product species of the explosive.

---

#### DISCUSSION

MATHIAS VAN THIEL

Lawrence Livermore National Laboratory, Livermore, California

These calculations were with your original parameter set; is that right? So your results will then

## A THEORETICAL STUDY FOR GAS-GAS SEPARATION IN HIGH TEMPERATURE AND HIGH PRESSURE FLUID

M. Koshi and H. Matsui

Department of Reaction Chemistry, The University of Tokyo,  
7-3-1 Hongo, Bunkyo-ku, Tokyo 113, Japan

T. Saito

Cray Research Japan Ltd.,

6-4 Ichiban-cho, Chiyoda-ku, Tokyo 102, Japan

K. Takayama

Institute of Fluid Science, Tohoku University,

2-1-1 Katahira, Sendai 980, Japan

The phase-separation in equimolar  $\text{H}_2\text{O}/\text{N}_2$  fluid mixtures was studied by molecular dynamics simulations at the conditions relevant to detonation environment. Calculations were performed for the NVT ensemble at  $T=2000$  K with the modified Buckingham (exp-6) potentials. Calculations of pair correlation functions and local mole fractions directly indicated the occurrence of the fluid phase-separation into  $\text{N}_2$ -rich and  $\text{H}_2\text{O}$ -rich phase at  $\rho > 1.35 \text{ g/cm}^3$ . Equations of state for the phase-separated mixtures were also calculated by the present molecular dynamics simulations. The compressibility factors and the internal energies for the phase-separated states were slightly lower than those for uniform mixtures. Comparisons of the equations of state derived from the van der Waals 1 fluid theory with the present results indicated that the van der Waals 1 fluid theory overestimated the compressibility factors and internal energies by  $<25\%$  in the range of  $\rho < 2.4 \text{ g/cm}^3$  ( $p < 40 \text{ GPa}$ ) at  $T=2000$  K. The rates of relaxation from uniform to phase-separated mixtures are important for the phase-separation behind shock or detonation waves. The present simulations indicated that the rates of demixing in the range of  $1.35 < \rho < 2.0 \text{ g/cm}^3$  are very fast ( $<30 \text{ ps}$ ). Direct simulations of the shock wave generation in the  $\text{H}_2\text{O}/\text{N}_2$  mixtures were performed to investigate the phase-separation behind shock waves. Some preliminary results are presented.

### INTRODUCTION

It is well known that the phase-separation in some gas mixtures can occur at temperatures and pressures above the critical point (gas-gas separation). Such phase separation is easily observed in  $\text{H}_2\text{O}/\text{N}_2$  and  $\text{H}_2\text{O}/\text{CO}_2$  mixtures at relatively low temperatures. Since  $\text{H}_2\text{O}$ ,  $\text{N}_2$ , and  $\text{CO}_2$  are the major gas-phase products of typical explosives containing C, H, N, and O atoms, the investigation of the dynamic behavior of mixtures containing  $\text{H}_2\text{O}$ ,  $\text{N}_2$ , and  $\text{CO}_2$  at high temperatures and high pressures is important for the prediction of the detonation properties. Recently, F.H.Ree<sup>1</sup> showed that the detonation products of explosives could separate into  $\text{N}_2$ -poor and  $\text{N}_2$ -rich fluid phase and that this gas-gas separation largely

affected detonation properties. The phase boundary was estimated by the solubility isotherms on the basis of the van der Waals 1 fluid theory. The occurrence of such phase separation is of great interest since not only the thermodynamic properties but also the rate of chemical reactions in the detonation waves are expected to be largely affected by the phase separation.

The phase separation at low temperatures may occur if the attractive interaction between unlike molecular pair is weaker than the attractive forces between like molecular pair.<sup>2,3</sup> However the driving force for the phase separation in the detonation waves is not clear, since the attractive force is not important at high temperatures. According to the Monte-Carlo

simulations by Kerley<sup>4</sup>, the phase separation could occur even if the interaction potentials between molecules are purely repulsive. For equimolar mixtures of molecules a and b with additive collision diameters ( $\sigma_{ab}=(\sigma_{aa}+\sigma_{bb})/2$ ) having the ratio of  $\sigma_{aa}/\sigma_{bb}=3$ , the fluid phase separation was found for  $r^6$  repulsive interactions at a pressure below the freezing point of the larger component. Such fluid phase separation was not found for mixtures interacting with  $r^{12}$  repulsive potentials. This results strongly suggested that the phase separation at high temperatures could occur in the mixtures of molecules with large differences in size and with very soft intermolecular repulsion. However  $r^6$  repulsion is too soft and the exponential repulsion is expected to be more appropriate for the real intermolecular interaction.

Recently, we performed direct molecular dynamics simulations for the high temperature phase-transition in  $H_2O/N_2$  equimolar mixtures with the modified Buckingham (exp-6) interaction potentials.<sup>5</sup> It was confirmed that the phase-separation could occur at high temperatures with exp-6 interaction potentials, and the dynamics of the phase separation from the initial uniform mixtures were investigated. This work is further developed in the present paper. The equations of state for the phase-separated mixtures are calculated by the molecular dynamics simulations for NVT ensemble and results are compared with the equations of state based on the van der Waals 1 fluid theory. Such comparison is practically important for the calculations of the detonation properties. The rates of the phase-separation are also important for the detonation properties. The rates of demixing from initial uniform mixtures in NVT ensemble are estimated in the present work. In addition, the phase behavior behind shock waves is also studied by the molecular dynamics simulations. Some preliminary results on the phase behavior behind strong shock waves are also presented.

## MOLECULAR DYNAMICS SIMULATIONS FOR NVT ENSEMBLE

Molecular dynamics (MD) simulations were performed for the equimolar  $H_2O/N_2$  mixtures at  $T=2000$  K with various densities. In order to make computation simple, the modified Buckingham (exp-6) potential,

$$\phi(r) = \frac{\epsilon}{\alpha - 6} \{ 6 \exp[\alpha(1 - \frac{r}{\sigma})] - \alpha(\frac{r}{\sigma})^{-6} \} \quad (1)$$

was used for the intermolecular potentials between  $H_2O-H_2O$ ,  $H_2O-N_2$ , and  $N_2-N_2$  molecular pairs. The potential parameters for  $H_2O$  and  $N_2$  are taken from reference [1]:  $\epsilon_{aa}/k=101.9$  K,  $\sigma_{aa}=4.09$  Å, and  $\alpha_{aa}=13$  for  $N_2$  (=molecule a), and  $\epsilon_{bb}/k=533$  K (at  $T=2000$  K),  $\sigma_{bb}=3.06$  Å and  $\alpha_{bb}=13$  for  $H_2O$  (=molecule b). The parameters for unlike pair,  $N_2-H_2O$ , are determined by the following combination rules:  $\sigma_{ab}=(\sigma_{aa}+\sigma_{bb})/2$ ,  $\epsilon_{ab}=(\epsilon_{aa}\epsilon_{bb})^{1/2}$ , and  $\alpha_{ab}=(\alpha_{aa}\alpha_{bb})^{1/2}$ . Although the use of same value of  $\alpha$  for  $H_2O$  and  $N_2$  is the subject of current debate in the literature, we used the same set of parameters used in the calculation of detonation properties by Ree<sup>1</sup> for convenience. MD calculations were carried out with the conditions of constant volume and constant temperatures (NVT ensemble). Equations of motion for 256 particles in a constant volume are integrated by using a leapfrog algorithm. Kind of molecules a and b on the initial fcc-lattice positions is determined by using random numbers. Small random displacements in the range of  $0 \sim d/10$  ( $d$  is the fcc-lattice constant) from initial positions are imposed before the integration. Temperature of the system is controlled by a velocity scaling method and the periodic boundary condition is assumed on a cubic cell. Calculations for the microcanonical (NVE) ensemble were also performed to determine the integration time step and the cut-off radius for the calculations of forces. The relative errors in the total Hamiltonian are within  $10^{-4}$  with a cut-off radius of 10 Å. Typically, the equations of motion are integrated over  $5 \times 10^4$  steps with the integration interval of  $1 \times 10^{-15}$  sec, but longer integration time is required at high density region to attain the equilibrium configuration from the initial uniform configuration. It was found that the pressure and the internal energy of the NVT ensemble were stabilized within the first 500 integration steps. Typically thermodynamic quantities are calculated by averaging over  $3 \times 10^4$  to  $5 \times 10^4$  integration steps. The pressure of the system was derived by adopting the virial theorem:

$$p = \frac{NkT}{V} - \frac{1}{3V} \sum_i \sum_j r_{ij} \frac{d\phi(r_{ij})}{dr_{ij}} \quad (2)$$

Here  $r_{ij}$  is the distance between particle  $i$  and  $j$ . The pair correlation functions  $g_{ij}(r_{ij})$  and the running coordination numbers  $N_{ij}(r_m)$  were calculated as a function of time to monitor the extent of the phase-separation. The running coordination number represents the average number of particle  $j$  in the sphere of radius  $r_m$  centered at the particle  $i$ . The value of  $N_{ij}$  is related to the pair correlation function  $g_{ij}$  by the following equation:

$$N_{ij}(r_m) = 4\pi \rho_j \int_0^{r_m} r^2 g_{ij}(r) dr \quad (3)$$

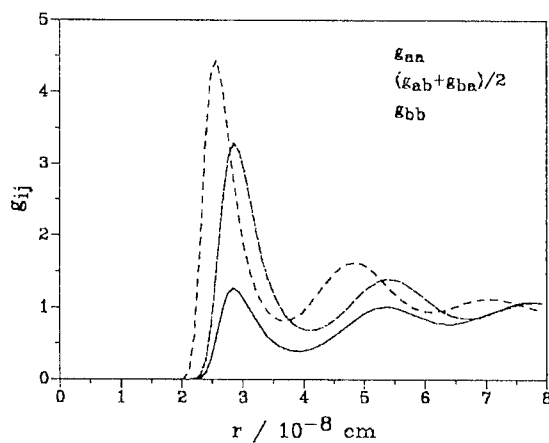


**FIGURE 1. PAIR CORRELATION FUNCTIONS FOR  $\text{H}_2\text{O}/\text{N}_2=1/1$  MIXTURE AT EQUILIBRIUM STATE:  $T=2000$  K,  $\rho=1.99$  g/cm<sup>3</sup>. (a= $\text{N}_2$ , b= $\text{H}_2\text{O}$ )**

Here,  $\rho_j$  is the density of the species  $j$ . The choice of a value of  $r_m$  is not critical for the properties of  $N_j(r_m)$ , as far as the value is in the range of  $0.8\sigma < r_m < 2.5\sigma$ . In the present work, we have chosen the value of  $r_m = \sigma_{ab}$  in all case.

Examples of the pair correlation function are shown in figure 1 for the case of  $\rho=1.99$  g/cm<sup>3</sup> at  $T=2000$  K. The corresponding pressure at the equilibrium state was calculated to be 22.6 GPa. By comparing the height of correlation functions of like-pairs ( $g_{aa}$  and  $g_{bb}$ ) with that of unlike-pair ( $g_{ab}$ ), it is evident that the fluid separation occurs at this density. The pair correlation functions shown in the figure

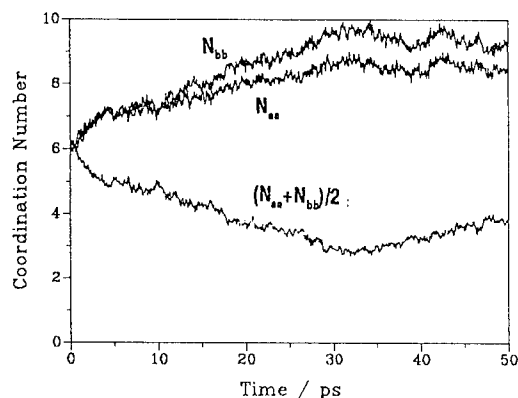


**FIGURE 2. TIME VARIATION OF THE RUNNING COORDINATION NUMBERS AT  $T=2000$  K,  $\rho=1.99$  g/cm<sup>3</sup>,  $\text{H}_2\text{O}/\text{N}_2=1/1$**

were obtained by averaging over the time steps from  $4 \times 10^5$  to  $5 \times 10^5$  (40 to 50 psec). It was confirmed that the calculated pressure, internal energy, and running coordination numbers were in steady state in these time periods for the density range of  $\rho < 2.0$  g/cm<sup>3</sup>. Since the present MD simulation started from the uniform distribution of molecules a and b, the transition to the phase separated mixture (i.e., demixing) has completed within 40 psec. In order to measure the rate of demixing, the running coordination numbers are plotted as a function of time in figure 2. The initial coordination numbers are the same (=6) for  $\text{N}_2$  and  $\text{H}_2\text{O}$ , indicating the uniform distribution of particles with total coordination number of 12 for one particle. The coordination number for  $\text{N}_2\text{-H}_2\text{O}$  gradually decreases to about 3, while the coordination numbers for  $\text{N}_2\text{-N}_2$  and  $\text{H}_2\text{O-H}_2\text{O}$  increase to about 9 after 30 psec. This example indicates that the rate of demixing from uniform to the phase separated state can be very fast (the order of several ten psec) at high temperatures. However, the rate of demixing in the MD simulations may depend on the number of particles used in the simulation and the initial configuration. It has been shown that the 'cluster-like' structure was formed in the phase-separated fluid<sup>25</sup>, and the rate of demixing could be largely dependent on the size of this 'cluster'. Although the rate of demixing with 108 particles was found to be similar to that calculated with 256 particles, further work is needed for the understanding of the relationship between the 'microscopic' and the 'bulk' rate of demixing.

For more precise definition of the phase separation, Hoheisel et al.<sup>23</sup> showed that the sum of

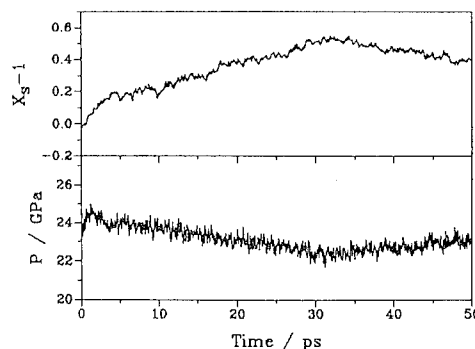


**FIGURE 3. TIME VARIATION OF PRESSURE AND SUM OF THE LOCAL MOLE FRACTIONS,  $X_{s-1}$ . CONDITIONS ARE THE SAME AS FIGURE 1.**

the local mole fractions could be used as a reliable distinction between homogeneous and inhomogeneous states in a mixture. The local mole fraction of the molecule a in a binary mixture,  $x_{aa}(r_m)$ , is defined by:

$$x_{aa}(r_m) = \frac{N_{aa}(r_m)}{N_{aa}(r_m) + N_{ab}(r_m)} \quad (4)$$

The sum of the local mole fractions,  $x_s(r_m) = x_{aa}(r_m) + x_{bb}(r_m)$ , represents deviations of the mean number of particles of the two kinds corresponding to specific cross interactions between unlike molecules. The value of  $x_s$  is unity for all  $r_m$  if the mixture is uniform and the function is normalized to unity at  $r_m \rightarrow \infty$ . For the inhomogeneous mixtures, particles of the same kind predominate the distribution, and values of  $x_s(r_m)$  for infinite  $r_m$  are larger than unity. Figure 3 shows a plot of  $(x_s - 1)$  as a function of time. Since the value of  $x_s$  represents the magnitude of the fluid phase separation, the rate of demixing can be defined by  $dx_s/dt$ . As can be seen in figure 3, the system relaxes to the equilibrium (phase separated) state without any incubation time at the density range of  $1.35 < \rho < 2.0$  g/cm<sup>3</sup>. Below the density range ( $\rho < 1.35$  g/cm<sup>3</sup>), phase separation was not indicated in our calculation. After initial rapid increase at  $t < 4$  psec, the value of  $x_s$  reaches gradually to the equilibrium values. It is found that the rate of initial rapid rise is independent of the density, whereas the rate of gradual approach to the equilibrium is slower at higher initial density. Correlation between the demixing rate and the diffusion rate has been suggested in our previous work.<sup>5</sup> The time profile of the pressure is also shown in figure 3. The equilibrium pressure is found to be slightly lower than that at the initial uniform mixture.

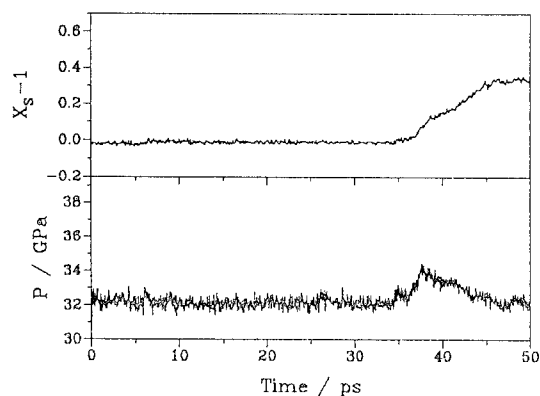


FIGURE 4. TIME VARIATION OF PRESSURE AND SUM OF LOCAL MOLE FRACTIONS AT  $T=2000$  K,  $\rho=2.12$  g/cm<sup>3</sup>,  $H_2O/N_2 = 1/1$ .

The dynamic features of the relaxation at high density region of  $\rho > 2.0$  g/cm<sup>3</sup> are found to be very different from the phase behavior at lower ( $1.35 < \rho < 2$  g/cm<sup>3</sup>) density. The time dependence of the value of  $x_s$  and pressure at  $\rho=2.12$  g/cm<sup>3</sup> are shown in figure 4. It is noted that there is a long incubation period that is never found at  $\rho < 2.0$  g/cm<sup>3</sup>. The phase separation suddenly starts after the long incubation time at about  $t=37$  psec. The pressure and internal energy remain constant during this incubation time, and the pair correlation functions show the amorphous-like structure. The mean square displacement (MSD) of the molecule in this incubation period is calculated to be less than  $5 \text{ \AA}^2$ , whereas the value of MSD linearly increases with time after the start of the phase separation at  $t > 37$  psec. The pressure also suddenly increases with the onset of the demixing, and then decreases to the lower equilibrium pressure than the initial value. The length of the incubation period is found to be very difficult to predict because of its stochastic nature: different incubation times are observed with different initial configurations even with the same density. This sudden occurrence of the phase separation may be caused by the "jump motion" of the molecule in the amorphous-like fluid mixture.

Since the present high pressure condition ( $\rho=2.12$  g/cm<sup>3</sup>,  $p=31$  GPa at  $T=2000$  K) can be attainable by strong shock waves, it is interesting to investigate the time scale for the demixing behind the shock waves.

#### EQUATION OF STATE FOR THE PHASE-SEPARATED BINARY MIXTURE

It is shown that the pressure of the phase-separated mixture in the NVT ensemble is lower than that for the uniform mixture. The compressibility factors for the uniform and the phase-separated binary  $H_2O/N_2$  mixture are compared in figure 5. The pressure and the internal energy for the uniform mixture are obtained by averaging the results of MD calculations over initial 500 to 2000 time steps. At the density range of  $\rho < 1.35$  g/cm<sup>3</sup>, where the phase separation does not occur, the averaged values of pressure and the internal energy obtained at 500 to 2000 time steps agreed well with the averaged values over 40000-50000 time steps. At the density range of  $\rho > 1.35$  g/cm<sup>3</sup>, where the phase separation occurs, the demixing process already proceeds at 500 to 2000 time steps. However, the effects of demixing to the pressure

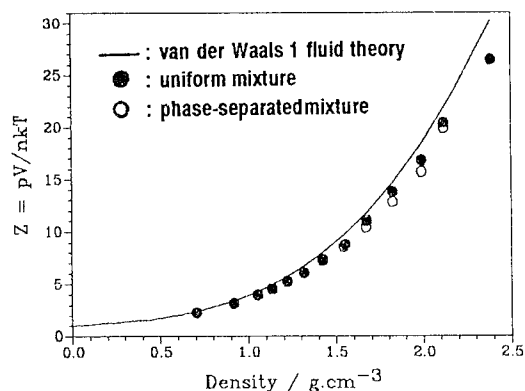


FIGURE 5. COMPRESSIBILITY FACTOR OF THE  $\text{H}_2\text{O}/\text{N}_2=1/1$  MIXTURE AT  $T=2000$  K

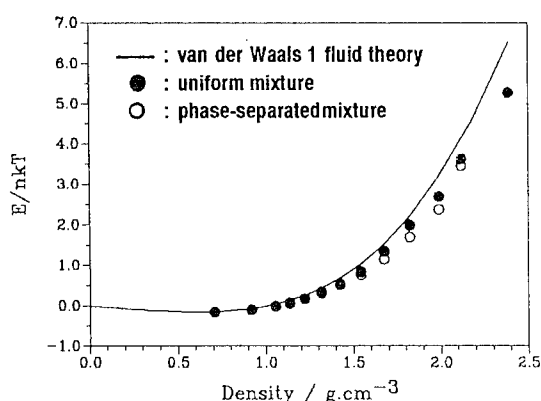


FIGURE 6. INTERNAL ENERGY,  $E/nkT$ , OF THE  $\text{H}_2\text{O}/\text{N}_2=1/1$  MIXTURE AT  $T=2000$  K

and internal energy at such initial stage can be neglected. As shown in figure 5, the difference of the compressibility factors between the uniform and the phase-separated mixtures is within 3% in the present NVT ensemble at the density range of  $\rho < 2.2 \text{ g/cm}^3$  and  $T=2000$  K. The internal energy as a function of density at  $T=2000$  K is also shown in figure 6. Similar to the pressure, the difference of the internal energy between the uniform and the phase-separated mixture is small (within 3.2 %). Although the influence of the phase separation on the pressure and internal energy is not large, the free energy is expected to be largely affected by the demixing because of the entropy of mixing. Direct evaluation of the free energy by the

MD simulations needs a more sophisticated method and it was not performed in the present work.

An analytical equation of state is desirable for the practical calculations of the detonation properties by taking into account the effects of the phase separation. The van der Waals 1 fluid theory is a widely used mixture theory in which a simplified potential is assumed to represent the mixture interaction potentials. For the exp-6 potentials, the improved version of the van der Waals 1 fluid model was proposed by Ree,<sup>7</sup> and was used in the modeling of the supercritical fluid phase separations in the detonation of condensed explosives.<sup>1</sup> In the van der Waals 1 fluid theory, the potentials for each molecular pairs are replaced by a hypothetical (effective) one-component potential. The improved van der Waals 1 fluid model<sup>7</sup> assumes that the actual potentials for each molecular pairs and the effective one-component potential both have the exp-6 form of equation (1), and the parameters for this effective one-component potential are given by:

$$\sigma_m = \sum_i \sum_j x_i x_j \sigma_{ij} \quad (5)$$

$$\epsilon_m (\sigma_m)^3 = \sum_i \sum_j x_i x_j \epsilon_{ij} (\sigma_{ij})^3 \quad (6)$$

$$\alpha_m \epsilon_m (\sigma_m)^3 = \sum_i \sum_j x_i x_j \alpha_{ij} \epsilon_{ij} (\sigma_{ij})^3 \quad (7)$$

Here,  $x_i$  is the mole fraction of species  $i$ ,  $\sigma_{ij}$ ,  $\epsilon_{ij}$  and  $\alpha_{ij}$  are the exp-6 potential parameters for  $ij$  molecular pairs, and  $\sigma_m$ ,  $\epsilon_m$ , and  $\alpha_m$  are the parameters for the effective one component potential. For the equimolar  $\text{H}_2\text{O}/\text{N}_2$  mixture, equations (5)-(7) yield  $\sigma_m=3.664 \text{ \AA}$ ,  $\epsilon_m/k=231.1 \text{ K}$ , and  $\alpha_m=13$ . Although the reliability of the improved van der Waals 1 fluid model has been verified by Monte Carlo simulations<sup>7</sup> over wide temperature and density range, applicability of this 'effective one component' treatment for the phase-separated fluid is not clear. To address this problem, the pressures and internal energies calculated in the present MD simulations are compared with those obtained by the improved van der Waals 1 fluid model.

To calculate thermodynamic properties by the van der Waals 1 fluid model, the equation of state for the single component fluid is required. An analytical expression for the free energy proposed by Kataoka<sup>8</sup> was used for the equation of state of a single component fluid with the exp-6 potentials. The Helmholtz free energy measured from the ideal gas was expanded in a series of temperature, density, and the potential parameter,  $\alpha$ . This Kataoka's expression consists of 75 terms and the coefficients of these terms



were determined on the basis of molecular dynamics simulations performed at very wide range of parameter values. Although Kataoka's equation of state is expected to be very accurate, present densities for the phase separation are out of range for this equation of state. Therefore additional MD simulations for the single component fluid were performed to test the validity of Kataoka's equation of state at high densities. It is found that the pressures and internal energies obtained in the present MD simulations agreed quite well with those derived from Kataoka's equation of state within the relative errors of 3% in the range of  $T=2000\text{K}$  and  $0.7 < \rho < 2.4 \text{ g/cm}^3$ . For the equation of state of a single component fluid interacting with exp-6 potential, it is concluded that Kataoka's equation of state is valid even at very high pressures and temperatures relevant to the detonation of explosives.

The compressibility factor and the internal energy calculated by the improved van der Waals 1 fluid model are compared with the results of the present MD simulations in figures 5 and 6. The van der Waals 1 fluid model always predicts higher values of compressibility factors and the internal energies than the MD values. The differences in compressibility factor and internal energy at the highest density of the present MD simulation ( $\rho=2.4 \text{ g/cm}^3$ ) are 18 and 32 %, respectively.

## MOLECULAR DYNAMICS SIMULATION OF SHOCK WAVES

It is confirmed that the supercritical fluid phase-separation can occur at high temperatures relevant to detonation. In the NVT ensemble, the rate of demixing is quite fast (less than 50 psec in the density range of  $1.35 < \rho < 2.0 \text{ g/cm}^3$ ). This indicates that the phase separation can occur just behind the shock front. It is interesting to investigate the dynamic nature of the demixing behind the shock waves. If the rate of demixing is really fast as observed in the NVT ensemble, the rate of the chemical reactions behind the shock waves should be largely affected by the occurrence of the demixing. Molecular dynamics simulations of strong shock waves in high density binary mixtures are tried and some preliminary results are presented here.

In order to observe the shock propagation in high density binary fluid, 2560 particles (1280  $\text{H}_2\text{O}$  and 1280  $\text{N}_2$  molecules) are placed in a rectangular box

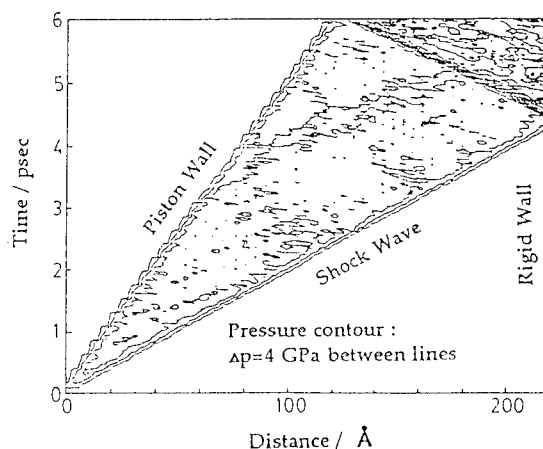


**FIGURE 7. X-T DIAGRAM OF A SHOCK WAVE IN  $\text{H}_2\text{O}/\text{N}_2=1/1$  MIXTURE:  $T_0=300 \text{ K}$ ,  $\rho_0=0.918 \text{ g/cm}^3$ , AND  $U_p=2000 \text{ m/sec}$**

whose side lengths of  $L_x=L_y$  and  $L_z=10L_x$ . The shock wave propagates along the  $z$ -axis. A periodic boundary condition is imposed only the  $x$  and  $y$ -direction and the walls at  $z=0$  and  $z=L_z$  are assumed to be elastic. After realizing an equilibrium condition in the unshocked fluid at temperature  $T_0=300 \text{ K}$ , the shock wave is generated by moving the elastic wall initially placed at  $z=0$  with the velocity of  $U_p$ . Typically, equations of motion are integrated over 10000 steps for the equilibration of the unshocked fluid. The spacial profiles of temperature, pressure, and internal energy along the  $z$ -direction are calculated as follows. The system is divided into small sections along the  $z$ -axis with a typical width of  $\Delta z=L_z/50$ . The thermodynamic properties for these small subsections with a volume of  $v=L_xL_y\Delta z$  are evaluated by averaging the corresponding quantities of the particle in each subsection. Therefore the spacial resolution of the thermodynamic properties is limited by the value of  $\Delta z$ . Equations of motion are integrated with a typical time step of  $2 \times 10^{-15} \text{ sec}$ .

An example of a shock wave propagation is shown in figure 7, in which the pressure contour is plotted on the  $x$ - $t$  plane. In this case, the size of the box is  $L_xL_yL_z=22 \times 22 \times 220 \text{ Å}^3$  and the pressure of the unshocked fluid is calculated to be 181 MPa. Shock wave is generated by moving the wall at  $z=0$  (piston) with the velocity  $U_p=2000 \text{ m/sec}$ . As can be seen in the figure, steady shock wave propagates with a constant shock speed of  $U_s=5060 \text{ m/sec}$ . Following averaged values for the thermodynamic properties behind incident shock wave are obtained:  $T=5930 \text{ K}$ ,  $P=10.75 \text{ GPa}$ , and  $\rho=1.51 \text{ g/cm}^3$ . Since a rigid wall is

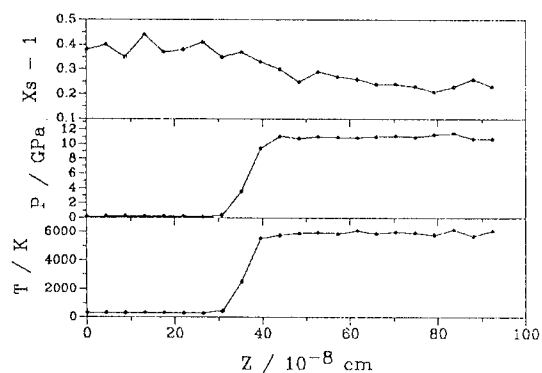


**FIGURE 8. SPACIAL PROFILES OF T, P, AND  $X_s$ , BEHIND SHOCK WAVE. SHOCK CONDITIONS ARE THE SAME AS IN FIGURE 7.**

assumed at the fixed position of  $z=L_z$ , propagation of the reflected shock wave is also observed at  $t > 4.4$  psec in figure 7. The spacial profiles of temperature or pressure behind shock wave are calculated with  $\Delta z = L_z/50 = 4.4 \text{ \AA}$ , which contains about 50 molecules on average. However 50 molecules are not enough to obtain the statistical quantities such as temperature and pressure. As a result, the snap shot profiles of the temperature and pressure have very large fluctuation. Since the simulated shock wave propagates with a constant velocity, the time averaging of the thermodynamic properties over  $t = 1.1$  to  $4.0$  psec is performed in the shock-fixed coordinate. Resulting spacial profiles of temperature and pressure are shown in figure 8.

Since we are interested in the demixing process behind the shock wave, the sum of the local mole fraction  $x_s$  is also plotted in figure 8. The value of  $x_s$  for the unshocked fluid at  $T_0 = 300 \text{ K}$  is 1.4, indicating the occurrence of the phase separation. On the other hand, the values of  $x_s$  behind the shock wave gradually decrease to about 0.25. In this case, the extent of the phase separation in the unshocked fluid is larger than that in the shocked fluid, and relaxation behind the shock wave proceeds from the phase-separated mixture to the more uniform mixture. This is caused by the large effect of temperature on the phase separation. It is also noted that the time variation of the  $x_s$  behind the shock wave is very fast, as can be seen in figure 8. The width of shock front in this figure is about  $12 \text{ \AA}$  and this value is 2.4 times longer than the length the mean free path for the molecular collision. Since the relaxation region for the

value of  $x_s$  is the same order as the width of the shock front, only a few collisions is required for the mixing process in this case.

## CONCLUDING REMARKS

Molecular dynamics simulations were performed to study the phase separation in high pressure and high temperature fluid relevant to the detonation. It is shown that the phase separation does occur even at high temperature where the repulsive intermolecular interaction is important. Pressure of the phase separated fluid in NVT ensemble is found to be lower than that of uniform mixtures. The improved van der Waals 1 fluid model with the exp-6 interaction are tested against the present results of the molecular dynamics simulations. In addition, direct simulation of the shock wave propagation in the binary fluid is tried to investigate the phase separation behind shock wave. The simulation indicated that the temperature effect on the phase separation is very important for the demixing (or mixing) processes. Wider range of temperature and pressure should be covered in the MD simulation in order to understand the general features of the phase-separation dynamics. More extensive calculations for the shock wave propagation in the mixture are being continued for this purpose.

## REFERENCES

1. Ree, F.H., "Supercritical fluid phase separations: Implications for detonation properties of condensed explosives", *J.Chem.Phys.*, Vol.84, 1986, p.5854.
2. Schoen, M., and Hoheisel, C., "Static and dynamic cross correlation in thermodynamically stable and unstable mixtures. I. A molecular dynamics simulation study using Lennard-Jones pair potential functions with identical  $\sigma$ -parameters", *Mol. Phys.*, Vol.53, 1984, p.1367.
3. Schoen, M., and Hoheisel, C., "Static and dynamics cross correlation in thermodynamically stable and unstable mixtures. II. Molecular dynamics studies on Lennard-Jones systems consisting of particles of unequal size", *Mol.Phys.*, Vol.57, 1986, p.65.

4. Kerley, G.I., "Equations of state and gas-gas separation on soft-sphere mixtures", *J.Chem.Phys.*, Vol.91, 1989, p.1204.

5. Koshi, M., and Matsui, H., *Molecular Simulation*, 1993, in press.

6. Miyagawa, H., Hiwatari, Y., Bernu, B., and Hansen, J.P., "Molecular dynamics study of binary soft-sphere mixtures: Jump motions of atoms in the glassy state", *J.Chem.Phys.*, Vol.88, 1988, p.3879.

7. Ree, F.H., "Simple mixing rule for mixtures with exp-6 interactions", *J.Chem.Phys.*, Vol.78, 1983, p.409.

8. Kataoka, Y., "Equation of state of the fluid defined by the modified Buckingham (exp-6) potential derived by molecular dynamics simulations", *Bull.Chem.Soc. Jpn.*, Vol.65, 1992, p.2093.

---

## DISCUSSION

DR. MATHIAS VAN THIEL

Lawrence Livermore National Laboratory, Livermore, California

(1) This is a nice piece of work - thank you for presenting it. Mike Costantino and S. F. Rice

["Supercritical Phase Separation in H<sub>2</sub>O-N<sub>2</sub> Mixture," *J. Phys. Chem.* **95**, 9034 (1991)] have done experiments in a DAC with mixtures of H<sub>2</sub>O and N<sub>2</sub> at -700K and 1 kbar. They see bubbles of one phase appearing in the other. This is a visual observation of phase separation.

(2) Similar Monte Carlo work by Francis Ree was reported by us in the Ninth International Symposium on Detonation (p. 425). It appears that all this work hangs together very nicely. It would be nice if we could get sufficient confidence in the Monte Carlo or MD calculations to determine the nonideality coefficients in the modified Lorentz Berthelot rule.

## REPLY BY MITSUO KOSHI:

(1) Thank you for your kind comments. The temperature dependence of the phase separation is very important and we also performed NVT-MD calculations at low temperatures, as expected. It would be very interesting to compare the experimental results of Mike and Rice with our calculations, if possible.

(2) Thank you again for your comment. Although direct comparison of our MD results with your Monte Carlo results could not be made because of the different conditions (T=4000 K in your work while T=2000K in our work), both results indicated that pressures for the phase-separated mixtures are higher than those for the uniform mixtures. I completely agree with you.

## MULTIPOLE EFFECTS ON THE EQUATION OF STATE FOR REACTION PRODUCTS OF EXPLOSIVES

HERMENZO D. JONES AND FRANK Z. ZERILLI

Dahlgren Division Detachment White Oak  
Naval Surface Warfare Center  
10901 New Hampshire Ave.  
Silver Spring, MD 20903-5640

The fluid constituents of the reaction products for CHNO explosives are described by a perturbation technique based on their intermolecular interactions, which may include angular dependent contributions. Standard solid-state approaches are applied to the solid component of the reaction products. Fluid phase separation is predicted in the high pressure regime. Calculated detonation velocities compared favorably with experimental data for PETN and RDX.

### INTRODUCTION

Prior to Ree's work<sup>(1)</sup>, it was generally accepted that multipolar effects on the reaction products of explosives would not be relevant in the description of detonation characteristics of explosives. Ree assumed a temperature dependent intermolecular potential to account for the angular dependence of the molecular interactions of some of the fluid constituents. His work predicted the presence of fluid-fluid separation even in the CJ regime for RDX. This work is an attempt to treat the angular dependent potentials in a more realistic manner and verify the existence of these phase changes in the high pressure region.

The description of the fluid constituents of the reaction products is based on liquid-state perturbation theory. The intermolecular potential is written as the sum of a spherically symmetric, exponential-6 (exp-6) interaction and angular dependent, multipole corrections. The isotropic contribution is treated with the formalism of Weeks, Chandler, and Anderson<sup>(2)</sup> (WCA). The multipole corrections are derived from the theory of Gubbins, Gray and Machado<sup>(3)</sup> (GGM). The same reference system formulated for the

isotropic part of intermolecular potential is employed in the evaluation of the contribution from the angular perturbation. These corrections are so large that the Pade approximation of Stell, Rasaiah and others<sup>(4-6)</sup> is used to represent the perturbative series in order to obtain convergence. This approximate treatment for the angular corrections is verified by comparisons with computations with a isotropic Lennard-Jones reference potential. Specifically, a calculation of the excess volume for a mixture of Xe/HBr is compared with the results of Calado, et al.<sup>(7)</sup>

Intermolecular potential parameters for the fluid constituents are chosen to be consistent with Hugoniot data. Only H<sub>2</sub>O and NH<sub>3</sub> were considered to have appreciable multipole moments.

A semi-empirical Gruneisen<sup>(8)</sup> EOS which employs a Murnaghan<sup>(9)</sup> form for the zero-degree isotherm is used to describe the solid carbon. The EOS parameters are obtained by matching thermal and shock wave data.

Chemical equilibrium calculations with the multipole corrections as described above for the reaction products of PETN and RDX, which consist of a heterogeneous mixture of fluid and solid constituents, are

performed with the Jones-Zerilli (JZ) Code.<sup>(10)</sup> Comparisons are these results and those of Ree<sup>(1)</sup>, where a temperature dependence is introduced into the intermolecular potential, are presented.

## EOS FOR FLUIDS

The interaction between two molecules is written as

$$\phi(\vec{r}_1, \vec{r}_2) = \phi_0(r) + \phi_1(\vec{r}_1, \vec{r}_2) \quad (1)$$

where

$$r = |\vec{r}_1 - \vec{r}_2| \quad (2)$$

and the  $\vec{r}_i$ 's are the position vector of the particles. In the above  $\phi_0(r)$  contains the electronic repulsion and van der Waals attraction, while  $\phi_1(r_1, r_2)$  consists of the multipole interactions. Taking the angular dependent term as a perturbation, the free energy is given by

$$f = f_{\text{int}} + f_0 + f^{(2)} + f^{(3)} + \dots \quad (3)$$

Here,  $f_{\text{int}}$  contains the contribution from the intramolecular vibrations and rotations, and  $f_0$  arises from the spherically symmetric reference potential. The superscripts refer to the order of the perturbative corrections associated with  $\phi_1$ .

An (exp-6) potential, given by

$$\phi(r) = \epsilon(6/\alpha) \exp[\alpha(1 - r/r^*)] - (r^*/r)^6 / (1 - 6/\alpha) \quad (4)$$

is used for the isotropic interaction for the reaction products.

The potential parameters denote the usual quantities. Specifically,  $\epsilon$  is the well depth,  $\alpha$  is the steepness parameter, and  $r^*$  is the position of the minimum of the potential. This is treated with the formalism of (WCA) where it is assumed that the repulsive forces are dominant in dense fluids. The exp-6 potential is divided, as suggested by Kang<sup>11</sup>, into a reference contribution, which is repulsive in character and a perturbation which is attractive. With the prescription of Verlet and Weis<sup>12</sup> the radial distribution function for the reference system is akin to one for hard spheres with a diameter which is a function of temperature and density.

The Helmholtz free energy arising from the spherically symmetric part can then be written analytically, aside from several simple numerical integrals. Additional details on the reference system and the free energy associated with  $\phi_0(r)$  are given in an earlier work.<sup>13</sup>

The angular dependent interaction is written as a sum of generalized spherical harmonics, but it is limited to dipole thru quadrupole terms. Lowest-order contributions to the free energy are evaluated by the techniques of (GGM).<sup>3</sup> These results are now combined in a Pade approximation<sup>4-6</sup> so that the total free energy per particle is written as

$$f = f_{\text{int}} + f_0 + f^{(2)} / (1 - f^{(3)} / f^{(2)}) \quad (5)$$

Equation (5) is a fundamental EOS from which all of the thermodynamics of the systems can be obtained.

A one-fluid model suggested by Ree<sup>14</sup> is used to described the fluid mixture. It has the advantage over similar approaches in that it removes the constraint that the steepness parameter of all the fluid constituents be the same. The free energy of the mixture can be written as that of a reference fluid characterized by averaged potential parameters given by

$$(r)^* = \sum_{i,j} x_i x_j (r_{i,j}^*)^3, \quad (6)$$

$$\epsilon = \sum_{i,j} x_i x_j \epsilon_{i,j} (r_{i,j}^* / r^*)^3, \quad (7)$$

$$\alpha = \sum_{i,j} x_i x_j \alpha_{i,j} (\epsilon_{i,j} / \epsilon) (r_{i,j}^* / r^*)^3, \quad (8)$$

where the  $x_i$ 's are the mole fractions, and the interaction parameters are taken as

$$r_{i,j}^* = k_{i,j} (r_i^* + r_j^*) / 2 \quad (9)$$

$$\epsilon_{i,j} = (\epsilon_i \epsilon_j)^{1/2},$$

$$\alpha_{i,j} = (\alpha_i \alpha_j)^{1/2} \quad (11)$$

## RESULTS FOR Xe/HBr MIXTURE

In order to verify the approximations in this approach to treating multipole effects, a calculation

for a mixture of Xe/HBr is considered. Since the experiments were carried out at low pressure, this is a very stringent test of the proposed theory. Here, a Lennard-Jones potential

$$\phi(r) = 4\epsilon(\sigma/r)^6 [(\sigma/r)^6 - 1] \quad (12)$$

is used for the spherically-symmetric potential. Constraints for the dipole moment and the quadrupole tensor elements for HBr are

$$\mu = \mu \hat{e}_z$$

$$Q_{xx} = Q_{yy} = Q/2$$

$$Q_{zz} = -Q$$

Induction forces, characterized by an isotropic polarizability  $\alpha_p$ , are also included in this calculation. Values of the potential parameters and the multipole moments of interest are given in Table I. The computed volume as a function of the composition at  $P=0$ ,  $T=195.4$  K is in good agreement with the experimental data as seen in Fig. 1. More importantly, the theoretical excess volume as a function of composition compares favorably with experiment as shown in Fig. 2. The curvature of the excess volume is very sensitive to the presence of multipolar effects.

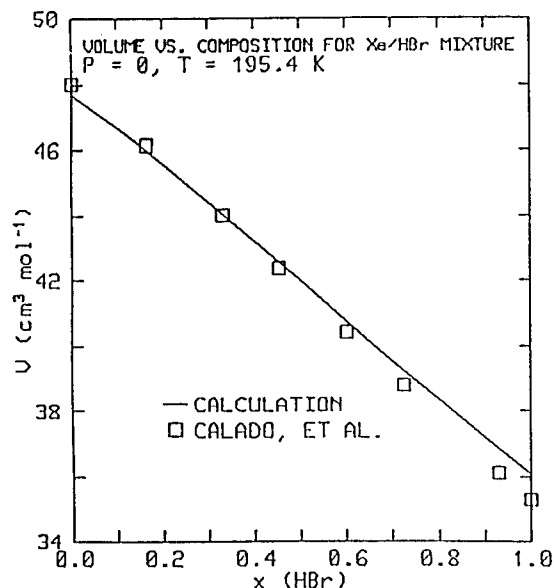


FIGURE 1. MOLAR VOLUME vs COMPOSITION FOR A Xe/HBr MIXTURE. THE DATA FROM CALADO, et al. REFERENCE 7 IS REPRESENTED BY THE SQUARES.

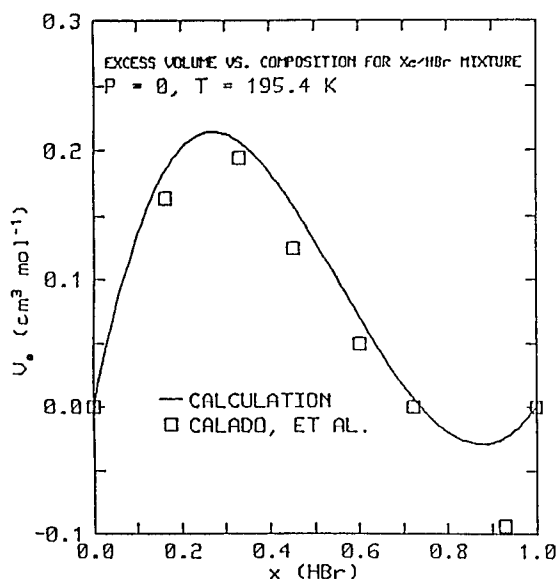


FIGURE 2. EXCESS MOLAR VOLUME vs COMPOSITION FOR A Xe/HBr MIXTURE. THE DATA FROM CALADO, et al. REFERENCE 7 IS REPRESENTED BY THE SQUARES.

TABLE I. POTENTIAL PARAMETERS FOR THE Xe/HBr MIXTURE

TABLE I					
	$\epsilon/K$ (°K)	$\sigma$ (Å)	$\mu \times 10^{18}$ (esu)	$Q \times 10^{26}$ (esu)	$\alpha_p$ (Å <sup>3</sup> )
Xe	231.5	3.961	-	-	4.10
HBr	248.5	3.790	0.788	4.0	-

## RESULTS FOR PETN AND RDX

The potential parameters used for the fluid constituents are given in Tables II and III. These were obtained by matching high-pressure data<sup>15-30</sup> to calculations using the liquid-state perturbation theory. With the exception of NH<sub>3</sub> and H<sub>2</sub>O the parameters are very close to those of Ree and a detailed analysis can be found in Refs. 13, 28 and 31. Theoretical Hugoniot for NH<sub>3</sub> and H<sub>2</sub>O are compared with experimental data in Figs. 3 and 4.

Diamond is chosen as the solid component of the reaction products. A complete description of the EOS used in these calculations is given in Ref. 10.

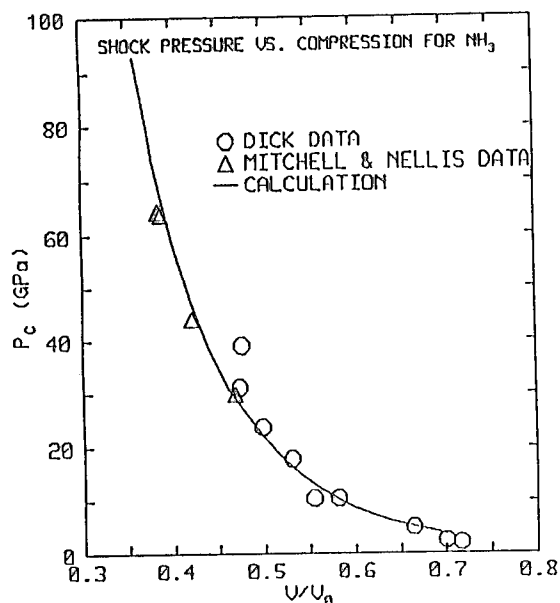


FIGURE 3. SHOCK PRESSURE vs RELATIVE VOLUME FOR LIQUID  $\text{NH}_3$ . THE EXPERIMENTAL MEASUREMENTS OF DICK REFERENCE 27 AND MITCHELL AND NELLIS REFERENCE 24 ARE REPRESENTED BY CIRCLES AND TRIANGLES, RESPECTIVELY.

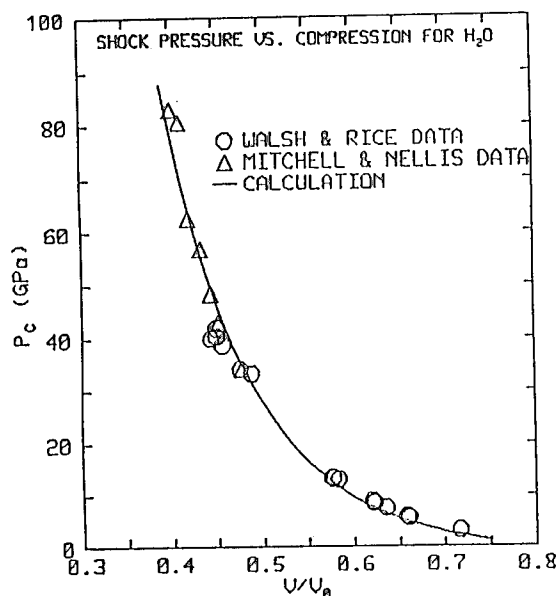


FIGURE 4. SHOCK PRESSURE vs RELATIVE VOLUME FOR LIQUID  $\text{H}_2\text{O}$ . THE EXPERIMENTAL DATA OF WALSH AND RICE REFERENCE 25 AND MITCHELL AND NELLIS REFERENCE 24 ARE REPRESENTED BY CIRCLES AND TRIANGLES, RESPECTIVELY.

TABLE II. ISOTROPIC FLUID EQUATION OF STATE PARAMETERS.

TABLE II			
FLUID EQUATION OF STATE PARAMETERS			
SPECIES	$r^*$	$\epsilon_0/k$	$\alpha$
$\text{CH}_4$	4.15	154.1	13.0
$\text{CO}$	4.12	100.0	13.3
$\text{CO}_2$	4.15	250.0	13.4
$\text{H}_2$	3.46	36.0	11.1
$\text{NH}_3$	3.84	150.0	12.6
$\text{H}_2\text{O}$	3.53	225.0	11.2
$\text{N}_2$	4.12	100.0	13.3
$\text{NO}$	3.97	112.9	13.0
$\text{O}_2$	3.89	125.0	13.0

$k_{\text{N}_2-\text{H}_2\text{O}} = 1.050$   
 $k_{\text{CO}_2-\text{H}_2\text{O}} = 0.920$

TABLE III. MULTIPOLE PARAMETERS

TABLE III				
	$\mu \times 10^{18}(\text{esu})$	$Q_{xx} \times 10^{26}(\text{esu})$	$Q_{yy} \times 10^{26}(\text{esu})$	$Q_{zz} \times 10^{26}(\text{esu})$
$\text{H}_2\text{O}$	1.86	2.63	-2.50	-0.13
$\text{NH}_3$	1.47	1.65	1.65	-3.30

The detonation properties of typical CHNO explosives are now considered with the allowance of a fluid-fluid separation associated with  $\text{N}_2$  and  $\text{H}_2\text{O}$ . Three separate phases are permitted in the chemical equilibrium calculations:

Fluid 1 -  $\text{N}_2$ ,  $\text{H}_2\text{O}$ ,  $\text{CO}_2$ ,  $\text{CO}$ ,  $\text{NH}_3$ ,  $\text{CH}_4$ ,  $\text{NO}$ ,  $\text{H}_2$ ,  $\text{O}_2$ ;

Fluid 2 -  $\text{N}_2$ ,  $\text{H}_2\text{O}$ ;

Solid - C(d).

The phase line for PETN along with its CJ point for an initial density of  $1.77 \text{ Mg/m}^3$  is shown in Fig. 5. In the miscible region the second fluid phase is empty, while across the phase line, most of the  $\text{N}_2$  of the system is located in the second phase. It is seen that the CJ point

lies in the miscible region, so that the multipole effects are not evident. This is in agreement with Ree's prediction.<sup>(1)</sup> Comparison of these two calculations with experimental data is given in Table IV. The approximate 10% disagreement between the predicted and experimental CJ pressure has been discussed earlier.<sup>(1)</sup>

**TABLE IV. CJ STATE PARAMETERS FOR PETN WITH AN INITIAL DENSITY OF 1.77 Mg/m<sup>3</sup>.**

TABLE IV			
CJ parameters for PETN ( $\rho_0 = 1.77 \text{ Mg/m}^3$ )			
	D (km/sec)	P (GPa)	T (K)
Exp <sup>(32)</sup>	8.31	32.0	-
JZ(Ree Approx)	8.21	28.1	4458
JZ(JZ)	8.26	28.7	4385

Predictions for the detonation characteristics of RDX with an initial density of 1.8 Mg/m<sup>3</sup> are sensitive to the multipolar effects, since the CJ point lies in the immiscible region, as seen in Fig. 5. The composition of the reaction products at the CJ point with units of moles/Kg of explosive is

Fluid 1 - N<sub>2</sub> (1.69), H<sub>2</sub>O (11.5), CO<sub>2</sub> (7.6),  
CO ( $1.8 \times 10^{-1}$ );  
NH<sub>3</sub> (1.2), CH<sub>4</sub> ( $7.0 \times 10^{-2}$ ), NO  
( $6.0 \times 10^{-3}$ ), H<sub>2</sub> ( $5.0 \times 10^{-2}$ );  
O<sub>2</sub> ( $1.9 \times 10^{-5}$ )

Fluid 2 - N<sub>2</sub> (11.2), H<sub>2</sub>O ( $1.51 \times 10^{-1}$ );

Solid - C (d) (5.7).

Inspection of Table V clearly shows that the presence of the fluid-fluid separation is necessary for agreement between experiment and theory. Again, the current results are nearly identical to those from the simpler approach of Ree.<sup>(1)</sup>

## SUMMARY

An analytical approach to the treatment of angular dependent intermolecular interactions for simple fluids has been constructed. A sample calculation for a excess volume of a Xe/HBr mixture was in good agreement with the results of Calado, et al.<sup>(7)</sup> Chemical equilibrium calculations for PETN and RDX were performed with the angular dependence for NH<sub>3</sub> and H<sub>2</sub>O explicitly included and compared

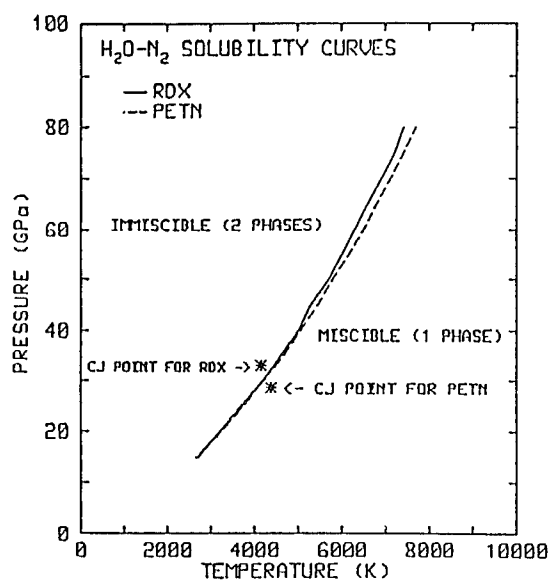


**FIGURE 5. H<sub>2</sub>O-N<sub>2</sub> SOLUBILITY CURVES FOR PETN AND RDX**

**TABLE V. CJ STATE PARAMETERS FOR RDX WITH AN INITIAL DENSITY OF 1.80 Mg/m<sup>3</sup>.**

TABLE V			
CJ parameters for RDX ( $\rho_0 = 1.80 \text{ Mg/m}^3$ )			
	D(km/sec)	P(GPa)	T(K)
Exp <sup>(33)</sup>	8.75	34.1	-
JZ(Ree Approx)	8.79	33.4	4232
JZ (JZ)	8.79	33.1	4171
JZ (JZ)	9.23	33.8	3879
without separation			

with the Ree approximation.<sup>(1)</sup> The fluid-fluid separation phase lines and the CJ states for the two explosives are nearly identical for the two approaches. It was found the separation of N<sub>2</sub> and H<sub>2</sub>O is important in the CJ regime for RDX, but not for PETN, which is in agreement with Ree's earlier work.<sup>(1)</sup>

## REFERENCES

1. Ree, F. H.; "Supercritical Fluid Phase Separations: Implications for Detonation Properties of Condensed Explosives," *J. Chem. Phys.*, Vol. 84, 1986, p. 5845.



2. Weeks, J. D.; Chandler, D.; and Anderson, H. C., "Role of Repulsive Forces in Determining the Equilibrium Structure of Simple Liquids," *J. Chem. Phys.*, Vol. 54, 1971, p. 5237.
3. Gubbins, K. E.; Gray, C. G.; and Machado, J.R.S., "Theory of Fluids of Non-Axial Quadrupolar Molecules," *Molec. Phys.*, Vol. 42, 1981, p. 817.
4. Stell, G.; Rasiah, J. C.; and Narang, H., "Thermodynamic Perturbation Theory for Simple Polar Fluids, I," *Molec. Phys.*, Vol. 23, 1972, p. 393.
5. Stell, G.; Rasaiah, J. C.; and Narang, H., "Thermodynamic Perturbation Theory for Simple Polar Fluids, II," *Molec. Phys.*, Vol. 27, 1974, p. 1393.
6. Rushbrooke, G. S.; Stell, G.; and Høye, J. S., "Theory of Polar Liquids. I. Dipolar Hard Spheres," *Molec. Phys.*, Vol. 26, 1973, p. 1199.
7. Calado, J. C. G.; Gray, C. G.; Gubbins, K. E.; Palavra, A. M.; Soares, V.A.M.; Staveley, L.A.K.; and Twu, H., "Thermodynamics of Binary Liquid Mixtures Involving HBr, HCl, and Xe," *J. Chem. Soc., Faraday Trans. I*, Vol. 74, 1978, p. 893.
8. Seitz, F., and Turnbull, D., Ed., *Solid State Physics*, Vol. 12, Academic Press, London, 1961, p. 275.
9. Murnaghan, F. D., "The Compressibility of Media Under Extreme Pressures," *Proc. Nat. Acad. Sci.*, Vol. 30, 1944, p. 244.
10. Jones, H. D.; and Zerilli, F. J., "Theoretical Equation of State for Aluminized Nitromethane," *J. Appl. Phys.*, Vol. 69, 1991, p. 389.
11. Kang, H. S.; Lee, C. S.; Ree, T.; and Ree, F. H., "A Perturbation Theory of Classical Equilibrium Fluids," *J. Chem. Phys.*, Vol. 85, 1985, p. 414.
12. Verlet, L.; and Weis, J., "Equilibrium Theory of Simple Liquids," *Phys. Rev.*, Vol. A5, 1972, p. 939.
13. Jones, H. D.; and Gray, M. W., "Theoretical Equation of State for Simple Liquids at High Pressures," *J. Appl. Phys.*, Vol. 53, 1982, p. 6604.
14. Ree, F. H., "Equilibrium Properties of High-Density Fluids," *J. Chem. Phys.*, Vol. 64, 1976, p. 4601.
15. Vodar, B. and Marteau, Ph., Ed., *High Pressure Science and Technology*, Vol. 2, Pergamon Press, New York, 1980, p. 1043.
16. Nellis, W. J.; and Mitchell, A. C., "Shock Compression of Liquid Argon, Nitrogen and Oxygen to 90 GPa," *J. Chem. Phys.*, Vol. 73, 1980, p. 6137.
17. Robertson, S. L.; and Babb, Jr., S. E., "Isotherms of Carbon Monoxide to 10 Kbar and 300° C," *J. Chem. Phys.*, Vol. 53, 1970, p. 1094.
18. Nellis, W. J.; Ree, F. H.; Van Thiel, M.; and Mitchell, A. C., "Shock Compression of Liquid Carbon Monoxide and Methane to 90 GPa," *J. Chem. Phys.*, Vol. 75, 1981, p. 3055.
19. Robertson, S. L.; and Babb, Jr., S. E., "Isotherms of Nitrogen to 400° C and 10,000 Bar," *J. Chem. Phys.*, Vol. 50, 1969, p. 4560.
20. Dick, R. D., "Shock Wave Compression of Benzene, Carbon Disulfide, Carbon Tetrachloride and Liquid Nitrogen," *J. Chem. Phys.*, Vol. 52, 1970, p. 6021.
21. Nellis, W. J.; Mitchell, A. C.; and Van Thiel, M., "Equation-of-State Data for Molecular Hydrogen and Deuterium at Shock Pressures in the Range 2-76 GPa," *J. Chem. Phys.*, Vol. 79, 1983, p. 1480.
22. Mills, L. C.; Liebenberg, D. H.; Bronson, J. C.; and Schmidt, L. C., "Equation of State Fluid n-H<sub>2</sub> From P-V-T and Sound Velocity Measurements to 20 Kbar," *J. Chem. Phys.*, Vol. 66, 1977, p. 3076.
23. Mills, R. L.; Liebenberg, D. H.; and Bronson, J. C., "Equation of State of Fluid n-D<sub>2</sub> From P-V-T and Sound Velocity Measurements to 20 Kbar," *J. Chem. Phys.*, Vol. 68, 1978, p. 2663.
24. Mitchell, A. C.; and Nellis, W. J., "Equation of State and Electrical Conductivity of Water and Ammonia shocked to the 100 GPa Pressure Range," *J. Chem. Phys.*, Vol. 76, 1982, p. 6273.
25. Walsh, J. M.; and Rice, M. H., "Dynamic Compression of Liquids From Measurements on Strong Shock Waves," *J. Chem. Phys.*, Vol. 26, 1957, p. 815.
26. Lyzenga, G. A.; Ahrens, T. J.; Nellis, W. J.; and Mitchell, A. C., "The Temperature of Shock-Compressed Water," *J. Chem. Phys.*, Vol. 76, 1982, p. 6282.
27. Dick, R. D., "Shock Compression Data For Liquids. III. Substituted Methane Compounds, Ethylene Glycol, Glycerol and Ammonia," *J. Chem. Phys.*, Vol. 74, 1981, p. 4053.

28. Ross, M.; and Ree, F. H., "Repulsive Forces of Simple Molecules and Mixtures at High Density and Temperature," *J. Chem. Phys.*, Vol. 73, 1980, p. 6146.
29. Ree, F. H., "A Statistical Mechanical Theory of Chemically Reacting Multiphase Mixtures: Application to the Detonation Properties of PETN," *J. Chem. Phys.*, Vol. 81, 1984, 1251.
30. Zubarev, V. N.; and Telegin, G. S., "The Impact Compressibility of Liquid Nitrogen and Solid Carbon Dioxide," *Dokl. Akad. Nauk USSR*, Vol. 142, 1962, p. 309 [*Sov. Phys. Dok.*, Vol. 7, 1962].
31. Ross, M.; Ree, F. H.; and Young, A. D., "Equation of State of Detonation Product Gases," *J. Chem. Phys.*, Vol. 79, 1983, p. 1.
32. Lee, E. L.; and Horning, H. C., "Equation of State of Detonation Product Gases," *Proc. Twelfth Symposium (International) on Combustion*, Poitiers, France, 14-20 July 1968, p. 493.
33. Price, D., "Dependence of Damage Effects Upon Detonation Parameters of Organic High Explosives," *Chem. Rev.*, Vol. 59, 1959, p. 801.

## SESSIONS ON SDT, DDT, AND XDT

**Cochairmen:** **Craig Tarver**  
**Lawrence Livermore National Laboratory**

**Boris Ermolaev**  
**Institute of Chemical Physics**

# INITIATION OF PRESOCKED HIGH EXPLOSIVES PBX-9404, PBX-9502, PBX-9501, MONITORED WITH IN-MATERIAL MAGNETIC GAUGING

Roberta N. Mulford, Stephen A. Sheffield, and Robert R. Alcon  
Los Alamos National Laboratory  
Los Alamos, New Mexico 87545

Desensitization of explosives by preshocking is being studied using the well-supported plane shock waves generated by a gas gun. Evolution of the waves in the explosive is monitored using in-material multiple magnetic gauges to measure particle velocity in the Lagrangian frame, over  $\approx 3\mu\text{s}$  of run. PBX-9404, PBX-9501, and PBX-9502 have been studied, at pressures up to 10.5 GPa. A substantial extension of the run to detonation is observed in PBX-9404, with the run beginning approximately at the end of the preshocked region. A reactive wave is observed while the preshock persists in both PBX-9404 and PBX-9501, but evidently does not contribute to the detonation wave or shorten the run to detonation. PBX-9502 is inert at pressures accessible with the gas gun, but serves to clarify the progress of multiple shocks over the off-Hugoniot EOS surface and the shock dynamics of wave coalescence.

## INTRODUCTION

Detonation characteristics of multiply shocked high explosives (HE) frequently differ noticeably from those of virgin explosive, beyond variations expected due to differing initial state. A precursor shock of sufficient pressure will hinder initiation by a subsequent shock of high pressure. This phenomenon is important to considerations of safety and relevant to many applications of energetic materials.

These studies complement previous investigations. Campbell and Travis<sup>1</sup> studied the overlap of two shocks in detonating material, and developed the idea that the run to detonation in preshocked explosive could best be estimated by the run anticipated for the second shock, measured from the point of coalescence of the preshock and the subsequent shock. Interaction of an established detonation with a preshocked region<sup>1</sup> yielded a quantitative minimum criterion for desensitization:  $P^{2.2}\tau = 1140$  (kbar,  $\mu\text{s}$ ), dependent on preshock pressure  $P$  and duration  $\tau$ . Their work includes data from a series of flyer plate preshock

experiments done by E. Gittings<sup>2</sup>, in which desensitization of impacted explosive was observed.

R. E. Setchell<sup>3</sup> used VISAR diagnostics to track behavior of materials subjected to preshocking by ramp waves which subsequently develop into shocks. The ramp waves evidently gradually compress granular materials, without provoking reaction at a pressure of 5.1 GPa. Even after shock formation, a considerable delay in transition to detonation was observed, relative to initiation by a simple shock. Subsequent experiments<sup>4</sup> using a separate ramp precursor wave showed similar desensitization behavior.

A similar study of the effect of short shocks and preshock pulses on detonation of PBX-9501 was done by Vorthman and Wackerle<sup>5</sup>, using in-material magnetic gauges to record particle velocities. A Lagrangian analysis code was used to estimate the effect of the preshock on the reaction rate.

Recent work by J. P. Plotard at Voujours<sup>6</sup> shows a marked increase of run to detonation with increased

preshock duration, in a material composed of TATB and HMX in comparable quantities.

## EXPERIMENTAL

Experiments were done on a single-stage light gas gun. An inert projectile is accelerated to impact an HE target. Use of a gas gun to generate the shock waves provides the distinct advantages of a well-characterized wave shape and well-supported shocks. The flat-topped pressure pulse simplifies consideration of the time-dependent behavior of the growth of the reactive wave.

Our gas gun can reach projectile velocities of up to 1.4 mm/ $\mu$ s, corresponding to pressures of up to about 10.5 GPa in PBX materials when single crystal sapphire impactors are used. Velocities are repeatable to 0.02 mm/ $\mu$ s. This maximum pressure is insufficient to cause initiation of PBX-9502 within an observable time, but will cause rapid growth to detonation in PBX-9404 or PBX-9501. Experiments have been performed on PBX-9502, to provide exactly quantifiable data on an effectively inert sample of PBX material, and on PBX-9404 and PBX-9501 to study initiation behavior under preshock conditions.

Use of embedded magnetic gauges provides unique measurements in the Lagrangian frame of the time evolution of the shocks, for a duration up to 3  $\mu$ s. Use of multiple gauges give independent measurements of particle velocity  $u_p$ , shock velocity  $U_s$  and, from impulse records, an estimate of the final stress. The precision of the gauges is about 1 to 2%.

The gauge package may consist of 5 nested particle velocity gauges and five impulse gauges (MIV gauge), arranged to record at well determined time intervals, or it may consist of ten particle velocity gauges (multiple magnetic gauge), to more closely monitor the time evolution of waves progressing through the material. Stirrup gauges are also used, to record input waves. The experimental setup is shown in Figure 1.

Current preshock experiments are done with a composite impactor. The stepped waves are generated using a thin (0.6 to 1.2 mm) piece of Kel-F or plexiglass on the front of a high impedance impactor. This experimental design allows accurate manipulation of time and pressure parameters, and generates reproducible flat-topped waves. Impedances of Kel-F and Vistal<sup>7</sup> are such that the first shock is about half of the stress of the second shock.

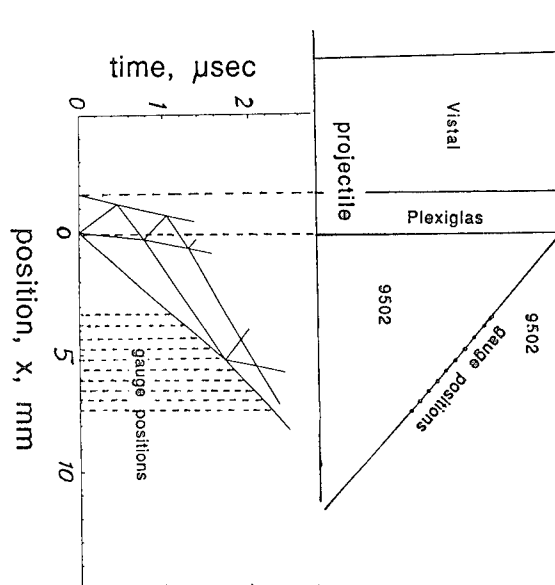


FIGURE 1. SETUP OF PRECURSOR SHOCK EXPERIMENTS

This projectile impacts onto a precisely machined flat explosive cylinder, into which the gauge package has been embedded at a 30° angle. Waves generated are one-dimensional for about 4  $\mu$ s. Signal recording is timed with redundant shorting pins, and velocity measured with an independent set of pins set perpendicular to the path of the projectile.

Experimental wave velocities are obtained by plotting gauge responses against the known gauge positions for the particle velocity gauges. Data are compared with pressures and particle velocities estimated using the MACRAME<sup>8</sup> code, employing a Gamma-law equation of state (EOS) for each material.

## RESULTS

Two experiments have been done with PBX 9404, and one with PBX-9501 to observe delayed detonation. In each of these experiments reaction after the second shock was observed. Four experiments have been completed on PBX 9502, which is basically an inert material under conditions achievable with our gun. Calculated pressures and measured particle velocities and wave velocities are tabulated in Table 1.

### PBX-9502

Since PBX 9502 behaves as an inert material at pressures below 10.5 GPa (when observed for only a

TABLE OF DATA

Experiment - 863			Experiment - 876			Experiment - 886			Experiment - 887		
Observed	MACRAME		Observed	MACRAME		Observed	MACRAME		Observed	MACRAME	
$u_1$	0.37	0.3882	$u_1$	0.56	0.5543	$u_1$	.57	.60	$u_1$	.625	.653
$u_2$	0.73	0.7066	$u_2$	0.96	0.9148	$u_2$	.97	.98	$u_2$	1.08	1.079
$u_3$	0.78	0.7651	$u_c$	0.96	0.9307	$u_c$	.97	1.00	$u_c$	1.08	1.093
$u_c$		0.7720	$U_1$	3.523	3.538	$U_1$	3.76	3.65	$U_1$	3.39	3.813
$U_1$	3.022	3.045	$U_2$	5.724	6.083	$U_2$	6.27	6.293	$U_2$	5.56	6.542
$U_2$	4.416	5.233	$U_c$	4.44	4.520	$U_c$	4.65	4.68	$U_c$	4.839	4.884
$U_3$	5.99	6.142	$P_1$		3.71	$P_1$		4.13	$P_1$		4.71
$U_c$		3.990	$P_2$		8.19	$P_2$		9.12	$P_2$		10.38
$P_1$		2.24	$P_c$		7.96	$P_c$		8.87	$P_c$		10.11
$P_2$		5.58									
$P_3$	6.102	6.63									
$P_c$		5.43									

few  $\mu$ s), it provides a convenient test of the technique and of material response to multiple shocks. For precursor shocks, the data supplements the measured low pressure points on the principle Hugoniot, while in the subsequent shock, points on the second shock Hugoniot of PBX 9502 relative to the initial shock are measured, giving new data on the PBX-9502 EOS. Although coalescence time falls consistently later than calculated from the principal Hugoniot, measured points on the second Hugoniot are very close to the principal Hugoniot, within the experimental error of previous<sup>9</sup> (plane wave lens) measurements in the region studied.

Experiments have focused on the region of the PBX 9502 Hugoniot which appears to show a discontinuity at approximately 7.5 GPa<sup>9</sup>. According to extant data,<sup>9</sup> this cusp should be too small to be resolved in a single-shock experiment. While single-wave experiments in PBX-9502 do not yield a two-wave structure in crossing this discontinuity, the steeper Rayleigh line of the second shock in a two shock experiment is more likely to be interrupted by this small cusp, generating two waves in the second shock, defining the location of this discontinuity. A front impactor made of Kel-F, a near impedance match to PBX-9502, eliminates the third reverberation in the gauge records, allowing a search for a two-wave structure in the second shock. Data from one experiment are shown in Figure 2.

In four experiments done at different pressures in PBX-9502, no two-wave structure has been observed. Possible reasons for the lack of an observable wave are that the cusp may be too small, the pressure pairs may bracket the exact region too widely, or the process responsible for the cusp may be slow on the timescale

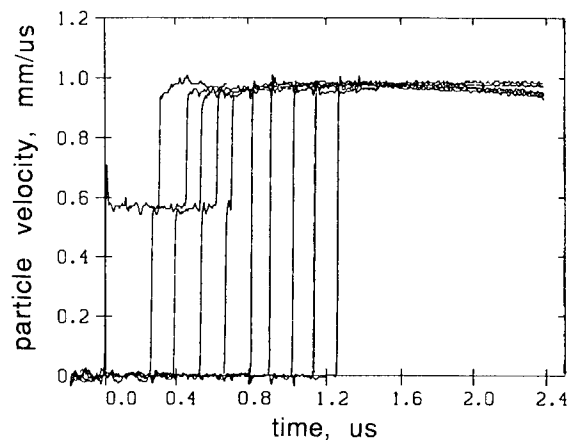


FIGURE 2. PARTICLE VELOCITY RECORDS FROM PBX-9502 PRECURSOR SHOCK EXPT.

of the shock propagation. A continuing series of experiments is investigating this region in small pressure increments, to locate exactly and characterize this apparent discontinuity and try to determine if it is due to a phase transition or other phenomenon.

Adequate data on the single wave arising after coalescence of the preshock and second shock allows the velocity of this wave to be measured. As expected, the velocity is decreased from that of the second shock. Examination of the coalescence in the  $x$ - $t$  plane indicates that a small rarefaction should be propagated back into the doubly shocked region to accommodate this state change. Estimation of the location of the second Hugoniot relative to the principal Hugoniot in the  $P$ - $u_p$  plane will predict the magnitude of the rarefaction wave. The MACRAME code gives a value of 0.15 GPa or 2.7% for the pressure change. This small wave is not resolved in the current data.

Hugoniot points measured in these experiments are plotted in Figure 3, showing that the second Hugoniot is very close to the principal Hugoniot for PBX-9502 at these pressures, and that the small rarefaction is unlikely to be larger than the resolution of the data.

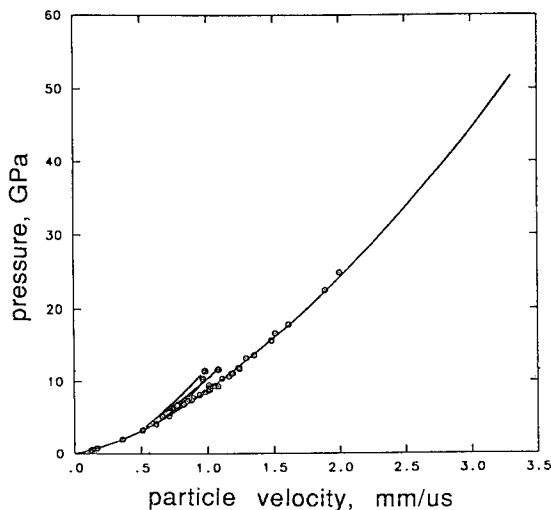


FIGURE 3. HUGONIOT DATA FOR PBX-9502<sup>9</sup>

#### PBX-9404

Initiation of PBX 9404 under preshocked conditions has been observed in detail, with the development of the reactive wave monitored at ten or more positions as the reaction progressed. Gauge records of the input shocks (precursor shock 2.3 GPa and second shock 5.6 GPa), and emerging reactive waves in PBX 9404 are shown in Figure 4.

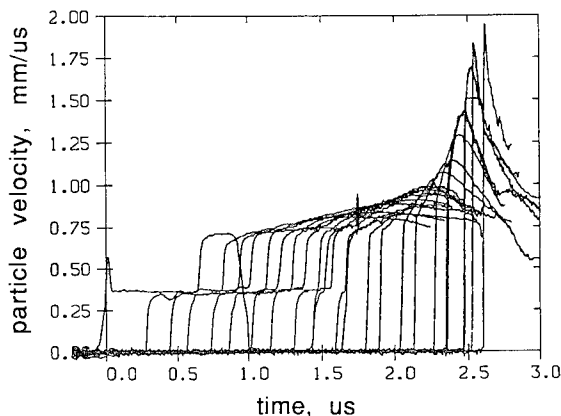


FIGURE 4. PARTICLE VELOCITY RECORDS FROM PBX-9404 PRECURSOR SHOCK EXPT.

Desensitization is clearly evident in the 9404, with the run to detonation showing an increase of 270% over that expected from the pop plot, measuring from the arrival of the second shock (in the preshocked material) to where detonation was observed to occur. Onset of detonation is approximated by the overtake of the shock by the reactive wave, giving a slightly early value. At this point the wave velocity is estimated to be 7.3 mm/ $\mu$ s (from the last two gauges) approaching the velocity of 8.1 mm/ $\mu$ s for PBX 9404. Pressure in this wave is estimated from the particle velocity to be about 15 GPa, well below the C-J pressure of 36 GPa. Nonetheless, detonation is delayed relative to the run anticipated from the pop plot for PBX-9404,<sup>10</sup> as shown in Figure 5.

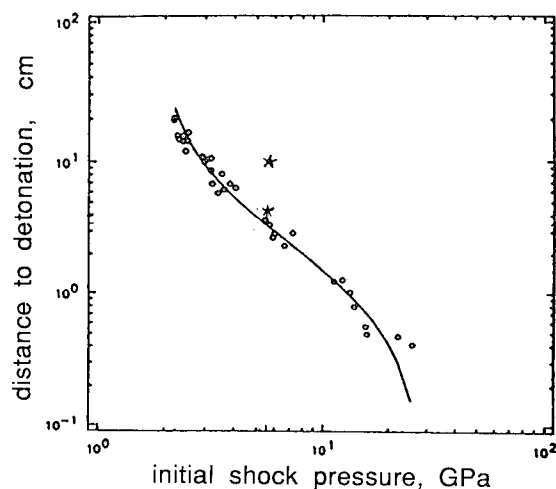


FIGURE 5. POP PLOT FOR PBX-9404<sup>9</sup>

Measuring from the coalescence of the second shock with the precursor also yields a slightly longer run than anticipated from the pop plot. The observed run is about 3% longer than the anticipated run, measuring only the region after coalescence of the two waves, giving nearly the behavior anticipated from the Campbell and Travis rule for the modified pop plot.

This slight extension may be explained by the shock interaction that takes place at the overtake of the preshock by the second shock. Shock dynamics requires a pressure reduction which is achieved by a small rarefaction wave traveling back into the doubly shocked region. Although, as in the PBX-9502, the small rarefaction is not observed directly, its passage is indicated by the reactive waves, appearing as a reduction in their velocity and a drop in their maximum particle velocity.<sup>11</sup> A contact discontinuity separates

the doubly shocked, low temperature region from the singly shocked material at higher temperature.

The reactive waves which are clearly emerging behind the second shock as it travels through the preshocked region evidently do not contribute at all to the development of the reactive wave after wave coalescence.<sup>11</sup>

Overtake of the precursor by the second shock is considerably earlier than calculated by the MACRAME code. Acceleration of the second wave by reaction is a possible reason for early overtake. Another possibility is that the EOS used in MACRAME is not doing a very good job of calculating the off-Hugoniot states.

#### PBX-9501

Limited data obtained for PBX-9501 are shown in Figure 6. PBX-9501 differs from PBX-9404 primarily in the choice of energetic binders. Both materials have HMX as the principal constituent (PBX 9404 has 94% and PBX 9501 has 95%). PBX-9404 uses a mixture of nitrocellulose(3%) and chloroethyl phosphate (CEF) (3.9%) as the binder, with a blue indicator, diphenyl amine (DPA)(0.1%).<sup>10</sup> PBX-9501 includes a mixture of estane (2.0%) and a eutectic consisting of bis(2,2-dinitropropyl-acetal (BDNPA) and -formal (BDNPF) (2.5%) as the binder.<sup>10</sup> The process of manufacture is very similar for both materials.<sup>10</sup> The relative sensitivities of the two binders differ somewhat, as do the shock impedances of the different binders relative to the HMX. The rheologies<sup>12</sup> of the two plastics are

believed to be a major factor in the very different skid responses of PBX-9404 and PBX-9501,<sup>10,12</sup> and provide a convenient variable related to hotspot behavior in preshock conditions.

An interesting feature of the several experiments done on PBX-9501, both single shock and double shock, is a set of small steps visible on the shock rise, and the long risetime consistently observed in this material. Risetimes of 35 ns in single shock experiments exceed risetimes usually seen, for example 15 ns in 9502 and 15-20 ns in 9404. Slight perturbations are seen in the shock rises, at particle velocities of 0.21 and 0.31 mm/ $\mu$ s. In the two-shock experiment, the first shock exhibits comparable cusps at particle velocities of 0.28 and 0.33 mm/ $\mu$ s, giving total risetimes of between 52 and 110 ns. These small perturbations are shown in Figure 6.

Elastic response may be responsible for these waves, although these perturbations are at much higher pressures than the expected yield of the binder in PBX-9501, about 0.65 GPa.<sup>12</sup> Elastic waves generally have a higher wave velocity than the plastic wave, and consequently appear as a larger perturbation with increasing run distance, as do these perturbations in PBX-9501.

A reactive wave is clearly present in material which has been preshocked, as is evident in Figure 5. As was observed in PBX-9404,<sup>11</sup> the reactive wave is not accelerating, and neither is its particle velocity increasing. The small rarefaction has already traversed the region of the material in which this reactive wave is present.

#### DISCUSSION

The small rarefaction generated at wave coalescence, while not observed in the PBX-9502 experiments, apparently has a real effect<sup>11</sup> on reactive waves in PBX-9404 and PBX-9501. The x-t diagrams showing reactive waves are shown in Figures 7 and 8. After the second shock arrives, reactive waves emerge in the doubly shocked material, which is at a low temperature for the given pressure. When they encounter the small rarefaction, their growth is hindered, or even, in the PBX-9501 case, reversed. After wave coalescence with its accompanying contact discontinuity, the material is at a high temperature, with the shock running into material at normal porosity. In this region, a reactive wave develops which ultimately grows to detonation. This wave is probably unrelated to the wave in the preshocked

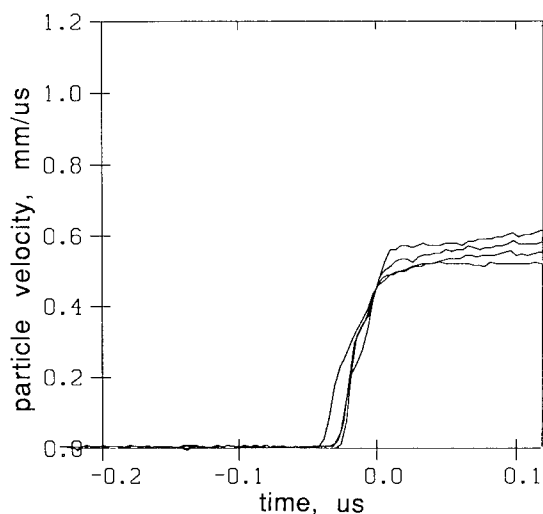


FIGURE 6. PARTICLE VELOCITY SHOCK FRONTS IN PBX-9501



region, since its growth to detonation is not accelerated by the preexisting reactive wave.

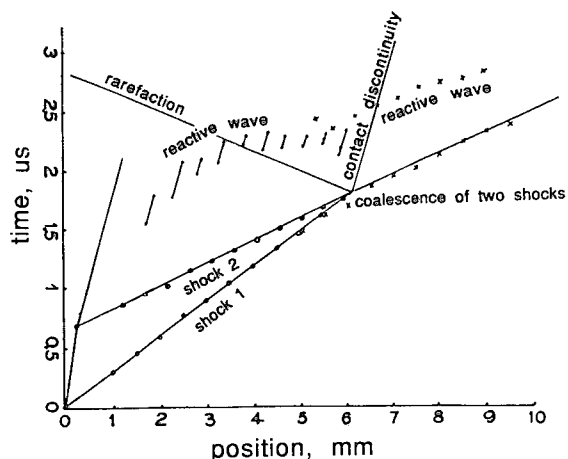


FIGURE 7. x-t DIAGRAM FOR PBX-9404 EXPT.

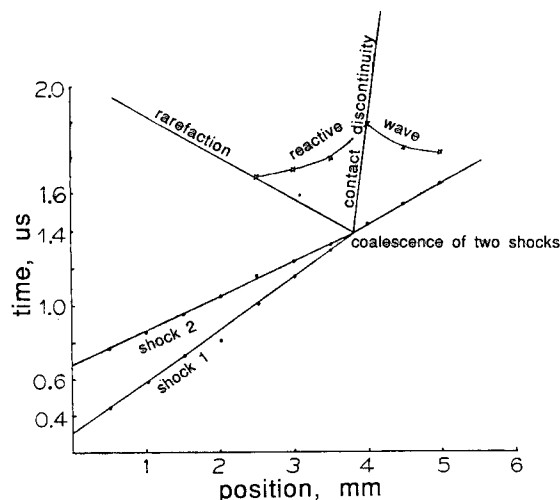


FIGURE 8. x-t DIAGRAM FOR PBX-9501 EXPT.

The small rarefaction and the contact discontinuity affect the bulk thermodynamic state of the material, rather than governing the reaction at hot spots. Only homogeneous initiation of detonation responds to bulk thermodynamic state, while heterogeneous initiation of detonation is largely sensitive to hot spots generated in the flow.

A homogeneous reaction mechanism has been suggested as active in doubly shocked material, because the density of the preshocked material is so high ( $2.1 \text{ g/cm}^3$  in this case), with porosity largely

removed. Heterogeneous character is never obliterated, because of the shock impedance mismatch between the binder and the HMX. Consequently hotspots will exist at any pressure in the plastic bonded material. The reactive waves throughout the experiment exhibit the profile of heterogeneous initiation, i.e., smooth growth behind the front. However, the growth is much slower than would be the case for a single-wave experiment.

While the reactive waves observed here resemble normal heterogeneous waves seen in single shock case, several factors suggest a homogeneous component active in the reactive waves observed in the preshocked region, in the doubly shocked material. The density of the preshocked material is high, so a very long run distance<sup>13</sup> is anticipated when compared to a heterogeneous detonation in a material at this porosity.

The velocity of the reactive wave is almost the same as that of the second shock in PBX-9404. In PBX-9501, the reactive wave actually decelerates relative to the second shock. The x-t planes shown in Figures 7 and 8 show the evolution of the reactive wave, with little acceleration until a wave is well established in the singly shocked region. The particle velocity at the shock arrival front never increases, strongly atypical of a heterogeneous mechanism, although the wave lacks the very localized profile and otherwise constant particle velocity seen in the classic homogeneous case.<sup>14</sup>

Homogeneous initiations may best be characterized by their extreme state-sensitivity.<sup>14</sup> The pressure drop in this rarefaction, from 5.60 to 5.54 GPa, corresponds to a drop of 20 K or less in the bulk temperature. A homogeneous wave is more likely to exhibit this extreme state sensitivity than one with substantial heterogeneous character.

A homogeneous reactive wave is unlikely to contribute to the heterogeneous initiation after wave coalescence, because the two processes proceed in different regions in the material. The x-t diagram and the long run to detonation from coalescence both suggest the non-interaction between the reactive wave in the preshocked region and that in the singly shocked material.

The usual model for preshock desensitization in PBX materials relies on hotspot removal. The  $P^2 \cdot \tau$  idea of Campbell and Travis suggests a time constant for hotspot removal. Sources of such a time constant may include compression time, time required for

cooling of the hotspots, or some kind of reaction or prereaction time.

Shock traversal of hotspots with accompanying local shear is expected to occur on a timescale orders of magnitude faster<sup>15</sup> than the  $\mu\text{s}$  timescale applicable in this case. Lee and Tarver<sup>16</sup> give a rate of  $44 \mu\text{s}^{-1}$ , or a time constant of 20 ns for ignition at hotspots. R. B. Frey<sup>17</sup> gives a time of 35 nsec for full temperature rise and onset of ignition in shear bands at a pressure of 1.03 GPa.

Material rheology, particularly binder rheology, may entail response times on the order of 1  $\mu\text{s}$ . The consistent value of  $\tau$  between explosives argues against the importance of microscopic material mechanical properties. Our data indicates differences in the behaviors of PBX-9404 and PBX-9501, with the PBX-9501 showing substantially less reaction in the preshocked region. This may argue for the effect of the binder or other microscopic properties. Viscous collapse times on the order of 0.5 to 1  $\mu\text{s}$  have been calculated theoretically<sup>18,19</sup> for hotspots. These times are for complete compression, rather than the shear discussed above.

The nitrocellulose energetic component in PBX-9404 reacts at a lower temperature (150C vs. 400C for estane, from DTA data<sup>20</sup>) with greater exothermicity than the estane<sup>20</sup> in PBX-9501. This extra heat release may explain the observed differences in reactivity in the preshocked region.

Thermal conduction is important in time-dependant behavior of hotspots. Hot spots result in local heating as opposed to bulk heating. Hot spot size, material thermal conductivity and the thermal differential between the hotspots and the bulk should be the governing factors in regulating the cooling of these hot spots.

Hotspot cooling should be about the same for both PBX-9404 and PBX-9501, since the major component, HMX, governs the thermal conductivity. Differences seen between PBX-9404 and PBX-9501 argue that bulk thermal conductivity leading to hot spot cooling is not the only factor governing the preshock desensitization, although allowances must be made for the different densities and grain sizes, hence different hotspot sizes and hotspot densities in the samples used.

Strain rate is related to both the compression time for the hotspots and this thermal conduction argument, since adiabatic compression keeps heating local, while

nonadiabatic compression allows dissipation of thermal energy during compression. In a shock, energy will remain localized as the bulk material reaches its final pressure and temperature, allowing reliable local ignition and rapid reactions in hotspots. Nonadiabatic compression permits compression with lower local temperature, (as well as bulk temperature) modifying hotspot reaction rates without manipulating other variables P and V. Thus loading rate allows some separation of hotspot behavior from bulk behavior. Varying strain rate can open up a channel for manipulation of hotspot behavior and temperature at the same bulk pressure and density.

Comparison of PBX-9404 and PBX-9501 data may provide a test of local cooling, because of the different rheology of the binders in the two materials. A long risetime for the first shock in PBX-9501 may be related to the malleability of the estane binder,<sup>11</sup> and modify the input wave enough to provide information on reactive behavior as a function of strain rate.

Experiments using ramp wave inputs will extend previous work and further illuminate the importance of maintaining local temperature during compression.

Prereaction inside hotspots during preshocking may be a factor in deactivating the hotspots without removing or compressing them completely. Prereaction is supposed to deactivate hotspots either by altering the chemistry of the local material, or by increasing the internal pressure sufficiently to make the hotspot void incompressible, preventing local shear or "crushup" and transfer of energy from subsequent shocks to the material. Reaction in the preshock is not visible in our experiments. Since increasing the pressure inside hotspots is a constant volume process, our particle velocity gauging will not indicate any activity if this process is active. Extending the run of the preshock (increasing " $\tau$ ") may reveal reaction and material acceleration during preshocking.

A reactive model developed by Pier Tang<sup>21</sup> reproduces the data and indicates nearly no reaction in the first wave, suggesting desensitization via mechanical changes during compression or temperature effects, rather than desensitization by partial chemical reaction.

## SUMMARY

Desensitization may be due to bulk thermal effects or to hot spot phenomena, specifically, pore collapse, temperature differences, and changes due to chemical

reaction behind the first wave.

A pressure drop is required by the shock dynamics of wave coalescence in the two-shock experiment. This pressure drop is not visible in PBX 9502 records, but may nonetheless be resulting in the extended run observed in PBX-9404 after coalescence of two waves. A reactive wave is emerging in the preshocked material, but apparently does not contribute to the detonation, as indicated by an extended rather than truncated run after coalescence. This fact and the sensitivity of this reactive wave to local conditions argue for some homogeneous character.

The increased reactive behavior of preshocked PBX-9404 over PBX-9501 may indicate that microscopic mechanical behavior is important in determining material reactivity under preshocked conditions, and dominates simple hotspot cooling under some conditions. Further experiments in which hotspot size and density are varied are necessary to confirm this idea.

Campbell and Travis<sup>1</sup> indicate that desensitization increases with increasing time between the first and second shocks, allowing more time for pore collapse, an idea supported in work done by R.E. Setchell.<sup>3,4</sup> However, Andreev et al.<sup>22</sup> indicate that material is more sensitive when the first wave creates more heterogeneities. We intend to further investigate separation of these mechanical and thermodynamic parameters by extending the work to include further comparison of PBX-9404 and PBX-9501, examination of a homogeneous detonating material with and without incompressible hot spots, and obtaining good estimates of relative temperatures in the single and double shock cases.

#### ACKNOWLEDGEMENTS

Pat Serrano did a very nice job of building the targets with the embedded gauges. Discussions with Chuck Forest and Ray Steele were very helpful in this work.

#### REFERENCES

1. A.W. Campbell and J. R. Travis, *Eighth Symposium (International) on Detonation*, NSWC MP 86-194, 1985, pp. 1057-1068.
2. E.F. Gittings, *Fourth Symposium (International) on Detonation*, ONR ACR-126, 1965, pp.373-380.
3. R. E. Setchell, *Combustion and Flame*, **43**, 255-264 (1981).
4. R. E. Setchell, *Combustion and Flame*, **54**, 171-182 (1983).
5. J. Vorthman and J. Wackerle, *Shock Waves in Condensed Matter*, 1983, Elsevier Science Publishers 1984, pp. 613-616.
6. Jean-Paul Plotard, Centre d'Etudes de Vaujours, Courtry, France, private communication.
7. Vistal is a trade name for pressed multicrystalline alumina (sapphire). It has an elastic limit of about 8 GPa.
8. MACRAME Computer Program, J. Fritz, Los Alamos National Laboratory, Group M-6.
9. J. J. Dick, C. A. Forest, J. B. Ramsay, and W. L. Seitz, *J. Appl. Phys.*, **63**, 4884-4888 (1988).
10. T. R. Gibbs and A. Popolato, *LASL Explosive Property Data*, University of California Press, Berkeley, California, 1980-, pp. 84, 85, 109.
11. R. N. Mulford, S. A. Sheffield, and R. R. Alcon, Joint AIRAPT/APS Conference, Colorado Springs, June 1993.
12. Ray Steele, Los Alamos National Laboratory, Group MEE-7, private communication.
13. A. W. Campbell, W. C. Davis, J. B. Ramsay, and J. R. Travis, *Physics of Fluids*, **4**, 511-521 (1961).
14. S. A. Sheffield, R. Engelke, and R. R. Alcon, Ninth Symposium (International) on Detonation, NSWC, 1989, pp. 39-49.
15. Jerry Dick, Material Research Society, Dec. 1982.
16. E.C. Lee and C.M. Tarver, *Phys. Fluids*, **23**, 2362 (1980)
17. R.B. Frey, *Seventh Symposium (International) on Detonation*, NSWC MP 82-334, 1981, pp. 36-44.
18. R.B. Frey, *Eighth Symposium (International) on Detonation*, NSWC MP 86-194, 1985, p. 68.
19. J. N. Johnson, P.K. Tang, and C.A. Forest, *J. Appl. Phys.*, **57**, 4323 (1985).

20. B.M. Dobratz and P.C. Crawford, *LLNL Explosive Handbook*, 1985 pp. 19-44, 19-96.
  21. Pier Tang, Los Alamos National Laboratory, private communication.
  22. S. G. Andreev, et al., *Combustion, Explosives, and Shock Waves*, **14**, pp. 102-105 (1977).
- 

#### DISCUSSION

ALAN FRANK

Lawrence Livermore National Laboratory, Livermore, California

Is there a significant difference in response of the HE if the initial shock is relaxed before the second shock?

#### REPLY BY ROBERTA MULFORD:

Desensitization via a short shock with relaxation before the second shock has been observed by Vorthman and Wackerle (1983) and discussed in terms of bulk temperature. Similar experiments, involving ramp compression instead of a preshock, have been extensively investigated by R. E. Setchell (1981, 1983). Transition to detonation is delayed considerably in that case, compared with the case of initial shock loading.

#### DISCUSSION

JACQUES BOILEAU

DRET, Paris, France

Has the HMX cristal size an effect on your results?

#### REPLY BY ROBERTA MULFORD:

Particle size distribution is an important factor governing sensitivity, along with density, because both affect the size and behavior of hot spots in the material. For this reason our next experiments will be performed on material of known particle size distribution, hydrostatically pressed to minimize density variations within the sample.

#### DISCUSSION

HAROLD J. GRYTING

Gryting Energetics Science Company, San Antonio, Texas

What criteria were used to select the binders for the explosives PBX-9501 and PBX-9502?

#### REPLY BY ROBERTA MULFORD:

Binders were selected with consideration, foremost, to compatibility with the pure HE, and to stability of the composite, especially retention of the plasticizer. The binder gives the composite the important physical properties of strength and high bulk density. Resistance of the composite to accidental initiation during handling is imparted by careful choice of binder. The binder in PBX-9501 was selected to give an added margin of handling safety over PBX-9404. The binder in PBX-9502 was selected for its combination of very high stability with handling safety.

## VELOCIMETRY STUDIES ON THE PROMPT INITIATION OF PBX 9502

Jerry Wackerle, H. L. Stacy and W. L. Seitz  
Los Alamos National Laboratory  
Los Alamos, NM 87545

We have extended the Ninth Detonation Symposium study of detonation reaction zones in PBX 9502 to prompt initiation phenomena in this plastic-bonded TATB explosive. A dual Fabry-Perot velocimeter was used to measure interface velocity histories on strongly shocked, thin (less than the 3-mm distance to detonation) explosives disks. A rounded character was resolved in the initial portion of the velocity histories. A shock-change analysis demonstrates that this observation requires that reaction rates immediately behind the shock front must be small relative to the subsequent rates in the evolution to detonation. We obtain good numerical hydrodynamic simulations of our measurements with the rate form Pier Tang developed in the previous reaction-zone study, with the empirical hotspot formulation of the first of three stages of his model providing the feature needed to match the new data. Our observations also could support some surface-burning concepts.

### INTRODUCTION

The use of interface velocimetry to investigate the reaction zones and reaction-rate representations in the prompt initiation and detonation of TATB-based explosives has been a continuing effort of our group for the past several years. The experimental aspects of this work have centered on the use of planar high-explosive driving systems to initiate detonation in disks of the subject explosive and the use of dynamic Fabry-Perot interferometry to observe interface velocity histories as waves are propagated from the explosive into appropriate window materials. Throughout, the study has included reactive numerical hydrodynamic calculations of the observations, with the objective of testing and refining reaction-rate models for their adequacy in representing the shock-induced decomposition behavior of the explosives. Investigations reported to the Eighth and Ninth Symposia on Detonation (References 1 and 2, hereafter denoted 8SD and 9SD) were focused on the properties of well-established detonations, and particularly on the slightly unsteady growth of the process, or "buildup of detonation," characteristic of the relatively long reaction zones in TATB-based explosives. A principal conclusion of these studies was that a relatively slow component in the later stages of the reaction-rate history is required for the accurate numerical modeling of detonation reaction zones in these explosives. Substantial improvements in the velocimetry system were realized between the two Symposia, and the better defined reaction-zone histories required a more complex reaction-rate form to properly model the observations reported in 9SD. Specifically, the single-stage, DAGMAR rate<sup>3,4</sup> used in 8SD was found inadequate to simulate *both* the relatively slow rates in the later stages of the detonation reaction zone and the relatively fast rates in the earlier stages inferred from the improved measurements. The more detailed

reaction-zone structures were successfully treated with a rate form having antecedents in the so-called JTF (Johnson-Tang-Forest) model,<sup>5</sup> and featuring significant improvements by Pier Tang.<sup>6</sup>

In this paper, we describe the extension and refinement of the same methods for an investigation of the reaction rates in the prompt initiation of PBX 9502 (95 wt percent TATB/5 wt percent Kcl F 800). A further improvement was realized in the experimental configuration of 9SD, which already was sufficient to resolve considerable detail in the detonation reaction zones. In this study, we obtained interface velocity histories on specimens with thicknesses less than the approximately 3-mm run distance needed to establish a nearly steady detonation reaction zone with our driving system. Within this experimental range, an initially rounded character was observed in velocity histories, and the quantitative measurements of the evolution of this feature during the prompt initiation buildup process provide the significant new experimental information of this paper.

As described below, both a shock-change analysis and numerical hydrodynamic modeling of the velocity histories demonstrate that the global reaction rates for PBX 9502 are relatively low immediately behind the shock front. By this, we mean that the initial rate is notably lower than the average rate required to effect buildup to detonation in the time observed, as would be characteristic of a form with a simple dependence on pressure and mass fraction reacted. Reaction-rate histories like those inferred are often characterized as requiring an "induction-time factor." This character is known to be appropriate for low-porosity explosives at lower input shock strengths, with times and distances to detonation several times larger than in the present work.

For example, Lagrange analyses of embedded-gauge data have shown this to be a feature of the reaction rates for low-porosity, plastic-bonded HMX explosives,<sup>3,7</sup> and for PBX 9502 under lower-pressure conditions.<sup>8</sup> To our knowledge, this work is the first demonstration of this reaction-rate property with relatively high shock pressures and prompt initiation conditions.

The experiments and results are described in the following section of this paper. This is followed by a shock-change analysis of the data, that demonstrates the relatively low rates behind the shock front. The next section describes one-dimensional numerical hydrodynamic calculations showing that the more advanced rate form used in 9SD to be capable of simulating this phenomenology. The discussion in a final section includes further calculations showing that surface-burning models—conceptually somewhat different than the JTF approach—also are consistent with the observations.

## EXPERIMENTS AND RESULTS

The experiments are described in considerable detail in 9SD; in this paper, we will limit the discussion to an overview of the method, some remarks on the more important modifications for this work, and some indications of the capabilities and resolution limits of the measurements.

The basic shot assembly is shown in Figure 1. The explosive driver system shown has been found to give reasonably planar, very reproducible input shock conditions, providing initial pressures and particle velocities in the explosive specimens of 20.5 GPa and 1.75 mm/ $\mu$ s, respectively. (The accepted wedge-test, or Pop-plot, data for PBX 9502 predict a run to detonation of about 2 mm and 0.3  $\mu$ s for this input shock strength, but our

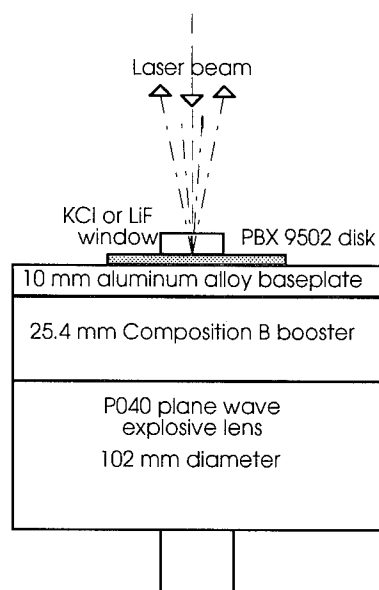


FIGURE 1. HIGH EXPLOSIVES ASSEMBLY

observations show a somewhat longer run is needed to establish a full detonation reaction-zone structure.) The PBX 9502 specimens were pressed from the same batch of material as before, and to very near the same initial density; the  $1.894 \pm 0.002$  g/cm<sup>3</sup> density for this study corresponds to a  $0.018 \pm 0.001$  void fraction. The test specimens were from 0.25 to 5.0 mm thick, with the disks less than 2-mm thick fabricated by machining the PBX 9502 after cementing it to the base plate. The diffuse reflection of the highly collimated, incident laser beam was accomplished by a slightly buffed, vapor-plated, aluminum coating on the appropriate window face; the aluminum layer was thin enough ( $<1$   $\mu$ m) and matched the window properties well enough to introduce negligible perturbations into the flow and interface-velocity histories. The single-crystal potassium chloride windows mostly used in this study have a slightly lower shock impedance than PBX 9502, so a slight rarefaction wave is reflected back into the reacting explosive. The lithium fluoride crystals have a shock impedance close to that of aluminum, and reflect a rather strong shock from the interface. Both crystal salts have linear refractive index-density relations, and are well-calibrated for the simple and accurate conversion of apparent interface velocities to the true values.<sup>9</sup>

A schema of the dual-channel velocimeter is shown in Figure 2. The argon ion laser provides an approximately 3-W collimated beam of a single, 514.5-nm frequency that is switched on for about 30  $\mu$ s by the light modulator and focused to 50- $\mu$ m spot on the aluminum window coating. The Doppler-shifted (after shock arrival) radiation is diffusely reflected from the interface and collected and collimated into a 50-mm-diameter beam by lens L5. This beam is divided by beam-splitter B2 and recorded through two channels of dynamic interferometers. Each channel includes a narrow bandpass filter to eliminate extraneous white light, a cylindrical lens (L3 and L4) to converge beams into one plane on the Fabry-Perot etalons, a focusing lens and a streak camera with the light gain boosted with a channel-plate intensifier. The Fabry-Perot etalons were set to shift the interferometer records one fringe per 1.5 mm/ $\mu$ s in interface velocity in the channel with the combination camera and a sensitivity of 1.93 mm/ $\mu$ s per fringe with the electronic streak camera.

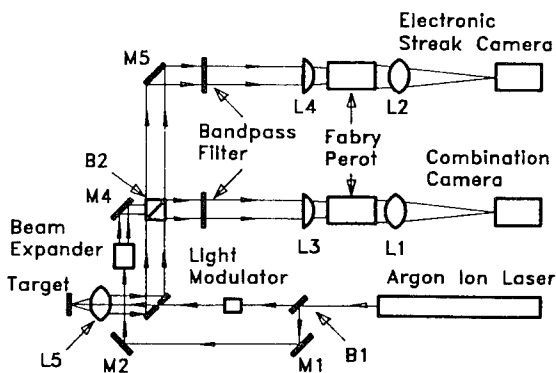
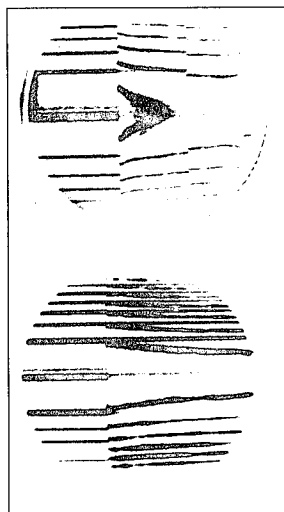


FIGURE 2. DUAL CHANNEL, FABRY-PEROT VELOCIMETER

The combination camera is the same rotating-mirror camera used for the 9SD study, with a format size determined by the 40-mm-diameter intensifier tube, and a writing speed of around 15.6 mm/ $\mu$ s. The electronic streak camera for the 9SD investigation was operated at a four times greater writing speed, but had a relatively narrow format for the fringe images, and as a consequence that study relied almost entirely on the rotating-mirror camera record for quantitative velocity data. The principal velocimeter improvement for the present work is the use of a wider-format electronic streak camera (a Hamamatsu Model C2780) that provides film records of a size and image quality quite comparable to those with the combination camera. The result was that interface velocity measurements with the two cameras had about the same 0.01- to 0.02-mm/ $\mu$ s estimated errors. We used our present electronic camera with 79-mm/ $\mu$ s writing speed and a 0.05-mm slit width, and the time resolution of the velocity histories is estimated to be 3 to 4 ns, which was mainly composed of the "fill time" required to reach good transmission through the Fabry-Perot etalon. As previously,<sup>2</sup> the estimated time resolution with the combination camera was 5 to 9 ns.

Typical dynamic interferographs are displayed in Figure 3. The comparable image quality is evident, and comparison with Figure 3 of 9SD emphasizes the improvement. The total writing time is about 2.7  $\mu$ s across the diameter of the combination camera record and about 0.5  $\mu$ s for the electronic camera. The records were chosen from an experiment with a 1.79-mm explosives specimen and a KCl window, and as seen both in the velocimeter records and in the reduced velocity histories, features are discernible in the electronic streak camera that are not apparent with the slower camera.

As previously, film records were read on a digitized optical comparator and processed with a computer



**FIGURE 3. VELOCIMETER RECORDS FROM THE COMBINATION CAMERA (TOP) AND THE ELECTRONIC STREAK CAMERA**

program relating the velocities to the position of the static (left side of records in Figure 3) and dynamic fringe positions and the precisely measured etalon spacing. The data-reduction calculation is a least-squares analysis treating all fringes simultaneously, and gives optimum accuracy and statistical significance to the previously cited estimates of errors in velocity.

Interface velocities obtained with KCl and LiF windows are shown in Figures 4 and 5, respectively. In both, the data using the electronic camera is shown as solid lines and chain-dot curves are from the combination camera. Shock transit times were not measured, and the relative timing of the velocity histories were derived from the numerical hydrodynamic calculations described later. The velocity histories starting at zero time in each set were for the appropriate windows in contact with the aluminum baseplate, and were used to calibrate the driver system for the hydrocode computations.

In the series with KCl windows, the PBX 9502 specimen thicknesses were 0.25, 0.51, 0.79, 1.02, 1.47, 1.79, 2.03, 3.0 and 5.0 mm. The deviation of the velocity histories from a simple step function is quite prominent at the first five levels, and data with the two cameras are in good agreement. In the rapid buildup region

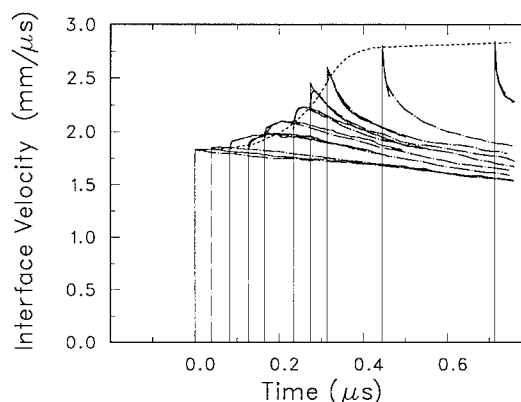


**FIGURE 4. VELOCITY HISTORIES AT PBX 9502-KCl INTERFACES**

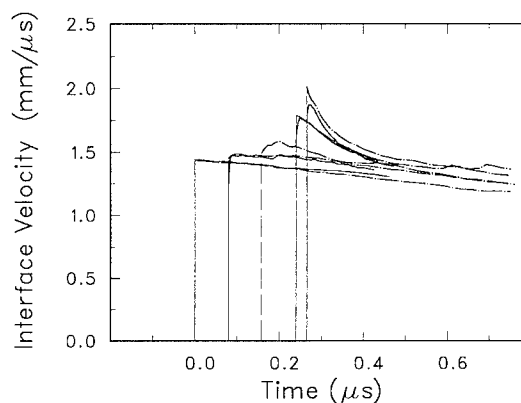


**FIGURE 5. VELOCITY HISTORIES AT PBX 9502-LiF INTERFACES**

of the shock front (estimated with the dashed line) at 1.79 and 2.03 mm, the rounding of the velocity histories occurs in 10 ns or less, and is discernible only with the electronic streak camera. A fully developed detonation and von Neumann spikes appear at the 3.0 and 5.0 mm levels, although some growth appears between the two. Both this growth and the character of these reaction-zone histories are consistent with the observations of 9SD.

Interface-velocity data with LiF windows were taken for only four PBX 9502 thicknesses, specifically 0.50, 0.99, 1.50 and 1.69 mm. The velocity ranges of Figures 4 and 5 are chosen different to roughly scale with the different shock impedance of KCl and LiF. Where data exist at common levels, the similarity of the histories with the two different window materials is quite striking. This suggests that the reaction rate process is not much affected by whether the wave reflected back into the reacting PBX 9502 is a modest rarefaction or a relatively strong shock. This observation is consistent with rate forms placing a strong dependence on the strength of the first shock, which is a feature of both the JTF model and the more empirical DAGMAR correlation cited earlier.

## SHOCK-CHANGE ANALYSIS

Throughout the analysis and modeling of this study, the assumption is that shocks in explosives are unreactive, and the issue addressed is the energy-release rates immediately behind the front. The unreactive shock front is a feature of nearly all the cited Los Alamos numerical modeling of initiation and detonation, if not always the rate formulations.<sup>10</sup> It is best justified experimentally by the fact that we observe the classic Zeldovich-von Neumann-Doering detonation reaction-zone structures whenever we have sufficient resolution in our measurements. Again in common with most of the cited Los Alamos work, we will represent the reactant-product equation of state of the explosive with the HOM form.<sup>10</sup> The assumptions of this state equation include that of temperature equilibrium, which can be argued as an inappropriate choice for heterogeneous explosives. However, it has been shown that the thermodynamic derivatives most critical to numerical modeling---the thermicity and sound speed---differ little between HOM and the so-called two-temperature or isentropic solid representations.<sup>11</sup> The constants and formulations for the solid and products state equation for this study are identical to those used in 9SD.

The combination of the fluid-dynamic (including shock) conservation equations and the Lagrangian time derivatives of the constitutive relations for reactive materials allows the derivation of a class of relations known as *shock-change equations*. Such expressions have been derived by many authors,<sup>12</sup> and describe the evolution of mechanical variables (particle velocity  $u$  and shock velocity  $U$ ) and the thermodynamic state variables (such as the pressure  $p$ , density  $\rho$ , specific energy  $e$  and mass fraction of reaction products  $\lambda$ ) behind the shock front, as influenced by the magnitudes of the variables behind the front, their gradients or material time derivatives, the reaction rate, and when appropriate, the curvature of the

shock wave. Such relations are best and most rigorously applied to observations of shocks propagating *within* an explosive, as would be measured with embedded gauges with negligible perturbations, rather than with our window-interface observations. However, because crystal KCl is a near match to PBX 9502 in shock impedance, we can make good estimates of reaction rates behind the front during the prompt initiation buildup with our data.

For a collection of material velocity histories, the appropriate shock-change equation is derived in one-dimensional, planar, Lagrangian distance-time,  $(h, t)$  coordinates, and relates the time derivative of the particle velocity at the shock front,  $du/dt$  or *front acceleration* to the material time derivative of the particle velocity, or *particle acceleration*,  $\dot{u}$ . (Unsubscripted variables are understood to be evaluated immediately behind the shock, and a sub-0 denote variables ahead of the shock.) These two quantities are expressed, respectively, by the slope of the dashed curve in Figure 4 and the slopes of the interface velocities, and are related through the directional derivative along the shock path

$$\frac{du}{dt} = \dot{u} + U \frac{\partial u}{\partial h}, \quad U = \frac{dh}{dt}, \quad (1)$$

where the gradient  $\partial u / \partial h$  is evaluated at constant time. The so-called master equation---essentially the material time derivative of the  $p(p, e, \lambda)$  equation of state can be written

$$\dot{p} - c^2 \dot{\rho} = p_\lambda \dot{\lambda}, \quad (2)$$

where the thermodynamic derivatives are  $c^2 = (\partial p / \partial \rho)_S$ ,  $S$  denoting the entropy,  $p_\lambda = (\partial p / \partial \lambda)_{p, e}$ , and  $\dot{\lambda}$  is the reaction rate. Some simple manipulation with Equations (1) and (2) and use of the mass and momentum conservation relations for both shock discontinuities and continuous flow give a shock-change relation

$$\frac{du}{dt} = \frac{F\dot{u} + G\dot{\lambda}}{H}. \quad (3)$$

Here  $F$ ,  $G$  and  $H$  are dimensionless functions defined as

$$F = W^2 - 1, \quad G = \frac{p_\lambda}{p}, \quad \text{and} \quad H = 1 + W^2 + \frac{U'u}{U}, \quad (4)$$

where  $W = (\rho c) / (\rho_0 U)$  is the reciprocal of the Mach number and  $U'$  denotes  $dU(u)/du = S(u)$  along the unreacted Hugoniot, which is constant with the common linear relation between shock and particle velocities.

Using the same equation-of-state representation and constants as in 9SD, we have calculated the functions in Equation (3) and plotted them against particle velocity over our range of observation in Figure 6. Also plotted is the function

$$(H/F) = \left( \frac{\dot{u}}{du/dt} \right)_{ro}, \quad (5)$$

the ratio of the particle acceleration to the front acceleration for a vanishing reaction rate. It is seen to be about 2.0 over most of the range of our data. Note that the ratio depends only on variables along the unreacted shock Hugoniot, and is independent of assumptions about the product equation of state or reactant-product mix rule. The principal dependence is on  $W$ , which in turn mainly depends on  $S(u)$ , which is fairly well known from experiment over the range of our data.



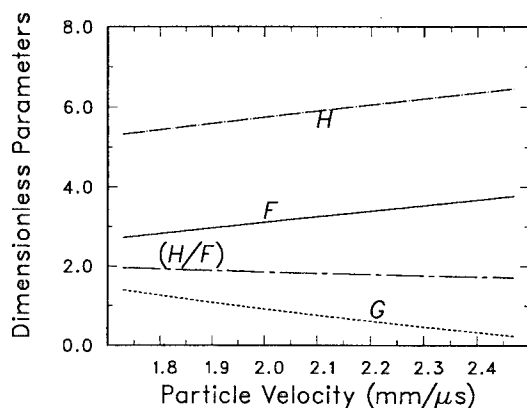


FIGURE 6. FUNCTIONS FOR SHOCK-CHANGE RELATIONS

Inspection of Figure 4 for the interface-velocity histories beginning at 0.8 to 0.23  $\mu\text{s}$  (0.25 to 1.47 mm) show that the conditions of Equation (5) are met throughout this region. The reaction rate behind the front would appear to be relatively small or vanishing over the range of shock strength assessed, which in the explosive is from 20.5 to 25 GPa. A more quantitative examination is aided by reference to Figure 7, which depicts the second-stage, "fast process" rate used in 9SD, and is a modified Forest Fire form well-calibrated to wedge data on PBX 9502. In Figure 4, we observe that the front acceleration in the earlier stages (from 0.25 to 0.75 mm) can be no more than 0.4  $\text{mm}/\mu\text{s}^2$ , while the expected fast rate of around 3  $\mu\text{s}^{-1}$  would lead to a  $du/dt$  three times this large if  $\dot{u}$  were merely vanishing, as in a so-called growing square wave. The observed particle accelerations would need to be negative to accommodate the fast-rate assumption, and they are positive enough to indicate a negligible rate behind the front. The experimental particle accelerations are, in fact, rather larger than is physical at some interfaces; possibly a different choice of the shock front would lead to more realistic results. This situation is remedied in the analysis at the 1.47-mm explosive thickness, where the observed  $\dot{u} \approx 20 \text{ mm}/\mu\text{s}^2$  and  $du/dt \approx 10 \text{ mm}/\mu\text{s}^2$  have just the ratio required for a vanishing rate.

Interpretation of the two interface-velocity histories in the rapid buildup region (records at 0.28 and 0.31  $\mu\text{s}$  on 1.73- and 2.02-mm PBX 9502 thicknesses) sample shock pressures in the explosive of approximately 28 and 32 GPa. The rounding is so brief that only the electronic-streak-camera data are useful, and it is difficult to choose the shock-front history well. The most reasonable interpretation is that the reaction rate behind the front is relatively small at the 1.73-mm level and that the rate cannot be assessed at 2.02 mm.

The interface-velocity histories for the 3.0- and 5.0-mm explosive thicknesses are in the region of a nearly steady detonation wave ( $du/dt \Rightarrow 0$ ), with a von Neumann spike pressure of about 35 GPa in our representation of PBX 9502. The particle acceleration is  $-30 \text{ mm}/\mu\text{s}^2$ , the front acceleration about 0.15  $\text{mm}/\mu\text{s}^2$ , and when corrected for the slight impedance mismatch,

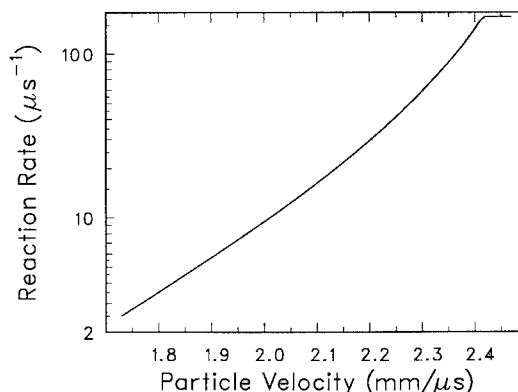


FIGURE 7. FAST-PROCESS RATE FOR PBX 9502

the particle velocity in the explosive is 2.47  $\text{mm}/\mu\text{s}$ . From the calculations graphed in Figure 4,  $F$ ,  $G$  and  $H$  are 3.8, 0.24 and 6.4 respectively, and Equation 3 gives a reaction rate of 194  $\mu\text{s}^{-1}$ , which in satisfying agreement with the 200- $\mu\text{s}^{-1}$  limiting value chosen for the fast process in 9SD.

While the above rate analysis for the detonation reaction zone is made on a basis of examining conditions immediately behind the front, it should be realized that the properties of steady detonations make the results valid even if there is some small, unresolved ( $<3 \text{ ns}$ ) induction-time factor in the rate. In this case, there would be a brief flat region in the interface velocity history, but then the initial particle acceleration is the same as without any induction time. This is because with steady waves there are linear relations between the pressure, density and particle velocity; basically resulting from a linear scaling of gradients and time derivative in the conservation relations for continuous flow. For our simple, planar case, the equivalence of the shock-change and steady-wave analyses are easily demonstrated. Denoting  $U_D$  as the constant detonation velocity, the appropriate steady-wave relations are

$$p = \rho_0 U_D u, \quad \dot{p} = \rho_0 U_D \dot{u}, \quad \text{and} \quad \dot{p} = \frac{\rho^2 \dot{u}}{\rho_0 U_D}. \quad (6)$$

If these relations are used to eliminate  $\dot{p}$  and  $\dot{\rho}$  from the continuous flow Equation (2) and the definitions of Equation (4) are imposed, then one immediately recovers the shock relation, Equation (3), for the steady-wave circumstance of a vanishing front acceleration.

## NUMERICAL HYDRODYNAMIC SIMULATIONS

To further illustrate the consequences of our "observations" of relatively low rates behind high-pressure shocks, we have conducted simulations of prompt initiation of PBX 9502 with our modification of a rudimentary, but rather accurate, numerical hydrocode. The CHARADE code is a method-of-characteristics based calculation, originally devised by J.N. Johnson for the study of JTF rate model described in Reference 5, but more recently refined by him and D. L. Tonks for fundamental studies of the constitutive relations for elastic-

plastic effects in metals.<sup>13</sup> The program operates on a rectangular Lagrangian ( $h, t$ ) mesh, using linear interpolation and explicit, linear extrapolation. Each time cycle, the mechanical and state variables at all positions are advanced through solutions between forward and backward propagating characteristics. The calculation presently treats only a single, forward-propagating shock, using a shock-change relation (in terms of stress gradients, rather than particle accelerations), offering a significant advantage for our problem compared with the inaccuracies and artifices attending the treatment of shocks with artificial-viscosity hydrocodes. Our principal modification to CHARADE is the addition of a variety of reaction-rate forms.

The CHARADE hydrocode presently is limited to two materials, so the capability it does have for programming velocity histories at the left boundary was utilized in calibrating for the explosives driving system. We found a velocity function for the rear face of the baseplate that gives good agreement with the interface velocities measured with the alkali halide windows (the zero-time profiles in Figures 4 and 5). This was then used with a combination of a baseplate and thick layer of PBX 9502 in computations of velocity histories in the embedded-gauge sense. These results included the history at the baseplate-explosive interface, which was used in simulating velocities between interfaces of PBX 9502 specimens and KCl windows, this somewhat limited the valid time of the calculations with thinner explosives specimens. All calculations were done with a 8.33- $\mu$ m mesh spacing and---with the usual Courant condition---time cycles were well below 1 ns.

As stated in the Introduction, the simulations were with the same reaction-rate model used in 9SD and described more fully in Reference 6. This rate form models the energy release as resulting from the combination of a hotspot explosion process and the bulk reaction by fast and relatively slow processes. The overall reaction rate can be written

$$\dot{\lambda} = \phi_h \dot{\lambda}_h + (1 - \phi_h - \phi_s) \dot{\lambda}_f + \phi_s \dot{\lambda}_s \quad (7)$$

Here the  $\lambda$ 's are all progress variables, going from zero to unity,  $\phi_h = 0.003$  the constant mass fraction of hotspots, and  $\phi_s = 0.15$  the slow component fraction. As is obvious from the associated fraction, the hotspot reaction *per se* contributes little to the overall reaction, but rather, it is the manner in which it enables the fast process---by some unspecified energy-transfer mechanism---that dominates the early stages of the shock-induced decomposition. This is formulated

$$\dot{\lambda}_f = (1 - \lambda_f) R_f \frac{(\lambda_h - f_0/\phi_h)}{(1 - f_0/\phi_h)} \quad (8)$$

where  $R_f$  is the modified Forest Fire rate in Figure 7 and  $f_0 = 0.01\phi_h$  is the minimum hotspot size for reaction. The evolution of the hotspot reaction is thus seen necessary to "turn on" the fast process. The formulation of  $\dot{\lambda}_h$  is unchanged from the JTF empirical hotspot model,<sup>5</sup> which is somewhat based in thermal explosion theory

and uses Arrhenius constants from thermal analysis data for calibration. However, the hotspot temperatures are most strongly dependent on shock pressure  $p_s$ , with slight modification from subsequent state changes, and can be expressed to good approximation as

$$\dot{\lambda}_h \equiv (1 - \lambda_h) R_h (p_s/p_N)^m \quad (9)$$

If we use  $p_N = 10$  GPa for normalization and  $m = 5.5$  as calibrated for PBX 9502, then the other constants entering in the complete hotspot rate function give  $R_h \equiv 0.61$ . In terms of hotspot activation times, this corresponds to  $\lambda_h = 0.5$  in about 22 ns with our initial shock conditions, in about 7.5 ns at the 1.47-mm (25-GPa) level, and in 1.2 ns at the detonation spike condition.

Results are shown in Figure 8 for CHARADE simulations of particle-velocity histories embedded gauges would record in a thick layer of PBX 9502, using the alternatives of an "instantaneous hotspot" assumption and the empirical hotspot model described above. The velocity histories calculated with the first assumption (top) bear little resemblance to our observations, and give a striking demonstration of the need for some representation of relatively low rates behind the shock front. Particularly notable is the negative particle accelerations throughout the buildup process, as the shock-change analysis shows is necessary to reconcile the front

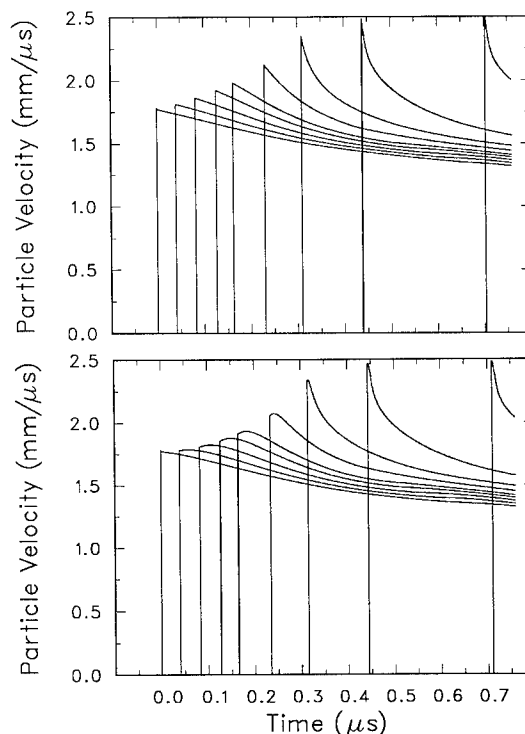


**FIGURE 8. SIMULATIONS OF VELOCITY HISTORIES IN PBX 9502 WITH THE INSTANTANEOUS HOTSPOT ASSUMPTION (TOP) AND WITH THE EMPIRICAL HOTSPOT MODEL**

accelerations with the full initial rates that effect the prompt initiation. The simulation with the rate form of 9SD (bottom) appears to match both the velocity histories and the buildup properties well. This is a result of the calibration of both the reactant-product equation of state and the many constants in the rate model to a wide variety of data on PBX 9502. The principal information for calibrating the hotspot rate model are measurements with embedded, magnetic-impulse-velocity gauges,<sup>8</sup> obtained in experiments at significantly lower shock strengths than this study. The constants for Equation (9) are essentially chosen to match these data and interpolate through the data range to give a negligible induction time for the detonation reaction zone. It appears to succeed fairly well in this purpose.

Our simulations of actual interface velocities with crystal KCl windows are shown in Figure 9. There is reasonable agreement, but the calculated values lie somewhat below observation and the initial accelerations are not as prominent as observed. The low detonation spikes calculated result more from the state equations chosen than from the rate form. As the larger observed accelerations were already found in conflict with the shock-change analysis, it is likely that part of the discrepancy lies in the experiments.

In another presentation to this Symposium, Pier Tang describes his further advances in theoretical modeling of reaction rates for heterogeneous explosives,<sup>14</sup> making some appealing arguments for an energy-release behavior at high pressures involving mechanisms more commonly associated with homogeneous explosives. He has simulated the observations of this work, and succeeded in obtaining agreement better than that shown here with a more physically rich model.

## DISCUSSION

The principal experimental fact of this work is that reaction rates are relatively low immediately behind the shock front in high-density, plastic-bonded TATB at higher initial shock strengths than previously realized, and we might question what alternative fictions we

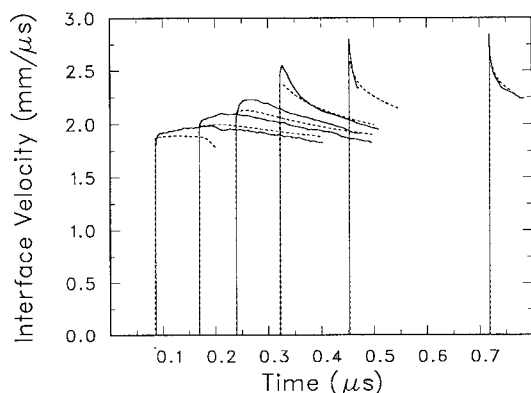


**FIGURE 9. CHARADE SIMULATIONS (DASHED CURVES) AND MEASURED INTERFACE-VELOCITY HISTORIES IN PBX 9502**

might construct around this observation. An existing, well-calibrated, hotspot model is found to simulate our measurements reasonably well, but this is not the only model that would serve this purpose. In particular, this can be done with a surface-burning model, with an initially very progressive burning topology, or hole burning. With such an approach, the instantaneous-hotspot assumption would be imposed, and the simple depletion used in the fast process---as manifested by  $(1-\lambda_f)$  fac-

tor in Equation (8)---replaced with the more appropriate form. We have conducted a very limited study of this possibility, replacing the factor in Equation (8) with both the empirical burning topology function devised for TATB explosives by Partom<sup>15</sup> and the form based in classic hole burning changing to grain burning by Starkenberg.<sup>16</sup> CHARADE simulations for both cases gave the qualitative features of our observations, and in particular the rounding of the velocity histories, but neither gave very good quantitative agreement over our data range. This probably was not a failure of concept, but rather resulted from the restricted scope of the study and the poor matching of the fast-rate factor  $R_f$  to the altered depletion factor. Although we have not attempted it, the replacement of simple depletion with a factor of  $\lambda^a(1-\lambda)^b$  as used in the nucleation and growth model<sup>17</sup> would no doubt serve as well.

We also can question if the relatively low rates behind the front are specific to high-density explosives such as plastic-bonded HMX and TATB, or also pertain to more porous explosives. An intriguing result in this regard comes from the study of 1.8-g/cm<sup>3</sup> (7 per cent porous) TATB in Reference 4. The Lagrange analysis of embedded-gauge data found that, unlike the case with plastic-bonded explosives,<sup>3,5,8</sup> no induction-time factor was needed in the DAGMAR rate correlation for this explosive. This question should be amenable to experimental resolution with our present methods.

A question less amenable to experimental resolution is whether there are in fact relatively low rates behind the fronts in detonation waves, and with a bit more time resolution in our velocimetry, we would observe velocity plateaus of nanosecond durations. Unless we drastically alter our Fabry-Perot system (reduce the reflectivity and finesse of the etalons), such measurements are beyond the capability of our multiple-beam interferometry. However, double-beam interferometry used in VISAR or ORVIS systems should provide the needed time resolution. A more serious concern is that nanosecond events correspond to a transit time of a strong shock or detonation through a few  $\mu\text{m}$  of condensed materials, which is less than the grain sizes of most of our explosives.

A final question is whether the demonstrated rate behavior in strongly shocked PBX 9502 has significant practical effects. The answer somewhat depends on the phenomena of interest. If the concern is initiation with very brief, high-pressure shock waves,<sup>18</sup> the observation and implications for rate models are important. If the interest is in shock and detonation wave propagation

phenomena, our results probably require less consideration. As part of the simulations depicted in Figure 8, we calculated the shock front trajectories for the instantaneous hotspot and empirical hotspot assumptions, and the results are nearly indistinguishable when displayed in distance-time coordinates. This shows both that explosive-wedge experiments are incapable of the detailed reaction-rate information we obtained, but that this information may be unimportant to practical initiation problems with reasonably well-supported shock waves. In a similar consideration, the details of the induction time to a full reaction rate should have little effect on the treatments of two- and three-dimensional detonation wave propagation with Detonation Shock Dynamics, providing the induction time is short compared with the time scale of the principal energy release.<sup>19</sup>

## ACKNOWLEDGMENTS

We greatly appreciate the film-reading efforts of Pamela Ulibarri. Ray Engelke made significant contributions to the experimental effort and Jim Johnson and Charles Forest provided both computer programs and expertise in using them. We also are indebted to these three gentlemen and to John Bdzil and Pier Tang for valuable discussions of the study. The work is supported by the United States Department of Energy under contract W-7405-ENG-36.

## REFERENCES

- Seitz, W. L., Stacy, H. L., and Wackerle, J., "Detonation Reaction-Zone Studies on TATB Explosive," *Proceedings of the Eighth Symposium (International) on Detonation*, 1985 pp. 123-132.
- Seitz, W. L., Stacy, H. L., Engelke, R., Tang, P. K., and Wackerle, J., "Detonation Reaction-Zone Structure of PBX 9502," in *Proceedings of the Ninth Symposium (International) on Detonation*, 1989, pp. 657-669.
- Wackerle, J., Rabie, R. L., Ginsberg, M. J., and Anderson, A. B., "A Shock Initiation Study of PBX-9404," *Symposium on High Dynamic Pressures*, Paris, Aug. 1978.
- Anderson, A. B., Ginsberg, M. J., Seitz, W. L., and Wackerle, J., "Shock Initiation of Porous TATB," *Seventh Symposium (international) on Detonation*, 1981, p. 385.
- Johnson, J. N., Tang, P.K., and Forest, C.A., "Shock Wave Initiation of Heterogeneous Reactive Solids," *Journal of Applied Physics*, Vol. 57, No. 9, 1985.
- Tang, P. K., "Initiation and Detonation of Heterogeneous High Explosives: A Unified Model," LA-11352-MS, 1988, LANL, Los Alamos, NM.
- Vorthman, J., Andrews, G., and Wackerle, J., "Reaction Rates from Electromagnetic Gauge Data," *Proceedings Eighth symposium (International) on Detonation*, 1985, p. 99.
- Forest, C. A., Wackerle, J., Dick, J. J., Sheffield, S. A., and Pettit, D. R., "Lagrangian Analysis of the MIV Gauge Experiments on PBX 9502 using the Mass-Displacement Moment Function," *Proceedings of the Ninth Symposium (International) on Detonation*, 1989, p. 683.
- Wackerle, J., Stacy, H. L., and Dallman, J. C., "Refractive Index Effects for Shocked Windows in Interface Velocimetry," *Proceedings of SPIE*, 1987, pp. 72-82.
- Mader, C. L. *Numerical Modeling of Detonation*, University of California Press, Berkeley, 1979.
- Wackerle, J. and Anderson, A. B., "Burning Topology in the Shock-Induced Reaction of Heterogeneous Explosives," *Shock Waves in Condensed Matter - 1983*, Elsevier Science Publishers B.V., 1984, pp. 601-604.
- See, for example, Davis, W. C. and Fickett, W., *Detonation*, University of California Press, 1979, pp. 101, 102, 131-133, and Section V of Reference 13.
- Johnson, J. N., and Tonks, D. L., *CHARADE: A Characteristics Code for Calculating Rate-Dependent Shock-Wave Response*, LA-11993-MS, 1991, LANL, Los Alamos, NM.
- Tang, P. K., "A Study of the Role of Homogeneous Process in Heterogeneous High Explosives", paper presented at this Symposium.
- Partom, Y. and Wackerle, J., "Surface Burn Model for Shock Initiation," *Preprints for the Ninth Symposium (International) on Detonation*, 1989, pp. 735-743.
- Starkenbergh, J., "A Model for the Initiation of Heterogeneous High Explosives Subject to General Compressive loading," *Proceedings of the Ninth Symposium (International) on Detonation*, 1989, pp. 604-617.
- Lee, E. L., and Tarver, C. M., "Phenomenological Model of Shock Initiation in Heterogeneous Explosives," *Physics of Fluids*, Vol. 23, No. 12, 1980, pp. 2362-2372.
- Seitz, W. L., "Short-Duration Shock Initiation of Triaminotrinitrobenzene (TATB)," *Shock Waves in Condensed Matter -1983*, Elsevier Science Publishers B.V., 1984, pp. 531-534.
- John Bdzil, personal communication, see also Bdzil, J. B., Fickett, W., and Stewart, D. S., "Detonation Shock Dynamics: A New Approach to Modeling Multi-Dimensional Detonation Waves" *Proceedings of Ninth Symposium International) on Detonation*, 1989 pp. 730-742.

## PROMPT AND DELAYED DETONATION FROM TWO-DIMENSIONAL SHOCK LOADINGS

R. R. Bernecker, A. R. Clairmont, Jr. and L. C. Hudson, III  
Naval Surface Warfare Center  
10901 New Hampshire Avenue  
Silver Spring, Maryland 20903-5640

Shock initiation studies of two high-energy propellants, RS075 and RS130, were conducted using a cylindrical (2-D) explosive driver system. Streak camera measurements include the distance and the time to detonation and have been used to delineate the boundary between prompt and delayed detonation for RS075. In addition, the data indicate that a relatively small diameter of the interior region is associated with the onset of delayed detonation. Numerical simulation of the shock driver system demonstrates that the radial pressure gradients across the entering shock front are severe at pressures near the boundary between prompt and delayed detonation. The combination of shock reactivity of the propellant, entering shock wave pressure profile, and the propellant Hugoniot is considered important in this system for defining the boundary between prompt and delayed detonation.

### INTRODUCTION

Many investigations have been conducted into the shock initiation process of near voidless samples of energetic materials (EMs) using "one-dimensional" (plane wave lenses) and "two-dimensional" (finite cylinders) explosive driver systems. Until recently though, there have been few systematic studies of the contrasting features of the build up process for detonation in these one-dimensional (1-D) and two-dimensional (2-D) systems. Moreover, one of the very intriguing aspects of 2-D shock initiation has been the observation of delayed detonation in certain high energy propellants.<sup>1</sup> We wish to report some of our observations (run distance and time to detonation) for a similar energetic material in which both prompt and delayed detonation have been observed with our 2-D shock loading arrangement. These observations are also compared to 1-D run distance and time to detonation data<sup>2</sup> for the same material.

To understand better any contrasting characteristics of the shock wave in the prompt and delayed detonation regime, numerical simulations of these 2-D experiments were begun. Thus far, the curvature of the shock wave and pressure-time profiles (as a function of peak, on-axis pressure) have been calculated at the attenuator/explosive interface. Additional calculations are be-

ing conducted to study the reactive build up process that leads to detonation. It is expected that the accumulated experimental data will be quite useful in guiding model development of the build up process for prompt initiation and that both will provide insight into the delayed detonation process.

In this study, two high energy propellants (RS075 and RS130) were evaluated; in other papers, elastomeric plastic-bonded explosives (PBXs) have been studied with the same 2-D driver.<sup>3,4</sup> Thus far, we have only observed delayed detonation for RS075.

### EXPERIMENTAL ARRANGEMENT AND TECHNIQUES

A 2-D test arrangement was developed to assess the shock reactivity of porous and cast energetic materials; it has been described, in part, in an earlier paper.<sup>3</sup> The basic aspects of the arrangement were initially used by D. Edwards of this Center in the late 1970s and are similar to those used by Klee and Ludwig.<sup>5</sup>

Our arrangement used the pentolite (1.56 g/cc) donor and the polymethylmethacrylate (PMMA) atten-

uator of the NOL large scale gap test (LSGT); both have diameters of 50.8 mm. A cylindrical, unconfined (in nearly all instances) sample of the EM (acceptor) was shock loaded by the wave exiting the PMMA material. Using the pressure calibration of the LSGT<sup>6</sup>, the entering (on-axis) pressure for the energetic material was calculated via the impedance matching technique. A high speed continuous-access streak camera (SC) was used to record both predetonation and detonation luminosity. A unique self illumination box, partially surrounding the donor and acceptor, was used to provide both front and back lighting; a very thin reflector system, attached to the EM, allowed the detection of various fronts. Fronts seen on the lateral surface of the charge were 1) a non-luminous shock (NLS) wave; 2) luminous and non-luminous rearward waves; and 3) the detonation wave.

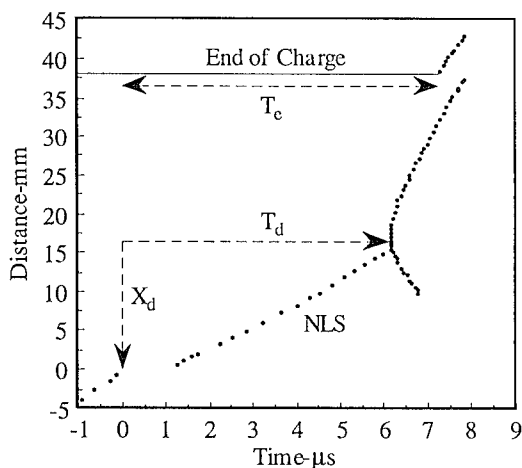


FIGURE 1. TYPICAL DIGITIZED REPRESENTATION OF STREAK CAMERA RECORD

Figure 1 is a schematic representation of a typical SC record for prompt initiation; time zero is when the PMMA shock wave (on-axis) enters the EM. The distance to detonation ( $X_d$ ) and time to detonation ( $T_d$ ), as seen on the lateral surface of the acceptor, can be accurately measured. In addition, the total transit time,  $T_c$ , can be determined;  $T_c$  is the time from arrival of the shock wave (on-axis) at the PMMA/acceptor interface to the arrival time (on-axis) of the detonation wave at the acceptor/air boundary. (The latter is defined by the propagation path of the detonation products at the end of the charge.) The detonation trace exhibits an extremely high velocity just beyond  $T_d$ , followed (in sufficiently long charges) by deceleration to a steady state detonation velocity. This behavior is typical when the onset of detonation occurs over some interior surface (whose diame-

ter is smaller than the charge diameter), followed by propagation of the detonation wave both axially and radially.<sup>7</sup>

The high energy research propellants, RS075 and RS130, were cast high energy double-base propellants containing HMX, ammonium perchlorate and aluminum. The cylindrical samples of RS075 had 50.7 mm diameters and varied in length from 24 to 102 mm; the cylindrical samples of RS130 had 38.1 mm diameters and varied in length from 32 to 83 mm.

## EXPERIMENTAL RESULTS

The initial experiments in this study were conducted with RS075; however, since the data base for RS130 shows more uniformity and also contains data on confined charges, the RS130 data are discussed first.

### RS130 Results

The data summarizing the RS130 experiments are shown in Table 1 where  $L$  is the length of the RS130 sample,  $L(G)$  is the length of the PMMA gap,  $P$  is the entering shock pressure in RS130, and  $V_e$  is the velocity of the product gases at the end of the RS130 sample;  $X_d$ ,  $T_d$  and  $T_c$  have been discussed above. Portions of the SC records are schematically shown in Figure 2 for some of the experiments.

Most of the RS130 samples had lengths of 38 mm

TABLE 1. RS130 EXPERIMENTS WITH REGULAR (LSGT) DRIVER SYSTEM

Shot No.	L (mm)	L(G) (mm)	P (GPa)	$X_d$ (mm)	$T_d$ (μs)	$T_c$ (μs)	$V_e$ (mm/μs)
A242	38.25	27.94	6.61	8.03	2.80	5.62	8.56
A226	32.03	31.19	6.06	9.58	3.46	5.07	8.56
A209	38.21	33.02	5.77	10.34	3.79	5.97	8.93
A207	38.20	34.57	5.54	12.56	4.63	6.44	8.83
A225	31.93	35.48	5.41	14.45	5.24	5.95	8.24
A208	38.23	36.86	5.08	16.52	6.13	7.25	8.34
A204	82.47	38.13	4.73	20.85	7.75	14.09	7.82
A237	82.47	38.61	4.60	31.57	10.52	15.56	8.86
A206	82.50	39.41	4.40	F	-	-	-
A241*	38.30	38.10	4.74	23.08	8.93	8.30	8.11
A236*	82.42	38.61	4.60	41.16	14.23	17.45	8.43

F - No Detonation

\* - 51.0 mm OD/38.1 mm ID Aluminum Tube

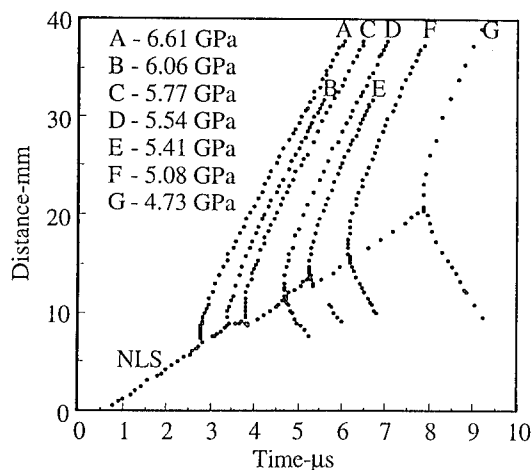


FIGURE 2. SOME STREAK CAMERA DATA FOR RS130 PROPELLANT

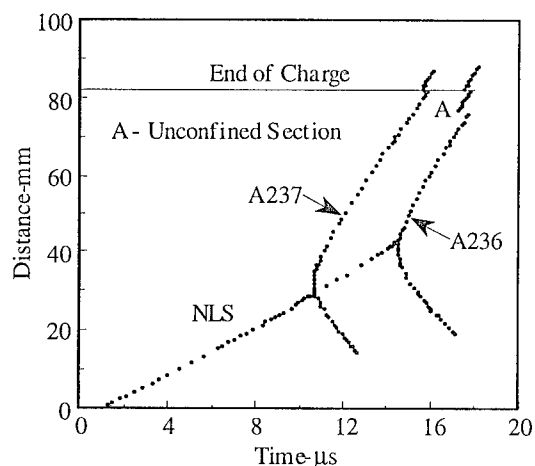


FIGURE 3. STREAK CAMERA DATA FOR UNCONFINED AND PARTIALLY CONFINED SAMPLES OF RS130 PROPELLANT

or less. Four samples had a length of approximately 82.5 mm. One of these samples was confined in an aluminum tube (ID of 38.1mm/OD of 51.0 mm) which was only 76.2 mm high (see A236 in Table 1). In Figure 3, the interesting SC data from A236 are compared to SC data from the unconfined, 82.5 mm long RS130 sample used in A237 (identical entering shock pressures). The presence, in the A236 data, of an unconfined portion of the detonating RS130 sample can be easily seen (at A). It is also interesting to note that the onset of detonation in the confined RS130 charge is not

earlier (nor has a shorter  $X_d$ ) than the unconfined charge of A237; the values for  $X_d$ ,  $T_d$ , and  $T_e$  in Figure 3 are all consistent with this conclusion.

#### RS075 Results

The data for the RS075 experiments are shown in Table 2. The initial experiments were run to explore the boundary between prompt and delayed initiation and utilized samples which were at least 76 mm long. (However, for most of the prompt initiation experiments, the sample lengths were, again, much less than 76 mm.) The data in Table 2 indicate that the boundary between the prompt and delayed detonation regimes is between 5.93 and 6.01 GPa. Portions of the SC records from the prompt initiation experiments are shown in Figure 4. As seen in Table 2, delayed detonation was observed in both 76 and 102 mm long samples at the same input pressure; portions of the SC records for the 102 mm long samples are shown in Figure 5.

TABLE 2. RS075 EXPERIMENTS WITH REGULAR (LSGT) DRIVER SYSTEM

Shot No.	L (mm)	L(G) (mm)	P (GPa)	$X_d$ (mm)	$T_d$ (μs)	$T_e$ (μs)	$V_e$ (mm/μs)
A235	24.00	24.18	7.65	10.57	3.87	3.83	9.25
A234	23.90	25.40	7.40	10.82	4.05	3.84	9.53
A191	24.89	26.62	7.15	12.51	4.73	4.22	8.22
A190	24.66	27.91	6.90	12.99	5.01	4.34	8.98
A123	39.37	28.40	6.81	12.50	4.74	6.05	9.30
A192	24.64	29.18	6.67	15.82	5.73	4.57	9.13
A120	75.84	30.48	6.44	14.89	5.56	11.35	6.78
A132	37.69	31.52	6.26	19.01	6.80	6.79	8.35
A121	75.97	33.02	6.01	21.19	9.51	13.06	8.87
A122	76.12	33.53	5.93	61.79	45.21	44.94	8.34
A119*	75.90	34.32	5.80	64.88	41.87	41.80	-
A137	101.40	34.32	5.80	61.01	44.73	47.68	7.00
A135	101.80	35.60	5.61	46.83	41.06	45.53	8.59
A136	76.10	35.60	5.61	48.70	40.85	42.26	8.38

\* - PMMA disk on top of charge

The SC data for the detonation region from the experiments with input pressures of 5.61 and 5.80 GPa are shown in Figure 6. Note that the data for the 76 mm samples, shocked at 5.61 and 5.80 GPa, partly overlay each other in Figure 6.

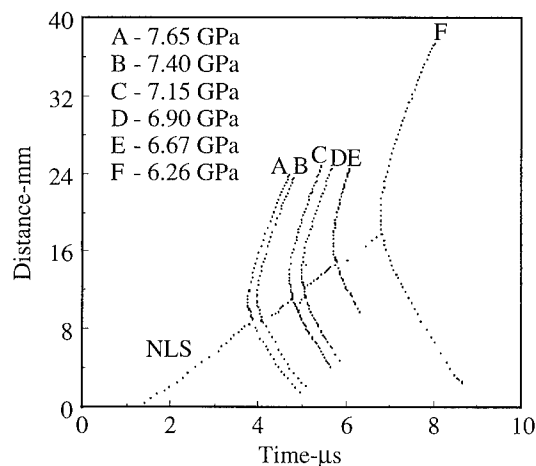


FIGURE 4. SOME STREAK CAMERA DATA FOR RS075 PROPELLANT

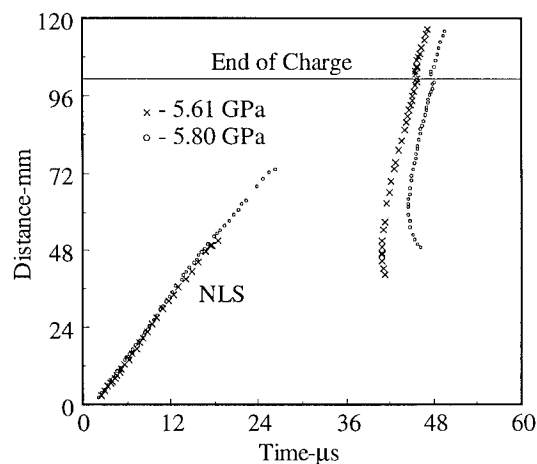


FIGURE 5. STREAK CAMERA DATA FOR DELAYED DETONATION REGIME OF RS075 PROPELLANT (EXPERIMENTS A135 AND A137)

The SC records of delayed detonation had many of the same features seen in the prompt initiation experiments. However, for the delayed detonation experiments, the NLS wave decelerated in both 76 and 102 mm long charges; also no rearward detonation waves were observed in any of the five delayed detonation experiments. In one of these experiments (A122), the motion of the upper surface was observed; its rate of expansion was about 0.27 mm/μs. For A119 and A122 (both 76 mm long samples), the NLS wave was detected at the end of the charge at 26.1 and 26.3 μs, respectively. For the longest samples, A135 and A137, the detonation velocity over the last 10 mm was 8.96 (+/- 0.15) and 8.09 (+/- 0.21) mm/μs, respectively.

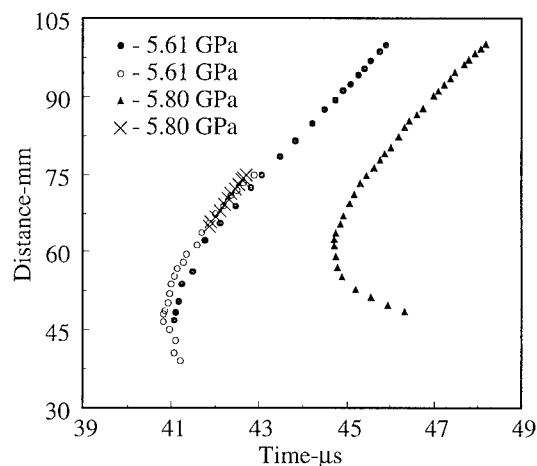


FIGURE 6. STREAK CAMERA DATA FOR DELAYED DETONATION REGIME OF RS075 PROPELLANT (EXPERIMENTS A119, A135, A136, AND A137)

## DISCUSSION

### Prompt Initiation

In earlier work,<sup>3,8</sup> it has been shown that the reciprocal of run distance ( $x^*$ ) from the wedge test yields a linear curve when plotted against pressure. In a similar manner, we have also shown that the reciprocal of  $X_d$  from our experiments also yields a linear curve when plotted against pressure. Both RS075 and RS130 propellants show the same relationships, as seen in Figure 7. What had not been described earlier was that  $t^*$  (wedge test) and  $T_d$  also yield a linear curve in the  $1/T_d$  or  $1/t^*$  vs. pressure plane; this feature is illustrated in Figure 8.

In 2-D experiments,  $X_d$  and  $T_d$  are associated not only with conditions for the onset of detonation on-axis but also with the ability of the detonation wave to traverse the sample radially. (That is, after the onset of detonation in the interior, the propagation of the detonation wave radially has the aspects of a "corner turning" process, as well.) The fact that these 2-D parameters mimic the wedge test data by having a linear relationship in the  $X^{-1}$  (or  $\text{Time}^{-1}$ ) vs. pressure plane is most intriguing and unexplainable at present.

Aspects of the SC records that are worthy of note are the presence/absence of rearward detonation waves in the prompt initiation work and the NLS wave; both are dependent upon the use of the reflector system. As seen



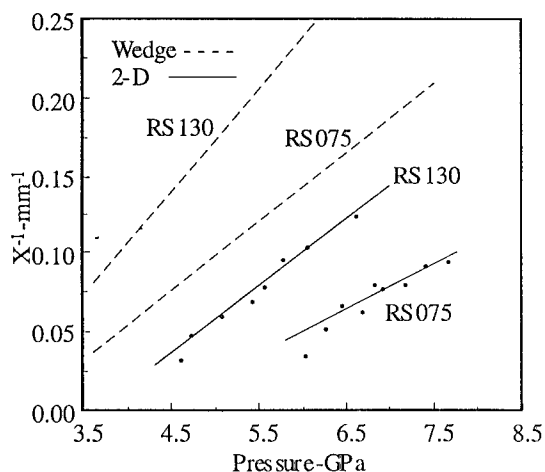


FIGURE 7. DISTANCE TO DETONATION - PRESSURE DATA FOR RS075 AND RS130 PROPELLANTS FROM WEDGE AND 2-D EXPERIMENTS

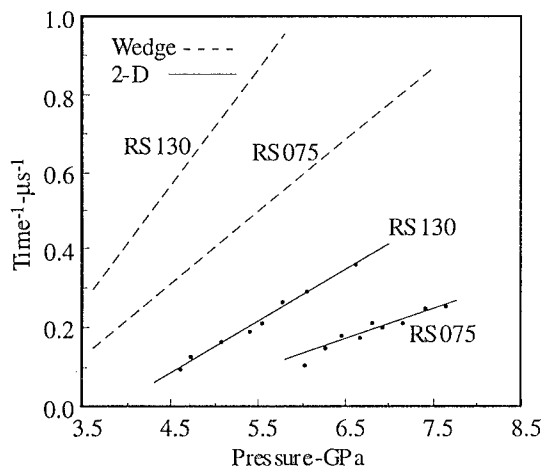


FIGURE 8. TIME TO DETONATION - PRESSURE DATA FOR RS075 AND RS130 PROPELLANTS FROM WEDGE AND 2-D EXPERIMENTS

in Figure 4, a rearward detonation wave is present in nearly every experiment with RS075 while rearward detonation waves are seen in Figure 2 (RS130) only at the lower pressures. Moreover, the velocities of these rearward detonation waves do not suggest a geometry effect as discussed in Reference 7. The interpretation of these observations is that rearward detonation waves propagate in an outer "shell" of the sample. The presence of the rearward detonation wave is determined by whether the thickness of the shell exceeds the critical diameter of EM. Thus, the sample diameter, the critical diameter of the EM, and the pressure profile (radially) of

the entering shock wave all determine whether a rearward detonation wave will be seen. (If the radial pressure gradients of the entering wave are fairly small, the shell is absent.)

The NLS wave is associated with the lower pressures at the lateral boundary of the sample. For most experiments with RS075 and RS130, the NLS wave provided poor representation of the buildup process occurring on-axis; this contrasts with some of our observations for other EMs.

#### Delayed Detonation

Delayed detonation in 2-D shock initiation systems has been described by Keefe<sup>1</sup> and Olinger.<sup>9</sup> Keefe used damage to a witness plate and timing pins to define the delayed detonation regime in confined samples while Olinger used a high speed framing camera, timing pins, and manganin gages in his work with unconfined samples. In our work, delayed detonation has been observed both with a streak camera (this paper) and with a high speed framing camera<sup>10</sup> for unconfined samples. In the framing camera work, only one out of three experiments successfully showed delayed detonation (pressure of 5.8 GPa); two failed at 5.6 GPa.

In this work, delayed detonation can easily be distinguished by evaluating the relationship between  $X_d$  and  $T_d$ . As shown in Figure 9, the experimental data for both RS075 and RS130 lie, within experimental error, along a line which passes through the origin and has a

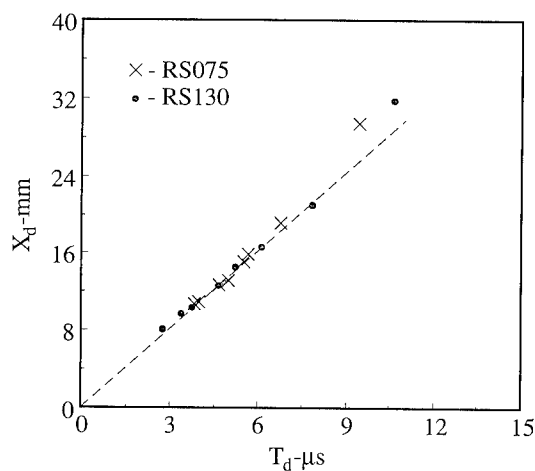


FIGURE 9. DISTANCE AND TIME TO DETONATION DATA FOR RS075 AND RS130 PROPELLANTS FROM 2-D EXPERIMENTS

slope of 2.70. (The data for  $X_d$  greater than 21 mm illustrate the effect on the buildup process from the rarefaction originating at the PMMA/sample interface.)

Although the data in Table 2 are somewhat limited, the use of 102 mm long samples has allowed us to determine that the onset of delayed detonation occurred (in the 102 mm sample) at about the time that the original shock wave reached the sample's end (see Figure 5). This shows that the mechanism driving the delayed detonation process did not involve a reflected rarefaction wave off the end of the sample. Since, at a constant input pressure, the  $X_d$  values for delayed detonation are very similar for both the 76 and 102 mm long samples (61 mm vs 65 mm for 5.80 GPa and 47 mm vs. 49 mm for 5.61 GPa), it appears that the sample length was not important for samples longer than 76 mm. Whether these limited data (distance and time to detonation) are statistically meaningful for generalizations which pertain to the delayed detonation regime in all EMs can only be determined from other studies.

There are other observations concerning delayed detonation which are interesting. First, while the data show that  $X_d$  increases with decreasing pressure in the prompt detonation regime (see Table 1 and 2), the delayed detonation data at 5.61 and 5.80 GPa have the opposite trend. Second, the SC data (Figure 5) show a very large geometry effect,<sup>7</sup> indicating that a relatively small diameter of the interior region is associated with the onset of delayed detonation. (This appears to be consistent with one of the proposed mechanisms for delayed detonation that has deconsolidation of the propellant in the interior of the sample; significantly after the passage of the initial shock front, leading to a porous sample that is more reactive under continued shock loading or secondary shock loading.) Finally, a definite judgement about delayed detonation in RS130 can not be made since only one RS130 sample failed to detonate.

#### Pressure-Time Loading From The Explosive Driver

Numerical simulations of our 2-D driver have been carried out by other workers. In those efforts, the description of the pressure wave entering the sample was basically limited to axial locations. However, from our earlier computational work<sup>11</sup>, it was appreciated that the rarefaction from the boundary of the pentolite/PMMA interface plays a major role in the pressure-time profile at the various locations, on-axis as well as off-axis. Hence, new numerical calculations of these 2-D shock initiation experiments were carried out with the DYNA2D hydrocode to extend that work.

The initial calculations<sup>12</sup> have only addressed the propagation of the detonation wave in the pentolite and the shock wave in the PMMA. The pentolite donor was modeled as a 2 cm x 2 cm cylinder; the PMMA attenuator was also modeled as a 2 cm dia. cylinder that was 3.5 cm long. The PMMA zoning in our "Case 1" calculation of Ref. 12 used 60 cells/cm in the radial direction and 54 cells/cm in the axial direction. The test of the "validity" of the calculations was the agreement of the calculated on-axis pressure in the PMMA with the experimental calibration reported in Reference 6. Very good agreement was found for distances beyond 12 mm from the pentolite/PMMA interface.<sup>12</sup> For the purposes of this paper, the features of that calculation discussed below are pressures calculated at various distances "off-axis".

In a 2-D explosive driver system, the entering shock wave has a curved front. Consequently, there are radial pressure gradients across the profile and only a portion (nearer the axis) can be considered approximately planar. To outline these effects, the calculations were first analyzed by comparing the on-axis pressure ( $P(\text{axis})$ ) with the maximum pressure ( $P(\text{off-axis})$ ) seen on a line parallel to the axis but 0.392 cm (9.96 mm in our PMMA gap) from the axis. A few data, at various distances away from the pentolite/PMMA interface, are shown in Table 3;  $L(G)$  is the PMMA distance from the pentolite/PMMA interface and  $P(\text{diff})$  is the difference between the two pressures.  $L(G)$  is also shown in "cards" in order to correlate directly with units used in Reference 1.

**TABLE 3. COMPARISON OF MAXIMUM PRESSURES SEEN ON-AXIS AND 10 mm OFF-AXIS FOR VARIOUS LENGTHS OF PMMA**

$L(G)$ (mm)	$L(G)$ ("cards")	$P(\text{axis})$ (GPa)	$P(\text{off-axis})$ (GPa)	$P(\text{diff})$ (GPa)
17.8	70	6.83	6.84	0.01
22.9	90	6.04	5.85	0.19
27.9	110	5.43	4.86	0.57
33.0	130	4.74	4.05	0.69
38.1	150	3.83	3.35	0.48
43.2	170	3.04	2.74	0.30
48.3	190	2.45	2.25	0.20

The data in Table 3 illustrate very nicely the influence of the rarefaction (arising from the lateral surface at the pentolite/PMMA interface<sup>11</sup>) that arrives

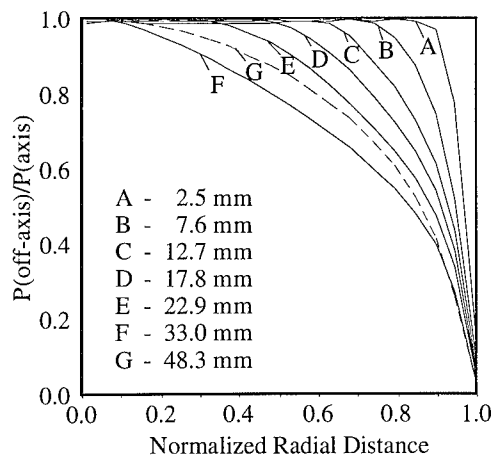


**FIGURE 10. PRESSURE PROFILES OF THE SHOCK WAVE AT VARIOUS LOCATIONS IN THE PMMA ATTENUATOR**

on-axis in the PMMA at about 34 mm. Thus, as the rarefaction approaches the axis at an angle (roughly 34 mm divided by 25.4 mm), the radial pressure profile begins to change dramatically. However, at longer distances (gaps) the pressure system become more uniform near the axis.

The second analysis of the DYNA2D data evaluated the pressure along several "off-axis lines" to produce a radial profile. These profiles are shown in Figure 10. This figure enhances the observations from Table 3. At the 48.3 mm location, the pressure profile begins to return to that seen at the shorter locations (<22.9 mm).

The data in Table 3 and Figure 10 appear to be significant for the interpretation of our 2-D experiments and gap tests in general and may be significant for the interpretation of the delayed detonation process in gap tests. From the wedge test data outlined in Figure 7, it is apparent from the slope that RS130 is more shock reactive than RS075. Our 2-D data are in accord with this. At a 33.5 mm gap (just below prompt initiation) for RS075, it is thought that the combination of shock reactivity of the propellant, entering shock wave pressure profile and the propellant Hugoniot characteristics defines the boundary between the prompt and delayed detonation regimes for unconfined RS075 in our 2-D experiments. That is, the shock reactivity of RS075 at PMMA lengths > 33.0 mm (see wedge data for pressures below 5.9 GPa) is still significant (both for the full density and any lower density material) but the pressure profile of the entering shock wave precludes a

prompt transition to detonation in the cast material. (It is assumed that  $X_d$  increases as the radial pressure gradients increases for a given on-axis pressure.)

The same rationale appears to be consistent with the probit profiles shown in Figures 4 and 5 of Reference 1 for confined charges. As the pressure profile characteristics improve at longer PMMA lengths (see Figure 10), the still significant reactivity of an EM (both cast and porous) leads to sufficient pressure build up for the delayed detonation process to reach fruition. Eventually, however, the shock reactivity will decrease sufficiently (at least for low porosity material) to preclude even delayed detonation. (Whether this picture is totally consistent with all observations for delayed detonations (from our limited SC data base and other studies) is uncertain; recall that the exact mechanism for delayed detonation is still unproven. These aspects provide further confirmation of the need for numerical modeling of the boundary (and regimes) of prompt and delayed detonation using accurate models of a) the p-t loading, b) the shock reactivity of the EM, and c) the high rate mechanical deformation of unconfined and confined samples. Experimental studies are also needed to understand the chemistry that drives the shock reactivity of propellants, and any other EMs, leading to delayed detonation.

Finally, the observation of severe radial pressure gradients for PMMA lengths of roughly 25 to 45 mm for the NOL LSGT donor system should be important in other tests, e.g., the NOL modified gap test.<sup>13</sup> It also provides an alternate explanation for changes in the  $X^{-1}_d$  - p relationship found for PBXN-109.<sup>3</sup>

## CONCLUSIONS

These 2-D distance and time to detonation measurements ( $X_d$  and  $T_d$ ) have been found to provide a good absolute measure of the shock reactivity of the EMs (slope in the  $X^{-1}$ -P plane) and a good relative measure of the shock sensitivity of the EMs (failure pressure (gap) for prompt detonation). It has been found that plots of  $X^{-1}$ -P and  $\text{Time}^{-1}$ -P are linear for both 1-D and 2-D data.

For the prompt initiation regime in RS130, it was observed that confinement did not reduce the time or distance to detonation at pressures near the failure boundary.

For delayed detonation in RS075, it was found that a)  $X_d$  increased with increasing pressure, the opposite of the prompt detonation observations; b) the SC data showed a very large geometry effect,<sup>7</sup> indicating that a relatively small diameter of the interior is associated with the onset of delayed detonation; and c) in sufficiently long samples, the build up process is driven by reaction which depends only upon the initial shock loading process (e.g., detonation occurs before the shock wave reflects off the far end).

A numerical simulation of the shock wave propagation through the attenuator of the shock driver system was used to demonstrate that the radial pressure gradients across the entering shock front are severe near those pressures that define the boundary between prompt and delayed detonation in RS075. It is postulated that the combination of shock reactivity of the propellant, entering shock wave profile, and the propellant Hugoniot relationship is important in defining the boundary between prompt and delayed detonation for our 2-D driver system.

#### ACKNOWLEDGEMENTS

The authors wish to thank Carl L. Groves for assistance in conducting the experiments and Harold W. Sandusky for support with the data acquisition and reduction software and hardware.

#### REFERENCES

1. Keefe, R. L., "Delayed Detonation in Card Gap Tests," in *Proceedings Seventh Symposium (International) on Detonation*, U.S. Naval Academy, Annapolis, MD, 16-19 Jun 1981, pp. 265-272.
2. Ramsay, J. B., Los Alamos National Laboratory, private communication.
3. Bernecker, R. R. and Clairmont, A. R., Jr., "Shock Initiation Studies of Cast Plastic-bonded Explosives," in *Combustion and Detonation Phenomena, 19th International Annual Conference of ICT 1988*, Jun 1988, p. 41:1-14.
4. Bernecker, R. R. and Clairmont, A. R., Jr., "Shock Initiation of Cast, Damaged, and Granulated PBXs," paper presented at this Symposium.
5. Klee, Ch. and Ludwig, D., "The Sensitivity to Initiation of HE-Wax Compounds at Different Temperatures," in *Proceedings Seventh Symposium (International) on Detonation*, U.S. Naval Academy, Annapolis, MD, 16-19 Jun 1981, pp. 336-342.
6. Erkman, J. O.; Edwards, D. J.; Clairmont, A. R., Jr.; and Price, D., *Calibration of the NOL Large Scale Gap Test; Hugoniot Data for Polymethyl Methacrylate*, NOL TR 73-15, Apr 1973, NOL, Silver Spring, MD.
7. Johansson, C. H.; Lundborg, N.; and Sjolín, T., "The Initiation of Explosives by Shock Waves," in *Eighth Symposium on Combustion*, Pasadena, CA, 1960, Williams and Wilkerson, Baltimore, MD, pp. 842-847.
8. Bernecker, R. R., "Concerning the Standardization of Gap Tests," 1990 JANNAF Propulsion Systems Hazards Subcommittee Meeting, CPIA Publication 538, Vol. I, Apr 1990, pp. 187-195.
9. Olinger, B., "Observations of Long Delays to Detonation in Propellants for Tests with Marginal Card Gaps," 1980 JANNAF Propulsion Systems Hazards Subcommittee Meeting, CPIA Publication 330, Vol. I, October 1980, pp. 239-244.
10. Unpublished data of A. R. Clairmont Jr.; T. Liddiard; and R. R. Bernecker.
11. Jacobs, S. J.; Sternberg, H. M.; Hudson, L.; and Bernecker, R. R., "Numerical Simulation of Donors for Gap Experiments," 1988 JANNAF Propulsion Systems Hazards Subcommittee Meeting, CPIA Publication 477, Vol. I, March 1988, pp. 79-86.
12. Bernecker, R. R. and Hudson, L. C., III, *Numerical Calibration of Donors for Some NAVSWC Gap Tests*, NSW TR 91-236, NSW, Silver Spring, MD, to be published.
13. Liddiard, T. P. and Forbes, J. W., *A Summary Report of the Modified Gap Test and the Underwater Sensitivity Test*, NSW TR 86-350, 12 Mar 1987, NSW, Silver Spring, MD.

## DISCUSSION

MANFRED HELD

Messerschmitt-Bölkow-Blohm, Schrobenuhausen,  
Germany

In your distance-time diagram for prompt initiation you have for the "nonluminous shock (NLS) wave" a straight line. No damping (decreasing of velocity) means not a shock wave--it is a reaction wave with constant velocity of about 2.5 - 2.7 mm/ $\mu$ s (estimated from your diagram). Sound velocity is less (you said  $\approx$  2.0 mm/ $\mu$ s). What is the nature or origin of this NLS on the charge surface?

## REPLY BY RICHARD BERNECKER:

The nonluminous shock (NLS) wave is associated with the shock wave, propagating through the test explosive, which arises from the PMMA shock loading. The pressure of the NLS wave is always lower than the pressure of the shock wave on-axis. Depending upon the radial pressure profile of the PMMA wave, the Hugoniot and the shock reactivity of the test explosive, that part of the shock wave very near the lateral surface of the test explosive may be reactive (velocity of the NLS wave increases with distance traveled) or nearly inert (velocity of the NLS is essentially constant). For the NLS wave in the delayed detonation experiments, its velocity eventually decreases with distance, indicative of an attenuating (non-reactive) shock wave near the far end of the propellant sample.

## TEMPERATURE EFFECTS ON FAILURE THICKNESS AND THE DEFLAGRATION-TO-DETONATION TRANSITION IN PBX 9502 AND TATB

B. W. Asay and J. M. McAfee  
Los Alamos National Laboratory  
Los Alamos, New Mexico 87545

Deflagration-to-detonation (DDT) behavior of TATB has been investigated at high temperatures and severe confinement. Comparison is made to other common explosives under similar confinement. TATB did not deflagrate to detonation under these conditions. The failure thickness of PBX 9502 at 170° and 240°C has also been determined. The limiting value at this temperature is approximately 2 mm. Estimates of the detonation velocity *versus* reciprocal size relationship can be made from a single experiment.

### INTRODUCTION

PBX 9502 (95/5 wt % of triamino-trinitrobenzene/Kel-F 800 plastic) is an explosive (HE) that, when examined at room temperature, is much less sensitive to shock initiation than many others. However, studies of its shock initiation behavior at high temperature ( $> 75^{\circ}\text{C}$ ) have begun only recently.

Using cylinders of PBX 9502, Campbell<sup>1</sup> found that the failure diameter is temperature dependent and that it varied inversely with the temperature when tested at  $-55^{\circ}$ ,  $24^{\circ}$ , and  $75^{\circ}\text{C}$ . He also showed that temperature effects on detonation velocity were functions of the diameter of the explosive. At small diameters, rate effects dominate (and the detonation velocity decreases as the temperature decreases) whereas at large diameters, density effects dominate (and the detonation velocity increases as the temperature decreases).

Ramsay<sup>2</sup> completed a study in which wedges of PBX 9502 were used to determine the failure thickness at the same temperatures as Campbell.<sup>1</sup> From theoretical considerations, the failure thickness should be one-half the failure diameter. Ramsay's study experimentally demonstrated this result, although the failure thickness was underestimated by 0.5 mm when the wedges were only 50-mm long.

Campbell and Engelke<sup>3</sup> showed that the failure diameter of an explosive increases as the reaction zone thickness increases. They also demonstrated the differences in the mechanism of detonation propagation between large- and small-diameter charges and between homogeneous and heterogeneous explosives.

Dallman and Wackerle<sup>4</sup> have obtained data showing the effect of temperature on the distance required to achieve detonation as a function of pressure (Pop plot).

They showed that as temperature increases, the Pop plot curve shifts toward lower pressures and the slope increases, indicating a significant increase in shock sensitivity. In fact, the sensitivity of PBX 9502 to shock at  $250^{\circ}\text{C}$  approaches that of PBX 9501 at ambient temperature.

Shocks are not the only mechanism whereby high explosive may be initiated. Deflagration can also result in detonation under the necessary conditions. The ability of many explosives to undergo deflagration-to-detonation transition has been evaluated. For example the DDT behavior of ball powders,<sup>5</sup> HMX,<sup>6</sup> tetryl,<sup>7</sup> and RDX<sup>8</sup> have all been studied. However, the DDT behavior of PBX 9502 has not been previously examined. Stimuli that can initiate DDT range from either gas-producing or gasless ignitors to a relatively mild compaction wave originating at a piston or other compressive source. The mechanism by which a reactive wave in an explosive changes from deflagration to detonation is not known precisely, but it has been established to be a function of many variables including confinement, porosity, reactivity, melting point, and combustion velocity.

Results of shock initiation studies at high temperature have obvious implications for the safety of components that incorporate TATB-based explosive. The results of DDT studies on other explosives are not sufficient to predict the response of PBX 9502 to DDT stimulus.

Continuing the characterization of PBX 9502, we present measurements of the failure thickness at temperatures up to  $240^{\circ}\text{C}$ . We also examine the high-temperature DDT behavior of the explosive component of PBX 9502, TATB, and compare it with several other explosives under varying conditions.

## EXPERIMENTAL RESULTS

### Deflagration-to-Detonation Transition in TATB

The purpose of this portion of the study was to determine if, under severe conditions of confinement and temperature, TATB powder would undergo DDT. TATB was used instead of PBX 9502 because we believed that the explosive alone is more sensitive without the addition of the binder. Studies have shown that TATB decomposes at temperatures above 325°C and melts at 450°C, but some researchers believe that partial reaction actually begins at temperatures as low as 250°C when the sample is maintained at temperature for extended periods of time. To avoid potential problems with decomposition, we chose a maximum temperature of 250°C. In all, three experiments were conducted, two at 200°C and one at 250°C.

The TATB used in this study was from lot 12-11-81-0503-151 obtained from Group M-1 at the Los Alamos National Laboratory. Analysis showed that 50.3% of the particles passed through a 45- $\mu$ m screen and 30.4% passed through a 20- $\mu$ m screen. TATB was placed into a steel tube in small increments and hand-packed lightly with a wooden dowel. The failure diameter of TATB at a density of 1.7 g/cm<sup>3</sup> and ambient temperature is 6.4 mm (Ref. 9). The failure diameter at lower densities and higher temperatures is unknown; however, based on experience with other explosives, we believe the tube diameter used in this study is sufficient to support steady detonation of this material.

In our previous DDT experiments<sup>6</sup> conducted at room temperature, the ignitor system was composed of a Pyrofuze<sup>®</sup> wire onto which was placed ~20 mg of a stoichiometric mixture of titanium and boron powder, followed by varying amounts of Class-A HMX powder. However, HMX decomposes and/or detonates at temperatures < 250°C. Thus, HNS (hexanitrostilbene) was used in place of the HMX for the high temperature experiment, with all other elements of the ignitor remaining the same.

The steel confining tube was 127-mm o.d., 25.4-mm i.d., and 305-mm long. A pressure transducer was used to monitor the pressure inside the tube to indicate the presence of decomposition. No pressure rise occurred before the desired ignition took place.

To examine the effects of confinement, the three tests used tubes with different types of confinement on the ends. The first experiment used the least

confinement and the last experiment used the greatest. The first shot (B-9686) had small end caps, 1-in. thick, that were secured to the tube with 0.25-in. threaded rod. For the next experiment (B-9688), the end caps were replaced with large 25.4-mm-thick steel plates that were tied together with 0.75-in. threaded rod. The bottom plate had small clearance holes through which the leads to the Pyrofuze<sup>®</sup> were passed. The same configuration was used for the last experiment (B-9712), except that grooves were machined into the bottom plate through which the Pyrofuze<sup>®</sup> leads were passed. This prevented the escaping gas from having clear passage through the clearance holes. The proof and tensile stress of the threaded rod were approximately 55 kpsi and 69 kpsi respectively.

The major results from this series are shown in Table 1. Packing densities were increased for each test to further increase the potential for detonation. The reaction of the TATB in each case was extremely vigorous. The threaded rods were broken during the first test and the end caps were destroyed. The rods did not break during the next two tests, but stretched considerably, and the ignitor blocks were severely eroded by the high-velocity, hot gas. However, it was clear that a detonation did not occur. Strong combustion was the only result. The unreacted TATB was severely compacted by the pressure generated by the reaction. The HE in the compact ceased to burn, once the confinement was lost. Densities of the recovered compacts are also shown in Table 1. No signs of reaction were evident in the recovered material. However, the outside surface was blackened somewhat. Only ash and char remained from the final test. The original HE was nearly all consumed.

To put these results into perspective, three other explosives were also tested. Four tests were conducted using PBX-9501 molding powder (95% HMX, 2.5% Estane, 2.5% BDNPA-F), followed by one test each with flaked TNT and nitromethane (NM). These explosives were placed into the same confinement as that used for Shot No. B-9712. The two solid explosives were poured into the tubes in small increments and tamped lightly. All shots were fired at 30°C except for one that used PBX 9501 at 150°C. The three tests with PBX 9501 at 30°C all detonated with runup distances of approximately 200 mm. The last test at 150°C detonated with a runup distance of 140 mm. Neither the flaked TNT nor the nitromethane detonated, although they exhibited vigorous reactions similar to those of TATB. For these cases however, the explosive was entirely consumed.

TABLE 1. RESULTS OF TATB DDT EXPERIMENTS

Shot No.	Bulk Density (g/cm <sup>3</sup> )	Temperature (°C)	TATB Consumed/ Original (g)	Compact Density (g/cm <sup>3</sup> )
B-9686	1.18	200	5/184	1.8
B-9688	1.23	200	84/190	1.6
B-9712	1.30	250	198/200	n/a

## Failure Thickness Of PBX 9502 As A Function Of Temperature

The wedges of PBX 9502 were similar to those described by Ramsay.<sup>2</sup> The wedges were 7-mm wide at the base with a 1-mm toe, 150-mm long, and 50-mm high. The wedge angle was made small to minimize multidimensional effects. The experimental configuration is shown in Fig. 1. The wedge and high-

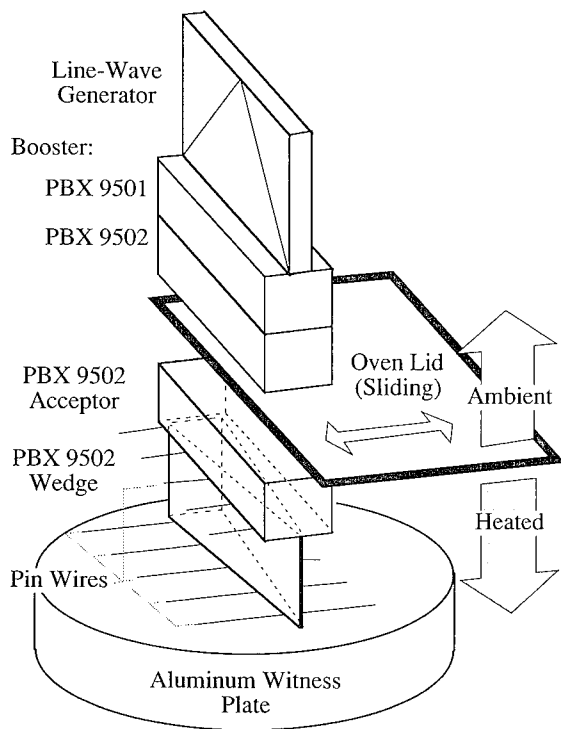


FIGURE 1. SCHEMATIC OF THE HEATED FAILURE-WEDGE EXPERIMENT

temperature acceptor were placed inside an insulated box equipped with a resistance heater and fan. Once the desired temperature was reached, the lid of the box was moved aside and the wedge assembly was raised to meet the composite booster assembly. A combination of PBX 9501 and PBX 9502 was used as the booster. After the shot, the point at which the detonation failed was clearly indicated in the aluminum witness plate. The failure thickness was then determined using this mark and geometric relationships. Fine wires were placed at intervals across the top and bottom of the wedge to register passage of the detonation. The time intervals between corresponding wires, combined with the wedge height, give measures of the detonation velocity at various thicknesses.

Figure 2 shows the failure-thickness data from this study compared with those of Campbell<sup>1</sup> and Ramsay.<sup>2</sup> Campbell's data are reported here as failure radii, to better compare with failure thickness.

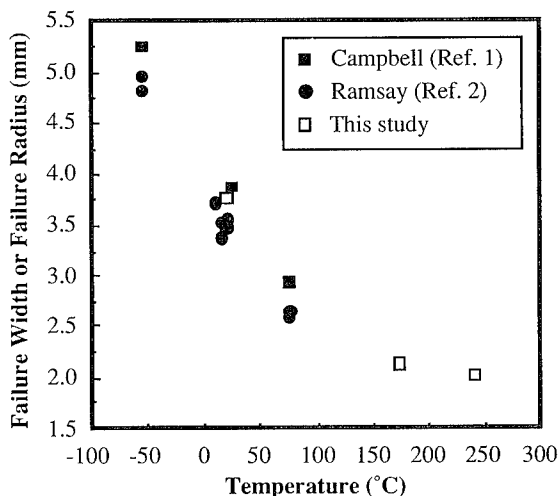


FIGURE 2. FAILURE WIDTH AS A FUNCTION OF TEMPERATURE FOR PBX 9502

Figure 3 reports the velocities obtained from the wires on the wedges. The data for the two lowest temperatures show a modest decrease in velocity as failure thickness is approached. The data at 240°C are too scattered to exhibit this trend unequivocally. Data not plotted in the figure at 20°C show, as expected, a substantial velocity decrement below failure thickness, indicating detonation failure.

The velocities obtained above failure thickness at 20°C are again plotted *versus* reciprocal wedge thickness in Fig. 4. The relationship found by Campbell and Engleke<sup>3</sup> as a function of reciprocal radius is also shown. The data from this single wedge experiment appear to be a reasonable approximation to the extensive rate-stick data shown in Fig. 4. The fitting form and the constants derived from linear least-squares fits for the three temperatures are given in Table 2. The infinite-dimension intercepts are within approximately 1%, and the slope coefficients (A) agree within approximately 5%. The constants for the data acquired at 240°C are quite uncertain, and therefore bear no interpretation.

## DISCUSSION

### DDT in TATB

Rapid pressurization in the combustion zone must be present if DDT is to occur in a given explosive. This pressurization serves to initiate and support the compaction wave that eventually results in shock formation and subsequent detonation. At ambient temperatures, the combustion velocity for TATB is at least an order of magnitude lower than that of HMX<sup>10</sup> at pressures from 2 to 15 kpsi. TATB will not sustain self-deflagration at pressures less than 1500 psi. From the results of this study, we believe the increases in initial temperature did not sufficiently accelerate the rate of



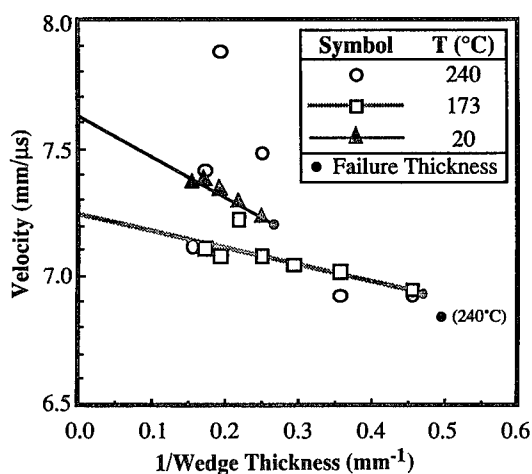


FIGURE 3. RECIPROCAL WEDGE THICKNESS VS DETONATION VELOCITY FOR PBX 9502 AT THREE TEMPERATURES

combustion to create the rapid pressure rise required. This is the case, even though TATB has a very high melting point, which has been found to correlate with early onset of unsteady burning and thus, DDT.<sup>11</sup>

Even the conditions conducive to convective combustion in these high-temperature experiments were not sufficient to overcome the low combustion velocity and concomitant slow pressure rise. The low combustion velocity is undoubtedly a function of many effects. There are endothermic steps involved in the early decomposition of TATB which would serve to lower the combustion velocity. It has also been postulated that ash formation on the particle surface can insulate the reactive material from the flame.

#### Failure Thickness Of PBX 9502 As A Function Of Temperature

Campbell and Engelke<sup>3</sup> showed that in heterogeneous explosives, two mechanisms control the energy release required to sustain detonation: hot spots and homogeneous burn. For heterogeneous explosives near failure diameter, only the hot spot mechanism sustains wave motion. The different state sensitivity of the rates for these two burning mechanisms is used to explain the differences in the diameter-effect curves between homogeneous and heterogeneous explosives. Campbell<sup>1</sup> found that for PBX 9502 at small diameters, the effect of temperature on detonation velocity is dominated by reaction-rate effects, whereas at large diameters, density effects predominate.

Our tests were conducted at near-failure thickness in a heterogeneous explosive. Thus we expected hot spots to control the energy release. The failure width approaches a near constant value of approximately 2 mm at high temperatures. These data compare favorably with those of Belyaev and Kurbangalina<sup>12</sup> where they measured the temperature effect on failure diameters of the homogeneous explosives nitroglycerin (NG) and liquid TNT. They reported a failure diameter reduction in the

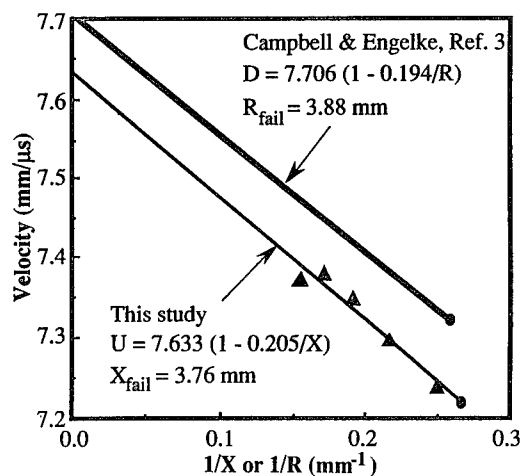


FIGURE 4. COMPARISON OF RATE-STICK TO WEDGE DATA AT 20°C

of TNT from ~60 mm to ~8 mm as the temperature increased from 80°C to 260°C, with asymptotic behavior similar to that found in this study.

This similarity of PBX 9502 to the homogeneous explosives NG and liquid TNT might be explained by asserting that PBX 9502 behaves like a homogeneous explosive. Evidence for this behavior at ambient temperatures is the relatively small decrement in detonation velocity at failure diameter.<sup>3</sup> Also, in this work, the two most certain slope coefficients (A in Table 2) indicate the velocity decrement is smaller at the higher temperature. We interpret this as the PBX 9502 exhibiting more homogeneous-like behavior as the initial temperature increases. It is unfortunate the highest temperature data are so uncertain. The physical explanation of this behavior may be that the length of the PBX 9502 reaction zone (1-2 mm)<sup>3</sup> is larger than the significant heterogeneities.<sup>13</sup>

If simple Arrhenius kinetics are assumed, then the behavior we have noted in PBX 9502 is readily explained. The high temperature minimum of the failure diameter in this material, and by extension, the reaction zone thickness, is reached in the vicinity of 250°C.

TABLE 2. LEAST-SQUARES FITS OF VELOCITY VS RECIPROCAL WEDGE THICKNESS

Temperature (°C)	$U_0$ (km/s)	std. dev. (km/s)	A (mm)	std. dev. (mm)	$r^2$
20	7.633	±0.042	0.205	±0.028	0.95
173	7.259	±0.068	0.093	±0.032	0.63
240	7.814	±0.345	0.255	±0.155	0.32
$U = U_0 (1 - A/X_{\text{wedge}})$ , $U$ (km/s), and $X_{\text{wedge}}$ (mm)					

## CONCLUSIONS

We have shown that even under severe confinement and high temperature, TATB will not transit from a deflagration to a detonation in 305 mm when ignited by a flame. These results further demonstrate the increase in the safety margin accomplished when TATB is used in place of HMX.

The failure thickness of PBX 9502 approaches 2 mm (or a failure diameter of 4 mm) at 250°C. This value appears to be a lower limit. PBX 9502 exhibits behavior similar to homogeneous explosives at elevated initial temperatures.

## REFERENCES

1. Campbell, A. W., "Diameter Effect and Failure Diameter of a TATB-Based Explosive," *Propellants, Explosives, and Pyrotechnics*, Vol. 9, 1984, pp. 183-187.
2. Ramsay, J. B., "Effect of Confinement on Failure in 95 TATB/5 Kel-F," *Proceedings of the 8th Symposium (Int.) on Detonation*, Albuquerque, NM, 15 July 1985, pp. 372-377.
3. Campbell, A. W. and Engelke, R., "The Diameter Effect in High-Density Explosives," *Proceedings of the 6th Symposium (Int.) on Detonation*, Coronado, CA, 24 August 1976, pp. 642-651.
4. Dallman, J. C. and Wackerle J., "Temperature Effect on the Initiation Sensitivity of TATB-Based PBXs," *Proceedings of the 10th Symposium (Int.) on Detonation*, Boston, MA, 15 July 1993.
5. Samirant, M., "DDT in RDX and Ball Powder: Behavior of the Porous Bed," *Proceedings of the 8th Symposium (Int.) on Detonation*, Albuquerque, NM, 15 July 1985, pp. 972-976.
6. McAfee, J. M.; Asay, B. W.; Campbell, A. W.; and Ramsay, J. B., "Deflagration-to-Detonation Transition in Granular HMX," *Proceedings of the 9th Symposium (Int.) on Detonation*, Portland, OR, 28 August 1989, pp. 265-279.
7. Bernecker, R. B.; Price, D.; Erkman, J. O.; and Clairmont, A. R., "Deflagration to Detonation Transition Behavior of Tetryl," *Proceedings of the 6th Symposium (Int.) on Detonation*, Coronado, CA, 24 August 1976, pp. 426-435.
8. Griffiths, N. and Groocock, J., M., "The Burning to Detonation of Solid Explosives," *J. Chem. Soc. Lond.*, Vol. 814, 1960, pp. 4154-4162.
9. Dobratz, B. M., "LLNL Explosives Handbook," Lawrence Livermore National Laboratory Report, UCRL-52997, 1981.
10. Boggs, T. L.; Price, C., F.; Zurn, D. E.; Atwood, A. I.; and Eisel, J. L., "Self-Deflagration Rates of 1, 3, 5, Triamino- 2, 4, 6, Trinitrobenzene (TATB)," *17th JANNAF Combustion Meeting*, November 1980, CPIA 329, Vol. 2, pp. 557-558.
11. Belyaev, A. F.; Korotkov, A. I.; and Sulimov, A. A., "Breakdown of Surface Burning of Gas-Permeable Porous Systems," *Fizika Goreniya i Vzryva*, Vol. 2, No. 3, 1966, pp. 47-58.
12. Belyaev, A. F., and Kurbangalina, R. Kh., "Effect of Initial Temperature on Critical Diameter of Nitroglycerin and Trinitrotoluene," *Russian Journal of Physical Chemistry*, Vol. 34, No. 3, March 1960.
13. Engleke, R., "Effect of the Number Density of Heterogeneities on the Critical Diameter of Condensed Explosives," *Phys. Fluids*, Vol. 26, No. 9, September 1983, pp. 2420-2424.

## DISCUSSION

J. GREGORY GLENN

High Explosives Research and Development Laboratory,  
Eglin Air Force Base, Florida

(1) Would you have experienced the same reaction with less confinement? What were the confinement limits?

(2) Does the adding of heat energy to the explosive assist the transition to detonation by aiding the breakdown (thermal decomposition) of the explosive at the hot spot sites?

## REPLY BY BLAINE ASAY:

(1) We showed that the fraction of TATB consumed increased with an increase in confinement.

(2) To first order, preheating the explosive has at least three effects. First, the hydrodynamic collapse of the hot spot yields a higher temperature. Second, the effective radius of the hot spot is increased because the explosive in the immediate vicinity requires less energy to react, thus extending the region of influence of the individual hot spots. Third, the amount of energy required to reach the activation energy of the bulk explosive has been reduced. These predicted responses ignore material effects which can change dramatically with temperature. For example, as binders soften and the explosive crystal morphology changes, we might expect different viscous behavior or modified fracture response. The influence that these changes have on the hot spot behavior can only be hypothesized at this time.

# INFLUENCE OF FRESH DAMAGE ON THE SHOCK REACTIVITY AND SENSITIVITY OF SEVERAL ENERGETIC MATERIALS

H. W. Sandusky and R. R. Bernecker  
Naval Surface Warfare Center  
Dahlgren Division Detachment White Oak  
Silver Spring, MD 20903-5640

The shock reactivity and sensitivity for single and multiple shocks are compared for a high-energy propellant (H-1) and two plastic-bonded explosives (PBXs). The same gap test donor arrangement provided the initiating shock in both the single- and multi-shock experiments. In the latter, there was an auxiliary (weak) shock loading of the sample before being reshocked, 1 to 5 ms later, by the donor. H-1 had a 66% reduction in the critical initiation pressure ( $P_{crit}$ ) relative to a single shock when the time between shocks was ~0.9 ms. When that time was increased to ~4.8 ms, sample deformation from the first shock had mostly relaxed and there was only a 10% reduction in  $P_{crit}$ . Multiple shocks reduced  $P_{crit}$  relative to a single shock in PBXW-114 by 29%, independent of time between shocks, and in PBXN-111 by 6%. The first shock was weaker in the PBXs than in H-1.

## INTRODUCTION

The origin of small amounts of porosity (<10% void volume) in an energetic material has a considerable effect on the shock sensitivity; that is, the critical shock pressure ( $P_{crit}$ ) necessary to initiate detonation. This has been observed for granular materials pressed to various porosities in the NOL large scale gap test (LSGT).<sup>1</sup> This has also been observed when simulating energetic materials damaged by an accident. One approach to simulating damage is to shred or chop the energetic material into pieces and then pack them into a container at uniform porosity prior to shock loading.<sup>2-4</sup> Another approach for elastomeric materials has been to quasi-statically strain them to failure prior to shock loading after a delay of 20 to 30 minutes.<sup>5</sup> Either approach allowed control over the extent and uniformity of the physical changes to the energetic material; however, those changes and any healing which occurred prior to shock loading may not reproduce the state of damage during an accident.

In other experiments, increased sensitivity resulted when samples were impacted by a gun projectile and then promptly reshocked, either by being driven into another sample<sup>6</sup> or by the air blast from the detonation of a nearby donor.<sup>2</sup> The time frame between damaging

the sample and reshocking it is the same order of magnitude as would be expected in certain accidents; that is, the damage is fresh. However, the first impact in these experiments delivered the strongest shock and severely damaged the unconfined sample, making it considerably more sensitive. Also, most energetic materials of the type studied are confined, which limits the macroscopic deformation and damage that would occur in an accident.

An experiment has been designed in which the sample is mildly damaged and then reshocked within milliseconds while the damage is still fresh. Except for one test, samples were unconfined. To produce only mild damage, the first shock must be weak (~0.1 GPa). Those damaged samples which were recovered (instead of being reshocked) exhibited little permanent distortion but often had cracking near the shock-entry surface.

## EXPERIMENTAL APPROACH

Three types of experiments were conducted for this study. Undamaged samples were shock loaded by a gap test donor while a streak camera recorded the distance ( $x_D$ ) and time ( $t_D$ ) for the onset of detonation, as seen on the lateral surface. In preparation for multi-shock experiments, samples were subjected to weak shocks

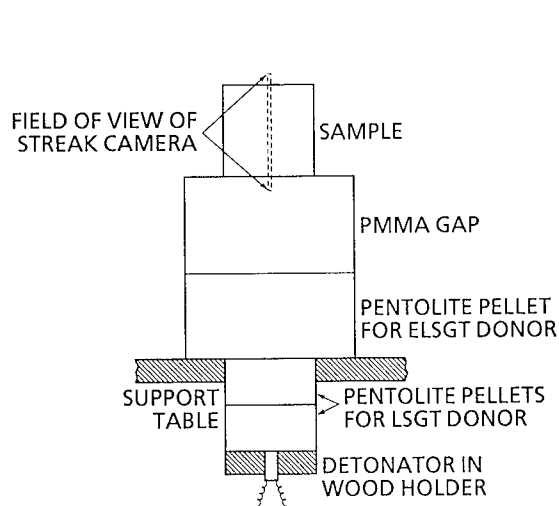


**FIGURE 1. SINGLE-SHOCK EXPERIMENTAL ARRANGEMENT**

while dynamic deformation and damage were recorded by framing photography and flash radiography. In multi-shock experiments, the sample was damaged with the pre-selected level of weak shock and then reshocked ( $<5$  ms) with the same type of gap test donor used for the undamaged samples. Values of  $x_D$  and  $t_D$  were obtained as in the single-shock experiments. Measurements from single- and multi-shock experiments are compared to show the effect of dynamic damage.

Single-shock experiments were conducted with the arrangement in Figure 1. The donor consists of pentolite pellets of 50/50 TNT/PETN pressed to 1.56 g/cc, and is a composite of the 50.8 mm diameter by 50.8 mm high NOL large scale gap test (LSGT) donor and one of the two 95.3 mm diameter by 47.65 mm high pentolite pellets from the NSWC expanded large scale gap test (ELSGT) donor<sup>7</sup>. The composite donor was desired for obtaining the more sustained shock pulse duration of the ELSGT donor (versus the LSGT donor) but with less explosive to avoid damaging the firing chamber. The shock pulse from the donor was attenuated by a 95.3 mm diameter polymethylmethacrylate (PMMA) gap, as in the ELSGT.

A calibration of shock pressure ( $P_G$ ) in the PMMA gap versus distance ( $x$ ) from the donor/gap interface has not been measured for the composite donor. For a water gap, calibrations of the composite and ELSGT donors were nearly the same.<sup>8</sup> It was assumed, therefore, that shock attenuation in a PMMA gap from a composite donor was equivalent to the ELSGT calibration<sup>9</sup> for gaps less than 98 mm ( $P_G = 1.82$  GPa). For longer gaps in the ELSGT calibration,  $P_G$  quickly decreases to  $\sim 0.8$

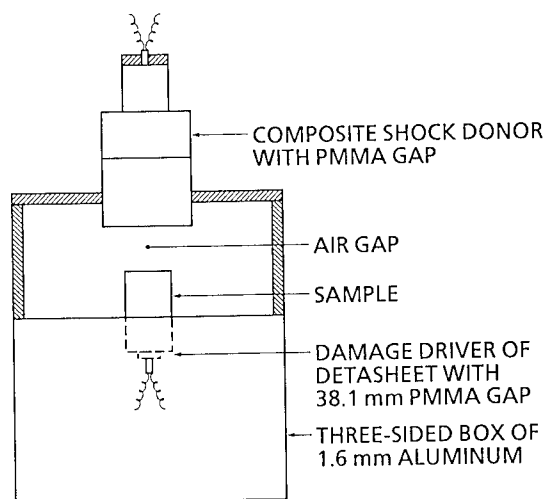


**FIGURE 2. MULTI-SHOCK EXPERIMENTAL ARRANGEMENT**

GPa and then levels off, which appears to be unrealistic. The ELSGT calibration for gaps less than 98 mm could be closely matched simply by scaling the distances in the LSGT calibration by a factor of 1.75.<sup>10</sup> It was assumed that  $P_G$  for gaps greater than 98 mm could also be scaled (by 1.75) and that shock attenuation for the longer gaps was still equivalent for the ELSGT and composite donors.<sup>10</sup> Given  $P_G$  and the Hugoniot of each sample material, the shock pressure in the samples ( $P_E$ ) was calculated by impedance matching.

Streak photography, with both back and front lighting of the slit region, was used to record shock propagation in the gap and on the periphery of the sample, the onset of detonation, the detonation wave on the periphery of the sample, and the breakout of the shock or detonation wave from the sample axis to the surrounding air. The lighting techniques and the application of a reflector to some of the samples to enhance recording of the non-luminous shock and detonation wave are described in Reference 11. Reflectors which had to be affixed to the samples were generally not used because of their unsuitability for damaged samples in multi-shock experiments. Rather, application of permanent inks (both black and white) on the samples and variations in front lighting assisted in improving streak images.

Only the bottom half of the arrangement in Figure 2 was used in preparatory experiments for selecting the level of weak shock for the multi-shock experiments. This shock originated from the detonation of several grams of Detasheet C, which was separated from the sample by a 38.1 mm thick PMMA spacer and a 1.6 mm

thick aluminum baffle. The aluminum baffle was large relative to the sample in order to shield the field of view of the sample, for several milliseconds, from the gases and fragments of the damage driver. The amount of Detasheet was adjusted to obtain the most dynamic deformation and interior damage possible without fragmenting the sample. The response of the sample to this shock was observed with backlit high-speed framing photography and flash radiography, and the samples were recovered for examination. The shock loading from the damage driver propelled the samples at velocities of 10 to 20 m/s.

The multi-shock arrangement in Figure 2 combines the damage driver just discussed with the gap test donor in Figure 1. The length of the air gap between the sample and the PMMA gap for the composite donor controlled the time between damaging and reshocking the sample. The donor was initiated when a thin ( $<0.15$  mm) switch on the 95.3 mm diameter PMMA spacer was short-circuited by the impacting sample. Streak photography was used to record the response of the sample to the shock from the composite donor, as in the single-shock experiments. This arrangement avoided any significant influence from the damage driver on the calibration of the gap test donor and sample damage was mild enough that the Hugoniot was assumed to be the same for undamaged samples. Thus,  $P_E$  versus  $x_D$  in undamaged and damaged samples could be correlated.

Three materials were examined for sensitization from mild dynamic damage. One is a solid rocket propellant, designated as H-1, which contains HMX, aluminum (Al), and ammonium perchlorate (AP) in an energetic binder. The other materials are plastic-bonded explosives (PBXs) with an inert hydroxy-terminated polybutadiene (HTPB) binder. PBXW-114 contains HMX and Al, and PBXW-115 (now PBXN-111) contains RDX, AP, and Al. Sample diameter for the two highly-loaded nitramine compositions, H-1 and PBXW-114, was 50.8 mm. For PBXW-115, whose unconfined critical diameter is 37.1 mm,<sup>12</sup> the sample diameter was increased to 75.0 mm. All samples were unconfined except for one multi-shock experiment in which an H-1 sample was radially confined by a 6.4 mm thick sleeve of Lexan.

## EXPERIMENTAL RESULTS

The data from single- and multi-shock experiments have been plotted as the inverse of  $x_D$  versus  $P_E$ . This presentation of data reveals both reactivity and sensitivity. Shock reactivity refers to the slope  $1/x_D$  versus  $P_E$ .<sup>4</sup> A greater slope in this plane corresponds to increased reactivity; that is,  $x_D$  is affected more by

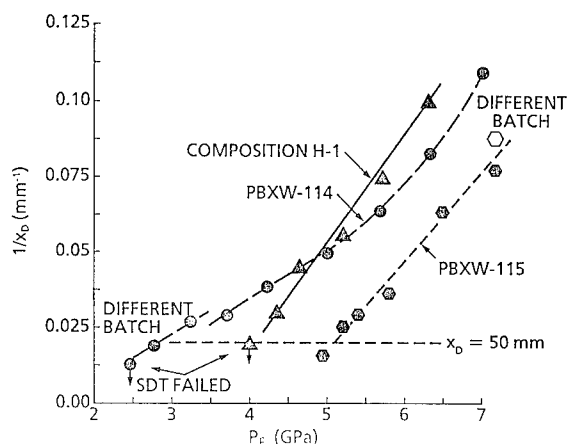


**FIGURE 3. INVERSE OF RUN DISTANCE TO DETONATION VERSUS SHOCK PRESSURE INTO THE SAMPLE FROM A COMPOSITE DONOR**

changes in  $P_E$ . The shock sensitivity, previously defined as  $P_{crit}$ , is defined for this study as the  $P_E$  in the shock reactivity plane corresponding to  $x_D = 50$  mm, since most samples used in the multi-shock experiments were  $\sim 50$  mm long. Allowing longer run lengths would not substantially reduce  $P_{crit}$  for the diameter of the donor and samples used because of rarefactions.

### Single-Shock Experiments

The response of these materials to a single shock is plotted in Figure 3. For H-1 and PBXW-114, the single-shock and most of the multi-shock data are tabulated in Reference 10. In addition to the presented data for composite donors, experiments with LSGT donors are reported for H-1 and PBXW-115 in References 11 and 13, respectively. As noted in Figure 3, two batches (mixes) of PBXW-114 were tested. The samples shocked at the three lowest pressures and those used in damage driver and multi-shock experiments were from the second batch. Both batches had the same density and were without porosity or defects that could be detected in radiographs. Even so, there was a 0.33 GPa change in  $P_{crit}$ . Also, there is a data point for PBXW-115 in Figure 3 from an earlier study<sup>13</sup> on a different batch than that used in the present study. As noted above,  $x_D = 50$  mm is marked in Figure 3 as a reference for selecting  $P_{crit}$ . The values of  $P_{crit}$  from the single-shock experiments are 4.04 GPa for H-1, 2.82 GPa for PBXW-114 (second batch), and 5.07 GPa for PBXW-115. These values of shock sensitivity are the basis for comparison with the multi-shock experiments.

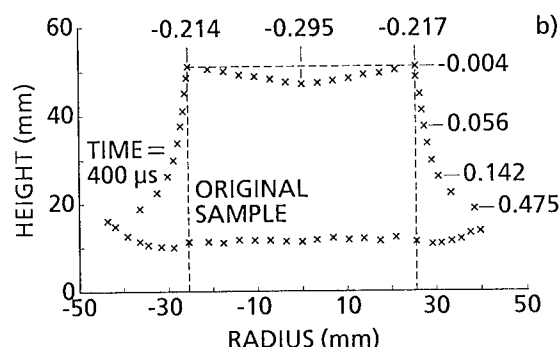
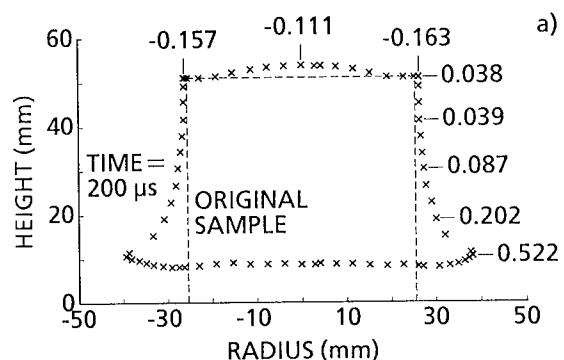


**FIGURE 4. RADIOGRAPHIC DATA OF DYNAMIC DEFORMATION IN H-1 AT (a) 200  $\mu$ s AND (b) 400  $\mu$ s AFTER INITIATING THE DAMAGE DRIVER**

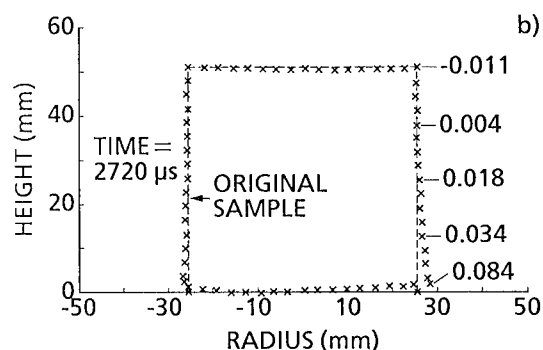
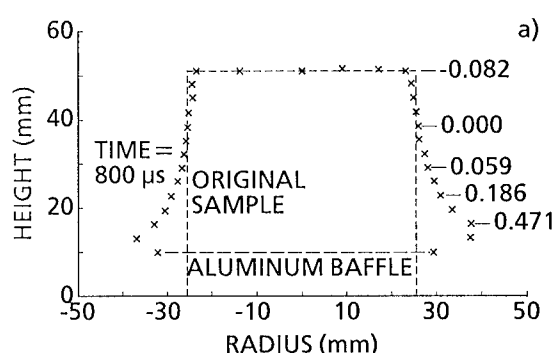


**FIGURE 5. PHOTOGRAPHIC DATA OF DYNAMIC DEFORMATION IN H-1 AT (a) 800  $\mu$ s AND (b) 2720  $\mu$ s AFTER INITIATING THE DAMAGE DRIVER**

### Damage Driver Experiments

The profile and external dimensions of an H-1 sample at four different times after initiation of the 4.4 g damage driver are shown in Figures 4 and 5. The bulge on the top of the sample in Figure 4a was attributed to incipient spall failure in the center region near that end of the sample. The void or low density region associated with incipient spall on the 200  $\mu$ s radiograph had closed by the time of the 400  $\mu$ s radiograph. This radiograph, which was taken near the time of maximum deformation, shows an overall axial strain of  $\sim 30\%$  near the center of the sample (Figure 4b). The strains listed in the figures were averaged over the diameter or height of the sample; local strains were probably much higher. Between the 200 and 400  $\mu$ s radiographs, the average axial strain rate was  $275 \text{ s}^{-1}$ . The sample had begun to relax by 800  $\mu$ s (Figure 5a) and had returned to almost its original dimensions by 2.7 ms. When the sample was recovered, there was no dimensional change or external indication of damage. Cutting the sample revealed no visible interior damage except for some cracking near

the incipient spall zone, which was observed by flexing a sample slice to open the cracks.

The Detasheet in the damage driver was reduced to 1.8 and 2.9 g, respectively, for PBXW-114 and PBXW-115 samples to avoid fragmentation of the shocked end and spalling of the opposite end. At these lower shock levels, the dynamic axial strain was much less than observed in H-1, but there was permanent damage near the circumference of the shock-entry surface. Radiographic data, like that in Figure 4, are shown for PBXW-114 at 1.0 and 4.7 ms in Reference 10.

Since the mass of the damage driver for each material was adjusted to obtain incipient spall failure, estimates of spall strength were possible. These estimates assumed that the particle velocity was half of the observed free surface velocity of the top center of the sample immediately following the reflection of the shock from the damage driver. Spall strengths of 85, 48, and 128 MPa were thus obtained for H-1, PBXW-114, and PBXW-115, respectively.

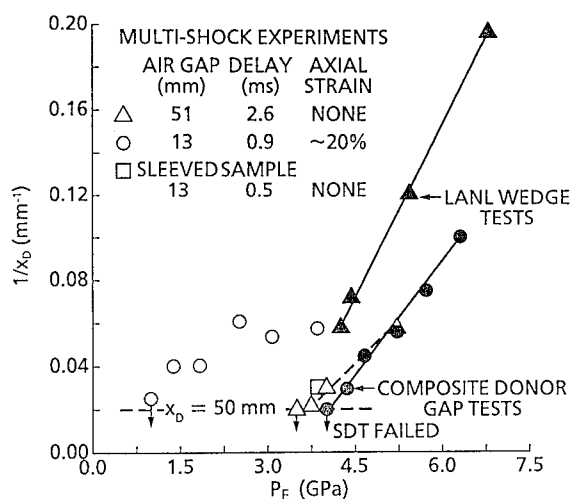


FIGURE 6. COMPARISON OF SINGLE- AND MULTI-SHOCK EXPERIMENTS ON H-1

#### Multi-Shock Experiments

While the mass of the damage driver was fixed for each material, as discussed above, the time delay between the shocks from the damage driver and composite donor was varied for H-1 and PBXW-114. Experiments on H-1 were conducted with air gaps between the sample and PMMA gap above it (Figure 2) of 12.7 and 50.8 mm, resulting in delay times of 0.9 and 2.6 ms, respectively. Multi-shock data for H-1 are plotted in Figure 6 along with the single-shock data from wedge testing<sup>14</sup> and the composite donor experiments shown in Figure 3. When the composite donor in the multi-shock experiments was initiated 2.6 ms after the damage driver, the H-1 samples had nearly relaxed to their original dimensions (Figure 5b) and there was only a 0.4 GPa decrease in  $P_{crit}$  relative to the undamaged samples in the single-shock experiments. If, however, the H-1 samples were reshocked after only a 0.9 ms delay, the samples were still deformed (Figure 4b) and there was at least a 2.65 GPa decrease in  $P_{crit}$ . This is based on the lowest  $P_E$  (1.39 GPa) at which detonation was observed and corresponds to a 66% decrease in  $P_{crit}$ . At a somewhat lower  $P_E$  (1.00 GPa), detonation failed but the recovered pieces of sample appeared to have extensively reacted in contrast to sample pieces which look much like the original sample when shock initiation has failed.<sup>11</sup> Thus,  $P_{crit}$  may actually be close to 1.00 GPa. For those samples which transited to detonation after a 0.9 ms delay between shocks,  $x_D$  varied from only 17 to 25 mm, while  $P_E$  decreased from 3.86 to 1.39 GPa.

The role of sample deformation in the increased sensitivity of H-1 was explored in an experiment in

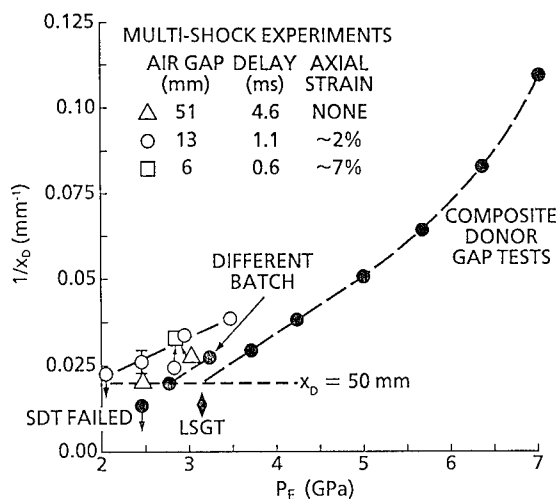


FIGURE 7. COMPARISON OF SINGLE- AND MULTI-SHOCK EXPERIMENTS ON PBXW-114

which the radial deformation of the sample was restrained by a 6.4 mm thick sleeve of clear Lexan, which was polished for photographic recording. The shock from the damage driver did not cause the sleeve to move relative to the sample. The presence of the sleeve increased the transit velocity of the sample across the air gap, which reduced the delay time between shocks from the 0.9 ms for an unconfined sample to 0.5 ms. The measured  $x_D$  of 32.7 mm was near that for samples which had mostly relaxed (2.6 ms delay) prior to entry of the second shock.

Multi-shock experiments on PBXW-114 were conducted with the same 12.7 and 50.8 mm air gaps as for H-1, resulting in somewhat longer delays of 1.1 and 4.6 ms, plus a shorter air gap of 6.4 mm with a delay time of 0.65 ms. Multi-shock data for PBXW-114 are compared in Figure 7 with the single shock data from Figure 3 and the LSGT sensitivity ( $P_G = 2.70$  GPa,<sup>15</sup> for which  $P_E = 3.42$  GPa). Although  $x_D$  at  $P_{crit}$  is unknown for the LSGT, 75 mm is estimated assuming that the effective unconfined charge diameter is twice the confined diameter and that a run to detonation beyond one unconfined charge diameter is unlikely. Most multi-shock experiments had a 1.1 ms delay between shocks, which reduced  $P_{crit}$  by 29% (0.8 GPa) to 2.0 GPa. For the experiment with the lowest  $P_E$  (2.46 GPa) at which detonation occurred for a 1.1 ms delay, it was uncertain whether  $x_D$  was 35.9 or 42.6 mm. To explore the effect of delay time, experiments with both a longer and shorter delay were conducted at the next higher  $P_E$  (2.95 GPa). At this  $P_E$ , there was little effect on  $x_D$  from either decreasing the delay to 0.65 ms (near the time of maximum deformation) or increasing the delay to 4.8 ms (minimal deformation). In an experiment with a 4.8

ms delay at a lower  $P_E$  (2.46 GPa), a measured  $x_D$  of 47.5 mm was definitely longer than that (35.9 to 42.6 mm) for an experiment with a 1.1 ms delay.

A single (25.4 mm) air gap in the PBXW-115 experiments resulted in a delay time of 2.4 ms. Multi-shock data on PBXW-115 are plotted in Figure 8 along with the single-shock data from wedge testing,<sup>16</sup> the LSGT and ELSGT sensitivities, modified LSGT gap tests with steel confinement of the sample,<sup>13</sup> and the composite donor experiments shown in Figure 3. The modified LSGT and composite donor experiments reasonably predict the LSGT and ELSGT sensitivities, respectively. The multi-shock tests show only a small (6% or 0.32 GPa) reduction in  $P_{crit}$  to 4.75 GPa, relative to a single shock, in samples which had insignificant deformation when the second shock entered.

## DISCUSSION

### Response to a Single Shock

A wide variation in  $P_{crit}$  to a single shock from a composite donor exists for these materials (Figure 3), with PBXW-114 having the lowest value. At high pressures ( $P_E > 5$  GPa), however, H-1 transits to detonation in a shorter run distance than PBXW-114. The relatively high  $P_{crit}$  for PBXW-115 reflects the lower amount of nitramine in the composition. The shock reactivities (slopes of  $1/x_D$  versus  $P_E$ ) of H-1 and PBXW-115 are linear and of similar magnitude. While the shock reactivity of PBXW-114 is comparable to the other two materials for  $P_E > 5$  GPa, the reactivity near  $P_{crit}$  is significantly less. As will be discussed, the shock reactivity of PBXW-115 in the wedge test behaves similarly. Comparable shock reactivity measurements were attained with LSGT donors on PBXW-108 (RDX, HTPB binder) and PBXW-109 (now PBXN-109; RDX, Al, HTPB binder).<sup>4</sup> While  $1/x_D$  versus  $P_E$  was linear for PBXW-108, it was non-linear for PBXW-109. In contrast to the PBXW-114 data, the region of higher reactivity in PBXW-109 occurred for the lower shock pressures near  $P_{crit}$ .

The role of shock pulse duration, which is dependent on donor size, differs for the materials. For H-1,  $P_{crit}$  for a composite donor with a PMMA gap is about the same for a LSGT donor in a water-filled aquarium, which effectively increases the shock duration.<sup>11</sup> For PBXW-114, which has an unconfined critical diameter of 6.1 mm,<sup>15</sup> differences in  $P_{crit}$  from a composite or LSGT donor are no more than from batch-to-batch variations (Figure 7). We are not certain there is a significant influence on  $P_{crit}$  for H-1 and PBXW-114 from the longer shock duration of the composite donor. For PBXW-115, which has an unconfined critical diameter

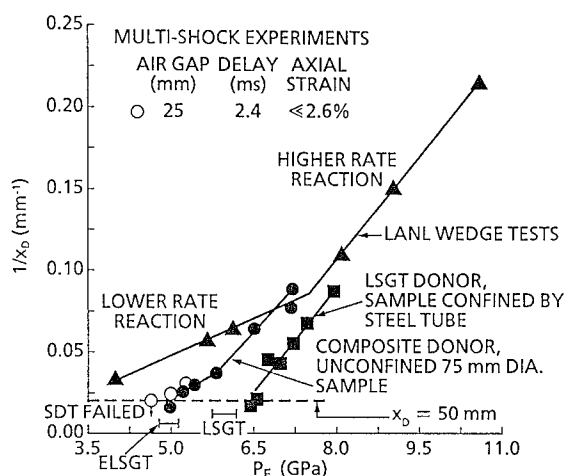


FIGURE 8. COMPARISON OF SINGLE- AND MULTI-SHOCK EXPERIMENTS ON PBXW-115

of 37.1 mm,<sup>12</sup>  $P_{crit}$  from a composite donor and the ELSGT are about the same (Figure 8); however,  $P_{crit}$  from a LSGT donor with steel confinement of the sample<sup>14</sup> and the LSGT are at least 1.0 GPa higher than for the larger donors. There is a significant influence from shock duration on  $P_{crit}$  for PBXW-115.

Wedge test donors provide a somewhat longer shock pulse duration than the composite donor, but the difference is less than that between the composite and LSGT donors.<sup>8</sup> It is surprising then that there is such a difference in  $P_{crit}$  from wedge and gap test donor data for H-1 whereas shock reactivities from the two tests are similar (Figure 6). Such differences were observed for two other high-energy propellants and are believed to result from observing the breakout of detonation along the axis of the sample in the wedge test versus the lateral surface in the gap test.<sup>17</sup> For PBXW-115, the wedge and composite donor data (Figure 8) overlap at  $P_E \approx 7$  GPa ( $x_D = 13.4$  mm), but  $P_{crit}$  for the wedge test is  $\sim 1$  GPa less than that for the composite donor gap test. This difference results from the unusual presence of a lower rate of reaction for  $P_E < 7.5$  GPa in the wedge test data. The shock reactivity of confined PBXW-115 in response to a LSGT donor is quite similar to that for the higher rate of reaction observed in wedge tests. Furthermore, rather than assign a straight line through the composite donor data as in Figure 3, in Figure 8 lines with slopes similar to those for the higher and lower reaction rates observed in wedge tests have been assigned to the highest and lowest values of  $P_E$ , respectively. The data suggests that the longer shock duration of the larger donors permits buildup to detonation by a reaction path that would otherwise quench for a shorter shock pulse.



## Response to Multiple Shocks

Changes in  $P_{crit}$  depend upon the amount and character of damage in the sample at the time of initiation by the strong shock. Since the extent of microscopic damage present could not be ascertained, there is no knowledge of whether the damage from the first shock is similar for the three materials. Note that impedance calculations for  $P_E$  assumed no porosity in the damaged sample, which would reduce  $P_E$ . Also, uniform sample contact with the PMMA gap for the composite donor was assumed when the sample was reshocked. Either porosity or nonuniform contact would further reduce the reported values of  $P_{crit}$ .

The largest change in  $P_{crit}$  (66%) from multiple shocks was for H-1 when it was still in a state of strain from the first shock. Allowing the sample to relax just another 1.7 ms or restraining the deformation from the first shock, with a sleeve around the sample, greatly reduced the change in  $P_{crit}$  from multiple shocks. Quasi-statically straining H-1 to failure and then shock loading the sample with a LSGT donor while immersed in water resulted in a 62% change in  $P_{crit}$  relative to an undamaged sample,<sup>5</sup> nearly the same as the worse case in the multi-shock experiments. Although the samples which had been strained to failure incurred much more damage than from the damage driver, there was only 1% porosity remaining at the time they were shocked.

The 29% and 6% reductions in  $P_{crit}$  from multiple shocks in PBXW-114 and PBXW-115, respectively, were less than in H-1, but the PBX samples received a weaker initial shock pulse and they were much less strained than H-1 when reshocked. In PBXW-114 the change in  $P_{crit}$  was relatively independent of the delay time between shocks, but the damage in PBXW-114 (and in PBXW-115) was more permanent than in H-1, indicating different high strain-rate mechanical behavior. The 0.32 GPa change in  $P_{crit}$  for PBXW-115 is essentially the same as that for PBXW-108 when 3% porosity had been introduced by compressively straining the samples and maintaining the strain during shock loading.<sup>4</sup>

In the H-1 experiments with a 0.9 ms delay between shocks,  $x_D$  and  $t_D$  were fairly independent of  $P_E$  (Figure 6). Plotting  $t_D$  versus  $x_D$ , using the tabulated data in Reference 11, revealed that a linear relationship exists for single shocks (prompt initiation) and for multiple shocks with a 2.6 ms delay between shocks. For the multi-shock experiments with a 0.9 ms delay between shocks, the samples reshocked at the two lowest pressures required significantly longer times to detonation than for prompt initiation, and samples reshocked at the next two lowest pressures required somewhat longer times to detonation than for prompt

initiation. Thus, it appears that these samples had characteristics of a delayed transition-to-detonation, as observed in other high-energy propellants.<sup>17</sup> This would possibly explain the appearance of reaction in the sample which failed to detonate for  $P_E = 1.00$  GPa. While the streak records from these experiments showed some unusual behavior, it is not clear whether that was due to the deformed state of the samples or delayed detonation.

When straining samples to failure, it could be argued that the effective porosity controlling shock sensitivity was the maximum achieved, since this represents the damage incurred in the material. Such a high porosity is also the initial state of a pressed explosive as the particles are poured into the die, and particulate deformation and/or fracture during pressing should incur just as much localized damage as straining a cast propellant to failure. Even so, shock sensitivity appears to be increased more by dynamic damage than by pressing a granulated material.<sup>18</sup>

## SUMMARY AND CONCLUSIONS

PBXs with HTPB binders did not incur large (>30%) increases in shock sensitivity when damaged here by a weak shock or by compressive strain<sup>4</sup>. Although the dynamic deformation by pre-shock was limited to avoid extensive fracture of the PBX samples, the damage was permanent. Thus, the 29% change in shock sensitivity for PBXW-114 appeared to be relatively independent of the time delay between shocks (0.6 to 4.6 ms). The less sensitive PBXW-115 had the smallest increase (6%) in sensitivity when pre-shocked, but there was only one delay time studied corresponding to essentially no axial strain in the samples when reshocked. The energetic binder in high-energy propellant H-1 permitted more dynamic deformation from a weak pre-shock, but there was little permanent damage. Once the deformation had relaxed, which required only 2.6 ms after the pre-shock, there was only a small change in sensitivity when reshocked. Reshocking H-1 when still deformed 0.9 ms after the pre-shock resulted in a 66% change in sensitivity and a change in mechanism from prompt initiation to delayed detonation. This large increase in sensitivity is comparable to that when H-1 had been quasi-statically strained to failure and shock loaded when ~1% porosity still remained.<sup>5</sup>

## ACKNOWLEDGMENTS

The experiments were performed and the records from them reduced by A. Robert Clairmont, Jr., J. Patrick Femiano, and Carl L. Groves.

## REFERENCES

1. Price, D.; Clairmont, A. R., Jr.; and Erkman, J. O., *The NOL Large Scale Gap Test. III. Compilation of Unclassified Data and Supplementary Information for Interpretation of Results*, NOLTR 74-40, 8 Mar 1974, Naval Surface Warfare Center, White Oak.
2. Lee, E. L.; James, E.; Green, L. G.; Von Holle, W.; Tarver, C.; Curran, D.; Murri, W.; and Seaman, D., "Response of Propellants to High Dynamic Stresses," *Hazard Studies for Solid Propellant Rocket Motors*, AGARD Conference Proceedings No. 367, 1984.
3. Sandusky, H. W. and Bernecker, R. R., "Compressive Reaction in Porous Beds of Energetic Materials," in *Proceedings of Eighth Symposium (International) on Detonation*, NSWC MP 86-194, Naval Surface Warfare Center, 1986, pp. 881-891.
4. Bernecker, R. R. and Clairmont, A. R., "Shock Initiation Studies of Cast, Damaged, and Granulated PBXs," paper presented at this Symposium.
5. Ritcher, H. P.; Boyer, L. R.; Graham, K. J.; Lepie, A. H.; and Zwierzchowski, N. G., "Shock Sensitivity of Damaged Energetic Materials," in *Proceedings of Ninth Symposium (International) on Detonation*, OCNR 113291-7, Vol. II, Office of the Chief of Naval Research, 1989, pp. 1295-1309.
6. Green, L.; James, E.; and Lee, E. "Energetic Response of Propellants to High Velocity Impact," in *Proceedings of Eighth Symposium (International) on Detonation*, NSWC MP 86-194, Naval Surface Warfare Center, 1986, pp. 284-293.
7. Liddiard, T. L. and Price, D., *The Expanded Large Scale Gap Test*, NSWC TR 86-32, March 1987, Naval Surface Warfare Center, White Oak, MD.
8. Bernecker, R. R., "Shock Sensitivity Tests, Insensitive Munitions, and Underwater Explosives," in *Proceedings of 1988 JANNAF Propulsion Systems Hazards Subcommittee Meeting*, CPIA Publ. 477, Vol. I, March 1988, pp. 69-78.
9. Tasker, D. G. and Baker, R. N., "A New, Unbiased Method for Analyzing Streak Data, The Calibration of the NSWC Expanded Large Scale Gap Test (ELSGT)," *Shock Compression of Condensed Matter-1989*, Ed. Schmidt, S. C., Johnson, J. N., Davis, L. W., Elsevier Science Publishers B. V., 1990.
10. Sandusky, H. W., "Influence of Fresh Damage on the Shock Sensitivity of an Energetic Material with an HTPB Binder," in *Proceedings of the 1991 JANNAF Propulsion Systems Hazards Subcommittee Meeting*, CPIA Publ. 562, March 1991, pp. 347-357.
11. Sandusky, H. W.; Bernecker, R. R.; and Clairmont, A. R., Jr., "Influence of Fresh Damage on the Shock Sensitivity of a High-Energy Propellant," in *Proceedings of 1990 JANNAF Propulsion Systems Hazards Subcommittee Meeting*, CPIA Publ. 538, Vol. 1, April 1990, pp. 335-348.
12. Forbes, J. W.; Lemar, E. R.; Baker, R. N., "Detonation Wave Propagation in PBXW-115," in *Proceedings of Ninth Symposium (International) on Detonation*, OCNR 113291-7, Vol. I, Office of the Chief of Naval Research, 1991, pp. 806-815.
13. Bernecker, R. R. and Clairmont, A. R., Jr., "Shock Reactivity and Sensitivity Measurements (2-D) of PBXs," TTCP Composite Explosives Meeting, Naval Surface Warfare Center, 18 Sept. 1990.
14. Grall, R. R. and Ramsay, J. B., "Shock Sensitivity of 90% - 100% TMD Composite Energetic Materials," in *Proceedings of 1990 JANNAF Propulsion Systems Hazards Subcommittee Meeting*, CPIA Publ. 538, Vol. 1, April 1990, pp. 203-209.
15. Hall, T. N. and Holden, J. R., *Navy Explosives Handbook - Explosion Effects and Properties - Part III. Properties of Explosives and Explosive Compositions*, NSWC MP 88-116, Oct. 1988.
16. Ramsay, J. B., Los Alamos National Laboratory, private communication.
17. Bernecker, R. R.; Clairmont, A. R., Jr.; and Hudson, L. C., III, "Prompt and Delayed Detonation from Two-Dimensional Shock Loadings," paper presented at this Symposium.
18. Richter, H. P.; Lepie, A. H.; Boyer, L. R.; Zwierzchowski, N. G., "Shock Sensitivity Increase with Porosity," in *Proceedings of 1990 JANNAF Propulsion Systems Hazards Subcommittee Meeting*, CPIA Publ. 538, Vol. 1, April 1990, pp. 297-304.

## DISCUSSION

J. F. GUERY

Societe National des Poudres et Explosifs  
Vert-le-Petit, France

In the classical definition, damage is an irreversible process. Nevertheless, do you think that the difference

in sensitivity is caused by the binder mechanical properties or by the fact that one is energetic?

**REPLY BY H.W. SANDUSKY**

There is no definitive answer, since both the mechanical properties and energy of the binder changed between the experiments on the high-energy propellants and the PBXs. As mentioned in the previous reply, I suspect that the weakly shocked propellant had irreversible damage which would manifest itself as a decreased modulus. The mechanical properties which permit such damage and the energetic binder in the high-energy propellant probably both contributed to its increased sensitivity.

**DISCUSSION**

**HAROLD J. GRYTING**  
Gryting Energetics Science Company  
San Antonio, Texas

Was the vacuum thermal stability determined on the parallel samples? . Sometimes for good chemical reasons, sensitivity and stability may go in opposite directions.

**REPLY BY H.W. SANDUSKY**

The vacuum thermal stability (VTS) values for PBXW-114 and PBXW-115 are 0.16 and 0.33 cc/g, respectively. VTS has not been measured for the high-energy propellant

**DISCUSSION**

**BLAINE ASAY**  
Los Alamos National Laboratory  
Los Alamos, New Mexico

You showed an increase in sensitivity only for samples that had not yet relaxed. However, Richter showed increased sensitivity in materials 30 min. after damage. What is the difference between these two studies?

**REPLY BY H.W. SANDUSKY**

In the studies of Richter et al.,<sup>4</sup> the high-energy propellant samples were extensively damaged by straining them to failure. In the present work, the propellant samples were deformed without external evidence of any permanent damage. The deformation from the weak shock probably created some porosity and microscopic cracks that closed during the several milliseconds after shocking when the sample relaxed to its original dimensions.

## SHOCK INITIATION STUDIES OF CAST, DAMAGED, AND GRANULATED PBXs

R. R. Bernecker and A. R. Clairmont, Jr.  
Naval Surface Warfare Center  
10901 New Hampshire Avenue  
Silver Spring, Maryland 20903-5640

Two-dimensional shock initiation experiments have been conducted with cast, strained, and granulated samples of two elastomeric, plastic-bonded explosives (PBXs). The shock reactivity and shock sensitivity of these two PBXs were evaluated in the  $1/X_d$ -pressure plane, where  $X_d$  is distance to detonation on the sample's lateral surface. For strained samples of PBXW-108 having porosities of 5% or less, it appears that at a given  $X_d$ , a 1 % increase in porosity corresponds to about a 0.1 GPa decrease in pressure. Different granules (cubes and shreds) were used to construct very porous PBXN-109 samples (18 to 25% porosity). There was a distinct difference in shock reactivity and sensitivity between samples composed of cubes and samples composed of shreds in the 2.8 to 4.6 GPa pressure range. Multiple hot spot mechanisms are proposed to explain these differences and are expected to contrast with the cast PBX hot spot process.

### INTRODUCTION

Accidents can expose an energetic material (EM) to unexpected shock loadings or impacts which can damage the explosive charge (e.g., introduce porosity). Since the damaged energetic material may be more shock reactive and sensitive than the original material, subsequent events can be affected by the change in the shock reactivity (and perhaps the critical diameter) of the damaged EM. Consequently, it is most desirable to have a firm understanding of the shock reactivity of the explosive, both in the initial state and in any potential damaged state.

For the present, the type of damage induced in an EM during an accident is too complex to reproduce for experimental studies of shock reactivity. One approach, utilized in this study, is to use an "idealized" representation of damaged material (granular bed of uniform particles) in order to 1) correlate experimental observations from studies where the granularity of the damaged material had different sizes and shapes and 2) provide useful quantitative data to guide and confirm the development of accurate models of shock reactivity in porous charges. Ultimately, it is necessary to extend such ex-

perimental observations to the time scale where the period between the "production" of damage (first shock loading, for example) and any subsequent shock loading is a fraction of a second (dynamic damage).<sup>1,2</sup>

In this study, shock reactivity/sensitivity data for plastic-bonded explosives (PBXs), both in the cast and granular state, have been obtained using a calibrated two-dimensional (2-D) shock loading arrangement. The shock reactivity/sensitivity data show the influence of both porosity and the size and shape of the granules on the shock reactivity/sensitivity of these PBXs.

### EXPERIMENTAL ARRANGEMENT AND TECHNIQUES

The basic aspects of the 2-D shock initiation arrangement used in this work have been described, in part, in earlier papers.<sup>3,4</sup> The explosive driver is a cylindrical pentolite charge (1.56 g/cc) while the attenuator material is polymethylmethacrylate (PMMA); both have nominal diameters of 50.8 mm.

The configuration of the test samples varied in this

study. In addition to the cast cylinders used in earlier work<sup>3,4</sup> and here, a special jig was used to create low porosity damaged (strained) samples from the castings. The jig consisted of two disks of PMMA (12.7 mm thick, 76.2 mm diameter) that were connected by three brass rods screwed into the lower disk. This jig, with its EM sample, was placed between the platens of a Tinius Olsen testing machine; the upper platen was slowly lowered (at a strain rate of about 0.001 1/s). The deformation of the compressed sample was retained by lowering nuts on the threaded rods to lock the top disk in place. The lower disk of the jig served as part of the attenuator system in these special experiments. The strained samples were tested 60 to 75 min after initial deformation. Unstrained samples (snug fit in the jig) were also tested.

For damaged samples containing porosities greater than 5 percent (a somewhat arbitrary number), the cast material must be "granulated" to produce granules which will be reconsolidated to produce samples of varying porosity. Confinement is required for these "pressed" porous elastomeric samples since the porous sample elastically unloads to its initial bulk density when the applied pressure is released. For the experiments reported here, the granular PBXs were confined in PMMA tubes with nominal dimensions of 38.1 mm ID and 50.8 mm OD; the lengths varied from 50 to 100 mm. The tubes were bonded at one end to the PMMA attenuator and sealed with a PMMA disk at the other (far) end. The samples were loaded using 12.7 mm high increments, with each increment manually pressed to the desired density. PBXW-108 granules and some of the PBXN-109 granules were manufactured as cubes. Because the size of the cubes showed some variation, the uniformity of the size of the cubes was controlled further by sieving. The cubes used here were nominally 2.1 mm on edge. Shreds of PBXN-109 were made via controlled machining of cast samples. Long strings ("linquini-like") were collected and cut to the desired length. The shreds of PBXN-109 were 2.5 mm wide and 0.79 mm thick; lengths were either 1.6 mm, 6.4 mm or 12.7 mm long.

A high speed continuous-access streak camera (SC) was used to record both predetonation and detonation luminosity. Fronts seen on the lateral surface of the charge were 1) a non-luminous shock (NLS) wave; 2) luminous and non-luminous rearward waves; and 3) the detonation wave. Data obtained from the SC records are the run distance to detonation,  $X_d$ , and the time to detonation,  $T_d$ , both as seen on the lateral surface of the charge, and, for the granular material, a detonation

velocity. Data are presented for two PBXs, PBXW-108 and PBXN-109. PBXW-108 is a mixture of RDX in an inert (HTPB) binder system while PBXN-109 contains RDX and aluminum in an inert (HTPB) binder system.

The entering (on-axis) pressure for the energetic material was calculated via the impedance matching technique. The shock loading from the driver system is based upon the calibration data of the NOL large scale gap test (LSGT) by Erkman et al.<sup>5</sup> The Hugoniot for the porous materials were calculated using the procedure of Erkman and Edwards.<sup>6</sup> The Gruneisen constants were calculated to be 1.13 for both PBXW-108 and PBXN-109.<sup>7</sup>

The densities of the unstrained cast (as manufactured) and strained PBX samples were carefully measured using the water immersion technique. For unstrained PBXW-108, the average density was 1.555 g/cc, while the corresponding value for PBXN-109 was 1.651 g/cc. These numbers are slightly lower than theoretical maximum densities (TMDs) determined by others, using a variety of methods. Our estimate of the TMD values, calculated from assumed densities of the ingredients, were 1.564 and 1.664 g/cc, respectively, for PBXW-108 and PBXN-109. The %TMDs of the porous charges reported in this paper were calculated using the experimentally determined density (1.555 or 1.651 g/cc) as the corresponding TMD value.

## PBXW-108 EXPERIMENTAL RESULTS

### Strained Samples

The maximum porosity for the strained samples was dictated by the compression characteristics of PBXW-108. Trial compression runs<sup>7</sup> were made to determine the strain level at which incipient external fracture could be determined. For PBXW-108, the maximum strain for our tests was selected to be about 25.4%, sufficiently below any signs of external fracture. As a result of the compression, the outline of the strained samples was "barrel-like" which contrasted with the right cylindrical profile of the unstrained samples. The compressed samples had "shear bands" ("raised" bands criss-crossing the external surface at roughly 45°).<sup>7</sup>

Most of the strained sample densities were determined by immersion in water, using data from the assembled "empty" jig and the assembled jig containing the test sample. Data for the strained and unstrained samples

**TABLE 1. DATA FOR THE STRAINED AND UNSTRAINED PBXW-108 JIG SAMPLES**

Shot No.	L(o) (mm)	L (mm)	Rho(o) (g/cc)	Rho (g/cc)	Strain %	L(G) (mm)	P (GPa)	X <sub>d</sub> (mm)	T <sub>d</sub> (μs)
A65*	75.95	72.52	1.559	-	4.5	35.59	-	18.6	12.5
A73	75.87	60.57	1.559	-	20.2	38.13	-	F	-
A74	76.56	57.15	1.556	1.508	25.4	36.83	4.52	19.5	13.1
A75	85.70	85.70	1.557	1.557	0.0	36.83	4.71	20.5	13.4
A81	76.28	56.90	1.554	1.472	25.4	37.36	4.24	22.0	14.2
A82	88.98	88.98	1.554	1.554	0.0	37.36	4.57	27.1	14.9
A83	76.28	56.90	1.553	1.502	25.4	38.11	4.18	32.7	17.3
A84	88.90	88.90	1.555	1.555	0.0	38.11	4.38	F	-

F - No Detonation

\* - Tested without the jig; one piece (50.8 mm dia) attenuator

are listed in Table 1 where L(o) is the original length of the sample, L is length of the compressed/tested sample, Rho(o) is the measured density of the sample (water immersion technique) before compression, Rho is the measured density of the sample (water immersion after compression), L(G) is the total length of the attenuator (gap), and P is the entering pressure (on-axis) in the test sample. One sample, used in shot number (Shot No.) A65, was compressed to about 25.4 % strain but removed from the jig prior to testing. Hence, its length (L) is greater than those samples used in shot number's A74, A81, and A83.

explored with the cubic granules. (The highest density "attainable" in our system for any PBX granulated sample was about 82 %TMD.) Figures 1 and 2 show schematic representations of the SC data for granular PBXW-108. Some traces have been displaced in time (see values in parentheses in upper left hand area) to clearly show the data pertaining to the NLS and detonation waves. Due to the granules' large size, the SC records show more irregularities than normal. Table 2 lists numerical data for the granular PBXW-108 samples. Detonation velocities and their standard deviations are calculated in the region at the far end of the sample.<sup>7</sup>

### Granular Samples

Two densities (1.268 g/cc (81.5 %TMD) and 1.166 g/cc (75.0 %TMD)) of granular PBXW-108 were

### PBXN-109 EXPERIMENTAL RESULTS

The cubic granules and shreds of PBXN-109 were evaluated at essentially the same porosity as the cubes of

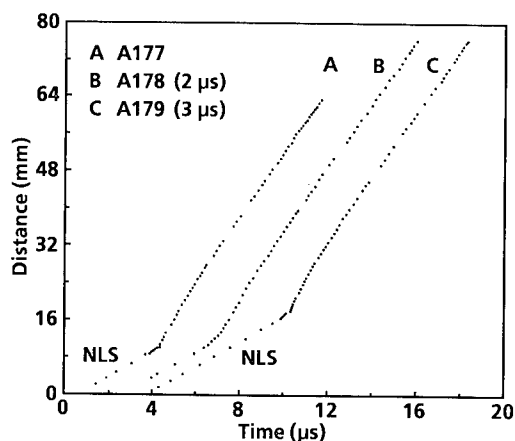


**FIGURE 1. STREAK CAMERA DATA FOR CUBES OF PBXW-108 AT 81.5% TMD**

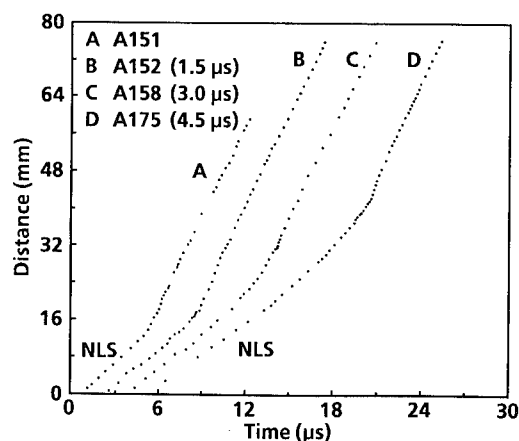


**FIGURE 2. STREAK CAMERA DATA FOR CUBES OF PBXW-108 AT 75.0% TMD**

**TABLE 2. PBXW-108 EXPERIMENTS WITH CUBIC GRANULES**

Shot No.	L (mm)	L(G) (mm)	P (GPa)	X <sub>d</sub> (mm)	T <sub>d</sub> (μs)	D (mm/μs)	Std Dev
A. 1.268 g/cc (81.5 %TMD)							
A177	63.42	33.02	4.08	10.1	4.36	6.85	0.03
A178	76.23	35.59	3.80	13.4	5.17	6.87	0.03
A179	76.28	38.10	3.30	18.0	7.33	6.78	0.03
B. 1.166 g/cc (75.0 %TMD)							
A151	63.47	2.99	3.72	13.9	5.36	6.39	0.10
A152	76.20	5.61	3.46	18.0	7.43	6.47	0.04
A158	76.23	8.10	3.00	31.3	11.13	6.40	0.04
A175	76.25	9.40	2.77	42.2	16.20	6.56	0.10

PBXW-108. Table 3 contains the data for the cubes at two densities, 81.8 %TMD and 75.1 %TMD, while Table 4 contains the data at the same two densities for the shreds. Figures 3 and 4 show schematic representations of the SC data for the cubes; Figure 5 shows SC data for the shreds.

## DISCUSSION

SC Characteristics of Granular Samples Exposed to 2-D Shock Loadings

The characteristics of the SC records for the porous granular charges contrast with the SC records for cast (strained and unstrained) materials. The most

**TABLE 3. PBXN-109 EXPERIMENTS WITH CUBIC GRANULES**

Shot No.	L (mm)	L(G) (mm)	P (GPa)	X <sub>d</sub> (mm)	T <sub>d</sub> (μs)	D (mm/μs)	Std Dev
A. 1.350 g/cc (81.8 %TMD)							
A156	63.47	30.48	4.63	17.5	6.24	5.85	0.04
A157	76.28	32.99	4.31	26.6	8.70	5.86	0.05
A176	76.25	35.03	4.07	F	-	-	-
A161	76.23	35.53	4.02	F	-	-	-
A090	89.13	40.64	3.00	F	-	-	-
A096	89.15	35.56	4.01	46.0	15.16	5.87	0.05
B. 1.240 g/cc (75.1 %TMD)							
A180	63.30	27.89	4.54	21.4	7.45	5.26	0.02
A181	63.27	29.24	4.37	29.0	9.48	5.32	0.04
A153	63.42	30.40	4.22	36.4	11.65	5.38	0.03
A159	76.28	33.10	3.91	F	-	-	-
A155	76.23	35.51	3.65	F	-	-	-

F - No Detonation

**TABLE 4. PBXN-109 EXPERIMENTS WITH SHREDDED GRANULES (6.4 mm LONG)**

Shot No.	L (mm)	L(G) (mm)	P (GPa)	X <sub>d</sub> (mm)	T <sub>d</sub> (μs)	D (mm/μs)	Std Dev
A. 1.350 g/cc (81.8 %TMD)							
A126	50.80	30.45	4.64	11.7	4.21	6.31	0.03
A110	63.53	35.59	4.00	18.2	6.22	6.24	0.02
A089	89.18	40.69	2.99	36.8	13.87	6.34	0.02
A124*	63.55	38.13	3.47	20.2	7.84	6.26	0.04
A125*	63.53	38.15	3.47	25.3	8.96	6.23	0.04
B. 1.240 g/cc (75.1 %TMD)							
A114	63.55	38.15	3.15	33.0	12.63	5.84	0.04
A111	63.58	44.50	2.15	F	-	-	-

F - No Detonation

\* - 12.7 mm long

\*\* - 1.6 mm long

striking feature is the near-absence of a geometry effect on the detonation trace. The detonation wave is seen propagating at a fairly constant velocity at the end of the porous charges, as evident by the standard deviations listed in Tables 2 to 4. The data<sup>8</sup> for cast PBXN-109 show an extremely high velocity just beyond X<sub>d</sub>, followed (in sufficiently long charges) by deceleration to a steady state detonation velocity, as also seen in Reference 4. While mild indications of a geometry effect can be seen in some of the traces in Figures 1 to 5, a constant velocity detonation wave is established a short distance beyond X<sub>d</sub>. This indicates that the onset of detonation occurs over a sample diameter that is only slightly smaller than the tube inner diameter (i.e., a diameter slightly smaller than 38 mm) for these porous charges.

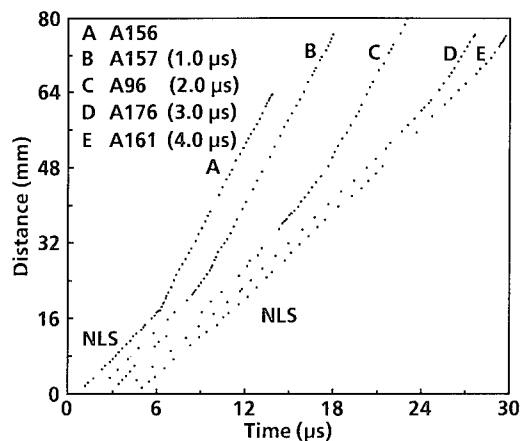


**FIGURE 3. STREAK CAMERA DATA FOR CUBES OF PBXN-109 AT 81.8% TMD**

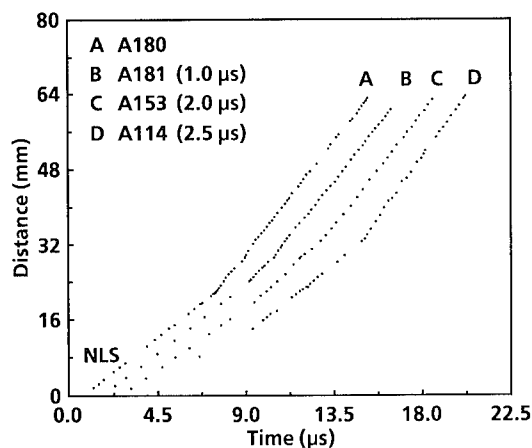


FIGURE 4. STREAK CAMERA DATA FOR CUBES AND SHREDS OF PBXN-109 AT 75.1% TMD

The detonation velocities calculated from Figures 1 to 5 (and summarized in Tables 2, 3, and 4) show 1) reasonably consistent values between experiments at a given density and 2) the expected decrease in detonation velocity with increasing porosity. Thus, for PBXW-108, the detonation velocity for a 81.5 %TMD sample of cubic granules is 6.83 mm/ $\mu$ s while it is 6.46 mm/ $\mu$ s for a 75.0 %TMD sample of cubic granules (see Table 2). On the other hand, the data in Tables 3 and 4 show a distinct difference in detonation velocities for different granule sizes/shapes of PBXN-109. For an 81.8 %TMD sample of cubic granules of PBXN-109, the detonation velocity is 5.86 mm/ $\mu$ s; this contrasts with the 6.30 mm/ $\mu$ s detonation velocity of the PBXN-109 shreds at the same density. The 75.1 %TMD samples of PBXN-109 show the same relative magnitudes; 5.32 mm/ $\mu$ s for cubes versus 5.84 mm/ $\mu$ s for shreds.

It is postulated that the difference in detonation velocities between the cubes and shreds of PBXN-109, both at 75.1 and 81.8 %TMD, can be associated with critical diameter considerations. For example, it is reasonable to believe that the critical diameter of the "smaller" shreds (smaller surface to volume (S/V) ratio) would be less than that of the cubes. This trend is consistent with data for granular cyclotol (RDX/TNT) mixtures.<sup>9</sup> Thus, the detonation velocities for the cubic material are believed to be farther from their infinite diameter values than the detonation velocities of the shreds. Hence, it can be seen that knowledge of the variation of critical diameter of these porous samples with porosity and granule size is also valuable. (On the other hand, numerical modeling of these (2-D) experi-

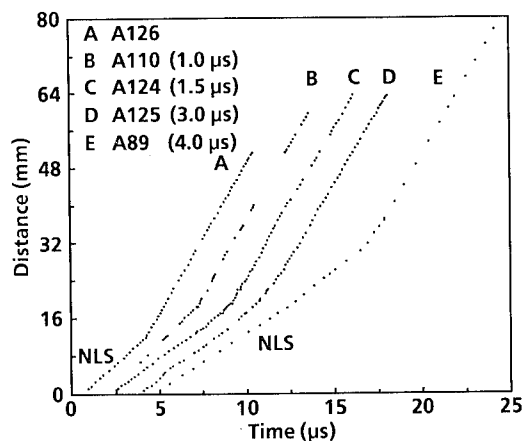


FIGURE 5. STREAK CAMERA DATA FOR SHREDS OF PBXN-109 AT 81.8% TMD

ments will use shock reaction kinetics which can be used, in additional calculations, to provide a good measure of these critical diameter relationships; see Reference 10, for example.) Experimental measurements of critical diameter considerations were not pursued here because of the large amount of granulated material that would have been needed.

#### Shock Reactivity of Cast, Damaged, and Granular PBXW-108

The SC records for both cast PBXW-108 and PBXN-109 are discussed in detail in Reference 8. The main parameter of interest in this paper is  $X_d$ . These data, for both cast PBXW-108 and cast PBXN-109, are displayed in the  $1/X_d$  - pressure plane of Figure 6. Over the wide pressure range studied for PBXW-108, a linear fit to the data is quite satisfactory and has been discussed for other EMs.<sup>4</sup>

In order to use the same  $1/X_d$  - pressure plane for damaged and granular PBXs, Hugoniot (and entering pressures) were calculated for the various porosities, using the methodology of Reference 6. Additionally, a two part attenuator was used in the case of the strained PBXW-108 samples. Thus, in the calculation of entering pressure for the strained samples, the calibration of the LSGT donor<sup>5</sup> had to be augmented to account for the 12.7 mm length of 76 mm diameter attenuator next to the sample. This was accomplished by using the data for unstrained PBXW-108 confined in the jig (see Table 1). A comparison of  $X_d$  values for unstrained samples in Table 1 and the  $1/X_d$  - pressure data of Figure 6 showed



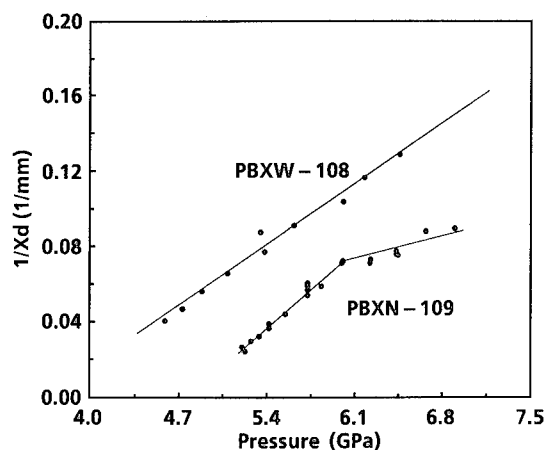


**FIGURE 6. DISTANCE TO DETONATION-PRESSURE DATA FOR CAST PBXW-108 AND PBXN-109**

that about 0.1 GPa had to be added to the entering pressure as calculated from impedance matching for PMMA lengths of 36 to 38 mm.

Consequently, the pressures for shot numbers's A74, A81, and A83 listed in Table 1 were calculated using a slightly shorter PMMA gap, an appropriate porous Hugoniot, and the impedance method. These data (from Table 1) are plotted in Figure 7, along with part of the data for cast and granular PBXW-108 samples. The data for strained samples are seen to lay to the left of the data for the cast samples, indicating, as expected, that the strained samples are more shock sensitive. Using the porosities of the strained samples from Table 1, it can be seen that for a given  $X_d$  value, a 1 % increase in porosity corresponds to about a 0.1 GPa decrease in pressure for porosities of 5% or less in PBXW-108. (It should be noted that it was the porous Hugoniot which produced most of the change in pressure from the cast data.) In Figure 7, a line has been drawn through the data for strained samples and parallel to the slope of the cast PBXW-108 data. This indicates that we expect the shock reactivity of the strained samples to approximate that of the cast samples.

The pressures in Figure 7 for porous samples (cubes) of PBXW-108 were calculated using the methodology of Erkman and Edwards and the linear Hugoniot for the cast material observed in the wedge test.<sup>11</sup> (That is, for the present, we have ignored the observation<sup>12</sup> that EMs containing RDX have two linear regions in the shock velocity-particle velocity Hugoniot

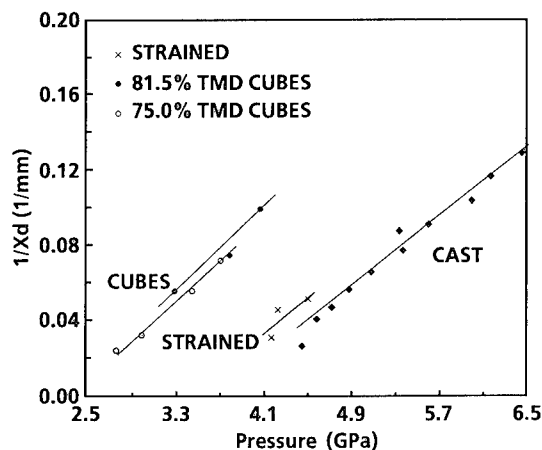


**FIGURE 7. DISTANCE TO DETONATION-PRESSURE DATA FOR CAST AND POROUS PBXW-108**

plane of cast and porous systems.) The  $X_d$  data for 75.0 %TMD samples in Figure 7 yield a linear relationship in this  $1/X_d$ -P plane, similar in slope to data for cast PBXW-108. Surprisingly, the data for the 81.5 %TMD samples, which show more scatter, appear to indicate that these samples are slightly more shock sensitive than the 75.0 %TMD samples. This is discussed below.

#### Shock Reactivity of Cast and Granular PBXN-109

Cast PBXN-109, as discussed in Reference 3, has two linear regions in the  $1/X_d$ -pressure plane when the pentolite/PMMA donor/attenuator arrangement (LSGT) is used; this is seen in Figure 6. When the same pentolite donor is used with bare cylinders of PBXN-109 in an aquarium arrangement, the lower pressure regime appears to be absent.<sup>3</sup> The presence of two linear regions may be associated, in part, with the radial pressure profiles provided by the 2-D shock loading of the pentolite/PMMA system.<sup>4</sup>

The distance to detonation data for the porous samples of PBXN-109 are shown in the  $1/X_d$ -pressure plane of Figure 8; some lower pressure data for cast PBXN-109 are also included. For the cubic granules of PBXN-109, the 75.0% TMD samples appear to be less sensitive than the 81.6% TMD samples; the same trend was observed for cubic granules of PBXW-108 and may be valid for the shreds of PBXN-109 as indicated by one datum. However, these sensitivity observations are currently attributed to a variety of factors, some experimental and some computational. For the latter, an

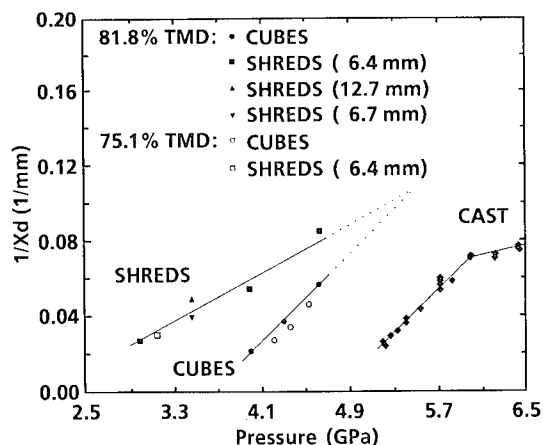


**FIGURE 8. DISTANCE TO DETONATION-PRESSURE DATA FOR CAST AND POROUS PBXN-109**

obvious one is the selection of a "correct" Hugoniot for the various densities. (The calculation of a Hugoniot for a porous, elastomeric material is state-of-the-art and subject to a fair amount of uncertainty.) Hence, it is assumed that the shock reactivity (slope in the  $1/X_d$ -P plane) and (relative) shock sensitivity (P at a given  $1/X_d$  value) data are very comparable for 75.0 and 81.6% TMD samples (both PBXW-108 and PBXN-109).

Figure 8 dramatically shows the difference between cubes and shreds of PBXN-109 in both shock reactivity and shock sensitivity. It is evident that there is a dramatic granule size/shape/surface-to-volume factor. Straight lines have been drawn through the 81.6% TMD data for both cubes and shreds in order to extrapolate beyond the experimental data base. One might expect, based upon these straight lines, the reactivities and sensitivities to become independent of the granule size/shape/surface-to-volume factor at the higher pressures. This interpretation has significant ramifications with respect to the understanding and development of hot spot models for porous, elastomeric materials.

For example, Bowman conducted numerical simulations of some of these 2-D shock initiation experiments for porous PBXW-108.<sup>13</sup> He found that disagreement between the predicted and experimental  $X_d$  values was so great as to suggest the observation of two different phenomena. We would like to think that the SC records for porous PBXN-109 in Figure 8 suggests that. Bowman used the Forest Fire model and a (pressure dependent) shock reaction rate relationship that has a hot

spot mechanism based upon that which drives shock initiation of cast (essentially TMD) material. However, at high porosities (75-80 %TMD), it is quite reasonable to expect that other hot spot mechanisms (plastic work, friction, etc.), not as important near TMD, to be operative. It seems quite appropriate to attribute the difference in shock reactivity and shock sensitivity between the PBXN-109 cubes and shreds to variations in importance of different hot spot processes in generating the reaction temperatures. Hence, the use of a model based upon the Forest Fire methodology is not applicable to the shock initiation of porous, elastomeric EMs. It is appreciated that the Forest Fire model has been successfully modeled the shock initiation of porous, neat explosives (e.g., PETN) or non-elastomeric (high modulus) explosives containing large fractions of crystalline materials (e.g., PBX 9404). However, the hot spot processes that dominate these explosives at high porosities are quite likely the same ones that occur at quite low porosities. Also, the grain sizes in PETN, PBX 9404, etc., were significantly smaller than granule sizes investigated here.

## CONCLUSIONS

In the  $1/X_d$ -P plane, it was determined that a 1% increase in porosity corresponds to about a 0.1 GPa decrease in pressure at a given  $X_d$  value for PBXW-108 at low porosities. For highly porous samples (75 and 82 %TMD) of PBXW-108 composed of cubic granules, the data show that the shock reactivity (slope in the  $1/X_d$ -P plane) is similar to that of the cast material but, of course, the shock sensitivity ( $1/X_d$  at a given pressure) is much higher. For PBXN-109, two types of granules were used to construct the very porous samples: cubes and shreds. Density variations (75 versus 82% TMD) had little influence on the shock reactivity and shock sensitivity for either the cubes or the shreds in the pressure region of 2.8 to 4.6 GPa. However, there was a distinct difference in shock reactivity and sensitivity between the samples containing cubes and the samples composed of shreds. However if the data for both types of granules are extrapolated to pressures greater than 5.7 GPa, the shock reactivity and sensitivity may become independent of the granules' size/shape.

These 2-D shock initiation experiments outline the change in shock reactivity and sensitivity of both cast and porous elastomeric plastic-bonded explosives. It has been proposed that the difference in shock reactivity and sensitivity seen for different sizes/shapes of granules represents the relative importance of multiple hot spot

processes occurring at the lower pressures.

## ACKNOWLEDGEMENTS

This research was funded by the Office of Naval Technology, Code 23 (now the Office of Naval Research, Code 23). The authors would like to thank Lewis C. Hudson III for reviewing this paper, Carl L. Groves for technical support (in all aspects) with these experiments and Brian C. Glancy for technical support during the compression testing.

## REFERENCES

1. Sandusky, H. W.; Bernecker, R. R.; and Clairmont, A. R., Jr., "Influence of Fresh Damage on the Shock Sensitivity of a High Energy Propellant," 1990 JANNAF Propulsion Systems Hazards Subcommittee Meeting, CPIA Publication 538, Vol. I, Apr 1990, pp. 335-348.
2. Sandusky, H. W. and Bernecker, R. R., "Influence of Fresh Damage on the Shock Sensitivity of Several Energetic Materials," paper presented at this Symposium.
3. Bernecker, R. R. and Clairmont, A. R., Jr., "Shock Initiation Studies of Cast Plastic-bonded Explosives," Combustion and Detonation Phenomena, 19th International Annual Conference of ICT 1988, Jun 1988, p. 41:1-14.
4. Bernecker, R. R.; Clairmont, A. R., Jr.; and Hudson, L. C., III, "Prompt and Delayed Detonation from Two-Dimensional Shock Loadings," paper presented at this Symposium.
5. Erkman, J. O.; Edwards, D. J.; Clairmont, A. R.; Jr.; and Price, D., *Calibration of the NOL Large Scale Gap Test; Hugoniot Data for Polymethyl Methacrylate*, NOL TR 73-15, Apr 1973, NOL, Silver Spring, MD.
6. Erkman, J. O. and Edwards, D. J., "Computed and Experimental Hugoniots for Unreacted Porous High Explosives," Proc. Sixth Symposium (International) on Detonation, ACR-221, U. S. Printing Office, Washington, D.C., 1976, p. 766.
7. Bernecker, R. R. and Clairmont, A. R., Jr., *Shock Initiation (2-D) Study of Some Porous Plastic-bonded Explosives: PBXW-108 and PBXN-109*, NSWC TR 93-80 (to be published), NSWC, Silver Spring, MD.
8. Bernecker, R. R. and Clairmont, A. R.; Jr., *Shock Initiation (2-D) Study of Two Cast, Elastomeric, Plastic-bonded Explosives: PBXW-108 and PBXN-109*, NSWC TR 93-82 (to be published), NSWC, Silver Spring, MD.
9. Zygmunt, B., "The Detonation Properties of Explosive-Water Mixtures," Propellants, Explos. Pyrotech, Vol 7, 1982, p. 107.
10. Bowman, A. L. and Fu, J. H. M., "Variation of Critical Diameter of Energetic Materials with Density," 1989 JANNAF Propulsion Systems Hazards Subcommittee Meeting, CPIA Publication 509, Vol. I, Feb 1989, pp. 105-112.
11. Ramsay, J. B., Los Alamos National Laboratory, private communication.
12. Bernecker, R. R., "The Calculation of Unreacted Hugoniots. I. TNT, RDX, and Their Mixtures," 1992 JANNAF Propulsion Systems Hazards Subcommittee Meeting, CPIA Publication 582, Vol. I, Apr 1992, pp. 285-302.
13. Bowman, A. L., Los Alamos National Laboratory, private communication.

## EFFECT OF A PRESOCK ON THE INITIATION OF HMX, TATB AND HMX/TATB COMPOSITIONS

J.P. Plotard, R. Belmas, M. Nicollet, M. Leroy

CEA-Centre d'Etudes de Vaujours - Moronvilliers  
BP n° 7 - 77181 Courtry - France

We use the results of an experimental and theoretical study to identify the microstructural origin of hot spots in pressed explosive compositions with inert binders. A numerical model is written to compute the initiation of the explosive by the viscoplastic collapse of the energetic material around the included pores. This model is used to analyse the initiation of HMX, TATB and HMX/TATB based compositions, and the possible desensitization of these compositions by a precursor shock.

### INTRODUCTION

In pressed explosive compositions, composed of grains of energetic material with a small amount of inert binder, the shock initiation is obtained by the interaction between the shock wave and the heterogeneities of the material. The energy carried by the shock is focused in points, called hot spots, and the explosive can be initiated.

These hot spots can be related to several heterogeneities: binder, porosity, gas in the pores. We performed an experimental study to determine the main source of hot spots in our explosive compositions. In this paper we present a summary of the experimental data which led to a numerical simulation of the shock initiation phenomena.

Then, the model is used to analyse the shock initiation of HMX, TATB, and HMX/TATB compositions, and the effect of a presock on the sensitivity of these compositions.

### HOT SPOTS: PHENOMENOLOGY EXPERIMENTS

In order to develop a hot spots model able to describe the shock initiation of explosive compositions, it is necessary to determine the physical origin of these points. Several heterogeneities have to be taken into account: porosity, binder,<sup>1,2</sup> and different mechanisms

can be invoked for hot spots formation, during pore collapse: hydrodynamic mechanism,<sup>3</sup> heating of trapped gases,<sup>4,5</sup> viscoplastic work in the explosive around the pores.<sup>6,7,8</sup>

The experimental study of these mechanisms is difficult, because the hot spots are very small, located in an opaque medium, and these phenomena involve high temperatures and pressures, short duration and decomposition of the material. Therefore, in order to overcome these difficulties, we performed comparative experiments to evaluate the relative importance of each mechanism regarding to the others. This experimental study was already published,<sup>9</sup> we just recall here the main results on which the assumptions of the model are based.

#### Relative Influence of Porosity and Binder

Experiments were performed on pressed TATB compositions and pure TATB samples pressed at different densities. In all cases, the same well characterized TATB powder was used.

Gap-Test: The experimental set-up is presented in figure 1. In addition to the go-no go results usually obtained by these experiments, we measure the run distance to detonation by observing the side of the sample with a streak camera. The experimental data are summarized in figures 2 and 3 for TATB samples with densities between 1.0 and 1.875, and a TATB

composition T2, which includes TATB powder, a few percent of binder and 2.3% of porosity. The removal of the binder from T2 leads to a 1.8 in density pure TATB sample.

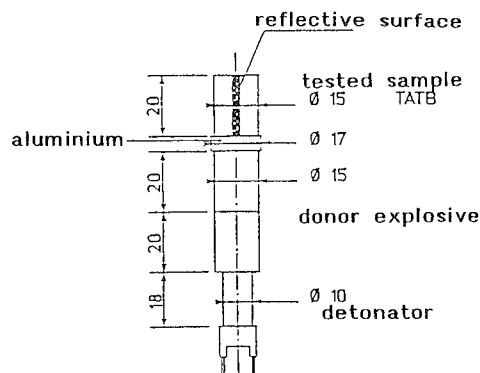


FIGURE 1. GAP TEST EXPERIMENTAL SET-UP

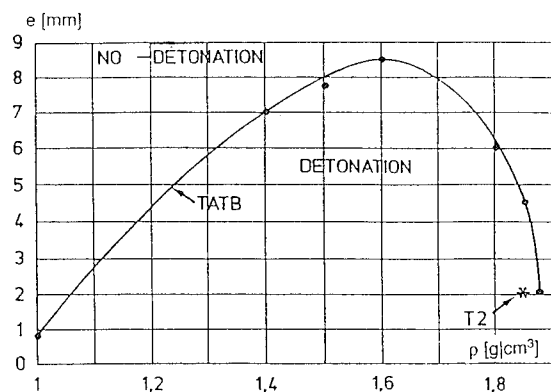


FIGURE 2. GAP-TEST DATA

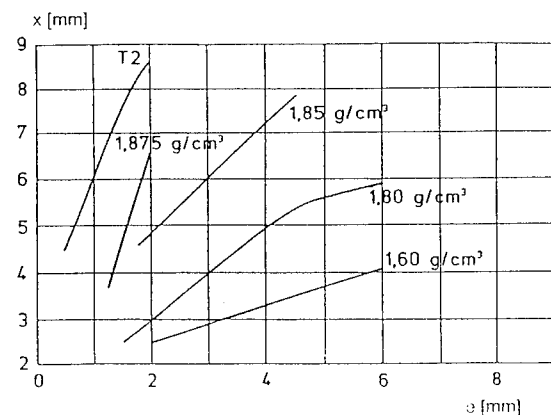


FIGURE 3. RUN DISTANCE TO DETONATION

The analysis of figures 2 and 3 shows that it is easier to initiate the powder without binder than the T2 composition. For the studied case, the binder has a negligible influence on the production of hot spots regarding to the influence of porosity.

Run distance to detonation: We performed wedge test experiments on three different TATB compositions based on the same explosive powder (table 1). The three binders have very different chemical and mechanical properties. We obtained the same results (figure 4) for T1 and T2, which have the same porosity, and the T3 composition, which has a lower porosity, is more difficult to initiate. These results confirm our previous conclusion on the weak influence of the binder on hot spots formation process.

TABLE 1. TATB COMPOSITIONS

Composition	TATB Powder	Binder	Porosity
T1	50 $\mu$ m	B1	2,6%
T2	50 $\mu$ m	B2	2,3%
T3	50 $\mu$ m	B3	1,4%

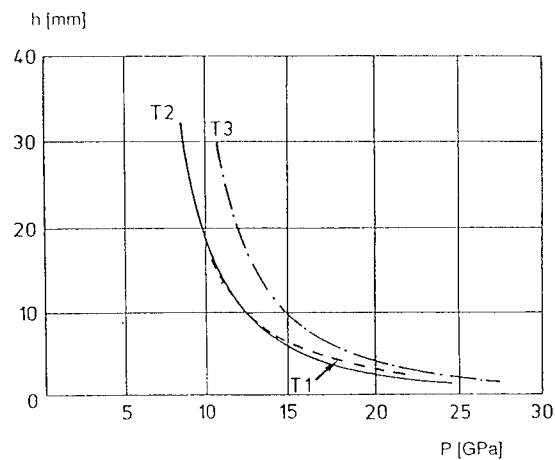
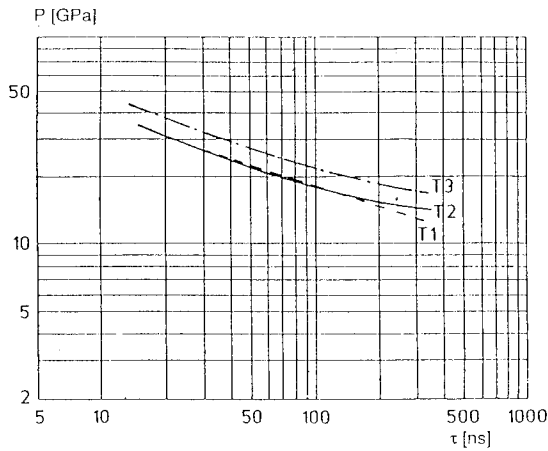


FIGURE 4. RUN DISTANCE TO DETONATION

Short duration shock initiation: The threshold curves (figure 5) obtained for T1, T2, and T3 lead to the same conclusion as before about the relative influence of binder and porosity.



**FIGURE 5. SHOCK SENSITIVITY TO SHORT DURATION SHOCK**

#### Effective Mechanism Governing Hot Spots Formation

We showed that in our pressed explosive compositions, the hot spots are created by the collapse of the pores. Some of the previously presented Gap-Test experiments, which were realised in the room atmosphere, were performed under vacuum. The same results, including the (x,t) diagrams, were obtained. Therefore the compression of the gas contained in the voids has no influence on the initiation of the explosive.

It is not so easy to have experimental data and make a choice between a hydrodynamic and a viscoplastic collapse of the voids. R.B. Frey<sup>8</sup> developed a non-dimensional analysis of this problem, his conclusion can be summarized as follows:

$$\text{if } N1 = \frac{a_o \frac{dP}{dt} \sqrt{\frac{\rho}{Y}}}{Y}$$

$$\text{and } N2 = \frac{a_o \sqrt{\rho P}}{\mu}$$

with  $a_o$  : initial pore radius (assumed spherical)  
 $P$  : pressure  
 $t$  : time  
 $Y$  : yield strength  
 $\rho$  : density  
 $\mu$  : viscosity

then, to have a hydrodynamic mechanism, the two quantities  $N1$  and  $N2$  must be greater than one.

In a shock wave,  $N1$  is always greater than one, but, as shown in figure 6, the criterion is not fulfilled by  $N2$  in our explosive compositions, in which the pores characteristic size lies between  $0.1 \mu\text{m}$  and  $1 \mu\text{m}$  and the viscosity, if not well known, can lie between  $100 \text{ Pa.s}$  and  $1000 \text{ Pa.s}$ , as proposed by several authors.<sup>6,10,11,12</sup>

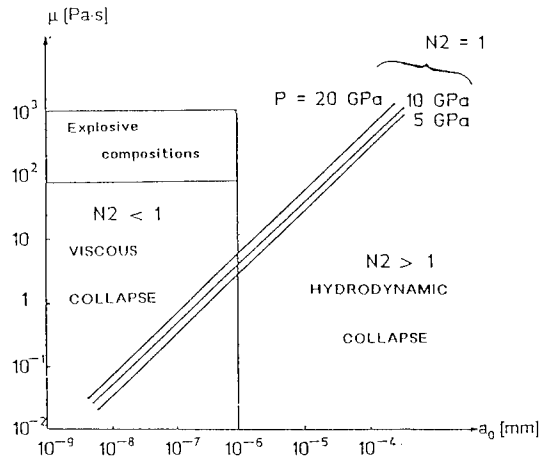


**FIGURE 6. ANALYSIS OF THE VISCOPLASTIC NATURE OF THE PORE COLLAPSE**

Therefore, this analysis, added to the experimental data, shows that in pressed explosive compositions, the hot spots formation process can be described by the viscoplastic collapse of the pores included in the material.

#### A HOT SPOTS FORMATION AND IGNITION MODEL

##### The Model

The pores are described as hollow spheres. The comparison of the two typical times, one for the viscous collapse  $\tau_c = \frac{4\mu}{P} \geq 10^{-7} \text{ s}$ , the other for the shock crossing through the pore

$$\tau_s = \frac{2a}{U} \leq 10^{-9} \text{ s}, \text{ shows that, at the beginning of the}$$

pore collapse, all the thermomechanical quantities are uniform all around the void. Therefore the implosion is spherical and the initial values of pressure, density, and temperature are those induced by the shock in the medium surrounding the pore.

A program was written in order to compute the heating of the explosive around the collapsing void, and its time to ignition. Based on the same assumptions and equations than other published models,<sup>6,7,8</sup> it calculates the evolution of a viscoplastic-heat-conducting-incompressible energetic material. The equations are:

$$r^3 - a^3 = r_o^3 - a_o^3$$

$$\rho \ddot{r} = \frac{\delta \sigma_r}{\delta r} - 12\mu \frac{\dot{r}}{r^2} + \frac{2Y}{r}$$

$$\rho C p \frac{\delta T}{\delta t} = \dot{C} + \dot{Q} + \dot{W}$$

in which

- $a_o$  initial pore radius
- $\mu$  viscosity
- $Y$  Yield strength
- $C$  Thermal conduction
- $Q$  Heat released by chemical reactions
- $W$  Heat created by the viscoplastic work

Therefore:

$$\dot{W} = 2Y \frac{\dot{r}}{r} + 12\mu \left( \frac{\dot{r}}{r} \right)^2$$

$$\dot{Q} = RZQ \exp(-E/RT)$$

$$\dot{C} = \lambda \left[ \frac{\delta T}{\delta r^2} + \frac{2\delta T}{r \delta r} \right]$$

All the parameters of these equations have a physical meaning, and can be known with a good accuracy but the viscosity. This last parameter can be calibrated by using the hot spots model together with pressure history curves measured with embedded manganin gauges in shocked explosive samples.

#### Determination of the Viscosity

The experimental set-up is presented in figure 7. The velocity of the projectile is chosen in order to have the needed shock pressure in the explosive. The pressure versus time curves are measured in the shocked explosive sample (figure 8). If the shock pressure is not too high (in the shown example, 9 GPa in the TATB composition T2), the curve presents two parts: a plateau followed by an increase of the pressure. The physical meaning of these two parts may be: the initiation of the hot spots followed by an increase of the pressure generated by the decomposition energy release.

The extrapolation, up to the zero depth, of the curve which represents the duration of the plateau as a function of the depth of measurement, gives the value of the initiation time of the hot spots for the

given pressure. This ignition time was determined for several shock pressures. The comparison of these experimental values with those obtained with the numerical model leads to a given value of the viscosity.

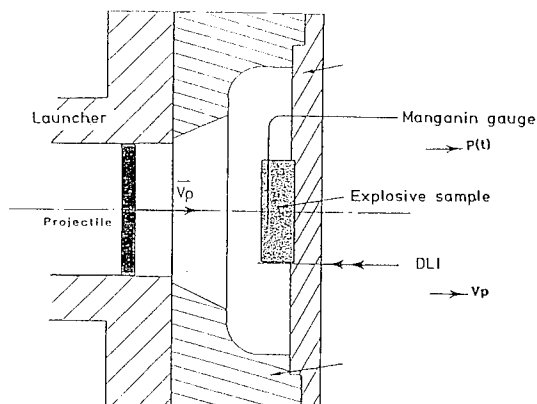


FIGURE 7. PRESSURE VS. TIME MEASUREMENT SET UP

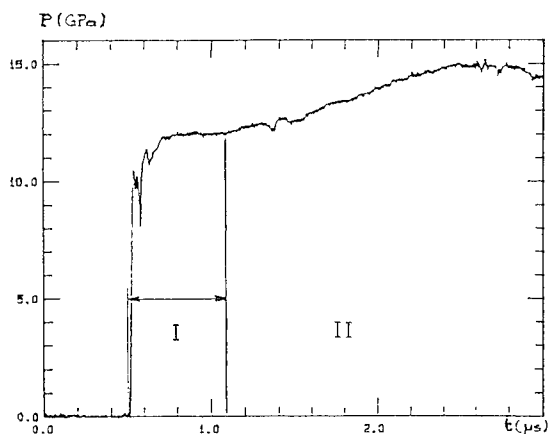


FIGURE 8. TYPICAL PRESSURE VS. TIME CURVE

But the so calibrated model is not able to simulate other experiments, like double-shocks impact. In fact, the duration of the first plateau is not only the ignition time of the hot spots, it includes also the time required to obtain a sufficient amount of gases which leads to a pressure increase in the explosive.

With the same experimental set-up it is possible to determine the threshold of shock initiation. Using the hot spots model with a given viscosity, it appears that,

the larger the pore, the easier the initiation (figure 9). Therefore, for a given shock pressure, the initiation time of the composition is the initiation time of the largest voids. The smaller pores, if initiated by the shock, modify the energy release history behind the shock, but have no influence on the first reactions initiation. The model used with the largest voids diameter and the good value of the viscosity will reproduce these threshold values.

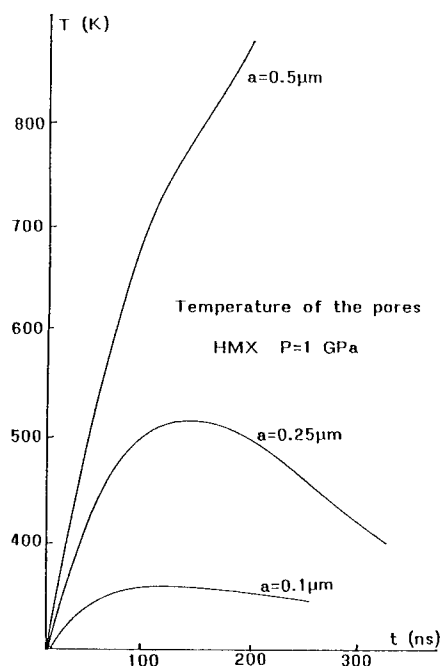


FIGURE 9. TEMPERATURE VS. TIME IN THE MEDIUM AROUND VOIDS OF SEVERAL INITIAL RADII

#### APPLICATION TO HMX, TATB, AND HMX/TATB COMPOSITIONS

The results obtained on three explosives compositions, X1, T2 and TX1 (defined in table 2) will be presented. From the pressure measurement reported in figures 10 and 11, the threshold pressure for X1 and T2 are respectively 1 and 4 GPa. The viscosity of HMX and TATB may be deduced from these values and the viscosity of the TATB is about five times the HMX one.

For the TX1 composition, the experimental threshold pressure is 2.5 GPa (figure 12). At this pressure the TATB is not initiated by the shock wave, and the composition is ignited by the HMX. The hot spots model, calibrated for the X1 composition with 1  $\mu\text{m}$  in

diameter pores, predicts the 2.5 GPa value for the threshold pressure of TX1 in which the larger pores are only 0.4  $\mu\text{m}$  in diameter (figure 13).

TABLE 2. EXPLOSIVES MICROSTRUCTURE

Composition	X1	T2	TX1
HMX wt % grain size	96 0-600	0	45 0-100
TATB wt % grain size ( $\mu\text{m}$ )	0	97 50-60	52 50-60
inert binder wt %	4	3	3
porosity and pores radii ( $\mu\text{m}$ )	1.7% $a_0 \leq 0.5$	2.3% $a_0 \leq 0.5$	0.5% intergranular $a_0 \leq 0.2$ 1.5% in the TATB $a_0 \leq 0.5$

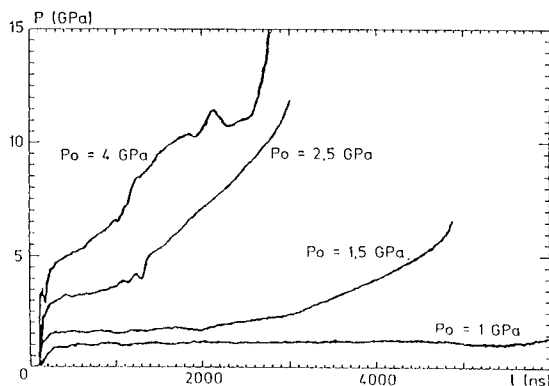


FIGURE 10. PRESSURE VS. TIME IN X1 COMPOSITION FOR SEVERAL INPUT PRESSURES

#### DOUBLE SHOCKS ON HMX, TATB, AND HMX/TATB COMPOSITIONS

If an explosive sample is subjected to a low pressure shock, the pores collapse and are not initiated. The pore collapse duration is a function of shock pressure, pore diameter and material viscosity.

If the explosive is subjected to a second shock (figure 14) of a higher pressure, even higher than the threshold pressure previously determined, it can be not initiated. This desensitization phenomenon depends on



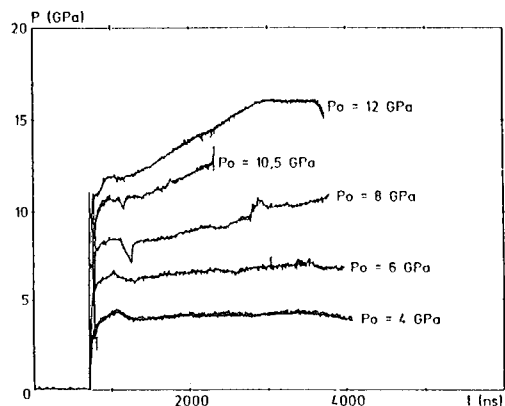


FIGURE 11. PRESSURE VS. TIME IN T2 COMPOSITION FOR SEVERAL INPUT PRESSURES

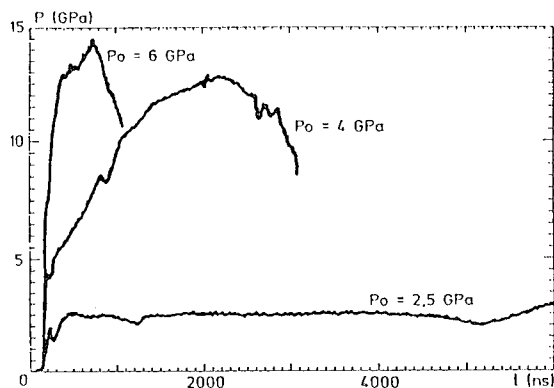


FIGURE 12. PRESSURE VS. TIME IN TX1 COMPOSITION FOR SEVERAL INPUT PRESSURES

first shock pressure and duration, and second shock pressure.

By example, for X1 composition, if  $P_1=0.5$  GPa and  $P_2=1.4$  GPa, computations with the hot spots model show that for  $\tau > 0.2 \mu s$ , the explosive is desensitized. This numerical value is in good agreement with experimental results (figure 15).

A TATB composition is more difficult to desensitize, because of its higher viscosity. But, as shown in figure 16, the same phenomenon can be obtained.

For a HMX/TATB composition, the initiation process is more complex. Experimental results are presented in figure 17. In this example,  $P_1=1.6$  GPa, lower than the initiation threshold pressure of the composition. At this shock pressure the pores directly connected with the HMX ( $a_0=0.2 \mu m$ ) are rapidly closed and none hot spots will be created in the HMX

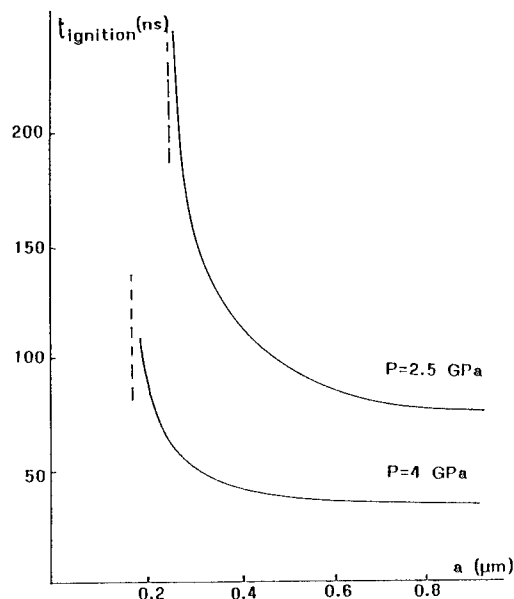


FIGURE 13. INITIATION TIME OF INTER-GRANULAR HOT SPOTS

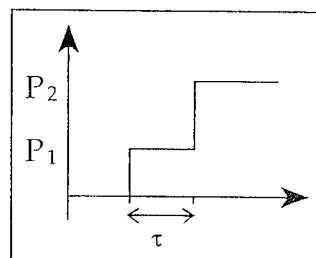


FIGURE 14. TYPICAL DOUBLE-SHOCK PROFILE

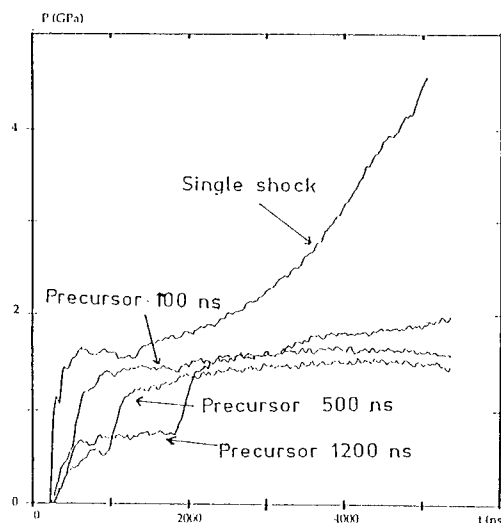


FIGURE 15. PRESSURE VS. TIME IN X1 SUBJECTED TO DOUBLE SHOCKS

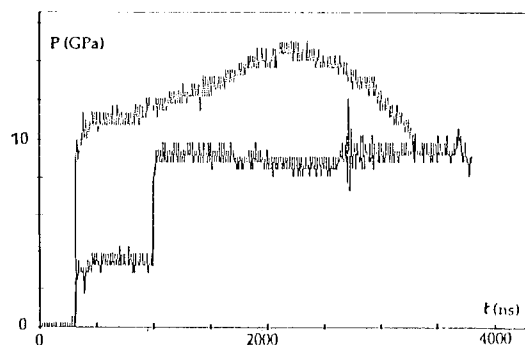


FIGURE 16. PRESSURE VS. TIME IN T2 COMPOSITION SUBJECTED TO DOUBLE SHOCKS

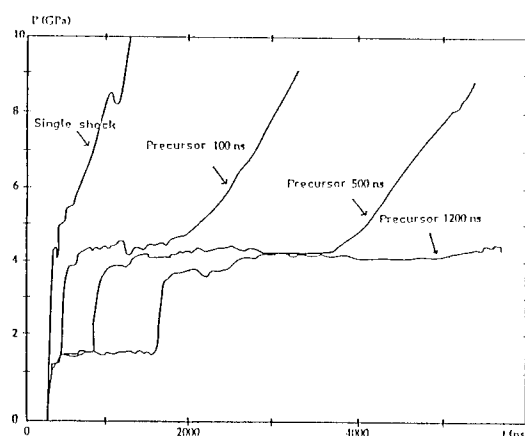


FIGURE 17. PRESSURE VS. TIME IN TX1 COMPOSITION SUBJECTED TO DOUBLE SHOCKS

by the  $P_2=4$  GPa shock. The TATB powder is the same than the one used in T2, with  $1\text{ }\mu\text{m}$  in diameter pores. As the TATB viscosity is greater than the HMX one, a longer time is required to get the closure of the pores. Therefore, if the duration of the precursor shock is less than 500 ns, the 4 GPa shock induced a heating of the TATB around the voids ( $800^\circ\text{C}$ ). The TATB can't be initiated, but by conduction of the thermal energy to an adjoining HMX grain, the TX1 composition is initiated.

As for a single shock, the initiation of the explosive composition is obtained by the initiation of the HMX, but this process requires a long time, governed by heat conduction. If the duration of the first shock is greater than 500 ns, TATB pores are also closed

enough to be desensitized.

## CONCLUSION

An experimental study and an analytical analysis showed that the viscoplastic pore collapse is the main process leading to the formation and ignition of the hot spots in our pressed explosive compositions. The hot spots model written with this assumption, and in which the microstructure of the explosive composition is introduced, is able to describe the initiation of HMX, TATB and HMX/TATB compositions, subjected to a single shock or to double shocks.

The desensitization of the explosive by a precursor shock can be quantified, and the delayed initiation of the TX1 composition subjected to such a solicitation may be explained by two kinds of porosity (in and between the grains) connected to each component.

This model calculates the initiation of the explosive. Associated with a grain burning model it will lead to a new kinetics able to compute the shock-to-detonation-transition in the heterogeneous explosives.<sup>13</sup>

## REFERENCES

1. E.H. Walker, "Derivation of the  $P^2t$  detonation criterion," 8th Symposium (International) on Detonation, Albuquerque (1985).
2. R. Belmas, "Amorçage d'une composition explosive par sollicitations mécaniques rapides," 3<sup>ème</sup> congrès de Pyrotechnie Spatiale, Juan-Les-Pins (1987).
3. C.L. Mader, J.D. Kershner, "The three dimensional hot spot model applied to PETN, HMX, TATB and NQ," LA-10203-MX UC-45 (September 1984).
4. Y. Partom, "A void collapse model for shock initiation," 7th Symposium (International) on Detonation, Annapolis (1981).
5. R. Belmas, Private communication.
6. B.A. Khasainov, A.A. Borisov, B.S. Ermolayev, "Shock wave predetonation processes in porous high explosives," 8th Symposium (International) on Detonation, Albuquerque (1985).
7. D.E. Maiden, "A hot spot model for calculating the threshold for shock initiation of pyrotechnics and explosives," 3<sup>ème</sup> congrès de Pyrotechnie Spatiale, Juan-Les-Pins (1987).

8. R.B. Frey, "Cavity collapse in energetic materials," 8th Symposium (International) on Detonation, Albuquerque (1985).
9. C. Castille, E. Germain, R. Belmas, "Origine physique des points chauds dans les compositions explosives pressées au TATB," Propellants, Explosives, Pyrotechnics 17,249-253 (1992).
10. J. Wakerle, J.O. Johnson, P.M. Halleck, "Shock initiation of high density PETN," 6th Symposium (International) on Detonation, Office of Naval Research, ACR-211, Arlington, VA (1970).
11. P.M. Halleck, J. Wackerle, Dynamic elastic-plastic properties of single crystal pentaerythritol tetranitrate," Journal of Applied Physics, vol. 47, n°3,(1976)
12. M.R. Baer, "Numerical studies of dynamic compaction of inert and energetic granular materials," Journal of Applied Mechanics 36, vol. 55 (1988).
13. R. Belmas, J.P. Plotard, C. Bianchi, "A physical model of shock to detonation transition in heterogeneous explosives," Paper presented at this Symposium.

---

## DISCUSSION

HAROLD J. GRYTING

Energetics Science Company, San Antonio, Texas

Was vacuum thermal stability determined before and after the shock damaged the explosives? If so, did it show changes in gas evolution? I like your explanations of the affect of a previous shock on shock sensitivity.

## REPLY BY J.P. PLOTARD:

No, we have not. Moreover, we showed that the duration of the first shock has an influence on the sensitivity of the explosive composition. We also know that a release of the sample modifies its sensitivity. Therefore a study of shocked samples may not be representative of the real state of the explosive when subjected to the second shock.

## NUMERICAL MODELING OF AN AQUARIUM TEST FOR A NONIDEAL EXPLOSIVE

Jaimin Lee, Jeong H. Kuk and Kyung Y. Choi

Agency for Defense Development  
Taejon, Korea

Fred W. Sandstrom  
Research Center for Energetic Materials  
Socorro, NM 87801, USA

An aquarium test of an ammonium nitrate-based emulsion explosive, a nonideal explosive, was numerically modeled by using a two-dimensional Lagrangian hydrodynamic code with a reaction rate. This reaction rate was determined from two-dimensional steady-state experiments by applying the detonation shock dynamics theory. The hydrodynamic calculation reproduced the experimental shock-front and bubble interface position in water. This agreement between the calculation and the experimental observation showed that the reaction rate faithfully modeled the nonideal detonation behavior.

### INTRODUCTION

For most military explosives (single-molecular explosives and their mixture), reaction rate is usually fast and sensitive to changes in thermodynamic state (pressure, temperature, etc.). As a result, they undergo shock-to-detonation transition (SDT) promptly over a wide range of input pressure. For a typical size of explosive piece ( $\sim 25$  mm), high order detonation consumes most of the explosive and reaction-rate effects on the propagation of the detonation wave can be mostly ignored. The simple rate-independent Chapman-Jouguet (CJ) theory can be used to model these explosives. These explosives are called ideal explosives.

For industrial explosives which are mostly composites of fuel and oxidizer(s), reaction rate is usually slow and relatively insensitive to the thermodynamic state. As a result, they undergo SDT gradually. For these explosives, the reaction-zone lengths ( $\sim 10$  mm) are a couple of orders of magnitude longer than they are in ideal explosives ( $\sim 0.25$  mm) and consequently, rate effects influence the detonation behavior of very large explosive pieces. These explo-

sives are often referred to as nonideal explosives owing to the fact that the CJ theory cannot be used to describe detonation in these explosives even in large samples.

For a nonideal explosive, the detonation velocity at a fixed diameter is much lower than the velocity at infinite diameter. This is mainly because that a significant fraction of explosive material remains unreacted at the sonic point, which is caused by weak state dependence of its reaction rate. Thus, the equation of state parameters calculated theoretically by using thermo/chemical equilibrium codes such as the BKW<sup>1</sup> or the TIGER code<sup>2</sup> which assume complete reaction at the sonic point (based on the CJ theory) cannot be used in modeling applications involving the nonideal explosives. Craig, Johnson, Mader and Lederman<sup>3</sup> first used the aquarium technique to measure and model the performance of nonideal explosives (water-gel and ANFO). The main idea was to obtain the equation of state parameters which could compensate the lack of reaction-rate information. The equation of state parameters are obtained from a thermo/chemical equilibrium code by adjusting the assumed heat-release rate to match the experimental data from an aquarium

test. This numerical-modeling technique, developed by Craig et al., involves heavy use of a thermo/chemical equilibrium code and a two-dimensional hydrodynamic code. This modeling technique is time consuming and its results can be applied only to a limited number of applications of which configurations are similar to that of the aquarium test. These shortcomings are due to the lack of reaction rates for nonideal explosives.

Lee<sup>4</sup>, and Lee, Persson and Bdzil<sup>5</sup> calibrated a reaction rate for an ammonium nitrate-based emulsion explosive, a nonideal explosive, by applying the detonation shock dynamics theory.<sup>6</sup> They first obtained a relationship between the detonation velocity normal to the detonation front ( $D_n$ ) and the front curvature ( $\kappa$ ) from experimental diameter-effect curve and detonation-front loci. Using the experimentally determined  $D_n(\kappa)$  and requiring that the eigenvalue condition (or the generalized CJ condition) be satisfied, they obtained the following reaction rate:

$$\frac{d\lambda}{dt} = 20.0 (1 - \lambda)^{1.89} \exp(-8.31 / \sqrt{P/\rho^{0.842}}) \quad (1)$$

where  $t$  is the time in  $\mu s$ ,  $P$  the pressure in GPa,  $\rho$  the density in  $g/cm^3$ , and  $\lambda$  the reaction extent, value of which varies from 0 for unreacted explosive material to 1 for completely reacted detonation products. Lee showed that the reaction rate, Equation (1), was very slow and insensitive to thermodynamic state. Using Equation (1), Lee<sup>4</sup> numerically modeled one-dimensional initiation tests (wedge tests), performed by Sandstrom<sup>7</sup> for a wide range of initial pressures. The calculated results agreed very well to the experimental observation, as shown in Figure 1.

Since the wedge test data carry information only about the early stage of the reaction behavior, the agreement between the predicted results and the experimental observation does not necessarily guarantee that the above reaction rate equation. A long-time rate behavior of Equation (1) also has to be tested.

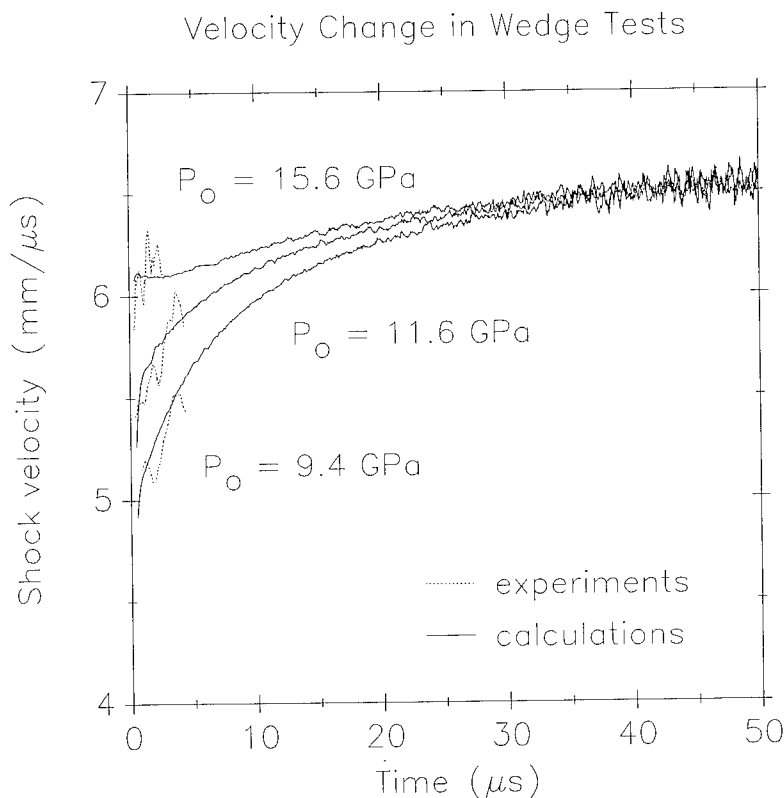


FIGURE 1. THE SHOCK VELOCITY CHANGES IN WEDGE TESTS. THE SOLID LINES REPRESENT RESULTS OF HYDRODYNAMIC CALCULATIONS BY USING EQUATION (1) AND DOTTED LINES EXPERIMENTAL RESULTS OBTAINED BY SANDSTROM<sup>7</sup>

In this paper, the reaction rate, Equation (1), for the AN-based emulsion explosive will be used to model an aquarium test for the same explosive. The successful reproduction of the aquarium test results will confirm that the above rate equation describes the non-ideal detonation behavior correctly.

## EXPERIMENTAL TECHNIQUES

Composition of the emulsion matrix is given by AN 77/water 16/mineral oil 6/emulsifier 1 in wt %, and its density is 1.353 g/cm<sup>3</sup> at 25°C. The emulsion matrix was mixed with 1 wt% of microballoons, C15/250 Glass Bubbles manufactured by 3M, St. Paul, MN, so that the density of the resulting explosive lowered down to 1.25 g/cm<sup>3</sup>. A 52.5 mm diameter and 610 mm length explosive charge confined in a PVC pipe with wall thickness of 3.9 mm was submerged in a large transparent water tank (aquarium). Experimental configuration is shown in Figure 2.

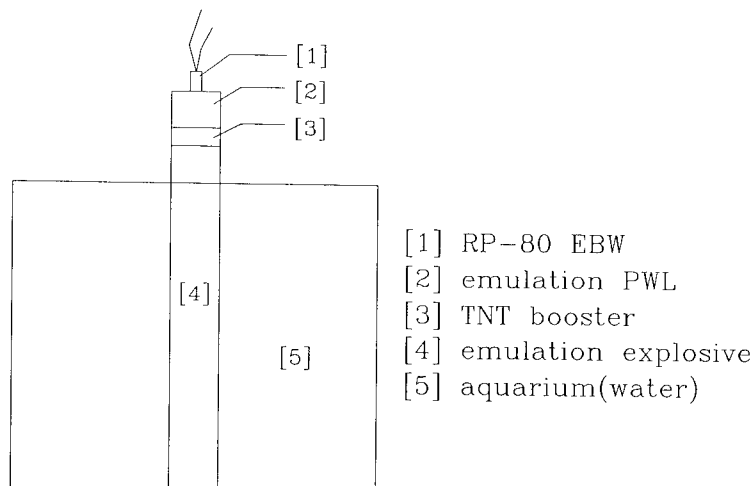
This charge was initiated from the top by using a 20 mm thick TNT booster and a plane-wave Lens. The aquarium was illuminated by a 150 W photoflood bulb, and the light was collimated by using a fresnel lens. At 90 and 115  $\mu$ s after initiation, the positions of the shock-wave front and the interface between the confining cylinder and water (bubble interface) were recorded with an image intensifier camera.

## CALCULATIONAL TECHNIQUES

The HOM equation of state<sup>8</sup> used in this modeling employs the Mie-Grüneisen equation of state with a shock Hugoniot as a reference for a solid phase and  $\beta$  equation of state with an isentrope passing through the CJ point as a reference for a gas phase. For a mixed phase such as a reacting explosive, two equations of state are mixed ideally.

Sandstrom<sup>7</sup> determined the shock Hugoniot of the emulsion explosive from a series of wedge tests:

### EXPERIMENTAL SETUP



inside diameter	length	wall thickness	aquarium	
			height	width
52.5	610	3.9	508	508

FIGURE 2. EXPERIMENTAL SETUP FOR THE AQUARIUM TEST

$$D = 2.036 + 1.923u \quad (2)$$

where  $D$  and  $u$  are detonation velocity and particle velocity in mm/ $\mu$ s, respectively. The heat capacity at constant pressure and the linear thermal expansion coefficient were measured to be 0.48 cal/g/K and  $5.6 \times 10^{-4}$  1/K. The Grüneisen parameter at ambient condition  $\Gamma_o$  was determined to be 1.626.

The state off the Hugoniot was calculated by using the Mie-Grüneisen equation of state, as is:

$$P_s - P_H = \frac{\Gamma}{v_s}(E_s - E_H) \quad (3)$$

where  $v$  and  $E$  are specific volume and specific internal energy, respectively. The subscript  $H$  refers to a property on the Hugoniot and the subscript  $s$  does a property of the unreacted solid explosive. The value of  $\Gamma/v$  was assumed to be the same with that of  $\Gamma_o/v_o$ .<sup>9</sup>

The equation of state for reaction products was determined by the following way. The internal energy of formation at zero K of the unreacted explosive was adjusted so that the calculated detonation velocity by

the BKW code was equal to the value (6.788 mm/ $\mu$ s) determined from the  $D_n(\kappa)$  function. The isentrope passing through the CJ point was calculated by using the BKW code. This isentrope was used as a reference line for the  $\beta$  equation of state, which is given by

$$P_g - P_R = \frac{1}{\beta v_g}(E_g - E_R) \quad (4)$$

where the subscript  $R$  denotes a property on the isentrope and the subscript  $g$  does a property of the reaction products. The value of  $\beta [= (\partial E_g / \partial P_g)_v / v_g]$  was determined on the isentrope.

For a reacting explosive, the internal energy and the volume were obtained by mixing those for the solid phase and the gas phase, assuming that the temperature and pressure of both phases were in equilibrium, respectively.

Calculational configuration for the aquarium test is shown in Figure 3. The size of the whole setup was set to  $\Phi 180 \times L330$  mm in axisymmetric cylindrical geometry. The TNT booster (26 mm in ra-

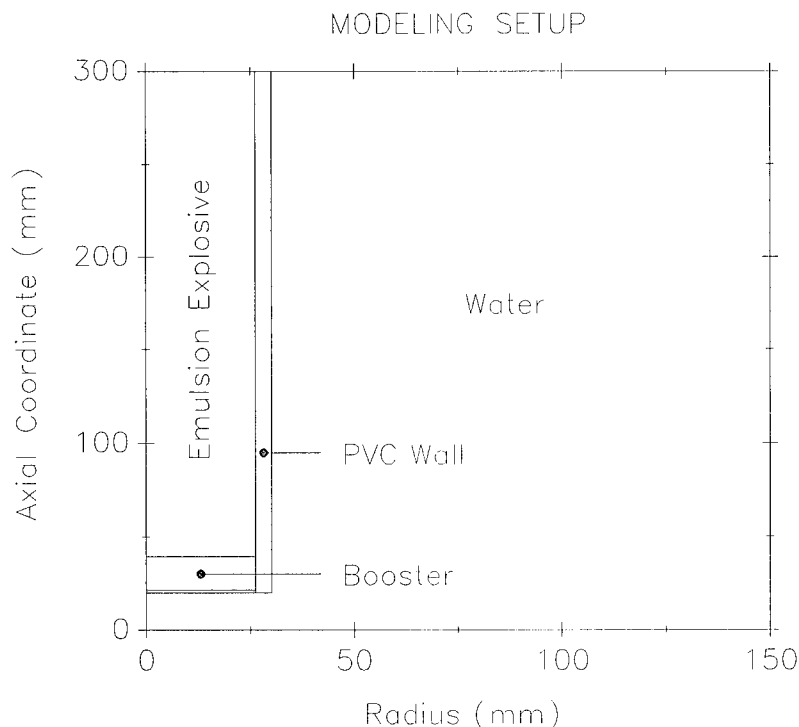


FIGURE 3. CALCULATIONAL SETUP FOR THE AQUARIUM TEST

dius and 19.5 mm in length) was divided into  $15 \times 13$  cells. The first row of the TNT cells was used as a hot spot. The rest of the TNT cells were burnt by using the CJ-volume burn technique.<sup>8</sup> The emulsion explosive (26 mm in radius and 300 mm in length) was divided into  $15 \times 200$  cells. These emulsion cells were burnt by using the reaction rate defined by Equation (1). The time step was set to  $0.05 \mu\text{s}$  so that it took about six time cycles for the detonation wave to pass through an emulsion cell. Lee<sup>4</sup> estimated the distance from the detonation front to sonic point was estimated to be 12 mm. Considering the compression of a cell behind the detonation front, this distance corresponded to about 11 cells in the present modeling. Approximately 60% of chemical energy was estimated to be released in this region. The confining PVC cylinder (3.9 mm in thickness and 300 mm in length) was divided into  $3 \times 200$  cells. The surrounding water (150 mm in thickness and 330 mm in length) was divided into  $75 \times 220$  cells. Ten mm thickness water layer was inserted under the booster in order to avoid distortion of booster cells.

## RESULTS AND DISCUSSIONS

The experimental record is shown in Figure 4. A Lagrangian hydrodynamic calculation was made by using the sharp-shock burn technique<sup>8</sup>, a programmed-burn technique, which is widely applied to steady-state detonation for ideal explosives. By assuming that the detonation velocity was  $4.94 \text{ mm}/\mu\text{s}$  and that no further reaction occurred, the equation of state parameters for detonation products of the emulsion explosive were calculated by the BKW code. In this case, 55% of AN was assumed to remain unreacted at the sonic point. By using these equation of state parameters, the positions of the shock front and the bubble interface were calculated by using the TDL code. The results are shown in Figure 5. The calculated positions of the shock front and the bubble interface were much off the experimental observation. This discrepancy between the calculated results and the experimental observation suggested that further reaction behind the sonic point should be taken into account in the calculation. It also clearly demonstrated that a

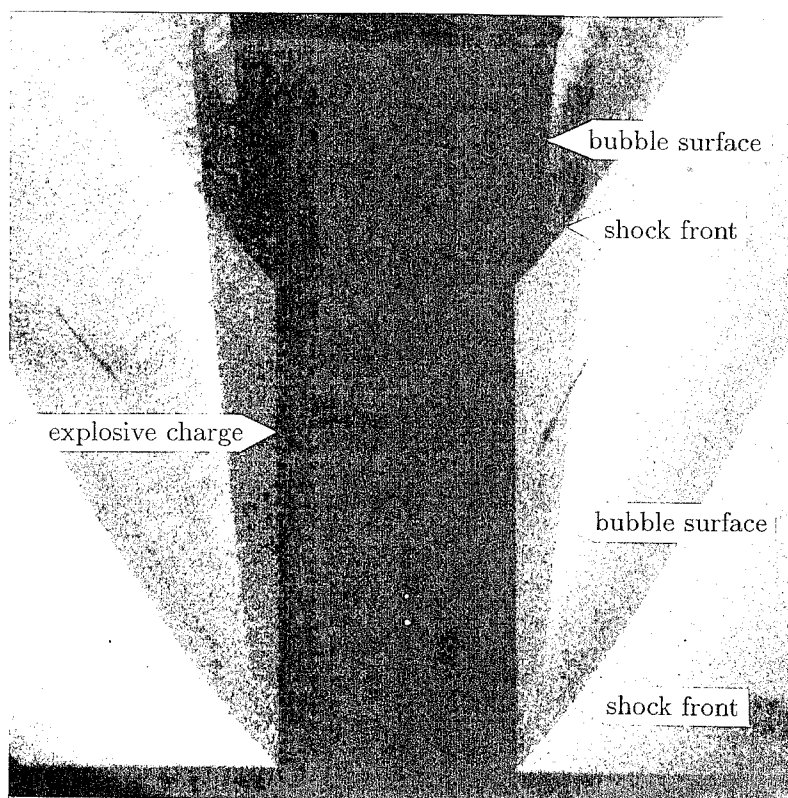


FIGURE 4. EXPERIMENTAL RECORD FOR THE AQUARIUM TEST



programmed-burn technique used widely for ideal explosives cannot be applied to a nonideal explosive.

Another hydrodynamic calculation was made by using the reaction rate, Equation (1). The results of this calculation are shown in Figure 6. The calculated shock position agreed well to the experimental observation, although slightly surpassed. The bubble interface position also showed the same trend except that the agreement between the calculated position and the experimental observation was slightly worse than that for shock-front position. The difference between the calculated results and the experimental observation suggested that slightly more energy was released in the hydrodynamic calculation than that in the aquarium test.

The detonation velocity determined from the front positions in the above hydrodynamic calculation was about  $5.3 \text{ mm}/\mu\text{s}$ , which agreed very well to the value obtained from rate-stick experiments ( $5.26 \text{ mm}/\mu\text{s}$ ). From the distance between two exposures of the deto-

nation front, the detonation velocity was determined to be  $4.94 \text{ mm}/\mu\text{s}$ . This low experimental velocity was believed to be resulted from density increase due to aging. The slightly high detonation velocity obtained in the hydrodynamic calculation ( $5.3 \text{ mm}/\mu\text{s}$ ), compared with the experimental velocity ( $4.94 \text{ mm}/\mu\text{s}$ ), explained the discrepancy between the calculated results and the experimental observation. The equation of state for the detonation products was believed to be partly responsible for the discrepancy in the bubble interface position.

The good agreement between the hydrodynamic calculation and experimental observation showed that the reaction rate, although determined from two-dimensional steady-state experiments which carried information only about reaction rate before the sonic point, faithfully modeled the rate after the sonic point. This agreement also demonstrated that the reaction-rate characteristics after the sonic point might not be much different from that before the sonic point.

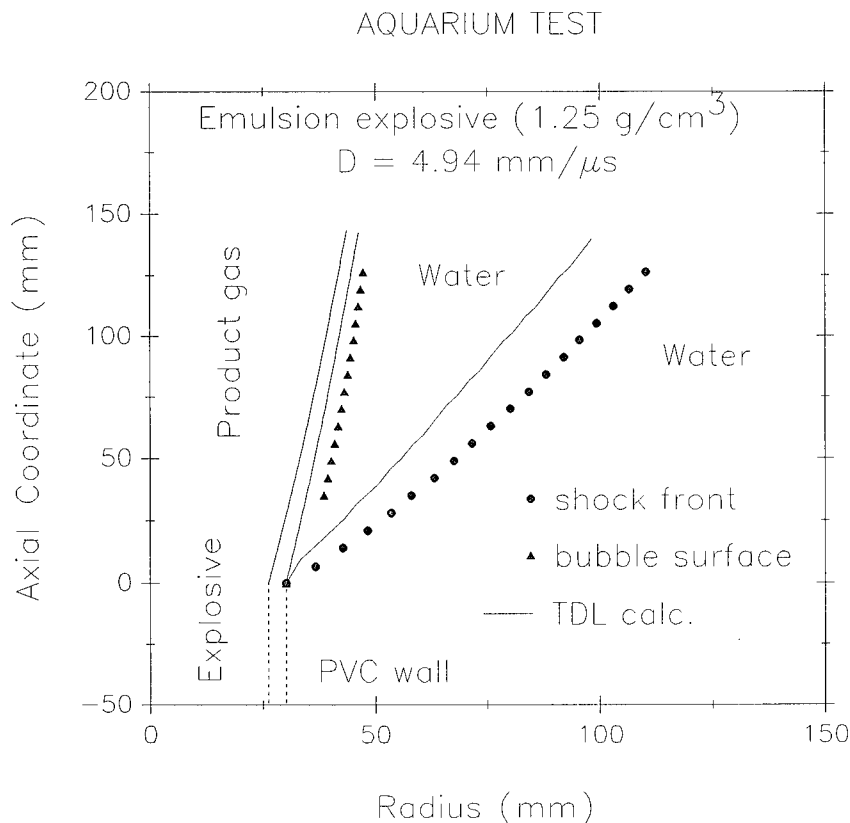


**FIGURE 5. RESULTS OF THE HYDRODYNAMIC CALCULATION BY USING THE SHARP-SHOCK BURN TECHNIQUE**

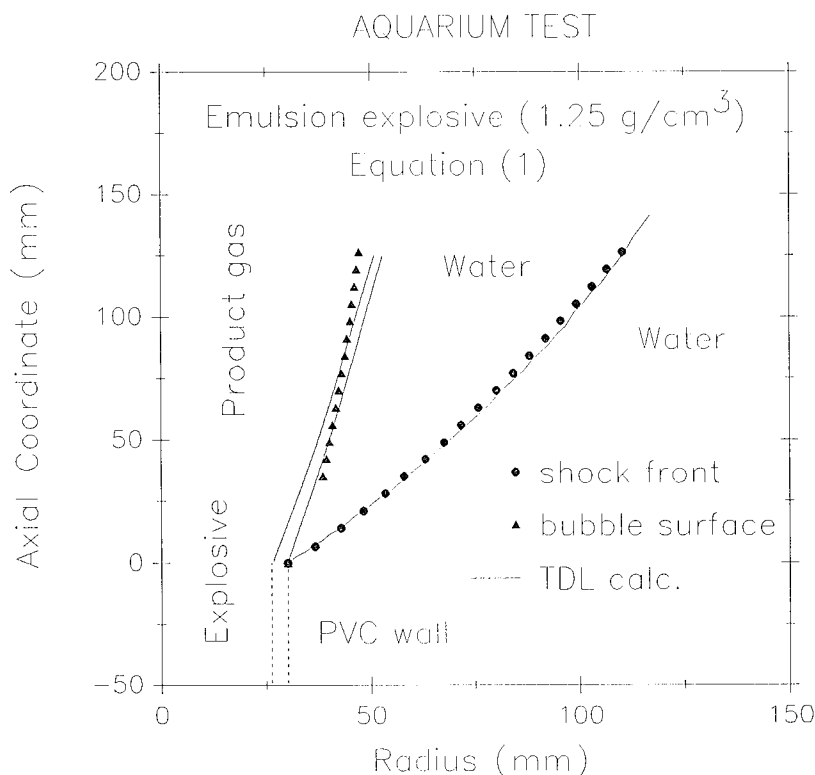


FIGURE 6. RESULTS OF THE HYDRODYNAMIC CALCULATION BY USING EQUATION (1)

## CONCLUSION

Nonideal explosives are used in a growing number of applications. Their reaction rate is slow and weakly state dependent. A significant amount of chemical energy is released behind the sonic point. Since the nonideal detonation behavior cannot be described by a simple detonation theory, it has been very difficult to model an application involving a nonideal explosive. A numerical modeling technique by using aquarium test results has been developed to model the nonideal detonation behavior. This technique is very time consuming and its results can be applied in a limited number of applications.

In this study, an aquarium test of a nonideal emulsion explosive was numerically modeled by using a rate equation obtained from two-dimensional steady-state experiments by applying the detonation shock dynamics theory. The results of this hydrodynamic calculation

agreed well to the experimental observation. This agreement suggested that the nonideal detonation behavior could be modeled by the reaction rate, Equation (1), although obtained from steady-state experiment data which carried only the information about energy release before the sonic point.

## ACKNOWLEDGEMENTS

We are deeply grateful to the Research Center for Energetic Materials (RCEM), Socorro, NM, USA for supporting the experimental work and the Agency for Defense Development (ADD), Taejon, Korea, for supporting the modeling work. One of the authors (J. Lee) expresses his thanks to Dr. Per-Anders Persson, Director of the RCEM, for guiding him through his study, Dr. J.B. Bdzil of Los Alamos National Laboratory, and W.C. Davis of Energetic Dynamics, for their teaching through numerous discussions.

## REFERENCES

1. Mader, C.L., *FORTTRAN BKW: A code for the detonation properties of explosives*, LASL LA-3704, 1963, Los Alamos Scientific Lab., Los Alamos, NM.
  2. Cowperthwaite, M.; and Zwisler, W.H., *TIGER computer program documentation*, March 1974, Stanford Research Institute, Menlo Park, CA.
  3. Craig, B.G.; Johnson, J.N.; Mader, C.L.; and Lederman, G.F., *Characterization of two commercial explosives*, LASL LA-7140, 1978, Los Alamos Scientific Lab., Los Alamos, NM.
  4. Lee, J., *Detonation shock dynamics of composite energetic materials*, Ph. D. Dissertation, New Mexico Institute of Mining and Technology, Socorro, NM, Dec. 1990.
  5. Lee, J.; Persson, P.-A.; and Bdzil, J.B., "Detonation shock dynamics of composite energetic materials", submitted to *Physics of Fluids*.
  6. Bdzil, J.B.; and Stewart, D.S., "Modeling two-dimensional detonation with detonation shock dynamics," *Physics of Fluids*, Vol. A1, 1989, p. 1261.
  7. Sandstrom, F.W., "Initiability: Shock initiation characteristics of composite energetic materials," *Semiannual Technical Report*, Research Center for Energetic Materials, A-07-89, Socorro, NM, Dec. 1989, pp. 27-36.
  8. Johnson, J.N.; Mader, C.L.; and Shaw, M.S., *2DL: A Lagrangian two-dimensional finite-difference code for reactive media*, LASL LA-8922-M, 1981, Los Alamos Scientific Lab., Los Alamos, NM.
  9. Walsh, J.M.; and Christian, R.H., "Equation of state of metals from shock wave measurements," *Physics Review*, Vol. 97, 1955, p. 1544.
- 

## DISCUSSION

EDWARD LEE

Lawrence Livermore National Laboratory,  
Livermore, California

Did you use your model to calculate the failure diameter of this material? If so, please comment on the results.

### REPLY BY J. LEE:

Hydrodynamic calculations determined the failure diameter of the emulsion explosive to be in a range from 30 to 36 mm, compared with the experimental value of 32 mm. This is only the result of preliminary calculations. More calculations will be performed to locate the failure diameter in a narrower range.

## DISCUSSION

P.K. TANG

Lawrence Livermore National Laboratory,  
Livermore, California

The value of the exponent 1.89 in the rate equation is very close to 2. It suggests a second-order type reaction and can likely represent some sort of diffusion process; that is why the rate is slow. Any comments?

### REPLY BY J. LEE:

The high reaction order suggests not only that the rate is slow but also that a significant amount of energy is released behind the sonic point. However, the rate equation was determined solely from hydrodynamic constraints given by conservation equations and equations of state to reproduce two-dimensional steady-state experimental data. As a result, it is only a fit to energy-release behavior which hydrodynamics require. The energy-release behavior can be modeled by different rate forms. Since the rate is not unique, it would be inappropriate to put a kinetic meaning to its reaction order.

**SESSIONS ON**  
**PHYSICAL CHEMISTRY**

**Cochairmen:**     **Richard Bardo**  
                         **Naval Surface Warfare Center**

**Conrad Bélanger**  
                         **Defence Research Establishment, Valcartier**

## OPTICAL TECHNIQUES FOR STRENGTH STUDIES OF POLYMER BONDED EXPLOSIVES

H.T. Goldrein, J. M. Huntley,  
S. J. P. Palmer, M. B. Whitworth,\* and J. E. Field  
Cavendish Laboratory, Madingley Road,  
Cambridge CB3 0HE, U.K.

Optical strain measurement techniques have two significant advantages over conventional strain gauges: they provide whole-field information, and they can be non-contacting. Three techniques have been developed for both quasi-static and dynamic studies of polymers, polymer bonded explosives (PBXs) and propellants: laser speckle photography; high resolution moiré photography; and digital speckle pattern interferometry.

### INTRODUCTION

The mechanical testing of materials conventionally involves the use of strain gauges or extensometers attached to the specimen to measure deformation. Extensometers provide an average value over a large section of material, while strain gauges provide a local measurement. Both methods involve attaching devices to the sample, and this often has a significant effect on the sample itself. It is also usually necessary to work with quite large samples (of dimension, say, a few cm) to be able to achieve a measurement.

When working with PBXs or propellants in particular, it is often useful to be able to study smaller samples (to minimise hazard risk), and to be able to measure strain with a non-contacting method. For these reasons the three techniques of laser speckle photography, high-resolution moiré photography and digital speckle pattern interferometry have been developed and applied to a variety of systems.

### LASER SPECKLE PHOTOGRAPHY

This is a well-established technique<sup>1</sup> and is the simplest of the three described here, though it involves substantial analysis to extract displacement and strain fields.

The slightly rough surface of the sample is illuminated by an expanded laser beam. The specimen appears speckled, due to light scattered from points on the specimen surface interfering with light scattered from nearby points constructively in some places, and destructively in others. Since these speckles are artefacts

of the surface relief, if the relief features move, so too will the speckles. Thus the speckles can be used as markers with which to measure surface displacement.

A double-exposure photograph of the speckle pattern on the surface of the specimen is taken, with one exposure before, and one after the sample is deformed. On the developed film, many pairs of dots are visible, the separation of the dots in each pair giving a measure of the in-plane displacement vector at that point on the sample. If a point on the film is now illuminated by an undiverged beam of laser light, then a classical Young's fringe pattern will be produced. This diffraction pattern is digitised, and processed by computer (by a two-dimensional fast-Fourier transform) to calculate the spatial frequency and orientation of the fringes.<sup>2</sup> This enables the local displacement vector at the point probed by the laser beam to be derived. The film is then moved (also under the control of a computer) so that the displacement at many points on the film can be determined. Typically, several hundred such fringe patterns have to be processed for each speckle photograph, and there may be many photographs in each deformation experiment. We have recently developed a parallel processing system which can analyse a fringe pattern in 160ms, and one photograph in under a minute.<sup>3</sup>

### Applications

For small samples of explosive, it is convenient to carry out mechanical testing in the Brazilian test geometry,<sup>4,5</sup> as illustrated in figure 1.

The test involves the diametral compression of a disc of PBX approximately 10mm in diameter. The sample fails in tension across the line of compression. In this test, the upper anvil is moved downwards at a constant rate of  $0.83\mu\text{m s}^{-1}$  which gives rise to a straining rate of ca.  $10^{-4}\text{s}^{-1}$ .

\* Now at FMBRA, Rickmansworth Road, Chorleywood, Hertfordshire, WD3 5SH, U.K.

The tensile strength of the material is then calculated from

$$\sigma_t = \frac{2P}{\pi Dt} \left\{ 1 - \left( \frac{b}{R} \right)^2 \right\}, \quad (1)$$

where  $P$  is the failure load,  $b$  is the contact half-width of the anvils, and  $D$ ,  $R$  and  $t$  are the diameter, radius, and thickness of the specimen respectively.

The validity of this equation is based on the assumptions that failure occurs at the point of maximum tensile stress (that is, at the centre) and that the compressive stress has no influence on the failure.

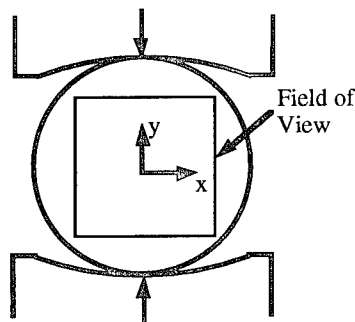


FIGURE 1. BRAZILIAN TEST GEOMETRY

With such a small sample, and with a typical strain-to-failure of a PBX of order 1 millistrain, the displacements which must be measured are only a few microns. The laser speckle technique can measure displacements across the whole of the specimen to an accuracy of better than  $0.1\mu\text{m}$ , and is non-contacting. For these reasons it has proved to be a useful technique for routine testing of PBXs.

#### Application 1 - Mechanical Testing of PBXs

Figure 2a,b shows the  $u_x$  and  $u_y$  displacement components of a sample of PBX, (X-0344, composition TATB/HMX/Kel-F 800/dye in the proportions 71.1/23.7/5.0/0.2% by mass), supplied by the Los Alamos National Laboratory. The sample dimensions ( $D \times t$ ) were  $6.5 \times 2\text{mm}$ , and the sample had been under load in the Brazilian test for 270 s. The contour spacing is  $0.5\mu\text{m}$  in figure 2(a), and  $1.0\mu\text{m}$  in figure 2(b). The region illustrated corresponds to the square in figure 1. From the displacement fields illustrated in figure 2, the strain fields can be deduced by numerical differentiation. The tensile strain distribution  $\epsilon_{xx}$  at the centre of the same disc under increasing load is illustrated in figure 3. Plates (a)–(d) represent  $\epsilon_{xx}$  at 108, 162, 216 and 270 s respectively. The contour spacing is 0.25 millistrain. Strain at the centre of the sample can be measured from these maps, and stress can be calculated from the load measured by a load cell in the testing machine. Thus stress-strain curves can be plotted as illustrated in figure 4.

#### Application 2 — Perforated Propellant Grains

A second illustration of the technique is the study of inert samples supplied by the United States Army Research Laboratory at Aberdeen, of perforated propellant grains, in order to study the contribution of the hexagonal array of burn holes to the mechanical properties. The sample was placed between two flat anvils, with its circular face (containing the array of burn holes) lying in the plane of the anvils. The specimen was loaded in compression by moving the upper anvil at a constant rate of  $0.83\mu\text{m s}^{-1}$  up to a maximum load of 40kg. The field of view is illustrated in figure 5.

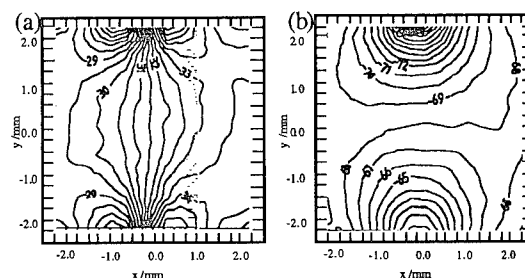


FIGURE 2.  $u_x$  (a) AND  $u_y$  (b) DISPLACEMENT COMPONENTS OF X-0344 UNDER LOAD IN THE BRAZILIAN TEST

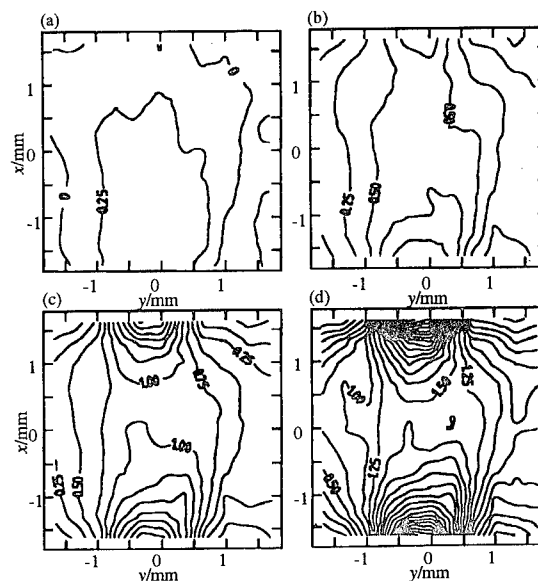


FIGURE 3. TENSILE STRAIN DISTRIBUTION  $\epsilon_{xx}$  AT THE CENTRE OF A DISC OF X-0344

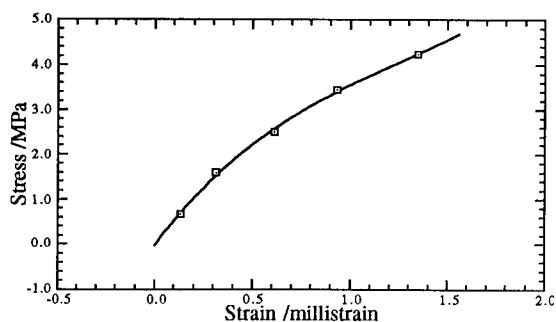


FIGURE 4. STRESS/STRAIN CURVE FOR X-0344 DERIVED FROM BRAZILIAN TEST

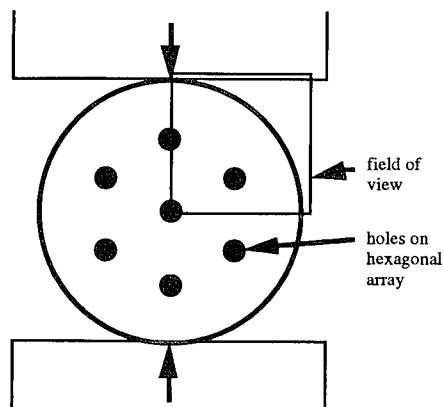


FIGURE 5. LOADING GEOMETRY FOR PERFORATED PROPELLANT GRAINS

In the displacement maps which appear as figure 6, it can be seen that strain is beginning to build up in the region under the anvil, the compressive strains here being approximately 2.0 millistrain. The  $u_x$  plot also shows some stress concentration between the burn holes.

### Application 3 — High Speed Speckle Photography

The previous applications have all dealt with quasi-static deformation of the sample. It is also possible to use speckle photography to record dynamic deformation events. A Beckman & Whitley 189 rotating-mirror high-speed camera and pulsed ruby laser have been modified for such a study.<sup>6</sup>

A pulse of light from a small flash tube placed inside the camera is arranged to illuminate a photodiode at the edge of each of the 25 relay lenses in the camera. This can only happen when the rotating mirror is pointing directly at the appropriate frame. The photodiodes then repeatedly Q-switch a ruby laser, which illuminates the sample, and records a speckle pattern. The camera is run once with the sample stationary, and once with the event in progress, thus double exposure speckle photographs are produced. These are then developed and analysed as before.

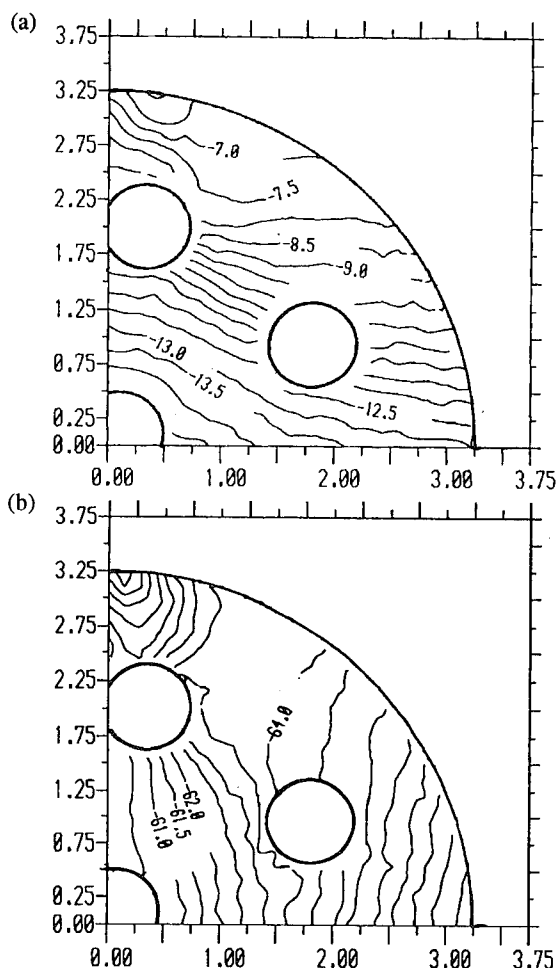


FIGURE 6. CONTOUR PLOTS OF IN-PLANE DISPLACEMENT COMPONENTS  $u_x$  (a) AND  $u_y$  (b) AT A LOAD OF 31.9 kg

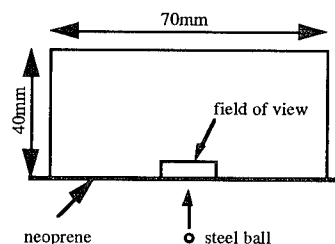


FIGURE 7. SPECIMEN GEOMETRY FOR BALL IMPACT EXPERIMENTS

In this example, experiments were carried out to measure the displacement field induced in a plate by solid particle impact. Figure 7 illustrates the geometry. The specimen was machined from a 6 mm sheet of cast polymethyl methacrylate (PMMA). The projectile, a 2mm steel ball impacted with a velocity of  $115 \pm 10 \text{ m s}^{-1}$ .

The results giving the horizontal displacement field from this experiment are illustrated in figure 8. The interframe time is  $1.65 \mu\text{s}$ , the field of view is  $14 \times 5.5 \text{ mm}^2$ , and the contour interval is  $2 \mu\text{m}$ .

### HIGH RESOLUTION MOIRE PHOTOGRAPHY

When two gratings are superimposed, beating between the gratings gives rise to a so-called moiré fringe pattern. In experimental mechanics this effect is used to measure in-plane displacements, out-of-plane slope, and surface form.<sup>7</sup> For example, in-plane displacements are determined by bonding a grating to the specimen surface. The fringe pattern formed by superimposing a stationary reference grating, either by direct contact or by imaging through a relay lens, then represents a contour map of the displacement component perpendicular to the grating lines. The sensitivity (i.e. fringe contour interval) is equal to the pitch of the specimen grating: with conventional moiré photography the maximum practical grating frequency is around  $40 \text{ lines mm}^{-1}$  ( $l \text{ mm}^{-1}$ ), corresponding to a sensitivity of  $25 \mu\text{m fringe}^{-1}$ . In the high resolution moiré technique<sup>8,9</sup> a masked lens is used to image the specimen grating. The lens and mask are designed to operate at a magnification of 1:1, with a frequency of  $150 \text{ l mm}^{-1}$  in both the specimen and image planes. Real time fringes are then recorded with a high speed camera allowing displacements to be measured with a sensitivity of  $6.7 \mu\text{m fringe}^{-1}$ , and with microsecond time resolution. This masked lens is illustrated in figure 9.

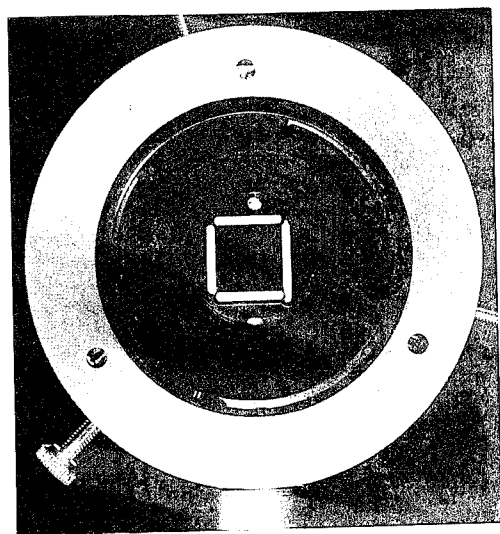


FIGURE 9. OBJECTIVE LENS WITH SLOTTED MASK FOR IMAGING HIGH FREQUENCY ( $150 \text{ lines mm}^{-1}$ ) SPECIMEN GRATINGS

Figure 10 shows the imaging system used. The masked lens ( $\text{OL}_1$ ) images the specimen grating (SG) onto the reference grating (RG), forming real-time moiré fringes, which are recorded by a high speed camera

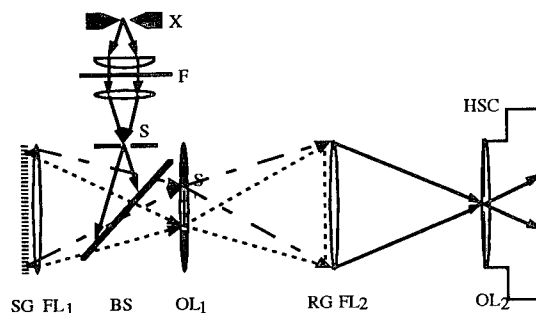


FIGURE 10. EXPERIMENTAL ARRANGEMENT FOR HIGH RESOLUTION MOIRE PHOTOGRAPHY

(HSC), an Imacon 792. Illumination is provided by a Xenon flash lamp (X) and beam-splitter (BS).  $\text{FL}_1$  and  $\text{FL}_2$  are field lenses. The theory of fringe formation is described in reference 9. The specimen grating is a thin reflective phase grating, formed either in epoxy resin, or (for low modulus samples) silicone rubber.

The recorded patterns are digitised and then analysed by computer, using a 2-D Fourier transform technique<sup>8,9</sup>.

### Application 1

One problem to which the high resolution moiré photography technique has been applied is the study of dynamic fracture of a rectangular PMMA plate containing a long crack. When loaded by a tensile stress pulse along one edge, a dilatational pulse enters the plate, trailed by shear waves which initiate at the plate edges as the pulse passes. High resolution moiré photography has been used to measure the displacement field in the vicinity of the (stationary) crack tip as the pure dilatational pulse passes. Figure 11 shows the high resolution moiré fringe patterns recorded by a high speed camera over a  $25 \text{ mm} \times 25 \text{ mm}$  field of view

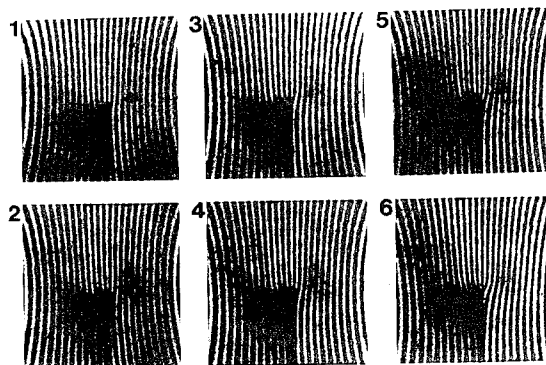


FIGURE 11. MOIRE FRINGE PATTERNS OBSERVED AT THE CRACK IN A PMMA PLATE



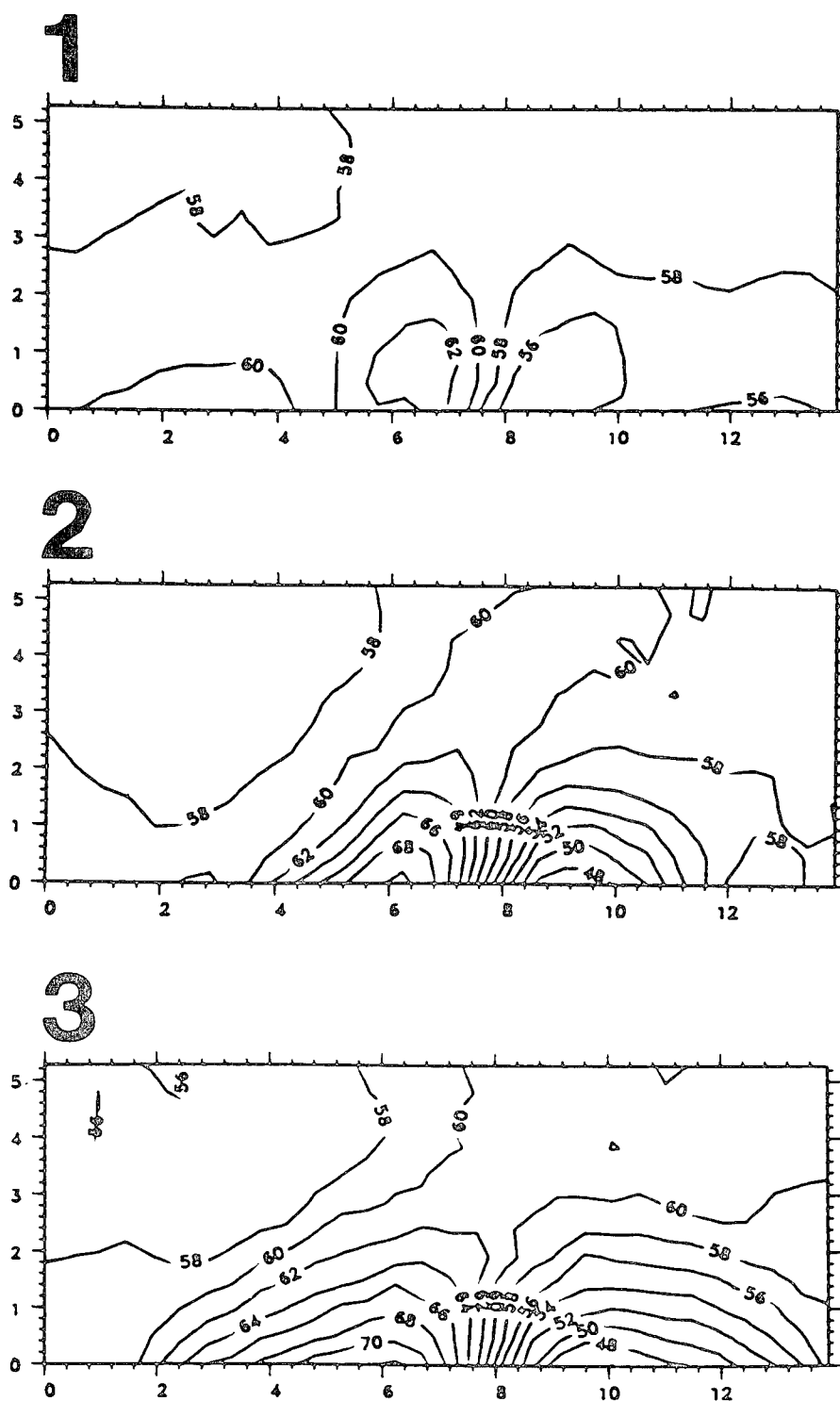
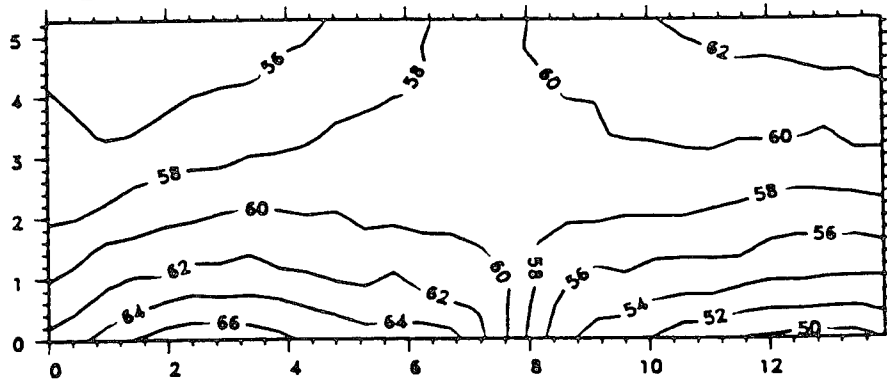
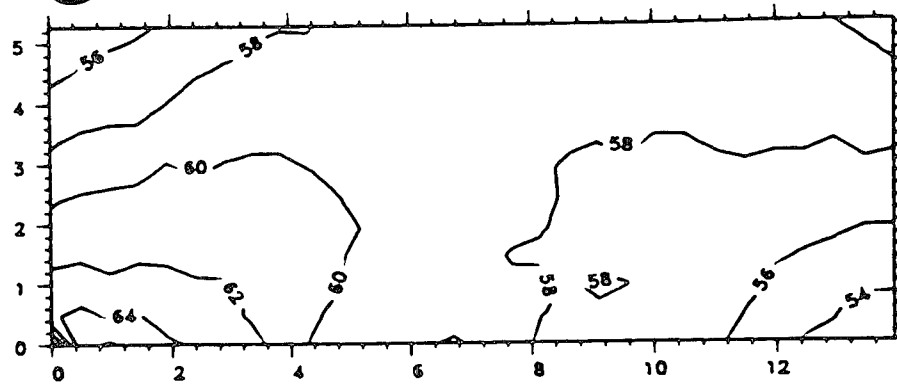


FIGURE 8. HORIZONTAL DISPLACEMENT COMPONENT FROM BALL IMPACT ON PMMA

4



5



6

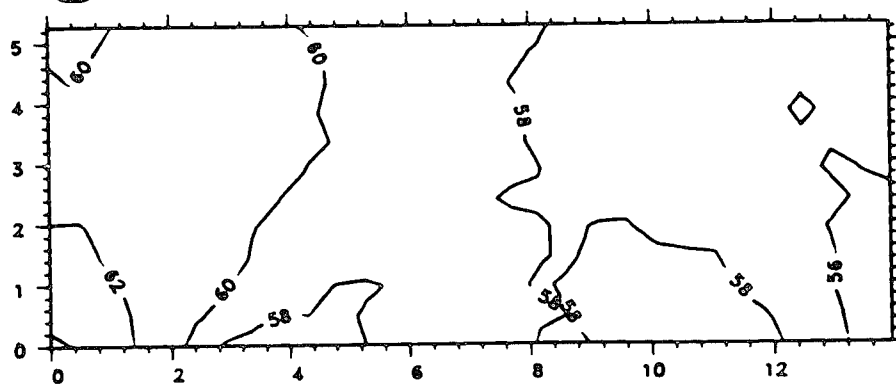


FIGURE 8. HORIZONTAL DISPLACEMENT COMPONENT FROM BALL IMPACT ON PMMA (CONT.)

centred on the crack tip. The first fringe pattern was recorded only 10.5  $\mu$ s after the arrival of a dilatational pulse incident from the left. Thus little displacement has occurred, and the fringes are only slightly modified from the mismatch fringes. Towards the end of the sequence, the fringes become more closely spaced, indicating increasing tensile horizontal strain ( $\epsilon_{xx}$ ). The interframe time is 5  $\mu$ s.

The horizontal component of the in-plane displacement field has been calculated as a function of time from these fringe patterns and from the corresponding mismatch fringes; it is shown in figure 12 as a sequence of contour maps, where dimensions are in mm, and the contour heights are in  $\mu$ m. The magnitude of the strain field can be seen to increase with time from the initial application of the dynamic load.

From these displacement fields, the mode-I stress intensity factor  $K_I^d$  can be calculated. It was compared with a theoretical solution based on a strain-gauge record of the input stress profile and the expected response for step pulse loading of an elastic plate. The predicted and measured K values are in agreement to within 5 to 10%.

#### Application 2

A second example is given by experiments carried out to investigate the effect of impact by rectangular projectiles on composite disc specimens. The discs simulate 2-D sections through artillery shells. The discs are 5 mm thick and consist of a central polycarbonate region with a diameter of 15.9 mm, 19.1 mm, or 22.2 mm, surrounded by a copper ring of external diameter 25.4 mm and wall thickness 1.6 mm. The intervening region was filled with a silicone rubber liner. Epoxy reflection gratings were applied to the polycarbonate region, and the aim was to measure the level of strains that were present in the polycarbonate region for different thicknesses of rubber. Phosphor bronze projectiles were fired by means of a rectangular bore gas gun, giving projectile velocities of  $56.0 \pm 1.1$  m s<sup>-1</sup>. High speed sequences, corresponding to each of the rubber thicknesses were recorded. By way of example, figure 13 shows the 19.1mm disc with a rubber thickness of 1.55 mm. The impact occurred horizontally from the left; the gratings were vertical so the fringes represent the horizontal displacement component, and compressive strains show up as a decrease in the fringe spacing. With a specimen grating frequency of 150 lines mm<sup>-1</sup>, the sensitivity is 6.7  $\mu$ m fringe<sup>-1</sup>. Only the central polycarbonate region is visible. The interframe time is 5  $\mu$ s. A compressive stress wave can be seen entering the polycarbonate from the left, crossing the disc in approximately 15  $\mu$ s. Figure 13 was analysed by the Fourier transform method, and the displacement field measured from the eight frames is shown in figure 14, where the contour interval is 2  $\mu$ m. Though not all the results are shown here, these experiments demonstrated the substantial reduction in strains which can be achieved through the use of a liner.

#### DIGITAL SPECKLE PATTERN INTERFEROMETRY

In digital speckle pattern interferometry, the sample is illuminated by two collimated beams of light as shown in figure 15. The resulting pattern of illumination is a set of cosine-squared fringes, modulated by a speckle pattern which is formed as described earlier. The camera of an image-processing system is focused on the surface of the specimen to observe these patterns. The fringe spacing is  $\lambda/(2\sin\alpha)$  where  $\lambda$  is the wavelength of light being used, 633nm in this case and  $\alpha$  is the angle of incidence. If  $\alpha$  is approximately 20° then the grating spacing is approximately 1 $\mu$ m. This is too fine for the camera to resolve and only the speckle pattern is visible.

If the sample is subjected to an in-plane displacement, then the speckles move as has already been noted with speckle photography. However, as the points contributing to their intensity move across the fine cosine grating, the intensity of the speckle will also vary sinusoidally at the grating frequency. If a speckle moves by 1 $\mu$ m, then it will change from bright to dark, and then to bright again. If the phase angle of the speckle along this sinusoid can be determined, then so too can the motion. There are three unknowns in this determination: the minimum intensity, the maximum intensity, and the phase angle, so one observation will not yield sufficient information to determine the phase uniquely. To provide this extra information, the length of one arm of the interferometer is altered by known fractions of a wavelength using the phase modulator shown in figure 15 and at least three measurements must be made. A sensitivity of order tens of nanometers is possible.

The main disadvantages of this are that at least three phase-stepped images must be acquired between which the specimen must not undergo any significant motion, so restricting the method to quasi-static tests, and that only one component of displacement can be obtained.

#### Applications

Brazilian test experiments were performed on inert PBX simulants in order to compare the effect of the polymer binders on the mechanical properties.

The interferometer was configured to measure horizontal in-plane displacements with a sensitivity of 0.433  $\mu$ m fringe<sup>-1</sup>. The Brazilian test loading rig was started, and phase-stepped speckle patterns were recorded every 25 s during the deformation. A sequence of such incremental phase maps for a composition with an hydroxy-terminated polybutadiene binder is shown in figure 16 in which black represents phase values of  $-\pi$ , and white is  $+\pi$ . Each map shows the change in horizontal displacement component that occurred in the 25 s between successive exposures. One fringe corresponds to a phase change of  $2\pi$  and a relative displacement of 0.433  $\mu$ m. The initial fringes are

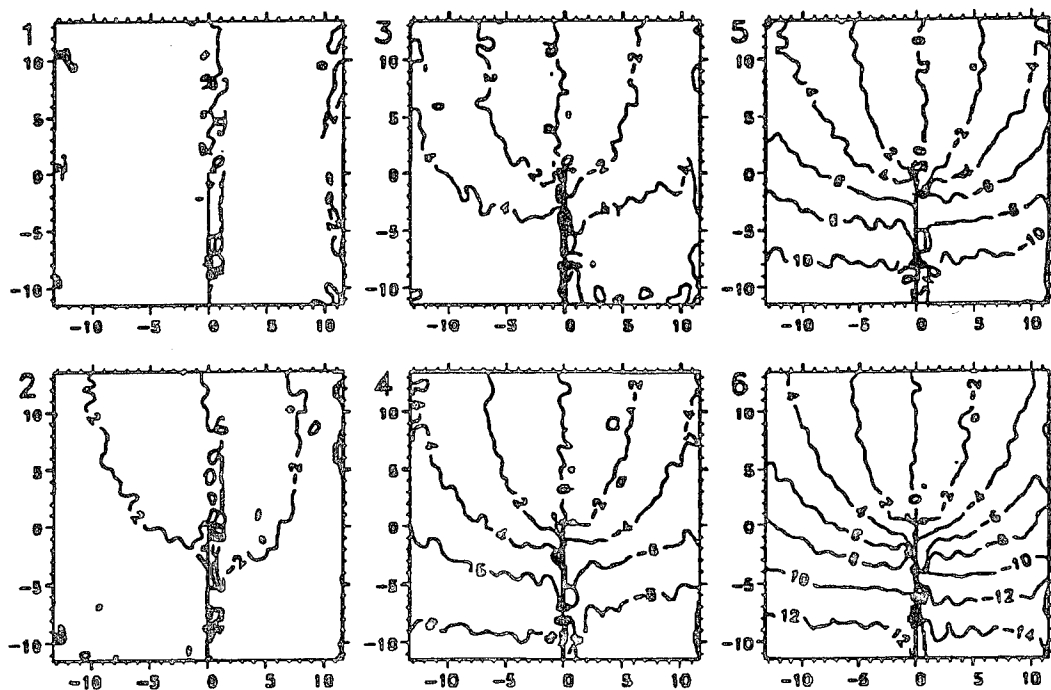


FIGURE 12. CONTOUR PLOTS OF THE HORIZONTAL IN-PLANE DISPLACEMENT COMPONENT OBTAINED FROM ANALYSIS OF FIGURE 11

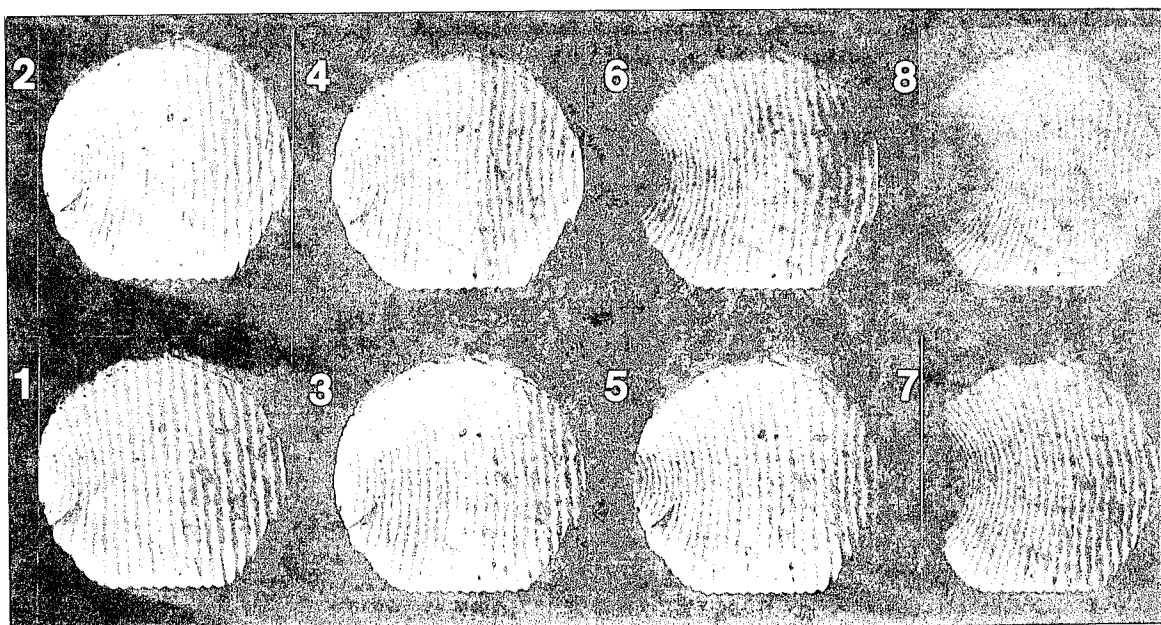


FIGURE 13. HIGH SPEED MOIRÉ SEQUENCE OF A COMPOSITE DISC UNDERGOING SLIDER IMPACT FROM LEFT TO RIGHT. INTERFRAME TIME =  $5\mu s$ .

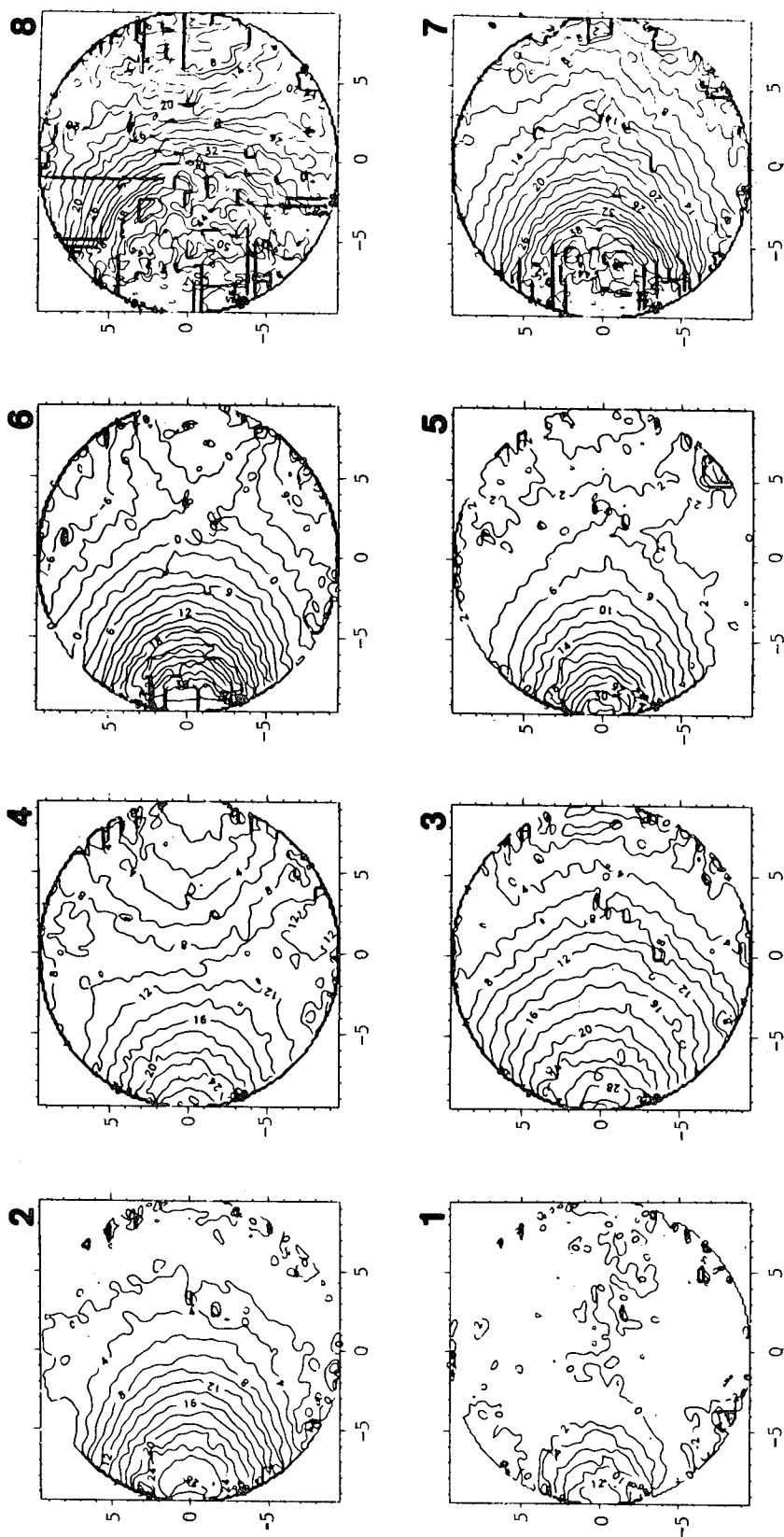


FIGURE 14. CONTOURS OF HORIZONTAL DISPLACEMENT COMPONENT FOR THE HIGH SPEED SEQUENCE SHOWN IN FIGURE 13. CONTOUR INTERVAL = 2 $\mu\text{m}$ .

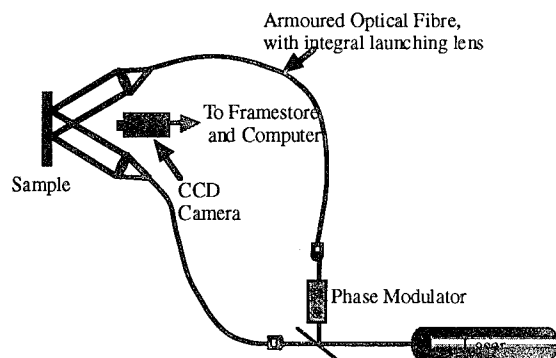


FIGURE 15. OPTICAL ARRANGEMENT FOR SPECKLE INTERFEROMETRY

essentially horizontal, indicating rigid body rotation of the disc. Tensile strain in the horizontal direction is proportional to the phase gradient in the  $x$  direction; the build-up of strain at the centre of the disc is clear from the tilting of the fringes to the vertical in that region. In the last frame the phase map has become very noisy at the centre of the disc. We believe this to be due to

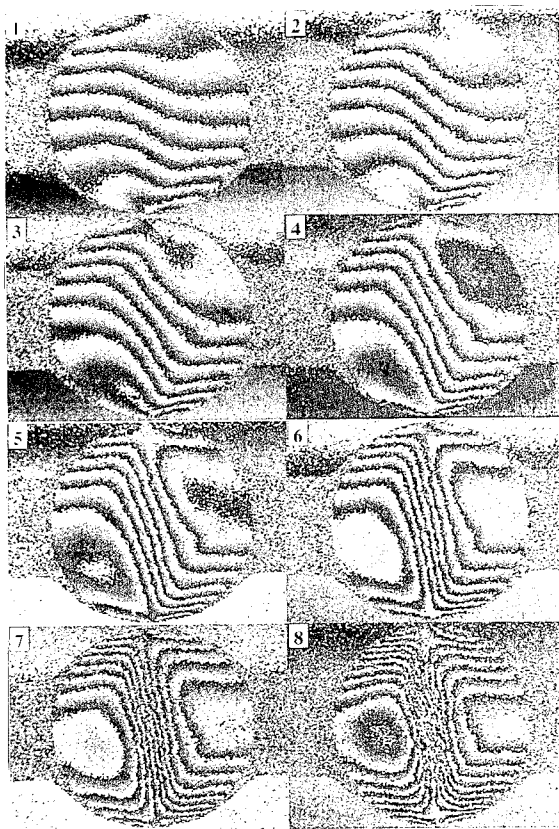


FIGURE 16. WRAPPED PHASE MAPS OF INERT PBX IN THE BRAZILIAN TEST

fracturing of the specimen, giving rise to excessive displacement and surface tilt, and hence to speckle decorrelation.

Subsequent analysis involves phase unwrapping (i.e. removal of the  $2\pi$  phase discontinuities) and numerical differentiation to calculate strain fields. Figure 17 shows maps of  $\epsilon_{xx}$  calculated from the frames of figure 16. The contour interval is 1 millistrain.

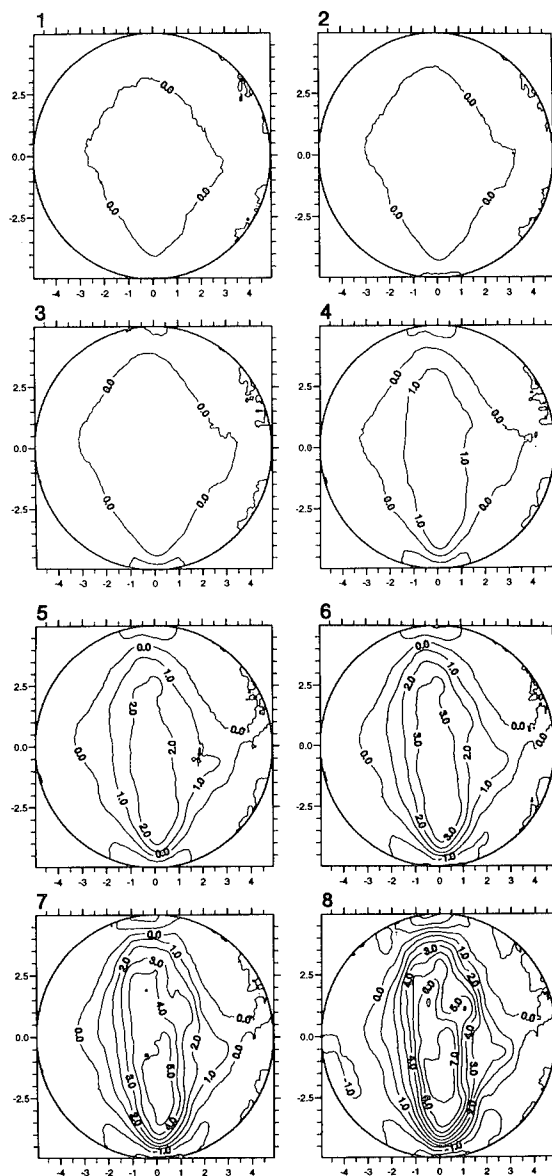


FIGURE 17. STRAIN MAPS DERIVED FROM FIGURE 16

## ACKNOWLEDGEMENTS

H.T.G. and S.J.P.P. thank A.W.E. Aldermaston, J.M.H. thanks the Royal Society, and M.B.W. thanks S.E.R.C. for their support. S.E.R.C. is also thanked for an equipment grant. The research was also supported in part by the U.S. European Office (Grant DAJA45-90-C-0023). A.W.E. Aldermaston and L.A.N.L. provided samples. The speckle interferometry experiments were carried out with Henrik Saldner at the University of Luleå, Sweden.

## REFERENCES

1. Dainty, J.C., Ed., *Laser Speckle and Related Topics in Applied Physics* Vol. 9, Springer, Berlin, 1975, pp. 203-253.
2. Huntley, J.M., Palmer, S.J.P., Field J.E., "Automatic Speckle Photography Fringe Analysis: Application to Crack Propagation and Strength Measurement", *Proc. SPIE*, Vol. 814, 1987, pp.153-160.
3. Huntley, J.M., Goldrein, H.T., Benckert, L.R., "Parallel processing system for rapid automated analysis of speckle photography and particle image velocimetry data", *Applied Optics* (in press).
4. Field, J.E., Parry, M.A., Palmer, S.J.P., Huntley, J.M., "Deformation and Explosive Properties of HMX Powders and Polymer Bonded Explosives", *9th Symposium (International) on Detonation*, Office of Naval Research, Portland, Oregon, Sept 1989, pp. 886-896.
5. Palmer, S.J.P., Field, J.E., and Huntley, J.M., "Deformation, strengths and strains to failure of polymer bonded explosives", *Proceedings of the Royal Society of London A*, Vol. 440, 1993, pp. 339-419.
6. Huntley, J.M., and Field, J.E., "High speed laser speckle photography", *Proc SPIE*, Vol. 1554A, 1991, pp. 756-765.
7. Sciammarella, C. A., "The moiré method - a review," *Experimental Mechanics*, Vol. 22, 1982, pp. 418-433.
8. Huntley, J.M., and Field, J.E., "High resolution moiré photography: application to dynamic stress analysis", *Optical Engineering*, Vol. 28, 1989, pp. 926-933.
9. Whitworth, M.B., and Huntley, J.M., "Dynamic stress analysis by high resolution reflection moiré photography", *Optical Engineering*, (submitted April 1993).

---

## DISCUSSION

HAROLD J. GRYTING

Gryting Energetics Science Company

Which of the three optical techniques you have developed would you recommend for tension and for compression strength information under slow deformation and fast (shock type) deformation?

## REPLY BY H.T. GOLDREIN:

Of the three techniques, only laser speckle photography and moiré photography can be used in dynamic situations. Of the two, the moiré approach is much more convenient, provided it is possible to put a grating on the specimen surface. Both these techniques can also be used in the quasi-static case. Digital speckle pattern interferometry can only be used in the quasi-static case, and will give only one displacement component at a time. However, its great strength is that displacement maps are produced within a few seconds of loading the sample, compared with minutes to hours for laser speckle photography. If a grating can be attached to the specimen surface, then moiré can be a good option in the low strain rate regime as well. All three techniques are equally useful for compressive or tensile loading.

## SHOCK RESPONSE OF PURE AND SENSITIZED (0.1 WT % ETHYLENEDIAMINE) NITROMETHANE: TIME-RESOLVED RAMAN MEASUREMENTS

G.I. Pangilinan and Y.M. Gupta  
Shock Dynamics Center and Physics Department  
Washington State University  
Pullman, Washington 99164-2814

Time-resolved Raman scattering measurements are performed on pure or sensitized (0.1 wt.% ethylenediamine) nitromethane shocked up to pressures of up to 140 kbars. In pure nitromethane, frequency hardening of the CN stretch, CH<sub>3</sub> stretch, and NO<sub>2</sub> stretch/CH<sub>3</sub> bend vibrations are observed from shocked liquid samples with 50 ns time resolution. Upon reaching peak pressures, the CN, NO<sub>2</sub> and CH<sub>3</sub> vibrational frequencies do not change in time; no softening is observed. In sensitized nitromethane shocked to 100 kbars, the CN frequency shift is observed to be the same as that in pure nitromethane, however, the background keeps rising in time even as peak pressure is reached. The background rise is due to a feature around the NO<sub>2</sub>/CH<sub>3</sub> bend vibrations that grows in time even when pressure in the material is constant. This feature, not observed in pure nitromethane shocked up to 140 kbars signals the onset of a chemical reaction in sensitized nitromethane. Possible origins of this feature are suggested.

A good understanding of shock induced chemical reactions at the atomic/molecular level is central to developing a microscopic theory of initiation in explosives. Although the large body of empirical data and continuum measurements obtained on a variety of explosives have contributed enormously to the use of high explosives in a broad range of applications, the development of a microscopic theory remains a challenging problem.<sup>1</sup> There exist many conceptual and practical difficulties in achieving this understanding. A major obstacle is the dearth of time-resolved, experimental measurements that may elucidate molecular changes in shocked energetic materials. Such measurements are difficult because of the single event nature of the experiments, the need for good spatial and temporal resolution in these fast reactions, and the pressure and temperature conditions of interest.

Over the past decade, considerable effort has been made in our laboratory to develop time-resolved optical spectroscopic methods to probe electronic and vibrational changes in shocked solids and liquids. Some representative examples of these developments may be seen in references 2-5. Recently, we have extended this work to shocked nitromethane. Because of its simple geometry and the lack of complexities associated with solid explosives, nitromethane has served as a good prototype energetic material for scientific investigations. Despite many of the advantages cited, the molecular mechanisms associated with energy releasing chemical reactions are not well characterized.<sup>6-11</sup> Furthermore, the sensitization of nitromethane under shock loading by the addition of

amines is not fully understood. Regarding the issue of amine sensitization, the recent comprehensive work by Constantinou<sup>11</sup> is noteworthy.

The present work utilizing Raman measurements is part of a broader study to develop an understanding of shock induced chemical reactions in nitromethane. This work has two main objectives. First, the manner by which a shock induced chemical reaction manifests itself in Raman scattering measurements will be determined. With a suitable definition of a reaction, the role of various parameters (pressure, temperature, degree of sensitization, and relevant times) required to initiate a chemical reaction will be examined. The second goal is to provide a molecular picture of shocked nitromethane just prior to reacting. Changes in the Raman active vibrations as nitromethane attains this precursor state will be important in understanding the initial chemical reactions in shocked nitromethane.

The overall experimental configuration to obtain time-resolved Raman measurements in shocked nitromethane are shown in Figure 1; further details about these measurements may be seen in Refs. 4 and 12. Briefly, a 150-300  $\mu\text{m}$  thick sample is sandwiched between two sapphire windows in a brass housing. A single stage light gas gun is used to accelerate a sapphire flyer plate, mounted on a projectile, to the desired velocity. Upon impact, a shock wave is propagated into the sample, and it reverberates between the sapphire/nitromethane boundaries until peak pressure is reached. The incident laser beam operated at 514 nm is focused onto the sample. The scattered light is sent to a system consisting of a spectrometer, a



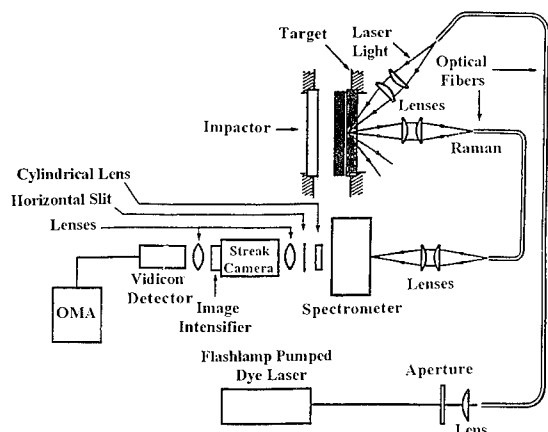


FIGURE 1. EXPERIMENTAL CONFIGURATION IN OBTAINING TIME RESOLVED RAMAN SCATTERING SPECTRA IN SHOCK NITROMETHANE

streak camera, a vidicon detector, and an optical multichannel analyzer. The wavelength dispersion of the spectrometer can be varied to yield wide spectral coverage ( $\sim 2500 \text{ cm}^{-1}$ ) or higher resolution ( $16 \text{ cm}^{-1}$  bandpass). The streak camera disperses the spectra in time, thus sending a two dimensional image to the vidicon detector. The output, controlled by the OMA consists of 30 spectra, with 50 ns resolution.

Typical time resolved spectra of nitromethane at ambient conditions is shown in Figure 2. Each spectrum corresponds to 50 ns duration. Nitromethane has 7 atoms per molecule giving rise to 15 vibrational modes.<sup>13-15</sup> In the  $C_{2v}$  point group, all 15 normal modes are Raman active. Of these modes, the strongest Raman peaks are the CN stretch ( $917 \text{ cm}^{-1}$ ), the  $\text{CH}_3$  stretch ( $2968 \text{ cm}^{-1}$ ), and the  $\text{NO}_2$  stretch ( $1400 \text{ cm}^{-1}$ ), which due to the wide spectral coverage chosen in Figure 2, is convoluted with a slightly weaker  $\text{CH}_3$  bending mode ( $1377 \text{ cm}^{-1}$ ).

Upon shockup to predetermined pressures, modifications to the nitromethane vibrations can be monitored. Figure 3 shows data from nitromethane shocked to 110 kbar peak pressure. Various time markers are indicated in the figure. Impact time corresponds to the time at which the flyer plate hits the front window. The shock wave then crosses through the thickness of the front window. Upon reaching the nitromethane sample, the shock wave reverberates through the nitromethane until peak pressure is attained. These spectra thus provide real time changes in the internal vibrations of nitromethane.

The spectral modifications can be seen from a comparison of spectra from ambient and shocked nitromethane shown in Figure 4. Unreacted shocked nitromethane is characterized by hardening of the CN,  $\text{CH}_3$ ,  $\text{NO}_2$  vibrations. This is especially clear for the CN and  $\text{CH}_3$  stretch modes. The  $\text{NO}_2$  stretch/ $\text{CH}_3$  bend harden the least, but gain intensity relative to the other modes.

## AMBIENT PRESSURE

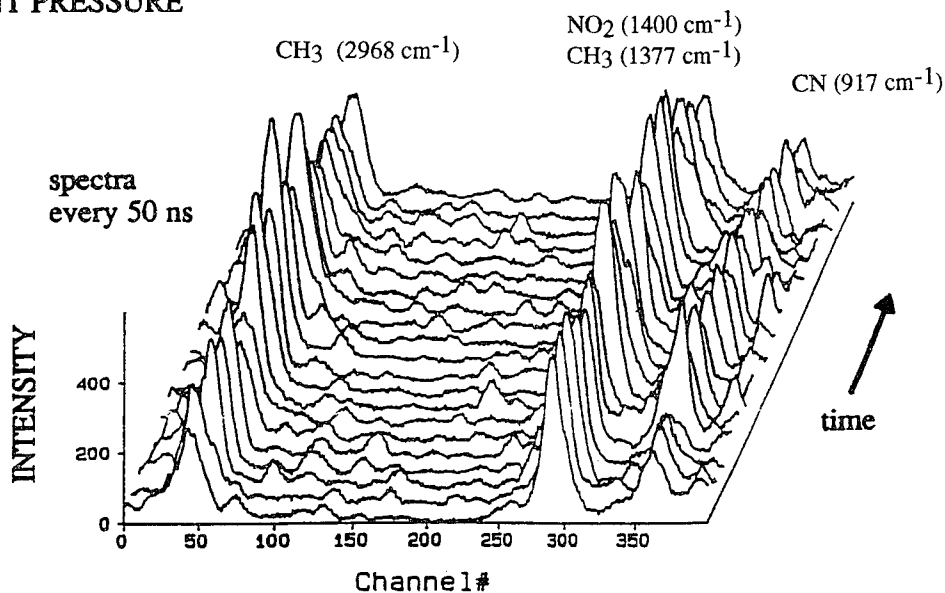


FIGURE 2. TIME RESOLVED SPECTRA OF NITROMETHANE WITH 50 NS RESOLUTION. SEEN ARE THE CN STRETCH,  $\text{CH}_3$  STRETCH, AND THE  $\text{NO}_2$  STRETCH CONVOLUTED WITH A WEAKER  $\text{CH}_3$  BEND VIBRATIONS.

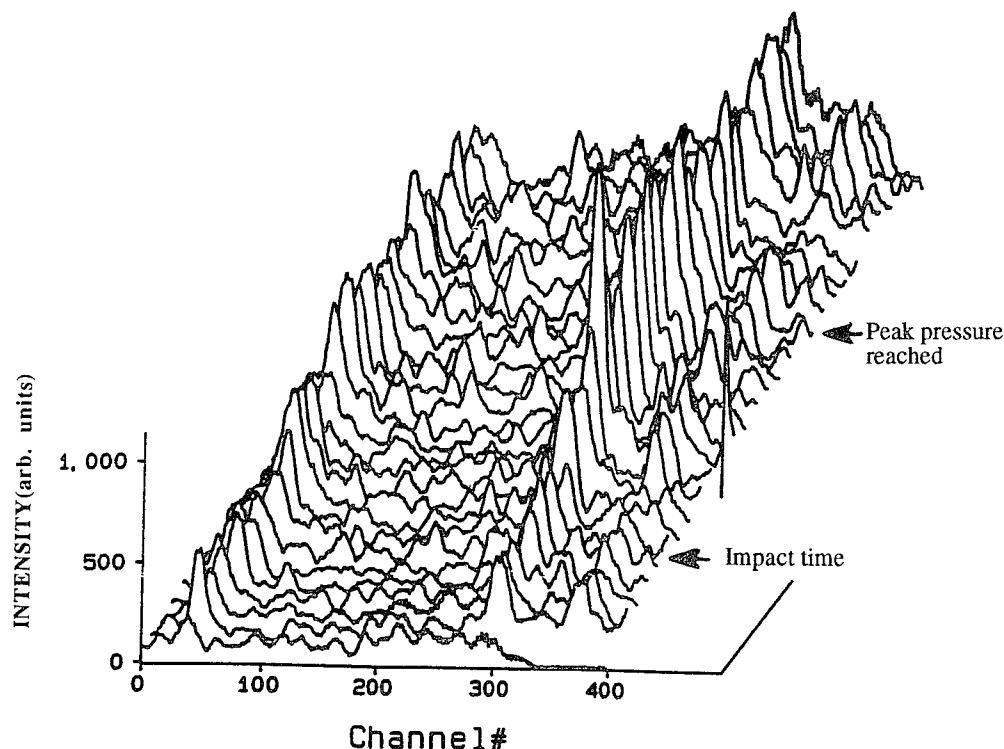


FIGURE 3. SPECTRA OF PURE NITROMETHANE SHOCKED UP TO 110 KBARS. INDICATED IN THE FIGURE IS THE IMPACT TIME, WHICH IS THE TIME THAT THE FLYER PLATE HITS THE SAPPHIRE FRONT WINDOW, AND THE TIME THAT THE PEAK PRESSURE IS REACH IN THE NITROMETHANE SAMPLE.

Experiments with higher frequency dispersion have been pursued to quantify the frequency shifts. The CN stretch vibration has been accorded the most attention due to the hypothesis<sup>6</sup> that CN scission is the rate determining step in the shock induced decomposition of nitromethane, and the  $\text{NO}_2$  and  $\text{CH}_3$  radicals that are released mediate the subsequent reactions. In this model of CN scission, barring vibrational mode couplings, the energy of the CN vibration is expected to soften prior to a reaction. Up to peak pressures of 140 kbars, the CN mode hardens and broadens under shock loading ( $51.5 \pm 3 \text{ cm}^{-1}$  at 140 kbars), and does not soften in the time window of the experiments. A similar effect is observed for the  $\text{CH}_3$  stretch which hardens and broadens at 140 kbars ( $82 \pm 3 \text{ cm}^{-1}$ ).

The onset of a reaction can be seen in Figure 5 from experiments performed at 110 kbar peak pressure on sensitized nitromethane. The evolution of a strong broad feature centered around the  $1400 \text{ cm}^{-1}$  and absent in Figure 3 dominates the spectra. This is currently viewed as the manifestation of a shock induced reaction. Experiments with higher dispersions around the CN stretch were completed, to monitor changes with the CN vibration in sensitized, and reacting nitromethane. Figure 6 shows the CN stretch in pure

and sensitized nitromethane at 100 kbar pressure. To account for sample thickness and light collection variations in the two shots, the spectra were normalized so that ambient spectra taken just before the two experiments had the same intensity. It is seen that no mode softening or intensity decrease is observed in the reacting sensitized nitromethane. The background level not shown in the figure, is higher in (c) due to the contributions from the broad peak observed in Figure 5. CN scission is therefore not the likely initial step in the shock induced decomposition of sensitized nitromethane.

At this point, we can only speculate on the origin of the broad feature that evolves in time in sensitized nitromethane. The first possibility is that it is a luminescence peak centered around 555 nm where intensity increases with time. This is probably due to luminescence from energy levels from a product state where intensity grows with time. Various molecules with luminescence around this energy region at ambient pressures are possible candidates, although pressure induced modifications in luminescence have to be considered. We have discounted the possibility that this luminescence originates from certain products that are formed in an excited state and subsequently emit photons. We have ascertained from other

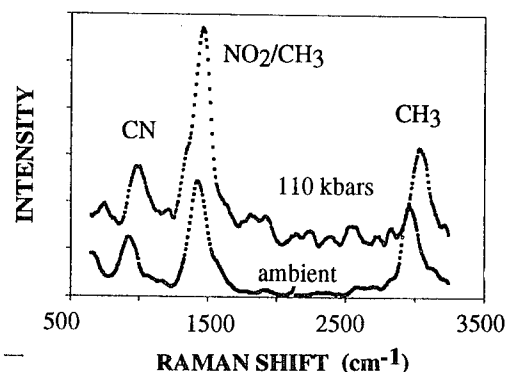


FIGURE 4. COMPARISON OF SPECTRA BETWEEN AMBIENT AND SHOCKED NITROMETHANE. QUALITATIVE SPECTRAL CHANGES CAN BE SEEN BY COMPARING LOW DISPERSION/WIDE COVERAGE SPECTRA FROM AMBIENT AND NITROMETHANE SHOCKED TO 110 KBAR PEAK PRESSURE. FREQUENCY HARDENING OF ALL PEAKS IS CLEAR BUT IS BETTER QUANTIFIED WITH HIGHER DISPERSION SPECTRA. ALSO SEEN IS A RELATIVE ENHANCEMENT OF THE  $\text{NO}_2$  STRETCH/ $\text{CH}_3$  BEND MODE.

experiments that this particular feature is observed only with laser excitation. It is also unlikely that this feature originates from the electronic levels of nitromethane in which the evolution arises from the breakdown of electric dipole selection rules brought about by the shock and the presence of the amine, since the intensity of the feature continues to increase even after peak pressure has been attained. The second possibility is that the feature is Raman excitation around  $1400\text{ cm}^{-1}$ , and is arising from reaction products whose concentration is increasing with time. The width may be due to a wide distribution of band strength. These possibilities are currently being pursued actively.

In summary, the onset of the reaction has been observed in Raman scattering measurements of sensitized nitromethane. The vibrational studies on shocked, unreacted nitromethane that describe the precursor state are currently being completed. These experimental results are expected to provide a molecular picture of nitromethane as shock-induced reactions are initiated. Ultimately, these Raman measurements, together with time-resolved absorption, reflection, and emission studies currently being performed in the Shock Dynamics Center will furnish a comprehensive microscopic picture of the energy releasing chemical reactions in shocked nitromethane.

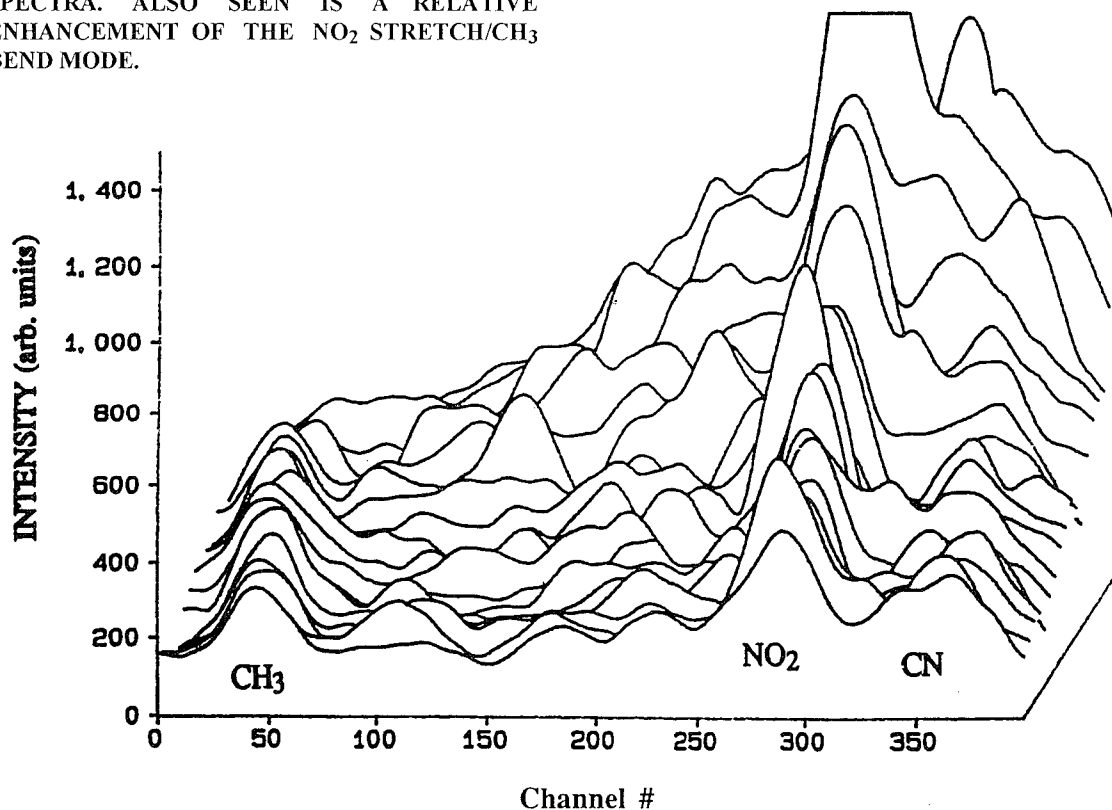


FIGURE 5. SMOOTHED SPECTRA OF SENSITIZED NITROMETHANE SHOCKED UP TO 110 KBARS, AS IN FIGURE 3. THE INTENSITY ENHANCEMENT OF THE  $\text{NO}_2/\text{CH}_3$  VIBRATION IS ALSO SEEN. THE EVOLUTION OF THE BROAD FEATURE AT LATER TIMES MARKS THE ONSET OF REACTION.

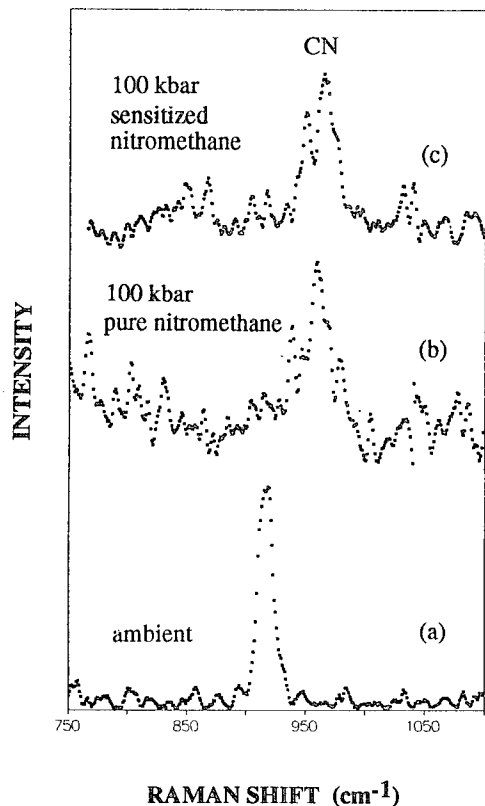


FIGURE 6. HIGHER DISPERSION SPECTRA OF THE CN STRETCH VIBRATION A) PURE NITROMETHANE AT AMBIENT PRESSURES, B) PURE NITROMETHANE AT 100 KBAR; AND C) SENSITIZED NITROMETHANE AT 100 KBAR. WITHIN ERROR LIMITS, NO INTENSITY, WIDTH, OR FREQUENCY DIFFERENCES ARE NOTICEABLE. NOT SEEN IN THE FIGURE IS A HIGHER BACKGROUND FOR (C) DUE TO CONTRIBUTIONS FROM THE BROAD FEATURE SHOWN IN FIGURE 5.

The authors are grateful for the technical support of Dave Savage and Kurt Zimmermann. Fruitful discussions with Constantinos P. Constantinou and Mike Winey are acknowledged. This work was supported by ONR Grant N00014-90-J-1400 (Project Monitor: Dr. R.S. Miller).

## REFERENCES

1. Fickett, W.; and Davis, W.C., Detonation, University of California Press, Berkeley and Los Angeles, California, 1979.
2. Horn, P.D. and Gupta, Y.M., "Luminescence R-line Spectrum of Ruby Crystals Shocked to 125 Kbar Along the C Axis," *Physical Review B*, Vol 39, 1989, p. 973.
3. Yoo, C.S.; Duvall, G.E.; Furrer, J.; and Granholm, "Effects of Pressure and Dilution on the Visible and Ultraviolet Spectrum of Liquid Carbon Disulfide Under Shock Compression," *Journal of Physical Chemistry*, Vol. 93, No. 8, 1989, p. 3012.
4. Yoo, C.S.; Gupta, Y.M.; and Horn, P.D., "Pressure Induced Resonance Raman Effect in Shocked Carbon Disulfide," *Chemical Physics Letters*, Vol. 159, 1989, p. 178.
5. Gustavsen, R.; and Gupta, Y.M., "Time-Resolved Spectroscopic Reflection Measurements in Shock Compressed Materials", *Journal of Applied Physics*, Vol. 69, No. 2, 1991, p. 918.
6. Cook, M.D.; and Haskins, P.J., "Decomposition Mechanisms and Chemical Sensitization in Nitro, Nitramine, and Nitrate Explosives," in the *Ninth Symposium on Detonation*, Royal Armament Research and Development Establishment, United Kingdom, 1989, p. 27.
7. Engelke, R.; Earl, W.L.; and Rohlfing, "Microscopic Evidence that the Nitromethane Acion is a Rate Controlling Species in the Detonation of Liquid Nitromethane," *Journal of Chemical Physics*, Vol. 85, 1986, p. 142.
8. Peyrard, M.; Odier, S.; Lavenir, E.; and Schnur, J.M., "Molecular Model for Cooperative Propagation of Shock-Induced Detonations in Energetic Solids and its Application to Nitromethane," *Journal of Applied Physics*, Vol. 57, No. 7, 1985, p. 2626.
9. Bardo, R.D., "Rate-determining Steps for Ignition of Shocked Nitromethane, in the "Ninth Symposium on Detonation, Naval Surface Weapons Center, Vol. 455, 1986, p. 843.
10. Engelke, R., "Effect of a Chemical Inhomogeneity on Steady-State Detonation Velocity," *Physics of Fluids*, Vol. 23, No. 5, 1980, p. 875.
11. Constantinou, C.P., "The Nitromethane-Amine Interaction," Ph.D. Dissertation, Cambridge University, 1992.
12. Gustavsen, R.; and Gupta, Y.M., to be published.

13. Malewski, G.; Pfeiffer, M.; and Reich, P.J., "Das Ramanspektrum von Nitromethan-<sup>15</sup>N," *Molecular Structure*, Vol. 3, 1969, p. 418.
14. Miller, P.J.; Block, S.; and Piermarini, G.J., "Effects of Pressure on the Vibrational Spectra of Liquid Nitromethane," *Journal of Chemical Physics*, Vol. 93, 1989, p. 462.
15. Hill, J.R.; Moore, D.S.; Schmidt, S.C.; and Storm, C.B., "Infrared Raman, and Coherent Anti-stokes Raman Spectroscopy of the Hydrogen/Deuterium Isotopomers of Nitromethane," *Journal of Physical Chemistry*, Vol. 95, No. 8, 1991, p. 3037.

## DISCUSSION

A. FRANK  
Lawrence Livermore National Laboratory, Livermore,  
California

What is your pump wavelength?

REPLY BY GERARDO PANGILINAN:

A 514-nm pump wavelength was used.

## DISCUSSION

JACQUES BOILEAU  
DRET, Paris, France

Comparison of nitromethane Raman spectrum under shock and under static pressure?

REPLY BY GERARDO PANGILINAN: :

Under static pressure, the only Raman spectrum reported in the literature is on the CN bond [Engelke, R., *et al*, *J. Phys. Chem.*, **92**, 6815 (1988)] of a CH<sub>3</sub>NO<sub>2</sub>/CD<sub>3</sub>NO<sub>2</sub> mixture at 21 kbars. The bond frequency interpolates well with our data. Lineshape changes at this static pressure are ascribed to isotopic mixing and are thus not meaningful to compare with our shock data.

Two reports on Raman frequency positions at static pressures are in the literature. Up to 17 kbars, before solidification, Miller, P. J., *et al* [*J. Phys. Chem.* **93**, 463 (1989)] reports that the CH<sub>3</sub> stretch, NO<sub>2</sub> symmetric stretch, and the CH<sub>3</sub> bend shift by 8, 7, and 2 cm<sup>-1</sup>. Our shock data obtained at much higher pressures reasonably agree with the large CH<sub>3</sub> stretch frequency shift. Our shock data, however, show that the NO<sub>2</sub> symmetric stretch shifts by only about half the CH<sub>3</sub> mode, and we did not observe at high pressures, further splitting of the NO<sub>2</sub> stretch/CH<sub>3</sub> bend modes suggested in the static data. No CN frequency shifts were mentioned in the report.

Cromer, D. T. *et al*, [*J. Phys. Chem.* **89**, 2315 (1985)] earlier reported Raman frequency positions of nitromethane obtained up to 117 kbar static pressures. Due to the large error bars in the report, only the CH<sub>3</sub> stretch, apart from the intermolecular modes, clearly showed hardening. Qualitatively, this CH<sub>3</sub> hardening agrees with our shock data. The NO<sub>2</sub> symmetric stretch is strikingly missing in that description.

## RADIATION OF CONDENSED EXPLOSIVES AND ITS INTERPRETATION (TEMPERATURE MEASUREMENTS)

M.F. Gogulya and M.A. Brazhnikov  
Institute of Chemical Physics, Russian  
Academy of Sciences, Kosygin Street  
4, Moscow 117977, Russia

Detonation temperature of some solid high explosives (TNT, RDX, TNT/RDX, HMX, RDX and HMX with wax) and liquid--nitromethane (NM) and molten TNT--was studied with a two-colour pyrometer. Not only the temperature of detonation front was measured, but also the temperature of detonation products after the interaction between detonation front and transparent windows of different impedances. The measured temperatures were used for determination of Chapman-Jouguet (C-J) temperature and Gruneisen parameter. The distinction between the detonation front temperature and the temperature of detonation products in the C-J point has been demonstrated for all explosives tested (except TNT and TNT/RDX mixture).

### INTRODUCTION

The electro-optical method for temperature measurements was proposed in the end of 1940's.<sup>1</sup> The first experimental data obtained with the help of an optical pyrometer, were reported by Gibson et.al.<sup>2,3</sup> The following solid explosives TNT, PETN, Tetryl, RDX, EDNA and liquid explosives NM, Nitroglycerol have been tested. Related works on detonation temperatures measurements were carried out by Voskoboinikov in the Soviet Union, practically at the same time.<sup>4</sup> The temperatures measured on liquid explosives were the same within the experimental error, but the results for solid ones didn't correlate with each other. Later widespread investigations of condensed explosives were undertaken.

The initial transparency of the liquid explosives makes it possible to carry out the end-on registration of the light beam, emitted from the detonation front. The emissive spectrum of detonation was investigated,<sup>5,6,7</sup> but only liquid explosives were tested. The authors came to the conclusion that the radiation emanating from the detonation front was nearly the same as that from the black body. This result was expanded

on all explosives studied. At the same time, non-thermal luminosity was observed in shocked inert materials; some possible explanations were proposed by Zel'dovich and Kormer.<sup>8,9,10</sup> Later it was experimentally found that the non-thermal radiation intensity was much higher in the case that the initial state of the material investigated was polycrystalline.<sup>11</sup>

The experiments with low-dense explosives (PETN, TNT) carried out by Akimova et.al.<sup>12</sup> has demonstrated the possibility to measure the detonation products temperature with the help of a transparent anvil. The same method was applied to the temperature determination by other researchers.<sup>13,14,15</sup> The techniques, when the investigated materials are in contact with some liquids or solids (transparent in the pressure range studied), open up fresh opportunities for the detonation products temperature study. But the utility of the only "window" seriously limits the advantages of the method, because supplementary investigations are required to correlate the experimental data with the temperatures in the C-J point.

Thus, at present research we undertake an attempt to use the advantages of the "window" techniques, utilizing anvils of different shock impedances.

## EXPERIMENT

The measurements were performed with an optical pyrometer at the wave lengths 420 nm and 720 nm; radiation was viewed end-on. The anvils utilized (lithium fluoride (LiF), plexiglas disks (PMMA), optical glass Cron-8, glycerol and water) had different shock impedances. Detonation light emitted from the area of 5 mm in diameter on the advancing detonation front or detonation products was focused on the end of the receiver of the photoelectric multiplier (FEU-119 and FEU-92) by condensing lens. The outputs of the amplifiers were recorded by two oscilloscopes via coaxial cables. The rise time of overall system with the digital-processing oscilloscope was measured to be less than 50 nsec, and with the cathode-ray oscillograph—to be less than 20 nsec. The calibration of the pyrometer was performed with a tungsten ribbon lamp, when the set-up was installed.

The explosives studied were the following—solids: TNT, RDX, TNT/RDX (50/50), HMX, RDX with wax, HMX with wax and liquids: NM, molten TNT. Some properties of the explosives are presented in Table 1.

TABLE 1.  
PROPERTIES OF HIGH EXPLOSIVES STUDIED

NAME	DEN- SITY (g/cc)	DETONATION VELOCITY (km/s)	NOTE
TNT	1.60	6.94	pressed
	1.45	6.58	molten
RDX	1.71	8.39	pressed
	1.71	8.39	pressed, cont. 1; 0.5; 0.25; wt % graphite
	1.80	8.77	agate-like
	1.67	8.34	pressed, cont. 5 wt % wax
TNT/ RDX (50/50)	1.67	7.60	pressed
HMX	1.80	8.75	pressed
	1.75	8.65	pressed, cont. 4 wt % wax
NM	1.13	6.30	liquid

The pressed granular explosives samples were 55 mm long, 40 mm in diameter. The densities of solid explosives charges were about 95% of single crystals density, except the agate-like RDX samples, which density was approximately of the single crystal ones (these charges were pressed from the pure fine RDX powder under the heating to 90 C with small amount of acetone). NM was contained in the aluminum tube of 60 mm long, 40 mm in diameter and 1 mm thick. Molten TNT at 90 C was contained in the aluminum tube of 50 mm long, 62 mm in diameter and 1 mm thick. The plane wave detonation was produced by lens made of RDX with wax.

The measured brightness temperatures were averaged over the two wavelengths, with an instrumental error about 150 K. The temperature difference on the wavelengths was less than value mentioned above.

Considering the detonation products as a mixture of non-reactive components, one may assume that the result of anvil-detonation products interaction depends on the shock impedance mismatch. If the detonation products behavior can be described in terms of the polytropic law, the temperature increase/decrease may be expected in the case that the anvil impedance is higher/lower than that of detonation products (see Fig. 1)

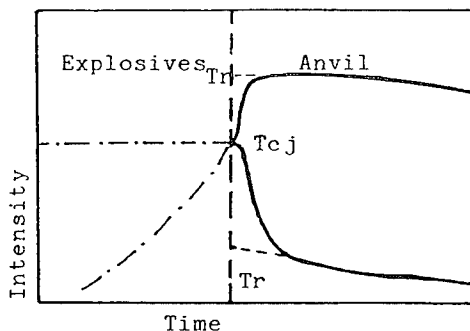


FIGURE 1. POSSIBLE INTENSITY RECORDS OF CONDENSED EXPLOSIVES

The restrictions applied by the set-up (such as the rise time) and the method used don't permit to determine the detonation temperature in direct wave correctly. Considering the reflected wave (shock or rarefaction wave) to be the isoentropic one and assuming the G/V ratio to be constant (G - Gruneisen parameter and V - specific volume), one may deduce the following temperature/specific volume relation in the C-J point:

$$Tr = Tc_j * \exp\{ (G/V) (V_{cj} - V_r) \},$$

where  $T_r$  - the detonation products temperature in the reflected wave,  $T_{cj}$  - the temperature in the C-J point,  $V_r$ ,  $V_{cj}$  - the specific volume of the products in the reflected wave and in the C-J point. If a polytropic index of detonation products and a shock adiabat of the window material are known, the specific volume difference may be estimated. Thus, basing on  $T_r$  experimental data for anvils of different shock impedances, the  $G/V$  and  $T_{cj}$  values can be determined.

## RESULTS OF DISCUSSION

The temperature time histories of the TNT pressed samples are shown in Fig. 2. The windows have different impedance mismatches with the detonation products. The curves are very much alike those expected. The  $T_{cj}$  value is practically equal, within the experimental error, to the temperature occurring, when the detonation complex is passing through the interface both in the case of LiF used (point 1 in Fig. 2) and in the case of water window (point 2 in Fig. 2).

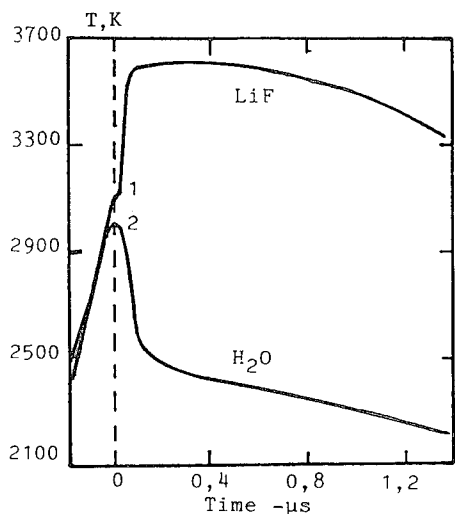


FIGURE 2. TEMPERATURE TIME HISTORIES OF TNT DETONATION PRODUCTS

The experimental profiles for the tested RDX pressed samples are shown in Fig. 3. The curves differ very much from those expected. The measured peak temperatures are unaffected by the anvil, materials used. This fact and the fact that the LiF interaction with the detonation products resulted to the temperature decrease lead us to the assumption of non-thermal character of detonation light being emitted till the wave complex achieved the interface.

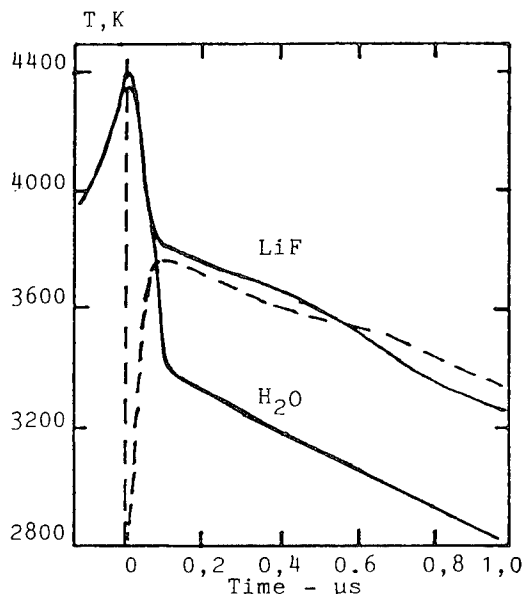


FIGURE 3. TEMPERATURE TIME HISTORIES OF RDX DETONATION PRODUCTS

In order to judge the nature of the phenomenon supplementary tests have been carried out. It's well known that an addition of small amount of carbon black powder to the inert heterogeneous composition may diminish its radiation under shock wave compression.<sup>16</sup> Two series of the experiments with LiF anvils were made. In the first series, the TNT mixture containing 1% of fine carbon black powder was examined. The experimental temperature values for the mixture and for the pure TNT are practically the same. This means that small additives of carbon powder didn't affect on the data within the experimental error. Another series of experiments was made in order to investigate the RDX mixtures with 0,25%, 0,50% and 1,0% content of the carbon black powder. The experimental curve for the mixture with 1% content of the powder is shown in Fig. 3 (dotted line). The carbon powder screened the detonation light from the internal parts of the charge. The curves with and/or without this additive are practically the same except the first portion of the curves, that duration is about 0,1  $\mu$ s. The reduced temperature peak was observed in the mixture with 0,25% content of carbon black powder. The peak luminosity may be explained in terms of non-thermal radiation; it would be erroneous to deduce the detonation temperature from the peak values. Basing on this assumption the experimental temperatures were determined from the curves extrapolation to the time point, when the detonation reached the interface. The temperatures so obtained and the "afterpeak" values lie within the experimental error.



Semi-transparent agate-like RDX charges were also tested. The experimental curves are shown in Fig. 4. It is evident from the comparison of these curves with those for pressed RDX samples, that the peak values are considerably diminished. This fact may be connected with the reduction of the initial heterogeneity of the samples examined, as it was found for the inert materials. The determination of the values to be the base for  $T_{cj}$  and  $G$  calculation was made in the same manner as for pressed RDX charges.

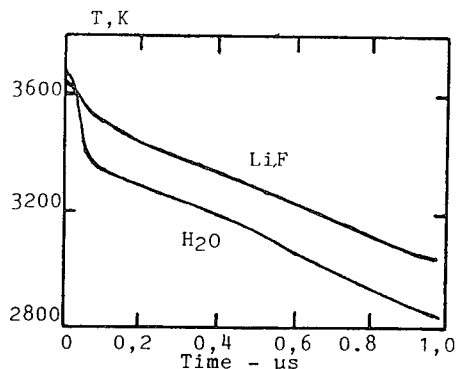


FIGURE 4. TEMPERATURE TIME HISTORIES OF AGATE-LIKE RDX DETONATION PRODUCTS

Thus, RDX and TNT demonstrate quite different behavior under the detonation decomposition. The initial physical properties of these materials also differ from each other (plasticity of TNT is in a contrast with the brittleness of the RDX crystals). These are the reasons to expect an intermediate character of the TNT/RDX mixture. One may assume the detonation mechanism in the case of mixed explosive to be different to the case of pure explosive. TNT/RDX experimental temperature profiles are shown in Fig. 5. Comparing these curves with those for RDX we confirm that the radiation of the mixture doesn't possess non-thermal properties. From this viewpoint the results are very much alike those obtained with TNT samples. But on the other hand it's evident that the shape of the temperature time history, when LiF was used, is of an intermediate character. The experimental data were determined in the same manner as in the case of pure TNT.

To some degree HMX is quite similar to RDX, but it has a higher density. Experimental data handling was made in the same way as for RDX pressed. The obtained data are presented in Fig. 6. The experiments with HMX have proved our assumption that the radiation of brittle explosives such as RDX or HMX may be of non-thermal character. The  $T_{cj}$  and  $G$  values coincide very closely in spite of the difference between the peak temperatures. It is important to

point out that having practically the same density and the same atomic composition, there is a distinction between agate-like RDX and HMX  $T_{cj}$  and  $G$  values.

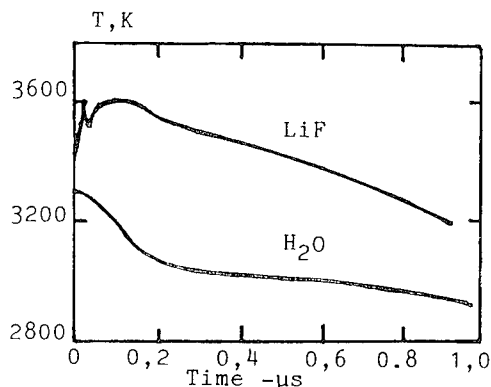


FIGURE 5. TEMPERATURE TIME HISTORIES OF RDX/TNT DETONATION PRODUCTS

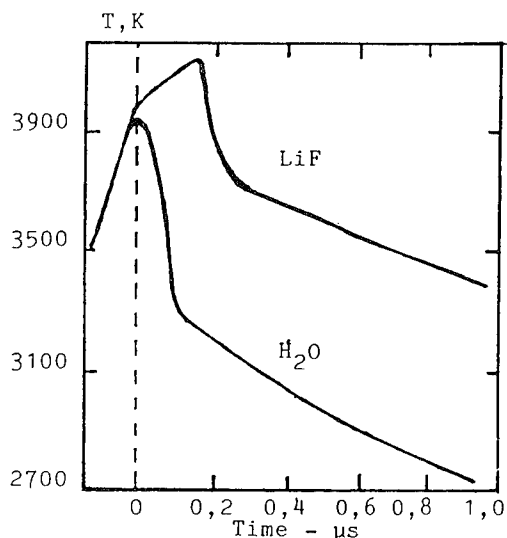


FIGURE 6. TEMPERATURE TIME HISTORIES OF HMX DETONATION PRODUCTS

The detonation mechanism of the explosives discussed above may be considered, to some extent, as a one-step process. This means that the rate of decomposition is too high to be indicated by the optical pyrometer, and that the detonation products may be treated as a mixture of inert materials. The real process is more complicated and this may be seen from the obtained results. But the simplification permits to calculate the  $T_{cj}$  values that are in good agreement with the present-day knowledge on detonation. And it's erroneous to base on this assumption when the explosives with wax (or with any other flegmatizing additive) are treated. The detonation process may be

considered as a two-step one. The first step is RDX decomposition, accompanied by heat release. This is a fast process to be indicated by our set-up. The second step is a stage of the additive destruction, accompanied by energy absorption. This is a slow process and its duration may be more than the observation time. The window material may affect on the two-step decomposition. Thus, the previous data handling couldn't be applied for these experiments. A number of anvils were utilized in order to investigate the materials affect the temperatures time histories. The experimental curves for the RDX with wax tests are shown in Fig. 7; the lower is the shock impedance of an anvil, the higher is the peak temperature observed. This means that the peak value is influenced by the material of the anvil; in this way, the rarefaction diminishes the rate of additive decomposition, i.e. rate of energy absorption. The peak of radiation doesn't correspond to the detonation wave passage through the interface. There is another problem if the wax screens the non-thermal radiation either totally or partially. One may point out that it's impossible to determine the  $T_{cj}$  value in the way, it was done before since the value itself is uncertain to some extent. The peak temperatures are the following: water - 3750 K, glycerol - 3640 K, glass - 3500 K, LiF - 3400 K.

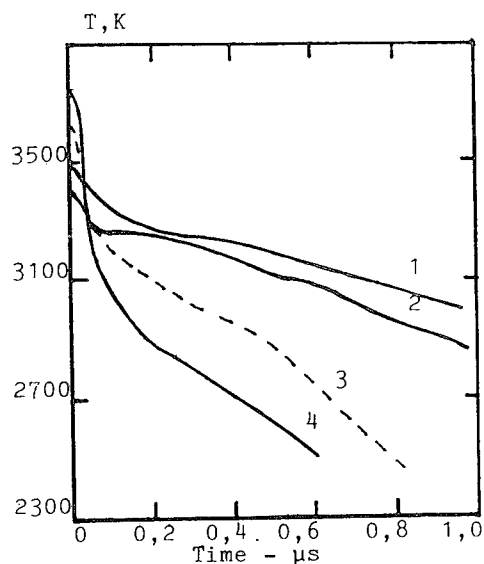


FIGURE 7. TEMPERATURE TIME HISTORIES OF RDX WITH WAX DETONATION PRODUCTS  
Anvils used: 1 - glass; 2 - LiF; 3 - glycerol; 4 - water.

It was possible to carry out only one test with HMX with wax mixture because of the small quantity of the material available. The test was made with LiF anvil. The experimental curve was very much like that obtained for the RDX with wax tests shown in Fig. 7.

The peak temperature was determined as 3550 K, and the "afterpeak" temperature is about 3350 K.

The experiments with NM (with different anvils used) showed the fall in the radiation, after the detonation products had interacted with any window material utilized. The only increase reported,<sup>17</sup> when sapphire had been used, was followed by the same drop in radiation. Several explanations have been supplied for the effect.<sup>14, 17, 18</sup> The detonation decomposition in the case of NM is too complicated to consider the interaction between NM detonation products and the anvil as an interaction of the anvil with some inert material. This point may be illustrated by the obtained results in Fig. 8. The curve for the test with LiF anvil lies lower, than that for the glass anvil. There is some analogy to the RDX with wax experiments, i.e. the anvil-detonation products interaction results to the processes affected, by the material of the window used. On the other hand, the drop in the radiation may be due to the cellular structure of the detonation front and, in this way, the determined front temperature (3700 K) is the result of temperature averaging over the area observed. Both ideas describe the same real process, but from different points of view and the problem is to correlate them. The ambiguity in the value of the detonation

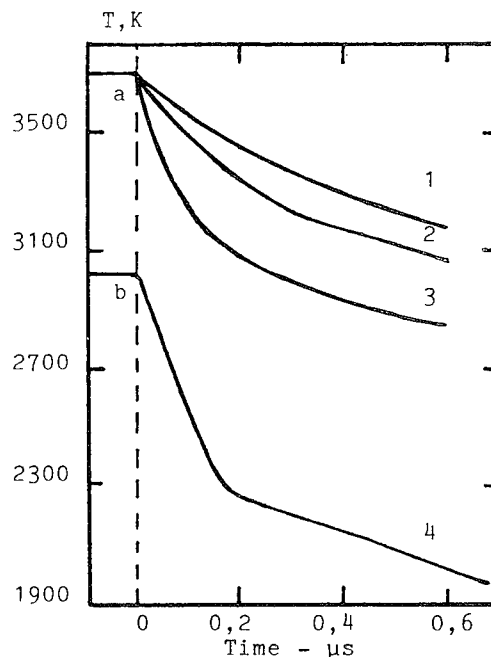


FIGURE 8. TEMPERATURE TIME HISTORIES OF NM (a) AND MOLTEN TNT (b) DETONATION PRODUCTS.  
Anvils used: 1 - glass; 2 - LiF; 3 - water; 4 - PMMA.

front temperature of NM (3200 K - 3800 K) may be explained by the grade of NM. The temperature of chemically pure NM is about 3700 K and that of commercial grade explosive is about 3400 K.

(3030 K) - Detonation Front Temperature.

Molten TNT was investigated with a PMMA anvil used. The experimental data are presented in Fig. 8. The detonation front temperature 3030 K is equal to the value determined in the Los Alamos Laboratory.<sup>19</sup>

All obtained data are listed in Table 2 and in Fig. 2 through Fig. 8.

In order to compare these results with those reported,<sup>14,15</sup> additional information is required. It is necessary to put the experimental data, the test condition and the applied methods of calculation to one-to-one correspondence. But this task seems to be impracticable because of the little information that can be extracted from the papers published.

#### NON-THERMAL LUMINOSITY

The idea of non-thermal radiation is closely related to the effect of the initial explosive structure on the detonation process and its temperature. One may assume that the detonation temperature of the perfect crystal is lower than the temperature of the heterogeneous compound of the same density. This assumption may be supported by the fact that less heterogeneous samples of RDX (agate-like) have less  $T_{cj}$  and  $G$  values. Two-step process may be proposed to describe this phenomenon. During the first stage the brittle RDX crystals being shocked are undergoing deformation and shake-down as a physical matter, the chemical decomposition is just being initiated. Non-thermal luminosity may be emitted during the "physical" decay of crystals as if they are the inert material. If the explosive has detonated, this means, in any way, that the crystals were broken-down. That is, the non-thermal radiation intensity isn't practically effected by

the detonation regime. The chemical decomposition (and the energy release), mainly, take place during the second step. When adding the fine carbon black powder to the RDX, the crystals become coated by the soot. The luminosity caused by crystals "cracking" is screened by this black coating. Carbon black is also a good lubricant and it may diminish the friction between crystals. Frictions, deformations, and "cracking" may be the possible causes of non-thermal radiation. During the second step the powder is being uniformly distributed in the volume, and its role is defined by the volume content.

Partially these assumptions were proved by the tests carried out with the thin RDX pressed pellets of 3 mm thick, with LiF anvils used. The detonation was initiated by the TNT charges of 1,60 and 1,35 g/sm<sup>3</sup> density. The measured peak values were practically the same as those measured for RDX pressed samples (long). The "afterpeak" temperatures fall down till the values 3400 K, 3200 K respectively.

The problems dealt with the interpretation of detonation front temperatures determined and temperature time histories observed are still unsolved; an attempt to calculate Gruneisen parameter for molten TNT, when PMMA anvil was used, has been unsuccessful. Basing on the value of detonation front temperature, that was assumed to be the  $T_{cj}$ , and on the value of the temperature of detonation products under rarefaction, the  $G$  parameter was calculated; the obtained value was too high.

#### SUMMARY

The results on solid and liquid explosives have demonstrated the advantages of the "window" technique utilizing anvils with different shock impedances, for study of the detonation products temperature in C-J point. The detonation products temperature of flegmatized explosives (explosives with wax), and decomposition of the additive were also studied with the help of this technique. It was shown that it would

TABLE 2. EXPERIMENTAL RESULTS

NAME	DENSITY (g/cc)	ANVIL	Pr (GPa)	Tr (K)	Pcj (GPa)	Tcj (K)	G
TNT	1.60	LiF water	25.9 14.1	3600 2500	20.3	3140	1.64
	1.45	PMMA	14.5	2400	17.2	(3030)	3.51
RDX	1.71	LiF water	37.5 20.3	3850 3450	31.4	3740	0.48
	1.80	LiF water	42.0 22.6	3550 3400	36.1	3520	0.19
TNT/RDX	1.67	LiF water	30.4 16.4	3600 3100	25.4	3460	0.65
HMX	1.80	LiF water	42.0 22.6	3800 3380	36.1	3700	0.50

be erroneous to interpret the detonation front temperatures observed as the temperature in C-J point without any additional assumptions.

#### ACKNOWLEDGEMENT

We would like to thank Prof. I.M. Voskobionikov for helpful discussions.

#### REFERENCES

1. Boyer, R.L., "Determination of Detonation Temperature in High Explosives," *Physical Review*, Vol. 74, No. 9, 1948, p. 1227, H8.
2. Gibson, F.C., et.al., Burmines Progress Report July 1, 1953 to June 30, 1955, Ordn Project TB-2-001, Army Project 599-01-004.
3. Gibson, F.C.; Bowser, M.L.; Summers, C.R.; Scott, F.N.; and Mason, C.M., "Use of an Electro-Optical Method to Determine Detonation Temperatures in High Explosives," *Journal of Applied Physics*, Vol. 29, No. 4, 1958, pp. 628-632.
4. Voskobionikov, I.M. and Apin, A.Ya, "Measurement of Detonation Front Temperature for Explosives," *Dokl.Akad.Nauk SSSR*, Vol. 130, No. 4, 1960, pp.804-806.
5. Kologrivov, V.N.; Anchurov, A.A., "Investigation of the Detonation Wave Emission Spectrum by the Spectrograph SP-75," *Usp. Nauchn, Photogr.*, Vol. 9, 1964, pp. 236-242.
6. Dremine, A.N. and Savrov, S.D., "Emission Spectrum of Detonation Wave in Nitromethane," *Zh. P.M.T.F.*, No. 1, 1965, pp. 103-105.
7. Trofimov, V.S. and Trojan, A.V., "Detonation Luminescence Spectrum of Nitromethane," *Fiz. Gor. i Vzry.*, Vol. 5, No. 2, 1969, pp. 280-282.
8. Zel'dovich, Ya.B.; Kormer, S.B.; Urtin, V.D., "Non-Equilibrium Luminosity of Shocked Compressed Crystals,  $T > 1$  eV," *Z.E.T.F.*, Vol. 55, No. 5, 1968, pp. 1631-1639.
9. Brooks, W.P., "Shock-Induced Luminescence in Quartz," *J.Appl. Phys.*, Vol. 36, No. 9, 1965, pp. 2788-2790.
10. Brannon, P.J.; Konrad, C.; Morris, R.W., et.al, "Studies of the Spectral and Spatial Characteristics of Shock-Induced Luminescence from X-Cut Quartz," *J.Appl.Phys.*, Vol. 54, No. 11, 1983, pp. 6374-6381.
11. Gogulya, M.F. and Brazhnikov, M.A., "The Radiation of Polycrystalline  $\text{NH}_4\text{Cl}$  and  $\text{NaCl}$  Samples under Shock Wave Compression," *Zh. Tekhnicheskoi Fiziki*, Vol. 61, No. 6, 1991, pp. 69-75.
12. Akimova, L.N.; Gogulya, M.F.; Galkin, B.N., "Detonation Parameters of the Low-Dense Condensed Explosives," *Fiz. Gor. i Vzry.*, Vol.14, No. 2, 1978, pp. 135-141.
13. Kato, Y. and Brochet, C., "Detonation Temperatures of Nitromethane Aluminum Gels," in *Dynamics of Shock Waves, Explosion and Detonation, Progress in Astronautics and Aeronautics*, New York, Vol. 94, AIAA, 1984, pp. 416-426.
14. Kato, Y.; Mori, N.; Sakai, H.; Tanaka, K.; Sakurai, T.; Hikita, T., "Detonation Temperature of Nitromethane and Some Solid High Explosives," *Preprint Eight Symposium (International) on Detonation*, New Mexico, Albuquerque, Convention Center Albuquerque Conf-85076, Vol. 1, July 15-19 1985, pp. 314-321.
15. He Xianchu; Han Chengbung and Kang Shufong, "The Measurements of Detonation Temperature of Condensed Explosives with Two Colour-Optical Fiber Pyrometer," *Preprint Eight Symposium (International) on Detonation*, New Mexico, Albuquerque, Convention Center Albuquerque, Conf-85076, Vol. 1, July 15-19 1985, pp. 322-329.
16. Paterson, S., "Source of the Light Recorded in Photographs of Detonating Explosives," *Nature*, Vol. 167, No. 4247, 1951, pp. 479-481.
17. Sorokin, S.B., "The Measurement of Detonation Products Temperature of Liquid Nitromethane Mixtures with Acetone," in *Proceedings of the High-Speed Mechanics*, Siberian Division USSR Academy of Sciences, Institute of Hydrodynamics, Novosibirsk, 1984, pp. 120-130.
18. Kato, Y.,; Bourianes, R. et Brochet, C. "Mesure de temperature de luminance des detonations d'explosifs transparents et opaques," in *Proc. of H.D.P. Symp.*, CEA, Paris, 1979, pp. 439-449.
19. Mader, C.L., "Numerical Modeling of Detonations," *Moscow, "Mir"*, 1985, p. 56

## TEMPERATURE MEASUREMENTS OF ENERGETIC MATERIALS CONTAINING ALUMINUM USING INFRARED DETECTORS

Diana L. Woody  
Naval Surface Warfare Center  
Silver Spring, MD 20903-5000

Jeffery J. Davis  
Department of Physics  
The American University  
Washington, DC 20012

This paper will discuss the results of the addition of aluminum on the reactivity and time of reaction of an energetic material. This experiment compared the infrared light emitted from the impact of a non-aluminized energetic material to that of a sample containing aluminum. The light emissions were used to approximate the temperatures of the reactions taking place in the impacted energetic samples. It was noted in these experiments that a 5  $\mu$ s delay existed in order for the aluminum to come into the reaction. The sample containing no aluminum showed a slower, more steady burning rate.

### INTRODUCTION

Metals are added to energetic compositions in order to obtain a higher amount of energy release from the original material. In the experiment of this paper, the effect of the addition of a metal to an energetic material was studied. The metal additive for this experiment was aluminum of 80  $\mu$ m particle size. The method of determining reaction was from the light emissions generated from the impacted energetic material samples. Comparison of intensity of emission vs. time plots registered the relative change in reactivity of the aluminum-containing sample to that of the sample containing no aluminum additive. The samples were impacted at low velocities with a small scale impact machine. The light emissions were observed with a two color infrared detector system. The emittance from the reacted sample was analyzed with Planck's equation in order to determine the temperature of the aluminum reaction.

In previous experiments the light emanating from the impacted sample was observed from the side of the sample. These studies showed that there was a 5  $\mu$ sec delay for the aluminum to take a part in the reaction.<sup>1</sup> Our results agree with those of large scale experiments. Cylinder tests have been

performed at the Lawrence Livermore National Laboratory by M. Finger et al. to study the detonability of the various materials depending upon the presence of aluminum.<sup>2</sup>

The results from the data of this paper indicate that there was a 5  $\mu$ s delay for the aluminized sample to show an appreciable temperature rise and for the aluminum to take a part in the reaction of the impacted material. This was indicated by the rapid rate increase of brightness release for the aluminized sample in comparison to that of the non aluminized sample. The sample containing no aluminum, on the other hand, showed a slower and steadier increase in temperature over time as evidenced in the temperature profile.

### EXPERIMENT

The experiment of this paper viewed the impacted sample from the sample's bottom face through a sapphire anvil. The emissions were limited to the cutoff wavelength of the sapphire anvil (6  $\mu$ m). Performance of the experiment with this limiting parameter gave a value that fell onto Planck's emittance curve thus giving an approximate temperature value for the aluminum reaction of each energetic material sample.

The impact of the crystal was obtained with the use of a drop weight and impact machine. The impact machine consisted of an anvil, drop weight, base, and release triggering device. The impact machine is described in detail in another publication.<sup>3</sup> The drop weight used was .377 kg. The distance from the bottom of the drop weight to the anvil of the impact machine was 157 cm. This height corresponded to the free fall velocities of 5.5 m/s.

The drop weight was designed to allow it to be accelerated to high velocities. Two holes on the outer rim through which the guide rails were run allowed for guided impacts in which the face of the drop weight was flat against the sample face upon impact. The tilt of the drop weight was less than 2 mrad.

Two energetic materials were used. These were PBXW-113 and PBXW-114. Both samples contained HMX and binders. PBXW-114 contained also aluminum powder. The energetic material sample was a cylinder disk typically 1.25 mm thick and 5 mm in diameter. The mass of the samples was between 35 mg to 45 mg.

The sample was placed on a sapphire anvil. The sapphire anvil was capable of transmitting infrared emissions ranging from the visible range out to six microns in the mid-infrared spectrum. The infrared transmission from the sample on the anvil was reflected by an Edmund Scientific gold front faced mirror, model # f32085 placed underneath the anvil, in the base, at a 45 degree angle to the anvil. The focusing lens was a Janos #A0707-112 barium fluoride infrared transmitting lens of diameter 2.5 centimeters. A two color infrared detector received the focused light. The experimental set up is shown in Fig. 1.

The Infrared Associates two color infrared detector consisted of a HgCdTe element and an InSb element. The field of view of the detector is 180 degrees. The InSb element was situated in front of the HgCdTe element so that the same unit area of flux of radiation was observed per element. The detector elements are constructed in the form of a sandwich which permits both elements to be near the focal plane of the instrument. Each element had dimensions of 0.101 cm by 0.101 cm with an active area of .010201 cm<sup>2</sup>. The detectors were housed in a liquid nitrogen cooled dewar and kept at an operating temperature of 77 K. The InSb element's spectral response was from 1  $\mu$ m to 5  $\mu$ m. The HgCdTe element was capable of detecting wavelengths from 5.5  $\mu$ m to 12  $\mu$ m but was wavelength limited to 6  $\mu$ m by the use of the sapphire anvil.

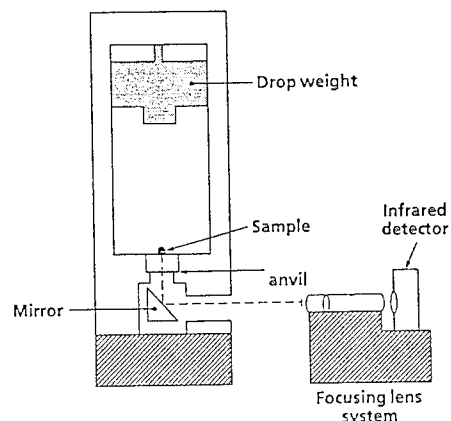


FIGURE 1. EXPERIMENTAL SETUP

The signal from each infrared detector was transmitted in the form of a voltage through an initial voltage amplifier and transferred to a 9424 LeCroy digital oscilloscope to be stored and transferred to a computer for further analysis and image reconstruction.

An accelerometer was used to trigger the acquisition of data from the oscilloscope upon impact. The accelerometer was placed inside the base of the hollowed out drop weight. This position presented the smallest delay in time between the impact of the drop weight and the triggering of the oscilloscope. By measuring the change in acceleration of the drop weight upon impact, the accelerometers were also used to determine the change in velocity of the drop weight by integrating the accelerometer trace on the digital oscilloscope.

## DATA ANALYSIS

Many experiments were performed. The results of two are shown. Figures 2 and 3 show graphs of infrared emission, measured as voltage vs time for the aluminized and non-aluminized samples. Figures 2a and 2b show the emission registered by the HgCdTe and InSb elements of the infrared detector for the reaction of the energetic sample containing no aluminum. Figures 3a and 3b show the emission registered by the HgCdTe and InSb elements of the infrared detector for the reaction of the energetic sample containing the aluminum additive.

The emission data from the two color detector was used along with the Planck's emittance equation to obtain an approximation of the temperature of the light emitted from the impacted sample. The

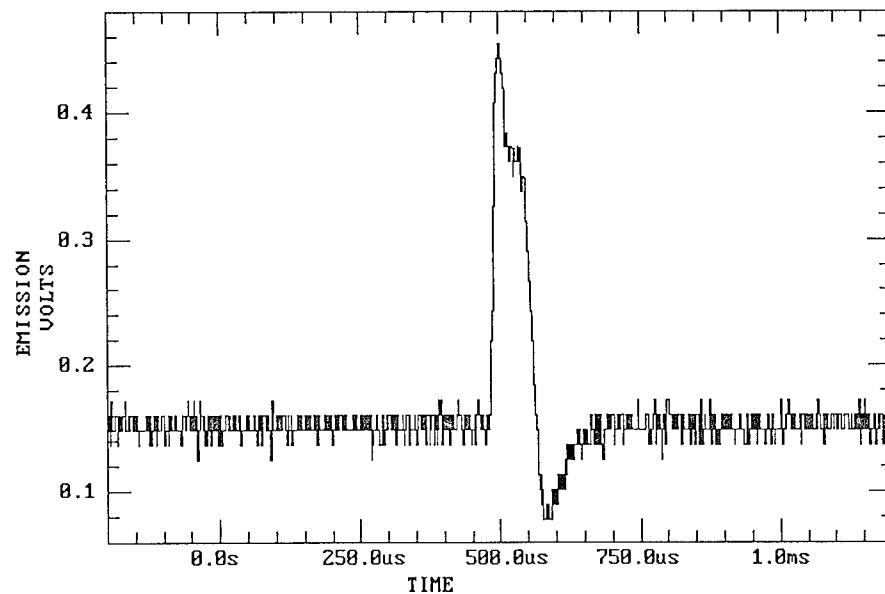


FIGURE 2A. EMISSION FROM HGCDTE ELEMENT FOR SAMPLE WITHOUT ALUMINUM

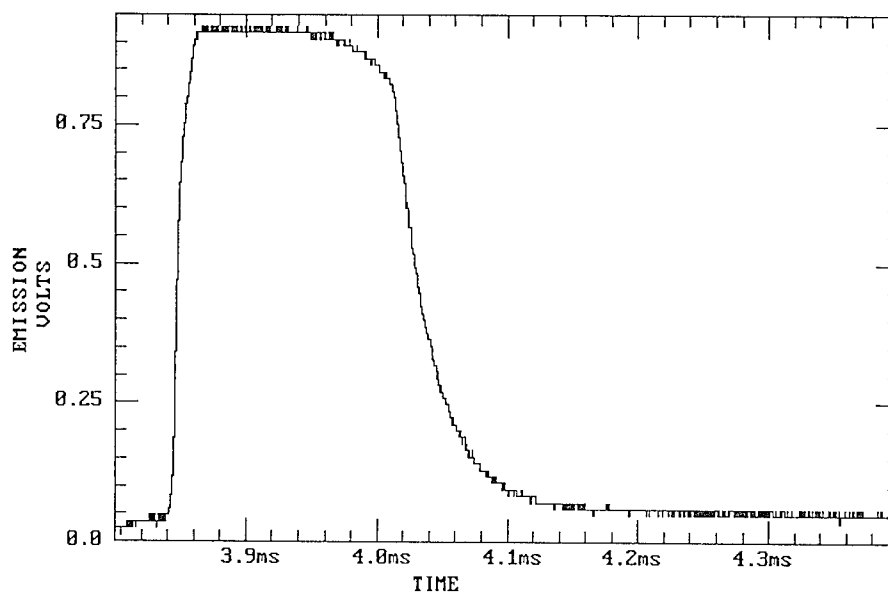


FIGURE 2B. EMISSION FROM INSB ELEMENT FOR SAMPLE WITHOUT ALUMINUM

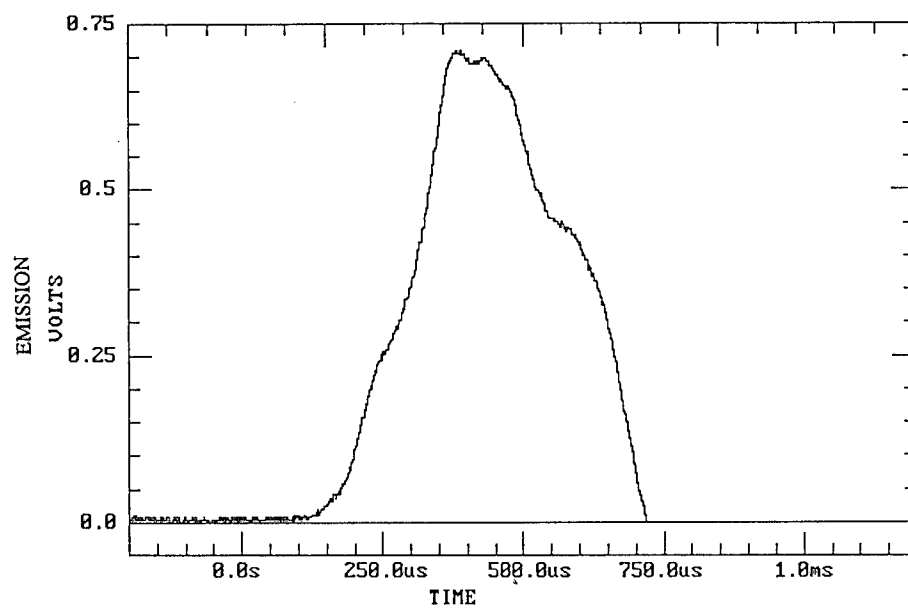


FIGURE 3A. EMISSION FROM HGCDTE ELEMENT FOR SAMPLE WITH ALUMINUM

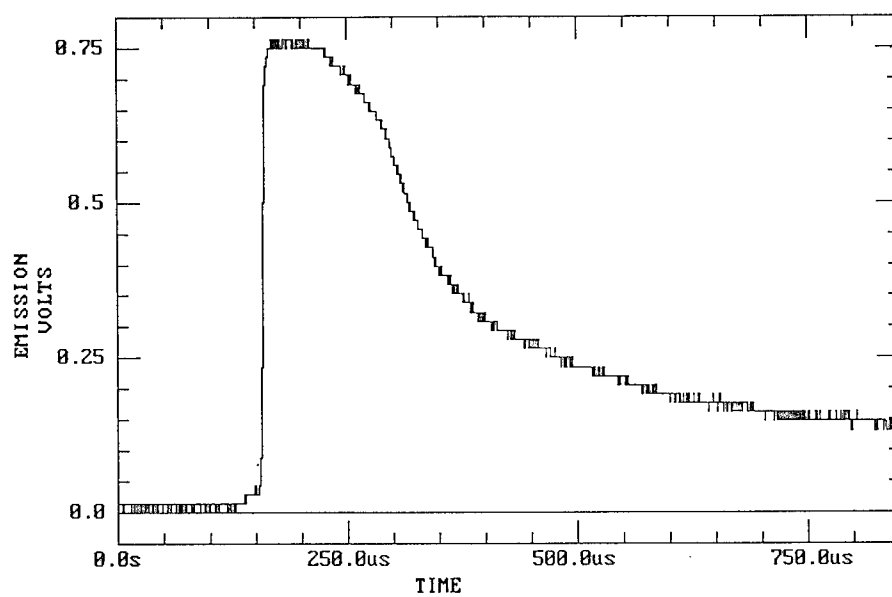


FIGURE 3B. EMISSION FROM INSB ELEMENT FOR SAMPLE WITH ALUMINUM



spectral radiant emittance equation is as follows from Planck's equation:

$$I_{\lambda} d\lambda = \frac{c_1}{\lambda} \left[ \frac{1}{e^{\left[ \frac{c_2}{\lambda T} \right]} - 1} \right] d\lambda \quad (1)$$

where

$$c_1 = 2\pi c^2 h = 3.74 \times 10^4 \text{ watts } \mu^4 / \text{cm}^{-2} \quad (2)$$

and

$$c_2 = \frac{ch}{k} = 1.44 \times 10^4 \mu \text{K} \quad (3)$$

This equation defines the flux of radiation into a hemisphere per unit area of source measured in Watts/cm<sup>2</sup>.<sup>4</sup>

Given the spectral range of the detector and the cutoff wavelength of the sapphire anvil, the equation was integrated over the 1 $\mu$ m to 6 $\mu$ m range. Since the InSb detector element is situated on top of the HgCdTe element, the area and amount of emission observed by each detector is the same. The ratio of the two emittance values observed by the InSb and the HgCdTe, R(T), was used along with Planck's equation to obtain approximate temperatures over time for the impacted energetic samples. This

eliminates the dimension factors as well as emissivity since I = flux of radiation per unit area of source in Watts/cm<sup>2</sup>.

A wavelength limited curve of temperature vs time was plotted for the first 20  $\mu$ sec of the reaction. This gives an approximate temperature profile over time for the reaction of the energetic samples. Figure 4 shows the temperature profile of the impact of the energetic material containing no aluminum additive and the energetic material containing an aluminum additive.

## CONCLUSIONS

The wavelength limiting experiment using a sapphire anvil at a cutoff wavelength showed that it was possible to approximate the temperature for the reaction if the approximation is limited to the near infrared range. The temperature profile of the impacted energetic materials gives an indication of the behavior of the materials during impact and the subsequent reaction. The sample containing no aluminum shows a steady temperature rise over time. The sample containing aluminum shows a peak emission after 5  $\mu$ sec and then a gradual cooling over time. Thus, the aluminum takes 5  $\mu$ sec to take part in the reaction.

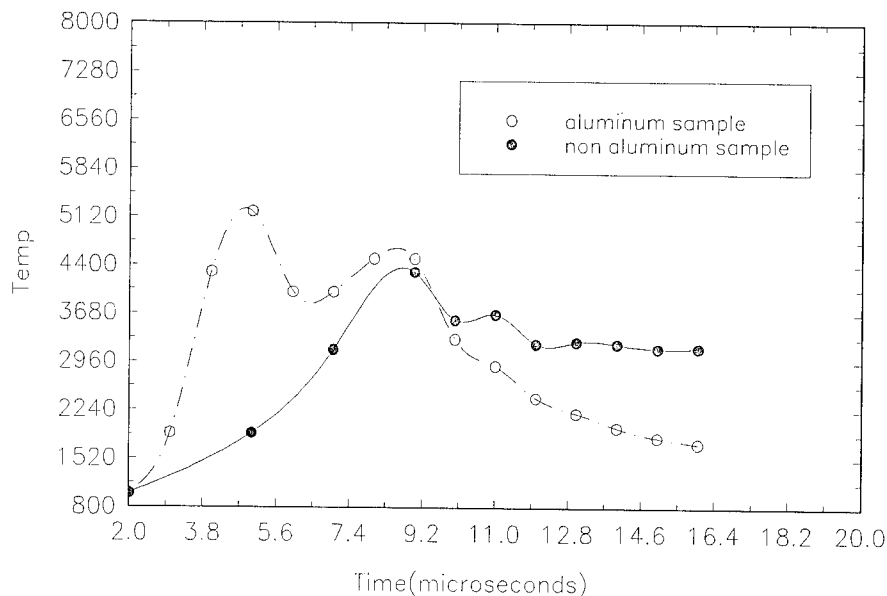


FIGURE 4. TEMPERATURE PROFILE FOR IMPACTED SAMPLES

## ACKNOWLEDGEMENTS

This research was performed under the sponsorship of the Independent Research program at the Naval Surface Warfare Center, Silver Spring, MD.

## REFERENCES

1. Woody, D. L.; Davis, J. J. and Coffey, C. S.; "Comparison of Infrared Emission from Impacted Aluminum to Non Aluminum Containing Energetic Materials," Proceedings of JANNAF Hazards Meeting, White Oak, MD, April 1992.
2. Finger, M.; Helm, F.; Lee, E.; Boat, R.; Cheung, H.; Walton, J.; Hayes, B. and Penn, L.; "Characterization of Chemical Explosives," Sixth Symposium on Detonation, Coronado, CA, August 1976.
3. Coffey, C. S.; Devost, V. F. and Woody, D. L.; "Towards Developing the Capability to Predict the Hazard Response of Energetic Materials Subjected to Impact," Ninth International Symposium on Detonation, Portland, OR, September 1989.
4. Jamieson, J. A., Infrared Physics and Engineering, McGraw-Hill Book Company, New York, 1963.

---

## DISCUSSION

THOMAS B. BRILL

University of Delaware, Newark, Delaware

Your peak temperature of 6000K for samples with Al is very high. The maximum adiabatic flame temperature reached by combustion of Al with organic oxidizers rarely exceeds 3000K. How do you account for the very high temperature assigned in your experiment?

### REPLY BY DIANA WOODY:

Previous calculations of the CJ parameters vs. Al concentration for energetic materials containing oxygen have shown that the typical temperatures for the reaction exceed 4000K. Refer to J. D. Jones and F. Zerilli, "Theoretical equation of State for Aluminized Nitromethane," *Journal of Applied Physics* 69 (7), 1 April 1991. Experimental data have shown similar results.

## DISCUSSION

PROFESSOR PASCAL BAUER

ENSMA, Poitiers, France

The experiments deal with brightness temperature measurements. They can be linked to thermodynamic temperature of the products provided one has an accurate knowledge of the value of the emissivity factor, because one may likely expect to get a grey body radiative behavior. How did you calibrate your setup in order to interpret such discrepancy?

RICHARD H. GRANHOLM

Dyno Nobel, Inc., West Jordan, Utah

How were you able to calibrate your system for temperature?

### REPLY BY DIANA WOODY:

For calibration, basically the optical setup was similar to that described for the impact study except that a variable temperature heat source was placed on the anvil simulating the infrared emission from the impacted crystal. A chopper wheel was placed in between the path of the signal and the infrared detector. The oscillating infrared signal from each detector element (InSb and HgCdTe) was registered as a voltage by the infrared detectors. The ratio of the InSb signal to that of the HgCdTe signal was calculated for each temperature measurement.

## DISCUSSION

DR. DIVYAKANT L. PATEL

Countermines Systems Directorate, U. S. Army,  
Fort Belvoir, Virginia

What type of aluminum is used in this experiment?

### REPLY BY DIANA WOODY:

An 80 micron aluminum was used.

## DISCUSSION

PHILLIP D. LIGHTFOOT

ICI Explosives, McMasterville, Quebec, Canada

How do you know if the emission from the sample is characteristic of a black body?

### REPLY BY DIANA WOODY:

It is assumed that emission resembles a grey body.

## LASER IGNITION OF EXPLOSIVES: A LIF STUDY OF THE RDX IGNITION ZONE

H. Östmark, K. Ekvall, M. Carlson, H. Bergman and A. Pettersson  
National Defence Research Establishment  
S-17290 Sundbyberg, SWEDEN

*This paper describes a method that combines laser ignition technique with laser induced fluorescence spectroscopy for studying the gas phase products in an ignition zone and the reactions that leads to a self sustained ignition. The experimental set-up consists of a tunable CO<sub>2</sub>-laser as ignition source, an excimer pumped dye-laser for inducing the fluorescence and a spectrometer equipped with an optical multichannel analyzer. This technique was used for measurements of relative NO and CN concentrations in the sub-ignition zone of RDX in pseudo-real time (time resolution better than 1  $\mu$ s). By using LIF technique for measuring the relative population of different vibrational levels, we were able to calculate the temperature in the gas phase reaction zone in front of the sample at sub-ignition to approximately 3100 K. Our measurements showed clearly that the chemical reactions in the sub-ignition zone play an important part long before a self-sustained reaction occurs, and thus influence the sensitivity of an explosive.*

### INTRODUCTION

In order to obtain a more detailed and fundamental understanding of the molecular level processes eventually leading to ignition, methods capable of making real time measurements of concentration, decomposition intermediates and temperature in the ignition zone have to be available. Slow thermal decomposition of High Explosives (HE) has been successfully studied with many methods, e.g. infrared multi-photon absorption in molecular beams,<sup>1</sup> thermal induced pyrolysis combined with mass spectroscopic detection,<sup>2-6</sup> FTIR spectroscopy,<sup>7</sup> measurements of the kinetic isotope effect by DSC,<sup>8</sup> emission spectroscopy,<sup>9</sup> STMBMS<sup>10</sup> and X-ray photoelectron spectroscopy.<sup>11</sup> These methods have mostly been used to study the thermal decomposition itself and then mainly the initial step of the decomposition, not the successive processes that leads to a self-sustained ignition. Very little work has been devoted to the study of processes in the sub-ignition/ignition zone.<sup>5,9,12,13</sup>

Laser Induced Fluorescence (LIF) spectroscopy has shown a large potential for combustion diagnostics<sup>14,15</sup> and has also been used in studies on propellant flames.<sup>16</sup> This paper shows how the Laser Ignition (LI)

method developed earlier<sup>5,17-19</sup> can be used in combination with LIF spectroscopy to study the sub-ignition/ignition reaction zone and to monitor changes in the products formation during the transition from slow thermal decomposition to a self-sustained deflagration, as well as for studying the chemical reactions occurring in an ignition zone. A concise survey of the possibilities for ignition studies offered by the LIF technique is also given.

All HE have an endothermic initial step (they are stable at room temperature), but for the development of a self-sustained reaction a switch-over to a set of exothermic reactions has to take place. This leads to the need of developing methods where all processes from a slow decomposition to the ignition of a self-sustained reaction can be studied. Earlier work on LI has shown this to be a very useful method for studying the influence of different parameters on the ignition of a pyrotechnic composition.<sup>18</sup> This method applied to HE has shown that the ignition energy is highly pressure dependent.<sup>17</sup> Similar results have been demonstrated for propellants<sup>20,21</sup> and pyrotechnics<sup>22,23</sup>. This indicates that the ignition process is a multi-phase process. In an earlier LI work<sup>17</sup> it has been shown that the ignition energy of an HE has two pressure regimes;

one at low pressure, where the ignition energy strongly depends on the pressure and one at high pressures (above 3 MPa), where the ignition is only slightly pressure dependent. This clearly demonstrates the necessity of being able to study the ignition processes at pressures of up to at least 4 MPa. At the same time it was shown that the ignition energy was different in air and in nitrogen, which shows the necessity of developing a method where different gases may be used at ambient and increased pressure. The explanation proposed for this behavior was that a multi-phase ignition takes place where both the gas and condensed phases have to interact in order to start a self-sustained reaction.

A brief summary of the literature on the decomposition process for RDX is presented elsewhere in this Symposium and will be used to facilitate the interpretation of the data acquired by the combination of LI with LIF in this paper.

#### LASER INDUCED FLUORESCENCE SPECTROSCOPY

LIF is based on laser excitation of atoms or molecules from the ground state to an excited electronic state. After a short time (from a few ns to some tens of  $\mu$ s) the atom or molecule reemits radiation which can be analyzed, and information on temperature<sup>24,25</sup> as well as concentration<sup>26</sup> may be deduced. Since the ground state, responsible for the excitation, is definite and the fluorescence from the corresponding upper state also occurs from definite vibrational and rotational levels, the selectivity using LIF is considerable. The LIF technique can also be used for imaging concentration<sup>27,28</sup> or temperature.<sup>29</sup> in one or two dimensions. Table 1 contains a collection of some of the species which have been detected at combustion and which could have some interest in ignition studies. The principle of LIF and an example of a LIF set-up can be seen in Figure 1. The experimental conduction of a LIF measurement is not complicated: the laser (normally an excimer or YAG pumped dye laser) is tuned to the absorption line and focused onto the sample, and the emitted LIF signal is detected, at right angles, using a scanning monochromator or a spectrometer, preferably equipped with an Optical Multichannel analyzer (OMA).

The advantage of LIF over conventional absorption spectroscopy is that instead of measuring a small dip in a large transmitted signal, a positive signal is measured against nearly zero background. Compared with emission spectroscopy this signal is up to  $10^6$  times larger. This enables the use of LIF technique for the

study of very fast processes and in strongly luminating systems such as high explosives. The use of LIF technique also has some disadvantages. Part of the relaxation occurs through non-radiative transitions, quenching, which leads to difficulties with the absolute determination of concentration as well as problems with the study of molecules with a large lifetime of the excited state as the sensitivity becomes very poor (e.g.  $\text{NO}_2$ ). LIF has its largest potential in the study of small molecules and radicals (composed of up to four or five atoms). LIF is a resonant process so normally only one type of molecule can be studied, but multiple species detection is possible if the absorption wavelength of different molecules coincide, e.g.  $\text{NO}$  and  $\text{NO}_2$ <sup>30</sup> or  $\text{OH}$ ,  $\text{CN}$  and  $\text{NH}$ .<sup>31</sup>

Fairchild and others<sup>32</sup> have developed a laser pyrolysis/laser fluorescence technique for real-time measurements of radicals/molecules in combustion processes, using a  $\text{CO}_2$ -laser and a Nd:YAG pumped dye-laser fired in sequence to monitor the reaction. The delay between the two lasers is controlled and can be varied by two delay generators. This paper presents a variation of this technique for studying the processes taking part in an ignition/decomposition reaction zone for RDX.

The use of LIF technique in the study of ignition processes has a large potential in that it is fast, selective, non-intrusive and enables imaging of both concentration and temperature.

TABLE 1. MOLECULES OF INTEREST IN IGNITION STUDIES WHICH CAN BE STUDIED WITH LIF TECHNIQUES. VALUES IN BRACKETS INDICATE THAT TWO-PHOTON EXCITATION HAS BEEN USED.

Molecule	Absorption wavelength (nm)	Reference
OH	284, 311	[28,34]
CN*	388	[34,35]
NH	336	[31,34]
NCO	399	[15]
$\text{NH}_2$	430-900	[37]
$\text{CH}_2\text{O}$	320-345	[38]
$\text{NO}^*$	226, (2-452)	[30,34]
$\text{NO}_2$	450-470	[26,30]
CH	431	[31,34,35]
N	(2-211)	[36]

\* Denotes that this molecule has been detected in an ignition zone in this paper.

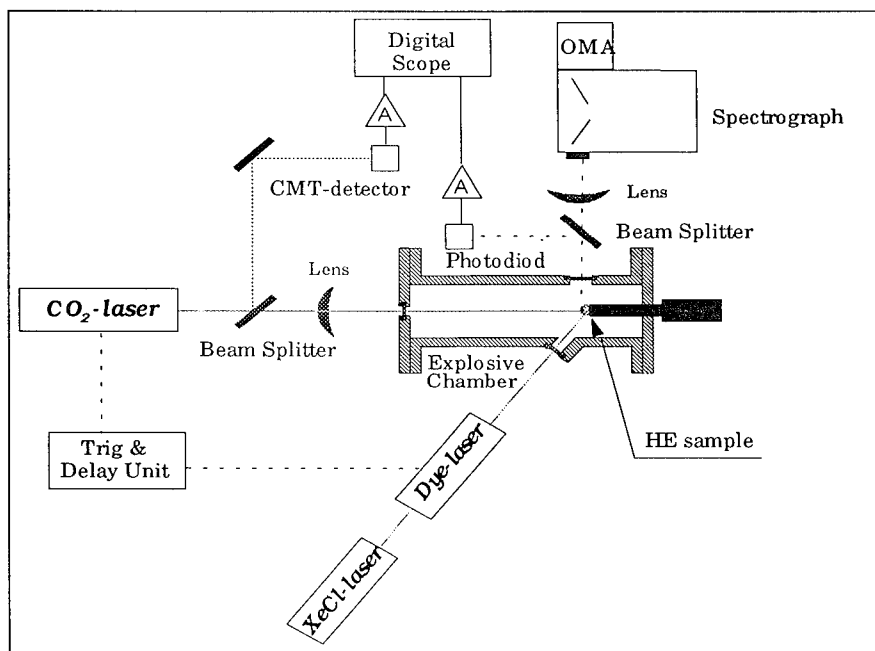


FIGURE 1. APPARATUS SET-UP FOR LASER-INDUCED FLUORESCENCE (LIF) SPECTROSCOPY IN A LASER INDUCED SUB-IGNITION/IGNITION REACTION ZONE

## EXPERIMENTAL

The LI/LIF spectroscopy set-up consists in short of a tunable (9-11  $\mu\text{m}$ ) continuous wave (180 W)  $\text{CO}_2$ -laser (Edinburgh PL6) for inducing the desired reaction (decomposition/ignition) in the HE, an excimer pumped dye laser (Lambda Physik EMG 201E + LPD 3002) for inducing the LIF signal and a spectrometer (Spex 500M) equipped with an OMA (OMA2000 EG&G) for detecting the LIF signal. A schematic overview of the apparatus set-up is shown in Figure 1. The experiments were conducted in the following way: The desired type of reaction was started by focusing the  $\text{CO}_2$ -laser (beam radius 0.25 mm, pulse width 10 ms, power 60 W and wavelength 10.59  $\mu\text{m}$ ) onto the explosive sample (pressed RDX pellets with 90% of the TMD, size 2 by 10 mm). The reaction was then studied by tuning the dye laser to the absorption line for the studied molecule and focusing the beam into the sub-ignition/ignition reaction zone, close to the surface of the pellet (less than 1 mm). The emitted LIF signal was then detected at right angles, using the spectrometer. The power of the  $\text{CO}_2$ -laser was measured by a power meter (Laser Precision Corp. Rk-5720/Rkt-1000-HD) and the pulse form by a Cadmium-Mercury-Telluride (CMT) detector and the total emitted light from the induced reaction was measured by a photo detector. The registration of these quantities was made on a digitizing oscilloscope (HP 54111D). All the

experiments were carried out in air and at atmospheric pressure.

Figure 2 shows an example of a LIF measurement of NO in the sub-ignition reaction zone of RDX. The measurement conditions for this registration were:  $\text{CO}_2$ -laser power 60 W and a pulse width of 10 ms, dye laser energy 3 mJ at 226.1 nm, detector gate width 200 ns and a time delay of 6 ms. When a vibrational transition is saturated, the observed fluorescence intensity is directly proportional to the population of the lower vibrational level prior to laser excitation and hence to the concentration of the molecules. The NO-molecule is excited with 226.1 nm which corresponds to transition  $\text{A}^2\Sigma(v'=0) \leftarrow \text{X}^2\Pi_{1/2}(v''=0)$  and a broad band fluorescence detection is made of transitions to several vibrational levels in the  $\text{X}^2\Pi_{1/2}$ -state. The three peaks to the right probably corresponds to fluorescence from CN and are also laser induced, but there is no direct excitation of these states. It is probably due to collision-induced energy transfer from excited NO molecules.

We also measured CN by exciting the  $\text{B}^2\Sigma(v'=0) \leftarrow \text{X}^2\Sigma(v''=0)$  transition with the dye laser at 388.3 nm, detecting at 421.6 nm, corresponding to the  $\text{B}^2\Sigma(v'=0) \rightarrow \text{X}^2\Sigma(v''=1)$  transition. The LIF signal from CN is shown in Figure 3. An attempt to measure the  $\text{NO}_2$  concentration in the sub-ignition zone failed. Aldén has

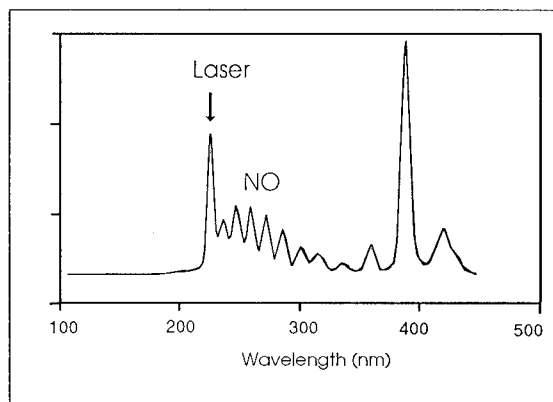


**FIGURE 2. LASER INDUCED FLORESCENCE (LIF) SPECTRUM FROM NO MOLECULES IN THE SUB-IGNITION REACTION ZONE OF RDX**

shown that  $\text{NO}_2$  concentration measurements can be carried out in a flame with LIF techniques.<sup>30</sup> However, using the same technique we were unable to get any reproducible concentration measurements on  $\text{NO}_2$  in the sub-ignition zone. This is probably due to the fact that  $\text{NO}_2$  measurements with LIF technique are very difficult and hard to evaluate.<sup>33</sup> We are instead planing to use a four-wave mixing technique<sup>39</sup> for the  $\text{NO}_2$  measurements.

By firing the  $\text{CO}_2$ -laser and the dye-laser in sequence it is possible to monitor the reaction at a specific time. The delay between the two lasers is controlled and can be varied by a delay generator (Stanford Research inc. DG535). The reaction can hereby be studied in pseudo real time. Figure 4 shows the relative concentrations of NO and CN as functions of time for a 10 ms wide, 60 W  $\text{CO}_2$ -laser pulse. One can here clearly see that during the  $\text{CO}_2$ -laser pulse the concentrations of NO and CN vary, even having a maximum during this time. This indicates that both NO and CN are reaction intermediates formed during the decomposition process, later reacting with other decomposition products or expanding away. Note especially that NO is not one of the normally assumed primary products in the RDX decomposition path.<sup>1-4</sup> This emphasizes the conclusion that when studying ignition (not decomposition) one has not only to consider the decomposition path but also the chemical reactions occurring in the ignition zone. The parts played by NO and CN in the nitramine combustion process are shown in a model by Melius.<sup>40</sup> Our results presented here serve to strengthen the conclusion that long before any self-sustained reaction can occur, the chemical reactions occurring in the sub-ignition zone

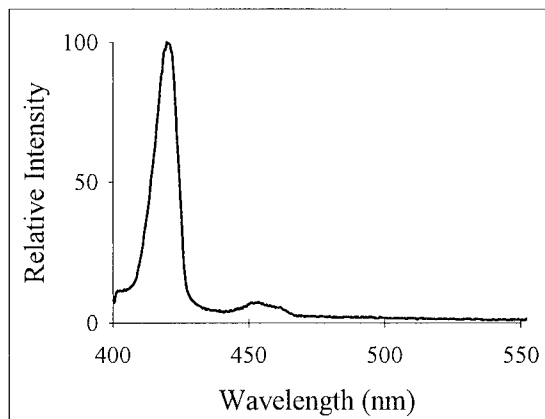


**FIGURE 3. LASER INDUCED FLUORESCENCE (LIF) SPECTRUM FROM CN MOLECULES IN THE SUB-IGNITION REACTION ZONE OF RDX**

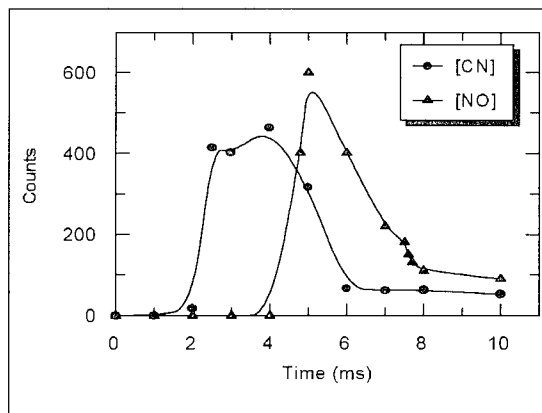


**FIGURE 4. TIME RESOLVED MEASUREMENT OF THE NO AND CN CONCENTRATION IN A RDX SUB-IGNITION REACTION ZONE FOR A  $\text{CO}_2$ -LASER PULSE WIDTH OF 10 MS**

have to be considered if the influences of physical state and chemical structure on the sensitivity of an explosive are to be fully understood.

#### TEMPERATURE MEASUREMENT

The possibility of measuring rotational temperature in a combustion environment has been shown by Lucht and others<sup>41</sup> and Cattolica<sup>42</sup>, who also suggested that the systematic and random errors might be reduced by measuring vibrational temperature instead. This would work because of the greater energy difference between the initial excitation levels. The Boltzman population of the vibrational levels is temperature dependent and this is used to estimate the vibrational temperature.

When a vibrational transition is saturated, the fluorescence intensity is directly proportional to the population of the lower vibrational level prior to laser excitation. By exciting a molecule to the same vibrational level (index notation 2) from two different ground state vibrational levels (index notation 0 and 1) and taking the ratio between the fluorescence intensities, the temperature can be deduced according to Equation 1:<sup>42</sup>

$$R = \frac{\Phi_{f(12)}/I_{12}}{\Phi_{f(02)}/I_{02}} = \frac{B_{12}g_1}{B_{02}g_0} \cdot \exp[-(E_1 - E_0)/kT_v] \quad (1)$$

Where  $\Phi_{f(ij)}$  is the fluorescence intensity from the excitation  $i \rightarrow j$ ,  $I_{ij}$  is the laser intensity at the excitation from  $i$  to  $j$ ,  $g_i$  is the degeneracy of state  $i$ ,  $T_v$  is the vibrational temperature and  $B_{ij}$  is the absorption coefficient from state  $i$  to  $j$ .

The spectral distribution of the fluorescence is identical for both initial levels since the excited level is the same. Any attenuation of the fluorescence by trapping will be identical. Since the laser power is high enough to saturate the fluorescence signal, we can neglect the small fluctuation in laser energy (that is  $I_{02} = I_{12}$ ) and any influence of quenching.

Temperature measurement in a non-stationary environment with two-line LIF technique requires two lasers to excite the two transitions with a small time delay between the two laser pulses (of the order of nanoseconds), enough to separate the fluorescence signals from the two transitions. In our case, though, we measure at a well defined spot in the sub-ignition zone where the conditions are non-turbulent. This enables us to use a single laser twice, for measuring two distinct ignition events. To minimize the influence of fluctuations, a number of measurements are made and the results averaged.

Figure 5 shows an example of the fluorescence intensities of the two different excitations. With the dye laser the NO-molecule is first excited at 226.1 nm ( $A^2\Sigma(v'=0) \leftarrow X^2\Pi_{1/2}(v''=0)$ ) and second at 236.3 nm ( $A^2\Sigma(v'=0) \leftarrow X^2\Pi_{1/2}(v''=1)$ ) and the broad band fluorescence is registered at 200-450 nm. By approximating the NO molecule as a harmonic oscillator, the degeneracy factors ( $g_0$  and  $g_1$ ) can be treated as equal. The emission coefficient  $B_{ij}$  is proportional to  $\lambda_{ij}^3$ , and  $\Delta E = 0.25$  eV. From Figure 5 the ratio of the

fluorescence intensities is calculated to 0.47 with an error,  $\Delta R$ , estimated to 10%. Equation 1 gives us the temperature 3100 K, and  $\Delta T$  is of the same order as  $\Delta R$  (10%).<sup>41</sup>

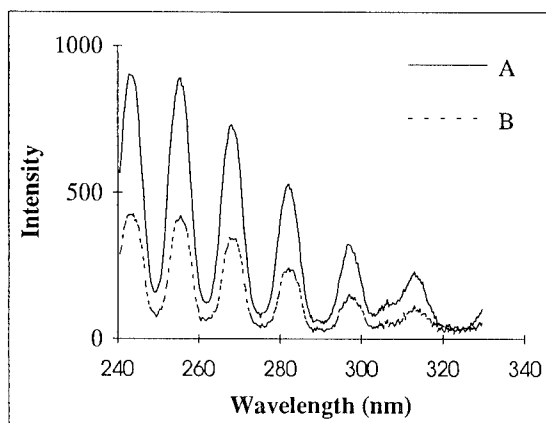


**FIGURE 5. FLUORESCENCE FROM NO EXCITED BY 226.1 NM (A) AND BY 236.3 NM (B) FROM WHICH AN INTENSITY RATIO CAN BE CALCULATED, AND THEN THE VIBRATIONAL TEMPERATURE OF NO IN THE SUB-IGNITION ZONE CAN BE ESTIMATED**

## CONCLUSIONS AND DISCUSSION

The combination of laser ignition with LIF spectroscopy enables the study of the gas phase reactions (e.g. concentration of NO, CN) in a sub-ignition/ignition zone in pseudo real time (time resolution better than 1  $\mu$ s).

The use of LIF technique in the study of ignition processes has a large potential in that it is fast, selective, non-intrusive, and enables imaging of concentration as well as temperature.

The combination of laser ignition technique and LIF spectroscopy clearly showed the importance of techniques able to study the chemical processes/reactions that occur in the sub-ignition zone. Our measurements showed clearly that these reactions play an important part long before a self-sustained reaction occurs and thus influence the sensitivity of an explosive.

This work will be continued in order to establish a one and two dimensional temperature and concentration field in a decomposition/ignition zone, preferably for additional decomposition products such as  $\text{NO}_2$ , NH, OH,  $\text{H}_2\text{CO}$  and CH.

## REFERENCES

1. Zhao, X., E.J. Hints, and Y.T. Lee, *Infrared multiphoton dissociation of RDX in a molecular beam*. Journal of Chemical Physics, 1988. **88**: p. 801-810.
2. Rauch, F.C. and A.J. Fanelli, *The Thermal Decomposition of Hexahydro-1,3,5-trinitro-s-triazine above the Melting Point: Evidence for Both a Gas and Liquid Phase Decomposition*. Journal of Physical Chemistry, 1969. **73**: p. 1604-1608.
3. Robertson, A.J.B., *Thermal Decomposition of Explosives*. Transaction of the Faraday Society, 1949. **45**: p. 85-93.
4. Bradley, J.N., et al., *Mass Spectrometric Study of the Thermal Decomposition of 1,3,5-Trinitrohexahydro-1,3,5-triazine (RDX)*. Journal of Chemical Society Trans Faraday., 1977. **73**: p. 1789-1795.
5. Östmark, H., H. Bergman, and K. Ekvall, *Laser Pyrolysis of Explosives Combined with Mass Spectral Studies of the Ignition Zone*. Journal of Analytical and Applied Pyrolysis, 1992. **24**: p. 163-178.
6. Östmark, H. *Laser Ignition of Explosives: A Mass Spectroscopic Study of the Pre-Ignition Reaction Zone*. in *Ninth Symposium (International) on Detonation*. 1989. Portland, Oregon:
7. Oyumi, Y. and T.B. Brill, *Thermal Decomposition of Energetic Materials 3. A High-Rate, In Situ, FTIR Study of the Thermolysis of RDX and HMX with Pressure and Heating Rate as Variables*. Combustion and Flame, 1985. **62**: p. 213-224.
8. Rogers, S.L., et al., *Comparative Mechanistic Thermochemical Decomposition Analyses of Liquid Hexahydro-1,3,5-Trinitro-1,3,5-Triazine (RDX) Using the kinetic Deuterium Isotope Effect Approach*. Thermochemical Acta, 1991. **177**: p. 151-168.
9. Leeuw, M.W., A.J.T. Rooijers, and A.C.V.d. Steen. *Fast Spectroscopic Analysis of Laser Initiated Decomposition Reactions in Explosives*. in *Proceedings of the Eighth Symposium (International) on Detonation*. 1985. Albuquerque, New Mexico: Naval Weapons Center NSWC-86-194.
10. Behrens, R., *The Application of Simultaneous Thermogravimetric Modulated Beam Mass Spectrometry and Time-of-Flight Velocity Spectra Measurements to the Study of the Pyrolysis of Energetic Materials*, in *Chemistry and Physics of Energetic Materials*, S.N. Bulusu, Editor. 1990, Kluwer Academic Publishers: Dordrecht. p. 327-346.
11. Sharma, J., et al., Journal of Physical Chemistry, 1987. **86**: p. 1857.
12. Grisch, F., et al., *Real time diagnostics of detonation products from lead azide using coherent anti-Stokes Raman scattering*. Applied Physics Letter, 1991. **59**: p. 3516-3518.
13. Nilsson, H. and H. Östmark. *Laser Ignition of Explosives: Raman Spectroscopy of the Ignition Zone*. in *Ninth Symposium (International) on Detonation*. 1989. Portland, Oregon: Office of Naval Research, OCNR 113291-7.
14. Eckbreth, A.C., P.A. Bonczyk, and J.F. Verdieck, *Laser Raman and Fluorescence Techniques for Practical Combustion Diagnostics*. Applied Spectroscopy Reviews, 1977. **13**(1): p. 15-164.
15. Crosley, D.R. and G.P. Smith, *Laser-Induced Fluorescence Spectroscopy for Combustion Diagnostics*. Optical Engineering, 1983. **22**(5): p. 545-553.
16. Edwards, P., D.P. Weaver and D.H. Campbell, *Laser-induced fluorescence in high pressure solid propellant flames*. Applied Optics, 1987. **26**(17): p. 3496-3509.
17. Östmark, H. and R. Gräns, *Laser Ignition of Explosives: Effects of Gas Pressure on the Threshold Ignition Energy*. Journal of Energetic Materials, 1990. **8**(4): p. 308-322.
18. Östmark, H. and N. Roman, *Laser Ignition of Pyrotechnic Mixtures: Ignition Mechanisms*. Journal of Applied Physics, 1993. **73**(4): p. 1993-2003.
19. Östmark, H. *Laser as a Tool in Sensitivity Testing of Explosives*. in *Eighth Symposium (International) on Detonation*. 1985. Albuquerque, New Mexico: Naval Surface Weapons Center.
20. Soufe, T. and A. Iwama, *Ignition of Composite Propellant at Sub atmospheric Pressures by means of Carbon Dioxide Laser*. Propellants and Explosives, 1979. **4**: p. 98-106.



21. Atwood, A.I., C.F. Price, and T.L. Boggs. *Initiability Measurements of Solid Propellants*. in *22nd International Annual Conference of ICT 1991*. 1991. Karlsruhe, Federal Republic of Germany: Fraunhofer-Institut für Chemische Technologie (ICT).
22. Holy, J.A. *Laser Initiation of  $TiH_x/KClO_4$* . in *Proceedings of the Eleventh International Pyrotechnics Seminar*. 1986. Vail, Colorado:
23. Holy, J.A. and T.G. Girmann. *The Effects of Pressure on the Laser Initiation of  $TiH_x/KClO_4$  and other Pyrotechnics*. in *Proceedings of the Thirteenth International Pyrotechnics Seminar*. 1988. Grand Junction, Colorado:
24. Zizak, G., N. Omenetto, and J.D. Winefordner, *Laser-excited atomic fluorescence techniques for temperature measurements in flames: A summary*. Optical Engineering, 1984. **23**(5): p. 749-755.
25. Gross, K.P. and R.L. McKenzie, *Single-pulse Gas Thermometry at Low Temperatures using two-photon Laser-Induced Fluorescence in  $NO-N_2$  mixtures*. Optics Letters, 1983. **8**(7): p. 368-370.
26. Dulcey, C.S., *Laser Induced Fluorescence in  $NO_2$ : Absolute Fluorescence Cross Sections and Quantum Yields*. Chemical Physics Letters, 1980. **76**(1): p. 80-84.
27. Aldén, M., et al., *Imaging laser-induced fluorescence of oxygen atoms in a flame*. Applied Optics, 1984. **23**(19): p. 3255-3256.
28. Dyer, M.J. and D.R. Crosley, *Two-dimensional imaging of OH laser-induced fluorescence in a flame*. Optics Letters, 1982. **7**(8): p. 382-384.
29. Seitzman, J.M., G. Kychakoff, and R.K. Hanson, *Instantaneous temperature field measurements using planar laser-induced fluorescence*. Optics Letters, 1985. **10**(9): p. 439-441.
30. Aldén, M., H. Edner, and S. Wallin, *Simultaneous spatial resolved NO and  $NO_2$  measurements using one- and two-photon laser-induced fluorescence*. Optics Letters, 1985. **10**(11): p. 529-531.
31. Crosley, D.R., *Semiquantitative Laser-Induced Fluorescence in Flames*. Combustion and Flame, 1989. **78**: p. 153-167.
32. Fairchild, P.W., G.P. Smith, and D.R. Crosley. *A Laser Pyrolysis/Laser Fluorescence Technique for Combustion Chemical Kinetics*. in *Nineteenth Symposium (International) on Combustion*. 1982. Haifa, Israel:
33. Östmark, H., personal conversation with M. Aldén, Department of Combustion Physics, Institute of Technology, Lund, Sweden, concerning LIF measurements of  $NO_2$ , 30 October 1992
34. Morley, C., *The Application of Laser Fluorescence to Detection of Species in Atmospheric Pressure Flames. Relative Quenching Rates of OH by  $H_2O$ ,  $H_2$  and  $CO$* . Combustion and Flame, 1982. **47**: p. 67-81.
35. Bonczyk, P.A. and J.A. Shirley, *Measurement of CH and Fluorescence*. Combustion and Flame, 1979. **34**: p. 253.
36. Agrup, S., U. Westblom, and M. Aldén, *Detection of atomic nitrogen using two-photon laser-induced stimulated emission*. Chemical Physics Letters, 1990. **170**: p. 406-410.
37. Halper, J.B., G. Hancock, M. Lenzi and K.H. Welge, *Laser induced fluorescence from amino(2A1). State selected radiative lifetimes and collisional deexcitation rates*. J. Chemical Physics, 1975. **63**(11): p. 4808-4816.
38. Becker, K.H., U. Shurath and T. Taarczyk, *Fluorescence determination of low formaldehyde concentrations in air by dye laser excitation*. Applied Optics, 1975. **14**(2): p. 310-313.
39. Ewart, P and M. Kaczmarek, *Two-dimensional mapping of temperature in a flame by degenerate four-wave mixing in OH*. Applied Optics, 1991. **30**(27): p. 3996-3999.
40. Melius, C.F, *Thermochemical modeling; II. Application to ignition and combustion of energetic materials*. in; S.N. Bulusu: Chemistry and physics of energetic materials. Kluwer Academic Publishers, Dordrecht: p. 51-78.
41. Lucht, R.P, N.M. Laurendeau, D.W. Sweeney, *Temperature measurement by two-line laser-saturated OH fluorescence in flames*. Applied Optics, 1982. **21**(20): p. 3729-3735.
42. Cattolica, R., *OH rotational temperature from two-line laser-excited fluorescence*. Applied Optics, 1981. **20**(7): p. 1156-1166.

## DISCUSSION

DR. RONALD E. BROWN  
Titan Corp., Pleasanton, California

Do you observe any change in the CN peak with the appearance of the 380 nm peak intensity with time; i.e., [CN]-decrease  $\rightarrow$  ["380"]-increase? Also: do you use, or is it practical to use, a boxcar to time-average?

### REPLY BY H. ÖSTMARK:

I have difficulty understanding the question. The 380 nm peak is observed only in the NO LIF spectrum and probably arises from CN. No direct correlation could be made with [CN] due to the fact that the CN LIF spectrum was acquired by using an excitation wavelength of 388 nm, which makes any measurements at 380 nm impossible.

Box-car technique can only be used for non-single shot experiments, and normally only for a single wavelength. We use an OMA with 960 active channels instead, and any time averaging is done digitally by PC computer. Since we aim for single-shot experiments, averaging is normally out of the question anyway.

## DISCUSSION

DR. DIVYAKANT L. PATEL  
Countermine Systems Directorate, U.S. Army, Fort Belvoir, Virginia

Can this technique be useful for studying detonation of RDX particles? For studying the detonation of RDX particles, this method required to modify, but it is difficult to use this technique for detonation of the RDX particles.

### REPLY BY H. ÖSTMARK:

LIF technique can be used for studying detonation products, but as LIF technique can be used only at moderate pressures, up to about 3 to 10 MPa, it can be applied only after an initial expansion has occurred.

## DISCUSSION

THOMAS P. BOGGS  
Naval Air Warfare Center, China Lake, California

What pressures were studied in this investigation?

Are you aware of the LIF studies of Tim and Donna Parr, and how do your results compare with theirs? For example, they show the transient products and the development with time and distance leading to a flame and self-sustained reaction.

### REPLY BY H. ÖSTMARK:

The pressure used in this experiment was 0.1MPa (air), but pressures in the 1-10 MPa range can be used.

I was not aware of these studies. Thank you for directing my attention to them.

# DETONATION REACTION STEPS FROZEN BY FREE EXPANSION AND ANALYZED BY MASS SPECTROMETRY

N. Roy Greiner, Herbert A. Fry, Normand C. Blais,  
and Ray Engelke  
Los Alamos National Laboratory  
Los Alamos, New Mexico 87545

Detonation reactions in small pellets of explosive are frozen by free expansion into a large vacuum chamber and analyzed by time-of-flight mass spectrometry. Sensitive explosives like PETN, RDX, and HMX show rapidly evolving reaction zones and mostly simple products like  $\text{H}_2\text{O}$ ,  $\text{CO}$ ,  $\text{N}_2$ , and  $\text{CO}_2$ . Less sensitive explosives like TATB, HNS, and TNT show slower evolution of the reaction zone, and more complex products in addition to the simple ones seen in PETN. Isotopic substitution shows that the more complex products contain moderate amounts of  $\text{NH}_3$ ,  $\text{HCN}$ ,  $\text{NO}$ ,  $\text{HNCO}$ , and  $\text{NO}_2$ . Other observations include polymerization of aromatic explosive molecules, adducts to the explosive molecules, and explosive molecules with functional groups missing. The more complex products are reservoirs of unreleased energy that may affect performance.

## INTRODUCTION

We think of new explosive synthesis and development as an exercise in molecular design. Molecular design requires knowledge of how the molecule will react in all the circumstances it is expected to meet. In the detonation process the ease by which the explosive undergoes transformation is related to shock sensitivity and reaction zone thickness; the mixture of products at the conditions of the Chapman-Jouguet (CJ) point in the detonation wave determines the performance. To guide the design of new explosive molecules we would like to know: (1) What product molecules give better performance? (2) What molecular structures give the better products? (3) How does structure influence sensitivity? and (4) How do we choose molecular structures that favor performance and disfavor sensitivity? Answers to these questions can be valuable guides to synthesis and can provide input for improved models of detonation processes.

Thus, the molecular design of new, more powerful, and less sensitive explosives requires detailed knowledge of reaction mechanisms and compositions of molecular products from explosives having a variety of molecular structures and performance parameters. Timely exploration of new chemical structures requires a fast-turnaround, small-scale method for analyzing the chemical reaction steps of both new explosives before costly scale up and model compounds exemplifying potential new combinations of fuel and oxidizer substructures. The reaction steps of interest to detonation science occur in times of a few to hundreds of nanoseconds at pressures from ten to hundreds of kilobars, conditions not found in typical research apparatus. To answer the above questions

effectively, it is necessary to characterize the chemistry of detonation products and the reaction steps by which explosives are transformed into products for a set of explosive molecules that exemplify combinations of potentially favorable structural features.

## EXPERIMENTAL

We describe a new apparatus and method for analyzing detonation reactions using laboratory-scale (30-250 mg) charges (Fig. 1). The new apparatus<sup>1</sup> is based on an older prototype<sup>2</sup> and consists of a time-of-flight mass spectrometer interfaced to a high-vacuum firing chamber through a skimmer and a laser-schlieren optical system for hydrodynamic characterization (Fig. 2). The fireball normally produced by a detonation is frozen sequentially from the outside inward in a continuum of stages by free adiabatic expansion into the vacuum. Reaction of a given volume element begins when the detonation wave arrives, and cooling by expansion begins when the rarefaction wave initiated at the free surface of the charge arrives at the volume element. Cooling of every element in the charge is thus initiated while that element is still at a density, pressure, and temperature characteristic of the detonation process. Experiments with layered charges demonstrate that very little mixing occurs between volume elements during the expansion. The chemical history of the detonation is thus frozen in time and imprinted on the structure of the expanding frozen fireball, with the outside of the fireball having a frozen composition characteristic of the initial stages of detonation and successive layers toward the inside having compositions characteristic of correspondingly later stages. Our apparatus isolates a core sample from the expanding fireball as an undisturbed

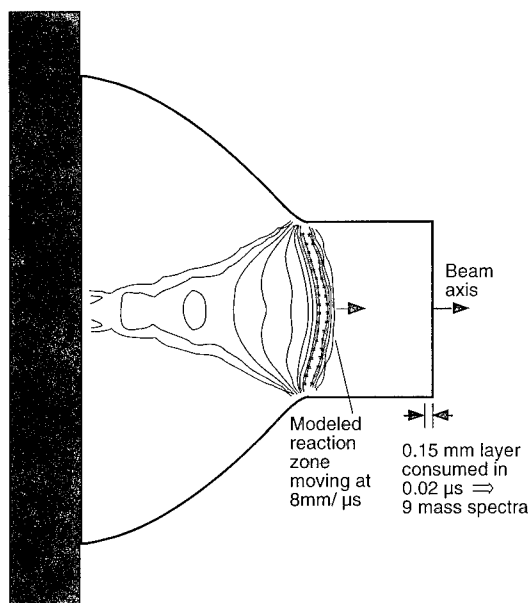


FIGURE 1. DIAGRAM OF A DETONATING CYLINDRICAL PELLET FROM THE HYDRODYNAMIC MODEL.

molecular beam and provides a series of mass spectra derived from successive segments of the core. The assembled data set from each pellet fired is a sequence of 95 mass spectra that identifies and characterizes the molecules resistant to change over a succession of sampling times. These sampling times are separated by about 5 ns, which corresponds to a succession of layers about 20  $\mu\text{m}$  thick in the detonating charge. These molecules are associated with the slower (rate-determining) steps or stable products in the reaction sequence and give valuable clues to reaction mechanisms. Our mass spectrometer automatically establishes expansion velocities of the core segments, and an electronic framing camera concurrently records a sequence of laser-schlieren images of the detonation and expansion.<sup>3</sup> The number of spectra over which a change is observed can be related, through the hydrodynamics of the detonation and expansion, to the rate of that change in the detonating sample.

## RESULTS AND DISCUSSION

### PETN and Other Sensitive Explosives

Figure 3 shows a sequence of spectra from the detonation of a PETN pellet. The first material arrives at scan 9 (top) and its velocity is 13 km/s. The major peaks at 18, 28, and 44 correspond to the parent peaks of the expected final products,  $\text{H}_2\text{O}$ ,  $\text{N}_2/\text{CO}$ , and  $\text{CO}_2$ , respectively, as predicted for the CJ composition by detonation product computer codes. The smaller transient peak at mass 30 is most likely NO. The spectra are relatively simple, and the sequence evolves rapidly to a fairly

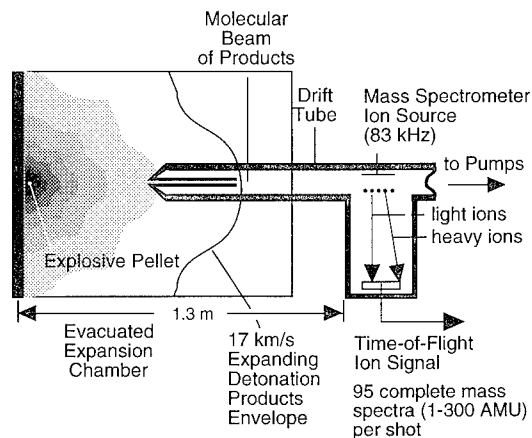


FIGURE 2. SCHEMATIC DIAGRAM OF THE APPARATUS.

constant spectrum that persists for many scans. Like the other sensitive explosives, RDX and HMX, under study with this method, PETN normally gives no substantial spectra of molecules larger than mass 44. Occasionally HMX gives a weak spectrum resembling HMX vapor,<sup>3</sup> but neither PETN nor RDX has ever been observed to produce unreacted vapor in our experiments.

These explosives also occasionally give a spectrum of clusters that appear to be composed of  $\text{NH}_4^+ \cdot n\text{H}_2\text{O}$ , where  $n$  has been observed to take values from 1-5. PETN in Fig. 4 shows a series of peaks at (approximately) 18, 36, 54, 72, and 90, in addition to the large peaks at 28 and 44. PETN-D6 in Fig. 5 shows peaks at 20 and 22, accompanied with the series 42, 62, and 82. Comparison with results from natural PETN indicates that these peaks are due to  $\text{D}_2\text{O}^+$  and a series of clusters containing  $\text{ND}_4^+ \cdot n\text{D}_2\text{O}$ , where  $n$  takes values from 0-4. The cluster spectra usually appear around scan 30 or later, if they appear at all, and they are almost always accompanied by exceptionally large peak(s) from  $\text{H}_2\text{O}^+$  and  $\text{NH}_4^+$ , as elucidated by isotopic substitution. The cluster peaks are usually just barely discernible from baseline noise, if they appear at all; the peaks shown in Figs 4 and 5 are some of the largest seen. However, the appearance of a very large 18 peak from natural isotopic explosives happens regularly and appears in approximately the same scans from each explosive studied. This strange behavior appears to be unique to mass 18 or its isotopic analogs, and it occurs in all of the explosives studied by us so far. Perhaps it might help explain the apparent low intensities of the 18 peak in most of the other scans from a given shot. This

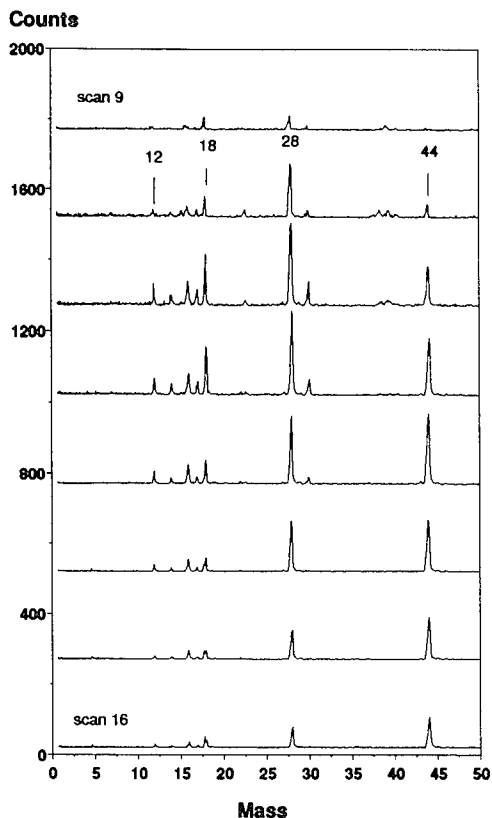


FIGURE 3. SERIES OF MASS SPECTRAL SCANS FROM THE DETONATION OF A PETN PELLET (NATURAL ISOTOPIC COMPOSITION). EACH SUCCESSIVE SCAN IS OFFSET FOR CLARITY.

phenomenon remains under study, but the results show that  $\text{NH}_4^+$  or  $\text{NH}_3$  is a product from rapidly quenched detonations, and that  $\text{H}_2\text{O}$  and  $\text{NH}_3$  are involved in some unexpected behavior in the detonation process.

The other transient species in PETN detonations, indicated by mass 30 in Fig. 3, is also seen in the early scans from all of the other explosives. RDX, HMX, HNS, and TATB show, in addition to mass 30, medium-size transient peaks at 26, 27, 29, 42, and 43. In RDX and HMX these peaks are about the size of the 30 peak in PETN, relative in each case to mass 28, and they grow in and disappear over a few scans, but in HNS and TATB they grow somewhat larger and disappear more slowly. Except for PETN- $\text{D}_8$ , no isotopic labeling experiments have been done on PETN, RDX, HMX or HNS. The fact that 28, 30, and 44 show no isotope shift with D substitution shows that they cannot have hydrogen in them. Thus mass 30 in PETN cannot be due to  $\text{CH}_2\text{O}$ .

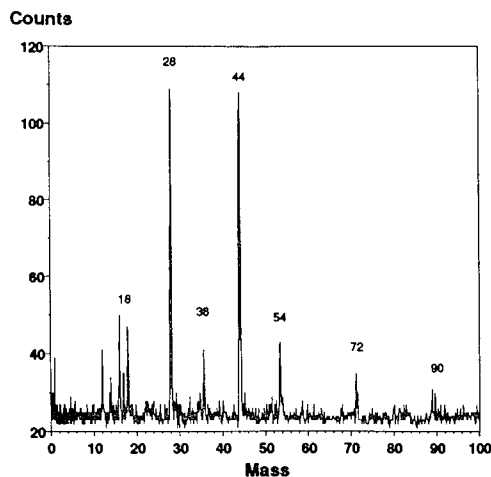


FIGURE 4. A LATE SCAN (33) FROM PETN.

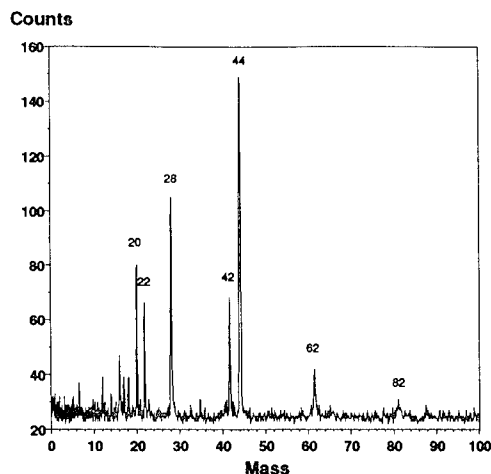


FIGURE 5. A LATE SCAN (30) FROM PETN- $\text{D}_6$ .

#### TATB and Other Insensitive Explosives

Figure 6 shows the first eight mass spectral scans after a (natural isotope) TATB pellet is fired. Although the expected 18, 28, and 44 peaks are present, the spectra are more complex than from PETN, there are large peaks in scans 12-16 that resemble the TATB spectrum, and sometimes smaller peaks indicative of dimerized TATB. Typically unreacted explosive begins to appear a couple scans after the first scan showing products, which would be expected if unreacted explosive is present as small grains of solid. The solid, because it is less elastic than the gases, would drag a bit as it is accelerated to the bulk velocity of the expanding gasses. Peaks corresponding to  $\text{NH}_4$ ,  $\text{HCN}$ ,  $\text{NO}$ , and  $\text{HCNO}$  are present and persist for many scans.

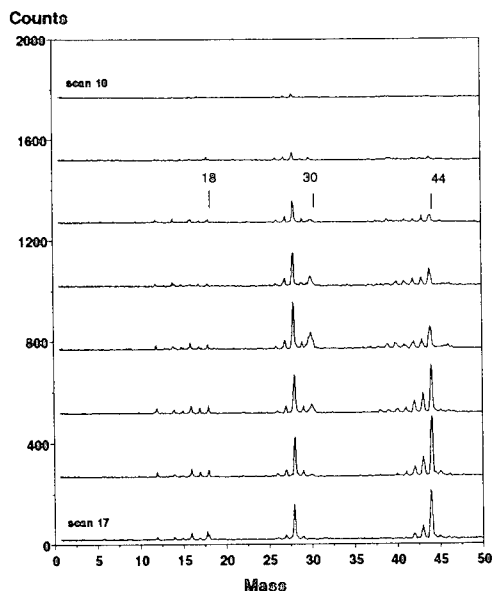


FIGURE 6A. A SERIES OF SCANS (10-17) FROM NATURAL ISOTOPIC TATB. LOW-MASS SPECTRUM.

HNS and TNT behave in a similar way, but in this paper we will focus on TATB.

Figure 7 shows a similar sequence from a TATB-D<sub>6</sub> shot. Comparison with natural TATB shows isotope shifts 18 to 20 and 22, 27 to 28, and 43 to 44. Some very small peaks are caused by a small amount of H contamination in the TATB-D<sub>6</sub>. These shifts show that in natural TATB 18 is both H<sub>2</sub>O<sup>+</sup> and NH<sub>4</sub><sup>+</sup>, 27 contains one H atom (HCN), and so does 43 (HNCO). Furthermore 28, 30, and 44 are not shifted, indicating that they contain no H. An unidentified peak appears at 14 mass units above the TATB-D<sub>6</sub> molecular ion, and the peak corresponding to the loss of OD is enhanced in scans 18-20. Unreacted TATB is seen over more scans than in Fig. 6, probably because the TATB-D<sub>6</sub> crystals were somewhat larger. TATB-<sup>15</sup>N<sub>6</sub> (Fig. 8) further confirms these identifications by showing isotope shifts from 14-15 indicating N atoms, 18-19 (NH<sub>4</sub><sup>+</sup>), 27-28 (HCN), 28-30 (N<sub>2</sub>), 30-31 (NO), and 43-44 (HNCO). This shot also shows that about one-half of the 28 peak in TATB at later times is N<sub>2</sub> and the other half must be CO, because it is not affected by any of the substitutions. Earlier scans in this shot show only mass 28 (CO) and no mass 30 (N<sub>2</sub>). Peaks due to NO and NO<sub>2</sub> do not appear in the spectrum of non-reacting TATB vapor, but they appear in our quenched detonation scans when TATB is present, indicating that these molecules are produced when TATB is forming products. Isotope shifts (or lack thereof) from TATB-(<sup>15</sup>NH<sub>2</sub>)<sub>3</sub> (Fig. 9) show that the N<sub>2</sub> comes about equally from the NH<sub>2</sub> and NO<sub>2</sub> groups, NH<sub>4</sub> comes from the NH<sub>2</sub> group, and when TATB

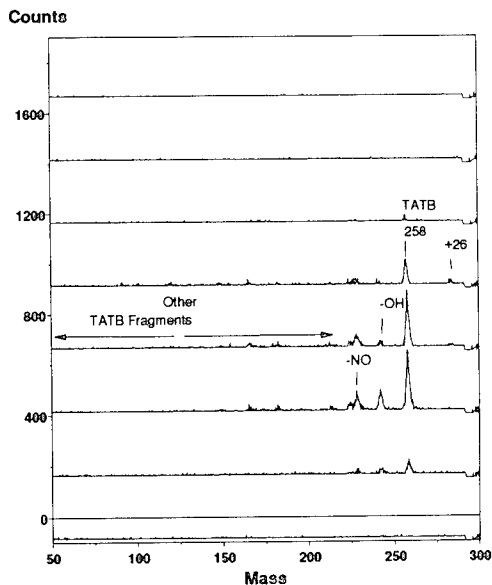


FIGURE 6B. A SERIES OF SCANS (10-17) FROM NATURAL ISOTOPIC TATB. HIGH-MASS SPECTRUM (COMPRESSED MASS SCALE).

gives a large H<sub>2</sub>O/NH<sub>4</sub> peak about equal signals are attributable to each ion. Spectra from shots with TATB-(<sup>15</sup>N<sub>3</sub>)<sub>3</sub> are not shown, but they are consistent with the above assignments.

In addition to the production of NO and NO<sub>2</sub>, alluded to above, reacting TATB shows a marked increase in the TATB-OH peak and a lesser increase in the TATB-NO peak toward the end of the reaction zone. Normal TATB often shows a small peak at mass 284, 26 mass units heavier than TATB and a small peak at about 568 mass units, twice as heavy as TATB. We have observed pentamers in the detonation of TNT, as well as the dimerization of another aromatic compound, anthracene, under shock compression. The further characterization of these phenomena is in progress.

Results from the new apparatus have given chemical characterizations of rapidly quenched reaction mixtures from a number of detonating explosives. The more sensitive explosives, PETN, RDX, and HMX, show simple, rapidly evolving sequences of spectra, with only a few low-mass intermediates. By contrast, the less-sensitive explosives, TATB and HNS show more complex and slowly evolving sequences of spectra, with more numerous and more intense low-mass intermediates and high-mass spectra strongly resembling vaporized, more or less intact, explosive molecules. Observed variations of these high-mass spectra during the reaction sequence are under investigation and may offer further clues to the detonation reaction mechanisms. Molecules such as NH<sub>3</sub>, HCN, NO,

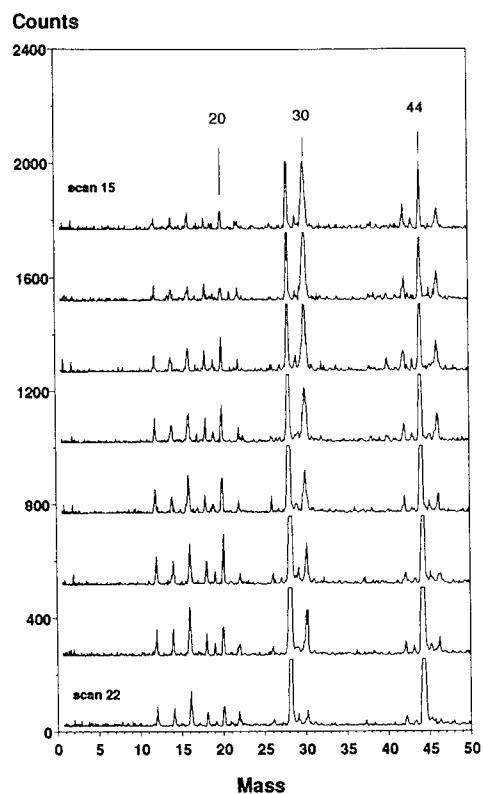


FIGURE 7A. TATB-D<sub>6</sub> SHOT, SCANS 15-22. LOW-MASS SPECTRUM

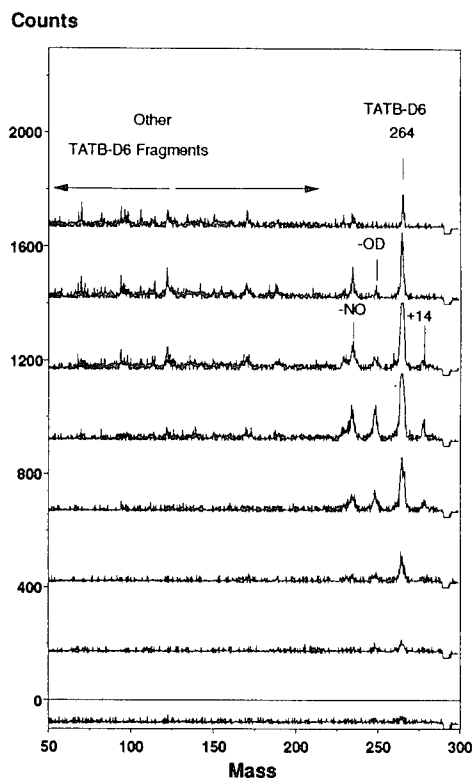


FIGURE 7B. TATB-D<sub>6</sub> SHOT, SCANS 15-22. HIGH-MASS SPECTRUM

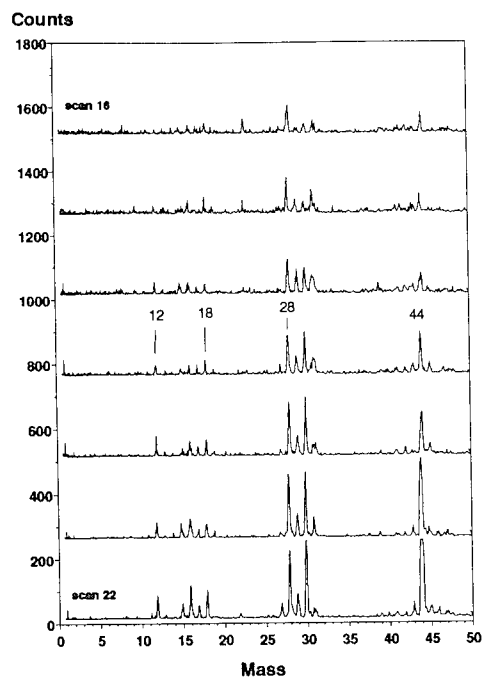


FIGURE 8. TATB-<sup>15</sup>N<sub>6</sub> SHOT, SCANS 16-22.

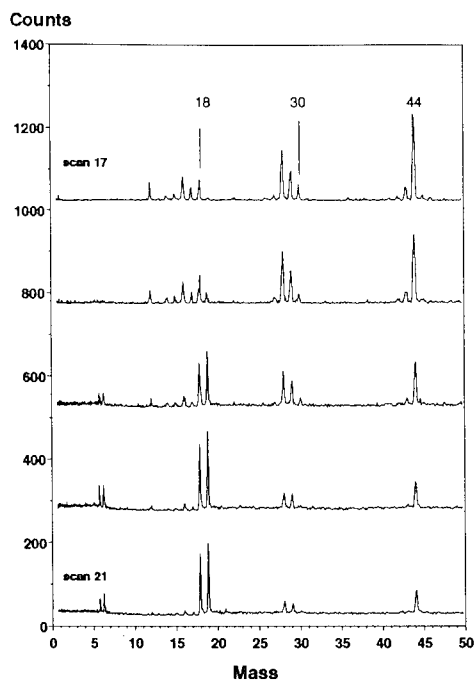


FIGURE 9. TATB-(<sup>15</sup>NH<sub>2</sub>)<sub>3</sub> SHOT, SCANS 17-21.

H<sub>2</sub>CO, H<sub>2</sub>CO, and NO<sub>2</sub>, have been confirmed as somewhat persistent intermediates in TATB detonations, and have peaks corresponding to observed intermediate peaks in the other explosives. These molecules could release additional energy if they were to react further to form H<sub>2</sub>O, N<sub>2</sub>, and CO<sub>2</sub>. Thus, the presence of these molecules indicates reservoirs of unreleased energy, which might account for observed performance inferior to expectations from equilibrium models. The late evolution of N<sub>2</sub> observed in the <sup>15</sup>N-substituted TATBs would also account for a slow energy release. The observation of partially reacted explosive over a series of scans early in the sequence appears to offer a measure of the extent of the reaction zone. These experiments allow us to resolve kinetic details of processes in the reaction zone of detonating explosives.

## ACKNOWLEDGEMENTS

We thank J. J. Romero and C. W. Wilson for valuable assistance in building the equipment and in conducting the experiments. We thank Don Ott for supplying the isotopic TATB samples. This research was supported by Laboratory Directed Research and Development funds at the Los Alamos National Laboratory.

## REFERENCES

1. Blais, N. C.; Fry, H. A.; and Greiner, N. R. "Apparatus for the Mass Spectrometric Analysis of Detonation Products Quenched by Adiabatic Free Expansion," *Review of Scientific Instruments*, Vol. 64, 1993, pp. 174-183.
2. Greiner, N. R. and Blais, N. C., "Free-Expansion Experiments and Modeling in Detonation: Chemistry and Hydrodynamics on a Laboratory Scale," *Proceedings of the Ninth Symposium (International) on Detonation*, Portland, Oregon, 28 Aug - 1 Sept 1989, pp. 953-961.
3. Greiner, N. R., "KIVA Reactive Hydrodynamics Code Applied to Detonations in High Vacuum," in *Chemistry and Physics of Energetic Materials*, S. N. Bulusu, ed., Kluwer Academic Publications, London, 1990, pp. 457-475.
4. F. Volk and H. Schubert, "Massenspektrometrische Untersuchungen von Explosivstoffen," *Explosivstoffe*, Vol. 1, 2, (1968).

## DISCUSSION

THOMAS B. BRILL

University of Delaware, Newark, Delaware

This is a valuable experiment for giving chemical details of the detonation reaction zone. Your data for

TATB, for example, show that CO and H<sub>2</sub>O are generated very early. CO formation requires that several reactions already take place. What are the possibilities for stretching the early reactions; perhaps by using lower shock energy? What would you say is the temperature that you created in your TATB sample?

## REPLY BY N. R. GREINER:

First I will answer the questions and then reply to the comment. Lower shock energy may perhaps stretch the reaction zone. This might be achieved by shocking a thin layer of the test explosive with a pellet of lower energy or lower density explosive as a driver. We have demonstrated the reliable performance of several such drivers. We have also shown in the case of TATB that thin layers containing larger crystals driven by normal TATB have a stretched reaction zone. Another way to observe stretched reaction zones might be to analyze material blown off the side of our cylindrical pellet rather than off the end, as we do now. Material from the sides would expand in two dimensions rather than one and might quench faster, thus arresting more of the early reaction zone. All of these approaches appear to be feasible, perhaps with a bit of development effort.

Estimation of temperature in detonations, particularly in heterogeneous solid explosives, is a complex problem. To give some idea of the complexity in a few sentences, consider the presence of voids and bulk solid crystals. Equalization of pressure after the arrival of the shock is probably achieved on the timescale of the transit time of a sound wave across a typical crystal and void dimension, in our case a few nanoseconds. Equalization of pressure requires that the collapsed voids be filled with very hot material, because it is at low density, much like a gas. The solid crystals heat up comparatively moderately under shock loading, because most of their support of the shock pressure is due to mechanical compression and very little due to heating. These temperature inhomogeneities exist even before reaction begins. In the face of such complexity, we have not attempted to determine temperature in our samples, except that they all started out at room temperature.

Indeed the first material to arrive at our mass spectrometer appears to have undergone extensive reaction. We have considered two explanations for this. One is that some of the first material is likely to have come from the collapse of voids embedded in the surface of the pellet facing the spectrometer. As explained above, this material will have experienced very hot conditions at low density, which favors rapid extensive reaction producing small molecules. Solid crystals at the surface probably have very little chance to react much, and they must undergo acceleration from the average bulk particle velocity (about 2 km/s) to the escape velocity (about 10 km/s) by entrainment in the expanding gaseous products. Because the acceleration takes time, the material coming from the crystals is retarded somewhat and arrives at the spectrometer a bit later than the gas that surrounded the crystals before



expansion. Even the gas mixture arriving at the spectrometer at any given scan time will contain material from the initiating hot spots as well as material from reactions that consume the solid crystals. So each scan gives a composite picture from a given layer, the later scans giving a composite picture from a later time in the reaction.

We think this method is a valuable tool for discovering chemical details of the detonation processes in a variety of explosives, but much work still needs to be done to realize the full potential of the method and to relate the results to chemical processes and performance.

## THE THERMAL DECOMPOSITION OF PURE AND AMINE-SENSITIZED NITROCOMPOUNDS

C. P. Constantinou and M. M. Chaudhri  
Cavendish Laboratory, University of Cambridge,  
Madingley Road, Cambridge, CB3 0HE.

We have used differential scanning calorimetry to study the thermal decomposition of nitromethane, trinitrotoluene, picric acid, tetryl and sensitized samples of each of these with a number of aliphatic amines. A complete description of the kinetics of each reaction is reported here. Each nitrocompound - amine mixture was found to show an additional stage of exothermic activity during its thermal decomposition. The mixtures also invariably showed a substantial drop in the peak decomposition and onset of decomposition temperatures. Furthermore, there were always sizeable decreases in the activation energy and the overall exothermicity was often found to increase considerably. Strong evidence is provided that the mechanism of sensitization is chemical in origin. The presence of an amine was found to change the rate-determining step of the decomposition of the nitrocompound. Various amines were found to sensitize nitromethane to different extents. The strength of the sensitizing influence does not correlate with the basicity of each amine. A sensitization factor is defined and is found to correlate well with the energy of an electronic transition from the nitrogen of an amino group to the anti-bonding orbital of the nitro-group. A mechanism is detailed for the sensitization, in terms of the formation of a charge-transfer complex between a nitrocompound and an amine.

### INTRODUCTION

Nitrocompounds are an important group of energetic materials. They are also known to be sensitized by amines through a chemical mechanism.<sup>1</sup> We report here on a comprehensive study of the thermal decomposition reactions of nitromethane, three aromatic polynitrocompounds (trinitrotoluene, tetryl, picric acid) and mixtures of each of these with diethylenetriamine (DETA). We also summarise our measurements on the thermal decomposition of mixtures of nitromethane with ammonia and a series of other amines: diethylamine (DEA), ethylenediamine (EDA) and *n,n*-dimethylethylamine (DMEA). To study these reactions, we have used differential scanning calorimetry (dsc) on samples enclosed in completely sealed containers. The underlying assumption in this technique, is that the rate of release of thermal energy from the sample is proportional to its rate of reaction.

Hutchinson et al.<sup>2</sup> have used dsc to study the thermal decomposition of tetryl. Earlier work<sup>3</sup> had indicated that this reaction proceeds via the formation of picric acid. They found that the material decomposed in the liquid phase with two distinct reaction stages. Their isothermal decomposition measurements can best be explained in terms of random nucleation.

The thermal decomposition of trinitrotoluene (TNT) has been a subject of recurring interest for most of this century. Some investigators<sup>4</sup> have attempted to isolate and identify intermediate species with a view towards elucidation of a stepwise decomposition mechanism. A more frequent approach<sup>5</sup> has involved the determination of apparent activation energy parameters for the overall sample consumption by comparing time-to-explosion or gas evolution data at several temperatures. There are wide discrepancies between the reported parameters as determined over different temperature ranges and under differing degrees of confinement. For example, quoted activation energies range from 59 to 182 kJ mol<sup>-1</sup>.

Nitromethane has received the greatest attention, as a model nitrocompound and a solvent.<sup>6-9</sup> The consensus is that the thermal decomposition of gaseous nitromethane involves unimolecular scission of the C-N bond. However, the reaction mechanism in the condensed phase has remained disputed.

Very little work has been carried out previously on the thermal decomposition of amine-sensitized nitrocompounds.

## EXPERIMENTAL METHODS

The solid nitrocompounds were obtained from Royal Armament Research and Development Establishment, U.K. Spectrophotometric grade nitromethane and amines were supplied by Aldrich Chemical Co. U.K. A 25% aqueous solution of ammonia, which was used, was also supplied by this company. The amines were purified in the laboratory by double distillation and were always used freshly distilled. The instrument used for the thermochemical measurements was a Mettler TA3000. The temperature calibration was based on the melting points of indium (429.7 K), lead (600.5 K) and zinc (692.6 K). The energy calibration was carried out against the heat of fusion of indium (28.45 kJ kg<sup>-1</sup>). Mixtures of nitromethane with the amines were prepared in air. Experiments on samples of nitromethane - diethylenetriamine (10% by volume) mixed in an argon atmosphere, with oxygen and water vapour levels restricted to below 6 ppm, showed no significant mechanistic deviation from the experiments on the samples mixed in air. The remaining solid mixtures were also prepared in air by adding the amine to the solid aromatic nitrocompound and thoroughly grinding the mixture into the form of a fine powder in a mortar and pestle. All nitrocompounds underwent a colour change when mixed with the amine. Samples of masses 2 to 10 mg were sealed in gold-plated stainless steel high pressure crucibles (Fisons Instruments, U.K.) under a mean pressure of 80 MPa using a specially designed hydraulic press. Such crucibles, when sealed, could contain pressures of up to 15 MPa. In all the experiments reported here, the sample crucible remained sealed throughout the duration of the reaction.

## RESULTS

Decomposition measurements were carried out under dynamic and isothermal conditions. In the former, the sample temperature is increased at a predetermined rate and in the latter the sample temperature is kept fixed. Isothermal scans are much more reliable for use in kinetic analyses. The dsc signal is assumed to be proportional to the velocity of reaction, which in turn is assumed to follow Arrhenius kinetics.

$$\frac{dQ}{dt} \propto \frac{d\alpha}{dt} = f(1-\alpha) A \exp\left(-\frac{E}{RT}\right) \quad (1)$$

R is the molar gas constant and T the absolute temperature. A is the pre-exponential factor in units of s<sup>-1</sup>. The signal can be integrated directly and normalised to give degree of decomposition,  $\alpha$ ,

against reduced time,  $\tau$ , plots. The reduced time is defined as the ratio of reaction time to the time taken for half the sample to decompose. Fourteen different kinetic functions were considered each corresponding to a different controlling mechanism. Any one of the normalised integrated kinetic functions  $\Phi(\alpha)$ , could be fitted by non-linear regression analysis to the  $\alpha$ - $\tau$  plot.  $\Phi(\alpha)$  relates to  $f(1-\alpha)$  according to equations (2) - (4):

$$\int_0^t \frac{d\alpha}{f(1-\alpha)} dt = \int_0^\alpha \frac{1}{f(1-\alpha)} d\alpha = F(\alpha) \quad (2)$$

$$F(\alpha) = K(T) \Delta t = A \exp\left(-\frac{E}{RT}\right) \Delta t \quad (3)$$

$$\Phi(\alpha) = \frac{F(\alpha)}{F(0.5)} = \frac{\Delta t}{\Delta t_{0.5}} = \tau \quad (4)$$

The kinetic function  $f(1-\alpha)$  could thus be identified from the reduced measurements. Furthermore, an Arrhenius plot of the natural logarithm of the maximum rate of release of thermal energy per unit sample mass ( $P_{\max}$ ) against reciprocal temperature provides, through its linearity or otherwise, a test for the validity of equation (1) and yields, through its slope, a value for the activation energy of decomposition, E. Once the kinetic function had been identified and a value for the activation energy was obtained, the frequency factor, A, could also be derived from equation (1).

## Dynamic Scans

Dsc provides a new technique for measuring the sensitization of nitrocompounds by amines<sup>1</sup>. The method is sensitive, accurate and reproducible. An example demonstrating the sensitization is given in Figure 1a, which shows the dsc traces of pure nitromethane and a nitromethane-DETA (10% by volume) mixture taken at a heating rate of 10 Kmin<sup>-1</sup>. The decomposition of the mixture, as indicated by the exotherm, begins at 453 K, and the rate of decomposition peaks at 493 K and 538 K. Nitromethane, on the other hand, starts decomposing at 593 K and its rate of decomposition peaks at 688 K. The total amount of energy released during the decomposition, which is related to the area under the curve, can also be seen to increase substantially from 3000 kJ kg<sup>-1</sup> in nitromethane, to 4100 kJ kg<sup>-1</sup> in the mixture. The amine, on the other hand, starts decomposing at a temperature of 643 K (not shown);

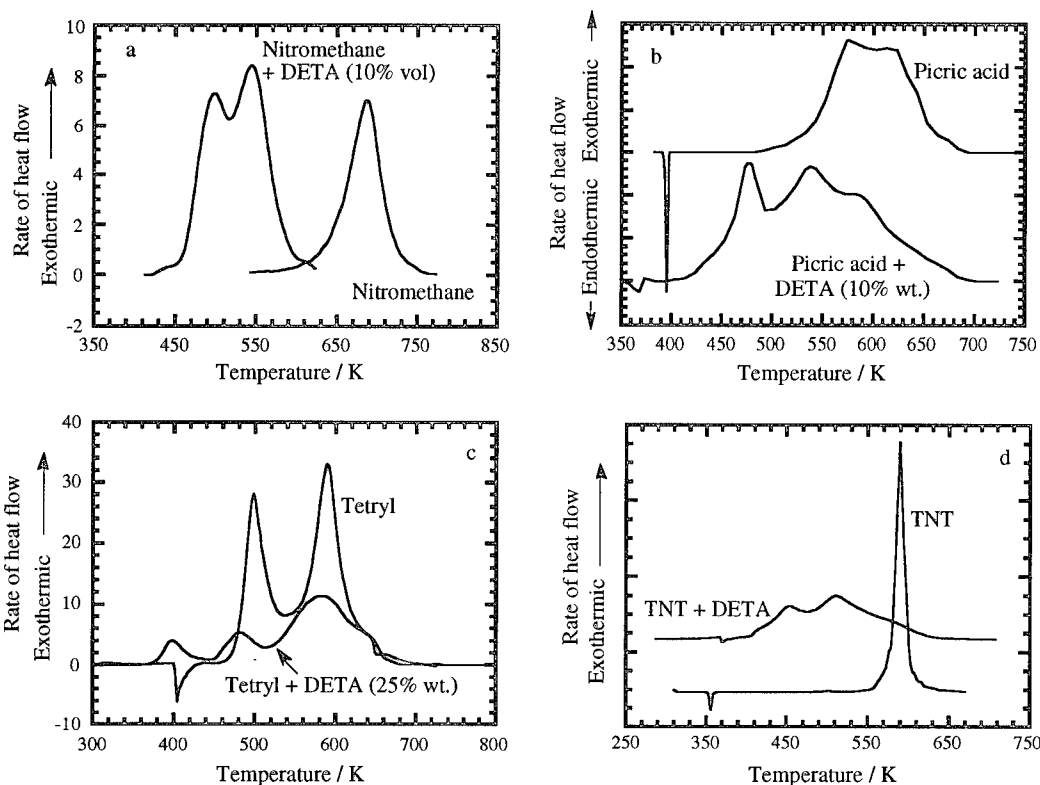


FIGURE 1. DSC TRACES OF NITROCOMPOUND AND NITROCOMPOUND - DETA MIXTURES TAKEN AT A HEATING RATE OF  $10 \text{ K MIN}^{-1}$ . THE UNITS ON THE ORDINATE AXIS ARE ARBITRARY.

it has an exothermicity of  $1337 \text{ kJ kg}^{-1}$  and its rate of decomposition peaks at  $753 \text{ K}$ . The drop in the decomposition temperature and the increase in the exothermicity are indications of the sensitization. The two peaks constitute evidence that the decomposition of the mixture takes place in two stages, each with its own rate-determining step.

Figures 1b - d show the dynamic dsc traces for pure and sensitized picric acid, tetryl and TNT. All the pure nitrocompounds were found to decompose in the liquid phase. The heat of fusion measured in this work for each polynitrocompound is in good agreement with the value quoted in the literature. In each case the decomposition of the mixture shows an additional reaction stage and starts at a lower temperature, as compared to that of the pure nitrocompound. Picric acid starts decomposing at a temperature of  $482 \text{ K}$ . On the other hand, the decomposition of its mixture with DETA (10% by weight) starts at  $400 \text{ K}$ . The onset of decomposition temperature is correspondingly decreased by the presence of the amine, for tetryl from  $455 \text{ K}$  to  $360 \text{ K}$

and for TNT from  $550 \text{ K}$  to  $405 \text{ K}$ . All the mixtures examined show sensitization as indicated by the lowering of the peak decomposition temperatures. The exothermicity is increased by the presence of the amine in the case of picric acid from  $2300 \text{ kJ kg}^{-1}$  to  $3600 \text{ kJ kg}^{-1}$ , whereas for TNT it is found to remain unchanged at  $3000 \text{ kJ kg}^{-1}$ . For tetryl, it was substantially decreased from  $5100 \text{ kJ kg}^{-1}$  to  $2840 \text{ kJ kg}^{-1}$ . The amine concentration in the tetryl - DETA mixture was 25% by weight. For the picric acid and TNT mixtures the amine concentration was 10% by weight.

#### Isothermal Scans

For each of the materials studied, a series of isothermal scans was obtained at temperatures just below the onset of detectable decomposition obtained in the dynamic scans. Typical measurements for nitromethane and nitromethane - DETA are shown in Figures 2 - 3.

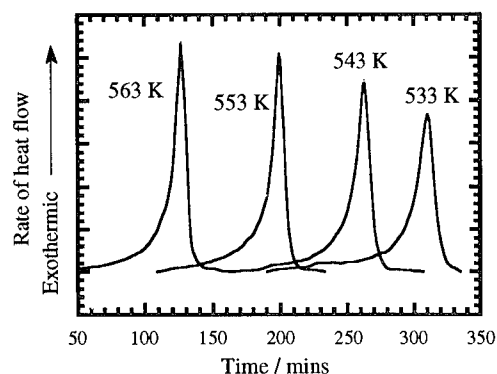


FIGURE 2. TYPICAL ISOTHERMAL DSC SCANS FOR NITROMETHANE AT THE TEMPERATURES INDICATED.

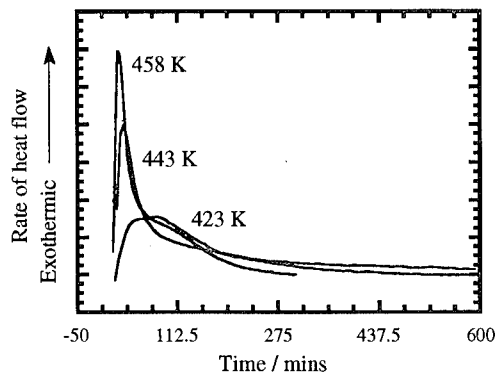


FIGURE 3. TYPICAL ISOTHERMAL DSC SCANS FOR NITROMETHANE - DETA (10% BY VOLUME) AT THE TEMPERATURES INDICATED.

In general, materials that showed more than one reaction stage in their dynamic dsc trace (such as the nitromethane - DETA mixture) could undergo complete decomposition isothermally at temperatures below the dynamic onset of the first stage of decomposition. This was not the case for tetryl and sensitized tetryl in which the two and three reaction stages respectively (Figure 1c), could be uncoupled. For tetryl and sensitized tetryl the isotherms used for the subsequent analysis correspond to the first reaction stage and have exothermicities of 2100 kJ kg<sup>-1</sup> and 425 kJ kg<sup>-1</sup>, respectively. The isotherms for all the other materials gave exothermicities which were identical to the corresponding dynamic traces, within the limits of experimental error.

The isothermal measurements were used to obtain an Arrhenius plot for each material. Such plots without exception showed good linearity which suggests that it is valid to apply Arrhenius kinetics to each of these reactions. The slope of each plot provided a value for the activation energy of the decomposition of each material. These values have been collected in Table 1 which also lists the exothermicity and the temperature at which the rate of decomposition peaks for each material. Peak decomposition temperatures for sensitized nitrocompounds refer to the first reaction stage. The value for the exothermicity of the mixture of nitromethane with ammonia is quoted as measured and has not been corrected for the mass of water present. The exothermicity of the corresponding mixture with gaseous ammonia would be expected to be higher. All the amines mentioned in Table 1 have their rate of decomposition peaking in the range 750 - 800 K and show much lower exothermicities than that of nitromethane. Each of these nitromethane - amine mixtures also shows two reaction stages in its decomposition.

In every case the activation energy of decomposition is found to drop substantially when a nitrocompound is mixed with an amine. Ammonia decreases the activation energy of nitromethane by the greatest extent, while primary amines are found to have a stronger influence in this respect than secondary or tertiary amines.

The isothermal measurements were also integrated and normalised to give fraction of sample decomposed against reduced time plots ( $\alpha$ - $\tau$  curves). These plots were fitted with reduced integrated kinetic functions in order to determine the mechanism of decomposition. Such plots are shown for nitromethane and nitromethane - DETA (10% by volume), along with the best theoretical fit, in Figures 4 - 5. Table 2 summarises the derived decomposition mechanism and gives a complete expression for the rate of decomposition of all these materials. The best fit to the experimental data for nitromethane in the range  $0.1 \leq \alpha \leq 1$  was provided by (Figure 4):

$$\Phi_1(\alpha) = \frac{1}{2 - C_0} \left[ \left( \ln \frac{1 - \alpha}{\alpha} \right) + \frac{1}{\alpha} - C_0 \right] \quad (5)$$

This is indicative of the greatest part of the decomposition reaction being governed by a cubic autocatalytic chemical process. Cubic autocatalysis arises when two of the products of decomposition take part in the rate-determining reaction step. The initial stages of the reaction ( $0 \leq \alpha \leq 0.1$ ) were best fitted by:

$$\Phi_2(\alpha) = \left[ \frac{\ln(1 - \alpha)}{\ln 0.5} \right]^{1/n} \quad (6)$$

TABLE 1. THE THERMAL DECOMPOSITION PARAMETERS OF NITROCOMPOUND AND NITROCOMPOUND - AMINE MIXTURES AS DETERMINED BY DSC. PEAK DECOMPOSITION TEMPERATURES REFER TO THE FIRST PEAK IN THE CASE OF MIXTURES.

material	activation energy / kJ mol <sup>-1</sup>	exothermicity / kJ kg <sup>-1</sup>	peak decomposition temperature /K	heat of explosion <sup>32</sup> / kJ kg <sup>-1</sup>
Nitromethane (NM)	130	3000	688	4544
NM+NH <sub>3</sub> (12.5% vol)	54.3	4000	488	-
NM+EDA (10% vol.)	82.5	4231	518	-
NM+DETA (10% vol.)	83.1	4100	493	-
NM+DEA (10% vol.)	87.4	4700	513	-
NM+DMEA (10%vol.)	89.0	4750	518	-
TNT	79.2	3000	589	5066
TNT+DETA (10% wt.)	45.3	3000	458	-
Picric acid (PA)	99.2	2300	588	5025
PA+DETA (10% wt.)	29.7	3600	478	-
Tetryl	148.3	5100	585	5527
Tetryl+DETA (25% wt.)	39.27	2840	403	-

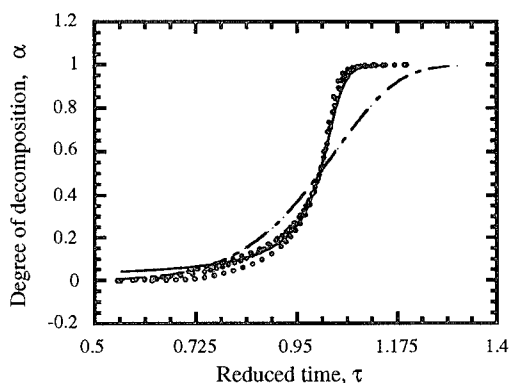


FIGURE 4. a-t PLOT FROM ISOTHERMAL DSC SCANS ON NITROMETHANE. THE POINTS REPRESENT EXPERIMENTAL DATA. THE FUNCTIONS  $\Phi_1(a)$  WITH  $C_0 = 60$  AND  $\Phi_2(a)$  WITH  $n=8$  ARE ALSO PLOTTED IN THE SOLID AND DOTTED CURVE, RESPECTIVELY.

This is the Avrami - Erofeev equation. It is indicative of random nucleation with the nuclei growing three-dimensionally in this case. Although liquids are often assumed to be homogeneous by their very nature, impurities, dissolved gases and vapour, as well as the sample-container interface can act as nucleation sites.

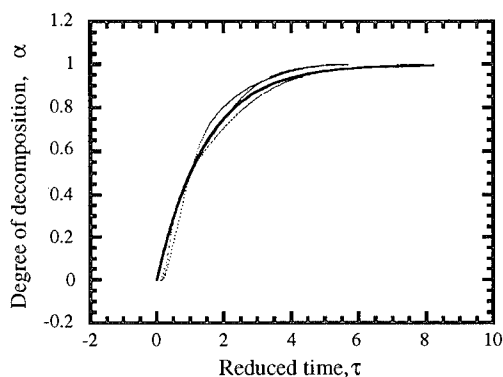


FIGURE 5. a-t PLOT FROM ISOTHERMAL DSC SCANS ON NITROMETHANE + DETA (10% VOL) THE POINTS REPRESENT EXPERIMENTAL DATA. THE SOLID CURVE IS A PLOT OF THE FUNCTION  $\Phi_3(a)$ .

Several workers have previously decomposed mixtures of nitromethane with various chemical species. The influence of many of the known products of decomposition has been tested in this way. Methyl radicals<sup>8</sup> and nitrogen dioxide were the only ones identified as capable of enhancing the rate of decomposition of nitromethane. Addition of small

TABLE 2. COMPLETE EXPRESSIONS FOR THE VELOCITY OF REACTION FROM THERMAL DECOMPOSITION EXPERIMENTS ON VARIOUS NITROCOMPOUNDS AND NITROCOMPOUND MIXTURES WITH AMINES. THE DECOMPOSITION MECHANISM IS ALSO INCLUDED. THE SENSITIZATION FACTOR IS DEFINED IN THE TEXT. NM INDICATES NITROMETHANE.

Material	Velocity of reaction, $\frac{d\alpha}{dt}$	Mechanism	Sensitization factor
NM in air	$(1-\alpha) \alpha^2 1.10 \times 10^{10} \exp[-(130000/RT)]$	cubic autocatalysis	1
NM in Argon	$(1-\alpha) \alpha^2 1.3 \times 10^9 \exp[-(130000/RT)]$	cubic autocatalysis	0.12
NM+ammonia (12.5%vol.)	$[-\ln(1-\alpha)]^{3/4} (1-\alpha) 2.9 \times 10^4 \exp[-(54300/RT)]$	random nucleation	649
NM + EDA (10% vol.)	$(1-\alpha) 4.3 \times 10^6 \exp[-(82500/RT)]$	unimolecular decay	143
NM + DETA (10% vol.)	$(1-\alpha) 1.4 \times 10^6 \exp[-(83100/RT)]$	unimolecular decay	40.4
NM + DEA (10% vol.)	$(1-\alpha) 7.7 \times 10^5 \exp[-(87400/RT)]$	unimolecular decay	7.9
NM + DMEA (10% vol.)	$\alpha (1-\alpha) 2.2 \times 10^6 \exp[-(89000/RT)]$	quadratic autocatalysis	7.7
TNT	$\alpha (1-\alpha) 4.5 \times 10^5 \exp[-(79200/RT)]$	quadratic autocatalysis	1
TNT + DETA (10% wt.)	$(1-\alpha) 3.0 \times 10^2 \exp[-(45300/RT)]$	unimolecular decay	4.6
Picric acid	$\alpha (1-\alpha) 2.0 \times 10^7 \exp[-(99200/RT)]$ or $[-\ln(1-\alpha)]^{3/4} (1-\alpha) 1.1 \times 10^7 \exp[-(99200/RT)]$	quadratic autocatalysis or random nucleation	1
Picric acid+DETA(10%wt.)	$[-\ln(1-\alpha)]^{-1} (1-\alpha) 1.7 \exp[-(29700/RT)]$	random nucleation	4.5 or 5.4
Tetryl	$[-\ln(1-\alpha)]^{1/2} (1-\alpha) 1.0 \times 10^{14} \exp[-(148300/RT)]$	random nucleation	1
Tetryl + DETA (25% wt.)	$(1-\alpha) 6.0 \times 10^2 \exp[-(39270/RT)]$	unimolecular decay	1.8

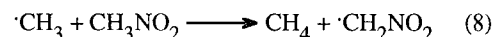
quantities of either in the initial reaction mixture was found to increase the rate of reaction. Oxygen, which is not amongst the known products, has also been shown to enhance the rate of decomposition of nitromethane.<sup>6</sup> In our work, the decomposition of nitromethane in argon rather than air was found to decrease the Arrhenius factor and to leave both the activation energy and the mechanism unchanged. Therefore, although the presence of oxygen increases the rate of decomposition, it does not appear to alter the rate-determining step. It is consequently proposed that the overall reaction in the thermal decomposition of nitromethane is possibly one between a methyl radical, nitromethane and nitrogen dioxide, as is shown below in equation (7):



The nitrogen dioxide amongst the products derives from the fission of the C-N bond in nitromethane and

the nitrogen oxide originates from the nitrogen dioxide in the reactants. The reaction determines the kinetics of the decomposition. It is highly exothermic. It can be estimated from the heats of formation of the various species that the heat of this reaction alone accounts for around half the exothermicity of nitromethane. The remaining energy is thought to come from the energy balance of subsequent, faster side reactions between the products.

It is thought likely that reaction (7) takes place in two stages:



The activation energy of reaction (8) is known<sup>7</sup> to lie between 33.5 and 42 kJ mol<sup>-1</sup>. The rate of this reaction is expected to be substantially higher than

that of reaction (9) which therefore would appear to be the rate-determining step. During this rate-determining step C-N breakage takes place in the presence of nitrogen dioxide.

The activation energy obtained for nitromethane is therefore likely to correspond to the energy required to break the C-N bond in the presence of nitrogen dioxide. The role of nitrogen dioxide would also explain the increase in the rate of decomposition when the sample is under pressure.<sup>9</sup> The formation of an activated complex which involves the interaction of two molecules, takes place more readily under an externally imposed pressure. The activation energy of decomposition would thus be expected to decrease if the sample is subjected to a hydrostatic or other loading, causing a subsequent increase in the rate of reaction. This feature of the decomposition, combined with the fact that reaction (7) is highly exothermic, is quite possibly important in the detonation of nitromethane.

The degree of decomposition against reduced time plot for the nitromethane - DETA mixture is depicted in Figure 5. The best fit to this and most of the corresponding graphs for the remaining nitromethane - amine mixtures was provided by:

$$\Phi_3(\alpha) = \frac{\ln(1-\alpha)}{\ln 0.5} \quad (10)$$

This indicates that in each case the thermal decomposition follows a unimolecular decay process best described by first order kinetics. The nitromethane - *n,n*-dimethylethylamine (10% by volume) mixture deviates from this behaviour; its decomposition is found to be autocatalytic. Quadratic autocatalysis arises when one of the products of decomposition takes part in the rate-determining reaction step.

The decomposition of the nitromethane mixtures with aqueous ammonia could best be described by the Avrami - Erofeev equation with  $n = 4$ . The kinetics here would appear to be governed by random nucleation. The presence of water is thought to influence this process. It is possible that a solution of gaseous ammonia in nitromethane would follow a unimolecular decay process described by first order kinetics.

It is evident from Table 2 that all the nitromethane-amine mixtures, with the possible exception of that involving *n,n*-dimethylethylamine, decompose through an identical governing mechanism which is distinctly different from that of nitromethane. It appears that the thermal decomposition of each of the mixtures is a first order unimolecular decay process governed by C-N

breakage.<sup>1</sup> Furthermore, it seems likely that this alteration of the chemical mechanism of decomposition is linked to the presence of the new chemical species suggested above. It would also appear that the altered rate-determining process is responsible for the chemical sensitization of nitromethane. The sensitization is thus not a consequence of a catalytic influence of an amine on nitromethane. It is a result of the introduction of a different and energetically more favourable decomposition pathway.

A sensitization factor has also been defined for every mixture in Table 2, as the ratio of the rate of decomposition of the sensitized to that of the pure nitrocompound, at a nominal temperature of 500 K and at a degree of decomposition,  $\alpha=0.5$ . All the mixtures studied show sensitization. Amongst the nitrocompounds examined, nitromethane is sensitized most. Ammonia, albeit in aqueous solution, has the strongest effect on nitromethane, with the amines sensitizing the latter in the order primary > secondary > tertiary.

The thermal decomposition of TNT was found to be governed by a quadratic autocatalytic chemical process (Table 2). In contrast, when the material is mixed with the amine the reaction it undergoes under increasing temperature is controlled by a unimolecular decay. Similarly, the first reaction sensitized tetryl undergoes in its thermal decomposition is controlled by a unimolecular decay. In contrast the thermal decomposition of pure tetryl is best described by the Avrami - Erofeev equation with  $n=2$ . This is indicative of random nucleation. The values determined here for the activation energy and for the Arrhenius constant are in excellent agreement with the values determined by previous workers.<sup>2</sup> Finally, our measurements on the decomposition of picric acid could be described equally well by quadratic autocatalysis or random nucleation. Sensitized picric acid deviates in its decomposition mechanism from that of the other sensitized nitrocompounds; it can best be described by random nucleation.

## DISCUSSION

All the nitrocompound-DETA mixtures examined showed sensitization as indicated by the lowering of their peak decomposition temperatures as compared to that of the pure nitrocompound. Mixtures of nitromethane with a range of amines or ammonia additionally displayed increased exothermicity. Every nitrocompound - amine mixture investigated gave rise to an additional peak in its dynamic dsc trace. This additional stage in their decomposition would seem to imply the existence of new chemical species in the mixtures.



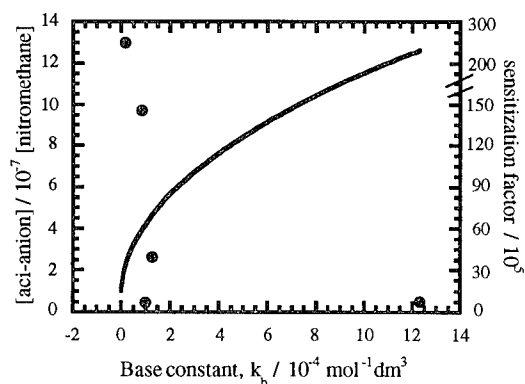


FIGURE 6. PLOT OF THE SENSITIZATION FACTOR (POINTS), AS DEFINED IN THE TEXT, AND THE RATIO OF THE ACI-ANION CONCENTRATION TO THAT OF NITROMETHANE (CURVE), FOR 10% BY VOLUME MIXTURES OF NITROMETHANE WITH THE AMINES, AGAINST AMINE BASICITY.

The activation energy of decomposition is shown to drop substantially when a nitrocompound is mixed with an amine. This provides strong evidence that the mechanism of sensitization is chemical in origin and occurs at the molecular level. It would seem from these results that the presence of an amine changes the rate-determining step of the decomposition of nitromethane and aromatic nitrocompounds, or it catalyzes their decomposition. Both of these possibilities, in addition to the decomposition of the amine, could influence the nature of the final products and hence change the overall exothermicity. The observed sensitization is a consequence of a reduction in the activation energy or a combination of such a reduction with an increase in the exothermicity. Any newly formed chemical species in the mixtures seem to be more reactive. It has been assumed previously<sup>10</sup> that there are no chemical changes in these systems which would give rise to new products at room temperature. This is supported by the <sup>13</sup>C nmr spectra of nitromethane-DETA mixtures, in which only an increase in the aci-anion concentration was detected.<sup>10</sup> We have used our dsc results to plot, in Figure 6, the sensitization factor (points), and the ratio of the aci-anion concentration to that of nitromethane (curve), for each of the nitromethane mixtures, against amine basicity. It is obvious from this figure that, for various nitromethane - amine mixtures, there is no systematic variation of the sensitization factor with the basicity of the amine. The concentration of the aci-anion does not, therefore, appear to influence the sensitization.

In a previous publication<sup>1</sup> we have identified the existence of a charge-transfer complex in nitrocompound-amine mixtures and showed that its presence can account for the observed sensitization. This molecular complex is formed by intermolecular charge-transfer from the nitrogen of the amino group to the antibonding orbital of the nitro group. This charge-transfer complex has been detected in nitromethane - amine as well as in all the nitrocompound - amine mixtures examined here, and is thought to cause weakening of the C-N bond. It is the only new chemical species that has been detected in these systems. It is expected, in each case, to be more reactive than the parent nitrocompound and as a consequence its presence will have a sensitizing effect. Its decomposition is thought to give rise to the additional stage observed in the thermal decomposition of the mixtures.

#### ACKNOWLEDGEMENTS

We would like to thank Dr. A. D. Yoffe, of this laboratory, for discussions and comments on the manuscript. Thanks are also due to Drs. P. Haskins and M. Cook of RARDE for their interest in this work. We gratefully acknowledge the Procurement Executive, Ministry of Defence for sponsoring this work. We are also indebted to the Safety Laboratory of CIBA-GEIGY for help with the experiments.

#### REFERENCES

1. Constantinou, C. P.; Mukundan, T.; and Chaudhri, M. M., "Sensitization of nitrocompounds by amines," *Phil. Trans. Roy. Soc. Lond. A*, Vol. 339, 1992, pp. 403 - 417.
2. Hutchinson, C. D.; Krishna Mohan, V.; and Millar, R. W., "Aminotetryls: Synthesis, Spectral Characterization, Thermal Decomposition and Explosive Properties," *Propellants, Explosives, Pyrotechnics*, Vol. 9, 1984, pp. 161-171.
3. Dubovitskii, F. I.; Manelis, G. B.; and Smirnov, L. P., "Kinetics of the thermal decomposition of n-methyl-n,2,4,6-tetranitroaniline (tetryl)," *Russian J. Phys. Chem.*, Vol 35, No. 3, 1961, pp. 255-260.
4. Rogers, R. N., "Combined Pyrolysis and thin layer chromatography: A method for the study of decomposition mechanisms," *Analytical Chemistry*, Vol. 39, 1967, pp. 730-733.
5. Wenograd, J., "The behaviour of explosives at very high temperatures," *Trans. Faraday Soc.*, Vol. 57, 1961, pp. 1612-1620.

6. Taylor, H. A.; and Vesselovsky, V. V., "The thermal decomposition of nitromethane," *J. Phys. Chem.*, 1935, Vol. 39, pp. 1095-1101.

7. Cottrell, T. L.; Graham, T. E.; and Reid, T. J., "The thermal decomposition of nitromethane," *Trans. Faraday Soc.*, Vol. 47, 1951, pp. 584-590.

8. Gray, P.; Yoffe, A. D.; and Roselaar, L., "Thermal decomposition of the nitroalkanes," *Trans. Faraday Soc.*, Vol. 51, 1955, pp. 1489-1497.

9. Lee, E. L.; Sanborn, R. H.; and Stromberg, H. D., "Thermal decomposition of high explosives at static pressures 10 - 50 kilobars," in *Proceedings of the Fifth Symposium (International) on Detonation*, Office of Naval Research - Department of the Navy, ACR-184, Aug 18-21, 1970, pp.331-337.

10. Engelke, R.; Earl, W. L.; and Rohlfing, C. M., "Microscopic evidence that the nitromethane aci-ion is a rate controlling species in the detonation of liquid nitromethane," *J. Chem. Phys.*, Vol. 84, 1986, pp. 142-146.

---

## DISCUSSION

JIMMIE C. OXLEY

New Mexico Institute, Socorro, New Mexico

Your work nicely explains how bases sensitize nitromethane. How does it address the sensitization by acids?

## REPLY BY C. P. CONSTANTINOU

This particular project exclusively addressed the nitrocompound-amine interaction. This effect is an order of magnitude more pronounced than any known sensitization of nitromethane by other compounds (such as sodium hydroxide, glacial acetic acid, nitric acid, or perchloric acid). It also appears that it has a distinct mechanism.

## DISCUSSION

DR. DIVYAKANT L. PATEL

Countermines Systems Directorate, U.S. Army,  
Fort Belvoir, Virginia

Do TNT and picric acid form eutectic mixtures with DETA?

## REPLY BY C. P. CONSTANTINOU

As can be seen from Figure 1, the melting point in the case of the solid nitrocompounds appears to change in the presence of the amine. It should be mentioned that DETA is a liquid and that there are chemical interactions in these mixtures.

## DISCUSSION

THOMAS B. BRILL

University of Delaware, Newark, Delaware

You noted that the rate does not correlate well with the basicity of the amine. Did you obtain the basicity values in the environment of the reaction? This is important because trends in amine basicity depend strongly on the environment.

## REPLY BY C. P. CONSTANTINOU

The basicity values quoted for the amines used in this work were obtained from the literature and have invariably been measured in aqueous solution. The relative magnitudes of these values were confirmed under our experimental conditions through electrical conductivity measurements.

I should emphasize that the measurements reported here are very critically dependent on sample (especially amine) purity.

## PRESSURE DEPENDENCE ON THE REACTION PROPAGATION RATE OF PETN AT HIGH PRESSURE

M. F. Foltz

Lawrence Livermore National Laboratory  
Livermore, California 94550

The reaction propagation rate (RPR) of the sensitive high explosive pentaerythritol tetranitrate (PETN) was measured in a diamond anvil cell (DAC) over the pressure range of 2-20 GPa. The experimental technique used is the same as that previously reported. The RPR data shows that it burns one to two orders of magnitude faster in the DAC than 1,3,5-triamino-2,4,6-trinitrobenzene (TATB) and nitromethane ( $\text{CH}_3\text{NO}_2$ ) respectively. The PETN RPR curve did not show simple pressure-dependent behavior like that of nitromethane, but instead varied abruptly like the RPR curve of TATB. In order to interpret these changes, static-pressure DAC mid-IR FTIR spectra were taken of micro-pellets of PETN embedded in KBr. The relationship between changes in the spectra, the RPR curve, and published single crystal PETN wedge test data are discussed.

### INTRODUCTION

Previous studies on the shock initiation of single-crystal pentaerythritol tetranitrate (PETN) have indicated a strong orientation dependence for sensitivity.<sup>1</sup> It has been proposed that greater shock sensitivity in the  $\langle 110 \rangle$  direction is due to anisotropic plastic flow, or on the molecular scale, to greater steric hindrance to dislocation motion. The experiments also revealed an apparent anomaly in the plot of run-distance-to-detonation vs input shock stress at 4.3 GPa. This run distance, the same as that interpolated for 9.6 GPa, is much shorter (i.e. the crystal is more sensitive) than predicted by linear fit of higher stresses. An initiation mechanism driven by decomposition reactions was suggested.

Another explanation for this anomaly would invoke a change in material properties due to one or more phase transitions. To test this hypothesis, the reaction rate of PETN was determined for static compression over the pressure regime of the anomaly. Observed changes were then interpreted by use of high-pressure mid-infrared spectroscopy. Future experiments are planned for elevated temperature to investigate the role of heating during shock loading. The goal of these studies is to understand on the molecular scale the mechanism behind the 4-GPa shock-initiated anomaly. Described below are the early results and preliminary interpretation of these experiments done on micro-samples ( $<1\text{-}\mu\text{g}$ ) of polycrystalline PETN confined under static high pressure in a diamond anvil

cell (DAC).

### EXPERIMENTAL

The experimental technique used is the same as that previously reported.<sup>2</sup> The Bassett-type DAC consists of two opposing 0.1-carat diamonds sandwiching a drilled stainless steel gasket. Pressure measurements were made by the standard ruby fluorescence technique, the argon ion laser (514-nm) focused onto ruby chips embedded in the sample. To load the cell, powdered PETN and ruby chips were compacted between the diamonds to form a gasket-contained micro-pellet. After pressure measurement, the same argon ion laser was defocused to fully illuminate the sample area. The transmitted laser speckle image of the PETN sample was magnified and projected onto the entrance slit of a streak camera. A single tightly focused light pulse from a frequency doubled Nd:YAG laser (532-nm) ignited the sample and triggered the streak camera to capture the reaction event on film. After ignition, the reaction front in the sample is recorded on film as a disturbance that moves radially outward from the ignition zone into an otherwise unperturbed speckle pattern. Light transmitted through the region of completely reacted material (products) produces an indistinct image on film. The velocity of the burn, or reaction propagation rate (RPR), was determined by measuring the slope of the disturbance from the film record. Since all samples vented when the burn front reached the gasket wall, new samples were required for each data point. The diamonds were

cleaned of any unreacted PETN, product, and gasket residue and the entire procedure repeated for all pressure points measured. The measured reaction propagation rates were plotted as a function of pressure to produce the RPR curve.

The RPR data of PETN yields a maximum DAC burn rate that is one to two orders of magnitude faster than those of TATB<sup>3</sup> and CH<sub>3</sub>NO<sub>2</sub>.<sup>2</sup> The RPR curve does not show the very simple pressure dependence typified by nitromethane, but has instead abrupt variations observed for TATB.<sup>3</sup> Such variations are suggestive of pressure-induced changes in molecular conformation and/or crystal lattice packing, i.e. phase changes. PETN is known to exist in two phases at ambient pressure, thermally phase converting above 130 °C from an orthorhombic lattice (Pcnc) to a high-temperature, metastable tetragonal (P4<sub>2</sub>1c) phase. The structures of both the ambient PETN(I)<sup>4a</sup> and metastable PETN(II)<sup>4b</sup> phases, as well as the mechanism of the thermal solid-solid polymorphic transformation,<sup>4b</sup> are known from x-ray studies.

To study pressure-induced molecular changes, and to infer from them the basis of the RPR fluctuations, static-pressure mid-IR FTIR spectra were taken over the pressure range of 0.3-16 GPa. Static-pressure Fourier transform infrared (FTIR) spectra of PETN samples were acquired with a benchtop Nicolet System 730 spectrometer (4 cm<sup>-1</sup> resolution). Micro-pellets were prepared by first pressing KBr (with embedded ruby chips for pressure measurement) to transparency into a drilled (120-150 µm diameter) gasket, then pressing a thin layer of PETN on top of the KBr "window". As a check of reproducibility and gross impurity contamination, standard 10% KBr macro-pellet and Nujol mull PETN spectra were also done. These spectra agree with published KBr-pellet<sup>5</sup> and Nujol mull<sup>6</sup> spectra.

Identification of even the ambient PETN FTIR spectrum is only tentative until isotopically labelled material has been analyzed. Work is underway to study fully deuterated PETN. Table I gives the frequencies of the very weak bands seen in the CH<sub>2</sub> stretching region of ~3000 cm<sup>-1</sup> and the very strong (vs) to weak (w) peaks in the "fingerprint region" of 1660-600 cm<sup>-1</sup>. Provisional identification is based on (a) published assignments of the fundamental vibrations of the O'-NO<sub>2</sub> group determined from nitro compounds and nitrate esters,<sup>7</sup> (b) comparison of PETN spectral features with those of pentaerythritol,<sup>8</sup> pentaerythritol tetrahalides,<sup>8</sup> *meso*-erythritol,<sup>8</sup> and other nitrate esters,<sup>6</sup> and (c) general normal mode identification guidelines.<sup>9,10</sup>

Table I. Mid-Infrared Spectral Features of PETN

Frequency (cm <sup>-1</sup> )	Comments,* Tentative Assignments	Ref.†
3022.97	vw, CH <sub>2</sub> stretch	g
2984.24	vw, CH <sub>2</sub> stretch	g
2910.24	vw, CH <sub>2</sub> stretch	g
1654.89	vs sh (overlap), NO <sub>2</sub> asymmetric stretch, split	a,g
1645.13	vs (overlap), NO <sub>2</sub> asymmetric stretch, split	a,g
1473.70	w, CH <sub>2</sub> ?	
1395.56	w (overlap), CH <sub>2</sub> scissors deformation	b,c,f
1384.91	w (overlap), CH <sub>2</sub> scissors deformation	b,c,f
1305.59	m, C-C skeletal mode?	d
1284.28	s, NO <sub>2</sub> symmetric stretch, split	a,c,f,g
1271.25	s, NO <sub>2</sub> symmetric stretch, split	a,c,f,g
1037.74	m, C-O'-N asymmetric stretch	e
1002.93	m, C-O'-N asymmetric stretch	e
938.61	w, C-O' stretch?	g
896.13	w sh, CH <sub>2</sub> wag & twist deformation?	c
869.58	m (overlap), C-C skeletal mode?	d
850.70	m (overlap), O'-N stretch?	c,f,g
754.42	m overlap, NO <sub>2</sub> out-of-plane bend	a,c,g
746.19	w sh, CH <sub>2</sub> rocking deformation??	c,g
703.25	m, NO <sub>2</sub> in-plane bend	a,c,g
623.26	w, O'-NO bend, split	a,g
618.56	w sh, O'-NO bend, split	a,g

\* vw = very weak, w = weak, m = medium, s = strong, vs = very strong, sh = shoulder, ? = least certain assignment

† Identification based on references #4-6, 8 and: (a) #7a; (b) #10c; (c) #10b; (d) #10a; (e) #7c; (f) #7b; and (g) #9.

## RESULTS

The RPR curve for high-pressure laser-ignition and burn of PETN in a DAC is shown in Fig. 1. The filled circle symbols connected by a dashed line correspond to values at 4.3 and 9.6 GPa interpolated from the measured data. A linear least squares fit for data taken below ~6-GPa gives a RPR value of 130.0 m/s for 4.3 GPa; a 5th order polynomial fit for data taken above ~8-GPa gives a similar RPR value of 135.9 m/s for 9.6 GPa. There are two dips in the curve, around 6.5 and 8 GPa, after which the rate again increases monotonically. As with all other energetic materials studied to date (e.g. CH<sub>3</sub>NO<sub>2</sub>; TATB; FEFO; the α-, β-, γ-, and ε-polymorphs of hexanitrohexaazaisowurtzitane), the PETN samples failed to burn to completion at the lowest pressures ignited. Under these conditions, up to three-quarters of the starting material remained unburnt in the gasket with some sooty residue at the burnt surfaces. With increasing pressure, the amount of residual unreacted material decreased rapidly.

Figure 2 shows the pressure dependence of the mid-IR spectral features listed in Table I. The behavior includes frequency shifting, peak splitting, loss of peak intensity, or peak broadening with increasing pressure. Solid lines are used for peaks of the highest intensity;

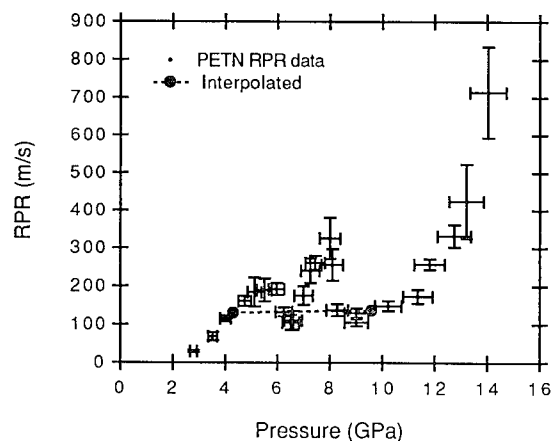


FIGURE 1. REACTION PROPAGATION RATE (RPR) OF HIGH-PRESSURE PETN CONFINED IN A DIAMOND ANVIL CELL.

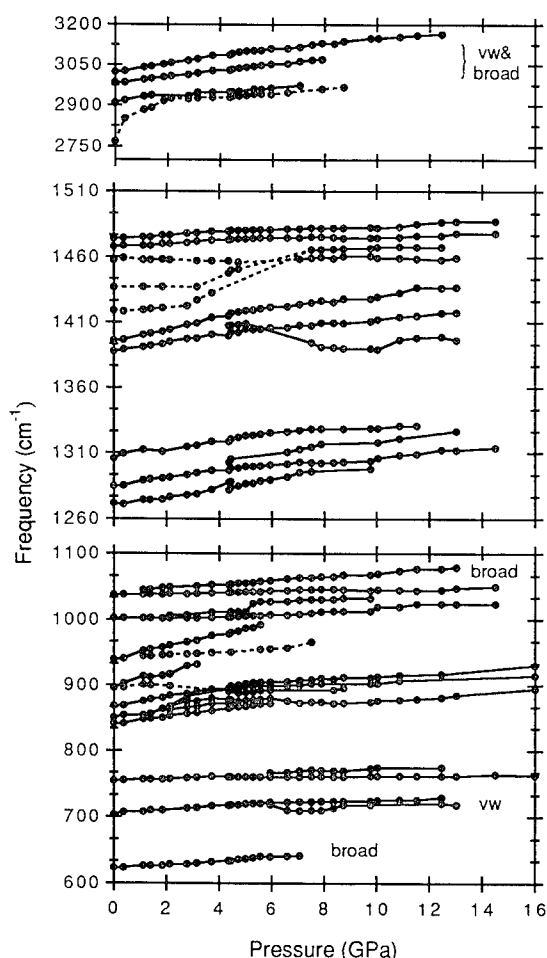


FIGURE 2. FREQUENCY SHIFT OF SOME MID-IR PETN SPECTRAL PEAKS (TABLE I).

dashed lines correspond to the more uncertain or speculative behavior of very weak or overlapping peaks. The  $\text{CH}_2$  deformation,  $\text{NO}_2$  symmetric stretch, and  $\text{C-O-N}$  modes in particular appear to be more noticeably affected by compression. Figure 3 illustrates the pressure effects of one deformation, the methylene scissors mode. New bands appear for pressures above  $\sim 4.5$  GPa along with intensity-switching of the 1385 and 1396  $\text{cm}^{-1}$  bands above 6.6 GPa. These spectral changes indicate the onset of phase transition(s). The transformation does not appear to proceed rapidly or go to completion, but sluggishness is typical of some solid-solid phase transitions.<sup>11</sup>

## DISCUSSION

Although the nature of a high-pressure phase conversion in PETN can be speculated, definitive identification should be done via high pressure x-ray measurements. Pressure-induced frequency shifts and intensity changes can be interpreted using the  $\text{PETNII} \rightarrow \text{PETNI}$  thermal phase conversion<sup>4b</sup> as a mechanistic template. The geometries of the molecules in these two phase are similar, the more noticeable differences being in bond angles like the  $\text{C-O-N}$  (average 1.5% decrease) and  $\text{O'-N-O}$  (+1.0% and -1.6%). A comparison of polymorphic mid-IR spectra would therefore be expected to show the greatest change in the  $\text{C-O-N}$ , and  $\text{O'-N-O}$  deformation modes. Differences in molecular packing lie in rotation  $\sim 60^\circ$  about the  $\text{C-C}$  bonds and in  $\sim 180^\circ$  rotation about and  $\sim 1\text{\AA}$  translation up the  $c$  axis. Since the intermolecular contacts change very little compared to intramolecular distortion, the  $\text{PETNII} \rightarrow \text{PETNI}$  conversion can be called a displacive transformation, proceeding relatively rapidly due to little or no opposition by an energy barrier.<sup>11</sup>

As a first approximation, pressure-induced molecular deformation could be considered a continuation of the phase II to phase I conversion mechanism. Under compression, the core tetrahedral carbon skeleton will continue to resist deformation. The remaining distortions available to relieve pressure-induced strain are motions about the  $\text{C-C}$  and  $\text{C-O'}$  bonds. During the  $\text{II} \rightarrow \text{I}$  cooling conversion, the symmetry of the space group increases while molecular symmetry decreases. Comparable pressure-induced bond motion will likely continue deforming the molecule to lower symmetry.<sup>11</sup> Resonance interaction within the  $\text{O'-NO}_2$  bonds, however, restrains the  $\text{C-O'-NO}_2$  ensemble to planarity during the  $\text{II} \rightarrow \text{I}$  transition, presenting a formidable barrier to torsion even under pressure.

Under static compression, PETN exhibits the greatest distortion in the  $\text{CH}_2$  deformation,  $\text{NO}_2$

symmetric stretch, and C-O'-N deformation modes. The splitting of the NO<sub>2</sub> stretching mode to higher and lower frequency can be due to an abrupt change in O'-NO<sub>2</sub> group resonance. For example, a lower bond frequency would denote a shorter N-O bond length of greater double-bond character, this in turn indicating a lengthening of O'-N bonds. A split in frequency suggests that the molecule is twisting asymmetrically, possibly by rotation about the C-O' bonds during the course of molecular translation/rotation. This interpretation is supported by the pressure-induced intensity loss and diffuseness the 620 cm<sup>-1</sup> O'-N-O bending mode. The intensity loss is due to a decrease in dipole moment as the O'-N-O angle opens up (i.e. the group becomes more linear). The splitting of the methylene deformation mode also suggests rotation about the C-O' bond. The strong blue shift and split of the (tentatively identified) 940 cm<sup>-1</sup> C-O' stretch again suggests an asymmetric distortion involving rotation about the C-O' bonds and affecting the C-O'-N angle.

In summary, it would appear that high static pressure forces the PETN molecules to undergo asymmetric deformation to a possibly lower symmetry conformation. As a result of undergoing these changes, there is a concurrent change in reaction propagation rate. Outside the region of greatest reaction rate change are the pressure points of 4.3 and 9.6 GPa called out in the LANL shock sensitivity work.<sup>1</sup> Interpolations from measured data indicate that the reaction rate at these pressures are comparable. In the LANL wedge test data, the degree of sensitivity was seen to be the same at these points. It was also surmised that the underlying cause of greater sensitivity at 4-GPa also affected data at 8 to 9 GPa since the LANL data from 8 to 9 GPa do not follow the "typical" linear trend but "pull" over toward the 4-GPa point. It can be seen from the mid-IR data of Fig. 2 and the RPR data of Fig. 1 that pressure-induced changes in these data are incomplete till pressures over 9 GPa. What is interesting is that even with the large changes seen in the (static pressure) RPR curve over the pressure regime of interest, the interpolated values should track so well with a trend seen in very different (shock initiation) experiment. This correlation suggests that heating the PETN samples in the DAC to 100 C (bulk temperature rise for 4.2 GPa)<sup>1</sup> prior to laser-ignition and burn and infrared analysis may not reveal many differences from the present data.

The underlying relationships between pressure-induced molecular deformation and reaction rate are not easily untangled. This is due to the multi-faceted role that pressure plays in affecting both bulk and molecular properties. The effect of pressure on the rate of reaction can be seen to involve (a) change in flame

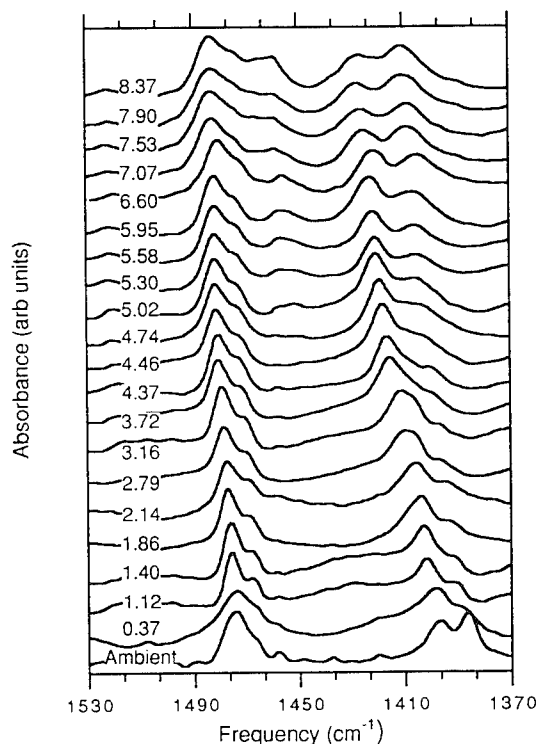


FIGURE 3. PRESSURE DEPENDENCE OF MID-IR PETN METHYLENE DEFORMATION MODES.

structure (i.e. whether a broad or narrow reaction zone), (b) change in the free energy of transition, either (i) gradual (static compression effects), or (ii) abrupt (phase change), and (c) change in kinematic (dynamic) coupling to the environment, which affects the rate at which the molecule passes through the transition state.<sup>13</sup>

Consider flame structure first. The width of the burn region, or flame structure, is mechanistically affected by the difference in density between the unreacted material and gaseous products. In lowering the pressure, the expanding gaseous products physically broaden the reaction burn zone and decrease the thermal gradient, which in turn reduces the reaction propagation rate. In addition to the mechanistic effect of flame structure are the pressure-induced chemical effects of (b) and (c) described above. When there is only a gradual change in potential energy surfaces due to compression, there will only be a gradual change in reaction rate with pressure. A prime example of this effect is seen in the DAC burn rate data of nitromethane.<sup>2</sup> Unlike the other energetic materials tested to date, no pressure-induced phase changes have been seen to occur in this system,<sup>12</sup> and there are no abrupt changes noted in the burn curve. The RPR

curve for  $\text{CH}_3\text{NO}_2$  monotonically increases with pressure until a maximum is reached  $\sim 30$  GPa, after which the reaction rate decreases. In this case, pressure affects the reaction rate of  $\text{CH}_3\text{NO}_2$  in all the ways described above except via phase change. The initial increase is due both to a mechanistic narrowing of the flame front with denser products, and to the static-compression slow shift in free energy. The gradual decrease in burn rate above 30 GPa is due to diffusion-limited reactions. The RPR curves of other energetic materials tested so far in the DAC typically show more complex RPR curves than that of  $\text{CH}_3\text{NO}_2$ . Nonetheless, these same materials also display pressure regimes over which the burn rate has a simple pressure dependence. In TATB, for example, a gradual change in RPR is seen for pressures less than 18-GPa and between 20 to 30 GPa.<sup>3</sup> In the PETN data presented here, a monotonic increase in reaction rate is seen for pressures below 5-GPa and above 9-GPa. Over these pressure regimes, therefore, it is expected that the burn rate is controlled predominantly by change in flame structure and the gradual effect of static compression on the free energy of the system.

Thermodynamically, a pressure-induced phase change will cause the potential energy surfaces describing the system to change abruptly. After the system phase transitions from one potential surface to another, different reaction pathways appear. The probability of following a given molecular reaction pathway is modified by the surrounding intermolecular environment which is different for each polymorph. In addition, the initial reaction step is affected not only by the change in local free energy surface, but also by the kinematic coupling of the crystal lattice to the reaction pathways.

## CONCLUSION

Earlier studies on the shock initiation of single-crystals of PETN indicated a strong orientation dependence for sensitivity.<sup>1</sup> The experiments also revealed an apparent anomaly in the plot of run-distance-to-detonation vs input shock stress at 4.3 GPa. An explanation proposed for this anomaly invokes a change in material properties due to one or more phase transitions. To test this hypothesis, the reaction rate of PETN was determined for static compression over the pressure regime of the anomaly. The reaction propagation rate (RPR) data shows that it burns one to two orders of magnitude faster in the diamond anvil cell (DAC) than TATB and nitromethane. The RPR curve of PETN did not show simple pressure-dependent behavior, but had abrupt dips at 6.5 and 8 GPa, after which the rate again increases monotonically. In order to interpret these changes, static-pressure mid-infrared

FTIR spectra were taken of high pressure PETN samples. Analysis of the behavior of the provisionally identified modes suggests that high static pressure forces PETN molecules to undergo asymmetric deformation to a possibly lower symmetry conformation. It is not clear the relative degree to which pressure-induced thermodynamic effects vs. kinetic effects control the reaction rate. One way to determine the role of thermodynamic properties in governing reaction rate would be to measure the thermal conductivity of the HE as a function of pressure, preferably across well-defined phase transitions. Reaction kinetics, on the other hand, are only gradually affected by pressure at a rate determined by the static compressibility of the material in the absence of phase conversion. The role of kinetics in controlling the relative reaction rates of phase conversion would need to be determined by studying the effects of isotopic labelling.

The RPR data obtained in these DAC studies may also prove to be very useful in understanding deflagration-to-detonation (DDT) processes under high confinement. The pressures and reaction rates attained in the DAC are similar to those observed in the DDT reaction regime of rapid compressive burning that proceeds shock formation and detonation.<sup>14</sup> Since most DDT experimental and theoretical work has focused on granular and porous materials, only low pressure conductive and convective combustion regimes of DDT have been addressed with any thoroughness to date. Diamond anvil cell RPR measurement techniques provide a small-scale, optically transparent environment for the study of the chemical and physical phenomena behind high-pressure pre-detonation reactions.

## ACKNOWLEDGEMENTS

The author would like to thank Craig Tarver, Jon Maienschein, and Albert Nichols, III for their advice and technical editing of this report.

\* Work performed under the auspices of the U.S. Department of Energy by the Lawrence Livermore National Laboratory under contract No. W-7405-ENG-48.

## REFERENCES

1. Dick, J. J., Mulford, R. N., Spencer, W. J., Pettit, D. R., Garcia, E. and Shaw, D. C., "Shock Response of Pentaerythritol Tetranitrate Single Crystals," *J. Appl. Phys.*, Vol. 70, No. 7, 1991, p. 3572.

2. Rice, S. F. and Foltz, M. F., "Very High Pressure Combustion: Reaction Propagation Rates of Nitromethane within a Diamond Anvil Cell," *Combustion and Flame*, Vol. 87, 1991, p. 109.
3. Foltz, M. F., "Pressure Dependence of the Reaction Propagation Rate of TATB at High Pressure," accepted for publication by *Propellants, Explosives, Pyrotechnics*.
4. (a) Booth, A. D. and Llewellyn, F. J., "The Crystal Structure of Pentaerythritol Tetranitrate," *Chem. Soc. (London) J.*, 1947, p. 837; (b) Cady, H. H. and Larson, A. C., "Pentaerythritol Tetranitrate II: Its Crystal Structure and Transformation to PETN I; an Algorithm for Refinement of Crystal Structures with Poor Data," *Acta Cryst.*, Vol. B31, 1975, p. 1864.
5. Carol, J. "Infrared Analysis of Erythritol Tetranitrate, Pentaerythritol Tetranitrate, and Mannitol Hexanitrate," *J. Assoc. Offic. Agr. Chemists*, Vol. 43, 1960, p. 259.
6. Pristera, F., Halik, M., Castelli, A. and Fredericks, W., "Analysis of Explosives Using Infrared Spectroscopy," *Anal. Chem.*, Vol. 32, 1960, p. 495.
7. (a) Brown Jr., J. F., "The Infrared Spectra of Nitro and Other Oxidized Nitrogen Compounds," *J. Amer. Chem. Soc.*, Vol. 77, 1955, p. 6341; (b) Kornblum, N., Ungnade, H. E., and Smiley, R. A., "The Infrared Absorption Spectra of Nitroparaffins and Alkyl Nitrates," *J. Org. Chem.*, Vol. 21, 1956, p. 377; (c) Carrington, R. A. G., "The Infra-red Spectra of Some Organic Nitrates," *Spectrochimica Acta*, Vol. 16, 1960, p. 1279.
8. Pouchert, C. J., Ed., *The Aldrich Library of Infrared Spectra, ed. III*, Aldrich Chemical Co., Inc., Milwaukee, WI, 1981.
9. (a) Conley, R. T., *Infrared Spectroscopy*, Second Ed., Allyn and Bacon, Inc., Boston, MA, 1972, pp. 97-100, 138-140, 181-186; (b) Bellamy, L. J., *The Infra-red Spectra of Complex Molecules*, John Wiley & Sons, New York, NY, 1975, pp. 13-29, 129-132, 331-339.
10. (a) Simpson, D. M., Sutherland, C. B. B. M., "Vibration Spectra of Hydrocarbon Molecules II. Skeletal Frequencies in Certain Branched Paraffins," *Proc. Royal Soc. London*, Vol. A199, 1949, p. 169; (b) Sheppard, N., Simpson, D. M., "The Infra-red and Raman Spectra of Hydrocarbons Part II. Paraffins," *Chem. Soc. London Quarterly Reviews*, Vol. 7, 1953, p. 19; (c) Francis, S. A., "Intensities of Some Characteristic Infrared Bands of Ketones and Esters," *J. Chem. Phys.*, Vol. 19, No. 7, 1951, p. 942.
11. Buerger, M. J., "Crystallographic Aspects of Phase Transformations," in *Phase Transformations in Solids*, Cornell University, Ithaca, NY, 23 Aug 1948.
12. (a) Trevino, S. F., Prince, E. and Hubbard, C. R., "Refinement of the Structure of Solid Nitromethane," *J. Chem. Phys.*, Vol. 73, 1980, p. 2996; (b) Cromer, D. T., Ryan, R. R. and Schiferl, D., "The Structure of Nitromethane at Pressures of 0.3 to 6.0 GPa," *J. Phys. Chem.*, Vol. 89, 1985, p. 2315; (c) Yarger, F. L. and Olinger, B., "Compression of Solid Nitromethane to 15 GPa at 298 K," *J. Chem. Phys.*, Vol. 85, 1986, p. 1534.
13. Nichols, A. L., III, private communication, Lawrence Livermore National Laboratory, Livermore, CA, March 1993.
14. Baer, M. R., Gross, R. J., and Nunziato, J. W., "An Experimental and Theoretical Study of Deflagration-to-Detonation Transition (DDT) in the Granular Explosive, CP," *Combustion and Flame*, Vol. 65, 1986, p. 15.

---

## DISCUSSION

LeROY GREEN

Lawrence Livermore National Laboratory, Livermore, California

There is an anomaly in the initiation of LX-17 (92.5% TATB, 7.5% Kel-F) at 18-20 GPa, reported in a previous Detonation Symposium (6th, Jackson et al., p. 755). It appears as a X3 increase in the flyer energy required as pressure is reduced through the pressure range. A normal "POP" plot does not show this effect.

## REPLY BY M. FRANCES FOLTZ:

It is interesting that the gun shot experiments show this anomaly for TATB at the same pressure as the first discontinuity in its burn rate curve. It is perhaps not



surprising because these measurements appear to be more sensitive than run-distance-to-detonation experiments for unresponsive materials such as TATB which do not have a clear-cut threshold for initiation as PETN does. In addition, representing "POP" plot data on a log-log scale can obscure all but very pronounced

nonlinear anomalies. There may also be anomalies in flyer plate experiments for PETN and  $\epsilon$ -hexanitrohexaazaisowurtzitane ( $\sim 2$  GPa), for example, at the discontinuity pressures seen in burn rate plots for these HEs.

# THE CALCULATION OF ELECTROSTATIC INTERACTIONS AND THEIR ROLE IN DETERMINING THE ENERGIES AND GEOMETRIES OF EXPLOSIVE MOLECULAR CRYSTALS

James P. Ritchie, Edward M. Kober, and Ann S. Copenhaver  
Los Alamos National Laboratory  
Los Alamos, NM 87544

Three different procedures were used to calculate electrostatic interactions in explosive molecular crystals. Potential Derived Charges (PDC's) and atom-centered multipole expansions (ACME's) provide reasonable fits of the molecular electrostatic potential. The ability of these approaches to reproduce observed crystal structures was also evaluated.

## INTRODUCTION

Properties of the crystalline phase are important in determining the behavior of explosives. The CJ state of an explosive depends sensitively upon its density for example.<sup>1</sup> In addition, the shock sensitivity of PETN is found to depend upon the crystal orientation with respect to the shock direction.<sup>2</sup> Moreover, HE's with large amounts of hydrogen-bonding in the crystal (such as TATB and nitroguanidine) are frequently found to be less sensitive than those without. Finally, the heat of sublimation, which is the enthalpy difference between the gaseous and crystalline phases, is required to obtain the heat of formation of a condensed phase explosive from estimates of its gaseous heat of formation. The latter quantity is readily estimated using a number of approaches.

The atom-atom potential method can be used to calculate the energy and geometry of a molecular crystal.<sup>3</sup> In this approach, the intermolecular interaction between molecules A and B in the crystal lattice is taken as a sum over atom pairs. The interaction energy between atoms is then partitioned into distinct energetic components, shown in Equation 1.

$$E_{AB} = \sum_{i \in A} \sum_{j \in B} \left( B_{ij} e^{-\alpha_{ij} R_{ij}} - \frac{A_{ij}}{R_{ij}^6} + E_{ele,ij} \right) \quad (1)$$

These terms attempt to describe, respectively, the closed shell repulsion between the atoms resulting from the Pauli exclusion principle, van der Waals attractions, and the electrostatic interactions between the atomic charge distributions. The last term may

be either attractive or repulsive. It is frequently represented as  $q_i q_j / R_{ij}$ , where the  $q$ 's represent atomic charges.

A Raleigh-Schroedinger perturbation analysis of intermolecular interactions has shown that the electrostatic interaction is the leading order term.<sup>4</sup> Most HE's contain strongly polar functionalities (such as nitro groups), and many contain strong hydrogen-bonding moieties (such as amine groups). It is, therefore, important to represent the electrostatic interaction as accurately as possible if a realistic description of crystal properties is to be obtained. (It is well-recognized that electrostatic interactions are important in hydrogen bonds.<sup>5</sup>)

In the past, a description of electrostatic interactions was difficult to obtain. The use of molecular electric moments for this purpose converges too slowly, if at all, for many common HE molecules. So, there was no reliable way of obtaining the atomic charges or multipoles that are required for the electrostatic calculation, except for the special case of small ions. More recently, however, it has become possible to obtain approximate charge distributions from *ab initio* molecular orbital theory for molecules the size of common explosives.<sup>6</sup> In addition, a number of procedures have been devised to obtain either atomic charges alone or multipoles for use in the electrostatic calculation.<sup>7</sup> In this paper, we examine three procedures for calculating electrostatic interactions. This has allowed us to characterize the role of these interactions in determining the crystalline geometry and energy of some explosives. In addition, diaminotetrazine, which is not an explosive, was ex-

aminated. This molecule is of interest because of its high nitrogen content.

## METHODS

Approximate molecular charge distributions were obtained from *ab initio* molecular orbital calculations for the molecules of interest using either the GAUSSIAN82<sup>8</sup> or GAUSSIAN92<sup>9</sup> computer program. The small split valence 3-21G basis was used throughout.<sup>6</sup> Molecular geometries were completely optimized within the common point group symmetry.

Atomic charges or multipoles were obtained from the approximate charge distributions using three different procedures. In the first of these, atomic charges are obtained from a mapping of the electron density onto the basis functions used in the molecular orbital calculation according to the prescription of Mulliken.<sup>10</sup> These Mulliken charges have been widely used in chemistry. A second procedure determines those atomic charge that best fit the electrostatic potential surrounding the molecule. Consequently, they are called potential-derived charges (PDC's).<sup>11</sup> Finally, atom-centered multipole expansions (ACME's) were determined from numerical integration of the charge distribution.<sup>12</sup>

Calculations for molecular crystals require accurate treatment of interactions on an infinite periodic lattice. The use of atom-atom potentials commonly gives rise to terms in  $R^{-1}$  and  $R^{-6}$ . Consequently there exist well-developed convergence schemes for these terms.<sup>13</sup> The exponential term used to describe overlap repulsions is a short-ranged function and does not require an accelerated convergence treatment. However, the multipole-multipole interactions arising from the use of ACME's required additional consideration beyond that readily available in the literature. Theoretical treatment of these terms has appeared,<sup>14</sup> but specific formula were unavailable. These are now presented in Table I without further discussion.<sup>15</sup>

These formulas were implemented in the PCK83 code of Williams.<sup>16</sup> This code performs lattice energy calculations using an input molecular geometry and Equation 1, as described in the program documentation and related publications. In addition to calculations of the energy, it was also desirable to energy optimize the cell parameters using the different treatments of the coulomb interactions. Consequently, derivatives of the multipole-multipole interactions were worked-out and implemented in the code.

## RESULTS AND DISCUSSION

**Fit of the Electrostatic Potential:** It is important to determine how well the PDC's and ACME's reproduce a molecule's electrostatic potential. ACME's require considerably more computer time to evaluate and their use can only be justified in the current investigation if they yield a more accurate fit of the potential. PDC's were specifically designed to provide the best fit possible using a model limited to atomic charges. The ACME's were truncated at quadrupoles for this comparison. MC's are not expected to be competitive with the other charge models and were consequently not considered in this comparison.

The evaluation was performed by comparing the differences in potential obtained from use of the above methods with that from analytical formulas on a grid of points surrounding the molecule. The grid points were 0.25 Å apart and formed a rectangular box. Grid points within a van der Waals distance of the molecule's atoms were ignored in this analysis. The fit of the potential was characterized by the root mean square (RMS) and relative root mean square (RRMS) error. These quantities were calculated for three ranges of potential values. In instances where the potential ( $V(r)$  in kJ/mol) range included positive and negative values these regions were: I:  $V(r) < -4.175$ , II:  $-4.175 \leq V(r) \leq 4.175$ , III:  $V(r) > 4.175$ . For charged species, the potential is uniformly positive or negative, depending upon the molecular charge. Consequently, the three ranges spanned the entire range by thirds. This division allowed a more accurate characterization of errors over a wide range of potential values. The results of the comparison are shown in Table II. Drawings of the molecules examined are shown in Figure 1.

Inspection of Table II shows that in many instances the use of ACME's provides an improvement over PDC's of a factor of two or more in reproducing the electrostatic potential. In some cases, however, the use of PDC's provides a somewhat better fit. Nonetheless, the average RMS and RRMS for PDC's (ACME's) is 4.36 (1.85), 0.087 (0.038) for region I and 5.21 (5.23), 0.078 (0.053) for region III. The RRMS was not calculated in region II when the potential can have zero as a value. The average RMS in that region for PDC's (ACME's) is: 3.36 (1.89). Thus, depending upon the molecule, the use of ACME's can provide a significantly better fit of the potential than PDC's.

### Electrostatics at Fixed Crystal Geometries:

To estimate the magnitude of the electrostatic energy in real crystals, the optimized molecular geometry was placed so that its center of mass and axes of the principle moments of inertia were in coincidence with those of the molecular geometry found in

**TABLE I.** ACCELERATED CONVERGENCE FORMULAS FOR LATTICE SUMS OF ELECTROSTATIC ENERGY USING ACME'S FOR TERMS UP TO QUADRUPOLES. THE ELECTROSTATIC TERM IN EQ. 1 IS:  $E_{ele} = \frac{1}{2} \sum_i^{cell} \sum_{j \neq i}^{lattice} R(r_{ij}) + (2\pi V)^{-1} \sum_{h_\lambda \neq 0} |F(\mathbf{h}_\lambda)|^2 \frac{\exp(-b^2)}{h_\lambda^2} - K \sum_k^{cell} q_k^2 + \frac{2\pi}{3V} \mu_{cell}^2$ .<sup>†</sup> THIS FORM REQUIRES THAT THE INTRAMOLECULAR CONTRIBUTIONS BE SUBTRACTED FROM THE SUMS TO OBTAIN THE DIRECT INTERMOLECULAR LATTICE ENERGY.

Real Space Term $R(r_{ij})$	Reciprocal Space Term $ F(\mathbf{h}) ^2$
<b>monopole-monopole</b> $q_i q_j r_{ij}^{-1} T_0$	$ S ^2$
<b>monopole-dipole</b> $[(\vec{\mu}_i \cdot \vec{r}) q_j - (\vec{\mu}_j \cdot \vec{r}) q_i] r_{ij}^{-3} T_1$	$2\pi i [(S)^* (\vec{U} \cdot \vec{h}) - (S) (\vec{U} \cdot \vec{h})^*]$
<b>monopole-quadrupole</b> $[(\vec{r} \cdot \vec{Q}_i \cdot \vec{r}) q_j + (\vec{r} \cdot \vec{Q}_j \cdot \vec{r}) q_i] r_{ij}^{-5} T_2$	$-\frac{4}{3} \pi^2 [(S) (\vec{h} \cdot \vec{V} \cdot \vec{h})^* + (S)^* (\vec{h} \cdot \vec{V} \cdot \vec{h})]$
<b>dipole-dipole</b> $[(\vec{\mu}_i \cdot \vec{\mu}_j) r_{ij}^{-3} - 3(\vec{\mu}_i \cdot \vec{r})(\vec{\mu}_j \cdot \vec{r}) r_{ij}^{-5}] T_2$	$-\frac{4}{3} \pi^2 [h^2  \vec{U} ^2 - 3 \vec{U} \cdot \vec{h} ^2]$
<b>dipole-quadrupole</b> $\{2[(\vec{r} \cdot \vec{Q}_i \cdot \vec{r}) \cdot \vec{\mu}_j - ((\vec{r} \cdot \vec{Q}_j \cdot \vec{r}) \cdot \vec{\mu}_i)] r_{ij}^{-5} - 5[(\vec{r} \cdot \vec{Q}_i \cdot \vec{r})(\vec{r} \cdot \vec{\mu}_j) - (\vec{r} \cdot \vec{Q}_j \cdot \vec{r})(\vec{r} \cdot \vec{\mu}_i)] r_{ij}^{-7}\} T_3$	$-\frac{8}{15} \pi^3 i [2h^2 \{(\vec{U})^* \cdot (\vec{V} \cdot \vec{h}) - (\vec{U}) \cdot (\vec{V} \cdot \vec{h})^*\} - 5[(\vec{U} \cdot \vec{h})^* (\vec{h} \cdot \vec{V} \cdot \vec{h}) - (\vec{U} \cdot \vec{h})(\vec{h} \cdot \vec{V} \cdot \vec{h})^*]]$
<b>quadrupole-quadrupole</b> $\left[ \frac{35}{3} (\vec{r} \cdot \vec{Q}_i \cdot \vec{r})(\vec{r} \cdot \vec{Q}_j \cdot \vec{r}) r_{ij}^{-9} - \frac{20}{3} [(\vec{r} \cdot \vec{Q}_i \cdot \vec{r})(\vec{r} \cdot \vec{Q}_j \cdot \vec{r})] r_{ij}^{-7} + \frac{2}{3} [\vec{Q}_i : \vec{Q}_j] r_{ij}^{-5} \right] T_4$	$\frac{16}{105} \pi^4 \left[ \frac{35}{3}  \vec{h} \cdot \vec{V} \cdot \vec{h} ^2 - \frac{20}{3} h^2  \vec{V} \cdot \vec{h} ^2 + \frac{2}{3} h^4 (\vec{V} : \vec{V})^* \right]$

<sup>†</sup>where  $\vec{r}$  is the vector from atom  $i$  to  $j$ .  $q_k, \vec{\mu}_k, \vec{Q}_k$  are the monopole, dipole, and quadrupole electric multipole moment.

$$T_0 = \text{erfc}(a)$$

$$T_1 = \text{erfc}(a) + 2Kr_{ij} \exp(-a^2)$$

$$T_2 = \text{erfc}(a) + Kr_{ij} \exp(-a^2)(4a^2 + 6)/3$$

$$T_3 = \text{erfc}(a) + Kr_{ij} \exp(-a^2)(8a^4 + 20a^2 + 30)/15$$

$$T_4 = \text{erfc}(a) + Kr_{ij} \exp(-a^2)(16a^6 + 56a^4 + 140a^2 + 210)/105$$

$$S = \sum_k^{cell} q_k \exp(2\pi i \vec{h} \cdot \vec{r}_k)$$

$$\vec{U} = \sum_k^{cell} \vec{\mu}_k \exp(2\pi i \vec{h} \cdot \vec{r}_k)$$

$$\vec{V} = \sum_k^{cell} \vec{Q}_k \exp(2\pi i \vec{h} \cdot \vec{r}_k)$$

$$\text{where } a^2 = \pi K^2 r_{ij}^2, \quad b^2 = \pi \frac{h^2}{K^2}$$

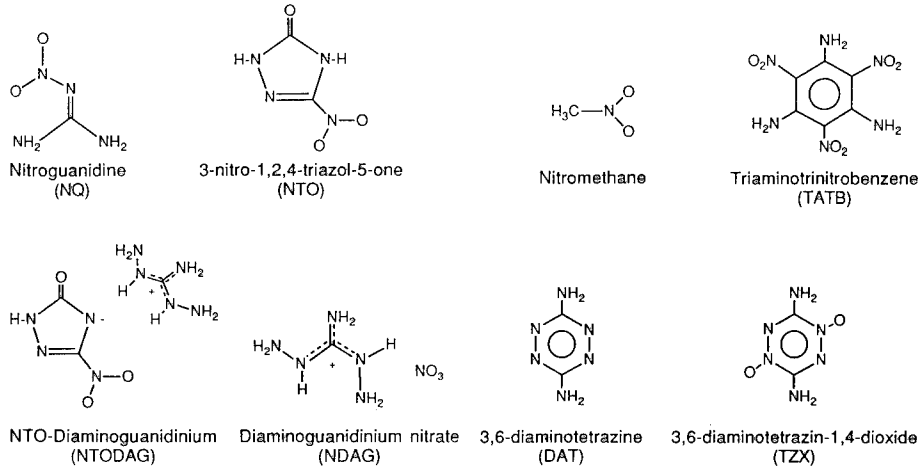


**FIGURE 1.** MOLECULAR STRUCTURES MAKING UP THE CRYSTALS STUDIED IN THIS PAPER.

**TABLE II.** FITS OF THE ELECTROSTATIC POTENTIAL OBTAINED FROM POTENTIAL DERIVED CHARGES (PDC'S) AND FROM ACME'S TO QUADRUPOLE LEVEL (ME 2). ANALYSIS WAS PERFORMED IN THREE SEPARATE RANGES OF THE POTENTIALS, AS INDICATED. VALUES OF THE POTENTIAL ARE IN kJ/mol. ROOT MEAN SQUARE (RMS) AND RELATIVE ROOT MEAN SQUARE, ( $RRMS = (Npts^{-1} \sum_i ((x_{i, obs} - x_{i, calc}) / x_{i, obs})^2)^{1/2}$ ) IN REGIONS SURROUNDING THE INDICATED MOLECULE ARE SHOWN.

	Npts	RMS	RRMS	Npts	RMS	RRMS	Npts	RMS	RRMS
<b>Nitroguanidine (NQ)</b>									
RANGE	-2.179e+02	-4.175e+00	-4.175e+00	-4.175e+00	-4.175e+00	4.175e+00	3.439e+02		
PDC	43992	2.162e+00	4.932e-02	2499	1.315e+00		46598	2.098e+00	6.399e-02
ME 2	43992	1.104e+00	4.513e-02	2499	1.587e+00		46598	2.226e+00	8.377e-02
<b>3-nitrotriazol-5-one (NTO)</b>									
RANGE	-1.859e+02	-4.175e+00	-4.175e+00	-4.175e+00	-4.175e+00	4.175e+00	2.397e+02		
PDC	41490	2.859e+00	1.097e-01	21009	8.609e-01		38416	4.198e+00	1.216e-01
ME 2	41490	1.086e+00	4.814e-02	21009	4.634e-01		38416	2.510e+00	5.748e-02
<b>Nitromethane</b>									
RANGE	-1.785e+02	-4.175e+00	-4.175e+00	-4.175e+00	-4.175e+00	4.175e+00	1.667e+02		
PDC	38639	1.841e+00	6.650e-02	6148	1.047e+00		42102	1.782e+00	6.394e-02
ME 2	38639	8.551e-01	2.269e-02	6148	4.395e-01		42102	2.148e+00	4.166e-02
<b>Triaminotrinitrobenzene (TATB)</b>									
RANGE	-1.599e+02	-4.175e+00	-4.175e+00	-4.175e+00	-4.175e+00	4.175e+00	2.064e+02		
PDC	49338	2.183e+00	1.049e-01	28636	6.753e-01		49261	3.896e+00	8.606e-02
ME 2	49338	9.654e-01	4.479e-02	28636	3.544e-01		49261	3.153e+00	4.954e-02
<b>NTO anion</b>									
RANGE	-6.406e+02	-4.673e+02	-4.673e+02	-2.941e+02	-2.941e+02	-2.941e+02	-1.216e+02		
PDQ	1469	1.350e+01	2.557e-02	19310	6.417e+00	1.742e-02	79701	1.525e+00	6.412e-03
ME 2	1469	6.671e+00	1.233e-02	19310	3.098e+00	8.393e-03	79701	6.532e-01	2.693e-03
<b>Diaminoguanidinium cation (W configuration, cation in NTODAG)</b>									
RANGE	1.294e+02	3.387e+02	3.387e+02	5.461e+02	5.461e+02	5.461e+02	7.535e+02		
PDC	97081	1.564e+00	5.311e-03	11485	9.966e+00	2.345e-02	152	1.330e+01	2.332e-02
ME 2	97081	5.254e-01	1.730e-03	11485	5.595e+00	1.322e-02	152	2.049e+01	3.232e-02
<b>Diaminoguanidinium cation (S configuration, cation in NDAG)</b>									
RANGE	1.239e+02	3.151e+02	3.151e+02	5.093e+02	5.093e+02	5.093e+02	7.010e+02		
PDC	102175	8.564e-01	3.147e-03	15647	7.493e+00	1.814e-02	257	1.747e+01	3.257e-02
ME 2	102175	3.214e-01	1.147e-03	15647	4.613e+00	1.109e-02	257	1.630e+01	2.863e-02
<b>Nitrate anion</b>									
RANGE	-6.774e+02	-5.015e+02	-5.015e+02	-3.256e+02	-3.256e+02	-3.256e+02	-1.486e+02		
PDC	2564	7.485e+00	1.330e-02	15402	2.272e+00	5.299e-03	51965	4.301e-01	1.561e-03
ME 2	2564	3.479e+00	6.000e-03	15402	7.855e-01	1.761e-03	51965	1.073e-01	3.898e-04
<b>1,4-dioxo-3,6-diaminotetrazine (TZX)</b>									
RANGE	-1.943e+02	-4.175e+00	-4.175e+00	-4.175e+00	-4.175e+00	4.175e+00	2.967e+02		
PDC	43912	3.345e+00	1.409e-01	15384	1.403e+00		54956	2.536e+00	1.129e-01
ME 2	43912	1.235e+00	6.641e-02	15384	7.601e-01		54956	2.284e+00	8.819e-02
<b>Diaminotetrazine (DAT)</b>									
RANGE	-1.851e+02	-4.175e+00	-4.175e+00	-4.175e+00	-4.175e+00	4.175e+00	1.604e+02		
PDQ	33730	7.800e+00	3.544e-01	21772	2.137e+00		43230	4.860e+00	2.686e-01
ME 2	33730	2.230e+00	1.330e-01	21772	1.171e+00		43230	2.382e+00	1.503e-01

the observed crystal structure. The electrostatic energy was then calculated at this molecular geometry, keeping all cell constants fixed at the observed values. In addition, the calculation was performed for two values of K, 0.0, and 0.2 Å<sup>-1</sup>, to determine the effect of the procedure for accelerated convergence obtained with K=0.2 versus normal convergence obtained with K=0.0. The calculated electrostatic energies using MC's, PDC's and ACME's are shown in Table III. For the latter case, term energy increments for charges ( $E_0$ ), dipoles ( $E_1$ ), quadrupoles ( $E_2$ ), and octapoles ( $E_3$ ) are shown.

The effect of the accelerated convergence procedure is seen by comparing the electrostatic energies

obtained with K=0.0 and 0.2 Å<sup>-1</sup>. The largest effect is found for the charge terms. A much smaller effect, on the order of a few percent at most, is found for the dipole terms and for quadrupole terms it is always less than a percent. This behavior is in accord with the shorter range of the higher moments. For monopoles, it is found that use of accelerated convergence results in changes as large as 10%, although many changes are much less. An exception to this generality is nitroguanidine (NQ), which has an acentric cell and where an unusually large difference in the dipole term using normal and accelerated convergence is noted. Apparently, long range interactions which are slow to converge arise from the dipole moment of the unit cell. Nitromethane

**TABLE III.** CALCULATED ELECTROSTATIC LATTICE ENERGIES FROM VARIOUS MODELS USING  $K=0.0$  AND  $0.2 \text{ \AA}^{-1}$ . WITH  $K=0.0$  MOLECULES WITHIN A  $10 \text{ \AA}$  SPHERE WERE INCLUDED. OPTIMIZED MOLECULAR GEOMETRIES WERE SUPERIMPOSED UPON OBSERVED CRYSTAL STRUCTURE COORDINATES AS DESCRIBED IN THE TEXT. ENERGIES IN kJ/mole.  $E_0, E_1, E_2, E_3$  AND SUM REFER TO THE INDIVIDUAL TERMS INVOLVING MONOPOLES, DIPOLES, QUADRUPOLES, OCTAPOLES, AND THE SUM OF THESE TERMS.

	K	MC	PDC	E0	E1	E2	E3	SUM
NQ	0.0	-56.1383	-75.7858	-23.1126	-35.3293	-8.7852	0.0176	-67.2095
	0.2	-57.8464	-78.4917	-27.3083	-41.3740	-8.8212	0.0119	-77.4916
NTO	0.0	-49.0554	-69.0363	-18.0496	-50.1642	-10.3494	-2.2446	-80.8078
	0.2	-52.9014	-70.4928	-17.8078	-50.6240	-10.3536	-2.2439	-81.0293
Nitro-methane	0.0	-56.0821	-33.3135	-13.1324	-18.4501	-1.5044	-1.2855	-34.3724
	0.2	-60.5602	-35.2294	-14.0745	-19.4050	-1.4975	-1.2845	-36.2615
TATB	0.0	-102.6632	-56.7937	-11.1111	-26.1713	-23.2284	-3.4906	-64.0014
	0.2	-100.7910	-56.5323	-10.9572	-26.0175	-23.3370	-3.4911	-63.8025
NTODAG	0.0	-456.1045	-521.3882	-375.4469	-147.5582	-24.6698	-0.0919	-547.7668
	0.2	-477.3539	-536.3023	-392.5094	-145.3748	-24.6436	-0.0908	-562.6186
NDAG	0.0	-518.6831	-540.6456	-485.6290	-76.5280	-15.6098	-2.3076	-575.4592
	0.2	-537.9923	-566.2153	-486.3985	-77.3460	-15.5230	-2.3099	-576.9576
TZX	0.0	-108.4899	-98.4557	-36.4657	-47.3883	-14.5291	-1.1781	-99.5612
	0.2	-108.0632	-98.1134	-36.2484	-47.2608	-14.5351	-1.1784	-99.2227
DAT	0.0	-48.6894	-67.4148	-14.1312	-58.8672	-16.4739	-5.5887	-95.0610
	0.2	-47.8922	-66.5370	-13.6711	-58.4092	-16.3241	-5.5883	-93.9927

and NTODAG also show a significant effect when accelerated convergence is used to perform the lattice sums. Other molecules show a lesser, but noticeable effect. Thus, it is difficult to know in advance whether the use of the accelerated convergence procedure in calculating lattice sums will make a noticeable difference and, consequently, its use is required for accurate *a priori* calculations.

The results in Table III also provide information about the convergence of the multipole expansions. First, it is observed that the contribution attributable to each multipole is not monotonically decreasing with increasing order. Except for the organic salts NTODAG and NDAG, the dipole term makes the largest contribution. In these salts, the dipole term is significantly larger than in the neutrals, but the charge term predominates. The quadrupole term is less by a factor of two or more than the dipole term in all cases, except TATB. In this instance, its contribution is about 10% smaller than the dipole term. Finally, the octapole contribution to the total energy is normally relatively small, amounting in most cases to about 5% or less of the total electrostatic energy. The worst behavior is shown by diaminotetrazine, and may arise from the presence of a large number of unshared electron pairs on the nitrogens. Overall, however, truncation of the expansion at quadrupoles is a reasonable approximation.

It is interesting to compare the calculated electrostatic lattice energies obtained with different methods. Use of PDC's and ACME's gives results that are significantly different from those obtained using MC's. These large differences reflect the fact that MC's are not designed for calculating intermolecular interactions. The present results show that MC's should not be used for this purpose. On the other hand, PDC's and ACME's give results that are frequently in close agreement. Some significant differences are noticeable, however. An especially large difference is found for DAT. In this case, inspection of Table II shows that ACME's reproduce the electrostatic potential significantly better than do PDC's. This is also true for TATB, where a significant difference in the calculated lattice energies is found. Consequently, when the ACME's produce a better fit of the electrostatic potential and a difference in the lattice energy obtained from the two methods occurs, the ACME's seem likely to be a better approximation to the exact electrostatic lattice energy.

Finally, the size of the electrostatic lattice energy is noteworthy. For the uncharged explosives, it ranges from a low of about -36 kJ/mol for nitromethane to a maximum of about -99 kJ/mol for TZX. Heats of sublimation for compounds similar to these vary over a wide range, but a value of 100 kJ/mol would certainly be reasonable. Thus, the electrostatic lattice energy is a significant fraction

of a heat of sublimation of an explosive. It is also noteworthy that the computed lattice energies of the salts are much larger than those of the other HE's. This is in accord with expectations, since salts typically do have large electrostatic energies and heats of sublimations. A final point is that the electrostatic lattice energy is found to be stabilizing in all crystals that were examined. It is thus an important contribution to the energy of molecular crystals, in agreement with the arguments of Claverie.<sup>4</sup>

**Calculation of Crystal Geometries:** Rather than attempting to develop potential functions specifically designed for explosives, we decided to carry out a number of crystal structure optimizations to determine the effect of using an accurate treatment of electrostatics in conjunction with an existing set of potentials. This approach will allow us to assess the relative importance of electrostatic effects more accurately and determine, at least qualitatively, the sensitivity of structural parameters to the electrostatic calculation. Perhaps this will indicate fruitful strategies in the development of a more general and accurate semi-empirical model.

Initially, parameters for the Buckingham-6 function were those recommended by Williams,<sup>3b,c</sup> et al. and are shown in Table IV. This set of potential functions was supplemented by an electrostatic calculation using one of the three models: MC's, PDC's, and ACME's truncated at the quadrupole level. After these optimization calculations were completed, which are summarized in Table V, we found that a number of crystals possessing extensive intermolecular hydrogen bonding were poorly calculated. Following Bondi,<sup>17</sup> we reasoned that a hydrogen on nitrogen or oxygen should be more positively charged and thus able to better penetrate an acceptor atom's electron cloud, thereby reducing its effective size. Accordingly, a set of crystal optimizations were performed in which the pre-exponential parameter of the appropriate hydrogens was decreased by 30%. This model was used with both the PDC's and ACME's for electrostatics. Results using this model are shown under the appropriate the P(N,O) or A(N,O) column of Table V. Finally, Williams recommends a foreshortening of the X-H, X=C,N,O intramolecular bond lengths of ca. 0.07 Å from standard lengths to account in part for poorly determined hydrogen positions from x-ray structure determinations. This recommendation was followed in choosing the molecular geometries in a set of calculations labelled P(X-H) and A(X-H). This choice necessitated the use of two force centers for hydrogens. The nuclear center was used for the electrostatic calculation, while a center foreshortened by 0.07 Å, but in the same direction from the heavy atom, was used for the other terms. In this way we attempted to use the Williams parameter set in the manner originally intended, but with an improved treatment of electrostatics.

**TABLE IV. POTENTIAL FUNCTION PARAMETERS USED IN THE BUCKINGHAM-6 EQUATION,  $E_{ij} = B_{ij} \exp(-\alpha_{ij} R_{ij}) - A_{ij}/R_{ij}^6$ , with  $A_{ij} = A_i A_j$ ,  $B_{ij} = B_i B_j$ , and  $\alpha_{ij} = \alpha_i + \alpha_j$ .**

	$A_i ((\text{\AA}^6 \text{kJ/mol})^{1/2})$	$\alpha_i (\text{\AA}^{-1})$	$B_i ((\text{kJ/mol})^{1/2})$
H	11.68	1.87	109.41
C	49.39	1.80	608.07
N	37.13	1.89	504.51
O	33.60	1.98	479.66

Inspection of Table V shows that the use of different electrostatic models gives very different lattice energies, reflecting the trends found in Table III. We were not able to find experimentally determined lattice energies or heats of sublimation for the compounds investigated here. Thus only a qualitative analysis of the calculated lattice energies can be given. In general, analogous models using either PDC's or ACME's yield very similar lattice energies. The MC's give crystal energies that differ from the other models significantly and are not expected to be very realistic. Lattice energies obtained using the other electrostatic models are of a reasonable magnitude and show larger values for the salts, as expected based upon the importance of coulomb interactions in them. Finally, a comparison of the electrostatic energies with the dispersion and repulsion energies can be made. The results in the table show that the electrostatic and repulsion energies are of opposite sign but frequently of similar magnitude. Thus, these two components of the energy nearly cancel. The salts obviously do not follow this trend.

One quantity of particular interest for explosives is the crystal density. As shown in the table, different electrostatic models give significantly different calculated densities. MC's yield the poorest results. The use of PDC's or ACME's with Williams's original parameters shows some improvement. The use of foreshortened X-H bonds provides an improvement over the use of the unaltered geometries. Additional improvement is found when the altered hydrogen parameters are used. This approach gives the best results, which are of comparable quality whether PDC's or ACME's are used. For these two models, the largest errors in the calculated densities are between 3-4%. For all the models a systematic underestimation of the density is apparent. Thus, for the purposes of density prediction alone, the model could be improved by applying a correction factor. Moreover, it is interesting to note that the difference in density of NQ at 25 C and -160 C is slightly over 2.5%.<sup>17</sup> Temperature is not included in our calculations at all, except insofar as the original derivation of the potential parameters was

**TABLE V.** ENERGY OPTIMIZED CRYSTAL STRUCTURES OBTAINED USING THE INDICATED ELECTROSTATIC MODEL. MC'S USED MULLIKEN CHARGES ON EACH NUCLEUS, PDC USED POTENTIAL DERIVED CHARGES, AND ACME'S USED ATOM-CENTERED MULTIPOLE EXPANSIONS. P(N,O) AND A(N,O) INDICATE THAT THE B HYDROGEN PARAMETER WAS DECREASED BY 30% FROM THE VALUE SHOWN IN TABLE IV. THE USE OF P(X-H) AND A(X-H) INDICATE FORSHORTENED X-H BONDS WITH THE INDICATED ELECTROSTATIC MODEL. CELL LENGTHS ARE IN Å, ANGLES IN DEGREES.  $\rho$  IS THE ANGLE BETWEEN THE AXIS OF THE ORIGINAL AND FINAL ORIENTATIONS OF THE ASYMMETRIC UNIT. T IS THE TRANSLATION OF THE ASYMMETRIC UNIT. D IS DENSITY IN g/cc. E(e) IS ELECTROSTATIC ENERGY, E(d) IS DISPERSION ENERGY, E(r) IS REPULSION ENERGY, E(t) IS SUM TOTAL. ALL ENERGIES IN kJ/mol. FIGURE IN PARENTHESES FOLLOWING CALCULATED PARAMETERS IS THE PERCENT ERROR.

NOTE: Legend on following page

<b>NQ</b> Nitroguanidine located in Space Group Fdd2 (#43). The molecule is on a general position. Z=16. <sup>a</sup>								
	Obs.	MC	PDC	P(N,O)	P(X-H)	ACME's	A(N,O)	A(X-H)
a	17.58	20.52 (16.7)	19.13 (8.8)	18.47 (5.1)	18.82 (7.1)	19.07 (8.5)	18.31 (4.1)	18.69 (6.3)
b	24.82	24.77 (-0.2)	25.90 (4.3)	25.41 (2.4)	25.71 (3.6)	25.93 (4.5)	25.45 (2.5)	25.75 (3.7)
c	3.58	3.51 (-2.0)	3.43 (-4.1)	3.41 (-4.8)	3.44 (-3.9)	3.46 (-3.4)	3.46 (-3.4)	3.48 (-2.8)
D	1.77	1.55 (-12.4)	1.63 (-8.1)	1.73 (-2.3)	1.66 (-6.2)	1.62 (-8.6)	1.72 (-3.0)	1.65 (-6.7)
$\rho$		11.2	8.5	6.9	7.3	7.8	5.7	6.2
T		0.60	0.25	0.15	0.20	0.20	0.09	0.14
E(e)		-50.87	-63.21	-69.48	-65.65	-60.91	-67.76	-63.76
E(d)		-74.65	-83.78	-97.98	-86.72	-82.41	-96.49	-85.38
E(r)		39.79	49.10	9.29	51.59	47.65	58.21	50.41
E(t)		-85.73	-97.79	-108.17	-100.78	-95.67	-106.04	-98.73
<b>NTO</b> 3-nitro-1,2,4-triazol-5-one located in Space Group P2 <sub>1</sub> /a (#14). The molecule is on a general position. Z=4. <sup>a</sup>								
	Obs.	MC	PDC	P(N,O)	P(X-H)	ACME's	A(N,O)	A(X-H)
a	9.10	8.80 (-3.3)	8.58 (-5.7)	8.56 (-5.9)	8.56 (-5.9)	8.48 (-6.8)	10.22 (12.3)	8.45 (-7.1)
b	5.51	5.78 (4.9)	6.03 (9.5)	6.03 (9.3)	6.04 (9.5)	6.17 (12.0)	5.03 (-8.8)	6.16 (11.7)
c	9.32	9.83 (5.5)	9.51 (2.0)	9.24 (-0.9)	9.39 (0.7)	9.89 (6.1)	9.85 (5.7)	9.69 (4.0)
$\rho$	100.9	85.6 (-15.1)	86.4 (-14.3)	86.8 (-14.0)	86.7 (-14.1)	96.6 (-4.2)	112.3 (11.3)	94.7 (-6.1)
D	1.88	1.73 (-7.9)	1.76 (-6.5)	1.81 (-3.5)	1.78 (-5.3)	1.68 (-10.7)	1.85 (-1.9)	1.72 (-8.6)
$\rho$		29.9	15.7	15.8	15.5	15.4	16.8	15.5
T		0.69	0.45	0.39	0.40	0.59	0.55	0.44
E(e)		-56.19	-63.30	-67.44	-65.07	-61.89	-63.44	-64.69
E(d)		-91.14	-93.09	-101.09	-95.12	-86.89	-105.51	-89.87
E(r)		55.12	57.13	62.99	58.63	54.47	67.36	57.14
E(t)		-92.21	-99.26	-105.54	-101.56	-94.31	-101.56	-97.42
<b>MeNO<sub>2</sub></b> Nitromethane located in Space Group P2 <sub>1</sub> 2 <sub>1</sub> 2 <sub>1</sub> (#19). The molecule is on a general position. Z=4. <sup>a</sup>								
	Obs.	MC	PDC	P(N,O)	P(X-H)	ACME's	A(N,O)	A(X-H)
a	5.24	5.24 (-0.1)	5.27 (0.6)		5.21 (-0.7)	5.28 (0.8)		5.22 (-0.4)
b	6.32	6.91 (9.4)	6.31 (-0.1)		6.30 (-0.3)	6.38 (1.0)		6.37 (0.7)
c	8.73	8.06 (-7.7)	8.77 (0.5)		8.69 (-0.4)	8.70 (-0.3)		8.61 (-1.3)
D	1.40	1.39 (-0.9)	1.39 (-0.9)		1.42 (1.4)	1.38 (1.4)		1.42 (1.1)
$\rho$		14.2	8.0		3.0	3.9		7.8
T		0.70	0.09		0.12	0.11		0.10
E(e)		-66.95	-35.56		-36.52	-34.25		-35.30
E(d)		-49.72	-48.39		-50.01	-47.82		-49.50
E(r)		34.56	29.20		30.16	28.42		29.46
E(t)		-82.11	-54.75		-56.37	-53.65		-55.34
<b>TATB</b> Triaminotrinitrobenzene located in Space Group P1 (#2). The molecule is on a general position. Z=2. <sup>a</sup>								
	Obs.	MC	PDC	P(N,O)	P(X-H)	ACME's	A(N,O)	A(X-H)
a	9.01	9.44 (4.8)	9.18 (1.9)	9.06 (0.6)	9.14 (1.5)	9.15 (1.6)	9.03 (0.2)	9.12 (1.2)
b	9.03	9.44 (5.6)	9.17 (1.5)	9.05 (0.2)	9.13 (1.1)	9.17 (1.5)	9.04 (0.2)	9.13 (1.1)
c	6.81	5.84 (-14.3)	6.79 (-0.4)	6.74 (-1.1)	6.79 (-0.4)	6.86 (-0.2)	6.74 (-1.0)	6.80 (-1.0)
$\alpha$	108.6	90.0 (-17.1)	110.8 (2.0)	111.0 (2.2)	110.8 (2.1)	110.4 (1.6)	110.2 (1.5)	110.4 (1.7)
$\beta$	91.8	90.0 (-2.0)	88.9 (-3.1)	88.6 (-3.5)	88.9 (-3.2)	90.2 (-1.7)	90.8 (-1.1)	90.4 (-1.6)
$\gamma$	120.0	120.0 (0.0)	120.0 (0.1)	120.1 (0.1)	120.0 (0.1)	120.1 (0.1)	120.1 (0.1)	120.1 (0.1)
D	1.94	1.90 (-1.8)	1.89 (-2.3)	1.96 (1.0)	1.91 (-1.6)	1.90 (-1.9)	1.97 (1.8)	1.91 (-1.1)
$\rho$		16.9	2.8	2.7	2.8	2.4	2.2	2.4
T		0.77	0.68	0.70	0.69	0.06	0.04	0.06
E(e)		-197.96	-61.18	-68.72	-63.05	-54.60	-62.38	-56.69
E(d)		-220.69	-194.95	-214.54	-197.52	-195.79	-217.04	-198.64
E(r)		138.16	101.01	114.75	103.10	97.08	112.07	99.48
E(t)		-280.49	-155.12	-168.51	-157.47	-153.31	-167.35	-155.85



TABLE V (CONT)

**NTODAG** 3-nitro-1,2,4-triazol-5-one-diaminoguanidine located in Space Group  $P1$  (#2). The salt is on a general position.  $Z=2$ . Ion #1=DAG<sup>+</sup>, Ion #2=NTO<sup>-</sup>.

	Obs.	MC	PDC	P(N,O)	P(X-H)	ACME's	A(N,O)	A(X-H)
a	6.73	8.52 (26.5)	8.34 (23.9)	8.12 (20.5)	8.22 (22.1)	8.16 (21.1)	7.85 (16.5)	7.95 (18.0)
b	6.75	7.18 (6.3)	6.50 (-3.7)	6.47 (-4.2)	6.57 (-2.7)	6.49 (-3.9)	6.40 (-5.2)	6.49 (-3.9)
c	9.84	10.54 (7.1)	10.22 (3.8)	9.93 (0.9)	10.11 (2.7)	10.10 (2.6)	9.85 (0.0)	9.99 (1.5)
$\alpha$	88.3	103.6 (17.4)	97.0 (9.8)	98.7 (11.7)	98.4 (11.5)	98.5 (9.3)	97.0 (9.8)	96.0 (8.8)
$\beta$	77.2	63.9 (-17.2)	67.8 (-12.1)	69.6 (-9.9)	68.9 (-10.7)	69.9 (-9.4)	71.2 (-7.7)	70.6 (-8.5)
$\gamma$	86.5	69.3 (-19.8)	74.7 (-13.7)	73.3 (-15.2)	74.0 (-18.5)	76.2 (-11.9)	76.5 (-11.6)	77.4 (-10.6)
D	1.67	1.52 (-9.1)	1.52 (-9.2)	1.62 (-3.2)	1.54 (-7.6)	1.53 (-8.6)	1.64 (-2.1)	1.56 (-6.4)
$\rho_1$		28.5	31.7	35.7	34.2	25.7	26.9	24.1
$\rho_2$		31.2	27.0	28.7	29.0	23.3	24.0	21.7
T1		4.29	2.58	2.33	2.47	2.17	1.83	1.91
T2		2.44	1.63	1.42	1.53	1.30	1.10	1.16
E(e)		-481.46	-509.99	-534.51	-520.35	-534.79	-570.16	-550.75
E(d)		-174.19	-174.84	-208.60	-178.99	-178.80	-216.66	-185.38
E(r)		122.53	125.53	150.56	129.46	137.70	172.28	146.43
E(t)		-533.12	-559.30	-592.55	-569.88	-575.89	-614.54	-589.70

**NDAG** Diaminoguanidine Nitrate located in Space Group  $P1$  (#2). The salt is on a general position.  $Z=2$ . Ion #1=DAG<sup>+</sup>, Ion #2=NO<sub>3</sub><sup>-</sup>.

	Obs.	MC	PDC	P(N,O)	P(X-H)	ACME's	A(N,O)	A(X-H)
a	6.04	6.90 (14.3)	6.69 (10.8)	6.58 (8.9)	6.69 (10.7)	6.84 (13.3)	6.79 (13.1)	6.91 (15.5)
b	6.97	7.32 (5.0)	7.22 (3.5)	6.97 (-0.1)	7.10 (1.9)	7.07 (1.5)	6.83 (-2.0)	6.98 (0.1)
c	7.76	7.32 (-5.7)	7.42 (-4.4)	7.26 (-6.4)	7.38 (-5.0)	7.48 (-3.7)	7.30 (-5.9)	7.42 (-4.5)
$\alpha$	97.3	86.3 (-11.4)	87.5 (-10.1)	86.7 (-11.0)	87.2 (-10.4)	85.3 (-12.4)	83.0 (-14.8)	83.4 (-14.3)
$\beta$	96.6	99.8 (3.3)	99.0 (2.5)	99.5 (3.0)	99.3 (2.8)	98.9 (2.4)	99.7 (3.3)	99.2 (2.9)
$\gamma$	102.1	106.7 (4.5)	106.0 (3.8)	107.1 (4.9)	106.7 (4.5)	107.8 (5.5)	109.0 (6.7)	108.4 (6.1)
D	1.61	1.45 (-10.1)	1.49 (-7.8)	1.61 (-0.1)	1.53 (-5.3)	1.49 (-7.8)	1.60 (-0.4)	1.51 (-6.1)
$\rho_1$		17.9	15.9	17.7	16.5	22.7	28.7	28.2
$\rho_2$		16.1	13.1	10.2	11.1	8.1	8.4	9.4
T1		0.33	0.24	0.11	0.16	0.15	0.46	0.17
T2		0.84	0.67	0.65	0.65	0.81	0.96	1.00
E(e)		-520.55	-542.12	-565.68	-552.82	-549.26	-576.07	-562.37
E(d)		-124.30	-131.57	-163.24	-136.97	-131.26	-162.77	-134.56
E(r)		98.23	106.97	130.99	112.03	108.33	133.85	112.75
E(t)		-546.62	-566.72	-597.93	-577.76	-572.19	-604.99	-584.18

**TZX** Space Group  $P2_1/a$  (#14), cell choice #3. Molecule is on an inversion center.  $Z=2$ .

	Obs.	MC	PDC	P(N,O)	P(X-H)	ACME's	A(N,O)	A(X-H)
a	6.77	7.07 (4.4)	6.72 (-0.7)	6.63 (-2.0)	6.70 (-1.0)	6.81 (0.7)	6.73 (-0.6)	6.79 (0.3)
b	7.35	7.44 (1.3)	7.55 (2.7)	7.47 (1.7)	7.52 (2.4)	7.55 (2.7)	7.46 (1.5)	7.52 (2.4)
c	5.25	5.06 (-3.7)	5.37 (2.3)	5.25 (-0.0)	5.32 (1.3)	5.38 (2.5)	5.26 (0.2)	5.06 (-3.7)
$\rho$	100.5	96.2 (-4.3)	97.8 (-2.7)	98.2 (-2.3)	98.2 (-2.3)	98.9 (-1.6)	99.3 (-1.1)	99.3 (-1.2)
D	1.86	1.81 (-2.8)	1.77 (-4.9)	1.86 (-0.2)	1.80 (-3.3)	1.75 (-6.0)	1.83 (-1.5)	1.78 (-4.4)
$\rho$		5.8	5.3	4.7	4.9	4.8	4.0	4.4
E(e)		-98.90	-88.78	-97.60	-92.49	-85.52	-93.92	-89.14
E(d)		-123.49	-118.83	-134.93	-122.02	-115.20	-130.87	-118.30
E(r)		80.13	75.93	87.46	78.42	72.28	83.07	74.51
E(t)		-142.26	-131.68	-145.07	-136.08	-128.44	-141.72	-132.93

**DAT** Space Group  $Amam$  (#63). Molecule is on two perpendicular mirrors.  $Z=4$ .

	Obs.	MC	PDC	P(N,O)	P(X-H)	ACME's	A(N,O)	A(X-H)
a	6.26	6.22 (-0.6)	6.17 (-1.4)	6.14 (-1.8)	6.18 (-1.2)	6.24 (-0.2)	6.19 (-1.0)	6.26 (-1.6)
b	7.84	9.01 (14.9)	8.89 (13.5)	8.60 (9.7)	8.72 (11.3)	8.45 (7.8)	8.10 (3.3)	8.25 (5.3)
c	9.42	8.94 (-5.1)	8.94 (-5.1)	8.77 (-7.0)	8.90 (-5.5)	9.46 (0.4)	9.35 (-0.7)	9.41 (-0.1)
D	1.61	1.49 (-7.8)	1.52 (-5.8)	1.61 (-0.3)	1.55 (-3.7)	1.49 (-7.4)	1.59 (-1.5)	1.53 (-4.9)
T		0.04	0.03	0.04	0.03	0.28	0.40	0.32
E(e)		-33.71	-49.61	-56.88	-55.17	-62.30	-78.73	-70.57
E(d)		-85.38	-90.29	-104.32	-93.33	-88.03	-105.16	-92.41
E(r)		45.91	53.02	63.14	55.54	57.98	75.91	63.99
E(t)		-73.18	-86.88	-98.06	-90.96	-92.35	-107.98	-98.99

- <sup>a</sup> Bryden, J. H.; Burkhardt, L. A.; Hughes, E. W.; and Donohue, J., *Acta Cryst.*, Vol. 9, 1956, p. 573.  
<sup>b</sup> Ritchie, J. P.; Cromer, D. T.; Stewart, R. F.; Wasserman, H. J.; and Ryan, R. R., *8th Symposium on Detonation*, 1985.  
<sup>c</sup> Gilardi, R., private communication. The crystal structure is for the  $\beta$ -polymorph.  
<sup>d</sup> Trevino, S. F.; Prince, E.; and Hubbard, C. R., *J. Chem. Phys.*, Vol. 73, 1980, p. 2996.  
<sup>e</sup> Cady, H. H.; and Larson A. C., *Acta Cryst.*, Vol. 18, 1965, p. 485.  
<sup>f</sup> Cromer, D. T.; Hall, J. H.; Lee, K.-Y.; and Ryan, R. R., *Acta Cryst.*, Vol. C44, 1988, p. 2206.  
<sup>g</sup> Ritchie, J. P.; Lee, K.-Y.; Cromer, D. T.; Kober, E. M.; and Lee, D. D., *J. Org. Chem.*, Vol. 55, 1990, p. 1994.  
<sup>h</sup> Ryan, R. R., et al., private communication.  
<sup>i</sup> Krieger, C.; Fischer, H.; and Neugebauer, F. A., *Acta Cryst.*, Vol. C43, 1987, p. 1320.

performed by fitting room temperature crystal structures. Thus, highly accurate predictions of crystal density may need to account for temperature explicitly. Except for nitromethane, all the crystal structures shown in Table V appeared to have been determined at approximately room temperature. Nitromethane was studied at -45 C.

Also shown in Table V is the percent error  $((x_{calc}/x_{obs}) \times 100)$  in calculated cell lengths and angles. MC's yield the poorest results. Surprisingly, however, there is little difference in the accuracy among the remaining models. For both cell lengths and angles root-mean-square percent errors of between 5.9% and 8.7% are found. These errors are larger than those found for the crystal density (between 1.8% and 7.2%). Thus, the accuracy of the crystal density predictions depends upon a cancellation of errors in the cell structural parameters. However, the tendency to systematically overestimate the cell lengths is evident.

Finally, in the crystal structure optimizations the asymmetric unit was allowed to undergo rigid rotation and translation to minimize the calculated energy. Any rotation or translation is measured relative to the observed orientation. The final rotations and translations are also shown in Table V in degrees and Å, respectively. Here again there is little distinction between the various electrostatic models, although MC's are qualitatively poorer.

## CONCLUSIONS

1. ACME's truncated at quadrupoles provide a fit of the electrostatic potential at least similar and many times superior to that given by PDC's. When unshared electron pairs are present in a molecule the improvement from the use of ACME's was most evident.
2. An efficient multipole treatment of electrostatic interactions on a periodic infinite lattice has been worked-out and implemented into a crystal modeling program.
3. The use of accelerated convergence techniques in the electrostatic lattice energy calculation results in reasonably small but noticeable differences when compared with explicit calculations within a given radius.
4. ACME's are reasonably well converged at the quadrupole level. For the basis set used in this work, octapoles contribute less than 5% to the total electrostatic energies calculated.
5. PDC's and ACME's frequently give very similar electrostatic lattice energies. Some differences were noted, however, for diaminotetrazine where there are a large number of unshared electron pairs.
6. The electrostatic lattice energy is a significant fraction of the total lattice energy, and is an important stabilizing force operating in a crystal.

7. The use of Mulliken charges provides uniformly poor results compared with any of the other electrostatic models.
8. Calculation of a compound's crystal density proved sensitive to the electrostatic model employed. This is the result of a cancellation of errors. The use of a slightly altered set of hydrogen parameters gave highly accurate computed densities. Larger errors were, however, found in other crystal structure parameters.

## ACKNOWLEDGEMENT

This work was jointly funded by the Department of Defense, Office of Munitions, and the Department of Energy.

## REFERENCES

1. Kamlet, M. J.; Jacobs, S. J., *J. Chem. Phys.*, Vol. 48, No. 23, 1968.
2. Dick, J. J.; Mulford, R. N.; Spencer, W. J.; Petit, D. R.; Garcia, E.; Shaw, D. C., *J. Appl. Phys.*, Vol. 70, 1991, p. 3572.
3. a) Pertsin, A.J.; Kitaigorodsky A. I., *The Atom-Atom Potential Method: Applications to Organic Molecular Solids*, Springer-Verlag, Berlin, 1987. b) Williams, D. E.; Cox, S. R., *Acta Cryst.*, Vol. B40, No. 404, 1984. c) Cox, S. R.; Hsu, L.-Y.; Williams, D. E., *Acta Cryst.*, Vol. A37, No. 293, 1981.
4. Claverie, P., *Intermolecular Interactions: From Diatomics to Biopolymers*, B. Pullman, Ed., Wiley, NY, 1978, Chap. 2.
5. a) Spackman, M. A., *J. Chem. Phys.*, Vol 85, 1986, p. 6587. b) Spackman, M. A., *J. Chem. Phys.*, Vol. 91, 1987, p. 3179. c) Ritchie, J. P.; Lee, K.-Y.; Cromer, D. T.; Kober, E. M.; Lee, D. D., *J. Org. Chem.* Vol. 55, 1990, p. 1994.
6. Hehre, W. J.; Radom, L.; Schleyer, P. v. R.; Pople, J. A., *Ab Initio Molecular Orbital Theory*, Wiley, NY, 1986.
7. a) Rein R., *Electronic Structure of Polymers and Molecular Crystals* Andie, J. M.; Ladik, J.; Delhalle, J., Eds., Plenum, NY, 1975. b) Sokalski, W. A.; Poirier, R. A., *Chem. Phys. Lett.*, Vol. 98, 1983, p. 86. c) Stone, A. J., *Chem. Phys. Lett.*, Vol. 83, 1981, p. 233. d) See also: Sokalski, W. A.; Sawaryn, A., *J. Chem. Phys* Vol. 87, 1987, p. 526 and references therein.

8. Binkley, J. S.; Frisch, M. J.; DeFrees, D. J.; Ragavachari, D. K.; Whiteside, R. A.; Schlegel, H. B.; Fluder, E. M.; Pople, J. A., Carnegie-Mellon University. The CTSS version at Los Alamos was implemented and enhanced by Dr. R. Martin.
9. Gaussian 92 Computer Program, Revision A, Frisch, M. J.; Trucks, G. W.; Head-Gordon, M.; Gill, P. M. W.; Wong, M. W.; Foresman, J. B.; Johnson, B. G.; Schlegel, H. B.; Robb, M. A.; Replogle, E. S.; Gomperts, R.; Andres, J. L.; Raghavachari, K.; Binkley, J. S.; Gonzalez, C.; Martin, R. L.; Fox, D. J.; DeFrees, D. J.; Baker, J.; Stewart, J. J. P.; Pople, J. A., Gaussian, Inc., Pittsburgh, PA, 1992. The authors thank Dr. R. Martin for his assistance in implementing the program at Los Alamos.
10. Mulliken, R. S., *J. Chem. Phys.*, Vol. 23, 1955, pp. 1833, 1841, 2338, 2343.
11. Breneman, C. M.; Wiberg, K. B., *J. Comp. Chem.*, Vol. 11, 1990, p. 361.
12. a) Hirshfeld, F. L., *Theor. Chim. Acta*, Vol. 44, 1977, p. 129. b) Ritchie, J. P., *J. Am. Chem. Soc.*, Vol. 107, 1985, p. 1829.
13. a) Ewald, P. P., *Ann. Physik*, Vol. 64, 1921, p. 253. b) Williams, D. E., *Acta Cryst.*, Vol. A37 1971, p. 452.
14. a) Nijboer, B. R. A.; De Wette, F. W., *Physica*, Vol. 23, 1957, p. 309. b) Nijboer, B. R. A.; De Wette, F. W., *Physica*, Vol. 23, 1958, p. 422. c) De Wette, F. W.; Nijboer, B. R. A., *Physica* Vol. 24, 1958, p. 1105. d) Harris, F. E., *Theoretical Chemistry: Advances and Perspectives*, Vol. 1, 1975, p. 147.
15. A full description will be given elsewhere.
16. Williams, D. E., *Quantum Chemistry Program Exchange*, University of Indiana, Bloomington, Indiana.
17. Bondi A., *J. Phy. Chem.*, Vol. 68, 1964, P. 441.
18. Compare x-ray structure at -160°C: Ritchie J. P.; Cromer, D.; Ryan, R.; Wasserman, H.; Stewart, R. F., *Proceedings of Ninth Symposium (International) on Detonation*, 1985.

## THERMODYNAMICS OF DETONATION PRODUCTS

S. McCahan  
University of Toronto  
Toronto, ON M5S 1A4

J.E. Shepherd  
Rensselaer Polytechnic Institute  
Troy, NY 12180

We examine the thermodynamic properties of two model equations of state. One is the widely used Jones-Wilkins-Lee equation,<sup>1,2</sup> and the other is the recently developed Byers Brown equation (THEOSTAR).<sup>3</sup> The JWL equation is probably one of the most widely used equations for hydrodynamic computations of solid explosive detonations and is in the convenient form of  $P(e, v)$ , i.e., pressure,  $P$ , is given in terms of specific internal energy,  $e$ , and specific volume,  $v$ . However, it is an incomplete and ad hoc equation and the ability to adequately represent thermodynamic properties at high densities has not been critically examined. On the other hand, THEOSTAR is based on extensive Monte Carlo simulations and statistical mechanics using realistic intermolecular potentials. The resulting equation of state is a complete representation of the Helmholtz energy  $A(T, v)$  but is not particularly suitable for hydrodynamic computations. Also, THEOSTAR is applicable in a somewhat restricted density regime.

### INTRODUCTION

As pointed out by Davis,<sup>4</sup> thermodynamics and statistical mechanics require certain properties of equations of state. In particular, the non-dimensional properties such as the Gruneisen coefficient, slope of the isentropes and fundamental derivatives (curvature of the isentropes) must take on particular limiting values and functional dependencies. We have determined what we believe to be reliable approximations to these properties from THEOSTAR. Similar computations with the JWL equation were used to identify discrepancies and the consequences of the approximate nature of that equation.

We have chosen the two frequently studied cases of PETN and PBX-9404 detonation products to illustrate our results. Since most hydrodynamic computations are concerned with the nearly isentropic flow behind the detonation we have examined properties on and near the product isentrope passing through the CJ (Chapman-Jouguet) point. The CJ point properties and composition were determined using the JCZ3 equation of state.<sup>5,6</sup> The composition was assumed to be fixed and only major products were considered. The JWL equation was evaluated using the parameters given in Dobratz<sup>7</sup> for initial densities of 1.770 g/cm<sup>3</sup> for PETN and 1.840 g/cm<sup>3</sup> for PBX-9404. THEOSTAR was evaluated using effective molecular potential parameters based on the usual single fluid

mixing rules and a product composition based on major species only. Real fluid properties were computed as the sum of a residual function and an ideal gas function determined from realistic specific heats<sup>8</sup> and formation data.

### RESULTS

The isentrope and the various thermodynamic properties for THEOSTAR were determined by a combination of analytical evaluation of residual properties and numerical solution of the resulting constraint equations. Results are given in Figures 1 through 4. In each of the graphs the x-axis represents the specific volume non-dimensionalized with respect to the detonation Chapman-Jouguet point. Although the JWL  $P(v)$  relation on the isentrope (Figure 1) appears reasonable, the Gruneisen coefficient,

$$G = v \left( \frac{\partial P}{\partial e} \right)_v \quad (1)$$

(Figure 2), the non-dimensional slope,

$$\gamma_s = -\frac{v}{P} \left( \frac{\partial P}{\partial v} \right)_s \quad (2)$$

(Figure 3), and the fundamental gas derivative,

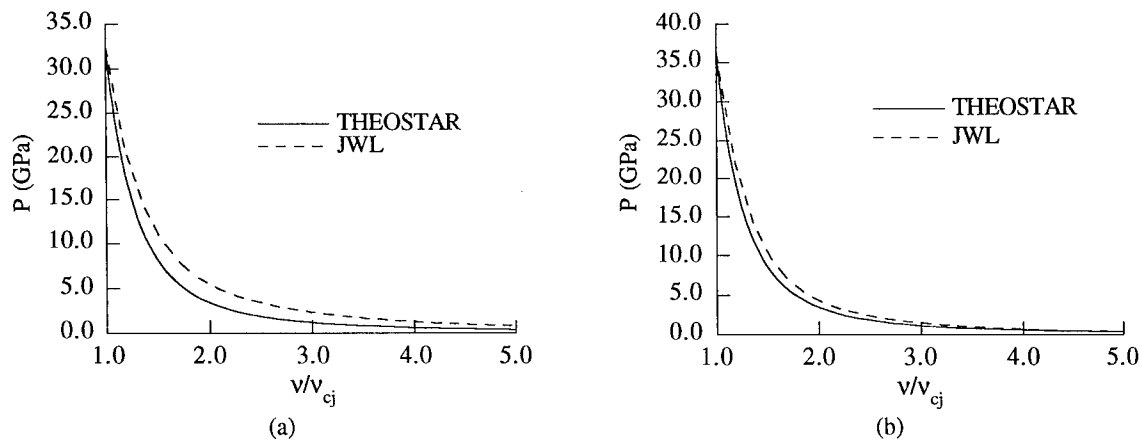


FIGURE 1. ISENTROPES CALCULATED USING THE JWL AND THEOSTAR EQUATIONS OF STATE; (a) PETN, (b) PBX-9404

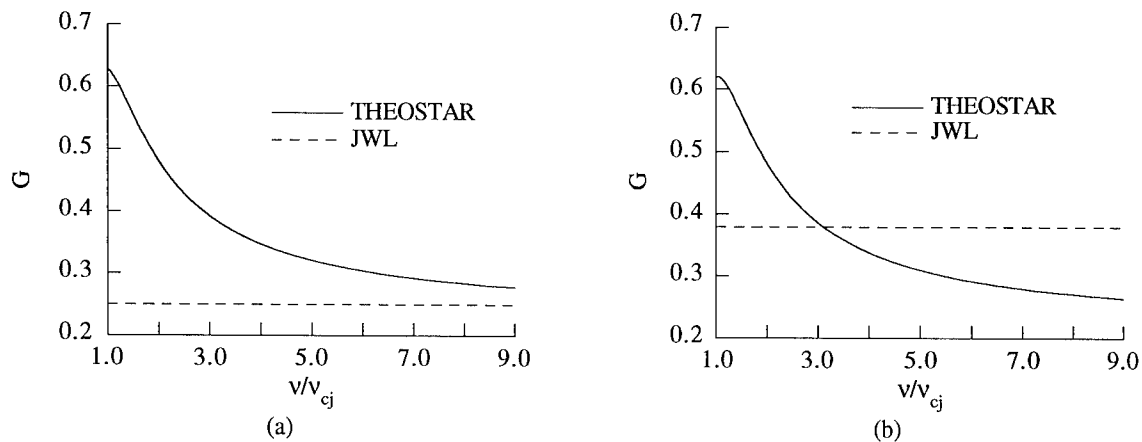


FIGURE 2. THE GRUNEISEN COEFFICIENT ALONG THE ISENTROPES VERSUS VOLUME CALCULATED USING THE JWL AND THE THEOSTAR EQUATIONS OF STATE; (a) PETN, (b) PBX-9404

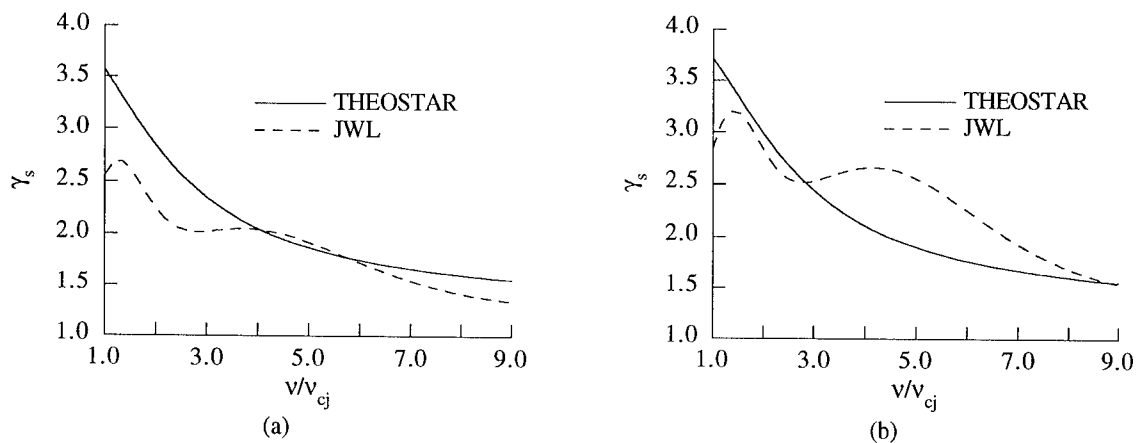
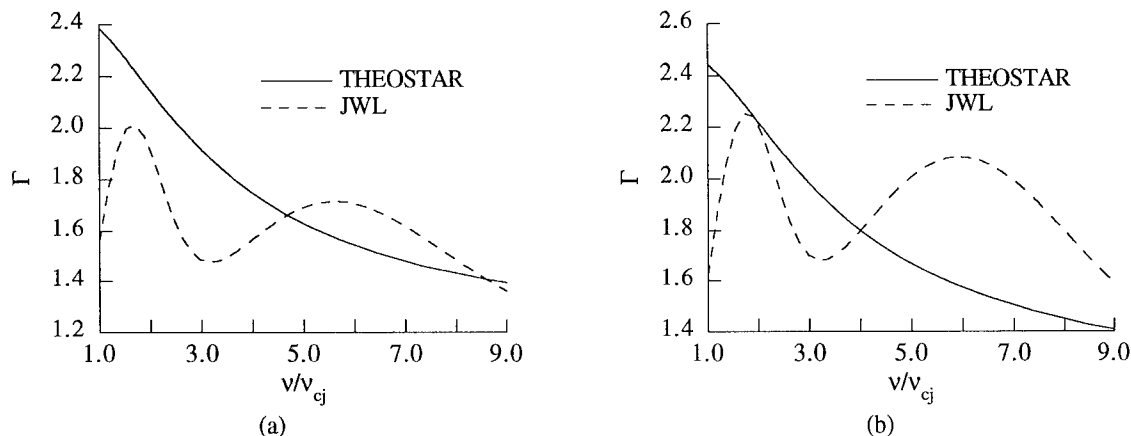


FIGURE 3. THE ISENTROPIC GAMMA FUNCTION ALONG THE ISENTROPE VERSUS VOLUME CALCULATED USING THE JWL AND THEOSTAR EQUATIONS OF STATE; (a) PETN, (b) PBX-9404



**FIGURE 4. THE FUNDAMENTAL GAS DERIVATIVE ALONG THE ISENTROPE VERSUS VOLUME CALCULATED USING THE JWL AND THEOSTAR EQUATIONS OF STATE; (a) PETN, (b) PBX-9404**

$$\Gamma = \frac{c^4}{2v^3} \left( \frac{\partial^2 v}{\partial P^2} \right)_s \quad (3)$$

(Figure 4), show significant differences between the realistic THEOSTAR results and the JWL values.

In the original studies<sup>1</sup> of the JWL equation, the peculiar non-monotone behavior shown in Figure 3 was observed and rationalized as a consequence of competing effects in the intermolecular potential. This notion appeared to be supported by LJD equation of state computations carried out at that time. However, the current results indicate that these oscillations are simply spurious consequences of the particular analytical form used for the JWL equation. The failure of the JWL equation to properly model the Gruneisen coefficient (Figure 2) is also well known but the consequences for hydrodynamic calculations are not well understood. The results given for the fundamental derivative (Figure 4) are unique to our knowledge. It has been demonstrated<sup>9</sup> that for many compressible flow phenomena it is essential to accurately represent the fundamental derivative.

What are the consequences of the behavior shown in Figures 1 to 4? A common interpretation is in terms of the ability to move material, experimentally measured by cylinder or plate push tests and theoretically determined by the Riemann integral,

$$\Delta u = \int \frac{dP}{\rho c}, \quad (4)$$

or the appropriate multidimensional analog. The velocity change at  $v/v_{cj} = 7$  is 5.384 km/s for THEOSTAR, and 6.043 km/s for JWL computed for PETN.

A more sensitive test is the examination of shock

adiabats centered on states located on the isentrope. This measure of the equation of state is appropriate for hydrodynamic problems in which there are significant shock waves catching up to the detonation from the rear and the potential for producing overdriven detonation waves. Figure 5 shows such shock adiabats. Both the discrepancies in the fundamental derivative and the Gruneisen coefficient contribute to the observed differences. Unfortunately, the upper limit on the density regime for THEOSTAR makes it impossible to compare the adiabats that start at the CJ point. This is a major flaw in the equation since it precludes computation of overdriven waves and comparison with available data. The upper limit on the density range for the PETN product mixture is 2.52 g/cm<sup>3</sup> ( $v/v_{cj} = 0.91$ ), and for the PBX-9404 product mixture 2.57 g/cm<sup>3</sup> ( $v/v_{cj} = 0.94$ ).

The other major drawback of THEOSTAR is the form of the expression. While the equation has the usual general form  $P(T, v)$ , it is not convenient for use in hydrodynamic calculations where the preferred equation form is  $P(e, v)$ . We have developed a general formalism<sup>10</sup> for determining an equation in the  $P(e, v)$  form given an equation of state such as THEOSTAR. However, implementing this procedure has proved difficult for equations that have a complex dependence on temperature.

## EQUATION OF STATE TRANSFORMATION

The general process consists of replacing temperature in the original equation with a function of internal energy and specific volume thus producing an expression that is not explicitly temperature dependent. Of course, a  $P(T, v)$  type equation of state does not, by itself, fully specify the behavior of a fluid. We must also choose a form for the specific heats and this

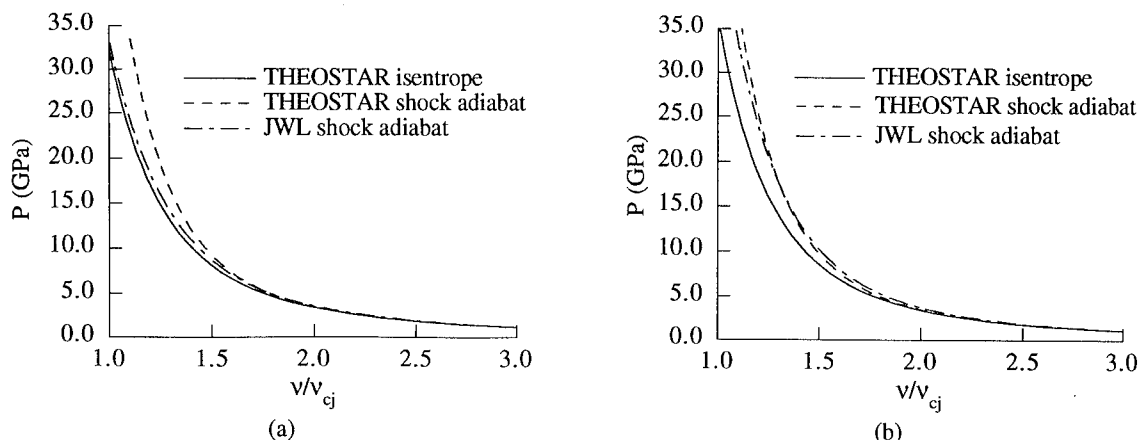


FIGURE 5. SHOCK ADIABATS CENTERED ON THE ISENTROPE VERSUS VOLUME CALCULATED USING THE JWL AND THEOSTAR EQUATIONS OF STATE; (a) PETN, (b) PBX-9404

expression must be combined with the original equation in order to produce a caloric,  $P(e, v)$ , form. The following simple example illustrates this procedure. Consider the Berthelot equation of state<sup>11</sup>;

$$P = \frac{RT}{v-b} - \frac{a}{Tv^2}, \quad (5)$$

where  $a$ ,  $b$  and  $R$  are constants. The Berthelot equation is chosen because it is the simplest cubic equation of state that has a temperature dependent residual internal energy. The residual internal energy,

$$e^r = e - e^{ig}(T, v), \quad (6)$$

represents the difference between the actual internal energy and the ideal gas energy compared at the same temperature and specific volume. By splitting the internal energy into residual and ideal gas parts we are essentially separating the part of the internal energy specified by the  $P(T, v)$  equation of state from the part that is determined by the form of the specific heats. It can be shown that the residual internal energy for the Berthelot equation is

$$e^r = \frac{-2a}{Tv}, \quad (7)$$

If we then select a constant specific heat formulation,

$$e^{ig} = c_v^{ig}T + C, \quad (8)$$

the resulting expression for the total internal energy can be solved for temperature;

$$T = \frac{(e - C) + \sqrt{(e - C)^2 + \frac{8c_v^{ig}a}{v}}}{2c_v^{ig}}, \quad (9)$$

This result is substituted back into the original equation of state to produce a  $P(e, v)$  type relation. It is clear from this example that as the temperature dependence of the residual internal energy or specific heat becomes more complex, an analytical solution becomes increasingly difficult. In fact, an analytical solution of this type is not possible for THEOSTAR.

The THEOSTAR expression for pressure has 64 terms many of which have a logarithmic dependence on temperature. The general form of the temperature dependence can be characterized as follows;

$$T^m [a + \ln(bT)]^n, \quad (10)$$

where  $a$  and  $b$  are constants. The exponent  $m$  is non-positive and the exponent  $n$  can be either negative or positive. This complex functionality makes the transformation process infeasible. However, the importance of the residual internal energy in the transformation suggests that the structure of the residual will strongly influence the construction of a caloric equation derived from an expression like THEOSTAR. Therefore, it is worth considering the form of the THEOSTAR residual internal energy.

Figure 6. shows three isotherms calculated for nitrogen. This plot suggests that it may be possible to formulate a simplified residual function if we are willing to consider a reduced temperature regime. Also,

by limiting the region of interest to an area specific to overdriven detonation waves in high explosives it may be possible to extend the upper limit on the density beyond the restrictive value set in the original equation. It is important that such a reformulation of the expression retain the important desirable features of THEOSTAR. So, the expression should adequately describe the residual internal energy in a functional form that is transformable using the method outlined above, and produce an expression that retains the information necessary to produce expressions for the Gruneisen coefficient and fundamental derivative as shown in Figures 2. and 4. While a fitting method may be a simple solution it is improbable that such a procedure could accomplish such ambitious goals. Instead, a more involved procedure which actually derives an equation of state from the molecular level tailored for the transformation process may be more appropriate.

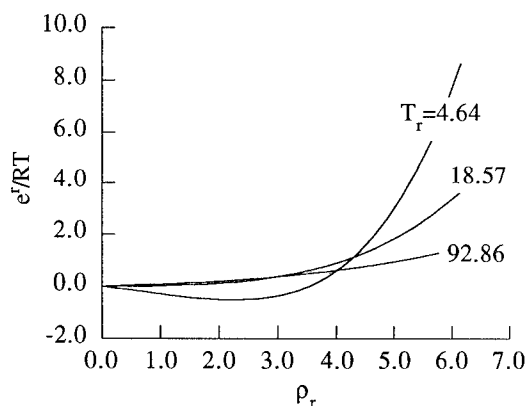


FIGURE 6. THE NON-DIMENSIONAL RESIDUAL INTERNAL ENERGY VERSUS THE REDUCED DENSITY ALONG VARIOUS ISOTHERMS CALCULATED USING THEOSTAR.<sup>10</sup>

## CONCLUSION

We conclude that the JWL equation of state does not accurately represent the Gruneisen coefficient or the fundamental derivative. These properties are important for describing shock steepening behavior. It would be preferable to formulate a more physically based equation which better represents these properties. However, such an equation must be in the appropriate form of  $P(e,v)$  for efficient hydrodynamic computation and must be applicable over a relatively wide range of states. We have developed a general method for finding an equation in the  $P(e,v)$  form given a canonical equation of state. The problem of implementing this procedure is examined. We consider this to be the first step in finding an improved analytical expression for the approximate high explosive

detonation product equation of state.

## REFERENCES

1. Kury, J.W.; Hornig, H.C.; Lee, E.L.; McDonnell, J.L.; Ornellas, D.L.; Finger, M.; Strange, F.M.; and Wilkins, M.L. "Metal Acceleration by Chemical Explosives," Proc. of the *Fourth Symposium (International) on Detonation*, Office of Naval Research, ACR-126, 1965, p. 3.
2. Lee, E.; Breithaupt, D.; McMillian, C.; Parker, N.; Kury, J.; Tarver, C.; Quirk, W.; and Walton, J., "The Motion of Thin Metal Walls and the Equation of State of Detonation Products," *Eighth Symposium (International) on Detonation*, Naval Surface Weapons Center, NSWC MP 86-194, 1985, p. 613.
3. Byers Brown, W., "Analytical Representation of the Excess Thermodynamic Equation of State for Classical Fluid Mixtures of Molecules Interacting with  $\alpha$ -Exponential-Six Pair Potentials up to High Densities," *J. Chem. Phys.*, Vol. 87, No. 1, 1987, p. 566.
4. Davis, W.C., "Equation of State for Detonation Products," *Eighth Symposium (International) on Detonation*, Naval Surface Weapons Center, NSWC MP 86-194, 1985, p. 785.
5. Jacobs, S.J., "On the Equation of State for Detonation Products at High Density," Proc. of the *Twelfth symposium (International) on Combustion*, (The Combustion Institute, Pittsburgh), 1969, p. 501.
6. Cowperthwaite, M.; and Zwisler, W.H., "The JCZ Equations of State for Detonation Products and Their Incorporation into the TIGER Code," Proc. of the *Sixth Symposium (International) on Detonation*, Office of Naval Research, ACR-221, 1976, p. 162.
7. Dobratz, B.M., *LNLL Explosive Handbook*, UCRL-52997, Livermore, CA, 16 March 1981, p. 8-21.
8. Cowperthwaite, M.; and Zwisler, W.H., *Vol. IV, TIGER User's Guide*, SRI publication Z106, Menlo Park, CA, 1974.
9. Thompson, P.A., *Compressible Fluid Dynamics*, RPI Bookstore, Troy, NY, 1972.
10. McCahan, S., *Thermodynamic Applications: Rapid Evaporation and Reacting Flow*, Ph.D. Dissertation, Rensselaer Polytechnic Institute, Troy, New York, 1992.
11. Van Ness, H.C.; and Abbott, M.M., *Classical Thermodynamics of Non Electrolyte Solutions, with Applications to Phase Equilibria*, McGraw-Hill, New York, NY, 1982, p. 148.



## PRODUCTS OF Al CONTAINING EXPLOSIVES DETONATED IN ARGON AND UNDERWATER

F. Volk, F. Schedlbauer  
Fraunhofer-Institut für Chemische Technologie (ICT)  
76327 Pfinztal (Berghausen), FRG

The detonation products of high explosives depend on the pressure and the confinement conditions under which the reaction proceeds. This holds true not only for less sensitive explosives such as nitroguanidine (NQ), 3-Nitro-1,2,4-triazol-5-one (NTO) but also for metal containing composite explosives with different binders. To better understand the reactions of aluminium (Al) with the detonation products, a series of explosives with different Al content were investigated. The objective was to determine the completeness of the Al reaction as well as the influence of the argon pressure. In a second part of the investigation, explosives with different Al content were detonated under water in a plastic balloon. The gaseous products and the solid residue were analyzed with regard to the formation of carbon soot and unreacted aluminium.

### INTRODUCTION

A better knowledge of the detonation products of high explosives is very useful for understanding the detonation behavior under different conditions such as confinement and as a function of pressure. The energy released during the detonation reaction depends on the energy of the explosive charge, the oxygen balance, the grain size of the ingredients, the degree of the confinement and the completeness of the reaction of metals such as aluminium (Al) with the reaction products of the explosive. In addition, equilibrium or non-equilibrium reactions influence not only the heat output but also the detonation velocity. For example, the products of nitroguanidine (NQ) containing explosives consist of a relatively high concentration of hydrocyanic acid (HCN), which is a metastable gas. The formation of this product decreases the detonation energy distinctly, which may explain the discrepancies between calculated and measured detonation velocity of NQ.<sup>1-5</sup> Another problem is the reaction behavior of

Al which reacts completely only within distinct limits of the energy output of the explosive charge and the oxygen balance. Recently, a series of small PETN-aluminium charges with various PETN/Al ratios were detonated both under water and in inert gas atmosphere in a closed bomb.<sup>7-9</sup>

The aim of this paper was to measure the detonation products of several explosives containing RDX, HMX, NQ and NTO with different binders and varying Al content. The investigations were done at various pressures of argon and under vacuum in order to find out the change of the reaction products under these conditions. In addition, plastic bonded high explosives with HMX and a polyiso-butylene (PIB) binder and varying Al content were detonated under water within a balloon. The aim of these tests was to measure not only the detonation gases, but also the solid products contained in water after the reaction. By analyzing the residue and the unreacted Al, provides the knowledge necessary to optimize the composition of underwater high explosives.

## EXPERIMENTS

### Experiments Performed In A 1.5 m<sup>3</sup> Container

Experiments were conducted in a stainless steel container with a volume of 1.5 m<sup>3</sup>. The cylindrical high explosive charge had a mass of about 300 g without booster. A No 8 detonator cap together with a 10 g RDX booster were used for the initiation. Because of the corner effect a second booster of about 18 g having the same diameter as the main charge was glued onto the charge.<sup>1, 2, 6</sup> A high efficiency vacuum pump was used for the reduced pressure experiments

After firing, gas samples were collected to measure the NO content in an NO<sub>x</sub>-analyzer and perform gas chromatographic and mass spectrometric analysis of the gas products. After the shot the solid residue was collected and analyzed for C, H, O, N as well as for unreacted Al. To establish a baseline for the analysis, the theoretical mass balance was calculated and compared with the experimental balance ratio of N/C, N/H and N/O.

### Underwater Experiments

A schematic picture of the test set-up is shown in Figure 1. An explosive charge of 30 g together with 2 g PETN booster was mounted inside a flexible rubber balloon filled with water. The shape of the charge was spherical. The balloons used for the experiments are commercially available and consist of Latex with a thickness below 1 mm. The diameter was about 800 mm. The balloon was filled with about 100 l of water and placed in a basin of water at a depth of 1.0 m. The basin had a diameter of 2.90 m and a depth of 2.00 m. The balloon was closed by special equipment which allowed one to easily collect the gaseous reaction products after the detonation. Two pressure gauges (turmaline and quartz) were fixed on the wall of the basin to measure and record the pressures.

The explosive charge was placed in the center of the water balloon together with a special underwater detonator. Before starting the experiment, the balloon was purged of any air bubbles and finally sealed. Then the balloon together with the explosive charge was lowered into the water. After the detonation of the charge the balloon immediately came up to the surface of the water. The reaction gases were collected in evacuated glass vessels for gas chromatographic and mass spectrometric analysis. Afterwards, the water from the balloon was pumped into plastic containers for a later filtration in order to separate the

solid residue, which was analyzed for carbon soot and unreacted aluminium after a drying process.

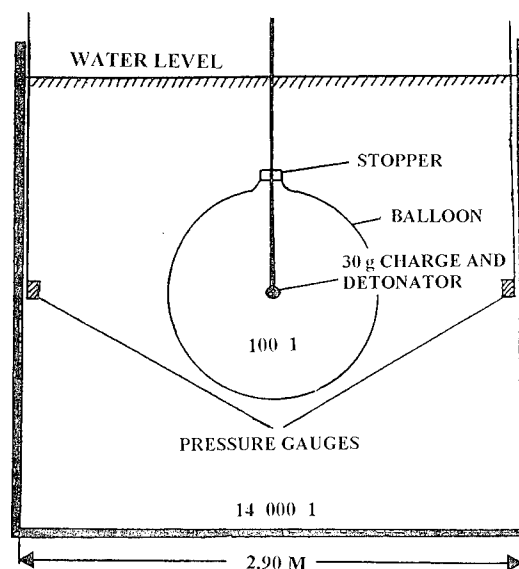


FIGURE 1. TEST SETUP

## RESULTS

### Detonation Products of Charges Without Aluminum (Al)

In order to be able to compare the detonation products of explosives without Al with those containing different amounts of Al, the investigation initially began with the following explosives charges:

2,4,6-TNT / NQ  
2,4,6-TNT / NTO  
RDX / GAP

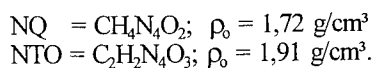
Explosive mixtures consisting of 2,4,6-TNT and nitroguanidine (NQ) and 2,4,6-TNT and 3-Nitro-1,2,4 triazol-5-one (NTO) are castable explosives. On the other hand, RDX or HMX with Glycidyl azide polymer (GAP) are composite explosives.

In earlier investigations we determined the influence of different argon pressures on the detonation products of TNT/NQ charges. These tests showed that very different detonation products were formed from the explosives when initiated in vacuum compared with those under 0.05 or 0.1 MPa of argon pressure.<sup>1-4</sup>

## Detonation Products of TNT/NQ and TNT/NTQ Charges

In order to compare nitroguanidine (NQ) with 3-Nitro-1,2,4-triazol-5-one (NTQ), explosive charges consisting of 45 % TNT/55 % NQ and 45 % TNT/55 % NTQ were manufactured by a casting process. Spherical NQ was used with a crystal density of 1.72 g/cm<sup>3</sup>. The density of NTQ was 1.91 g/cm<sup>3</sup>.

The detonation experiments were performed with an argon pressure of 1 bar (0.1 MPa) and the results are listed in Table 1. There are interesting similarities between NQ and NTQ when comparing the oxygen balance and the heat of formation. Only the sum formulas and the densities exhibit differences:



From this standpoint it is obvious that the detonation products and the detonation enthalpies ( $\Delta H_{\text{det}}$ ) are also similar, as is the carbon content in the soot. There are, however, only differences in the gas formation. The enthalpy of detonation was 3763 for the NQ and 3843 kJ/kg for the NTQ containing charge.

TABLE 1. DETONATION PRODUCTS OF TNT/NQ AND TNT/NTQ CHARGES IN 0.1 MPa Ar

sample no.	1450/3c	1475/1
composition, %	45 TNT/ 55 NQ	45 TNT/ 55 NTQ
Ar pressure (MPa)	0.1	0.1
O <sub>2</sub> -balance (%)	-47.6	-44.7
charge mass (g)	331.	328.4
$\Delta H_f$ (kJ/kg)	-657.	-657.4
products (mol%)		
H <sub>2</sub>	5.0	3.7
CH <sub>4</sub>	0.24	0.5
CO	14.3	15.8
CO <sub>2</sub>	10.3	17.7
N <sub>2</sub>	25.6	25.4
NO	0.13	0.1
HCN	3.6	1.9
NH <sub>3</sub>	4.9	1.8
C <sub>2</sub> H <sub>4</sub>	0.1	-
H <sub>2</sub> O	20.0	13.3
C <sub>s</sub>	15.9	19.8
$\Delta H_{\text{det}}$ (kJ/kg)	3763	3843
C in residue (% of total C)	35.7	35.6
gas formation (mol/kg)	35.7	31.35

## Detonation Products of RDX/GAP Charges in Different Argon Pressures and in Vacuum

In order to test the pressure dependence and evaluate the explosive products, composite charges

containing 80 % RDX and 20 % glycidyl azide polymer binder (GAP) were tested in vacuum, in 0.05 MPa Ar and 0.10 MPa Ar (see Table 2). With increasing pressure a decrease of H<sub>2</sub> and CO and an increase of CO<sub>2</sub>, H<sub>2</sub>O and solid carbon (C<sub>s</sub>) are observed. The enthalpy of detonation increases from 4002 to 4933 kJ/kg, the carbon content in the residue from 9.8 to 40.1 % of total carbon; but the gas formation decreases from 45.6 to 38.4 mol/kg. Similar behavior was found for explosive charges consisting of 80 % HMX and 20 % GAP; these results are therefore not reported here.

TABLE 2. DETONATION PRODUCTS OF RDX/GAP CHARGES IN DIFFERENT Ar PRESSURES

sample no.	1459/1	1459/2	1459/3
composition, %	80 RDX / 20 GAP		
Ar pressure (MPa)	Vacuum	0.05	0.1
O <sub>2</sub> -balance (%)	-44.86	-44.86	-44.8
charge mass (g)	329.2	329.7	319.4
$\Delta H_f$ (kJ/kg)	-149.1	-148.9	-151.5
products (mol%)			
H <sub>2</sub>	21.6	19.4	10.3
CH <sub>4</sub>	-	-	0.23
CO	31.6	24.7	15.1
CO <sub>2</sub>	4.0	6.7	8.4
N <sub>2</sub>	25.4	25.5	25.3
NO	0.1	0.09	0.06
HCN	0.03	0.08	0.52
NH <sub>3</sub>	-	-	0.10
C <sub>2</sub> H <sub>4</sub>	0.1	-	-
H <sub>2</sub> O	13.4	15.1	23.8
C <sub>s</sub>	3.9	8.4	16.2
$\Delta H_{\text{det}}$ (kJ/kg)	4002	4258	4933
C in residue (% of total C)	9.8	21.1	40.1
gas formation (mol/kg)	45.6	43.1	38.4

## Detonation Products of Charges with Aluminium (Al)

For the manufacturing of Al containing explosives, in all cases aluminium Alcan 400 with a particle size of ~ 4 µm was used. In the following, the results of tests will be described in which composite explosive charges with increasing Al content were investigated. In all cases, the components of the charges are RDX, Al and GAP. Explosive charges containing Al are distinguished by a large heat output which is due to the formation of Al<sub>2</sub>O<sub>3</sub>.

# **Detonation Products of Charges with Different Contents of RDX, Al and GAP in Vacuum and at 0.05 and 0.1 MPa Ar**

The results of composite explosive charges consisting of 70 % RDX, 15 % Al and 15 % GAP binder are listed in Table 3. The reaction products follow the same trend discussed earlier: with increasing pressure, H<sub>2</sub> and CO decrease, CO<sub>2</sub> increases slightly, and H<sub>2</sub>O and solid carbon both increase. The energy output maximizes at a pressure of 0.05 MPa Argon. Only a small amount of Al remains unreacted in the carbon soot. The reason for this is apparently the relatively good oxygen balance of about -48,4 g O<sub>2</sub>/100 g explosive

**TABLE 3. DETONATION PRODUCTS OF 70 RDX/ 15 Al/ 15 GAP IN DIFFERENT Ar PRESSURES**

sample no.	1462/1	1462/2	1462/3
composition, %	70 RDX / 15 Al/ 15 GAP		
Ar pressure (MPa)	Vacuum	0.05	0.1
O <sub>2</sub> -balance (%)	-48.4	-48.35	-48.34
charge mass (g)	328.4	329.3	328.9
ΔH <sub>f</sub> (kJ/kg)	-106.6	-110.1	-110.7
products (mol%)			
H <sub>2</sub>	33.0	30.4	23.2
CH <sub>4</sub>	0.08	0.02	0.04
CO	34.0	30.4	23.6
CO <sub>2</sub>	0.05	0.23	2.0
N <sub>2</sub>	24.2	24.6	24.5
NO	0.07	0.08	0.07
HCN	0.06	0.08	0.46
C <sub>2</sub> H <sub>4</sub>	0.08	-	0.01
H <sub>2</sub> O	-	1.7	8.3
C	2.3	6.4	11.5
Al <sub>2</sub> O <sub>3</sub>	5.9	6.0	6.1
Al	0.24	0.14	0.2
ΔH <sub>det</sub> (kJ/kg)	5632	5737	6237
Al in residue (% of total Al)	2.0	1.1	1.6
C in residue (% of total C)	6.2	17.2	30.4
gas formation (mol/kg)	39.0	37.3	33.9

How the detonation reaction proceeds in explosives charges with increasing Al content can be seen in Tables 4 and 5, which contain the results of 65 % RDX/20 % Al/15 % GAP and 60 % RDX/25 % Al/15 % GAP. For these high Al concentrations there is a lack of oxygen as we see from the water content in the products. The same holds for CO<sub>2</sub> which in all cases exhibits concentrations of lower than one mol percent. Nevertheless it is remarkable that the amount of unreacted Al in both tables is very low. This is due to the relatively good O<sub>2</sub> balance and to the high enthalpy of detonation as we will see later.

**TABLE 4. DETONATION PRODUCTS OF CHARGES CONTAINING RDX, Al, AND GAP IN DIFFERENT Ar PRESSURES**

sample no.	1463/1	1463/2	1463/3
composition, %	65 RDX / 20 Al/ 15 GAP		
Ar pressure (MPa)	Vacuum	0.05	0.1
O <sub>2</sub> -balance (%)	-51.35	-51.33	-51.29
charge mass (g)	329.7	330.0	329.7
ΔH <sub>f</sub> (kJ/kg)	-127.5	-128.8	-130.8
products (mol%)			
H <sub>2</sub>	33.9	31.9	26.9
CH <sub>4</sub>	0.05	0.05	0.05
CO	34.8	33.6	26.8
CO <sub>2</sub>	0.1	0.1	0.5
N <sub>2</sub>	22.9	23.3	22.9
NO	0.10	0.10	0.10
HCN	0.06	0.43	2.4
C <sub>2</sub> H <sub>4</sub>	0.06	0.11	0.01
H <sub>2</sub> O	-	-	4.3
C	-	2.0	7.5
Al <sub>2</sub> O <sub>3</sub>	7.74	8.1	8.3
Al	0.32	0.2	0.2
ΔH <sub>det</sub> (kJ/kg)	6628	6613	6764
Al in residue (% of total Al)	2.0	1.2	1.0
C in residue (% of total C)	-	5.5	20.2
gas formation (mol/kg)	36.9	35.1	32.7

**TABLE 5. DETONATION PRODUCTS OF CHARGES CONTAINING RDX, Al, and GAP IN DIFFERENT Ar PRESSURES**

sample no.	1464/1	1464/2	1464/3
composition, %	60 RDX / 25 Al/ 15 GAP		
Ar pressure (MPa)	Vacuum	0.05	0.1
O <sub>2</sub> -balance (%)	-54.47	-54.44	-54.40
charge mass (g)	329.6	329.1	328.7
ΔH <sub>f</sub> (kJ/kg)	-138.8	-139.9	-141.8
products (mol%)			
H <sub>2</sub>	33.1	28.5	30.0
CH <sub>4</sub>	0.04	0.05	0.09
CO	33.6	27.6	26.5
CO <sub>2</sub>	0.01	0.03	0.19
N <sub>2</sub>	21.9	21.2	21.6
NO	0.07	0.06	0.08
HCN	0.03	0.02	1.92
C <sub>2</sub> H <sub>4</sub>	0.06	0.09	0.05
H <sub>2</sub> O	-	2.9	1.0
C	0.5	8.5	7.7
Al <sub>2</sub> O <sub>3</sub>	9.7	10.6	10.7
Al	1.0	0.4	0.12
ΔH <sub>det</sub> (kJ/kg)	7370	7563	7481
Al in residue (% of total Al)	4.7	1.9	0.6
C in residue (% of total C)	1.5	23.4	21.2
gas formation (mol/kg)	33.5	29.4	30.1

## Detonation Products of Charges Containing RDX, NQ, Al and HTPB Binder

Until now, explosive charges were tested which exhibited a relatively large enthalpy of detonation and oxygen balances which were better than -55 %. In order to study the detonation behavior of composite explosives with a smaller energy content, instead of the energetic binder GAP, a polybutadiene binder (HTPB) was used for the manufacture of these explosives. In addition, a large portion of the RDX was substituted by nitroguanidine which has less energy than RDX. The results of charges with 30 % RDX, 38 % NQ, 17 % Al and 15 % HTPB binder under different pressure conditions are listed in Table 6. Besides the normal behavior of the products with increasing pressure (decrease of  $H_2$  and CO, increase of  $CO_2$ ,  $H_2O$  and  $C_s$ ), a large amount of hydrocyanic acid (HCN) is formed at 0.05 and 0.10 MPa Ar. Also the formation of  $NH_3$  is dominant with increasing argon pressure. It is also of interest that in the vacuum test nearly all Al reacted whereas at ambient pressure 34.6 % of Al remained unreacted. This is the reason that the heat output at ambient pressure is less than that at 0.01 and 0.05 MPa argon.

TABLE 6. DETONATION PRODUCTS OF CHARGES CONTAINING RDX, NQ, Al, AND HTPB BINDER IN DIFFERENT Ar PRESSURES

sample no.	1485/1	1485/2	1485/3
composition, %	30 RDX / 38 NQ/ 17 Al/ 15 HTPB		
Ar pressure (MPa)	Vacuum	0.05	0.1
$O_2$ -balance (%)	-74.1	-74.0	-74.10
charge mass (g)	331.3	325.9	330.9
$\Delta H_f$ (kJ/kg)	-432.7	-433.7	-433.2
products (mol%)			
$H_2$	34.0	15.4	6.7
$CH_4$	-	1.1	1.9
CO	25.6	11.5	7.7
$CO_2$	-	3.4	4.8
$N_2$	21.3	17.8	17.9
$N_2O$	-	-	0.4
NO	-	0.08	0.06
HCN	2.1	9.36	5.3
$NH_3$	-	8.6	8.5
$C_2H_4$	-	0.49	1.1
$H_2O$	-	5.8	12.2
$C_s$	10.8	18.7	23.7
$Al_2O_3$	6.05	6.5	4.73
Al	0.15	1.26	5.0
$\Delta H_{det}$ (kJ/kg)	4935	4954	4569
Al in residue (% of total Al)	1.2	8.9	34.6
C in residue (% of total C)	28.1	41.6	52.1
gas formation (mol/kg)	36.8	29.3	26.2

Very similar results were obtained when testing the following composition which contained NTO instead of NQ: 30 % RDX, 38 % NTO, 17 % Al and HTPB binder.

Table 7 contains the test results of 3 shots, each performed at 0.1 MPa (1 bar argon). The results show not only the reproducibility at the same argon pressure, but also how sensitively the enthalpy of detonation depends on the composition of the products, in this case, on the amount of unreacted Al.

TABLE 7. DETONATION PRODUCTS OF CHARGES CONTAINING RDX, NTO, Al, AND HTPB BINDER IN 0.1 MPa Ar

sample no.	1482/1	1482/2	1482/3
composition, %	30 RDX / 38 NTO/ 17 Al/ 15 HTPB		
Ar pressure (MPa)	0.1	0.1	0.1
$O_2$ -balance (%)	-74.04	-74.2	-73.94
charge mass (g)	314.1	317.2	316.2
$\Delta H_f$ (kJ/kg)	-447.5	-443.8	-449.7
products (mol%)			
$H_2$	7.5	8.6	8.9
$CH_4$	1.85	1.9	1.7
CO	10.4	10.6	10.4
$CO_2$	6.1	6.2	5.7
$N_2$	17.0	17.4	17.5
NO	0.19	0.2	0.2
HCN	3.93	4.3	3.9
$NH_3$	8.4	7.0	6.0
$C_2H_4$	1.8	1.8	1.5
$H_2O$	7.4	8.4	9.8
$C_s$	25.7	23.3	24.3
$Al_2O_3$	5.5	4.5	4.3
Al	4.2	5.8	5.8
$\Delta H_{det}$ (kJ/kg)	4816	4459	4460
Al in residue (% of total Al)	27.6	39.0	40.7
C in residue (% of total C)	49.9	46.6	49.8
gas formation (mol/kg)	25.3	26.8	27.0

Other tests for which charges have been used with a further replacement of RDX by NTO (such as 20 % RDX, 48 % NTO, 17 % Al and 15 % HTPB) exhibited no reproducible detonation products. In some tests more than 34 % of unreacted Al were found in the residue. The oxygen balance in this case was -74.4 %, the carbon content in the residue 71.3 % of total carbon and the energy output 3633 kJ/kg.

### Detonation Products of Underwater High Explosive Containing HMX, Al and Polyisobutylene Binder (PIB)

Two underwater high explosives consisting of 65 % HMX, 25 % Al and 10 % polyisobutylene binder (PIB) and 60 % HMX, 30 % Al and 10 % PIB were also investigated in the 1.5 m<sup>3</sup> container at 0.1 MPa argon pressure, in order to compare the reaction products with those which will be formed in real underwater experiments. The results are listed in Table 8. It is of interest to note that not only the 25 % Al but also the 30 % Al containing charge PHXA-82 exhibits a fairly good detonation reaction with an enthalpy output of 7027 kJ/kg, even though there is an amount of 20.6 % of unreacted Al in the residue.

**TABLE 8. DETONATION PRODUCTS OF AN UNDERWATER HIGH EXPLOSIVE CONTAINING HMX, Al, AND POLYISOBUTYLENE BINDER**

sample no.	PHXA-81	PHXA-82
composition, %	65 HMX/25 Al/ 10 PIB	60 HMX/30 Al/ 10 PIB
Ar pressure (MPa)	0.1	0.1
O <sub>2</sub> -balance (%)	-63.45	-66.05
charge mass (g)	220.0	221.5
$\Delta H_f$ (kJ/kg)	-96.2	-119.7
products (mol%)		
H <sub>2</sub>	26.1	28.9
CH <sub>4</sub>	1.7	1.4
CO	21.3	22.3
CO <sub>2</sub>	3.2	2.5
N <sub>2</sub>	20.1	18.9
HCN	3.2	2.6
C <sub>2</sub> H <sub>4</sub>	1.7	1.4
H <sub>2</sub> O	3.6	0.8
C <sub>2</sub>	7.1	6.9
Al <sub>2</sub> O <sub>3</sub>	7.9	9.4
Al	4.1	4.9
$\Delta H_{det}$ (kJ/kg)	6583	7027
Al in residue (% of total Al)	20.8	20.6
C in residue (% of total C)	17.7	18.0
gas formation (mol/kg)	31.3	29.8

### PRODUCTS OF UNDERWATER DETONATIONS

As mentioned before, the mass of the underwater high explosive was 30 g and the PETN booster 2.0 g. The detonation was initiated using special underwater cap No 8. All underwater high explosives were manufactured using a polyisobutylene binder (PIB) treated with paraffin oil in a mixer. The results of three explosives with different Al content are listed

in Table 9. One sees that with increasing Al content the concentration of H<sub>2</sub> and CO increases, but CO<sub>2</sub> and H<sub>2</sub>O decreases. This behavior is the result of the reaction of Al with gaseous products such as CO<sub>2</sub> and H<sub>2</sub>O which prevents the Boudouard reaction from going to the right side:

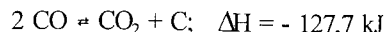


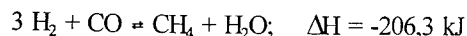
**TABLE 9. PRODUCTS OF UNDERWATER DETONATIONS FROM EXPLOSIVES WITH DIFFERENT ALUMINUM CONTENT**

sample no.	PHXA-78	PHXA-49	PHXA-81
composition, %	75 HMX 15 Al 10 PIB	70 HMX 20 Al 10 PIB	65 HMX 25 Al 10 PIB
charge mass (g)	32.	32.	32.
booster, PETN (g)	2.	2.	2.
O <sub>2</sub> -balance (%)	-60.03	-63.19	-66.35
$\Delta H_f$ (kJ/kg)	-9.2	-21.1	-33.0
products (mol%)			
H <sub>2</sub>	9.8	10.6	17.5
CH <sub>4</sub>	5.7	5.0	7.6
CO	17.0	17.0	21.6
CO <sub>2</sub>	4.1	4.2	2.9
N <sub>2</sub>	23.7	22.1	22.3
N <sub>2</sub> O	0.03	0.04	0.03
NO	0.03	0.07	0.06
HCN	++	>0.45	>0.45
NH <sub>3</sub>	?	?	?
C <sub>2</sub> H <sub>4</sub>	0.4	0.6	0.7
H <sub>2</sub> O	17.9	16.7	5.6
C <sub>2</sub>	13.8	12.3	7.7
Al <sub>2</sub> O <sub>3</sub>	4.9	6.1	8.4
Al	2.6	4.8	5.6
$\Delta H_{det}$ (kJ/kg)	6684	6973	7090
Al in residue (% of total Al)	21.0	28.2	24.9
C in residue (% of total C)	33.5	30.6	18.6
gas formation (mol/kg)	31.4	29.4	28.6

As a result, carbon formation is reduced. Nevertheless, the formation of unreacted Al increases because the oxygen balance decreases with Al content. The highest value of the enthalpy of detonation is 70-90 kJ/kg, corresponding to an Al content of the explosive of 25 wt.%. In this connection it is of interest that the formation of methane (CH<sub>4</sub>) is abnormally high.

In order to enable a comparison of products from the underwater detonation with products of a containment shot in argon atmosphere, the corresponding results are listed in Table 10. Although there is only a small difference in the amount of unreacted Al in the residue (20.8 % compared with 24.9 %), we see a large difference in the formation of CH<sub>4</sub>: 1.7 mol% when contained in argon atmosphere, but 7.6 mol% analyzed from the

underwater shot. The explanation for this behavior could be the different conditions of the reaction gas present after detonation. In the container filled with 1.5 cm<sup>3</sup> argon, a very strong expansion of the reaction products occurs. As a result the reaction



is less probable than it will be in the balloon, where the hot reaction products are very close together, so that formation of CH<sub>4</sub> in the cooling phase is favored. The second underwater shot shown in Table 10 points out that the reproducibility of explosives with a high Al content is limited. So we see a very high content of unreacted Al.

TABLE 10. COMPARISON OF THE PRODUCTS FROM THE CONTAINMENT AND THE UNDERWATER EXPERIMENT

sample no.	Containment Experiment PHXA-81	Underwater Experiment PHXA-81
composition, %	65 HMX/25 Al/10 Binder	65 HMX/25 Al/10 Binder
Ar pressure (MPa)	0.1	-
O <sub>2</sub> -balance (%)	-63.45	-66.35
charge mass (g)	220.	32.
booster (g)	10. (RDX)	2. (PETN)
blasting foil (g)	20.	-
$\Delta H_f$ (kJ/kg)	-96.2	-33.0
products (mol%)		
H <sub>2</sub>	26.1	17.5 14.4
CH <sub>4</sub>	1.7	7.6 6.0
CO	21.3	21.6 19.4
CO <sub>2</sub>	3.2	2.9 3.1
H <sub>2</sub> O	20.1	22.3 21.2
NO	-	0.06 0.12
HCN	3.2	++ ++
NH <sub>3</sub>	?	? ?
C <sub>2</sub> H <sub>4</sub>	1.7	0.7 0.63
H <sub>2</sub> O	3.6	5.6 10.2
C	7.1	7.7 10.0
Al <sub>2</sub> O <sub>3</sub>	7.9	8.4 6.1
Al	4.1	5.6 9.1
$\Delta H_{det}$ (kJ/kg)	6583	7090 6386
Al in residue (% of total Al)	20.8	24.9 42.6
C in residue (% of total C)	17.7	18.6 24.5
gas formation (mol/kg)	31.3	28.6 28.9

## CONCLUSION

It has been shown that analysis of reaction products formed during detonation in a 1.5 m<sup>3</sup> stainless steel container under different conditions is very useful for the energy optimization of explosives for a blast, as well as for a better understanding of non-equilibrium and incomplete metal reactions.

Likewise, investigation of the detonation products of underwater high explosives in a plastic balloon allows one to elucidate the reaction mecha-

nism and the energy output of detonations by chemical analysis. It was found that the post detonation reactions in the cooling phase of the products significantly differed in the amount of methane formed.

## REFERENCES

1. Volk, F. and Schedlbauer, F., "Detonation Products of Less Sensitive High Explosives Formed Under Different Pressures of Argon and in Vacuum," in *Proc. 9th Symp. (Int.) on Detonation*, pp. 962-971, 1989, Portland, Oregon, Office of Naval Research.
2. Volk, F., "Energy Output of Insensitive High Explosives by Measuring the Detonation Products," *Phil. Trans. R. Soc. London A* (1992) **339**, pp. 335-343.
3. Volk, F., "Analysis of Reaction Products of Propellants and High Explosives," *Chemistry and Physics of Energetic Materials*, edited by S. N. Bulusu, ARDEC, Picatinny Arsenal, Dover, New Jersey, 1990.
4. Volk, F., "Detonation Gases and Residues of Composite Explosives," *Journal of Energetic Materials* **4** (1986), pp. 93-113.
5. Greiner, R. N.; Phillips, D. G.; Johnson, J. D. and Volk, F., "Diamonds in Detonation Soot," *Nature, Lond.* **333**, pp. 440-442, 1988.
6. Held, M., "Corner Turning Distance and Detonation Radius," *Prop. Expl. Pyrot.* **14**, (1989), pp. 153-161.
7. Carlson, D.; Doherty, R.; Ringbloom, V.; Deiter, J. and Wilmot, G., "Chemistry of Underwater Explosive Detonations," in *Proc. 9th Symp. (Int.) on Detonation*, 1989, pp. 908-919.
8. Wilmot, G. and Deiter, J., "Detonation Chemistry of Underwater Explosives - Gaseous Products," *1992 Annual DEA-A-76-G-1218 Meeting on Energetic Materials for Munitions*, Naval Air Warfare Center, China Lake, California, 22-24 Sept. 1992.
9. Deiter, J. and Wilmot G., "Analysis of Condensed-Phase Detonation Products From Underwater Explosives," *1992 Annual DEA-A-76-G-1218 Meeting on Energetic Materials for Detonations*, China Lake, California, 22-24 Sept. 1992.

## THERMAL STABILITY STUDIES ON NITROARENES

Jimmie Oxley, James Smith, Hong Ye,  
Jiang Wang, and Hongtu Feng  
Chemistry Department  
New Mexico Institute of Mining and Technology  
Socorro, New Mexico 87801

Robert L. McKenney and Paul R. Bolduc  
High Explosive Research and Development  
Eglin Air Force Base, Florida 32542

The thermal stabilities of a number of nitrobenzenes were examined in solution and in condensed phase. In general, increasing the number of nitro groups decreased thermal stability. For nitrobenzenes with other substituents, the placement of species relative to the nitro groups appeared to be more important than the number of nitro groups. Changing the substituent on 1-X-2,4,6-trinitrobenzene from X = H to NH<sub>2</sub> to CH<sub>3</sub> to OH accelerated decomposition; this effect was attributed to increased ease of intramolecular proton transfer to an ortho nitro group, thus weakening the carbon nitrogen bond. In solution, the effect of increasing substitution on trinitrobenzene was uniformly that of decreasing the thermal stability of the species. However, in condensed-phase, results suggested that crystal habit may be more important than molecular structure. Extrapolation of condensed-phase data obtained for the mono-, di-, and tri-methyl-trinitrobenzenes to the homologous trinitroanilines tentatively suggests that TATB may have high thermal stability in the solid state but not in solution.

### INTRODUCTION

For a number of years the military has been interested in "insensitive" explosives, but to date, there are few which are generally agreed to be insensitive. TATB (1,3,5-triamino-2,4,6-trinitrobenzene) is one of these. Researchers have attempted to correlate sensitivity to a variety of stimuli with chemical structure; the difficulty with that approach as applied to nitroarenes is thoroughly explored in reference 1. Looking for correlations between thermal stability and chemical structure, one notices that there is a general trend for nitroarenes to be more stable than nitramines which, in turn, are more stable than nitrate esters. At temperatures over which thermal stability is

normally examined, each of these classes of explosives has a common mode of decomposition available--loss of NO<sub>2</sub>.<sup>2-12</sup> Thus, the trend in thermal stabilities is in line with the X-NO<sub>2</sub> bond energies: nitrate ester O-NO<sub>2</sub>, 40 kcal/mol; nitramine N-NO<sub>2</sub>, 47 kcal/mol; and nitroarene C-NO<sub>2</sub>, 70 kcal/mol.<sup>9</sup> Of course, stability is influenced by factors other than just the atom directly linked to the nitro group. Such factors as whether the bonded atom is part of a ring structure or whether there is the possibility of electron delocalization are also important.

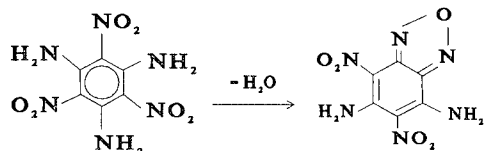
Among the nitroarenes TATB has abnormally high thermal and impact stabilities, yet good performance. To examine the source of this unusual thermal stability, we have examined the stability of several homologous series: 2,4,6-trinitroaniline, 1,3-diamino- 2,4,6-trinitrobenzene (DATB), and TATB; 2,4,6-trinitrotoluene (TNT), 2,4,6-trinitroxylyene, and 2,4,6-trinitromesitylene; and 2,4,6-trinitrophenol (picric acid),

\* Work performed at New Mexico Institute of Mining and Technology with funding from the Armament Division, Eglin Air Force Base through Office of Naval Research grant N-000-1489J3143.



2,4,6-trinitroresorcinol (styphnic acid), and 2,4,6-trinitrophenol (picric acid).

Although the thermal decomposition mechanisms of nitrotoluenes and TNT have received much attention,<sup>2-5</sup> the thermal decomposition studies of nitroaniline and TATB have been comparatively neglected.<sup>6-8</sup> It has been suggested that the key to TATB insensitivity is the thermoneutral formation of benzofurazan and benzofuroxan rings in the first step of its decomposition.<sup>8</sup>



Owing to the insolubility of TATB, thorough analysis of its decomposition behavior has been hampered, and much of its behavior is inferred by analogy. Politzer, et. al<sup>12</sup> have carried out extensive theoretical analyses on a variety of trinitrobenzene derivatives, including the hydroxy derivatives for which the thermal stability decreases as the number of hydroxyl groups increases. They suggested that proton transfer from hydroxyl to nitro results in formation of nitronic acid and that an increased number of hydroxyl-substituents facilitate this reaction. However, this same mode of reactivity is available to nitrotoluenes and nitroanilines.<sup>4</sup> Yet the trend in thermal stability reported for the mono-, di-, and tri-amino-substituted trinitrobenzenes is the opposite of that postulated for the hydroxyl-substituted nitroarenes. The reason for this contradiction is not immediately obvious.

At temperatures over which the thermal stability of nitroarenes is normally studied, two modes of decomposition are generally postulated: homolysis of the C-NO<sub>2</sub> bond or proton transfer to nitro, resulting in formation of nitronic acid. The latter reaction may be inter- or intra-molecular, and several subsequent decomposition pathways are available. The relative dominance of these decomposition pathways changes with temperature; Brill has reviewed the manner in which this affects observed sensitivities.<sup>1</sup>

## EXPERIMENTAL SECTION

The thermal stabilities of various nitroarenes were examined by differential scanning calorimetric (DSC) analysis and by conventional isothermal techniques; the latter was applied primarily to solution samples. Enough solid sample was added to 100  $\mu$ L of benzene to form a solution between 0.7

and 5 wt% reactant; since most samples had low solubility in benzene, 1.2wt% was most commonly used. The prepared solution (15  $\mu$ L) was transferred by syringe into a 40-50  $\mu$ L melting point capillary tube (0.9-1.1 mm I.D.). For isothermal thermolysis of neat samples, samples (0.2 mg) were weighed into the reaction tube. Tubes were flame sealed and heated in a molten metal bath for the desired length of time. At the completion of heating, the tip of the tube was broken. For neat samples, 60  $\mu$ L of acetone was added; and the tube was resealed and heated in a boiling water bath until no more sample appeared to dissolve. The fraction of sample remaining was determined by injection of the sample solution into a Varian 3600 gas chromatograph (GC) equipped with an Alltech fused silica 5-BP capillary column (8 foot) and flame-ionization detector (FID). Thermal stability was assessed from the rate constants determined from first-order plots. The larger the fraction reacted, the higher the rate constant, and the lower the thermal stability. Solid-state decomposition was also analyzed by the programmed DSC. For DSC results, the temperature at which the exothermic maximum appeared (at 20°/minute scan rate) was considered an indication of thermal stability--the lower the temperature, the lower the stability. For a number of solids, activation energy and frequency factor were determined by the ASTM<sup>13</sup> variable heating rate method; and using these values and the Arrhenius relationship, the rate constant at 340°C was calculated.

## SOLUTION RESULTS

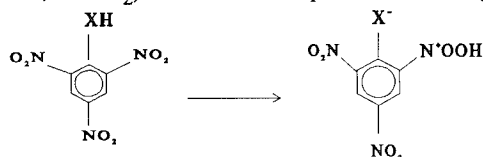
Initially the decomposition of the nitroarene species was examined in solution. Solution eliminates the sometimes confusing effects of particle size, crystal habit, and melting point. In solution, the intrinsic chemistry of the molecule can be followed in a pseudo-first-order fashion. Furthermore, reactive intermediates can sometimes be trapped before they undergo subsequent reactions.

### The Effect of Substituent Type

The relative thermal stabilities of chemical species are subject to the temperature regime of the comparison. Most nitroarenes examined were studied over a 100°C temperature range around 340°C. For some, 340°C was the highest temperature at which rates could be measured by our manual techniques (reactions complete in less than 4 seconds were difficult to follow). For some, 340°C was the lowest temperature. Therefore,

thermal stabilities were compared at 340°C. Since activation energies differ widely, thermal stabilities change their relative ordering in different temperature regimes. In fact, in a few cases thermal stabilities ordered by the temperature of the DSC exothermic maximum (20°/minute) were not consistent with those obtained by ordering the compounds by the 340°C isothermal rate constant.

Nitrobenzenes, as a class, are more thermally stable than the hetero-substituted nitrobenzenes. By DSC analysis of neat samples as well as isothermal studies in benzene, trinitrobenzene (TNB) appears more stable than any of the singly-substituted trinitrobenzenes examined. Since symmetrical trinitroaniline (NH<sub>2</sub>-TNB) is more thermally stable than symmetrical trinitrotoluene (TNT or CH<sub>3</sub>-TNB) and TNT is more stable than picric acid (HO-TNB), the thermal stability appears to correlate with the acidity of the hydrogen-containing substituent (Table I). This type of correlation would be in line with the decomposition mode of substituted nitrobenzenes, where the rate-determining step is intramolecular proton transfer from the hydrogen-containing substituent to a neighboring NO<sub>2</sub> group (where X = O, NH, or CH<sub>2</sub>). This would explain the stability of



unsubstituted nitrobenzenes since the major mode of decomposition available to them would be by homolysis of the C-NO<sub>2</sub> bond rather than C-NO<sub>2</sub>H formed by intramolecular proton transfer. The latter process has an activation energy roughly half of the former. (Note formation of C-NO<sub>2</sub>H would still be available by intermolecular pathways, but the accessibility of intramolecular versus intermolecular routes has been adequately demonstrated in the enhanced thermal instability of o-nitrotoluene compared to p-nitrotoluene.<sup>2)</sup>

Yet, even if proton acidity explains some of the thermal stability trends observed with singly-substituted trinitrobenzenes; this rationale cannot be applied to 2,4,6-trinitroanisole (CH<sub>3</sub>O-TNB), the most unstable of the mono-substituent trinitrobenzenes examined, nor to 2,4,6-trinitrobromobenzene (Br-TNB), the most stable. It might be argued that poor thermal stability of trinitroanisole is not a result of proton transfer; but of CH<sub>3</sub><sup>+</sup> transfer to the neighboring nitro group since, indeed, CH<sub>3</sub><sup>+</sup> is labile. The bromo group is not particularly labile; in fact, mass spectral fragmentation patterns show that under electron

impact, all three nitro groups are lost before the bromine. The reason that trinitrobromobenzene is somewhat less thermally stable than trinitrobenzene is not obvious.

#### The Effect of Nitro Groups

Within the nitrobenzene group, thermal stability decreased slightly as the number of nitro groups increased. Presumably, since the C-NO<sub>2</sub> is subject to homolysis, the more C-NO<sub>2</sub> bonds, the more rapid the decomposition. With in the nitrotoluene and nitroaniline classes, there was also a trend for thermal stability to decrease with increasing number of nitro groups; but the relative position of the nitro groups appeared to be more important than the total number of nitro groups. Para-nitrotoluene and nitroaniline were much more stable than the ortho analogs (Table I). 2,4-Dinitro-toluene and aniline were more thermally stable than the 2,6-configuration where both nitro groups are ortho to the hetero substituent (CH<sub>3</sub> or NH<sub>2</sub>) site. However, symmetrically substituted trinitrotoluene and trinitroaniline were not less stable than the 2,6-dinitro-substituted analogs. In fact, in some tests, the latter appeared slightly more stable, leading to speculation about possible stabilization by para nitro substituents (Table I). As discussed above, converting the C-NO<sub>2</sub> bond to C-NO<sub>2</sub>H lowers the bond dissociation energy by about half. Therefore, the presence of ortho substituents capable of transferring a proton to the nitro group increases the rate of decomposition of the species.

#### The Effect of Multiple Hetero Substituents

It has been speculated that TATB possesses its unusually good thermal stability because there are no hydrogen atoms directly attached to the aromatic ring. Due to the insolubility of DATB and TATB, we have not yet tested their thermal stability in solution. However, for a number of trinitrobenzenes the rate of decomposition in benzene solution (1.2%) was measured. In general, as the number of hetero substituents on the trinitrobenzene (TNB) ring increased, the thermal stability decreased. For those with labile protons, this increased reactivity is understandable since it facilitates the formation of C-NOOH. The present data implies that trinitromesitylene [(CH<sub>3</sub>)TNB] does not possess the superior stability attributed to TATB (Table I).

#### CONDENSED-PHASE RESULTS

Because most explosives are actually stored and used as solids, it is necessary to extend the range of

our kinetic studies from solutions to the condensed phase. Isothermal thermolysis studies are in progress. These have proved arduous because the reproducibility of the data is constrained by our ability to extract all the remaining reactant from the resulting residue. We have not yet attempted to study the reaction kinetics of DATB and TATB by this method because their low solubility makes most analyses impractical. For these reasons, most of the 340°C rate constants cited for the condensed-phase studies are calculated rather than measured. Most of the rate constants were calculated from the activation energies and frequency factors obtained using the ASTM programmed DSC method.<sup>13</sup> Where Arrhenius parameters and rate constants have been determined isothermally, they are considered more reliable. Assessing relative thermal stabilities with the present data, materials with large rate constants (340°C) and low-temperature DSC exotherms are considered thermally unstable. Where isothermal rate constants have been obtained, these are labeled "Iso." to distinguish them from rate constants calculated by the DSC ASTM method "DSC." The temperature of the DSC exothermic maximum "exo. °C" and the melting point "m.p. °C" are also given.

Most of the trends observed in solution appeared to apply to the condensed-phase decomposition, though, of course, the condensed-phase decompositions were faster than those in solution. Presumably, the rationale used to explain the thermal stability trends in solution can equally well be applied to the condensed phase.

#### The Effect of Substituent Type and of Nitro Groups

In solution we observed that the thermal stability of a substituted symmetrical trinitrobenzene (TNB) was related to the acidity of the protons on the substituent and their ability to attack the nitro group. (In the case of trinitroanisole, the thermal instability was attributed to the lability of the methyl group.) These trends hold in the condensed-phase decomposition (Table II). Within the nitrobenzene group, thermal stability decreased as the number of nitro groups increased (Table II). As in solution, the relative position of the nitro groups was more important than the total number of nitro groups. Para- nitrotoluene and nitroaniline remained much more stable than ortho isomers (Table II).

In the condensed-phase studies, the relative thermal stabilities of 2,4-dinitrotoluene and 2,6-dinitrotoluene were reversed. Furthermore, symmetrically substituted trinitrotoluene appears greatly destabilized compared with the other species.

This difference in relative stabilities between solution and condensed phase decomposition may be related to the packing of the molecules and their ability to undergo intermolecular reactions. However, the same differences have not been observed in the nitroaniline group (Table II).

#### The Effect of Multiple Hetero Substituents

The intriguing difference between solution-phase and condensed-phase thermal stability studies is in the effect of multiple hetero substituents ( $\text{CH}_3$ ,  $\text{NH}_2$ ,  $\text{OH}$ ). In the solution studies we observed that addition of other substituents to trinitrobenzene (TNB) decreased thermal stability. However, in methyl- and bromo-substituted homologous series we observed just the opposite in the solid-state decomposition. In fact, their rate of decomposition increased as the melting point decreased.

Condensed-Phase Rate Constant ( $\times 10^3$ ) Calculated for 340°C			
$(\text{CH}_3)\text{-TNB} > (\text{CH}_3)_2\text{-TNB} > (\text{CH}_3)_3\text{-TNB}$			
Iso.	25	11	1.2
DSC	18	8.8	3.2
exo. °C	328	351	368
Sol'n	1.0	3.0	4.7
m.p. °C	80	187	240

Condensed-Phase Rate Constant ( $\times 10^3$ ) Calculated for 340°C			
$\text{Br-TNB} > \text{Br}_2\text{-TNB} > \text{Br}_3\text{-TNB}$			
Iso.	4.2		1.4
DSC	3.1	1.8	0.39
exo. °C	374	399	400
m.p. °C	124	140	297

The trend observed with the homologous series  $(\text{CH}_3)\text{-TNB}$ ,  $(\text{CH}_3)_2\text{-TNB}$ ,  $(\text{CH}_3)_3\text{-TNB}$  suggests that in the condensed phase crystal structure considerations may be more important than the structure of the individual molecule. Although trinitromesitylene was the least stable of the homologues in solution, in condensed phase it was the slowest to decompose. Trinitromesitylene melts substantially higher than the other two trinitrotoluenes due to its high molecular weight and symmetry. Since it is generally true that the more mobile liquid phase decomposes more rapidly than the solid phase, the species which melt first begin to decompose much faster than those which remain solid. The advantage gained in melting at a lower temperature may overcome the "intrinsic" or solution thermal stability if the differences in intrinsic rate are not great and the melting points differ widely.

TABLE I: SOLUTION (1.2%) RATE CONSTANTS ( $\times 10^3$ ) MEASURED AT 340°C

The Effect of Substituent Type					
TNB < 0.2	Br-TNB < 0.42	NH <sub>2</sub> -TNB 0.6	CH <sub>3</sub> -TNB 1.0	OH-TNB 7.6	CH <sub>3</sub> O-TNB 16
The Effect of Nitro Groups					
(NO <sub>2</sub> )C <sub>6</sub> H <sub>5</sub> < 0.08	1,4 0.09	(NO <sub>2</sub> ) <sub>2</sub> C <sub>6</sub> H <sub>5</sub>	1,3 < 0.2	(NO <sub>2</sub> ) <sub>3</sub> C <sub>6</sub> H <sub>3</sub> 0.23	
p-NA < 0.02	o-NA 0.13	p-NT < 0.24	o-NT 0.9		
p-NA < 0.02	o-NT < 0.13	2,4-DNA < 0.15	TNA 0.6	2,6-TNA 0.6	
p-NT < 0.2	o-NT < 0.85	2,4-DNT 1.0	TNT < 1.0	2,6-DNT 1.6	
The Effect of Multiple Hetero Substituents					
(CH <sub>3</sub> ) <sub>2</sub> -TNB < 1.0		(CH <sub>3</sub> ) <sub>2</sub> -TNB < 3.0		(CH <sub>3</sub> ) <sub>3</sub> -TNB 4.7	
(CH <sub>3</sub> ) <sub>2</sub> -TNB < 1.0		(NH <sub>2</sub> )(CH <sub>3</sub> )-TNB < 1.2		(NH <sub>2</sub> )(CH <sub>3</sub> ) <sub>2</sub> -TNB 2.7	
HO-TNB < 7.6		(HO) <sub>2</sub> -TNB < 420		(HO) <sub>3</sub> -TNB 1100	

NA=nitroaniline; NT=nitrotoluene; DNA=dinitroaniline; DNT=dinitrotoluene; TNB=trinitrobenzene

In the hydroxytrinitrobenzene homologous series, the condensed-phase thermal stabilities are in the same relative order as the solution stabilities. This is not surprising in view of the large differences observed in their solution rate constants and the small differences in their melting points.

#### Condensed-Phase Rate Constant ( $\times 10^3$ )

Calculated for 340°C

	HO-TNB	(HO) <sub>2</sub> -TNB	(HO) <sub>3</sub> -TNB
Iso.	56	1800	too fast
DSC	23	101	18000
exo. °C	332	300	215
Sol'n	7.6	420	1100
m.p. °C	124	180	163

	(CH <sub>3</sub> ) TNB	(NH <sub>2</sub> )(CH <sub>3</sub> ) TNB	(NH <sub>2</sub> ) <sub>2</sub> (CH <sub>3</sub> ) TNB
DSC	18	31	82
exo. °C	328	323	306
Sol'n	1.0	1.1	2.6
m.p. °C	80	140	228

The aminomethyl-trinitrobenzene series is not a true homologous series, but it is interesting to note that their condensed phase rate constants also follow those observed in solution. Like the hydroxytrinitrobenzene series, these species have

such high intrinsic rate constants that crystal lattice considerations are overwhelmed.

Since in some cases we have observed that condensed-phase isothermal rate constants show thermal stability trends opposed to those observed in solution, it raises the question whether the touted stability of TATB is simply a result of an inability to disrupt its crystal structure either by melting or by dissolution. Therefore, determining the isothermal solution and condensed-phase rate constants for the aminotrinitrobenzene series is a matter of great interest. Due to the insolubility of both DATB and TATB, neither the isothermal solution nor the isothermal condensed-phase thermolyses have been performed. With the data from programmed DSC scans, the trend is unclear.

#### Condensed-Phase Rate Constant ( $\times 10^3$ )

Calculated for 340°C

	TNA (NH <sub>2</sub> )TNB	DATB (NH <sub>2</sub> ) <sub>2</sub> TNB	TATB (NH <sub>2</sub> ) <sub>3</sub> TNB
DSC	1.5	6.2	1.0
exo. °C	387	360	397
m.p. °C	192	286	449

Unique to this homologous series, the di-substituted trinitrobenzene decomposes most

TABLE II: CONDENSED-PHASE RATE CONSTANTS ( $\times 10^3$ ) CALCULATED FOR 340°C

The Effect of Substituent Type					
	TNB <	NH <sub>2</sub> -TNB <	CH <sub>3</sub> -TNB <	HO-TNB <	CH <sub>3</sub> O-TNB
DSC rate	0.2	1.07	18	23	55
DSC exo. °C	435	387	328	332	318
The Effect of Nitro Groups					
	1,4	(NO <sub>2</sub> ) <sub>2</sub> C <sub>6</sub> H <sub>4</sub>	1,3 <	(NO <sub>2</sub> ) <sub>3</sub> C <sub>6</sub> H <sub>4</sub>	
DSC rate	0.083		0.06	0.15	
DSC exo. °C	443		453	435	
	p-NA <	o-NA	p-NT <	o-NT	
DSC rate	1.6	2.5	0.9	3.4	
DSC exo. °C	394	388	397	389	
	p-NA	o-NA	2,4-DNA	TNA	2,6-DNA
DSC rate	1.6	2.5	2.4	1.5	2.3
DSC exo. °C	394	388	390	387	393
Solution	0.02	0.12	0.15	0.7	0.8
m.p. °C	150	75	183	192	140
	p-NT <	o-NT <	2,4-DNT <	TNT	2,6-DNT
DSC rate	0.9	3.4	6.4	18	3.1
DSC exo. °C	397	389	351	328	371
Solution	0.24	0.84	1.0	1.0	1.6
m.p. °C	53	-5	70	80	65

NA=nitroaniline; NT=nitrotoluene; DNA=dinitroaniline; DNT=dinitrotoluene; TNB=trinitrobenzene

quickly. Although a definitive answer must await a successful completion of our attempts to do the isothermal studies, we venture to rationalize these results as follows. We propose that like the other series the tri-substituted trinitrobenzene is the least stable in solution. In the condensed phase, however, the crystal lattice strength partially reverses that trend. For TATB, which due to hydrogen bonding, symmetry, and molecular weight, has an extremely high melting point, the lattice considerations are more important than the "intrinsic" instability of the molecule; therefore, it decomposes most slowly. For DATB, however, which has a substantially lower melting point than TATB, the intrinsic chemistry of the molecule is not overcome, and it decomposes the fastest in the series.

## CONCLUSIONS

Both in solution and in the condensed-phase decomposition, the thermal stability of nitroarenes decreased as the number of nitro groups was increased from one to three and as other substituents capable of attack on the ortho nitro group were added. In the solution studies, an increase in the number of methyl or hydroxyl groups

on trinitrobenzene increased the thermal instability. The destabilization is due to the presence of groups ortho to the nitro groups which can transfer a proton to the nitro. Such transfer lowers the C-NO<sub>2</sub> bond strength. Sufficient isothermal condensed-phase studies have not yet been performed, but present data suggests that the solution trend for added substituents to destabilize trinitrobenzene may be reversed in the condensed phase. For the homologous series (CH<sub>3</sub>)-TNB, (CH<sub>3</sub>)<sub>2</sub>-TNB, (CH<sub>3</sub>)<sub>3</sub>-TNB the thermal stability increased with the addition of methyl. This increased stability was attributed not to a change in the elementary chemistry but to an increase in the crystal lattice integrity as the molecular weight and symmetry increased. Since decomposition is slower in the solid state than in the liquid, the high melting species may appear more thermally stable than low melting ones, even though the intrinsic molecular stability of the high melting species is lower. Such a balance of the thermal stability of the molecular structure and that of the crystal lattice lead to homologous series which show stability trends parallel and to some which are opposed to those in solution. Although definitive results are not yet available for the aminotrinitrobenzene series, the possibility exists that the remarkable stability observed for TATB may be a function of its crystal lattice stability rather

than some intrinsic property of the molecule. Verification of this speculation awaits reliable isothermal solution and condensed-phase kinetics for DATB and TATB. If this speculation proves to be the case, it will add another factor to the design of future insensitive explosives.

## REFERENCES

- Brill, T.; James, K.J. submitted *J. Phys. Chem.*
- Minier, L.; Brower, K.; Oxley J.C. *J. Org. Chem.* 1991, 56, 3306.
- Tsang, W.; Robaugh, D.; Mallard, W.G.; J. *Phys. Chem.* 1986, 90, 5968.  
Lewis, K.E.; McMillen, D.F.; Golden, D.M.; J. *Phys. Chem.* 1980, 84, 226.  
Gonzalez, A.C.; Larson, C.W.; McMillen, D.F.; Golden, D.M. *J. Phys. Chem.* 1985, 89, 4809.  
He, Y.Z.; Cui, J.P.; Mallard, W.G.; Tsang, W.; *J. Am. Chem. Soc.* 1988, 110, 3754.
- Oxley, J.C.; Smith, J.L.; Wang, W. manuscript in preparation.
- McKinney, T.M.; Warren, L.F.; Goldberg, I.B.; Swanson, J.T., *J. Phys. Chem.* 1986, 90, 1008.  
Turner, A.G.; Davis, L.P. *J. Am. Chem. Soc.* 1984, 106, 5447.  
Shackelford, S.A.; Beckmann, J.W.; Wilkes, J.S. *J. Org. Chem.* 1977, 42, 4201.  
Suryanarayanan, K.; Capellos, C. *Int. J. Chem. Kinet.*, 1974, 6(1), 89.  
Maksimov, Yu. Ya; Sapronovich, V.F; Polyakova, N.V. *Tr. Mosk. Khim.-Tekhnol. Inst.* 1974, 83, 51.  
Dacons, J.C.; Adolph, H.G.; Kamlet, M.J. *J. Phys. Chem.*, 1970, 74, 3035.
- Sharma J.; Garrett, W.L.; Owens, F.J.; Vogel, V.L. *J. Phys. Chem.* 1982, 86, 1657.  
Rogers, R.N. *Thermochim. Acta* 1975, 11, 131.  
Zeman, S. *Thermochim. Acta.* 1979, 31, 269.
- Catalano, E.; Rolon, C.E. *Thermochimica Acta* 1983, 61, 37 and 53.  
Farber, M.; Srivastava, R.D. *Combust. Flame* 1981, 42, 165.
- Sharma, J.; Hoffsommer, J.C.; Glover, D.J.; Coffey, C.S.; Santiago, F.; Stolovy, A.; Yasuda, S. in *Shock Waves in Condensed Matter*; Asay, J.R.; Graham, R.A.; Straub, G.K., Eds.; Elsevier; New York, 1984; pp 543-546.
- Melius, Carl F. *Proceedings, 25th JANNAF Combust. Meetg., Huntsville, AL, 1988.*
- Oxley, J.C.; Kooh, A.B.; Szekeres, R.; Zheng, W. *Proceed. of ADPA Energetic Materials Technology, New Orleans, 1992*, 188.  
Oxley, J.C. Hiskey, M.A., Naud, D.; Szekeres, R. *J. Phys. Chem.* 1992, 96, 2505-2509.  
Hoffsommer, J.C.; Glover, D.J. *Combust. Flame* 1985, 59 303.  
Behrens, R.; Bulusu, S *J. Phys. Chem* 1992, 96, 8877 and 8891.
- Hiskey, M.A.; Brower, K.R.; Oxley, J.C. *J. Phys. Chem.* 1991, 95, 3955.  
Ng, W.L.; Field, J.E.; Hauser, H.M. *J.C.S. Perkin II*, 1976, 637.  
Oyumi, Y.; Brill, T.B. *Comb. Flame.* 1986, 66, 9.
- Politzer, P.; Seminario, J.M.; Bolduc, P.R. *Chem. Phys. Let.* 1989, 158(5), 463.  
Murray, J.S.; Lane, P.; Politzer, P.; Bolduc, P.R. *Chem. Phys. Let.* 1990, 168(2), 135.  
Murray, J.S.; Lane, P.; Politzer, P.; Bolduc, P.R.; McKenney, Jr., R.L. *J. Mol. Struct.* 1990, 209, 349.
- ASTM Method E 698-79 (reapproved 1984) "Standard Test Method for Arrhenius Kinetic Constants for Thermally Unstable Materials."

## DISCUSSION

JACQUES BOILEAU  
DRET, Paris, France

It would be interesting in this frame to study the stability of hexanitrostilbene (HNS) and dinitro-*p*-tolylstyrene, which are stable above 300 °C.

## REPLY BY JIMMIE OXLEY:

Yes, we have attempted to study HNS, but like TATB its poor solubility makes it difficult to examine by the techniques used in this work. I assume we would have the same problem with dinitro-*p*-tolylstyrene. Our DSC study of HNS is published (Minier, L. and Oxley, J.C., *Thermochem. Acta* 1990, 166, 241-249). Furthermore, HNS is not quite analogous to the compounds studied here because of the pi bond.

## DISCUSSION

C. P. CONSTANTINOV  
Washington State University, Pullman, Washington

In your determination of the reaction rate constants, are you not assuming first-order kinetics? What

influence would different governing mechanisms have on your trends?

**REPLY BY JIMMIE OXLEY:**

Yes, we are assuming first-order kinetics. This is a correct assumption in the case of solution-phase thermolyses. However, in the condensed-phase decompositions, the reactions can be approximated as first-order only to the first 20% decomposition. We are using only those initial data for our comparisons.

**DISCUSSION**

JIM RITCHIE

Los Alamos National Laboratory, Los Alamos, New Mexico

(1) What is the deuterium kinetic isotope effect?

(2) H-transfer is usually quite easy, but you are using methyl (Me) transfer to describe the reactivity of

anisole. Is there any precedent for transfer of methyl being easier than H transfer?

**REPLY BY JIMMIE OXLEY:**

(1) The DKIE of d3-TNT has been reported by several groups, and there are many publications including our own discussing the evidence that o-nitrotoluenes exhibit both intra- and intermolecular DKIE. In the thermolysis of neat TNT at 280 °C, we find a DKIE of 1.73. When d3-TNT is heated in benzene at 340 °C, we calculate a value of 1.59. The same rationale appears to hold for trinitroaniline. We find that it exhibits an intermolecular DKIE of 1.52 when heated in deutro-benzene at 340 °C.

(2) We are not claiming transfer of methyl is easier than H. We are saying that in trinitroanisole the tendency is to transfer methyl rather than proton. The protons of the methoxy group in trinitroanisole are not particularly acidic. Trinitroanisole does not form salts by loss of proton as does picric acid. On the other hand, one could envision nucleophilic attack at the methyl with  $^-OC_6H_2(NO_2)_3$  as the leaving group.

**SESSIONS ON**  
**UNDERWATER EXPLOSIVES**

**Cochairmen:**     **Ruth Doherty**  
                         **Naval Surface Warfare Center**

**Masatake Yoshida**  
                         **National Chemical Laboratory for Industry**



## DETONATION CHEMISTRY OF UNDERWATER EXPLOSIVES

J. S. Deiter and G. B. Wilmot  
Naval Surface Warfare Center  
Silver Spring, MD. 20903

Gaseous and solid products were recovered and analyzed from detonations of metallized explosives done in open air and in a closed bomb both in inert gas and underwater. Analyses have shown, both underwater and in an inert atmosphere, that the aluminum metal reacts primarily in the condensed phase with the oxide layer on the particle growing from the outside inward. Relationships were detected between the initial particle size distribution of the aluminum and the distribution of the oxide products. Gas analytical data for the inert gas and underwater detonations in a closed bomb show the expected trend toward increasingly fuel-rich products as the amount of aluminum in PETN/Al charges was increased.

### INTRODUCTION

A common method of increasing the total energy of an explosive formulation is to add selected metals. This has been a useful strategy in formulating compositions for air blast and underwater explosives where total energy output is an important parameter. Although addition of metal to explosive formulations improves measured overall performance, especially underwater bubble performance and blast effects,<sup>1</sup> the theoretically predicted maximum energy for metallized compositions has not been attained. Without a fundamental understanding of the chemistry of metals in an explosive environment, the probability of attaining optimum performance is in question.

Modeling the chemistry and physics of an underwater detonation is difficult due to the effect of a water environment on detonation behavior. The present models for calculating detonation pressure and detonation velocity for metallized compositions assume thermodynamic equilibria without including reaction kinetics; however, current work is expanding to include kinetics. These models cannot be used very well to predict underwater explosive performance. A shock with high peak pressure transmitted through water is more rapidly degraded than a shock with lower peak pressure but a broader pressure-time profile.<sup>2</sup>

In order to elucidate the reaction products and mechanisms of underwater detonation of explosives, detailed chemical and physical analyses were done on the detonation products of metallized compositions. While the primary focus of the study was on the mechanisms of metal reactions in underwater explosions, quantitative analysis of the gaseous products was needed to establish the mass balance and product distribution. The gas

composition data can be compared to the composition predicted by thermochemical performance codes to obtain information on freeze-out temperatures and reaction kinetics. This paper describes the experimental results on the solid and gaseous products from detonations of pentaerythritol (PETN) and aluminum (Al) compositions. The kinetic and mechanistic implications of the condensed-phase products produced and the measured gaseous product distribution as a function of the metal content of the explosive charge will be discussed.

### EXPERIMENTAL

Several analysis techniques have been used to study the condensed-phase products. A Siemens Diffractometer 500 was used for obtaining X-ray diffraction (XRD) spectra, which were used to identify and quantitate the crystalline detonation products. The XRD data also gave the relative amounts of the crystalline polymorphs of alumina. A Topcon DS-130C scanning electron microscopy (SEM) was used, at high magnification, to determine the morphological characteristics of the solid products, and a Fisons 8003 energy dispersive x-ray spectrometer (EDS) was utilized for elemental analysis of the products, including assessment of homogeneity and determination of the radial compositional gradients in single particles. A Dionex 2020i ion chromatograph (IC) system was employed to quantify the amount of unreacted metal remaining in the recovered products.

The analysis of the gaseous products was done with a Hewlett Packard 5890A gas chromatograph (GC) and by Fourier transform infrared (FTIR) spectroscopy.

The FTIR analysis serves as a check on the GC analysis for carbon monoxide and carbon dioxide and also gives the amounts of some of the low concentration organic gases such as methane. For gases such as carbon dioxide which are appreciably soluble in water, an analysis is also done on the gases recovered under vacuum from a sample of the water from the bomb. An analysis for water as a product of the detonation can not be done for the underwater shots.

## RESULTS AND DISCUSSION

A series of small PETN/Al charges containing 0-20 mass % Alcan H-5 atomized aluminum were detonated both underwater and in an inert atmosphere in the closed bomb. After detonation, the solid and gaseous products were recovered from the closed bomb and analyzed. The cylindrically shaped charges used in this study were 5/8-inch in diameter and approximately 3/4 inch in length (mass: 6-7 grams). PETN was chosen for our efforts since it is an ideal explosive with high oxygen content and it does not by itself yield any solid products during detonation.<sup>3</sup> Additionally, the aluminum in PETN/aluminum explosive formulations has recently been shown by Tao et al.<sup>4</sup> to react quickly and nearly completely at 10% aluminum content.

Earlier work on the underwater detonation of PETN/Al charges<sup>5,6</sup> was done in a 0.8 m diameter weather balloon filled with water and suspended in a 10 ft. diameter by 10 ft. high tank filled with water. This setup was an attempt to obtain approximately free-field conditions during detonation. A method utilizing a closed bomb for trapping the solid and gaseous reaction products from detonation of 6-gram charges underwater and in an inert atmosphere was developed.<sup>7</sup> Recent detonations of charges of the PETN/Al series have been done in a closed stainless steel bomb 6 in. internal diameter and 12 in. high (volume 5.6 liters). A comparison of balloon and closed bomb gas product analyses (TABLE 1) indicates that the gaseous products are very similar for the balloon and closed bomb underwater tests. The particle distributions and morphologies of the aluminum products are also quite similar. Since equivalent results were obtained, the closed bomb appears to be the method of choice since it is less time-consuming and allows more complete product recovery and consequently more accurate gas analysis results. Since detonations both in inert gas and underwater can be done in the closed bomb, product data for comparing detonations under these two conditions can be readily obtained.

TABLE 1. COMPARISON OF BALLOON VS CLOSED BOMB GAS PRODUCT ANALYSIS

PETN-90% Al-10% (Underwater Conditions)		
Gas	Balloon (%)	Closed Bomb (%)
H <sub>2</sub>	11.5	11.1
N <sub>2</sub>	27.2	25.9
CO	42.4	44.0
CO <sub>2</sub>	18.9	16.5
No. Shots	6	6

If the detonation is to be done under water, approximately 3.5 liters of distilled water is placed in the bomb. This fills approximately 60% of the bomb's volume. The charge, pressed to 96% TMD, with its EBW detonator (detonator contains pure PETN) is suspended under the water about 4 cm. above the bottom. The head space in the bomb is then flushed with an inert gas, usually argon, and filled to a pressure of about 0.7 atmospheres with the gas. If data are desired on detonation in a gas, no water is added and the inert gas is added to a pressure of approximately one atmosphere. After the charge is detonated, several samples of the gas products are recovered via a sampling valve before the bomb is opened. The condensed-phase solid products are then recovered from the opened bomb or by filtration from the water if the detonation was conducted under water.

### X-ray Diffraction

A portion of the recovered solid product from each of the charges which are listed in Table 2 was analyzed by XRD. Figure 1 is the total XRD spectrum obtained from the charge SDGW-4, containing 90% PETN and 10% Al, which was subjected to a "balloon test". Because reproducibility was good, Figure 1 is representative of the spectra obtained from the solid detonation products from all balloon tests. The most prevalent crystalline component detected in the solid detonation products, as suggested by the semiquantitative XRD analysis, was the metastable  $\gamma$ -form of  $\text{Al}_2\text{O}_3$ . No characteristic XRD lines for aluminum oxide in the stable form of  $\alpha$ - $\text{Al}_2\text{O}_3$  (corundum) were detected in the solid detonation products recovered from balloon tests. There has been very little experimental work on morphological characterization of solid detonation products; however, Price<sup>8</sup> reported that the major form of alumina from detonation of 40/38/17/5 RDX/TNT/Al/Wax underwater was determined to be  $\gamma$ - $\text{Al}_2\text{O}_3$ .

Small but distinct peaks were present at the characteristic Al lines in the XRD spectrum of solid products recovered from each balloon test which indicated that a small amount of unreacted aluminum was present. This also is shown in Figure 1. Although unreacted aluminum has been observed by other researchers in detonation product determinations,<sup>9</sup> it was in a much less highly oxidized system and the particle size of the aluminum was much larger (Alcan 400  $\mu\text{m}$ ). Therefore, unreacted Al, even in the small amounts detected, was unexpected because of the high oxygen balance of the explosive detonated in this study. Also, small particle-size (approximately 3.7  $\mu\text{m}$ ) aluminum was used in this formulation. This should also have promoted complete reaction of the aluminum.

Charge SDGW-6, containing 90% PETN and 10% Al, was detonated underwater within the 5.6 liter bomb. Charge SDGW-7, also containing 90% PETN and 10% Al, was detonated in an inert atmosphere. XRD results from solid products acquired from each test setup are shown in Figures 2 and 3. Again,  $\gamma$ - $\text{Al}_2\text{O}_3$  was the form of alumina recovered from the detonation in inert gas; while both  $\gamma$  and  $\alpha$ - $\text{Al}_2\text{O}_3$  were present in the

TABLE 2: ANALYTICAL RESULTS FROM RECOVERED DETONATION PRODUCTS

Sample ID#	Composition of Sample (%)		Test Setup <sup>a</sup>	Charge Weight (grams)	Unreacted Al (wt%)	Detonation Products
	PETN	Al				
SDGW-4 -water	90	10	1	5.46	0.21	$\gamma$ - $\text{Al}_2\text{O}_3$ ; Al
SDGW-5 -water	90	10	1	5.47	0.18	$\gamma$ - $\text{Al}_2\text{O}_3$ ; Al
SDGW-6 -inert	90	10	2	5.46	0.29	$\alpha$ -, $\gamma$ - $\text{Al}_2\text{O}_3$ ; Al
SDGW-7 -water	90	10	2	5.43	0.46	$\alpha$ -, $\gamma$ - $\text{Al}_2\text{O}_3$ ; Al
SDGW-8 -inert	80	20	2	5.95	0.49	$\alpha$ -, $\gamma$ - $\text{Al}_2\text{O}_3$ ; Al
SDGW-9 -water	80	20	2	6.23	0.74	$\alpha$ -, $\gamma$ - $\text{Al}_2\text{O}_3$ ; Al
SDGW-10 -inert	80	20	2	6.00	0.38	$\alpha$ -, $\gamma$ - $\text{Al}_2\text{O}_3$ ; Al
SDGW-11 -water	80	20	2	6.20	0.93	$\alpha$ -, $\gamma$ - $\text{Al}_2\text{O}_3$ ; Al

<sup>a</sup>1 = Balloon Test; 2 = closed bomb

products from the underwater detonation;  $\alpha$ - $\text{Al}_2\text{O}_3$  was more prevalent in the products from underwater detonation. Additionally, the detonation products from both charges contained small quantities of unreacted Al, with more Al present in the solid products from the underwater detonations. The presence of a larger quantity of unreacted Al in the solid products recovered from the charge detonated under water may be related to the confinement of the charge; in the presence of water, the sustained detonation temperature may not be sufficient to allow total reaction of the metal.

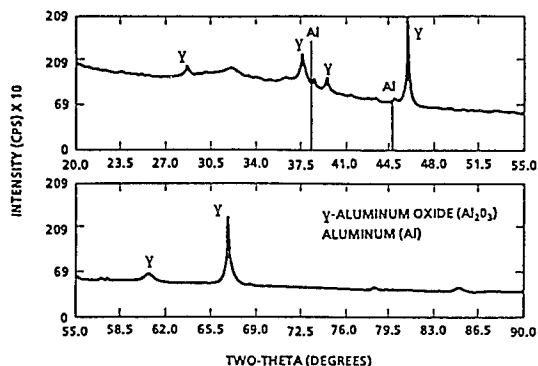


FIGURE 1. XRD SPECTRUM OF SOLID PRODUCTS FROM SDGW-4 (90/10 PETN/Al) DETONATED IN AN INERT ATMOSPHERE

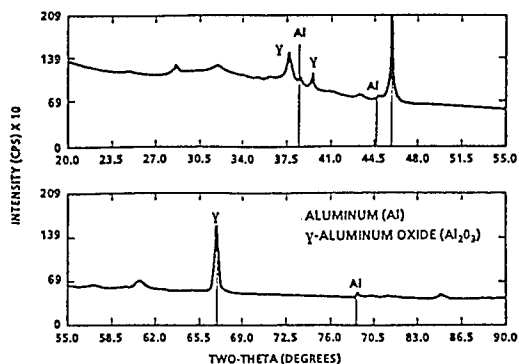


FIGURE 2. XRD SPECTRUM OF SOLID PRODUCTS FROM SDGW-6 (90/10 PETN/Al)

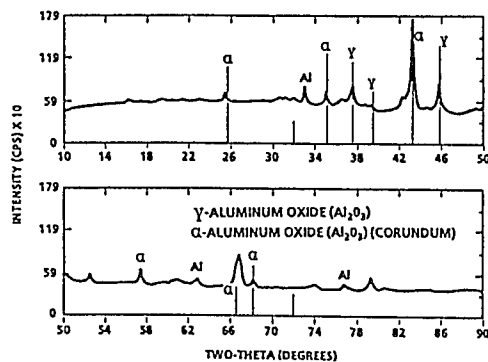


FIGURE 3. XRD SPECTRUM OF SOLID PRODUCTS FROM SDGW-7 (90/10 PETN/Al) DETONATED UNDER WATER IN CLOSED BOMB

The solid residue from specimens SDGW-8 and SDGW-9, containing 80/20 PETN/Al, which were detonated underwater and in an inert atmosphere within the closed bomb, exhibited XRD results, shown in Figures 4 and 5, which were similar to the data obtained from residue of charges containing 10% Al. However, a small increase in the amount of unreacted Al was detected in these specimens containing 20% metal when compared to the charges containing 10% metal. In addition, charge SDGW-9, which was detonated under water, exhibited approximately 50% more unreacted Al than charge SDGW-8, which was detonated in an inert atmosphere. Copper and copper oxide were identified in the residue from each charge containing 20% Al. These products are from the copper sleeve surrounding the PETN detonator. The copper products were not able to be filtered from the residue after detonation because they were considerably smaller in size than the copper products produced from detonation of charges containing 10% metal.

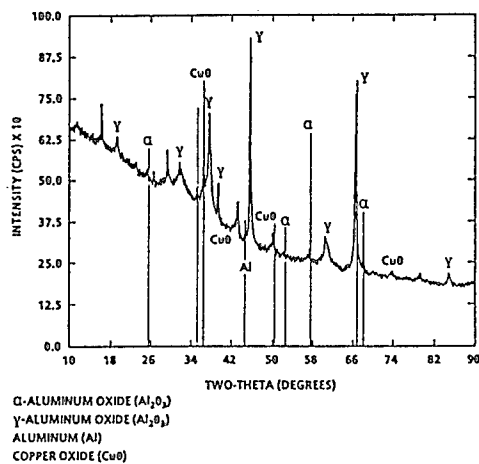


FIGURE 4. XRD SPECTRUM OF SOLID PRODUCTS FROM SDGW-8 (80/20 PETN/Al) DETONATED IN INERT ATMOSPHERE IN CLOSED BOMB

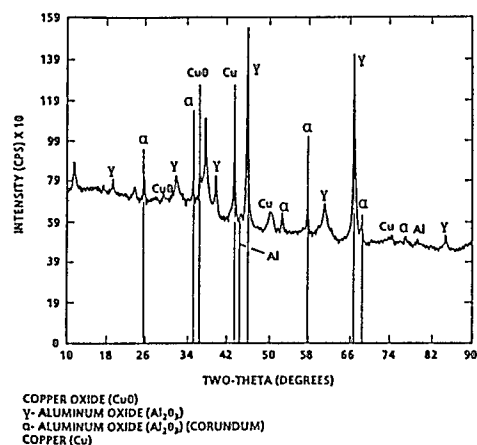


FIGURE 5. XRD SPECTRUM OF SOLID PRODUCTS FROM SDGW-9 (80/20 PETN/Al) DETONATED UNDER WATER IN CLOSED BOMB

### Scanning Electron Microscopy

Morphology studies were conducted with the use of a scanning electron microscope (SEM). Normally, the process for preparing specimens for analysis with SEM requires the application of a conductive surface coating which is necessary to eliminate or reduce the electric charge which builds up rapidly in a poorly conducting specimen when scanned by a beam of high-energy electrons from the SEM electron gun. However, the conductive coating interferes with the detection of surface characteristics at high magnification because there is the possibility that it could mask true surface characteristics. Additionally, EDS includes elements of the conductive surface coating in the spectra of the solid products. Therefore, none of the solid detonation products was subjected to a conductive coating. In order

to proceed with the analysis, a quad backscatter detector, which is an accessory to the SEM, was used for studying the surface of the samples. It uses atomic number contrast of the elemental components within the specimen to produce a SEM image without the use of high energy. (When the composition of the material under analysis is composed of an element or elements of decidedly different atomic number, the degree of backscatter or absorption becomes smaller with increasing element density).

Morphological characteristics of the solid reaction products from every PETN/Al charge detonated underwater or in an inert atmosphere within the closed bomb or the "balloon test" were quite similar. The solid products were composed of relatively spherical particles with cratered, porous surfaces. Some particles were agglomerated or fused together. Figures 6-9 are representative of them. The particles produced from the detonation had an average diameter of  $5.4\mu m$  and were larger than the Al starting material ( $3.7\mu m$  average particle size).

These morphological characteristics suggest that the particles were produced at both high temperature and pressure by condensed-phase oxidation of the original Al particles. For comparison, aluminum particles were extracted from the molding powder which was used to produce all the explosive charges. As shown in Figure 10, they had the smooth, spherical morphology typical of atomized aluminum particles.

In order to study the internal morphology of individual particles from the products of a detonation, several particles from the detonation products of SDGW-7, recovered from detonation underwater in the closed bomb, were cross-sectioned. Their characteristics are shown in Figure 11. The observation was made that the particles, with a diameter of approximately  $5\mu m$  or larger, contained a non-porous solid inner core which was surrounded by a porous composition. Particles with a diameter less than approximately  $4\mu m$  were porous; no solid inner core was observed. These observations suggest that the particle size of the Al starting material had an effect on the morphology of solid reaction products produced from an underwater detonation.

Because the size of the aluminum starting material appeared to be different from that of the products produced in either an underwater or closed bomb detonation, a particle size analysis was conducted. 2000 particles from products recovered from charges detonated either in an inert atmosphere or underwater in the closed bomb were counted and measured. The average diameter as well as particle size ranges are reported in Table 3.

These results indicated that charges containing 90/10 PETN/Al or 80/20 PETN/Al detonated either underwater or in an inert atmosphere produce morphologically similar products; however, the average diameter of the products appears to be dependent upon the test condition since particles produced in the underwater detonation were larger than those produced in an inert atmosphere. A possible cause for the

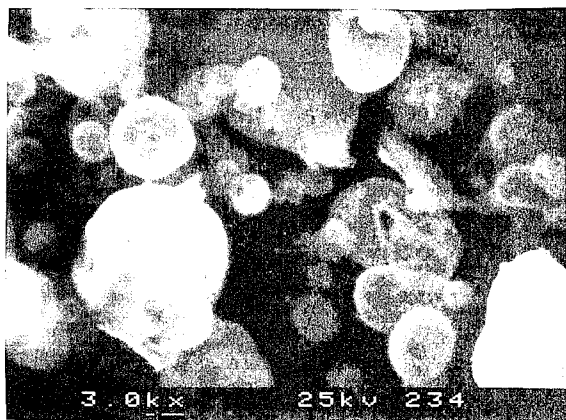


FIGURE 6. PRODUCTS FROM SDGW-4 (90/10 PETN/Al) RECOVERED FROM BALLOON TEST



FIGURE 7. PRODUCTS FROM SDGW-6 (90/10 PETN/Al) DETONATED INERT IN CLOSED BOMB

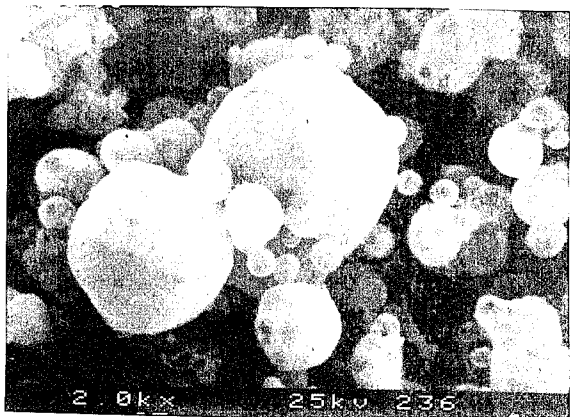


FIGURE 8. PRODUCTS FROM SDGW-8 (80/20 PETN/Al) DETONATED INERT IN CLOSED BOMB



FIGURE 9. PRODUCTS FROM SDGW-9 (80/20 PETN/Al) DETONATED UNDER WATER IN CLOSED BOMB

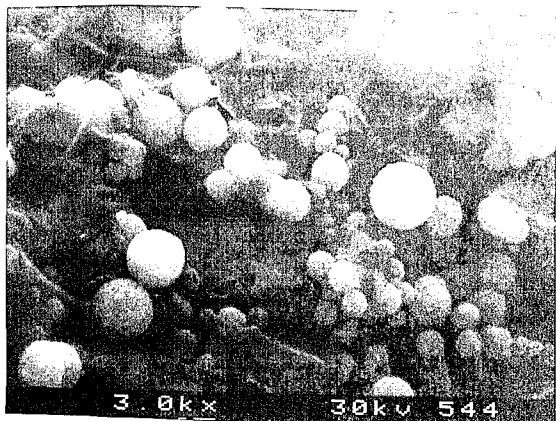


FIGURE 10. ALUMINUM STARTING MATERIAL USED FOR ALL CHARGES

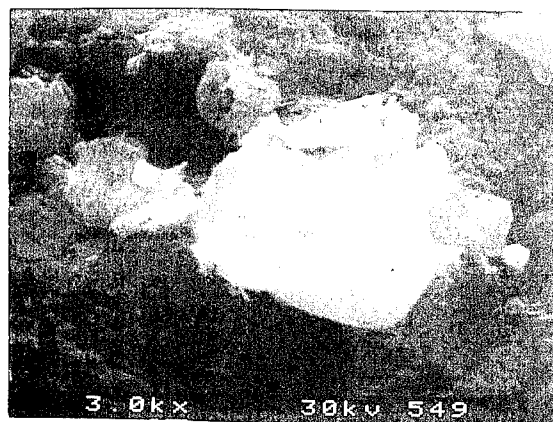


FIGURE 11. CROSS-SECTIONED PRODUCTS FROM SDGW-7 (90/10 PETN/Al)

difference is that the recovered products have been more damaged by impact with the inside of the closed bomb during detonation in an inert gas.

TABLE 3. AVERAGE DIAMETER OF ALUMINUM POWDER AND SOLID PRODUCTS (Based on 2,000 particles)

Sample	Average Diameter ( $\mu\text{m}$ )	Range ( $\mu\text{m}$ )
Al powder	3.7	0.7 - 6.3
SDGW-8 -inert	4.7	1.4 - 13.8
SDGW-7 -water	5.3	1.2 - 12.3
SDGW-9 -water	5.1	1.0 - 11.0

The solid detonation products produced in an underwater environment has an average diameter which is approximately 30% larger than the Al starting material. The particles are larger since they are going from pure Al to  $\text{Al}_2\text{O}_3$ , which is also less dense than Al. These results indicate that a water environment sufficiently affects the reaction of the aluminum component in an explosive so that low density spherically shaped particles are formed. The porosity within and on the surface of the particles may be caused by outgassing during the cooling process. Apparently this is size and temperature dependent, because, from the reported observations, the aluminum starting material with an approximate diameter greater than  $4\mu\text{m}$  may contain a solid unmelted core surrounded by various reaction products in a thick porous layer after detonation.

A comparison was made between the measured particle distribution of the Al starting material and the distribution of products recovered from SDGW-7, which contained 90/10 % PETN/Al. The plotted data are shown in Figure 12. It indicates that the shape of the distributions are similar. If all the Al metal in the charge would react during detonation and transform into  $\text{Al}_2\text{O}_3$ , the addition of oxygen to Al should add approximately 30% to the mass of Al. Therefore, if the particle distribution of the Al powder were increased by 30%, the plotted data would be similar to the distribution represented by circles in Figure 12. This plot is quite similar to the data obtained for the products produced in inert gas and underwater in the closed bomb. There appears to be a relationship between the particle sizes of Al starting material and the resulting detonation particles

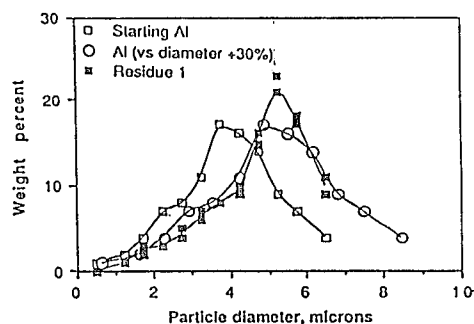


FIGURE 12. OBSERVED PARTICLE DISTRIBUTIONS FROM UW DETONATION OF SDGW-7 (90/10 PETN/Al) AND AL POWDER

in PETN charges containing 10% metal which have been detonated underwater and in inert gas.

### Energy Dispersive X-ray Spectrometry

In order to determine the elemental composition and homogeneity of recovered solid products from an underwater detonation, EDS techniques were employed. With the SEM in a spot mode of operation, (scanning an area of only one pixel) at a magnification of 3,000X, an EDS spectrum was obtained at every  $1\mu\text{m}$  interval across the cross-sectioned particle, shown in Figure 11, from products of SDGW-7. The particle had a diameter of  $8\mu\text{m}$ , so the interval at  $4\mu\text{m}$  was considered the center of the particle. Also, the exterior of the particle was analyzed. Then the ratio of peak heights from Al and oxygen (O) at each interval was calculated in order to determine the relative amount of Al present in a specific location across the diameter of the particle.

The plotted EDS results, shown in Figure 13, indicate the significant variations in the amounts of Al to O from one interval to the next. The study showed evidence that an internal core (at  $4\mu\text{m}$ ) was composed primarily of aluminum with very little oxygen existing within the particle. This was very different from the exterior of the particle, which was significantly richer in oxygen and lower in aluminum ( $0\mu\text{m}$  and  $8\mu\text{m}$  in Figure 13). Due to the nature of the electron beam interaction volume within the particle, the  $1\mu\text{m}$  analysis intervals overlapped slightly. Therefore, it was possible that a much sharper rise in the data at the core of the particle could have been obtained. Also, because the particle was randomly cross-sectioned, it is possible that the exact center or core of the particle was not analyzed, which could have further emphasized the rise in the plotted data. This procedure was repeated with similar results on particles from other charges which had a diameter of  $6\mu\text{m}$  or larger. When EDS techniques were applied to cross-sectioned particles with an average diameter of less than approximately  $4\mu\text{m}$ , the peak height ratio was flat across the width of the particles, indicating that no core area was present which was high in Al and low in O. Also, these particles were porous throughout their entire diameter.

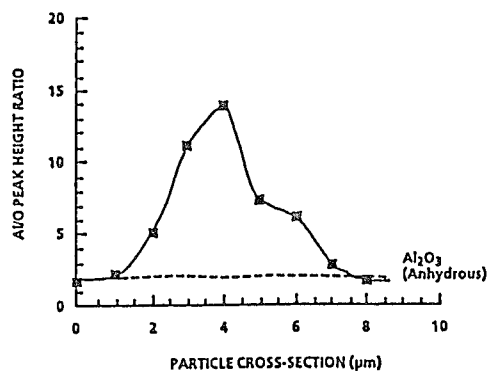


FIGURE 13. EDS Al/O PEAK HEIGHT RATIOS ACROSS  $8\mu\text{m}$  RESIDUE PARTICLE FROM SDGW-7 (90/10 PETN/Al)

A standard composition of anhydrous aluminum oxide ( $\text{Al}_2\text{O}_3$ ) was subjected to the same EDS conditions as detonation products from the closed bomb tests. Then, a comparison was made between the standard and the EDS spectrum obtained from the exterior of a typical recovered particle from the detonation of charge SDGW-11. The dashed line in Figure 13 shows the Al/O peak height ratio of anhydrous aluminum oxide. It was found that the spectrum from the surface of the particle was virtually identical to the alumina standard. Therefore, the EDS data indicate that the exterior of the product particles was  $\text{Al}_2\text{O}_3$ .

### Ion Chromatography and Gas Chromatography

The amount of unreacted Al in the solid products was determined by treatment of a 3-mg sample of solid products with 0.5 mL 1M NaOH in a septum-sealed vial. The amount of hydrogen generated was determined by gas chromatography, under chromatographic conditions described in Reference 3, and compared to the amount of hydrogen produced by a 0.5-mg sample of pure Al powder similarly treated with NaOH. The total aluminum content (Al metal and  $\text{Al}_2\text{O}_3$ ) were determined by ion chromatography after the aluminum products were put into solution. Table 2 shows the amount of unreacted Al determined, as a weight percent of the total aluminum.

Less than 1 mass % of unreacted Al was present in recovered products from the series of explosive charges after detonation both under water and in an inert atmosphere within a conventional steel bomb. The amounts of unreacted Al appeared to increase proportionally as the amount of Al in the PETN charge was increased. In addition, the amount of unreacted metal from charges detonated under water was consistently slightly greater than from charges detonated in an inert atmosphere in the closed bomb.

### Gas Analytical Data

Some trends in the composition of the gaseous products as a function of aluminum content and detonation environment (underwater vs inert gas) have been identified and compared to theoretical calculations. Figure 14 compares the TIGER code calculated  $\text{CO}/\text{H}_2$  constant volume ratios (points connected by lines in Figure 14) with the measured ratios of the detonation gases recovered from 90/10% PETN/Al charges. The experimental and calculated data appear to be quite similar.

The gas analytical data for both the inert gas and underwater detonations show the expected trend toward increasingly fuel-rich products as the amount of aluminum in the PETN/Al charges is increased. No significant solid carbon residues have been found and all the carbon goes to gaseous products. This gives us the amount of water produced and allows us to determine the oxygen distribution from this quantity, from the analysis of the solid products (aluminum oxide and aluminum) and from the gas analysis. An estimate of the freeze-out

temperature for the shifting water-gas equilibrium ( $\text{CO}_2 + \text{H}_2 = \text{CO} + \text{H}_2\text{O}$ ) as the gaseous products expand and cool can be obtained from these results. The data obtained to date indicate that the water-gas equilibrium (freeze-out temperature) occurs at approximately 2,000 - 2,300 °K with a trend towards lower temperatures with increasing aluminum content.

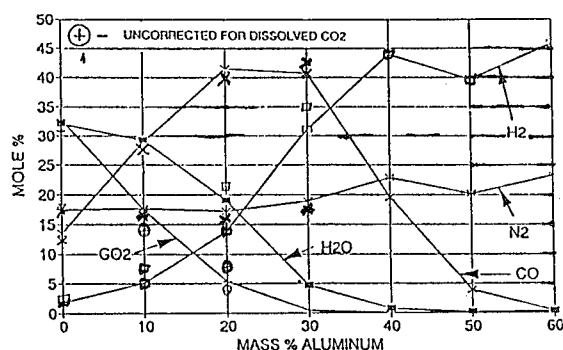


FIGURE 14. DETONATION GASES FROM PETN/Al: CALCULATED USING TIGER CODE (POINTS CONNECTED BY LINES) AND MEASURED

### CONCLUSIONS

XRD results indicated that, in the closed bomb, the major alumina product formed during either underwater or inert atmosphere detonations was  $\gamma\text{-Al}_2\text{O}_3$ . Additionally, a small quantity of  $\alpha\text{-Al}_2\text{O}_3$  (corundum) was detected.

It has been shown by XRD, IC, and GC that a small quantity of unreacted Al metal also was recovered in detonation products from all charges containing 10-20% Al detonated either underwater or in an inert atmosphere in a conventional steel bomb. The amount of unreacted metal increased as the mass % of metal in the charge increased. In addition, the quantity of unreacted Al metal was consistently greater in the products from underwater detonations than in products from charges detonated in an inert atmosphere.

SEM data showed that during underwater detonations, the solid reaction products formed which were composed of relatively spherical particles with a cratered, porous surface.

EDS results indicated that during an underwater detonation the explosive charges used in this study produced two compositionally different types of solid products. One type was composed solely of alumina, while the other type was composed of a non-porous core which was high in Al and low in O surrounded by a porous layer composed primarily of  $\gamma\text{-Al}_2\text{O}_3$ .

The particle size analyses indicated that the average diameter of the recovered products from underwater detonation was 5.4  $\mu\text{m}$ . This was 30% greater than the average diameter of 3.7  $\mu\text{m}$  for the aluminum starting material. The products from detonation which were approximately 5  $\mu\text{m}$  or larger contained a non-porous inner core surrounded by a porous layer. Particles with a diameter less than 4  $\mu\text{m}$  were porous; no solid inner core was observed. EDS results showed for the larger particles that the core had a higher aluminum/oxygen ratio while the porous region was  $\gamma\text{-Al}_2\text{O}_3$ . Smaller particles showed only  $\gamma\text{-Al}_2\text{O}_3$  with no unreacted aluminum in their centers.

These analyses have convincingly shown, for both underwater and an inert atmosphere, that the aluminum metal reacts primarily in the condensed phase with the oxide layer on the particle growing from the outside inward. The experimental results which support this conclusion are: (1) the close relationship found between the initial particle size distribution of the aluminum and the size distribution of the oxide products and (2) the increase in aluminum/oxygen ratios in the interior of the larger particles.

## REFERENCES

1. Christian, E. A., "The Contribution of Aluminum to the Effectiveness of an Explosion. I. Underwater Performance of One-pound Charges," NAVORD 3760, 1 August 1954.
2. Bjarnholt, G. and Holmberg, R., "Explosive Expansion Works in Underwater Detonation," Sixth Symposium (International) on Detonation, August 1976.
3. Ornellas, D. L., "Calorimetric Determination of the Heat and Products of Detonations", Ninth Symposium on Detonation Vol. III, Portland, Oregon, September 1989.
4. Tao, W.C., Tarver, C. M., Breithaupt, D. R., McGuire, R. R. and Ornellas, D. L., 14th Symposium on Explosives and Pyrotechnics, Franklin Research Center, Burlingame, CA., 13-15 February 1990.
5. Carlson, D., Doherty, R., Ringbloom, V., Deiter, J. S., and Wilmot, G. B., 9th Symposium (International) on Detonation, 31 August 1989.
6. Carlson, D., Deiter, J. S., and Doherty, R., 21st International ICT Conference, Fraunhofer-Institut für Chemische Technologie, Karlsruhe, Germany, July 1990.
7. Deiter, J. S., and Wilmot, G. B., "Composition of Solid Products from Underwater Detonation of Pentaerythritol Tetranitrate - Aluminum Explosives," 21st International Annual Conference of Fraunhofer-Institut für Chemische Technologie (ICT), V-19, July 1990.
8. Price, D., "Composition of Solid Residues from Aluminized Explosives," NAVORD Report No. 4087, 16 Sept 1955 (declassified 6/16/76).
9. Volk, F., "Detonation Gases and Residues of Composite Explosives", Journal of Energetic Materials Vol. 4, 93-113 (1986).

## DISCUSSION

DR. RONALD E. BROWN

Titan Corporation, Research & Technology, Pleasanton, California

Would you expect some percentage of aluminum particle fracture as a result of the isothermic oxidation reaction, and thus some particle size reduction (adjusted for density changes of the product)?

## REPLY BY J. SCOTT DEITER:

The size of the closed bomb may influence the reaction and resultant physical changes. There are plans to investigate this possible effect in larger bombs. We have not observed particle "fracture"; we have observed Al particle "melting." The particle distributions increase during the reaction as Al changes to  $\text{Al}_2\text{O}_3$ . The data are contained in the paper.

## DISCUSSION

DR. ROBERT SARRACINO

AECI Explosives, Modderfontein, South Africa

Have you compared your results with those from combustion studies--if there are any combustion studies?

## REPLY BY J. SCOTT DEITER:

Yes, we have looked at results of combustion studies by Dr. W. Tao (Lawrence Livermore), as well as those of Dr. Volk (ICT, Germany). Our gas analysis data compare favorably with data on PETN-Al reactions studied by Dr. Volk.



## **DISCUSSION**

**ANDREW VICTOR**

Victor Technology, Ridgecrest, California

Between the balloon tests and your bomb tests (both in water and in inert gas), have you found any correlation between quasi-static pressure (or pressure reverberations) and the per cent of Al oxidized or the depth of

oxidation in individual particles?

**REPLY BY J. SCOTT DEITER:**

For identical PETN-Al charges, we have consistently seen a slight increase in unreacted Al in those tests conducted under water. This may be due to confinement of the charge in an underwater test configuration.

## UNDERSTANDING COMPOSITE EXPLOSIVE ENERGETICS: IV. REACTIVE FLOW MODELING OF ALUMINUM REACTION KINETICS IN PETN AND TNT USING NORMALIZED PRODUCT EQUATION OF STATE

William C. Tao, Craig M. Tarver, John W. Kury, Chet G. Lee, and Donald L. Ornellas  
Chemical Sciences Division  
High Explosives Application Facility (HEAF)  
Lawrence Livermore National Laboratory  
Livermore, California 94550

Using Fabry-Perot interferometry techniques, we have determined the early time rate of energy release from detonating PETN and TNT explosives filled with 5 to 20 wt% of either 5  $\mu\text{m}$  or 18  $\mu\text{m}$  spherical aluminum (Al). From the measured particle velocity data, we are able to infer the reaction rate of aluminum with the detonation products, and calculate the extent of reaction at 1-3  $\mu\text{s}$  after the detonation. All of the metal in PETN formulations filled with 5 wt% or 10 wt% of either 5  $\mu\text{m}$  or 18  $\mu\text{m}$  aluminum reacted within 1.5  $\mu\text{s}$ , resulting in an increase of 18 - 22% in energy compared to pure PETN. For TNT formulations, between 5 to 10 wt% aluminum reacts completely within the same timeframe. A reactive flow hydrodynamic code model based on the Zeldovich-von Neumann-Doring (ZND) description of the reaction zone and subsequent reaction product expansion (Taylor wave) is used to address the reaction rate of the aluminum particles with detonation product gases. The detonation product JWL equation of state is derived from that of pure PETN using a parametric normalization methodology.

### INTRODUCTION

Over the last three decades, there has been a consistent effort in the energetic community in trying to understand the fundamental chemical, thermodynamic, and hydrodynamic interactions between the different components in a composite explosive.<sup>1-5</sup> These energetic mixtures, typically used for cratering and fragmentation, consist of a high-solids loading of fuels (e.g. HMX, RDX, TNT), oxidizers (ammonium perchlorate, sodium nitrate), metallic additives (aluminum, boron, zirconium), and binder/plasticizer (viton, estane).

Several key experiments have shown the effect of particle size, solids loading percent, confinement, and temperature on the energy release rate. Finger et al.<sup>2</sup> measured the late time energy release from the expansion of a copper cylinder filled with different particle size of AP. Their results illustrated that within a constant confinement, a given cylinder diameter, the formulation with the larger AP particle size yielded a slower rate of energy release. As

the cylinder diameter increased, the equilibrium energy from a formulation with a constant AP particle size increased proportionately. The rate of energy release also increased with larger confinement. McGuire et al.<sup>3</sup> studied the effect of detonation temperature on the rate of reaction and energy release. By varying slightly the composition of three explosives, they were able to change the detonation temperature dramatically, while maintaining a similar expansion isentrope (i.e., similar Chapman-Jouguet pressure and volume) for each of the formulation. The rate of energy release is faster and the equilibrium energy is higher for the composition with a higher detonation temperature.

During the last several years, we have performed a systematic study of the reaction rate of aluminum metal additives in different composite explosive matrices.<sup>6,7</sup> Our goal is to develop a comprehensive composite explosive model that can predict the effect of particle size, metal to oxygen ratio, and other formulation related parameters on the energy release profile. In our study, we simplify the problem by choosing a bicomponent composite explosive consisting of PETN or TNT mixed with either 5 or 18  $\mu\text{m}$  spherical aluminum particles. In each case, the detonation products of the monomolecular explosive serve as the oxidizer for the reacting aluminum fuel.

\* LLNL work performed under USDOE Contract W-7405-Eng-48 with funding support from the DOE/DOD Office of Munitions.

In the case of PETN, the high detonation temperature serves to increase the mass transport rate and shorten the aluminum reaction timescale. More important, the immediate conversion to detonation products in PETN due to a very narrow reaction zone (<1 ns) allows us to study the reaction between aluminum and the PETN detonation products without having to consider the nature of the reaction zone, decomposition rates, and possible reaction with the intermediate detonation products.<sup>6-8</sup> The moderate reaction zone of TNT (~120 ns), along with a poorer aluminum to oxidizer ratio in the detonation product mixture, should drastically affect the rate of energy release. In this work we measure the interface particle velocity of the metal-filled mixture using Fabry-Perot laser interferometry.<sup>9</sup> The hydrodynamics is subsequently analyzed by a reactive flow model based on the Zeldovich-von Neumann-Doring (ZND) description of the reaction zone and subsequent reaction product expansion (Taylor wave).<sup>10</sup> This model provides a basis for inferring the early time reaction rate of the aluminum particles with the detonation products as well as the extent of aluminum oxidation. To test the validity of the model, we apply the results to predict the hydrodynamics of a different geometry, in which we measure the acceleration history of a tantalum (Ta) plate by the PETN/Al and TNT/Al composite explosives.

#### MATERIALS PREPARATION AND FABRY-PEROT INTERFEROMETRY

The monomolecular explosive, PETN and TNT, are intimately mixed with the 5 and 18  $\mu\text{m}$  aluminum by acetone slurry coating, and the resulting powder pressed into 25.4 mm diameter right cylindrical pellets with thicknesses measuring 12 mm and 18 mm. These dimensions were chosen such that the detonation behavior within the experimental timeframe of several  $\mu\text{s}$  will reach steady state and remains one-dimensional in nature without perturbations from radial rarefactions.<sup>6</sup> All of the pellets are pressed to greater than 95% of the theoretical maximum density.

Each experiment consists of shock initiating the pellet with a thin Kapton flyer accelerated by a capacitor-discharge electric gun, and measuring either the interface particle velocity or the Ta metal free-surface velocity with Fabry Perot Laser Interferometry.<sup>9,11</sup> The reflective interface for the particle velocity measurement is a thin layer of gold sandwiched in between the explosive pellet and a NaCl or LiF crystal, the latter used as an acoustic impedance matching barrier to minimize axial rarefaction and reflected shocks. For the metal acceleration experiments, we replace the gold and impedance matching crystal with a Ta plate with thicknesses of 0.262 mm or 0.522 mm scaled

to the different pellet thicknesses, 12 mm or 18 mm, respectively.<sup>10</sup> Table I summarizes the explosive formulations and the experimental details for the impedance-matched particle velocity measurements and the Ta plate-push experiments. Figure 1 illustrates schematically the Fabry-Perot experiment setup.

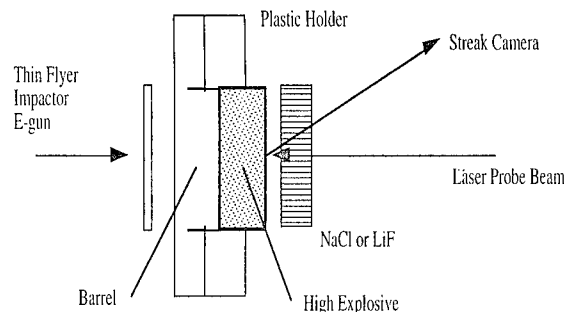


**FIGURE 1. CONFIGURATION OF THE FABRY-PEROT EXPERIMENT FOR MEASURING THE INTERFACE PARTICLE VELOCITY OF AN EXPLOSIVE PELLET**

**TABLE 1. PETN/Al AND TNT/Al FORMULATIONS AND EXPERIMENTAL DETAILS**

Name	HE	HE/Al (wt%)	Al ( $\mu\text{m}$ )	Xstals	HE (mm)	Ta (mm)
RX40AA	PETN	95/5	5	NaCl	18	0.522
RX40AB	PETN	90/10	5	NaCl	18	0.522
RX40AC	PETN	80/20	5	NaCl	18	0.522
RX40AF	PETN	95/5	18	LiF	12	0.262
RX40AG	PETN	90/10	18	LiF	12	0.262
RX40AH	PETN	80/20	18	LiF	12	0.262
RX40CA	TNT	95/5	5	NaCl	12	0.262
RX40CB	TNT	90/10	5	NaCl	12	0.262
RX40CF	TNT	95/5	18	LiF	18	0.522
RX40CG	TNT	90/10	18	LiF	18	0.522

#### COMPOSITE EXPLOSIVE MODEL DEVELOPMENT

The Ignition and Growth reactive flow model has been applied to shock initiation and detonation of many solid explosives.<sup>10</sup> The model uses two Jones-Wilkins-Lee (JWL) equations of state (EOS), one for the unreacted explosives and one for the reaction products of the form:

$$\text{JWL Equation of State} \quad (1)$$

Hugoniot States

$$P = A(1 - \omega/R_1 V)e^{-R_1 V} + B(1 - \omega/R_2 V)e^{-R_2 V} + \omega E/V,$$

where  $E = E_0 + 1/2P(1 - V)$  and  $V = \text{relative volume}$ ;

### Isentrope

$$P_S = A e^{-R_1 V} + B e^{-R_2 V} + C_V / V^{\omega+1},$$

where  $P$  is pressure,  $V$  is relative volume, and  $A, B, R_1, R_2, \omega$ , and  $C_V$  are constants. The reaction rate law is of the form:

$$\frac{dF}{dt} = I(1-F)^b(\rho/\rho_0 - 1 - a)^x + G_1(1-F)^c F^d P^y + G_2(1-F)^e F^g P^z, \quad (2)$$

where  $F$  is the fraction of explosive reacted,  $t$  is the time,  $\rho$  is the current density,  $\rho_0$  is the initial density,  $P$  is the pressure, and  $I, G_1, G_2, a, b, x, c, d, y, e, g$ , and  $z$  are constants. For Zeldovich-von Neumann-Doring (ZND) type detonation waves, the first term in Equation (2) ignites some of the explosive during shock compression. The second term represents the rapid decomposition of the explosive forming the reaction product gases  $\text{CO}_2, \text{H}_2\text{O}$ , and  $\text{N}_2$ . The third term models the relatively slow diffusion controlled reactions which follow the main reaction such as solid carbon coagulation or, in the case of aluminized explosives, the oxidation of aluminum particles by the product gases ( $\text{H}_2\text{O}, \text{CO}_2$  and perhaps  $\text{CO}$ ). For PETN/Al formulations, PETN has a very fast reaction (the reaction zone thickness is less than a couple nanoseconds, the resolution of the Fabry-Perot interferometer) so its energy release is modeled with a large value of  $G_1$ , and the aluminum reaction with the detonation products is modeled by the third term in the equation with  $e=g=z=1$  as in a diffusion controlled reaction. For TNT/Al, the pure TNT detonation reaction zone has been studied previously<sup>13,14</sup> and is approximately 120 nanoseconds long. Therefore the second term in Equation (2) for TNT/Al formulations is the usual TNT reaction rate, and the third term models the diffusion controlled reaction between the aluminum and the TNT detonation products. Since the detonation temperature of PETN is higher than that of TNT, and its products are better oxidized, it is expected that the oxidation rate of aluminum by PETN's reaction products is faster than for TNT's reaction products.

### CONSISTENT ESTIMATION OF JWL PRODUCT EQUATION OF STATE

Since we cannot measure directly the detonation products or the partially reacted aluminum composition within the reaction zone or at any stage during the expansion, we need a method to choose the parameters of the product JWL EOS, outlined in Equation (1), to consistently represent the metal filled explosive's pressure and energy over a wide range of volume expansion.

An explosive with a detonation product JWL EOS

proven to be accurate over a wide range of pressure and volume expansion can serve as a reference for choosing the JWL EOS parameters for the metal filled explosive. The product JWL EOS for PETN, derived from one-dimensional early time experiments, has been found applicable over a wide range of volume expansion and input pressure. It is therefore reasonable to use the JWL EOS for pure PETN as a reference for estimating the product equation of state for metal filled explosives. Table 2 illustrates the result of a TIGER thermodynamic calculation for PETN with 5 wt% of aluminum loading. For volume expansions less than 1.5, we are interested in the pressure difference between PETN and the metal filled explosive. Similarly, we calculate the energy release from the PETN/Al formulation and compare it with that from pure PETN, as illustrated in Table 3, for volume expansions greater than 1.5. The next step in estimating the new product JWL EOS for this PETN/Al mixture involves adjusting the parameters of the PETN JWL EOS and fitting the change in pressure and energy release, until a consistent set of JWL parameters are found that can simultaneously account for both the change in pressure and energy release over the entire volume expansion range. Table 4 summarizes the new JWL parameters for several PETN/Al formulations.

**TABLE 2. TIGER THERMODYNAMIC EQUILIBRIUM CALCULATION OF THE EARLY TIME PRESSURE OUTPUT FROM DETONATING PETN/AL LOADED WITH 5 WT% OF ALUMINUM. THE PRESSURE IS THEN REFERENCED TO THAT OF PURE PETN AT THE SAME VOLUME EXPANSIONS UP TO  $V/V_0 = 1.4$ .**

BKWR Equation of State (5 wt% Al fully reacted)			
	PETN (exp.)	PETN	PETN/Al
$\rho$ (g/cc)	1.763	1.763	1.775
$D$ (mm/ $\mu$ s)	8.27	8.33	8.12
$P_{cj}$ (kbar)	315	306	307
$T_{cj}$ (K)		3337	3767
$V_{cj}$		0.424	0.414
$V_{cj}/V_0$		0.747	0.734
Pressure on CJ Isentrope (Kbar)		$\Delta P$ for PETN/Al relative to PETN	
$V/V_0$	PETN	PETN/Al	(% diff.)
0.65	467.6	441.6	-5.6
0.70	371.1	352.2	-5.1
0.75	301.9	289.9	-4.0
0.80	250.7	243.8	-2.8
0.85	212.1	207.9	-2.0
0.90	181.7	179.3	-1.3
0.95	157.2	155.7	1.0
1.00	136.9	135.9	-0.7
1.20	83.4	83.0	-0.5
1.40	54.2	54.6	-0.7

TABLE 3. TIGER THERMODYNAMIC EQUILIBRIUM CALCULATION OF THE LATE TIME ENERGY RELEASE FROM DETONATING PETN/Al LOADED WITH 5 WT% OF ALUMINUM. THE ENERGY OUTPUT IS THEN REFERENCED TO THAT OF PURE PETN AT THE SAME VOLUME EXPANSIONS FROM  $V/V_0 = 1.5$  TO 6.5.

BKWR Equation of State (5 wt% Al fully reacted)						
$V/V_0$	PETN	PETN/Al	Delta E (% diff.)	PETN/Al Delta E (Cal/g)	Delta E (Kcal/cc) PETN	Delta E (Kcal/cc) PETN/Al
1.5	1.0	1.010	1.0	730.0	1.283	1.296
2.2	1.0	1.014	1.4	996.1	1.744	1.768
4.1	1.0	1.023	2.3	1214.0	2.107	2.155
6.5	1.0	1.030	3.0	1301.0	2.243	2.309
Amb.	1.0	1.085	8.5	1560.0	2.553	2.769

TABLE 4. SUMMARY OF THE MODIFIED JWEL PARAMETERS FOUND FROM FITTING SIMULTANEOUSLY THE DIFFERENCE IN THE PRESSURE OUTPUT AND ENERGY RELEASE FROM PETN/Al COMPOSITE EXPLOSIVES. THE PRODUCT JWEL EQUATION OF STATE IS GENERATED FOR A DETONATION PRODUCT SET IN WHICH ALL OF THE ALUMINUM FULLY REACTED.

JWL Product Equation of State				
	PETN	PETN/Al (95/5)	PETN/Al (90/10)	PETN/Al (80/20)
Density (g/cc)	1.763	1.775	1.800	1.893
D (mm/ $\mu$ s)	8.27	8.10	8.00	7.88
P <sub>cj</sub> (Kbar)	315	320	325	320
Gamma	2.828	2.639	2.545	2.673
E <sub>0</sub>	0.108	0.120	0.120	0.123
R <sub>1</sub>	6.00	4.90	4.50	5.55
R <sub>2</sub>	2.60	2.30	2.00	2.23
w	0.57	0.52	0.50	0.42
A (Mbar)	10.322	5.942	5.022	8.126
B (Mbar)	0.906	0.441	0.269	0.654
E @ $V/V_0 = 1.5$	1.00	1.010	1.022	1.047
E @ $V/V_0 = 10$	1.00	1.064	1.061	1.055

## EXPERIMENTAL RESULTS

The interface particle velocity Fabry-Perot results for 12 mm of RX40AA and RX40AB with a NaCl crystal, and 12 mm of RX40AF with a LiF crystal are illustrated in Fig. 2. For the 5  $\mu$ m Al compositions, RX40AA and RX40AB, the results in Fig. 2 suggest that the rate and extent of aluminum oxidation are similar for both 5 and 10 wt% aluminum loading. The particle velocity result for the 18  $\mu$ m aluminum 5 wt% RX40AF suggests that there is a significant decrease in the energetics from the reaction between aluminum and the PETN detonation products.

To determine the fraction of the chemical energy release that is due to  $Al_2O_3$  formation, and thus the fraction reacted parameter in the model where the aluminum and

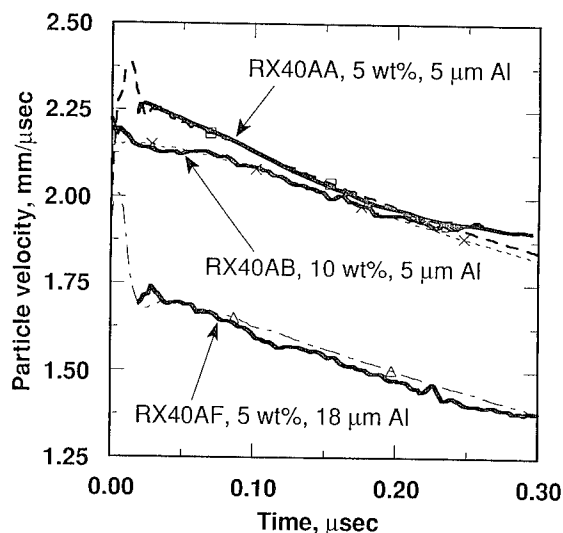


FIGURE 2. FABRY-PEROT PARTICLE VELOCITY MEASUREMENTS OF 18 mm OF DETONATING PETN/Al COMPOSITE LOADED WITH 5 WT% (RX40AA) AND 10 WT% (RX40AB) OF 5  $\mu$ m SPHERICAL ALUMINUM, AND 5 WT% OF 18  $\mu$ m (RX40AF) ALUMINUM. THE DASHED CURVES ARE ZND MODEL CALCULATIONS USING NORMALIZED JWEL EQUATIONS OF STATE.

reaction products rate is switched on, the theoretical heat of reaction of the pure explosive is compared to that for the aluminized compositions assuming that all aluminum reacts to  $Al_2O_3$ . However, since the aluminum reacts with  $H_2O$ ,  $CO_2$ , or  $CO$  that was produced as part of the pure explosives' reaction, the loss of the heat of formation of these gases as the aluminum reduces them to  $H_2$  or carbon must also be considered. Since it is unknown when aluminum reacts with  $H_2O$  or  $CO_2$  or, if it reacts with  $CO_2$  whether it reduces  $CO_2$  to  $CO$  or carbon, there is a few percent uncertainty in the contribution of  $Al_2O_3$  formation to the overall heat of reaction. Allowing both  $H_2O$  and  $CO_2$  to react with aluminum, the fraction of total energy that is due to the pure explosive detonating to form products, and the fraction due to the subsequent reaction between the detonation products and aluminum, are summarized in Table 5 for the various PETN/Al and TNT/Al formulations.

We now apply our Ignition and Growth reaction rate law, outlined in Equation (2), along with the product JWEL EOSs summarized in Table 4 to interpret the various Fabry Perot particle velocity results in Fig. 2. Starting with the 5  $\mu$ m, 5 and 10 wt% formulations, RX40AA and RX40AB, we approximate a percentage of the total energy released promptly by the PETN, and assume the remaining energy to be slowly released as the aluminum reacts. The model is then applied to the particle velocity results to infer a mass

**TABLE 5. THE TOTAL ENERGY RELEASED IN DETONATING PETN/Al AND TNT/Al FORMULATIONS SEPARATED INTO TWO FRACTIONS. THE FIRST PART IS FROM THE PURE EXPLOSIVE, AND THE SECOND FRACTION IS FROM THE REACTION BETWEEN THE ALUMINUM AND THE DETONATION PRODUCTS.**

Al wt%	PETN/Al formulations		TNT/Al formulations	
	% from PETN	% from Al	% from TNT	% from Al
5	86	14	85	15
10	74	26	70	30
20	58	42	-	-

regression rate for the aluminum oxidation,  $G_2$ , and the fraction of Al reacted,  $F$ . The dashed curves in Fig. 2 represent the fit of the composite model to the experimental data, and Table 6 summarizes the fitted constants for the third term of the Ignition and Growth rate law in Equation (2). A pressure exponent of one supports the assumption of a diffusion controlled reaction for aluminum oxidation.

**TABLE 6. THE MASS REGRESSION PARAMETERS OF THE REACTION RATE LAW IN EQUATION (2) FOUND FROM REACTIVE-FLOW MODELING. THE PARAMETER  $G_1$  FOR DETONATING PURE PETN WAS DETERMINED SEPARATELY USING SIMILAR IMPEDANCE MISMATCH EXPERIMENTS.**

$G_1(1 - F)^x F^y P^z + G_2(1 - F)^x F^y P^z$		
	PETN/Al, spherical Al	
	5 $\mu\text{m}$	18 $\mu\text{m}$
$G_1$ (Mbars $^{-z}$ /μs)	1000.0	1000.0
$G_2$ (Mbars $^{-z}$ /μs)	66.0	18.4
x	1.0	1.0
y	1.0	1.0
z	1.0	1.0

We can check the validity of our composite explosive model by predicting the rate of energy release from aluminum reaction with different aluminum particle sizes; from 5  $\mu\text{m}$  to 18  $\mu\text{m}$ . A logical assumption is that the reaction mechanism for aluminum combustion remains the same for different particle size aluminum, and the mass regression parameter  $G_2$  for 18  $\mu\text{m}$  aluminum will decrease proportionally by the ratio of the surface to volume ratios of the 5 and 18  $\mu\text{m}$  aluminum particles. This is true for a surface regression and inward combustion reaction mechanism for aluminum reaction. The values in Table 6 for 18  $\mu\text{m}$  aluminum, which reflects a decrease of  $G_2$  from 66 to 18.4, are used to predict the particle velocity history of PETN/Al

compositions loaded with 18  $\mu\text{m}$  aluminum. The accuracy of our prediction is illustrated in Fig. 2 as dashed curves along with experimental measurements of RX40AF loaded with 5 wt% of 18  $\mu\text{m}$  aluminum particles. We are confident, from the results in Fig. 2, that we have a consistent modeling methodology for predicting the reaction rate and energy release rate of aluminum loaded bicomponent composite explosives.

## DISCUSSION

### PETN/Al Ta Acceleration Free-Surface Velocity Measurements

The validity of the composite explosive model depends on whether a consistent methodology of reactive-flow and normalized equation of state may be used to interpret different impedance matched and mismatched experiments. Figure 3 illustrates the Fabry-Perot free-surface velocity measurements of a 0.522 mm Ta plate accelerated by 18 mm of detonating PETN/Al composite loaded with 5 wt% of 5  $\mu\text{m}$  spherical aluminum. The Ta plate jumps off with a velocity of 1.5 mm/μs, and accelerates to ~3 mm/μs within the first 2 μs. In Fig. 4, we illustrate acceleration histories of a 0.522 mm Ta plate accelerated by 18 mm of either 10 wt% or 20 wt% 5  $\mu\text{m}$  aluminum loaded PETN formulations. There appears to be minimal difference

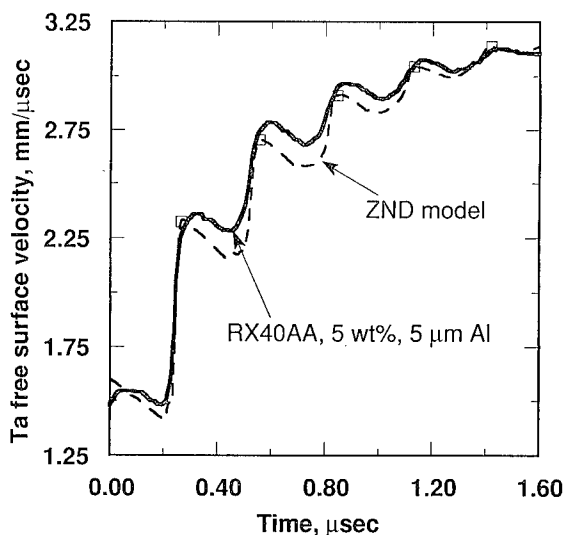


**FIGURE 3. FABRY-PEROT FREE-SURFACE VELOCITY MEASUREMENTS OF A 0.522 mm Ta PLATE ACCELERATED BY 18 mm OF DETONATING PETN/Al COMPOSITE LOADED WITH 5 WT% OF 5  $\mu\text{m}$  SPHERICAL ALUMINUM. THE DASHED CURVES ARE ZND MODEL CALCULATIONS USING NORMALIZED JWEL EQUATIONS OF STATE.**

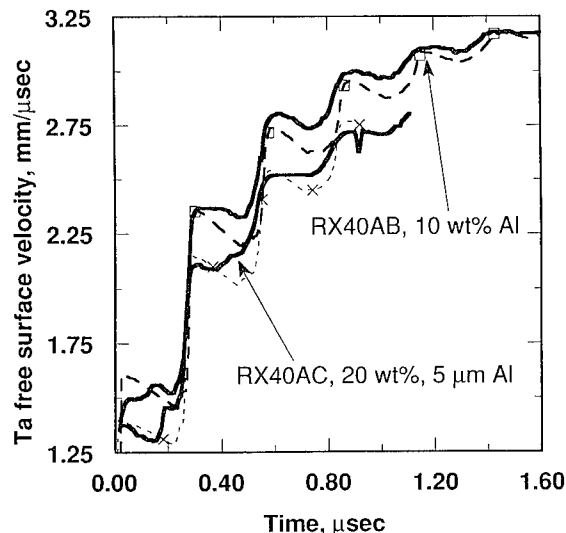


**FIGURE 4. FABRY-PEROT FREE-SURFACE VELOCITY MEASUREMENTS OF A 0.522 mm Ta PLATE ACCELERATED BY 18 mm OF DETONATING PETN/Al COMPOSITE LOADED WITH EITHER 10 OR 20 WT% OF 5  $\mu$ m SPHERICAL ALUMINUM**

between the acceleration histories of the Ta plates for either the 5 wt% or 10 wt% 5  $\mu$ m aluminum loaded PETN, suggesting that all of the 5  $\mu$ m aluminum reacted fully with the PETN detonation product gases to form alumina. The dashed curves in both Fig. 3 and Fig. 4 represent the ZND reactive flow model calculation of the Ta plate-push experiments, using the unreacted and product EOSs for PETN/Al from Table 4 and model parameters from Table 6. The model, using the parameters derived from particle velocity measurements, were able to predict the Ta-plate jump-off velocity and the steady state end velocity fairly well.

Figure 5 illustrates the results of a Ta plate accelerated by detonating PETN/Al explosives filled with 18  $\mu$ m aluminum. The reaction rate parameters in Table 6 for the oxidation of 18  $\mu$ m aluminum in PETN were used to model the results in Fig. 5. Note that the  $G_2$  parameter for 18  $\mu$ m aluminum was scaled from that for 5  $\mu$ m aluminum, which was derived from a single set of particle velocity measurements.

#### TNT/AlTa Acceleration Free-Surface Velocity Measurements

In a similar manner, we have generated the normalized unreacted and product JWL equation of state for TNT formulations loaded with 5 and 10 wt% of aluminum. The JWL parameters for compositions in which the aluminum is assumed to react fully to completion are summarized in

Table 7. Figure 6 illustrates the acceleration history of 0.262 mm of Ta driven by 12 mm of detonating TNT loaded with either 5 wt% or 10 wt% of 5  $\mu$ m spherical aluminum. The dashed curve is a model calculation of the Ta free-surface velocity using reaction rate parameters for 5  $\mu$ m aluminum in TNT as listed in Table 8. Unlike the fast reacting PETN, TNT reacts slower and has a finite, measurable reaction zone thickness. Therefore, the mass regression parameter for TNT,  $G_1 = 360$ , results in reaction time for pure TNT of approximately 120 ns. Compared to the rate of reaction between aluminum and the detonation products, the reaction of TNT is still much faster, and we can assume that the TNT reacts first to form detonation products followed by aluminum combustion and oxidation with the products.

At first glance, a comparison between the  $G_2$  parameters in Table 8 with those in Table 6 suggests that aluminum in TNT reacts faster than aluminum in PETN. The term in Equation (2) describing the diffusion controlled aluminum reaction, however, is not just the parameter  $G_2$  but the entire third term of the equation,  $G_2(1 - F)^{X_F Y P^Z}$ . For TNT, the pressure at any point of the reaction is much lower than that for PETN. Therefore, the rate of aluminum reaction with TNT is slower than that with PETN, and the trend is consistent with the lower temperature and poorer oxidation conditions of the TNT detonation products.

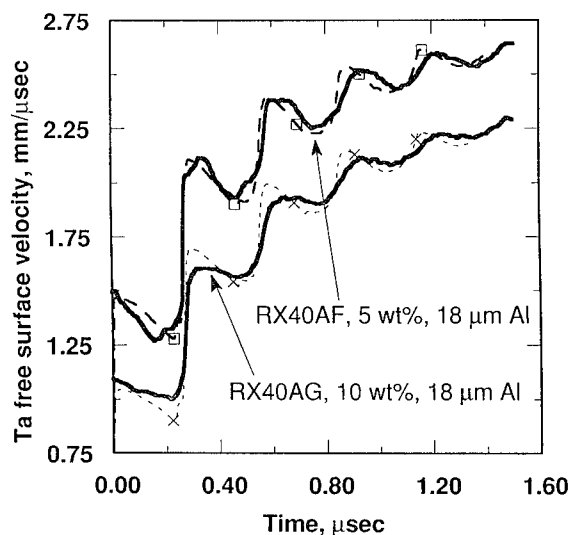


**FIGURE 5. FABRY-PEROT FREE-SURFACE VELOCITY MEASUREMENTS OF A 0.262 mm Ta PLATE ACCELERATED BY 12 mm OF DETONATING PETN/Al COMPOSITE LOADED WITH EITHER 5 OR 10 WT% OF 18  $\mu$ m SPHERICAL ALUMINUM**

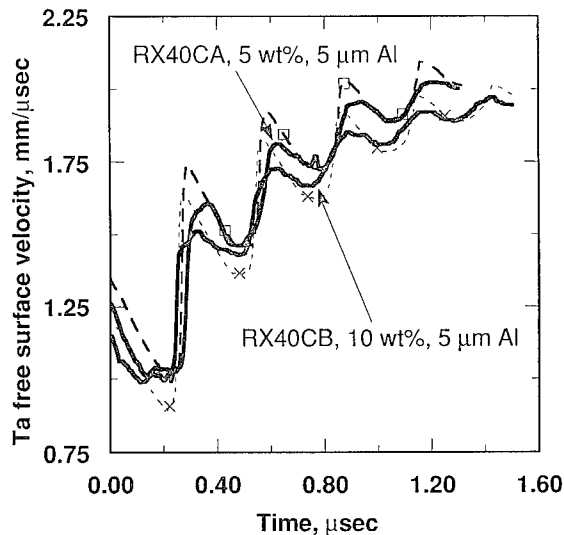


FIGURE 6. FABRY-PEROT FREE-SURFACE VELOCITY MEASUREMENTS OF A 0.262 mm Ta PLATE ACCELERATED BY 12 mm OF DETONATING TNT/Al COMPOSITE LOADED WITH EITHER 5 WT% OR 10 WT% OF 5  $\mu$ m SPHERICAL ALUMINUM

TABLE 7. NORMALIZED UNREACTED AND PRODUCT JWEL EQUATION OF STATE FOR DETONATING TNT/Al LOADED WITH 5 OR 10 WT% OF ALUMINUM

JWL Unreacted and Product Equations of State			
	Unreacted	TNT/Al (95/5)	TNT/Al (90/10)
Density (g/cc)	-	1.635	1.670
D (mm/ $\mu$ s)	-	6.80	6.80
P <sub>cj</sub> (Kbar)	-	195	190
Gamma	-	2.877	3.064
E <sub>0</sub>	-	0.076	0.082
R <sub>1</sub>	10.0	8.8	7.4
R <sub>2</sub>	1.0	3.4	2.4
w	.5675	0.57	0.45
A (Mbar)	202.8	19.736	17.653
B (Mbar)	-0.0375	1.466	0.535
E @ V/V <sub>0</sub> = 1.5	-	0.635	0.654
E @ V/V <sub>0</sub> = 10	-	0.682	0.700

#### PETN/Al and TNT/Al Fraction Reacted

Figure 7 illustrates the fraction of total energy release as a function of time for PETN/Al compositions loaded with 5, 10, and 20 wt% of either 5  $\mu$ m or 18  $\mu$ m aluminum. Note that the reaction of 5, 10, and 20 wt% of aluminum with the PETN detonation product only accounts for 14%,

TABLE 8. THE MASS REGRESSION PARAMETERS OF THE REACTION RATE LAW IN EQUATION (2) FOUND FROM REACTIVE-FLOW MODELING. THE PARAMETER  $G_1$  FOR DETONATING PURE TNT WAS DETERMINED SEPARATELY USING SIMILAR IMPEDANCE MATCHING EXPERIMENTS.

$G_1(1-F)^x F^y P^z + G_2(1-F)^x F^y P^z$		
	TNT/Al, spherical Al	
	5 $\mu$ m	18 $\mu$ m
$G_1$ (Mbars $^{-z}$ / $\mu$ s)	360.0	360.0
$G_2$ (Mbars $^{-z}$ / $\mu$ s)	90	25
x	1.0	1.0
y	1.0	1.0
z	1.0	1.0

26%, and 42%, respectively, of the total energy released by the composite explosive within the early time frame of the impedance mismatched experiments. The rest of the energy is assumed to be released instantaneously by the fast reacting PETN. The 5 to 20 wt% of 5  $\mu$ m aluminum in PETN fully reacts within a  $\mu$ s, while about 80% of the 5 and 10 wt% 18  $\mu$ m aluminum reacted and about 75% of the 20 wt% 18  $\mu$ m reacted within the same timeframe.

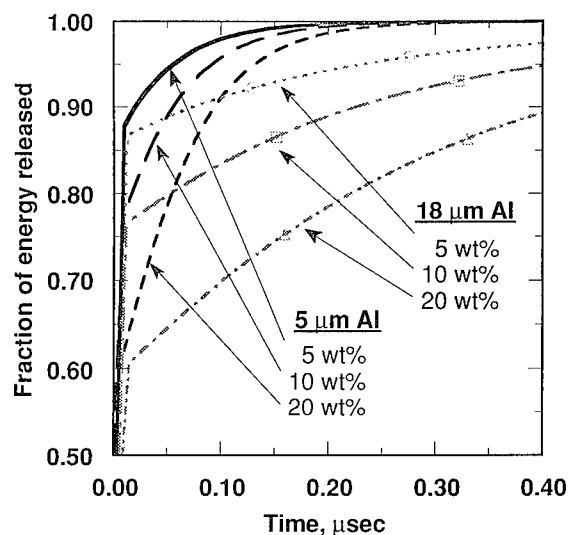
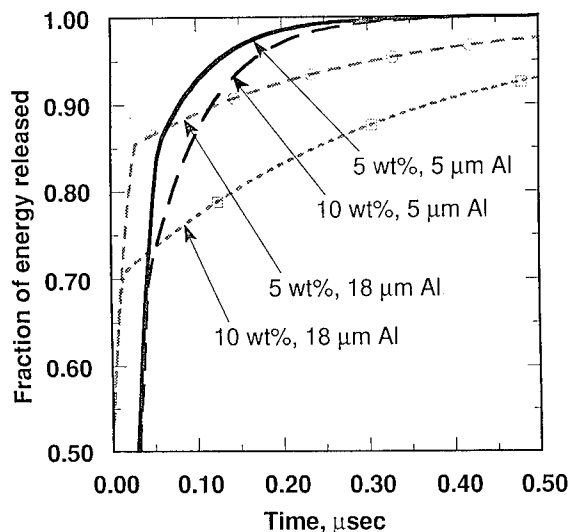


FIGURE 7. FRACTION OF TOTAL ENERGY RELEASE AS A FUNCTION OF TIME FOR PETN/Al COMPOSITE EXPLOSIVES LOADED WITH 5, 10, OR 20 WT% OF 5  $\mu$ m AND 18  $\mu$ m ALUMINUM. THE PURE PETN IS ASSUMED TO INSTANTANEOUSLY RELEASE ITS ENERGY WITHIN A FEW ns.



Figure 8 is a similar graphical summary of the rate of total energy released for TNT/Al compositions with different wt% and particle size aluminum loadings.



**FIGURE 8. FRACTION OF TOTAL ENERGY RELEASE AS A FUNCTION OF TIME FOR TNT/Al COMPOSITE EXPLOSIVES LOADED WITH 5 OR 10 WT% OF 5  $\mu$ m AND 19  $\mu$ m ALUMINUM**

## SUMMARY

In this study, the reaction rates of two different diameters spherical particles of aluminum with reaction product gases from detonating PETN and TNT are inferred from impedance matched and metal acceleration experiments using reactive flow modeling for the first few microseconds following detonation. The 5 wt% and 10 wt% aluminum in PETN formulations react completely in one to two microseconds yielding more energy for metal acceleration than pure PETN. The 20 wt% aluminum in PETN formulations do not react completely and do not accelerate metal better than pure PETN; so 20 wt% aluminum is too much metal additive for early time energy delivery applications. In TNT, 5 to 10 wt% of 5  $\mu$ m spherical aluminum reacts completely while 10 wt% of 18  $\mu$ m aluminum may not. Therefore the limiting percentage of aluminum in TNT for early metal acceleration applications is near 10 wt%. Larger scale experiments are being planned to determine later time energy release rates in aluminized explosives. Experiments are also being performed to determine whether H<sub>2</sub>O, CO<sub>2</sub>, or CO is the most effective oxidizer of aluminum under detonation conditions. This technique is also being applied to practical HMX/AP/Al formulations. In these explosives and propellants, there exists a complex tradeoff

between the AP and aluminum reactions. AP decomposition produces large amounts of O<sub>2</sub> for the aluminum to reduce, but at the same time lowers the overall detonation temperature. This severely hinders the aluminum reaction which is very sensitive to temperature near the melting point of Al<sub>2</sub>O<sub>3</sub>, 2400K, which often creates a crust around the aluminum particles.

## ACKNOWLEDGEMENT

The authors wish to thank LeRoy Green for his valuable technical discussions. Mr. Wardell Black and his crew at Site 300 have contributed much to the preparation of the test samples.

## REFERENCES

1. E. L. Lee and H. C. Hornig, Twelfth Symposium (International) on Combustion, 1969, p. 493.
2. M. Finger, H. C. Hornig, E. L. Lee, and J. W. Kury, "Metal Acceleration by Composite Explosives", Fifth Symposium (International) on Detonation, ACR-184, 1979, p. 137.
3. R. R. McGuire, D. L. Ornellas, and I. B. Akst, "Detonation Chemistry, Diffusion Control in Non-Ideal Explosives", Propellants and Explosives, 4 No. 2, 1979, pp. 23-26.
4. R. R. McGuire and M. Finger, "Composite Explosives for Metal Acceleration: The Effect of Detonation Temperature", Eighth Symposium (International) on Detonation, 1985, p. 1018.
5. J. W. Kury, H. C. Hornig, E. L. Lee, J. L. McDonnell, D. L. Ornellas, M. Finger, F. M. Strange, and M. L. Wilkens, "Metal Acceleration by Chemical Explosives," Fourth Symposium (International) on Detonation, White Oak, Maryland, Oct. 12-15, Office of Naval Research, ACR-126, 1965, pp. 3-13.
6. W. C. Tao, C. M. Tarver, R. D. Breithaupt, R. R. McGuire, and D. L. Ornellas, "Understanding Composite Explosive Energetics: I. The Role of Metallic Additives," Proceedings of the 14th Symposium on Explosives and Pyrotechnics, Burlingame, California, Franklin Research Center, February 1990.
7. W. C. Tao, C. M. Tarver, D. R. Breithaupt, and D. L. Ornellas, "Understanding Composite Explosives Energetics: II The Combustion Kinetics of Metallic Additives in Different Oxidizing Environments," Proceedings of the 27th JANNAF Combustion Meeting, F. E. Warren AFB, Cheyenne, WY, Nov. 5-9, 1990.

8. L. G. Green, E. L. Lee, D. Breithaupt, and J. Walton, *Shock Waves in Condensed Matter 1987* (S. C. Schmidt and N. C. Holmes, eds) Elsevier Science Publishers B.V., 1988, p. 507.
9. C. F. McMillan, D. R. Goosman, N. L. Parker, L. L. Steinmetz, H. H. Chau, T. Huen, R. K. Whipkey, and S. J. Perry, "Velocimetry of Fast Surface at LLNL using Fabry-Perot Interferometry," *Rev. Sci. Instrum.*, 59(1), 1-20, 1988.
10. Y. B. Zeldovich and A. S. Kompaneets, Theory of Detonation, Academic Press, New York (1960).
11. R. C. Weingart, R. S. Lee, R. K. Jackson, and N. L. Parker, "Acceleration of Thin Flyers by Exploding Metal Foils: Application to Initiation Studies," Sixth Symposium (International) on Detonation, San Diego, California, Aug. 24-27, Office of Naval Research, ACR-221, 1976, pp. 653-663.
12. M. Cowperthwaite and W. H. Zwisler, TIGER Computer Program Documentation, SRI International Report on Contract AT(04-3)-115, 1974.
13. C. M. Tarver, R. D. Breithaupt, and J. W. Kury, "Current Experimental and Theoretical Understanding of Detonation Waves in Heterogeneous Solid Explosives," UCRL-95462, International Symposium on Pyrotechnics and Explosives, Beijing, China, 1987, p. 692-700.
14. L. G. Green, C. M. Tarver, and D. J. Erskine, "Reaction Zone Structure in Supracompressed Detonating Explosives," Ninth Symposium (International) on Detonation, Portland, Oregon, Aug. 27 - Sept. 1, 1989, p. 670.

## AN ALUMINUM REACTION TIME LIMIT IN UNDERWATER DETONATION OF AN ENCASED ALUMINIZED EXPLOSIVE

J. W. ENIG  
ENIG ASSOCIATES, INC.  
SILVER SPRING, MD 20904-2633

Oblique shock and Prandtl-Meyer expansion calculations, applied to the problem of the failure of the aluminum reaction in an aluminized explosive to support the detonation front under conditions of light case confinement under water, provide the following: the changing pressure and temperature environment that the aluminum particle at the explosive/case interface sees as it traverses the detonation front that is determined by a CHNO explosive such as RDX; the effects of the confining case material, case thickness, and angle  $\beta$  between the detonation front and the case/explosive interface on the detonation flow in the vicinity of the case/products interface; and an estimate of the length of time  $t_{AH}$  the aluminum particle has at elevated temperatures in the explosive products before the aluminum reaction will be quenched, if at all, by the lateral expansion wave from the case/water interface.

### INTRODUCTION

The reaction of aluminum with the detonation products in all explosives is still to this day poorly understood, but there is much evidence, albeit indirect, that the exothermic reaction that consumes aluminum takes place over a much longer time-scale than that which consumes, say, RDX or HMX.<sup>1,2</sup>

At the Naval Surface Warfare Center, White Oak, MD, cylinders of PBXN-109, 8.5" (25.19 cm) in diameter and 8.5" in length, were encased by steel or polyvinyl chloride (PVC) of different thicknesses, as shown in Fig. 1, and detonated under water. If it is assumed that the detonation wave is spherical and originates at the detonator, then the detonation wave makes an angle  $\beta$  with the case as shown schematically in Fig. 1. Along the case/explosive interface,  $\beta$  can be taken as  $90^\circ$  in the immediate vicinity of the detonator (assuming a hemispherical detonation wave in the explosive), which abruptly changes to  $0^\circ$  when the detonation wave reaches the corner, and thereafter increases toward  $90^\circ$ . Experimental evidence indicates that for the PVC-encased PBXN-109 the aluminum in the explosive is not reacting on a short-enough time scale to support the detonation front and the underwater shock wave, i.e., the PVC does not provide the confinement, and therefore the sufficiently high pressure and temperature, which the aluminum needs in order to react to completion.

To explain the apparent failure of the aluminum reaction in an aluminized explosive to support the detonation front under conditions of

light case confinement under water, we have undertaken to determine the changing pressure and temperature environment that an aluminum particle sees as it traverses the detonation front that is determined by a CHNO explosive such as RDX. In particular, we seek the effects of the confining case material, case thickness, and detonation front inclination to the case/explosive interface on the detonation flow in the vicinity of the case/products interface, just behind the Chapman-Jouguet (CJ) detonation front. The means of finding these effects is through the application of oblique shock and Prandtl-Meyer expansion theories to the pseudo-stationary flows used to approximate the unsteady flows.

### BACKGROUND

The lateral expansion must affect the reaction zone and the detonation front itself: a curved detonation front, progressing with constant velocity  $D$ , obtains in a long stick of explosive.<sup>3</sup> Inasmuch as we inquire into the effect of lateral rarefactions on the aluminum reaction behind the explosive (e.g., RDX) reaction zone, and not on the explosive reaction zone itself, we ignore such curvature effects and consider the problem of a detonation wave of negligible (i.e., zero) reaction zone thickness advancing with its normal velocity  $D$  from its point of initiation.

With the use of oblique shock theory<sup>4</sup> and Prandtl-Meyer expansion theory,<sup>5</sup> we examine that neighborhood of the detonation products and

surrounding case in water, whose dimensions are small compared to the explosive charge radius. In a simpler version of this problem, Taylor and Jones<sup>6</sup> provided a solution for the case of a TNT detonation moving parallel to planar interface, and Sternberg and Piacesi<sup>7</sup> considered the problem of the detonation of a slab of pentolite explosive surrounded by iron, where the angle  $\beta$  between the tangent to the detonation front and the metal varies from  $0^\circ$  to  $90^\circ$ ;  $90^\circ$  corresponds to the case treated by Taylor and Jones.<sup>6</sup> Recently, Walsh<sup>8</sup> used oblique shock theory to estimate the jump-off velocity for different case materials and different explosives at different values of  $\beta$  for detonations in air; the lateral expansion wave in the case, originating at the case/air interface, is not actually calculated. Also, oblique shocks in various metals, which are driven by Composition B-3, PBXN-9404, and TNT with the detonation perpendicular to the interface, i.e.,  $\beta = 90^\circ$ , have been investigated by flash radiographic techniques and analyzed by oblique shock theory.<sup>9</sup>

We describe work here beyond the cases considered in references 7 and 8; we consider an explosive (PBXN-109) encased in a thin shell of metal, itself surrounded by water, with attention focused on the expansion wave at the metal/explosive products interface arising from the lateral expansion at the water/metal interface (Fig. 2). We provide an estimate of the length of time an aluminum particle has at elevated temperatures in the explosive products before the aluminum reaction will be quenched, if at all, by that lateral expansion wave. This "length of time" is a function of the angle  $\beta$ . For  $\beta = 90^\circ$  and a thin metal case, the most accurate solutions have been obtained by the methods of characteristics by Hoskin, *et al*<sup>10</sup> and Fickett and Scherr.<sup>11</sup>

## ANALYSIS BY OBLIQUE SHOCK AND PRANDTL-MEYER EXPANSION THEORIES

At every shock angle  $\beta$ , we apply steady-state theory in order to construct separate pressure  $P$  versus streamline deflection  $\theta$  shock polar for each material (i.e., metal and explosive). The continuity of pressure and streamline deflection across the contact discontinuity (i.e., metal/explosive products interface) yields the appropriate solution for  $P$  and  $\theta$ . The method of solution for the interaction of products and metal follows Sternberg and Piacesi.<sup>7</sup> We extend their work and derive the effect of the surrounding water on the flow in a metal case of finite thickness and describe how this flow could effect the pressure and temperature that an aluminum particle sees as it moves along the product/metal interface.

The detonation products at the Chapman-Jouguet (CJ) state are defined by

$$P = P(E, V) \quad (1)$$

$$E_j = E_o + (P_j - P_o)(V_o - V_j)/2 \quad (2)$$

$$(P_j - P_o)/(V_o - V_j) = (\rho_o D)^2, \quad (3)$$

where  $P$ ,  $V$ , and  $E$  are, respectively, the pressure, specific volume, and specific internal energy of the products.  $\rho = 1/V$  is the density;  $D$  is the CJ

detonation velocity. The subscripts  $o$  and  $j$  refer to unreacted explosive and CJ states, respectively. Eq.(1) is the equation of state of the detonation products. From Eq.(1), we obtain the local sound speed  $c$  defined by

$$c^2 = V^2 [P(\partial P / \partial E)_V - (\partial P / \partial V)_E]. \quad (4)$$

## Regular Reflection in Detonation Products

For the case of regular reflection in the neighborhood of A of Fig. 3, we consider a coordinate system moving with the point A. The appropriate equations are

$$q_o = D / \sin \beta \quad (5)$$

$$u_i = D / \tan \beta \quad (6)$$

$$u_i = c_j \quad (7)$$

$$\rho_i u_i = \rho_o D \quad (8)$$

$$\tan(\beta - \epsilon) = u_i / u_i \quad (9)$$

$$q_i = u_i / \sin(\beta - \epsilon), \quad (10)$$

where subscripts  $o$  and  $i$  refer to the conditions, respectively, ahead of and behind the detonation front.  $q$  is the flow velocity along the streamline;  $u_i$  and  $u_i$  are, respectively, the normal and tangential velocity components; and Eq. (7) is the Jouguet condition. For prescribed  $\beta$ ,  $\rho_o$ , and  $D$  and  $c_j$ , the streamline deflection angle  $\epsilon$  is determined from Eqs. (1)-(4) and (6)-(9).

Across the reflected shock, we have

$$P_2 = P(E_2, V_2) \quad (11)$$

$$E_2 = E_i + (P_2 - P_i)(V_i - V_2)/2 \quad (12)$$

$$P_2 = P_i + u_{ir}^2 (V_i - V_2) / V_j^2 \quad (13)$$

$$u_{ir} = q_i \sin v \quad (14)$$

$$u_{2i} = u_{ir} / \tan v \quad (15)$$

$$\rho_2 u_2 = \rho_i u_{ir} \quad (16)$$

$$u_2 = u_{2i} \tan(v - \epsilon + \theta). \quad (17)$$

$u_{ir}$  is the normal component of the flow velocity into the reflected shock;  $v$  is the angle between the incoming streamline and the reflected shock; the subscript 2 refers to the region in the products behind the reflected shock;  $\theta$  is the streamline deflection angle (from the horizontal). Eqs. (5)-(17) are 13 equations in the 14 unknowns,  $q_o$ ,  $u_i$ ,  $u_i$ ,  $\rho_i$ ,  $\epsilon$ ,  $q_i$ ,  $E_2$ ,  $P_2$ ,  $V_2$ ,  $u_{ir}$ ,  $v$ ,  $u_{2i}$ ,  $u_2$ , and  $\theta$ , from which we obtain for the prescribed parameters the reflected shock polar

$$P_2 = F(\theta_2) \quad (18)$$

(shown in Fig. 4(a)) that is the locus of possible reflected shock pressure  $P_2$  and streamline deflection angle  $\theta_2$  solutions -- the exact pair to be determined below. Methods of shock polar construction and their properties are described in detail by Sternberg and Piacesi<sup>7</sup> and Enig.<sup>12</sup>

## Mach Reflection in Detonation Products

For certain shock angles  $\beta$ , regular reflection is not possible. Mach reflection in the detonation products as shown in Fig. 5 is an alternative. Here, an incident detonation front, a reflected shock, and a curved Mach detonation front (Mach stem) meet at the triple point T. We choose a coordinate system that moves with the point T. The shock angle  $\beta$  is again the angle between the incident detonation front and a horizontal line parallel to the interface between the metal casing and the unreacted explosive.

Exactly as in the case for regular reflection above, the  $P_2, \theta_2$  locus of possible states behind the reflected shock is given by Eq.(18).

The locus of possible pressure  $P_3$  and streamline deflection angle  $\theta_3$  behind the curved Mach front is derived from the following equations:

$$P_3 = P(E_3, V_3) \quad (19)$$

$$E_3 = E_0 + (P_3 - P_0)(V_0 - V_3)/2 \quad (20)$$

$$u_0^2 = V_0^2(P_3 - P_0)/(V_0 - V_3) \quad (21)$$

$$\sin \eta = u_0/q_0 \quad (22)$$

$$u_3 = u_0 \tan \eta \quad (23)$$

$$u_3 = u_0 V_3/V_0 \quad (24)$$

$$u_3 = u_3 \tan(\eta - \theta) \quad (25)$$

and Eq. (5), which are 8 equations in the 9 unknowns,  $P_3, E_3, V_3, u_0, \eta, q_0, u_3, \theta$ , and  $\theta$ , from which we obtain the Mach wave shock polar

$$P_3 = G(\theta_3) \quad (26)$$

(shown in Fig. 4(a)) that is the locus of possible  $P_3, \theta_3$  solutions. In Fig. 5,  $\eta$  is the angle between the horizontal and the tangent to the curved Mach front;  $u_0$  is the detonation velocity normal to the Mach front. The flow speed  $q_3$  behind the Mach front is given by

$$q_3 = u_3 \csc(\eta - \theta). \quad (27)$$

Across the slip line TC, which originates at the triple point T, the pressure must be continuous and the flow parallel, i.e.,  $P_3 = P_2$  and  $\theta_3 = \theta_2$ . (However,  $q_3 \neq q_2$ .) Therefore, from Eqs. (18) and (26),  $P_3$  and  $\theta_3$  are found at the triple point T. This is just the point of intersection T of the two shock polars in Fig. 4(a).

### Shock Polar for the Expansion Wave in the Detonation Products

For  $\beta$  sufficiently large (i.e., as  $\beta \rightarrow 90^\circ$ ), the pressure at the interface between detonation products and metal case is lower than the incident CJ detonation pressure  $P_j$ . This occurs through a Prandtl-Meyer expansion fan shown in Fig. 4 and described by Eq. (4) and the following equations for the products:

$$P = P(E, V), \quad dE + PdV = 0, \quad qdq = -VdP \\ qd\theta = (M^2 - 1)^{1/2} dq, \quad \sin \alpha = 1/M, \quad M = q/c,$$

where  $q$  is the velocity along the streamline,  $\theta$  the angle between the horizontal and the streamline,  $M$  the Mach number, and  $\alpha$  the Mach angle. The resulting  $P, \theta$  locus is called the "expansion polar" and is derived by solving these equations subject to boundary conditions that depend on the CJ values,  $\beta$ , and  $\epsilon$ .

In order to derive the expansion polar, and for purposes of numerical solution, it is more convenient to replace Eq.(4) and the equations immediately above by the following equivalent set:

$$d\theta/dP = -(V/q^2)(q^2/c^2 - 1)^{1/2} \quad (28)$$

$$dq/dP = -V/q \quad (29)$$

$$dE/dP = -PV^2/c^2 \quad (30)$$

$$dV/dP = -V^2/c^2 \quad (31)$$

$$\sin \alpha = c/q. \quad (32)$$

The initial conditions at the "head" of the rarefaction (expansion) fan are the following:

$$\theta = \epsilon, \quad q = q_1, \quad E = E_j, \quad V = V_j \quad \text{at } P = P_j. \quad (33)$$

The incident Mach line angle is  $\alpha_1 = \beta - \epsilon$ ; the angle

that the head of the expansion fan makes with the horizontal is  $\phi_1 = \epsilon - \alpha_1$ . At the "tail" of the expansion fan, i.e., where  $P = P_{ptail} < P_j$  and  $\theta = \theta_{ptail}$ , the Mach line angle made with the stream velocity  $q_{ptail}$  is

$\alpha_{ptail} = \sin^{-1}(c_{ptail}/q_{ptail})$ ;  $\phi_{ptail} = \theta_{ptail} - \alpha_{ptail}$  is the angle that the tail of the expansion fan makes with the horizontal. Thus, the locus of possible expansion states is given by the expansion polar. A typical expansion polar, RQ in Fig. 4(a), is

$$P_{ptail} = I(\theta_{ptail}). \quad (34)$$

### Shock Wave in the Metal Case

Let the subscript 4 refer to the constant state behind the shockwave in the metal liner as shown in Figs. 3 or 5. The locus of possible states  $P_4, \theta_4$  is given by the shock polar

$$P_4 = J(\theta_4) \quad (35)$$

that is derived from

$$H(P_4, V_4) = 0 \quad (36)$$

$$q_{on}^2 = V_{on}^2(P_4 - P_0)/(V_{on} - V_4) \quad (37)$$

$$\sin \lambda = q_{on}/q_0 \quad (38)$$

$$q_{4t} = q_0 \cos \lambda \quad (39)$$

$$q_{4n} = q_{on} V_4/V_{on} \quad (40)$$

$$q_{4n} = q_{4t} \tan(\lambda - \theta) \quad (41)$$

and Eq.(5). Eq.(36) is the Hugoniot in the metal;  $\lambda$  is shock angle in the metal;  $V_{on}$  is the specific volume of the metal case; and

$$q_4 = q_{on}/\sin(\lambda - \theta) \quad (42)$$

is the flow speed in the metal.

Now we are prepared to determine whether there exists regular reflection, Mach reflection, or a centered rarefaction fan at the point where the detonation front meets the metal. The metal shock polar MN shown in Fig. 4(a) yields regular reflection (see Fig. 3) as determined by the intersection A of the two polars  $P_4 = J(\theta_4)$  and  $P_2 = F(\theta_2)$ . If, however, the metal shock polar is M'N' of Fig. 4(a), Mach reflection (see Fig. 5) occurs, where P and  $\theta$  along WT of Fig. 5 is given by P and  $\theta$  along WT of Fig. 4(a). Clearly, W and T are different states. Finally, for the third case, if the metal shock polar M'N' (of Fig. 4(a)) intersects the expansion polar, a centered rarefaction fan  $R_1$  (see Fig. 2) results, where Q of Fig. 4(a) determines the values of P and  $\theta$  at the tail of the rarefaction fan, i.e., the constant state  $P_{ptail} = P_4$  and  $\theta_{ptail} = \theta_4$  in TAIHK of Fig. 2.

### Shock Wave in the Water and Expansion Wave in the Metal Case

To find the effect of the water on the metal case and, therefore, on the detonation products, a problem not considered by Sternberg and Piacesi,<sup>8</sup> we construct the shock polar for the water from the equations analogous to Eqs. (36)-(41). In particular, let the subscript 6 refer to the constant state behind the shock wave IS in the water as shown, for example, in Fig. 2. The locus of possible states  $P_6, \theta_6$  is given by the shock polar

$$P_6 = J(\theta_6) \quad (43)$$

that is derived from

$$H_2(P_6, V_6) = 0 \quad (44)$$

$$q_{\text{on}}^2 = V_{\text{om}}^2 (P_6 - P_o) / (V_{\text{om}} - V_6) \quad (45)$$

$$\sin \sigma = q_{\text{on}} / q_o \quad (46)$$

$$q_{6t} = q_o / \cos \sigma \quad (47)$$

$$q_{6n} = q_{\text{on}} V_6 / V_{\text{om}} \quad (48)$$

$$q_{6n} = q_{6t} \tan(\sigma - \theta_6) \quad (49)$$

and Eq.(5). Eq.(44) is the Hugoniot in the water;  $\sigma$  is shock angle in the water;  $V_{\text{om}}$  is the specific volume of the water; and

$$q_6 = q_{\text{on}} / \sin(\sigma - \theta_6) \quad (50)$$

is the flow speed in the water.

Inasmuch as the impedance for water is less than that for the metal, the pressure at the metal/water interface is lower than behind the shock in the metal. This occurs through a Prandtl-Meyer expansion fan HIF shown in Fig. 2. The expansion fan is calculated using Eqs. (28)-(32) and the following initial conditions:

$$\theta = \theta_4, q = q_4, E = E_4, V = V_4 \text{ at } P = P_4. \quad (51)$$

Their solution provides, in particular, the position of the head IH and tail IF of the rarefaction fan HIF. The intersection of the water shock polar, Eq.(43), and the expansion branch of the polar defining the reflection states in the metal determines the streamline deflection through the fan.

The incident Mach line angle is  $\alpha_4 = \sin^{-1}(c_4/q_4)$ ; the angle that the head IH of the expansion fan makes with the horizontal is  $\zeta_4 = \theta_4 - \alpha_4$ . At the tail IF, i.e., where  $P = P_{\text{mtail}} < P_4$  and  $\theta = \theta_{\text{mtail}} > \theta_4$ , the Mach line angle made with the stream velocity  $q_{\text{mtail}}$  is  $\alpha_{\text{mtail}} = \sin^{-1}(c_{\text{mtail}}/q_{\text{mtail}})$ ;  $\zeta_{\text{mtail}} = \theta_{\text{mtail}} - \alpha_{\text{mtail}}$  is the acute angle that the tail IF of the expansion fan makes with the horizontal. The intersection of the locus of possible expansion states with the water shock polar Eq.(43), i.e., when  $P_{\text{mtail}} = P_6$  and  $\theta_{\text{mtail}} = \theta_6$ , determines the constant pressure state on both sides of the metal/water interface. The intersection of these two polars is shown in Fig. 4(b), where the point W,A,Q refers to any of the three points W, A, or Q of Fig. 4(a) as appropriate

### Quenching of the Aluminum Reaction

The length  $d$ , the distance between the intersection (point A) of the metal and the detonation front and point H of Fig. 2, is just the distance that an aluminum particle travels along the metal/products interface before its pressure and temperature are lowered by the rarefaction wave originating at I:

$$d = h(1 + \tan|\zeta_4| / \tan \lambda) / (\tan|\zeta_4| \cos \theta_4 + \sin \theta_4). \quad (52)$$

Thus, in a coordinate system moving with the point A, the aluminum particle moving along the products/metal interface with streamline velocity  $q_2$  traverses the distance  $d$  (from A to H) in the time

$$t_{\text{AH}} = d/q, \quad (53)$$

where

$$q = \begin{cases} q_2 & \text{for regular reflection} \\ q_3 & \text{for Mach reflection} \\ q_{\text{ptail}} & \text{for expansion wave,} \end{cases} \quad (54)$$

before its pressure and temperature are lowered by the rarefaction wave originating at I. If that aluminum particle has not reacted in the time  $t_{\text{AH}}$ , it may never react thereafter.

In the limiting case when  $\beta = 0^\circ$ , there is only one-dimensional flow: the transmitted shock in the case reaches the case/water interface; a rarefaction wave is reflected back into the case; the total transit time in the case,  $\tau$ , is given by

$$\tau/h = (1 - v_4/c_4)/U + 1/c_4, \quad (55)$$

where  $U$  and  $v$  are, respectively, the shock and particle velocities of the transmitted shock in a fixed laboratory coordinate system. Of course,  $\tau$  is just the value of  $t_{\text{AH}}$  at  $\beta = 0^\circ$ .

In a fixed laboratory coordinate system, the aluminum particle travels the distance  $vt_{\text{AH}}$  along the interface before meeting the head of the rarefaction fan originating at the metal/water interface, where

$$v = (q_o^2 - 2q_o q \cos \theta_4 + q^2)^{1/2} \quad (56)$$

and  $q$  is given by Eq.(54). Equation (56) is obtained by superposing the vector  $-q_o$  onto the flow vector  $q$ .  $v$  is just the "jump-off" velocity of the products into the metal case!

Both  $d$  and  $t_{\text{AH}}$  are directly proportional to the metal case thickness  $h$ ;  $h$  is the only characteristic length in the problem. Thus, Eqs.(52) and (53) express the geometric effect of confinement: the thicker (thinner) the metal case, the larger (smaller) the value of  $t_{\text{AH}}$ , and the more (less) likely is the aluminum particle to react. Actually, we would expect a reasonably sharp critical value  $t_{\text{crit}}$  such the  $t_{\text{AH}} < t_{\text{crit}}$  implies that the chemical kinetic, heat conduction, and diffusion processes that determine the aluminum reaction do not cause appreciable reaction. In such a case, a failure wave along which the aluminum reaction is quenched would propagate along the detonation front away from the point A of Fig. 2.

### SAMPLE CALCULATIONS FOR PBXN-109

Calculations for the explosive PBXN-109 were made in which the detonation angle  $\beta$  was varied from  $0^\circ$  to  $90^\circ$  for metal cases of different compositions. As examples, different detonation angles that show regular reflection ( $\beta=30^\circ$ ), Mach reflection ( $\beta=70^\circ$ ), and a Prandtl-Meyer expansion fan ( $\beta=85^\circ$ ) in the products are shown, respectively, in Figs. 6,7, and 8, where the confining case is made of copper. All three figures are drawn to scale, except that in Fig. 7, the length of the Mach stem is completely arbitrary inasmuch as pseudo-stationary oblique shock theory provides no means of estimating the length of the Mach stem.

TIGER code equilibrium calculations provide the following Chapman-Jouguet values when aluminum is assumed to react completely in the reaction zone:

$$P_j = 0.23137 \text{ Mbar}, V_j = 0.45062 \text{ cm}^3/\text{g}, E_j = 0.049659 \text{ Mbar} \cdot \text{cm}^3/\text{g}, c_j = 0.56846 \text{ cm}/\mu\text{sec}, D = 0.751869 \text{ cm}/\mu\text{sec}.$$

When the aluminum is assumed to act as an "inert," i.e., there is no chemical reaction in the reaction zone, the Chapman-Jouguet values are  $P_j = 0.248647 \text{ Mbar}$ ,  $V_j = 0.457601 \text{ cm}^3/\text{g}$ ,  $E_j = 0.049334 \text{ Mbar} \cdot \text{cm}^3/\text{g}$ ,  $c_j = 0.613351 \text{ cm}/\mu\text{sec}$ ,  $D = 0.798857 \text{ cm}/\mu\text{sec}$ .

The TIGER code gives higher values of  $P_4$  and  $D$  when aluminum is considered as an inert than when it reacts completely. In the former case, the equilibrium temperature is 2208°K; in the latter case, 4158°K. However, the reaction of aluminum results in less moles, but of a higher  $\gamma$ -value gas.

In the PBXN-109 calculations, the product gas was assumed to be a  $\gamma$ -law gas:  $E = PV/(\gamma-1)$ , with  $\gamma=3.09949$  if the aluminum reacts and 3.30635 if it does not, satisfying the above Chapman-Jouguet values. The equation of state of the metal case employed the Hugoniot relationship that is derived from an experimental linear shock velocity versus particle relationship. For our purposes, such an approximate equation of state is sufficiently accurate. The Hugoniot for water is that of Hantel and Davis.<sup>13</sup>

The computer code CYLINDR was written by the author to do all of the calculations.

#### Products Pressure $P_4$ and Temperature $T_1$ at Case/Products Interface

A number of calculations were performed in which the case material was polyvinyl chloride (PVC), aluminum 921T, steel, copper, or uranium. The constant pressure  $P_4$  at the case/products interface AH of Figs. 2, 3, and 4 is plotted as a function of  $\beta$  for  $0^\circ \leq \beta \leq 90^\circ$  in Figs. 9-13 and depicted in the figure by an X; the aluminum in the explosive is assumed to act as an inert; the plots for the reacting aluminum are similar and not shown here. As expected, the pressures at the PVC/products interface are substantially lower than those at the uranium interface, with the pressures for the aluminum, steel, and copper cases falling in between.

For PVC cases, regular and Mach reflection in the products do not occur at any value of  $\beta$ ; only a Prandtl-Meyer expansion wave is present. For aluminum cases, there is no Mach reflection in the products. For steel cases, Fig. 11 shows the transition from regular to Mach reflection occurs at  $\beta=61^\circ$ . As  $\beta$  becomes sufficiently large, Mach reflection is replaced by regular reflection, which in turn is replaced by a Prandtl-Meyer expansion as  $\beta$  increases even further. For copper cases (Fig. 12), Mach reflection occurs at  $\beta=63^\circ$ . For uranium cases, the transition to Mach reflection occurs in the region of  $56^\circ < \beta < 57^\circ$ . For the copper and uranium cases, we did not run enough values of  $\beta$  to tell whether or not Mach reflection transitions to regular reflection with increasing  $\beta$  before the Prandtl-Meyer expansions for large  $\beta$  are reached.

Comparison of Figs. 9 and 11 for, respectively, the PVC and steel cases, shows that for PVC, the maximum value of  $P_4$ , 0.188 Mbars, occurs at  $\beta=0^\circ$ ; the minimum value, 0.080 Mbars, occurs at  $\beta=90^\circ$ . For steel,  $0.378 \leq P_4 \leq 0.405$  Mbars in the regular reflection region; Mach reflection reaches even higher pressures; and the minimum value, 0.172 Mbars, occurs at  $\beta=90^\circ$ . *This can explain why underwater experiments with PVC cases indicate that the aluminum reaction may not occur, or at least if having started can fail, because lateral rarefaction waves can lower the pressure and temperature too much.*

Interpolation of the TIGER-calculated temperatures along the isentrope through the Chapman-Jouguet point give values of  $T_1 \approx 2036^\circ\text{K}$  at  $P_4=0.172$  Mbars and  $T_1 \approx 1704^\circ\text{K}$  at  $P_4=0.080$  Mbars, where  $T_1$  is the temperature of the products at the case/products interface. In other words, PVC causes the products temperature to be 332°K lower than if the case were steel. However, it must be pointed out that all temperatures calculated in equilibrium codes are suspect.

#### Calculations of $t_{AH}$

Using Eqs.(52) and (53), the reduced (dimensional) time  $t_{AH}/h$  needed by an aluminum particle to travel the distance  $d$  along the case/products interface is plotted as a function of  $\beta$  and depicted by a + in Figs. 9-13. Note that in order to use the same range of ordinate values as used by  $P_4$ , we actually plot  $t_{AH}/10h$  versus  $\beta$  in Figs. 9-12 and  $t_{AH}/20h$  versus  $\beta$  in Fig. 13.

Figures 9-13 for the inert aluminum show the somewhat suprising result that for fixed  $h$  the time  $t_{AH}$  changes relatively little as a function of  $\beta$ , compared to what might be expected from viewing the motion of the aluminum particle in a coordinate system moving with the point A of Figs. 2 and 3 and point W of Fig. 5. For the PVC case, the maximum value of  $t_{AH}$  is 30% larger than the minimum value. For the aluminum, steel, copper, and uranium cases, these ratios are, respectively, 62, 6, 18, and 40%.

For  $\beta = 90^\circ$ ,  $t_{AH}/h = 3.398, 1.828, 3.246, 4.014,$  and  $6.911 \mu\text{sec/cm}$ , for, respectively, PVC, aluminum, steel, copper, and uranium cases. Thus, the PVC and steel cases give almost equal values of  $t_{AH}/h$  for  $\beta=90^\circ$ ; the PVC does not follow the trend of increasing  $t_{AH}/h$  with increasing case density.

#### Discussion of the Experiments

The forgoing analysis has shown the not suprising result that confinement by denser cases leads to higher pressures at the case/products interface and that the lowest pressures (and temperatures) behind the detonation front occur at  $\beta=90^\circ$ .

If aluminum reaction failure occurs, it is reasonable to expect that this would occur at the case/products interface for large  $\beta$ , i.e., near  $90^\circ$ , where the pressure and temperature in the products are below some threshold values that depend on the time duration  $t_{AH}$ . The larger the value of  $t_{AH}$  for given pressure and temperature, the greater the probability or degree of aluminum reaction. In fact, it would be expected that there might be some trade-off between interface product pressure  $P_4$  (and temperature  $T_1$ ) and time duration  $t_{AH}$ .

In Fig.1, the experimental values of  $h$  are given: 0.318 cm for the PVC case and 0.397, 0.794, and 1.588 cm for the three steel cases. Using the values of  $t_{AH}/h$  given above for  $\beta=90^\circ$ , it follows that  $t_{AH} = 1.08 \mu\text{sec}$  for  $P_4=0.080$  Mbars for the PVC case and 1.29, 2.58, and 5.15  $\mu\text{sec}$  for  $P_4=0.172$  Mbars for the three steel cases.

From Fig. 1, we see that aluminum reaction failure might occur at the end plate in the vicinity of the detonator before the detonation wave has reached the cylindrical surface, i.e., before  $\beta$  abruptly decreases to  $0^\circ$ . Pseudo-stationary oblique shock theory does not provide an answer as to what happens when the (assumed) hemispherical detonation wave reaches the corner defined by the end plate and the cylindrical shell of the case. The detonation angle  $\beta$  jumps discontinuously from  $90^\circ$  to  $0^\circ$  in a neighborhood of the corner. For a steel case, for example, we cannot assume that  $P_4$  jumps from 0.172 Mbar (at  $\beta \approx 90^\circ$ ) to 0.404 Mbar (at  $\beta = 90^\circ$ ) in the neighborhood of the corner point and as a result that the aluminum reaction will now begin (if it had been quenched for  $\beta = 90^\circ$ ). This is because the reflected shock wave is not moving into a constant Chapman-Jouguet detonation state, but instead is reflected into a Prandtl-Meyer expansion fan (of lower pressure and density) with a singularity at the corner (where all of the characteristics come together at the origin). This, no doubt, causes a rarefaction wave to move along the products/case interface away from the corner and in the direction of the unreacted explosive. Therefore, as  $\beta$  increases away from  $0^\circ$ , the pressure at the interface downstream of the reflected shock must lie well below 0.404 Mbar

#### THE CASE JUMP-OFF VELOCITY INTO AIR

For PBXN-109, the jump-off velocity  $v_{fs}$  of the copper case surrounded by air is given as a function of  $\beta$  in Table I; the aluminum in the explosive is assumed to react. Here,  $v_{fs} = (q_0^2 - 2q_0 q_{\text{metal}} \cos \theta_6 + q_{\text{metal}}^2)^{1/2}$ ,  $v_{\text{vert}} = q_{\text{metal}} \sin \theta_6$ , and  $\theta_{\text{metal}} = \sin^{-1}(v_{\text{vert}}/v_{fs})$ , where  $v_{\text{vert}}$  is the vertical component of  $v_{fs}$  in the direction perpendicular to the axis of symmetry of the case, and  $\theta_{\text{metal}}$  is the angle (the vector)  $v_{fs}$  makes with the horizontal.

Table I.  $P_4$ ,  $v_{fs}$ ,  $v_{\text{vert}}$ , AND  $\theta_{\text{metal}}$  AS A FUNCTION OF  $\beta$  FOR PBXN-109 IN A COPPER CASE SURROUNDED BY AIR.

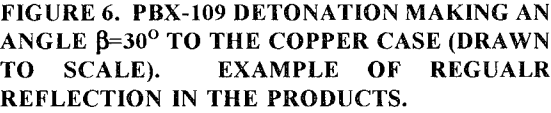
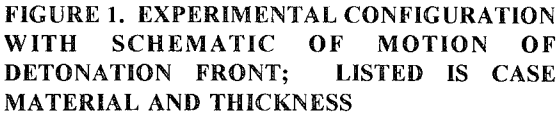
$\beta$ deg	$P_4$ Mbar	$v_{fs}$ cm/ $\mu$ sec	$v_{\text{vert}}$ cm/ $\mu$ sec	$\theta_{\text{metal}}$ deg
5	0.383	0.1658	0.1658	89.429
10	0.382	0.1649	0.1649	88.869
20	0.378	0.1612	0.1611	87.819
30	0.372	0.1554	0.1552	86.922
40	0.365	0.1479	0.1475	86.225
50	0.357	0.1396	0.1392	85.740
55	0.354	0.1358	0.1354	85.559
57	0.354	0.1347	0.1343	85.487
59	0.357	0.1343	0.1339	85.397
60	0.361	0.1349	0.1345	85.324
61	0.430*	0.1530*	0.1523*	84.611*
62	0.417	0.1490	0.1483	84.706
63	0.405	0.1451	0.1445	84.800
65	0.382	0.1378	0.1372	84.984
67	0.361	0.1310	0.1305	85.163
70	0.331	0.1216	0.1212	85.423
75	0.287	0.1075	0.1072	85.852
80	0.224	0.0874	0.0872	86.591
85	0.188	0.0751	0.0750	87.048
89	0.165	0.0674	0.0674	87.349

\*Mach reflection begins here; regular reflection occurs for smaller values of  $\beta$ .

#### REFERENCES

1. M. Finger, H.C. Hornig, E.L. Lee, and J.W. Kury, "Metal Acceleration by Composite Explosives," in *Fifth Symposium (International) on Detonation* (Office of Naval Research Report ACR-184, August 1970) p.137.
2. G. Bjarnholt, "Effects of Aluminum and Lithium Fluoride Admixtures on Metal Acceleration Ability of Comp B," in *Sixth Symposium (International) on Detonation* (Office of Naval Research Report ACR-221, August 1976) p.510.
3. W. Fickett and W.C. Davis, *Detonation* (University of California Press, Berkeley, California, 1979).
4. R. Courant and K.O. Friedrichs, *Supersonic Flow and Shock Waves* (Interscience Publishers, Inc., New York, 1956).
5. A. Ferri, *Elements of Aerodynamics of Hypersonic Flows* (Macmillan Company, New York, 1949); see Chapter 2.
6. G.I. Taylor and H. Jones, "Note on the Lateral Expansion Behind a Detonation Wave," *Phys. Ex.* 1942, 271/AC, 2093.
7. H.M. Sternberg and D. Piacesi, "Interaction of Oblique Detonation Waves with Iron," *Phys. Fluids* 9, 1307 (1966).
8. J.M. Walsh, "On the Problem of the Oblique Interaction of a Detonation Wave with an Explosive-Metal Interface," in *Proceedings of Shock Waves in Condensed Matter Symposium*, Monterey, CA (1987), p.3.
9. T. Neal, "Perpendicular Explosive Drive and Oblique Shocks," in *Sixth Symposium (International) on Detonation* (Office of Naval Research Report ACR-221, Aug. 1976), p. 602.
10. N.E. Hoskin, J.W.S. Allan, W.A. Bailey, J.W. Lethaby, and I.C. Skidmore, "The Motion of Plates and Cylinders Driven by Detonation Waves at Tangential Incidence," in *Fourth Symposium (International) on Detonation* (Office of Naval Research Report ACR-126, October 1965), p. 14.
11. W. Fickett and L.M. Scherr, "Numerical Calculation of the Cylinder Test," Los Alamos Scientific Laboratory Report LA-5906 (July 1975).
12. J.W. Enig, "The Unsteady Regular and Mach Reflection Resulting From the Interaction of Spherical Explosion Shock Waves in Water," in *Sixth Symposium (International) on Detonation* (Office of Naval Research Report ACR-221, August 1976), p. 570.
13. L.W. Hantel and W.C. Davis, "Spherical Explosions in Water," in *Fifth Symposium (Intern.) on Detonation* (Office of Naval Research Report ACR-184, Aug. 1970) p.599.





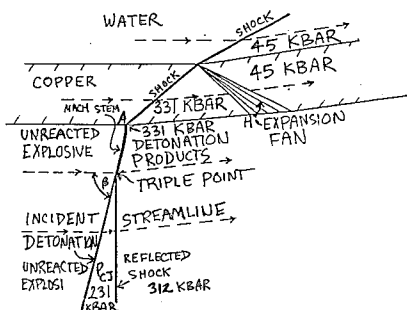


FIGURE 7. MACH REFLECTION IN PRODUCTS FOR  $\beta=70^\circ$  IN PBX-109 (DRAWN TO SCALE EXCEPT FOR THE LENGTH OF THE MACH STEM)

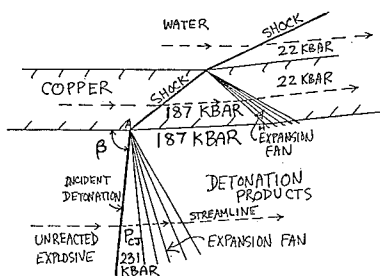


FIGURE 8. EXPANSION FAN IN PBX-109 PRODUCTS FOR  $\beta=85^\circ$  (DRAWN TO SCALE)

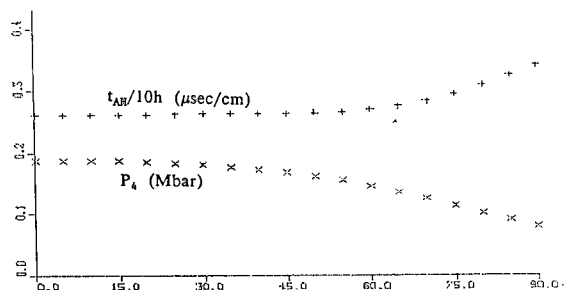


FIGURE 9.  $P_4$ (MBARS) AND  $t_{AH}/10h$  ( $\mu$ SEC/CM) AS A FUNCTION OF  $\beta$  FOR PBX-109 IN A POLYVINYL CHLORIDE (PVC) CASE SURROUNDED BY WATER

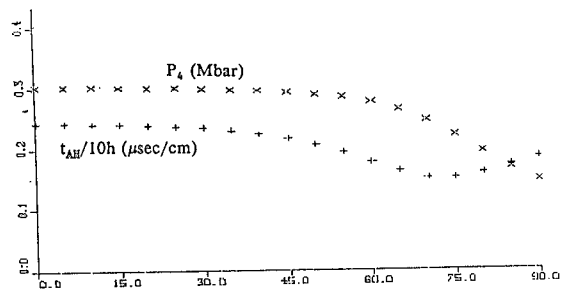


FIGURE 10.  $P_4$ (Mbar) AND  $t_{AH}/10h$  ( $\mu$ SEC/CM) AS A FUNCTION OF  $\beta$  FOR PBX-109 IN AN ALUMINUM CASE SURROUNDED BY WATER

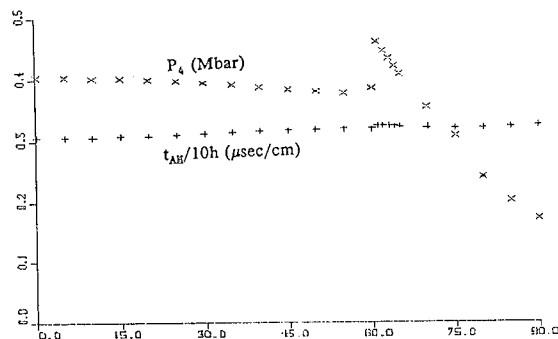


FIGURE 11.  $P_4$ (Mbar) AND  $t_{AH}/10h$  ( $\mu$ SEC/CM) AS A FUNCTION OF  $\beta$  FOR PBX-109 IN A STEEL CASE SURROUNDED BY WATER

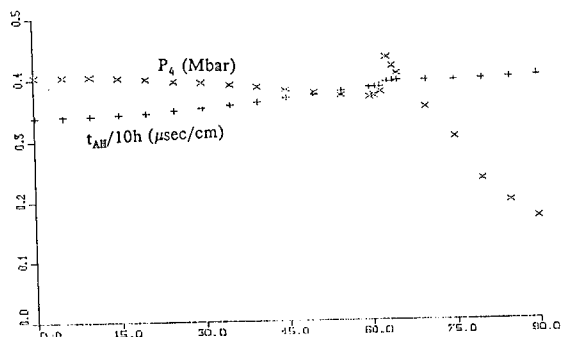


FIGURE 12.  $P_4$ (MBARS) AND  $t_{AH}/10h$  ( $\mu$ SEC/CM) AS A FUNCTION OF  $\beta$  FOR PBX-109 IN A COPPER CASE SURROUNDED BY WATER

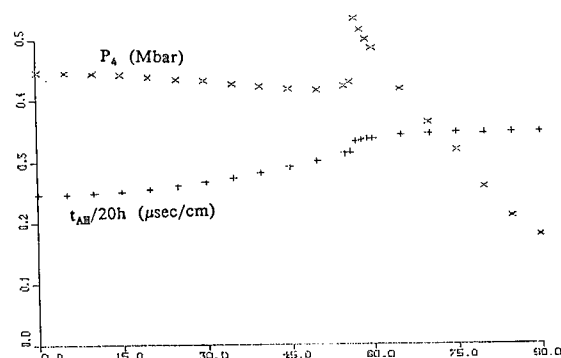


FIGURE 13.  $P_4$ (Mbar) AND  $t_{AH}/20h$  ( $\mu$ SEC/CM) AS A FUNCTION OF  $\beta$  FOR PBX-109 IN A URANIUM CASE SURROUNDED BY WATER

## **DISCUSSION**

**JOSEPH M. POWERS**

University of Notre Dame, South Bend, Indiana

Would you expect the heat release from the aluminum to influence the lead shock?

## **REPLY BY J. W. ENIG**

The reaction of aluminum with the detonation products is poorly understood to this day, but there is

much evidence, albeit indirect, that the exothermic reaction that consumes aluminum takes place over a much longer time scale than that which consumes, say, TNT, RDX, or HMX. Fine aluminum particles will tend to be consumed more readily in the CHNO reaction zone than are larger particles. That fraction of aluminum consumed upstream of the sonic surface will support the detonation front and the lead shock in the water. The aluminum reacting "late" may support the lead in the water, but only after some time interval has elapsed.

## A REACTION MODEL FOR ALUMINIZED PBX APPLIED TO UNDERWATER EXPLOSION CALCULATIONS\*

G. BAUDIN, D. BERGUES  
DGA / CENTRE D'ETUDES DE GRAMAT  
46500 GRAMAT - FRANCE

The detonation of two aluminized high explosives, B3100 (42% HMX, 9% AP, 19% Al, 30% binder) and B3103 (51% HMX, 19% Al, 30% binder), and a reference high explosive identical to B3103 except for the aluminum which was replaced by LiF, was studied in small-scale ballistic tests. Liner velocity measurements conducted using a Fabry-Perot interferometer revealed slow oxidation of the aluminum in the Taylor rarefaction wave. A model based on the experimental results was developed, identified through symmetrical plane test experiments and then validated in several other small-scale ballistic tests. The use of this model in numerical simulation of underwater explosions shows good agreement between experiments and calculations, thereby offering an interesting perspective for numerical simulation in this type of configuration.

### INTRODUCTION

Aluminized high explosives, frequently used in underwater charges, exhibit a particular behavior related to aluminum oxidation. A classical detonation model using a JWL equation of state does not provide an accurate description of detonation of these non-ideal explosives. Aluminum oxidation in condensed high explosives has been the object of several studies that conclude with contradictory results. In most of these works, the effect of aluminum appears behind the detonation wave, but the interpretations provided vary greatly depending on the author. There are two major explanations: (i) aluminum oxidation in the detonation front associated with heat exchanges or chemical recombination in the Taylor rarefaction wave,<sup>4,8,12</sup> (ii) gradual combustion of aluminum in the rarefaction wave.<sup>1,9,16,17</sup> The difficulties encountered in demonstrating the reaction mechanism of aluminum in various high explosives are increased by the fact that its energy contribution may depend on its content, its grain-size distribution and the chemical

species formed in the detonation products. In this paper, the reaction behavior of aluminum in HMX- and ammonium perchlorate-based high explosives is analyzed in order to develop a model for predicting high explosive performance in aerial small-scale tests and underwater explosions.

This analysis is based on a large amount of experimental data resulting from various small-scale tests of ballistic capability,<sup>10</sup> as well as calculations carried out using a specific thermochemical code which takes into account the mass fraction of aluminum oxidized in the detonation front.

### EXPERIMENTAL RESULTS

The reaction behavior of aluminum was studied in two compositions, B3100 (42% HMX, 9% AP, 19% Al, 30% binder) and B3103 (51% HMX, 19% Al, 30% binder), with a nitroglycerine-based energetic binder. A reference explosive, B3212, identical to B3103 except for the aluminum (Al), which was replaced by lithium fluoride (LiF), was also used. The lithium fluoride is a constituent known to have thermodynamic characteristics close to that of aluminum<sup>6</sup> and to remain inert in a reactive medium.

\* Work performed under the auspices of the French Ministry of Defence by the Centre d'Etudes de Gramat under S.T.P.E. contract.

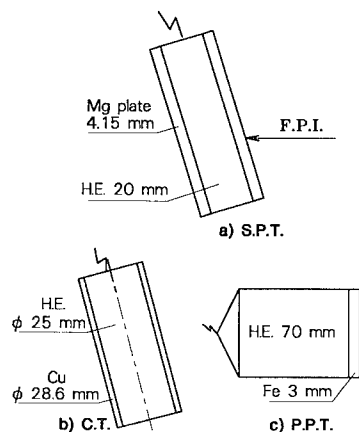


FIGURE 1. EXPERIMENTAL SET-UP

The three high explosives were subjected to small-scale ballistic tests. Figure 1 shows the three test configurations used in this study: the symmetrical plane test using magnesium plates (SPT), the copper cylinder test (CT), and the steel plate push test (PPT). In these tests, detonation velocity is measured using self-shorting pins and the liner velocity is measured using a Fabry-Perot laser interferometer. The velocities presented in this paper are average records obtained over several shots; the resulting reproducibility is approximately 2% on the final velocity values.

Analysis of these results is based mainly on comparison of liner accelerations produced by the three explosives in the SPT and PPT configurations. According to the SPT and PPT results presented in Figure 2, it is difficult to evaluate the influence of aluminum (Al) and ammonium perchlorate (AP) on the first velocity jump. An analysis of the first microseconds of each velocity record shown in Figure 3 reveals that AP and Al have no particular effect at the very beginning of metal liner acceleration.

After a few microseconds, the liner velocity values obtained for the aluminized explosives are significantly higher than the result observed for the explosive containing LiF. Acceleration of the metal liners is gradual and appears to continue at the end of the velocity recordings. This gradual acceleration is sustained by the energy released through decomposition of the explosive, weighted by the efficiency of the configuration. Assuming that the efficiency of each configuration is independent of the explosive, the more sustained acceleration of the liner observed in each configuration for explosives B3103 and B3100 is thus due to the Al energy contribution. A closer look at the detonation velocity for explosives B3103 and B3212 indicates that Al is not oxidized in the Chapman-Jouguet plane; these velocity values are very close (7810 m/s for B3103 and 7790 m/s for B3212).

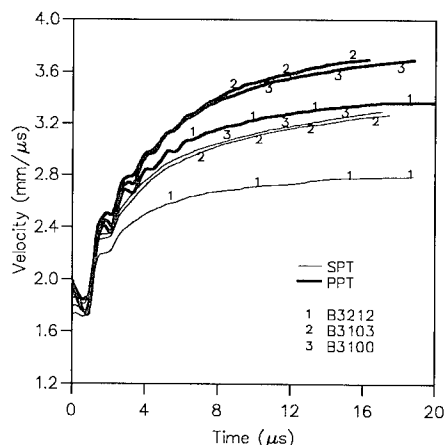


FIGURE 2. PPT AND SPT: PLATE VELOCITY FOR B3100, B3103, AND B3212

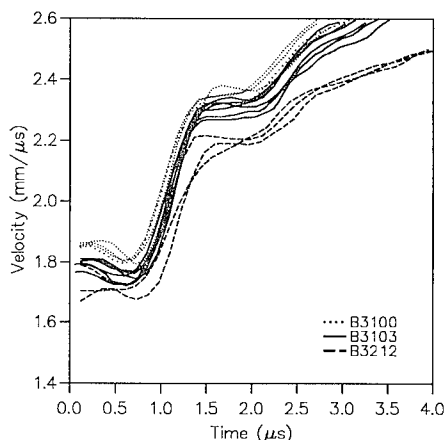


FIGURE 3. FIRST MICROSECONDS OF SPT VELOCITY RECORDINGS

These two important results lead to elimination of the hypothesis, assumed by certain authors,<sup>4,8,12</sup> of complete oxidation of Al in the detonation front, and to retain an oxidation mechanism in the Taylor rarefaction wave from the Chapman-Jouguet point. The sonic point (CJ) is reached before the end of irreversible reactions.

Another important result is the very small divergence in the metal liner velocities when using explosives B3100 and B3103 in SPT and PPT (Figure 2). Explosive B3100, with a lower HMX content, provides as much energy as B3103. The advantage of adding AP is therefore obvious with regards to ballistic performance. Substituting AP for a fraction of HMX ensures a very slight increase in the density of the explosive—the difference in density between HMX and AP is not great and AP is only 9 % of the formulation—, as well as a significant supply of oxygen, favoring the formation of propellant gases CO and CO<sub>2</sub>, to the detriment of solid carbon, thereby improving conversion of Al into Al<sub>2</sub>O<sub>3</sub>. The small size of AP grains leads to

assume a very fast reaction of the products of AP decomposition with the products of HMX decomposition.

Aluminum oxidation can occur according to several chemical reaction patterns. Given the composition of the products resulting from decomposition of the HMX, binder and AP, calculated using the BKW code<sup>13</sup>, the most probable patterns involve reduction of H<sub>2</sub>O and CO<sub>2</sub>. Reducing H<sub>2</sub>O produces hydrogen (H<sub>2</sub>), whereas reducing CO<sub>2</sub> can produce either CO or solid carbon (C). The BKW code indicates the presence of a simultaneous reduction of H<sub>2</sub>O and CO<sub>2</sub> without formation of solid carbon, while analyses of the detonation products of various aluminized explosives carried out by Volk and al.<sup>20</sup> give greater importance to the reduction of CO<sub>2</sub> with a significant formation of solid carbon. The energy contribution Q<sub>Al</sub> of this reaction pattern is 20.126 MJ/kg of aluminum.

In the present paper, the latter reaction pattern has been chosen. It is based on complete decomposition of AP in the Chapman-Jouguet plane and on gradual oxidation of Al into Al<sub>2</sub>O<sub>3</sub> in the rarefaction wave. The rate of conversion  $\alpha(t)$  of Al into Al<sub>2</sub>O<sub>3</sub> can then be calculated behind the detonation front from the kinetic energy transmitted to the plate in the symmetrical plane test<sup>10</sup> using explosives B3103 et B3212 :

$$\alpha(t) = \frac{1}{2\eta\psi Q_{Al}} \left( V_{B3103}^2(t) - V_{B3212}^2(t) \right) \quad (1)$$

$\xi$  is the ratio of the projected metallic mass with respect to the explosive mass (0.4),  $\psi$  is the Al mass fraction (0.19) and  $\eta$  is the average efficiency of the configuration (SPT : 0.533). The aluminum-to-alumina conversion rate, shown in Figure 4, reaches 30% after 20  $\mu$ s of velocity recording.

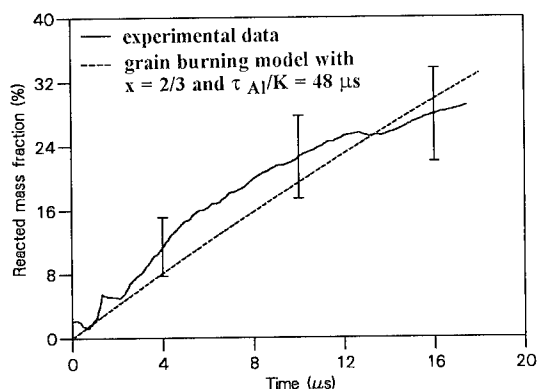


FIGURE 4. ALUMINUM-TO-ALUMINA CONVERSION RATE IN THE RAREFACTION WAVE

Given the increase of the Al conversion rate versus time in fig. 4, it can reasonably be expected that the aluminum will continue to oxidize for several microseconds more. These results show that the magnitude of

the time characteristic of aluminum oxidation is several tens of microseconds, i.e. much greater than the decomposition time of the other constituents in the explosive which is usually a few hundred nanoseconds. The aluminum-to-alumina conversion velocity  $d\alpha/dt$ , derived from the  $\alpha(t)$  curve, provides interesting information that can be used to identify the adjustable parameters of an aluminum reaction kinetic pattern.

## MODELLING

On the basis of the preceding analyses, the detonation state of the explosives studied can be defined by a reaction scenario similar to the one proposed by Finger et al.<sup>9</sup> (1970) and used by Veyssi re<sup>18-19</sup> for gaseous explosives:

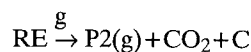
- (1) reaction initiation in the most reactive constituent,
- (2) decomposition of the HMX, binder and AP in the stationary zone, sustaining the detonation,
- (3) heating of the aluminum particles to their ignition temperature through absorption of the energy from the detonation products,
- (4) Al oxidation when its temperature is greater than its ignition temperature, releasing a large amount of energy in the rarefaction wave.

It is therefore considered that the aluminum particles are not thermally in balance with the remaining explosive and its decomposition products, allowing the model to be used for various detonation states.<sup>5</sup> The initiation phase, also required in applying the model to various detonation states, results in local reactions around the hot spots that develop in the nitroglycerine, which has an adiabatic explosion time significantly less than those of the other explosive constituents.

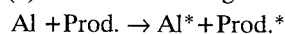
### a) Reaction kinetics

The mass fractions of nitroglycerine (NG) and aluminum (Al) contained in the explosive are denoted  $\mu$  and  $\psi$ . The remaining explosive, with a mass fraction of  $1-\mu-\psi$ , is designated RE. In the proposed reaction pattern, reactions develop around hot spots in the nitroglycerine (NG). These reactions then spread into the remaining explosive RE when a sufficient fraction of nitroglycerine has decomposed. Aluminum oxidation takes place as soon as its temperature reaches the ignition level. Denoted  $f$ ,  $g$  and  $\alpha$  the reacted mass fraction of NG, RE and Al, the stages taken into account in this model are:

- (1) decomposition of the mass fraction  $\mu$  of nitroglycerine,
 
$$\mu \xrightarrow{f} \text{P1(g)} + \text{CO}_2$$
- (2) decomposition of the mass fraction  $(1-\mu-\psi)$  of explosive,

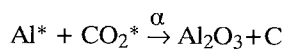


(3) aluminum heating

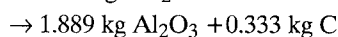
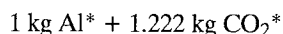
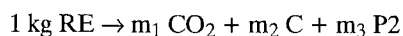
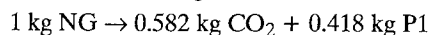


where  $\text{Prod.} = [\text{P1(g)} + \text{P2(g)} + \text{CO}_2 + \text{C}]$ ,  $\text{Al}^*$  is the heated aluminum and  $\text{Prod}^*$  the cooled products,

(4) aluminum oxidation when its temperature reaches the ignition temperature,



P1 and P2 represent respectively the products of nitroglycerine reactions and of the remaining explosive without the  $\text{CO}_2$  and the solid carbon. Formulation of the reaction kinetics requires the mass balance of the chemical reactions. The amounts of carbon and  $\text{CO}_2$  produced in reactions (1) and (2) are calculated according to the KAMLET<sup>2</sup> method. A balance in mass is achieved in the chemical reactions (1), (2) and (4) in the following manner:



with

$$m_1 = \frac{0.044(n_1 - 13.22\mu)}{1 - \mu - \psi}$$

$$m_2 = \frac{0.012n_2}{1 - \mu - \psi} \quad \text{and} \quad m_3 = 1 - m_1 - m_2$$

$n_1$  and  $n_2$  are the number of moles of  $\text{CO}_2$  and C produced after complete decomposition of 1 kg of explosive without oxidation of the aluminum.

The reaction rates are expressed according to the conventional method used in kinetic chemistry. The variations in the mass concentrations of nitroglycerine and the products P1 formed in reaction (1) are given by the equations:

$$\frac{d[\text{NG}]}{dt} = -\frac{[\text{NG}]^{A1}}{\tau_{\text{NG}}} \quad (2)$$

$$\frac{d[\text{P1}]}{dt} = -0.418 \frac{d[\text{NG}]}{dt} \quad (3)$$

According to reaction (2),

$$\frac{d[\text{RE}]}{dt} = -\frac{[\text{RE}]^{A2}}{\tau_{\text{RE}}} \quad (4)$$

$$\frac{d[\text{P2}]}{dt} = -m_3 \frac{d[\text{RE}]}{dt} \quad (5)$$

Reaction (4) leads to the following kinetic laws:

$$\frac{d[\text{Al}]}{dt} = -\frac{[\text{Al}]^{A3}[\text{CO}_2]^{B3}}{\tau_{\text{Al}}} \quad (6)$$

$$\frac{d[\text{Al}_2\text{O}_3]}{dt} = -1.889 \frac{d[\text{Al}]}{dt} \quad (7)$$

$$\frac{d[\text{C}]}{dt} = -m_2 \frac{d[\text{RE}]}{dt} - 0.333 \frac{d[\text{Al}]}{dt} \quad (8)$$

$$\frac{d[\text{CO}_2]}{dt} = 1.222 \frac{d[\text{Al}]}{dt} - 0.582 \frac{d[\text{NG}]}{dt} - m_1 \frac{d[\text{RE}]}{dt} \quad (9)$$

Transformation (3) is described by the usual heat transfer equations.<sup>3</sup>

The reacted explosive fraction being denoted as  $r$ , the mass fractions are governed by the following equation:

$$r = (1 - \psi)\lambda + \psi\alpha \quad (10)$$

with

$$\lambda = \left( \frac{\mu}{1 - \psi} \right) f + \left( 1 - \frac{\mu}{1 - \psi} \right) g \quad (11)$$

and the  $[\text{Al}]$ ,  $[\text{NG}]$ ,  $[\text{RE}]$  and  $[\text{CO}_2]$  concentrations are expressed as follows:

$$[\text{NG}] = \mu(1 - f) \quad (12) \quad \text{and} \quad [\text{Al}] = \psi(1 - \alpha) \quad (13)$$

$$[\text{RE}] = (1 - \mu - \psi)(1 - g) \quad (14)$$

$$[\text{CO}_2] = 0.044n_1 + 0.582\mu(f - g) - 1.222\psi\alpha \quad (15)$$

Variations in the mass concentrations of aluminum, nitroglycerine, and the remaining explosive RE are then written in the form:

$$\frac{d\alpha}{dt} = \psi^{A3-1} \frac{(1 - \alpha)^{A3} [\text{CO}_2]^{B3}}{\tau_{\text{Al}}} \quad (16)$$

$$\frac{df}{dt} = \frac{(1 - f)^{A1}}{\tau_{\text{NG}}} \mu^{A1-1} \quad (17)$$

$$\frac{dg}{dt} = \frac{(1 - g)^{A2}}{\tau_{\text{RE}}} (1 - \mu - \psi)^{A2-1} \quad (18)$$

The first of these three equations can be simplified when the value of  $(0.044n_1)/(1.222\psi)$  involved in  $[\text{CO}_2]$  is close to 1. Simplification can be performed in this way for explosives B3103 and B3100 for which this ratio is equal to 1.09. Heat exchanges between the aluminum and the reaction products of the nitroglycerine and of the remaining explosive are phenomena for which the characteristic time is greater than the characteristic time of reactions (1) and (2) for particle diameters greater than a micrometer. Analysis of the experiment data has shown that the characteristic time of aluminum oxidation is quite long compared to the characteristic time of the other chemical reactions. These two observations lead to the conclusion that reactions (1) and (2) have ended when aluminum oxidation begins. In this case,  $f$  and  $g$  can be chosen to be equal to 1 in the  $[\text{CO}_2]$  expression, leading to non-oxidation of aluminum in the detonation front, in agreement with the experimental results. The aluminum oxidation velocity can then be expressed in a simple manner:

$$\frac{d\alpha}{dt} = \frac{k}{\tau_{\text{Al}}} (1 - \alpha)^x \quad (19)$$

where

$$k = 1.222^{B3} \psi^{x-1} \quad \text{with} \quad x = A3 + B3$$

This expression of the aluminium reaction kinetics calls upon two values: the order of reaction  $x$  and a time constant  $\tau_{Al}/k$  which may depend on the local thermodynamic state of the aluminum. Identification of these values on the  $\alpha(t)$  curve, derived from the kinetic energy values of the metal liner in the SPT test produced by B3103 and B3212 (Figure 4), require additional hypotheses on how  $\tau_{Al}$  is influenced by temperature or pressure. In a first approach, the time constant is considered to be independent of the thermodynamic conditions. Several combinations of the values of  $x$  and  $\tau_{Al}$  have been explored. The best results are obtained for  $x=2/3$  and  $\tau_{Al}/k=48 \mu s$ , leading to an acceptable reproduction of the  $\alpha(t)$  curve in Figure 4. The value of the order of reaction  $x$  corresponds to grain burning of spherical particles having the same diameter. In this particular instance,  $\tau_{Al}/k$  takes the form

$$\frac{\tau_{Al}}{k} = \frac{d_{Al}}{6V_r} \quad (20)$$

where  $V_r$  is the grain burning velocity of spherical particles and  $d_{Al}$  their mean diameter. The advantage of this model is its ability to reproduce the influence of the diameter of aluminum particles. A good agreement is obtained with the experimental results of Tao et al.<sup>17</sup> on the dependence of reaction on Al particle size.

Using a grain burning mode of the aluminum particles, this model can be improved in several ways. By taking into account the distribution of the particle diameters, it is possible to search for the grain size distribution that leads to optimal explosive efficiency. Another improvement is achieved by using the Saint-Venant relation between burning velocity  $V_r$  and pressure, thus taking into account confinement of the explosive in different configurations.  $V_r$  can be expressed in the form

$$V_r = V_r^{CJ} \left( \frac{P}{P_{CJ}} \right)^y \quad (21)$$

where  $V_r^{CJ}$  and  $y$  are adjustable parameters.

The expressions for the time characteristics  $\tau_{NG}$  and  $\tau_{RE}$  retained in this model for reactions (1) and (2) are those of Johnson, Tang and Forest<sup>11,15</sup> used in their model of hot-spot initiation of HMX-based high explosives. For nitroglycerine,  $\tau_{NG}$  is the adiabatic explosion time calculated for a mean hot spot temperature  $\theta$

$$\tau_{NG} = \frac{\theta^2}{\theta_{act}\beta Z} \exp\left(\frac{\theta_{act}}{\theta}\right) \quad (22)$$

$Z$ ,  $\theta_{act}$  and  $\beta$  are respectively the pre-exponential factor, the activation temperature, and the adiabatic temperature rise. For the remaining explosive RE,  $\tau_{RE}$  is given by the Forest-Fire<sup>11</sup> model corrected at low pressures by the term  $G_0(P/P_0)$  with a reference pressure  $P_0$ :

$$\tau_{RE} = \frac{f-f_0}{1-f_0} \left[ G_0 \frac{P}{P_0} + A \left( \frac{P}{P_0} \right)^n + B \left( \frac{P}{P_0} \right)^7 \right]^{-1} \quad (23)$$

The values for the orders of reaction A1 and A2 involved in the decomposition velocity of nitroglycerine and the remaining explosive are not readily available. They are assumed to be equal to 1, as in the Johnson, Tang and Forest model.

The mean hot spot temperature reached under shock is calculated using an empirical equation<sup>11</sup>:

$$\theta_c = \theta_0 \left( 1 - m \frac{\theta_0}{\theta_{act}} \ln \left( \frac{P_c}{P_0} \right) \right)^{-1} \quad (24)$$

After the shock, the change in the temperature of the hot spots is described by an adiabatic compression process:

$$\frac{d\theta}{dt} = \theta \Gamma k \frac{dP}{dt} \quad (25)$$

where  $\Gamma$  is the Gruneisen coefficient and  $k$  the isentropic compressibility coefficient given by the equations of state of the inert explosive.

#### b) Heat transfer between aluminum and decomposition products

Calculation of the ignition time for aluminum particles is achieved through simple processing of the heat transfers between aluminum and the explosive decomposition products. The ignition time for a spherical particle, isolated and immersed instantaneously in the gaseous products generated during decomposition of the HMX, binder and ammonium perchlorate, can be calculated by assuming the hypotheses used by Veyssière<sup>18-19</sup> in a model developed for gaseous explosives with aluminum particles. This author assumes that the temperature balance is reached instantaneously at all points within the particle, this hypothesis being confirmed for particles with a diameter less than 100  $\mu m$ , and that these particles are subject to convected and radiated heat exchanges. The aluminum ignition mechanism used in this model is based on a diffusion limited process of the chemical species throughout the alumina layer present at the surface of the particles. These particles ignite when their temperature reaches the melting point of alumina (2290 K).

The equation used to calculate the differential of the aluminum temperature  $T_{Al}$  is derived from the energy conservation equation applied to spherical particles and from theoretical considerations concerning the three-phase mixture composed of aluminum, alumina and gaseous products. This is expressed as follows:

$$\begin{aligned} \frac{dT_{Al}}{dt} = & T_{Al} \Gamma_{Al} k_{Al} \frac{dP}{dt} \\ & + \frac{h}{\rho_{Al} C_p} \left( \frac{S}{V} \right)_{Al} \frac{T_{Al} - T}{1-\psi} + \psi Q_{Al} \frac{d\alpha}{dt} \end{aligned} \quad (26)$$



where  $\left(\frac{S}{V}\right)_{Al}$  is equal to  $\frac{6}{d_{Al}}$ .

$\Gamma_{Al}$  and  $k_{Al}$  are respectively the Gruneisen coefficient and the isentropic compressibility coefficient of aluminum.  $C_p$  is its heat capacity at constant pressure and  $h$  represents the heat exchange between the aluminum and the gaseous products. Integration of this equation is performed from the aluminum temperature reached at the shock front. In steady detonation, the shock front is assumed to be at Von-Neuman pressure. The temperature of shock-loaded aluminum is developed in a polynomial form identified on the Hugoniot curve, calculated from the Hugoniot:

$$(T_{Al})_c = 300 + 0.48 \cdot 10^{-9} P_c + 0.29 \cdot 10^{-20} P_c^2 + 0.46 \cdot 10^{-33} P_c^3 \quad (27)$$

where  $P_c$  is the shock pressure expressed in CGS units.

The coefficient  $h$  is a physical parameter that can be evaluated in the Chapman-Jouguet state using the heat exchange equations used in the Selman<sup>14</sup> method. This can also be used to reproduce aluminum ignition time.

c) Equations of state for the explosive during decomposition

The thermodynamic states of this reaction system are described by Helmholtz  $F$  free energy, written as a function of the specific volume  $V$ , temperature  $T$ , the parameter  $\lambda$  representing the overall progress of reactions (1) and (2) and the aluminum-to-alumina conversion rate  $\alpha$ . Pressure  $P$ , internal energy  $E$  and entropy  $S$  are derived using the classical thermodynamic equations. The free energy differential is expressed as follows:

$$dF = -PdV - SdT - f_\lambda d\lambda - f_\alpha d\alpha \quad (28)$$

which can be used to calculate the entropy differential

$$dS = \frac{1}{T} \left( \frac{\partial E}{\partial T} \right)_{V,\lambda,\alpha} dT + \frac{1}{T} \left( \left( \frac{\partial E}{\partial V} \right)_{T,\lambda,\alpha} + P \right) dV + \frac{1}{T} \left( \left( \frac{\partial E}{\partial \lambda} \right)_{V,T,\alpha} + f_\lambda \right) d\lambda + \frac{1}{T} \left( \left( \frac{\partial E}{\partial \alpha} \right)_{V,T,\lambda} + f_\alpha \right) d\alpha \quad (29)$$

Entropy is exact and the equality of the crossed derivatives of the multiplying coefficients of  $dT$ ,  $dV$ ,  $d\lambda$  and  $d\alpha$  leads to thermodynamic identities that must be verified by the equations of state. Simplifying hypotheses are needed to derive the equations of state. The following hypotheses are used:

- (a) affinity  $f_\alpha$  remains constant and equal to  $Q_{Al}$
- (b) the heat capacity at constant volume depends strictly on the parameter  $\lambda$ .

On the basis of these hypothesis, the thermodynamic identities lead to the following pressure and energy equations:

$$P(V, T, \lambda, \alpha) = \left( \frac{\delta f_1(V, \lambda)}{\delta V} \right)_\lambda + \eta(V, \lambda) T \quad (30)$$

$$E(V, T, \lambda, \alpha) = f_1(V, \lambda) + C_v(\lambda) T + \alpha Q_{Al} \quad (31)$$

The functions  $\eta(V, \lambda)$ ,  $f_1(V, \lambda)$  et  $C_v(\lambda)$  are selected for linear forms of the parameter  $\lambda$ :

$$\eta(V, \lambda) = \lambda \eta_g(V) + (1-\lambda) \eta_s(V) \quad (32)$$

$$C_v(\lambda) = \lambda C_{vg} + (1-\lambda) C_{vs} \quad (33)$$

$$f_1(V, \lambda) = \lambda f_g(V) + (1-\lambda) f_s(V) \quad (34)$$

where indices  $s$  and  $g$  represent the solid explosive and the decomposition products when the aluminum remains inert. The quantity  $\eta$  is expressed as a function of the Gruneisen coefficient and the heat capacity at constant volume:

$$\eta(V) = \frac{\Gamma C_v}{V} \quad (35)$$

The Gruneisen coefficient and the heat capacity of the solid explosive and the decomposition products are assumed to be constant. For the solid, potential  $f_s$  is the sum of the repulsive and attractive potentials:<sup>7</sup>

$$f_s = A \left( \frac{V}{V_0} \right)^{-a} - B \left( \frac{V}{V_0} \right)^{-b} \quad (36)$$

The coefficients are identified to reproduce the Hugoniot curve deduced from a linear relation between the shock velocity and the material velocity.

For the decomposition products, potential  $f_g$  is derived from a JWL equation, the aluminum being considered inert, assuming a constant heat capacity:<sup>2,3</sup>

$$f_g = -Q_{ch} + \frac{A}{R_1} e^{-R_1 \frac{V}{V_0}} + \frac{B}{R_2} e^{-R_2 \frac{V}{V_0}} + \frac{C}{\omega V^\omega} \quad (37)$$

It can either be identified to reproduce the isentrope given by the Chapman-Jouguet state calculated using a thermochemical code,<sup>2,5</sup> or identified to reproduce the explosive small-scale test experiments in which the aluminum is replaced by lithium fluoride.

## ASYMPTOTIC BEHAVIOR OF THE MODEL IN STEADY DETONATION

In the explosive's initiation phase, all the kinetic stages of the model must be considered. In steady detonation, the kinetic processes can be reduced to a few stages. Since detonation occurs at very high pressures (Von-Neuman pressure), the characteristic reaction time of nitroglycerine around the hot spots is significantly lower than that of the other reactions; the nitroglycerine is consumed rapidly and  $f$  is instantly equal to 1. The reaction velocity of the remaining explosive (RE) is thus simplified considerably:

$$\frac{dg}{dt} = \frac{(1 - g)}{\tau_{RE}} \quad (38)$$

As pressure is high in the reaction zone, the term  $G_0(P/P_0)$  involved at low pressure in the time constant  $\tau_{RE}$  is negligible in comparison with the other terms, and the reaction kinetics are reduced to the “Forest–Fire”, required to process the reaction zone in steady detonation.

This latter equation, associated with the aluminum combustion law, represents the asymptotic behavior of the original reaction model.

The adjustable parameters in this model are then reduced to the “Forest–Fire” parameters, the equation of state parameters, heat exchange coefficient  $h$ , aluminum particle burning velocity  $V_r$ , and the  $y$  exponent of the Saint–Venant law. The parameters are adjusted to reproduce the plate acceleration in the symmetrical plane test.

## NUMERICAL SIMULATIONS

### a) Model identification and validation in ballistic capability tests

In the explosives studied, the aluminum grain–size distribution is centered around a diameter of 16  $\mu\text{m}$  with a low mean deviation. The present case is thus assumed to be one where the diameter is the same for the entire particle population. The low level of dependence between the aluminum reaction rate derived from Figure 4, and pressure in the SPT test leads to the choice of a null value for the  $y$  exponent of the Saint–Venant law.

The aluminum particle burning velocity is therefore the only adjustable parameter that may be used to control the energy released in the Taylor rarefaction wave. A preliminary estimation of its value can be made on the basis of the  $\alpha(t)$  curve presented in Figure 4.

The value of the heat exchange coefficient  $h$  is evaluated using the heat exchange equations<sup>3,14</sup> applied to the Chapman–Jouguet state. These equations give a very high value, to the order of several  $\text{MJ/m}^2\text{K}$ , which confirms the results of the SPT and PPT experiments showing that aluminum oxidation begins in a flow region neighboring the end of the stationary reaction zone.

The parameters of potential  $f_g$  of the B3103 reaction products are identified to reproduce the acceleration of the magnesium plates in the SPT test where aluminum is replaced by lithium fluoride (explosive

B3212). This costly solution can be replaced by identification of these parameters on an isentrope from the Chapman–Jouguet point calculated using a thermochemical code when the aluminum remains inert. A simple thermochemical computation method was developed for this purpose to calculate the Chapman–Jouguet characteristics of  $\text{CHNOFCAl}$  explosives<sup>2</sup> as a function of the oxidized aluminum mass fraction in the Chapman–Jouguet plane. This method also provides a calculation of the isentropic rarefaction wave from the Chapman–Jouguet state. When applied to explosive B3103, it shows that the pressure calculated along the isentrope taken from the Chapman–Jouguet point is in good agreement with that identified for explosive B3212 (Figure 5).

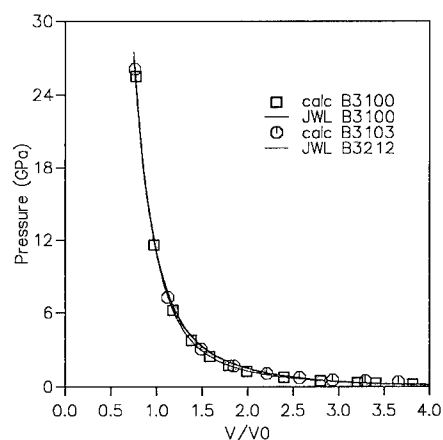


FIGURE 5. B3100, B3103 AND B3212 ISENTROPIC RAREFACTION WAVES

For explosive B3100, the parameters of potential  $f_g$  are identified to reproduce both the beginning of the SPT magnesium plate velocity recording and the isentropic rarefaction wave from the Chapman–Jouguet point given by the thermochemical computation method.

Numerical simulations of the SPT experiments were carried out using the finite–element Lagrangian code EPIC2. Comparisons between the experiment and calculations are shown in Figure 6 for explosives B3103 and B3100.

This model, identified to reproduce the SPT liner velocity for explosives B3103, B3100 and B3212, was then validated in PPT and CT experiments. The PPT numerical simulation for B3103, B3100 and B3212 gives results that are in good agreement with the experiments (Figure 6). Good numerical results are also obtained for the cylinder test (Figure 6).

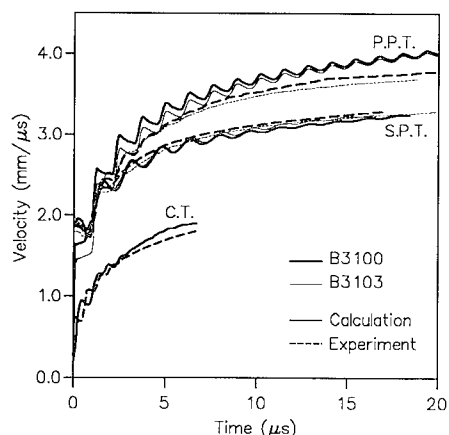


FIGURE 6. LINER VELOCITIES: SPT, PPT AND CT TESTS

#### b) Application in calculating underwater explosions

In order to validate the model for applications similar to those used in the armed forces, underwater charges of approximately 10 kg were fired. Conducted as part of a French and British joint program, these experiments were carried out by DRA/Fort Halstead. Testing involved in particular B3103 and TNT explosives. TNT was selected due to its almost ideal behavior in detonation. Instrumentation consisted of 12 tourmaline pressure sensors placed horizontally along 3 radii ( $-30^\circ$ ,  $0^\circ$ ,  $+30^\circ$ ). In order to allow application of the principles of similitude,<sup>21</sup> the sensors were positioned at a distance  $x$  from the axis of the explosive charge,  $x$  being between 1.25 m and 4.25 m. The corresponding reduced distance  $z$  thus varied from 0.6 to 2 ( $z = xW^{-1/3}$  where  $W$  is the weight of the charge in kg), a range where the relations between the pressure logarithm and the reduced distance logarithm are known to be linear. The maximum pressure  $P_{\text{Max}}$  and the reduced impulse  $I_R$ , were taken for each signal, the value of the latter being calculated as follows:<sup>21</sup>

$$I_R = \frac{1}{W^{1/3}} \int_0^{6.7\theta} P dt$$

where  $\theta$  is the interval during which the pressure drops from  $P_{\text{Max}}$  to  $P_{\text{Max}}/e$ .

Numerical simulations of these experiments were conducted in parallel at CEG using a spherical one-dimensional lagrangian code containing the presented model. For TNT, a simple detonation wave-front model was used. The numerical signals  $P(t)$  noted at various lagrangian abscissas were processed by DCN/Toulon-Etudes, as they involved experimental signals. Figures 7 and 8 show that the calculated and experimental results for parameters  $P_{\text{Max}}$  and  $I_R$  are in good agreement.

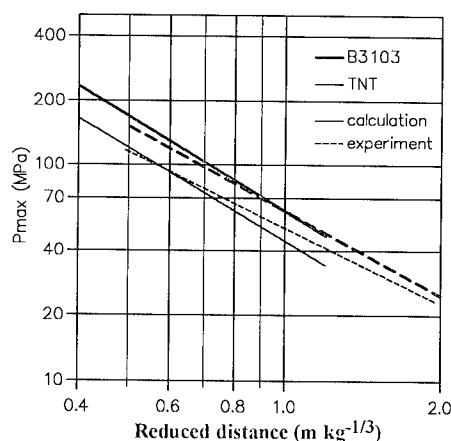


FIGURE 7. UNDERWATER EXPLOSIONS: MAXIMUM PRESSURE

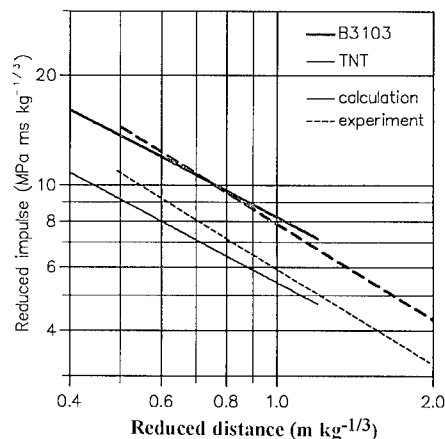


FIGURE 8. UNDERWATER EXPLOSIONS: REDUCED IMPULSE

#### CONCLUSION

A model was developed for numerical simulation of various types of detonation states in high explosives containing aluminum. It was used to simulate steady detonation in small-scale experiments with the aim of simulating underwater explosion of large charges containing aluminized compositions.

The parameters of this model were adjusted to reproduce SPT. The model was then validated in PPT and CT. The results of the numerical simulations achieved using this model were in good agreement with the experimental data. They demonstrated that the grain burning model of the aluminum particles correctly reproduced the energy released through oxidation for the expansion velocities encountered in various small-scale tests. They also showed that Al oxidation begins in a flow region neighboring the end of the stationary zone, thus revealing that a heat balance is rapidly attained between the decomposition products of the explosive and the aluminum particles.

Although the expansion velocities were clearly lower in the underwater explosions than in the small-scale tests, numerical simulations of this type of configuration correctly reproduce all phenomena observed in the experiments conducted.

## ACKNOWLEDGEMENTS

The authors extend their thanks to Dr. Haskins' workgroup at DRA/Fort Halstead (England) for conducting the underwater explosion experiments, to SNPE/CRB for producing the explosives and supplying certain experimental data, and DCN/Toulon-Etudes (with special thanks to Ph. Boyce) for processing calculated pressure profiles. They also thank the members of the detonics team at the Centre d'Etudes de Gramat who contributed to this work, especially Mr. Lagarde for data processing.

## REFERENCES

1. Afanas'eva E.A., Levin V.A., "Aluminum-particle ignition and combustion behind shock and detonation waves", Translated from *Fizika Goreniya i Vzryva*, Moscou, Vol. 23, No. 1, 1987, pp. 8-14.
2. Baudin G., "Un code thermochimique adapté au calcul des caractéristiques de détonation des explosifs aluminisés", in *Proceedings of EURO-PYRO*, Strasbourg France, 1993, p. 409.
3. Baudin G., Bergues D., "Aluminum combustion in HMX/AP based high explosives", in *Proceedings of MWDDEA AF-71-F/G 7304 Physic of explosives*, Paris France, 1991, Vol. 1, p. 193.
4. Belyaev A.F., Frolow Yu.V., Korotkov A.I., "Combustion and ignition of particles of finely dispersed aluminum", *Fizika Goreniya i Vzryva*, Moscou, Vol. 4, No.3, pp. 323-329.
5. Bergues D., Baudin G., Trumel H., "A shock-to-detonation transition model for high-energy rocket propellant applied to predict jet initiation threshold", in *Proceedings of 10<sup>th</sup> Symposium on detonation*, Boston, 1993.
6. Bjarnholt G., "Effects of aluminum and lithium fluoride admixtures on metal acceleration ability of Comp B", in *Proceedings of 6<sup>th</sup> Symposium on detonation*, Coronado, 1976, p. 510.
7. Cochran S.G., Chan J., *Shock initiation and detonation models in one and two dimensions*, VC/D 18024, LLNL, Livermore, January 20 1979.
8. M. Cowperthwaite, *Nonideal detonation in composite CHNO explosives containing aluminum*, PYD 8570, SRI International, Menlo Park, February 28 1991.
9. Finger M., Horning H.C., Lee E.L., Kury J.W., "Metal acceleration by composite explosives", in *Proceedings of 5<sup>th</sup> Symposium on detonation*, Pasadena, 1970, p. 137.
10. Gimenez P., Bedoch J.P., Saint-Martin C., Baudin G., de Longueville Y., "F.P.I. velocimetry techniques applied to various problems in detonics", in *Proceedings of 9<sup>th</sup> Symposium on detonation*, Portland, 1989, p.1351.
11. Johnson J.N., Tang P.K., Forest C.A., "Shock waves initiation of heterogeneous reactive solids", *J. Appl. Phys.*, Vol. 57 (9), 1 May 1985.
12. Mader C.L., *Numerical modelling of detonations*, Los Alamos Series in Basic and Applied Sciences, University of California Press, Berkeley - Los Angeles - London, 1979.
13. Mader C.L., *FORTTRAN BKW: A code for the computing the detonation properties of explosives*, LA 3704, LANL, Los Alamos, 1967.
14. Selman J.R., Hsiao Y.J., "Single particle acceleration and heating in a shock wave", Department of Chemical Engineering Illinois, Institute of Technology, Chicago, IL 60616, 1985.
15. Tang P.K., *Initiation and detonation of heterogeneous high explosives: a unified model*, LA-11352-MS, LANL, Los Alamos, 1988.
16. Tao W.M., Tarver C.M., Breithaupt D.R., McGuire R.R., Ornellas D.L., *Understanding Composite Explosive Energetics: 1 The role of metallic additives*, UCRL - 102581, LLNL, Livermore, February 1990.
17. Tao W.M., Tarver C.M., Breithaupt D.R., McGuire R.R., Ornellas D.L., *Understanding Composite Explosive Energetics: 2 Particle size effects and reaction modeling development*, UCRL-JC-104280, LLNL, Livermore, June 1991.
18. Veyssieres B., "Ignition of aluminum particles in a gaseous detonation", *Dynamics of Shock Waves, Explosions and Detonations*, edited by J.R. Bowen, N. Manson, A.K. Oppenheim and R.I. Soloukhin, *Progress in Astronautics and Aeronautics*, Vol. 87, 1983.
19. Veyssieres B., "Structure of the detonations in gaseous mixtures containing aluminum particles in suspension", *Dynamics of Shock Waves, Explosions and Detonations*, edited by J.R. Bowen, N. Manson, A.K. Oppenheim and R.I. Soloukhin, *Progress in Astronautics and Aeronautics* Vol. 106, 1986.
20. Volk F., Barthelt H., Schedlbauer F., Wagner J., "Detonation products of insensitive cast high explosives", in *Proceedings of 8<sup>th</sup> Symposium on detonation*, Albuquerque, 1985, pp. 577-586.
21. Cole R.H., *Underwater explosions*, Dover Publications Inc., New York, NY, 1948.

## DISCUSSION

RUTH DOHERTY

NSWC White Oak, Silver Spring, Maryland

In your paper you assume that all oxidation of aluminum is done by  $\text{CO}_2$ . In light of the data from Volk *et al.* and Deiter *et al.*, that there is oxidation of Al by water as well, how do you justify excluding oxidation by water from your model?

### REPLY BY GÉRARD BAUDIN:

In our paper, we assume that the most important mechanism of aluminum oxidation is the  $\text{CO}_2$  reduction. This assumption is based on Volk *et al.* analysis of detonation products presented at the 8th Symposium on Detonation. Following Volk's results, we calculated that only 18% in molar fraction of  $\text{H}_2\text{O}$  and up to 50% in molar fraction of  $\text{CO}_2$  were reduced. Moreover, we demonstrated in a private communication that aluminum oxidation with  $\text{H}_2\text{O}$  alone is not a reasonable mechanism, because thermochemical calculations with this assumption lead to detonation velocities significantly lower than experimental data for our explosives. The thermochemical calculations of CJ state with aluminum oxidation with  $\text{CO}_2$  alone, lead to detonation velocities closer to experimental data. Therefore, the reduction of  $\text{CO}_2$  alone is a mechanism sufficient to calculate the energy released by aluminum oxidation.

The model could be improved accounting aluminum oxidation with both  $\text{H}_2\text{O}$  and  $\text{CO}_2$ , with the disadvantage of increasing the number of parameters to be fitted.

## DISCUSSION

PER-ANDERS PERSSON

Research Center for Energetic Materials, Socorro, New Mexico

With thermal equilibrium between the Al and the reaction products surrounding it as you have assumed, do you think of the Al as liquid or solid?

### REPLY BY GÉRARD BAUDIN:

With regard to aluminum behavior modeling, the solid-liquid phase transition is taken into account in the equation of state used in the thermochemical calculations performed in the paper. In the reactive model, we don't take into account this phase transition in the equation of state used to calculate the aluminum temperature. In our model, the heat exchanges between the aluminum particles and the gaseous products are taken into account; the thermal equilibrium is reached in the rarefaction wave near the CJ surface.

## NONIDEAL DETONATION IN A COMPOSITE CHNO EXPLOSIVE CONTAINING ALUMINUM\*

M. Cowperthwaite  
SRI International  
Menlo Park, California 94025-3493

This theoretical study was performed to provide a better understanding of the behavior of aluminum in the nonideal detonation process in H6. An H6 composition called H6N was used for our study, and nonideal detonation was modeled as a one-dimensional ZND wave. Comparison of the designated CJ JWL parameters for H6 and CJ parameters, calculated with the TIGER code, for H6N with different mass fractions ( $1-\hat{\alpha}$ ) of the Al frozen showed that the flow in the reaction zone is supported by a mass fraction of Al in the range  $0.70 \leq \hat{\alpha} \leq 0.77$ . Variation of the BKW CJ composition with  $\hat{\alpha}$  was used to identify the major exothermic reactions of Al supporting detonation and a physical model was developed for calculating  $\hat{\alpha}$ . Comparison of the relative positions of the CJ JWL and JWLS isentropes for H6 and frozen BKW isentropes for H6N showed that, for practical purposes, 0.73 of the available Al supports detonation but none of the remaining Al supports the flow in the release wave.

### INTRODUCTION

The objective of this theoretical study of nonideal detonation was to provide a better understanding and description of the behavior of aluminum in the CHNO-Al explosive called H6. The nonideal detonation process was assumed to be one-dimensional and was modeled as a ZND wave<sup>1</sup> with a steady region followed by an unsteady region. Because Al is presumed to react in and behind the steady-state reaction zone (SSRZ) at the wave front in such a nonideal detonation, it was necessary to estimate how much of the Al reacts in the SSRZ to support the propagation of detonation and how much of it reacts behind the SSRZ to support the unsteady flow in the ensuing release wave. Two sets of calculations were therefore performed to estimate (1) the amount and the exothermic reactions of Al that support the propagation of nonideal detonation in H6 and (2) the amount of Al that supports the flow in the release wave.

### OUR FORMULATION FOR H6

For computational purposes, our formulation for H6 was called H6N and assigned the empirical formula  $C_{1.8869} H_{2.6123} N_{1.5796} O_{1.9667} Al_{0.7642}$  for the composition obtained by neglecting calcium salts in the Naval formulation for H6:<sup>2</sup> 74.20/20.16/4.69/0.05/0.37

by weight Comp B/Al/Comp D2/CaCl<sub>2</sub>/CaSiO<sub>4</sub>. Our calculated specific heat of formation for H6N is  $\Delta h_f = -9.08$  cal/g. H6N was assigned the initial density  $\rho_0 = v_0^{-1} = 1.76$  g/cm<sup>3</sup> and the same Chapman-Jouguet (CJ) parameters as the designated JWLCJ parameters for H6:<sup>3</sup>  $D = 7.47$  mm/ $\mu$ s,  $\hat{p} = 240$  kbar, and  $\hat{k} = 3.092$ .

These CJ parameters were assigned to H6N because Steinberg and Hudson<sup>4</sup> used them in constructing their modified JWLS isentrope for H6 and because our procedure for estimating the amount of Al reacting in the release wave in our second set of calculations is based on this JWLS isentrope. Throughout this paper, as indicated above, we use  $D$ ,  $\hat{p}$ , and  $\hat{k}$  to denote the detonation velocity, the pressure, and the adiabatic index, and we use the superscript  $\hat{\phantom{x}}$  to denote the CJ state.

### QUANTIFYING THE ROLE OF AL IN THE SSRZ

Our first set of calculations to estimate the amount and the exothermic reactions of Al that support the flow in the SSRZ in H6 was performed using the TIGER code<sup>5</sup> as follows.

### TIGER CJ Calculations

Our procedure for estimating the amount of Al that supports the propagation of detonation in H6 is based on the TIGER code's capability to calculate CJ states with different amounts of the Al frozen. This capability is conveniently used by first incorporating

\*This work was monitored by Dr. J. W. Forbes of the Naval Surface Warfare Center (NSWC) and supported by NSWC under Contract No. N60921-90-C-0068.

into the TIGER library an element called X that has the same thermodynamic properties as Al, and then specifying that a portion of the Al in the initial composition is X. In a CJ calculation, the Al labeled as X remains frozen because no other species in the TIGER library contains X.

To perform these CJ calculations, we use the parameter  $\hat{\alpha}$  as a reaction coordinate to denote the mass fraction of Al that is allowed to react with the detonation products of RDX and TNT in the SSRZ. When all the Al in the composition is labeled X,  $\hat{\alpha} = 0$  and none of the Al is allowed to support propagation of detonation. When none of the Al in the composition is labeled X,  $\hat{\alpha} = 1$  and all the Al is allowed to support detonation and attain chemical equilibrium with the detonation products at the CJ point where the flow becomes sonic at the end of the reaction zone.

We accordingly used TIGER to perform CJ calculations for H6N with values of  $\hat{\alpha}$  from 0 to 1 and compared the resulting sets of CJ parameters with the designated set of JWLCJ parameters for H6 to provide a means of estimating how much Al supports the propagation of detonation. Three series of calculations were performed using a newly calibrated OLD EOS<sup>5</sup> for solid and liquid Al based on shock wave data,<sup>6</sup> but with solid and liquid  $\text{Al}_2\text{O}_3$  treated as incompressible materials.

The first and second series of calculations were performed with the BKW and BKWR EOS used to describe the detonation products of Composition B. The BKW calculations were performed with the following values for the empirical BKW parameters ( $\alpha = 0.5$ ,  $\beta = 0.10$ ,  $K = 11.83$ ,  $\theta = 400$ ) and with the values for the BKW covolumes [ $C(Y^i)$ ] of the detonation products ( $Y^i$ ) in the SRI TIGER library. The BKWR calculations were performed with the following values for the BKW parameters and covolumes of detonation products generated at Lawrence Livermore National Laboratory (LLNL)<sup>7</sup> [ $\alpha = 0.5$ ,  $\beta = 0.176$ ,  $K = 11.80$ ,  $\theta = 1850$  and  $C(\text{CO}_2) = 610$ ,  $C(\text{H}_2\text{O}) = 270$ ,  $C(\text{NH}_3) = 384$ ,  $C(\text{N}_2) = 404$ ,  $C(\text{CO}) = 440$ ,  $C(\text{CH}_4) = 550$ ,  $C(\text{H}_2) = 98$ ] and with the values for the covolumes of the other detonation products in the SRI TIGER library. Table 1 lists the BKW CJ parameters, with  $T$  and  $u$  used to denote temperature and particle velocity. The BKWR CJ parameters are not presented here because of space limitations. These calculated BKW and BKWR values of  $D$  and  $\hat{p}$  were plotted against  $\hat{\alpha}$ , and the values associated with a given value of  $\hat{\alpha}$  were compared with the designated JWL values of  $D$  and  $\hat{p}$  for H6.

The following observations were made as a result of these comparisons:

- (1) The values of  $D$  and  $\hat{p}$  calculated using the BKW EOS and values of  $\hat{\alpha}$  in the neighborhood of  $\hat{\alpha} = 0.75$  differ slightly from the designated JWL values of  $D$  and  $\hat{p}$  for H6.
- (2) The values of ( $D = 7.50$  mm/ $\mu\text{s}$ ,  $\hat{p} = 227.3$  kbar) and ( $D = 7.78$  mm/ $\mu\text{s}$ ,  $\hat{p} = 240.6$  kbar)

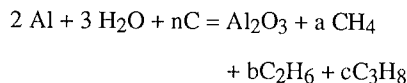
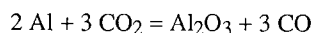
calculated with the BKWR EOS for values of  $\hat{\alpha} = 0.75$  and  $\hat{\alpha} = 0.25$  show that we can only match either the designated CJ detonation velocity or the designated CJ pressure for H6 by varying the amount of Al frozen in CJ calculations performed with the BKWR EOS.

Because of these observations, further calculations were limited to the BKW EOS, and a third series of CJ calculations was performed to quantify our first observation and provide a base set of CJ states for our following treatment of the release wave. Values of  $\hat{\alpha}$  close to  $\hat{\alpha} = 0.75$  were used in this third series of calculations to determine a set of CJ states that define essentially the smallest neighborhood of  $\hat{p}$  and  $D$  states containing the designated values of  $\hat{p}$  and  $D$  for H6. The results of these calculations showed that this neighborhood is spanned by values of  $\hat{\alpha}$  in the range  $0.70 \leq \hat{\alpha} < 0.77$ . The difference in  $\hat{p}$  between H6N and H6( $\delta\hat{p}$ ) is equal to 0.3 kbar for  $\hat{\alpha} = 0.70$  and to -3.7 kbar for  $\hat{\alpha} = 0.77$ . The difference in  $D$  between H6N and H6 ( $\delta D$ ) is equal to 0.06 mm/ $\mu\text{s}$  for  $\hat{\alpha} = 0.70$  and to -0.01 mm/ $\mu\text{s}$  for  $\hat{\alpha} = 0.77$ .

#### The Exothermic Reactions of Al with the Detonation Products of H6N and a Simple Model for their Termination

Although different time scales for the exothermic reactions of Al supporting detonation are simulated by varying the value of  $\hat{\alpha}$  in CJ calculations, these reactions and models for estimating the amount of Al consumed by them must be considered to obtain a better understanding of the role of Al in the detonation process. Conditions for the termination of these exothermic reactions must be established for the sake of consistency in the present treatment of nonideal detonation, because the reactive flow equations show that the global chemical energy release rate must be zero when the flow becomes sonic at the CJ plane in a one-dimensional detonation wave.

The major exothermic reactions of Al supporting detonation were identified by investigating how the composition of the calculated CJ states for H6N depend on  $\hat{\alpha}$ . When we applied the principle of mass balance to the variation of the CJ composition of H6N as the value of  $\hat{\alpha}$  varies from 0.25 to 0.75, we found that the major exothermic reactions of Al supporting the propagation of detonation in H6 can be represented by the chemical equations



with  $a + 2b + 3c = n$  and  $2a + 3b + 4c = 3$ . Essentially, the Al robs the  $\text{CO}_2$  and  $\text{H}_2\text{O}$  of oxygen, and the hydrogen from the water reacts with solid carbon to produce hydrocarbons.

Our treatment of the termination of these Al reactions at a CJ point was based on the idea that a spherical particle of Al becomes coated with a layer of

TABLE 1. CJ PARAMETERS FOR H6N, WITH DIFFERENT MASS FRACTIONS  $1 - \hat{\alpha}$  OF THE Al FROZEN, CALCULATED USING THE BKW EQUATION OF STATE

Mass Fraction of Al Reacted	$\hat{\alpha} = 0.0$	$\hat{\alpha} = 0.25$	$\hat{\alpha} = 0.50$	$\hat{\alpha} = 0.75$	$\hat{\alpha} = 1.0$
D (mm/ $\mu$ s)	7.86	7.82	7.69	7.48	7.21
$\hat{p}$ (atm $\times 10^3$ )	259.5	255.5	247.0	234.3	218.9
$\hat{k}$	3.138	3.158	3.154	3.148	3.127
$\hat{T}$ (kelvins)	2350	2870	3343	3807	4294
$\hat{v}$ (cm <sup>3</sup> /g)	0.4309	0.4315	0.4314	0.4312	0.4305
$\hat{u}$ (mm/ $\mu$ s)	1.90	1.88	1.85	1.80	1.75
Total moles of fluid per kilogram of H6N	24.43	23.04	21.60	20.20	18.78
Moles of (Al <sub>2</sub> O <sub>3</sub> ) <sub>i</sub> per kilogram of H6N	0.00	0.96	1.92	2.88	3.84

Al<sub>2</sub>O<sub>3</sub>, which prevents its further reaction. Following our CJ calculations for H6N with  $\hat{\alpha} \approx 0.75$ , we treated the Al as a compressible solid and the Al<sub>2</sub>O<sub>3</sub> as an incompressible liquid. In this case, when we apply the principle of mass balance to the mass fraction  $\hat{\alpha}_i$  of an Al particle (having an initial radius  $R_i$  greater than a critical radius  $R_c$ ) that reacts to form a layer of Al<sub>2</sub>O<sub>3</sub> having a critical thickness  $\hat{l}$ , we obtain a model for calculating  $\hat{\alpha}$ , when  $\hat{\alpha}_i = 1$  for particles with  $R_i \leq R_c$ .

To formulate our model for the termination of the Al reactions, we consider a particle with an initial radius  $R_i > R_c$ , an initial mass  $m_i$ , and an initial specific volume  $v_o$ , and we let  $R_i$ ,  $\hat{m}_i$ , and  $\hat{v} = v(T, \hat{p})$  denote, respectively, the radius, mass, and specific volume of the Al in the inner core of this particle when its protective layer of Al<sub>2</sub>O<sub>3</sub> has attained the critical thickness  $\hat{l}$  at a CJ point. We also use (AW) and (MW), respectively, to denote the atomic and molecular weights of Al and Al<sub>2</sub>O<sub>3</sub> and use  $v_i$  to denote the specific volume of our incompressible Al<sub>2</sub>O<sub>3</sub>. We then apply the principle of mass balance to the amount of Al,  $\hat{\alpha}_i \hat{m}_i$ , that reacts to form Al<sub>2</sub>O<sub>3</sub> as follows. The two equations for  $\hat{m}_i$ ,

$$\hat{m}_i = m_i (1 - \hat{\alpha}_i) = \frac{4\pi R_i^3}{3 v_o} (1 - \hat{\alpha}_i) \quad (1)$$

and

$$\hat{m}_i = \frac{4\pi}{3} \frac{(\hat{R}_i)^3}{\hat{v}} \quad (2)$$

are first combined to obtain the following equation relating  $(R_i/R_i)$  to  $\hat{\alpha}_i$ :

$$\left(\frac{\hat{R}_i}{R_i}\right)^3 = \frac{\hat{v}}{v_o} (1 - \hat{\alpha}_i) \quad (3)$$

The condition that  $\hat{\alpha}_i \hat{m}_i$  grams of Al are converted into Al<sub>2</sub>O<sub>3</sub> is then used to derive another equation relating  $(R_i/R_i)$  to  $\hat{\alpha}_i$  and  $\hat{l}$  as

$$\frac{\hat{\alpha}_i \hat{m}_i (\text{MW})}{2 (\text{AW})} = \frac{4\pi}{3 v_i} \left[ (\hat{R}_i + \hat{l})^3 - (\hat{R}_i)^3 \right] \quad (4)$$

and the molar volume of Al<sub>2</sub>O<sub>3</sub> [ $V_i(\text{Al}_2\text{O}_3)$ ] and the atomic volume of Al [ $V_o(\text{Al})$ ] are introduced so that Equation (4) can be rewritten as

$$\frac{\hat{\alpha}_i V_i (\text{Al}_2\text{O}_3)}{2 V_o (\text{Al})} = \left[ \left( \frac{\hat{R}_i}{R_i} + \frac{\hat{l}}{R_i} \right)^3 - \left( \frac{\hat{R}_i}{R_i} \right)^3 \right] \quad (5)$$

Equations (3) and (5) are then combined to obtain the equation

$$\left[ \left( \frac{\hat{v}}{v_o} (1 - \hat{\alpha}_i) \right)^{1/3} + \frac{\hat{l}}{R_i} \right]^3 = \frac{\hat{\alpha}_i V_i (\text{Al}_2\text{O}_3)}{2 V_o (\text{Al})} + \frac{\hat{v}}{v_o} (1 - \hat{\alpha}_i) \quad (6)$$

and the condition that  $\hat{\alpha}_i = 1$  when  $R_i = R_c$  is used to obtain the following equation relating  $\hat{l}$  and  $R_c$ :

$$\frac{\hat{l}}{R_c} = \left[ \frac{V_i (\text{Al}_2\text{O}_3)}{2 V_o (\text{Al})} \right]^{1/3} \quad (7)$$

The combination of Equations (6) and (7) then gives our equation for estimating  $\hat{\alpha}_i$  for particles with  $R_i > R_c$  in terms of the ratio  $R_c/R_i$  and the thermodynamic properties of Al and Al<sub>2</sub>O<sub>3</sub> as



$$\left[ \left( \frac{\hat{v}}{v_0} (1 - \hat{\alpha}_i) \right)^{1/3} + \left( \frac{V_i(\text{Al}_2\text{O}_3)}{2 V_0(\text{Al})} \right)^{1/3} \frac{R_c}{R_i} \right]^3 = \frac{\hat{\alpha}_i V_i(\text{Al}_2\text{O}_3)}{2 V_0(\text{Al})} + \frac{\hat{v}}{v_0} (1 - \hat{\alpha}_i) \quad (8)$$

Here, we will call an equation relating  $\hat{\alpha}_i$  and  $R_c/R_i$  an  $\hat{\alpha}_i = \alpha(R_c/R_i)$  relationship. The  $\hat{\alpha}_i = \alpha(R_c/R_i)$  relationship for estimating  $\hat{\alpha}_i$  for particles with  $R_i/R_c > 1$ , when the Al is assumed to be incompressible, is obtained from Equation (8) by setting  $\hat{v}/v_0 = 1$ .

### Our Model for the Amount of Al Supporting Detonation

Equation (8) is the basic equation in our simple model for quantifying the termination of the exothermic reactions of Al with the detonation products of H6. We use it here, first to determine properties of our model and then to derive the equation for  $\hat{\alpha}$ .

According to our assumptions, propagation of detonation is completely supported by Al particles with initial radii  $R_i \leq R_c$ , but is only partially supported by Al particles with initial radii  $R_i > R_c$  because they become coated by a layer of  $\text{Al}_2\text{O}_3$  1 thick. Equation (7), with the values of  $V_i^s(\text{Al}_2\text{O}_3) = 25.7 \text{ cm}^3/\text{mol}$  and  $V_l^s(\text{Al}_2\text{O}_3) = 26.00 \text{ cm}^3/\text{mol}$  for incompressible solid and liquid  $\text{Al}_2\text{O}_3$  from the TIGER library and the value of  $V_0(\text{Al}) = 9.67 \text{ cm}^3/\text{gram atom}$  for Al, gives the equations

$$\hat{l}_s = 1.099 R_c \quad \hat{l}_l = 1.104 R_c \quad (9) \text{ and } (10)$$

for protective solid and liquid layers of  $\text{Al}_2\text{O}_3$ . Equation (10), with the subscript l dropped for notational convenience, is considered here only because  $\text{Al}_2\text{O}_3$  appears as a liquid in our CJ calculations with H6N.

We now use Equation (8) to obtain more detailed properties of our model by calculating values of  $\hat{\alpha}_i$  associated with values of  $R_i > R_c$  for compressible solid Al with different values of  $R_c$  and  $\hat{l}$ . The Al was assumed to be solid rather than liquid in these calculations because X appears as a solid in our CJ calculations performed with H6N.

When our unreacted Al is compressible, values of  $\hat{v}$  must be known, before we can use Equation (8) to determine values of  $\hat{\alpha}_i$  associated with values of  $R_c/R_i$ . We used the values  $\hat{T} = 3087 \text{ K}$  and  $\hat{p} = 237.4 \text{ kbar}$  from the CJ calculation with  $\hat{\alpha} = 0.75$  and the value  $\hat{v}$  calculated from the OLD EOS to calculate  $\hat{v}/v_0 = 1.061$ . Substituting this value of  $\hat{v}/v_0$  and Equation (10) into Equation (8) gives the equation

$$\left[ \left( 1.061 (1 - \hat{\alpha}_i) \right)^{1/3} + 1.104 \frac{R_c}{R_i} \right]^3 = 1.061 + 0.2834 \hat{\alpha}_i \quad (11)$$

which can be solved for  $\hat{\alpha}_i$  when  $R_c/R_i$  is specified. The values of  $\hat{\alpha}_i$  associated with values of  $R_i$  for the

specified values of  $R_c$  given in Table 2 were calculated from Equation (11) by calculating values of  $R_c/R_i$  for values of  $\hat{\alpha}_i$  in the range  $0 < \hat{\alpha}_i < 1$  and then assigning the different values to  $R_c$ .

A similar calculation with  $\hat{v}/v_0 = 1$  in Equation (8), showed that the relationship between  $\hat{\alpha}_i$  and  $R_i$  is essentially the same for incompressible solid Al and compressible solid Al, governed by the OLD EOS used in the CJ calculations, because the expansion of the Al produced by raising its temperature to 3087 K is offset by the compression produced by raising its pressure to 237.4 kbar.

We now derive our expression for calculating the mass fraction of Al,  $\hat{\alpha}$ , supporting detonation in an explosive such as H6 when an  $\hat{\alpha}_i = \alpha(R_c/R_i)$  relationship is given and we know the mass fractions of Al with different initial particle sizes and the critical radius for completion of reaction. We let  $M_{Al}$  denote the mass of Al in our explosive composition and use  $M_{Al}^i$ ,  $n_i$ , and  $\beta_{Al}^i$  to denote the mass, number, and mass fraction of Al particles with an initial radius  $R_i$  and initial mass  $m_i = (4\pi/3)v_0$ . In this case,  $M_{Al}^i = n_i m_i$ ,  $\beta_{Al}^i = M_{Al}^i/M_{Al}$ , and the expression for the conservation of mass for the Al particles is  $\sum \beta_{Al}^i = 1$ . The definition of  $\hat{\alpha}_i$  leads to the following expression for the mass fraction of Al supporting detonation:

$$\begin{aligned} \hat{\alpha} M_{Al} &= \sum \alpha(R_c/R_i) n_i m_i \\ &= \frac{4\pi}{3v_0} \sum n_i R_i^3 \alpha(R_c/R_i) \end{aligned} \quad (12)$$

which we rewrite for convenience as

$$\hat{\alpha} = \sum \beta_{Al}^i \alpha(R_c/R_i) \quad (13)$$

Equation (13) is our expression for estimating the mass fraction of Al reacting to support detonation when the mass fractions of particles with initial radii  $R_i$  are known, the  $\hat{\alpha}_i = \alpha(R_c/R_i)$  relationship is known, and we assign a value to  $R_c$ .

To estimate a value of  $R_c$  for H6, we used Equation (13), the  $\hat{\alpha}_i = \alpha(R_c/R_i)$  relationship given by Equation (11), and the results of our BKW CJ calculation for H6N with  $\hat{\alpha} = 0.75$  along with a known Al particle size distribution for an H6 charge made at Los Alamos National Laboratory (LANL). This H6 charge, made at LANL for SRI's Lagrange gage study of H6 supported by NSWG,<sup>7</sup> had a composition RDX/TNT/Al/D-2 Wax by weight 45.89/28.87/19.80/5.44. With  $D_i$  and  $R_i$  used, respectively, to denote the mean and assigned initial diameters and radii of the Al particles, an analysis of the Al particle size distribution data supplied by LANL showed that  $\beta_{Al}^i = 0.004$  and  $R_i = 45 \mu\text{m}$  for  $D_i > 90 \mu\text{m}$ ,  $\beta_{Al}^i = 0.002$  and  $R_i = 27 \mu\text{m}$  for  $D_i$  in the range  $60 \mu\text{m} > D_i > 45 \mu\text{m}$ ,  $\beta_{Al}^i = 0.988$  and  $R_i = 19 \mu\text{m}$  for  $D_i$  in the range  $45 \mu\text{m} > D_i > 30 \mu\text{m}$ ,  $\beta_{Al}^i = 0.004$  and  $R_i = 12 \mu\text{m}$  for  $D_i$  in the range  $30 \mu\text{m} > D_i > 20 \mu\text{m}$ , and  $\beta_{Al}^i = 0.02$  and  $R_i = 8 \mu\text{m}$  for  $D_i$  in the range  $20 \mu\text{m} > D_i > 10 \mu\text{m}$ .

TABLE 2. MASS FRACTIONS  $\hat{\alpha}_i$  OF COMPRESSIBLE SOLID Al PARTICLES WITH INITIAL RADII  $R_i > R_c$  CONVERTED INTO AN INCOMPRESSIBLE LAYER OF LIQUID  $Al_2O_3$  FOR DIFFERENT VALUE OF  $R_c$

$\hat{\alpha}_i$	$R_i/R_c$	$R_i$ ( $\mu m$ )		
		$R_c = 5 \mu m$	$R_c = 10 \mu m$	$R_c = 15 \mu m$
0.1	24.96	124.8	249.6	374.4
0.2	12.13	60.6	121.3	181.9
0.3	7.84	39.2	78.4	117.6
0.4	5.66	28.3	56.6	84.9
0.5	4.35	21.7	43.5	65.2
0.6	3.45	17.2	34.5	51.7
0.7	2.78	13.9	27.8	41.7
0.8	2.25	11.2	22.5	33.7
0.9	1.77	8.9	17.7	26.6

We then used these values of  $\beta_{Al}^i$  and  $\hat{R}_i$ , and values of  $\alpha(R_c/R_i)$  calculated from plots of  $\hat{\alpha}_i$  versus  $R_i$  constructed from Table 2 for  $R_c = 5 \mu m$  and  $R_c = 10 \mu m$  in Equation (13) to calculate the corresponding values of  $\hat{\alpha}$ . These calculations gave the values  $\hat{\alpha} = 0.55$  for  $R_c = 5 \mu m$  and  $\hat{\alpha} = 0.849$  for  $R_c = 10 \mu m$ . Because the particles with initial radii different from  $19 \mu m$  contribute 0.007 to the value of  $\hat{\alpha}$  when  $R_c = 5 \mu m$  and 0.009 to the value of  $\hat{\alpha}$  when  $R_c = 10 \mu m$ , we assigned the value  $R_i = 19 \mu m$  to all the Al particles in H6N and used the plot of  $\hat{\alpha}_i$  versus  $R_i/R_c$  constructed from Table 2 to show that the value of  $\hat{\alpha} = 0.75$  is associated with a value of  $R_i/R_c = 2.5$ , which gives a value of  $R_c = 7.6 \mu m$  and a value of  $\hat{l} = 8.4 \mu m$ .

These calculations led to the following result:

Our simple model for the amount of Al supporting detonation in a CHNO-Al explosive, with its CJ parameters evaluated from our BKW calculation for H6N with  $\hat{\alpha} = 0.75$  and a realistic particle size distribution for Al, predicts that the critical diameter and critical thickness for the completion and prevention of reaction of the Al particles, respectively, are  $D_c \approx 15 \mu m$  and  $\hat{l} \approx 8 \mu m$  for CJ states with temperatures  $\hat{T} \approx 3807$  K and pressures  $\hat{p} \approx 237$  kbar.

Because our value of  $\hat{l} \approx 8 \mu m$  was obtained in a thermodynamic type of calculation, a study of the kinetic processes involved in the formation of the protective layer of  $Al_2O_3$  should be undertaken to substantiate this result.

## QUANTIFYING THE ROLE OF Al IN THE RELEASE WAVE

Our second set of calculations to estimate the amount of Al supporting the flow in the release wave in H6 was also performed using the TIGER code. With our present definitions of nonideal detonation and  $\hat{\alpha}$ ,  $(1 - \hat{\alpha}) M_{Al}$  grams of Al pass through the SSRZ and enter the unsteady release wave behind the CJ plane. From a physical point of view, we speculate that reaction of Al starts again in the release wave because the covering of  $Al_2O_3$  becomes damaged and the inner

cores of Al particles become exposed to the detonation products.

In applying TIGER to the flow in the release wave, we can again freeze the  $(1 - \hat{\alpha}) M_{Al}$  grams of Al or allow it to react with the detonation products of RDX and TNT. When all this Al is kept frozen, the flow in the release wave is isentropic and the release adiabat is represented by an isentrope. When some of this Al is allowed to react, however, the flow in the release wave is not isentropic and the entropy increases until the Al stops reacting and the flow again becomes isentropic.

Accordingly, our approach in using TIGER to estimate the amount of Al supporting the release wave in H6 was to calculate and compare frozen isentropes for H6N to the JWL isentropes for H6 given in the literature<sup>3,4</sup> and, if necessary construct a reactive release adiabat to match the appropriate JWL isentrope.

## The CJ JWL and CJ JWLS Isentropes for H6

The JWL EOS for detonation products, developed at LLNL<sup>3</sup> in terms of the reduced energy  $E$ , the reduced volume  $V = v/\rho_0^*$ , and  $p$ , contains five other parameters  $w$ ,  $A$ ,  $B$ ,  $R_1$ , and  $R_2$ . The equation for a JWL isentrope can be written as

$$p = C(p_i, V_i) V^{-(w+1)} + A e^{-R_1 V} + B e^{-R_2 V} \quad (14)$$

The value of  $C(p_i, V_i)$  that satisfies Equation (14) when  $p = p_i$  and  $V = V_i$  defines the particular isentrope that passes through the point  $(p_i, V_i)$ . The values of these parameters defining the JWL EOS for H6 with an initial density  $\rho_0^* = 1.76$  g/cm<sup>3</sup> and the designated CJ parameters ( $\hat{p} = 240$  kbar,  $\hat{k} = 3.097$ ,  $\hat{V} = 0.7556$ ) are  $w = 0.2$ ,  $A = 7.5807$  Mbar,  $B = 0.08513$  Mbar,  $R_1 = 4.9$ , and  $R_2 = 1.1$ . With these values of the parameters, the CJ JWL isentrope for H6 is defined by the value  $C = 0.01143$  Mbar.

Sternberg and Hudson<sup>4</sup> developed their modified JWLS EOS for H6 for use in underwater explosion dynamic calculations

$$p = C (p_i, V_i) V^{-(w+1)} + A_1 e^{-R_1 V}$$

$$+ A_2 e^{-R_2 V} + \sum_{j=3}^6 A_j V^{-\beta_j} \quad (15)$$

The parameters defining this JWLS EOS have the same values for  $R_1$  and  $R_2$  as the JWL EOS, and the values  $A_1 = 16.964$  Mbar,  $A_2 = 0.1509$  Mbar,  $A_3 = -0.06096$  Mbar,  $A_4 = 0.2701$  Mbar,  $A_5 = -0.3708$  Mbar,  $A_6 = 0.05807$  Mbar,  $\beta_3 = 2.0$ ,  $\beta_4 = 2.5$ ,  $\beta_5 = 3.0$ , and  $\beta_6 = 3.5$ . With these values of the parameters, the CJ JWLS isentrope for H6 is defined by the value  $C = 0.01642$  Mbar.

Points on these CJ JWL and CJ JWLS isentropes in the (V-p) plane were calculated for V in the range  $0.7556 \leq V \leq 10$  and are listed in Table 3. This range of V was chosen because these JWL and JWLS essentially become polytropic isentropes with  $k = 1 + w$  when V is greater than 7 and V is greater than 10, respectively. Values of the pressure are also given in kilobar because TIGER uses these units of pressure. Examination of the (p-V) points in Table 3 shows that, as the pressure falls from 236.8 katm, the CJ JWL isentrope for H6 lies above the CJ JWLS isentrope for H6 until V attains a value of  $V \approx 1.75$  but thereafter lies below it.

#### Frozen BKW Isentropes for H6N

TIGER was used to construct frozen BKW isentropes passing through the following CJ points: ( $\hat{p} = 237.2$  katm,  $\hat{V} = 0.4313$  cm<sup>3</sup>/g,  $\hat{\alpha} = 0.70$ ), ( $\hat{p} = 235.5$  katm,  $\hat{V} = 0.4312$  cm<sup>3</sup>/g,  $\hat{\alpha} = 0.73$ ), ( $\hat{p} = 234.4$  katm,  $\hat{V} = 0.4312$  cm<sup>3</sup>/g,  $\hat{\alpha} = 0.75$ ), and ( $\hat{p} = 233.2$  katm,  $\hat{V} = 0.4312$  cm<sup>3</sup>/g,  $\hat{\alpha} = 0.77$ ), with values of  $\hat{p}$  and  $\hat{D}$  that span the designated values of  $\hat{p}$  and  $\hat{D}$  for H6. Points on these frozen isentropes in the (V-p) plane with  $\hat{\alpha} = 0.7$ ,  $\hat{\alpha} = 0.75$ , and  $\hat{\alpha} = 0.77$  are listed in Table 4. The JWL and JWLS isentropes passing through the designated CJ state of H6 were then compared with these frozen BKW isentropes.

#### Comparison of the CJ JWL and JWLS Isentropes for H6 and Frozen BKW Isentropes for H6N

The (V,p) points in Tables 3 and 4 were plotted to provide a means of (1) estimating how much Al reacts with the detonation products of RDX and TNT behind the reaction zone in H6N and (2) estimating how much Al supports detonation by determining which CJ state with  $\hat{\alpha}$  in the range  $0.70 \leq \hat{\alpha} \leq 0.77$  most suitably represents the designated CJ state in H6. A pressure scale, exhibiting quantitative differences between the CJ JWL and JWLS isentropes for H6, must be chosen for these plots to make our comparisons of these JWL and frozen BKW isentropes meaningful.

We, accordingly, chose a pressure scale which shows that the areas under the JWLS and JWL isentropes in the (V-p) plane are significantly different

for the volume range  $1.5 \leq V \leq 10$ , and we plotted the (V, p) points for the isentropes given in Table 3 and 4.

A comparison of these plots of the JWL, JWLS and frozen BKW isentropes led to the following observations:

- (1) The CJ JWLS and CJ JWL isentropes are significantly different over the volume range  $2 \leq V \leq 10$  where the JWLS pressure exceeds the JWL pressure, and this excess pressure increases from a value of 8.5% at  $V = 2$  to attain an approximate maximum value of 32.2% at  $V = 4$  and then decreases to a value of 29.6% at  $V = 10$ .
- (2) The CJ JWLS isentrope and the frozen BKW isentrope with  $\hat{\alpha} = 0.70$  differ significantly for values of V in the range  $1.2 \leq V \leq 1.9$  but not for values of V in the range  $0.756 \leq V \leq 1.2$  or the range  $1.9 \leq V \leq 10$ .
- (3) The frozen BKW isentropes for H6N with  $\hat{\alpha}$  in the range  $0.70 \leq \hat{\alpha} \leq 0.77$  and s in the range  $1.538 \text{ cal K}^{-1}/\text{g} \leq s \leq 1.556 \text{ cal K}^{-1}/\text{g}$  are essentially indistinguishable until the pressure falls to a value of  $\approx 7$  katm at  $V \approx 3.2$  and thereafter are barely distinguishable.
- (4) Because of the proximity of the frozen BKW isentropes with  $\hat{\alpha}$  in the range  $0.70 \leq \hat{\alpha} \leq 0.77$ , there is no significant difference between the JWLS isentrope and the frozen BKW isentrope with  $\hat{\alpha} = 0.70$  over the volume range  $2 \leq V \leq 10$ , where the JWLS and JWL isentropes are significantly different.

These observations about the JWL, JWLS, and BKW isentropes in the (V-p) plane showed that the frozen BKW isentropes for H6N, with values of  $\hat{\alpha}$  in the range  $0.70 \leq \hat{\alpha} \leq 0.75$  and CJ states neighboring the designated CJ state for H6, are significantly different from the CJ JWL isentrope for H6 but lie close to the CJ JWLS isentrope for H6. Also, because the values of the CJ parameters for H6N with  $\hat{\alpha} = 0.73$  lie closer to the designated JWL CJ parameters than those with  $\hat{\alpha} = 0.70$ , the frozen isentrope passing through the CJ state ( $\hat{D} = 7.50$  mm/ $\mu$ s,  $\hat{p} = 235.5$  kbar,  $\hat{V} = 0.7589$ ,  $\hat{\alpha} = 0.73$ ) can be used to represent the detonation process in H6 with 0.73 of the available Al reacting to support the propagation of detonation and the remaining amount of available Al frozen in the release wave. Thus, there is no need to model the release wave in H6 as a reactive adiabat.

#### CONCLUSIONS

Theoretical studies of the explosive H6N, 74.20/20.61/4.69 by weight Comp B/Al/Comp D2, were undertaken to obtain a better understanding and description of Al in the nonideal detonation process in H6. With this nonideal detonation modeled as a one-dimensional ZND wave, work was performed to (1) estimate how much Al reacts to support the

TABLE 3. VALUES OF THE PRESSURE (p) AND RELATIVE VOLUME (V) FOR THE JWLS AND JWLS ISENTROPES THROUGH THE DESIGNATED JWLS CJ POINT OF H6

Relative Volume V	JWL		JWLS	
	p (kbar)	p (katm)	p (kbar)	p (katm)
0.7556	240.00	236.80	240.00	236.80
1.0	96.15	94.90	89.38	88.21
1.5	28.24	27.90	25.10	24.75
2.0	14.83	14.63	16.10	15.88
3.0	6.19	6.11	8.03	7.92
4.0	3.21	3.17	4.25	4.19
5.0	2.01	1.98	2.63	2.60
6.0	1.45	1.43	1.88	1.85
7.0	1.14	1.13	1.48	1.46
8.0	0.96	0.94	1.24	1.22
9.0	0.82	0.81	1.06	1.05
10.0	0.72	0.71	0.93	0.92

TABLE 4. VALUES OF PRESSURE (p) AND RELATIVE VOLUME (V) FOR FROZEN BKW ISENTROPES PASSING THROUGH THE CALCULATED CJ POINT OF H6N WITH  $\hat{\alpha} = 0.70$ ,  $\hat{\alpha} = 0.75$ , AND  $\hat{\alpha} = 0.77$

$\hat{\alpha} = 0.70$		$\hat{\alpha} = 0.75$		$\hat{\alpha} = 0.77$	
Relative Volume V	Pressure p (atm)	Relative Volume V	Pressure p (atm)	Relative Volume V	Pressure p (atm)
7.5909E-01	2.3720E+05	7.5891E-01	2.3440E+05	7.5891E-01	2.3320E+05
8.7789E-01	1.5240E+05	8.7472E-01	1.5070E+05	8.7490E-01	1.5000E+05
1.0169E+00	9.7970E+04	1.0185E+00	9.6900E+04	1.0190E+00	9.6450E+04
1.1896E+00	6.2970E+04	1.1938E+00	6.2310E+04	1.1954E+00	6.2030E+04
1.4078E+00	4.0470E+04	1.4161E+00	4.0060E+04	1.4194E+00	3.9890E+04
1.6859E+00	2.6010E+04	1.7000E+00	2.5760E+04	1.7056E+00	2.5660E+04
2.0416E+00	1.6720E+04	2.0645E+00	1.6560E+04	2.0733E+00	1.6500E+04
2.5837E+00	1.0750E+04	2.6066E+00	1.0650E+04	2.5960E+00	1.0610E+04
3.2120E+00	6.9070E+03	3.2718E+00	6.8490E+03	3.2982E+00	6.8250E+03
4.0410E+00	4.4400E+03	4.1290E+00	4.4040E+03	4.1659E+00	4.3890E+03
5.1498E+00	2.8530E+03	5.2800E+00	2.8320E+03	5.3328E+00	2.8230E+03
6.6581E+00	1.8340E+03	6.8446E+00	1.8210E+03	6.9221E+00	1.8150E+03
8.7402E+00	1.1790E+03	9.0112E+00	1.1710E+03	9.1238E+00	1.1680E+03
1.1656E+01	7.5770E+02	1.2049E+01	7.5290E+02	1.2214E+01	7.5090E+02

propagation of detonation, (2) identify the major exothermic reactions of Al with the detonation products of RDX and TNT and formulate a quantitative model to account for their termination in the CJ state, and (3) estimate how much Al reacts to support the flow in the release wave.

CJ TIGER calculations were performed on H6N with different amounts of the Al frozen to provide a means of estimating the amount of Al that reacts to support the propagation of detonation in H6. Comparison of these calculated CJ parameters with the designated CJ parameters for H6 ( $D = 7.47$  mm/ $\mu$ s,  $\hat{p} = 240$  kbar) led to two major conclusions. First, we can only match either the designated detonation velocity for H6 or its designated CJ pressure by varying the amount of Al frozen in CJ calculations performed with the BKWR EOS. Second, the values of  $D$  and  $\hat{p}$  calculated

with the BKW EOS for values of  $\hat{\alpha}$  in the range  $0.70 \leq \hat{\alpha} \leq 0.77$  differ slightly from the designated values of  $D$  and  $\hat{p}$  for H6. As  $\hat{\alpha}$  increases from 0.70 to 0.77, the difference in  $\hat{p}$  between H6N and H6 ( $\delta\hat{p}$ ) decreases smoothly from 0.3 katm to -3.7 katm, and the corresponding difference in  $D$  ( $\delta D$ ) decreases smoothly from 0.06 mm/ $\mu$ s to -0.01 mm/ $\mu$ s.

Variation of the calculated BKW CJ composition of H6N with  $\hat{\alpha}$  was investigated to identify the major exothermic reactions of Al supporting detonation, and a phenomenological model for their termination was based on the physical idea that particles of Al become coated by protective layers of  $Al_2O_3$  which prevent their further reaction. Our investigation of the dependence of the calculated CJ composition of H6N on  $\hat{\alpha}$  showed that the major exothermic reactions supporting detonation can be represented by two

chemical equations: one, the reaction of Al with  $\text{CO}_2$  to form  $\text{Al}_2\text{O}_3$  and  $\text{CO}$ , the other, the reaction of Al with  $\text{H}_2\text{O}$  and solid C to form  $\text{Al}_2\text{O}_3$  and hydrocarbons. Our simple physical model for calculating the amount of Al ( $\alpha$ ) supporting detonation was based on the assumption that a spherical particle of Al with an initial radius  $R_i$  greater than a critical radius  $R_c$  stops reacting because its protective layer attains a critical thickness  $l$  at the CJ point. The principle of mass balance was applied to the mass fraction  $\alpha_i$  of a particle with  $R_i > R_c$  to obtain an equation for  $\alpha_i$  in terms of  $l/R_i$  and certain nondimensional volume ratios for Al and  $\text{Al}_2\text{O}_3$ . This equation for  $\alpha_i$  was subjected to the condition  $\alpha_i = 1$  for  $R_i \leq R_c$  to obtain a relationship between  $l$  and  $R_c$  and an  $\alpha_i = \alpha(R_c/R_i)$  relationship for calculating  $\alpha_i$  for a particle with an initial radius  $R_i$  when  $R_c$  is specified and the thermodynamic states of Al and  $\text{Al}_2\text{O}_3$  at the CJ point are known. The equation for  $\alpha$  was obtained by multiplying  $\alpha_i$  by the mass fraction  $\beta_{\text{Al}}$  of particles with  $R_i$  and summing over  $i$ .

A known particle size distribution for an H6 charge made at LANL was used with the thermodynamic states for Al and  $\text{Al}_2\text{O}_3$  from our CJ calculation for H6N with  $\alpha = 0.75$  to predict that the critical diameter and thickness for the completion and prevention of reaction of Al particles, respectively, are  $\approx 15 \mu\text{m}$  and  $\approx 8 \mu\text{m}$  for CJ states with temperatures  $T \approx 3807 \text{ K}$  and pressures  $p \approx 237 \text{ kbar}$ .

Comparison of the JWL and JWLS isentropes for H6 and the frozen BKW isentropes for H6N with  $\alpha$  in the range  $0.70 \leq \alpha \leq 0.77$  led us to conclude that, for practical purposes, 0.73 of the available Al reacts to support the propagation of detonation in H6, but none of the remaining Al supports the flow in the release wave. Nonideal detonation in H6 can thus be represented by the frozen isentrope for H6N with  $\alpha = 0.73$  that passes through the CJ state whose parameters differ from those of the designated JWL CJ state of H6 by  $\delta D = +0.40\%$ ,  $\delta p = -0.55\%$ , and  $\delta V = +0.43\%$ .

We conclude that the results of our theoretical study provide a more quantitative description of the detonation process in H6 and of the role of Al in the nonideal detonation process in CHNO-Al explosive. However, because this description is based on TIGER calculations with both phases of  $\text{Al}_2\text{O}_3$  treated as incompressible materials and because we expected to find that a significant amount of Al supports the release wave, additional work should be performed to determine how the CJ parameters for H6N with different values of  $\alpha$  depend on the thermodynamic description used for  $\text{Al}_2\text{O}_3$  in the TIGER library.

## REFERENCES

1. Fickett, W. and Davis, W. C., *Detonation*, University of California Press, Berkeley and Los Angeles, CA, 1979, Chapter 2.
2. Hall, T.N. and Holden, J. R., *Navy Explosives Handbook*, NSWC MP 88-116, NSWC, Dahlgren, VA, Silver Spring, MD, October 1988.

3. Dobratz, B. M., *LLNL Explosives Handbook*, UCRL-52997, Lawrence Livermore Laboratory, Livermore, CA, March 1981.
4. Sternberg, H. M. and Hudson, L., "Equations of State for Underwater Explosives," in *Proceedings of the International Symposium on Pyrotechnics and Explosives*, Beijing, China, 12 October 1987, pp. 680-686.
5. Cowperthwaite, M. and Zwislner, W. H., TIGER Computer Program Documentation, SRI Publication No. Z106, SRI International, Menlo Park, CA, January 1973.
6. Seitz, F. and Turnbull, D., Eds., *Solid State Physics*, Vol. 6, Academic Press, New York and London, 1958.
7. Finger, M. et al., "The Effect of Elemental Composition on the Detonation Behavior of Explosives," in *Sixth Symposium (International) on Detonation*, Hotel del Coronado, Coronado, CA, August 24-27, 1976, pp. 710-722.
8. Cowperthwaite, M. and Rosenberg, J. T., *Lagrange Gage Studies of Composition B and H-6*, SRI Final Report, SRI Project PYU-1764, SRI International, Menlo Park, CA, May 1982.

## DISCUSSION

P. A. PERSSON

Materials Center for Energetic Materials  
Socorro, New Mexico.

Do you assume thermal equilibrium (*i.e.*, the same temperature) in the  $\text{Al}_2\text{O}_3$  and the unreacted Al?

## REPLY BY M. COWPERTHWAITTE:

Because TIGER is a thermodynamic code, its chemical equilibrium calculations are performed for systems in thermal and mechanical equilibrium. Consequently, the results of TIGER calculations for CHNO-Al compositions with some of the Al frozen will show that  $\text{Al}_2\text{O}_3$  and the frozen Al, call X, attain the same temperature in the Chapman-Jouguet state.

## DISCUSSION

FRED VOLK

Fraunhofer Institut für Chemische Technologie  
Pfinztal, Germany

According to the results of our Al-reaction investigation, we can say that not only the  $\text{O}_2$  balance but

also the energy output determine the completeness of the Al reaction. The same holds for using energetic or non-energetic binders, producing different detonation heats or detonation temperatures.

**REPLY BY M. COWPERTHWAITE:**

The amount of Al that reacts in a detonation wave obviously depends on the relative rates of kinetic processes. The results of detonation calculations, showing that more than 50% of the Al reacts to support detonation, indicate to me that the temperature in the reaction zone is high enough and the reaction zone is long enough to promote reaction of the Al with the detonation products of the explosive.

**DISCUSSION**

HAROLD J. GRYTING

Gryting Energetics Science Company  
San Antonio, Texas

Are the calculations applicable to determine whether more or less aluminum should be used in underwater or air burst explosives for (1) improvement of underwater bubble energy, (2) underwater shock and (3) open air blast potential. (For example, in modifying H-6 or HBX-3 or their PBX "analogs" for better performance).

**NO REPLY FROM THE AUTHOR**

## MODELLING SHOCK INITIATION AND DETONATION IN THE NON-IDEAL EXPLOSIVE PBXW-115

David L. Kennedy  
ICI Australia Operations Pty. Ltd.  
PO Box 196, Kurri Kurri NSW 2327, Australia

David A. Jones  
DSTO Materials Research Laboratory  
PO Box 50, Ascot Vale 3032, Australia

We analyse the detonics of the non-ideal explosive PBXW-115 (also called PBXN-111). Two chemical equilibrium codes were used to predict its ideal CJ state, with estimates of its ideal detonation velocity differing by over  $1.3 \text{ mm} \cdot \mu\text{s}^{-1}$ . A small divergent detonation theory was calibrated to unconfined detonation velocity measurements, and used to describe the CJ state at different charge diameters. It was predicted that the detonation was being supported by about 15% reaction at the critical diameter, with the velocity about  $1.7 \text{ mm} \cdot \mu\text{s}^{-1}$  below the ideal value. A finite element hydrocode was used to simulate a variety of initiation and detonation tests, with the results generally in excellent agreement with the experimental data. It was found that many experimental techniques (including those for the measurement of ideal detonation velocity, CJ zone length, and Pop-plots) require substantially different interpretation for non-ideal explosives.

### INTRODUCTION

Composite explosives are used extensively in both commercial and military applications. The partial or complete physical separation of their oxidiser and fuel phases results in mass diffusion reducing their reaction rates and increasing their reaction zone lengths in comparison with monomolecular explosives. As a consequence, they exhibit non-ideal performance, where their detonation velocities can be considerably lower than the ideal value predicted by equilibrium thermodynamic calculations. They typically have large critical diameters. These factors all contribute to increased difficulty and expense when performing characterisation experiments, as the charge weights involved are necessarily larger than those involving ideal explosives. This raises the question as to how relevant existing experimental techniques are for the investigation of the detonics of such explosives.

This paper will present a detailed evaluation of the experimental techniques applied to the non-ideal explosive PBXW-115 (also known as PBXN-111). These include detonation velocity and critical diameter for both unconfined and confined charges, corner turning ability, and shock front curvature, all obtained at NSWC by Forbes and coworkers<sup>1,2</sup> for the US variant. Bocksteiner et al.<sup>3</sup> at MRL have measured detonation velocity and critical diameter for both unconfined and confined charges of the Australian variant, examining the effects of RDX and Al particle size. Held<sup>4</sup> has applied a small-sample technique to the measurement of the ideal detonation velocity of the German variant.

The results will include a description of the ideal Chapman-Jouget (CJ) detonation state as provided by two

equilibrium thermodynamic codes, an analysis of steady detonation in axisymmetric geometry, and time-resolved numerical simulations using the hydrocode DYNA2D.<sup>5</sup>

### IDEAL DETONATION – THE IDEAL CJ STATE

The nominal density of W-115 is about  $1.79 \text{ g} \cdot \text{cm}^{-3}$ , corresponding to voidage levels of less than 2%. It is cast cured, with its nominal composition being 20% cyclotri-methylene trinitramine (RDX), 43% ammonium perchlorate (AP), 25% aluminium (Al), and 12% hydroxy terminated polybutadiene (HTPB) as binder.

Two chemical equilibrium codes were used to calculate its CJ state for an ideal detonation, with the results presented in Table 1. The first was BKW,<sup>6</sup> based on the Becker-Kistiakowsky-Wilson equation of state (EoS) for the gaseous products and the Cowan EoS for the solid products. The second was the ICI code IDeX (standing for Ideal Detonation of eXplosives), using an intermolecular EoS<sup>7</sup> for the gaseous products and the Murnaghan EoS for the solid products.

TABLE 1. IDEAL CJ STATE OF W-115

Parameter	BKW	IDeX
Detonation velocity ( $\text{mm} \cdot \mu\text{s}^{-1}$ )	8.010	6.665
Detonation pressure (GPa)	27.51	22.53
Detonation temperature (K)	5175	5295
Heat of reaction ( $\text{MJ} \cdot \text{kg}^{-1}$ )	6.328	8.396
CJ Gamma	3.175	2.534

The predictions from the two codes differ to a greater extent than has been observed for any other explosive. This is

due to the different product species allowed by the two codes, as summarised in Table 2. In particular, IDeX predicts that the excess carbon would be present as diamond rather than graphite, and that significant amounts of ammonia and methane would be formed, none of which were included in the BKW database. The IDeX predictions have been adopted, for the pragmatic reason that the subsequent CPeX analysis (described below) based on the BKW predictions could not be made to fit the experimental detonation velocity data.

TABLE 2. PREDICTED SPECIES PRESENT AT CJ POINT

Species	Mole number (1kg explosive)	
	BKW	IDeX
C (diamond)	n.a.#	6.43
C (graphite)	9.64	Nil
Al <sub>2</sub> O <sub>3</sub>	4.63	4.63
NH <sub>3</sub>	n.a.#	4.62
CO	0.443	3.42
H <sub>2</sub>	8.66	2.76
H <sub>2</sub> O	6.75	2.65
HCl	2.90	2.62
N <sub>2</sub>	4.53	2.22
CH <sub>4</sub>	n.a.#	1.56
Cl <sub>2</sub>	0.382	0.52
CO <sub>2</sub>	0.0158	0.0669
NO	0.00409	0.00827
H	0.0510	n.a.#

#Not available in product species database.

## REACTIVE EQUATION OF STATE MODEL

The unreacted or explosive phase is described by a Mie-Grüneisen EoS in the form

$$e_x = e_r + \frac{v_{x0}}{\Gamma_{x0}}(p_x - p_r) \quad (1)$$

where  $p$  is pressure,  $v$  is specific volume,  $e$  is specific internal energy, and  $\Gamma$  is the Grüneisen coefficient. The subscripts are:  $x$  for the unreacted explosive,  $0$  for the initial state, and  $r$  for the reference (principal) isentrope. The latter is represented by the Birch-Murnaghan finite strain equation in the form described by Jeanloz<sup>8</sup> as

$$p_r = 3K_0 \varphi (2\varphi + 1)^{5/2} [1 + a_1 \varphi] \quad (2)$$

$$\text{and} \quad e_r = \frac{9}{2} K_0 v_{r0} \varphi^2 [1 + (2a_1/3)\varphi] \quad (3)$$

$$\text{where} \quad \varphi = \frac{1}{2} \left[ (v_{x0}/v_x)^{2/3} - 1 \right] \quad (4)$$

The required coefficients in equations (2) to (4) are determined from the Hugoniot

$$U = c_0 + s u \quad (5)$$

where  $U$  is shock velocity and  $u$  particle velocity, as

$$K_0 = \rho_{x0} c_0^2 \quad \text{and} \quad a_1 = (3/2)(4s - 5) \quad (6)$$

The reacted or product phase, denoted by the subscript  $p$ , is described by a polytropic EoS with a density-dependent index, namely

$$e_p = \frac{p_p v_p}{\gamma_p - 1} - q_p \quad (7)$$

where

$$\gamma_p = \gamma_0 + \gamma_1/v_p + \gamma_2/v_p^2 \quad (8)$$

and where  $q_p$  is the heat of reaction. The constants in equation (8) are determined by requiring that it return the correct values for  $(\partial \ln p / \partial \ln v)_s$  at the ideal CJ state and at infinite expansion.

The equation of state for the reacting mixture is then completely specified by invoking the simple mixture rules

$$p \equiv p_x \equiv p_p, \quad v \equiv v_x \equiv v_p, \quad e = (1 - \lambda)e_x + \lambda e_p \quad (9)$$

where  $\lambda$  is the extent of reaction, varying from 0 for the unreacted explosive to 1 for the detonation products. The associated reaction rate was developed for composite porous explosives by Kirby and Leiper,<sup>9</sup> namely

$$\dot{\lambda} = (1 - \lambda) \left\{ \frac{p_{hs} a_h}{\tau_h} + \frac{p a_i}{\tau_i} + \frac{p a_f}{\tau_f} \right\} \quad (10)$$

$$\text{where} \quad p_{hs} = \begin{cases} \frac{p}{4} \left( \frac{3p}{4p_{cr}} \right)^3 & \text{for } p < 4p_{cr}/3 \\ p - p_{cr} & \text{for } p \geq 4p_{cr}/3 \end{cases} \quad (11)$$

The subscripts are:  $h$  for hotspot,  $i$  for intermediate, and  $f$  for final stages of the reaction. There are four adjustable parameters — three characteristic reaction times  $\tau$ , and the critical pressure  $p_{cr}$  that inhibits the onset of the hotspot reaction. The  $a$  factors in equation (10) describe the assumed geometry of the burn front, controlling the switching on and off of the hotspot, intermediate and final reaction rate terms. They are functions of  $\lambda$ , and are Gaussian in shape, namely

$$a_h = \begin{cases} \exp \left\{ -[(\lambda - C_i)/W_h]^2 \right\} & \text{for } 0 \leq \lambda \leq C_i \\ \exp \left\{ -[(\lambda - C_i)/W_i]^2 \right\} & \text{for } C_i < \lambda \leq 1 \end{cases} \quad (12)$$

$$a_i = \begin{cases} 0 & \text{for } 0 \leq \lambda \leq C_i \\ 1 - a_h & \text{for } C_i < \lambda \leq C_f \\ \exp \left\{ -[(\lambda - C_f)/W_f]^2 \right\} - a_h & \text{for } C_f < \lambda \leq 1 \end{cases} \quad (13)$$

$$a_f = \begin{cases} 0 & \text{for } 0 \leq \lambda \leq C_f \\ 1 - a_h - a_i & \text{for } C_f < \lambda \leq 1 \end{cases} \quad (14)$$

where the Gaussian parameters are defined in terms of the mass fractions,  $\Phi$ , of the three stages as:

$$\text{Centroids} \quad \begin{cases} C_i = \Phi_h^2 \\ C_f = (\Phi_h + \Phi_i)^2 \end{cases} \quad (15)$$

$$\text{Half-widths} \quad \begin{cases} W_h = 2C_i/(1 + C_i) \\ W_i = \Phi_h(1 - \Phi_h) \\ W_f = \Phi_f(1 - \Phi_f) \end{cases} \quad (16)$$



## STEADY NONIDEAL DETONATION -- CPeX ANALYSIS

The above reactive equation of state was embedded into the analytical non-ideal detonation model CPeX (standing for Commercial Performance of explosives). This model was developed to describe the detonics of non-ideal explosives by Kirby and Leiper,<sup>9</sup> who extended the small divergent detonation theory of Wood and Kirkwood.<sup>10</sup> It describes the flow along the central streamtube between the detonation front and the CJ plane for unconfined cylindrical geometry by using the shooting method described by Braithwaite et al.<sup>11</sup> to solve the system of partial differential equations including the Euler equations of motion, the equation of state, the reaction rate, and an empirical relationship between the wave front curvature  $R_s$  and the charge diameter  $d$ . In previous versions of CPeX, this relationship had the form

$$R_s = (d - Bx_{CJ})/A \quad (17)$$

where  $x_{CJ}$  is the CJ zone length at the diameter  $d$ , and where  $A$  and  $B$  are empirical constants. However, in practice,  $x_{CJ}$  is not known beforehand, so that an iterative procedure must be employed to determine the necessary model constants. This work employs a simpler form suggested by Leiper,<sup>12</sup> namely

$$\frac{d}{R_s} = \alpha + \beta \frac{d_{cr}}{d} \quad (18)$$

where  $\alpha$  and  $\beta$  are empirical constants and  $d_{cr}$  is the critical diameter below which detonation will not propagate.

The adjustable parameters in the reaction rate law were varied until the predicted variation of detonation velocity with unconfined charge diameter matched the experimental measurements of Forbes et al.<sup>1</sup> as shown in Figure 1. This figure also includes CPeX fits to an ideal and a non-ideal explosive for comparative purposes. The former is the fine RDX Composition B (COMP B) data of Malin.<sup>13</sup> The latter is a proprietary ICI blend of porous ammonium nitrate prill plus fuel oil (ANFO) with an AN/water-in-oil emulsion.<sup>14</sup>

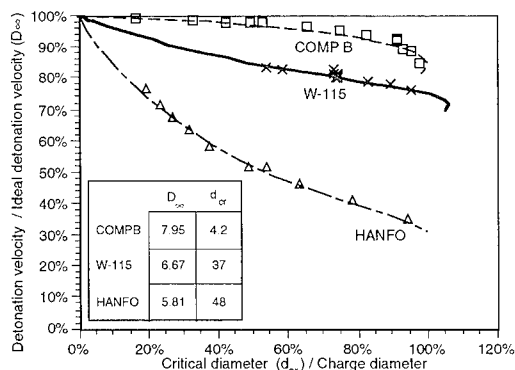


FIGURE 1. DETONATION VELOCITY FOR UNCONFINED CYLINDRICAL CHARGES

The ideal detonation velocity assumed in the CPeX fit for W-115 is about  $0.5 \text{ mm} \cdot \mu\text{s}^{-1}$  faster than that determined by a linear extrapolation of Forbes' data. It is believed that the experimental data have been obtained over too small a range of diameters, being limited to within a factor of two of the critical diameter. As an illustrative example, the "ideal" detonation velocity inferred for HANFO from measurements

made on charges up to twice the critical diameter is about  $1.5 \text{ mm} \cdot \mu\text{s}^{-1}$  lower than the value predicted from ideal thermodynamic calculations, and inferred from measurements over a wider range of charge diameters (namely up to six times the critical diameter).

The parameter values for W-115 are summarised in Table 3, applying specifically to the NSW composition.<sup>1,2</sup> For reasons not yet identified, the Australian variant<sup>3</sup> has a critical diameter roughly twice that of the NSW material. Since an experimental Hugoniot was not available for W-115, one was derived from those of its components using the mixture rule described by Afanasenkov et al.<sup>15</sup> — this Hugoniot is similar to that measured experimentally for the propellant SPIS-44 with composition 20/49/21/10% HMX/AP/Al/binder, for which  $U = 2.774 + 1.855u$ .<sup>16</sup>

TABLE 3. CPeX MODEL CONSTANTS FOR W-115

Parameter	Symbol	Value
Initial density	$\rho_0$	$1.79 \text{ g} \cdot \text{cm}^{-3}$
Hugoniot intercept	$c_0$	$2.80 \text{ mm} \cdot \mu\text{s}^{-1}$
Hugoniot slope	$s$	1.83
Grüneisen coefficient	$\Gamma_{x0}$	2.60
Curvature parameter	$\alpha$	0.165
Curvature parameter	$\beta$	0.692
Polytropic coefficient	$\gamma_0$	1.343
Polytropic coefficient	$\gamma_1$	$0.2045 \text{ cm}^3 \cdot \text{g}^{-1}$
Polytropic coefficient	$\gamma_2$	$0.005112 \text{ cm}^6 \cdot \text{g}^{-2}$
Hotspot mass fraction	$\Phi_h$	0.15
Intermediate mass fraction	$\Phi_i$	0.60
Final mass fraction	$\Phi_f$	0.25
Critical hotspot pressure	$p_{cr}$	5.5 GPa
Hotspot time constant	$\tau_h$	$11.8 \mu\text{s} \cdot \text{GPa}^{-1}$
Intermediate time constant	$\tau_i$	$100.0 \mu\text{s} \cdot \text{GPa}^{-1}$
Final time constant	$\tau_f$	$66.0 \mu\text{s} \cdot \text{GPa}^{-1}$

Initially, the CPeX fit for W-115 was based on the plausible assumption that the hotspot or initial reaction consumed the RDX, that the intermediate phase of the reaction involved the AP plus binder, and that the Al was the last to react. The appropriate mass fractions would then be  $\Phi_h = 20\%$ ,  $\Phi_i = 55\%$  and  $\Phi_f = 25\%$ . However, a superior fit to the velocity data was achieved by modifying the hotspot mass fraction to be  $\Phi_h = 15\%$  (with  $\Phi_i = 60\%$ ). This may indicate that the Gaussian shape factors developed for highly porous explosives and described in equations 12 to 16 are not as appropriate for non-porous explosives. Alternatively, it may be argued that the use of a single parameter,  $\lambda$ , is not sufficient to simultaneously account for the release of energy via the chemical reactions, the switch from unreacted to reacted equations of state, and the geometry of the burn front.

It should be noted that the adopted values of the constants describing the late stages of the reaction (ie.  $\Phi_i$ ,  $\Phi_f$ ,  $\tau_i$  and  $\tau_f$ ) are not unique — other assumed values could give equally acceptable fits to the detonation velocity data. This is explained by examining the reaction rate in greater detail. Figure 2 shows how the predicted CJ extent of reaction varies with charge diameter. Detonation in the ideal explosive COMP B fails when its CJ extent of reaction falls below 96%, whereas both the non-ideal compositions continue to propagate down to about 15% reaction. The maximum CJ extent of reaction achieved over the range of diameters

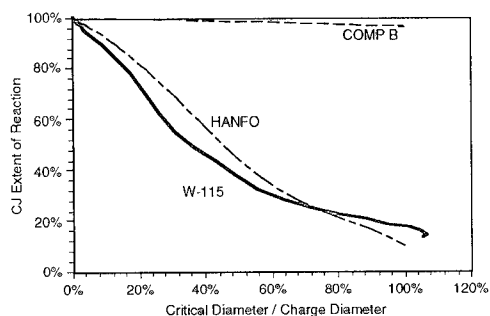


FIGURE 2. CPeX CJ EXTENT OF REACTION

sampled for W-115 is about 35%. Consequently, that part of the reaction rate for  $\lambda > 0.35$  has not been fitted to experimental data, and so must be considered conjectural.

Figure 3 examines this in greater detail, by presenting the full reaction rate surface  $\lambda(p, \lambda)$  for each explosive. The  $(p_{CJ}, \lambda_{CJ})$  locus (traced out by varying charge diameter) for unconfined detonation is superimposed on this surface, together with the two  $(p, \lambda)$  histories followed by Lagrangian particles on the central streamtube between the shock front and the CJ plane for unconfined detonations in the smallest and largest diameters characterised experimentally. It can be seen that the detonation velocity measurements performed to date have sampled only a very restricted subset of the reaction rate surface for W-115, so that any predictions of late-time reactions involving the AP and Al must be of dubious accuracy. In order to extract accurate values for the time constants  $\tau_i$  and  $\tau_f$  from a CPeX analysis, it would be necessary to measure the detonation velocity of unconfined charges exceeding 250 mm diameter and 1500 mm length.

The measurements for COMP B have sampled across the full range of extents of reaction, but only for a restricted part of the pressure domain. Consequently, descriptions of low pressure shock initiation based only on the CPeX fit would be suspect unless augmented by specific initiation experiments. However, the reaction rate surface for HANFO is very well covered by the experimental detonation velocity data, permitting accurate predictions of its detonics.

## CJ PRESSURE

Figure 4 presents the CPeX predictions for the pressures at the shock front, and at the CJ plane. It can be seen that they are predicted to vary by a factor of about three over the full range of diameters that will support detonation.

## HYDROCODE MODELLING OF W-115

The equation of state and reaction rate law described above for the CPeX model were embedded in the explicit finite element hydrocode DYNA2D<sup>5</sup> to permit the simulation of time-dependent reactive flow in non-ideal explosives. The constants derived for W-115 by the CPeX analysis, and displayed in Table 3, were used in the DYNA2D simulations without any further adjustment.

## STEADY-STATE AXISYMMETRIC DETONATION

Figure 5 summarises the DYNA2D predictions of detonation velocity in axisymmetric geometry. All charges

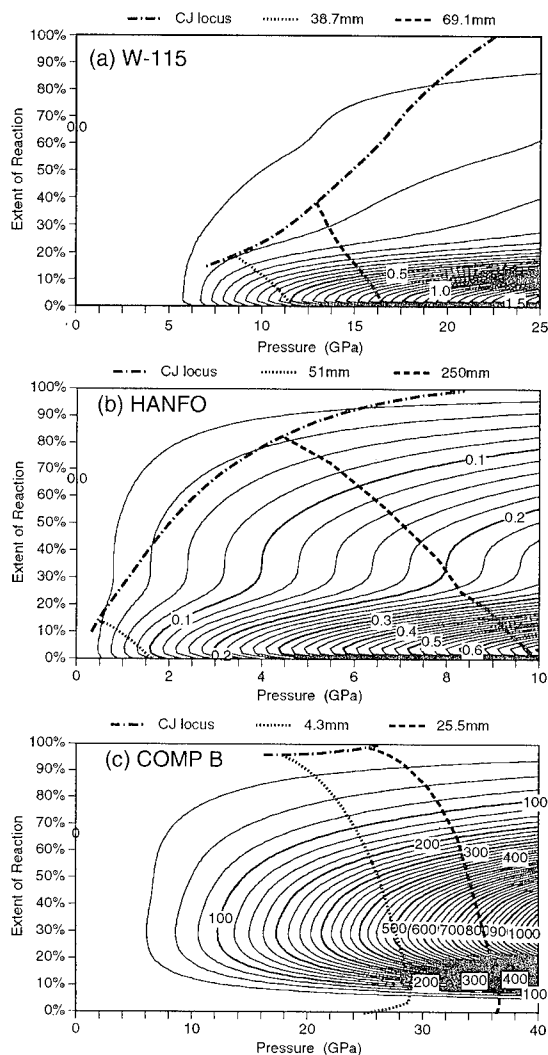


FIGURE 3. CONTOURS OF REACTION RATE  $\lambda(p, \lambda)$

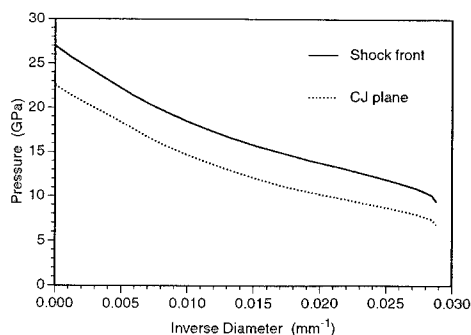


FIGURE 4. CPeX SHOCK AND CJ PRESSURES

were 300 mm in length to ensure that steady state conditions were reached. There is excellent agreement between the

numerical simulations and the experimental data<sup>1</sup> for both unconfined and confined detonations in 2.5 mm thick brass.

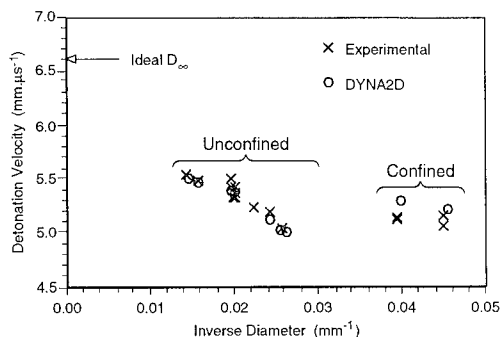


FIGURE 5. W-115 DETONATION VELOCITY

The experimental<sup>1</sup> pass / fail diameters for W-115 were 38.7 / 35.1 mm unconfined, and 22.2 / 19 mm confined (in 2.5 mm brass). The simulations were in excellent agreement, predicting 38 / 37 mm unconfined and 22 / 19 mm confined. Figure 6 shows how the predicted shock velocity in a 37 mm rate stick decayed with distance from the booster. The wave propagated for over four charge diameters before dying. Dick<sup>17</sup> has observed similar behaviour for a HMX-based composite propellant. This suggests that the 153 mm length charges used at NSWC were only just long enough to ensure steady state behaviour in diameters close to critical.

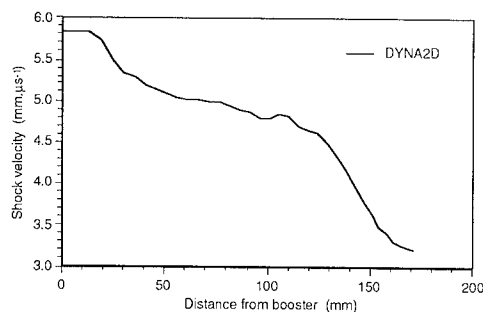


FIGURE 6. FAILURE IN 37MM DIAMETER

This high level of agreement for unconfined detonation confirms not only the model constants, but also serves to verify the assumptions made in the CPeX model to relate flow divergence to shock front curvature. Such assumptions are not required for the DYNA2D simulations. Furthermore, the similar excellent agreement for confined detonation provides additional confirmation of the model, having sampled a different combination of lateral expansion and extent of reaction.

## WAVE FRONT CURVATURE AND CJ ZONE LENGTHS

Figure 7 presents the comparison between the NSWC measurements<sup>1</sup> and the DYNA2D simulations of shock front radius of curvature for unconfined charges, plotted to illustrate the linear behaviour expressed in equation (18). The scatter reflects the difficulty in measuring the curvature both experimentally and in the simulations. This data was used in the CPeX fit, but not explicitly by the DYNA2D simulations. The good agreement thus helps to confirm the flow pattern assumed in the CPeX theory.

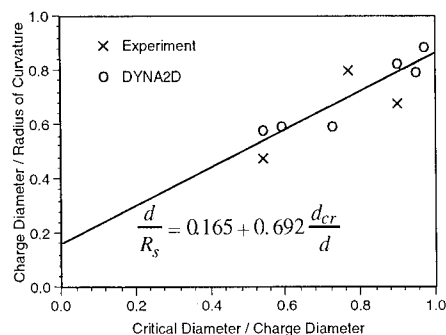


FIGURE 7 SHOCK FRONT CURVATURE

Wave curvature experiments are often performed in order to estimate the CJ zone lengths via application of the Wood-Kirkwood theory.<sup>10</sup> The zone lengths calculated by Forbes et al.<sup>1</sup> are compared with the CPeX predictions in Figure 8. The agreement is poor, with the CPeX CJ zone lengths being up to a factor of two higher than Forbes' calculations based on

$$\frac{D_{\infty} - D}{D_{\infty}} = C \frac{x_{CJ}}{R_s} \quad (19)$$

where  $D_{\infty}$  is the ideal value of the detonation velocity,  $D$  the measured value, and  $R_s$  the wave curvature for the charge diameter of interest.  $C$  is a constant dependent upon the equation of state. Wood and Kirkwood derived equation (19) as a specific solution to their more general theory by making a number of assumptions. In particular, they assumed that the reaction rate is Arrhenius in form, so that the reaction rate immediately behind the shock is low, and then rises to a sharp maximum very close to complete reaction. This leads firstly to CJ parameters ( $p$ ,  $v$  and  $\lambda$ ), that are only slightly perturbed from their ideal values, and secondly to a pressure profile that is essentially flat-topped at the von Neumann spike value. These conditions are not too dissimilar from the behaviour summarised in Figures 2 and 3 for the ideal explosive COMP B. However, these Figures show that these assumptions are clearly inappropriate for both non-ideal explosives, W-115 and HANFO. Hence, the simplistic form of the Wood-Kirkwood theory, represented by equation (19), should not be applied to non-ideal explosives.

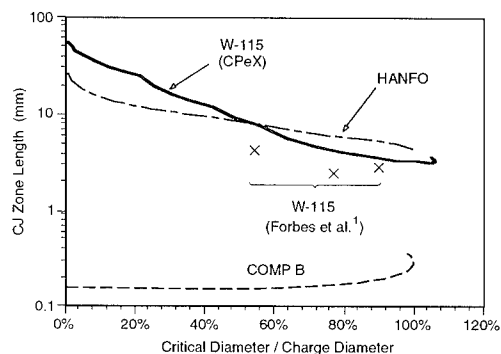


FIGURE 8. CPeX CJ ZONE LENGTHS

It is apparent from Figure 8 that the CJ zones for the two non-ideal explosives extend over much larger regions of space than is the case for the ideal one. In particular, it is predicted that experiments intended to characterise an ideal

steady-state planar detonation in W-115 must be performed on a massive scale — the ideal CJ zone predicted by CPeX exceeds 60 mm in length and 15  $\mu$ s in duration.

## CORNER TURNING

Forbes et al.<sup>1,2</sup> have characterised the corner-turning ability of W-115, measuring the breakout times through the curved surfaces of bowl-shaped acceptor charges. The bowls were initiated through their flat rear surfaces by boosters of 51 mm diameter and 153 mm in length. The curved surface of each bowl had a radius of curvature of 51 mm (measured from the edge of the booster). Four different booster configurations were used — (1) bare W-115, (2) bare COMP B, (3) bare COMP B with a steel plate covering the flat surface of the bowl, and (4) W-115 confined in a brass tube with 16.5 mm thick walls.

In order to control the distortion of the finite element mesh at the booster/bowl junction, it was necessary to introduce a 6 mm radius of curvature there in the numerical simulations with DYNA2D — the effect of this change on the predicted breakout times is unknown, but is believed to be small. Figure 9a presents the predicted pressure contours 9  $\mu$ s after the shock from the booster has entered the bowl, while Figure 9b shows the extent of reaction after the shock has completely enveloped the bowl (with the material motion removed in order to facilitate comparison).

The comparison with experiment is shown in Figure 10, and is seen to be excellent for the bare boosters, cases (1), (2), and (3). This agreement indicates that the reaction rate surface for W-115 (shown in Figure 3a) is accurate in regions beyond that directly calibrated by the detonation velocity measurements. In particular, the breakout through the outer edges of the bowl for case (1), the unconfined W-115 booster, is controlled by the reaction rate surface in the lower pressure regime below 5 GPa. The break-outs for cases (2) and (3) with the COMP B boosters are dominated by high pressures, exceeding 20 GPa, developed along the axis of the bowls.

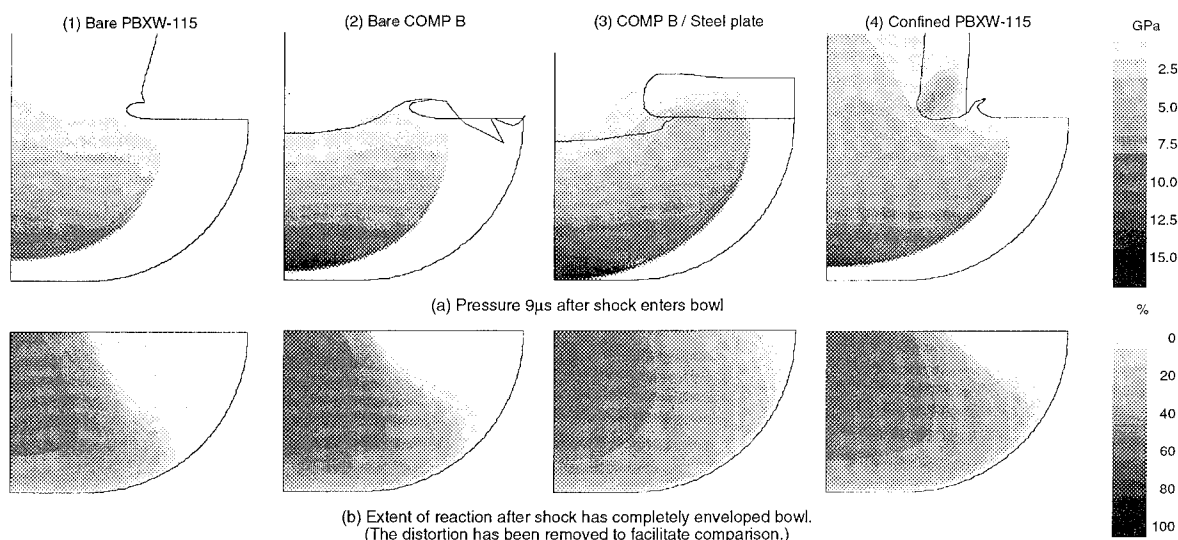


FIGURE 9. EFFECT OF BOOSTER TYPE ON CORNER TURNING IN BOWL OF W-115

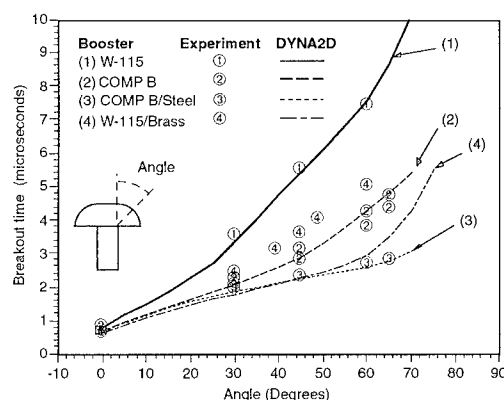


FIGURE 10. CORNER TURNING BREAKOUT TIMES

detonation is plotted against the initial shock pressure.

The simulation has grossly underestimated the breakout times for case (4), the W-115 booster confined in a thick (16.5 mm) wall brass tube. This confinement increases both the peak value and the duration of the pressure in the booster and the acceptor charge. Consequently, the simulation has sampled portions of the reaction rate surface outside the region characterised by the unconfined detonation velocity measurements. The poor agreement with experiment suggests that the reaction rates shown in Figure 3a for W-115 have been overestimated past about 35% extent of reaction.

## WEDGE TEST AND POP-PLOTS

The wedge test is often used to characterise the shock initiation behaviour of explosives. A plane-wave generator sends a relatively flat-topped planar shock into a wedge of acceptor explosive — observation of the emergence of the shock through the angled face of the wedge gives a continuous record of run up to detonation. The results are displayed on a Pop-plot, where the measured run distance to

Several simulations were performed to examine the behaviour of W-115 in this test. Figure 11 summarises the predicted shock velocity versus time histories over a 50 mm run distance induced by various input shock pressures. In the simulations, these pressures were created by the impact of thick aluminium flyer plates.

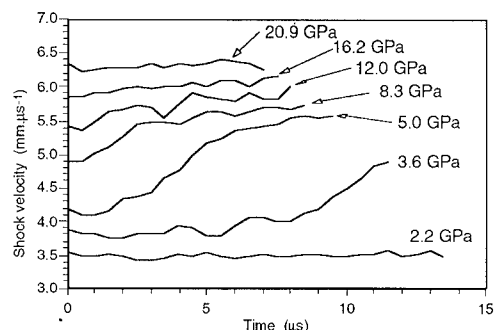


FIGURE 11. PREDICTED SHOCK ACCELERATION OVER 50 MM IN WEDGE TEST

These trajectories are notable for the absence of the sharp transition between low velocity shock and high velocity detonation that is characteristically observed with ideal explosives. They are qualitatively similar to those published for other non-ideal explosives. Dick<sup>17</sup> suggested that the gradual increase of velocity with time shown by the traces for a HMX / AP / Al / binder propellant (not unlike W-115) was evidence of overdriven detonation. In spite of all trajectories showing gradual acceleration, workers at RCEM<sup>18,19</sup> derived a Pop-plot for an emulsion explosive, concluding that it was much less shock sensitive than TNT.

The present work suggests that these interpretations of wedge test data for non-ideal explosives are incorrect. Figure 12 extends the trajectories of Figure 11 out to a distance of 500 mm. Two features are apparent. Firstly, the trajectories for the 2.2 and 3.6 GPa initial shocks now show clear (albeit diffuse) transitions between low and high velocity regimes. Secondly, none of the trajectories have attained a steady-state velocity even after 500 mm of run, though they are all asymptotically approaching the expected ideal detonation velocity of 6.67 mm.μs<sup>-1</sup>.

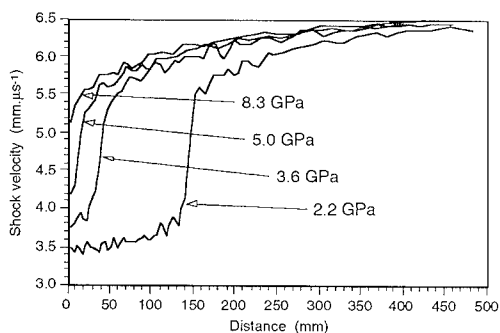


FIGURE 12. PREDICTED SHOCK ACCELERATION OVER 500 MM IN WEDGE TEST

This behaviour can be explained by referring to the reaction rate surfaces in Figure 3. For W-115, the  $\lambda$  surface can be divided into two regimes.

Firstly, for initial shock pressures above 5 GPa, the peak reaction rate occurs at minimal extents of reaction, causing rapid consumption of the RDX component. Any rapid acceleration of the shock velocity will occur during this short phase, quickly giving rise to velocities typical of detonation in small diameters, i.e. about 5.0  $\approx$  5.5 mm.μs<sup>-1</sup>. However, once the extent of reaction exceeds 20% or so, the reaction rate decreases sharply, and so approach to the ideal detonation state will be gradual.

Secondly, for initial shock pressures below 5 GPa, the initial reaction rate is low, so that the shock propagates with minimal acceleration. However, as the reaction proceeds and the pressure builds up, the condition is reached where the reaction rate increases sharply. The shock then transitions to a higher velocity, though, as above, it is supported essentially by consumption of the RDX. Further acceleration is consequently slow.

In contrast, ideal explosives at low porosity will have reaction rate surfaces similar to that shown in Figure 3c for COMP B. Here, the initial reaction rate at low to medium shock pressures is low, so that initial shock velocities are low with minimal acceleration. However, once several percent reaction has occurred, the increase of pressure causes the rapid acceleration of the reaction rate, resulting in an abrupt transition. Furthermore, the reaction rate remains high, so that the reaction soon goes to completion, and the ideal detonation velocity is quickly attained. Hence, there is always a strong distinction between detonation and non-detonation.

This analysis suggests that reduction of wedge test traces, and interpretation of their resultant Pop-plots, requires substantial modification for non-ideal explosives. Pop-plots are traditionally used for two distinct purposes. Firstly, they are used to derive kinetics for detonation models, as exemplified by the Forest-Fire model<sup>20</sup>. However, this paper has shown how this can be accomplished instead by detonation velocity measurements on non-ideal explosives. Secondly, they are used to rank the shock sensitivity of different explosives for hazard studies. For this purpose, it is sufficient to know the conditions under which incident shocks lead to self-propagating reactive waves releasing substantial amounts of energy. Hence, it is necessary to replace the identification of transition to detonation by the identification of transition between low and high velocity shocks.

Once this is done, Figures 11 and 12 show that W-115 is predicted to exhibit such transitions for incident shock pressures below about 5.0 GPa. The run distances predicted to occur using a 50 mm wedge are shown in Figure 13, together with the published<sup>21</sup> experimental Pop-plot for W-115. The two-stage nature of this experimental Pop-plot is highly unusual. The preceding discussion of the simulations indicates that the lower pressure branch corresponds to a regime where transitions have a physical interpretation. However, the higher pressure branch corresponds to a regime where the shock front is predicted to show only smooth acceleration, and hence the slope will probably be sensitive to the techniques adopted for data reduction.

The wedge test behaviour of other non-ideal explosives can now be explained.

In the propellant studied by Dick<sup>17</sup>, HMX would play the role of the RDX in W-115 — Figure 1 of Dick's paper does indeed show a strong similarity to Figure 11 of this work,

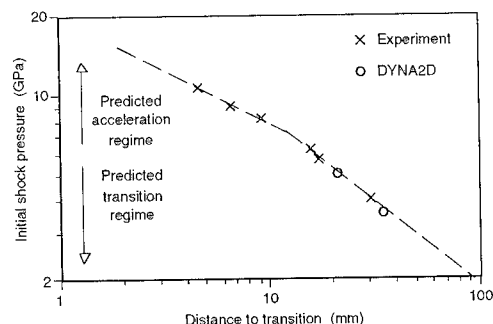


FIGURE 13. W-115 POP-PLOT

though shifted to higher initial shock pressures in line with the lower inherent shock sensitivity of HMX when compared with RDX.

The emulsion studied at RCEM<sup>18,19</sup> is expected to have a reaction rate surface not unlike that of the HANFO shown in Figure 3b. This exhibits only the first regime discussed above, where the reaction rate is always greatest at or immediately behind the shock front, so that acceleration is always smooth, and transitions would never occur. Hence, both the published Pop-plot for this emulsion, and the claim that it is less sensitive than TNT, are suspect.

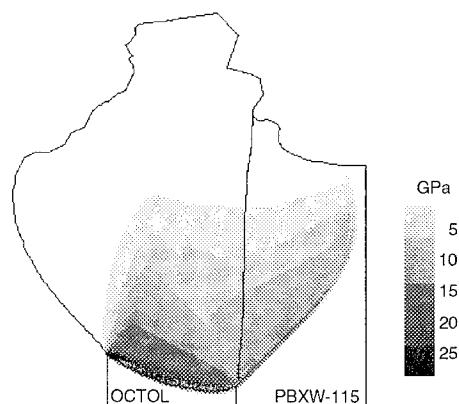
#### IDEAL DETONATION VELOCITY EXPERIMENTS

Held<sup>4</sup> has recently described a technique to measure the ideal detonation velocity using only small samples, and has applied it to the German variant of W-115. A donor charge with high detonation velocity drives a bow wave into a parallel adjacent acceptor test charge with lower detonation velocity, which is inferred from the measurement of the breakout through the face opposite the initiation point. Held assumed that if a steady detonation was established in the acceptor, then it must represent an ideal detonation.

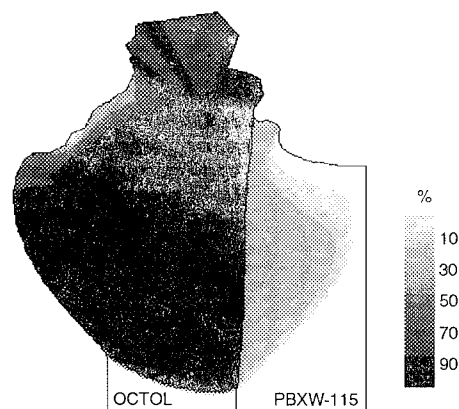
Figure 14 shows the predicted detonation wave shapes immediately prior to breakout for the case of an Octol donor driving a bow wave into W-115. Although the bow wave in the W-115 is shown as being curved, DYNA2D predicts that it does straighten out prior to full breakout. (The W-115 used in the experiment had the composition 40 / 24 / 24 / 12% AP / RDX / Al / binder. This was treated by increasing  $\Phi_h$  to 18% and decreasing  $\Phi_i$  to 57%. The simulation had to be performed using slab charges in planar geometry, in place of the actual half cylinders.)

The charges used by Held were 60 mm in length, which is roughly the same order as the ideal CJ zone length predicted by CPeX (shown in Figure 8). Consequently, DYNA2D is predicting that a steady non-ideal detonation has been created in the W-115, with the extent of reaction having reached a maximum of less than by 50% by the time that the detonation front begins to break out through the end face.

The predicted breakout times for the non-ideal detonation are compared with the experimental results in Figure 15, with the agreement being excellent, confirming the accuracy of the DYNA2D simulation. The conclusion is that the small sample technique does not measure ideal detonation velocity as intended. Much longer and larger diameter charges would be required to accomplish this objective.



(a) Pressure



(b) Extent of Reaction

FIGURE 14. DYNA2D PROFILES FOR IDEAL DETONATION VELOCITY METHOD

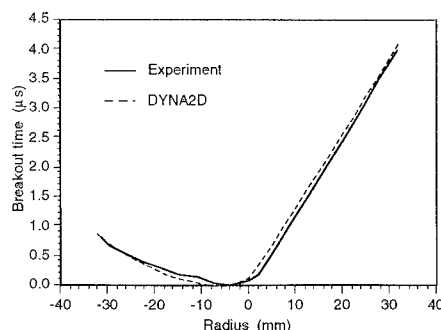


FIGURE 15. BREAKOUT TIMES FOR IDEAL DETONATION VELOCITY METHOD

#### CONCLUDING REMARKS

The application of the CPeX small-divergent detonation theory, and the DYNA2D simulations performed for this paper, have both been built around the assumption that the ideal detonation velocity of W-115 is  $6.67 \text{ mm} \cdot \mu\text{s}^{-1}$  as

predicted by the chemical equilibrium code IDeX.<sup>7</sup> At the time of writing, there is no direct experimental evidence to support this assumption. However, the ensuing excellent agreement between the predictions and almost all the available experimental data provides strong indirect evidence that this assumption is correct, and hence that the detonics of W-115 are strongly non-ideal.

The only piece of experimental data which could not be reproduced by the DYNA2D simulations was the breakout time in the corner turning experiment using a heavily confined W-115 booster. It is believed that this experiment sampled a portion of the reaction rate surface outside the region characterised by the unconfined detonation velocity measurements. This suggests that the reaction rate for W-115 (as shown in Figure 3a) has been overestimated for  $\lambda > 0.35$ .

The analysis presented in this paper illustrates that the reaction rate surface of the non-ideal explosive W-115 is fundamentally different from that of the ideal explosive, Composition B. It is strongly believed that this is a specific example of a more general truth.

Many of the experimental tests in use today were developed to characterise the detonics of ideal explosives, and at a fundamental level, require the reaction rate surface to have particular features. When applying such tests to non-ideal compositions, it is essential to understand the basis of what the test is actually measuring in order to know if it is still applicable. In particular, if knowledge of the full range of detonation behaviour is required for an explosive like W-115, there is no way to avoid at least some experiments performed on massive charges.

Many of the theories and the data reduction techniques that are applied to detonation experiments assume that non-ideal behaviour can be treated as a small perturbation in ( $p$ ,  $v$ ,  $\lambda$ ) space from the ideal CJ conditions. However, a steady-state detonation that is supported by only about 15% reaction cannot be considered to represent a small perturbation from ideal. Due to the work by Forbes and co-workers at NSW, there is now an extensive database of experimental information available on at least one non-ideal explosive for use in confirming the myriad emerging theories of non-ideal detonics.

## ACKNOWLEDGEMENTS

A number of people have provided invaluable advice, information, and discussion. This paper would not have been possible without access to the comprehensive experimental database generated by Jerry Forbes and co-workers at NSW. Dan Whelan and Gunter Bocksteiner provided information and insights on the behaviour of the Australian variant of W-115. Chuck Mader advised on the application of BKW to non-ideal systems. Bob Sheahan and Gwyn Harries provided many insights into non-ideal detonics. Graeme Leiper contributed much advice on the application of CPeX to W-115, while Alan Minchinton explained many of the finer details of the CPeX model.

The authors acknowledge with thanks the permission of ICI Australia and of DSTO to publish this paper.

## REFERENCES

1. Forbes, J. W.; Lemar, E. R.; and Baker, R. N., "Detonation Wave Propagation in PBXW-115", *Ninth Symposium (International) on Detonation*, Office of the Chief of Naval Research, OCNR 113291-7, 1989, pp.806-815.
2. Forbes, J. W.; Lemar, R.; and Baker R., "Detonation wave corner turning in PBXW-115", *Bulletin of American Physical Society*, Vol 35, No. 3, March 1990, p.808.
3. Bocksteiner, G.; and Wolfson, M., *Detonation velocity measurements on Australian PBXW-115*, Materials Research Laboratory report, Melbourne, in press 1993.
4. Held, M., "Steady Detonation Velocity  $D_{\infty}$  of Infinite Radius Derived from Small Samples", *Propellants, Explosives and Pyrotechnics*, Vol 17, 1992, pp. 275-277.
5. Hallquist, J. O., *User's Manual for DYNA2D*, UCID-18756, Rev. 3, March 1988, Lawrence Livermore National Laboratory, Livermore, CA.
6. Mader, C. L., *FORTTRAN BKW: A code for computing the detonation properties of explosives*, LA-3704, Los Alamos Scientific Laboratory.
7. Freeman, T. L.; Gladwell, I.; Braithwaite, M.; Byers-Brown, W.; Lynch, P. L.; and Parker, I. B., "Modular software for modelling the ideal detonation of explosives", *Math. Engng. Ind.*, Vol 3, No.2, 1990, pp.97-109.
8. Jeanloz, R., "Shock Wave Equation of State and Finite Strain Theory", *Journal of Geophysical Research*, Vol 94, No B5, 1989, pp. 5873-5886.
9. Kirby, I. J.; and Leiper, G. A., "A small divergent detonation theory for intermolecular explosives", *Proceedings of the Eighth Symposium (International) on Detonation*, Albuquerque, 1985, pp. 176-185.
10. Wood, W. W.; and Kirkwood, J. G., "Diameter effect in condensed explosives. The relationship between velocity and radius of curvature of the detonation wave", *Journal of Chemical Physics*, Vol 22, 1954, pp. 1920-1924.
11. Braithwaite, M.; Farran, T.; Gladwell, I.; Lynch, P. M.; Minchinton, A.; Parker, I. B.; and Thomas, R. M., "A detonation problem posed as a differential/algebraic boundary value problem", *Math. Engng. Ind.*, Vol 3, No. 1, 1990, pp. 45-57.
12. Leiper, G. A., private communication to D. L. Kennedy regarding literature survey of wave curvature, 1988.
13. Malin, M. E.; Campbell, A. W.; and Mautz, C. W., "Particle-Size Effects in Explosives at Finite and Infinite Diameters", *Journal of Applied Physics*, Vol 28, No. 1, 1957, pp. 63-69.
14. Sheahan, R. M., private communication to D. L. Kennedy regarding detonation velocity measurements, 1992.

15. Afanasenkov, A. N.; Bogolomov, V. M.; and Vostobionikov, I. M., "Generalised shock Hugoniot of condensed substances", *Zhur. Prok. Mekh. Tekh.*, Vol 10, 1969, pp. 137-147.
16. Gibbs, T. R.; and Popolato, A.; Eds., *LASL Explosive Property Data*, University of California Press, Berkeley, 1980, p. 416.
17. Dick, J. J., "Nonideal detonation and initiation behaviour of a composite solid rocket propellant", *Seventh Symposium (International) on Detonation*, Naval Surface Weapons Center, NSWC MP 82-334, 1982, pp. 620-623.
18. Sandstrom, F. W., *Shock initiation characteristics of composite energetic materials*, Research Center for Energetic Materials, New Mexico, RCEM Semiannual Technical Report A-03-89, 1989, pp. 22-25.
19. Lee, J.; Sandstrom, F. W.; Craig, B. G.; and Persson, P. A., "Detonation and shock initiation properties of emulsion explosives", *Ninth Symposium (International) on Detonation*, Office of the Chief of Naval Research, OCNR 113291-7, 1989, pp.573-584.
20. Mader, C. L., *Numerical Modelling of Detonation*, University of California Press, Berkeley, 1979, pp. 208-250.
21. Sandusky, H. W.; and Bernecker, R. R., "Influence of fresh damage on the shock reactivity and sensitivity of several energetic materials", presented at this Symposium, 1993.

---

## DISCUSSION

### PER-ANDERS PERSSON

Research Center for Energetic Materials, Socorro, New Mexico

May I offer my humble congratulations to an excellent and very clarifying paper. Could you please give some additional detail on the uniqueness of the shape and size of the three Gaussian distribution parameters  $a_h$ ,  $a_i$ ,  $a_f$  and the methods by which these are determined? For example, in the PBWX-115, what experiments gave the data for aluminum?

### REPLY BY D. L. KENNEDY:

The form of the geometrical terms was determined by Leiper and Kirby during the early 1980s, prior to their paper in the 8th Detonation Symposium (see Reference 9). They performed a number of numerical simulations to examine the progress of the burn front following shockwave passage through multiphase explosives comprised of random distributions of gas, liquid, and solid phases; each phase having a size distribution typical of those found in commercial explosives. They then found that the Gaussian functions expressed here by equations 12 to 16 gave reasonable analytical fits to the results of their numerical simulations.

These Gaussians provide a smooth transition between each of the three stages (hotspot, intermediate, and final) of the reaction. Hence, for example, the intermediate stage begins to burn as the hotspot stage begins to extinguish, with the crossover point corresponding to the mass fraction of the hotspots.

The model is most sensitive to the values adopted for the mass fractions of the hotspot, intermediate, and final stages. These values are usually assigned by identifying the various stages with different physical or chemical features of the explosive. For W-115, it was natural to assume that the RDX would be consumed in the initial (hotspot) stage. It was then assumed that the AP would react next. However, in view of the conclusion that the reaction rate has been overestimated for extents of reaction exceeding 35%, it may be necessary to assume that the Al reacts as the intermediate stage. The only way to be sure is to map out the full detonation velocity versus charge diameter behavior for several compositions, varying the ratio of AP to Al.



## TIME-DEPENDENT EQUATIONS OF STATE FOR ALUMINIZED UNDERWATER EXPLOSIVES

R. H. Guirguis and P. J. Miller  
Detonation Physics Branch  
Naval Surface Warfare Center  
Dahlgren Division, White Oak Detachment  
Silver Spring, MD 20903-5640

The paper resolves the current discrepancy concerning the equation of state of the products of aluminized underwater explosives, which appears to depend on the size of the charge and degree of confinement, by introducing the rate of late reactions in the formulation. A time-dependent Jones-Wilkins-Lee equation of state, that takes into account the variation of the products during the course of these late reactions and the effects of dissociation in limiting the amount of energy release, is presented. The experimental data from underwater explosion tests and large-scale cylinder tests are used to derive the rate of late reactions in typical underwater explosives.

### INTRODUCTION

Underwater explosives are often designed to release a substantial amount of their energy late in the explosion process, after the bubble has expanded a few times the initial charge size. These are highly non-ideal composite explosives containing significant amounts of metal particles, commonly aluminum (Al), and other non-ideal components, such as ammonium perchlorate (AP), added to complete the aluminum oxidation. In ideal explosives, the reaction times are finite but much smaller than hydrodynamic times. If the size of the charge is larger, but not much larger than the critical diameter, the flow behind the detonation wave is divergent, causing a small amount of energy to be released beyond the sonic Chapman-Jouguet (CJ) surface. In non-ideal explosives, however, a significant amount of energy is released beyond that surface. And in highly non-ideal underwater explosives, energy release may persist even after the bubble has expanded several times the volume of the charge.

These highly non-ideal explosives bridge the gap between propellants and explosives. On a scale representing the different regimes of pressure generated by energetic materials, we have on one end the rocket propellants, in which burning only occurs on the limited exposed surface of the propellant cavity, producing pressures in tens up to few hundred bars. Gun propellant in powder form is already subdivided into a large number of small grains, thus presenting a much larger burning surface, and producing a few kilobars of pressure. The powder is ignited by a relatively slow subsonic flame that pressurizes the propellant ahead of it and starts the

projectile moving in the gun barrel, before all the powder is ignited. The expansion of the products keeps the pressure lower than in explosives.

Between propellants and high explosives, the components of underwater explosives are ignited by a supersonic detonation wave, before any global expansion can take place. Some of the metal in the explosive may react before the CJ surface. But the detonation front is mostly sustained by a small fraction of fast reacting ideal components, such as HMX or RDX, resulting in detonation pressures in tens up to a hundred kilobar. The detonation products of these ideal components, dispersed within the bulk of the explosive, provide the surface area, heat, and oxidizers necessary to start the non-ideal components burning. But these non-ideal components burn at relatively slow rates, through the Taylor rarefaction region, and even after the bubble has expanded several times the initial volume. On the opposite end, we have the traditional explosives, first the non-ideal, then the ideal explosives in which most of the reactions are completed by the CJ plane, resulting in hundreds of kilobars of pressure.

These underwater explosives pack large amounts of energy per unit volume because of the significant fraction of metals in their formulation. They perform particularly well underwater for two independent reasons. Water, being  $10^3$  times denser than air, confines the products longer at high temperatures and pressures, allowing the metals more time to react to completion. And because delaying the release of energy reduces the fraction lost in heating the water.<sup>1</sup> Unfortunately, if the explosive charge is small or if it is not properly confined, the non-ideal components may not react to completion,<sup>2</sup> and in extreme cases, may not react at all,<sup>3</sup> making it difficult to characterize these explosives using traditional methods, such as small-scale cylinder tests, wedge tests, etc.

What makes characterizing non-ideal explosives in

This work was performed under the auspices of ONR 6.2 Explosives and Undersea Warheads Block Program and the Explosives and Warheads Division in NSWCWDET.

general difficult is that the reaction times of some of the components are comparable to the hydrodynamic time scales. The detonation structure is controlled by the fluid flow, the chemical reactions (to be more specific, the rate of energy release), and both the reactants and products equations of state (EOS). Long-range diffusional processes are usually neglected because they are slow. The ambient pressure being much smaller than the pressures generated by the detonation, the EOS of the reactants can be decoupled from the problem. In ideal explosives, because the reaction times are much smaller than the hydrodynamic time scales, chemical reactions can be also decoupled from the problem. Decoupling a physical process from the problem does not mean the process is not occurring. Instead, it means we can solve the problem without *simultaneously* considering (modeling) it. The solution is then substituted in the equations governing the decoupled process and the solution for that particular process separately obtained.

A short reaction time also makes it possible to scale the properties and effects of the detonation. Since both the detonation structure and its effects on the surrounding medium are described by 1<sup>st</sup> order (hyperbolic) PDE's, scaling is possible, if *all* characteristic times of the problem proportionately change with the size of the charge. Because chemical reaction times are not controlled by the size, the detonation problem scales only when the reaction times are much shorter than other characteristic times of the problem, in which case, the reaction process decouples from the problem. Long-range diffusion being governed by PDEs involving 2<sup>nd</sup> order derivatives is another example of processes that could prevent scaling. Fortunately, diffusion drops out because it is too slow. In general, if a physical process is too slow or too fast, it can be decoupled from the problem.

Scaling and decoupling the different physical processes contributing to the detonation are very convenient tools when we experimentally characterize an explosive. In the cylinder test of an ideal explosive, for example, the cylinder expansion is mostly affected by the EOS of the products. As a result, the EOS can be determined by comparing calculated and measured wall velocities, independently of the rate of reaction. Once the EOS of the products is known, it is easier to evaluate the rate of reaction from a different class of experiments. When the wall expansion data of a 2-inch cylinder test of an ideal explosive are scaled by a factor of 0.5, they coincide with the corresponding 1-inch test data, confirming that we can indeed derive from the test a unique EOS independent of the size. By definition, non-ideal explosives include components that have reaction times comparable to hydrodynamic times. We can still conduct cylinder tests of non-ideal composite explosives, but if we ignore the reaction process, the derived EOS will depend to some degree on the diameter of the charge. And in highly non-ideal explosives, the products resulting from the late reactions will not be represented in the EOS, if the diameter of the charge is smaller than some critical value.

We can distinguish three different time regimes in underwater detonations. The early time regime covers the energy released shortly after the leading shock front, up to the CJ surface. This energy directly affects the curvature of the detonation front, making curvature measure-

ments suitable for deriving its rate of release. The intermediate regime spans the energy released in the Taylor rarefaction, up to the point where the gas flow effects become unimportant. Measuring the lateral expansion of the products of a cylindrical charge detonating underwater may provide a good basis for characterizing the energy released in this regime. The late energy release regime starts after the bubble has engulfed the whole charge and has expanded to the point where the flow effects inside the bubble become negligible compared to the thermodynamic effects of the energy being released. Characterizing this late energy release is the subject of this paper.

In this paper, we try to resolve the current discrepancy concerning the equation of state of the products of aluminized underwater explosives, which appears to depend on the size of the charge and degree of confinement, by introducing the rate of late reactions in the formulation. A time-dependent Jones-Wilkins-Lee (JWL) EOS, that takes into account the change in the composition of the products during the course of these late reactions, is presented. Because aluminum reactions are highly energetic, the dissociation effects can play a significant role in limiting the amount of energy released and are also introduced in JWL EOS. The paper explains how to use the experimental data of underwater explosions and large-scale cylinder tests to derive the rate of late reactions in typical underwater explosives.

## EQUILIBRIUM JWL EOS FOR REACTING PRODUCTS

The pressure in the traditional JWL EOS is expressed in terms of the energy  $E$  and volume  $V$  per unit volume of the explosive charge.  $E$  and  $V$  are not intensive thermodynamic properties. As a result, we get a different JWL EOS if the same explosive powder is pressed to a different initial density  $\rho_0$ . RDX and HMX are described by different JWL EOS, although both produce the same products. By definition, the EOS should only depend on the composition of the products and not on the initial density or any other property related to their history. Substituting  $E = \rho_0 e$  and  $V = \rho_0 \vartheta$  in JWL EOS, where  $e$  and  $\vartheta$  are the specific energy and volume, and denoting  $\rho_0 R_1$  by  $R_1$  and  $\rho_0 R_2$  by  $R_2$ , we get

$$p(\vartheta, e) = A \left(1 - \frac{\omega}{R_1 \vartheta}\right) e^{-R_1 \vartheta} + B \left(1 - \frac{\omega}{R_2 \vartheta}\right) e^{-R_2 \vartheta} + \frac{\omega e}{\vartheta} \quad (1)$$

in which all parameters,  $A$ ,  $B$ ,  $R_1$ ,  $R_2$ , and  $\omega$ , depend on the products' composition only. Assuming that the specific heat is a weak function of the volume, we can define an average  $C_v$  such that :

$$e(T, \vartheta) = \frac{\varepsilon}{\vartheta^{\omega}} + C_v T + \frac{A}{R_1} e^{-R_1 \vartheta} + \frac{B}{R_2} e^{-R_2 \vartheta} \quad (2)$$

The constant of integration  $\varepsilon$  is a free parameter that can be adjusted to assign a particular temperature to a given state, for example, the temperature at the CJ state.

In Eqs. 1 and 2, it is implicitly assumed that the products are frozen.  $e$  is the sensible energy, i.e., energy that manifests itself as increase in temperature and pressure. If the products are still reacting, the internal energy  $e$  should be replaced by  $e - (1 - \lambda)Q$ , and the parameters  $A$ ,  $B$ ,  $R_1$ ,  $R_2$ ,  $\omega$ ,  $\epsilon$ ,  $C_v$  become functions of  $\lambda$  in order to account for the changing composition of the products. That is, if we assume that the chemical reaction can be described in terms of a single reaction progress variable  $\lambda$ , and  $Q$  is the energy stored per unit mass. The resulting EOS,  $p(\vartheta, e, \lambda)$ ,  $e(T, \vartheta, \lambda)$ , is coupled to the rate  $d\lambda/dt$  through its dependence on  $\lambda$ . That is why it is concisely described as a time-dependent EOS.

In order to introduce the effects of dissociation in JWL EOS, we derive a formula to describe these effects in simple chemical reactions, such as  $H_2 + 1/2 O_2 = H_2O$ ,  $CO + 1/2 O_2 = CO_2$ , etc., and assume it applies to the more complex reactions involved in the chemical equilibrium of explosive products. We define a measure  $\delta$  of the fraction of energy released

$$\delta(T, p) \equiv \frac{H_{\text{reactants}}(T, p) - H_{\text{products}}(T, p)}{-\Delta H_f(T, p)} \quad (3a)$$

If no dissociation occurs, such as at low temperatures,  $\delta = 1$  by definition. At high temperatures, dissociation is significant and the transformation from reactants to products releases less energy, yielding  $\delta < 1$ . Here, we introduce the first of two approximations intended to simplify the use of  $\delta$  in practical problems. We replace  $\Delta H_f(T, p)$  in Eq. 3a by  $\Delta H_{f, 298}^\circ$ .

Using NASA Equilibrium Code,  $\delta$  was calculated for a stoichiometric  $H_2 - O_2$  mixture at  $p = 0.01, 0.1, 1, 10, 100$  atm, and in the range of temperatures  $T = 300 - 5,000$  K. Figure 1 displays the results for the two cases  $p = 0.1$  and  $p = 1$  only. At low temperatures, up to 2000 K, dissociation have very little effect and the reaction releases most of  $\Delta H_{f, 298}^\circ$ , as illustrated in Fig. 1a.  $\delta$  is slightly larger than 1 in this range because  $\Delta H_{f, 298}^\circ < \Delta H_{f, T}^\circ$  for  $T > 298$  K. As the temperature increases beyond 3000 K,  $\delta$  eventually becomes negative and asymptotically approaches a constant negative value  $\delta_\infty$  ( $\approx -2.96$ ), where  $H_2, O_2$  are fully dissociated, producing H, O atoms only. The results in Fig. 1a also suggest that  $\delta$  can be expressed as

$$\delta(T, p) = \frac{1 + \delta_\infty}{2} - \frac{1 - \delta_\infty}{2} \tanh\left\{\frac{T - \alpha(p)}{\beta(p)}\right\} \quad (4a)$$

In Fig. 1b, the results are plotted on a transformed ordinate such as to yield the straight line  $(T - \alpha)/\beta$ , if Eq. 4a is a proper fit, and the value of the two parameters  $\alpha$ ,  $\beta$ . The upper and lower bounds are  $\tanh^{-1}(\pm 0.99) = \pm 2.6467$ . The intersection with the lower bound gives the temperature beyond which dissociation becomes significant, and the intersection with the upper bound the temperature beyond which  $H_2, O_2$  are fully dissociated. Both  $\alpha$ ,  $\beta$  increase with pressure, confirming the well known fact that pressure inhibits dissociation.  $\alpha$ ,  $\beta$  were also calculated for  $p = 0.01, 10, 100$  atm and the results

plotted on a log-log scale. Both plots were found to be nearly straight lines, indicating that  $\alpha \sim p^a$  and  $\beta \sim p^b$ .

The EOS being expressed in terms of  $(\vartheta, e)$ , however, it would be more convenient to define a measure

$$\delta(T, \vartheta) \equiv \frac{e_{\text{reactants}}(T, \vartheta) - e_{\text{products}}(T, \vartheta)}{-\Delta e_f(T, \vartheta)} \quad (3b)$$

But it is much easier to describe the effect of pressure on dissociation than that of volume, although, in principle, nothing prevents a formulation in terms of  $\delta(T, \vartheta)$ . Here, we introduce the second approximation - we replace  $\delta(T, \vartheta)$  by  $\delta(T, p)$  in Eq. 3b, where  $p$  is the pressure of the products. We also repeat the first approximation - we assume that  $\Delta e_f(T, \vartheta)$  does not change much and can be replaced by a constant  $-Q$ , the same way  $\Delta H_f(T, p)$  was replaced by  $\Delta H_{f, 298}^\circ$  in Eq. 3a.

Introducing the effects of chemical reaction and dissociation in Eqs. 2 and 1, we get

$$e(T, \vartheta, \lambda) = \left\{1 - \lambda \delta(T, p)\right\} Q + \frac{\epsilon(\lambda)}{\vartheta^{\omega(\lambda)}} + C_v(\lambda) T + \frac{A(\lambda)}{R_1(\lambda)} e^{-R_1(\lambda)\vartheta} + \frac{B(\lambda)}{R_2(\lambda)} e^{-R_2(\lambda)\vartheta} \quad (5)$$

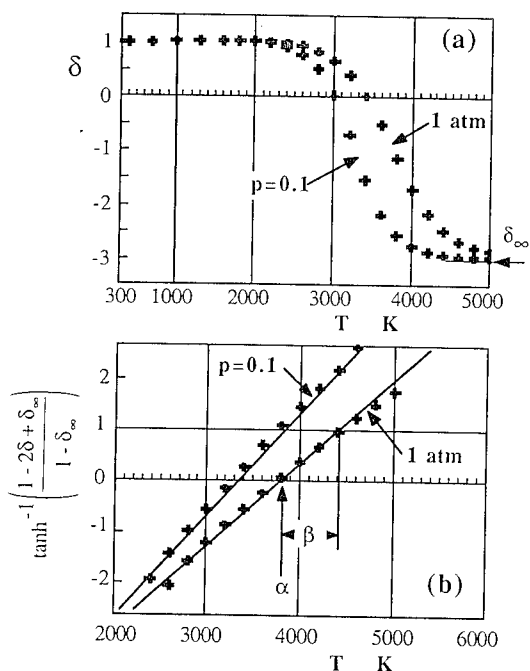


FIGURE 1. MEASURE OF DISSOCIATION FOR A STOICHIOMETRIC  $H_2-O_2$  MIXTURE

$$p(\vartheta, \epsilon, \lambda) = A(\lambda) \left\{ 1 - \frac{\omega(\lambda)}{R_1(\lambda)\vartheta} \right\} e^{-R_1(\lambda)\vartheta} + B(\lambda) \left\{ 1 - \frac{\omega(\lambda)}{R_2(\lambda)\vartheta} \right\} e^{-R_2(\lambda)\vartheta} + \frac{\omega(\lambda) \{ \epsilon - [1 - \lambda \delta(T, p)] Q \}}{\vartheta} \quad (6)$$

Technically, since  $A$ ,  $B$ ,  $R_1$ ,  $R_2$ ,  $\omega$ ,  $\epsilon$ ,  $C_v$  all depend on the composition of the products, we have to modify each  $\lambda$  in these functions by  $\delta$ , yielding  $A(\lambda\delta)$ ,  $B(\lambda\delta)$ , etc. But for the sake of simplicity, and because these parameters will be derived from the equilibrium isentrope corresponding to a given value of  $\lambda$ , as explained below, we elected to write them here as functions of  $\lambda$  alone. While each of Eqs. 1, 2 separately defines a thermodynamic property once their arguments are specified, Eqs. 5 and 6 are coupled by virtue of  $\delta(T, p)$ . If  $(T, \vartheta, \lambda)$  are specified, we cannot get  $\epsilon$  from Eq. 5 alone, even if the function  $\delta(T, p)$  is explicitly defined. Instead, we have to iterate on  $p$  in  $\delta(T, p)$  until  $\epsilon$  resulting from Eq. 5 reproduces the same pressure when substituted in Eq. 6.

Finally, the simplicity of taking the effects of dissociation into account through a single function  $\delta(T, p)$  is misleading. To evaluate  $\delta(T, p)$ , we have to solve the equilibrium problem, which involves the minimization of Gibbs free energy. But Gibbs free energy is affected by the EOS, thus recoupling both the equilibrium problem and the problem of deriving the EOS together again. However, for the limited purpose of introducing the effects of dissociation in JWL EOS, we can assume  $\delta$  is a correction defined by Eq. 4a, where  $\delta_\infty$ ,  $\alpha(p)$ ,  $\beta(p)$  are free parameters that can be adjusted to reproduce the experimental results. All what Eq. 4a implies is that at low temperatures, dissociation is negligible, at very high temperatures, the products fully dissociate, and that pressure inhibits dissociation, all of them are reasonable postulates. In fact, since in most applications involving explosives, we do not have an independent source of energy that can increase the temperature beyond the limit where  $\delta$  becomes negative, and since at the high pressures produced by explosives, dissociation beyond  $\delta=0$  is unlikely, Eq. 4a can be simplified and rewritten as

$$\delta(T, p) = -\tanh\left\{\frac{T - \alpha(p)}{\beta(p)}\right\}, \quad (T < \alpha, 0 \leq \delta \leq 1) \quad (4b)$$

where  $\alpha$  is the temperature at which  $\delta=0$ , and  $1/\beta$  is the slope  $-(\partial\delta/\partial T)_p$  at that point.

### Difference Between $\lambda$ , $\delta$

Although in Eqs. 5 and 6,  $\lambda$  and  $\delta$  appear always together as a product ( $A(\lambda)$  is actually  $A(\lambda\delta)$ , etc.), we cannot replace  $\lambda\delta$  by a single variable because  $\lambda$  and  $\delta$  have different meanings. If we consider the combustion of aluminum, for example,  $\lambda$  is the fraction of aluminum

that has reacted, while  $\delta$  is the fraction of energy released. For the same  $\lambda$ , the amount of energy released  $\lambda\delta Q$  is reduced at high temperatures and low pressures because  $AlO$  and  $Al_2O$  are formed instead of  $Al_2O_3$ . In general, the combustion of aluminum particles is limited by the slow diffusion of the gas oxidizers to the particle surface.  $d\lambda/dt$  can be thought of as proportional to the rate of diffusion  $\times$  particle surface area. But aluminum chemical reactions are much faster than the rate of species diffusion. Once a specific amount of aluminum reacts, we can assume it instantaneously reaches chemical equilibrium with the surrounding gases. The reaction follows a sequence of *successive-equilibrium* steps. If half of the aluminum has already reacted, for example, we obviously assume that the other half is frozen and is not involved in the equilibrium process.

### EOS OF A MIXTURE OF REACTANTS AND PRODUCTS

The JWL EOS in Eqs. 5, 6 describes a mixture of reacting products. Because  $A$ ,  $B$ ,  $R_1$ ,  $R_2$ ,  $\omega$ ,  $\epsilon$  are functions of  $\lambda$ , they can be adjusted to describe a mixture containing solid reactants. Solids being much less compressible than gases, however, the resulting functions  $A(\lambda)$ ,  $B(\lambda)$ , etc., may be stiff. In addition, experimental data suitable for deriving  $\delta_\infty$ ,  $\alpha(p)$ ,  $\beta(p)$  are not readily available. Below, we describe an alternative approximate approach that treats solid reactants separately and uses the TIGER code to account for dissociation.

Let us assume a typical underwater explosive composed of  $\lambda^{oRDX}$  RDX,  $\lambda^{oAl}$  Al,  $\lambda^{oAP}$  AP, and  $\lambda^{oB}$  binder, where  $\lambda^o$  denotes the initial mass fraction. We divide the different components of the explosive into two categories. The ideal components are assumed to react to completion by the CJ plane. The non-ideal components (everything else) are assumed not to release any of their energy before the CJ plane and, therefore, do not contribute to the detonation pressure and velocity. This assumption allows us to use the measured detonation pressure and velocity to derive an adjusted average value for the chemical energy stored in the ideal components,  $e_o(0)$ , that is consistent with the EOS of the products.

For simplicity, we assume here that RDX is the only ideal component. But the methodology is general and can be applied if the components are divided differently, for example, if a fraction of the aluminum is included as a part of the ideal components. Below, the subscript RDX can be replaced by ideal, and Al, AP, B, by non-ideal 1, 2, and 3. Moreover, because the experimental data currently available is not enough to distinguish between individual reactions, we lump all non-ideal components into one, with a single variable  $\lambda$  to describe the mass fraction that has already reacted. The mass fraction of the products in the mixture of products and unreacted non-ideal components is given by

$$\lambda_{\text{products}} = \lambda_{RDX}^o + \lambda (\lambda_{Al}^o + \lambda_{AP}^o + \lambda_B^o) \quad (7)$$

The word "products" should not be interpreted as meaning only gases, because the products may contain solid or liquid phases, such as  $Al_2O_3$  particles.

We assume that both Al and AP particles remain in the solid phase at their initial density ( $\rho_{Al}^0=2.7$ ,  $\rho_{AP}^0=1.95$  gm/cc), until they react and become gas or solid products. The binder (typically,  $\rho_B \approx 0.9$  gm/cc) is the softest of the unreacted components and is assumed to be pressed to zero volume in the high pressure environment of the detonation products. Thus,

$$\frac{V}{\rho_0} \equiv \vartheta = \lambda_{\text{products}} \vartheta_{\text{products}} + (1-\lambda) \left( \frac{\lambda_{Al}^0}{\rho_{Al}^0} + \frac{\lambda_{AP}^0}{\rho_{AP}^0} \right) \quad (8a)$$

where  $\vartheta$  and  $V$  are the specific and relative volumes of the mixture, and  $\rho_0$  is the density of the explosive. In reality, Al and AP particles are slightly compressed at high pressures and the binder retains some of its volume, resulting errors that cancel out to some extent.

Because Al and AP particles are assumed incompressible, their internal energy remains fixed until they react. The binder is assumed infinitely soft. When compressed to zero volume, its internal energy is not increased either. If we further assume that the core remains cold, the heat transferred from the hot gas products to the outer layer of a particle is completely carried to the products side of the energy balance when this layer reacts or evaporates. Thus,

$$\frac{E}{\rho_0} \equiv e = \lambda_{\text{products}} e_{\text{products}} + (1 - \lambda_{\text{products}}) Q \quad (8b)$$

where  $e$  and  $E$  denote the internal energy of the mixture per unit mass and per unit initial volume, and  $Q$  is the energy stored per unit mass of non-ideal components.

If we know the volume and internal energy of the mixture, Eqs. 8a, 8b give the corresponding values  $\vartheta$  and  $e$  of the products, and if the EOS of the products is known, we can get the pressure and temperature. Only the products are described by the JWL EOS. The unreacted components are either incompressible or infinitely soft. Here, we don't use Eqs. 5 and 6. Instead, we use Eqs. 1 and 2, and account for the energy released due to the reaction of the non-ideal components separately, by using Eq. 8b.

To account for dissociation effects, we use the TIGER equilibrium code. TIGER also accounts for the effects of condensed phases in the products, such as  $Al_2O_3$  particles. For a particular composition defined by  $\lambda$ , the equilibrium isentrope starting from the corresponding CJ point is calculated and the results fitted to

$$p(\vartheta, \lambda) = A(\lambda) e^{-R_1(\lambda)\vartheta} + B(\lambda) e^{-R_2(\lambda)\vartheta} + \frac{c(\lambda)}{\vartheta^{\omega(\lambda)+1}} \quad (9)$$

in order to get  $A$ ,  $B$ ,  $R_1$ ,  $R_2$ ,  $\omega$ .  $c(\lambda)$  determines which isentrope, of the set covering the whole  $p$ - $\vartheta$  plane Eq. 9 describes, and is immaterial to our analysis. Technically, we should use TIGER to calculate the equilibrium isentropes for a sequence (for example,  $\lambda=0.1, 0.2, \dots, 1$ ) of compositions  $\lambda^0_{RDX} RDX + \lambda \times (\lambda^0_{Al} Al + \lambda^0_{AP} AP + \lambda^0_B \text{ binder})$ . But in view of the other simplifications

adopted in the calculations, such an elaborate procedure would be unjustified. Instead, we solve the equilibrium problem only once at  $\lambda=1$ , calculate  $A(1)$ ,  $B(1)$ ,  $R_1(1)$ ,  $R_2(1)$ ,  $\omega(1)$ , and assume that we can interpolate between the two extremes  $\lambda=0$ ,  $\lambda=1$ . Thus,  $A(\lambda)=(1-\lambda)A(0) + \lambda A(1)$ ,  $B(\lambda)=(1-\lambda)B(0) + \lambda B(1)$ , etc. We also assume  $\epsilon(\lambda)=(1-\lambda)\epsilon(0) + \lambda\epsilon(1)$  and  $C_v \approx 0.5$  cal/gm K.

TIGER code also calculates the pressure and temperature at the CJ point and the detonation velocity at  $\lambda=1$ . These are the CJ parameters if all components finished reacting by the CJ plane. From these values, the conservation equations across the detonation wave, and JWL EOS for the products, we calculate the total chemical energy stored in the reactants  $e_0(1)$ , including all ideal and non-ideal components, and  $\epsilon(1)$ .

Using a similar procedure, the measured detonation pressure and velocity in the explosive are used to calculate  $e_0(0)$  and  $\epsilon(0)$ . Here, because RDX is the only ideal component,  $A$ ,  $B$ ,  $R_1$ ,  $R_2$ ,  $\omega$  at  $\lambda=0$  are readily known from the JWL EOS of pure RDX;  $R_1 = \rho^0_{RDX} R_1$ ,  $R_2 = \rho^0_{RDX} R_2$ ,  $\rho^0_{RDX} = 1.77$  gm/cc. But contrary to  $\lambda=1$ , the mixture at  $\lambda=0$  contains solid unreacted components. Here, we assume that the Hugoniot energy relation  $e_H = e_0 + 1/2 p_H (\vartheta_0 - \vartheta_H)$  applies to the products of RDX separately. This assumption does not introduce any errors if the unreacted solid phases are incompressible.

Finally, from the energy stored in RDX alone  $e_0(0)$ , and the total energy stored in the explosive  $e_0(1)$ , the energy stored per unit mass of non-ideal components  $Q$  is evaluated. The parameters  $A$ ,  $B$ ,  $R_1$ ,  $R_2$ ,  $\omega$ ,  $\epsilon$ ,  $e_0$  at  $\lambda=0, 1$ , and  $Q$ , are listed in Table 1 for a typical underwater explosive, as well as the measured CJ conditions (in bold letters), and those predicted by TIGER if all components finished reacting by the CJ plane. The isentropes at  $\lambda=0$ ,  $\lambda=1$  are plotted in Fig. 2, starting from the corresponding CJ points.

In the procedure described above, it is clear that we have accounted for the effects of dissociation on the parameters  $A$ ,  $B$ ,  $R_1$ ,  $R_2$ ,  $\omega$ ,  $\epsilon$ . But because we did not use JWL EOS as implemented by Eqs. 5 and 6, it is not readily obvious how dissociation affects the energy released by the reaction of the non ideal components. The effects of dissociation were introduced at only one point, when we calculated  $Q$  from the CJ conditions at  $\lambda=1$  predicted by TIGER, where all components of the explosive were assumed in equilibrium.  $Q$  includes the effects of dissociation, but only at one state, the CJ state. Mathematically, this is equivalent to introducing the approximation  $[1-\lambda\delta(T,p)]Q = (1-\lambda)\delta(T_{CJ}, p_{CJ})Q$  in Eqs. 5 and 6. During isentropic expansion, both temperature and pressure decrease. But since they have opposite effects on dissociation, the errors produced in  $\delta$  when  $T < T_{CJ}$  and  $p < p_{CJ}$  cancel out to some extent.

## SOURCE OF DATA

Two kinds of experimental data are used in this work to derive the rate of late reactions - data from underwater explosions and data from cylinder tests. In underwater explosion tests, the pressure-time history is measured at several locations in the water. Although we

TABLE 1. JWL PARAMETERS AND CJ CONDITIONS

$\lambda = 0$		$\lambda = 1$	
A = 7.783 Mbar	$R_1 = 4.485$	A = 6.527 Mbar	$R_1 = 5.1523$
B = 0.07071 Mbar	$R_2 = 1.068$	B = 0.1064 Mbar	$R_2 = 1.0305$
$\omega = 0.3$	$\epsilon = 0.05580$	$\omega = 0.1551$	$\epsilon = 0.04845$
$\rho_o = 1.780$ g/cc		$\rho_o = 1.780$ g/cc	
$p_{CJ} = 0.120$ Mbar	$D_{CJ} = 0.570$ cm/ $\mu$ s	$p_{CJ} = 0.204$ Mbar	$D_{CJ} = 0.690$ cm/ $\mu$ s
$T_{CJ} = 3150$ K		$T_{CJ} = 5925$ K	
$e_o = 0.03015$ Mbar.cc/gm		$e_o = 0.09568$ Mbar.cc/gm	
Q = 0.081906 Mbar.cc/gm of non-ideal components			

can derive  $d\lambda/dt$  from the raw data, in the analysis presented below, we elected to start from  $p=f^n(V)$  in the bubble, derived by Hudson and Sternberg<sup>2</sup> (H&S) from the pressure history in the water using 1-D calculations. This was done in order to emphasize the thermochemical differences between underwater explosions of ideal and non-ideal explosives, instead of the hydrodynamic aspects of the problem.<sup>1</sup> In the cylinder test, the wall expansion is usually measured using a streak camera. To model the effects of the late energy release on the wall expansion, a simplified version of Eqs. 5, 6, in which A, B,  $R_1$ ,  $R_2$ ,  $\omega$  are independent of  $\lambda$  and  $\delta=1$ , was added to DYNAD2 EOS library, as well as an ODE solver for  $d\lambda/dt$  derived from the underwater explosions data.

## UNDERWATER EXPLOSIONS

H&S  $p=f^n(V)$  in the bubble resulting from the detonation of a 60 lb charge of a typical underwater explosive<sup>1</sup> is plotted in Fig. 2 on the same p-V plane showing the isentropes  $\lambda=0$  and  $\lambda=1$ . H&S  $p=f^n(V)$  mostly falls in between the two isentropes, but does not violate any thermodynamic principles when its projection on p-V crosses the isentrope  $\lambda=1$ .<sup>4</sup> The kink observed in the region  $V \approx 1.5-5$  is attributed to the delayed chemical reactions of Al and AP. But other reasons are also possible.<sup>5</sup>

First, we calculate  $\lambda(V)$ ,  $T(V)$ . In adiabatic expansion,

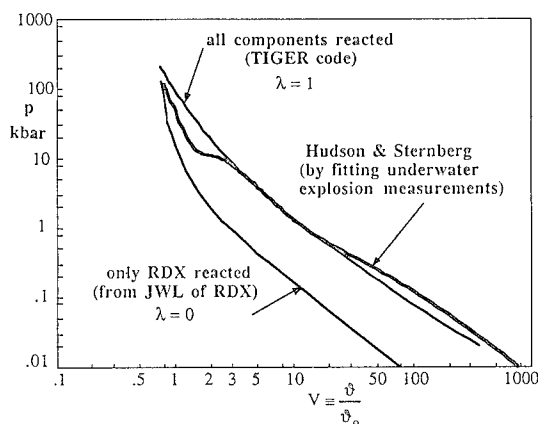


FIGURE 2. PRESSURE INSIDE BUBBLE DUE TO UNDERWATER EXPLOSION OF A 60 LB CHARGE

sion,  $dE = -pdV$ . Integrating H&S  $p=f^n(V)$  between the CJ point and any other point V, we calculate  $\Delta E = E(p_{CJ}, V_{CJ}) - E(p, V)$ . Using Eqs. 1, 7, 8a, 8b, and the interpolated values of A, B,  $R_1$ ,  $R_2$ ,  $\omega$ , we calculate  $\Delta e = e(p_{CJ}, \vartheta_{CJ}, 0) - e(p, \vartheta, \lambda)$ , the pressure being known as a function of  $\vartheta = V/\rho_o$  from H&S  $p=f^n(V)$ . We iterate on  $\lambda$  until  $\Delta e = \Delta E/\rho_o$ , then use Eq. 2 and the interpolated value of  $\epsilon$  to get  $T(V)$ . The results are given in Table 2.  $\lambda(V)$  in the region  $V=0.8-6$ , where the transition from  $\lambda=0$  to  $\lambda=1$  mostly occurs, is also illustrated in Fig. 3.

$\lambda$  decreases as the bubble expands from  $V=1$  to 1.5, and also from  $V=5$  to 6. It is unlikely that the energy already released can be absorbed back. We attribute the discrepancy to errors committed when  $p=f^n(V)$  in the bubble was derived from the pressure-time history in the water. In spherical geometry, the pressure quickly decays after the shock. The excess in pressure resulting from the delayed energy release is effectively derived from the difference between the measured pressure pulse and a corresponding profile representing the pressure pulse if no energy is released after the CJ plane, both of which are quickly decaying. In Fig. 2, the departure of H&S  $p=f^n(V)$  from the isentrope  $\lambda=0$  is so large in the region  $V_{CJ}=0.79$  to  $V \approx 1.5$ , that it almost results a flat plateau in the subsequent region  $V=1.5-3$ . To avoid these errors, a small-scale test was recently designed to carry underwater explosions in planar geometry.<sup>6</sup>

So far, time did not appear in the solution. Only the thermochemistry within the bubble was considered.  $\lambda(V)$ ,  $p(V)$ ,  $T(V)$  are known. We only need  $V(t)$  in order

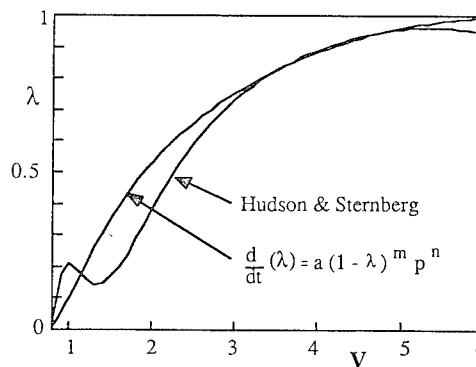


FIGURE 3. PROGRESS OF LATE REACTIONS

TABLE 2. THERMOCHEMICAL PROPERTIES OF THE BUBBLE

V	0.79	1.0	1.5	2.0	2.5	3.0	3.5	4.0	4.5	5.0	6.0
$\lambda$	0	0.212	0.167	0.382	0.592	0.733	0.826	0.889	0.932	0.956	0.943
p kbar	120	48.6	14.0	11.6	10.2	8.4	6.9	5.6	4.7	3.96	2.95
T K	3150	2247	1790	2541	3388	3954	4309	4535	4671	4721	4515

to determine  $d\lambda/dt=f^0(p,T,\lambda)$ . 1-D calculations were used to solve the underwater expansion of a uniform bubble which pressure is given by H&S  $p=f^0(V)$ , starting at  $(V_{CJ}, p_{CJ})$  where  $\lambda=0$ . The assumption of a uniform bubble is consistent with the definition given in the introduction that the late regime starts after the transitional flow structures inside the bubble have decayed. But the solution starts at the CJ state. During the early phases, we assume that the effects of the flow gradients inside the bubble on the time-evolution  $V(t)$  average out.

In reality, the bubble is not uniform, even if it is produced by an ideal explosive. Suppose the underwater explosion is created by the detonation of a spherical charge initiated at the center. The particles near the center go through a short Taylor wave, then remain confined at high temperature and pressure until the detonation wave consumes the charge and the rarefaction waves that emanate from the interface with the water propagate back to the center. As a result, the particles near the center complete their reaction relatively early, almost at constant volume. The particles near the surface of the explosive charge, on the other hand, start expanding as soon as the detonation wave reaches them. They react slowly, and if the charge is not properly confined, may not react at all.<sup>3</sup> In an underwater explosion, however, because the water confines the charge, the particles near the surface partially react, but not to completion.

The time each particle spends at high temperature and pressure is different, depending on its initial location in the explosive charge, the size of the charge, and the impedance of the confining medium. Nevertheless, each particle follows a similar thermodynamic path. Each particle jumps to the conditions behind the detonation shock front, reaches CJ conditions after a relatively short time, then expands from CJ to the low subambient pressures achieved when the bubble overexpands to its maximum radius. In ideal explosives, the chemical reactions are mostly completed by the CJ plane. All particles in the bubble will follow the same thermodynamic path, even though some expand faster than others. When projected on a p-V plane, all particle paths fall on the same isentrope, independent of the size of the charge and degree of confinement. But because of the late reactions in non-ideal explosives, the different rates of expansion result in different thermodynamic paths.<sup>4</sup> If the detonation products EOS is derived by fitting the pressure history in the water without considering the time-dependency caused by the late reactions, the resulting EOS will depend on the size and degree of confinement.

After getting  $V(t)$ ,  $\lambda(V)$  is calculated by solving  $d\lambda/dV=d\lambda/dt \times (dV/dt)^{-1}$ , where

$$\frac{d\lambda}{dt} \equiv a(1-\lambda)^m p^n \quad (10)$$

and the parameters a, m, and n adjusted until the resulting  $\lambda(V)$  matches the one derived earlier from pure thermochemical considerations. Because Eq. 10 cannot sustain a drop in  $\lambda$ , fitting the data to Eq. 10 results in the smooth curve  $\lambda(V)$  illustrated in Fig. 3, starting from  $\lambda=0$ , continuously increasing throughout, and asymptotically reaching  $\lambda=1$ , as it should. We get  $a=0.025$ ,  $m=0.53$ , and  $n=0.15$ , when the time t is expressed in  $\mu s$  and the pressure p in Mbars.

Using the derived rate  $d\lambda/dt$ , we recalculated  $p(V)$ . Figure 4a displays the effect of smoothing  $\lambda(V)$ . After  $V=2.5$ , the derived rate yields the same results as H&S  $p=f^0(V)$ . Here, we had to use the actual charge radius ( $R_0=15.4$  cm for a 60 lb charge) in order to replicate the same time scales of the underwater explosion test used in deriving  $p=f^0(V)$ . If generated by an ideal explosive, or in general, if the EOS is time-independent, we can solve the explosion problem assuming a charge radius  $R_0=1$ , then scale the results up by multiplying both radii and times by the actual radius.

The effect of using a smaller charge on the thermodynamic path in the p-V plane is illustrated in Fig. 4b. Because the time-dependency is introduced in the current formulation, it is now possible to see the difference, unlike a time-independent EOS, which would give the same  $p(V)$  for a 60 or a 2 lb charge. In Fig. 4b, we get smaller pressures when we use a 2 lb charge ( $R_0=5$  cm), because of the relatively faster expansion of the bubble.

## CYLINDER TEST

The time-dependent JWL EOS was also used to model 4 and 8-inch cylinder test data of another underwater explosive ( $\rho_0=1.88$  g/cc,  $p_{CJ}=150$  kbar,  $D_{CJ}=5.9$  km/s), also containing large amounts of Al and AP.<sup>6</sup> The

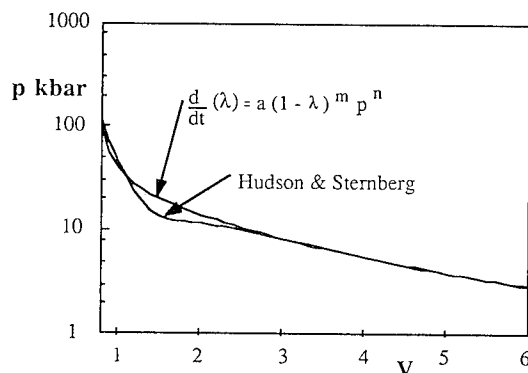
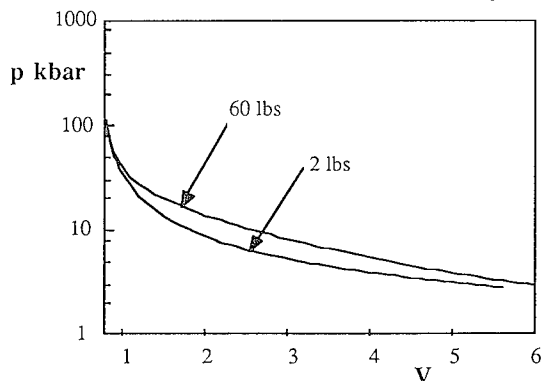


FIGURE 4A. PRESSURE INSIDE THE BUBBLE

tests were conducted in LLNL.<sup>7</sup> We couldn't fit both early and late regimes of the cylinder expansion using a traditional JWL EOS. As obvious from Fig. 5, an excellent fit was obtained when a time-dependent JWL EOS was used instead. In Fig. 5, both measured and calculated values are scaled down to the usual 1-inch cylinder test data representation. The measured data points were smoothed to get rid of the noise in the wall velocity. The calculations were carried out using a simplified version of Eq. 6, in which the parameters  $A=6.95$  Mbar,  $B=0.0313$  Mbar,  $R_1=5.4$ ,  $R_2=1.4$ ,  $\omega=0.4$  are independent of  $\lambda$ ,  $\delta=1$ , and using the rate expression in Eq. 10 with  $a=0.0065$ ,  $m=1/2$ ,  $n=1/6$ .

## CONCLUSIONS

$d\lambda/dt$  was derived from underwater explosion data. But the same rate expression reproduced the measured wall velocities of 4 and 8-inch cylinder tests of a different underwater explosive, also containing significant amounts of Al and AP. The major difference between the two rates is the coefficient  $a$  in Eq. 10, which is larger in



**FIGURE 4B. EFFECT OF EXPLOSIVE CHARGE SIZE ON PRESSURE INSIDE THE BUBBLE**

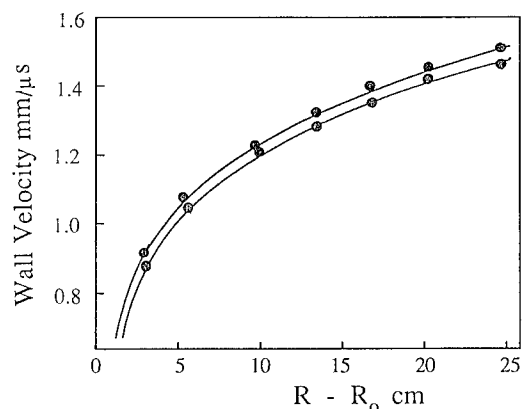


**FIGURE 5. COMPARISON OF MEASURED (POINTS) AND CALCULATED (SOLID LINES) WALL VELOCITIES FOR 4 AND 8-INCH CYLINDER TESTS**

the case of the underwater explosion. Assuming a uniform bubble makes it easier to try different expressions for  $d\lambda/dt$ . But it errantly increases  $V(t)$  and, in

turn,  $d\lambda/dt (=d\lambda/dV \times dV/dt)$ . At  $t=0$ , the pressure of the whole bubble is assumed at  $p_{CJ}$  instead of just a narrow region behind the detonation front. As a result, the initial high rate of expansion of the bubble persists until the rarefaction waves from the interface with the water reach the center of the charge and reflect back. In reality, the expansion slows down considerably as the rarefaction waves dissipate the high pressure region behind the front. However, once  $d\lambda/dt$  is derived, we can repeat the simulations without the uniform bubble assumption and adjust the coefficient  $a$  until the measured pressure pulse is reproduced. This was done in the cylinder test simulations, but not in the underwater explosion.

## REFERENCES

1. Miller, P. J. and Guirguis, R. H., "Effects of Late Chemical Reactions in Non-Ideal Underwater Explosives on the Energy Partition in the Bubble," *Proceedings of the Joint AIRAPT/APS*, 1993, Colorado Springs, CO.
2. Hudson, L. and Sternberg, H., *Equations of State and Underwater Detonation of Composite Explosives*, ATR-87-0035, Advanced Technology and Research Corporation, Laurel, MD, 1987.
3. Forbes, J., Lemar, R., and Baker, R., "Detonation Wave Propagation in PBXW-115," Ninth Symposium (International) on Detonation, 1989, ONR, Arlington, VA, OCNR 113291-7, Vol. 1, pp. 806-815.
4. Guirguis, R. H., "Rate of Late Reactions in the Underwater Explosion of PBXW-115," *Proceedings of the JANNAF PSHS*, 1993, CPIA, Columbia, MD.
5. Guirguis, R. H., "Modeling the Late Reactions in Aluminized Underwater Explosives," *Proceedings of the JANNAF PSHS*, 1992, CPIA, Columbia, MD.
6. Miller, P. J. and Guirguis, R. H., "Experimental Study and Model Calculations of Metal Combustion in Al/AP Underwater Explosives," *Proceedings of the MRS Symposium*, 1992, MRS, Pittsburg, PA, Vol. 296, pp. 299-304.
7. Simpson, R., private communications, 1992, LLNL, Livermore, CA.

## DISCUSSION

PHILIPPE G. BOYCE  
CTSN-MDTC, BP. 28  
83800 Toulon, France

Have you actually applied your model to an underwater explosion? Did you compare the measured and calculated values of shock wave and bulk characteristics?

## REPLY BY R. GUIRGUIS:

Yes, we did. See references 1 and 6 in the paper.



**SESSIONS ON**

**DDT AND SDT**

**Cochairmen:**     **Harold Sandusky**  
                         **Naval Surface Warfare Center**

**Michel Samirant**  
**French German Research Institute (ISL)**

## THE INFLUENCE OF PARAMETER VARIATIONS ON THE DEFLAGRATION TO DETONATION TRANSITION

Ries Verbeek, Albert van der Steen  
and Ed de Jong  
TNO Prins Maurits Laboratory  
P.O. Box 45, 2280 AA Rijswijk  
THE NETHERLANDS

The results are presented of the influence of parameter variations on the outcome of DDT tube tests. The parameters that have been varied are the density of the explosive material, the particle size and the geometry of the tube. The influence of particle size and density on the run-up length to detonation appeared to be ambiguous. The level of confinement of the explosive material was found to have a clear and large influence. In thin-walled tubes evidence was found for the formation of so-called plugs, i.e. regions of explosive material that are compressed to almost 100 % TMD.

### INTRODUCTION

In the research on the Deflagration to Detonation Transition (DDT) at the TNO Prins Maurits Laboratory the emphasis is put on reaching a better understanding of the influence of various parameters on the deflagration to detonation transition in solid explosives. The parameters of interest are, e.g., the density of the explosive material, the particle size, the strength of the igniter and the confinement of the explosive. The DDT program consists of two parts. One part comprises the simulation of the DDT process with use of a computer program, while in the other part a tube test is used to study the DDT phenomenon. Both simulation results and experimental results of the tube test have been reported at earlier Detonation Symposia<sup>1,2</sup>.

The modelling work comprises a one-dimensional computer simulation of the tube test where the explosive system is treated as a fluid mixture of two components: the unreacted explosive and the reaction products. It is very successful as a tool to reach a better understanding of the DDT process and to examine the behaviour of the explosive system by means of parameter variations.

At the development of the tube test care was taken to produce a well defined system in order to make the experiments as reproducible as possible. To this end, e.g., a soft, well-defined ignition is used while also the explosive material is directly pressed into the tube in order to obtain a homogeneous density distribution. At the previous Detonation Symposium experimental results have been presented of two tube types. Since then the research has been extended to several new tube geometries. Also narrower

fractions of the particle size distribution width of the explosive have been used and different densities of the explosive material have been applied. In this paper the results are presented of this extended research.

### EXPERIMENTAL SET-UP

The experiments are performed in thick-walled stainless steel tubes, that are honed to obtain a constant inner diameter and a smooth inner surface. The tubes are closed at both ends with steel screw caps. The tubes are completely filled with the explosive material to be investigated apart from a part with a length of 10 to 25 mm at one end of the tube that is used for the igniter system. In most experiments at the opposite end of the tube the part of the tube that is covered at its outside by the screw cap is filled with a stainless-steel cylindrical piece, since it is not possible to carry out measurements in this part of the tube. At the igniter end one hole with a diameter of 3.8 mm is drilled through the screwcap parallel to its axis to provide a feedthrough for the igniter leads. The remaining space in the hole is filled up afterwards with glue. Along the length of the tube several holes of 1 mm diameter are bored to provide feedthroughs for the measuring probes. Also in this case the holes are filled up as much as possible by using teflon tubes around the probes and by the use of glue, in order to preserve the confinement as much as possible. The probes are located at intervals in the order of 30 mm of each other and are placed spirally along the tube with a difference in angle of 120° with respect to each other in order not to impair the strength of the tube.

Several tube geometries are used to test the influence of charge diameter and confinement on the DDT process. The used tubes include thick walled tubes of varying inner diameter (16 - 36 mm i.d.; 44 - 64 mm o.d.) and relatively thin walled tubes of 16 mm i.d. and 34 mm o.d. The tube lengths range from 330 mm to 360 mm. In table 1 the dimensions of each type of tube used are given.

**TABLE 1. OVERVIEW OF USED TUBE GEOMETRIES**

Tube type	I.D. (mm)	O.D. (mm)	Length (mm)
I	36.2	64	327
II	28.2	54	358
III	16.2	44	334
IV	16.2	34	334

The explosive material to be investigated is loaded into the tube by inserting the material into the tube in increments of equal length and then pressing it to the desired density. This procedure is carried out in order to reduce inhomogeneities in the explosive density as much as possible and to avoid the occurrence of a gap between the explosive material and the tube wall. For these experiments an RDX/wax composition (95 wt% RDX, 4.5 wt% polyethylene wax, 0.5 wt% graphite) has been used with a batch particle size between 200 and 1200  $\mu\text{m}$ . Experiments have been performed with two fractions of this material with a narrower particle size distribution width, namely 600  $\mu\text{m} < d < 710 \mu\text{m}$  and 850  $\mu\text{m} < d < 1000 \mu\text{m}$ , that is obtained from the raw material by sieving it. Up to now three different densities of the material have been used namely 1.28  $\text{mg}/\text{mm}^3$ , 1.35  $\text{mg}/\text{mm}^3$  and 1.42  $\text{mg}/\text{mm}^3$ .

The explosive material is ignited in a relatively gentle and well defined way. The igniter consists of a PVC cylinder at the center of which a small cylindrical cavity is made (diameter 5 mm, depth 2 mm) that contains 90 mg of a pyrotechnic mixture. The pyrotechnic mixture is ignited by applying an electrical current to a NiCr resistance wire that is in contact with the mixture. As igniter material a mixture of lead oxide, tetrazene and boron (85.5/5.0/9.5 wt%) is used. This mixture mainly produces hot particles and only a limited amount of gaseous reaction products, thereby providing a rather soft ignition.

The position of the flame front is detected with use of ionisation probes (Dynasen Inc., type CA-1207), inserted into the tube through the holes in the wall of the tube. The electrical signals are registered by a multichannel transient recorder. A trigger signal is supplied by the output of an optical fiber, positioned at a small distance besides the igniter assembly. After each experiment the fragments of the test tube are gathered and examined and they serve as an extra means of evaluation of the result of the test.

For each tube type experiments were performed with the two explosive compositions described above (with different particle size distributions). In such a series of experiments one or more of the indicated explosive densities

were used. The specific data for each series are presented in tables 2 through 5.

## EXPERIMENTAL RESULTS

A typical example of experimental results obtained with the type I tube is shown in figure 1. In this figure the location of the flame front is given as a function of time for two experiments with a different average particle size. The time is taken relative to the response times of the first ionisation probe. The example is very typical for most DDT experiments. Initially a convective combustion is observed with an almost constant velocity in the order of 0.4  $\text{mm}/\mu\text{s}$ . Then the speed of the front gradually accelerates until a constant speed is reached, the detonation velocity. From the figure it is clear that the distance and time, needed to reach detonation, is larger for the experiment where coarser particles were used. This can also be observed in table 2 in which a summary is given of the results of the experiments performed with this type of tube. In the table the results given for the detonation distance represent an average of the results for all experiments performed with that particle size and density.

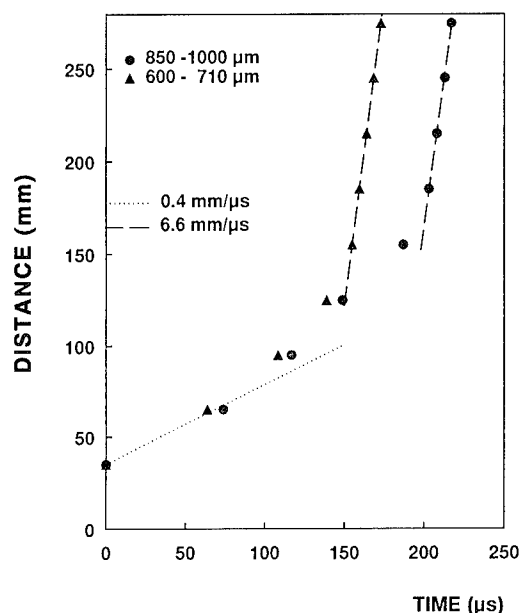


**FIGURE 1. EXPERIMENTAL RESULTS FOR TUBE TYPE I FOR TWO EXPERIMENTS WITH DIFFERENT PARTICLE SIZE FRACTIONS**

**TABLE 2. RESULTS OF TUBE TYPE I**

Fraction ( $\mu\text{m}$ )	Density ( $\text{mg}/\text{mm}^3$ )	Detonation distance (mm)
600 - 710	1.28	140 $\pm$ 10
850 - 1000	1.28	195 $\pm$ 20

A summary of the results obtained with a smaller kind of tube (type II) is presented in table 3. In this series of experiments besides two different particle sizes also two different densities were used. Although the scatter in some of the data is rather large, the data in the table indicate that a density increase has a different influence for different particle sizes. Increasing the density has the effect of increasing the detonation distance for a particle size of 600-710  $\mu\text{m}$ , while the opposite is true for a particle size of 850-1000  $\mu\text{m}$ . Viewed from a different angle, at a density of 1.28  $\text{mg}/\text{mm}^3$  the detonation distance is shorter for a smaller particle size and at a density of 1.35  $\text{mg}/\text{mm}^3$  the opposite is true.

TABLE 3. RESULTS OF TUBE TYPE II

Fraction ( $\mu\text{m}$ )	Density ( $\text{mg}/\text{mm}^3$ )	Detonation distance (mm)
600 - 710	1.28	135 $\pm$ 10
850 - 1000	1.28	190 $\pm$ 5
600 - 710	1.35	180 $\pm$ 50
850 - 1000	1.35	155 $\pm$ 10

In some experiments the data suggest the presence of an intermediate almost stationary stage between the convective burning stage and the detonation stage. In this intermediate stage the flame front propagates with a practically constant velocity in the order of 1  $\text{mm}/\mu\text{s}$  until a sudden transition to detonation occurs. Figure 2 shows an example of such an experiment for a density of 1.35  $\text{mg}/\text{mm}^3$  and a particle size of 850-1000  $\mu\text{m}$ .

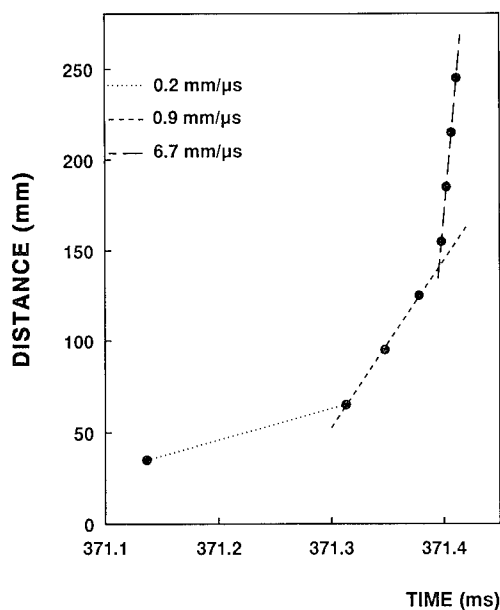


FIGURE 2. EXPERIMENTAL RESULT OBTAINED WITH TUBE TYPE II

TABLE 4. RESULTS OF TUBE TYPE III

Fraction ( $\mu\text{m}$ )	Density ( $\text{mg}/\text{mm}^3$ )	Detonation distance (mm)
600 - 710	1.28	155 $\pm$ 20
850 - 1000	1.28	190 $\pm$ 20
600 - 710	1.42	140 $\pm$ 20
850 - 1000	1.42	230 $\pm$ 20

The results obtained with an again smaller kind of tube (type III) are summarized in table 4. In these experiments again two different particle sizes were used as well as two different densities (1.28  $\text{mg}/\text{mm}^3$  and 1.42  $\text{mg}/\text{mm}^3$ ). The results for the experiments with a density of 1.28  $\text{mg}/\text{mm}^3$  agree rather well with the results obtained with the other tubes for the same density but the experiments with a density of 1.42  $\text{mg}/\text{mm}^3$  are not in line with the experiments with tube type II for a density of 1.35  $\text{mg}/\text{mm}^3$ . This is illustrated in figures 3 and 4 where the results from tubes I, II and III for a given particle size fraction are combined into one figure, showing the detonation distance as a function of density. The scatter in some of the data is rather high but not high enough to explain the apparently contradictory results, obtained for the two particle size fractions.

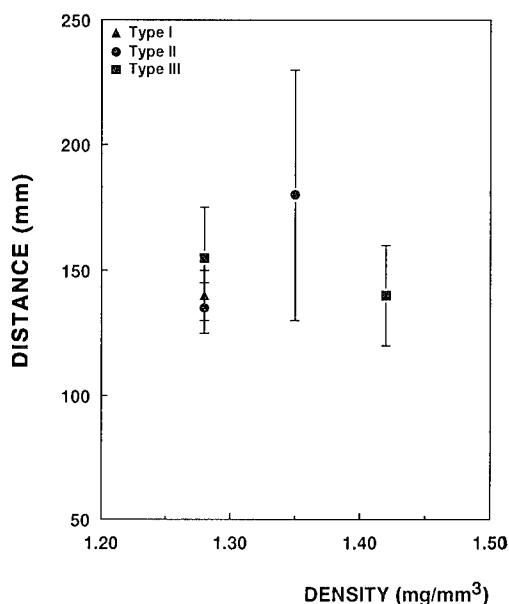
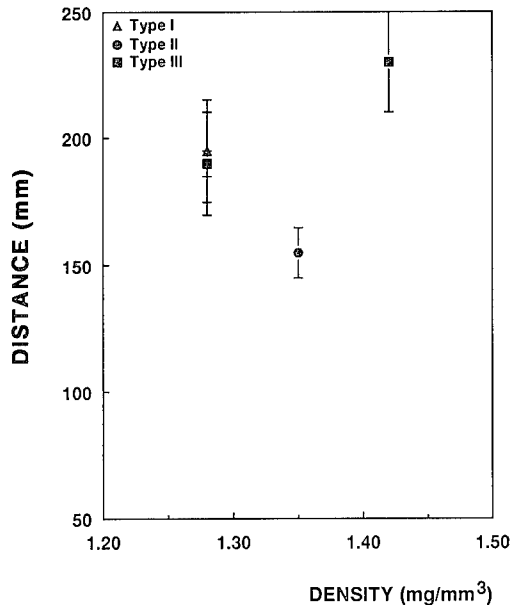


FIGURE 3. DETONATION DISTANCE AS A FUNCTION OF DENSITY FOR TUBE TYPE I, II AND III AND FOR A PARTICLE SIZE FRACTION OF 600 - 710  $\mu\text{m}$ .



**FIGURE 4. DETONATION DISTANCE AS A FUNCTION OF DENSITY FOR TUBE TYPE I, II AND III AND FOR A PARTICLE SIZE FRACTION OF 850 - 1000  $\mu\text{m}$**

In table 5 the results are displayed of experiments performed with the type IV tubes. The inner diameter of this tube is the same as for type III but in this case the wall thickness is only 9 mm instead of about 14 mm for the other tubes.

**TABLE 5. RESULTS OF TUBE TYPE IV**

Fraction ( $\mu\text{m}$ )	Density ( $\text{mg}/\text{mm}^3$ )	Detonation distance (mm)
600 - 710	1.28	230
850 - 1000	1.28	>250
600 - 710	1.35	235
850 - 1000	1.35	-
600 - 710	1.42	255
850 - 1000	1.42	-

In this tube it appeared to be very difficult to reach a transition to detonation. In explosive materials with a larger average particle size (850 - 1000  $\mu\text{m}$ ) a transition to detonation before the tube end was observed only once (for a density of 1.28  $\text{mg}/\text{mm}^3$ ). For materials with smaller particle sizes a transition did occur but only at rather large distances from the igniter. On the other hand the tube fragments seem to indicate that in the experiments where the signals from the ionisation probes did not show a detonation, still detonation pressures were reached at the very end of the tube.



**FIGURE 5. TEST TUBE FRAGMENTS FOR AN EXPERIMENT WITH A TYPE IV TUBE**

The analysis of the test tube fragments resulted in a quite different picture for this type of tube than for the other types. For tube types I, II and III the first part of the tube is usually fragmented into large strips, while the last part of the tube, where the transition to detonation has occurred, is fragmented into many small pieces. For tube type IV however, the tubes are for a large part intact, but show two large bulges, always at approximately the same places. In the part of the tube between the two bulges the deformation of the tube is relatively small (see figure 5). The final transition to detonation, if any, only takes place at a location between the second bulge and the end of the tube.

## DISCUSSION

In spite of the effort that has been put into improving the reproducibility of the experiments still some scatter exists in the results. Although an even better control of experimental parameters is still possible, the most important reason for the variation in the results is probably the inherent irreproducibility of the DDT process itself, due to the large influence on the process of variations in the geometry of the explosive material on microscopic scale. The scatter in the results however is generally small enough to be able to examine the influence of parameter variations on the DDT process.

From the combined results in figures 3 and 4 it appears that for densities of 1.28  $\text{mg}/\text{mm}^3$  and 1.42  $\text{mg}/\text{mm}^3$  a larger particle size results in a longer distance to detonation but for a density of 1.35  $\text{mg}/\text{mm}^3$  the opposite seems to be true. Figure 4 shows that the detonation distance as a function of density for a particle size of 850-1000  $\mu\text{m}$  has a clear minimum at a density of 1.35  $\text{mg}/\text{mm}^3$ . In figure 3, however, for a particle size of 600-710  $\mu\text{m}$ , instead a maximum is observed for this same density but in this case the scatter is very high. Although the appearance of a maximum is possibly due to the inaccuracy of the results, a minimum is clearly not observed.

The fact that the density dependence is not a monotonous function is not unexpected, since different phenomena play a role here. A higher density will generally result in a higher gas generation rate in the first stage of the burning process but will on the other hand present a larger resistance to convective combustion and will also often reduce the sensitivity for shock initiation. Which of the mentioned effects dominates depends on a number of parameters, leading to a different result in different circum-

stances. Further research will have to clarify whether the occurrence of a maximum in figure 3 is a real effect or that this result is due to the inherent irreproducibility of the DDT process.

A clear and reasonably reproducible transition to detonation has only been observed in the experiments with the thick walled tubes, type I, II and III. From the similarity of the results for a density of  $1.28 \text{ mg/mm}^3$  we can conclude that the difference in diameter between these tubes has a negligible influence on the results. In the experiments with the relatively thin-walled tubes, type IV, a transition often did not occur or did only occur near the end of the tube, even if the other parameters were equal to those of the thick walled tubes. A certain level of confinement is clearly necessary in order to invoke the final acceleration to detonation. However, what is actually happening in the case of a relatively low confinement is not yet clear. From the analysis of the tube fragments of tube type IV a certain picture puts itself forward. The tubes appear to reach their largest expansion at two points while in between a region with rather low deformation is found. This indicates that the pressure of the reaction products has reached much higher values at those points than in the area in between. An explanation for this peculiar phenomenon might be that in the region with low deformation a so-called "plug" has formed, i.e. a region where the explosive material has been compressed to a density of almost 100% TMD, where no convective combustion can take place and where the explosive material burns relatively slowly in a conductive mode. The formation of such "plugs" has been observed earlier in other experiments<sup>3</sup> and has also been predicted by numerical modelling of the DDT process<sup>2</sup>. In this view the explosive material at the side of the plug that is closest to the igniter cannot sufficiently vent its product gases and consequently quickly builds up a very high pressure which causes large deformation and fracture of the tube. The material at the other side of the plug is ignited by a compressive combustion wave travelling through the plug and the build-up process repeats itself. The fact that in many experiments a final transition to detonation is observed close to the end of the tube can be ascribed to the relatively larger tube strength in this region due to the end screw caps.

## CONCLUSION

In the experimental DDT program at TNO-PML interesting results have been obtained as a result of varying parameters such as the density, the particle size and the confinement. The dependency of the results on the density and particle size appeared to be ambiguous. The observations on the influence of the confinement on the DDT process indicate the occurrence of a plug in the case of thin-walled tubes. Further investigations into these points will be very worthwhile.

## ACKNOWLEDGEMENTS

The authors wish to acknowledge R. Oostdam and F.A.M.H. Jacobs for preparing and performing the experiments.

## REFERENCES

1. Verbeek, H.J., "Modelling of DDT in Granular Explosives", in *Proceedings of the Eighth Symposium (International) on Detonation*, Albuquerque, NM, 15 - 19 Jul 1985, pp. 669 - 677.
2. Verbeek, H.J. and Van der Steen, A.C., "Combined Experimental and Theoretical Investigations into the Deflagration to Detonation Transition", in *Proceedings of the Ninth Symposium (International) on Detonation*, Portland, Oregon, 28 Aug - 1 Sep 1989, pp. 320 - 328.
3. McAfee, J.M.; Asay, B.W.; Campbell, A.W. and Ramsay, J.B., "Deflagration to Detonation in Granular HMX", in *Proceedings of the Ninth Symposium (International) on Detonation*, Portland, Oregon, 28 Aug - 1 Sep 1989, pp. 276 - 279.

## A NEW LOOK AT THE RUN DISTANCE CORRELATION AND ITS RELATIONSHIP TO OTHER NON-STEADY-STATE PHENOMENA

P. W. Cooper  
Sandia National Laboratories  
Albuquerque, New Mexico 87185

A review of a portion of the published data on run distance versus input shock pressure led to the formulation of a simple single constant correlation equation:  $P^2 X = a$ . This equation can be used in lieu of the now traditional "Pop-Plot" equation. The advantages provided by this simple form are that "a" is now a quantitative single valued parameter which describes an explosive's shock sensitivity. It also allows for direct correlation to other non-steady-state phenomena such as the critical energy fluence for initiation, the detonation velocity-charge radius effect and the critical or failure diameter.

### INTRODUCTION

When an explosive material is subjected to an input shock wave, it does not detonate instantly. The shock wave proceeds into the unreacted explosive while chemical reaction initiated behind the shock builds up. The increase in pressure due to the chemical decomposition causes the reaction to speed up and eventually catch up with the shock front. At that point, steady-state detonation is achieved and the reaction then proceeds into the remaining explosive material at the steady-state detonation velocity.

The distance which the non-reactive shock wave had traveled into the explosive up to the point where the chemical reaction caught up and became a detonation, is called the run distance,  $X$ . This distance is affected by the magnitude of the input shock pressure,  $P$ , and increases with decreasing pressure. Experimentally determined values of input shock pressures and run distances can be correlated by a fit to a straight line on a log plot of the data. The representation of the data in this form is called a Pop-Plot.<sup>1</sup> This fit corresponds to a power equation:

$$\log P = b' - n \log X \quad (1)$$

or:  $PX^n = b \quad (2)$

where  $b'$  is the  $\log X$  intercept, and  $n$  is the magnitude of the slope.

Published values of the coefficient  $b'$  for various explosives range from -0.3 to +1.6, and for the exponent  $n$ , from 0.15 to 1.1.

### REFITTING THE DATA

A portion of the published body of data for the run distance correlation has been recently reviewed.<sup>1,2</sup> It was found that a simpler fit, where the exponent  $n$  is equal to 1/2 for all explosives, also fits the data. thus we can say:

$$P = a' X^{-1/2}, \quad \text{or: } P^2 X = a \quad (3)$$

Statistical analysis of the data spread for each explosive shows similar and overlapping standard deviations for either correlation (see Table 1), thereby giving equal mathematical validity to each. Figure 1 shows typical data for three different explosives, demonstrating the range from tight to very loose data spread and correlation. In this figure, the solid lines are the new  $P^2 X = a$  correlation and the dashed lines are the previously published fits for the Pop-Plot power curves.

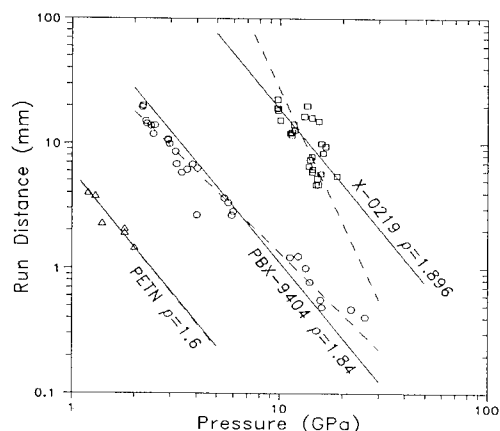


FIGURE 1. EXAMPLES OF BOTH CORRELATIONS FOR THREE DIFFERENT EXPLOSIVES

Table 1 shows the Pop-Plot constants along with the coefficient  $a$  for the new correlation. Also shown are the number of experiments run for each particular explosive, as well as the standard deviations of the difference between the predicted values of run distance from the experimental values for each correlation.

TABLE 1. CORRELATIONS OF RUN DISTANCE TO INPUT SHOCK PRESSURE

EXPLOSIVE	DENSITY	POP-PLOT EXPONENT	POP-PLOT COEFF.	"a"	NUMBER OF SHOTS	std.dev. ("a")	std.dev. (pop)
PETN	1.0	0.401	-0.311	0.298	14	0.1019	0.1221
PETN	1.4	0.399	0.142	2.7	6	0.0520	0.0434
PETN	1.6	0.494	0.383	5.9	6	0.0564	0.0571
Tetryl	1.5	0.812	0.753	14.7	16	0.2507	0.0257
Tetryl	1.4	0.987	0.838	14.9	14	0.3281	0.0227
PETN	1.72	0.589	0.643	16.7	12	0.0845	0.0671
Tetryl	1.3	1.114	0.867	17.5	9	0.4917	0.0634
PETN	1.75	0.0395	0.560	18.1	10	0.0571	0.0642
Tetryl	1.6	0.650	0.727	19.8	17	0.1309	0.0277
PBX9404	1.721	0.700	0.951	39.5	7	0.1318	0.0352
XTX-8003	1.53	0.372	0.735	43.9	3	0.0093	0.0397
Tetryl	1.7	0.424	0.792	47.1	13	0.0771	0.0440
PBX9501	1.8	0.698	1.105	81.9	5	0.1346	0.0414
PBX9405	1.761	0.701	1.165	95.3	7	0.1154	0.0477
PBX9404	1.84	0.616	1.076	111.5	29	0.1686	0.0936
PBX9501	1.833	0.674	1.178	113.1	7	0.1083	0.0328
LX-04	1.859	0.469	1.006	113.3	3	0.0355	0.0355
DATB/Estane (95/5)	1.625	0.785	1.316	119.3	4	0.0210	0.0084
X-0250-040-19	1.45	0.415	0.993	144.4	3	0.0724	0.0342
PBX9501	1.844	0.506	1.103	156.2	4	0.0319	0.0312
X-0224	1.812	0.500	1.110	166.5	3	0.0251	0.0251
FKM Class	1.814	0.434	1.044	166.9	5	0.0564	0.0500
VII Propellant							
PBX9011	1.79	0.657	1.184	175.6	5	0.0861	0.0158
VOP-7 Class	1.910	0.576	1.174	175.7	8	0.1200	0.0891
VII Propellant							
HMX	1.891	0.594	1.178	177.9	8	0.0535	0.0296
VTQ-2 Class	1.852	0.481	1.136	205.0	11	0.0486	0.0484
VII Propellant							
TATB	1.714	0.415	1.069	219.0	5	0.0975	0.1131
TNT(pressed)	1.63	0.501	1.174	223.6	8	0.0519	0.0518
VTQ-3 Class	1.857	0.423	1.097	225.1	6	0.0445	0.0175
VII Propellant							
X-0219-50-14- 10	1.912	0.123	0.917	238.8	3	0.1268	0.0863
VRO Class VII Propellant	1.833	0.409	1.115	263.9	6	0.0557	0.0345
VTG-5A Class	1.839	0.412	1.125	265.6	6	0.0457	0.0257
VII Propellant							
VRE Class VII Propellant	1.836	0.366	1.086	276.2	7	0.0821	0.0664



VWC-2 Class	1.835	0.375	1.092	281.0	8	0.0657	0.0373
VII Propellant							
Comp B	1.72	0.697	1.416	294.4	8	0.1066	0.0598
RDX/Wax/Elvax	1.711	0.727	1.429	315.0	3	0.1784	0.0658
(95/2.5/2.5)							
TP-N1028 Class	1.846	0.454	1.210	325.5	9	0.0360	0.0282
VII Propellant							
TATB	1.806	0.420	1.310	424.9	9	0.0660	0.0527
UTP20930 Class	1.838	0.376	1.189	449.1	8	0.0704	0.0323
VII Propellant							
Baratol	2.613	0.338	1.235	567.0	5	0.0811	0.0570
Destex	1.69	0.383	1.285	602.5	7	0.0810	0.0399
TATB	1.841	0.462	1.352	617.6	6	0.0895	0.0927
TATB	1.808	0.381	1.417	793.8	8	0.0772	0.0734
TATB	1.876	0.403	1.417	943.3	3	0.0313	0.0100
TATB/KELF800/ KELF827	1.883	0.356	1.412	1009.7	3	0.0372	0.0181
(95/2.5/2.5)							
TNT (cast)	1.624	0.151	1.302	1101.8	4	0.0951	0.0807
PBX-9502	1.896	0.307	1.387	1390.8	4	0.0906	0.0523
TNT (cast)	1.627	0.337	1.418	1605.0	6	0.0587	0.0715
TATB/Estane	1.833	0.319	1.466	1731.4	4	0.1471	0.0380
(94/6)							
TATB/KELF800/ KELF827	1.912	0.348	1.485	1741.2	3	0.0667	0.0574
(85/7.5/7.5)							
X-0219	1.896- 1.929	0.282	1.404	1882.9	29	0.1451	0.1941
NQ (needle grain)	1.688	0.266	1.516	1909.1	5	0.0779	0.0352
TATB/PS/DOP	1.821	0.270	1.472	2259.0	7	0.1847	0.0895
(94/4.5/1.5)							
TATB/Estane	1.846	0.263	1.489	2387.2	3	0.1713	0.0127
(94/6)							
TATB/KELF800	1.930	0.292	1.511	2828.7	4	0.0620	0.0057
(85/15)							
TATB/Elvax/Wax	1.802	0.191	1.470	2957.3	3	0.2431	0.0157
(94/3/3)							
TATB/PS/DOP	1.797	0.298	1.523	3182.3	3	0.0647	0.0104
(92/6/2)							
NQ (large grain)	1.7	0.151	1.441	3229.5	9	0.2829	0.4630
X-0228	1.660	0.145	1.468	3719.6	6	0.2650	0.2680
TATB/Elvax/Wax	1.739	0.090	1.387	4721.0	3	0.2484	0.0410
(90/5/5)							
X-0241	1.676	0.148	1.479	5757.5	3	0.2266	0.0159
Averages						0.1099	0.0592

What, if any are the advantages of changing the present accepted correlation to a new simpler one other than mathematical tidiness?

### CORRELATION TO OTHER PARAMETERS

This new and simpler correlation has only one experimentally determined parameter,  $\alpha$ , that defines an explosive's shock sensitivity. The larger the value of  $\alpha$ , the less sensitive the explosive. When attempting to correlate the effect of other physical parameters upon the shock sensitivity, the single variable can be easily used. An example of this is shown in Figure 2, where the new run distance coefficient for PETN is shown as a function of the initial unreacted density. This allows one to estimate run distance versus pressure at densities for which there is no previous experimental data.

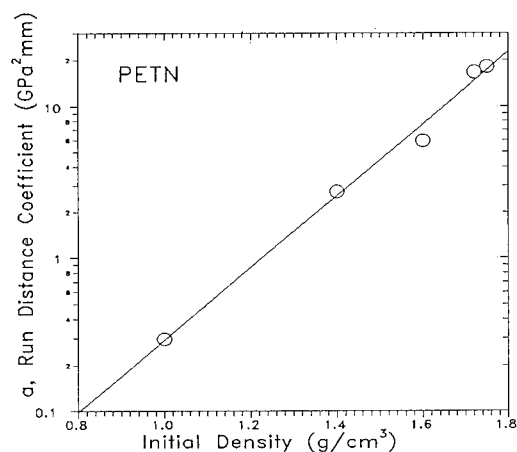


FIGURE 2. RUN DISTANCE COEFFICIENT AS A FUNCTION OF INITIAL DENSITY

## CRITICAL ENERGY FOR INITIATION

Another criteria used to describe the initiation of explosives by an input shock wave is the critical energy fluence,  $E_c$ . This term is defined as:

$$E_c = \frac{P^2 t_o}{\rho_o U} \quad (4)$$

where  $P$  is the input shock pressure,  $t_o$  is the input shock pulse duration,  $\rho_o$  is the initial unreacted explosive density, and  $U$  is the velocity of the non-reactive shock wave entering the explosive. It is generally accepted that  $E_c$  is a constant, with a different value for each explosive. Detonation will occur only if the input shock parameters yield a value greater than  $E_c$ . Figure 3 shows  $E_c$  plotted against the new run distance coefficient for a number of different explosives and indicates there is a connection between  $E_c$  and the run distance phenomenon.

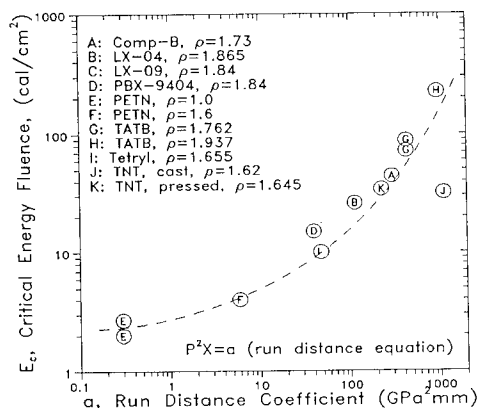


**FIGURE 3. CRITICAL ENERGY FLUENCE CORRELATED TO THE RUN DISTANCE COEFFICIENT**

Let's examine that relationship further. Picture an input square wave shock pulse entering an explosive target. The non-reactive shock travels into the target at constant velocity  $U$ . When the back end of the input shock pulse arrives at the input surface of the target, a rarefaction wave then races into the previously shocked material. The rarefaction wave velocity  $R$ , is greater than the shock velocity and eventually catches up with the shock front. Beyond the catch up point, the shock front pressure decreases with distance because it is now being eroded by the encroaching rarefaction wave. Figure 4 shows this process.

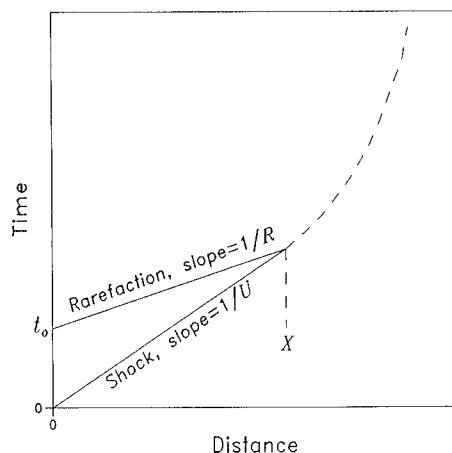


**FIGURE 4. THE  $x-t$  DIAGRAM OF A SHOCK AND THE FOLLOWING RAREFACTION FROM AN ENTERING SQUARE WAVE PULSE**

If we assume the run distance to detonation will be limited by the catch up distance described above, then the critical run distance for a given input pressure is  $x$ , the catch up distance. The given input pressure also determines both the shock velocity  $U$  and the rarefaction velocity  $R$ . Examination of Figure 4 yields:

$$t = \frac{1}{U} x, \text{ and} \quad (5)$$

$$t = t_o + \frac{1}{R} x \quad (6)$$

Equating (5) to (6) gives:

$$t_o = x \left( \frac{1}{U} - \frac{1}{R} \right) \quad (7)$$

Combining equations (7), (4), and (3) yields:

$$E_c = \frac{a(U^{-1} - R^{-1})}{\rho_o U} \quad (8)$$

Since  $U$  and  $R$  are dependent upon and increase with increasing pressure,  $E_c$  therefore also will depend somewhat upon pressure.  $E_c$  was evaluated in this manner for a number of explosives as a function of pressure and the results of these calculations are shown in Figure 5 and in Table 2. Figure 5 shows critical energy fluence of PETN as calculated in this manner compared to the value found in the references.

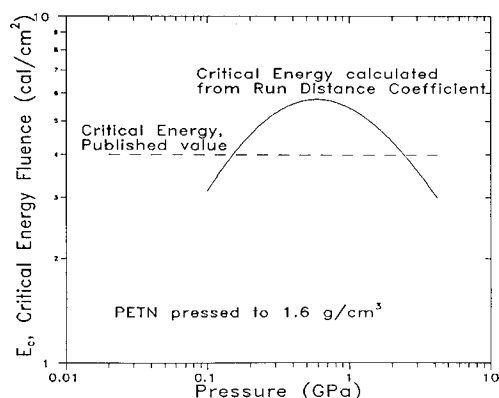


FIGURE 5. CALCULATED AND EXPERIMENTAL VALUES OF CRITICAL ENERGY FLUENCE OF PETN AT 1.6 g/cm<sup>3</sup> DENSITY

Notice in Figure 5 that the calculated value of the critical energy fluence goes through a maximum at some particular value of input pressure. It is not clear what the significance of this is, if any. Table 2 shows the results of this same calculation for several other explosives along with the experimental values from the literature.

TABLE 2. CALCULATED AND EXPERIMENTAL VALUES OF CRITICAL ENERGY FLUENCE FOR SEVERAL EXPLOSIVES

EXPLOSIVE	PRESSURE RANGE (GPa)	PRESSURE (GPa) AT PEAK $E_c$	CALCULATED RANGE OF $E_c$ (GPa <sup>2</sup> mm)	Experimental $E_c$ FROM LITERATURE <sup>4</sup>
Comp B	0.5 - 50	3.0	30 - 105	44
LX-04	0.5 - 50	2.5	20 - 86	26
LX-09	0.5 - 30	2.0	17 - 51	25
PBX-9404	0.3 - 30	2.0	10 - 35	15
PETN (1.0)	0.02 - 0.7	0.11	1 - 1.75	2
PETN (1.6)	0.1 - 4	0.6	3 - 5.75	4
TATB (1.762)	0.5 - 30	2.1	35 - 124	72 - 88
TATB (1.937)	0.5 - 50	5.5	100 - 227	226
Tetryl	1.0 - 15	3.5	7.5 - 10.5	10

## DETONATION RATE AND DIAMETER

If a cylinder of explosive is detonated in the axial direction the side losses of pressure affect the rate of the detonation. As the diameter decreases, the detonation velocity decreases. This process continues until a diameter is reached below which detonation cannot be sustained, that is called the critical or failure diameter. The detonation rate versus diameter relationship can be approximated by the correlation equation:

$$(D/D_\infty) = 1 - A_R R^{-1} \quad (9)$$

where  $D$  is the detonation velocity at a given charge radius,  $D_\infty$  is the "infinite radius" detonation velocity,  $R$  is the charge radius, and  $A_R$  is the rate coefficient, a constant, different for different explosives. The rate coefficient  $A_R$ , can be correlated to the failure radius  $R_f$ . This is shown in Figure 6 for several explosives whose velocity versus failure radius was found in the literature.<sup>2</sup>

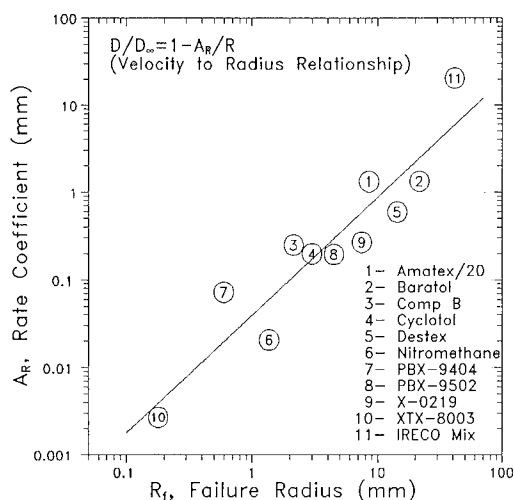
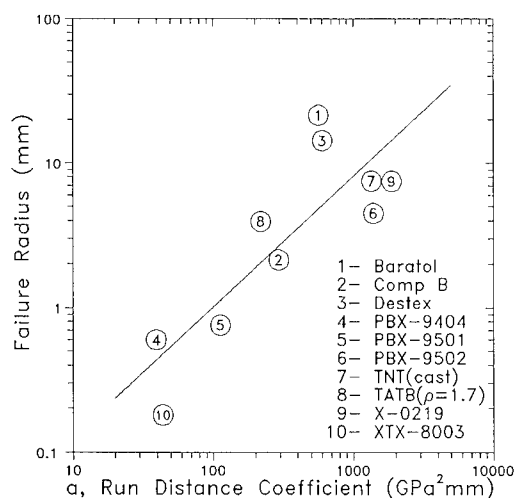


FIGURE 6. CORRELATION OF FAILURE RADIUS TO VELOCITY-RADIUS COEFFICIENT

Both the rate coefficient  $A_R$ , and the failure radius  $R_f$  appear to be correlatable to the run distance coefficient  $\alpha$ . A preliminary correlation for a limited number of explosives for which data was available<sup>2,3,4</sup> shown in Figure 7 where failure radius is correlated to run distance coefficient.



**FIGURE 7. PRELIMINARY CORRELATION OF FAILURE RADIUS TO RUN DISTANCE COEFFICIENT**

## CONCLUSION

A limited review of run distance data has yielded a new correlation of pressure and run distance. The new single parameter  $\alpha$ , the new run distance coefficient can be used to tie together and perhaps to predict other non-steady-state phenomena such as critical initiation energy fluence, the detonation velocity to radius effect, and detonation failure radius.

Only a limited data base has as yet been interrogated, more work is required to refine these correlations and make them useful for the design engineer or analyst.

## ACKNOWLEDGMENT

This work was performed at Sandia National Laboratories and was supported by the U. S. Department of Energy under contract number DE-AC04-76DP00789

## REFERENCES

1. Ramsay, J. B. and Popolato, A., "Analysis of Shock Wave and Initiation Data for Solid Explosives," in *Proceedings of the Fourth Symposium (International) on Detonation*, Office of Naval Research, ACR-126 (U.S. Government Printing Office, Washington D.C.), 1965, pp. 233-238.
2. Gibbs, T. R. and Popolato, A., Eds., *LASL Explosive Property Data*, University of California Press, Berkeley, Ca., 1980.
3. Campbell, A. W. and Engelke, R., "The Diameter Effect in High-Density Heterogeneous Explosives," *Proceedings of the Sixth Symposium (International) on Detonation*, Office of Naval Research, ACR-221 (U.S. Government Printing Office, Washington D.C.), 1976, pp. 642-652.
4. Dobratz, B. M., Ed., *LLNL Explosives Handbook*, UCRL-52997, 31 Jan. 1985, Lawrence Livermore National Laboratory, Livermore, Ca.

## DISCUSSION

JOHN B. RAMSAY

Los Alamos National Laboratory  
Los Alamos, New Mexico

The use of  $P^2$  to look at the correlations of failure diameter, etc., is fascinating and should be carefully considered. However, the use of  $P^2x$  for initiation modeling and calculations will lead to non-conservative estimates and I would not recommend its use.

**No reply from the author.**

## DISCUSSION

JACQUES BOILEAU

DRET, Paris, France

Did you try correlating the failure diameter for the same product but in two different phases, solid and liquid (molten), e.g., TNT or hydrazine nitrate?

**No reply from the author.**

## MULTIPLE SHOCK INITIATION OF LX-17

C. M. Tarver, T. M. Cook, P. A. Urtiew, and W. C. Tao  
Lawrence Livermore National Laboratory  
Livermore, CA 94550

The response of the insensitive TATB-based high explosive LX-17 to multiple shock impacts is studied experimentally in a four inch gas gun using embedded manganin gauges and numerically using the ignition and growth reactive flow model of shock initiation and detonation. Pressure histories are reported for LX-17 cylinders which are subjected to sustained shock pulses followed by secondary compressions from shocks reflected from metal discs attached to the backs of the explosive targets. These measured and calculated pressure histories show that the threshold for hot spot growth in LX-17 is 7 GPa, that LX-17 can be dead pressed at slightly lower pressures, and that the reaction rates behind reflected shocks increase greatly as the impedance of the metal increases. A study of the response of LX-17 to the collision of two reacting, diverging shocks forming a Mach stem wave inside the LX-17 charge demonstrated that this interaction can result in a high pressure region of sufficient size and strength to cause detonation under certain conditions.

### INTRODUCTION

The single shock initiation and detonation wave propagation of the insensitive TATB-based high explosive LX-17 (92.5% TATB and 7.5% Kel-F binder pressed to  $1.905 \text{ g/cm}^3$ ) has been studied experimentally and theoretically over a wide range of initial pressures, temperatures and shock pulse durations.<sup>1-6</sup> However, many hazard and vulnerability scenarios for explosives confined by inert materials involve multiple shock compressions of the explosive. The objectives of this research are to experimentally measure the reactivity of LX-17 in multiple shock environments and to extend the ignition and growth reactive flow model to account for changes in reaction rates during multiple compressions. Two series of experiments fired in a four inch gas gun facility are reported in which manganin gauges are embedded at various locations in the explosive charge to determine the pressure histories of shocked, reacting LX-17. One series studied the effect of reflected shocks on the reaction rates on previously shocked LX-17. The second series studied the generation and effects of Mach stems produced in LX-17 by the collision of two

reacting, diverging shocks formed by separated impacts of the explosive targets. The ignition and growth reactive flow model of shock initiation and detonation is used to determine the reaction rates of LX-17 in these multiple shock environments.

### REFLECTED SHOCK EXPERIMENTS

In the reflected shock experiments, stainless steel flyer plates are accelerated by a four inch diameter gas gun to various velocities and then impact 20 mm thick discs of LX-17. The LX-17 discs are backed by 10 mm thick discs of either aluminum, copper or tantalum to produce reflected shocks of varying amplitudes in the reacting LX-17. Pairs of manganin pressure gauges were placed at 5, 10, and 15 mm depths in the LX-17 to record the arrival of the initial shock wave, the pressure increase due to reaction behind that shock, the arrival of the reflected shock, and further reaction behind that shock. The initial shock pressure regime of interest is 7 - 10 GPa, because LX-17 is known to produce little or no reaction below 6.5 GPa and to transition to detonation within 20 mm at pressures exceeding 10 GPa. Table 1 lists the twelve

TABLE 1. REFLECTED SHOCK EXPERIMENTS

FLYER VELOCITY(mm/ $\mu$ s)	PRESSURE (GPa)	METAL DISC
0.75	4.4	Al
1.00	6.8	Cu
1.09	7.2	Al
1.09	7.2	Cu
1.10	7.3	Ta
1.11	7.3	Ta
1.14	7.6	Cu
1.153	7.7	Ta
1.175	7.9	Al
1.19	8.1	Ta
1.191	8.2	Cu
1.23	8.6	Al

reflected shock experiments, the flyer velocities, the metal used to create the reflected shock, and the approximate initial shock pressures. Measured pressure histories are compared to those calculated by the ignition and growth model in the Results section.

#### COLLIDING SHOCK EXPERIMENTS

The objectives of these experiments are to produce a Mach stem shock interaction at various depths in LX-17 targets by the collision of two separate diverging shocks and to measure the resulting pressure histories. These experiments simulate hazard scenarios in which two (or more) fragments impact LX-17 in close proximity. This is different scenario from the production of Mach stem shocks by oblique reflection of a shock at explosive-metal interface.<sup>7</sup> Several designs of the impactor and the gauged LX-17 targets were fired, but the most successful geometry used a stainless steel flyer sabot with a 10 mm wide annulus with an inner diameter of 20 mm that protruded 10 mm. This sabot impacted an LX-17 target in which six embedded manganin gauges were placed along a 24 degree wedge to cover various depths and radial positions in the LX-17. Placing the gauges along a wedge surface eliminates the gauge interaction problem. This technique has been successfully used in several applications.<sup>6,8</sup> Gauge records were obtained in the two single shock regions and in the collision region where the two diverging shocks meet. Comparison of these gauge records and the corresponding calculations are shown in the Results section.

#### IGNITION AND GROWTH MODELING

The ignition and growth reactive flow model for

LX-17 has been normalized to a great deal of single shock wave data for sustained and short duration shock pulses.<sup>1-5</sup> A limited number of double shock results have been reported.<sup>3,5</sup> However, almost all previous experiments have involved shocks exceeding 10 GPa pressure so that detonation would occur in less than 25 mm. The exceptions are: the infrared radiometry experiments of Von Holle<sup>3</sup> which established an ignition threshold for LX-17 of 6.5 GPa, two six inch gas gun experiments<sup>3</sup> at 7 - 8 GPa to obtain a detonation and a reactive shock in 100 mm of explosive, and one embedded gauge experiment at 8.4 GPa by Erickson shown in Figure 6 of Reference 3. Therefore the experiments reported in this paper cover the 7 - 10 GPa pressure regime much more thoroughly than previous work.

The ignition and growth model consists of: two Jones-Wilkins-Lee (JWL) equations of state fitted to the available experimental data on the unreacted explosive and its reaction products and a reaction rate law of the form:<sup>9</sup>

$$\frac{dF}{dt} = I(1-F)^b(\rho/\rho_0-1-a)^x + G_1(1-F)^c F^d p^y + G_2(1-F)^e F^g p^z \quad (1)$$

where F is the fraction reacted,  $\rho$  is the density,  $\rho_0$  is the initial density, p is pressure and I, G<sub>1</sub>, G<sub>2</sub>, a, b, c, d, e, g, x, y, and z are constants. The first term represents the ignition of hot spots created by void collapse just behind the leading shock front, the second term represents the growth of isolated hot spots in a deflagration-type process, and the third term

TABLE 2. IGNITION AND GROWTH MODEL PARAMETERS

EXPLOSIVE JWEL	PRODUCT JWEL	RATE PARAMETERS
Density = 1.905 g/cm <sup>3</sup>		I = 4.0x10 <sup>6</sup>
A = 632.07 Mbar	A = 6.5467 Mbar	b = 0.667
B = -0.04472 Mbar	B = 0.071236 Mbar	a = 0.22
R <sub>1</sub> = 11.3	R <sub>1</sub> = 4.45	x = 7.0
R <sub>2</sub> = 1.13	R <sub>2</sub> = 1.2	G <sub>1</sub> = 1.2
w = 0.8958	w = 0.35	c = 0.667
C <sub>V</sub> = 2.487x10 <sup>-5</sup> Mbar/K	C <sub>V</sub> = 1.0x10 <sup>-5</sup> Mbar/K	d = 0.333
T <sub>0</sub> = 298K	E <sub>0</sub> = 0.069 Mbarcc/cc	y = 1.0
		G <sub>2</sub> = 400.0
		e = 0.333
		g = 1.0
		z = 3.0

represents the rapid completion of reaction as the hot spots coalesce and the remaining explosive reacts at high temperature and pressure. Table 2 lists the JWEL and reaction rate parameters used in this study. The calculated pressure histories are compared to both kinds of experiments in the Results section.

## RESULTS

### Reflected Shocks

The experimental and calculational results are shown in order of increasing initial shock pressure in Figures 1 - 8. Figure 1 compares measured and calculated pressure histories for a steel flyer impacting an LX-17 disc with an aluminum backing plate at a velocity of 0.75 mm/μs. This impact produces a 4.4 GPa shock into LX-17 which, upon reflection from Al, jumps to 6.7 GPa. In previous work,<sup>3</sup> these shock pressures produced no measurable growth of reaction in LX-17. This experiment confirms those results. Neither the gauges nor the ignition and growth model yielded any evidence of exothermic reaction and pressure increase. The calculated arrival times of the initial and reflected shocks and the calculated peak pressures at the three gauge positions agree with experiment, indicating that the unreacted equation of state is accurate in this pressure regime. The small pressure oscillations in the records and calculations are due to the impedance mismatch between the teflon gauge insulation and the LX-17. The gauges exhibit more pronounced pressure decays behind the initial shock than do the calculations, which use an idealized elastic-plastic material model for unreacted LX-17. The pressure decay may be a gauge problem or it may be due to energy loss (endothermic) processes occurring in the shocked LX-17. If so, an endothermic process can easily be added to the ignition and growth model to account for the work done collapsing and heating voids

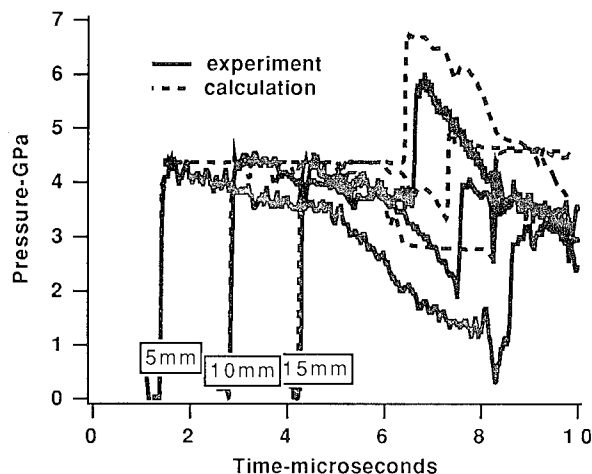
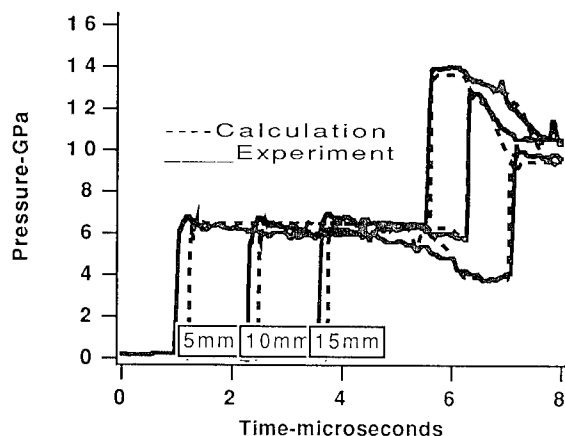


FIGURE 1. PRESSURE HISTORIES FOR LX-17 IMPACTED AT 0.75mm/μs WITH AN ALUMINUM REFLECTOR DISC

in LX-17. Similar processes have been observed for HMX-based explosives in the 1 - 3 GPa shock pressure regime.<sup>8,10</sup>

Figure 2 illustrates the phenomenon of "dead pressing" in LX-17 for an experiment with a copper backing plate and an impact velocity of 1.0 mm/μs. This impact creates a shock pressure of 6.8 GPa, which is insufficient to cause any growth of reaction during the time duration of this experiment. The subsequent reflected shock from the copper interface reaches 14 GPa, which would cause a transition to detonation in less than 10 mm if it were the initial shock.<sup>11</sup> However, this reflected shock causes little or no growth of reaction in the experimental records in Fig. 2. The LX-17 must have been "dead pressed" by the initial shock. Dead pressing is a well-known phenomenon in solid explosives which occurs when all of the porosity



**FIGURE 2. DEAD PRESSING IN LX-17 IMPACTED AT 1mm/μs WITH A COPPER REFLECTOR DISC**

is compressed out of the explosive without igniting hot spots, resulting in a voidless material that can not be shock initiated.<sup>12</sup> Even some primary explosives can be dead pressed.<sup>13</sup> Perfect single crystals of solid explosives are difficult or even impossible to detonate.<sup>14</sup> In this experiment the 6.8 GPa initial shock compressed the 2% porosity out of the LX-17 sample without causing hot spots to grow behind the shock. There may have been some chemical reaction in the hydrodynamically heated regions surrounding the original voids, but not enough to sustain the reaction and cause hot spot spreading. Therefore the heated spot just died out by thermal diffusion.<sup>15</sup> Then the reflected shock traveling through the precompressed LX-17 found no remaining ignition sites and just propagated as an inert shock.

The standard ignition and growth model had never considered dead pressing so it would have predicted rapid reaction behind the reflected shock. A condition was added to the ignition term of Equation (1) to prevent any reaction from ever occurring if a critical range of shock compressions (or pressures) is applied to the explosive. The calculated pressure histories in Fig. 2 included this added ignition criteria and therefore show no reaction upon shock reflection in good agreement with the gauge records. From the results of higher pressure experiments which do not dead press, the maximum shock pressure for dead pressing LX-17 is approximately 7 GPa. The minimum shock pressure which will compress all of the possible hot spot sites out of LX-17 is unknown, but it is likely to be less than 1 GPa. In the shock desensitization study of Campbell and Travis<sup>16</sup> on the more shock sensitive explosives PBX 9404 and Composition B, the range of shock pressures causing desensitization varied from 0.7 to 2.3 GPa. At shock pressures exceeding 2.3 GPa, hot spots

rapidly grow in PBX 9404,<sup>9</sup> and below 0.7 GPa not all of the voids are compressed out, because it is possible to produce very late time reactions.<sup>17</sup>

When LX-17 is impacted at pressures exceeding 7 GPa, sufficient reaction occurs behind the initial shock front to create growing hot spots which react rapidly when subjected to a reflected shock. Table 1 lists four experiments with impact velocities close to 1.1 mm/μs, all of which yielded similar pressure histories before shock reflection. Figure 3 shows the experimental and calculated pressure histories from one of these four experiments, which had an impact velocity of 1.09 mm/μs and an aluminum backing disc. The 10 mm deep gauges failed so only the 5 and 15 mm deep gauge records are shown. At both of these depths, the initial shock front pressure increases very little from its initial strength of 7.2 GPa, but reaction growth behind the shock increases the pressure to approximately 10 GPa before the reflected shock arrives. Since the reflection disc is aluminum, the reflected shock raises the pressure from 10 GPa to only 14 GPa at the 15 mm deep gauge, and the reaction accelerates slightly behind this shock.

The calculated pressure histories in Fig. 3 use the parameters listed in Table 2, which include two minor changes from those in previous papers<sup>1-5</sup> that improved the simulations at lower shock pressures without changing previous higher shock pressure results. The sound speed in the unreacted LX-17 equation of state was lowered by approximately 5% to improve the shock arrival times and calculated shock

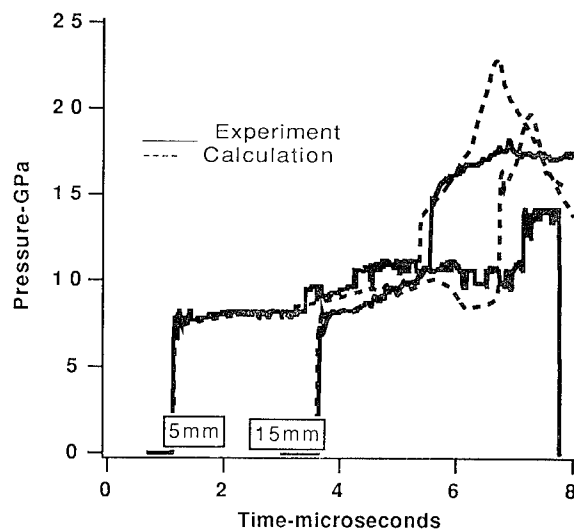


**FIGURE 3. PRESSURE HISTORIES IN LX-17 SUBJECT TO AN IMPACT OF 1.09mm/μs WITH AN AL REFLECTOR DISC**



pressures. This was accomplished by lowering  $A$ , essentially the bulk modulus, in Table 2. The hot spot growth rate, the second term in Equation (1), was modified to cause less growth near the shock front and slightly more growth at higher fractions reacted. This was accomplished by changing coefficient  $d$  in Table 2 from 0.111 to 0.333 so that the growth rate is slower at small values of  $F$  (0.01 to 0.1) and faster as  $F$  approaches 0.5. The growth coefficient  $G_1$  was increased to renormalize the growth rate to previous calculations. The use of the previous equation of state and reaction rate law parameters yield similar results to those reported here, except that the shock front pressures increase slightly too rapidly and the subsequent reactions are slightly slow. A close look at the calculation for the 8.4 GPa experiment in Fig. 6 of Reference 3 reveals that the calculated shock front pressure at the 15 mm gauge was also slightly high. Thus the coefficients in Table 2 describe LX-17 slightly better at lower shock pressures (less than 10 GPa) without affecting higher pressure and short pulse duration results.

The calculated shock front and early growth histories agree well with experiment in Fig. 3, but the calculated reaction rate behind the reflected shock at the 15 mm depth appears to be too fast. This is due to the fact that the reflected shock pressures are quite high and the fraction reacted exceeds 0.5, at which point the third term in Equation (1), which represents the rapid completion of reaction at high pressures and temperatures necessary for the transition to detonation, dominates the reaction rate. In experiments using two shock compressions, the temperature, which actually controls reaction rates, is much lower than if the same pressure had been attained by one shock, and thus reaction rates are slower behind reflected shocks than high pressure single shocks. The current ignition and growth model uses pressure to control reaction rates so it can not differentiate between one and two shock processes. As the shock pressures and the impedances of the metal reflector discs increase in the higher impact velocity experiments, the completion reaction rate simulates the experimental records more closely.

Figure 4 compares the records from an experiment which had an impact velocity of 1.14 mm/ $\mu$ s and a copper reflecting disc. This causes an initial shock of 7.6 GPa and very little shock front growth, but the growth of reaction takes the pressure to 13 GPa before reflection. Reflection off copper drives the pressure to 23 GPa, and the subsequent reaction occurs very rapidly. The calculations agree well with experiment, except at the 15 mm deep gauge where the reflected shock pressure is low and the following

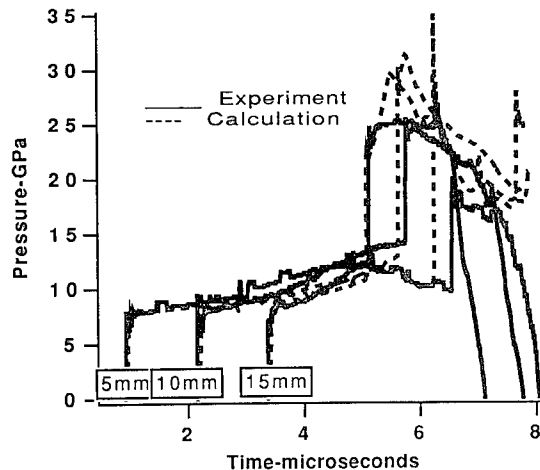


FIGURE 4. PRESSURE HISTORIES FOR LX-17 SUBJECTED TO AN IMPACT OF 1.14mm/ $\mu$ s WITH A COPPER REFLECTOR DISC

reaction slightly fast creating a peak pressure higher than measured. The rapid pressure dropoff exhibited by the gauges in Fig. 4 after the reflected shock is typical of manganin gauge failure after being subjected to detonations or other very high pressure flows. The pressures actually remain above 20 GPa, as shown by the calculated pressure histories.

Figures 5 - 8 contain the measured and calculated pressure histories for four of the higher impact velocity experiments listed in Table 1 in order of increasing impact velocity. As the initial shock pressure increases, more shock front growth is observed and hot spot growth rates also increase. Reflected shock pressures are also higher causing these waves to be essentially detonations back through the partially reacted LX-17 for the high impedance discs in Fig. 7 (copper) and Figs. 5 and 6 (tantalum). The calculations are in good agreement with the gauge records for these four higher impact velocities.

## COLLIDING SHOCKS

The sabot with a 10 mm wide circular protusion impacts the LX-17 target at 1.48 mm/ $\mu$ s producing two 10 GPa shock waves 10 mm in diameter and 20 mm apart. These reacting, diverging shocks are known to be incapable of growing to detonation individually.<sup>11</sup> Figure 9 shows the six pressure histories recorded in the wedge of LX-17. By the time the initial shock reaches the first gauge depth of 10 mm, its shock pressure has decreased to 5 GPa. This same shock front has higher pressures at the second and third gauges in Fig. 9, because those gauges, although they are located deeper into the LX-17 at 13 and 17 mm, respectively, are

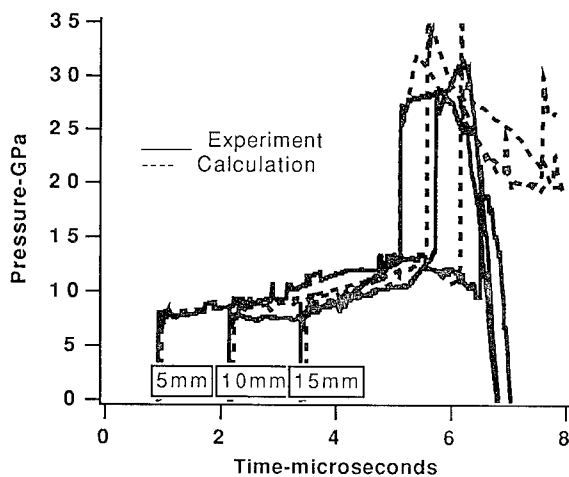


FIGURE 5. PRESSURE HISTORIES FOR LX-17 IMPACTED AT  $1.153 \text{ mm}/\mu\text{s}$  WITH A TANTALUM REFLECTOR DISC

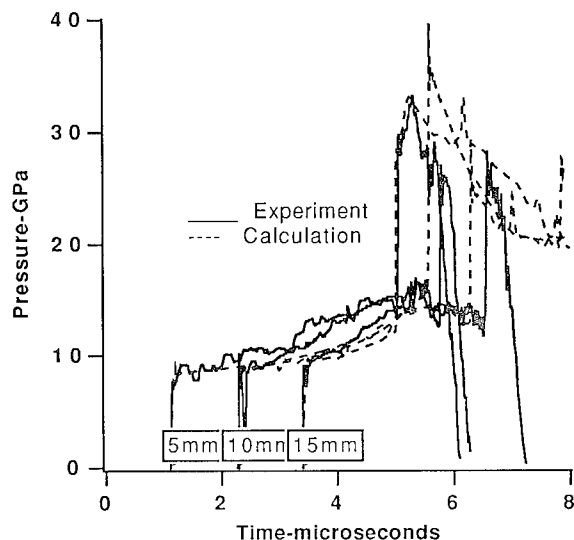


FIGURE 6. PRESSURE HISTORIES FOR LX-17 IMPACTED AT  $1.19 \text{ mm}/\mu\text{s}$  WITH A TANTALUM REFLECTOR DISC

directly in front of the steel impactor and thus suffer less pressure decrease due to the edge rarefaction waves. The two shocks collide producing the high pressure interaction and subsequent rapid reaction to 25 GPa recorded by gauges 4 and 5 at depths of 19.9 mm and 23.2 mm, respectively. The last gauge record in Fig. 9 detected the arrival of the other decaying shock at 26.4 mm depth plus some subsequent compression and reaction.

The two-dimensional ignition and growth calculations are also shown in Fig. 9. The decay of the

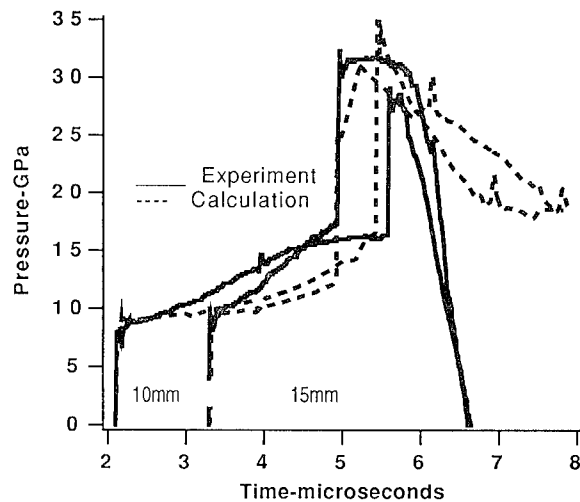


FIGURE 7. PRESSURE HISTORIES FOR LX-17 IMPACTED AT  $1.19 \text{ mm}/\mu\text{s}$  WITH A COPPER REFLECTOR DISC

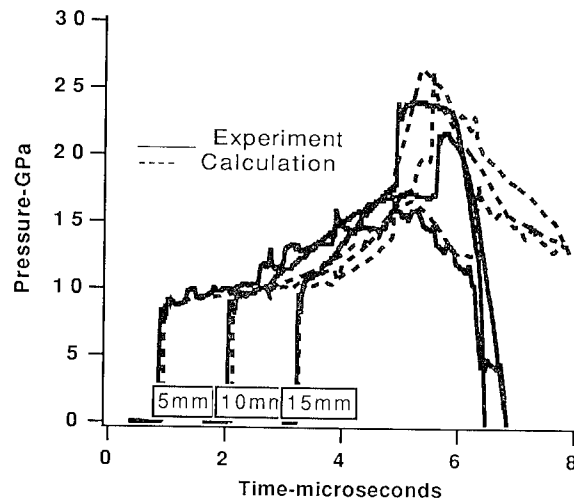


FIGURE 8. PRESSURE HISTORIES FOR LX-17 IMPACTED AT  $1.23 \text{ mm}/\mu\text{s}$  WITH AN ALUMINUM REFLECTOR DISC

initial shock pressures to 5 GPa is calculated accurately, and the Mach stem correctly causes detonation at the fourth and fifth gauges. The calculated sixth gauge record shows a low pressure shock being overtaken by the detonation wave in less than a microsecond, whereas the gauge did not appear to be in the path of the detonation. Other experiments and calculations have demonstrated that the direction of growth of the Mach stem induced rapid reaction region varies considerably. The calculated direction of detonation spreading was incorrect in Fig. 9. However, both the gauges and the modeling clearly show that the collision of two failing

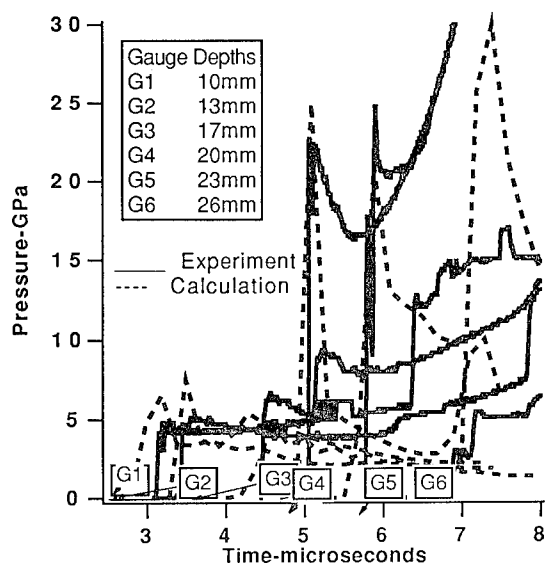


FIGURE 9. PRESSURE HISTORIES IN LX-17 IMPACTED AT 1.48 mm/ $\mu$ s BY TWO DIVERGING SHOCKS WHICH COLLIDE TO PRODUCE A MACH STEM

shocks did produce sufficient pressure over a large enough volume to cause a detonation wave approximately 20 mm into the LX-17 charge.

## CONCLUSIONS

The main conclusion of this study is that multiple shock waves can increase the reaction rates in LX-17 and perhaps cause detonation when one shock would not. The experimental embedded gauge study provides a data base to which the ignition and growth model is normalized. The model can then be used to evaluate other hazard and vulnerability scenarios that can not be tested. Since explosives are usually confined by metal and other inert materials, the reflected shock study provided essential knowledge of the effects of shock wave reflection on LX-17 reaction rates. The production of Mach stems and subsequent detonations by colliding shock waves indicates that the explosive may be vulnerable to multiple fragment impacts over certain ranges of velocity, size, timing and spacing of these impacts. Additional experiments and modeling of colliding shocks in LX-17 is required to fully explore this hazard scenario.

Work performed under the auspices of the U.S. Department of Energy by the Lawrence Livermore National Laboratory under contract No. W-7405-ENG-48.

## REFERENCES

1. Tarver, C. M. and Hallquist, J. O., Seventh Symposium (International) on Detonation, Naval Surface Weapons Center NSWC MP82-334, White Oak, MD, 1981, p.488.
2. Cochran, S. G. and Tarver, C. M., Shock Waves in Condensed Matter-1983, J. R. Asay, R. A. Graham, G. K. Straub, eds., Elsevier Science Publishers, B. V., 1984, p. 593.
3. Bahl, K.; Bloom, G.; Erickson, L.; Lee, R.; Tarver, C.; Von Holle, W.; and Weingart, R., Eighth Symposium (International) on Detonation, Naval Surface Weapons Center NSWC MP86-194, White Oak, MD, 1985, p. 1045.
4. Urtiew, P. A.; Erickson, L. M.; Aldis, D. F.; and Tarver, C. M., Ninth Symposium (International) on Detonation, Office of the Chief of Naval Research OCNR113291-7, Portland, OR, 1989, p. 112.
5. Tarver, C. M., Propellants, Explosives and Pyrotechnics 15, 132 (1990).
6. Urtiew, P. A.; Cook, T. M.; Maienschein, J. L.; and Tarver, C. M., "Shock Sensitivity of IHE at Elevated Temperatures," paper presented at this Symposium.
7. Ferm, E. N. and Hull, L. M., "Reflected Shock Initiation of Explosives," paper presented at this Symposium.
8. Tarver, C. M.; Urtiew, P. A.; Chidester, S. K.; and Green, L. G., Propellants, Explosives and Pyrotechnics 18, 117 (1993).
9. Tarver, C. M.; Hallquist, J. O.; and Erickson, L. M., Eighth Symposium (International) on Detonation, Naval Surface Weapons Center NSWC MP86-194, White Oak, MD, 1985, p. 951.
10. Kennedy, J. E. and Nunziato, J. W., J. Mech. Phys. Solids 24, 107 (1976).
11. Jackson, R. K.; Green, L. G.; Bartlett, R. H.; Hofer, W. W.; Kramer, P. E.; Lee, R. S.; Nidick, Jr., E. J.; Shaw, L. L., and Weingart, R. C., Sixth Symposium (International) on Detonation, Office of Naval Research ACR-221, Coronado, CA, 1976, p. 755.

12. Muraour, H., Rev. Inst. Fr. Petrole 5, 148 (1950).
  13. Dickson, P. M.; Parry, M.; and Field, J. E., Ninth Symposium (International) on Detonation, Office of the Chief of Naval Research OCNR 113291-7, Portland, OR, 1989, p. 1100.
  14. Dick, J. J.; Mulford, R. N.; Spencer, W. J.; Pettit, D. R.; Garcia, E.; and Shaw, D. C., J. Appl. Phys. 70, 3572 (1991).
  15. Nichols, A. L.; Tarver, C. M.; and Chidester, S. K., "Modeling Thermal Explosion and Hot Spot Growth in HMX and TATB," manuscript in preparation.
  16. Campbell, A. W. and Travis, J. R., Eighth Symposium (International) on Detonation, Naval Surface Weapons Center NSWC 86-194, White Oak, MD, 1985, p. 1057.
  17. Liddiard, Jr., T. P., Fourth Symposium (International) on Detonation, Office of Naval Research ACR-126, White Oak, MD, 1965, p. 487.
- 

## DISCUSSION

MICHAEL GUNGER

Orlando Technology, Inc., Shalimar, Florida

Does dimensionality affect the results of the calculation primarily in pulse duration?

## REPLY BY CRAIG TARVER:

These experiments used cylindrically symmetric 90-mm-diameter explosive charges. The Manganin gauges were placed near the axis of the charge. Two-dimensional dyna calculations confirmed that the experiments were one-dimensional for more than 10  $\mu$ s. The effects of side and/or rear rarefaction waves are taken into account in all of our gauge experiments.

## NOVELTIES OF DETONATION PHENOMENON STUDY

A.N.Dremin

Institute of Chemical Physics (Chernogolovka),  
Russian Academy of Sciences, Moscow region,  
Chernogolovka, 142432, Russia

Two experimental findings and two theoretical concepts have appeared as novelties in the study of detonation phenomena since the advent of ZND theory, these are revisited. The experimental findings are the discovery of unstable detonation and the contradiction between the rather weak dependence of a liquid explosives' detonation velocity on charge diameter and the finite value of the liquid explosives' detonation failure diameter. The theoretical concepts are the non-equilibrium excitation and destruction of complex molecules inside a detonation wave shock front, and chemical reaction breakdown behind the front. The concepts, ideas and their origins are discussed.

### INTRODUCTION

The detonation phenomenon has been known since the last century. The phenomenological thermodynamic analysis performed by Michelson,<sup>1</sup> Chapman<sup>2</sup> and Jouguet,<sup>3</sup> without taking into account chemical reaction kinetics, has resulted in the generalization of shock wave theory. The detonation wave has been represented as a shock wave with energy evolution due to instantaneous chemical reaction in the wave front. This was the most prominent step in the progress of detonation theory. The inclusion of chemical reaction kinetics (Zeldovich,<sup>4</sup> Neuman,<sup>5</sup> Döring<sup>6</sup>) has led to the ZND detonation model. The model is more complicated due to the inclusion of a compression wave. In essence detonation has changed into deflagration moving behind the shock front with the front velocity. That is, the explosive at detonation is only compressed within the shock front and its decomposition takes place behind the front in a state of shock-compressed thermodynamic equilibrium, the effect of heating to a high temperature by shock compression.

The ZND model made its appearance about 50 years ago. Since then some novelties of the experimental and theoretical study of detonation phenomena have been revealed. The objective of this paper is to remind the reader of these novelties [*observations and concepts, Ed.*].

### EXPERIMENTAL OBSERVATIONS

The first two novelties are experimental. The first to be discovered was unstable detonation. In essence the concept of unstable detonation had been introduced into detonation theory by Shchelkin in 1959.<sup>7</sup> Before then everybody investigating gaseous detonation believed that the rather complicated detonation front luminescence, that had been observed experimentally, was some manifestation of the so-called many-headed spin detonation. Shchelkin was the first to realize and announce that, in fact, it was the manifestation of kinetic instability in gaseous detonation waves. According to Shchelkin, chemical reaction originates non-simultaneously in time and space over the detonation wave front surface during the unstable detonation. The detonation instability has been observed experimentally in gaseous explosive mixtures<sup>8,9</sup> as well as in some liquid explosives.<sup>10</sup> The unstable detonation physical model differs fundamentally from the ZND detonation model.<sup>11,12</sup>

The second experimental finding, which is inconsistent with the ZND theory, is the contradiction between the rather weak dependence of a liquid explosive's detonation velocity with charge diameter, on the one hand, and the finite value of a liquid explosive's detonation failure diameter, on the other. Really, according to available theories (for example references <sup>13</sup> and <sup>14</sup>) the

failure diameter is proportional to the explosive's detonation chemical reaction time; the larger the time then the larger the critical diameter for detonation. And to the contrary, the smaller the time, the less the detonation velocity depends on the diameter. So, as the time approaches zero the dependence of detonation velocity on charge diameter has to disappear, and the failure diameter has also to approach zero. By contrast liquid explosives, whose detonation velocities as a rule do not practically depend on charge diameter, have failure diameters that are not zero and can amount to significant values. For example, nitromethane has a detonation velocity at room temperature of 6.3 km/s which does not change significantly near its failure diameter. Nevertheless, the failure diameter of nitromethane detonation is rather big (15 mm).<sup>10</sup> The contradiction had no interpretation in the context of the ZND theory.

## THEORETICAL CONCEPTS

Investigations of the nature of detonation front instabilities, as well as of the cause of a liquid explosive's weak dependence of detonation velocity with charge diameter (even for considerable values of failure diameter) have resulted in the introduction of two new concepts into detonation theory: the "break-down" (BD) and "shock discontinuity" (SD) concepts.

### Break-Down Concept

The BD has come to light in the course of the investigation of detonation processes in liquid explosives.<sup>10</sup> The majority of the investigations have been performed with nitromethane and its mixture with acetone. The explosive's detonation front is unstable. Clearly, the most feasible approach was to use the concept of an unstable detonation decomposition in order to look for the cause of the above-mentioned contradiction. By this was meant that the theory of unstable detonation failure diameter had to be developed. The theory had been elaborated on the basis of a decomposition mechanism, worked out by Shchelkin and Troshin<sup>8</sup> in the early sixties, for unstable detonation in gases.

**Reaction Sites and Triple Shocks** Shchelkin's and Troshin's explosive detonation transformation mechanism differs from that of the ZND detonation theory in the following manner. In the ZND theory, the detonation front is stable and the explosive reaction originates behind the detonation shock front in the explosive shock-compressed state simultaneously over the wave front. In Shchelkin's and Troshin's case the detonation front is unstable; the explosive reaction originates nonsimultaneously over the detonation shock front at triple-shock interactions due to double collisions at

discrete sites.<sup>8</sup> These interactions appear over the entire surface of the detonation shock front due to the complex instability of the shock wave chemical reaction.<sup>7</sup>

According to Shchelkin and Troshin the explosive reaction sites will not appear over the detonation shock front if the double collisions do not take place. In their view the triple-shocks, originating in the detonation shock front, are due exclusively to repeated collisions with each other or with the gas containing tube walls; each separate interaction dying out eventually. However, the collisions give rise to new explosion sites which lead to the origin of new triple-shocks. The new triple-shocks collide again and the process continues.

This sequence of events continues throughout the stationary detonation front except at the front edge at the lateral free surface of the explosive charge. In this case the last triple-shocks, moving to the charge's free surface at the front edge of the detonation, have no opposing shocks to collide with. Consequently, new explosion sites cannot appear near the surface, and similarly, no new triple-shocks are created there. It is therefore, impossible for neighboring explosion sites, located further from the surface, to appear. So, the presence of the charge's free surface leads to the progressive extinction of explosion sites in the direction away from the surface, that is, a reaction quenching wave appears to move from the charge free surface towards its axis.

**Experiments** The reaction-quenching waves have actually been observed in specially-arranged experiments. In the experiments the explosive's detonation wave, moving inside a metal tube, transits through a sudden enlargement of the tube diameter. The detonation wave front occupies the entire cross section of the first tube. In accordance with the foregoing, the triple-shock collisions with the first tube wall result in the explosion sites appearing in the same manner as at their collisions between themselves. Owing to that fact, there is no reaction-quenching wave during detonation wave motion inside metal tubes. (It stands to reason that the tube's inner surface is smooth). Just as described above, the last triple-shock interactions at the unstable detonation wave front edge will have nothing to collide with when they emerge from the end of the first tube, and the reaction-quenching wave appears there and extinguishes the detonation. It has been verified in these experiments that the reaction-quenching waves actually appear at the end of the first tube.

**Failure Diameter** It turns out that the quenching waves spread over the detonation wave front towards the charge axis only to a certain depth. Moreover, it has been found that the detonation wave moves along the

charge axis with constant velocity if the first tube radius is larger than the depth; and the detonation wave generally ceases if the reaction-quenching waves shut down the entire cross-section of the tube. It has been shown that for unstable detonation in liquid explosives the depth coincides with the explosive's detonation failure radius.<sup>15</sup> A theory of failure diameter was developed based on this experimental finding.<sup>15,16</sup> The fact that the reaction-quenching wave can only penetrate to a certain depth, from the charge lateral free surface towards its axis, is a convincing explanation of the independence of the liquid explosive's detonation wave velocity from the charge diameter. It follows that as the explosive detonation wave moves along the charge axis it "knows" nothing about the events, which take place in neighboring regions located some distant away from the charge axis, if the charge diameter is larger than the failure diameter.

**Reaction-quenching Waves in Stable Detonation** From the above-presented considerations, the reaction-quenching wave is crucial to the nature of detonation instabilities and the failure diameter of liquid explosives. This reaction-quenching wave was predicted on the basis of Shchelkin's and Troshin's hot-spot mechanism for explosive reaction during unstable detonation. However, it turns out that the reaction-quenching waves also occur for stable detonation in liquid explosives.<sup>10</sup> This finding had led to the notion that the reaction-quenching waves are not caused by the extinction of explosion sites, as described above, but due to some general phenomenon which is an inherent characteristic of all explosion processes in all energetic materials (gases, liquids, solids). In essence, it was the discovery of the BD phenomenon which led to the determination of the limiting conditions for detonation shock initiation, detonation stability as well as detonation failure diameter.<sup>17</sup>

What is the main point of the BD phenomenon? When does it occur? The BD leads to an abrupt cessation of explosive chemical reaction. It takes place behind the shock wave front if adiabatic cooling, caused by the rarefaction wave, compensates for self-heating in the explosive due to its **exothermic** reaction.<sup>10,18</sup> More precisely, the probability of BD occurring is governed by competition between two rates: the explosive chemical reaction rate which leads to an increase in explosive temperature and a commensurate rate increase; and the rate of adiabatic cooling in the explosive which decreases the chemical reaction rate.

### Shock Discontinuity Concept

The fourth and last of the present novelties in the investigations of condensed ideal explosives detonation

phenomena is the shock-discontinuity (SD) concept. It is evident that the processes of the explosive energy evolution process, under the effect of shock, are governed by the mechanism of shock wave induced explosive reaction. The elucidation of the mechanism has resulted in the creation of the SD concept. The SD denotes the whole process of the complex, non-equilibrium, athermal excitation and decomposition of polyatomic explosive molecules within the shock wave front.<sup>19</sup>

**Superheating of the Translational Mode** The superheating (disequilibrium) of the translational temperature in complex molecules inside the shock front is crucial to the process. Now the rate of material loading is very high inside the shock discontinuity zone (the zone time width being circa  $10^{-13}$  s). Consequently, the disequilibrium in the translational temperature  $T_{oh}$  arises because the kinetic part of the shock compression energy - which is equally distributed behind the shock front among all the translational, vibrational and rotational degrees of freedom of polyatomic molecules - is absorbed only by the translational degrees of freedom within the zone.  $T_{oh}$  is a maximum when  $T_{oh} = 2(N - 1)(T - T_0)$ , where  $N$  is the number of atoms comprising the molecule, and  $T_0$  and  $T$  are the equilibrium temperatures at the initial and shock-compressed explosive states.<sup>19</sup> The  $T_{oh}$  is of the order of tens times the shock-compressed explosive equilibrium temperature.

**Reaction Mechanisms** During the time it takes the most slowly excited bonds of the explosive molecule to be excited (circa  $10^{-10}$  s, which is the shock wave front width) the translational temperature falls to its equilibrium value; then non-equilibrium athermal excitation and the decomposition of some complex explosive molecules occur simultaneously. Since the excitation and decomposition are **endothermic** processes the pressure has to increase inside the detonation shock front. The main processes behind the front are the explosive molecules interaction with active particles (radicals, ions and excited molecules) as well as the particles with each other. The overall interaction process is **exothermic** and therefore the pressure decreases behind the front. (It should be noted that it is not improbable that reaction occurs within the shock front; however, the total transformation of explosive molecules is **endothermic**, and therefore the pressure increases inside the front.)

### CONCLUSIONS

Thus, four novelties have been introduced into the investigations of detonation phenomena in the 50 years since the advent of ZND theory. Two of them are experimental: first the discovery of unstable detonation; second the elucidation of the cause of the weak depen-

dence of unstable detonation velocity on the charge diameter in liquid explosives, even at considerable sizes of failure diameter. These experimental findings have resulted in the creation and introduction to detonation theory of two new theoretical concepts. One was named the breakdown (BD) concept of chemical reaction; the other the shock discontinuity (SD) concept. The SD denotes the whole process of the excitation and decomposition of complex polyatomic molecules within the shock wave front ( $10^{-10}$  s). Although the shock discontinuity zone width ( $10^{-13}$  s) is considerably smaller than that of the shock front, the whole process was named the SD since its main effect is to superheat the explosive molecules' translational temperature; this originates just inside the shock discontinuity zone, owing to the tremendous rate of substance loading within the zone.

**Competition Between SD and BD Processes** The BD and the SD are interrelated in all detonation phenomena; the BD follows SD. The SD is characterized by the **endothermic** processes of excitation and decomposition of complex polyatomic molecules inside the detonation shock front; however, the BD manifests itself behind the front, where the **exothermic** processes of molecular interaction with active particles, and the particles with each other, occur. If the wave intensity increases, so does the number of active particles originating inside the detonation shock front. At the same time, the explosive shock compression equilibrium temperature increases and hence, the rate of explosive energy release increases behind the detonation shock front; this reduces the probability of BD.

By contrast, if the wave intensity diminishes, the explosive shock compression temperature falls as does the number of active particles originating inside the detonation shock front. This reduces the rate of explosive energy release behind the shock front and thus, increases the probability of BD. Consequently, the more the SD manifests itself, the less probable the BD is. And in contrast, the less the SD occurs, the more probable the BD is.

The foregoing means that the BD most readily occurs in explosives which transform, under shock loading, according to the "slow kinetic" processes (these are usually weak homogeneous explosives, e.g., practically all gaseous mixtures as well as some liquid explosives). The BD occurs with the most difficulty in explosives which transform according to the "fast kinetic" processes (these are usually the more powerful explosives).

Detonation waves in homogeneous weak explosives are usually unstable, with chemical reaction originating and terminating continuously and nonsimultaneously

over their detonation wave fronts.<sup>10-12</sup> The origin of the detonation failure diameter in explosives has been elaborated.<sup>15,16</sup> According to the theory the failure diameter is governed by the depth beyond which the BD wave, originating at the charge lateral free surface, can spread over the detonation front towards the charge axis.

The detonation wave front in powerful homogeneous explosives is stable; the BD does not occur between the shock-to-detonation transition and the CJ state in their strong detonation fronts. However, it does occur at the charge's lateral free surface. It has been shown experimentally that the BD governs the failure diameter of both powerful and weak homogeneous explosives with stable detonations fronts.<sup>10</sup> However, the theories of detonation failure diameter for these explosives have not yet been developed.

The detonation front in solid heterogeneous explosives (cast, pressed, etc.) has to be stable since the BD does not take place over almost all the detonation wave front. The BD occurs behind the detonation wave front, at the charge axis, only when the charge diameter is smaller than the failure diameter. However, it should be mentioned that chemical reaction has been seen to extinguish and reinitiate in the detonation wave front at the lateral surface of some cast explosive charges.<sup>20,21,22</sup>

## REFERENCES

1. Michelson, V. A., *Utshenie Zapiski Imperatorskogo Moskovskogo Universiteta*, Moskava, Issue 10, 1893, pp. 1-92.
2. Chapman, D. L., "On the Rate of Explosions in Gases," *Philos. Mag.*, Vol. 47, 1899, pp. 90-104.
3. Jouguet, E., *Mathem. J.*, Vol. 6, 1904, p. 5.
4. Zeldovich, Ya. B., "On the Theory of Gas Detonation," *Zur. Experim. i. Teor. Fiz.*, Vol. 10, No. 5, 1940, pp. 542-568.
5. Von Neuman, J., *OSRD Rept.*, N. 549, 1942.
6. Doring, W., "Uber der Detonations Vergang in Gases," *Ann. Phys.*, Vol. 43 (5), 1943, pp. 421-436.
7. Shchelkin, K. I., "Two Kinds of Unstable Burning," *Zur. Experim. i. Teor. Fiz.*, Vol. 36, 1959, pp. 600-606.
8. Shchelkin, K. I., and Troshin, Ya. K., "Gasodinnamika Gorenija," *Akademija Nauk*, Moskva, 1963.
9. Voicechovsky, B. V., Mitrofanov, V. V., and Topthijan, M. E., "Detonation Front Structure in Gases," *Akademija Nauk*, Novosibirsk, 1963.
10. Dremine, A. N., Savrov, S. D., Trofimov, V. S. and Shvedov, K. K., *Detonacionnie Volni v*



*Kondensirovannich Sredach*, Nauka, Moskva, 1970, "Detonation Waves in Condensed Media," Translated from Russian by Foreign Technology Division, Wright-Patterson Air Force Base, Ohio, Aug. 1972.

11. Dremin, A. N., "Pulsating Detonation Front," *Fizika Gorenija i Vzriva*, No. 4, 1983, pp. 159-169.
12. Dremin, A. N., "Mechanism of Unstable Detonation Front Origin," in *Proc. of the 13th Int. Colloq. on Expl. and React. Systems*, Nagoyana, July 28 - Aug. 2, 1991, Japan (to be published in the AIAA Journal in 1993).
13. Rosing, V. O., Chariton, Yu. B., *Dokl. Akad. Nauk SSSR*, Vol. 26, 1940, pp. 360-365.
14. Bolkhovitinov, L. G., *Vzrivnoe Delo*, No. 76/33, 1976, p. 150.
15. Dremin, A. N., "The Critical Detonation Diameter of Liquid Explosives," *Dokl. Acad. Nauk SSSR*, Vol. 147, No. 4, 1962, pp. 870-873.
16. Dremin, A. N., and Trofimov, V. S., "On the Nature of the Critical Diameter," in *Proceedings of the Tenth Symposium (Int) on Combustion*, The Combustion Institute, Pittsburg, Pennsylvania, 1965, pp. 839-843.
17. Dremin, A. N., "Critical Phenomena in the Detonation of Liquid Explosives," in *Proceedings of the Twelfth Symposium (Int) on Combustion*, Poitiers, France, 1968, pp. 691-699.
18. Trofimov, V. S., and Veretennikov, V. A., "On Detonation Front Structure in Condensed Explosives," *Khimitscheskaja Fizika Processor Gorenija i Vzriva, Detonacija*, Nauka, Chernogolovka, 1977, pp. 9-11.
19. Dremin, A. N., Klimenko, V. Yu., Davidova, O. N., and Zolodeva, T. A., "Multiprocess Detonation Model," in *Proceedings of the Ninth Symposium (Int) on Detonation*, Portland, Oregon, 1989, pp. 724-729.
20. Howe, P., Frey, R., and Melani, G., *Combustion Science and Technology*, Vol. 14, Nos. 1, 2, 3, 1976, pp. 63-74.
21. Kozack, G. D., Kondrikov, B. N., Oblomky, V. B., "Spinning Detonation in Solid Explosives," *Fizika Gorenija i Vzriva*, No. 4, 1989, Vol. 25, pp. 86-91.
22. Kozack, G. D., Kondrikov, B. N., Oblomky, V. B., "Spinning Wave and Liquid Explosives, Detonation Failure," *Fizika Gorenija i Vzriva*, No. 2, 1992, pp. 93-98.

## DISCUSSION

ANDREW VICTOR

Victor Technology, Ridgecrest, California

The very high transient temperatures you postulate lead one to expect some dissociation at inner orbital levels. This would lead to X-ray emission. Do you know if X-radiation has been passively measured from detonations? Also, one would think that if the detonation occurred in a very high electric field, a longer delay between recombination of these high energy states might lead to much higher energy release to the environment; what do you think?

## REPLY BY ANATOLIY DREMIN:

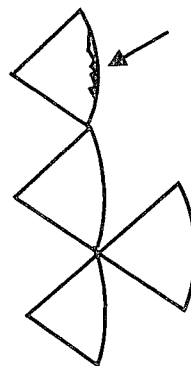
Thank you for the question. In answer to the second part of the question, in my talk I was referring to the possible overheating of the translational temperature in composite multiatomic organic molecules. It originates because of the tremendous rate of substance loading inside the shock wave front, when the molecules' inner degrees of freedom have no time to be excited. As the translational energy is redistributed between the inner degrees of freedom, the translational temperature falls to the equilibrium temperature.

## DISCUSSION

PER-ANDERS PERSSON

Research Center for Energetic Materials, Socorro, New Mexico

In the cellular structure detonation, do you envision a "mini-cellular" structure also of the overdriven parts of the detonation front?



## REPLY BY ANATOLIY DREMIN:

One can observe cellular structure also in the overdriven parts of the detonation front (so-called fine instability pattern).

## VISUALIZATION AND MODELLING OF DELAYED DETONATION IN THE CARD GAP TEST

B. SALVETAT - J.F. GUERY  
SNPE Centre de Recherches du Bouchet  
BP 2 - 91710 Vert le Petit - FRANCE

In the 80s, delayed detonations occurred in safety tests, such as card gap test, on XLDB propellants. We have performed experimental and numerical studying to describe a scenario leading to these detonations. The model developed is able to reproduce the phenomenology of events. There is a good agreement between experiments and computation on where and when the detonation occurs.

### INTRODUCTION

In the early 80's, detonations below traditional thresholds occurred in safety tests on Cross Linked Double Base Propellant. They were observed several times in card gap tests and reported by Kincaid<sup>1</sup>. A research was then performed to study the mechanisms of these Unknown Detonation Transitions (XDT's). The first step consisted in identifying experiments where these detonations might occur : they were detected in the French and NOL card gap tests, flyer plate impact tests, high velocity shot gun tests for different sizes, and more recently in the bullet impact threat<sup>2</sup>. Systematic experiments were performed in order to identify the threshold levels leading to a detonation, below the threshold level for shock to detonation transition (SDT). We were able to determine when the detonation occurred and identify it as a delayed detonation.

For a XLDB propellant, with a total solid of 75% (AP, HMX, Al), a complete study has been performed both numerically and experimentally, in order to determine the scenario leading to this detonation. For the experiments, the French card gap test was chosen.

### EXPERIMENTAL STUDIES

The french card gap test includes :

- a booster charge consisting of two samples of compressed RDX/wax. The booster (40 mm diameter, 80 mm length) is initiated by a blasting cap ;

- a variable gap made of cellulose acetate cards (46 mm diameter, 0.19 mm thickness) which attenuates the shock ;

- the propellant sample (200 mm length, 40 mm diameter) which is confined in a steel tube (4 mm thickness) ;

- a compressed RDX/wax acceptor (40 mm length, 40 mm diameter) for punching a hole in a steel witness plate. The compressed RDX/wax acceptor detonates if it has been initiated by the propellant detonation. All these elements are held in a cardboard tube and suspended with a rope.

The test technique used at SNPE consists in determining the number of acetate cards (N) which do not transmit the detonation : one must get three negative trials at this card number. The increment used is 5 cards. Thus there is at least one detonation with N-5 acetate cards. The test is calibrated to determine a shock pressure from the attenuator thickness.

### DETONATION THRESHOLDS

In some published work it was detected that one may get two distinct detonation thresholds for a given XLDB propellant. These multilevel results can be characterized by a transit time measurement. It is also noticed that the threshold obtained with the higher level of shock is constant. When the second threshold is detected at "low" level of shock, the frequency of

detonation is variable. This threshold is also variable when compared to a different "grain" of the same propellant composition. Studies have been performed to identify these two kinds of detonation :

First, measurement of the shock transit time through the sample length were made. Transit time is measured by placing pin switches at each end of the propellant sample. At the top of the sample, a mechanical pin switch detects the shock arrival. These switches are composed of two wires and an electrical conductive cap. When the shock induced by the booster through the card appears, the conductive cap puts the two wires in contact completing an electrical circuit. At the bottom of the sample, an ionisation pin is placed which reacts when the detonation occurs. The detonation of the propellant produces the ionisation of the gas near the pin and an electrical circuit is established. Timing is recorded by a chronometer, whose accuracy is 0,1  $\mu$ s.

With an XLDB propellant and a gap below 140 cards (26.6 mm), we obtain a transit time lower than 30  $\mu$ s. Above 145 cards (27.5mm), we obtain a detonation with a transit time greater than 45  $\mu$ s, that is the reason why the unknown detonation is called "delayed detonation". This method was applied to other propellants but the XDT phenomenon appears only on XLDB propellants. The next experiments were conducted in order to know where and when the detonation occurs in both SDT and XDT cases.

## A MODIFIED TEST

A modified test was developed to allow a high speed camera instrumentation. The main objective is the visualization of the propellant, so the steel tube confinement is taken away. To avoid smoke from the booster detonation products, an horizontal mask was introduced around the acetate cards. A few tests were performed with 145 and 150 cards to confirm the occurrence of delayed detonations during these experiments. With all these tests we obtained detonations with transit time ranging from 45.4  $\mu$ s to 52  $\mu$ s. To determine the timing of the events (shock wave and detonation), an instrumented test was performed, which enables us to adjust the beginning of the film. A set of mechanical pin switches and ionisation pins are employed on an unconfined sample. The test is realized with 145 cards (27.5mm). The results we obtained with

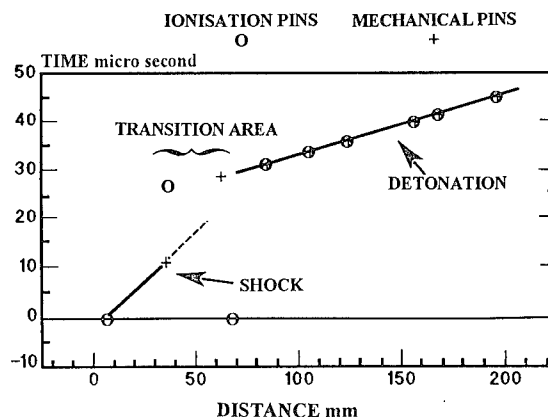


FIGURE 1. TIMING DATA OF SHOCK AND DETONATION

each kind of pin are presented in figure 1. The time reference is given by the first mechanical pin.

The graphical representation of these results indicates that :

- there is a delayed detonation with a transit time of 45  $\mu$ s ;
- the detonation has a constant velocity, around 8000 m/s, after 65 mm ;
- the transition area takes place between 30 and 60 mm and the detonation occurs in this area between 20 and 30  $\mu$ s ;
- at 35 mm in the propellant, the first shock wave arrives at 11 $\mu$ s and the detonation at 26.5  $\mu$ s. The knowledge of these times enables the synchronization of the high speed camera. This camera has a recording speed ranging from 500 000 f/s to 4 000 000 f/s and a recording length of 50 frames. The speed chosen gives a picture each 2  $\mu$ s. The light is produced by a pyrotechnic flash distant of 30 cm from the sample, with a 100  $\mu$ s lighting time.

## NO DETONATION RESULTS

During the first test with 145 cards, no detonation occurred. Thus, one can see the effects of a non-reactive shock wave in the propellant :

- (1) - detonation of the booster at  $t_0 - 12 \mu$ s ;
- (2) -  $t_0$  : at this time the shock wave reaches the propellant, the acetate card diameter increases ;
- (3) - at  $t_0 + 30 \mu$ s, the top of the sample opens in a corolla of fine particules ;
- (4) - at the end, the first third of the sample is destroyed.

## SDT RESULTS

To insure SDT conditions, we used 100 acetate cards:

- (1) -  $t_0$  : the shock wave enters the propellant ;
- (2) -  $t_0 + 2 \mu s$  : the detonation occurs ;
- (3) -  $t_0 + 12 \mu s$  : the detonation propagates at constant velocity.

## XDT RESULTS

A delayed detonation is obtained with 145 cards :

- (1) -  $t_0$  : the shock wave reaches the propellant ;
- (2) - until  $t_0 + 36 \mu s$  : a non reactive shock wave has propagated in the propellant ;
- (3) -  $t_0 + 36 \mu s$  : a detonation emerges at about 30 mm ;
- (4) - the detonation propagates along the sample.

When the delayed detonation has occurred, it behaves as a normal detonation, with the same velocity as in SDT phenomena.

At the end of experimental investigation, the phenomenon of delayed detonation was clearly identified. We have determined where and when the detonation occurred. The second step consists in understanding how this delayed detonation can occur. In such a test where geometrical effects are important, the numerical simulation is an efficient tool. The purpose of numerical modelling is to use theoretical models for predicting what can happen in the propellant, and what can be the differences between SDT and XDT.

## NUMERICAL STUDY

We first modelled the shock to Detonation Transition. We have used Lee and Tarver reactive model<sup>3</sup> implemented in the explicit two-dimensional hydrodynamic finite element code DYNA 2D<sup>4</sup>. The propellant is described by two uncomplete JWL equations of state for solid phase and detonation products :

$$P(v, T) = Ae^{-R_1 v} + Be^{-R_2 v} + \frac{\alpha c_v T}{v}$$

We assume pressure and temperature equilibrium between the two phases. The volumes are assumed additive. The mixture is defined by the mass fraction reacted  $\lambda$ , where :

$$0 \leq \lambda \leq 1,$$

$$\lambda = 0 \text{ for no reaction,}$$

$$\lambda = 1 \text{ for complete conversion from solid phase to reaction products.}$$

The chemical reaction rate for conversion of unreacted explosive to reaction products consists of two physically realistic terms : an ignition term to initiate the reaction after the shock wave has compressed the material and a growth term to spread and complete this initial reaction.

$$\frac{d\lambda}{dt} = I(\lambda_m - \lambda)(\rho / \rho_0 - 1)^m + G(1 - \lambda)^{x_1} \lambda^{x_2} P^{x_3}$$

The reactive model is fitted with Lagrangian Analysis, Wedge Test and flyer plate experiments. The numerical simulations are in good agreement with experimental data for the SDT phenomenon<sup>5</sup>, but this model is unable to predict delayed detonations.

In order to determine the stress and strain history in the material when the delayed detonations occur, we performed non-reactive simulations. The propellant is described by an elastoplastic constitutive law for the deviatoric part of the stress tensor and a Mie-Gruneisen equation of state for the pressure term. Experimentally, the delayed detonation occurs 30  $\mu s$  after the shock has entered the propellant. The computations show that the material is first submitted to a strong shock wave that rapidly decays, which is characteristic of the card gap test. Afterwards, the material opens in a corolla, gets in tension by two-dimensionnal effects. Then, 30  $\mu s$  after the first shock comes a second compression generated by two-dimensionnal effects. Anytime XDT occurs, the material is damaged in tension, which is one of the reasons why we have studied propellant damage models.

## PROPELLANT DAMAGE

Experimentally, propellant damage is the result of nucleation, growth and coalescence of microscopic cracks. Because of propellant nature, cracks spread quickly, leading to a fracture similar to a brittle one. The damage models based on these assumptions are the NAG models (for Nucleation and Growth) developed at SRI International<sup>6</sup>. We combined the BFRAC model for brittle materials with our version of DYNA 2D. In the BFRAC model, damage is modelled by a crack distribution. This distribution is exponential at the nucleation step :

$$N = N_0 \exp\left(-\frac{R}{R_n}\right)$$

Here,  $R$  is the crack radius and  $N$  the number of cracks greater than  $R$ . Cracks are assumed penny shaped. The nucleation rate depends on the tensile stress following :

$$\frac{dN}{dt} = N_0 \left( \exp\left(\frac{\sigma - \sigma_{n0}}{\sigma_1}\right) - 1 \right)$$

for  $\sigma > \sigma_{n0}$  the growth rate is given by :

$$\frac{dR}{dt} = \frac{1}{4\eta} (\sigma - \sigma_{go}) R$$

with :

$$\sigma_{go} = \frac{\sqrt{\pi}}{4R} K_{Ic}$$

Cracks can open elastically. The crack opening is given by :

$$\delta = \frac{4(1 - \nu^2)}{\pi E} R \sigma$$

The total strain is the sum of crack opening and solid material strain.

$$\varepsilon = \varepsilon^s + \varepsilon^c$$

The cracks open in tension following :

$$\varepsilon^c = \frac{16(1 - \nu^2)}{3E} N R^3 \sigma$$

The crack opening causes stress relaxation in the material. A global damage variable  $\tau$  is defined by :

$$\tau = A \int_{R_{\min}}^{R_{\max}} R^3 dN$$

$\tau$  represents the volume fraction of fragmented material.

In these equations,  $\nu$  is Poisson coefficient,  $E$  is young modulus,  $K_{Ic}$  is the stress intensity factor,  $N_0$ ,  $R_n$ ,  $\sigma_{n0}$ ,  $\sigma_1$ ,  $\eta$ ,  $\Lambda$  are model parameters.

We fitted the BFRAC parameters with the results of plate impact experiments. The crack damage was quantified in size and location for the recovered targets using Scanning Electronic Microscope observations. After this "post mortem" determination, we validated the model in time, using free surface velocity measurements (VISAR experiments).

## CARD GAP TEST SIMULATIONS

We performed simulations of the standard card gap test at 200 cards. Tensions near the top of the sample lead to fracture creation. The shock wave, subsonic with respect to the downstream medium, is overtaken by rarefaction waves. The first shock vanishes quickly. Only the top of the sample is highly damaged. The simulations give crack distributions and surface area in the propellant. When fracture is followed by the second recompressive wave (30  $\mu$ s after the shock), subsequent burning may occur in the freshly damaged propellant. The undamaged propellant acts as a confinement and the reaction can be amplified, until it propagates as a detonation in the undamaged zone.

Because we have the same timing, both experimentally and numerically, we can suppose that the

TABLE 1. BFRAC PARAMETERS FOR THE PROPELLANT

$\rho_0$	1.85	g/cm <sup>3</sup>			
$C_0$	2241	m/s	s	2.13	
G	75	MPa	$\sigma_Y$	5	MPa
$1/4\eta$	15000	/MPa/s	$K_{Ic}$	1.28	MPa cm <sup>1/2</sup>
$R_n$	0.0021	cm	Rmax	0.02	cm
$N_0$	60.10 <sup>6</sup>	/cm <sup>3</sup> /s	$\sigma_{n0}$	80	MPa
$\sigma_1$	20	MPa	$\Lambda$	4	

succession of shock - tension - and recompression is sufficient to initiate a delayed detonation on a XLDB propellant.

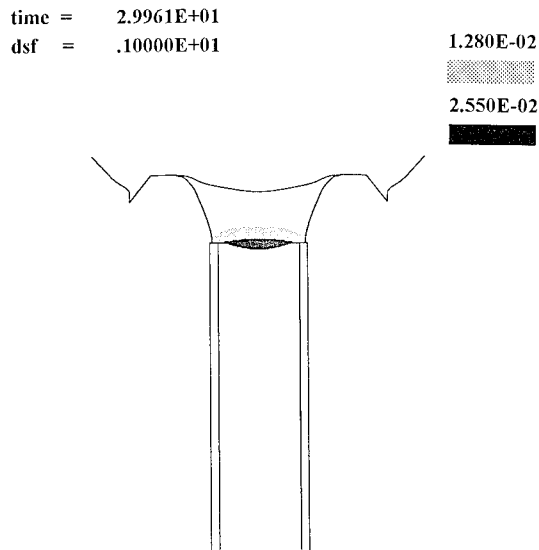


FIGURE 2. THE SHOCK ENTERS THE UNDER PROPELLANT (FRINGE OF PRESSURE - Mbar)

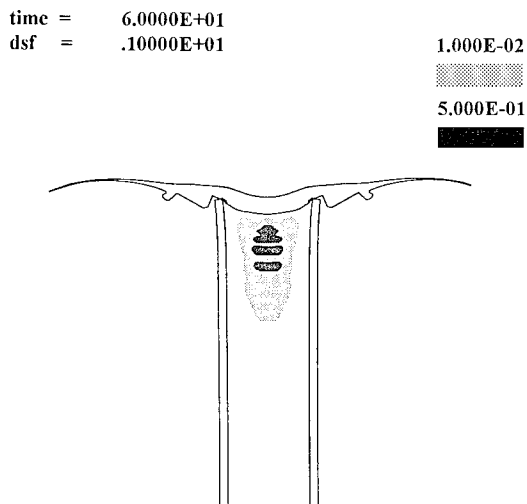


FIGURE 3. FRINGE OF DAME

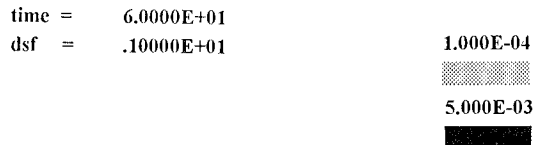


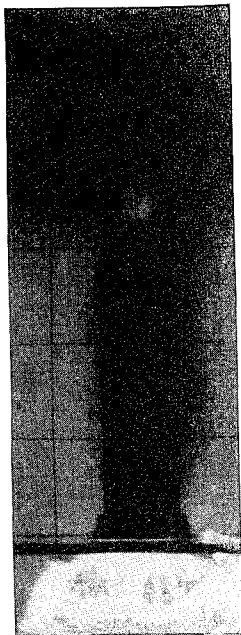
FIGURE 4. THE DAMAGED ZONE IS UNDER COMPRESSION

## CONCLUSIONS

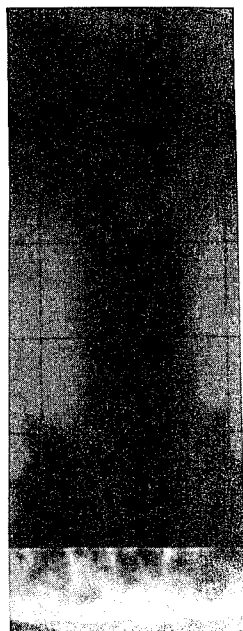
We have shown in this example how material properties, geometry and aggression were important for the delayed detonation phenomenon. The numerical model is a way for taking it into account. We also performed simulations of other tests leading to a delayed detonation, high velocity shot gun, flyer plate impact, bullet impact, validating and quantifying the scenario.

The next step will consist in using crack distributions given by the damage model as sources of hot spots for a reactive model. Then, we will be able to simulate delayed detonation phenomena correctly.

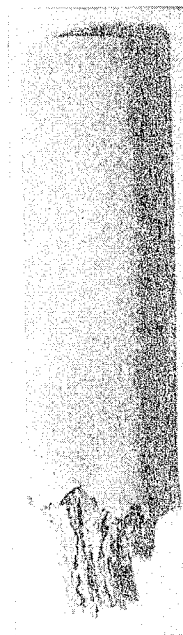
For the analysis of an unknown phenomenon, the coupled approach of experiments and numerical modelling is fundamental. The phenomenon is first observed experimentally. The initial conditions are quantified. Thus, numerical modelling with existing models is used to predict the response. When existing theoretical models are not sufficient, the simulations are an efficient tool to quantify the more likely causes and elaborate new theories. These theories need to be validated both experimentally and numerically in various experiments.



$t_0$

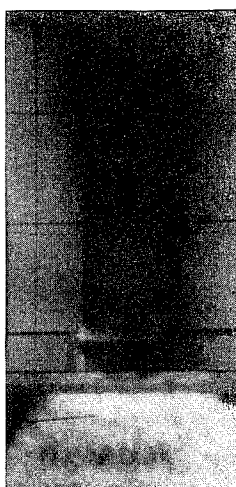


$t_0 + 50 \mu s$

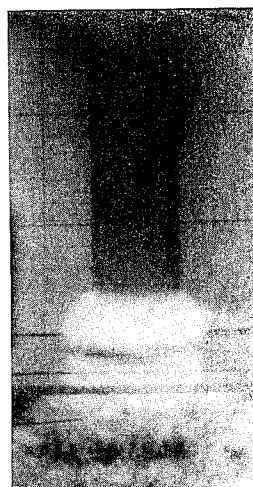


sample after

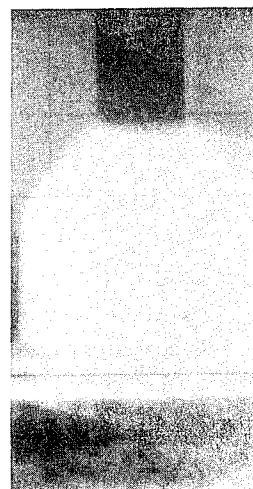
NO DETONATION RESULTS



$t_0$

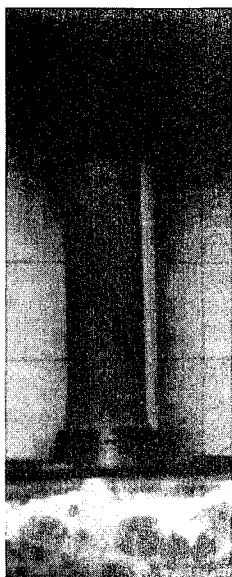


$t_0 + 2 \mu s$

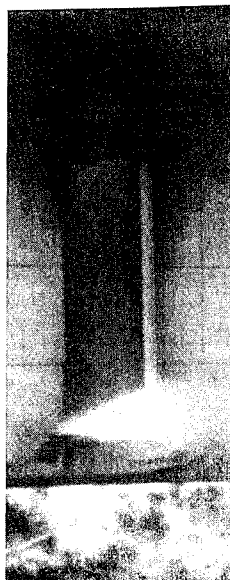


$t_0 + 12 \mu s$

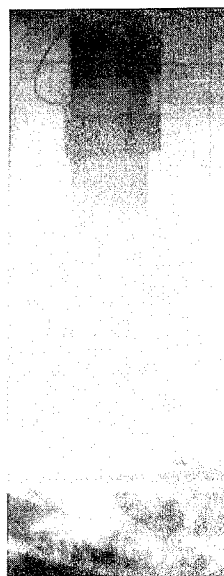
SDT RESULTS



$t_0$



$t_0 + 36 \mu s$



$t_0 + 48 \mu s$

#### XDT RESULTS

#### REFERENCES

1. Kincaid, J.F, "The determination of the propensity for detonation of high Performance Propellants", *ICT Jahrestagung*, Karlsruhe, Germany, 1982, pp 155-168
2. Brunet J, Hamaide S, Nouguez B, Pitiot F, "Bullet impact behavior of solid propellant grains", *AGARD Conference Proceedings*, Bonn, Germany, 1991, pp 17/1-17/9
3. E.L. Lee, C.M. Tarver, "Phenomenological model of shock initiation in heretogeneous explosives" *Phys. Fluids*, Vol 23, No 12, 1980, pp 2362- 2372
4. Hallquist J.O, "User's manuel for LSDYNA2D" Livermore Software Technology Corporation, 1990
5. Quidot M, Hamaide S, Groux J, Gimenez P, Isler J, "Fragment impact initiation of cast PBX in relation with shock sensitivity tests", paper presented at this symposium
6. Curran D.R, Seaman L, Shockey D.A, "Dynamic failure of solids", *Physics reports*, vol 147, n° 586, pp 255-388, 1987

*This work was performed under the auspices of the Service Technique des Poudres et Explosifs. The authors want to thank R. Heysen who performed the visualizations.*

#### DISCUSSION

J. GREGORY GLENN  
Wright Laboratory, Eglin Air Force Base, Florida

What was the pressure of the compressive wave that caused the detonation?

#### REPLY BY JEAN FRANCIS GUERY:

In the computations, the order of magnitude of the pressure is 25 kbar for the first shock and 10 kbar for the compressive wave 30  $\mu s$  later at a depth of 5 mm on the axis of the sample.



# DEFLAGRATION-TO-DETONATION IN GRANULAR HMX: IGNITION, KINETICS, AND SHOCK FORMATION

J. M. McAfee, B. W. Asay, and J. B. Bdzil  
Los Alamos National Laboratory  
Los Alamos, New Mexico, 87545

Experimental studies and analysis of the deflagration-to-detonation transition (DDT) in granular HMX are continued. Experiments performed using a direct-gasless igniter exhibit the same phenomenology as those ignited with a piston. Simple kinetics and mechanics describe the formation of the ~100% TMD plug in terms of competing pressurization processes. A mass-conservation analysis of the experimentally observed structures shows how the low velocities characteristic of convective burning are amplified to shock-wave velocities through non-convective processes.

## INTRODUCTION

In the Ninth Detonation Symposium,<sup>1</sup> we presented a descriptive model of the deflagration-to-detonation transition (DDT) of granular HMX confined in steel tubes. The particular experiments described and analyzed in that paper were ignited by a combustion-driven piston. We have since performed experiments on the same material, igniting directly with a high-temperature gasless igniter instead of a piston. We briefly describe these experiments and correlate the previous analysis with these observations.

Further experimentation and consideration of the observed phenomena, particularly in the region below the plug, have led us to expand and correct the original descriptive model. The nature of the burning in the compacted material is crucial to understanding the observed phenomena. Preliminary discussion on the nature and application of autocatalytic kinetics to this problem is given by McAfee, Asay, and Ferm.<sup>2</sup> Here we will expand and modify that exposition and consider ideas about intergranular gas pressure and energy transport in granular beds.

## EXPERIMENTAL RESULTS

The directly-ignited experiments were similar to those described by Campbell.<sup>3</sup> The same lot of granular HMX used in the previous studies<sup>1</sup> was hand packed to 35% porosity in mild steel tubes (~76-mm outer diameter, 12.7-mm inner diameter) and ignited with the previously described Ti/B/Pyrofuse® system. Beginning 13 mm above the igniter, coaxial ionization pins were placed in a double-spiral pattern with a net vertical spacing of 2 mm. Pin response was recorded by time-interval meters to an accuracy of  $\pm 3$  ns. Some of the steel tubes burst during the tests. Those that did not were axially sectioned and the profile of the inner diameter measured. The terminal observations for all the tests showed similar structures, although the burst tubes were not quantitatively measured. Figure 1(a) shows the pin data and wall profile for Shot No. B-9827.

The expanded-tube profile and pin-report times are plotted *versus* distance from the igniter. The expansion data are an average of the two sides of the axial section. Figure 1(b) shows the incremental velocities (pin separation divided by report-time difference) for pairs of pins in the leading trajectory. The six pins that reported late are plotted, but are not considered for velocity. The pins used in this experiment were not particularly well constructed, and some significant fraction had different threshold behavior, thus the occasionally anomalous report times.

The pin data indicate the transition to detonation occurred at approximately 52 mm. The tube expansion and inner-bore surface characteristics are consistent with this position for the transition. The expansion measurements are confounded in this area because the axial section passed through two of the pin holes at 50 and 52 mm. There are four regions evident in the wall-expansion data: (i) = 0 to ~10 mm, (ii) = ~10 to ~30 mm, (iii) = ~30 to ~50 mm, and (iv) = ~50 mm to the end of the tube. Region (i) does not have corresponding pin data. The expansion indicates a relatively low pressure. Region (ii) corresponds to an approximately constant-velocity front as measured by the incremental velocities, and the pressure increases moderately. Region (iii) indicates rapidly increasing pressure, and the pins show a rapid increase in velocity. In region (iv), the reduced expansion is typical, not significant, and due to confinement loss near the end of the tube. The last four pins give the detonation velocity of the original-density material.

The incremental velocities indicate the tube-profile in regions (iii) and (iv) is each composed of two distinct velocity regimes. In region (iii), the velocities increase rapidly from less than 1 km/s to over 9 km/s in slightly over a 10-mm distance. In fact, the last velocity (9.13 km/s) is marginally above the detonation velocity of Theoretical Maximum Density (TMD) HMX<sup>4</sup>. Even though this velocity is determined by only two pin reports, it clearly is not the beginning of a detonation because the next velocity up the tube is much less, constant, and spans three pins. As discussed in Reference 1, velocities greater than detonation can be

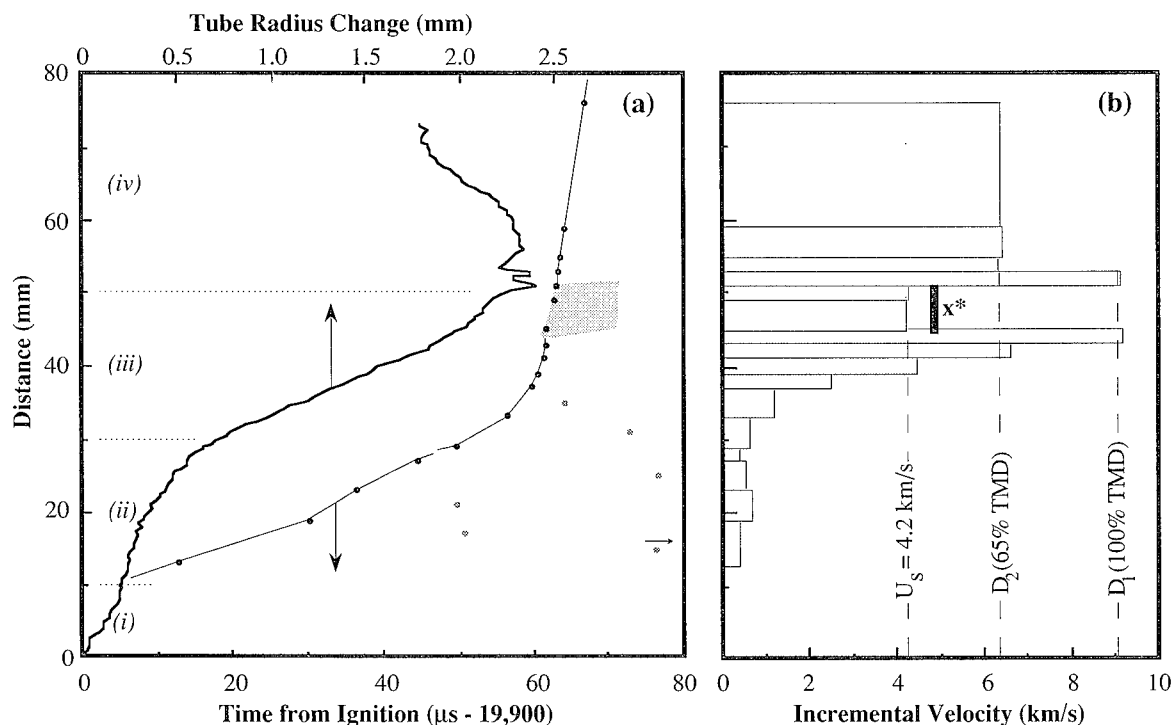


**FIGURE 1. TUBE PROFILE, PIN RECORD, AND INCREMENTAL VELOCITIES FOR SHOT NO.B-9827**

obtained by connecting data points from regions with distinctly different physical properties and histories. Our model of the DDT process postulates a contact-surface discontinuity between a burning region and a near 100% TMD region we have identified as the plug. These current data are interpreted by this model. The region immediately above this discontinuity (velocity = 4.2 km/s) corresponds to the shock that is the upper boundary of the plug. The region below the discontinuity is reacting rapidly and is described by a locus of a fixed (but arbitrary) amount of reaction in the approximately 90% TMD compact. The amount of reaction for this particular locus is determined by the threshold behavior of the diagnostic pins.

It is informative to compare the pin-measured 6-mm run distance of the 4.2-km/s shock and the run-to-detonation ( $x^*$ ) derived from the full-density HMX Hugoniot and Pop Plot<sup>4</sup> for that velocity. The calculation results in a shock pressure of 5 GPa and an  $x^*$  of 6.5 mm. This value of  $x^*$  is plotted on the incremental velocity-distance graph in Fig. 1.

Region (iv) exhibits a two-pin incremental velocity of 9.09 km/s, followed by a four-pin velocity equal to the detonation velocity of 65% TMD HMX (6.4 km/s). The detonation, initiated in the compact, overtakes the initial compaction wave, and subsequently proceeds (more slowly) in original density material. The observation of these two distinct detonation velocities indicates the existence and position of a compaction

wave in these directly ignited experiments, the same as for the piston-ignited experiments.<sup>1</sup>

## DISCUSSION

### Ignited Experiments

One of the continuing controversies in descriptions of the DDT is the significance of convective combustion (See citations in Reference 1). By definition, convective combustion requires that the velocities of the two (or more) phases be different. Our previous experiments using piston-driven ignition, by their very nature, compacted the bed before ignition or any of the structures required for transition to detonation were established. The initial piston compaction of the granular bed to approximately 90% TMD essentially eliminated the possibility of significant gas flow relative to the solid matrix in scales larger than a grain size.

The current ignition-started experiments remove the constraint of precompaction by piston motion. However, the phenomenology observed is the same as for the piston-started experiments. Undoubtedly, the very early stages of burning in ignited experiments are convective. The pressures, Reynolds numbers, and gas-evolution rates are small enough that gas can flow through the initial bed. However, the gas permeation into the nascent bed is limited. For those materials that can transit to detonation, the burning rate is high enough

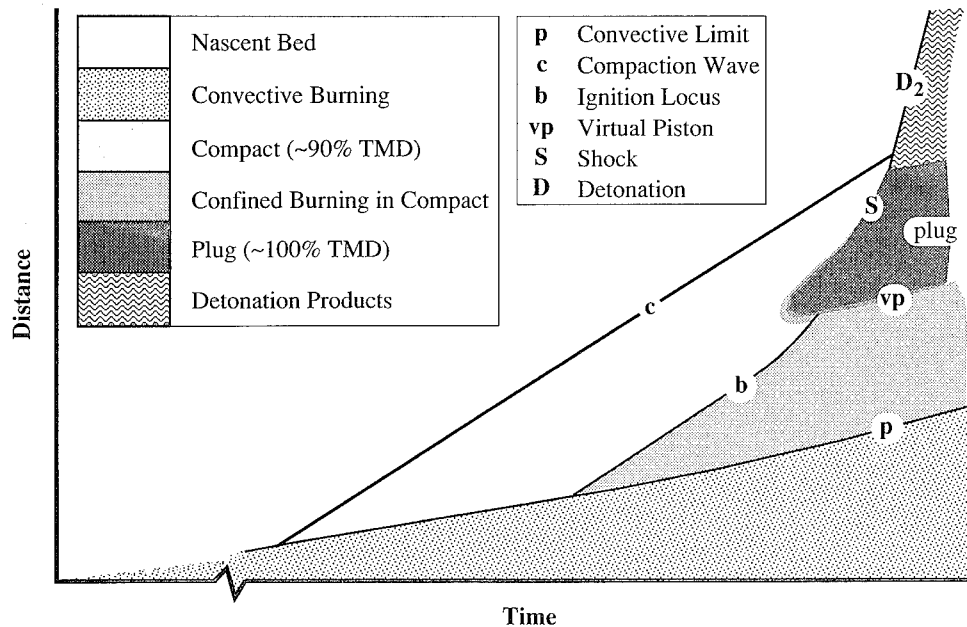


FIGURE 2. SCHEMA OF THE DDT PROCESS IN GRANULAR HMX

that product gas is produced faster than it can flow away. The subsequent build-up of pressure and the resulting compaction of the bed are well described by Campbell.<sup>3</sup> By placing diaphragms at various distances in the HMX bed, Campbell determined that convection was significant for only the first 10 to 15 mm. Additionally, Asay and others<sup>5</sup> have ignited granular HMX below a confined bed of SiC particles of similar size distribution and porosity as the nascent HMX bed. Measurements of the pressure at stations within the effectively-rigid bed indicate bulk gas penetration at a velocity on the order of only 10 m/s for driving pressures of approximately 0.3 GPa. Therefore, convection in beds of these porosities is too slow to have anything but a slight influence on the higher-velocity trajectories and long ignition-time phenomena observed in both piston- and ignition-driven experiments.

The wall profile of region (i) in Fig. 1 indicates a build-up of pressure over an approximately 10-mm distance. The small expansion of the wall indicates this region was exposed to the lowest pressure in the bed. We believe the important effects of convection in these DDT experiments are confined to this relatively short region. Once the gas generation rate is sufficient to overcome convective losses, the flow is choked and pressure builds, compacting the bed above the convection limit.

The pin and wall-expansion data in regions (ii), (iii), and (iv) are completely consistent with the data and phenomenology presented for piston-driven experiments.<sup>1</sup> Therefore, the boundary between the low-pressure convective region and the compact is equivalent to a combustion-driven mechanical piston.

### Descriptive Model

In Fig. 2, we present a schema of the DDT process for ignited HMX. The boundary between the initial convective region and the compact is labeled **p**. This is the same nomenclature used in Reference 1 to indicate the trajectory of the mechanical piston because the function is the same. The time axis is broken to indicate that the interval from the first ignition to compaction-wave formation is long relative to the events occurring after compact formation. There are three differences between this diagram and that given in Reference 1: The initial convective region is included, the early-time plug is rounded in shape and somewhat diffuse, and no coalescing stress waves are drawn. Only the last of the three changes is significant. Consideration of the dispersive and dissipative nature of porous beds convinces us that acoustic propagation and subsequent coalescence of characteristics are not an accurate description. Instead, we believe the sensitivity to porosity of the local pressurization by reaction-product gases, in conjunction with the compaction behavior of the bed (for the time scales of interest), leads to plug formation. We will explore this assertion in some detail, and propose a model for the ignition of the compact.

### Pressure Calculation

We can estimate the interstitial pressure  $P$  in the porous compact due to reaction products by assuming incompressible solid and a constant gas temperature with the ideal gas law. Initial conditions are:  $\phi_0$  = volume fraction of voids, and  $1 - \phi_0$  = volume fraction of solid.

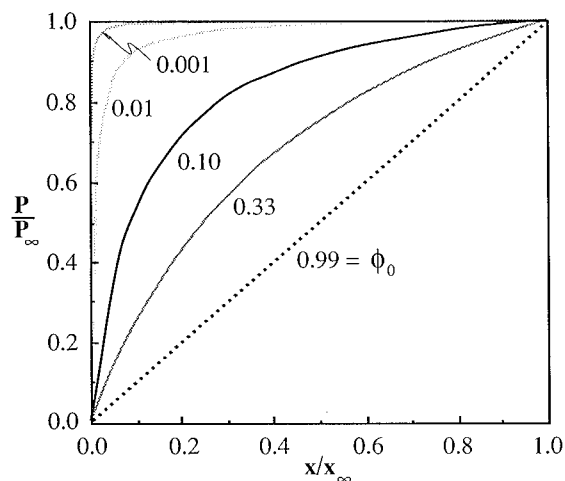


FIGURE 3. THE EFFECT OF INITIAL POROSITY ON THE INTERSTITIAL PRESSURE AS A FUNCTION OF REACTION PROGRESS

As the solid reacts to form gas (i.e., the reaction products), material and volume conservation give the following where  $x$  is the volume fraction of solid reacted to gas:  $x + \phi_0$  = gas volume fraction, and  $1 - x - \phi_0$  = volume fraction of solid remaining. The number of moles of gas  $n$  and the volume for that gas  $v$  are therefore

$$n = x \frac{\rho_{\text{solid}}}{M_{\text{gas}}} \quad \text{and} \quad v = x + \phi_0 \quad (1)$$

where  $\rho_{\text{solid}}$  = solid density and  $M_{\text{gas}}$  = average molecular weight of the product gas. Therefore, the pressure of the gas  $P$  can be approximated by the ideal gas law

$$P = \frac{n}{v} RT = \frac{x}{x + \phi_0} \frac{\rho_{\text{solid}}}{M_{\text{gas}}} RT = \beta \frac{x}{x + \phi_0} \quad (2)$$

where  $R$  is the gas constant,  $T$  the absolute temperature, and  $\beta$  is the accumulation of the constants.

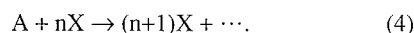
As the burning of the solid goes to completion ( $t \rightarrow \infty$ ), the final amount of solid reacted to gas  $x_\infty$  and the final pressure  $P_\infty$  are given by

$$x_\infty = 1 - \phi_0 \quad \text{and} \quad P_\infty = \beta(1 - \phi_0). \quad (3)$$

In Fig. 3 we plot the pressures calculated from Eq. (2) normalized to the completion values in Eq. (3) for several values of the initial porosity  $\phi_0$ . For small porosities ( $\phi_0 \leq 0.1$ ), a large fraction of the final pressure can be developed for a small fraction reacted ( $x/x_\infty \leq 0.05$ ). We will use this fact later in our description of plug formation.

### Autocatalytic Kinetic Model

The decomposition of HMX is autocatalytic.<sup>6</sup> In all autocatalytic decompositions, there must be a source for the initial product concentration  $x_0$ . We assert  $x_0$  is proportional to the strength of the compaction wave (i.e., the work performed on the bed). The compaction wave provides the energy for the initial decomposition by shear, compression, and friction. The experimental observations reported in Reference 1 show faster pistons give shorter induction periods, therefore the time between compaction and ignition,  $\tau$ , depends inversely on  $x_0$ . This dependence can be estimated for autocatalytic kinetics. The general decomposition of reactant  $A$  into product  $X$  is



Taking the rate of reaction proportional to the concentration of both the reactant and the product, for  $n = 1$ , the simple autocatalytic rate law and its integral are

$$\frac{dx}{dt} = kax = k(a_0 - x)(x + x_0) \quad \text{and} \quad kt = \frac{1}{(a_0 + x_0)} \ln \frac{a_0(x_0 + x)}{x_0(a_0 - x)}, \quad (5)$$

where  $k$  is the rate constant,  $a$  and  $x$  are concentrations at time  $t$ ,  $a_0$  and  $x_0$  are initial concentrations, and  $x$  is the progress variable. The total product concentration is  $x = x_0 + x(t)$ . Initially ( $t = 0$ ),  $x = 0$  and  $a = a_0$ , while at the final equilibrium ( $t \rightarrow \infty$ ),  $x \rightarrow a_0$  and  $a \rightarrow 0$ .

Some of the properties of this rate law, particularly the induction period, are detailed in Reference 2. The induction time is defined by the abscissa-intersection of the tangent to the rate curve as shown in Fig. 4. (As an example, we choose  $x_0 = 0.0001$  for this and the following graphs.) The induction period  $\tau$  depends primarily on the rate constant and the initial product concentration  $x_0$ , because for cases of interest, the initial product concentration is small,  $x_0 \ll a_0$ , and  $a_0 \approx 1$ .

$$k\tau = \frac{1}{(a_0 + x_0)} \left[ \ln \left( \frac{a_0(2 - \sqrt{3})}{x_0} \right) - \sqrt{3} \right] \quad (6)$$

The rate  $dx/dt$  at time  $\tau$  is approximately 0.18 of the maximum rate. The value for  $x(\tau)$  is 0.045. For this kinetics model, the rate-curve shape is nearly independent of initial product concentration after the induction time. That is, once the induction time is reached and the "fast burning" starts, reaction-rate time histories are similar regardless of the initial product concentration. Therefore, the ignition line **b** in Fig. 2 is not a propagating wave with a distinct boundary, but a locus of constant reaction rate or product concentration. Experimental measurements of the ignition locus have often incorrectly been associated with convective burning.

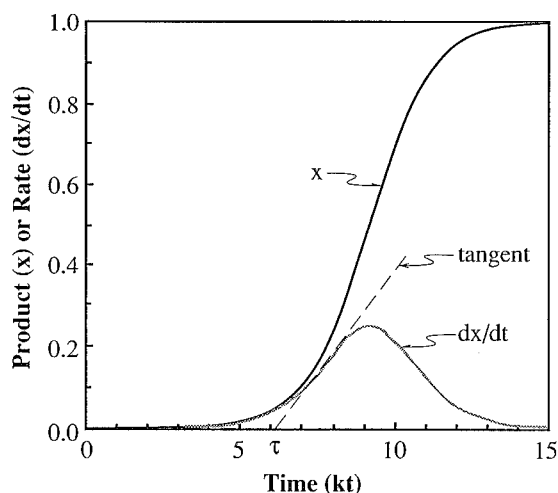


FIGURE 4. PRODUCT CONCENTRATION AND RATE FOR THE SIMPLE AUTOCATALYTIC REACTION. THE INDUCTION PERIOD IS DEFINED BY THE TANGENT TO THE RATE CURVE.

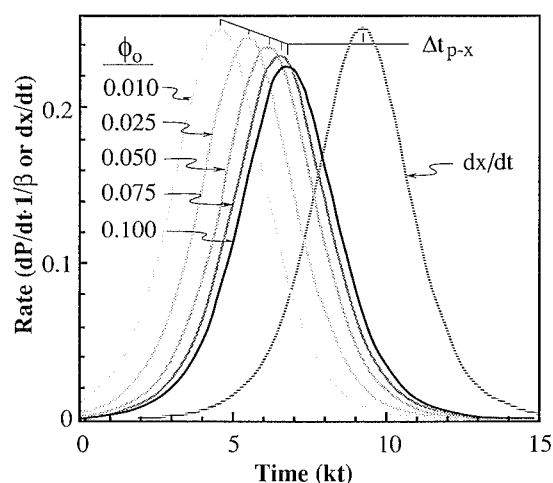


FIGURE 6. PRESSURE RATE AS A FUNCTION OF INITIAL POROSITY. THE PRODUCT RATE  $dx/dt$  IS INDEPENDENT OF POROSITY.

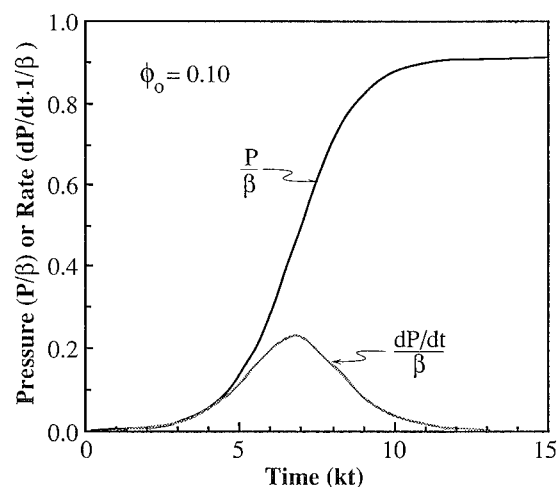


FIGURE 5. THE INTERGRANULAR PRESSURE AND RATE FOR AN INITIAL POROSITY OF 0.10

The pressure history is similar in shape to the product concentration. The interstitial pressure calculated from Eq. (2), and its time derivative (the pressure rate,  $dP/dt$ ) are graphed in Fig. 5 for an initial porosity of 0.10. Comparison with Fig. 4 shows  $P$  and  $dP/dt$  lead  $x$  and  $dx/dt$  by approximately  $2.2kt$  for these conditions. This is a consequence of the fact shown earlier that large pressures result from little reaction if the initial porosity is low.

In Fig. 6 we plot the pressure-rate for several values of the initial porosity for a constant initial product

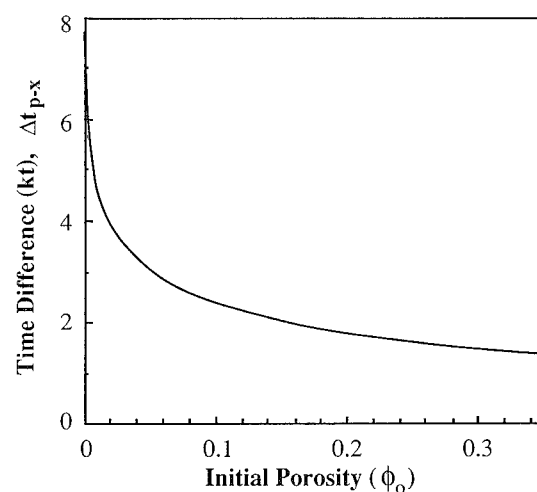


FIGURE 7. TIME DIFFERENCE BETWEEN MAXIMUM PRODUCT RATE AND MAXIMUM PRESSURE RATE

concentration. The amount of time by which the pressure-rate leads the product-concentration rate is a function of  $\phi_0$ . By taking the proper time derivatives and using the above approximations, it is straightforward, though tedious, to show that the time difference  $\Delta t_{p-x}$  between the maximum pressure-rate and the maximum concentration-rate is independent of the initial product concentration. This is plotted in Fig. 7 and given by

$$\Delta t_{p-x} = \ln\{(1 + \phi_0)/\phi_0\}. \quad (7)$$

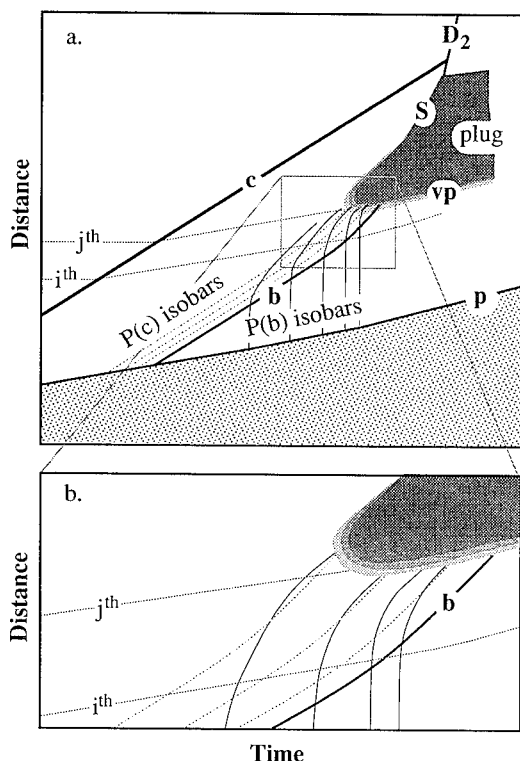


FIGURE 8. PARTICLE PATHS SHOWING THE TIMING OF PRESSURE INTERACTIONS FOR PLUG FORMATION

#### Plug Formation

The interaction of the burn region and the compact can be understood with the help of Figs. 8 and 9. Low levels of product in the compact (derived from the decomposition started by the compaction wave) provide intergranular pressure to resist further compaction. This is represented by the isobars  $P(c)$  plotted as dotted lines parallel to and earlier than  $b$ . Pressure generated in the burning region (below  $b$ ) propagates into the compact (above  $b$ ) as increased stress in the solid matrix. The isobars  $P(b)$  represent the influence of the burning region on the compact and are schematic. They indicate pressure equilibrium behind the ignition locus and their trajectory in the compact above  $b$ . The final pressure-stress field for a given location is a superposition of  $P(c)$ ,  $P(b)$ , and the compaction stress,  $\sigma_c$ .

As the product concentration continues to slowly rise, the intergranular pressure above  $b$  can temporarily keep pace with the rapidly increasing stress transmitted from the burning region below because the intergranular pressure leads the product concentration (Figs. 6 and 7). The variation of this time difference with compaction state provides a feedback mechanism that tends to prevent further collapse of the bed. Eventually, for a given particle in the bed, one of two events will occur: The compaction-initiated reaction will transit to fast burning (i.e., the particle will pass through the  $b$  locus).

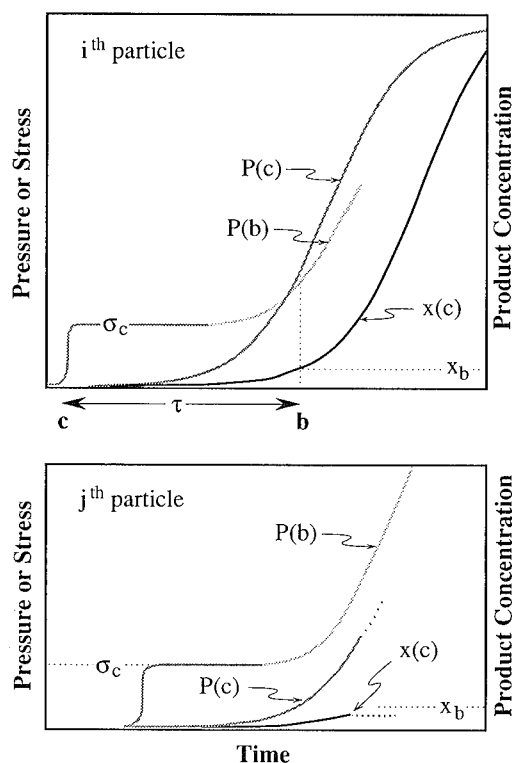


FIGURE 9. PRESSURE, STRESS, AND PRODUCT CONCENTRATION PROFILES FOR THE TWO PARTICLES

Or, the rapidly increasing pressure from below  $b$  will overcome the strength of the solid matrix and the product pressure, and the bed will further collapse to a compaction state consistent with the high pressure in the burn region (i.e., the plug will form).

Which eventuality is determined by the length of time the particle has had to react after compaction and before being affected by the pressure from the burn region (transmitted as stress through the compact). Lower particles (e.g., the  $i^{\text{th}}$  in Figs. 8 and 9) have a sufficient portion of their induction time unaffected to produce enough product, and therefore pressure, to prevent further compaction until rapid burning starts. The higher particles (e.g., the  $j^{\text{th}}$ ) are intercepted sooner after compaction by stresses generated from the burning region. Therefore, there is insufficient intergranular pressure to resist further compaction, and collapse occurs.

Schematically, Fig. 9 shows the intergranular stress and pressure histories of two such particles. For the  $i^{\text{th}}$  particle, the stress generated from the compaction wave  $\sigma_c$  is supported by the solid matrix. The product gas pressure  $P(c)$  increases soon enough to resist compaction by the stress transmitted from the burn region  $P(b)$ . The ignition locus  $b$  is reached and the  $i^{\text{th}}$  particle becomes part of the burn region.

For the  $j^{\text{th}}$  particle,  $P(b)$  begins to affect the compact before there is sufficient product pressure to stiffen the bed. The rapid increase in stress overcomes the combination of the compact's strength and low intergranular pressure, and compacts the bed further. This additional compaction quenches the decomposition,<sup>7</sup> thus preventing further product evolution. At compactions near TMD, the gas-phase and gas-producing reactions stop because there is essentially no free volume and the increase in thermal conduction rapidly cools the residual gas. Even deconsolidative burning is slowed by more than an order of magnitude.<sup>8</sup> Therefore, the ignition locus effectively terminates when it intersects the plug. Further reaction of the plug region is governed by the condensed-phase kinetics appropriate to shock-induced reactions.

The experimental evidence clearly indicates the acceleration of the ignition locus, as we have discussed elsewhere.<sup>1,2</sup> We believe that the accelerating ignition locus combines synergistically with the pressurization-density effects to generate the plug. High velocities for the ignition locus below the virtual piston ( $\sim 6.5$  km/s in Fig. 1) can be thought of as providing a near constant-volume ignition of the compact in the vicinity the plug. The pressure will therefore grow rapidly, quickly accelerating the virtual piston and thus forming and accelerating the shock.

### Velocity Amplification

The compaction, ignition, and plug-formation processes are the mechanisms that generate shock-level velocities in this system. Convective burning kinetics and compaction properties of the bed will determine the compaction-wave velocity  $u_c$  relative to the convective limit interface velocity  $u_p$ .<sup>1</sup> Mass balance across the compaction wave gives

$$u_c = \rho_c u_p / (\rho_c - \rho_o) \quad (8)$$

where  $\rho_c$  is the compact density and  $\rho_o$  the nascent-bed density. Because the ignition locus  $b$  follows from the compaction wave  $c$ , the reactive velocity in the system is amplified from tens of m/s (characteristic of convection) to hundreds of m/s (characteristic of the compaction wave).

Amplification of velocities from the order of  $u_c$  to shock speeds can also be estimated using mass balance across  $S$  (Fig. 2). Using eq. (8), we rewrite the equation given in Reference 1 as

$$U_s = \rho_s u_{vp} / (\rho_s - \rho_c) - u_c \quad (9)$$

where  $U_s$  is the shock velocity,  $\rho_s$  is the plug density ( $\sim 100\%$  TMD), and  $u_{vp}$  is the virtual-piston velocity. The shock velocity relative to the virtual-piston velocity is largely determined by the denominator (nominally  $\sim 0.1$ ). This is the amplification necessary to reach shock speeds of km/s, enough for a shock-to-detonation transition (SDT). There is no direct measurement of  $u_{vp}$ ,

but the current experimental results for  $U_s$  and  $u_c$  indicate that  $u_{vp}$  is on the order of  $u_c$ .

### CONCLUSIONS

We have shown, using detailed experimental observations, simple mechanics and kinetics, that the transition from deflagration to detonation in granular HMX is a straightforward consequence of material and porous-bed properties. Convective flow and hot-gas ignition contribute only to the early-time, low-velocity phenomena. The formation of a compaction wave in undisturbed material begins the series of non-convective events that lead to a final shock-to-detonation.

This model demonstrates the necessity of a rapid pressurization in the initial bed. The pressurization rate ( $dP/dt$ ) must be large enough such that product gasses cannot infinitely diffuse into the granular bed. With strong enough confinement, the flow is choked because of limited permeability, and the bed above this burning is compacted. The launching of a compaction wave above the convectively-ignited and burning region is the first velocity amplification in the process. The second amplification involves the formation and acceleration of the plug, and is sufficient to reach shock velocities.

We believe this scenario and analysis generally describe the DDT in granular and porous materials. The lack of convective phenomena after compaction leads us to speculate that computational modeling of this and similar systems can be accomplished by invoking the complexity of multi-velocity, multi-phase flow only in the precompaction regimes. After compaction, a single-velocity description is appropriate. Therefore, two- and three-dimensional models of the deflagration-to-detonation transition may be computationally within reach in the near future.

### REFERENCES

1. McAfee, J. M., Asay, B. W., Campbell, A. W., and Ramsay, J. B., "Deflagration to Detonation in Granular HMX," Ninth Symposium (International) on Detonation, Portland, OR, 1989, pp. 265-278.
2. McAfee, J. M., Asay, B. W., and Ferm, E. N., "Deflagration to Detonation in Granular HMX: Structure and Kinetics in the Predetonation Region," 1991 JANNAF Propulsion Systems Hazards Subcommittee Meeting, Albuquerque, NM, 1991.
3. Campbell, A. W., "Deflagration-to-Detonation Transition in Granular HMX," 1980 JANNAF Propulsion Systems Hazards Subcommittee Meeting, Monterey, CA, 1980, pp. 105-130.
4. Gibbs, T. R. and Popolato, A., LASL Explosive Property Data, University of California Press, Berkeley, CA, 1980, pp. 42-51.
5. Asay, B. W. and Laabs, G. W., Los Alamos National Laboratory document, M-8-QR-92-4, 1992. Or Chitanvis, C. Z., Bdzil, J. B., and Asay, B. W., "The

Permeation of High-Pressure Gas Through a Porous Bed," to be published.

6. Rogers, R. N. and Janney, J. L., "Thermochemical Evaluation of Zero-Order Processes Involving Explosives," *Proceedings of the Seventh International Conference on Thermal Analysis*, Vol. II, Chichester, GB, 1981, p. 1434.
7. For the time scales of interest, quenching of the decomposition in this region is shown experimentally in Reference 1 by the observation of the high-density plug after the transition to detonation.
8. Fifer, R. A. and Cole, J. E., "Transition from Laminar Burning for Porous Crystalline Explosives," *Seventh Symposium (International) on Detonation*, Annapolis, MD, 1981, pp. 164-174.



# A PHYSICAL MODEL OF SHOCK TO DETONATION TRANSITION IN HETEROGENEOUS EXPLOSIVES

R. Belmas, J. P. Plotard, C. Bianchi

CEA-Centre d'Etudes de Vaujours-Moronvilliers  
BP n°7 - 77181 Courtry - France

We present the basic equations and the capabilities of the AMORC kinetics. Devoted to the study of the shock to detonation transition in heterogeneous explosives, this kinetics is composed of two physical models which describe the hot spots formation and ignition, and the explosive grains burning. Taking into account the microstructure of the explosive compositions, the AMORC kinetics is an efficient tool for safety studies and explosive compositions formulation.

## INTRODUCTION

The study of the behavior of explosive devices subjected to mechanical stimuli requires numerical modelisations of the shock to detonation transition. Several models, able to compute the shock initiation of heterogeneous explosives, were developed in different laboratories. The most famous and used are the Ignition and Growth Model,<sup>1,2</sup> the Forest-Fire Rate and the Explicit Hot Spot Model.<sup>3,4</sup> These models are efficient tools but their empirical formulations and, in some cases, the important number of parameters needed, limit their applications.

In another connection, all the laboratories working about the formulation of explosive compositions are looking for insensitive high explosives. A kinetics of decomposition of the explosive, which takes into account the microstructure of the explosive composition, would help the researchers in their choices.

The AMORC model, presented in this paper, is based on an explicit description of the microstructure of the explosive and needs very few fitting parameters (our knowledge is not yet sufficient to have none). It results of the association of two models, developed and calibrated separately: one devoted to the initiation of the first reactions by the hot spots process, the other to the explosive grain burning.

## HOT SPOT FORMATION AND IGNITION

An experimental and theoretical study performed on pressed TATB compositions<sup>5</sup> showed that the hot spots are created by the local viscoplastic strains in the vicinity of collapsing voids. As a result of this study, a hot spots model was developed,<sup>6</sup> based on the collapse of spherical microvoids included in the energetic material.

In this model, we perform the numerical integration of the motion and thermal equations, taking into account the viscoplastic behavior of the explosive and the conductive heat transfer. This model is efficient to analyse the hot spot formation and ignition as a function of several parameters, like incident shock pressure, cavities sizes, mechanical and thermochemical characteristics of the explosive. It is very useful in safety studies and analysis of the influence of microstructural properties on the initiation of explosives. However, it is far too complex to be incorporated in a kinetics implemented in a hydrodynamic code.

We wrote a simplified hot spots model, easier to use in a code and which gives the same results about the evolution of the microvoids (radius, temperature) that those obtained previously with the reference numerical model.

## Motion Equation

The evolution of the radius of the pore is governed by the equation :

$$-\rho \ddot{a} = P - P_Y + 4\mu \frac{\dot{a}}{a} + 1.5\rho a \dot{a}^2$$

with  $\rho$  : explosive cristal density  
 $a$  : pore radius  
 $P$  : pressure  
 $P_Y$  :  $-2/3 Y \ln \phi$   
 $\mu$  : viscosity  
 $Y$  : yield stress  
 $\phi$  : porosity

The asymptotic solution of this equation is :

$$a = a_0 \exp \left[ \int_0^t -\frac{P - P_Y}{4\mu} dt \right]$$

We use this formula for  $a(t)$  in the simplified model because it leads to a very good agreement with the results of the reference model (figure 1).

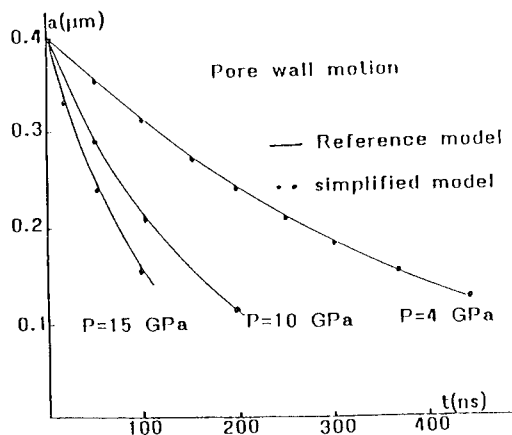


FIGURE 1. COMPRESSION OF SIMPLIFIED MODEL AND REFERENCE MODEL

## Viscoplastic Heating and Thermal Conduction

The pore wall temperature increase, due to the viscoplastic strains of the explosive, is given by :

$$d\theta_{vp} = \left[ \frac{12\mu}{\rho C_p} \frac{\dot{a}}{a^2} - \frac{2Y}{\rho C_p} \frac{\dot{a}}{a} \right] dt$$

where  $C_p$  is the heat capacity, and  $a$ , the pore radius, is given by the motion asymptotic solution.

The cooling of the material, resulting of the thermal conduction, is calculated with a simplified analytical model based on an approximated heat balance in a spherical geometry (figure 2).

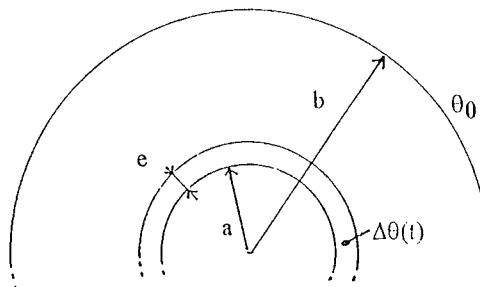


FIGURE 2. DEFINITION OF A HOT SPOT TYPICAL GEOMETRY

We calculate the temperature (assumed uniform) in a thin shell of explosive surrounding the void. During  $dt$ , this temperature increases of  $d\theta_{vp}$  as a result of viscoplastic heating, and the approximated heat balance is given by :

$$\frac{4\pi\lambda ab}{b-a} (\theta(t) + d\theta_{vp} - \theta_0) dt = 4\pi\rho C_p a^2 f a_0 d\theta_c$$

where  $d\theta_c$  is the cooling due to thermal conduction. Then, the pore wall temperature is given by :

$$\theta(t+dt) = \theta(t) + d\theta_{vp} - d\theta_c + d\theta_d$$

$d\theta_d$  is the increase in temperature produced by the explosive decomposition, and is calculated with a simple zero order Arrhenius kinetics.

The thickness of the shell,  $e$ , is equal to  $f a_0$ , where  $f$  is a function of the non-dimensional variable

$\chi = \frac{\rho C_p a^2 \dot{a}}{\lambda a_0}$ ,  $\lambda$  is the heat conductivity of the explosive. This function is determined in order to fit the results delivered by the reference hot spot model, as shown in figure 3.

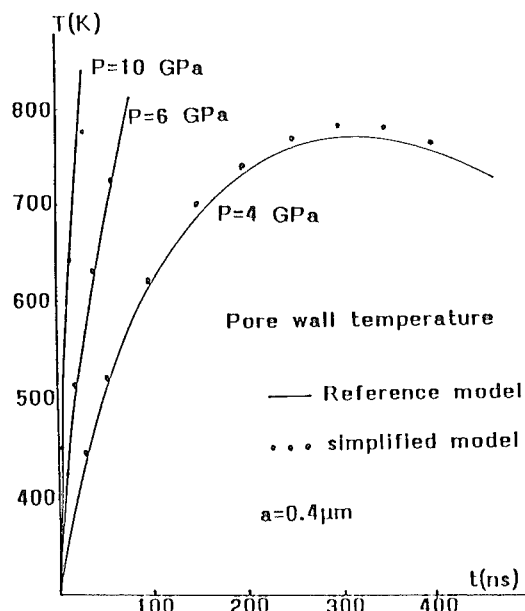


FIGURE 3. PORE WALL TEMPERATURE CALCULATED WITH THE SIMPLIFIED MODEL AND THE REFERENCE ONE

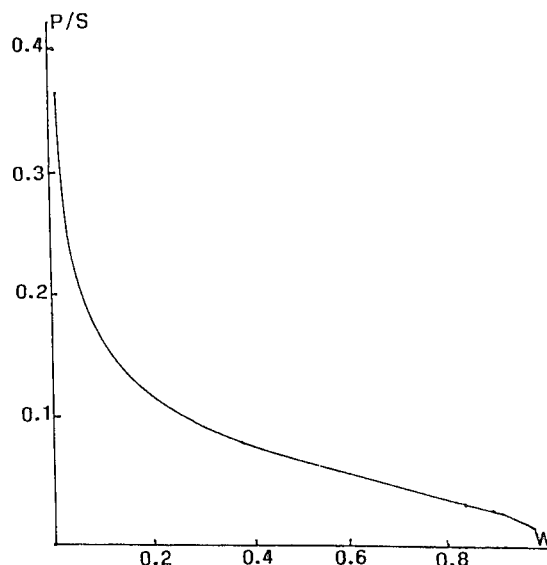


FIGURE 4. EVOLUTION OF GRAIN MORPHOLOGY DURING THE DECOMPOSITION

### EXPLOSIVE GRAIN BURNING

The influence of grain size on the microstructural burning is well known. Fine grains generally burn faster than coarse ones. In addition, the importance of grain morphology on the decomposition phenomena was demonstrated.<sup>7</sup> The assumed mechanism based on these works is composed of three phases: hot-spots ignition on the surface, grain surface growth, and grain burning.

The association of a powder morphology analysis with a grain mathematical erosion method leads to an evolution of the yield  $P/S$  (perimeter/surface of the grains) characteristic of the real powder. As an example, for the TATB powder used in our TATB compositions, the calculated evolution of  $P/S$  as a function of the unburned mass fraction  $W$  is plotted in figure 4.

### THE AMORC MODEL

The AMORC model is the association of the hot spots model with the grain burning law. The decomposition term of the kinetics is given by:

$$-\frac{1}{W} \frac{dW}{dt} = F(N) \cdot \frac{P}{S} \cdot V_c(P)$$

where -  $f(N)$  is a function of the number of hot spots,  $N$ , calculated by the hot spots model, in which a pore size distribution is introduced.

-  $V_c(P)$  is the pressure dependent burning velocity, measured in strand burner tests.

### VALIDATION OF AMORC KINETICS

The AMORC kinetics is implemented in a one dimensional hydrodynamic code. The reference hot spots model is able to calculate the threshold initiation shock pressure and to predict the desensitization of the explosive by a precursor shock.<sup>6</sup> The kinetics must reproduce the pressure versus time curves measured at several depths in shocked explosive samples.

In figure 5 are plotted the profiles of pressure as a function of time, measured with manganin gauges in a TATB composition (T2) for an initial sustained shock of 11 GPa, and calculated with the AMORC kinetics. Figure 6 presents the comparison between measurements

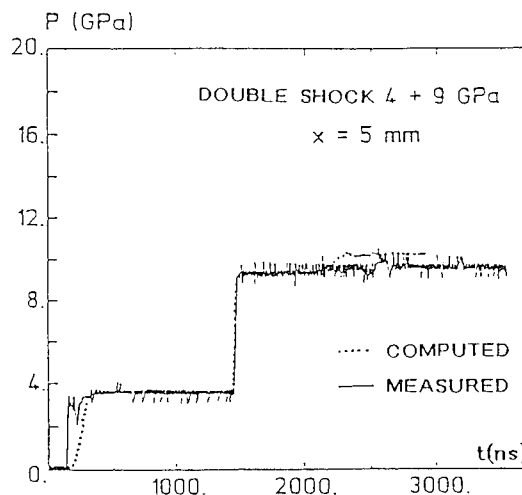
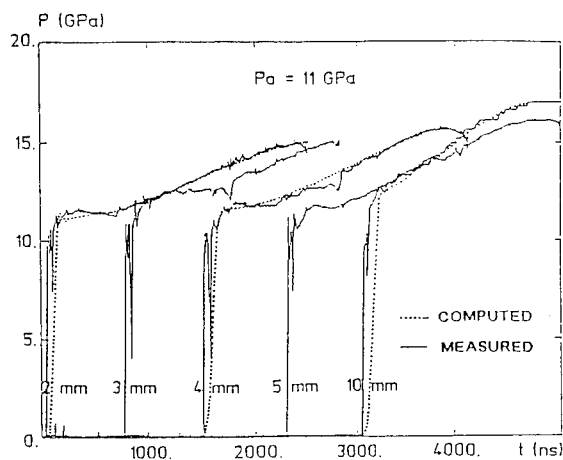
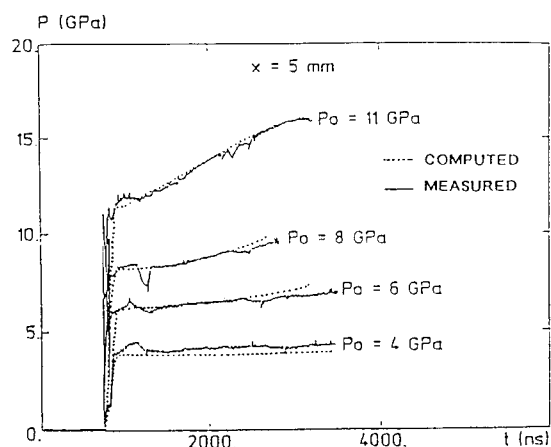


**FIGURE 7. EXAMPLE OF DESENSITIZATION OF TATB COMPOSITION BY PRESCHOCKING**



**FIGURES 5 AND 6. COMPARISON BETWEEN MEASURED AND COMPUTED PRESSURE EVOLUTION IN SHOCKED T2 EXPLOSIVE THE CURVES ARE ARBITRARILY POSITIONED ON THE TIME AXIS**

and calculations at a 5 mm depth in the same explosive composition for different initial shock pressures. A good agreement is obtained in all cases. The run distance to detonation as a function of the input pressure was also calculated.

As shown in figure 7, computations with AMORC reproduce the desensitization of the explosive by a precursor shock.

## NEW APPLICATIONS

In the two parts of the kinetics, the microstructure of the explosive is explicitly introduced, and the temperature of the medium is taken into account to determine the ignition of the hot spots. The physical description of the initiation process allows preliminary numerical studies of new explosive compositions, in which the porosity, the grain size or grain morphology are modified. The explicit calculation of the temperature in the ignition process has an important application in safety studies. Two examples are shown now as an illustration of the AMORC capabilities.

### Influence of the Initial Temperature

In figure 8 are reported the pressure profiles calculated for T2 composition of 300 K or preheated at 500 K and subjected to the same shock. These results exhibit a small but significant sensitization of the explosive when it is heated before impacted. This result agrees with experimental data.<sup>8</sup>

### Influence of the Microstructure

Let C1, C2 and C3 be three TATB compositions composed of spherical grains of three different diameters. These three compositions are defined in table 1. The smaller the grain size, the smaller the pores. The pressure calculated after a 5 mm propagation of the shock in the explosive samples are reported in figure 9.

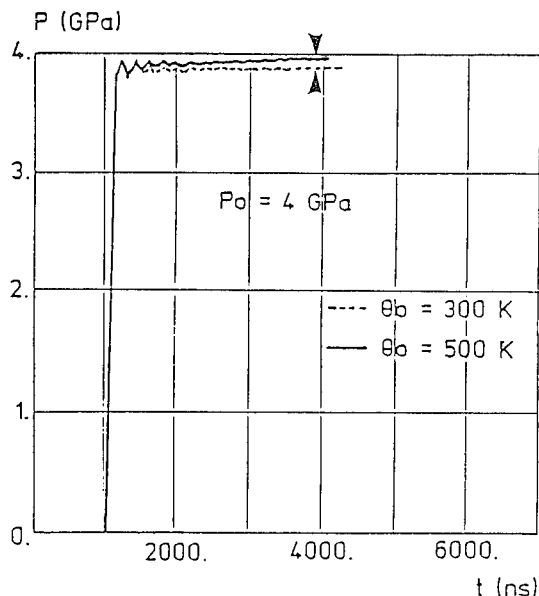


FIGURE 8. EFFECT OF THE TEMPERATURE ON THE SENSITIVITY OF EXPLOSIVE COMPOSITIONS

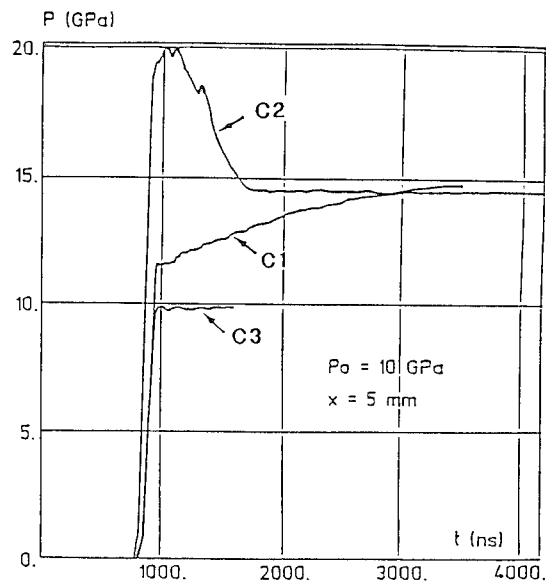


FIGURE 9. EFFECT OF THE MICROSTRUCTURE ON THE SENSITIVITY OF EXPLOSIVE COMPOSITIONS

TABLE 1. MICROSTRUCTURE OF THE EXPLOSIVE COMPOSITIONS

	Grains diameter ( $\mu\text{m}$ )	Pores radius ( $\mu\text{m}$ )
C1	50	0.4
C2	10	0.2
C3	1	0.1

For C1 composition, the large pores lead to hot spots ignition and the coarse grains burn slowly. For C2, ignition is also obtained and the smaller grain size results in a faster pressure increase. The use of smaller grains increases the sensitivity of the explosive composition.

For C3, the voids are too small to produce an ignition of the explosive. In this case a smaller grain size results in a lower sensitivity of the explosive composition. This phenomenon, called crossing of sensitivity, was previously experimentally observed.<sup>9,10</sup>

## CONCLUSION

AMORC is a physical model of shock to detonation transition based on the microstructural events involved in shock initiation of heterogeneous explosives. This kinetics takes into account the two basic phenomena: hot spots formation and ignition, and grain burning. Implemented in a one dimensional hydrodynamic code and validated, it is nowadays available for a great number of applications in the area of physics of explosives, safety studies and explosive compositions formulation.

## REFERENCES

1. Lee, E. L. and Tarver, C. M., "Phenomenological Model of Shock Initiation in Heterogeneous Explosives," *Physics of Fluids*, Vol. 4, pp. 511-521 (1980).
2. Tarver, C. M.; Hallquist, J. O. and Erickson, L. M., "Modeling Short Pulse Duration Shock Initiation of Solid Explosives," *8th Symposium (International) on Detonation*, Albuquerque, New Mexico (1985), NSW MP 86-194, 1985.
3. Johnson, J. N.; Tang, P. K. and Forest, C. A., "Shock Wave Initiation of Heterogeneous Reactive Solids," *J. of Applied Physics*, Vol. 57, pp. 4323-4334 (1985).
4. Tang, P. K., Johnson, J. N. and Forest, C. A., "Modeling Heterogeneous High Explosive Burn With an Explicit Hot Spot Process," *8th Symposium (International) on Detonation*, Albuquerque, New Mexico (1985), NSW MP 86-194, 1985.
5. Castille, C.; Germain, E. and Belmas, E., "Origine Physique Des Points Chauds Dans Les Compositions Explosives Pressées Au TATB," *Propellants, Explosive and Pyrotechnics* 17, pp. 249-253 (1992).
6. Plotard, J. P.; Belmas, R. and Nicollet, M., "Effect of a Preshock on the Initiation of HMX, TATB and HMX/TATB Compositions," paper presented at this symposium.
7. Cherin, H. and Gohar, P., "The Influence of Grains Morphology on the Behavior of explosives," *9th Symposium (International) on Detonation*, Portland, Oregon (1990).
8. Urtiew, P. A.; Erickson, L. M.; Aldis, D. F. and Tarver, C. M., "Shock Initiation of LX-17 as a Function of its Initial Temperature," *9th Symposium (International) on Detonation*, Portland, Oregon (1990).
9. Moulard, H., "Particular Aspect of the Explosive Particule Size Effect on Shock Sensitivity of Cast PBX Formulations," *9th Symposium (International) on Detonation*, Portland, Oregon (1990).
10. Honodel, C. A. & al, "Shock Initiation of TATB Formulations," *7th Symposium (International) on Detonation*, Annapolis, Maryland (1981), NSW MP 82-334 (1981).

## DISCUSSION

J. F. GUERY

Research Center CRB, Vert-le-Petit, France

With the assumptions you made on hot spot location and grain burning, this model seems well suited for compress explosives. Have you tried to apply it to cast explosives which have better mechanical properties, and what assumptions should be made?

### REPLY BY ROBERT BELMAS:

It must first be noticed that the mechanical properties taken into account in the hot spot model are those of the explosive crystals around the intergranular or intergranular voids and not those of the explosive composition.

In the case of cast explosives with a very low porosity but a high percentage of binder, the model can apply if we approach this problem considering a cavity in the explosive (size approximately equal to the space between two grains) filled with binder. Thus, the collapse must be simulated taking into account the binder's mechanical properties.

An incompressible binder will tend to limit the collapse and make the ignition more difficult than a compressible one. Experimental observations of the influence of the binder type on SDT are in agreement with this.

## DISCUSSION

J. PEI CHI CHOU

Dyna East Corp., Philadelphia, Pennsylvania

(1) What is the effect of pore diameter on your pore collapse model?

(2) How did you decide what value of viscosity to use?

### REPLY BY ROBERT BELMAS:

(1) The time to ignition is very sensitive to the pore diameter. The smaller this diameter, the more difficult the ignition. This is mainly due to the fact that small porosities have a weak thermal inertia and are easily cooled by heat conduction. As a result, their temperature rises slowly and, in some cases, finally decreases despite the heat generation due to viscoplastic work.

(2) The value of the viscosity is determined as follows:

(a) Evaluation of the largest pore sizes (using microscopic observations, for example.

(b) Experimental determination of the shock pressure threshold under which no decomposition phenomenon occurs (press measurements with manganin

gauges are well suited for this determination).

(c) This threshold is assumed to result from a nonignition of the hot spots issued from the largest porosities (the easier to ignite). Then we determine with the hot spot model the value of viscosity leading to a nonignition of the largest voids for the so-considered pressure threshold. This viscosity is the only fitting parameter of the model.

## THE ANALYSIS OF MODIFIED GAP TEST DATA FOR SEVERAL INSENSITIVE EXPLOSIVES

E. R. Lemar, T. P. Liddiard, J. W. Forbes,  
G. T. Sutherland, and W. H. Wilson  
Naval Surface Warfare Center  
Dahlgren Division, White Oak Detachment  
Silver Spring, Maryland 20903-5640

The Modified Gap Test (MGT) is used to determine the shock sensitivities of several plastic bonded (PBX) explosives, including some with large failure diameters. The explosives in this study are PBXN-103, PBXN-110, PBXN-111 (formerly called PBXW-115), PBXW-121, PBXW-122, PBXW-123, IRX-1, IRX-3, SW-21, and LG/UW-4. This study shows that the sustained reaction thresholds of explosives with large failure diameters (up to 150 mm) can be accurately determined. Even though explosives with failure diameters greater than 51 mm cannot detonate in the MGT, a relative ranking of the initiation thresholds of these explosives can be obtained from the shape of the response curves. It is found that a correlation exists between break points on the surface velocity versus input stress curves and the failure diameter for explosives with very large failure diameters.

### INTRODUCTION

The Modified Gap Test (MGT) is used to determine first reaction,  $P_e^R$ , and sustained ignition,  $P_e^I$ , stress thresholds for explosives. The first reaction threshold is the minimum stress in the acceptor charge,  $P_e$ , that produces a detectable reaction. Detectable reaction in the MGT is defined as reaction in the acceptor sufficient to raise the rear free-surface velocity to a value just above that calculated for a non-reacting explosive. It is assumed that the onset of first reaction is not a function of sample size and confinement but is affected by preparation techniques and particle size. The sustained ignition threshold is the minimum stress in the acceptor that will lead to detonation when the acceptor diameter is larger than the failure diameter and the acceptor thickness exceeds the run-to-detonation length for the input stress-time shock impulse. The sustained ignition threshold is dependent on donor geometry. It is known that larger donor explosive systems result in longer pulse durations. Several of the explosives reported here have large failure diameters and cannot detonate in the MGT. However, the measured first reaction and sustained ignition thresholds are believed to be valid.

In using free-surface velocity as an indication of chemical reaction, it is necessary to keep in mind that a hydrodynamic phenomenon is being measured. Chemical reaction does not specifically mean combustion or ignition. The original solid material must be heated until it forms gases which can, in turn, burn. This heating and decomposition (pyrolysis) can be considered an ignition phenomenon leading to combustion and initiation.

A technical report<sup>1</sup> and a paper<sup>2</sup> summarize all previous MGT test results. This paper presents MGT data on several additional cold cast explosives. The explosives studied, their densities, and main ingredients are given in Table 1. The details of the present work can be found in Reference 3.

### EXPERIMENTAL PROCEDURE

The MGT setup shown in Figure 1 uses the donor-gap system of the NSWC Large Scale Gap Test (LSGT).<sup>4</sup> Two charges are tested simultaneously. The 50.8 mm diameter, 50.8 mm long, donor charges are pentolite pressed to a density of 1.56 g/cm<sup>3</sup>. The deto-



nators are Reynolds RP-80 exploding bridgewire types. The PMMA gaps are machined to the desired length from 50.8 mm diameter cast rods. The acceptor samples are 50.8 mm in diameter and 12.7 mm long. The MGT shock loads the explosive acceptor with a quasi-triangular shaped stress-time pulse which is not uniform across the acceptor. The peak stresses in the MGT can range from 5 to 150 kbar with pulse widths at half-peak stress from 1 to 2  $\mu$ s.<sup>5</sup> These shock waves realistically simulate environments that occur in many explosive devices. A baffle consisting of a steel plate on 19 mm thick plywood impedes the forward flow of gases from the detonated donors. A steel baffle between the two acceptors holds a calibration scale and prevents disturbances in one acceptor from prematurely reaching the other. A wire across the field of view supplies a reference line on the photographic record.

TABLE 1. DENSITIES AND INGREDIENTS OF EXPLOSIVES IN THIS STUDY

Explosive	$\rho_e$ (g/cm <sup>3</sup> )	Ingredients
IRX-1	1.42	Coarse HMX/HTPB
IRX-3	1.58	Coarse HMX/HTPB/Al
SW-21	1.50	Fine HMX/Other
PBXN-110*	1.67	HMX/Other
PBXN-111**	1.79	AP/Al/RDX/HTPB
LG/UW-4	1.98	AP/Al/TMETN/Other
PBXN-103	1.90	AP/Al/TMETN/Other
PBXW-121	1.75	NTO/Al/HTPB/RDX
PBXW-122	1.75	NTO/AP/Al/HTPB/RDX
PBXW-123	1.91	AP/Al/TMETN/Other

\* Formerly PBXW-113 II

\*\* Formerly PBXW-115

HTPB	Hydroxy-terminated polybutadiene
NTO	3-nitro-1,2,4-triazol-5-one
TMETN	Trimethylolethane Trinitrate

The test is backlit by an exploding-wire light source collimated by a Fresnel lens. A disadvantage of this lighting method is that a shadowgraphing system is sensitive to relatively minor disturbances such as the presence of ejecta and very weak air shock waves. Although these disturbances can partially obscure the acceptor outline, good results can usually be obtained. To help reduce the ejecta from the samples, a 2 mil thick layer of Mylar film, held in place by a thin coating of silicone grease, was placed over the entire rear surface of the acceptor in some of the shots.

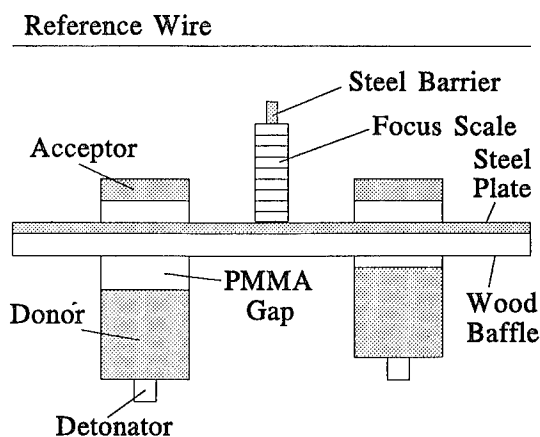


FIGURE 1. THE MODIFIED GAP TEST SETUP

Details concerning the exploding-wire light sources can be found in Appendix A of Reference 1.

The tests were recorded with a Jacobs high speed, focal plane shutter, framing camera. While this camera is ideally suited to the MGT, it is unique in the field of high-speed photography, and it is unique to this facility. The Jacobs camera is discussed in References 1 and 6 and Appendix A in Reference 7.

#### ACCEPTOR RESPONSE

Due to lateral release waves, the shock front entering the acceptor is curved and the highest peak stress is along the axis. As a consequence, the shock wave causes the flat free surface of the acceptor to become dome shaped. When the shock wave moves through the acceptor without chemical reaction, the free surface takes on a velocity (on axis) approximately twice that of the particle velocity immediately behind the shock front. The acceptor surface, acting as a piston, produces an air shock wave which is clearly recorded.

The acceptor does not remain intact in the MGT, even when no reaction is induced. Spalling undoubtedly takes place even at the lowest input stresses used in this study. There is a distinct difference in the free-surface motion between explosives containing elastomer binders and explosives such as TNT. In the explosives with elastomer binders, the acceptor velocity falls off for approximately the first 15  $\mu$ s and then stays fairly constant for the remainder of the observation time. In contrast, TNT-like acceptors spall suddenly and appear to move with constant velocity within a few microseconds after the shock wave reaches the free surface.

With backlighting, the actual acceptor free surface is not directly observed in most cases due to sprays of particles or gases that are ejected from the acceptor surface. In most cases, at low stress inputs, an identifiable but hazy ejecta front can be observed between the air shock and the acceptor surface. At higher input stresses, the ejecta may overtake and penetrate the main air shock front. They are then quickly retarded by air drag in front of the main shock front and merge with the main shock front.

For most of the tests at stresses near or below the threshold for chemical reaction, the ejecta front completely obscures the acceptor dome profile so that only the ejecta front is observed. However, in shot number JK-116B, PBXW-122, the actual surface becomes visible in the latter part of the record. The position versus time plot from this record is shown in Figure 2. It clearly shows that after 90 to 100  $\mu$ s, the acceptor surface lags about 3 mm behind the ejecta front.

In later shots, a 2 mil thick layer of Mylar film was placed over the entire surface of the acceptor and held in place by a thin coating of silicone grease. This provided a sharp image of the acceptor in the case of PBXW-122, even up to a peak stress of 88 kbar in the explosive. Separation does not occur between the Mylar film and the acceptor surface if the film covers the entire flat free surface and no appreciable chemical reaction occurs. (This was determined using PMMA acceptors in an early calibration of the LSGT.<sup>8</sup>) In contrast to the behavior of PBXW-122, PBXW-123 records show some ejecta disturbances for all gap thicknesses used. Thus, what works well for one explosive may not work as well for other explosives. Fortunately, the disturbances in the case of PBXW-123 were

not enough to obscure the acceptor profile and data were obtained that correspond to the actual acceptor surface motion.

## DATA ANALYSIS

The measured free-surface velocity of the acceptor,  $U_a$ ; the calculated peak stress entering the acceptor,  $P_e$ ; and the calculated unreacted free-surface velocity,  $U_a^*$ , are used in analyzing MGT results. The calculated values are obtained by using the LSGT calibration<sup>9</sup> and standard 1-D impedance matching techniques. These calculations are described in Reference 3.

A typical plot of the acceptor surface position,  $x$ , versus time,  $t$ , is shown in Figure 3 (Shot No. JK-120B, PBXW-123,  $P_e = 42.7$  kbar) along with the air shock front curve. Note that beyond the point  $x = 13$  mm,  $t = 16$   $\mu$ s for this test,  $x$  becomes linear with increasing  $t$ . The velocities corresponding to the linear portion of the  $x$ -vs- $t$  curves are the values used throughout this work.

As one would expect, the calculated unreacted velocity is greater than the measured unreacted velocity in the cases covered here. The tensile strength of the acceptor material and subsequent spalling are not accounted for in the calculations, and the calculations assume one-dimensional (1-D), rather than two-dimensional (2-D), shock wave propagation. In addition, the Hugoniot constants for a number of the explosives are not well known. Even though the measured and calculated unreacted portions of the  $U_a$ -vs- $P_e$  curves differ, this difference should remain nearly constant at any given value of  $P_e$  as long as no chemical re-

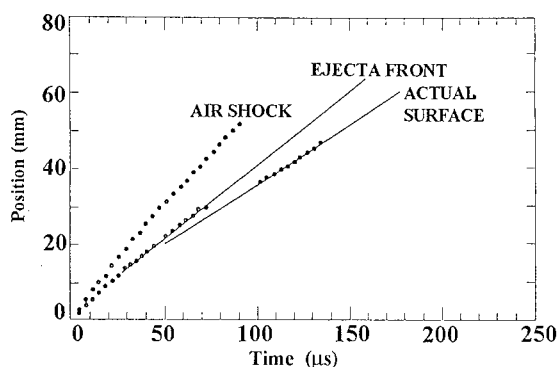


FIGURE 2. POSITION-TIME PLOT FOR PBXW-122, SHOT NO. JK-116B

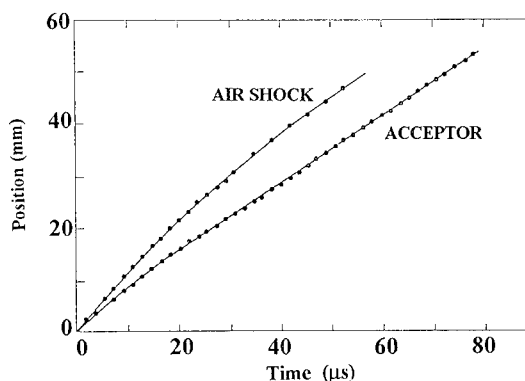


FIGURE 3. POSITION-TIME PLOT FOR AIR SHOCK AND ACCEPTOR SURFACE FOR PBXW-123, SHOT NO. JK-120B

action is present. This small difference in velocity has little, if any, effect on the sustained ignition threshold determination since even small amounts of reaction cause large increases in free-surface velocity.

In this work, a nearly constant velocity difference of 0.11 to 0.13 mm/ $\mu$ s is obtained between the measured and calculated unreacted velocities. Therefore, offsets of -0.11 to -0.13 mm/ $\mu$ s are added to the calculated velocities to compensate for these velocity differences. The corrected calculated free-surface velocity is then subtracted from the measured free-surface velocity to give the excess velocity,  $U_a - U_a^*$ . The excess velocity is then plotted against the input stress. ( $U_a - U_a^*$ ) versus  $P_e$  curves for all of the explosives given in Table 1 are shown in Reference 3. The two stress thresholds,  $P_e^R$  and  $P_e^I$ , are listed in Table 2 along with the corresponding PMMA gap lengths,  $X_g^R$  and  $X_g^I$ . It is seen in the table that the value of  $P_e^I$  for PBXN-110 actually covers a band of values from about 35 to 45 kbar. A wide range of values for the stress required to produce detonations in the LSGT was also found for PBXN-110 which confirms that the thresholds for detonation of PBXN-110 are not as sharply defined as for most explosives.

**TABLE 2. GAP LENGTHS AND STRESSES IN THE EXPLOSIVE FOR THE FIRST REACTION AND SUSTAINED IGNITION THRESHOLDS**

Explosive	First Reaction		Sustained Ignition	
	$X_g^R$ (mm)	$P_e^R$ (kbar)	$X_g^I$ (mm)	$P_e^I$ (kbar)
IRX-1	47.5	27	40.6	39
IRX-3	46.5	30	38.6	46
LG/UW-4	26.4	72	26.4	72
PBXN-103	46.2	32	37.6	50
PBXN-110	49.8	26	43.7 - 39.1	35 - 45
PBXN-111	51.6	24	38.4	48
PBXW-121	46.5	30	37.3	49
PBXW-122	33.5	57	25.9	70
PBXW-123	27.4	69	27.4	69
SW-21	48.0	27	39.1	43

Typically, for cast materials with small failure diameters, the excess velocity levels off after the initial rise at  $P_e^R$  until the sustained ignition threshold,  $P_e^I$ , is reached. This is shown schematically by the solid curve in Figure 4.  $P_e^I$  is the point where the curve rises more or less abruptly toward detonation. For explosives with large failure diameters, the rate of rise of the

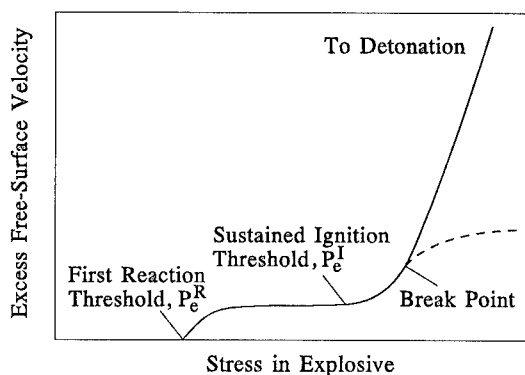


**FIGURE 4. SCHEMATIC OF EXCESS FREE-SURFACE VELOCITY VERSUS PEAK STRESS IN A CAST EXPLOSIVE**

curve above  $P_e^I$  decreases abruptly above a breakpoint, as indicated by the dashed line in the figure.

Five explosives in Table 2 show the effects of long reaction zones. The points at which fall-off occurs, i.e., the break points indicated in Figure 5, occur in the same order as the increasing failure diameter,<sup>10-14</sup>  $d_c$ , listed in Table 3. From these data, it seems certain that inward moving lateral rarefactions, as well as the initial non-uniform stress loading, interfere with the chemical reactions behind the wave front.

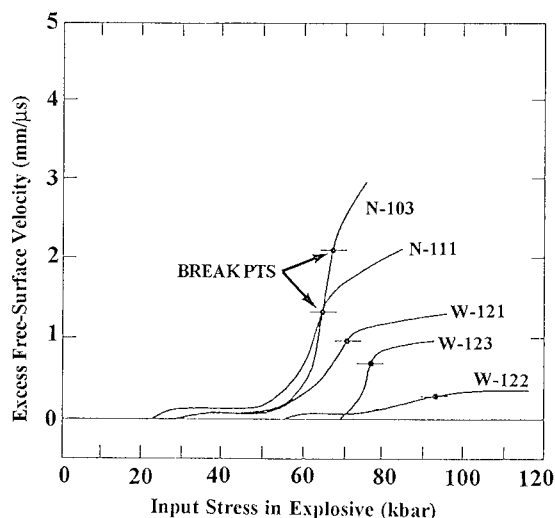


**FIGURE 5. EXCESS FREE-SURFACE VELOCITY VERSUS STRESS IN THE EXPLOSIVE SHOWING THE EFFECT OF RAREFACTIONS**

**TABLE 3. THE EXCESS FREE-SURFACE VELOCITY AT THE BREAK POINTS FOR SEVERAL EXPLOSIVES SHOWING CORRELATION WITH FAILURE DIAMETER**

Explosive	$U_a - U_a^*$ (mm/ $\mu$ s)	$d_c$ (mm)	Ref
PBXN-103	2.1	28	10
PBXN-111	1.4	37	11
PBXW-121	1.0	$\approx 90$	12
PBXW-123	0.7	$> 127$	13
PBXW-122	0.3	$\approx 180$	14

## DISCUSSION

Physical factors can overwhelm chemical ones for MGT sensitivity. The most dominant effect on sensitivity is explosive preparation. Whether the explosive is cast or pressed makes a significant difference in sensitivity. The addition of aluminum and/or inert binders desensitizes explosives. Increasing the amount of energetic material in a composite causes a corresponding increase in shock sensitivity. The particle size of the most shock-sensitive component has a great influence on the sensitivity.<sup>15,16</sup> It is slightly easier to ignite charges with larger particles. An increase in porosity also increases sensitivity.

The explosives in this study are all cold cast. They can be grouped into four categories based on their main explosive ingredient: HMX, RDX, TMETN, or NTO. The three HMX-based research explosives<sup>15,16</sup> (IRX-1, IRX-3, and SW-21) are designed to study the effects of changes in the main explosive components, particle sizes, and binders. PBXN-110 is HMX based, PBXN-111 is RDX-based, and PBXW-121 and PBXW-122 are NTO-based. LG/UW-4, PBXN-103, and PBXW-123 are TMETN-based underwater explosives.

For the explosives in this study, stress thresholds for first reaction range from 24 to 72 kbar. Stresses of 35 to 72 kbar are required for sustained ignition in the 12.7 mm thick acceptors. The excess velocity (and the amount of reaction) remains at a low and nearly constant value between the first reaction and sustained ignition points. It is reasonable to assume that the plateau indicates the ignition of the most sensitive component. This reaction would, in turn, ignite the other components which could also be ignited by higher initiating stresses above the plateau.

Of the two thresholds,  $P_e^R$  and  $P_e^I$ ,  $P_e^I$  appears to be the more useful. It has been shown that a good correlation exists between  $P_e^I$  and the detonation threshold in the LSGT for a number of explosives.<sup>1,3,10</sup> However, the data for the rubbery explosives, PBXW-121, PBXW-122, and PBXW-123, do not correlate. It seems likely that this lack of correlation is linked to the relatively long reaction zones of these rubbery explosives. Since the MGT sustained reaction thresholds for these materials are lower than the LSGT detonation thresholds, and these reactions would probably lead to detonation in large enough samples, the MGT (not the LSGT) should be used to determine the shock sensitivity of these materials.

$P_e^R$  may have little, if any, effect on initiation of detonation if the reaction occurring between  $P_e^R$  and  $P_e^I$  in the MGT, indicated by the excess free-surface velocity, is at a very low level, such as that occurring in PBXN-103 or PBXW-121.<sup>3</sup> On the other hand, the high level of reaction at  $P_e^I$  relative to  $P_e^R$  displayed by some explosives indicates that violent sub-detonation reactions are possible in large charges at input stresses lower than one might expect from the LSGT. For example, four of the explosives in Table 1, IRX-1, IRX-3, PBXN-110, and SW-21 contain a large percentage of HMX and have high levels of chemical reaction between  $P_e^R$  and  $P_e^I$ . These four are readily detonated in the MGT. A significant reaction between  $P_e^R$  and  $P_e^I$  in the MGT may lead to catastrophic reactions in large configurations. Therefore, practical explosive formulations should keep the reaction level between  $P_e^R$  and  $P_e^I$  small.

## SUMMARY AND CONCLUSIONS

This study shows that the sustained reaction thresholds of explosives with large failure diameters (up to 150 mm) can be accurately determined. In addition, even though explosives with failure diameters greater than 51 mm cannot detonate in the MGT, a relative ranking of the initiation thresholds of these explosives can be obtained from the shape of the response curves. It is found that a correlation exists between break points on the surface velocity versus input stress curves and the failure diameter for explosives with very large failure diameters.

## ACKNOWLEDGEMENTS

This work was performed for and funded by the Office of Naval Research, Code 4525, as part of the Explosives and Undersea Warheads Technology Block

Program PE602314N. The authors wish to acknowledge many useful discussions on the contents of this paper with S. Jacobs, R. Bernecker, and D. Tasker. R. Doherty and L. Roslund have given technical and moral support for this work.

## REFERENCES

1. Liddiard, T. P. and Forbes, J. W., *A Summary Report of the Modified Gap Test and the Underwater Sensitivity Test*, NSWC TR 86-350, 12 Mar 1987.
2. Liddiard, T. P.; Forbes, J. W.; and Price, D., "Physical Evidence of Different Chemical Reactions in Explosives as a Function of Stress," *Proceedings, Ninth Symposium (International) on Detonation*, Portland, OR, 28 Aug - 1 Sep 1989, Vol. II, pp. 1235-1242.
3. Lemar, E. R.; Liddiard, T. P.; Forbes, J. W.; Sutherland, G. T.; and Wilson, W. H., *The Analysis of Modified Gap Test Data for Several Selected Insensitive Explosives*, NAVSWC TR 89-290, Sep, 1993.
4. Price, D.; Clairmont, A. R., Jr.; and Erkman, J. O., *The NOL Large Scale Gap Test. III. Compilation of Unclassified Data and Supplementary Information for Interpretation of Results*, NOLTR 74-40, 8 Mar 1974.
5. Kamegai, M. and Erkman, J., "Numerical Analysis of a Diverging Shock Wave in Plexiglas Cylinders," *Fifth Symposium (International) on Detonation*, Pasadena, CA, 18-21 Aug 1970, pp. 477-485.
6. Jacobs, S. J.; McLanahan, J. D., Jr.; and Whitman, E. C., "A High Speed Shutter Framing Camera," *Society of Motion Picture and Television Engineers*, Vol. 72, No. 12, Dec 1963, pp. 923-926. Also in *Proceedings of the Sixth International Congress on High Speed Photography*, The Hague, Netherlands, Tjeenk-Haarlem, 1963, pp. 57-64.
7. Liddiard, T. P. and Forbes, J. W., *Shockwaves in Fresh Water Generated by the Detonation of Pentolite Spheres*, NSWC TR 82-488, 26 May 1983.
8. Liddiard, T. P., Jr., "The Compression of Polymethyl Methacrylate by Low Amplitude Shock Waves," *Fourth Symposium (International) on Detonation*, U. S. Naval Ordnance Laboratory, White Oak, MD, 12-15 Oct 1965, Office of Naval Research (ACR-126), pp. 214-221.
9. Erkman, J. O.; Edwards, D. J.; Clairmont, A. R., Jr.; and Price, D., *Calibration of the NOL Large Scale Gap Test; Hugoniot Data for Polymethyl Methacrylate*, NOLTR 73-15, 4 Apr 1973.
10. NSWC memorandum from R12 (Montesi, L. J.) to R11 (Leahy, J.), *LSGT Results of PBXW-121 and PBXW-121 Mod.*, 1 May 1989.
11. Forbes, J. W.; Lemar, E. R.; and Baker, R. N., "Detonation Wave Propagation in PBXW-115," *Proceedings, Ninth Symposium (International) on Detonation*, Portland, OR, 28 Aug - 1 Sep 1989, Vol. I, pp. 806-815.
12. NSWC memorandum from R12 (Carlson, K.) to R10B (Haiss, H.), *ELSGT Testing of PBXW-121 and PBXW-122*, 8 May 1989.
13. Wilson, W. H.; Forbes, J. W.; Gustavson, P. K.; and Sutherland, G. T., *Experimental Study of Detonation in PBXW-123, A Large Failure Diameter, Non-Ideal Explosive*, Tenth Symposium (International) on Detonation, Boston, MA, 12-16 Jul 1993.
14. Spahn, P. et al., "Design of a Booster for Initiating Navy Explosive PBXW-122," *Proceedings of the 41st Annual Bomb and Warhead Technical Meeting*, Vol. 1 (unclassified papers), NOSC, San Diego, CA, 15-16 May 1991.
15. Sutherland, G. T.; Lemar, E. R.; Forbes, J. W.; Anderson, E.; Ashwell, K. D.; and Baker, R. N., Sensitivity and performance Trends of Selected HMX Based Explosives with HTPB Binder Systems, *Proceedings of the 1993 JANNAF Propulsion Systems Hazards Subcommittee Meeting*, May, 1993.
16. Sutherland, G. T.; Lemar, E. R.; Forbes, J. W.; Miller, P.; Anderson, E.; Ashwell, K. D.; and Baker, R. N., *Shock Wave and Detonation Wave Response of Selected HMX Based Research Explosives with HTPB Binder Systems*, *Proceedings of the American Physical Society Topical Conference*, Colorado Springs, CO, June, 1993.

## **DISCUSSION**

J. GREGORY GLENN  
Wright Laboratory, Eglin Air Force Base, Florida

Do the explosives with very large critical diameters exhibit non-ideal behavior during detonation?

## **REPLY BY RAY LEMAR:**

Because explosives with very large critical diameters do not detonate in the Modified Gap Test, no direct measure of non-ideal behavior during detonation can be observed. However, the sustained ignition thresholds for these materials can usually be measured.

## SESSIONS ON EMULSION EXPLOSIVES

**Cochairmen:** Allen Tulis  
IIT Research Institute

Albert van der Steen  
Prins Maurits Laboratory TNO

# DETONATION BEHAVIOUR OF 'WATER - IN - OIL' TYPE EMULSION EXPLOSIVE CONTAINING GLASS MICROBALLOONS OF SELECTED SIZES

M. Munawar Chaudhri  
Cavendish Laboratory, University of Cambridge, Cambridge CB3 0HE, U.K.,

Lars-Åke Almgren  
Komminister vägen 51, S-16152 Bromma, Sweden,

and

Algot Persson  
SveDeFo, Swedish Detonic Research Foundation, Box 320 58, S-12611 Stockholm, Sweden.

Detonation velocities of water-in-oil emulsion explosives containing glass microballoons of selected diameters have been measured. The microballoons were of diameters <45, 45-63, 63-90, 90-125, and 125-150  $\mu\text{m}$ ; the explosives densities were 1.03 to 1.21  $\text{g.cm}^{-3}$ . The charges were confined in thin-walled pvc tubes of internal diameters of 10.5, 16, 25, 29, 38, and 62 mm and in all cases the detonation velocity increased linearly with decreasing  $1/(\text{charge diameter})$ . Using the plate dent test, the C-J pressures of the emulsion explosives were estimated to be 60-80 kbar. Although the estimated infinite-diameter detonation velocity was dependent upon the weight percentage of the glass, for emulsion explosives of similar densities and for charge diameters smaller than 29 mm, the charges containing the smaller diameter microballoons gave higher detonation velocities. This behaviour has been explained on the hot spots caused by microjetting in the microballoons collapsing at the detonation front. A computer model of this jetting process, supporting this suggestion is given.

## INTRODUCTION

During the last twenty years new types of commercial explosives, usually called emulsion explosives, have been developed.<sup>1</sup> These new explosives have several advantages over other industrial explosives; these advantages include good explosive performance, high water resistance, and virtually no toxic effects. Basically, an emulsion explosive is a water-in-oil type of emulsion, with salt solution in water forming the micro emulsion cells surrounded by fuel oil. In the pure emulsion form, these explosives are very insensitive. In fact, it is not known so far whether, in the pure form and without containing any voids or gaseous pockets, they can be detonated at all, irrespective of their confinement or charge diameter.

To sensitize emulsion explosives, glass or plastic microballoons of diameters of up to  $\sim 200 \mu\text{m}$  and of sufficient quantities are added to them. Indeed, by carefully controlling the weight ratios of the microballoons added to the emulsion, cap-sensitive explosives are prepared, which show very uniform detonation velocities. However, what was not known about these explosives was the influence of the size of

the microballoons on the magnitude of the detonation velocity, its variation with charge diameter, and the detonation failure diameter. In 1981 at Nitro Nobel, Sweden, we carried out a detailed experimental study of the influence of glass microballoons of different sizes on the detonation behaviour of an emulsion explosive. The results of this study were presented in a report.<sup>2</sup> The present paper is based on the experimental work described in ref.2. Subsequently, other similar investigations<sup>3-5</sup> have also been reported. In general, these investigations' results agree with the experimental findings reported earlier.<sup>2</sup> Here we give a detailed account of the work.

## EXPERIMENTAL

The glass microballoons were obtained from Minnesota Mining and Manufacturing Company, U.S.A and in the as-received form their diameters were in the range of 10 - 250  $\mu\text{m}$ . They were separated into groups of different diameters using dry mechanical sieving. The weight percentages of the various groups are shown in Table 1 below.



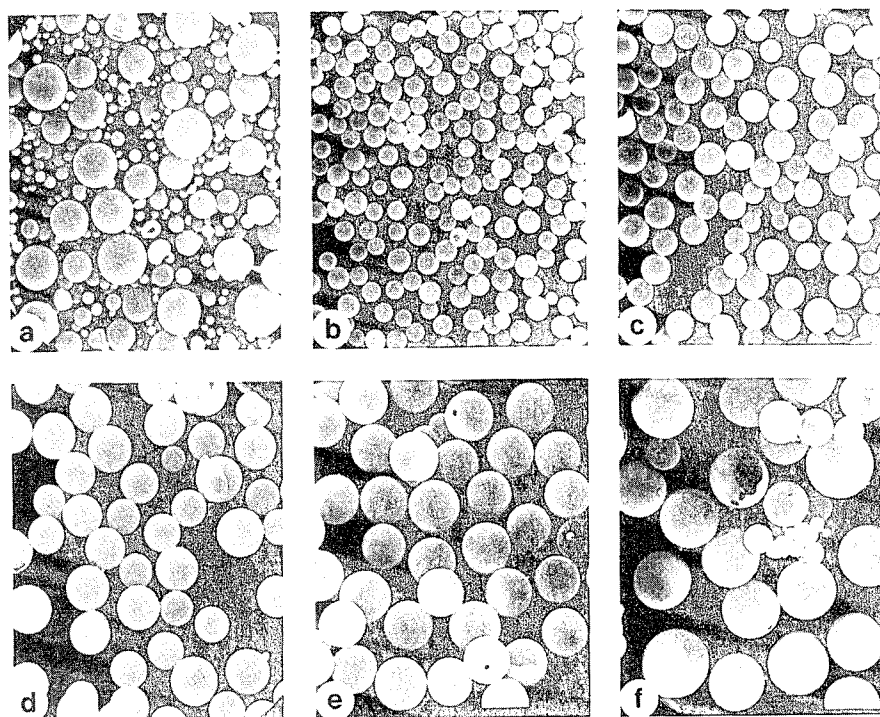


FIGURE 1. SCANNING ELECTRON MICROGRAPHS OF THE SIEVED GLASS MICROBALLOONS OF DIFFERENT DIAMETERS. (a)  $<45 \mu\text{m}$ ; (b)  $45\text{--}63 \mu\text{m}$ ; (c)  $63\text{--}90 \mu\text{m}$ ; (d)  $90\text{--}125 \mu\text{m}$ ; (e)  $125\text{--}150 \mu\text{m}$ ; (f)  $150\text{--}250 \mu\text{m}$ . MAGNIFICATIONS: (a)  $\times 150$ ; (b) to (f)  $\times 50$ .

TABLE 1. THE WEIGHT PERCENTAGES AND BULK DENSITIES OF GLASS MICROBALLOONS OF DIFFERENT DIAMETERS.

Diameter ( $\mu\text{m}$ )	Weight percentage	density ( $\text{g.cm}^{-3}$ )
$<45$	29.25	0.209
$45 - 63$	13.60	0.082
$63 - 90$	26.31	0.063
$90 - 125$	26.90	0.060
$125 - 150$	3.9	0.052
$150 - 250$	0.04	not measured
$>250$	$\sim 0.00$	not measured.

Scanning electron micrographs of typical balloons of different diameters are shown in Figure 1(a-f) and it will be seen that the sieving has worked satisfactorily and that there is little adhesion between balloons. Some balloons were deliberately broken to measure their wall thicknesses, which were found to be in the range of  $0.3$  to  $0.6 \mu\text{m}$ .

The emulsion explosives, consisting of emulsion matrix and glass microballoons, were prepared in the

laboratory. The emulsion matrix was always prepared with the same weight proportions of salts, distilled water, paraffin oil and wax, and emulsifier. The various salts used were: ammonium nitrate, sodium nitrate, and sodium perchlorate. To prepare the emulsion matrix, the salts were dissolved in distilled water heated to  $90$  to  $95^\circ\text{C}$  and in a separate container the fuel (i.e. oils and waxes) was heated to  $75^\circ\text{C}$ . The molten fuel was poured into a heated 3-litre plastic bowl and stirred rapidly with a kitchen whisk while the salt solution was gradually added to the fuel. This resulted in the immediate formation of the emulsion matrix, which had a physical appearance like that of Vaseline. The matrix density varied from one preparation to another and it was measured to be  $1.431 \pm 0.001 \text{ g.cm}^{-3}$ , which meant that during the preparation some air was inadvertently mixed in. Glass microballoons, which were stored at a temperature of  $75^\circ\text{C}$  to remove any moisture from them, of a desired diameter range and amount were then mixed into the hot matrix using the slowest speed of the whisk. This resulted in the formation of the emulsion explosive, which was much whiter than the matrix. By adding different weight percentages of the microballoons to the emulsion matrix, we were able to obtain emulsion explosives of densities in the range of  $1.03$  to  $1.31 \text{ g.cm}^{-3}$ . The emulsion explosives so formed and while still hot were filled into cylindrical seamless pvc tubes of internal diameters of  $10.5$ ,  $16.0$ ,  $25.0$ ,  $29.0$ ,  $38.0$ , and

62.0 mm and lengths in the range of 200 to 550 mm. The wall thicknesses of the tubes were 0.5 to 1 mm. One tube of 200 mm diameter and 1100 mm in length was also used. In a few cases, a 25 mm diameter steel tube, having a wall thickness of 3 mm, was also filled with the emulsion explosives.

The detonation behaviour of an emulsion explosive charge was examined by electrically detonating a no. 8 cap placed axially inside it at one end. The detonation velocity of the charge was measured by electrical and optical methods. The electrical circuit used for the former was based on an earlier design.<sup>6</sup> In the charge, twisted pieces of 0.4 mm diameter enamelled copper wire were inserted diametrically at several selected positions along its length. As a detonation front passed over a twisted-wire assembly, it electrically shorted the two pieces, which, in turn, discharged the corresponding capacitor; the discharge current signal was recorded by a transient digitizer (Data Lab. DL 1080). In this manner, capacitor-discharge signals, corresponding to the shorting of the various wire-assemblies, were recorded. From a knowledge of the distances between the wire assemblies and the time intervals between the capacitor discharge signals, the detonation velocity of the charge was measured. The accuracy of the measurements was better than 2%. A typical pin record is shown in Figure 2. In the optical method, the initiation and propagation of detonation in a bare emulsion explosive charge was photographed with a high speed Kerr cell camera. As before, a no. 8 cap was used for the initiation of detonation and the charge was lit with the light from two argon flash bombs.

The C-J detonation pressures of the emulsion explosives were measured with a plate dent test.<sup>7</sup> The test charge, 25 mm in diameter and 400 - 500 mm long, was placed coaxially on a steel cylinder 50 mm thick and 125 mm in diameter which, in turn, was coaxially placed on a 100 mm thick similar steel cylinder of the same

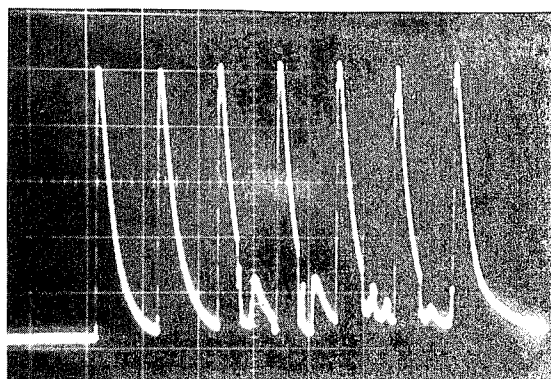


FIGURE 2. A TYPICAL RECORD OF SIGNALS FROM THE TWISTED WIRE ASSEMBLIES PLACED DIAMETRICALLY ALONG THE LENGTH OF AN EMULSION EXPLOSIVE CHARGE CONFINED IN A PVC TUBE. HORIZONTAL SCALE: 1 DIV = 10  $\mu$ s.

diameter. The entire assembly was then placed on a flat piece of ground, with the explosive charge vertical. The charge was detonated with a no. 8 cap and this resulted in a dent, approximately part of a sphere in shape, in the plate. Its depth, below the original flat surface of the steel, was measured with a dial gauge having an accuracy of 0.01 mm. Calibration tests were carried out using 25 mm diameter and 50 to 100 mm long charges of PETN, TNT and Hexotol, the C-J pressures of which for different densities are well documented.<sup>7</sup>

## RESULTS

We found that an emulsion matrix (i.e. without any glass microballoons) charge confined in a 25 mm internal diameter steel tube of a wall thickness of 3 mm could not be detonated using a no. 8 cap or a no. 8 cap with a PETN primer 25 mm in diameter and 25 in length. In fact, we were unable to detonate an emulsion matrix charge contained in a 62 mm diameter pvc tube. In other words, the emulsion matrix was very insensitive. On the other hand, if enough glass microballoons were added to the emulsion matrix, so that the density of the physical mixture was reduced to below  $\sim 1.26 \text{ g.cm}^{-3}$ , it could be detonated with a no. 8 cap. This clearly shows the marked sensitization effect of the addition of the glass microballoons. It is interesting to report that even glass microballoons of diameters less than 45  $\mu$ m were very effective in sensitizing the emulsion matrix. Figure 3 shows the variation of the detonation velocity with  $1/(\text{charge diameter})$  for two emulsion explosives, each containing microballoons of diameter  $<45 \mu$ m, but having densities of 1.08 and 1.16  $\text{g.cm}^{-3}$ . The charges

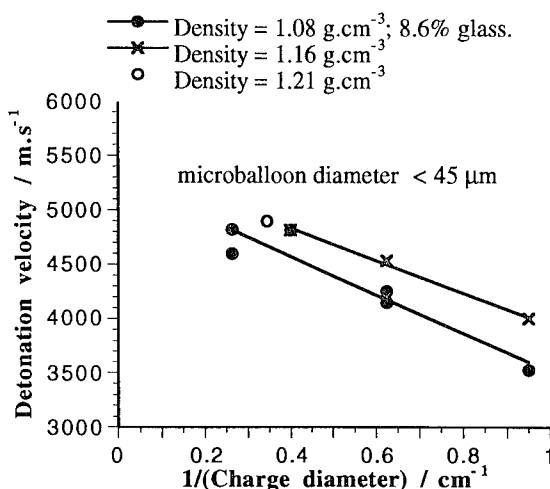


FIGURE 3. DETONATION VELOCITY VERSUS  $1/(\text{CHARGE DIAMETER})$  OF EXPLOSIVES CONTAINING GLASS MICROBALLOONS OF DIAMETERS  $<45 \mu$ m AND DENSITIES OF 1.08 AND 1.16  $\text{g.cm}^{-3}$ .

of both densities supported a detonation down to a charge diameter of 10.5 mm; we did not examine whether a detonation would have propagated in smaller diameter charges. For both the densities, the detonation velocity increased linearly as  $1/(\text{charge diameter})$  decreased. This observation is different from that made by Lee and Persson<sup>5</sup>, who found the curves to be concave towards the  $1/(\text{charge diameter})$  axis. Also, the higher density charge gave higher detonation velocities at all charge diameters studied. In Figure 3 we also show a data point for a 29 mm diameter charge of a density of  $1.21 \text{ g.cm}^{-3}$  and we note that the detonation velocity is similar to the expected value for the  $1.16 \text{ g.cm}^{-3}$  charge.

The influence of the variation of charge density on the detonation velocity was more pronounced when glass microballoons of diameters in the range of 63-90  $\mu\text{m}$  were added to the emulsion matrix. Figure 4 shows the results for charge densities of 1.03 to  $1.18 \text{ g.cm}^{-3}$ . These emulsion explosives were unable to support a detonation for a charge diameter of 10.5 mm or smaller. It will be seen from Figure 4 that for the smaller charge diameters of 16 and 25 mm, the detonation velocity was higher for the lower charge densities. However, for charge diameters of 38 mm or greater, the higher the charge density, the greater was the detonation velocity. Also, for all the densities, the detonation velocity increased linearly with decreasing  $1/(\text{charge diameter})$ .

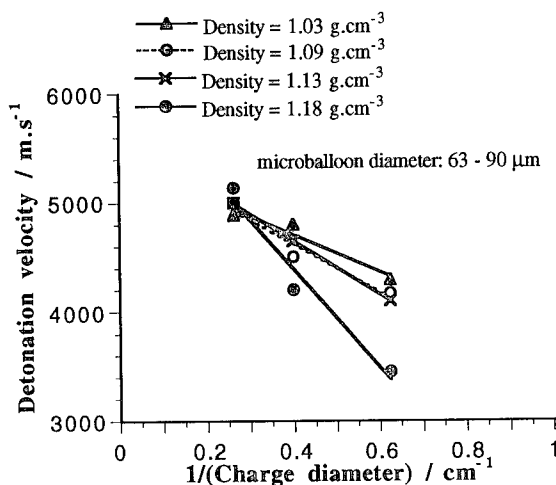


FIGURE 4. THE INFLUENCE OF CHARGE DENSITY ON DETONATION VELOCITY VERSUS  $1/(\text{CHARGE DIAMETER})$  CURVES FOR EMULSION EXPLOSIVES WITH GLASS MICROBALLOONS OF DIAMETERS IN THE RANGE OF 63-90  $\mu\text{m}$ .

The marked influence of the glass microballoons' diameter on the detonation velocity of a charge was evident when detonation velocities of charges of similar densities and of different diameters, but containing microballoons of different sizes were compared. Figure 5 shows such a comparison. It is interesting that the charges containing smaller diameter microballoons show

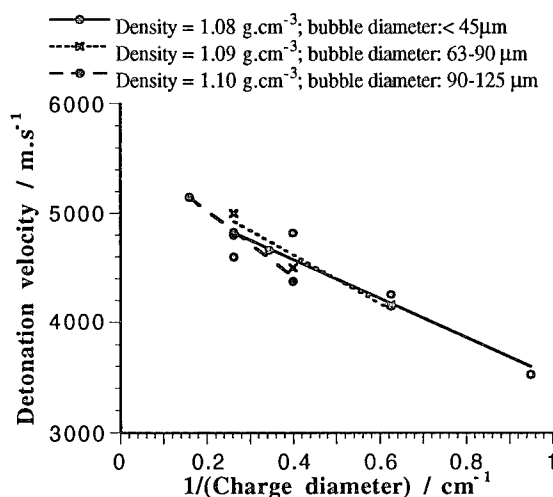


FIGURE 5. DETONATION VELOCITY VERSUS  $1/(\text{CHARGE DIAMETER})$  BEHAVIOUR OF EMULSION EXPLOSIVES OF SIMILAR DENSITIES, EACH HAVING MICROBALLOONS OF DIFFERENT DIAMETERS. NOTE THAT THE EXPLOSIVE CONTAINING THE SMALLEST DIAMETER MICROBALLOONS HAS THE SMALLEST FAILURE DIAMETER.

a smaller failure diameter. The failure diameter of the emulsion explosive containing glass microballoons of diameters  $<45 \mu\text{m}$  was smaller than 10.5 mm and the failure diameters of the other two explosives containing glass microballoons of diameters 63 - 90  $\mu\text{m}$ , and 90 - 125  $\mu\text{m}$  were greater than 10.5 mm, but less than 16 mm. However, the extrapolated infinite diameter velocities are larger for the charges containing the larger diameter microballoons. These velocities are 5290, 5510, and 5630  $\text{ms}^{-1}$  for charges containing balloons of diameters  $<45 \mu\text{m}$ , 63-90  $\mu\text{m}$ , and 90-125  $\mu\text{m}$ , respectively.

We note from Table 1 that the bulk density of the glass microballoons decreases with increasing balloon diameter. Also, we would expect that, for charges of infinite diameters, the detonation velocity will be controlled by the proportion of the inert material, i.e. glass. Therefore, we compare the detonation behaviour of two emulsion explosives containing approximately the same percentage of glass in the form of the microballoons. One explosive contained the as-received unsieved microballoons and the other had microballoons of diameters in the range of 90-125  $\mu\text{m}$ . However, the densities of the emulsion explosives were 1.15 and  $1.06 \text{ g.cm}^{-3}$ , respectively. These emulsion explosives also yielded detonation velocities which decreased linearly with increasing  $1/(\text{charge diameter})$  (see Figure 6). In both cases, the detonation failed to propagate for a charge diameter of 10.5 mm. Moreover, we note from Figure 6 that for infinite charge diameters, the values of the detonation velocities converge, even though there is a

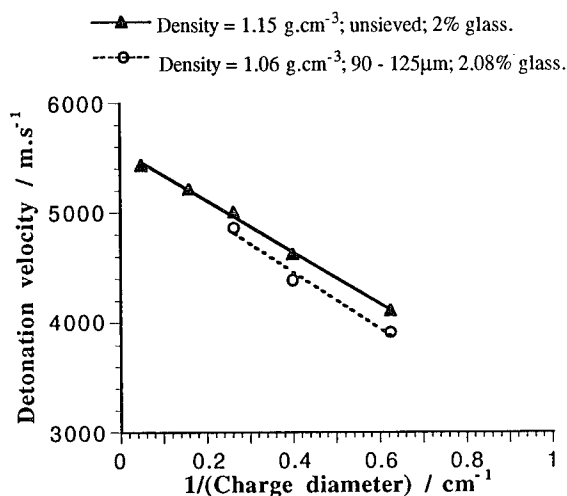


FIGURE 6. DETONATION VELOCITY VERSUS  $1/(\text{CHARGE DIAMETER})$  BEHAVIOUR OF EMULSION EXPLOSIVES CONTAINING  $\sim 2\%$  GLASS, BUT HAVING DIFFERENT DIAMETER MICROBALLOONS.

significant difference in their densities. The infinite diameter velocities are estimated to be 5580 and 5490  $\text{ms}^{-1}$  for charges of densities 1.15 and 1.06  $\text{g.cm}^{-3}$ , respectively.

High-speed photographic sequences also showed that the detonation propagated smoothly in the emulsion explosives containing microballoons of selected sizes. A typical sequence is shown in Figure 7. The charge has a square cross section 25 mm x 25 mm and it is 210 mm long. Its density is 1.07  $\text{g.cm}^{-3}$  and it contains microballoons of diameters in the range of 90-125  $\mu\text{m}$ . The charge was initiated with a no. 8 cap and, without showing any acceleration, the detonation reached a uniform velocity of 4500 - 5000  $\text{ms}^{-1}$ . It will be noticed that the reaction products have a four-fold symmetry, which is due to the square cross section of the charge.

The plate dent tests worked satisfactorily with the emulsion explosive charges. From the measurements of the dent depths and the experimental data for several explosives given by Smith<sup>7</sup>, we estimated the C-J pressures of different emulsion explosive charges; the values were found to be in the range of 60 - 80 kbar. It is worth remarking that the higher the C-J pressure, the deeper and wider was the dent.

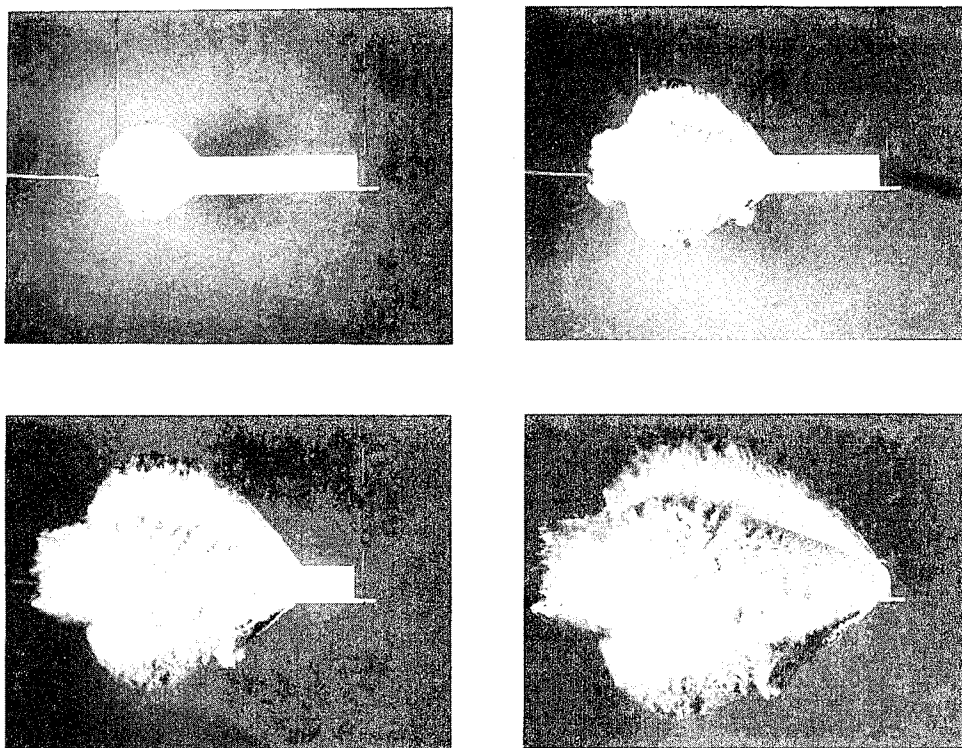


FIGURE 7. HIGH SPEED PHOTOGRAPHIC SEQUENCE TAKEN WITH A KERR CELL CAMERA OF THE DETONATION OF AN UNCONFINED EMULSION EXPLOSIVE CHARGE OF CROSS SECTION  $25 \times 25 \text{ mm}^2$ , DENSITY  $1.07 \text{ g.cm}^{-3}$ , AND CONTAINING GLASS MICROBALLOONS OF DIAMETERS 90-125  $\mu\text{m}$ . INTERFRAME TIME: 9  $\mu\text{s}$ ; EXPOSURE TIME OF EACH FRAME: 0.3  $\mu\text{s}$ .

## DISCUSSION

The results presented in Figures 3 to 6 clearly show that the glass microballoons greatly enhance the sensitivity of the emulsion matrix. Another important finding is that the sensitivity of an emulsion explosive is not only controlled by its density. This has been concluded by studying the behaviour of charges of similar densities, but which contained glass microballoons of different diameters (see Figure 5). It will be seen from this figure that whereas the failure diameter of the emulsion explosive containing the 90-125  $\mu\text{m}$  diameter glass microballoons was 16 mm, in the emulsion explosive charge of a similar density, but containing glass microballoons of diameters less than 45  $\mu\text{m}$ , the detonation propagated steadily for a charge diameter of 10.5 mm. Since the number density of the microballoons in the charge containing the smaller diameter microballoons is considerably higher than in that containing the larger size microballoons, the experimental observations suggest that the greater the number density of the microballoons, the smaller will be the failure diameter of the charge. However, it should be noted that the increase in the percentage of the glass added to the emulsion matrix reduces the theoretical exothermicity per unit mass of the mixture. So, when too much glass is added, the reaction may not even be self-sustained. We, however, did not examine experimentally such a situation.

The pressure measurements made with the plate dent test show that a detonating emulsion charge containing glass microballoons generates C-J pressures in the range of 60-80 kbar, depending upon its density and composition. These pressures are too low to sustain the propagation of a detonation in the emulsion matrix without any microballoons. Further support to this conclusion comes from the fact that, if no microballoons were added to the emulsion matrix confined in a steel tube, it could not be detonated, even with a PETN booster charge. It appears, therefore, that in the emulsion charges containing the glass microballoons, the detonation is supported by localised reaction occurring at individual microballoons. This brings us to the mechanism responsible for the localised reaction. Previous work<sup>8-10</sup> with individual gas-filled microscopic bubbles has shown that their collapse by a relatively weak shock can generate high enough temperatures to cause the initiation of an explosion in an explosive crystal's surface on which the bubble collapses. Moreover, the amount of heat transferred in a submicrosecond period from the hot gas within the collapsed bubble to the explosive surface was sufficiently high<sup>9,10</sup>. However, since in a glass microballoon the gaseous pressure is considerably smaller than one atmosphere, it would appear that the compression heating of any contained gases may not be of vital significance here.<sup>10</sup> As suggested by us before<sup>10,11</sup>, it is the impact on the front wall by the jet of the shock-heated material formed in the collapsing balloon, which plays an important part. Our high-speed photographic sequence of the collapse of a 9.5 mm diameter hollow aluminium sphere under water by an approximately 20 kbar shock has shown<sup>11</sup> the formation

of the fast jet. This jet can even hit the front wall of the balloon before the main shock does so. At the jet impact site a very high temperature hot spot is formed where localised reaction takes place and which supports the detonation. Using an axially symmetric 2-dimensional model, we have studied the interaction of a shock wave with a 5 mm diameter spherical cavity in water. The strength of the shock hitting the cavity is 15 kbar. The water jet formed (see Figure 8) during the collapse reaches a maximum velocity of around  $3000 \text{ m.s}^{-1}$ . At the jet impact on the opposite wall of the cavity the pressure rises to 65 kbar, which is shown as a pressure-time history of the tip of the jet in Figure 9. Note that the primary shock wave has not crossed the jet impact area and the strength of the primary shock reduces to 1 kbar at the lobes of the cavity (shown as thick solid lines in Figure 8). It will be seen that our computer model supports the experimental observations.<sup>11</sup> We may add that if in an emulsion explosive charge there is a large percentage of broken glass microballoons, it fails to detonate. This further suggests that any sensitization by the addition of solid physical discontinuities, such as broken glass microballoons or solid beads<sup>12</sup>, is likely to be insignificant compared to that by the intact microballoons.

By extrapolating the experimental detonation velocity vs  $1/(\text{charge diameter})$  curves, infinite diameter detonation velocities were obtained. Also, using the TIGER CODE and JCZ-3 equation of state, the infinite diameter detonation velocities of the emulsion explosives of different densities and containing 2% and 10% by

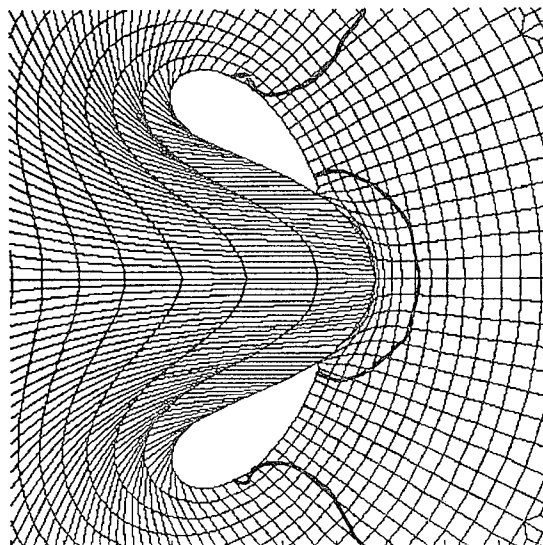


FIGURE 8. COMPUTER MODEL OF THE FORMATION OF A FAST JET WHEN A 5 MM DIAMETER SPHERICAL CAVITY IN WATER COLLAPSES UNDER THE INFLUENCE OF A 15 KBAR SHOCK

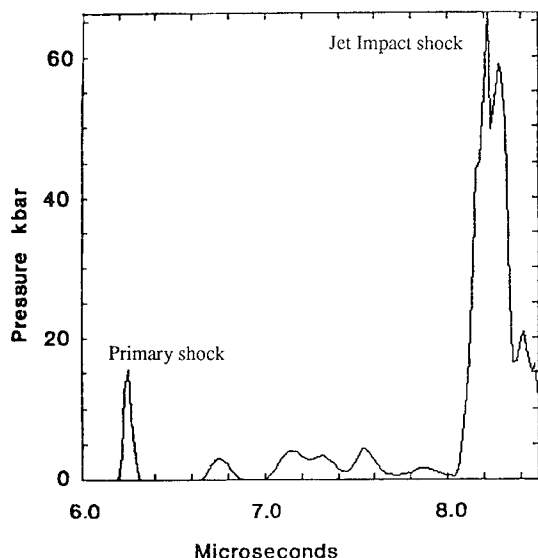


FIGURE 9. PRESURE-TIME HISTORY OF THE MATERIAL (i.e. WATER) OF THE JET.

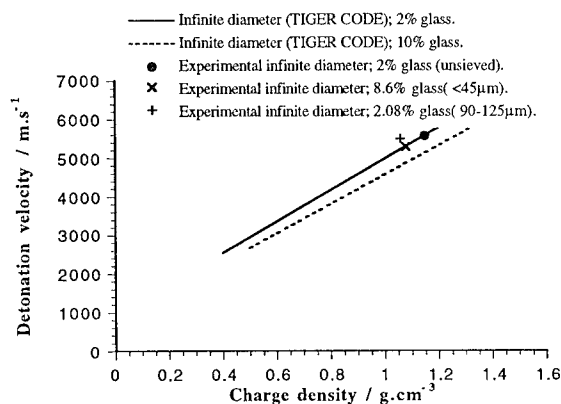


FIGURE 10. THEORETICAL INFINITE DIAMETER DETONATION VELOCITIES OF EMULSION EXPLOSIVE OF DIFFERENT DENSITIES HAVING 2% AND 10% BY WEIGHT OF GLASS. THREE EXPERIMENTAL DATA POINTS ARE ALSO SHOWN, WHICH ARE REASONABLY CLOSE TO THE THEORY.

weight of glass were calculated. The results are shown in Figure 10; also shown in the figure are our experimental values for the emulsion explosives containing 2% and 8.6% glass by weight, obtained from Figures 3 and 6. It is interesting to note from Figure 10 that the

agreement between theory and experiment is reasonably good. At small charge diameters, the important factor is the number density of glass microballoons. Since, in the group of microballoons of less than 45  $\mu\text{m}$  in diameter, there is a high proportion of balloons of diameters 10-20  $\mu\text{m}$ , it would appear likely that such small diameter balloons are also important.

## CONCLUSIONS

By adding carefully sieved glass microballoons of selected diameters to a water-in-oil emulsion explosive, it has been shown that the number density and diameters of the microballoons play very important parts in determining its explosive behaviour. Thus, the higher the number density of the microballoons, the smaller was the failure diameter of the explosive. The detonation velocity was found to increase linearly with decreasing  $1/(\text{charge diameter})$ . Furthermore, at charge diameters smaller than 29 mm and for a given explosive density, the detonation velocity was higher for the explosive containing the smaller diameter microballoons. The infinite diameter velocities have been found to be controlled by the percentage of the added glass and were found to be in reasonable agreement with the theoretical values calculated using the TIGER CODE and JCZ-3 equation of state. It has been suggested that the detonation is sustained by reaction localised at microballoons where high-temperature hot spots are formed due to the impact of fast jets during the microballoons' collapse. A computer model of the collapse process, which agrees with our experimental observations, has also been given.

## ACKNOWLEDGEMENTS

We should like to thank Nitro Nobel, Sweden for permission to publish this work. We also thank Junhua Deng of SveDeFo for his help with the computer modelling.

## REFERENCES

1. Wade, C. G., "Water-in-Oil Emulsion Explosive Composition," U.S. Patent No. 4110134, 1978.
2. Chaudhri, M. M.; Almgren, L.-A., "The Factors Controlling the Detonation Behaviour of Emulite," Technical Report No. DL 1982: 07, March 1982, Nitro Nobel, Stockholm, Sweden.
3. Hattori, K; Fukatsu, Y; and Sakai, K., "Effect of the Size of Glass Microballoons on the Detonation Velocity of Emulsion Explosives," Kogyo Kayaku, Vol. 43, 1982, pp. 295-301.
4. Yoshida, M; Iida, M; Tanaka, K; Fujiwara, S; Kusakabe, M; and Shino, K., "Detonation Behaviour of Emulsion Explosives Containing Glass Microballoons," *Eight Symposium (International) on Detonation*, NSWC MP 86-194, Naval Surface Weapons Center, White Oak, Silver Spring, Maryland, 1985, pp. 993-1000.

5. Lee, J.; and Persson, P.-A., "Sensitization of Emulsion Explosives by Microballoons" "Working Group Meeting on Sensitivity of Explosives," Socorro, NM, 15-18 March 1987.

6. Campbell, A. W.; Malin, M. E.; Boyd, T. J. Jr.; and Hull, J. A., Precision Measurement of Detonation Velocities in Liquid and Solid Explosives," Review of Scientific Instruments, Vol. 27, 1956, pp. 567-574.

7. Smith, L. C., "On Brisance, and a Plate Denting Test for the Estimation of Detonation Pressure," Explosivestoffe, Nr. 5, 1967, pp. 106-110 and 130-134.

8. Bowden, F. P.; and Chaudhri, M. M., "Initiation of Explosion in  $\text{AgN}_3$  and  $\beta\text{-PbN}_6$  single crystals by a collapsing bubble," Nature, Vol. 220, 1968, pp. 690-694.

9. Chaudhri, M. M.; and Field, J. E., "The Role of Rapidly Compressed Gas Pockets in the Initiation of Condensed Explosives," Proceedings of the Royal Society, Vol. A340, 1974, pp. 113-128.

10. Chaudhri, M. M., "The Initiation of Fast Decomposition in Solid Explosives by Fracture, Plastic Flow, Friction, and Collapsing Voids," *Ninth Symposium (International) on Detonation*, OCNR 113291-7, Office of the Chief of Naval Research, Arlington, Virginia, 1989, pp. 857-867.

11. Chaudhri, M. M.; Almgren, L.-A.; and Persson, A., "High Speed Photography of the Interaction of Shock Waves with Voids in Condensed Media," *Fifteenth International Congress on High Speed Photography and Photonics*, SPIE Vol. 348, 1983, pp. 388-394.

12. Engelke, R., "Effect of a Physical Inhomogeneity on Steady-State Detonation Velocity," *Physics of Fluids*, Vol. 22, 1979, pp. 1623-1630.

## DISCUSSION

EDWARD L. LEE

Lawrence Livermore National Laboratory, Livermore, California

There is a vast gulf between the analyses presented in the papers by Chaudhri, Almgren, & Persson; Khasainov, Ermolaev & Presles; and Gois, Campos & Mendes. Chaudhri's results clearly indicate hydrodynamic closure of  $\mu$ -balloons. Khasainov, Ermolaev & Presles consider spherical viscoplastic plate collapse in the same region of shock intensity. Gois, Campos & Mendes do not clearly differentiate.

## REPLY BY MUNAWAR CHAUDHRI:

I am glad that Dr. Lee has pointed out major differences in the mechanisms of balloon sensitization which we proposed and that put forward by Dr. Presles. Our mechanism is based on high-speed framing photography with which we observed the collapse of hollow glass and aluminum spheres in water by 17-20 kbar shocks (see Ref. 11 of the paper). It was found that the shock caused an asymmetrical collapse of the sphere, producing a very high-speed jet; on impact on the downstream wall of the sphere a strong shock was generated. It is at this impact site where a hot spot is formed and fresh reaction is initiated. Our 2-D modeling also showed that when a 15-kbar water shock hits a 5-mm-diameter cylindrical cavity, a jet traveling at 3000 m/s is produced, which generates on impact a new shock of 65 kbar (see Figs. 8 and 9). We believe that similar asymmetrical collapse and jetting will also take place in 20-200- $\mu$ m-diameter glass microballoons present in an emulsion explosive when they are impacted by a strong ( $\sim$ 20 kbar) shock. In fact, in some other experiments it has been shown that when a 150- $\mu$ m bubble in water collapses asymmetrically, fast jetting occurs. Moreover, as the measured C-J pressure in the emulsion explosive is  $\sim$ 60 kbar, the microjets in the collapsing balloons will be even faster than 3000 m/s.

The mechanism proposed by Presles appears to be dependent upon the rise of temperature by the viscous flow/plasticity of the wall of a glass microballoon collapsing spherically (experimental evidence of such a collapse has yet to be provided). To calculate the temperature rise, he assumed a value of 0.5 GPa for the yield stress of the glass. In fact, it is known that in a quasi-static tensile test no plastic yielding occurs at room temperature in soda-lime glass (probably from which the microballoons are made) and fused silica for stress values of 3.5 and 5.6 GPa, respectively.<sup>1,2</sup> Under shock loading conditions (*i.e.*, very high rate of strain), the yield stress values of both of these glasses are likely to increase considerably. In other words, the viscoplastic collapse model proposed by Presles seems unrealistic.

In the paper presented by Gois, no mechanism of sensitization appears to have been proposed, as also noted by Dr. Lee.

## REFERENCES

1. F. P. Mallinder and B. A. Proctor, "Elastic Constants of Fused Silica as a Function of Large Tensile Strain," *Physics and Chemistry of Glasses*, Vol. 5, 91-103 (1964).
2. D. M. Marsh, "Plastic Flow in Glass," *Proceedings of The Royal Society*, Vol. A279, 420-435 (1964).

## EFFECT OF GLASS MICROBALLONS ON SHOCK WAVE SENSITIVITY AND DETONATION CRITICAL DIAMETER OF CONDENSED EXPLOSIVES

B.A. Khasainov, B.S. Ermolaev

Institute of Chemical Physics  
Academy of Sciences of Russia  
Kossygin street 4, Moscow 117334 RUSSIA

and

H.N. Presles

Laboratoire d'Energétique et de Détonique,  
URA CNRS 193, ENSMA, 86034 Poitiers FRANCE

A viscoplastic model for cavity collapse induced by shock loading was used to gain an insight into the mechanisms responsible for the sensitization of emulsion and liquid high explosives by glass microballoons (GMB). Heat released during the GMB collapse is localized mainly at its inner interface and is transferred to the surrounding explosive by conduction. Ignition delay increases as the shock wave amplitude decreases. Critical pressures exist below which the explosive is not ignited. For a given explosive, the ignition delay and critical pressure depend mainly on GMB parameters and concentration. Reasonable values of ignition delay and critical pressure are predicted for a wide range of values for glass viscosity. An analysis of available experimental data on critical detonation diameters of GMB-explosive mixtures reveals a striking linear correlation between the critical diameter and the reciprocal of the specific surface of GMB. This analysis shows also that the ignition delay may play an important role in the problem of critical diameter.

### INTRODUCTION

Explosive safety problems motivated researchers to pay attention to detonation performance and critical detonation diameters of emulsion and liquid high explosives sensitized by hollow glass microballoons, but data on shock wave sensitivity are not available.<sup>1-3</sup>

It is well known that pores or cavities in porous explosives increase their shock sensitivity by collapsing to produce hot spots which are centers for additional growth of reaction. Depending on the Reynolds number  $Re = a_0(\rho P_{SO})^{1/2}/(4\mu)$  there are two modes of collapse: a hydrodynamic-collapse mode,<sup>4</sup> associated with values of  $Re \gg 1$ , and a viscous-collapse mode associated with values of  $Re < 1$  (here  $a_0$  is the cavity radius,  $\rho$  and  $\mu$  are the explosive density and viscosity,  $P_{SO}$  is the shock strength).<sup>5</sup> For  $Re > 1$  fast asymmetrical collapse coupled with generation of jets occurs. The pressure increases essentially in the vicinity of the collapsed void, the hot

spot size is about  $a_0$ , and its life time is controlled by a rarefaction wave.<sup>4</sup> At  $Re < 1$  viscous stress at the void surface is so important that the process of void collapse behind the shock is spherically symmetric and relatively slow. The explosive adjacent to the cavity is heated by viscous and plastic work and cooled by heat conduction.<sup>5</sup> The viscous collapse is not accompanied by any significant increase of pressure, hence the hot spot life time is controlled by heat conduction and appears to be essentially longer than in the hydrodynamic case.

In this paper the viscoplastic model of hot spot generation is used to analyze the effect of glass microballoons (GMB) on shock wave sensitivity of explosives. An analysis of available experimental data on critical detonation diameters of GMB sensitized explosives shows that this explosive property is linearly proportional to the reciprocal of GMB specific surface.



## DESCRIPTION OF THE MODEL

The behavior of GMB in shocked liquid explosive may differ significantly from that of air bubbles due to the properties of the thin glass shell and especially the viscosity of glass that at normal conditions is very high. Hence it is likely that the Reynolds number behind a shock is small and the collapse of GMB immersed in the explosive will occur in a viscoplastic mode, that is, spherical uniform compression of GMB will take place without fragile destruction. The GMB collapse will be described on the basis of the approach developed by Carrol and Holt.<sup>6</sup> Let us consider a representative effective cell consisting of three spherical regions: GMB internal cavity with initial radius  $a_0$ , glass layer with outer radius  $g_0$  and thickness  $h_0$  and explosive layer with external radius  $b_0$ . With known properties of the explosive and GMB it is easy to compute the cell parameters:

$$g_0 = \frac{d_0}{2}; h_0 = g_0 \left\{ 1 - \sqrt[3]{1 - \frac{M_1 \rho_2}{\rho_1 (\rho_2 / \rho_{mixt} + M_1 - 1)}} \right\}$$

$$a_0 = g_0 - h_0; b_0 = g_0 \sqrt[3]{1 - (1 - M_1) \rho_{mixt} / \rho_2}$$

Here  $d_0$  is the mean outer diameter of GMB,  $\rho_1$  and  $\rho_2$  are the densities of glass and explosive,  $M_1$  is the mass fraction of GMB in the explosive mixture,  $\rho_{mixt}$  is the mixture density. Table 1 shows characteristics of ideal effective spherical cell for the emulsion explosive ( $\rho_1 = 2300 \text{ kg/m}^3$  and  $\rho_2 = 1400 \text{ kg/m}^3$ ).<sup>1</sup> One can see that the estimated GMB thickness is about  $1.5 \text{ } \mu\text{m}$ .

TABLE 1. PARAMETERS OF A TYPICAL CELL DEDUCED FROM DATA OF LEE AND PERSSON.<sup>1</sup>

Explosive			Effective cell			
$d_0$ ( $\mu\text{m}$ )	$M_1$ (%)	$\rho_{mixt}$ ( $\text{kg/m}^3$ )	$a_0$ ( $\mu\text{m}$ )	$g_0$ ( $\mu\text{m}$ )	$h_0$ ( $\mu\text{m}$ )	$b_0$ ( $\mu\text{m}$ )
153	5.36	909	75.1	76.5	1.4	105
153	1.72	1210	75.0	76.5	1.6	144
108	3.0	1202	52.2	54.0	1.7	98
64	4.32	1204	30.6	32.0	1.4	57

Let us consider the behavior of an effective spherical cell behind a shock with the amplitude  $P_{s0}$  and the duration  $\tau_s$ . Assuming that the glass viscosity is so high that  $Re < 1$ , one can treat the process of GMB collapse as spherically symmetrical and neglect the wave reverberations in the cell.<sup>5</sup> We also assume that

glass and explosive can be treated respectively as viscoplastic and purely viscous media, and that their densities depend only on the shock strength. In addition, because heat exchange between GMB and air in the cavity is not considered, the pressure change in the cavity during the GMB collapse is adiabatic. With these assumptions, the behavior of a spherical effective cell is described by the continuity, impulse and energy conservation equations that are written separately for glass and explosive (subscript  $i=1$  and 2 respectively) as:

$$\frac{\partial}{\partial r}(r^2 v) = 0; \rho_i \left( \frac{\partial v}{\partial t} + v \frac{\partial v}{\partial r} \right) = \frac{\partial \sigma_r}{\partial r} + \frac{2}{r} (\sigma_r - \sigma_\theta) \quad (1, 2)$$

$$\rho_i c_i \left( \frac{\partial T}{\partial t} + v \frac{\partial T}{\partial r} \right) = \lambda_i \frac{\partial^2 (rT)}{r \partial r^2} - 2Y_i \frac{v}{r} + 12\mu_i \frac{v^2}{r^2} + W_i \quad (3)$$

Stresses are related to pressure as follows:

$$\sigma_r - \sigma_\theta = Y_i + 2\mu_i \left( \frac{\partial v}{\partial r} - \frac{v}{r} \right), \quad \sigma_r + 2\sigma_\theta = -3P$$

The boundary and initial conditions are:

$$r = a: \sigma_{r1} = -P_g \equiv -P_{g0} (a_0/a)^3 \gamma, \quad \partial T_1 / \partial r = 0$$

$$r = g: \sigma_{r1} = \sigma_{r2}, \quad \lambda_1 (\partial T / \partial r)_1 = \lambda_2 (\partial T / \partial r)_2, \quad T_1 = T_2$$

$$r = b: \partial T_2 / \partial r = 0$$

$$t = 0: a = a_0, \quad g = g_0, \quad b = b_0, \quad v = 0, \quad T_i = T_{0i}$$

Here  $r$  is the radial coordinate,  $t$  the time,  $v$  the radial velocity,  $\sigma_r$  and  $\sigma_\theta$  the radial and tangential stresses,  $Y$  the yield strength ( $Y_2=0$ ),  $\rho$  the density and  $c$  the heat capacity,  $\lambda$  the heat conductivity,  $T$  the temperature,  $\gamma$  and  $P_{g0}$  are the polytropic index and the initial pressure of air,  $W$  the heat release rate from chemical reaction:  $W_1=0$ ,  $W_2=p_2 Q Z \exp(-E/RT_2)$ , where  $Q$ ,  $Z$  and  $E$  are the heat of chemical reaction, the preexponential factor and the activation energy of the explosive.

To take into account the effects of temperature on the viscosity and yield strength we used the following dependencies:

$$\mu_i = \begin{cases} \mu_{oi}, & T < T_{mi} \\ \mu_{oi} \exp[T_{mi}(1/T - 1/T_{mi})], & T \geq T_{mi} \end{cases} \quad (4)$$

$$Y_i = \begin{cases} Y_{oi} [(T_{mi} - T)/(T_{mi} - T_0)]^{n_i}, & T \leq T_{mi} \\ 0, & T > T_{mi} \end{cases}$$

here  $\mu_{oi}$ ,  $T_{mi}$ ,  $T_0$ ,  $Y_{oi}$  and  $n_i$  are constants ( $T_{\mu 2}=0$  and  $Y_{02}=0$  for the explosive),  $T_0$  - standard temperature.

To close the system of Equations (1-3) one needs a relationship between the pressure in the GMB and the shock amplitude  $P_s(t)$ . It is assumed to be constant ( $P_s=P_{s0}$ ) during time  $\tau_s$  and then to decrease with time as  $P_s=P_{s0}\exp[-(t-\tau_s)/\tau_s]$ . Integrating Equations (1,2) over the radial coordinate from  $r=a(t)$  to  $r$  and taking into account boundary conditions at the inner interface of GMB, one can calculate the pressure profile  $P(r,t)$  in the cell. Integrating this profile once more gives the average pressure in the solid phase of the cell as

$$P_s = \phi P_g + (1 - \phi) \frac{3}{(b^3 - a^3)} \int_a^b P(r,t) r^2 dr \quad (5)$$

where  $\phi=(a/b)^3$  is the GMB porosity, and  $P_g=P_g(t)$  is the mean pressure in the cavity. However this relationship between the mean cell pressure and shock strength is not valid when dependencies (4) are taken into account. Therefore we used mainly constant viscosity and yield strength and replaced  $P(r,t)$  in Equation (5) by  $P(b,t)$ . For small GMB mass fractions this assumption is valid because the main drop of pressure takes place in a narrow layer of glass adjacent to the cavity and does not affect the pressure averaged over the cell volume. If properties of the glass and explosive are constant, then the governing system of equations splits into dynamic and thermal parts.

The governing equations were transformed to nondimensional form using typical scales for viscoplastic cavity collapse:  $P_{s0}$  is used as a characteristic scale for pressure and yield strength,  $a_0$  is used as a space scale;  $t_\mu=4\mu_1/P_{s0}$ ,  $v_\mu=a_0/t_\mu$  and  $T_\mu=3P_{s0}/(\rho_1 c_1)$  are used as time, velocity and temperature scales.<sup>5</sup> Integrating Equations (1,2) in the case of constant  $\mu_1$  and  $Y_1$  one can obtain a system of ordinary differential equations describing the behavior in time ( $\tau=t/t_\mu$ ) of the dimensionless radii of the cavity, GMB and cell (respectively  $A=a/a_0$ ,  $G=g/a_0$  and  $B=b/a_0$ ):

$$\begin{aligned} A[1 - F_1(1-\delta_2)\frac{A}{G} - \frac{3}{2}F_2]\frac{d^2A}{d\tau^2} = \\ - \frac{1}{Re^2} \left\{ \frac{\pi_s - \pi_g - \Sigma}{1 - F_0} + [1 - F_1(1-N_2)\frac{A^3}{G^3}] \frac{1}{A} \frac{dA}{d\tau} \right\} + \\ \frac{3}{2} \left( \frac{dA}{d\tau} \right)^2 [1 - 2F_2 - F_3 + \frac{2}{3}F_1(1-\delta_2)(2 - \frac{A^3}{2G^3})\frac{A}{G}] \quad (6) \end{aligned}$$

$$G^2 \frac{dG}{d\tau} = B^2 \frac{dB}{d\tau} = A^2 \frac{dA}{d\tau} \quad (7)$$

$$\tau = 0: A = 1, G = g/a_0, B = b/a_0, dA/d\tau = 0$$

Here  $Re = a_0(\rho_1 P_{s0})^{1/2}/(4\mu_1)$ ,  $\delta_2 = \rho_2/\rho_1$ ,  $N_2 = \frac{\mu_2}{\mu_1}$ ,

$$\sigma_1 = \frac{Y_1}{P_{s0}}, \pi_s = \frac{P_s}{P_{s0}}, \pi_g = \frac{P_g}{P_{s0}}, \Sigma = 2\sigma_1 \ln(G/A),$$

$$F_0 = (A/B)^3, F_1 = [1 - (G/B)^3]/(1 - F_0),$$

$$F_2 = (A/B)[(G^2 - A^2)/B^2 + \delta_2(B^2 - G^2)/B^2]/(1 - F_0),$$

$$F_3 = F_0(A/B)[B/A - B/G + \delta_2(B/G - 1)]/(1 - F_0).$$

The ordinary differential Equations (6,7) were solved numerically along with the energy Equation (3), with the partial derivatives approximated by an implicit finite-difference scheme. The computation region includes two domains:  $a \leq r \leq g$  (glass) and  $g \leq r \leq b$  (explosive). Because the boundaries of the cell change with time, the radial coordinate  $r$  was transformed to a nondimensional coordinate  $X$  similar to a Lagrange one. With this new variable the surface of the cavity  $r=a(t)$  is located at  $X=1$ , the outer interface of GMB  $r=g(t)$  corresponds to  $X=2$  and the outer surface of the cell  $r=b(t)$  is located at  $X=3$ .

When the dependencies (4) are taken into account, the governing equations do not split and additional integral terms appear in Equation (6):

$$\frac{1}{\mu_{01}} \frac{d \ln(A)}{d\tau} \int_a^b \frac{a^3}{r^3} \frac{\partial \mu_1}{\partial r} dr \quad \text{and} \quad \frac{1}{Y_{01}} \int_a^b \ln(r) \frac{\partial Y_1}{\partial r} dr$$

These terms lead to an increasing number of iterations at each time step.

## COMPUTATION RESULTS AND DISCUSSION

A model mixture of nitromethane (NM) with a small amount of PMMA was considered.<sup>2</sup> Table 2 lists base line input data in the model. There is an important difficulty with the glass viscosity. Due to the absence of reliable techniques to measure shear viscosity of condensed substances under shock loading, the uncertainty in this viscosity may reach a few orders of magnitude. Besides one can expect that the glass viscosity may drop essentially with temperature. Consequently, base values of the glass viscosity were chosen practically arbitrarily and a wide range parametric study of the influence of glass viscosity was undertaken with viscosity either constant or dependent on temperature. The explosive viscosity was assumed constant. Shock temperatures of pure nitromethane were used to simulate shock heating of the explosive.<sup>7</sup> Shock

heating of glass was neglected. Chemical kinetics parameters for pure nitromethane were used for the explosive decomposition.<sup>8</sup> If otherwise not stated, the results shown below correspond to infinite duration  $\tau_s$  of the initiating shock.

In general, the solution to our problem, depends on the following basic parameters  $Re$ ,  $Fo_1$  and  $Fo_2$ . The most important parameter is the Reynolds number  $Re = a_0(\rho_1 P_{so})^{1/2} / (4\mu_1)$  which governs the mode of GMB collapse. The Fourier number  $Fo_1 = t_\mu \lambda_1 / (\rho_1 c_1 h_0^2)$  is the ratio of the characteristic collapse time to the typical heat transfer time through the layer of glass and  $Fo_2 = t_\mu \lambda_2 / (\rho_2 c_2 g_0^2)$  determines the efficiency of the hot spot cooling by heat conduction into the explosive. The number of these parameters prohibits our making a parametric study of the problem.

#### EFFECT OF GMB ON EXPLOSIVE IGNITION

Let us consider a typical solution for the basic set of input parameters listed in Table 2 for a typical GMB with  $d_0 = 40 \mu m$  and  $h_0 = 1.5 \mu m$  at  $M_1 = 0.5\%$ . Figure 1 shows the computed temperature profiles in the effective cell at different times for the shock strength  $P_{so} = 20$  kbar ( $t_\mu = 19.8 \mu s$ ,  $Re = 9.59 \cdot 10^{-4}$ ). Table 3 lists the changes with time of the cell radii, collapse velocity and temperatures  $T_a$  and  $T_g$  at two characteristic points of the cell - at the inner [ $X=1$  or  $r=a(t)$ ] and outer [ $X=2$  or  $r=g(t)$ ] faces of GMB. One observes that the dissipative heating is essentially localized in the internal layers of the cell and mostly in the glass. The temperature is maximal at the inner face of GMB and decreases when the radius decreases. The difference between  $T_a$  and  $T_g$  results from the dependence of the dissipative sources on the radial coordinate and the effectiveness of heat transfer through glass that is

TABLE 2. INPUT DATA OF THE MODEL

Property	Glass	Explosive
Density, $\rho$ , kg/m <sup>3</sup>	2130	1140
Heat capacity, $c$ , J/(kg·K)	1200	1260
Heat conductivity, $\lambda$ , W/(m·K)	0.25	0.247
Viscosity, $\mu$ , Pa·sec	$10^4$	2
Yield strength, $Y$ , kbar	5	0
Preexponential factor, $Z \cdot 10^{-10}$ , s <sup>-1</sup>	-	6.76
Heat effect, $Q \cdot 10^{-6}$ , J/kg	-	4.66
Activation energy, $E$ , kcal/mole	-	30

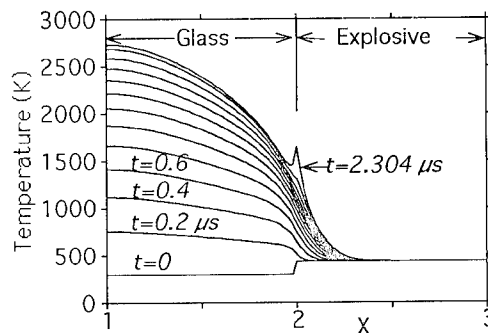


FIGURE 1. TEMPERATURE PROFILES ( $\Delta t = 0.2 \mu s$ )

controlled by  $Fo_1$ . The explosive is heated in a relatively thin layer adjacent to the outer face of GMB. With our input data, the increase of temperature at the outer surface of the cell ( $r=b$ ) is negligibly small.

The temperature rise of the explosive at the contact boundary with the glass is the most interesting result from the point of view of the GMB sensitizing effect. The computed dependence  $T_g(t)$  for  $P_{so} = 20$  kbar is shown by curve 1 on Figure 2 and by the last column in Table 3. At first, explosive behaves as an inert substance heated mainly by a conductive heat transfer from the hot parts of the GMB (test run with zero heat conductivities of glass and explosive showed that the GMB collapse practically did not result in heating of explosive inner layers). For temperatures above 1050 K, the temperature growth rate increases rapidly and becomes nearly infinite due to the heat release by the chemical reaction. The time when the slope of the  $T_g(t)$  profile becomes

TABLE 3. BASE LINE SOLUTION

t ( $\mu s$ )	a ( $\mu m$ )	g ( $\mu m$ )	b ( $\mu m$ )	da/dt (m/s)	$T_a$ (r=a)	$T_g$ (r=g)
0.0	18.50	20.00	85.87	0.00	300	436
0.2	17.70	19.32	85.83	-3.70	756	509
0.4	17.01	18.75	85.81	-3.23	1118	636
0.6	16.40	18.25	85.78	-2.86	1415	742
0.8	15.86	17.82	85.76	-2.56	1662	831
1.0	15.38	17.44	85.75	-2.31	1873	906
1.2	14.93	17.10	85.73	-2.11	2054	971
1.4	14.53	16.79	85.72	-1.93	2212	1029
1.6	14.16	16.52	85.71	-1.78	2351	1083
1.8	13.82	16.30	85.70	-1.65	2475	1139
2.0	13.50	16.04	85.69	-1.54	2585	1204
2.2	13.20	15.83	85.69	-1.44	2685	1318
2.3	13.05	15.73	85.68	-1.39	2733	1664

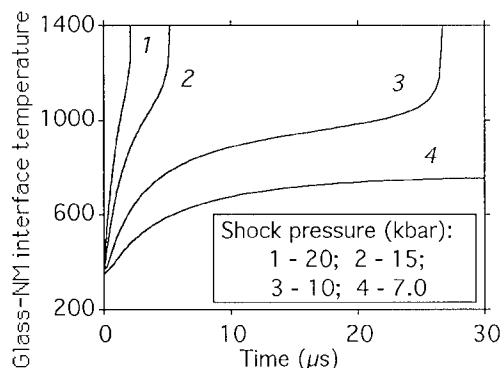


FIGURE 2. TEMPERATURE EVOLUTION OF THE GLASS-NM INTERFACE

nearly infinite is taken here to be the ignition delay time  $t_{ign}$ . In this example, at  $t=t_{ign}=2.304\mu s$  the cavity radius is about 70% of its initial value and the cavity collapse velocity is  $\approx 1.4$  m/s. If one reduces the applied pressure  $P_{so}$  from 20 kbar to 15 and 10 kbar (curves 2 and 3 in Figure 2), explosive heating becomes slower and the ignition delay grows. Finally at  $P_{so}=7$  kbar (curve 4) heating of the explosive is not sufficient for the ignition and the explosive temperature at  $r=g$  passes through a maximum at  $t\approx 36\mu s$  and then decreases.

Let us consider the influence of the governing parameters of the model on the ignition delay  $t_{ign}$ . Figure 3 demonstrates the dependence of  $t_{ign}$  on shock strength  $P_{so}$  at different values of the GMB parameters (curve 1 corresponds to the basic set of input parameters). One can see that  $t_{ign}$  increases as  $P_{so}$  decreases and that the increase in  $t_{ign}$  becomes very important as the pressure approaches a certain threshold value denoted by  $P_{cr}$ . Ignition of the explosive does not take place when  $P_{so} < P_{cr}$ . This critical pressure characterizes the shock sensitivity of the explosive to ignition and increases rapidly with increase of GMB thickness: curves 6, 1 and 4 correspond to  $h_0=0.75, 1.5$  and  $3 \mu m$  (at nominal  $d_0=40 \mu m$ ). Ignition delay decreases with increase of GMB diameter (compare curves 2, 1 and 5 that correspond to  $d_0=20, 40$  and  $80 \mu m$  at fixed  $h_0=1.5 \mu m$ ). The relative thickness of GMB,  $2h_0/d_0$ , is the same for curves 5 and 6 and four times larger for curves 2 and 4. Note that curves 5 and 6 coincide and curve 4 is located above curve 2. Thus the sensitizing effect of GMB depends on the relative GMB thickness and decreases essentially for larger  $2h_0/d_0$ . However this conclusion is valid until

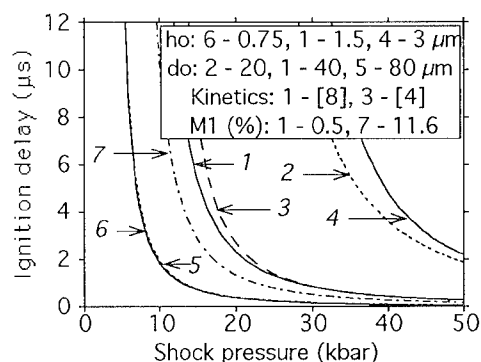


FIGURE 3. IGNITION DELAY VS PRESSURE

$Fo_1 = t_{\mu} \lambda_1 / (\rho_1 c_1 h_0^2) > O(1)$ . Indeed, the effect of  $h_0$  at smaller  $Fo_1$  or larger  $h_0$  becomes more important than that of  $d_0$  because dissipated energy localizes in the inner hotter layers of GMB and the colder external layers of GMB cannot ignite the explosive. In other words, at small  $Fo_1$ , the characteristic heated layer around the cavity becomes smaller than GMB thickness. As a result, thick-walled GMBs may "block" heating of the explosive.

### EFFECT OF VISCOSITY

Figure 4 shows the influence of the glass viscosity on the GMB sensitizing effect (curve 4 corresponds to the basic set of input parameters with  $\mu_1=10^4$  Pa·s). One can see that for  $\mu_1=10^1-10^4$  Pa·s (curves 1-4) the effect of viscosity on the critical pressure  $P_{cr}$  is quite weak but non monotonous. This feature is due to the effect of two opposite trends: decrease of  $\mu_1$  increases energy dissipation rate,<sup>5</sup> and temperature growth rate at the inner interface of GMB, however the amount of heat dissipated in the cell does not depend on the viscosity and the drop of  $Fo_1 \sim \mu_1$  again increases the blocking effect of GMB. Hence a large decrease in glass viscosity may even increase  $t_{ign}$  and  $P_{cr}$ . The increase of the glass viscosity in comparison with its base value (curves 5 and 6) shifts the critical pressure and ignition time to higher values because the collapse time  $t_{\mu}$  grows and  $Fo_2$  becomes higher than 1. Hence, decrease of energy dissipation rate is accompanied by enhanced heat transfer from the GMB into the bulk of the explosive. This is why further increase of the glass viscosity makes ignition of the explosive impossible in the considered pressure range. Thus, the viscoplastic mechanism can provide the GMB sensitizing effect in a

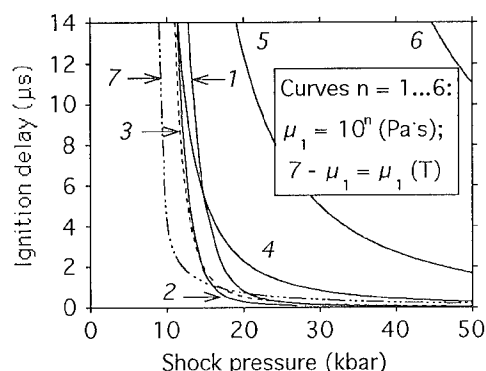


FIGURE 4. INFLUENCE OF GLASS VISCOSITY

wide range of glass viscosity from  $\approx 10$  to  $10^6$  Pa·s, where the lower limit corresponds to the condition  $Re < 1$  and the upper one to  $Fr < 1$ .

We also used variable viscosity  $\mu_1$  and yield strength  $Y_1$  of glass described by Equation (4) with parameters providing 20-50 fold decrease of  $\mu_1$  in the range of expected temperature rises. Both  $\mu_1(T)$  and  $Y_1(T)$  effects decrease the ignition delay and critical pressure slightly, i.e., increase GMB sensitizing effect (curve 7 in Figure 4).

The effects of some other parameters on the ignition delay were also studied. For example, the influence of the GMB mass fraction at constant values of  $d_0$  and  $h_0$  is illustrated by curves 1 and 7 in Figure 3. One can see that  $P_{cr}$  and  $t_{ign}$  decrease with increase of  $M_1$ , because at the same time the volume fraction of cavities  $\phi_0 = (a_0/b_0)^3$  increases and, hence, according to Equation (5)  $P_{cr}$  decreases proportionally to  $(1-\phi_0)$ . The effect of chemical kinetics is demonstrated by curves 1 and 3 which correspond to the kinetics parameters for NM used by Chaiken<sup>8</sup> and Mader.<sup>4</sup>

Finally the effect of shock duration  $\tau_s$  on  $t_{ign}$  and  $P_{cr}$  was studied. The ignition delay does not depend on  $\tau_s$  if  $\tau_s$  is larger than a "nominal" ignition delay  $t_{ign}^{nom}$  which corresponds to the same  $P_{s0}$  and infinite shock duration and which was presented above for different cases. When  $\tau_s$  becomes smaller than  $t_{ign}^{nom}$ , the ignition delay begins to grow and the sensitizing effect of GMB disappears when  $\tau_s$  is 3-4 times lower than  $t_{ign}^{nom}$ .

## COMMENTS ON THE GMB EFFECT ON CRITICAL DIAMETER

Unfortunately, the predicted trends cannot be verified now due to the lack of experimental data. That is why we can rely only on critical detonation diameters of GMB sensitized explosives. We plan to perform a detailed analysis of detonation limits in these explosives in the future. Now, however, we can demonstrate the effect of ignition delay in near-critical conditions qualitatively by analyzing available data on critical diameters of detonation in GMB sensitized explosives. A linear correlation of critical diameters with the reciprocal of the GMB specific surface is obtained as a result of this analysis.

Let us consider initiation and growth of chemical reaction behind a detonation wave front in a GMB-explosive mixture. Taking into account the model described above, a local chemical reaction will be initiated in a thin layer of explosive surrounding the GMB while the main part of explosive is still relatively cold. Hence, the subsequent evolution of the chemical reaction might proceed as a burning wave, and GMB spacing,  $L_p$ , must affect strongly the critical diameter (in our notations  $L_p = 2b_0(\pi/6)^{1/3}$  for a cubic set distribution of GMB). To estimate the effect of  $L_p$  we introduce a few assumptions. First, we neglect the ignition delay in comparison with the characteristic time of chemical reaction or burning (later we shall see that this assumption contradicts some experimental data). Then we use simulation results,<sup>9</sup> which predict that "the critical diameter of heterogeneous explosives scales with a chemical reaction rate", i.e., fast reactions give small critical diameters and vice versa. Finally, we ignore the dependence of the reaction rate on shock pressure, because experimental data show that the critical detonation velocity  $D_c$  (and, hence, shock pressure) is weakly dependent on GMB parameters for a given explosive (see Table 4). With these assumptions, the chemical reaction rate is proportional to the total surface of ignited hot spots per unit volume and the critical diameter  $d_c$  is inversely proportional to the product of the number of GMB per unit volume,  $N$ , and GMB surface,  $\pi d_0^2$ . Taking into account that  $N$  is reciprocally proportional to  $L_p^3$ , we arrive at

$$d_c \sim (Nd_0^2)^{-1} \sim (d_0^2/L_p^3)^{-1} \sim L_p^3/d_0^2 \sim 1/A_s \quad (8)$$

Here  $A_s$  is the specific surface of the GMB in the explosive. This simple formula predicts that the

experimental critical diameters for the given explosive must lie on a unique straight line when plotted against  $L_p^3/d_0^2$  independently of GMB mass fraction and size (note that  $L_p$  approaches  $d_0$  with increase of GMB mass fraction). It is important that for any explosive the continuation of this straight line should pass through the origin of the reference frame if our three assumptions are valid. The slope of the line (8) should decrease with increase of explosive burning rate (or reactivity) and, generally, confinement strength. It should be emphasized that this simple formula cannot be used for very large  $L_p^3/d_0^2$  corresponding to small GMB fractions when  $d_c$  approaches the critical diameter of homogeneous explosive.

Experimental critical diameters are plotted versus  $L_p^3/d_0^2$  in Figure 5 and the respective experimental conditions are listed in Table 4. Examination of the plots in figure 5 provides striking evidence for the validity of the linear relationship between  $d_c$  and  $L_p^3/d_0^2$  developed in expression (8), i.e., the critical diameter of GMB sensitized explosive changes linearly with the reciprocal of the GMB specific surface in a wide range of GMB concentrations. For example, experimental points corresponding to line 1 are described by the following correlation equation,<sup>10</sup>

$$d_c = 0.464 + 0.0159 L_p^3/d_0^2 \quad (9)$$

where  $L_p$  and  $d_0$  are measured in  $\mu\text{m}$  and  $d_c$  in mm. The correlation coefficient is 0.992.

However two different trends can be observed: lines 1-4 follow the strict proportionality predicted by Equation (8), and line 5 declines from it and cuts the ordinate axis at  $d_c = 8$  mm. It is quite surprising that line 6 obtained for glass beads,<sup>12</sup> has nearly the same

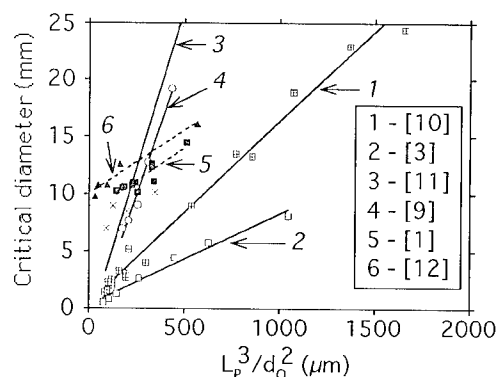


FIGURE 5. CRITICAL DIAMETERS OF GMB SENSITIZED EXPLOSIVES

behavior as line 5. This second trend may be explained by withdrawing the assumption of zero ignition delay, for then an additive term should appear in Equation (8) and the strict proportionality should be replaced by a linear one. Indeed, we propose two arguments in favor of this statement: i) following the model described above, in the case of line 5, the ignition delay of AN-based explosive must be quite important because the GMB thickness is higher and the critical detonation velocity and, hence, the pressure are lower than in other cases (see Table 4); ii) line 6 is obtained utilizing very fine glass beads and beads of the same size as GMBs did not sensitize explosive at all.<sup>12</sup>

## CONCLUSIONS

The initiation of chemical reaction in the shocked explosives containing glass microballoons (GMB) was analyzed by using a viscoplastic model for hot spot formation. Due to a great difference in the viscosities of glass and explosive, heat dissipated during

TABLE 4. GMB EFFECT ON CRITICAL DETONATION DIAMETERS (SEE FIGURE 5)

No of line	Ref.	Base component of explosive	Matrix density (g/cc)	Range of GMB fractions (%)	$d_0$ ( $\mu\text{m}$ )	$h_0$ ( $\mu\text{m}$ )	Range of $D_c$ (km/s)	Range of $d_c$ (mm)	Range of $L_p$ ( $\mu\text{m}$ )
1	10	NM	1.14	0.25 - 10 <sup>m</sup> )	43, 74, 109 <sup>s</sup> )	1	3.4-3.8	1.4 - 24.5	53-242
2	3	AN	1.34	2.5 - 77 <sup>v</sup> )	60 <sup>p</sup> )	0.5 <sup>e</sup> )	-	0.5 - 8 <sup>l</sup> )	64-224
3	11	EGMN	1.3	0.4 - 7.3 <sup>m</sup> )	80 <sup>p</sup> )	0.75 <sup>e</sup> )	3.3-3.6	7.0 - 54	83-182
4	9	AN	-	10.0 - 25 <sup>v</sup> )	83 <sup>s</sup> )	-	3.0-3.5	7.0 - 19.2	105-143
5	1	AN	1.41	1.0 - 12 <sup>m</sup> )	64, 71, 110, 130, 153 <sup>s</sup> )	1.5 <sup>e</sup> )	2.5-3.0	10.2 - 14.5	68-229
6	12	NM <sup>b</sup> )	1.12	0.5 - 9 <sup>m</sup> )	2.5 <sup>s</sup> )	-	-	9.8 - 16	6-15

NM - nitromethane; AN - ammonium nitrate; EGMN - ethylene glycol mononitrate; <sup>b</sup>) data correspond to glass beads, not GMB; <sup>e</sup>) evaluated on the basis of original data; <sup>m</sup>) GMB mass fractions, <sup>p</sup>) polydispersed GMBs, <sup>s</sup>) sieved fractions; <sup>l</sup>) critical thickness measured in wedge explosive set-up, <sup>v</sup>) GMB volume fractions.

the GMB collapse localizes in a layer of glass and the temperature of the explosive increases due to the conductive heat transfer from the hotter inner parts of the GMB. Chemical reaction is initiated at the contact boundary between glass and explosive. Critical shock pressures exist below which ignition of the explosive does not take place. Given an explosive, the sensitizing effect of GMB decreases when the ratio of GMB thickness to its diameter increases, however the effect of GMB thickness may be more important than its diameter. The GMB sensitization effect can be explained as a result of two opposite trends: the presence of GMB provides hot spot formation at relatively low shock strengths (about 10 kbar), but at the same time maximal overheating is localized at the inner surface of the GMB and, hence, thick-walled GMBs may block heating and prevent ignition of the explosive.

Analysis of available experimental data for heterogeneous explosive mixtures with GMB reveals a striking linear correlation of the critical detonation diameter and the reciprocal of the GMB specific surface. It would be interesting to check if this correlation is valid for porous solid explosives. This analysis shows also that the ignition delays cannot be ignored in the problem of critical detonation diameter.

Because some simplifying assumptions were used in our analysis of the GMB sensitizing effect, the results presented in this paper are mainly qualitative. Our next step to provide a better understanding of the GMB sensitizing effect would be based on experimental verifications of computed trends and evaluation of glass viscosity under shock loading.

We are grateful to Dr P. Vidal (L.E.D., Poitiers, France), Dr M. Cowperthwaite (S.R.I. International, USA) for their assistance and Dr. P.A. Taylor (S.N.L., Albuquerque, USA) for useful comments.

## REFERENCES

1. Lee, J.; Persson, P.A., "Detonation behavior of emulsion explosives", *Propellants, Explosives, Pyrotechnics*, Vol. 15, 1990, p. 208.
2. Presles, H.N.; Campos, J.; Heuze, O.; Bauer, P., "Effects of microballoons concentration on the detonation characteristics of nitromethane - PMMA mixture", *Ninth Symposium (International) on Detonation*, OCNR 113291-7, 1989, p. 925.
3. Yoshida, M.; Iida, M.; Tanaka K.; Fujiwara, S.; Kusakabe, M.; and Shino K., "Detonation behavior of emulsion explosives containing glass microballoons", *Eighth Symposium (International) on Detonation*, NSWC MP 86-194, 1985, p. 993.
4. Mader, C.L., *Numerical Modeling of Detonation*, Univ. of California Press, Berkeley, 1979.
5. Khasainov, B.A.; Borisov, A.A.; Ermolaev, B.S.; Korotkov A.I., "Two-phase visco-plastic model of shock initiation of detonation in high density pressed explosives", *Seventh Symposium (International) on Detonation*, Annapolis, MD, NSWC MP 82-334, 1981, p. 435.
6. Carrol, M.; Holt, A.C., "Static and dynamic pore-collapse relations for ductile porous materials" *J. Appl. Phys.*, Vol. 43, 1972, p.1626.
7. Cowperthwaite, M.; Shaw, R., "Equation of state for liquids. Calculation of the shock temperature of carbon tetrachloride, nitromethane and water in the 100-kbar region", *J. of Chem. Phys.*, V.53, No 3, 1970, p. 555.
8. Chaiken, R.F., "Correlation of shock pressure, shock temperature and detonation induction time in nitromethane", *Symp. on High Dynamic Pressures*, CEA, Paris, 1978, p. 41.
9. Leiper, G.A.; Cooper, J., "Reaction rates and the charge diameter effect in heterogeneous explosives", *Ninth Symposium (International) on Detonation*, OCNR 113291-7, 1989, p. 197.
10. Presles, H.N.; Vidal, P.; Gois, J.C.; Khasainov, B.A.; Ermolaev, B.S., "Influence of Glass Microballoons Size on the Detonation of Nitromethane Based Mixtures", Paper accepted for presentation at the XIV<sup>th</sup> ICDERS, Coimbra, Portugal, 1993.
11. Chan, S.K., "A model for predicting the critical diameter of bubble sensitized explosives", *Symp. on High Dynamic Pressures*, CEA, Paris, 1978, p. 233.
12. Engelke, R., "Effect of number density of heterogeneities on the critical diameter of condensed explosives", *Phys. Fluids*, Vol. 26 (9), 1983, p.2420.

## DISCUSSION

EDWARD L. LEE

Lawrence Livermore National Laboratory, Livermore, California

There is a vast gulf between the analyses presented in the papers by Chaudhri, Almgren, & Persson; Khasainov, Ermolaev & Presles; and Gois, Campos & Mendes. Chaudhri's results clearly indicate hydrodynamic closure of  $\mu$ -balloons. Khasainov, Ermolaev & Presles consider spherical viscoplastic collapse in the *same* region of shock intensity. Gois, Campos & Mendes do not clearly differentiate.

## REPLY BY B. A. KHASAINOV, B. S. ERMOLAEV, AND H.-N. PRESLES:

A scale effect during closure of voids and microballoons in shock waves is controlled by Reynolds number,  $Re$ , described in our paper. Large microballoons ( $Re \gg 1$ ) must follow hydrodynamic mechanism of closure with formation of jets observed by Chaudhri in the case of millimeter-size balloons. The hydrodynamic mechanism of this kind of void collapse in liquid explosives was studied numerically by Mader.

However, collapse of smaller microballoons may follow viscoplastic mechanism if the balloon material viscosity is so high that  $Re < 1$ . At small  $Re$  the jet cannot be formed and the shape of the microballoon must be close to spherical during collapse of the balloon. These assumptions made in our work are supported by the numerical results of P. S. Chou, D. Liang, and Z. Ritman ("The Viscoplastic Hot Spots in Pore Collapse" this symposium). They used the two-dimensional code DEFEL to simulate the closure of a *cylindrical* void in a viscoplastic compressible medium. Their results clearly demonstrate that at relatively small  $Re \approx 0.17$  (void radius  $a_0 = 0.3 \mu\text{m}$ , shock pressure  $P_{SO} = 3 \text{ GPa}$ , viscosity  $\mu = 1 \text{ Pa}\cdot\text{s}$ ) "viscoplasticity of the material retards the motion of the surface of the pore, thus decreases the impact between the upstream and downstream surfaces." The shape of the void is nearly symmetric after about a twofold decrease of its volume, and local ignition of the solid explosive takes place at an early stage of pore deformation.

Thus, for small Reynolds numbers, the shock-induced collapse of *spherical* microballoons must have a viscoplastic nature.



## SHOCK INITIATION OF NITROMETHANE - PMMA MIXTURES WITH GLASS MICROBALLONS

J. C. Gois, J. Campos and R. Mendes  
Laboratory of Energetics and Detonics  
Faculty of Sciences and Technology  
University of Coimbra  
3000 Coimbra, Portugal

The effect of glass microballoons (GMB) as sensitizer on shock initiation of a homogeneous mixture of nitromethane/polymethylmetacrylate (NM/PMMA) is described. GMB size is between 10 and 150  $\mu\text{m}$ , 1  $\mu\text{m}$  glass wall and density of 200  $\text{kg/m}^3$ . Detonation velocity, referred to infinite diameter, decreases linearly with increasing GMB concentration. The theoretical approach, using BKW, H9 and H12 EoS, proves the non ideal detonation behaviour for large concentration of GMB. NM/PMMA mixture is a very insensitive explosive with large critical diameter. The shock sensitivity of NM/PMMA-GMB mixtures was measured with slapper and gap experiments. Slapper experiments (12  $\mu\text{F}$ , 25-40 kV) proves the strong sensitizer effect of GMB. Donor charge of gap experiments was pure NM. The initiation delay and the distance of run to detonation were measured, simultaneously, in gap experiments, by the short-circuit of a parallel double axial resistive wire, inside the acceptor charge, and by the crush depth of an aluminum bar, placed under the acceptor. The Pop-plot shows that NM/PMMA-GMB mixtures, with 1% and 2% of small GMB - average diameter of 45  $\mu\text{m}$ , are initiated by induced shock pressure less than 3 GPa. This minimum initiation shock pressure increases with increasing GMB size and with decreasing GMB concentration, suggesting that the initiation mechanism, by hot spots formation due to the collapse of GMB, reducing critical diameter of NM/PMMA, depends on distance between particles. Small GMB proves to be a strong sensitizer of NM/PMMA mixture.

### INTRODUCTION

Glass microballoons (GMB) are generally used to sensitize emulsion explosives. Detonation velocity, initiation sensitivity and critical diameter depend on concentration of GMB.<sup>1-3</sup> Nitromethane (NM) is a very known pure chemical homogeneous explosive. Its low sensitivity is ideal to understand the sensitizer role of GMB. The large discrepancy between the density of NM (1.135) and GMB (0.2) not allows a homogeneous distribution of GMB inside NM. This requirement can be obtained increasing NM viscosity, by adding a few percent of polymethylmetacrylate (PMMA), completely solved at initial NM. NM/PMMA mixture has large critical diameter and seems to be more insensitive than pure NM.<sup>4</sup> Studies of mixtures of NM, containing physical heterogeneities, show detonation properties

more as solids than liquids, because, under shock conditions, the heterogeneities produce hot spots, which increase the energy release rate in the NM.<sup>5-8</sup> Presles et al.<sup>5</sup> studied the effect of GMB concentration on steady-state detonation of NM/PMMA-GMB mixtures. Recently Gois et al.<sup>6-7</sup> studied the effect of GMB size on steady-state detonation velocity and critical diameter characteristics. GMB allow support steady detonation in cylindrical charges with smaller diameter than the critical diameter of the base NM/PMMA mixture.<sup>6-7</sup> The aim of the present study is to contribute to a better understanding of the specific role of GMB as sensitizer on NM/PMMA mixture.

Shock initiation of an explosive describes the process in which a shock wave, passing through the explosive material, grows into a detonation wave. These kind of experiments can be done submitting one

of the wedges of explosive test sample under a large plane shock wave generator (from a donor explosive charge through an inert barrier, electrically exploding metal foils - slapper, or gas guns)<sup>9-10</sup> and observing when and where the rapid change of shock velocity occurs in the explosive sample. A sequence of such shots, varying initial shock pressure on the explosive, allows to define a graph of distance of run to detonation  $L_\tau$  and its induced delay  $\tau$ , as a function of induced shock pressure  $P$ . These graphs are known, in logarithmic scale, as the Pop-plot.<sup>11</sup> The Pop-plot and Hugoniot data has been used to describe and compare shock sensitivity of heterogeneous explosives.<sup>12-13</sup> In present study the shock sensitivity of the NM/PMMA-GMB mixtures was measured by slapper and gap experiments.

## EXPLOSIVE MIXTURES

Two types of GMB were used. QCel 300 and QCel 520 FPS (supplied by PQ Corporation) both with  $1\ \mu\text{m}$  wall thickness, shown in Figure 1, and an effective density about  $200\ \text{kg}\cdot\text{m}^{-3}$ .

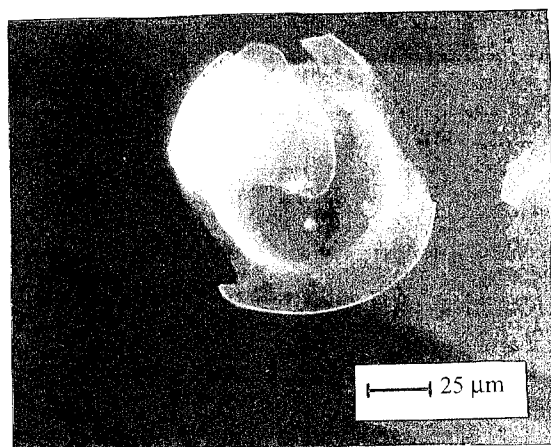


FIGURE 1. BROKEN GMB SHOWING WALL THICKNESS

The effect of particle size on shock sensitivity was studied sieving QCel 300 GMB in ten granulometric sizes and selecting two of them. Cumulative distribution of these used three class of GMB, referred to its mean diameter  $\bar{d}_p$ , were measured by laser diffraction spectrometry and shown in Figure 2.

In order to allow a homogeneous distribution of GMB inside explosive, NM viscosity was increased up to  $0.864\ \text{Pa}\cdot\text{s}$  (measured by a Brookfield viscometer with Spindle A at  $100\ \text{rpm}$  at  $21^\circ\text{C}$ ) by adding 4 weight mass percent of PMMA. NM/PMMA-GMB mixtures were defined by the mass fraction  $X$  of GMB.

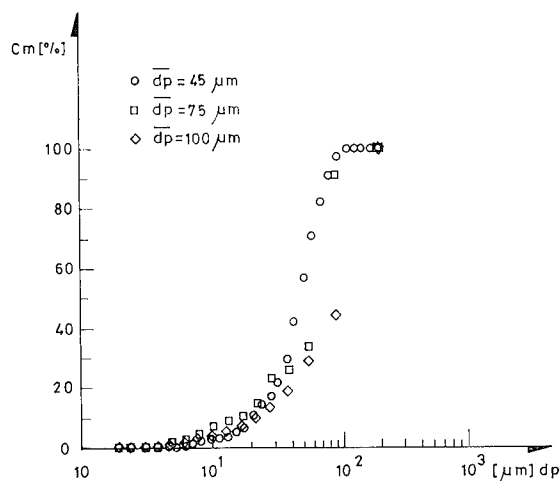


FIGURE 2. CUMULATIVE DISTRIBUTION OF THREE USED GRANULOMETRIC CLASS OF GMB

Air concentration, from inside GMB, in NM/PMMA-GMB mixtures, can be obtained multiplying mass fraction  $X$  by  $4.36 \times 10^{-3}$ ,  $7.37 \times 10^{-3}$  and  $10 \times 10^{-3}$  constants, respectively for granulometric class of  $\bar{d}_p = 45, 75$  and  $100\ \mu\text{m}$ . Results show the influence of the glass mass of GMB on NM/PMMA-GMB measured global density.

TABLE 1. DENSITY OF NM/PMMA-GMB MIXTURES, AS A FUNCTION OF MASS FRACTION  $X$  AND MEAN DIAMETER OF GMB,  $\bar{d}_p$ .

$\rho$ [kg/m <sup>3</sup> ]	$\bar{d}_p$ [μm]		
	45	75	100
$X$ [%]			
0	1 135	1 135	1 135
1	1 092	1 052	1 012
2	1 043	969	911

## DETONATION VELOCITY AND CRITICAL DIAMETER

Detonation velocity of NM/PMMA-GMB mixtures, confined in PMMA and steel tubes, as a function of the reciprocal charge diameter, shown downward concave curves.<sup>6</sup> This diameter effect curve was not observed for the base NM/PMMA mixture. Figure 3 shows the detonation velocity  $D_\infty$ , referred to infinite diameter, decreasing linearly with increasing GMB concentration.

$D_{\infty}$  values for low GMB concentrations show a good correlation with theoretical predictions using THOR code, with BKW, H9 and H12 EoS, as a function of NM/PMMA-GMB density.<sup>14</sup> High GMB concentration, up to  $X=6\%$ , proves the influence of GMB on non ideal detonation behaviour.

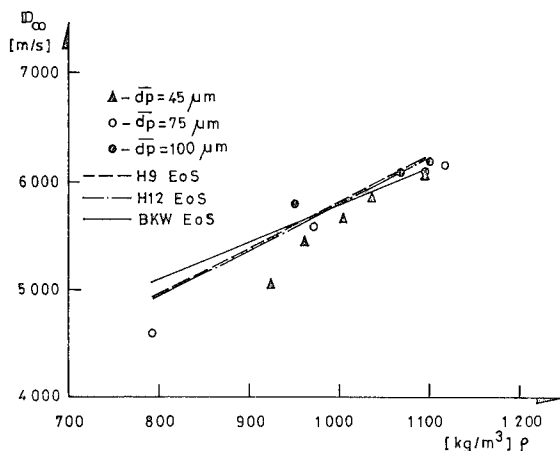


FIGURE 3. THEORETICAL AND EXPERIMENTAL  $D_{\infty}$ , AS A FUNCTION OF NM/PMMA-GMB DENSITY

NM/PMMA-GMB mixtures allow steady detonation in cylindrical charges with much smaller diameter (3 mm with plastic confinement), than original NM/PMMA mixture (30 mm).<sup>7</sup> Independently of GMB size and for moderate GMB concentration ( $5 < X < 10\%$ ) the minimum critical diameter is nearly the same.<sup>7</sup>

## SHOCK INITIATION EXPERIMENTS AND RESULTS

### Slapper Experiments and Results

Shock initiation threshold has been measured using slapper apparatus developed by TNO-PML\*. This experimental apparatus is a device which can accelerate plastic flyers to velocities high enough to initiate explosives. A strong current, generated by a capacitor discharge (12  $\mu$ F, 25-40 kV) feeds an aluminium foil of 60  $\mu$ m of thickness. This foil evaporates instantaneously and the high pressure developed accelerates plastic flyer (kapton - diameter 9 mm and thickness 125  $\mu$ m) inside a PVC barrel of 5 mm of length. Terminal flyer velocity was from 6.5 to 9 km/s. In order to confine the explosive mixture, the bottom of tube sample was closed by another kapton plate. Two optical fibers were introduced, parallel to

the axis, into the wall of detonation tube, near top, to verify the existence or not of initiation and to measure detonation velocity. Four optical fibers, on top of detonation tube, allow to evaluate the detonation front curvature.

Calibration of the flyer velocity  $U_f$  as a function of current density  $J_B$ , shown in Figure 4, follows the equations:

$$J_B = \text{probe factor} \times V_{I_{\max}}/S \quad (1)$$

$$U_f = 12.2 \times J_B^{0.71} \quad (2)$$

where the tension  $V_{I_{\max}}$  is the measured value for maximum current  $I_{\max}$ , and  $S$  represents the section of the foil.

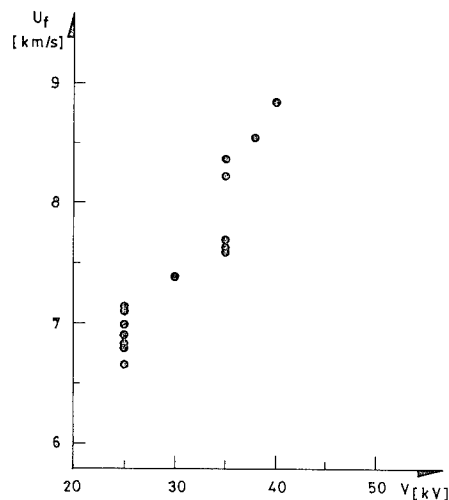


FIGURE 4. VELOCITY OF THE KAPTON FLYER, AS A FUNCTION OF DISCHARGE TENSION OF CAPACITORS

The evolution of the induced shock pressure  $P$  on kapton, as a function of its particular velocity  $U_p$ , ( $P=2.57-2.32 \times U_p + 0.63 \times U_p^2$ )<sup>15</sup> allows the calculation of induced pressure on kapton, from measured value of  $U_f$  ( $U_p \approx U_f/2$ ). Shock impedance correction, between kapton and explosive, has been made to determine shock induced pressure on explosive sample.<sup>16</sup> Shock initiation results of NM/PMMA-GMB mixtures, as a function of discharge tension of capacitors, is shown in Figure 5 (D-detonation, F-failure). Failures only happen for mixtures with large size of GMB (average diameter of 100  $\mu$ m). The minimum shock intensity, produced by slapper apparatus, is strong enough to detonate all the others mixtures.

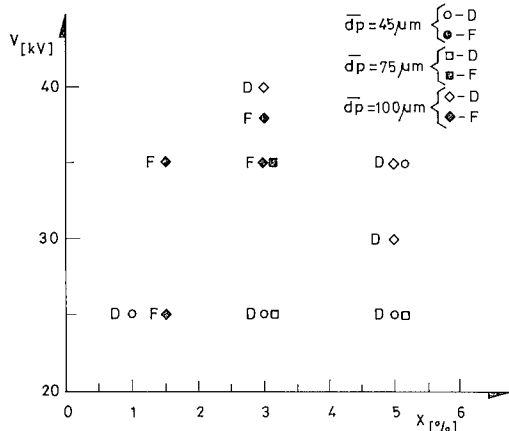


FIGURE 5. DETONATION OR FAILURE OF NM/PMMA-GMB MIXTURES, AS A FUNCTION OF DISCHARGE TENSION OF CAPACITORS AND GMB CONCENTRATION

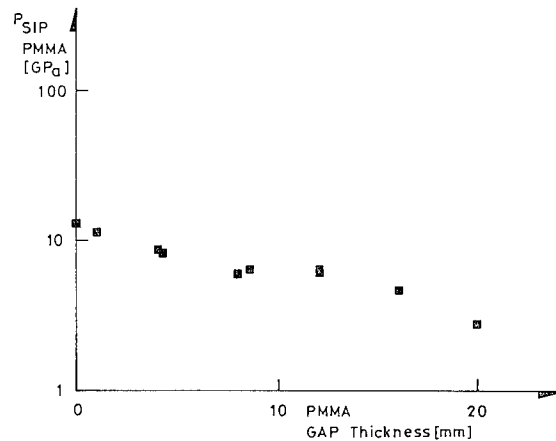


FIGURE 7. INDUCED SHOCK PRESSURE VARIATION, AS A FUNCTION OF PMMA THICKNESS OF GAP

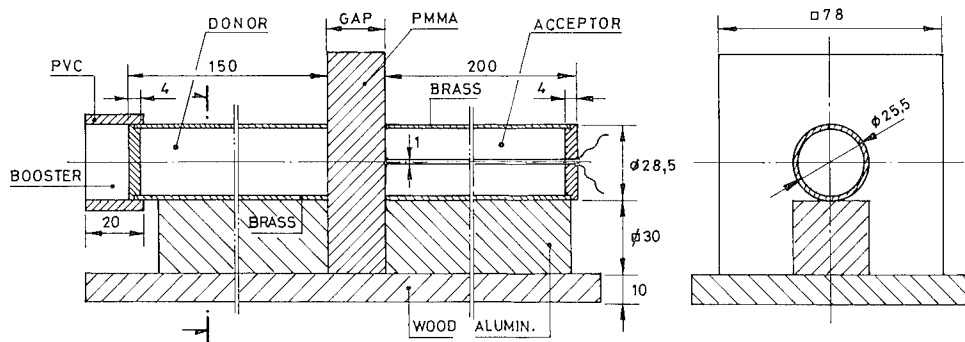


FIGURE 6. GAP EXPERIMENTAL ASSEMBLY

### Gap Experiments

The gap assembly, shown in Figure 6, has pure NM as donor charge and a plate of PMMA as gap. The donor and acceptor charges have internal diameter of 25.5 mm. Wall confinement was brass tube with 1.5 mm of thickness. This condition ensure an almost plane wave detonation of NM donor.<sup>17</sup> An ionization probe method was used to measure the detonation velocity of NM (donor).<sup>18</sup> Figure 7 shows the induced shock pressure on the acceptor, as a function of PMMA gap thickness. This pressure was measured by shock induced polarization<sup>19</sup> on a PMMA plate, of 1 mm of thickness, fixed at the end of PMMA gap, instead of the acceptor charge. The extrapolation to zero thickness of PMMA gap, shown in Figure 7, leads to value of NM detonation pressure, with good agreement with literature.<sup>16</sup> In order to verify the existence or not of detonation on acceptor, a parallel double thin resistive wire (100  $\mu m$  diameter and 174  $\Omega/m$ ) was fixed inside and along axis of acceptor charge, and connected to a

strong tension source as a tension divisor, with a variable resistance  $R_v$  formed by the parallel double resistive wire and a constant resistance  $R_c$ .

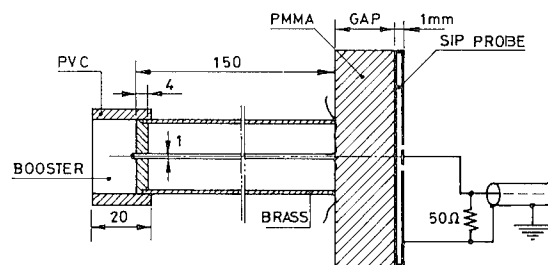


FIGURE 8. CALIBRATION APPARATUS TO MEASURE SHOCK INDUCED PRESSURE

The detonation wave, inducing a short-circuit between the wires, generates a variation of tension that shows its position along the wires.<sup>18</sup> Using the followed equation,

$$V_{out} = \frac{R_c}{R_c + 2\rho(L_0 - x) + R_i} V_{ref} \quad (3)$$

where  $V_{ref}$  and  $V_{out}$  represents the source and output tensions,  $R_i$  the assembly internal resistance of source and cables,  $R_v = 2\rho(L_0 - x)$ , being  $\rho$  the resistivity of the wire,  $L_0$  the length of the explosive acceptor tube and  $x$  the distance of run to detonation. It is possible to determine, from the recorded output voltage  $V_{out}$ , as a function of time  $t$ , the corresponding  $L(t)$ . An example is shown in Figure 9. An aluminium bar, with cross section of 30x30 mm, placed under acceptor charge, shows clearly the initiation section, as it can be seen in Figure 10.

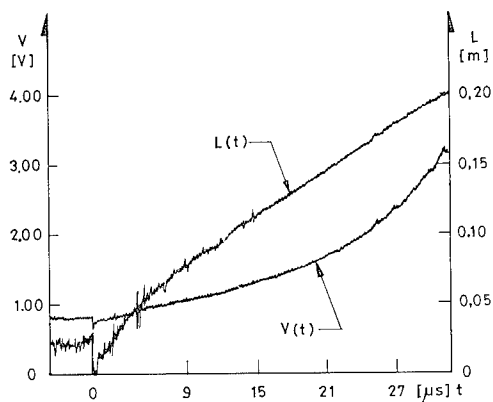


FIGURE 9. EVOLUTION OF MEASURED TENSION AND RUN DISTANCE, AS A FUNCTION OF TIME

Figures 11 and 12 show, for 1 and 2% of GMB,  $dp = 45 \mu m$ , the evolution of shock front velocity and the level of depth crushing of the witness bar, respectively as a function of time and length. The evolution of crush depth on witness aluminium bar, shows a good correlation with the shock front velocity. A delay between witness bar depth evolution and shock front velocity sometimes is observed.

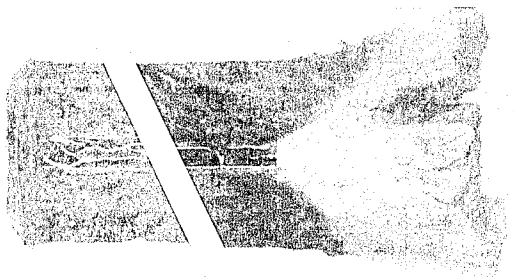


FIGURE 10. ALUMINUM WITNESS BAR

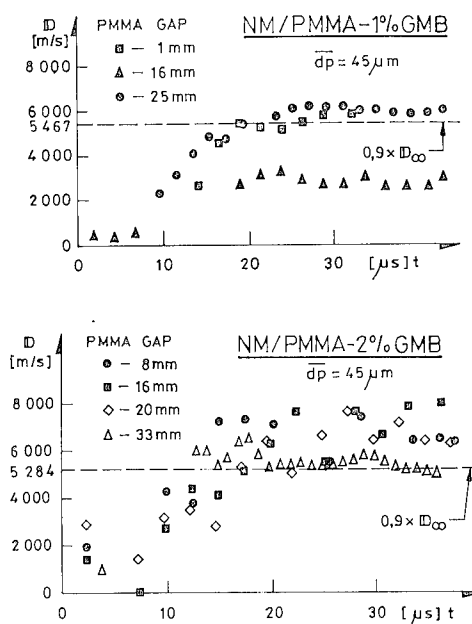


FIGURE 11. SHOCK FRONT VELOCITY IN ACCEPTOR CHARGE, AS A FUNCTION OF TIME

## DISCUSSION OF RESULTS

Induced delay  $\tau$  and distance of run to detonation  $L_\tau$  were determined, as a function of the induced pressure from gap, assuming the transition level for detonation velocity of  $0.9 D_\infty$ .<sup>12</sup> Figures 13 and 14 show the Pop-plot evolution of induced time and distance of run to detonation, as a function of induced shock pressure. It can be seen that NM/PMMA-GMB mixtures containing small GMB (average diameter of  $45 \mu m$ ) initiate even with the largest experimental gaps (25 mm for  $X=1\%$  and about 35 mm for  $X=2\%$ ), corresponding to induced shock pressures less than 3 GPa.

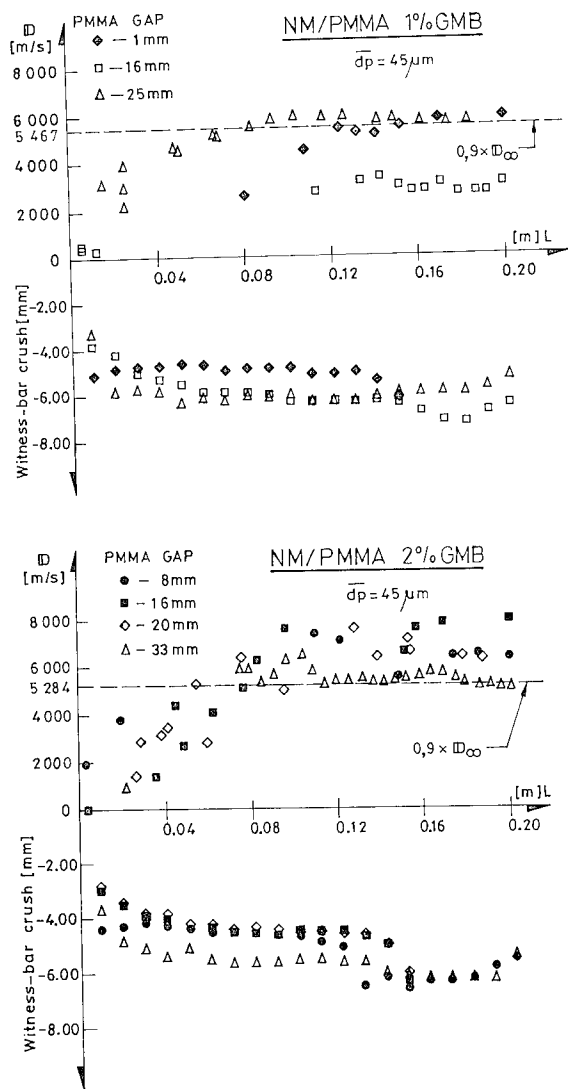


FIGURE 12. SHOCK FRONT VELOCITY IN ACCEPTOR CHARGE, AS A FUNCTION OF DISTANCE

Obtained results with slapper and gap experiments show that the minimum shock initiation of NM/PMMA-GMB mixtures is very dependent on the particle size of GMB.

Hot spots energy released rate, due to GMB collapse, seems to be responsible for the low critical diameter of NM/PMMA-GMB mixtures.<sup>7</sup> In a similar way, it seems to contribute to sensitize the studied explosive mixtures, increasing its sensitivity with decreasing GMB size and with increasing GMB concentration. These facts suggest that initiation mechanism is also related with the distance between GMB.

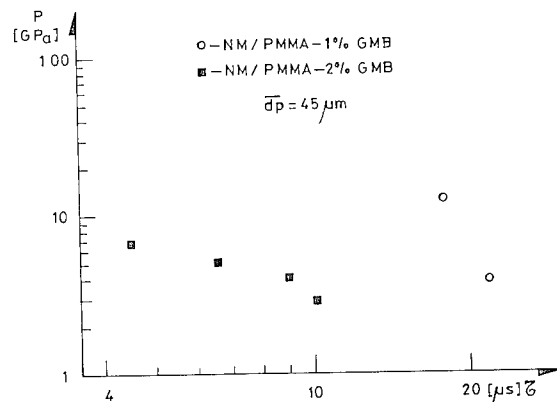


FIGURE 13. INDUCED SHOCK PRESSURE, AS A FUNCTION OF INDUCED TIME

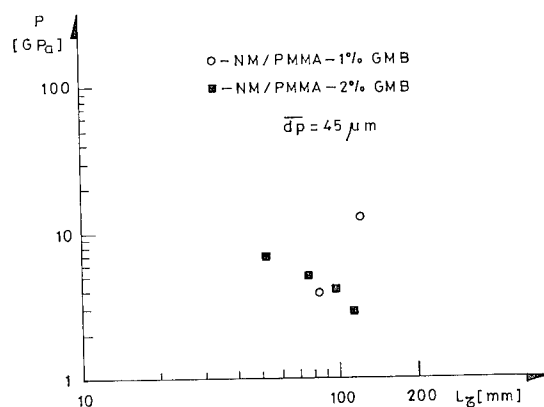


FIGURE 14. INDUCED SHOCK PRESSURE, AS A FUNCTION OF DISTANCE OF RUN TO DETONATION

## CONCLUSIONS

The detonation velocity, of NM/PMMA-GMB mixtures, referred to infinite diameter, decreases linearly with increasing GMB concentration. Critical diameter of these mixtures, confined in plastic tubes and reported to the mass fraction of GMB, shows clearly the strong effect of a few concentration of GMB.

The shock sensitivity of NM/PMMA-GMB mixtures was measured by slapper and gap experiments. Using slapper apparatus, 12  $\mu\text{F}$  and 25-40 kV, failures only happen for NM/PMMA-GMB mixtures with large size of GMB (average diameter of 100  $\mu\text{m}$ ). For all the others mixtures, the minimum

shock intensity, produced by this slapper apparatus, was strong enough to initiate.

To measure the high sensitivity of NM/PMMA-GMB mixtures, with small size of GMB ( $d_p=45\text{ }\mu\text{m}$ ), a gap experimental apparatus was used, composed by pure NM as donor and a PMMA plate as gap. The existence or not of detonation was verified by a parallel double thin resistive wire and an aluminum bar, placed under the acceptor, that shows clearly the initiation section. The induced shock pressure was calibrated by shock induced polarization, as a function of PMMA gap thickness. NM/PMMA-GMB mixtures, with 1 and 2% of small size of GMB, ( $d_p=45\text{ }\mu\text{m}$ ), show to be initiated respectively by a minimum pressure shock of 3.5 GPa and 2.75 GPa. The observed dispersion of results proves the existence of a very complex and heterogeneous mechanism of initiation. The minimum initiation shock pressure increases with increasing GMB size and with decreasing GMB concentration, suggesting that the initiation mechanism, by hot spots formation due to the collapse of GMB, reducing critical diameter of NM/PMMA original mixture, depends on distance between particles. Small GMB proves to be a strong sensitizer of NM/PMMA mixtures.

\* The authors are grateful to TNO-PML (The Netherlands) by their slapper experimental facilities and helpful.

## REFERENCES

1. Tanaka, K., Yoshida, M., Iida, M. and Fujiwara, S., "Detonation Properties of Water Gels", *Proceedings of the Symposium International on Pyrotechnics and Explosives*, China Academic Publishers, Beijing, Oct. 12-15, 1987, pp. 328-332.
2. Yoshida M., Iida M., Tanaka, K., Fujiwara, S., Kusakabe, M. and Shiino, K., "Detonation Behaviour of Emulsion Explosives Containing Glass Microballoons" *Proceedings of the Eighth Symposium International on Detonation*, NSWC MP 86 -194, 1985, pp. 993-1000.
3. Okamoto, T., Sato, S. and Sunagawa, T., "High Performance Water Gel Explosives", *Proceedings of the Symposium International on Pyrotechnics and Explosives*, China Academic Publishers, Beijing, Oct. 12-15, 1987, pp. 313-317.
4. Kato, Y. and Brochet, C., "Cellular Structure of Detonation in Nitromethane Containing Aluminum Particles", *Proceedings of the Sixth Symposium International on Detonation*, Office of Naval Research, White Oak, Aug. 24-27, 1976, pp. 124-132.
5. Presles, H.N., Campos, J., Heuzé, O. and Bauer, P., "Effects of Microballoons Concentration on the Detonation Characteristics of Nitromethane-PMMA Mixtures", *Proceedings of the Ninth Symposium International on Detonation*, Portland, Oregon, August 28 - September 1, 1989, pp. 925-929.
6. Gois, J. C., Presles, H. N. and Vidal, P., "Effect of Hollow Heterogeneities on Nitromethane Detonation", *Thirteenth International Colloquium on the Dynamics of Explosions and Reactive Systems*, 27 July - 2 August, Nagoya, Japan, 1991, to be published in *Progress in Astronautics and Aeronautics*.
7. Gois, J. C., Presles, H. N., Vidal, P., Khasainov B. A. and Ermolaev, B. S., "Influence of Glass Microballoons Size on the Detonation of Nitromethane Based Mixtures", Accepted for presentation at the *Fourteenth International Colloquium on the Dynamics of Explosions and Reactive Systems*, August 1-6, Coimbra, 1993.
8. Engelke, R., "Effect of a Chemical Inhomogeneity on Steady-State Detonation Velocity", *Physics of Fluids*, Vol. 22, 1979, pp. 1623-1630.
9. Weingart, R.C., Lee, R. S., Jackson, R. K. and Parker, N. L., "Acceleration of Thin Flyers by Exploding Metal Foils: Applications to Initiation Studies", *Proceedings of the Sixth Symposium International on Detonation*, Naval Surface Weapons Center, White Oak, August 24-27, 1976, pp. 653-663.
10. Moulard, H., "Critical Conditions for Shock Initiation of Detonation by Small Projectile Impact", *Proceedings of the Seventh Symposium International on Detonation*, US Naval Academy, Annapolis, Maryland, June 16-19, 1981, pp. 316-324.
11. Ramsey, J. B. and Popoplato, A., "Analysis of Shock Wave and Initiation Data for Solid Explosives", *Proceedings of the Fourth Symposium International on Detonation*, White Oak, MD, ACR 126, pp. 233, 1965.
12. Mader, C., *Numerical Modeling and Technology of Explosives and Propellants*, University of Poitiers, May 12-15, 1988.

13. Mader, C. and Forest, C. A. , "Two Dimensional Homogeneous and Heterogeneous Detonation Wave Propagation", *Los Alamos Scientific Laboratory, Report n° LA-6259*, USA, 1976.
14. Campos, J., "Thermodynamic Calculation of Solid and Gas Combustion Pollutants Using Different Equations of State", *Preprints of First Conference International on Combustion Technologies for a Clean Environment*, Vilamoura, September 1-6, Portugal, 1991, pp. 30.4.1-30.4.11.
15. Marsh S. Eds, *LASL Shock Hugoniot Data*, University of California Press, 1980, pp. 444-451.
16. Fisson, F., *Étude de Grandeurs Caracteristiques de la Détonation d'Explosifs Liquides*, Ph. D. Dissertation, ENSMA Poitiers, France, 1976.
17. Vidal, P., *Contribution à l'Etude des Conditions d'Extinction de la Détonation dans les Mélanges Liquides a Base d'Acide Nitrique*, Ph. D. Dissertation, ENSMA, Poitiers, France, 1990.
18. Mendes, R., Campos, J., Gois, J. C. and Moutinho, C., "Shock Initiation and Detonation Stability of Industrial Explosives", Accepted for presentation at the *Twentht Fourth International Annual Conference of ICT*, June 29 - July 2, Karlsruhe, 1993.
19. Hauver, G. E., "Shock-Induced Polarization in Plastics. Experimental Study of Plexiglas and Polysterene", *Journal of Applied Physics*, Vol. 36, No. 7, 1965, pp. 2113-2118.

---

## DISCUSSION

EDWARD L. LEE

Lawrence Livermore National Laboratory  
Livermore, California

There is a vast gulf between the analyses presented in the papers by Chaudhri, Almgren and Persson; Khasainov, Ermolaev and Presles; and Gois, Campos and Mendes. Chaudhri's results clearly indicate hydrodynamic closure of  $\mu$ -balloons. Khasainov, Ermolaev and Presles consider spherical-viscoplastic plate collapse in the *same* region of shock intensity. Gtois, Campos and Mendes do not clearly differentiate.



## ISOTHERMAL AND SHOCK COMPRESSION OF HIGH DENSITY AMMONIUM NITRATE AND AMMONIUM PERCHLORATE

F.W. Sandstrom and P.A. Persson  
Research Center for Energetic Materials  
New Mexico Institute of Mining and Technology  
Socorro, NM 87801

B. Olinger  
Los Alamos National Laboratory  
Los Alamos, NM 87545

Bulk sound speed measurements, isothermal volume compression/X-ray diffraction experiments and shock loading experiments (maximum pressure  $\approx 20$  GPa) have been performed for high initial density ( $\geq 94\%$  TMD) ammonium nitrate (AN) and ammonium perchlorate (AP). The experimental data, and full density Hugoniot calculated from that data, suggest the presence of low pressure, shock induced phase transitions in both the AN and AP. The AP phase transition occurs at  $\approx 4$  GPa, and exhibits characteristics of a high density to low density phase transition, but the present data are not conclusive. The AN phase change occurs at a shock pressure of less than 3.5 GPa, but the associated volume change is relatively large, indicating the presence of a previously unidentified high pressure, high density phase.

### INTRODUCTION

Given the extensive use of AN and AP in explosive and propellant applications, relatively little data has been reported pertaining to the static or shock loading of either material with regard to their shock Hugoniot or equations of state. Dremin et al.<sup>1</sup> have reported shock Hugoniot data for AN at an initial density of  $0.86 \text{ g/cm}^3$ . They subsequently calculated a full density Hugoniot based on sound speed measurements in solid density AN ( $c_b = 2.20 \text{ mm}/\mu\text{s}$ ) and a generalized Hugoniot formula proposed by Afanasenkov et al.<sup>2</sup>:

$$U_s = c_b + 2U_p - 0.1U_p^2/c_b, \quad (1)$$

where  $U_s$  is shock velocity,  $U_p$  is particle velocity and  $c_b$  is the bulk sound speed. The resulting  $U_s$ ,  $U_p$  fit obtained for the solid AN Hugoniot was  $U_s = 2.20 + 1.96U_p$ . However, rather poor agreement was observed between the experimental porous Hugoniot and a porous Hugoniot calculated assuming a caloric equation of state. Erkman and Edwards,<sup>3</sup> using a Mie-Grüneisen equation of state and Dremin's calculated solid AN Hugoniot as a thermodynamic reference, calculated a Hugoniot for porous AN at  $\rho_0 = 0.86 \text{ g/cm}^3$ , and also found rather poor agreement with Dremin's experimental data, particularly at lower pressures.

They attributed the lack of agreement to a shock induced phase change that cannot be accounted for in Equation (1). Sandusky et al.<sup>4</sup>, in analyzing shock loading experiments on single crystals of AP, considered the  $U_s$ ,  $U_p$  fit proposed by Martynyuk et al.<sup>5</sup>:  $U_s = 2.84 + 2.0U_p$ . The origin of this fit appears to be based on a bulk sound speed measurement for solid AP ( $c_b = 2.84 \text{ mm}/\mu\text{s}$ ),<sup>6</sup> and Equation (1). However, Sandusky et al. found that the relation  $U_s = 2.84 + 1.6U_p$  best fit shock compression data for  $1.92 \text{ g/cm}^3$  AP pressings at 15.5 and 17.8 GPa.<sup>7</sup>

This paper reports the results of sound speed measurements, isothermal compression/X-ray diffraction experiments, and shock loading experiments used to evaluate the shock Hugoniot of AN and AP at high initial density ( $\geq 94\%$  TMD) to pressures of approximately 20 GPa. From this data, full density Hugoniot have subsequently been calculated assuming a Mie-Grüneisen equation of state.

### EXPERIMENTAL

The AN and AP samples used for the sound speed and shock Hugoniot experiments were prepared by pressing. The AN starting material was a commercially

available reagent grade in flake form. The AP starting material used was an ultra-high purity grade with a nominal grain size of 200  $\mu\text{m}$ . The cylindrical (25 mm diameter) pressings were made at nominal thicknesses of 3, 4.5 and 6 mm. Samples used in the shock compression experiments were cut into 16 mm wide x 22 mm long rectangles to accommodate the experimental geometry. Individual sample densities were determined using gas pycnometry. Although the samples were stored at room temperature under desiccant, some slight warping and cracking occurred in the AN pressings with time.

Longitudinal ( $c_l$ ) and shear ( $c_s$ ) sound velocities were measured using pairs of X- and Y-cut quartz crystals, respectively, as sending and receiving transducers for sound waves. Transit times through individual samples were measured with an oscilloscope and a differential timer. Bulk sound velocities ( $c_b$ ) were calculated from the relation

$$c_b = (c_l^2 - 4/3 c_s^2)^{1/2}. \quad (2)$$

Isothermal compression experiments were performed using a high pressure X-ray diffraction technique<sup>8</sup>. A beryllium annulus (3.5 mm OD, 0.3 mm ID, 0.2 mm thick) containing either the AN or AP, NaF pressure standard, and a 4:1 methanol-ethanol mixture, was compressed between two tungsten-carbide Bridgman anvils. A Cu-K $\alpha$  X-ray beam was directed through the annulus and diffraction patterns were recorded at different applied stresses. The AN and AP samples for these experiments were taken from the pressings. Zero pressure, room temperature diffraction patterns confirmed that the initial state of the AN and AP were the orthorhombic phase IV,  $\rho_o = 1.728 \text{ g/cm}^3$ , and the orthorhombic phase I,  $\rho_o = 1.951 \text{ g/cm}^3$ , respectively. Volume compressions of the AN or AP were determined by correlating the pressurized diffraction data with the ambient diffraction data. Pressures were deduced from the volume compression of the NaF standard. The isothermal pressure and volume data can be conveniently expressed in a form similar to the shock Hugoniot

$$U_{st} = c_t + s_t U_{pt} + q U_{pt}^2, \quad (3)$$

where the t subscript denotes isothermal conditions. The isothermal shock and particle velocity analogs,  $U_{st}$  and  $U_{pt}$ , respectively, are obtained from pressure and volume along the isotherm using the Hugoniot conservation relations that apply to shock loading:

$$U_{st} = (PV_o/(1 - V/V_o))^{1/2} \quad (4)$$

and

$$U_{pt} = (PV_o (1 - V/V_o))^{1/2}. \quad (5)$$

In the isothermal equation (3),  $c_t$  is related to the isothermal bulk sound speed at zero pressure in the same way that the adiabatic bulk sound speed is related to the  $c_o$  term in the Hugoniot equation.

The shock compression experiments utilized explosively generated plane shock waves to simultaneously drive shocks through small samples of 6061 Al and the AN and AP pressings mounted on 6061 Al base plates. Each experiment typically used three each 4.5 mm thick 6061 Al samples, and three each of the AN and AP samples at nominal thicknesses of 3, 4.5 and 6 mm. Transit times of shocks through the samples were recorded with flash gaps and a multiple slit streak camera.<sup>9</sup> The film records were analyzed using the DASEOS computer code<sup>10</sup>, which makes corrections for wave curvature, transit times through flash gap armor and flash gap closure times, and performs the analytical impedance match solutions for the shocked states of the individual AN and AP samples using the 6061 Al as a standard. The variable thicknesses of the AN and AP samples were used in an effort to evaluate any effects of shock induced chemical decomposition (e.g., systematic increases in shock velocity with increasing sample thickness).

## EXPERIMENTAL RESULTS AND DISCUSSION

The results of the sound speed measurements on the AN and AP using 3 mm thick samples are summarized in Table 1. Each data point represents the average of four measurements on two different samples. Sound speed data reported by other workers<sup>1,6,11</sup> is shown for comparison. Our longitudinal sound velocities ( $c_l$ ) for the AP pressings are consistent with the data reported by Reese et al. for AP pressings using various grain size starting materials, but also illustrates the effect that grain size can have on the measurements. The isothermal bulk sound speed ( $c_t$ ) obtained from a linear fit to the  $U_{st}$ ,  $U_{pt}$  isothermal compression data is also in good agreement with the bulk sound speed value reported for AP at TMD.<sup>6</sup> On the other hand, our measured AN adiabatic sound speed is considerably higher than the value reported by Dremin et al. The discrepancy is even more pronounced in light of the differences in density. The reason for the discrepancy is not readily apparent, but could be the result of inhomogeneities and/or anisotropy of the AN pressings used for our measurements. Similarly, the isothermal bulk sound speed obtained from a linear fit to the  $U_{st}$ ,  $U_{pt}$  isothermal compression data is also significantly higher than the value reported by Dremin et al. The difference here is interesting in light of the fact that the values are both representative of AN at TMD. For many materials, the adiabatic bulk sound

TABLE 1. SOUND VELOCITY MEASUREMENTS  
FOR AN AND AP

This Work						
	TMD (g/cm <sup>3</sup> )	$\rho_0$ (g/cm <sup>3</sup> )	$c_l$ (mm/ $\mu$ s)	$c_s$ (mm/ $\mu$ s)	$c_b$ (mm/ $\mu$ s)	$c_t^a$ (mm/ $\mu$ s)
AP	1.951	1.87	2.81	1.57	2.16	2.81
AN	1.728	1.60	4.06	1.81	3.48	3.01
Other Work						
	TMD (g/cm <sup>3</sup> )	$\rho_0$ (g/cm <sup>3</sup> )	$c_l$ (mm/ $\mu$ s)	$c_s$ (mm/ $\mu$ s)	$c_b$ (mm/ $\mu$ s)	$c_t^a$ (mm/ $\mu$ s)
AP <sup>11</sup>	1.951	1.90 (500 $\mu$ m)	2.18	—	—	—
AP <sup>11</sup>	1.951	1.90 (76 $\mu$ m)	2.97	—	—	—
AP <sup>6</sup>	1.951	1.95	—	—	2.84	—
AN <sup>1</sup>	1.728	1.73	—	—	2.20	—

<sup>a</sup> Isothermal bulk sound velocities shown are for AN and AP @ TMD

speeds are typically the same or slightly higher than the isothermal bulk sound speeds.<sup>12</sup>

The isothermal compression/X-ray diffraction data for the AN and AP are summarized in Table 2, along with the resulting linear fits to the calculated  $U_{st}$ ,  $U_{pt}$  points. No phase changes were observed in the AN up to the maximum pressure of 7.7 GPa. However, a diffraction pattern of the AP taken at 4.7 GPa indicates that a phase change had occurred. Unfortunately, we were unable to solve the diffraction pattern and therefore could not calculate the volumetric compression any further, although the pattern was characteristic of an asymmetrical crystal structure such as triclinic or monoclinic. This result is in sharp contrast to the cubic structure of AP(II), which occurs at temperatures above 240°C at atmospheric pressure. The linear fits to the  $U_{st}$ ,  $U_{pt}$  data were chosen over a quadratic fit (Equation 3) primarily due to a lack of low pressure (< 1 GPa) data. It has been shown for some low Z materials that a quadratic fit (downward concave in the  $U_{st}$ ,  $U_{pt}$  plane) in the low pressure region gives a more accurate representation of isothermal compression data, since the initial compression can be rapid.<sup>12</sup> In the case of the AN, a downward concave quadratic fit to the  $U_{st}$ ,  $U_{pt}$  data might give an intercept value in closer agreement to the bulk sound speed of Dremine et al., but attempts at forcing a fit through this value did not represent the current data accurately.

The results of the shock compression/impedance match experiments for the AN and AP are summarized

TABLE 2. SUMMARY OF ISOTHERMAL  
COMPRESSION DATA FOR AN AND AP  
 $T \approx 25^\circ\text{C}$

AN					
$\rho_0$ (g/cm <sup>3</sup> )	$P_t$ (GPa)	$V_t$ (cm <sup>3</sup> /g)	$U_{st}$ (mm/ $\mu$ s)	$U_{pt}$ (mm/ $\mu$ s)	
1.728	1.66	.532	3.44	.280	
1.728	2.79	.517	3.89	.415	
1.728	4.15	.497	4.14	.581	
1.728	5.52	.480	4.33	.738	
1.728	6.95	.471	4.65	.866	
1.728	7.70	.464	4.75	.939	
Isothermal Hugoniot: $U_{st} = 3.01 + 1.87 U_{pt}$					
AP					
$\rho_0$ (g/cm <sup>3</sup> )	$P_t$ (GPa)	$V_t$ (cm <sup>3</sup> /g)	$U_{st}$ (mm/ $\mu$ s)	$U_{pt}$ (mm/ $\mu$ s)	
1.951	1.33	.478	3.18	.214	
1.951	1.34	.477	3.15	.218	
1.951	2.80	.459	3.72	.386	
1.951	3.14	.449	3.60	.447	
1.951	3.57	.442	3.63	.504	

Isothermal Hugoniot:  $U_{st} = 2.81 + 1.84 U_{pt}$

in Tables 3 and 4 respectively. Plots of the  $P$ ,  $V$  and  $U_s$ ,  $U_p$  shock Hugoniots, along with the corresponding isothermal compression data, are shown in Figures 1 and 2. Each shock Hugoniot data point shown represents the average shocked states of the three AN and AP samples on each shot. At higher shock pressures (> 12 GPa), both the AN and AP exhibit similar shot-to-shot trends. These trends appear to be artifacts of the explosive/inert driver systems rather than being representative of any physical behavior of the AN or AP. However, at lower shock pressures, data scatter for the AN was greater than for the AP, both for individual samples on a given shot as well as for the shot-to-shot averages. The shock arrival traces for the AN at low pressures tended to be very nonuniform compared to the AP traces on the same shots, and for the AN at higher pressures (Figure 3). Further scrutiny of the low pressure AN data did not reveal any systematic behavior with respect to individual sample densities (which typically varied from approximately 1.60 g/cm<sup>3</sup> to 1.67 g/cm<sup>3</sup>), or with sample thickness. The erratic low pressure AN shock traces can presumably be attributed to sample inhomogeneity and/or anisotropy, which could also explain the disagreement between our sound speeds and the value reported by Dremine et al. However, at this point we cannot definitively rule out materials strength effects, or more significantly, non-equilibrium effects of a low pressure, shock induced phase transition.

TABLE 3. AN PRINCIPAL HUGONIOT DATA  
AVERAGE  $\rho_o = 1.636 \pm 0.026 \text{ g/cm}^3$

$\rho_o$ (g/cm <sup>3</sup> )	$U_s$ (mm/ $\mu$ s)	$U_p$ (mm/ $\mu$ s)	P (GPa)	V (cm <sup>3</sup> /g)
1.637	2.98	.715	3.49	.464
1.636	3.59	.802	4.71	.475
1.635	4.41	.983	7.09	.475
1.636	4.18	1.16	7.90	.442
1.647	4.95	1.56	12.75	.415
1.632	5.22	1.62	13.82	.422
1.643	6.06	1.80	17.96	.428
1.626	6.14	2.03	20.29	.411
1.632	6.15	2.12	21.28	.401

Shock Hugoniot:  $U_s = 1.82 (\pm 0.03) + 2.13 (\pm 0.20) U_p$

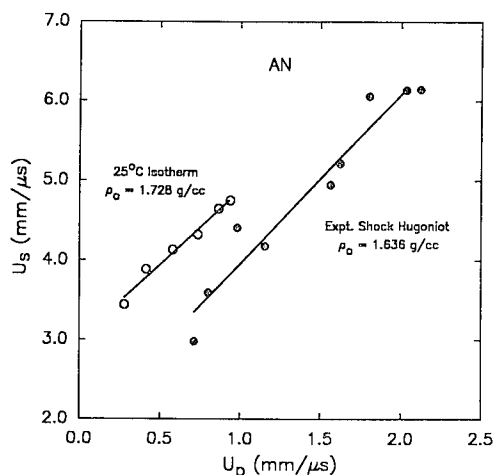


TABLE 4. AP PRINCIPAL HUGONIOT DATA  
AVERAGE  $\rho_o = 1.879 \pm 0.026 \text{ g/cm}^3$

$\rho_o$ (g/cm <sup>3</sup> )	$U_s$ (mm/ $\mu$ s)	$U_p$ (mm/ $\mu$ s)	P (GPa)	V (cm <sup>3</sup> /g)
1.881	3.65	.659	4.52	.436
1.885	3.82	.760	5.48	.425
1.885	4.14	.958	7.48	.408
1.908	4.30	1.02	8.36	.400
1.890	4.82	1.51	13.75	.364
1.882	5.11	1.56	15.04	.369
1.859	5.57	1.78	18.42	.366
1.868	5.90	1.97	21.74	.357
1.857	5.92	2.06	22.64	.351

Shock Hugoniot:  $U_s = 2.56 (\pm 0.01) + 1.65 (\pm 0.07) U_p$

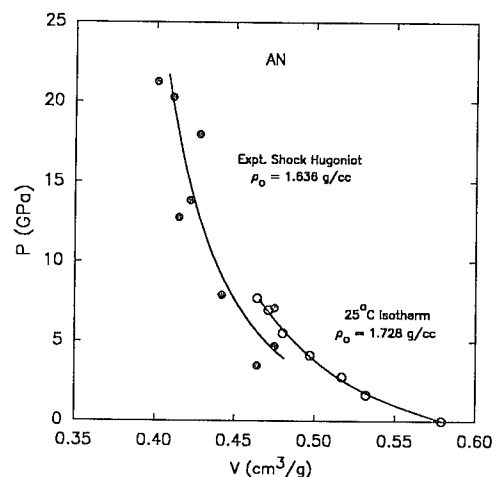


FIGURE 1. AN EXPERIMENTAL ISOTHERMS AND SHOCK HUGONIOTS (SOLID LINES ARE LEAST SQUARES FITS)

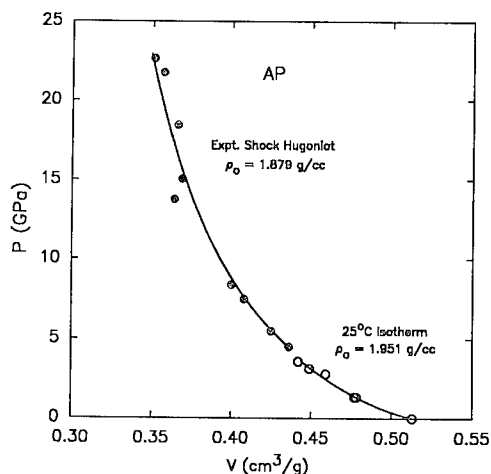
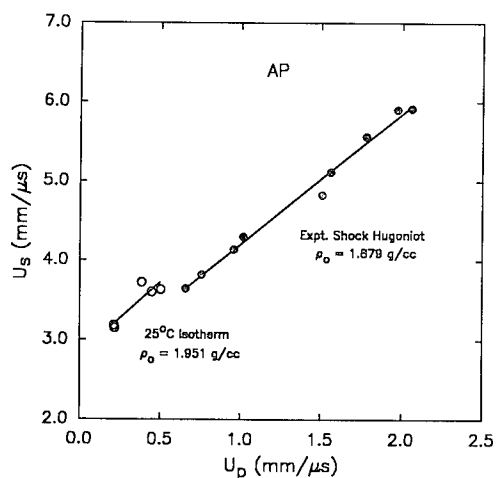


FIGURE 2. AP EXPERIMENTAL ISOTHERMS AND SHOCK HUGONIOTS (SOLID LINES ARE LEAST SQUARES FITS)

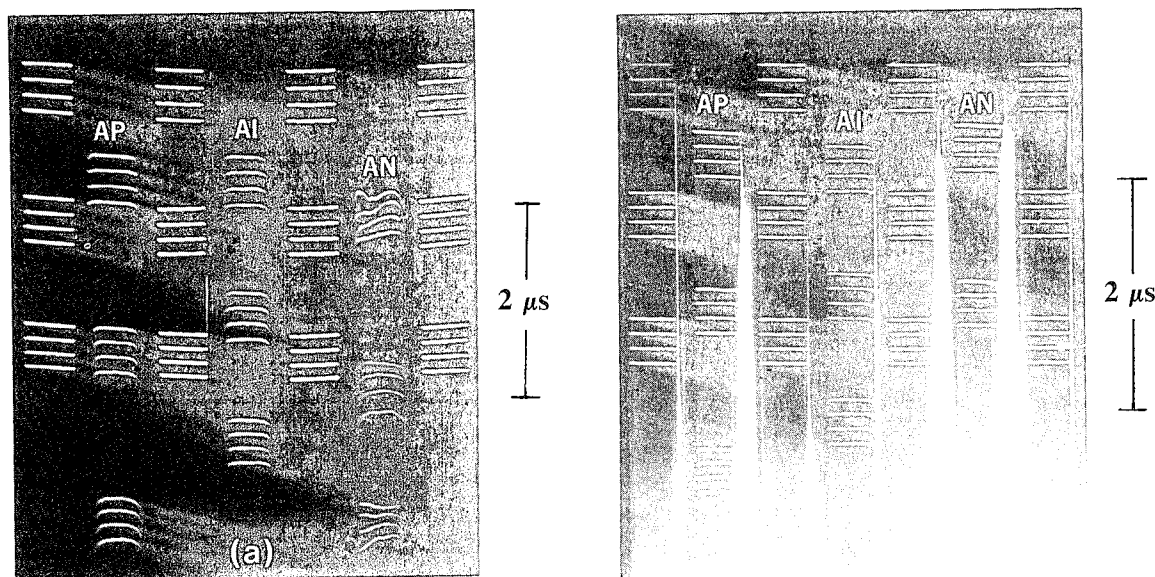


FIGURE 3. LOW (a) AND HIGH (b) SHOCK PRESSURE STREAK CAMERA RECORDS

In the absence of phase transitions, the experimental isotherms should be good approximations to the full density shock Hugoniots at lower pressures, while the measured shock Hugoniots are for slightly porous initial states. For AP, the positions of the  $U_s$ ,  $U_p$  and  $P$ ,  $V$  isotherms and Hugoniots (Figure 2) conform to the different initial densities. The porous Hugoniot lies below, and has the same or slightly steeper slope than the isotherm in the  $U_s$ ,  $U_p$  plane, and is to the right of the isotherm in the  $P$ ,  $V$  plane. For AN, while the porous  $U_s$ ,  $U_p$  Hugoniot lies below, and is slightly steeper than the isotherm, the porous  $P$ ,  $V$  Hugoniot lies to the left of the isotherm, which is characteristic of a material that undergoes a shock induced phase transition (Figure 1). This evidence for the existence of a low pressure ( $< 3.5$  GPa), shock induced phase change in the AN is interesting in light of the fact that no phase changes were observed in the isothermal compression experiments up to 7.7 GPa. One reason for this may be the absence of heating in the isothermal compression experiments. Bridgman<sup>13</sup> has identified a sixth phase of AN at pressures above 0.88 GPa and temperatures greater than 169°C in static compression experiments. Deal<sup>14</sup> has suggested that the shearing mechanisms present under shock loading may also be required to induce the phase transition. Visual extrapolation of the AN  $P$ ,  $V$  shock Hugoniot to zero pressure also suggests that the transition goes to a higher density, metastable phase. In contrast, although a phase change in the AP was observed in the isothermal compression experiments, the  $P$ ,  $V$  isotherm and shock Hugoniot data are essentially continuous, indicating that if a shock induced phase transition does exist, the volume change associated with it is very small.

Effects of chemical decomposition of the shocked AN and AP pressings have been considered inasmuch that no gross systematic increases in shock velocities through the different thicknesses of the samples were observed, even at the highest shock pressures. In cases where velocity changes were observed, the changes could be attributed to variations in density between samples, or in the case of some of the low pressure AN shots, inhomogeneity of the samples. On the other hand, when the polycrystalline samples were shocked, localized hot spots and some chemical decomposition undoubtedly occurred. Sandusky et al. reported evidence of chemical decomposition in single crystals of AP shocked to pressures of only  $\approx 2.5$  GPa. However, prior studies<sup>15,16</sup> of the shock initiation behavior of energetic materials containing relatively large quantities of AN and AP have demonstrated that in some cases, several tens of microseconds are required for a given shock to grow to a steady detonation. We feel that the time scales of our shock loading experiments ( $\approx 2 \mu s$  or less) are too short for these chemical reactions to contribute significantly to the propagation of shocks through the samples.

#### CALCULATION OF FULL DENSITY HUGONIOTS

The solid density Hugoniots for AN and AP were calculated from the isothermal compression and shock loading data using the Mie-Grüneisen equation of state

$$E = E_r + (V/\gamma)(P - P_r). \quad (6)$$

This equation states that the pressure and energy at a given volume can be related to these quantities on a reference curve, denoted by the  $r$  subscript (e.g., an experimental isotherm or shock Hugoniot), through an average value of the Grüneisen parameter

$$\gamma = V(\partial P/\partial E)_V. \quad (7)$$

For the calculations discussed here,  $\gamma$  is assumed to be a constant function of volume only, where

$$\gamma/V = \gamma_0/V_0. \quad (8)$$

From thermodynamic considerations,  $\gamma_0$  can be expressed as

$$\gamma_0 = 3\alpha c_s^2/C_p \quad (9)$$

or

$$\gamma_0 = 3\alpha c_t^2/C_v \quad (10)$$

where  $\alpha$  = the linear coefficient of thermal expansion ( $3\alpha = \beta$  = the volumetric coefficient of thermal expansion for an isotropic solid);  $c_s$  and  $c_t$  are the adiabatic and isothermal sound speeds respectively; and  $C_p$  and  $C_v$  are the constant pressure and constant volume heat capacities, respectively. The sound speeds and heat capacities are related by

$$c_t^2/c_s^2 = C_v/C_p, \quad (11)$$

and  $C_v$  can be calculated from  $C_p$  using the equation

$$C_v = C_p - (3\alpha)^2 T c_t^2. \quad (12)$$

The isothermal sound speeds,  $c_t$ , for the AN and AP were initially taken as the intercept values ( $U_{pt} = 0$ ) from the linear fits to the isothermal shock-particle velocity ( $U_{st}$ ,  $U_{pt}$ ) data. However, because of our limited number of data points, and the fact that at low pressures the uncertainty in  $V$  dominates the  $(1 - V/V_0)$  term in Equations (4) and (5), the  $U_{pt} = 0$  intercept value has a large statistical error associated with it. Consequently, we have used Equations (11) and (12) to evaluate both  $c_t$  and  $C_v$  values for the AN and AP at solid density. This process involves substituting known values of  $c_s$  for  $c_t$  in Equation (12) to calculate an initial  $C_v$ . We then recalculated using the  $c_t$  value from Equation (11), which was found using the initial  $C_v/C_p$  value. This process was repeated until the values converged.

The inputs used for AN at 1.728 g/cm<sup>3</sup> were  $3\alpha = 9.82 \times 10^{-4}/K$ ,  $C_p = 1670$  J/kg-K, and  $c_s = 2200$  m/s.<sup>Ref. 1,17</sup> The resulting values of  $c_t$  and  $C_v$ , 1630 m/s and 918 J/kg-K, differ significantly from

the input  $c_s$  and  $C_p$  values. However, calculations made using our measured  $c_s$  (3480 m/s) or the intercept value of  $c_t$  (3010 m/s) resulted in a negative value for  $C_v$  on the first iteration. Assuming that the reported  $c_s$  (2200 m/s) value for solid AN is valid, the calculated  $c_t$  may not be totally unreasonable; this would imply that the initial isothermal compression of AN is indeed rapid, and that the  $U_{st}$ ,  $U_{pt}$  data would be better represented by a quadratic rather than linear fit in this region. On the other hand, although current literature values of  $C_p$  for AN are estimates, they all indicate that  $C_p$  can vary considerably with temperature. Hence, our simple equations probably do not address this complex behavior. The calculated value of  $\gamma_0$  for AN from Equations (9) and (10) is 2.8, which is quite large compared to other explosives reported in the literature. These values typically vary from  $\approx 0.5$  to 1.5. Dremin et al. calculated  $\gamma_0 = 0.9$  for AN. For the Hugoniot calculations reported here, we assumed  $\gamma_0 = 1.0$  for AN.

The inputs used for the AP at 1.951 g/cm<sup>3</sup> were  $3\alpha = 1.2 \times 10^{-4}/K$ ,  $C_p = 1297$  J/kg-K, and  $c_s = 2840$  m/s.<sup>Ref. 6,17</sup> The  $c_t$  and  $C_v$  values obtained for the AP were 2800 m/s and 1260 J/kg-K, respectively. It is interesting to note that the calculated value for  $c_t$  is in very good agreement with the intercept value from the linear fit to the AP isothermal shock-particle velocity data (2810 m/s). The calculated value for  $\gamma_0$  for AP was 0.8.

Details of the isotherm to Hugoniot calculations are outlined in Reference 12. The porous to solid Hugoniot calculations were made using the relations

$$U_{sH} = \frac{V_0}{V_0 - V} U_{pH} \quad (13)$$

and

$$U_{pH}^2 = \frac{1 - (\gamma/2V)(V_{\infty} - V)}{1 - (\gamma/2V)(V_0 - V)} (V_0 - V) \frac{U_s U_p}{V_{\infty}} \quad (14)$$

where the H subscript denotes parameters on the solid Hugoniot, and  $V_{\infty}$  is the average initial volume of the AN and AP pressings. For both calculations we have assumed that  $C_v$  and the ratio  $\gamma_0/V_0 = \gamma/V$  are constant. These assumptions were maintained even though the experimental shock Hugoniots for both the AN and AP are thought to be representative of different phases than the isothermal compression curves. The  $C_v$  value used for calculating the solid AN Hugoniots was taken to be 1670 J/kg-K. Subsequent calculations taking  $C_v = 918$  J/kg-K showed that the effect of changing this value was very small.

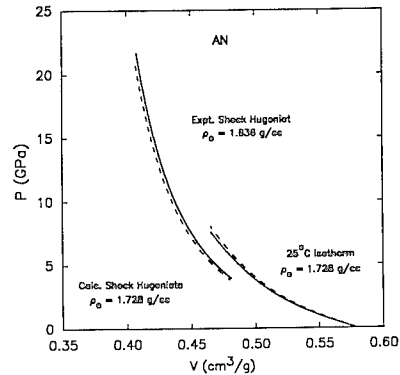
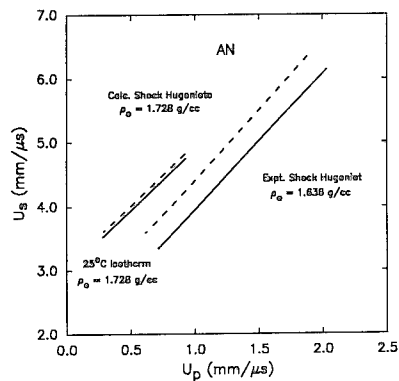


FIGURE 4. AN EXPERIMENTAL ISOTHERMS AND SHOCK HUGONIOTS (SOLID LINES), AND CALCULATED FULL DENSITY HUGONIOTS (DASHED LINES) LEAST SQUARES FITS TO CALCULATED HUGONIOTS ARE  $U_s = 3.07 + 1.89 U_p$  FOR  $0.28 \leq U_p \leq 0.94$ , AND  $U_s = 2.23 + 2.18 U_p$  FOR  $0.72 \leq U_p \leq 2.12$ .

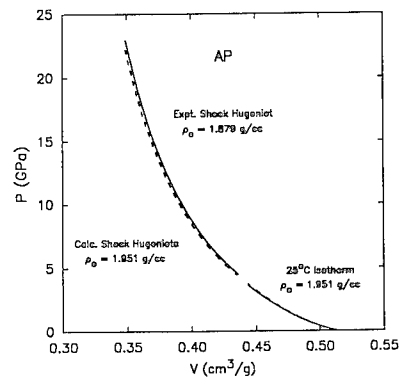
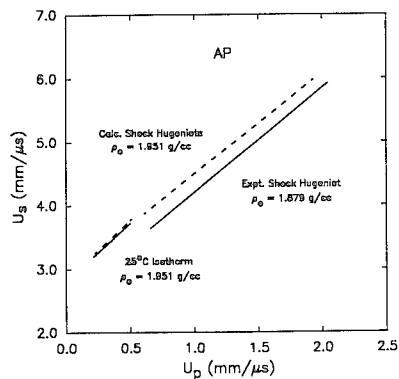


FIGURE 5. AP EXPERIMENTAL ISOTHERMS AND SHOCK HUGONIOTS (SOLID LINES), AND CALCULATED FULL DENSITY HUGONIOTS (DASHED LINES). LEAST SQUARES FITS TO CALCULATED HUGONIOTS ARE  $U_s = 2.81 + 1.84 U_p$  FOR  $0.21 \leq U_p \leq 0.50$ , AND  $U_s = 2.90 + 1.59 U_p$  FOR  $0.66 \leq U_p \leq 2.10$ .

The experimental isotherms, Hugoniot, and calculated solid Hugoniot are shown in Figures 4 and 5 for the AN and AP, respectively. The displacements between the calculated low and high pressure  $U_s$ ,  $U_p$  and  $P$ ,  $V$  AN Hugoniot continue to suggest the presence of a low pressure, shock induced phase transition to a new higher density phase for this material. In the case of the AP, both the calculated low and high pressure  $U_s$ ,  $U_p$  and  $P$ ,  $V$  Hugoniot are nearly continuous. The negative change in slope from the calculated low pressure to high pressure  $U_s$ ,  $U_p$  Hugoniot could be the result of a shock induced phase transition from a high density to low density phase, but the present data are not conclusive. It is interesting to note that our calculated high pressure Hugoniot for AN ( $U_s = 2.23 + 2.18 U_p$ ) and AP ( $U_s = 2.90 + 1.59 U_p$ ) agree very well with previous estimates (Dremin et al., AN  $U_s = 2.20 + 1.96 U_p$ , and Sandusky et al., AP  $U_s = 2.84 + 1.6 U_p$ ).

## CONCLUSION

The isothermal and shock compression of AN and AP at high initial density demonstrates evidence for the existence of low pressure ( $\leq 4$  GPa), shock induced phase transitions in both materials. For the AN, the presence of a new high density, high pressure phase is clearly illustrated by the data, although the shocked state at which the transition occurs is not clearly defined. For the AP, aside from the fact that a phase change was observed to occur in the isothermal compression experiments, the evidence for a shock induced phase transition is less conclusive, although the data illustrates characteristics of a high density to low density transition. Our limiting assumptions regarding the equation of state and calculation of solid density Hugoniot from the experimental isotherms and porous Hugoniot likely do not adequately address the materials' strength effects or the complex thermo-

dynamic properties associated with the shock loading of either the AN or the AP. For this reason, low pressure shock loading experiments using carefully prepared samples, and coupled with more sophisticated diagnostics (e.g., wave profile measurements) are in order. These experiments would presumably shed considerable light on the nature of the phase transitions.

## ACKNOWLEDGEMENTS

We gratefully acknowledge the support of the members and staff of the Research Center for Energetic Materials, a National Science Foundation Industry/University Research Cooperative. Special thanks to G. Faulks and K. Paisano, NAWC, China Lake, for preparing the AP pressings, L. Stretz and M. Barr, LANL, for preparing the AN pressings, and J.N. Fritz, LANL, for much discussion and constructive criticism.

## REFERENCES

1. Dremine, A.N.; Shevdov, K.K.; and Avdonin, O.S., "Shock Compressibility and Temperature of Certain Explosives in the Porous State," *Comb. Exp./Shock Waves*, Vol. 6, No. 4, 1970, p. 449.
2. Afanasekov, A.N.; Bogomolov, V.M.; and Voskobinikov, I.M., "Generalized Shock Hugoniot of Condensed Substances," *Zh. Prikl. Mekh. Fiz.*, Vol. 10, No. 4, 1970, p. 660.
3. Erkman, J.O.; and Edwards, D.J., "Computed and Experimental Hugoniots for Unreacted Porous High Explosives," *Proceedings of the Sixth Symposium (International) on Detonation*, NSWC, White Oak, MD, 24-27 Aug 1976, pp. 766-776.
4. Sandusky, H.W.; Glancy, B.C.; Carlson, D.W.; Elban, W.L.; and Armstrong, R.W., "Deformation and Shock Loading Studies on Single Crystals of Ammonium Perchlorate," *Proceedings of the Ninth Symposium (International) on Detonation*, Portland, OR, 28 Aug-1 Sep 1989, pp. 1260-1270.
5. Martynyuk, V.F.; Khasainov, B.A.; Sulimov, A.A.; and Sukoyan, M.K., "Estimating Heat Production in the Detonation of Poured Density Ammonium Perchlorate," *Comb. Exp./Shock Waves*, Vol. 23, No. 1, 1987, p. 58.
6. Belyaev, A.F.; Bobolev, V.K.; Korotkov, A.I.; Sulimov, A.I.; and Chuiako, S.V., "Shock Initiated Detonation: Determination of Critical Initiation Pressures," in *Transition of Combustion of Condensed Systems to Detonation*, Chapter 5, Part B, Section 29, pp. 182-189, Moscow, 1973. Translated by P. Newman, SAND76-6016, 1976, Sandia National Laboratories, Albuquerque, NM.
7. Salzman, P.K.; Irwin, O.R.; and Andersen, W.H., "Theoretical Detonation Characteristics of Solid Composite Propellants," *AIAA Journal*, Vol. 45, No. 11, 1965, p. 2238.
8. Halleck, P.M.; and Olinger, B., "A Method for the Accurate Measurement of Lattice Compression of Low-Z materials at Pressures up to 12 GPa by X-Ray Diffraction," *Rev. Sci. Instrum.*, Vol. 45, No. 11, 1974, p. 1408.
9. McQueen, R.G.; Marsh, S.P.; Taylor, J.W.; Fritz, J.N.; and Carter, W.J., "The Equation of State of Solids from Shock Wave Studies," *High Velocity Impact Phenomena*, R. Kinslow, Ed., Academic Press, New York, NY, 1970, pp. 293-417.
10. Fritz, J.N., *M-6 Technical Notes Number 13 ed. 2: DASEOS, A Data Analysis Code for Shock Wave Experiments*, LA-UR 86-3763, 1986, LANL, Los Alamos, NM.
11. Reese, B.O.; Blackburn, J.H.; Seely, L.B.; and Evans, M.W., "Longitudinal Sound Velocities of Granular Compacts of Ammonium Perchlorate and Potassium Chloride," *Comb. Flame*, Vol. 11, 1967, p. 262.
12. Olinger, B.; and Cady, H.H., "The Hydrostatic Compression of Explosives and Detonation Products to 10 GPa and their Calculated Shock Compression: Results for PETN, TATB, CO<sub>2</sub> and H<sub>2</sub>O," *Proceedings of the Sixth Symposium (International) on Detonation*, NSWC, White Oak, MD, 24-27 Aug 1976, pp. 700-709.
13. Bridgman, P.W., "Polymorphic Changes under Pressure of the Univalent Nitrates," *Proc. Am. Acad. Arts Sci*, Vol. 51, 1916, p. 581.
14. Deal, W.E., Personal Communication, 27 Oct 1992.
15. Lee, J.; Sandstrom, F.W.; Craig, B.G.; and Persson, P.A., "Detonation and Shock Initiation Properties of Emulsion Explosives," *Proceedings of the Ninth Symposium (International) on Detonation*, Portland, OR, 28 Aug-1 Sep 1989, pp. 573-583.
16. Dick, J.J., "Nonideal Detonation and Shock Initiation Behavior of Composite Solid Rocket Propellant," *Proceedings of the Seventh Symposium (International) on Detonation*, U.S. Naval Academy, Annapolis, MD, 16-19 Jun 1981, pp. 620-623.
17. Dobratz, B.M.; and Crawford, P.C., *LLNL Explosives Handbook, Properties of Chemical Explosives and Explosive Simulants*, UCRL-52997 Change 2, Jan 1985, LLNL, Livermore, CA.



## DISCUSSION

MICHAEL COWPERTHWAIT  
SRI International, Menlo Park, California

The Hugoniot curve is close to the isentrope only when  $C_p \approx C_v$ . Did you check that  $C_p/C_v \approx 1$ ?

REPLY BY F. W. SANDSTROM AND  
P. A. PERSSON:

Initially, I should point out that the low-pressure Hugoniots were calculated from experimental isotherms rather than isentropes. In the case of the AP, the ratio of the literature value of  $C_p$  to our calculated value of  $C_v$  was indeed very close to unity. For the AN this same ratio was approximately 1.8. The extent to which this value is representative of the behavior of AN is not clear; reported values of  $C_p$  for AN are estimates, and indicate complex behavior as a function

of temperature. Consequently, our limiting assumptions and simple equations for calculating  $C_v$  probably do not adequately address this behavior. In any event, we found that the value of  $C_v$  chose had very little effect on the low-pressure Hugoniot curve calculated from the isotherm. There was, however, a marked dependence on the value used for  $\gamma_0$ , where higher values led to unrealistically steep Hugoniots for the AN in the low-pressure region.

In the high-pressure region, we also assumed constant  $C_v$  and  $\gamma/V$  to calculate the solid Hugoniots from the experimental shock Hugoniots centered at slightly porous initial states. The absence of systematic, measurable shock velocity changes through the samples of different thicknesses indicated that extensive chemical reaction does not take place in the samples in the time duration of the experiments. This could otherwise have caused large deviations from the assumed  $C_v$  behavior. In future experiments, it would be desirable to measure not only the shock loading profiles, but the release isentropes as well.

**SESSIONS ON**

**HOT SPOTS**

**Cochairmen:**     **William Deal, Jr.**  
                             **Los Alamos National Laboratory**

**Anatolij Dremin**  
**Institute of Chemical Physics**

## A NUMERICAL STUDY OF DROP WEIGHT IMPACT TESTING OF SOLID ROCKET PROPELLANTS

K.P. Duffy and A.M. Mellor  
Vanderbilt University  
Nashville, TN 37235

The high strain rate material behavior determines the sensitivity of composite solid rocket propellants to drop weight impact. The small scale drop weight impact sensitivity of the material is thought related to the large scale system level response and thus the safety of a solid rocket motor containing that propellant. Here we summarize one area of work performed under a drop weight impact research program, numerical modeling.

Current techniques for using dynamic finite element analysis to model sample deformation in the drop weight test are explained. Local estimates of, for example, shear stress in the propellant are shown, and by knowing how these variables are distributed, a better understanding of the mechanisms which lead to ignition is achieved. The results indicate a sample stress state which supports a postulated shear initiation mechanism. Results of a parametric study on several material property constants suggest postulated initiation mechanisms are most sensitive to changing factors associated with the flow of the material.

### INTRODUCTION

Safety of devices containing energetic materials, in particular explosives and solid rocket propellant, has received renewed emphasis in part due to standards recently agreed by the Department of Defense for so-called insensitive munitions (IM), to be fielded after October 1993 (or in production after October 1995).<sup>1</sup> Weapon systems are subjected to a number of tests in which they are stimulated by thermal or mechanical energy input. The latter include projectile impact, fragment impact, and sympathetic detonation, in which propagation of detonation from an initiated round is to be prevented.

Energetic materials themselves are also routinely subjected to small-scale laboratory hazards tests. A long-term goal of research on these screening tests is their improvement so quantitative information is obtained. Such data, if characteristic of the energetic material, could assist not only in formulating propellants and explosives of decreased sensitivity, but also in relating small-scale test behavior to the results from full-scale systems tests. Although significant differences exist between configuration, confinement, energy level, rate, and duration of stimulus, modeling of small-scale tests may provide some confidence in model extrapolation to accident scenarios on fielded munitions. One such test involves drop weight impact which ranks the

impact sensitivity of energetic materials. In this test, the kinetic energy of a falling weight is transferred to a sample of energetic material resting on an anvil, extruding the sample radially between the striker and anvil. Small-scale testing, exemplified by the drop weight method, is used for primarily two reasons: it is simple and inexpensive relative to full-scale system tests, and only small samples of energetic test material are required.

It is well known that the energy, and hence heat, must be localized into regions of high temperature called hot spots in order to cause ignition. Many hot spot mechanisms have been hypothesized.<sup>2-9</sup>

For the drop weight test, in particular, shear and friction are significant factors in the energy localization process. Coffey<sup>7</sup> has conducted drop weight experiments that show the ignition location of these hot spots is not in the high pressure center of the propellant, but near the high strain outer edge. Coffey et al.<sup>10</sup> measured higher values of critical energy in a binder/AP energetic material when polished anvils were used relative to rough anvils. As Baker and Mellor<sup>11</sup> explain, the energy required to reach a certain temperature increases with decreasing friction. This effect is small if the temperature is distributed uniformly over the thickness of the impacted sample. However, if focused in narrow layers near the surface, called shear bands,

significantly higher temperature increases can occur.<sup>11</sup> These shear bands are regions of localized plastic flow and form when the total derivative of flow stress with respect to strain equals zero.

The present research is directed towards obtaining a fundamental understanding of the impact ignition process. Three complementary approaches are under way: (1) instrumented critical energy drop weight experiments, (2) macro and microscopic analytic modeling of sample deformation, and (3) finite element modeling of sample deformation and hot spot creation. Early results of (1) and (2) are discussed briefly below with more details in Baker et al.<sup>12</sup> and Baker and Mellor.<sup>11</sup> and <sup>13</sup> Here a summary of the finite element modeling is presented, with complete details in Duffy.<sup>14</sup>

Current experimental work involves critical energy testing of a set of nine AP composite research propellants with systematically varied formulations. The influence of AP particle size and size distribution, total solids loading, aluminum, HMX and binder material (HTPB, CTPB, or PBAN) on critical energy and, thus, impact sensitivity is studied. These data will be interpreted in terms of an ignition mechanism where shear near the sample edge is the operative hot spot mechanism, either via friction heating or shear banding. Impact velocity is altered to study how critical energy varies with strain rate. Results from this work will be presented in future publications.

In related work, Baker et al.<sup>12</sup> tested three hydroxy-terminated polybutadiene/AP/aluminum (HTPB/AP/Al) propellants on an instrumented drop weight impact machine. Critical energy was determined for a range of impact velocities from low values ( $\approx 5$  m/s) where only localized chemical reaction occurred to higher values ( $> 10$  m/s) where ignition and complete sample consumption were observed. The calculated energies for reaction generally increased with increasing impact velocity. For one propellant, a monotonic increase in energy with velocity was found, while a limiting energy was obtained for another. In a third propellant, the energy increased over a lower range of velocity, but showed unstable behavior at higher velocities. Baker et al.<sup>12</sup> suggest these trends may follow the material property trends with strain rate. Ideally, critical energy results could be used to predict energetic material response in many types of impact scenarios. However, the critical energy drop weight experiment does not provide this energy localization information so modeling of the sample deformation is required.

In conjunction with the ongoing experimental program, dynamic finite element calculations using the hydrocode DYNA2D have been performed for a realistic drop weight machine geometry. Initial modeling work was done to

identify the sources of the oscillations observed in accelerometer records from the experiments.<sup>15</sup> These computations suggested more optimum instrumentation locations and machine designs which could be used to simplify testing. However, the major goal of the finite element modeling is to identify where and how the input drop weight energy is focused. Eventually, for rocket propellants, such computations might relate the input energy to stresses applied to the largest oxidizer crystals at the outer edge of the sample, thus providing a link with the lattice dislocation pileup theory of hot spot formation proposed by Coffey.<sup>6</sup> and <sup>8-9</sup>

Strain rates in the drop weight test are on the order of  $10^4$  s<sup>-1</sup> which is similar to real life low velocity impact scenarios. Hence, high strain rate behavior of the energetic material is important to the creation of hot spots, initiation, and subsequent ignition of the propellant. The mechanical properties of the energetic material change significantly as the strain rate is increased. Understanding this behavior is fundamental in the development of less sensitive, and hence safer rocket motors. Duffy and Mellor<sup>16</sup> discuss factors which affect the mechanical properties of polymers in general and Duffy<sup>14</sup> provides an overview of two different approaches for material modeling: constitutive and molecular based theories.

The sophistication of propellant mechanical property specification necessary to accurately model its response with DYNA2D is explored as well as the importance of accepting or modifying a number of parameters within DYNA2D which are assigned default values. The modeling is divided into two areas: an initial homogeneous propellant model, and a more detailed inhomogeneous propellant model in which differing amounts of ammonium perchlorate (AP) oxidizer particles are inserted in the binder matrix to more realistically model the propellant deformation behavior. Due to space limitations, the inhomogeneous results will be discussed elsewhere.

## DESCRIPTION OF DYNA2D

In conjunction with the experimental drop weight impact program, the hydrodynamic finite element code DYNA2D from Lawrence Livermore National Laboratory is used.<sup>17</sup> The present computations are performed on a DEC VAX 8800. DYNA2D is an explicit, central difference, Lagrangian code developed primarily to handle large deformations of energetic materials used in military applications. A comprehensive description of the code is found in Goudreau and Hallquist.<sup>18</sup> A contact/impact algorithm, which allows sliding friction definitions between material interfaces, is implemented in the code.<sup>19</sup> This sliding feature and the code's capability to rezone tangled elements were primary reasons DYNA2D was selected for these computations.

## DEFINITION OF MODEL SETUP

The axisymmetric finite element grid shown in Figure 1a models the experimental drop weight machine used by Baker et al.<sup>12</sup> At time zero the drop weight and striker are given an initial velocity from 5–15 m/s (corresponding to the experimental velocities). DYNA2D then predicts the time dependent deformation of the sample. The initial coarse striker and anvil mesh is shown in Figure 1b. Refinements (discussed later) result in the more detailed mesh shown in Figure 1c.

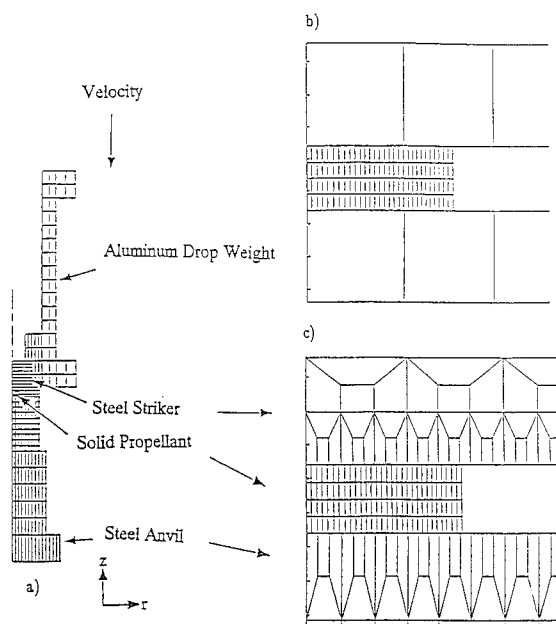


**FIGURE 1. a) DYNA2D MESH OF THE DROP WEIGHT IMPACT MACHINE. EXPANDED VIEWS OF PROPELLANT/STEEL INTERFACES (b = ORIGINAL MESH, c = REFINED MESH). LENGTH FROM TOP OF DROP WEIGHT TO BOTTOM OF ANVIL IS 19 CM RADIUS AND 0.1 CM THICKNESS.**

A range of 0.2 to 0.5 was estimated for the dynamic friction coefficient between the sample/striker and the sample/anvil interfaces.<sup>20</sup> Very

limited data exist that characterize friction coefficients at interfaces between polymeric materials and metals. Some energetic material data have been found for Composition B-3 (A), an explosive with TNT, RDX, and a small percentage of wax,<sup>21</sup> and these data exhibit a dependence on pressure and surface finish. As the pressure increases, the friction coefficient decreases. The maximum pressures encountered in the DYNA2D simulations are on the order of 1000 MPa at the specimen centerline, which suggests low friction coefficients are more realistic than high values. Although the anvil surface finish in the drop weight tests of Baker et al.<sup>12</sup> is not known, and only the low end pressures encountered in the drop weight test at slow impact velocities match the ranges for the previously mentioned experimental data, it does not appear unreasonable to use the aforementioned range for the friction coefficient.

The material properties of the steel and aluminum sections are shown in Table 1. Initially, the 0.1 cm thick by 0.25 cm radius propellant sample is modeled with a 4×30 element grid (see Figure 1b), and following So and Francis,<sup>20</sup> an isotropic, linearly elastic, linearly plastic, homogeneous constitutive material model is used (Material Model 3 in DYNA2D). The initial propellant material properties listed in Table 1 are estimates based on tensile data for a PBAN composite propellant.<sup>20</sup> Solid propellant has a Poisson's ratio,  $\nu$ , of near 0.5. However, using a value too close to 0.5 in the code was expected to lead to computational difficulties because of a term involving  $(1-2\nu)^{-1}$  in the constitutive equations.<sup>22</sup> As a result,  $\nu = 0.48$  was used as an initial value.

A series of parametric studies<sup>24</sup> and <sup>25</sup> showed improved results using a dynamic friction coefficient of 0.2 at the steel/propellant interface, a sample Poisson's ratio of 0.499 and refined striker and anvil meshes (Figure 1c). These values are used in the ensuing model also.

## MECHANICAL PROPERTY PARAMETRIC STUDY

For all the previous computations, the propellant has been modeled as a linearly-elastic,

**TABLE 1. MATERIAL PROPERTIES<sup>a</sup> FOR PRESENT DYNA2D COMPUTATIONS**

Material	Elastic Modulus, $E_{elas}$ (dyne/cm <sup>2</sup> )	Poisson's Ratio, $\nu$	Density $\rho$ (g/cm <sup>3</sup> )	Yield Stress, $\sigma_y$ (dyne/cm <sup>2</sup> )	Plastic Modulus, $E_{plas}$ (dyne/cm <sup>2</sup> )
Steel	$2.07 \times 10^{12}$	0.3	7.8	NA	NA
Al	$7.24 \times 10^{11}$	0.33	2.7	NA	NA
Propellant Sample	$6.895 \times 10^8$	0.48–0.499	1.833	$6.895 \times 10^7$	$6.895 \times 10^7$

<sup>a</sup>Values for steel and aluminum taken from Hodgman;<sup>23</sup> values for sample taken from So and Francis<sup>20</sup>.

linearly-plastic (LE-LP) material (Figure 2) using the material constants listed in Table 1. A mechanical property parametric study has been performed using variations in the propellant material constants: yield stress ( $\sigma_y$ ), elastic ( $E_{elas}$ ) and plastic ( $E_{plas}$ ) moduli.

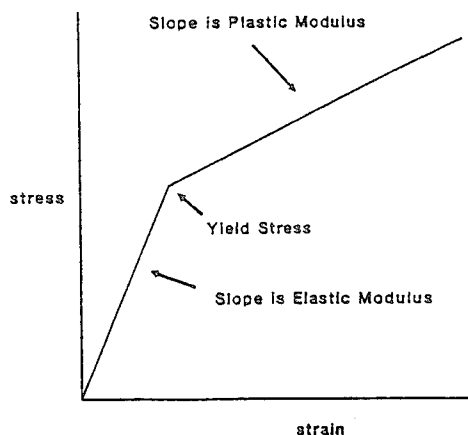


FIGURE 2. LINEARLY ELASTIC, LINEARLY PLASTIC STRESS-STRAIN CURVE INDICATING THE THREE MATERIAL CONSTANTS CHANGED

#### Current Mechanical Property Data

The purpose of the parametric study was to determine if changes in the material constants led to significant changes in the computed stress state in the propellant which could then be related to suggested initiation mechanisms. A search of the current mechanical property data literature was successful in providing some material constants over a range of strain rates. As discussed earlier, mechanical properties for most energetic materials are strong functions of temperature and strain rate,<sup>26-28</sup> and thus various temperature/strain rate shifting techniques were used to estimate the mechanical property values at strain rates corresponding to the drop weight test.

For example, Ho and Fong<sup>28</sup> used a Hopkinson pressure bar to determine mechanical properties of selected gun and rocket propellants over a strain rate range of 1 to 1000 s<sup>-1</sup> and a temperature

range of -60 to 60° C. They obtained an empirical correlation for yield stress as:

$$\sigma_y = K_1 + K_2 \log(\dot{\epsilon} a_t) \quad (1)$$

where  $K_1$  and  $K_2$  are straight line constants for the different propellants tested,  $\dot{\epsilon}$  is strain rate and  $a_t$  is a shifting factor which relates curves at various temperatures to a reference temperature. Considering an HTPB propellant and the range of strain rates to which it is subjected in the drop weight test (10 to 10000 s<sup>-1</sup>), the yield stress variations are calculated by Eq. (1) as approximately 7.5 to 35 MPa.

Atlantic Research determined some of the mechanical properties of the research propellants used in the experimental drop weight program.<sup>29</sup> Results from compression tests at 3.33 s<sup>-1</sup> and a temperature of -40° C (shifting applied) resulted in elastic moduli values over the range 2 to 26 MPa.<sup>25</sup> Unfortunately, the effective strain rate after shifting was probably not in the range of the drop weight test due to the low crosshead speed used in the test. Therefore, higher values for the elastic modulus are assumed. No data were available for post yield plastic moduli so reasonable approximations are made.

The resulting parametric variations performed are listed in Table 2. All values are presented as constant multiples of Case 3, which is taken as the baseline case.

A schematic of the axisymmetric finite element model is shown in Figure 3. To compare the results of the eleven cases, the five elements shown in Figure 3 were examined. The initial impact velocity for all runs was 8.4 m/s.

#### Comparative Criteria: Maximum Shear Stress and Strain Energy

Next, criteria for the comparisons were established. Two such criteria were selected: the maximum shear stress ( $\tau_{max}$ ) and the strain energy ( $E_{strain}$ ). These were chosen because, in the drop weight test, if critical (but yet undetermined) values of these parameters are reached, initiation may occur.<sup>9</sup> and <sup>12</sup> The maximum shear stress is defined as:

TABLE 2. MECHANICAL PROPERTY VARIATIONS

Yield Stress Variations $E_{plas} = 26 \text{ MPa}$ $E_{elas} = 69 \text{ MPa}$	Plastic Modulus Variations $\sigma_y = 20 \text{ MPa}$ $E_{elas} = 69 \text{ MPa}$	Elastic Modulus Variations $\sigma_y = 20 \text{ MPa}$ $E_{plas} = 26 \text{ MPa}$
1) $1.75 \times \sigma_y(3)$	—	9) $2 \times E_{elas}(3)$
2) $1.33 \times \sigma_y(3)$	7) $1.5 \times E_{plas}(3)$	11) $1.5 \times E_{elas}(3)$
3) $20 \text{ MPa}$	3) $26 \text{ MPa}$	3) $69 \text{ MPa}$
4) $0.66 \times \sigma_y(3)$	6) $0.375 \times E_{plas}(3)$	8) $0.5 \times E_{elas}(3)$
5) $0.35 \times \sigma_y(3)$	—	—

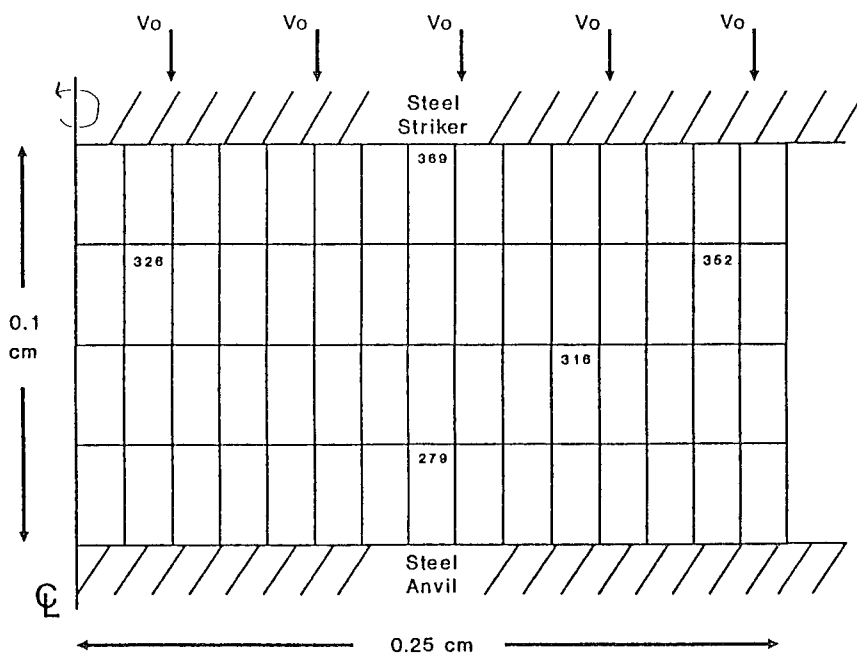


FIGURE 3. AXISYMMETRIC FINITE ELEMENT MODEL INDICATING ELEMENTS COMPARED IN THE PARAMETRIC STUDY

$$\tau_{\max} = \sqrt{\left(\frac{\sigma_x - \sigma_y}{2}\right)^2 + \tau_{xy}^2} \quad (2)$$

and is readily obtained from the DYNA2D postprocessor, ORION. The strain energy is defined as the work done on the sample over a selected strain interval and is given by:

$$E_{\text{strain}} = \int \sigma_{\text{eff}} d\epsilon_{ij} \quad (3)$$

where  $\sigma_{\text{eff}}$  is the effective stress and  $\epsilon_{ij}$  is the strain tensor, both also available from the postprocessor. They are then input to a spreadsheet, and the strain energy integral is evaluated numerically. As mentioned earlier, friction is also a potential source of initiation in the drop weight test. So<sup>30</sup> used a DYNA2D simulation to estimate the energy contained in shear bands caused by the friction stresses at the sliding interfaces between the propellant and steel. He found that this energy was approximately equal to the auto-ignition energy for his HTPB/AP propellant, and therefore, attributed propellant ignition to the frictional heat generated at the interface. However, several unsubstantiated assumptions and extrapolations were required to calculate the frictional energy. Thus, a similar friction initiation criterion was not explored for the present mechanical property study.

## Results and Discussion

Normalized time histories of maximum shear

stress for element 316 (see Figure 3) are shown in Figures 4a through c for changes in yield stress, plastic and elastic moduli, respectively. These results are direct functions of the changes in the input stress strain curves. For example, in the yield stress variations (Figure 3a) the curves appear to break away from the top curve at about 10, 20, 30 and 35  $\mu\text{s}$ . The corresponding normalized shear stress ratios are 1.75, 3, 5, 6.25. Ratios of the normalized shear stress values to the Case 3 value of 5 equal 0.35 (Case 5 to 3), 0.6 (Case 4 to 3), and 1.25 (Case 4 to 3). Note that these ratios are nearly identical to the yield stress ratios in Table 2. The plastic modulus variations (Figure 4b) all have the same yield stress, and hence the normalized  $\tau_{\max}$  curves break at the same point ( $\approx 30 \mu\text{s}$ ). After that point, the magnitude of the normalized shear stress is a direct function of the value of the plastic modulus. Thus, at any time the difference in the shear stress value is a direct function of the change in material property. Similar trends are observed for the elastic modulus changes as well. These results suggest that energetic materials with larger values of mechanical properties (i.e., harder materials) are more susceptible to accidental initiation since they are capable of building up greater stresses for a given loading-time history than softer materials.

More quantitative spatial comparisons were made by examining how changes in the material constants affected the two initiation criteria at the same instant in time (70  $\mu\text{s}$ ). For example, normalized  $\tau_{\max}$  values versus normalized  $\sigma_y$  for the five different elements are shown in Figure 5. The higher values of  $\tau_{\max}$  for the elements along

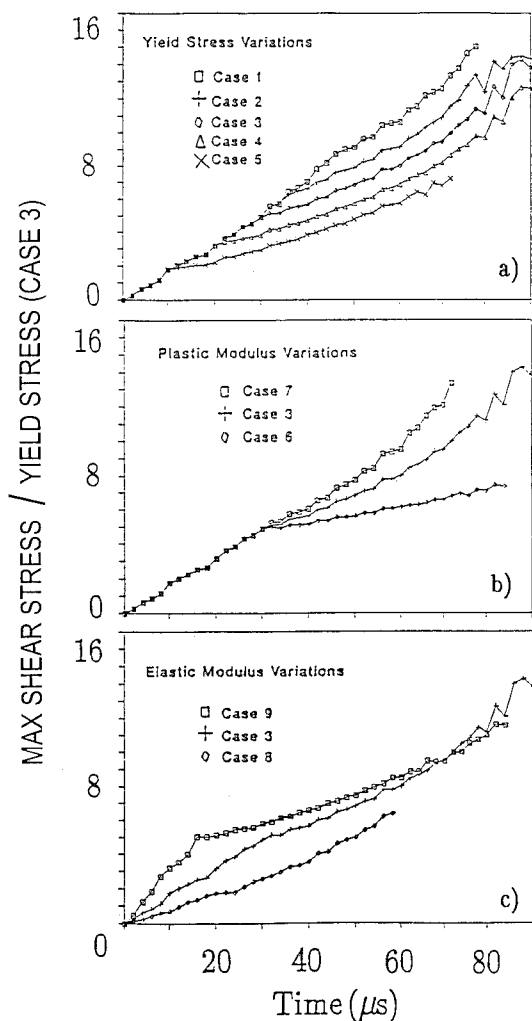


FIGURE 4. EFFECT OF a) YIELD STRESS, b) PLASTIC MODULUS, AND c) ELASTIC MODULUS ON NORMALIZED MAXIMUM SHEAR STRESS

the steel/propellant interfaces and near the propellant outer edge agree well with experiments in which initiation was observed at these high shear stress locations.<sup>9</sup> The slopes of all of these curves are sensitivity coefficients that express the degree of change in the initiation criterion for a given change in the material constant. The dimensionless sensitivity coefficients are used to simplify the explanation of the results and are determined from the best-fit lines of the data. Similar curves were generated for the other material constants and for the strain energy criterion. The results are summarized in Figures 6 and 7. The values below the corresponding element numbers are the respective sensitivity

coefficients; the average value for the five elements is given above the propellant mesh. Note that for changes in the elastic modulus, a bi-linear representation was used with the break points as noted.

From Figures 6 and 7 it is evident that both the shear stress and strain energy criteria are most sensitive to choice of  $\sigma_y$  and  $E_{plas}$  at the outer specimen edge. Plastic modulus at the specimen/machine interfaces is also important for either criterion. The shear stress criterion is not sensitive to elastic modulus, while the strain energy value is equally sensitive to  $E_{elas}$  and  $E_{plas}$  at the lower values of the former.

## CONCLUSIONS

The accuracy of simulations for modeling the response of energetic material subjected to various stimuli is limited by, among other submodels, the constitutive relations used to describe the component material behavior. For elastic materials such as steel, these relations and the corresponding constants are well-understood. However, for energetic materials, the behavior is more complicated. For small displacements and/or low strain rates, simplifying assumptions make the problem tractable to model in a finite element code. But for large displacement and/or high strain rates, typically found in tests such as drop weight impact, accurate material property characterization of the energetic material is required over the entire sample deformation time since different modes of failure occur at different rates. This information is now becoming available due in large part to research efforts in the solid rocket and gun propellant communities.

For the DYNA2D modeling presented here, considerable effort was made to optimize the calculations under the assumption of a homogeneous propellant sample. The results indicate a sample stress state that supports a postulated shear initiation mechanism.<sup>6</sup> and 7 Models were constructed which use the available material property data to account for changes with temperature and strain rate. The use of the simple linearly elastic, linearly plastic constitutive relation is justified since it mimics the actual stress-strain curves of selected propellants nearly as well as a more complicated non-linear visco-elastic relation without requiring the large number of model parameters (determined by experiments) that the latter does.

A mechanical property parametric study was performed on solid propellant material constants, assuming a linearly elastic, linearly plastic model, for a finite element simulation of the drop weight impact test. An assessment was made of the relative importance of changes in the yield stress and elastic and plastic moduli using two different initiation criteria, maximum shear stress and strain energy. Comparisons were made at



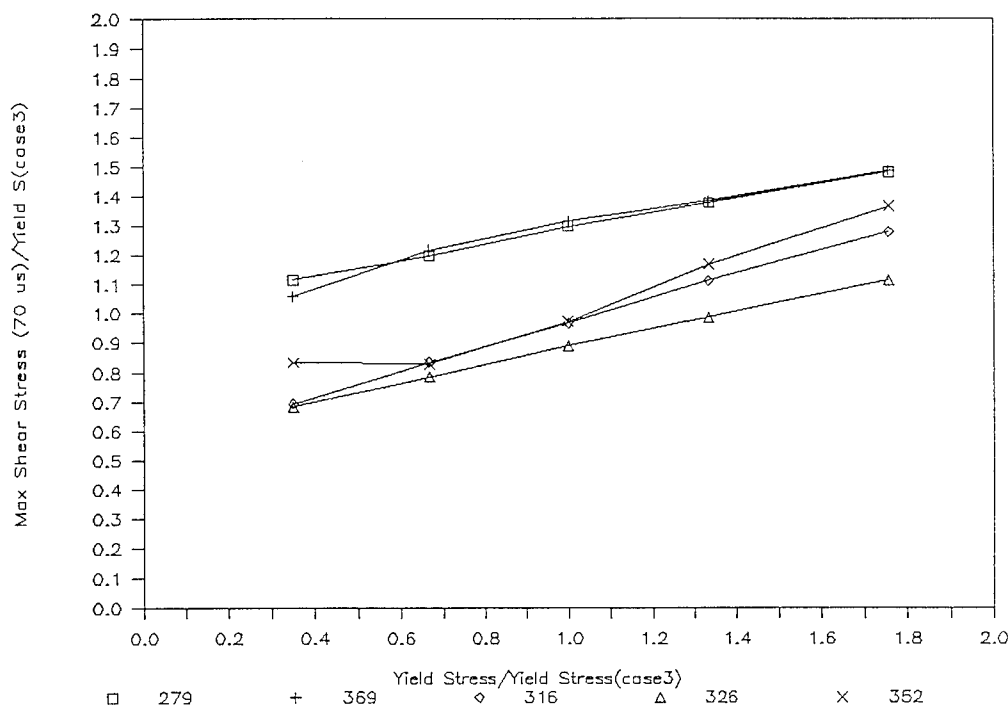


FIGURE 5. NORMALIZED MAXIMUM SHEAR STRESS AS A FUNCTION OF NORMALIZED YIELD STRESS

different locations in the propellant sample. For both initiation criteria and the three material constants, the maximum sensitivity coefficients occurred in the element located nearest the outer edge which agrees with experimental observations of the ignition location. High sensitivities at sample/machine interfaces were also indicated by the computations. The maximum shear stress findings suggest only changes in yield stress and plastic modulus significantly affect the results. The strain energy study demonstrates all three constants are important, but changing the elastic modulus has little significance at high modulus values. These three particular mechanical properties do not have exact physical significance for a real propellant, more properly modeled as a non-linear viscoelastic material. In a more realistic representation, results of the present study indicate that ignition criteria will be most sensitive to those parameters affecting flow of the material.

However, some propellant stress-strain curves can be approximated by an LE-LP curve, and these results suggest that it is more important to obtain accurate values for the yield stress and the modulus after yield than the elastic modulus. Furthermore, to those modeling a high rate impact event using the LE-LP approximation, any approximate value for the elastic modulus may be adequate.

#### ACKNOWLEDGEMENT

Support for this work was provided by the Army Research Office under Contract No. DAAL03-89-K-0061, Program Manager Dr. D. M. Mann. The views, opinions and/or findings contained in this paper are those of the authors and should not be construed as an official Department of the Army position, policy, or decision, unless so designated by other documentation.

#### REFERENCES

1. Maykut, A., "Insensitive munitions requirements and their impact on rocket motor design," *Central States Section/The Combustion Institute*, Nashville, TN, 22 April 1991.
2. Heavens, S.N. and Field, J.E., "The ignition of a thin layer of explosives by impact," *Proceedings of the Royal Society of London, Series A*, Vol. 338, 1974, pp. 77-93.
3. Winter, R.E. and Field, J.E., "The role of localized plastic flow in the impact initiation of explosives," *Proceedings of the Royal Society of London, Series A*, Vol. 343, 1975, pp. 399-413.

		.29	
.31			.51
		.42	
	.26		

			.51						
.52								1.13	
					.56				
			.51						

		.49			
.26					.53
			.37		
		.49			

			.45					
.18								.62
					.31			
			.47					

			.15 .02				
.11 .02							.12 .01
					.08 .01		
			.16 .02				

[illegible]

FIGURE 7. STRAIN ENERGY SENSITIVITY COEFFICIENTS FOR THE FIVE ELEMENTS STUDIED

- 784

11. Baker, P.J. and Mellor, A.M., "Relating sample deformation to observations in the dropweight impact test," AIAA Paper 92-3631, 28th Joint Propulsion Conference, Nashville, 1992.
12. Baker, P.J., Mellor, A.M. and Coffey, C.S., "Critical impact initiation energies for three HTPB propellants," *Journal of Propulsion and Power*, Vol. 8, No. 3, 1992, pp. 578-585.
13. Baker, P.J. and Mellor, A.M., "Modeling propellant sample deformation in the drop weight impact test," Central States Section/The Combustion Institute, Columbus, OH, 1992.
14. Duffy, K.P., "Dynamic finite element simulations of the response of solid rocket propellant subjected to impact," Masters Thesis, Mechanical Engineering, Vanderbilt University, Nashville, TN, 1993.
15. Duffy, K.P., "Numerical analysis of the drop weight impact machine using DYNA2D," Final Technical Report, Fall Semester, Mechanical Engineering Honors Program, Vanderbilt University, 1990.
16. Duffy, K.P. and Mellor, A.M., *Journal of Propulsion and Power*, to appear, 1993.
17. Hallquist, J.O., "User's manual for DYNA2D," Univ. of Cal., Lawrence Livermore National Laboratory, Report UCID-18756, Rev. 1, 1982.
18. Goudreau, G.L. and Hallquist, J.O., "Recent developments in large-scale finite element Lagrangian hydrocode technology," Computer Methods in Applied Mechanics and Engineering, Vol. 33, 1982, pp. 725-757.
19. Hallquist, J.O., "A numerical treatment of sliding interfaces and impact," Computational Techniques for Interface Problems, K. Park and D. Gartling, (Eds.), A.M.D. Vol. 30, ASME, United Engineering Center, New York, 1978.
20. So, W.T. and Francis, E.C., "Impact test analysis," *Journal of Spacecraft and Rockets*, Vol. 28, 1991, pp. 658-662.
21. Dobratz, B.M. and Crawford, P.C., "LLNL explosives handbook," Univ. of Cal., Lawrence Livermore National Laboratory, Report UCRL-52997, Change 2, 1985.
22. Francis, E.C., United Technologies, Chemical Systems Division, Personal Communication, 1990.
23. Hodgman, E.C., Handbook of Chemistry and Physics, 42nd Edition, The Chemical Rubber Publishing Co., Cleveland, 1961.
24. Barr, E.J., "Finite element analysis of low velocity impact tests for solid rocket propellants," Masters Thesis, Mechanical Engineering, Vanderbilt University, Nashville, TN, 1992.
25. Duffy, K., Baker, P., Barr, E. and Mellor, A., "Dynamic analysis of drop weight impact rocket propellant ignition," AIAA Paper 91-2193, 27th Joint Propulsion Conference, Sacramento, 1992.
26. Lieb, R. and Leadore, M., "Mechanical response comparison of gun propellants evaluated under equivalent time-temperature conditions," ARL Technical Report, Army Research Lab, Aberdeen Proving Ground, MD, to be published, July, 1993.
27. Lieb, R. and Leadore, M., "Time-temperature shift factors for gun propellants," Technical Report ARL-TR-131, Army Research Lab, Aberdeen Proving Ground, MD, to be published, May, 1993.
28. Ho, S. and Fong, C., "Temperature dependence of a high strain-rate impact fracture behaviour in highly filled polymeric composite and plasticized thermoplastic propellants," *Journal of Materials Science*, Vol. 22, 1987, pp. 3023-3031.
29. Graham, P.H., Atlantic Research Corporation, 22nd Monthly Status Report, Task 8, Contract DAAH01-88-D-0138, to US Army Missile Command, 1990.
30. So, W.T. (1991), "Dynamic finite element analysis of drop weight impact test of solid propellant," United Technologies, Chemical Systems Division, Internal Report.

# A FRICTIONAL WORK PREDICTIVE METHOD FOR THE INITIATION OF SOLID HIGH EXPLOSIVES FROM LOW-PRESSURE IMPACTS

S. K. Chidester, L. G. Green,

and C. G. Lee

Lawrence Livermore National Laboratory

Livermore, California 94550

"Experiments were performed and a methodology developed using the hydrodynamic code DYNA2D to predict the projectile threshold velocity for a positive response of the explosive LX-10-1 (94.5% HMX, 5.5% Viton A) to the projectile impact. The predictions are based on the frictional work for ignition of the explosive under the test conditions, about 0.37 cal/cm<sup>2</sup>. This value was then used to successfully predict the threshold velocity for reaction of a different geometry. Damaged explosive was found to have a lower threshold velocity for reaction, about two thirds that of undamaged. The insensitive explosive LX-17 (92.5% TATB, 7.5% KelF) could not be made to react under maximum test conditions, even when heated to 260°C.

## INTRODUCTION

There is an extensive data base of explosive response to projectile impact.<sup>1-9</sup> The listed references are only examples of a much larger literature. For the work being reported here, the threshold velocity for violent reaction from projectile impact of encased solid high explosive (HE) was determined experimentally for a well-defined geometry that was amenable to calculation. The measured and calculated pressure in the HE was less than 0.3 GPa for 150  $\mu$ sec at the reaction threshold. Since 0.3 GPa is well less than the threshold for shock initiation of the particular explosive used, the questions of ignition mechanism and course of reaction become pertinent. The thrust of the study was to help answer questions about explosive response under conditions of impact that were less than that required for direct shock initiation but still resulted in violent events. One answer, not necessarily unique, is that when frictional work on the HE at the HE/metal interface using one geometry was calculated, it was possible to use this result to calculate the threshold for response of the HE in a different geometry.

The goal of these tests was to provide information that would aid in the prediction of HE response in accident situations where the initiating stimulus was less than that required for direct shock initiation. Before these tests were run, a prediction of

threshold impact velocity was made (70m/s) using a rough average of previously reported<sup>10</sup> threshold frictional work from skid tests (1 cal/cm<sup>2</sup>) and the experimental value for coefficient of friction of 0.5(+/-) measured in the same tests for PBX-9404. The actual testing proved the threshold impact velocity to be much less, and the pre-test prediction was not only wrong, it was not conservative. This work presents a methodology for more accurately predicting the reaction threshold for HE involved in an accident such as an airplane crash or a severe land transportation accident. In addition to equations to describe the mechanical response of the system being considered that take into account the different velocities of the elastic and plastic waves at low pressure such as were seen in reference,<sup>11</sup> one also needs to know the energy required for ignition at the threshold velocity and pressure of the impact and the coefficient of friction between the explosive and whatever is translating across it or through it under pressure. The main focus of this work is on LX-10-1 (94.5% HMX, 5.5% Viton A binder, density 1.86g/cm<sup>3</sup>). Additional work was done on LX-17 (92.5% TATB, 7.5% KelF binder, density 1.90g/cm<sup>3</sup>), a very insensitive explosive. The explicit two-dimensional finite element code, DYNA2D,<sup>12</sup> was used to model the tests and predict the HE response. The finite element mesh of the projectile and target were generated using MAZE.<sup>13</sup> The post-processing of the DYNA2D analysis was done

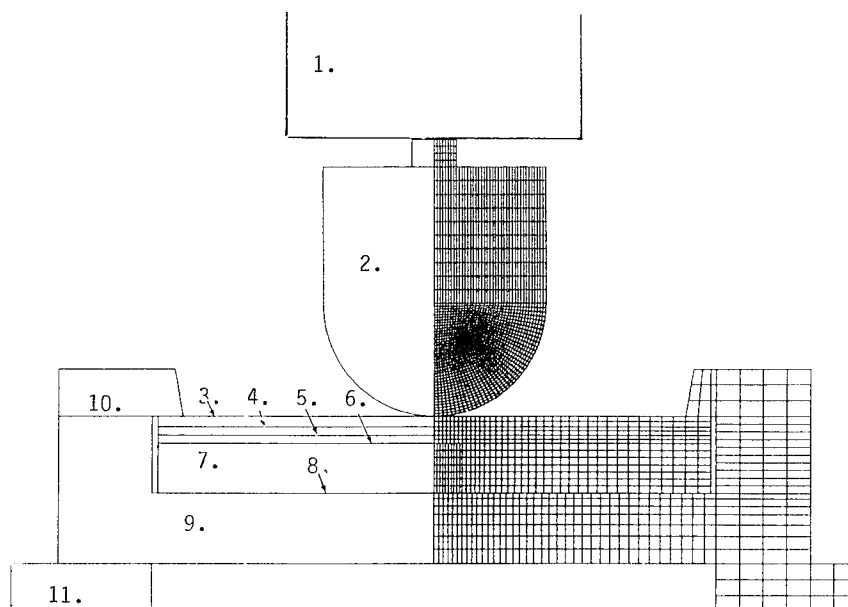


**FIGURE 1. SCHEMATIC REPRESENTATION OF FLAT PLATE IMPACT EXPERIMENTS AND CALCULATIONAL MESH**

Material	Thickness mm	Density gm/cm <sup>3</sup>	Modul GPa	Yield stress KPa	Ultimate Stress KPa
1. Sabot, 1.0kg					
2. 2.6kg Ta impactor		16.65	186	241	310
3. Ta foil	2.79	16.65	186	241	310
4. 6061-T6 A1	2.34	2.71	69	290	310
5. 6061-T6 A1	2.12	2.71	69	290	310
6. Halthane	0.25	1.27	-	-	-
7. LX-10-1	12.85	1.86	17	55	83
8. Silastic	0.18	1.27	-	-	-
9. 4130 Steel	19.05	7.85	207	910	1034
10. 4130 Steel	12.70	7.85	207	910	1034
11. 77 kg Reaction mass					

**TABLE 1. MATERIAL PROPERTIES USED IN CALCULATIONS AND KEY TO FIGURE 1**

with ORION.<sup>14</sup>

#### EXPERIMENTAL

Most of the experiments were done using a smooth-bore 76mm dia. gas gun to project a 0.46kg sabot carrying a 2.56kg Ta slug rounded on the impact

surface against a metal encased explosive target. See Fig. 1 for details of plane geometry target assembly and Table 1 for key to components in Fig. 1. Pressure gauges, both PVF2 and manganin, were used to monitor impact pressure on some of the experiments. They provided a check on the calculations done to describe the impact process. Previous work with LX-10-1 had

established the two-wave structure<sup>11</sup> that develops from impact shocks in LX-10-1 at amplitudes in the 0.3 to 1.0 GPa range. The equations used in the present calculations were fit to the previous work.

Single impact experiments on flat-plate target assemblies of LX-10-1 were carried out over a range of velocities and are tabulated in Table 2. None of the violent reactions observed were actually detonations of the LX-10-1. Small amounts of LX-10-1 were recovered from each experiment and the metal that was in contact with the explosive showed no evidence of the metal flow that is characteristic of a metal in contact with a detonating explosive. Even though these reactions were not detonations, they were extremely violent. The 76kg inertial block that was placed behind the experiment was projected ten meters or more and the Ta foil that covered the target explosive was rolled up into little cylinders and driven up to a centimeter into the rolled homogenous armor that protected the gas gun.

Single impact experiments on concave spherical geometry targets with an initial radius of curvature of about 5 cm that were derived from the plane geometry targets are tabulated in Table 3. While the data is not as extensive as would be desired, it does

fall within the prediction envelope that was developed for this geometry from the plane geometry experiments. Reaction levels were somewhat higher than for the plane geometry experiments and may have resulted in detonation of some of the LX-10-1 involved in the experiment.

Multiple impact experiments were also carried out on LX-10-1 and are tabulated in Table 4. They were done by subjecting the target assembly to an initial impact from the steel back side with either the tantalum slug or the large steel slug, then impacting it with a tantalum slug as was done with the single impact tests. Some single impact targets which had been hit on the front surface by a Ta impactor were subjected to a second impact if they failed to react from the first impact. Multiple impacts resulted in lower threshold velocities and somewhat less violent reactions. There was definitely more LX-10-1 left unreacted after the double impact experiments than from the single impact experiments. As with the single impact experiments, there was no evidence of detonation, only violent reaction.

Impact experiments carried out on the insensitive high explosive (IHE) LX-17 are tabulated in table 5. The gas gun was not able to reach the threshold

Ta impactor vel. m/s	Experiment number	LX-10-1 reaction	Comments
25.3	E2-4	None	Dent in target 3.33 mm deep x 26.14 mm dia.
29.4	E2-16	None	LX-10-1 at 73°C prior to impact
31.5	E2-8	Explosion	
31.7	E2-6	None	
32.3	E2-5	None	Dent in target 4.12 mm deep x 29.84 mm dia.
32.3	E2-9	None	
35.3	E2-10	Explosion	
35.3	E2-7	Explosion	
40.0	E2-3	Explosion	
61.3	E2-2	Explosion	
106.7	E2-1	Explosion	Violence of explosion less than others.

TABLE 2. SUMMARY OF SINGLE IMPACT PLANE GEOMETRY EXPERIMENTS ON LX-10-1

Ta impactor vel. m/s	Experiment number	LX-10-1 reaction	Comments
41.7	E3-1	None	
42.8	E3-4	Explosion	Possible detonation
45.7	E3-3	Explosion	Possible detonation
50.2	E3-2	Explosion	Possible detonation

**TABLE 3. SUMMARY OF SINGLE IMPACT EXPERIMENTS ON SPHERICAL LX-10-1 TARGETS DERIVED FROM PLANE GEOMETRY TARGETS**

Ta impactor vel. m/s	Experiment number	Reaction from second impact	Comments
12.3	E2-9.1	None	Initial impact on front at 32.3 m/s, 2.56 kg Ta impactor
20.2	E2-13	None	Initial impact on back at 37.8 m/s, 1.71 kg steel impactor
21.2	E2-15	Explosion	Initial impact on back at 39.6 m/s, 1.71 kg steel impactor
22.6	E2-6.1	Explosion	Initial impact on front at 31.7 m/s, 2.56 kg Ta impactor
29.5	E2-14	Explosion	Initial impact on back at 41.5 m/s, 1.71 kg steel impactor
31.3	E2-4.1	Explosion	Initial impact on front at 25.3 m/s, Ta impactor
32.3	E2-11	Explosion	Initial impact on front at 42.7 m/s, Ta impactor
33.4	E2-5.1	Explosion	Initial impact on front at 33.4 m/s, Ta impactor

**TABLE 4. SUMMARY OF MULTIPLE IMPACT EXPERIMENTS ON LX-10-1**

Impactor vel. m/s	Impactor	Temperature °C	LX-17 reaction	Experiment number
104.9	2.56 kg Ta	ambient	None	E2-12
122.3	1.71 kg steel	250	None	E2-H1
138.4	120 kg steel	260	None	E2-H2
141.2	120 kg steel	260	None	E2-H3

**TABLE 5. SUMMARY OF PLANE GEOMETRY IMPACT EXPERIMENTS ON LX-17**

velocity for reaction even for the experiments where the LX-17 was heated to 260°C prior to impact. All experiments on the IHE were conducted at the maximum capability of the gas gun, about 141m/s for the lightest projectile weight used.

## DISCUSSION

The mechanical aspects of the impact are dealt with rather well. Comparison of the maximum dent dimensions with the calculations in the Table 6

Impact vel. m/s	Depth of dent, mm		Diameter of dent, mm	
	Experiment	Calculation	Experiment	Calculation
25.3	3.33	3.48	26.14	26.29
32.3	4.12	4.29	29.84	30.45

**TABLE 6. COMPARISON OF MEASURED AND CALCULATED DENTS IN TWO PLANE GEOMETRY IMPACT EXPERIMENTS**

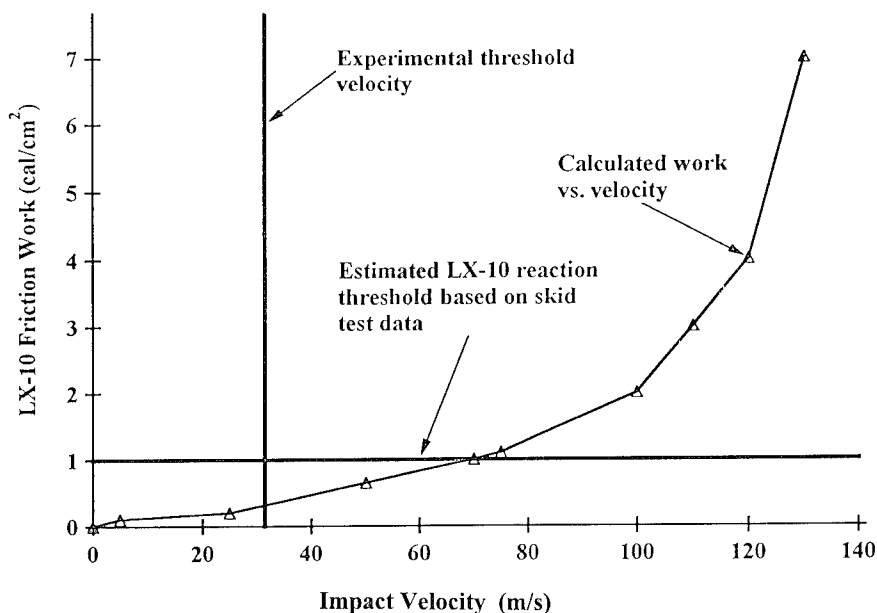


**FIGURE 2. FRICTIONAL WORK ON LX-10-1 SURFACE VS. 2.56 KG TANTALUM SLUG IMPACT VELOCITY**

summary shows reasonable agreement between calculation and experiment. Figure 1 is both a schematic of the plane geometry experiment and a representation of the undeformed mesh used in the calculations. Table 1 lists the material properties used in the calculations.

Figure 2 is a graphical representation of the frictional work done on the LX-10-1 in the plane geometry experiments by the impact of the tantalum impactor. The assumption of a friction coefficient of 0.5 uniquely determines the value of the frictional work. The frictional work can be no better than the uncertainty in the value of the coefficient of friction. An earlier measurement of the coefficient of friction between PBX-9404,<sup>15</sup> which has about the same volume percent HMX as LX-10-1, and aluminum, gave a value that varied between 0.47 and 0.52, with an average value of about 0.50. It can easily be seen in Figure 2 that a different threshold energy requirement

or a different coefficient of friction could move the impact threshold for reaction around considerably. There may also be a minimum area of ignition which could affect the threshold velocity, but that has not been considered here.

#### SUMMARY

The coefficient of friction and the minimum ignition energy to ignite a surface under the test conditions can be used to calculate a reasonable threshold velocity level for impact ignition. The calculations can be applied to different geometries and can relate the change in threshold velocity with change in geometry.

Work performed under the auspices of the U.S. Department of Energy by the Lawrence Livermore National Laboratory under contract No. W-7405-ENG-48.



## REFERENCES

1. Dewey, J. and Slade, D., "High Order Initiation of Two Military Explosives by Projectile Impact," Ballistic Research Laboratory Report N. 1021, 1957.
2. Eldh, D.; Persson, B.; Ohlin, B.; Johansson, C. H.; Ljungberg, S.; and Sjolín, T., "Shooting Test with Plane Impact Surface for Determine the Sensitivity of Explosives," Explosivstoffe, No. 5, 1963.
3. Roslund, L. A.; Watt, J. M.; and Coleburn, N. L., "Initiation of Warhead Explosives by the Impact of Controlled Fragments in Normal Impact (U)," NOLTR 73-124, 1975.
4. Bahl, K. L.; Vantine, H. C.; and Weingart, R. C., "The Shock Initiation of Bare and Covered Explosives by Projectile Impact," Seventh Symposium (International) on Detonation, 1981.
5. Walker, F. E. and Wasley, R. J., "Initiation Patterns Produced in Explosives by Low-Pressure, Long-Duration Shock Waves," Combustion and Flame 22, 53-58, 1974.
6. Dobratz, B. M. and Crawford, P. C., "LLNL Explosive Handbook," LLNL report No. UCRL-52997 Change 2, 1985.
7. Schnurr, N. M., "Thermal Initiation Caused by Fragment Impact on Cased Explosives," Los Alamos National Laboratory report No. LA-UR-89-2467, 1989.
8. Green, L., "Shock Initiation of Explosives by Impact of small Diameter Cylindrical Projectiles," Seventh Symposium (International) on Detonation, 1981.
9. Ferm, E. N. and Ramsay, J. B., "Spherical Projectile Impact on Explosives," Ninth Symposium (International) on Detonation, 1989.
10. Green, L.; Weston, A.; Van Velkinburg, J., "Mechanical and Frictional Behavior of Skid Test Hemispherical Billets," UCRL-51085, Lawrence Livermore National Laboratory, Livermore, CA, July, 1971, pp. 42-45.
11. Tarver, C. M.; Urtiew, P. A.; Chidester, S. K.; Green, L. G., "Shock Compression and Initiation of LX-10," Propellants, Explosives, Pyrotechnics 18, xx-xx, 1993.
12. Whirley, R. G.; Engelmann, B. E., "DYNA2D a Nonlinear, Explicit, Two-Dimensional Finite Element Code for Solid Mechanics," UCRL-MA-110630, 1992.
13. Hallquist, J. O., "MAZE- An Input Generator for DYNA2D and NIKE2D - Users Manual," UCID-19029, June 1983.
14. Hallquist, J. O., "ORION - An Interactive Color Post-Processor for Two Dimensional Finite Element Codes - Users Manual," UCID-19310, January 1982.
15. Hoge, K. G., "Friction and Viscoelastic Properties of Highly Filled Polymers: Plastic-Bonded Explosives, UCRL-70588, Lawrence Radiation Laboratory, Livermore, CA, July, 1967, Fig. 14.

## DISCUSSION

MICHAEL GUNGER

Orlando Technology Inc., Shalimar, Florida

Are the friction values used functions of other quantities such as temperature, strain rate, etc.?

## REPLY BY LEROY GREEN:

No. The referenced work by Ken Hoge did look at coefficient of friction vs. sliding velocity and surface finish, but the changes were generally less than 20 percent. We simply used a representative value.

## DISCUSSION

J. E. KENNEDY

Los Alamos National Laboratory,  
Los Alamos, New Mexico

Can you compare these experiments and results with those from Susan tests, which involve low-velocity crushing impact?

## REPLY BY LEROY GREEN:

For LX-10, the Susan test threshold occurs at a pressure of about 500 bars, which causes rupture of the aluminum case around the LX-10 and the extrusion of the explosive through the case cracks, but not a complete failure of the case. The actual work done on the explosive in the extrusion process is difficult to

calculate, and because the pressure is significantly lower than for the current experiments, the rate of doing work on the explosive is much less. The tests appear to have much in common, but they are not the same. For a

very insensitive explosive such as LX-17, however, the correspondence would be much closer and the results of one test would give a very good indication of what could be expected from the other.

## AN INVESTIGATION OF COMPRESSION AND SHEAR WAVE PROPAGATION IN EXPLOSIVES\*

M. Cowperthwaite and Y. M. Gupta<sup>†</sup>  
SRI International  
Menlo Park, California 94025-3493

Theoretical and experimental studies of the one-dimensional (1D) flows produced in an explosive subjected to compression and shear (CS) loading were performed to investigate the onset of shear-induced reaction (SIR). In this theoretical study, the 1D flow equations were written in terms of the reference configuration because measurements of longitudinal particle velocity ( $u_1$ ) and shear particle velocity ( $u_2$ ) are made by Lagrange gages in SRI's CS experiments. A complete, elastic equation of state (EOS) for a reacting explosive was used to derive the simplest 1D reactive flow equations governing the first Piola-Kirchhoff stresses  $p_{11}$  and  $p_{21}$ , and flows influenced by compression-induced reaction (CIR), shear-enhanced reaction (SER), and SIR were considered to provide a framework for interpreting the measured  $u_1$ -histories. In the experimental study, multiple Lagrange gages embedded in Composition B3 (CB3) targets were used to make  $u_1$  and  $u_2$  measurements in normal and parallel-inclined impact (PII) experiments designed to produce equivalent compression waves. The  $u_1$  histories gave evidence of SER and SIR in different batches of CB3 shocked, respectively, into the 10- and 15-kbar regions. The  $u_2$  measurements showed that the shear deformation produced in CB3 by PII remains close to the impact surface.

### INTRODUCTION

This work was performed to provide a better understanding and description of an explosive's response to compression and shear (CS) loading and to obtain evidence for the occurrence of shear-induced reaction (SIR).

SIR in explosives was postulated in the 1940s by Bridgman,<sup>1</sup> and the results of explosive sensitivity tests, such as the drop-weight<sup>2</sup> and fragment impact tests, provide some evidence for its occurrence. It is difficult to use the results from such tests to establish the occurrence of SIR, however, because the tests are not well instrumented and the explosives are subjected to different combinations of deformations that are not easily amenable to quantitative analysis. Recognizing these limitations, Gupta<sup>3</sup> proposed that the one-dimensional compression and shear (1DCS) loading technique could be used to perform a more definitive study of SIR in explosives. In this 1DCS wave

technique,<sup>4,5</sup> the gas gun is used to perform parallel-inclined impact (PII) experiments with multiple Lagrange particle velocity gages embedded in the target, and the magnetic field is oriented to determine either longitudinal particle velocity ( $u_1$ ) histories or shear particle velocity ( $u_2$ ) histories from gage measurements. In using this 1DCS technique to address the problem of SIR in explosives,  $u_1$  histories are measured in normal impact (NI) and PII experiments designed to produce compression waves (CWs) of the same strength that are nonreactive in the time frames of the experiments. In this case, because the loading conditions differ only by a shear component, significant differences between the sets of particle velocity histories recorded in the NI and PII experiments can be taken as evidence for the onset and occurrence of SIR in the explosive subjected to PII. Such NI and PII experiments designed to produce CWs of the same strength will here be called equivalent NI and PII experiments.

Series of  $u_1$  and  $u_2$  measurements were made on Composition B3 (CB3) in a series of equivalent NI and PII experiments in our present application of the 1DCS technique to explosives; the equations of motion for 1DCS flows were written in Lagrange form and combined with an equation of state (EOS) for a reactive elastic solid to provide a framework for interpreting the results of our CS gas gun experiments.

\*This work was monitored by Dr. D. Mann of the U.S. Army Research Office and performed under Contract No. DAA29-84-0018.

<sup>†</sup>Y. M. Gupta, Consultant to SRI International, Physics Department, Washington State University, Pullman, WA 99163.

## PARALLEL-INCLINED IMPACT EXPERIMENT

### Experimental Techniques

In our CS experiments, multiple Lagrange gages are used to record particle velocity histories in a target that is subjected to a PII in the gas gun. Figure 1 shows a schematic view of a flyer about to strike a target in a PII experiment but does not show the gages embedded in the target. Upon impact, compressive and shear disturbances, parallel respectively to the directions  $X_1$  and  $X_2$ , are produced at the impact surface because the normal to the flyer plate  $X'_1$  is not parallel to its direction of motion  $X_1$ . These compressive and shear disturbances propagate into the target and back into the flyer and will be 1D with respect to  $X_1$  until they are influenced by lateral rarefaction waves.

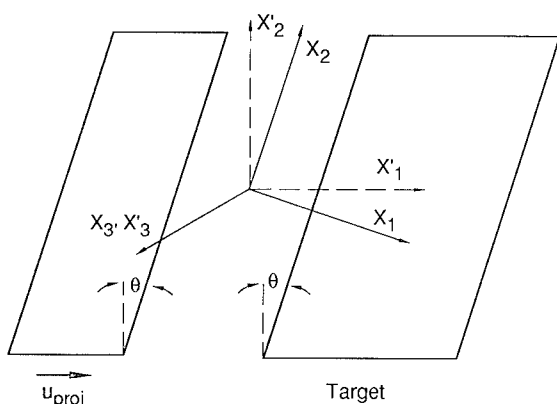


FIGURE 1. SCHEMATIC VIEW OF EXPERIMENTAL TECHNIQUE TO PRODUCE COMPRESSION AND SHEAR WAVES.

THE  $X'_i$  REFERS TO THE LABORATORY SYSTEM;  $X_i$  REFERS TO THE COORDINATE SYSTEM FIXED ON IMPACT PLATES.

The Lagrange electromagnetic particle velocity (EPV) gages embedded in the target are based on the principle that an electric conductor of length  $l$  moving with a velocity  $u$  in a fixed magnetic field  $B$  will generate an electromotive force  $E$  given by the equation  $E = l \cdot (u \times B)$ . It follows from this equation that we can orient the magnetic field to make either  $u_1$  - time ( $t$ ) measurements or ( $u_2$  -  $t$ ) measurements. The voltage signals from the EPV gages are recorded, using the usual methods, by analog and digital oscilloscopes.

To measure compression response in a target, the angle in Figure 1 is set to zero in the NI experiments and to  $15^\circ$  or  $20^\circ$  in the PII experiments, and the magnetic field is aligned to measure  $u_1(t)$ .

To measure shear response in a PII experiment, the angle  $\theta$  in Figure 1 is set to  $15^\circ$  or  $20^\circ$  and the magnetic field is aligned so that the voltages generated by the EPV gages have only  $u_2$  contributions. Even with good field alignment, shear particle velocity measurements are not as accurate as longitudinal particle velocity measurements.

The target assembly for the shear wave experiments is identical to that for the plane compression experiments.

### Governing Equations

Our theoretical description of the PII experiment is based on the assumption that the flow produced by the impact is 1D with respect to the direction normal to the plane of impact.

To specify the strain, it is convenient to introduce a different notation from that used in Figure 1, and let  $h_1$ ,  $h_2$ ,  $x_1$ , and  $x_2$  denote, respectively, the Lagrange and Eulerian coordinates normal and parallel to the plane of impact. In this case, when  $u_1(h_1) = 0$  for  $t \leq \tau_1$  and  $u_2(h_1) = 0$  for  $t \leq \tau_2 \leq \tau_1$ , we can write the following equations for the deformation gradients:

$$\frac{\partial x_1}{\partial h_1} = 1 + \int_{\tau_1}^t \frac{\partial u_1}{\partial h_1} dt, \quad \frac{\partial x_1}{\partial h_2} = 0 \quad (1)$$

$$\frac{\partial x_2}{\partial h_1} = 1 + \int_{\tau_2}^t \frac{\partial u_2}{\partial h_1} dt, \quad \frac{\partial x_2}{\partial h_2} = 1$$

and use the matrix of deformation gradients  $F$  to construct a strain tensor  $V$  from the equation<sup>6</sup>

$$V = \frac{1}{2} (C - I) \quad (2)$$

where  $I$  denotes the unit matrix, and the right Cauchy-Green tensor  $C = F^+F$ , where  $F^+$  is the transpose of  $F$ . The combination of Equations (1) and (2) gives the elements of  $V$  describing the strain produced in our PII experiments as

$$V_{11} = \frac{1}{2} \left[ \left( \frac{\partial x_1}{\partial h_1} \right)^2 + \left( \frac{\partial x_2}{\partial h_1} \right)^2 - 1 \right] \quad (3)$$

$$V_{12} = V_{21} = \frac{1}{2} \left( \frac{\partial x_2}{\partial h_1} \right), \quad V_{22} = 0 \quad (4)$$

The equation expressing the conservation of mass for our PII experiment is written conveniently in terms of the specific volume  $v$  as

$$\frac{\partial v}{\partial t} = v_0 \frac{\partial u_1}{\partial h_1} \quad (5)$$

where the subscript  $o$  denotes the initial state of the material. Equation (5) is readily obtained from the Lagrange expression for mass balance,  $v = v_0 J = v_0 \text{Det}$

F with  $J = (\partial x_1 / \partial h_1)$  from Equation (1), by differentiating with respect to  $t$ .

The natural equations expressing the conservation of linear momentum for our PII loading are written in terms of the components  $P_{ij}$  of the first Piola-Kirchhoff<sup>6</sup> (PK) stress tensor as

$$\frac{\partial u_1}{\partial t} = -v_0 \frac{\partial P_{11}}{\partial h_1} \quad (6)$$

$$\frac{\partial u_2}{\partial t} = -v_0 \frac{\partial P_{21}}{\partial h_1} \quad (7)$$

The  $P_{jk}$  are related to the components  $\sigma_{ij}$  of the Cauchy stress tensor by the equation

$$P_{jk} = J \sigma_{ij} \frac{\partial h_k}{\partial x_i} \quad (8)$$

and for PII loading satisfy the equations

$$P_{11} = \sigma_{11}, \quad P_{12} = -\sigma_{11} \frac{\partial x_2}{\partial h_1} + \frac{\partial x_1}{\partial h_1} \sigma_{21} \quad (9)$$

$$P_{21} = \sigma_{12} = \sigma_{21}, \quad P_{22} = -\sigma_{12} \frac{\partial x_2}{\partial h_1} + \frac{\partial x_1}{\partial h_1} \sigma_{22}$$

To complete our balance equations, we write the equation for the time rate of change of the specific internal energy ( $e$ ) for adiabatic flow in the reference configuration as

$$\frac{\partial e}{\partial t} = -P_{ij} v_0 \frac{\partial u_i}{\partial h_j} \quad (10)$$

The energy equation for our PII experiment then follows from Equation (10) as

$$\frac{\partial e}{\partial t} = -v_0 \left( P_{11} \frac{\partial u_1}{\partial h_1} + P_{21} \frac{\partial u_2}{\partial h_1} \right) \quad (11)$$

A more complete description of a material's response to PII is provided by its EOS. To be more specific, we assume that the impacted material is an inert elastic solid and denote its specific entropy and temperature by  $s$  and  $T$ . We then use the differential form for the  $e = e(s, v_0 \partial x_i / \partial h_j)$  EOS,<sup>7</sup>

$$de = Tds - v_0 p_{ij} d(\partial x_i / \partial h_j) \quad (12)$$

and Equation (11) to obtain the following equation for the entropy production in an inert elastic solid subjected to PII,

$$T \frac{\partial s}{\partial t} = -v_0 (P_{11} - p_{11}) \frac{\partial u_1}{\partial h_1} - v_0 (P_{21} - p_{21}) \frac{\partial u_2}{\partial h_1} \quad (13)$$

## FLOW EQUATIONS FOR A REACTIVE ELASTIC SOLID SUBJECTED TO CS LOADING

Reactive flow equations are obtained by combining Equation (10) with an equation for  $e$  describing the reactive mixture of interest. We consider the simplest case here, by assuming that our elastic explosive undergoes a global decomposition to produce solid reaction products and a mixture that is in mechanical and thermal equilibrium. We use  $\lambda$  to denote the mass fraction of the explosive that has decomposed, and we use  $Q$  and  $A$ , respectively, to denote the heat of decomposition and the affinity of the decomposition reaction. In this case, our reactive mixture can be described by an  $e = e(s, v_0 \partial x_i / \partial h_j, \lambda)$  EOS<sup>8</sup> and for PII,

$$\frac{\partial e}{\partial t} = T \frac{\partial s}{\partial t} - v_0 p_{11} \frac{\partial u_1}{\partial h_1} - v_0 p_{21} \frac{\partial u_2}{\partial h_1} - A \frac{\partial \lambda}{\partial t} \quad (14)$$

We now assume that the entropy production in regions free from shocks is dominated by reaction, set  $P_{ij} = p_{ij}$  accordingly, and combine Equations (11) and (14) to obtain the basic equation governing our reactive flow as

$$\frac{\partial s}{\partial t} = \frac{A}{T} \frac{\partial \lambda}{\partial t} = \left( \frac{\partial s}{\partial \lambda} \right)_{c, x'_1, x'_2} \frac{\partial \lambda}{\partial t} \quad (15)$$

where  $x'_1 = \partial x_1 / \partial h_1$  and  $x'_2 = \partial x_2 / \partial h_1$ .

The combination of Equation (15) with the  $s = s(p_{11}, v_0 x'_1, v_0 x'_2, \lambda)$  and  $s = s(p_{21}, v_0 x'_1, v_0 x'_2, \lambda)$  EOS then leads to the equations

$$\begin{aligned} & \frac{\partial p_{11}}{\partial t} - \left( \frac{\partial p_{11}}{\partial x'_1} \right)_{s, x'_2, \lambda} \frac{\partial u_1}{\partial h_1} \\ &= \left( \frac{\partial p_{11}}{\partial x'_2} \right)_{s, x'_1, \lambda} \frac{\partial u_2}{\partial h_1} + \left( \frac{\partial p_{11}}{\partial \lambda} \right)_{c, x'_1, x'_2} \frac{\partial \lambda}{\partial t} \end{aligned} \quad (16)$$

$$\begin{aligned} & \frac{\partial p_{21}}{\partial t} - \left( \frac{\partial p_{21}}{\partial x'_1} \right)_{s, x'_2, \lambda} \frac{\partial u_1}{\partial h_1} \\ &= \left( \frac{\partial p_{21}}{\partial x'_2} \right)_{s, x'_1, \lambda} \frac{\partial u_2}{\partial h_1} + \left( \frac{\partial p_{21}}{\partial \lambda} \right)_{c, x'_1, x'_2} \frac{\partial \lambda}{\partial t} \end{aligned} \quad (17)$$

where  $(\partial p_{ji} / \partial \lambda)_{c, x'_1, x'_2} = -(\partial e / \partial \lambda)_{p_{ji}, x'_1, x'_2} / (\partial e / \partial p_{ji})_{x'_1, x'_2, \lambda}$  with  $j = 1, 2$ .

## Model Reactive Solid for Interpreting the Gas Gun Experiments

To include chemical reaction in our treatment of the PII experiment, we adopt the classical ZND model<sup>9</sup> of detonation and assume that the front of the wave produced in such an experiment is a nonreactive shock discontinuity. Because we are interested primarily in

the dependence of the longitudinal particle velocity on the chemical reaction, it is convenient to restrict our attention to an EOS for the reactive mixture that provides the simplest treatment of this dependence.

We accordingly chose an EOS compatible with the simplest type of inert flow that may be produced by PII. This flow is ideal in the sense that it consists of a CW in which  $(\partial u_2/\partial t) = 0$ , followed by a shear wave (SW) in which  $(\partial u_1/\partial t) = 0$ . Because  $(\partial u_2/\partial h_1) = 0$  in the CW and  $(\partial u_1/\partial h_1) = 0$  in the SW, it follows from Equations (6) and (7), and Equations (16) and (17) with  $\partial \lambda/\partial t = 0$ , that the condition for the uncoupling of the longitudinal and shear motions is

$$\left(\frac{\partial p_{11}}{\partial x_2}\right)_{s, x_1', \lambda} = \left(\frac{\partial p_{21}}{\partial x_1}\right)_{s, x_2', \lambda} = 0 \quad (18)$$

Ignoring the classical theory of elasticity, we write a simple EOS that satisfies these conditions as

$$e = e_0^* - \lambda Q + v_0 \frac{A_1(s)}{(n-1)} (x_1')^{-(n-1)} + \frac{v_0}{2} A_2(s) (x_2')^2 \quad (19)$$

where  $e_0^*$  denotes the energy of formation of the explosive,  $A_1(s)$  and  $A_2(s)$  are functions of the entropy, and  $n > 1$ .

Differentiating Equation (19) partially with respect to the independent variables shows that  $A = Q$ , and gives the following equations for  $T$ ,  $p_{11}$ , and  $p_{21}$ :

$$T = \frac{v_0}{(n-1)} \frac{dA_1}{ds} (x_1')^{-(n-1)} + \frac{v_0}{2} \frac{dA_2}{ds} (x_2')^2 \quad (20)$$

$$p_{11} = A_1(s) (x_1')^{-n} \quad (21)$$

$$p_{21} = -A_2(s) x_2' \quad (22)$$

with  $A_1(s_0) = 0$  to make  $p_{11} = 0$  when  $x_1' = 1$ .

Combining Equation (15) and the equations obtained by differentiating Equations (21) and (22) with respect to  $t$  gives the reactive flow equations (RFE) for our model material subjected to PII as

$$\frac{\partial p_{11}}{\partial t} = \frac{\partial v}{\partial t} \left(\frac{\partial p_{11}}{\partial v}\right)_{s, x_2', \lambda} + Q \frac{\partial \lambda}{\partial t} \left(\frac{\partial p_{11}}{\partial e}\right)_{x_1', x_2', \lambda} \quad (23)$$

$$\frac{\partial p_{21}}{\partial t} = \frac{\partial u_2}{\partial h_1} \left(\frac{\partial p_{21}}{\partial x_2'}\right)_{s, x_1', \lambda} + Q \frac{\partial \lambda}{\partial t} \left(\frac{\partial p_{21}}{\partial e}\right)_{x_1', x_2', \lambda} \quad (24)$$

where  $(\partial p_{11}/\partial e)_{x_1', x_2', \lambda} = (dA_1/ds)/(x_1')^n T = (n-1)/v$  in the CW and  $(\partial p_{21}/\partial e)_{x_1', x_2', \lambda} = -(dA_2/ds)x_2'/T$  in the SW.

For convenience in using Equations (23) and (24) to interpret flows produced by NI and PII and construct a framework for our CS experiments, we

supplement the term SIR with the terms compression-induced reaction (CIR) and shear-enhanced reaction (SER).

We first consider flows produced by NI in our model material and introduce the subscript H to denote the shock front. For NI, we need only consider CIR and flows governed by Equation (23), because  $x_2' = u_2 = 0$ . For flier velocities not large enough to produce CIR in the time-frame of the experiments, the Lagrange  $(u_1 - t)$  records are step-like. The jump from  $u = 0$  to  $u = u_H(h_1)$  in the very steep portion of the records represents the shock, and the horizontal portion with  $\partial u_1/\partial t = \partial p_{11}/\partial h_1 = 0$  represents the flow behind the shock. When  $u_H$  is independent of  $h_1$ ,  $\partial u_1/\partial h_1 = 0$  behind the shock, and it follows from the equation

$$\frac{d(u_1)_H}{dt} = \frac{\partial u_1}{\partial t_H} + U \left(\frac{\partial u_1}{\partial h_1}\right)_H \quad (25)$$

that the shock velocity  $U$  must also be constant. It then follows from the equation

$$\left(\frac{\partial p_{11}}{\partial u_1}\right)_H \frac{d(u_1)_H}{dt} = \frac{\partial p_{11}}{\partial t_H} - \rho_0 U \frac{\partial u_1}{\partial t_H} \quad (26)$$

that  $(\partial p_{11}/\partial t)_H = 0$ , and  $\partial p_{11}/\partial t = 0$  also behind the shock because  $\partial \lambda/\partial t = 0$  in Equation (23).

For flier velocities large enough to produce CIR, many types of flow can be produced by the influence of the chemical energy release rate (CERR) on the  $p_{11}$  and  $u_1$  fields. Here, we concentrate on a type of reactive flow that has been observed in multiple Lagrange studies of explosives such as TNT<sup>10</sup> and PBX9404,<sup>11</sup> and is pertinent to our investigation of CB3 here. In this type of reactive flow, the shock propagates with the nonreactive features described above until it is influenced by reaction. Initially at Lagrange positions influenced by CIR,  $\partial p_{11}/\partial t > 0$  because  $(\partial u_1/\partial h_1) = 0$ ,  $\partial p_{11}/\partial h_1 < 0$  because  $\partial^2 p/\partial h_1 \partial t < 0$ , and the particles accelerate  $\partial u_1/\partial t > 0$ . As the flow develops, however,  $\partial p_{11}/\partial h_1$  and  $\partial u_1/\partial t$  become zero at these Lagrange positions because  $\partial^2 p/\partial h_1 \partial t > 0$ , and the  $(p_{11} - t)$  profiles intersect to form an envelope where the  $(u_1 - t)$  profiles exhibit their maxima.

We next consider PII experiments with our model material and NI flier velocities associated with the nonreactive step shocks produced in the NI experiments. In the event of SIR, the flow is governed by Equations (23) and (24) and the chemical energy liberated influences the  $p_{11}$  and  $u_1$  fields as well as the  $p_{21}$  and  $u_2$  fields. Definitive evidence for SIR is then that the  $(u_1 - t)$  records obtained in these PII experiments are significantly different from the step-like  $(u_1 - t)$  records obtained from the inert shock produced in the NI experiments. Because  $\partial u_1/\partial h_1 = 0$  in the CW, we expect SIR to influence the  $p_{11}$  field and the  $(u_1 - t)$  records in a similar manner to that described for CIR above.

We finally consider equivalent NI and PII experiments performed on our model material with flier velocities large enough to produce CIR. Interpreting

the differences exhibited by two such equivalent sets of  $(u_1 - t)$  records is difficult because (1) CIR influences both the  $p_{11}$  and  $u_2$  fields and the  $p_{11}$  and  $u_1$  fields in the region subjected to shear, and (2) SER can increase the CERR in the region subjected to shear. Here, because reactive flow is so complicated, we can only speculate about differences that may be exhibited by equivalent sets of  $(u_1 - t)$  records. Two limiting cases come to mind with respect to SER. In the first case, the influence of SER on the chemical energy release rate is insignificant. We then expect the downstream  $(u_1 - t)$  records obtained in the PII experiment to show less influence of the reaction than those obtained in the NI experiment, because we expect  $\partial p_{11}/\partial t$  in the region close to the impact surface to be smaller for PII than for NI. In the second case, SER increases the CERR to such an extent that  $\partial p_{11}/\partial t$  in the region close to the impact surface is significantly larger in the PII experiment than in the NI experiment. We then expect the first  $(u_1 - t)$  record from the PII experiment to show more influence of chemical reaction than the first  $(u_1 - t)$  record from the NI experiment.

## EXPERIMENTAL METHODS AND RESULTS

### Multiple Lagrange Gage Composition B3 Targets

Targets of CB3 (60% RDX, 40% TNT by weight) were used in all the gas gun experiments. These targets were made as pucks by casting CB3 around sets of Lagrange particle velocity gages held in a gage assembly. The casting was performed at SRI International's Test Facility, and preliminary castings were sectioned to verify that the casting procedure produced uniform CB3 with no cavities and with the gages firmly embedded in the explosive. The gage assemblies used for casting four cylindrical targets 40 mm in diameter and 20 mm high, each containing three Lagrange gages, were made at SRI. These gages were positioned 0.5, 2.5, and 4.5 mm above the base plate of the assembly, which interfaces with the impact surface of the explosive target. The 10-mm-long active gage elements were made from 0.05-mm-diameter copper wires and carefully soldered to 0.25-mm-diameter copper posts, which, after the casting process, came out of the back surface of the explosive target.

### Gas Gun Experiments

We performed 18 gas gun experiments with five batches of CB3. These shots were performed in sets and were labelled in chronological order as follows: (84-2-26, 84-2-27, 84-2-28), (84-2-33, 84-2-34, 84-2-35, 84-2-36), (85-2-8, 85-2-9, 85-2-10, 85-2-11), (86-2-16, 86-2-17, 86-2-18), and (86-2-64, 86-2-65, 86-2-66, 86-2-67). Experimental details for these shots are given in Table 1, and we first use these data to make some general conclusions about the  $u_1$  and  $u_2$  measurements before discussing the shots in detail. Examination of the initial particle velocity  $(u_1)_H$  data in Table 1 shows that the values of  $(u_1)_H$  recorded in the different batches of CB3 are consistent except for the batch used in Shots 86-2-17 and 86-2-18. We surmise that some unknown problem with the casting process is responsible for this result and consequently omit these results from our

discussion. Estimates of the initial values of  $p_{11}$   $(p_{11})_H$  in the CWs, based on the Rankine-Hugoniot conditions and the gage data, show that values of  $(u_1)_H \approx 0.4$ ,  $\approx 0.3$ , and  $\approx 0.2$  mm/ $\mu$ s are associated with values of  $(p_{11})_H$  of  $\approx 20$ ,  $\approx 15$ , and  $\approx 10$  kbar, respectively. Table 1 also shows that no good sets of  $u_2$  histories were recorded in the CB3 targets in our present series of CS experiments. Because no significant shear particle velocities were recorded beyond the first gage position, we concluded that the shear deformation produced in CB3 by PII does not propagate very far away from the impact surface.

We now consider our CS experiments in more detail, remembering that the experimental time frame at a gage position is  $\sim 3.5$   $\mu$ s. Our first series of experiments, Shots 84-2-26 through 84-2-28, was designed to produce CWs in CB3 with  $(p_{11})_H$  in the 20-kbar region. A set of complete  $(u_1 - t)$  records was obtained for CB3 subjected to PII but not for CB3 subjected to NI. Because only one complete  $(u_1 - t)$  record was obtained in the NI experiment, we were unable to make a meaningful comparison of the two sets of records. Comparison of the three  $u_1$ -histories produced by PII, however, indicated that the front of the CW is significantly influenced by the CERR and also that the flow may be influenced by SER. Consequently, all our other CS experiments were designed to produce values of  $(p_{11})_H$  in the 15- and 10-kbar regions.

Our second series of experiments, Shots 84-2-33 through 84-2-36, was designed to produce CWs in CB3 with  $(p_{11})_H$  in the 10-kbar region. Shot 84-2-26 was performed as a repeat of Shot 84-2-34 to test the reproducibility of our experimental technique, but the excessive noise recorded at some of its gage positions invalidated this test. The sets of  $(u_1 - t)$  records obtained in Shots 84-2-33 and 84-2-34 are shown in Figure 2.

Superpositioning the sets of  $(u_1 - t)$  records in Figures 2a and 2b shows that the flows in Shots 84-2-33 and 84-2-34 develop in the same way, as decaying step shocks in the  $(u_1 - t)$  and  $(p_{11} - h_1)$  planes, until they are influenced by exothermic reaction and become significantly different. The flow behind such a decaying shock with  $\partial u_1/\partial t = \partial p_{11}/\partial h_1 = 0$  satisfies the condition  $\partial p_{11}/\partial t = d(p_{11})_H/dt < 0$  and is represented in the  $(p_{11} - t)$  plane by a single  $(p_{11} - t)$  profile until at different Lagrange positions  $\partial p_{11}/\partial t > 0$  because of the exothermic reaction. The maxima exhibited by the  $(u_1 - t)$  records, in Figures 2a and 2b, indicate that the exothermic CERR influences the spatial variation of  $\partial p_{11}/\partial t$  at Lagrange positions neighboring the first gage in Shot 84-2-33 and the first two gages in Shot 84-2-34 in such a way that the flows first satisfy the conditions  $\partial p_{11}/\partial h_1 < 0$  and  $\partial^2 p_{11}/\partial t \partial h_1 < 0$ , and then the conditions  $\partial p_{11}/\partial h_1 < 0$  and  $\partial^2 p_{11}/\partial t \partial h_1 > 0$ , until  $\partial p_{11}/\partial h_1 = 0$ . Moreover, the flow produced by PII is influenced more by the exothermic CERR than the flow produced by NI. Whereas both  $(u_1)$  histories at the first gage position are essentially identical for 1.76  $\mu$ s, thereafter, the  $u_1$  produced by PII rises to a peak value of 0.275 mm/ $\mu$ s at 3.0  $\mu$ s but the  $u_1$  produced by NI remains essentially constant for another 0.5  $\mu$ s before rising to a peak value of 0.239 mm/ $\mu$ s at 2.78  $\mu$ s. Remembering that differences between sets of  $(u_1 - t)$

TABLE 1. SUMMARY OF COMPRESSION-SHEAR EXPERIMENTS  
PERFORMED IN COMPOSITION B3<sup>a</sup>

Shot No.	Flyer Velocity (mm/ $\mu$ s)	Angle (degrees)	Initial Particle Velocity (mm/ $\mu$ s)	Comments
84-2-26 <sup>b</sup>	0.558	0°	0.416	Third gage broke
84-2-27 <sup>c</sup>	0.579	15°	None	No good records
84-2-28 <sup>b</sup>	0.575	15°	0.414	Reactive flow
84-2-33 <sup>b</sup>	0.295	0°	0.215	Reactive flow
84-2-34 <sup>b</sup>	0.292	15°	0.220	Reactive flow
84-2-35 <sup>c</sup>	0.302	15°	None	No good records
84-2-36 <sup>b</sup>	0.300	15°	None	First gage record too noisy
85-2-8 <sup>b</sup>	0.301	0°	0.216	Reactive flow
85-2-9 <sup>b</sup>	0.305	15°	0.200	Reactive flow
85-2-10 <sup>b</sup>	0.308	20°	0.200	Reactive flow
85-2-11 <sup>c</sup>	0.312	15°	None	No good records
86-2-16 <sup>b</sup>	0.294	0°	None	First gage record too noisy
86-2-17 <sup>b</sup>	0.304	15°	0.140	Essentially nonreactive
86-2-18 <sup>b</sup>	0.294	15°	0.136	Second gage faulty
86-2-64 <sup>b</sup>	0.293	0°	0.230	Essentially nonreactive
86-2-65 <sup>b</sup>	0.302	15°	0.230	Essentially nonreactive
86-2-66 <sup>b</sup>	0.452	15°	0.310	Reactive flow
86-2-67 <sup>b</sup>	0.429	0°	0.320	Reactive flow

<sup>a</sup>A 1/4-inch-thick fused silica flyer was used in Shot 84-2-26; 3/8-inch-thick fused silica flyers were used in all the others.

<sup>b</sup>Magnetic field aligned to measure longitudinal particle velocity.

<sup>c</sup>Magnetic field aligned to measure shear particle velocity.

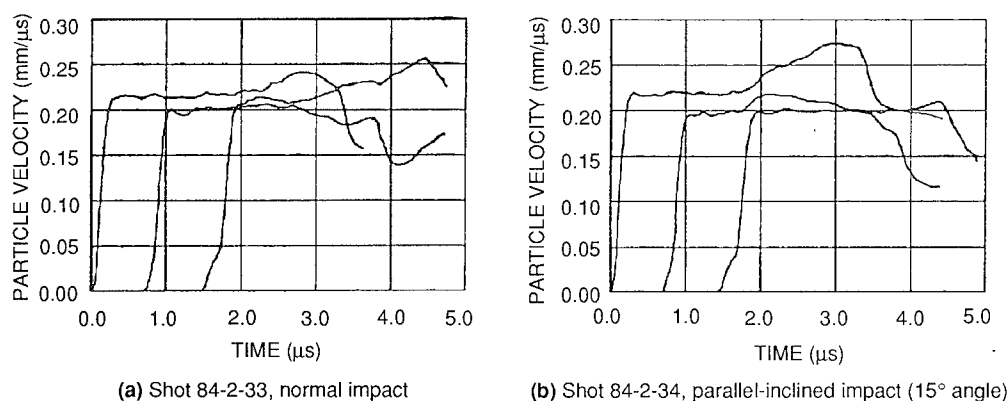


FIGURE 2. COMPOSITE PLOTS OF LAGRANGE LONGITUDINAL PARTICLE VELOCITY HISTORIES IN CB3 PRODUCED BY NORMAL IMPACT IN SHOT 84-2-33 AND BY PARALLEL-INCLINED IMPACT (15° ANGLE) IN SHOT 84-2-34.

records produced by PII and NI cannot be taken as evidence for SIR when the flow produced by NI is influenced by CIR, we here attribute these differences exhibited by the  $(u_1 - t)$  records at the first two gage positions in Shots 84-2-23 and 84-2-34 to the occurrence of SER.

The third series of experiments, Shots 85-2-8 through 85-2-11, was also designed to produce CWs in CB3 with  $(p_{11})_H$  in the 10-kbar region. Although the  $(u_1 - t)$  records will not be shown here because of space limitations, it is important to note that the flows were influenced by CIR and developed initially in the  $(u_1 - t)$  and  $(p_{11} - h_1)$  planes as constant rather than decaying step shocks.

The two pairs of shots performed in the fifth series of experiments, Shots 86-2-64 and 86-2-65 and Shots 86-2-66 and 86-2-67, were designed respectively to produce values of  $(p_{11})_H$  in the 10- and 15-kbar regions, because (1) anomalous  $(u_1 - t)$  records were obtained in Shots 86-2-17 and 86-2-18 and (2) the front of the CW with  $(p_{11})_H$  in the 20-kbar region was influenced by exothermic reaction in Shot 84-2-28. The  $(u_1 - t)$  records from the first pair of shots are shown in Figures 3a and 3b, and those from the second pair of shots in Figures 4a and 4b. Superpositioning the composite plots in Figures 3a and 3b shows that these flows in the  $(u_1 - t)$  and  $(p_{11} - h_1)$  planes develop initially on decaying step shocks and are essentially identical. Comparison of the composite plots in Figures 3a and 3b



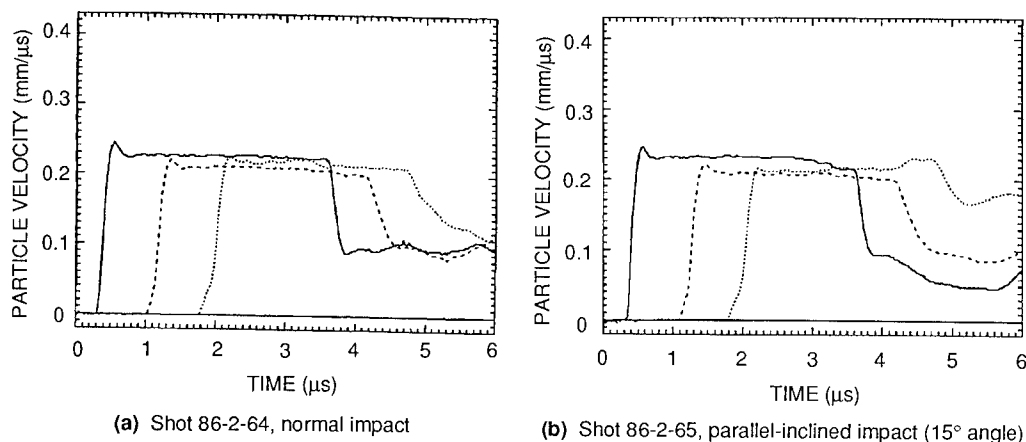


FIGURE 3. COMPOSITE PLOTS OF LAGRANGE LONGITUDINAL PARTICLE VELOCITY HISTORIES IN CB3 PRODUCED BY NORMAL IMPACT IN SHOT 86-2-64 AND BY PARALLEL-INCLINED IMPACT (15° ANGLE) IN SHOT 86-2-65.

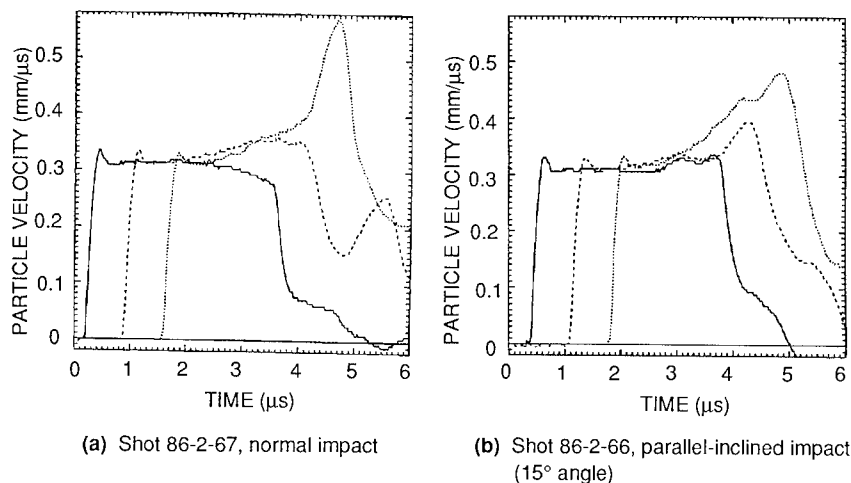


FIGURE 4. COMPOSITE PLOTS OF LAGRANGE LONGITUDINAL PARTICLE VELOCITIES IN CB3 PRODUCED BY NORMAL IMPACT IN SHOT 86-2-67 AND BY PARALLEL-INCLINED IMPACT (15° ANGLE) IN SHOT 86-2-66.

with those in Figures 2a and 2b, however, shows that our CB3 targets shocked into the 10-kbar region exhibit contrasting behavior. Whereas all these flows develop initially on decaying step shocks, the flows produced in the second series of experiments were significantly influenced by the exothermic CERR but those produced in the fifth series of experiments show little evidence of exothermic reaction. Our only explanation for this result, as for the anomalous ( $u_1 - t$ ) records obtained in the fourth series of experiments, is that our CB3 targets prepared in different castings had different physical properties.

Superpositioning the composite plots in Figures 4a and 4b shows that these flows produced by PII and NI are identical for about 2.3  $\mu$ s but then are significantly influenced by the exothermic CERR and become markedly different. Because of the complexity of reactive flow, it is sufficient for our purpose here to

consider the flows at the first gage position. In the neighborhood of the first gage, both flows develop with  $\partial p_{11}/\partial h_1 = 0$  until  $\partial p_{11}/\partial h_1 > 0$  in the flow produced by NI after about 2.5  $\mu$ s, and  $\partial p_{11}/\partial h_1 < 0$  and  $\partial^2 p_{11}/\partial t \partial h_1 < 0$  in the flow produced by PII after about 2.6  $\mu$ s. This difference between the flows produced at the first gage position is here taken as evidence for the occurrence of SIR, because the flow close to the impact surface produced by PII shows the influence of an exothermic CERR but that produced by NI does not.

## CONCLUSIONS

Theoretical and experimental studies of CS wave propagation in an explosive were performed to investigate the occurrence of SIR and provide a better understanding of its influence on the 1D flow produced in an explosive by the type of PII experiment pioneered by Gupta.<sup>4</sup>

In our theoretical study, we took a simplistic approach to the propagation of CS waves in explosives by treating the explosive and its products as an elastic solid governed by a complete EOS that decouples the longitudinal and shear deformations when the flow is nonreactive. This complete EOS was combined with the energy equation to derive the most convenient reactive flow equations for interpreting the 1D adiabatic flows produced in solids by NIs and PIIs. Flows influenced by CIR, SIR, and SER were then considered to provide an understanding of the influence of the CERR on the  $u_1$  field and a framework for interpreting the results of our gas gun experiments.

Our experimental study was based on the premise that significant difference between the sets of  $u_1$  histories recorded in an explosive subjected to NI and PII producing equivalent nonreactive CWs can be taken as evidence for the occurrence of SIR produced by PII. Eighteen NI and PII experiments were performed in a gas gun with CB3 targets, and multiple Lagrange gages embedded in these targets were used to make  $u_1$  and  $u_2$  measurements. The 18 experiments were divided into five sets that were performed with targets made from different batches of CB3. The results of our  $u_1$  measurements gave evidence for the occurrence of SER in the first batch of CB3, which was shocked initially into the 10-kbar region, as well as evidence for the occurrence of SIR in the fifth batch of CB3, which was shocked initially into the 15-kbar region. The results of the  $u_2$  measurements led to the conclusion that the shear deformation produced in CB3 by PII remains close to the impact surface. This conclusion showed that our simplistic EOS for a reactive solid is unrealistic as far as shear deformation is concerned.

Although the results of our gas gun experiments with CB3 provide some evidence for the occurrence of SIR and SER produced by PII, they are inconsistent and therefore not completely definitive. Because experimental conditions were essentially the same in the second, third, and fourth sets of experiments, inconsistencies among the sets of  $u_1$ -histories recorded in these experiments must be attributed to differences among the CB3 targets. Consequently, our casting procedure was not as well controlled as we had originally thought.

We conclude that the results of our theoretical and experimental studies provide some evidence for the occurrence of SER and SIR in explosives subjected to PII, but not enough to establish that SIR plays a significant role in the shock initiation of explosives. Future theoretical studies of SIR should be based on a more realistic description of the explosive that can be used to develop a more quantitative procedure for interpreting the sets of  $u_1$  histories recorded in equivalent NI and PII experiments. Future gas gun investigations of SIR should be performed with explosive targets with similar physical properties produced by well-proved casting

techniques.

## REFERENCES

1. Bridgman, P. W., "The Effects of High Mechanical Stress in Certain Solid Explosives," *J. Chem. Phys.*, Vol. 15, 1947, pp. 311-313.
2. Coffey, C. S.; Frankel, M. J.; Liddiand, T. P.; and Jacobs, S. J., "Experimental Investigation of Hot Spots Produced by High Rate Deformation and Shocks," in *Seventh Symposium (International) on Detonation*, U.S. Naval Academy, Annapolis, M. D., June 16-19, 1981, pp. 970-975.
3. Gupta, Y. M., "New Opportunities for Research in Energetic Materials," Wrightsville Beach, NC, November 1977.
4. Gupta, Y. M., "Shear Measurements in Shock-Loaded Solids," *Appl. Phys. Lett.* Vol. 34, 1976, pp. 694-697.
5. Gupta, Y. M.; Keough, D. D.; Walter, D. F.; Dao, K. C.; Henley, D.; and Urweider, A., "Experimental Facility to Produce and Measure Compression and Shear Waves in Impacted Solids," *Rev. Sci. Instr.*, Vol. 51, No. 2, 1980, pp. 183-194.
6. Thurston, R. N., "Waves in Solids," in *Encyclopedia of Physics*, Vol. VIa/4, *Mechanics of Solid IV*, Springer-Verlag, New York, 1974, pp. 109-146.
7. Gibbs, J. W., *The Scientific Papers of J. Willard Gibbs*, Vol. 1, *Thermodynamics*, Dover Publications, Inc., New York, 1961, pp. 184-214.
8. Cowperthwaite, M., "Compression and Shear Wave Propagation in Explosives," SRI Project PYU-6834, January 1989, Menlo Park, CA.
9. Fickett, W. and David, W. C., *Detonation*, University of California Press, Berkeley, Los Angeles, 1979, pp. 42-51.
10. Cowperthwaite, M. and Rosenberg, J. T., "A Multiple Lagrange Gage Study of the Shock Initiation Process in Cast TNT," in *Sixth Symposium (International) on Detonation*, Hotel del Coronado, Coronado, CA, August 24-27, 1976, pp. 786-793.
11. Weingard, R.; et al., "Manganin Stress Gages in Reacting High Explosive Environment," *Symposium H.D.P., Behavior of Dense Media Under High Dynamic Pressures*, Paris, France, August 27-31, 1978, pp. 451-461.

## DISCUSSION

DONALD J. BUTZ

Battelle Memorial Institute, Columbus, Ohio

Were all the experiments conducted at the same sample temperature, and have you yet modeled the effect of initial temperature or SIR/SER thresholds or mechanisms?

### REPLY BY M. COWPERTHWAITE:

I cannot give you a definitive answer about the sample temperature because it was not measured. In my simple treatment of compression and shear waves in explosives the initial temperature is not accounted for, for simplicity.

## DISCUSSION

W. E. DEAL

Los Alamos National Laboratory, Los Alamos, New Mexico

Did you look at the TNT samples to see if the crystallite size was comparable to the dimensions of the gauge? Large crystallite size in cast TNT has in the past caused me trouble in experimental reproductivity. I went to pressed TNT to achieve reproducible experiments.

### REPLY BY M. COWPERTHWAITE:

We sectioned some targets to verify that the gauges were firmly embedded in the Composition B3, but I cannot make any comment about the size of the TNT crystallite.

## COMPARISON OF DAMAGE-CREATED VOIDS WITH OTHER VOID TYPES IN ENERGETIC MATERIALS\*

John B. Ramsay  
Los Alamos National Laboratory, Los Alamos, New Mexico 87545

Herbert P. Richter  
Naval Air Warfare Center, China Lake, California 93555

and  
Richard R. Bernecker  
Naval Surface Warfare Center, White Oak, Silver Spring, Maryland 20903-3252

Discontinuities (voids and particulates) affect the phenomena of initiation of most explosives. Only liquids and single crystals are free of significant heterogeneity. Solid explosives cannot be pressed or cast to full density (100% TMD) and thus contain voids. Even vacuum-cast and pressure-cured explosives contain up to 0.8% porosity. Experimental evidence shows that the particular natures of these discontinuities significantly change this sensitivity. The observations are preliminary, but they are significant in our understanding of heterogeneous initiation.

Over the past several years, initiation of damaged and rubblized cast-cured, multi-component, multiparticulate energetic materials has been extensively studied. Three types of voids are recognized: (1) voids created by microballoons, (2) tensile damage attributed to debonding between solid particles and an elastomeric binder, and (3) porosity created during the initial pressing of the energetic material or by recompaction of shredded or particulated material. The data discussed here show that the shock sensitivity of heterogeneous energetic materials is significantly affected by the specific nature of the included voids, in addition to their concentration. Only a slight change in sensitivity was observed when microballoons were added to a multiparticulate material.

### INTRODUCTION

Introduction of discontinuities increases the sensitivity of energetic material to initiation by shock waves. Experimental evidence shows that the particular nature of these discontinuities significantly changes this sensitivity. The observations are preliminary, but they are significant in our understanding of heterogeneous initiation.

Discontinuities (voids and particulates) affect the phenomena of initiation of most explosives. Only liquids and single crystals are free of significant heterogeneity. Solid explosives cannot be pressed or cast to full density (100% TMD) and thus contain voids. Even vacuum-cast and pressure-cured explosives contain up to 0.8% porosity. Campbell and Travis<sup>1</sup> showed that

single crystals of HMX are not initiated by the pressure-time loading generated in detonating PBX 9404. Campbell et al.<sup>2</sup> and Lindstrom<sup>3</sup> showed that the shock sensitivity of an explosive was inversely related to the density (increase in void fraction). The manufacture of precision explosive components requires extreme care to control the density within narrow limits and thus ensure required initiation behavior. Low-density discontinuities, such as microballoons, are deliberately added to increase the shock sensitivity of blasting explosives. Travis<sup>4</sup> found no correlation between the density of a discontinuity and the efficacy of initiation of nitromethane. In numerical modeling of Travis' experiments, Mader<sup>5</sup> showed that high-temperature regions, sufficient to promptly initiate nitromethane, are formed by the collapse of a void and by the interaction of the shock wave downstream from a discontinuity. These studies involved the use of isolated discontinuities. Much work has been done to elucidate the effect of particle size on the shock sensitivity of polycrystalline explosives. In some carefully formulated experiments, Moulard<sup>6</sup> showed that, for HMX, the relationship between pressure and shock sensitivity was a function of

\* A portion of this work was performed under Contract No. W-7405-ENG-36 with the Los Alamos National Laboratory, Los Alamos, New Mexico. Other support was provided by Naval Air Warfare Center, Weapons Division, Independent Research Program.

the particle size distribution. At relatively low shock pressures, large-grain HMX was more sensitive than fine-grain HMX and, at relatively higher pressures, the fine-grain HMX was the more sensitive. Van der Steen et al.<sup>7</sup> reported data showing an effect of the RDX particle shape on shock sensitivity, as measured by a corner-turning gap test.

Discontinuities in solid energetic materials are introduced by damage. Damaged energetic materials have fracture surfaces and voids, particularly around particulate surfaces. Depending on the nature of the material and the extent of damage, porosity in the material can be closed or connected. With polymeric materials, a healing process takes place with time after the damage occurs. This healing process decreases the void volume, but the material remains weak. As a result of damage, a material may have different surface-area scales. The largest is that arising from the initial particle size distributions used in the formulation, followed by a smaller area created by the fracture surfaces. Both affect the response of a material in a hazardous environment. Kegler and Schall<sup>8</sup> showed that even the detonation process was affected by damage, over and above the effect of the change in density. Using a PETN-rubber explosive, they showed a greater decrease in detonation velocity with damage-induced density decrements than could be accounted for by the density change alone.

Over the past several years, initiation of damaged and rubblized cast-cured, multicomponent, multiparticulate, energetic materials has been studied extensively. Bernecker and Clairmont<sup>9</sup> presented data on the cast-cured RDX/inert-binder explosive, PBXW-108, and on an aluminized version of the same formulation, PBXN-109, in the 75% to 92% TMD range and at 100% TMD. Low-density samples were prepared by shredding or by chopping the material to produce regular-shaped grains, each of which contained many individual particles of RDX. The grains were then recompact to form the samples at various fractions of the original density. In a few experiments, the shock sensitivity was measured with the PBXW-108 under compressive loading at 97% TMD. The shock sensitivity for shredded (2.5-mm-wide, 0.8-mm-thick, and 6.4-mm-long) PBXN-109 was greater than that for cubes (2.1 mm on edge) of the same material at the same density. The decrease in shock sensitivity with compressively induced damage was approximately that expected for the decrease in density for a pressed explosive. This will be discussed later. In another report, Bernecker<sup>10</sup> showed a similar difference between cubes and shreds for a multiparticulate cast-cured material.

Sandusky and Bernecker<sup>11</sup> investigated the effect of time on damage-induced sensitivity. They damaged samples of cast-cured material with a weak shock and then used a gap test assembly to measure the sensitivity of the damaged material approximately 1 ms after the damage occurred. The residual porosity was sufficiently small that it could not be measured with flash x-radiography. With a very elastic formulation (H-1), they observed a 66% decrease in the critical gap pressure for material damaged 0.9 ms earlier. If there was a 2.5-ms delay between the damage and the initiating shock wave,

the reduction in critical gap pressure was only 10% for the same level of damage. Green et al.<sup>12</sup> used a gun-driven technique to create a damaged sample that was then projected against an undamaged sample of the same material. Delayed detonation (XDT) occurred as function of the geometry of the impact and the impact velocity.

A major increase in sensitivity occurs between 100% and 90% TMD. None of the techniques commonly used to measure sensitivity was suitable for obtaining quantitative information on shock sensitivity and porosity. Hence, two complementary lines of investigation were developed to measure the initiation sensitivity of these energetic materials from 90% to 100% TMD. Richter et al.<sup>13</sup> induced tensile damage by stretching a sample and subsequently measuring the critical gap thickness required for initiation. The porosity produced during straining and that remaining after failure was measured using dilatometers. As an example, samples of the same formulation used by Sandusky were tensilely strained to failure (300% elongation) and tested 20-30 minutes later. With a 1% residual porosity, a 50% decrease in critical gap pressure was observed. No microscopic examination of the stretched material was made with these test samples. As observed with similar energetic materials, we assume that the volume increase resulted from debonding between the binder and the particulate material. This debonding occurs first around the largest particles; in this case, the ammonium perchlorate (AP). Both Bernecker and Richter showed that the damage, or void volume, created in cast-cured material "healed" with time. Also the longer the time between the creation of the damage and the testing, the smaller the increase in shock sensitivity.

The shock sensitivities of special blends containing differing amounts of 44- $\mu$ m glass microballoons were studied by Grall and Ramsay.<sup>14</sup> The material was a cast-cured composition consisting of aluminum, AP, and HMX, with polyethylene glycol (PEG) as the binder and trimethylolethane trinitrate (TMETN) as a plasticizer. The materials are identified as RB-100 to RB-90, in which the number refers to the percent of TMD determined by the volume percent of microballoons. Shock sensitivity for RB-90 increases only slightly over that measured for RB-100. Results are explained on the basis of the particle size distribution of the energetic materials, relative to the microballoon diameter. The particle sizes of the HMX were 3- to 13- $\mu$ m (diam) and those of the AP were  $\approx$  90  $\mu$ m. The 44- $\mu$ m microballoons did not affect the shock sensitivity to the extent expected by the authors.

In this paper, three types of voids are recognized: (1) voids created by microballoons, (2) tensile damage attributed to debonding between solid particles and an elastomeric binder, and (3) porosity created during the initial pressing of the energetic material or by recompact-ing shredded or particulated material. Shock sensitivity data from Refs. 9, 13, and 14 on cast energetic materials, as well as data from the available literature on pressed explosives, are interpreted to show quantitatively different responses for materials with the three types of voids. For materials with the same porosity, tensile

damage creates the most sensitive material; pressed explosives and recompacted cast-cured material are less sensitive; and the addition of microballoons to this multi-particulate material creates the smallest change in sensitivity. When data for pressed or recompacted material are normalized, we have an interesting representation of shock sensitivity as a function of density.

## A COMPARISON OF VOID TYPE WITH SHOCK SENSITIVITY

Two basic types of shock initiation data are available, wedge data and gap test data. Wedge data are obtained with approximately one-dimensional, well-supported input pressure waves. These data are generally limited in number. Wedge test data used in these correlations are those for PETN,<sup>15</sup> PBX 9404,<sup>15</sup> tetryl,<sup>15</sup> TATB,<sup>15</sup> HMX,<sup>16,17</sup> and the RB-90 to RB-100 series. (Note: some of the data used to define the Pop plot for low-density HMX were obtained by a transit time technique rather than by a wedge test.<sup>16</sup>) Typically, wedge data are represented by the Pop plot, a log-log curve (linear) of run distance to detonation vs input pressure. We compare the data by using the pressures required for a 10-mm run to detonation ( $P_{10\text{mm}}$ ), computed from the Pop-plot relation for each material. These values were normalized to the  $P_{10\text{mm}}$  for the highest density of that particular formulation for which data were available ( $P_0$ ). The results obtained are listed in Table 1. Figure 1 plots  $P_{10\text{mm}}/P_0$  vs % TMD for these materials. Two salient features are in the figure: the effect on the shock sensitivity of microballoon voids, relative to the effect of

pressing voids in the explosive, and the concordance of the  $P/P_0$  plot for the various pressed explosives. Although this second feature is unexpected, it is very descriptive. Among the explosives, the agreement in the results is approximately the same as the estimated experimental errors present in the wedge test. The explanation may lie in the fact that voids in pressed explosives are inherently of the same type; that is, small, intergranular voids, initially present in the pressing powder, that were not removed during the pressing operation.

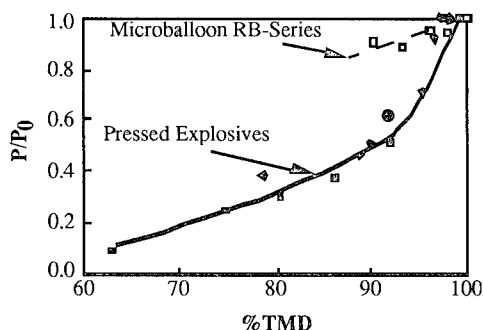


FIGURE 1. NORMALIZED PRESSURE FOR A 10-mm RUN TO DETONATION FOR VARIOUS EXPLOSIVES. THE VALUE OF  $P_0$  WAS ESTABLISHED AS THE PRESSURE REQUIRED FOR A 10-mm RUN IN THE HIGHEST-DENSITY MATERIAL FOR WHICH DATA WERE AVAILABLE. SYMBOLS:  $\circ$  PBX 9404;  $\blacklozenge$  PETN;  $\blacksquare$  TETRYL;  $\blacklozenge$  TATB;  $\blacksquare$  HMX

TABLE 1. NORMALIZED PRESSURE IN EXPLOSIVE VERSUS % TMD AS MEASURED BY THE WEDGE TEST

PBX 9404 <sup>15</sup>		PETN <sup>15</sup>	
Maximum Density = 1.873 g/cm <sup>3</sup>		Maximum Density = 1.778 g/cm <sup>3</sup>	
$P_0(10\text{mm}) = 2.88 \text{ GPa}$		$P_0(10 \text{ mm}) = 1.45 \text{ GPa}$	
%TMD	$P/P_0$	%TMD	$P/P_0$
0.982	1.00	0.984	1.00
0.918	0.617	0.967	0.912
		0.900	0.501
		0.787	0.381
Tetryl <sup>15</sup>		RB- Series <sup>14</sup>	
Maximum Density = 1.74 g/cm <sup>3</sup>		Maximum Density = 1.745 g/cm <sup>3</sup>	
$P_0(10\text{mm}) = 2.34 \text{ GPa}$		$P_0(10 \text{ mm}) = 5.69 \text{ GPa}$	
%TMD	$P/P_0$	%TMD	$P/P_0$
0.977	1.00	1.00	1.00
0.920	0.513	0.98	0.94
0.862	0.372	0.96	0.95
0.805	0.302	0.93	0.88
0.747	0.245	0.90	0.90
TATB <sup>15</sup>		HMX <sup>16,17</sup>	
Maximum Density = 1.94 g/cm <sup>3</sup>		Maximum Density = 1.905 g/cm <sup>3</sup>	
$P_0(10\text{mm}) = 10.47 \text{ GPa}$		$P_0(10 \text{ mm}) = 3.89 \text{ GPa}$	
%TMD	$P/P_0$	%TMD	$P/P_0$
0.972	1.00	0.993	1.00
0.954	0.708	0.630	0.090
0.888	0.457		

The effect of a third void type, damage produced by straining, was not investigated with the wedge test. Gap test data (aquarium and PMMA gaps) are available for undamaged RB-100 and RB-90; for undamaged and tensilely damaged specimens of another formulation, H-1; and for 97% TMD PBXW-108, which was compressively damaged. The formulation H-1 is a high-energy, multicomponent, multiparticulate material containing aluminum, AP, and HMX with a polyethylene glycol (PEG) binder and nitroglycerin(NG)/TMETN as a plasticizer. Los Alamos large-scale gap test data (brass gaps) are available for TNT<sup>15</sup> and PBX 9404,<sup>15</sup> as a function of density. Numerical model calibrations<sup>18</sup> of the pressure in the gap material were available for both gap tests. These pressures are used to standardize the data from the two types of gap tests. The gaps for 50% go/no-go were used to calculate a  $P/P_0$ , where  $P_0$  is the gap pressure for the highest available density. The normalized pressures vs %TMD for these materials are listed in Table 2.

Gap test data are compared in Fig. 2. As with the wedge test data, the standard explosives appear to fall on a common curve. One data point<sup>9</sup> for compressively

damaged PBXW-108 falls near this curve. However, tensilely damaged H-1 shows a 60% decrease in normalized pressure with the introduction of 0.8% voids. The effect shown and the data presented here are typical of other cast-cured, multicomponent, multiparticulate materials that were examined after tensile damage. Richter et al.<sup>13</sup> have shown that the void volume at the time of testing is the critical variable, not the void volume at the time of maximum elongation. Void-volume relaxation is very rapid after stretching. Most tests were conducted 20-30 minutes after damage. The effect of damage-induced voids on H-1, with less than 1% residual voids, is significantly greater than the effect of an equal volume of pressing voids in more standard explosives or the 3% voids in the compression-damaged PBXW-108. A very limited number of tests were done on tensilely damaged RB-90 and RB-100. The behavior of the RB-90 appears to agree with that observed for H-1, whereas RB-100 shows no change in sensitivity with 0.4% additional voids. This discrepancy has not been investigated further. The difference in the effect on sensitivity with addition of microballoons, as measured by the gap test, is analogous to that measured with the wedge test.

TABLE 2. NORMALIZED PRESSURE IN THE GAP MATERIAL VERSUS % TMD AS MEASURED BY VARIOUS GAP TESTS

TNT <sup>15</sup>		PBX 9404 <sup>15</sup>	
Los Alamos Large-Scale Gap Test		Los Alamos Large-Scale Gap Test	
Maximum Density = 1.654 g/cm <sup>3</sup>		Maximum Density = 1.873 g/cm <sup>3</sup>	
P <sub>0</sub> = 10.08 GPa		P <sub>0</sub> = 8.20 GPa	
%TMD	P/P <sub>0</sub>	%TMD	P/P <sub>0</sub>
0.986	1.00	0.996	1.00
0.964	0.795	0.986	0.861
0.964	0.793	0.979	0.842
0.910	0.725	0.974	0.842
0.908	0.734	0.972	0.785
0.868	0.741	0.960	0.760
0.820	0.723	0.846	0.673
0.819	0.734	0.747	0.666
0.738	0.689	0.657	0.644
0.619	0.569	0.491	0.578

H-1 <sup>9</sup>		RB-Series <sup>14</sup>	
NWC Aquarium Gap Test		NWC Aquarium Gap Test	
Maximum Density = 1.831 g/cm <sup>3</sup>		Maximum Density = 1.745 g/cm <sup>3</sup>	
P <sub>0</sub> = 2.81 GPa		P <sub>0</sub> = 2.98 GPa	
%TMD	P/P <sub>0</sub>	%TMD	P/P <sub>0</sub>
1.00	1.00	1.000	1.000
0.997	0.618	0.900	0.894
0.993	0.454		
0.992	0.796		
0.996	0.443		

PBXW-108 <sup>9</sup>	
Maximum Density = 1.56 g/cm <sup>3</sup>	
P <sub>0</sub> = 4.84 GPa	
%TMD	P/P <sub>0</sub>
1.000	1.00
0.970	0.92
0.750	0.69
0.815	0.66

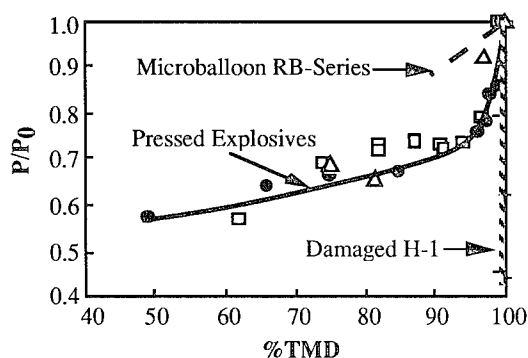


FIGURE 2. NORMALIZED PRESSURE FOR GAP TEST DATA. THE PRESSURES USED WERE THOSE IN THE GAP MATERIAL. SYMBOLS:  $\square$  TNT;  $\bullet$  PBX 9404;  $\Delta$  PBX 108(E)

Voids created by stretching H-1 and several other cast-cured materials are described as closed cell; that is, the void develops initially next to embedded crystals and there is no interconnection between voids. One energetic material (#110 of Fig. 5 in Ref. 9) produced an open-cell porosity, and its increase in sensitivity was approximately half that observed for H-1. The interconnected type of damage produced in 110 is a combination of two damage types. Initial straining produces closed cell damage as with H-1, followed by tearing of the polymer network which is similar to damage in a cut or chopped material. The reduced sensitivity increase per measured porosity in 110 is consistent with a combination of highly sensitizing voids on crystal surfaces and less sensitizing cut surface porosity.

Our  $P/P_0$ -vs-%TMD representation of the data for the normal explosives, for both the wedge and gap tests, appears to fall on common curves for each test method. This was unexpected. However, the data in Fig. 2 are incomplete. Los Alamos large-scale gap test data for RDX and TATB do not fall on the gap-test curve, nor do some NOL gap test data for several explosives. The curves presented here may be completely fortuitous, or the pressure may not have been measured for material of sufficiently high density to establish  $P_0$ . We have no explanation at the present time. The possibility should be investigated further.

## CONCLUSIONS

The data discussed here show that the shock sensitivity of heterogeneous energetic materials is significantly affected by the specific nature of the included voids, in addition to their concentration. Only a slight change in sensitivity was observed when microballoons were added to a multiparticulate material. Standard pressed explosives and cast-cured PBXW-108 appear to follow a common normalized behavior, with 5 vol% voids decreasing the normalized pressure by 40% for the wedge test data and 30% for the gap test data. Tensilely damaged multiparticulate formulations containing an energetic plasticizer (such as TMETN or NG) show a 60%

reduction in normalized pressure when 0.8% residual voids are introduced. An exception to this extreme rate of change in sensitivity was found for one material, in which tensile damage created interconnected-cell porosity. Particle shape and size (i. e., cubes vs shreds) create sensitivity differences at the same per cent of TMD, at least in the region of 75% TMD. Common curves can describe the relationship between normalized pressure and percent TMD for wedge data, as well as for gap test data.

The major impetus and funding for the work reported here have terminated and only a small number of current projects remain. Therefore, we believe that it is important to review and interpret the available data as best we can. We admit that the conclusions reported here are based on only minimal data, some of which should be repeated. Sufficient experimental data do support the conclusion that the nature of the interaction of the energetic material and voids significantly affects the shock sensitivity; this includes characteristic particle and void sizes and shapes. Tensile damage may be more important than compressive damage, although no unequivocal data support this postulate. Energetic plasticizers (such as TMETN, and NG) may contribute to an increased sensitivity in the presence of damage-created voids. The relationship between normalized pressure and per cent TMD for standard explosive formulations should be explored further. All the measurements discussed here have been made at high pressure, relative to the pressures involved in an accident. Differences in shock sensitivity, as reported here, may invert in different pressure regions, particularly at lower pressures. We need more complete understanding of the effects of compressive and tensile damage, confounding with the effects of composition on shock sensitivity to predict and control catastrophic events in accident environments.

## REFERENCES

1. Campbell, A. W. and Travis, J. R., "The Shock Desensitization of PBX-9404 and Composition B-3," **Proc. of the 8th Symp. (Int.) on Detonation**, Albuquerque, New Mexico, July 15-19, 1985, pp. 1057-1068.
2. Campbell, A. W., Davis, W. C., Ramsay, J. B., and Travis, J. R., *J. Appl. Phys.* **4**(1), 511-521 (April 1961).
3. Lindstrom, I. E., *J. Appl. Phys.* **41**(1), 337-350 (1970).
4. Travis, J. R., "Experimental Observations of Initiation in Nitromethane by Shock Interactions at Discontinuities," **Proc. of the 4th Symp. (Int.) on Detonation**, U.S. Naval Ordnance Laboratory, White Oak, Maryland, October 12-15, 1965, pp. 386-393.
5. Mader, C.L., **Numerical Modeling of Detonations**, pp. 171-186, University of California Press, Berkeley, (1979).



6. Moulard, H., "Particular Aspect of the Explosive Particle Size Effect on Shock Sensitivity of Cast PBX Formulations," **Proc. of the 9th Symp. (Int.) on Detonation**, Portland, Oregon, August 28-September 1, 1989, pp. 18-24.
7. Van der Steen, A. C., Verbeek, H. J., and Meulenbrugge, J. J., "Influence of RDX Crystal Shape on the Shock Sensitivity of PBXs," **Proc. of the 9th Symp. (Int.) on Detonation**, Portland Oregon, August 28-September 1, 1989, pp. 83-88.
8. Kegler, W., and Schall, R., "Mechanical and Detonation Properties of Rubber Bonded Sheet Explosives," **Proc. of the 4th Symp. (Int.) on Detonation**, U. S. Naval Ordnance Laboratory, White Oak, Maryland, October 12-15, 1965, pp. 496-501.
9. Bernecker, R. R., and Clairmont, A. R., "Shock Initiation of Cast, Damaged, and Granulated PBXs," **Proc. of the 10th Symp. (Int.) on Detonation**, Boston, Massachusetts, July 12-16, 1993.
10. Bernecker, R. R., unpublished communication, 1992.
11. Sandusky, H. W. and Bernecker, R. R., "Influence of Fresh Damage on Shock Sensitivity of Several Energetic Materials," **Proc. of the 10th Symp. (Int.) on Detonation**, Boston, Massachusetts, July 12-16, 1993.
12. Green, L., James, E., and Lee, E., "Energetic Response of Propellants to High Velocity Impact," **Proc. of the 8th Symp. (Int.) on Detonation**, Albuquerque, New Mexico, July 15-19, 1985, pp. 284-293.
13. Richter, H. P., Boyer, L. R., Graham, K. J., Lepie, A. H., and Zwierchowski, N. G., "Shock Sensitivity of Damaged Energetic Materials," **Proc. of the 9th Symp. (Int.) on Detonation**, Portland, Oregon, August 28-September 1, 1989, pp. 1295-1300.
14. Grall, R. R. and Ramsay, J. B., "Shock Sensitivity of 90%-100% TMD Composites Materials," **JANNAF Propulsion Systems Hazards Subcommittee Meeting**, CPIA Publication 538, Vol. I, April 1990, pp. 203-210.
15. Gibbs, T. R. and Popolato, A., **LASL Explosive Property Data** (University of California Press, 1980).
16. Dick, J. J., *Combustion and Flame* **54**, 121-129 (1983).
17. Rabie, R. L., Forest, C. A., and Dick, J. J., unpublished communication, 1992.
18. Bowman, A. L., Sommer, S., and Fu, J. H., "Calibration Curves for Four Standard Gap Tests," Los Alamos National Laboratory report LA-11763-MS (March 1990).

---

## DISCUSSION

JACQUES BOILEAU  
DRET, Paris, France

(1) In order to diminish the sensitivity due to a decohesion of composite elastic energetic material, it is interesting to add some tensioactive product (wetting agent), to have a better contact between the energetic crystal and the binder; that is made in France.

(2) We use in France an efficient apparatus, the Farris Balance, to measure the decohesion of elastic composite materials under stretch and the healing of that decohesion under a recompression of the sample. That apparatus allows us to distinguish the disposition of internal voids with only a contact between crystal and binder, or with the primitive adhesion between both.

## REPLY BY RICHARD BERNECKER:

(1) It is our expectation that bonding (wetting) agents will not affect the shock sensitivity of a cast, undamaged energetic material. On the other hand, the use of a bonding agent has the potential to influence both the shock reactivity (extent of subdetonation reaction) and the shock sensitivity of damaged energetic material. An interesting aspect of the last statement is whether there is a time regime in which the influence of the bonding agent is most effective for a given level of damage). With respect to resistance to damage, studies at NAWC have shown that with particle sizes of 10 microns or less, energetic materials do not benefit significantly from added bonding agents. With larger particle sizes, the materials do show improved resistance to damage with bonding agents.

(2) At NAWC, liquid dilatometers, similar in concept to the Farris instrument, are used to measure dewetting between binder and filler. The paper includes data, on void volumes of a series of propellants, generated with these instruments during tension and shear deformation studies.

## THE INFLUENCE OF MICROSTRUCTURE ON THE SENSITIVITY OF EXPLOSIVE COMPOSITIONS

H. CHERIN

Commissariat à l'Energie Atomique

Centre d'Etudes du RIPAULT

B. P. N° 16 - 37260 MONTS - FRANCE

The objective of the study presented below is the perfection of a predictive method which enables us to confer the desired behavior to explosive compositions, as much from the point of view of performance as for safety, by taking into account the microstructural parameters of the explosive.

The study was divided into two phases :

◆ Modelling of burning : establishment of analytical laws governing the burning of spherical particles distributions. Application to granulometric mixtures of TATB. Experimental check-up of expected changes in burning kinetics.

◆ Study of morphological changes (size, shape, porosity) undergone by an explosive powder during pressing and shock wave propagation.

### INTRODUCTION

The "Centre d'Etudes du RIPAULT" is responsible for the conception, development, and manufacture of explosive compositions. Pyrotechnic safety being nowadays an extremely important objective, we have installed an approach aiming to define and produce explosive compositions which are optimized from the safety point of view by choices of the nature of the explosive and the binder, of the percentages of the basic components, and of the microstructural parameters.

The objective of the study of microstructure presented here was the perfection of predictive methods enabling the microstructural and morphological parameters of the explosive powder to be fixed, in order to direct the reactive behavior of the explosive composition in the desired direction. The first phase of this work consisted in modelling the burning of the explosive grains. In fact, whatever the observed

pyrotechnic phenomenon is (burning, burning to deflagration to detonation transition, or shock-to-detonation transition), the explosive grains first step of the decomposition is always the explosive grains burning. To develop predictive models, the influence of the morphological parameters of the powder on the burning rate had therefore to be known. The establishment of analytical laws governing the degree of the decomposition of spherical particles as a function of time and of particles size distribution allowed the definition of granulometric profiles, corresponding to specific burning kinetics. The results of this modelling were then applied to mixtures of TATB batches approaching the theoretical granulometric profiles previously studied.

The second part of the study is related to the morphological changes of a powder that has undergone pressing and the propagation of a shock wave. The aim was to understand the actual parameters of the powder when it is about to undergo burning.

## GRAIN BURNING MODELLING

### The Different Mechanisms

Any decomposition mechanism is the result of different stages, characterized by the following parameters :

- an induction time for the reaction, during which no significant phenomenon is observed,
- a reaction rate, for the initial and intermediate stages of the decomposition,
- an overall reaction time.

These parameters are themselves functions of the intensive parameters of the studied system (particularly temperature and pressure).

When the parameters to be optimized are determined, the approach consists in studying the influence of the morphological properties on the change in these parameters, with the help of a theoretical model providing a good simulation of the physical process. The only morphological parameter to take into account is the grains size distribution, since it is in fact the only criterion accessible to the experimenter (the shape and the porosity of the grains are not today controllable during the synthesis operations).

Concerning the burning process, we have observed that some elementary mechanisms describe most of decomposition reactions [1] :

- homogeneous combustion of the explosive grains,
- surface germination of active sites, surface decomposition growth, then (when the surface is completely covered with decomposition products), transition towards homogeneous combustion,
- surface germination, then decomposition growth in volume,
- germination-growth within the solid phase.

### Results

All the decomposition mechanisms described above have been subjected to an analytical study enabling a relation for the reaction degree as a function of time and of granulometric distribution. The

hypotheses under which the modellings were based are the following :

- the germination of the active decomposition sites is instantaneous,
- the growth rate of the active sites is the same for all the particles,
- the variations of the intensive parameters (pressure, temperature) are not taken into account. This is justified by the fact that, in most explosive decomposition models, the change in morphology and the effect of the intensive parameters are considered to be separated (the decomposition rate is expressed in the form of a product of a morphological factor and a factor including the pressure).

The simulation of the decomposition of different spherical particles distributions, presented in figure 1, for each possible mechanism, allowed the following points to be brought out.

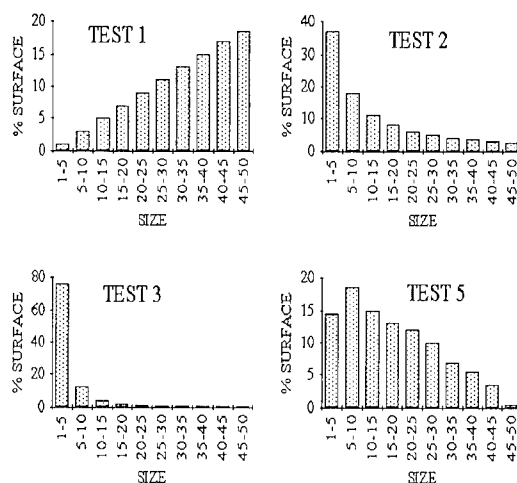


FIGURE 1. THEORETICAL DISTRIBUTIONS

- The shape of the granulometric distribution significantly influences all the decomposition kinetic parameters (initial value of the reaction rate and change of this value with time, induction time, and overall combustion time).
- For all mechanisms, the highest initial rates are produced by the TEST 3 type distribution. This is also the population which gives the highest

intermediate reaction rates, up to a reaction degree by 0.5.

- The longest overall combustion times are observed for the samples with a particle surface percentage growing with the particle size, or for the TEST 5 type distribution.

Within the hypothesis of a mechanism of germination, surface decomposition growth and finally homogeneous combustion, all these parameters have been calculated for TEST 5 and 3 type distributions. The results are shown in table 1.

	Induction time $\alpha = 0,99$	Initial rate $\alpha = 0,97$	Intermediate rate $\alpha = 0,50$	Overall combustion time $\alpha = 0,01$
TEST 5	1	1	1	1
Ratio of values TEST 3 TEST 5	0,7	1,2	3,3	0,84

All values are relative to those of the TEST 5 population taken as a reference

**TABLE 1. DECOMPOSITION PARAMETERS OF TEST 3 AND TEST 5 DISTRIBUTIONS**

## EXPERIMENTAL APPLICATION

### Granulometric Characteristics of the Samples

The explosive selected for the experimental study was TATB. The combustion kinetics were determined on different powder samples (mass : 8 mg), with a SETARAM 111 differential scanning calorimeter, operating in isothermal mode. The temperature of the observations was fixed at 320°C, sufficiently far from the decomposition temperature (363°C, maximum of peak observed in thermal analysis) to obtain easily manageable decomposition rates.

In order to reproduce experimentally the granulometric distributions presented in figure 1, we made mixtures of TATB-based batches, differing significantly in their granulometry. The characteristics of these batches are given in table 2.

	Average grain size ( $\mu\text{m}$ )	Specific area ( $\text{m}^2/\text{g}$ )
4116	0,6	18
FU 12	1,5	10
Medium	15	0,9
Standard	40	0,3

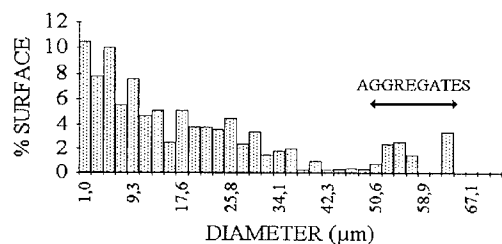
**TABLE 2. CHARACTERISTICS OF INITIAL BATCHES**

Mixtures MG1 and MG2 were produced from the mass fractions indicated in table 3. These fractions were chosen in order to reproduce the granulometric profile TEST 3 for mixture MG1 and TEST 5 for mixture MG2.

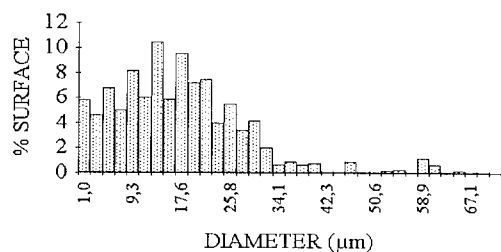
	MG1	MG2
4116	60	5
FU 12	25	10
Medium	10	25
Standard	5	60

**TABLE 3. INITIAL BATCHES MASS PERCENTAGES IN MIXTURES**

The size distribution histograms for each of these mixtures, obtained by image analysis, are shown in figure 2 (surface percentage as a function of diameter). These distributions were not completely identical to those used in the calculations, but were fairly close. The presence of aggregates of small particles in the sample with a high percentage of TATB 4116 (MG1) is worth noting, since the existence of such clusters can induce specific behavior, as can be seen in the following. The size of these aggregates can reach several tens of micrometers.



2a - MG1 mixture



2b - MG2 mixture

FIGURE 2. SIZE DISTRIBUTION HISTOGRAMS

## Results

Figure 3 shows the reaction degree as a function of the reduced time  $t/t_{0.5}$  (where  $t_{0.5}$  is the time corresponding to the decomposition of 50% of the initial mass of the explosive), for mixtures MG1 and MG2 and the starting batches with extreme granulometries (4116 and standard).

The analysis of these results shows that up to a reaction degree by 0.5, TATB 4116 tends to adopt similar behavior to that of standard TATB : this similarity arises from the fact that the small particles are associated in aggregates, whose combustion kinetics is identical to those of the elementary particles of standard TATB. Beyond a degree by 0.5, the decomposition of 4116 batch is significantly different, since the loss of cohesion of the aggregates at a given burning stage allows the reaction to spread out over a larger area. The behavior of the MG2 batch is due to the fact that, in this mixture, the surface of the large grains is covered with small particles, which induces a specific initial reactivity. Beyond a degree by 0.5, the burning of this mixture tends to approach the standard

TATB one, the largest particles being those which determine the burning rate at the end of the reaction.

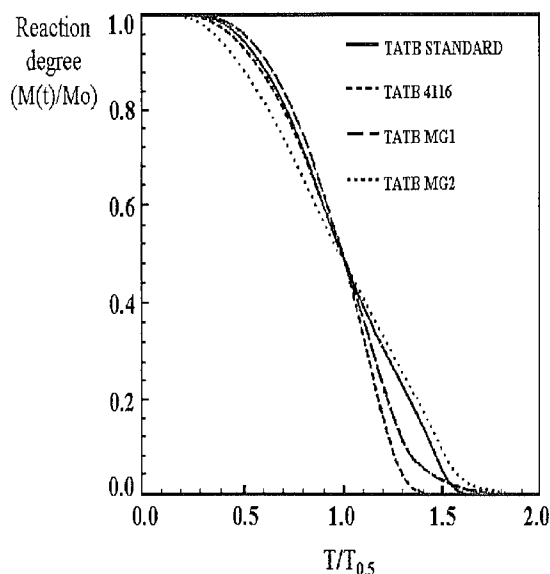


FIGURE 3. DSC CURVES FOR TATB BATCHES

Table 4 presents a summary of the different burning kinetics parameters for TATB mixtures, and for the initial batches with extreme grain sizes.

	Induction time (s)	Initial rate ( $s^{-1} \cdot 10^6$ )	Intermediate rate ( $s^{-1} \cdot 10^6$ )	Overall time (s)
	$\alpha = 0,99$	$\alpha = 0,97$	$\alpha = 0,50$	$\alpha = 0,01$
4116	1279	118	406	5194
FU12	842	111	319	6465
Medium	678	111	216	6989
Standart	1126	101	260	7018

TABLE 4. DECOMPOSITION PARAMETERS OF TATB BATCHES

The high values for the induction times measured for the 4116 and MG1 samples are due to the presence of the aggregates previously described. The introduction of large particles favors loss of cohesion of these clusters, so the MG1 mixture shows a lower induction time than the 4116 batch. The value of this

parameter also decreases for MG2 mixture in comparison with standard TATB. The highest intermediate rates are observed with the 4116 and MG1 batches. The longest overall combustion time is observed for the standard TATB.

If we assume that the decomposition mechanism of TATB consists of a process of germination, surface decomposition growth and homogeneous combustion, most of the experimental values confirm the modelling results :

- the highest intermediate burning rates were obtained for high percentage of small particles,
- the longest overall burning times correspond to the mixtures with high concentration of large particles.

Only the conclusions relating to the induction times could not be validated because the numerical simulations do not take into account the aggregates of particles with very small size. For the same reason, the initial rates are not as different as predicted by the model. They are however in the right order, from TATB 4116 to standard.

The results of this study also show that it is possible to define granulometric distributions enabling the burning kinetics of an explosive powder to be significantly modified, by introducing very small quantities of particles with different size.

## NUMERICAL SIMULATION OF THE SHOCK-TO-DETONATION TRANSITION

In order to understand the influence of the granulometric distribution profile on the transient phenomena during the detonation build-up, we have carried out numerical simulations of the shock-to-detonation transition on the spherical particles distributions studied above, and on the TATB mixtures derived from them. These simulations were carried out with a kinetics, implemented in a one-dimensional hydrodynamic code, that allows the description of the shock initiation of heterogeneous explosives. This kinetics has been described elsewhere [2]. The principles are briefly described below.

### Description of the Kinetics

The shock-to-detonation transition is the result of

two basic phenomena :

- hot spots formation and ignition,
- explosive grains burning.

In order to simulate closely the microstructural phenomena at the origin of shock initiation, the kinetics is composed of two models :

- the first one describes the formation and ignition of hot spots, due to the collapse of the pores under the effect of shock waves,
- the second one describes the explosive grains burning after ignition of hot spots and takes into account :
  - . the morphology of the grains and its change during the decomposition,
  - . the burning rate (dependent on pressure) of the basic explosive,
  - . the number of hot spots created by the mechanical stimulus.

This kinetics provides results in very good agreement with experimental data, such as the threshold initiation pressure, pressure growth in the explosive during the transition, depth-to-detonation...

### Simulation of the Decomposition by Image Analysis

The knowledge of the morphological changes of the grains during decomposition is necessary for the kinetics to work correctly. This can be understood by the variations of the surface/volume ratio. This geometric parameter can be determined by image analysis techniques [3]. From the basic processes of mathematical morphology, all the decomposition mechanisms previously mentioned can be simulated. The morphological changes during the decomposition can thus be quantified by the evolution of the grain perimeter/surface ratio, characteristic of the studied powder. This ratio is representative of the surface/volume ratio. These data, introduced into the kinetics simulating the shock-detonation transition provides results such as those shown in figure 4. The pressure curves in the explosive are drawn every 500 nanoseconds. With this kind of diagrams, it is easy to determine the threshold ignition pressure by varying the magnitude of the initial shock pressure, and the depth to detonation for each value of this pressure.

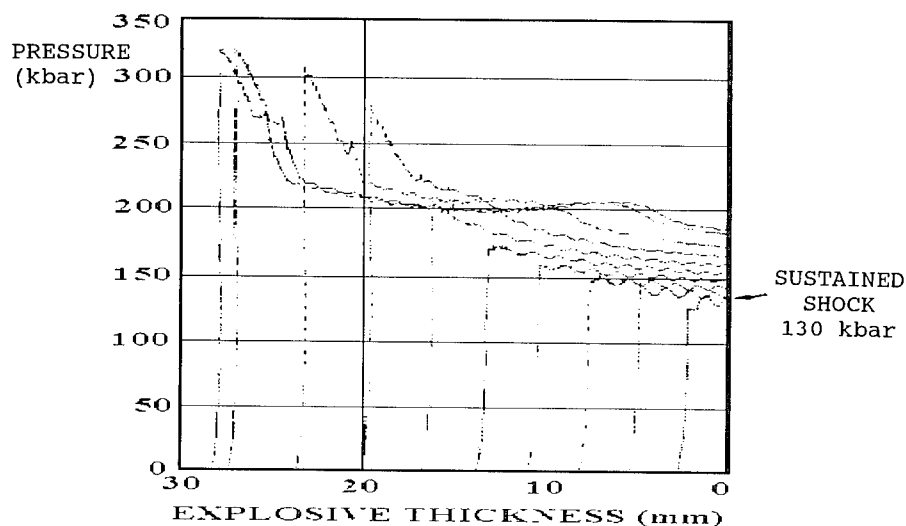


FIGURE 4. PRESSURE PROFILE IN EXPLOSIVE THICKNESS

#### Applications

To perform the calculations simulating the shock-to-detonation transition, we assumed that all the populations studied were pressed up to a density by 98 % TMD (Theoretical maximum density).

The results for the different spherical particles distributions are shown on figure 5. We see that, whatever the intensity of the initial shock is, the TEST 3 distribution gives a depth-to-detonation significantly lower than those obtained with the other three populations. These differences become less important for higher shock pressures.

This kind of result is useful to guide the formulator in the choice of a granulometric distribution. For example, the choice of a TEST 1 population will lead to an enhanced safety level for shock stimuli.

The depths-to-detonation for a sustained shock of 130 kbar have been calculated for TATB 4116, standard, MG1, and MG2. The results are as follows :

depth (mm)	4116	MG1	Standard	MG2
	15,7	10,3	12,8	8,9

The depth-to-detonation is lower for MG2 than for standard TATB. This is due to the small particles in the MG2 mixture.

This depth is lower for MG1 than for 4116 batch, as a result of the presence in MG1 mixture of large particles desaggregating the clusters. It must be noted that the ignition depths calculated for batches with a

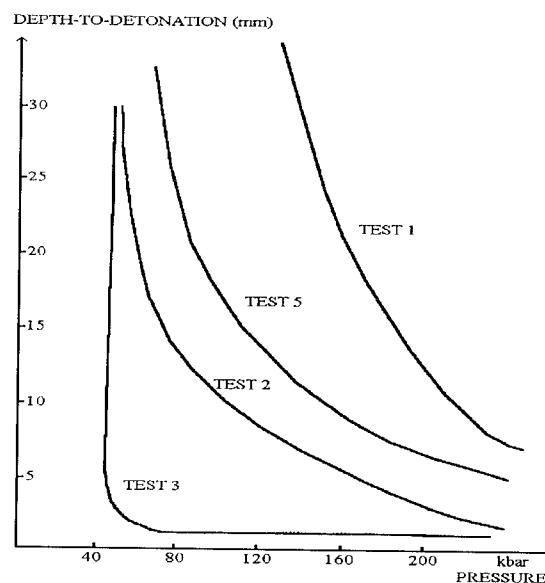


FIGURE 5. DEPTHS TO DETONATION FOR THEORETICAL DISTRIBUTIONS

high concentration of micronic particles are higher than those calculated for the standard and MG2. This is in disagreement with the results of the modelling of the behavior of spherical particles, and is explained by the fact that the simulations of the decomposition by image analysis do not take into account the loss of cohesion of the aggregates, which occurs very rapidly during the reaction and restores their intrinsic reactivity to the small particles. This point will be the subject of a modification of the burning simulation tools using image analysis.

### MORPHOLOGICAL CHANGES OF THE GRAINS AFTER PRESSING AND PROPAGATION OF A SHOCK WAVE

The morphological characteristics of an explosive powder will undergo significant changes during its use, particularly during pressing or when submitted to a shock wave. It is thus necessary, in order to improve our models, to be able to estimate the new morphological parameters of a powder that has undergone such loadings, since this new morphological state will govern the reaction kinetics at the moment of decomposition.

The explosive used for this study was a 0-100  $\mu\text{m}$  HMX powder, pressed to a density by 1.2  $\text{g}/\text{cm}^3$ . The impulse shock pressures were of course lower than the initiation threshold. Three tests were carried out for impulse shocks pressures by 8, 12, and 20 kbar.

The pressed and shocked samples were broken up using ultrasounds, to obtain a dispersed powder, and they were then submitted to the following characterizations :

- scanning electron microscopy,
- determination of specific area (B.E.T. method),
- determination of porosity (between 15 and 300 Å) using krypton desorption,
- determination of size distribution and grain shape using image analysis.

These analysis techniques are described in [4]. All results concerning the initial powder, the pressed powder, and the shocked samples are given in table 5.

### Change in Specific Area

Excluding the uncertainty on specific area measurements, relatively high in this range of small areas ( $\pm 5\%$ ), the variations of this parameter does not show a logical trend with respect to the stimuli experimented by the different samples. This shows the inadequacy of this kind of measurement to study powder morphological changes.

	Initial powder	Pressed powder	Shocked powders		
			8 kbar	12 kbar	20 kbar
Specific area ( $\text{m}^2/\text{g}$ )	0,5	0,55	0,39	0,31	0,43
Porous volume ( $\text{mm}^3/\text{g}$ )	1,02	1,35	-	0,86	0,61
Grain size ( $\mu\text{m}$ )	0 - 90	30 - 110	15 - 90	15 - 70	3 - 50
Shape index	0,10 - 0,60	0,10 - 0,60	0,15 - 0,70	0,20 - 0,80	0,25 - 0,90

TABLE 5. MORPHOLOGICAL PARAMETERS

### Change in Porosity

The increase observed for the pressed powder in comparison with the initial powder can be explained by the breaking of some grains and/or aggregates during pressing, allowing the appearance of pores previously inaccessible to gas.

### Changes in Size and Shape of Grains

The comparison of the initial powder and the pressed powder shows a significant increase in size, probably due to the formation of aggregates during pressing, without change of the shape. With respect to the pressed powder, the shocked powders exhibit :

- a significant reduction in grain size,
- a significant increase in shape index.

These phenomena are more significant as the shock pressure increases. The comparison between the pressed powder and the 20kbar shocked powder is particularly revealing (figure 6).

The propagation of a shock across the pressed powder results in breaking grains and aggregates, leading to a much finer powder, and by a significant increase of the sphericity of the particles. This leads to a morphology much less complex than the initial one.



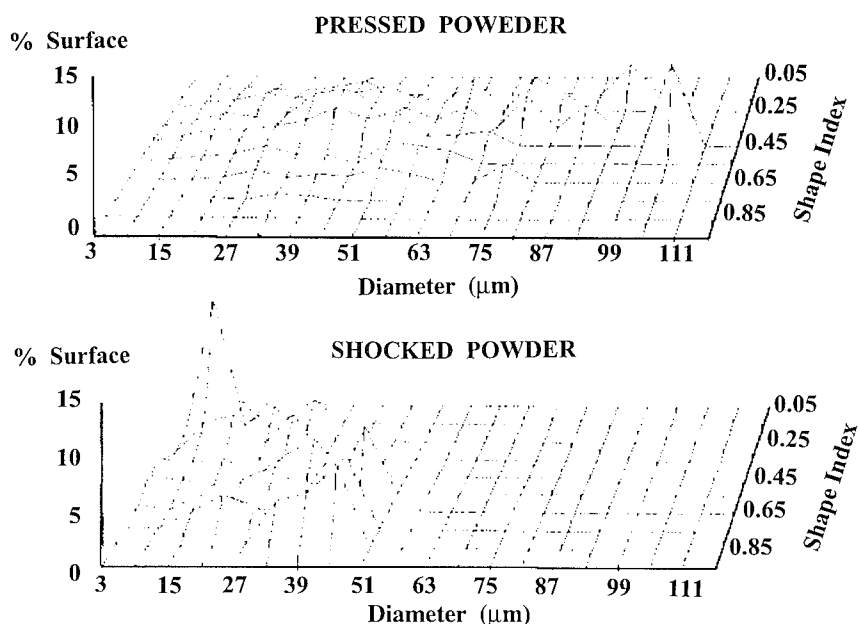


FIGURE 6. CHANGES IN SIZE AND SHAPE

The morphological changes undergone by the powder during pressing and shock propagation are thus important. This study needs to be continued, following two main lines :

- ♦ influence of molding : investigation of changes undergone by the pressed powder at a density close to that of the explosive compositions,
- ♦ influence of dynamic stimuli : study of the effects induced by sustained shocks.

## CONCLUSION

The results of this study have shown the important influence of morphological and microstructural parameters on the reactive behavior of explosive compositions, and the possibility to adjust the values of these parameters in order to confer the desired behavior to the explosives. All the tools, necessary to modelling (decomposition of spherical particles, image analysis simulation of powders burning, shock-to-detonation transition calculations) are now available. The next step of this study will consist to improve our knowledge of the morphological changes of the explosive powder during pressing and after the shock wave crossing. However, the results actually available enable us to start the final stage of this study, that is to say design and development of optimized explosive compositions.

## ACKNOWLEDGEMENTS

We thank E. MEILLOT and M. LEROY (C.E.A., Centre d'Etudes de Vaujours-Moronvilliers) for the calculations of the shock-to-detonation transition.

## REFERENCES

- [1] Introduction à la cinétique hétérogène  
B. DELMON.  
Editions TECHNIP, Paris, 1969.
- [2] A physical model of shock-to-detonation transition in heterogeneous explosives.  
R. BELMAS, C. BIANCHI, M. LEROY.  
10th Symposium (International) on Detonation, Boston, USA - 1993
- [3] The influence of grain morphology on the behavior of explosives.  
S. DUFORT, H. CHERIN, P. GOHAR.  
9th Symposium (International) on Detonation, Portland, USA - 1989
- [4] Shock-induced changes of the morphological characteristics of an explosive powder.  
H. CHERIN, D. BOURNISIEN, D. LEMOINE.  
8th International Pyrotechnics Seminar, Breckenridge, USA, July 1992.

## INFLUENCE OF CRYSTAL DEFECTS ON SENSITIVITY OF EXPLOSIVES

F. BAILLOU, J.M. DARTYGE, C. SPYCKERELLE, J. MALA

*S.N.P.E.*

Centre de Recherches du Bouchet - BP 2  
91710 Vert le Petit  
FRANCE

For studying influence of crystal defects on shock sensitivity, seven different batches of RDX crystals have been specially prepared corresponding to different manufacturing processes and have been formulated with an HTPB binder (78 wt% RDX, 22 wt% HTPB). Our experimental results show that sensitivity depends on the amount of defects present inside the crystals. To determine a correlation between defects and sensitivity, analysis by physicochemical techniques have been performed. One shows that sensitivity increases with the number and size of defects. The chemical nature of the internal defects seems to have a second-order influence on sensitivity.

### INTRODUCTION

A great deal of research work has been carried out to develop and characterize insensitive molecules having good performances with a lower vulnerability. A new approach to make less sensitive explosives, different from a search for new molecules, consists in improving the physical structure of classic explosive crystals in order to decrease their sensitivity while keeping their performances. It appears that defects present in explosives crystals play an important role in the sensitivity of materials<sup>1,2</sup>. This study consists in identifying the relationship between structural properties and shock sensitivity of explosives.

For studying influence of crystal defects on shock sensitivity, SNPE has specially

prepared different batches of RDX crystals corresponding to different manufacturing processes. The wedge test has been used to determine sensitivity. For this purpose, RDX-based compositions, using the different batches of crystals, have been specially formulated with the same binder, weight composition and the same loading density. Thus, for a given particle size distribution, the only possible variation parameters are the grain morphology and structure in connection with the manufacturing process.

In order to determine the relationship between the sensitivity of these materials and their physical structure, the possible defects existing inside the crystals have been characterized by using X - ray diffraction and optical microscopy.

Analysis by physicochemical techniques and tests of recrystallization from solvent with different coloring matters have been carried out respectively to identify the nature of defects and to perform their topographic study.

## EXPERIMENTAL WORK

### Explosive Compositions

Sensitivity is not measured directly on the crystals because the results would be too much dependent on external (extragranular) porosity. To eliminate the problems due to this porosity, the sensitivity tests have been carried out on cast PBX compositions. We have specially prepared samples with the same binder (HTPB), the same

weight composition (78 % RDX, 22 % HTPB) and the same loading density. Characteristics of cast PBX compositions are given in Table 1.

Seven different batches of RDX crystals have been used for the investigation (one for each composition). The grain size distributions for the different batches are presented in Figure 1 and the major characteristics for each manufacturing process are summarized in Table 1.

Except the batch corresponding to the fourth composition (C1), all the others get particle size distributions which are almost similar.

TABLE 1. CHARACTERISTICS FOR THE DIFFERENT BATCHES OF RDX CRYSTALS AND DENSITY OF THE CAST PBXs

COMPOSITION	LOADING DENSITY OF CAST PBX (kg/m <sup>3</sup> )	MEDIAN RDX PARTICLE SIZE (μm)	MAJOR CHARACTERISTICS OF THE PROCESS FOR RDX
A1	1490	194	recrystallization from acetone and sieving
A2	1493	174	recrystallization from acetone and sieving
B	1496	175	raw material from synthesis
C1	1495	475	recrystallization from cyclohexanone
C2	1495	165	recrystallization from cyclohexanone and grinding
C3	1497	130	recrystallization from cyclohexanone and sieving
M	1489	189	recrystallization from methyl ethyl ketone and sieving

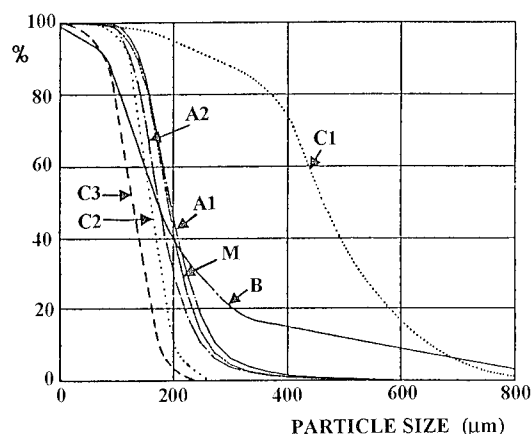


FIGURE 1. PARTICLE SIZE DISTRIBUTIONS FOR THE SEVEN BATCHES OF RDX CRYSTALS

#### Shock Sensitivity

The different composite explosives are submitted to sustained shock waves in wedge test experiments where a space/time diagram of the shock wave to detonation transition is recorded by a streak camera. The impact velocity of 10 mm thick aluminium plates has been varied from 820 m/s to 1850 m/s so the pressure induced in the explosive wedge varies from 4 GPa to 10 GPa. The wedge angle is 20°. This test allows to determine the variation of the run distance to detonation versus shock pressure (pop - plot).

Figure 2 shows sustained shock initiation diagrams obtained for the seven cast PBX compositions. The relation between the run distance to detonation and the applied pressure is expressed as :

$$\ln P = a + b \ln X \quad (1)$$

where X is the run distance to detonation in mm, P the induced pressure in GPa, a and b the coefficients of the least squares straight line (Table 2).

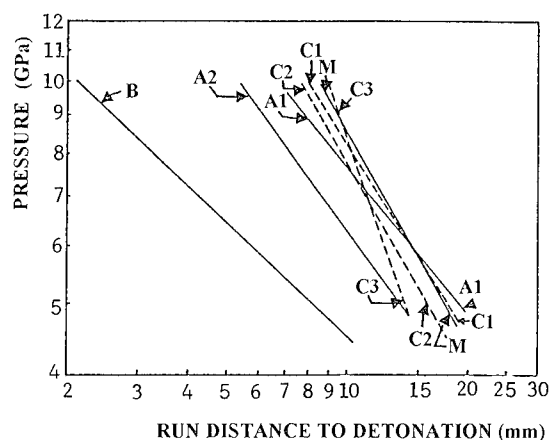


FIGURE 2. SUSTAINED SHOCK INITIATION DIAGRAMS

TABLE 2. RELATION BETWEEN THE RUN DISTANCE TO DETONATION AND THE APPLIED PRESSURE FOR THE SEVEN CAST PBX COMPOSITIONS : COEFFICIENTS a AND b

CAST PBX COMPOSITION	a	b
A1	3.585	- 0.6733
A2	3.526	- 0.7334
B	2.647	- 0.4912
C1	4.015	- 0.8315
C2	4.246	- 0.9564
C3	5.592	- 1.516
M	4.268	- 0.9217

The pop - plot results show that the most sensitive material is the PBX which contains raw RDX, with initiation distances far below those of the other six compositions.

In order to determine the relationship between sensitivity and physical structure, we have tried to characterize the possible defects existing inside these crystals. Two techniques are used : X - ray diffraction and optical microscopy.

#### X-Ray Diffraction

Physical microstructure of RDX crystals has been characterized by X - ray diffraction. Characterization techniques that have been used employ a X - ray powder diffractometer using transmission geometry with curved crystal monochromator (Cu K $\alpha$ 1) or reflection geometry with Ni filter, and a focusing camera. Whatever the sample may be, lines positions and intensities agree with the theoretical ones and there is no line broadening effect : no

microstructural defect was detected.

#### Optical Microscopy

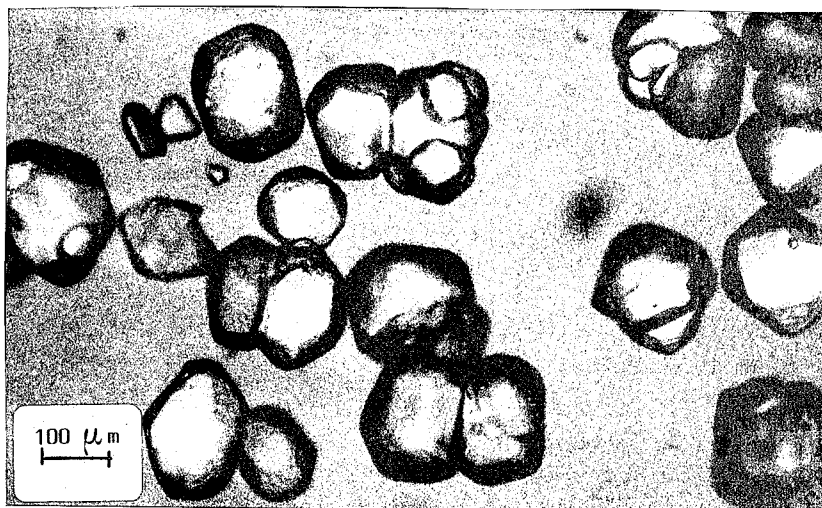
A visualization of crystals by optical microscopy has been considered. A small amount of RDX crystals was placed on a microscope slide and immersed in a fluid of matching refractive index to get a good view inside the crystals. The refractive indices of RDX are 1.578, 1.597 and 1.602<sup>3</sup>. The refractive index of the immersion liquid is 1.518. Typical pictures from a microscopic examination of the seven RDX are presented on Figures 3 to 7. The most important morphological and structural characteristics are summarized in Table 3.

TABLE 3. MICROSCOPIC EXAMINATION FOR THE SEVEN RDX BATCHES

COMPOSITION	MORPHOLOGY AND STRUCTURE OF RDX CRYSTALS
A1 (Figure 3)	A lot of crystals have no void. A few crystals comprise some voids which get a maximum size below 5 $\mu\text{m}$
A2 (Figure 4)	The crystals contain a lot of cavities the size of which can reach 60x30 $\mu\text{m}^2$ . Some crystals comprise "bubbles" inside the cavities.
B (Figure 5)	The crystals contain cavities the size of which can reach 100 x 20 $\mu\text{m}^2$ . The largest voids are in the biggest crystals.
C1	The samples show surface irregularities and a lot of cavities with a size which varies between 15 et 50 $\mu\text{m}$ . Some crystals comprise "bubbles" inside the cavities.
C2	The samples are made of irregularly-shaped particles. Crystals comprise cavities with a size varying from 15 to 20 $\mu\text{m}$ . Some cavities contain "bubbles".
C3 (Figure 6)	The crystals show cavities with a size which varies between 15 et 30 $\mu\text{m}$ . Some crystals contain "bubbles" inside the cavities.
M (Figure 7)	The particle shapes, quantity of cavities and their sizes are similar to the previous one.

*MORPHOLOGY AND STRUCTURE OF RDX CRYSTAL*

*FIGURE 3.*



*FIGURE 4.*



*FIGURE 5.*



*MORPHOLOGY AND STRUCTURE OF RDX CRYSTAL*

*FIGURE 6.*



*FIGURE 7.*

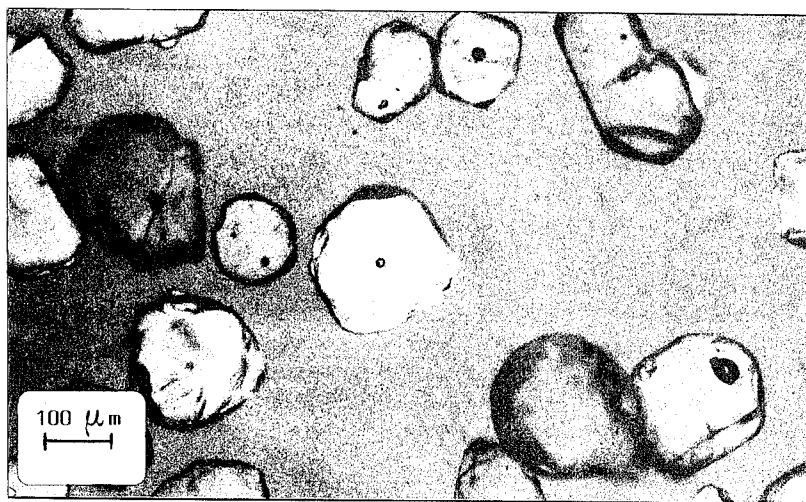


*FIGURE 8.*



## The Nature of Defects

To have an idea on the nature of this internal porosity, analysis by physicochemical techniques and tests of recrystallization from a solvent with coloring matters have been carried out in the case of a RDX sample recrystallized from cyclohexanone.

Analysis by gas phase chromatography, ion chromatography and infrared spectrometry have shown that cavities contain recrystallization solvent, mineral salts including carbonates. An example of the main impurity rates is given in Table 4 with an accuracy of 5 %.

Analysis is not complete, in particular, proportioning of phosphate has not been performed. This can partly explain the difference between the total quantity of anion ( $14.5 \cdot 10^{-6}$  mole/kg) and cation ( $23.9 \cdot 10^{-6}$  mole/kg).

Tests of recrystallization from cyclohexanone with different coloring matters have been carried out in order to perform a topographic study of defects. Picture 8 shows RDX crystals recrystallized from cyclohexanone with "organol" red. The visualization of these crystals by optical microscopy techniques shows that solvent is contained within the cavities.

TABLE 4. RATE OF IMPURITIES

CYCLOHEXANONE		0.06 wt %
ANION (mole/kg)		CATION (mole/kg)
Cl <sup>-</sup>	$3.61 \cdot 10^{-6}$	Na <sup>+</sup> $1.11 \cdot 10^{-5}$
NO <sub>2</sub> <sup>-</sup>	$3.22 \cdot 10^{-6}$	
NO <sub>3</sub> <sup>-</sup>	$2.39 \cdot 10^{-6}$	K <sup>+</sup> $1.11 \cdot 10^{-5}$
SO <sub>4</sub> <sup>2-</sup>	$2.39 \cdot 10^{-7}$	
CO <sub>3</sub> <sup>2-</sup>	$5 \cdot 10^{-6}$	Ca <sup>2+</sup> $1.72 \cdot 10^{-6}$

## DISCUSSION AND CONCLUSIONS

Figure 2 shows that sensitivity depends strongly on the manufacturing process of the RDX crystals and consequently on their quality. This is particularly clear if one looks at the two compositions A1 and A2 for which RDX was recrystallized from a same solvent (acetone). Composition A2 for which RDX manufacturing process parameters have been shifted from their classical values in order to obtain a "bad" material (RDX crystals with numerous and larger cavities, greater amount of trapped solvent, Table 5), gets an increased sensitivity compared to composition A1, while the particle size distributions are nearly the same.

TABLE 5. RATE OF SOLVENT FOR THE DIFFERENT BATCHES OF RDX CRYSTALS

Composition	A1	A2	C1	C2	C3	M
Rate of solvent (%)	0.005	0.12	0.06	0.04	0.04	0.02

The three formulations C1, C2 and C3, involving RDX recrystallized from cyclohexanone, have like behaviours under

shock waves, though composition C1 comprises coarser RDX particles. Their internal porosities are similar.



Composition M which has approximately the same type of defects (geometrically speaking) as C2 and C3, leads to a nearly similar level of sensitivity. Nevertheless, it seems to be a little less sensitive at low pressure. Anyway, this last observation cannot be explained by the particle size which is slightly larger for composition M than for the other ones. Perhaps, this trend is due to the nature of the solvent.

According to MOULARD<sup>4</sup>, compositions B and A2 which use small RDX particles compared to C1 should be less sensitive in the low pressure range. This is not the case and the reason seems to be the presence of larger cavities in the explosive grains. Composition B which is the most sensitive, gets the largest cavities.

Thus, there seems to be a correlation between shock sensitivity and magnitude of the internal porosity within the explosive grains. Sensitivity increases with the number and size of internal defects, at least, as long as the size of these defects is between some microns and some tens of microns. The difference of sensitivity between these cast PBX compositions can be explained by the formation of hot spots which is an essential step in the shock initiation process.

The chemical nature of the impurities contained within the cavities (trapped solvents for example) seems to have only a second-order influence on sensitivity, except if one considers that it may play an indirect role in the void dimensions themselves. This point has yet to be precised.

In order to get a better knowledge of the internal porosity and its link with sensitivity, further works are needed to determine, qualitatively and quantitatively, the main parameters which could play a role in the formation and efficiency of the hot spots. Some of these works are planned now, such as : determination of the water contents, characterization of the "bubbles" that have been

observed within the pores, determination of the existence or not of trapped gas (air for example), etc...

## ACKNOWLEDGEMENTS

The authors wish to thank J. Groux for his help in the experimental part of this study.

This work has been performed under the auspices of French MOD (DRET).

## REFERENCES

1. Mishra I.B. and Vande Kieft L.J., "Novel Approach to Insensitive Explosives", in *proceedings of the 19th International Annual Conference of ICT*, Karlsruhe, 1988, pp 25-1 to 25-21.
2. Van Der Steen A.C. ; Verbeek H.J. and Meulenbrugge J.J., "Influence of RDX Crystals Shape on the Shock Sensitivity of PBXes", in *proceedings of the Ninth Symposium International on Detonation*, Portland (Oregon), 1989, pp 83 to 88.
3. Dobratz B.M. ; Craxford P.C., "Properties of Chemical Explosives and Explosive Simulants", LLNL Explosives Handbook, 1985.
4. Moulard H., "Particular Aspect of the Explosive Particle Size Effect on Shock Sensitivity of Cast PBX Formulations", in *proceedings of the Ninth Symposium International on Detonation*, Portland (Oregon), 1989, pp 18 to 24.

# THE INITIATION OF EXPLOSIVE CRYSTALS BY SHOCK OR IMPACT

C.S. Coffey  
Naval Surface Warfare Center  
White Oak Laboratory  
Silver Spring, MD 20903-5640

The initiation of chemical reaction in crystalline explosives by shock or impact occurs by a collection of microscopic quantum mechanical processes. A brief review is given of the microscopic processes believed responsible for initiation due to the shear that occurs during plastic flow due to shock or impact. These results are then extended to macroscopic quantities and compared with experimental observations.

## INTRODUCTION

The plastic flow and associated energy dissipation properties of crystalline solids are determined by the creation and motion of dislocations. Much of our recent efforts have been devoted towards understanding how these processes generate hot spots and ignition sites in explosive crystals during high rate deformation due to shock or impact. Here, the intent is to extend this microscopic analysis to the macroscopic level. It will be seen that many of the features of the microscopic analysis appear in the macroscopic picture including the observation that shear is the important driver for the dissipation, hot spot formation and ignition processes. Further, it will be shown that impact and shock ignition are connected processes with impact described by the first order terms in the microscopic treatment and the shock and detonation processes described by the higher order terms. The transition from the slower first order impact processes to the very rapid detonation-like higher order processes occurs because the high speed dislocations, responsible for high rate plastic deformation, generate phonons of sufficient energy to resonantly excite the internal vibrational modes of the molecules of the shocked crystal.

## MICROSCOPIC PROCESSES OF ENERGY LOCALIZATION

Under the influence of an applied shear stress a dislocation can move at speeds that can approach the shear wave sound speed. In the process of moving, the dislocation will significantly perturb the crystal lattice in the vicinity of the dislocation core. The interaction of the dislocation with the lattice can be written in terms of the interaction Hamiltonian

$H_I \propto \vec{\sigma} \cdot \vec{\epsilon}$ . Expressing the strain,  $\epsilon$ , in terms of the lattice displacement produced by the dislocation and the stress field,  $\sigma$ , as the stress generated by a classical edge dislocation,<sup>1</sup> the interaction Hamiltonian becomes<sup>2</sup>

$$H_I = \frac{\Delta x}{4\pi(1-\nu)} \frac{Gb}{r} \left[ \sin\theta + \cos\theta \right] \times \left( \frac{\cos\theta}{d_2} - \frac{\sin\theta}{d_1} \right) \quad (1)$$

The shear modulus  $G$  provides a measure of the coupling between the dislocation and the lattice. To simplify matters, it will be assumed that  $G$  is a constant, independent of crystal slip directions.<sup>3</sup> The quantity  $b$  is the Burgers length,  $\nu$  is the Poisson ratio,

$r$  is the distance from the dislocation core,  $\theta$  is the angle between the shear stress and the strain, and  $d_1$  and  $d_2$  are the lattice spacings. The lattice displacement,  $\Delta x$ , can be transformed directly into a quantum mechanical expression.<sup>4</sup>

Treating the moving dislocation as a superposition of plane waves, the energy dissipation rate for  $N$  moving edge dislocation is<sup>5,6</sup>

$$\frac{dE}{dt} = N\Gamma G^2 \int (n_q + 1) dq + N \sum_j \frac{1}{\hbar} \omega_{j,j-1} X$$

$$\sum_{f,u=1}^{\infty} \left| \sum \frac{\langle f|H'|1\rangle \langle 1|H'|u\rangle}{E_1 - E_u - \hbar \sum_{j=1}^{\infty} \omega_{j,j-1}} \right|^2 - K \frac{dT}{dx'} \quad (2)$$

where

$$\Gamma = \frac{1}{32\pi^3 \rho} \left( \frac{Rb}{1-\nu} \right)^2 \frac{1}{v_0 d^2}$$

$R$  is the radius of the dislocation core,  $\rho$  is the density, and  $v_0$  is the shear wave speed. For simplicity, it was assumed that the lattice spacings were nearly equal,  $d = d_1 = d_2$ . The quantity  $H'$  is the interaction Hamiltonian coupling the moving dislocation with the internal molecular vibrational modes. The last term in Eqn. (2) describes the thermal conduction of energy from the shear zone. For most shock or impact situations this term will only be important when the thermal gradient is large as would be the case with very narrow energy concentrations or for relatively long impact times.

A dislocation moving with a speed  $v$  encounters and perturbs the lattice potential  $v/d$  times per second. This lattice perturbation generates a spectrum of phonons centered at the frequency  $\omega = 2\pi v/d$  and the approximation was made that these phonons can be treated as being concentrated at the center frequency.<sup>5,6</sup> In addition it was assumed that the empirical dislocation velocity-applied shear stress relation obtained by Gilman can be applied to explosive molecules,  $v = v_0 \exp(-\tau_0/\tau)$ .<sup>7,8</sup> The quantity  $\tau$  is the applied shear stress,  $\tau_0$  is a characteristic shear stress of the material and, as above,  $v_0$  is the shear wave speed. While it remains to be shown that the relation applies to complicated molecular crystals, it does give the correct asymptotic limits for the dislocation velocity in both the low and high shear stress regimes.

When these approximations are introduced into equation (2) the rate of energy dissipation becomes<sup>6</sup>

$$\frac{dE}{dt} \approx \frac{4\pi\Gamma G^2 N}{d} e^{-\tau_0/\tau} + N \sum_j \frac{1}{\hbar} \omega_{j,j-1} X$$

$$\sum_{f,u=1}^{\infty} \left| \sum \frac{\langle f|H'|1\rangle \langle 1|H'|u\rangle}{E_1 - E_u - \hbar \sum_{j=1}^{\infty} \omega_{j,j-1}} \right|^2 - K \frac{dT}{dx'} \quad (3)$$

where  $\omega_{j,j-1} = (2\pi v_0/d) \exp(-\tau_0/\tau)$ .

The first term of (3) arises from the first order transitions and is responsible for the dissipation due to low and medium velocity dislocations. Consequently, it reflects the energy dissipation rate due to impact and low level shock.

The higher order terms in (3) are mainly responsible for energy dissipation due to relatively large amplitude shocks, since for these terms to be important resonance must occur,  $\omega_{j,j-1} = (E_j - E_{j-1})/\hbar \approx 10^{13}$  rad/s. This requires that the dislocation velocity approach its maximum value,  $v \rightarrow v_0$ , which only happens at high shear stress when  $\tau \gg \tau_0$ . As resonance is approached, a transition takes place between the relatively slow first order processes and the very rapid higher order processes. With this a very rapid increase in the energy dissipation rate occurs. The high energy optical phonons, centered in a band about  $\omega = 2\pi v/d$ , and their large number densities combine to produce multi-phonon resonant excitation of the internal vibrational modes of the molecules of the host crystal located on or near the path of the moving dislocations. At resonance the transition probability between adjacent vibrational levels approaches unity. Only for the more widely spaced lowest vibrational levels are non-resonant conditions likely to occur. Consequently, the energy dissipation-molecular excitation rate in molecular crystals subjected to high amplitude shear will be determined by the product of only a few non-resonant lowest level transition probabilities. This results in an extremely fast process in which energy is transferred directly from the moving dislocations to excite the internal vibrational modes and even dissociate the molecules in the shear regions of the host crystal.

The energy dissipated by the moving dislocations and deposited locally in the lattice to form a hot spot can be obtained by integrating equations (2) or (3) with respect to time.

## THE NUMBER OF MOVING DISLOCATIONS

The number density of moving dislocations,  $N = N(t)$ , created by a source can be estimated on the basis of a generalized source of size  $l_0$  beyond which the dislocation pairs have to move before the source can again function to create a new dislocation pair.<sup>9</sup> The rate of dislocation generation by such a source is

$$\frac{dN}{dt} = 2 \frac{v(\tau, t)}{l_0} P_c(\tau, t) = 2 \frac{V_0}{l_0} e^{-\tau_d \tau(t)} P_c(\tau, t) \quad (4)$$

where  $P_c(\tau, t)$  is the probability that the source will create a dislocation at a shear stress  $\tau(t)$ . For large shear stress,  $P_c(\tau, t) \rightarrow 1$ . The number of dislocations created by the source is obtained by integrating (4) with respect to time. However, the number of dislocations moving at any time requires that account be taken of those dislocations that were forced to stop at blocking obstacles such as grain boundaries.

If only  $N_0$  dislocations are allowed on a slip plane and the average distance between slip planes is  $D$ , the width of a shear zone created by a single source is<sup>9,10</sup>

$$W = \frac{D}{N_0} \int \frac{dN}{dt} dt \quad (5)$$

This implies that the energy dissipated by the moving dislocations is localized in the regions of high shear and high dislocation density near the dislocation sources.

## MICROSCOPIC TO MACROSCOPIC TRANSITION

In order to express these microscopic results in terms of the appropriate macroscopic quantities it is necessary to determine the shear stresses within the crystals that comprise the solid. For a randomly oriented aggregate of crystals this requires that the shear stresses be averaged over all slip planes of the crystals and that the origin of these stresses due to the contact forces between interacting particles within the aggregate be properly accounted for. First, the average shear stress is determined for a collection of randomly oriented crystals.

## EXTENSION TO MULTI-CRYSTALLINE EXPLOSIVES

Up to this point the development has been for a single crystal for which a shear stress  $\tau$  has been

applied parallel to one of its slip planes and along the slip direction. To relate these single crystal results to a aggregate of randomly oriented crystals, we first determine the average shear stress that the slip planes in each crystal in the aggregate experiences, and then determine the shear stress onto the slip direction of each crystal.

Let the direction of the applied shear stress,  $\tau_A$ , be along the  $z$  axis, and let the plane of the applied shear be the  $x, z$  plane of a standard  $x, y, z$  coordinate system. Assume a unit hemi-sphere centered at the origin of the  $x, y, z$  coordinate system where the angles  $\theta$  and  $\Phi$  are measured from the  $x$  and  $z$  axes respectively. It is only necessary to consider the first half of the hemi-sphere above the  $x, y$  plane. In the spherical coordinate system, the probability that the unit vector normal to a slip plane of a randomly oriented crystal will lie in the interval  $\theta, \theta + d\theta$  and  $\Phi, \Phi + d\Phi$ , is just the ratio of the differential area element on the unit sphere to the area of half the hemi-sphere,  $p(\theta, \Phi) = \sin\theta d\theta d\Phi / \pi$ . Since the slip plane lies in the plane of the infinitesimal area element, the projection of the applied shear stress onto the slip plane is  $\tau_A \sin\theta \sin\Phi$ . In a similar fashion, let  $\Psi$  be the angle between the direction of the slip axis and the projected shear stress. The probability that this projected shear stress will lie within an angle  $\Psi, \Psi + d\Psi$  of the crystal slip direction is just  $d\Psi / (\pi/2)$ , determined by the ratio of an elemental arc length and the perimeter length of a one quarter of a unit circle. The probable projection of this shear stress onto the crystal slip direction is  $\cos\Psi d\Psi / (\pi/2)$ . Since these probabilities are independent, the average shear stress,  $\langle \tau \rangle$ , in a slip plane and slip direction that is experienced by these randomly oriented crystals is

$$\langle \tau \rangle = \frac{2}{\pi^2} \int \tau_A \sin^2\theta \, d\theta \int \sin\Phi \, d\Phi \int \cos\Psi \, d\Psi \quad (6)$$

The appropriate limits of integration are from 0 to  $\pi$  on  $\theta$ , and 0 to  $\pi/2$  on  $\Psi$  and  $\Phi$ , which gives the average shear stress along the slip direction as  $\langle \tau \rangle = \tau_A / \pi$ . Only the averaged component of the applied shear stress will be considered here. However, many crystals will have slip planes and directions that are more closely aligned with the applied shear stress and consequently experience greater dissipation. These will introduce fluctuations into the average initiation properties.

## SHEAR STRESS IN AN AGGREGATE

To determine the shear stress acting within a crystal in an aggregate requires a departure from the usual approach in which the stresses within a solid are developed in terms of the stresses applied to the

surface elements enclosing a small volume of the solid. While the volume may contain a number of crystalline particles of different sizes, shapes, crystal orientation and defect content, it is customary to average over all of the particles and treat the material within the volume as a continuum.<sup>11</sup> The stresses that appear on the surface elements of the volume are the averages of the stresses on the particles within the volume.

To describe dislocation motion and plastic flow it is necessary to treat the forces acting within a crystal due to nonuniform loading either by the contact forces that it experiences through its interactions with its neighboring crystals or from the spatial variation of the applied force. This can be done by writing the force in a particle as the gradient of the local energy within the particle

$$F = -\nabla E \quad (7)$$

Dividing by an infinitesimal cross sectional area gives the local stress vector within a particle. The shear stresses arise because of the gradient of the forces within the crystal. For example, if the  $z$  axis is taken as the direction of wave propagation, the magnitude of the shear stress components within a particle are determined from the gradient of the pressure  $P_z$  in the directions perpendicular to  $z$

$$\tau_{zx} = \frac{\partial P_z}{\partial x} dx \quad (8)$$

and

$$\tau_{zy} = \frac{\partial P_z}{\partial y} dy \quad (9)$$

Similar relations hold in the  $x$  and  $y$  directions.

Here, the concern is with the heating that occurs within the crystals in an aggregate as they undergo plastic deformation due to shock or impact. It is possible to estimate the maximum shear stress in a crystal contained in an aggregate system composed of many crystal particles and a few voids. In most systems of interest the voids are small in size and number so that heating due to adiabatic compression of gas within the voids during shock or impact is not a major concern. Often the voids are filled with a soft polymer and contain no gas. The maximum shear gradient within a crystal due to uneven loading is approximately

$$\frac{\partial P_z}{\partial x} \approx \frac{\partial P_z}{\partial y} \approx \frac{\Delta P_z}{\delta l} \quad (10)$$

where  $\delta l$  is the thickness of the shear zone over which the deformation occurs. If, for an unfilled void, the pressure gradient within a crystal is approximated to

first order by the average pressure on the surface of the volume element,  $P$ , an estimate of the maximum shear stress within the particle is

$$\tau_{\max} \approx \frac{P}{\delta l} \quad (11)$$

where  $l$  is the average particle size. If the particle size and the shear zone size are about the same then

$$\tau_{\max} \approx P \quad (12)$$

Either approximation can be substituted into equations (2) or (3) to predict the maximum local heating due to dislocation motion and plastic flow in the shear zone. In the case of a polymer filled void the compressible polymer will oppose the pressure imbalance due to the uneven loading of the crystal by its neighbor and act to reduce the maximum shear stress in equation (11) or (12).

## NUMBER OF SOURCES AND HOT SPOTS

Ignore for the moment the shear stress due to an externally applied force gradient. The number of active dislocation sources,  $N_s$ , within an aggregate can be estimated by observing that the sources within a crystal are active only when they are adjacent to a void or more compliant region into which plastic flow can occur. At this time it is not apparent how to specify the number of potentially active sources that exist in a crystal. Here, it will be assumed that there will always be an adequate number of such sources per crystal and that plastic flow is only limited by the number of voids. If all of the particles and voids are approximately the same size,  $l$ , the number of active dislocation sources due to the presence of voids is approximately

$$N_s \approx (1 - \frac{\%TMD}{100}) l^{-3} \quad (13)$$

where % TMD is the per cent of Theoretical Maximum Density of the aggregate. As the % TMD approaches 100 the number of active dislocation sources approaches zero because the number of internal voids or more compliant regions in the aggregate vanish so that shear induced plastic deformation becomes impossible. Thus, regardless of the dislocation number density or crystal orientation, heating within the crystal due to dislocation motion and plastic deformation into void or polymer filled regions vanishes as the % TMD  $\rightarrow$  100. If, however, rarefactions are allowed to enter from the confining walls of the aggregate localized plastic flow and heating will occur.

## COMPARISON WITH EXPERIMENT

Support for these predictions can be found in the results of the NOL Gap test.<sup>12</sup> In the NOL Gap test the explosive is confined in a heavy walled steel cylinder so that the shock stimulus is nearly a plane wave and the shear stress arising from a curved wave front is negligible. It has been observed that it is increasingly difficult to shock initiate any explosive in this test as its % TMD approached 100.<sup>13,14</sup> This is not the case for the lightly confined versions of the gap test in which the explosive is confined in thin walled cylinders. The light confinement allows rarefactions which produces a curved shock wavefront within the explosive and consequently a radial stress gradient and shear stress will develop. Thus, shear induced plastic flow and local heating will be present and ignition can occur even as the % TMD approaches 100.<sup>15</sup>

These results apply to experiments on single crystals of explosive as well. In a recent series of experiments by A. M. Frank at the Lawrence Livermore National Laboratory, large single crystals of HMX were impacted with flier plates to shock pressures up to 12.8 Gpa and the initial stages of initiation were observed photographically with a 15 ns time resolution.<sup>16</sup> Since these were well prepared crystals with no internal voids, the % TMD = 100, so the only shear that could arise was from stress gradients due to relief waves entering from the edge of the crystal. It was observed that, shortly after impact, reactions first occurred along the edges and corners of the impacted face of the crystals. These are the regions where rarefactions first enter and where shear plastic flow will first develop. Consequently these are the regions where hot spots and ignition are first expected to occur.

The same shear dependence of explosive/propellant initiation is found in low level impact experiments. In numerous impact experiments on explosives and propellants in which the ignition threshold was investigated it was observed that, at threshold, ignition of explosive crystals always occurred in regions of high shear and never in regions of just high pressure.<sup>17,18</sup> Usually, the high shear regions where ignition first occurred were also regions of low pressure,  $P < 10^7$  pa.

It appears possible to predict a simple but approximate relationship between impact ignition sensitivity and the shear modulus,  $G$ . Let  $E_p$  be the energy of plastic flow. The amount of energy deposited in the lattice by the moving dislocations is proportional to  $E_p G^2 |H'|^{-2}$ , where  $G$  has been extracted out of the

interaction Hamiltonian,  $H_i = GH''$ . At threshold this is the average energy necessary to cause ignition,  $E_i$ . If it is assumed that the energy of plastic flow is proportional to the total impact energy,  $E_2$ , so that  $E_p = kE$ , then  $E_i \propto G^2 E \{k |H'|^{-2}\}$ . For a drop weight impact,  $E = Mgh$ , so that  $E_i \propto G^2 h \{Mg |H'|^{-2}\}$  where  $h$  is the drop height and the term within the brackets is a constant. It has been the experience of this observer that for many materials the energy to ignition,  $E_i$ , is approximately a constant,  $\approx 2$  to 4 j/gm.<sup>19</sup> When this is the case  $G^2 h \approx \text{constant}$ . For example, for PETN, TNT, and TATB the shear moduli are 5, 2 and  $1 \times 10^{10}$  dynes/cm<sup>2</sup> respectively and the drop heights to 50% ignition are approximately 12, 70 and  $\geq 300$  cm respectively. This approximate relation has an intuitive appeal since  $G$  is a measure of the coupling of dislocation motion and plastic flow energy to the lattice and  $h$  determines the impact energy.

The difference between the shock and impact initiation responses of crystalline explosives is mainly due to the rate at which plastic deformation occurs. On the microscopic level the rate of plastic deformation is determined by the number and velocity of the moving dislocations. For low level impacts the dislocation velocity,  $v$ , is small. Consequently only low energy phonons are created by just the first order terms in the energy dissipation expression, (2) or (3), are important. Local heating and subsequent ignition of the explosive crystals proceed relatively slowly.

For high amplitude shocks the dislocation velocity can approach the local shear wave sound speed in the crystal. The high energy optical phonons generated by these high speed dislocations are capable of resonantly exciting the internal vibrational modes of the explosive molecules,  $\omega \geq 10^{13}$  rad/s. This gives rise to an extremely fast multiphonon excitation process in which the higher order resonant terms dominate the energy dissipation rate. The time to molecular dissociation is determined by the inverse of the product of just the few nonresonant transition probabilities. This time is expected to be on the order of nanoseconds or less, typical of that of a detonation.<sup>20,21</sup>

The transition from the slow first order processes to the very rapid multiphonon processes is similar to the change in reaction rate that is observed in the transition from mild impact driven reactions to the extremely rapid reactions of high pressure detonation. Liddiard, Forbes and Price reported a series of shock ignition experiments in which the amplitude of the shock stimulus was varied for different explosives.<sup>22</sup> They observed the transition from relatively slow,

low amplitude, reactions to rapid detonation-like events for these materials. Using the Gilman expression for dislocation velocity,<sup>7,8</sup> this transition should occur at  $\langle \tau \rangle \approx \tau_0$ . From the relation  $\langle \tau \rangle \approx P/\pi$ , the transitions were observed to occur at shear stresses from about .3 to about 3 Gpa for explosives that ranged from Pentolite to TATB. Gilman observed that the characteristic shear stress,  $\tau_0$ , at which high speed dislocations began to develop in LiF was about .6 Gpa.<sup>7,8</sup> Also, it was observed that pressed charges transitioned to detonation more rapidly than cast charges of the same material. This is expected since the pressed charges have greater dislocation number densities than the cast materials.

## CONCLUSIONS

The energy dissipation that occurs in a crystalline explosive during rapid plastic deformation by shock or impact is a quantum mechanical process which is not accessible by classical mechanics. Originating from the perturbations produced in the crystal lattice by moving dislocations, this process allows energy to be localized in regions of dislocation concentrations. Ignition due to impact or shock are shown to be connected processes. The transition from a relatively slow rate of molecular excitation due to first order processes to a very rapid rate of excitation by higher order processes is predicted. This analysis has been extended to the macroscopic level and its predictions are compared with experimental observations.

## ACKNOWLEDGEMENTS

This work was supported by the Office of Naval Research and by the Naval Surface Warfare Center Independent Research Funds. In particular, the author wishes to thank Dr. Donald Liebenberg of the ONR and Mr. Raymond H. Riedl of NSWC for their support and encouragement.

## REFERENCES

- Hirth, J. P. and Lothe, J., *Theory of Dislocations* (McGraw-Hill New York, 1968).
- Coffey, C. S., Phys. Rev. B 24, 6984 (1981).
- A more complete determination would take into account the directional dependence of the shear modulus.
- Reissland, J. A., *The Physics of Phonons* (Wiley, London, 1973).
- Coffey, C. S., Phys. Rev. B 32, 5335 (1984).
- Coffey, C. S., J. Appl. Phys. 70 (8), 4248 (1991).
- Gilman, J. J., Aust. J. Phys. 13, 327 (1960).
- Gilman, J. J. and Johnston, W. G., in *Solid State Physics*, edited by F. Seitz and D. Turnbull (Academic, New York, 1962), Vol. 13, p. 147.
- Coffey, C. S., J. Appl. Phys. 66, 1654 (1989).
- It is not necessary that  $D = d$ .
- Landau, L. D. and Lifshitz, E. M., *Fluid Mechanics*, Pergamon Press, London, 1959.
- Price, D. and Liddiard, T. P., NOLTR 66-87, Naval Ordnance Laboratory, White Oak, MD. 1966.
- Price, D.; Clairmont, A. R. and Erkman, J. O., NOLTR 74-40, Naval Ordnance Laboratory, White Oak, MD. 1974.
- Price D., Lecture 9, NSWC MP 81-399, 1981.
- Spear, R. J. and Nanut, V. in Proc. of the 9th Symp. on Detonation, OCNR 113291-7, 1989, p. 98.
- Frank, A. M. Energetics Materials Program Review, Equipment and Diagnostics, UCRL-LR-109534-92-2, 1992, p. 25.
- Armstrong, R. W.; Coffey, C. S.; DeVost, V. F. and Elban, W. L., J. Appl. Phys. 68, 979 (1990).
- Coffey, C. S.; Frankel, M. J.; Liddiard, T. P. and Jacobs, S. J., Proc. 7th Symp. on Detonation, NSWC MP 82-334, (1981).
- Coffey, C. S., DeVost, V. F. and Woody, D. L., Proc. 9th Symp. on Detonations, (1989).
- Sheffield, S. A.; and Bloomquist, D. D., Proc. 7th Symp. on Detonation, NSWC MP 82-334 (1981), p. 1004.
- Hayes, B. and Tarver, C. M., Proc. 7th Symp. on Detonation, NSWC MP 82-334, (1981), p. 1029.
- Liddiard, T. P.; Forbes, J. W. and Price, D., Proc. of 9th Symposium on Detonation, 1989, p. 1235.

## DISCUSSION

A. N. DREMIN

Institute of Chemical Physics, Chernogolovka, Russia

What is the time scale of multi-phonon up-pumping at shock initiation of detonation?

## REPLY BY C. S. COFFEY:

Typically, these multi-phonon processes occur in picoseconds. At detonation shock levels the dislocation velocities,  $v$ , approach the shear wave

sound speed,  $\approx 2 \times 10^3 \text{ m/s}$ . The frequencies of the phonons generated by these rapidly moving dislocations are in the vicinity of the internal vibrational frequencies of the explosive molecules,  $\omega = 2\pi v/d \approx 10^{13} \text{ rad/s}$ , where  $d$  is the molecular spacing distance  $\approx 10^{-9} \text{ m}$ . Large numbers of phonons are generated by these rapidly moving dislocations. This causes a very rapid excitation of the internal vibrational levels of the molecules that lie along the paths of the moving dislocations. Molecular dissociation by this resonant driven up-pumping process occurs in times of a few picoseconds.



# SHOCK SOLICITATION OF PETN SINGLE CRYSTALS PRESENTING DEFECTS AND VISUALIZATION OF HOT SPOTS INITIATION

Denis SPITZER and Michel SAMIRANT

French-German Research Institute of Saint-Louis (ISL)  
5 rue du Général-Cassagnou  
68301 SAINT LOUIS CEDEX (France)

Crystallization techniques such as temperature gradient and solvent evaporation are used to obtain centimetric PETN single crystals for shock \*solicitation tests. Optical microscopy with refractive index matching, light emission by fluorescence and ESM, reveal the size of the defect and the orientation conservation according to the carrier crystal. The X-ray Lang topography techniques characterize the crystallographic volume distortion induced by the located defect. A quasi spherical optical defect induces a 3\*3\*3 larger deformed crystallographic volume. Shock solicitation ranging from 4 to 11 GPa highlights the hot-spot formation leading to shock to detonation transition in the vicinity of the optical size defects at about 5 GPa. These experiments, together with the emission study, show the heterogeneous character of the initiation mechanism for low stresses and the rather homogeneous one for higher stresses within the scope of the available spatial precision.

## INTRODUCTION

A lot of work showed that adiabatic gas compression<sup>1,2</sup>, hydrodynamic pore collapse including thermal effect<sup>3,4,5,6,7,8,9,10,11</sup> by viscoplastic heating were the sources of "hot-spots" formation in energetic materials leading to their initiation under shock loading.

The role of crystal defects in PETN single crystal sensitivity was studied by J. J. Dick. He determined<sup>12</sup> that microscopic damage produced by radiation enhances their shock to detonation sensitivity characterized by lowering the run to detonation distance over that of relatively defect free crystals. By measuring the shock transit time in 2 to 3 mm thick PETN <111> slices L. Soulard<sup>13</sup> noted reduced transit times in some cases for stresses near 3 GPa. He attributed this fast reaction to the potential presence of optical scale defects in some samples.

Up to now, however, no work has been done to visualize the hot-spots formation in the vicinity of optical size defects in PETN shocked single crystals.

The present work briefly describes the PETN crystal synthesis done at ISL and the defect analysis methods employed to characterize the defect parameters: their size and location in the sample. X-ray topography enables us to determine the crystallographic distortion volume induced by the optical defect.

The samples are first solicited on the <110> direction determined by J. J. Dick<sup>14</sup> as the most sensitive one. The solicitation on <001> has been started. The stress range covered is between 4 to 11 GPa. During solicitation the light emission in the vicinity of a well known defect is recorded by a Thomson CSF TSN 506 streak camera. The record obtained enables us to determine: the run to detonation distance, the hot-spot time induction and the time of emission appearing under shock loading.

\*Editor's Note: For "solicitation" read "compression"

## PENTAERYTHRITOL TETRANITRATE (PETN)

PETN ( $C(CH_2ONO_2)_4$ ) crystallizes in the tetragonal space group  $P4_2/c$  with two molecular units into the crystal cell. The cell parameters are  $a = 0.938$  nm and  $c = 0.67$  nm.<sup>15</sup> The perfect crystal density is  $1.778$  g/cm<sup>3</sup>.

## CRYSTALLIZATION TECHNIQUES

PETN crystals are prepared with two different techniques: growing under temperature gradient condition and solvent evaporation. The crystals are prepared from commercial 200/800  $\mu$ m polycrystalline PETN in solution in acetone or ethyl acetate. Temperature gradient techniques use a saturated solution and a constant temperature difference of about 8°C. The initial seed can be either suspended to a wire yielding large crystals which present a great amount of macroscopic scale defects (50 to 300  $\mu$ m) in the suspending wire region produced as the crystallization process starts, or supported on a before warmed pyrex plate leading to a lower defect density in the wire region (see figure 1).

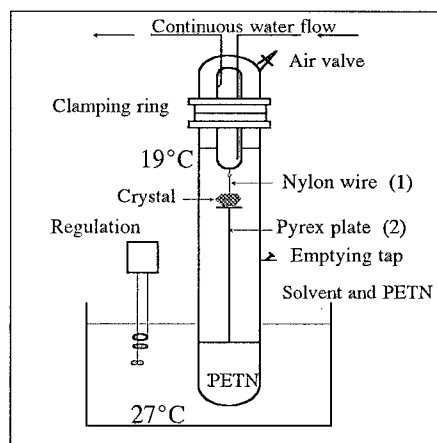


**FIGURE 1. SCHEMATIC REPRESENTATION OF THE TEMPERATURE GRADIENT CRYSTALLIZATION TECHNIQUES USED: (1) SUSPENDED SEED, (2) SUPPORTED SEED**

We also use the solvent evaporation technique, which gives crystals of relatively high purity with very few optical defects. Solutions at about 5% under the saturation yield were left in large bottles with reduced contact with the atmosphere, at a temperature of 27°C. This technique yields optically clear flat crystals. The "as-grown" crystals used for sollicitation and X-ray

topography experiments exhibit well defined  $\{110\}$  and  $\{101\}$  facets. The typical sample size usable for shock sollicitation is  $25 \times 14 \times 10$  mm<sup>3</sup>.

## OPTICAL MICROSCOPY

The set-up of this technique is the result of a cooperation with Ch. Baras, L. Borne, and H. Royer (ISL). The arrangement is shown in figure 2. The crystal is illuminated by a white light or Laser source. Microscopes are limited by the frontal distance of their objectives. The crystal is observed through a Zeiss objective ( $f = 63$  mm) and the image recorded on a  $9 \times 12$  cm Kodak TMAX 100 film.

To overcome the diffraction by the crystal faces, the sample is mounted in a glass cell containing an index matching liquid. PETN is slightly birefringent.<sup>12</sup> The ordinary index for propagation along the C axis is  $1.5559 \pm 0.0006$  and the extraordinary index is  $1.553 \pm 0.001$ . To match the refractive index, we used two types of mixing. The first one contains about 70% CS<sub>2</sub> ( $n = 1.626$  at 20°C) and 30% n-Hexan ( $n = 1.375$  at 20°C). The second one with a lower toxicity contains 98% Anethol ( $n = 1.560$  at 20°C) and 2% ethanol ( $n = 1.361$  at 20°C). The global index of each mixing is adjusted with an Abbe refractometer. By fixing the refractive index of the liquid between the two indexes of the PETN crystal we can simultaneously visualize the defects and the limits of the sample, which enables the coordinate measurement. The elimination of the surface disturbance allows us to scan and analyze crystals up to thicknesses of about 15 mm.

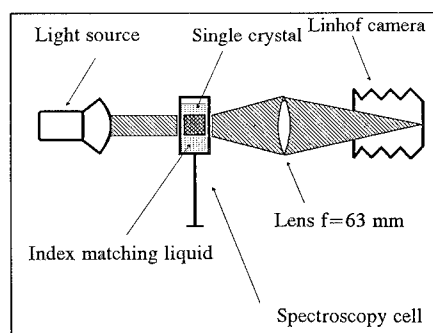


**FIGURE 2. PRINCIPLE OF MICROSCOPY WITH REFRACTIVE INDEX MATCHING**

Microscopy analysis is done according to two crystal directions: the  $\langle 110 \rangle$  and the  $\langle 001 \rangle$ . The technique allows us to characterize defects with dimen-

sions down to micrometric sizes. The size is characterized (see figure 3) by the coordinates  $x_d$ ,  $y_d$ , and  $z_d$ . The position of the defect with respect to the limits of the sample are defined by  $x$ ,  $y$ ,  $z$ . These parameters will also be applied to the X-ray topography and the shot experiments.

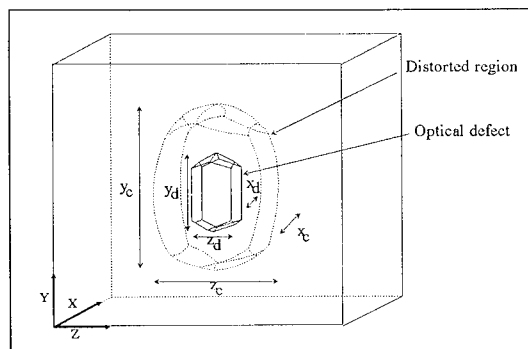


**FIGURE 3. DEFINITION OF THE DEFECT SIZE AND COORDINATE PARAMETERS OF THE DEFECT**

$x$ ,  $y$ ,  $z$ : relative position of the defect in the sample,  
 $x_d$ ,  $y_d$ ,  $z_d$ : size of the optically characterized defect,  
 $x_c$ ,  $y_c$ ,  $z_c$ : size of the distorted crystallographic region.  
 Defect with crystal orientation:  $|y| > |x|$ ,  $|z|$ ,  
 Defect with orthogonal orientation:  $|z| > |x|$ ,  $|y|$ .

The main result shown on pictures 4 and 5 for the crystal used for shot T 111 is that the defect conserves the symmetry and orientation of the carrier crystal.

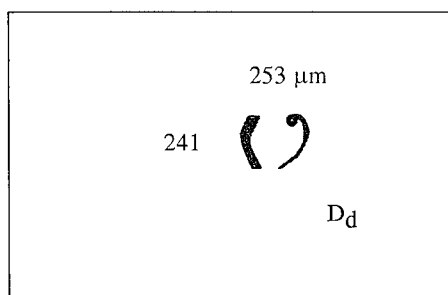


**FIGURE 4. <110> VIEW OF THE CRYSTAL FOR SHOT T 111 (OPTICAL DEFECT LABELLED  $D_d$ )**

#### **LASER FLUORESCENCE ANALYSIS**

Numerous defect observations with the optical technique revealed that the defects have the habit of the

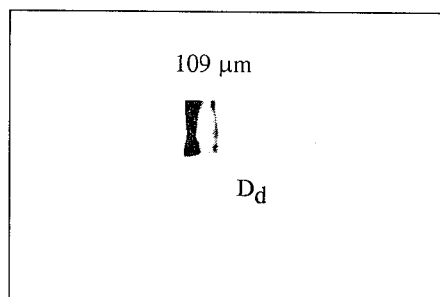


**FIGURE 5. <001> VIEW OF THE CRYSTAL FOR SHOT T 111 (OPTICAL DEFECT LABELLED  $D_d$ )**

carrier crystal. Most of them are bubbles, or crystal shaped figures presenting the same symmetry as the main crystal and partially filled with solvent. In some cases, there were defects with a crystallite aspect. In two other cases, using crystals from our reserve being about 15 years old, we observed defects containing a mobile acetone solution. To test the crystallite hypothesis we used the fluorescence analysis. Therefore, we put a small amount of Rhodamin 6 G ( $10^{-4}$  mol/l) in an acetone seed supported reactor. Rhodamin presents the property to emit a fluorescent light when solvated and excited with a short wave length. An Argon laser illuminates the sample obtained in the Rhodamin bath, which is mounted in its glass cell and surrounded with the  $CS_2/n$ -Hexan mixing. The characteristic view in figure 6 shows that inside each defect, there is still a great amount of solvent. So the hypothesis of a crystallite presenting approximately the same density as the perfect crystal is not realistic.



**FIGURE 6. FLUORESCENCE VIEW OF A CRYSTAL PRESENTING DEFECTS**

#### **ELECTRON SCANNING MICROSCOPY**

We use electron scanning microscopy (ESM) to show that the perfection criterion of a crystal, especially in the case of an organic crystal, should be considered with attention. The designations "perfect crystal" or "optical clear crystal" given currently do not mean

that the crystal contains no defects. With index matching microscopy we reach a great resolution and magnification but, we cannot see all the defects, even those with micrometric sizes, especially for crystals up to a thickness of 13 mm used for shock solicitation.

Ten samples were prepared from single crystals obtained by the solvent evaporation technique or the temperature gradient with supported seed. Each sample is cut from another crystal. These crystals are "optically perfect" crystals. It is therefore rather easy to cleave them along the (110) plane. Because of the heating by the electron beam, the mass of the sample is limited to 2.5 g for safety reasons. The ESM analysis is operated under an acceleration tension of 15 KV. The cleaved surface to be observed is covered by an about 400 Å thick gold layer. The optical observation of each sample did not reveal any optical size defect.

The main result shown on figures 7 and 8 is again the conservation of the habit and the orientation of the carrier crystal by the defects. These two views are typical of the defects observed during the scanning of the cleavage surface of all samples. Another important result is the characterization of the topographic aspect of the defect itself. View 7 shows that the inside walls of the defects are rather rough. They are covered by tiny crystallites which are the result of the dynamic equilibrium crystallization-dissolution in the residual solvent. This solvent is present immediately after the growing of the crystal or migrates to the defect during the residual tension release in the crystal net. This can also lead to a partial filling of the defect with crystalline PETN. This is not evidenced by the optical observation due to the light scattering limits of the defect.



FIGURE 7. ESM VIEW OF A (110) SURFACE PRESENTING A HOLE,  $\varnothing 55 \mu\text{m}$

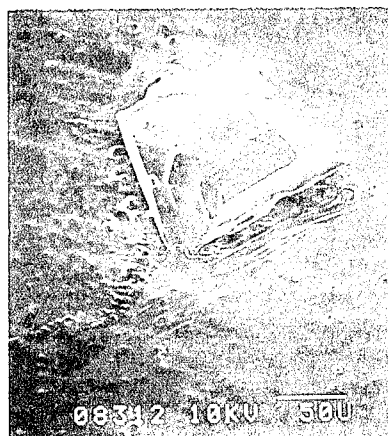


FIGURE 8. ESM VIEW OF A (110) SURFACE PRESENTING A BUMP,  $\varnothing 130 \mu\text{m}$

#### X-RAY TOPOGRAPHY

These experiments in cooperation with Professor C. Burggraf in Strasbourg, have led to the measuring of the crystallographic spatial extension of the distorted region created by the existence of an optically characterized defect. The appearance of a defect during the crystallization creates a defective crystal organization in the vicinity of the optical defect. We used the two Lang topography techniques: the section and the projection topography. The characteristics of the samples studied by these techniques are given in table 1. They are cut from a set of 10 crystals presenting visible defects. The slices are obtained with a circular saw using a kerozen lubrication. Their thickness is adjusted with a precision of 1/100th mm according to the desired orientation. The experimental set-ups used for the projection and the section topography are respectively given in figures 9 and 10.

The projection technique was used by Halfpenny and al.<sup>16</sup> on samples that were slightly thinner than ours and led to the identification of solvent inclusions, growth sector boundaries, growth sectors, and dislocations. Due to its relatively low linear absorption coefficient  $\mu_0$ , PETN allows us to have sample thicknesses up to 3.5 mm. Both techniques use a Molybden X-ray source with the  $K\alpha_1$  wave length being 0.709 Å. The X-ray beam is collimated on the  $K\alpha_1$  wave length with the front double slit of the set-up.

In both set-ups, the crystal sample is mounted on an adjustable support in the center of a double goniometric ( $\theta, 2\theta$ ) plate and the diffracted intensity is registered on a Kodirex film. A high reflecting plane (220) is chosen for each slice (see figure 11). The sample is set under the Bragg angle by adjusting the maximum of

Sample no.	Axis	Xs (mm)	Ys (mm)	Zs (mm)	Mass (g)
1	<110>	3.70	11.25	08.18	0.5992
2	<110>	3.29	10.10	10.23	0.4849
3	<110>	2.61	12.77	09.77	0.4426
4	<001>	2.78	14.70	13.15	0.9007
5	<001>	2.74	13.87	12.14	0.8081
6	<001>	2.90	15.95	14.86	1.2158
7	<001>	2.42	14.50	14.80	0.8683
8	<001>	2.60	13.42	12.83	0.7717
9	<001>	2.35	15.11	15.80	0.7346
10	<001>	2.82	13.38	12.47	0.7995
11	<001>	3.35	15.13	10.00	0.8777
12	<001>	2.28	13.65	06.12	0.3266
13	<001>	2.53	13.65	09.75	0.5286
14	<110>	2.77	14.28	10.28	0.6427
15	<110>	2.72	15.40	10.05	0.7373
16	<110>	2.57	12.56	15.86	0.8748

TABLE 1. CHARACTERISTICS AND DIMENSIONS OF THE SLICES USED FOR X-RAY TOPOGRAPHY

diffracted intensity. In the case of the projection topography, the sample is fixed with the photographic plate and they are moved together according to the X-ray beam. To obtain a good contrast on the film, we need about 130 cycles. One cycle being a back and forth travel. For large sample sizes ( $z = 12$  to  $15$  mm) the experiment duration is 5 to 6 hours.

For this reason we limit the exploration to a width of  $\pm 3$  mm around the optical defect region. The parameters determined are respectively the "width" ( $z_c$ ) and the "height" ( $y_c$ ) (see figure 3).

In the case of the section topography, we maintain the crystal sample and the recording plate fixed according to the beam. After an exposure duration of about 8 minutes we record a section view of the slice at the position of the beam penetration. We sweep the crystal along the  $z$  parameter in  $100 \mu\text{m}$  steps. The section topography allows us to determine the 3 extension parameters of the crystallographic distorted region. These are the "height" ( $y_c$ ), the "depth" ( $x_c$ ), and the

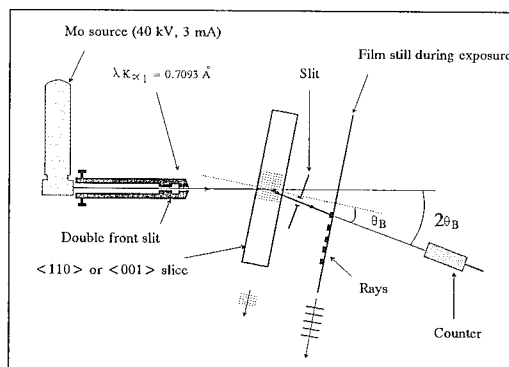


FIGURE 9. SCHEMATIC REPRESENTATION OF THE SECTION TOPOGRAPHY SET-UP

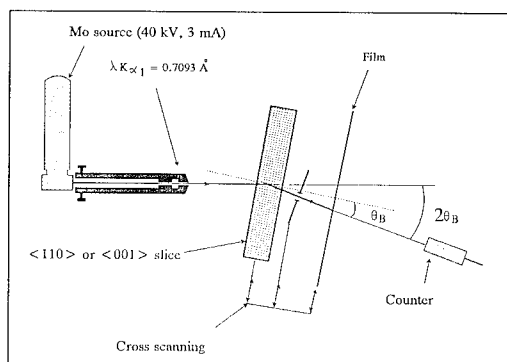


FIGURE 10. REPRESENTATION OF THE PROJECTION TOPOGRAPHY SET-UP

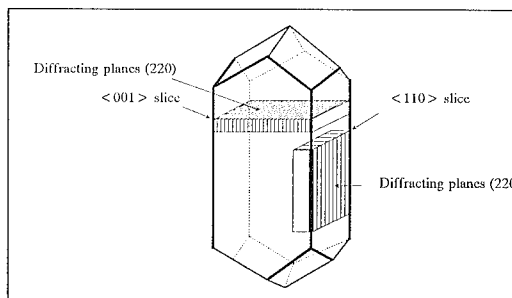


FIGURE 11. TYPE OF SLICES SUBMITTED TO X-RAY TOPOGRAPHY

"width" ( $z_c$ ). The section views obtained are magnified and read with a microdensitometer. The spatial resolution is  $4.6 \mu\text{m}$ . In both methods the contrast appears if the net does not verify locally the Bragg condition corresponding to the (220) planes. The resulting diffracted intensity is then lower than the one diffracted by the perfect crystal. A schematic representation of the contrast is given for the section case in figure 12.

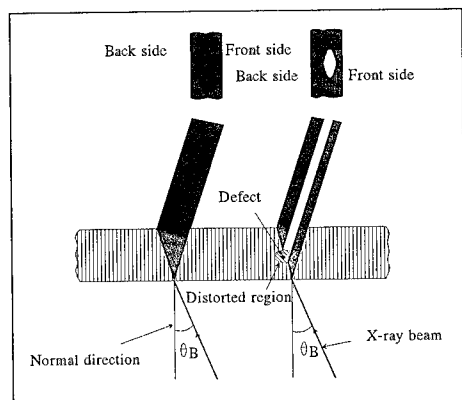


FIGURE 12. EXPLANATION OF THE CONTRAST PRODUCED IN THE SECTION TOPOGRAPHY BY A DEFECT

Typical results of both techniques are given by figure 13 and 14 and table 2.

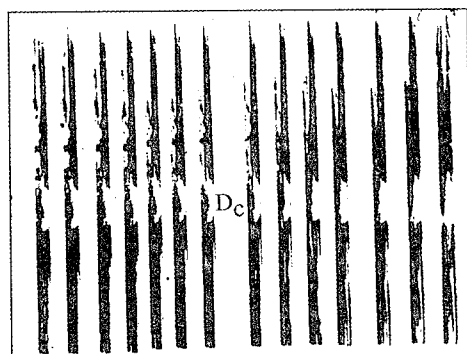


FIGURE 13. SECTION TOPOGRAPHY OF A  $\langle 001 \rangle$  SAMPLE PRESENTING A DEFECT (CRYSTALLOGRAPHIC DISTORTED VOLUME LABELLED  $D_c$ )

Table 2 is the result of a study of 16 defects. In all cases, we noted that the general shape of the optical defect is conserved by the distorted crystallographic region. The two kinds of forms are homothetic. We can determine the crystallographic deformation by the ratio  $R$  defined as:

$$R = \frac{1}{3} \left( \frac{x_c}{x_d} + \frac{y_c}{y_d} + \frac{z_c}{z_d} \right)$$

Three classes of optical defects are defined with the relative dimension being: for the defect with crystal orientation  $|y_d| > |x_d| + 20 \mu\text{m}$  or  $|y_d| > |z_d| +$

$20 \mu\text{m}$ ; for the quasi spherical defect  $|x_d| = |y_d| = |z_d| \pm 20 \mu\text{m}$ , and for the defect with orthogonal orientation  $|z_d| > |x_d| + 20 \mu\text{m}$  or  $|z_d| > |y_d| + 20 \mu\text{m}$ .

The evolution of  $R$  depends on the orientation and the relative size of the optical defect. When the optically characterized defect has the same "habitus" as the carrier crystal, it creates a much lower distortion than if it has an orthogonal orientation. In the latter case, it leads to a crystallographic distorted volume about eight times larger than in the former case. The intermediate case (the quasi spherical defect) gives a ratio  $R$  between 2.65 and 3.27.



FIGURE 14. PROJECTION TOPOGRAPHY OF THE SAME SLICE AS IN FIGURE 13 CRYSTALLOGRAPHIC DISTORTED VOLUME LABELLED  $D_c$ )

Defect orientation	Distortion ratio R
Crystal orientation	1.56
"	1.78
"	1.86
"	1.92
"	1.98
"	2.03
"	2.14
"	2.20
"	2.27
Quasi spherical defect	2.65
"	2.96
"	3.07
"	3.27
Orthogonal orientation	4.35
"	4.69
"	5.15

TABLE 2. EVOLUTION OF THE RATIO  $R$  WITH THE ORIENTATION AND RELATIVE DEFECT SIZE

## SHOCK SOLICITATION, EXPERIMENTAL SET-UP

### The Impact Principle

Single crystals are solicited by shock ranging from 4 to 11 GPa with a  $\Phi$  25 mm, 7 mm thick copper impactor launched by a 30 mm powder gun with an evacuated chamber (figure 15 and 16). The projectile corresponding velocity is 600 m/s to 1400 m/s. The impact velocity is determined by three gauges in the barrel near the gun mouth (figure 16). The third velocity gauge in direct contact with the copper disk is the time reference for the observations.

To predict the parameters of the input shock, we run the hydrodynamic code Dyna 2d. A PETN Hugoniot in the direction  $\langle 110 \rangle$  was determined by J. J. Dick. The simulations show (figure 17) that the shock duration is about 1 to 1.2  $\mu$ s and that it is well sustained for a run distance (x) of 7 to 8 mm in the sample. The shock duration is about 15 times longer than the shock wave transit time in a 300  $\mu$ m defect.

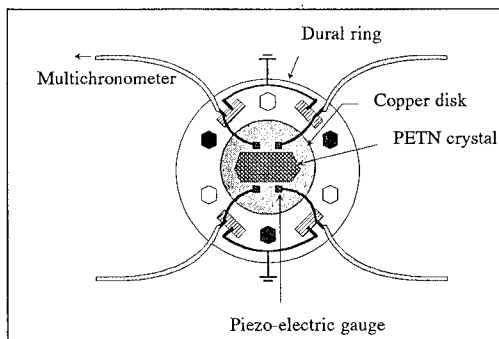


FIGURE 15. FRONT VIEW OF THE TARGET

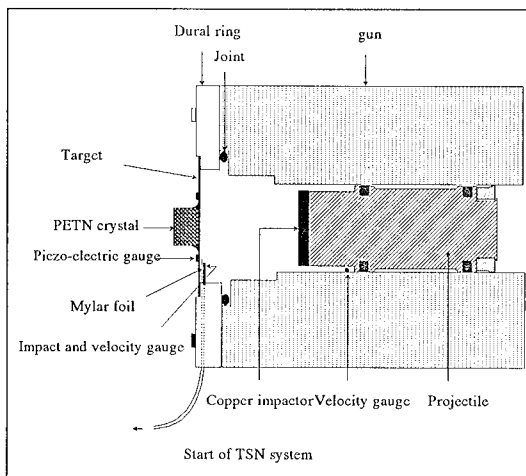


FIGURE 16. SIDE VIEW OF THE IMPACT SET-UP

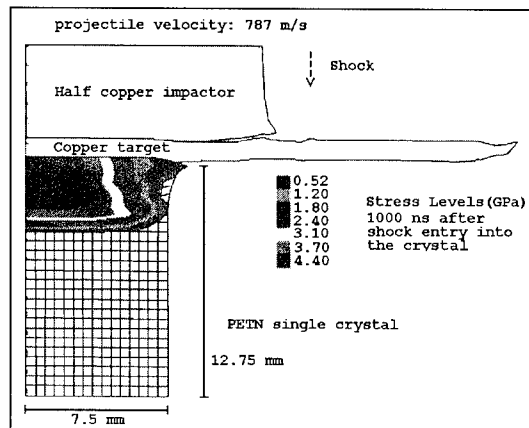


FIGURE 17. AN EXAMPLE OF A DYNA 2D SIMULATION

To determine the shock entry time with a good precision we use piezo-electric copolymers supplied by F. Bauer (ISL). Their rise time is between 2 and 5 ns. For each shot we mount a gauge on each corner of a 22\*10 mm<sup>2</sup> rectangle centered on the shock axis and register the current output on a TSN 632 multichronometer. The entry time into the crystal is determined by the average value of the four signals. The dispersion of the signals gives the tilt angle. The maximum value is one mrad.

### The Shot Experiment

The light emission coming out of the crystal as the shock wave goes through it, especially in the vicinity of a defect, is recorded with a TSN 506 streak camera coupled with a TSN 550 time marker. Two types of techniques are used. The front view (see figure 18) is obtained by a reflecting mirror set either one meter in front of the gun or on a glass holder at a very short distance of the crystal back face. This last technique gives a higher magnification of the crystal image. The 300 to 500  $\mu$ m wide slit is glued on the back side of the crystal and centered on the defects to be studied. The lateral position of the defect (y) is determined according to marks fixed vertically to the slit. The general intensity of the emission through the slit is measured with an optical fiber and a photomultiplier (figure 18).

## EXPERIMENTAL RESULTS

The shots performed until now were mostly done on the  $\langle 110 \rangle$  axis and some on the  $\langle 001 \rangle$  one. Their characteristics are given in table 3.

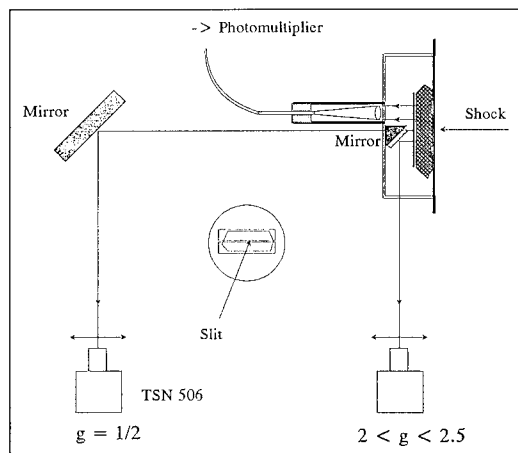


**FIGURE 18. SCHEMATIC REPRESENTATION OF BOTH VISUALIZATION SET-UPS**

Shot no. and axis	Crystal thick. (mm)	Shock vel. (mm/ $\mu$ s)	Long stress (GPa)	Defect size ( $\mu\text{m}^3$ ) $x_d \cdot y_d \cdot z_d$	Defect deep (x), mm	Run to deto. (mm)
T108 <110>	3.54	4.552	5.15	250*635*330	1.92	no
T109 <110>	2.95	4.535	4.95	252*860*608	0.91	no
T111 <110>	8.17	4.538	4.98	109*253*241	4.92	5.91
T112 <110>	6.27	4.722	7.33	115*198*268	4.32	no
T113 <110>	7.85	4.768	7.98	261*422*335	3.42	no
T114 <110>	5.49	4.850	9.21	324*460*382	3.26	no
T302 <110>	12.75	4.552	5.16	58*67*97	4.76	7.11
PM02 <110>	8.80	4.624	5.07	136*274*219	5.86	6.39
T304 <001>	9.22	4.721	10.4	122*258*95	4.63	no

**TABLE 3. SHOT CHARACTERISTICS**

The crystal before solicitation is studied with the optical index matching microscope and the defect size and position are measured. Crystals presenting defects near the center and in a 3 to 5 mm depth are selected.

Typical streak camera views are shown in figures 19 and 20. We discuss three points: the run to detonation distance, the effectiveness of a defect for a given stress and the emission while the shock wave is traveling in the crystal.

### 1) The run to detonation distance (rdd):

The (rdd) is shorter for low stresses which corresponds to J. J. Dick's results:<sup>17</sup> 5.91 mm at 4.98 GPa, 6.39 mm at 5.07 GPa and 7.11 mm at 5.16 GPa.

### 2) Defect Effectiveness:

We observe the creation of hot-spots on optical size defects for a stress level of 5 GPa. The shots T 111 and PM02 show that defects having respective sizes of  $109 \times 253 \times 241 \mu\text{m}^3$  and  $136 \times 274 \times 219 \mu\text{m}^3$  led to the creation of a hot-spot bringing about a shock to detonation transition. This kind of transition is shown on the camera view in figure 19. As for shot PM02, the shot image reveals, that the initiation in the crystal is not homogeneous but spatially heterogeneous. The position of the shock wave is calculated with the Hugoniot of the <110> direction ( $U=2.74+1.81u$  determined by J. J. Dick<sup>18</sup>). For each shot we note a time difference between the theoretical shock position and the reaction itself. The time difference for the shot T 111 is  $267 \pm 10$  ns and for shot PM02,  $114 \text{ ns} \pm 10$  ns. The time precision of  $\pm 10$  ns is the effective time precision we can reach through the space and time measuring on the shot photograph registered on a 100 Iso polaroid film. We associate this delay to the duration of the collapse of the pore. A smaller defect ( $58 \times 67 \times 97 \mu\text{m}^3$ ) solicited under the same stress conditions did not lead to any light emission.

The study for higher stress ranges of respectively 7-8 GPa and 9-10 GPa shows that the optical defects ranging from 100 to  $400 \mu\text{m}$  do not lead to a local reaction. Figure 20 shows a typical shot with no emission on the selected defect. This type of shot will be performed with slightly thicker crystals.

### 3) Crystal light emission

The last parameter studied is the light emitted by the shocked PETN crystal. This emission, the origin of which is not known, has been noted by J. J. Dick<sup>17</sup> in shocked PETN at the stress level of 3 to 5 GPa, but has also been detected in shocked x-cut quartz<sup>19</sup> and z-cut lithium niobate.<sup>20</sup> The nonexplosive character of those two crystals shows that the emission origin has to be investigated in the nature of the physical interaction shock-crystal net itself.

Figures 19 and 20 show the typical difference observed for the studied stress ranges. For all shots in the 4 to 5 GPa range, the emission starts when the shock enters into the crystal. The main difference with higher stress levels is that at these stresses, the camera does not reveal any kind of emission. This behavior is



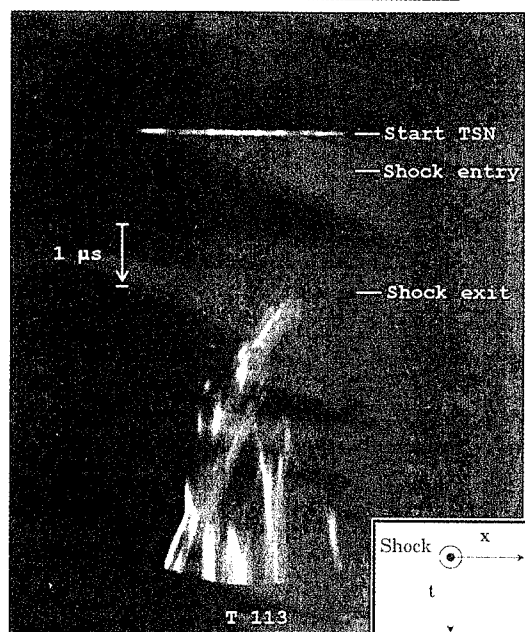
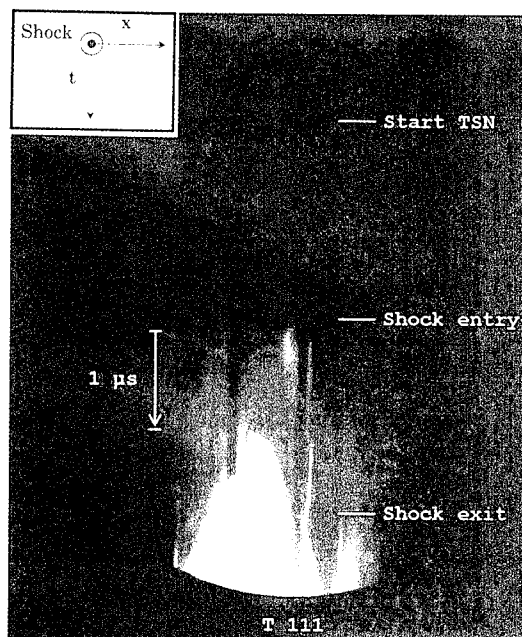
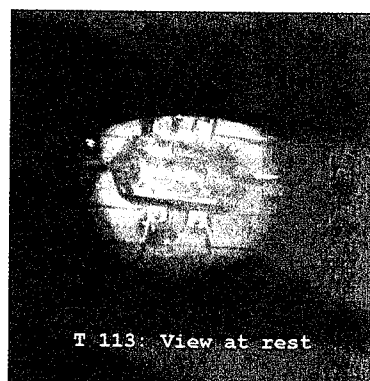
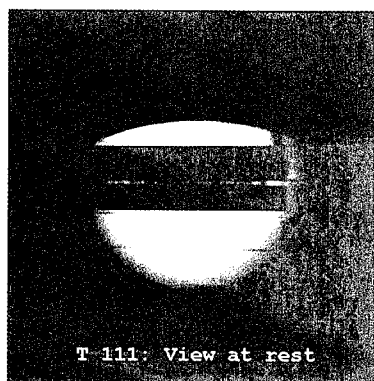


FIGURE 19. SHOT T 111, 4.98 GPa

FIGURE 20. SHOT T 113, 7.98 GPa

also observed for stresses slightly above the elastic limit of the shocked quartz and lithium niobate crystals. To characterize this emission with more precision, we set a photomultiplier (PM) in front of the slit beside the reflecting mirror (see figure 18). In these experiments the scope that records the PM signal is directly triggered by the output signal of one of the four piezoelectric time gauges. The time between the shock entry and the start of recording is about 20 ns. In one of the first shots (PM02), we showed that the emission starts exactly when the shock wave enters into the crystal. The emission intensity recorded grows as the wave travels through the crystal and rises suddenly when the detonation takes place. This kind of shot will be performed for higher stress solicitation (7-10 GPa).

## CONCLUSIONS

Optical microscopy with refractive index matching, analysis of fluorescent light emission, electron scanning microscopy were done on PETN single crystals to characterize the optical size defects. X-ray topography showed that a crystal defect optically characterized creates a spatial crystal net distortion. The dimensions of that distortion are three times the defect dimensions in the case of a rather spherical defect. This kind of result can probably be used in an initiation model.

The shot experiments highlight the role of the optical defects in the shock to detonation transition at about 5 GPa. Hot-spots were effectively detected in

the vicinity of their position. Induction times can be determined. A possible role of optical defects has not been yet detected at higher stress levels.

The emission study showed that the light emission is observed at stresses near the elastic limit and not above it.

These studies reveal that optical defects are effective sites of energy accumulation but that the initiation mechanism is based on defects differing in size and nature depending on the stress range.

## REFERENCES

1. Chaudhri, M. and Field, J. E.; *Proc. Lond. A* 340:pp. 113-128, 1974.
2. Partom, Y.; in *Seventh Symposium (International) on Detonation*, Naval Surface Weapons Center, Annapolis, Maryland, pp 506-516, 1981.
3. Mader, C. L.; *Phys. Fluids*, Vol. 8, pp. 1811-1816, 1965.
4. Mader, C. L.: *Numerical Modeling of Detonations*, Los Alamos Series in Basic and Applied Sciences, University of California Press, Berkeley, California, 1979.
5. Taylor, P. A.; in *Eighth Symposium (International) on Detonation*, Naval Surface Weapons Center, Albuquerque, New Mexico, pp. 26-34, 1985.
6. Setchell, R. E. and Taylor, P. A.; in *Prog. Astronaut. Aeronaut.*, Vol. 94, pp. 350-368, 1984.
7. Khasainov, B. A.; Borisov, A. A.; Ermolaev, B. S. and Korotkov, A. I.; in *Seventh Symposium (International) on Detonation*, Naval Surface Weapons Center, Annapolis, Maryland, pp. 435-447, 1981.
8. Khasainov, B. A.; Borisov, A. A. and Ermolaev, B. S.; *Prog. Astronaut. Aeronaut.*, Vol. 87, pp. 492-504, 1983.
9. Kang, J.; Butler, P. B. and Baer, M. R.; *Combustion and Flame*, Vol. 89, pp. 117-139, 1992.
10. Carroll, M. M. and Holt, A. C.; *J. Appl. Phys.*, Vol. 43, pp. 1626-1636, 1972.
11. Butcher, B. M.; Carroll, M. M. and Holt, A. C.; *J. Appl. Phys.*, Vol. 45, p. 3864, 1974.
12. Dick, J. J.; *J. Appl. Phys.*, Vol. 53(9), pp. 6161-6167, 1982.
13. Soulard, L.; *Thesis*, ISL, 1990.
14. Dick, J. J.; *Appl. Phys. Lett.*, Vol. 44(9), pp. 859-861, 1994.
15. Booth, A. D. and Llewellyn, F. J.; *J. Chem. Soc.*, pp. 837-846, 1947.
16. Halfpenny, P. J.; Roberts, K. J. and Sherwood, J. N.; *J. Appl. Cryst.*, Vol. 17, pp. 320-327, 1984.
17. Dick, J. J.; Mulford, R. N.; Spencer, W. J.; Pettit, D. R.; Garcia, E. and Shaw, D. C.; *J. Appl. Phys.*, Vol. 70(7), pp. 3572-3587.
18. Dick, J. J.; *Shock Waves in Condensed Matter*, pp. 903-907, 1986.
19. Brannon, P. J.; Konrad, C.; Morris, R. W.; Jones, E. D. and Asay, J. R.; *J. Appl. Phys.*, Vol. 54(11), pp. 6374-6381.
20. Brannon, P. J.; Morris, R. W. and Asay, J. R., *J. Appl. Phys.*, Vol. 57(5), pp. 1676-1679.

## DETONATION PARAMETERS OF CONDENSED HIGH EXPLOSIVE CHARGES WITH LONG CERAMIC ELEMENTS

I.A. Balagansky,\* S.V. Razorenov and A.V. Utkin

\*Institute of Electrical Technology  
Novosibirsk, 630090, Russia  
Institute of Chemical Physics of  
Russia Academy of Sciences,  
Chernogolovka, Moscow region, 142432, Russia

Two series of experiments were carried out with charges of high explosives being in contact with long SiC ceramic plates or shells. The longitudinal sound velocity in the SiC ceramic is equal to 11.1–11.2 km/s, what is significantly more than detonation velocity in the explosive. In result the long ceramic elements influence on detonation process and change the high explosive (HE) detonation parameters. In the first series of experiments the detonation propagated along the axis of SiC cylinder shell filled by NM ( $\rho_0=1.14$  g/cm<sup>3</sup>), cast TNT or TNT/RDX 35/64 mixture with densities 1.6 and 1.67 g/cm<sup>3</sup>, respectively. Measurements of pressure profiles were made with manganin gauges placed on the end of charge. In the second experimental series the pressure profiles and average detonation velocity were measured with manganin gauges at the interface between plane plates of SiC 10 mm thick and pressed or cast TNT, TNT/RDX 36/64 or pressed phlegmatized RDX. The existence of a detonation regime with abnormally high detonation pressure and velocity was established in the result of these experiments. Some nonstationary regime and increase of detonation pressure were observed. In tests with ceramic plates an increase of detonation velocity in studied explosives has been registered. The peculiarities of detonation are obviously due to the effect of ceramic elements on detonation parameters.

### INTRODUCTION

It is well-known that hard shells containing any explosive effect on its detonation parameters. The case when the velocity of shock wave in shell material exceeds the velocity of detonation wave front is of special interest. In this case the increase of pressure and velocity of detonation can be up to 20–25%.<sup>1,2</sup> Presently it is known a great number of materials with the shock wave velocity exceeding the detonation velocity of condensed explosives, in particular, the ceramic materials such as boron nitride, boron carbide, cremnium carbide, alumina and others.<sup>3</sup> At the investigation of ceramic materials behavior in shock waves such characteristics of ceramics are

important as a very high velocity of wave processes, being as a rule higher 10 km/s and dynamic elastic limits being about 10 GPa. For high-module ceramic materials a relative weak relaxation of shock waves as they advance in the sample is also characteristic of.

In the present work the experimental investigations were carried out concerning the effect of materials with high sound velocity being in contact with condensed explosives, on the process of detonation propagation. The samples were the plates or thick shells made in selfbinding cremnium carbide (SiC). The sound velocity measured in the samples was 11.1–11.2 km/s. It should be noted that a phase transition proceeds in cremnium carbide at 24 GPa, which is

connected with change of the volume. Two series of experiments were made for different sets up and various sorts of condensed explosives in which the velocity and pressure of detonation waves were determined.

## EXPERIMENTAL RESULTS

In the first set of the tests the registration of pressure profiles for detonation propagation in thick SiC cylindrical shells filled by explosives was realized with the use of manganin gauges.<sup>4</sup> The length of the shell was 60 mm, the internal diameter and wall thickness were 48 mm and 13 mm, correspondingly. The shell internal surface and the ends of shell were polished. Fig. 1 shows the scheme of the experimental set up. The experiments were made with nitromethane of 1,14 g/cm<sup>3</sup> density, cast TNT and TNT/RDX 36/64 of 1,6 and 1,67 g/cm<sup>3</sup> densities. The detonation waves in the explosive charges and shock waves within the shell were generated by a plane wave explosive lens. In the case of nitromethane an additional 40 mm thick explosive charge of phlegmatized RDX was placed between the explosive lens and experimental assembly. For every explosive two types of experiments were carried out, when between the explosive lens and the shell the ring of porous foam-plastic was put or not. Manganin gauges of pressure with characteristic dimensionality 5 x 5 mm<sup>2</sup> and 20  $\mu$ m thickness in 80  $\mu$ m thick teflon insulation were located between two copper plates. The thickness of the copper plates were varied from 1,2 to 2,6 mm (the first plate) and from 5 to 10 mm (the second plate). In each of experiments the pressure

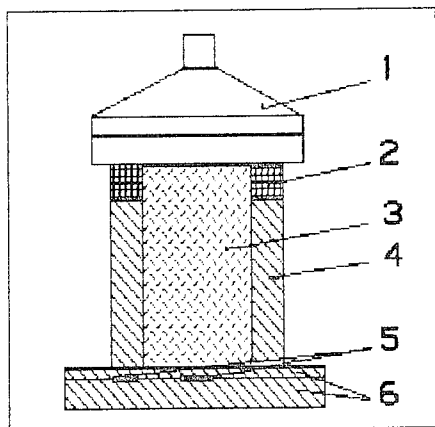


FIGURE 1. SCHEME OF EXPERIMENTS WITH CERAMIC SHELLS: 1 - EXPLOSIVE LENS, 2 - FOAM-PLASTIC RING, 3 - HIGH EXPLOSIVE, 4 - CERAMIC SHELL, 5 - MANGANIN GAUGES, 6 - COPPER PLATES.

was registered by two gauges, one of which is placed along the axis of the shell and the other - under the shell wall.

Fig. 2 demonstrates the profiles of pressure for nitromethane with (Fig. 2b) or without the foam-plastic ring (Fig. 2a). The pressure profiles obtained in copper plates by manganin gauges are shown by solid lines. The dashed lines are the pressure profiles calculated for ceramics and explosives with making use of known shock wave adiabats of these materials. At first the periphery gauge registers the shock wave propagated in ceramic shell with the amplitude not higher 0,5 GPa. Several microsecond later the second gauge registers the appearance of a detonation wave. The maximal pressure measured by a central gauge depends on the initial conditions what can be seen in Fig. 2. The second spike of pressure distant 0,8  $\mu$ s from the first is conditioned by the scheme of experimental set up and connected with circulation of wave in the copper screen.

Results of tests with other explosives are summarized in Table 1, with Chapman Jouguet (C-J) parameters ( $P_{CJ}$ ,  $D_{CJ}$ ) for studied explosives<sup>5</sup> and maximal pressures in explosives ( $P_{HE}$ ) and ceramics ( $P_C$ ) being presented too. The latter were calculated from the registered pressure profiles with help of the known adiabats. The experimental error of pressure determination in the tests was less than 5%. In some tests with foam-plastic ring the pressure profiles were not fixed due to destruction of gauges under the shock wave.

From analysis of the undertaken experiments it is followed that transition of the detonation regime to the stationary does not take place at the conditions. That is obvious from comparison of tests with the foam-plastic ring and without it. In both cases the conditions of initiation of explosives were the same: the explosive charge was initiated by the shock wave with 5 GPa amplitude and more than 5  $\mu$ s duration. At these conditions of initiation the transition length to the stationary detonation for most condensed explosives is about 10 mm. This length for the cast TNT equals ~16 mm<sup>5</sup> at the same conditions, what is significantly smaller than the ceramic shell length. Nonstationary regimes of detonation in conducted experiments are explained by the influence of ceramic shell. The shock wave propagating in the shell leaves behind the detonation wave and changes the initial conditions of detonation initiation in the charge. This may lead to formation overcompressed detonation and increasing pressure in the detonation wave as compared with C-J parameters, what indeed was observed in experiments with nitromethane and hexogen.

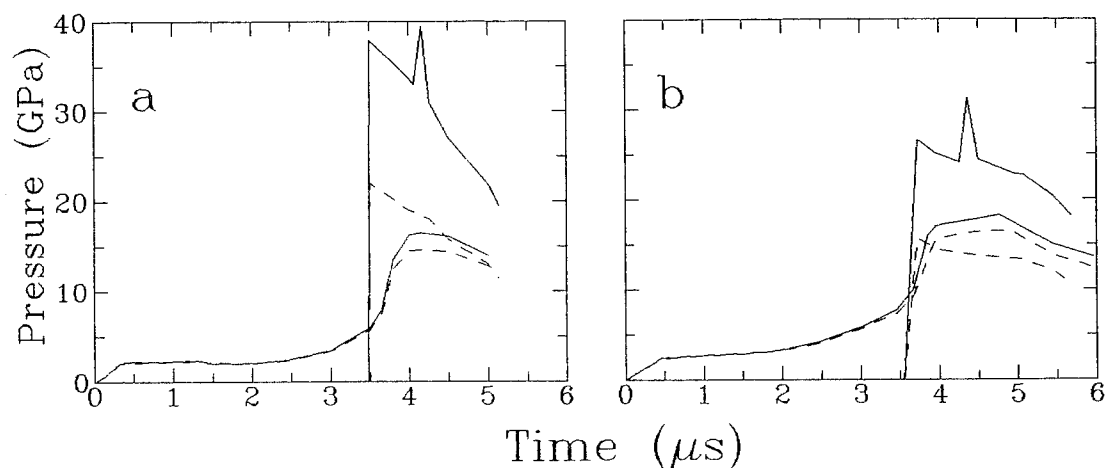


FIGURE 2. PRESSURE PROFILES RECORDED BY MANGANIN GAUGES IN CERAMIC SHELL EXPERIMENTS WITH NITROMETHANE: a - WITHOUT FOAM-PLASTIC RING, b - WITH FOAM-PLASTIC RING.

TABLE 1. THE RESULTS OF EXPERIMENTS WITH CERAMIC SHELLS

HE	$\rho$ , g/cm <sup>3</sup>	$P_{CJ}$ , GPa	$D_{CJ}$ , km/s	Ring	$P_{HE}$ , GPa	$P_C$ , GPa
Nitromethane	1.14	14.1	6.3	no	22.0	16.5
				yes	15.5	16.0
Cast TNT	1.6	19.0	6.9	no	24.0	7.5
				yes	17.0	15.8
Cast TNT/RDX 36/64	1.7	25.0	8.0	no	25.0	11.0
				yes	-	-
RDX	1.1	10.0	6.3	no	12.5	12
				yes	-	-

In the second series of experiments the pressure profiles and the average velocity of propagation of detonation wave were measured at the contact boundary of charges (pressed and cast TNT, composition TNT/RDX 36/64, and pressed flegmatized hexogen) with the plane SiC plate 10 mm thick and 60 x 60 mm surface size. The scheme of experiments is presented in Fig. 3. The thickness of charges was 20–25 mm. Detonation wave propagating along the polished surface of the plate was generated in the charge by a plane wave explosive lens. The air layer between the ceramic plate and explosive lens was about 10 mm.

Manganin gauges in teflon insulation 200  $\mu$ m thick were used in a form of strip of 0.5 mm width, 20  $\mu$ m thickness and 30–40 mm length, oriented parallelly to

the front of detonation wave and located between the charge and plate. Registration of pressure was carried out by two gauges distant 15–20 mm one from the other in the direction of detonation wave propagation. Thus, in these experiments the pressure in detonation wave and the average velocity of its propagation were fixed simultaneously.

In some experiments a copper or aluminum plate was arranged between gauges and the explosive charge. These experiments have shown that metallic plates do not lead to any peculiarities in pressure profiles. Only a small pressure jump connected with a circulation of wave in plate appears before the detonation front.

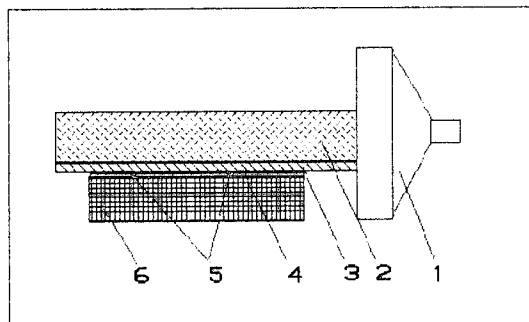


FIGURE 3. SCHEME OF EXPERIMENTS WITH CERAMIC PLATES: 1 - EXPLOSIVE LENS, 2 - HIGH EXPLOSIVE, 3 - ALUMINUM OR COPPER PLATES, 4 - INSULATION OF GAUGES, 5 - MANGANIN GAUGES, 6 - CERAMIC PLATE.

The pressure profiles registered in the second series of experiments for cast TNT/RDX 35/64 are presented in Fig. 4. The analysis of experimental profiles shows that measured pressures on the boundary with ceramic plate are lower than pressures in the C-J point and velocities of the detonation waves are higher than velocities of stationary detonation. In the case of hexogen the increase of detonation velocity was  $\sim 12\%$ . The data of treatment of experimental oscillograms are presented in Table 2. It is summarized there the maximal pressures ( $P_1$  and  $P_2$ ) measured by both gauges in direction of detonation wave propagation and the average detonation velocities, calculated with time of wave passing between the two pressure maxima fixed by the gauges.

## CONCLUSION

Thus, the experimental investigations permitted us to find out the detonation regimes undescribed yet. In experiments with shells no stationary regime and increase of detonation pressure were observed. In tests with ceramic plates some increase of detonation velocity in studied explosives has been registered. The observed peculiarities of detonation wave propagation

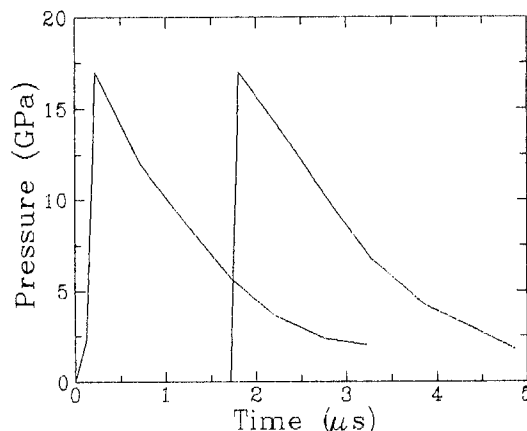


FIGURE 4. PRESSURE PROFILES RECORDED BY MANGANIN GAUGES IN CERAMIC PLATE EXPERIMENTS WITH CAST TNT/RDX 36/64.

in these explosives are obviously conditioned by the effect of ceramic elements on detonation parameters of high explosives. The shock waves propagating in ceramic elements generate a shock wave in explosive charge, changing, therefore, its initial state ahead of the detonation wave front. In addition, this leads to change of the explosive-ceramic boundary conditions. Both these points prevent from forming the stationary detonation or, at least, significantly increase the size of transition zone to the stationary detonation regime.

## ACKNOWLEDGEMENT

Authors would like to thank A.V. Labudin and L.G. Ermolov for the help in preparation and realization of experiments.

## REFERENCES

1. Eden G. and Belcher R.A., "The Effects of Inert Walls on the Velocity of Detonation in EDC35, " in *Ninth Symposium (Int.) on Detonation*, 1989 Vol. 1, pp. 322-330.

TABLE 2. THE RESULTS OF EXPERIMENTS WITH CERAMIC PLATES

HE	$\rho$ , g/cm <sup>3</sup>	$P_{CJ}$ , GPa	$D_{CJ}$ , km/s	$H_{pl}$ , mm	$P_1$ , GPa	$P_2$ , GPa	$D$ , km/s
TNT	1.6	19.0	6.94	Cu; 1.6	14.0	16.4	7.02
TNT	1.6	19.0	6.94	no	12.2	14.6	7.08
RDX	1.6	25.6	8.0	Al; 1.34	20.0	19.5	8.41
RDX	1.6	25.6	8.0	no	17.0	17.8	9.0

2. Merzievsky L.A., Fadeenko Y.I., Filimonov V.A. and Chistiakov V.P., "Accelerated Propagation of Detonation in Charges with Filled by Litium Space", *Fiz. Gor. Vzd. (in Russian)*, 1976, N2, pp. 233-240.
  3. Kipp M.E. and Grady D.E., "Shock Compression and Release in High-Strength Ceramics", in *Shock Waves in Condensed Matter*, 1989, Ed.: Schmidt S.C., Johnson J.N., Davison L.W., Els.Sci.Publ. B.V., 1990, pp. 377-380.
  5. Kanel G.I., Utkin A.V. and Fortov V.E., "The Equations of State and Macrokinetics of Decomposition of Solid Explosives in Shock and Detonation Waves," *Thermal Physics Reviews*, Ed.: Scheindlin A.E. and Fortov V.E., Vol. 3, Part 3, pp. 1-86.
  4. Lyle J.W., Scrivener R. L. and McMillan A.R., "Dynamic Piezoresistive Coefficient of Manganin to 392 kbar", *J.Appl.Phys.*, 1969, Vol. 40, N11, pp. 4663-4664.
- 

#### DISCUSSION

BRIAN D. LAMBOURN  
AWE (A), Aldermaston, Reading, England

Your calculations show that the detonation velocity and detonation pressure oscillate as the wave propagates along the boundary with the ceramic. Have you observed the oscillations experimentally?

#### REPLY BY I. A. BALANGSKY

No reply was received.

## SESSIONS ON RESPONSE TO STIMULUS

**Cochairmen:**

**John Kury**  
**Lawrence Livermore National Laboratory**

**Manfred Held**  
**Messerschmitt-Bölkow-Blohm GmbH**



## INTERPRETATION OF TIME-TO-EXPLOSION TESTS

Joseph E. Shepherd  
Department of Mechanical Engineering  
Rensselaer Polytechnic Institute  
Troy, NY 12180-3590

Thomas B. Brill  
Department of Chemistry  
University of Delaware  
Newark, DE 19716

The heater-explosive interface is experimentally probed, physically modeled, and numerically simulated to illustrate that a dynamic temperature boundary condition is needed to predict time-to-explosion data accurately. The curvature of plots of  $\ln t_{ex}$  vs.  $1/T$  for RDX measured by T-jump/FT-IR spectroscopy in the 1-10 s range are explained by numerical simulation and the Semenov model. Proper treatment of the explosive-heater interface and a reliable thermal model are as important as the chemical rate law for computing the time-to-explosion.

### INTRODUCTION

The time before an explosion occurs at a given temperature is important to safe handling and using of explosives. Numerous tests have been devised to measure critical temperature and time-to-explosion for small-scale assemblies<sup>1-9</sup>. Modeling is then used to predict the behavior of the explosion on a larger scale and in different geometries<sup>6,10-15</sup>. However, semilog plots of time-to-explosion vs.  $1/T$  are frequently curved<sup>1,2,6,8,9,14,16</sup> so that a single Arrhenius equation does not describe the process. Extrapolation is risky. The implication is that the time-to-explosion is controlled by the dynamic blend of physical and chemical rates. Previous test results have been interpreted by use of numerical models of thermal diffusion within the explosive. We suggest that the description of the contact region between the heater and explosive is also very significant. Consideration of the heater, vapor film between the heater and explosive, and temperature boundary condition may be necessary to predict time-to-explosion correctly.

An optimized experimental design to investigate the explosive-heater interface would involve a small, highly responsive heater in contact with a thin layer of explosive of small mass. Such a condition exists in the T-jump/FT-IR technique<sup>9</sup>, where a thin Pt ribbon filament is in contact with 200  $\mu\text{g}$  of thinly spread explosive.

A detailed thermal model demonstrated<sup>9</sup> that steady-state spatial temperature distribution of the

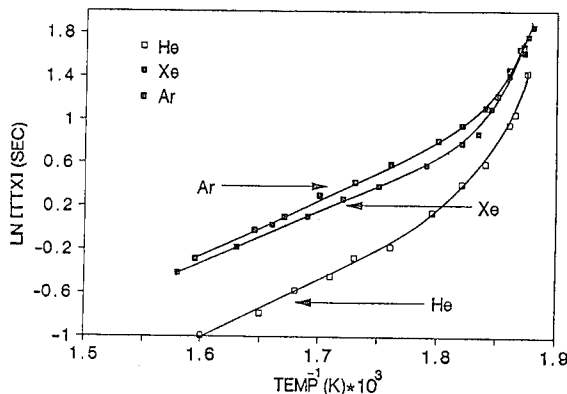


FIGURE 1. EXPERIMENTAL T-JUMP/FT-IR DATA FOR TIME-TO-EXPLOSION OF RDX AS A FUNCTION OF COVER GAS (4.08 ATM).

filament could be predicted from the average filament resistance if the effects of energy loss through radiative and convective heat transfer to the surrounding gas and the filament support were taken into account. Both the effects of gas molar mass and pressure on the steady-state temperature were correctly predicted by the model. However, the time-to-explosion data can rarely be interpreted with a single activation energy because of the pronounced curvature of the Arrhenius plots (Fig. 1). In addition, there appears to be a definite limiting lower temperature, below which, explosions cannot be obtained.

The reasons for these behaviors are not obvious. Numerous explanations have been advanced for the non-Arrhenius effects in terms of heat transfer and competing chemical mechanisms. The T-jump/FT-IR instrument is a sophisticated device but the actual sample temperature cannot be measured as a function of time during the test. Only the steady-state temperature is known through independent calibration testing. The sample temperature history could significantly influence the time-to-explosion results. There may be physical effects such as a vapor layer between the sample and filament that inhibit the heat transfer and affect the time-to-explosion. The very small sample size and delicate nature of the filament (about 6  $\mu\text{m}$  thick) aid in parameterizing the model but make it difficult to measure the actual sample temperature or visualize the sample-filament interface. A detailed physical model and numerical simulation of the instrument transient operation, sample heat-up and explosion process have been developed.

### TRANSIENT ANALYSIS OF THE T-JUMP/FT-IR EXPERIMENT

Our model is an extension of our previous determination of the steady-state response of the heated filament<sup>9</sup>. There are three aspects to the model. First, a detailed thermal model of the filament has been constructed and calibrated against experiments with inert materials. Second, a model of the electronic feedback circuit used to control the filament has been developed. Third, we use a standard thermal explosion model for the heating, thermal decomposition and explosion of the sample. These models are implemented as a set of coupled differential equations. The filament is spatially resolved but the sample is treated as a homogeneous mass. A time-accurate numerical solution of this system of equations is used to determine the thermal response and time-to-explosion of the sample.

The thermal model includes conduction along the filament, convection into the surrounding gas, thermal radiative exchange, time-dependent resistance heating and energy exchange between the surroundings and explosive sample. This model is identical to that developed previously<sup>9</sup> for the steady-state response study. The filament is very thin so that only the conduction in the axial direction is considered. Under these conditions the transient energy balance equation for the filament is:

$$A_f \rho_f c_p \frac{\partial T}{\partial t} = A_f k_f \frac{\partial^2 T}{\partial x^2} - wh(T - T_g) - 2w\epsilon\sigma(T^4 - T_g^4) + i^2 \frac{\rho_e}{A_f} + \dot{q}_s \quad (1)$$

The symbols are:  $T$ , temperature of the filament at axial location  $x$  and time  $t$ ;  $A_f$ , cross sectional area of the filament;  $\rho_f$ , mass density of the filament;  $c_p$ , specific heat of the filament;  $k_f$ , thermal conductivity of the filament;  $w$ , width of filament;  $h$ , natural convection coefficient;  $T_g$ , temperature of the gas and the cell;  $\epsilon$ , filament emissivity;  $\sigma$ , Stefan-Boltzmann constant ( $5.67 \times 10^{-8} \text{ W m}^{-2} \text{ K}^{-4}$ );  $i$ , current through the filament at time  $t$ ;  $\rho_e$ , electrical resistivity of the filament;  $\dot{q}_s$ , thermal energy per unit length

transferred from the sample into the filament. A typical filament is made of platinum and is 38 mm long, 2 mm wide and 6.3  $\mu\text{m}$  thick. Values of other parameters and details of the solution procedure are discussed elsewhere<sup>9</sup>.

At the ends of the filament  $x = 0$  and  $x = L$ , the temperature of filament is fixed at the ambient temperature of the cell  $T(x = L, t) = T(x = 0, t) = T_g$ . The electrical resistivity of the filament is a function of temperature, approximated in this study as  $\rho_e = \rho_e^0 (1 + \alpha(T - T^0))$ . The convection heat transfer coefficient  $h$  is computed from an engineering heat transfer correlation for natural convection from a thin ribbon. The magnitude of  $h$  is proportional to the gas thermal conductivity and is an increasing function of pressure. As a consequence, the calibration of the probe will depend on the gas composition and pressure<sup>9</sup>.

The electronic feedback controller is a key part of the T-jump/FT-IR instrument<sup>9</sup>. There are two aspects to the controller. One circuit ramps up the average filament temperature at fixed rate of 2000 K/s until the set temperature is reached and then another high-gain feedback loop regulates the current to keep the total resistance of the filament constant. The average temperature and total resistance are computed within the model by integrating the numerical solution of the temperature field across the filament at each time step:

$$\bar{T} = \frac{1}{L} \int_0^L T(x) dx \quad (2)$$

$$R = R(\bar{T}) = \rho_e^0 \frac{L}{A} (1 + \alpha(\bar{T} - T^0))$$

The linear relation between resistance and temperature implies that the average temperature will be constant after the initial transient. However, due to thermal diffusion in the axial direction, the temperature at the sample location (the midpoint of the filament) will vary even though the average temperature is held constant. This effect is illustrated in Fig. 2. The temperature transient effect shown in Fig. 2 can be understood as an interaction between the control circuit and the thermal response of the filament. Initially, the effect of thermal conduction is negligible and the temperature is essentially spatially uniform along the filament except for very thin thermal boundary layers at the ends near the cold supports and the region of the sample. With increasing time, thermal conduction transports energy from the filament into the supports and the thermal layers at the end penetrate into the central region of the filament. Since the average temperature is held constant, the temperature at the midpoint of the filament must increase with time to compensate for the decrease in the end regions. The time constant for axial diffusion is quite long (seconds), so that the temperature variation of the filament midpoint (Fig. 3), and therefore the sample, is substantial during the induction phase of the explosion. The sudden change of slope at 1.15 s indicates the occurrence of the thermal explosion.

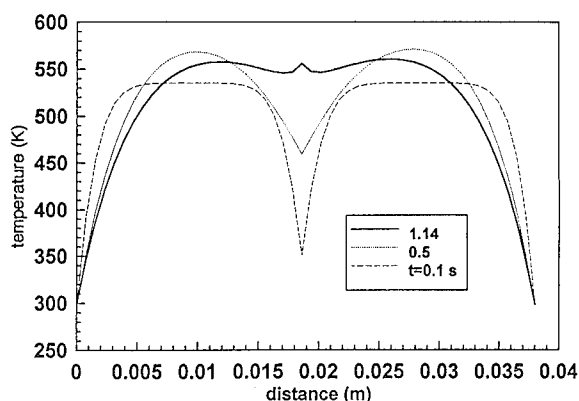


FIGURE 2. FILAMENT TEMPERATURE VS. DISTANCE ALONG FILAMENT FOR SEVERAL TIMES. A REACTIVE SAMPLE IS PLACED AT THE MIDPOINT OF THE FILAMENT AND AN ARGON COVER GAS AT 1 ATM IS USED.

The feedback controllers for the filament are modeled by assuming that the electronic circuits are linear, first-order systems. The initial temperature ramp is produced by controlling the current  $i$  through the filament with the model equation (3), where  $t_{c1}$

$$\frac{di}{dt} + \frac{i}{t_{c1}} = g_1 \left( \left. \frac{dT}{dt} \right|_{set} - \frac{dT}{dt} \right) \quad (3)$$

is the controller response time constant,  $g_1$  is the gain factor and  $dT/dt|_{set} = 2000 \text{ K/s}$  is the ramp set point. Once the average temperature is within 25 K of the set point temperature, control of the current is switched from average temperature rate to average temperature. The controller for the average temperature was modeled in the similar fashion.

$$\frac{di}{dt} + \frac{i}{t_{c2}} = g_2 (\bar{T}|_{set} - \bar{T}) \quad (4)$$

The average temperature of the filament  $\bar{T}$  and its time derivative are computed from the solution to the thermal model of the filament, Eqn. 1. The time constants and gains for the two controller models were determined by comparing the computed results against the actual measured controller outputs<sup>9</sup>. Values used for the present simulations were:  $t_{c1} = 0.01 \text{ s}$ ,  $g_1 = 1 \text{ A/K}$ ,  $t_{c2} = 0.01 \text{ s}$ ,  $g_2 = 10 \text{ A/K-s}$ . Because of the low value of the gain parameters used in the controller models, the set points had to be chosen slightly higher than the actual values desired for the steady-state solution. This was determined by separate calibration computations of the steady-state solutions without sample effects. The computed average temperature of the filament is shown in Fig. 3. The clean results indicate that the control circuit model is quite effective at imitating the actual controller.

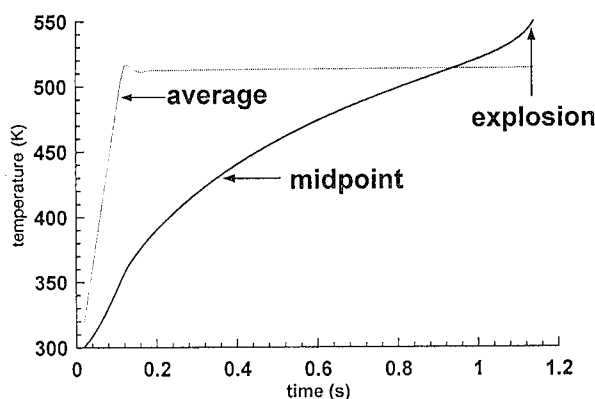
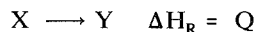


FIGURE 3. FILAMENT AVERAGE AND MIDPOINT TEMPERATURES AS A FUNCTION OF TIME. A REACTIVE SAMPLE IS PLACED AT THE MIDPOINT AND AN ARGON COVER GAS AT 1 ATM IS USED.

The sample chemical reaction and energy balance were modeled by assuming that the sample could be treated as a homogeneous mass. We feel that this is justified since the sample is thin enough (less than  $100 \mu\text{m}$ ) that the characteristic thermal diffusion time of  $25 \mu\text{s}$  is much less than the typical explosion time of 0.1 to 10 s. The explosion process was initially modeled using a one-step reaction mechanism and a constant heat of reaction  $Q$ .



A more realistic model for chemical reaction could be constructed using the time-resolved species measurements produced in T-jump/FT-IR analyses<sup>17</sup> and other recent data on the chemical reaction kinetics of RDX as described in the Appendix. This will be considered in subsequent studies of this problem. For the purposes of the present study, this simple model has been used to illustrate the interaction between instrument response and chemical reaction kinetics.

If the mass fraction of the original sample that has been converted to product is  $\lambda$ , then Eqn. 5 is the rate expression for a first-order, irreversible,

$$\frac{d\lambda}{dt} = (1-\lambda) A \exp(-E_a/\bar{R}T_s) \quad (5)$$

global process, where  $A$  is the pre-exponential constant,  $E_a$  is the activation energy and  $\bar{R}$  is the universal gas constant. The temperature of the sample  $T_s$  is determined by the balance between competing energy transfer and generation processes. The key energetic processes are the heat transfer from the filament to the sample, the energy release or absorption associated with chemical reaction and the energy used to vaporize the sample. Treating the sample as homogeneous, a control-volume analysis of the energy balance yields the following equation for the sample temperature  $T_s$ :

$$m c_{p,s} \frac{dT_s}{dt} = m Q \frac{d\lambda}{dt} - \dot{q}_s x_s \quad (6)$$

The energy equation for the sample and that for the filament are coupled through the term  $\dot{q}_s$ , the rate at which energy is transferred from the sample to the filament (per unit length of filament). Other symbols are:  $m$ , the sample mass;  $c_{p,s}$ , sample specific heat;  $x_s$ , the length of the sample. While the effect of vaporization is also known to be important at high temperatures, this is beyond the scope of the present study.

Additional models are required to describe the heat transfer rate between the sample and the filament. A simplified heat transfer model is  $\dot{q}_s = h_s(T_s - T_f)$ , where  $h_s$  is the heat transfer coefficient between the sample and filament. In the limit of intimate contact,  $h_s \rightarrow \infty$ ; for an adiabatic sample,  $h_s \rightarrow 0$ . Note that the heat transfer plays a dual role. The initial energy transfer is from the filament to the sample  $\dot{q}_s < 0$ . After the sample temperature is increased sufficiently and exothermic reaction commences, the heat transfer is from the sample to the filament,  $\dot{q}_s > 0$ . The initial value of the heat transfer coefficient must be large enough so that the exothermic reactions are initiated, but if it is too large, the loss of energy during the explosion phase will slow down the reactions.

Note that superficially, this model appears to be identical to the classical Semenov model<sup>18</sup> of a non-adiabatic thermal explosion. Substituting the film heat transfer and reaction models into the thermal

$$m c_{p,s} \frac{dT_s}{dt} = m Q (1 - \lambda) A \exp(-E_a / \tilde{R} T_s) - S h_s (T_s - T_f(t, L/2)) \quad (7)$$

explosion equation, we have equation 7, where  $S = w x_s$  is the surface area available for heat transfer between the sample and filament. However, there are two key differences between the present model and the Semenov problem. The transient nature of  $T_f$  at the sample location and the thermal impedance of the filament both contribute to this effect. The temperature  $T_f$  in the present problem is not fixed but is the filament midpoint temperature as determined by the solution to the filament energy equation. The reaction equation, filament and sample energy balances must all be simultaneously solved in order to determine the evolution of the sample temperature. As indicated in Fig. 3, the sample temperature is an increasing function of time. Boddington, et al.<sup>19</sup>, have considered the Semenov problem with a linearly increasing temperature  $T_f$  to develop an asymptotic model of heat flux DSC operation but did not consider the additional complications of the heating surface and control circuit response. These factors are especially important in the T-jump instrument.

Unlike the standard Semenov problem, thermal explosions will occur in our T-jump model even if the

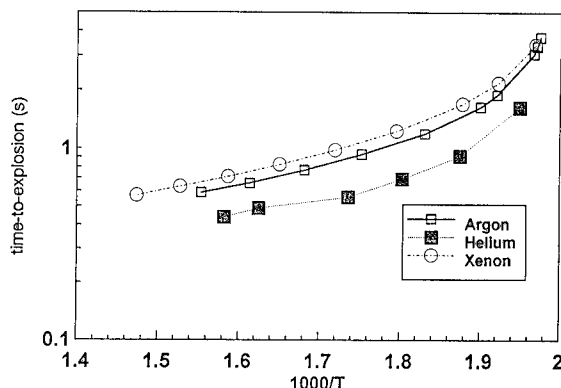


FIGURE 4. TIME-TO-EXPLOSION COMPUTATIONS FOR T-JUMP EXPERIMENT FOR RDX WITH ZINN-MADER ONE-STEP REACTION MODEL PARAMETERS AND 4.08 ATM (60 PSI) COVER GASES OF ARGON, HELIUM AND XENON. THE TEMPERATURE SHOWN IS THE STEADY-STATE MIDPOINT TEMPERATURE.

film coefficient  $h_s = \infty$  since the filament itself provides a thermal resistance. If  $T_f$  was fixed, then the only possible solution for  $h_s = \infty$  would be  $T_s = T_f$ . However the filament itself provides the thermal resistance in the present case and the limit  $h_s = \infty$  does provide some interesting results that are discussed subsequently.

To illustrate the results of the model, the decomposition of RDX was modeled using the rate parameters of Zinn and Mader<sup>12</sup>,  $A = 3.2 \times 10^{18} \text{ s}^{-1}$  and  $E_a = 183 \text{ kJ/mol}$ . For simplicity, we have supposed intimate thermal contact ( $h_s = \infty$ ) between the explosive and the filament. Numerical solutions to the model equations were obtained by simple explicit integration schemes<sup>9</sup>.

Calculated time-to-explosion vs the final filament temperature data are shown for RDX in Fig. 4 for three cover gases, helium, argon and xenon at 4 atm. Note the very strong curvature and the appearance of a limiting lower temperature indicating a critical condition. The effect of temperature and the ambient gas composition are both similar to what is shown in the data of Fig. 1. However, it is clear that the one-step model with the Zinn-Mader parameter values produces times-to-explosion that are in quantitative disagreement with the T-jump time-to-explosion data.

The results of these computations can be understood by appealing to several simple limiting cases and the results of the simpler Semenov model. First, recognize that there are at least two characteristic times in this problem that are significant. At one extreme is the characteristic thermal explosion time for an adiabatic sample at a specified initial temperature  $T$ . This is the classical adiabatic explosion time, which for our simple model reaction is approximately

$$t_{ad} = \frac{\tilde{R}T}{E_a} \frac{C_p T}{Q} A^{-1} \exp(E_a / \tilde{R}T). \quad (8)$$

Using the Zinn-Mader model parameters, the value of  $t_{ad}$  varies from 0.5 s at 500 K to 0.13 ms at 625 K.

At the other extreme is the characteristic heating time for the sample *neglecting the effects of reaction*. For the case of a fixed filament temperature and heat transfer coefficient, the time required to achieve 67% of the final temperature rise is:

$$t_h = \frac{mC_p}{h_s} \quad (9)$$

If  $h_s = 500 \text{ W m}^{-2} \text{ K}^{-1}$ , then  $t_h = 0.175 \text{ s}$ . The actual heating time of the sample is somewhat different in the T-jump instrument due to the operation of the controller circuit and also the interaction between filament and sample energy balances. Both the adiabatic explosion times and the nonreactive heating time are indicated on Fig. 5. The ratio of the two time scales plays an important role in understanding the results of the T-jump test. This ratio is known as the Semenov parameter  $\psi = t_h/t_{ad}$ , a quantity that plays a key role in the steady and unsteady behavior of nonadiabatic explosions<sup>18</sup>.

At high temperatures, the large differences between the T-jump simulation and the adiabatic explosion time are due to the finite time required to heat up the sample at the center of the filament and the thermal energy transfer between the filament and surroundings during the explosion process. We have already shown that even though the average filament resistance reaches its final value after less than 0.1 s, the temperature profile is far from steady-state at this point and the center temperature changes significantly as the profile relaxes (Figs. 2 and 3). The sample temperature does not approach the steady-state value until about 1.5 s for the largest temperature jumps ( $\Delta T$  of about 300 K).

So for high temperatures,  $t_h > t_{ad}$ , the explosion time is dominated by the time required just to heat up the sample. This accounts for the apparent low activation energy at high temperature. At low temperature,  $t_{ad} \gg t_h$  and the explosion time is dominated by the time required for the actual explosion process, the heating being relatively fast by comparison. However, if the temperature is reduced below some minimum level, the explosion time increases rapidly above the adiabatic value, indicating a quenching or critical effect. This is a consequence of the thermal response of the filament.

As the explosive reacts exothermically, the energy produced diffuses away through the filament and is transferred to the surrounding gas by convection and radiation. A critical condition is reached when the rate of energy loss equals the energy production rate. This occurs at a temperature around 500 K for the RDX parameters. As the critical condition is approached, the time-to-explosion increases rapidly with temperature, resulting in the observed curvature

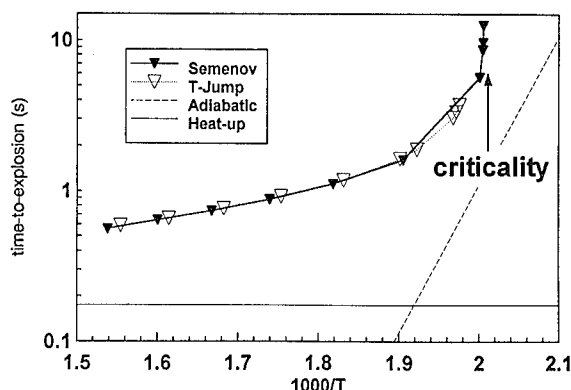


FIGURE 5. COMPARISON OF TIME-TO-EXPLOSION FOR T-JUMP SIMULATION (4 ATM Ar), ADIABATIC EXPLOSION TIME, SIMPLE SEMENOV MODEL AND NONREACTIVE CHARACTERISTIC HEATING TIME.

of the semilogarithmic plots of time-to-explosion vs reciprocal temperature. No solutions are found for final temperatures less than the critical value. In contrast to the solution for a large sphere or semi-infinite slab<sup>12</sup>, the time-to-explosion is not simply related to the adiabatic thermal explosion time at high temperatures.

This behavior is very similar to that observed with the Semenov model discussed above. However, now we consider the thermal resistance to be provided by a combination of processes at the filament-sample interface and the filament itself. So the heat transfer coefficient has some effective value  $h^*$  and the filament temperature in the sample energy equation is taken to be the steady-state value  $T_{s, \max}$  at the midpoint. The result of simulations with the Semenov model using the heat transfer coefficient of  $500 \text{ W m}^{-2} \text{ K}^{-1}$  is shown in Fig. 5. The superb agreement is fortuitous because this value of  $h_s$  is somewhat arbitrary. On the basis of the Pt filament alone, a larger heat transfer coefficient would exist. However, the effect of a gas layer and other barriers to heat transfer would lower the value of  $h_s$ . Further modeling is necessary to refine the value of  $h_s$ . On the other hand, it appears that despite the complexity of the control circuit and the filament thermal response, a simple model mimics the overall response of the T-jump instrument. This suggests that the critical behavior of the Semenov model can be used to explain the limiting lower temperature observed in the T-jump simulations.

The critical behavior of the Semenov model has been extensively studied for both the classical model and models related to DSC<sup>19</sup>. There is a critical value of the Semenov parameter  $\psi = e^{-1}$  that determines the boundary between slow reaction and explosion. The existence of this critical parameter implies that there is a critical value of the filament temperature, below which reaction will not take place. This accounts for the strong upward curvature or increase in the apparent activation

energy at lower temperatures.

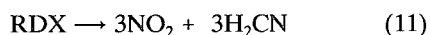
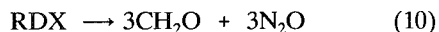
In conclusion, we have developed a transient thermal model for the T-jump fast thermolysis experiment. The experimentally observed trends in the time-to-explosion can be explained as the interaction of instrument response, heat transfer and chemical reaction. Transient thermal effects and thermal losses to the filament and surroundings play a very important role in determining the time-to-explosion. We postulate that similar considerations are important in analyzing other thermal explosion tests. Proper treatment of the explosive-heater interface and a reliable thermal model of the surroundings appear to be as important as the chemical rate law in determining the time-to-explosion. The effective activation energy variations that have been deduced from previous time-to-explosion data may in many cases be artifacts that are consequences of such thermal and physical effects rather than actual chemical mechanism changes.

#### ACKNOWLEDGEMENTS

T. B. B. thanks the Wright Laboratory, Armament Directorate, Eglin AFB, FL for financial support, and P. J. Brush for the data for Fig. 1.

#### APPENDIX

Time did not permit incorporation of the most recent relevant kinetic and mechanism details for RDX. According to T-jump/FT-IR spectroscopy, RDX thermally decomposes by two temperature dependent stoichiometric branches 10 and 11<sup>20</sup>. Reaction 10 is exothermic and is favored at lower temperature, while 11 is endothermic by

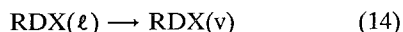


approximately the same amount as 10 is exothermic and is favored at higher temperature<sup>17,21</sup>. We emphasize that the reactions are stoichiometric and not elementary because the fuel species  $\text{CH}_2\text{O}$  and  $\text{HCN}$  form from an ill-defined residue that is left as the nitrogen oxides  $\text{N}_2\text{O}$  and  $\text{NO}_2$  are liberated<sup>17</sup>. The rate constants for 10 and 11 are 12 and 13, respectively.<sup>22</sup>  $E_a$  values are kcal/mol.

$$k_{10} = 10^{13} e^{-36/RT} \quad (12)$$

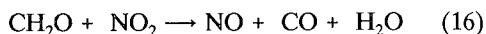
$$k_{11} = 2 \times 10^{16} e^{-45/RT} \quad (13)$$

For vaporization of RDX, the rate constant 15 has been estimated<sup>22</sup>. The first large heat



$$k_{14} = 7.5 \times 10^{16} e^{-22.6/RT} \quad (15)$$

release reaction that initiates the explosion of RDX is the reaction of the  $\text{CH}_2\text{O}$  fuel from 10 and the  $\text{NO}_2$  oxidizer from 11 according to 16<sup>17,20</sup>. Rate data for 16 are available<sup>23</sup>. The rates and heats of



reactions 10, 11, 14 and 16 could be incorporated into equation 7 in place of the simple one step reaction. This is planned in a future project.

#### REFERENCES

1. Henkin, H. and McGill, R., Indust. Eng. Chem., Vol. 44, 1952, p. 1391.
2. Wenograd, J., Trans. Farad. Soc., Vol. 57, 1961, p. 1612.
3. Rogers, R. N., Thermochim. Acta, Vol. 11, 1975, p. 131.
4. Catalano, E., McGuire, R., Lee, E. L., Wrenn, E., Ornellas, D., and Walton, J., Sixth Symposium (International) on Detonation, Office of Naval Research, ACR-221, Coronado, CA, 1976, p. 214.
5. Jaeger, D. L., Los Alamos Scientific Laboratory Report LA-8332, August, 1980.
6. McGuire, R. R. and Tarver, C. M. Seventh Symposium (International) on Detonation, U.S. Naval Academy, Annapolis, MD, 1981, p. 56.
7. Stolovy, A., Namenson, A. I., Aviles, J. B., Jr., Jones, E. C., Jr., and Kidd, J. M., J. Energetic Mat., Vol. 5, 1987, 181.
8. Brill, T. B. and Brush, P. J., Ninth Symposium (International) on Detonation, Portland, Oregon, 1989, p. 228.
9. Brill, T. B. and Brush, P. J., James, K. J., Shepherd, J. E. and Pfeiffer, K. J., Appl. Spectrosc., Vol. 46, 1992, p. 900.
10. Frank-Kamenetskii, D. A., Acta Physicochim. (USSR), Vol. 10, 1939, p. 365.
11. Chambré, P. L., J. Chem. Phys., Vol. 20, 1952, p. 1795.
12. Zinn, J. and Mader, C. L., J. Appl. Phys., Vol. 31, 1960, p. 323.
13. Gray, P., Lee, P. R. and MacDonald, J. A., Combust. Flame, Vol. 13, 1969, p. 461.
14. Zinn, J. and Rogers, R. N., J. Phys. Chem., Vol. 66, 1962, p. 2646.
15. Merzhanov, A. G. and Abramov, V. G., Prop. Explos., Vol. 6, 1981, p. 130.
16. Freeman, E. S. and Gordon, S. J. Phys. Chem., Vol. 60, 1956, p. 867.
17. Brill, T. B. and Brush, P. J., Phil. Trans. Roy. Soc. Lond. A, Vol. 339, 1992, p. 377.
18. Semenov, N. N., Z. Physik, Vol. 42, 1928, p. 571.

19. Boddington, T., Gray, P. and Kay, S. R., Proc. R. Soc. Lond. A, Vol. 425, 1989, p. 269.
20. Brill, T. B., Brush, P. J., Patil, D. G. and Chen, J. K., Twenty-Fourth Symp. (International) on Combustion, The Combustion Institute, Pittsburgh, PA, 1992, p. 1907.
21. Brill, T. B. in Non-Intrusive Combustion Diagnostics, K. K. Kuo, Ed. Begell House, New York, 1993, in press.
22. Melius, C. F. in Chemistry and Physics of Energetic Materials, S. Bulusu, Ed. Kluwer Academic Publ., Dordrecht, The Netherlands, 1990, p. 51.
23. Lin, C. Y., Wang, H. T., Lin, M. C. and Melius, C. F. Int. J. Chem. Kin., Vol. 22, 1990, 455.

---

## DISCUSSION

A.C. VAN DER STEEN

Prins Maurits Laboratory TNO, Rijswijk, Netherlands

(1) In experiments following the Wenograd methods we performed some years ago, we found a perfect relation between  $\ln t$  and  $1/T$ . Probably we have to compare our results to see what is causing the differences.

(2) The heat transfer is even more complicated because a gas layer is formed between the explosive and the metal. This could even cause an increasing induction time with increasing temperature. Did you observe anything like that?

## REPLY BY T. B. BRILL AND J. SHEPHERD:

(1) Wenograd reported linear and nonlinear data depending on the compound. I agree that we should compare data.

(2) In the beginning of this modeling project, we planned to include a gas film layer between the heater and the explosive. However, this condition is so complicated that the nature of the gas layer, if it is present, must be better understood before expanding the time to model it. For example, it is not reasonable to use the simplified evaporation model with radial flow as developed for  $\text{CO}_2$  by Cantrell [R. H. Cantrell, *AIAA J.*, Vol. 1, 1944 (1963)] for a reacting explosive like RDX. We did find, however, that varying the heat transfer coefficient at the interface does not change the essential details of the results. A reasonable interfacial gas layer model for an explosive might evolve from a video study of how the sample behaves on the surface. An even simpler experiment than described in our paper is necessary because the model of the heater and the explosive is already complicated without adding further details about the interface.

## ON THE THEORY OF IGNITION OF A REACTIVE SOLID BY A NON-CONSTANT ENERGY FLUX

G. A. Leiper, G. F. Roach  
Aerospace and Automotive Research,  
ICI Explosives, Stevenston, Scotland.  
Department of Mathematics, University  
of Strathclyde, Glasgow, Scotland.

In this note we investigate the time to ignition of a reactive solid as a consequence of a time dependent heat flux at the boundary. The approach adopted here reproduces as special cases results obtained in the pioneering works of Bradley<sup>1</sup> and Linan and Williams<sup>2</sup> where the authors considered a similar problem but with a constant heat flux. Indications are also given of how the work of these authors may be adjusted to accommodate non-constant heat flux conditions.

### INTRODUCTION

Energetic materials are capable of supporting the propagation of a self-sustaining combustion wave. Whilst the characteristics of this wave are readily measured by experiment they are difficult to predict accurately from purely theoretical grounds, due to the complex reactive fluid dynamics occurring in condensed propellant flames.

The use of mathematical models to investigate the ignition transient suffered by energetic material exposed to thermal stimuli has been the subject of intensive study. Many models have been developed first to investigate the ignition phenomenon, and then to provide a means of predicting ignition limits for a variety of stimuli over a range of propellant systems. The basis of all models is a solution of the heat flow equation with a chemical source term, and boundary conditions describing the external stimulus.

Early workers developed both semi-analytic and numerical solutions to the model, given that the boundary condition was a simple source term. Limited success was found in predicting the time to ignition for simple propellants from well behaved thermal surface fluxes.

The search for more accurate results led to the development of more complex models, with the addition of extra regions, describing in detail the behaviour of the surface subject to the thermal flux; for example gasification from the surface, and early chemical decomposition reactions within the gasifying propellant. Indeed reaction between the propellant and the gaseous atmosphere above the surface can also be included.

Such approaches give a full and reliable model, but one which is difficult to use in simulations of overall ignition trains in propellant devices. In particular, if the external stimulus is that due to two-phase flow of reacting ignition material across the propellant surface, the computational overhead due to inclusion of a detailed ignition model, prevents the solution of models of a useful size.

In this work, a simple but reasonably complete model of ignition is developed based on the earlier work of Bradley and of Linan and Williams. The basis of the model is that of surface ignition of a solid propellant by an arbitrary time dependent surface heat flux. The propellant is assumed to react by a single channel first order Arrhenius reaction rate without reaction depletion.



The aim of this development is to produce a model capable of easy inclusion in an ignition model of a sodium azide based propellant subjected to the flow of reacting solid and gaseous igniter products at grazing incidence.

The approach adopted here reproduces as special cases results obtained in the pioneering works of Bradley<sup>1</sup> and Linan and Williams<sup>2</sup> where the authors considered a similar problem but with a constant heat flux. Indications are also given of how the work of these authors may be adjusted to accommodate non-constant heat flux conditions.

## MATHEMATICAL FORMULATION

Let  $x, y, z$  denote the usual, non-dimensional, Cartesian coordinates with respect to a fixed origin.

We consider a homogeneous reactive solid occupying the half-space  $x > 0$  and assume that the solid is heated by a time-dependent energy input at the surface  $x = 0$ . Following Bradley<sup>1</sup> and Linan and Williams<sup>2</sup> we ignore reactant depletion and the order of the reaction. Consequently, the heating of the solid can be described in terms of a one-dimensional initial boundary value problem of the form

$$u_t = u_{xx} + F(x, t, u, u_x), \quad 0 < x < \infty, 0 < t < T \quad (2.1)$$

$$u(x, 0) = \phi(x), \quad 0 < x < \infty \quad (2.2)$$

$$u_x(0, t) = g(t), \quad 0 < t < T \quad (2.3)$$

where  $u \equiv u(x, t)$  denotes the non-dimensional temperature in the solid at the point  $x$  at the non-dimensional time  $t$ . The function  $F$  is known and describes the reaction in the solid whilst  $\phi$  and  $g$  are given data functions.

Using the well known properties of the heat kernel

$$K(x, t) := \frac{1}{\sqrt{4\pi t}} \exp\left\{-\frac{x^2}{4t}\right\}, \quad t > 0 \quad (2.4)$$

it is a straightforward matter to show that the initial boundary value problem (2.1)-(2.3) is equivalent to the non-linear integral equation

$$u(x, t) = -2 \int_0^t K(x, t - \tau) g(\tau) d\tau + \int_0^\infty N(x, \xi, t) \phi(\xi) d\xi +$$

$$+ \int_0^t \int_0^\infty \{N(x, \xi, t - \tau) \times F(\xi, \tau, u(\xi, \tau), u_\xi(\xi, \tau))\} d\xi d\tau \quad (2.5)$$

where

$$N(x, \xi, t) := K(x - \xi, t) + K(x + \xi, t), \quad t > 0. \quad (2.6)$$

It will be equation (2.5) which will be the focus of the following analysis. We would remark that in arriving at (2.5) we have not been concerned with how the energy flux at the boundary  $x = 0$  is generated. This is almost always due to an associated gas phase. This aspect will be considered in detail in a separate communication, as indeed will be the effects of reactant depletion and the phenomenon of ignition within the solid, and will be accompanied by a comparison with the results obtained by Bush and Williams<sup>3,4</sup>.

## ANALYSIS OF THE INERT STAGE

In the present case the reaction term  $F$  in (2.1) has the form

$$F(x, t, u, u_x) = A \exp\left\{-\frac{E'}{u}\right\} \quad (3.1)$$

where  $A$  and  $E'$  are non-dimensional constants, the former is a measure of chemical and external heating rates and the latter specifies the activation energy.

Following Bradley<sup>1</sup> and Linan and Williams<sup>2</sup> we define:

$$A = \exp\left\{\frac{E'}{u_1}\right\}, \quad u_1 > 1. \quad (3.2)$$

Substituting (3.1) and (3.2) into (2.1) yields

$$u_t = u_{xx} + \exp\left\{\left(\frac{E'}{u_1}\right)\left(\frac{u - u_1}{u}\right)\right\}. \quad (3.3)$$

In the limit as  $(E'/\mu_1) \rightarrow \infty$  we see that the reaction term is exponentially small for  $\mu < \mu_1$  and exponentially large for  $\mu > \mu_1$ . We shall assume initially that  $t$  is sufficiently small to ensure that  $\mu < \mu_1$  throughout the solid, in which case (3.3) reduces to the familiar heat equation. Consequently, for this inert stage (2.1)-(2.3) reduces to

$$u_t = u_{xx}, \quad 0 < x < \infty, \quad 0 < t < T \quad (3.4)$$

$$u(x, 0) = \phi(x), \quad 0 < x < \infty \quad (3.5)$$

$$u_x(0, t) = g(t), \quad 0 < t < T \quad (3.6)$$

We shall consider (3.4)-(3.6) in the particular case when

$$\phi(x) = 1, \quad 0 < x < \infty \quad (3.7)$$

$$g(t) = -1 + h(t), \quad 0 < t < \infty. \quad (3.8)$$

We assume that the required solution  $u$  has the form

$$u(x, t) = v(x, t) + w(x, t) \quad (3.9)$$

where

$$v_t = v_{xx}, \quad 0 < x < \infty, \quad 0 < t < T \quad (3.10)$$

$$\mathbf{P1}: \quad v(x, 0) = 1, \quad 0 < x < \infty \quad (3.11)$$

$$v_x(0, t) = -1, \quad 0 < t < T \quad (3.12)$$

and

$$w_t = w_{xx}, \quad 0 < x < \infty, \quad 0 < t < T \quad (3.13)$$

$$\mathbf{P2}: \quad w(x, 0) = 0, \quad 0 < x < \infty \quad (3.14)$$

$$w_x(0, t) = h(t), \quad 0 < t < T. \quad (3.15)$$

The problem **P1** was the one considered by Bradley<sup>1</sup> and by Linan and Williams<sup>2</sup>. Solutions to problem **P2** provide the adjustments which have to be made to solutions of **P1** as a consequence of a time-dependent energy flux boundary condition.

Arguing as in Section 2 we see that for **P1** the equation (2.5) reduces to

$$v(x, t) = 2 \int_0^t K(x, t - \tau) d\tau + \int_0^\infty N(x, \xi, t) d\xi. \quad (3.16)$$

Using the definitions (2.4) and (2.6) and integrating the result directly shows that (3.16) reduces to

$$v(x, t) = 1 + 2\sqrt{\frac{t}{\pi}} \exp\left\{\frac{-x^2}{4t}\right\} - \operatorname{erfc}\left\{\frac{x}{2\sqrt{t}}\right\} \quad (3.17)$$

which is the result obtained by Bradley<sup>1</sup> and Linan and Williams<sup>2</sup>.

Similarly, for **P2**, arguing as in Section 2 we see that (2.5) reduces to

$$w(x, t) = -2 \int_0^t K(x, t - \tau) h(\tau) d\tau. \quad (3.18)$$

Hence the solution of (3.4)-(3.6) can be expressed in the form

$$u(x, t) = 1 + 2\sqrt{\frac{t}{\pi}} \exp\left\{\frac{-x^2}{4t}\right\} - \operatorname{erfc}\left\{\frac{x}{2\sqrt{t}}\right\} - 2 \int_0^t K(x, t - \tau) h(\tau) d\tau. \quad (3.19)$$

For convenience we rewrite (3.19) in the form

$$u(x, t) = v(x, t) - 2I(x, t) \quad (3.20)$$

where

$$I(x, t) = \int_0^t K(x, t - \tau) h(\tau) d\tau = \int_0^t K(x, s) h(t - s) ds \quad (3.21)$$

having used the substitution  $s = t - \tau$ .

It is clear, from (2.4), that  $I$  is monotonic decreasing with respect to  $x$ . However the situation is not so straightforward regarding the behaviour with respect to  $t$ . Nevertheless, if we notice that

$$\frac{\partial I}{\partial t} = \frac{1}{\sqrt{4\pi t}} \exp\left\{\frac{-x^2}{4t}\right\} h(0) + \int_0^t K(x, s) \frac{\partial h}{\partial t}(t - s) ds \quad (3.22)$$

then  $I$  will be monotonic increasing with respect to  $t$  if  $h$  is chosen so that  $\frac{\partial I}{\partial t} \geq 0$  for all  $t$ .

Alternatively  $I$  will be monotonic decreasing with respect to  $t$  if  $h$  is chosen so that  $\frac{\partial I}{\partial t} \leq 0$  for all  $t$ .

It should be noted that monotonicity is not by any means the only possibility, certain choices of  $h$  could deny this. In any event the presence of the term  $I$  in (3.20) will introduce different times to ignition than that obtained by Bradley<sup>1</sup> and Linan and Williams<sup>2</sup>.

The monotonicity with respect to  $x$  of  $u(x, t)$  given by (3.20) indicates that the break-down of the inert heat-conduction approximation, that is when  $u(x, t) = u_1$ , occurs at the surface  $x = 0$ . There-

fore, to this approximation,  $u_1$  can be regarded as the ignition temperature since (3.3) indicates that thermal runaway occurs when  $u$  reaches  $u_1$ .

Setting  $x = 0$  in (3.19) yields

$$u(0, t_1) =: u_1 = 1 + 2\sqrt{\frac{t_1}{\pi}} - 2 \int_0^t K(0, s)h(t_1 - s)ds \quad (3.23)$$

where  $t_1$  = time to ignition.

Thus, (3.19) gives the temperature field in the material at any time  $t$  and for given  $h$  whilst (3.22) provides an expression for the time to ignition. In addition (3.19) indicates the surface temperature at any time  $t$  for given  $h$ . Numerical results for various forms of  $h$  are given in §5.

## TRANSITION TO IGNITION

To analyse the transition from inert heating to vigorous reaction we re-introduce the reaction term (3.1) and consider the non-linear problem

$$u_t = u_{xx} + A \exp \left\{ -\frac{E'}{u} \right\} \quad (4.1)$$

$$u(x, 0) = \phi(x), \quad 0 < x < \infty \quad (4.2)$$

$$u_x(0, t) = g(t), \quad 0 < t < T. \quad (4.3)$$

We now specify that the ignition time will be  $t_1$  and define a corresponding inert ignition temperature  $u_1$  given by (3.23). Equation (4.1) can then be rewritten in the form

$$u_t = u_{xx} + A \exp \left\{ -\frac{E'}{u_1} \right\} \times \exp \left\{ \frac{E'}{u_1} \left( \frac{u - u_1}{u} \right) \right\}. \quad (4.4)$$

Solving (4.4), (4.2), (4.3) and setting  $t = t_1$ , the condition for thermal runaway, will then yield  $A$ . To this end (2.5) yields

$$u(x, t) = u_I(x, t) + \int_0^t \int_0^\infty N(x, \xi, t - \tau) \times F(\xi, \tau, u(\xi, \tau)) d\xi d\tau \quad (4.5)$$

where

$u_I(x, t)$  = inert solution given by (3.19),  
is a known quantity and

$$F(x, t, u) = A \exp \left\{ -\frac{E'}{u_1} \right\} \exp \left\{ \frac{E'}{u_1} \left( \frac{u - u_1}{u} \right) \right\}.$$

The Volterra equation (4.5) can now be analysed by standard techniques. However numerical experiments (iterations) may be adequate.

## NUMERICAL ANALYSIS

The integral equations developed in the preceding sections were solved using standard integration procedures. Extensive use was made of the quadrature routines available in the Numerical Algorithm Group (NAG) software library.

The inert temperature field, equation (3.23), was integrated using DO1AHF, an adaptive finite interval routine, using the method of Paterson. The reactive temperature field, equation (4.5), cannot be guaranteed to be well behaved, and was therefore solved by consecutive applications of one dimensional routines DO1AMF, for the inner, and DO1AJF for the outer integral. Both routines use an adaptive finite interval strategy. The equations were solved in the dimensionless variables set out by Bradley.

The physical constants used in the solution were those published by Chan<sup>5</sup> for a typical sodium azide based propellant. Boundary heat fluxes were taken to approximate those found experimentally by Chan, Lee and Leiper<sup>6</sup> for a Boron-Potassium Nitrate ignition system acting upon a flat surface at grazing incidence.

The following diagrams and table illustrate the various aspects of the above analysis.

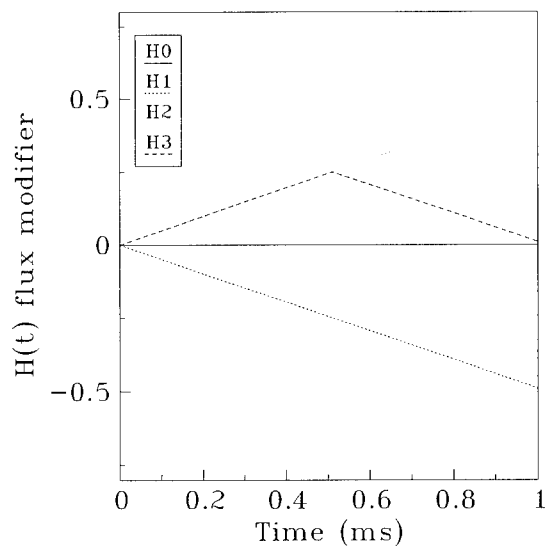


FIGURE 1. VARIOUS FLUX FUNCTIONS USED IN THE ANALYSIS

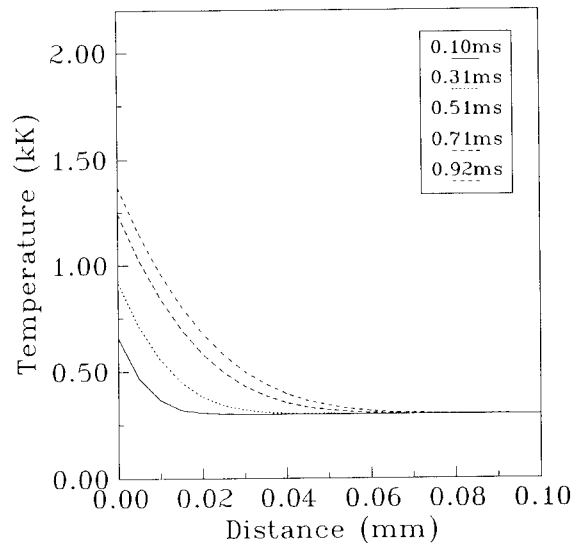


FIGURE 3. VARIATION OF TEMPERATURES WITH TIME AND DISTANCE INTO THE SURFACE FOR THE CASE OF FLUX FUNCTION H0

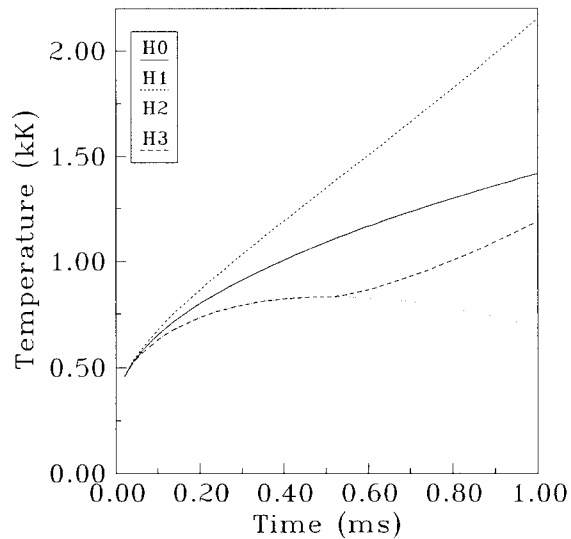


FIGURE 2. SURFACE TEMPERATURE PREDICTED BY EQUATION (3.23) FOR FLUX FUNCTIONS IN FIGURE 1

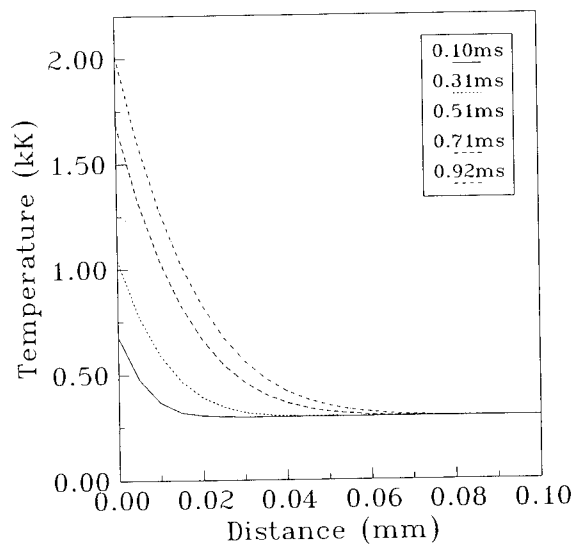


FIGURE 4. VARIATION OF TEMPERATURES WITH TIME AND DISTANCE INTO THE SURFACE FOR THE CASE OF FLUX FUNCTION H1

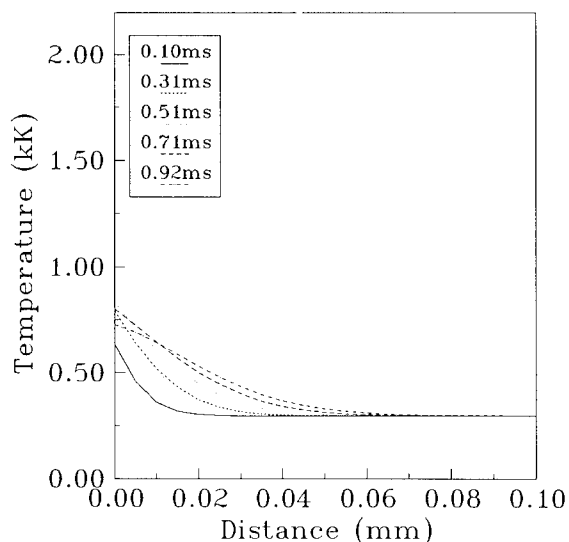


FIGURE 5. VARIATION OF TEMPERATURES WITH TIME AND DISTANCE INTO THE SURFACE FOR THE CASE OF FLUX FUNCTION H2

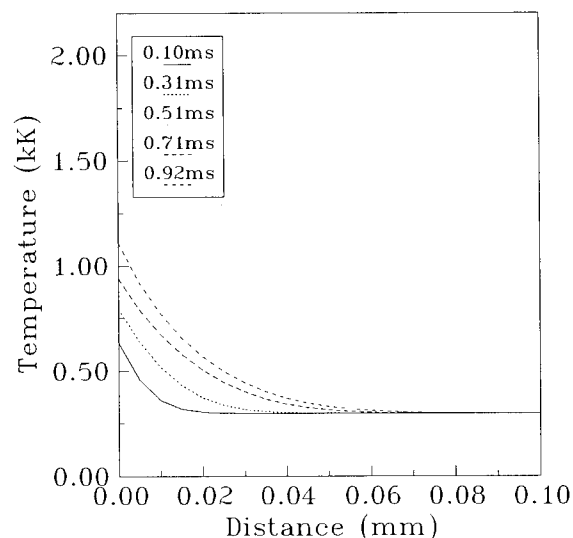


FIGURE 6. VARIATION OF TEMPERATURES WITH TIME AND DISTANCE INTO THE SURFACE FOR THE CASE OF FLUX FUNCTION H3

TABLE 1. IGNITION DELAY TIMES AND SURFACE TEMPERATURES AT IGNITION PREDICTED BY EQUATION (3.23) FOR FLUX FUNCTIONS GIVEN IN FIGURE 1

	Time (ms)	Time (ms)	Temperature (K)
	Eq. 3.17	Eq. 3.23	Eq. 3.23
H0	0.511	0.511	1,098.0
H1		0.221	900.6
H2		1.120	843.0
H3		0.910	1,101.0

#### REFERENCES

1. Bradley, H. H., *Theory of ignition of a reactive solid by constant energy flux*, Combustion Sci. and Tech. 2, 1970, 11-20.
2. Linan, A. and Williams, F.A., *Theory of ignition of a reactive solid by constant energy flux*, Combust. Sci. Tech. 3, 1971, 91-98.
3. Bush, W. B. and Williams, F. A., *Radiant ignition of a surface-cooled reactive solid*, Acta. Astronautica, 2, 1975, 445-462.
4. Bush, W. B. and Williams, F. A., *Influence of strong conductive gas-phase cooling on radiant ignition of a reactive solid*, Combust. Flame 27, 1976, 321-329.
5. Chan, S. K., *Hot plate ignition characteristics of a sodium azide propellant*, 16th International Pyrotechnics Seminar, Jonkoping, Sweden, 1991.
6. Chan, S. K., Lee, J. M. and Leiper, G. A., Private Communication.

## A STUDY OF THE SENSITIVITY AND DECOMPOSITION OF KETO-RDX

H. Bergman, H. Östmark, K. Ekvall and A. Langlet  
National Defence Research Establishment  
S-172 90 Sundbyberg, SWEDEN

*The thermal decomposition and thermal stability of 1,3,5-trinitro-2-oxo-1,3,5-triazacyclo-hexane (keto-RDX or K-6) was studied. The keto-RDX synthesis is described and mass spectra (electron impact, 20 and 70 eV and chemical ionization), which are similar to RDX spectra registered under like conditions, are presented. The LI-MS (laser induced mass spectroscopic) results imply that the first steps in the decomposition of keto-RDX is the elimination of NO<sub>2</sub> and subsequent breakdown of the triazacyclohexane ring. The thermal stability, activation energy ( $E_a = 140$  kJ/mole) and frequency factor ( $K_0 = 9 \cdot 10^9$  s<sup>-1</sup>) were measured using chemiluminescence (NO detection only). Microcalorimetry, drop-weight test, friction test, DSC and ignition temperature measurements were also conducted. Quantum mechanical calculations (semi-empirical MNDO method with PM3 set at the unrestricted Hartree-Fock level) were conducted to correlate the sensitivity and thermal decomposition to those of RDX. No significant differences in bond breaking energies for RDX and keto-RDX were found.*

### INTRODUCTION

RDX is one of the most commonly used high explosives. Thus, a great deal of sensitivity data on RDX has been published, and its thermal decomposition path has been widely examined.<sup>1-4</sup> None of the decomposition studies, however, are conclusive, and no agreement on any single decomposition path has been reached. RDX could well have a thermal decomposition following many different paths. In order to better understand how the sensitivity and the decomposition path is related to the molecular structure we have synthesized a substance, keto-RDX (1,3,5-trinitro-2-oxo-1,3,5-triazacyclohexane), which is very similar to RDX, differing only by the incorporation of a carbonyl group into the six-membered ring. We have then measured the sensitivity and studied the thermal decomposition of keto-RDX and tried to correlate these results with those of RDX. Data from the following tests and studies are presented in this paper: Drop weight test, friction test, chemiluminescence, DSC, temperature of ignition test according to Woods metal bath, microcalorimetry, mass spectra and LI/MS (laser ignition mass spectra). Semi-empirical quantum mechanical (QM) calculations of the N-NO<sub>2</sub> bond scission energies for both RDX and keto-RDX were also carried out and compared with the experimental

results. Keto-RDX also has an interestingly high density ( $\rho = 1.93$  g/cm<sup>3</sup>).<sup>5</sup> The idea to correlate the sensitivity with the structure for closely related molecules is not new, but in earlier studies only one or two tests were normally used for the correlation.<sup>6,7</sup> In a study on the thermal sensitivity and decomposition of NTO a more complete set of tests has been used.<sup>8</sup> This set of tests, expanded with others (drop weight, friction and microcalorimetry), is the base for this study of the thermal sensitivity and decomposition of keto-RDX.

### RDX DECOMPOSITION

One of the purposes of this paper is to compare the decomposition paths of two closely related high explosives, keto-RDX and RDX. To facilitate the interpretation of the keto-RDX decomposition data, a short review of the RDX decomposition is given here.

In a very early study Robertson<sup>9</sup> noted the effect of neighboring molecules on the decomposition of RDX, and showed that one of the decomposition paths is the transfer of an oxygen atom from the NO<sub>2</sub> group to the CH<sub>2</sub> group. Analysis of gases evolved at the decomposition showed the presence of NO, N<sub>2</sub>O, N<sub>2</sub>, CO, CO<sub>2</sub>, CH<sub>2</sub>O and H<sub>2</sub>O. Another mechanism was proposed by Rauch<sup>10</sup> showing that NO<sub>2</sub> mainly derives

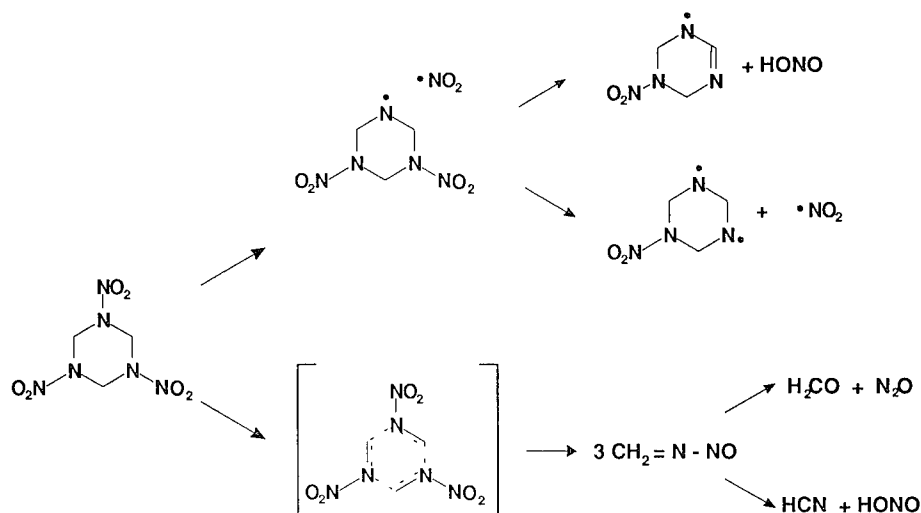


FIGURE 1. DECOMPOSITION PATHS FOR RDX AS PROPOSED BY ZHAO<sup>1</sup>

from a gas phase decomposition and that  $\text{H}_2\text{CO}$  and  $\text{N}_2\text{O}$  arose from a liquid phase decomposition. In addition to the above-mentioned decomposition products,  $\text{HCOOH}$ ,  $\text{NH}_3$  and hydroxymethyl formamide have also been observed.<sup>11,12</sup> This implies that the decomposition mechanism leading to the formation of the pyrolysis products is more complicated than simply a uni-molecular decomposition.

A collision-free IRMPD (IR multiphoton decomposition) experiment by Zhao<sup>1</sup> shows that the collision-free decomposition of RDX follows at least two different reaction channels (shown in Figure 1): via concerted symmetric triple fission and by N-N bond scission.

Mass spectroscopic studies by Bradley<sup>4</sup> and Faber<sup>13</sup> show that RDX exhibits yet another mode of decomposition, namely one in which the ring is stripped from its  $\text{NO}_2$  groups in conjunction with the elimination of one or more hydrogens, forming dihydro-sym-triazin. A closely related mechanism has been proposed by Liebman<sup>14</sup> who proposed the elimination of three  $\text{HONO}$  or  $\text{HNO}_2$  molecules from the ring, forming sym-triazine. The existence of triazine in an RDX decomposition/ignition zone have recently been experimentally verified.<sup>15,16</sup> The existence of decomposition products that cannot be explained by any of the collision-free decomposition paths indicates that different decomposition mechanisms operate in the gas phases compared to those in condensed phases which, of course, implies that a larger set of decomposition paths and reaction products has to be used when trying to conclude the sensitivity from the molecular structure. Oyumi and Brill found<sup>12</sup> that at higher pressures larger

fractions of  $\text{N}_2\text{O}$  and  $\text{CH}_2\text{O}$  are present among the decomposition products. They also emphasize the importance of the state of the material in which the reactions take place, and suggest that the decomposition mechanism is linked to the physical processes operating in the material. The slow thermal decomposition processes of both liquid and solid state RDX exhibit a first order kinetic deuterium isotope effect (KDIE), indicating that the C-H bond rupture is its rate-controlling mechanistic step.<sup>2,3</sup>

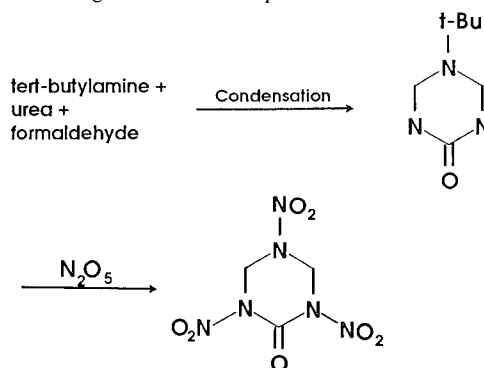


FIGURE 2. THE SYNTHESIS OF 1,3,5-TRINITRO-20-EXO-1,3,5-TRIAZACYCLO-HEXANE (KETO-RDX)

#### SYNTHESIS

Keto-RDX was obtained by a two-step synthesis. The six-membered ring is formed by reacting urea, formaldehyde, and *t*-butyl amine (step 1)<sup>17</sup> giving 2-oxo-5-*tert*-butyltriazone (5-*tert*-butyltriazone, TBT). The intermediate was then nitrated (step 2): 26 ml of nitric acid was cooled to  $-10^\circ\text{C}$ . Keeping the temperature

below  $-5^{\circ}\text{C}$ , 52 ml acetic anhydride was added, drop by drop, after which 3 g of TBT was added in small portions, still keeping the temperature below  $-5^{\circ}\text{C}$ . The reaction mixture was kept at  $-2.5^{\circ}\text{C}$  over night, and a white precipitate was formed. The mixture was allowed to warm up slowly to  $5^{\circ}\text{C}$  after which it was poured over crushed ice, filtered and the solid precipitate was washed with water. This method yielded 2 g dry keto-RDX (a 44 % yield). The keto-RDX used in this study was purified by recrystallizations from ethyl acetate.

## SENSITIVITY TESTS

Both the drop-weight sensitivity and the friction sensitivity of keto-RDX were measured. The impact sensitivity was measured with a 2 kg drop weight BAM apparatus. The results are based on tests on both sides of the 50% probability level using an up-and-down method. The friction sensitivity was measured with a Julius Petri friction apparatus, using the same technique. The calculations were performed with the ML14 computer code. The results from these calculations can be found in Table 1 where data for RDX is also given for comparison.

**TABLE 1. SENSITIVITY DATA FOR RDX AND KETO-RDX, THE 50% LEVEL WITH A 95% CONFIDENCE INTERVAL**

TEST	RDX	keto-RDX
drop weight test	7,4 Nm	$1,5 \pm 0,5$ Nm
friction test	12 kp	$10,8 \pm 2,4$ kp

## CHEMILUMINESCENCE AND DSC

The basic thermal stability of keto-RDX was measured with DSC using a Mettler FP 82. The sample was heated from room temperature with a heating rate of  $5^{\circ}\text{C}/\text{min}$ . The substance shows a strong exotherm with onset at  $188^{\circ}\text{C}$  and a maximum at  $195^{\circ}\text{C}$  ( $225^{\circ}\text{C}$  for RDX). An ocular inspection showed no trace of melting, it seemed more as if a gaseous bubble interacted with the solid and formed a liquid phase. The same phenomenon has been observed when RDX has been tested with the same parameters.

The chemiluminescence (CL) method has earlier been used for decomposition studies at low temperatures.<sup>8</sup> These studies indicated that the CL would be useful for determining the kinetic parameters of keto-RDX at low temperatures, and we used it for studying the low temperature NO development. An apparatus (fully described in (ref 8)) using the chemical

reaction between NO and ozone was constructed. This method was developed for analysis of propellants and is not yet fully tested on high explosives. This means that the measurements should be regarded as preliminary and not as final results. Because of this a comparison with the NO production for TATB, RDX and NTO is also presented. In Figure 3 the production rate of NO is shown as a function of temperature for keto-RDX, RDX, TATB and NTO. A preliminary calculation for keto-RDX in the temperature interval  $90 - 120^{\circ}\text{C}$  gave us an activation energy ( $E_a$ ) of  $140 \text{ kJ/mole}$  and a frequency factor ( $K_0$ ) of  $9 \cdot 10^9 \text{ s}^{-1}$ . Figure 4 shows the production rate of NO at  $135^{\circ}\text{C}$  as a function of time. Here it can clearly be seen that keto-RDX starts to decompose at this temperature.

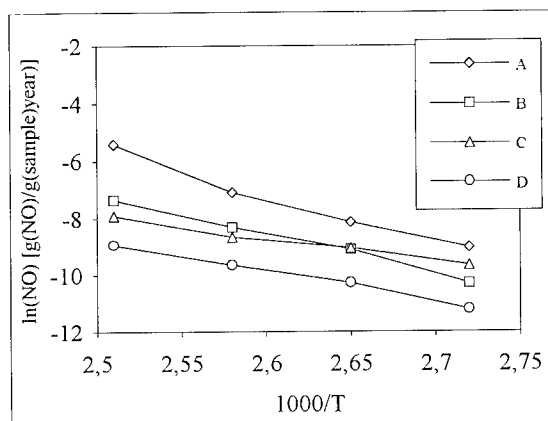


**FIGURE 3. THE PRODUCTION RATE OF NO AS A FUNCTION OF TEMPERATURE FOR (A) KETO-RDX, (B) NTO, (C) TATB AND (D) RDX**

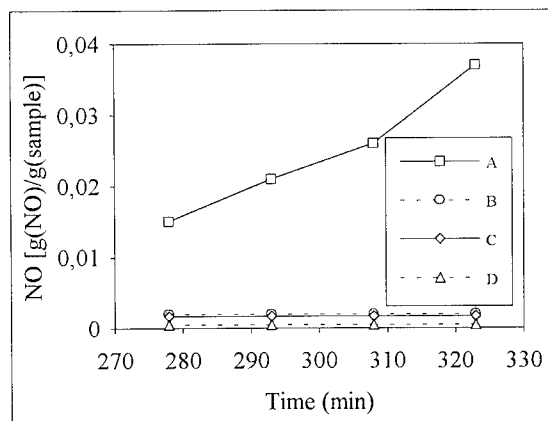


**FIGURE 4. THE PRODUCTION RATE OF NO AS A FUNCTION OF TIME AT  $135^{\circ}\text{C}$  FOR (A) KETO-RDX, (B) NTO, (C) TATB AND (D) RDX**

## IGNITION TEMPERATURE TEST

The sensitivity to thermal ignition was measured according to (ref 18) using Wood's metal bath. The



ignition temperature was found to be 170°C. The ignition temperature for keto-RDX is relatively low; Tetryl tested in the same apparatus under the same conditions gave a lowest temperature of ignition at 207.5°C.

## MICROCALORIMETRY

A LKB Thermal Activity Monitor equipped with the BOMIC 2277 software was used to monitor the stability of keto-RDX at 65°C. A micro calorimeter measures the sum of all chemical and physical reactions that takes place in the sample. The apparatus used is very accurately thermostated and the accuracy of the apparatus is better than 1  $\mu$ W. In figure 5 the activity at 65°C over a period of 30 days is shown for keto-RDX and RDX. It can be seen here that the activity is significantly higher for keto-RDX than for RDX.

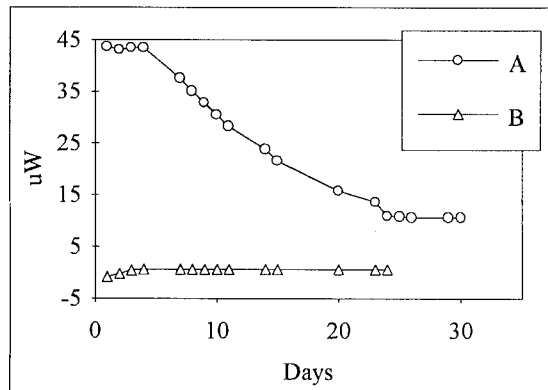


FIGURE 5. MICROCALORIMETRY REGISTRATION OF (A) KETO-RDX AND (B) RDX

## MASS SPECTROSCOPY

It has been shown earlier that the thermal fragmentation path of RDX shows similarities to its mass spectral fragmentation.<sup>19</sup> As keto-RDX is very similar to RDX, a mass spectroscopic study is a natural starting point for acquiring new information about the decomposition mechanism. A review of mass spectroscopy on explosives can be found in reference<sup>20</sup> which also gives the assignment of the different RDX peaks used in the analysis of the keto-RDX spectra.

The mass spectroscopic study was conducted on a JEOL 300D double focusing magnetic sector instrument equipped with a PC-based computer system with Technivent Vector/2 software for data analysis. All mass spectra were acquired using the solid sample inlet with a heating rate of about 50°/min. Both electron impact, (EI), 20 and 70 eV and chemical ionization, (CI), spectra were acquired. The CI spectra were obtained

using methane as the reagent gas. The mass spectra of RDX were registered for comparison and, if possible, to correlate the fragmentation paths of RDX and keto-RDX. In Figure 6 the mass spectra of keto-RDX and RDX are shown. Mass spectra for TBT, the keto-RDX intermediate  $C_7H_{15}N_3O$ , were also acquired.

In comparing the mass spectra for RDX and keto-RDX registered with 20 eV one can see that the fragmentation is seen to be very similar for the two substances. However, two differences can be noted: The mass fragment at  $m/z$  175 ( $C_3H_5N_5O_4$ ) for RDX is found at  $m/z$  189 ( $C_3H_3N_5O_5$ ) for keto-RDX and the mass fragment  $m/z$  102 ( $C_2H_4N_3O_2$ ) for RDX is found at  $m/z$  116 ( $C_2H_2N_3O_3$ ) for keto-RDX.

In the mass spectra obtained at 70 eV the differences are not as conclusive. However, in the mass spectra for keto-RDX the  $m/z$  56 is much more intense than it is for RDX. In the RDX spectra the  $m/z$  42 is very strong whereas in the keto-RDX spectra the signal is much lower. Another slight difference is that in the keto-RDX spectra the  $m/z$  44 is stronger compared to that in RDX while the  $m/z$  30 is weaker. The observations of the  $m/z$  175 and 189 in the 20 eV spectra also apply here.

As can be seen in Figure 6 both keto-RDX and RDX exhibit a molecular peak in the electron impact spectra, even at 70 eV. This observation combined with the ones mentioned above indicates that keto-RDX and RDX have similar decomposition paths and that the molecular sensitivity approximately is equal.

In the CI spectra for keto-RDX the  $m/z$  237 (molecule mass), 161, 149, 130, 120, 75, 56 and 46 were detected.

## LI/MS

In order to get a better understanding of the pure thermal decomposition of keto-RDX the Laser Induced Mass Spectrometry (LI/MS) method<sup>15, 16</sup> was used. This method cannot distinguish between reactions taking place in different interaction phases since the capillary is placed in the ignition zone and collects products from all participating phases. However, this method can give information on which reactions are taking place in the decomposition/reaction zone. The experimental set-up consists of an explosive chamber, a 180W continuous wave carbon dioxide laser (Edinburgh PL6) used to heat the sample, thus starting a decomposition/ignition of the high explosive, and a mass spectrometer (JEOL 300D double focusing magnetic sector instrument or Finnigan OWA 1020 quadrupole instrument). As an interface between the reaction chamber and the mass spectrometer a nearly chemically

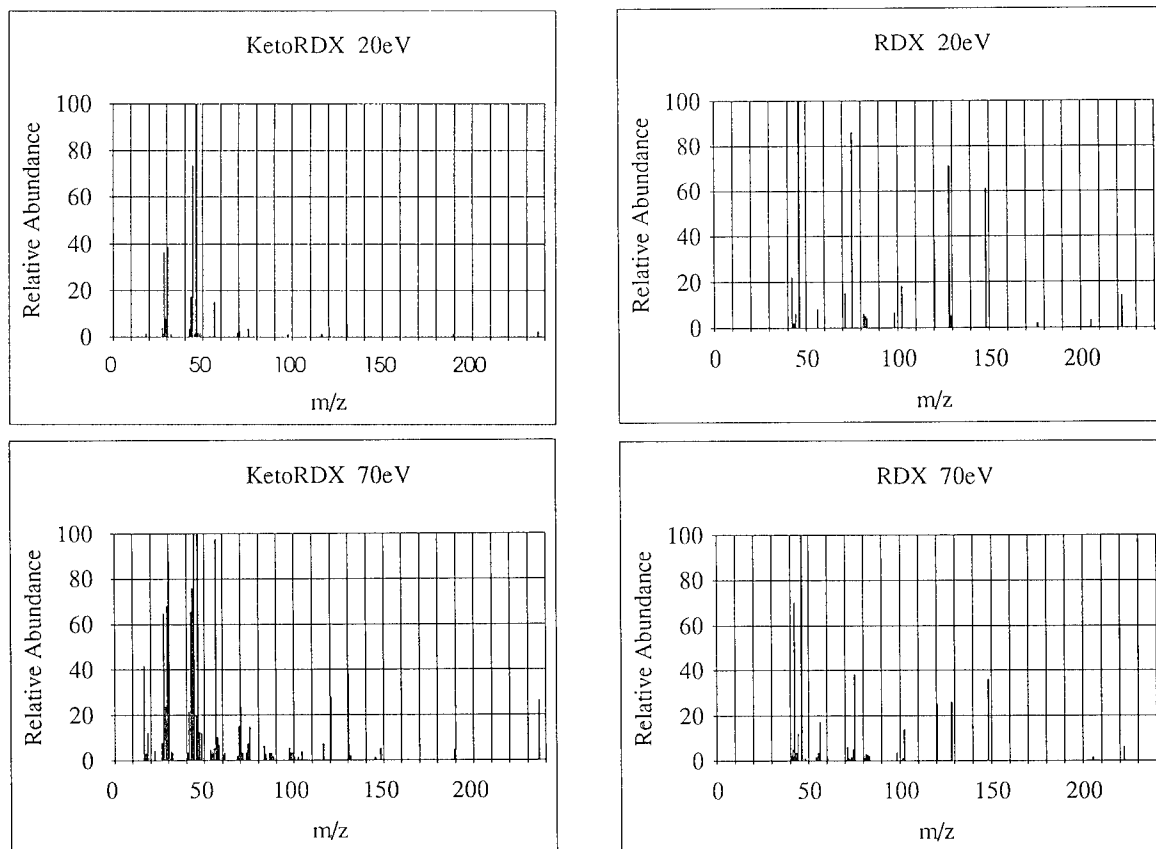


FIGURE 6. MASS SPECTRA FOR KETO-RDX AND RDX 20 AND 70 eV RESPECTIVELY

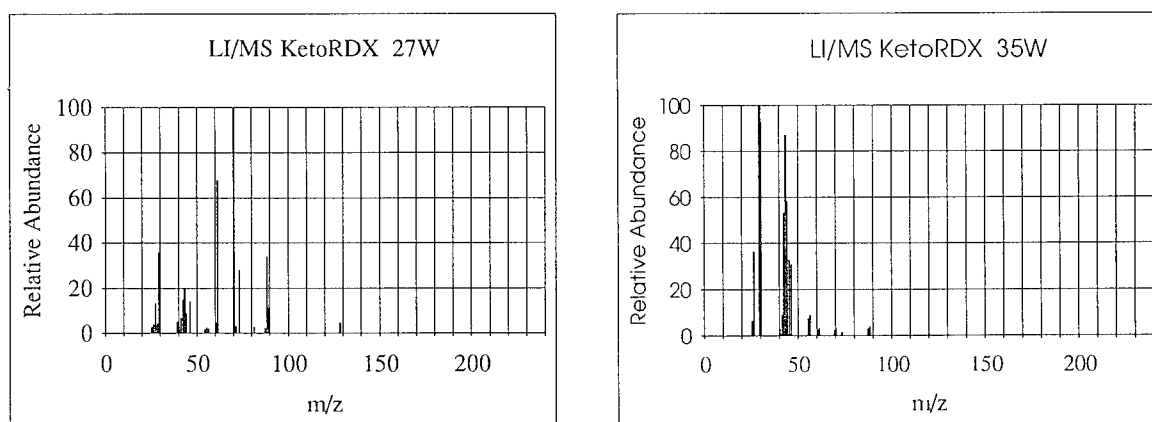


FIGURE 7. LI/MS SPECTRA OF THE KETO-RDX DECOMPOSITION

inert fused silica capillary was used. The use of a capillary also enabled the use of increased pressure in the explosive chamber, up to 2.5 MPa. A complete description of the laser ignition technique, and how to combine it with different spectroscopical techniques, can be found in reference.<sup>15, 16, 21-23</sup>

The LI/MS spectra were acquired in a helium atmosphere (0.4 MPa). The decomposition was started by a laser pulse with a pulse width of 4 ms and a power in the interval 25 - 40 W. Figure 7 shows an example of a registration.

An interesting observation is that keto-RDX gives more fragments with higher mass than RDX.<sup>15, 16</sup> In the sub-ignition zone of RDX we could not detect any significant mass peaks larger than  $m/z$  70 (some heavier peaks were detected but only in very small amounts). This implies that keto-RDX has a thermal decomposition path which differs fundamentally from that of RDX. A probable thermal decomposition path for keto-RDX is an elimination of a  $\text{NO}_2$  group followed by a break down of the ring.

## QUANTUM MECHANICAL CALCULATIONS

For the semi-empirical calculations the MOPAC 6.0 computer program<sup>24</sup> was used with the MNDO (modified neglect of diatomic overlap) formalism<sup>25</sup> using the PM3 parameter set<sup>26</sup> at the unrestricted Hartree-Fock (UHF) level of theory. The MNDO/PM3 combination was shown by Akutsu et al. to give the best results for both nitro alifates and nitro aromates<sup>27,28</sup> so it should be equally good for nitramines. RDX can have  $\text{C}_{3v}$ ,  $\text{C}_s$  and  $\text{C}_1$  molecular symmetry and keto-RDX can have  $\text{C}_s$  or  $\text{C}_1$  symmetry. In the calculations presented here we have used the conformation with the highest symmetry ( $\text{C}_{3v}$  for RDX and  $\text{C}_s$  for keto-RDX). In a more extensive QM study all molecular conformations have to, of course, be considered. As said before, RDX and possibly keto-RDX, have multiple decomposition paths, of which only three, and then only the first step, will be considered in this QM study, namely: N-N bond fission, concerted symmetric triple fission and HONO elimination.

The potential energy surface for the uni-molecular bond scission of RDX and keto-RDX (N-N bond) was generated by fixing the N-N bond and then fully optimizing the geometry in a number of steps around the equilibrium value. The bond scission energy,  $\Delta E^*$ , was found to be 22 kcal/mole for RDX. The same calculations were performed for the two types of (non-equivalent) N-N bonds in keto-RDX with the following bond scission energies:  $\Delta H_{\text{bond1}} = 26.4$  kcal/mole and  $\Delta$

TABLE 2. KETO-RDX DECOMPOSITION PEAKS AND POSSIBLE ASSIGNMENTS

Mass number	Assignment	Strength	Comments
18	$\text{H}_2\text{O}$	2	
26	CN	2	
27	HCN	2-3	Increases with laser power
28	$\text{N}_2$ , CO	1	
29/30	$\text{H}_2\text{CO}$	1	
30	(NO)	1	
41		3	
42	$\text{N}(\text{CH}_2)\text{N}$ , $(\text{CH}_2)\text{N}$ , $\text{C}(\text{O})\text{N}$	1	Ring fragments
43	$\text{NCOH}$ , $\text{OCNH}$	1	
44	$\text{N}_2\text{O}$ , $\text{CO}_2$	1	
45		2	
46	$\text{NO}_2$	2	
55	$(\text{CO})\text{N}(\text{CH})$	4	Ring fragments
56	$(\text{CO})\text{N}(\text{CH}_2)$ , $\text{N}(\text{CO})\text{N}$	3	Ring fragments
57		3	
60	$\text{NNO}_2$	3	
61/60/46/45	$\text{CH}_3\text{NO}_2$	2	
61	$\text{HNNO}_2?$	2	
69		3	
70	Oxadiazole	2-3	
87	$\text{CHNNO}_2\text{CH}_2$	4	
88	$(\text{NO}_2)\text{NCO}$ , $\text{CH}_2\text{NNO}_2\text{CH}_2$	2	
89		2	Highest mass having an intense peak
120		4	Only visible at low laser power
128	$\text{CHN}(\text{CO})\text{-N}(\text{NO}_2)\text{CH}$	4	Decreases with increasing laser power.

$H_{\text{bond2}} = 21.5$  kcal/mole, respectively. The concerted symmetric triple fission energies were 68.2 kcal/mole for RDX and 67.1 kcal/mole for keto-RDX. The QM calculations is summarized in Figure 8. Clearly the result of this study is that no significant difference in the bond breaking energies for RDX and keto-RDX exists (at this level of theory).

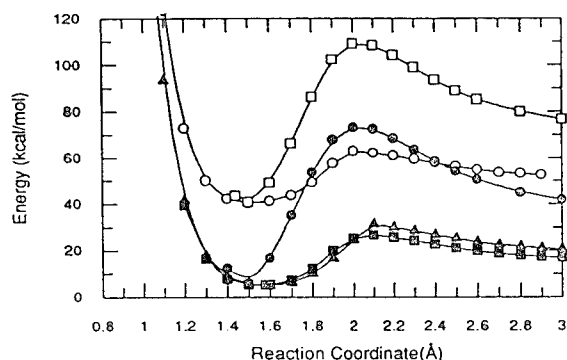


**FIGURE 8. POTENTIAL ENERGY SURFACE FOR THE UNIMOLECULAR BOND SCISSION (N–NO<sub>2</sub>) AND FOR THE CONCERTED SYMMETRIC TRIPLE FISSION FOR RDX (□ = TRIPLE FISSION, ○ = NO<sub>2</sub> ELIMINATION) AND KETO-RDX (● = TRIPLE FISSION, ▲ = 1-NO<sub>2</sub> ELIMINATION, ■ = 5-NO<sub>2</sub> ELIMINATION)**

Using semi-empirical methods for calculating absolute heat of reaction or heat of formation in a reaction involving either bond breaking or bond formation normally gives questionable results. However, when one is only interested in comparing different reaction channels, or when studying closely related molecules, reasonable results may be obtained.<sup>29</sup> We will try to verify these results through *ab initio* quantum mechanical calculations. In these studies the geometry of the transition states will also be calculated.

## DISCUSSION AND CONCLUSIONS

Keto-RDX and RDX have very similar mass decomposition paths and keto-RDX can therefore be used as a model substance when trying to correlate structure with sensitivity. Both keto-RDX and RDX exhibit molecular peaks of approximately the same magnitude in the EI spectra at 70 eV, which indicates that the molecular sensitivity is approximately the same for the two substances.

Keto-RDX is found to be more sensitive to impact than RDX but the sensitivity to friction is equal.

We can clearly see from the CL and DSC measurements that keto-RDX is much more thermally unstable than RDX. The reaction at 135°C in the CL measurements may be caused by auto catalysis.

The existence of several ignition reaction products with high *m/z* indicates that concerted symmetric triple fission is less important for keto-RDX than for RDX. A probable decomposition path is the elimination of NO<sub>2</sub> followed by a breakdown of the ring.

QM calculations show that no significant difference in the bond breaking energies for RDX and keto-RDX exists (at the MNDO/PM3 level of theory). This is contradictory to the large difference in thermal sensitivity. The interpretation may be that the sensitivity of keto-RDX is not determined by the initial decomposition but by reactions occurring later, which are possibly auto catalytic.

## REFERENCES

1. Zhao, X., E.J. Hints, and Y.T. Lee, *Infrared multiphoton dissociation of RDX in a molecular beam*. J. Chem. Phys., 1988. **88**: p. 801-810.
2. Rogers, S.L., et al., *Comparative Mechanistic Thermochemical Decomposition Analyses of Liquid Hexahydro-1,3,5-Trinitro-1,3,5-Triazine (RDX) Using the kinetic Deuterium Isotope Effect Approach*. Thermochimica Acta, 1991. **177**: p. 151-168.
3. Bulusu, S., et al., *Deuterium Kinetic Isotope Effect in the Thermal Decomposition of 1,3,5-Trinitro-1,3,5-triazacyclohexane and 1,3,5,7-Tetranitro-1,3,5,7-tetraazacyclooctane: Its Use as an experimental Probe for Their Shock-Induced Chemistry*. J. Phys. Chem., 1986. **90**: p. 4121-4126.
4. Bradley, J.N., et al., *Mass Spectrometric Study of the Thermal Decomposition of 1,3,5-Trinitronexahydro-1,3,5-triazine (RDX)*. J. Chem. Soc. Trans Faraday., 1977. **73**: p. 1789-1795.
5. Gilardi, R., J.L. Flippen-Anderson, and C. George, *Structures of 1,3,5-Trinitro-2-oxo-1,3,5-triazacyclohexane (I) and 1,4-Dinitro-2,5-dioxo-1,4-diazacyclohexane (II)*. Acta Cryst., 1990. **C46**: p. 706-708.
6. Brill, T.B., *Structure-Thermolysis Relationships for Energetic Materials*, in *Chemistry and Physics of Energetic Materials*, S.N. Bulusu, Editor. 1990, Kluwer Academic Publishers: Dordrecht.

7. Storm, C.B., J.R. Steine, and J.F. Kramer, *Sensitivity Relationship in Energetic Materials*, in *Chemistry and Physics of Energetic Materials*, S.N. Bulusu, Editor. 1990, Kluwer Academic Publishers: Dordrecht.
8. Östmark, H., H. Bergman, and G. Åqvist, *The Chemistry of 3-nitro-1,2,4-triazole-5-one (NTO): Thermal Decomposition*. *Thermochimica Acta*, 1993. **213**: p. 165-175.
9. Robertson, A.J.B., *Thermal Decomposition of Explosives*. *Trans. Faraday Soc.*, 1949. **45**: p. 85-93.
10. Rauch, F.C. and A.J. Fanelli, *The Thermal Decomposition of Hexahydro-1,3,5-trinitro-s-triazine above the Melting Point: Evidence for Both a Gas and Liquid Phase Decomposition*. *J. Phys. Chem.*, 1969. **73**: p. 1604-1608.
11. Cosgrove, J.D. and A.J. Owen, *The Thermal Decomposition Kinetics of 1,3,5-Trinitro-hexahydro-1,3,5-triazine (RDX) -- Part I: The Products and Physical Parameters*. *Combustion and Flame*, 1974. **22**: p. 13-18.
12. Oyumi, Y. and T.B. Brill, *Thermal Decomposition of Energetic Materials 3. A High-Rate, In Situ, FTIR Study of the Thermolysis of RDX and HMX with Pressure and Heating Rate as Variables*. *Combustion and Flame*, 1985. **62**: p. 213-224.
13. Faber, M. and R.D. Srivastava, *Mass spectrometric investigation of the thermal decomposition of RDX*. *Chem. Phys. Lett.*, 1979. **64**(2): p. 307-310.
14. Liebman, S.A., et al., *Time-Resolved Analytical Pyrolysis Studies of Nitramine Decomposition with a Triple Quadrupole Mass Spectrometer System*. *J. Anal. Appl. Pyrolysis*, 1987. **12**: p. 83-95.
15. Östmark, H., H. Bergman, and K. Ekvall, *Laser Pyrolysis of Explosives Combined with Mass Spectral Studies of the Ignition Zone*. *J. Anal. Appl. Pyrolysis*, 1992. **24**: p. 163-178.
16. Östmark, H. *Laser Ignition of Explosives: A Mass Spectroscopic Study of the Pre-Ignition Reaction Zone*. in *Ninth Symposium (International) on Detonation*. 1989. Portland, Oregon:
17. Lear, R.D. and R. McGuire, *High Explosives*. *Energy and Technology Review*, 1988. (January-February): p. 22.
18. *Swedish Defence Standard FSD 0214 underbilaga 101.2*, Temperature of Ignition, Wood's metal bath, 14 Feb. 1992.
19. Stals, J., *Trans. Faraday Soc.*, 1971. **6**: p. 67.
20. Yinon, J., *Mass spectrometry of explosives: Nitro compounds, nitrate esters and nitramines*. *Mass Spec. Rev.*, 1982. **1**: p. 257-307.
21. Östmark, H. and N. Roman, *Laser Ignition of Pyrotechnic Mixtures: Ignition Mechanisms*. *J. Appl. Phys.*, 1993. **73**(4): p. 1993-2003.
22. Östmark, H. and R. Gräns, *Laser Ignition of Explosives: Effects of Gas Pressure on the Threshold Ignition Energy*. *J. Energetic Materials*, 1990. **8**(4): p. 308-322.
23. Nilsson, H. and H. Östmark, *Laser Ignition of Explosives: Raman Spectroscopy of the Ignition Zone*. in *Ninth Symposium (International) on Detonation*. 1989. Portland, Oregon: Office of Naval Research, OCNR 113291-7.
24. Stewart, J.J.P., *MOPAC: A Semiempirical Molecular Orbital Program*. *J. Computer-Aided Molecular Design*, 1990. **4**(1): p. 1-105.
25. Dewar, M.J.S. and W. Thiel, *Ground States of Molecules. 38. The MNDO Method. Approximations and Parameters*. *J. Am. Chem. Soc.*, 1977. **99**(15): p. 4899-4907.
26. Stewart, J.J.P., *Optimization of Parameters for Semiempirical Methods I. Method*. *J. Comp. Chem.*, 1989. **10**(2): p. 209-220.
27. Akutsu, Y., et al., *Calculation of Heats of Formation for Nitroaromatics with PM3 and MM2*. *J. Energetic Materials*, 1992. **10**: p. 173-182.
28. Akutsu, Y. and S. Tahara, *Calculation of Heats of formation for Nitro Compounds by Semi-empirical Methods and Molecular Mechanics*. *J. Energetic Materials*, 1991. **9**: p. 161-172.
29. Shi, Y. and S.M. Senkan, *MNDO-PM3 Calculations of Activation Energies for the Addition of Chlorinated C1 and C2 Radicals to Chlorinated Ethylenes and Acetylenes*. *J. Phys. Chem.*, 1991. **95**(13): p. 5181-51856.

## CHEMICAL SENSITISATION IN C-NITRO EXPLOSIVES

M. D. Cook and P. J. Haskins  
Defense Research Agency  
Fort Halstead, Sevenoaks, Kent TN14 7BP, UK

Ab-initio molecular orbital calculations are reported for a number of decomposition reactions of nitro compounds. These calculations highlight the importance of C-N bond scission as the primary step. It is postulated that the amine sensitisation of nitro compounds is the result of a bimolecular reaction which lowers the activation energy for this process. Of a range of compounds investigated as possible sensitisers, only those containing an amine functional group showed this effect. The products of this initial step are predicted to undergo further reaction by a diazo mechanism.

### INTRODUCTION

There is much interest at present in understanding detonation chemistry. Firstly, to help with the development of new initiation and growth models for use with hydrocodes and secondly, to help with the search for new explosive molecules. We have published a number of papers over the last few years reporting results of ab-initio molecular orbital calculations on a variety of small model energetic molecules including nitromethane, methyl nitramine, methylnitrate and hydrazoic acid. The majority of the work to date has been concentrated on nitro compounds since they exhibit a marked sensitisation effect when mixed with amines. This is a chemical rather than a physical effect, and thus provides a useful probe to help investigate the detonation chemistry.

We have previously reported<sup>1</sup> the results of ab-initio molecular orbital calculations on the sensitisation of nitromethane by amines. The technique used was to compare the activation energy calculated for breaking both the C-H and C-N bonds in nitromethane both with and without an amine, in this case ammonia, present. An ammonia molecule was used as a "model" amine to simplify the calculations. The results of these calculations showed that the presence of the ammonia molecule lowered the activation energy for C-N bond scission by ca. 27 percent. It was concluded from these calculations that this new low energy pathway is

primarily the result of a bimolecular process in which a new bond is created, to form a protonated methylamine molecule as the nitromethane C-N bond is broken. However, only a restricted geometry whereby the ammonia nitrogen was aligned along the nitromethane C-N bond was reported.

In this paper we report the results of calculations on a further ring-like geometry for the reaction of nitromethane with ammonia, and explain the subsequent chemistry. Further to these calculations, we have also extended the study to a series of nitro-alkanes which include: nitroethane, 2-nitro-propane and 2-methyl-2-nitropropane. We also report a number of calculations to examine the effect of other classes of compounds on the sensitivity of nitromethane.

We have shown experimentally<sup>1</sup> that both trinitrobenzene and trinitrotoluene are sensitised by amines and, to the same extent. This implies that the sensitisation effect is independent of the methyl group. In this paper we report a detailed theoretical study of this system.

### POTENTIAL ENERGY SURFACE CALCULATIONS

All the calculations reported here have employed the Gaussian<sup>2</sup> series of ab-initio molecular orbital

codes, running on both a Cray YMP and Silicon Graphics workstations. The majority of calculations were carried out with a modest sized (6-31g split valence) basis set in order to save computational time. Some calculations included polarisation functions on the first row atoms, and a few have been carried out using a much larger 6-311g\*\* basis set. Additional calculations have also been performed at post SCF levels, primarily using Moller-Plesset MBPT to either second (MP2) or fourth (MP4) order. The MP4 calculations include single, double, triple and quadruple excitations.

### AMINE / NITROMETHANE CALCULATIONS

We have previously reported detailed calculations on bond scission in nitromethane. State-of-the-art calculations on the unimolecular  $\text{CH}_3\text{--NO}_2$  scission in nitromethane using a 6-311g\*\* basis set at the MP4 level of accuracy gave a bond dissociation energy for this process of 65.6 kcal/mol. This compares favourably with the experimental value of 60.3 kcal/mol. Similar calculations on C-H and N-O bond scission in nitromethane gave bond dissociation energies of 106.5 kcal/mol and 147.5 kcal/mol respectively. Potential energy surfaces of each of these bond scission processes are shown in figure 1.

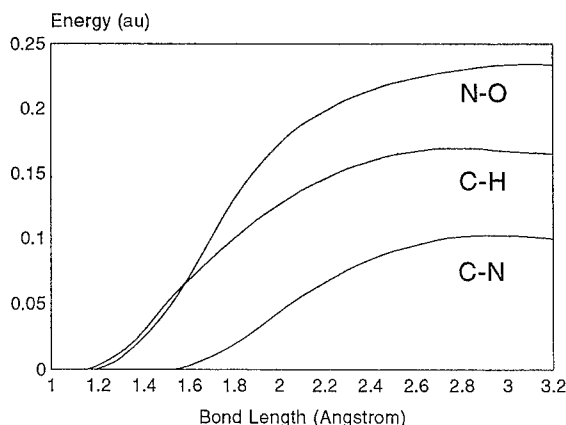


FIGURE 1. NITROMETHANE BOND SCISSION SURFACES

Experiments show that addition of small quantities of amines to nitromethane drastically reduces both its shock sensitivity and critical diameter.<sup>3</sup> The effect is chemical in origin. To investigate this sensitisation mechanism we have carried out calculations on both the isolated molecule and a nitromethane-amine super-molecule system. An ammonia molecule was chosen as the amine to reduce computer time. In our first calculations, the ammonia molecule was placed,

and constrained to remain, with its nitrogen atom looking along the axis of the nitromethane molecule as shown in figure 2. The supermolecule structure was then optimised to find the ground state configuration. From this starting point a potential energy surface was then calculated using the C-N nitromethane bond as the reaction co-ordinate. These calculations gave an activation energy of 50 kcal/mol for C-N bond scission and protonated methylamine and  $\text{NO}_2$  as products. In later calculations a less restrictive geometry starting from the optimised ring structure shown in figure 3 was used. The advantage of this structure was that a total optimisation of the geometry of the system could be achieved, only the reaction co-ordinate being imposed. In these calculations the reaction co-ordinate was the ammonia nitrogen - nitromethane carbon distance. The bi-molecular reaction which ensues as this reaction co-ordinate is reduced yields methylamine and nitrous acid as the products. The potential surface for the system is shown in figure 4. The activation energy for the overall reaction was found to be 54 kcal/mol and the reaction was exothermic by 9 kcal/mol. It therefore appears highly likely that the amine sensitisation of nitromethane proceeds by a bi-molecular reaction which yields nitrous acid and a new amine in a concerted process or alternatively, a protonated amine and  $\text{NO}_2$  which may subsequently react to form the same products. The products are interesting since



FIGURE 2. NITROMETHANE - AMMONIA LINEAR ARRANGEMENT

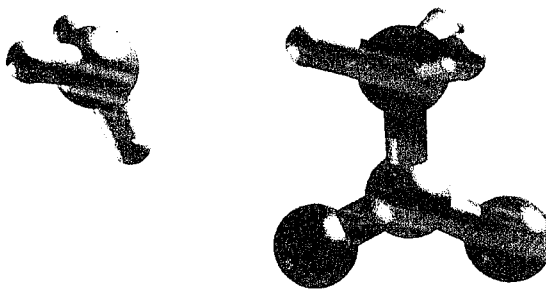


FIGURE 3. NITROMETHANE - AMMONIA RING ARRANGEMENT

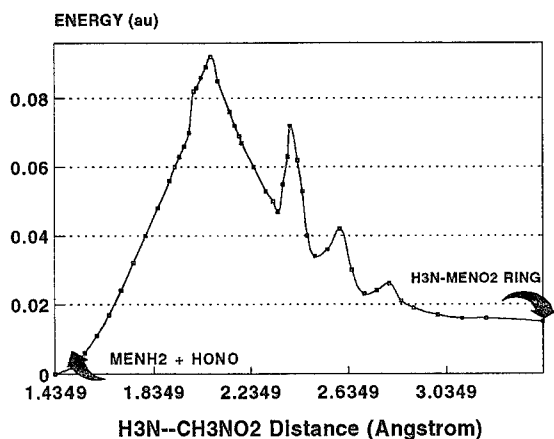


FIGURE 4. NITROMETHANE - AMMONIA BIMOLECULAR REACTION POTENTIAL SURFACE

it will be recognised that these are the reactants of the well-known diazo reaction. It is well-known that the diazo reaction occurs readily even under ambient conditions, and subsequent decomposition of diazo compounds is exothermic and yields gaseous nitrogen. This mechanism can explain why a small quantity of amine might give a large effect, since an amine one order higher than the initial amine is returned as one of the products, making the process autocatalytic. The mechanism predicts that all orders of amine will sensitise nitromethane, but not necessarily to the same degree since the autocatalytic process must terminate when a quaternary ammonium salt is returned (as product from the reaction with a tertiary amine). Whilst the above discussion applies to amine sensitised nitro compounds, it is highly likely that nitrous acid will also be formed at an early stage in the decomposition of pure nitro compounds, and may well play an important role in subsequent reactions.

#### OTHER POSSIBLE EXPLANATIONS OF THE SENSITISATION MECHANISM

We have previously<sup>1</sup> discussed the alternative explanation for the sensitisation of nitromethane suggested by Engelke et al. A further explanation for the sensitisation effect has also been put forward by Constantinou.<sup>4</sup> This explanation is in terms of a charge transfer complex formed between a nitromethane and an amine molecule. It is argued that the energy between the HOMO of an amine molecule and the LUMO of a nitromethane molecule is lower than the gap between the nitromethane HOMO and LUMO. The calculated energy gap between the HOMO of the amine and LUMO of the nitromethane is 2.46eV for ammonia, 2.18eV for methylamine, 2.01eV for

dimethylamine and 1.83eV for trimethylamine. On the basis of these figures, Constantinou argues that primary amines would be expected to sensitise nitromethane more than secondary; more than tertiary (as found by experiment). The energy gap for the amine HOMO / nitromethane LUMO is about 2-3eV, this is a large energy gap and suggests a charge transfer absorption, rather than a charge transfer complex. It is highly likely that this charge transfer absorption is responsible for the slight yellow tint when amines are added to nitromethane. However, even if complexes were formed their stabilities would lie in the reverse order to that suggested.

#### NITROALKANE / AMINE CALCULATIONS

Potential energy surfaces for C-N bond scission have also been generated for a series of nitroalkanes including nitromethane, nitroethane, 2-nitro-propane and 2-nitro-2-methyl propane. The calculations were carried out in the same manner as described for nitromethane above. Initially, a ground state geometry optimisation was carried out for each molecule. The C-N bond was then stretched and the rest of the geometry optimised at each point. Problems were encountered with obtaining a well-behaved surface with the latter two compounds for homolytic C-N bond scission even when using post SCF corrections. However, a good estimation of the homolytic bond scission energy was obtained from SCF optimisations of the initial molecule and the radical products. It may be noted that the values quoted for nitromethane are different from those given earlier, this results from the smaller basis set used here.

As with nitromethane, the calculations carried out to examine the effect of amines on these compounds used an ammonia / nitroalkane supermolecule approach. The ammonia molecule was placed at the alkyl end of each molecule with the ammonia nitrogen constrained to be aligned along the nitroalkane C-N bond. The whole supermolecule structure was first optimised. Using this geometry as a starting point, the

TABLE 1. ACTIVATION ENERGIES FOR R-NO<sub>2</sub> BOND SCISSION

Compound	Ea (R-NO <sub>2</sub> )	Ea (H <sub>3</sub> N--R-NO <sub>2</sub> )
MeNO <sub>2</sub>	53	47
EtNO <sub>2</sub>	52	43
Pr <sup>1</sup> NO <sub>2</sub>	50	38
Bu <sup>1</sup> NO <sub>2</sub>	44	33

Using 6-31 g basis set, energies in kcal/mol



C-N distance was incrementally increased and the rest of the geometry optimised at each point. The calculated activation energies are shown in table 1 below.

It is clear from the results in table 1 above that all the nitroalkanes investigated are sensitised by ammonia.

#### THE SENSITISATION EFFECTS OF OTHER COMPOUNDS ON NITROMETHANE

Calculations have also been carried out to investigate the effect of a number of potential sensitisers on nitromethane. The compounds examined in this study were: water, methanol, methanal, acetonitrile, 2-propanone, and dimethyl ether. The calculations were performed in the same manner as those for ammonia, the potential sensitiser being placed at the methyl end and aligned along the C-N bond of the nitromethane molecule. Once again a potential energy surface was created by first optimising the supermolecule and then incrementally increasing the C-N bond and optimising the rest of the geometry at each point. The potential surface for each system was then compared to that for C-N bond scission in an isolated nitromethane molecule. The potential surfaces for all these compounds are plotted in figure 5. The results of this study clearly indicated that only ammonia would be expected to exhibit any significant lowering of the activation energy for C-N bond scission.

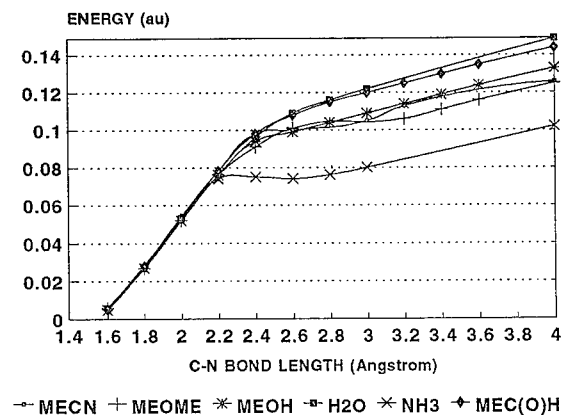


FIGURE 5. EFFECT OF SMALL MOLECULES ON NITROMETHANE C-N BOND SCISSION

#### TRINITROBENZENE / AMINE CALCULATIONS

It has been demonstrated experimentally,<sup>1</sup> in drop weight experiments, that both trinitrotoluene and trinitrobenzene exhibit a marked sensitisation effect when amines are added to them. Moreover, the measured sensitisation effect is of the same magnitude for

both compounds. This suggests that there is a common sensitisation mechanism operating in both compounds, and indicates that this might involve the aromatic ring. As pointed out in reference 1 these results do not support the importance of the aci-quinone structure (which could only be formed from TNT).

Calculations have been carried out to investigate the mechanism of sensitisation of trinitrotoluene (TNT) and trinitrobenzene (TNB) by amines. Most of the calculations have been carried out on TNB. Initially, calculations were performed in which an ammonia molecule was placed such that the ammonia nitrogen was in the plane of the aromatic ring. On optimisation of this initial structure the ammonia molecule displayed a pronounced preference to be above the aromatic ring. Further calculations showed that the ammonia molecule had two minimum ground state locations. These were with the nitrogen atom of the ammonia above an NO<sub>2</sub> group or in-between a hydrogen atom and a nitro group, but still above the plane of the ring. These two optimised ground state structures, shown in figures 6 and 7, were then used as the basis for further calculations.

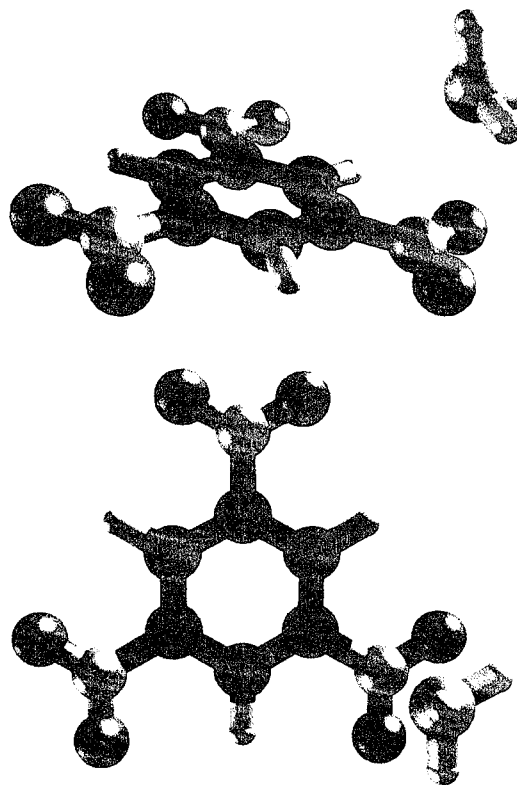


FIGURE 6. TNB - AMMONIA MINIMUM ENERGY CONFORMATION IN WHICH THE AMMONIA SITS ABOVE THE NO<sub>2</sub> GROUP

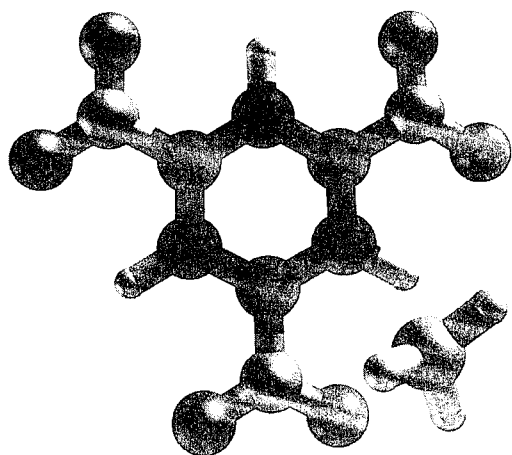


FIGURE 7. TNB - AMMONIA MINIMUM ENERGY CONFORMATION IN WHICH THE AMMONIA SITS ABOVE AND IN-BETWEEN C-H AND NO<sub>2</sub> GROUPS

Starting with the second arrangement in which the ammonia molecule sits between a hydrogen atom and a nitro group, a potential energy surface was generated by incrementally decreasing the distance between the ammonia nitrogen and the carbon atom attached to the hydrogen atom. The initial distance between these two atoms as ca. 3.3Å. Compression of this configuration of the two molecules, over a small energy barrier (ca. 9 kcal/mol), to a distance of ca. 1.6Å (ring C and ammonia N distance) resulted in a second stable structure. This structure has been previously reported as the Mesenheimer complex.<sup>5</sup> In this configuration the ammonia nitrogen atom is bonded to the ring carbon which has a tetrahedral bond arrangement (figure 8), the integrity of the benzene ring however, remains intact. Further calculations were performed to examine whether this structure was responsible for the sensitisation effect. However, the results of these calculations showed that the bond strengths, particularly of the neighbouring C-NO<sub>2</sub> groups, were not affected. It was therefore concluded that this addition compound was not responsible for the sensitisation effect.

Attention was then turned to the other optimized supermolecule structure having the ammonia molecule directly above a nitro group. Calculations were performed in which the distance between the ammonia nitrogen and the carbon atom attached to the nitro group was incrementally reduced and the remaining geometry optimised at each step. A potential energy surface was thus generated as shown in figure 9. Calculations on this system showed that under compression, a bimolecular reaction of the amine and TNB

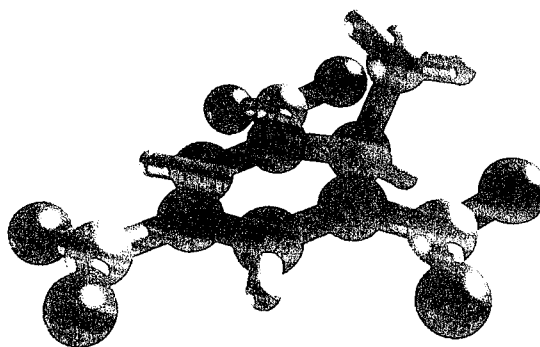


FIGURE 8. MEISENHEIMER COMPLEX

can occur through the C-NO<sub>2</sub> group analogous, to that with nitromethane. The activation energy of this process was calculated to be 58.8 Kcal/mol compared to 89.5 Kcal/mol for unimolecular C-NO<sub>2</sub> bond scission. The products of this reaction were predicted to be nitrous acid and 3,5 dinitro aniline. As with the nitromethane / ammonia sensitisation, these products would be expected to undergo the diazo reaction to give gaseous products.

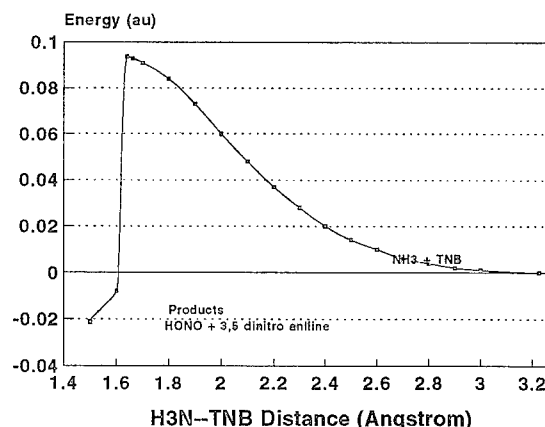


FIGURE 9. TNB - AMMONIA POTENTIAL SURFACE

Preliminary studies on TNT appear to suggest an entirely analogous sensitisation process to that for TNB. However, calculations on triaminotrinitrobenzene (TATB) indicate that displacement of a nitro group by bimolecular reaction with an amine does not occur with this molecule. Hence, it is predicted that TATB would not be expected to show any significant sensitisation effect in the presence of amines.

## DISCUSSION

The ab-initio MO calculations we have reported in this paper strongly suggest that sensitisation of nitromethane by amines occurs by way of a bimolecular reaction. The products of this first step being nitrous acid and the methylated amine. For all amines with the exception of tertiary's, the methylated amine is capable of reaction with further nitromethane molecules. The intermediate amines and nitrous acid can then readily undergo the diazo reaction, and subsequent exothermic decomposition. Calculations on a series of nitro alkanes have shown the same amine sensitisation mechanism would appear to operate for this class of compounds. Further calculations have shown that other classes of small molecules including aldehydes, ketones, ethers and alcohols have no inclination to undergo similar reaction with nitromethane. It is therefore concluded, that these compounds are unlikely to significantly sensitise nitromethane. This is in general agreement with experimental observations.<sup>6</sup>

Calculations to investigate the amine sensitisation mechanism of TNB have revealed that the mechanism is analogous to that with nitromethane. It was found that the minimum ground state configuration was with the amine above the plane of the TNB aromatic ring. Two structures were identified, one with the amine above a nitro group, and another with the amine between a nitro group and a hydrogen. The latter structure, was found to be capable of forming an addition compound thought to be the Meisenheimer complex.<sup>5</sup> The former structure, with the amine above a nitro group was found to be responsible for the sensitisation effect. Preliminary studies show that a similar mechanism should operate with TNT, but not with TATB.

In this paper we have presented new theoretical evidence to support our earlier hypothesis<sup>1</sup> concerning the mechanism by which amines sensitise nitro

compounds. In addition, our results indicate the important role played by nitrous acid and diazo type reactions in the detonation chemistry of nitro compounds. It is to be hoped that future studies of this type will further increase our knowledge of these processes, and thereby enhance our capability to tailor the safety and performance characteristics of explosives.

## REFERENCES

1. M.D. Cook, P.J. Haskins, "Decomposition Mechanisms and Chemical Sensitisation in Nitro, Nitramine and Nitrate Explosives," Ninth Symposium (International) on Detonation, Portland, Oregon, USA, 1989.
2. Gaussian 92, M.J. Frisch, M. Head-Gordon, G.W. Trucks, J.B. Foresman, H.B. Schlegel, K. Raghavachari, M.A. Robb, J.S. Binkley, C. Gonzalez, D.J. Defrees, D.J. Fox, R.A. Whiteside, R. Seeger, C. F. Melius, J. Baker, R.L. Martin, L.R. Kahn, J.J.P. Stewart, S. Topiol, and J.A. Pople, Gaussian, Inc., Pittsburgh, PA, 1992.
3. R. Engelke, *Phys Fluids*, 23, 875, (1980).
4. C.P. Constantinou "The Nitromethane-Amine Interaction," Ph.D Thesis, Cambridge University, 1992.
5. M.R. Crampton and B. Gibson, *J. Chem. Soc. Perkin II*, 1981, 533.
6. Angus Chemical company, "Symposium on Safety and Handling of Nitromethane in Military Applications," Monroe, Louisiana, 14-15 November, 1984. C.M. Mason and E.G. Aiken, "Methods for Evaluating Explosives and Hazardous Materials," U.S. Bureau of Mines Information Circular 8541, 1972.

## THE INFLUENCE OF PARTICLE SIZE AND MECHANICAL PROPERTIES ON THE SENSITIVITY OF HIGH EXPLOSIVE CHARGES (PBX)

F. Schedlbauer, A. Kretschmer  
Fraunhofer-Institut für Chemische Technologie (ICT)  
76327 Pfinztal-Berghausen, FRG

It is well known that the particle size of the crystalline explosive materials influences the sensitivity of explosive charges. The finer the particles the less sensitive are charges against external stimuli. It is also well known that the mechanical properties of plastic bonded explosives (PBX) changes based on the particle size of the filler. In previous investigations we determined that increased sensitivity occurring with fine particles was solely due to the change in mechanical properties. In order to confirm these results, formulations with fine, coarse and bimodal particles having the same Youngs Modulus were made in order to eliminate the influence of the mechanical properties. Two other types of binder were investigated along with HMX as an explosive component (with different particle sizes). Not only the particle sizes are responsible for the sensitivity but also the binder type. To compare and evaluate these PBX's various tests were carried out: Impact-, Bullet Impact- and Gap-Test. The results of these investigations are presented and discussed.

### INTRODUCTION

In Low Vulnerability Ammunition the explosive charge embedded in bombs, shape charges, warheads etc. plays an important role. During the last decade extensive efforts were undertaken to develop and manufacture so called IHE (Insensitive High Explosive) corresponding to the criteria of UN-test-serie 7.

Nitramines are used in explosive and propellant formulations. A particular energetic material of interest is HMX. Efforts are being directed towards further understanding the role of small particles in order to gain a better ability to produce less sensitive explosive and propellant formulations with improved processing, handling, storage and transportation characteristics. This will result in better protection for personell and equipment.

It is generally known and confirmed by many

experiments that explosive charges containing smaller particles of crystalline material exhibit reduced sensitivity to threats such as shock and impact /1-4/. However some test results were observed during our investigations showing the opposite behavior. These differences indicate that there must be some other important parameters such as

- \* Quantity and Type of the Explosive Filler
- \* Particle Size
- \* Mechanical Properties
- \* Porosity

### APPROACH

The goal of this study is to demonstrate that, when mechanical properties are held constant, explosive charges containing smaller particles exhibit reduced sensitivity. This was done by adjusting the formulations to obtain a constant Youngs Modulus.

## EXPERIMENTAL

Two baseline formulations were chosen and investigated to determine:

- \* the influence of the amount of HMX
- \* the influence of the particle size
- \* the influence of the binder composition

on the basis of the same Youngs Modulus.

In addition the following parameters were varied:

- \* quantity of explosive
- \* particle size distribution
- \* NCO/OH ratio
- \* volume fraction plasticizer

The weight percent of HMX of the formulations tested, was 80 % and 85 %, respectively. The average particle size of the monomodal explosive was 250  $\mu\text{m}$  and 10  $\mu\text{m}$ , respectively and a bimodal distribution with 80 %/20 % was also used. The binder system consisted of HTPB and IPDI with NCO/OH ratios of 0.9, 0.95 and 1.0 and the volume fraction of plasticizer was 20 %, 40 % and 60 %, respectively.

### Mechanical Properties

To obtain castable and curable charges the parameters can be modified only within a small area. While the filler quantity is constant the binder system must be varied to obtain the desired Youngs Modulus. Two possibilities to do this are changing the NCO/OH ratio and/or adding plasticizer (IDP).

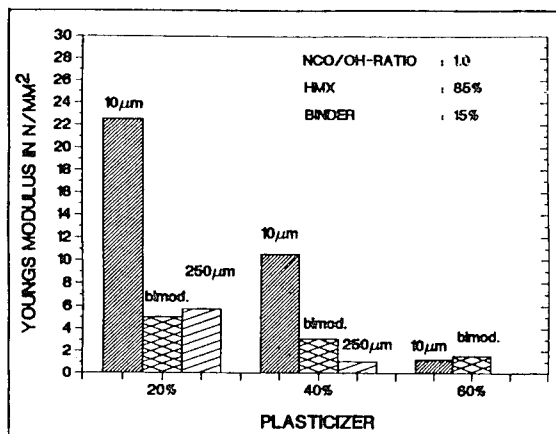


FIGURE 1. YOUNGS MODULUS VS. PLASTICIZER CONTENT

TABLE 1. MECHANICAL PROPERTIES OF FORMULATIONS WITH 85% HMX NCO/OH - RATIO: 1

Plasticizer	Particle Size Distribution of HMX		
	100% 10 $\mu\text{m}$	80% 250 $\mu\text{m}$ 20% 10 $\mu\text{m}$	100% 250 $\mu\text{m}$
20	$\sigma_B$ : 1,60 N/mm <sup>2</sup> $\epsilon_R$ : 10 % E : 22,6 N/mm <sup>2</sup>	$\sigma_B$ : 0,27 N/mm <sup>2</sup> $\epsilon_R$ : 16 % E : 5,1 N/mm <sup>2</sup>	$\sigma_B$ : 0,15 N/mm <sup>2</sup> $\epsilon_R$ : 11 % E : 5,8 N/mm <sup>2</sup>
40	$\sigma_B$ : 1,12 N/mm <sup>2</sup> $\epsilon_R$ : 15 % E : 10,6 N/mm <sup>2</sup>	$\sigma_B$ : 0,17 N/mm <sup>2</sup> $\epsilon_R$ : 13 % E : 3,1 N/mm <sup>2</sup>	$\sigma_B$ : 0,07 N/mm <sup>2</sup> $\epsilon_R$ : 15 % E : 1,1 N/mm <sup>2</sup>
60	$\sigma_B$ : 0,40 N/mm <sup>2</sup> $\epsilon_R$ : 36 % E : 1,3 N/mm <sup>2</sup>	$\sigma_B$ : 0,11 N/mm <sup>2</sup> $\epsilon_R$ : 12 % E : 1,6 N/mm <sup>2</sup>	Not Cured

In Table 1 the mechanical properties of the formulation with 85 % HMX as a function of the particle size distribution and the amount of IDP are shown. The results of the Youngs Modulus are plotted in Figure 1.

The mechanical properties of the composition with 80 % HMX can be seen in Table 2 and Figure 2. In both cases the NCO/OH ratio was 1. In Figure 3 the dependence of the Youngs Modulus on the NCO/OH ratio for this formulation is demonstrated.

TABLE 2. MECHANICAL PROPERTIES OF FORMULATIONS WITH 80% HMX NCO/OH - RATIO: 1

Plasticizer	Particle Size Distribution of HMX		
	100% 10 $\mu\text{m}$	80% 250 $\mu\text{m}$ 20% 10 $\mu\text{m}$	100% 250 $\mu\text{m}$
20	$\sigma_B$ : 0,52 N/mm <sup>2</sup> $\epsilon_R$ : 40 % E : 3,0 N/mm <sup>2</sup>	$\sigma_B$ : 0,31 N/mm <sup>2</sup> $\epsilon_R$ : 12 % E : 5,3 N/mm <sup>2</sup>	$\sigma_B$ : 0,16 N/mm <sup>2</sup> $\epsilon_R$ : 17 % E : 3,2 N/mm <sup>2</sup>
40	$\sigma_B$ : 0,41 N/mm <sup>2</sup> $\epsilon_R$ : 49 % E : 1,7 N/mm <sup>2</sup>	$\sigma_B$ : 0,19 N/mm <sup>2</sup> $\epsilon_R$ : 17 % E : 2,8 N/mm <sup>2</sup>	$\sigma_B$ : 0,10 N/mm <sup>2</sup> $\epsilon_R$ : 20 % E : 1,4 N/mm <sup>2</sup>
60	$\sigma_B$ : 0,17 N/mm <sup>2</sup> $\epsilon_R$ : 93 % E : 0,4 N/mm <sup>2</sup>	$\sigma_B$ : 0,16 N/mm <sup>2</sup> $\epsilon_R$ : 10 % E : 3,4 N/mm <sup>2</sup>	Plasticizer Exudation

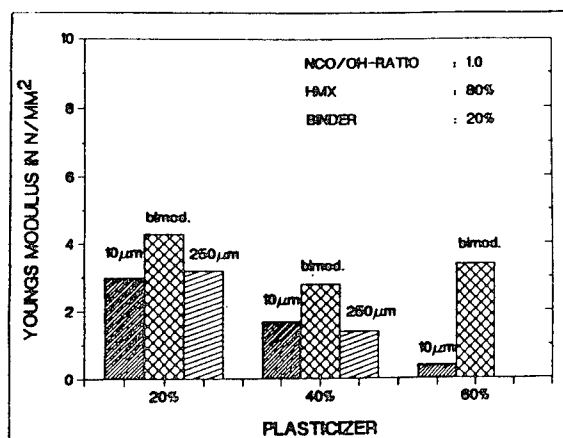


FIGURE 2. YOUNGS MODULUS VS. PLASTICIZER CONTENT

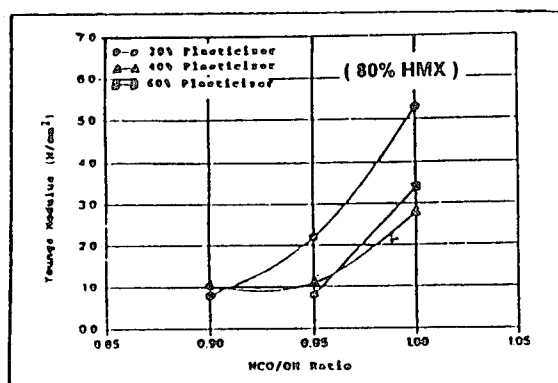


FIGURE 3. YOUNGS MODULUS VS. NCO/OH-RATIO

After this very time consuming work the formulations shown in Table 3 were selected for further investigations.

TABLE 3. SELECTED FORMULATIONS

Particle Size	10 µm	250 µm	bimodal
85% HMX	HX 166	HX 164	HX 161
Youngs Mod.	1,3 N/mm <sup>2</sup>	1,1 N/mm <sup>2</sup>	1,6 N/mm <sup>2</sup>
Deton. Rate	7990 m/s	7750 m/s	8090 m/s
80% HMX	HX 133	HX 142	HX 127
Youngs Mod.	3,0 N/mm <sup>2</sup>	3,2 N/mm <sup>2</sup>	3,4 N/mm <sup>2</sup>
Deton. Rate	7770 m/s	7420 m/s	8000 m/s

The impact and friction sensitivity for all compositions is nearly in the same range (Table 4). No great differences are seen in the chemical stability, however, there is a slight decrease in the ignition temperature going from the bimodal HMX to the smaller and then to the coarser material (Table 5).

TABLE 4. IMPACT AND FRICTION SENSITIVITY

Comp.	HMX			Binder HTPB %	Impact Sensitivity Nm	Friction Sensitivity N
	100% 10 µm %	80% 250µm 20% 10µm %	100% 250 µm %			
HX 127	-	80	-	20	8,3	353
HX 133	80	-	-	20	10,8	>353
HX 142	-	-	80	20	6,8	283
HX 161	-	85	-	15	8,3	353
HX 166	85	-	-	15	8,3	316
HX 164	-	-	85	15	7,4	316
HMX 80% 250 µm/20% 10 µm					2,0	118
HMX 10 µm					2,0	103
HMX 250 µm					1,5	118

TABLE 5. CHEMICAL STABILITY

Comp.	HMX			Binder HTPB %	Ignition Temp. °C	Vacuum Stabl. ml/g	Weight Loss 105 °C 72 h %
	100% 10 µm %	80% 250µm 20% 10µm %	100% 250µm %				
HX 127	-	80	-	20	285	0,05	0,13
HX 133	80	-	-	20	253	0,19	0,14
HX 142	-	-	80	20	251	0,07	0,12
HX 161	-	85	-	15	260	0,10	0,11
HX 166	85	-	-	15	255	0,16	0,09
HX 164	-	-	85	15	253	0,06	0,10

## VULNERABILITY TESTS

The sensitivity to shock was determined by the Large-Scale-Gap-Test (LSGT). The donor charge consists of 95 % RDX and 5 % wax. The sizes of the donor and the acceptor charges are 100 mm in length and 50 mm in diameter. Plexiglas discs of 1 mm thickness were used for the gap between the explosive and the test sample.

The results of the LSGT are shown in Figure 4. Composition B serves as a reference charge. Charges with 20 % binder are all less sensitive compared with the samples with 15 % binder. Of even greater interest is that the charges with fine particles are in every case the least sensitive and charges with coarse material show the highest sensitivity. In the case of 85 % HMX the same value as Comp.B is obtained.

The sensitivity to bullet impact was determined with a measuring system developed by the ICT. Contrary to the UN-recommendations ICT uses a 20 mm projectile with a flat nose. The muzzle velocity is about 1010 m/s. The test sample is placed in steel container 5 mm thick and 50 mm in length and diameter. The front plate is made up of a 2 mm thick steel cover. A pressure gauge is located 1.1 m behind the test set-up to measure and record the pressure maxima.

The test results are presented in Figure 5. All of the investigated charges are clearly insensitive in comparison with Comp. B. The pressure values confirm that no detonation has occurred. While Comp.B showed a maximum pressure of 7 bars the tested charges had only 1 bar or below. The large spread of the data for formulations with a bimodal particle size distribution is noteworthy. In these tests

the coarse HMX was again found to be the most sensitive.

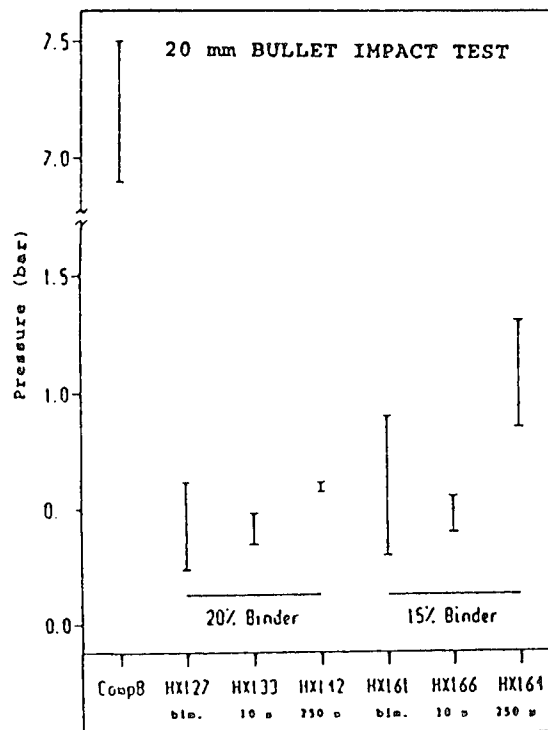


FIGURE 5. TEST RESULTS

## DISCUSSION

These tests have proved that the fine particles give a more insensitive material at the same mechanical properties. But the reason for this behavior is still an open question.

Investigations of the purchasable HMX and RDX with particle sizes upon 100  $\mu$ m by polarized light show a lot of defects /5/. These can be e.g. voids filled with mother liquor or gases which can create hot spots. Figure 6 clearly shows the differences between the raw material and the recrystallized HMX. Is the application of coarse nitramines a reason for a higher sensitivity? New experiments must be carried out to test this assumption. It is clear that fine particles have less defects and so they are less sensitive. This has been confirmed by many tests.

Another point leading to increasing sensitivity is the porosity of the charges themselves. Normally it is not possible to achieve the Theoretical Maximum Density (TMD) in reality. But the higher the TMD the less sensitive are the explosive charges because not hot spots exist.

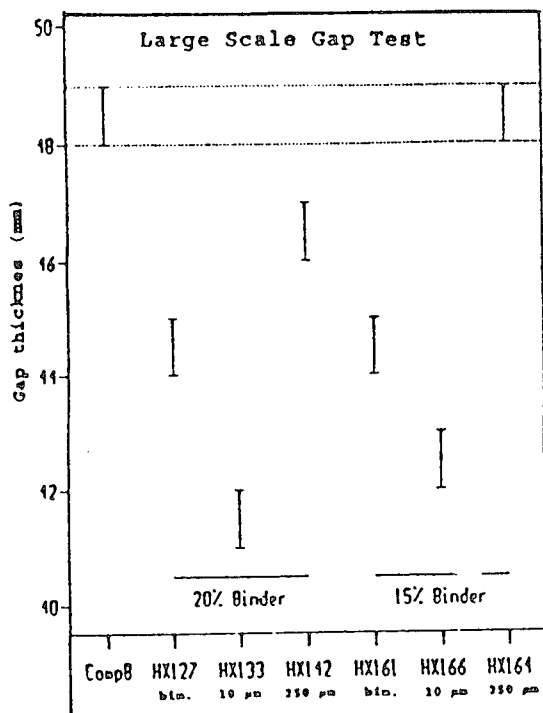


FIGURE 4. TEST RESULTS

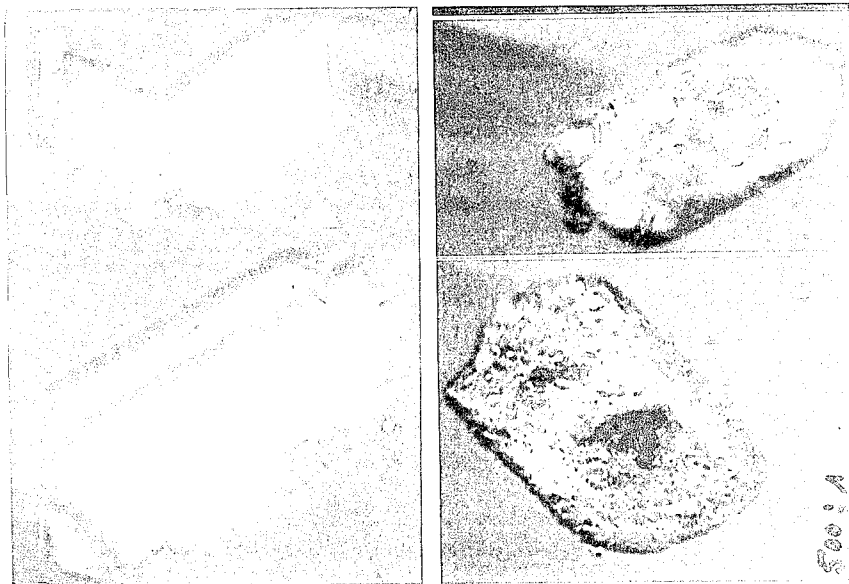


FIGURE 6. RAW AND RECRYSTALLIZED HMX

Follow-up investigations were made to examine the influence of the mechanical properties. To obtain very low Young's Modulus uncured resins like polyisobutylene (PIB) and silicone oil (Si oil) were used for a binder material. The problem in this case was to get charges with high densities. These investigations are not completed because a new aspect comes up during the interpretation of the bullet impact

test. In Fig. 7 the results show big differences between PIB and Si-oil. This needs further investigation.

#### CONCLUSIONS

These investigations provide conclusive confirmation that when the Young's Modulus is held constant, explosive charges containing fine particles are less sensitive than charges with coarse material. Charges with a bimodal particle size distribution are of intermediate sensitivity. These conclusions were reached through testing of charges in which the percentages of HMX and the binder composition were constant.

Further investigations are necessary to clear the questions of the influence of crystal defects, porosity and binder systems.

#### REFERENCES

- /1/ Schedlbauer, F. et al., "Grundlagenforschung auf dem Gebiet der unempfindlichen Sprengstoffe" ICT-Bericht T/R721/J0038/H1701
- /2/ Moulard, H., Kury, J.W., Declos, "The Effect of RDX Particle Size on the Shock Sensitivity of Cast PBX Formulations", 8. Symposium (International) on Detonation (Albuquerque, New Mexico) 0902

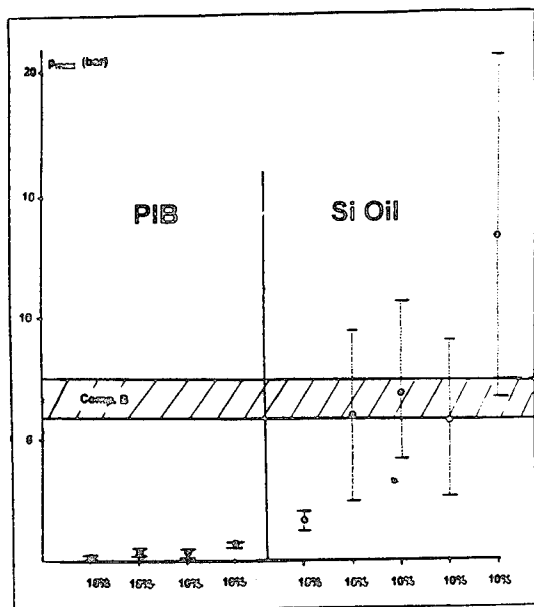


FIGURE 7. TEST RESULTS



- /3/ Moulard, H., "Particular Aspect of Explosive Particle Size Effect on Shock Sensitivity of Cast Formulations", 9. Symposium (International) on Detonation (Portland, Oregon) 0018
- /4/ Moulard, H., "Experimentelle Untersuchung des Einflusses der Korngrößenverteilung des Oktogens auf die Empfindlichkeit von zwei gegossenen monomodalen Sprengstoffzusammensetzungen mit Kunststoffbinder", ISL-Bericht RT 508/89
- /5/ Private communication L. Borne ISL

---

#### DISCUSSION

LEWIS ROTHSTEIN  
Consultant, Newport News, Virginia

Could the desensitizing difference between silicon oil vs. PBI be due to differences in specific heat as well as to, or rather than, difference in viscosity?

NO REPLY FROM THE AUTHOR

#### DISCUSSION

JOHN KURY  
Lawrence Livermore National Laboratory,  
Livermore, California

As you indicated, void content is an important factor in determining shock sensitivity. The variations in detonation velocity values given in Table 3 indicate significant porosity differences for your explosives. What are the test densities and maximum theoretical densities for your compositions?

NO REPLY FROM THE AUTHOR

#### DISCUSSION

HAROLD J. GRYTING, Ph.D.  
Gryting Energetics Science Company,  
San Antonio, Texas

This appears to be a very fertile field of investigation. What were the binders that you used and could you differentiate the affects of different binders from the affects of the varied mechanical properties by the sensitivity and stability tests that you conducted?

NO REPLY FROM THE AUTHOR

**SESSIONS ON**  
**NEW FORMULATIONS**

**Cochairmen:**     **Gary Parsons**  
                         **Wright Laboratory/Armament Directorate**

**Joël Mala**  
                         **Societe Nationale Des Poudres et Explosifs**

## CONCEPTION, SYNTHESIS AND CHARACTERIZATION OF A NEW INSENSITIVE HIGH EXPLOSIVE : DANTNP

P. CHARRUE, Ch. WARTENBERG, , F. LAVAL  
Commissariat à l'Energie Atomique  
Centre d'Etudes du RIPAUT  
BP n° 16 - 37260 MONTS  
FRANCE

Previous studies by Quantum Chemistry methods of the electronic structure of organic explosives molecules allowed us to develop a predictive approach which permits to evaluate before synthesis the most important safety parameters of an aimed molecule, shock sensitivity and thermal stability.

On the basis of these results, we are presenting a new insensitive high explosive, the 5 nitro-4,6 bis ((5nitro, 1H-1,2,4 triazole-3yl) amino) pyrimidine or DANTNP. This molecule is based on the amino nitro 1,2,4 triazole pattern which gives high detonic characteristics and good insensitivity properties when grafted on aromatic ring.

The synthesis method and the main characteristics of the DANTNP are discussed. The experimental data of this new explosive are compared to the theoretical values obtained from our conceiving methodology. This new explosive is close to TATB in term of safety paramaters but the detonic properties observed on cylinder test show an improvement of 10 % compared to TATB. This result permits us to validate the hereby developped methodology and the way of research on new insensitive high explosives based on ANT pattern.

### INTRODUCTION

One of the most important objective for the synthesis level of new explosives consists of searching molecules showing both a good energetic power and maximum safety guarantees. In other words, this objective could be globally translated by the need of a material, conciliating insensitivity characteristics close to TATB and increasing detonation properties. It can be compared to the TATB and the HMX as shown in Table 1.

Such specifications are not very accessible with known explosives. Then the problem is that of defining a new molecular pattern in order to satisfy the whole requirements.

In the last fifteen years, we concentrated all our

TABLE 1. REQUIREMENTS FOR THE CONCEPTION OF NEW INSENSITIVE EXPLOSIVES

	TATB	HMX	REQUIREMENTS
SHOCK SENSITIVITY (5 kg Sorgues impact test)	>72cm	>15cm	>50cm
FRICTION SENSITIVITY (Julius Peters Apparatus)	>353N	118N	> 353N
THERMAL STABILITY (D.S.C.)	350°C	280°C	>300°C
DETONATION PRESSURE	280kbar	390kbar	>330kbar

efforts on the study of the relationship between explosive behaviour and chemical structure. What we know today about this problem allows us to use predictive methods for two purposes.

→ To conceive a molecular formula in order to obtain specific properties,

→ To evaluate, before any synthesis operation, the performance level of a new molecule project, as for the aspects connected to the safety (shock sensitivity, thermal stability) or to the detonation properties (pressure and detonation velocity).

This approach allows to focus on the synthesis activity to the only molecules satisfying "a priori" the whole of the requirements.

### CONCEPTION OF THE DANTNP MOLECULE

The conception of this molecule is based on the insensitivity objective. For this purpose we have used the method developed by A. DELPUECH and J CHERVILLE [1], which permits to foresee the shock sensitivity of the explosive, using the study of electronic structure of the molecule by quantum mechanics. Applied to the picrylazoles family, this method revealed the interest of the 3-Amino-5 nitro - 1,2,4 Triazole (or ANT) pattern as insensitivity generator when it is used as picryl ring substituent. The developed formula of the ANT is as follows :

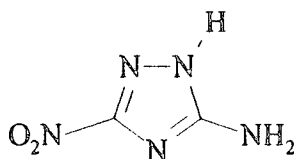


FIGURE 1. STRUCTURE OF ANT

The presence of nitro group gives to ANT explosive type properties. Acquisition of characteristics satisfying to the requirements of table 1 consists of choosing the aromatic ring which, when associated with ANT, will contribute to :

- ensure a low sensitivity, according to the principles drawn from theoretical investigations on the picrylazoles.
- reinforce the thermal stability.
- preserve the energetic performances of the molecule.

The high thermal stability of nitrogenous aromatics heterocycles led us to consider this chemical family for the conception of the DANTNP. More exactly, we have chosen the nitropyrimidine, substituted in  $\alpha$  and  $\alpha'$  position from the nitro group with ANT pattern. As a result the following formula of DANTNP new explosive appears :

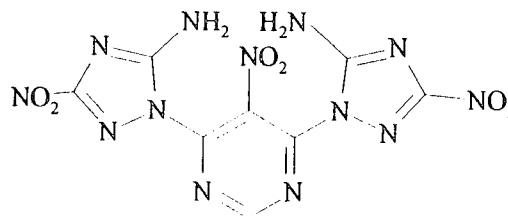


FIGURE 2. STRUCTURE OF DANTNP

The density of this molecule, calculated by the CADY'S method is :  $\rho_{\text{calc}} = 1.85$ .

The evaluation of detonation characteristics needs the use of the thermochemical code ETARC. Its application to DANTNP gives, on CJ point and at CADY'S density, the following values for pressure and detonation velocity :

$$D_{\text{CJ}} = 8100 - 8200 \text{ m/s}$$

$$P_{\text{CJ}} = 350 \text{ kbar}$$

Beside the values at CJ point, ETARC code plots the evolution of the work transmitted to an external medium by the expansion of the detonation products. The curves of TATB and DANTNP are presented on figure 3. We can observe, in favour of DANTNP, a difference of 15 to 20 % on the work given by two explosives.

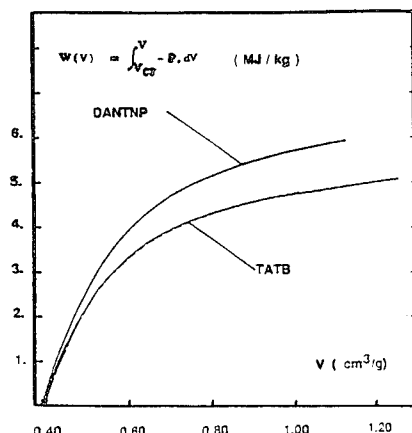


FIGURE 3. WORK COMMUNICATED TO AN EXTERNAL MEDIUM - ETARC CALCULATIONS PLOT

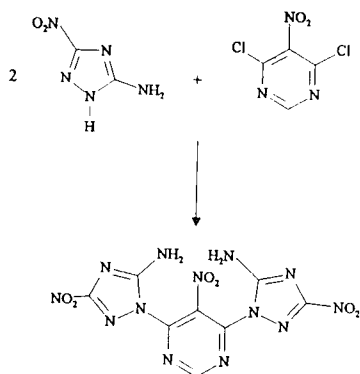
These whole considerations permit to obtain the table of estimated characteristics of DANTNP :

- shock sensitivity (5kg) : > 60 - 70 cm
- Thermal stability : > 300°C
- Detonation velocity : 8100 - 8200 m/s
- Detonation pressure : 350 kbar.

Concerning the safety, the expectations are in agreement with requirements. Moreover, the progressiveness of detonation product expansion permits to reach the desired objective in spite of the detonation velocity which is lower than the 8500 m/s expected. It is possible that this expansion mode (sustained shock) will be an advantage in numerous applications.

## DANTNP SYNTHESIS

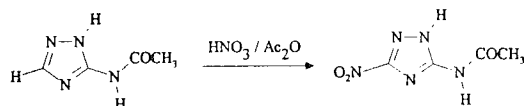
Synthesis method of the DANTNP molecule is based on the condensation reaction of 2 ANT patterns on a di-halogenous nitro pyrimidine ring [4].



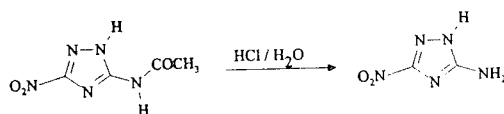
SCHEME 1 : SYNTHESIS OF DANTNP

## ANT SYNTHESIS

The synthesis method used is inspired by the one described in publications [5]. It consists of a nitration of the Amino Triazole, preceded by an acetylation of the amine group, this one used to protect the chemical function during the nitration. Hydrolysis of the Acetamido nitro triazole gives the ANT product.



SCHEME 2 : NITRATION OF ACETAMIDO-1,2,4-TRIAZOLE

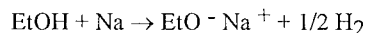


SCHEME 3 : SYNTHESIS OF ANT

The ANT is obtained with a 30 % yield in good purity grade. The synthesis have been scaled up to pilot plant. The ANT obtained is used for DANTNP synthesis without additional purification.

## DANTNP SYNTHESIS

The condensation reaction occurs between the dichloro-nitro-pyrimidine and the ANT sodium salt. The salt is made "in situ" in ethanol medium with sodium metal.



The dichloronitro pyrimidine is directly introduced in the reactive medium. The chloride reactivity, increased with the presence of the nitro group on  $\alpha$  position, gives a very high reaction rate, the DANTNP precipitating instantaneously.

## DANTNP CHARACTERIZATION

### A - CRISTAL STRUCTURE

The DANTNP is a whity powder which has a density of 1.865, determinated from the RX diffraction spectrum.

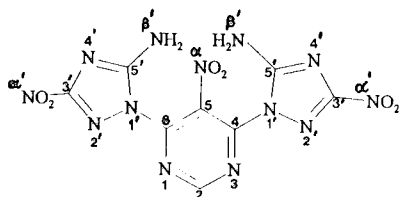
The cristal structure was calculated from diffraction data obtained with powder as synthetised, this because non single cristal have been made at the present time.

The cristal structure is orthorhombic  
The parameters of the cristal are as follows:

a = 16.8005(10)Å  
b = 11.9365(8)Å  
c = 6.7409(6)Å  
d = 1.864 g.cm<sup>3</sup>  
V = 1351.81Å<sup>3</sup>

## B - STRUCTURE IDENTIFICATION

The structure identification is based on the results obtained by NMR <sup>15</sup>N and <sup>13</sup>C. The spectra (figures 4 and 5) agree with the molecular structure expected. Particularly, we can check that the substitution reaction on the dichloro-nitro-pyrimidine is realised with the secondary amine of the triazole ring (presence of a typical peak of primary amine on <sup>15</sup>N spectrum).



## INDEXING NMR SPECTRUM

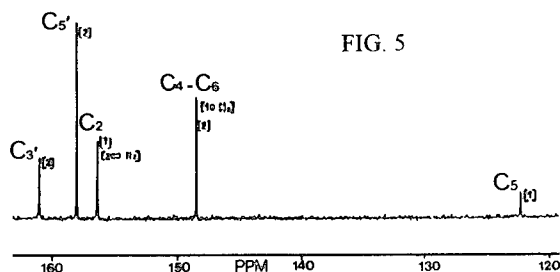
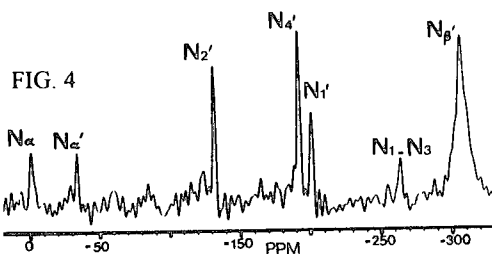


FIGURE 4. NMR <sup>15</sup>N SPECTRUM OF DANTNP  
FIGURE 5. NMR <sup>13</sup>C SPECTRUM OF DANTNP

## C - SAFETY CHARACTERISTICS

The results of characterization tests are :

- shock sensitivity  
(Sorgues drop hammer test 5 kg) : 70 cm
- friction sensitivity  
(Julius Peters apparatus) : no reaction
- thermal stability : 350°C  
(decomposition temperature DSC)
- déflagration point : 328°C.

The results agree perfectly with the estimated values when the molecule was designed.

We noted a very good response of the DANTNP to the Vacuum Test. The gas volume evolved during 70 hours at 170°C is less than 10 ml for 100 g of explosive.

## DETONATION CHARACTERISTICS

The first objective of these test is to confirm the data obtained from ETARC code applied to the DANTNP molecule. The cylinder test gives in a single shot the whole information expected :

- Detonation velocity of the explosive.
- Expansion mode of the detonation products.
- Bulk energy delivered by the detonation with the limit speed of expansion of the copper cylinder.

Experimental set-up is described on figure 6.

We have developed, at laboratory scale, several DANTNP plastic bonded compositions, the aim being to obtain the highest possible density with the minimum percentage of binder in order to be close to the behavior of the pure explosive.

Finally, at a pilot scale, we have chosen a composition containing 2,5 % weight of an adapted thermoplastic binder.

In order to obtain the upper density, we have determined the molding parameters. So the maximum obtained density is :

d = 1,810 (≈ 98 % of the theroretical molding density)

All the results described hereafter have been obtained with such a composition.

**TABLE 2. COMPARATIVE RESULTS ON CYLINDER TEST SHOT**

COMPOSITION (%wt)	TATB (97.5%)	DANTNP (97.5%)
Composition density	1.903	1.810
Détonation velocity (in m/s) extrapolated at crystal density of the explosive	8150	8200
Maximum expansion speed of the cylinder (in m/s)	2000	2090

Table 2 compares the results obtained in the same conditions with DANTNP composition and TATB composition.

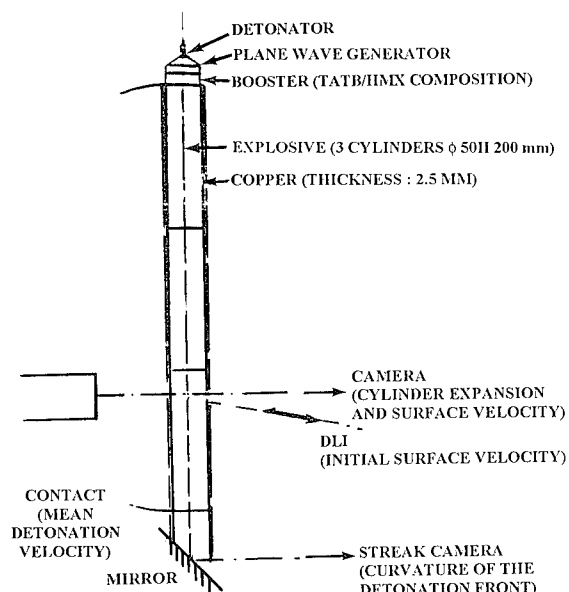


**FIGURE 6. CYLINDER TEST EXPERIMENTAL SET-UP AND MEASUREMENTS**

The values show a detonation velocity of the DANTNP composition which is higher than the detonation velocity measured on TATB composition and this in spite of a low density.

The maximum speed of expansion observed with DANTNP shows, that at constant volume, there is an energetic transfer to copper cylinder which is larger than the one obtained with a high performance TATB based composition.

At a constant weight, the difference raises to 15 %. The increasing speed of the cylinder recorded by DLI shows that the acceleration induced by the DANTNP is lower than the one with TATB.

## CONCLUSIONS

The conception of a new insensitive explosive using predictive methods developed on CEA/DAM was validated with the synthesis and the characterization of DANTNP. This molecule is conform to the safety criteria evaluated "a priori" using theoretical quantum chemistry method. The energetic experimental behaviours are in agreement with the preliminaries calculations made with ETARC code.

The knowledge acquired through the development of the DANTNP validates the bulk conceiving technique of energetic and insensitive molecular patterns resulting from our predictive approach. The interest in using the amino nitro triazole group as insensitiveness generator is hereby reinforced. The ANT pattern permits to imagine a larger family of molecules with different properties and manufacturing costs when associated with appropriate ring.

## REFERENCES

1. A. DELPUECH, J. CHERVILLE, *Propellants and Explosives*, 1978, 3(6)169, 1979, 4(2)61, 1979, 4(6)121.
2. A. DELPUECH, J. CHERVILLE, C. MICHAUD, *The Seventh Symposium on Detonation*, Annapolis, Maryland, U.S.A., 1981.
3. F. BUGAUT, S. BERNARD, R. CHIRAT, *9th International Symposium on Detonation*, Portland, Oregon, U.S.A., 1989.

4. F. LAVAL, Ch. WARTENBERG,  
M. L. MORIGNAT, *Brevet sur DANTNP*, U.S.  
patent 4, 970, 311, 13-11-90.

5. M. S. PEVZNER et Co, *Khimiya Geterotsikliches  
kikh Soedimenti* 8 1132, 1979

6. H. H. CADY, *Informal Report*, LA - 7760 - MS -  
1979

---

#### DISCUSSION

J. F. GUERY  
Centre de Recherche du Bouchet, Vert-Le-Petit, France

Have you performed other shock sensitivity tests?

#### REPLY BY P. CHARRUE:

The objective of our work was to validate the results given by predictive methods; therefore, we have not performed other shock tests. Complementary tests will be carried out within the complete characterization of the explosive composition.

#### DISCUSSION

DR. DIVYAKANT L. PATEL  
Countermining Systems Directorate, U.S. Army,  
Fort Belvoir, Virginia

How much does 1 kg of DANTNP cost? If it costs \$3000, it is much more expensive than TATB.

#### REPLY BY P. CHARRUE:

Today, the cost of DANTNP is about \$3000/kg. At such a level of development (pilot plant) this cost is normal; but production of DANTNP on a larger scale will reduce the cost rapidly.



## DEVELOPMENT AND CHARACTERIZATION OF A COLD-CAST COMPOSITE/MOLECULAR EXPLOSIVE

J.D. Renick

Field Command, Defense Nuclear Agency  
Kirtland AFB, NM 87117-5669

K. Bell

New Mexico Engineering Research Institute  
Albuquerque, NM 87131

A composite/molecular explosive mixture called ATX-27R, whose formulation and processing is based on recent advances in nonaqueous emulsion and cold-cast technology, has been developed and characterized with respect to its mechanical, thermal, and detonation properties. Principal ingredients are ethylene diamine dinitrate and ammonium nitrate in the composite phase, and 27 percent by weight of RDX as an additive. Thermal analysis indicates that a 20-ton spherical ATX-27R charge can be cast with a temperature margin of approximately 21°C between predicted temperature for thermal runaway and peak casting temperature. Detonation properties were evaluated in unconfined cylindrical charge and 1000-lb spherical charge experiments in air. Detonation performance is similar to that of pentolite, but with an improved oxygen balance.

### INTRODUCTION

Extensive research has been conducted since World War II utilizing hemispherical and spherical explosive charges to study blast effects in air. Experiments have been conducted over ideal surfaces to observe airblast environments in the regular and mach reflection regions,<sup>1</sup> and over nonideal surfaces to study both clean and dusty percurd flows.<sup>2</sup> Experiments have been conducted for a wide range of charge sizes from sub-gram-size used in laboratory experiments<sup>3</sup> to charges of up to 4500 tons in field tests.<sup>4</sup> Baker<sup>5</sup> and Esparza<sup>6</sup> provide reviews with extensive references of airblast research conducted using spherical explosive charges.

Several different explosives have been used in these experiments. Most experiments conducted with melt/cast charges (i.e., TNT, pentolite, Comp B) produce irregular blast environments due to imperfections in the castings. Pressed charges such as PBX-9404 and LX-10 provide exceptionally high quality repeatable airblast environments, however the press-

ing/machining fabrication process severely limits the size charge that can be produced.

The weight of bare spherical explosive charges used in free-air experiments has, for practical reasons, been limited to around 1000 lbs. The ability to make certain flow measurements and to construct scaled structural response models has been limited by this relatively small scale. For this reason, researchers have had a long-standing interest in conducting larger scale spherical charge experiments of up to 20 tons TNT equivalent.

The emergence of emulsion technology within the commercial explosives industry and in particular, the development of cold-cast technology<sup>7,8,9,10</sup> in the 1980s, introduced the potential for producing high quality cast charges with the detonation performance of pentolite or better, and which, because of the potential for casting at low temperatures, could be safely cast into spherical charges of up to 20 tons. The Defense Nuclear Agency initiated a research program in 1989

to investigate how this technology might be applied to the production of large high-quality explosive spheres for use in airblast phenomenology studies.

## DESCRIPTION

Researchers at the Defense Nuclear Agency (DNA), the New Mexico Engineering Research Institute (NMERI), the Energetic Materials Research and Technology Center (EMRTC), and IRECO Inc., have developed and characterized a composite/molecular explosive mixture called ATX-27R, whose formulation and processing is based on recent advances in nonaqueous emulsion and cold-cast technology. The acronym "ATX" (Advanced Technology Explosive) refers to the basic composite explosive and "27R" indicates that the mixture contains approximately 27 percent RDX. The ATX nomenclature was selected as a generic designation of the composite component long before the composite formulation was established.

Existing evidence indicated that a simple elemental composition would improve the detonation performance relative to ideal/theoretical behavior,<sup>11</sup> therefore, the formulation was developed under the restriction that it would contain only the elements C, H, N and O. This excluded the use of metallic salts such as calcium nitrate and sodium nitrate. Aluminum was also excluded from the formulation because a satisfactory detonation/combustion model for aluminized explosives was unavailable. The intent was that current thermochemical equilibrium models (BKWR) would provide a reasonable theoretical description of the detonation state and reaction products expansion for use in hydrodynamic prediction codes, and that the detonation performance would be relatively insensitive to the effects of scale and confinement. Finally, it was desired that the oxygen deficiency of the reaction products be minimized to reduce afterburning effects in air. The nominal composition of ATX-27R is described in Table 1.

An earlier formulation was investigated which contained nitroguanidine (NQ) in the salt phase. The idea here was that a highly uniform dispersion of a molecular explosive throughout the salt phase might improve the detonation performance. However, poor solubility of NQ in the salt solution was observed and it was deleted from the formulation.

The favorable effects of adding RDX to the emulsion were to increase energy, density, and sensitivity to shock initiation. The unfavorable effects were to decrease thermal stability, increase mixture viscosity, and to decrease the shear strength of the cast product. A loading of around 27 percent RDX was

TABLE 1. ATX-27R NOMINAL COMPOSITION

<u>Salt Phase</u>	67.8%
EDD (Ethylene Diamine Dinitrate)	33.2%
AN (Ammonium Nitrate)	33.2%
U (Urea)	1.4%
<u>Fuel Phase</u>	4.8%
Oil	3.1%
Emulsifier	1.7%
<u>Additive Phase</u>	27.4%
RDX	27.0%
Casting Agent	0.4%
<u>Total</u>	100.0%

determined to provide an acceptable compromise between these various factors.

The emulsion is formed by heating the salt solution and fuel to approximately 120 °C and mixing them under high shear conditions. The emulsion is then allowed to cool to room temperature where its consistency resembles that of a soft grease. RDX and the casting agent are added to the cool emulsion and blended, and the mixture drawn into a casting mold under vacuum through a slitter plate to remove entrained air. Solidification time can be regulated through selection of appropriate emulsifiers and casting agents. Typical times are 4 to 8 hours for 1000-lb charges and 1 to 2 days (predicted) for 20-ton charges.

A major challenge in the production process is to ensure sufficient stability of the emulsion such that it is able to withstand shear loads required during blending of the RDX at room temperature while allowing an acceptable "pot life" for a well-controlled casting process. During the casting process a rise in temperature of 48 °C occurs as a result of the heat of crystallization. Cooling time, which is dependent on charge size, is typically three to four days for 1000-lb spherical charges and is estimated to be around two weeks for 20-ton spherical charges. Cast densities of 1.565 g/cm<sup>3</sup> (98 percent of TMD) are typical.

Mechanical properties of the cast mixture were found to be strongly dependent on the maximum temperature experienced during casting. After removing the charge from the casting mold, the surface of the charge is "heat treated" by exposing it to circulating air at 50 °C for 12 hrs. The result is an

increase in shear strength from around 15 lb/in<sup>2</sup> to over 100 lb/in<sup>2</sup>. This additional strength is important for large charges where the explosive must withstand bearing and shear loads from the charge support sling which is quite austere in design.

The ATX-27R formulation results in a theoretical oxygen balance (reaction to CO<sub>2</sub>) of -24.2 percent compared to -21.6 percent for RDX and -74.0 percent for TNT. Because it is generally desirable to minimize the effects of afterburning for detonations in air, this result is considered favorable.

### THERMAL PROPERTIES

Thermal analysis data were obtained from DSC, DTA, and ARC tests. The results are summarized in Table 2.

TABLE 2. RESULTS OF ATX-27R THERMAL EXPERIMENTS

Method	Sample Weight	Exotherm Onset
DSC	9.7 mg	174 °C
DTA	0.50 g	167 °C
ARC	0.48 g	152 °C

Thermal properties for critical temperature predictions were determined in Henkin and 1.4-kg, 2.0-kg, and 18.2-kg cook-off experiments. The temperatures, dimensions, and shape factors used in the thermal modeling calculations are shown in Table 3. An Arrhenius plot for these global decomposition rate data is shown in Figure 1. Parameters for use in the Frank-Kamenetskii model for thermal runaway considering heat losses by conduction are given in Table 4. A plot of critical temperature versus charge radius for spherical charges using the Frank-Kamenetskii model for several different explosives are plotted along with the curve for ATX-27R in Figure 2. Critical temperature of 111°C and 96°C are predicted for 1000-lb and 20-ton spherical charges, respectively. Considering the 48°C temperature rise due to crystallization, the maximum temperature expected during casting is approximately 75°C depending on the initial casting temperature. This results in a temperature margin of only 21°C for a 20-ton charge. Uncertainties in the prediction could reduce this margin further.

TABLE 3. PARAMETERS USED IN THERMAL ANALYSIS

Method	T <sub>c</sub> <sup>a</sup>	a <sup>b</sup>	Shape Factor
Henkin <sup>c</sup>	211°C	0.038 cm	0.88
1.4-kg C/O <sup>d</sup>	142°C	5.370 cm	2.50
2-kg C/O	132°C	0.225 cm	2.50
18.2-kg C/O	123°C	14.030 cm	3.32

a Critical temperature

b Characteristic dimension, radius or half-thickness

c 40-mg

d Cook-off experiment

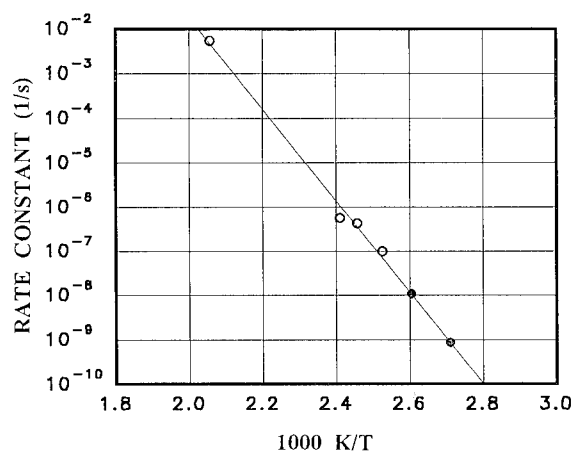


FIGURE 1. ARRHENIUS PLOT FOR ATX-27R DECOMPOSITION RATE COEFFICIENTS DERIVED FROM COOK-OFF DATA. DATA (OPEN CIRCLES) ARE FOR EXPERIMENTS DESCRIBED IN TABLE 3 USING THE FRANK-KAMENETSKII MODEL FOR THERMAL RUNAWAY. ARRHENIUS EXPRESSION FIT TO DATA IS  $k = 7.68 \times 10^{18} \exp(-47184/RT) \text{ s}^{-1}$ . PREDICTIONS FOR THE CRITICAL TEMPERATURES OF 1000-LB AND 20-TON SPHERICAL CHARGES ARE SHOWN BY THE FILLED CIRCLES.

One concern about the way in which the thermal runaway prediction model is developed is that it is based on thermal data from small samples at temperatures which are above the melting temperature

of the salt phase, yet that model is used to predict the thermal behavior of a very large solid charge where the critical temperature is predicted to be below the melting temperature of the salt phase. It is also possible that for the small-sample high-temperature tests, the fuel may be stratified to the top leaving particulate RDX in the molten salt solution, whereas in the solid state, the fuel is uniformly dispersed. It is also assumed that even though the sample is molten, no convective currents exist because of the relatively high viscosity, i.e., heat transfer occurs by conduction only.

TABLE 4. VALUES FOR FRANK-KAMENETSKII EQUATION PARAMETERS

Thermal Conductivity	0.0007 cal/cm-s-K
Density	1.565 gm/cm <sup>3</sup>
Shape Factor	3.32 (sphere)
Gas Constant	1.9872 cal/K-gmole
Activation Energy	47184 cal/gmole
Pre-exponential	$7.68 \times 10^{18} \text{ s}^{-1}$
Heat of Reaction	500 cal/g

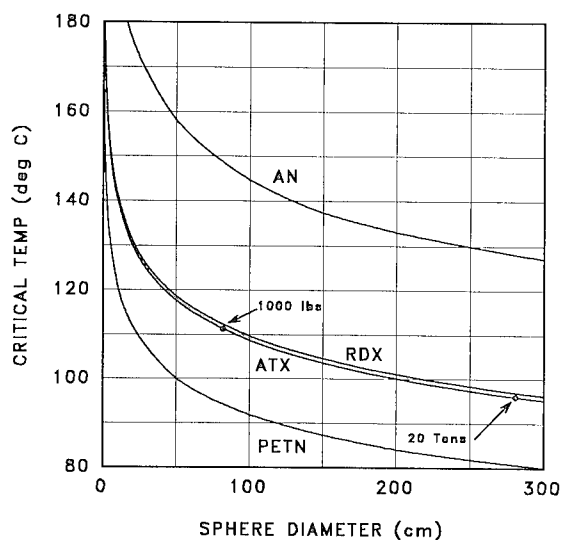


FIGURE 2. CRITICAL TEMPERATURE PREDICTION BASED ON FRANK-KAMENETSKII MODEL FOR THERMAL RUNAWAY VS. SPHERICAL CHARGE DIAMETER FOR ATX-27R, COMPARISON WITH RDX, PETN, AND AN.

Because of these concerns and the relatively narrow temperature margin predicted to exist for the cast/cure operation, a very large cook-off experiment (approximately 2000 lbs) to be conducted at a temperature slightly less than the melting temperature, will be required prior to casting of a 20-ton ATX-27R spherical charge to add confidence to the thermal runaway predictions.

## SAFETY TESTS

Results of various safety tests on ATX-27R are summarized as follows. The  $H_{50}$  height for the IRECO drop weight apparatus using the Bruceton up-down procedure was 33.9 in compared to 17.0 in for RDX. No reaction was observed in bullet impact tests (23 of 23, .22 calibre, 55 gr at 3500 ft/s). A large-scale drop test onto concrete was conducted with a 22-lb cylindrical sample from a height of 44 ft with no reaction. No explosion was observed in unconfined burn tests of 25-mm cubes. Cap tests using #8 blasting caps resulted in failure to detonate in 5 of 5 tests. The minimum booster was determined to be 36 grams. Weight loss of 0.34 percent was observed in gas evolution test of a 50-g sample at 75 °C for 48 hours. Card gap tests using schedule 80 steel pipe at a diameter of 1.44 inches (failure diameter is less than 1 inch in schedule 80 steel pipe) resulted in detonation 50 percent of the time for 126 cards compared to 111 cards for TNT ( $\rho=1.615 \text{ g/cm}^3$ ). Electrostatic discharge sensitivity was measured at 0.30 J compared to 0.14 J for RDX. Friction sensitivity, measured with an ABL apparatus, resulted in no ignition for 10 trials at 900 lb/in<sup>2</sup>.

## DETONATION PROPERTIES

The theoretical detonation state for this explosive was calculated using TIGER. For a density of 1.565 g/cm<sup>3</sup>, detonation pressure and velocity were calculated as 245 kbar and 8.08 km/s respectively. Detonation velocity was measured in unconfined cylindrical charge experiments at different diameters. The resolution of the time-of-arrival recording system limited the determination of detonation velocity to only two significant figures, and we believe that uncertainties in loading density introduced the scatter observed in the experimental results. Failure diameter was determined to be less than 1.5 in. Ideal detonation performance was observed for diameters of 4 inches and above. The diameter-effect curve for ATX-27R is shown in Figure 3. Additional cylinder experiments will be conducted in the future to better define diameter effects on detonation velocity.

Theoretical detonation velocity and highly uniform

and symmetric propagation of the detonation front was observed in the detonation of three 32-in-diameter 966-lb spherical charges. Typical detonation breakout times (center initiation) at 22 evenly distributed points on the surface of the top half of the charges, when adjusted for detonator offset from the true charge center, varied by no more than  $\pm 400$  ns, approximately twice the time resolution of the digital recording system used in those experiments.

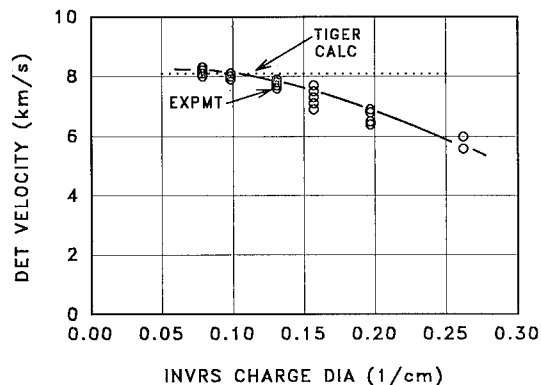


FIGURE 3. DIAMETER-EFFECT CURVE FOR ATX-27R

The free-air curve for ATX-27R was determined in the three 966-lb spherical charge experiments from time-of-arrival measurements along free-air radials using the Gilmore equation-of-state for air.<sup>12,13</sup> The results are shown in Figure 4 where the Goodman free-air curve for a 966-lb spherical pentolite charge<sup>14</sup> and the results of hydrocode prediction<sup>15</sup> of the ATX-27R free-air curve are included for comparison. A JWL model of the expansion of the reaction products was used in the hydrocode predictions. The JWL parameters were determined by fitting the JWL equation to the combined isentropes for the BKWR and JCZ equation-of-state models in TIGER calculations. These results are shown in Figure 5. The JWL parameters are listed in Table 5. The calculated ATX-27R free-air curve compares quite well with the experimental free-air curve. The difference in attenuation between the pentolite and ATX-27R is attributed to reduced afterburning for ATX-27R due to the improvement in oxygen balance relative to that of pentolite.

## SUMMARY

A thorough characterization of the mechanical, thermal, and detonation properties of ATX-27R has been accomplished. Detonation properties are similar to those of pentolite but with an improved oxygen balance. Thermal stability is such that a 20-ton

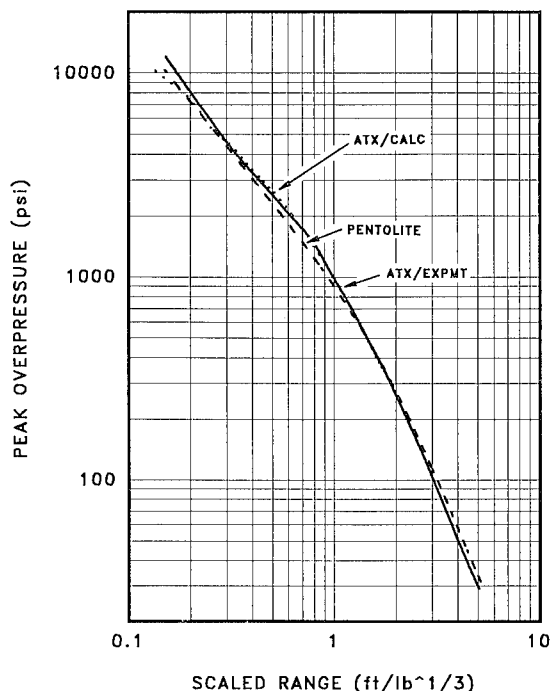


FIGURE 4. FREE-AIR CURVE FOR SPHERICAL ATX-27R CHARGES, COMPARISON BETWEEN EXPERIMENTAL AND CALCULATIONAL RESULTS, AND COMPARISON WITH GOODMAN'S FREE-AIR CURVE FOR PENTOLITE

TABLE 5. VALUES OF JWL PARAMETERS FOR FIT TO TIGER-CALCULATED ISENTROPE

$\rho_0$	= 1.565 gm/cm <sup>3</sup>
$D$	= 8.08 km/s
$E_0$	= 0.084 Mbar-cm <sup>3</sup> /cm <sup>3</sup>
$e_0$	= 1282 cal/g
$A$	= 4.587641 Mbar
$B$	= 0.078517 Mbar
$C$	= 0.008222 Mbar
$R_1$	= 4.182585
$R_2$	= 1.048391
$\omega$	= 0.28639

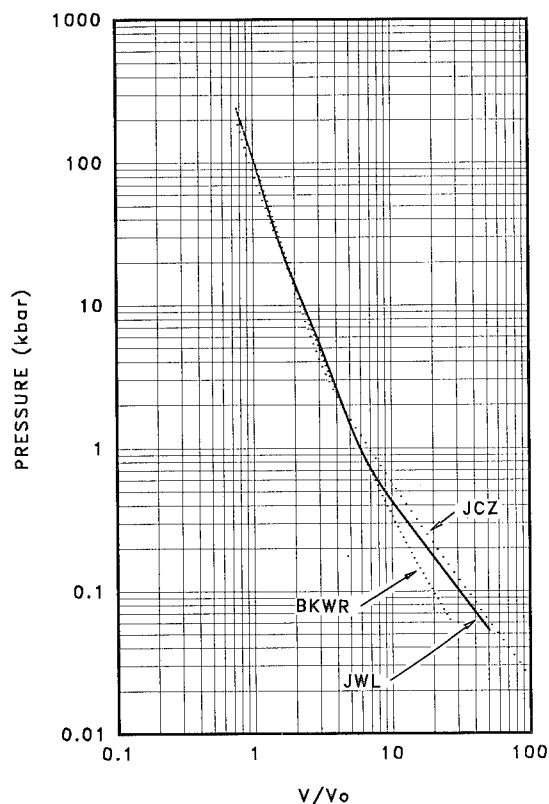


FIGURE 5. RESULTS OF JW FIT TO TIGER CALCULATED ISENTROPES USING BKWR AND JCZ MODELS

spherical charge can be safely cast, however, a very large scale cook-off test is required to increase confidence in the thermal runaway prediction model. A JW equation-of-state based on a theoretical isentrope was shown to be adequate for airblast prediction purposes. LLNL is presently developing a JW equation-of-state based on copper cylinder tests, and additional unconfined cylinder tests are planned to provide a better definition of the diameter-effects curve. The near-ideal behavior of ATX-27R for diameters above 4 inches is believed to be due to the simple CHNO elemental composition.

#### ACKNOWLEDGEMENTS

The authors gratefully acknowledge the numerous people at DNA, NMERI, EMRTC, and IRECO who contributed to this effort. We are especially grateful to the DNA Project Manager, Mr. Matt Holm, for his support and leadership.

#### REFERENCES

1. Ben-Dor, G., *Shock Wave Reflection Phenomena*, Springer-Verlag, Inc., New York, NY, 1992.
2. Reisler, R.E., *et al*, "Height of Burst Studies with a High Sound Speed Layer", in *Proceedings of the Tenth International Symposium on Military Applications of Blast Simulation*, Bad Reichenhall, FRG, 21-25 Sep 1987.
3. Reichenbach, H. and Kuhl, A.L., "HOB Experiments with 0.5-g Charges", in *Proceedings of the Eleventh International Symposium on Military Applications of Blast Simulation*, Albuquerque, NM, 10-15 Sep 1989.
4. Lutton, R.T., "MISTY PICTURE Overview", in *Proceedings of the MISTY PICTURE Symposium*, Test Directorate, Defense Nuclear Agency, Kirtland AFB, NM, 7-10 Dec 1987.
5. Baker, W.E., *Explosions in Air*, University of Texas Press, Austin and London, 1973.
6. Esparza, E.D., "Blast Measurements and Equivalency for Spherical Charges at Small Scaled Distances", *International Journal of Impact Engineering*, Vol. 4, No. 1, pp. 22-40, 1986.
7. Abegg, T.M. and Peterson, J.A., "Microcellular Composite Energetic Materials and Method for Making Same", U.S. Patent No. 4632714, Dec 30, 1986.
8. Jessop, H.A., *et al*, "Anhydrous Melt Emulsion Explosives", U.S. Patent No. 4600450, Feb 8, 1984.
9. Cranney, D.H., Gordon, D.L., and Hales, R.H., "Cast Explosives Composition and Method", U.S. Patent No. 4678524, Jul 7, 1987.
10. Healy, N.A., "Anhydrous Melt Emulsion Explosives", U.S. Patent 4248644, Feb 3, 1981.
11. Lee, J., *et al*, "Detonation and Shock Initiation Properties of Emulsion Explosives", in *Proceedings of the Ninth Symposium (International) on Detonation*, Portland, OR, Aug 28-Sep 1, 1989, pp. 573-584.
12. Gilmore, F.R., *Equilibrium Composition and Thermodynamic Properties of Air to 24,000 K*, RM-1543, The Rand Corporation, Santa Monica, CA, August 1955.

13. Gilmore, F.R., *Additional Values for the Equilibrium Composition and Thermodynamic Properties of Air*, RM-2328, The Rand Corporation, Santa Monica, CA, December 1959.

14. Goodman, H.J., *Compiled Free-Air Blast Data on Bare Spherical Pentolite*, BRL Report No. 1092, Aberdeen Proving Grounds, MD, February, 1960.

15. CRT ltr:JLT:Ser 6248N: of 19 Jun 1992, to Field Command, Defense Nuclear Agency, Kirtland AFB, NM.

---

#### DISCUSSION

KENNETH GRAHAM  
Atlantic Research Corporation, Gainesville, Virginia

Is EDDN now commercially available? What was your source of EDDN?

#### REPLY BY JOSEPH RENICK:

We used EDDN furnished by the U.S. Air Force. It is not commercially available but can be easily manufactured as needed. Sources were identified recently who were willing to produce EDDN.

## EFFECT OF INERT BINDER MECHANICAL PROPERTIES OF KINETIC PARAMETERS IN HMX-BASED CAST PBX

S. LECUME, P. GIMENEZ, J. MALA, J.F. GUERY

*S.N.P.E.*

Centre de Recherches du Bouchet - BP 2  
91710 VERT LE PETIT  
FRANCE

A comparative study was performed on four HMX - based explosives. Polyurethane, silicon, fluorinated and HTPB binders were selected. A correlation between binder mechanical properties and decomposition rates, calculated by a Forest Fire model, has been found out and constitutes the main result of our investigation. An approach based on measurements of induction time and wave propagation in sustained shock experiments is then proposed in order to fit the results by a LEE TARVER kinetic law.

### INTRODUCTION

For engineering purpose, we have investigated the shock to detonation transition in four similar HMX-based explosives differentiated by the inert binder used, in order to determine the binder contribution to the explosive behaviour. First, the steady detonation was studied. The binder effects on the main performances were analysed.

Then, for describing the transient detonation behaviour whatever the binder used, an empirical method which involves a Forest Fire model is proposed. In order to improve the treatment of the ignition phase, a new method for fitting some of the parameters of the Lee - Tarver

model has been developed from induction time results and applied to one of the studied compositions.

### COMPOSITIONS STUDIED

Four HMX - based cast PBXs have been formulated for the study. The volume rate in octogen is constant, 70 %, and the grain size distribution of HMX is always the same ; the mean specific surface area of the grains is about  $0.4 \text{ m}^2/\text{g}$ .

The major characteristics of the four compositions are indicated in table 1.



TABLE 1. CHARACTERISTICS OF THE COMPOSITIONS

Explosive	Binder	HMX % (by weight)	Density (kg/m <sup>3</sup> )
B2208	Polyurethane	82	1635
B2209	Silicon	81.5	1642
B2210	Fluorinated	72	1854
B2241	HTPB	82.8	1613

## STEADY STATE DETONATION

Detonation characteristics such as velocity, pressure and ballistic performance were measured for the four compositions, under steady propagation conditions.

### Detonation Velocity

Detonation velocities were measured in cylindrical cartridges of various diameters. The extrapolation of the experimental results to an infinite diameter gives the ideal detonation velocities  $D_{\infty}$ . These values are given in table 2. Despite the word "inert" used to qualify the binders, one can see that detonation velocity is greatly influenced by the choice of the binder. For example, the velocity is about 7 % more for B2208 than for B2209 and the difference cannot be explained by a change in density.

Using the TIGER code, the detonation velocity was calculated for two participation rates of the binder in the detonation ( $\lambda=0$  and  $\lambda=1$ ). For the simulation of the non - participation of the binder ( $\lambda=0$ ), the assumption of an independent decomposition for the explosive and the binder is made. However, the temperature and pressure equilibrium condition is met.

The comparison between experimental and

theoretical values (see table 2) shows that involving the binder in the detonation has generally a negative effect on performance.

TABLE 2. DETONATION VELOCITY

Explosive	Experimental $D_{\infty}$ (m/s)	$D_{TIGER}$ (m/s)	
		$\lambda = 0$	$\lambda = 1$
B2208	8237	8378	7921
B2209	7686	7977	7509
B2210	8100	8164	8166
B2241	8219	8356	7859

### Detonation Pressure

Detonation pressures were deduced from the measurements of the velocity of the shock wave induced in a PMMA block located at the end of the explosive cartridge. Large differences may be noted (see table 3). Replacing HTPB binder by the fluorinated one resulted in an increase of detonation pressure larger than 25 %.

TABLE 3. DETONATION PRESSURE

Explosive	B2208	B2209	B2210	B2241
P (GPa)	26.8	25.9	31.4	24.6

### Ballistic Performance

Ballistic performance was assessed using a symmetrical lateral driving test. Several experiments with plates of different thicknesses enable to determine the relationship between the lateral driving angle  $\varphi$  and the metal/explosive mass ratio  $\mu$ . From the knowledge of this relationship and the detonation velocity, the value

of the kinetic energy  $E$  transmitted to the liner is calculated with the following formula<sup>1</sup> :

$$E = \rho_o \mu D^2 [1 - \cos(\varphi)] \quad (1)$$

The value of the energy maximum,  $E_{\max}$ , is got from there and is given in table 4. The fluorinated binder leads to an increase for  $E_{\max}$  of about 18 % compared to the silicon and HTPB binders and 6 % compared to the polyurethane binder.

TABLE 4. BALLISTIC PERFORMANCE

Explosive	B2208	B2209	B2210	B2241
$E_{\max}$ (J/cm <sup>3</sup> )	2098	1872	2224	1896

#### TRANSIENT REGIME

##### Correlation Between Reaction Rate of the Compositions and Hugoniot of the Components

Wedge test experiments have been performed for three explosives (B2208, B2209 and B2210) for studying the role of the binder in the SDT process. Experimentally, the travelling distance to detonation is a function of the initial shock strength, and leads to the diagram commonly known as "Pop-plot", and corresponding to the following formula :

$$\ln X = \alpha_1 + \alpha_2 \ln P \quad (2)$$

where  $X$  means the run distance to detonation (in m) and  $P$  the shock pressure (in Pa). Table 5 gives the two parameters  $\alpha_1$  and  $\alpha_2$ .

TABLE 5. POP-PLOT COEFFICIENTS

Explosive	B2208	B2209	B2210
$\alpha_1$	26.86	31.43	28.62
$\alpha_2$	-1.39	-1.61	-1.47

Figure 1 shows the Pop - plots for B2208, B2209 and B2210. B2209 is the most sensitive composition, the difference between B2208 and B2210 is slight.

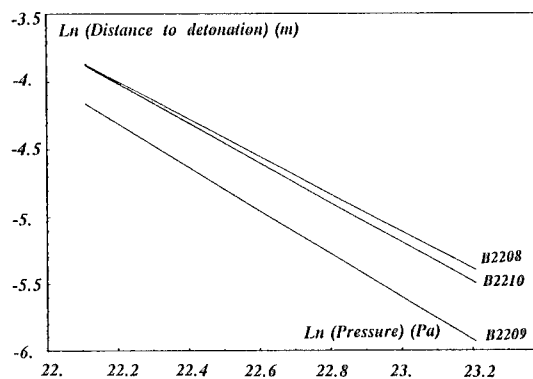


FIGURE 1. POP-PLOT FOR B2208, B2209 AND B2210

From the wedge test results and the experimentally determined  $U_s = C + S U_p$  Hugoniot of the components (see Table 6), shock - induced decomposition is calculated by a Forest Fire model<sup>2</sup>. In order to be able to determine the reaction rates, reactive and unreactive Hugoniot of the compositions have been inferred from those for components by means of a mixing rule<sup>3</sup>.

TABLE 6. HUGONIOT PARAMETERS

Component	Polyurethane binder	Silicon binder	Fluorinated binder	unreacted HMX <sup>4</sup>
C (m/s)	1444	1262	998	2740
S	2.297	1.875	2.128	2.60
$\rho_0$ (kg/m <sup>3</sup> )	980	1015	1740	1900

Then, we have tried to obtain a unique formulation of the reaction rate which could be valid whatever the binder used. This has led to the next formula :

$$d\lambda/dt = A \Delta u (1-\lambda) \widetilde{P}^N \quad (3)$$

with :

$$\widetilde{P} = P/\rho_0(C_0^2 - C_b^2) \quad (4)$$

where  $\lambda$  is the fraction reacted,  $P$  the shock pressure,  $\Delta u$  the particle velocity gap between the binder and the HMX crystals which is induced by the shock and can be considered as a parameter characterizing the shear which occurs within the sample,  $\rho_0$  the density of the composition,  $C_0$  and  $C_b$  respectively the sound speed in the composition and the binder.

The two parameters  $A$  and  $N$  should be dependent on the nature, the amount and the grain size of the explosive filler. For our HMX compositions,  $A = 17.82 \cdot 10^6$  (in  $m^{-1}$ ) and  $N = 3.98$ . A representation of the relationship (3) is given in figure 2.

As it can be seen from the relation 3, for a given octogen content, the reaction rate can be correlated with the mechanical properties of the binder represented only by its Hugoniot parameters. The parameter  $\Delta u$ , which roughly takes into account the shear, allows us to estimate the reaction rate of a composition by means of a

single curve (see figure 2), whatever the binder, as soon as its mechanical properties are known (see figure 3).

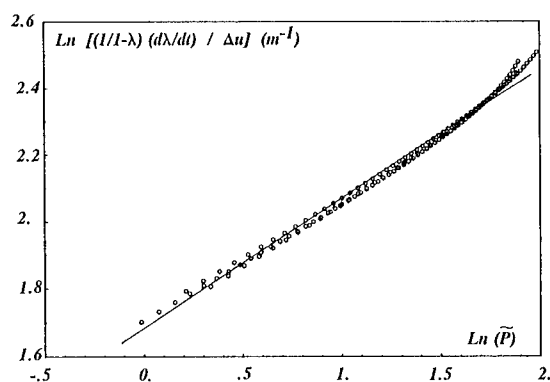


FIGURE 2. REACTION RATE VS PRESSURE

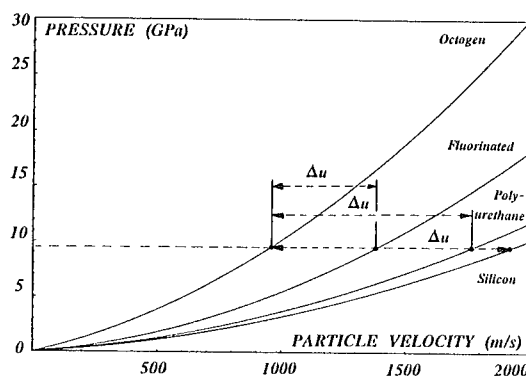


FIGURE 3. OCTOGEN AND BINDER HUGONIOTS.

## Fitting the Lee-Tarver Kinetic Law

We wanted to fit a more sophisticated kinetic law than a Forest Fire one from the previous experimental results, while taking into account induction time results. These last results were obtained from sustained shock experiments instrumented by means of pressure gauges. The explosive sample was glued onto an aluminium plate and this plate was impacted by an aluminium projectile launched by means of a light gas gun or a powder gun. At the interface of the explosive sample and aluminium plate, pressure histories were recorded in the range of 0.8 to 8 GPa.

From pressure signals, we have chosen to define the induction time  $\tau$  as the duration while no significant pressure increase was observed.

For B2210, which has been the only composition studied, the experimentally induction time results are presented in table 7.

TABLE 7. INDUCTION TIME FOR B2210

P (GPa)	0.87	1.92	3.29	42.9	*	*	*
$\tau$ ( $\mu$ s)	3.94	2.33	1.88	1.50	0.65	0.50	0.40

\* results obtained from C.E.G

The Lee- Tarver reactive model<sup>5</sup> was chosen. The explosive is described by two JWL equations of state for the unreacted solid phase and detonation products :

$$P = A e^{-R_1 v} + B e^{-R_2 v} + \omega C_v T / v \quad (5)$$

Pressure and temperature equilibrium is assumed. The decomposition reaction rate consists of two terms, an ignition and a growth

term :

$$\begin{aligned} d\lambda/dt &= I (1-\lambda)^m [(\rho/\rho_0)-1]^n + \\ G (1-\lambda)^x \lambda^y P^z &= \dot{\lambda}_I + \dot{\lambda}_G \end{aligned} \quad (6)$$

where  $\lambda$  is the reacted fraction,  $t$  the time,  $\rho_0$  the initial density,  $\rho$  the density of the unreacted explosive,  $P$  the pressure and  $I, m, n, G, x, y, z$  are constants.

Just behind the shock front, only the ignition term should not be equal to zero, at least as long as  $\lambda$  is less than a critical value  $\lambda^*$ , for which the increase of pressure becomes macroscopically significant. We assume that  $\lambda^*$  is independent of pressure.

For sustained shock experiments, the density remains nearly constant after the shock. Let us note  $\rho^*$  its value, we have :

$$\lambda^* \# \int_0^\tau I (1-\lambda)^m [(\rho^*/\rho_0)-1]^n dt \quad (7)$$

We can define the relationship between the shock and the induction time by the following formula<sup>6</sup> :

$$\begin{aligned} \int_0^\tau [(\rho^*/\rho_0)-1]^n dt &= [(\rho^*/\rho_0)-1]^n \tau \quad (8) \\ &= \int_0^{\lambda^*} d\lambda / [I (1-\lambda)^m] = A \end{aligned}$$

where  $A$  is a constant. One can note that the criterium  $[(\rho^*/\rho_0)-1]^n \tau = A$  can be considered as a SDT criterium as well as the classical  $P^n \tau = \text{constant}$ .

From the results given by the sustained shock experiments  $(P, \tau)$ , we can deduce the values of  $n$  and  $A$ .

In order to define completely the ignition term of the Lee-Tarver model, we have chosen  $m=1$  and calculated  $I$  from the next formula :

$$I = -\ln(1 - \lambda^*) / A \quad (9)$$

Thus, two parameters  $I$  and  $n$  can be fitted. The other parameters are obtained with the hydrocode DYNA2D<sup>7</sup> in an iterative way, by

fitting at the same time the induction time and wedge test data. For instance, following Lee and Tarver, we choose  $x=2/3$  and  $y=2/9$  which give a reasonable behaviour for the evolution of the surface area of hot spots.

For B2210, the JWL parameters for the unreactive solid and the products are indicated in Table 8.

TABLE 8. J.W.L. EQUATION OF STATE PARAMETERS

	A (Mbar)	B (Mbar)	R <sub>1</sub>	R <sub>2</sub>	$\omega$	E <sub>0</sub> (Mbar)
unreacted explosive	-3.75 10 <sup>-2</sup>	9186	1.317	15.08	1	--
reaction products	15.76	0.275	5.858	1.417	0.4	0.099

Table 9 gives the values of the Lee-Tarver kinetic law parameters, deduced from the previous method in the case of  $\lambda^* = 0.01$ .

TABLE 9. LEE-TARVER KINETIC LAW COEFFICIENTS

I	m	n	G	x	y	z
0.4317	1.0	2.495	250	2/3	2/9	2.2

We have simulated, with DYNA2D, impact experiments with in situ pressure gauge measurements corresponding to a shock pressure close to 5 GPa, in order to test this set of parameters.

The figure 4 shows a comparison between the computed pressure signals at four different depths within the explosive sample (corresponding to 0, 3, 6 and 10 mm) and the experimental pressure histories  $p(t)$ . The agreement for the

induction times is rather satisfactory but the growth step is not reproduced very correctly, probably due to the fact that the growth term in equation (6) is fitted only on wedge test results.

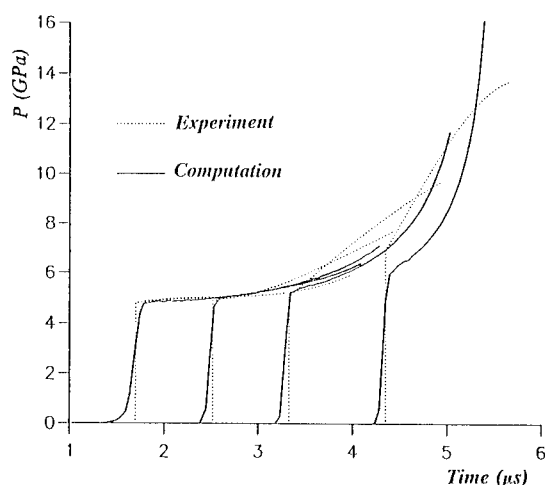


FIGURE 4. COMPARISON OF COMPUTED AND EXPERIMENTAL  $p(t)$  FOR B2210

## CONCLUSIONS

A series of HMX - based PBXs only utilizing inert binders has been tested. According to the binder, important differences in performance may be noted under steady propagation conditions, even if the nature and the content of the explosive filler remains the same.

An empirical method using a Forest Fire model has been developed. It allows us to estimate the reaction rate of an HMX-based composition if one knows the mechanical properties (Hugoniot) of its binder. It may certainly be improved and its application may be extended to other kinds of binders and/or explosive fillers.

A tentative to fit a Lee-Tarver kinetic law on a small number of experimental data including induction times and wedge test results has been carried out.

This work has been performed under the auspices of the French M.O.D (S.T.P.E).

## ACKNOWLEDGEMENTS

The authors wish to thank the people at the Centre de Recherches du Bouchet who have contributed to this work.

## REFERENCES

1. Défourneaux M., Jacques L., "Explosive deflection of a liner as a diagnostic of detonation flows", in *proceedings of the Fifth Symposium on Detonation*, Pasadena, 1970, pp 457 - 466

2. Forest C.A., "Burning and detonation", in *proceedings of the Seventh Symposium on Detonation*, Anapolis, Maryland, 1981, pp 234 - 243
3. Romain J.P., "*Equations d'état et stabilité des fronts d'onde de choc en milieu métallique homogène et hétérogène*", Thesis N°234, Poitiers, 1977
4. Olinger B., "The linear and volume compression of  $\beta$  HMX and RDX to 9 GPa", in *proceedings of the International Symposium on High Dynamic Pressures*, Paris, 1978, pp 3 - 8
5. Lee E.L., Tarver C.M., "*Phenomenological model of shock initiation in heterogeneous explosives*", *Phys. fluid* N°23, december 1980, pp 2362 - 2372
6. Guery J.F., private communication
7. Hallquist J.O., "*User's manual for DYNA2D*", LLNL 18756, jan.1984

---

## DISCUSSION

A. C. VAN DER STEEN  
Prins Maurits Laboratory TNO, Rijswijk,  
Netherlands

What are the specific densities of the binders you applied?

## REPLY BY S. LECUME

The fluorinated binder density is approximately twice as big as the polyurethan and silicon binder; the values are, respectively, 1.74 g/cm<sup>3</sup>, 0.98 g/cm<sup>3</sup>, and 0.92 g/cm<sup>3</sup>.

**DISCUSSION**

HAROLD J. GRYTING

Gryting Energetics Science Company,  
San Antonio, Texas

other chlorinated material or chlorine gas during  
stability tests or in storage?

**REPLY BY S. LECUME**

Does the silicon binder release any HCl or

No, the components of our silicon binder  
do not comprise any chlorine.

**SESSIONS ON**  
**SAFETY RELATED TOPICS**

**Cochairmen:**     **Joseph Lannon**  
                             **U.S. Army Armament Research, Development**  
                             **and Engineering Center**

**Henric Östmark**  
                             **National Defence Research Establishment**



## SIMULATED FRAGMENT ATTACK ON CASED MUNITIONS

Pauline Roberts\*, J.E. Field.

Cavendish Laboratory,  
Madingley Road,  
Cambridge, CB3 0HE.  
England.

\*also DRA, Fort Halstead, Nr. Sevenoaks, Kent, England.

The mechanisms which, under simulated fragment attack, can lead to ignition in sections of cased charges have been studied using high-speed photography. The front-end geometry and velocity of the projectiles, the casing material and explosive filling of the target were altered to determine their effect on these mechanisms.

### INTRODUCTION

The response of cased munitions to high velocity impact is an area of major concern to weapon designers. The impact, caused by bullet or shrapnel fragment during either intentional or accidental attack can elicit a variety of responses from the munition. The most violent response is the prompt shock initiation of the explosive filling, leading to detonation of the whole charge. If the shock pressure resulting from the impact is not high enough to shock initiate the charge, it may nevertheless penetrate the casing and cause ignition of the charge within. This may or may not be followed by a deflagration-to-detonation transition (DDT), depending upon the degree of confinement, which will in any case have been reduced by the impact, and the nature of the explosive filling. The impact, whether it penetrates the casing or not, may not cause a sustained ignition of the filling though it is still possible that the damage which results from this impact may increase the sensitivity of the charge to further impacts.

The series of experiments detailed here address the problem of observing inside a cased charge whilst it is undergoing simulated fragment attack at impact velocities below which shock initiation is caused. Shock initiation mechanisms have been extensively investigated due to the seriousness of response. Early work by Dewey and Slade<sup>1</sup> and Brown and Whitbread<sup>2</sup> using right circular cylinders fired at bare and lightly-covered explosives, impacting on the flat end of the cylinders, showed that the critical velocity for initiation of the sample was independent of the length of the projectile, as long as the length was greater than about half the diameter. If the material of the projectile was changed, then the critical velocity was altered so that the impact shock pressure remained constant.

If the charges were more heavily confined, Howe *et al.*<sup>3</sup> found that shock initiation did not always explain the detonation thresholds that were observed, and that the length of the projectile was important when

considering explosive fillings such as TNT, where shear effects were also found to contribute to the initiation process.

Cook *et al.*<sup>4</sup> have carried out much work in this area, particularly on the effect of the charge casing on the munition's response. They have shown that for thin barriers of steel and aluminium, it is possible to model initiation using a modified 1-D critical energy-per-unit-area criterion, but that for initiation through thicker barriers, this model is not applicable. Liang *et al.*<sup>5</sup> used the DEFEL 2-D finite element dynamic code incorporating the Mie-Gruneisen equation of state to calculate the pressure and temperature distributions within explosive charges impacted by flat-ended projectiles. They found that shock initiation mechanisms were dominant for bare charges, but that for heavily confined charges, viscoplastic heating of the explosive was important and that adiabatic shear band heating in the explosive near the periphery of the plug was a possible ignition mechanism.

Using thin barriers, Haskins *et al.*<sup>6</sup>, in projectile attack trials on PE4, investigated whether altering the front-end projectile geometry affected the critical velocity for initiation. They concluded from theoretical and experimental results that flat-ended projectiles, which transmit a 1-D shock into the explosive, were the most efficient at causing initiation. Projectiles with cone angles of less than  $\sim 120^\circ$ , which have a subsonic contact periphery velocity, and flat-ended projectiles impacting thick barriers, produce divergent shocks in the explosive material and are therefore less efficient at causing initiation. They also investigated the effect of charge-liner materials and found that rubber liners reduced the impact shock, providing the rubber's Hugoniot curve did not lie between that of the casing and the explosive.

At impact velocities below the shock initiation threshold, there is the possibility of the charge undergoing a wide variety of reactions from DDT to

ricochet of the projectile with no apparent reaction. Although the hazard will generally decrease with lowering impact velocity, any response, from DDT to burning leading to case venting, may be transmitted to other munitions stored in close proximity. The initial impact may thus escalate from a small-scale event into a more devastating large-scale accident. Much work has been carried out by Boggs *et al.*<sup>7</sup> into quantifying the range of responses a munition may exhibit under various stimuli, including bullet and fragment attack, so that a mechanistic understanding of the reactions and predictive capability could be achieved for a given munition. Whilst most of the research effort has understandably been concentrated on the most hazardous SDT and DDT responses, the aim of the experiments detailed in this paper was to investigate and understand the mechanisms which cause ignition of the charge in the first place. Further responses were noted but are not the primary interest of this work.

## EXPERIMENTAL

There are a number of putative mechanisms for ignition, including heating due to rapid viscous flow ahead of the projectile, adiabatic shear band formation and heating of the explosive filling in contact with the points of casing failure. In order to isolate the effects of these mechanisms, various parameters and conditions in the experimental arrangement were altered. High-speed photography was used to observe directly the ignition sites and give a photographic insight into the ignition mechanisms.

The front-end geometry of the impacting projectile was varied in three ways to alter the flow conditions and shear stresses ahead of the projectile. The projectiles were either flat-ended, hemispherical-ended or 30° cone-ended (see Table 1). A flat-ended projectile would be expected to cause shear failure of the casing and push the plug of casing ahead of the projectile into the explosive. This geometry was also expected to cause the highest amount of shear stress and viscous flow in the filling. At the other extreme, a 30° cone-ended projectile should cause tensile failure of the casing, followed by penetration of the filling by the

projectile and the deformed points at casing fracture. In the case of the hemispherical-ended projectile, the casing should undergo tensile and shear failure under impact and the explosive filling would be affected by shear stresses and rapid viscous flow ahead of the projectile though to a lesser extent than for the flat-ended projectile.

In order to isolate the effect of whether the casing fracture surfaces cause ignitions in the explosive, the casing of the target was cut at the projectile entry point, leaving effectively a bare charge. The targets were then tested for their response to the three types of projectile.

The effect of casing material (see Table 2) was also investigated by using both copper and steel. Due to the different physical properties of these two materials and their different modes of failure (copper undergoing ductile failure at higher strain rates than steel, which is more prone to brittle fracture) it was thought that the casing material may alter the likelihood of ignition.

Voids were introduced between the casing and the filling and at varying distances from the casing within the filling to assess their effect on the sensitivity of the target to ignition. These voids were included to simulate the effect of voids occurring in charges through debonding from the casing and imperfect processing.

The impact experiments were performed using a single-stage, twin-solenoid operated gas-gun with helium as the propellant gas because of its low molecular weight. The gun barrel was 2 m long and of 13.2 mm bore. The projectiles were made of silver steel (density 7.8 g cm<sup>-3</sup>) and sabot-driven to keep the mass of explosive to a minimum to comply with safety constraints. The sabots were made of nylon 666 rod (density 1.1 g cm<sup>-3</sup>) with a recess for the projectile at the front and material reamed out at the rear to reduce the weight of the combination, as shown in figure 1. The projectile was fired at the target at velocities in the range 350 to 650 m s<sup>-1</sup>. Although the flat-ended projectile imparts a shock into the explosive filling, it is below the critical shock initiation pressure and therefore shock initiation was not expected to occur.

TABLE 1. FRONT-END GEOMETRY AND DIMENSIONS OF PROJECTILES

front-end geometry	diameter (mm)	length (mm)	mass (g)
flat	5.2	16	2.6
hemispherical	5.2	16	2.4
30° cone	5.2	20	2.3

TABLE 2. PHYSICAL PROPERTIES OF THE TARGET CASING MATERIALS

casing material	density (g cm <sup>-3</sup> )	Young's modulus (GPa)	thermal conductivity (kJ s <sup>-1</sup> m <sup>-1</sup> K <sup>-1</sup> )	specific heat capacity (J kg <sup>-1</sup> K <sup>-1</sup> )
copper	8.91	130	7.14	390
steel (mild)	7.86	210	0.97	470

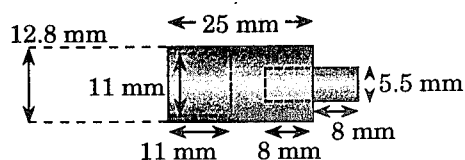


FIGURE 1. SCHEMATIC DIAGRAM OF THE SABOT-PROJECTILE COMBINATION

In addition to varying the front-end geometry of the projectiles, the impact velocities were varied to determine whether different mechanisms become more dominant at different velocities.

There were 5 types of explosive filling used as targets, as detailed in table 3.

The targets were 19 mm diameter  $\times$  6 mm thick discs of explosive, encased by 1.5 mm of either copper or mild steel and sandwiched between two 10 mm thick blocks of polycarbonate, as shown in figure 2. The blocks also acted as sabot strippers, although as a result,

TABLE 3. TARGET FILLINGS

explosive	composition (wt %)	density ( $\text{g cm}^{-3}$ )
PE4	RDX (88%)/grease (12%)	1.60
cyclotol	RDX (60%)/TNT(40%)	1.68
octol	HMX(70%)/TNT(30%)	1.80
LX-14	HMX (95.5%)/estane (4.5%)	1.83
PBX	HMX (88%)/binder (12%)	1.74

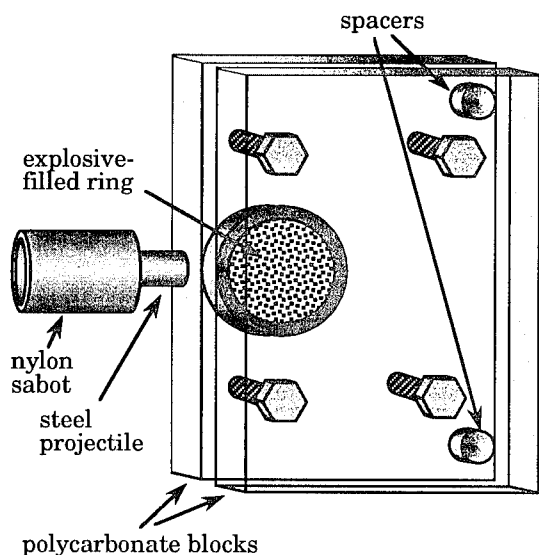


FIGURE 2. SCHEMATIC DIAGRAM OF THE TARGET ARRANGEMENT

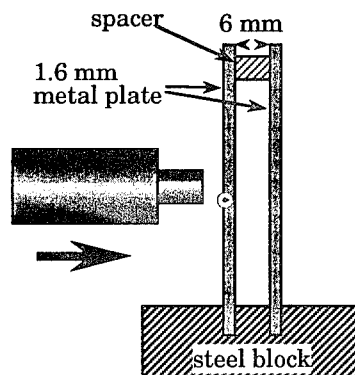


FIGURE 3. SCHEMATIC DIAGRAM OF THE PROJECTILE PENETRATION TARGET ARRANGEMENT

a second shock was imparted to the explosive on impact of the sabot. The effect of this impact is clearly visible in some shots, but since it occurred at least 15  $\mu\text{s}$  after the projectile had impacted, it had no effect on the initial ignition mechanisms.

Projectile penetration experiments, to determine the amount of kinetic energy lost by the projectile in this process, were also performed on sheets of copper and steel of the same thickness as the target casings. These experiments were performed using metal sheet/air gap/metal sheet and metal sheet/cyclotol/metal sheet arrangements for comparison (see figure 3).

The velocity of the projectile was measured by timing it between two laser beams a known distance apart. The timer was connected to an up-down counter which was used to fire the camera at the correct time, irrespective of projectile velocity.

The impacts on targets were recorded using an Imacon 792 camera operating in framing mode, with framing rates of between  $5 \times 10^4$  and  $1 \times 10^6$  frames per second, and those for the projectile penetration experiments using an Imacon 790 in streak mode at  $1100 \text{ ns mm}^{-1}$ . In addition, an IMCO Ultramac camera, with programmable interframe and exposure times, was used for some of the cyclotol filled target experiments.

## EXPERIMENTAL RESULTS

### Projectile Penetration of Steel and Copper Casings

At the impact velocities in this study, the flat-ended projectiles produced sufficiently high shear strain rates in both metals to shear out a plug of casing, with initially relatively little deformation of the surrounding material. Figure 5 shows a steel projectile penetrating an unfilled copper casing, with the plug (p) clearly visible after penetration. Photographs obtained of the same event with a steel ring were almost identical, and examination of the rings and plugs afterwards confirmed that the failure was very similar in the two cases, although the subsequent deformation around the point of failure was rather greater for the copper rings.

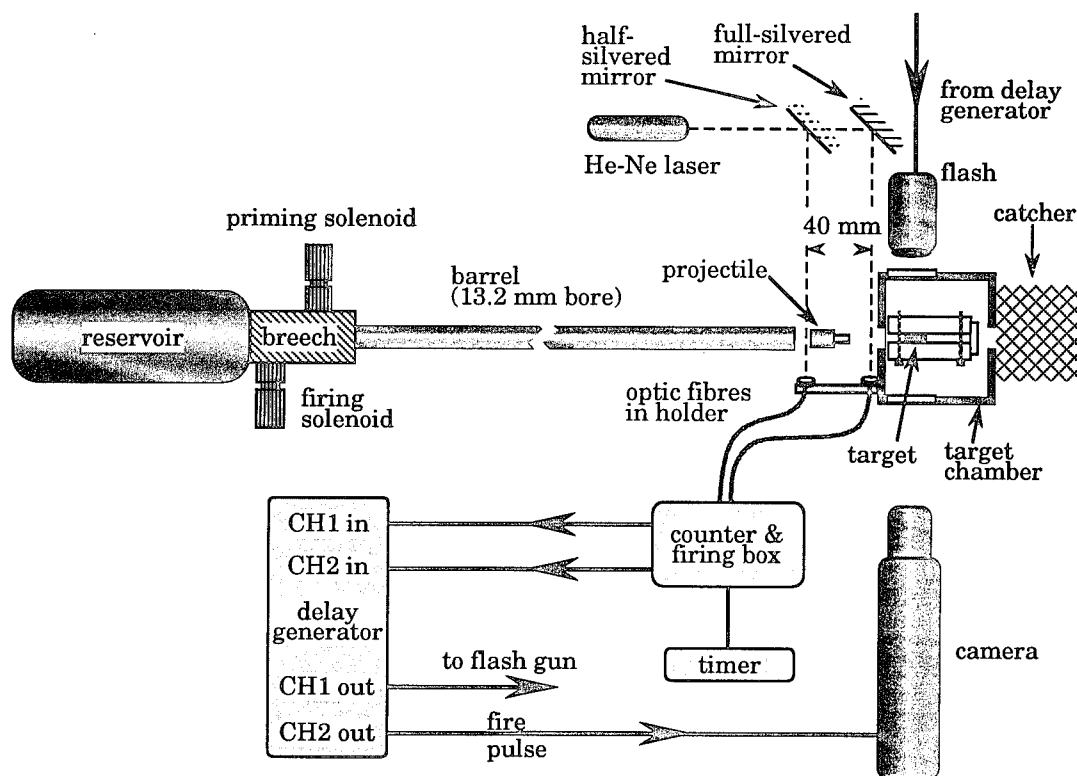


FIGURE 4. SCHEMATIC DIAGRAM OF THE EXPERIMENTAL ARRANGEMENT

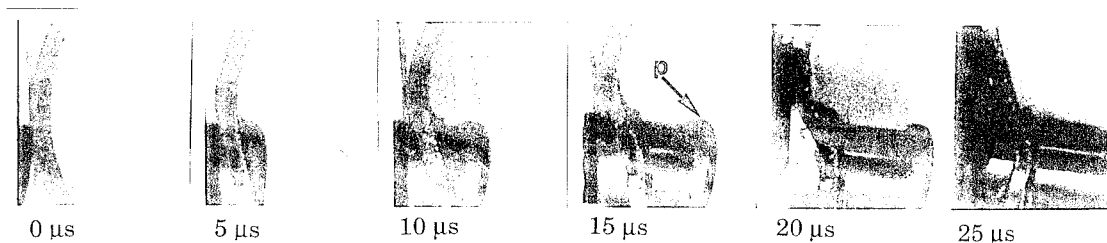


FIGURE 5. FLAT-ENDED PROJECTILE IMPACT OF AN UNFILLED COPPER CASING AT  $400 \text{ ms}^{-1}$ . (FRAMING RATE  $2 \times 10^5 \text{ fps}$ )

With pointed projectiles, the strain rates in the metal during penetration are far less than for the flat-ended projectiles. The copper casing undergoes ductile failure and the projectile emerges relatively undamaged. However, the harder steel casing causes the point to be deformed by the initial impact, and it does not survive the penetration, emerging with a rounded profile as shown in Figure 6.

Hemispherical-ended projectiles impacting copper led to predominantly ductile failure on penetration, with a thin layer of copper being stretched across the front of the projectile. On impacting mild steel, the penetration occurred by plugging, with a well-defined plug of steel being removed in a similar manner to that seen with the

flat-ended impacts. This may involve a combination of ductile and adiabatic shear failure.

From streak photographs of the penetration of flat-ended projectiles through steel and copper plates, the kinetic energy lost in the process was estimated. Steel projectiles of  $2.5 \text{ g}$  impacting  $1.6 \text{ mm}$  steel plate with a velocity of  $500 \text{ m s}^{-1}$  were estimated to have lost  $100 \text{ J}$  of kinetic energy. If this energy is deposited adiabatically into a thin region ( $\approx 50 \mu\text{m}$ ) of shear band at the edge of the plug, then an initial temperature rise of greater than  $2000 \text{ K}$  would be achieved, and although this would be quenched very quickly by conduction into the body of the plug, it might be expected to constitute a viable ignition source for the explosive within.

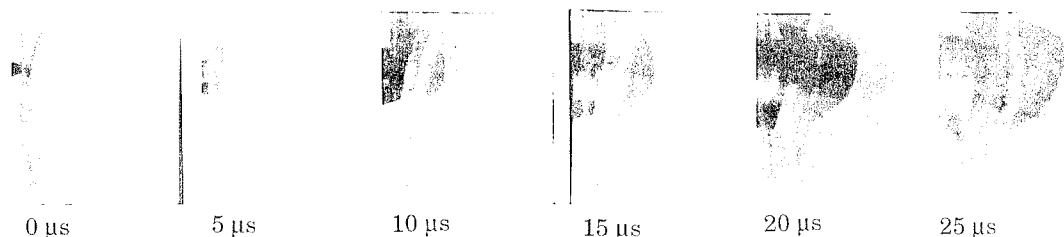


FIGURE 6. 30° CONE-ENDED PROJECTILE IMPACT OF AN UNFILLED STEEL CASING AT 400 ms<sup>-1</sup>. (FRAMING RATE 2 x 10<sup>5</sup> fps)

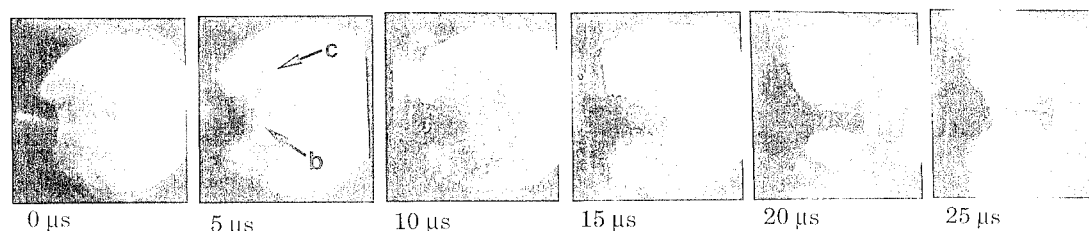


FIGURE 7. FLAT-ENDED PROJECTILE IMPACT OF A COPPER-CASED LX-14 TARGET AT 506 ms<sup>-1</sup>. (FRAMING RATE 2 x 10<sup>5</sup> fps)

Repeating these tests with explosive sandwiched between the plates enabled the amount of energy lost by the projectile in passing through the explosive layer to be calculated. For a cast cyclotol composition, this was of the order of 10 – 20 J mm<sup>-1</sup>.

#### Ignition Tests on Explosive Compositions

Table 4 shows threshold flat-ended impact velocities for observed ignition sites for the compositions tested. Values are given for both bare and cased charges. Where ignition was not observed in the high-speed photographs, the composition was usually recovered unburned from the test-box.

Subsequent experiments, to observe different types of ignition mechanism, were mostly restricted to cyclotol, octol and LX-14, which had the lower threshold velocities.

#### Effect of Projectile Front-End Geometry

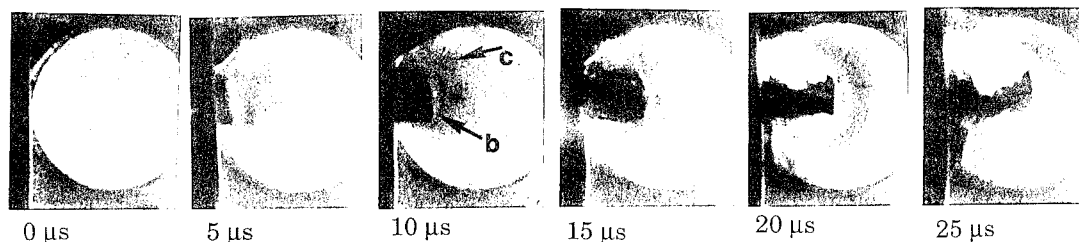
Above the threshold velocity for flat-ended

projectiles quoted in table 4, similar ignition sites were readily observed in the cyclotol, octol and LX-14 compositions in the absence of any voids. The main source of ignition appeared to be due to the rapid flow of the explosive around the front of the projectile, with additional reaction sometimes seen associated with the compressive wave moving ahead of the projectile into the surrounding material. Figure 7 shows reaction in a target of LX-14 and the outbreak of burning (b) in the damaged material ahead of the projectile, together with some possible ignition behind the compressive wave front (c). There is further ignition at the failed edge of the casing on impact of the sabot (frame 3). There does not seem to be ignition associated with the initial failure of the casing.

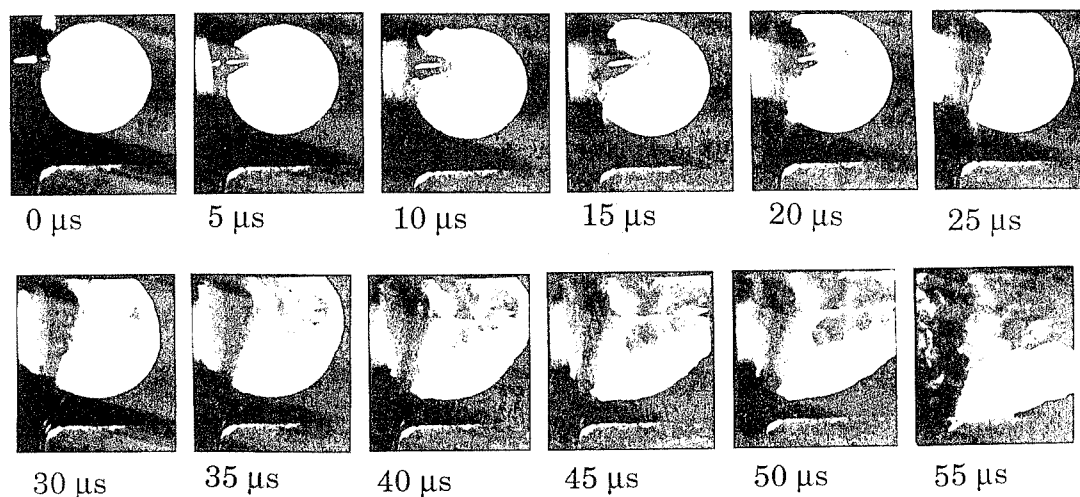
Figure 8 shows a similar impact on a target with cut and removed casing, and the ignition is very similar to that observed in the fully cased sample. The bright flash of light in frame 4 is probably due to compression of air trapped under the end of the casing by the sabot.

TABLE 4. THRESHOLD VELOCITIES FOR FLAT-ENDED IMPACTS

Composition	Threshold velocity (m s <sup>-1</sup> )			Comments
	Copper	Steel	Bare	
PE4	> 610	> 610	> 610	some ignition with voids
cyclotol	530	550	520	
octol	550	–	540	tests in steel inconclusive
LX-14	400	–	< 500	not yet tested in steel
PBX	> 580	> 580	> 580	not yet tested with voids



**FIGURE 8. FLAT-ENDED PROJECTILE IMPACT OF A CUT COPPER-CASED LX-14 TARGET AT  $506 \text{ ms}^{-1}$ . (FRAMING RATE  $2 \times 10^5 \text{ fps}$ )**



**FIGURE 9. FLAT-ENDED PROJECTILE IMPACT OF A COPPER-CASED OCTOL TARGET AT  $570 \text{ ms}^{-1}$ . (FRAMING RATE  $2 \times 10^5 \text{ fps}$ )**

Further ignition due to sabot impact is apparent in some of the high-speed photographs. Figure 9 is a sequence showing a flat-ended projectile impacting a cased sample of octol, taken using an IMCO Ultramac image converter camera. The sabot impact occurs in frame 3. In the later frames, two regions of burning are clearly visible, one in the damaged material behind the projectile as it crosses the ring and the other across a broader area moving away from the sabot impact.

No ignitions were observed with either pointed or hemispherical-ended projectiles up to the maximum velocities tested ( $\sim 610 \text{ m s}^{-1}$ ), nor were there any subsequent ignitions due to sabot impact on the already damaged material of the type observed with the flat-ended projectiles.

#### Effect of Voids

Voids of diameter 1.5 mm were introduced into samples of octol and cyclotol at various distances from the point of projectile impact. Since the mechanism by which a void acts as an ignition site is by heating due to shock induced adiabatic collapse of the void, it would be expected that the effectiveness of the void would decrease with distance from the point of impact.

Figure 10 shows the collapse of a void at the casing under the point of impact of a flat-ended projectile on a sample of cyclotol. There is a second, similar void at 12 mm from the point of impact. The heating of the trapped gas in the first void causes it to luminesce, and burning of the surrounding material is apparent in frame 4. The second void does not undergo such strong compression as it is much further away from the point of impact and thus similar luminescence does not occur. Almost all of the explosive was burned in this test, in contrast to those tests in which no voids were present when most of it was recovered, indicating that the first void was the main source of ignition.

Figure 11 shows the effect of a flat-ended projectile impacting a sample of cased octol with a void 3 mm from the point of impact. The projectile is below the surface of the charge and cannot be seen, but the shock wave causing the collapse is visible as a darkening of the surface of the charge, and the collapse of the void is complete, as indicated by the flash of light, roughly  $6 \mu\text{s}$  after the shock wave reaches it. Burning of the surrounding material is visible in the subsequent frames. Impact of the sabot, with further associated reaction, is visible in frame 7.

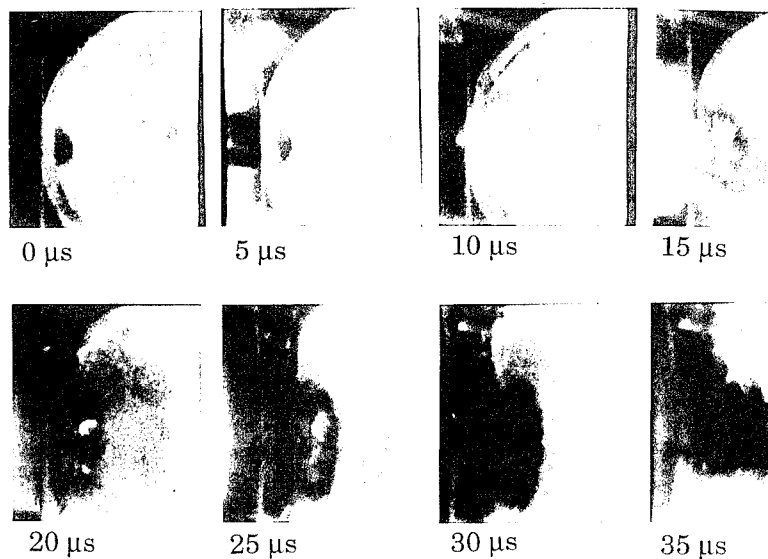


FIGURE 10. FLAT-ENDED PROJECTILE IMPACT AT  $556 \text{ ms}^{-1}$  OF A STEEL-CASED CYCLOTOL TARGET WITH A VOID AT THE SITE OF IMPACT AND SECOND VOID NEAR THE TARGET CENTRE. (FRAMING RATE  $2 \times 10^5 \text{ fps}$ )

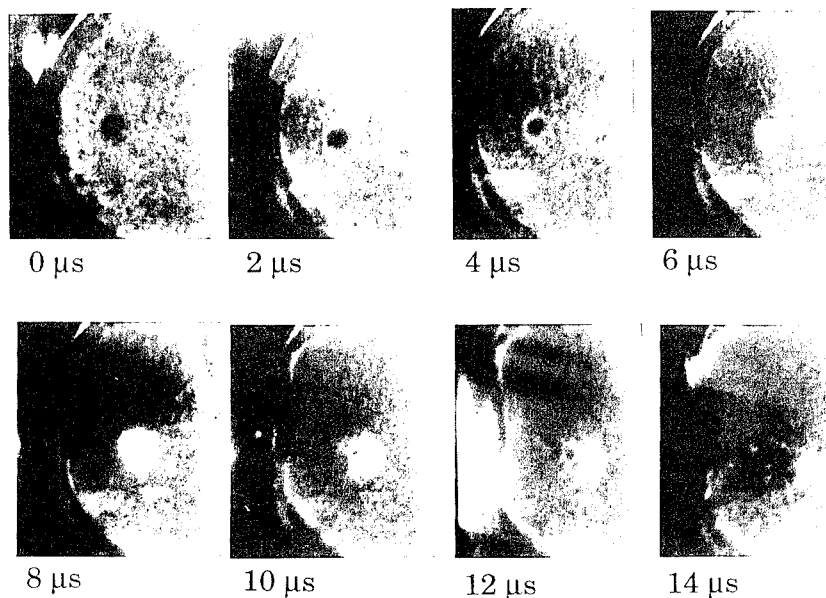


FIGURE 11. FLAT-ENDED PROJECTILE IMPACT AT  $564 \text{ ms}^{-1}$  OF A STEEL-CASED OCTOL TARGET WITH A VOID 3 mm FROM THE SITE OF IMPACT. (FRAMING RATE  $5 \times 10^5 \text{ fps}$ )

Impacts with pointed and hemispherical-ended projectiles were far less effective at rapidly collapsing voids, giving little or no light output and no ignitions.

#### DISCUSSION

High-speed photography of the impact of flat-ended

projectiles on copper and steel targets shows that at the impact velocities studied, the projectile penetrates by shearing a plug of metal from the target. Assuming that this is basically an adiabatic shear process, the fracture energy will lead to the edges of the plug being hot, and this might provide a possible source of ignition as the plug is driven through the explosive composition.

Calculation of the temperature rise at the edge of the plug from measurement of the energy lost by the projectile suggests that very high temperatures may be achieved. However, even if quenching of this hot region by conduction of heat into the body of the plug is ignored, which may be justifiable on the timescales involved, the temperature rise in any one small region of the explosive which comes into contact with the edge of the plug will be limited by the duration of that contact. This duration is roughly determined by the impact velocity and the casing thickness if the filling is assumed to be stationary as the plug moves through it; in these experiments it would be of the order of 4  $\mu$ s.

The high-speed photographs of ignition in LX-14 and octol show that the outbreak of reaction is associated with the leading edge of the projectile or plug. However, there is little difference between the observed ignition mechanisms for cased and uncased explosives, despite the lack of a hot plug in the latter case, which suggests that the source of ignition is more to do with the rapid flow of the material ahead of the projectile. This should be similar for the two situations, though with a bare charge, the projectile will be moving faster through not having been slowed by collision with the casing, and the edges of the leading face will be sharper than the slightly rounded edge of the sheared plug. Both of these effects will tend to produce higher material flow velocities in the bare charge than in the cased charge for any given impact velocity.

The threshold velocity for ignition of octol appeared to be lower for copper casing than for steel, despite the higher thermal conductivity of copper, which should lead to a much more rapid cooling of the edges of the plug and make it less effective as a source of ignition. This also suggests that the hot plug may not be the predominant source of ignition in these impacts.

Changing the front end of the projectile to a conical shape alters the nature of the casing failure, the strength and divergence of the shock wave which is transmitted to the explosive through the casing, and reduces the flow velocity of the material around the projectile once it has entered the explosive. The rapid adiabatic shear failure of the casing seen with the flat-ended projectile is absent; in the case of the copper casing, the projectile penetrates reasonably intact by ductile failure of the metal whereas with steel, the front of the projectile is flattened by the impact and it is quite blunt when it reaches the explosive. All these factors should reduce the effectiveness of the projectile as an ignition source, and this was indeed found to be the case, with no observed ignitions up to 610 m s<sup>-1</sup>. Hemispherical-ended projectiles, which caused ductile failure in copper but shear failure in steel, also failed to produce ignitions even in steel casings, again indicating that the fractured plug may be less important than the material flow.

These observations are not inconsistent with the calculations of Liang *et al.*<sup>5</sup> who showed that the

temperature rise in an explosive due to the shear and flow of material ahead of a projectile could be expected to produce local temperatures high enough to cause ignition.

## CONCLUSIONS

High-speed photography of projectile impacts on cased and uncased charges has permitted direct observation of the ignition sites within the explosive. These observations suggest that the rapid flow of material around the front of the projectile may be more important as an ignition source than the hot fracture surface of the plug of casing which is sheared out in the course of casing penetration.

## ACKNOWLEDGEMENTS

P.R. thanks DRA, Fort Halstead for supporting her research. SERC are thanked for equipment grants. The research was supported in part by the U.S. European Office on Contract DAJA 95-90-C-002. We thank Dr. P.M. Dickson for his advice and help with the experimental techniques.

## REFERENCES

1. Dewey, J. and Slade, D., "High order initiation of two military explosives by projectile impact", ARBRL-TB-1021, 1957, Ballistic Research Laboratory, Aberdeen Proving Ground, MD.
2. Brown, S. and Whitbread, E., "The initiation of detonation by shock waves of known intensity and duration", Colloque Internationale C.N.R.S., Les Ondes de Detonation, editions Du Centre National De la Recherche Scientifique 15, Paris, 1962, p.97.
3. Howe, P.M., Watson, J. and Frey, R.B., "Response of confined explosive charges by projectile impact", Seventh Symposium (International) on Detonation, Annapolis, MD, 1981, pp. 1048-1054.
4. Cook, M.D., Haskins, P.J. and James, H.R., "Projectile impact initiation of explosive charges", Ninth Symposium (International) on Detonation, Portland, Oregon, 1989, pp.1441-1450.
5. Liang, D., Chou, P.C. and Hashemi, J., "Shock and shear effects in explosives due to impact", Shock compression of condensed matter, Williamsburg, Virginia, 1991, pp. 345-348.
6. Haskins, P.J., Cook, M.D. and James, H.R., "Effect of case thickness and projectile geometry on the shock initiation threshold for a given explosive", AGARD Conference preprints, Bonn, Germany, 1991, paper 18.
7. Boggs, T.L. et al, "Hazards of energetic materials and their relation to munitions survivability", AGARD conference preprints, Bonn, Germany, 1991, paper 16.



## DISCUSSION

ANDREW VICTOR

Victor Technology, Ridgecrest, California

In field tests of projectile attack we may observe time delays from impact to ignition of sizeable fractions of a second and even many minutes. What is the longest delay time from impact to ignition observed in your tests?

## REPLY BY PAULINE ROBERTS:

In my experiments, I have observed delays of approximately 120  $\mu$ s before ignition occurs. However, my simulated sections of cased charge, within their polycarbonate blocks, do not experience the degree of confinement that would be present in an actual munition and thus the delay time stated should be treated with caution.

## DETONATION AND REACTION OF CLASS 1.1 EXPLOSIVES AND PROPELLANTS DUE TO WATER JET IMPACT

S.G. Giltner, O.C. Sitton, and P.N. Worsey  
Rock Mechanics and Explosives Research Center  
University of Missouri - Rolla  
Rolla, Missouri 65401

Water jet impact sensitivity tests for energetic materials developed at the University of Missouri - Rolla, are described. The tests were developed as part of a program to investigate the demilitarizing of ordnance using high pressure water jets. As high pressure water has been proven effective for the excavation of HE ordnance, water jet initiation sensitivity of explosives and propellants must be quantified.

Testing has focused on the determination of reaction thresholds. Two tests were developed producing water jets with velocities of 0.5 to 5 mm/ $\mu$ s and 6 mm/ $\mu$ s to 11 mm/ $\mu$ s. Each test is recorded by high speed photography to record jet velocity and any visible reaction. Reaction products are retained for analysis, specifically the  $\text{NO}_x^-$  ions which are indicative of the reaction of military explosives and propellants.

A total of 1500 tests have been performed on 34 energetic materials. All but the most insensitive explosives tested have reacted to impact by water jets. Descriptions of the various reaction levels achieved are presented.

### INTRODUCTION

Researchers at the Rock Mechanics and Explosives Research Center (RMERC) of the University of Missouri-Rolla (UMR) have been working for the United States Navy defense contractors and nuclear weapons industry to determine the water jet impact sensitivity of Plastic Bonded eXplosives (PBX's) and Class 1.1 propellants. The purpose of this research is to establish safe procedures for the cutting and washout of these materials from missile warheads and rocket motors using high pressure water jets. This exotic extraction technique was considered as normal methods of demil such as steaming are ineffective on the newer "insensitive" explosives such as PBX's in comparison to the traditional melt cast explosives.

In light of the new high pressure water excavation process having been proven, it was important that the sensitivity of the energetic materials to water jet impact be quantified. Due to the size and type of some ordnance in inventory, avoidance of a water jet impact initiated reaction is critical. Therefore the testing not only focused on the determination of sustained reaction thresholds but also on the point at

which brief reactions occur.

As a result of extensive development and testing, a small scale test apparatus was devised. The apparatus is similar to a water cannon, but due to its small size it was named the "water derringer". Simplistically, the water derringer comprises a plunger, enclosed in a steel jacket, which is forced by an explosive charge to expel a small slug (5 cc or less) of water through an accelerating nozzle at an explosive target.

The derringer is used for water jet velocities of 0.5 mm/ $\mu$ s to 5 mm/ $\mu$ s. To obtain velocities in excess of 5 mm/ $\mu$ s, a second experimental procedure known as the shaped charge test is used. The standardized shaped charge test comprises the formation and ejection of a focused jet of water by the detonation of a shaped charge incorporating a water gel liner.

The explosives and Class 1.1 propellants tested to date for water jet impact sensitivity include: PBX 9404; PBXN 3, 4, 5, 6, 101, 103, 105, 106, 107, and 108; AFX 109, 201, and 708; PETN, Cyclotol, DDP, CYH, VTQ-3, FKM, GBG, and VTG-5A. In addition, limited tests have been performed on PBX 9407, 9501,

9502, AFX 400, Comp A-3, Comp B, Comp D-2, LX-10-2, HMX, Ammonium Perchlorate, NC, and NG/NC.

Although a large amount of data has been collected on these materials, only a small sample of results can be presented due to the limited available space in these proceedings. In addition to references mentioned later, various detailed information on these tests can be found in Summers, *et. al.* 1985 and 1988).

## EQUIPMENT AND FACILITIES

Separate descriptions of the derringer and shaped charge tests are given in later sections. However before discussing these two tests, an overview of the facilities and equipment common to both tests is provided.

### Explosion Chamber

Due to the violent nature of both tests and the potential for the violent reaction of up to 50 grams of high explosives, the tests are performed within an explosion chamber. This chamber is located in a controlled indoor environment within part of the RMERC Explosives Laboratory. The explosion chamber has an internal capacity in excess of 25 m<sup>3</sup> and is rated at 1 kg of TNT with a vacuum applied. The chamber is a 1.4 m internal diameter steel cylinder with four ports along the sides. A single side port is used as a viewing window for the high speed camera while the other ports are used for the passage of gas sampling tubes and the high voltage firing and flash synchronization cabling required.

### High Speed Photography of The Derringer and Shaped Charge Tests

In order to ascertain jet velocity and to observe any light emitted by a reaction, high speed photography is utilized in the testing. The Explosives Laboratory at RMERC operates a Cordin framing camera model no. 10-010A which is capable of recording at a framing rate from 50,000 to 1,250,000 frames per second. For the photographic recording of the derringer tests, a framing rate between 100,000 and 200,000 frames per second is used. For the shaped charge tests a framing rate of 500,000 frames per second is used.

The high speed light source used for the derringer tests is a multiple array of 2 or 3 Vivitar 2800 Zoom Thyristor Flash Guns. The shaped charge tests are self illuminated by the detonation of the shaped charges and therefore do not require flash units.

## THE DERRINGER TEST

Two derringer designs are available to produce either focused or unfocused water jets (see Worsey, *et. al.* 1990 for details). The two designs are almost

identical in outward appearance and represent a balance between size, weight, survivability and cost. Highly focused jet impact has been developed for the investigation of the reaction of high explosives to

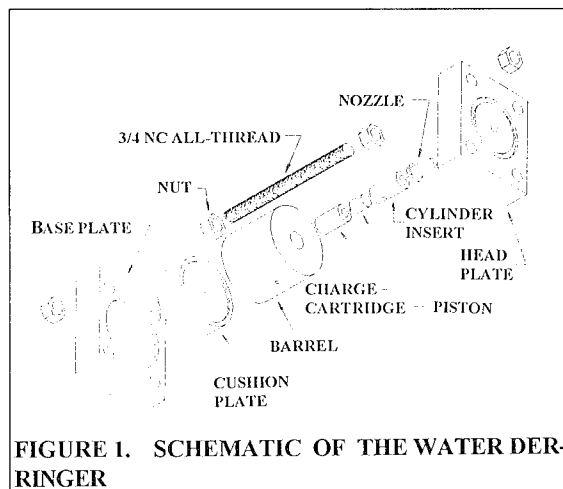


FIGURE 1. SCHEMATIC OF THE WATER DERRINGER

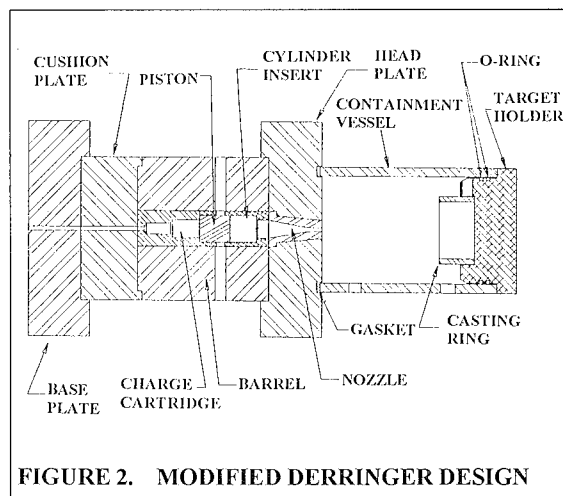


FIGURE 2. MODIFIED DERRINGER DESIGN

machining by high pressure water jet, whereas the unfocused, or diverging, jet is used to investigate their reaction to high pressure water jet washout. A schematic breakdown of the derringer is presented in Figure 1.

The present modified design, as illustrated in Figure 2, has a mass of approximately 21 kg, has good survivability and lasts approximately 50 shots when firing 1 gram propulsion charges before a major overhaul is required.

In the derringer tests small volumes of water (5 cc or less) are rapidly accelerated by a piston to velocities of up to 5 mm/ $\mu$ s. In order to power this acceleration it is necessary to use an explosive driver. The booster charge comprises secondary high explosive

marketed as Detasheet™ by Dupont. Depending on the velocity required, up to 6 grams of this plastic explosive may be used. The detonator used is a Reynolds RP80 Exploding Bridgewire Detonator (EBW) with a functioning time of less than 3  $\mu$ s. The piston/cylinder arrangement was experimentally designed to eliminate contamination of the containment vessel by the gaseous products of the propulsion charge.

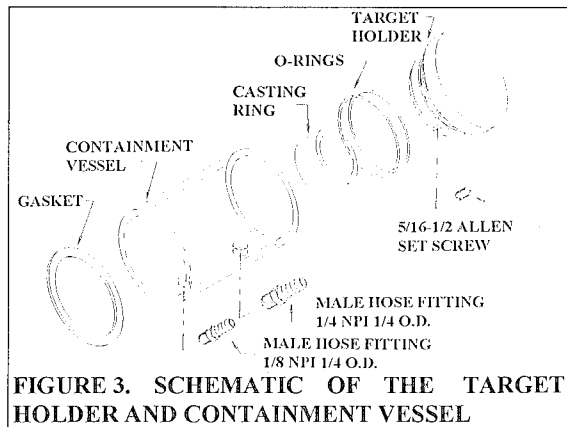


**FIGURE 3. SCHEMATIC OF THE TARGET HOLDER AND CONTAINMENT VESSEL**

#### Target Holder/Containment Vessel

The explosive target is imbedded in plaster of Paris and held in position directly above and in-line with the derringer nozzle by an aluminum target holder. The target is set at a fixed standoff of 100 mm from the nozzle by a clear acrylic tube which serves as a containment vessel between the target holder and derringer. The containment vessel retains any reaction products, which are subsequently collected by flushing and chemically analyzed. The transparency of the vessel allows the high speed camera to photograph the water jet impacting the target explosive. A schematic of the target holder and containment vessel is given in Figure 3 and a photograph of the assembled unit in Figure 4.

The containment vessel is secured in place so that a gas-tight seal of 35 kPa is maintained with the derringer head plate throughout the test.

#### Gas Sampling And Analysis Equipment

Gas samples are collected in each derringer test to determine if any low level reactions occur. Low level nitrite emissions may be caused by the chemical reaction of certain compounds under high pressure rather than an explosive reaction, an example being ammonium perchlorate.

The gas sampling procedure now used is an improvement of the original design. This gas sampling

equipment is illustrated in Figure 5 and described in detail by Giltner, *et. al.* 1993.

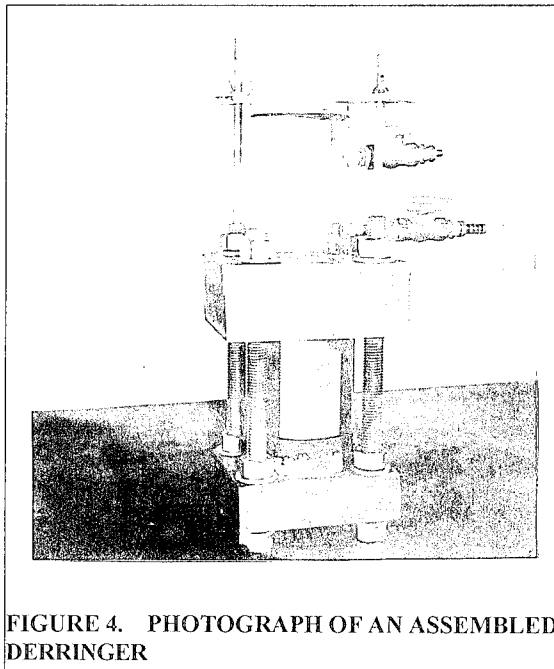


**FIGURE 4. PHOTOGRAPH OF AN ASSEMBLED DERRINGER**

The sparger solution consists of 2.0 ppm  $\text{SO}_4^{2-}$  in 2.2 mM  $\text{NaHCO}_3$ /1.8 mM  $\text{Na}_2\text{CO}_3$ . The carbonate/bicarbonate solution is also the mobile phase for the ion chromatograph method which eliminates the solvent peak. The 2.0 ppm  $\text{SO}_4^{2-}$  serves as an internal standard in the method which corrects for the loss of water during sparging and any errors related to sample injection. The gas samples are bubbled into this solution during gas sample acquisition. The nitrite ion in acid or neutral water is unstable and will break down or convert to other products, so the basic

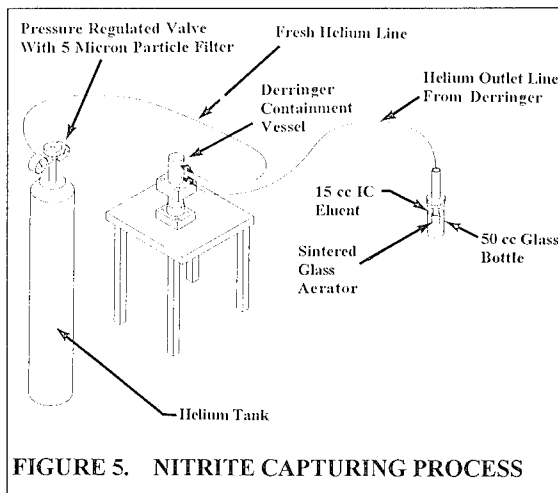


**FIGURE 5. NITRITE CAPTURING PROCESS**

$\text{NaHCO}_3/\text{Na}_2\text{CO}_3$  mixture will trap the ion and not allow it to convert to undesirable by-products.

The gas sample analysis used employs a computerized HP 1090 M liquid chromatograph equipped with an anion column, a diode-array UV/VIS, and a conductivity detector. Based on standardization run results it is calculated that the test results are

accurate to better than 3%. A lengthy detailed procedure for the use of the ion chromatograph in this test is given in the standard operating procedure (Worsey, *et al.* 1990) and by Giltner, *et al.* 1993. Examples of the ion chromatograph output for no reaction and a brief reaction as identified by the presence of the nitrite ion ( $\text{NO}_2^-$ ) are given in Figure 6 and 7 respectively.

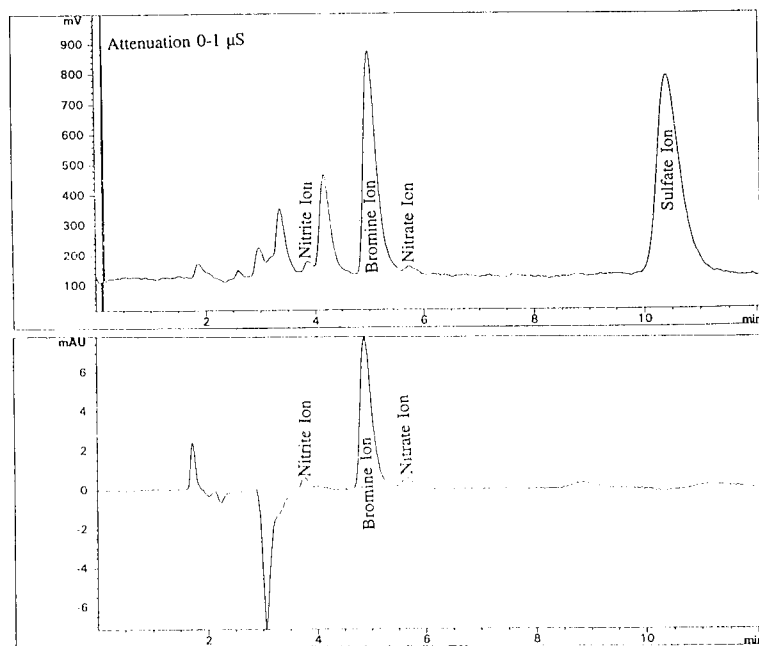


FIGURE 6. SAMPLE I.C. OUTPUT FOR NO REACTION

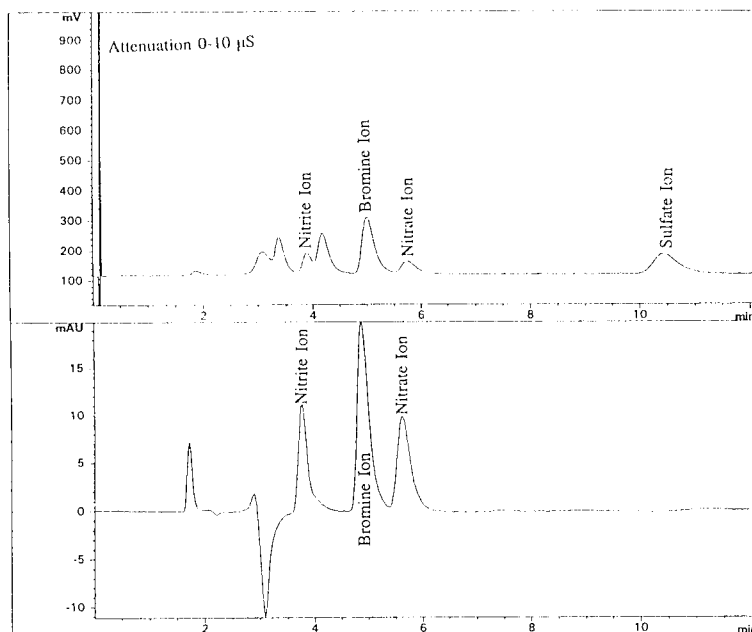


FIGURE 7. SAMPLE I.C. OUTPUT FOR A BRIEF REACTION

Example chromatograms resulting from the 206 nm measurements is shown in Figures 6 and 7 as the DAD1 A signal. The chromatogram obtained from the conductivity measurement is shown as Signal Z in these figures. The sulfate ion is conductive in solution but does not absorb in the UV region and cannot be seen on the 206 nm trace. Therefore, a known and constant amount of bromine was added to each sample as an external standard for the quantification of the DAD1 A chromatogram. As bromine is conductive in solution it is also shown in the conductivity trace.

There are several distinct advantages to the analysis methods developed for these studies. The nitrite and nitrate ions are detected and quantified using two independent techniques. Since spectra of the nitrite and nitrate peaks were obtained in real time, a comparison of the spectra at half peak height on the upslope and downslope and at the apex of the peak allowed a determination of the purity of the peak. This provided online verification that the nitrite, bromine and nitrate peaks were indeed those species and not contaminated by an unsuspected reaction product.

## THE SHAPED CHARGE TEST

The shaped charge test is employed where water jet velocities exceeding 5 mm/ $\mu$ s are desired. The conical shaped charge used is a standard well perforating charge which is acquired from the manufacturer without a liner.

A three millimeter water gel liner is cast and set in the shaped charge immediately before each test. The test assembly is illustrated in Figure 8 and described in detail by Klosterman, *et. al.* 1988 and Canon, *et. al.* 1988. Carrageenan gel, which is 97.5% water by weight, is used as the shaped charge liner. The shape and thickness of the gel is precisely controlled by a precision machined mandrel.

The explosive target is placed in contact with a witness plate made of 25 mm thick hot rolled steel on the target rest (with adhesive backing if necessary). In order to vary the jet velocity and impact pressure, the standoff distance is changed in increments of 100 mm. Most high explosives may be detonated using this test at 100 to 200 mm standoffs and only a small number of

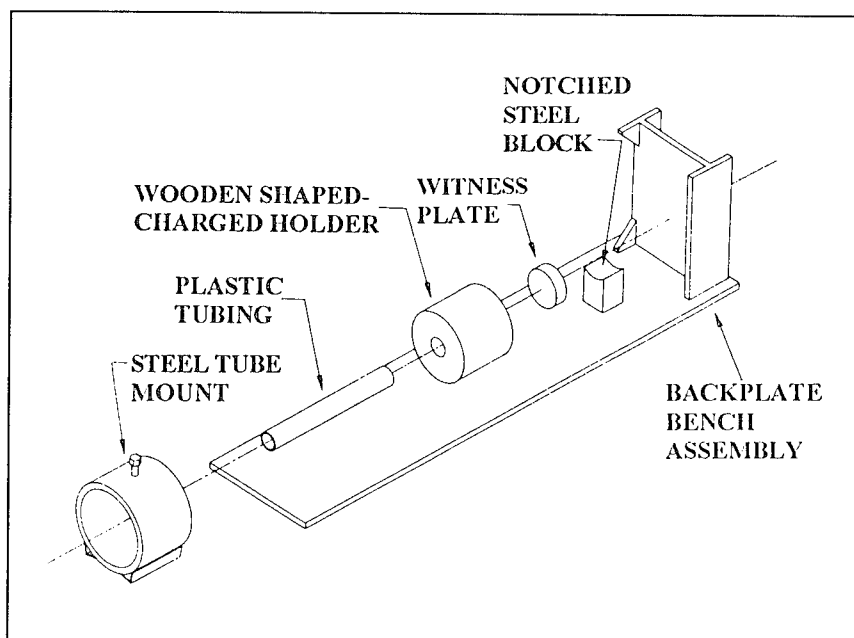


FIGURE 8. SHAPED CHARGE TEST ASSEMBLY

insensitive high explosives have failed to provide a sustained detonation.

A deflagration or detonation of the explosive target is confirmed by both measuring the rate of any visible reaction from the high speed photographs and from examination of the witness plate for either scarring or imprinting. Due to the destructive nature of this test, it is not possible to confine and isolate the reaction gases liberated from the target material. Therefore no gas samples are collected in the shaped charge test.

An example of the detonation of an explosive target is given in Figure 9 with an imprint due to a target detonation in Figure 10. The clear imprint in the mild steel witness plate shown in Figure 10 is indicative of a detonation. The high speed photograph indicates the extreme bright white light of a detonation and the analysis of successive photographs indicates the extremely high rate of reaction. In many cases the shock wave from the detonating explosive is of

sufficient strength to produce a spall on the back of the witness plate or in extreme cases fragment the witness plate into several pieces. In comparison, a deflagration emits a warmer less bright light with a comparatively slow target consumption rate. As the deflagration of an explosive target does not create a shock wave, the steel witness plate shows no sign of disruption except for severe scorching on the surface.

#### SAMPLE PHOTOGRAPHIC RESULTS

Examples of the photographs obtained using the described derringer photographic setup are given in Figures 11, 12 and 13. The first photograph (Figure 11) illustrates a focused jet before impact with the explosive target. The second photograph (Figure 12) is an example of the limited fireball emanating from the surface of an explosive target during a brief initiation. In this reaction mode the target is initiated by the first striking of the jet. It has been noted that reactions are more likely to occur when the jet front is spread over the majority of the target surface and impacts uniformly giving a "slapping" action. Whereas, the initial front of the jet causes reaction in this mode, the effect of the main column of the jet is to extinguish the reaction by the erosion, dispersion and quenching of the reacting material. This is obviously for only weak reactions where the rate and strength of the propagation is far less than that of the water jet. Where strong deflagrations or detonations are experienced, total target consumption can be expected. An example of such a violent reaction is given in Figure 13, which is a single frame from the detonation of an explosive target in which the complete containment vessel was obliterated.

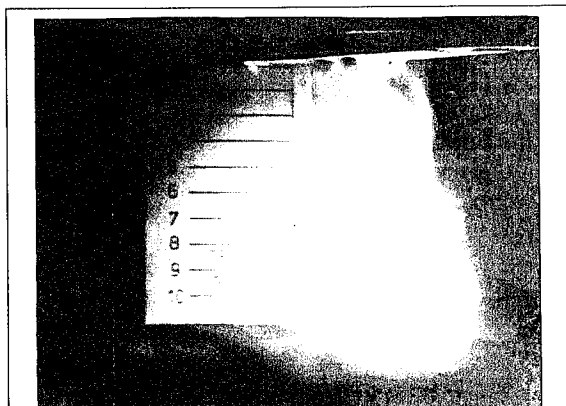


FIGURE 9. DETONATION OF AN EXPLOSIVE TARGET BY WATER JET IMPACT

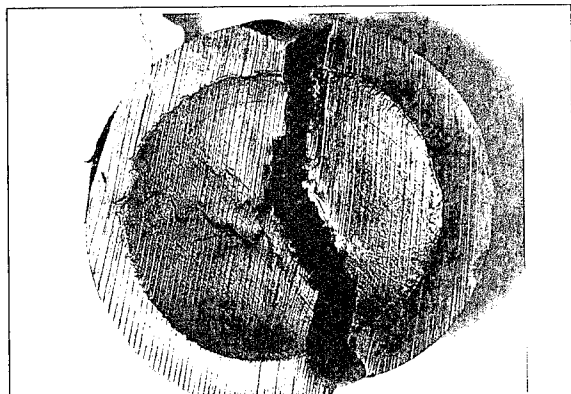


FIGURE 10. WITNESS PLATE SHOWING IMPRINT DUE TO TARGET DETONATION

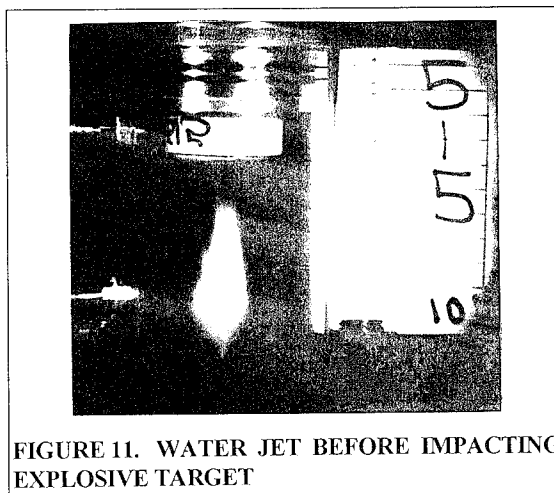
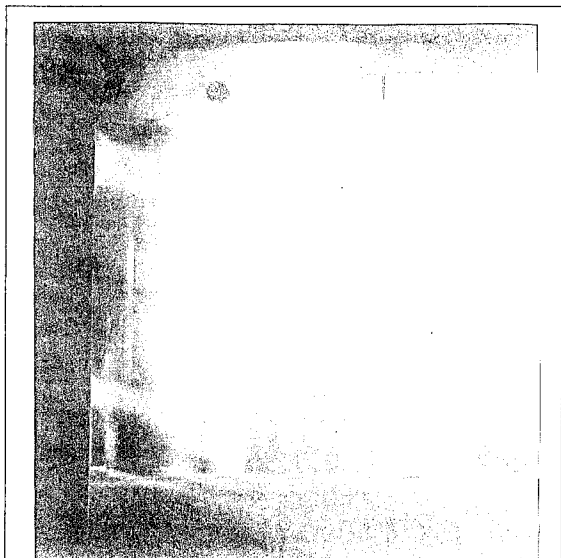
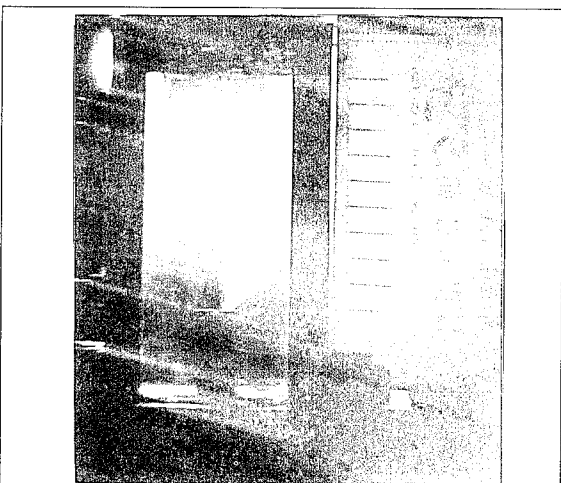


FIGURE 11. WATER JET BEFORE IMPACTING EXPLOSIVE TARGET



**FIGURE 12. IMPACT OF WATER JET CAUSING BRIEF VISIBLE REACTION**



**FIGURE 13. DETONATION OF AN EXPLOSIVE TARGET BY WATER JET IMPACT IN THE DERRINGER TEST**

As mentioned previously, the main objective of the high speed photography is to measure the water jet velocity and observe any visible reaction of the target, whether brief or sustained, to the water jet impact. From this information a histogram of jet velocity versus visible and no visible reactions can be established (Figures 14, 15, 16, and 17). As can be seen in these figures, a transition zone exists where visible and no visible reactions overlap. However as the jet velocity continues to increase, visible reactions become dominant. The transition zone shown is typical for most Class 1.1 propellants and is the main area of

interest for determining safety data for water jet washout.

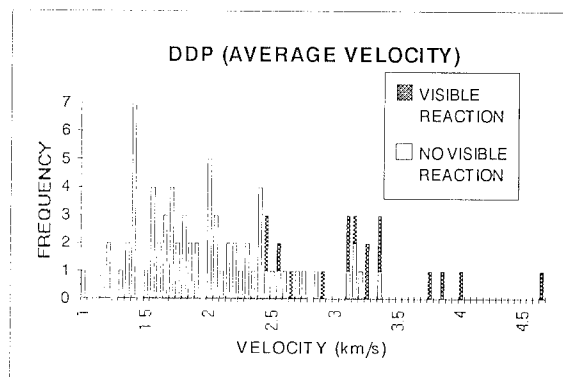


**FIGURE 14. FREQUENCY FOR A RANGE OF AVERAGE JET VELOCITIES, DDP TARGETS**

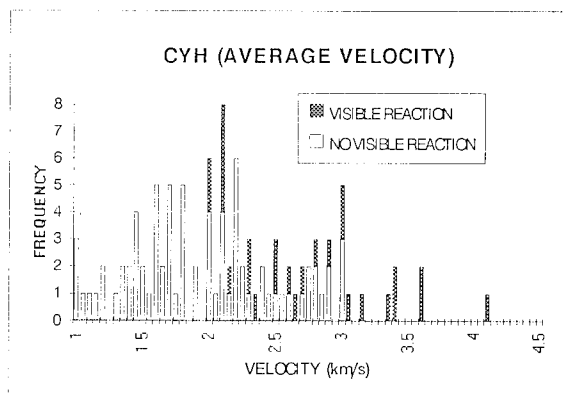


**FIGURE 15. FREQUENCY FOR A RANGE OF AVERAGE JET VELOCITIES, CYH TARGETS**

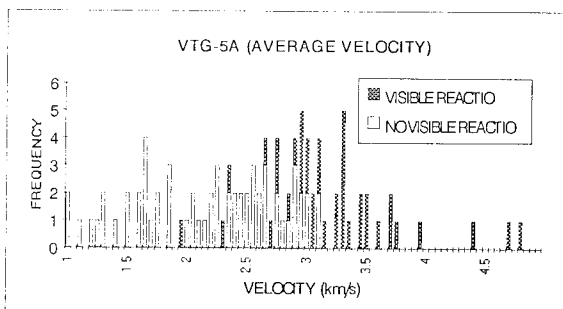


**FIGURE 16. FREQUENCY FOR A RANGE OF AVERAGE JET VELOCITIES, VTG-5A TARGETS**



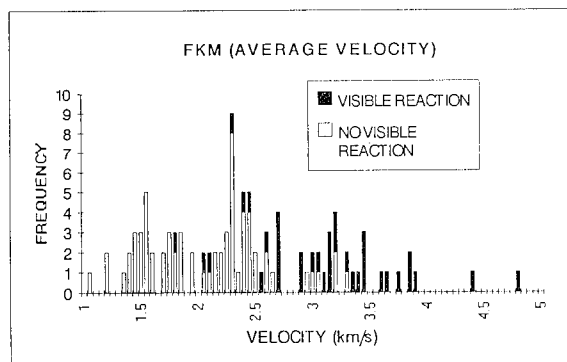


FIGURE 17. FREQUENCY FOR A RANGE OF AVERAGE JET VELOCITIES, FKM TARGETS

Another item of interest is the impact velocity threshold for visible reactions. Table 1 lists the impact velocity threshold values for DDP, CYH, VTG-5A, FKM, ammonium perchlorate (AP), nitrocellulose (NC), HMX, and a NG/NC double-base.

TABLE 1. VISIBLE REACTION THRESHOLDS

TARGET	AVERAGE VELOCITY THRESHOLD (km/s)	IMPACT VELOCITY THRESHOLD (km/s)
DDP	2.45	1.50
CYH	2.00	2.25
FKM	1.83	1.88
VTG-5A	1.95	1.60
AP	2.90	3.15
NC	2.30	2.44
HMX	2.25	2.70
Double-Base	3.00	2.63

#### SAMPLE ION CHROMATOGRAPH RESULTS

Illustrated in Figures 18, 19, 20, and 21 are the accompanying plot of jet velocity versus nitrite concentration for DDP, CYH, VTG-5A, and FKM which typifies most Class 1.1 propellants. It is evident that nitrite levels suddenly increase around a different velocity for each propellant type with generally strong reactions occurring over 2 to 2.5 km/s. A small amount of background flutter is shown for DDP and CYH and is typical of explosives containing ammonium perchlorate.

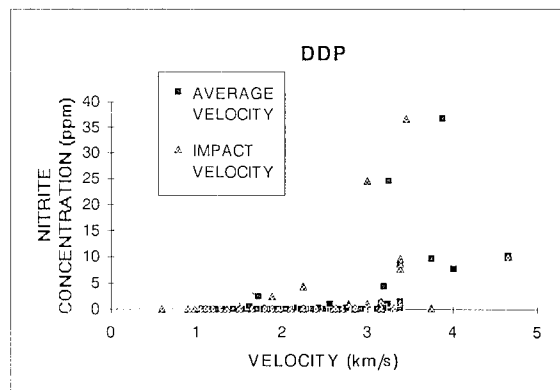


FIGURE 18. PLOT OF JET VELOCITIES VERSUS NITRITE CONCENTRATION 0-10 ppm FOR DDP TESTS

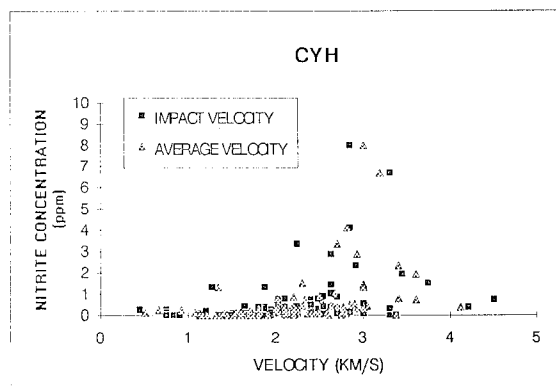


FIGURE 19. PLOT OF JET VELOCITIES VERSUS NITRITE CONCENTRATION 0-10 ppm FOR CYH TESTS

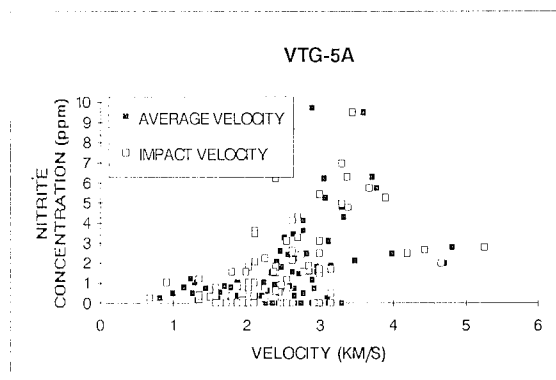
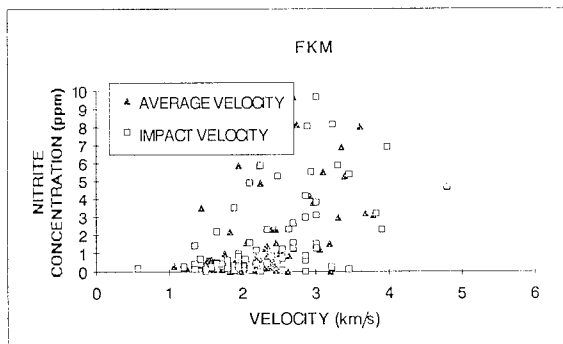


FIGURE 20. PLOT OF JET VELOCITIES VERSUS NITRITE CONCENTRATION 0-10 ppm FOR VTG-5A TESTS



**FIGURE 21. PLOT OF JET VELOCITIES VERSUS NITRITE CONCENTRATION 0-10 ppm FOR FKM TESTS**

## SUMMARY

A total of 34 different explosives and propellants have been investigated to date using the water derringer and shaped charge techniques. These tests have proven invaluable in the derivation of initiation threshold data for water jet impact. Excellent results have been achieved which have formed the basic safety data on which the water jet washout and machining of explosives and propellants has been based.

Tentative comparisons between other sensitivity tests have been made and from verbal discussions with Sandia National Laboratories personnel it appears that the waterjet impact sensitivity of an explosive may be directly linked to slapper detonator impact sensitivities (Cooper, 1990). Data on common and similar explosives give similar detonation impact threshold velocities for both tests. It is thought that this similarity is due to the closeness of the densities of Kapton and water.

## ACKNOWLEDGMENTS

We would like to express our appreciation to the sponsors of this work and the technical personnel responsible for testing and fabrication of the derringer components, specifically Mike Sturdevant, Terry Croxford, Scott Link, and John Pierce for operating tests, Dr. Greg Galecki for nozzle manufacturing processes and supervision of machine shop personnel, machine shop personnel James Blaine and Doug Hopper, and the analytical chemistry personnel responsible for the ion chromatography Dr. Beistel, April Wright and Ralph Grant.

## REFERENCES

- Canon C.M., Klosterman J.K. and Worsey P.N., "Fluid Jet Explosive Test Studies", Final Report of Investigations to Mason and Hanger - Silas Mason Company Inc., Pantex Plant, H5111600, 49 pages, July 1988.
- Cooper P., Sandia National Laboratories, personal communication, October 1990.
- Giltner, S.G., Sitton, O.C. and Worsey, P.N., "The Reaction of Class 1.1 Propellants to Water Jet Impact", Proceedings 24th International Annual Conference of ICT, Karlsruhe, Federal Republic of Germany, 41, 1-13, 29 June - 2 July, 1993.
- Klosterman J.K. and Worsey P.N., "Fluid Jet Impact Sensitivity Test Manual", Mason & Hanger-Silas Mason Company, Pantex, H5111600, 161 pages, July 1988.
- Summers D.A. and Worsey P.N. "Evaluation of Washout Procedures for Missile Casings", Final Report US Naval Weapons Support Center, Crane IN, N00164-84-C-0205, 58, November 1985.
- Summers D.A., Wu W., Worsey P.N. and Craig L.E. "PBX Demilitarization", US Navy Publication NWSC/CR/RDTR-427, Ordnance Engineering Dept., Naval Weapons Support Center, Crane, IN, 79 pages, September 1988.
- Worsey P.N., Summers, D.A. and Craig L.E. "Waterjet Impact Sensitivity Test Manual", US Navy Publication NWSC/CR/RDTR-541, Ordnance Engineering Department, Naval Weapons Support Center, Crane, IN, 191 pages, June 1990.
- Worsey P.N. and Giltner S.G., "Water Jet Impact Sensitivity Testing of DDP Class 1.1 Propellant", Report of Investigations to Naval Weapons Support Ctr., Ordnance Engineering, Code 4022 bld. 3031 Crane, IN 47522-5090, Restricted Access, pp. 22, September, 1992.
- Worsey P.N. and Giltner S.G., "Water Jet Impact Sensitivity Testing of CYH Class 1.1 Propellant (REVISED)" Report of Investigations to Naval Weapons Support Ctr., Ordnance Engineering, Code 4022 bld. 3031 Crane, IN 47522-5090, Restricted Access, 23 pages, November 1992.
- Worsey P.N. and Giltner S.G., "Water Jet Impact Sensitivity Testing of VTG-5A Class 1.1 Propellant", Report of Investigations to Naval Weapons Support Ctr., Ordnance Engineering, Code 4022 bld. 3031 Crane, IN 47522-5090, Restricted Access, 23 pages, 10 March, 1993.
- Worsey P.N. and Giltner S.G., "Water Jet Impact Sensitivity Testing of AP, HMX, NC, and NG/NC Components", Report of Investigations to Naval Weapons Support Ctr., Ordnance Engineering, Code 4022 bld. 3031 Crane, IN 47522-5090, Restricted Access, pp. 32, June, 1993.

## DISCUSSION

MANFRED HELD

Messerschmitt-Bölkow-Blohm GmbH, Schrobenehausen, Germany

1. Do you really mean initiation or ignition?
2. How do you measure the reaction levels; burning, deflagration, partial detonation, detonation?

## REPLY BY P. N. WORSEY

1. This question appears to assume that 'initiation' refers solely to detonation, whereas, 'initiation' simply refers to the onset of any visible reaction.
2. The reaction levels for the most part are determined by the photographic results from which the target reaction rates may also be determined. For the shaped charge tests, additional information is provided by post test examination of the witness plate.

## DISCUSSION

STEVEN HALLET

Mason & Hanger, Amarillo, Texas

1. Due to the method of generating the water stream, the water actually impacts the explosive surface as a series of droplets rather than as a continuous stream. Have you observed a step or cumulative effect resulting from these sequential impacts of the droplets (primarily related to a time exposure threshold)?
2. Is the impact pressure delivered by each of these droplets uniform (water hammer phenomenon)?

## REPLY BY P. N. WORSEY

1. It appears to be a cumulative effect.
2. Most investigators determine the water hammer pressure by  $P = \rho cV$ . Therefore, the pressure delivered by each droplet is independent of mass and depends only on density and velocity. Hence, if water droplets have the same velocity, they provide the same water hammer pressure. If the velocity is not the same, then the pressures are different.

# SIMULATING SYMPATHETIC DETONATION EFFECTS

J. Gregory Glenn  
Wright Laboratory  
Eglin AFB, FL 32542-5434  
and  
Mike Gunger  
Orlando Technology, Incorporated  
Shalimar, Florida 32579

A model and test method have been developed to predict the propensity for stored munitions to sympathetically detonate. The model incorporates the JWL equation-of-state to determine case wall impact velocities. Impact pressures are determined through the Hugoniot of the respective materials. A divergence term is used to incorporate two dimensional effects into a one dimensional framework. The experimental technique uses high explosives to launch flat plates into acceptor charges. Instrumentation can be used to observe the response of the acceptor explosive. Data is presented on AFX 644(1), an Air Force developed explosive composed of TNT, NTO and aluminum. Detonation initiated at a plate velocity of 1.9 mm/μsec and failed at 1.8 mm/μsec, corresponding experimentally determined pressures in the explosive at 12.7 mm were 81 and 63 kb respectively.

## INTRODUCTION

Attempts to suppress sympathetic detonation when it occurs by way of shock initiation between donor and acceptor have been unsuccessful especially in large munitions. A great deal of effort has been devoted to development of explosive formulations without a real understanding of the shock environment. Observation of large scale test results showed that interactions between the donor and acceptors in adjacent and diagonal positions are complex. Thickness, velocity and divergence of the donor's expanding case vary in relationship to the acceptors. Recent efforts have concentrated on methods to predict transmitted pressures so the explosive formulator could establish a sensitivity goal or threshold. This effort consisted of two activities, a model which could predict shocks strength and acceptor explosive response and an experimental method for impacting explosive samples with large flat plates which simulate the stimulus provided by a detonating donor.

## SIMPLIFIED MODEL DEVELOPMENT

The development of a simplified model to predict the results of the flyer plate test was considered essential for numerous reasons. Principally, it was felt that if the event was well understood, a model could be developed and also, with a simplified model, the necessity of understanding both the equations of state and numerical methods employed in a large, multi material, multi dimensional finite difference code such as the OTI\*HULL code, could be avoided. This is particularly true of resolution requirements which in a simplified

model can be avoided altogether. For the development and checkout of the model, the OTI\*HULL code was used. The model is broken into three parts: (1) the cylinder expansion, (2) impact, case wall pressure divergence and (3) the acceptor explosive evaluation. Each of these parts will be addressed separately. A more detailed description of this model can be found in a DTIC tech report, WL/MN-TR-93-7030.

### Cylinder Expansion

The model currently allows the user three separate means of determining the donor case wall impact velocity. The first method as shown in equation 2 is a straight forward integration of the expansion isentrope. The second, attempts to better match cylinder expansion data through the use of impulse-momentum. The last is a combination of the first two methods. The JWL equation of state (EOS) is given as

$$P = ae^{-r_1 v} + be^{-r_2 v} + cv^{-(w+1)} \quad (1)$$

The integration of the expansion isentrope can be found in numerous references but for this application the method given by Miller is most suitable<sup>3</sup>. To avoid repetition, only a summary will be given here.

$$E = E(v=1) - \left( \frac{a}{r_1} e^{-r_1 v} + \frac{b}{r_2} e^{-r_2 v} + \frac{c}{w} v^{-w} \right) \quad (2)$$

From the Gurney relation.

$$Eg = E_{19} \left( \frac{M}{V} \right) \left( 1 + 0.5 \rho / \frac{M}{V} \right) \quad (3)$$
$$v = \sqrt{2Eg}$$

Then setting  $E(v=1)$  equal to the heat of detonation, the energy given by equation 2 can then be substituted into equation 3 for  $E_{19}$  giving the velocity as a function of volume expansion.

A plot using this method can be seen in Figure 1 with a hydrocode calculation also shown for comparison. Late time data is fit very well but early time response, which is controlled by momentum transfer, is not.

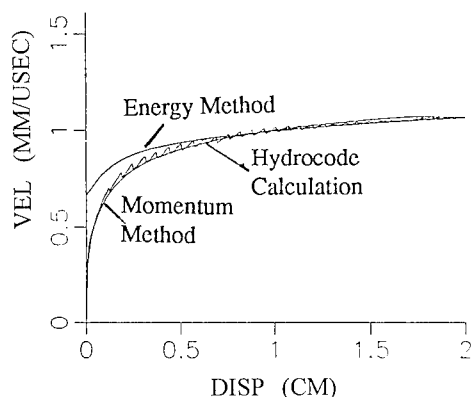


FIGURE 1. ONE INCH COPPER CYLINDER TEST FOR AFX-1100

To overcome this difficulty, a model based upon impulse and momentum as given by equation 4 was developed.

$$\int F dt = \int M dv \quad (4)$$

F = force  
dt = loading duration  
M = mass  
dv = change in velocity

Substituting the pressure, inside case wall area and mass into equation 4 yields:

$$v_i = v_{i-1} + \frac{PA_{i-1}dt}{M} \quad (5)$$

$A_{i-1} = \text{Area}$

Since this equation by itself does not yield a unique result, all quantities are scaled to the one inch copper cylinder test. The equations are cast in plane geometry so that dt is taken as the transit time of the detonation wave over 1 cm (10 mm). This result is further broken down into n divisions. Further, the initial case wall volume ratio ( $V/V_0 = 1$ ) implies that the Chapman Jouget pressure is never attained. To avoid this difficulty, the CJ volume is calculated as:

$$V_j = \frac{\gamma}{\gamma+1} V_0 \quad (6)$$

This value is subtracted from the initial volume (1) so that the volume input to the JWL EOS is reduced for a time by this amount. However, once the reaction zone passes a given part of the cylinder, this volume reduction no longer applies. It is assumed that when the shock wave reaches the cylinder free surface, this volume reduction is removed. To calculate the shock velocity in the case wall due to the impact of a detonation wave, the following equation is applied.

$$\left[ \frac{u_1 - u}{\gamma D / (\gamma + 1)} \right]^2 = \frac{2}{\gamma(\gamma + 1)} \frac{(P/P_1 - 1)^2}{\gamma(\gamma + 1) P/P_1 + (\gamma - 1) / (\gamma + 1)} \quad (7)$$

Where

$U_1, P_1, D, \gamma$  refer to the CJ condition.

Since the equations are cast in plane geometry, only radial expansion can be considered. However, it has been found necessary to allow the volume to expand axially as a function of the particle velocity. This can be expressed as:

$$h = h_{i-1} + up \cdot k \quad (8)$$

Where h is the increase in the height of the computational cylinder. The particle velocity (up) can be calculated from the momentum equation as:

$$up = P / \rho_o U_s \quad (9)$$

The shock velocity can be calculated from the Gamma gas law. The appropriate value of gamma is given by the JWL EOS.

$$k = 1 - (c/m_{cu}) / (c/m) + xp_{cu} (r_i/r_{icu}) \quad (10)$$

cu = reference to one inch copper cylinder test  
r = initial inside radii for the respective cylinder

Note that this term reduces to zero for the one inch test with no axial expansion ( $xp_{cu}$ ). Values for the axial expansion constant are generally in the range of 0.1 to 0.2 for the one inch test. Results for this model are shown in Figures 1 and 2 with the first being a copper cylinder test and the second a steel cylinder with a cross section corresponding to a munition item.

Velocities are limited to the Gurney velocity. At a volume ratio of approximately 2, the impulse-momentum calculation can be terminated and the remaining expansion calculated as a function of energy. This method is preferred since the energy method is significantly faster and produces better late time results.

The casewall motion as a function of displacement is now determined. The casewall thickness as a function of expanding radius can be calculated through the continuity equation as:

$$t_{cu} = r - \sqrt{r_i^2 - r_o^2 + r^2} \quad (11)$$

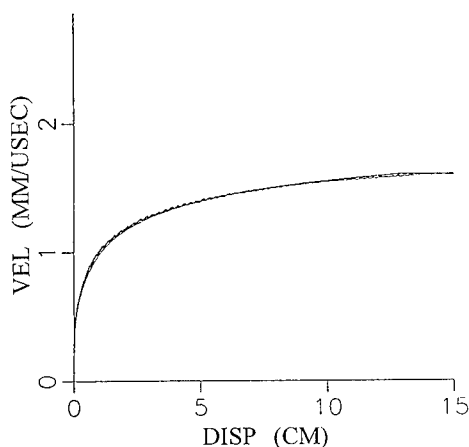


FIGURE 2. STEEL CYLINDER CASEWALL VELOCITY TESTING USING AFX-1100

where

- $r$  = the current radius
- $r_i$  = initial inside radius
- $r_o$  = initial outside radius

#### Impact - Pressure Divergence

The results of the previous section indicate the impact velocity can be calculated to within a few percent. From the impact velocity, the initial pressure in the casewall can be determined. Without divergence, that pressures will be uniform throughout the material thickness. However, through hydrocode analysis, a significant amount of pressure divergence can be observed in the casewall. Figure 3 depicts the results of three impact scenarios involving a purely one-dimensional flat plate impact, a flat plate impacting a right circular cylinder and a curved plate impacting a right circular cylinder.

The pressure pulse response in the casewall and in the explosive can be seen in Figure 4. Note that the pulse duration is the same for all three cases.

These calculations were performed using the Lagrange module in OTI\*HULL at a resolution required to predict the analytical one-dimensional flat plate pressure. The ratio of impacting plate thickness to acceptor plate is 0.5. The impacting velocity is 1.5 mm/ $\mu$ sec. As can be seen, each case begin at the same initial pressure which can be calculated through the momentum equation and material Hugoniot.

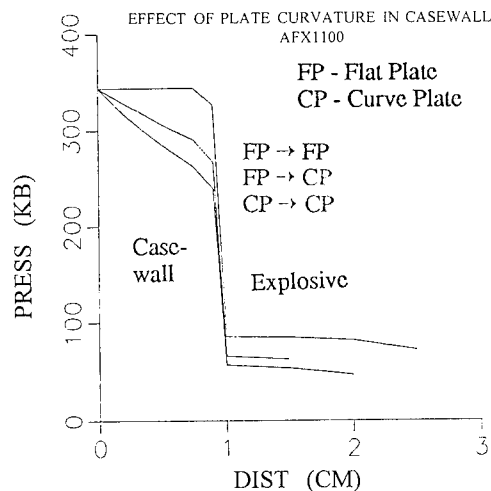


FIGURE 3. PRESSURE PROFILE FOR THREE IMPACT EVENTS IN CASEWALL AND EXPLOSIVE

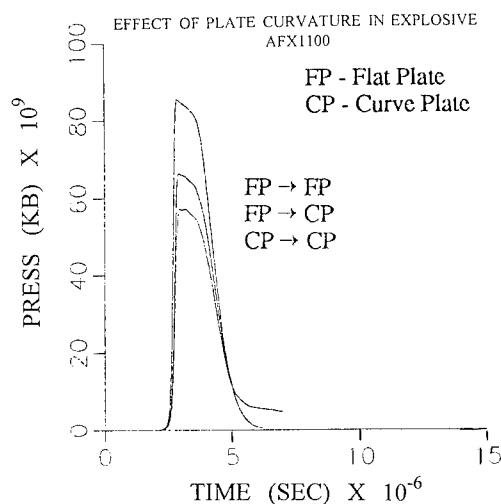
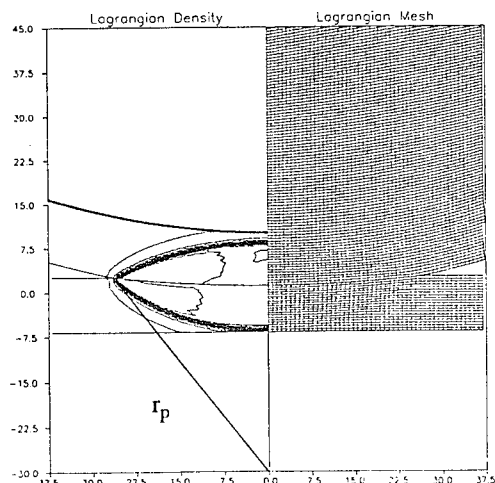


FIGURE 4. EFFECT OF PLATE CURVATURE ON PRESSURE PULSE IN EXPLOSIVE

Figures 5 and 6 depict impact scenarios involving different plate thicknesses and impact velocities.

Note the difference in wave curvature and extent. The resulting pressure wave due to the impact begins at the impact point and terminates at the end of the impacting plate. The magnitude of the initial shock wave pulse can be reduced either through wave divergence or rarefactions resulting from free surface interaction. The problem then is to determine the minimum diameter equivalent flat plate which reproduces the conditions involved in the original impact problem. Work involving spherical fragments indicated that the equivalent flat plate was controlled by lateral free surface relief which occurred when the plate closing rate was exceeded by



**FIGURE 5. LAGRANGIAN CALCULATION OF 24MM THICK FLAT PLATE IMPACT**  
**V=1.7 MM/μSEC**

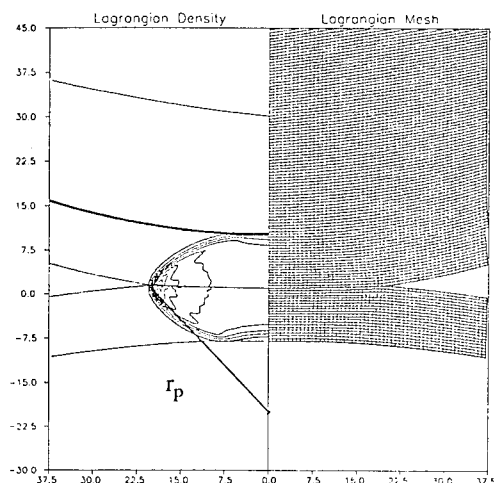


**FIGURE 6. LAGRANGIAN CALCULATION OF 25MM THICK FLAT PLATE IMPACT**  
**V=1.05 MM/μSEC**

the velocity of rarefaction waves which were set equal to the ambient sound speed in the material<sup>5</sup>. Since the spheres were solid, a one dimensional region was considered to exist in the impacted material prior to relief due to the rarefaction waves. For a sphere impacting a plane surface with time referenced to the center of the sphere, the equivalent plate diameter was given as:

$$d_i = 2y\sqrt{1 + Co^2/u_i^2} \quad (12)$$

Victor extended this to curved plates with the equivalent plate given as<sup>5</sup>:

$$d_i = 2r_a(v_r/Co_c)(r_d + L)/(r_a + r_d + L) \quad (13)$$

where

- $r_a$  is the radius of the acceptor
- $v_r$  is the velocity at donor radius  $r$
- $r_d$  is the initial donor radius
- $L$  is the shortest distance between donor and acceptor

Green's expanding wave approximation<sup>6</sup>

$$Peqv = Po \left[ \frac{1}{1 + \sqrt{2} \left( \frac{xi}{do} \right)} \right] \quad (14)$$

Where

- $xi$  is the distance into the acceptor
- $do$  is the equivalent flat plate diameter

could be used when rarefactions entered the one dimensional region with depths less than the critical diameter.

As mentioned previously, considerable divergence exists within the case wall and must be taken into account. In addition, rarefactions also enter due to rear surface relief and may control the plate diameter. Hydrocode results suggests that a better approximation to the equivalent flat plate can be determined by replacing the ambient sound speed in either equations 12 or 13 with the shock velocity appropriate to the impact velocity determined through the momentum equation.

Since the pressure diverges, an iterative approach must be taken. In addition, compression of the donor case wall due to impact must be accounted for in the determination of the pressure pulse duration.

From hydrocode calculations varying impact velocity, plate thickness and curvature, a divergence term which relates the impact pressure ( $P_o$ ) to the incident pressure ( $P_{eqv}$ ) (see Figure 6) is given as:

$$Peqv = Po * (\cos xi / rp) \quad (15)$$

where  $rp$  is the radius of the pressure pulse and  $xi$  is the flat plate radius. Figure 7 is a plot of an AFX-1100 loaded munition item in a side-by-side impact scenario at various expansions. The pressures plotted were calculated in the explosive using both the OTI\*HULL code and equation 15.

Included in the model is the ability to insert a liner in the case wall. Again, Figure 7 shows the results of including the liner. It is interesting to note that without the liner, donor case wall expansions greater than 3.5 cm, produced detonations in side-by-side impact calculations involving AFX-1100 explosives. Tests of this same event produced no detonation in side-by-side configurations. With the addition of the 2.5 mm thick liner, the model recreated the test results. In addition, the pressures so

calculated were almost identical to previous coarsely zoned calculations without a liner which also reproduced the test results. For small expansions, the isentrope pressure may be significant. This pressure is added such that the total interface pressure is given as:

$$P = P_{eqv} + P_{jwl} \quad (16)$$

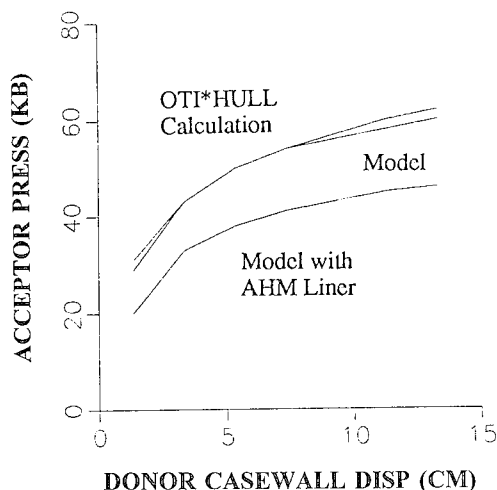


FIGURE 7. COMPARISON BETWEEN OTI\*HULL CALCULATIONS AND MODEL RESULTS FOR AFX-1100 LOADED MUNITION SIDE-BY-SIDE

It is assumed that the isentrope pressure pulse duration at the peak is of the order of the reaction zone length which is of almost zero duration relative to the case pulse. The pressure pulse is then triangular with a duration at the base given by the case wall thickness.

The hydrocode results indicate that for the pulse controlled by the plate thickness, a 1-D region in the explosive does exist primarily due to the shock velocity difference between the undetonated explosive and the metal case wall. After this region, the expanding wave equation by Green provides good results.

With the peak pressure and duration in the explosive determined, the likelihood of sympathetic detonation can be determined in many ways. The model currently uses 2 methods to evaluate sympathetic detonation. The first uses the Pop-plot in the form:

$$run = CPeqv^{-d} \quad (17)$$

to determine the required time the pressure must be supported. It is also assumed that the minimum pressure at which a go was recorded in the wedge test sets the go/no

go pressure. If the pressure is supported above the go/no for a length greater than some critical parameter, in this case critical diameter, the explosive is assumed to detonate according to the Pop plot. In the event critical diameter data is unavailable, minimum pressure governs.

## FLYER PLATE TEST DEVELOPMENT

Results of previous work indicated the need to reproduce the boundary conditions observed in the pallet test, (storage configuration test) in a controlled manner. It was observed from calculations that a large, flat flyer plate traveling at a velocity corresponding to that calculated in the pallet test produced results which agreed in both magnitude and duration. As a result, an investigation to develop this capability was initiated. Since it was expected that the entire test apparatus would be destroyed upon initiation of the acceptor charge, the system requirements included fast manufacturing and small capital investment. The method developed from these requirements is a modification of a technique developed at Sandia National Laboratories.<sup>7</sup> Through hydrocode analysis and test constraints, the current configuration consists of a plate 177.8 mm in diameter with a thickness up to 12.7 mm. In order to recreate the boundary conditions observed in munition stacks, the velocity range required is 1.4 to 2.2 mm/ $\mu$ sec.<sup>1</sup> The basic requirement consists of using a thick walled cylinder (>76 mm thick) to ensure shock wave rarefactions from the free surface do not interfere with the plate acceleration. In addition to the thick walled cylinder, an air gap is used to enhance planarity of the flyer plate driver shock. The pressure distribution across the plate face must be as uniform as possible to prevent plate distortion.

The booster charge currently in use is AFX-1100, a desensitized form of tritonal. The detonation train consists of a 50 x 25 mm pentolite booster, 25 x 25 mm A-5 pellet and an RP-83 detonator. Between the booster charge and the flyer plate is a thin wall pmma ring which serves as a spacer to ensure the air gap is at a constant height ( $\approx$  1-3 mm). The launch tube is actually an assembly which consists of an inner and outer tube as shown in Figure 8. This configuration allows the explosive charge and the flyer plate to be loaded and aligned prior to installation in the outer tube which both simplifies range operations and greatly reduces alignment errors. The flyer plate, explosive, air gap device and steel cylinders are precision machined to  $\pm 0.127$  mm. The ratio of flyer plate/case wall thickness has been found to be a major parameter in the determination of both peak pressure and pulse duration in the explosive due to divergence in the case wall.



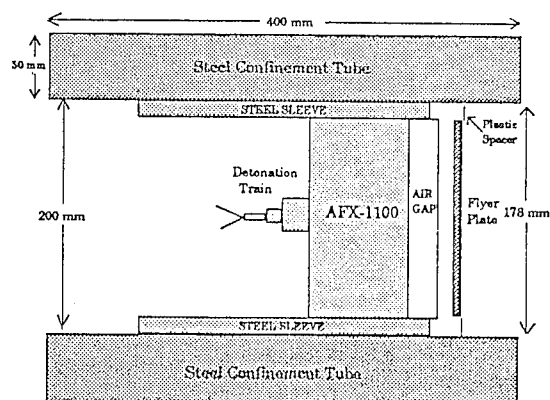


FIGURE 8. FLYER PLATE TEST ITEM

Both the hydrocodes and the post test data verified that the fragments had thinned from 10 mm to 6 mm.<sup>2</sup> Therefore, the flyer plate thickness used for this investigation was 6 mm. Experimental determination of flyer plate velocity is through flash radiography. In addition to velocity data, the radiographs also provide information on the plate planarity and verification spallation does not occur. Figure 9 is a flash x-ray of a plate traveling at 2.0 mm/ $\mu$ sec.

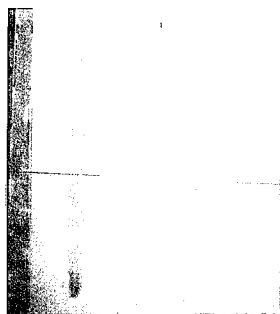


FIGURE 9. FLASH X-RAY OF FLYER PLATE

Calibration of the flyer plate velocity as a function of charge length was next performed. To this end, a series of four tests were performed. A booster charge calibration curve consisting of the four shots is shown in Figure 10.

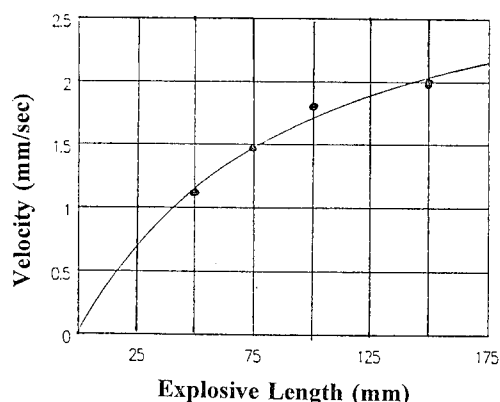


FIGURE 10. PLOT OF FLYER VELOCITY VERSUS CHARGE LENGTH

The equation that was derived from this plot is shown below.

$$y = ((a + cx) / (1 + bx)) \quad (18)$$

$$a = 0.0086, b = 0.0106, c = 0.03512$$

With the flyer plate velocity curve established, live acceptors could now be tested. The live acceptors are explosively filled right circular cylinders with Piezoelectric pins embedded into the explosive. The cylinders are 1018 cold rolled steel 250 mm long by 200 mm outside diameter and 180 mm inside diameter. The acceptors have 17 pin holes drilled along the long axis and centered on the can. Piezoelectric pins are placed in these holes in a stair stepped fashion away from the inside surface of the acceptor casewall. The 17 pins make up two channels of data with the center pin touching the inside surface of the acceptor casewall. Manganin gauges have also been used to measure pressure directly. Figure 11 is a side view of the can with the gauge installed.

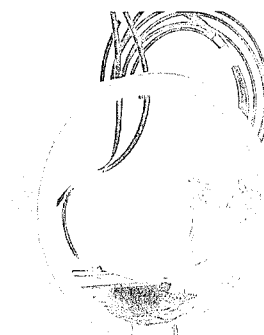


FIGURE 11. GAUGE INSTALLED IN ACCEPTOR

Because there were concerns that the pressure signal might not impact the gauge normal to the sensing element, a special manganin/constantan strain compensated gauge was used. The gauge was embedded in the explosive 13 mm from the inside surface of the cylindrical wall. To ensure correct placement, x-rays were made of the instrumented cans. As a backup to the instrumentation, a 250 x 250 x 25 mm thick witness plate was used to indicate if the acceptor went high order. The final setup is performed with the acceptor charge positioned on the witness plate as shown in Figure 12.

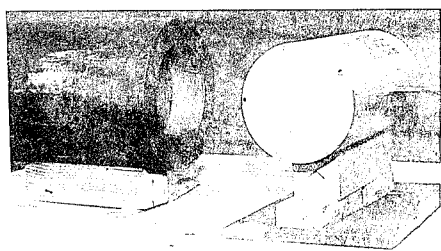


FIGURE 12. FLYER PLATE TEST SETUP

## EXPERIMENTAL RESULTS

Figure 13 depicts the comparison of the simplified model data to the experimental method. The test series utilized an insensitive high explosive (IHE) AFX-6441 in the acceptor charges. The experimental data was gathered using piezoelectric pins. All of the data was fitted. The IHE used in the acceptor exhibited a go-no-go point at a pressure of  $\approx 70$  Kbars which corresponds to a shock velocity of  $4.04 \text{ mm}/\mu\text{sec}$ . As can be seen the flyer velocity at  $1.9 \text{ mm}/\mu\text{sec}$  produces a shock velocity of approximately  $4.2 \text{ mm}/\mu\text{sec}$  which results in a detonation. The run up equation derived from ELSGT tests is  $\log X^* = -3.24 \log P^* + 5.21$ . A shock velocity of  $4.2 \text{ mm}/\mu\text{sec}$  corresponds to a pressure of 81 Kbars which results in a run of 185 mm. The detonation velocity of this explosive is  $7.1 \text{ mm}/\mu\text{sec}$ . From Figure 13 by 120 mm the transition to detonation is almost complete. The implication is that the induced pressure is actually higher or the pop plot is in error. The model predicts a detonation for the  $1.9 \text{ mm}/\mu\text{sec}$  flyer against this explosive using a 12.7 mm critical diameter, and no detonation at  $1.48 \text{ mm}/\mu\text{sec}$ . Interface shock velocities predicted by the model are approximately 4% higher in all cases.

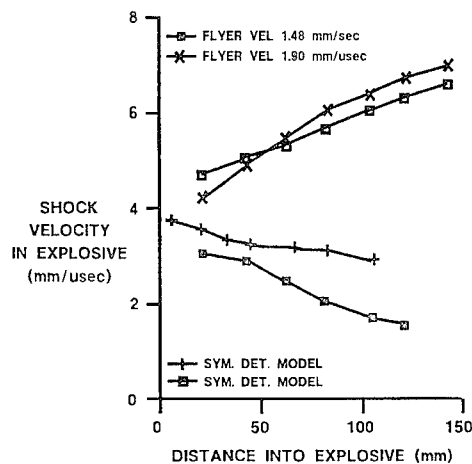


FIGURE 13. VELOCITY - VS - DISTANCE

Figure 14 is the manganin stress data for the  $1.9 \text{ mm}/\mu\text{sec}$  flyer velocity. The predicted pressure at this point (13 mm into the explosive) was 55 kbars. The constantan strain gauge revealed that the manganin gauge started receiving a non-planar stress wave approximately 100 nanoseconds into the event. It is believed that the true peak pressure signal was lost due to this problem. The technique is still being perfected and more tests will be performed to obtain the actual pressure.

The pulse duration for this test as shown in Figure 14 is given as 0.986 microseconds. This compares to a predicted pulse duration of 1.07 microseconds. It is not known the exact effect the non-planar wave has on pulse duration.

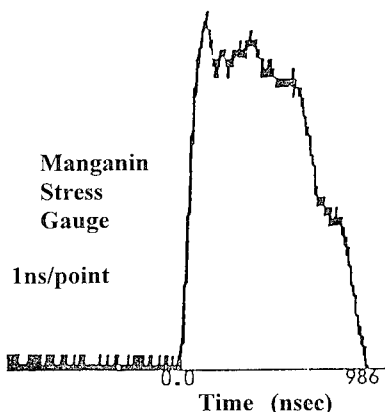


FIGURE 14. MANGANIN GAUGE DATA

## DISCUSSION AND CONCLUSIONS

The purpose of this research effort was to develop a means of predicting the likelihood of sympathetic detonation in the storage configuration for explosive fills under development. Since it is not clear which mechanism or combination of mechanisms is responsible for sympathetic detonation (these may vary from explosive to explosive), the goal was to develop a test which accurately reproduces the conditions observed in the storage configuration. If the boundary conditions can be reproduced, then those mechanisms should exhibit themselves. While it is possible to instrument rounds in the storage configuration, this experiment allows much greater control of the acceptor environment.

Results of the model indicate interface pressures approximately 12% above those recorded in the experiment. However, at 12.7 mm, the calculated pressure for the 1.9 mm/ $\mu$ sec impact test is 83 kb or 2% above the experimental result. Assuming the run up was induced by the calculated interface pressure of 93 kb, the predicted run up is 118 mm, significantly closer to that observed in the experiment than would be predicted by an 81 kb initiation. The model, as mentioned previously, predicts sufficient stimulus to achieve detonation. Only the physical size of the acceptor charge prevents this. This suggests the interface values predicted by the model are reasonably accurate but the rate of shock wave decay may be too low. The calculated pressures at 12.7 mm into the explosive for the 1.48 mm/ $\mu$ sec impact point is 51 kb. The one dimensional region in the explosive varies but was generally controlled by lateral relief.

Differences between the model and the experiment may be due to curvature in the impacting plate, small errors in impact velocity, or differences in the Hugoniot modeled and that tested. Regardless, the model predicts with a high degree of accuracy the interface condition in the round-to-round acceptor experiment giving the explosives formulator a quick and accessible tool to determine the likelihood of sympathetic detonation. Similarly, the flyer plate test has proven to be a versatile and valuable tool in assessing safety margins or lack thereof of rounds in the storage configuration.

## REFERENCES

1. Glenn, J.G., Gunger, M.E. McCormick, H.C., and Aubert, S.A., *Sympathetic Detonation Predictive*

*Methods*, WL/MN-TR-93-7001, Eglin AFB FL. 32542-5434.

2. Glenn, J.G., and Gunger, M.E., *Simulating Sympathetic Detonation Effects*, WL/MN-TR-93-7030, Eglin AFB FL. 32542-5434.
3. Miller, P.J., *Determining JWL Equation of State Parameters Using the Gurney Approximation*, 9th Symposium on Detonation, paper 203, August 89.
4. Ferm, E.N., Ramsey, J.B., *Spherical Projectile Impact on Explosives*, 9th Symposium on Detonation, paper 41, August 1989.
5. Victor, A.C., *Simple Analytical Relationships for Munitions Hazard Assessment*, DDESB Explosives Safety Seminar, August 1992.
6. Green, L., *Shock Initiation of Explosives by Impact of Small Diameter Cylindrical Projectiles*, 7th Symposium on Detonation, pg. 273-277, June 1981.
7. Benham, R.A., and Kampfe, W.R., *Ultra-High Velocity Impacts Utilizing a Rocket Sled and an Explosively Accelerated Flyer Plate*, Shock and Vibration Bulletin, No. 55, Pt. 2, June 1985, PP 51 - 56.

---

## DISCUSSION

ROY LUCHT, LOS ALAMOS NATIONAL LABS,  
NEW MEXICO

Can this technique be used to investigate XDT phenomena?

## REPLY BY MIKE GUNGER

Yes. The acceptor charge can be tailored such that voids, cracks or other damage can be known prior to the experiment. Since the acceptor charge is confined, multiple stress wave transits can be induced. Also, considerable plastic deformation occurs in the confining case which provides opportunities for sheer or other damage mechanisms to manifest themselves in the explosive.

## ELECTROSTATIC DISCHARGE (ESD) HAZARDS OF ENERGETIC MATERIALS

Josephine Covino and F. E. Hudson III  
Naval Air Warfare Center Weapons Division  
China Lake, California 93555-6001

David R. Dreitzler  
U.S. Army Missile Command  
Brian Hammant  
Defense Research Agency  
Richard J. Lee  
Naval Surface Warfare Center

Recent incidents have renewed interest in the phenomenon of electrostatic discharge (ESD) in energetic materials as a mechanism for induced inadvertent ignition and sustained combustion. In the last ten years, ESD research has focused on developing experimental techniques to evaluate ESD hazards of energetic materials. In this paper, logic/protocol is described for assessing the ESD sensitivity of a system consisting of stimulus, energetic material properties, energetic material sensitivity, and system response. However, most of the research has only addressed energetic material properties and sensitivity. At China Lake, ESD sensitivity evaluation of energetic materials consists of a calculation percolation coefficient and measurements of resistivity, dielectric constant, dielectric breakdown, resistive-capacitive (R-C) discharge, and breakdown to ignition experiments. Representative data on energetic and nonenergetic propellant formulations are presented and discussed. ESD sensitivity as a function of damaged energetic material is also presented. The data shows that damaged energetic material is more sensitive to ESD when compared to undamaged material.

### INTRODUCTION

On January 11, 1985, in Heilbron, Germany, a large rocket motor with a Kevlar-case containing an aluminized HTPB (hydroxyl-terminated polybutadiene) propellant ignited, killing three people.<sup>1-2</sup> The subsequent investigation suggested that ignition could have been caused by an electrostatic discharge (ESD) through the motor following the separation of dissimilar dielectric materials in a cold, dry climate. These findings prompted the propulsion community to study the ESD hazard of solid rocket propellants. In recent years, ESD research has focused on developing experimental techniques and a hazards protocol to fully evaluate the ESD hazards of energetic systems.

Static charge relative to ESD hazards can be generated by several means: (1) *Tribo-electric effect*, when a non-conductive surface first contacts and then separates from a second surface; (2) *Polarization*, when materials acquire a static charge under the influence of an electric field; (3) *Thermo-ionic emission*, electron emission caused by raising the particle temperature; (4) *Mechanical fracture*, electron emission prompted by ruptured, strained, or otherwise mechanically broken bonds within solids; and (5) *Charging by freezing*, where potential differences are induced during freezing. Through these mechanisms, a considerable electrostatic charge can be created during the handling and manufacturing of a solid rocket motor. For example, recorded electric potentials on a propellant core may exceed several thousand volts at the end of a man-

drel pull-out operation. Rocket motor manufacturers and government facilities have implemented extensive preventive measures for reducing charge accumulation. These measures include the use of graphite (both as a propellant ingredient and motor cases) and of systematic grounding. Since preventive measures cannot ensure complete mitigation, it is important to understand the behavior and sensitivity of propellants (particularly composite propellants) to ESD.

A severe hazard arises when energetic materials used in ammunition and propulsion systems are charged to a potential where breakdown occurs, or when a change in grounding conditions allows breakdown. Discharge processes generate charge carriers, which reduce the impedance of the energetic material and result in a rapid current increase. This can lead to arcing, establishment and growth of discharge paths, followed by catastrophic discharge. The resulting pressure and temperature increase in the very narrow discharge path may induce ignition and combustion.

Prior to the resurgence of ESD hazards of energetic materials, ESD sensitivity levels of rocket motor propellants were determined by capacitive discharge. This test method is based on experimental work performed by the U.S. Bureau of Mines<sup>3</sup> over many years. However, a detailed methodology has not been standardized and differs among government agencies and propellant manufacturers. The use of this methodology established that a propellant, considered insensitive to

ESD at 70°F, could in fact be sensitive at a lower temperature. This observation compels the retesting of existing, fielded propellants at other temperatures.

To assess ESD sensitivity of a complete system, a logic/protocol was developed by The Technical Cooperation Program (TTCP) Subgroup W Action Group 11 (WAG-11). This protocol addresses the ESD hazards of a weapon system, containing energetic materials (EM), in terms of basic physical and chemical parameters of the materials and their local environment. The approach adopted divides the protocol into four categories: (1) Stimulus, (2) Energetic Material (EM) Properties, (3) EM Sensitivity and (4) System Response.

To date most of the research has only addressed the EM properties and sensitivity because of the need to obtain a fundamental understanding of ESD hazards. From a research perspective, the stimulus and the system response categories are difficult to address because they are complex and very system specific. Therefore, the emphasis in this work has been to characterize the EM response to an ESD stimuli and to better understand the mechanisms involved, and not to focus on system specific response. In this paper all four categories will be discussed. However EM properties and sensitivity will be emphasized.

To assess ESD sensitivity of munitions, a series of tests were developed at the Naval Air Warfare Center Weapon Division (NAWC), China Lake, Calif. These tests measure the EM electrical properties. This methodology is based on preliminary work performed at the Soci t  Nationale Des Poudres et Explosifs (SNPE) by Kent and Rat.<sup>4</sup>

In this work the test methodology was employed on both inert formulations and real propellants, allowing validation for inert samples with predictive extension to energetic materials. This paper attempts to correlate the chemical composition of inert and energetic formulations with electrical properties and ESD sensitivity. In order to fully understand the EM response to electrical stimuli, the effects of damage to ESD sensitivity were also evaluated.

## EXPERIMENTAL METHOD

### ESD Hazard Assessment Protocol

The ESD protocol, shown in Figure 1, is divided into four areas: stimulus, EM properties, EM sensitivity and system response.

**ESD Stimulus.** The stimulus in the ESD protocol results from the separation of electrical charge due to relative motion between materials. This motion can be caused by rubbing (tribo-electrification) or by separation. In addition, pyro-electrification (charging induced by thermal cycling) and piezo-electrification (charging induced by mechanical stress or strain) are possible. The basic physical properties that characterize an electrostatic process are the charge,  $Q$ , which has been separated, the electric field strength,  $E$ , resulting from the charge, and the energy,  $J$ , available in the charge. When considering

the location of the charge prior to an electrostatic event, possible scenarios include:

1. Charge transfer from an external source to the energetic material, as in discharge from a human body. This discharge can result in ignition of the EM.

2. Charge transfer from tribo-electric effects, thermal cycling, etc. An ESD can occur when the energetic material is discharged to an external electrical load.

Other factors influencing charge transfer to the energetic material include: (1) The case properties (e.g., is the case material conductive, insulating, or dissipative); (2) The discharge time constant; (3) The mechanics of the dielectric breakdown.

**Material Description.** The material description can be divided into five broad categories: the energetic material, the case and liner, the interface between the energetic material, case and liner interfaces, the condition of the material constituents, and the effect of environment.

**Electrical Properties of Material.** The particle sizes, types, morphologies, concentrations, homogeneity of solids, binder cross-linking densities, and solubility of solids into the binder all alter the electrical properties of the energetic material. They can also alter the dielectric breakdown strength,  $E_{bk}$ , surface and volume resistivities, and the dielectric constant of the material. The resistivity and dielectric constant combine to determine the discharge time of the electrostatic energy. For example, the aluminum (Al) concentration, morphology, size, and oxide coating all affect the dielectric strength. Flake Al, when compared to spherical Al, tend to enhance local breakdown and reduce the  $E_{bk}$ .

**Effects of the Case/Liner Insulating Material.** Volume and surface resistivities of the case/liner insulating material control the material time constant. If the case is conductive (metallic) and therefore grounded, charge cannot accumulate on the surface. Because of this grounding it would be impossible for energy to be transferred to the energetic material. On the other hand, if the case is an insulator, the charge accumulation on it is a function of the volume resistivity, surface resistivity, dielectric constant, dielectric breakdown field strength, etc. This accumulated charge can be coupled into the energetic material. The rate, quantity, and mechanism of this energy coupling are also determined by the material's time constant, bulk, and surface resistivities of each material, and the surface resistivity of the case.

**Interface Between Energetic Material, Case, and Liner.** The interface in this report refers to the region between energetic and the inert materials (insulator and case). At the interface, the energetic material (propellant or explosive) may be binder-rich. Air gaps may also exist in this region. Such a dielectric mismatch can focus the deposition of the energy into the energetic material. The effectiveness of the energy transfer is controlled by the surface electrical properties of the material involved.

**Condition of the Material.** The condition of the energetic material is the degree of damage it experiences during its life cycle. The degree of damage affects the electrical behavior.

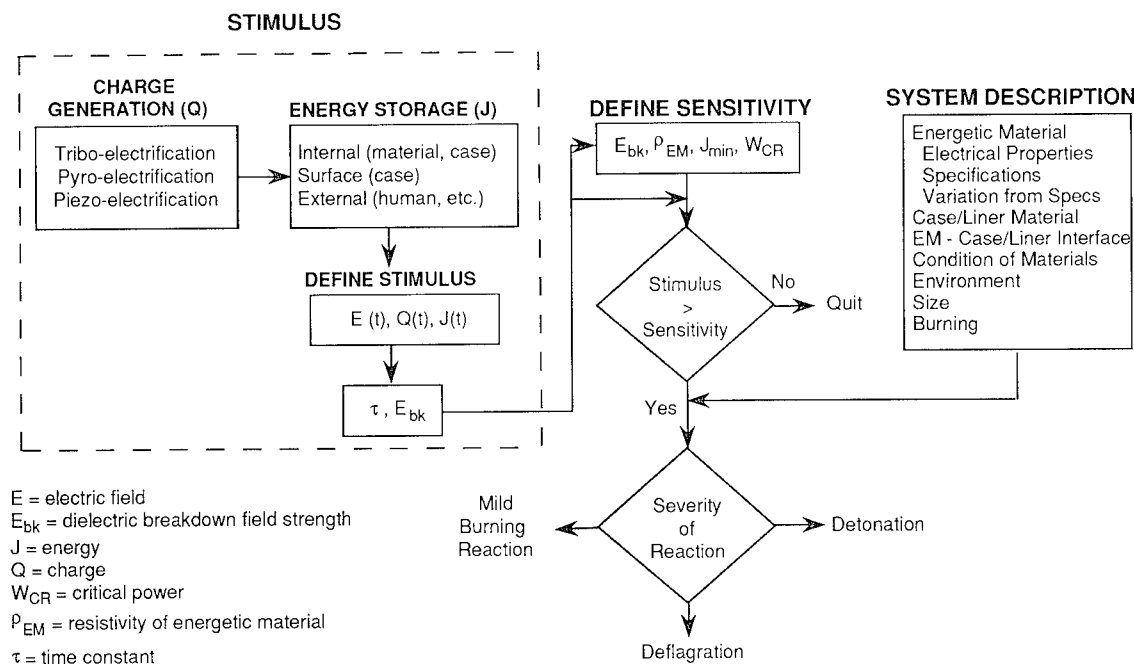


**FIGURE 1. FLOW CHART OF ESD PROTOCOL**

In general, a damaged material has a greater void content, and also has more defect sites and altered mechanical properties. These material changes can reduce  $E_{bk}$ , the volume resistivity, etc., and can possibly make the material more reactive to an ESD stimulus.

**Environmental Parameters.** Environmental parameters also play a very significant role in the electrical response of a material. For example, temperature, humidity, charging time, etc., can significantly alter the  $E_{bk}$ , volume resistivity, dielectric constant, etc. Furthermore, internal or external pressure can also alter the material's response to an ESD stimulus. For example, the material may be squeezed between two electrodes, or the cell configuration may be pressurized by the introduction of inert gas. These processes can induce microcracks, shearing of the binder, burning rate modifications, and so on.

**ESD Sensitivity Factors.** Before electrostatic energy can be deposited in the EM, a conductive path is necessary. For non-conducting EMs, dielectric breakdown is a necessary first step. For partially conducting materials, e.g., those containing a nitrate ester (e.g. nitroglycerin), or high Al concentrations, a catastrophic breakdown process will be necessary to maximize the breakdown energy.

Classic dielectric breakdown is obtained when a critical electric field  $E_{bk}$  is exceeded. Typically, a large field is generated between two metallic electrodes. Prior to breakdown there is little or no electrical current flow. At breakdown, electrical current begins to flow in discharge channels. As current flow continues the discharge channels grow, and are heated by the electrical energy deposited by the discharge. This heating will cause chemical reaction if the temperature is high enough.

**Time and Frequency Factors.** The dielectric strength  $E_{bk}$  depends on the time signature and thus the frequency spectrum of the electrical discharge.  $E_{bk}$  is usually at a minimum for low frequency (DC) discharges. When the electric field is applied, it takes time for the breakdown to occur. Breakdown delay times may range from one nanosecond to many seconds depending on the applied field and the material. Consequently, an impulsive electric field of short duration compared to the breakdown delay, will not induce breakdown. EMs are less sensitive to short duration impulsive discharges.

**Minimum Resistivity.** If the volume resistivity is low (below a minimum value,  $\rho_{min}$ , which has to be defined), the electrical energy will be distributed through the bulk of the material, i.e., it will not be concentrated in a narrow arc channel. A high energy density is necessary for initiation of burning in the EM, typically  $\sim 10$  MJ/m. By distributing the discharge through the bulk, the energy density and therefore the sensitivity of the EM to ESD is minimized. The charge distribution through the bulk allows energy to be safely discharged to ground.

**Minimum Initiation Energy and Power.** Chemical reaction always occurs in the EM at dielectric breakdown sites. The rate of energy deposition (the electrical power) controls the arc dynamics and hence the arc channel volume. However, there is a critical volume of EM necessary for the subsequent chemical reaction to be self-supporting. In other words, the chemical energy and power released by the volume of EM that reacts must exceed the heat energy and power lost to the surrounding unreacted EM by thermal or mechanical transport. This volume must, therefore, be large enough for the chemical energy and power to exceed the losses. The channel volume depends, in turn, on the electrical energy deposited; consequently there is a minimum energy,  $E_{min}$ , and power,

$W_{min}$ , necessary for sustained ignition to occur. Note that the losses depend on the geometry and confinement of the EM.

**Maximum Power.** There is a maximum power,  $W_{max}$ , beyond which sustained reaction may not be initiated. If the power is too high, the subsequent explosion of the arc channel generates a hole in the EM. This occurs so rapidly that joule heating of the arc channel is reduced as the resistance of the channel approaches zero. The transport of electrical energy into a mechanical shock maximizes the volume of the arc channel and minimizes the temperature rise.

**Severity of Response.** If the energetic material is a primary explosive, it can exhibit prompt detonation as a result of ESD. However, it is assumed that with this exception, all energetic materials will experience an event that is initially deflagratory, since the shock component of any ESD is usually too small to induce prompt detonation.

**Growth of Deflagration.** The final response level will be determined by conditions that may cause a transition from deflagration to detonation (DDT) and whether these requirements are satisfied. Those conditions that will have the most significant effect are: composition, history, charge size, and environmental effects.

#### EM Properties and Sensitivity

Electrical properties are necessary for evaluating any propellant for ESD sensitivity. The specific methodology which is used at NAWC consists of: Step 1-Percolation Calculations; Step 2-Resistivity Measurements; Step 3-Dielectric Constant Measurements; Step 4-Dielectric Breakdown; Step 5-The R-C Discharge Test and Step 6-Breakdown to Ignition Measurements. By using this procedure, propellants can be ranked for ESD sensitivity. Presently, the ESD phenomena is being examined by looking at propellants' ingredients as the electrical building blocks to model development. These studies will allow identification of some of the basic parameters necessary to assess the propensity of propellants to ignite upon ESD. It is expected that such data will also enable ESD phenomena to be modelled and provide a predictive tool for assessing the sensitivity of future formulations.

**Step 1. Percolation Calculations.** In an attempt to understand why certain propellants are ESD sensitive and others are not, Kent and Rat<sup>4</sup> used percolation theory.<sup>5-7</sup> Factorial examination of propellant active ingredients shows that the Al particle size and the electrical properties of the binder are major factors in determining the propellant's electrical properties. Kent and Rat<sup>4</sup> found that, for a constant Al concentration, as the particle size decreases (i.e., the number of Al particles increases), the propellant sensitivity to capacitive discharge increases. Percolation ( $P_{imp}$ ) calculations were performed on five inert and four energetic formulations shown in Tables 1 and 2, respectively. The energetic propellants all contain ammonium perchlorate (AP) as the nonconducting solid (oxidizer), while the inert propellants contain sodium chloride (NaCl). The  $P_{imp}$  values for both the inert and energetic formulations are listed in Table 3.

From the percolation values, one can rank the sensitivity of the inert propellants from least to most sensitive: KJ-17, KJ-14, KJ-15, and KJ-16. KJ-18 cannot be considered because it contains only Al particles; thus a percolation value cannot be calculated. The ranking is directly related to the Al concentration. The KJ-16  $P_{imp}$  value is higher than other samples. This results from the coarse (550- $\mu$ m) NaCl that was used for the finest fraction of nonconducting particles.

One can also rank the energetic formulations, propellant C, propellant B, propellant D, and propellant A. The  $P_{imp}$  value for propellant C has a wide distribution because it contains variable amounts of ZrC (actually a semiconductor) as the conducting particles. The percolation breakdown coefficient calculation does not include many critical propellant parameters and cannot describe the propellant system fully or accurately.

TABLE 1. INERT PROPELLANT FORMULATIONS.<sup>a</sup>

Sample	Wt%			
	3- $\mu$ m Al	Coarse NaCl (~550 $\mu$ m)	Fine NaCl (~150-200 $\mu$ m)	Total NaCl
KJ-17	5	37.2	37.8	75
KJ-14	20	37.2	22.8	60
KJ-15	35	37.2	7.8	45
KJ-16	50	30.0	0	30
KJ-18	80	0	0	0

<sup>a</sup>All propellants contain 20 wt% HTPB as binder.

Density in g/cc: Al = 2.702, NaCl = 2.165,

binder = 0.93,  $\rho$  (binder) =  $3 \times 10^{10} \Omega \cdot m$ .

TABLE 2. ENERGETIC PROPELLANT FORMULATIONS

Propellant <sup>a</sup>	Conducting materials		Wt% of total nonconducting solids (AP)
	Material	Wt%	
A	Al	~18-20	~65-70 <sup>b</sup>
B	Al	~18-20	~65-70 <sup>b</sup>
C	ZrC	~1-4	...
D	Al	~18-20	~65-70

<sup>a</sup>All propellants contain 10-15 wt% HTPB as the binder.

<sup>b</sup>Propellants A and B have modal distribution of the AP.

TABLE 3.  $P_{imp}$  VALUES

Wt% of 3- $\mu$ m Al	Sample	$P_{imp} \Omega \cdot m$
Inert propellant samples		
5	KJ-17	$1.4 \times 10^{13}$
20	KJ-14	$8.8 \times 10^{13}$
35	KJ-15	$4.4 \times 10^{14}$
50	KJ-16	$1.6 \times 10^{17}$ (only coarse NaCl)
80	KJ-18	Only Al particles
Energetic propellant samples <sup>a</sup>		
	A	$129 \times 10^{10}$
	B	$20.6 \times 10^{10}$
	C	$8 \times 10^8 - 5 \times 10^{10}$
	D	$64 \times 10^{10}$

<sup>a</sup>The modal distribution of the AP causes the large energetic differences shown.

**Step 2. Resistivity Measurements.** Kent and Rat's experiments suggest that the temperature behavior of a propellant's volume resistivity may be important in ESD sensitivity.<sup>4</sup> Using specially constructed instrumentation, the volume resistivity was measured for the HTPB binder, inert propellant samples, and energetic propellant samples as a function of temperature, time of voltage application, voltage, relative humidity, and sample thickness. Details on measurement techniques and methodology can be found in ASTM<sup>8</sup> and Keithley.<sup>9</sup> In general, volume resistivities for HTPB propellants range from  $10^{12}$  -  $10^{13}$   $\Omega$ -cm; for PBAN propellants,  $10^{10}$   $\Omega$ -cm; for Composite Modified Double Base propellants,  $10^8$   $\Omega$ -cm; and for Cross Linked Double Base and NEPE based propellants,  $10^7$   $\Omega$ -cm. These comparison measurements were made at an applied voltage ranging from 20 - 500 volts using 0.635-cm (0.25-in.) thick samples after 60 seconds from initial voltage application.

**Step 3. Dielectric Constant Measurements.** The dielectric constant of propellants and propellant ingredients as a function of frequency, temperature, and relative humidity characterizes the energy storage capability and energy discharge potential. Dielectric properties may be measured using a parallel plate capacitor. For details on dielectric theory and measurement techniques, see ASTM<sup>10</sup> and Smyth.<sup>11</sup>

In this work, the dielectric constant was measured as a function of temperature, relative humidity, sample thickness, and frequency for inert propellants, HTPB binder, and energetic propellants. These data, taken at 1 kHz, are representative of the similarities and differences between the samples. The dielectric constants for inert samples and propellants A and B range from 4 - 16. The measured dielectric constant for the HTPB binder was 3. For details, see Covino and Hudson III.<sup>12</sup> In general, the more Al in a propellant formulation, the higher the dielectric constant and the more ESD sensitive the propellant is expected to be. However, the behavior of the dielectric constant with respect to NaCl concentration is more complex. As seen in Figure 2, the dielectric constant decreases as the volume percent of fine NaCl increases. This behavior with total volume percent of NaCl changes little for the first 20% and then decreases linearly with respect to concentration. This result suggests the lowest dielectric constant is due to the lowest concentration of conducting particles.

Neglecting the effects of breakdown voltage, the higher the dielectric constant, the more energy can be stored in a material. In this case, the amount of energy that these inert and energetic propellant samples can store is directly proportional to the Al concentration and inversely proportional to the NaCl concentration (for the inert samples) and to the AP concentration (for the energetic samples).

Dissipation measurements were made for both inert and energetic propellant samples. For the inert samples, the dissipation factor increases inversely with temperature. The dissipation factor is very small for the HTPB binder and exhibits a complicated temperature dependence. The dissipation factor for propellant A is temperature independent, but for propellants B and C increases

inversely with temperature. From the dissipation factor data, some understanding can be gained of how well and for how long the material can hold a given charge. The larger the dissipation factor, the less likely it is for that material to hold a charge. At lower temperatures, it is easier for all these materials (except for the HTPB binder and propellant A) to lose or dissipate the applied charge.

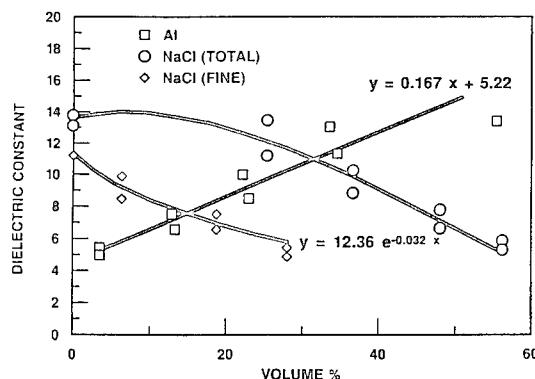


**FIGURE 2. AVERAGE DIELECTRIC CONSTANT VS. FORMULATION FOR INERT PROPELLANT SAMPLES**

**Step 4. Dielectric Breakdown.** The dielectric breakdown voltage of a material is the voltage that may be sustained across the sample just prior to transition from a dielectric material (nonconductor) to a conductor.<sup>13</sup> This breakdown voltage is important in understanding the behavior of the material in an ESD event. The dielectric strength of a material is the dielectric breakdown voltage divided by the thickness. Any one of four methods for applying a test voltage may be used in determining the dielectric breakdown voltage: (1) ramped voltage, (2) stepped voltage, (3) switched capacitor, and (4) pulsed-transformer methods (a coil method developed at NAWC). During the dielectric breakdown, the applied voltage on the sample and the current going through the sample are measured. More details on the theory and experimental methods can be found in ASTM<sup>14</sup> and IEEE.<sup>15</sup>

Dielectric breakdown measurements are used to establish the voltage at which a material will no longer electrically insulate. Many propellants are too conductive to be considered a dielectric. In these cases, the tests quantify the conditions required for transition from an initially more resistive to a less resistive state. Rupture or decomposition of material is positive evidence of voltage breakdown. When neither of these physical evidences is apparent, it is common practice to reapply the voltage which, in most cases, will give a positive indication.

Dielectric breakdown data and dielectric breakdown field strength were measured for all inert samples as a function of electrode configuration, method of voltage application, and temperature. Figure 3 shows that the dielectric strengths of the inert propellants showed no temperature dependence for the breakdown field strength. Dielectric strengths decrease with increasing volume percent of Al for all voltage application methods and electrode configurations. The measured dielectric strength of



pure 3- $\mu$ m Al was  $0.47 \times 10^6$  V/m, which suggests that Al, although the major contributor to dielectric strength, is not the only contributor. The effect of NaCl (AP in real propellants) on breakdown strength is mainly geometrical rather than electrical. The NaCl particle sizes affect the Al particle spacing, which is directly related to the dielectric breakdown voltage. The ESD sensitivity of energetic propellants is a function of AP modal distribution and concentration. Propellants containing the larger AP particle sizes are more ESD sensitive. From the inert samples, it appears that the major contributor to the dielectric field strength is the aluminum concentration. The NaCl (total) concentration introduces second-order effects, while the fine NaCl has third-order effects.

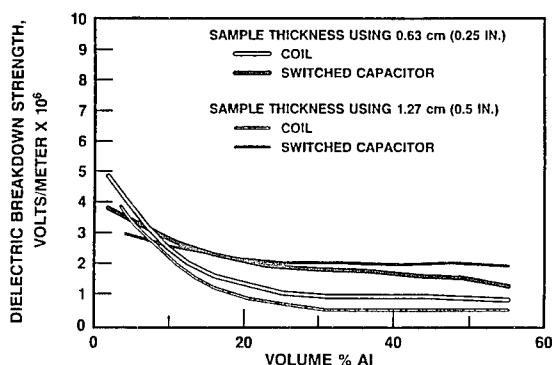


FIGURE 3. DIELECTRIC STRENGTH OF INERT PROPELLANTS VS. VOLUME PERCENT ALUMINUM

Table 4 summarizes the dielectric breakdown data for propellants A and B. These data were collected using the ramp method with 2-in. electrodes. Neither propellant was temperature dependent, and the magnitude of the dielectric field strengths for both propellants was about the same. This result is not surprising since the two formulations are quite similar. The dielectric strength for propellant C at all temperatures was greater than  $9 \times 10^6$  V/m.

TABLE 4. DIELECTRIC STRENGTH DATA FOR ENERGETIC PROPELLANT SAMPLES A AND B (2-IN. ELECTRODES)

Temperature (RH <sup>a</sup> <30%)	Dielectric strength $\times 10^6$ V/m	
	0.63-cm sample	1.27-cm sample
<b>Propellant A</b>		
40°F (4.44°C)	0.75	0.85
70°F (21.11°C)	1.12	1.25
90°F (32.22°C)	0.78	0.94
<b>Propellant B</b>		
40°F (4.44°C)	0.69	0.58
70°F (21.11°C)	0.62	0.66
95°F (35°C)	0.69	0.62

<sup>a</sup>Relative humidity.

Microstructural modeling of the electrical breakdown was performed by Gyure and Beale<sup>16</sup> using the formulation data in Table 1. The model calculated the spacing of the Al particles in the interstitial region. Figure 4 shows how the calculated spacing was used to plot the experimental breakdown voltage. As shown, a good linear fit exists with the experimental data for the inert propellant

formulations. The slope of the line is the breakdown field strength of the HTPB binder, which is 18 mV/m (about 6 times the free space value). This value is in very good agreement with the calculated value. Such good agreement between experimental results and the microscopic model derived by Gyure and Beale<sup>16</sup> is excellent proof that the only influence of NaCl (or AP in real propellants) on the breakdown is its effect on the spacing of the Al particles (i.e., NaCl has a geometrical effect only).

**Step 5. R-C Discharge Test (Large Scale).** A variety of ESD R-C discharge tests have been developed and are detailed in Brown et al.<sup>3</sup> and Kent and Rat<sup>4</sup>. In the NAWC logic/protocol, a R-C discharge test was incorporated because of its demonstrated utility in establishing the R-C discharge characteristics of large samples of energetic materials. This test showed that the propellant is sensitive to ESD events, particularly at the colder temperatures. Details of this R-C discharge test can be found in Covino and Dreitzler.<sup>17</sup> ESD tests were performed on propellants A and B as a function of temperature and applied energy, are summarized in Figure 5. These data show that both propellants are ESD sensitive. The sensitivity of propellant B also increases as the temperature decreases.

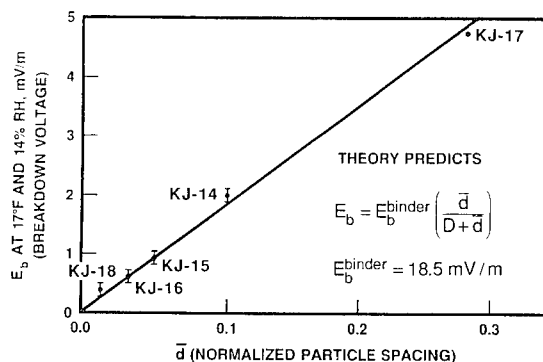


FIGURE 4. BREAKDOWN VOLTAGE VS. NORMALIZED PARTICLE SPACING FOR THE INERT PROPELLANTS

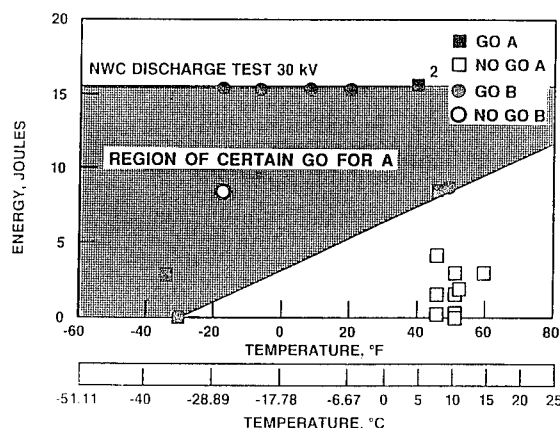


FIGURE 5. R-C DISCHARGE DATA FOR PROPELLANTS A AND B

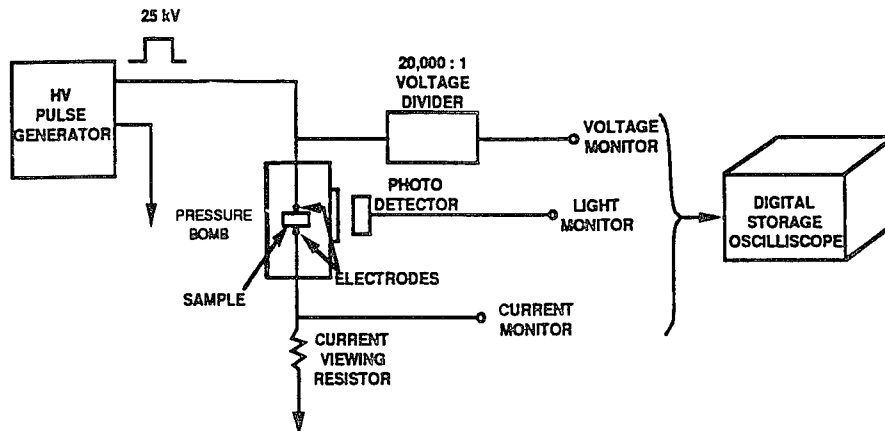


FIGURE 6. SCHEMATIC OF THE ESD IGNITION CIRCUIT USED FOR EXPERIMENTS

**Step 6. Breakdown to Ignition Measurements.** Breakdown voltage and ESD ignitability as a function of pressure are important parameters that must be addressed in order to understand the ESD hazard in solid rocket propellants. To evaluate such parameters, we designed an ESD ignition experiment, schematically represented in Figure 6. For all measurements a 25-kV applied voltage was used. The rate of energy transfer (current flow) is controlled by a resistor in series with the propellant sample being tested. However, the total energy is controlled by changing the length of time that the voltage is applied to the sample. With this circuit two different experiments were performed: GO/NO GO ignition experiments and energy-to-first light experiments.

These measurements show that confinement, geometry, electrode, circuit parameters, and distance between the electrode and propellant are among some critical parameters that influence the likelihood of ignition by ESD. It is important to note that the pressure effects seen by ESD ignition are also seen in laser-ignition studies.<sup>18</sup>

#### ESD Sensitivity of Damaged Propellant

Investigation into the hazards of damaged propellants have shown that damage increases shock sensitivity and reactivity.<sup>19</sup> To evaluate the effect of damage on ESD sensitivity, damaged and undamaged propellants were investigated. Propellant E is a model mix formulated at OLAC Phillips Laboratory, Edwards AFB, California.

The mix is 20 wt% 3 and 6 $\mu$ m Al, 68 wt.% AP (200 and 16  $\mu$ m) and 8.6 wt.% HTPB binder. Propellant F is an HTPB propellant with 18-20 wt.% Al and 65-70 wt.% modal distributed AP. The propellant formulations differ in the amount, particle size, and morphology of the Al and AP. The electrical and physical properties are tabulated in Table 5. Samples were damaged by shooting a 19 mm steel sphere at a 11.4 x 11.6 x 3.8 cm block of undamaged propellant. The impact, at velocity of about 900 m/sec, was perpendicular to the face of the block. Typical damage consisted of shredded propellant surrounding a hole through the block. Samples were sectioned out of the damaged regime, while undamaged

samples were recovered from the pristine region of the impact block. The void content of damaged material was determined by using Archimedes' method to measure the density. The difference in the density was attributed to voids in the propellant. Damaged propellant E had a void content of 1.66% while damaged propellant F contained 2.20% voids.

TABLE 5. PROPELLANT PROPERTIES

PROPERTIES	PROPELLANT E	PROPELLANT F
Volume resistivity	$2.66 \times 10^{11} \Omega\text{-cm}$	$2.28 \times 10^{11} \Omega\text{-cm}$
Dielectric constant	26.6	19.8
Density (undamaged)	1.81 g/cc	1.75 g/cc
Density (damaged)	1.78 g/cc	1.71 g/cc
Void content	1.66 %	2.20 %

ESD ignition experiments for both the damaged and undamaged propellant samples were performed using the circuit shown in Figure 6 without the use of the photodetector nor the pressure bomb. Comparison of ESD ignition times and energies indicate that the damaged propellant ignited more readily than the undamaged one. For both propellants, damaged samples require less time to ignite than the undamaged samples. Damaged propellant E ignited in 22.9 ms while undamaged propellant E required 27.9 ms. The average ignition times for propellant F were 22.7 ms (damaged) and 29.4 ms (undamaged). For both propellants, damaged propellants required less energy (from an ESD discharge) for ignition when compared to undamaged ones. Damaged propellant E required  $1.7 \pm 0.8$  J to ignite while undamaged propellant E required  $5.7 \pm 1.5$  J. Similarly, damaged propellant F required  $1.6 \pm 1$  J to ignite and undamaged propellant F required  $3.8 \pm 1$  J.

#### SUMMARY AND CONCLUSIONS

The ESD logic/protocol was applied to HTPB-based inert propellants to learn more about the mechanisms of ESD events. The protocol was also applied to energetic propellant formulations in an attempt to check predictions deduced from the inert propellants and to validate the logic/protocol with real propellants. Data taken on the inert propellant samples showed that the volume resistivity, dielectric constant, and dielectric strength are very

sensitive to composition. The overall electrical properties of the materials are influenced by the HTPB binder and to a lesser extent by the concentration and particle size of the Al (conducting) particles. The oxidizer (nonconducting) particles contribute only geometrically to influence the spacing of the Al particles. ESD ignitability studies are required in order to further advance the state of the art in ESD mechanistic understanding.

In conclusion, the HTPB class of propellants should be modified as follows to make them less susceptible to ESD events: (1) Change the HTPB binder to a more conductive type; (2) Reduce the concentration of conducting particles to less than 20 volume percent; (3) Decrease the particle size of the conducting particles and make them more uniform; (4) Increase the solids loading and broaden the modal distribution of the nonconducting particles. This increase should be made in such a manner that the conducting particle packing allows the particles to be as far from each other as possible; (5) Add trace concentrations of conducting species. At the present time, these formulation changes would significantly degrade weapon performance. However, an ESD safe propellant can only be achieved if tradeoffs studies between performance and ESD hazards are made.

Such formulation changes would allow the electrical properties to be modified as follows: (1) The resistivity of the propellants would be lowered; (2) The dielectric constant would be reduced and the dissipation factor increased; (3) The dielectric strength should be large so that the breakdown cannot readily be reached under normal operating procedures; (4) The ignition energy (i.e., that energy required for sustained ignition) should be relatively high in order to ensure that no ignition can take place during normal handling of the rocket motors.

Data has been presented in this paper which directly substantiates that damaged propellants are more ESD sensitive when compared to undamaged ones. Comparisons of ESD ignition times and energies indicate that damaged propellants ignite more readily than undamaged ones. This increased sensitivity can be attributed to cracks, jagged edges, and increased surface area which enhances combustion processes in damaged propellants. However, this work has only addressed damage caused by impact. Other types of damage could also increase the vulnerability to ESD. Damage caused by strain, aging, or thermal cycling may be areas for future evaluation.

The electrical phenomena and ESD ignitability addressed in the logic/protocol are all interrelated. A technology has been developed that allows the investigation and ranking of ESD sensitivity in propellants and suggests methods of mitigation. However, further work is still required to understand the mechanism of ESD-triggered events. Before the above suggested propellant changes are made and the propellant is qualified to be used in a solid rocket motor, the ESD sensitivity should be reevaluated on the revised formulation.

## REFERENCES

1. Mardikguian M 1985 *Electrostatic Discharge - Understand, Simulate and Fix ESD Problems* (Gainesville Va: Interference Control Technologies Inc) p vi.
2. U.S. Army Missile Command 1985. J A Knauer, ed, Tech Report no RK-85-9 V IIIA (Huntsville Ala: USAMC).
3. Brown F W, Kusler D J and Gibson F C 1953 *Bureau of Mines Report of Investigation no 5002*.
4. Kent R and Rat R J 1985 *J. Electrostatics* V 17 No 299 pp 299-312.
5. Hammersley J M and Hanscomb D C 1964 *Monte Carlo Methods* (London: Spottiswoode Ballentyne) pp 134-41.
6. Hammersley J M and Broadbent S R 1957 *Proc. Cambridge Phil. Soc.* V 53 pp 629-41.
7. Frisch H L and Hammersley J M 1963 *J. Soc. Ind. Appl. Math* V 11 pp 894-918.
8. American Society for Testing and Materials 1983 *ASTM Standard D257-78* pp 84-104.
9. Keithley Instruments Inc 1984 *Low Level Measurement for Effective Low Current, Low Voltage, and High Impedance* 3rd ed (Cleveland Ohio: Keithley) pp 63-66.
10. American Society for Testing and Materials 1971 *ASTM Standard D150-70* p 27.
11. Smyth C P 1955 *International Chemical Series Dielectric Behavior and Structure* (NY: McGraw-Hill).
12. Covino J and Hudson III F E 1991 *J. Propulsion and Power* Mar-Apr 1991.
14. American Society for Testing and Materials 1981 *ASTM Standard D149-81* pp 1-13.
13. West A R 1984 *Solid State Chemistry and its Applications* (NY: John Wiley and Sons) pp 534-40.
15. Institute of Electrical and Electronic Engineers 1969 *IEEE Standard 4-1969* pp 37-125
16. Gyure M F and Beale P D *Physical Review B*, Vol. 46, No. 7, pg. 3736-3746. 1992.
17. Covino J and Dreitzler D R 1988 *Combustion and Detonation Phenomena 19th International Conference of ICT* (Fed Rep Germany pub) p 80-1.
18. Atwood A I, Price C F, Richter H P, and Boggs T L 1988 *Combustion and Detonation Phenomena 19th International Conference of ICT* (Fed Rep Germany pub) p 1-1.
19. Boggs T L, Price C F, Richter H P, Atwood A I, Lepic A H, Zwierzchowski N G, and Boyer, L R 1988. *Combustion and Detonation Phenomena 19th International Conference of ICT* (Fed Rep Germany pub) p 30-1.

## **DISCUSSION**

FLOYD J. HILDERBRANDT  
U.S. Army ARDEC, Picatinny Arsenal, New Jersey

(1) Has any effort been made to evaluate the change in hazard between a glazed and unglazed propellant?

(2) Are they using an approaching electrode or is the testing a fixed gap?

### **REPLY BY JOSEPHINE COVINO:**

(1) No, we have not looked at glazing effects. However, we looked at silicon grease coating of the samples. The silicone grease reduces surface discharges during the experiments.

(2) The details of the test configurations are in the paper.

## **DISCUSSION**

RICHARD H. GRANHOLM  
Dyno Nobel, Inc., West Jordan, Utah

Can you say more on the effect of voids in the material on its sensitivity to ESD?

### **REPLY BY JOSEPHINE COVINO:**

The last section, "ESD Sensitivity of Damaged Propellants," addresses all the data that we have to date.

**SESSIONS ON**  
**HOT SPOT MODELS**

**Cochairmen:**    **Jerry Wackerle**  
                         **Los Alamos National Laboratory**

**Per-Anders Persson**  
                         **Research Center for Energetic Materials**

## A STUDY OF THE ROLE OF HOMOGENEOUS PROCESS IN HETEROGENEOUS HIGH EXPLOSIVES

P. K. Tang

Los Alamos National Laboratory  
Los Alamos, New Mexico 87545

In a new hydrodynamic formulation of shock-induced chemical reaction, we can show formally that the presence of certain homogeneous reaction characteristics is becoming more evident as shock pressure increase even in heterogeneous high explosives. The homogeneous reaction pathway includes nonequilibrium excitation and deactivation stages prior to chemical reaction. The excitation process leads to an intermediate state at higher energy level than the equilibrium state, and as a result, the effective activation energy appears to be lower than the value based on thermal experiments. As the pressure goes up higher, the homogeneous reaction can even surpass the heterogeneous process and becomes the dominant mechanism.

### INTRODUCTION

It has been recognized that various fundamental physical and chemical processes take place in the shock-induced chemical reaction of high explosives (HE).<sup>1</sup> Not all of them play the same significant role over a wide range of hydrodynamic condition, however. Quite often, only one becomes perhaps the dominant mechanism within a certain range while the rest are dormant or inconsequential by comparison. Wherever there is seemingly a substantial change in the appearance of reaction behavior, a switch of mechanism should be suspected. Identification of the various elementary processes and their relative contribution to the total reaction can eventually lead not only to the better understanding but also to the control of reaction behavior for specific purpose. A case in point is the variation of density and grain size on the initiability of HE.

High explosives without any form of physical heterogeneity are rarely used in applications for they are difficult to initiate; however, chemical reaction is observed when the shock intensity is high. In fact, many studies on homogeneous HE have been carried out mainly to investigate the chemical aspects without the complication associated with heterogeneity. Among the major differences observed between the shock-induced chemical reaction and the thermal reaction is that the former exhibits a lower activation energy based on a simple Arrhenius kinetics formulation,<sup>2</sup> considering the fact that high pressure effect alone usually inhibits chemical reaction for some major explosives.<sup>3</sup> The result prompts us to suspect that the chemical reaction under shock loading for homogeneous HE is beyond the simple Arrhenius kinetics.

In static loading, heterogeneity in material causes stress concentration; thus, it is not surprising to expect localization of mechanical energy dissipation under

dynamic conditions. The nonuniformity of energy transformation from mechanical to thermal type results in nonuniform temperature distribution along with the associated consequence. In HE with physical heterogeneity, the response to shock loading depends on the physical structure in addition to the chemical properties. Within the HE, regions associated with heterogeneity are more susceptible to shock effect, resulting in the concentration of shock energy at some specific sites. Due to the higher energy absorption in these locations, the temperature is therefore higher than their surroundings, and chemical decomposition starts sooner. The regions with shock energy localization are called "hotspots" and serve as the center of ignition. If the hotspot burn is intense enough and if the number of hotspots is large enough, then the burning can propagate into the bulk of the HE, enabling the reaction to grow to its ultimate intensity. In this scenario, the hotspot burn is the first stage in a chain of steps that follow. As a result, the overall reaction follows the shock front quite closely. The hotspot burn itself depends on the shock intensity and also on the characteristic of the region, typically linked to the packing density as well as the grain size.

For high compaction and very fine-grained HE, however, the hotspot mechanism is not as effective at low pressure because of cooler temperatures associated with small hotspots. In this case, the initiation of HE cannot rely on the hotspot burn; an alternate route must be available if the HE can be initiated at all. The new avenue is the homogeneous process which does not require the hotspot burn as the very first step. So it is not surprising to find out that for very fine-grained and/or for high compaction HE, the initiation behavior is quite similar to that found in liquids and single crystals.<sup>4</sup>

The question remains how shock causes chemical reaction in homogeneous explosives. The logical answer would simply be shock heating and the reaction model follows the Arrhenius kinetics with assumed large

activation energy.<sup>5</sup> The driving force is just the bulk temperature. After a period of induction, a reactive wave is formed behind the shock and moves forward to catch the initial shock. Since the reactive wave has the characteristic of a detonation but travels at a greater speed than the leading shock, it is thus called superdetonation. The chemical reaction wave first falls behind the shock but gains on it until the two merge to form a single detonation wave. However, in recent experiments on nitromethane, instead of a superdetonation wave, a growing amplitude reaction wave is observed<sup>6</sup> and is not easily explained by the simple Arrhenius kinetics formulation. Along with the observed lower activation energy<sup>2</sup> and pressure effect,<sup>3</sup> we develop a new concept in the homogeneous reaction.

### HOMOGENEOUS REACTION

High explosive element is treated as a dynamic system consisting of many degrees of freedom (modes), each with its own characteristic time. Subjected to external stress, these modes respond to the stimulus in different ways according to the times. If the longest time among all degrees of freedom is still shorter than the characteristic time of the imposing stress, then, a quasi-steady case is resulted. For example, high pressure static compression, such as found in diamond anvil experiment, can produce a temperature rise so that uniformity inside the explosive element is expected. On the other hand, if the characteristic times of some modes are longer than the characteristic time of the stimulus, these modes will not sense the effect of the stimulus until sometime later. Thus, the impact is concentrated only on those modes with shorter response times. Using shock as the mechanical stress and temperature as an indication of the effect, we expect to see faster temperature rise in some degrees of freedom and slower rise in others. As time elapses, these temperatures should converge to the equilibrium value. But before that occurs, the thermal nonequilibrium condition prevails. So we must make the distinction between a simple high-pressure state and a shock state: the former is in thermal equilibrium but the latter, at least for a period of time, is not. During the nonequilibrium period, chemical process can occur in quite a different manner. To express the higher temperature condition of those particular modes, we introduce the concept of overheat:

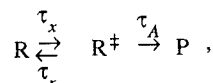
$$\theta^\ddagger = F\theta. \quad (1)$$

$\theta$  is the equilibrium temperature of the medium,  $\theta^\ddagger$  the temperature of the excited state. Evidently the overheat factor,  $F$ , is greater than 1, but it eventually approaches to 1 as the equilibrium condition reaches. If these excited modes are in the pathway to chemical reaction, using the Arrhenius kinetics formulation, a process time  $\tau_A$  is expressed as

$$\tau_A = Z^{-1} \exp\left(\frac{\alpha}{F\theta}\right) = Z^{-1} \exp\left(\frac{\alpha}{\theta}\right). \quad (2)$$

$Z$  is the frequency factor, and  $\alpha$  the activation temperature. Since  $F$  is typically greater than 1, Eq. (2) illustrates the consequence that, expressing in term of the equilibrium temperature which is generally obtainable

from the equation of state under equilibrium conditions, the apparent activation temperature  $\alpha/F$  would be smaller than its counterpart,  $\alpha$ , in a normal chemical reaction. Thus we conclude that the lower activation energy appearing in shock initiation of explosives is quite likely a manifestation of a certain nonequilibrium state along the reaction pathway. Such a reduction in the activation temperature can be substantial and likely invalidates the very large activation energy condition usually assumed in asymptotic analysis. At this moment, we should point out the similarity between the heterogeneous hotspots and the nonequilibrium state discussed here, although one is acting in the microstructure level and another in the intramolecular level. To facilitate the homogeneous reaction involving an excited state, we find that the principle of the transition state theory provides an excellent framework to accommodate the formulation of shock-induced chemical reaction.<sup>7</sup> Without going into any background information in great detail, we propose the following scheme:



where  $R$  and  $P$  represent the reactant and the product, and  $R^\ddagger$  the excited state of the reactant.  $\tau_x$  is the excitation time for the creation of the excited state,  $\tau_r$  the process time of the deactivation step.  $\tau_A$  is the chemical process time based on the excited state temperature as given in Eq. (2). Based on this reaction scheme, the overall reaction rate is as follows.

$$\frac{d\lambda}{dt} = \frac{1}{\tau_H} (1 - \lambda), \quad (3)$$

$$\text{with} \quad \tau_H = \tau_x \left[ 1 + \frac{\tau_A}{\tau_x} \left( 1 + \frac{\tau_x}{\tau_r} \right) \right]. \quad (4)$$

$\lambda$  is the reaction fraction and  $t$  the time.  $\tau_H$  is the effective global homogeneous or simply the homogeneous time. In arriving at the above result, a quasi-steady assumption is made on the excited state. Although we have constructed the reaction scheme hydrodynamically, the times  $\tau_x$  and  $\tau_r$  do have their quantum-mechanical origin.<sup>8</sup> They are treated as constant in the current formulation, or at least in the range in which they are significant.  $\tau_x$  is typically in the nanosecond range. An important point to make is that  $\tau_r$  can be orders of magnitude smaller than  $\tau_x$ ,<sup>9</sup> indicating that the reverse process is much faster than the excitation process,  $\tau_r \ll \tau_x$ , then we simplify

$$\tau_H = \tau_x \left( 1 + \frac{\tau_A}{\tau_r} \right). \quad (5)$$

As seen in Eq. (2), the overheat factor  $F$  has the effect of decreasing  $\tau_A$ ; therefore, the amount of overheat required is to make  $\tau_A$  much smaller than  $\tau_r$  so that the overall reaction can proceed at a significant rate. The study of the limiting behavior of the homogeneous time leads to the conclusion that  $\tau_H$  is actually composed of two times: the modified Arrhenius time

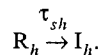
and the excitation time. Due to the Arrhenius nature of the time  $\tau_A$ , at low shock pressure level, the temperature is low so that  $\tau_A/\tau_r \gg 1$ , and we obtain  $\tau_H = \tau_A (\tau_x/\tau_r) \equiv \tau_{MA}$  which is defined as the modified Arrhenius time. The fact that  $\tau_{MA}$  can be orders of magnitude larger than  $\tau_A$  by the factor  $\tau_x/\tau_r$  is supported by the observed reduction of frequency factor  $Z$ .<sup>2</sup> At the other extreme where the pressure and therefore the temperature are very high, then  $\tau_A/\tau_r \ll 1$  and  $\tau_H = \tau_x$ . Their behaviors are illustrated in Fig. 1 for TATB. The change-over pressure condition from chemical kinetic-dominated to excitation-dominated is about 320 kbar. Also shown is the conventional Arrhenius time without the overheat factor. In this paper, we do not pursue the homogeneous model alone further except to mention that we have obtained preliminary results similar to those observed in nitromethane experiments.<sup>6</sup> Our main goal here is to construct a unified or hybrid model including both homogeneous and heterogeneous reaction pathways, and to explore the condition for the presence of the homogeneous process and the impact on heterogeneous HE reaction behavior.

## HETEROGENEOUS REACTION

Historically this model was developed first, but a peculiar behavior involving a specific characteristic time prompted us to look into a new reaction pathway in parallel to the regular heterogeneous reaction route. That particular characteristic time is related to the energy transfer between the hotspot burned product and the unburned bulk explosive, and the unusual behavior is the rapid increase of rate at high pressure. At this point, a review of the model and the refinement to account for the nonequilibrium process is deemed necessary.

In the original unified reaction model for the heterogeneous HE, we propose the following major steps:<sup>10</sup>

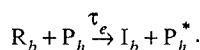
1. Hotspot shock process leading to the formation of an intermediate state, a state of higher temperature than the bulk,



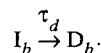
2. Hotspot decomposition, consumption of the intermediate state,



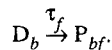
3. Heating of the bulk of explosive by the hotspot burned product, creation of the intermediate state for that region,



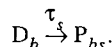
4. Decomposition of the intermediate in the bulk of explosive, generation of decomposition product,



5. Decomposition product becomes final product through fast reaction,



6. Decomposition product transforms into final product through slow reaction,



The symbols R, I, D, and P represent reactant, intermediate, decomposition product, and final product.  $P_h^*$  represents the "cool" hotspot product. Subscripts  $h$  and  $b$  are for hotspots and bulk of explosives;  $f$  and  $s$  for fast and slow processes. The intermediate state means that it is "hot;" and the decomposition product is the direct descendant of the decomposition process but does not represent the final product. To reach the final product, there are two reaction branches: one is fast, the other slow, which accounts for the slow reactions including carbon coagulation.  $\tau_{sh}$ ,  $\tau_h$ ,  $\tau_e$ ,  $\tau_d$ ,  $\tau_f$ , and  $\tau_s$  represent the shock, hotspot, energy transfer, decomposition, fast, and slow process times, respectively.

After some simplifications, the above set of reaction steps leads to three rate equations for the hotspots, the bulk and the slow burn. The model worked quite well until we tried to match the interface velocity experiments where we found we had to impose a limit on the energy transfer rate.<sup>11,12</sup> It appears that for PBX 9502 (95% TATB, 5% Kel-F), at the detonation front a rather constant reaction characteristic time of a few nanoseconds is needed. The investigation of the origin of the process at high pressure leads to the replacement of the decomposition process, step 4, by

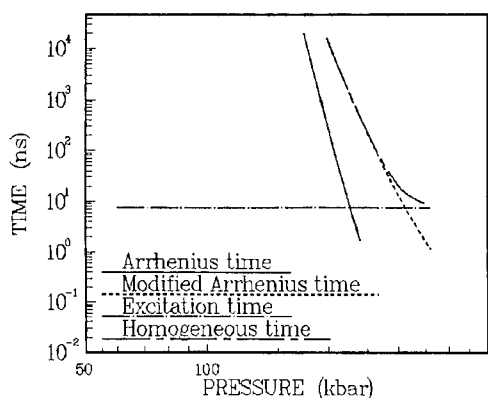
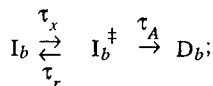


FIGURE 1. THE BASIC PROCESS TIMES IN THE HOMOGENEOUS MODEL: SIMPLE ARRHENIUS TIME  $\tau_A$ , MODIFIED ARRHENIUS TIME  $\tau_{MA}$ , EXCITATION TIME  $\tau_x$  AND HOMOGENEOUS TIME  $\tau_H$



this is where we first applied the transition state principle.<sup>13</sup> Since the temperature of the state  $I_b$  is already quite high due to the energy transfer from the hotspot burned product, the nonequilibrium temperature associated with  $I_b^{\ddagger}$  should be even higher; therefore we conclude that  $\tau_A \ll \tau_r$ , the reaction is dictated by the excitation process time  $\tau_x$ , see Eq. (5). So instead of one rate equation for the bulk burning, we have one exclusively for the energy transfer, and followed by another for the excitation as we will see shortly.

We summarize the result here. The total reaction fraction  $\lambda$  is divided into three major components: hotspot, bulk reaction, slow reaction,

$$\lambda = \eta\lambda_h + (1 - \eta - \psi)\lambda_b + \psi\lambda_s. \quad (6)$$

The designated amounts that go into the hotspots and the slow reaction are  $\eta$  and  $\psi$ ; the balance falls into the bulk as the subscripts  $h$ ,  $s$ , and  $b$  imply. The major portion is usually burned in the bulk.  $\lambda_h$ ,  $\lambda_s$  and  $\lambda_b$  are the reaction fractions of the corresponding components, and they are zero for the completely unreacted portion and one for the burned product. Each component has its own reaction stage with a unique characteristic time. In addition to the rate equations for various reaction fractions,  $E_b$  represents the fraction of the bulk of the explosive being heated by the hotspot burned product; a quantity was considered as decomposition product previously.<sup>10</sup>

First, the hotspot burn,

$$\frac{d\lambda_h}{dt} = \frac{1}{\tau_h} (1 - \lambda_h). \quad (7)$$

The hotspot process time  $\tau_h$  is assumed to take the form of thermal explosion time based on the hotspot temperature which, in turn, is linked to the initial shock pressure using an empirical formulation. The calibration is essentially based on the low impact gauge records. The second stage is the energy transfer,

$$\frac{dE_b}{dt} = \frac{\eta}{\tau_e} (1 - E_b) \frac{(\lambda_h - f_0/\eta)}{(1 - f_0/\eta)}. \quad (8)$$

Equation (8) represents the effect of energy transfer from the hotspot burned product to the unburned explosive.  $\tau_e/\eta$  is the characteristic time for overall energy transfer, including the hotspot mass fraction effect, the amount of heat source.  $f_0$  represents a threshold condition. Even though the energy transfer mechanism is not known and cannot be modeled directly, it is probably through conduction at low pressure level but becomes turbulent mixing at high pressure. That is the reason why we choose to relate the energy transfer time to pressure. The method is similar to the burn rate for solid propellants. The calibration is done based on the wedge test results (Pop plot) similar to the Forest Fire rate.

The chemical process is controlled by the excitation process after the energy transfer stage,

$$\frac{d\lambda_b}{dt} = \frac{1}{\tau_x} (E_b - \lambda_b); \quad (9)$$

and finally, the slow reaction follows the bulk burn,

$$\frac{d\lambda_s}{dt} = \frac{1}{\tau_s} (\lambda_b - \lambda_s). \quad (10)$$

Calibration of  $\tau_x$ ,  $\tau_s$  and  $\psi$  is achieved by matching interface velocity and plate push experiments. Figure 2 shows the variations of the hotspot process time  $\tau_h$ , the overall energy transfer time  $\tau_e/\eta$ , the excitation time  $\tau_x$ , and the slow process time  $\tau_s$  with respect to the change of the hydrodynamic condition represented by pressure, for PBX 9502. We can draw the conclusion that the hotspot process controls the rate in the lowest pressure range. As the pressure goes up higher, the energy transfer becomes the limiting factor. These two processes dictate the initiation behavior of the HE. In the detonation phase, the reaction is essentially controlled by the nonequilibrium excitation, Eq. (9). The slow reaction, Eq. (10), affects the late time behavior, and contributes to the nonsteady detonation phenomenon.<sup>14</sup>

One feature standing out quite vividly is the rapid decrease of the overall energy transfer time at the high pressure level, even in log-log scale. Such a strong hydrodynamic dependence through pressure is suspected - perhaps too strong to be physically reasonable. We currently use the following relation,

$$\tau_e = [G_0 p + \exp(\sum a_i p^i)]^{-1}, \quad (11)$$

where  $G_0$  and  $a_i$  are constant. The exponential part is known as the Forest Fire with typically more than ten terms. Such a complex expression is used to accelerate the rate in the high pressure region, a condition required to match the Pop plot. The formulation quite likely misrepresents the physical origin, that is, the energy transfer as we intend it to be. If a simpler power law is used to express the energy transfer, for example,

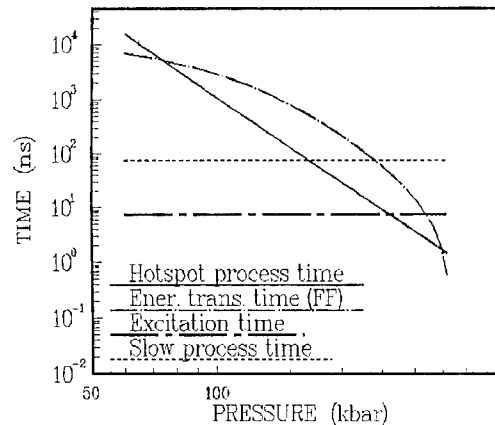


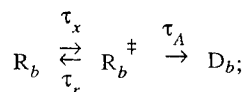
FIGURE 2. THE FOUR MAJOR PROCESS TIMES IN THE HETEROGENEOUS MODEL: HOTSPOT PROCESS TIME  $\tau_h$ , OVERALL ENERGY TRANSFER TIME  $\tau_e/\eta$ , EXCITATION TIME  $\tau_x$ , AND SLOW PROCESS TIME  $\tau_s$ .

$$\tau_e = (G_0 p + G_n p^a)^{-1}, \quad (12)$$

where  $G_n$  and  $a$  are constant obtained by fitting the lower pressure portion of Eq. (11). The results are shown in Fig. 3. Since Eq. (12) yields a lower rate than Eq. (11) in high pressure, a compensation must be made to account for the difference between the two. The logical and physically sound choice is to add a new branch in parallel to the heterogeneous branch. This new pathway has to be of the homogeneous type which does not require hotspot burn and certainly becomes effective only at high pressure level. However, a simple Arrhenius time, also shown in Fig. 3, would not work since it would produce too fast a reaction rate; therefore, we conclude that the proper homogeneous time must be the one we have presented previously. At this point, we cannot speculate on the adequacy of the form of Eq. (12), but for the time being, it does serve the purpose and it is simple in form.

### HYBRID MODEL

We believe the homogeneous process does contribute to the reaction even for heterogeneous high explosives, but its presence is felt mainly at high pressure. Realizing this fact, however, we should not generate a new set of rate equations by simply adding the two rates together as given in Eq. (3) and Eqs. (7) through (10). A formal treatment of multiple reaction stages involving both branches must be carried out. In addition to the heterogeneous pathways 3 and 4 as seen earlier, we add a new branch for the bulk of explosive,



here we assume the homogeneous reaction affects the

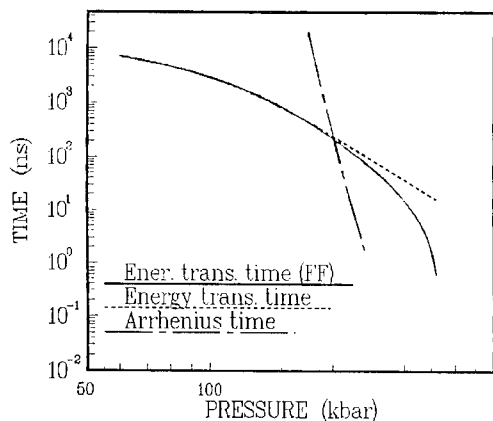


FIGURE 3. THE ENERGY TRANSFER TIME BASED ON THE FOREST FIRE, THE NEW ENERGY TRANSFER TIME, AND THE SIMPLE ARRHENIUS TIME

bulk of explosive only. After extensive mathematical manipulation, Eqs. (8) and (9) are replaced by:

$$\frac{dE_b}{dt} = (1 - E_b) \left[ \frac{\eta (\lambda_h - f_0/\eta)}{\tau_e (1 - f_0/\eta)} + \frac{1}{\tau_H} \right], \quad (13)$$

and

$$\frac{d\lambda_b}{dt} = \frac{1}{\tau_x} (E_b - \lambda_b) + \frac{1}{\tau_H} (1 - E_b) \left( 1 - \frac{\tau_A}{\tau_x} \right). \quad (14)$$

$\tau_H$  is the characteristic time of the homogeneous branch defined previously in Eq. (5). The second terms on the right-hand sides of Eqs. (13) and (14) represent the additional contribution due to the homogeneous process. Its presence in Eq. (13) makes the apparent energy transfer time shorter or the rate faster as reflected in the original formulation using the Forest Fire expression. It should be noted that the benefit of the homogeneous contribution to the decomposition product is not realized until  $\tau_A$  is smaller than  $\tau_x$ . However, the homogeneous pathway does not require any precursor burn from the heterogeneous hotspots as indicated in the burn rate. It should be emphasized that although the homogeneous time  $\tau_H$  appears to link to the pressure, in fact, the relationship is to the temperature through  $\tau_A$  as given in Eq. (2). It is through this particular connection that the homogeneous process remains effective longer as we will see later. Overall, we find that  $\tau_h$  and  $\tau_e$  and the hotspot mass fraction  $\eta$  are affected exclusively by the physical microstructure; whereas  $\tau_x$ ,  $\tau_r$ ,  $\tau_A$ , and  $\tau_s$  and the slow mass fraction  $\psi$  are intrinsic to the fundamental molecular chemical property. For granular explosives, the heterogeneous process is essentially a surface burn mechanism, whereas the homogeneous branch directly affects the interior. Figure 4 shows all the principal process times in the hybrid model.

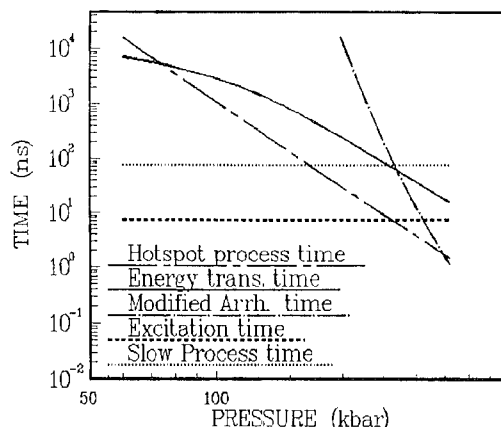


FIGURE 4. ALL MAJOR PROCESS TIMES IN THE HYBRID MODEL

## SIMULATION OF THIN EXPLOSIVE CHARGE EXPERIMENTS

Since the contribution of the homogeneous process is significant only in the high pressure regime, its presence can only be indirectly implicated in hydrodynamic experiments near detonation phase. Although the interface velocity experiment on very thin explosives was designed for other purpose,<sup>15</sup> it does provide an excellent opportunity to test the hybrid model. The reason will be made clear shortly. A very thin HE in the range of 0.25 mm and up was initiated by a driver consisting of a planewave lens, a piece of Comp B and a layer of aluminum. The driver provides a near prompt initiation on PBX 9502. The HE charge was sandwiched between the aluminum and a transparent window of potassium chloride (KCl). Measurement of the interface velocity between the HE and the window was made using the Fabry-Perot technique. Two calculations are made in each case: one based on the original heterogeneous model with the Forest Fire expression for the energy transfer time (dash curve), and another using the hybrid model with the simplified energy transfer time relation and with the homogeneous process explicitly included (solid curve). Markers are from experiments. Result is presented in Fig. 5 for a thickness of 0.25 mm. Instead of a sharp peak observed in thicker HE, a rounded top is seen in the experimental record. This feature indicates the decreasing reaction rate due to the quenching effect even with a very strong initial shock. The heterogeneous model calculation seems quite satisfactory and captures all the features including the reverberation inside the HE, but it still slightly underestimates the experiment. With an adequate amount of overhear, the result of the hybrid model matches the experiment almost perfectly. In this configuration, it is realized that although the HE is initiated rather promptly by the driving system, the reaction cannot really sustain itself to reach the final detonation due to the pressure release, causing rapid

reaction rate reduction. If the reaction is solely supported by the energy transfer process through the pressure dependence in the pure heterogeneous reaction model, then indeed the reaction would drop rather quickly, and so does the velocity as seen in simulation. However, even with significant pressure drop, the temperature decrease would not be as great. As a result, the temperature condition can support reaction by the homogeneous reaction pathway, in the hybrid model. With a proper amount of overhear, the net result is additional growth in reaction intensity as reflected in the interface velocity record. For increasingly thicker HE charges, 0.5 mm, 1.0 mm, and 2.0 mm, seen in Figs. 6, 7, and 8, the rounded top feature gradually diminishes as the two different model calculations converge. Although there is no significant difference between the two simulations numerically, the important point to make is the better representation of the physical phenomenon in the high pressure region using the hybrid model.

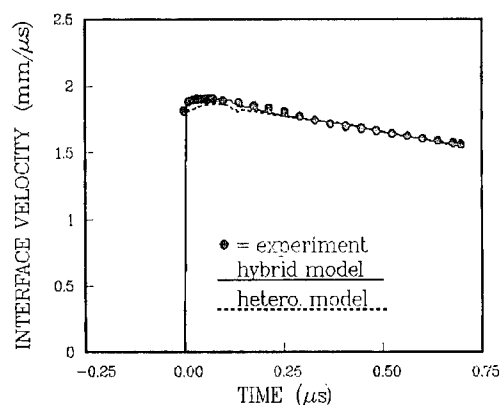


FIGURE 6. 0.5-MM PBX 9502, EXPERIMENT AND CALCULATIONS

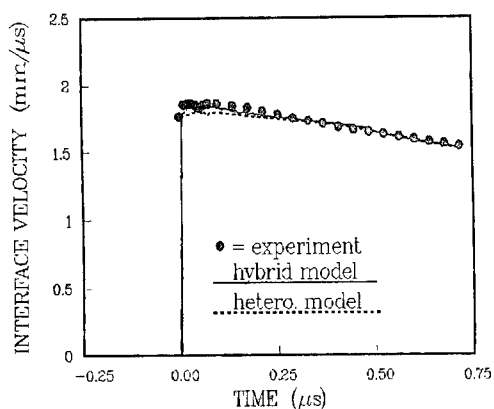


FIGURE 5. 0.25-MM PBX 9502, EXPERIMENT AND CALCULATIONS

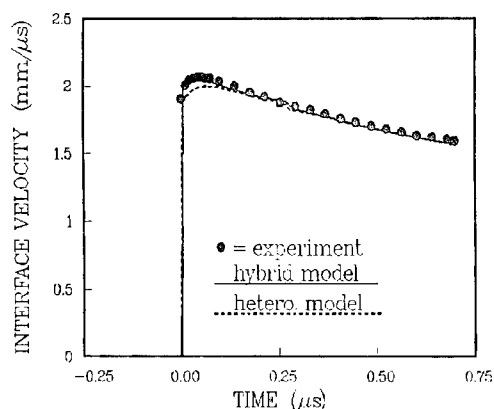


FIGURE 7. 1.0-MM PBX 9502, EXPERIMENT AND CALCULATIONS

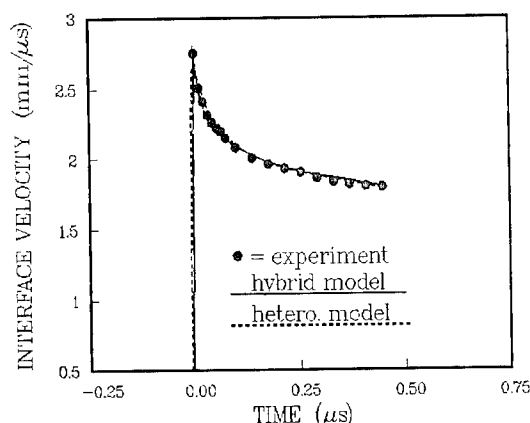


FIGURE 8. 2.0-MM PBX 9502, EXPERIMENT AND CALCULATIONS

## CONCLUSIONS

Based on the process time characteristics, we can identify the significance of various fundamental processes in different hydrodynamic regimes. For heterogeneous explosives, the low pressure initiation behavior is controlled by the hotspots and followed by the energy transfer. The homogeneous branch works in parallel to the heterogeneous branch. Although limited mainly in the high pressure regime, the homogeneous process does contribute to the total reaction. Its effectiveness, however, relies on the nonequilibrium condition associated with shock. A novel idea to account for this effect is introduced by using the concept of overheat. The overheat factor represents the ability of a few selective modes to absorb the shock energy more effectively than others; and the excitation time is a measure of how fast that can be accomplished before equilibration settles in. The equilibration process is characterized by the deactivation process time. As the pressure gets higher, the reaction rate is first controlled by the modified Arrhenius process but eventually reaches a plateau dominated by the excitation process. Further increase in shock strength would not increase the rate. Finally, a slow reaction component appears following the main burn. The appearance of a strong pressure dependence in energy transfer using the Forest Fire formulation seems to be an attempt to accommodate the effect of the homogeneous process.

## ACKNOWLEDGMENTS

The experimental data are taken from Reference 15. The author wishes to thank J. Wackerle, W. Seitz and H. Stacy for their generous support, and C. Forest for the thermal nonequilibrium treatment of the equation of state. The author is also indebted to J. Dick, S. Shaw, and J. Wackerle, all of Los Alamos, for valuable discussions and suggestions. The work is supported by the United States Department of Energy under contract W-7405-ENG-36.

## REFERENCES

1. Dremmin, A. N.; Klimenko, V. Yu.; Davidova, O.N.; and Zoludeva, T. A., "Multi-process Detonation Model," in *Proceedings of the Ninth Symposium (International) on Detonation*, Portland, OR, Aug 1989, pp. 724-729.
2. Dick, J. J., "Pop Plot and Arrhenius Parameters for <110> Pentaerythritol Tetranitrate Single Crystals," in *Proceedings of the APS Topical Conference on Shock Wave in Condensed Matter*, Spokane, WA, Jul 1985, pp. 903-907.
3. Lee, E. L.; Sanborn, R. H.; and Stromberg, H. D., "Thermal Decomposition of High Explosives at Static Pressures 10-50 Kilobars," in *Proceedings of the Fifth Symposium (International) on Detonation*, Pasadena, CA, Aug 1970, pp. 331-337.
4. Kipp, M. E.; and Setchell, R. E., "A Shock Initiation Model for Fine-Grained Hexanitrostilbene," in *Proceedings of the Ninth Symposium (International) on Detonation*, Portland, OR, Aug 1989, pp. 209-218.
5. Campbell, A. W.; Davis, W. C.; and Travis, J. R., "Shock Initiation of Detonation in Liquid Explosives," *Phys. of Fluids*, Vol. 4, No. 4, 1961, p. 498.
6. Sheffield, S. A.; Engelke, R.; and Alcon, R. R., "In-Situ Study of the Chemically Driven Flow Fields in Initiation Homogeneous and Heterogeneous Nitromethane Explosives," in *Proceedings of the Ninth Symposium (International) on Detonation*, Portland, OR, August, 1989, pp. 39-49.
7. Eyring, H., "The Activated Complex in Chemical Reactions," *Journal of Chemical Physics*, Vol. 3, No. 1, 1935, p. 107.
8. Bardo, R. D., "The Lattice Density of States Concept and Its Role in Determining the Shock Sensitivity of PETN and Nitromethane," in *Proceedings of the Ninth Symposium (International) on Detonation*, Portland, OR, August, 1989, pp. 235-245.
9. Moore, D. S.; Schmidt, S. C.; Shaw, M. S.; and Johnson, J. D., "Coherent Anti-Stokes Raman Spectroscopy of Shock-Compressed Liquid Carbon Monoxide," *Journal of Chemical Physics*, Vol. 95, No. 8, 1991, p. 5603.
10. Tang, P. K., "Initiation and Detonation of Heterogeneous High Explosives: A Unified Model," LA-11352-MS, Sep 1988, LANL, Los Alamos, NM.
11. Seitz, W. L.; Stacy, H. L.; Engelke, R.; Tang, P. K.; and Wackerle, J., "Detonation Reaction-Zone Structure of PBX 9502," in *Proceedings of the Ninth Symposium (International) on Detonation*, Portland, OR, Aug 1989, pp. 657-669.
12. Tang, P. K., "Modeling Hydrodynamic Behavior in Detonation," *Propellants, Explosives, Pyrotechnics*, Vol. 16, No. 5, 1991, p. 240.
13. Tang, P. K., "Transition State Theory Applying to the Study of Reaction Processes in Detonation,"

LA-11903-MS, Jul 1990, LANL, Los Alamos, NM.

14. Tang, P. K.; Seitz, W. L.; Stacy, H. L.; and Wackerle, J., "A Study on the Contribution of Slow Reaction in Detonation," in *Proceeding of the APS Topical Conference on Shock Compression of*
15. Wackerle, J.; Stacy, H. L.; and Seitz, W. L., "Velocimetry Studies on the Prompt Initiation of PBX 9502," paper presented at this Symposium.

*Condensed Matter*, Albuquerque, NM, Aug 1989, pp. 279-282.

## AN ENERGY TRANSPORT MODEL FOR THE SHOCK INITIATION OF COMPOSITE EXPLOSIVES AND PROPELLANTS

A. J. Lindfors and O. E. R. Heimdahl  
Naval Air Warfare Center  
Weapons Division  
China Lake, CA. 93555-6001

A large body of shock initiation data has been developed on composite explosives and propellants. These energetic materials often consist of multiple energetic species, complex energetic binders and other inert additives. Due to this highly composite nature many of the materials show marked differences in their behavior under shock loading when compared to single energetic species/single binder systems. The wedge test was used to determine the build-up to detonation, and a new method for describing the build-up was developed. This method considers the build-up as internal energy transport with self-generation. The self-generation is described in terms of the acceleration of the shock front, and shows that it may be used to describe the relative shock sensitivity of the materials tested.

### INTRODUCTION

Over the past several years a large number of shock insensitive propellants and explosives have been developed. These propellants and explosives are often complex heterogeneous composites. They contain mixtures of energetic species, various inert solids, and complex binder systems. Due to this composite nature many of the materials show markedly different behavior when subjected to shock than do simpler energetic materials.

An important experimental technique used to characterize and study initiation is the wedge test. The wedge test provides run and time to detonation as a function of input pressure data which is used to characterize shock sensitivity. However, for some highly composite systems this data can be somewhat puzzling. Frequently there appear to be breaks in the data which represent mechanism changes or favored reactions of competing energetic species. Current shock initiation models do not treat these breaks. In an attempt to better understand this behavior a new method for treating the data was developed.

Since the wedge test primarily provides shock velocity histories it was necessary to describe the initiation process in these terms. Determining the reactivity as a function of change in shock velocity<sup>1</sup> or particle velocity has been approached by a number of workers,<sup>2,3</sup> who have used the motion induced in an inert material to deduce the amount of reactivity in an energetic material. In this new approach, however, the shock velocity history is used to define the internal energy build-up. The build-up process is considered to be one of internal energy transport with internal generation.

In this build-up process the input energy from the shock wave provides the impetus for the internal generation as in a flux system, and the internal generation is provided by hot-spots. These hot-spots may be voids, high density inclusions, exothermic reaction, or local energetic molecule decomposition. This internal generation provides energy to the front and the rate of generation increases at the front. This leads to the self-supporting detonation wave. The generation rates for various energetic materials can then be compared and give a measure of relative shock sensitivity.

In this paper the wedge test and the energetic materials tested are described. The proposed model is developed and then applied to the experimental results. An application of the model to shock sensitivity is demonstrated to be consistent with another model, and the results are subsequently discussed. In addition, a study was undertaken and described to determine the effect of the assumptions used in developing the model.

### WEDGE TEST EXPERIMENTS

#### Technique

In the wedge test a planar shock wave is introduced into the energetic material to be tested. As the shock progresses through the energetic material energy is accumulated at the shock front, which builds-up to a detonation. The objective of the wedge test is to determine the point at which the shock wave is transformed to a detonation wave. This point is characterized by a unique time and distance to detonation for a specific set of input conditions.

A streak camera is used to record the wedge test event. The surface of the wedge is mirrored to reflect light into the camera. When either the shock wave or detonation wave reaches the surface, the surface distorts so that the light is no longer reflected into the camera. When the shock wave is transformed to the detonation wave the slope of the reflected light trace on the film changes. Thus, the shock velocity history can be determined from the film record. A schematic of the wedge test set-up is shown in Figure 1.

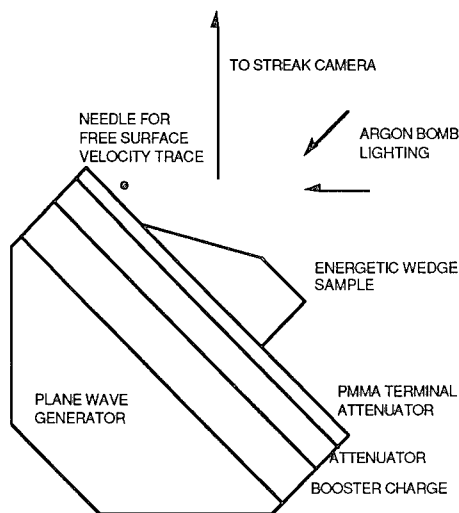


FIGURE 1. SCHEMATIC OF THE WEDGE TEST SET-UP

#### Propellants Tested

Three propellants with complex formulations were studied. The propellant formulations consisted of RDX or HMX, AN, nitrate ester plasticized energetic binders, and other additives. All the formulations contained 60% by weight of solids. The first formulation used RDX, and AN with the addition of a small amount, 0.8 wt. %, of high density lead carbonate as a burn-rate modifier. The second formulation consisted of HMX, and AN with no burn-rate modifiers. The third and final propellant contained RDX, and AN with no burn-rate modifiers. The three propellant formulations are designated HEP-1, HEP-2 and, HEP-3 respectively. The propellants were processed using small particle size solids and mixed extensively under a vacuum to minimize density discontinuities. The resulting formulations were of very good quality and 99%+ of theoretical maximum density.

#### Explosives Tested

Two explosives were used in this study. One explosive, used as a control, contained all RDX, and was a cast cure single non-energetic binder system. This explosive is designated here as PBX-1. The second explosive used was a mixture of TATB, HMX, and an HTPB binder. This explosive is designated PBX-2. As in the case of the propellants the resulting

mixes were of good quality and resulted in samples at 99%+ of TMD.

#### TRANSPORT MODEL DEVELOPMENT

The data obtained for the three propellants and two explosives studied exhibited the complex initiation behavior which is not addressed by the current initiation models. In attempt to interpret this behavior an energy transport model was developed. The model development is outlined in this section.

Consider a volume of material in slab geometry, as shown in Figure 2, where  $A = \Delta y \Delta z$ , and internal self-generation,  $G$ , is present. The equation for self-generation given by Equation 1 can be derived as follows:

$$e_0 A + G \Delta x = e_1 A$$

$$e_1 A - e_0 A = G \Delta x$$

which for the one-dimensional case gives

$$\Delta e = e_1 - e_0 = G \Delta x$$

Thus, as  $\Delta x$  approaches 0:

$$de/dx = G \quad (1)$$

To determine the energy generated, and subsequently the self-generation term, as the shock wave moves through the material a simple analysis in the P-V plane was used. Several P-V curves are drawn in Figure 3 showing the unreacted material, partially reacted material and fully reacted material. Since it is

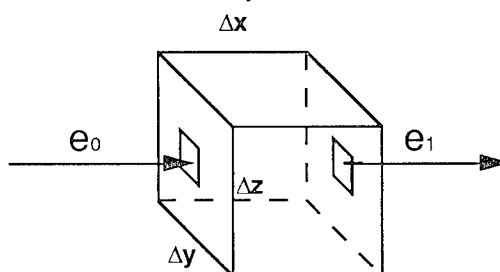


FIGURE 2. SCHEMATIC OF THE ENERGY TRANSPORT MODEL IN SLAB GEOMETRY

not possible to explicitly determine from the wedge test experiment the amount of reaction that has occurred, an assumption for the new volume generated was needed. This model assumes that the new volume is the same as that generated during the initial shock compression. The errors associated with the assumption of constant volume during reaction were studied by a reactive flow computer code and are more fully covered in the reactive modelling section.

Under this assumption, two energy terms are generated. The first is the specific energy generated

from the shock compression of the material. The second is the specific energy generated due to shock interaction. The second term may involve energetic decomposition, hot-spot generation, and/or bulk shock heating. The sum of these two terms gives the total energy generated during the shock process. By subtracting the energy due to compression from the total specific energy generated, and using the nomenclature in Figure 3, the energy generated is found to be given by Equation 2.

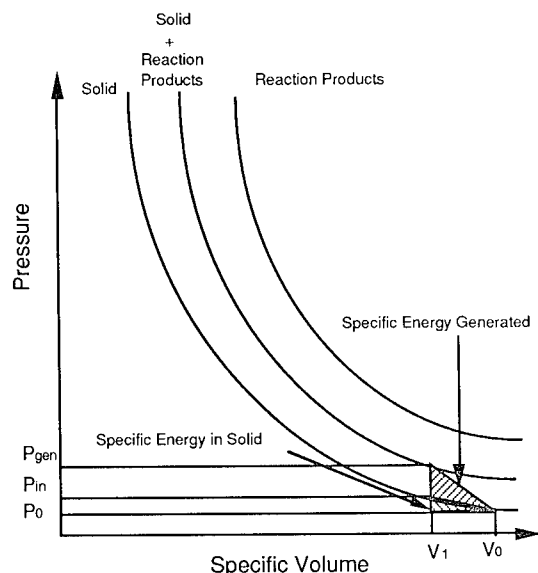


FIGURE 3. P-V DIAGRAM SHOWING ENERGY TERMS

$$e_{gen} = [1/2 (P_{gen} - P_{in})(V_0 - V_1)] \quad (2)$$

Since the wedge test only provides data in the form of shock velocity and shock acceleration, an expression for the energy generated is needed in these terms alone. To accomplish this, the shock Hugoniot for the material is needed. In this model the shock Hugoniot for the P-V curve of partially reacted material is assumed to be an average of the solid Hugoniot and the fully reacted Hugoniot. Though, this does introduce some errors, it is felt that they are not substantial, and are about 2-3%. Therefore, from:

$$P_1 = U_1 u_1 / V_0 \quad (3)$$

$$U_1 = C_1 + S_1 u_1 \quad (4)$$

$$U_2 = C_2 + S_2 u_2 \quad (5)$$

where U and u are shock and particle velocity respectively, and the subscripts 1 and 2 indicate unreacted and partially reacted respectively. Conserving mass, the following expression is derived.

$$1 - (V_0 / V_1) = u_1 / U_1 \quad (6)$$

Then substituting Equations 3, 4, 5, and 6 into Equation 2 gives the energy generated in terms of shock velocity only in Equation 7.

$$2e_{gen} = \left( \frac{U_1 - C_1}{S_1} \right)^2 \left[ \left( \frac{U_2 - C_2}{U_1 - C_1} \right) \left( \frac{S_1}{S_2} \right) \left( \frac{U_2}{U_1} \right) - 1 \right] \quad (7)$$

Using Equation 7 an energy build-up as a function of distance may be determined for a given wedge test record. Figure 4 shows a least-squares fit to the energy generated data, for the first wedge shot listed in Table 1, where the run-to-detonation was 1.75 millimeters. As steady state detonation is achieved the slope of the line tends to zero.

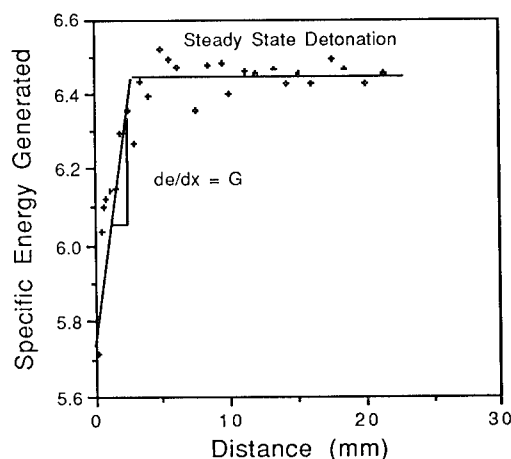


FIGURE 4. ENERGY GENERATION IN THE BUILD-UP TO DETONATION

## EXPERIMENTAL RESULTS

### Wedge Tests and Self-Generation Values

The experimental results of the wedge tests performed, as well as the self-generation term, G, are listed in Table 1. The shots where no transition to detonation occurred are indicated by the double asterisk (\*\*). In this case the energy generation term is negative as the energy losses equal or exceed the energy gains as the shock decays.

For each streak camera record the film was read and converted to real time and space. The space and time data may be converted to shock velocity using a number of fitting techniques<sup>4</sup>. However, in this case the shock velocities were determined using three point running fits to the space time data. The subsequent shock velocities were used in Equation 7 to generate the incremental energy gain as the shock transits the material. Incremental energy gain as a function of distance are plotted in Figure 5 for three of the HEP-1 experiments.



TABLE 1. EXPERIMENTAL RESULTS

Material	P <sub>0</sub> (GPa)	x* (mm)	t* (μs)	G (de/dx)
HEP-1	10.00	1.75	0.22	0.288
HEP-1	7.04	6.25	1.25	0.200
HEP-1	6.73	9.60	1.96	0.155
HEP-1	5.40	14.52	2.49	0.118
HEP-1**	4.35	-----	-----	<0
HEP-1**	3.20	-----	-----	<0
HEP-2	9.98	1.54	0.27	0.266
HEP-2	8.41	12.10	2.48	0.140
HEP-2	8.10	13.52	2.87	0.103
HEP-2	6.90	14.32	3.11	0.010
HEP-3	10.70	11.71	2.46	0.132
HEP-3	8.48	13.72	2.96	0.054
HEP-3	7.11	15.30	3.31	0.039
HEP-3	6.18	17.73	3.93	0.009
HEP-3**	5.65	-----	-----	<0
PBX-1	11.31	1.91	0.33	1.892
PBX-1	4.36	12.06	2.91	0.530
PBX-1	7.14	4.87	0.93	1.060
PBX-1	3.37	20.68	5.25	0.294
PBX-1**	2.47	-----	-----	<0
PBX-1	7.48	4.05	0.80	1.170
PBX-2	12.05	14.06	2.03	0.050
PBX-2	7.65	21.74	3.33	0.021
PBX-2	6.10	27.35	4.32	0.007

\* Indicates Transition to Detonation

\*\* Indicates No Transition to Detonation

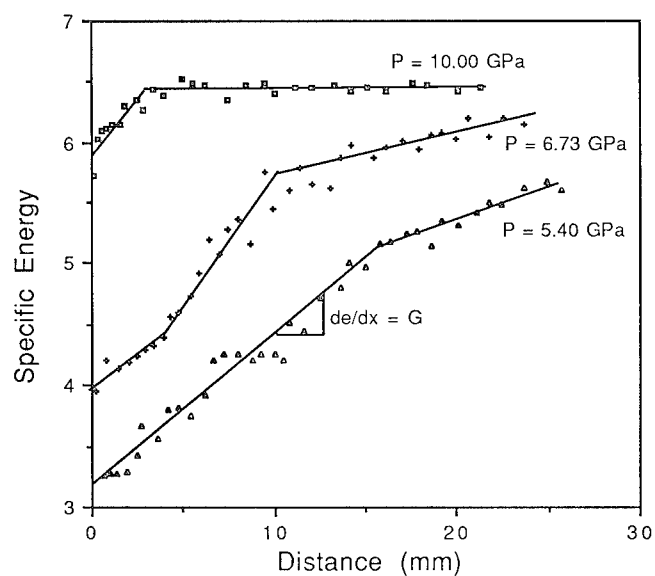


FIGURE 5. SPECIFIC ENERGY PLOTS FOR THREE HEP-1 WEDGE EXPERIMENTS

## Application to Shock Sensitivity

A determination of shock sensitivity can be made from plots of the self-generation term versus input shock pressure. This is shown in Figure 6 for HEP-1, HEP-2, HEP-3, and PBX-2. The plot for PBX-1 is shown separately in Figure 7 as its data range would overshadow the differences in sensitivity in Figure 6. The fits for the data are quite linear over the range of shock pressures and fit the form of Equation 8.

$$G = a + bP \quad (8)$$

Where:

G = Self-generation rate

P = Shock input pressure

a, b = constants for a given formulation

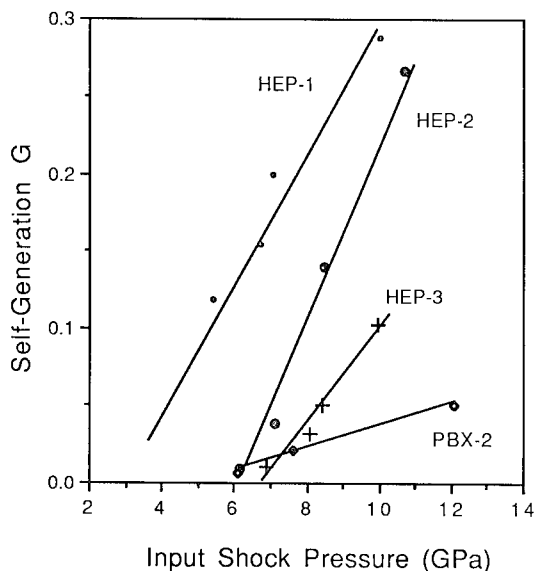


FIGURE 6. SELF-GENERATION PLOTS FOR HEP-1, HEP-2, HEP-3, AND PBX-2

The interpretation of sensitivity behavior of an energetic material using these plots is done by observing the behavior of the constants a and b. The value a defines the horizontal position of line, and thus defines the relative self-generation for a given input pressure, and b is the slope of the line.

For example, as one moves to the left and the slope increases there is an increase in sensitivity. This is indicated in the following manner. For a given input shock pressure the material with the higher self-generation rate is the more sensitive. Thus the materials may be ranked in shock sensitivity in the following manner; from least to most sensitive: PBX-2 < HEP-3 < HEP-2 < HEP-1 < PBX-1.

The traditional method for plotting the data from the wedge test has been in the  $\log P$  versus  $\log x^*$  plane.

Where P is the shock input pressure and  $x^*$  is the distance to detonation. Typically this type of plot has been called the Pop-plot after Alphonse Popolato. On the next page the Pop-plots are shown in Figure 8 for the formulations plotted previously. In the  $\log x^* - \log P$  plane, shock sensitivity increases as one moves to the left. As can be seen in the Pop-plots the materials show the same relative shock sensitivity as in the self-generation plots.

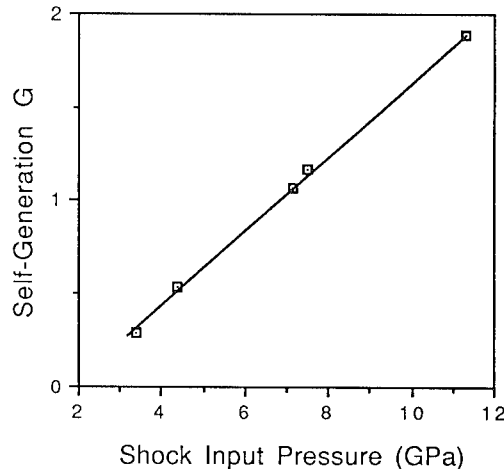


FIGURE 7. SELF-GENERATION PLOT FOR PBX-1

## DISCUSSION

It has been shown that an energy transport model can describe the build-up to detonation in the propellants and explosives tested including both composite materials and a single energetic species/single binder system.

Greater interest however, lies in determining when competing mechanisms or favored energetic decomposition are taking place. Some evidence of this may be shown in the break in slope in some of the energy generation plots, prior to steady-state conditions. Decomposition of the RDX and, HMX appear to drive the reaction in the propellants at lower input pressures. However at higher input pressures decomposition of ammonium nitrate may begin to take place. The investigations of Stinecipher,<sup>5</sup> and Lee<sup>6</sup> on the contribution of ammonium nitrate in a reaction show indications that this does take place.

In the PBX-2 system there were no significant slope breaks in the build-up process. Which suggests that the decomposition of the TATB and the HMX is continuous at all input pressures where a run-to-detonation is achieved.

In several of the experiments the energy generated versus distance plots have still not reached steady state, that is to say constant velocity for detonation. This is not unusual, for in many wedge tests the detonation velocity observed does not coincide

with the detonation velocity measured in other tests such as a detonation velocity experiment. However, from the analysis it is clear that the slope of the self-generation versus distance plot must tend to zero slope for all experiments where detonation is achieved. This would undoubtedly be the case if the scale of the wedge test were increased. In the experiments where no run-to detonation was achieved it is assumed that the energy losses equaled or exceeded the energy gains due to reaction.

### Checking Assumptions By Hydrocode

The assumption that the reaction takes place at a constant volume is probably the most problematic. To check this assumption a reactive flow model with Pressure-Volume gauge points was run using a Forest Fire model<sup>7</sup> for the PBX-1 material. The Forest Fire reactive model is directly linked to the wedge test through the linear Pop plot fit. This reactive model is appropriate for simple shock to detonation geometries.

An overlay of P-V plots calculated for two such gauge points separated by a distance of 2.5 millimeters new pressure, corresponding to an increase in shock is shown in Figure 9. The energy of the shock is shown in the figure as the energy under the solid Hugoniot, while the energy generated is given by the

velocity. Thus, the error associated with the constant volume reaction, shown in the figure as an area in the vertex of a Pressure-Volume triangle, appears to be quite small. However, if the same assumption were used where the gauge points are separated by large distances the error would be considerably larger.

### CONCLUSIONS

The shock sensitivity of several complex propellants and explosives were assessed in the wedge test. The results indicated that these propellants and explosives show quite different behavior under shock loading when compared to simpler energetic materials. A new method was developed to study their initiation behavior and relative shock sensitivity. This method, called the Energy Transport Model, showed quite consistent behavior for both composite and single species energetic materials.

Future work on this model will include refining the assumptions stated earlier and include the input of more explicit shock Hugoniot for partially reacted material. In addition it is hoped that the energy transport approach may be useful in assessing other phenomena, such as decay of detonation due to critical diameter effects.

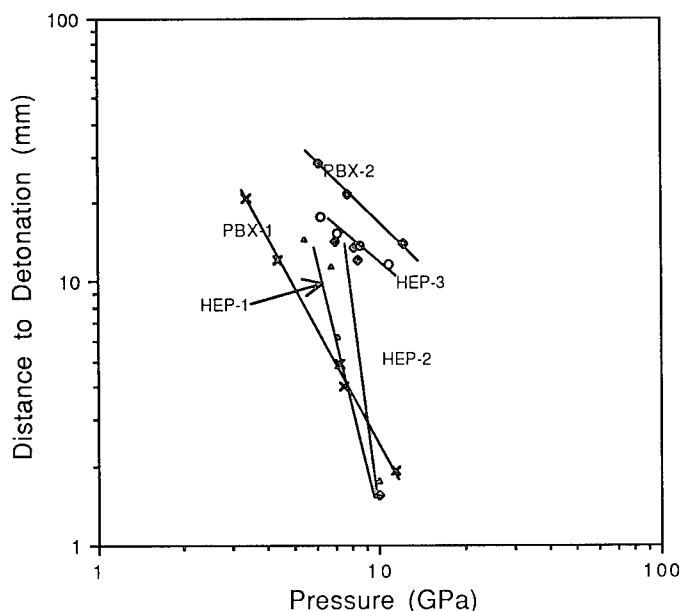


FIGURE 8. DISTANCE TO DETONATION VERSUS PRESSURE PLOTS (POP-PLOTS) FOR THE TEST MATERIALS

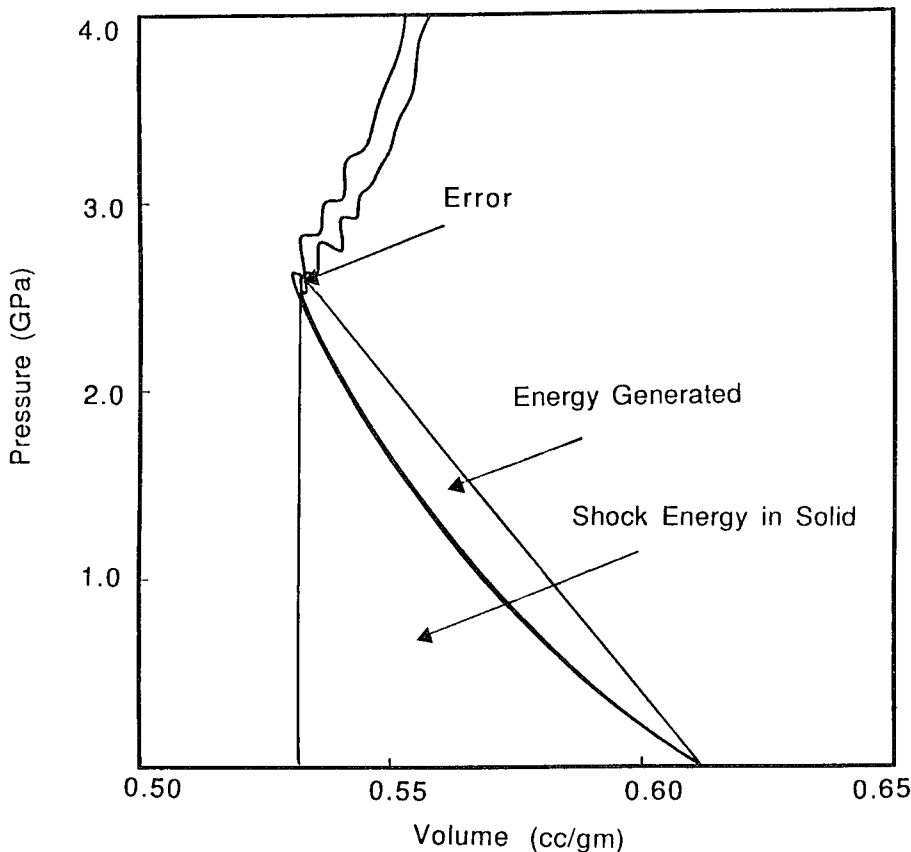


FIGURE 9. PRESSURE VOLUME PLOTS USING THE FOREST-FIRE MODEL FOR TWO GAUGE POINTS LOCATED AT 2.5 MM AND 5 MM FROM THE INTERFACE IN PBX-1

#### REFERENCES

1. Lobanov, V. F.; "Initiating Wave Parameters Determination for TG 50/50," *Combustion, Explosion and Shockwaves*, Vol. 22, No. 5, Sep-Oct 1986.
2. Tasker, D. B.; "Shock Initiation and Subsequent Growth of Reaction in Explosives and Propellants: The Low Amplitude Shock Initiation Test LASI," *Proceedings of the Seventh Symposium (International) on Detonation*, Office of Naval Research, Annapolis, MD, 16-19 June 1981, pp. 295-298.
3. Liddiard, T. P. and Forbes, J. W.; "Initiation of Burning and Detonation in Cast H-6 and Cast PBXW-109," *Proceedings of the Seventh Symposium (International) on Detonation*, Office of Naval Research, Annapolis, MD, 16-19 June 1981, pp. 308-315.
4. Gibbs, T. R. and Popolato, A.; eds., *LASL Explosive Property Data*, University of California Press, Berkeley, CA, 1980, pp. 294-296.
5. Stineciph, M. M.; "Eutectic Composite Explosives Containing Ammonium Nitrate," *Proceedings of the Seventh Symposium (International) on Detonation*, Office of Naval Research, Annapolis, MD, 16-19 June 1981, pp. 801-810.
6. Lee, J.; et al., "Detonation and Shock Initiation Properties of Emulsion Explosives," *Proceedings of the Ninth Symposium (International) on Detonation*, Office of Naval Research, Portland, OR, 28 Aug- 1 Sep 1989, pp. 263-270.
7. Lundstrom, E.; "Evaluation of Forest Fire Burn Model of Reaction Kinetics of Heterogeneous Explosives," *NWC TP 6898*, Naval Weapons Center, China Lake, CA, May 1988.

## DISCUSSION

HAROLD H. GRYTING  
Gryting Energetics Science Company

In the presentation a PBX-1 and PBX-2 were referred to. According to the summary these do not appear to refer to PBXN-1 and PBXN-2. If available, can you give the formulations of "PBX-1 and PBX-2"?

## REPLY BY A. J. LINDFORS:

The formulations PBX-1 and PBX-2 do not stand for PBXN-1 and PBXN-2. They are my own designations.

PBX-1 is an RDX based explosive containing 86% RDX and 14% acrylate binder. PBX-2 contains 50% TATB, 20% HMX and 30% HTPB binder.

PBX-1 and PBX-2 have detonation velocities of 8.10 mm/ $\mu$ sec and 6.60 mm/ $\mu$ sec respectively.

## MODELING SHOCK INITIATION IN COMPOSITION B\*

M.J. Murphy and E.L. Lee  
Lawrence Livermore National Laboratory  
Livermore, CA 94550

A.M. Weston  
KMI Services  
Livermore, CA 94550

A.E. Williams  
Naval Research Laboratory  
Washington, D.C. 20375-5000

A hydrodynamic modeling study of the shock initiation behavior of Composition B explosive was performed using the "Ignition and Growth of Reaction in High Explosive" model developed at the Lawrence Livermore National Laboratory. The HE responses were computed using the CALE and DYNA2D hydrocodes and then compared to experimental results. The data from several standard shock initiation and HE performance experiments was used to determine the parameters required for the model. Simulations of the wedge tests (pop plots) and failure diameter tests were found to be sufficient for defining the ignition and growth parameters used in the two term version of the computational model. These coefficients were then applied in the response analysis of several Composition B impact initiation experiments. A description of the methodology used to determine the coefficients and the resulting range of useful application of the ignition and growth of reaction model is described.

### INTRODUCTION

The Lee and Tarver phenomenological model<sup>1</sup> of shock initiation in explosives discussed in this paper has been in use at LLNL for more than a decade. The purpose of this paper is to provide a practical description of the utility of the model as well an approach for determining parameters used in the model. The model is based on an ignition and growth of reaction phenomenology for modeling high explosives as they transition from the unreacted state to the reacted state. The JWL form of equation of state (EOS) is used to simulate the pressure-volume-energy relationship for the material in both the unreacted and reacted states. The key to the model is a pressure and fraction reacted dependent rate law that controls the transition from the unreacted phase to the reacted phase.

Two forms of the rate law have been described in previous detonation symposia.<sup>2,3</sup> The two-term model<sup>2</sup> consists of an ignition term and a single growth of reaction term. This methodology has been shown to be useful for a wide range of shock and impact initiation studies. The three term model published in the 8th Detonation Symposium consists of an ignition term with two growth terms.<sup>3</sup> This model has been shown to be more effective for high intensity, short duration shocks.<sup>3,4</sup> For shock initiation problems not involving a high pressure, short duration pressure pulse, we feel that the two term model is more adequate.

The utility of the ignition and growth of reaction methodology has been demonstrated for a few well characterized materials. The primary deficiency of this model is the limited number of materials that have been parameterized for the model. The purpose of this paper is to show that available explosives shock initiation and performance data are sufficient for defining an appropriate set of coefficients for using the model in CALE,<sup>5</sup> DYNA2D,<sup>6</sup> or other hydrocodes.

\* Work performed under the auspices of the U.S. Department of Energy by the Lawrence Livermore National Laboratory under contract No. W-7405-ENG-48.

## IGNITION AND GROWTH MODEL DESCRIPTION

The ignition and growth concept of shock initiation in high explosives has been the subject of numerous studies and modeling efforts. The LLNL I & G model was developed based on the concept that the ignition and growth of "hot spots" is the dominant mechanism in the shock initiation and detonation of high explosives. In addition, the LLNL model was developed to yield stable detonation waves based on the Zeldovich-von Neumann-Doering model.<sup>7</sup> Thus, the detonation model consists of a leading shock front in which no explosive has reacted, followed by a well defined reaction zone in which the pressure decreases to the Chapman-Jouguet value as the fraction of the explosive reacted approaches unity. The I&G model is concerned only with simulating the reaction zone, where the transition from the fully unreacted to the fully reacted state occurs. Prior to the reaction starting, the explosive is modeled with its unreacted EOS. After the reaction has completed, the explosive is modeled with the JWL equation of state for the detonation products. The fraction of explosive reacting per cycle during the transition from the unreacted to the reacted state is controlled by the reaction rate relation.

The transition region, or reaction zone, is treated as a mixture based on the two equations of state. Although the most physical method for equilibration of the mixture EOS would rely on defining the entropy at a fixed volume for each phase, the method adopted in the DYNA and CALE codes utilizes simultaneous pressure and "temperature" equilibrium. Studies have shown that the differences in the two methods are not significant.<sup>8</sup>

### Reaction Rate Relation

The reaction rate relation shown below is the mathematical expression of the reaction rate behavior just described.

$$df/dt = I(1-F)^{2/9}(\rho/\rho_0-1-a)^4 + G_1(1-F)^{2/9}F^{2/3}p^Z$$

In this equation there are four user defined variables ( $I$ ,  $a$ ,  $G_1$ , &  $Z$ ) and several exponent terms that are normally constants and not defined by the user. Most of the exponents used in this relation are fixed in value since the reaction rate phenomenology is found to be similar for the majority of explosives.

There is a maximum limit,  $F_{\text{igmax}}$ , for the contribution of the ignition terms after which the rate relation is controlled by the growth term. Shock ignition experiments indicate that the amount of explosive contributing to ignition process is related to the material porosity. Thus, the contribution of the

ignition terms in the rate equation is quite small with a  $F_{\text{igmax}}$  that ranges from 0.02 to 0.1. However, through empirical correlation with test results, particularly short duration, high pressure pulses, the values of  $F_{\text{igmax}}$  commonly used have been somewhat larger (0.2 to 0.5).

The form factor  $(1-F)^{2/9}$  simply represents surface burning as the material is consumed. The amount of material ignited by shock is also found to be proportional to the pressure squared (or compression to the fourth power), thus, the exponent of 4 on the compression term. The compression rate is also used in the ignition term so that finite compression rate processes such as ramp waves can be modeled.

Once the material is ignited the second term dominates the response. The form factor  $F^{2/3}(1-F)^{2/9}$ , represents the area of the burning material starting as burning "holes" and ending as burning "grains". The exponent 2/9 causes the surface factor to maximize at the value of  $F$  where "holes" would connect. The growth term has also been shown to be pressure dependent with the exponent  $z$  ranging from 2 to 3.

### COEFFICIENT DETERMINATION FROM STANDARD TESTS

There are several types of material properties data used to determine an appropriate set of coefficients for modeling shock initiation with the I & G model. The parameters used in the equations of state for the unreacted and reacted high explosive are typically based on existing shock Hugoniot data and explosive performance data respectively. The rate parameters used in the I & G rate of reaction equation are preferably derived from detailed embedded pressure gage records. However, this approach is both costly and time consuming. An alternate approach for determining the rate terms uses a combination of existing data from standard tests for the material combined with extrapolation of the remaining unknown parameters from similar known materials. The alternate approach was recently used quite successfully for the determination of a set of parameters for Comp-B based on existing data and an extrapolation from the published PBX-9404 parameters. The set of parameters developed for Comp-B are summarized in Table 1. Values for PBX-9404 and LX-17 are also shown for comparison. Note that there are two sets of Comp-B values listed in the table. The two sets of values are for the two most common types of Comp-B referenced in the literature. The first set is for a higher density "weapon" grade pressed material developed by LANL and the second set is for lower density cast military Comp-B. Parameters for both the 2 & 3 term versions of the model are listed. The 2<sup>nd</sup> growth term in the 3 term model is not used, causing the 3 term model to look like the 2 term model.

Explosive	LANL COMP B	Military COMP B	PBX-9404	LX-17
Unreacted Equation of State and Constitutive Values				
$\rho_o$ (g/cm <sup>3</sup> )	1.712	1.630	1.842	1.903
A (Mbars)	778.1	1479.0	9522.0	778.1
B (Mbars)	-0.05031	-0.05261	-0.05944	-0.05031
R <sub>1</sub>	11.3	12.0	14.1	11.3
R <sub>2</sub>	1.13	1.20	1.41	1.13
$\omega$	0.8938	0.9120	0.8867	0.8938
C <sub>v</sub> (Mbars/K)	2.487 X 10 <sup>-5</sup>	2.487 X 10 <sup>-5</sup>	2.781 X 10 <sup>-5</sup>	2.487 X 10 <sup>-5</sup>
T <sub>c</sub> (K)	298.0	298.0	298.	298.
E (Mbars-cm <sup>3</sup> /cm <sup>3</sup> )	6.624 X 10 <sup>-3</sup>	6.759 X 10 <sup>-3</sup>	7.348 X 10 <sup>-3</sup>	6.624 X 10 <sup>-3</sup>
Yield Strength (Mbars)	0.002	0.002	0.002	0.002
Shear Modulus (Mbars)	0.0354	0.0354	0.0454	0.0354
<u>Von Neumann Spike Values</u>				
D (mm/ $\mu$ sec)	7.98	7.70	8.80	7.596
p (Mbars)	0.334	0.268	0.3981	0.3374
$\rho_o/\rho$	0.6933	0.7228	0.7210	0.6954
u <sub>p</sub> (mm/ $\mu$ sec)	2.45	2.26	2.455	2.336
Reacted Product Equation of State and CJ Values				
A (Mbars)	5.242	5.5748	8.524	6.5467
B (Mbars)	0.07678	0.0783	0.1802	0.071236
R <sub>1</sub>	4.2	4.5	4.6	4.45
R <sub>2</sub>	1.1	1.2	1.3	1.2
$\omega$	0.34	0.34	0.38	0.35
C <sub>v</sub> (Mbars/K)	1.0 X 10 <sup>-5</sup>	1.0 X 10 <sup>-5</sup>	1.0 X 10 <sup>-5</sup>	1.0 X 10 <sup>-5</sup>
E <sub>o</sub> (Mbars-cm <sup>3</sup> /cm <sup>3</sup> )	0.085	0.081	0.102	0.069
<u>Chapman-Jouguet (CJ) Values</u>				
D (mm/ $\mu$ sec)	7.98	7.70	8.80	7.596
p (Mbars)	0.295	0.250	0.370	0.275
$\rho_o/\rho$	0.7293	0.7413	0.740	0.7492
u <sub>p</sub> (mm/ $\mu$ sec)	2.16	1.99	2.29	1.91
Reaction Rate Parameters for 2 Term Model				
I ( $\mu$ sec <sup>-1</sup> )	44.0	44.0	44.0	50.0
G (Mbars <sup>-2</sup> $\mu$ sec <sup>-1</sup> )	414.0	514.0	850.0	500.0
Z	2.0	2.0	2.0	3.0
Reaction Rate Parameters for 3 Term Model*				
I ( $\mu$ sec <sup>-1</sup> )	44.0	44.0	44.0	50.0
b	2/9	2/9	2/9	2/9
a	0.01	0.01	0.01	0.0
x	4.0	4.0	4.0	4.0
G <sub>1</sub> (Mbars <sup>-2</sup> $\mu$ sec <sup>-1</sup> )	414.0	514.0	850.0	500.0
c	2/9	2/9	2/9	2/9
d	2/3	2/3	2/3	2/3
y	2.0	2.0	2.0	3.0
G <sub>2</sub> (Mbars <sup>-2</sup> $\mu$ sec <sup>-1</sup> )	0.0	0.0	0.0	0.0
e	0.0	0.0	0.0	0.0
g	0.0	0.0	0.0	0.0
Z	0.0	0.0	0.0	0.0
F <sub>igmax</sub>	0.3	0.3	0.3	0.3
F <sub>G1max</sub>	1.0	1.0	1.0	1.0
F <sub>G2min</sub>	1.0	1.0	1.0	1.0

\* Note: The parameters listed here for the second growth term are all 0.0 causing the 3 term model to look like the 2 term model.

TABLE 1. COEFFICIENTS FOR THE IGNITION AND GROWTH OF REACTION MODEL



## Unreacted Equation of State

The form of equation of state used for the unreacted material is the JWL form. The parameters used to fit the EOS for the Comp-B material are based on Hugoniot data, the CJ state, and the von Neumann spike state. The Hugoniot data is typically taken from reference 9. The CJ state data can be found in many sources including reference 10. The von-Neumann spike state is determined from embedded gage experiments<sup>11</sup> or estimated from  $U_s - U_p$  Hugoniot data with  $U_s$  equal to the detonation velocity. In addition, it is assumed that the von Neumann spike state, the CJ state, and ambient state ( $P=0.0$ ,  $v=1.0$ ) are collinear in PV space.

There are three key boundary conditions that the EOS model for the unreacted material must match. At a relative volume of 1.0, the pressure must be 0.0 and  $dp/dv$  must be the bulk modulus. In addition, the von-Neumann spike state must also lie on the Hugoniot of the unreacted explosive. This state is calculated using the  $U_s - U_p$  data, density, and detonation velocity. The values used for the Comp-B studied in this paper are summarized in Table 1.

## Reated Equation of State

The coefficients used in the reacted, or products, equation of state for the Comp-B material are the published values found in the LLNL HE handbook.<sup>10</sup> For new materials, or materials not published in the LLNL HE handbook, Souers and Kury have recently published a description of several alternative methods used at LLNL for determining the JWL EOS coefficients for an explosive material.<sup>12</sup>

## Ignition Terms

The ignition rate terms used in the model consist of an ignition term coefficient (I) and a compression threshold factor (a).

$$\text{ignition rate} = I(1-F)^{2/9}(\rho/\rho_0-1-a)^4$$

The ignition term for PBX 9404 and LX-17, HMX & TATB based explosives respectively, ranges from 44 to 50.<sup>2</sup> We selected an ignition term value of 44.0 because of the shock initiation similarities of RDX and HMX. The compression threshold term was not included in the early forms of the model as it was based on experimental data with shock initiation intensity at levels well beyond the compression threshold limit. The introduction of the compression threshold term was first described in the 3 term model published in the 8th detonation symposium.<sup>3</sup> The compression thresholds for PBX-9404 and LX-17 published in reference 3 are 0.0

and 0.22 respectively. Recent experiments<sup>13</sup> on LX-10, a high HMX explosive with similar sensitivity to PBX-9404, indicate that a value of 0.01 for PBX-9404 is more appropriate. These experiments produced delayed high order deflagrations at pressures well below conventional values for SDT.

## Growth of Reaction Terms

The growth of reaction terms used in this study are based on the single growth rate term version of the I & G model. This form of the model uses a growth of reaction rate law that consist of two variables, a growth term coefficient ( $G_1$ ) and an exponent term (Z) for the pressure dependence factor.

$$\text{growth rate} = G_1(1-F)^{2/9}F^{2/3}p^Z$$

There are several sources of data that are useful for determining appropriate values of the growth rate parameters  $G_1$  & Z. We have found that the influence of the pressure exponent term, Z, is most easily observed in simulations of run distance to detonation (pop plot). The pop plots<sup>10</sup> for PBX-9404, LX-17, & Comp-B are shown in Figure 1. It can be seen that the slope for PBX-9404 & Comp-B are about the same while the slope for LX-17 is greater. Thus, the pressure exponent for both PBX-9404 & Comp-B is 2.0 while the pressure exponent for LX-17 is 3.0. We feel that a pressure exponent for most HMX & RDX based explosives of 2.0 is appropriate.

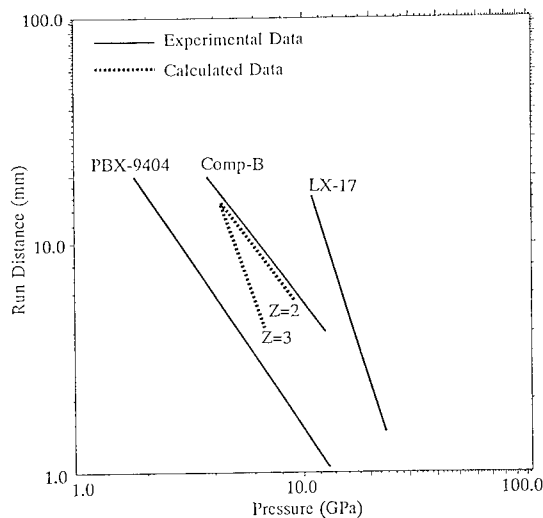


FIGURE 1. POP-PLOTS FOR PBX-9404, COMP-B, AND LX-17

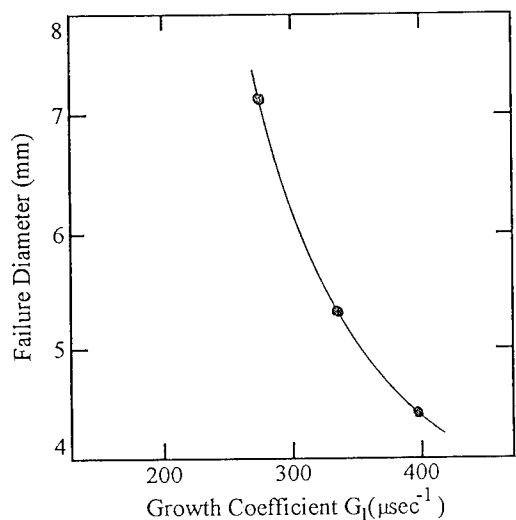


FIGURE 2. WEAPON GRADE COMP-B FAILURE DIAMETER VERSUS GROWTH COEFFICIENT ( $G_1$ )

The remaining term to be defined in the growth part of the reaction rate law is the growth term coefficient,  $G_1$ . We have found that it is possible to determine  $G_1$  by correlating to the failure diameter of the material. Simulations of the weapon grade Comp-B failure diameter with various values of  $G_1$  were used to define the curve shown in Figure 2. This figure shows that for a failure diameter of about 4.4 mm the corresponding value of  $G_1$  is 414. The published value of failure diameter for the weapon grade Comp-B is 4.3 mm.<sup>14</sup>

We have also used the published large scale gap test results as an independent method for checking the validity of the parameters used in the model.<sup>15</sup> The LSGT results provide an additional data point for modeling SDT at the initiation threshold.

#### COMP-B RESPONSE FROM TUNGSTEN IMPACT

Several Comp-B initiation experiments were conducted at NRL for the evaluation of the Comp-B parameters listed in Table 1. The experiment consisted of two stage gas gun firings of tungsten spheres into tantalum covered Comp-B targets. The tungsten spheres had diameters of 9, 14, 18, and 25 mm and were fabricated from a sintered material<sup>16</sup> with density of 17.77 g/cc. The tantalum cover was 3.65 mm thick with density 16.6 g/cc. The Comp-B target was 5 cm thick and 25 cm in diameter. This material was fabricated with a pellet fill - melt cast processing

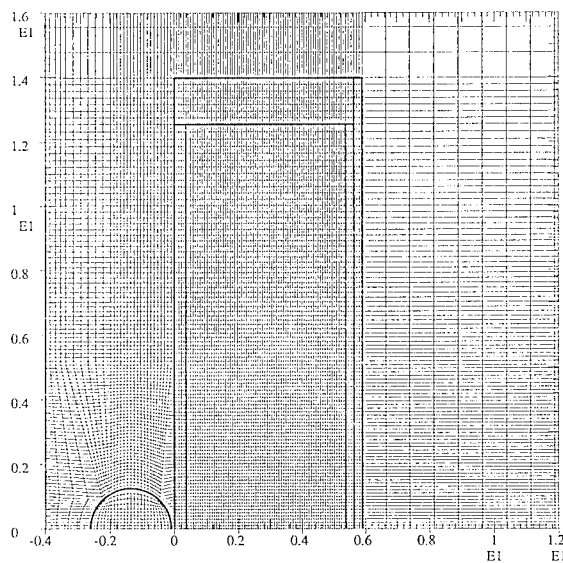


FIGURE 3. CALE MESH OF NRL COMP-B TUNGSTEN SPHERE IMPACT EXPERIMENTS

method that yielded an average density of 1.63 g/cc. The computational mesh used in the CALE code analysis of the experiments is shown in Figure 3. The calculations were performed prior to the experiments in order to select the tungsten sphere velocities that would fall on both sides of the threshold initiation curve.

#### Model for the Comp-B Tested

The melt cast 1.630 g/cc density military Comp-B is slightly different than the 1.712 g/cc pressed LANL weapon grade Comp-B that was initially used to determine a set of ignition and growth parameters. A new set of parameters was developed for the 1.630 g/cc density material by first adjusting the unreacted and reacted equations of state. A new value of the  $G_1$  term used in the reaction rate equation was then determined. The new value of  $G_1$  is such that the 1.630 g/cc Comp-B has the same initiation characteristics as the 1.712 g/cc Comp-B. Although the 1.630 density material is more porous which would tend to make it more ignitable, it also has a higher TNT content which should have the opposite effect. Both sets of parameters used in the model are listed in Table 1.

#### Experimental Results

A comparison of the pre-test calculations of the threshold initiation curve with the experimental results is shown in Figure 4. The solid line is the predicted

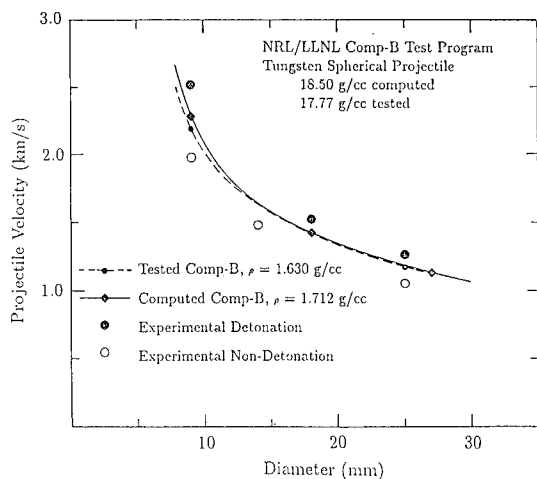


**FIGURE 4. DETONATION THRESHOLD CURVE FOR MILITARY COMP-B**

threshold initiation curve for the 1.712 g/cc density material while the dashed line is for the 1.630 g/cc density material. The solid black circles are the experimental detonation points and the open circles are the experimental non-detonations. These results further indicate that the parameters defined for the reactive flow model, based on standard published data, provide for an excellent prediction of the initiation characteristics of military Comp-B.

Using the military Comp-B model, we have found that the computed difference in impact velocities that separate prompt SDT from a very low level burning reaction is on the order of 0.25 km/s. Within this velocity range the timing of the response from shock to detonation varied substantially depending upon the diameter of the impacting sphere. Both the experimental data and the analysis for the 9 mm sphere indicate prompt SDT less than 5  $\mu$ sec after projectile impact. The experimental data for the 25 mm sphere indicates a transition time of about 19  $\mu$ sec. The 19  $\mu$ sec delay time for the transition corresponds to the timing of the pressure wave reflection at the rear cover plate of the Comp-B. A plot of the pressure in the Comp-B at 18  $\mu$ sec, presented in Figure 5., shows the shock just before arriving at the rear cover. Note that the peak value of pressure wave is 8 GPa increasing to full detonation pressure of 29.5 GPa in the next 3 microseconds. In the NRL experiments, the range

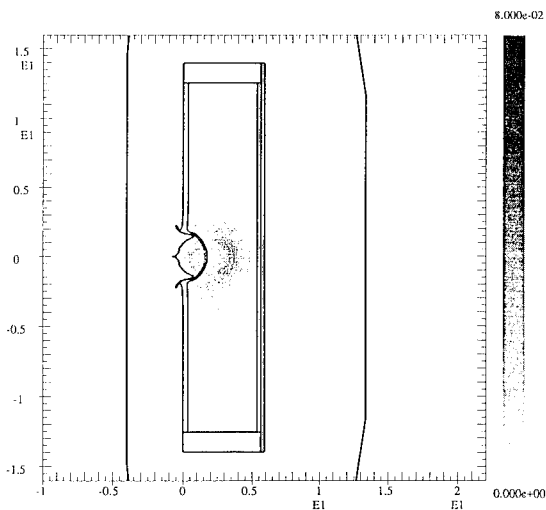


**FIGURE 5. PRESSURE PLOT IN COMP-B AT 18  $\mu$ SEC FROM 25 MM SPHERE IMPACT**

of peak pressures at the Ta/Comp-B interface for the 9 mm to 25 mm tungsten spheres are consistent with results published by Moulard<sup>17</sup> as well as the LANL data previously discussed.

Additional experiments with a 76 mm Lexan sphere are now planned. The computed detonation thresholds will be further delayed until after a second reflection off the tantalum cover plate in these experiments. The computations show that the Lexan sphere will not penetrate into the HE prior to detonation and the pressure history entering the HE will be lower than that measured for existing SDT data by a factor of 3. These planned experiments will be a severe test of the COMP-B model described in this paper.

## CONCLUSIONS

We have demonstrated that data from standard HE and shock physics experiments are sufficient to determine the coefficients used in the LLNL ignition and growth of reaction in high explosives model. Specifically,

- 1) Shock velocity/particle velocity Hugoniot data is used to define the unreacted (solid) EOS of the explosive material. This data is fit to a JWLEOS form rather than a form based on a linear  $U_s U_p$  relationship.

- 2) Cylinder test data and/or other performance test data is used to define the reacted (explosive products) EOS of the explosive material. This is typically the standard JWL EOS for the HE.
- 3) Only two coefficients need to be determined in the reaction model to describe the initiation behavior of most solid explosives pressed or cast to a density within a few percent of TMD. The growth term used in the model is determined from HE response experiments, including the wedge, failure diameter, & various gap tests, where the success or failure to propagate detonation is measured. The pressure exponent is determined by the slope of the run distance versus pressure relation.
- 4) We have shown for a specific example, Comp-B, that this relatively simple estimation procedure based on plane wave tests yields model parameters which provide a good description of more complex tests.

#### REFERENCES

1. Lee, E.L. and Tarver, C.M., *Phenomenological Model of Shock Initiation in Heterogeneous Explosives*, Phys. Fluids 23(12), December 1980, pp 2362-2372.
2. Tarver, C.M. and Hallquist, J.O., *Modeling Two-dimensional Shock Initiation and Detonation Wave Phenomena in PBX 9404 and LX-17*, Seventh Symposium (International) on Detonation, Annapolis, MD, June 1981, pp 488-497.
3. Tarver, C.M.; Hallquist, J.O.; and Erickson, L.M., *Modeling Short Pulse Duration Shock Initiation of Solid Explosives*, Eighth Symposium (International) on Detonation, Albuquerque, NM, July 1985, pp 951-961.
4. Bahl, K.L.; Breithaupt, R.D.; Tarver, C.M.; and Von Holle, W.G., *Fabry Perot Velocimetry on Detonating LX-17 in Planar and Spherically Divergent Geometries*, Ninth Symposium (International) on Detonation, Portland, OR, Aug 1989, Vol. 1, pp 133-141.
5. Tipton R., *CALE USERS MANUAL, Version 101491*, Lawrence Livermore National Laboratory, Livermore, CA 94550, 10/14/91.
6. Whirley, R.G.; Engelmann, B.E.; and Hallquist, J.O., *DYNA2D, A Nonlinear, Explicit, Two-Dimensional Finite Element Code For Solid Mechanics*, UCRL-MA-110630, April, 1992.
7. Fickett, W. and Davis, W.C., *Detonation*, University of California Press, 1979, Chapter 2 Section 2C, pp 42-51.
8. Wackerle, J. and Anderson, A.B., *Burning Topology in the Shock-Induced Reaction of Heterogeneous Explosives*, Shock Waves in Condensed Matter - 1983, Elsevier Science Publishers B.V., 1984, pp 601-604.
9. Marsh, S.P., *LASL Shock Hugoniot Data*, University of California Press, 1980.
10. Dobratz, B.M. and Crawford, P.C., *LLNL Explosives Handbook*, UCRL-52997 Change 2, January 31, 1985.
11. Cowperthwaite, M. and Rosenberg, J.T., *Lagrange Gage Studies in Ideal and Non-Ideal Explosives*, Seventh Symposium (International) on Detonation, Annapolis, MD, June 1981, pp. 1072-1083.
12. Souers, P.C. and Kury, J.W., *Comparison of Cylinder Data and Code Calculations for Homogeneous Explosives*, UCRL-JC-110661, May, 1992, to be published in Journal of Propellants, Explosives, & Pyrotechnics.
13. Tarver, C.M.; Urtiev, P.A.; Chidester, S.K.; and Green, L.G., *Shock Compression and Initiation of LX-10*, accepted for publication in Propellants, Explosives, & Pyrotechnics, June 1992.
14. Campbell, A.W. and Engelke, R., *The Diameter Effect in High-Density Heterogeneous Explosives*, Sixth Symposium (International) on Detonation, Coronado, CA, August 24 - 27, 1976, ACR-221, pp 647.
15. Tarver, C.M. and James, E., *Two-Dimensional Reactive Flow Modeling of the Minimum Priming Charge, LANL Large Scale Gap and NOL Large Scale Gap Test*, UCRL-94210, February, 1986.
16. Teledyne-Firth-Sterling, *Material X-21C*.
17. Moulard H., *Critical Conditions for Shock Initiation of Detonation by Small Projectile Impact*, Seventh Symposium (International) on Detonation, Annapolis, MD, June 1981, pp 316-324.

## DISCUSSION

MANFRED HELD

Messerschmitt-Bolkow-Blohm, Schrobenehausen,  
Germany

In pop-plots derived from instrumented gap tests, I have found exponents of about 3 for pressed HE charges and of about 2 for cast TNT-based HE charges. My interpretation is that charges with more irregularities (*i.e.*, hot spots) have the exponent 3 and quicker build up distance compared with charges having greater homogeneity.

## REPLY BY MICHAEL MURPHY:

In our study we showed that the exponent on the pressure term in the growth component of the ignition and growth of the reaction model could be correlated to the slope of the pop-plot. An exponent of 3 on the pressure term correlated well for the insensitive LX-17 explosive, while a pressure exponent of 2 correlated better for Comp-B, PBX-9404, and other RDX/HMX-based explosives. Please note, however,

that this exponent is applied to the pressure term in the growth component of the reaction rate equation and is not necessarily the actual slope of the pop-plot.

## DISCUSSION

JACQUES BOILEAU

DRET, Paris, France

Did you observe in your experimental results an effect due to the particular size and/or distribution and particle shape of the RDX crystals, or to the chemical origin of RDX (Bachmann process vs. Woolwich process)?

## REPLY BY MICHAEL MURPHY:

Unfortunately, we did not have the opportunity to conduct experiments with different variations of Comp-B. We are in the process of conducting characterization studies of the material used in the experiments and this information will be made available for correlation to other work involving different particle size and distributions.

## COMPUTATIONAL ANALYSIS OF SLIP IN PETN

James P. Ritchie  
Los Alamos National Laboratory  
Los Alamos, NM 87544

Molecular mechanics calculations have been performed to model slip in PETN. The results are in qualitative agreement with experiment. Molecular deformations are found to be an important consideration influencing ease of slip. This factor has not been mentioned previously.

### INTRODUCTION

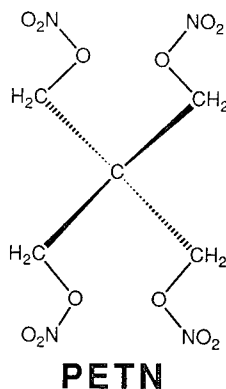
The ease of dislocation motion in crystalline PETN has been of considerable recent interest. Dick proposed that it causes the orientation dependence of the shock initiation of PETN crystals.<sup>1</sup> As part of that analysis,  $[110]\langle 1\bar{1}1 \rangle$  was proposed as the primary slip system. This was subsequently verified experimentally by Gallagher et al.<sup>2</sup> Dick's prediction of the primary slip system was based on the concept of steric hindrance. Briefly, it is supposed that a shock stimulates shear slip thereby causing a "clashing" of molecules on different sides of the slip plane. The greater this "clashing," the more effectively initiated are chemical reactions that lead to detonation.

Despite this interest, the physical factors that control the ease of slip in crystalline PETN have not been determined. Dick's analysis was based upon the number of close intermolecular contacts that occur during translation along a Burgers vector. It was performed using non-deformable molecules and, as noted by Dick, frequently leads to intermolecular contacts that are exceptionally short and physically unrealistic. In any case, inspection of Figure 1 shows that the slip system  $[001]\langle 010 \rangle$  results in larger "close contacts" than found for  $[110]\langle 1\bar{1}1 \rangle$ . Thus, a simple analysis of this type, while identifying certain important interactions and concepts, is limited in its predictive ability. Moreover, the highly anisotropic nature and organic composition of PETN are very different from metals and inorganic ions that have been intensely studied in the material sciences. Consequently, concepts developed from

those studies must be applied with care for PETN. Crystalline PETN also differs importantly from organic polymers, the material properties of which are of great interest, in that it lacks cross-linking between monomeric units through covalent bonds. In contrast, PETN molecules interact with each other through much weaker non-bonding interactions and, also unlike many organic polymers, form high-quality crystals.

One feature of PETN not previously mentioned in discussions of its ease of dislocation motion is the possibility of the individual molecules to deform easily. Inspection of the drawing below shows that, with the exception of the terminal oxygens of the nitro group, the atoms of the molecule are bonded together with single bonds.

Internal rotation about an axis parallel with a single bond is usually quite easy. For example, in the gas phase, the barrier to rotation in ethane



is 2.9 kcal/mol.<sup>3</sup> Similarly, in methyl nitrate, rotational barriers about the C-O and O-NO<sub>2</sub> bonds of approximately 3.0 and 7.5 kcal/mol, respectively, have been measured.<sup>4</sup> PETN contains similar bond types and should thus be easily deformable, meaning that the bonding topology of the molecule can remain unchanged while the molecular geometry is varied widely with relatively little expense in energy. In the crystal, however, deformations of the molecular geometry are severely restricted by the presence of neighboring molecules. It is thus possible to obtain an accurate x-ray crystal structure of PETN.<sup>5</sup> These studies do not show any anomalously large thermal parameters, as would be expected if large librations of the molecule or its constituent parts were occurring. During edge dislocation motion, however, the molecular environment changes and, in any case, the additional energy required to initiate the motion is available. These factors can lead to substantial deformation of the PETN molecule that might significantly influence the ease of slip.

In order to gain insight into the factors described above, a series of molecular mechanics calculations have been performed. The results agree qualitatively with available experimental data and show that molecular deformations are an important consideration in determining the ease of slip in crystalline PETN.

## METHODS

Calculations were performed using the program AMBER 4.0,<sup>6</sup> which was developed and has been heavily applied in the study of biochemical systems. It has a molecular mechanics package in it that was used in this work. In this approach, the energy of a system of molecules is calculated using Equation 1. The first three terms describe the energy cost associated with bond, angle, and dihedral angle distortions from the equilibrium values. These terms are calculated for the bonded atom pairs in a molecule. Intermolecular interactions are calculated using the fourth term in Equation 1, which is a Lennard-Jones interaction. Standard values of equilibrium bond lengths and angles as well as the associated force constants have been determined previously<sup>7</sup> for other systems. These parameters were used without alteration in the calculations described in this report. It was necessary to develop a number of additional parameters to describe the nitro group and the atomic charges in PETN. These were obtained by performing some quantum mechanical calculations using PM3<sup>8</sup> and GAUSSIAN82<sup>9</sup> and following published recommendations.<sup>10</sup> The resulting values of these parameters are shown in Table I.

A representative computational set-up is shown in Figure 2. Two blocks, each made up of 3x3x2

$$E_{tot} = \sum_{bonds} K_r(r - r_{eq})^2 + \sum_{angles} K_\theta(\theta - \theta_{eq})^2 + \sum_{dihedrals} \frac{V_n}{2}[1 + \cos(n\phi - \gamma)] + \sum_{i < j} \left[ \frac{A_{ij}}{R_{ij}^{12}} - \frac{B_{ij}}{R_{ij}^6} + \frac{q_i q_j}{\epsilon R_{ij}} \right] \quad (1)$$

unit cells of PETN, were constructed using the observed x-ray and neutron crystal coordinates.<sup>5</sup> Each unit cell contains two molecules, so this system as a whole contained 72 molecules or 2088 atoms. Slip on other planes (not illustrated) was examined using a similar set-up that differed in the total number and orientation of the unit cells. Using this initial set-up, the geometry of the individual molecules were then energy optimized, subject to the constraint that the carbon atoms remain fixed. This constraint was employed to ensure that the model system resemble the real system and to minimize edge effects resulting from the small system size. The resulting geometry was then used in the slip calculations, described next.

Slip was modeled by displacing one of the PETN blocks over the other along a single repeat vector in 20 incremental steps. Geometrical parameters of the molecules in the blocks, excepting those associated with carbons, were energy optimized at each step. The final geometry of one step was then rigidly displaced by the required increment to produce the starting geometry for the next. Again, the carbons were constrained to remain at their equilibrium lattice positions within each unit cell. Although such calculations are highly idealized, simple models frequently play an important role in illuminating basic concepts.

## RESULTS AND DISCUSSION

Five slip systems were examined. Three of these were proposed to be stimulated by an initiating shock wave in orientations that were relatively sensitive (S) or insensitive (I) as determined by Dick: [110]<111>, (I); [100]<001>, (I); and [100]<011>, (S). Slip on [110]<111> was actually proposed by Dick, but this system is symmetry equivalent to

**TABLE I.** PARAMETER VALUES USED IN THIS WORK TO DESCRIBE PETN. THE SYMBOL NN REPRESENTS THE NITRO-NITROGEN, OTHERS FOLLOW AMBER CONVENTIONS. LENGTHS IN Å, ANGLES IN DEGREES, FORCE CONSTANTS IN CORRESPONDING UNITS.

Mulliken Charges from 3-21G Calculations  
Numbering from Table I, Ref. 5a.

Atom	$q_i$		
C <sub>1</sub>	-0.479		
C <sub>2</sub>	-0.030		
N <sub>3</sub>	0.771		
O <sub>4</sub>	-0.476		
O <sub>5</sub>	-0.346		
O <sub>6</sub>	-0.388		
H <sub>7</sub>	0.294		
H <sub>8</sub>	0.294		
Bond	$k_r$	$r_{eq}$	
NN-O	450.0	1.1955	
OS-NN	300.0	1.4026	
Angle	$k_\theta$	$\theta$	
O-NN-OS	70.0	115.0	
O-NN-O	70.0	130.33	
NN-OS-CT	70.	113.2	
Dihedrals	$V_n/2$	$\gamma$	$n$
X-NN-OS-X	0.9	180.0	2.0
Non-bonded	Rvdw	Evdw	(NAMNB = STDA)
NN	1.6	0.2	

[110]< $\bar{1}11$ >; eg. Figure 1. Another system examined was [110]<001>, which had been proposed as the primary slip system based upon the magnitude of the Burgers vector.<sup>11</sup> Finally, [001]<010> was examined because slip on this system results in the largest intermolecular contacts when a rigid molecule analysis is performed, as shown in Figure 1. It might have been proposed as the primary slip system on this basis.

Some snapshots of representative lattices are shown in Figures 3 and 4. These show lattice geometries on a strongly and slightly hindered slip system, respectively. Some edge effects that cause the lattices to lack perfect periodicity are apparent. Nevertheless, these effects are small and nearly absent in the lattice interiors. Interestingly, molecular deformations occurring during slip were largely localized to the slip plane. Further comparison of the "slipped" lattice geometries illustrated in Figures 3 and 4 shows more deep-seated molecular deformations in the [100]<011> case. Here, the entire CH<sub>2</sub>ONO<sub>2</sub> arm of PETN that initially cuts across the slip plane is severely displaced and distorted from its original geometry. In addition, PETN molecules on opposite sides of the slip plane are crowded closer together. In contrast, slip on [110]< $\bar{1}11$ > results in only a slight deformation of the molecules on the slip plane. Some rotation of the NO<sub>2</sub> group from its initial position is evident, but the remainder of the molecules remain essentially undisturbed. Thus, in these cases, it is found that the number and distance of intermolecular contacts previously found in

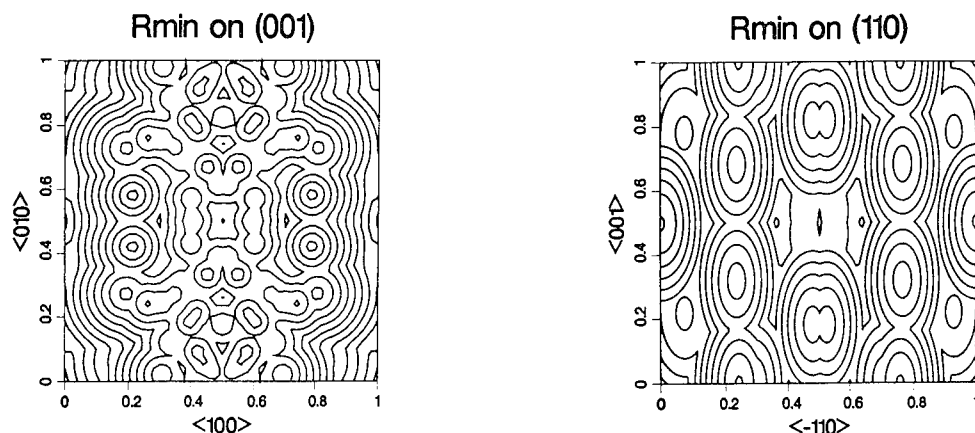


**FIGURE 1.** CONTOUR PLOTS SHOWING VALUES OF THE SHORTEST INTERMOLECULAR CONTACTS ( $R_{min}$ ) OCCURRING AS TWO BLOCKS OF PETN FIXED AT THE OBSERVED CRYSTAL GEOMETRY ARE SLIPPED OVER ONE ANOTHER ON THE INDICATED SLIP PLANE. THE AXES REPRESENT ONE REPEAT VECTOR IN THE DIRECTION INDICATED. THE VALUE OF  $R_{min}$  IS 2.45 Å IN EACH CORNER OF THE PLOTS. THE FIRST CONTOUR ENCOUNTERED TRAVELING AWAY FROM ANY CORNER IS 2.4 Å. ADDITIONAL CONTOURS OCCUR AT 0.2 Å INCREMENTS.



Model for slip on [100] PETN

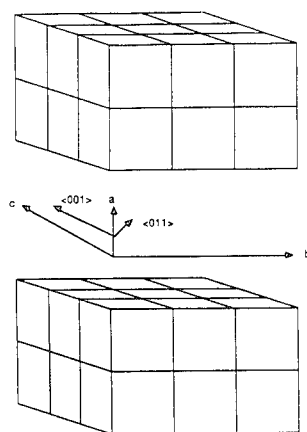


**FIGURE 2.** COMPUTATIONAL SET-UP USED TO MODEL SLIP ON THE [100] PLANE OF PETN. THE CRYSTALLOGRAPHIC AXES ARE ILLUSTRATED. THE TWO LARGE BLOCKS ARE COMPRISED OF  $3 \times 3 \times 2$  UNIT CELLS, EACH OF WHICH CONTAINS TWO MOLECULES. THE SEPARATION BETWEEN THE TWO LARGE BLOCKS IS AN ARTIFACT OF THE DRAWING TO CLARIFY THE PRESENTATION. IN THE CALCULATIONS, THE SEPARATION IS THAT FOUND IN THE CRYSTAL STRUCTURE.

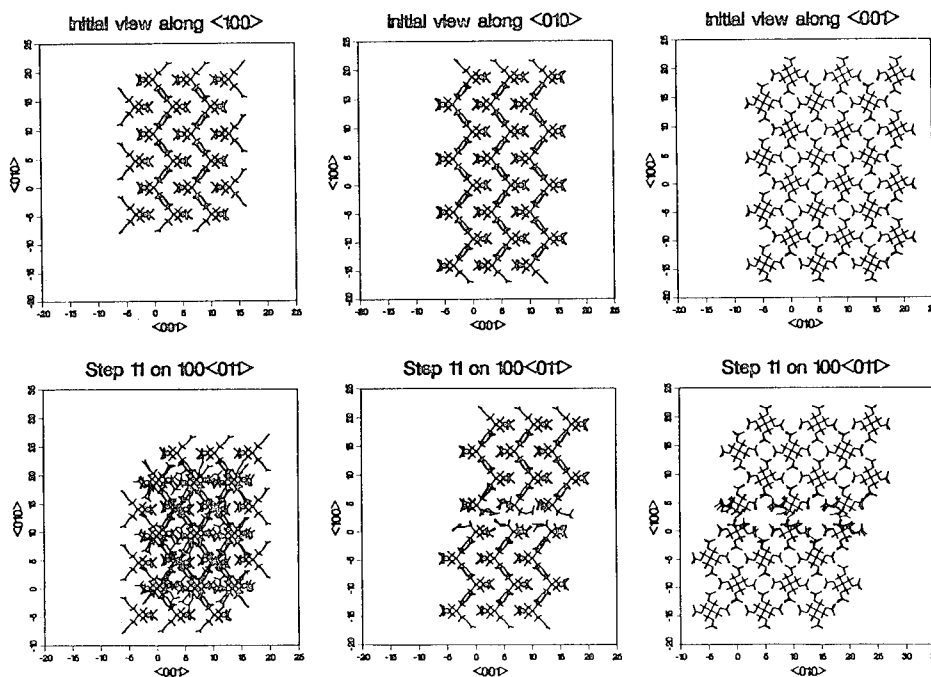


**FIGURE 3.** ORTHOGRAPHIC PROJECTIONS OF MODEL LATTICES OBTAINED FROM SLIP ON [100]<011>. INITIAL LATTICE AND THAT FOUND FOR STEP 11, WHICH IS AN ENERGY MAXIMUM ARE SHOWN. LINES CONNECTING ATOMS WERE DRAWN IF THE DISTANCE BETWEEN THE ATOMS WAS LESS THAN A TYPICAL INTERMOLECULAR MOLECULAR DISTANCE; I.E., LESS THAN 1.6 Å FOR BONDS BETWEEN HEAVY ATOMS AND LESS THAN 1.2 Å FOR BONDS TO HYDROGEN. THUS, THE ABSENCE OF LINES CUTTING THE [100] PLANE INDICATES THAT NO CLOSE CONTACTS ARE OCCURRING.

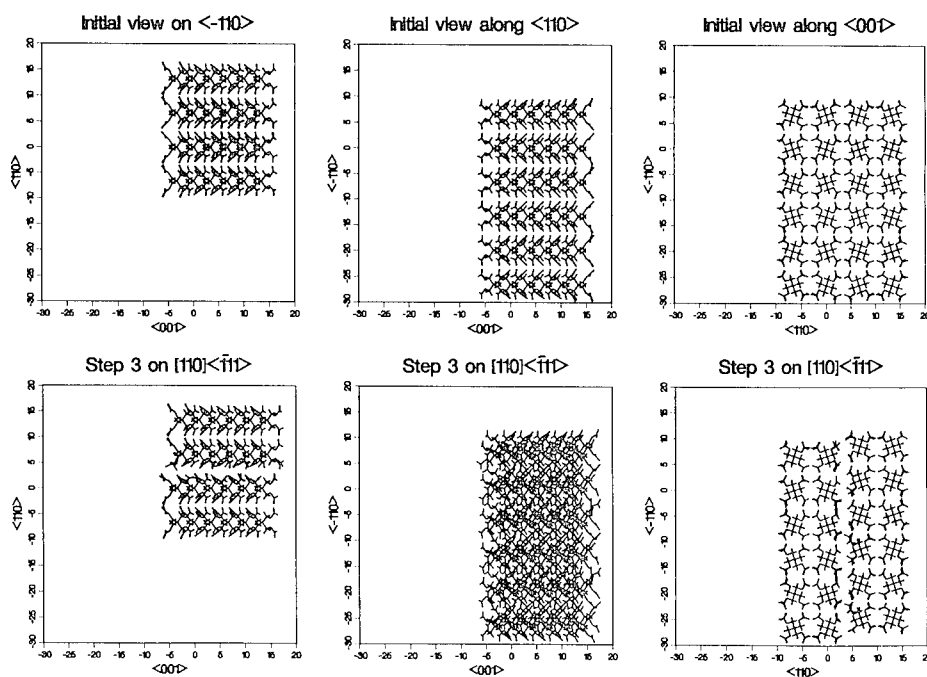


FIGURE 4. AS IN FIGURE 3 FOR SLIP ON  $[110]\langle\bar{1}11\rangle$ . STEP 3 IS A LOCAL ENERGY MAXIMUM. ALSO, NOTE THAT THE LATTICE AXES HAVE BEEN ROTATED FROM THOSE SHOWN IN FIGURE 3, SO THAT THEY ARE ORTHOGONAL OR PARALLEL TO THE SLIP PLANE. THIS CLARIFIED THE PRESENTATION.

the analysis using rigid molecules<sup>1</sup> is reflected by the extent of molecular deformation found in molecular mechanics calculations.

The molecular mechanics calculations show that the molecules deform to avoid close contacts during slip. Further information about this point can be obtained by inspection of Figure 5. There the closest intermolecular contact in lattices of rigid and deformable molecules are contrasted. The differences are dramatic and demonstrate that close contacts are only slightly reduced from equilibrium values, even when slip occurs on highly hindered planes. It should also be noted in Figure 5 that the values of  $R_{min}$  for the rigid lattices do not correspond exactly with those found previously and shown in Figure 1, for example. This is because the initial lattices used in the molecular mechanics calculations did not correspond precisely with the observed crystal geometries. This is because of imperfections in the potential functions and the small size of the lattices.

Finally the maximum energy required for slip of the model lattices must be considered. In order to compare results with somewhat different lattices

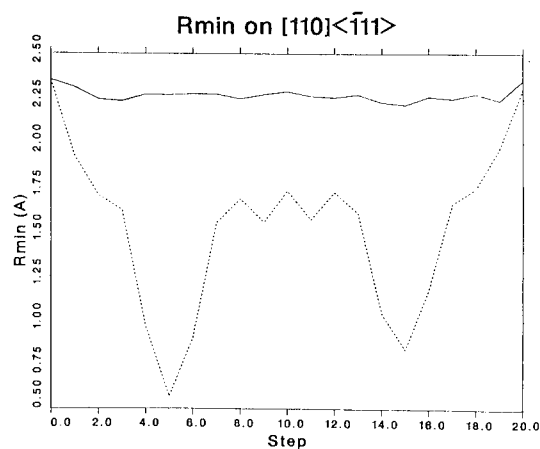


FIGURE 5. MINIMUM INTERMOLECULAR DISTANCES FOR SLIP ON THE INDICATED SYSTEM. THE DASHED LINE SHOWS SLIP WITH RIGID MOLECULES, WHILE THE SOLID LINE WAS OBTAINED FROM ANALYSIS OF THE MOLECULAR MECHANICS CALCULATIONS.

and numbers of molecules, the following procedure was devised. The steric energy of the  $n$ 'th step is defined in Equation 2.

$$E_{s,n} = (E_n - E_o - ASE*OSA) / CSA \quad (2)$$

There,  $E_n$  and  $E_o$  are the energies obtained from the molecular mechanics calculations at the  $n$ 'th and original positions, respectively. However, this energy difference does not account for molecules that "slip off the edge" of the computational lattice, as schematically illustrated in Figure 6. The energy of these molecules is higher than those in the original lattice, despite the fact that they are not sterically strained by a surrounding crystal environment. This is because these molecules are not stabilized by van der Waals type interactions with partners on the other side of the slip plane. Thus, the energy of two widely separated PETN blocks is destabilized relative to the original lattice where the two blocks are in direct contact. This destabilization was calculated directly by molecular mechanics and divided by the original contact surface area to obtain the areal surface energy (ASE). A crude correction of the molecular mechanics energy difference at the  $n$ 'th step was then obtained by accounting for the energy of the overhanging surface area as ASE\*OSA. This procedure led in some cases to negative steric energies for the final steps when the full ASE was used. Reduction of this term by half gave consistently positive steric energies and can be rationalized by noting that the overhanging surface area still interacts with the remainder of the lattice because of the long-range of van der Waals type interactions, while the full ASE is obtained with no interaction between blocks. In any case, this quantity is relatively small compared with the energy difference between the molecular

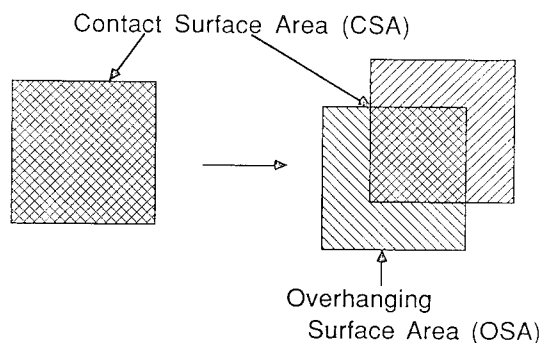


FIGURE 6. DIAGRAM ILLUSTRATING THE CONTACT AND OVERHANGING SURFACE AREAS.

mechanics energies of any two steps. In addition, variations in the procedure described above did not alter the ranking based upon the maximum energy required for slip. More importantly, however, it was necessary to compare the calculated steric energies for the different lattices employed. This was accomplished by dividing the total steric energy by the contact surface area. The result is thus an energy per unit area and allows at least qualitative comparison of the computed results.

The results obtained as described above are shown in Figure 7. It is immediately evident that slip on  $[100]<011>$  is most difficult. This is in agreement with previous analysis. Remarkably, slip is found to be easiest on  $[110]<\bar{1}11>$ . This direction is symmetry equivalent to  $[110]<\bar{1}\bar{1}1>$  found in Dick's previous analysis<sup>1</sup> and experimentally observed.<sup>2</sup> The energy difference between this system and the other three remaining ones is significant. However it is conceivable that reasonable variations in the potential function parameters could narrow the difference or even change its sign. Nonetheless, the energy differences calculated agree with experiment and the corresponding molecular deformations for slip on  $[110]<\bar{1}11>$  are less than those found on the other slip systems. These factors show that the ease of slip in crystalline PETN is markedly influenced by molecular deformations.

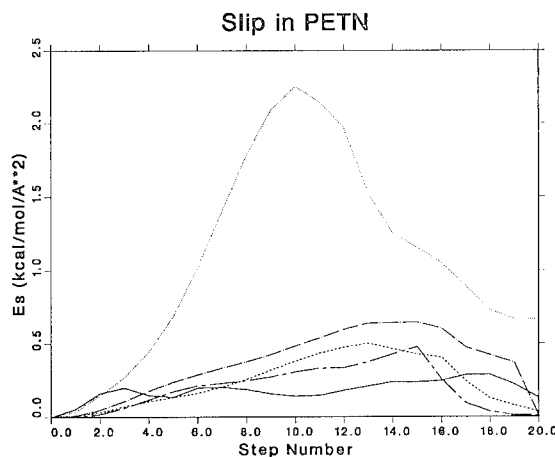


FIGURE 7. STERIC ENERGIES CALCULATED AS DESCRIBED IN THE TEXT AT EACH STEP ALONG THE FOLLOWING SLIP SYSTEMS: LINE,  $[110]<\bar{1}11>$ ; DASH,  $[110]<001>$ ; CHAIN-DASH,  $[001]<010>$ ; CHAIN-DOT,  $[100]<001>$ ; DOT,  $[100]<011>$ .

Although the calculated energies shown in Figure 7 are only qualitatively reliable, it is interesting to note the following. The faces of a unit cell of PETN are  $88 \text{ \AA}^2$  and  $63 \text{ \AA}^2$ , or  $75 \text{ \AA}^2$  as a single representative value. If it is considered that one of the two molecules of a unit cell lies in a face then an average surface area per molecule can be obtained as  $75 \text{ \AA}^2$ . To obtain an energy per surface molecule, this figure must be divided by two to account for the presence of molecules on both sides of the surface. Now, this figure when multiplied by the  $E_s$  maxima shown in Figure 7 gives an average energy per surface molecule. It is, roughly, 80 kcal/mol for slip on  $[100]<011>$ , 19 kcal/mol for slip on  $[110]<001>$ ,  $[100]<001>$ , and  $[001]<010>$ ; and but 10 kcal/mol for slip on  $[110]<111>$ . Therefore, this crude analysis gives energies that are larger, less than, and significantly less than a presumed O-NO<sub>2</sub> bond strength of very roughly 40 kcal/mol.<sup>12</sup> This result is interesting because shock orientations supposed to stimulate slip on  $[100]<011>$  lead to detonation, while shock orientations supposed to stimulate slip in the other directions do not.

## SUMMARY AND CONCLUSIONS

Molecular mechanics calculations show that rotation about the several bonds in PETN are likely to occur during slip and plays an important role in determining the ease of slip. This factor had not been discussed in previous accounts of the subject. This study also demonstrates the application of computational techniques not previously applied to these problems.

## REFERENCES

1. Dick, J. J.; Mulford, R. N.; Spencer, W. J.; Pettit, D. R.; Garcia, E.; and Shaw D. C., *J. Appl. Phys.*, Vol. 70, 1991, p. 3572.
2. Gallagher, H. G.; Halfpenny, P. J.; Miller, J. C.; and Sherwood, J. N., *Phil. Trans. R. Soc. Lond. A339*, Vol. 293, 1992.
3. Weiss, S.; and Leroi, G., *J. Chem. Phys.*, Vol. 48, 1968, p. 962.
4. van der Viken, B. J.; Guirgis, G. A.; and Durig, J. R., *J. Mol. Struct.*, Vol. 142, P. 105.
5. a) Conant, J. W.; Cady, H. H.; Ryan, R. R.; Yarnell, J. L.; and Newsam, J. M., LA-7756-MS, December 1979. b) Trotter, J., *Acta Cryst.*, Vol. 15, 1963, p. 698.

6. Parlman, D. A.; Case, D. A.; Caldwell, J. C.; Scibel, G. L.; Singh, U. C.; Weiner, P.; and Kollman, P. A., AMBER 4.0, University of California, San Francisco, 1991.
7. Weiner, S. J., Kollman, P. A. Kollman, Nguyen, D. T.; and Case, D. A., *J. Comput. Chem.*, Vol. 7, 1986, p. 230.
8. Stewart, J. J. P., *J. Comp. Chem.*, Vol. 10, 1989, P. 221.
9. Binkley, J. S. Frisch, M. J., DeFrees, D. J. Raghavachari, D. K., Whiteside, R. A.; Schlegel, H. B.; Fluder, E. M.; and Pople, J. A., Carnegie-Mellon University. The CTSS version was implemented and enhanced by R. L. Martin.
10. Hopfinger, A. J.; and Pearlstein, R. A., *J. Comput. Chem.*, Vol. 5, 1984, p. 486.
11. Halfpenny, P. J.; Roberts, K. J.; and Sherwood, J. N., *J. Mater. Sci.*, Vol. 19, 1984, p. 1629.
12. The figure is for methyl nitrate. See: G.N. Spokes, S.W. Benson, *J. Am. Chem. Soc.*, Vol. 89, 1967, p. 6030.

## DISCUSSION

M. SAMIRANT

French German Research Institute, Ste.-Louis Cedex, France

You present new results on the potential and the energies for slip in PETN crystals depending on orientation. Do these results agree with shock-sensitivity measurements obtained by Jerry Dick?

## REPLY BY JAMES RITCHIE:

The molecular mechanics calculations reported in this paper give  $[110]<111>$  (which is symmetry equivalent to  $[110]<\bar{1}\bar{1}1>$ ) as the primary slip system in crystalline PETN. As shown in Figure 7, slip on other systems requires more energy. This is in qualitative agreement with Dick's earlier analysis.

## DISCUSSION

DENIS SPITZER

French German Research Institute, Ste.-Louis Cedex,  
France

(1) As you studied the MRSS slip system  $100\langle 001 \rangle$  for shock direction  $\langle 101 \rangle$ , have you ever seen or observed a possible explanation or reason that would explain the observed transition to intermediate velocity (by Dick)?

(2) Have you studied also the MRSS slip system  $110\langle 111 \rangle$  which corresponds to the less sensitive orientation ( $\langle 100 \rangle$ )?

## REPLY BY JAMES RITCHIE:

(1) The molecular mechanics calculations give no indication of the causes underlying this phenomenon.

(2) Yes, please see Figure 7 of the final paper. It did not appear in earlier versions.

## THE VISCOPLASTIC HOT SPOTS IN PORE COLLAPSE

P. C. Chou, D. Liang, and Z. Ritman  
Drexel University  
Philadelphia, PA 19104

The shock induced pore collapse in heterogeneous solid explosives is studied by the two-dimensional hydrocode DEFEL. The calculations include the effects of compressibility, plastic flow stress, viscosity and heat conduction. The temperature dependent Arrhenius reaction rate model is applied. It is shown that hot spots are formed, primarily due to viscoplastic heating, before the pore is completely closed. For the moderate shock pressure studied, chemical reaction is initiated at these hot spots, and slow burn is propagating out, but does not lead into detonation. The burning rate is enhanced by multi-pore interaction. This "viscoplastic hot spot" model is compared with the "hydrodynamic hot spot" model of Mader.

### INTRODUCTION

The mechanism of shock initiation of detonation in heterogeneous explosives is known to involve the strengthening of shock wave by hot spots, Campbell,<sup>1</sup> Mader,<sup>2</sup> and Taylor.<sup>3</sup> When a shock wave first encounters a density inhomogeneity, such as pores, boundaries between grains, or solid inclusions, hot spots are formed. These hot spots initiate chemical reaction, or burning, and release energy. For moderate strength shock waves, the initial pressure and temperature are not high enough to cause detonation, only slow burning. The energy released from this burning does strengthen the shock wave. As the shock wave passes over more inhomogeneities, hotter hot spots are formed and the shock wave grows stronger and stronger. Eventually, this shock wave develops into a sustaining detonation wave.

This shock initiation mechanism has been supported by experimental evidence. Mader<sup>2</sup> further demonstrated this mechanism by hydrocode numerical simulations. He used the Particle-in-Cell code and 2DE code to simulate hot spot formation in the liquid explosive nitromethane with voids (pores). The shock wave drove the upstream free surface of the void to impact the downstream surface, which resulted in higher temperatures than that behind the shock. When the temperature dependent Arrhenius reaction rate law was introduced, burning or explosion was initiated at the hot spot. For moderate strength shocks, this burning did not lead into detonation. When four voids were simulated, two in a row behind another two, the results showed that the downstream ones generated higher temperatures than the upstream ones. This shows, qualitatively, that hot spots strengthen the shock, and with a large number of hot spots, detonation wave could eventually form.

These simulations were with nonviscous, nonconducting, liquid nitromethane.

Taylor<sup>3</sup> has made similar simulations, but the material was solid with elastic-plastic properties. A shock pressure of 3.0 GPa was applied on a 0.6 micron diameter pore. During collapse, a maximum temperature of 1800 °K was obtained due to plastic work and compression. The pressure and temperature fields after the impact between the upper-stream and down-stream sides of the pore were also calculated. The effects of heat transfer and shear banding were not included. He also limited the analysis to a single pore; the effect of the strengthening of the shock by multiple pore was not treated.

Mader and Kershner<sup>4</sup> also studied this problem with the three-dimensional code, 3DE. The interaction of a shock wave with a matrix of spherical pores in several solid explosives were simulated. The resulting hot-spot formation, interaction, and buildup towards detonation or failure have been modeled. The simulations indicate clearly the process of the shock wave enhancement as it propagates and interacts with more pores. They treated the solid explosives as compressible fluids, with proper equations of state, and called it the "hydrodynamic hot-spot" model. The solid mechanic properties of plastic flow stress, viscosity and heat transfer were not included.

Recently, we have used the DEFEL code to simulate pore collapse in the solid explosive HNS, Chou, Ritman, and Liang<sup>5</sup>. Visco-plastic constitutive equations for solid are used. It is shown that unlike the case of liquid explosives, hot spots are formed before the pore is fully closed. The high temperature in the hot spots is due to shear bands, or shear concentrations, and compression, in regions next to the

pore where the strain rate and the pressure are very high, and the visco-plastic work and compressive work supply the energy for temperature increase. The effect of pore size and heat conduction are also discussed, but chemical reactions are not included. The experimental result of sensitivity reversal, where a medium-sized grain (and pore) is more sensitive than both finer and coarser ones, is explained by the code results in terms of maximum temperature. For large pores, the heat conduction effect is not significant, thus temperature increases with the decreasing pore diameter. For small pores, the conduction effect becomes more dominant, overcoming the viscosity effect, thus temperature decreases with decreasing diameter.

In this paper, we extend the work of Chou et al.<sup>5</sup> by incorporating the Arrhenius reaction rate law and simulating the chemical energy release and the spreading of the burning front. The effect of the strengthening of the shock by multi-pore interaction is also included. It is shown that the viscoplastic heating is a main source of hot spot. For heterogeneous solid explosives, this could be called the "viscoplastic hot spot" model.

## HYDROCODE AND CONSTITUTIVE EQUATIONS

The simulations are done by the hydrocode DEFEL, a two-dimensional finite-element Lagrangian code, which incorporates different forms of equations of state and constitutive equations. Heat transfer capability and reaction rate models are also included.

Detailed discussions of the constitutive equations in DEFEL are given in Chou<sup>5,6</sup>. The equations are summarized here for convenience. The stresses are calculated according to Bingham model, in which the three-dimensional total stress is considered to be composed of a hydrodynamic pressure part, an elastic-plastic deviator part, and a viscous part as follows,

$$\sigma_{ij} = -P \delta_{ij} + S_{ij}^{c-p} + \sigma_{ij}^v \quad (1)$$

where  $\sigma_{ij}$  is the stress tensor,  $S_{ij}$  the deviator stress tensor,  $P$  the hydrodynamic pressure, and  $\sigma_{ij}^v$  the viscous stress tensor.

The hydrodynamic pressure  $P$  is computed from the Mie-Grüneisen equation of state,

$$P = (K_1 \eta + K_2 \eta^2 + K_3 \eta^3) (1 - \Gamma \eta/2) + \Gamma E_s (1 + \eta) \quad (2)$$

where  $P$  is the pressure,  $E_s$  is the internal energy,  $\eta = (\rho/\rho_0) - 1$  is the compression,  $\rho$  and  $\rho_0$  are the den-

sity and initial density,  $K_1, K_2, K_3$  are material constants, and  $\Gamma$  is the Mie-Grüneisen coefficient.

In our previous work,<sup>5</sup> the elastic-plastic deviator stress tensor was computed by the Johnson-Cook equation.<sup>7</sup> In the present work, for simplicity, a constant flow stress of  $\sigma_c = 200$  MPa is used. The viscous stresses are computed by the Stokes's law

$$\sigma_{ij}^v = 2\mu \dot{\epsilon}_{ij} \quad (3)$$

where  $\dot{\epsilon}_{ij}$  is the deviatoric strain-rate tensor,  $\mu$  is the coefficient of viscosity and a constant  $\mu = 10$  Poise is taken in the present simulations. Note that this is a generalization of Frey's treatment<sup>8</sup> of viscosity in one-dimensional cases.

The governing equation for heat conduction is

$$k \nabla^2 T = -Q + \rho c \frac{\partial T}{\partial t} \quad (4)$$

where  $c$  is the specific heat,  $k$  the thermal conductivity, and  $Q$  the rate of work per unit volume, which includes compressive, viscous, and plastic work. The rate of work per unit volume is

$$Q = -P \dot{\epsilon}_v + (S_{ij} + 2\mu \dot{\epsilon}_{ij}) \dot{\epsilon}_{ij} \quad (5)$$

where  $\dot{\epsilon}_v$  is the volumetric strain rate,  $S_{ij}$  are the deviatoric stresses. The constants of  $c = 1.013$  J/(g°K) and  $k = 0.45$  J/(ms°K) are used in the present simulation.

For cases with chemical reaction, the Arrhenius rate model used is in the form

$$\partial F / \partial t = (1 - F) Z \exp(E_a / RT) \quad (6)$$

where  $F$  is the burn fraction,  $Z$  the frequency factor,  $E_a$  the activation energy,  $R$  the universal gas constant, and  $T$  the absolute temperature. Details of the application of this model is given in Ref. 6.

## RESULTS WITHOUT CHEMICAL REACTION

The initial geometry and the finite-element mesh are shown in Fig. 1. The lateral boundary at  $R = 2.28$   $\mu\text{m}$  is not shown. The mesh is different from those used in Chou<sup>5</sup>; finer meshes are used in the region near the pore surface where large deformation is expected. The radial boundary is larger to simulate a pore in an infinite medium.

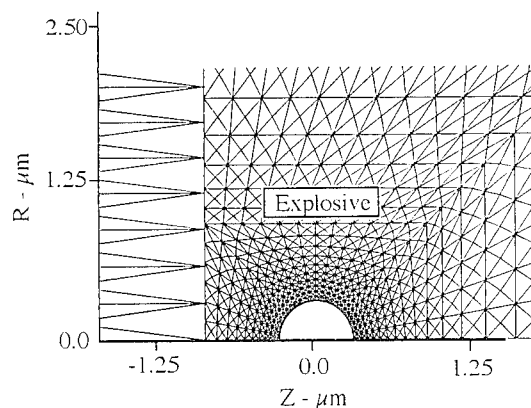
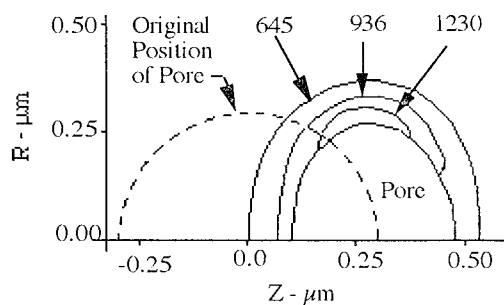
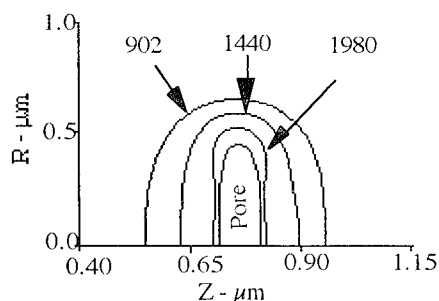


**FIGURE 1. THE INITIAL GRID GEOMETRY WITH WIDE BOUNDARY**

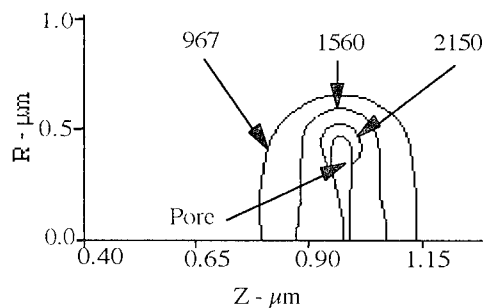
Simulations are carried out for five values of pore diameters:  $60\mu\text{m}$ ,  $6\mu\text{m}$ ,  $0.6\mu\text{m}$ ,  $0.3\mu\text{m}$  and  $0.16\mu\text{m}$ . Figure 2 shows the calculated isotherms at different times for the case of the initial pore diameter of  $0.6\mu\text{m}$ .



(a)  $t = 0.8$  nanosecond



(b)  $t = 2.0$  nanosecond



(c)  $t = 2.4$  nanosecond

**FIGURE 2. THE CALCULATED ISOTHERMS ( $^{\circ}\text{K}$ ) AT DIFFERENT TIMES AFTER IMPACT**

It can be seen that the temperature increases during collapse, and the highest value is always near the upper surface of the pore, where the curvature is the highest. This is the region where maximum strain rate and shear banding occur, Chou.<sup>5</sup>

Results on pore size and heat conduction effects, similar to those of Ref. 5, are also obtained. Figure 3 shows the highest temperature near the pore boundary versus the initial pore diameter. Without heat conduction, the maximum temperature increases first when the diameter reduces from  $60\mu\text{m}$ , and then remains constant when the diameter is less than  $6\mu\text{m}$ . With heat conduction, the maximum temperature reaches a highest value at  $d = 0.6\mu\text{m}$  and decreases when the diameter is further reduced. This "sensitivity reversal" effect, which was observed experimentally by Setchell and Taylor,<sup>9</sup> is in agreement with the results in Ref. 5.

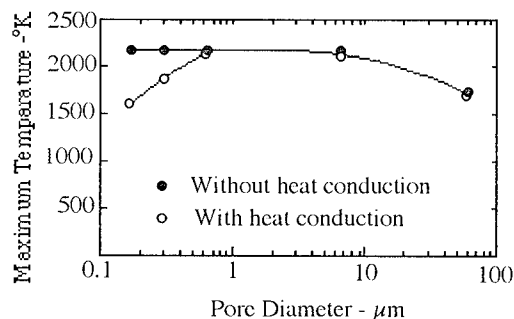


**FIGURE 3. THE MAXIMUM TEMPERATURE VERSUS PORE DIAMETER**

## RESULTS WITH CHEMICAL REACTION

For the simulation of pore collapse with chemical reaction, we chose the explosive PBX-9404 impacted by a steel impactor at  $600\text{ m/s}$ , which is approximately the threshold shock initiation velocity.



The same pore diameter,  $0.6\ \mu\text{m}$ , as in the non-reaction case is used to study the formation of hot spot with a temperature dependent reaction rate model. We use the same properties of PBX-9404 as in Chou.<sup>6</sup> The coefficients of viscosity and heat conduction are assumed to be the same as those of HNS. The initial mesh is exactly as shown in Figure 1.

Once burning started, the gas phase of the reaction product expands rapidly and fills the pore. The elements of the gas phase distort into narrow triangles which increase the computation time and cause numerical instability. To remedy this, mesh rezoning technique is carried out periodically for the central part of the gas phase elements. Figure 4(a) shows the mesh geometry where the layer of elements next to the pore has burned and expanded. Figure 4(b) shows the mesh geometry after the gas filled completely the pore cavity. The central part where elements are randomly oriented contains the rezoned elements.

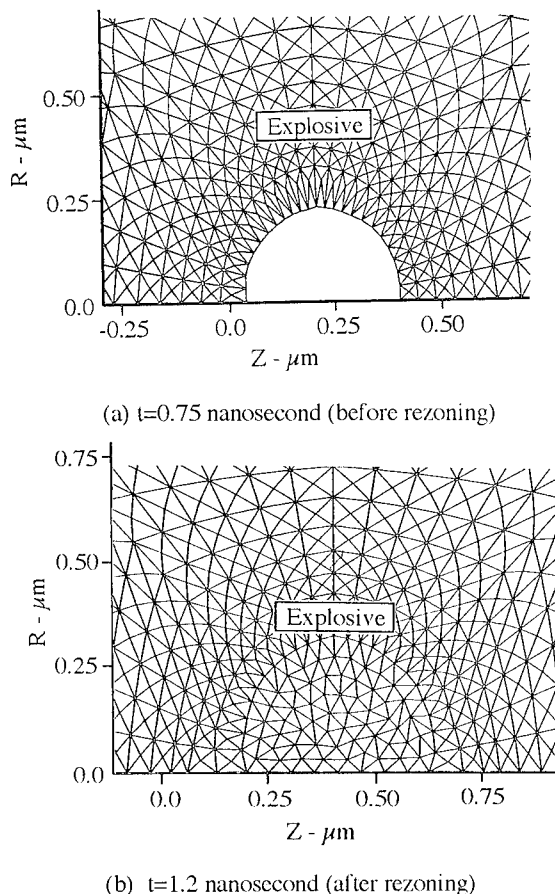


**FIGURE 4. MESH DEFORMATION AT TWO DIFFERENT TIMES**

Figure 5 gives the contours of burn fraction at different times. Fig. 5(a) shows that reaction starts, approximately at 0.75 nanosecond, from the region

where the temperature is the highest. At  $t = 6$  ns, as shown in Fig. 5(b), the gas product has filled completely the pore cavity. Please note that Fig. 5(b), (c) and (d) are in the same scale, but (a) is in a larger scale for clarity. At 12 and 18 ns, Fig. 5(c) and (d), the gas bubble expands and moves forward along the axis.

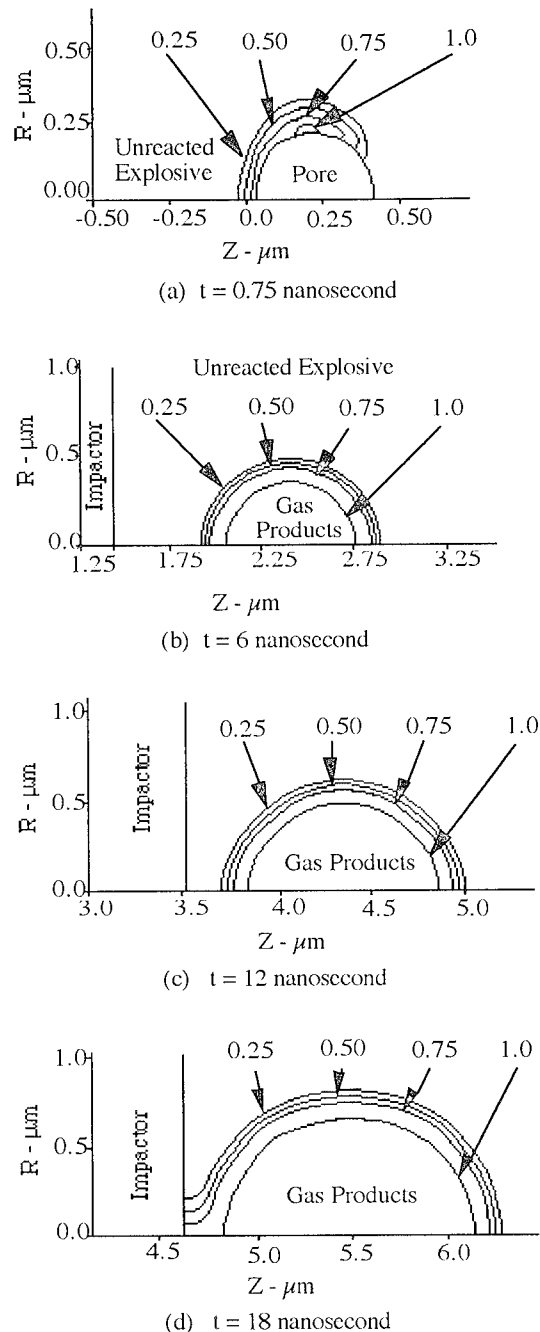


**FIGURE 5. BURN FRACTION CONTOURS AT DIFFERENT TIMES**

The expansion of the gas bubble is the result of two effects. One is the expansion outward of the burned gas, the other is the propagation of the burn surface relative to the material in front, as more solid explosive is burned. The heat conduction from a burned element raises the temperature of a neighboring element, and causes it to burn.

To study the speed of the burning wave front, we integrated the reacted explosive over the complete explosive at different time, and the result is shown in Figure 6. The burn surface propagating speed relative to the material is also calculated and shown in Figure 7. The chemical reaction started at about 0.75 ns after the impact as shown in Fig. 5(a). At this stage or shortly after this, the chemical reaction takes place in certain region (hot spot) where the material is heated by the compression and visco-plastic work and its temperature raised to above the threshold value for Arrhenius chemical reaction. During this stage, the burn surface velocity is very high. At about 5 to 10

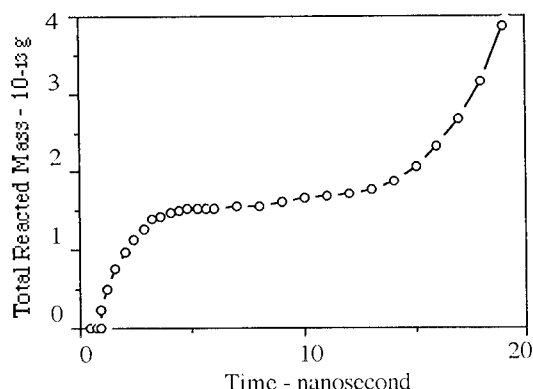


FIGURE 6. THE TOTAL MASS OF BURNED EXPLOSIVE VERSUS TIME

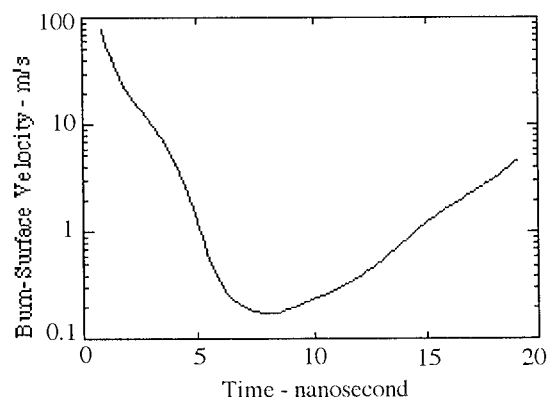


FIGURE 7. THE PROPAGATION VELOCITY OF BURN SURFACE RELATIVE TO THE MATERIAL IN FRONT OF IT

nanosecond, the burn surface has advanced beyond the originally viscoplastically-heated region, and the burn-surface velocity drops to very low values.

As can be seen from Fig. 6 and Fig. 7, the burning rate gradually builds up again. The propagating velocity increment is due to the expansion of the gas products which compresses and deforms the surrounding explosive and raises its temperature. The increase of the total burned mass, as shown in Fig. 6, is also caused by the larger volume engulfed by the burn surface as its radius increases.

This example of a 0.6  $\mu\text{m}$  pore, subjected to a shock pressure of 3 GPa, shows that chemical reaction, or burning, can be initiated and propagating, but the burning does not develop into a detonation wave.

## THE STRENGTHENING EFFECT OF MULTI-PORE

As shown by Mader<sup>2</sup> and Mader and Kershner,<sup>4</sup> a hot spot from a single pore collapse can cause burning which strengthens the shock and increases the temperature, but not to an extent for detonation. Every subsequent pore it passes, the shock is strengthened further. After many pores, eventually the shock develops into detonation.

In order to demonstrate the multi-pore strengthening effect for solid explosives, multi-pore arranged along the axial direction is needed, and will be done in the near future. In the present paper, we demonstrate that even two pores arranged along a line parallel to the wave front can produce a maximum temperature higher than that of a single pore.

Simulating multi-pore interactions with a two-dimensional code is best done by the plane-strain approximation. A plane strain simulation of a single pore is performed, with the same initial mesh as shown in Fig. 1 for the axial symmetric case. The lateral boundary from the plane of symmetry is 7.6 times the pore radius. During the time period of interest, waves reflected from the lateral boundary will affect the flow field. However, its effect is rather small; we shall use this case to approximate a single pore in an infinite matrix of explosive.

To study the interaction between two parallel pores, we used a narrow strip of explosive with one pore, and with a fixed and frictionless lateral boundary, as shown in Fig. 8(a). The explosive elements are allowed to slide along this boundary, but not to cross it. Its effect is identical to the case of an image pore at the same distance above the boundary. Therefore, the narrow boundary case provides a qualitative description of the influence of multi-pores. Figure 8(b) shows the wide boundary (or single pore) case.

The mesh geometry of the narrow boundary case is shown in Fig. 9. Fig. 10 shows a comparison of the burn fraction contours between the wide and the narrow boundary cases. At 8 nanosecond,

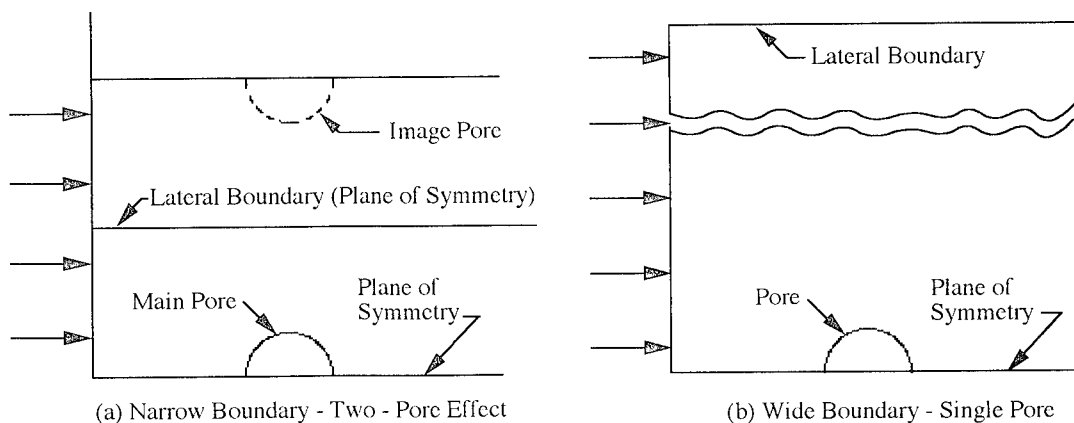


**FIGURE 8. SIMULATION OF TWO-PORE STRENGTHENING EFFECT BY NARROW LATERAL BOUNDARY**

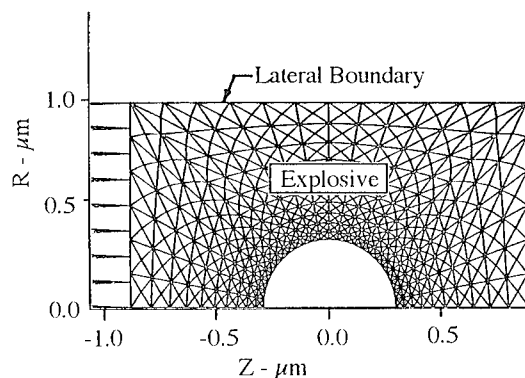


**FIGURE 9. THE INITIAL GRIND GEOMETRY WITH NARROW BOUNDARY**

there is very little difference; both contours are close to circular form. At 20 nanosecond, the narrow boundary case shows clearly the confining effect of the boundary (or the image hole), and more explosive burned. A direct comparison of the reacted explosive mass at different time is plotted in Fig. 11. At the early stage, chemical reaction of the wide boundary case is much faster. This is probably due to the higher pore collapse velocity; there is less restraint from the fixed boundary. As a result, more viscoplastic work generated, and higher temperature reached. At later time, the reacted mass of the narrow-boundary case overtakes that of the wide-boundary case. This demonstrates the effect of confining boundary (or neighbor pore) of increasing the pressure and temperature, and resulting in higher burning rate.

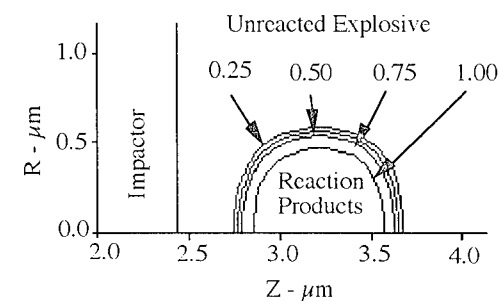
## DISCUSSIONS

As mentioned before, simulation of hot spot formation during pore collapse by hydrocode have been performed previously by Mader<sup>1,3</sup> and Talor.<sup>2</sup> Mader considered the explosive as a pure compressible fluid, without any solid properties; Taylor included

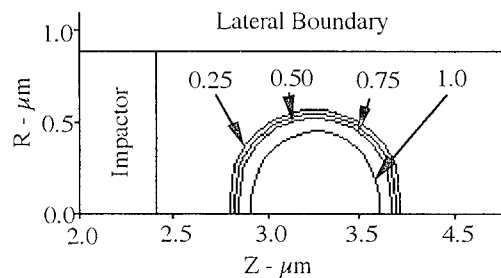
the effect of plastic strength, but did not include the viscosity and heat conduction effects. Both of their results show that hot spots are formed primarily due to the impact of the upstream surface of the pore upon the downstream surface. The high temperature regions appear after the pore is completely closed.

Our present results show that the viscoplastic property of the explosive can cause regions of shear concentration (or shear bands), where very high shear strain and shear strain rate occur, before the pore is closed. These regions are the source of hot spots. This "viscoplastic hot spot" model is consistent with the shear band theories of Frey,<sup>8</sup> Howe,<sup>10</sup> and Field.<sup>11</sup> Note also that the viscoplasticity of the material retards the motion of the surface of the pore, thus decreases the impact between the upstream and downstream surfaces.

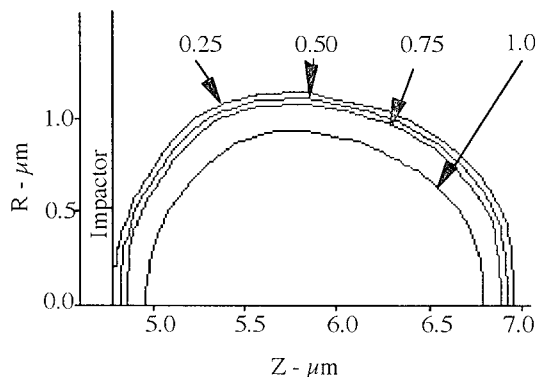
The heat conduction effect is important in the propagation of the burning front. Without heat conduction, the burning may not spread to the neighboring material where the temperature is below the threshold value. The spreading of the burning front is consistent with the concept of the ignition and growth model of shock initiation.



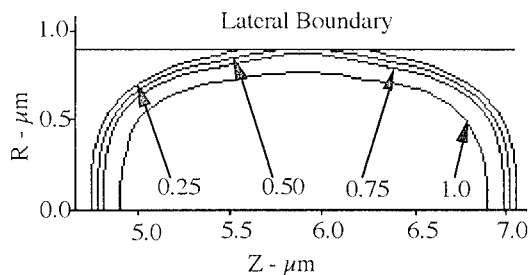
(a) Wide boundary and  $t = 8$  nanosecond



(c) Narrow boundary and  $t = 8$  nanosecond



(b) Wide boundary and  $t = 20$  nanosecond



(d) Narrow boundary and  $t = 20$  nanosecond

**FIGURE 10. THE COMPARISON OF BURN FRACTION CONTOURS BETWEEN WIDE (a and b) AND NARROW (c and d) BOUNDARIES**

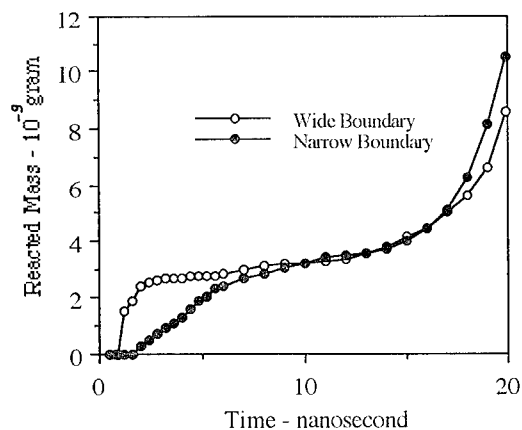


**FIGURE 11. THE MASS OF REACTED EXPLOSIVE VERSUS TIME**

## REFERENCES

1. Campbell, A.W., Davis, W.C., Ramsay, J.B., and Travis, J.R., "Shock Initiation of Solid Explosive," *Physics of Fluids*, Vol.4, p.511,1961.
2. Mader, C.L., *Numerical Simulation of Detonation*, Univ. of California Press, 1979.
3. Tabor, A.T., "The Effects of Material Microstructure on The Shock Sensitivity of Porous Granular Explosive," *Proc. of the Eighth Symposium (International) on Detonation*, 1985.
4. Mader, C.L., and Kershner, J.D., "The Three-Dimensional Hydrodynamic Hot-Spot Model," *Proc. of the Eighth Symposium (International) on Detonation*, 1985.
5. Chou, P.C., Ritman, Z., and Liang, D., "Viscoplastic and Heat Conduction Effects in Pore Collapse," Presented at Symposium on Shear Instabilities and Viscoplasticity Theories, Sept. 14-16, 1992 San Diego, Cal.; Also to appear in *Jour. of Mechanics of Materials*.

6. Chou, P.C.; Liang, D.; and Flis, W.J., "Shock and Shear Initiation of Explosive," Shock Waves, No.1, 1991, p. 285-292.
7. Johnson, G.R. and Cook, W.H., "A constitutive model and data for metals subjected to large strains, high strain rates, and high temperatures," Proc. 7th Inter. Symp. Ballistics, The Hague, The Netherlands, 1983, pp. 541-548.
8. Frey, R.B., "The Initiation of Explosive Charges by Rapid shear," Proc. of the seventh Symposium (International) on Detonation, 1981.
9. Setchel, R.E., and Taylor P.A., "The Effect of Grain Size on Shock Initiation Mechanisms in Hexanitrostiblene (HNS) Explosive," Progress in Astronautics and Aeronautics, Vol. 94, Dynamics of Shock Wave, Explosions, and Detonations, Edited by Bowen J.R., Manson N., Oppenheim A.K., and Soloukhin R.I..
10. Howe, P., "On the Role of Shock and Shear Mechanism in the Initiation of Detonation by Fragment Impact," Proc. of the Eighth Symposium (International) on Detonation, 1985.
11. Field, J.E., Palmer, S.J.P., Sundarajan, R., and Swallowe, G.M., Proc. of the Eighth Symposium (International) on Detonation, 1985.

## DISCUSSION

J. E. KENNEDY

Los Alamos National Laboratory, Los Alamos, New Mexico

Your analysis shows a decrease in temperature rise (sensitivity) at particle/pore sizes below 1  $\mu\text{m}$ , and the

implied conclusion from this result is that explosives may become less sensitive at this small particle size. My comment is that not many explosives have been studied at such small sizes; most studies of "fine-grain" explosives look at materials 1-10  $\mu\text{m}$  in diameter or larger. Your finding is consistent with a tendency for fine-grain explosives to behave increasingly like homogeneous explosives rather than heterogeneous ones.

## REPLY BY P. C. CHOU:

The shock sensitivity is often experimentally studied by varying the grain size. In this paper, the discussion is based on the pore size. The pore size is dependent on the grain size and the initial density of the explosive charge. The mean pore diameter is much smaller than the mean grain size in denser explosive charges. For example, in the HNS charge with density of 1.60  $\text{g}/\text{cm}^3$  (92% of TMD), with an average grain size of 8.8  $\mu\text{m}$  x 4.0  $\mu\text{m}$ , the average pore size is 0.61  $\mu\text{m}$ . Therefore, in this case, the pore size is about one tenth of the grain size (P. A. Taylor, 8th Detonation Symposium). Taylor also found that the HNS explosive with average pore diameter 0.61 (grain size 8.8  $\mu\text{m}$  x 4.0  $\mu\text{m}$ ) is more shock-sensitive than both the one with larger average pore diameter of 5.3  $\mu\text{m}$  (average grain size 167  $\mu\text{m}$  x 51  $\mu\text{m}$ ) and the one with smaller average pore diameter of 0.15  $\mu\text{m}$  (average grain size 1.5  $\mu\text{m}$  x 1.4  $\mu\text{m}$ ). Our results are, qualitatively, in agreement with this.

J. P. Plotard et al. used pore diameters of 0.4 and 1 micron for explosive X1 (96% HMX) (10th Detonation Symposium). D. E. Maiden measured the pore diameter distributions of PBX-9404 at density of 1.89  $\text{g}/\text{cm}^3$  and PETN at a density of 1.77  $\text{g}/\text{cm}^3$  by mercury porosimetry analysis. The average pore diameters are 0.0233 micron and 0.163 micron, respectively, much smaller than one micron (UCRL-96360).

## THE SIMULATION OF SHOCK INITIATION OF LESS SENSITIVE EXPLOSIVES USING THE HYDROCODE AUTODYN

Ries Verbeek and Albert van der Steen  
TNO Prins Maurits Laboratory  
P.O. Box 45, 2280 AA Rijswijk  
THE NETHERLANDS

One-dimensional simulations of the shock initiation of RDX-based PBXes have been carried out in order to reach a better understanding of experimental sensitivity data, obtained for these kind of explosives both at TNO-PML and at ISL. In the simulations the Lee-Tarver ignition and growth model has been used. The emphasis in the simulations has been put on examining the relative influence of the ignition and growth terms on the initiation behaviour. From the results it appears that the growth terms are the dominating factor and determine to a high degree the run-up length to detonation. This indicates that the burning surface area of the explosive particles gives a very important contribution to the sensitivity for shock initiation of heterogeneous explosives.

### INTRODUCTION

At the TNO Prins Maurits Laboratory a research program is being carried out on the characterisation and development of less sensitive explosives. In this respect the influence of the properties of the RDX crystals on the shock sensitivity of RDX based PBXes is investigated. An account of the study and optimisation of the crystal properties and of the first experimental results on shock sensitivity was presented at the previous Detonation Symposium<sup>1</sup>. In a companion paper that is presented at this symposium<sup>2</sup> the results of the continuation of these experiments are given.

The explosives that are being studied are HTPB based PBXes containing 85 wt% RDX with a density of 1.58 mg/mm<sup>3</sup>. The explosive load consists of a bimodal mixture of RDX particles, a coarse fraction with an average size in the order of 300  $\mu$ m and a fine fraction with an average size in the order of 30  $\mu$ m. The research concentrates on the influence on the shock sensitivity of the particle size and shape. In the experimental work reported in reference 1 the shock sensitivity was determined with use of a 50 mm diameter gap test, providing the sensitivity for shocks of long duration. Currently also the shock sensitivity is measured for the impact of thin plastic flying plates, that provide shock pulses of high amplitude and short duration.

In reference 1 mainly the influence of the particle morphology on the shock sensitivity was considered. Also evidence was seen however that the sensitivity for shock initiation was larger when the average particle size was lower (see figure 1). This result is in contradiction with experimental results obtained at ISL, reported at previous Detonation Symposiums<sup>3,4</sup>. In this research effort, that is similar to the TNO-PML research, PBXes are tested that

contain 70 wt% RDX and have a density of 1.45 mg/mm<sup>3</sup>. The explosive is a monomodal formulation with RDX particles that have an average size of either 428  $\mu$ m, 134  $\mu$ m or 6  $\mu$ m. Shock sensitivity results were reported for both flying-plate experiments (short shock duration) and wedge-test experiments (long shock duration). In the wedge test experiments the relation between the shock sensitivity and the particle diameter appeared to be pressure dependent (see figure 2). For initiation pressures above 10 GPa PBXes with smaller particle size are more sensitive while below 5 GPa the opposite is true. In the region in between the sensitivity curves cross each other. The particle size dependency in the low pressure region is completely opposite to the dependency obtained at TNO-PML. This is remarkable and can not easily be explained by the differences between the two experimental programs (bimodal composition versus monomodal composition, 85 % solid load versus 70 % solid load, 1.58 mg/mm<sup>3</sup> density versus 1.45 mg/mm<sup>3</sup> density, emphasis on low pressure region versus emphasis on high pressure region).

### SIMULATION OF SHOCK INITIATION

In order to gain more insight in the reasons for the observed behaviour a series of computer simulations have been carried out. In these simulations use is made of the computer code Autodyn-2D, a commercial hydrocode developed by Century Dynamics Inc.<sup>5,6</sup>. With this program shock dynamic calculations can be carried out for many kinds of inert materials and explosives. In order to be able to describe a shock initiation experiment with this code a shock initiation model has to be incorporated into the code. Currently two shock initiation models are available in Autodyn, the Forest Fire model and the Lee-Tarver model.

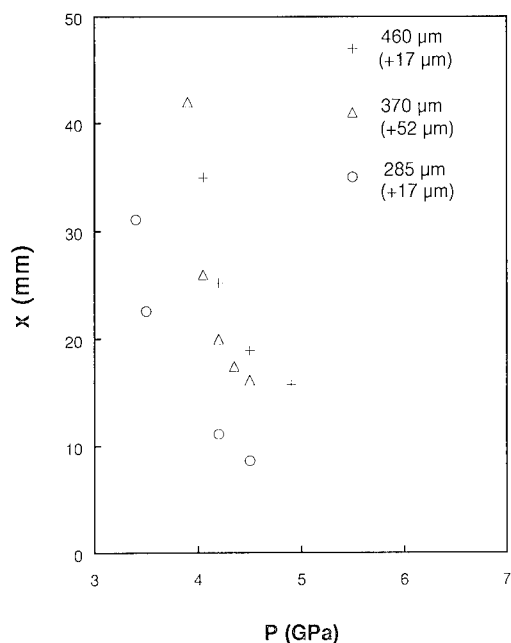


FIGURE 1. EXPERIMENTAL RUN-UP LENGTHS TO DETONATION FROM REFERENCE 1. DATA ARE PRESENTED FOR 3 BIMODAL COMPOSITIONS. THE PARTICLE SIZES ARE INDICATED IN THE FIGURE.

The Forest Fire model<sup>7</sup> is a phenomenological initiation model that is based on the so-called Popplot, i.e. an experimentally determined relation between the initiating shock pressure and the distance to detonation. Due to its simplicity the model is not suitable for carrying out parameter studies, but since the necessary empirical parameters can be obtained relatively easily it is a good tool to compare the shock initiation properties of explosives with those of other explosives. Its use at TNO-PML is restricted to this kind of applications. The implementation of Forest Fire is an internally developed addition to the hydrocode Autodyn.

The Lee-Tarver or ignition and growth model<sup>8,9</sup> on the other hand is not based on a simple empirical relation but is founded on the knowledge that the shock initiation of heterogeneous explosives is controlled by the formation and subsequent reaction of the hot spots that are created when the shock pulse compresses the heterogeneous solid. In its current form<sup>9</sup> the model consists of three terms, the first of which represents the formation and initial reaction of hot spots during shock compression, while the second and third terms correspond to respectively the initial slow burning of the ignited explosive grains and to the rapid completion of the reaction when the reaction sites begin to coalesce. It assumes the form:

$$\frac{\partial F}{\partial t} = I \cdot (1-F)^b \cdot (\mu \cdot a)^x + G_1 \cdot (1-F)^c \cdot F^d \cdot P^y + G_2 \cdot (1-F)^e \cdot F^g \cdot P^z \quad (1)$$

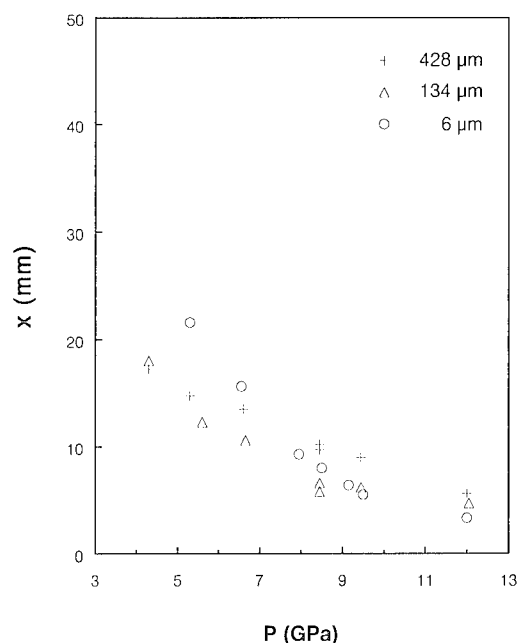


FIGURE 2. EXPERIMENTAL RUN-UP LENGTHS TO DETONATION FROM REFERENCE 4. DATA ARE PRESENTED FOR 3 MONOMODAL COMPOSITIONS. THE PARTICLE SIZES ARE INDICATED IN THE FIGURE.

where  $F$  is the fraction reacted explosive,  $t$  is the time,  $\mu$  is the compression and  $I, a, b, x, G_1, c, d, y, G_2, e, g$  and  $z$  are constants. Three more constants are added to the model:  $F_{\text{igmax}}$ ,  $F_{G1\text{max}}$  and  $F_{G2\text{min}}$  which limit the contributions of the three terms to respectively a maximum reacted fraction  $F_{\text{igmax}}$  for the first term, a maximum fraction  $F_{G1\text{max}}$  for the second term and a minimum fraction  $F_{G2\text{min}}$  for the last term. This brings the total of unknown constants in the model to 15.

Although this model is still phenomenological of nature its relation to a number of distinct, physical stages in the shock initiation process offers the possibility to link variations on some parameters in the model to variations in explosive properties such as particle size, crystal shape, surface smoothness etc. Its main use therefore at TNO-PML is as a tool to qualitatively examine the influence on shock initiation behaviour of changes in parameters of the explosive material.

## SET-UP OF SIMULATIONS

The simulations that have been carried out were not intended to exactly reproduce the experimental results but instead to provide insight in the influence of various parameters. To this end some parameter variations have been performed with use of the Lee-Tarver model. In first instance only 2 parameters of the possible 15 have been varied, being the proportionality constants  $I$  and  $G_1$  of respectively the ignition term and the first growth term.

The values of the remaining parameters used are given in table 1. These values largely agree to the values used in the simulations that were reported in reference 3. For these parameter values one-dimensional simulations have been carried out of the shock initiation of an RDX based PBX by a sustained shock pulse with pulse heights between 4 and 10 GPa. Such series of simulations have been performed for several  $I$ ,  $G_1$  combinations. While  $I$  was fixed to a value of  $10 \mu s^{-1}$  simulations have been carried out with  $G_1$  varying between  $0.05 \text{ GPa} \cdot \mu s^{-1}$  and  $0.3 \text{ GPa} \cdot \mu s^{-1}$  and with  $G_1$  fixed to  $0.1 \text{ GPa} \cdot \mu s^{-1}$   $I$  was varied between  $10^{-3} \mu s^{-1}$  and  $10^4 \mu s^{-1}$ .

TABLE 1. LEE-TARVER MODEL PARAMETERS

$I (\mu s^{-1})$	$10^{-3} - 10^4$
$a$	0
$b$	0.1
$x$	4
$G_1 (\text{GPa} \cdot \mu s^{-1})$	$0.05 - 0.3$
$c$	0.667
$d$	0.083
$y$	1
$G_2 (\text{GPa} \cdot \mu s^{-1})$	$2.25 \times 10^{-3}$
$e$	0.222
$g$	0.667
$z$	3
$F_{igmax}$	0.3
$F_{G1max}$	0.5
$F_{G2min}$	0.5

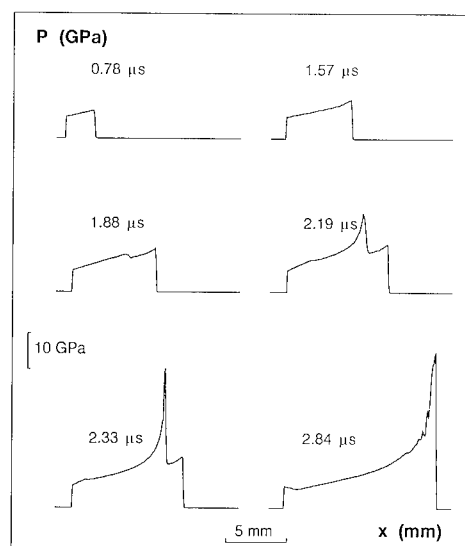


FIGURE 3. DEVELOPMENT OF PRESSURE PROFILES IN TIME FOR INITIATION WITH A 6 GPa SHOCK

## SIMULATION RESULTS

In figure 3 a typical example is given of the development of the pressure profile. Initially a steadily progressing shock wave is observed of which the amplitude is only slightly increasing. At a later stage well behind the shock front a pressure spike develops that subsequently quickly grows to a large amplitude and starts to gain on the shock front. After some time this pressure spike overtakes the shock front and a full detonation has developed. The explanation for this behaviour can be found in figure 4. In this figure for the same points of time the profiles of the reacted fraction  $F$  are shown. The figure shows that at the shock front only part of the material has reacted and that the growth of reaction continues behind the front, eventually accelerates and reaches completion well behind the front, giving rise to a local pressure spike. For shock pulses of low strength this results in a very long reaction zone, the length of which is determined mainly by the length of the growth stage.

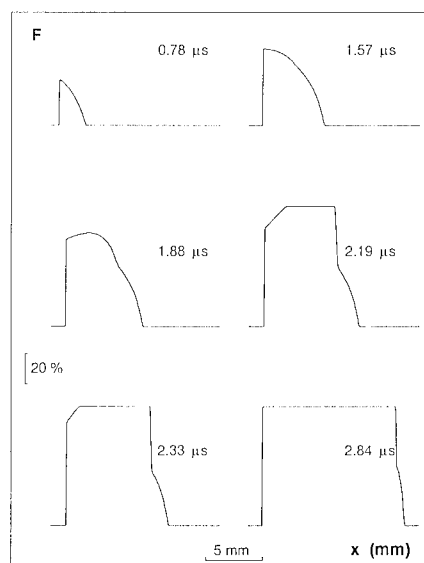


FIGURE 4. REACTED FRACTION PROFILES FOR THE SIMULATION OF FIGURE 3

The following figures show the influence on the initiation distance of variations in the parameters  $I$  and  $G_1$ . In our simulations the initiation distance and time are defined as the distance respectively time needed for the pressure spike to overtake the initial shock wave. In figure 5 the influence of varying the parameter  $G_1$  of the growth term is demonstrated while all other parameters are kept constant. The influence appears to be very strong. Figure 6 shows the influence of varying the parameter  $I$  of the ignition term. The influence of this term appears to be much smaller. I had to be increased by a factor of 10000 to reduce the initiation distance by no more than 25%. Increasing  $I$  still further did not result in a further reduction of the initiation distance. At the same time, decreasing  $I$  below  $0.1 \mu s^{-1}$  did not result in a longer initiation distance. The influence of the parameter  $I$  therefore appears to be very limited.



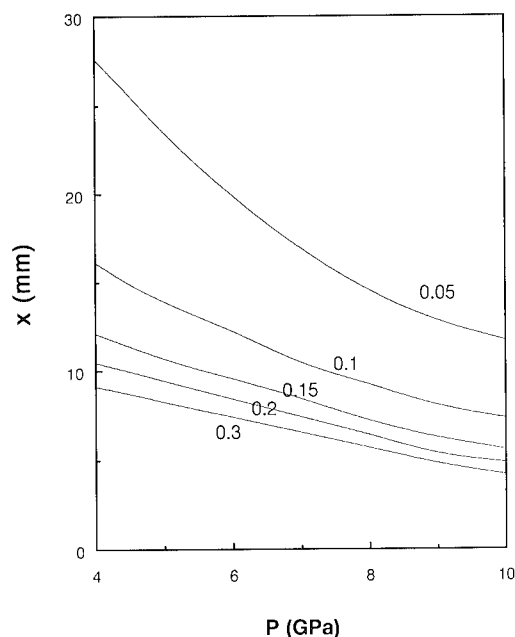


FIGURE 5. INITIATION DISTANCE AS A FUNCTION OF SHOCK PRESSURE FOR 5 DIFFERENT VALUES OF THE PARAMETER  $G_I$

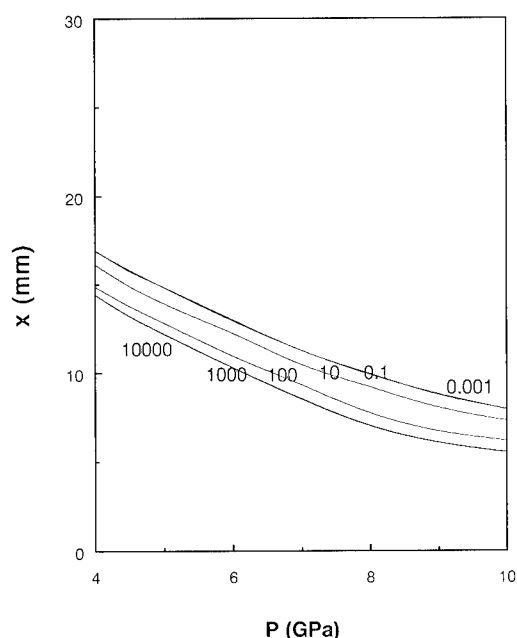


FIGURE 6. INITIATION DISTANCE AS A FUNCTION OF SHOCK PRESSURE FOR 6 DIFFERENT VALUES OF THE PARAMETER  $I$

The reason for this phenomenon is that the ignition term is only active till a reacted fraction  $F_{igmax}$  is reached. Above that limit only the growth terms contribute to the reaction rate. Since the reaction rate during the growth stages is usually much smaller than the reaction rate in the ignition stage the length of the growth stage mainly determines the initiation distance. This also explains the fact that above a certain value of  $I$  increasing  $I$  further has no effect. In that case the reacted fraction already immediately reaches the value  $F_{igmax}$  and is then controlled by the growth terms. Increasing  $I$  further brings no change to this situation. The reason that decreasing  $I$  below a certain value also has no effect is that the ignition term is then much smaller than the growth term (which is also active at small values of  $F$ ). The ignition term in that case only serves to raise  $F$  to a value slightly above 0 since the growth terms are zero for  $F=0$  but then the growth terms take over completely.

## EVALUATION OF SIMULATIONS

The above results show that the growth terms dominate the initiation behaviour. As yet only two parameters have been varied:  $I$  and  $G_I$ . Other parameters that will have a large influence on the initiation distance are the proportionality constant  $G_2$  of the second growth term, the pressure exponent  $z$  of that term and the limits  $F_{G1max}$ ,  $F_{G2max}$  and  $F_{igmax}$ . Varying these parameters will strongly influence the build-up to detonation, but will not essentially change the picture sketched above. Namely the ignition term determines the sensitivity of the material for shock impact and the initial growth rate but the growth terms mainly determine the reaction behaviour, the time necessary to reach complete reaction and whether or not the reaction does come to completion or fails.

## COMPARISON OF SIMULATIONS WITH EXPERIMENTS

When comparing the outcome of the simulations with experimental results it is necessary to provide a link between physical and chemical properties of the explosive and the parameters of the Lee-Tarver model. A direct correspondence between the properties and the parameters does not exist but for some properties a clear relation exists with one of the terms in the model. In this respect we can expect that e.g. the particle size has a large influence on the growth terms because of the much larger burning surface that is provided by small grains. We would therefore expect that the parameter  $G_I$  will be larger for smaller particle sizes. The influence of the particle size on the ignition term is more difficult to estimate and will be different for the different mechanisms that might be responsible for ignition like e.g. void closure, microjetting, plastic work at void peripheries, particle friction etc. Possibly these mechanisms are less likely to occur for small particle sizes. The particle shape and smoothness will probably have little influence on the parameters of the growth terms but will certainly affect the ignition process, although it is not clear how to correlate them with the parameters of the ignition term.

We might conclude from the above that the main effect of decreasing the particle diameter will be an increase of the value of  $G_1$ , resulting in a shorter run distance to detonation. This is in agreement with the experimental observations obtained at PML, but in the ISL experiments this dependency is only seen in the high pressure region, while at low pressures the opposite is true. This behaviour seems to be in contradiction with the outcome of the simulations, since especially at low initiating pressures the growth terms are by far the dominating factor. If a cross-over effect is to be expected, it should go the opposite way, since at high pressures the reaction rate during the ignition phase is relatively more important.

A clear explanation for the experimental results has not been provided yet by the simulations. Of course in the experiments many more parameters play a role than have been considered above. E.g. the role of the binder, the influence of the distribution width of the particle diameter, the density and in the case of the PML experiments the influence of the bimodality of the mixture have not been taken into account. To clarify these points more experimental data will be needed in combination with more parameter variations. To this end more simulations will be performed where also the influence of varying the other parameters in the Lee-Tarver model will be examined. Further the influence of two-dimensional effects will be examined as well as the shock initiation properties of short shock pulses.

## CONCLUSION

The simulations indicate that the growth terms are by far the dominating factor at shock initiation of detonation. This indicates that the burning surface of the explosive particles is one of the most important factors that determine the run up distance to detonation. The simulations could not yet fully explain the experimental results obtained at various institutes. More experimental data and more parameter variations in the simulation will be needed to clarify the link between simulation parameters and experimental parameters and to provide more insight into the influence of material properties on the shock sensitivity of explosives.

## REFERENCES

1. Van der Steen, A.C., Verbeek, H.J. and Meulenbrugge, J.J., "Influence of RDX Crystal Shape on the Shock Sensitivity of PBXes", in *Proceedings of the Ninth Symposium (International) on Detonation*, Portland, Oregon, 28 Aug - 1 Sep 1989, pp 83 - 88.
2. Van der Steen, A.C., De Jong, E.G., Prinse, W.C., Hordijk, A.C. and Duvalois, W., "Crystal quality and Shock Sensitivity of RDX-Based PBXes", in *Proceedings of the Tenth International Symposium on Detonation*, Boston, MA, 12-16 Jul 1993.
3. Moulard, H., Kury, J.W. and Delclos, A., "The Effect of RDX Particle Size on the Shock Sensitivity of Cast PBX Formulations", in *Proceedings of the Eighth Symposium (International) on Detonation*, Albuquerque, NM, 15 - 19 Jul 1985, pp 902 - 913.
4. Moulard, H., "Particular Aspect of the Explosive Particle Size Effect on Shock Sensitivity of Cast PBX Formulations", in *Proceedings of the Ninth Symposium (International) on Detonation*, Portland, Oregon, 28 Aug - 1 Sep 1989, pp 18 - 24.
5. Birnbaum, N.K. and Cowler, M.S., "Numerical Simulation of Impact Phenomena in an Interactive Computing Environment", in *Proceedings of the International Conference on Impact Loading and Dynamic Behaviour of Materials "IMPACT 87"*, Bremen, FRG, May 1987.
6. Birnbaum, N.K., Cowler, M.S., Itoh, M., Katayama, M. and Obata, H., "AUTODYN - an Interactive Non-Linear Dynamic Analysis Program for Microcomputers through Supercomputers", in *Proceedings of the 9th International Conference on Structural Mechanics in Reactor Technology*, Lausanne, Switzerland, August 1987.
7. Forest, C.A., *Burning and Detonation*, Los Alamos Scientific Laboratory Report LA-7245, 1978, LASL, Los Alamos, NM.
8. Lee, E.L. and Tarver, C.M., "Phenomenological Model of Shock Initiation in Heterogeneous Explosives", *Phys. Fluids*, Vol. 23, No. 12, 1980, pp 2362 - 2372.
9. Tarver, C.M., Hallquist, J.O. and Erickson, L.M., "Modelling Short Pulse Duration Shock Initiation of Solid Explosives", in *Proceedings of the Eighth Symposium (International) on Detonation*, Albuquerque, NM, 15 - 19 Jul 1985, pp 951 - 961.

# AN ASSESSMENT OF THE PERFORMANCE OF THE ORIGINAL AND MODIFIED VERSIONS OF THE FOREST FIRE EXPLOSIVE INITIATION MODEL

John Starkenberg  
U.S. Army Research Laboratory  
Aberdeen Proving Ground, MD 21005-5066

The Forest Fire explosive initiation model is useful because it can be calibrated from readily available sensitivity data. Often, it is the only choice available for a given energetic material. However, assumptions used in the Forest Fire derivation limit its accuracy and applicability. Present computations show that, while Forest Fire adequately predicts run to detonation for sustained-shock loading, it is grossly in error when applied to pulsed-shock loading. On the other hand, it exhibits qualitatively correct results for finite-rate compression or ramp-wave loading. As part of the present effort, several relatively simple modifications which extend the applicability of Forest Fire have been developed. These include improved mixture modeling, use of a higher order reactive Hugoniot and incorporation of surface area burning into the reaction rate model. The effect of the choice of mixture model on flow field prediction may be substantial. The influence of the reactive Hugoniot, on the response to pulsed-shock loading is significant. The inclusion of a surface burning model has a profound effect on the computational results. When combined with a quadratic reactive Hugoniot, it provides a good representation of the responses to a pulsed-shock stimulus.

## INTRODUCTION

"Forest Fire" is the first and simplest of a number of models treating the initiation of detonation in energetic materials. It is useful because it can be calibrated from readily available sensitivity data.<sup>1,2,3,4</sup> Other models are more sophisticated and capture more of the micromechanical phenomenology involved in initiation of heterogeneous explosives.<sup>5,6,7</sup> Often, however, Forest Fire is the only choice available for a given energetic material. A problem arises in that, on the basis of the assumptions used in its derivation, Forest Fire is quite limited in its range of applicability. It can be expected to adequately predict the distance of run to detonation for sustained-shock loading as it is directly calibrated to do just that. However, in the complex environments associated with accidental initiation, pulsed-shock and finite-rate compression (or ramp-wave) loading is common.<sup>8</sup>

Indeed, Forest Fire is routinely employed in these environments and beyond its limits.<sup>9,10,11</sup> The

consequences of this on the accuracy of the results achieved have heretofore been unclear, as the literature does not include assessments of Forest Fire performance for pulsed shocks or ramp waves. The present paper is, in part, an attempt to rectify this situation.

In the course of pursuing this understanding, it became clear that several relatively simple modifications might extend the applicability of Forest Fire. These modifications include improved mixture modeling, use of a more realistic reactive Hugoniot, and incorporation of surface area burning into the reaction rate model. These modifications not only improve the performance of the model but also serve to illustrate the sources of the shortcomings in the original Forest Fire.

## FOREST FIRE

A brief discussion of the Forest Fire model is included here to provide necessary background. A more detailed exposition has been provided by Lundstrom.<sup>4</sup>

Forest Fire is a single-step model that applies to a two-phase mixture of reactants and products in mechanical and thermal equilibrium. The reactant mass fraction is used to characterize reaction progress. Forest Fire incorporates a reactive shock model and an empirical reaction rate law.

The reactive shock is described by a reactive Hugoniot, connecting the unreacted ambient state with the Chapman-Jouget state. This Hugoniot gives shock velocity as a linear function of particle velocity. While the reactive Hugoniot is a part of the Forest Fire derivation and directly affects the reaction rate law, it is not generally used to describe reactive shock waves in hydrocode implementations where shock waves are modeled using artificial viscosity. In this case, the propagation rate law is integrated through the viscous shock. It should be emphasized that, although Forest Fire has no explicit ignition step, the reaction associated with the shock wave, whether determined by integration or by the reactive Hugoniot, plays this role.

The reaction rate law is derived assuming that bulk reaction takes place. That is, the reaction rate is proportional to the mass fraction of unreacted material and "hot spots," and surface burning phenomena are specifically excluded. The pressure dependence is obtained with reference to the "Pop plot," representing commonly available sensitivity data for high explosives (run distance to detonation as a function of initial shock pressure) obtained in the "wedge test."<sup>12</sup> The "single curve build-up hypothesis" interprets the Pop plot as the path to detonation in the pressure-distance plane so that the solutions obtained automatically reproduce wedge test results. The derivation is simplified by assuming that the pressure derivative behind the shock vanishes. This condition is met only when the shock wave transitions to detonation as a growing square wave. The derived Forest Fire rate is a function of the state variables immediately downstream of the shock wave. This is fitted as a function of pressure and applied at all points downstream of the shock. The original fit is a polynomial in pressure of as many as fifteen terms.

## COMPUTATIONAL METHODS

Some discussion of the computational approaches used in this study is appropriate. Computations were made using the One-Dimensional Explicit Shock (ODES) code. The use of a one-dimensional code naturally limits the study to consideration of one-dimensional phenomena. However, this is quite sufficient to cover response to sustained-shock, pulsed-shock, and ramp-wave loading.

The most significant feature of ODES is its explicit

modeling of shock waves. This approach is appropriate whenever the flow between the upstream and downstream states is quasi-steady. Generally, mass momentum and energy conservation along with overtaking characteristic and other appropriate conditions are solved for downstream conditions with upstream conditions given. Shock waves may be either inert or reactive. In a reactive shock, some degree of reaction is associated with the shock jump. This eliminates the requirement to resolve parts of the reactive flow field which are concentrated in a narrow region. In the case of a Chapman-Jouget detonation, the entire reactive flow field is unresolved. However, it should be noted that such spatial concentration does not guarantee that the quasi-steady condition is met. In conjunction with the Forest Fire model, the reactive Hugoniot is used to close the system of equations describing the shock wave and is directly responsible for determining the amount of reaction associated with the shock. In addition to shock waves, ODES also gives explicit treatment to gradient discontinuities (such as the heads and tails of isentropic waves) and allows them to transition to shock waves. This is useful for modeling finite-rate compressions.

This approach stands in contrast to that taken in multidimensional codes employing artificial viscosity. In that case, the reactive Hugoniot is abandoned and the Forest Fire rate is integrated from the unreacted state through the viscous shock. The approach has low physical fidelity, and results are reported to be improved by including the artificial viscous stress along with the pressure in calculating the reaction rate. This has the effect of increasing the amount of reaction associated with the shock wave which may be lower than that associated with the reactive Hugoniot. Specifically, this represents the method that has been implemented in the 2DE code.<sup>3,13</sup> During most of the development of a detonation, the amount of reaction associated with the shock is small and the process is dominated by downstream reaction. The final transition to detonation occurs rapidly over a short distance. Thus, use of this technique can be expected to have little effect on predicted distances of run to detonation.

## FOREST FIRE PERFORMANCE

### Sustained-Shock Stimulus

Sustained-shock computations were made using a "thick" (semi-infinite) copper flyer impacting a PBX-9404 sample to produce the stimulus. The velocity of the flyer was varied to produce different initial shock pressures.

Figure 1 shows pressure versus position at various

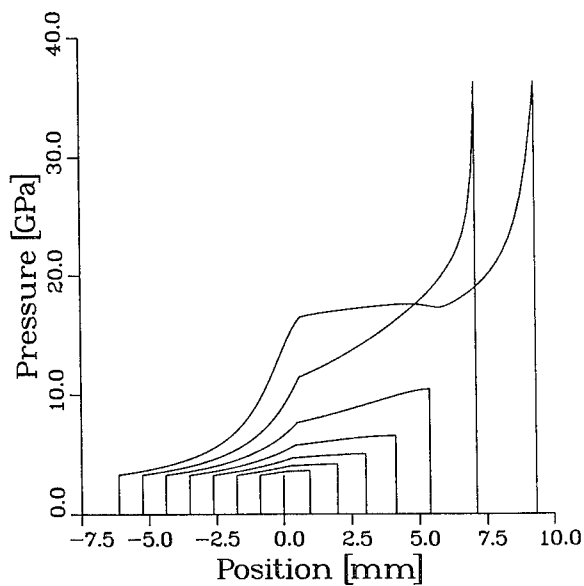


FIGURE 1. SEQUENCE OF PRESSURE PROFILES SHOWING DETONATION DEVELOPMENT IN PBX-9404 FOLLOWING IMPACT OF A THICK COPPER FLYER AT 550 m/s

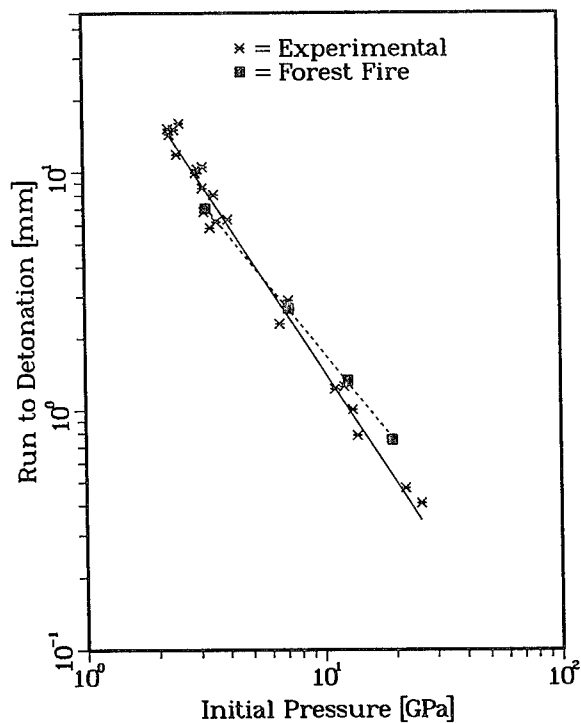


FIGURE 2. COMPARISON OF EXPERIMENTAL POP PLOT WITH FOREST FIRE PREDICTIONS FOR PBX-9404

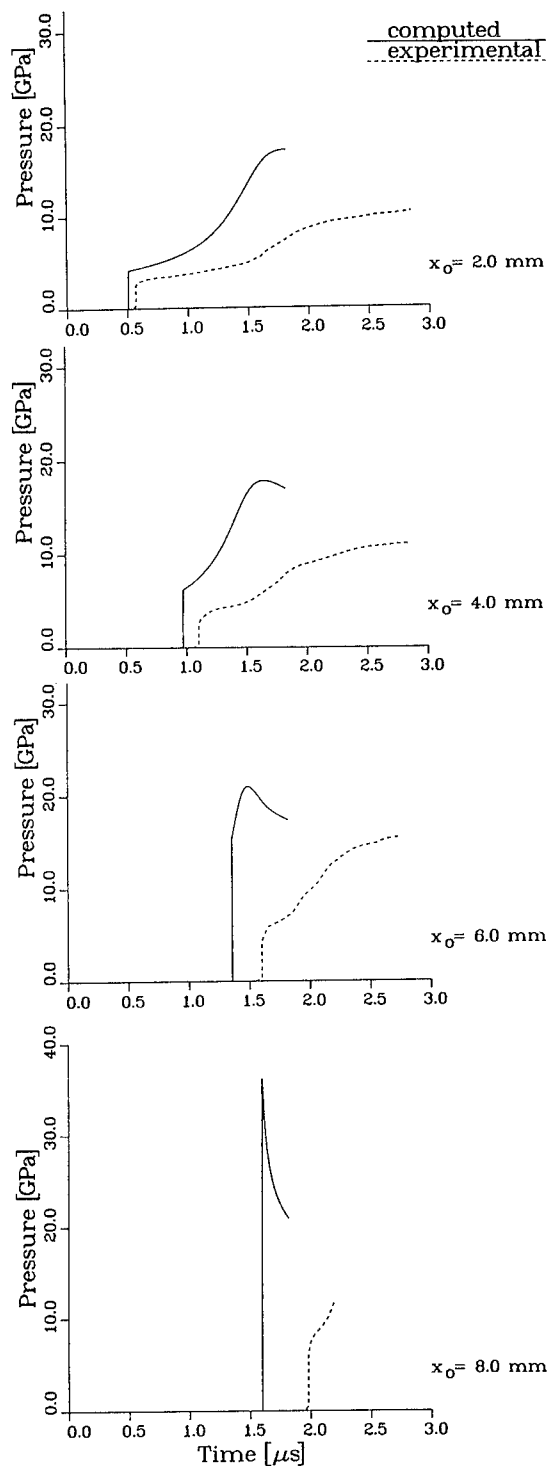


FIGURE 3. COMPARISON OF EXPERIMENTAL PRESSURE HISTORIES WITH FOREST FIRE PREDICTIONS AT FOUR LAGRANGIAN STATIONS FOR SUSTAINED-SHOCK INITIATION OF PBX-9404

times during the transition to detonation for a shock wave produced by flyer impact at 550 m/s. An approximation to a growing square wave prevails during most of the build-up process. Forest Fire was derived to predict the distance of run to detonation as a function of initial pressure (or Pop plot), and it is no surprise that it does this well (although the slope of the computed Pop plot differs somewhat from the experimental value as shown in Figure 2).<sup>14</sup>

In contrast, the predicted pressure histories at several Lagrangian stations produced by the 550-m/s flyer impact, shown in Figure 3, exhibit poor agreement with experimental measurements.<sup>15</sup>

Two related aspects of the computed results merit attention. First, the shock pressures are too high, and the shock propagates too rapidly. Since shock waves are treated explicitly here, the linear reactive Hugoniot determines the amount of reaction in the shock which may be too great. Second, reaction proceeds too promptly following shock passage. This produces a strong compression overtaking the shock, which also contributes to its increased pressure and velocity. It appears that improvement might be obtained by implementing a surface area model to delay reaction.

#### Pulsed-Shock Stimulus

Experimental data for the critical impact of thin mylar flyers on PBX-9404 are fit well by a straight line in a log-log plot of flyer velocity versus flyer thickness.<sup>16</sup> This is shown in Figure 4.

The critical velocities computed using Forest Fire differ grossly from the experimentally determined

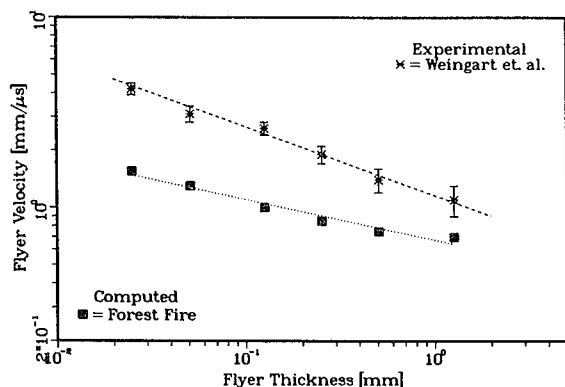


**FIGURE 4. COMPARISON OF EXPERIMENTAL CRITICAL CONDITIONS WITH FOREST FIRE PREDICTIONS FOR INITIATION OF PBX-9404 BY THIN MYLAR FLYERS**

values. The predicted sensitivity is much too high, and the variations appear slightly nonlinear, especially for the thickest flyers. In the experimental study mentioned earlier,<sup>15</sup> pressure histories were also measured for a thin copper flyer impacting a PBX-9404 sample at the same 550-m/s velocity. A comparison of the pressure measured at a station 1.0 mm from the impact point with results from the corresponding numerical simulation is shown in Figure 5.

Again, the initial shock pressure is too high, and reaction proceeds too promptly following shock passage. This is sufficient to negate the quenching effects of the rarefactions. The resulting error is biased toward safety when Forest Fire is used to predict initiation hazards. That is, Forest Fire predicts initiations that should not occur.

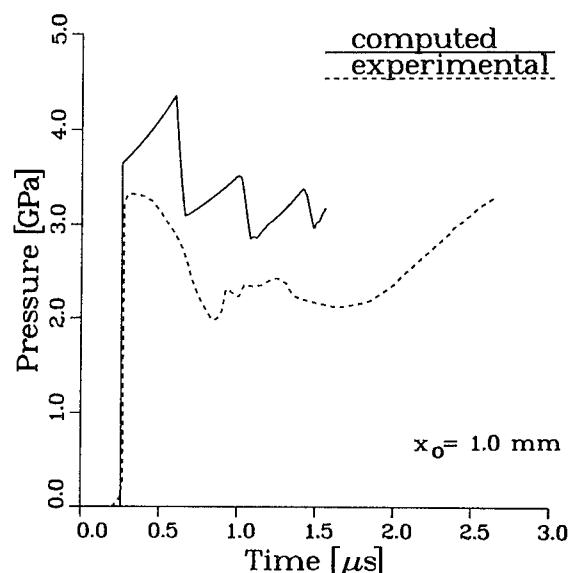


**FIGURE 5. COMPARISON OF EXPERIMENTAL PRESSURE HISTORY WITH FOREST FIRE PREDICTIONS IN A PBX-9404 SAMPLE AT A STATION INITIALLY 1.0 mm FROM THE POINT OF IMPACT OF A 0.76-mm-THICK COPPER FLYER MOVING AT 550 m/s**

#### Ramp Wave Stimulus

An experimental study of the response of an explosive to ramp waves was conducted by Setchell.<sup>17</sup> In this study, the desired loading was produced by the impact of a copper flyer on a pyroceram layer covering a PBX-9404 sample. The constitutive nature of pyroceram causes the impact shock wave to disperse into a compression wave having a finite rise time. The

rise time can be controlled by adjusting the thickness of the pyroceram cover. In these experiments, evidence of reaction increased as the rise time decreased.

Because a constitutive model for pyroceram was not readily available, it was not possible to simulate these experiments directly. However, ramp waves can be generated computationally by specifying the pressure history at a boundary which is free to move accordingly.

Two such computations were made to assess the response of Forest Fire to ramp waves. In the first of these, boundary conditions corresponding to a linear pressure increase from ambient to a final value of 5.0 GPa over an interval of 1.0  $\mu$ s were applied. In the second, the interval was cut in half. In each case, the boundary pressure was maintained at 5.0 GPa after reaching that value. For comparison, another computation was made in which a pressure-step boundary condition was used to produce a shock wave of the same strength.

Figure 6 is a position-time plot comparing the wavefronts for the three computations. The shock wave transitions to detonation earliest, while the ramp waves transition first to reactive shock waves and then to detonations in order of increasing rise time. Pressure histories at a station initially 3 mm from the impact point are shown in Figure 7. The ramp waves produce higher pressures than the shock wave at this station. The computed results are qualitatively consistent with the observations of Setchell,<sup>17</sup> but their accuracy cannot be assessed. Indeed, close correspondence to experimental results should not be expected. Lower sensitivity to ramp waves is merely a reflection of the fact that no shock wave ignites the explosive and that it resides at lower pressures for longer periods as the rise time increases. This result should be produced by any model in which reaction rate is a monotonically increasing function of pressure.

## MODIFICATIONS

### Adiabatic Reaction

Forest Fire has been derived assuming that the reactant and product phases are in mechanical and thermal equilibrium. While the mechanical equilibrium assumption is generally plausible, thermal equilibrium has long been recognized as unlikely.<sup>5,6</sup> The conditions of mechanical and thermal equilibrium in conjunction with known equations of state for each of the phases are sufficient to define an equation of state for the reacting mixture from which mixture pressure and phase specific

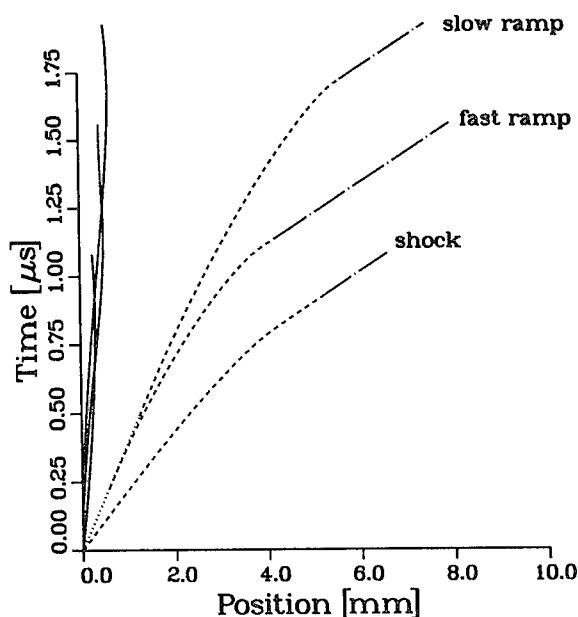


FIGURE 6. COMPARISON OF PREDICTED PATHS TO DETONATION IN THE POSITION-TIME PLANE FOR PBX-9404 SUBJECTED TO "SLOW-RAMP," "FAST-RAMP," AND SHOCK WAVE COMPRESSIONS

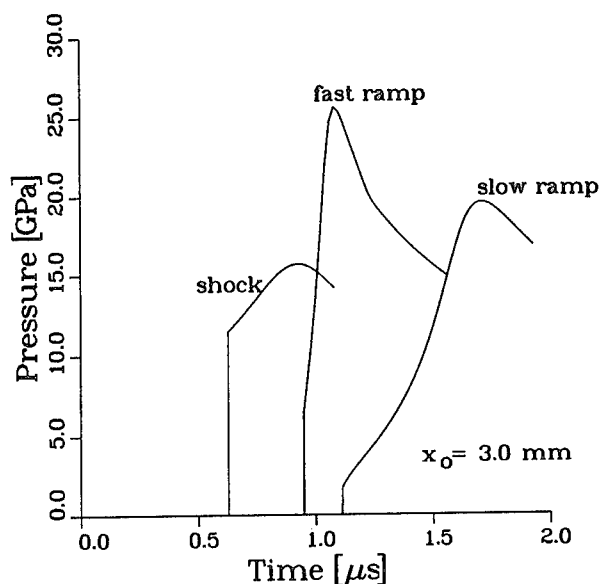


FIGURE 7. COMPARISON OF PREDICTED PRESSURE HISTORIES AT A STATION INITIALLY 3.0 mm FROM THE POINT OF APPLIED LOADING FOR PBX-9404 SUBJECTED TO "SLOW-RAMP," "FAST-RAMP," AND SHOCK WAVE COMPRESSIONS

volumes and internal energies may be determined as functions of mixture specific volume and internal energy and product mass fraction in an iterative procedure. This may be functionally expressed as

$$p = p(v, e, y),$$

$$v_r = v_r(v, e, y),$$

$$e_r = e_r(v, e, y),$$

$$v_p = v_p(v, e, y),$$

$$e_p = e_p(v, e, y),$$

where the subscripts  $r$  and  $p$  refer to reactants and products respectively. Here, the product mass fraction,  $y$ , is used instead of the original reactant mass fraction,  $1-y$ , because its progression from zero to one as reaction progresses provides a more natural description of the process.

An alternative has been offered in conjunction with the JTF initiation model which substitutes an isentropic reactant condition for thermal equilibrium.<sup>6</sup> This approach allows the previously given form of the mixture equation of state to be retained but suffers from the disadvantages of requiring time-consuming iterative integration of the isentrope equation as well as advection of the initial state along the isentrope throughout the flow field. Further, this formulation is limited to a particular form of the reactant equation of state.

If the partial differential equation describing conservation of energy of the mixture is split between the phases such that thermal isolation of the reactant phase is imposed, both the reactant and product internal energies may be determined in the primary integration. For one-dimensional flow, the energy conservation equations for the mixture and each phase are

$$\frac{\partial e}{\partial t} + u \frac{\partial e}{\partial x} + p v \frac{\partial u}{\partial x} = h_d R$$

$$\frac{\partial e_r}{\partial t} + u \frac{\partial e_r}{\partial x} + p v_r \frac{\partial u}{\partial x} = 0$$

$$\frac{\partial e_p}{\partial t} + u \frac{\partial e_p}{\partial x} + p v_p \frac{\partial u}{\partial x} = (e_r + h_d - e_p) \frac{R}{y}.$$

Note that the chemical energy released is treated as a potential energy of the reactants so that  $h_d$  is a positive

constant. Since the mixture and phase internal energies are related by a saturation condition, only two of the foregoing equations are needed in a computational implementation.

In this case, the mixture equation of state must give the mixture pressure and phase specific volumes as functions of mixture specific volume, phase internal energies, and product mass fraction.

$$p = p(v, e_r, e_p, y),$$

$$v_r = v_r(v, e_r, e_p, y),$$

$$v_p = v_p(v, e_r, e_p, y).$$

This can be achieved assuming only mechanical equilibrium in conjunction with the phase equations of state, which may have any form.

The effect on pressure history is shown in Figure 8. Results at a station initially 4.0 mm from the point of impact of a 550-m/s copper flyer obtained under the adiabatic reaction assumption differ significantly from those obtained under the thermal equilibrium assumption (also see Figure 3b). Adiabatic reaction produces a shorter run to detonation. The effect on the

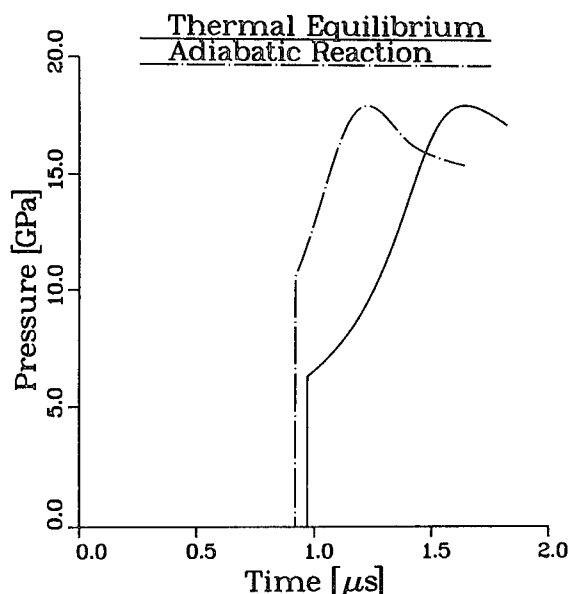


FIGURE 8. EFFECT OF MIXTURE MODEL ON THE PREDICTED PRESSURE HISTORY IN A PBX-9404 SAMPLE AT A STATION INITIALLY 4.0 mm FROM THE POINT OF IMPACT OF A THICK COPPER FLYER MOVING AT 550 m/s



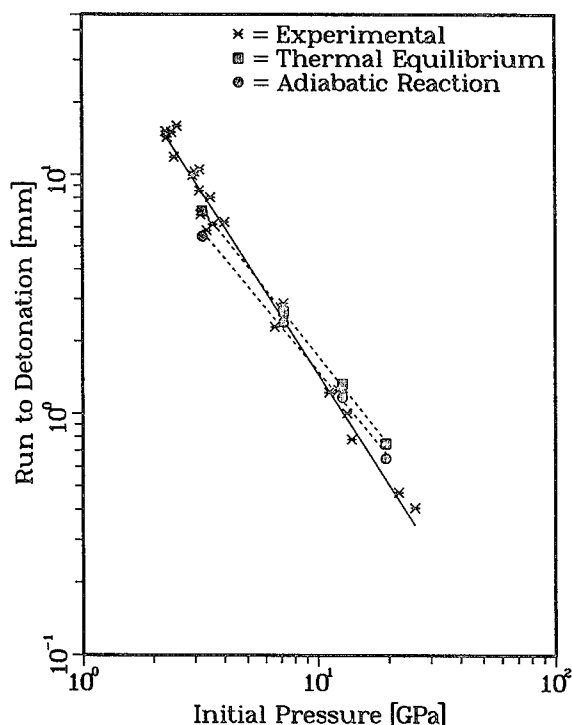


FIGURE 9. EFFECT OF MIXTURE MODEL ON THE PREDICTED POP PLOT OF PBX-9404

Pop plot is shown in Figure 9. There is a 10% to 25% reduction in the predicted run distance. Because of the way Forest Fire is calibrated, agreement with experimental data is better when using the original model. Since the mixture equation of state is used in the determination of the Forest Fire reaction rate coefficients, strictly speaking, these coefficients should be redetermined any time the equation of state is changed. However, it was not practical to do this for the present computations.

### Reactive Hugoniot

The reactive Hugoniot is used to close the system of equations describing a reactive shock wave. The use of an inert shock in conjunction with the Forest Fire model as suggested by Lundstrom<sup>4</sup> was not considered advantageous. This would require numerical resolution of the entire reactive flow field.

At least some portion of the reactive region may have a scale significantly smaller than that of the total flow field, and its resolution may carry a significant computation-time penalty. Use of a reactive shock wave is most advantageous as the wave approaches detonation and more and more reaction is included in the shock wave.

The inert shock Hugoniot for the reactants is given by

$$U = c_i + s_i u.$$

Forest Fire is derived using a linear reactive Hugoniot which connects the ambient state to the Chapman-Jouget state.

$$U = c_i + s_r u,$$

where

$$s_r = (D_{cj} - c_i) / u_{cj}.$$

The results computed using Forest Fire exhibit a level of reaction in low pressure shock waves which is too great to be consistent with experimental observations. More realistic representations are provided by higher order reactive Hugoniots which are initially tangent to the inert shock Hugoniot and depart more gradually from inert behavior before approaching the Chapman-Jouget state.

$$U = c_i + s_i u + s_n u^n,$$

where

$$s_n = [(D_{cj} - c_i) / u_{cj} - s_i] / u_{cj}^{n-1}.$$

The linear and quadratic (n=2) reactive Hugoniots are illustrated in Figure 10 along with the inert Hugoniot.

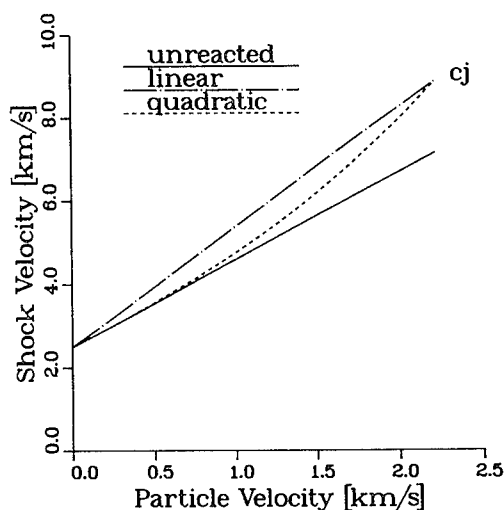


FIGURE 10. UNREACTED AND LINEAR AND QUADRATIC REACTIVE HUGONIOTS FOR PBX-9404

**TABLE 1. EFFECT OF REACTIVE HUGONIOT ORDER ON DISTANCE OF RUN TO DETONATION AND CRITICAL IMPACT VELOCITY FOR PBX-9404**

	Sustained-Shock Run to Detonation for Copper Flyer at 550 m/s	Pulsed-Shock Critical Impact Velocity for 0.0254-mm Mylar Flyer
Linear Hugoniot	7 mm	850 m/s
Quadratic Hugoniot	7 mm	1,200 m/s

The reactive Hugoniot appears explicitly in the Forest Fire derivation, and, again, the Forest Fire coefficients should be redetermined any time it is changed. Results presented here, comparing shock initiation computations for the quadratic Hugoniot with those for the linear Hugoniot, however, are for the original Forest Fire rate law.

Computations were made for both sustained- and pulsed-shock loading. The results are summarized in Table 1. The distances of run to detonation are indistinguishable while the critical impact velocity is substantially altered. In general, this indicates that the reaction associated with the shock wave or the ignition model strongly affects predictions of the response to pulsed-shock loading.

### Surface Burning

The Forest Fire reaction rate model is consistent with bulk reaction. The reaction rate is given by

$$R(y,p)=(1-y)F(p),$$

where product mass fraction,  $y$ , is used to characterize reaction progress and  $F(p)$  is the Forrest Fire pressure fit. The reaction rate may be generalized as the product of function of mass fraction and a function of pressure.

$$R(y,p)=S(y)F(p).$$

Considerable research points to the presence of surface burning mechanisms.<sup>18,19</sup> Applicability to pulsed-shock loading problems may be improved by adding surface area dependence to the reaction rate model. The surface area dependence may be identified with the mass fraction dependent function while the original pressure dependence is retained. A simplification of a previously proposed surface area model may be readily applied to the generalized form of the Forest Fire rate law.<sup>20</sup> In this case,

$$S(y)=A \begin{cases} (y/y_t)^{2/3} & 0 \leq y \leq y_t \\ [(1-y)/(1-y_t)]^{2/3} & y_t \leq y \leq 1. \end{cases}$$

This model is consistent with transition from outward "hole burning" to inward "grain burning" at a point specified by a single calibration parameter,  $y_t$ , referred to as the transition mass fraction. Small values of  $y_t$  imply early transition to grain burning. This parameter can be set with reference to available pulsed-shock response data. The leading coefficient is determined by equating the integral of the surface area function with respect to mass fraction to the similar integral of the Forest Fire bulk reaction model. This gives  $A=5/6$  and helps to ensure that the sustained-shock response of the model is not significantly altered. The surface area function has been plotted for two values of  $y_t$  and is compared with the bulk reaction function in Figure 11. Since the surface area (and, hence, the reaction rate) vanishes for unreacted explosive, this model cannot be used in conjunction with ramp-wave loading unless an ignition model is supplied.

The surface burning model may be calibrated to reproduce the experimental critical response shown in Figure 4 at a specific flyer thickness. This has been done for a 0.254-mm-thick flyer, which lies at the middle of the range of flyer thicknesses considered. In the case of the surface burning model, the initial reaction rate is highly sensitive to the initial reacted mass fraction which, in turn, depends strongly on the form of the reactive Hugoniot.

In conjunction with the linear reactive Hugoniot, the calibration gives  $y_t = 0.55$ . Further computations for the thinnest and thickest flyers yield poor predictions of critical impact velocity as shown in Figure 12.

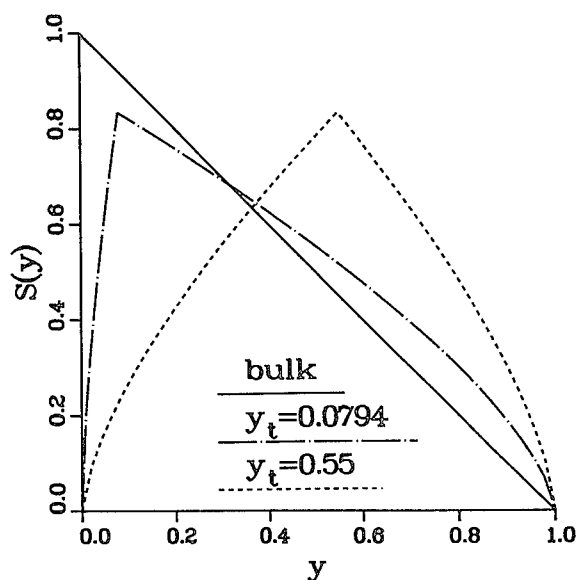


FIGURE 11. BULK AND SURFACE REACTION FUNCTIONS

Another calibration using the quadratic reactive Hugoniot gives  $y_t = 0.0794$ . This produces substantially better results, also shown in Figure 12. It appears that a still higher order Hugoniot and smaller transition mass fraction would provide further improvement. It is notable that the best results are achieved with a very small value of the transition mass fraction corresponding to a very early transition to grain burning.

The effect of using the quadratic reactive Hugoniot on the predicted Pop plot is shown in Figure 13. The fact that agreement with experiment is improved throughout the entire range of initial pressures may be regarded as fortuitous.

## SUMMARY

Forest Fire is limited in its applicability beyond prediction of run to detonation for sustained-shock loading. The reactive flow field is inadequately represented, even in this case. Forest Fire's prediction of response to pulsed-shock loading is grossly in error. The predicted response to ramp-wave loading is qualitatively correct but could not be quantitatively assessed. There is no reason to believe that Forest Fire can be accurately applied in this case.

The assumption of adiabatic reaction (or isentropic reactants) is more physically realistic than that of

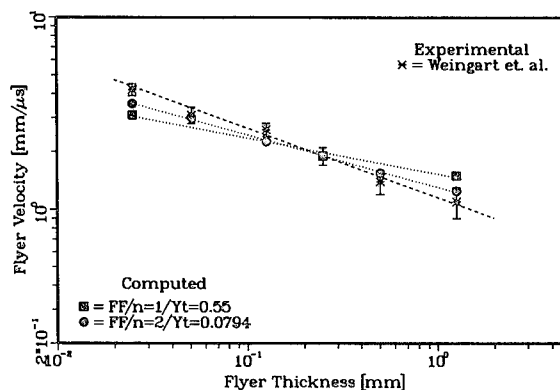


FIGURE 12. COMPARISON OF EXPERIMENTAL CRITICAL CONDITIONS FOR INITIATION OF PBX-9404 BY THIN MYLAR FLYERS WITH PREDICTIONS USING FOREST FIRE WITH EITHER LINEAR OR QUADRATIC REACTIVE HUGONIOTS AND A SURFACE REACTION MODEL

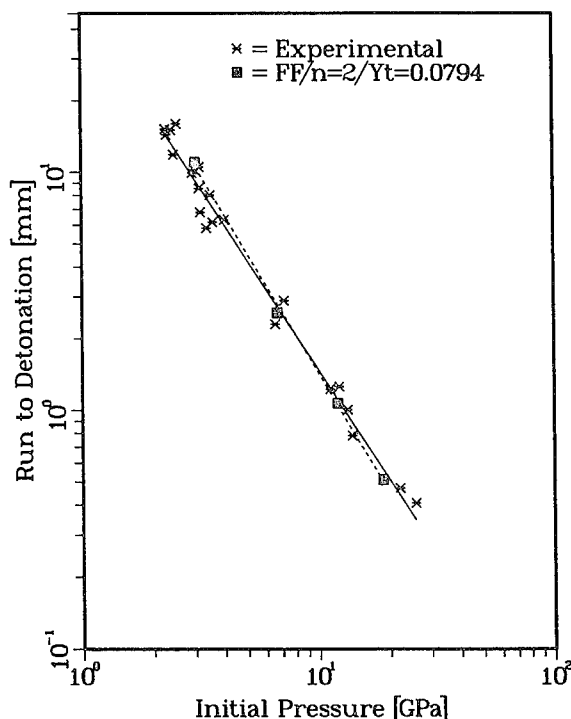


FIGURE 13. COMPARISON OF EXPERIMENTAL POP PLOT FOR PBX-9404 WITH PREDICTIONS USING FOREST FIRE WITH A QUADRATIC REACTIVE HUGONOT AND A SURFACE REACTION MODEL

thermal equilibrium. The effect of this assumption on flow field prediction may be substantial. Implementation of adiabatic reaction through the energy conservation equations provides a more economical computational tool.

Reaction occurring within the shock wave constitutes Forest Fire's ignition model. The amount of such reaction is determined either by integration of the reaction rate law through a viscous shock or by use of a reactive Hugoniot in conjunction with an explicit shock model. The influence of the ignition reaction on the response to pulsed-shock loading is significant.

## SYMBOLS

$c_i$  inert ambient sound speed  
 $D_{cj}$  Chapman-Jouget detonation velocity  
 $e$  mixture specific internal energy  
 $e_r$  reactant specific internal energy  
 $e_p$  product specific internal energy  
 $h_d$  heat of detonation  
 $n$  reactive Hugoniot order  
 $p$  pressure  
 $R$  reaction rate  
 $S$  surface area function  
 $s_i$  inert Hugoniot coefficient  
 $s_r$  reactive Hugoniot coefficient  
 $s_n$  reactive Hugoniot coefficient  
 $v$  mixture specific volume  
 $v_r$  reactant specific volume  
 $v_p$  product specific volume  
 $y$  product mass fraction  
 $y_t$  transition mass fraction  
 $U$  shock velocity  
 $u$  particle velocity  
 $u_{cj}$  Chapman-Jouget particle velocity

The inclusion of a surface burning model also has a profound effect on the computational results. When combined with the quadratic reactive Hugoniot, it provides a good representation of the responses to a pulsed-shock stimulus. The best results are achieved with calibration corresponding to a very early transition to grain burning.

## REFERENCES

1. Mader, C. L., *An Empirical Model of Heterogeneous Shock Initiation of 9404*, Los Alamos Scientific Laboratory Report LA-4475, 1970.
2. Mader, C. L.; and Forest, C. A., *Two Dimensional Homogeneous and Heterogeneous Detonation Wave Propagation*, Los Alamos Scientific Laboratory Report LA-6259, 1976.
3. Mader, C. L., *Numerical Modeling of Detonation*, University of California Press, Berkeley, 1979.
4. Lundstrom, E. A., *Evaluation of Forest Fire Burn Model of Reaction Kinetics of Heterogeneous Explosives*, Naval Weapons Center Technical Publication 6898, 1988.
5. Lee, E. L.; and Tarver, C. M., "Phenomenological Model of Shock Initiation in Heterogeneous Explosives," *Physics of Fluids*, Vol. 23, No. 12, 1980, pp. 2362-2372.
6. Johnson, J. N.; Tang, P. K.; and Forest, C. A., "Shock Wave Initiation of Heterogeneous Reactive Solids," *Journal of Applied Physics*, Vol. 57, No. 9, 1985.
7. Tang, P. K.; Johnson, J. N.; and Forest, C. A., "Modeling Heterogeneous High Explosive Burn with an Explicit Hot Spot Process," *Proceedings of the Eighth Symposium (International) on Detonation*, 1985, pp. 52-61.
8. Starkenberg, J.; Dorsey, T. M.; Benjamin, K. J.; and Arbuckle, A. L., "A Computational Assessment of the Role of Shielding in Preventing the Sympathetic Detonation of Munitions," *Proceedings of the Ninth Symposium (International) on Detonation*, 1989, pp. 1489-1501.
9. Bowman, A. L.; Forest, C. A.; Kershner, J. D.; Mader, C. L.; and Pimbley, G. H., "Numerical Modeling of Shock Sensitivity Experiments," *Proceedings of the Seventh Symposium (International) on Detonation*, 1981, pp. 479-487.

10. Starkenberg, J.; Huang, Y. K.; and Arbuckle, A. L., *Numerical Modeling of Projectile Impact Shock Initiation of Bare and Covered Composition B*, Ballistic Research Laboratory Technical Report ARBRL-TR-02576, 1984.
11. Cost, T. L.; Thomas, W. B.; Vance S. L.; and Jones, D. J., "Bullet and Fragment Impact Testing and Analysis for the Army IM Database," *Proceedings of the 1992 JANNAF Propulsion Systems Hazards Subcommittee Meeting*, 1992, pp. 227-235.
12. Ramsay, J. B.; and Popolato, A., "Analysis of Shock Wave and Initiation Data for Solid Explosives," *Proceedings of the Fourth Symposium (International) on Detonation*, 1965, pp 233-238.
13. Kershner, J. D.; and Mader, C. L., *2DE, A Two-Dimensional Continuous Eulerian Hydrodynamic Code for Computing Multicomponent Reactive Hydrodynamic Problems*, Los Alamos Scientific Laboratory Report LA-4846, 1972.
14. Gibbs, T. R.; and Popolato, A., (editors), *LASL Explosive Property Data*, University of California Press, Berkeley, 1980.
15. Wackerle, J.; Rabie, R. L.; Ginsberg, M. J.; and Anderson, A. B., "A Shock Initiation Study of PBX-9404," *Symposium on High Dynamic Pressures*, Paris, 1978.
16. Weingart, R. C.; Jackson, R. K.; Honodel, C. A.; and Lee, R. S., "Shock Initiation of PBX-9404 by Electrically Driven Flyer Plates," *Propellants and Explosives*, Vol. 5, 1980, pp. 158-162.
17. Setchell, R. E., "Ramp-Wave Initiation of Granular Explosives," *Combustion and Flame*, Vol. 43, 1981, pp. 255-264.
18. Howe, P. M.; Frey, R. B.; Taylor, B. C.; and Boyle, V. M., "Shock Initiation and the Critical Energy Concept," *Proceedings of the Sixth Symposium (International) on Detonation*, 1976, pp. 11-19.
19. Wackerle, J.; and Anderson, A. B., "Burning Topology in the Shock-Induced Reaction of Heterogeneous Explosives, *Shock Waves in Condensed Matter*, J. R. Asay, R. A. Graham, G. K. Straub (editors) Elsevier Science Publishers B. V., 1984.
20. Starkenberg, J., "A Model for the Initiation of Heterogeneous High Explosives Subject to General Compressive Loading," *Proceedings of the Ninth Symposium (International) on Detonation*, 1989, pp. 604-617.

## THE CALCULATION OF THE CONSTANTS FOR THE FOREST FIRE MODEL

D. Liang, W. J. Flis\*, and P. C. Chou  
Drexel University  
Philadelphia, PA 19104

\*Dyna East Corporation  
3201 Arch Street, Philadelphia, PA 19104

A numerical approach has been developed for computing the constants of the Forest Fire reaction-rate model following both the original Forest-Mader<sup>1,2</sup> approach and the Lundstrom<sup>3</sup> approach. The Mie-Grüneisen and JWL equations of state are used in this approach because data are available for many explosives. The calculations are carried out for PBX-9404 explosive using both approaches and different Hugoniot. The computed results reveal only a very small difference in predicted reaction rates between the two different assumptions of reaction (Forest-Mader) and no reaction (Lundstrom) across the shock front. Results also show little effect of using different Hugoniot (nonreactive, reactive, or adjusted to pass through the C-J point) on the calculated rate. Therefore one can choose either the Forest-Mader or Lundstrom approach and use any reasonable Hugoniot available.

### INTRODUCTION

The Forest Fire reaction rate model is developed originally by Forest<sup>2</sup> and Mader,<sup>1</sup> based on the assumption of single curve build-up and square wave. The HOM equation of state, reactive Hugoniot ( $U_s-U_p$ ) and Pop plot were used in their model to develop the reaction rate constants. In this original model, the chemical reaction takes place across the shock front, that is, the burn fraction on the shock front changes with shock pressure.

Lundstrom,<sup>3</sup> assuming no reaction on the shock front, proposed another approach. He uses only the HOM equation of state and Pop plot to generate rate constants. The reactive Hugoniot is no longer needed. How much these different assumptions, reaction and no reaction on the shock front, will affect the calculated reaction rate remains to be answered.

Both the Forest and Lundstrom approaches require a nonreactive Hugoniot for the HOM equation of state of the unreacted explosive. The Forest approach needs also a reactive Hugoniot. How or where do we get these Hugoniot? What is the experimental Hugoniot, is it reactive or nonreactive? There is no clear answer for these questions. But one thing that may help and can be easily done is to check how sensitive is the predicted reaction rate to these Hugoniot. If it is not, then we can safely use any one available

The Forest Fire model has been very successful in the simulation of many practical problems. But its application has been limited to only a few explosives because

of the unavailability of reaction rate constants. This could be due to the lack of constants for the HOM equation of state and Pop plot, or due to the difficulty in the derivation and calculation. A clarified numerical approach for calculating rate constants is needed and the most available equations of state should be selected for both unreacted and reacted explosive. We think that the Mie-Grüneisen and JWL equations of state are the best choice, because data are available for most explosives.

We shall briefly discuss the Forest and Lundstrom approaches first, and then present our numerical approach for calculating reaction rate at different shock pressure, following both Forest and Lundstrom and using the Mie-Grüneisen and JWL equations of state. A least-squares technique for developing constants in the exponential form of the Forest Fire model from computed data of rate versus pressure will also be presented. The calculated results for PBX-9404 and the conclusions based on them will be discussed in the last two sections.

### FOREST'S APPROACH

Forest and Mader calculated the constants of the Forest Fire model using the HOM equation of state, the experimentally determined (reactive) shock Hugoniot, and the Pop plot, under the assumptions of single-curve build-up and square wave. They described the Forest Fire model in a system of Lagrangian mass-time ( $m$ ,  $\tau$ ) coordinates. Their governing equations are

$$U_\tau = -P_m \quad (1)$$

$$V_\tau = U_m \quad (2)$$

$$E_\tau = -PV_\tau \quad (3)$$

where subscripts denote partial derivatives. Equation (3) is suitable for nonreactive flow. We modified it by adding a term,

$$E_\tau = -PV_\tau - QW_\tau \quad (4)$$

where  $Q$  is the chemical energy per unit mass. The terms on the right-hand side denote the pressure work and the chemical energy release, respectively.

The general form of the equation of state is

$$P = P(V, E, W) \quad (5)$$

where  $W$  is the mass fraction of unburned explosive. Differentiation yields

$$P_\tau = P_V V_\tau + P_E E_\tau + P_W W_\tau \quad (6)$$

where  $P_V$ ,  $P_E$ , and  $P_W$  are known for a given equation of state, and can be numerically, and sometimes analytically, computed along the shock line. The other three derivatives,  $P_\tau$ ,  $V_\tau$ ,  $E_\tau$ , can also be calculated along the shock line. Therefore,  $W_\tau$  can be found numerically. Forest computed  $W_\tau$  on the shock as a function of shock pressure and extended it to the region behind the shock as a function of local pressure. The derivation is outlined below. Let  $m_s(\tau)$  be the mass position of the shock front; therefore  $dm_s(\tau)/d\tau = \rho_o U_s$ , where  $U_s$  is the shock velocity and

$$\begin{aligned} \dot{P}_1 &= \frac{dP[m_s(\tau), \tau]}{d\tau} = P_\tau + \\ &+ P_m \frac{dm_s(\tau)}{d\tau} = P_\tau + \rho_o U_s P_m \end{aligned} \quad (7)$$

$$\begin{aligned} \dot{U}_1 &= \frac{dU[m_s(\tau), \tau]}{d\tau} = U_\tau + \\ &+ U_m \frac{dm_s(\tau)}{d\tau} = -P_m + \rho_o U_s U_m \end{aligned} \quad (8)$$

where subscript 1 denotes parameters just behind the shock front. The two unknowns on the left-hand sides of Eqs. (7) and (8) can be computed from the Pop plot, which is of the form

$$\ln X = A + B \ln P \quad (9)$$

where  $X$  is the run distance,  $P$  is the initial shock pressure, and  $A$  and  $B$  are constants. Also needed are the jump conditions across the shock,

$$P_1 = U_s U_1 / V_o \quad (10)$$

$$V_1 U_s = V_o (U_s - U_1) \quad (11)$$

$$\begin{aligned} E_1 &= P_1 (V_o - V_1) / 2 + Q (1 - W_1) \\ &= U_1^2 / 2 + Q (1 - W_1) \end{aligned} \quad (12)$$

and the experimental Hugoniot,

$$U_s = C + s U_1 \quad (13)$$

The first term in the right-hand side of Eq. (12) is the pressure work, and the second term, which we have added, is the chemical energy released.

Differentiating Eq. (9) along the shock line yields

$$\dot{P}_1 = \frac{dP_1}{dx} \frac{dx}{d\tau} = -U_s \frac{dP_1}{dX} = -\frac{U_s P_1}{BX} \quad (14)$$

Now, from Eqs. (10), (11), and (13), we get

$$P_1 = \rho_o U_s U_1 = \rho_o (C + s U_1) U_1, \text{ therefore}$$

$$\dot{U}_1 = \frac{\dot{P}_1}{\rho_o (C + 2s U_1)} \quad (15)$$

Substituting Eqs. (14) and (15) into (7) and (8), respectively, and assuming  $P_m = 0$  (the square-wave assumption), we obtain

$$P_\tau = \dot{P}_1 = -\frac{U_s P_1}{BX} \quad (16)$$

$$V_\tau = U_m = \frac{\dot{P}_1}{\rho_o^2 U_s (C + s U_1)} \quad (17)$$

Substituting Eqs. (4), (16), and (17) into (6), we get

$$W_\tau = \left[ \frac{P_V - P_1 P_E}{\rho_o^2 (C + 2s U_1)} - U_s \right] \frac{P_1}{(P_w + P_E Q) B X} \quad (18)$$

## LUNDSTROM'S APPROACH

By assuming no reaction on the shock front, Lundstrom<sup>3</sup> proposed a new method to calculate reaction rate without using the reactive shock Hugoniot. According to the hot-spot-initiation concept, only a very small amount of explosive burns on the shock front. Thus, the assumption of a nonreactive shock front is consistent with this concept.

Along the shock line, then,  $W_1=1$ , so that the equation of state becomes

$$P_1 = P(V_1, E_1, W_1=1) \quad (19)$$

Note that in Forest's approach above,  $W_1$  does not remain constant along the shock, but decreases with shock

pressure  $P_1$ , decreasing to zero when  $P_1$  reaches the C-J value,  $P_{CJ}$ .

Differentiating Eq. (19) and considering Eq. (12), we get

$$\dot{P}_1 = P_V \dot{V}_1 + P_E \dot{E}_1 = P_V \dot{V}_1 + P_E U_1 \dot{U}_1 \quad (20)$$

Combining Eqs. (10) and (11) to eliminate  $U_s$  and then differentiating the resulting equation, we get

$$(V_o - V_1) \dot{P}_1 - P_1 \dot{V}_1 = 2U_1 \dot{U}_1 \quad (21)$$

Combining Eqs. (20) and (21) can eliminate  $V_1$ , to yield

$$\dot{U}_1 = \frac{P_1 - (V_o - V_1)P_V}{(P_1 P_E - 2P_V)U_1} \dot{P}_1 \quad (22)$$

Functionally, this equation is equivalent to Eq. (15). Note, however, that while Eq. (15) is based on a reactive Hugoniot, this equation is based on the assumption that no reaction takes place on the shock front.

Using Eq. (22) instead of (15), and following a similar procedure as for Forest's approach, we can get the reaction-rate equation,

$$W_\tau = \left\{ \frac{[P_1 - P_V(V_o - V_1)](P_V - P_1 P_E)}{P_1(P_1 P_E - 2P_V)} - 1 \right\} \times \frac{U_s P_1}{(P_W + P_E Q) B X} \quad (23)$$

## EQUATIONS OF STATE AND MIXTURE RULE

Both reacted and unreacted phases are modeled, each by an independent equation of state, connected by a mixture rule.

For the unreacted phase of explosive, we use the Mie-Grüneisen equation of state,

$$P_s = (K_1 \mu_s + K_2 \mu_s^2 + K_3 \mu_s^3)(1 - 0.5 \Gamma_o \rho_o V_s \mu_s) + \Gamma_o \rho_o E_s \quad (24)$$

where  $\mu_s = V_o / V_s - 1$ ,  $E_s$  is the internal energy per unit mass, and constants  $K_1$ ,  $K_2$  and  $K_3$  may be computed from the nonreactive Hugoniot  $U_s = C_n + s_n U_1$ ,

$$K_1 = \rho_o C_n^2 \quad (25)$$

$$K_2 = [1 + 2(s_n - 1)] K_1 \quad (26)$$

$$K_3 = [2(s_n - 1) + 3(s_n - 1)^2] K_1 \quad (27)$$

The Grüneisen coefficient  $\Gamma_o$  may be calculated from the identity

$$\Gamma_o = \frac{\alpha K_1}{\rho_o C_v} \quad (28)$$

where  $\alpha$  is the cubic thermal expansion coefficient,  $K_1$  is the bulk elastic modulus, and  $C_v$  is the specific heat at constant volume.

The Jones-Wilkins-Lee (JWL) equation of state is used for the explosive reaction products,

$$P_g = A \left( 1 - \frac{\omega V_o}{R_1 V_g} \right) \exp(-R_1 \frac{V_g}{V_o}) + B \left( 1 - \frac{\omega V_o}{R_2 V_g} \right) \exp(-R_2 \frac{V_g}{V_o}) + \frac{\omega E_g}{V_g} \quad (29)$$

where  $A$ ,  $B$ ,  $R_1$ ,  $R_2$ , and  $\omega$  are material constants, and  $E_g$  is internal energy per mass.

We use the mixture rule,

$$V = W V_s + (1 - W) V_g \quad (30)$$

$$E = W E_s + (1 - W) E_g \quad (31)$$

$$P = P_s = P_g \quad (32)$$

Temperature equilibrium is not enforced; instead, we use the following equation in the region near the shock front,

$$E_g = E_s + Q \quad (33)$$

This is equivalent to neglecting heat transfer between the two phases.

## NUMERICAL PROCEDURE FOR FOREST'S APPROACH

Forest calculated the reaction rate on the shock front numerically.

The equation of state on the shock front can be expressed as

$$P_1 = P(V_1, E_1, W_1) \quad (34)$$

There are six unknowns ( $P_1$ ,  $U_s$ ,  $U_1$ ,  $V_1$ ,  $E_1$ ,  $W_1$ ) in five equations, (10-13 and 34). Given  $P_1$ , we can find  $U_s$ ,  $U_1$ , and  $V_1$  from Eqs. (10), (11), and (13), and get  $W_1$  and  $E_1$  from Eqs. (34) and (12). To calculate  $W_1$ , iteration and the mixture rule are needed.



Knowing  $P_1$ ,  $U_s$ ,  $U_1$ ,  $V_1$ ,  $E_1$  and  $W_1$ , one can numerically obtain  $P_V$ ,  $P_E$ , and  $P_W$  easily from the equation of state and mixture rule. For example, by holding  $E_1$  and  $W_1$  unchanged, increasing  $V_1$  to  $V_1 + \Delta V_1$ , and using the equation of state and mixture rule, we can get a new pressure which changes, say, from  $P_1$  to  $P_1 + \Delta P_1$ , and then get  $P_V = \Delta P_1 / \Delta V_1$ . Similarly,  $P_E$  and  $P_W$  can be obtained.

Substituting  $P_1$  and the obtained values of  $U_s$ ,  $U_1$ ,  $P_V$ ,  $P_E$ ,  $P_W$  into Eq. (18), we get a value of  $W_\tau$  corresponding to the given pressure of  $P_1$ . Changing  $P_1$ , we can obtain a set of data in the  $W_\tau$ - $P_1$  plane and a reaction-rate equation  $W_\tau = f(P_1)$  by fitting these data.

This procedure clearly shows that the reaction rate is calculated on the shock front. But, practically, it is used in the whole flow field with local pressure instead of shock pressure.

On the shock front, the equations of state can be expressed as

$$P_s = (K_1 \mu_{s1} + K_2 \mu_{s1}^2 + K_3 \mu_{s1}^3) \times (1 - 0.5 \Gamma_o \rho_o V_{s1} \mu_{s1}) + \Gamma_o \rho_o E_{s1} \quad (35)$$

$$P_g = A \left(1 - \frac{\omega V_o}{R_1 V_{g1}}\right) \exp(-R_1 \frac{V_{g1}}{V_o}) + B \left(1 - \frac{\omega V_o}{R_2 V_{g1}}\right) \exp(-R_2 \frac{V_{g1}}{V_o}) + \frac{\omega E_{g1}}{V_{g1}} \quad (36)$$

Combining Eqs. (12), (31) and (33) yields

$$E_{s1} = U_1^2 / 2 \quad (37)$$

$$E_{g1} = U_1^2 / 2 + Q \quad (38)$$

Substituting Eqs. (37) and (38) into Eqs. (35) and (36), respectively, yields

$$P_s = (K_1 \mu_{s1} + K_2 \mu_{s1}^2 + K_3 \mu_{s1}^3) \times (1 - 0.5 \Gamma_o \rho_o V_{s1} \mu_{s1}) + \Gamma_o \rho_o U_1^2 / 2 \quad (39)$$

$$P_g = A \left(1 - \frac{\omega V_o}{R_1 V_{g1}}\right) \exp(-R_1 \frac{V_{g1}}{V_o}) + B \left(1 - \frac{\omega V_o}{R_2 V_{g1}}\right) \exp(-R_2 \frac{V_{g1}}{V_o}) + \frac{\omega (U_1^2 / 2 + Q)}{V_{g1}} \quad (40)$$

Knowing  $P_s = P_g = P_1$  and  $U_1$ , we can get  $V_{s1}$  and  $V_{g1}$  from Eqs. (39) and (40), respectively, by linearly inter-

polative iteration, then get  $W_1$  by Eq. (30) and  $E_1$  by Eq. (12).

Given  $P_1$ ,  $U_s$ ,  $U_1$ ,  $V_1$ ,  $E_1$  and  $W_1$ , we first compute  $P_V$ ,  $P_E$ ,  $P_W$ , and then calculate  $W_\tau$  by substituting  $P_1$ ,  $U_s$ ,  $U_1$ ,  $P_V$ ,  $P_E$  and  $P_W$  into Eq. (18).

Changing  $V_1$  to  $V_1 + \Delta V_1$ , and calculating the new pressure by solving Eqs. (30), (32), (39), and (40), we can get  $P_V = \Delta P_1 / \Delta V_1$ .

By changing  $E_1$  a little, say  $\Delta E_1 = 0.001 E_1$ , then from Eqs. (31) and (33) we can get

$$E_{s1} = U_1^2 / 2 + \Delta E_1 \quad (41)$$

$$E_{g1} = U_1^2 / 2 + Q + \Delta E_1 \quad (42)$$

Substituting these two equations into Eqs. (35) and (36), we get

$$P_s = (K_1 \mu_1 + K_2 \mu_1^2 + K_3 \mu_1^3) \times (1 - 0.5 \Gamma_o \rho_o V_{s1} \mu_1) + \Gamma_o \rho_o (U_1^2 / 2 + \Delta E_1) \quad (43)$$

$$P_g = A \left(1 - \frac{\omega V_o}{R_1 V_{g1}}\right) \exp(-R_1 \frac{V_{g1}}{V_o}) + B \left(1 - \frac{\omega V_o}{R_2 V_{g1}}\right) \times \exp(-R_2 \frac{V_{g1}}{V_o}) + \frac{\omega (U_1^2 / 2 + Q + \Delta E_1)}{V_{g1}} \quad (44)$$

Solving Eqs. (30), (32), (43), and (44) yields the pressure change  $\Delta P$  and  $P_E = \Delta P / \Delta E_1$ .

Changing  $W_1$  to  $W_1 + \Delta W_1$ , solving Eqs. (30), (32), (39), and (40), we can get  $\Delta P$  and  $P_W = \Delta P / \Delta W_1$ .

## NUMERICAL PROCEDURE FOR LUNDSTROM'S APPROACH

Lundstrom also calculated the reaction rate on the shock front. He did not use the reactive Hugoniot, but instead assumed no reaction on the shock front regardless of shock strength. Therefore, along the shock line,  $W_1$  becomes a constant of 1 and the equation of state reduces to Eq. (19). So there are five unknowns ( $P_1$ ,  $U_s$ ,  $U_1$ ,  $V_1$ ,  $E_1$ ) and four equations (10-12 and 19).

Considering  $W_1 = 1$ , we have

$$P_1 = (K_1 \mu_1 + K_2 \mu_1^2 + K_3 \mu_1^3) \times (1 - 0.5 \Gamma_o \rho_o V_1 \mu_1) + \Gamma_o \rho_o E_1 \quad (45)$$

Substituting Eq. (12) into Eq. (45), we further get

$$(K_1\mu_1 + K_2\mu_1^2 + K_3\mu_1^3)(1 - 0.5\Gamma_0\rho_0V_1\mu_1) - 0.5\Gamma_0\rho_0P_1V_1 = (1 - 0.5\Gamma_0)P_1 \quad (46)$$

For a given  $P_1$ ,  $V_1$  can be obtained by iterating on Eq. (46), and then  $E_1$  and  $U_1$  by Eq. (12), and finally  $U_s$  by Eq. (10).

To calculate  $P_V$ , first increase  $V_1$  to  $V_1 + \Delta V_1$ , then return to Eq. (45) to calculate  $\Delta P_1$ . Determination of  $P_E$  is trivial since it is clear from Eq. (45) that  $P_E = \Gamma_0\rho_0$ , a constant. Calculating  $P_W$  is the same as in the Forest approach: first decrease  $W_1$  a little, then solve Eqs. (30), (32), (39), and (40) to calculate  $\Delta P$ .

## CALCULATION OF COEFFICIENTS OF REACTION RATE EQUATION

After getting a set of data of  $W_\tau$  and  $W_1$  versus  $P_1$  by either of the above procedures, we use the least-squares method to fit these data to a reaction-rate equation in exponential form,

$$\begin{aligned} W_\tau &= W \exp(a_0 + a_1P + a_2P^2 + \dots + a_{n-1}P^{n-1}) \\ &= W \exp\left(\sum_{j=0}^{n-1} a_j P^j\right) \end{aligned} \quad (47)$$

This is the first-order Forest Fire reaction-rate equation. To determine coefficients  $a_j$  by least squares, we take the logarithm of Eq. (47),

$$\ln(W_\tau / W)_i = \sum_{j=0}^{n-1} a_j P_i^j \quad (48)$$

For each set of  $N$  data ( $N \geq n$ ) to be fitted, we calculate

$$Z_i = \ln(W_{1\tau} / W_1)_i \quad (i = 1, 2, \dots, N) \quad (49)$$

and

$$Y_i = \sum_{j=0}^{n-1} a_j P_i^j \quad (i = 1, 2, \dots, N)$$

Then the sum of the squares of the differences between the values predicted with Eq. (48) and those to be fitted is

$$\Delta^2 = \sum_{i=1}^N (Y_i - Z_i)^2 \quad (50)$$

Constants  $a_j$  are determined by solving simultaneously the equations,

$$\frac{\partial \Delta^2}{\partial a_k} = \sum_{i=1}^N 2(Y_i - Z_i) \left(\frac{\partial Y}{\partial a_k}\right)_i = \sum_{i=1}^N 2(Y_i - Z_i) P_i^k = 0$$

or

$$\sum_{i=1}^N \left( \sum_{j=0}^{n-1} a_j P_i^j - Z_i \right) P_i^k = 0 \quad (k = 0, 1, \dots, n-1)$$

This set of equations can be changed into

$$\sum_{j=0}^{n-1} a_j \sum_{i=1}^N P_i^{j+k} + \sum_{i=1}^N Z_i P_i^k = 0 \quad (k = 0, 1, \dots, n-1) \quad (51)$$

These comprise  $n$  linear equations in  $n$  unknown coefficients, easily solved by computer.

For the zero-order Forest Fire model, Eqs. (47), (48), and (49) have the following corresponding forms,

$$\begin{aligned} W_\tau &= \exp(a_0 + a_1P + a_2P^2 + \dots + a_{n-1}P^{n-1}) \\ &= \exp\left(\sum_{j=0}^{n-1} a_j P^j\right) \end{aligned} \quad (52)$$

$$Y_i = \sum_{j=0}^{n-1} a_j P_i^j \quad (i = 1, 2, \dots, N) \quad (53)$$

$$Z_i = \ln(W_{1\tau})_i \quad (i = 1, 2, \dots, N) \quad (54)$$

and the fitting procedure is exactly the same as described above for the first-order reaction-rate equations.

## COMPUTED RESULTS

Both Forest and Lundstrom calculated the reaction rate on the shock front, and extended the result to the region behind. Both used the Pop plot and made assumptions of single-curve build-up and square wave.

In the present studies, the nonreactive shock Hugoniot is needed for the Mie-Grüneisen equation of state. The reactive Hugoniot is also needed in Forest's method. But data of nonreactive and reactive Hugoniots of most explosives are not available. Experimental Hugoniots of most explosives are available, although these vary from source to source. But whether these experimentally measured Hugoniots should be taken as nonreactive or reactive is still open to question. Therefore, we have investigated the sensitivity of the reaction rate to the Hugoniots used in the calculation.

To demonstrate this problem, we take PBX-9404 explosive as an example. Its nonreactive and reactive Hugoniot were given by Mader<sup>1</sup> as

$$U_s = 2423 + 1.883 U_1 \quad (\text{m/s}) \quad (55)$$

$$U_s = 2460 + 2.530 U_1 \quad (\text{m/s}) \quad (56)$$

respectively. The second constant of Eq. (56) may also be adjusted to force the Hugoniot to pass through the C-J point,

$$U_s = 2460 + 2.774 U_1 \quad (\text{m/s}) \quad (57)$$

This equation can be obtained from the bulk sound speed and detonation velocity of the explosive and the adiabatic coefficient of expansion of the detonation products.

Calculated results with Eqs. (55-57) are shown in Figures 1 through 4. In these figures, the curves are marked "F" and "L" to denote Forest's and Lundstrom's approaches, respectively; "non", "exp", and "CJ" refer to the nonreactive (Eq. 55), experimental (Eq. 56), and adjusted (Eq. 57) Hugoniot, respectively. For example, L(exp) indicates that the result is calculated using Lundstrom's method with the experimental Hugoniot for the equation of state, while F(non-CJ) denotes Forest's method, the nonreactive Hugoniot for the equation of state, and the adjusted Hugoniot in the reaction-rate equation (18).

Figure 1 includes nine computed curves, F(non-CJ), F(non-exp), F(non-non), L(non), F(exp-exp), F(exp-CJ), L(exp), F(CJ-CJ) and L(CJ). The nonreactive Hugoniot is used for the equation of state in the first four curves. The experimental or adjusted one is used in the rest of the curves. Mader's data are also plotted in this figure. As it can be seen, these curves are very close to each other, especially in the low and middle pressure range. When the pressure goes up to about 0.2 Mbar they separate into two groups. The first group with slightly lower reaction rates are all calculated using the nonreactive Hugoniot for the equation of state. Mader used the nonreactive Hugoniot in his HOM equation of state, so his curve falls into this group. The curves in the second group with slightly higher reaction rates are computed with experimental or adjusted Hugoniot for the equation of state.

It is evident that different assumptions about the chemical reaction across the shock front and the use of different Hugoniot do not much affect the calculated reaction rate and pressure relation. The only appreciable differences are at high pressures, where they are of little practical significance, because our previous simulation with Forest Fire model<sup>4</sup> shows that when the shock pressure reaches about 0.07 Mbar, the turning point in Fig. 1, detonation will start and propagate.

Figure 2 shows the comparison between Mader's and our results with nonreactive Hugoniot for the equation of state. They are not far from each other.

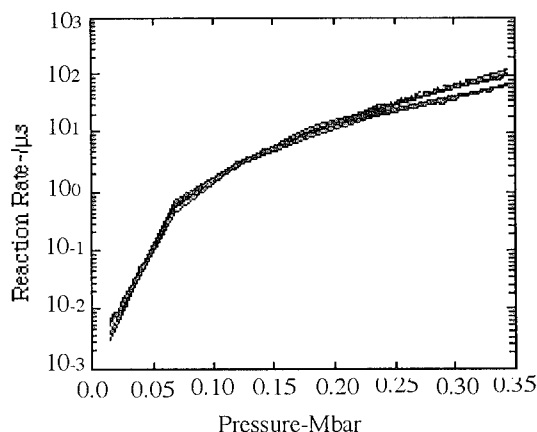


FIGURE 1. NINE COMPUTED CURVES AND MADER'S CURVE

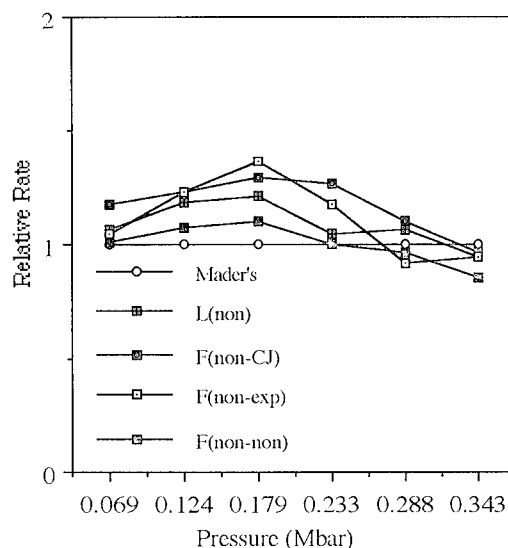


FIGURE 2. THE COMPARISON OF OUR RESULTS USING NONREACTIVE SHOCK HUGONIOT FOR THE EQUATION OF STATE WITH MADER'S DATA

The results calculated with experimental and adjusted Hugoniot for the equation of state are compared with Mader's data in Figures 3 and 4, respectively.

These results show that our calculated reaction rate increases with shock pressure faster than Mader's below about 0.18 Mbar but then slows down. It can also be seen that results based on different Hugoniot are not very different from one another or from Mader's data, especially at lower shock pressure.

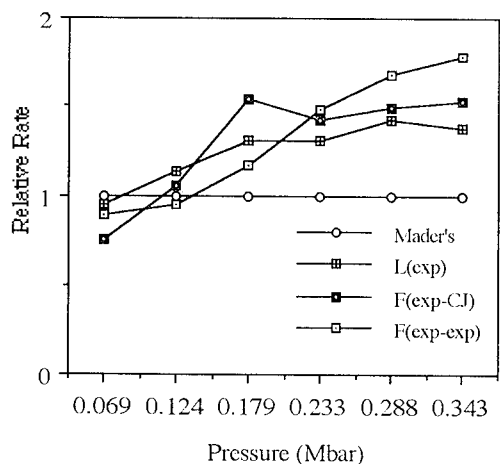


FIGURE 3. THE COMPARISON OF OUR RESULTS USING EXPERIMENTAL SHOCK HUGONIOT FOR THE EQUATION OF STATE WITH MADER'S DATA

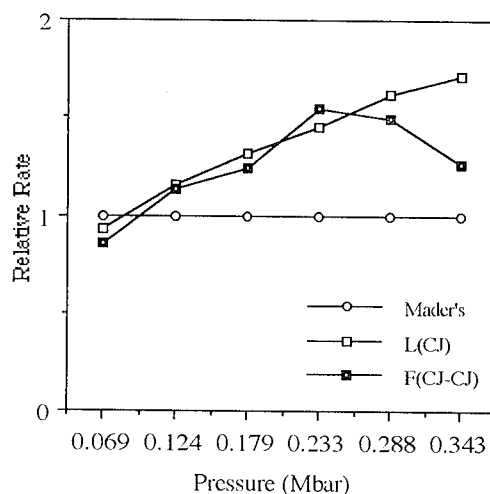


FIGURE 4. THE COMPARISON OF OUR RESULTS WITH ADJUSTED SHOCK HUGONIOT FOR THE EQUATION OF STATE WITH MADER'S DATA

## CONCLUSIONS

From the calculated results and the discussion above, we offer the following conclusions:

1. The Mie-Grüneisen and JWL equations of state can be properly combined to calculate Forest Fire constants.
2. Forest and Lundstroms' methods yield similar results. This indicates that assuming a reactive or nonreactive shock front makes little difference.
3. The choice of Hugoniot to use for Forest's rate equation (18) is not critical.
4. If the nonreactive Hugoniot is not available, the experimental or adjusted Hugoniot can be used for the equation of state.

## REFERENCES

1. Mader, C. L., "Numerical Simulation of Detonation", Univ. of California Press, 1979.
2. Forest, C. A., "Burning and Detonation," *Proc. of the Seventh Symposium (International) on Detonation*, 1981.
3. Lundstrom, E. A., "Evaluation of Forest Fire Burn Model of Reaction Kinetics of Heterogeneous Explosives," *NWC TP 6898*, Naval Weapons Center, China Lake, CA, 1988.
4. Chou, P. C.; Liang, D. and Flis, W. J., "Shock and Shear Initiation of Explosive," *Shock Waves*, No. 1, 1991, P. 285-292.

**INDEXES OF THE PROCEEDINGS FOR THE  
NINTH SYMPOSIUM (INTERNATIONAL)  
ON DETONATION, 1989**

**INDEXES OF THE PROCEEDINGS FOR  
THE NINTH SYMPOSIUM (INTERNATIONAL)  
ON DETONATION, 1989**

Sharon L. Crane, William E. Deal, John B. Ramsay,  
Alita M. Roach, and Bruce E. Takala\*

The *Proceedings* of the nine Detonation Symposia have become the major archival source of information of international research in explosive phenomenology, theory, experimental techniques, numerical modeling, and high-rate reaction chemistry. In many cases, they contain the original reference or the only reference to major progress in the field. For some papers, the information is more complete than the complementary article appearing in a formal journal; yet for others, authors elected to publish only an abstract in the *Proceedings*. For the large majority of papers, the Symposia *Proceedings* provide the only published reference to a body of work. This report indexes the Ninth *Proceedings* of the Detonation Symposia by paper titles, topic phrases, authors, and first appearance of acronyms and code names.

## INTRODUCTION

The indexes comprise four parts: a listing of the paper titles and authors in order of appearance in the Ninth Symposium *Proceedings*, an alphabetical listing of topic phrases, an index of all authors, and an index to first appearance of acronyms and code names of compositions and components that are defined. Each index also lists the page number of the Ninth Symposium. {Editor's note: *The authors provided a paper containing the complete indexes of all the first nine Symposia.*<sup>1</sup> Unfortunately, space limitations allow only the indexes for the Ninth Symposium to be published here. *Indexes of the first eight symposia were published in the ninth symposium.*<sup>2</sup>}

---

\*Major, US Army

## TITLES INDEX

In this first index, the chronological order of the papers is preserved, beginning with the first paper presented. We list the page number, paper title, co-authors, and nation of the first author.

## TOPIC PHRASE INDEX

Here we list topic phrases alphabetically with reference to the page number. We considered using key words, which are cryptic and more mnemonic, rather than the longer and more descriptive topic phrases, but we decided on the latter because they provide more information for selecting the correct reference. The compilers have used their own judgment in selecting and defining the topic phrases and

hope that the phrases are self-explanatory. At the present time, a significant cross-referencing capability is lacking within the index, and users are cautioned to check several different possible topics when searching.

## AUTHOR INDEX

This index is a simple listing of all authors, giving the page number references. All except family names were contracted to initials. We have attempted to combine different presentations of an author's name (e.g., J. Ramsay and J. B. Ramsay) into a uniform entry. Please notify the compilers of any errors.

## ACRONYM AND CODE NAME INDEX

This index is an attempt to cite the *first use* of an acronym or code name for neat explosives, ingredients, and formulations, for which a definition of the term is also provided.

Many explosive compounds and compositions are named as a contraction of the chemical name (e.g., PSF); for others, the history of the name is lost in research laboratories (e.g, HMX ); and others have no relationship to the composition (e.g., TS3659).

A large number of papers within the first nine Symposia *Proceedings* refer to compositions only by acronym or code name, with no formal definition of composition. Composition B (Comp B) is cited in many papers, yet at least 10 citations for Composition B provide similar but different compositions. Also, in some instances, the same explosive compound was defined by three or more different acronyms.

We intended that each citation be the earliest reference within the Ninth *Proceedings* to the use of the acronym coupled with a meaningful chemical definition. Errors in finding and entering the citations may have occurred. If readers detect errors, please contact one of the authors.

## REFERENCES

1. Crane, S.L., Deal, W.E., Ramsay, J.B., Roach, A.M., and Takala, B.E., *Indexes of the Proceedings for The Nine Symposia (International) On Detonation, 1951-89*, LAUR 93-2237, Los Alamos National Laboratory, Los Alamos, NM 87545.
2. Crane, S.L., Deal, W.E., Ramsay, J.B., and Takala, B.E., "Indexes for the Proceedings of the Symposia (International) On Detonation - 1951 Through 1989," *Proceedings of the Ninth Symposium (International) on Detonation*, Portland, Oregon, August 28 - September 1, 1989, p.1543.

# TITLES INDEX - NINTH SYMPOSIUM

<u>Page</u>		<u>Page</u>	
3	<b>Combined Pressure Shear Ignition of Explosives;</b> V. Boyle, R. Frey, and O. Blake; USA	123	<b>Initiation and Detonation Properties of the Insensitive High Explosive TATB/Kel-F 8009 5/5;</b> C. D. Hutchinson, G. C. W. Foan, H. R. Lawn, and A. G. Jones; UK
18	<b>Particular Aspect of the Explosive Particle Size Effect on Shock Sensitivity of Cast Formulations;</b> H. Moulard; France	133	<b>Fabry Perot Velocimetry on Detonating LX-17 in Planar and Spherically Divergent Geometries;</b> K. L. Bahl, R. D. Breithaupt, C. M. Tarver, and W. G. Von Holle; USA
25	<b>Particle Size Effects in the Initiation of Explosives Containing Reactive and Non-Reactive Continuous Phases;</b> R. L. Simpson, F. H. Helm, P. C. Crawford, and J. W. Kury; USA	142	<b>Reaction Rates of PBH-9D Explosive;</b> Zhao Feng, Sun Chengwei, Sun Peiqi, and Ouyaqng Denghuan; China (PRC)
39	<b>In-Situ Study of the Chemically Driven Flow Fields in Initiating Homogeneous and Heterogeneous Nitromethane Explosives;</b> S. A. Sheffield, and R. Engelke, and R. R. Alcon; USA	153	<b>Pulsed-Laser-Excited Raman Spectra of Shock-Compressed Triaminotrinitrobenzene;</b> W. M. Trott, and A. M. Renlund; USA
50	<b>Decomposition of High Explosives in Shock and Detonation Waves;</b> V. Fortov, G. I. Kanel, T. N. Fortova, S. I. Malyrenko, and A. V. Utkin; USSR	162	<b>Laser Ignition of Explosives: A Mass Spectroscopic Study of the Pre-Ignition Reaction Zone;</b> H. Nilsson and H. Östmark; Sweden
58	<b>Initiation of Explosive Crystals by Shock or Impact;</b> C. S. Coffey; USA	172	<b>The Use of Time-Resolved Spectrometries in the Study of Initiation of Explosives at Molecular Level;</b> A. E. Delpuech; France
66	<b>Initiation Threshold of High Explosives in Small Flyer Plate Experiments;</b> H. R. Kleinhan, F. Lungenstra, and H. Zöellner; Germany	180	<b>Vibrational Spectroscopic Investigations of Shock-Compressed Liquid Nitrogen and Shock-Compressed Liquid Nitromethane;</b> D. S. Moore and S. C. Schmidt; USA
77	<b>A Two-Dimensional Lagrangian Technique for Shock Initiation Diagnosis;</b> Huan Shi and Ding Jing; China (PRC)	190	<b>Absorption Spectroscopy of Shocked Benzene;</b> N. C. Holmes, G. Otani, P. McCandless, and S. F. Rice; USA
83	<b>Influence of RDX Crystal Shape on the Shock Sensitivity of PBXs;</b> A. C. van der Steen, H. J. Verbeek, and J. J. Meulenbrugge; Netherlands	197	<b>Reaction Rates and the Charge Diameter Effect in Heterogeneous Explosives;</b> G. A. Leiper and J. Cooper; UK
89	<b>A Lagrange Gauge Study of the Shock Initiation Process in an Intermolecular Explosive EAK;</b> M. Cowperthwaite, J. T. Rosenberg, and A. G. Taliancich; USA	209	<b>A Shock Initiation Model for Fine-Grained Hexanitrostilbene;</b> M. E. Kipp and R. E. Setchell; USA
98	<b>Anomalous Shock Sensitivity/Density Relationship for Pressed Booster Explosives from a Small-Scale Gap Test;</b> R. J. Spear and V. Nanut; Australia	219	<b>A Theoretical Picture of Shock-to-Detonation Transition in a Homogeneous Explosive;</b> A. K. Kapila and J. W. Dold; USA and France
112	<b>Shock Initiation of LX-17 as a Function of Its Initial Temperature;</b> P. A. Urtiew, L. M. Erickson, D. F. Aldis, and C. M. Tarver; USA	228	<b>Chemical Phenomena Associated with the Initiation of Thermal Explosions;</b> T. B. Brill and P. J. Brush; USA
		235	<b>The Lattice Density of States Concept and Its Role in Determining the Shock Sensitivity of PETN and Nitromethane;</b> R. D. Bardo; USA
		246	<b>Unified Formulation of the Reactivity of Condensed Explosives;</b> R. Cheret; France



# TITLES INDEX (Cont.) - NINTH SYMPOSIUM

<u>Page</u>		<u>Page</u>	
250	<b>The Choice Problem of Equation Determining the Condensed Reacting Media Characteristics in Numerical Modeling of Shock Processes;</b> V. S. Trofimov; USSR	396	<b>The Measurement of Electrical Conductivity in Detonating Condensed Explosives;</b> D. G. Tasker and R. J. Lee; USA
252	<b>Global Calibration of Constitutive Relationships in Explosive Reaction Zone;</b> Huan Shi and Ding Jing; China (PRC)	407	<b>Synthesis of Ultrafine Diamonds in Detonation Waves;</b> V. M. Titov, V. F. Anischkin, and I. Yu. Mal'kov; USSR
259	<b>DDT--Determination of the Successive Phases of Phenomena;</b> M. Samirant; France	417	<b>Carbon in Detonations;</b> J. D. Johnson; USA
265	<b>Deflagration to Detonation in Granular HMX;</b> J. M. McAfee, B. W. Asay, A. W. Campbell, and J. B. Ramsay; USA	425	<b>Phase Changes in Carbon and Nitrogen Systems: Their Effects on the Detonation Properties of High Explosives;</b> F. H. Ree and M. van Thiel; USA
280	<b>Model Calculations and Experimental Measurements of the Response of HMX Porous Beds to Deflagration and Shock;</b> D. F. Aldis, E. L. Lee, R. L. Simpson, and A. M. Weston; USA	435	<b>The Detonation Parameters of New Powerful Explosive Compounds Predicted with a Revised VLW Equation of State;</b> Wu Xiong, Sun Jian, and Xiao Lianjie; China (PRC)
293	<b>Compressive Combustion of Granular Materials Induced by Low-Velocity Impact;</b> M. R. Baer and J. W. Nunziato; USA	443	<b>Theoretical Model of Explosive Detonation Products: Tests and Sensitivity Studies;</b> G. I. Kerley; USA
306	<b>Compaction Wave Acceleration in Granular Energetic Material: Simulation with a Reactive Shock Wave Model;</b> D. E. Kooker; USA	452	<b>A New Simulation Method for the Efficient Calculation of Benchmarks for Detonation Products Equations of State;</b> M. S. Shaw; USA
320	<b>Combined Experimental and Theoretical Investigations into the Deflagration-to-Detonation Transition;</b> H. J. Verbeek and A. C. van der Steen; Netherlands	461	<b>Calculations of Detonation Pressures for a Homologous Series of Polynitroaliphatic Explosives Using a Fluid Perturbation Equation of State and a New Chemical Equilibrium Computer Program;</b> F. J. Zerilli and H. D. Jones; USA
329	<b>Numerical Simulation of Deflagration-to-Detonation Transition for TS 3659 Propellants;</b> T. Hsieh and K. Kim; USA	471	<b>A Detonation Pressure Measurement System Employing High Resistance Manganin Foil Gauge;</b> S. Y. Song and J. W. Lee; Korea
341	<b>Dynamic Compaction and Compressive Reaction Studies for Single and Double-Base Ball Propellants;</b> B. C. Glancy, H. W. Sandusky, P. J. Miller, and A. D. Krall; USA	478	<b>Heat of Detonation, the Cylinder Test, and Performance in Munitions;</b> I. B. Akst; USA
354	<b>DDT Studies of a High Energy Spherical Ball Propellant;</b> R. R. Bernecker; USA	489	<b>Theoretical Prediction of High Explosives Efficiency: Application to NTO;</b> F. Bugaut, S. Bernard, and R. Chirat; France
363	<b>An Improved Model of the Deflagration-to-Detonation Transition in Porous Beds;</b> C. F. Price, A. I. Atwood, and T. L. Boggs; USA	498	<b>Determining JWL Equation of State Parameters Using the Gurney Equation Approximation;</b> P. J. Miller and K. E. Alexander; USA
379	<b>Shock Behavior of Explosives about the C-J Point;</b> P. W. Cooper; USA	506	<b>Studies about the Equations of State of the Detonation Products;</b> N. Carion, J. Aveille, P. Andriot, F. Chaisse, G. Guri, M. T. Kerihuel, and M. Leroy; France
388	<b>Electrically Enhanced Detonation and Equations of State for Detonation Products;</b> M. Cowperthwaite; USA	513	<b>Sensitivites of Adiabatic and Grüneisen Gammas to Errors in Molecular Properties of Detonation Products;</b> W. Byers Brown and M. Braithwaite; UK

# TITLES INDEX (Cont.) - NINTH SYMPOSIUM

<u>Page</u>		<u>Page</u>	
525	<b>Reactive Flow Measurements and Calculations of <math>ZrH_2</math>-Based Composite Explosives;</b> M. J. Murphy, R. L. Simpson, R. D. Breithaupt, and C. M. Tarver; USA	641	<b>The Fundamentals of Metal Combustion in Composite Explosives Revealed by High Speed Microphotography;</b> W. C. Tao, A. M. Frank, R. E. Clements, and J. E. Shepherd; USA
537	<b>Detonation Characteristics of Gun Propellants;</b> B. W. Asay, A. W. Campbell, M. J. Ginsberg, and J. B. Ramsay; USA	657	<b>Detonation Reaction-Zone Structure for PBX 9502;</b> W. L. Seitz, H. L. Stacy, R. Engelke, P. K. Tang, and J. Wackerle; USA
545	<b>Detonation Properties of Mixtures of HMX and Emulsion Explosives;</b> J. D. Renick, P. A. Persson, and J. A. Sanchez; USA	670	<b>Reaction Zone Structure in Supracompressed Detonating Explosives;</b> L. G. Green, C. M. Tarver, and D. J. Erskine; USA
554	<b>The Prospects for Composite Explosive;</b> Guo Yuxian; China (PRC)	683	<b>Lagrangian Analysis of MIV Gauge Experiments on PBX 9502 Using the Mass-Displacement Moment Function;</b> C. A. Forest, J. Wackerle, J. J. Dick, S. A. Sheffield, and D. R. Pettit; USA
560	<b>Detonation Velocity and Pressure of the Non-Ideal Explosive Ammonium Nitrate;</b> A. Miyake, A. C. van der Steen, and H. H. Kodde; Japan and The Netherlands	693	<b>The Heterogeneous Explosive Reaction Zone;</b> C. L. Mader and J. D. Kershner; USA
566	<b>Shock Sensitivites of Energetically Substituted Benzofuroxans;</b> M. L. Chan, C. D. Lind, and P. Ploitzer; USA	701	<b>Using Small Scale Tests to Estimate the Failure Diameter of a Propellant;</b> C. M. Tarver and L. G. Green; USA
573	<b>Detonation and Shock Initiation Properties of Emulsion Explosives;</b> J. Lee, F. W. Sandstrom, B. G. Craig, and P. A. Persson; USA	713	<b>Molecular Dynamics Simulation of the Effect of Molecular Dissociation and Energy Absorption on Detonation Structure in Energetic Solids;</b> S. G. Lambrakos, M. Peyrard, E. S. Oran; USA
585	<b>Effect of Pressure of Shock Sensitivity of Emulsion Explosives;</b> G. Om Reddy and F. P. Beitel Jr.; India and USA	724	<b>Multiprocess Detonation Model;</b> A. N. Dremin, V. Yu. Klimenko, O. N. Davidova, and T. A. Zoludeva; USSR
593	<b>Development of a Model of Reaction Rates in Shocked Multicomponent Explosives;</b> K. Kim; USA	730	<b>Detonation Shock Dynamics: A New Approach to Modeling Multi-Dimensional Detonation Waves;</b> J. B. Bdzil, W. Fickett, and D. S. Stewart; USA
604	<b>A Model for the Initiation of Heterogeneous High Explosives Subject to General Compressive Loading;</b> J. Starkenberg; USA	743	<b>Nonequilibrium Effects of Slow Diffusion Controlled Reactions on the Properties of Explosives;</b> M. van Thiel and F. H. Ree; USA
621	<b>Calculation of Detonation Properties of Emulsion Explosives;</b> K. Tanaka, M. Iida, Y. Nakayama, N. Ishikawa, M. Yoshida, and S. Fujiwara; Japan	751	<b>Computation of a Diverging Comp-B Detonation;</b> B. G. Bukiet; USA
626	<b>Chemistry of Underwater Explosive Detonations;</b> D. Carlson, R. Doherty, V. Ringbloom, J. S. Deiter, and G. B. Wilmot; USA	757	<b>A Theoretical Analysis of the Sonic Point Properties in a Plane Detonation Wave;</b> L. Brun and F. Chaisse; France
633	<b>Estimation of Performance of Underwater Explosives;</b> D. A. Cichra and R. M. Doherty; USA	766	<b>Investigations of the Influence of Polymorphous Transformation on the Process of Detonation of Mixtures Containing HE and Substances Undergoing Transformation;</b> E. Włodarczyk, R. Trebinski, W. Trzcinski, and W. Witkowski; Poland
640	<b>Underwater Explosion of Emulsion Explosives;</b> K. Hattori, Y. Kato, K. Tokita, Y. Fukatsu, N. Mori, and A. Torii; Japan		

# TITLES INDEX (Cont.) - NINTH SYMPOSIUM

<u>Page</u>		<u>Page</u>	
773	<b>Examples of Detonation Shock Dynamics for Detonation Wave Spread Applications;</b> D. S. Stewart and J. B. Bdzil; USA	897	<b>Physical and Chemical Nature of Hot Spots in TATB and HMX;</b> J. Sharma, B. C. Beard, J. Forbes, C. S. Coffey, and V. M. Boyle; USA
784	<b>Application of Whitham's Shock Dynamics Theory to the Propagation of Divergent Detonation Waves;</b> B. D. Lambourn and D. C. Swift; UK	906	<b>Hot Spot Formation in a Collapsing Void of Condensed-Phase, Energetic Material;</b> P. B. Butler, J. Kang, and M. R. Baer; USA
798	<b>Propagation of Detonation Waves from an Impact Region;</b> R. S. Lee, W. C. Tao, and L. D. Couch; USA	918	<b>Broad Bandwidth Study of the Topography of the Fracture Surfaces of Explosives;</b> M. Y. D. Lanzerotti, J. J. Pinto, and A. Wolfe; USA
806	<b>Detonation Wave Propagation in PBXW-115;</b> J. W. Forbes, E. R. Lemar, and R. N. Baker; USA	925	<b>Effects of Microballoon Concentration on the Detonation Characteristics of Nitromethane-PMMA Mixtures;</b> H. N. Presles, J. Campos, O. Heuzé, and P. Bauer; France
816	<b>Non-Steady Flow in a Detonator;</b> Jia Quansheng, Chen Fumei, and Wang Tinzhen; China (PRC)	933	<b>Detonation Characteristics of Dense Gaseous Explosive Mixtures;</b> P. Bauer, M. Dunand, H. N. Presles, and O. Heuzé; France
822	<b>Polysulfone SIP Gage for Flying Plate Explosive Components;</b> T. W. Warren and R. R. Weinmaster; USA	939	<b>Detonation Temperature of Some Liquid and Solid Explosives;</b> Y. Kato, N. Mori, H. Sakai, T. Sakurai, and T. Hikita; Japan
831	<b>The Effects of Inert Walls on the Velocity of Detonation in EDC35, an Insensitive High Explosive;</b> G. Eden and R. A. Belcher; UK	947	<b>The Studying of Detonation Temperatures of Solid High Explosives;</b> Shi Huisheng, Han Chengbang, Kang Shufang, and Huang Lihong; China (PRC)
842	<b>Experimental and Numerical Study of Oblique Interactions of Detonation Waves with Explosive/Solid Material Interfaces;</b> J. Aveillé, N. Carion, J. Vacellier, and J. M. Servas; France	953	<b>Free-Expansion Experiments and Modeling in Detonation: Chemistry and Hydrodynamics on a Laboratory Scale;</b> N. R. Greiner and N. Blais; USA
853	<b>Experimental and Numerical Study of Corner-Turning Detonation;</b> A. W. Gibb; Canada	962	<b>Detonation Products of Less Sensitive High Explosives Formed Under Different Pressures of Argon and in Vacuum;</b> F. Volk and F. Schedlbauer; Germany
857	<b>The Initiation of Fast Decomposition in Solid Explosives by Fracture, Plastic Flow, Friction, and Collapsing Voids;</b> M. M. Chaudhri; UK	972	<b>Explosive Potential of Carbohydrate-Metal Composites;</b> A. J. Tulis, J. L. Austing, W. K. Sumida, D. E. Baker, and D. J. Hrdina; USA
868	<b>Characterization of Defect Microstructure in High Explosives Single Crystals by Synchrotron X-Ray Tomography;</b> W. C. Tao and J. H. Kinney; USA	987	<b>A Review of Paramagnetic Resonance Products in Condensed Phase Energetic Materials;</b> M. D. Pace; USA
869	<b>Cavity Collapse in a Heterogeneous Commercial Explosive;</b> N. K. Bourne and J. E. Field; UK	995	<b>Properties of Bis(2, 2, 2-Trinitroethyl-N-Nitro) Ethylenediamine and Formulations Thereof;</b> Dong Haishan; China (PRC)
879	<b>Response of Composite Propellants to Shock Loading;</b> Bai Chunhua and Ding Jing; China (PRC)	1008	<b>Use of Oxynitrotriazole to Prepare an Insensitive High Explosive;</b> A. Becuwe and A. Declos; France
886	<b>Deformation and Explosive Properties of HMX Powders and Polymer Bonded Explosives;</b> J. E. Field, M. A. Parry, S. J. P. Palmer, and J. M. Huntley; UK		

# TITLES INDEX (Cont.) - NINTH SYMPOSIUM

<u>Page</u>		<u>Page</u>	
1014	Effects of Binder Concentration on the Properties of Plastic-Bonded Explosives; R. D. Steele, L. A. Stretz, G. W. Taylor, and T. Rivera; USA	1140	Time-Resolved Mass Spectrometry Technique for Studying Fast Transient CHNO Explosive Decomposition Kinetics; R. D. Skocypec and K. L. Erickson; USA
1019	Chemistry of Nitromethane at Very High Pressure; S. F. Agnew, B. I. Swanson, J. Kenney, and I. Kenney; USA	1151	Laser Ignition of Explosives: Raman Spectroscopy of the Ignition Zone; H. Nilsson and H. Östmark; Sweden
1027	Decomposition Mechanisms and Chemical Sensitization in Nitro; Nitramine, and Nitrate Explosives, M. D. Cook and P. J. Haskins; UK	1162	The Effect of the Pentafluorothio (SF <sub>5</sub> ) Group on the Properties of Explosive Nitro Compounds: New SF <sub>5</sub> Explosives; M. E. Sitzman and D. L. Ornellas; USA
1037	Decomposition of Energetic Materials on the Drop-Weight-Impact Machine; G. A. Buntain, T. L. McKinney, T. Rivera, and G. W. Taylor; USA	1170	Chemistry of Detonation Soot: Diamonds, Graphite, and Volatiles; N. R. Greiner and R. Hermes; USA
1047	Behavior of an Unreacted Composite Explosive on Low Velocity Impact; C. Loupias and A. Fanget; France	1185	Molecular Models for Explosives: Applications to NTO; J. P. Ritchie, and E. M. Kober; USA
1052	Response of Rocket Propellants to Projectile Impact; S. Y. Ho; Australia	1193	Reaction and Diffusion in Detonation; N. J. B. Green, M. J. Pilling, and S. H. Robertson; UK
1060	Characterization of Booster-Rocket Propellants and Their Simulants; L. J. Weirick; USA	1199	A Thermochemical Model for Shock-Induced Chemical Reactions in Porous Solids: Analogs and Contrasts to Detonation; M. B. Boslough; USA
1070	Experimental Study and Numerical Modeling of Thermal Initiation and Combustion of High Heterogeneous Explosives; C. Castille, D. Bainville, P. Reynier, and R. Belmas; France	1217	Reactive Modeling in Shock Initiation of Heterogeneous Explosives; M. Quidot and J. Groux; France
1076	Electrostatic Sensitivity Testing of Explosives at Los Alamos; T. E. Larson, P. Dimas, and C. E. Hannaford; USA	1224	Reactive Flow Analysis and Its Applications; G. A. Leiper and D. L. Kennedy; UK and Australia
1084	Molecule-Surface Collision Induced Excitation and Dissociation: n, i-C <sub>3</sub> F <sub>7</sub> NO, C <sub>6</sub> F <sub>5</sub> NO, 2-Methyl, 5-Vinyl Tetrazole and C(NO <sub>2</sub> ) <sub>4</sub> with MgO(100) Surfaces at E <sub>incident</sub> ≤ 7.5eV; E. Kolodny, P. S. Powers, L. Iwata, H. Reisler, C. Wittig, I. B.	1235	Physical Evidence of Different Chemical Reactions in Explosives as a Function of Stress; T. P. Liddiard, J. W. Forbes, and D. Price; USA
1100	Initiation and Propagation in Primary Explosives; P. M. Dickson, M. A. Parry, and J. E. Field; UK	1243	Towards Developing the Capability to Predict the Hazard Response of Energetic Materials Subjected to Impact; C. S. Coffey, D. F. DeVost, and D. L. Woody; USA
1110	Prompt Detonation of Secondary Explosives by Laser; D. L. Paisley; USA	1253	"Frozen Hot Spots" in Shocked EDC35; an Insensitive High Explosive; G. Eden, R. A. Belcher, M. I. Andrew, and W. R. Marlow; UK
1118	Laser Initiation of Secondary Explosives; A. M. Renlund, P. L. Stanton, and W. M. Trott; USA	1260	Deformation and Shock Loading Studies on Single Crystals of Ammonium Perchlorate Relating to Hot Spots; H. W. Sandusky, B. C. Glancy, D. W. Carlson, W. L. Elban, and R. W. Armstrong; USA
1131	Intense Electron Beam Detonation of TATB Explosives; D. Demske, N. Brazell, W. E. Farley, S. Miller, and R. Warnes; USA		

Page

- 1271 **The Influence of Grain Morphology on the Behavior of Explosives;** S. Dufort, H. Cherin, and P. Gohar; France
- 1276 **Role of Adiabatic Shear Bands in Initiation of Explosives by Drop-Weight Impact;** V. Krishna Mohan, V. C. Jyothi Bhasu, and J. E. Field; UK
- 1284 **Gap Tests as a Method of Discriminating Shock Sensitivity;** S. A. Aubert, G. H. Parsons, J. G. Glenn, and J. L. Thoreen; USA
- 1295 **Shock Sensitivity of Damaged Energetic Materials;** H. P. Richter, L. R. Boyer, K. J. Graham, A. H. Lepie, and N. G. Zwierzchowski; USA
- 1310 **Burning Rates of Two Cast Nitramine Explosives Using a Hybrid Closed Bomb-Strand Burner;** W. C. Tao, M. S. Costantino, and D. L. Ornellas; USA
- 1322 **Explosiveness and Shock-Induced Deflagration Studies of Large Confined Explosive Charges;** P. J. Hubbard and R. Tomlinson; UK
- 1335 **Initiation and Detonation Measurements on Liquid Nitric Oxide;** G. L. Schott, W. C. Davis, and W. C. Chiles; USA
- 1351 **Mechanisms of Detonation and Failure in Weak Chemically Sensitized Mining Safety Explosives;** M. Kennedy and I. D. Kerr; UK
- 1360 **Experimental Studies on the Detonation of an Explosive by Multi-Point Initiation;** Yu Jun, Fu Xinghai and Zhang Guanren; China (PRC)
- 1364 **Detonation Properties of Explosive Foams;** C. J. Anderson, K. Von Rosen, A. W. Gibb, and I. O. Moen; Canada
- 1371 **F.P.I. Velocimetry Techniques Applied to Various Problems in Detonics;** P. Gimenez, J. P. Bedoch, C. Saint-Martin, G. Baudin, and Y. de Longueville; France
- 1378 **Detonation Product Equation of State for Baratol;** J. W. Kury and R. D. Breithaupt; USA

Page

- 1385 **Design and Development of Precision Linear Shaped Charges;** M. G. Vigil; USA
- 1404 **Jet Initiation Mechanisms and Sensitivities of Covered Explosives;** M. Chick, T. J. Bussell, R. B. Frey, and A. Bines; Australia and USA
- 1416 **Initiation Phenomena with Shaped Charge Jets;** M. Held; Germany
- 1427 **Spherical Projectile Impact on Explosives;** E. N. Ferm and J. B. Ramsay; USA
- 1441 **Projectile Impact Initiation of Explosive Charges;** M. D. Cook, P. J. Haskins, and H. R. James; UK
- 1451 **Correlation of Explosive Sensitivity to Compressional Inputs;** M. Kornhauser; USA
- 1460 **Sensitivity of Several Explosives to Ignition in the Launch Environment;** J. Starkenberg, D. L. McFadden, D. L. Pilarski, K. J. Benjamin, V. M. Boyle, and O. R. Lyman; USA
- 1480 **Study of Explosive Shell Fillings with Defects in Simulated Gun Launch Conditions;** C. Bélanger; Canada
- 1489 **A Computational Assessment of the Role of Shielding in Preventing the Sympathetic Detonation of Munitions;** J. Starkenberg, T. M. Dorsey, K. J. Benjamin, and A. L. Arbuckle; USA
- 1510 **Output Measurements and Modeling of HNS Mild Detonating Fuse;** R. G. Jungst and M. E. Kipp; USA
- 1529 **Detonator Response Measurements with a Standardized Piezoelectric Polymer (PVDF) Gauge;** L. M. Moore, R. A. Graham, R. P. Reed, and L. M. Lee; USA
- 1543 **Indexes for the Proceedings of the Symposia (International) on Detonation 1951 through 1985;** S. L. Crane, W. E. Deal, J. B. Ramsay, and B. E. Takala; USA

# TOPIC PHRASE INDEX - NINTH SYMPOSIUM

	Page		Page
1DUCT model of HMX porous bed response . . .	280	Benzofuroxans, substituted, shock sensitivity . . .	566
2D axisymmetric shock initiation . . . . .	77	Berger's vector . . . . .	58
2DUCT model of HMX porous bed response . . .	280	Beryllium wall, effect on D of EDC35 . . . . .	831
Absorption spectroscopy, shocked benzene . . . .	190	Bimodal formulations . . . . .	18
Accelerated combustion in DDT . . . . .	259	Binder concentration, effect on PBX properties .	1014
Accumulation mechanism for polyatomic molecules . . . . .	724	Birch's isotherm . . . . .	50
Acoustic & optical phonon modes . . . . .	235	Bis(2,2,2-trinitroethyl(-N-nitro) ethylenediamine	995
Acoustic approximation for detonation gases . . .	560	BKW calculations, emulsion HE, D vs density . .	573
Activation energy from time-to-explosion . . . . .	228	Blast wave, 500-kg emulsion HE test . . . . .	621
Adiabatic gamma, sensitivity to molecular props.	513	Boltzman EOS, gaseous HEs . . . . .	933
Adiabatic shear bands, role in initiation . . . . .	1276	Boron nitride, polymorphic transformation, detonation. . . . .	766
ADNBF, shock sensitivity . . . . .	561	Bow wave shock initiation . . . . .	1404
ADNBF, shock sensitivity, phys., chem. properties . . . . .	560	Brass wall, effect on EDC35 detonation velocity .	831
ADNT performance . . . . .	478	Brazilian test & laser speckle, tensile strength . .	886
AFATL 8-inch gap test . . . . .	1284	BTF performance . . . . .	478
AFX-902 performance . . . . .	478	Bubble energy, underwater HEs . . . . .	633
Aggregate reactivity . . . . .	246	Bubbles & voids, initiation by . . . . .	857
Air-compression & deformation, HE sensitivity .	1460	Buckingham-Kees potential . . . . .	513
Aluminized explosives, performance . . . . .	478	Burn model, 1D SDT of RDX, mesh size, P . . .	1224
Aluminum particle reaction, underwater explosion	641	Burn rates, nitramines, high pressure . . . . .	1310
AMMO, time to explosion . . . . .	228	Burning-front velocity vs initial temperature . . .	1070
Ammonia-nitromethane complex calculations . . .	1027	C-NO <sub>2</sub> , time-to explosion . . . . .	228
AN emulsion HE, D vs density . . . . .	573	Calibration, global, HE reaction zone . . . . .	252
AN, detonation velocity & pressure . . . . .	560	Cap sensitivity of emulsion HEs . . . . .	585
AN, emulsion HE with 70% . . . . .	621	Capacitor discharge testing of HEs . . . . .	1076
AP, shock loading . . . . .	879	Capture & analysis of detonation products . . . .	621
AP, single crystals, shock loading . . . . .	1260	Carbamates & dicarbamates, SF <sub>5</sub> . . . . .	1162
AP, time to explosion . . . . .	228	Carbohydrate-metal composites, potential as HEs	972
Aquarium gap test, damaged energetic material .	1295	Carbon behind shock front . . . . .	396
Aqueous emulsion HEs . . . . .	545	Carbon clusters and melt line, soot examination .	417
Arc experiment . . . . .	730	Carbon condensation . . . . .	417
Area of shock loading, initiation threshold . . . .	66	Carbon condensation, in shocked benzene . . . . .	190
Arrhenius kinetics, HNS . . . . .	209	Carbon EOS . . . . .	443
Arrhenius one-step unimolecular reaction . . . . .	219	Carbon resistor pressure gauge . . . . .	537
Arrhenius to non-Arrhenius kinetics . . . . .	235	Carbon, condensation effects . . . . .	743
ARTOO, 2D Lagrangian propagation code . . . . .	209	Carbon, phase changes, effect on detonation . . . .	425
Azide, time to explosion . . . . .	228	Carrol & Holt particle-to-particle stress . . . . .	363
B 2214, properties . . . . .	1008	CARS data, liquid N <sub>2</sub> & NM . . . . .	180
Ball propellant data, four porosity levels . . . . .	363	Cast TNT, reaction extent history . . . . .	252
Ball propellant, DDT studies . . . . .	354	Cast-cured PBX, modeling of wedge tests . . . . .	1217
Ball propellants, compaction, single-, double-based . . . . .	341	CAT finite-element thermal ignition code . . . . .	1070
Ballistic impact chamber (BIC) test . . . . .	1243	Cavity collapse in emulsion HEs . . . . .	869
Balloon test, underwater HE detonation . . . . .	626	CH-6, small-scale gap test . . . . .	98
Baratol Hugoniot . . . . .	379	Characterization, booster-rocket propellants . . . .	1060
Baratol products EOS . . . . .	1378	Chemical equilibrium code . . . . .	461
Baratol, detonation product EOS . . . . .	1378	Chemically sensitized mining safety HEs . . . . .	1351
Baratol, UK, wave shapes in rods . . . . .	784	Chemico-acoustic interactions . . . . .	219
BDNPA/BDNPAF concentration, effects on HE .	1014	Chemistry in free expansion of HE products . . . .	953
Benzene, shocked, absorption spectroscopy . . . .	190	Chemistry of detonation soot . . . . .	1170
		Chemistry of underwater HE detonations . . . . .	626
		Chemistry, NM, high pressure . . . . .	1019

# TOPIC PHRASE INDEX (Cont.) - NINTH SYMPOSIUM

	Page		Page
Chemistry, thermal explosion . . . . .	228	Condensed explosives, reactivity . . . . .	246
CHEMKIN chemical kinetics, void collapse calc. . . . .	906	Condensed HEs, detonating, electrical conductivity . . . . .	396
CHNO HE decomposition kinetics . . . . .	1140	Condensed reacting media . . . . .	250
CID, collision-induced dissociation, experiments . . . . .	1084	Condensed-phase particle conservation equations . . . . .	363
CJ point, shock properties of reaction products . . . . .	379	Conductivity, in detonating condensed HE . . . . .	396
CJ pressure vs homolog sequence number . . . . .	461	Confined acceptor charges, jet initiation . . . . .	1416
CJ zone length, calculated . . . . .	806	Confinement effect, failure diameter, PBXW-115 . . . . .	806
Closed-bomb strand burner, hybrid . . . . .	1310	Confinement effect, SSGT . . . . .	98
Cluster formation, carbon . . . . .	743	Confinement effect, violence, deflagration . . . . .	1322
Clusters, carbon & nitrogen . . . . .	743	Constitutive model, for 2D code DYNA2D . . . . .	280
CMC probe, composite manganin-constantan . . . . .	77	Constitutive relations, global method calibration . . . . .	252
CN-stretching mode, NM . . . . .	180	Contact shock initiation, spherical projectile on HE . . . . .	1427
Coaxial HE conductivity experiments . . . . .	396	Continuum mixture model, fine-grained HNS . . . . .	209
Cochran-Chan rate constants, PBH-9D . . . . .	142	Convective combustion, early phase of DDT . . . . .	329
Cold LX-17, buildup . . . . .	133	Converging detonation, 2D Lagrangian model . . . . .	1217
Collapse of cavities in HE . . . . .	869	Copper cylinder test, heat of detonation . . . . .	478
Collapse of single pore by shock wave . . . . .	593	Corner turning & desensitization . . . . .	1224
Collapsing void, condensed HE, hot-spot formation . . . . .	906	Corner-turning data, EDC35 vs U.S. IHEs . . . . .	123
Collapsing voids, initiation of fast decomposition . . . . .	857	Corner-turning data, PBXW-115 . . . . .	806
Collisional energy transfer . . . . .	1084	Cover-plate thickness, effect on jet initiation . . . . .	1404
Combustion propagation . . . . .	1070	CP, detonator in flying-plate tests . . . . .	824
Combustion, compressive, granular materials . . . . .	293	Critical energy per unit area, initiation . . . . .	66
Common distance vs shock velocity in wedge test . . . . .	1217	Critical impact diameter, thin flyer-plate impact . . . . .	66
Comp A-3 Type II, ignition thresholds . . . . .	1460	Critical temperature for TATB . . . . .	1070
Comp B performance . . . . .	478	Crystal defects, role in forming hot spots . . . . .	1260
Comp B, computation of diverging detonation . . . . .	743	Crystal diameter effects in HEs . . . . .	98
Comp B, computation of diverging detonation . . . . .	751	Crystal microstructure & defects . . . . .	1260
Comp B, detonation pressure profile . . . . .	471	Crystal orientation, incident laser energy . . . . .	172
Comp B, fracture surface topography . . . . .	918	Crystal shape effect, PBX . . . . .	83
Comp B, Hugoniot . . . . .	379	Crystals, HE, impact initiation . . . . .	58
Comp B, pressure shear ignition . . . . .	3	Curvature of detonation front, mining safety HEs . . . . .	1351
Comp B, reaction products . . . . .	962	Curvature, detonation velocity relation . . . . .	784
Comp B-3, diameter effect . . . . .	197	Cutback experiments, thin flyer-plate experiments . . . . .	798
Comp C-4, performance . . . . .	478	Cyclic polynitroaliphatic SF <sub>5</sub> HE . . . . .	1162
Compaction wave acceleration, granular material . . . . .	306	Cyclotol 75/25 Hugoniot . . . . .	379
Compaction wave, DDT . . . . .	265	Cylinder test, 42 HMX/9 AP/19 Al/30 binder . . . . .	1371
Compaction, single-, double-based ball propellants . . . . .	341	Cylinder test, 88 RDX/12 PBHT . . . . .	1371
Composite emulsion explosives, performance . . . . .	573	Cylinder test, 96 HMX/4 Viton . . . . .	1371
Composite explosive, HMX/emulsion . . . . .	545	Cylinder test, heat of detonation . . . . .	478
Composite HE, higher-energy prospects . . . . .	554	Cylinder test, ZrH <sub>2</sub> -based composites . . . . .	525
Composite HE, low-velocity projectile impact . . . . .	1047	Cylindrical & spherical detonation, mixtures . . . . .	766
Composite HEs, underwater performance . . . . .	633	Cylindrical case expansion, JWLL, Gurney equation . . . . .	498
Composite manganin-constantan ring probe . . . . .	77	Damage characterization, energetic materials . . . . .	1295
Composite propellants, response to shock loading . . . . .	879	Damaged energetic materials, shock sensitivity . . . . .	1295
Compressional input, correlation to HE sensitivity . . . . .	1451	DDNP, EMV particle velocity meas. in detonator . . . . .	810
Compressive burning, DDT, experiment & theory . . . . .	320	DDT in primary HEs . . . . .	1100
Compressive combustion, granular materials . . . . .	293	DDT model, compacted porous beds, NWC . . . . .	363
Compressive heating, ignition and launch . . . . .	1460	DDT model, TS 3659 propellant . . . . .	329
Compressive loading of heterogeneous HEs . . . . .	604	DDT modeling, granular materials . . . . .	293
Compressive reaction, ball propellants . . . . .	341		
Condensed carbon yield in detonation . . . . .	407		

# TOPIC PHRASE INDEX (Cont.) - NINTH SYMPOSIUM

	Page		Page
DDT parameter, particle diameter, largest influence . . . . .	320	Detonation products, $\gamma$ s, molecular properties . . .	513
DDT studies, RDX & RDX/wax, steel confinement . . . . .	259	Detonation products, carbon clusters . . . . .	417
DDT studies, spherical ball propellant . . . . .	354	Detonation propagation, PBXW-115 . . . . .	806
DDT tube test, RDX/wax, experiments & model . . . . .	320	Detonation properties, 95 TATB/5 Kel-F 800 . . .	123
DDT tube tests, HMX, radiographs, model . . . . .	265	Detonation properties, AN emulsion, model . . .	621
DDT, granular HMX . . . . .	265	Detonation properties, explosive foams . . . . .	1364
DDT, numerical modeling . . . . .	259	Detonation properties, NTO . . . . .	1001
DDT, porous beds . . . . .	259	Detonation properties, ZOX . . . . .	985
DDT, porous beds of ball propellants . . . . .	341	Detonation shock dynamics, 2D model, DSD . . .	730
DDT, simulation of compaction wave . . . . .	306	Detonation shock dynamics, deton. wave spread . .	773
DDT, successive phases, gauges . . . . .	259	Detonation structure, molecular dynamics . . . . .	713
DDT, wedge test run to detonation . . . . .	320	Detonation Symposia indexes, 1981-1985 . . . . .	1543
Dead pressing, failure of DDT at high density . .	1100	Detonation temperature, liquid & solid HEs . . .	939
Decomposition mechanisms, arbitrary . . . . .	633	Detonation temperature, solid HEs . . . . .	947
Decomposition mechanisms, C-N bond, NM, NH <sub>3</sub> .	1027	Detonation velocity for HMX/emulsion . . . . .	545
Decomposition, fast transient, kinetics . . . . .	1140	Detonation velocity vs $\rho$ , 60 PETN/40 PU foam .	1364
Decomposition, new HE, drop weight impact . .	1037	Detonation velocity vs $\rho$ , emulsion HEs . . . . .	573
Decomposition, NM, drop-weight impact . . . . .	1019	Detonation velocity vs $\rho$ , NM foam . . . . .	1364
Defect microstructure in HE single crystals . . .	868	Detonation velocity vs particle size, composite HEs . . . . .	554
Deflagration, shock-induced, desensitization . .	1322	Detonation velocity, curvature function . . . . .	784
Deflagrations induced by direct thermal means . .	1322	Detonation velocity, density, AN, model . . . . .	560
Deformation & HE properties of HMX powder . .	886	Detonation velocity, EDC35 . . . . .	822
Delay to detonation vs shock ampl., PETN, NM .	235	Detonation velocity, wall effect on EDC35 . . . .	831
Demilitarization of large charges . . . . .	1322	Detonation wave propagation from impact region .	798
Density of HMX/emulsion vs % HMX . . . . .	545	Detonation wave spread, deton. shock dynamics .	773
Density snapshots, PBX 9502 . . . . .	683	Detonation wave, decomposition of HE . . . . .	50
Density vs shock sensitivity . . . . .	98	Detonator response measurement with PVDF gauge . . . . .	1529
Denton's correlation for heat transfer to porous bed . . . . .	363	Detonator, non-steady flow . . . . .	816
Design, precision linear shaped charges . . . . .	1385	DETOVA code for DDT . . . . .	329
Detonability experiments . . . . .	18	Diameter effect in liquid NO . . . . .	1335
Detonability of carbohydrate-metal composites . .	972	Diameter effect, NM-PMMA-GMB . . . . .	925
Detonability of mixtures of C, BN, Si . . . . .	766	Diameter effect, non-ideal explosives . . . . .	197
Detonation calorimetry, Cu cylinder test . . . .	478	Diamond in detonation products . . . . .	417
Detonation calorimetry, Spectrometer, model . .	953	Diamond-anvil cell, NM decomposition . . . . .	1019
Detonation characteristics, gun propellants . . .	537	Diamonds, graphite & volatiles in detonation soot	1170
Detonation development, thin flyer-plate impact .	66	Diamonds, synthesis in detonation waves . . . . .	407
Detonation enhanced by electric current flow . .	388	Diffusion role in detonation chemistry . . . . .	1193
Detonation front curvature, HNS . . . . .	209	Diffusion-controlled reactions of HEs . . . . .	743
Detonation mechanisms, mining safety HEs . . .	1351	DINGU, performance . . . . .	478
Detonation model, multiprocess, Russian . . . .	724	DIP mass spectrum from TNT soot . . . . .	1170
Detonation parameters, predicting with VLW EOS	435	Discontinuous diameter-effect curves . . . . .	197
Detonation pressure measurement, manganin foil	471	Dislocations, RDX, PETN . . . . .	1276
Detonation pressure, AN, Japanese-Dutch tests .	560	Dispersal, explosive, heated Al particles into water . . . . .	641
Detonation pressures, calculation . . . . .	461	Disposal of surplus ammunition . . . . .	1322
Detonation product EOS . . . . .	506	Distance-time plot of double impact of piston . .	306
Detonation product EOS, Baratol . . . . .	1378	Divergence testing, EDC35 . . . . .	123
Detonation product EOS, Monte Carlo method . .	452	Divergence, IHE . . . . .	123
Detonation products EOS, EED, e-p-v . . . . .	388	Divergent detonation waves, Whitham's theory . .	784
Detonation products into argon & vacuum . . . .	962	Divergent spherical generator, calibration . . . .	1371



# TOPIC PHRASE INDEX (Cont.) - NINTH SYMPOSIUM

	<u>Page</u>		<u>Page</u>
Diverging & converging detonation experiments .	1217	Emulsion HEs, detonation properties, calculated .	621
Diverging detonation, computation, Comp B . . .	743	Emulsion HEs, performance vs diam & density .	573
Diverging detonation, computation, Comp B . . .	751	Emulsion HEs, shock sensitivity . . . . .	585
Diverging detonation, mushroom-shaped sample .	1217	Emulsion HEs, underwater explosion . . . . .	641
DNBF, shock sensitivity . . . . .	561	EMV particle-velocity gauge . . . . .	816
DNBF, shock sensitivity, phys. & chem.		Energy level diagram . . . . .	235
properties . . . . .	566	Energy localization, predicting hazard response .	1243
DNNC, time to explosion . . . . .	228	Energy loss, multipoint initiation . . . . .	1360
Double-base propellants, pressure shear ignition .	3	Energy output of HEs, parameters . . . . .	962
Double-based ball powder, DDT . . . . .	259	Energy thresholds for direct laser initiation . . . .	1118
DREV setback simulator . . . . .	1480	Energy to ignition, impact ignition & growth . . .	1243
Drop weight impact, HE decomposition . . . . .	1037	Energy transfer, phenomenological models . . . .	713
Drop weight impact, HMX & PBX deformation .	886	Energy-per-unit-area criterion, impact on HE . .	1441
Drop weight impact, radiometry & spectroscopy .	1037	EOS clusters, CHEQ code . . . . .	743
Drop-weight impact, HE decomposition . . . . .	1019	EOS for detonation products . . . . .	388
Drop-weight impact, shear bands role in initiation	1276	EOS of dense gaseous HEs . . . . .	933
Drop-weight-impact tests, fluctuating response .	1243	EOS of detonation products . . . . .	388
DSC, emulsion HEs . . . . .	585	EOS of detonation products, TATB . . . . .	506
DSD, examples for detonation wave spread . . .	773	EOS, Baratol detonation product . . . . .	1378
DXD-01, detonation pressure profile . . . . .	471	EOS, C and N . . . . .	425
DYNA2D, 2D Lagrange code, porous bed		EOS, comparison of various HEs . . . . .	621
analysis . . . . .	280	EOS, detonation products, Monte Carlo method .	452
DYNA2D, reactive flow analysis . . . . .	1224	EOS, detonation temperature . . . . .	939
EAK, Lagrange gauge study of initiation . . . .	89	EOS, fluid perturbation, calc. detonation pressure	461
Ector electron-beam HE detonation . . . . .	1131	EOS, HE, model . . . . .	443
EDC29 & EDC32, wave shapes in rods . . . . .	784	EOS, JCZ3 . . . . .	933
EDC35 IHE, frozen hot spots in shocked . . . .	1253	EOS, JWJ . . . . .	25
EDC35, inert wall effect, detonation velocity . .	822	EOS, JWJ . . . . .	133
EDC35, initiation & detonation . . . . .	123	EOS, JWJ . . . . .	142
EDC35, wall effect on detonation velocity . . . .	831	EOS, JWJ . . . . .	209
EDD performance . . . . .	478	EOS, JWJ . . . . .	498
EDNA, time to explosion . . . . .	228	EOS, JWJ . . . . .	670
EE, emulsion explosives, calc. of det. properties	621	EOS, JWJ . . . . .	701
EED, electrically enhanced detonation model . .	388	EOS, JWJ . . . . .	1217
Efficiency, HE, theoretical prediction . . . . .	489	EOS, JWJ parameters using Gurney equation . .	498
Elastic modulus vs strain rate, Octorane 86A . .	1047	EOS, LX-14 . . . . .	425
Elastic-plastic flow in alumina . . . . .	842	EOS, Mie-Grüneisen . . . . .	50
Electric gun experiments, particle size effects .	25	EOS, Mie-Grüneisen . . . . .	329
Electric gun, initiation studies . . . . .	66	EOS, NTO . . . . .	489
Electrical conductivity, detonating condensed HE	396	EOS, PANDA code . . . . .	443
Electrically driven thin flyer plates . . . . .	66	EOS, Percus-Yevick . . . . .	933
Electrically enhanced detonation . . . . .	388	EOS, VLW, predicting detonation parameters . .	435
Electromagnetic gauges, NM SDT . . . . .	39	EOS, TATB, virial, detonation products . . . . .	506
Electromagnetic velocity gauge, radial flow . . .	77	EPR, products from condensed phase HEs . . . .	939
Electron beam initiation of TATB HEs . . . . .	1131	Equivalence of EED & unsupported detonation .	388
Electron micrograph, shocked HMX . . . . .	897	ESD test, electrostatic discharge, common HEs .	1076
Electrostatic sensitivity testing of HEs . . . . .	1076	ETARC, a thermochemical code . . . . .	489
Embedded gauges, LX-17 initiation vs		Ethylene/air detonation velocity vs initial pressure	933
temperature . . . . .	112	Excess transit time, thin flyer-plate impact . . . .	798
Emission spectroscopy, drop weight impact on HE	1019	Excitation and dissociation, molecular collision .	1084
Emulsion explosives, mixtures with HMX . . . .	545	Expanded large-scale gap test (ELSGT) . . . . .	1284
Emulsion HE, diameter effect . . . . .	197	Explosive foams, detonation properties . . . . .	1364

# TOPIC PHRASE INDEX (Cont.) - NINTH SYMPOSIUM

	Page		Page
Explosive properties, effect of SF <sub>6</sub> group . . . . .	1162	Fume chemistry, diffusion & reaction model . . .	1193
Explosive reaction zone, calibration for models . .	252	Gamma law EOS of PBH-9D . . . . .	142
Explosiveness in setback simulator tests . . . . .	1480	Gammas, Grüneisen & adiabat, errors, molec. props. . . . .	513
Explosiveness of large charges . . . . .	1322	Gap test modeling . . . . .	1451
Explosiveness, test for shear ignition . . . . .	3	Gap test, IHE . . . . .	123
Fabry-Perot interferometry, applied to detonics .	1371	Gap tests, shock sensitivity . . . . .	1284
Fabry-Perot interferometry, electron beam initiation . . . . .	1131	Gap tests, small & large scale . . . . .	566
Fabry-Perot laser interferometry, ZrH <sub>2</sub> composites	525	Gas-gun SDT experiments . . . . .	39
Fabry-Perot velocimeter, Baratol deton. products	1378	Gas-phase chemistry on hot-spot formation . . . .	906
Fabry-Perot velocimetry, 1D, PBX 9502 . . . . .	657	Gas-phase conservation equations . . . . .	363
Fabry-Perot velocimetry, LX-17 . . . . .	133	Gas-phase influence on laser ignition . . . . .	162
Failure diameter test assembly . . . . .	708	Gas-phase reactions in ignition zone . . . . .	1151
Failure diameter, calculating . . . . .	1351	Gaseous HEs, dense, detonation characteristics .	933
Failure diameter, emulsion or composite HEs . .	573	Gauge, pressure, carbon resistor . . . . .	537
Failure diameter, gun propellants . . . . .	537	Gauss quadrature points . . . . .	293
Failure mechanisms, mining safety HEs . . . . .	1351	Gaussian 86 code, potential energy calculations .	1027
Failure thickness modeling, PBX 9407 . . . . .	1224	GAUSSIAN82 computer program . . . . .	1185
Failure-diameter test assembly . . . . .	701	Geochemical detonation in supercooled magma .	1199
Fast decomposition of HE, initiation . . . . .	857	Gibbsian EOS . . . . .	513
FCT, flux-corrected transport method . . . . .	320	Glass transition point of Kel-F-800 . . . . .	123
Flame front position in DDT . . . . .	320	Global method, calibration of constitutive relations	252
Flow-resistance law of Jones & Krier . . . . .	329	Glucose/NG, TIGER calculations . . . . .	972
Fluid EOS parameters . . . . .	461	GMB, concentration effect on NM-PMMA deton.	925
Fluid perturbation EOS, calc. detonation pressure	461	Grain fracture . . . . .	280
Flyer plate experiments, small . . . . .	66	Grain morphology, effect on HE behavior . . . .	1271
Flyer plate impact, thin . . . . .	798	Grain size and combustion . . . . .	1271
Flyers driven by multipoint-initiated HE . . . . .	1360	Grain-burning modes . . . . .	280
Flying-plate explosive components, SIP gage . .	822	Grain-burning process . . . . .	50
Foam HEs, Detonability limits . . . . .	1364	Granular beds, HMX, DDT . . . . .	265
Foil acceleration, LX-17 . . . . .	133	Granular material, simulation of compaction wave	306
Forest Fire, PBH-9D . . . . .	142	Granular materials, compressive combustion . .	293
Formic acid, EOS parameters . . . . .	443	Graphite, diamonds, & volatiles in detonation soot	1170
Fractal dimension vs spectral slope . . . . .	918	Graphite, polymorphic transformation, detonation	766
Fracture strength, PBXs . . . . .	886	Grüneisen Γ, sensitivity to molecular properties .	513
Fracture surface topography of HEs . . . . .	918	Grüneisen EOS for inert materials . . . . .	670
Fracture, cause for initiation . . . . .	842	Gun launch, simulated, defects in shell fillings .	1480
Fracture, initiation of fast decomposition . . . .	857	Gun propellants, detonation characteristics . . .	537
Frank-Kamenetski equation, thermal explosion . .	3	Gurney equation, determining JWL parameters . .	498
Free-expansion, HE products, chem. & hydrodynamics. . . . .	953	Gurney-JWL energy relation . . . . .	498
Free-radical in HE by paramagnetic resonance . .	987	H-19 propellant, characterization . . . . .	1060
Free-radical products in HE, a review . . . . .	987	H/HN performance . . . . .	478
Free-radical products, EPR . . . . .	939	Hazard response to impact, energetic materials .	1243
Friction sensitivity, shear ignition study . . . .	3	HBX-1 Hugoniot . . . . .	379
Friction, initiation of fast decomposition . . . .	857	Heat detonations, porous solids, model . . . . .	1199
Front-tracking method in RCM code . . . . .	751	Heat of detonation, Cu cylinder test . . . . .	478
Frozen hot spots, shocked EDC35 IHE . . . . .	1253	Heat of detonation, SF <sub>6</sub> model compound . . . . .	1162
FT-1 composite propellant, shock loading . . . .	879	Heat-sensitive-film techniques . . . . .	886
FT-2 composite propellant, shock loading . . . .	879	Heated HE, ESD sensitivity . . . . .	1076
FTIR spectroscopy, thermal explosions . . . . .	228	Heaviside function . . . . .	293
Full-surface multipoint initiation, baratol . . . .	1360	Heavy-fragment impact sensitivity, ONTA . . . .	1008
		Heterogeneity, effect on performance . . . . .	197

# TOPIC PHRASE INDEX (Cont.) - NINTH SYMPOSIUM

	Page		Page
Heterogeneous commercial HE . . . . .	869	HOM EOS . . . . .	751
Heterogeneous HE reaction zone, calculated . . .	693	HOM EOS of PBH-9D . . . . .	142
Heterogeneous HE, thermal ignition & combustion . . . . .	1070	Homogeneous HE, liquid NO . . . . .	1335
Heterogeneous initiation, SDT . . . . .	39	Homogeneous HE, SDT theory . . . . .	219
High-confinement DDT, WC140, TS3659, WC231 . . . . .	341	Homogeneous initiation, SDT, <i>in situ</i> . . . . .	39
High-order behavior, diameter effect . . . . .	197	Homologous series of polynitroaliphatic HEs . . .	461
High-pressure activator . . . . .	3	HONDO finite-element material code . . . . .	363
High-rate deformation, HE crystals . . . . .	58	Hopkinson bar, miniaturized . . . . .	886
High-resistance manganin foil gauge, det. pressure	471	Hopkinson bar, modified, tests on rocket propellant . . . . .	1052
High-speed-machining test of NTO . . . . .	1001	Hot spots . . . . .	842
High-strain-rate impact tests, rocket propellant .	1052	Hot spots . . . . .	886
Highest energy of energetic composite materials .	554	Hot spots by dynamic compaction . . . . .	341
Highly localized structures, molecular dynamics .	713	Hot spots, AP, single crystals . . . . .	1260
HMX performance, cylinder test, Q . . . . .	478	Hot spots, frozen, shocked EDC35 IHE . . . . .	1253
HMX porous bed response, deflagration & shock	280	Hot spots, multiprocess detonation . . . . .	724
HMX powders & polymer HEs, deform. & deton.	886	Hot spots, reactive porous beds . . . . .	259
HMX, detonation temperature measurement . . .	947	Hot spots, shear bands in crystals . . . . .	58
HMX, fracturing data, four porosity levels . . .	363	Hot spots, time evolution, model . . . . .	1193
HMX, granular, DDT . . . . .	265	Hot-spot formation . . . . .	1243
HMX, mixtures with emulsion explosives . . . . .	545	Hot-spot formation, collapsing void, condensed HE . . . . .	906
HMX, monocrystal decomp. vs shock pressure .	172	Hot-spot generation & extinction . . . . .	604
HMX, nature of hot spots in TATB & HMX . . .	897	Hot-spot generation, model of reaction rate . . .	593
HMX, prompt laser initiation . . . . .	1110	Hot-spot reaction in DDT . . . . .	293
HMX, propagation of detonation from impact . .	798	Hot-spot residue, physical nature . . . . .	897
HMX, quasi-static compaction pressure . . . . .	280	HTPB PBXs, RDX crystals . . . . .	83
HMX, reflection spectra & ignition threshold . .	1100	Hugoniot calculations, porous reactive material .	1199
HMX, surface-to-volume ratio . . . . .	280	Hugoniot data, various materials . . . . .	1441
HMX, thermochemical data, application to NTO	489	Hugoniot measurements, rocket propellants . . .	1060
HMX, thermophysical & material property data .	293	Hugoniot, reaction products . . . . .	379
HMX, time to explosion . . . . .	228	Hydrazine nitrate/hydrazine hydrate solution, prop. . . . .	939
HMX, x-t DDT data . . . . .	306	Hydrazine nitrate/water solution, properties . . .	939
HMX/AP/ZrH <sub>2</sub> /Estane, meas. of reactive flow .	525	Hydrocarbon-air compressed mixtures . . . . .	933
HMX/W Hugoniot, $\rho/\rho_{CJ}$ vs $u/u_{CJ}$ . . . . .	379	Hydrogen bonding, TATB . . . . .	153
HMX/water, initiation, particle size effects . . .	25	Hydrostatic compression instrument . . . . .	1295
HN/HH, detonation-front temperature . . . . .	939	Ideal mixing, accuracy . . . . .	443
HN/H <sub>2</sub> O, detonation-front temperature . . . . .	939	IDEX code, adiabatic $\gamma$ & Grüneisen $\Gamma$ . . . . .	513
HNB performance, Cu cylinder test, Q . . . . .	478	Igniter effect on DDT . . . . .	320
HNDZ, time-to explosion . . . . .	228	Igniters for DDT, Pb <sub>3</sub> O <sub>4</sub> /tetrazene/B . . . . .	320
HNS linear-shaped-charge design . . . . .	1385	Igniters for KNO <sub>3</sub> /Zr . . . . .	320
HNS MDF, output measurements & modeling . .	1519	Ignition & growth flow, computer models . . . .	701
HNS powders, isothermal compressibility . . . .	209	Ignition & growth model, LX-17 . . . . .	112
HNS, chemistry in free expansion of HE products	953	Ignition & growth model, SDT, composite HE . .	593
HNS, fine-grained, reactive model . . . . .	209	Ignition & growth rate, LX-17, velocimetry . . .	133
HNS, laser initiation . . . . .	1118	Ignition & growth reaction rate law, ZND model	670
HNS, mild detonating fuse output measurements .	1510	Ignition energy vs pressure . . . . .	162
HNS, products in pre-ignition reaction zone . . .	162	Ignition mechanisms, launch environment . . . .	1460
HNS, prompt laser initiation . . . . .	1110	Ignition thresholds, TNT, LX-14, Comp A-3 . . .	1460
HNS, reflection spectra & ignition threshold . . .	1100	Ignition vs buildup, SSGT, Australian . . . . .	98
HNS, slapper detonator . . . . .	209	Ignition wave in DDT, HMX . . . . .	265
Hollow-sphere configuration modeling . . . . .	906		

# TOPIC PHRASE INDEX (Cont.) - NINTH SYMPOSIUM

	<u>Page</u>		<u>Page</u>
IHE EDC35, effect of wall on detonation velocity	831	Ionization probes in DDT studies	320
IHE EDC35, frozen hot spots in shocked	1253	IR absorption spectra, TATB	153
IHE gap test, EDC35 (95 TATB/5 Kel-F)	123	IR absorption, NM, diamond-anvil cell	1019
IHE gap tests, (ELSGT) at AFATL	1284	JA2, detonation characteristics	537
Impact hazard response, energetic materials	1245	JCZ3 EOS, dense gaseous HEs	933
Impact initiation, HE crystals	58	Jet initiation mechanism, covered HE	1404
Impact initiation, HEs by projectile	1441	Jet initiation, confined acceptor charges	1416
Impact initiation, propellants	1052	Jet penetration equation, covered, bow shock	1404
Impact on HEs, spherical projectile	1427	Jet penetration velocity vs run to detonation	1404
Impact region, propagation of detonation from	798	Jets from single-cavity collapse	869
Impact, low-velocity projectile, composite HE	1047	Jets, shaped-charge, initiation phenomena	1416
Impedance matching effect, measured det. T	947	Jones & Krier porous-bed drag	363
Impulse time integral, PBX 9502	683	Jones-Krier flow-resistance law	329
Impulse-gauge data, PBX 9502	683	Jones-Wilkins-Lee EOS	293
Indexes of Detonation Symposia, 1951-1985	1543	JWL coefficients, reactive modeling	1217
Induction test, safety analysis models	1070	JWL EOS	670
Influence on detonation, polymorphous transform.	766	JWL EOS forms	701
Initial temperature vs burning-front velocity	1070	JWL EOS of PBH-9D	142
Initiation & propagation, primary HEs	1100	JWL EOS parameter determination, Gurney	498
Initiation by adiabatic shear	886	equation.	498
Initiation by electron beam of TATB HEs	1131	JWL EOS, LX-17	133
Initiation by fracture, plastic flow & void collapse	842	JWL EOS, pinned wedge tests	25
Initiation by impact, propellants	1052	JWL EOS, porous HNS	209
Initiation diagnosis, shock, 2-D	77	Kim's model of gas generation	329
Initiation mechanism, jet on covered HE	1404	KIVA hydrodynamic & chemistry code	956
Initiation model for heterogeneous HEs	604	Lagrangian analysis of EMV experiments	816
Initiation of fast decomposition in solid HE	857	Lagrangian analysis of pressure measurements	1217
Initiation of HEs by projectile impact	1441	Lagrangian analysis, MIV gauge, PBX 9502	683
Initiation phenomena, shaped-charge jets	1416	Lagrangian analysis, reaction rates of PBH-9D	142
Initiation process, Lagrangian gauge study, EAK	89	Lagrangian gauge studies	252
Initiation properties, 95 TATB/5 Kel-F 800	123	Lagrangian gauge study of initiation	89
Initiation study, time-resolved spectrometry	172	Lagrangian gauges, 2D	816
Initiation threshold experiments, IHE	1131	Large-scale blast-pad test, NG/ -lactose	972
Initiation threshold, small flyer-plate experiments	66	Large-scale gap test, benzofuroxans	566
Initiation, impact, excitation & dissociation	1084	Laser ignition of HEs, preignition reaction	162
Initiation, impact, HE crystals	58	Laser ignition of HEs, Raman spectroscopy	1151
Initiation, laser, secondary HEs	1118	Laser initiation of secondary HEs	1118
Initiation, liquid NO	1335	Laser initiation, prompt, secondary HEs	1110
Initiation, multipoint, slab, optical data vs xray	1360	Laser Raman spectroscopy, ignition zone	1151
Initiation, NM homogeneous & heterogeneous	39	Laser-probe mass spectrography	172
Initiation, particle-size effects, HMX	25	Laser-speckle & Brazilian test	886
Initiation, plastic flow, fracture, friction, voids	857	Lattice deformation, HE crystals	58
Initiation, prompt laser, secondary HEs	1110	Lattice density of states in HE	235
Initiation, shock, LX-17 vs temperature	112	Launch environment, sensitivity of HEs to	
Intercrystalline friction	857	ignition	1460
Intercrystalline potential, HE crystals	58	Lead-foil electrostatic testing technique	1076
Interface velocimetry, PBX 9502	657	Less-sensitive HEs, capture of detonation products	962
Intermolecular HE EAK, Lagrange gauge study	89	LI/MS laser-ignited/mass spectrometry	162
Intermolecular HE, prospects	554	Lindemann theory	235
Intermolecular potential parameters, HE products	513	Linear shaped charges, design & development	1385
Internal cavities in sample, setback simulator	1480	Liquid Hugoniot, universal	39
Ionization pins for DDT experiments	259	Liquid NO, initiation & detonation	1335

# TOPIC PHRASE INDEX (Cont.) - NINTH SYMPOSIUM

	<u>Page</u>		<u>Page</u>
Lorentz-type electromagnetic gauges . . . . .	766	Mixture theory, HE EOS . . . . .	443
Low-order behavior, diameter effect . . . . .	197	Model calculation of HMX porous-bed response .	280
Low-pressure HEs, PETN/polyurethane foam . .	1364	Model for dislocation, HE crystals . . . . .	58
Low-velocity impact, compressive combustion . .	259	Model for initiation of heterogeneous HEs . . . .	604
Low-velocity impact, granular materials . . . . .	293	Model for spherical projectile impact on HE . . .	1427
LSC, linear shaped charges, collapse & jetting . .	1385	Model of reaction rates in shocked HEs . . . . .	593
LSCAP code, linear-shaped-charge analysis . . .	1385	Model of shock initiation . . . . .	1224
LX-10 booster for LX-17 . . . . .	133	Model, DDT in porous beds . . . . .	363
LX-14, EOS . . . . .	425	Model, multiprocess detonation . . . . .	724
LX-14, ignition threshold . . . . .	1460	Model, thermochemical, shock-induced reaction .	1199
LX-17, Fabry-Perot velocimetry . . . . .	133	Modeling a spherically-expanding Comp B deton.	751
LX-17, shock initiation vs temperature . . . . .	112	Modeling by mathematical morphology theory . .	1271
LX-17, supracompressed, reaction-zone structure	670	Modeling detonation waves, deton. shock	
M2, detonation characteristics . . . . .	537	dynamics . . . . .	730
M5, detonation characteristics . . . . .	537	Modeling gap tests, sensitivity vs compression . .	1451
Mach detonation disk, UFD charge design . . . .	407	Modeling HNS MDF output . . . . .	1519
Mach reflection, HE-inert interfaces . . . . .	842	Modeling of thermal ignition & combustion . . .	1070
Macrokinetics of shock-wave decomposition . . .	50	Modeling, mild detonating fuse output . . . . .	1510
Magnetic gauging experiments . . . . .	39	Modeling, reacting media, choice of equations . .	250
Manganin foil gauge . . . . .	3	Modified gap test, mechanical shocks, 27 HEs . .	1235
Manganin gauge, high resistance, detonation		Modified steel DDT tube . . . . .	354
press. . . . .	471	Molecular beam, freely expanding HE products . .	953
Manganin gauges in TNT & RDX . . . . .	50	Molecular collision excitation & dissociation . . .	1084
Manganin gauges, multiple . . . . .	25	Molecular dissociation, effect on deton. structure	713
Manganin-constantan ring gauge . . . . .	816	Molecular dynamics simulation of deton. structure	713
Manganin-constantan ring probe . . . . .	77	Molecular models for HEs, NTO . . . . .	1185
Mass displacement moment, PBX 9502 . . . . .	683	Molecular orbital calculations, C-N bond scission	1027
Mass spectrometer study of detonation products .	953	Molecular population behind shock wave . . . . .	172
Mass spectrometry, fast-transient kinetics . . . .	1140	Molecular properties, gamma sensitivity to errors	513
Mass spectroscopy of HE, preignition reaction . .	162	Molecular reactivity, HE . . . . .	246
MDF, HNS, output measurements & modeling . .	1519	Molecular/composite explosives . . . . .	545
MDF, mild detonating fuse, HNS . . . . .	1510	Molecule-surface collision-induced dissociation .	1084
Mechanisms for jet initiation of HE . . . . .	1404	Monomodal formulations, particle effect . . . . .	18
Melt line, carbon . . . . .	417	Monte Carlo method, detonation product EOS . .	452
Mercuric-s-nitrotetrazole, initiation . . . . .	1100	Morphology of grains, effect on HE behavior . .	1271
Mercury fulminate, initiation & propagation . . .	1100	Moving dislocations, HE crystals . . . . .	58
Metal combustion in composite HEs . . . . .	641	MRL & NOL SSGT . . . . .	98
Micro-indentation studies, unshocked HE crystals	1260	Multiboundary HE geometry, 2D program . . . .	730
Microballoon concentration, NM-PMMA deton. .	925	Multidimensional detonation waves, modeling . .	730
Microflash photography, impact on propellants . .	1052	Multilayered shields, sympathetic detonation . . .	1489
Microphotography, metal combustion, compos.		Multiphase mixture model, granular materials . .	293
HE . . . . .	641	Multiple Lagrange gauge experiments . . . . .	89
Microscopic processes, simulations . . . . .	713	Multipoint initiation . . . . .	1360
Microstructure, PBXs . . . . .	886	Multiprocess detonation model . . . . .	724
Mie scattering, from shocked benzene spectra . .	190	Munitions performance, Q, Cu cylinder test . . .	478
Mie-Grüneisen EOS for DDT . . . . .	329	Munitions, shielding, sympathetic detonation . . .	1489
Mie-Grüneisen equation . . . . .	50	Murnaghan solid compressibility . . . . .	209
Mild detonating fuse, modeling & output . . . . .	1510	N-NO <sub>2</sub> , time-to explosion . . . . .	228
Mining safety HEs, detonation & failure . . . . .	1351	Navier-Fourier fluid . . . . .	246
MIV gauge experiments, PBX 9502 . . . . .	683	New, more powerful HE, predicting, VLW EOS . .	435
Mixing thermal model, heterogeneous reactants .	1199	NH <sub>2</sub> deformation modes, TATB . . . . .	153
Mixture EOS . . . . .	670	Nitramine burning rates, high pressure . . . . .	1310

# TOPIC PHRASE INDEX (Cont.) - NINTH SYMPOSIUM

	<u>Page</u>		<u>Page</u>
Nitramine HEs, decomposition mechanisms . . . .	1027	Optical fiber gauges for DDT experiments . . . .	259
Nitrate HEs, decomposition mechanisms . . . . .	1027	ORA 86, properties, detonation velocity . . . . .	1008
Nitro HEs, decomposition mechanisms . . . . .	1027	Orvis interferometer, TNT & RDX . . . . .	50
Nitrogen, phase changes, effect on detonation . .	425	Overdriven Comp B Hugoniot . . . . .	379
Nitroxy radicals of HEs . . . . .	987	Overdriven shock Hugoniots, four HEs . . . . .	443
NM decomposition, diamond-anvil cell . . . . .	1019	Oxynitrotriazole, using to prepare an IHE . . . . .	1008
NM HE foams . . . . .	1364	P-t data for compressive fronts . . . . .	354
NM Hugoniot . . . . .	379	P-u <sub>p</sub> measurement methods for HE products . . . .	379
NM performance . . . . .	478	PANDA, an HE EOS code . . . . .	443
NM, ammonia complex calculations . . . . .	1027	Paramagnetic resonance products in HE . . . . .	987
NM, overdriven shock Hugoniot . . . . .	443	Parameters for CJ, ignition & growth calculation	133
NM, sensitized, SDT . . . . .	39	Particle impact on PETN & RDX crystals . . . . .	1276
NM, shock sensitivity, lattice density . . . . .	235	Particle shape, shock sensitivity effect . . . . .	83
NM, shocked, vibrational spectroscopy . . . . .	172	Particle velocity histories in EAK . . . . .	89
NM, vibrational spectroscopy . . . . .	180	Particle-breakup model for DDT . . . . .	329
NM-PMMA-GMB, Microballoon concentration . .	925	Particle-size characteristics of UK TATB . . . . .	123
NO, initiation & detonation . . . . .	1335	Particle-size effects, D and curvature . . . . .	18
NOL & MRL SSGT . . . . .	98	Particle-size effects, initiation, HMX . . . . .	25
NOL large-scale gap test . . . . .	83	Particle-size effects, sensitivity, RDX . . . . .	18
NOL SSGT, decreased sensitivity at lower TMD	98	Particle-velocity histories, PBH-9D . . . . .	142
Nonequilibrium, diffusion-controlled reactions . .	743	Particle-velocity profiles, LX-17 . . . . .	112
Nonideal explosive, AN, D & P . . . . .	560	Path-line method, MIV gauge, PBX 9502 . . . . .	683
Nonideal explosives, diameter effect . . . . .	197	PBH-9D, reaction rates . . . . .	142
Nonideal explosives, reaction rates . . . . .	197	PBX 0280, ignition threshold . . . . .	1460
Nonsteady flow in a detonator . . . . .	816	PBX 9404 performance, Q, Cu cylinder test . . . .	478
NO <sub>2</sub> deformation modes, TATB . . . . .	153	PBX 9404, calculated reaction zone . . . . .	693
NO <sub>2</sub> groups, role in molecular excitation . . . .	172	PBX 9404, Hugoniot, shock around CJ point . . .	379
NQ, performance . . . . .	478	PBX 9404, model application to shock initiation .	604
NSWC impact machine, hazard response . . . . .	1243	PBX 9404, overdriven shock Hugoniot . . . . .	443
NTO, isentropic expansion . . . . .	489	PBX 9404, reaction zone structure . . . . .	670
NTO, molecular model . . . . .	1185	PBX 9404, short-duration-shock response . . . . .	604
NTO, performance, Q . . . . .	478	PBX 9404, sustained-shock response . . . . .	604
NTO, properties & performance . . . . .	1001	PBX 9404, time-resolved conductivity test . . . .	396
NTO, theoretical and thermochemical data . . . .	489	PBX 9407, sustained 1D shock initiation . . . . .	1224
NTO/binder formulations . . . . .	1001	PBX 9501 properties, binder effect . . . . .	1014
NTO/RDX/binder formulations . . . . .	1001	PBX 9501, critical thickness . . . . .	396
Nucleation of hot spots . . . . .	50	PBX 9501, detonation parameters for EED . . . .	388
Numerical modeling of reactive media . . . . .	250	PBX 9501, time-resolved conductivity test . . . .	396
Numerical modeling, DDT . . . . .	259	PBX 9501, time-resolved conductivity, detonating	396
Numerical simulation, DDT, TS 3659 propellant	329	PBX 9502 performance, Q, Cu cylinder test . . . .	478
NWC porous-bed code . . . . .	363	PBX 9502, Hugoniot, shock around CJ point . . .	379
N <sub>2</sub> liquid, shocked, vibrational spectroscopy . . .	172	PBX 9502, MIV gauge experiments . . . . .	683
N <sub>2</sub> , liquid, vibrational spectroscopy . . . . .	180	PBX 9502, properties, binder effect . . . . .	1014
O-NO <sub>2</sub> , time-to explosion . . . . .	228	PBX 9502, reaction-zone structure . . . . .	657
Oblique detonation wave interaction at interfaces	842	PBX properties, effect of binder concentration . .	1014
Octol, Hugoniot . . . . .	379	PBX shock sensitivity, RDX crystal shape effect .	83
Octol, thin flyer-plate impact . . . . .	66	PBX, cast . . . . .	18
Octorane 86A, low-velocity projectile impact . .	1047	PBX, cast-cured, wedge test modeling . . . . .	1217
ODTX test . . . . .	1070	PBX-N5, thin flyer-plate impact . . . . .	66
OMA, optical multichannel analyzer . . . . .	1019	PBXs, fracture strength . . . . .	886
Onionskin experiment . . . . .	730	PBXW-113, ignition threshold . . . . .	1460
ONTA, use to prepare an IHE . . . . .	1008	PBXW-115, detonation propagation . . . . .	806

# TOPIC PHRASE INDEX (Cont.) - NINTH SYMPOSIUM

	Page		Page
PBXW-115, failure thickness . . . . .	396	Polar species, treatment in EOS . . . . .	513
PBXW-115, time-resolved HE conductivity test . . . . .	396	Polymorphous transformation effect on detonation . . . . .	766
Pentafluorothio group, effect on HE properties . . . . .	1162	Polysulfone Hugoniot . . . . .	822
Pentolite, Hugoniot, shock around CJ point . . . . .	379	Polysulfone SIP gauge for flying-plate detonators . . . . .	822
Percus Yevick, PY, EOS, dense gaseous HEs . . . . .	933	Polyvinylidene, PVDF . . . . .	1529
Performance, NQ, TATB, DINGU, NTO, EAR . . . . .	478	Pop plot, sensitized NM . . . . .	39
Performance, NTO . . . . .	1001	Pop plots, particle size effects . . . . .	18
Performance, ZOX, zero-oxygen-balance HE . . . . .	995	Pore collapse by shock wave . . . . .	593
Permeability of deformed/fractured materials . . . . .	363	Pore radial motion . . . . .	906
Permeability parameters . . . . .	280	Porous bed, HMX, response, deflagration & shock . . . . .	280
PETN performance, Q, Cu cylinder test . . . . .	478	Porous beds, DDT . . . . .	259
PETN, chemistry, free expansion of HE products . . . . .	953	Porous beds, dynamic compression, ball propellant . . . . .	341
PETN, detonation temperature measurement . . . . .	947	Porous nitramines, DDT . . . . .	259
PETN, detonation velocity vs density (D vs $\rho$ ) . . . . .	443	Porous solids, thermochemical model, shock . . . . .	1199
PETN, dislocations, shear bands . . . . .	1276	Postdetonation kinetics, diffusion coefficient . . . . .	1193
PETN, explosive foam . . . . .	1364	Potential energy calculations, Gaussian 86 code . . . . .	1027
PETN, impacted, spectral emission . . . . .	1037	Predicting detonation parameters with VLW EOS . . . . .	435
PETN, laser initiation . . . . .	1118	Predicting hazard response, energetic mat., impact . . . . .	1243
PETN, monocrystal decomposition vs P . . . . .	172	Predicting ideal detonation velocities . . . . .	513
PETN, overdriven shock Hugoniot . . . . .	443	Predicting threshold for jet initiation . . . . .	1404
PETN, particle-size effect, electrostatic sensitivity . . . . .	1076	Preignition reaction zone . . . . .	162
PETN, prompt laser initiation . . . . .	1110	Premature ignition of HE . . . . .	1460
PETN, Raman spectra . . . . .	1118	Premature initiation . . . . .	1480
PETN, reflection spectra & ignition threshold . . . . .	1100	Premature simulator . . . . .	1451
PETN, sensitivity coefficients for CJ properties . . . . .	513	Pressed-booster explosives, shock sensitivity . . . . .	98
PETN, shock sensitivity, lattice density . . . . .	235	Pressure at detonation front, baratol . . . . .	1378
PETN, time to explosion . . . . .	228	Pressure cycling, effect on burning rate . . . . .	1310
PETN, time-resolved mass spectra, decomposition . . . . .	162	Pressure desensitization, water-based emulsion HEs . . . . .	585
PETN, time-resolved spectrometry . . . . .	172	Pressure-particle velocity of HE products . . . . .	379
PETN, underwater detonation, chemistry . . . . .	626	Pressure-specific vol, supracompressed detonation . . . . .	670
Phase changes, C & N . . . . .	425	Primary HEs, physical & thermodynamic data . . . . .	1100
Phase diagram, carbon . . . . .	417	Proceedings indexes, Det. Symposia, 1951-1985 . . . . .	1543
Phase separation, diffusion-controlled reactions . . . . .	743	Products in preignition reaction zone . . . . .	162
Phonon modes, acoustic & optical . . . . .	235	Products of detonation for SF <sub>5</sub> model compound . . . . .	1162
Photodissociation of expansion-cooled C <sub>3</sub> F <sub>7</sub> NO . . . . .	1084	Profilometer study of HE fracture surfaces . . . . .	918
Photography, cavity collapse in emulsion HEs . . . . .	869	Projectile impact, propellants . . . . .	1052
Photography, fast decomposition in solid HEs . . . . .	857	Projectile impact, small-caliber, composite HE . . . . .	1047
Photography, high-speed, drop-weight impact . . . . .	886	Projectile, spherical, impact on HEs . . . . .	1427
Photolytic initiation . . . . .	987	Propagation of detonation from impact region . . . . .	798
Photomicrographs of emulsion HEs . . . . .	585	Propellant failure diam, estimated, small-scale test . . . . .	701
Piezoelectric polymer PVDF gauge measurements . . . . .	1529	Propellants, booster rocket, characterization . . . . .	1060
Pinned wedge test, HMX . . . . .	25	Propellants, composite, response to shock loading . . . . .	879
Piston-driven compaction experiments, simulation . . . . .	306	Propellants, gun, detonation characteristics . . . . .	537
Piston-driven DDT in granular HMX . . . . .	265	Propellants, projectile impact . . . . .	1052
Planar geometry, detonating LX-17 . . . . .	133	Prospects for composite HE . . . . .	554
Plane deton. wave, analysis, sonic point properties . . . . .	757	PSF, polysulfone film gauge . . . . .	822
Plastic deformation, HE crystals . . . . .	58	Pulsed-laser-excited Raman spectra, TATB . . . . .	153
Plastic flow, initiation of fast decomposition . . . . .	857	PVDF gauge charge vs stress . . . . .	1529
Plastic flow, role in initiation . . . . .	842	PVDF gauge, detonation response measurements . . . . .	1529
Plastic-bonded-explosives, binder concentration . . . . .	1014		
Plug in DDT, HMX, model . . . . .	265		

# TOPIC PHRASE INDEX (Cont.) - NINTH SYMPOSIUM

	Page		Page
Pyrometer, measurement of detonation temperature . . . . .	939	Reaction rate model for shocked HEs . . . . .	593
P <sub>2</sub> t vs pressure sensitivity curve . . . . .	1451	Reaction rate parameters, LX-17 . . . . .	112
Q, heat of detonation . . . . .	479	Reaction rates of PBH-9D . . . . .	142
Quasi-steady reaction wave . . . . .	219	Reaction rates, nonideal explosives . . . . .	197
QUATUOR thermochemical code, gaseous HEs . . . . .	933	Reaction thresholds, rocket propellants . . . . .	1060
Radial flow in drop-weight-impact experiments . . . . .	886	Reaction zone structure of PBX 9502 . . . . .	657
Radiography of impacted HEs . . . . .	1019	Reaction zone structure, resolved . . . . .	670
Radiolysis-stimulated detonation . . . . .	1131	Reaction zone structure, supracompressed HE . . . . .	670
Radiometric experiments, RDX particle size . . . . .	25	Reaction zone, heterogeneous HE, calculated . . . . .	693
Raman spectra of PETN . . . . .	1118	Reaction zone, mass spectroscopy of HE . . . . .	162
Raman spectra, shock-compressed TATB . . . . .	153	Reactions in porous solids, model . . . . .	1199
Raman spectrometry, ultra fast . . . . .	172	Reactive flow analysis & models . . . . .	1224
Raman spectroscopy, coherent anti-Stokes . . . . .	180	Reactive flow meas., calc., ZrH <sub>2</sub> -based composites . . . . .	525
Raman spectroscopy, laser, ignition zone . . . . .	1151	Reactive Huygens construction . . . . .	730
Random choice hydrodynamics code, RCM . . . . .	751	Reactive model, HNS . . . . .	209
Random choice method, diverging detonation . . . . .	743	Reactive modeling, wedge test . . . . .	1217
Rate of chemical energy release, heterogeneous HE . . . . .	197	Reactive shock model, compaction simulation . . . . .	306
Rat's stick geometry, detonation shock dynamics . . . . .	773	Reactivity of condensed explosives . . . . .	246
Rate stick, 2D, calculated . . . . .	730	Rearward compressive wave in DDT . . . . .	354
Rates of conductivity change . . . . .	407	Reflectance-change apparatus . . . . .	265
Rates of energy transfer & reaction . . . . .	235	Reflection spectra of PETN, HMX, & HNS . . . . .	1100
RCM, random choice method code . . . . .	751	Regular reflection at HE-inert interfaces . . . . .	842
RDX crystal shape, effect on shock sensitivity . . . . .	83	Relative sensitivity of HEs . . . . .	1460
RDX crystals in HTPB PBXs . . . . .	83	Release & recompression of detonation products . . . . .	506
RDX performance . . . . .	478	Resolved reaction zone structure . . . . .	670
RDX, chemistry in free expansion of HE products . . . . .	953	Resolved reactive zone . . . . .	693
RDX, decomposition in shock wave . . . . .	50	Richtmeyer-Meshkov instability . . . . .	869
RDX, detonation temperature measurement . . . . .	947	Rods & slabs, steady-state wave shapes . . . . .	784
RDX, detonation velocity vs density . . . . .	443	Run to detonation vs jet penetration velocity . . . . .	1404
RDX, dislocations, shear bands . . . . .	1276	RX-08-EL, burning rate . . . . .	1310
RDX, EMV particle velocity meas. in detonator . . . . .	816	RX-25-BF, EOS & reaction-rate parameters . . . . .	525
RDX, EOS parameters . . . . .	50	RX-25-BH, EOS & reaction-rate parameters . . . . .	525
RDX, Grades A & B, small-scale gap test . . . . .	98	RX-26-AF propagation of detonation from impact . . . . .	798
RDX, laser ignition, Raman spectra, ignition zone . . . . .	1151	RX-26-AF, impact at low temperature . . . . .	798
RDX, laser initiation . . . . .	1118	RX-26-AF, supracompr., reaction zone structure . . . . .	670
RDX, particle effects on sensitivity . . . . .	18	RX-35-AP, burning rate . . . . .	1310
RDX, pore collapse parameters . . . . .	906	Schlieren photog., cavity collapse, emulsion HE . . . . .	869
RDX, products in preignition reaction zone . . . . .	162	SCW, strong compressive wave from igniter, DDT . . . . .	354
RDX, RDX/wax, DDT phases . . . . .	259	SDT in EAK, Lagrange gauge study . . . . .	89
RDX, time-resolved spectrometry . . . . .	172	SDT process, conceptual interpretation . . . . .	593
RDX/NQ/Al, detonation products in Ar, vacuum . . . . .	962	SDT transition data, emulsion HE . . . . .	573
RDX/wax, DDT . . . . .	320	SDT, damaged energetic materials . . . . .	1295
Reaction behavior in condensed phase . . . . .	363	SDT, model of reaction rates . . . . .	593
Reaction degree, . . . . .	142	SDT, NM, sensitized . . . . .	39
Reaction diagram, pressure-temperature, NM . . . . .	1019	SDT, theory, homogeneous HE . . . . .	219
Reaction diffusion theory in detonation . . . . .	1193	Secondary HEs, laser initiation . . . . .	1118
Reaction growth process . . . . .	1243	Secondary HEs, prompt laser initiation . . . . .	1110
Reaction of molten Al with water . . . . .	641	Sensitivity curve of HE, theoretical . . . . .	1451
Reaction products, condensed HEs, EPR . . . . .	939	Sensitivity experiments, PBX, particle size effect . . . . .	18
Reaction products, shock properties at C-J point . . . . .	379		



# TOPIC PHRASE INDEX (Cont.) - NINTH SYMPOSIUM

	<u>Page</u>		<u>Page</u>
Sensitivity of HE, correlation to compression input . . . . .	1451	Shock-induced deflagration in shells . . . . .	1322
Sensitivity of HEs to air compression, deformation . . . . .	1460	Shock-induced reactions, thermochemical model . . . . .	1199
Sensitivity of HEs to ignition in launch environment. . . . .	1460	Shock-light coupling, initiation . . . . .	172
Sensitivity testing of HEs, electrostatic . . . . .	1076	Shock-loading area, initiation threshold . . . . .	66
Sensitivity, shock, substituted benzofuroxans . . . . .	561	Shocked multicomponent HEs, model, reaction rate . . . . .	593
Sensitization by voids . . . . .	857	Short-duration-shock response of PBX 9404 . . . . .	604
Sensitizer droplets, role in modeling initiation . . . . .	1351	Short-shock experiments, 1D, PBX 9502 . . . . .	657
Setback simulator . . . . .	1460	Shotgun tests, rocket propellant . . . . .	1052
Setback simulator, DREV . . . . .	1480	Silicon, polymorphic transformation, detonation . . . . .	766
SF <sub>5</sub> (pentafluorothio) group HEs, new . . . . .	1162	Simulants, booster-rocket propellants, characteriz. . . . .	1060
Shaped charge jet initiation . . . . .	1404	Simulated gun launch . . . . .	1480
Shaped charge penetration . . . . .	537	Simulation of compaction wave, granular material . . . . .	306
Shaped charges, linear, design & development . . . . .	1385	Single crystals of HE, theory of shock initiation . . . . .	235
Shaped-charge jets, initiation phenomena . . . . .	1416	Single crystals, AP, shock loading . . . . .	1260
Shaw-Johnson (SJ) diffusion model . . . . .	953	SIP gauge for flying-plate detonators . . . . .	822
Shear bands, hot spots in HE crystals . . . . .	58	Slabs & rods, steady-state wave shapes . . . . .	784
Shear bands, RDX, PETN . . . . .	1276	Slapper detonator, HNS . . . . .	209
Shear bands, TNT-double base propellant . . . . .	3	Small-scale gap test, SSGT . . . . .	98
Shear ignition test . . . . .	3	Small-scale intermediate gap test . . . . .	566
Shear sensitivity test . . . . .	3	Small-scale tests, estimate failure diam, propellant . . . . .	701
Sheet-explosive deflagration donors . . . . .	1322	Solid-explosive foam (PETN) . . . . .	1364
Shell HE fillings with defects, simulat. gun launch . . . . .	1480	Sonic point properties in plane detonation wave . . . . .	757
Shielding, sympathetic detonation, computation . . . . .	1489	Soot analysis from TNT/NQ, PBX, RDX/NQ/Al . . . . .	962
Shock & deformation mitigation by shields . . . . .	1489	Soot recovery from detonation . . . . .	417
Shock behavior of reaction products at C-J point . . . . .	379	Soot, chemistry of detonation . . . . .	1170
Shock dynamics, Whitham's theory, divergent det. . . . .	784	Spall strengths, rocket propellants . . . . .	1060
Shock ignition of single crystals, lattice densities . . . . .	235	Species at final state . . . . .	906
Shock initiation, LX-17 vs temperature . . . . .	112	Spectral emission, impacted PETN . . . . .	1037
Shock initiation, reactive modeling . . . . .	1217	Spectral slope vs fractal dimension . . . . .	918
Shock initiation, role of free radicals . . . . .	987	Spectrometry, time-resolved, initiation study . . . . .	172
Shock loading, response of composite propellants . . . . .	879	Spectroscopy, absorption, shocked benzene . . . . .	190
Shock polar solutions . . . . .	842	Spectroscopy, vibrational, shocked liq. N <sub>2</sub> & NM . . . . .	172
Shock sensitivity of HMX . . . . .	25	Spectroscopy, vibrational, shocked liq. N <sub>2</sub> & NM . . . . .	180
Shock sensitivity of substituted benzofuroxans . . . . .	566	Spherical explosion, Comp B . . . . .	743
Shock sensitivity testing, EDC35 . . . . .	123	Spherical generator, divergent, calibration . . . . .	1371
Shock sensitivity, damaged energetic materials . . . . .	1295	Spherical projectile impact on HEs . . . . .	1427
Shock sensitivity, EAK . . . . .	89	Spherically-diverging detonation, LX-17 . . . . .	133
Shock sensitivity, emulsion HEs . . . . .	585	Squib-driven DDT experiment . . . . .	280
Shock sensitivity, gap tests . . . . .	1284	SSS, 1-D hydrocode for reactive media . . . . .	142
Shock sensitivity, modified gap test . . . . .	1235	Stages in DDT process for porous charges . . . . .	354
Shock sensitivity, PETN, NM . . . . .	235	Starch-metal composites, detonability . . . . .	972
Shock sensitivity, pressed booster explosives . . . . .	98	Stationary deflagration in DDT . . . . .	259
Shock sensitivity, RDX crystal shape effect . . . . .	83	Steady-state waveshapes in rods & slabs . . . . .	784
Shock sensitivity, substituted benzofuroxans . . . . .	561	Steady-wave (rate stick) experiments, PBX 9502 . . . . .	657
Shock wave energy (SWE) for HEs . . . . .	633	Stochastic simulation . . . . .	1193
Shock wave, decomposition of HE . . . . .	50	Strand burner, hybrid closed bomb . . . . .	1310
Shock-capture method . . . . .	293	Streak images of Al wire combustion in water . . . . .	641
Shock-decomposition processes . . . . .	724	Structures & energies, calculated, isomers of NTO . . . . .	1185
		Subdetonation reaction, 27 HEs, data base . . . . .	1235
		Subignition decomposition, chemical products . . . . .	897

# TOPIC PHRASE INDEX (Cont.) - NINTH SYMPOSIUM

	Page		Page
Sugar-metal composites, detonability . . . . .	972	TIGER calculations, baratol . . . . .	1378
Supercritical phase separations . . . . .	425	TIGER calculations, pinned-wedge tests . . . . .	25
Superdetonation, SDT . . . . .	39	TIGER code calculation for starch/Al . . . . .	972
Supracompressed HE, reaction-zone structure . . . . .	670	TIGER code calculations of DDT . . . . .	320
Surface cavities in sample, setback simulator . . . . .	1480	Time to onset of compressive reaction, DDT . . . . .	306
Surface-burning model . . . . .	604	Time-dependent absorp. spectroscopy, C <sub>6</sub> H <sub>6</sub> . . . . .	190
Surface-coating disruption, RDX grain . . . . .	98	Time-resolved conductivity, detonating HE . . . . .	396
Sustained 1D shock initiation, PBX 9407 . . . . .	1224	Time-resolved infrared spectral photog., TRISP . . . . .	153
Sustained ignition, mechanical shock, 4-86 kbar . . . . .	1235	Time-resolved mass spectra . . . . .	162
Sustained-shock experiments, PBX 9502 . . . . .	657	Time-resolved mass spectrometry . . . . .	1140
Sustained-shock response of PBX 9404 . . . . .	604	Time-resolved spectrometries in initiation . . . . .	172
SWE, shock wave energy for HEs . . . . .	633	Time-to-exotherm, thermocouple measurement . . . . .	228
Sympathetic detonation, shielding role . . . . .	1489	TNT Hugoniot . . . . .	379
Synthesis of diamonds, detonating condensed HE . . . . .	407	TNT labeled with <sup>13</sup> C . . . . .	407
Synthesis of polynitro SF <sub>5</sub> model compound . . . . .	1162	TNT performance, Q, Cu cylinder test . . . . .	478
TATB HEs, electron-beam initiation . . . . .	1131	TNT reaction products . . . . .	962
TATB performance . . . . .	478	TNT soot, mass spectrum, ODTX . . . . .	1170
TATB, 1D Lagrangian experiments & simulation . . . . .	252	TNT, 2D Lagrangian probe . . . . .	77
TATB, detonation products EOS . . . . .	506	TNT, cast, numerical modeling . . . . .	250
TATB, hot spots' nature . . . . .	897	TNT, chemistry in free expansion of HE products . . . . .	953
TATB, hydrogen bonding . . . . .	153	TNT, decomposition in shock wave . . . . .	50
TATB, LX-17 shock initiation vs temperature . . . . .	112	TNT, detonation pressure profile . . . . .	471
TATB, propagation of detonation from impact . . . . .	798	TNT, detonation temperature measurement . . . . .	947
TATB, Raman spectra of shock-compressed . . . . .	153	TNT, detonation velocity vs density . . . . .	443
TATB, thermochemical data . . . . .	489	TNT, detonation-front temperature . . . . .	939
TATB/Kel-F 800 95/5, initiation & detonation . . . . .	123	TNT, EMV particle velocity meas. in detonator . . . . .	816
TATB/T2 Hugoniot . . . . .	379	TNT, fracture surface topography . . . . .	918
Temperature effect on LX-17 shock initiation . . . . .	112	TNT, ignition threshold . . . . .	1460
Temperature effects, propellant detonation . . . . .	537	TNT, overdriven shock Hugoniot . . . . .	443
Temperature evaluation, SDT explosion phase . . . . .	219	TNT, pressed & cast, shock wave properties . . . . .	50
Temperature profiling, FTIR . . . . .	228	TNT, pressed with liquid in pores . . . . .	724
Temperature, detonation, measurement, HN/HH . . . . .	939	TNT, pressure shear ignition . . . . .	3
Temperatures, calculated on an isentrope . . . . .	1199	TNT, reaction zone structure . . . . .	670
Temperatures, calculated, TATB, vs pressure . . . . .	153	TNT, thin-flyer plate impact . . . . .	66
Tetrazole, time to explosion . . . . .	228	TNT/NQ, detonation products in argon & vacuum . . . . .	962
Tetryl, detonation front temperature . . . . .	939	TNT/RDX, 90/10 to 30/70 . . . . .	407
Tetryl, detonation pressure profile . . . . .	471	Topography, fracture surface of HEs . . . . .	918
Tetryl, detonation temperature measurement . . . . .	947	Torvik's method, Hugoniot for mixtures . . . . .	34
Tetryl, products in preignition reaction zone . . . . .	162	TP-H1207C propellant, characterization . . . . .	1060
Tetryl, small-scale gap test . . . . .	98	TRISP feasibility, CHNO decomposition kinetics . . . . .	1140
Thermal explosion chemistry, gas products, time . . . . .	228	TRISP, time-resolved infrared spectral photography . . . . .	153
Thermal ignition & combustion, heterogeneous HE . . . . .	1070	TS 3659, DDT studies . . . . .	354
Thermal initiation, role of free radicals . . . . .	987	TS3659 propellant, numerical simulation of DDT . . . . .	329
Thermite Hugoniot, calculated . . . . .	1199	TS3659, compressive reaction . . . . .	341
Thermochemical model, shock-induced reactions . . . . .	1199	TS3659, thermophysical & material property data . . . . .	293
Thermocouples, measuring time to exotherm . . . . .	228	TS3659, x-t DDT data . . . . .	306
Thermograms of emulsion HEs . . . . .	585	Two-stage light-gas gun, shocked C <sub>6</sub> H <sub>6</sub> . . . . .	190
Three-rate-equation model, initiation of PBX 9502 . . . . .	657	Two-step combustion model, granular materials . . . . .	293
Threshold for jet initiation, predicting . . . . .	1404	TZL-4, time to explosion . . . . .	228
Threshold for laser initiation, PETN, HMX, HNS . . . . .	1100	UFD particle-size distributions . . . . .	407
Threshold impact velocity of jet vs diameter . . . . .	1416	UFD, ultrafine-diamonds from detonating HE . . . . .	407

# TOPIC PHRASE INDEX (Cont.) - NINTH SYMPOSIUM

	<u>Page</u>		<u>Page</u>
UGS propellant, characterization . . . . .	1060	Wave-front curvature . . . . .	806
Ultrafast laser microphotography . . . . .	641	Wavelength dependence, laser initiation . . . . .	1118
Underwater detonation, AN emulsion HEs . . . . .	621	WC140, compressive reaction . . . . .	341
Underwater explosion, emulsion HEs . . . . .	641	WC140, thermophysical & material property data . . . . .	293
Underwater HE detonation, chemistry . . . . .	626	WC231, thermophysical & material property data . . . . .	293
Underwater HEs, performance estimate . . . . .	633	Weak detonation, polymorphous transformation . . . . .	766
Underwater sensitivity test . . . . .	1235	Wedge test, baratol . . . . .	1378
Underwater shock input, TATB, HMX, & AP . . . . .	897	Wedge test, emulsion properties . . . . .	573
Unreacted Hugoniot, emulsion HE . . . . .	573	Wedge test, liquid NO, cold, gas gun . . . . .	1335
Variable-density HE, foams . . . . .	1364	Wedge test, modeling, PBX, 2D JWL . . . . .	1217
Velocimetry, Fabry-Perot interferometry . . . . .	1371	Wedge test, particle-size effect on PBX . . . . .	18
Vibrational energy transfer in HE . . . . .	235	Wedge tests, HMX formulations . . . . .	25
Vibrational modes, TATB Raman spectra . . . . .	153	Wedge tests, pinned, HMX, particle size . . . . .	25
Vibrational spectroscopy, molecular initiation . . . . .	172	Whitham's shock dynamics theory, divergent . . . . .	784
Vibrational spectroscopy, shocked liq. N <sub>2</sub> & NM . . . . .	180	Wilkins EOS of detonation products, TATB . . . . .	506
Vibron level, lattice density, PETN & NM . . . . .	235	Wire heating, high-speed microphotography . . . . .	641
Violence of HE response compared to sensitivity . . . . .	1460	WONDY, 1D Lagrangian propagation code . . . . .	209
Virial EOS of detonation products, TATB . . . . .	506	Wood-Kirkwood reaction zone length . . . . .	806
Virtual piston in DDT . . . . .	265	Wood-Kirkwood theory, nonideal explosives . . . . .	197
VISAR on TNT & RDX . . . . .	50	X-0242, performance & sensitivity . . . . .	1014
VISAR PSF gauge, data comparison . . . . .	822	X-0420 performance . . . . .	478
VISAR, meas. of HNS mild detonating fuse . . . . .		X-0430, performance & sensitivity . . . . .	1014
output . . . . .	1510	X-0432 performance . . . . .	478
VISAR, reaction-zone struct., supracompressed . . . . .		X-0438, performance & sensitivity . . . . .	1014
HE . . . . .	670	X-0444, performance & sensitivity . . . . .	1014
VLW EOS, predicting detonation parameters . . . . .	435	X-ray study of DDT in granular HMX . . . . .	265
Void collapse, role in initiation . . . . .	842	X-ray tomography of HE defects . . . . .	868
Void gas effect on temperature measurement . . . . .	947	XM39, detonation characteristics . . . . .	537
Voidage, effect on reaction rate . . . . .	197	XNOVAK code for DDT . . . . .	329
von Neumann-spike pressure, LX-17 . . . . .	133	XPS spectra, HMX, RDX . . . . .	897
V <sup>2</sup> d jet initiation criterion . . . . .	1416	XPS, x-ray photoelectron spectroscopy . . . . .	897
WAK-2 propellant, characterization . . . . .	1060	ZOX properties and formulations . . . . .	995
Wall effect on EDC35 detonation velocity . . . . .	831	ZOX, chemical and detonation properties . . . . .	985
Wave propagation in EDC35 . . . . .	1243	ZrH <sub>2</sub> -based composites, reactive flow meas., calc. . . . .	525
Wave shapes, steady-state, rods & slabs . . . . .	784		

# AUTHOR INDEX - NINTH SYMPOSIUM

Page	Page	Page
Agnew, S. F. . . . . 1019	Carlson, D. W. . . . 626, 1260	Frank, A. M. . . . . 641
Akst, I. B. . . . . 478	Castille, C. . . . . 1070	Frey, R. B. . . . . 3, 1404
Alcon, R. R. . . . . 39	Chaisse, F. . . . . 506, 757	Fu Xinghai . . . . . 1360
Aldis, D. F. . . . . 112, 280	Chan, M. L. . . . . 566	Fujiwara, S. . . . . 621
Alexander, K. E. . . . 498	Chaudhri, M. M. . . . 857	Fukatsu, Y. . . . . 640
Anderson, C. J. . . . . 1364	Chen Fumei . . . . . 816	Gibb, A. W. . . . . 853, 1364
Andrew, M. I. . . . . 1253	Chen Peiqi . . . . . 142	Gimenez, P. . . . . 1371
Andriot, P. . . . . 506	Cheret, R. . . . . 246	Ginsberg, M. J. . . . . 537
Anisichkin, V. F. . . . 407	Cherin, H. . . . . 1271	Glancy, B. C. . . . . 341, 1260
Arbuckle, A. L. . . . . 1489	Chick, M. C. . . . . 1404	Glenn, J. G. . . . . 1284
Armstrong, R. W. . . . 1260	Chiles, W. C. . . . . 1335	Gohar, P. . . . . 1271
Asay, B. W. . . . . 265, 537	Chirat, R. . . . . 489	Graham, K. J. . . . . 1295
Atwood, A. I. . . . . 363	Cichra, D. A. . . . . 633	Graham, R. A. . . . . 1529
Aubert, S. A. . . . . 1284	Clements, R. E. . . . 641	Green, L. G. . . . . 670, 701
Austing, J. L. . . . . 972	Coffey, C. S. . . . . 58, 897, 1243	Green, N. J. B. . . . . 1193
Aveillé, J. . . . . 506, 842	Cook, M. D. . . . . 1027, 1441	Greiner, N. R. . . . . 953, 1170
Baer, M. R. . . . . 293, 906	Cooper, J. . . . . 197	Groux, J. . . . . 1217
Bahl, K. L. . . . . 133	Cooper, P. W. . . . . 379	Guo Yuxian . . . . . 554
Bai Chunhua . . . . . 879	Costantino, M. S. . . . 1310	Guri, G. . . . . 506
Bainville, D. . . . . 1070	Cowperthwaite, M. . . 89, 388	Han Chengbang . . . . 947
Baker, D. E. . . . . 972	Craig, B. G. . . . . 573	Hannaford, C. E. . . . 1076
Baker, R. N. . . . . 806	Crane, S. L. . . . . 1543	Haskins, P. J. . . . . 1027, 1441
Bardo, R. D. . . . . 235	Crawford, P. C. . . . . 25	Hattori, K. . . . . 640
Baudin, G. . . . . 1371	Crouch, L. D. . . . . 798	Held, M. . . . . 1416
Bauer, P. . . . . 925, 933	Davidova, O. N. . . . . 724	Helm, F. H. . . . . 25
Bdzil, J. B. . . . . 730, 773	Davis, W. C. . . . . 1335	Hermes, R. . . . . 1170
Beard, B. C. . . . . 897	de Longueville, Y. . . 1371	Heuze, O. . . . . 925, 933
Beccuwe, A. . . . . 1008	Deal, W. E. . . . . 1543	Hikita, T. . . . . 939
Bedoch, J. P. . . . . 1371	Deiter, J. S. . . . . 626	Ho, S. Y. . . . . 1052
Beitel Jr., F. P. . . . . 585	Delclos, A. . . . . 1008	Holmes, N. C. . . . . 190
Belanger, C. . . . . 1480	Delpuech, A. E. . . . . 172	Hrdina, D. J. . . . . 972
Belcher, R. A. . . . . 831, 1253	Demske, D. . . . . 1131	Hsieh, T. . . . . 329
Belmas, R. . . . . 1070	DeVost, D. F. . . . . 1243	Huan Shi . . . . . 77, 252
Benjamin, K. J. . . . . 1460, 1489	Dick, J. J. . . . . 683	Huang Lihong . . . . . 947
Bernard, S. . . . . 489	Dickson, P. M. . . . . 1100	Hubbard, P. J. . . . . 1322
Bernecker, R. R. . . . 354	Dimas, P. . . . . 1076	Huntley, J. M. . . . . 886
Bhasu, V. C. Jyothi . . 1276	Ding Jing . . . . . 77, 252, 879	Hutchinson, C. D. . . . 123
Bines, A. . . . . 1404	Doherty, R. M. . . . . 626, 633	Iida, M. . . . . 621
Blais, N. C. . . . . 953	Dold, J. W. . . . . 219	Ishiokawa, N. . . . . 621
Blake, O. . . . . 3	Dong Haishan . . . . . 995	Iwata, L. . . . . 1084
Boggs, T. L. . . . . 363	Dorsey, T. M. . . . . 1489	James, H. R. . . . . 1441
Boslough, M. B. . . . . 1199	Dremin, A. N. . . . . 724	Jia Quansheng . . . . . 816
Bourne, N. K. . . . . 869	Dufort, S. . . . . 1271	Johnson, J. D. . . . . 417
Boyer, L. R. . . . . 1295	Dunand, M. . . . . 933	Jones, A. G. . . . . 123
Boyle, V. M. . . . . 3, 897, 1460	Eden, G. . . . . 831, 1253	Jones, H. D. . . . . 461
Braithwaite, M. . . . . 513	Elban, W. L. . . . . 1260	Jun Wung Lee . . . . . 471
Brazell, N. . . . . 1131	Engelke, R. . . . . 39, 657	Jungst, R. G. . . . . 1510
Breithaupt, R. D. . . . 133, 525, 1378	Erickson, K. L. . . . . 1140	Kanel, G. I. . . . . 50
Brill, T. B. . . . . 228	Erickson, L. M. . . . . 112	Kang Shufang . . . . . 947
Brown, W. Byers . . . . 513	Erskine, D. J. . . . . 670	Kang, J. . . . . 906
Brun, L. . . . . 757	Fanget, A. . . . . 1047	Kapila, A. K. . . . . 219
Brush, P. J. . . . . 228	Farley, W. E. . . . . 1131	Kato, Y. . . . . 640, 939
Bugaut, F. . . . . 489	Ferm, E. N. . . . . 1427	Kennedy, D. L. . . . . 1224
Bukiet, B. G. . . . . 751	Fickett, W. . . . . 730	Kennedy, M. . . . . 1351
Buntain, G. A. . . . . 1037	Field, J. E. . . . . 869, 886, 1100,	Kenney, I. . . . . 1019
Bussell, T. J. . . . . 1404	1276	Kenney, J. . . . . 1019
Butler, P. B. . . . . 906	Foan, G. C. W. . . . . 123	Kerihuel, M. T. . . . . 506
Campbell, A. W. . . . . 265, 537	Forbes, J. W. . . . . 806, 897, 1235	Kerley, G. I. . . . . 443
Campos, J. . . . . 925	Forest, C. A. . . . . 683	Kerr, I. D. . . . . 1351
Capellos, C. . . . . 1084	Fortov, V. E. . . . . 50	Kershner, J. D. . . . . 693
Carion, N. . . . . 506, 842	Fortova, T. N. . . . . 50	Kim, K. . . . . 329, 593

# AUTHOR INDEX (Cont.) - NINTH SYMPOSIUM

Page	Page	Page
Kinney, J. H. . . . . 868	Paisley, D. L. . . . . 1110	Steele, R. D. . . . . 1014
Kipp, M. E. . . . . 209, 1510	Palmer, S. J. P. . . . . 886	Stewart, D. S. . . . . 730, 773
Kleinhanss, H.R. . . . 66	Parry, M. A. . . . . 886, 1100	Stretz, L. A. . . . . 1014
Klimenko, V. Yu. . . . 724	Parsons, G. H. . . . . 1284	Sumida, W. K. . . . . 972
Kober, E. M. . . . . 1185	Persson, P. -A. . . . . 545, 573	Sun Chengwei . . . . 142
Kodde, H. H. . . . . 560	Pettit, D. R. . . . . 683	Sun Jian . . . . . 435
Kolodney, K. . . . . 1084	Peyrard, M. . . . . 713	Swanson, B. I. . . . . 1019
Kooker, D. E. . . . . 306	Pilarski, D. L. . . . . 1460	Swift, D. C. . . . . 784
Kornhauser, M. . . . . 1451	Pilling, M. J. . . . . 1193	Takala, B. E. . . . . 1543
Krall, A. D. . . . . 341	Pinto, J. J. . . . . 918	Taliancich, A. G. . . . 89
Kury, J. W. . . . . 25, 1378	Politzer, P. . . . . 566	Tanaka, K. . . . . 621
Lambourn, B. D. . . . 784	Powers, P. S. . . . . 1084	Tang, P. K. . . . . 657
Lambrakos, S. G. . . . 713	Presles, H. N. . . . . 925, 933	Tao, W. C. . . . . 641, 798, 868, 1310
Lanzerotti, M. Y. D. . . 918	Price, C. F. . . . . 363	Tarver, C. M. . . . . 112, 133, 525, 670, 701
Larson, T. E. . . . . 1076	Price, D. . . . . 1235	Tasker, D. G. . . . . 396
Lawn, H. R. . . . . 123	Quidot, M. . . . . 1217	Taylor, G. W. . . . . 1014, 1037
Lee, E. L. . . . . 280	Ramsay, J. B. . . . . 265, 537, 1427, 1543	Thoreen, J. L. . . . . 1284
Lee, J. . . . . 573	Reddy, G. O. . . . . 585	Titov, V. M. . . . . 407
Lee, L. M. . . . . 1529	Ree, F. H. . . . . 425	Tokita, K. . . . . 640
Lee, R. J. . . . . 396	Ree, F. H. . . . . 743	Tomlinson, R. . . . . 1322
Lee, R. S. . . . . 798	Reed, R. P. . . . . 1529	Torii, A. . . . . 640
Leiper, G. A. . . . . 197, 1224	Reisler, H. . . . . 1084	Trebinski, R. . . . . 766
Lemar, E. R. . . . . 806	Renick, J. D. . . . . 545	Trofimov, V. S. . . . . 250
Lepie, A. H. . . . . 1295	Renlund, A. M. . . . . 153, 1118	Trott, W. M. . . . . 153, 1118
Leroy, M. . . . . 506	Reynier, P. . . . . 1070	Trzcinski, W. . . . . 766
Liddiard, T. P. . . . . 1235	Rice, S. F. . . . . 190	Tulis, A. J. . . . . 972
Lind, C. D. . . . . 566	Richter, H. P. . . . . 1295	Urtiew, P. A. . . . . 112
Loupias, C. . . . . 1047	Ringbloom, V. . . . . 626	Utkin, A. V. . . . . 50
Lungenstrass, F. . . . 66	Ritchie, J. P. . . . . 1185	Vacellier, J. . . . . 842
Mader, C. L. . . . . 693	Rivera, T. . . . . 1014, 1037	van der Steen, A. C. . . 83, 320, 560
Mal'kov, I. Yu. . . . . 407	Robertson, S. H. . . . 1193	van Thiel, M. . . . . 425, 743
Malyrenko, S. I. . . . . 50	Rosenberg, J. T. . . . . 89	Verbeek, H. J. . . . . 83, 320
Marlow, W. R. . . . . 1253	Saint-Martin, C. . . . . 1371	Vigil, M. G. . . . . 1385
McAfee, J. M. . . . . 265	Sakai, H. . . . . 939	Volk, F. . . . . 962
McCandless, P. . . . . 190	Sakurai, T. . . . . 939	Von Holle, W. G. . . . 133
McFadden, D. L. . . . 1460	Samirant, M. . . . . 259	Von Rosen, K. . . . . 1364
McKinney, T. L. . . . . 1037	Sanchez, J. A. . . . . 545	Wackerle, J. . . . . 657, 683
Meulenbrugge, J. J. . . 83	Sandstrom, F. W. . . . 573	Wang Tinzheng . . . . 816
Miller, P. J. . . . . 341, 498	Sandusky, H. W. . . . 341, 1260	Warnes, R. . . . . 1131
Miller, S. . . . . 1131	Schedlbauer, F. . . . . 962	Warren, T. W. . . . . 822
Mishra, I. B. . . . . 1084	Schmidt, S. C. . . . . 180	Weinmaster, R. R. . . . 822
Miyake, A. . . . . 560	Schott, G. L. . . . . 1335	Weirick, L. J. . . . . 1060
Moen, I. O. . . . . 1364	Seitz, W. L. . . . . 657	Weston, A. M. . . . . 280
Mohan, V. K. . . . . 1276	Servas, J. M. . . . . 842	Wilmot, G. B. . . . . 626
Moore, D. S. . . . . 180	Setchell, R. E. . . . . 209	Witkowski, W. . . . . 766
Moore, L. M. . . . . 1529	Sharma, J. . . . . 897	Wittig, C. . . . . 1084
Mori, N. . . . . 640, 939	Shaw, M. S. . . . . 452	Wlodarczyk, E. . . . . 766
Moulard, H. . . . . 18	Sheffield, S. A. . . . . 39, 683	Wolfe, A. . . . . 918
Murphy, M. J. . . . . 525	Shepherd, J. E. . . . . 641	Woody, D. L. . . . . 1243
Nakayama, Y. . . . . 621	Shi Huisheng . . . . . 947	Wu Xiong . . . . . 435
Nanut, V. . . . . 98	Simpson, R. L. . . . . 25, 280, 525	Xiao Lianjie . . . . . 435
Nilsson, H. . . . . 162, 1151	Sitzmann, M. E. . . . . 1162	Yoshida, M. . . . . 621
Nunziato, J. W. . . . . 293	Skocypec, R. D. . . . . 1140	Yu Jun . . . . . 1360
Oran, E. S. . . . . 713	So-young Song . . . . . 471	Zerilli, F. J. . . . . 461
Ornellas, D. L. . . . . 1162, 1310	Spears, R. J. . . . . 98	Zhang Guan-Ren . . . . 1360
Ostmark, H. . . . . 162, 1151	Stacy, H. L. . . . . 657	Zhao Feng . . . . . 142
Otani, G. . . . . 190	Stanton, P. L. . . . . 1118	Zöellner, H. . . . . 66
Ouyang Denghuan . . . 142	Starkenber, J. . . . . 604, 1460, 1489	Zoludeva, T. A. . . . . 724
Pace, M. D. . . . . 987		Zwierzchowski, N. G. 1295

# ACRONYM AND CODE NAME INDEX - NINTH SYMPOSIUM

Page		Page			
A-3	106	.91 RDX/9 wax	O	1236	other material
ADNBF	566	.7 amino-4,6 dinitrobenzofuroxan	Octogen	1236	.HMX
AF 902	487	.95 NQ/5 Viton A	Octol	69	.64 RDX/36 TNT
AFX-108 E	1236	.82 RDX/18 O	Octorane 86A	1047	.84 HMX/16 PU
AFX1100	1284	.66 TNT/16 OD2 wax/18 Al	ORA86	1008	.86 HMX/14 inert binder
AMMO	232	.azidomethyl methyloxetane	PBH-9D	144	.HMX, plastic bonded
ATEC	539	.acetyl triethyl citrate	PBX-0280	1463	.95 RDX/5 Estane
B 2214	1008	.12 HMX/72 NTO/16 inert binder	PBX-0280/PE	1463	.95 RDX/5 polyethylene
Baratol UK	793	.70 TNT/30 BaNO <sub>3</sub>	PBX-9010	1082	.90 HMX/10 Kel-F 800
BDNPA	1018	.bis (2,2-dinitropropyl)-acetal	PBX-9011	1083	.90 HMX/10 Estane
BDNPA-F	1236	.eutectic	PBXC-117	1236	.71 RDX/17 Al/12 other
BDNPF	1018	.bis (2,2-dinitropropyl)-formal	PBXC-121	1236	.82 HMX/18 other
CAB	539	.cellulose acetate butyrate	PBXN-103	1236	.23 TT/40 AP/27 Al/10 other
Cedosol 10	1082	.B <sub>10</sub> H <sub>12</sub> (CsNO <sub>3</sub> ) <sub>2</sub>	PBXW-106 E	1236	.75 RDX/18 BDNPA-F/7 other
CH6	100	.97.5 RDX/0.5 polyisobutylene/0.5 calcium stearate/0.5 graphite	PBXW-108 I	1236	.85 RDX/15 other
CMBD	7	.NC/NG/HMX/Al/AP	PBXW-109 E	1236	.64 RDX/20 Al/16 other
Comp A3	1463	.91 RDX/9 polyethylene	PBXW-109 I	1236	.65 RDX/20 Al/15 other
Comp B-3	1236	.60 RDX/40 TNT	PBXW-113 II	1236	.68 HMX/12 other
CW3	1323	.analog of 60 RDX/40 TNT	PBXW-114 II	1236	.78 HMX/10 Al/12 other
CX-84A	1482	.84 RDX/16 HTPB	PBXW-115	806	.20 RDX/43 AP/25 Al/12 HTPB
Cyclotol 25/75	1236	.25 RDX/75 TNT	PBXW-7	106	.36 RDX/60 TATB/5 Viton A
Cyclotol 60/40	1236	.60 RDX/40 TNT	PHX31	963	.85 RDX/15 Cariflex 1107
D-2	1236	.84 D2 wax/14 NC/2 lecithin	PSF	822	.polysulfone
DNNC	232	.1,3,5,5-tetranitro-hexahydropyrimidine	RX-08-EL	1312	.73 HMX/25 FEFO/I PCL 240/other
EDC-29	793	.95 HMX/5 polyurethane	RX-08-FL	7	.75.9 HMX/22.2 FEFO/1.9 polyvinyl binder
EDC-32	793	.85 HMX/15 Viton	RX-08-GB	26	.61 HMX/36 FEFO/3.1 urethane
EDC-35	123	.95 TATB/5 Kel-F 800	RX-08-GG	26	.61 HMX/36 FEFO/3.1 urethane
EE	585	.emulsion explosive	RX-25-BF	526	.38 HMX/36 AP/22 ZrH <sub>2</sub> /4 Estane
EJC-90	1236	.26 HMX/14 NC/32 NG/5 AP/18 Al/5 O	RX-25-BH	526	.19 HMX/47 AP/30 ZrH <sub>2</sub> /4 Estane
eutectic	1015	.50 BDNPA/50 BDNPF	RX-25-BP	526	.38 HMX/36 AP/22 ZrH <sub>2</sub> /4 Estane
FT-1	879	.21 thiokol/8 Al/65AP	RX-25-BQ	526	.38 HMX/36 AP/22 ZrH <sub>2</sub> /4 Estane
FT-2	879	.11 HTPB/18 Al/68 AP	RX-35-AP	1313	.60 HMX/40 NG, TA, PEG binder
H/HN	487	.21 hydrazine/79 hydrazine nitrate	S-2	1236	.63 RDX/22 TNT/15 Al
H19	1061	.32 Al/5 AP/51 KCl/9 HTPB/2 DOA	TBP	1236	.tris- -chloroethyl phosphate
HBX-1	1236	.40 RDX/36 TNT/19 Al/5 D-2	TO	1001	.1,2,4-triazole-5-one
HBX-3	1236	.30 RDX/26 TNT/38 Al/6 D-2	TPH12076	1061	.Al/AP/HTPB
heat powder	1082	.88 Fe/12 KP	Trotyl	1236	.TNT
HH	940	.hydrazine hydrate	TS3659	297	.79.9 NC/21.6 NG
HNDZ	232	.1,3,3,5,7,7-hexanitrodiazacyclooctane	TT	1236	.trimethylolethane trinitrate
HX72	963	.80 RDX/20 PB	TZL-4	232	.1,5-dinitro-tetrazole
HX78	963	.55 NQ/30 RDX/15 PB	UFD	407	.ultrafine diamonds
HXA123	963	.70 RDX/15 PB/15 Al	UGS	1062	.20 DBP/5 Al/65 Na <sub>2</sub> O <sub>4</sub> /9 HDAP
JA2	539	.59 NC/15 NG/25 DEGDN	WAK2	1062	.Al/HMX/AP
KHNO	1082	.potassium salt of hexanitro diphenylamine	WC140	297	.98 NC
LAC	975	.lactose	WC231	297	.74.8 NC/25.2 NG
LX-03-0	1236	.70 HMX/20 DATB/10 Viton A	X-0242	1015	.94 HMX/3 Estane/5 eutectic
M2	539	.75 NC	X-0420	487	.94 DINGU/5 Exon/1 titanate
M5	539	.82 NC/20 NG	X-0430	1015	.88 HMX/6 Kraton/6 Tufflo oil
MDF	1510	.mild detonating fuse or fuze	X-0432	487	.57 DINGU/43 TNT
NF	995	.nitroform	X-0444	1015	.88 HMX/6 Estane/6 eutectic
NME	1019	.nitromethane	XM39	539	.76 RDX/15 NG/12 CAB/8 ATEC
NTO	1001	.3-nitro-1,2,4 triazole-5-one	ZOX	995	.2,2,2-trinitro ethyl-N-nitroethylenediamine
			ZOX	995	.zero-oxygen-balance explosive
			ZPCP	1083	.azidopentamine cobalt (III) perchlorate

**REGISTRANTS  
AND  
AUTHOR INDEX**

# TENTH INTERNATIONAL DETONATION SYMPOSIUM REGISTRANTS

Irving B. Akst  
1032 Duncan Street  
Pampa, TX 79055

John Anderson  
Mining Resource Engineering Limited  
1555 Sydenham Road, RR#8  
Ontario, K7L 4V4, CANADA

Mark Andrews  
Sandia National Laboratories  
P.O. Box 5800  
Albuquerque, NM 87185-5800

James D. Aplin  
U.S. Air Force  
13 Roundabend Road  
Shelimar, FL 32579

Nasit Ari  
Kaman Sciences Corp  
P.O. Box 7463  
Colorado Springs, CO 80933

Blaine W. Asay  
Los Alamos National Laboratory  
Los Alamos, NM 87545

Alice I. Atwood  
Naval Air Warfare Center  
China Lake, CA 93555-6001

James L. Austing  
IIT Research Institute  
10 West 35th Street  
Chicago, IL 60616-3799

Joseph B. Aviles, Jr.  
Integrated Systems Technology, Inc.  
710 West Tantalum Drive  
Ft. Washington, MD 20744

Melvin R. Baer  
Sandia National Laboratories  
P.O. Box 5800  
Albuquerque, NM 87185-5800

Françoise Baillou  
Societe Nationale des Poudres et Explosifs  
Vert le Petit, B.P. 2, 91710, FRANCE

Ernest Baker  
U.S. Army Armament Research,  
Development and Engineering Center  
Picatinny Arsenal, NJ 07806-5000

Richard D. Bardo  
Naval Surface Warfare Center  
10901 New Hampshire Avenue  
Silver Spring, MD 20903-5640

Jude W. Barry  
Aerojet Propulsion Division  
P. O. Box 13222  
Sacramento, CA 95813-6000

Gerard Baudin  
DGA  
Gramat, 46500, FRANCE

Pascal Bauer  
ENSMA  
Rue Guillaume VII  
Poitiers (Cedex), 86034, FRANCE

John B. Bdzil  
Los Alamos National Laboratory  
Los Alamos, NM 87545

Clifford D. Bedford  
Naval Surface Warfare Center  
10901 New Hampshire Avenue  
Silver Spring, MD 20903-5640

Richard Behrens, Jr  
Sandia National Laboratories  
Livermore, CA 94551-0969

Conrad Bélanger  
Defence Research Establishment,  
Valcartier  
2459, Pie XI Blvd., North  
Québec, GOA 1R0, CANADA

Ken Bell  
NM Engineering Research Inst.  
Campus P.O. Box 25  
Albuquerque, NM 87106-4339

Donald R. Beltz  
ICI Explosives USA Inc.  
P.O. Box 271  
Tamaqua, PA 18252

Helena U.I. Bergman  
National Defence Research Establishment  
S-17290  
Sundbyberg, SWEDEN

Didier Bergues  
DGA / Centre d'Etudes de Gramat  
Gramat, 46500, FRANCE

Richard R. Bernecker  
Naval Surface Warfare Center  
10901 New Hampshire Avenue  
Silver Spring, MD 20903-5640

Naury Birnbaum  
Century Dynamics, Inc.  
7702 Edgewater Drive  
Oakland, CA 94621

Dean Blackburn  
Trojan Corporation  
P.O. Box 310  
Spanish Fork, UT 84660-0310

Thomas L. Boggs  
Naval Air Warfare Center  
China Lake, CA 93555

Jacques Boileau  
DRET  
15 Rue des Lions Saint Paul  
Paris, 75004, FRANCE

Lloyd L. Bonzon  
Sandia National Laboratories  
P.O. Box 5800  
Albuquerque, NM 87185-5800

Lionel Borne  
French German Research Institute (ISL)  
5, Rue de General Cassagnou  
Saint-Louis Cedex, 68301, FRANCE

Philippe Gerard Boyce  
CTSN - MDTC  
Site Mourillon  
Toulon NAVAL, 83800, FRANCE

Vicky L. Brady  
Naval Air Warfare Center  
China Lake, CA 93555

Martin Braithwaite  
ICI Explosives, Group Technical Centre  
K29  
Stevenston  
Ayrshire, KA20 3LN, SCOTLAND

Paul C. Braithwaite  
Thiokol Corporation  
P.O. Box 707, M/S 244  
Brigham City, UT 84302-0707

Jean Paul Brignolle  
SNPE  
1111 Jefferson Davis Highway  
Arlington, VA 22202

Thomas B. Brill  
University of Delaware  
Newark, DE 19716

Ronald E. Brown  
California Research and Technology  
Division  
5117 Johnson Drive  
Pleasanton, CA 94588

Richard V. Browning  
Los Alamos National Laboratory  
Los Alamos, NM 87544



# TENTH INTERNATIONAL DETONATION SYMPOSIUM REGISTRANTS (Cont.)

Charles D. Brumley  
Holsten Defense Corp.  
4509 West Stone Drive  
Kingsport, TN 37660-9982

Louis Brun  
Commissariat a l'Energie Atomique  
Courtry, 77181, FRANCE

Que T. Bui-Dang  
Naval Air Warfare Center  
China Lake, CA 93555-6001

Bruce G. Bukiet  
New Jersey Institute of Technology  
Newark, NJ 07102

P. Barry Butler  
University of Iowa  
2208 Engineering Bldg.  
Iowa City, IA 52242

Donald J. Butz  
Battelle Memorial Institute  
505 King Avenue  
Columbus, OH 43201-2693

William Byers-Brown  
University of Manchester  
Devonshire House  
Buxton, Derbyshire, SK17 6RQ,  
ENGLAND

Magnus Carlson  
National Defence Research Establishment  
Sundbyberg, S-17290, SWEDEN

Jean-François Cau  
DGA / Centre d'Etudes de Gramat  
Gramat, 46500, FRANCE

Francis Chaissé  
Commissariat a l'Energie Atomique  
Courtry, 77181, FRANCE

May L. Chan  
Naval Air Warfare Center  
China Lake, CA 93555

Pierre Charrue  
Commissariat a l'Energie Atomique  
Monts, 37260, FRANCE

Jay B. Chase  
Lawrence Livermore National Laboratory  
P.O. Box 808  
Livermore, CA 94550

Munawar Chaudhri  
University of Cambridge  
Madingley Road  
Cambridge, CB4 3NB, ENGLAND

Philip J. Cheese  
Defense Research Agency  
Fort Halstead  
Sevenoaks, Kent, TN14 7BP, ENGLAND

John C. Cheng  
EG&G Mound Applied Technologies, Inc.  
P. O. Box 3000  
Miamisburg, OH 45343-3000

Hervé Cherin  
Commissariat a l'Energie Atomique  
Monts, 37260, FRANCE

Christopher R. Cherry  
Sandia National Laboratories  
P.O. Box 5800  
Albuquerque, NM 87185-5800

R. Frank Chiappetta  
Blasting Analysis International, Inc.  
2516 28th Street, S.W.  
Allentown, PA 18103

Young-il Choo  
Lockheed Missiles and Space Co.  
Sunnyvale, CA 94088-3504

Jean Philippe Choquin  
Commissariat a l'Energie Atomique  
Courtry, 77181, FRANCE

Pei Chi Chou  
Dyna East Corp.  
3201 Arch Street  
Philadelphia, PA 19104

Dorothy A. Cichra  
Naval Surface Warfare Center  
10901 New Hampshire Avenue  
Silver Spring, MD 20903-5640

Michael D. Coburn  
Los Alamos National Laboratory  
P. O. Box 1663  
Livermore, CA 87544

Charles S. Coffey  
Naval Surface Warfare Center  
10901 New Hampshire Avenue  
Silver Spring, MD 20903-5640

Steve L. Collignon  
Naval Surface Warfare Center  
10901 New Hampshire Avenue  
Silver Spring, MD 20903-5640

Constantinos P. Constantinou  
Department of Physics  
Pullman, WA 99164-2814

Malcolm D. Cook  
Defence Research Agency  
Fort Halstead  
Sevenoaks, Kent, TN14 7BP, ENGLAND

Paul W. Cooper  
Sandia National Laboratories  
P.O. Box 5800  
Albuquerque, NM 87185-5800

John Corley  
Wright Laboratory/Armament Directorate  
2306 Perimeter Road  
Eglin AFB, FL 32542-5910

Josephine Covino  
Naval Air Warfare Center  
China Lake, CA 93555-6001

Michael Cowperthwaite  
SRI International - Poulter Laboratory  
333 Ravenswood Avenue  
Menlo Park, CA 94025

O.B. Crump  
Sandia National Lab  
P.O. Box 5800  
Albuquerque, NM 87185

Carl James Dahn  
Safety Consulting Engineers, Inc.  
2131 Hammond Drive  
Schaumburg, IL 60173

John C. Dallman  
Los Alamos National Laboratory  
P.O. Box 1663  
Los Alamos, NM 87545

Frank W. Davies  
Ktech Corporation  
901 Pennsylvania NE  
Albuquerque, NM 87110

Jeffery J. Davis  
Naval Surface Warfare Center  
10901 New Hampshire Avenue  
Silver Spring, MD 20903-5640

William C. Davis  
Los Alamos National Laboratory  
693 46th Street  
Los Alamos, NM 87544

David Davison  
Shock Transients, Inc.  
P.O. Box 5357  
Hopkins, MN 55343

William E. Deal, Jr.  
Los Alamos National Laboratory  
Los Alamos, NM 87545

# TENTH INTERNATIONAL DETONATION SYMPOSIUM REGISTRANTS (Cont.)

Marc Defourneaux  
NIMIC  
Brussels, 1110, BELGIUM

J. Scott Deiter  
Naval Surface Warfare Center  
10901 New Hampshire Avenue  
Silver Spring, MD 20903-5640

Peter M. Dickson  
University of Cambridge  
Madingley Road  
Cambridge, CB3 0HE, ENGLAND

Remon J. Dihu  
IIT Research Institute  
10 West 35th street  
Chicago, IL 60616

Brigitta Dobratz  
KEN Co.  
543 Todd Loop  
Los Alamos, NM 87544

Ruth M. Doherty  
Naval Surface Warfare Center  
10901 New Hampshire Avenue  
Silver Spring, MD 20903-5640

Paul J. Dotson  
Los Alamos National Laboratory  
Mail Stop B214  
Los Alamos, NM 87545

Anatolij N. Dremine  
Institute of Chemical Physics  
Russian Academy of Sciences  
Moscow, 142432, RUSSIA

Kevin P. Duffy  
Vanderbilt University  
24th and Garland  
Nashville, TN 37235

Alan Eachus  
Angus Chemical  
1500 East Lake Cook Road  
Buffalo Grove, IL 60089

Katrin A. Ekwall  
National Defence Research Establishment  
Sundbyberg, S-17290, SWEDEN

Wayne L. Elban  
Loyola College  
Baltimore, MD 21210

Julius W. Enig  
Enig Associates, Inc.  
Suite 500  
11120 New Hampshire Avenue  
Silver Spring, MD 20904-2633

Kenneth L. Erickson  
Sandia National Laboratories  
P.O. Box 5800  
Albuquerque, NM 87185-5800

Boris S. Ermolacv  
Institute of Chemical Physics  
Kossygin Street, 4  
Moscow, 117334, RUSSIA

David Ewick  
Ensign Bickford Aerospace Co.  
P. O. Box 427  
Simsbury, CT 06070

Anita Fehsal  
U.S. Army Armament Research,  
Development and Engineering Center  
Picatinny Arsenal, NJ 07806-5000

Nicholas M. Ferriter  
2 Stevens Forest  
Columbia, MD 21045

Bernd Fießler  
IABG mbH Dept. TAF  
Einsteinstraße 20  
Ottobrunn, 8012, GERMANY

Milton Finger  
Lawrence Livermore National Laboratory  
P.O. Box 808  
Livermore, CA 94550

Stephen Finnegan  
Naval Air Warfare Center  
Weapons Division  
China Lake, CA 93555-6001

Susan H. Fischer  
Sandia National Laboratories  
P.O. Box 5800  
Albuquerque, NM 87185-5800

Barry D. Fishburn  
U.S. Army Armament Research,  
Development and Engineering Center  
Picatinny Arsenal, NJ 07806-5000

Kevin J. Fleming  
Sandia National Laboratories  
1515 Eubank S.E.  
Albuquerque, NM 87123

William J. Flis  
Dyna East Corporation  
3201 Arch Street  
Philadelphia, PA 19104

Mary F. Foltz  
Lawrence Livermore National Laboratory  
P.O. Box 808  
Livermore, CA 94550

Jerry W. Forbes  
Naval Surface Warfare Center  
10901 New Hampshire Avenue  
Silver Spring, MD 20903-5640

Joseph C. Foster, Jr.  
Wright Laboratory/Armament Directorate  
Eglin Air Force Base, FL 32542-6009

Alan M. Frank  
Lawrence Livermore National Laboratory  
P.O. Box 808  
Livermore, CA 94550

Robert B. Frey  
Army Research Laboratory  
Aberdeen Proving Ground, MD  
21005-5066

Wolfgang Fücke  
Battelle Ingenieurtechnik GmbH  
Am Römerhof 35  
Frankfurt/Main 90, D-6000, GERMANY

Robert F. Gentner  
U.S. Army Armament Research,  
Development and Engineering Center  
Picatinny Arsenal, NJ 07806-5000

Brian C. Glancy  
Naval Surface Warfare Center  
10901 New Hampshire Avenue  
Silver Spring, MD 20903-5640

J. Gregory Glenn  
Wright Laboratory/Armament Directorate  
Eglin Air Force Base, FL 32542-5434

José Carlos Gois  
Mech. Eng. Department  
Avenida Universidade de Coimbra  
Coimbra, 3000, PORTUGAL

Vladimir M. Gold  
U.S. Army Armament Research,  
Development and Engineering Center  
Picatinny Arsenal, NJ 07806-5000

H. Timothy Goldrein  
Cambridge University  
Madingley Road  
Cambridge, CB3 0HE, ENGLAND

David Lynn Gordon  
Ireco Incorporated  
3000 West 8600 South  
West Jordan, UT 84088

Reinhard Grabski  
Institut der Feuerwehr Sachsen-Anhalt  
Biederitzer Str. 5  
Heyrothsberge, D-39175, GERMANY

# TENTH INTERNATIONAL DETONATION SYMPOSIUM REGISTRANTS (Cont.)

Kenneth J. Graham  
Atlantic Research Corporation  
5945 Wellington Road  
Gainesville, VA 22065-1699

Robert A. Graham  
Sandia National Laboratories  
P.O. Box 5800  
Albuquerque, NM 87185-5800

Robert Grande  
Naval Surface Warfare Center  
10901 New Hampshire Avenue  
Silver Spring, MD 20903-5640

Richard H. Granholm  
Ireco Incorporated  
3000 West 8600 South  
West Jordan, UT 84088

Lars Arne Granlund  
Nitro Nobel AB  
Gyttorp  
Nora, S-71382, SWEDEN

LeRoy G. Green  
Lawrence Livermore National Laboratory  
P.O. Box 808  
Livermore, CA 94550

N. Roy Greiner  
Los Alamos National Laboratory  
Los Alamos, NM 87545

Harold J. Gryting  
Gryting Energetics Science Co.  
7126 Shadow Run  
San Antonio, TX 78250-3483

Jean Francois Guery  
Research Center CRB  
Rue Lavoisier  
Vert-le-Petit, 91710, FRANCE

Rafaat H. Guirguis  
Naval Surface Warfare Center  
10901 New Hampshire Avenue  
Silver Spring, MD 20903-5640

Michael Gunger  
Orlando Technology, Inc.  
P.O. Box 855  
Shalimar, FL 32579

Yogendra M. Gupta  
Washington State University  
Physical Science 948A  
Pullman, WA 99164-2814

Steven G. Hallett  
Mason & Hanger  
P.O. Box 30020, Bldg 11-2  
Amarillo, TX 79177

Steven Hancock  
33591 Stephano Ct.  
Fremont, CA 94555

Matti M.J. Harkoma  
Ministry of Defence  
PL 5  
Lakiala, FINLAND

Peter J. Hart  
Ordnance Board, MOD  
Lillie Road  
London, SW6 1TR, ENGLAND

Peter J. Haskins  
Defence Research Agency  
Fort Halstead  
Sevenoaks, Kent, TN14 7BP, ENGLAND

J. Edmund Hay  
U. S. Bureau of Mines  
P. O. Box 18070  
Pittsburgh, PA 15236

Manfred Held  
c/o Messerschmitt-Bölkow-Blohm GmbH  
AG  
Postfach 1340  
Schrobenhausen, 8898, GERMANY

Walter Herrmann  
Sandia National Laboratories  
P.O. Box 5800  
Albuquerque, NM 87185-5800

Olivier Heuzé  
CEA  
Villeneuve - Saint Georges, 94195,  
FRANCE

Floyd J. Hildebrant  
U.S. Army Armament Research,  
Development and Engineering Center  
Building 65S  
Picatinny Arsenal, NJ 07806-5000

Sook-Ying Ho  
EOD/Materials Research Laboratory,  
DSTO  
P. O. Box 1750  
Adelaide, 5108  
SOUTH AUSTRALIA

Michael L. Hobbs  
Sandia National Laboratories  
P.O. Box 5800  
Albuquerque, NM 87185-5800

Ron E. Hollands  
Royal Ordnance Plc  
Glascoed, GWENT, WALES, UK

Peter J. Honey  
Defense Research Agency  
Fort Halstead  
Sevenoaks, Kent, TN14 7BP, ENGLAND

Irene E. Hooton  
Defence Research Establishment,  
Valcartier  
2459, Pie XI Blvd., North  
Québec, GOA 1R0, CANADA

Yasuyuki Horie  
Dept. Civil Eng.  
Box 7908  
Raleigh, NC 27695-7908

Philip M. Howe  
Los Alamos National Laboratory  
P.O. Box 1663  
Los Alamos, NM 87545

Peter J. Hubbard  
Defence Research Agency  
Fort Halstead  
Sevenoaks, Kent, TN14 7BP, ENGLAND

Pascal Hubert  
Aerospatiale  
66, Route de Vernaud  
Les Mureaux, 78130, FRANCE

Lawrence Hull  
Los Alamos National Laboratory  
Los Alamos, NM 87545

Rondall W. Hurd  
Mason & Hanger  
P.O. Box 30020, Bldg 11-2  
Amarillo, TX 79177

John D. Immele  
Los Alamos National Laboratory  
Los Alamos, NM 87545

Jean Isler  
SNPE Research Center  
Vert le Petit, 91710, FRANCE

Barbara Jackson  
Naval Surface Warfare Center  
10901 New Hampshire Avenue  
Silver Spring, MD 20903-5640

Richard K. Jackson  
U. S. Department of Energy  
Washington, DC 20545

Hugh R. James  
Atomic Weapons Establishment (Foulness)  
Foulness Island  
Southend-on-Sea, Essex, SS3 9XE,  
ENGLAND

# TENTH INTERNATIONAL DETONATION SYMPOSIUM REGISTRANTS (Cont.)

Leif Jerberyd  
Defence Materiel Administration  
Stockholm, S-115 58, SWEDEN

Henry J. John, Jr.  
Naval Air Warfare Center  
China Lake, CA 93555-6001

James D. Johnson  
Los Alamos National Laboratory  
Los Alamos, NM 87545

James N. Johnson  
Los Alamos National Laboratory  
Los Alamos, NM 87545

David A. Jones  
Materials Research Laboratory  
P. O. Box 50  
Victoria, 3032, AUSTRALIA

Orval T. Jones  
Sandia National Laboratories  
P.O. Box 5800  
Albuquerque, NM 87185-5800

Eleonore G. Kayser  
Naval Surface Warfare Center  
10901 New Hampshire Avenue  
Silver Spring, MD 20903-5640

Dale K. Kenemuth  
Dept. of the Navy - SSP  
9904 Copenhagen Drive  
Potomac, MD 20854

David L. Kennedy  
ICI Explosives  
P.O. Box 196, George Booth Drive  
NSW, 2327, AUSTRALIA

James E. Kennedy  
Los Alamos National Laboratory  
Los Alamos, NM 87545

Alain L. Kerdraon  
GIAT Industries  
Bourges, 18005, FRANCE

Jean-Yves Kermarrec  
DME/STPE  
26 Boulevard Victor  
Armées, Paris 00460, FRANCE

Patrick Kernen  
NIMIC  
Brussels, 1110, BELGIUM

James D. Kershner  
Los Alamos National Laboratory  
Los Alamos, NM 87545

Kibong Kim  
Naval Surface Warfare Center  
10901 New Hampshire Avenue  
Silver Spring, MD 20903-5640

Sun-Hwan Kim  
Hanwha Corporation  
50 Kojan-Dong  
Inchon, S. KOREA

Hans-Rudolf Kleinhanss  
Institut für Experimentalphysik  
Steffenstrasse 21  
Düsseldorf, D-40545, GERMANY

Stephen C. Korn  
Wright Laboratory/Armament Directorate  
101 West Eglin Blvd, STE 135  
Eglin AFB, FL 32542-6810

Herman Krier  
University of Illinois at Urbana-Champaign  
1206 W. Green Street  
Urbana, IL 61801

Kurtis K. Kuhrt  
Mason & Hanger, Silas Mason Co., Inc.  
Box 30020, Bldg 11-2  
Amarillo, TX 79177

John W. Kury  
Lawrence Livermore National Laboratory  
P.O. Box 808  
Livermore, CA 94550

Patrick M. Ladd  
Naval Surface Warfare Center  
10901 New Hampshire Avenue  
Silver Spring, MD 20903-5640

Gerald R. Laib  
Naval Surface Warfare Center  
10901 New Hampshire Avenue  
Silver Spring, MD 20903-5640

David E Lambert  
Wright Laboratory/Armament Directorate  
Eglin AFB, FL 32452

Brian D. Lambourn  
MOD (PE), AWE (A)  
Aldermaston  
Reading, Berkshire, RG7 4PR,  
ENGLAND

Teresa A. Land  
Lawrence Livermore National Laboratory  
P.O. Box 808  
Livermore, CA 94550

Abraham Langlet  
National Defence Research Establishment  
Sundbyberg, S-172 90, SWEDEN

Yvonne Lanzerotti  
U.S. Army Armament Research,  
Development and Engineering Center  
Picatinny Arsenal, NJ 07806-5000

Donald B. Larson  
Lawrence Livermore National Laboratory  
P.O. Box 808  
Livermore, CA 94550

Khine Latt  
Office of Naval Research  
Ballston Tower #1  
Arlington, VA 22217-5120

Serge Lecume  
Societe Nationale Des Poudres et Explosifs  
Centre de Recherches du Bouchet  
Vert-le-Petit, 91710, FRANCE

Edward L. Lee  
Lawrence Livermore National Laboratory  
P.O. Box 808  
Livermore, CA 94550

Jaimin Lee  
Agency for Defense Development  
Yuseong P.O. Box 35 (1-3-7)  
Taejon, 305-600, KOREA

Richard J. Lee  
Naval Surface Warfare Center  
10901 New Hampshire Avenue  
Silver Spring, MD 20903-5640

Ronald S. Lee  
Lawrence Livermore National Laboratory  
P.O. Box 808  
Livermore, CA 94550

Carl-Otto Leiber  
BICT  
D-5357 Swisttal  
Heimarzheim, GERMANY

Graeme A. Leiper  
ICI Explosives  
K80, ICI plc  
Stevenston, Ayrshire, KA20 3LN,  
SCOTLAND

E. Ray Lemar  
Naval Surface Warfare Center  
10901 New Hampshire Avenue  
Silver Spring, MD 20903-5640

# TENTH INTERNATIONAL DETONATION SYMPOSIUM REGISTRANTS (Cont.)

Deshou Liang  
Mech. Engineering and Mechanics  
Chestnut and 32nd streets  
Philadelphia, PA 19104

Larry Libersky  
New Mexico Institute of Mining  
Technology  
Campus Station  
Socorro, NM 87801

Phillip D. Lightfoot  
ICI Explosives  
801 Richelieu Boulevard  
QUEBEC, J3G 1T9, CANADA

Allen J. Lindfors  
Naval Air Warfare Center  
China Lake, CA 93555-6001

Ola A. Listh  
National Defence Research Institute (FOA)  
Sundbyberg, S-17290, SWEDEN

Pai Lu  
U.S. Army Armament Research,  
Development and Engineering Center  
Picatinny Arsenal, NJ 07806-5000

Roy A. Lucht  
Los Alamos National Laboratory  
Los Alamos, NM 87545

Peter Luebeck  
University of Cambridge  
Madingley Road  
Cambridge, CB3 0HE, ENGLAND

Eric A. Lundstrom  
Naval Air Warfare Center  
China Lake, CA 93555

Jon L. Maienschein  
Lawrence Livermore National Laboratory  
P.O. Box 808  
Livermore, CA 94550

Joël Mala  
Societe Nationale Des Poudres et Explosifs  
Centre de Recherches du Bouchet  
Vert-le-Petit, 91710, FRANCE

Allan C. Mason  
British Aerospace, Defence  
6 Southbank View  
Worcester, DY11 7RZ, ENGLAND

Ruth Maticic  
Naval Surface Warfare Center  
10901 New Hampshire Avenue  
Silver Spring, MD 20903-5640

Daniel A. Matuska  
Orlando Technology, Inc.  
P.O. Box 855  
Shalimar, FL 32579

John M. McAfee  
Los Alamos National Laboratory  
P.O. Box 1663  
Los Alamos, NM 87545

Susan McCahan  
Department of Mechanical Engineering  
5 Kings College Road  
Toronto, Ontario, M5S 1A4, CANADA

Evelyn McDougal  
U.S. Army Research Laboratory  
Aberdeen Proving Ground, MD  
21005-5066

Grant McIntosh  
Defence Research Establishment Valcartier  
Box 8800  
Courcelette, G0A 1R0, QUEBEC

Arthur M. Mellor  
Vanderbilt University  
Box 1592  
Nashville, TN 37235-1592

Arthur P. Metzner  
Naval Surface Warfare Center  
101 Strauss Avenue  
Indian Head, MD 20640-5035

George H. Miller  
Lawrence Livermore National Laboratory  
P.O. Box 808  
Livermore, CA 94550

Philip J. Miller  
Naval Surface Warfare Center  
10901 New Hampshire Avenue  
Silver Spring, MD 20903-5640

Dennis E. Mitchell  
Sandia National Laboratories  
P.O. Box 5800  
Albuquerque, NM 87185-5800

Wanda J. Morat  
Naval Surface Warfare Center  
10901 New Hampshire Avenue  
Silver Spring, MD 20903-5640

John R. Moser  
Hercules Incorporated  
P.O. Box 98  
Magna, UT 84044-0098

Henry Moulard  
French German Research Institute (ISL)  
5, Rue de General Cassagnou  
Saint-Louis Cedex, 68301, FRANCE

Roberta N. Mulford  
Los Alamos National Laboratory  
P. O. Box 1663  
Los Alamos, NM 87545

John J. Mullay  
ICI Explosives  
P. O. Box 577  
Tamaqua, PA 18252

Michael J. Murphy  
Lawrence Livermore National Laboratory  
P.O. Box 808  
Livermore, CA 94550

Kirk E. Newman  
Naval Surface Warfare Center  
Yorktown, VA 23691-5110

Albert L. Nichols III  
Lawrence Livermore National Laboratory  
P.O. Box 808  
Livermore, CA 94550

George Nickel  
Los Alamos National Laboratory  
P.O. Box 1663  
Los Alamos, NM 87545

Shulin S.N. Nie  
Swedish Detonic Research Foundation  
(SveDeFo)  
Box 32058  
S-126 11 Stockholm, SWEDEN

John P. O'Brien  
O'Brien Design Associates  
366 Ross Hill Road  
Charlestown, RI 02813

Simone Odier  
Université Pierre et Marie Curie  
Tour 22-4  
Paris CEDEX 05, 75252, FRANCE

Henric L. Östmark  
National Defence Research Establishment  
Sundbyberg, S-17290, SWEDEN

Douglas B. Olson  
EMRTC - New Mexico Tech  
Campus Station  
Socorro, NM 87801

# TENTH INTERNATIONAL DETONATION SYMPOSIUM REGISTRANTS (Cont.)

Jimmie C. Oxley  
New Mexico Institute  
Research Center for Energetic Materials  
Socorro, NM 87801

M. Dale Pace  
Naval Research Laboratory  
4555 Overlook Ave., S.W.  
Washington, DC 20375-5342

Gerardo Ines Pangilinan  
Dept. of Physics  
Shock Dynamics Laboratory  
Pullman, WA 99164-2814

John I. Paradise  
Advanced Technology Applications Suite  
100  
Vernon Hills, IL 60061

Gary H. Parsons  
Wright Laboratory/Armament Directorate  
Eglin Air Force Base, FL 32542-6009

Yehuda Partom  
Institute of Advanced Technology  
4030-2 W. Braker Lane  
Austin, TX 78759

Divyakant L. Patel  
Countermines Systems Directorate,  
SATBE-NAA  
Fort Belvoir, VA 22060-5606

Wayne L. Patrick  
Mason & Hanger - Silas Mason Co., Inc.  
17575 Highway 79  
Middletown, IA 52638

Deanne J. Pauley  
Los Alamos National Laboratory  
Los Alamos, NM 87545

Per-Anders Persson  
Research Center for Energetic Materials  
RCCEM  
Campus Station  
Socorro, NM 87801

Anna K. Pettersson  
National Defence Research Establishment  
Sundbyberg, S-172 90, SWEDEN

Jean-Paul Plotard  
Commissariat a l'Energie Atomique  
Courtry, 77181, FRANCE

Glenn Pomykal  
L-084  
Box 808  
Livermore, CA 94550

Brigitte R. Pouligny  
Commissariat a l'Energie Atomique  
B. P. No. 2  
Le Barp, 33114, FRANCE

Henri N. Presles  
ENSMA  
Rue Guillaume VII  
Poitiers (Cedex), 86034, FRANCE

John B. Ramsay  
Los Alamos National Laboratory  
Los Alamos, NM 87545

Joseph D. Renick  
Defense Nuclear Agency  
1680 Texas St. SE  
Kirtland AFB, NM 87117-5669

Anita M. Renlund  
Sandia National Laboratories  
P.O. Box 5800  
Albuquerque, NM 87185-5800

Herbert P. Richter  
Naval Air Warfare Center  
China Lake, CA 93555-6001

James P. Ritchie  
Los Alamos National Laboratory  
Los Alamos, NM 87545

Alita Roach  
Los Alamos National Laboratory  
Los Alamos, NM 87545

Gary F. Roach  
University of Strathclyde  
Livingstone Tower  
Glasgow, G1 1XH, SCOTLAND

Pauline J. Roberts  
University of Cambridge  
Maddingley Road  
Cambridge, CB3 0HE, ENGLAND

Nils Roman  
National Defence Research Establishment  
S-17290  
Sundbyberg, SWEDEN

John T. Rosenberg  
Lockheed Missile and Space Co.  
Sunnyvale, CA 94088-3504

Leslie A. Roslund  
Naval Surface Warfare Center  
10901 New Hampshire Avenue  
Silver Spring, MD 20903-5640

Lewis R. Rothstein  
124 Selden Rd.  
Newport News, VA 23606

Tsutomu Saito  
Institute of Fluid Science  
Tohoku University  
2-1-1 Katahira, Sendai, 980, JAPAN

Bchzad Salimi  
Los Alamos National Laboratory  
P.O. Box 1663  
Los Alamos, NM 87545

Michel M.S. Samirant  
French German Research Institute (ISL)  
5, Rue de General Cassagnou  
Saint-Louis Cedex, 68301, FRANCE

Mohsen Sanai  
SRI International  
333 Ravenswood Avenue  
Menlo Park, CA 94025-3493

José Angel Sanchidrian  
Union Espanola de Explosivos, S.A.  
c/ Claudio Coello, 124  
Madrid, 28006, SPAIN

Frederick W. Sandstrom  
Research Center for Energetic  
Materials (RCCEM)  
Campus Station  
Socorro, NM 87801

Harold W. Sandusky  
Naval Surface Warfare Center  
10901 New Hampshire Avenue  
Silver Spring, MD 20903-5640

Robert S. Sarracino  
AECI Explosives  
Technical Department  
Post Bag X2  
Modderfontein 1645  
SOUTH AFRICA

Dale R. Schaeffer  
EG&G Mound Applied Technologies, Inc.  
P. O. Box 3000  
Miamisburg, OH 45343-3000

Fritz Schedlbauer  
Fraunhofer Institut für  
Joseph von Fraunhofer Strasse 7  
Berghausen, GERMANY

Robert G. Schmitt  
The University of Iowa  
Iowa City, IA 52242

# TENTH INTERNATIONAL DETONATION SYMPOSIUM REGISTRANTS (Cont.)

Günther Schniedermann  
Bundesinstitut für Chemisch-  
Großes Cent  
Swisttal 1, GERMANY

Herbert J. Scholles  
Rheinmetall GmbH  
Heinrich-Erhard - Str.2  
Unterlues, 29343, GERMANY

Toshimori Sekine  
National Institute for Research in Inorganic  
1-1 Namiki  
Tsukuba, 305, JAPAN

Shai Sela  
ESP Ltd.  
P.O. Box 7191  
Tel-Aviv, 01071, ISRAEL

Robert E. Setchell  
Sandia National Laboratories  
P.O. Box 5800  
Albuquerque, NM 87185-5800

M. Sam Shaw  
Los Alamos National Laboratory  
P.O. Box 1663  
Los Alamos, NM 87545

Stephen A. Sheffield  
Los Alamos National Laboratory  
P. O. Box 1663  
Los Alamos, NM 87545

James M. Short  
Naval Surface Warfare Center  
10901 New Hampshire Avenue  
Silver Spring, MD 20903-5640

Ronald L. Simmons  
Naval Surface Warfare Center  
Indian Head, MD 20640

Philippe Simonetti  
Atomic Energy Commission (CEA)  
Monts, 37260, FRANCE

Randall L. Simpson  
Lawrence Livermore National Laboratory  
P.O. Box 808  
Livermore, CA 94550

Oliver C Sitton  
University of Missouri-Rolla  
Rolla, MD 65401

David P. Smith  
Emmanuel College  
Cambridge, CB2 3AP, ENGLAND

P. Clark Souers  
Lawrence Livermore National Laboratory  
P.O. Box 808  
Livermore, CA 94550

Patrick Spahn  
Naval Surface Warfare Center  
10901 New Hampshire Avenue  
Silver Spring, MD 20903-5640

Arthur F. Spencer  
U.S. Air Force  
Eglin AFB, FL 32542-5910

Denis Spitzer  
French German Research Institute (ISL)  
5, Rue de General Cassagnou  
Saint-Louis Cedex, 68301, FRANCE

John Starkenberg  
U.S. Army Research Laboratory  
Aberdeen Proving Ground, MD  
21005-5066

LeRoy M. Stayton  
Naval Air Warfare Center  
China Lake, CA 93555-6001

Daniel Stec, III  
Geo-Centers, Inc.  
762 Route 15 South  
Lake Hopatong, NJ 07840

Donald Scott Stewart  
University of Illinois  
104 S. Wright Street  
Urbana, IL 61801

Leonard I. Stiel  
Polytechnic University  
333 Jay Street  
Brooklyn, NY 11201

Carlyle B. Storm  
Los Alamos National Laboratory  
Los Alamos, NM 87545

Stephen R. Struck  
Wright Laboratory/Armament Directorate  
2306 Perimeter Road, Site 9  
Eglin AFB, FL 32542-5910

Gerrit Sutherland  
Naval Surface Warfare Center  
10901 New Hampshire Avenue  
Silver Spring, MD 20903-5640

Janet Sutton  
Naval Surface Warfare Center  
10901 New Hampshire Avenue  
Silver Spring, MD 20903-5640

Jeffrey W. Swegle  
Sandia National Laboratories  
P.O. Box 5800  
Albuquerque, NM 87185-5800

Damian Swift  
Atomic Weapons Establishment (AWE)  
Aldermaston  
Reading, Berkshire, RG7 4PR,  
ENGLAND

Katsumi Tanaka  
Chemical Research  
Tsukuba, Ibaraki 305, JAPAN

Pier K. Tang  
Los Alamos National Laboratory  
Los Alamos, NM 87545

William C. Tao  
Lawrence Livermore National Laboratory  
P.O. Box 808  
Livermore, CA 94550

Craig M. Tarver  
Lawrence Livermore National Laboratory  
P.O. Box 808  
Livermore, CA 94550

Douglas G. Tasker  
Naval Surface Warfare Center  
10901 New Hampshire Avenue  
Silver Spring, MD 20903-5640

David Tassia  
Naval Surface Warfare Center  
10901 New Hampshire Avenue  
Silver Spring, MD 20903-5640

Robert E. Tompkins  
Alliant Techsystems Inc.  
600 Second Street N.  
Hopkins, MN 55343

Allen J. Tulis  
IIT Research Institute  
10 West 35th Street  
Chicago, IL 60616-3799

Richard Turcotte  
ICI Explosives Canada  
Explosives Technical Center  
McMasterville, Quebec, J3G 1T9,  
CANADA

Paul A. Urtiew  
Lawrence Livermore National Laboratory  
P.O. Box 808  
Livermore, CA 94550

# TENTH INTERNATIONAL DETONATION SYMPOSIUM REGISTRANTS (Cont.)

Albert C. van der Steen  
Prins Maurits Laboratory TNO  
Lange Kleiweg 137  
Rijswijk, 2280 AA  
THE NETHERLANDS

Mathias van Thiel  
Lawrence Livermore National Laboratory  
P.O. Box 808  
Livermore, CA 94550

H.J. (Ries) Verbeek  
Prins Maurits Laboratory TNO  
Lange Kleiweg 137  
Rijswijk, 2280 AA  
THE NETHERLANDS

Andrew C. Victor  
Victor Technology  
712 North Peg Street  
Ridgecrest, CA 93555

Pierre Vidal  
ENSMA  
Rue Guillaume VII  
Poitiers (Cedex), 86034, FRANCE

Ari A. Virekunnas  
Ministry of Defence  
PL 31  
Lakiala, FINLAND

Fred Volk  
Fraunhofer Institut (FCT)  
Josef von Fraunhofer Strasse  
GERMANY

William G. Von Holle  
LLNL/DNA  
6940 South Kings Highway  
Alexandria, VA 22310

Wallace E. Voreck  
Consultant - Schlumberger  
2551 Loop 35, Apt. 1218  
Alvin, TX 77583

Jerry Wackerle  
Los Alamos National Laboratory  
Los Alamos, NM 87545  
Samuel S. Waggener  
Naval Surface Warfare Center  
Dahlgren, VA 22448-5000

Hauke Wagner  
Institut der Feuerwehr Sachsen-Anhalt  
Biederitzer Str. 5  
Heyrothsberge, D-39175, GERMANY

Chris A. Weickert  
Defence Research Establishment Suffield  
Box 4000  
Medicine Hat, Alberta, T1A 8K6,  
CANADA

Samuel T. Weir  
Lawrence Livermore National Laboratory  
Box 808  
Livermore, CA 94550

Rita Weshefsky  
U.S. Army Armament Research,  
Development and Engineering Center  
Picatinny Arsenal, NJ 07806-5000

Albert M. Weston  
KMI  
c/o Lawrence Livermore National  
Laboratory  
Livermore, CA 94550

William W. Whaley  
Los Alamos National Laboratory  
1501 Crystal Drive, Apt. 625  
Arlington, VA 22202

Michael S. Wieland  
U. S. Bureau of Mines  
Cochrans Mills Road  
Pittsburgh, PA 15236

John D. Willett  
Nuclear Metals, Inc.  
Mail Stop 7  
Concord, MA 01742

Andrew E. Williams  
Naval Research Laboratory  
Washington, DC 20375-5345

Michael Winey  
Dept. of Physics  
Shock Dynamics Laboratory  
Pullman, WA 99164-2814

Diana L. Woody  
Naval Surface Warfare Center  
10901 New Hampshire Avenue  
Silver Spring, MD 20903-5640

Delbert F. Wright  
Lawrence Livermore National Laboratory  
P.O. Box 808  
Livermore, CA 94550

Masatake Yoshida  
National Chemical Lab for Industry  
1-1 Higashi  
Ibaraki, 305, JAPAN

Frank J. Zerilli  
Naval Surface Warfare Center  
10901 New Hampshire Avenue  
Silver Spring, MD 20903-5640

Martin Zimmer  
Wright Laboratory/Armament Directorate  
101 W. Eglin Blvd, Suite 101  
Eglin Air Force Base, FL 32542-6810

I. Harold Zimmerman  
Lawrence Livermore National Laboratory  
Box 808  
Livermore, CA 94550



## AUTHOR INDEX

This index lists the authors of papers in these proceedings. Bold page numbers opposite an author's name indicate that he or she is the first listed author of the paper.

Alcon, R.R.	166, 459	Chick, M.	<b>69</b>
Almgren, L.-Å.	741	Chidester, S.K.	<b>786</b>
Anderson, C.J.	<b>294</b>	Choi, K.Y.	515
Anderson, M.U.	166	Chou, P.C.	<b>979</b> , 1003
Asay, B.W.	<b>104</b> , <b>485</b> , 716	Clairmont, Jr., A.R.	476, 499
Atwood, A.I.	320	Coffey, C.S.	219, <b>824</b>
Axenrod, T.	358	Collyer, A.M.	<b>175</b>
		Constantinou, C.P.	<b>570</b>
Baer, M.R.	409	Cook, M.D.	89, 148, <b>870</b>
Baillou, F.	<b>816</b>	Cook, T.M.	139, 696
Baker, E.L.	<b>394</b> , 433	Cooper, J.	267
Baker, R.N.	347	Cooper, P.W.	<b>690</b>
Balagansky, I.A.	<b>841</b>	Copenhaver, A.S.	586
Balduc, P.R.	608	Covino, J.	<b>936</b>
Baudin, G.	122, <b>646</b>	Cowperthwaite, M.	<b>656</b> , <b>793</b>
Bdzil, J.B.	716	Crane, S.L.	<b>1013</b>
Beard, B.C.	347	Crump, O.B.	351
Bedford, C.D.	<b>358</b>	Curran, P.O.	320
Behrens, Jr., R.	181		
Bélanger, C.	<b>305</b>	Dallman, J.C.	<b>130</b>
Bell, K.	891	Dartyge, J.M.	816
Belmas, R.	507, <b>724</b>	Dave, P.R.	358
Bergman, H.	555, <b>862</b>	Davis, J.J.	549
Bergues, D.	122, 646	Davis, William C.	<b>369</b>
Bernecker, R.R.	<b>476</b> , 490, <b>499</b> , 802	de Jong, E.	685
Bianchi, C.	724	Deal, W.E.	1013
Blais, N.C.	563	Deiter, J.S.	<b>619</b>
Borne, L.	<b>286</b>	Dickson, P.M.	242
Braithwaite, M.	377	Dreizler, D.R.	936
Brazhnikov, M.A.	542	Dremin, A.N.	<b>704</b>
Brill, T.B.	849	Duffy, K.P.	<b>777</b>
Brun, L.	<b>43</b>		
Bukiet, B.G.	<b>19</b>	Ekvall, K.	555, 862
Bussell, T.J.	69	Engelke, R.P.	563
Byers Brown, W.	<b>377</b>	Enig, J.W.	<b>637</b>
		Erickson, K.L.	<b>340</b>
Calef, D.F.	3	Ermolaev, B.S.	749
Campos, J.	758		
Carion, N.	37	Feng, H.	608
Carlson, M.	555	Ferm, E.N.	<b>78</b> , 104
Castille, C.	<b>207</b>	Field, J.E.	242, 525, 909
Cau, J.F.	<b>224</b>	Finnegan, S.A.	<b>320</b>
Chabin, P.	276	Fleming, K.J.	<b>351</b>
Chaissé, F.	<b>50</b>	Flis, W.J.	1003
Charrue, P.	<b>885</b>	Foltz, M.F.	181, <b>579</b>
Chaudhri, M.M.	570, <b>741</b>	Forbes, J.W.	63, 347, 731
Chaykovsky, M.	358	Forohar, F.	358
Cheese, P.J.	148	Fortov, V.E.	<b>58</b>
Cherin, H.	<b>808</b>	Frey, R.B.	69
Chevalier, J.M.	<b>37</b>	Fried, L.E.	3

# AUTHOR INDEX (Cont.)

Fry, H.A.	563	Land, T.A.	181
Gilardi, R.	358	Langlet, A.	862
Giltner, S.G.	918	Lanzerotti, M.Y.D.	190
Gimenez, P.	113, 276, 898	Lascaux, P.	43
Glenn, J.G.	928	Laval, F.	885
Gogulya, M.F.	542	Lecume, S.	898
Gois, J.C.	758	Lee, C.G.	628, 786
Gold, V.M.	433	Lee, E.L.	963
Goldrein, H.T.	525	Lee, J.	515
Graham, R.A.	166	Lee, R.J.	936
Green, L.G.	786	Leiper, G.A.	267, 856
Greiner, N.R.	563	Lemar, E.R.	731
Grixti, M.A.	89	Leroy, M.	507
Groux, J.	113	Liang, D.	979, 1003
Guery, J.F.	709, 898	Libersky, L.D.	199
Guirguis, R.H.	27, 675	Liddiard, T.P.	347, 731
Gunger, M.	928	Lindfors, A.J.	955
Gupta, Y.M.	536, 793	Luebcke, P.E.	242
Gustavsen, R.L.	166		
Gustavson, P.K.	63	Maienschein, J.L.	139
		Mala, J.	276, 816, 898
Hamaide, S.	113	Matsui, H.	441
Hammant, B.	936	McAfee, J.M.	485, 716
Haselman, Jr., L.C.	425	McCahan, S.	596
Haskins, P.J.	89, 148, 870	McKenney, R.L.	608
Heimdahl, O.E.R.	955	Mellor, A.M.	777
Helm, F.H.	215	Mendes, R.	758
Ho, S.Y.	94	Menikoff, R.	19
Hobbs, M.L.	409	Metzner, A.P.	219
Hudson III, F.E.	936	Miller, P.J.	675
Hudson III, L.C.	476	Mulford, R.N.	459
Hull, L.M.	11, 78	Murphy, M.J.	963
Huntley, J.M.	525	Murray, S.B.	294
Isler, J.	113	Ni, A.L.	58
		Nicollet, M.	507
James, H.R.	89		
Johnson, A.M.	175	Oeconomos, J.N.	50
Jones, D.A.	665	Östmark, H.	555, 862
Jones, H.D.	449	Olinger, B.	766
		Ornellas, D.L.	628
Kennedy, D.L.	665	Oxley, J.	608
Khasainov, B.A.	749		
Kneib, J.-M.	43	Palmer, S.J.P.	525
Kober, E.M.	586	Pangilinan, G.I.	536
Koshi, M.	441	Pauley, D.J.	104
Kretschmer, A.	876	Persson, A.	741
Kuk, J.H.	515	Persson, P.-A.	199, 766
Kury, J.W.	215, 628	Petschek, A.G.	199
		Pettersson, A.	555
Lackner, K.S.	19	Pinco, M.E.	294
Lambourn, B.D.	386	Pinto, J.	190
		Plotard, J.P.	507, 724

# AUTHOR INDEX (Cont.)

Presles, H.-N.	749	Stiel, L.I.	433
Pringle, J.K.	320	Stuart Smith, K.	89
		Sutherland, G.T.	63, 731
Quidot, M.	113	Swift, D.C.	175, 386
Ramsay, J.B.	802, 1013	Takala, B.E.	1013
Razorenov, S.V.	841	Takayama, K.	441
Ree, F.H.	419, 425	Tang, P.K.	947
Renick, J.D.	891	Tao, W.C.	628, 696
Renlund, A.M.	340	Tarver, C.M.	3, 139, 628, 696
Rho, M.-K.	358	Thomson, D.J.	190
Richter, H.P.	802	Trott, W.M.	340
Ritchie, J.P.	157, 586, 971	Trumel, H.	122
Ritman, Z.	979		
Roach, A.M.	1013	Urtiew, P.A.	139, 696
Roach, G.F.	856	Utkin, A.V.	58, 841
Roberts, Pauline J.	909		
Ruggerio, A.J.	3	van der Steen, A.C.	685, 987
		van Thiel, M.	419, 425
Saito, T.	441	Verbeek, R.	685, 987
Salvetat, B.	709	Volk, F.	601
Samirant, M.	831		
Sandstrom, F.W.	515, 766	Wackerle, J.	130, 468
Sandusky, H.W.	490	Wang, J.	608
Schedlbauer, F.	601, 876	Wartenberg, Ch.	885
Seitz, W.L.	468	Watt, J.W.	347
Sharma, J.	347	Weston, A.M.	963
Shaw, M.S.	401	Whitworth, M.B.	525
Sheffield, S.A.	166, 459	Williams, A.E.	963
Shepherd, J.E.	596, 849	Wilmot, G.B.	619
Shutov, A.V.	58	Wilnich, J.	320
Siekhaus, W.J.	181	Wilson, W.H.	63, 731
Simpson, R.L.	215	Wolfe, A.	190
Sitton, O.C.	918	Woody, D.L.	549
Smith, J.	608	Worsey, P.N.	918
Soulès, F.	207		
Spitzer, D.	831	Ye, H.	608
Spyckerelle, C.	276, 816		
Stacy, H.L.	468	Zerilli, F.J.	449
Starkenber, J.	992	Zwierzchowski, N.G.	320